TRANSLATIONAL ADVANCES IN ALZHEIMER'S, PARKINSON'S, AND OTHER DEMENTIA: MOLECULAR MECHANISMS, BIOMARKERS, DIAGNOSIS, AND THERAPIES, VOLUME II

EDITED BY: Jiehui Jiang, Kuangyu Shi, Yiyun Henry Huang, Chih-Yu Hsu, Woon-Man Kung and Kenneth S. Hettie

PUBLISHED IN: Frontiers in Aging Neuroscience, Frontiers in Pharmacology and Frontiers in Molecular Neuroscience

frontiers Research Topics

Frontiers eBook Copyright Statement

The copyright in the text of individual articles in this eBook is the property of their respective authors or their respective institutions or funders. The copyright in graphics and images within each article may be subject to copyright of other parties. In both cases this is subject to a license granted to Frontiers.

The compilation of articles constituting this eBook is the property of Frontiers.

Each article within this eBook, and the eBook itself, are published under the most recent version of the Creative Commons CC-BY licence. The version current at the date of publication of this eBook is CC-BY 4.0. If the CC-BY licence is updated, the licence granted by Frontiers is automatically updated to the new version.

When exercising any right under the CC-BY licence, Frontiers must be attributed as the original publisher of the article or eBook, as applicable.

Authors have the responsibility of ensuring that any graphics or other materials which are the property of others may be included in the CC-BY licence, but this should be checked before relying on the CC-BY licence to reproduce those materials. Any copyright notices relating to those materials must be complied with.

Copyright and source acknowledgement notices may not be removed and must be displayed in any copy, derivative work or partial copy which includes the elements in question.

All copyright, and all rights therein, are protected by national and international copyright laws. The above represents a summary only. For further information please read Frontiers' Conditions for Website Use and Copyright Statement, and the applicable CC-BY licence.

ISSN 1664-8714
ISBN 978-2-83250-577-9
DOI 10.3389/978-2-83250-577-9

About Frontiers

Frontiers is more than just an open-access publisher of scholarly articles: it is a pioneering approach to the world of academia, radically improving the way scholarly research is managed. The grand vision of Frontiers is a world where all people have an equal opportunity to seek, share and generate knowledge. Frontiers provides immediate and permanent online open access to all its publications, but this alone is not enough to realize our grand goals.

Frontiers Journal Series

The Frontiers Journal Series is a multi-tier and interdisciplinary set of open-access, online journals, promising a paradigm shift from the current review, selection and dissemination processes in academic publishing. All Frontiers journals are driven by researchers for researchers; therefore, they constitute a service to the scholarly community. At the same time, the Frontiers Journal Series operates on a revolutionary invention, the tiered publishing system, initially addressing specific communities of scholars, and gradually climbing up to broader public understanding, thus serving the interests of the lay society, too.

Dedication to Quality

Each Frontiers article is a landmark of the highest quality, thanks to genuinely collaborative interactions between authors and review editors, who include some of the world's best academicians. Research must be certified by peers before entering a stream of knowledge that may eventually reach the public - and shape society; therefore, Frontiers only applies the most rigorous and unbiased reviews.
Frontiers revolutionizes research publishing by freely delivering the most outstanding research, evaluated with no bias from both the academic and social point of view. By applying the most advanced information technologies, Frontiers is catapulting scholarly publishing into a new generation.

What are Frontiers Research Topics?

Frontiers Research Topics are very popular trademarks of the Frontiers Journals Series: they are collections of at least ten articles, all centered on a particular subject. With their unique mix of varied contributions from Original Research to Review Articles, Frontiers Research Topics unify the most influential researchers, the latest key findings and historical advances in a hot research area! Find out more on how to host your own Frontiers Research Topic or contribute to one as an author by contacting the Frontiers Editorial Office: frontiersin.org/about/contact

TRANSLATIONAL ADVANCES IN ALZHEIMER'S, PARKINSON'S, AND OTHER DEMENTIA: MOLECULAR MECHANISMS, BIOMARKERS, DIAGNOSIS, AND THERAPIES, VOLUME II

Topic Editors:
Jiehui Jiang, Shanghai University, China
Kuangyu Shi, University of Bern, Switzerland
Yiyun Henry Huang, Yale University, United States
Chih-Yu Hsu, Fujian University of Technology, China
Woon-Man Kung, Chinese Culture University, Taiwan
Kenneth S. Hettie, Stanford University, United States

Citation: Jiang, J., Shi, K., Huang, Y. H., Hsu, C.-Y., Kung, W.-M., Hettie, K. S., eds. (2022). Translational Advances in Alzheimer's, Parkinson's, and Other Dementia: Molecular Mechanisms, Biomarkers, Diagnosis, and Therapies, Volume II. Lausanne: Frontiers Media SA. doi: 10.3389/978-2-83250-577-9

Table of Contents

09 ***Editorial: Translational Advances in Alzheimer's, Parkinson's, and Other Dementia: Molecular Mechanisms, Biomarkers, Diagnosis, and Therapies, Volume II***

Jiehui Jiang, Kuangyu Shi, Yiyun Henry Huang, Chih-Yu Hsu, Kenneth Scott Hettie and Woon-Man Kung

13 ***Poly (ADP-ribose) Interacts With Phosphorylated α-Synuclein in Post Mortem PD Samples***

Laura N. Puentes, Zsofia Lengyel-Zhand, Ji Youn Lee, Chia-Ju Hsieh, Mark E. Schneider Jr., Kimberly J. Edwards, Kelvin C. Luk, Virginia M.-Y. Lee, John Q. Trojanowski and Robert H. Mach

27 ***Acupuncture Can Regulate the Peripheral Immune Cell Spectrum and Inflammatory Environment of the Vascular Dementia Rat, and Improve the Cognitive Dysfunction of the Rats***

Pan Pan, Zhinan Ma, Zhen Zhang, Zhenzhen Ling, Yao Wang, Qiuping Liu, Xiaolin Lin, Pan Xu, Dan Yang, Hui Zhi, Runmin Wang and Xuezhu Zhang

39 ***Optimal Combinations of AT(N) Biomarkers to Determine Longitudinal Cognition in the Alzheimer's Disease***

Rong-Rong Lin, Yan-Yan Xue, Xiao-Yan Li, Yi-He Chen, Qing-Qing Tao and Zhi-Ying Wu for Alzheimer's Disease Neuroimaging Initiative

53 ***Miro1 Impairment in a Parkinson's At-Risk Cohort***

David Nguyen, Vinita Bharat, Devon M. Conradson, Pawan Nandakishore and Xinnan Wang

61 ***Amyloid-Beta Influences Memory* via *Functional Connectivity During Memory Retrieval in Alzheimer's Disease***

Binyin Li, Miao Zhang, Ikbeom Jang, Guanyu Ye, Liche Zhou, Guiying He, Xiaozhu Lin, Hongping Meng, Xinyun Huang, Wangxi Hai, Shengdi Chen, Biao Li and Jun Liu

73 ***Reduced Risk of Atrial Fibrillation Following Cholecystectomy: A Nationwide Population-Based Study***

Tung Ching Ho, Yu-Ching Chen, Che-Chen Lin, Hsu-Chih Tai, Cheng-Yu Wei, Yung-Hsiang Yeh and Chung Y Hsu

83 ***Operational Determination of Subjective Cognitive Decline, Mild Cognitive Impairment, and Dementia Using Sum of Boxes of the Clinical Dementia Rating Scale***

Yu-Wan Yang, Kai-Cheng Hsu, Cheng-Yu Wei, Ray-Chang Tzeng and Pai-Yi Chiu

92 ***Using Machine Learning for Predicting the Best Outcomes With Electrical Muscle Stimulation for Tremors in Parkinson's Disease***

Onanong Phokaewvarangkul, Peerapon Vateekul, Itsara Wichakam, Chanawat Anan and Roongroj Bhidayasiri

106 ***Disrupted Dynamic Functional Connectivity in Distinguishing Subjective Cognitive Decline and Amnestic Mild Cognitive Impairment Based on the Triple-Network Model***

Chen Xue, Wenzhang Qi, Qianqian Yuan, Guanjie Hu, Honglin Ge, Jiang Rao, Chaoyong Xiao and Jiu Chen

118 ***Nanopore Single-Molecule Sequencing for Mitochondrial DNA Methylation Analysis: Investigating Parkin-Associated Parkinsonism as a Proof of Concept***
Theresa Lüth, Kobi Wasner, Christine Klein, Susen Schaake, Ronnie Tse, Sandro L. Pereira, Joshua Laß, Lasse Sinkkonen, Anne Grünewald and Joanne Trinh

132 ***Topological Alterations of Working Memory Impairment in Aged Patients With Vascular Dementia***
Cao Zheng, Rong-Sheng Zhang, Ting Wan and Jun-Sheng Zhao

140 ***Transcriptomic and Network Meta-Analysis of Frontotemporal Dementias***
Virginie Bottero, Fahed Alrafati, Jose A. Santiago and Judith A. Potashkin

153 ***Methamphetamine and Modulation Functionality of the Prelimbic Cortex for Developing a Possible Treatment of Alzheimer's Disease in an Animal Model***
Bai-Chuang Shyu, Zhi-Yue Gao, José Jiun-Shian Wu, Alan Bo Han He, Cai-N Cheng and Andrew Chih Wei Huang

170 ***Can Levodopa Challenge Testing Predict the Effect of Deep Brain Stimulation? One-Year Outcomes in a Chinese Cohort***
Wei Lin, Dongliang Shi, Dan Wang, Likun Yang, Yuhai Wang and Lingjing Jin

177 ***Severe and Regionally Widespread Increases in Tissue Urea in the Human Brain Represent a Novel Finding of Pathogenic Potential in Parkinson's Disease Dementia***
Melissa Scholefield, Stephanie J. Church, Jingshu Xu, Stefano Patassini, Federico Roncaroli, Nigel M. Hooper, Richard D. Unwin and Garth J. S. Cooper

186 ***Association Between Plasma Amyloid-β and Neuropsychological Performance in Patients With Cognitive Decline***
Gyihyaon Yun, Hye Jin Kim, Hyug-Gi Kim, Kyung Mi Lee, Il Ki Hong, Sang Hoon Kim, Hak Young Rhee, Geon-Ho Jahng, Sung Sang Yoon, Key-Chung Park, Kyo Seon Hwang and Jin San Lee

196 ***Alleviative Effect of Alpha-Lipoic Acid on Cognitive Impairment in High-Fat Diet and Streptozotocin-Induced Type 2 Diabetic Rats***
Chih-Yuan Ko, Jian-Hua Xu, Yangming Martin Lo, Rong-Syuan Tu, James Swi-Bea Wu, Wen-Chung Huang and Szu-Chuan Shen

208 ***Age Matching Is Essential for the Study of Cerebrospinal Fluid sTREM2 Levels and Alzheimer's Disease Risk: A Meta-Analysis***
Shimin Hu, Na Pan, Chunyan Liu, Yuping Wang and Tingting Zhang

219 ***Region-Specific Neurovascular Decoupling Associated With Cognitive Decline in Parkinson's Disease***
Song'an Shang, Hongying Zhang, Yuan Feng, Jingtao Wu, Weiqiang Dou, Yu-Chen Chen and Xindao Yin

231 ***Genetic Pathways and Functional Subnetworks for the Complex Nature of Bipolar Disorder in Genome-Wide Association Study***
Chan-Yen Kuo, Tsu-Yi Chen, Pei-Hsiu Kao, Winifred Huang, Chun-Ruei Cho, Ya-Syuan Lai, Giou-Teng Yiang and Chung-Feng Kao

246 *^{18}F-THK5351 Positron Emission Tomography Imaging in Neurodegenerative Tauopathies*

Michinori Ezura, Akio Kikuchi, Nobuyuki Okamura, Aiko Ishiki, Takafumi Hasegawa, Ryuichi Harada, Shoichi Watanuki, Yoshihito Funaki, Kotaro Hiraoka, Toru Baba, Naoto Sugeno, Shun Yoshida, Junpei Kobayashi, Michiko Kobayashi, Ohito Tano, Shun Ishiyama, Takaaki Nakamura, Ichiro Nakashima, Shunji Mugikura, Ren Iwata, Yasuyuki Taki, Katsutoshi Furukawa, Hiroyuki Arai, Shozo Furumoto, Manabu Tashiro, Kazuhiko Yanai, Yukitsuka Kudo, Atsushi Takeda and Masashi Aoki

254 *Characteristics of Autonomic Dysfunction in Parkinson's Disease: A Large Chinese Multicenter Cohort Study*

Zhou Zhou, Xiaoting Zhou, Xiaoxia Zhou, Yaqin Xiang, Liping Zhu, Lixia Qin, Yige Wang, Hongxu Pan, Yuwen Zhao, Qiying Sun, Qian Xu, Xinyin Wu, Xinxiang Yan, Jifeng Guo, Beisha Tang and Zhenhua Liu

264 *Effects of Chemogenetic Inhibition of D1 or D2 Receptor-Containing Neurons of the Substantia Nigra and Striatum in Mice With Tourette Syndrome*

Lixue Lin, Yuye Lan, He Zhu, Lingling Yu, Shuang Wu, Wangyixuan Wan, Yang Shu, Hongchun Xiang, Tengfei Hou, Hong Zhang, Yan Ma, Wen Su and Man Li

282 *Flavones 7,8-DHF, Quercetin, and Apigenin Against Tau Toxicity* via *Activation of TRKB Signaling in ΔK280 Tau$_{RD}$-DsRed SH-SY5Y Cells*

Ni-Ni Chiang, Te-Hsien Lin, Yu-Shan Teng, Ying-Chieh Sun, Kuo-Hsuan Chang, Chung-Yin Lin, Hsiu Mei Hsieh-Li, Ming-Tsan Su, Chiung-Mei Chen and Guey-Jen Lee-Chen

299 *Structural Covariance Network as an Endophenotype in Alzheimer's Disease-Susceptible Single-Nucleotide Polymorphisms and the Correlations With Cognitive Outcomes*

Hsin-I Chang, Yu-Tzu Chang, Chi-Wei Huang, Kuo-Lun Huang, Jung-Lung Hsu, Shih-Wei Hsu, Shih-Jen Tsai, Wen-Neng Chang, Chen-Chang Lee, Shu-Hua Huang and Chiung-Chih Chang

314 *Association of the Polygenic Risk Score With the Probability of Prodromal Parkinson's Disease in Older Adults*

Maria I. Maraki, Alexandros Hatzimanolis, Niki Mourtzi, Leonidas Stefanis, Mary Yannakoulia, Mary H. Kosmidis, Efthimios Dardiotis, Georgios M. Hadjigeorgiou, Paraskevi Sakka, Alfredo Ramirez, Benjamin Grenier-Boley, Jean-Charles Lambert, Stefanie Heilmann-Heimbach, Maria Stamelou, Nikolaos Scarmeas and Georgia Xiromerisiou

324 *Liraglutide Improves Cognitive and Neuronal Function in 3-NP Rat Model of Huntington's Disease*

Samar M. Shawki, Mohammed A. Saad, Rania M. Rahmo, Walaa Wadie and Hanan S. El-Abhar

340 *Quantitative Electroencephalography as a Biomarker for Cognitive Dysfunction in Parkinson's Disease*

Kevin Novak, Bruce A. Chase, Jaishree Narayanan, Premananda Indic and Katerina Markopoulou

354 *Positron Emission Tomography in Animal Models of Tauopathies*

Lei Cao, Yanyan Kong, Bin Ji, Yutong Ren, Yihui Guan and Ruiqing Ni

369 ***Effects of α-Lipoic Acid on Phagocytosis of Oligomeric Beta-Amyloid$_{1–42}$ in BV-2 Mouse Microglial Cells***

Chih-Yuan Ko, Jian-Hua Xu, Yu-Wei Chang, Yangming Martin Lo, James Swi-Bea Wu, Wen-Chung Huang and Szu-Chuan Shen

383 ***Preservation of Retinal Function Through Synaptic Stabilization in Alzheimer's Disease Model Mouse Retina by Lycium Barbarum Extracts***

Jinfeng Liu, Larry Baum, Shasha Yu, Youhong Lin, Guoying Xiong, Raymond Chuen-Chung Chang, Kwok Fai So and Kin Chiu

394 ***Netrin-1 Ameliorates Postoperative Delirium-Like Behavior in Aged Mice by Suppressing Neuroinflammation and Restoring Impaired Blood-Brain Barrier Permeability***

Ke Li, Jiayu Wang, Lei Chen, Meimei Guo, Ying Zhou, Xiaofeng Li and Mian Peng

407 ***Colonic Leucine-Rich Repeat Kinase 2 Expression Is Increased and Associated With Disease Severity in Patients With Parkinson's Disease***

Peng-Hsiang Liao, Han-Lin Chiang, Chia-Tung Shun, Jen-Fan Hang, Han-Mo Chiu, Ming-Shiang Wu and Chin-Hsien Lin

415 ***Intrinsic Brain Activity Alterations in Patients With Mild Cognitive Impairment-to-Normal Reversion: A Resting-State Functional Magnetic Resonance Imaging Study From Voxel to Whole-Brain Level***

Qili Hu, Qianqian Wang, Yunfei Li, Zhou Xie, Xiaomei Lin, Guofeng Huang, LinLin Zhan, Xize Jia and Xiaohu Zhao

427 ***Magnetic Resonance Imaging Markers for Cognitive Impairment in Parkinson's Disease: Current View***

Yanbing Hou and Huifang Shang

438 ***Deciphering the Roles of Metformin in Alzheimer's Disease: A Snapshot***

Wang Liao, Jiaxin Xu, Bo Li, Yuting Ruan, Tian Li and Jun Liu

448 ***Computer-Aided Classification Framework of Parkinsonian Disorders Using ^{11}C-CFT PET Imaging***

Jiahang Xu, Qian Xu, Shihong Liu, Ling Li, Lei Li, Tzu-Chen Yen, Jianjun Wu, Jian Wang, Chuantao Zuo, Ping Wu and Xiahai Zhuang

457 ***Stereopsis and Eye Movement Abnormalities in Parkinson's Disease and Their Clinical Implications***

Fang Ba, Tina T. Sang, Wenjing He, Jaleh Fatehi, Emanuel Mostofi and Bin Zheng

468 ***A Spatiotemporal Brain Network Analysis of Alzheimer's Disease Based on Persistent Homology***

Jiacheng Xing, Jiaying Jia, Xin Wu and Liqun Kuang

480 ***The Frontal and Cerebellar Metabolism Related to Cognitive Dysfunction in Multiple System Atrophy***

Cong Shen, Qi-Si Chen, Chuan-Tao Zuo, Feng-Tao Liu and Jian Wang

490 ***^{18}F-APN-1607 Tau Positron Emission Tomography Imaging for Evaluating Disease Progression in Alzheimer's Disease***

Xiaojun Xu, Weiwei Ruan, Fang Liu, Yongkang Gai, Qingyao Liu, Ying Su, Zhihou Liang, Xun Sun and Xiaoli Lan

499 ***Cerebrospinal Fluid Biomarkers in Cerebral Amyloid Angiopathy: New Data and Quantitative Meta-Analysis***
Nils G. Margraf, Ulf Jensen-Kondering, Caroline Weiler, Frank Leypoldt, Walter Maetzler, Sarah Philippen, Thorsten Bartsch, Charlotte Flüh, Christoph Röcken, Bettina Möller, Georg Royl, Alexander Neumann, Norbert Brüggemann, Benjamin Roeben, Claudia Schulte, Benjamin Bender, Daniela Berg and Gregor Kuhlenbäumer

510 ***Role of Specialized Pro-resolving Mediators in Reducing Neuroinflammation in Neurodegenerative Disorders***
Jana Ponce, Arzu Ulu, Corrine Hanson, Erin Cameron-Smith, John Bertoni, Jenna Wuebker, Alfred Fisher, Ka-Chun Siu, Vivien Marmelat, Jiri Adamec and Danish Bhatti

521 ***The Disease Modification Conundrum in Parkinson's Disease: Failures and Hopes***
Zoltan Mari and Tiago A. Mestre

528 ***Mild Cognitive Impairment Subtypes Are Associated With Peculiar Gait Patterns in Parkinson's Disease***
Marianna Amboni, Carlo Ricciardi, Sofia Cuoco, Leandro Donisi, Antonio Volzone, Gianluca Ricciardelli, Maria Teresa Pellecchia, Gabriella Santangelo, Mario Cesarelli and Paolo Barone

538 ***Unified Deep Learning-Based Mouse Brain MR Segmentation: Template-Based Individual Brain Positron Emission Tomography Volumes-of-Interest Generation Without Spatial Normalization in Mouse Alzheimer Model***
Seung Yeon Seo, Soo-Jong Kim, Jungsu S. Oh, Jinwha Chung, Seog-Young Kim, Seung Jun Oh, Segyeong Joo and Jae Seung Kim

552 ***A Novel Elastomeric UNet for Medical Image Segmentation***
Sijing Cai, Yi Wu and Guannan Chen

563 ***Identification of Potential Driver Genes and Pathways Based on Transcriptomics Data in Alzheimer's Disease***
Liang-Yong Xia, Lihong Tang, Hui Huang and Jie Luo

576 ***Aberrant Volume-Wise and Voxel-Wise Concordance Among Dynamic Intrinsic Brain Activity Indices in Parkinson's Disease: A Resting-State fMRI Study***
Yuan Tian, Hai-Bo Chen, Xin-Xin Ma, Shu-Hua Li, Chun-Mei Li, Shao-Hui Wu, Feng-Zhi Liu, Yu Du, Kai Li and Wen Su

585 ***Therapeutic Devices for Motor Symptoms in Parkinson's Disease: Current Progress and a Systematic Review of Recent Randomized Controlled Trials***
Joji Fujikawa, Ryoma Morigaki, Nobuaki Yamamoto, Teruo Oda, Hiroshi Nakanishi, Yuishin Izumi and Yasushi Takagi

610 ***Directional DBS of the Fornix in Alzheimer's Disease Achieves Long-Term Benefits: A Case Report***
Juan A. Barcia, María Aurora Viloria, Raquel Yubero, Leyre Sanchez-Sanchez-Rojas, Amanda López, Bryan Andrew Strange, María Cabrera, Leonides Canuet, Pedro Gil and Cristina Nombela

619 ***Molecular Mechanisms and Therapeutic Strategies for Levodopa-Induced Dyskinesia in Parkinson's Disease: A Perspective Through Preclinical and Clinical Evidence***
Ritam Bandopadhyay, Nainshi Mishra, Ruhi Rana, Gagandeep Kaur, Mohammed M. Ghoneim, Sultan Alshehri, Gulam Mustafa, Javed Ahmad, Nabil. A. Alhakamy and Awanish Mishra

642 ***Intelligent Healthcare System Using Patients Confidential Data Communication in Electrocardiogram Signals***
Ming Zhao, Shuo-Tsung Chen, Tzu-Li Chen, Shu-Yi Tu, Cheng-Ta Yeh, Fang-Yu Lin and Hao-Chun Lu

651 ***Statistical Parametric Mapping in Amyloid Positron Emission Tomography***
Natasha M. Smith, Jeremy N. Ford, Arsalan Haghdel, Lidia Glodzik, Yi Li, Debra D'Angelo, Arindam RoyChoudhury, Xiuyuan Wang, Kaj Blennow, Mony J. de Leon and Jana Ivanidze

662 ***Deep Learning-Based Multilevel Classification of Alzheimer's Disease Using Non-invasive Functional Near-Infrared Spectroscopy***
Thi Kieu Khanh Ho, Minhee Kim, Younghun Jeon, Byeong C. Kim, Jae Gwan Kim, Kun Ho Lee, Jong-In Song and Jeonghwan Gwak

678 ***Effects of Sex on the Relationship Between Apolipoprotein E Gene and Serum Lipid Profiles in Alzheimer's Disease***
Jiajia Fu, Yan Huang, Ting Bao, Ruwei Ou, Qianqian Wei, Yongping Chen, Jing Yang, Xueping Chen and Huifang Shang

688 ***Alzheimer's Disease Diagnosis and Biomarker Analysis Using Resting-State Functional MRI Functional Brain Network With Multi-Measures Features and Hippocampal Subfield and Amygdala Volume of Structural MRI***
Uttam Khatri and Goo-Rak Kwon for the Alzheimer's Disease Neuroimaging Initiative

frontiers | Frontiers in Aging Neuroscience

TYPE Editorial
PUBLISHED 10 October 2022
DOI 10.3389/fnagi.2022.1045828

Check for updates

OPEN ACCESS

EDITED AND REVIEWED BY
Allison B. Reiss,
New York University, United States

*CORRESPONDENCE
Woon-Man Kung
nskungwm@yahoo.com.tw

SPECIALTY SECTION
This article was submitted to Alzheimer's Disease and Related Dementias,
a section of the journal
Frontiers in Aging Neuroscience

RECEIVED 16 September 2022
ACCEPTED 20 September 2022
PUBLISHED 10 October 2022

CITATION
Jiang J, Shi K, Huang YH, Hsu C-Y, Hettie KS and Kung W-M (2022) Editorial: Translational advances in Alzheimer's, Parkinson's, and other dementia: Molecular mechanisms, biomarkers, diagnosis, and therapies, volume II.
Front. Aging Neurosci. 14:1045828.
doi: 10.3389/fnagi.2022.1045828

COPYRIGHT
© 2022 Jiang, Shi, Huang, Hsu, Hettie and Kung. This is an open-access article distributed under the terms of the Creative Commons Attribution License (CC BY). The use, distribution or reproduction in other forums is permitted, provided the original author(s) and the copyright owner(s) are credited and that the original publication in this journal is cited, in accordance with accepted academic practice. No use, distribution or reproduction is permitted which does not comply with these terms.

Editorial: Translational advances in Alzheimer's, Parkinson's, and other dementia: Molecular mechanisms, biomarkers, diagnosis, and therapies, volume II

Jiehui Jiang [1], Kuangyu Shi [2,3], Yiyun Henry Huang [4], Chih-Yu Hsu [5], Kenneth Scott Hettie [6] and Woon-Man Kung [7,8]*

[1]School of Life Science, Institute of Biomedical Engineering, Shanghai University, Shanghai, China, [2]Department of Nuclear Medicine, Inselspital, Bern University Hospital, University of Bern, Bern, Switzerland, [3]Department of Informatics, Technical University of Munich, Munich, Germany, [4]Department of Radiology and Biomedical Imaging, PET Center, Yale University School of Medicine, New Haven, CT, United States, [5]School of Transportation, Fujian University of Technology, Fuzhou, China, [6]Molecular Imaging Program at Stanford (MIPS), Department of Radiology, Otolaryngology, Head and Neck Surgery, Stanford University School of Medicine, Palo Alto, CA, United States, [7]Division of Neurosurgery, Department of Surgery, Taipei Tzu Chi Hospital, Buddhist Tzu Chi Medical Foundation, New Taipei City, Taiwan, [8]Department of Exercise and Health Promotion, College of Kinesiology and Health, Chinese Culture University, Taipei, Taiwan

KEYWORDS

Alzheimer's disease, Parkinson's disease, dementia, neurodegenerative disorders, big data mining, imaging methods, bioinformatic applications

Editorial on the Research Topic
Translational advances in Alzheimer's, Parkinson's, and other dementia: Molecular mechanisms, biomarkers, diagnosis, and therapies, volume II

Neurodegenerative dementia, such as Alzheimer's disease (AD), Parkinson's disease (PD), and other dementia has garnered increasing attention (Livingston et al., 2020) from an extensive array of researchers. The application of imaging techniques allows clinicians to explore disease process from micro and/or macro perspectives. Increasing numbers of scientists are also focusing on the relationship between genes and diseases (Jansen et al., 2019). Furthermore, bioinformatics analysis, artificial intelligence methodologies, and molecular imaging techniques have been widely used (Bloem et al., 2021; Buckley, 2021; Li et al., 2021). We can better understand disease mechanisms and etiologies through multidisciplinary approaches, allowing for identification of novel biomarkers for prompt diagnosis. Ultimately, revolutionary treatments for disease management may be developed.

Despite the replacement of some editors in the current Research Topic *"Translational advances in Alzheimer's, Parkinson's, and other dementia: Molecular mechanisms, biomarkers, diagnosis, and therapies, volume II"* by Frontiers in Aging Neuroscience, we aimed to update the advancement of scientific knowledge to improve patient care, considering the anteceding Volume I. After intensive evaluation of numerous international submissions, 57 articles are published in Volume II. We hope this collection will facilitate the gaining of new knowledge and to stimulate a wider application of the available tools for future research. The articles contained in this Research Topic highlight significant insights and innovations in the discipline. These manuscripts can be categorized to the following themes.

Genetics

Chang et al. explored the relationship across 15 genetic loci, apolipoprotein E4 (*ApoE4*) status, structural covariance networks of gray matter volume, and clinical scale score. Results suggested that AD-susceptible loci interacted with *ApoE4*, structural networks, and are associated with the cognitive outcomes. Xia et al. identified the candidate gene *GJA1*, which was likely to be a target of AD. Fu et al. explored the effect of sex on lipids (cholesterol and low-density lipoprotein) in AD and normal controls with different *APOE* genes. Lüth et al. established a mitochondrial DNA (mtDNA) methylation workflow using Nanopore sequencing and explored its implication in PD. The study of Maraki et al. suggested that there was an association between polygenic risk score and prodromal markers of PD. The accumulation of genetic variants was related to cognitive deficits.

Kuo et al. proposed 87 enriched pathways that are significant for bipolar disorder *via* genetic pathway analytics strategies. In addition, there were 3 subnetworks with multiple hotspots linked with several Gene Ontology processes for bipolar disorder. In another meta-analysis, Bottero et al. found dysregulated genes expression in frontal areas and Brodmann's area 8 for patients with frontotemporal dementia (FTD). They also compared the similarities and differences between sporadic and familial FTD.

Biomarkers: Molecular

Identification of novel molecular markers for diagnosis and treatment of neurodegenerative disease is important. Using data from Alzheimer's Disease Neuroimaging Initiative (ADNI) cohort, Lin R. R. et al. compared different amyloid-beta (Aβ), tau, and neurodegeneration (AT(N)) biomarkers with cognitive progression. The biomarkers included cerebrospinal fluid (CSF) Aβ42, amyloid positron emission tomography (PET) ([18F]flutemetamol), phosphorylated tau (p-tau), tau PET ([18F]flortaucipir), total tau (t-tau), hippocampal volume, temporal cortical thickness, [18F]fluorodeoxyglucose (FDG) PET, and plasma neurofilament light (NfL). Margraf et al. evaluated the biomarkers in CSF of patients with probable cerebral amyloid angiopathy, including Aβ40, Aβ42, t-tau, and phosphorylated tau 181 (p-tau^{181}). Xu X. et al. analyzed 31 AD patients with ^{18}F-APN-1607 PET imaging. This tracer has high binding affinity for 3- and 4-repeat tau deposits. Data showed that this tracer is effective to evaluate change pattern of tau protein deposition in AD patients. Ezura et al. categorized patients with corticobasal syndrome (CBS), progressive supranuclear palsy (PSP), and AD based on ^{18}F-THK5351 PET. They reported sites including precentral gyrus and inferior temporal gyrus, which were susceptible to disease-related pathologies.

Using immunofluorescence-based assays, Puentes et al. explored if Poly (ADP-ribose) Polymerase-1 (PARP-1) enzymatic product (PAR) promotes the aberrant cytoplasmic accumulation of hyperphosphorylated (S129) forms of alpha-synuclein (pαSyn) in transgenic murine and post mortem PD/Parkinson's disease dementia (PDD) patient samples. Liao P. H. et al. reported an increased colonic leucine-rich repeat kinase 2 (LRRK2) expression in PD patients, where the level was related to disease severity. Nguyen et al. proposed that the mitochondrial protein Miro1 is a promising molecular marker. It has potential to detect both PD and at-risk populations. Scholefield et al. measured the amount of brain urea in PD patients. Increased urea level provides an understanding about the pathogenic mechanism in PD patients with dementia.

Biomarkers: Signaling and imaging

On the basis of quantitative electroencephalography, Novak et al. used a wavelet-transform based time-frequency algorithm to assess the instantaneous predominant frequency (IPF) at 60 ms intervals. Results demonstrated that there was an altered relative time spent by the IPF in cognitively impaired PD individuals.

For diagnosis of AD and its prodromal stages, Ho T. K. K. et al. validated the capability of functional near-infrared spectroscopy. They further used deep learning models to do the multi-class classification. The Convolutional Neural Network-Long Short-Term Memory (CNN-LSTM) model obtained the highest accuracy.

Shen et al. enrolled 27 multiple system atrophy (MSA) with predominant parkinsonism (MSA-P) patients and 57 MSA with predominant cerebellar ataxia (MSA-C) patients. They found a relationship between ^{18}F-FDG uptake and neuropsychological scores, especially in frontal lobe and cerebellum. Ba et al. assessed stereopsis and eye movement abnormalities in PD using 2D and Titmus stereotests, followed by 3D active shutter system. They suggested that visual parameters may potentially serve as

the clinical biomarkers for PD. Amboni et al. reported that the gait pattern recorded by digital cameras was associated with mild cognitive impairment (MCI) patients of PD. Shang et al. compared the neurovascular decoupling index between PD with normal cognition (NC) and PD with MCI, including global and regional cerebral blood flow-regional homogeneity (CBF-ReHo) correlation coefficients and CBF-ReHo ratios. Results showed regionally specific neurovascular decoupling in PD-MCI, was most prominent in visual-spatial areas. Hu Q. et al. focused on the metrics of intrinsic brain activity in MCI patients who revert to AD, including amplitude of low-frequency of fluctuation (ALFF), fraction amplitude of low-frequency fluctuation (fALFF), ReHo, and degree centrality (DC). Changed activity of these MCI reverters helps us to explore AD. Khatri et al. provided a diagnostic framework to identify AD and to differentiate whether MCI will be converted to AD. They used biomarkers obtained from resting-state functional magnetic resonance imaging (rs-fMRI), including ALFF, fALFF, ReHo, DC, and salience networks (SN).

To investigate the relationship between Aβ and cognitive decline in AD, Li B. et al. performed a simultaneous memory task functional MRI and amyloid PET experiment. They reported a decreased functional connectivity during the memory retrieval stage. There was a negative correlation between Aβ deposition and connectivity. Moreover, functional connectivity mediated an adverse effect of Aβ on memory. Yun et al. reported the relationship across plasma Aβ analysis, amyloid PET scanning, and neuropsychological tests. Zheng et al. focused on patients with vascular dementia caused by aneurysmal subarachnoid hemorrhage (aSAH). They investigated the topological characteristics of brain network. Results discovered a decreased characteristic path length in the aSAH patients. Xue et al. analyzed dynamic functional connectivity (DFC) based on the sliding time-window correlation. They found significant alteration of DFC in brain between subjective cognitive decline (SCD) and amnestic mild cognitive impairment (aMCI), which could be applied for precise preclinical AD diagnosis. Xing et al. used time-sliding window method to explore the spatiotemporal evolution of brain functional networks. It could provide information about abnormalities of the functional organization of AD patients. Tian et al. also used the sliding time window approach to study brain activity of PD patients.

Computer-aided diagnosis/image processing

Xu J. et al. developed a computer-aided classification framework, which could be used to identify PD, multiple system atrophy (MSA), and PSP. This framework consisted of MRI-assisted PET segmentation, feature extraction and prediction, and automatic subject classification. Smith et al. used the Statistical Parametric Mapping technique to create a database, which enhanced the diagnostic performance in AD through its quantitative approach.

Seo et al. provided an approach based on deep learning, which could generate brain parenchyma mask and target volumes-of-interest (VOIs) for mouse brain to solve the problem about skull-stripping and brain region segmentation of PET images. Cai et al. proposed an Elastomeric UNet (EUNet) structure for medical image segmentation. It performed well on a self-built dataset and publicly benchmark retinal datasets.

Therapies

Pan et al. found that acupuncture could regulate the peripheral immune function and inflammation of the vascular dementia rats. Additionally, it could improve the cognitive dysfunction of the rats. Shyu et al. explored the effect of methamphetamine to enhance cognitive function or to alleviate AD symptoms in rats. Lin L. et al. investigated the mechanisms of tourette syndrome (TS) in a mice model. Outcomes revealed that substantia nigra pars compacta (SNpc) and dorsal striatum (dSTR) may be the targets for treatment. A research from Ko, Xu, Lo., et al. reported that alpha-lipoic acid (ALA) could ameliorate cognition impairment in high-fat diet (HFD) plus streptozotocin (STZ) induced diabetic rats.

Another paper by Ko, Xu, Chang., et al. investigated the enhancing effect of vitamin-like ALA on phagocytosis of oligomeric amyloid-beta ($oA\beta_{1-42}$) in mouse microglial cell lines. Chiang et al. reported that 7, 8-dihydroxyflavone (7, 8-DHF), quercetin, and apigenin targeting on heat shock protein family B (small) member 1 (HSPB1), nuclear factor erythroid 2-like 2 (NRF2), and tropomyosin-related kinase B (TRKB) could reduce tau aggregation and protect cell lines against tau neurotoxicity, which may be used to treat AD.

Liu et al. reported that *Lycium barbarum* extracts (LBE) may be a potential neuroprotectant for AD through synapse preservation through a brief research report. Shawki et al. revealed the role of an antidiabetic drug liraglutide in Huntington's disease (HD).

Lin W. et al. investigated PD patients who underwent subthalamic nucleus deep brain stimulation (STN-DBS). They found that the levodopa (L-DOPA) challenge test could not predict the quality of life (QoL) outcomes after implantation surgery. However, it could be incorporated into a regression prediction model to predict the effect of DBS. Barcia et al. reported one case about DBS surgery on AD. They assessed the safety of DBS in this AD patient using the fornix as stimulation target. Except for verbal fluency, the cognition of patient seems to return to baseline level after 24 months stimulation. Combined with machine learning, Phokaewvarangkul et al. used a Parkinson's glove and applied electrical muscle stimulation (EMS) for resting tremor during "on" period. They concluded

that the LSTM model had the highest accuracy for predicting pulse amplitude which elicited the longest tremor reset time.

Reviews

There are 8 crucial reviews included in this Research Topic. As neuroinflammation is a hallmark for the progression of AD and PD, Ponce et al. reviewed the anti-inflammatory and pro-resolving effects of polyunsaturated fatty acid (PUFA)-derived mediators (Specialized Pro-resolving Mediators–SPM) in neurodegenerative disorders. Hu S. et al. reviewed studies discussing the association of soluble triggering receptor expressed on myeloid cells 2 (sTREM2) levels in CSF and AD risk. They also provided upcoming recommendations. Bandopadhyay et al. discussed the molecular mechanisms and therapeutic approaches for L-DOPA-induced dyskinesia in PD patients. Although metformin is a first-line medication for Type 2 Diabetes Mellitus (T2DM), it also showed beneficial effects on neurodegenerative disorders. Liao W. et al. reviewed the mechanisms of metformin in AD pathology. Mari and Mestre. provided a mini review about the PD modification clinical trials and discussed what to do in the future.

Cao et al. reviewed the recently developed PET tracers for evaluation of pathophysiology in tauopathy animal models. They also discussed several considerations for future tauopathy animal studies. Hou and Shang reviewed the current biomarkers based on MRI for cognitive impairment in PD.

Fujikawa et al. reviewed the development of invasive and non-invasive medical devices to alleviate motor symptoms in PD.

Miscellaneous

Yang et al. explored the clinical application of the sum of boxes of the Clinical Dementia Rating (CDR) Scale. They found that it could be used to determine SCD, MCI, and dementia. Zhou et al. assessed the prevalence and clinical features of autonomic dysfunction in Chinese patients with PD. This study included a large multicenter cohort of 2,556 individuals. For postoperative delirium (POD), Li K. et al. reported the anti-inflammatory and blood-brain barrier (BBB) protective effects of Netrin-1 (NTN-1) (an axonal guidance molecule) in an inflammatory environment in mice.

To explore the association between gallstone disease (GD) and atrial fibrillation (AF), Ho T. C. et al. focused on a longitudinal large scale population-based cohort and reported that GD patients had an increased AF risk. Furthermore, cholecystectomy was related to a reduction of AF risk. Zhao et al. developed an intelligent healthcare system that could hide patients' confidential data into electrocardiogram (ECG) signals.

Author contributions

JJ and KS wrote the draft. KSH copyedited for the language. YHH, C-YH, and W-MK reviewed and revised the manuscript. All authors listed have made a substantial, direct, and intellectual contribution to the work and approved it for publication.

Conflict of interest

The authors declare that the research was conducted in the absence of any commercial or financial relationships that could be construed as a potential conflict of interest.

Publisher's note

All claims expressed in this article are solely those of the authors and do not necessarily represent those of their affiliated organizations, or those of the publisher, the editors and the reviewers. Any product that may be evaluated in this article, or claim that may be made by its manufacturer, is not guaranteed or endorsed by the publisher.

References

Bloem, B. R., Okun, M. S., and Klein, C. (2021). Parkinson's disease. *Lancet* 397, 2284–2303. doi: 10.1016/S0140-6736(21)00218-X

Buckley, R. F. (2021). Recent advances in imaging of preclinical, sporadic, and autosomal dominant Alzheimer's disease. *Neurotherapeutics* 18, 709–727. doi: 10.1007/s13311-021-01026-5

Jansen, I. E., Savage, J. E., Watanabe, K., Bryois, J., Williams, D. M., Steinberg, S., et al. (2019). Genome-wide meta-analysis identifies new loci and functional pathways influencing Alzheimer's disease risk. *Nat. Genet* 51, 404–413. doi: 10.1038/s41588-018-0311-9

Li, W., Zhao, H., Qing, Z., Nedelska, Z., Wu, S., Lu, J., et al. (2021). Disrupted network topology contributed to spatial navigation impairment in patients with mild cognitive impairment. *Front. Aging Neurosci.* 13, 630677. doi: 10.3389/fnagi.2021.630677

Livingston, G., Huntley, J., Sommerlad, A., Ames, D., Ballard, C., Banerjee, S., et al. (2020). Dementia prevention, intervention, and care: 2020 report of the Lancet commission. *Lancet* 396, 413–446. doi: 10.1016/S0140-6736(20)30367-6

frontiers in Aging Neuroscience

ORIGINAL RESEARCH
published: 18 June 2021
doi: 10.3389/fnagi.2021.704041

Poly (ADP-ribose) Interacts With Phosphorylated α-Synuclein in Post Mortem PD Samples

*Laura N. Puentes[1], Zsofia Lengyel-Zhand[2], Ji Youn Lee[2], Chia-Ju Hsieh[2], Mark E. Schneider Jr.[2], Kimberly J. Edwards[1], Kelvin C. Luk[3], Virginia M.-Y. Lee[3], John Q. Trojanowski[3] and Robert H. Mach[2]**

[1] Department of Systems Pharmacology and Translational Therapeutics, Perelman School of Medicine, University of Pennsylvania, Philadelphia, PA, United States, [2] Department of Radiology, Perelman School of Medicine, University of Pennsylvania, Philadelphia, PA, United States, [3] Department of Pathology and Laboratory Medicine, Institute on Aging and Center for Neurodegenerative Disease Research, Perelman School of Medicine, University of Pennsylvania, Philadelphia, PA, United States

Poly (ADP-ribose) (PAR) is a negatively charged polymer that is biosynthesized by Poly (ADP-ribose) Polymerase-1 (PARP-1) and regulates various cellular processes. Alpha-synuclein (αSyn) is an intrinsically disordered protein (IDP) that has been directly implicated with driving the onset and progression of Parkinson's disease (PD). The mechanisms by which α-synuclein (αSyn) elicits its neurotoxic effects remain unclear, though it is well established that the main components of Lewy bodies (LBs) and Lewy neurites (LNs) in PD patients are aggregated hyperphosphorylated (S129) forms of αSyn (pαSyn). In the present study, we used immunofluorescence-based assays to explore if PARP-1 enzymatic product (PAR) promotes the aberrant cytoplasmic accumulation of pαSyn. We also performed quantitative measurements using *in situ* proximity ligation assays (PLA) on a transgenic murine model of α-synucleinopathy (M83-SNCA*A53T) and post mortem PD/PDD patient samples to characterize PAR–pαSyn interactions. Additionally, we used bioinformatic approaches and site-directed mutagenesis to identify PAR-binding regions on αSyn. In summary, our studies show that PAR–pαSyn interactions are predominantly observed in PD-relevant transgenic murine models of αSyn pathology and post mortem PD/PDD patient samples. Moreover, we confirm that the interactions between PAR and αSyn involve electrostatic forces between negatively charged PAR and lysine residues on the N-terminal region of αSyn.

Keywords: poly (ADP-ribose), PARP-1, alpha-synclein, Parkinson's disease (PD), neurodegeneration

OPEN ACCESS

Edited by:
Jiehui Jiang,
Shanghai University, China

Reviewed by:
Michele Salemi,
Oasi Research Institute, Scientific Institute for Research, Hospitalization and Healthcare (IRCCS), Italy
Rosana Chehin,
CCT Consejo Nacional de Investigaciones Científicas y Técnicas (CONICET) Tucuman, Argentina

****Correspondence:***
Robert H. Mach
rmach@pennmedicine.upenn.edu

Received: *01 May 2021*
Accepted: *26 May 2021*
Published: *18 June 2021*

Citation:
Puentes LN, Lengyel-Zhand Z, Lee JY, Hsieh C-J, Schneider ME Jr, Edwards KJ, Luk KC, Lee VM-Y, Trojanowski JQ and Mach RH (2021) Poly (ADP-ribose) Interacts With Phosphorylated α-Synuclein in Post Mortem PD Samples. Front. Aging Neurosci. 13:704041. doi: 10.3389/fnagi.2021.704041

INTRODUCTION

A characteristic feature in the pathogenesis of Parkinson's disease (PD) involves the accumulation of alpha-synuclein (αSyn) protein within the cytoplasm of brain cells (Maries et al., 2003; Waxman and Giasson, 2009) — an event that underlies the molecular basis of PD pathology (Bridi and Hirth, 2018; Zeng et al., 2018). While the exact mechanisms associated with PD progression are unknown, it is well understood that the intracellular aggregation of αSyn is directly linked to the neurodegeneration found in PD (Maries et al., 2003). αSyn is a protein that primarily

exists as a natively unfolded soluble monomer (Lashuel et al., 2013). In neurons, αSyn is believed to function in a variety of synaptic processes, including vesicle trafficking and recycling (Kahle et al., 2000; Murphy et al., 2000; Cabin et al., 2002). Depending on the environment, αSyn can undergo a variety of dynamic conformational changes, which include the formation of α-helix-rich tetramers (Dettmer et al., 2015), partially folded α-helical forms (due to interactions with biological membranes), transitioning into oligomeric species, and producing toxic fibrils that are insoluble and resistant to protease activity (Vermaas and Tajkhorshid, 2014). The resulting effect of the latter is a loss in the original protein function and damage in the affected neurons (Perez and Hastings, 2004). In PD, αSyn accumulates into higher-order aggregates known as Lewy bodies (LBs) and Lewy neurites (LNs) (Spillantini et al., 1997).

In the last decade, extensive research has been done exploring the role of nuclear protein Poly (ADP-ribose) Polymerase-1 (PARP-1) in promoting neurodegeneration (Outeiro et al., 2007; Yunjong et al., 2014). Studies have shown that PARP-1 hyperactivation depletes NAD^+, induces an accumulation of Poly (ADP-ribose) (PAR), and triggers mitochondrial damage in Alzheimer's disease (AD) (Martire et al., 2015), Huntington's disease (HD) (Cardinale et al., 2015), amyotrophic lateral sclerosis (ALS) (Kim et al., 2004), ischemic brains (Moroni, 2008), and PD (Yunjong et al., 2014). PAR is primarily synthesized by PARP-1 from NAD^+ in the nucleus of cells (Luo and Kraus, 2012); it regulates cellular processes such as modulating protein localization through covalent (aspartic, glutamic, or lysine residues) and non-covalent interactions via PAR-binding motifs (PBMs) on target proteins (Pleschke et al., 2000). Several lines of evidence show that increased levels of intracellular PAR promote liquid demixing and irreversible aggregation of intrinsically disordered proteins (IDPs) (Altmeyer et al., 2015). Moreover, PAR and PARylated proteins have been shown to interact directly with pathogenic protein states, such as, Aβ (Martire et al., 2013), TDP43 (McGurk et al., 2018), and hnRNP-A1 (Duan et al., 2019). Thereby, affecting the aggregation kinetics of these proteins, potentiating toxicity, and promoting cell-to-cell transmission. As such, it has been suggested that the association of PAR and protein aggregates may serve as a feed-forward mechanism that amplifies neurotoxicity and drives neurodegeneration (Narne et al., 2017). A seminal study by Kam et al. (2018), revealed that αSyn preformed fibrils (PFF) increase intracellular oxidant levels which result in DNA damage and activation of PARP-1, leading to the intraneuronal accumulation of PAR and cell death via Parthanatos (Kam et al., 2018). It was also reported that PAR binds αSyn PFF resulting in a more stable PFF that displays faster fibrillization kinetics and higher neurotoxicity.

In the present study, we employed the use of a human neuroblastoma line overexpressing wild type αSyn (SH-SY5Y-αSyn) to gather physiologically relevant information on the role of PAR in promoting the accumulation of phosphorylated αSyn (pαSyn). We also performed *in situ* proximity ligation assays (PLA) to gain respective insight into the pathophysiological significance of PAR–pαSyn interactions, and utilized site-directed mutagenesis, immunodot blots, and molecular docking studies to elucidate the nature of these interactions. Altogether, our results support the notion that PAR plays a role in the aggregation pathway of αSyn and reinforce the importance of investigating small-molecule inhibitors of PARP-1 as disease modifying therapies for PD.

RESULTS

PAR Colocalizes With Phosphorylated (S129) αSyn Aggregates *in vitro*

In physiological settings, approximately 4% of soluble αSyn is phosphorylated at amino acid residue S129 (pαSyn) (Anderson et al., 2006; Tenreiro et al., 2014). Correlations have been established between pαSyn status and pathological conditions (Oueslati, 2016; Wang et al., 2012). In LBs, it is estimated that up to 90% of αSyn is phosphorylated at S129 (Anderson et al., 2006). Furthermore, pαSyn is observed in other synucleinopathies (neurodegenerative diseases characterized by abnormal accumulation of αSyn aggregates) as well, including dementia with LBs (DLB) (Kim et al., 2014) and multiple system atrophy (MSA) (Wakabayashi et al., 1998). In addition, increased levels of pαSyn have also been reported in PD-like transgenic murine models (Neumann et al., 2002).

The processes by which native αSyn transitions from a monomeric state to a pathogenic aggregate form are unknown. As such, identifying the underlying factors that drive abnormal αSyn assembly are vital to understand the pathogenesis of PD. In this study, we asked whether the addition of exogenous PAR could promote the cytoplasmic accumulation of pαSyn *in vitro* (**Figure 1A**). To address this question, we employed the use of a protein transfection system, *BioPORTER,* to deliver a physiologically relevant dose of PAR polymer (50 nM) into SH-SY5Y-αSyn cells (**Figure 1B**). The rationale for the use of *BioPORTER* – instead of a genotoxic agent like MNNG (Lábaj et al., 2003; Carrozza et al., 2009; Gassman et al., 2012) – was to develop a neuronal-like cell model that recapitulated the effects of PARP-1 hyperactivation (i.e., elevated PAR) in a genomically stable setting. Additionally – and in parallel – we also used *BioPORTER* to deliver 50 nM of adenosine diphosphate (hydroxymethyl)pyrrolidinediol (ADP-HDP) (Slama et al., 1995) into SH-SY5Y-αSyn cells to assess if the stable NH-analog of ADP-ribose was sufficient to induce intracellular αSyn aggregation. After a 48 h incubation, the cells were immunostained with an antibody directed toward pαSyn. Using fluorescence microscopy, we identified pαSyn inclusions (∼1 μm length) in the cytoplasm of PAR treated cells (**Figures 1C,D**). We also noted that PAR signal overlapped with ∼ 60% of these cellular pαSyn inclusions when co-immunostained with a PAR-specific antibody (**Figures 1E,F**).

Our studies showed that the addition of exogenous PAR led to the accumulation of cytosolic pαSyn inclusions (**Figures 1C,D**) by 48 h. By contrast, these pαSyn inclusions were not observed in the ADP-HDP treated or vehicle control samples (**Figures 1C,D**). In addition, quantification of co-immunostained samples using image processing software, indicated that while over half of the pαSyn inclusions were colocalized with PAR signal (**Figures 1G,H**), the majority of PAR signal was not colocalized with pαSyn (**Figure 1F**). The latter was not surprising given

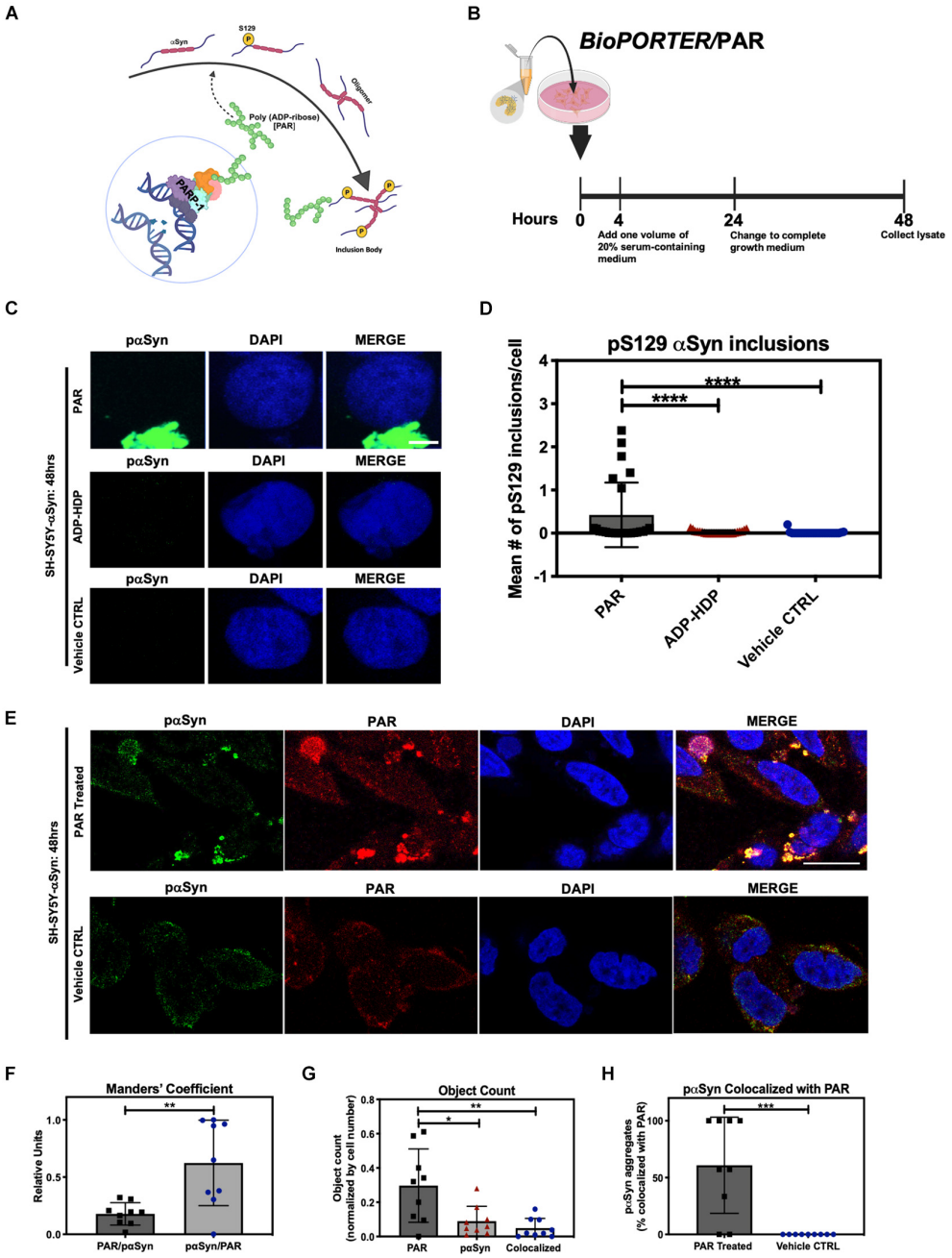

FIGURE 1 | Poly (ADP-ribose) (PAR) colocalizes with pαSyn. **(A)** Proposed mechanism of PAR-induced pαSyn accumulation, whereby PARP-1 hyperactivation due to DNA damage results in excess PAR production, leading to cytoplasmic pαSyn accumulation and pathogenic PAR–pαSyn interactions. **(B)** Experimental scheme of *BioPORTER*-mediated transfection of PAR polymer into SH-SY5Y-αSyn neuroblastoma cells. **(C)** Representative immunostain of pαSyn (green) and DAPI (blue) in SH-SY5Y-αSyn cells 48 h post treatment with either 50 nM PAR or ADP-HDP vs. *BioPORTER* alone (vehicle control). Scale bar 5 μm. **(D)** Quantification of pαSyn inclusions (aggregates larger than 1 μm) in PAR treated, ADP-HDP treated, and *BioPORTER* alone (vehicle control) samples. Bars represent mean ± SD. Two-way ANOVA followed by Tukey's *post hoc* test ($n = 3$). $^{****}P < 0.0001$. **(E)** Representative IF immunostain of pαSyn (green), PAR polymer (red), and DAPI (blue) in SH-SY5Y-αSyn cells 48 h post treatment with 50 nM PAR vs. *BioPORTER* alone (vehicle control). Scale bar 10 μm. **(F)** Manders' overlap coefficient analysis between total PAR over pαSyn inclusions (PAR/pαSyn) and pαSyn inclusions over total PAR (pαSyn/PAR) in the PAR treated samples, whereby an overlap coefficient of 0.5 implies that 50% of both objects (i.e., pixels) overlap. Bars represent mean ± SD. Student's two-tailed *t*-test ($n = 3$). $^{**}P < 0.002$. **(G)** Average object count in the PAR treated samples for the following objects: PAR, pαSyn inclusions, and colocalized PAR-pαSyn inclusions. Object counts were normalized by DAPI signal (i.e., cell number). Bars represent mean ± SD. Two-way ANOVA followed by Tukey's *post hoc* test ($n = 3$). $^{*}P < 0.02$, $^{**}P < 0.0045$. **(H)** Colocalization analysis comparing the number of pαSyn inclusions colocalized with PAR immunostain in PAR treated and *BioPORTER* alone (vehicle control) samples. Images were captured using Zeiss LSM 710 confocal (40×/1.4 Oil) microscope. Bars represent mean ± SD. Student's two-tailed *t*-test ($n = 3$). $^{***}P < 0.0005$. Graphical symbols represent *fields-of-view* containing 50–70 cells each.

the diverse roles that PAR plays in the cell (David et al., 2009; Leung, 2014).

PAR Interacts With Phosphorylated (S129) αSyn *in vitro*

To directly measure the interactions between PAR and pαSyn in our cell model, we employed *in situ* PLA (Alam, 2018), which allowed us to record the prevalence of PAR–pαSyn interactions with greater sensitivity and specificity when compared to traditional immunoassays.

In addition to PAR/*BioPORTER* delivery, we also added a small molecule PARG inhibitor (PDD 00017273) (James et al., 2016) to limit the degradation of the exogenous PAR. PARG is an enzyme that regulates intracellular PAR levels via its exo- and endoglycosidase activities (Le May et al., 2012). Thus, to reduce PAR catabolism, we pre-treated SH-SY5Y-αSyn cells with 1 μM PARG inhibitor PDD 00017273, 1 h prior to *BioPORTER* delivery of 50 nM PAR. Results from the PLA showed an increase in signal for both the PAR and PAR + PARGi treated samples when compared to ADP-HDP treated and vehicle control samples at 4 h (**Figure 2A**), 24 h (**Figure 2B**), and 48 h (**Figures 2C,D**). Notably, PLA signal for the PAR + PARGi treatment condition remained constant for all three time points (4, 24, and 48 h), while PLA signal for the PAR-only condition decreased from ∼18 PLA dots/cell at 4 h to ∼12 PLA dots/cell at 24 h to ∼5 PLA dots/cell at 48 h. Results from a PAR ELISA confirmed that the decrease in PLA signal for the PAR-only condition was likely due to a decrease in PAR levels from 4 to 48 h; this decrease was presumably due to the degradation of PAR by PARG and ADP-ribosylhydrolase 3 (ARH3) (Mashimo et al., 2013) (**Supplementary Figure 1A**). Interestingly, we also recorded an increase in PLA signal for ADP-HDP treated samples at 4 h (**Figure 1A**). Additional studies revealed that this increase in signal was likely due to elevated PAR levels at 4 h resulting from ADP-HDP-mediated PARG inhibition (**Supplementary Figure 1B**). After 24 h, the PLA signal for the ADP-HDP treated samples returned to baseline levels (**Figure 2B**), this decrease was likely due to the rapid degradation of ADP-HDP by phosphodiesterases in the cell (Wang et al., 2014).

Altogether, the evidence from our cell model suggests that the exogenous addition of PAR promotes the formation of hyperphosphorylated αSyn inclusions in the cytoplasm of SH-SY5Y-αSyn cells and that PAR likely stabilizes pαSyn inclusions, as evidenced by our PAR–pαSyn colocalization and PLA studies.

PAR and pαSyn Interactions Are Prevalent in a PD-Like Transgenic Mouse Model of α-Synucleinopathy

In order to assess if PAR–pαSyn interactions are present in αSyn pathology, we used a transgenic (Tg) murine model of α-synucleinopathy (M83 SCNA*A53T) that develops a PD-like phenotype with age (Bétemps et al., 2014). The Tg murine line (M83) used in this study overexpresses a form of human αSyn that harbors a point mutation at amino acid residue 53 (A53T); this point mutation has been directly implicated in familial early onset PD (Li et al., 2002). Information on the animals used in this study can be found in **Supplementary Table 2**.

The Tg mice were separated into two groups: M83 Tg young (less than 12 months) and M83 Tg aged (12 months or older). To control for age-related effects, we also used a non-transgenic murine line (B6C3F1/J) in our studies. Following euthanasia, murine brains were dissected and hemisected in the sagittal plane. Immunostaining for endogenous PAR was carried out to assess PARP-1 activity. Our studies revealed that PAR signal intensity increased with age in both M83 Tg and non-Tg mice (**Supplementary Figure 2A**), an increase that was particularly pronounced in the cerebral cortex, hippocampus, and cerebellum. We also observed a notable increase in signal in the cortex, cerebellum, thalamus, and brain stem regions of an M83 Tg aged (17 months) mouse compared to an age-matched control. Likewise, a study by Mao et al. (2020) recently showed that both PAR and PARP-1 are elevated in SNpc and cortical brain regions of M83 Tg mice compared to WT controls.

In addition to PAR, we also immunostained for pαSyn to assess whole brain expression in both M83 Tg and non-Tg mice (**Supplementary Figure 2B**). Notably, we observed a remarkable increase in pαSyn expression in an M83 Tg aged (17 months) sample – with maximum signal output measured in the brainstem, midbrain, thalamus, hypothalamus, and cerebral cortex regions (**Supplementary Figure 2B**).

To measure the prevalence of PAR–pαSyn interactions, we performed *in situ* PLA on frozen brain sections from all three animal groups: M83 Tg young, M83 Tg aged and non-Tg (B6C3F1/J). To limit non-specific PLA signal, adjacent brain tissue sections were incubated without primary antibody, subsequent imaging parameters (i.e., exposure time and depth of field) were then adjusted in order to acquire detectable signal above background. To ensure consistency between experimental models, we used the same primary antibodies (anti-PAR and anti-pαSyn, **Supplementary Table 1**) for our cell and animal brain tissue PLA. Results from our studies revealed that PLA signal for PAR–pαSyn was strongest in M83 Tg vs. non-Tg mice (**Figures 2E,F**). Analogously, M83 Tg aged vs. M83 Tg young mice differed significantly in PLA signal (**Figures 2E,F**) – with the strongest signal differential detected in the brainstem region of the M83 Tg aged group (**Figures 2G,H**). Similarly, increased PLA signal was also observed in an M83 Tg aged mouse (18 months) when using primary antibodies against PAR and total αSyn (anti-PAN-αSyn) (**Supplementary Figure 2C**), thus confirming that PAR interacts with both phosphorylated and non-phosphorylated αSyn. In addition, we noted that M83 Tg brain tissue samples with the highest pαSyn expression also had the greatest PLA signal output, suggesting that pαSyn-PAR PLA signal may be directly tied to the amount of pathology (i.e., pαSyn expression) present in a given sample.

Overall, our studies revealed that PLA signal was highest in anatomical brain regions most commonly associated with αSyn pathology in the M83 Tg aged group (Leung, 2014) (**Figures 2E,F**); these findings are in accordance with our observations from the SH-SY5Y-αSyn cell model, which show that PAR–pαSyn interactions are prevalent in pathogenic states involving both αSyn aggregation and elevated PAR levels.

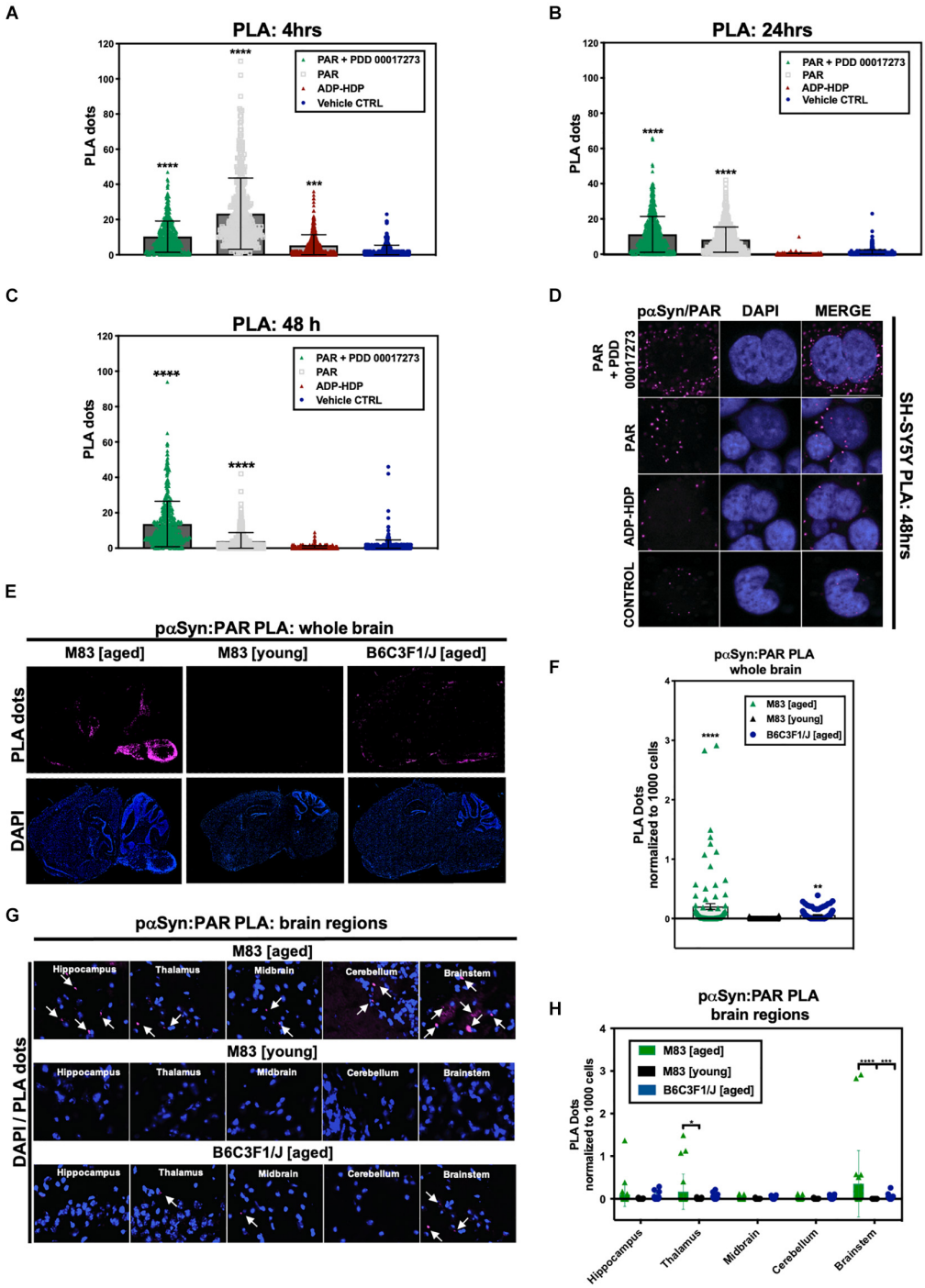

FIGURE 2 | Poly (ADP-ribose) interacts with phosphorylated (S129) αSyn in pathological settings. Quantification from proximity ligation assays (PLA) measuring pαSyn and PAR interactions in SH-SY5Y-αSyn cells at **(A)** 4 h, **(B)** 24 h, and **(C)** 48 h post treatment with either PAR, PAR + 1 μM PDD00017273 (PARGi) or ADP-HDP vs. *BioPORTER* alone (vehicle control). Bars represent means ± SD. One-way ANOVA followed by Tukey's *post hoc* test ($n = 3$). ***$P < 0.0004$, ****$P < 0.0001$ **(D)** Representative DAPI and PLA ROI images showing PLA dots (pink); these dots indicate direct interactions between pαSyn and PAR in PAR treated, ADP-HDP treated and *BioPORTER* alone (vehicle control) samples at 48 h. Scale bar 10 μm. **(E)** Representative DAPI (bottom panel) and PLA (top panel) whole brain images from M83 Tg aged, M83 Tg young, and B6C3F1/J aged mice. **(F)** Quantification of whole brain PLA levels in M83 Tg aged, M83 Tg young and B6C3F1/J mice ($n = 3$ per group). Each bar represents means ± SD. One-way ANOVA. **$P < 0.002$, ****$P < 0.0001$. **(G)** Representative PLA staining (white arrows) of ROIs obtained from 20× merge images. **(H)** Quantification of different brain regions in M83 Tg aged, M83 Tg young, and B6C3F1/J aged mice. Images were captured using Zeiss Axio Widefield (20×/0.8) microscope. Bars represent means ± SD. Two-way ANOVA followed by Tukey's *post hoc* test ($n = 3$). *$P < 0.025$, ***$P < 0.0002$, ****$P < 0.0001$.

PAR–pαSyn Interactions Are Observed in Post Mortem Brain Tissue From PD/PDD Patients

To determine the clinical relevance of PAR–pαSyn interactions in PD, we performed immunoassays (**Figures 3A–F**) and PLA (**Figures 4A–C**) on human post mortem striatum, midfrontal gyrus, and hippocampus brain regions derived from PD and PDD (Parkinson's Disease Dementia) patients, as well as, non-PD controls. Results from these studies revealed heterogeneity in pαSyn (**Figure 3E**) and PAR (**Figure 3F**) immunostaining for all patient samples, however, PD/PDD patient samples had overall increased pαSyn and PAR expression when compared to control (**Figures 3A,B**). We also observed higher signal overlap (i.e., colocalization) between PAR and pαSyn staining in the PD/PDD patient samples, as determined by Manders' overlap coefficient (**Figure 3D**). Cumulatively, the PD/PDD patient group had higher pαSyn (**Figure 3B**), PAR (**Figure 3C**), and PLA (**Figures 4A–C**) signal. Interestingly, we found that patients with pathological αSyn scores classified as severe (3+) (McKeith et al., 2017) had higher PAR (**Figure 3F**) and PLA (**Figure 4B**) signal output (*patient information can be found in* ***Supplementary Table 3***). Thus, suggesting that PLA signal may be associated with disease progression and severity.

To supplement our PD/PDD PLA results, we also performed PAR–pαSyn PLA (**Figure 4D**) and pαSyn immunostains (**Figure 4E**) on cerebellum tissue samples from patients diagnosed with multiple system atrophy (MSA) – another main type of α-synucleinopathy – along with healthy region-matched controls (**Supplementary Figures 3A,B**). From this, we observed PLA staining patterns that closely matched pαSyn pathology in MSA (**Figures 4D,E**). As a result, we were able to validate PLA signal in two different α-synucleinopathies. From our studies, we found that including technical controls (i.e., imaging adjacent tissue sections in the absence of primary antibodies), along with validation of signal in more than one disease type, led to reliable results from our PLA studies.

In summary, although there was heterogeneous expression of pαSyn and PAR in the patient tissue samples, we found there to be a statistically significant increase in PLA signal in the PD/PDD patient group relative to age-matched controls. *The data obtained from these experiments, to our knowledge, is the first direct evidence showing pathologically relevant PAR–pαSyn associations on human post mortem brain tissue samples from PD/PDD and MSA patient groups*. Further studies are warranted in order to better understand the role of PAR-bound pαSyn in the disease progression of PD/PDD and other synucleinopathies. Such a finding could have wide ranging implications for the development of disease modifying therapies (such as PARP-1 inhibitors) for patients harboring familial PD genetic variants (i.e., A30P, E46K, and A53T).

PAR Binds αSyn via Electrostatic Interactions Involving Lysine Residues

A previous study (Kam et al., 2018) showed that PAR binds αSyn via non-covalent interactions on the N-terminal region of αSyn – thus, suggesting that the interactions between PAR and αSyn are electrostatic in nature. In order to identify the amino acid residues involved in αSyn-PAR binding, a protein alignment tool (NPS@PATTINPROT search) was used to align the native αSyn protein sequence to two published PAR binding motifs (PBM) (Pleschke et al., 2000; Gagné et al., 2008). We identified two sites on αSyn as potential PAR-binding sites (**Figure 5A**): a site between amino acids residues 43–54 and another site between amino acid residues 48–58.

To better characterize αSyn-PAR interactions, we substituted positively charged lysine residues at the two PAR-binding sites predicted by the NPS@PATTINPROT tool (**Figure 5A**). Using site-directed mutagenesis, we generated three mutants of αSyn with compromised PAR-binding sites by replacing lysine residues with neutral alanine residues (**Figure 5A**). Two of the αSyn mutants had a single point mutation at amino acid residues K43 and K58, respectively, while the third mutant had two point mutations at positions K43 and K45 (**Figures 5A,B**). To test if PAR binding was affected in the different αSyn mutant fibrils, we performed PAR-binding immunodot blot (**Figure 5C**). WT and mutant αSyn fibrils were spotted onto a membrane along with a PAR-binding protein, histone H4 (positive control) and BSA (negative control). Incubation with PAR polymer, followed by immunoblotting with a PAR-specific antibody (10H), revealed that both histone H4 and αSyn WT fibril bound to PAR. Interestingly, we observed a *decrease in PAR binding for all three mutants* when compared to αSyn WT fibril (**Figure 5C**).

To assess if the decrease in PAR binding on the alanine mutant fibrils was a direct result of substituting positively-charged lysine residues – and not just due to the introduction of a point mutation, we performed an additional PAR-binding immunodot blot with αSyn A53T fibrils. From this, we observed that PAR binds the αSyn A53T mutant with similar signal intensity compared to αSyn WT fibril (**Supplementary Figure 3C**). Based on these results, we confirm that PAR binding to αSyn is primarily mediated by *electrostatic interactions at positions 43–58 of the N-terminal region*. Our data also indicates that PAR binds to a known familial point mutation of αSyn (A53T) (**Supplementary Figure 3C**). The latter has direct relevance in patients who harbor the A53T variant of αSyn – as this variant has been shown to be aggregation prone and has been directly linked to autosomal dominant early onset PD.

PAR, MSA, and Beyond

The cryo-EM structure of Sarkosyl-insoluble αSyn filaments isolated from five MSA cases was recently reported (Schweighauser et al., 2020). The structure revealed two different filament types, type I and type II. Both filament types consist of two different protofilaments having an extended N-terminus and compact C-terminal body. In addition, the interface between the two different protofilaments consist of a non-proteinaceous density in the region of K43 and K45 in one protofilament, and K58 of the other protofilament. Since replacement of these lysine residues with an alanine residue diminished PAR binding (**Figure 5C**), and since PAR and pαSyn interact in both PD/PDD (**Figures 4A–C**) and MSA brain tissue (**Figure 4D**), we conducted a series of computational chemistry studies (**Figure 5D**) to evaluate the interaction of a PAR-dimer

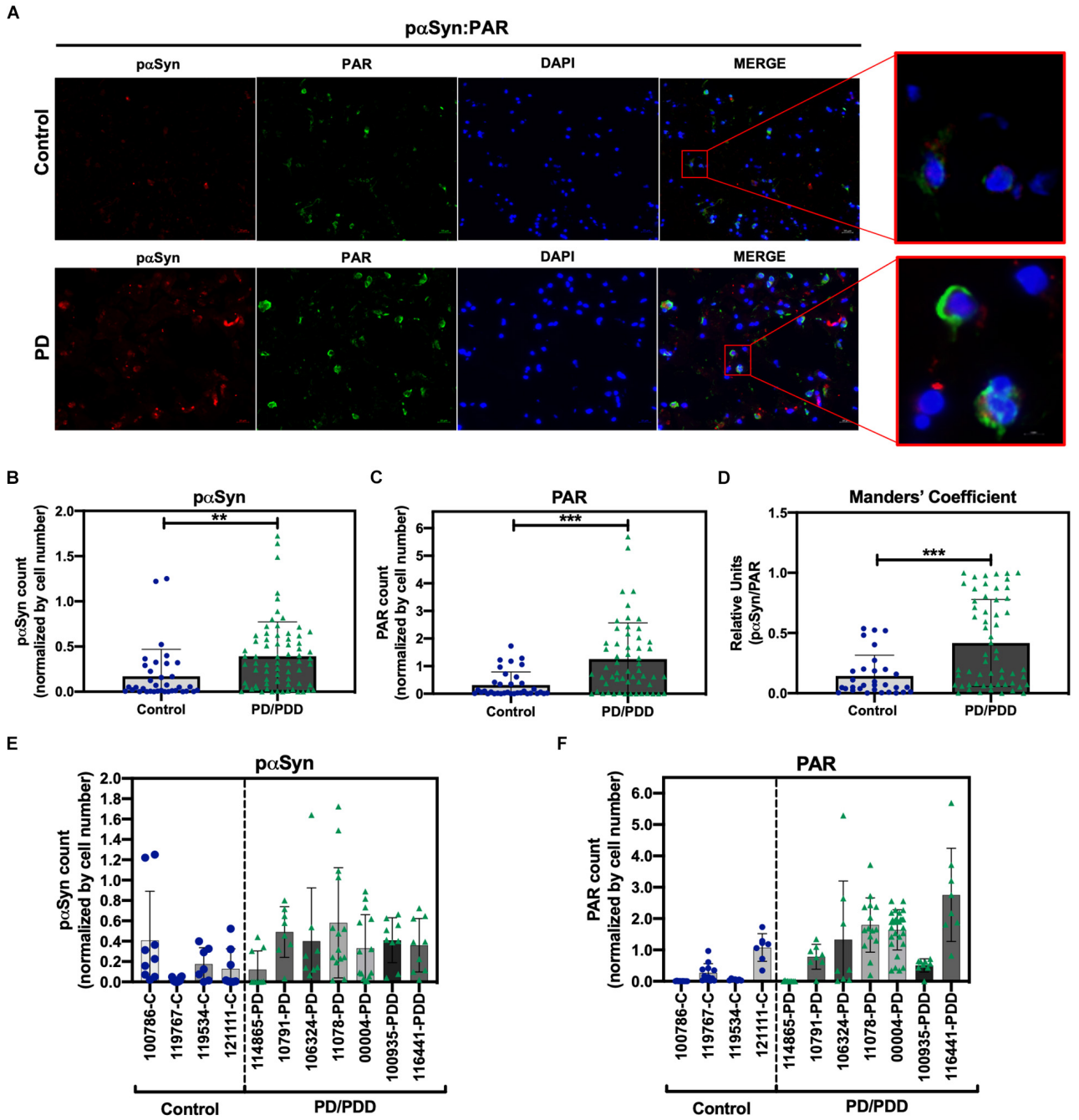

FIGURE 3 | Increased S129 pαSyn and PAR levels in PD/PDD patient samples. **(A)** Representative IF immunostain of pαSyn (red), PAR (green), and DAPI (blue) in non-PD control (***top panel***, tissue ID 121111, middle frontal gyrus) and PD/PDD (***bottom panel***, tissue ID 116441, middle frontal gyrus) patient samples. Merge channel regions of interest (ROI) show colocalization between pαSyn and PAR staining. Scale bar 20 μm. Images were captured using Zeiss Axio Widefield (20×/0.8) microscope. **(B)** Quantification of pαSyn levels, normalized by DAPI count, in control vs. PD/PDD patients. **(C)** Quantification of PAR levels, normalized by DAPI count, in control vs. PD/PDD patients. **(D)** Quantification of pαSyn/PAR overlap in control vs. PD/PDD patients using Manders' overlap coefficient. Graphical symbols represent *fields-of-view* containing 100–150 cells each. Immunostain quantification of **(E)** pαSyn and **(F)** PAR expression for all human PD/PDD and non-PD post mortem brain samples used in this study. For all experiments, bars represent means ± SD. Student's two-tailed *t*-test [n = 4 (control) and 7 (PD/PDD) patient samples per group]. $^{**}P < 0.0028$, $^{***}P < 0.0001$. Graphical symbols represent *fields-of-view* containing 100–150 cells each.

(**Supplementary Figure 3D**) with the cryo-EM structure of αSyn, specifically the type I filament (Schweighauser et al., 2020). From this, we found a very strong fit of the PAR-dimer in the space occupied by this non-proteinaceous density – with strong ionic interactions between these lysine residues and the diphosphate moiety of the PAR-dimer and hydrogen

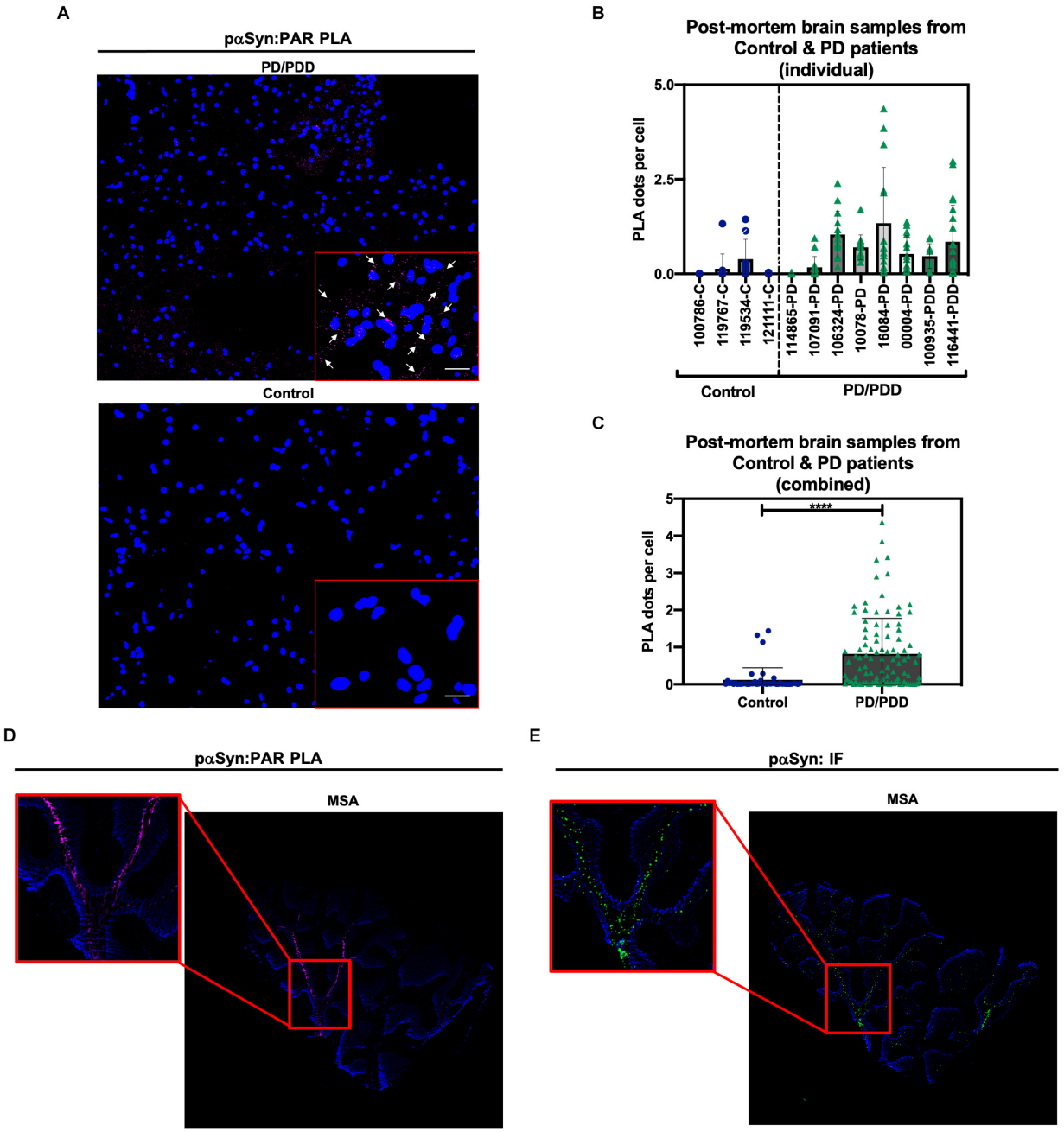

FIGURE 4 | Poly (ADP-ribose) predominantly interacts with pαSyn in PD/PDD post mortem patient samples. **(A)** Representative PLA and DAPI images in non-PD control (***top panel***, tissue ID 121111, middle frontal gyrus) and PD/PDD patient samples (***bottom panel***, tissue ID 116441, middle frontal gyrus). ROI overlaid on merge channel. ROI scale bar 10 μm. Images were captured using Zeiss Axio Widefield (20×/0.8) microscope. Representative white arrows showing PLA positive signal. **(B)** Quantification of PLA dot count per cell in individual non-PD control vs. PD/PDD patient samples. Bars represent means ± SD. **(C)** Combined PLA analysis for all control and PD/PDD tissue samples. Bars represent means ± SD. Student's two-tailed *t*-test [$n = 4$ (control) and 8 (PD/PDD) patient samples per group]. $^{****}P < 0.0001$. For **(B,C)** each graphical symbol represents the average number of PLA dots normalized to cell count (DAPI) for each *field-of-view*. 10–15 fields were captured for each patient sample. **(D)** PLA (pink) and DAPI (blue) signal from cerebellum sections derived from an MSA patient. **(E)** Standard immunostain of adjacent cerebellum sections from an MSA patient showing pαSyn (green) and DAPI (blue) channel images. Red boxes indicate PLA signal **(D)** and matching pαSyn IF **(E)** in adjacent MSA tissue sections. Images were captured using Zeiss Axio Widefield (20×/0.8) microscope.

bond interactions between tyrosine-39 and histidine-50 with the adenine group and ribose groups (**Figure 5D**). Based on these results, it is conceivable that the non-proteinaceous density in the cryo-EM structure of αSyn filaments reported in MSA *may be PAR*; however, additional research is warranted to confirm this hypothesis.

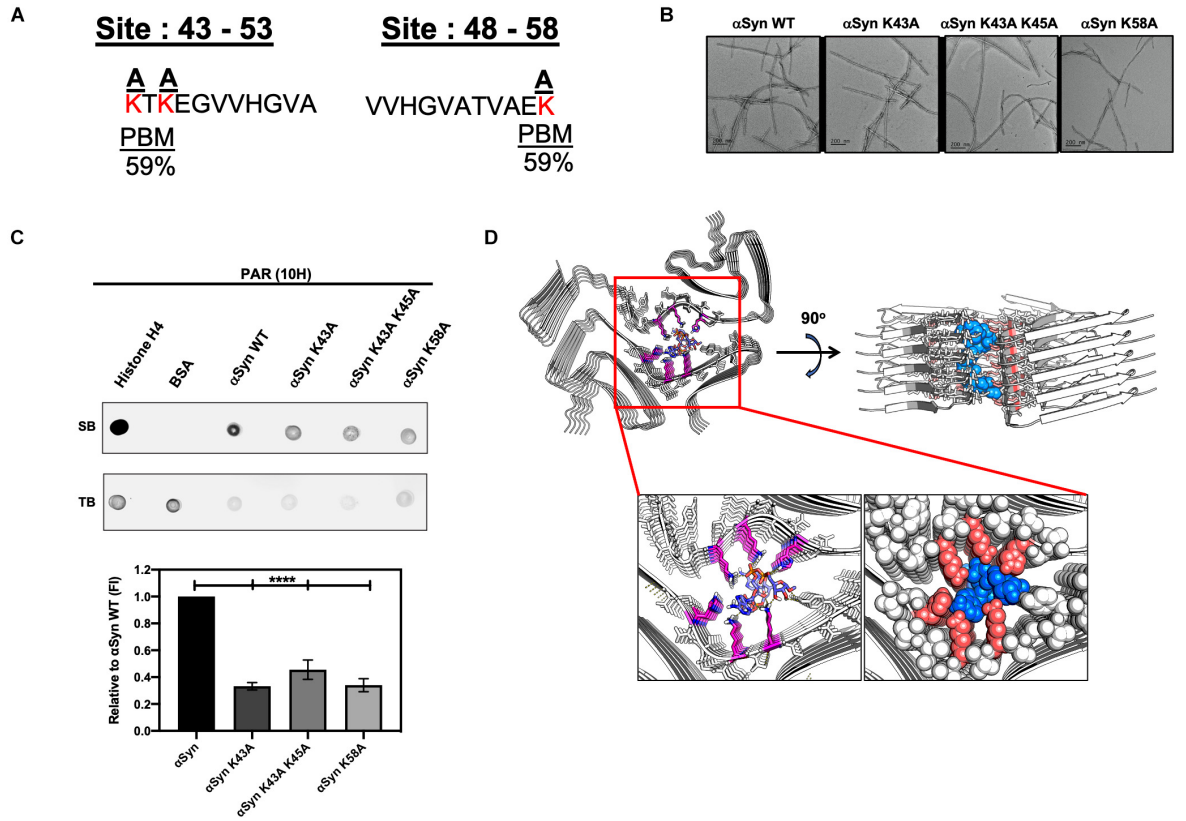

FIGURE 5 | Poly (ADP-ribose) interacts with αSyn via electrostatic forces in the N-terminal region of the protein. **(A)** Alignment of the full αSyn sequence with PBMs yielded a 59% PAR-binding probability at amino acid residues 43–54 and 48–58 on αSyn. Lysine amino acid residues (red) at the two sites were substituted to neutral alanine residues. **(B)** Three mutants of αSyn were generated with compromised PAR-binding sites. Two of the αSyn mutants had a point mutation at amino acid residues K43 and K58, respectively, while the third mutant had two point mutations at positions K43 and K45. All mutants were fully fibrillated within 72 h. Scale bar 200 nm. **(C)** PAR immunodot blot (***top panel***), whereby WT and mutant αSyn fibrils were spotted onto a membrane, along with, histone H4 (positive control), and BSA (negative control) and incubated with PAR polymer to assess PAR binding. Semi-quantitative analysis (***bottom panel***) of WT and mutant αSyn fibril signal intensity normalized to WT αSyn signal. One-way ANOVA ($n = 3$). $^{****}P < 0.0001$. **(D)** Cryo-EM structure of MSA Type I αSyn fibril interacting with the PAR-dimer complex with a low free binding energy of –15.6 kcal/mol.

DISCUSSION

Poly (ADP-ribose) is a highly branched polymer that has been best characterized as a recruiter of DNA repair factors during single-strand DNA break repair. However, in recent years the role of PAR outside of the nucleus has become clearer, and the role of this polymer in neurodegeneration stands as a promising avenue for better understanding the molecular basis of neurotoxicity leading to neurodegeneration. Specifically, the interaction between PAR and αSyn may represent a critical step in the formation of Lewy bodies and Lewy neurites. Our observation that significant interactions between PAR–pαSyn are present in post mortem PD/PDD and MSA patient samples suggests that this interaction may be prevalent in disease. Understanding this interaction and relating it to disease progression may have wide implications in treating the synucleinopathies since non-toxic PARP inhibitors could represent an important disease-modifying therapy (Berger et al., 2018).

Another novel finding in our present work is the identification of the amino acid residues that could be responsible for the binding of PAR to αSyn. Our studies confirm that PAR and αSyn interact via electrostatic forces involving positively charged lysine residues on αSyn. Our computational chemistry studies also suggest that the non-proteinaceous density in αSyn fibrils isolated from MSA brain may be PAR; additional studies are clearly needed to confirm this hypothesis.

In summary, our results confirm previously reported findings, suggesting that PAR is involved in the formation of disease-associated αSyn aggregates in PD. Furthermore, our studies are significant since they represent the first demonstration of the presence of PAR–pαSyn interactions in post mortem samples of PD, PDD, and MSA brain. Our data also suggest that the interaction of PAR with αSyn occurs via the electrostatic interactions of negatively charged PAR with positively charged lysine residues toward the N-terminus of the protein. The computational chemistry studies described here also suggest that the non-proteinaceous density found in αSyn isolated from MSA brain may be PAR and suggest further studies aimed at confirming this hypothesis.

Study Design

The primary objectives of this study were to investigate PAR binding to pαSyn in cell and murine models of αSyn aggregation, as well as human post mortem brain samples. In addition, we also aimed to identify the amino acid residues involved in αSyn–PAR binding. These controlled laboratory experiments involved the use of immunostaining, PLA, molecular biology, and computational chemistry techniques.

Immunostaining and PLA results were analyzed using CellProfiler 3.0 (McQuin et al., 2018) software, whereby, specialized pipelines were implemented to identify and count PAR and pαSyn staining (Cell/particle counting pipeline) or PLA dot signal (modified Speckle Counting pipeline; whereby PLA dots were identified within cells' cytoplasm). For animal studies, sample size for each age group was $n = 3$. Age groups were determined via PAR immunostaining, whereby, mice that were 12 months of age and older displayed higher PAR intensity. The oldest mice in our study were between 17 and 18 months of age, therefore, we defined 17 months as the end point for our murine data collection. Mice that were older than 12 months were included in the "aged" group, whereas mice that were younger than 12 months were included in the "young" group. Similarly, we used littermate controls for the "aged" group to account for age-related effects. Information on the strain, sex, and age of the mice used in this study can be found in **Supplementary Table 2**. For studies on post mortem tissue samples, PD/PDD cases were characterized by PD type pathology (**Supplementary Table 3**).

MATERIALS AND METHODS

PAR Polymer

Purified PAR polymer chains (commercially obtained from TREVIGEN) were synthesized from PARP-1 in the presence of NAD^+, cleaved and subsequently purified. PAR chain lengths ranged in size from 2 to 300 ADP-ribose subunits, with a final concentration of 10 μM.

Cell Culture

SH-SY5Y-αSyn cells were transfected using Lipofectamine 2000 (Invitrogen) with pcDNA3.1 expression vector following manufacturer's protocol. The expression vector contained the full-length human wild type αSyn cDNAs, cloned in the polylinker region at the KpnI and ApaI sites. Stable transfected cell lines were selected and maintained in complete medium containing 300 μg/ml G418 (Invitrogen) (Mazzulli et al., 2006). The cells were maintained in DMEM/F12 media with GlutaMAX supplement (Thermo Fisher Scientific, Cat#10565018), 10% heat-inactivated fetal calf serum (FBS), 100 units/ml penicillin and 100 μg/ml streptomycin (Pen-Strep), in a humid atmosphere of 5% CO_2 and 95% O_2 at 37°C.

BioPORTER Experiments

SH-SY5Y-αSyn cells were seeded at concentrations of 16,000 cells/well in Nunc® Lab-Tek Chamber Slide™ system (8 wells, 0.8 cm^2/well) (Millipore, C7182-1PAK) for fluorescent microscopy experiments (IF and PLA) 24 h before incubation with either PAR + *BioPORTER*, ADP-HDP + *BioPORTER* or *BioPORTER* alone (vehicle control). *BioPORTER* Protein Delivery Reagent "QuikEase Kit" (Genlantis, Cat#BP502424) was prepared according to the manufacturer's protocol, briefly described as follows. Either PAR or ADP-HDP were diluted in 100 μL PBS to a final concentration of 50 nM, the diluted solution was then added to a QuikEase Single-Use Tube containing the dried BioPORTER reagent, mixed by pipetting 3–5 times, incubated at room temperature (RT) for 5 min and gently vortexed (post-incubation) for 3–5 s. Opti-MEM I Reduced Serum Medium (Life Technologies Inc., Cat#31985062) was used to bring the final volume in each QuikEase Single-Use Tube to 500 μL. The cells were washed once with Reduced Serum Medium 1 h before *BioPORTER* delivery, then replenished with 200 μL of Opti-MEM I (Thermo Fisher Scientific, Cat#31985062). *BioPORTER* medium mix was added at a 1:1 volume ratio in the cells grown in chamber slides. The cells were subsequently incubated for 4 h at 37°C. After 4 h, one volume of 20% serum-containing medium was added directly to the chamber slides, 24 h post-*BioPORTER* delivery, the medium was aspirated from the chamber slides and replenished with complete growth medium (DMEM/F12 media with GlutaMAX supplement). 48 h after *BioPORTER* delivery, the cells were washed 2× with PBS and processed for downstream experiments.

Animals

M83-SNCA*A53T mice expressing human A53T variant αSyn were obtained from The Jackson Laboratory, Bar Harbor, ME (JAX stock #004479). All mice were on B6;C3H genetic background. Animals were housed under controlled temperature and lighting conditions and had free access to food and water. All animal procedures were approved by IACUC and were in accordance with the National Institutes of Health Guide for the Care and Use of Laboratory Animals.

Human Post Mortem Brain αSyn Pathology Analysis

Human brain samples were obtained from University of Pennsylvania's Center for Neurodegenerative Disease Research Brain Bank and were evaluated with standardized histopathological methods as described (Toledo et al., 2014; Brettschneider et al., 2015; Robinson et al., 2018).

Immunofluorescence (IF) Staining

Forty-eight hours post-*BioPORTER* delivery, SH-SY5Y-αSyn cells (seeded on chamber slides at 16,000 cells per well) were fixed on ice with 4% paraformaldehyde for 8 min. The cells were then washed 3× with PBS and permeabilized with 0.1% Triton X-100 for 10 min at RT. After permeabilization, the cells were washed 3× with PBS-T (PBS with 0.1% Tween-20) at RT. After the third wash, 200 μL of 10% goat serum (Thermo Fisher, Cat#50062Z) was added to each well for 1 h at 37°C to block non-specific immuno binding. After blocking, the cells were sequentially incubated with primary antibodies (**Supplementary Table 1**) targeting PAR (10H) and

pαSyn (ps129) overnight at 4°C. Following primary antibody incubation, the cells were washed 3X with PBS-T. After the third wash, the cells were then sequentially incubated with secondary antibodies (**Supplementary Table 1**) for 1 h at 37°C, washed 3X with PBS-T, and stained with DAPI. Coverslips were placed on each slide and the slides were allowed to dry overnight at 4°C. Images were captured using Zeiss LSM 710 confocal (40x/1.4 Oil) and Zeiss Axio Widefield (20x/0.8) microscopes.

Human post mortem tissue sections were treated with TrueBlack (TrueBlack Lipofuscin Autofluorescence Quencher) according to manufacturer's protocol, in order to eliminate lipofuscin autofluorescence before immunostaining.

Following the blocking step with 10% goat serum, murine tissue sections underwent an additional blocking step with anti-mouse IgG (**Supplementary Table 1**) for 1 h at 37°C in order to reduce non-specific signal from secondary antibodies directed against PAR antibody (10H), which is a mouse monoclonal primary antibody.

Proximity Ligation Assay (PLA)

Forty-eight hours post-*BioPORTER* delivery, chamber slides cells (SH-SY5Y-αSyn cells) were processed with regards to fixation and permeabilization using the IF protocol described in the previous section. *In situ* PLA was performed according to the manufacturer's protocol, briefly described as follows. Following permeabilization, cells were blocked using Duolink® Blocking Solution for 1 h at 37°C. PAR primary antibody (**Supplementary Table 1**) was diluted in Duolink® Antibody Diluent, added to the cells and incubated overnight at 4°C. Following overnight incubation with PAR primary antibody, the cells were washed 2× with Duolink® Wash Buffer A, then incubated with Duolink® PLA Probe (goat anti-mouse *MINUS*) for 1 h at 37°C. After incubation with PLA Probe *MINUS,* the cells were washed 2× with Wash Buffer A, blocked with Duolink® Blocking Solution for 1 h at 37°C and incubated overnight at 4°C with primary antibody targeting pαSyn (**Supplementary Table 1**). Following overnight incubation, the cells were washed 2X with Wash Buffer A and incubated with Duolink® (PLA Probe goat anti-rabbit *PLUS*) for 1 h at 37°C. Following the sequential addition of primary antibodies and corresponding PLA Probes, the cells were processed with respect to ligation (Duolink® Ligation buffer and Ligase), amplification (Duolink® Amplification buffer and Polymerase) and imaging using Zeiss Axio Widefield (20×/0.8) microscope. Human post mortem tissue sections were treated with TrueBlack (TrueBlack® Lipofuscin Autofluorescence Quencher) according to manufacturer's protocol, in order to eliminate lipofuscin autofluorescence before PLA. Murine tissue sections underwent an additional blocking step with anti-mouse IgG (**Supplementary Table 1**) for 1 h at 37°C to reduce non-specific signal from goat anti-mouse *MINUS*.

αSyn Protein Expression and Purification

Protein expression and purification was done following previously published protocol (Lengyel-Zhand et al., 2020). Briefly, the plasmid encoding the human αSyn sequence was transformed into *Escherichia coli* BL21(DE3) and the cells were grown on agar/LB plates with ampicillin (100 μg/mL) overnight at 37°C. The next day a single colony was inoculated into 100 mL Luria–Bertani (LB) containing ampicillin (100 μg/mL). The culture was incubated at 37°C overnight with shaking at ∼200 rpm. The following day, 10 mL of the overnight culture was diluted with 1 L of LB media supplemented with ampicillin and this culture was incubated at 37°C until OD_{600} reached 0.6 – 0.7. Protein expression was induced by addition of isopropyl-β-D-thiogalactoside (IPTG) to a final concentration of 1 mM and continued to grow at 18°C overnight. After induction, cells were harvested by centrifugation at 4°C (20 min, 4,000 *g*). The typical yield of wet-cell paste was 2 g/L. Cells were suspended in a lysis buffer (5 mL for 1 g of cell paste) containing 25 mM Tris, 20 mM imidazole, 50 mM NaCl (pH 8) with a protease inhibitor (phenylmethylsulfonyl fluoride, 0.5 mM final concentration and protease inhibitor cocktail from Cell Signaling Technology). Cells were lysed by sonication on ice for 10 min (20 s on, 20 s off). The crude cell lysate was then centrifuged at 20,000 *g* for 30 min, and the supernatant was mixed with Ni-NTA resin (Clontech, 3 mL) and kept on a rocker at RT for 30 min. The resin was then washed with 100 mL wash buffer (25 mM Tris, 20 mM imidazole, 50 mM NaCl, pH 8). The protein was eluted with a buffer containing 25 mM Tris, 300 mM imidazole, 50 mM NaCl (pH 8). Fractions containing the protein were identified by UV-Vis spectroscopy, combined and was treated with β-mercaptoethanol (200 mM final concentration) overnight at RT to cleave the C-terminal intein. The next day, the protein was concentrated to 3 mL and dialyzed against buffer containing 25 mM Tris, 50 mM NaCl, pH 8. After dialysis, the protein mixture was loaded onto Ni-NTA column and the pure αSyn protein was collected in the flow through fractions. The combined protein fractions were concentrated and dialyzed against buffer containing 50 mM Tris, 150 mM NaCl, pH 7.5. The purity of the protein was confirmed by SDS-PAGE. Protein concentration was determined by measuring the absorbance at 280 nm and using the calculated (ExPASy) extinction coefficient of 5,960 $M^{-1}cm^{-1}$.

Site-Directed Mutagenesis

αSyn mutations were generated by performing site directed mutagenesis using the following primers:

αSyn K43A
Forward: 5′- TCCGCAACCAAGGAGGGA -3′
Reverse: 5′- TCCCTCCTTGGTTGCGGA - 3′
αSyn K43A K45A
Forward: 5′- GGCTCCGCAACCGCGGAGGGAGTG - 3′
Reverse: 5′- CACTCCCTCCGCGGTTGCGGAGCC - 3′
αSyn K58A
Forward: 5′-GTGGCTGAGGCGACCAAA - 3′
Reverse: 5′-TTTGGTCGCCTCAGCCAC - 3′

All plasmids and inserts were sequenced and confirmed to be free of any errors.

PAR Binding Motifs (PBM)

hxbxhhbbhhb (h are hydrophobic residues, b are basic residues, and x is any amino acid residue) (Pleschke et al., 2000). [HKR]-X-X-[AIQVY]-[KR]-[KR]- [AILV]-[FILPV] (Pleschke et al., 2000; Gagné et al., 2008).

Preparation of αSyn Fibrils

Purified αSyn monomer (100 μM) was incubated in buffer containing 50 mM Tris (pH 7.5), 150 mM NaCl and 0.05% NaN_3 for 72 h at 37°C with shaking at 1,000 rpm in a Fisher Scientific Mixer.

Transmission Electron Microscopy (TEM)

The 100 μM fibril stock solution was diluted 4× with water and samples (5 μL) were spotted onto glow-discharged formvar/carbon-coated, 200-mesh copper grids (Ted Pella). After 1 min, grids were washed briefly with water and stained with one 10 μL drop of 2% w/v uranyl acetate for 1 min. The excess stain was removed by filter paper and the grids were dried under air. Samples were imaged with a Tecnai FEI T12 electron microscope at an acceleration voltage of 120 kV. Images were recorded on a Gatan OneView 4K Cmos camera.

PAR Immunodot Blot

PAR-binding motif (PBM) were identified by aligning the PBM consensus to αSyn using the PATTINPROT search engine (NPS@PATTINPROT). For immunodot analysis, either 1 mg fibrils, Histone H4 (positive control), or bovine serum albumin (negative control) were blotted onto a 0.2 μm nitrocellulose membrane (Bio-Rad). Membranes were left to dry for 60 min, then incubated in DPBS supplemented with 0.05% Tween-20 (PBS-T) for 10 min. The membrane was then incubated with 50 nM PAR polymer in PBS-T for 2 h with rocking at RT. The membrane was washed 5× with PBS-T (5 min each) and blocked with PBSMT (5% milk in PBS-T) for 2 h at RT. After the blocking step, the membrane was incubated in primary antibody (**Supplementary Table 1**) in PBS-T at 4°C overnight. After 5 washes in PBSMT (5 min each), the membrane was incubated with secondary antibody (**Supplementary Table 1**) in PBSMT for 1 h at RT. The membrane was washed 3× in PBSMT, 2× in PBS-T, and 2× in DPBS (5 min each). The membrane was then imaged using Li-COR ODYSSEY CLx scanner. Spot intensities were measured using Image Studio software. Revert 700 protein stain was used for total protein staining measurement. Blotted membranes were incubated with protein stain for 5 min, rinsed with Revert 700 wash buffer, and imaged using Li-COR ODYSSEY CLx scanner.

Molecular Docking

The PAR-dimer structure used in our studies was based on Lambrecht et al. (2015) and drawn on ChemDraw Profession 15.1 (PerkinElmer Informatics, Inc.). It was then imported to Chem3D Ultra 15.1 (PerkinElmer Informatics, Inc.) to minimize the PAR-dimer by MMFF94 force field for preparation of molecular docking. Molecular docking studies were performed via AutoDock 4.2 (Morris et al., 2009) plugin on PyMOL[1]. Cryo-EM structure of MSA Type I αSyn fibril (PDB ID 6XYO, Resolution 2.6 Å) was obtained from RCSB Protein Data Bank[2]. Polar hydrogens were added to the fibril structure. Non-polar hydrogens were removed from the PAR-dimer. A grid box with a dimension of 30 × 30 × 30 $Å^3$ was applied to the MSA Type I αSyn fibril structure covering the non-proteinaceous density pocket at the protofilament interface. The Lamarckian Genetic Algorithm with a maximum of 2,500,000 energy evaluations was used to calculate 100 αSyn fibril-PAR binding poses. The αSyn fibril-PAR complex with the most contacts and low free binding energy was reported.

Quantification and Statistical Analysis

All measurements were taken from distinct samples. Data points in each graph are mean (±SD); where "*n*" indicates the number of biological replicates for each experiment. *T*-tests, one-way ANOVA, and two-way ANOVA followed by Tukey's *post hoc* test were performed and are described in each figure legend. Statistical significance was set at $P < 0.05$. All statistical analyses were carried out using Graphpad prism 8 software.

DATA AVAILABILITY STATEMENT

The original contributions generated for this study are included in the article/**Supplementary Material**, further inquiries can be directed to the corresponding author.

ETHICS STATEMENT

The animal study was reviewed and approved by IACUC and was in accordance with the National Institutes of Health Guide for the Care and Use of Laboratory Animals.

AUTHOR CONTRIBUTIONS

LP performed all the cell-based studies and *ex vivo* animal and patient experiments, along with the computational protein alignment. ZL-Z helped to produce all the purified proteins and fibrils used in this project and performed TEM, ThT, and PAR immunodot blot analysis. LP and ZL-Z designed the primers for mutagenesis. JL maintained cell cultures and aided in the experimental set-up for PLA. C-JH performed molecular docking studies. MS maintained αSyn protein expression and purification. KE provided assistance with PLA. KL provided support with animal model and experimental design. VL and JT provided support with experimental design and characterization of human post mortem brain tissue from PD/PDD and non-PD patients. All authors contributed to the article and approved the submitted version.

[1] pymol.org
[2] www.rcsb.org

FUNDING

This research was supported by the Michael J. Fox Foundation (RM), U19-NS110456 (RM), T32GM008076 (LP) and supported in part by 1U19AG062418 (JT, VL, and KL).

ACKNOWLEDGMENTS

SH-SY5Y-αSyn cells were a gift from Harry Ischiropoulos, University of Pennsylvania. The plasmid encoding the human αSyn sequence was a gift from James Petersson, University of Pennsylvania.

SUPPLEMENTARY MATERIAL

The Supplementary Material for this article can be found online at: https://www.frontiersin.org/articles/10.3389/fnagi.2021.704041/full#supplementary-material

Supplementary Figure 1 | Poly (ADP-ribose) (PAR) ELISA. **(a)** PAR ELISA on SH-SY5Y-αSyn cells treated with 50 nM PAR/*BioPORTER* at 4 and 48 h. $^*P < 0.05$. Bars represent means ± SD. Student two-tailed *t*-test ($n = 3$). **(b)** PAR ELISA on SH-SY5Y-αSyn cells treated with ADP-HDP for 4, 24, and 48 h. Bars represent means ± SD. One-way ANOVA followed by Tukey's *post hoc* test. $^*P < 0.05$.

Supplementary Figure 2 | Characterization of PAR and pαSyn expression in murine brain sections. Representative images of endogenous PAR **(a)** and pαSyn **(b)** levels in sagittal brain sections from B6C3F1/J (top panel) and M83 Tg (bottom panel) mice at three different age groups (8, 12, and 17 months). **(c)** PLA on PAR-pαSyn (left) and PAR-PAN-αSyn (right) sagittal brain sections from M83 Tg mice at 18 months of age. All sections were 10 μm thick and all images were captured using a Li-COR ODYSSEY CLx scanner.

Supplementary Figure 3 | Cerebellum PLA and A53T dot blot. **(a)** PLA and DAPI signal from cerebellum sections derived from a control "non-MSA" patient. **(b)** Standard immunostain of adjacent cerebellum sections from a control patient showing pαSyn and DAPI signal. Images were captured using Zeiss Axio Widefield (20×/0.8) microscope. **(c)** Representative PAR immunodot blot to assess PAR-αSyn A53T binding. Signal intensity was normalized to αSyn WT signal. Histone H4 and BSA were used as positive and negative controls for PAR binding, respectively. **(d)** Chemical structure of PAR-dimer used in molecular docking studies.

Supplementary Table 1 | Antibody information.

Supplementary Table 2 | Animal information.

Supplementary Table 3 | Patient information.

Supplementary Table 4 | Microscopy settings.

REFERENCES

Alam, M. S. (2018). Proximity Ligation Assay (PLA). *Curr. Protoc. Immunol.* 123:e58. doi: 10.1002/cpim.58

Altmeyer, M., Kai, J. N., Teloni, F., Pozdnyakova, I., Pellegrino, S., Grøfte, M., et al. (2015). Liquid demixing of intrinsically disordered proteins is seeded by poly(ADP-ribose). *Nat. Commun.* 6:8088.

Anderson, J. P., Walker, D. E., Goldstein, J. M., de Laat, R., Banducci, K., Caccavello, R. J., et al. (2006). Phosphorylation of Ser-129 is the dominant pathological modification of α-synuclein in familial and sporadic Lewy body disease. *J. Biol. Chem.* 281, 29739–29752. doi: 10.1074/jbc.m600933200

Berger, N. A., Besson, V. C., Boulares, A. H., Bürkle, A., Chiarugi, A., Clark, R. S., et al. (2018). Opportunities for the repurposing of PARP inhibitors for the therapy of non-oncological diseases. *Br. J. Pharmacol.* 175, 192–222. doi: 10.1111/bph.13748

Bétemps, D., Verchère, J., Brot, S., Morignat, E., Bousset, L., Gaillard, D., et al. (2014). Alpha-synuclein spreading in M83 mice brain revealed by detection of pathological α-synuclein by enhanced ELISA. *Acta Neuropathol. Commun.* 2, 29–29.

Brettschneider, J., Del Tredici, K., Lee, V. M. Y., and Trojanowski, J. Q. (2015). Spreading of pathology in neurodegenerative diseases: a focus on human studies. *Nat. Rev. Neurosci.* 16, 109–120. doi: 10.1038/nrn3887

Bridi, J. C., and Hirth, F. (2018). Mechanisms of α-synuclein induced synaptopathy in Parkinson's disease. *Front. Neurosci.* 12:80. doi: 10.3389/fnins.2018.00080

Cabin, D. E., Shimazu, K., Murphy, D., Cole, N. B., Gottschalk, W., McIlwain, K. L., et al. (2002). Synaptic vesicle depletion correlates with attenuated synaptic responses to prolonged repetitive stimulation in mice lacking α-synuclein. *J. Neurosci.* 22, 8797–8807. doi: 10.1523/jneurosci.22-20-08797.2002

Cardinale, A., Paldino, E., Giampà, C., Bernardi, G., and Fusco, F. R. (2015). PARP-1 inhibition is neuroprotective in the R6/2 mouse model of Huntington's disease. *PLoS One* 10:e0134482. doi: 10.1371/journal.pone.0134482

Carrozza, M. J., Stefanick, D. F., Horton, J. K., Kedar, P. S., and Wilson, S. H. (2009). PARP inhibition during alkylation-induced genotoxic stress signals a cell cycle checkpoint response mediated by ATM. *DNA Repair (Amst.)* 8, 1264–1272. doi: 10.1016/j.dnarep.2009.07.010

David, K. K., Andrabi, S. A., Dawson, T. M., and Dawson, V. L. (2009). Parthanatos, a messenger of death. *Front. Biosci. (Landmark Ed.)* 14:1116–1128. doi: 10.2741/3297

Dettmer, U., Newman, A. J., Soldner, F., Luth, E. S., Kim, N. C., von Saucken, V. E., et al. (2015). Parkinson-causing α-synuclein missense mutations shift native tetramers to monomers as a mechanism for disease initiation. *Nat. Commun.* 6, 7314–7314.

Duan, Y., Du, A., Gu, J., Duan, G., Wang, C., Gui, X., et al. (2019). PARylation regulates stress granule dynamics, phase separation, and neurotoxicity of disease-related RNA-binding proteins. *Cell Res.* 29, 233–247. doi: 10.1038/s41422-019-0141-z

Gagné, J.-P., Isabelle, M., Lo, K. S., Bourassa, S., Hendzel, M. J., Dawson, V. L., et al. (2008). Proteome-wide identification of poly(ADP-ribose) binding proteins and poly(ADP-ribose)-associated protein complexes. *Nucleic Acids Res.* 36, 6959–6976. doi: 10.1093/nar/gkn771

Gassman, N. R., Stefanick, D. F., Kedar, P. S., Horton, J. K., and Wilson, S. H. (2012). Hyperactivation of PARP triggers nonhomologous end-joining in repair-deficient mouse fibroblasts. *PLoS One* 7:e49301. doi: 10.1371/journal.pone.0049301

James, D. I., Smith, K. M., Jordan, A. M., Fairweather, E. E., Griffiths, L. A., Hamilton, N. S., et al. (2016). First-in-class chemical probes against poly(ADP-ribose) glycohydrolase (PARG) inhibit DNA repair with differential pharmacology to Olaparib. *ACS Chem. Biol.* 11, 3179–3190. doi: 10.1021/acschembio.6b00609

Kahle, P. J., Neumann, M., Ozmen, L., Muller, V., Jacobsen, H., Schindzielorz, A., et al. (2000). Subcellular localization of wild-type and Parkinson's disease-associated mutant α-synuclein in human and transgenic mouse brain. *J. Neurosci.* 20, 6365–6373. doi: 10.1523/jneurosci.20-17-06365.2000

Kam, T.-I., Mao, X., Park, H., Chou, S. C., Karuppagounder, S. S., Umanah, G. E., et al. (2018). Poly(ADP-ribose) drives pathologic α-synuclein neurodegeneration in Parkinson's disease. *Science* 362:eaat8407. doi: 10.1126/science.aat8407

Kim, S. H., Engelhardt, J. I., Henkel, J. S., Siklós, L., Soós, J., Goodman, C., et al. (2004). Widespread increased expression of the DNA repair enzyme PARP in brain in ALS. *Neurology* 62, 319–322. doi: 10.1212/01.wnl.0000103291.04985.dc

Kim, W. S., Kågedal, K., and Halliday, G. M. (2014). Alpha-synuclein biology in Lewy body diseases. *Alzheimers Res. Ther.* 6:73.

Lábaj, J., Slamenová, D., and Kosikova, B. (2003). Reduction of genotoxic effects of the carcinogen N-methyl-N'-nitro-N-nitrosoguanidine by dietary lignin in

mammalian cells cultured in vitro. *Nutr. Cancer* 47, 95–103. doi: 10.1207/s15327914nc4701_12

Lambrecht, M. J., Brichacek, M., Barkauskaite, E., Ariza, A., Ahel, I., and Hergenrother, P. J. (2015). Synthesis of dimeric ADP-ribose and its structure with human poly(ADP-ribose) glycohydrolase. *J. Am. Chem. Soc.* 137, 3558–3564.

Lashuel, H. A., Overk, C. R., Oueslati, A., and Masliah, E. (2013). The many faces of α-synuclein: from structure and toxicity to therapeutic target. *Nat. Rev. Neurosci.* 14, 38–48. doi: 10.1038/nrn3406

Le May, N., Iltis, I., Amé, J. C., Zhovmer, A., Biard, D., Egly, J. M., et al. (2012). Poly (ADP-Ribose) glycohydrolase regulates retinoic acid receptor-mediated gene expression. *Mol. Cell* 48, 785–798. doi: 10.1016/j.molcel.2012.09.021

Lengyel-Zhand, Z., Ferrie, J. J., Janssen, B., Hsieh, C. J., Graham, T., Xu, K. Y., et al. (2020). Synthesis and characterization of high affinity fluorogenic α-synuclein probes. *Chem. Commun.* 56, 3567–3570. doi: 10.1039/C9CC09849F

Leung, A. K. L. (2014). Poly(ADP-ribose): an organizer of cellular architecture. *J. Cell Biol.* 205, 613–619. doi: 10.1083/jcb.201402114

Li, J., Uversky, V. N., and Fink, A. L. (2002). Conformational behavior of human α-synuclein is modulated by familial Parkinson's disease point mutations A30P and A53T. *NeuroToxicology* 23, 553–567. doi: 10.1016/s0161-813x(02)00066-9

Luo, X., and Kraus, W. L. (2012). On PAR with PARP: cellular stress signaling through poly(ADP-ribose) and PARP-1. *Genes Dev.* 26, 417–432. doi: 10.1101/gad.183509.111

Mao, K., Chen, J., Yu, H., Li, H., Ren, Y., Wu, X., et al. (2020). Poly (ADP-ribose) polymerase 1 inhibition prevents neurodegeneration and promotes α-synuclein degradation via transcription factor EB-dependent autophagy in mutant α-synucleinA53T model of Parkinson's disease. *Aging Cell* 19:e13163.

Maries, E., Dass, B., Collier, T. J., Kordower, J. H., and Steece-Collier, K. (2003). The role of alpha-synuclein in Parkinson's disease: insights from animal models. *Nat. Rev. Neurosci.* 4, 727–738.

Martire, S., Fuso, A., Rotili, D., Tempera, I., Giordano, C., De Zottis, I., et al. (2013). PARP-1 modulates amyloid beta peptide-induced neuronal damage. *PLoS One* 8:e72169. doi: 10.1371/journal.pone.0072169

Martire, S., Mosca, L., and d'Erme, M. (2015). PARP-1 involvement in neurodegeneration: a focus on Alzheimer's and Parkinson's diseases. *Mech. Ageing Dev.* 146-148, 53–64. doi: 10.1016/j.mad.2015.04.001

Mashimo, M., Kato, J., and Moss, J. (2013). ADP-ribosyl-acceptor hydrolase 3 regulates poly (ADP-ribose) degradation and cell death during oxidative stress. *Proc. Natl. Acad. Sci. U.S.A.* 110, 18964–18969. doi: 10.1073/pnas.1312783110

Mazzulli, J. R., Mishizen, A. J., Giasson, B. I., Lynch, D. R., Thomas, S. A., Nakashima, A., et al. (2006). Cytosolic catechols inhibit alpha-synuclein aggregation and facilitate the formation of intracellular soluble oligomeric intermediates. *J. Neurosci.* 26, 10068–10078. doi: 10.1523/jneurosci.0896-06.2006

McGurk, L., Gomes, E., Guo, L., Mojsilovic-Petrovic, J., Tran, V., Kalb, R. G., et al. (2018). Poly(ADP-Ribose) prevents pathological phase separation of TDP-43 by promoting liquid demixing and stress granule localization. *Mol. Cell* 71, 703.e–717.e.

McKeith, I. G., Boeve, B. F., Dickson, D. W., Halliday, G., Taylor, J. P., Weintraub, D., et al. (2017). Diagnosis and management of dementia with Lewy bodies. Fourth consensus report of the DLB Consortium. *Neurology* 89, 88–100.

McQuin, C., Goodman, A., Chernyshev, V., Kamentsky, L., Cimini, B. A., Karhohs, K. W., et al. (2018). CellProfiler 3.0: next-generation image processing for biology. *PLoS Biol.* 16:e2005970. doi: 10.1371/journal.pbio.2005970

Moroni, F. (2008). Poly(ADP-ribose)polymerase 1 (PARP-1) and postischemic brain damage. *Curr. Opin. Pharmacol.* 8, 96–103. doi: 10.1016/j.coph.2007.10.005

Morris, G. M., Huey, R., Lindstrom, W., Sanner, M. F., Belew, R. K., Goodsell, D. S., et al. (2009). AutoDock4 and AutoDockTools4: automated docking with selective receptor flexibility. *J. Comput. Chem.* 30, 2785–2791. doi: 10.1002/jcc.21256

Murphy, D. D., Rueter, S. M., Trojanowski, J. Q., and Lee, V. M.-Y. (2000). Synucleins are developmentally expressed, and α-synuclein regulates the size of the presynaptic vesicular pool in primary hippocampal neurons. *J. Neurosci.* 20, 3214–3220. doi: 10.1523/jneurosci.20-09-03214.2000

Narne, P., Pandey, V., Simhadri, P. K., and Phanithi, P. B. (2017). Poly(ADP-ribose)polymerase-1 hyperactivation in neurodegenerative diseases: the death knell tolls for neurons. *Semin. Cell Dev. Biol.* 63, 154–166. doi: 10.1016/j.semcdb.2016.11.007

Neumann, M., Kahle, P. J., Giasson, B. I., Ozmen, L., Borroni, E., Spooren, W., et al. (2002). Misfolded proteinase K–resistant hyperphosphorylated α-synuclein in aged transgenic mice with locomotor deterioration and in human α-synucleinopathies. *J. Clin. Invest.* 110, 1429–1439. doi: 10.1172/jci200215777

Oueslati, A. (2016). Implication of alpha-synuclein phosphorylation at S129 in synucleinopathies: what have we learned in the last decade? *J. Parkinsons Dis.* 6, 39–51. doi: 10.3233/jpd-160779

Outeiro, T. F., Grammatopoulos, T. N., Altmann, S., Amore, A., Standaert, D. G., Hyman, B. T., et al. (2007). Pharmacological inhibition of PARP-1 reduces α-synuclein- and MPP+-induced cytotoxicity in Parkinson's disease in vitro models. *Biochem. Biophys. Res. Co* 357, 596–602. doi: 10.1016/j.bbrc.2007.03.163

Perez, R. G., and Hastings, T. G. (2004). Could a loss of α-synuclein function put dopaminergic neurons at risk? *J. Neurochem.* 89, 1318–1324. doi: 10.1111/j.1471-4159.2004.02423.x

Pleschke, J. M., Kleczkowska, H. E., Strohm, M., and Althaus, F. R. (2000). Poly(ADP-ribose) binds to specific domains in DNA damage checkpoint proteins. *J. Biol. Chem.* 275, 40974–40980. doi: 10.1074/jbc.m006520200

Robinson, J. L., Lee, E. B., Xie, S. X., Rennert, L., Suh, E., Bredenberg, C., et al. (2018). Neurodegenerative disease concomitant proteinopathies are prevalent, age-related and APOE4-associated. *Brain* 141, 2181–2193. doi: 10.1093/brain/awy146

Schweighauser, M., Shi, Y., Tarutani, A., Kametani, F., Murzin, A. G., Ghetti, B., et al. (2020). Structures of α-synuclein filaments from multiple system atrophy. *Nature* 585, 464–469. doi: 10.1038/s41586-020-2317-6

Slama, J. T., Aboul-Ela, N., Goli, D. M., Cheesman, B. V., Simmons, A. M., and Jacobson, M. K. (1995). Specific inhibition of poly(ADP-ribose) glycohydrolase by adenosine diphosphate (hydroxymethyl)pyrrolidinediol. *J. Med. Chem.* 38, 389–393. doi: 10.1021/jm00002a021

Spillantini, M. G., Schmidt, M. L., Lee, V. M., Trojanowski, J. Q., Jakes, R., and Goedert, M. (1997). α-Synuclein in Lewy bodies. *Nature* 388, 839–840.

Tenreiro, S., Eckermann, K., and Outeiro, T. F. (2014). Protein phosphorylation in neurodegeneration: friend or foe? *Front. Mol. Neurosci.* 7:42. doi: 10.3389/fnmol.2014.00042

Toledo, J. B., Van Deerlin, V. M., Lee, E. B., Suh, E., Baek, Y., Robinson, J. L., et al. (2014). A platform for discovery: the University of Pennsylvania integrated neurodegenerative disease biobank. *Alzheimers Dement* 10, 477.e–484.e.

Vermaas, J. V., and Tajkhorshid, E. (2014). Conformational heterogeneity of α-synuclein in membrane. *Biochim. Biophys. Acta Biomem.* 1838, 3107–3117. doi: 10.1016/j.bbamem.2014.08.012

Wakabayashi, K., Yoshimoto, M., Tsuji, S., and Takahashi, H. (1998). α-Synuclein immunoreactivity in glial cytoplasmic inclusions in multiple system atrophy. *Neurosci. Lett.* 249, 180–182. doi: 10.1016/s0304-3940(98)00407-8

Wang, Y., Shi, M., Chung, K. A., Zabetian, C. P., Leverenz, J. B., Berg, D., et al. (2012). Phosphorylated α-synuclein in Parkinson's disease. *Sci Transl Med* 4, 121ra20.

Wang, Z., Gagné, J.-P., Poirier, G. G., and Xu, W. (2014). Crystallographic and biochemical analysis of the mouse poly(ADP-Ribose) glycohydrolase. *PLoS One* 9:e86010. doi: 10.1371/journal.pone.0086010

Waxman, E. A., and Giasson, B. I. (2009). Molecular mechanisms of alpha-synuclein neurodegeneration. *Biochim. Biophys. Acta* 1792, 616–624.

Yunjong, L., Kang, H. C., Lee, B. D., Lee, Y. I., Kim, Y. P., and Shin, J. H. (2014). Poly (ADP-ribose) in the pathogenesis of Parkinson's disease. *BMB Rep.* 47, 424–432.

Zeng, X.-S., Geng, W.-S., Jia, J.-J., Chen, L., and Zhang, P.-P. (2018). Cellular and molecular basis of neurodegeneration in Parkinson disease. *Front. Aging Neurosci.* 10:109. doi: 10.3389/fnagi.2018.00109

Conflict of Interest: The authors declare that the research was conducted in the absence of any commercial or financial relationships that could be construed as a potential conflict of interest.

Copyright © 2021 Puentes, Lengyel-Zhand, Lee, Hsieh, Schneider, Edwards, Luk, Lee, Trojanowski and Mach. This is an open-access article distributed under the terms of the Creative Commons Attribution License (CC BY). The use, distribution or reproduction in other forums is permitted, provided the original author(s) and the copyright owner(s) are credited and that the original publication in this journal is cited, in accordance with accepted academic practice. No use, distribution or reproduction is permitted which does not comply with these terms.

frontiers in Aging Neuroscience

ORIGINAL RESEARCH
published: 19 July 2021
doi: 10.3389/fnagi.2021.706834

Acupuncture Can Regulate the Peripheral Immune Cell Spectrum and Inflammatory Environment of the Vascular Dementia Rat, and Improve the Cognitive Dysfunction of the Rats

Pan Pan[1,2,3†], Zhinan Ma[1,2†], Zhen Zhang[1,4], Zhenzhen Ling[1,5], Yao Wang[1,2], Qiuping Liu[1,2], Xiaolin Lin[6,7], Pan Xu[1,2], Dan Yang[1,2], Hui Zhi[1,2], Runmin Wang[1,2] and Xuezhu Zhang[1,2]*

[1] First Teaching Hospital of Tianjin University of Traditional Chinese Medicine, Tianjin, China, [2] National Clinical Research Center for Chinese Medicine Acupuncture and Moxibustion, Tianjin, China, [3] Yunnan University of Traditional Chinese Medicine, Kunming, China, [4] Weifang Traditional Chinese Hospital, Weifang, China, [5] Department of Immune Regulation, Immunology Frontier Research Center, Osaka University, Osaka, Japan, [6] Tianjin University of Traditional Chinese Medicine, Tianjin, China, [7] Hangzhou Hospital of Traditional Chinese Medicine, Hangzhou, China

Objective: The aim of this study is to analyze the effects of acupuncture on peripheral immune function, inflammation, and cognitive impairment in vascular dementia (VD) rats.

Methods: In this study, 2-month-old healthy male Wistar rats (260–280 g) were assigned to the groups as follows: normal group (Gn, n = 10), sham-operated group (Gs, n = 10), and operated group (Go, n = 45). The Go group was established by permanent, bilateral common carotid artery occlusion (BCCAO). Two months after operation, the operated rats were screened by hidden platform trial and the rats with cognitive dysfunction were further randomly divided into impaired group (Gi), acupoint group (Ga), and non-acupoint group (Gna) with 10 rats in each group. The Ga group was given acupuncture treatment for 14 days with a rest for every 7 days. After treatment, the Morris water maze (MWM) test was performed to evaluate the spatial learning and memory abilities of rats. The lymphocyte subsets in peripheral blood and spleen of rats were measured by flow cytometry. The levels of cytokines [i.e., interleukin (IL)-1β, IL-2, IL-4, IL-10, tumor necrosis factor-α (TNF-α), and interferon-γ (INF-γ)], chemokines (i.e., macrophage inflammatory protein-2 (MIP-2)), and other inflammatory mediators (i.e., cyclooxygenase-2 (COX-2) and inducible nitric oxide synthase (iNOS)) in peripheral blood and hippocampus were measured by enzyme linked immunosorbent assay (ELISA).

Results: Compared with the Gn group, the Gi rats presented long escape latencies to find the platform. After acupuncture treatment, the escape latencies of the Ga group were rescued markedly when compared with the Gi group ($P < 0.05$). The proportion of CD4 + T lymphocytes in both spleen and peripheral blood in the Ga group increased ($P < 0.05$) in comparison with the Gi group. There is an obvious reduction in IL-1β ($P < 0.05$), IL-2 ($P < 0.05$), TNF-α ($P < 0.01$), INF-γ ($P < 0.01$), MIP-2 ($P < 0.05$), and iNOS ($P < 0.01$), coming along with the increased levels of IL-4 and IL-10 ($P < 0.01$) in the Ga group when compared with the Gi group. In addition, the hippocampus

OPEN ACCESS

Edited by:
Jiehui Jiang,
Shanghai University, China

Reviewed by:
Julien Rossignol,
Central Michigan University, United States
Banikalyan Swain,
University of Florida, United States

***Correspondence:**
Xuezhu Zhang
xzzhang@tjutcm.edu.cn

† These authors have contributed equally to this work

Received: *08 May 2021*
Accepted: *18 June 2021*
Published: *19 July 2021*

Citation:
Pan P, Ma ZN, Zhang Z, Ling ZZ, Wang Y, Liu QP, Lin XL, Xu P, Yang D, Zhi H, Wang RM and Zhang XZ (2021) Acupuncture Can Regulate the Peripheral Immune Cell Spectrum and Inflammatory Environment of the Vascular Dementia Rat, and Improve the Cognitive Dysfunction of the Rats. Front. Aging Neurosci. 13:706834. doi: 10.3389/fnagi.2021.706834

proinflammatory factors IL-1β ($P < 0.01$), IL-2 ($P < 0.01$), TNF-α ($P < 0.05$), INF-γ ($P < 0.05$), MIP-2 ($P < 0.05$), iNOS ($P < 0.01$), and COX-2 decreased in the Ga group, whereas the anti-inflammatory factors IL-4 and IL-10 ($P < 0.01$) increased.

Conclusion: There are abnormal immune function and peripheral inflammation in VD rats. Acupuncture can regulate the peripheral immune function and inflammation of the VD rats and can improve the cognitive dysfunction of the rats.

Keywords: vascular dementia, cognitive function, acupuncture, inflammation, immune cell, immunomodulatory

INTRODUCTION

Vascular dementia (VD) is a serious cognitive dysfunction syndrome caused by cerebrovascular disease, which is the second most common type of dementia after Alzheimer's disease (O'Brien and Thomas, 2015). The epidemiological data show that the incidence of VD is 0.98% in 71- to 79-year-old people and 4.09% in 80- to 89-year-old people (Plassman et al., 2007). However, in reality, vascular factors may have a greater impact on dementia, since some dementia-related infarcts are difficult to identify in the clinic (Smith, 2017).

In the clinic, dementia caused by ischemic brain damage is the most common type (Venkat et al., 2015). In this study, we used the bilateral common carotid artery occlusion (BCCAO) method to establish the VD rat model, which may be more stable and reliable to study the physiopathological mechanisms of cognitive impairment related to chronic cerebral ischemia (Zhang et al., 2014). The long-term decrease in cerebral blood flow caused by the ligation of bilateral common carotid arteries (BCCAs), resulting in a series of pathological changes similar to VD, such as the sparsity of brain white matter (Cho et al., 2017; Nyitrai et al., 2018), hippocampus and cortex damage (Mori et al., 2017; Nyitrai et al., 2018), increased inflammation (Hei et al., 2018; Ranjithkumar et al., 2019), microglia activation (Yuan-Cheng et al., 2018; Impellizzeri et al., 2019), oxidative stress (Zhang et al., 2017), and blood–brain barrier damage (Edrissi et al., 2016). In addition, cognitive impairment is the core symptom of dementia. Some behavioral tests also prove that the BCCAO model has poor performance in the eight-arm maze, Morris water maze (MWM), elevated T-maze, Y-maze, and object recognition test (Venkat et al., 2015), indicating that the model has a cognitive impairment such as learning and memory.

In the pathological process of ischemic brain damage and hypoxemia–hypoperfusion dementia, the chronic hypoperfusion and thromboembolism events can cause a decrease in cerebral blood flow, hypoxia, oxidative stress, and inflammatory reaction and, finally, can cause a cognitive impairment (Venkat et al., 2015). More recently, some studies have demonstrated that neuroinflammation plays a critical role in the pathophysiology of ischemic brain damage (Iadecola, 2010). According to the knowledge of the past, peripheral immune cells cannot enter the central nervous system due to the existence of the blood–brain barrier. However, more recent observations have supported that peripheral inflammation and abnormal immune function may aggravate neuroinflammation and promote neuron damage (An et al., 2014; Prinz and Priller, 2017). A typical example is that a peripheral inflammation induced by the intraperitoneal injection of lipopolysaccharide (LPS) can cause immune activation and neuroinflammation in the brain, and even cognitive impairment (Zakaria et al., 2017; Harland et al., 2020). Another example is that mice, lacking peripheral T cells, manifest cognitive dysfunction (Kipnis et al., 2004). These findings suggested that peripheral inflammation and immune dysfunction may have the adverse effects on the function of the central nervous system and may lead to the changes in cognitive function (Doyle et al., 2015; Prinz and Priller, 2017). At present, several studies have shown that the peripheral inflammation and immune function and the inflammation levels of patients with VD are abnormal (Guoping et al., 2015; Busse et al., 2017; Shang et al., 2018), while correcting the abnormalities of peripheral inflammation and immune function in patients with VD may help improve the cognitive function. Some drugs used in the treatment of Alzheimer's disease have entered the clinical trials to modulate peripheral immune system and to improve peripheral inflammation (Dionisio-Santos et al., 2019); however, research on the peripheral immune system of VD is still rare.

Lots of evidence showed that acupuncture has immunomodulatory and anti-inflammatory effects (Zhao et al., 2015; Wan et al., 2016; Chen et al., 2017) and it has a certain curative effect on VD (Yu et al., 2006; Peng et al., 2007; Shi et al., 2012). However, the mechanism of acupuncture for VD has not been fully clarified. Existing research shows that acupuncture may improve cognitive impairment and protect neurons by enhancing antioxidant capacity (Wang et al., 2015), reducing the inflammation in the hippocampus (Fang and Sui, 2016), improving the energy metabolism level of brain tissue (Zhao et al., 2011), and promoting the angiogenesis of the hippocampus (Cai et al., 2015). There is no study to observe the regulation of acupuncture on peripheral immune function of the VD animals until now, and the relationship between acupuncture-induced peripheral immune phenotype changes and VD cognitive dysfunction is still unknown.

Therefore, we proposed a hypothesis that acupuncture treatment can improve the peripheral immune function and inflammation of VD, which may partially explain the therapeutic effect of acupuncture.

MATERIALS AND METHODS

Experimental Animals

In this study, 2-month-old healthy male Wistar rats (260–280 g) were randomly divided into normal group (Gn, $n = 10$), sham-operated group (Gs, $n = 10$), and operated group (Go, $n = 45$).

After 1 week of acclimation, the VD model was established by permanent BCCAO (i.e., 2VO). Before the operation, the rats were anesthetized intraperitoneally with 40 mg/kg of pentobarbital sodium. After the BCCAs were exposed through a neck median incision, we lightly separated them from the vagus nerve and then ligated the bilateral blood vessels with a 4–0 silk thread. After ligation, the skin incision was sutured, the iodophor was disinfected, and a 0.2 ml of gentamicin sulfate (i.e., 40 mg/ml) injection was sprayed locally to prevent wound infection. In the Gs group, the same operation was performed with the exception of arterial ligation. Throughout the surgery process, the operation was as gentle as possible to reduce the pain of the animal.

All animal experiments were performed by the guidelines of the Committee for Animal Care at Tianjin University of Traditional Chinese Medicine. Every effort had been made to minimize the number and suffering of the experimental animals.

Acupuncture Manipulation

Two months after operation, the hidden platform trial of the MWM test was used to screen the operated rats. The screening ratio (SR) was calculated according to the formula as follows: SR = (the total mean escape latency of Go on the fifth day – the total mean escape latency of Gn on the fifth day)/the total mean escape latency of Gn on the fifth day × 100%. The SR which is higher than 20% was considered as the rats with cognitive dysfunction. The rats with cognitive dysfunction (n = 30) were further randomly divided into impaired group (Gi, n = 10), acupoint group (Ga, n = 10), and non-acupoint group (Gna, n = 10). The Ga group was given acupuncture treatment (with needles of 0.25 × 4.0 mm, Hwato, China) for 30 s. Acupuncture treatment was performed in the location of points [i.e., Tangzhong (CV17), Zhongwan (CV12), Qihai (CV6), Zusanli (ST36), and Xuehai (SP10)] as described in **Table 1**. The Gi rats were grasped with the same amount of time and the same extent of strength as that in the Ga group. In the Gna group, the rats were stimulated at sham sites, not related to any traditional acupuncture point, which are located at the hypochondrium on both sides of the body (i.e., 3 mm above the iliac crest) for 105 s per location (i.e., 210/2 = 105), to maintain the same stimulation techniques and time as performed in the Ga group. The treatment was continued for 14 days with a rest for every 7 days. The specific experimental steps are shown in **Figure 1**.

TABLE 1 | Acupuncture points and their anatomical positions.

Points	Anatomical positions	Time(s)
Tangzhong (CV17)	On the anterior median line of the chesty, at the level of the fourth intercostal space	30
ZhongWan (CV12)	On the anterior median line of the upper abdomen, 10 mm below the xiphosternal synchondrosis	30
Qihai (CV6)	On the anterior median line of the lower abdomen, 4 mm below the umbilicus	30
Xuehai (SP10)	On the medal aspect of the thigh when the knee is flexed 4 mm above the mediosuperior border of the patella, on the bulge of the medial portion of m quadriceps femoris	30
Zusanli (ST36)	Three millimeters below head of fibula under knee joint, and 1 mm from the anterior crest of the tibia	30
Non-acupoints	On the hypochondrium, 3 mm above iliac crest	105

Morris Water Maze Test

After treatment for 14 days, the MWM test was performed to evaluate the spatial learning and memory abilities of rats. The MWM is a circular device (i.e., 150 cm in diameter and 50 cm in height) filled with water, and the temperature of the water was maintained at 22 ± 1°C. The water surface was divided into four quadrants of equal size, and four starting positions were located in the middle of each quadrant at the edge of the tank.

The MWM test includes four stages, namely, hidden platform trial, probe trial, reversal trial, and visible platform trial. Before the hidden platform trial, a circular platform (i.e., 10 cm in diameter and 30 cm in height) was placed in the center of any quadrant and submerged 2 cm below the water surface. The rats were allowed to swim freely in the pool to familiarize themselves with the environment for two times. During the hidden platform trial, the rats were placed into the water from one of the four starting positions to find the platform. The order of the start locations was varied, and any given sequence was not repeated on the days of the acquisition phase. The rats should find the platform within 90 s, and the escape latency was recorded. If the rats failed to locate the platform within 90 s, they would be placed on the platform for 10 s to get familiar with the environment and the escape latencies of 90 s were recorded. All rats were trained two times a day for 4 days, and the average escape latency of each day was statistically analyzed.

At the end of the hidden platform trial, the probe trial was performed immediately with the platform removed. The rats were allowed to swim freely in the pool for 60 s, and the latencies of the first target-site crossover, time in the middle annulus, and the number of crossings over the former platform location was recorded.

During the reversal trial, the platform was moved to the opposite quadrant of the hidden platform trial. The rats were trained two times a day for 3 days, and the training methods were the same as the hidden platform trial.

All the rats performed the visible platform trial on the last day with the platform 2 cm above the water surface. The experimental process of the visible platform trial was the same as the probe trial.

Flow Cytometry

After the MWM test, the rats were fasted for 12 h and then anesthetized intraperitoneally with 40 mg/kg of pentobarbital sodium. Then, the peripheral blood was collected with the ethylenediaminetetraacetic acid tube, Hebei Xinle Science & Technology Company, Hebei, China for the flow cytometry and ELISA. At the same time, the spleen and hippocampus

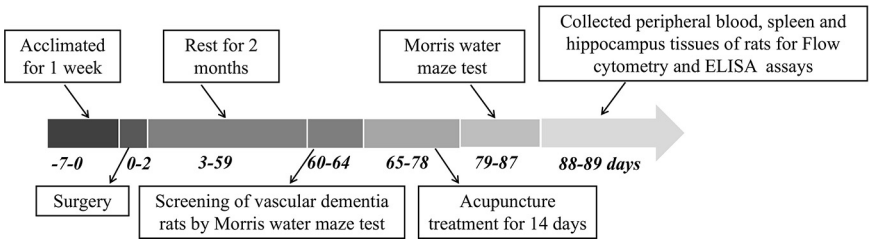

FIGURE 1 | Detailed time course schema of experiments.

tissues were also collected for further analysis. Erythrocytes were lysed two times with red blood cell lysis buffer (Solarbio, Beijing, China) for 15 and 10 min and then suspended two times with 1 × phosphate-buffered saline (PBS) to purify the cells. Spleens were collected as soon as possible and homogenized with the plunger of a syringe. The single-cell suspension was obtained by using a 300-μm cell filter. Then, cell suspensions were centrifuged at 300 × *g* for 10 min at room temperature and then resuspended in 3 ml of 1 × PBS. Erythrocytes were treated with red blood cell lysis buffer and washed two times with 1 × PBS. Finally, suspensions were resuspended in the appropriate volume of 1 × PBS, and the final concentration was approximately 1 × 10^6 cells/ml and calculated by using the cell counting plate and a microscope, Olympus Corporation, Tokyo, Japan. The flow cytometry tubes were divided into negative isotype control and sample tubes with 100 μl of single-cell suspension in each tube. According to the instructions of the kit, APC-CD3 (BD Biosciences, Chicago, Illinois, United States), FITC-CD4 (BD Biosciences, Chicago, Illinois, United States), PE-CD8a (BD Biosciences, Chicago, Illinois, United States), and PE-CyTM7-CD45 (BD Biosciences, Chicago, Illinois, United States) were added into the sample tubes, and also PE-CyTM7-CD45 and T/B/NK Cell Cocktail (BD Biosciences, Chicago, Illinois, United States) were added into the isotype control tubes. After vortexed and incubated at room temperature away from the light for 20 min, each tube was added with 2 ml of 1 × PBS solution and centrifuged at 450 × *g* for 5 min. Then, the cells in the lower layer were collected, washed two times, and suspended in 1 × PBS solution, and subsequently analyzed by using flow cytometry within 1 h after staining. Lymphocytes were gated by sideward scatter and PE-CyTM7-CD45. At least 15,000 gated events were collected using FACSCalibur (BD Biosciences, United States). The data were analyzed using FlowJo X (BD Biosciences, Ashland, Oregon, United States) software. The flow cytometry gating scheme for detecting each lymphocyte subgroup is shown in this figure. First of all, according to the physical properties of lymphocytes, the lymphocyte gate is set up according to the parameters of forward scatter and sideward scatter, and then, the lymphocyte gate **(A)** is further confirmed by SSC/CD45, second, to analyze the cells in the gate, the proportion of T cells (CD3 + cells) is determined by CD3/CD45, the proportion of B cells (CD3-CD45RA + cells) is determined by CD3/CD45RA, and the proportion of NK cells (CD3-CD161a + cells) is determined by CD3/CD161a **(B)**, and finally, the proportion of CD3 + CD4 + T cells (CD3 + CD4 + cells) was determined by CD3/CD4, and the proportion of CD3 + CD8 + T cells (CD3 + CD8 + cells) was determined by CD3/CD8 **(C)**.

ELISA

The peripheral blood of rats (n = 5) was centrifuged at 1,500 × *g* for 10 min at 4°C. The serum was separated and stored at −80°C until use. The hippocampus was homogenized with 1 × PBS and centrifuged at 3,000 × *g* for 10 min at 4°C, and then, the supernatant was stored at −80°C for further analysis. According to the protocols of the ELISA kit (IBL International, Germany), the levels of interleukin IL-1β, IL-2, IL-4, IL-10, TNF-α, INF-γ, MIP-2, COX-2, and iNOS were detected.

Statistical Analysis

All the data were processed with the SPSS (IBM Corporation, Chicago, Illinois, United States) 17.0 statistical software. The data were expressed as mean ± SEM. The data of the hidden platform trial and reversal trial were analyzed by the two-way repeated-measure ANOVA with the least significant difference (LSD). The comparison between groups was performed using the one-way ANOVA with LSD. $P < 0.05$ was considered statistically significant.

RESULTS

Acupuncture Ameliorated the Cognitive Disabilities of VD Rats

As shown in **Figure 2A**, there were no significant differences in escape latency between the Gn and Gs groups ($P > 0.05$), suggesting that the operation did not affect the learning and memory ability of rats. Compared with the Gn group, the operated rats presented long escape latencies to find the platform ($P < 0.01$), indicating that the learning and cognitive function of operated rats was impaired. After acupuncture treatment, the escape latencies of the Ga group were rescued markedly when compared with the Gi group ($P < 0.01$). During the whole training process, the escape latency of the Gna group was higher than that of the Ga group ($P < 0.05$).

In the probe trial, both the time spent in the former platform quadrant and the number of crossing over the former platform location are showed in **Figures 2C,D**.

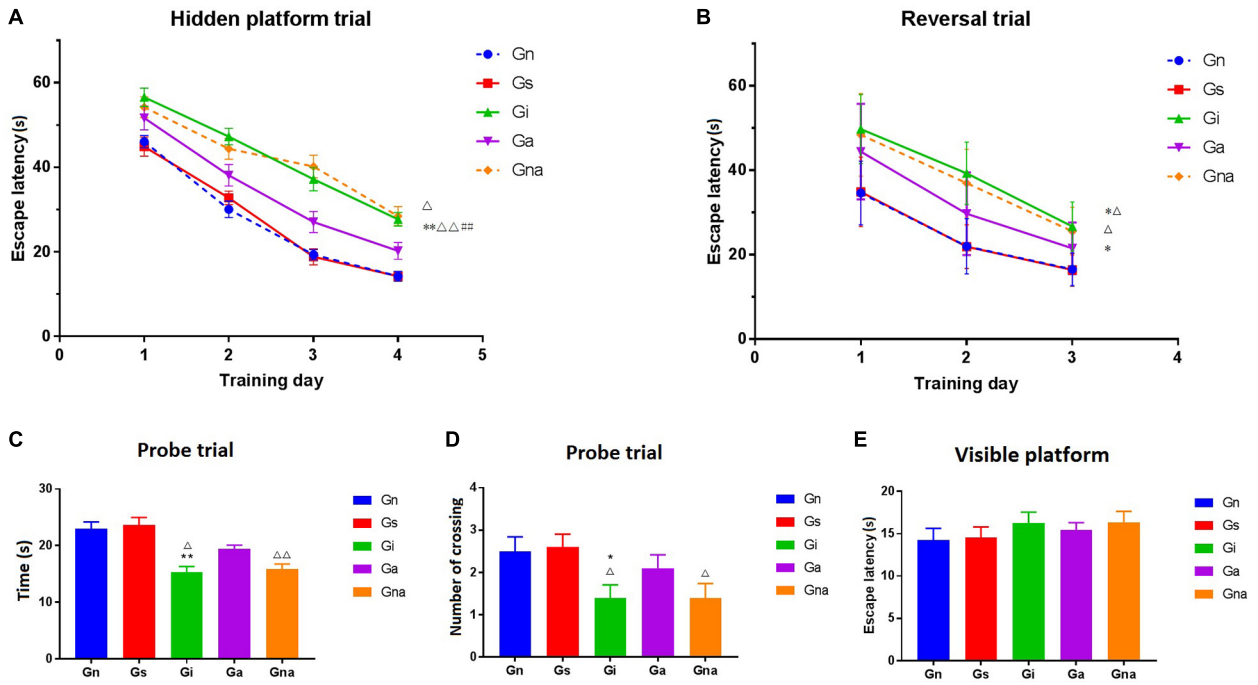

FIGURE 2 | Acupuncture improved the spatial learning and memory ability of VD mice in the Morris water maze. **(A)** Escape latency of each group in the hidden platform trial. **(B)** Escape latency of each group in the reversal trial. **(C)** Time spent in the former platform quadrant in the probe trial. **(D)** The number of crossing over the former platform location in the probe trial. **(E)** Escape latency of each group in the visible platform. The data are expressed as the mean ± SEM (n = 10). $^{*}P < 0.05$, $^{**}P < 0.01$, vs. Gn group; $^{\#}P < 0.05$, $^{\#\#}P < 0.01$, vs. Gs group; $^{\triangle}P < 0.05$, $^{\triangle\triangle}P < 0.01$, vs. Ga group. Gn, normal group; Gs, sham-operated group; Gi, impaired group; Ga, acupoint group; Gna, non-acupoint group.

No obvious differences were found between the Gn and Gs groups ($P > 0.05$). The time of staying in the quadrant of the original platform of the Gi group was significantly shorter than that of the Gn group ($P < 0.01$), and the times of crossing the original platform were also less than that of the Gn group ($P < 0.05$). The retention time of the former platform of the Ga group was much longer than that of the Gi group ($P < 0.05$). Similar results were obtained from the former platform crossings between the two groups. There were no significant differences between the Gna and Gi groups ($P > 0.05$).

Figure 2B shows the time of finding the hidden platform (i.e., in a different quadrant than the one used in the original platform). The results showed that the time of searching for the hidden platform in the Gi and Gna groups was significantly longer than that in the Ga, Gn, and Gs groups ($P < 0.05$).

In the visible platform trial, there were no significant differences in escape latency among the five groups ($P > 0.05$) (**Figure 2E**), indicating that the above experiments were not affected by the difference in motivation and motor skills and could objectively reflect the cognitive function of rats.

Acupuncture Can Improve the Peripheral Immune Function of VD Rats

We studied whether acupuncture affected the proportion of lymphocyte subsets in peripheral blood and spleen. The flow cytometry gating scheme for detecting each lymphocyte subgroup is shown in **Figure 3**. The flow cytometric analysis showed that there were no differences in the proportion of lymphocytes in peripheral blood and spleen between the Gs and Gn groups ($P > 0.05$), suggesting that operation did not affect the proportion of lymphocyte subsets in rats. As shown in **Figures 4**, **5**, the proportion of T lymphocytes and CD4 + T lymphocytes in peripheral blood and spleen of the Gi group was significantly lower than that of the Gn and Gs groups ($P < 0.05$), while the proportion of B lymphocytes in the spleen of the Gi group was significantly higher than that of the Gn and Gs groups ($P < 0.01$), indicating that the peripheral immune function of VD rats was abnormal.

Besides, the proportion of CD4 + T lymphocytes in both spleen and peripheral blood in the Ga group increased ($P < 0.05$) compared with the Gi group. The proportion of CD4 + T lymphocytes in both spleen and peripheral blood in the Ga group was lower than that in the Gn group, and there were no significant differences between the two groups, but the proportion of CD4 + T lymphocytes in the Ga group showed an upward trend. There were no significant differences between the Gs and Gna groups ($P > 0.05$), suggesting that the acupuncture points were of therapeutic specificity.

Acupuncture Regulates the Expression of Peripheral Inflammatory Factors in VD Rats

To verify the peripheral inflammatory level of VD rats and the effect of acupuncture on them, the serum cytokines (i.e., IL-1β,

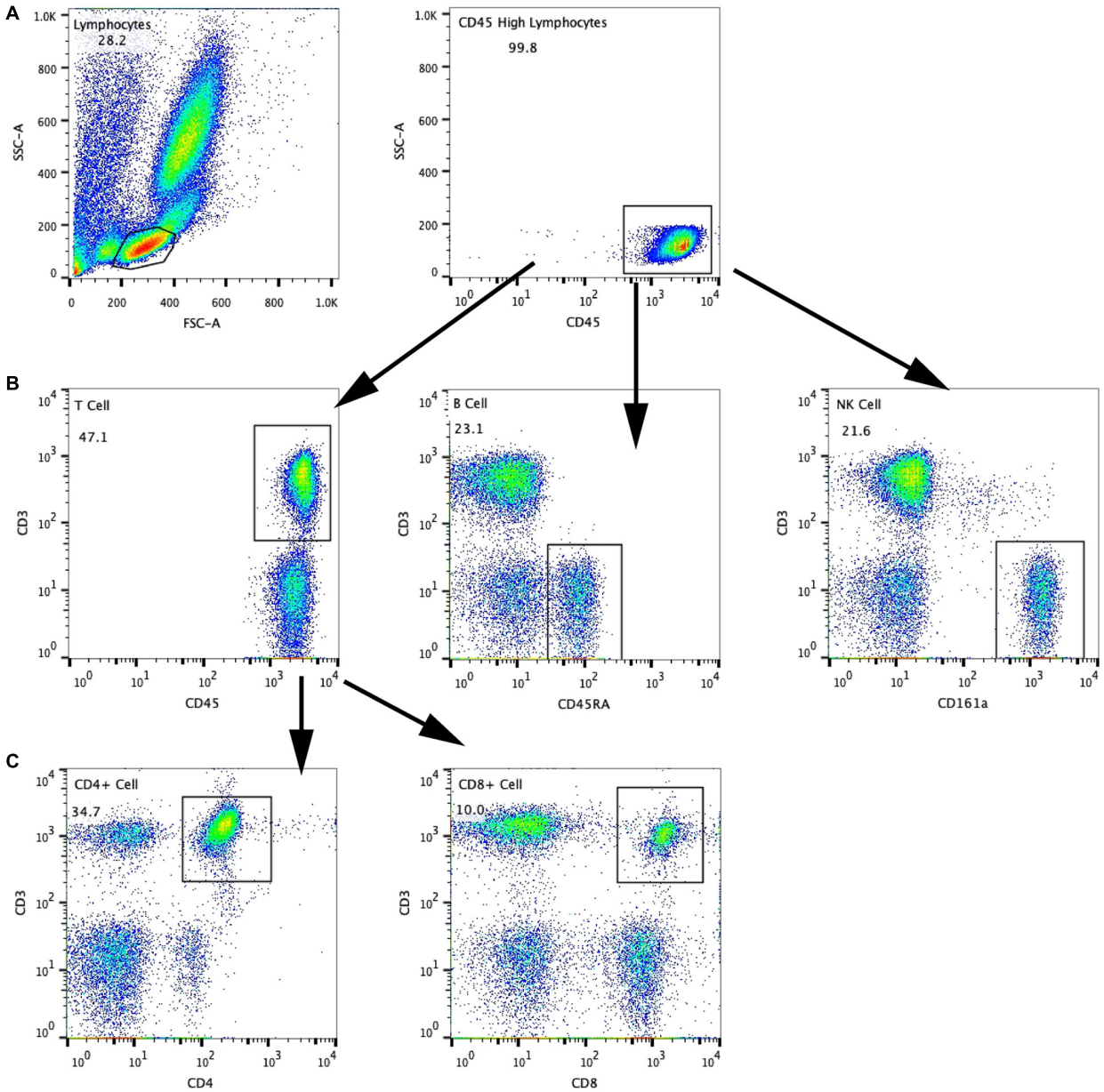

FIGURE 3 | The flow cytometry gating scheme for detecting each lymphocyte subgroup is shown in this figure. First of all, according to the physical properties of lymphocytes, the lymphocyte gate is set up according to the parameters of forward scatter and sideward scatter, and then, the lymphocyte gate **(A)** is further confirmed by SSC/CD45, second, to analyze the cells in the gate, the proportion of T cells (CD3 + cells) is determined by CD3/CD45, the proportion of B cells (CD3-CD45RA + cells) is determined by CD3/CD45RA, and the proportion of NK cells (CD3-CD161a + cells) is determined by CD3/CD161a **(B)**, and finally, the proportion of CD3 + CD4 + T cells (CD3 + CD4 + cells) was determined by CD3/CD4, and the proportion of CD3 + CD8 + T cells (CD3 + CD8 + cells) was determined by CD3/CD8 **(C)**.

IL-2, IL-4, IL-10, TNF-α, and INF-γ) and other inflammatory mediators (i.e., COX-2 and iNOS) of each group were detected by ELISA (**Figure 6**). There were no significant differences in serum cytokines and inflammatory mediators between the Gs and Gn groups ($P > 0.05$), indicating that operation did not affect the serum inflammatory level in rats. As shown in **Figure 6**, the cytokines of IL-1β, IL-2, TNF-α, INF-γ, and MIP-2 and the inflammatory mediators of COX-2 and iNOS in the serum of the Gi group increased remarkably, while IL-4 and IL-10 decreased, which showed significant differences when compared with Gn and Gs groups (all $P < 0.01$). All the results prompted that VD rats have a higher level of inflammation. After acupuncture treatment, there is a significant reduction in IL-1β ($P < 0.05$), IL-2 ($P < 0.05$), TNF-α ($P < 0.01$), INF-γ ($P < 0.01$), MIP-2 ($P < 0.05$), and iNOS ($P < 0.01$), coming along with the increased levels of IL-4 and IL-10 ($P < 0.01$) in the Ga group

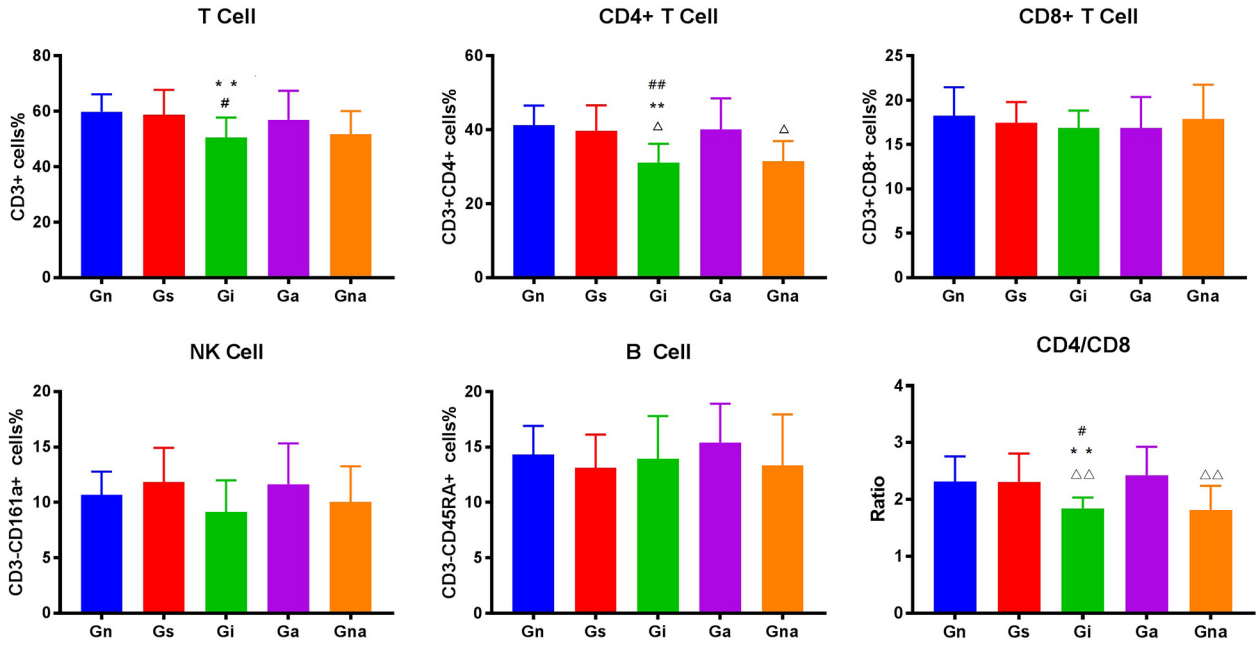

FIGURE 4 | Effect of acupuncture on peripheral blood lymphocyte subsets. The data are expressed as the mean ± SEM (n = 10). $^{**}P < 0.01$, vs. Gn group; $^{\#}P < 0.05$, $^{\#\#}P < 0.01$, vs. Gs group; $^{\triangle}P < 0.05$, $^{\triangle\triangle}P < 0.01$, vs. Ga group. Gn, normal group; Gs, sham-operated group; Gi, impaired group; Ga, acupoint group; Gna, non-acupoint group.

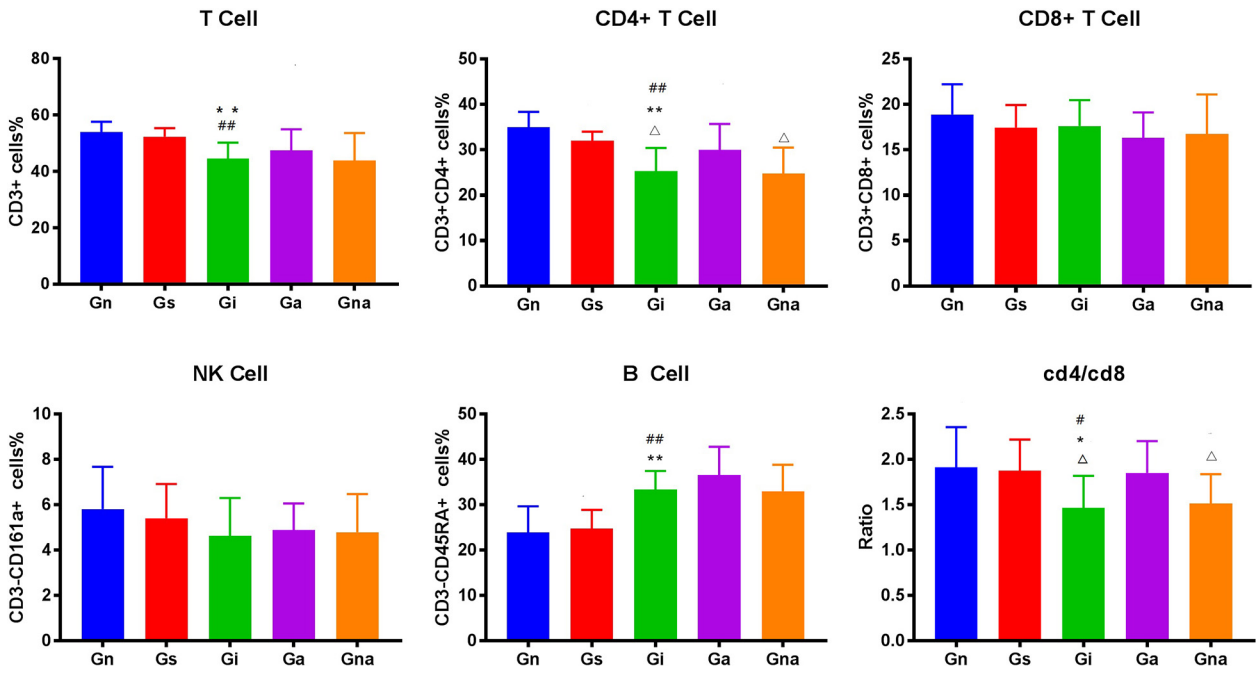

FIGURE 5 | Effect of acupuncture on splenic lymphocyte subsets. The data are expressed as the mean ± SEM (n = 10). $^{*}P < 0.05$, $^{**}P < 0.01$, vs. Gn group; $^{\#}P < 0.05$, $^{\#\#}P < 0.01$, vs. Gs group; $^{\triangle}P < 0.05$, $^{\triangle\triangle}P < 0.01$, vs. Ga group. Gn, normal group; Gs, sham-operated group; Gi, impaired group; Ga, acupoint group; Gna, non-acupoint group.

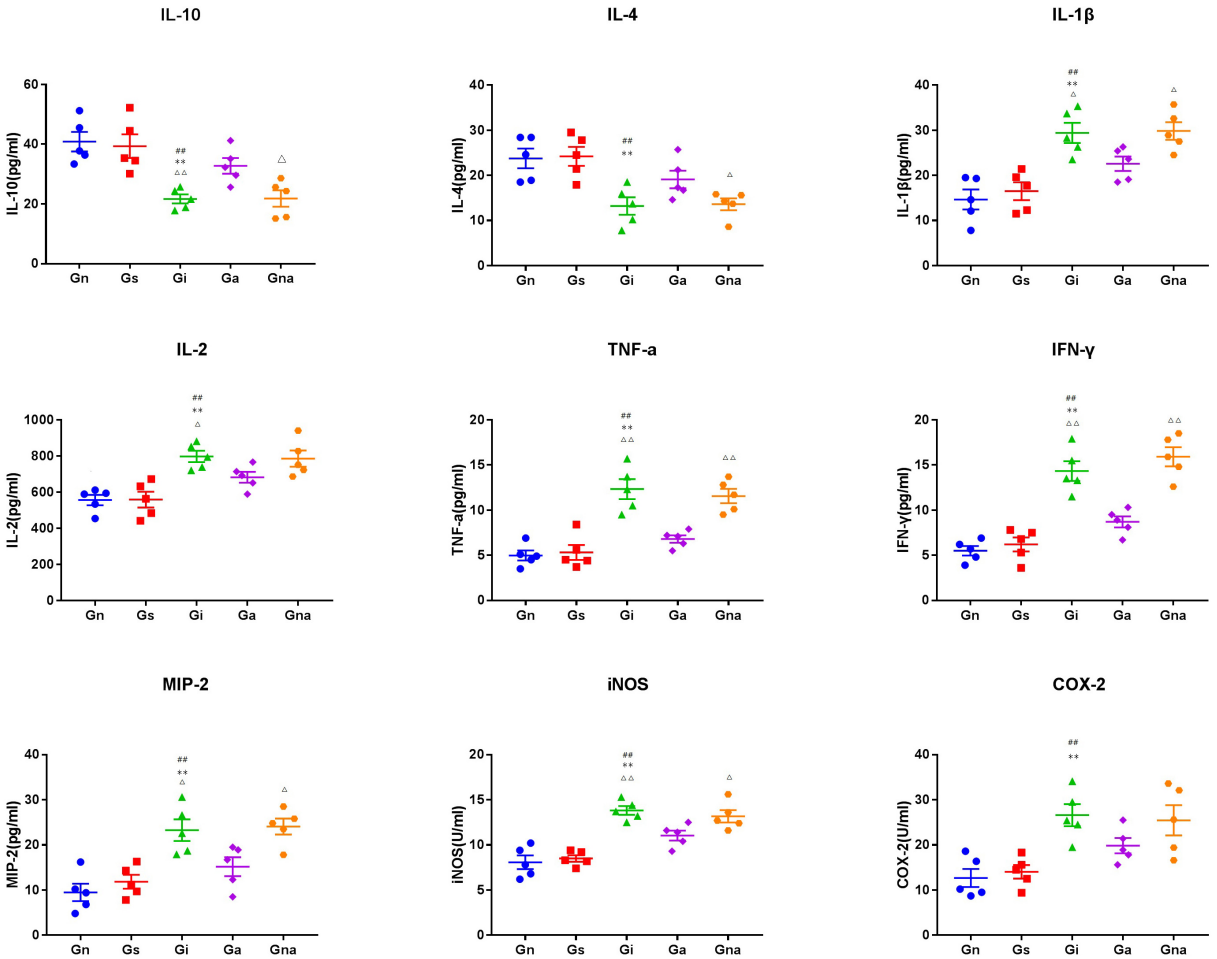

FIGURE 6 | Effect of acupuncture on the levels of related inflammatory mediators in serum. The data are expressed as the mean ± SEM (n = 5). $^{**}P < 0.01$, vs. Gn group; $^{\#}P < 0.05$, $^{\#\#}P < 0.01$, vs. Gs group; $^{\triangle}P < 0.05$, $^{\triangle\triangle}P < 0.01$, vs. Ga group. Gn, normal group; Gs, sham-operated group; Gi, impaired group; Ga, acupoint group; Gna, non-acupoint group.

compared with the Gi group. To sum up, acupuncture treatment has the potential to decrease the level of serum inflammatory factors and to relieve the inflammatory reaction in VD rats. Also, due to the specificity of acupuncture points, there were no significant differences between the Gi and Gna groups ($P > 0.05$).

Acupuncture Can Reduce Inflammatory Factors in the Hippocampus of VD Rats

The levels of cytokines (i.e., IL-1β, IL-2, IL-4, IL-10, TNF-α, and INF-γ), chemokines (i.e., MIP-2), and other inflammatory mediators (i.e., COX-2 and iNOS) in the hippocampus were detected by the ELISA kits (**Figure 7**). There were no significant differences in all indexes between the Gs and Gn groups ($P > 0.05$), excluding the effect of the operation on the level of hippocampal inflammation in rats. Compared with the Gn and Gs groups, the levels of cytokines, such as IL-1β, IL-2, TNF-α, INF-γ, MIP-2, COX-2, and iNOS, in the hippocampus in the Gi group were increased, while IL-4 and IL-10 were decreased (all $P < 0.01$), which were similar to the results of serum cytokines. It further suggested that there was inflammation in VD rats. However, compared with the Gi group, the hippocampal proinflammatory factors in the Ga group IL-1β ($P < 0.01$), IL-2 ($P < 0.01$), TNF-α ($P < 0.05$), INF-γ ($P < 0.05$), MIP-2 ($P < 0.05$), iNOS ($P < 0.01$), and COX-2 were decreased after acupuncture treatment, whereas the anti-inflammatory factors IL-4 and IL-10 ($P < 0.01$) were increased, indicating that acupuncture could improve the inflammation in the hippocampus of VD rats. This effect was not observed in the Gna group compared with the Gi group ($P > 0.05$), indicating the specificity of acupuncture.

DISCUSSION

Currently, there is no specific drug for VD (Sun, 2018), as a treatment option, acupuncture shows its potential in the treatment of VD (Liu et al., 2014). In this study, we confirmed that acupuncture treatment could improve the cognitive impairment of the VD rats. Moreover, we also found that there are abnormalities of peripheral inflammation and immune

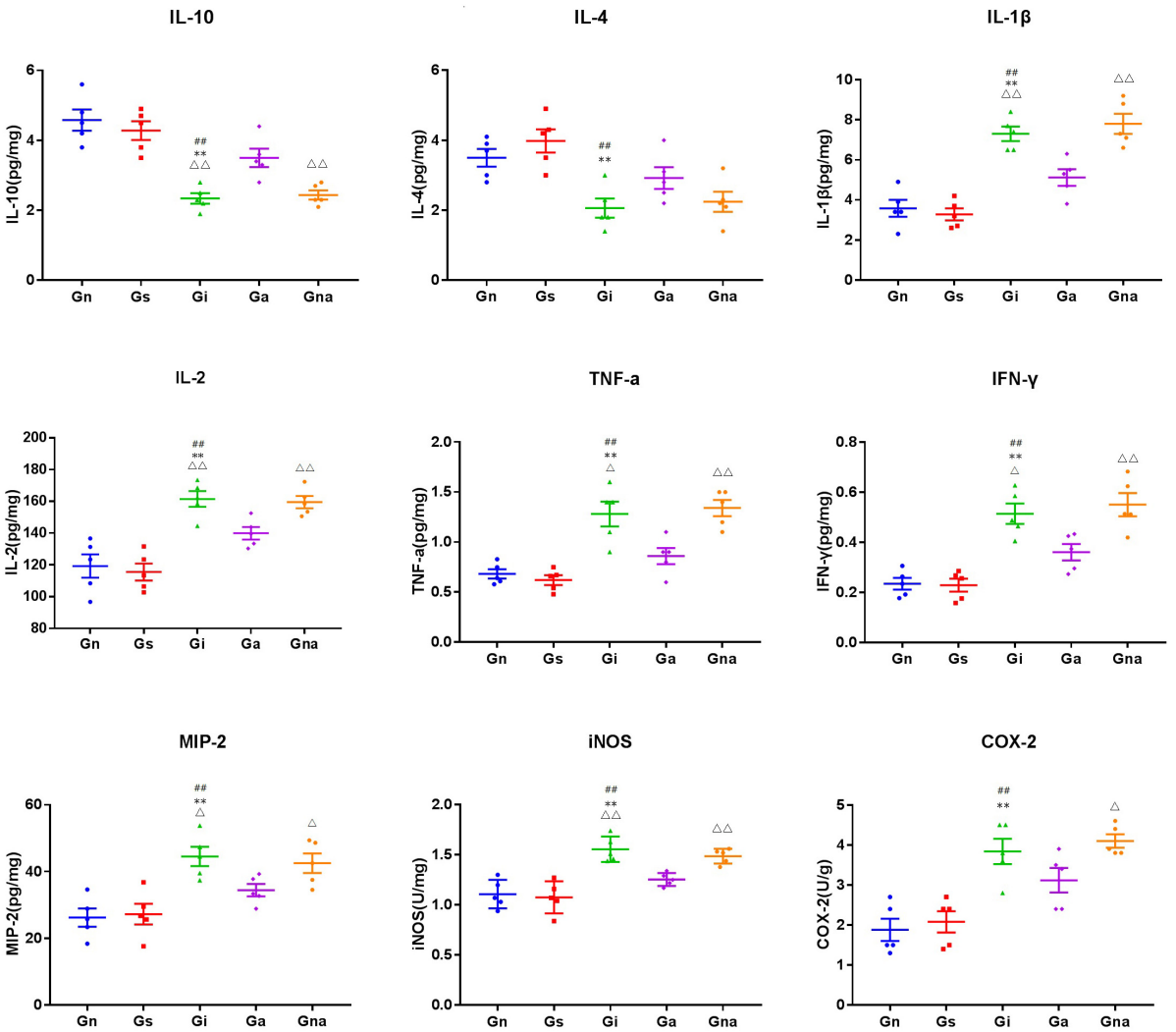

FIGURE 7 | Effect of acupuncture on the levels of related inflammatory mediators in the hippocampus. The data are expressed as the mean ± SEM (n = 5). $^{**}P < 0.01$, vs. Gn group; $^{\#}P < 0.05$, $^{\#\#}P < 0.01$, vs. Gs group; $^{\triangle}P < 0.05$, $^{\triangle\triangle}P < 0.01$, vs. Ga group. Gn, normal group; Gs, sham-operated group; Gi, impaired group; Ga, acupoint group; Gna, non-acupoint group.

function in the VD rats, and acupuncture can regulate this abnormality.

Specifically, on the one hand, we found that the proportion of T cells and CD4+ helper T cells in the peripheral blood and spleen of the Gi group decreased in varying degrees, accompanied by the decrease in the ratio of CD4/CD8, which means that there is an abnormal immune function in the VD rats. T lymphocyte plays a key role in cell-mediated adaptive immunity. Lots of evidence supported the involvement of T lymphocytes in neuroinflammation and brain injury after ischemia (An et al., 2014). The abnormal function of CD4 + T cells may lead to serious cognitive impairment (Jeon et al., 2016), and some clinical evidence (Busse et al., 2017) has also proven that the proportion of T cells and CD4+ helper T cells decreased in the peripheral blood of patients with VD. Combined with our results, we speculated that adaptive immunity may be involved in the pathological process of cognitive impairment after cerebral ischemia, especially T cells and CD4+ helper T cells. However, after the acupuncture treatment, the proportion of T cells and CD4+ helper T cells increased to a certain extent, and the cognitive impairment was improved. This indicates that the therapeutic effect of acupuncture may be related to T cells and CD4+ helper T cells. Some animal studies have also shown that T cells and CD4+ helper T cells contribute to nerve repair and neurogenesis (Brait et al., 2012; Wang et al., 2017). Another interesting finding is that in the spleen of model rats, the proportion of B cells increased significantly, whereas the increase in peripheral blood was not obvious. This phenomenon seems to suggest that B lymphocytes are involved in the process of cognitive impairment after multiple infarctions. Some evidence also shows that although B lymphocytes have a certain protective effect in the early stage of cerebral ischemia, the autoimmunity

mediated by B lymphocytes may be an important mechanism of cognitive impairment after stroke (Doyle Kristian and Buckwalter Marion, 2017). However, after acupuncture, the proportion of B cells did not change. A reasonable explanation is that the therapeutic effect of acupuncture may not be mediated by B cells, or acupuncture may not change the proportion of B cells but may change its subsets or functions, which needs further research. On the other hand, we found that there was inflammation in the peripheral blood of model rats, which showed the upregulation of inflammatory mediators such as IL-1β, IL-2, TNF-α, INF-γ, MIP-2, COX-2, and iNOS and the downregulation of anti-inflammatory factors such as IL-4 and IL-10, which was consistent with the results of some studies. Some data showed that IL-1β, IL-2, IL-6, TNF-α, INF-γ, and other inflammatory factors in peripheral blood of patients with VD increased in varying degrees (Guoping et al., 2015; Schmitz et al., 2015), while IL-4 and IL-10 decreased in varying degrees (De Luigi et al., 2002; Liu et al., 2018). A large number of data show that peripheral inflammation can cause neuroinflammation and cognitive impairment (Badshah et al., 2016; Miryam and Goar, 2016; Zhang et al., 2018) and can aggravate the symptoms of VD model rats (Levine et al., 2015). After acupuncture, inflammatory mediators such as IL-1β, IL-2, TNF-α, INF-γ, MIP-2, COX-2, iNOS, and other inflammatory mediators were downregulated in varying degrees, while IL-4 and IL-10 were upregulated. This indicates that acupuncture reduced the level of peripheral inflammation, improved the peripheral immune environment, and reversed peripheral inflammation and the corrected peripheral immune abnormalities can reduce neuroinflammation and cognitive impairment (Dadsetan et al., 2016; Balzano et al., 2020). This may be one of the mechanisms of acupuncture improving the cognitive function of VD model rats.

Finally, in addition to improving peripheral immune function and inflammation, we also found that acupuncture can improve the inflammation level of the hippocampus. The results of ELISA indicate that there was inflammation in the hippocampus, and the level of inflammation was alleviated after acupuncture treatment.

CONCLUSION

Our results found that the VD rats have an abnormal immune function and peripheral inflammation, while acupuncture can regulate the immune cell phenotype and peripheral inflammation of VD rats, reduce the expression of proinflammatory factors in the hippocampus, and improve the cognitive impairment of VD rats. This shows that acupuncture can be used as an efficacious therapeutic approach for VD in the future.

DATA AVAILABILITY STATEMENT

The raw data supporting the conclusions of this article will be made available by the authors, without undue reservation.

ETHICS STATEMENT

The animal study was reviewed and approved by the guidelines of the Committee for Animal Care at Tianjin University of Traditional Chinese Medicine.

AUTHOR CONTRIBUTIONS

PP and XZ contributed to the conception and design of the study. ZM and ZZ organized the database. ZL and YW performed the statistical analysis. PP and ZM wrote the first draft of the manuscript. QL, XL, PX, DY, HZ, and RW wrote sections of the manuscript. All the authors participated in and completed the whole experiment, contributed to manuscript revision, read, and approved the submitted version.

FUNDING

The study was supported by the National Natural Science Foundation of China (81473766) and the Science and Technology support program of Tianjin City (20YFZCSY00810).

REFERENCES

An, C., Shi, Y., Li, P., Hu, X., Gan, Y., Stetler, R. A., et al. (2014). Molecular dialogs between the ischemic brain and the peripheral immune system: dualistic roles in injury and repair[J]. *Prog. Neurobiol.* 115, 6–24. doi: 10.1016/j.pneurobio.2013.12.002

Badshah, H., Ali, T., and Kim, M. O. (2016). Osmotin attenuates LPS-induced neuroinflammation and memory impairments via the TLR4/NFκB signaling pathway[J]. *Sci. Rep.* 6:24493.

Balzano, T., Dadsetan, S., Forteza, J., Cabrera-Pastor, A., Taoro-Gonzalez, L., Malaguarnera, M., et al. (2020). Chronic hyperammonemia induces peripheral inflammation that leads to cognitive impairment in rats: reversed by anti-TNF-α treatment[J]. *J. Hepatol.* 73, 582–592. doi: 10.1016/j.jhep.2019.01.008

Brait, V. H., Arumugam, T. V., Drummond, G. R., and Sobey, C. G. (2012). Importance of T lymphocytes in brain injury, immunodeficiency, and recovery after cerebral ischemia[J]. *J. Cereb. Blood FlowMetab.* 32, 598–611. doi: 10.1038/jcbfm.2012.6

Busse, M., Michler, E., von Hoff, F., Dobrowolny, H., Hartig, R., Frodl, T., et al. (2017). Alterations in the peripheral immune system in dementia [J]. *J. Alzheimers Dis. JAD* 58:1303. doi: 10.3233/jad-161304

Cai, R. L., Cheng, H. L., Zhou, T., Chen, G. Q., Chen, X. S., and Wu, S. B. (2015). Effects of electroacupuncture on learning-memory ability and expression of hippocampal vascular endothelial growth factor (VEGF), VEGF receptor 1 and 2 genes in vascular cognitive impairment rats[J]. *Acupunct. Res.* 40, 25–29.

Chen, L., Xu, A., Yin, N., Zhao, M., Wang, Z., Chen, T., et al. (2017). Enhancement of immune cytokines and splenic CD4+ T cells by electroacupuncture at ST36 acupoint of SD rats[J]. *PLoS One* 12:e0175568. doi: 10.1371/journal.pone.0175568

Cho, K. O., Kim, S. K., and Kim, S. Y. (2017). Chronic cerebral hypoperfusion and plasticity of the posterior cerebral artery following permanent bilateral common carotid artery occlusion[J]. *Korean J. Physiol. Pharmacol.* 21, 643–650. doi: 10.4196/kjpp.2017.21.6.643

Dadsetan, S., Balzano, T., Forteza, J., Cabrera-Pastor, A., Taoro-Gonzalez, L., Hernandez-Rabaza, V., et al. (2016). Reducing peripheral inflammation with infliximab reduces neuroinflammation and improves cognition in rats with

hepatic encephalopathy[J]. *Front. Mol. Neurosci.* 9:106. doi: 10.3389/fnmol.2016.00106

De Luigi, A., Pizzimenti, S., Quadri, P., Lucca, U., Tettamanti, M., Fragiacomo, C., et al. (2002). Peripheral inflammatory response in alzheimer's disease and multiinfarct dementia[J]. *Neurobiol. Dis.* 11, 308–314. doi: 10.1006/nbdi.2002.0556

Dionisio-Santos, D. A., Olschowka, J. A., and O'Banion, M. K. (2019). Exploiting microglial and peripheral immune cell crosstalk to treat Alzheimer's disease[J]. *J. Neuroinflammation* 16:74.

Doyle, K. P., Quach, L. N., Solé, M., Axtell, R. C., Nguyen, T. V., Soler-Llavina, G. J., et al. (2015). B-Lymphocyte-mediated delayed cognitive impairment following Stroke[J]. *J. Neurosci.* 35, 2133–2145. doi: 10.1523/jneurosci.4098-14.2015

Doyle Kristian, P., and Buckwalter Marion, S. (2017). Does B lymphocyte-mediated autoimmunity contribute to post-stroke dementia?[J]. *Brain Behav. Immun.* 64, 1–8. doi: 10.1016/j.bbi.2016.08.009

Edrissi, H., Schock, S. C., Cadonic, R., Hakim, A. M., and Thompson, C. S. (2016). Cilostazol reduces blood brain barrier dysfunction, white matter lesion formation and motor deficits following chronic cerebral hypoperfusion[J]. *Brain Res.* 1646, 494–503. doi: 10.1016/j.brainres.2016.06.036

Fang, Y., and Sui, R. (2016). Electroacupuncture at the wangu acupoint suppresses expression of inflammatory cytokines in the hippocampus of rats with vascular dementia[J]. *Afr. J. Tradit. Comp. Altern. Med.* 13, 17–24.

Guoping, P., Wei, W., Xiaoyan, L., Fangping, H., Zhongqin, C., and Benyan, L. (2015). Characteristics of the peripheral T cell immune response of patients at different stages of vascular cognitive impairment[J]. *Immunol. Lett.* 168, 120–125. doi: 10.1016/j.imlet.2015.09.015

Harland, M., Torres, S., Liu, J., and Wang, X. (2020). Neuronal mitochondria modulation of LPS-induced neuroinflammation[J]. *J Neurosci* 40, 1756–1765. doi: 10.1523/jneurosci.2324-19.2020

Hei, Y., Chen, R., Yi, X., Long, Q., Gao, D., and Liu, W. (2018). HMGB1 neutralization attenuates hippocampal neuronal death and cognitive impairment in rats with chronic cerebral hypoperfusion via suppressing inflammatory responses and oxidative stress[J]. *Neuroscience* 383, 150–159. doi: 10.1016/j.neuroscience.2018.05.010

Iadecola, C. (2010). The overlap between neurodegenerative and vascular factors in the pathogenesis of dementia[J]. *Acta Neuropathol.* 120, 287–296. doi: 10.1007/s00401-010-0718-6

Impellizzeri, D., Siracusa, R., Cordaro, M., Crupi, R., Peritore, A. F., Gugliandolo, E., et al. (2019). N-Palmitoylethanolamine-oxazoline (PEA- OXA): a new therapeutic strategy to reduce neuroinflammation, oxidative stress associated to vascular dementia in an experimental model of repeated bilateral common carotid arteries occlusion[J]. *Neurobiol. Dis.* 125, 77–91. doi: 10.1016/j.nbd.2019.01.007

Jeon, S. G., Kim, K. A., Chung, H., Choi, J., Song, E. J., Han, S. Y., et al. (2016). Impaired memory in ot-II transgenic mice is associated with decreased adult hippocampal neurogenesis possibly induced by alteration in th2 cytokine Levels[J]. *Mol. Cells* 39, 603–610. doi: 10.14348/molcells.2016.0072

Kipnis, J., Cohen, H., Cardon, M., Ziv, Y., and Schwartz, M. (2004). T cell deficiency leads to cognitive dysfunction: implications for therapeutic vaccination for schizophrenia and other psychiatric conditions[J]. *Proc. Natl. Acad. Sci. U.S.A.* 101, 8180–8185. doi: 10.1073/pnas.0402268101

Levine, D. A., Galecki, A. T., Langa, K. M., Unverzagt, F. W., Kabeto, M. U., Giordani, B., et al. (2015). Trajectory of cognitive decline after incident stroke[J]. *J. Am. Med. Assoc.* 314:41. doi: 10.1001/jama.2015.6968

Liu, F., Li, Z. M., Jiang, Y. J., and Chen, L. D. (2014). A meta-analysis of acupuncture use in the treatment of cognitive impairment after stroke[J]. *J. Altern. Comp. Med.* 20, 535–544. doi: 10.1089/acm.2013.0364

Liu, Q. Q., Zhong, D., Zhang, X., and Li, G. Z. (2018). IL-10 targets Th1/Th2 balance in vascular dementia[J]. *Eur. Rev. Med. Pharmacol. Sci.* 22, 5614–5619.

Miryam, N. C., and Goar, G. (2016). LPS-induced murine neuroinflammation model: main features and suitability for pre-clinical assessment of nutraceuticals[J]. *Curr. Neuropharmacol.* 14, 155–164. doi: 10.2174/1570159x14666151204122017

Mori, M. A., Meyer, E., Soares, L. M., Milani, H., Guimarães, F. S., de Oliveira, R. M. W., et al. (2017). Cannabidiol reduces neuroinflammation and promotes neuroplasticity and functional recovery after brain ischemia[J]. *Prog. Neuro Psychopharmacol. Biol. Psychiatry* 75, 94–105. doi: 10.1016/j.pnpbp.2016.11.005

Nyitrai, G., Spisák, T., Spisák, Z., Gajári, D., Diószegi, P., Kincses, T. Z., et al. (2018). Stepwise occlusion of the carotid arteries of the rat: MRI assessment of the effect of donepezil and hypoperfusion-induced brain atrophy and white matter microstructural changes[J]. *PLoS One* 13:e0198265. doi: 10.1371/journal.pone.0198265

O'Brien, J. T., and Thomas, A. (2015). Vascular dementia[J]. *Lancet* 386, 1698–1706.

Peng, W. N., Zhao, H., Liu, Z. S., and Wang, S. (2007). Acupuncture for vascular dementia[J]. *Cochrane Database Syst. Rev.* 2:CD004987.

Plassman, B. L., Langa, K. M., Fisher, G. G., Heeringa, S. G., Weir, D. R., Ofstedal, M. B., et al. (2007). Prevalence of dementia in the United States: the aging, demographics, and memory study[J]. *Neuroepidemiology* 29, 125–132. doi: 10.1159/000109998

Prinz, M., and Priller, J. (2017). The role of peripheral immune cells in the CNS in steady state and disease[J]. *Nat. Neurosci.* 20, 136–144. doi: 10.1038/nn.4475

Ranjithkumar, R., Alhadidi, Q., Shah, Z. A., and Ramanathan, M. (2019). Tribulusterine containing tribulus terrestris extract exhibited neuroprotection through attenuating stress kinases mediated inflammatory mechanism: in vitro and in vivo studies[J]. *Neurochem. Res.* 44, 1228–1242. doi: 10.1007/s11064-019-02768-7

Schmitz, M., Hermann, P., Oikonomou, P., Stoeck, K., Ebert, E., Poliakova, T., et al. (2015). Cytokine profiles and the role of cellular prion protein in patients with vascular dementia and vascular encephalopathy[J]. *Neurobiol. Aging* 36, 2597–2606. doi: 10.1016/j.neurobiolaging.2015.05.013

Shang, J., Yamashita, T., Fukui, Y., Song, D., Li, X., Zhai, Y., et al. (2018). Different associations of plasma biomarkers in alzheimer's disease, mild cognitive impairment, vascular dementia, and ischemic stroke[J]. *J. Clin. Neurol.* 14, 29–34. doi: 10.3988/jcn.2018.14.1.29

Shi, G. X., Liu, C. Z., Li, Q. Q., Zhu, H., and Wang, L. P. (2012). Influence of acupuncture on cognitive function and markers of oxidative DNA damage in patients with vascular dementia[J]. *J. Tradit. Chin. Med.* 32, 199–202. doi: 10.1016/s0254-6272(13)60011-4

Smith, E. E. (2017). Clinical presentations and epidemiology of vascular dementia[J]. *Clin. Sci.* 131, 1059–1068. doi: 10.1042/cs20160607

Sun, M. K. (2018). Potential therapeutics for vascular cognitive impairment and dementia[J]. *Curr. Neuropharmacol.* 16, 1036–1044. doi: 10.2174/1570159x15666171016164734

Venkat, P., Chopp, M., and Chen, J. (2015). Models and mechanisms of vascular dementia[J]. *Exp. Neurol.* 272, 97–108. doi: 10.1016/j.expneurol.2015.05.006

Wan, F., Niu, X., Song, Y. L., and Si, Y. C. (2016). The role of chinese herbs and acupuncture on the inflammation reaction after cerebral ischemia[J]. *Curr. Pharm. Design* 22, 709–719. doi: 10.2174/1381612822666151204001348

Wang, G. Y., Taylor, T., Sumich, A., Merien, F., Borotkanics, R., Wrapson, W., et al. (2017). Associations between immunological function and memory recall in healthy adults[J]. *Brain Cogn.* 119, 39–44. doi: 10.1016/j.bandc.2017.10.002

Wang, X. R., Shi, G. X., Yang, J. W., Yan, C. Q., Lin, L. T., Du, S. Q., et al. (2015). Acupuncture ameliorates cognitive impairment and hippocampus neuronal loss in experimental vascular dementia through Nrf2-mediated antioxidant response[J]. *Free Radical Biol. Med.* 89, 1077–1084. doi: 10.1016/j.freeradbiomed.2015.10.426

Yu, J., Zhang, X., Liu, C., Meng, Y., and Han, J. (2006). Effect of acupuncture treatment on vascular dementia[J]. *Neurol. Res.* 28, 97–103. doi: 10.1179/016164106x91951

Yuan-Cheng, K., Li, Z., Ying, S., Li, Y., Ren, W. L., Wei, W. S., et al. (2018). MicroRNA-26b regulates the microglial inflammatory response in hypoxia/ischemia and affects the development of vascular cognitive impairment[J]. *Front. Cell. Neurosci.* 12:154. doi: 10.3389/fncel.2018.00154

Zakaria, R., Wan Yaacob, W. M., Othman, Z., Long, I., Ahmad, A. H., and Al-Rahbi, B. (2017). Lipopolysaccharide-induced memory impairment in rats: a model of Alzheimer's disease[J]. *Physiol. Res.* 66, 553–565. doi: 10.33549/physiolres.933480

Zhang, D., Xiao, Y., Lv, P., Teng, Z., Dong, Y., Qi, Q., et al. (2017). Edaravone attenuates oxidative stress induced by chronic cerebral hypoperfusion injury: role of ERK/Nrf2/HO-1 signaling pathway[J]. *Neurol. Res.* 40, 1–10. doi: 10.1080/01616412.2017.1376457

Zhang, F., Zhang, J. G., Yang, W., Xu, P., Xiao, Y. L., and Zhang, H. T. (2018). 6-Gingerol attenuates LPS-induced neuroinflammation and cognitive impairment partially via suppressing astrocyte overactivation[J]. *Biomed. Pharmacother.* 107, 1523–1529. doi: 10.1016/j.biopha.2018.08.136

Zhang, Z. H., Shi, G. X., Li, Q. Q., Wang, Y. J., Li, P., Zhao, J. X., et al. (2014). Comparison of cognitive performance between two rat models of vascular dementia[J]. *Int. J. Neurosci.* 124, 818–823. doi: 10.3109/00207454.2014.880435

Zhao, C., Bao, C., Li, J., Zhu, Y., Wang, S., Yang, L., et al. (2015). Moxibustion and acupuncture ameliorate crohn's disease by regulating the balance between Th17 and Treg cells in the intestinal mucosa[J]. *Evid. Based Comp. Altern. Med.* 2015:938054.

Zhao, L., Shen, P., Han, Y., Zhang, X., Nie, K., Cheng, H., et al. (2011). Effects of acupuncture on glycometabolic enzymes in multi-infarct dementia rats[J]. *Neurochem. Res.* 36, 693–700. doi: 10.1007/s11064-010-0378-x

Conflict of Interest: The authors declare that the research was conducted in the absence of any commercial or financial relationships that could be construed as a potential conflict of interest.

Copyright © 2021 Pan, Ma, Zhang, Ling, Wang, Liu, Lin, Xu, Yang, Zhi, Wang and Zhang. This is an open-access article distributed under the terms of the Creative Commons Attribution License (CC BY). The use, distribution or reproduction in other forums is permitted, provided the original author(s) and the copyright owner(s) are credited and that the original publication in this journal is cited, in accordance with accepted academic practice. No use, distribution or reproduction is permitted which does not comply with these terms.

frontiers in Aging Neuroscience

ORIGINAL RESEARCH
published: 06 August 2021
doi: 10.3389/fnagi.2021.718959

Optimal Combinations of AT(N) Biomarkers to Determine Longitudinal Cognition in the Alzheimer's Disease

Rong-Rong Lin, Yan-Yan Xue, Xiao-Yan Li, Yi-He Chen, Qing-Qing Tao and Zhi-Ying Wu* for Alzheimer's Disease Neuroimaging Initiative†*

Department of Neurology and Research Center of Neurology in Second Affiliated Hospital, and Key Laboratory of Medical Neurobiology of Zhejiang Province, Zhejiang University School of Medicine, Hangzhou, China

OPEN ACCESS

Edited by:
Jiehui Jiang,
Shanghai University, China

Reviewed by:
Nilo Riva,
San Raffaele Hospital (IRCCS), Italy
Nobuyuki Kimura,
National Center for Geriatrics and Gerontology (NCGG), Japan

***Correspondence:**
Zhi-Ying Wu
zhiyingwu@zju.edu.cn
Qing-Qing Tao
qingqingtao@zju.edu.cn

†*Data used in preparation of this article were obtained from the Alzheimer's Disease Neuroimaging Initiative (ADNI) database (adni.loni.usc.edu). As such, the investigators within the ADNI contributed to the design and implementation of ADNI and/or provided data, but did not participate in analysis or writing of this report. A complete listing of ADNI investigators can be found at: http://adni.loni.usc.edu/wp-content/uploads/how_to_apply/ADNI_Acknowledgement_List.pdf*

Received: *01 June 2021*
Accepted: *05 July 2021*
Published: *06 August 2021*

Citation:
Lin R-R, Xue Y-Y, Li X-Y, Chen Y-H, Tao Q-Q and Wu Z-Y (2021) Optimal Combinations of AT(N) Biomarkers to Determine Longitudinal Cognition in the Alzheimer's Disease. Front. Aging Neurosci. 13:718959. doi: 10.3389/fnagi.2021.718959

Background: National Institute on Aging—Alzheimer's Association (NIA-AA) proposed the AT(N) system based on β-amyloid deposition, pathologic tau, and neurodegeneration, which considered the definition of Alzheimer's disease (AD) as a biological construct. However, the associations between different AT(N) combinations and cognitive progression have been poorly explored systematically. The aim of this study is to compare different AT(N) combinations using recognized biomarkers within the Alzheimer's Disease Neuroimaging Initiative (ADNI) cohort.

Methods: A total of 341 participants were classified into cognitively unimpaired (CU; $n = 200$) and cognitively impaired (CI; $n = 141$) groups according to the clinical manifestations and neuropsychological tests. Cerebrospinal fluid (CSF) Aβ42 and amyloid-PET ([18F]flutemetamol) were used as biomarkers for A; CSF phosphorylated tau (p-tau) and tau-PET ([18F]flortaucipir) were used as biomarkers for T; CSF total tau (t-tau), hippocampal volume, temporal cortical thickness, [18F]fluorodeoxyglucose (FDG) PET, and plasma neurofilament light (NfL) were used as biomarkers for (N). Binary biomarkers were obtained from the Youden index and publicly available cutoffs. Prevalence of AT(N) categories was compared between different biomarkers within the group using related independent sample non-parametric test. The relationship between AT(N) combinations and 12-year longitudinal cognition was assessed using linear mixed-effects modeling.

Results: Among the CU participants, A–T–(N)– was most common. More T+ were detected using p-tau than tau PET ($p < 0.05$), and more (N)+ were observed using fluid biomarkers ($p < 0.001$). A+T+(N)+ was more common in the CI group. Tau PET combined with cortical thickness best predicted cognitive changes in the CI group and MRI predicted changes in the CU group.

Conclusions: These findings suggest that optimal AT(N) combinations to determine longitudinal cognition differ by cognitive status. Different biomarkers within a specific component for defining AT(N) cannot be used identically. Furthermore, different strategies for discontinuous biomarkers will be an important area for future studies.

Keywords: Alzheimer's disease, biomarkers, AT(N) system, longitudinal cognition, linear mixed-effects model

INTRODUCTION

Alzheimer's disease (AD) is the most common cause of dementia, and one of the main causes of complications and death in the aging population. A series of complex pathobiological processes is involved in the pathogenesis of AD, including the deposition of extracellular amyloid plaques, tau-related intracellular neurofibrillary tangles (NFTs), neuronal loss and atrophy (Long and Holtzman, 2019). Recently, the National Institute on Aging—Alzheimer's Association (NIA-AA) proposed a research framework based on the pathological characteristics mentioned above (Jack et al., 2018). The framework establishes a classification system consisting of biomarkers of Aβ (A), tau (T), and neurodegeneration (N), and lists a classic AD biomarker grouping including cerebrospinal fluid (CSF), MRI, and PET. However, it is not perfectly concordant among biomarkers within a specific component (A, T, or N) (Jack et al., 2018; Knopman et al., 2018), and all examinations are usually difficult to perform on patients, which may limit its clinical application. Many studies have compared different biomarkers in a certain component (Mattsson et al., 2015; Hansson et al., 2018; La Joie et al., 2018), and have manifested that these biomarkers partially play different roles in the diagnosis, staging, and the progression of Alzheimer's pathology. For example, CSF is suitable for early diagnosis (Mattsson et al., 2015), and tau PET is related to cross-sectional cognition of AD patients (La Joie et al., 2018). This means that different biomarkers need to be selected according to different clinical needs. But only one study assessed different combinations of AT(N) biomarkers using BioFINDER participants (Mattsson-Carlgren et al., 2020). Here, we used a more comprehensive biomarker group and focused on the relationship between different AT(N) combinations and longitudinal cognition decline. We postulated that the prevalence of AT(N) categories and prediction of longitudinal cognition would vary by different combinations of biomarkers in cognitively unimpaired (CU) and cognitively impaired (CI) participants.

MATERIALS AND METHODS

Participants

All participants in this study were from the Alzheimer's Disease Neuroimaging Initiative (ADNI), a longitudinal multicenter study designed to develop clinical, imaging, genetic, and biospecimen biomarkers for tracking the progression of AD. Regional ethics committees of all institutions approved the ADNI study. Written informed consent was obtained from all participants. The key eligibility criteria were based on the ADNI protocol. Cognitively unimpaired (CU) participants must be free of memory complaints and cognitively normal, with MMSE scores between 24 and 30 (inclusive) and a CDR of 0. Cognitively impaired (CI) participants must have a subjective memory concern and were divided into two subgroups, namely: mild cognitively impaired (MCI) participants and AD dementia participants. The MCI participants reported MMSE scores between 24 and 30 (inclusive), a memory complaint, have objective memory loss measured by education-adjusted scores on Wechsler memory scale logical memory II, a CDR of 0.5, absence of significant levels of impairment in other cognitive domains, essentially preserved activities of daily living, and an absence of dementia. The AD dementia participants met NINCDS/ADRDA criteria for probable AD (McKhann et al., 1984), with MMSE scores between 20 and 26 (inclusive) and a CDR of 0.5 or 1.0. Demographic and clinical information, neuroimaging, and biomarker data were downloaded from the ADNI data repository (adni.loni.usc.edu).

CSF and Plasma Biomarker Analysis

Cerebrospinal fluid β-amyloid (1-42), phospho-tau (181P), and total tau were analyzed using the electrochemiluminescence immunoassays (ECLIA) Elecsys following a Roche Study Protocol (Hansson et al., 2018). Plasma neurofilament light (NfL) was obtained using the single molecule array (Simoa) technique.

Neuroimaging Acquisition and Processing

The 3T MRI scans were processed before being downloaded as previously described (Jack et al., 2008, 2010). FreeSurfer (ADNI phase 1, grand opportunity, and phase 2 data were run with FreeSurfer version 5.1, while phase 3 with version 6.0) was used for further analysis. Two MRI measures were used, including hippocampal volume and cortical thickness. The volume of bilateral hippocampal was extracted as the regions of interest (ROI), and was adjusted for the intracranial volume (ICV) by calculating the residual term (ε) from a linear regression of hippocampal volume (y) vs. ICV (x) within 128 ApoE-negative CU participants (Jack et al., 2014). The adjusted hippocampal volume can be interpreted as a deviation from the expected hippocampal volume calculated from the given ICV. An AD signature cortical thickness was composed of mean thickness in the entorhinal, inferior temporal, middle temporal, and fusiform cortices (Dickerson et al., 2009).

Amyloid, tau, and metabolic imaging were performed using [18F]florbetapir, [18F]flortaucipir and [18F]fluorodeoxyglucose (FDG) PET, respectively. The [18F]florbetapir standardized uptake value ratios (SUVRs) were calculated by averaging the four cortical regions, frontal, which are anterior/posterior cingulate, lateral parietal, and lateral temporal cortices (Klunk et al., 2004; Xue et al., 2020), and dividing the ROIs by the whole cerebellum reference region. For tau PET, the inferior temporal cortex (ITC) and the Braak V/VI region (specific regions were shown in **Supplementary Table 1**) were selected as target ROIs. ITC and Braak V/VI indicated early and late stages of tangle pathology, respectively (Braak et al., 2006; Johnson et al., 2016). The [18F]flortaucipir data were corrected for partial volume effects using the geometric transfer matrix approach and divided by the inferior cerebellar GM reference region (Baker et al., 2017). The predefined meta-ROIs in FDG PET of AD were composed of the angular gyrus, posterior cingulate, and ITC normalized to the pons and vermis (Herholz et al., 2002).

Cognition Assessment

Cognition was assessed using the longitudinal Mini-Mental State Examination (MMSE) and Clinical Dementia Rating Sum of

TABLE 1 | Characteristics of ADNI participants.

	CU	CI	P	MCI	AD	P
No.	200	141	CU vs. CI	101	40	MCI vs. AD
Age at baseline, y[a]	70.95 ± 6.27	72.25 ± 7.08	0.074417	72.47 ± 6.69	71.72 ± 8.06	0.57102
Female	115 (57.5%)	60 (42.6%)	<0.05	41 (40.6%)	19 (47.5%)	0.454664
Education, y	16.77 ± 2.39	15.98 ± 2.82	<0.05	16.21 ± 2.98	15.40 ± 2.31	0.077458
ApoE e4 positive	71 (35.7%)	61 (43.3%)	<0.01	38 (37.6%)	23 (57.5%)	0.097857
MMSE at baseline	29.11 ± 1.10	27.61 ± 2.32	<0.0001	28.15 ± 1.74	26.28 ± 2.99	<0.0001
CDRSB at baseline	0.13 ± 0.47	1.32 ± 1.11	<0.0001	0.98 ± 0.65	2.19 ± 1.51	<0.0001
CSF Aβ42, ng/L	1332.84 ± 643.16	1029.24 ± 660.36	<0.0001	1159.51 ± 703.67	700.33 ± 375.32	<0.0001
CSF Aβ42 positive	61 (30.5%)	82 (58.2%)	<0.0001	48 (47.5%)	34 (85.0%)	<0.0001
Amyloid PET SUVR	1.11 ± 0.18	1.26 ± 0.26	<0.0001	1.20 ± 0.24	1.42 ± 0.22	<0.0001
Amyloid PET positive	63 (31.5%)	92 (65.2%)	<0.0001	56 (55.4%)	36 (90.0%)	<0.0001
CSF p-tau, ng/L	22.21 ± 10.85	29.65 ± 17.95	<0.0001	26.67 ± 15.16	37.15 ± 22.06	<0.001
CSF p-tau positive	83 (41.5%)	95 (67.4%)	<0.0001	62 (61.4%)	33 (82.5%)	<0.05
Tau PET in ITC SUVR	1.99 ± 0.28	2.65 ± 1.20	<0.0001	2.28 ± 0.74	3.60 ± 1.57	<0.0001
Tau PET in ITC positive	41 (20.5%)	80 (56.7%)	<0.0001	46 (45.5%)	34 (85.0%)	<0.0001
Tau PET in Braak5/6 SUVR	1.81 ± 0.19	2.17 ± 0.70	<0.0001	1.95 ± 0.33	2.72 ± 1.02	<0.0001
Tau PET in Braak5/6 positive	40 (20.0%)	72 (51.1%)	<0.0001	40 (39.6%)	32 (80.0%)	<0.0001
Hippocampal volume, cm^3	−0.059 ± 0.808	−1.09 ± 1.11	<0.0001	−0.80 ± 1.03	−1.83 ± 0.95	<0.0001
Hippocampal volume positive	51 (25.5%)	95 (67.4%)	<0.0001	60 (59.4%)	35 (87.5%)	<0.001
Temporal meta-ROI thickness, mm	3.01 ± 0.15	2.80 ± 0.28	<0.0001	2.86 ± 0.25	2.65 ± 0.28	<0.0001
Temporal meta-ROI thickness positive	41 (20.6%)	90 (63.8%)	<0.0001	56 (55.4%)	34 (85.0%)	<0.01
CSF t-tau, ng/L	244.13 ± 98.70	306.61 ± 152.66	<0.0001	281.77 ± 130.47	369.34 ± 185.41	<0.01
CSF t-tau positive	90 (45.0%)	95 (67.4%)	<0.0001	62 (61.4%)	33 (82.5%)	<0.01
FDG-PET meta-ROI SUVR[a]	1.33 ± 0.11	1.22 ± 0.14	<0.0001	1.26 ± 0.13	1.11 ± 0.12	<0.0001
FDG-PET meta-ROI SUVR positive	34 (24.1%)	85 (62.0%)	<0.0001	52 (52.5%)	33 (86.8%)	<0.0001
plasma NfL, ng/L	35.92 ± 15.72	43.66 ± 20.62	<0.01	41.82 ± 20.90	48.28 ± 19.44	<0.05
plasma NfL positive	66 (47.8%)	81 (69.8%)	<0.01	52 (62.7%)	29 (87.9%)	<0.01

Aβ, β-amyloid; amyloid PET, [18F]florbetapir PET; CDRSB, Clinical Dementia Rating Sum of Boxes; CI, cognitively impaired; CU, cognitively unimpaired; FDG-PET, [18F]fluorodeoxyglucose PET; ITC, inferior temporal cortex; MMSE, Mini-Mental State Examination; NfL, neurofilament light; p-tau, phosphorylated at Thr181; ROI, region of interest; tau PET, [18F]flortaucipir PET; SUVR, standardized uptake value ratio. Data are presented as mean (SD) or n (%).

[a]The population sample was normally distributed using Kolmogorov-Smirnov Z-test, continuous biomarkers were compared between different groups using Student's t-test.

Boxes (CDRSB). According to the interquartile range (IQR; 6–8 years), we selected seven-time points from baseline to 12 years (baseline, 2, 4, 6, 8, 10, and 12 years, respectively) for the longitudinal cognitive assessment.

AT(N) Definitions

AT(N) biomarkers included CSF Aβ42 (A1), amyloid PET ([18F]florbetapir) (A2), CSF p-tau (T1), tau PET ([18F]flortaucipir) SUVR in the ITC (T2) and Braak V/VI region (T3), hippocampal volume ([N]1), temporal meta-ROI cortical thickness ([N]2), CSF t-tau ([N]3), AD-characteristic FDG PET SUVR ([N]4), and plasma NfL ([N]5). For CSF Aβ positivity, we used a published cutoff (CSF Aβ42 level, <880 ng/L; Hansson et al., 2018). For amyloid PET, we selected a cutoff of 1.11, which is the upper 95% confidence interval above the mean of a young normal control group (Joshi et al., 2012). Binarization of other biomarkers (T and [N]) was performed using cutoffs established by the Youden index (Aβ-positive MCI vs. Aβ-negative CU, with the Aβ status defined by the CSF Aβ42). Furthermore, the mean ± 2 SD from Aβ-negative CU controls (+2 SD for amyloid PET, tau PET, CSF tau, and plasma NfL; −2 SD for CSF Aβ42, hippocampal volume, temporal cortical thickness, and FDG PET), along with 90% sensitivity for AD, were used as a sensitivity analysis.

Statistical Analyses

Demographics and continuous biomarkers were compared between different groups using Mann–Whitney *U*-test or Student's *t*-test according to normality of the population sample using Kolmogorov-Smirnov *Z*-test, and binary biomarkers using Fisher's exact test. Associations between biomarkers were analyzed using Spearman's rank correlation (ρ), Cohen's kappa coefficient (κ), and percentage agreement (concordance). Prevalence estimates for AT(N) categories were calculated with 95% confidence intervals generated using bootstrap resampling (n = 1,000). Prevalence of AT(N) categories was compared between different biomarkers within the group using related independent sample non-parametric test (McNemar test for A and Cochran's *Q*-test for T or [N]). The relationships

between AT(N) combinations and cognitive trajectories (12-year longitudinal MMSE and CDRSB scores) were examined using a linear mixed-effects (LME) model (including age, sex, and education as covariates, and time as a categorical variable) with subject-specific intercepts and slopes. The goodness of LME models with different AT(N) combinations was assessed by marginal R^2, which represented the fixed effect of LME models. All analyses were performed using IBM SPSS Statistics 20, with significance of the two-tailed test set to $p < 0.05$.

RESULTS

Study Participants

Demographics are presented in **Table 1**, and more detailed information is shown in **Supplementary Table 2**. A significant difference in age was not observed between CU and CI participants, while more females, higher education level, and a lower prevalence of APOE e4 were observed in the CU group. No significant differences were observed in age, sex, education, or APOE e4 between participants with MCI and AD (subgroups of CI). MMSE scores, Aβ42, hippocampal volume, temporal cortical thickness, and FDG PET decreased sequentially, while CDRSB scores, amyloid and tau PET, and CSF tau and NfL increased sequentially among the CU, MCI, CI, and AD groups. As plasma NfL levels were reported to be positively associated with age ($\rho = 0.471$, $p < 0.01$) (Mattsson et al., 2017a, 2019), we divided participants into younger and older groups based on the median value (age = 72.25 y) and identified a significant difference in NfL levels between these groups ($p < 0.001$). Therefore, the prevalence of (N)+ using NfL was likely to vary by age in the present cohort, so we calculated the cutoff based on age stratification.

Biomarker Relationships

Cutoffs were defined as CSF Aβ42 <880 ng/L (A1), amyloid PET >1.1 SUVR (A2), p-tau > 21.11 ng/L (T1), ITC tau PET >2.122 SUVR (T2), Braak V/VI tau PET >1.938 SUVR (T3), adjusted hippocampal volume <-0.4477 cm^3 (N1), temporal meta-ROI thickness <2.9214 mm (N2), CSF t-tau > 233.6 ng/L (N3), FDG PET meta-ROIs <1.2599 SUVR (N4), and plasma NfL levels >30.35 ng/L in younger participants and >36.45 ng/L in older participants. Similar cutoffs were obtained using 90% sensitivity for AD, while mean ± 2 SD from Aβ-negative CU controls resulted in more conservative cutoffs (**Supplementary Table 3**).

Continuous biomarkers within each component were correlated: CSF Aβ42 vs. amyloid PET ($\rho = -0.671$; **Figure 1A**), p-tau vs. ITC tau PET ($\rho = 0.379$) and Braak V/VI ($\rho = 0.380$), as well as between the 2 tau PET measures ($\rho = 0.851$; **Figures 1B–D**); hippocampal volume vs. temporal cortical thickness ($\rho = 0.584$), vs. FDG PET ($\rho = 0.448$), and vs. NfL ($\rho = -0.395$); temporal cortical thickness vs. FDG PET ($\rho = 0.426$), and vs. NfL ($\rho = -0.321$); and FDG PET vs. NfL ($\rho = -0.326$). Weak correlations were observed between CSF t-tau and other neurodegeneration biomarkers: CSF t-tau vs. hippocampal volume ($\rho = -0.239$), vs. temporal cortical thickness ($\rho = -0.215$), vs. FDG PET ($\rho = -0.145$, $p < 0.05$) and vs. NfL ($\rho = 0.188$; all $p < 0.001$, except as specifically indicated; **Figures 1E–N**).

Using binary data, there was a substantial agreement between amyloid biomarkers (**Figure 1A**), between the two tau PET measures (**Figures 1B–D**), and a moderate agreement between the two MRI imaging measures (**Figure 1E**). Fair agreement was identified between p-tau and tau PET (**Figures 1B,C**), between MRI imaging measures, FDG PET, and NfL (**Figures 1G,H,J,K,N**), whereas slight agreement between CSF t-tau and other neurodegeneration biomarkers (**Figures 1F,I,L,M**).

Prevalence Measures in CU Participants

The prevalence of AT(N) categories in CU and CI participants is summarized in **Figures 2, 3** and **Supplementary Tables 4, 5**. When only considering A and T in the CU group, A-T- was the most common category (range 43.5% [A1T1; 95% confidence interval, 36.6–50.5%] to 62.0% [A2T2; 95% confidence interval, 55.0–68.8%]). When comparing A biomarkers, slightly more were negative when using CSF Aβ42 instead of amyloid PET ($p > 0.05$). The highest positivity for T was observed when CSF p-tau were used for both A+ or A– ($p < 0.001$) (**Figure 2A**). Based on these results, the use of CSF p-tau may substantially increase the positive rate of the T component compared to tau PET in CU participants.

When adding (*N*) biomarkers, the most prevalent category was A-T-(N)- (range 26.1% [A2T1(N)5; 95% confidence interval, 18.7–33.3%] to 50.8% [A2T2(N)2; 95% confidence interval, 44.1–58.0%]). Although eight possible categories were identified for each AT(N) variants, A+T+(N)+, A+T-(N)+, and A-T+(N)+ had very low frequencies when using MRI imaging and FDG PET. A+T+(N)-, A+T-(N)+, and A-T+(N)- were almost lacking in the combination of CSF p-tau and t-tau since a strong correlation ($\rho = 0.980$, $p < 0.001$) and almost perfect agreement ($\kappa = 0.876$; concordance = 93.8%) was observed between them, as previous study reported (Blennow et al., 1995). Among the different biomarkers for (N), CSF t-tau and plasma NfL were the most prevalent biomarkers resulting in (N)+ cases ($p < 0.001$) (**Figure 3A**).

Prevalence Measures in CI Participants

A+T+ was the main category when only A and T biomarkers were used for CI participants (range 39.7% [A1T3; 95% confidence interval, 31.8–48.4%] to 54.6% [A2T1; 95% confidence interval, 45.7–63.5%]). A and T categories of different AT(N) variants in the CI group showed similar trends to the CU [i.e., higher prevalence of A+ using amyloid PET ($p < 0.05$) and lower prevalence of T+ using tau PET ($p < 0.005$)] (**Figure 2B**). There were significant differences in A and T categories between the two subgroups of CI (Fisher exact test, all $p < 0.001$). In participants with MCI, A-T- were the most common categories when using tau PET in Braak V/VI (**Figure 2C**). In the AD group, A+T+ accounted for approximately 75% (range 70% [A1T3; 95% confidence interval, 55.8–85.3%] to 82.5% [A2T1; 95% confidence interval, 69.8–93.3%]); the difference from other groups was the lower prevalence of T+ obtained using CSF p-tau than tau PET in the case of A- ($p > 0.05$) (**Figure 2D**).

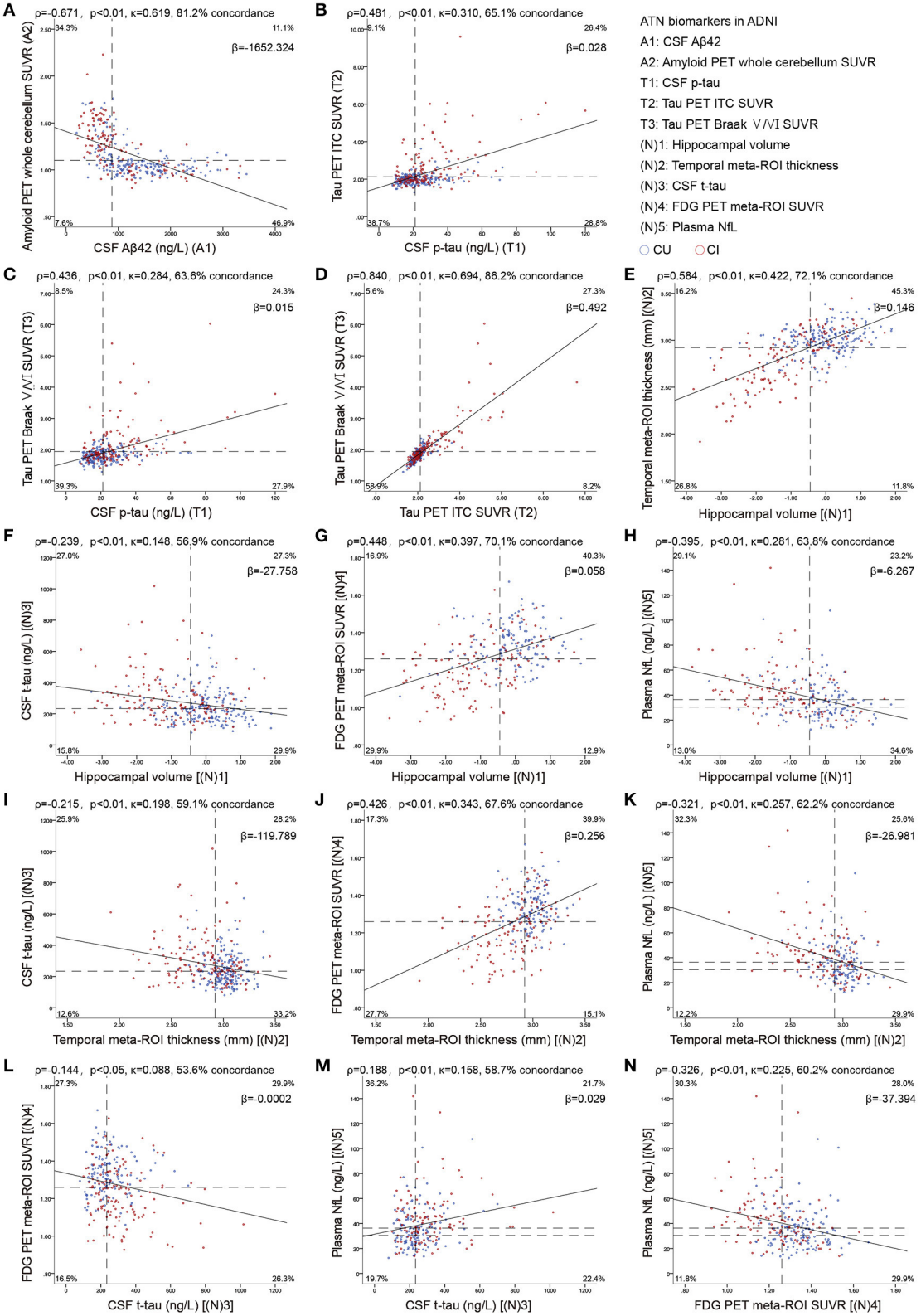

FIGURE 1 | Scatterplots show the association between continuous measures for amyloid **(A)**, tau **(B–D)**, and neurodegeneration **(E–N)** biomarkers. Dashed lines indicate cutoff points. Spearman's correlations (ρ) with *p*-values, Cohen's kappa statistic (κ), concordance (percentage showing both biomarkers positive or negative), *(Continued)*

FIGURE 1 | and the slope (β) of regression curve are shown at the top of each panel. For A comparisons, the upper left and the lower right quadrants indicate concordance positive (+/+) and negative (–/–). For T comparisons, lower left and upper right quadrants indicate concordance positive and negative, respectively. For the comparisons of (N)3 with (N)5, the upper right and lower left quadrants indicate concordance positive and negative, respectively. For the four remaining (N) comparisons, concordant positives are shown in the upper left quadrant, whereas concordant negatives are shown in the lower right quadrant. Percentage figures across quadrants indicate distribution (percentagewise) of participants. Aβ, β-amyloid; AT(N), β-amyloid, tau, and neurodegeneration classification system; CI, cognitively impaired; CU, cognitively unimpaired; ITC, inferior temporal cortex; NfL, neurofilament light; p-tau, tau phosphorylated at Thr181; ROI, region of interest; SUVR, standardized uptake value ratio; t-tau, total tau.

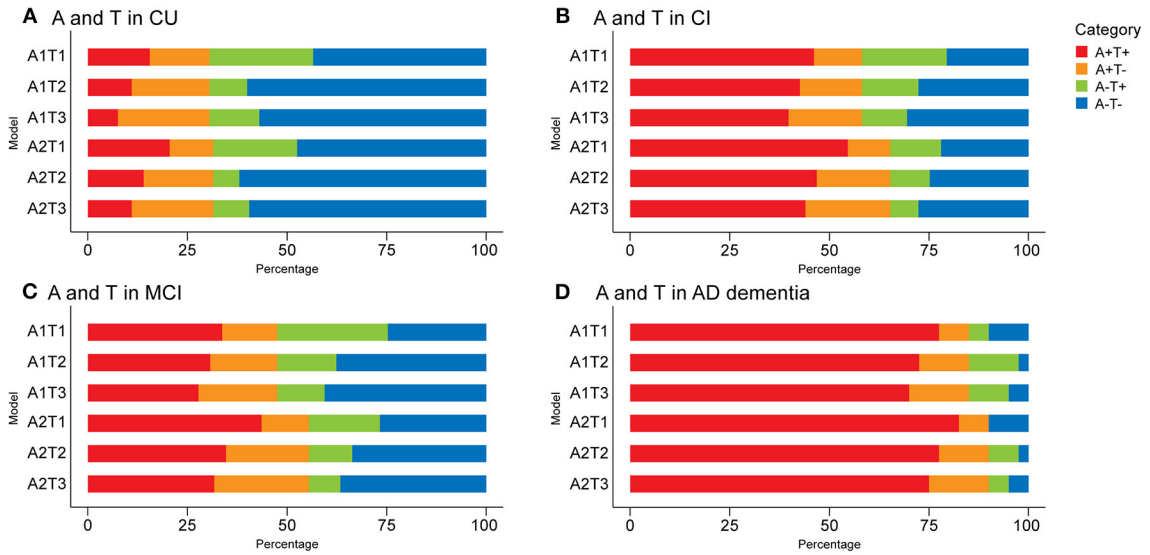

FIGURE 2 | Prevalence of different AT(N) categories in different AT variants among cognitively unimpaired (CU) **(A)** and cognitively impaired (CI) **(B)** participants in the ADNI. Mild cognitively impaired (MCI) **(C)** and Alzheimer's disease (AD dementia) **(D)** are two subgroups of the CI group. CSF Aβ42 (A1); amyloid PET whole cerebellum standardized uptake value ratio (SUVR) (A2); CSF tau phosphorylated at Thr181 (T1); tau PET inferior temporal cortex SUVR (T2); tau PET Braak V/VI SUVR (T3). AT(N), β-amyloid, tau, and neurodegeneration classification system.

When adding (N) biomarkers, the most prevalent category was A+T+(N)+ (range 29.9% [A1T3(N)4; 95% confidence interval, 23.3–38.6%] to 51.8% [A2T1(N)3; 95% confidence interval, 43.2–60.3%]), and the frequencies of T+(N)- and T-(N)+ in the combination of CSF p-tau and t-tau were relatively low (**Figure 3B**). As mentioned above, A-T-N- was the main category when using tau PET in Braak V/VI combined with some N biomarkers in the MCI group (**Supplementary Figure 1A**). The AD group had the most A+T+(N)+ (range 60.6% [A1T3(N)5; 95% confidence interval, 44.1–76%] to 80% [A2T1(N)3; 95% confidence interval, 67.6–92.1%]) among the three groups. Again, several categories were lacking or had low frequencies (A-T+N- and A-T-N+ when using tau PET) (**Supplementary Figure 1B**). The prevalence of all the (N) biomarkers resulting in (N)+ cases was approximative, except it was relatively low when using FDG PET in CI individuals ($p > 0.05$) (**Figure 3B**).

Longitudinal Cognition

The overall findings for longitudinal cognition using continuous predictors are summarized in **Figures 4, 5** and **Supplementary Tables 6–9**. In CU participants, age and education significantly affected cognition (age, $p = 0.027$ and education, $p = 0.048$ in CDRSB; age, $p = 0.025$ and education, $p < 0.001$ in MMSE), consistent with previous findings (Compton et al., 2000; Ardila and Moreno, 2001). When using a single AT(N) biomarker to predict cognitive changes, just the MRI imaging contributed significantly (temporal cortical thickness, [N]2, $p = 0.047$, $R^2 = 7.54\%$ in CDRSB; hippocampal volume, [N]1, $p = 0.025$, $R^2 = 10.76\%$ in MMSE) (**Figures 4G,H**). The best AT(N) variants capturing changes in cognition in CDRSB and MMSE were A2T3(N)2 (amyloid PET, tau PET in Braak V/VI regions, and temporal cortical thickness) and A2T1(N)1 (amyloid PET, CSF p-tau, and hippocampal volume), respectively, but not all included biomarkers contributed significantly (A2, $p = 0.795$, T3, $p = 0.396$, and [N]2, $p = 0.064$, $R^2 = 7.84\%$ in CDRSB; A2, $p = 0.043$, T1, $p = 0.081$, and [N]1, $p = 0.037$, $R^2 = 12.29\%$ in MMSE) (**Figures 4B,E**). We considered whether random effects accounted for a greater proportion of the variance because the marginal R^2 for CU participants was relatively low. Then, we calculated conditional R^2 using MRI imaging biomarkers (temporal cortical thickness for CDRSB and hippocampal volume for MMSE). After considering the random effect, the conditional R^2 increased to 19.32% and 33.55% for the CDRSB and MMSE scores, respectively. These results indicated that longitudinal cognition in CU participants

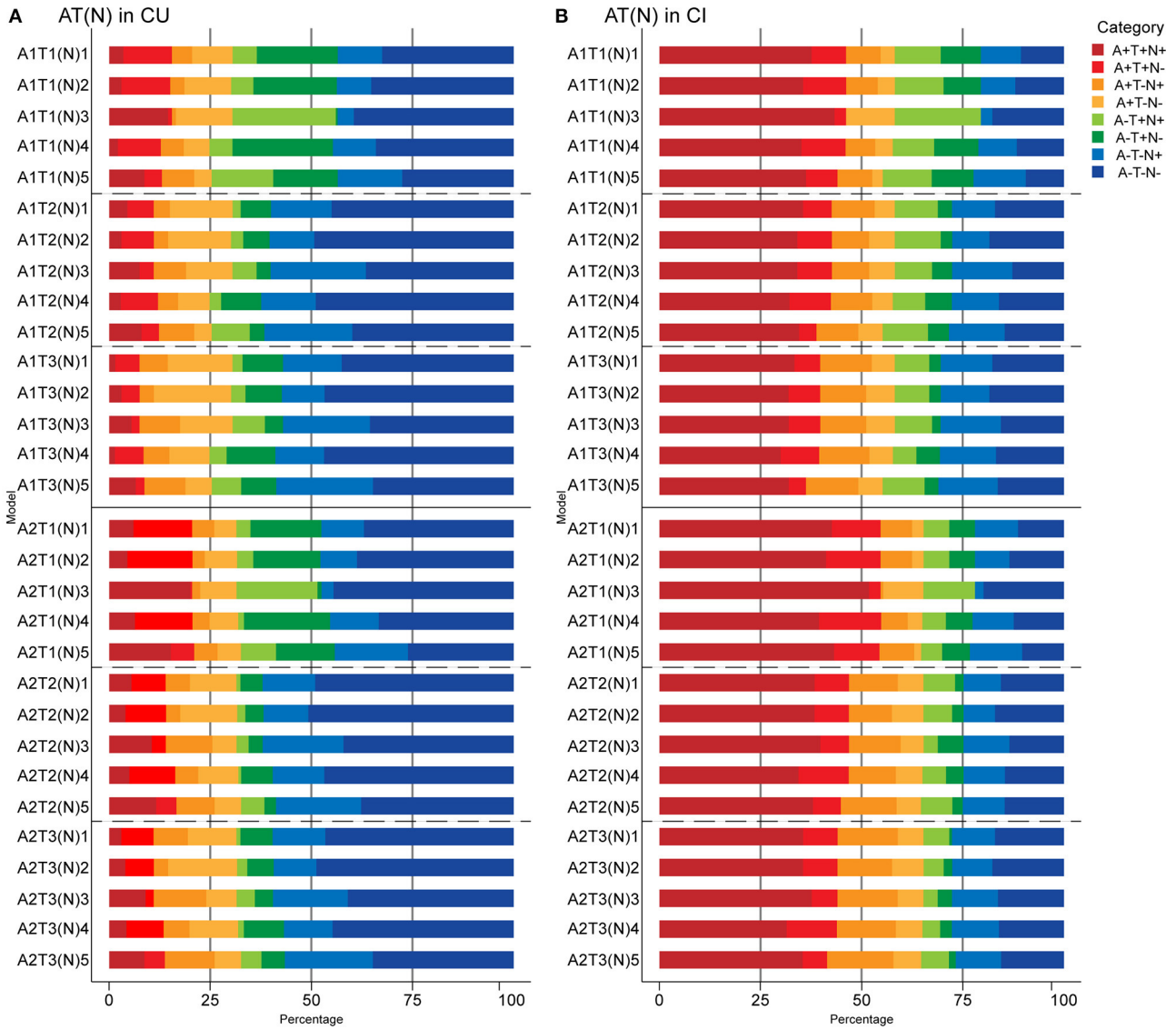

FIGURE 3 | Prevalence of different AT(N) categories in different AT(N) variants among cognitively unimpaired (CU) **(A)** and cognitively impaired (CI) **(B)** participants in the ADNI. CSF Aβ42 (A1); amyloid PET whole cerebellum standardized uptake value ratio (SUVR) (A2); CSF tau phosphorylated at Thr181 (T1); tau PET inferior temporal cortex SUVR (T2); tau PET Braak V/VI SUVR (T3); hippocampal volume [(N)1]; temporal meta-ROI thickness [(N)2]; CSF total tau [(N)3]; FDG PET meta-ROI SUVR [(N)4]; plasma neurofilament light [(N)5]. AT(N), β-amyloid, tau, and neurodegeneration classification system.

was mainly associated with individual characteristics, and MRI measurements were the best biomarkers to predict cognitive changes.

In CI participants, individual characteristics were not significantly associated with cognitive decline. Almost all single AT(N) biomarkers could predict longitudinal cognition, except CSF p-tau ($p = 0.061$) and t-tau ($p = 0.051$) in CDRSB, and the marginal R^2 using MRI imaging and tau PET was relatively higher than others (**Supplementary Table 6**). The AT(N) variants combining CSF Aβ42, tau PET, and temporal cortical thickness were the best predictors in both CDRSB and MMSE, and almost all included variables contributed significantly (CDRSB: A1T2[N]2, A1, $p = 0.061$, T2, $p = 0.013$, [N]2, $p < 0.001$, $R^2 = 37.94\%$; A1T3[N]2, A1, $p = 0.040$, T3, $p = 0.036$, [N]2, $p < 0.001$, $R^2 = 37.53\%$; MMSE: A1T3[N]2, A1, $p = 0.018$, T3, $p < 0.001$, [N]2, $p < 0.001$, $R^2 = 36.43\%$; A1T2[N]2, A1, $p = 0.026$, T2, $p = 0.001$, [N]2, $p = 0.001$, $R^2 = 35.57\%$) (**Figures 5B,C,E,F**). Then, we found that the interaction between time and AT(N) variants significantly improved the goodness of fit (AIC and BIC) using a paired *t*-test ($p < 0.001$ for CDRSB and MMSE), and interactions dominated the main effects. Again, CSF Aβ42, tau PET, and temporal cortical thickness were the best combinations in both scales, and all interactions were significant (CDRSB: A1T2[N]2, A1, $p > 0.05$, T2, $p > 0.05$, [N]2, $p > 0.05$,

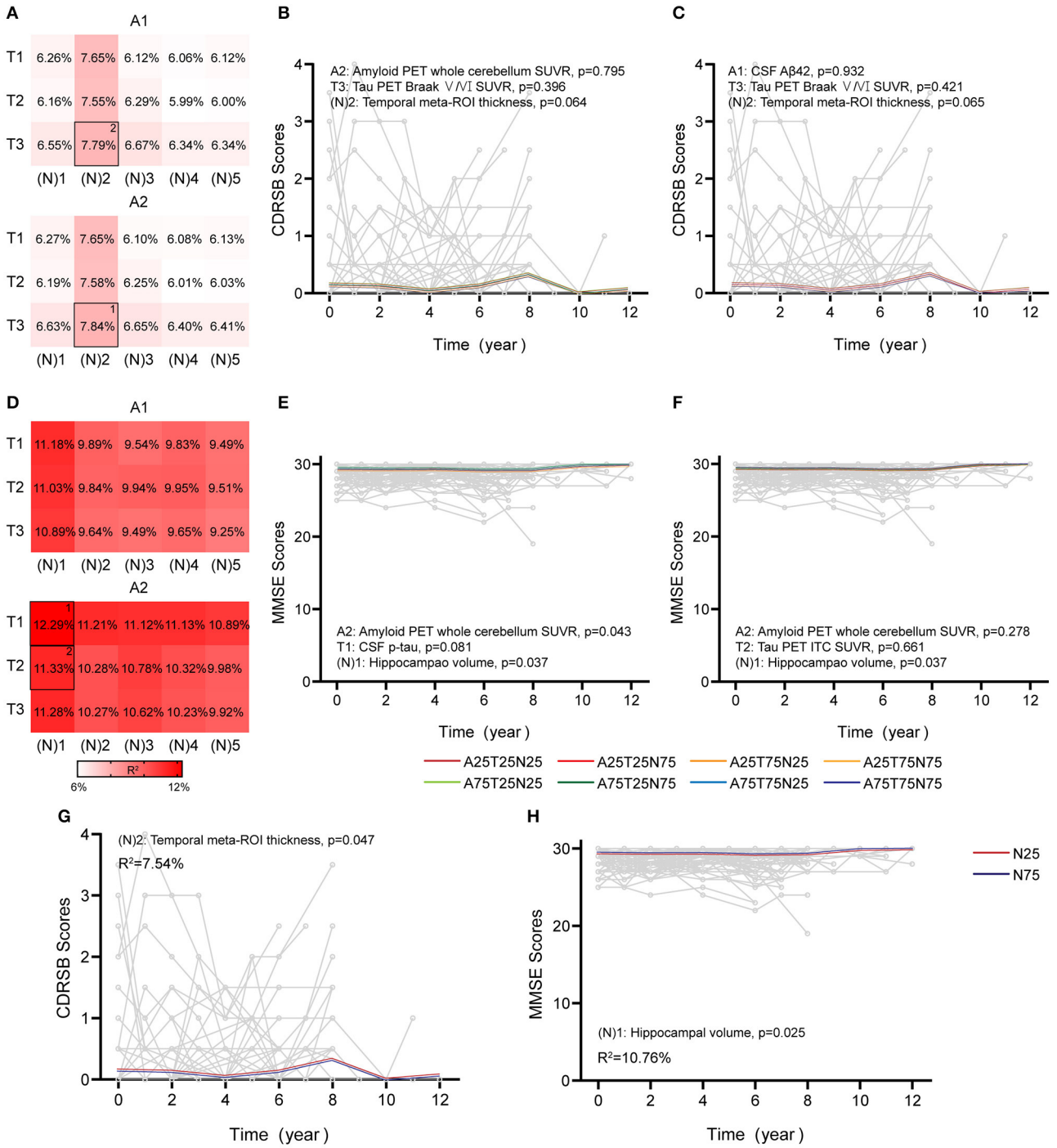

FIGURE 4 | Associations between different AT(N) combinations and longitudinal cognition in the CU group. Marginal R^2 for different AT(N) variants to predict longitudinal clinical dementia rating sum of boxes (CDRSB) and mini-mental state examination (MMSE) for cognitively unimpaired (CU), respectively (divided by A biomarkers) **(A,D)**. The selected models in **(B,C)** and **(E,F)** are the top two best models for different cognitive scales. The LME models with significant AT(N) biomarkers to predict longitudinal are CDRSB and MMSE, respectively **(G,H)**; AT(N) variants chosen in the model, *p*-values, and marginal R^2 are shown at the top (CDRSB) or bottom (MMSE) of each panel; 25 and 75 refer to 25th and 75th quartiles, where a lower value indicates a more abnormal biomarker. Aβ, β-amyloid; AT(N), β-amyloid, tau, and neurodegeneration classification system; ITC, inferior temporal cortex; p-tau, tau phosphorylated at Thr181; ROI, region of interest; SUVR, standardized uptake value ratio.

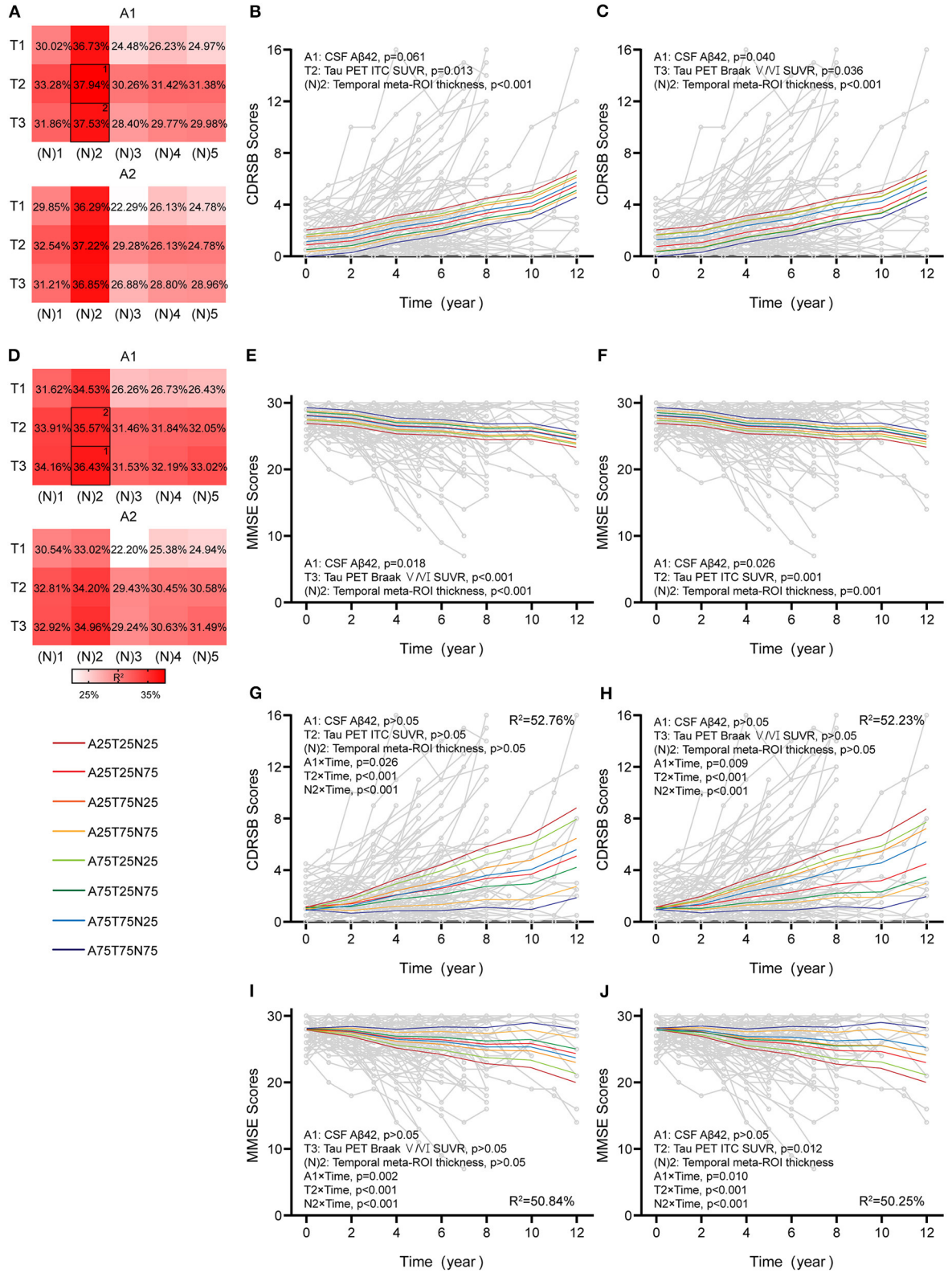

FIGURE 5 | Associations between different AT(N) combinations and longitudinal cognition in the CI group. Marginal R^2 for different AT(N) variants to predict longitudinal clinical dementia rating sum of boxes (CDRSB) and mini-mental state examination (MMSE) for cognitively impaired (CI), respectively (divided by **A** biomarkers) **(A,D)**.

(Continued)

FIGURE 5 | The selected models in **(B,C)** and **(E,F)** are the top two best models for the different cognitive scales. The top two best models with an interaction between time and AT(N) variants to predict longitudinal CDRSB and MMSE, respectively **(G–J)**; AT(N) variants chosen in the model and *p*-values, and marginal R^2 are shown at the top (CDRSB) or bottom (MMSE) of each panel; 25 and 75 refer to 25th and 75th quartiles, where a lower value indicates a more abnormal biomarker. Aβ, β-amyloid; AT(N), β-amyloid, tau, and neurodegeneration classification system; ITC, inferior temporal cortex; ROI, region of interest; SUVR, standardized uptake value ratio.

A1×Time, $p = 0.026$, T2×Time, $p < 0.001$, [N]2×Time, $p < 0.001$, $R^2 = 52.76\%$; A1T3[N]2, A1, $p > 0.05$, T3, $p > 0.05$, [N]2, $p > 0.05$, A1×Time, $p = 0.009$, T3×Time, $p < 0.001$, [N]2×Time, $p < 0.001$, $R^2 = 52.23\%$; MMSE: A1T3[N]2, A1, $p > 0.05$, T3, $p > 0.05$, [N]2, $p > 0.05$, A1×Time, $p = 0.002$, T3×Time, $p < 0.001$, [N]2×Time, $p < 0.001$, $R^2 = 50.84\%$; A1T2[N]2, A1, $p > 0.05$, T2, $p > 0.05$, [N]2, $p > 0.05$, A1×Time, $p = 0.010$, T2×Time, $p < 0.001$, [N]2×Time, $p < 0.001$, $R^2 = 50.25\%$) (**Figures 5G–J**).

Finally, similar findings were observed when using the LME model with time as a covariate to verify the results using continuous predictors (**Supplementary Table 9**).

Sensitivity Analyses

We repeated the AT(N) prevalence analyses using alternative cutoffs (**Supplementary Table 10**). Using cutoffs from 90% sensitivity for AD, except for more amyloid positivity using CSF Aβ42 in CU participants, other results were consistent with the data obtained from the main cutoffs. However, cutoffs defined by the mean ± 2 SD from Aβ-negative CU controls were more conservative. The lowest prevalence of T+ was obtained when using CSF rather than PET, and temporal cortical thickness in all the participants was negative.

DISCUSSION

In this study, we found that different combinations of AT(N) biomarkers exerted different effects on the category prevalence and predictions of cognitive decline. First, the difference in the composition of AT(N) categories between CU and CI individuals is not surprising. Categories representing the AD continuum were the most common in CI participants, while more subjects with non-AD pathological changes were observed in the CU group (Rami et al., 2011; Jack et al., 2018; Knopman et al., 2018; Carandini et al., 2019). Moreover, different AT(N) variants resulted in considerable differences in prevalence, such as a lower prevalence of T+ when using tau PET in all groups and a higher prevalence of N+ when using fluid biomarkers in the CU group. Finally, different AT(N) combinations have different associations with cognitive changes, with differences observed between CU and CI groups (MRI was more influential in CU participants and tau PET in CI participants). Taken together, these results indicate that different combinations lead to different AT(N) classifications of individuals and different predictions of longitudinal cognition. Our results have important implications for choosing AT(N) combinations according to different needs of research or clinical applications. For instance, we tend to use dynamic fluid examinations for early screening and prevention, and cognition may be predicted by non-invasive MRI imaging in the CU group. Imaging measures that represent the magnitude of the neuropathological load or damage accumulated over time, especially tau PET, may greatly assist with the accurate clinical staging and determination of the prognosis of patients with cognitive impairment.

Biomarkers of AD mainly include fluids and imaging. Here, we chose seven classic biomarkers mentioned in the NIA-AA Research Framework 2018 (Jack et al., 2016, 2018) and plasma NfL, a candidate neurodegeneration marker identified recently (Mattsson et al., 2017a, 2019). However, different biomarkers in the specific AT(N) component may be discordant (Vos et al., 2016; Jack et al., 2018). In our study, the continuous relationship between CSF Ab42 and amyloid PET was "L-shaped" rather than linear (**Figure 1A**) (Landau et al., 2013; Palmqvist et al., 2015). This may be due to a temporal offset between them (Mattsson et al., 2015; Palmqvist et al., 2016; Vlassenko et al., 2016). In addition, the correlation between CSF p-tau and tau PET was imperfect because p-tau seems to plateau later in the disease (Fagan et al., 2014) whereas the tau PET signal continues to increase (Mattsson et al., 2017b). Among biomarkers in the (N) component, MRI imaging tends to reflect cumulative neuronal loss and shrinkage of the neuropil (Bobinski et al., 2000; Zarow et al., 2005; Barkhof et al., 2007), CSF t-tau, and plasma NfL manifest the intensity of neuronal injury dynamically (van Rossum et al., 2012; Zetterberg, 2016), and FDG PET likely indicates both processes (Alexopoulos et al., 2014). These differences may explain the discordance among (N) biomarkers.

Regarding the AT(N) prevalence, we noted that both AT(N) categories and variants differed between CU and CI participants. Normal AD biomarkers (A-T-[N]-) and non-AD pathological change (A-T+[N]-, A-T+[N]+, and A-T-[N]+) account for most CU individuals, whereas the Alzheimer's continuum (A+T+[N]-, A+T+[N]+, A+T-[N]-, and A+T-[N]+) accounts for CI individuals, especially AD (A+T+[N]-, A+T+[N]+) (Jack et al., 2018). Nevertheless, approximately 1/4 of CU individuals are classified as AD continuum without cognitive symptoms. Cognition is also a continuum and the definition of CU is independent of biomarker findings according to the NIA-AA research framework (Jack et al., 2018). In our study, the overall prevalence of A+ in CU participants was similar, consistent with a metaanalysis (Jansen et al., 2015). However, greater increases in amyloid positivity were observed between the two groups when using amyloid PET. This may be because the CSF analysis detects cerebral Aβ accumulation earlier than PET (Mattsson et al., 2015; Palmqvist et al., 2016; Vlassenko et al., 2016). The same findings were obtained for tau positivity when comparing CSF and PET due to a temporal lag (Mattsson et al., 2017b; McDade and Bateman, 2018). Among the neurodegeneration biomarkers, CSF t-tau and plasma NfL were more common in CU participants, whereas no evident

differences were observed in CI participants. These results are consistent with several studies showing that CSF t-tau and blood NfL levels are increased before symptom onset (Mattsson et al., 2017a; Preische et al., 2019).

We repeated prevalence calculations using different cutoffs to verify the prevalence across AT(N) categories and found that the results were not completely consistent. This finding highlights that the optimization of categorization strategies is important for future studies.

Here, we analyzed the predictive effect of different AT(N) variants on longitudinal cognition evaluated using both the CDRSB and MMSE. CDRSB may enable a more detailed analysis of subtle changes with different stages of dementia severity (O'Bryant et al., 2008). First, optimal variants differ by clinical stage. Only MRI measures were significantly associated with cognitive changes in CU participants, whereas the best model for predicting cognition in CI participants included CSF Aβ42, tau PET, and cortical thickness. When using a single AT(N) biomarker for the prediction, no obvious difference was identified between CSF and PET amyloid plaques. This finding may indicate that CSF Aβ42 and amyloid PET can be used interchangeably as several studies have reported (Blennow and Zetterberg, 2018; Hansson et al., 2018). When considering the AT(N) combinations, we found that the amyloid pathology contributed the least to longitudinal cognition in the CI group. This implies that cognitive impairment is weakly related to extracellular Aβ burden and is presumably driven by other factors (Villemagne et al., 2011, 2013; de Wilde et al., 2019), consistent with the characteristics of "A" as state biomarkers (Knopman et al., 2018). However, CSF p-tau is increased earlier in the disease course than tau PET (Blennow and Zetterberg, 2018; La Joie et al., 2018; Mattsson-Carlgren et al., 2020). Therefore, between the two subgroups of CI, the difference in tau PET was more significant than that in CSF p-tau. These results might explain why tau PET far exceeded CSF p-tau levels in the longitudinal prediction of cognition in the CI group. The early tangle pathology identified using tau PET was a better predictor of CDRSB than MMSE, consistent with the characteristics of the scales. Compared to other N biomarkers, MRI measures, especially cortical thickness, were the best. Since hippocampal volume is strongly related to ICV (Jack et al., 2015), different methods for adjusting the volume by ICV associated with sex, age, and study populations may affect study power (Schwarz et al., 2016). A study proposed using thickness measurements, rather than volumes, to assess neurodegeneration in AD cohorts with a large age range (Schwarz et al., 2016). Our results also suggested that cortical thickness may predict cognition more precisely. Among all N biomarkers, the lowest marginal R^2 was obtained when using CSF t-tau to predict longitudinal cognition in CI participants. Firstly, CSF t-tau was reported to be related to multiple variables (age, sex, or education), which may attenuate the association with cognition under adjustment for such covariables (Mielke et al., 2019). Furthermore, recent findings showed that t-tau may be less specific to AD pathology (Buckley et al., 2019; Mielke et al., 2021), and its longitudinal trajectory along the AD continuum is still controversial (Vemuri et al., 2010; Kester et al., 2012; Toledo et al., 2013; Lleo et al., 2019). Similar findings were obtained when considering interactions in CI participants, but the interactions dominated the main effects. Although AT(N) variants were able to predict cognitive changes, their marginal effects relied on the time level. Overall, we obtained relatively robust results for this cohort (MRI for CU participants and the combination of tau PET and cortical thickness for CI participants). Compared to a recent study recruiting participants from Swedish BioFINDER (Mattsson-Carlgren et al., 2020), we confirmed the importance of tau PET in the AD diagnosis and staging, and highlighted that cortical thickness may have a highly significant contribution to cognitive decline.

This study has several limitations. First, the sample size in our study was moderate, which may affect the study power. Especially in the prediction of longitudinal cognition, the sample size of the AD group was too small, which may lead to deviations. So, it limited more refined analysis of subgroups. Secondly, we did not consider the Aβ42/Aβ40 ratio because the Aβ40 of many participants was missing in the database (detailed information was shown in **Supplementary Table 2**). Additionally, though our research has obtained relatively robust results, it still warrants independent validation in other larger cohorts covering all biomarkers in this study. Furthermore, the greater individual heterogeneity of CU participants may explain the low marginal R^2. Then, differences were observed among different cutoff strategies, and the cutoffs using in the study were sample specific, which may be biased to the sample. Therefore, more approaches for selecting cutoffs or alternatives to binarization (semicontinuous scale; Jack et al., 2016) must be tested. Finally, we only analyzed typical AD biomarkers in this study. With the emergence of an increasing number of biomarkers, they may also need to be included.

Collectively, the proposed AT(N) framework provides a more precise division of the Alzheimer's continuum based on the pathology (Jack et al., 2018), but different biomarkers for defining AT(N) cannot be used interchangeably. Each component of biomarkers included in the AT(N) system classification plays different roles in the stating and staging of AD, and the optimal combinations for predicting cognition may differ by cognitive status. Furthermore, different strategies for discontinuous biomarkers will be an important area for future studies.

DATA AVAILABILITY STATEMENT

The original contributions presented in the study are included in the article/**Supplementary Material**, further inquiries can be directed to the corresponding author/s.

ETHICS STATEMENT

The studies involving human participants were reviewed and approved by the Alzheimer's Disease Neuroimaging Initiative (ADNI) study. The patients/participants provided their written informed consent to participate in this study.

AUTHOR CONTRIBUTIONS

R-RL: analysis and interpretation of the data and drafting the manuscript. Y-YX, X-YL, and Y-HC: data acquisition, analysis, and interpretation of the data. Q-QT: funding, design of the study, and critical revision of the manuscript. Z-YW: funding, conceptualization and design of the study and critical revision of the manuscript. All authors reviewed the manuscript, contributed to the manuscript revising and editing critically for important intellectual content, given final approval of the version, agreed to be accountable for all aspects of the work presented here, and read and approved the final manuscript.

FUNDING

This study was supported by grants from the Key Research and Development project of Zhejiang Province (2019C03039), the National Natural Science Foundation of China (81970998), and the Natural Science Foundation of Zhejiang province (LBY21H090003).

ACKNOWLEDGMENTS

Data collection and sharing for this project was funded by the Alzheimer's Disease Neuroimaging Initiative (ADNI) (National Institutes of Health Grant U01 AG024904) and DOD ADNI (Department of Defense award number W81XWH-12-2-0012). ADNI was funded by the National Institute on Aging, the National Institute of Biomedical Imaging and Bioengineering, and through generous contributions from the following: AbbVie, Alzheimer's Association; Alzheimer's Drug Discovery Foundation; Araclon Biotech; BioClinica, Inc.; Biogen; Bristol-Myers Squibb Company; CereSpir, Inc.; Cogstate; Eisai Inc.; Elan Pharmaceuticals, Inc.; Eli Lilly and Company; EuroImmun; F. Hoffmann-La Roche Ltd and its affiliated company Genentech, Inc.; Fujirebio; GE Healthcare; IXICO Ltd.; Janssen Alzheimer Immunotherapy Research & Development, LLC.; Johnson & Johnson Pharmaceutical Research & Development LLC.; Lumosity; Lundbeck; Merck & Co., Inc.; Meso Scale Diagnostics, LLC.; NeuroRx Research; Neurotrack Technologies; Novartis Pharmaceuticals Corporation; Pfizer Inc.; Piramal Imaging; Servier; Takeda Pharmaceutical Company; and Transition Therapeutics. The Canadian Institutes of Health Research is providing funds to support ADNI clinical sites in Canada. Private sector contributions are facilitated by the Foundation for the National Institutes of Health (www.fnih.org). The grantee organization is the Northern California Institute for Research and Education, and the study is coordinated by the Alzheimer's Therapeutic Research Institute at the University of Southern California. ADNI data are disseminated by the Laboratory for Neuro Imaging at the University of Southern California.

SUPPLEMENTARY MATERIAL

The Supplementary Material for this article can be found online at: https://www.frontiersin.org/articles/10.3389/fnagi.2021.718959/full#supplementary-material

REFERENCES

Alexopoulos, P., Kriett, L., Haller, B., Klupp, E., Gray, K., Grimmer, T., et al. (2014). Limited agreement between biomarkers of neuronal injury at different stages of Alzheimer's disease. *Alzheimers Dement.* 10, 684–689. doi: 10.1016/j.jalz.2014.03.006

Ardila, A., and Moreno, S. (2001). Neuropsychological test performance in Aruaco Indians: an exploratory study. *J. Int. Neuropsychol. Soc.* 7, 510–515. doi: 10.1017/s1355617701004076

Baker, S. L., Maass, A., and Jagust, W. J. (2017). Considerations and code for partial volume correcting [(18)F]-AV-1451 tau PET data. *Data Brief* 15, 648–657. doi: 10.1016/j.dib.2017.10.024

Barkhof, F., Polvikoski, T. M., van Straaten, E. C., Kalaria, R. N., Sulkava, R., Aronen, H. J., et al. (2007). The significance of medial temporal lobe atrophy: a postmortem MRI study in the very old. *Neurology* 69, 1521–1527. doi: 10.1212/01.wnl.0000277459.83543.99

Blennow, K., Wallin, A., Agren, H., Spenger, C., Siegfried, J., and Vanmechelen, E. (1995). Tau protein in cerebrospinal fluid: a biochemical marker for axonal degeneration in Alzheimer disease? *Mol. Chem. Neuropathol.* 26, 231–245. doi: 10.1007/BF02815140

Blennow, K., and Zetterberg, H. (2018). Biomarkers for Alzheimer's disease: current status and prospects for the future. *J. Intern. Med.* 284, 643–663. doi: 10.1111/joim.12816

Bobinski, M., de Leon, M. J., Wegiel, J., Desanti, S., Convit, A., Saint, L. L., et al. (2000). The histological validation of post mortem magnetic resonance imaging-determined hippocampal volume in Alzheimer's disease. *Neuroscience* 95, 721–725. doi: 10.1016/s0306-4522(99)00476-5

Braak, H., Alafuzoff, I., Arzberger, T., Kretzschmar, H., and Del, T. K. (2006). Staging of Alzheimer disease-associated neurofibrillary pathology using paraffin sections and immunocytochemistry. *Acta Neuropathol.* 112, 389–404. doi: 10.1007/s00401-006-0127-z

Buckley, R. F., Mormino, E. C., Chhatwal, J., Schultz, A. P., Rabin, J. S., Rentz, D. M., et al. (2019). Associations between baseline amyloid, sex, and APOE on subsequent tau accumulation in cerebrospinal fluid. *Neurobiol. Aging* 78, 178–185. doi: 10.1016/j.neurobiolaging.2019.02.019

Carandini, T., Arighi, A., Sacchi, L., Fumagalli, G. G., Pietroboni, A. M., Ghezzi, L., et al. (2019). Testing the 2018 NIA-AA research framework in a retrospective large cohort of patients with cognitive impairment: from biological biomarkers to clinical syndromes. *Alzheimers Res. Ther.* 11:84. doi: 10.1186/s13195-019-0543-7

Compton, D. M., Bachman, L. D., Brand, D., and Avet, T. L. (2000). Age-associated changes in cognitive function in highly educated adults: emerging myths and realities. *Int. J. Geriatr. Psychiatry* 15, 75–85. doi: 10.1002/(sici)1099-1166(200001)15:1<75::aid-gps81>3.0.co;2-m

de Wilde, A., Reimand, J., Teunissen, C. E., Zwan, M., Windhorst, A. D., Boellaard, R., et al. (2019). Discordant amyloid-beta PET and CSF biomarkers and its clinical consequences. *Alzheimers Res. Ther.* 11:78. doi: 10.1186/s13195-019-0532-x

Dickerson, B. C., Bakkour, A., Salat, D. H., Feczko, E., Pacheco, J., Greve, D. N., et al. (2009). The cortical signature of Alzheimer's disease: regionally specific cortical thinning relates to symptom severity in very mild to mild AD dementia and is detectable in asymptomatic amyloid-positive individuals. *Cereb. Cortex* 19, 497–510. doi: 10.1093/cercor/bhn113

Fagan, A. M., Xiong, C., Jasielec, M. S., Bateman, R. J., Goate, A. M., Benzinger, T. L., et al. (2014). Longitudinal change in CSF biomarkers in autosomal-dominant Alzheimer's disease. *Sci. Transl. Med.* 6:226ra30. doi: 10.1126/scitranslmed.3007901

Hansson, O., Seibyl, J., Stomrud, E., Zetterberg, H., Trojanowski, J. Q., Bittner, T., et al. (2018). CSF biomarkers of Alzheimer's disease concord with amyloid-beta

PET and predict clinical progression: a study of fully automated immunoassays in BioFINDER and ADNI cohorts. *Alzheimers Dement.* 14, 1470–1481. doi: 10.1016/j.jalz.2018.01.010

Herholz, K., Salmon, E., Perani, D., Baron, J. C., Holthoff, V., Frolich, L., et al. (2002). Discrimination between Alzheimer dementia and controls by automated analysis of multicenter FDG PET. *Neuroimage* 17, 302–316. doi: 10.1006/nimg.2002.1208

Jack, C. J., Bennett, D. A., Blennow, K., Carrillo, M. C., Feldman, H. H., Frisoni, G. B., et al. (2016). A/T/N: an unbiased descriptive classification scheme for Alzheimer disease biomarkers. *Neurology* 87, 539–547. doi: 10.1212/WNL.0000000000002923

Jack, C. J., Bernstein, M. A., Borowski, B. J., Gunter, J. L., Fox, N. C., Thompson, P. M., et al. (2010). Update on the magnetic resonance imaging core of the Alzheimer's disease neuroimaging initiative. *Alzheimers Dement.* 6, 212–220. doi: 10.1016/j.jalz.2010.03.004

Jack, C. J., Wiste, H. J., Knopman, D. S., Vemuri, P., Mielke, M. M., Weigand, S. D., et al. (2014). Rates of beta-amyloid accumulation are independent of hippocampal neurodegeneration. *Neurology* 82, 1605–1612. doi: 10.1212/WNL.0000000000000386

Jack, C. R., Bennett, D. A., Blennow, K., Carrillo, M. C., Dunn, B., Haeberlein, S. B., et al. (2018). NIA-AA research framework: toward a biological definition of Alzheimer's disease. *Alzheimers Dement.* 14, 535–562. doi: 10.1016/j.jalz.2018.02.018

Jack, C. R., Bernstein, M. A., Fox, N. C., Thompson, P., Alexander, G., Harvey, D., et al. (2008). The Alzheimer's disease neuroimaging initiative (ADNI): MRI methods. *J. Magn. Reson. Imaging* 27, 685–691. doi: 10.1002/jmri.21049

Jack, C. R., Wiste, H. J., Weigand, S. D., Knopman, D. S., Mielke, M. M., Vemuri, P., et al. (2015). Different definitions of neurodegeneration produce similar amyloid/neurodegeneration biomarker group findings. *Brain* 138, 3747–3759. doi: 10.1093/brain/awv283

Jansen, W. J., Ossenkoppele, R., Knol, D. L., Tijms, B. M., Scheltens, P., Verhey, F. R., et al. (2015). Prevalence of cerebral amyloid pathology in persons without dementia: a meta-analysis. *JAMA* 313, 1924–1938. doi: 10.1001/jama.2015.4668

Johnson, K. A., Schultz, A., Betensky, R. A., Becker, J. A., Sepulcre, J., Rentz, D., et al. (2016). Tau positron emission tomographic imaging in aging and early Alzheimer disease. *Ann. Neurol.* 79, 110–119. doi: 10.1002/ana.24546

Joshi, A. D., Pontecorvo, M. J., Clark, C. M., Carpenter, A. P., Jennings, D. L., Sadowsky, C. H., et al. (2012). Performance characteristics of amyloid PET with florbetapir F 18 in patients with Alzheimer's disease and cognitively normal subjects. *J. Nucleic Med.* 53, 378–384. doi: 10.2967/jnumed.111.090340

Kester, M. I., Scheffer, P. G., Koel-Simmelink, M. J., Twaalfhoven, H., Verwey, N. A., Veerhuis, R., et al. (2012). Serial CSF sampling in Alzheimer's disease: specific versus non-specific markers. *Neurobiol. Aging* 33, 1591–1598. doi: 10.1016/j.neurobiolaging.2011.05.013

Klunk, W. E., Engler, H., Nordberg, A., Wang, Y., Blomqvist, G., Holt, D. P., et al. (2004). Imaging brain amyloid in Alzheimer's disease with Pittsburgh Compound-B. *Ann. Neurol.* 55, 306–319. doi: 10.1002/ana.20009

Knopman, D. S., Haeberlein, S. B., Carrillo, M. C., Hendrix, J. A., Kerchner, G., Margolin, R., et al. (2018). The National Institute on Aging and the Alzheimer's Association Research Framework for Alzheimer's disease: perspectives from the Research Roundtable. *Alzheimers Dement.* 14, 563–575. doi: 10.1016/j.jalz.2018.03.002

La Joie, R., Bejanin, A., Fagan, A. M., Ayakta, N., Baker, S. L., Bourakova, V., et al. (2018). Associations between [(18)F]AV1451 tau PET and CSF measures of tau pathology in a clinical sample. *Neurology* 90, e282–e290. doi: 10.1212/WNL.0000000000004860

Landau, S. M., Lu, M., Joshi, A. D., Pontecorvo, M., Mintun, M. A., Trojanowski, J. Q., et al. (2013). Comparing positron emission tomography imaging and cerebrospinal fluid measurements of beta-amyloid. *Ann. Neurol.* 74, 826–836. doi: 10.1002/ana.23908

Lleo, A., Alcolea, D., Martinez-Lage, P., Scheltens, P., Parnetti, L., Poirier, J., et al. (2019). Longitudinal cerebrospinal fluid biomarker trajectories along the Alzheimer's disease continuum in the BIOMARKAPD study. *Alzheimers Dement.* 15, 742–753. doi: 10.1016/j.jalz.2019.01.015

Long, J. M., and Holtzman, D. M. (2019). Alzheimer disease: an update on pathobiology and treatment strategies. *Cell* 179, 312–339. doi: 10.1016/j.cell.2019.09.001

Mattsson, N., Andreasson, U., Zetterberg, H., and Blennow, K. (2017a). Association of plasma neurofilament light with neurodegeneration in patients with Alzheimer disease. *JAMA Neurol.* 74, 557–566. doi: 10.1001/jamaneurol.2016.6117

Mattsson, N., Cullen, N. C., Andreasson, U., Zetterberg, H., and Blennow, K. (2019). Association between longitudinal plasma neurofilament light and neurodegeneration in patients with Alzheimer disease. *JAMA Neurol.* 76, 791. doi: 10.1001/jamaneurol.2019.0765

Mattsson, N., Insel, P. S., Donohue, M., Landau, S., Jagust, W. J., Shaw, L. M., et al. (2015). Independent information from cerebrospinal fluid amyloid-beta and florbetapir imaging in Alzheimer's disease. *Brain* 138, 772–783. doi: 10.1093/brain/awu367

Mattsson, N., Scholl, M., Strandberg, O., Smith, R., Palmqvist, S., Insel, P. S., et al. (2017b). (18)F-AV-1451 and CSF T-tau and P-tau as biomarkers in Alzheimer's disease. *EMBO Mol. Med.* 9, 1212–1223. doi: 10.15252/emmm.201707809

Mattsson-Carlgren, N., Leuzy, A., Janelidze, S., Palmqvist, S., Stomrud, E., Strandberg, O., et al. (2020). The implications of different approaches to define AT(N) in Alzheimer disease. *Neurology* 94, e2233–e2244. doi: 10.1212/WNL.0000000000009485

McDade, E., and Bateman, R. J. (2018). Tau positron emission tomography in autosomal dominant Alzheimer disease: small windows, big picture. *JAMA Neurol.* 75, 536–538. doi: 10.1001/jamaneurol.2017.4026

McKhann, G., Drachman, D., Folstein, M., Katzman, R., Price, D., and Stadlan, E. M. (1984). Clinical diagnosis of Alzheimer's disease: report of the NINCDS-ADRDA Work Group under the auspices of Department of Health and Human Services Task Force on Alzheimer's Disease. *Neurology* 34, 939–944. doi: 10.1212/wnl.34.7.939

Mielke, M. M., Przybelski, S. A., Lesnick, T. G., Kern, S., Zetterberg, H., Blennow, K., et al. (2021). Comparison of CSF neurofilament light chain, neurogranin, and tau to MRI markers. *Alzheimers Dement.* 17, 801–812. doi: 10.1002/alz.12239

Mielke, M. M., Syrjanen, J. A., Blennow, K., Zetterberg, H., Skoog, I., Vemuri, P., et al. (2019). Comparison of variables associated with cerebrospinal fluid neurofilament, total-tau, and neurogranin. *Alzheimers Dement.* 15, 1437–1447. doi: 10.1016/j.jalz.2019.07.009

O'Bryant, S. E., Waring, S. C., Cullum, C. M., Hall, J., Lacritz, L., Massman, P. J., et al. (2008). Staging dementia using Clinical Dementia Rating Scale Sum of Boxes scores: a Texas Alzheimer's research consortium study. *Arch. Neurol.* 65, 1091–1095. doi: 10.1001/archneur.65.8.1091

Palmqvist, S., Mattsson, N., and Hansson, O. (2016). Cerebrospinal fluid analysis detects cerebral amyloid-beta accumulation earlier than positron emission tomography. *Brain* 139, 1226–1236. doi: 10.1093/brain/aww015

Palmqvist, S., Zetterberg, H., Mattsson, N., Johansson, P., Minthon, L., Blennow, K., et al. (2015). Detailed comparison of amyloid PET and CSF biomarkers for identifying early Alzheimer disease. *Neurology* 85, 1240–1249. doi: 10.1212/WNL.0000000000001991

Preische, O., Schultz, S. A., Apel, A., Kuhle, J., Kaeser, S. A., Barro, C., et al. (2019). Serum neurofilament dynamics predicts neurodegeneration and clinical progression in presymptomatic Alzheimer's disease. *Nat. Med.* 25, 277–283. doi: 10.1038/s41591-018-0304-3

Rami, L., Fortea, J., Bosch, B., Sole-Padulles, C., Llado, A., Iranzo, A., et al. (2011). Cerebrospinal fluid biomarkers and memory present distinct associations along the continuum from healthy subjects to AD patients. *J. Alzheimers Dis.* 23, 319–326. doi: 10.3233/JAD-2010-101422

Schwarz, C. G., Gunter, J. L., Wiste, H. J., Przybelski, S. A., Weigand, S. D., Ward, C. P., et al. (2016). A large-scale comparison of cortical thickness and volume methods for measuring Alzheimer's disease severity. *Neuroimage Clin.* 11, 802–812. doi: 10.1016/j.nicl.2016.05.017

Toledo, J. B., Xie, S. X., Trojanowski, J. Q., and Shaw, L. M. (2013). Longitudinal change in CSF tau and abeta biomarkers for up to 48 months in ADNI. *Acta Neuropathol.* 126, 659–670. doi: 10.1007/s00401-013-1151-4

van Rossum, I. A., Vos, S. J., Burns, L., Knol, D. L., Scheltens, P., Soininen, H., et al. (2012). Injury markers predict time to dementia in subjects with MCI and amyloid pathology. *Neurology* 79, 1809–1816. doi: 10.1212/WNL.0b013e3182704056

Vemuri, P., Wiste, H. J., Weigand, S. D., Knopman, D. S., Trojanowski, J. Q., Shaw, L. M., et al. (2010). Serial MRI and CSF biomarkers in normal aging, MCI, and AD. *Neurology* 75, 143–151. doi: 10.1212/WNL.0b013e3181e7ca82

Villemagne, V. L., Burnham, S., Bourgeat, P., Brown, B., Ellis, K. A., Salvado, O., et al. (2013). Amyloid beta deposition, neurodegeneration, and cognitive decline in sporadic Alzheimer's disease: a prospective cohort study. *Lancet Neurol.* 12, 357–367. doi: 10.1016/S1474-4422(13)70044-9

Villemagne, V. L., Pike, K. E., Chetelat, G., Ellis, K. A., Mulligan, R. S., Bourgeat, P., et al. (2011). Longitudinal assessment of Abeta and cognition in aging and Alzheimer disease. *Ann. Neurol.* 69, 181–192. doi: 10.1002/ana.22248

Vlassenko, A. G., McCue, L., Jasielec, M. S., Su, Y., Gordon, B. A., Xiong, C., et al. (2016). Imaging and cerebrospinal fluid biomarkers in early preclinical alzheimer disease. *Ann. Neurol.* 80, 379–387. doi: 10.1002/ana.24719

Vos, S., Gordon, B. A., Su, Y., Visser, P. J., Holtzman, D. M., Morris, J. C., et al. (2016). NIA-AA staging of preclinical Alzheimer disease: discordance and concordance of CSF and imaging biomarkers. *Neurobiol. Aging* 44, 1–8. doi: 10.1016/j.neurobiolaging.2016.03.025

Xue, M., Sun, F., Ou, Y., Shen, X., Li, H., Huang, Y., et al. (2020). Association of cerebrospinal fluid neurogranin levels with cognition and neurodegeneration in Alzheimer's disease. *Aging* 12, 9365–9379. doi: 10.18632/aging.103211

Zarow, C., Vinters, H. V., Ellis, W. G., Weiner, M. W., Mungas, D., White, L., et al. (2005). Correlates of hippocampal neuron number in Alzheimer's disease and ischemic vascular dementia. *Ann. Neurol.* 57, 896–903. doi: 10.1002/ana.20503

Zetterberg, H. (2016). Neurofilament light: a dynamic cross-disease fluid biomarker for neurodegeneration. *Neuron* 91, 1–3. doi: 10.1016/j.neuron.2016.06.030

Conflict of Interest: The authors declare that the research was conducted in the absence of any commercial or financial relationships that could be construed as a potential conflict of interest.

Publisher's Note: All claims expressed in this article are solely those of the authors and do not necessarily represent those of their affiliated organizations, or those of the publisher, the editors and the reviewers. Any product that may be evaluated in this article, or claim that may be made by its manufacturer, is not guaranteed or endorsed by the publisher.

Copyright © 2021 Lin, Xue, Li, Chen, Tao and Wu. This is an open-access article distributed under the terms of the Creative Commons Attribution License (CC BY). The use, distribution or reproduction in other forums is permitted, provided the original author(s) and the copyright owner(s) are credited and that the original publication in this journal is cited, in accordance with accepted academic practice. No use, distribution or reproduction is permitted which does not comply with these terms.

frontiers in Molecular Neuroscience

BRIEF RESEARCH REPORT
published: 09 August 2021
doi: 10.3389/fnmol.2021.734273

Miro1 Impairment in a Parkinson's At-Risk Cohort

*David Nguyen[1], Vinita Bharat[1], Devon M. Conradson[1], Pawan Nandakishore[2] and Xinnan Wang[1]**

[1] Department of Neurosurgery, Stanford University School of Medicine, Stanford, CA, United States, [2] Colaberry Inc, Boston, MA, United States

There is a lack of reliable molecular markers for Parkinson's disease (PD) patients and at-risk individuals. The detection of the pre-symptomatic population of PD will empower more effective clinical intervention to delay or prevent disease onset. We have previously found that the mitochondrial protein Miro1 is resistant to mitochondrial depolarization-induced degradation in fibroblasts from a large number of PD patients and several at-risk individuals. Therefore, Miro1 has the potential to molecularly label PD populations. In order to determine whether Miro1 could serve as a molecular marker for the risk of PD, here we examine the Miro1 response to mitochondrial depolarization by biochemical approaches in induced pluripotent stem cells from a cohort of at-risk individuals. Our results show that the Miro1 phenotype is significantly associated with PD risk. We propose that Miro1 is a promising molecular marker for detecting both PD and at-risk populations. Tracking this Miro1 marker could aid in diagnosis and Miro1-based drug discoveries.

Keywords: Parkinson's disease, IPSC, mitophagy, risk, Miro1

OPEN ACCESS

Edited by:
Jiehui Jiang,
Shanghai University, China

Reviewed by:
Evandro Fei Fang,
University of Oslo, Norway
Daniele Bottai,
University of Milan, Italy

****Correspondence:***
Xinnan Wang
xinnanw@stanford.edu

Specialty section:
This article was submitted to Brain Disease Mechanisms, a section of the journal Frontiers in Molecular Neuroscience

Received: *30 June 2021*
Accepted: *19 July 2021*
Published: *09 August 2021*

Citation:
Nguyen D, Bharat V, Conradson DM, Nandakishore P and Wang X (2021) Miro1 Impairment in a Parkinson's At-Risk Cohort. Front. Mol. Neurosci. 14:734273. doi: 10.3389/fnmol.2021.734273

INTRODUCTION

Parkinson's disease (PD) is the second most common movement disorder, characterized by selective loss of dopaminergic neurons in the substantia nigra. Currently, the diagnosis of PD is based on symptom evaluations with a high probability of misdiagnosis (Dickson, 2018), and there are no reliable biomarkers for PD patients or at-risk individuals, presenting a roadblock to drug development (Bartels, 2016). Early detection in individuals before symptom onset is particularly important, since early intervention will undoubtedly improve treatment efficacy.

We have discovered that a mitochondrial protein, Miro1, is useful for marking a subset of PD patients (Hsieh et al., 2019). Miro1 is attached to the outer mitochondrial membrane and can recruit microtubule motors to mitochondria to mediate their transport (**Figure 1A**; Guo et al., 2005; Fransson et al., 2006; Wang and Schwarz, 2009). Miro1 is removed from the surface of depolarized mitochondria to arrest their motility and to facilitate their subsequent clearance via mitophagy (**Figure 1A**; Wang et al., 2011; Hsieh et al., 2016, 2019; Shaltouki et al., 2018). The molecular players that mediate Miro1 removal from damaged mitochondria include Parkinson's-related proteins—LRRK2, PINK1, and Parkin (Wang et al., 2011; Hsieh et al., 2016). Mutations in *LRRK2*, *PINK1*, or *Parkin* cause familial PD (Kitada et al., 1998; Bonifati, 2002; Valente et al., 2004; Zimprich et al., 2004), and are also associated with the risk of sporadic PD (Cookson, 2010). Therefore, mitophagy may play a key role in Parkinson's pathogenesis and in additional age-dependent neurodegenerative diseases (Pickrell and Youle, 2015; Fang et al., 2019; Lautrup et al., 2019).

We have previously measured the Miro1 response to mitochondrial depolarization using biochemical assays in skin fibroblasts from a broad spectrum of PD patients, and discovered that 94% of the patients' fibroblast cell lines fail to remove Miro1 following depolarization (Hsieh et al., 2019). These patients include both familial patients with pathogenic mutations and sporadic patients with no known genetic mutations. Importantly, we have found that the Miro1 defect occurs in five asymptomatic genetic carriers. Those observations suggest that the Miro1 marker may be employed to detect the pre-symptomatic population which will benefit most from early therapeutic intervention. Therefore, it is imperative to determine the frequency of our Miro1 marker in an expansion of non-manifesting genetic carriers, as well as individuals who show prodromal symptoms such as rapid eye movement sleep behavior disorder (RBD) and hyposmia. In the current work, we filled this gap of research by examining our Miro1 marker in induced pluripotent stem cells (iPSCs) from a cohort of genetic carriers and prodromal individuals. These cells represent the entire collection of the first released iPSC repository from Parkinson's Progression Markers Initiative (PPMI). We discovered a significant association of the Miro1 defect with the risk of PD, yielding important insights into the possibility of detecting the pre-symptomatic phase of this disease.

MATERIALS AND METHODS

Subject Details

No animal models or human subjects were used in this study. The iPSC work was approved by the Stanford Stem Cell Oversight Committee. iPSCs were obtained under an MTA from the National Institute of Neurological Disorders and Stroke (NINDS) human and cell repository or PPMI, which is in a partnership with multiple institutions that deposited iPSCs, approved study protocols, and ensured consent from donors. All iPSC lines in this study are summarized in **Supplementary Table 1**. PPMI is an international, multi-center, and progressing study designed to identify PD biomarkers by the MJFF[1]. The study design, subject recruitment criteria, site selection, and study assessment have been detailed in Parkinson Progression Marker Initiative (2011).

Cell Culture and Western Blotting

Induced pluripotent stem cells were cultured in mTeSR Plus Kit (05825, Stemcell Technologies) and maintained in a 37°C, 5% CO_2 incubator with humidified atmosphere. The media were refreshed every 1–2 days and split every 4–6 days. CCCP (C2759, Sigma-Aldrich) was prepared at 40 mM in DMSO fresh every time and applied at 40 μM in fresh culture medium (1:1000 dilution) for 6 h. Cells were subsequently lysed in NP40 Cell lysis buffer (FNN0021, ThermoFisher Scientific) with protease inhibitor cocktail (539134, Calbiochem). Cell debris was removed by centrifugation at 17,000 *g* for 10 min at 4°C. Cell lysates were mixed 1:1 with 2× Laemmli buffer (4% SDS, 20% Glycerol, 120 mM Tris–HCl, 0.02% bromophenol blue, 700 mM 2-mercaptoethanol) and boiled for 5 min prior to being loaded into an SDS-PAGE. 10% polyacrylamide gels (acrylamide:bis-acrylamide = 29:1) and Tris-Glycine-SDS buffer (24.8 mM Tris, 192 mM glycine, 0.1% SDS) were used for electrophoresis. After electrophoresis, nitrocellulose membranes (1620115, Bio-Rad) were used in semi-dry transfer with Bjerrum Schafer-Nielsen buffer [48 mM Tris, 39 mM glycine, 20% Methanol (v/v), pH 9.2]. Transferred membranes were first blocked overnight in phosphate-buffered saline containing 5% fat-free milk and 0.1% tween-20 at 4°C, and then incubated with the following primary antibodies: mouse anti-Miro1 (WH0055288M1, Sigma-Aldrich) at 1:1,000, mouse anti-ATP5β (AB14730, AbCam) at 1:1,000, or rabbit anti-GAPDH (5174S, Cell Signaling Technology) at 1:1-3,000, at 4°C overnight in blocking buffer. HRP-conjugated goat anti-mouse (115-035-003, Jackson ImmunoResearch Laboratories) or goat anti-rabbit (111-035-144, Jackson ImmunoResearch Laboratories) were used at 1:10-20,000. Pierce ECL Western Blotting Substrate (32109, ThermoScientfic) were used for ECL immunoblotting. Membranes were scanned using a Bio-Rad ChemiDoc XRS system. Experiments were repeated for more than three times. Cell passaging numbers were within the range of 12–17 and did not affect the phenotype.

Quantification of Western Blotting Data

All experiments were performed in a blinded format. The intensities of protein bands were measured by ImageJ (ver. 1.48V, NIH). The intensity of each band was normalized to that of the loading control GAPDH from the same blot, and expressed as a fraction of that of "Healthy-1 with DMSO treatment" from the same experiment; this control was included in every independent experiment. Values of Mean ± S.E.M of Miro1 were reported in **Supplementary Table 1**. The ratio of Miro1 was calculated by dividing the mean of Miro1 intensities treated with CCCP by the mean of Miro1 with DMSO of the same subject, and imported into the heat map. Student *T* Test was performed for comparing normalized Miro1 band intensities within the same subject ("with DMSO" vs "with CCCP"), and *P* values were reported in **Supplementary Table 1**. The number of subjects with a P value > 0.05 together with subjects that showed significant Miro1 upregulation after CCCP, or the number of subjects with $P < 0.05$ for Miro1 reduction after CCCP was counted, respectively, and used in Fisher Exact Test in **Figure 1C**. $n = 3$–55 independent experiments.

Multivariance regression or Anova was used to determine the interactions among multiple variables for affecting Miro1 ratio and *P* values were calculated by linear fit in **Figures 2**, **3**. During the analysis, Hoehn and Yahr Scale and Mini-Mental Status Examination were detected to show an interaction. Partial regression plots were subsequently generated to help decipher the relationship between an individual variable and the response variable in a multivariable regression problem. Seven partial regression plots, one for each individual variable in the regression problem (Hoehn and Yahr Scale, Mini-Mental

[1]http://www.ppmi-info.org/study-design/

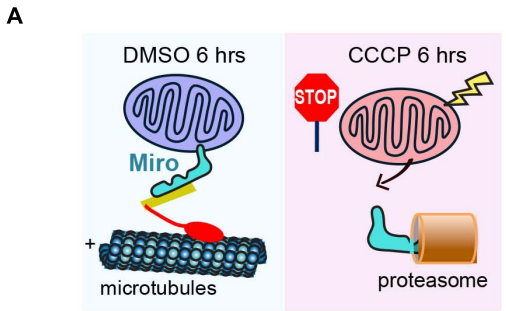

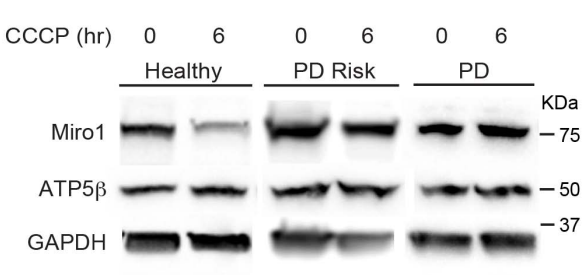

C

Diagnosis	No. (Miro1 DMSO v.s. CCCP P<0.05)	No. (Miro1 DMSO v.s. CCCP P>0.05)	P (Fisher Exact) Compared to Healthy
Healthy	9 (100%)	0 (0%)	
PD	5 (16.7%)	25 (83.3%)	<0.00001
PD Risk (Carrier)	6 (14.3%)	36 (85.7%)	<0.00001
PD Risk (Hyposmia)	3 (60%)	2 (40%)	0.1099
LRRK2+, Hyposmia	1 (16.7%)	5 (83.3%)	0.002

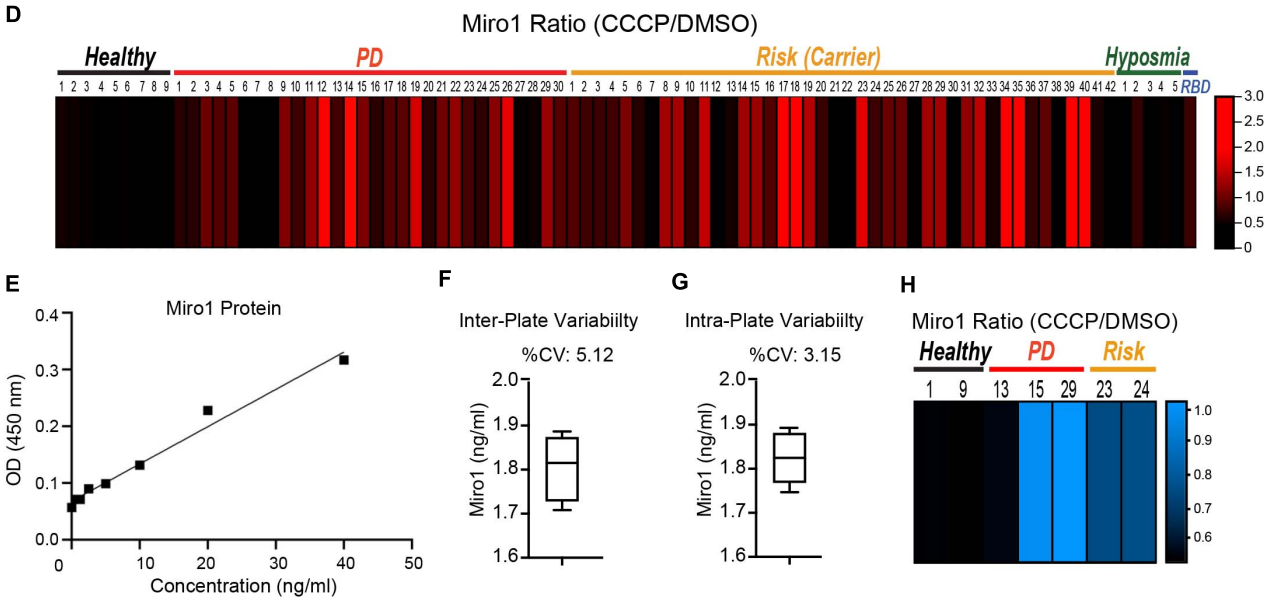

FIGURE 1 | The Miro1 Response to CCCP in iPSCs. **(A)** Schematic representation of our readout. **(B)** Examples of the readout using Healthy-2, PD-29, and Risk-39. Cell lysates were blotted as indicated. **(C)** Summary of the Western blotting results. Normalized Miro1 intensities of "with DMSO" and "with CCCP" within the same subject are compared by Student *T* Test, and the number of subjects with $P > 0.05$ together with subjects that show significant Miro1 upregulation after CCCP, or the number of subjects with $P < 0.05$ for Miro1 reduction after CCCP, is indicated in the column of "No. (Miro1 DMSO vs CCCP $P > 0.05$ or <0.05)." Fisher Exact Test is used to determine the *P* value of a specific group in comparison with "Healthy." **(D)** The heatmap shows the relative ratio of mean normalized Miro1 intensities ("with CCCP" divided by "with DMSO") of the same subject measured by Western blotting. Data are from **Supplementary Table 1**. $n = 3–55$. **(E–G)** Validation of ELISA for Miro1. **(E)** A representative standard curve is shown. LLOD = 0.112 ng/ml. Dynamic range = 0.625–40 ng/ml. **(F)** Inter-plate variability is demonstrated by measuring the same sample (Healthy-1) in 4 different plates. **(G)** Intra-plate variability is shown by measuring the same sample (Healthy-1) 4 times in the same plate. **(H)** The heatmap shows the relative ratio of mean Miro1 values ("with CCCP" divided by "with DMSO") of the same subject measured by ELISA. Data are from **Supplementary Table 1**. $n = 3–4$.

Status Examination, onset age), their interaction terms, and the intercept were generated. Out of all the partial regression plots for interaction terms, the plot of Hoehn and Yahr Scale and Mini-Mental Status Examination with linear fit showed significance ($P = 0.012$). This plot and additional representative partial regression plots were shown in **Figure 4**.

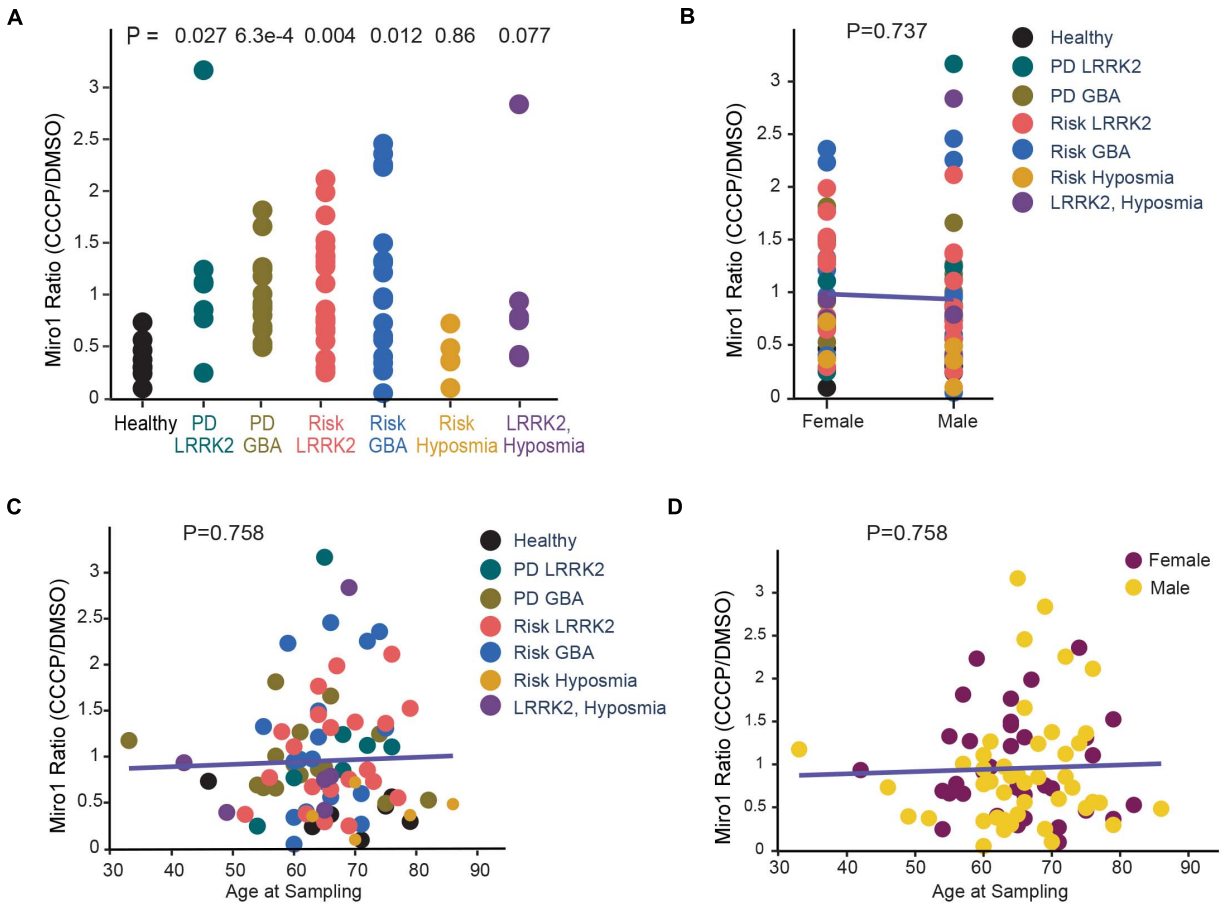

FIGURE 2 | Correlation Analysis of Miro1 Ratio in iPSCs. **(A)** One-Way Anova is used to determine the significant difference among all groups. **(B)** Two-Way Anova is used to determine the interaction between sex and genetic background with Miro1 ratio as the response variable. **(C, D)** Multivariable regression is used to determine the interaction between age and genetic background **(C)**, or age and sex **(D)**, with Miro1 ratio as the response variable. All *P* values are calculated by linear fit.

Enzyme-Linked Immunosorbent Assay

All experiments were performed as blinded tests. 40 μM CCCP in DMSO or the same volume of DMSO alone was applied to iPSCs for 6 h, and then cells were lysed in NP40 Cell lysis buffer (FNN0021, ThermoFisher Scientific) with protease inhibitor cocktail (539134, Calbiochem). Cell debris was removed by centrifugation at 17,000 *g* for 10 min at 4°C. The Rhot1 ELISA kit (EKL54911, Biomatik) was used according to the manufacturer's instructions. The specificity and stability were validated by Biomatik. The dynamic detection range, sensitivity (lower limit of detection–LLOD), and precision (inter- and intra-assay) were determined by both Biomatik and us (**Figures 1E–G**), and the results were comparable. Briefly, 50 μl of cell lysate prepared from above, or serial dilutions of the standard (0–40 ng/ml) were added and incubated for 2 h at 37°C. Each well was then incubated with 100 μl of Detection Reagent A for 1 h at 37°C. Next, plates were washed, and each well was incubated with 100 μl of Detection Reagent B for 1 h at 37°C. Plates were washed again, and 90 μl of Substrate Solution was added to each well for 15–25 min at 37°C. The colorimetric reactions were stopped by 50 μl of Stop Solution and absorbance was read at 450 nm by a microplate reader (Infinite 200 Pro, Tecan). An experiment for generating the standard curve was included in each plate and the representative standard plot was shown in the figure. Each data point was from 3 to 4 independent experiments with 2 technical repeats each time. Student *T* Test was performed for comparing Miro1 signals within the same subject (DMSO vs CCCP). A loading control, GAPDH, was detected by Western blotting in each experiment and there was no significant difference in loading between "DMSO" and "CCCP" for each cell line. Raw data and *P* values are reported in **Supplementary Table 1**.

Statistics

Throughout the paper, the distribution of data points was expressed as box-whisker or dot-plot, except otherwise stated. Statistical analyses were performed using Prism, Excel, or Python's statsmodels package. For all experiments, between 3 and 55 independent experiments were performed. The number of experimental replications (n) can be found in Figure

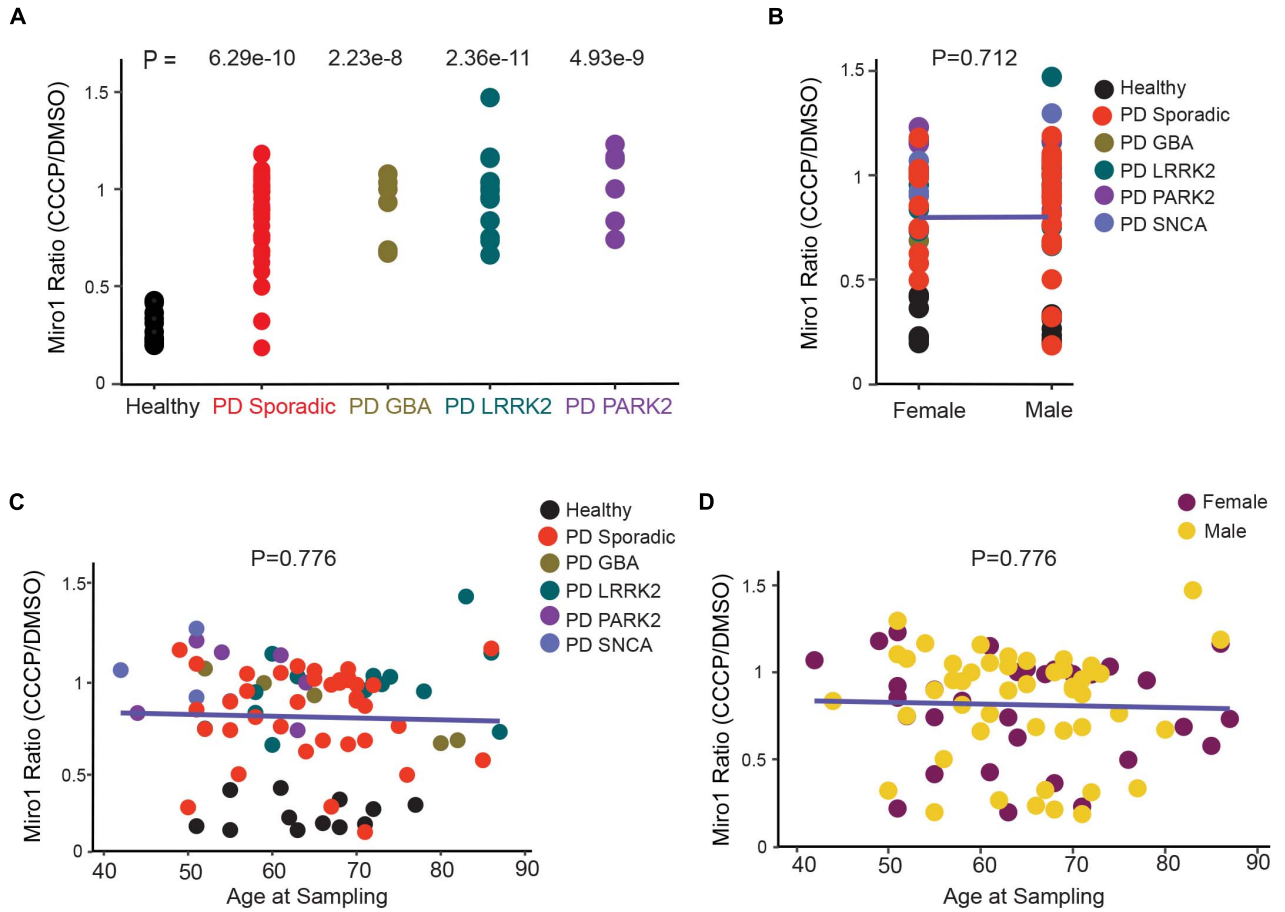

FIGURE 3 | Correlation Analysis of Miro1 Ratio in Fibroblasts. **(A)** One-Way Anova is used. **(B)** Two-Way Anova is used to determine the interaction between sex and genetic background with Miro1 ratio as the response variable. **(C, D)** Multivariable regression is used to determine the interaction between age and genetic background **(C)**, or age and sex **(D)**, with Miro1 ratio as the response variable. All *P* values are calculated by linear fit.

Legends and **Supplementary Table 1**. We did not exclude any data.

RESULTS

Miro1 Is Resistant to Degradation in iPSCs From Individuals at Risk for PD

We employed the same methods we previously utilized in fibroblasts that detected Miro1 degradation following mitochondrial depolarization (Hsieh et al., 2019). We cultured iPSCs and applied CCCP, a mitochondrial uncoupler, to depolarize the mitochondrial membrane potential ($\Delta\Psi m$; Hsieh et al., 2016, 2019). In healthy controls at 6 h following CCCP treatment, Miro1 was significantly degraded as detected by Western blotting (**Figures 1A,B**); this time point is prior to the completion of mitophagy when multiple mitochondrial markers are degraded (Hsieh et al., 2016, 2019). We applied this method to a total of 87 iPSC lines we obtained from the PPMI and NINDS human and cell repository (**Supplementary Table 1**). This cohort included 9 wild-type controls (8 healthy subjects and 1 corrected wild-type), 30 PD patients bearing mutations in *SNCA*, *LRRK2*, or *GBA* without the presence of signs for other neurological disorders, 42 asymptomatic genetic carriers (named "Risk"), and 6 individuals exhibiting prodromal symptoms such as hyposmia or RBD but without PD diagnosis (named "Risk-Hyposmia" and "Risk-RBD," respectively; **Supplementary Table 1**). 57 individuals have a positive family history. We performed our experiments in a blinded manner. Cell passaging numbers were within the range of 12–17 which had no influence on the phenotype. Notably, we discovered a unifying impairment in degrading Miro1 at 6 h after CCCP treatment in 25 PD (83.3%) and 36 Risk (genetic carriers) lines (85.7%; **Figure 1C** and **Supplementary Table 1**). By contrast, Miro1 was efficiently removed following depolarization in every single control subject (0%; **Figure 1C** and **Supplementary Table 1**). This phenotype was clearly demonstrated when we imported Miro1 ratio of each individual (Miro1 intensities "with CCCP" divided by "with DMSO") into a heat map. The majority of the PD and at-risk subjects showed high Miro1 ratios whereas all heathy subjects displayed low Miro1 ratios (**Figure 1D**). The frequency of the Miro1 phenotype in iPSCs was significantly higher in

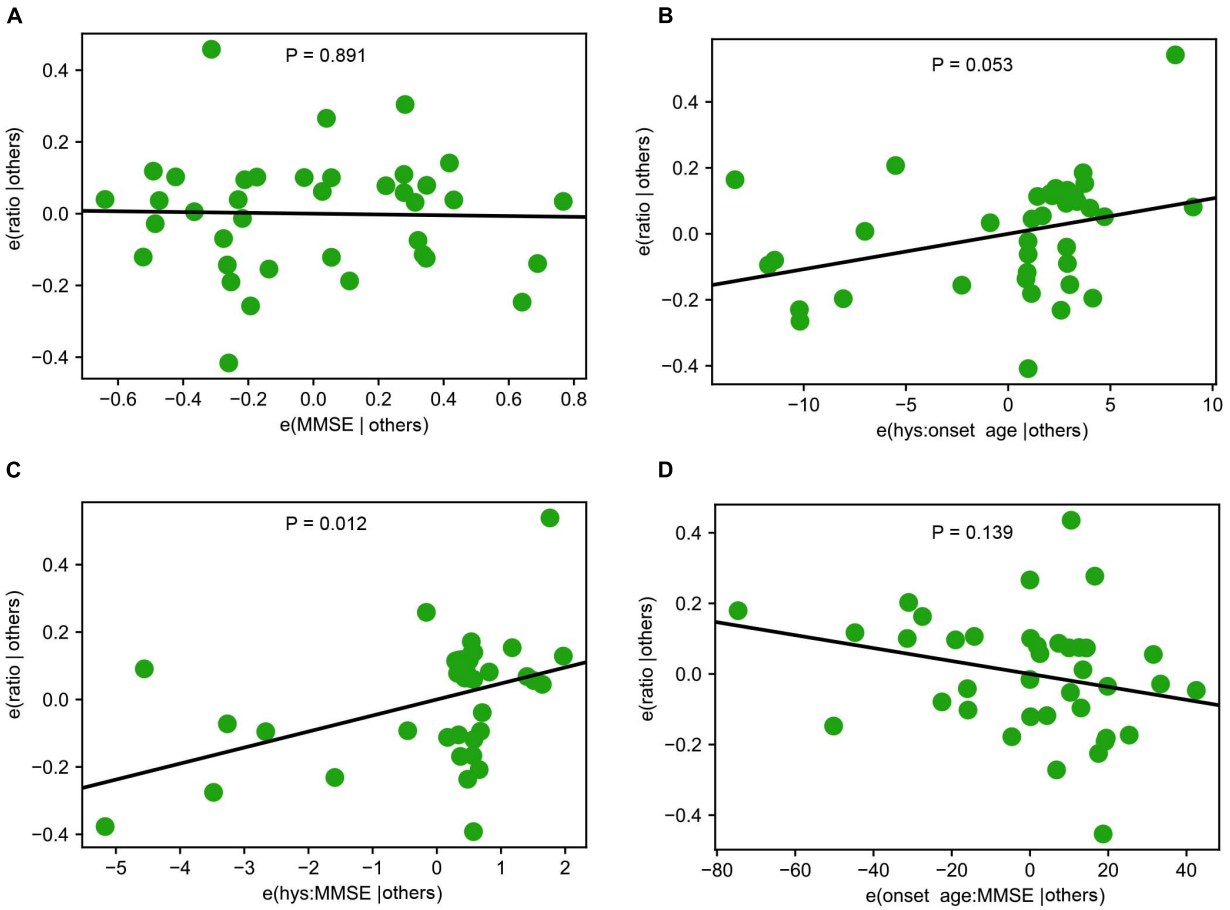

FIGURE 4 | Interactions among Demographic and Clinical Variables. **(A)** A representative partial regression plot shows the influence of a single variable, Mini-Mental Status Examination (MMSE), on Miro1 ratio. **(B–D)** Representative partial regression plots show the interactions of two variables for influencing Miro1 ratio. **(B)** Hoehn and Yahr Scale (hys) and onset age. **(C)** MMSE and hys. **(D)** Onset age and MMSE.

patients and non-manifesting carriers than healthy subjects (**Figure 1C**). Interestingly, at-risk individuals with hyposmia alone failed to show a statistical difference from healthy controls, but individuals who were positive for both *LRRK2* mutations and hyposmia had a significantly higher rate of the Miro1 phenotype (**Figure 1C**). We next validated the results from Western blotting with an alternative method: Enzyme-Linked Immunosorbent Assay (ELISA; Hsieh et al., 2019; **Figures 1E–G**). We examined seven cell lines used in **Figure 1D**. For each individual line, the ELISA result of the Miro1 response to mitochondrial depolarization was consistent with that from Western blotting (**Figures 1D,H** and **Supplementary Table 1**), demonstrating the robustness of both methods for detecting Miro1 in iPSCs. Similarly, we have previously found that both Western blotting and ELISA are reliable for detecting Miro1 in fibroblasts (Hsieh et al., 2019). Therefore, we have established two methods to measure Miro1 in patients' cells which could be useful for clinical practice. Miro1 ratio (Miro1 intensities "with CCCP" divided by "with DMSO") was also significantly correlated with PD and genetic risk (**Figure 2A**), but not with age (at sampling) or sex (**Figures 2B–D**). There were no interactions among age, sex, and genetic background for affecting Miro1 ratio (**Figures 2B–D**). Taken together, these observations show that the failure to remove Miro1 following mitochondrial depolarization is a common cellular defect in this cohort of at-risk individuals.

Comparison of the Miro1 Defect Between PD Patients and At-Risk Individuals

Having assembled a large dataset of the Miro1 marker in both iPSCs (this paper) and fibroblasts (Hsieh et al., 2019) from PD patients and non-manifesting genetic carriers (**Figures 1, 2** and **Supplementary Table 1**; Hsieh et al., 2019), we performed cross-sectional analyses of the overall outcome. We first compared the frequency of the Miro1 defect in total PD patients between this cohort using iPSCs and the previous cohort using fibroblasts (Hsieh et al., 2019), and found that it was largely consistent (83.3% in iPSCs, 94% in fibroblasts). We next examined the frequency in specific subgroups (sample size $\geq$ 5; **Figures 2A, 3A**). The rate of the Miro1 defect was slightly lower in PD patients bearing mutations in *LRRK2* or *GBA* in this cohort using

iPSCs than that in the previous cohort using fibroblasts (iPSCs: 83.3 and 93.3%; fibroblasts: 100 and 100%, for *LRRK2* and *GBA*, respectively). We then compared the occurrence of the Miro1 phenotype in iPSCs from PD patients and asymptomatic genetic carriers harboring mutations in the same gene. Notably, non-manifesting genetic carriers bearing mutations in *LRRK2* or *GBA* showed a similar rate of the Miro1 defect as symptomatic patients carrying mutations in the same gene (carriers: 86.4 and 83.3%; PD: 83.3 and 93.3%, for *LRRK2* and *GBA*, respectively).

Lastly, we examined whether there were interactions among genetic background, demographics, and clinical manifestations of PD patients for influencing the Miro1 phenotype using the Western blotting data from fibroblasts we previously published in Hsieh et al. (2019), given the large sample size of this PD cohort (12 healthy subjects and 71 PD patients). Although each individual variable alone including age, sex, Unified PD Rating Scale, Hoehn and Yahr Scale, and Mini-Mental Status Examination did not affect Miro1 ratio, there was a significant interaction between Hoehn and Yahr Scale and Mini-Mental Status Examination (**Figures 3B–D, 4**), suggesting that Miro1 ratio might respond to PD progression combined with cognitive impairment.

DISCUSSION

The lack of reliable molecular biomarkers for PD hinders the development of an effective treatment. Although the signature symptoms of PD occur late in life in most patients, the underlying molecular changes and neuronal cell death may have started years prior to symptom onset. Therefore, the identification of a molecular marker that defines the pre-symptomatic population will enable more effective therapeutic intervention. In this study, we have explored the mitochondrial protein Miro1 as a common molecular signature for detecting the pre-disease-onset phase of PD. We have discovered a significant association of the Miro1 defect with PD and its risk using iPSCs, mirroring our previous discovery using fibroblasts (Hsieh et al., 2019). Our findings demonstrate the translational value of Miro1 for marking a subset of Parkinson's symptomatic and asymptomatic individuals.

The frequency of the Miro1 marker is comparable between non-manifesting genetic carriers and PD patients with mutations in the same gene (*LRRK2* or *GBA*). Given the incomplete penetrance of these mutations (Healy et al., 2008; Marongiu et al., 2008; Nishioka et al., 2009; Anheim et al., 2012), longitudinal studies will be especially valuable to determine the disease conversion rate of at-risk individuals who test positive for the Miro1 defect. Our analyses also detect an interaction between Hoehn and Yahr Scale and Mini-Mental Status Examination for influencing the Miro1 phenotype in PD patients (**Figure 4**), suggesting that Miro1 could be utilized to monitor PD progression in combination with cognitive impairment. Interestingly, the Miro1 defect occurs in several individuals with hyposmia or RBD. Compared with genetic carriers, the sample sizes for RBD and hyposmia are much smaller, due to the unavailability of sufficient donors. Future work is needed to examine our Miro1 marker in larger cohorts of RBD and hyposmia. It will be similarly beneficial to expand the sample size for genetic carriers and to examine the Miro1 phenotype in additional neurodegenerative diseases. Our work opens new avenues to detecting and treating the disease by using Miro1 as a marker and target, but also raises important questions about the mechanisms underlying the Miro1 impairment in distinct types of PD and the downstream consequences. Our previous work has mechanistically linked depolarization-triggered Miro1 degradation and mitophagy to several PD-causing genes, including *PINK1*, *Parkin*, *LRRK2*, and *SNCA* (Wang et al., 2011; Hsieh et al., 2016, 2019; Shaltouki et al., 2018). Further investigations are warranted to reveal the interplay of Miro1 with additional PD-associated genes such as *GBA*, and the Miro1-dependent pathways in sporadic PD. A systemic characterization of Miro1 protein levels and response to mitochondrial damage with age in heathy and diseased cells will also shed light on Miro1's role in normal and pathological aging.

DATA AVAILABILITY STATEMENT

The original contributions presented in the study are included in the article/ **Supplementary Material**; further inquiries can be directed to the corresponding author/s.

AUTHOR CONTRIBUTIONS

DN, VB, and DC designed and performed the experiments. DN, VB, and PN analyzed the data, made the figures, and wrote the manuscript. XW conceived and supervised the project, designed the experiments, and wrote the manuscript. All authors contributed to the article and approved the submitted version.

FUNDING

This work was funded by the Michael J. Fox Foundation (MJFF, #18195) and Stanford WHSDM Center. PPMI was funded by MJFF and funding partners, including Abbvie, Avid, Biogen, Bristol-Myers Squibb, COVANCE, GE Healthcare, Genentech, GlaxoSmithKline, Lilly, Lundbeck, Merck, Meso Scale Discovery, Pfizer, Piramal, Roche, Servier, and UCB.

ACKNOWLEDGMENTS

We thank the MJFF for providing cell lines and advice, and the Steinberg lab for assistance.

SUPPLEMENTARY MATERIAL

The Supplementary Material for this article can be found online at: https://www.frontiersin.org/articles/10.3389/fnmol.2021.734273/full#supplementary-material

REFERENCES

Anheim, M., Elbaz, A., Lesage, S., Durr, A., Condroyer, C., Viallet, F., et al. (2012). Penetrance of Parkinson disease in glucocerebrosidase gene mutation carriers. *Neurology* 78, 417–420. doi: 10.1212/WNL.0b013e318245f476

Bartels, T. (2016). Conformation-specific detection of alpha-synuclein: the search for a biomarker in Parkinson disease. *JAMA Neurol.* 74, 146–147. doi: 10.1001/jamaneurol.2016.4813

Bonifati, V. (2002). Deciphering Parkinson's disease–PARK8. *Lancet Neurol.* 1:83. doi: 10.1016/s1474-4422(02)00036-4

Cookson, M. R. (2010). The role of leucine-rich repeat kinase 2 (LRRK2) in Parkinson's disease. *Nat. Rev. Neurosci.* 11, 791–797. doi: 10.1038/nrn2935

Dickson, D. W. (2018). Neuropathology of Parkinson disease. *Parkinsonism Relat. Disord.* 46(Suppl. 1), S30–S33. doi: 10.1016/j.parkreldis.2017.07.033

Fang, E. F., Hou, Y., Palikaras, K., Adriaanse, B. A., Kerr, J. S., Yang, B., et al. (2019). Mitophagy inhibits amyloid-beta and tau pathology and reverses cognitive deficits in models of Alzheimer's disease. *Nat. Neurosci.* 22, 401–412. doi: 10.1038/s41593-018-0332-9

Fransson, S., Ruusala, A., and Aspenstrom, P. (2006). The atypical Rho GTPases Miro-1 and Miro-2 have essential roles in mitochondrial trafficking. *Biochem. Biophys. Res. Commun.* 344, 500–510. doi: 10.1016/j.bbrc.2006.03.163

Guo, X., Macleod, G. T., Wellington, A., Hu, F., Panchumarthi, S., Schoenfield, M., et al. (2005). The GTPase dMiro is required for axonal transport of mitochondria to *Drosophila* synapses. *Neuron* 47, 379–393. doi: 10.1016/j.neuron.2005.06.027

Healy, D. G., Falchi, M., O'Sullivan, S. S., Bonifati, V., Durr, A., Bressman, S., et al. (2008). Phenotype, genotype, and worldwide genetic penetrance of LRRK2-associated Parkinson's disease: a case-control study. *Lancet Neurol.* 7, 583–590. doi: 10.1016/S1474-4422(08)70117-0

Hsieh, C. H., Li, L., Vanhauwaert, R., Nguyen, K. T., Davis, M. D., Bu, G., et al. (2019). Miro1 marks Parkinson's disease subset and miro1 reducer rescues neuron loss in Parkinson's models. *Cell Metab.* 30, 1131–1140.e7. doi: 10.1016/j.cmet.2019.08.023

Hsieh, C. H., Shaltouki, A., Gonzalez, A. E., Bettencourt da Cruz, A., Burbulla, L. F., St Lawrence, E., et al. (2016). Functional impairment in miro degradation and mitophagy is a shared feature in familial and sporadic Parkinson's disease. *Cell Stem Cell* 19, 709–724. doi: 10.1016/j.stem.2016.08.002

Kitada, T., Asakawa, S., Hattori, N., Matsumine, H., Yamamura, Y., Minoshima, S., et al. (1998). Mutations in the parkin gene cause autosomal recessive juvenile parkinsonism. *Nature* 392, 605–608. doi: 10.1038/33416

Lautrup, S., Sinclair, D. A., Mattson, M. P., and Fang, E. F. (2019). NAD(+) in brain aging and neurodegenerative disorders. *Cell Metab.* 30, 630–655. doi: 10.1016/j.cmet.2019.09.001

Marongiu, R., Ferraris, A., Ialongo, T., Michiorri, S., Soleti, F., Ferrari, F., et al. (2008). PINK1 heterozygous rare variants: prevalence, significance and phenotypic spectrum. *Hum. Mutat.* 29:565. doi: 10.1002/humu.20719

Nishioka, K., Ross, O. A., Ishii, K., Kachergus, J. M., Ishiwata, K., Kitagawa, M., et al. (2009). Expanding the clinical phenotype of SNCA duplication carriers. *Mov. Disord.* 24, 1811–1819. doi: 10.1002/mds.22682

Parkinson Progression Marker Initiative (2011). The Parkinson progression marker initiative (PPMI). *Prog. Neurobiol.* 95, 629–635. doi: 10.1016/j.pneurobio.2011.09.005

Pickrell, A. M., and Youle, R. J. (2015). The roles of PINK1, parkin, and mitochondrial fidelity in Parkinson's disease. *Neuron* 85, 257–273. doi: 10.1016/j.neuron.2014.12.007

Shaltouki, A., Hsieh, C. H., Kim, M. J., and Wang, X. (2018). Alpha-synuclein delays mitophagy and targeting Miro rescues neuron loss in Parkinson's models. *Acta Neuropathol.* 136, 607–620. doi: 10.1007/s00401-018-1873-4

Valente, E. M., Abou-Sleiman, P. M., Caputo, V., Muqit, M. M., Harvey, K., Gispert, S., et al. (2004). Hereditary early-onset Parkinson's disease caused by mutations in PINK1. *Science* 304, 1158–1160. doi: 10.1126/science.1096284

Wang, X., and Schwarz, T. L. (2009). The mechanism of Ca2+ -dependent regulation of kinesin-mediated mitochondrial motility. *Cell* 136, 163–174. doi: 10.1016/j.cell.2008.11.046

Wang, X., Winter, D., Ashrafi, G., Schlehe, J., Wong, Y. L., Selkoe, D., et al. (2011). PINK1 and Parkin target Miro for phosphorylation and degradation to arrest mitochondrial motility. *Cell* 147, 893–906. doi: 10.1016/j.cell.2011.10.018

Zimprich, A., Biskup, S., Leitner, P., Lichtner, P., Farrer, M., Lincoln, S., et al. (2004). Mutations in LRRK2 cause autosomal-dominant parkinsonism with pleomorphic pathology. *Neuron* 44, 601–607. doi: 10.1016/j.neuron.2004.11.005

Conflict of Interest: PN is employed by Colaberry Inc. XW is a co-founder, adviser, and shareholder of AcureX Therapeutics Inc, and a shareholder of Mitokinin Inc.

The remaining authors declare that the research was conducted in the absence of any commercial or financial relationships that could be construed as a potential conflict of interest.

Publisher's Note: All claims expressed in this article are solely those of the authors and do not necessarily represent those of their affiliated organizations, or those of the publisher, the editors and the reviewers. Any product that may be evaluated in this article, or claim that may be made by its manufacturer, is not guaranteed or endorsed by the publisher.

Copyright © 2021 Nguyen, Bharat, Conradson, Nandakishore and Wang. This is an open-access article distributed under the terms of the Creative Commons Attribution License (CC BY). The use, distribution or reproduction in other forums is permitted, provided the original author(s) and the copyright owner(s) are credited and that the original publication in this journal is cited, in accordance with accepted academic practice. No use, distribution or reproduction is permitted which does not comply with these terms.

frontiers in Aging Neuroscience

ORIGINAL RESEARCH
published: 01 September 2021
doi: 10.3389/fnagi.2021.721171

Amyloid-Beta Influences Memory *via* Functional Connectivity During Memory Retrieval in Alzheimer's Disease

Binyin Li[1†], Miao Zhang[2†], Ikbeom Jang[3,4], Guanyu Ye[1], Liche Zhou[1], Guiying He[1], Xiaozhu Lin[2], Hongping Meng[2], Xinyun Huang[2], Wangxi Hai[2], Shengdi Chen[1], Biao Li[2,5] and Jun Liu[1]**

[1] Department of Neurology and Institute of Neurology, Ruijin Hospital, Shanghai Jiao Tong University School of Medicine, Shanghai, China, [2] Department of Nuclear Medicine, Ruijin Hospital, Shanghai Jiao Tong University School of Medicine, Shanghai, China, [3] MGH/MIT/HMS Athinoula A. Martinos Center for Biomedical Imaging, Massachusetts General Hospital, Boston, MA, United States, [4] Department of Radiology, Harvard Medical School, Boston, MA, United States, [5] Collaborative Innovation Center for Molecular Imaging of Precision Medicine, Ruijin Center, Shanghai, China

Objective: Amnesia in Alzheimer's disease (AD) appears early and could be caused by encoding deficiency, consolidation dysfunction, and/or impairment in the retrieval of stored memory information. The relationship between AD pathology biomarker β-amyloid and memory dysfunction is unclear.

Method: The memory task functional MRI and amyloid PET were simultaneously performed to investigate the relationship between memory performance, memory phase-related functional connectivity, and cortical β-amyloid deposition. We clustered functional networks during memory maintenance and compared network connectivity between groups in each memory phase. Mediation analysis was performed to investigate the mediator between β-amyloid and related cognitive performance.

Results: Alzheimer's disease was primarily characterized by decreased functional connectivity in a data-driven network composed of an *a priori* default mode network, limbic network, and frontoparietal network during the memory maintenance (0.205 vs. 0.236, $p = 0.04$) and retrieval phase (0.159 vs. 0.183, $p = 0.017$). Within the network, AD had more regions with reduced connectivity during the retrieval than the maintenance and encoding phases (chi-square $p = 0.01$ and < 0.001). Furthermore, the global cortical β-amyloid negatively correlated with network connectivity during the memory retrieval phase ($R = -0.247$, $p = 0.032$), with this relationship mediating the effect of cortical β-amyloid on memory performance (average causal mediation effect = −0.05, $p = 0.035$).

Conclusion: We demonstrated that AD had decreased connectivity in specific networks during the memory retrieval phase. Impaired functional connectivity during memory retrieval mediated the adverse effect of β-amyloid on memory. These findings help to elucidate the involvement of cortical β-amyloid (Aβ) in the memory performance in the early stages of AD.

Keywords: amyloid, magnetic resonance imaging, Alzheimer disease, memory, neural connectivity

OPEN ACCESS

Edited by:
Kuangyu Shi,
University of Bern, Switzerland

Reviewed by:
Wang Min,
Shanghai University, China
Valentina Echeverria Moran,
Bay Pines VA Healthcare System, United States

***Correspondence:**
Biao Li
lb10363@rjh.com.cn
Jun Liu
jly0520@hotmail.com

[†] These authors contributed equally to this work

Received: *06 June 2021*
Accepted: *05 August 2021*
Published: *01 September 2021*

Citation:
Li B, Zhang M, Jang I, Ye G, Zhou L, He G, Lin X, Meng H, Huang X, Hai W, Chen S, Li B and Liu J (2021) Amyloid-Beta Influences Memory via Functional Connectivity During Memory Retrieval in Alzheimer's Disease. Front. Aging Neurosci. 13:721171. doi: 10.3389/fnagi.2021.721171

INTRODUCTION

Alzheimer's disease is marked by prominent memory deficiency in the early stage. It is controversial whether the observed amnesia is due to disrupted encoding, the consolidation of episodic information, or an impairment in the retrieval of stored memory information. Several studies have suggested that the ineffective encoding of new information in the brain triggers episodic memory deficits (Pasquier et al., 2001; Weintraub et al., 2012), while more evidence supported a retrieval deficit in early Alzheimer's disease (AD) (Grober and Kawas, 1997; Albert et al., 2001; Li et al., 2016). Transgenic AD mouse models also suggested that the direct activation of hippocampal memory engram cells resulted in memory retrieval, revealing a major impairment of retrieval, rather than storage, in early AD (Roy et al., 2016).

Many studies have been conducted to show that memory is retrieved by neural networks (Palm, 2013). The integration between neural networks supports autobiographic memory retrieval, with network connectivity increasing when memories are accessible and recollected (St Jacques et al., 2011). In AD, the inability to encode and retrieve memory is present at the earliest stage of the disease and deteriorates throughout the course of the disease (Aggarwal et al., 2005). The aggregated β-amyloid (Aβ), which accumulates as the first pathological marker of AD, was involved in neural network dysfunction (Palmqvist et al., 2017). Clinically, episodic memory processing-related medial temporal lobe activation was negatively associated with higher global Aβ levels (Mormino et al., 2012; Vannini et al., 2012).

Together, these findings suggest that Aβ pathology might exert an influence on neural network dysfunction, and this disruption causes worse memory performance in AD. However, this hypothesis has not been tested in humans. To address this caveat in the literature, detailed alterations in cortical connectivity networks during different memory phases (encoding, maintenance, and retrieval) in 36 patients with AD and 36 normal participants by task functional MRI (fMRI) were characterized. Simultaneously, cortical Aβ deposition were measured using PET. The level of Aβ pathology in the cortex was evaluated for its effect on memory-related cortical functional networks. To assess the clinical relevance of the observed functional alterations, the Aβ pathologies were related to measures of memory performance.

Our primary hypothesis was that AD functional connectivity changed within specific cortical networks during memory retrieval. With this, the cortical Aβ deposition would correlate with the functional connectivity, and this relationship would mediate the influence of cortical Aβ on memory performance. The findings would further our understanding of the mechanisms underlying memory deficiency in AD and the effect of Aβ pathology on memory-related functional neural networks.

MATERIALS AND METHODS

Participants

In the cohort recruitment, AD was diagnosed using the syndromal categorical cognitive staging scheme and positive amyloid deposition by PET, based on the National Institute on Aging-Alzheimer's Association workgroups (Jack et al., 2018). According to cognitive status, neuro psychologic test performance, and Aβ positivity determined by an agreement between one nuclear medicine specialist and one memory-disorder specialist, 36 Aβ positive (Aβ+) AD participants and 36 Aβ negative (Aβ-) normal controls were included in this study.

All participants underwent neuropsychological tests that included the Mini-Mental State Examination (MMSE, Chinese Version) (Katzman et al., 1988), global clinical dementia rating (CDR > 0.5 for AD diagnosis), Zung Self-rating Anxiety Scale, Self-rating Depression scale, Activities of Daily Living questionnaire (for caregivers), the Beijing version of the Montreal Cognitive Assessment (MoCA), and the Chinese version of Addenbrooke's Cognitive Examination-Revised (ACER) with subtests of memory, language, attention, fluency, and visual-spatial processing (Fang et al., 2014).

The present study was approved by the Ethics Committee (internal review board) of the Shanghai Jiao Tong University-affiliated Ruijin Hospital, China. According to the Declaration of Helsinki, all participants in the study or their caregivers signed written informed consent before being included.

Task Design in fMRI

The task used an event-related design, with a total of 34 encoding objects and 56 retrieval objects (**Figure 1**). During the encoding phase, the participants studied 34 unique objects (with a 3 × 3 degree visual angle), which were presented in pairs and had 2–6 randomized interstimulus intervals. In the following 2-min maintenance phase, the screen was blank and no stimulus was presented. Then, in the retrieval phase, there were 56 test trials that presented objects with the same visual angle. The objects were presented sequentially, followed by 2- to 6-s interstimulus intervals. The participants were asked to judge whether the objects were "old" (studied) or "new" (unstudied). The participants had up to 4 s to respond. Among these trials, half presented old (studied) objects and half presented new (unstudied) objects. Task accuracy was defined as the percentage of the correct answer in 56 recognition objects.

The participants viewed an MRI-compatible display monitor *via* a mirror mounted to the head coil. All responses were recorded by an MRI-compatible optical mouse. The order of object presentation was randomized across all participants. The duration of the task slightly varied from 11 to 13 min because of the interstimulus interval randomization and different reaction times.

Acquisition of MR and PET Images

The MRI data were acquired on a whole-body PET–MR scanner (Biograph mMR; Siemens Healthcare, Erlangen, Germany).

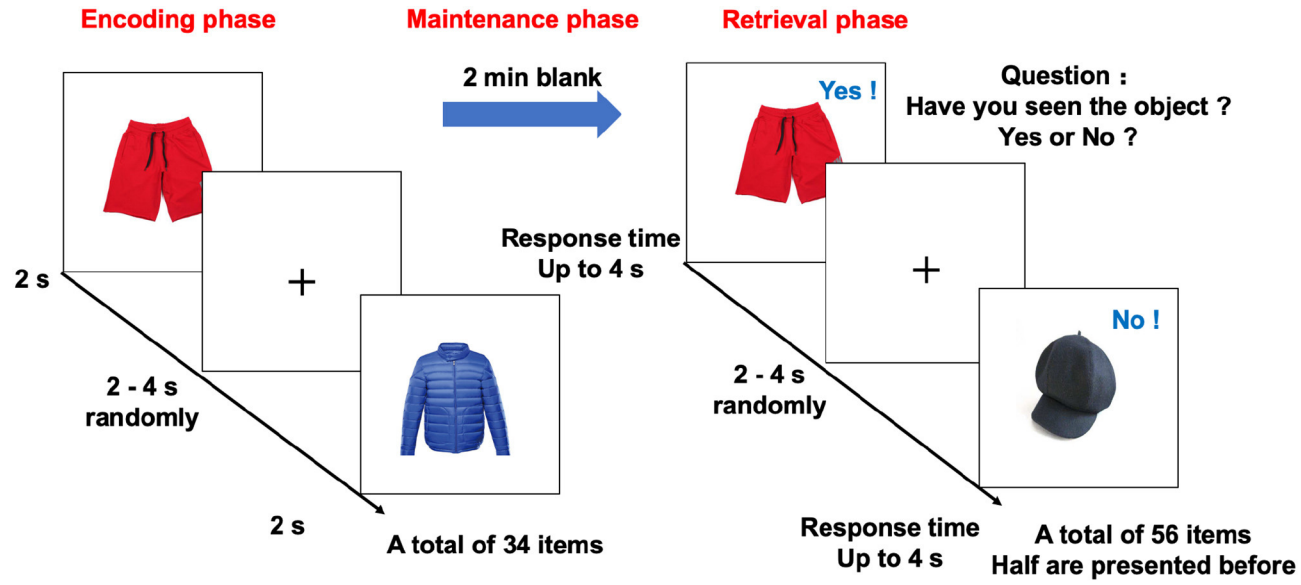

FIGURE 1 | Design of the memory task in the fMRI study. The memory task in the fMRI study, included encoding, blank (memory maintenance), and retrieval phases. In the encoding phase, 34 objects were sequentially presented for 2 s. After a 2-min blank, the participants indicated whether the object was present or absent in the encoding phase as quickly as possible using two buttons of an MR-compatible button box. During retrieval, each object appeared on the screen until there was a response or up to 4 s before the next letter was shown. The inter-object interval was randomly set between 2 and 4 s. fMRI, functional magnetic resonance imaging.

Blood oxygen level-dependent (BOLD) MRIs using echo-planar imaging weighted sequence were performed during the tasks (260 functional images, 3,000-ms repetition time, 30-ms echo time, matrix = 64 × 64, a 90° flip angle, 35 slices, no slice gap, and a voxel size of 3 × 3 × 3.75 mm^3). The T1-weighted three-dimensional structural image was acquired with TR = 1,900 ms, TE = 2.44 ms, and 192 slices covering the whole brain.

The PET scans were performed simultaneously using an ^{18}F florbetapir (AV45) tracer to image Aβ. The participants received an intravenous injection of AV45 at a mean dose of 3.7 MBq/kg body weight after finishing the task fMRI. Then, static AV45-PET data were acquired in sinogram mode 50 min after injection using the following parameters: 128 slices (gap, 0.5 mm) covering the whole brain, a matrix size of 344 × 344, a voxel size of 2.6 × 2.6 × 3.1 mm^3, reconstructed with high-definition PET (21 subsets, 4 iterations), and post-filtered with an isotropic full-width half-maximum (FWHM) Gaussian kernel of 2 mm. The attenuation correction for PET was performed using MR-based attenuation maps derived from a dual-echo Dixon-based sequence.

An automatic pipeline was employed to extract cortical standardized uptake value ratios (SUVRs) by PETSurfer FreeSurfer 6.0 (https://surfer.nmr.mgh.harvard.edu/fswiki/PetSurfer) using the cerebellum cortex as the reference region. In detail, structural T1 images were used to create a high-resolution segmentation using the Schaefer function atlas (Schaefer et al., 2018) to run the partial volume correction (PVC) methods. The PET/anatomical image registration was then performed and visually checked. To minimize the partial volume effect from cortical atrophy in AD, the extended Muller–Gartner method as a PVC method (Müller-Gärtner et al., 1992; Greve et al., 2016) was applied. Surface-based SUVR maps were smoothed on the two-dimensional surface by a Gaussian kernel of 5 mm in FWHM.

fMRI Activation Analysis: Standard Univariate Analysis

Functional and T1 MRI data were pre-processed by Freesurfer v6.0 and FsFast v5.0 (surfer.nmr.mgh.harvard.edu). The pre-processing pipeline for fMRI included templating from the middle time point of raw functional data, masking, functional-anatomical registration, motion correction, slice-timing, and resampling the raw time courses to the left and right hemispheres. Quality control of functional-anatomical registration was performed by both the automatic rating from Freesurfer and visual inspection. Two-dimensional spatial smoothing was performed for surface data with a Gaussian kernel of 5 mm in FWHM.

The encoding and retrieval phases were evaluated separately using a surface-based stream. For the first-level general linear model (GLM) analysis (within-subject), contrasts (encoding stimulus against interstimulus rest and recognition stimulus against interstimulus rest) were calculated by the gamma hemodynamic response function within the cortical surface at each voxel. Each case was inspected after the first-level analysis by visualization to ensure that they registered well with the FreeSurfer average surface (common space). All cases were concatenated for further analysis.

In the second level (between-subject) analysis, task accuracy-related activation maps were generated in all participants by GLM with task accuracy as a regressor. Significant clusters were

TABLE 1 | Demographic and clinical characteristics.

	AD	Control	P
Number	36	36	
Sex (M/F)	17/19	15/21	0.232
Age	68.78 ± 7.63	69.05 ± 7.11	0.778
Education	12.08 ± 2.53	13.27 ± 2.83	0.076
MMSE	19.88 ± 5.49	28.05 ± 1.86	< 0.001
MoCA	15.36 ± 6.71	26.54 ± 2.41	< 0.001
ACER	56.50 ± 18.8	89.30 ± 6.73	< 0.001
Attention	11.61 ± 3.81	17.02 ± 1.13	< 0.001
Memory	15.42 ± 4.92	21.61 ± 3.73	< 0.001
Fluency	6.19 ± 3.38	10.11 ± 2.15	< 0.001
Language	19.00 ± 5.74	24.97 ± 1.68	< 0.001
Visuospatial	11.13 ± 4.69	15.72 ± 0.55	< 0.001
Task accuracy	0.23 ± 0.09	0.62 ± 0.38	< 0.001
Cortical thickness	2.28 ± 0.15	2.39 ± 0.11	< 0.001

Data are expressed as the mean ± standard deviation. A two-sample independent permutation t-test was conducted to test between-group differences. The chi-square test was used for categorical variables. ACER, Addenbrooke's Cognitive Examination-Revised; MoCA, Montreal Cognitive Assessment.

computed after permutation resampling by bootstrapped Monte Carlo simulations (10,000 iterations) at $p = 0.001$ to correct for multiple comparisons across all brain voxels. Finally, we collected clusters of that size or larger during the simulation and corrected them to a threshold of $p < 0.05$ (Greve and Fischl, 2018). The coefficients of activation were extracted after mapping on the native surface using an inverse affine transform for further analysis.

Memory Phase-Related Time Courses

We re-preprocessed the fMRI by the pipeline implemented in the CONN toolbox (version19.c) (https://www.nitrc.org/projects/conn) within MATLAB, similar to a previous study (Nour et al., 2019). This pre-processing included slice timing correction, the realignment of functional scans and normalization to MNI space, and spatial smoothing (Gaussian kernel of 8 mm in FWHM). In the denoising step, linear regression was used to remove the influence from (1) the BOLD signal from the white matter and CSF voxels (five components each, derived using the anatomical component-based correction implemented using the ART toolbox), (2) six residual head motion parameters and their first order temporal derivatives, (3) the scrubbing of artifact or outlier scans, and (4) the effect of task-condition using event regressors (encoding and retrieval stimulus) convolved with the hemodynamic response function. Finally, the de-noising step included temporal bandpass filtering (0.008–0.09 Hz) and the linear de-trending of the time courses.

Following pre-processing, the whole BOLD time courses were split into three memory phases (encoding, maintenance, and retrieval) for each participant and then extracted individual mean time courses within 200 cortical nodes, which were defined by the Schaefer function atlas (Schaefer et al., 2018). The 200 nodes can be assigned to seven *a priori* functional networks, namely, the visual network, somatomotor network, dorsal attention network (DAN), ventral attention network (VAN), limbic network, frontoparietal network (FPN), and default mode network (DMN).

Data-Driven Detection of Empirical Networks

The functional connectivity between two brain regions (nodes) was defined as the Fisher z-transformed Pearson's correlation coefficient between the mean BOLD time course in each region (Rubinov and Sporns, 2010). The functional connectivity in the maintenance phase from the control group was used to generate an undirected weighted covariance matrix, C, where c_{ij} represents the functional connectivity between nodes i and j (i.e., edge strength between nodes). After setting negative weights to 0, the Louvain algorithm (implemented in the MATLAB Brain Connectivity Toolbox, https://sites.google.com/site/bctnet/) was used to get the control group-level empirical networks (Bostanciklioglu, 2020) in the maintenance phase (see **Supplementary Material**).

The community detection analysis was restricted to the 136 nodes allocated to the limbic network, DMN, DAN, VAN, and FPN suggested by a previous cognition study (Nour et al., 2019). Given the stochastic nature of the Louvain algorithm, a consensus clustering approach was used to ensure the robustness of the final community structure by the Agreement and Consensus functions in the Brain Connectivity Toolbox (Blondel et al., 2008, Cohen and D'Esposito, 2016, Hearne et al., 2017) (see **Supplementary Material** for details). Finally, these nodes were clustered into three new empirical networks from controls.

Empirical Network Connectivity Comparison in Each Memory Phase

The network component analysis was performed using a node-wise connectivity comparison between the networks, which showed group differences in the mean functional connectivity. For functional connectivity in each phase, it entered into a group analysis that gauged the differences in AD and controls using codes similar to the NBS (v1.2) algorithm (Zalesky et al., 2010). Different from the traditional NBS, all the t-values of the links were calculated in a general linear model after regressing out age and sex (Berron et al., 2020). Applying a two-sided suprathreshold, the differences in node–node functional connectivity between two groups were visualized as binary outcomes in each memory phase in the BrainNet viewer (Xia et al., 2013).

The BOLD information content was also gauged using an entropy measure for discrete-time courses called sample entropy (Richman and Moorman, 2000) (setting embedding dimension m = 2 and the range in standard deviation from all-time courses). The measure should be higher for time courses with lower predictability and random disorder and conversely reduced for more ordered and predictable time courses (Yao et al., 2013).

Statistical Analyses

Statistical analyses were performed by R (Version 3.6.2). The AD and controls were compared using an independent t-test or

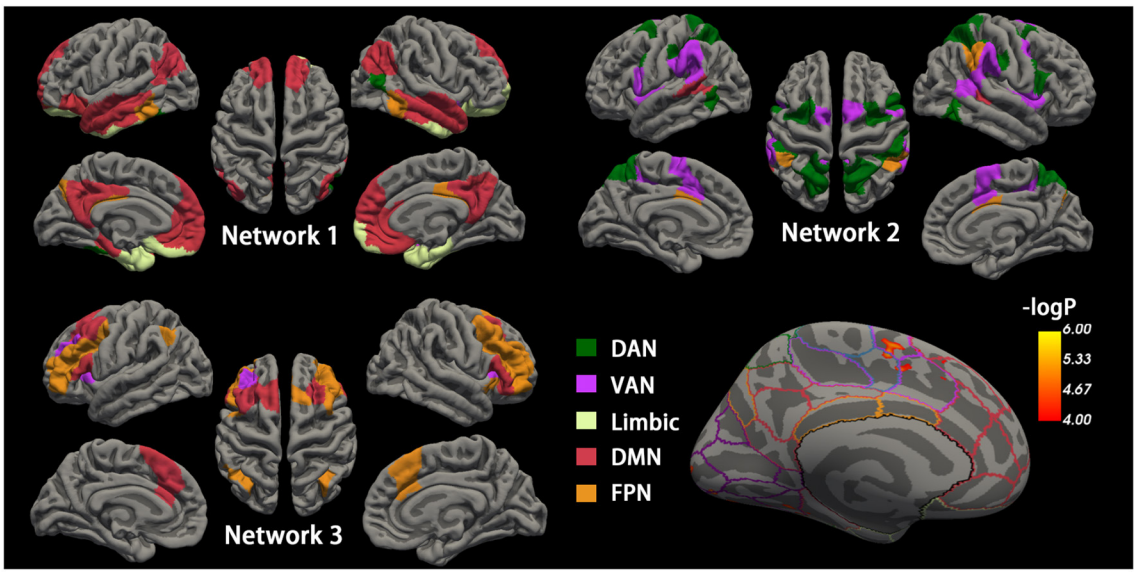

FIGURE 2 | Cortical networks during the maintenance phase and accuracy-related neural activation. Top-left, top-right, and bottom-left cortical mappings illustrated the nodes of the three empirical networks identified by the community detection algorithm during the maintenance phase, colored by *a priori* network assignments from the Schaefer cortical parcellation. Network 1 is mainly composed of the DMN and limbic network, and Network 2 consists of DMN and FPN. Network 3 generally includes DAN and VAN. The bottom right shows the surface maps of the activated cortex in the retrieval phases related to accuracy. The border on the surface indicates the network identical to the above Schaefer cortical parcellation. The activation is observed in the region of VAN. DMN, default mode network; FPN, frontoparietal network; DAN, dorsal attention network; VAN, ventral attention network.

chi-square test for continuous or nominal variables, respectively. Pearson's correlation was used to test the relationships between connectivity in each phase and cortical Aβ SUVR. All significant results were double-checked by the *RVAideMemoire* package in R, performing a resampling test with 10,000 permutations.

To explore the effect of Aβ on cognition, General Linear Regressions was further used to set network connectivity and cortical amyloid as predictors of cognitive performance, adjusted for age, education, and sex. The hypothesis that cortical Aβ influenced memory performance was tested *via* modulating network connectivity by a mediation analysis using the "mediation" package in R, implementing a non-parametric bootstrap method with bias-corrected and accelerated confidence intervals and 10,000 simulation draws.

All tests were two-tailed, and values of corrected $p < 0.05$ were considered statistically significant unless specified otherwise. **Supplementary Figure 1** summarizes our analysis approach.

RESULTS

Participants and Task-Related Activation

A total of 36 AD and 36 normal controls satisfied the criteria and were included. The two groups were matched in age, education, and sex (**Table 1**), and AD had worse cognitive performance in all cognitive domains assessed by the MMSE, MoCA, and ACER, as expected. In the fMRI memory task, the AD group had lower accuracy than the control group. Furthermore, task accuracy had significant correlations with the MoCA ($R = 0.61$, $p < 0.001$), ACER ($R = 0.652$, $p < 0.001$), and ACER memory scores ($R = 0.696$, $p < 0.001$).

As expected, in the standard fMRI GLM analysis, there were widespread activations associated with task accuracy in the visual, frontoparietal, and attention networks of the left hemisphere during memory retrieval (voxel-wise $p < 0.001$ and cluster-wise corrected $p < 0.05$ after correction by randomized permutation simulator). Besides the visual network, the most prominent activation was in the left superior frontal cortex (Talairach Montreal Neurological Institute coordinates: −5.8, −7.8, 53.5; $p = 0.001$, activation $\beta = 5.429$, lower right in **Figure 2**). It was located in the ventral attention network, and mainly correlated with ACER memory ($R = 0.435$, $p < 0.001$), ACER ($R = 0.348$, $p < 0.001$), and MoCA ($R = 0.373$, $p < 0.001$). In contrast, in the encoding phase, there was no significant linear or quadratic relationship between neural activation and task accuracy in the second-level voxel-wise analysis.

Empirical Networks From *a priori* Network Assignments

To investigate memory phase-related functional connectivity changes within task-relevant cortical networks, a data-driven community detection algorithm (Blondel et al., 2008, Lancichinetti and Fortunato, 2012) was first used to partition the 200 cortical nodes into three group-level networks: Network 1 consisting of 56 nodes, Network 2 with 50 nodes, and Network 3 with 30 nodes (**Figure 2**). All three empirical networks were visually symmetrical in the cortex. The "empirical" Network 1 node assignments overlapped with the *a priori* network

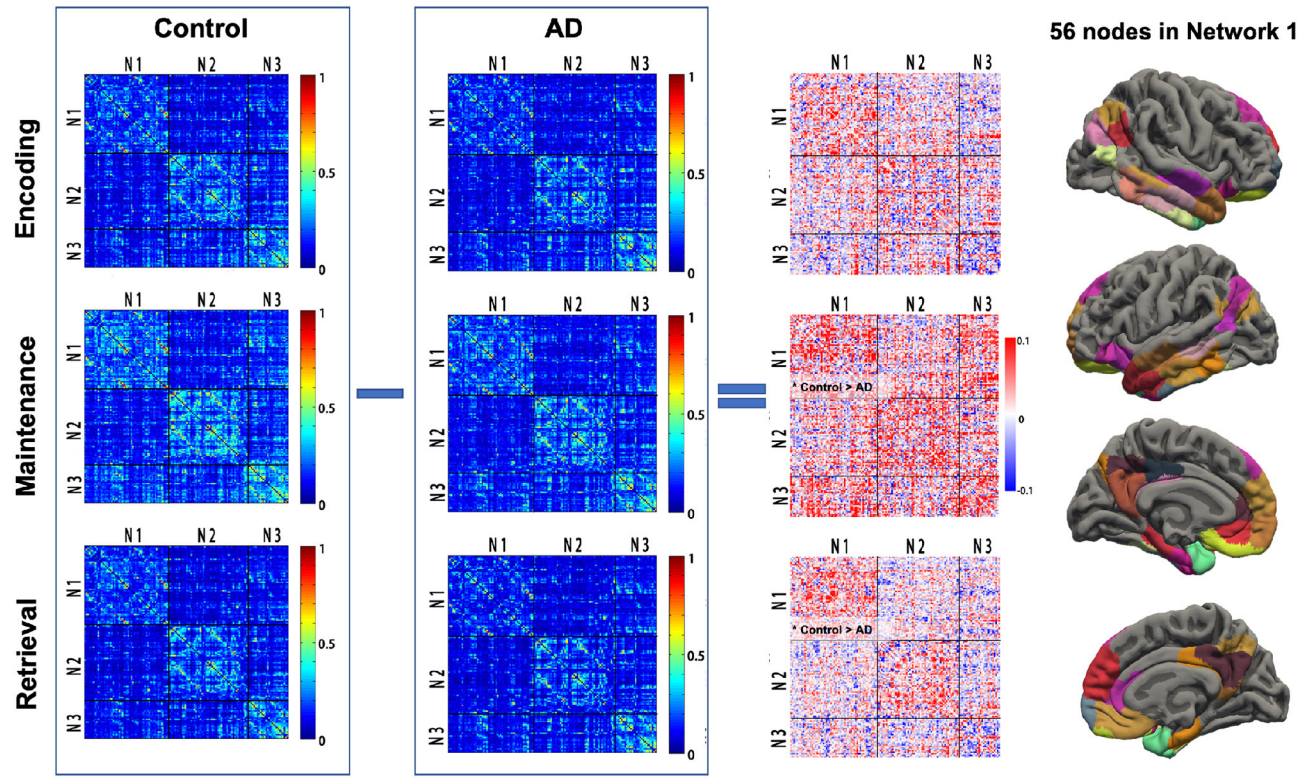

FIGURE 3 | Task phase-related functional connectivity in AD and controls. The first and second columns: averaged functional connectivity (FC) matrices in each task phase of controls and AD. Each cell of the matrix represents the FC strength (Fisher *z*-transformed *r*-value) between the cortical nodes. The third column: The difference of FC (control—AD) in each task phase between AD and controls. Black lines indicate the boundary separating nodes allocated to the empirical Networks 1–3. The fourth column illustrated the 56 cortex nodes in Network 1. *Control > AD, significantly reduced mean FC in the Network 1-Network 1 matrix in AD; AD, Alzheimer's disease; N1, Network 1; N2, Network 2; N3, Network 3.

assignments from the Schaefer functional atlas in DMN, limbic network, and FPN. Network 2 mainly overlapped with the dorsal and ventral attention networks and the spatial activation maps from the standard fMRI activation analysis. Network 3 generally included regions assigned to FPN and its adjacent DMN regions.

For each participant, the phase-related functional connectivity was defined as the connectivity between two nodes during the phase. Thus, each participant had three connectivity matrices within each network and three matrices between networks (i.e., Network 1–Network 2, Network 2–Network 3, Network 1–Network 3). The mean matrices for the AD and control group are shown in **Figure 3**.

Connectivity Within Network 1 Is Reduced in AD

The group difference of the mean functional connectivity within the three empirical networks between the AD and controls was first investigated. The AD group had significantly reduced connectivity within Network 1 during maintenance (0.205 vs. 0.236, $p = 0.04$) and retrieval (0.159 vs. 0.183, $p = 0.017$). No difference in functional connectivity within Network 1 was observed in the encoding phase. The specificity of group differences was investigated in two additional analyses, where, first, there was no solid group difference in the mean functional connectivity during each memory phase in Network 2 ($p = 0.081$, 0.088, and 0.449 for encoding, maintenance, and retrieval, respectively) and Network 3 ($p = 0.073$, 0.914, and 0.934 for encoding, maintenance and retrieval, respectively). Second, the mean connectivity between the networks (Network 1 and Network 2, Network 2 and Network 3, Network 1 and Network 3) in each memory phase was not different between AD and controls either (all $p > 0.250$, **Figure 3**).

AD Had More Nodes With Reduced Connectivity in Network 1 During Retrieval

As decreased mean connectivity was found within Network 1 of the AD group during retrieval, node-wise functional connectivity was further compared between AD and controls during encoding, maintenance, and retrieval in Network 1. In AD, during the retrieval phase, 29 in 56 nodes were found to have significantly reduced links (32 edges), and they were located in the medial prefrontal cortex, posterior cingulate cortex, middle temporal and inferior parietal cortex of the left hemisphere, and the inferior temporal and medial prefrontal cortex of right hemisphere. The majority of nodes with reduced connectivity were assigned to DMN (yellow nodes in **Figure 4**), followed by

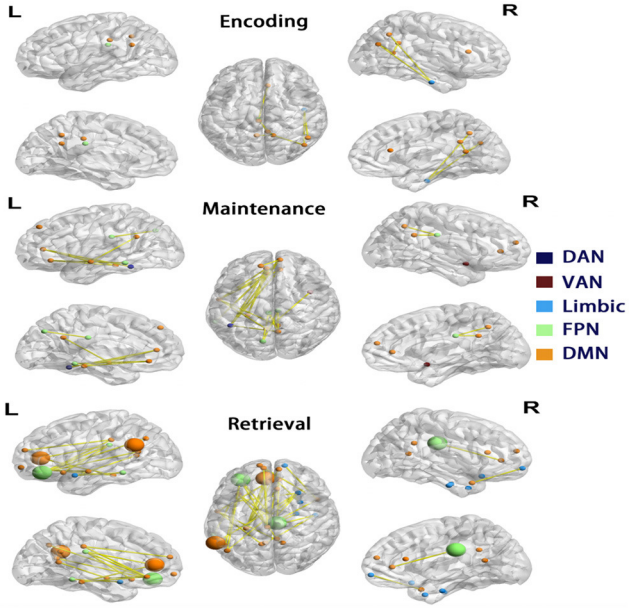

FIGURE 4 | Differences in functional connectivity of Network 1. Each row showed nodes with significantly reduced connectivity in AD compared to controls in each phase, visualized by BrainNet Viewer (Xia et al., 2013). The nodes are colored by the a priori network assignments in the Schaefer atlas. Larger sized nodes indicate significant decreased functional entropy in the AD, as well as decreased functional connectivity. DMN, default mode network; FPN, frontoparietal network; DAN, dorsal attention network; VAN, ventral attention network.

the limbic network and FPN (blue and green nodes in **Figure 4**). In the maintenance phase, fewer (16 in 56) nodes were found with reduced links (21 edges) in AD (chi-square $p = 0.01$, compared to the retrieval phase). The reduced connectivity had a similar pattern to that in the retrieval phase, predominantly in the DMN of the left hemisphere. During encoding, only 10 nodes with 9 reduced links in AD (Chi-Square $p < 0.001$, compared with the retrieval phase; $p = 0.179$ compared with the maintenance phase, **Figure 4**) was observed.

To elucidate the nature of the reduced connectivity in AD, entropy as a measure of BOLD time course predictability (Yao et al., 2013) was investigated in each phase. The AD showed reduced entropy in five nodes (temporal pole, olfactory cortex, medial prefrontal cortex, and inferior prefrontal cortex in the left and cingulate cortex in the right hemisphere) during the retrieval phase, which were all in Network 1 (of these, four nodes had reduced functional connectivity in AD, shown as larger nodes in **Figure 4**). The results indicated that decreased functional connectivity appeared to be partially characterized by more regular and predictable BOLD time courses in AD during the retrieval phase.

Relationship Between Cortical Aβ, Network 1 Connectivity, and Cognition

Across the two groups, there was a negative relationship between global cortical Aβ and the mean connectivity within Network 1 [$R = -0.247$, 95% confidential interval: (-0.453, -0.016), $p = 0.032$] during the retrieval phase. The relationship between Aβ and the mean connectivity during encoding or maintenance was not significant ($R = -0.113$, $p = 0.336$; $R = -0.142$, $p = 0.228$). Only the cortical Aβ had a robust adverse impact on Network 1 connectivity. There was no significant relationship between cortical Aβ and the mean connectivity within Network 2 or Network 3 in any of the memory phases (**Figure 5**). However, in the AD group, significant relationships between global cortical Aβ and the mean connectivity were not observed within Network 1 ($p = 0.887$) in the retrieval phase, neither in the encoding nor maintenance phases ($p = 0.746/0.342$). The relationships between Aβ and the mean connectivity in the CN group was also not significant ($p > 0.16$).

For completeness, an additional analysis was conducted to test the relationship between Aβ and accuracy-related neural activation during the retrieval phase. Amyloid deposition in activated regions and the global cortex both had a negative effect on task accuracy-related neural activation ($R = -0.365$, $p = 0.001$; $R = -0.267$, $p = 0.023$). In the GLM adjusting age, sex, and education, the cortical Aβ in activated regions had associations with ACER memory ($\beta = -0.43$, SE $= 0.108$, $p < 0.001$), and mean connectivity in Network 1 during retrieval ($\beta = -0.24$, SE $= 0.116$, $p = 0.043$). Noting that the mean connectivity in Network 1 during retrieval associated with ACER memory ($R = -0.304$, $p = 0.008$), the mediation effect from Aβ on memory was observed by connectivity in Network 1 [mediation effect $= -0.08$, 95% confidential interval: (-0.15, -0.02), $p = 0.037$]. It suggested the transmission of the effect of Aβ variability on memory through functional connectivity in Network 1.

The global Aβ also had a significantly negative relationship with MoCA ($\beta = -0.34$, SE $= 0.112$, $p = 0.003$) and ACER ($\beta = -0.3$, SE $= 0.114$, $p = 0.011$). Similarly, the mediation analysis indicated that the effect of Aβ on memory performance was mediated through mean connectivity in Network 1 during retrieval: average causal mediation effect $= -0.05$, 95% confidential interval: (-0.13, -0.01), $p = 0.035$ (**Figure 6**). The mediation effect was also significant for the effect of Aβ on ACER. However, the mean connectivity within Network 2 or Network 3 had no significant mediation effect on memory and ACER.

DISCUSSION

It was found that AD participants were mainly characterized by decreased functional connectivities in the Network 1 community (dominantly composed of DMN, the limbic network, and FPN) during the maintenance and retrieval phase in the memory task. In detail, AD had more nodes with reduced connectivity in Network 1 during the retrieval phase than any other phases. The nodes were in the medial prefrontal cortex, posterior cingulate cortex, middle temporal cortex, inferior parietal cortex of the left hemisphere, and inferior temporal and medial prefrontal cortex of the right hemisphere. The global cortical Aβ was associated with decreased mean connectivity in Network 1 only during retrieval. The mediation analysis indicated that cortical

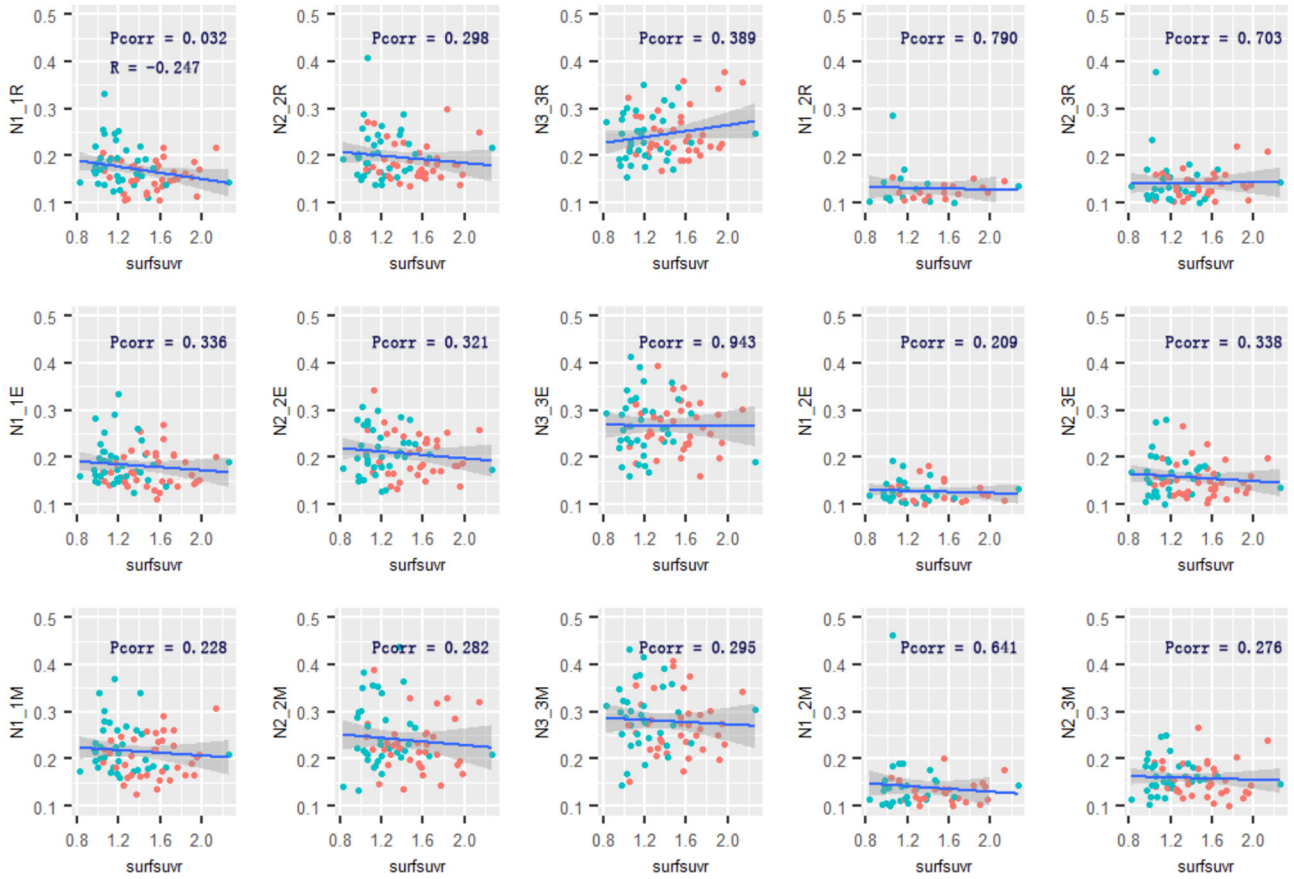

FIGURE 5 | Relationship of cortical Aβ and Network 1–3 connectivity. The cortical Aβ deposition was associated with Network 1-Network 1 functional connectivity in the retrieval phase. No other associations were observed. R and Pcorr represented correlation coefficient and significance across two groups. Pcorr in the correlation analysis was corrected by 10,000 permutations. The gray zone around blue lines represent the 95% confidence interval for predictions from the linear model. surfsuvr = surface standardized uptake value ratios; N1_1, Network 1-Network 1; N2_2, Network 2-Network 2; N3_3, Network 3-Network 3; N1_3, Network 1-Network 3; N2_3, Network 2-Network 3; R, Retrieval; E, Encoding; M, Maintenance.

Aβ might affect memory performance by modulating retrieval-related functional connectivity within Network 1.

As memory maintenance is believed to require more neocortex regions (Gazzaley et al., 2004, Woodward et al., 2006, Takahama and Saiki, 2014), regions were clustered with assignments to *a priori* networks based on functional connectivity during the maintenance phase. Network 1 was composed of four *a priori* networks, with its regions being spatially well organized in the bilateral temporal cortex, medial prefrontal cortex, posterior cingulate cortex, and occipitotemporal regions (**Figure 2**). The pattern of Network 1 was like the joint anterior-temporal and posterior-medial system (Libby et al., 2012), which works interactively for encoding and retrieval memory (Collins and Dickerson, 2019, Cooper and Ritchey, 2019). The reduced functional connectivity within Network 1 is consistent with evidence found in resting-state fMRI, both in AD and cognitively unimpaired Aβ+ individuals (Harrison et al., 2019, Berron et al., 2020). Importantly, AD reduced mean functional connectivity, specifically in the maintenance and retrieval phases of memory. As in a previous work, retrieval deficiencies could be the cause of poor performance (Li et al., 2016). An intervention study provided additional evidence for the importance of the retrieval phase in recognition (Smith et al., 2013). Taken together, these suggested that Network 1 successfully clustered regions that were working together for memory maintenance and retrieval, and it was impaired in AD.

Significant positive correlations between the Network 1 connectivity and ACER memory performance were observed in the retrieval phase. The DMN was dominant in Network 1 as it was clustered, and these results are consistent with studies that highlight the importance of DMN activation (Smith et al., 2018) and cortical network reorganization for better cognitive performance (Shine et al., 2016; Shine and Poldrack, 2018), especially when large shifts of attention are required during cognitive operations.

The task accuracy-related activation during retrieval was located in the left superior frontal cortex, within VAN/Network 2. In the working memory model, retrieval, which is generally defined as attention allocation efficiency (Germano and Kinsella,

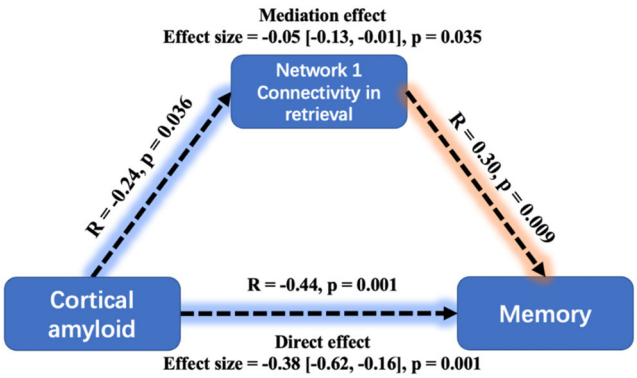

FIGURE 6 | Mediation analysis between cortical amyloid, task-related Network 1connectivity, and memory performance. A greater cortical amyloid deposition has a significant but indirect association with worse memory performance, mediated *via* the mean connectivity during retrieval within Network 1. Mediation effects were computed by 10,000 bootstrapped samples and the 95% confidence intervals were reported.

2005, Wang et al., 2010), requires a phonological loop and central executive. In this study, task activation also correlated with memory performance, suggesting the failure to recruit VAN may also hamper the cognitively demanding selection.

As we found that the hallmark of the AD had decreased mean connectivity in Network 1 during memory retrieval, we further performed node-wise functional connectivity comparisons. As expected from the above results, more nodes had reduced connectivity during the retrieval phase than other phases in AD. Some nodes were clustered in the left posterior cingulate cortex, originally assigned to the left DMN. The DMN being involved in the cognitive process has been studied. During the memory process, the functional connectivity between DMN sub-networks increases in the retrieval of episodic memories (Sestieri et al., 2011). In AD, reduced resting-state functional connectivity was observed in posterior DMN nodes in the precuneus/posterior cingulate cortex (Badhwar et al., 2017). Other than that, another hub in the DMN, the medial prefrontal cortex, was observed to have reduced connectivity. Similarly, previous research on schema memories showed the activation of the medial prefrontal cortex (mPFC) associated with successful memory for schema items (Liu et al., 2017). Importantly, the results showed a strongly left-lateralized connectivity change in the retrieval phase in AD. This fits with earlier studies showing similar left-lateralized effects in early AD using resting-state fMRI (Berron et al., 2020), volumetric gray matter measurements (Shi et al., 2009), FDG-PET (Weise et al., 2018), and amyloid PET (Raji et al., 2008).

To elucidate the nature of decreased functional connectivity in AD, the node-wise entropy in Network 1 was calculated. Nodes with reduced entropy (i.e., reduced BOLD signal predictability) only showed clear spatial correspondence with nodes of reduced connectivity relative to CN during the retrieval phase. This indicated that some regions in Network 1 with decreased functional connectivity were more predictable and less random with reduced complexity. The results revealed retrieval-related connectivity-entropy coupling and showed a difference in AD from normal aging (Yao et al., 2013).

For the adverse effect of amyloid, the negative correlation between cortical amyloid and ACER memory performance was observed. The finding was consistent with previous amyloid studies, which found that higher amyloid deposition correlated with lower immediate memory and delayed recall scores in mild cognitive impairment (MCI) participants and amyloid-positive healthy controls (Doraiswamy et al., 2012; Sperling et al., 2013).

It was once argued that amyloid pathology and neurodegeneration have adverse and, in part, synergistic effects on prospective cognition (Bilgel et al., 2018). In addition to the linear relationship found between Aβ and cognition (Knopman et al., 2018), Aβ load was revealed to have a nonlinear role in moderating the BOLD activation effect on behavioral task performance (Foster et al., 2018, Kennedy et al., 2018). Taken together, these findings suggested the involvement, but lack of direct effect, of Aβ on the cognitive deficiency. Several of these results are in accordance with this hypothesis. First, the correlation between cortical amyloid and memory performance/task activation was not regionally specific. Second, the mediation analyses indicated a significant effect of Aβ on memory performance, and yet mediated through a direct effect on Network 1 connectivity during the retrieval phase. These results suggested that global cortical amyloid might exert an influence on memory performance through an effect on functional connectivity during memory retrieval within Network 1, which mainly included DMN, limbic network, and FPN. Participants with higher cortical amyloid depositions exhibited the pronounced Network 1 connectivity decreases, which were linked to worse memory performance.

The study has some strengths that extend the current literature, including the measurement of cortical amyloid, connectivity, and entropy in the same participants and the examination of memory phase-related functional connectivity. One key limitation is that it was not possible to make strong inferences regarding the direction of causality from purely observational studies. Related to this, there may be unmeasured biomarkers (e.g., tau) and neuronal variables that exert a more direct causal influence on memory performance. These concerns can only be addressed in fully randomized interventional experimental designs. Second, as regionally specific effects from amyloid were not found, findings were the results of the global effects of AD pathology in the cortex. More effort was needed to make sure that the neural activities in certain regions were more vulnerable to local pathological change. Finally, while there were significant correlations between Aβ and connectivity across two groups, their linear relationships were insignificant in AD or the control group, respectively. It could be due to the limited sample size in each group and the few participants in the AD continuum such as MCI. Further work should include participants in different AD stages and explore the effect of Aβ pathology evolution.

CONCLUSION

Reduced mean functional connectivity was found in patients with AD. They had more brain regions exhibiting decreased connectivity compared to controls during memory retrieval in the default mode, limbic, and frontoparietal networks. Importantly, it was found that mean cortical Aβ deposition is directly related to the network-specific functional connectivity during the memory retrieval phase. The cortical Aβ may also impair memory performance through its relationship with connectivity. The findings can help in the mapping of impaired functional connectivity during memory phases and explaining Aβ-related memory deficiencies in patients with AD.

DATA AVAILABILITY STATEMENT

The raw data supporting the conclusions of this article will be made available by the request to the corresponding authors, without undue reservation.

ETHICS STATEMENT

The studies involving human participants were reviewed and approved by The ethical committee of Ruijin Hospital, Shanghai Jiao Tong University School of Medicine. The patients/participants provided their written informed consent to participate in this study.

AUTHOR CONTRIBUTIONS

ByL analyzed and interpreted all imaging data and drafted the manuscript. MZ performed PET-MR and was the equal contributor in writing the manuscript. XL, HM, and XH performed PET-MR scanning. WH synthesized the AV45 tracer. GY, LZ, and GH helped with clinical data collection. SC supervised the research. BL and JL supervised, reviewed, and modified the manuscript. All authors read and approved the final manuscript.

FUNDING

This study was supported by grants from the National Key Research and Development Program (2016YFC1306505), Shanghai Rising-Star Program (21QA1405800), the National Natural Science Foundation of China (81873778 and 81801045), the Science and Technology Commission of Shanghai Municipality (18JC1420303), the Three-year planning of Shanghai Shen-Kang Promoting Hospital's Clinical Skills and Innovative Ability Project (16CR3110B), and Shanghai Municipal Key Clinical Specialty (shslczdzk03403).

ACKNOWLEDGMENTS

We would like to thank our anonymous reviewers for their thoughtful comments on the manuscript. We are also grateful to all the research participants. We thank Prof. Hank Kung and Lin Zhu for kindly gifting us the Florbetapir precursor and suggestions to improve this manuscript. We are also grateful to all of the study participants for their patience and cooperation.

SUPPLEMENTARY MATERIAL

The Supplementary Material for this article can be found online at: https://www.frontiersin.org/articles/10.3389/fnagi.2021.721171/full#supplementary-material

REFERENCES

Aggarwal, N. T., Wilson, R. S., Beck, T. L., Bienias, J. L., and Bennett, D. A. (2005). Mild cognitive impairment in different functional domains and incident Alzheimer's disease. *J. Neurol. Neurosurg. Psychiatry* 76, 1479–1484. doi: 10.1136/jnnp.2004.053561

Albert, M. S., Moss, M. B., Tanzi, R., and Jones, K. (2001). Preclinical prediction of AD using neuropsychological tests. *J. Int. Neuropsychol. Soc.* 7, 631–639. doi: 10.1017/S1355617701755105

Badhwar, A., Tam, A., Dansereau, C., Orban, P., Hoffstaedter, F., and Bellec, P. (2017). Resting-state network dysfunction in Alzheimer's disease: a systematic review and meta-analysis. *Alzheimer's Demen. Diagn. Assess. Dis. Monitor.* 8, 73–85. doi: 10.1016/j.dadm.2017.03.007

Berron, D., van Westen, D., Ossenkoppele, R., Strandberg, O., and Hansson, O. (2020). Medial temporal lobe connectivity and its associations with cognition in early Alzheimer's disease. *Brain* 143, 1233–1248. doi: 10.1093/brain/awaa068

Bilgel, M., An, Y., Helphrey, J., Elkins, W., Gomez, G., Wong, D. F., et al., (2018). Effects of amyloid pathology and neurodegeneration on cognitive change in cognitively normal adults. *Brain* 141, 2475–2485. doi: 10.1093/brain/awy150

Blondel, V. D., Guillaume, J.-L., Lambiotte, R., and Lefebvre, E. (2008). Fast unfolding of communities in large networks. *J. Statistic. Mech. Theory Experim.* 2008:P10008. doi: 10.1103/PhysRevE.83.036103

Bostancikliogl u, M. (2020). An update on memory formation and retrieval: an engram-centric approach. *Alzheimers. Dement.* 16, 926–937. doi: 10.1002/alz.12071

Cohen, J. R., and D'Esposito, M. (2016). The segregation and integration of distinct brain networks and their relationship to cognition. *J. Neurosci.* 36, 12083–12094. doi: 10.1523/JNEUROSCI.2965-15.2016

Collins, J. A., and Dickerson, B. C. (2019). Functional connectivity in category-selective brain networks after encoding predicts subsequent memory. *Hippocampus* 29, 440–450. doi: 10.1002/hipo.23003

Cooper, R. A., and Ritchey, M. (2019). Cortico-hippocampal network connections support the multidimensional quality of episodic memory. *Elife* 8:e45591. doi: 10.7554/eLife.45591

Doraiswamy, P. M., Sperling, R. A., Coleman, R. E., Johnson, K. A., Reiman, E. M., Davis, M. D., et al., (2012). Amyloid-beta assessed by florbetapir F 18 PET and 18-month cognitive decline: a multicenter study. *Neurology* 79, 1636–1644. doi: 10.1212/WNL.0b013e3182661f74

Fang, R., Wang, G., Huang, Y., Zhuang, J. P., Tang, H. D., Wang, Y., et al., (2014). Validation of the Chinese version of Addenbrooke's cognitive examination-revised for screening mild Alzheimer's disease and mild cognitive impairment *Dement. Geriatr. Cogn. Disord.* 37, 223–231. doi: 10.1159/000353541

Foster, C. M., Kennedy, K. M., Horn, M. M., Hoagey, D. A., and Rodrigue, K. M. (2018). Both hyper- and hypo-activation to cognitive challenge are associated with increased beta-amyloid deposition in healthy aging: a nonlinear effect. *Neuroimage* 166, 285–292. doi: 10.1016/j.neuroimage.2017.10.068

Gazzaley, A., Rissman, J., and D'Esposito, M. (2004). Functional connectivity during working memory maintenance. *Cogn. Affect. Behav. Neurosci.* 4, 580–599. doi: 10.3758/CABN.4.4.580

Germano, C., and Kinsella, G. J. (2005). Working memory and learning in early Alzheimer's disease. *Neuropsychol. Rev.* 15, 1–10. doi: 10.1007/s11065-005-3583-7

Greve, D. N., and Fischl, B. (2018). False positive rates in surface-based anatomical analysis. *Neuroimage* 171, 6–14. doi: 10.1016/j.neuroimage.2017.12.072

Greve, D. N., Salat, D. H., Bowen, S. L., Izquierdo-Garcia, D., Schultz, A. P., Catana, C., et al., (2016). Different partial volume correction methods lead to different conclusions: An (18)F-FDG-PET study of aging. *Neuroimage* 132, 334–343. doi: 10.1016/j.neuroimage.2016.02.042

Grober, E., and Kawas, C. (1997). Learning and retention in preclinical and early Alzheimer's disease. *Psychol. Aging* 12, 183–188. doi: 10.1037/0882-7974.12.1.183

Harrison, T. M., Maass, A., Adams, J. N., Du, R., Baker, S. L., and Jagust, W. J. (2019). Tau deposition is associated with functional isolation of the hippocampus in aging. *Nat. Commun.* 10, 1–12. doi: 10.1038/s41467-019-12921-z

Hearne, L. J., Cocchi, L., Zalesky, A., and Mattingley, J. B. (2017). Reconfiguration of brain network architectures between resting-state and complexity-dependent cognitive reasoning. *J. Neurosci.* 37, 8399–8411. doi: 10.1523/JNEUROSCI.0485-17.2017

Jack, C. R., Bennett, D. A., Blennow, K., Carrillo, M. C., Dunn, B., Haeberlein, S. B., et al., (2018). NIA-AA Research framework: toward a biological definition of alzheimer's disease. *Alzheim. Demen. J. Alzheimer's Assoc.* 14, 535–562. doi: 10.1016/j.jalz.2018.02.018

Katzman, R., Zhang, M. Y., Ouang Ya, Q., Wang, Z. Y., Liu, W. T., Yu, E., et al., (1988). A Chinese version of the Mini-Mental State Examination; impact of illiteracy in a Shanghai dementia survey. *J. Clin. Epidemiol.* 41, 971–978. doi: 10.1016/0895-4356(88)90034-0

Kennedy, K. M., Foster, C. M., and Rodrigue, K. M. (2018). Increasing beta-amyloid deposition in cognitively healthy aging predicts nonlinear change in BOLD modulation to difficulty. *Neuroimage* 183, 142–149. doi: 10.1016/j.neuroimage.2018.08.017

Knopman, D. S., Lundt, E. S., Therneau, T. M., Vemuri, P., Lowe, V. J., Kantarci, K., et al., (2018). Joint associations of beta-amyloidosis and cortical thickness with cognition. *Neurobiol. Aging* 65, 121–131. doi: 10.1016/j.neurobiolaging.2018.01.017

Lancichinetti, A., and Fortunato, S. (2012). Consensus clustering in complex networks. *Sci. Rep.* 2:336. doi: 10.1038/srep00336

Li, B. Y., Tang, H. D., and Chen, S. D. (2016). Retrieval deficiency in brain activity of working memory in amnesic mild cognitive impairment patients: a brain event-related potentials study. *Front. Aging Neurosci.* 8:54. doi: 10.3389/fnagi.2016.00054

Libby, L. A., Ekstrom, A. D., Ragland, J. D., and Ranganath, C. (2012). Differential connectivity of perirhinal and parahippocampal cortices within human hippocampal subregions revealed by high-resolution functional imaging. *J. Neurosci.* 32, 6550–6560. doi: 10.1523/JNEUROSCI.3711-11.2012

Liu, Z. X., Grady, C., and Moscovitch, M. (2017). Effects of prior-knowledge on brain activation and connectivity during associative memory encoding. *Cereb. Cortex* 27, 1991–2009. doi: 10.1093/cercor/bhw047

Mormino, E. C., Brandel, M. G., Madison, C. M., Marks, S., Baker, S. L., and Jagust, W. J. (2012). Aβ Deposition in aging is associated with increases in brain activation during successful memory encoding. *Cereb. Cort.* 22, 1813–1823. doi: 10.1093/cercor/bhr255

Müller-Gärtner, H. W., Links, J. M., Prince, J. L., Bryan, R. N., McVeigh, E., Leal, J. P., et al., (1992). Measurement of radiotracer concentration in brain gray matter using positron emission tomography: MRI-based correction for partial volume effects. *J. Cereb. Blood Flow Metabol.* 12, 571–583. doi: 10.1038/jcbfm.1992.81

Nour, M. M., Dahoun, T., McCutcheon, R. A., Adams, R. A., Wall, M. B., and Howes, O. D. (2019). Task-induced functional brain connectivity mediates the relationship between striatal D2/3 receptors and working memory. *eLife* 8:10. doi: 10.7554/eLife.45045.010

Palm, G. (2013). Neural associative memories and sparse coding. *Neural Netw.* 37, 165–171. doi: 10.1016/j.neunet.2012.08.013

Palmqvist, S., Scholl, M., Strandberg, O., Mattsson, N., Stomrud, E., Zetterberg, H., et al., (2017). Earliest accumulation of beta-amyloid occurs within the default-mode network and concurrently affects brain connectivity. *Nat. Commun.* 8:1214. doi: 10.1038/s41467-017-01150-x

Pasquier, F., Grymonprez, L., Lebert, F., and Van der Linden, M. (2001). Memory impairment differs in frontotemporal dementia and Alzheimer's disease. *Neurocase* 7, 161–171. doi: 10.1093/neucas/7.2.161

Raji, C. A., Becker, J. T., Tsopelas, N. D., Price, J. C., Mathis, C. A., Saxton, J. A., et al., (2008). Characterizing regional correlation, laterality and symmetry of amyloid deposition in mild cognitive impairment and Alzheimer's disease with Pittsburgh Compound B. *J. Neurosci. Methods* 172, 277–282. doi: 10.1016/j.jneumeth.2008.05.005

Richman, J. S., and Moorman, J. R. (2000). Physiological time-series analysis using approximate entropy and sample entropy. *Am. J. Physiol.-Heart Circulat. Physiol.* 278, H2039–H2049. doi: 10.1152/ajpheart.2000.278.6.H2039

Roy, D. S., Arons, A., Mitchell, T. I., Pignatelli, M., Ryan, T. J., and Tonegawa, S., (2016). Memory retrieval by activating engram cells in mouse models of early Alzheimer's disease. *Nature* 531, 508–512. doi: 10.1038/nature17172

Rubinov, M., and Sporns, O. (2010). Complex network measures of brain connectivity: uses and interpretations. *Neuroimage* 52, 1059–1069. doi: 10.1016/j.neuroimage.2009.10.003

Schaefer, A., Kong, R., Gordon, E. M., Laumann, T. O., Zuo, X. N., Holmes, A. J., et al., (2018). Local-Global parcellation of the human cerebral cortex from intrinsic functional connectivity MRI. *Cereb. Cortex* 28, 3095–3114. doi: 10.1093/cercor/bhx179

Sestieri, C., Corbetta, M., Romani, G. L., and Shulman, G. L. (2011). Episodic memory retrieval, parietal cortex, and the default mode network: functional and topographic analyses. *J. Neurosci.* 31, 4407–4420. doi: 10.1523/JNEUROSCI.3335-10.2011

Shi, F., Liu, B., Zhou, Y., Yu, C., and Jiang, T. (2009). Hippocampal volume and asymmetry in mild cognitive impairment and Alzheimer's disease: meta-analyses of MRI studies. *Hippocampus* 19, 1055–1064. doi: 10.1002/hipo.20573

Shine, J. M., Bissett, P. G., Bell, P. T., Koyejo, O., Balsters, J. H., Gorgolewski, K. J., et al., (2016). The dynamics of functional brain networks: integrated network states during cognitive task performance. *Neuron* 92, 544–554. doi: 10.1016/j.neuron.2016.09.018

Shine, J. M., and Poldrack, R. A. (2018). Principles of dynamic network reconfiguration across diverse brain states. *Neuroimage* 180, 396–405. doi: 10.1016/j.neuroimage.2017.08.010

Smith, J. C., Nielson, K. A., Antuono, P., Lyons, J. A., Hanson, R. J., Butts, A. M., et al., (2013). Semantic memory functional MRI and cognitive function after exercise intervention in mild cognitive impairment. *J. Alzheimers. Dis.* 37, 197–215. doi: 10.3233/JAD-130467

Smith, V., Mitchell, D. J., and Duncan, J. (2018). Role of the default mode network in cognitive transitions. *Cereb. Cortex* 28, 3685–3696. doi: 10.1093/cercor/bhy167

Sperling, R. A., Johnson, K. A., Doraiswamy, P. M., Reiman, E. M., Fleisher, A. S., Sabbagh, M. N., et al., (2013). Amyloid deposition detected with florbetapir F 18 ((18)F-AV-45) is related to lower episodic memory performance in clinically normal older individuals. *Neurobiol. Aging* 34, 822–831. doi: 10.1016/j.neurobiolaging.2012.06.014

St Jacques, P. L., Kragel, P. A., and Rubin, D. C. (2011). Dynamic neural networks supporting memory retrieval. *Neuroimage* 57, 608–616. doi: 10.1016/j.neuroimage.2011.04.039

Takahama, S., and Saiki, J. (2014). Functional connectivity supporting the selective maintenance of feature-location binding in visual working memory. *Front. Psychol.* 5:507. doi: 10.3389/fpsyg.2014.00507

Vannini, P., Hedden, T., Becker, J. A., Sullivan, C., Putcha, D., Rentz, D., et al., (2012). Age and amyloid-related alterations in default network habituation to stimulus repetition. *Neurobiol. Aging* 33, 1237–1252. doi: 10.1016/j.neurobiolaging.2011.01.003

Wang, Y., Song, Y., Qu, Z., and Ding, Y. (2010). "Task difficulty modulates electrophysiological correlates of perceptual learning. *Int. J. Psychophysiol.* 75, 234–240. doi: 10.1016/j.ijpsycho.2009.11.006

Weintraub, S., Wicklund, A. H., and Salmon, D. P. (2012). The neuropsychological profile of Alzheimer disease. *Cold Spring Harb. Perspect. Med.* 2:a006171. doi: 10.1101/cshperspect.a006171

Weise, C. M., Chen, K., Chen, Y., Kuang, X., Savage, C. R., and Reiman, E. M. (2018). Left lateralized cerebral glucose metabolism declines in amyloid-beta positive persons with mild cognitive impairment. *Neuroimage Clin.* 20, 286–296. doi: 10.1016/j.nicl.2018.07.016

Woodward, T. S., Cairo, T. A., Ruff, C. C., Takane, Y., Hunter, M. A., and Ngan, E. T. (2006). Functional connectivity reveals load dependent neural systems underlying encoding and maintenance in verbal working memory. *Neuroscience* 139, 317–325. doi: 10.1016/j.neuroscience.2005.05.043

Xia, M., Wang, J., and He, Y. (2013). BrainNet Viewer: a network visualization tool for human brain connectomics. *PLoS ONE* 8:e68910. doi: 10.1371/journal.pone.0068910

Yao, Y., Lu, W. L., Xu, B., Li, C. B., Lin, C. P., Waxman, D., et al., (2013). The increase of the functional entropy of the human brain with age. *Sci. Rep.* 3:2853. doi: 10.1038/srep02853

Zalesky, A., Fornito, A., and Bullmore, E. T. (2010). Network-based statistic: identifying differences in brain networks. *Neuroimage* 53, 1197–1207. doi: 10.1016/j.neuroimage.2010.06.041

Conflict of Interest: The authors declare that the research was conducted in the absence of any commercial or financial relationships that could be construed as a potential conflict of interest.

Publisher's Note: All claims expressed in this article are solely those of the authors and do not necessarily represent those of their affiliated organizations, or those of the publisher, the editors and the reviewers. Any product that may be evaluated in this article, or claim that may be made by its manufacturer, is not guaranteed or endorsed by the publisher.

Copyright © 2021 Li, Zhang, Jang, Ye, Zhou, He, Lin, Meng, Huang, Hai, Chen, Li and Liu. This is an open-access article distributed under the terms of the Creative Commons Attribution License (CC BY). The use, distribution or reproduction in other forums is permitted, provided the original author(s) and the copyright owner(s) are credited and that the original publication in this journal is cited, in accordance with accepted academic practice. No use, distribution or reproduction is permitted which does not comply with these terms.

frontiers in Aging Neuroscience

ORIGINAL RESEARCH
published: 02 September 2021
doi: 10.3389/fnagi.2021.706815

Reduced Risk of Atrial Fibrillation Following Cholecystectomy: A Nationwide Population-Based Study

Tung Ching Ho[1,2], Yu-Ching Chen[2], Che-Chen Lin[3], Hsu-Chih Tai[4], Cheng-Yu Wei[4,5], Yung-Hsiang Yeh[6] and Chung Y. Hsu[7]*

[1]Department of Cardiology, Chang Hua Hospital, Changhua County, Taiwan, [2]Department of Bioinformatics and Medical Engineering, College of Information and Electrical Engineering, Asia University, Taichung, Taiwan, [3]Management Office for Health Data, China Medical University Hospital, Taichung, Taiwan, [4]Department of Exercise and Health Promotion, College of Kinesiology and Health, Chinese Culture University, Taipei, Taiwan, [5]Department of Neurology, Chang Bing Show Chwan Memorial Hospital, Changhua County, Taiwan, [6]Digestive Disease Center, Chang Bing Show Chwan Memorial Hospital, Changhua County, Taiwan, [7]Graduate Institute of Clinical Medicine Science and School of Medicine, College of Medicine, China Medical University, Taichung, Taiwan

Background: Gallstone disease (GD) is associated with a high risk of cardiovascular disease. However, it is unknown whether GD contributes to atrial fibrillation (AF). We aimed to investigate the association between GD and AF.

Methods: We performed a population-based cohort study using data from the Taiwan National Health Insurance Research Database between 2001 and 2011. A GD cohort of 230,076 patients was compared with a control cohort consisting of an equal number of patients matched for age, sex, cardiovascular and gastrointestinal comorbidities.

Results: In total, 5,992 (49.8/10,000 person-years) patients with GD and 5,804 (44.5/10,000 person-years) controls developed AF. GD increased AF risk with a hazard ratio (HR) of 1.20 [95% confidence interval (CI), 1.16–1.25]. In patients with GD but without cholecystectomy, the HR of AF reached 1.57 (95% CI = 1.50–1.63). After cholecystectomy, the HR of AF significantly decreased to 0.85 (95% CI = 0.81–0.90). Among the three age groups with GD (<45, 45–64, and ≥65 years), the adjusted HRs of AF were 1.59 (95% CI = 1.08–2.33), 1.31 (95% CI = 1.18–1.45), and 1.18 (95% CI = 1.13–1.22), respectively. Compared with patients with a CHA_2DS_2-VASc score equal to 0, the HRs of AF risk among total cohort patients and a score equal to 1, 2, 3, and ≥ 4 were 1.28 (95% CI = 1.15–1.43), 2.26 (95% CI = 2.00–2.56), 3.81 (95% CI = 3.35–4.34), and 5.09 (95% CI = 4.42–5.87), respectively.

Conclusion: This population-based longitudinal follow-up study showed that patients with GD had an increased AF risk. Moreover, cholecystectomy was related to reduced AF risk. Cardiovascular checkups may be necessary for patients with GD, especially those who are young and have other typical risk factors.

Keywords: atrial fibrillation, risk factors, gallstone disease, cholelithiasis, cholecystectomy, prevention

OPEN ACCESS

Edited by:
Jiehui Jiang,
Shanghai University, China

Reviewed by:
Juanjuan Jiang,
Anhui Polytechnic University, China
Chia-Yen Dai,
Kaohsiung Medical University, Taiwan

****Correspondence:***
Cheng-Yu Wei
yuyu@seed.net.tw

Received: *08 May 2021*
Accepted: *22 July 2021*
Published: *02 September 2021*

Citation:
Ho TC, Chen Y-C, Lin C-C, Tai H-C, Wei C-Y, Yeh Y-H and Hsu CY (2021) Reduced Risk of Atrial Fibrillation Following Cholecystectomy: A Nationwide Population-Based Study. Front. Aging Neurosci. 13:706815. doi: 10.3389/fnagi.2021.706815

INTRODUCTION

Atrial fibrillation (AF) is the most common sustained cardiac arrhythmia in adults. Although AF prevalence varies among ethnic populations, its prevalence progressively increases with advancing age. It occurs in <1% of individuals aged 60–65 years but in 8% to 10% of individuals aged >80 years (Kannel and Benjamin, 2009; Rodriguez et al., 2015). AF can lead to acute or chronic severe outcomes, including embolic stroke, extracranial systemic thromboembolism, dementia, heart failure (HF), myocardial infarction, and venous thromboembolism (Staerk et al., 2017). Patients with AF may experience various symptoms such as palpitations, shortness of breath, exercise intolerance, chest pain, fatigue, dizziness, and light-headedness (Reynolds et al., 2006; Zimetbaum, 2017). However, up to 90% of AF events may be symptomless, particularly in the elderly (Page et al., 1994). Therefore, early recognition and diagnosis of AF are crucial, particularly in people with risk factors (RFs).

Some unmodifiable and modifiable RFs are well established for AF (Staerk et al., 2017). The unmodifiable RFs include genetics age gender, and race (Marcus et al., 2010; Rodriguez et al., 2015). The modifiable RFs include physical inactivity, smoking, obesity, diabetes mellitus (DM), obstructive sleep apnea (OSA), and hypertension (Alonso et al., 2013; Schnabel et al., 2015). However, the mechanisms that cause AF are unclear. AF may occur in the absence of known structural or electrophysiological abnormalities (Staerk et al., 2017). Epidemiological studies have revealed many potential RFs for AF. In the field of digestive disorders, gastroesophageal reflux disease (GERD; Huang et al., 2012), inflammatory bowel disease (IBD; Choi et al., 2019), gastrointestinal cancers (Jakobsen et al., 2019), and liver disease (Lee et al., 2017; Huang et al., 2018) have been reported to be associated with significantly increased AF risk.

Gallstone disease (GD; cholelithiasis) is a common digestive disorder and significantly increases cardiovascular disease (CVD) risk (Bortnichak et al., 1985; Jiang et al., 2013; Olaiya et al., 2013; Wei et al., 2014, 2019; Lv et al., 2015; Wirth et al., 2015; Zheng et al., 2016, 2018; Fan et al., 2017; Upala et al., 2017; Fairfield et al., 2019). However, no studies on AF risk in patients with GD have been conducted. Therefore, we investigated the relationship between GD and later AF development by using a prospective, nationwide, and case-cohort study design. If gallbladder removal reduces AF incidence, it would serve as evidence for GD being a risk factor for AF. Therefore, we further compared patients with GD who did not undergo cholecystectomy with those who underwent cholecystectomy.

MATERIALS AND METHODS

Data Source

The Taiwan National Health Insurance program is a universal, single-payer health insurance program covering 99% of the residents of Taiwan. The Taiwan government has transferred medical claims data to the National Health Research Institutes (NHRI), which has established and managed a database named the National Health Insurance Research Database (NHIRD). The NHIRD contains medical claims data, including a registry of beneficiaries, disease record files, and other medical services. The NHIRD uses the *International Classification of Diseases, Ninth Revision, Clinical Modification* (*ICD-9-CM*) for coding diseases. The NHRI has released the database (for research use) and assigned a unique encoded number for accessing the annual medical history of each insured individual. Moreover, this study was approved by the Ethics Review Board of China Medical University (CMUH104-REC2-115).

Study Population

This study investigated the AF risk in patients with GD. This study had two stages. We established a GD cohort and a control cohort to observe AF occurrence. The GD cohort involved aged ≥20 years patients from January 1, 2001, to December 31, 2009, and assigned the index date as the first date of newly diagnosed GD (*ICD-9-CM* 574), which included gallbladder stones (cholecystolithiasis), intrahepatic bile duct stones (hepatolithiasis) and extrahepatic bile duct stones (choledocholithiasis; Lammert et al., 2016). The GD cohort was further subgrouped in asymptomatic (*ICD-9-CM* 574.2, 574.5, and 574.9) and symptomatic GD (*ICD-9-CM* 574.0, 574.1, 574.3, 574.4, 574.6, 574.7, and 574.8). The patients with symptomatic GD are meant to have specific or nonspecific symptoms or complications, such as biliary colic, intolerance to fatty foods, and infections (Lammert et al., 2016). Furthermore, we categorized GD into two subgroups: with and without cholecystectomy. An equal number of control individuals without GD were randomly selected by using the propensity matching method. The matching criteria were age, sex, cardiovascular and gastrointestinal comorbidities. The cardiovascular comorbidities included hypertension (*ICD-9-CM* 401–405), DM (*ICD-9-CM* 250), coronary artery disease (CAD, *ICD-9-CM* 410–414), chronic kidney disease (CKD, *ICD-9-CM* 585, 586, 588.8, and 588.9), hyperlipidemia (*ICD-9-CM* 272), and HF (*ICD-9-CM* 428). The gastrointestinal comorbidities included GURD (*ICD-9-CM* 533, 530.11, and 530.81), IBD (*ICD-9-CM* 555, 556), hepatitis C (*ICD-9-CM* 070.41, 070.44, 070.51, 070.54, 070.70, 070.71, and V02.62), and nonalcoholic fatty liver disease (NAFLD, *ICD-9-CM* 571.8). We assigned the index date for control individuals as a random month and day but with the same index year as the matched cases. The GD and control cohorts excluded individuals without AF diagnosis (*ICD-9-CM* 427.31) and various kinds of cancer (*ICD-9-CM* 140–239) before the index date. Follow-up ceased when an individual withdrew from the insurance program, an AF event occurred, or the date reached December 31, 2011 (**Figure 1**).

CHA_2DS_2-VASc [Congestive heart failure, Hypertension, Age ≥75 years (doubled), Diabetes, prior Stroke or transient ischemia attack (doubled)—Vascular disease, Age 65–74 years, and Sex category (female)] was used for predicting AF in patients with GD. The score was calculated for each patient by assigning 1 point for HF, hypertension, DM, vascular disease (*ICD-9-CM* 410, 412, 420.20, 420.21, 420.22, 420.23, 420.24, 420.29, 429.79, 440.0, 440.20, 440.21, 440.22, 440.23, 440.24, 440.3, 440.4, 443.81, 443.89, and 443.9), sex category (female), and age (65–74 years) and 2 points for any history of ischemic stroke or transient

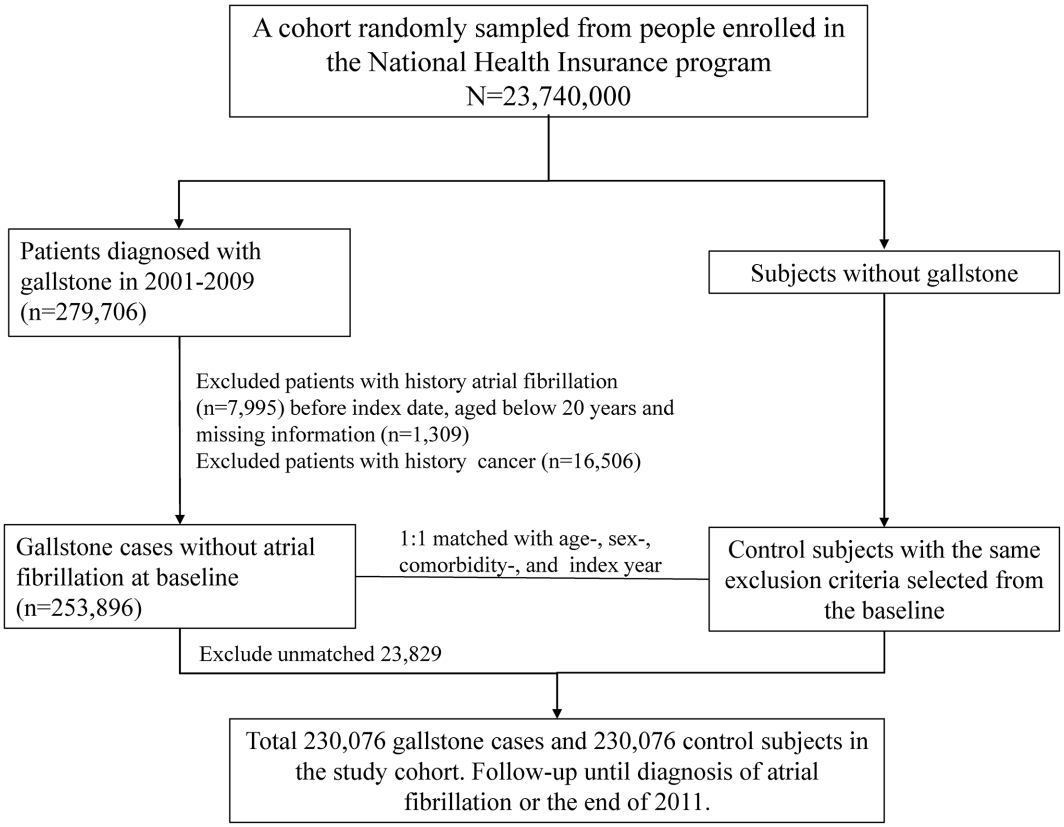

FIGURE 1 | Flowchart for study population selection.

ischemia attack (*ICD-9-CM* 433–438) and age ≥75 years (Lip et al., 2010; Camm et al., 2012; January et al., 2014).

Statistical Analysis

To present the distribution of the study cohorts, we indicate the number and percentage for all the category variables (including age group, sex, and comorbidities). To assess the distribution difference between the two cohorts, we used the standard mean difference. The incidence destiny of AF for each cohort was calculated as the number of patients with AF divided by the total number of patients followed up. The cumulative incidence curve was measured using the Kaplan–Meier method, and the curve difference was tested using the log-rank test. To analyze the difference in AF risk between the GD cohort and the control cohort, we estimated the hazard ratios (HRs) and 95% confidence intervals (CIs) by using the crude and adjusted Cox proportional hazard models. Moreover, we used Cox models to determine the influence of cholecystectomy and various GD subtypes on AF risk. Furthermore, we applied a subgroup analysis for comparing patients with GD with control individuals through the stratification of variables, including age group, sex, and comorbidities. Additionally, Cox models were used to estimate AF risk associated with CHA_2DS_2-VASc score. SAS 9.4 software (SAS Institute, Cary, NC, USA) was used to perform the analyses, and R software (R Foundation for Statistical Computing, Vienna, Austria) was used to determine the incidence curves. The significance level was set at $p < 0.05$ for 2-sided testing.

RESULTS

This study involved two cohorts: a cohort of 230,076 patients with GD and a control cohort consisting of an equal number of healthy individuals (**Table 1**). In the study cohort, the majority of the participants were ≥65 years old (approximately 43%), and the proportions of men and women were approximately equal. Furthermore, the comorbidities, including hypertension, DM, CAD, CKD, hyperlipidemia, HF, GURD, IBD, hepatitis C, and NAFLD, were similar between the GD cohort and the control cohort.

AF occurred in 5,804 and 5,992 participants in the control and GD cohorts, respectively (**Table 2**). The AF incidences were 44.5 and 49.8 per 10,000 person-years in the control and GD cohorts, respectively. **Figure 2** shows that the cumulative incidence curves of AF were significantly higher in the GD without cholecystectomy cohort and lower in the GD with cholecystectomy than in the control cohort (log-rank test, $p < 0.001$). After adjusting for age, sex, and comorbidities, the GD group was significantly associated with increased AF risk compared with the control group (HR = 1.20, 95% CI = 1.16–1.25). Moreover, **Table 2** shows that relative to the

TABLE 1 | Demographic characteristics and comorbidities in GD and control groups.

Variable	Control cohort N = 230076 (%)	Gallstone cohort N = 230076 (%)	Standard mean difference[§]
Age group, years			
< 45	50,821 (22.1)	50,634 (22.0)	0.002
45–64	80,433 (35.0)	82,529 (35.9)	0.02
≥65	98,822 (43.0)	96,913 (42.1)	0.017
Mean (SD)	59.9 (17.0)	59.6 (16.8)	0.01
Sex			
Female	117,990 (51.3)	116,694 (50.7)	0.01
Male	112,086 (48.7)	11,382 (49.3)	0.01
Cardiovascular comorbidity			
Hypertension	46,670 (20.3)	44,124 (19.2)	0.03
DM	29,727 (12.9)	27,762 (12.1)	0.03
CAD	22,315 (9.70)	20,887 (9.08)	0.02
CKD	3,726 (1.62)	3,756 (1.63)	0.001
Hyperlipidemia	11,840 (5.15)	11,222 (4.88)	0.01
HF	6,263 (2.72)	7,036 (3.06)	0.02
Gastrointestinal comorbidity			
GURD	13,598 (5.91)	14,536 (6.32)	0.02
IBD	295 (0.17)	411 (0.18)	0.002
Hepatitis C	2,216 (0.96)	2,916 (1.27)	0.03
NAFLD	8,290 (3.60)	8,082 (3.51)	0.005

GD, gallstone disease; DM, diabetes mellitus; CAD, coronary artery disease; CKD, chronic kidney disease; HF, heart failure; GURD, gastroesophageal reflux disease; IBS, inflammatory bowel; NAFLD, nonalcoholic fatty liver disease [§]Standard mean difference ≤0.10 indicates a negligible difference between the two cohorts.

control cohort, the patients with GD who did not undergo cholecystectomy had a 1.57-fold increased AF risk (95% CI = 1.50–1.63), whereas patients with GD who underwent cholecystectomy had a 0.85-fold decreased AF risk (95% CI = 0.81–0.90). Simultaneously, compared with the patients with GD and without cholecystectomy, the HR of AF for patients with GD who underwent cholecystectomy was 0.54 (95% CI = 0.51–0.57). The incidence and HR of AF were calculated according to various GD subtypes. Compared with the patients without GD, those with asymptomatic and symptomatic GD had 1.33- and 1.07-fold increased AF risk (95% CI = 1.27–1.39 and 1.02–1.12), respectively.

Figure 3 shows the stratified analysis for patients with GD and the control cohort. Relative to the control cohort, the adjusted HRs of AF were 1.59 (95% CI = 1.08–2.33), 1.31 (95% CI = 1.18–1.45), and 1.18 (95% CI = 1.13–1.22) for patients with GD in the age groups of < 45, 45–64, and ≥65 years, respectively. The female and male patients with GD had a 1.19- and 1.22-fold increased AF risk compared with female (95% CI = 1.13–1.25) and male (95% CI = 1.16–1.29) control individuals, respectively. Among the noncomorbid patients, those with GD had a significantly higher AF risk than those in the control cohort (HRs for hypertension, DM, CAD, CKD, hyperlipidemia, HF, GURD, IBD, hepatitis C, and NAFLD were 1.25, 1.23, 1.22, 1.21, 1.21, 1.22, 1.25, 1.20, 1.20 and 1.22 respectively).

Table 3 shows the incidence and HRs of AF in three study cohorts stratified based on CHA_2DS_2-VASc score. In total study cohort patients, including GD and non-GD patients, the incidence rate of AF increased from 9.08 per 10,000 person-years for patients with a CHA_2DS_2-VASc score of 0 up to 172.1 per 10,000 person-years for those with a CHA_2DS_2-VASc score of at least 4. The HR of AF was 5.09 (95% CI = 4.42–5.84) for those with a CHA_2DS_2-VASc score of at least 4 as compared with those with a CHA_2DS_2-VASc score of 0. In GD patients with and without cholecystectomy, the incidence rates and HRs were also gradually increased as the CHA2DS2-VASc score increased from 0 to at least 4.

DISCUSSION

This study demonstrated that GD was independently associated with an increased AF risk in a population-based cohort, suggesting that GD may play a crucial role in determining AF risk. Furthermore, we found that patients with GD who underwent cholecystectomy were 0.85- and 0.54-fold less likely to develop AF compared with individuals without GD and patients with GD who did not undergo cholecystectomy, respectively. This result may provide further evidence that GD is one of the potential RFs for AF. GD is a common disorder that affects approximately 10%-20% of the global adult population (Lammert et al., 2016). Simultaneously, GD and AF share several RFs, including age, physical inactivity, obesity, and DM (Lammert et al., 2016; Staerk et al., 2017; Ibrahim et al., 2018). Many original and meta-analysis studies have highlighted the importance of recognizing GD as a risk factor for CVD and stroke (Bortnichak et al., 1985; Jiang et al., 2013; Olaiya et al., 2013; Wei et al., 2014, 2019; Lv et al., 2015; Wirth et al., 2015; Zheng et al., 2016, 2018; Fan et al., 2017; Upala et al., 2017; Fairfield et al., 2019). AF is known to be a major cause of systemic embolism and stroke (Staerk et al., 2017), but the association between GD and AF has remained unclear. This is the first longitudinal follow-up study to reveal that GD increases AF risk.

In the study, both asymptomatic and symptomatic GD without gallbladder removal exhibited a high AF risk. In fact, 80% of the patients with GD were asymptomatic, but these patients exhibited approximately a 1%-3% annual and 7%-26% lifetime risk of developing complications related to biliary colic or gallstones (Friedman et al., 1989; Friedman, 1993;

TABLE 2 | Incidence and HRs of AF in GD and control groups.

GD treatment	*N*	Event	PYs	Rate	HRs	
					Model 1	Model 2
Without GD	230,076	5,804	130,5065	44.5	ref	
With GD	230,076	5,992	120,3452	49.8	1.20 (1.16, 1.25)***	
GD without cholecystectomy	97,408	3,814	440,837	86.5	1.57 (1.50, 1.63)***	ref
GD with cholecystectomy	132,668	2,178	762,615	28.6	0.85 (0.81, 0.90)***	0.54 (0.51, 0.57)***
Asymptomatic GD	107,561	3,396	518,529	65.5	1.33 (1.27, 1.39)***	
Symptomatic GD	122,515	2,596	684,898	37.9	1.07 (1.02, 1.12)**	

*Model 1 and model 2 adjusted for age, sex, cardiovascular, and gastrointestinal comorbidities. AF, atrial fibrillation; PYs, person-years; Rate, incidence rate, per 10,000 person-years; HRs, hazard ratios; ref, reference. **$p < 0.01$, ***$p < 0.0001$.*

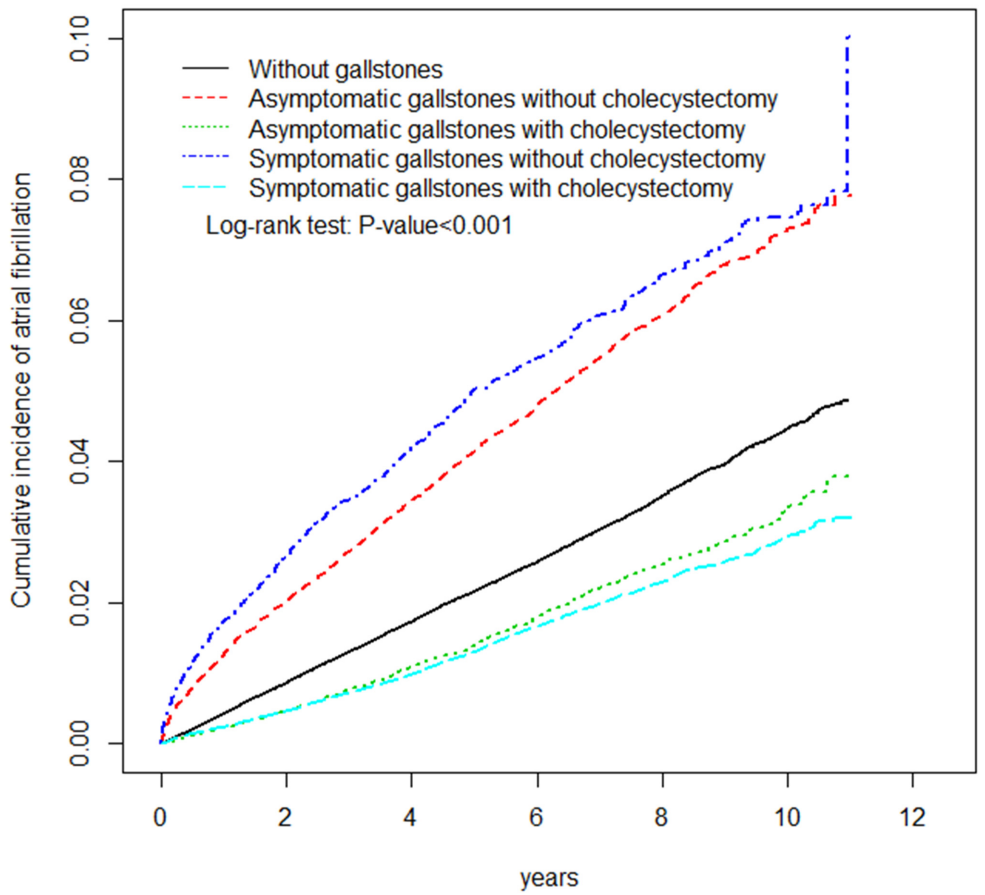

FIGURE 2 | The adjusted cumulative incidence curves of atrial fibrillation between patients with or without gallstone disease.

Ibrahim et al., 2018). Conventionally, expectant management is the standard treatment for asymptomatic GD, except for patients with chronic hemolytic anemia or who are Native Americans (Ibrahim et al., 2018). Our previous findings have suggested that patients with GD have a high risk of stroke, but cholecystectomy reduces the risk of ischemic and hemorrhagic stroke among both asymptomatic and symptomatic patients (Wei et al., 2014, 2019). Therefore, patients with GD should receive frequent cardiovascular checkups. In addition, GD and AF must be studied in further detail.

In the stratified analysis based on age (45, 45–64, and ≥65 years), GD exhibited an obvious association with AF. This suggests that attention should be paid to preventing embolic stroke, particularly in young GD patients. Although epidemiological data have shown a high prevalence of GD and low prevalence of AF in women (Lammert et al., 2016; Staerk et al., 2017), both female and male patients with GD had an obvious risk of AF in the study. The GD groups had a significantly higher AF risk than the control groups without comorbidities. Thus, GD might be a newfound risk factor for AF.

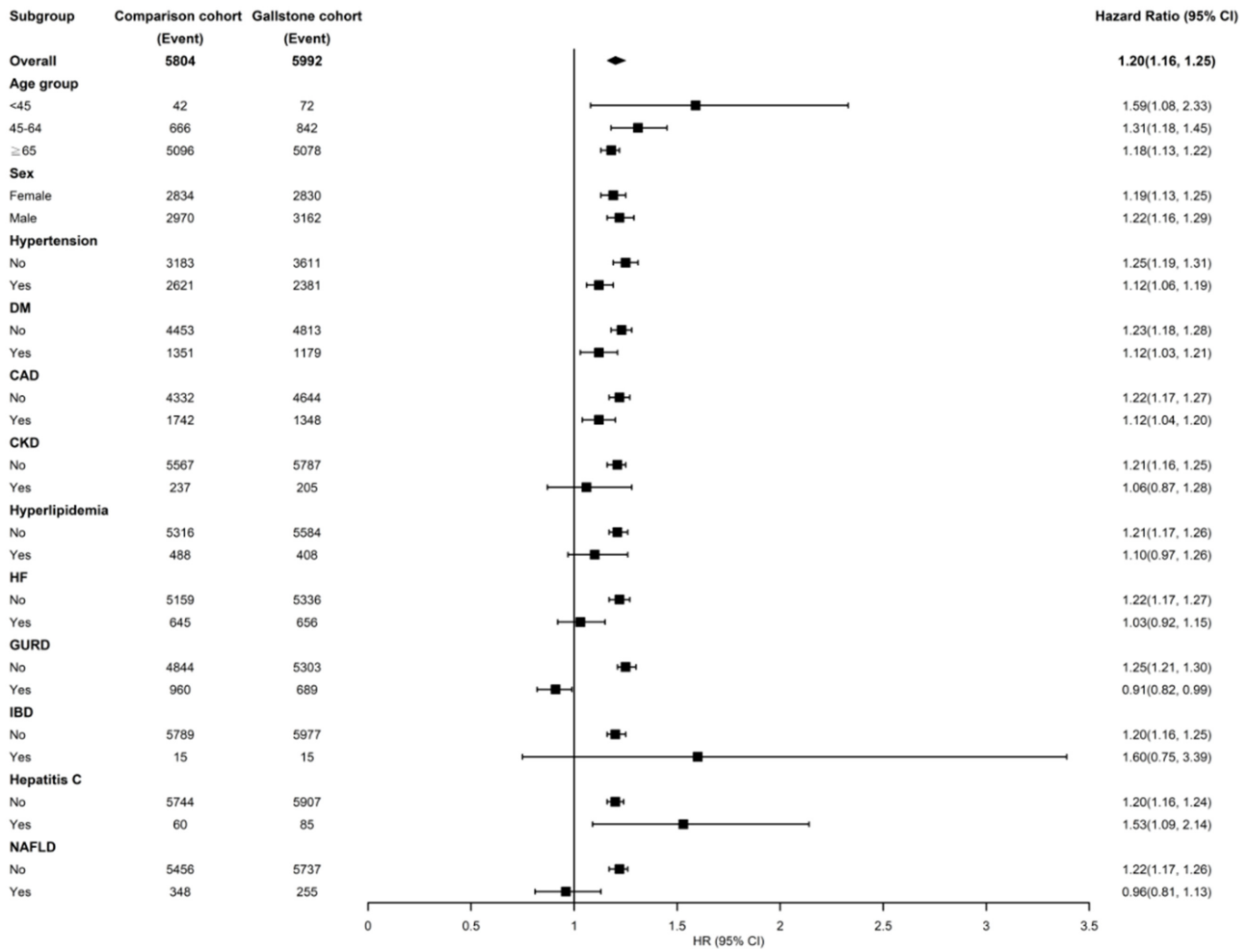

FIGURE 3 | Incidence and hazard ratios of atrial fibrillation stratified by age, sex, and comorbidities in the patients of gallstone disease. DM, diabetes mellitus; CAD, coronary artery disease; CKD, chronic kidney disease; HF, heart failure; GURD, gastroesophageal reflux disease; IBS, inflammatory bowel; NAFLD, nonalcoholic fatty liver disease.

Although CHA_2DS_2-VASc score was originally developed for stroke risk prediction in patients with AF (Lip et al., 2010; Camm et al., 2012; January et al., 2014), transportability of the score across different populations has been investigated. One research showed the CHA2DS2-VASc score is useful in predicting poor 12-month outcomes following myocardial infarction in diabetic patients without AF (Hudzik et al., 2016). Moreover, some studies have demonstrated the score achieves high performance for predicting new-onset AF in middle-aged adults and patients with cancer (Saliba et al., 2016; Hu and Lin, 2017; Hu et al., 2019). To our knowledge, the current investigation is the first to assess the predictive role of CHA_2DS_2-VASc score for the incidence and HR of AF. Because many of the individual RFs included in the score are also RFs for AF, AF risk increased with increasing CHA_2DS_2-VASc score among total patients and GD patients with and without cholecystectomy.

AF is defined as a supraventricular tachyarrhythmia with uncoordinated atrial activation and consequently ineffective atrial contraction (January et al., 2014). Many established and potential RFs for AF induce structural and histopathologic changes in the atrium, which are characterized directly or indirectly by fibrosis, inflammation, and cellular and molecular changes (Staerk et al., 2017). Although the actual pathophysiology through which GD leads to AF remains undetermined, certain observational evidence might offer possible explanations. GD can lead to inflammation that is characterized by bile retention or microbiota in the gallbladder (Lammert et al., 2016). The inflammation can cause oxidative damage in the atrium, which may be followed by AF. Inflammatory biomarkers, such as C-reactive protein and interleukin-6, increase in AF (January et al., 2014; Gutierrez and Van Wagoner, 2015; Harada et al., 2015). Therefore, cholecystectomy is assumed to reduce AF risk through the elimination of the inflammatory mechanism.

Some of the hepatobiliary and gastrointestinal diseases were independently associated with an increased AF risk.

TABLE 3 | Incidence and HRs of AF in study cohort patients stratified by CHA_2DS_2-VASc score.

CHA_2DS_2-VASc	*N*	Event	PYs	Rate	HR (95% CI)
Total study cohort patients					
0	106,900	579	637,602	9.08	ref
1	163,602	1,533	986,007	15.6	1.28 (1.15, 1.43)***
2	73,853	2,670	393,492	67.9	2.26 (2.00, 2.56)***
3	51,643	2,774	245,102	113.2	3.81(3.35, 4.34)***
≥4	64,154	4,240	246,313	172.1	5.09 (4.42, 5.87)***
GD without cholecystectomy					
0	87,484	386	533,446	7.24	ref
1	139,938	1,106	857,101	12.9	1.35 (1.19, 1.54)***
2	56,059	1,908	314,054	60.8	2.46 (2.12, 2.85)***
3	36,708	1,867	186,091	100.3	4.09 (3.49, 4.81)***
≥4	42,555	2,715	176,987	153.4	5.53 (4.64, 6.59)***
GD with cholecystectomy					
0	19,416	193	104,156	18.5	ref
1	23,664	427	128,906	33.1	1.14 (0.94, 1.39)
2	17,794	762	79,438	95.9	1.69 (1.36, 2.08)***
3	14,935	907	59,011	153.7	2.63 (2.11, 3.29)***
≥4	21,599	1,525	69,326	220.0	3.17 (2.49, 4.03)***

*HRs, hazard ratios; AF, atrial fibrillation; GD, gallstone disease; PYs, person-years; Rate, incidence rate, per 10,000 person-years; HRs, hazard ratios; ref, reference. ***p < 0.0001.*

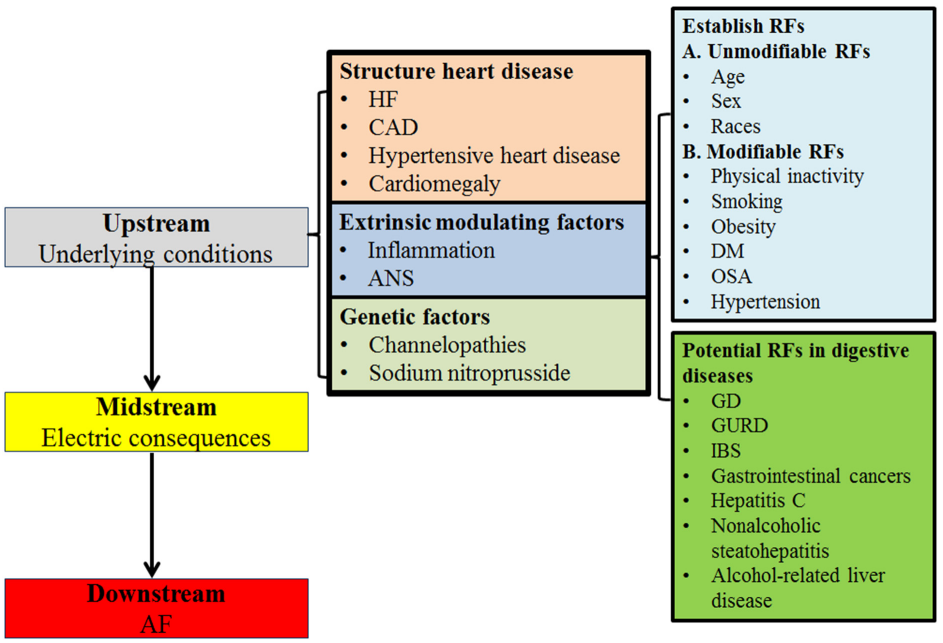

FIGURE 4 | Mechanisms of AF. HF, heart failure; CAD, coronary artery disease; ANS, Autonomic nervous system; RFs, risk factors; DM, diabetes mellitus; OSA, obstructive sleep apnea; GD, gallstone disease; GURD, gastroesophageal reflux disease; IBD, inflammatory bowel disease.

IBD including ulcerative colitis and Crohn's disease, that are significantly associated with AF incidence (HR = 1.36, 95% CI = 1.20–1.55), could be caused by an inflammatory mechanism (Choi et al., 2019). The incidence and risk of new-onset AF significantly increased, especially in lung and gastrointestinal cancers, possibly due to systemic inflammation (Jakobsen et al., 2019). Liver diseases, including hepatitis C, nonalcoholic steatohepatitis, alcohol-related liver disease, and primary liver cancer, increased the prevalence and incidence of new-onset AF, as they share the underlying link of autonomic dysfunction and inflammation (Huang et al., 2018). Liver cirrhosis increased the risk of AF (HR = 1.46; 95% CI = 1.18–1.80), likely due to cirrhotic cardiomyopathy, vasoactive intestinal peptide, and galectin-3 (Lippi et al., 2015; Xi et al., 2015; Lee et al., 2017; Huang et al., 2018). GERD increased AF risk (HR = 1.31, 95% CI = 1.06–1.61), possibly because of vagal nerve overstimulation, inflammation, autoimmune response, or acid stimulation of the lower esophagus (Huang et al., 2012). Accumulating evidence suggests autonomic dysfunction may contribute to the GD by impairing motility in the gallbladder and sphincter of Oddi (Chawla et al., 2001; Villanacci et al., 2016). Besides inflammatory mechanisms, autonomic dysfunction, which has been observed

in patients with GD, may be responsible for the association between GD and an increased risk of AF (Kanoupakis et al., 2000). **Figure 4** lists the plausible mechanisms of nonvalvular AF and associating RFs (Iwasaki et al., 2011; Staerk et al., 2017).

Gallstones are classified into cholesterol gallstones (90%) and pigment stones (10%). The mechanism of cholesterol gallstones is caused by disturbance of biliary cholesterol homeostasis. The pathophysiology of pigment gallstones results from hepatic hypersecretion of bilirubin, bile stasis, or bacterial infection (Lammert et al., 2016). The biochemical or inflammatory process caused by abnormal metabolism of cholesterol or bilirubin might induce left atrium remodeling and then induced AF development (Camm et al., 2012). The cholecystectomy might eliminate partially reversible factors of AF progression.

One of the advantages of this study is its use of nationwide population-based data which are highly representative of the general population. However, certain limitations of our study must be considered. First, limited to usage specifications of the NHIRD, the research period of enrollment was from 2001–2009 and the end of follow-up date was up to the end of December 31, 2011. If the research has longer collection and follow-up, the validity should be higher. Second, we did not consider whether patients had undergone open or laparoscopic cholecystectomy. The AF outcome with different procedures warrants further evaluation. Third, the detailed GD subtypes could not be used due to clinical coding habits. Fourth, AF subtypes (paroxysmal, persistent, long-standing persistent, or permanent) could not be classified because of the lack of specific *ICD-9-CM* codes. Fifth, evidence derived from a retrospective cohort study is generally lower in statistical quality than that derived from randomized trials due to potential bias related to adjustments for confounding variables. Sixth, the patient data recorded in the NHIRD are anonymous, and therefore, detailed personal information regarding smoking and sleep habits, body mass index, physical inactivity, lifestyle, or family history could not be obtained, although these are RFs for AF. Changes in lifestyle and body weight may affect the results. Simultaneously, relevant clinical variables, such as symptoms, signs, imaging results, pathology findings, and serum laboratory data, were unavailable in the NHIRD. However, records related to AF, GD, and cholecystectomy diagnoses were highly reliable. Further prospective observational and interventional studies are necessary to support the findings.

This large data-based longitudinal follow-up and retrospective study revealed an association between GD (both asymptomatic and symptomatic) and increased AF risk. Cholecystectomy is related to reduce AF risk. Our findings suggest that gastroenterologists and gastrointestinal surgeons must pay close attention to patients with GD in light of the risk of AF, particularly in patients with conventional stroke RFs.

DATA AVAILABILITY STATEMENT

The original contributions presented in the study are included in the article, further inquiries can be directed to the corresponding author.

ETHICS STATEMENT

The studies involving human participants were reviewed and approved by Ethics Review Board of China Medical University. The ethics committee waived the requirement of written informed consent for participation.

AUTHOR CONTRIBUTIONS

TCH and Y-CC proposed the research idea and wrote the manuscript. C-CL supported the data analysis. H-CT provided the clinical suggestions. C-YW wrote the manuscript and prepared the manuscript for submission. Y-HY and CYH supported the literature review. All authors contributed to the article and approved the submitted version.

FUNDING

This study was supported in part by the Taiwan Ministry of Health and Welfare Clinical Trial Center (MOHW108-TDU-B-212-133004), China Medical University Hospital, the Academia Sinica Stroke Biosignature Project (BM10701010021), the MOST Clinical Trial Consortium for Stroke (MOST 108-2321-B-039-003), the Tseng-Lien Lin Foundation (Taichung, Taiwan), and the Katsuzo and Kiyo Aoshima Memorial Funds (Japan).

ACKNOWLEDGMENTS

This manuscript was edited by Wallace Academic Editing.

REFERENCES

Alonso, A., Krijthe, B. P., Aspelund, T., Stepas, K. A., Pencina, M. J., Moser, C. B., et al. (2013). Simple risk model predicts incidence of atrial fibrillation in a racially and geographically diverse population: the CHARGE-AF consortium. *J. Am. Heart Assoc.* 2:e000102. doi: 10.1161/JAHA.112.000102

Bortnichak, E. A., Freeman, D. H., Jr., Ostfeld, A. M., Castelli, W. P., Kannel, W. B., Feinleib, M., et al. (1985). The association between cholesterol cholelithiasis and coronary heart disease in framingham, massachusetts. *Am. J. Epidemiol.* 121, 19–30. doi: 10.1093/oxfordjournals.aje.a113978

Camm, A. J., Lip, G. Y., De Caterina, R., Savelieva, I., Atar, D., Hohnloser, S. H., et al. (2012). 2012 focused update of the ESC Guidelines for the management of atrial fibrillation: an update of the 2010 ESC Guidelines for the management of atrial fibrillation. developed with the special contribution of the european heart rhythm association. *Eur. Heart J.* 33, 2719–2747. doi: 10.1093/eurheartj/ehs253

Choi, Y. J., Choi, E. K., Han, K. D., Park, J., Moon, I., Lee, E., et al. (2019). Increased risk of atrial fibrillation in patients with inflammatory bowel disease: a nationwide population-based study. *World J. Gastroenterol.* 25, 2788–2798. doi: 10.3748/wjg.v25.i22.2788

Chawla, A., Puthumana, L., and Thuluvath, P. J. (2001). Autonomic dysfunction and cholelithiasis in patients with cirrhosis. *Dig. Dis. Sci.* 46, 495–498. doi: 10.1023/a:1005630711669

Fairfield, C. J., Wigmore, S. J., and Harrison, E. M. (2019). Gallstone disease and the risk of cardiovascular disease. *Sci. Rep.* 9:5830. doi: 10.1038/s41598-019-42327-2

Fan, L. L., Chen, B. H., and Dai, Z. J. (2017). The relation between gallstone disease and cardiovascular disease. *Sci. Rep.* 7:15104. doi: 10.1038/s41598-017-15430-5

Friedman, G. D. (1993). Natural history of asymptomatic and symptomatic gallstones. *Am. J. Surg.* 165, 399–404. doi: 10.1016/s0002-9610(05)80930-4

Friedman, G. D., Raviola, C. A., and Fireman, B. (1989). Prognosis of gallstones with mild or no symptoms: 25 years of follow-up in a health maintenance organization. *J. Clin. Epidemiol.* 42, 127–136. doi: 10.1016/0895-4356(89)90086-3

Gutierrez, A., and Van Wagoner, D. R. (2015). Oxidant and inflammatory mechanisms and targeted therapy in atrial fibrillation: an update. *J. Cardiovasc. Pharmacol.* 66, 523–529. doi: 10.1097/FJC.0000000000000313

Harada, M., Van Wagoner, D. R., and Nattel, S. (2015). Role of inflammation in atrial fibrillation pathophysiology and management. *Circ. J.* 79, 495–502. doi: 10.1253/circj.CJ-15-0138

Hu, W. S., Hsieh, M. H., and Lin, C. L. (2019). A novel atrial fibrillation prediction model for Chinese subjects: a nationwide cohort investigation of 682 237 study participants with random forest model. *Europace* 21, 1307–1312. doi: 10.1093/europace/euz036

Hu, W. S., and Lin, C. L. (2017). Comparison of CHA(2)DS(2)-VASc, CHADS(2) and HATCH scores for the prediction of new-onset atrial fibrillation in cancer patients: a nationwide cohort study of 760,339 study participants with competing risk analysis. *Atherosclerosis* 266, 205–211. doi: 10.1016/j.atherosclerosis.2017.10.007

Huang, C. C., Chan, W. L., Luo, J. C., Chen, Y. C., Chen, T. J., Chung, C. M., et al. (2012). Gastroesophageal reflux disease and atrial fibrillation: a nationwide population-based study. *PLoS One* 7:e47575. doi: 10.1371/journal.pone.0047575

Huang, W. A., Dunipace, E. A., Sorg, J. M., and Vaseghi, M. (2018). Liver disease as a predictor of new-onset atrial fibrillation. *J. Am. Heart Assoc.* 7:e008703. doi: 10.1161/JAHA.118.008703

Hudzik, B., Szkodziński, J., Hawranek, M., Lekston, A., Poloński, L., and Gąsior, M. (2016). CHA2DS2-VASc score is useful in predicting poor 12-month outcomes following myocardial infarction in diabetic patients without atrial fibrillation. *Acta Diabetol.* 53, 807–815. doi: 10.1007/s00592-016-0877-6

Ibrahim, M., Sarvepalli, S., Morris-Stiff, G., Rizk, M., Bhatt, A., Walsh, R. M., et al. (2018). Gallstones: Watch and wait, or intervene? *Cleve. Clin. J. Med.* 85, 323–331. doi: 10.3949/ccjm.85a.17035

Iwasaki, Y. K., Nishida, K., Kato, T., and Nattel, S. (2011). Atrial fibrillation pathophysiology: implications for management. *Circulation* 124, 2264–2274. doi: 10.1161/CIRCULATIONAHA.111.019893

Jakobsen, C. B., Lamberts, M., Carlson, N., Lock-Hansen, M., Torp-Pedersen, C., Gislason, G. H., et al. (2019). Incidence of atrial fibrillation in different major cancer subtypes: a Nationwide population-based 12 year follow up study. *BMC Cancer* 19:1105. doi: 10.1186/s12885-019-6314-9

January, C. T., Wann, L. S., Alpert, J. S., Calkins, H., Cigarroa, J. E., Cleveland, J. C., et al. (2014). 2014 AHA/ACC/HRS guideline for the management of patients with atrial fibrillation: a report of the american college of cardiology/american heart association task force on practice guidelines and the heart rhythm society. *Circulation* 130, e199–e267. doi: 10.1161/CIR.0000000000000041

Jiang, Z. Y., Sheng, X., Xu, C. Y., Li, W. W., Chang, X. X., Sun, L. Y., et al. (2013). Gallbladder gallstone disease is associated with newly diagnosed coronary artery atherosclerotic disease: a cross-sectional study. *PLoS One* 8:e75400. doi: 10.1371/journal.pone.0075400

Kannel, W. B., and Benjamin, E. J. (2009). Current perceptions of the epidemiology of atrial fibrillation. *Cardiol. Clin.* 27, vii13–vii24. doi: 10.1016/j.ccl.2008.09.015

Kanoupakis, E. M., Manios, E. G., Mavrakis, H. E., Kaleboubas, M. D., Parthenakis, F. I., and Vardas, P. E. (2000). Relation of autonomic modulation to recurrence of atrial fibrillation following cardioversion. *Am. J. Cardiol.* 86, 954–958. doi: 10.1016/s0002-9149(00)01129-2

Lammert, F., Gurusamy, K., Ko, C. W., Miquel, J. F., Méndez-Sánchez, N., Portincasa, P., et al. (2016). Gallstones. *Nat. Rev. Dis. Primers* 2:16024. doi: 10.1038/nrdp.2016.24

Lee, H., Choi, E. K., Rhee, T. M., Lee, S. R., Lim, W. H., Kang, S. H., et al. (2017). Cirrhosis is a risk factor for atrial fibrillation: a nationwide, population-based study. *Liver Int.* 37, 1660–1667. doi: 10.1111/liv.13459

Lip, G. Y. H., Nieuwlaat, R., Pisters, R., Lane, D. A., and Crijns, H. J. G. M. (2010). Refining clinical risk stratification for predicting stroke and thromboembolism in atrial fibrillation using a novel risk factor-based approach: the euro heart survey on atrial fibrillation. *Chest* 137, 263–272. doi: 10.1378/chest.09-1584

Lippi, G., Cervellin, G., and Sanchis-Gomar, F. (2015). Galectin-3 in atrial fibrillation: Simple bystander, player or both? *Clin. Biochem.* 48, 818–822. doi: 10.1016/j.clinbiochem.2015.04.021

Lv, J., Qi, L., Yu, C., Guo, Y., Bian, Z., Chen, Y., et al. (2015). Gallstone disease and the risk of ischemic heart disease. *Arterioscler. Thromb. Vasc. Biol.* 35, 2232–2237. doi: 10.1161/ATVBAHA.115.306043

Marcus, G. M., Alonso, A., Peralta, C. A., Lettre, G., Vittinghoff, E., Lubitz, S. A., et al. (2010). European ancestry as a risk factor for atrial fibrillation in African Americans. *Circulation* 122, 2009–2015. doi: 10.1161/CIRCULATIONAHA.110.958306

Olaiya, M. T., Chiou, H. Y., Jeng, J. S., Lien, L. M., and Hsieh, F. I. (2013). Significantly increased risk of cardiovascular disease among patients with gallstone disease: a population-based cohort study. *PLoS One* 8:e76448. doi: 10.1371/journal.pone.0076448

Page, R. L., Wilkinson, W. E., Clair, W. K., McCarthy, E. A., and Pritchett, E. L. (1994). Asymptomatic arrhythmias in patients with symptomatic paroxysmal atrial fibrillation and paroxysmal supraventricular tachycardia. *Circulation* 89, 224–227. doi: 10.1161/01.cir.89.1.224

Reynolds, M. R., Lavelle, T., Essebag, V., Cohen, D. J., and Zimetbaum, P. (2006). Influence of age, sex and atrial fibrillation recurrence on quality of life outcomes in a population of patients with new-onset atrial fibrillation: the fibrillation registry assessing costs, therapies, adverse events and lifestyle (FRACTAL) study. *Am. Heart J.* 152, 1097–1103. doi: 10.1016/j.ahj.2006.08.011

Rodriguez, C. J., Soliman, E. Z., Alonso, A., Swett, K., Okin, P. M., Goff, D. C., et al. (2015). Atrial fibrillation incidence and risk factors in relation to race-ethnicity and the population attributable fraction of atrial fibrillation risk factors: the multi-ethnic study of atherosclerosis. *Ann. Epidemiol.* 25, 71–76. doi: 10.1016/j.annepidem.2014.11.024

Saliba, W., Gronich, N., Barnett-Griness, O., and Rennert, G. (2016). Usefulness of CHADS2 and CHA2DS2-VASc scores in the prediction of new-onset atrial fibrillation: a population-based study. *Am. J. Med.* 129, 843–849. doi: 10.1016/j.amjmed.2016.02.029

Schnabel, R. B., Yin, X., Gona, P., Larson, M. G., Beiser, A. S., McManus, D. D., et al. (2015). 50 year trends in atrial fibrillation prevalence, incidence, risk factors and mortality in the Framingham Heart Study: a cohort study. *Lancet* 386, 154–162. doi: 10.1016/S0140-6736(14)61774-8

Staerk, L., Sherer, J. A., Ko, D., Benjamin, E. J., and Helm, R. H. (2017). Atrial fibrillation: epidemiology, pathophysiology and clinical outcomes. *Circ. Res.* 120, 1501–1517. doi: 10.1161/CIRCRESAHA.117.309732

Upala, S., Sanguankeo, A., and Jaruvongvanich, V. (2017). Gallstone disease and the risk of cardiovascular disease: a systematic review and meta-analysis of observational studies. *Scand. J. Surg.* 106, 21–27. doi: 10.1177/1457496916650998

Villanacci, V., Del Sordo, R., Salemme, M., Cadei, M., Sidoni, A., and Bassotti, G. (2016). The enteric nervous system in patients with calculous and acalculous gallbladder. *Dig. Liver Dis.* 48, 792–795. doi: 10.1016/j.dld.2016.03.014

Wei, C. Y., Chuang, S. H., Lin, C. L., Kung, W. M., Tai, H. C., Tsai, K. W., et al. (2019). Reduced risk of stroke following cholecystectomy: a nationwide population-based study. *J. Gastroenterol. Hepatol.* 34, 1992–1998. doi: 10.1111/jgh.14678

Wei, C. Y., Chung, T. C., Chen, C. H., Lin, C. C., Sung, F. C., Chung, W. T., et al. (2014). Gallstone disease and the risk of stroke: a nationwide population-based study. *J. Stroke Cerebrovasc. Dis.* 23, 1813–1820. doi: 10.1016/j.jstrokecerebrovasdis.2014.04.024

Wirth, J., di Giuseppe, R., Wientzek, A., Katzke, V. A., Kloss, M., Kaaks, R., et al. (2015). Presence of gallstones and the risk of cardiovascular diseases:

the EPIC-Germany cohort study. *Eur. J. Prev. Cardiol.* 22, 326–334. doi: 10.1177/2047487313512218

Xi, Y., James Chao, Z. Y., Yan, W., Abbasi, S., Yin, X., Mathuria, N., et al. (2015). Neuronally released vasoactive intestinal polypeptide alters atrial electrophysiological properties and may promote atrial fibrillation. *Heart Rhythm* 12, 1352–1361. doi: 10.1016/j.hrthm.2015.03.003

Zheng, Y., Xu, M., Heianza, Y., Ma, W., Wang, T., Sun, D., et al. (2018). Gallstone disease and increased risk of mortality: Two large prospective studies in US men and women. *J. Gastroenterol. Hepatol.* 33, 1925–1931. doi: 10.1111/jgh.14264

Zheng, Y., Xu, M., Li, Y., Hruby, A., Rimm, E. B., Hu, F. B., et al. (2016). Gallstones and risk of coronary heart disease: prospective analysis of 270 000 men and women from 3 US cohorts and meta-analysis. *Arterioscler. Thromb. Vasc. Biol.* 36, 1997–2003. doi: 10.1161/ATVBAHA.116.307507

Zimetbaum, P. (2017). Atrial fibrillation. *Ann. Intern. Med.* 166, ITC33–ITC48. doi: 10.7326/AITC201703070

Conflict of Interest: The authors declare that the research was conducted in the absence of any commercial or financial relationships that could be construed as a potential conflict of interest.

Publisher's Note: All claims expressed in this article are solely those of the authors and do not necessarily represent those of their affiliated organizations, or those of the publisher, the editors and the reviewers. Any product that may be evaluated in this article, or claim that may be made by its manufacturer, is not guaranteed or endorsed by the publisher.

Copyright © 2021 Ho, Chen, Lin, Tai, Wei, Yeh and Hsu. This is an open-access article distributed under the terms of the Creative Commons Attribution License (CC BY). The use, distribution or reproduction in other forums is permitted, provided the original author(s) and the copyright owner(s) are credited and that the original publication in this journal is cited, in accordance with accepted academic practice. No use, distribution or reproduction is permitted which does not comply with these terms.

frontiers in Aging Neuroscience

ORIGINAL RESEARCH
published: 07 September 2021
doi: 10.3389/fnagi.2021.705782

Operational Determination of Subjective Cognitive Decline, Mild Cognitive Impairment, and Dementia Using Sum of Boxes of the Clinical Dementia Rating Scale

Yu-Wan Yang[1], *Kai-Cheng Hsu*[1,2,3], *Cheng-Yu Wei*[4], *Ray-Chang Tzeng*[5] *and Pai-Yi Chiu*[6,7]*

[1] Department of Neurology, China Medical University Hospital, Taichung, Taiwan, [2] Department of Medicine, China Medical University, Taichung, Taiwan, [3] Artificial Intelligence Center for Medical Diagnosis, China Medical University Hospital, Taichung, Taiwan, [4] Department of Exercise and Health Promotion, College of Kinesiology and Health, Chinese Culture University, Taipei, Taiwan, [5] Department of Neurology, Tainan Municipal Hospital, Tainan, Taiwan, [6] Department of Neurology, Show Chwan Memorial Hospital, Changhua, Taiwan, [7] Department of Nursing, College of Nursing and Health Sciences, Da-Yeh University, Changhua, Taiwan

Objectives: The Clinical Dementia Rating (CDR) Scale is the gold standard for the staging of dementia due to Alzheimer's disease (AD). However, the application of CDR for the staging of subjective cognitive decline (SCD) and mild cognitive impairment (MCI) in AD remains controversial. This study aimed to use the sum of boxes of the CDR (CDR-SB) plus an SCD single questionnaire to operationally determine the different stages of cognitive impairment (CI) due to AD and non-AD.

Methods: This was a two-phase study, and we retrospectively analyzed the Show Chwan Dementia registry database using the data selected from 2015 to 2020. Individuals with normal cognition (NC), SCD, MCI, and mild dementia (MD) due to AD or non-AD with a CDR < 2 were included in the analysis.

Results: A total of 6,946 individuals were studied, including 875, 1,009, 1,585, and 3,447 with NC, SCD, MCI, and MD, respectively. The cutoff scores of CDR-SB for NC/SCD, SCD/MCI, and MCI/dementia were 0/0.5, 0.5/1.0, and 2.5/3.0, respectively. The receiver operating characteristic (ROC) analysis showed that the area under the curve (AUC) values of the test groups were 0.85, 0.90, and 0.92 for discriminating NC from SCD, SCD from MCI, and MCI from dementia, respectively. Compared with the Cognitive Abilities Screening Instrument or the Montreal Cognitive Assessment, the use of CDR-SB is less influenced by age and education.

Conclusion: Our study showed that the operational determination of SCD, MCI, and dementia using the CDR-SB is practical and can be applied in clinical settings and research on CI or dementia.

Keywords: sum of boxes of the Clinical Dementia Rating, normal cognition, subjective cognitive decline, mild cognitive impairment, dementia

OPEN ACCESS

Edited by:
Kuangyu Shi,
University of Bern, Switzerland

Reviewed by:
Golden Masika,
University of Dodoma, Tanzania
Antonella Lopez,
University of Bari Aldo Moro, Italy

***Correspondence:**
Pai-Yi Chiu
paiyibox@gmail.com

Received: *06 May 2021*
Accepted: *10 August 2021*
Published: *07 September 2021*

Citation:
Yang Y-W, Hsu K-C, Wei C-Y, Tzeng R-C and Chiu P-Y (2021) Operational Determination of Subjective Cognitive Decline, Mild Cognitive Impairment, and Dementia Using Sum of Boxes of the Clinical Dementia Rating Scale. Front. Aging Neurosci. 13:705782. doi: 10.3389/fnagi.2021.705782

INTRODUCTION

The Clinical Dementia Rating (CDR) Scale is a semi-structured interview and a golden standard protocol for investigating people with dementia of the Alzheimer type or probable Alzheimer's disease (AD) (Hughes et al., 1982; Morris, 1997). Many studies have indicated that non-medical personnel reliably apply the CDR Scale to identify and determine the stage of dementia (McCulla et al., 1989; Chaves et al., 2007). Based on the combination of clinical history acquisition and a simple cognitive test, the CDR has become widely used in longitudinal studies and clinical trials to standardize the staging of AD and related disorders (Vos et al., 2013; Williams et al., 2013).

The pre-dementia phases of AD or other dementia, which include subjective cognitive decline (SCD) and mild cognitive impairment (MCI), have gradually attracted the attention of researchers; therefore, robust studies for predicting progression among people in these phases are in full swing (Palmer et al., 2007; Mitchell and Shiri-Feshki, 2009; Snitz et al., 2018; Mazzeo et al., 2019). Although the CDR has been used in many clinical trials or studies, its reliability is suboptimal in very mild dementia (VMD) cases with CDR = 0.5 (Rockwood et al., 2000; Schafer et al., 2004; Duara et al., 2010). However, many studies have indicated that the sum of boxes of the CDR (CDR-SB) can provide additional information to the CDR in detecting VMD and distinguishing these patients from patients with MCI (Lynch et al., 2006; Julayanont and DeToledo, 2020). The CDR-SB score has a wider dynamic range (0–18) than the CDR (0–3) and can be analyzed as an interval variable.

Evidence of CDR utility in dementia diagnosis is robust (McCulla et al., 1989; Morris, 1997; Lynch et al., 2006; Chaves et al., 2007; O'Bryant et al., 2008; Vos et al., 2013; Williams et al., 2013; Julayanont and DeToledo, 2020; Huang et al., 2021). However, the clinical application of CDR-SB in cognitive evaluation among people with SCD or MCI is still lacking. Moreover, when diagnosing dementia due to non-AD, that is, dementia with Lewy bodies (DLB), vascular dementia (VaD), or dementia due to Parkinson's disease (PDD), the question of using the CDR in AD remains to be answered. Less clinical evidence has been provided, and some modifications may be necessary (Lima-Silva et al., 2020).

In our recent experience and studies using artificial intelligence (AI) for the diagnosis of cognitive impairment (CI) and dementia, the CDR and CDR-SB have become perfect references for machine learning in our newly designed questionnaires (Chiu et al., 2019a; Chang et al., 2020; Zhu et al., 2020a,b). Therefore, we highly recommend CDR as a further AI study. For future studies that compare individuals with NC, SCD, and MCI on the risks, prevention, and follow-up for progression to dementia, a reliable, simple, and useful tool is urgently needed. The CDR, which assesses the patient cognition and acquires daily function from their caregivers, is a good candidate staging tool that can fulfill the criteria for clinically urgent and unmet needs.

To test the clinical utility of the CDR-SB for the diagnosis of the different CI stages of AD and non-AD, we designed and analyzed the data from a relatively large dementia database that has been created for registering more than 10,000 individuals. Each individual had detailed clinical data, such as demographic, clinical history, CDR, cognitive and neuropsychological tests, brain imaging, and laboratory findings. Nearly all of them had a definite diagnosis of CI stages and disease subtypes identified by well-experienced neurologists or a consensus group composed of neurologists, psychiatrists, neuroradiologists, nuclear medicine physicians, neuropsychologists, and technicians. CI diagnoses were made using the CDR and other neuropsychological tests. Criteria for AD or vascular cognitive impairment (VCI) were established by the National Institute on Aging and Alzheimer's Association Workgroup (NIA-AA) (McKhann et al., 2011) or the 2011 American Heart Association (AHA) criteria. DLB, Parkinson's disease (PD), PDD, and other disorders (OD) were diagnosed according to the clinical or diagnostic criteria for those disorders. We aimed to define the operational criteria for the differential diagnosis of normal cognition (NC), SCD, MCI, and dementia by determining the cutoff scores using the CDR-SB. In addition, in this study, we hope to provide further evidence of practical diagnostic criteria studying the different CI stages by using the CDR-SB in AD and other brain disorders.

MATERIALS AND METHODS

This study is a retrospective analysis of the dementia registry database from the Show Chwan Healthcare System, currently applied in three centers in Taiwan (two in central Taiwan and one in southern Taiwan). In the database, the detailed clinical history of each participant was recorded using a structured questionnaire called the History-Based Artificial Intelligent Clinical Dementia Diagnostic System (HAICDDS), which has been well-validated (Lin et al., 2018; Chiu et al., 2019a,b, 2020; Tsai and Chiu, 2019; Chang et al., 2020; Wang et al., 2020; Zhu et al., 2020a,b; Huang et al., 2021). In addition, CDR was used for staging dementia, and the daily function was assessed using the Instrumental Activities of Daily Living (IADL) Scale (Lawton and Brody, 1969) and Barthel Index (BI) (Mahoney and Barthel, 1965). Cognitive function was assessed using the Cognitive Abilities Screening Instrument (CASI) (Teng et al., 1994) and Montreal Cognitive Assessment (MoCA) (Freitas et al., 2012). Neuropsychiatric symptoms were assessed using the Neuropsychiatric Inventory (NPI) (Cummings et al., 1994). The CASI and MoCA for all participants were performed by trained neuropsychologists. Informants of the participants were interviewed by well-trained neuropsychologists to perform CDR, IADL, BI, and NPI. Diagnosis of the severity and subtype of dementia or CI was performed by neurologists after the clinical data, such as clinical history, neuropsychological tests, brain imaging, and laboratory data, were completed. Difficult or undetermined cases were discussed in the consensus meetings.

Diagnosis of NC, SCD, MCI, and Dementia

Normal cognition was diagnosed when the participant had a global CDR (Morris, 1993) score of 0 and without subjective memory or other cognitive complaints. Cognitive tests, such as MoCA and CASI, should be in the normal range. The cutoff scores of the NC/MCI of the CASI (83/82) and the MoCA (20/19) were derived from our previous study published in 2019 (Chiu

et al., 2019b). SCD was diagnosed when the participant had a global CDR score of 0 or 0.5 and subjective memory or other cognitive complaints. The cognitive tests, such as MoCA and CASI, should also be in the normal range as in NC. MCI was diagnosed based on the criteria for MCI of the NIA-AA in 2011 (Albert et al., 2011) as a change in cognition with impairment in one or more cognitive tests (CASI or MoCA), but there is no evidence of impairment in social or occupational functioning (IADL > 6) with a CDR score of 0.5. The cutoff scores of MCI/dementia of the CASI (74/73) and the MoCA (14/13) were also derived from the same study published in 2019 (Chiu et al., 2019b). Dementia diagnosis was made according to the criteria for dementia developed by the NIA-AA (Kim et al., 2017). Participants with dementia had impairments in two or more cognitive domains and a decline in daily function (IADL < 7).

Diagnosis of Disease Subtypes

Alzheimer's disease was diagnosed according to the criteria for probable AD developed by the NIA-AA (McKhann et al., 2011). Participants who had evidence of insidious onset and progressive cognitive decline on subsequent evaluations based on information from informants and cognitive testing in the amnestic or other cognitive domains were diagnosed as patients with AD. Vascular cognitive disorder (VCD)/VaD diagnosis was determined according to the 2011 AHA criteria for VCD (Gorelick et al., 2011). CI and clear imaging evidence for vascular disease were available. CI should be due to vascular disease with a temporal relationship between vascular disease and the onset of cognitive deficits. DLB diagnosis was made according to the revised consensus criteria for probable DLB developed by the fourth report of the DLB consortium (McKeith et al., 2017). For probable DLB diagnosis, "two or more core clinical features" or "one core clinical feature, but with one or more indicative biomarkers" is required. Core clinical features include fluctuation in cognition, visual hallucinations, spontaneous parkinsonism, and rapid eye movement (REM) sleep behavior disorder. Indicative biomarkers include abnormal uptake in the metaiodobenzylguanidine scintigraphy and dopamine transporter imaging and REM sleep without atonia in polysomnography. PD/PDD diagnosis was processed according to the 2015 (Postuma et al., 2015) and 2007 (Emre et al., 2007) criteria for probable PD and PDD, respectively. Participants should have parkinsonism, defined as bradykinesia, in combination with either resting tremor, rigidity, or both. Clinically probable PD requires the absence of absolute exclusion criteria and the presence of red flags counterbalanced by supportive criteria. CI or dementia should be diagnosed after a well-established PD for more than 1 year. OD diagnosis with CI or dementia was determined according to their clinical or diagnostic criteria.

Study Procedures

This study is a two-phase study that included the design and test phases. In the design phase, the data from 2015 to 2017 were analyzed. Individuals with NC, SCD, MCI, and dementia due to AD and those without AD were included in the analysis. Non-AD groups included cerebrovascular disease (CVD), VCI, PD with and without dementia, DLB, and OD. The cutoff scores of the CDR-SB for NC/SCD/MCI/mild dementia (MD) were derived.

In the test phase, the data from 2018 to 2020 were analyzed. This study aimed to separate NC/SCD/MCI due to vascular disease, PD, or other brain disorders from pure NC/SCD/MCI without brain disorders. According to clinical criteria or studies, individuals with established brain disorders are essential in diagnosing the progression to the same disease entity (Vanneste, 2000; Starkstein and Jorge, 2005; Emre et al., 2007; Gorelick et al., 2011). However, most of the pure NC/SCD/MCI without other brain disorders are considered to progress to AD instead of VaD, Lewy body disease (LBD), or dementia due to the existing brain disorder (Hsiung et al., 2006; Maioli et al., 2007; Rountree et al., 2007). Therefore, pure NC/SCD/MCI and NC/SCD with vascular disease and vascular CI/no dementia (VCIND) were divided into the AD and VCI/VaD groups, respectively. PD with NC/SCD/MCI or DLB and NC/SCD/MCI with other well-diagnosed brain disorders were divided into the LBD and OD groups, respectively. The NC/SCD/MCI diagnostic criteria in all disease groups were based on the neurocognitive tests with the cutoff scores described in the "Diagnosis of NC, SCD, MCI, and dementia" section. Individuals with NC, SCD, MCI, and MD due to AD or non-AD with a global CDR < 2 were included in the analysis. The cutoff scores of the CDR-SB for NC/SCD/MCI/MD derived from the design phase were all tested in the AD and non-AD groups.

Statistics

The Chinese version of SPSS 22.0 for Windows (IBM, SPSS Inc., Chicago, IL, USA) was used for the statistical analyses. The demographic data in the design phase are summarized descriptively. Comparisons of the demographic data, neuropsychological tests, CDR-SB, IADL, CASI, BI, MoCA, and a composite score of the NPI (Cummings, 1988) were compared between the different groups and analyzed using one-way ANOVA with either Bonferroni or Dunnett's T3 *post-hoc* analysis according to the homogeneity of variance. Sex, CDR, and CI stages and subtypes were analyzed using the chi-square test. Youden's index was applied (maximum = sensitivity ± specificity −1) to determine the cutoff scores for differentiating between the cognitive stages. Spearman's correlation coefficients among age, education, CDR-SB, and CI stages using CDR-SB, MoCA, CASI, and NPI were summarized.

RESULTS

Design Phase

The demographic data of participants in the design phase are summarized in **Table 1**.

A total of 3,498 individuals were included in the design phase. Among them, 233 had NC, 268 had SCD, 599 had MCI, and 2,398 had dementia. According to the diagnosed disease subtypes, 1,622 had AD or NC/SCD/MCI that were not due to VCI, PD, or OD, 777 with CVD/VCI, 793 with LBD (PD/DLB), and 306 with OD, which included 126 with NPH, 106 with TBI, 27 with frontotemporal dementia (FTD), 11 with primary progressive aphasia, and 36 with other diseases. The comparison

TABLE 1 | Demographic data of the participants in the design phase.

	Mean (SD)
N	3,498
Age, years	74.5 (11.4)
Sex, female, *N* (%)	1,975 (56.3)
Education, years	5.1 (4.7)
CDR, 0/0.5/1/2/3, *N*	294/1390/881/624/309
CDR-SB	5.9 (5.3)
CASI	54.4 (28.2)
MoCA	11.2 (8.5)
IADL	4.2 (3.3)
BI	76.6 (34.4)
NPI	8.2 (10.7)
CI severity, NC/SCD/MCI/Dementia	233/268/599/2398
Subtypes, AD/VCI/LBD/OD	1622*/777/793/306
Cutoff scores, NC/SCD/MCI/Dementia	
AD group	0/0.5/1.0/2.5
Non-AD group	0/0.5/1.0/3.0
All participants	0/0.5/1.0/2.5

N, number; SD, Standard deviation; CDR, Clinical Dementia Rating Scale; CDR-SB, Sum of boxes of the Clinical Dementia Rating Scale; CASI, Cognitive Abilities Screening Instrument; MoCA, Montreal Cognitive Assessment; IADL, Instrumental Activities of Daily Living; BI, Barthel Index; NPI, Neuropsychiatric Inventory; CI, cognitive impairment; NC, normal cognition; SCD, subjective cognitive decline; MCI, mild cognitive impairment; AD, Alzheimer's disease; VCI, vascular cognitive impairment; LBD, Lewy body disease; OD, other disorders.

**Participants with NC/SCD/MCI without the cerebrovascular disease (CVD), LBD, or other brain disorders were divided and analyzed in the AD group.*

of demographic characteristics showed significant differences at different stages of CI (**Table 1**).

The cutoff scores of CDR-SB for NC/SCD, SCD/MCI, and MCI/MD in the AD group were 0/0.5, 0.5, 1.0, and 2.0/2.5, respectively. The receiver operating characteristic (ROC) analysis showed that the area under the curve (AUC) in this group was 0.87, 0.86, and 0.95 for discriminating SCD from NC, MCI from SCD, and dementia from MCI, respectively.

The cutoff scores of CDR-SB for NC/SCD, SCD/MCI, and MCI/MD in the non-AD group were 0/0.5, 0.5, 1.0, and 2.5/3.0, respectively. The ROC analysis showed that the AUC in this group was 0.92, 0.97, and 0.96 for discriminating SCD from NC, MCI from SCD, and dementia from MCI, respectively.

The cutoff scores of CDR-SB for NC/SCD, SCD/MCI, and MCI/MD in all the participants were 0/0.5, 0.5, 1.0, and 2.0/2.5, respectively. The ROC analysis showed that the AUC in this group was 0.89, 0.90, and 0.96 for discriminating SCD from NC, MCI from SCD, and dementia from MCI, respectively.

Test Phase

The demographic data of participants in the test phase are summarized in **Table 2**.

A total of 4,381 individuals were included in the test phase. For the diagnosis of CI stages in all participants, 642 patients with NC, 741 with SCD, 986 with MCI, and 2,012 with MD were included. For the diagnosis of normal or CI without other diseases, 436 patients had NC, 544 had SCD, and 650 had MCI. For the diagnosis of normal or CI comorbid with other diseases, there were 1,036 patients with AD dementia, 664 with CVD/VCI, 778 with LBD (PD/DLB), and 273 with OD, which included 81 patients with TBI, 60 with NPH, 37 with a brain tumor, 26 with FTD, 24 with primary progressive aphasia, and 45 with other diseases. The comparison of demographic characteristics showed significant differences among the different stages of CI (**Table 2**).

To determine the cutoff scores in different stages, the NC, SCD, or MCI participants without CVD or parkinsonism were included in the AD group. Participants with CVD, VCI without dementia, or VaD were included in the VCI group. Participants with PD, MCI of PD (PDMCI), PDD, or DLB were included in the LBD group. Participants with other brain disorders were included in the OD group.

The cutoff scores of CDR-SB for NC/SCD, SCD/MCI, and MCI/MD derived from the design phase were applied to the AD group. The ROC analysis showed that the AUC in this group was 0.83, 0.86, and 0.92 for discriminating SCD from NC, MCI from SCD, and MD from MCI, respectively. For the CVD/VCI group, the ROC analysis showed that the AUC in this group was 0.79, 0.96, and 0.93 for discriminating SCD from NC, MCI from SCD, and MD from MCI, respectively. For the LBD group, the ROC analysis showed that the AUC in this group was 0.91, 0.99, and 0.93 for discriminating SCD from NC, MCI from SCD, and MD from MCI, respectively. For the OD group, the ROC analysis showed that the AUC in this group was 0.88, 0.97, and 0.87 for discriminating SCD from NC, MCI from SCD, and MD from MCI, respectively. For all participants, the ROC analysis showed that the AUC in this group was 0.84, 0.90, and 0.92 for discriminating SCD from NC, MCI from SCD, and MD from MCI, respectively (**Table 3**; **Figure 1**).

Spearman's correlation coefficients among age, education, CDR-SB, MoCA, CASI, NPI, and CI stages are summarized in **Table 4**. The CDR-SB and CI stages had decreased correlation with age ($r = 0.43$ and 0.38 for CDR-SB and CI, respectively) or education ($r = -0.34$ and -0.31 for CDR-SB and CI, respectively). On the contrary, cognitive tests such as MoCA and CASI both had a moderate correlation with age ($r = -0.59$ and -0.58 for MoCA and CASI, respectively) or education ($r = 0.62$ and 0.54 for MoCA and CASI, respectively), and all had $p < 0.001$. Furthermore, NPI had the highest correlation with CDR-SB ($r = 0.35$, 0.30, -0.15, and -0.15 for CDR-SB, CI stages, MoCA, and CASI, respectively), with $p < 0.001$ (**Table 4**).

DISCUSSION

This study has demonstrated several important findings that may provide practical methods for clinical settings and epidemiological research. First, the CDR-SB, NC/SCD, MCI, and dementia were used for the operational diagnosis of the prodromal phase of dementia. In addition, this operational diagnostic method is not only applicable to older adults without comorbidity of a brain or systemic disorder but also suitable for persons with CVD, LBD, or other brain disorders, such as TBI and NPH. Second, all subjects underwent regular neurological

TABLE 2 | Comparison of the demographic data among participants with normal cognition, subjective cognitive decline, mild cognitive impairment, and mild dementia in the test phase.

	NC, mean (SD)	SCD, mean (SD)	MCI, mean (SD)	MD, mean (SD)	f/χ^2	*p*-value
N	642	741	986	2,012		
Age, years	63.2 (13.6)	66.3 (12.0)	70.4 (11.0)	77.2 (10.1)	345.3	<0.001[a]
CDR, 0/0.5/1	642/0/0	248/493/0	0/986/0	0/1045/967	4516.2	<0.001[a]
CDR-SB	0.0 (0.1)	0.4 (0.3)	1.3 (0.6)	4.4 (2.4)	1990.5	<0.001[b]
Female, *N* (%)	292 (45.5)	381 (51.4)	478 (47.5)	1170 (58.2)	44.8	<0.001[c]
Education	9.9 (6.9)	8.9 (4.6)	7.5 (5.4)	4.7 (4.8)	242.3	<0.001[d]
IADL	7.8 (0.9)	7.8 (0.6)	7.0 (1.5)	3.2 (2.6)	1830.9	<0.001[e]
MoCA	23.0 (5.9)	22.3 (5.3)	18.3 (5.3)	9.0 (5.4)	1864.0	<0.001[e]
CASI	85.7 (13.2)	85.4 (9.3)	78.2 (9.6)	52.0 (18.3)	1622.5	<0.001[e]
NPI	2.1 (4.0)	2.9 (4.6)	4.9 (7.2)	6.7 (8.9)	90.2	<0.001[b]
Diagnostic group AD/VCI/LBD/OD	436*/77/107/22	544*/73/104/20	650*/102/177/57	1036/412/390/174	179.6	<0.001[f]

NC, normal cognition; SCD, subjective cognitive decline; MCI, mild cognitive impairment; MD, mild dementia; AD, Alzheimer's disease; VCI, vascular cognitive impairment; LBD, Lewy body disease; OD, other disorders; CDR, Clinical Dementia Rating Scale; CDR-SB, Sum of boxes of the Clinical Dementia Rating Scale; IADL, Instrumental Activities of Daily Living; MoCA, Montreal Cognitive Assessment; CASI, Cognitive Abilities Screening Instrument; NPI, Neuropsychiatric Inventory.

**Participants with NC/SCD/MCI without CVD, parkinsonism, or other brain disorders were divided and analyzed in the AD group. Post-hoc analysis: a: NC < SCD < MCI < MD; b: NC = SCD < MCI < MD; c: NC < SCD < MD, NC = MCI, SCD = MCI, MCI < MD; d: NC > SCD > MCI > MD; e: NC = SCD > MCI > MD; f: NC = SCD ≠ MCI ≠ MD.*

TABLE 3 | Comparison of sensitivity, specificity, area under the curve (AUC), and cutoff score among participants with Alzheimer's disease*, vascular cognitive impairment, Lewy body disease, other disorders, and all participants with a sum of boxes of the clinical dementia rating scale in the test phase.

	AD*	VCI	LBD	OD	All
N	2,666	664	778	273	4,381
SCD vs. NC					
N, SCD/NC	544/436	73/77	104/107	20/22	642/741
Sensitivity	0.68	0.63	0.87	0.80	0.71
Specificity	0.98	0.94	0.97	0.95	0.98
AUC	0.83	0.79	0.91	0.88	0.84
AUC 95%CI	0.81–0.86	0.72–0.87	0.87–0.96	0.77–0.99	0.82–0.86
Cutoff	0/0.5	0/0.5	0/0.5	0/0.5	0/0.5
MCI vs. SCD					
N, MCI/SCD	650/544	102/73	177/104	57/20	986/741
Sensitivity	0.73	0.91	0.99	0.97	0.81
Specificity	0.90	0.96	0.97	0.85	0.92
AUC	0.86	0.96	0.99	0.97	0.90
AUC 95%CI	0.84–0.89	0.94–0.99	0.97–1.00	0.93–0.99	0.89–0.92
Cutoff	0.5/1.0	0.5/1.0	0.5/1.0	0.5/1.0	0.5/1.0
MD vs. MCI					
N, MD/MCI	1036/650	412/102	390/177	174/57	2012/986
Sensitivity	0.74	0.80	0.82	0.81	0.80
Specificity	0.97	0.92	0.97	0.84	0.91
AUC	0.92	0.93	0.93	0.87	0.92
AUC 95%CI	0.91–0.93	0.90–0.95	0.91–0.95	0.82–0.91	0.91–0.93
Cutoff	2.0/2.5	2.5/3.0	2.5/3.0	2.5/3.0	2.0/2.5

AD, Alzheimer's disease and participants with NC/SCD/MCI without CVD, parkinsonism, or other brain disorders; VCI, vascular cognitive impairment; LBD, Lewy body disease; OD, other disorders; SCD, subjective cognitive decline; NC, normal cognition; MCI, mild cognitive impairment; MD, mild dementia.*

examinations, thus ensuring the reliable detection of dementia and cognitive function. Moreover, we used two phases (design and test phases) to validate our hypothesis. The results of the two phases were surprisingly persistent. Furthermore, the data used in this study were sourced from the Show Chwan Dementia registry database, and the sample size was large enough to support the study results. Third, the test group results successfully replicated that of the design group. The findings

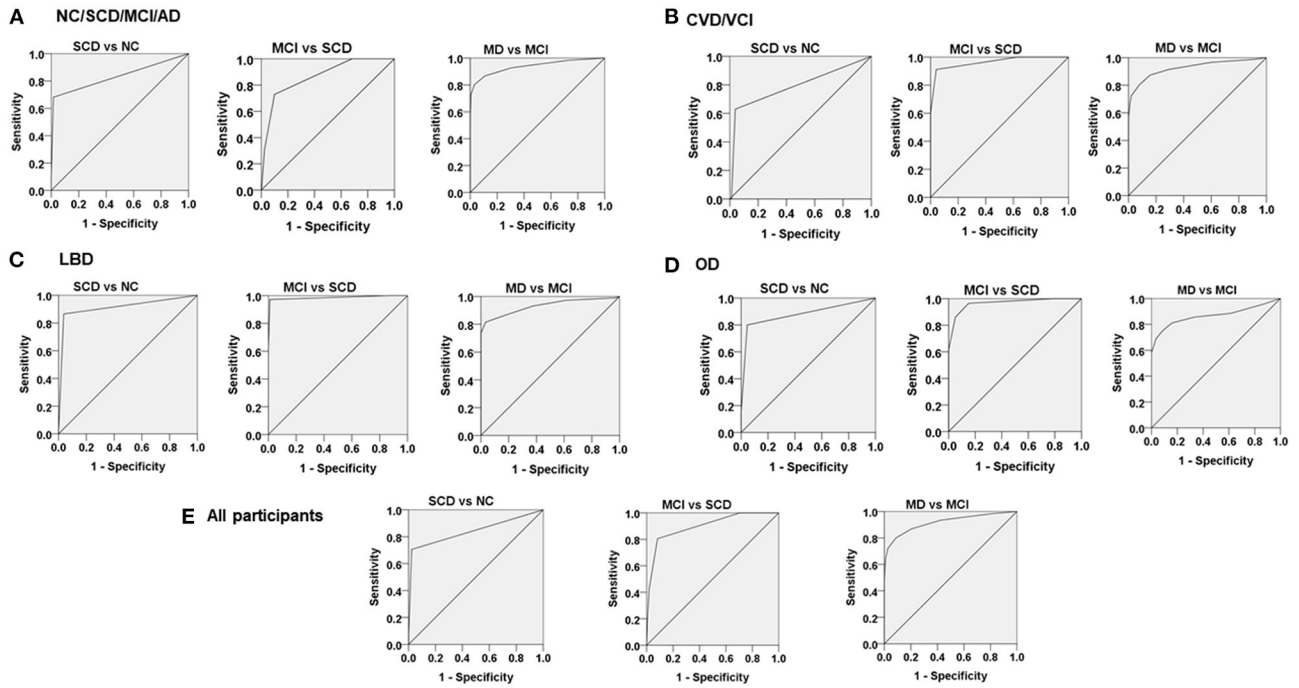

FIGURE 1 | The receiver operating characteristic (ROC) analysis to determine the cutoff scores of the sum of boxes of the Clinical Dementia Rating Scale for normal cognition/subjective cognitive decline (SCD), SCD/mild cognitive impairment (MCI), and MCI/mild dementia among **(A)** the AD group, **(B)** the CVD/VCI group, **(C)** the LBD group, **(D)** the OD group and **(E)** all participants.

TABLE 4 | Spearman's correlation coefficients between age, education, and different diagnostic tools for cognitive impairment.

	Age	Education	CDR-SB	MoCA	CASI	NPI	CI stages
Age	1.00						
Education	−0.49**	1.00					
CDR-SB	0.43**	−0.34**	1.00				
MoCA	−0.59**	0.62**	−0.69**	1.00			
CASI	−0.58**	0.54**	−0.71**	0.97**	1.00		
NPI	0.04*	−0.08**	0.35**	−0.15**	−0.15**	1.00	
CI stages	0.38**	−0.31**	0.83**	−0.66**	−0.64**	0.30**	1.00

CDR-SB, sum of boxes of the Clinical Dementia Rating Scale; MoCA, Montreal Cognitive Assessment; CASI, Cognitive Abilities Screening Instrument; NPI, Neuropsychiatric Inventory; CI stages, cognitive impairment stages grouped using the CDR-SB in all participants.
*$p < 0.01$; **$p < 0.001$.

from both groups were derived from huge study cohorts called the HAICDDS cohorts. These cohorts continue to be followed up, and further longitudinal studies of NC/SC/MCI to dementia progression are warranted and expected. Finally, the universal single-payer healthcare system of Taiwan minimizes barriers to seeking medical treatment (Cheng, 2003; Cheng et al., 2011). This healthcare system decreases selective bias or enrollment difficulty in the study population.

Although AD is the most common cause of dementia, not all types of dementia are AD. Cerebrovascular disease is present in most individuals with dementia, and the dementia risk is increased about 2-fold after stroke (Wolters and Ikram, 2019). Furthermore, VaD is estimated to be ∼30% in Asia, somewhat higher than in North America and Europe (Jhoo et al., 2008; Chan et al., 2013). Risk factors for vascular MCI are treatable, and appropriate treatment can prevent or delay dementia progression. Therefore, this group is an excellent candidate for secondary prevention. However, community-dwelling older adults with vascular MCI are often undetected and are not clinically identified until they develop evident dementia (Meguro and Dodge, 2019). LBD, such as PD and DLB, is the second most common degenerative neurological disorder. LBD is a movement disorder and also presents with multi-domain CI throughout the stages of this disease (Emre et al., 2007; Postuma et al., 2015; McKeith et al., 2017). However, CDR and CDR-SB are seldom used in these patients. Other brain disorders, such as NPH, TBI, and FTD, also demonstrated CI in memory, orientation, judgment, and visuospatial functions throughout the

stages of these diseases, although the characteristics of these diseases might have some differences. The assessment of most of the cognitive domains is already provided in the CDR Scale; therefore, we propose that the CDR and CDR-SB will help assess the different stages of various brain disorders. This study successfully demonstrates that CDR-SB is practical for detecting dementia and CI with fair accuracy. Moreover, CDR-SB can be reliably applied by non-medical personnel to identify and determine the stage of dementia. This result will be useful for public healthcare and dementia prevention in the community.

Some researchers have proposed that in the context of dementia, the global scale of CDR (CDR-GS) had superior pooled specificity compared with the CDR-SB, while similar sensitivities were demonstrated between the CDR-GS and CDR-SB by Huang et al. (2021). Some crucial factors, such as old age, high educational level, high MCI or dementia prevalence in a developing country, and a lack of observations of informants in these studies, may affect the estimation of the result. In this study, we demonstrated that CDR-SB is sufficient to detect dementia and CI in the pre-dementia stages. Based on the premise of memory, orientation/visuospatial functions, judgment/executive functions, community affairs, home hobbies, and personal care being the most involved not only in AD but also in other subtypes of dementia, we have proposed that the CDR-SB is a good tool and provides an operational diagnostic method. However, we would like to collaborate with other researchers using different languages to validate the findings of this study.

This study had several limitations. First, our study was conducted in only three centers in Taiwan using a hospital-based population. The findings and results of CDR-SB may not be generalizable to all individuals with different stages and disease subtypes. Second, the comparison among the different groups in our study was retrospective and cross-sectional. Therefore, further longitudinal follow-up studies to investigate the dementia progression rates in NC, SCD, and MCI participants are warranted.

CONCLUSION

Our findings suggest that the operational determination of SCD, MCI, and dementia using the CDR-SB is practical and can be applied both in clinical settings and on a dementia registration platform. Compared with CASI or MoCA for the CI staging, using CDR-SB was less influenced by age and education.

DATA AVAILABILITY STATEMENT

The original contributions presented in the study are included in the article/supplementary material, further inquiries can be directed to the corresponding author/s.

ETHICS STATEMENT

The studies involving human participants were reviewed and approved by Show Chwan Memorial Hospital. Written informed consent for participation was not required for this study in accordance with the national legislation and the institutional requirements.

AUTHOR CONTRIBUTIONS

Y-WY undertook the literature search and data analysis, edited the author contributions, and was mainly responsible for the revisions and drafts of the manuscript. P-YC participated in the data analysis and contributed to the revisions and final draft of the manuscript. K-CH and C-YW contributed to the revisions of the manuscript. R-CT undertook the literature search and contributed to revisions. All authors contributed to the article and approved the submitted version.

FUNDING

This study was financially supported by the Show Chwan Memorial Hospital No. RD-105032 and the research grants from the Ministry of Science and Technology (K-CH, 110-2321-B-039-003- and 110-2314-B-039-010-MY2).

ACKNOWLEDGMENTS

We thank National Center for High-performance Computing (NCHC) of National Applied Research Laboratories (NARLabs) in Taiwan for providing the computational and storage resources. The authors thank Dr. Hsing-Ju Wu at the Research Assistant Center of the Show Chwan Memorial Hospital for editing the manuscript.

REFERENCES

Albert, M. S., DeKosky, S. T., Dickson, D., Dubois, B., Feldman, H. H., Fox, N. C., et al. (2011). The diagnosis of mild cognitive impairment due to Alzheimer's disease: recommendations from the National Institute on Aging-Alzheimer's Association workgroups on diagnostic guidelines for Alzheimer's disease. *Alzheimers Dement.* 7, 270–279. doi: 10.1016/j.jalz.2011.03.008

Chan, K. Y., Wang, W., Wu, J. J., Liu, L., Theodoratou, E., Car, J., et al. (2013). Epidemiology of Alzheimer's disease and other forms of dementia in China, 1990-2010: a systematic review and analysis. *Lancet* 381, 2016–2023. doi: 10.1016/S0140-6736(13)60221-4

Chang, Y. F., Loi, W. Y., Chiu, P. Y., and Huang, H. N. (2020). Classification of dementia severity in Taiwan based on history-based clinical diagnosis system. *Am. J. Alzheimers Dis. Other Dement.* 35:1533317520970788. doi: 10.1177/1533317520970788

Chaves, M. L., Camozzato, A. L., Godinho, C., Kochhann, R., Schuh, A., de Almeida, V. L., et al. (2007). Validity of the clinical dementia rating scale for the detection and staging of dementia in Brazilian patients. *Alzheimer Dis. Assoc. Disord.* 21, 210–217. doi: 10.1097/WAD.0b013e31811ff2b4

Cheng, C. L., Kao, Y. H., Lin, S. J., Lee, C. H., and Lai, M. L. (2011). Validation of the National Health Insurance Research Database with ischemic stroke cases in Taiwan. *Pharmacoepidemiol. Drug Saf.* 20, 236–242. doi: 10.1002/pds.2087

Cheng, T. M. (2003). Taiwan's new national health insurance program: genesis and experience so far. *Health Aff (Millwood)* 22, 61–76. doi: 10.1377/hlthaff.22.3.61

Chiu, P. Y., Hung, G. U., Wei, C. Y., Tzeng, R. C., and Pai, M. C. (2020). Freezing of speech single questionnaire as a screening tool for cognitive dysfunction in patients with dementia with lewy bodies. *Front. Aging Neurosci.* 12:65. doi: 10.3389/fnagi.2020.00065

Chiu, P. Y., Tang, H., Wei, C. Y., Zhang, C., Hung, G. U., and Zhou, W. (2019a). NMD-12: a new machine-learning derived screening instrument to detect mild cognitive impairment and dementia. *PLoS ONE* 14:e0213430. doi: 10.1371/journal.pone.0213430

Chiu, P. Y., Wei, C. Y., and Hung, G. U. (2019b). Preliminary study of the history-based artificial intelligent clinical dementia diagnostic system. *Show Chwan Med. J.* 18, 18–27. doi: 10.3966/156104972019061801003

Cummings, J. L. (1988). Intellectual impairment in Parkinson's disease: clinical, pathologic, and biochemical correlates. *J. Geriatr. Psychiatry Neurol.* 1, 24–36. doi: 10.1177/089198878800100106

Cummings, J. L., Mega, M., Gray, K., Rosenberg-Thompson, S., Carusi, D. A., and Gornbein, J. (1994). The Neuropsychiatric Inventory: comprehensive assessment of psychopathology in dementia. *Neurology* 44, 2308–2314. doi: 10.1212/WNL.44.12.2308

Duara, R., Loewenstein, D. A., Greig-Custo, M. T., Raj, A., Barker, W., Potter, E., et al. (2010). Diagnosis and staging of mild cognitive impairment, using a modification of the clinical dementia rating scale: the mCDR. *Int. J. Geriatr. Psychiatry* 25, 282–289. doi: 10.1002/gps.2334

Emre, M., Aarsland, D., Brown, R., Burn, D. J., Duyckaerts, C., and Mizuno, Y., et al. (2007). Clinical diagnostic criteria for dementia associated with Parkinson's disease. *Mov. Disord.* 22, 1689–1707. doi: 10.1002/mds.21507

Freitas, S., Simoes, M. R., Alves, L., Vicente, M., and Santana, I. (2012). Montreal Cognitive Assessment (MoCA): validation study for vascular dementia. *J. Int. Neuropsychol. Soc.* 18, 1031–1040. doi: 10.1017/S135561771200077X

Gorelick, P. B., Scuteri, A., Black, S. E., DeCarli, C., Greenberg, S. M., Iadecola, C., et al. (2011). Vascular contributions to cognitive impairment and dementia: a statement for healthcare professionals from the American Heart Association/American Stroke Association. *Stroke* 42, 2672–2713. doi: 10.1161/STR.0b013e3182299496

Hsiung, G. Y. R., Donald, A., Grand, J., Black, S. E., Bouchard, R. W., Gauthier, S. G., et al. (2006). Outcomes of cognitively impaired not demented at 2 years in the Canadian Cohort Study of Cognitive Impairment and Related Dementias. *Dement. Geriatr. Cogn. Disord.* 22, 413–420. doi: 10.1159/000095751

Huang, H. C., Tseng, Y. M., Chen, Y. C., Chen, P. Y., and Chiu, H. Y. (2021). Diagnostic accuracy of the Clinical Dementia Rating Scale for detecting mild cognitive impairment and dementia: a bivariate meta-analysis. *Int. J. Geriatr. Psychiatry* 36, 239–251. doi: 10.1002/gps.5436

Hughes, C. P., Berg, L., Danziger, W. L., Coben, L. A., and Martin, R. L. (1982). A new clinical scale for the staging of dementia. *Br. J. Psychiatry* 140, 566–572. doi: 10.1192/bjp.140.6.566

Jhoo, J. H., Kim, K. W., Huh, Y., Lee, S. B., Park, J. H., Lee, J. J., et al. (2008). Prevalence of dementia and its subtypes in an elderly urban korean population: results from the Korean Longitudinal Study on Health And Aging (KLoSHA). *Dement. Geriatr. Cogn. Disord.* 26, 270–276. doi: 10.1159/000160960

Julayanont, P., and DeToledo, J. C. (2020). Validity of the clinical dementia rating scale sum of boxes in staging and detection of cognitive impairment in Mexican Americans. *J. Geriatr. Psychiatry Neurol.* doi: 10.1177/0891988720973755

Kim, J., Na, H. K., Byun, J., Shin, J., Kim, S., Lee, B. H., et al. (2017). Tracking cognitive decline in amnestic mild cognitive impairment and early-stage Alzheimer dementia: mini-mental state examination versus neuropsychological battery. *Dement. Geriatr. Cogn. Disord.* 44, 105–117. doi: 10.1159/000478520

Lawton, M. P., and Brody, E. M. (1969). Assessment of older people: self-maintaining and instrumental activities of daily living. *Gerontologist* 9, 179–186. doi: 10.1093/geront/9.3_Part_1.179

Lima-Silva, T. B., Mioshi, E., Bahia, V. S., Cecchini, M. A., Cassimiro, L., Guimaraes, H. C., et al. (2020). Disease progression in frontotemporal dementia and Alzheimer disease: the contribution of staging scales. *J. Geriatr. Psychiatry Neurol.* 34, 397–404. doi: 10.1177/0891988720944239

Lin, C. M., Hung, G. U., Wei, C. Y., Tzeng, R. C., and Chiu, P. Y. (2018). An informant-based simple questionnaire for language assessment in neurodegenerative disorders. *Dement. Geriatr. Cogn. Disord.* 46, 207–216. doi: 10.1159/000493540

Lynch, C. A., Walsh, C., Blanco, A., Moran, M., Coen, R. F., Walsh, J. B., et al. (2006). The clinical dementia rating sum of box score in mild dementia. *Dement. Geriatr. Cogn. Disord.* 21, 40–43. doi: 10.1159/000089218

Mahoney, F. I., and Barthel, D. W. (1965). Functional evaluation: the barthel index. *Md. State Med. J.* 14, 61–65. doi: 10.1037/t02366-000

Maioli, F., Coveri, M., Pagni, P., Chiandetti, C., Marchetti, C., Ciarrocchi, R., et al. (2007). Conversion of mild cognitive impairment to dementia in elderly subjects: a preliminary study in a memory and cognitive disorder unit. *Arch. Gerontol. Geriatr.* 44, 233–241. doi: 10.1016/j.archger.2007.01.032

Mazzeo, S., Padiglioni, S., Bagnoli, S., Bracco, L., Nacmias, B., Sorbi, S., et al. (2019). The dual role of cognitive reserve in subjective cognitive decline and mild cognitive impairment: a 7-year follow-up study. *J. Neurol.* 266, 487–497. doi: 10.1007/s00415-018-9164-5

McCulla, M. M., Coats, M., Van Fleet, N., Duchek, J., Grant, E., and Morris, J. C. (1989). Reliability of clinical nurse specialists in the staging of dementia. *Arch. Neurol.* 46, 1210–1211. doi: 10.1001/archneur.1989.00520470070029

McKeith, I. G., Boeve, B. F., Dickson, D. W., Halliday, G., Taylor, J. P., Weintraub, D., et al. (2017). Diagnosis and management of dementia with Lewy bodies: fourth consensus report of the DLB Consortium. *Neurology* 89, 88–100. doi: 10.1212/WNL.0000000000004058

McKhann, G. M., Knopman, D. S., Chertkow, H., Hyman, B. T., Jack Jr, C. R., Kawas, C. H., et al. (2011). The diagnosis of dementia due to Alzheimer's disease: recommendations from the National Institute on Aging-Alzheimer's Association workgroup on diagnostic guidelines for Alzheimer's disease. *Alzheimers Dement.* 7, 263–269. doi: 10.1016/j.jalz.2011.03.005

Meguro, K., and Dodge, H. H. (2019). Vascular mild cognitive impairment: identifying disease in community-dwelling older adults, reducing risk factors, and providing support. The Osaki-Tajiri and Kurihara projects. *J. Alzheimers Dis.* 70, S293–S302. doi: 10.3233/JAD-180899

Mitchell, A. J., and Shiri-Feshki, M. (2009). Rate of progression of mild cognitive impairment to dementia–meta-analysis of 41 robust inception cohort studies. *Acta Psychiatr. Scand.* 119, 252–265. doi: 10.1111/j.1600-0447.2008.01326.x

Morris, J. C. (1993). The Clinical Dementia Rating (CDR): current version and scoring rules. *Neurology* 43, 2412–2414. doi: 10.1212/WNL.43.11.2412-a

Morris, J. C. (1997). Clinical dementia rating: a reliable and valid diagnostic and staging measure for dementia of the Alzheimer type. *Int. Psychogeriatr.* 9, 173–176. doi: 10.1017/S1041610297004870

O'Bryant, S. E., Waring, S. C., Cullum, C. M., Hall, J., Lacritz, L., Massman, P. J., et al. (2008). Staging dementia using Clinical Dementia Rating Scale Sum of Boxes scores: a Texas Alzheimer's research consortium study. *Arch. Neurol.* 65, 1091–1095. doi: 10.1001/archneur.65.8.1091

Palmer, K., Berger, A. K., Monastero, R., Winblad, B., Backman, L., and Fratiglioni, L. (2007). Predictors of progression from mild cognitive impairment to Alzheimer disease. *Neurology* 68, 1596–1602. doi: 10.1212/01.wnl.0000260968.92345.3f

Postuma, R. B., Berg, D., Stern, M., Poewe, W., Olanow, C. W., Oertel, W., et al. (2015). MDS clinical diagnostic criteria for Parkinson's disease. *Mov. Disord.* 30, 1591–1601. doi: 10.1002/mds.26424

Rockwood, K., Strang, D., MacKnight, C., Downer, R., and Morris, J. C. (2000). Interrater reliability of the Clinical Dementia Rating in a multicenter trial. *J. Am. Geriatr. Soc.* 48, 558–559. doi: 10.1111/j.1532-5415.2000.tb05004.x

Rountree, S. D., Waring, S. C., Chan, W. C., Lupo, P. J., Darby, E. J., and Doody, R. S. (2007). Importance of subtle amnestic and nonamnestic deficits in mild cognitive impairment: prognosis and conversion to dementia. *Dement. Geriatr. Cogn. Disord.* 24, 476–482. doi: 10.1159/000110800

Schafer, K. A., Tractenberg, R. E., Sano, M., Mackell, J. A., Thomas, R. G., Gamst, A., et al. (2004). Reliability of monitoring the clinical dementia rating in multicenter clinical trials. *Alzheimer Dis. Assoc. Disord.* 18, 219–222.

Snitz, B. E., Wang, T., Cloonan, Y. K., Jacobsen, E., Chang, C. H., Hughes, T. F., et al. (2018). Risk of progression from subjective cognitive decline to mild cognitive impairment: the role of study setting. *Alzheimers Dement.* 14, 734–742. doi: 10.1016/j.jalz.2017.12.003

Starkstein, S. E., and Jorge, R. (2005). Dementia after traumatic brain injury. *Int. Psychogeriatr.* 17, S93–S107. doi: 10.1017/S1041610205001973

Teng, E. L., Hasegawa, K., Homma, A., Imai, Y., Larson, E., Graves, A., et al. (1994). The cognitive abilities screening instrument (CASI): a practical test for cross-cultural epidemiological studies of dementia. *Int. Psychogeriatr.* 6, 45–58. doi: 10.1017/S1041610294001602

Tsai, C. F., and Chiu, P. Y. (2019). Modified instrumental activities of daily living scale to differentiate severity of cognitive dysfunction in Parkinson's disease. *Show Chwan Med. J.* 18, 107–116. doi: 10.3966/156104972019121802004

Vanneste, J. A. L. (2000). Diagnosis and management of normal-pressure hydrocephalus. *J. Neurol.* 247, 5–14. doi: 10.1007/s004150050003

Vos, S. J., Xiong, C., Visser, P. J., Jasielec, M. S., Hassenstab, J., Grant, E. A., et al. (2013). Preclinical Alzheimer's disease and its outcome: a longitudinal cohort study. *Lancet Neurol.* 12, 957–965. doi: 10.1016/S1474-4422(13)70194-7

Wang, C. T., Hung, G. U., Wei, C. Y., Tzeng, R. C., and Chiu, P. Y. (2020). An informant-based simple questionnaire for visuospatial dysfunction assessment in dementia. *Front. Neurosci.* 14:44. doi: 10.3389/fnins.2020.00044

Williams, M. M., Storandt, M., Roe, C. M., and Morris, J. C. (2013). Progression of Alzheimer's disease as measured by Clinical Dementia Rating Sum of Boxes scores. *Alzheimers Dement.* 9, S39–S44. doi: 10.1016/j.jalz.2012.01.005

Wolters, F. J., and Ikram, M. A. (2019). Epidemiology of vascular dementia. *Arterioscler. Thromb. Vasc. Biol.* 39, 1542–1549. doi: 10.1161/ATVBAHA.119.311908

Zhu, F., Li, X., McGonigle, D., Tang, H., He, Z., Zhang, C., et al. (2020a). Analyze informant-based questionnaire for the early diagnosis of senile dementia using deep learning. *IEEE J. Transl. Eng. Health Med.* 8:2200106. doi: 10.1109/JTEHM.2019.2959331

Zhu, F., Li, X., Tang, H., He, Z., Zhang, C., Hung, G. U., et al. (2020b). Machine learning for the preliminary diagnosis of dementia. *Sci. Program.* 2020:5629090. doi: 10.1155/2020/5629090

Conflict of Interest: The authors declare that the research was conducted in the absence of any commercial or financial relationships that could be construed as a potential conflict of interest.

Publisher's Note: All claims expressed in this article are solely those of the authors and do not necessarily represent those of their affiliated organizations, or those of the publisher, the editors and the reviewers. Any product that may be evaluated in this article, or claim that may be made by its manufacturer, is not guaranteed or endorsed by the publisher.

Copyright © 2021 Yang, Hsu, Wei, Tzeng and Chiu. This is an open-access article distributed under the terms of the Creative Commons Attribution License (CC BY). The use, distribution or reproduction in other forums is permitted, provided the original author(s) and the copyright owner(s) are credited and that the original publication in this journal is cited, in accordance with accepted academic practice. No use, distribution or reproduction is permitted which does not comply with these terms.

frontiers in Aging Neuroscience

ORIGINAL RESEARCH
published: 10 September 2021
doi: 10.3389/fnagi.2021.727654

Using Machine Learning for Predicting the Best Outcomes With Electrical Muscle Stimulation for Tremors in Parkinson's Disease

*Onanong Phokaewvarangkul[1], Peerapon Vateekul[2], Itsara Wichakam[1], Chanawat Anan[1] and Roongroj Bhidayasiri[1,3]**

[1] Department of Medicine, Faculty of Medicine, Chulalongkorn Centre of Excellence for Parkinson's Disease and Related Disorders, Chulalongkorn University and King Chulalongkorn Memorial Hospital, Bangkok, Thailand, [2] Department of Computer Engineering, Faculty of Engineering, Chulalongkorn University, Bangkok, Thailand, [3] The Academy of Science, The Royal Society of Thailand, Bangkok, Thailand

Recent studies have identified that peripheral stimulation in Parkinson's disease (PD) is effective in tremor reduction, indicating that a peripheral feedback loop plays an important role in the tremor reset mechanism. This was an open-label, quasi-experimental, pre- and post-test design, single-blind, single-group study involving 20 tremor-dominant PD patients. The objective of this study is to explore the effect of electrical muscle stimulation (EMS) as an adjunctive treatment for resting tremor during "on" period and to identify the best machine learning model to predict the suitable stimulation level that will yield the longest period of tremor reduction or tremor reset time. In this study, we used a Parkinson's glove to evaluate, stimulate, and quantify the tremors of PD patients. This adjustable glove incorporates a 3-axis gyroscope to measure tremor signals and an EMS to provide an on-demand muscle stimulation to suppress tremors. Machine learning models were applied to identify the suitable pulse amplitude (stimulation level) in five classes that led to the longest tremor reset time. The study was registered at the www.clinicaltrials.gov under the name "The Study of Rest Tremor Suppression by Using Electrical Muscle Stimulation" (NCT02370108). Twenty tremor-dominant PD patients were recruited. After applying an average pulse amplitude of 6.25 (SD 2.84) mA and stimulation period of 440.7 (SD 560.82) seconds, the total time of tremor reduction, or tremor reset time, was 329.90 (SD 340.91) seconds. A significant reduction in tremor parameters during stimulation was demonstrated by a reduction of Unified Parkinson's Disease Rating Scale (UPDRS) scores, and objectively, with a reduction of gyroscopic data ($p < 0.05$, each). None of the subjects reported any serious adverse events. We also compared gyroscopic data with five machine learning techniques: Logistic Regression, Random Forest, Support Vector Machine (SVM), Neural Network (NN), and Long-Short-Term-Memory (LSTM). The machine learning

OPEN ACCESS

Edited by:
Woon-Man Kung, Chinese Culture University, Taiwan

Reviewed by:
Antonio Parziale, University of Salerno, Italy
Satyabrata Aich, Inje University, South Korea

***Correspondence:**
Roongroj Bhidayasiri
rbh@chulapd.org

Received: *19 June 2021*
Accepted: *16 August 2021*
Published: *10 September 2021*

Citation:
Phokaewvarangkul O, Vateekul P, Wichakam I, Anan C and Bhidayasiri R (2021) Using Machine Learning for Predicting the Best Outcomes With Electrical Muscle Stimulation for Tremors in Parkinson's Disease. Front. Aging Neurosci. 13:727654. doi: 10.3389/fnagi.2021.727654

model that gave the highest accuracy was LSTM, which obtained: accuracy = 0.865 and macro-F1 = 0.736. This study confirms the efficacy of EMS in the reduction of resting tremors in PD. LSTM was identified as the most effective model for predicting pulse amplitude that would elicit the longest tremor reset time. Our study provides further insight on the tremor reset mechanism in PD.

Keywords: Parkinson's disease, electrical muscle stimulation, machine learning, tremor, Parkinson's glove, resetting mechanism

INTRODUCTION

Tremor is found in 70% of patients with Parkinson's disease (PD), usually occurring at rest (Hughes et al., 1993; Deuschl et al., 1998). Resting tremors can cause considerable disability for an individual with PD (Hughes et al., 1993), often leading to stigmatization, feelings of shame, and psychological difficulties (Zimmermann et al., 1994; Simpson et al., 2013). The standard treatment of parkinsonian tremors are dopaminergic and anticholinergic medications, but the outcomes are often unreliable when compared to treatment outcomes for other cardinal motor symptoms, such as bradykinesia and rigidity (Jimenez and Vingerhoets, 2012). Moreover, there are no evidence-based therapeutic guidelines that provide the efficacy of specific dopaminergic medications for parkinsonian tremors (Ferreira et al., 2013; Connolly and Lang, 2014). Current therapeutic options for patients who fail to respond adequately to standard treatment include surgical interventions or infusion therapies, which can be associated with various side effects (Benabid et al., 1996; Koller et al., 1997; Krack et al., 1998a,b; Limousin et al., 1998; Pinter et al., 1999; Marjama-Lyons and Koller, 2000; Pogarell et al., 2002; Crosby et al., 2003; Katzenschlager et al., 2003; Ferreira et al., 2013). Therefore, there is a real need to identify a new efficacious treatment, with fewer adverse events, for this symptom.

Although not exactly known, the mechanism of tremorogenesis in PD is complex, generated by interactions between central and peripheral (local mechanical-reflex) loops (Hallett, 1998; Deuschl et al., 2000; McAuley and Marsden, 2000; Deuschl et al., 2001) with the contralateral primary motor cortex likely to be the major driver for tremor in activities selected by the basal ganglia (putamen, globus pallidus, and subthalamic nucleus) (Helmich et al., 2012; Hirschmann et al., 2013). The amplitude of tremor is probably determined by a network within the cerebellum acting through the thalamus (Helmich et al., 2011). The role of peripheral mechanisms for tremor in PD is less clear, but is considered to be involved in the maintenance and modulation of the amplitude of tremor (Deuschl et al., 2000; McAuley and Marsden, 2000). While central tremor generation is the main target for most current PD treatments (e.g., thalamotomy or thalamic DBS), some evidence has indicated that peripheral stimulation involving either mechanical resonance (such as bone, joint, and soft tissue) or feedback resonance (represented as a reflex mechanism) can also generate or modulate tremor even when driven from a central origin (McAuley and Marsden, 2000). In one early study, supramaximal electrical peripheral nerve stimulation inhibited rhythmic EMG activity in parkinsonian tremor for a period of around 200 ms with the duration of inhibition varying inversely with ongoing tremor (Britton et al., 1993). Another study also demonstrated a significant attenuation of parkinsonian tremor (up to 62%) following electrical muscle stimulation (EMS) of the afferent muscles (Javidan et al., 1992). As muscles can generate tremor, direct and strong mechanical conditions imposed upon the muscle might be able to reset tremor, even if that tremor originates from a central source.

Based on promising results from early studies (Mones and Weiss, 1969; Bathien et al., 1980; Lee and Stein, 1981; Britton et al., 1992, 1993), recent investigators have explored the potential of EMS as a treatment of parkinsonian tremor. While efficacy has been replicated in a number of recent studies, others have reported conflicting results associated with potential side effects (Javidan et al., 1992; Maneski et al., 2011; Zhang et al., 2011; Gallego et al., 2013; Bo et al., 2014; Dosen et al., 2014). Our group recently explored the benefits of EMS in the reduction of medically refractory resting tremor in PD patients in both open-label and randomized-controlled studies (Jitkritsadakul et al., 2015, 2017). Significant reductions in transient tremor were achieved during EMS which correlated with a reduction in the clinical tremor score obtained from the Unified Parkinson's Disease Rating Scale (UPDRS) (Jitkritsadakul et al., 2015, 2017). This preliminary evidence supported the possibility of a tremor reset mechanism from EMS (Jitkritsadakul et al., 2015). From direct visual observation, following a 10-s stimulation period, tremor reduction remained stable for a further 10 s after withdrawal of EMS before returning to baseline levels (Jitkritsadakul et al., 2015). Using a 30-s square-wave stimulation, some patients had visual tremor reductions for up to 3 min before their tremor re-emerged to the pre-stimulation level—we interpreted this period as a tremor reset time (Jitkritsadakul et al., 2017). It seems that a longer period of stimulation may produce a longer period of tremor reduction (Jitkritsadakul et al., 2015, 2017).

Recent advances in machine learning analytics in PD have allowed the development of methods that can recognize human motion using training information obtained from multiple sensors. Deep learning, as a type of machine learning that typically involves multilayered neural networks to perform a variety of input-output modeling tasks, has been shown to be capable of detecting tremor (Yao et al., 2019), motor fluctuations (Aich et al., 2020), and freezing of gait (Sigcha et al., 2020) in PD; however, no prior studies have investigated the role of machine learning for predicting the best outcomes with EMS for tremor in PD. We hypothesized that EMS had a direct

tremor reduction effect, and the higher pulse amplitude and/or the greater stimulation time may produce a longer tremor reset time. Therefore, the objectives of this study were to: (1) evaluate the effect of EMS and the tremor reduction in PD; (2) assess the level of pulse amplitude that produces significant tremor reduction with the longest tremor reset time; and (3) identify the best machine-learning model for predicting stimulation levels that yield the longest tremor reset time.

MATERIALS AND METHODS

This was an open-label, quasi-experimental, pre- and post-test design, single-blind, single-group study involving 20 PD patients. The study was conducted at Chulalongkorn Centre of Excellence for Parkinson's Disease and Related Disorders[1] The study protocol was approved by the Institutional Review Board, Faculty of Medicine, Chulalongkorn University (IRB 483/57). The IRB granted us to permission this treatment as an adjunctive treatment during "on" period when patients were optimized on oral medications. Information regarding this research study was provided and written informed consent was obtained from every subject at enrollment in accordance with the declaration of Helsinki. The study was registered at the www.clinicaltrials.gov under the name "The Study of Rest Tremor Suppression by Using Electrical Muscle Stimulation" (NCT02370108) with the translation of study protocol provided as the **Supplementary Material 1**. **Supplementary Figure 1** provides a complete detailed CONSORT flowchart. A TREND checklist is provided as the **Supplementary Material 2**. All subjects met the clinical diagnosis criteria for PD according to the United Kingdom Parkinson's Disease Society Brain Bank criteria (Hughes et al., 1993). As tremors in Parkinson's disease patients are heterogeneous presentation and classified in 3 different types of tremor patterns, including class I tremor, class II tremor, and class III tremor. In order to reduce clinical heterogeneity of tremor, we recruited only PD patients with type 1, classic Parkinsonian tremor according to the consensus statement of the Movement Disorder Society (Deuschl et al., 1998). In addition, all patients must have drug resistant tremor as defined as the subjects either failed to experience a clinically relevant and useful improvement in tremor under an optimized antiparkinsonian therapy with various agents, or side effects encountered under an effective anti-tremor therapy were intolerable. We also recruited only subjects whose tremor were unresponsive to at least 2 oral dopaminergic medications and anticholinergics (Jitkritsadakul et al., 2015). None of participants received device-aided therapies, such as infusion therapy or deep brain stimulation. Similar details of inclusion and exclusion criteria were shown in our previous study (Jitkritsadakul et al., 2015). The calculation of the sample size was based on the results of the RMS of the angular velocity before and during stimulation from previous publication (Jitkritsadakul et al., 2015), which suggested that at least 7 subjects were required for the comparison for tremor outcomes in this study (**Supplementary Material 3**).

[1]www.chulapd.org

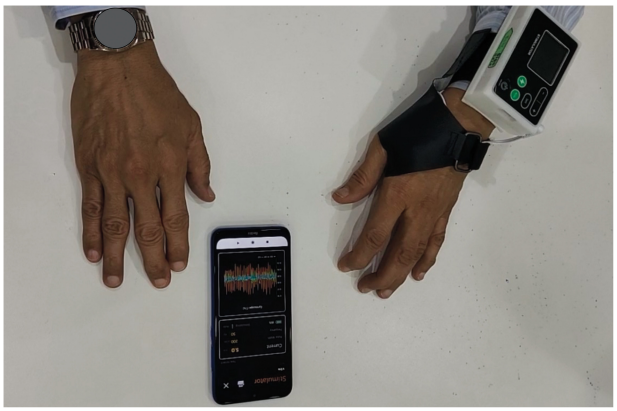

FIGURE 1 | The Parkinson's glove. The Parkinson's glove is a specially designed adjustable glove, which incorporates a tremor detection module and an electrical muscle stimulation module to detect and suppress resting hand tremors. The control panel was developed using an Android application on a mobile phone connected via Bluetooth to the Parkinson's glove.

Procedures

Before enrollment, all recruited patients received stable anti-parkinsonian medications for at least 30 days. A movement disorder neurologist (OP) conducted individual interviews with participants to obtain their demographics and clinical data relevant to the study. Parkinsonian and tremor assessments, both clinical and objective, were done for each patient to determine the severity of PD symptoms during both "off" and "on" periods. Physical examinations of each patient were recorded by video for later review. Parkinsonian symptoms were clinically assessed according to the UPDRS and Hoehn and Yahr (HY) scale. Marked tremor criteria are clinically defined by a sum score of at least 8 out of 32 on UPDRS tremor items 16, 20, and 21 (tremor score), or, if the tremor is present on one side only, by a tremor score of at least 6 out of 32 (Zimmermann et al., 1994; Pogarell et al., 2002). Parkinsonian tremors were objectively assessed with the tremor detection module of a Parkinson's glove during both "off" and "on" periods, however, the assessment of tremor during stimulation was done during "on" periods only (2–3 h after the last intake of medications) in order to evaluate the additional benefits of EMS for tremor reduction. Standard oral medications for PD tremor usually give a maximum of 50% tremor reduction for each dose (Kartzinel et al., 1976; Pogarell et al., 2002), therefore, in this study, tests during the "on" period were only conducted to see whether EMS could provide additional benefits to tremor reduction as an adjunctive treatment to current oral medications.

Parkinson's Glove

In this study, we used the Parkinson's glove to evaluate, stimulate, and quantify parkinsonian tremors. A Parkinson's glove is a unique adjustable glove used to treat tremors, which

integrates both a tremor detection module and an EMS module, and is worn on the most tremulous hand (**Figure 1**). The tremor detection module was a 3-axis gyroscope that measures tremor signals from angular displacements of motion (Gallego et al., 2010). A fast Fourier transform algorithm was calculated and graphed for tremor amplitude and frequency. The EMS module was designed to function identically to the approved EMS standard, and received approval for electronic product testing from the electrical and electronic products testing center (PTEC) in Thailand. The EMS module provided continuous stimulation with a square-wave pulse to the affected muscles via two surface electrodes under either manual or automatic control. The controller, with an embedded sensor, was placed over the patient's wrist. The control panel was developed using an Android application on a mobile phone connected via a Bluetooth connection to the Parkinson's glove. Real-time tremor signals and stimulation protocols were transferred automatically and recorded in the internal memory of a mobile phone, which could then be uploaded onto a Cloud system for further analysis. Similar details for the Parkinson's glove development are shown in our previous study (Jitkritsadakul et al., 2017). A patent application number of the Parkinson's glove has been filed to the Thai Intellectual Property Office (Application number 1701000170).

Tremor Experiment

Tremor assessment was conducted in a quiet room. All participants wore the Parkinson's glove on their most tremulous hand with two self-adhesive electrodes placed over the thenar muscle as well as the first and second interosseous muscles. Participants were instructed to sit comfortably in an armchair and asked to close their eyes while counting backward to encourage the resting tremor. After turning on the Parkinson's glove, the tremor detection module was used to quantify the intensity of tremor signals throughout the session. Meanwhile, an EMS module was used to stimulate the patient's hand muscles to reduce tremors. Stimulation was performed manually by the attending physician to identify the most effective stimulation protocol for tremor reduction. There are three main stimulation parameters for an EMS: pulse amplitude, pulse width, and frequency. As depicted in **Figure 2**, pulse amplitude is the intensity of the stimulation, measured in milliampere (mA), pulse width is the duration of each stimulus, measured in microseconds (μs), and frequency is the number of stimuli delivered per second, measured in hertz (Hz). In this study, each subject only underwent the experimental procedure once, and the total experiment time was approximately 30 min for each subject. We divided the experiment into 3 sections as follows (**Figure 3**).

1. Before stimulation: The period when the tremor detection module is turned on, but the EMS module is still turned off. Tremor signals were measured continuously by the tremor detection module to give baseline data. This section usually took 5 min.
2. During stimulation: The period when the tremor detection module and the EMS module were both turned on. Two stimulation parameters, frequency (50 Hz) and pulse width (150 μs), were kept constant while the attending physician increased the stimulation intensity by slowly raising the pulse amplitude by 1 mA approximately every 10 s (1 mA, 2 mA, 3mA,. . ., etc.) until the tremor was reduced and the criteria for tremor reduction achieved. If a maximum pulse amplitude was identified, the physician then provided continuous stimulation at that pulse amplitude for approximately further 30 s before turning off the EMS. Criteria for significant tremor reduction in this study were determined by direct observation, including (1) a more than 50% tremor reduction from the clinical rating scale (UPDRS tremor score), and/or (2) a more than 50% tremor reduction identified by real-time gyroscope signals. For patients who did not meet these significant tremor reduction criteria, the physician turned off the stimulation if a visualized tetanic muscle contraction was achieved without pain. Tremor signals were measured continuously by the tremor detection module during the whole stimulation period. This section usually took 10–15 min.
3. After stimulation: The period when the EMS module was turned off, but the tremor detection module remained on. After turning off the EMS, tremor signals were measured continuously by the tremor detection module until the tremor signals returned to pre-stimulation levels. The duration of tremor reduction from EMS initiation until tremor re-emergence to pre-stimulation levels is termed the tremor reset time (Jitkritsadakul et al., 2015). This section usually took 10 min.

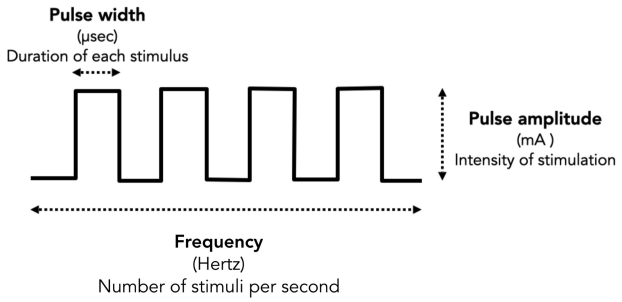

FIGURE 2 | Stimulation parameters. There are main three stimulation parameters determine for the size and intensity of each stimulus of an EMS including pulse amplitude, pulse width, and frequency. Pulse amplitude is the intensity of the stimulation, measured in milliampere (mA). Pulse width is the duration of each stimulus, measured in microseconds. Frequency is the number of stimuli delivered each second, measured in hertz (Hz).

Safety profiles were assessed by recording the frequencies and severity of reported adverse events during stimulation and in a 1-month follow-up period. Any new symptoms or worsening of pre-existing symptoms was documented for each participant.

Data Collecting Process

The control panel for the Parkinson's glove was developed as an Android application for mobile phones using a

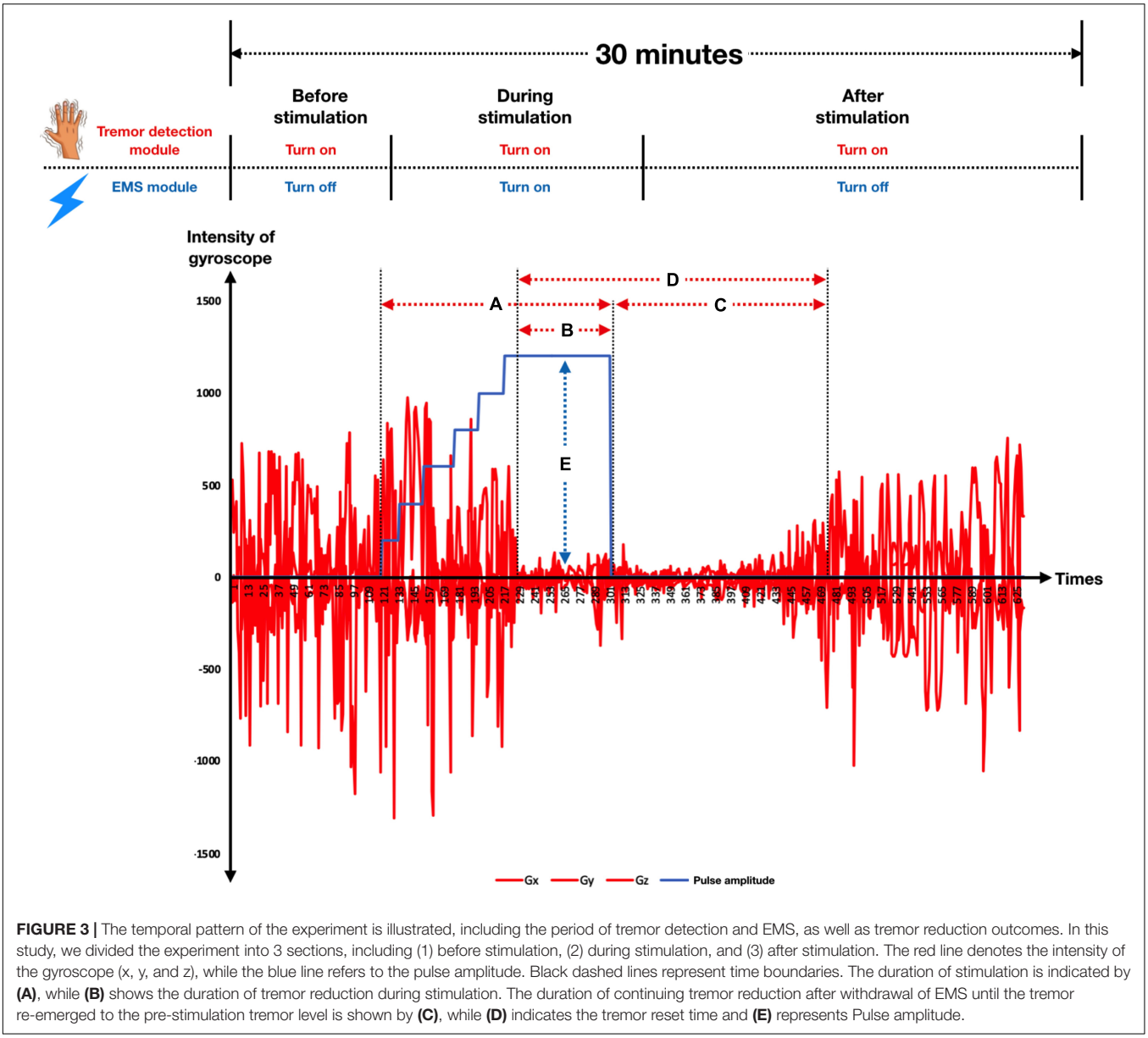

FIGURE 3 | The temporal pattern of the experiment is illustrated, including the period of tremor detection and EMS, as well as tremor reduction outcomes. In this study, we divided the experiment into 3 sections, including (1) before stimulation, (2) during stimulation, and (3) after stimulation. The red line denotes the intensity of the gyroscope (x, y, and z), while the blue line refers to the pulse amplitude. Black dashed lines represent time boundaries. The duration of stimulation is indicated by **(A)**, while **(B)** shows the duration of tremor reduction during stimulation. The duration of continuing tremor reduction after withdrawal of EMS until the tremor re-emerged to the pre-stimulation tremor level is shown by **(C)**, while **(D)** indicates the tremor reset time and **(E)** represents Pulse amplitude.

Bluetooth connection so that the investigators could control and save tremor signals and stimulation parameters (**Figure 1**). Real-time tremor signals in every axis and stimulation protocol were saved to the internal memory of a mobile phone and automatically uploaded to a Cloud system as.csv files for further analysis. Raw motion signals from the gyroscope were calculated using the root mean square of angular velocity for each axis (RMS_x, RMS_y, RMS_z) and tremor frequency for each axis. After receiving the collected data, regression analysis was used to determine the predictive factors for the longest tremor reset time, and a supervised machine learning approach used to identify the suitable stimulation levels that will yield the longest tremor reset time.

Data Analysis

The baseline characteristics and tremor parameters were summarized using either means and standard deviations (SD), or frequencies and percentages as appropriate. The Wilcoxon–Mann–Whitney test was used to compare the efficacy of stimulation based upon the tremor parameters between the before-stimulation and during-stimulation measurements. The Chi-square test was used for categorical data. Correlation analysis was performed using Spearman's correlation to determine the relationship between stimulation parameters and tremor reduction outcomes. The correlation coefficient (r) was interpreted as the strength of correlation as either weak, moderate, or high correlation (Taylor, 1990). Multiple linear regression analysis was carried out to predict the factors that lead to the longest tremor reset time. The multiple correlation

coefficient is an index of how well a dependent variable can be predicted from a linear combination of independent variables. It ranges from 0 (zero multiple correlations) to 1 (perfect multiple correlations) and the value of R^2 is the coefficient of determination. A $p < 0.05$ (two-tailed) was considered statistically significant. Statistical analysis for this study was based on the SPSS program version 23.0 software (SPSS Inc., Chicago, IL).

Automatic Pulse Amplitude Prediction Models

Normally, physicians use manually controlled variation of stimulation to achieve an appropriate pulse amplitude setting for EMS, based on tremor intensity. However, as tremor intensity can fluctuate between individual PD patients, this method is impractical in a real-life scenario. To overcome this challenge, it is crucial to develop a machine learning model to automatically predict the suitable pulse amplitude for individual patients. In this study, the pulse amplitude level (target variable) is divided into five stimulation classes suggested by physicians as shown in **Table 1**, representing low to high stimulation levels.

Developments using standard machine learning require several steps, including data preprocessing, model construction, and model evaluation (Bizzego et al., 2019). The first step, data pre-processing, was the capture of raw motion signals from the gyroscope (G_x, G_y, G_z) along with pulse amplitude (I_t) and timestamp (t). Then, these gyroscope signals were aggregated using Root Mean Square (RMS) during an interval of 1 s resulting in RMS of each axis (RMS_x, RMS_y, RMS_z), so each observation (row) represented a signal of 1 s interval using RMS, with the main outcome for prediction stimulation level, categorized into one of the five classes (low to high). We also investigated the effect of the stimulation level at the previous timestep (t−1) since stimulation adjustment is usually gradual; for example, the pulse amplitude level "3" is normally changed to either "2" or "4," not suddenly jumped to "0" or "5." Therefore, there were four inputs in total (RMS_x, RMS_y, RMS_z, I_{t-1}). During the training phase, we applied a training strategy called "the teacher forcing algorithm" (Williams and Zipser, 1989) by supplying observed sequence values as inputs. In our case, we supplied the pulse amplitude level from the previous step, adjusted by physicians into the model. For the testing phase, the model was evaluated on the data collected from the physician's process. Thus, it is a limitation of this study that the previous stimulation level used for the model was based on observed data, not from the model prediction so in the discussion section, we have provided a suggestion of how to deploy our model in real-life scenarios. Also, some data points needed to be removed due to manual pulse amplitude adjustments, e.g., no pulse amplitude assigned during the tremor period as shown in **Figure 3**. These data points are removed because they are bad examples for the model and can weaken model performance. In summary, the main outcome for prediction was stimulation level, which was categorized into five classes (low to high) as shown in **Table 1**. There were two feature sets; (1) only gyroscope signals and (2) gyroscope signals with the previous stimulation level.

TABLE 1 | Categorized stimulation class into 5 classes based on pulse amplitude levels.

Pulse amplitude level (mA)	Stimulation class (low to high)
0	0
1–5	1
6–10	2
11–15	3
> = 16	4

mA, milliampere; Greater stimulation class represents higher pulse amplitude level.

The second development step concerns model construction. A machine learning model was applied to learn from the cleaned data using a multiclass classification that aimed to predict the pulse amplitude class (of the five) of stimulation required. Here we employed and compared five prediction techniques: (1) logistic regression, (2) random forest, (3) support vector machine (SVM) (Boser et al., 1992), (4) Neural Network (NN), and (5) long-short-term-memory (LSTM) (Hochreiter and Schmidhuber, 1997). Since this is a classification task, logistic regression was chosen as our baseline technique. Random forest is an ensemble of decision trees. It is developed to overcome the instability that a single classification or regression tree exhibits with minor perturbations of training data. Each tree is constructed using perturbed training data by sampling both rows (samples) and columns (variables); thus, it produces a variation among the trees in the ensemble. The settings for random forest were: the number of trees is 100, the number of sampled features is a squared root of total features, and observations are sampled using bootstrapping (sampling with replacement). SVM, one of more popular machine learning algorithms designed for a classification task, finds a separation hyperplane that maximizes between two classes, as shown in **Figure 4** (Larhmam, 2018). The settings of SVM were: the kernel is radial basis function (RBF) and regularized parameter (C) is 1. Neural Network is built up with two hidden layers with 100 hidden units. Implementation of linear regression, random forest, SVM, and NN are all based on the scikit-learn library in Python.

For the deep learning approach, LSTM was chosen since it is a recurrent neural network, commonly used for time–series data. It takes information from both the previous steps (short-term memory) and the long-term dependencies into account as shown in **Figure 5** (Olah, 2015). The model is uni-directional, not bi-directional since we aim to predict the next time step; thus, future data cannot be used. The settings of LSTM were: there are two layers with 100 hidden units, follow by a dense layer with softmax activation and Adam optimization applied with the learning rate of 0.001. The implementation is based on the Tensorflow/Keras library.

The third, and final, step of model development is the evaluation. Here, all prediction models were applied and compared based on threefold cross validation as shown in **Figure 6**. Each fold contains a different set of patients, where the results are averaged on all three testing sets rather than just one set of testing data, so avoiding an overfitting result. In our data set, there were 20 PD patients, so there were 7, 7,

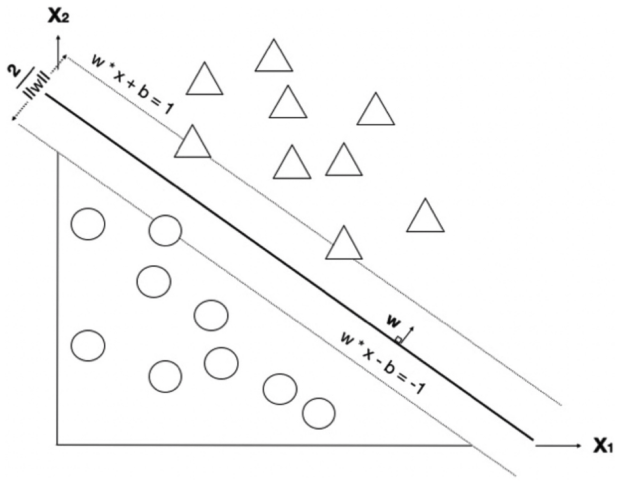

FIGURE 4 | A decision boundary for support vector machine (SVM) that tries to maximize the boundary between two classes. Image shows a maximum-margin hyperplane and margin for an SVM trained on two classes. Samples on margins are called support vectors. x refers to each feature; there are two features in this example (x_1 and x_2). Each circle refers to a datum point, where blue and green refer to different classes. There are two learning parameters from the model; w and b are weights and bias, respectively. The margin between the two classes is 2/||w|| .

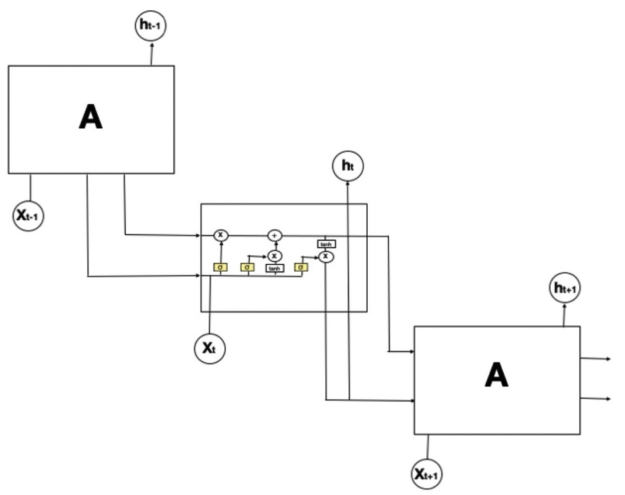

FIGURE 5 | The structure of long-short-term-memory (LSTM). The repeating module in an LSTM contains four interacting layers. In this figure, an LSTM model is expanded into 3-time steps (t−1, t, t+1). The middle box refers to the model at the current time with an input x_t. Since LSTM is a recurrent neural network, it also obtains two outputs from the previous time step: the lower arrow is the short-term memory output (h_{t-1}) and the upper arrow is the long-term memory.

and 6 patients in each fold, respectively. The data is separated into threefold by patients in order to avoid information leaking should data of the same patient be in both training and testing datasets. **Table 2** illustrates the data statistics collected from 20 PD patients showing the number of records for each fold along with percentage of each stimulation class. However, each fold may have a slight difference in class distribution since the data is separated based on patients.

Evaluation measures, precision (P), recall (R or called sensitivity), and F1 (the harmonic mean between precision and recall) were calculated based on a confusion matrix that has True Positive (tp), True Negative (tn), False Positive (fp), and False Negative (fn) as the components. The calculation method of P, R, and F1 is shown in the equation below. Since there are five classes, the overall performance is an averaging of performance from all classes called "Macro Averaging" (Macro-Precision, Macro-Recall, and Macro-F1).

$$P = \frac{tp}{tp+fp}, \quad R = \frac{tp}{tp+fn}, \quad F1 = 2\frac{RP}{R+P}$$

To imitate this manual process of stimulation adjustment, it is intended that stimulation levels are automatically calibrated by the model based on the previous stimulation level predicted by the model. The amount of pulse amplitude can be gradually increased by 1 mA to reach the maximum level (0, 5, 10, 15, 20 mA for levels 0, 1, 2, 3, 4, respectively). For the stimulation duration, EMS can be continued until RMS_x and RMS_y are reduced by at least 2.5 times those recorded at the start, indicating a significant tremor reduction.

RESULTS

Patients Demographic and Characteristics

The demographic and baseline clinical characteristics are summarized in **Table 3**. All 20 PD patients were of the tremor predominant subtype, which was confirmed by kinematic studies for a classic type 1 Parkinsonian tremor according to the consensus statement (Deuschl et al., 1998). From **Table 4**, the reduction of the UPDRS score during stimulation, the reduction of the UPDRS tremor score during stimulation and the UPDRS tremor score for the most affected hand was greater than before stimulation ($p < 0.001$, each) and a consistent reduction of RMS in the x-, y-, and z-axis was achieved ($p < 0.001$, $p = 0.001$, and $p < 0.001$, respectively). However, there was no statistical difference in tremor frequency between the before-stimulation and the during-stimulation measurements in all axes. Mean maximum pulse amplitude was 9.45 (SD ± 4.29) mA (min–max: 3–17, average pulse amplitude was 6.25 (SD ± 2.84) and mean stimulation period was 440.7 (SD ± 560.82) seconds (min–max: 42–2382). During EMS, the duration of tremor reduction during stimulation lasted for 200.35 (SD ± 170.21) seconds (min–max: 42–596) and the duration of continuing tremor reduction after the withdrawal of EMS until the tremor re-emerged to the pre-stimulation level was 129.55 (SD ± 226.7) seconds (min–max: 0–1032). The tremor reset time was 329.90 (SD ± 340.91) seconds (min–max: 73–1628). None of the subjects reported any serious adverse events, including numbness, burning sensation, or fatigue occurring at the stimulation sites during the examination or at the 1-month follow-up visit.

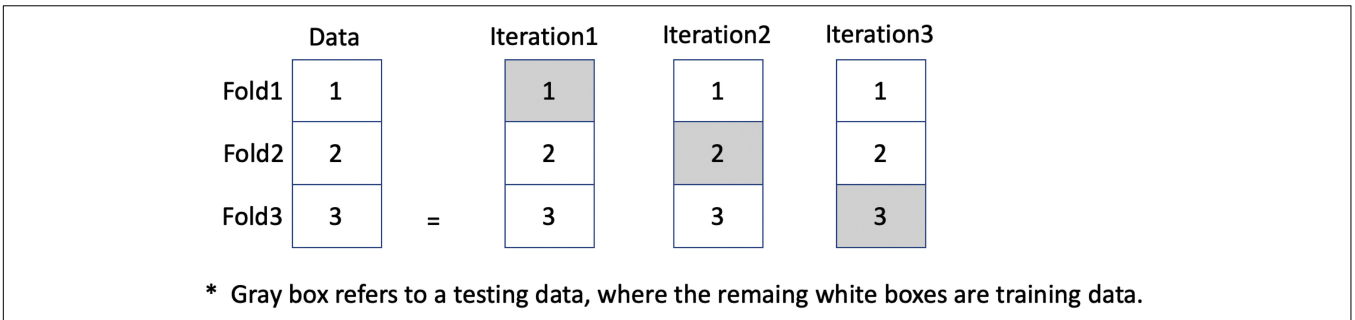

FIGURE 6 | An illustration of threefold cross validation in order to avoid overfitting results. Gray box refers to testing data, where the remaining white boxes are training data.

TABLE 2 | Data statistics of data collected from 20 PD patients.

		Class 0	Class 1	Class 2	Class 3	Class 4	Total
Fold1	#records	3,191	1,280	573	406	87	5,537
7 PD's	%records	57.16	25.60	9.39	6.45	1.38	100
Fold2	#records	1,798	1,879	1,076	228	0	4,981
7 PD's	%records	34.68	43.33	18.54	3.44	0	100
Fold3	#records	3,303	775	2,558	796	9	7441
6 PD's	%records	43.34	20.65	21.37	14.21	0.41	100
Total	#records	2,511	1,169	882	453	34	5,049
	%records	49.73%	23.15%	17.47%	8.97%	0.67%	100%

Each row refers to an interval of 1 s. Only two patients with data in Class 4; thus, there are only twofolds with Class 4's data.

Results of Correlation Analysis

Correlation analysis was performed to evaluate the relationship between stimulation parameters and tremor reduction outcomes according to **Table 5**. Significant correlations between tremor reset time and the following stimulation parameters were identified: max pulse amplitude ($r = 0.567$, $p = 0.008$), average pulse amplitude ($r = 0.495$, $p = 0.035$), stimulation time ($r = 0.586$, $p = 0.007$), and duration of tremor reduction during stimulation ($r = 0.773$, $p < 0.001$). In addition, significant correlations between tremor reset time and the following tremor reduction outcomes were identified: delta UPDRS tremor limb ($r = 0.505$, $p = 0.023$), delta RMS_x ($r = 0.456$, $p = 0.043$), and delta RMS_y ($r = 0.459$, $p = 0.042$). Delta is the difference of outcome between before and during stimulation. Furthermore, significant correlations between average pulse amplitude and the following stimulation parameters were identified: max pulse amplitude ($r = 0.787$, $p < 0.001$), duration of continuing tremor reduction after the withdrawal of EMS until the tremor re-emerged to the pre-stimulation level ($r = 0.474$, $p = 0.035$), and tremor reset time ($r = 0.495$, $p = 0.027$). In addition, significant correlations between average pulse amplitude and the following tremor reduction outcomes were identified: delta RMS_x ($r = 0.686$, $p = 0.001$), delta RMS_y ($r = 0.789$, $p < 0.001$), and delta RMS_z ($r = 0.746$, $p < 0.001$). Finally, significant correlations between stimulation and the following stimulation parameters were identified: max pulse amplitude ($r = 0.552$, $p = 0.012$), duration of tremor reduction during stimulation ($r = 0.866$, $p < 0.001$), and tremor reset time ($r = 0.586$, $p = 0.007$).

Results of the Multiple Linear Regression Analysis

An additional multiple linear regression analysis with a stepwise method was carried out to predict factors that would yield the longest period of tremor reset time. After including multiple parameters to the stepwise model, including; average pulse amplitude, max pulse amplitude, stimulation time, LED, Hoehn and Yahr stage, Age, disease duration, TMSE score, UPDRS III—off period, UPDRS III tremor—off period, UPDRS III tremor limb– off period, UPDRS III—on period, UPDRS III tremor—on period, and UPDRS III tremor limb– on period. We found the average pulse amplitude and the stimulation time were predictive factors for the tremor reset time in a mathematic model: $D = -98.336 + 48.559\ (E) + 0.282\ (A)$; where "D" represents tremor reset time (seconds), "E" represents the average pulse amplitude (mA), and "A" represents stimulation time (seconds). In this model, the multiple correlation coefficient was 0.712, while the coefficient of the determinant was 50.7%. Based on the conclusions provided by the model, a higher average pulse amplitude and a greater stimulation time results in a longer tremor reset time.

Results of Automatic Pulse Amplitude Prediction Models

We aimed to find the most effective algorithm to identify which tremor patterns should be stimulated and which pulse amplitude should be provided to obtain the longest tremor reset time. Five machine learning techniques: Logistic Regression (LR),

TABLE 3 | A demographic study of all patients participated in this study.

Items	Description (*N* = 20)	Min–Max
Age (year ± SD)	63.40 ± 9.91	51–85
Hoehn and Yahr (Score ± SD)	2.53 ± 0.85	1–4
LED (mg/day ± SD)	761.20 ± 329.69	300–1759
Disease duration (year ± SD)	8.45 ± 3.26	4–18
TMSE (Score ± SD)	26.55 ± 2.80	21–30
Tremor outcome: before stimulation		
• Off UPDRS—III	30.90 ± 12.08	14–56
• Off UPDRS—III tremor	9.15 ± 3.63	2–16
• Off UPDRS—III tremor limb	3.65 ± 0.58	2–4
• On UPDRS—III	17.95 ± 7.52	6–33
• On UPDRS—III tremor	5.50 ± 2.31	1–9
• On UPDRS—III tremor limb	2.20 ± 0.52	1–3
• RMS angular velocity X axis	13.19 ± 19.46	0.36–66.46
• RMS angular velocity Y axis	16.04 ± 30.45	0.17–127.65
• RMS angular velocity Z axis	8.25 ± 12.80	0.09–46.59
• Frequency X axis	5.82 ± 1.76	2.32–10.43
• Frequency Y axis	5.29 ± 1.82	2.33–8.91
• Frequency Z axis	5.59 ± 1.60	2.71–8.24
Tremor outcome: during stimulation		
• On UPDRS—III during stimulation	16.65 ± 7.53	5–32
• On UPDRS—III tremor during stimulation	4.20 ± 2.35	0–8
• On UPDRS—III tremor limb during stimulation	0.85 ± 0.49	0–2
• RMS angular velocity X axis	5.10 ± 11.11	0.18–50.70
• RMS angular velocity Y axis	6.29 ± 15.31	0.14–68.77
• RMS angular velocity Z axis	3.55 ± 9.39	0.11–43.04
• Frequency X axis	6.47 ± 1.35	3.10–8.96
• Frequency Y axis	5.68 ± 1.22	3.10–7.57
• Frequency Z axis	5.88 ± 1.87	2.32–11.22
Stimulation parameters		
• Maximum pulse amplitude (mA ± SD)	9.45 ± 4.29	3–17
• Average pulse amplitude (mA ± SD)	6.25 ± 2.84	2.06–12.95
• Stimulation period (second ± SD)	440.70 ± 560.82	42–2382
• The duration of tremor reduction during stimulation (second ± SD)	200.35 ± 170.21	42–596
• The duration of continuing tremor reduction after the withdrawal of EMS until the tremor re-emerged to the pre-stimulation level (second ± SD)	129.55 ± 226.71	0–1032
• Tremor reset time (second ± SD)	329.90 ± 340.91	73–1628

UPDRS, Unified Parkinson's Disease Rating Scale; LED, Levodopa Equivalent Dosage; BMI, Body Mass Index; TMSE, Thai Mental Status Examination; EMS, Electrical muscle stimulation.

TABLE 4 | Comparison of tremor parameters between the before-stimulation and during-stimulation measurements.

Items	Before stimulation (Value ± SD)	During stimulation (Value ± SD)	*p*-value
On UPDRS III	17.95 ± 7.52	16.65 ± 7.53	< 0.001
On UPDRS III tremor section	5.50 ± 2.31	4.20 ± 2.35	< 0.001
On UPDRS III tremor limb	2.20 ± 0.52	0.85 ± 0.49	< 0.001
RMS angular velocity X axis	13.19 ± 19.46	5.10 ± 11.11	< 0.001
RMS angular velocity Y axis	16.04 ± 30.45	6.29 ± 15.31	0.001
RMS angular velocity Z axis	8.25 ± 12.80	3.55 ± 9.39	< 0.001
Frequency X axis	5.82 ± 1.76	6.47 ± 1.35	0.135
Frequency Y axis	5.29 ± 1.82	5.68 ± 1.22	0.354
Frequency Z axis	5.59 ± 1.60	5.88 ± 1.87	0.872

UPDRS, Unified Parkinson's Disease Rating Scale; RMS, Root Mean Square. All statistical analysis was performed by Wilcoxon Signed Rank test.

TABLE 5 | Correlation of stimulation parameters and tremor reduction outcomes.

Parameters	Stimulation parameters		Tremor reduction outcome	
	Parameters	***r***	**Outcome**	***r***
Tremor reset time	Max pulse amplitude	0.567* ($p = 0.008$)	Delta UPDRS tremor limb	0.505* ($p = 0.023$)
	Average pulse amplitude	0.495* ($p = 0.035$)	Delta RMS X	0.456* ($p = 0.043$)
	Stimulation time	0.586* ($p = 0.007$)	Delta RMS Y	0.459* ($p = 0.042$)
	The duration of tremor reduction during stimulation	0.733* ($p < 0.001$)		
Average pulse amplitude	Max pulse amplitude	0.787* ($p < 0.001$)	Delta RMS_X	0.686* ($p = 0.001$)
	The duration of continuing tremor reduction after the withdrawal of EMS until the tremor re-emerged to the pre-stimulation level	0.474* ($p = 0.035$)	Delta RMS_y	0.789* ($p < 0.001$)
	Tremor reset time	0.495* ($p = 0.027$)	Delta RMS_z	0.746* ($p < 0.001$)
Stimulation time	Max pulse amplitude	0.552* ($p = 0.012$)		
	The duration of tremor reduction during stimulation	0.866* ($p < 0.001$)		
	Tremor reset time	0.586* ($p = 0.007$)		

*All correlation analysis was performed by Spearman Rho's correlation; Statistically significant was determined with *$p < 0.05$; delta: the difference of outcome between before and during stimulation; RMS_x, RMS Gyroscope axis X; RMS_y, RMS Gyroscope axis Y; RMS_z, RMS Gyroscope axis Z.*

TABLE 6 | Choices of parameters used in the grid search for RF, SVM, and NN on both feature sets.

Parameters	Range of parameters	The best parameters	
		Feature Set: Only gyroscope signals	**Feature Set: Gyroscope signals with previous stimulation**
RF (RandomForestClassifier)			
The number of trees *(n_estimators)*	[50, 100, 200, 300, 400, 500]	200	100
The bootstrap option *(bootstrap)*	[True, False]	True	True
The criterion *(criterion)*	["gini," "entropy"]	"gini"	"gini"
The minimum number of samples *(min_samples_leaf)*	[2, 5, 10, 20, 30]	5	2
SVM (SVC)			
C *(C)*	[0.5, 1, 2]	2	1
Kernel *(kernel)*	["linear," "poly," "rbf," "sigmoid"]	"rbf"	"rbf"
NN (MLPClassifier)			
The size of hidden layers *(hidden_layer_sizes)*	[(50), (100), (200), (50, 50), (100, 100), (200, 200)]	(100, 100)	(100, 100)
The activation function *(activation)*	["tanh," "relu"]	"relu"	"relu"
The optimizer *(solver)*	["lbfgs," "sgd," "adam"]	"adam"	"adam"

TABLE 7 | Performance in terms of "macro-F1" comparison between Logistic Regression, Random Forest, NN, and SVM with two feature sets.

Model	Only gyroscope (Value ± SD)	Gyroscope with previous stimulus (Value ± SD)	Improvement (%)
Logistic regression	0.211 ± 0.121	0.317 ± 0.144	50.47%
Random forest	0.261 ± 0.110	0.734 ± 0.274	180.85%
SVM	0.261 ± 0.128	0.436 ± 0.183	67.25%
NN	**0.296 ± 0.096**	0.683 ± 0.264	130.56%
LSTM	0.295 ± 0.090	**0.736 ± 0.282**	149.51%

The last column shows a percentage of improvement by adding the previous stimulation level (I_{t-1}). Boldface refers to the most effective in each category in the first two column. SVM, support vector machine; NN, Neural Network; LSTM, long-short-term-memory.

Random Forest (RF), SVM, NN, and LSTM, were evaluated based on threefold cross validation. There were two feature sets in the experiment: (1) only gyroscope signals (3 inputs: RMS_x, RMS_y, RMS_z) and (2) gyroscope signals with the previous stimulation level (4 inputs: RMS_x, RMS_y, RMS_z, I_{t-1}); thus, the same procedures were employed similarly on both feature sets.

TABLE 8 | Performance in terms of "accuracy" comparison between Logistic Regression, Random Forest, NN, and SVM with two feature sets.

Model	Only gyroscope (Value ± SD)	Gyroscope with previous stimulus (Value ± SD)	Improvement (%)
Logistic regression	0.292 ± 0.285	0.472 ± 0.363	61.62%
Random forest	0.431 ± 0.292	0.846 ± 0.292	68.18%
SVM	0.404 ± 0.297	0.680 ± 0.295	96.39%
NN	**0.513 ± 0.252**	0.840 ± 0.254	63.84%
LSTM	0.497 ± 0.212	**0.865 ± 0.259**	73.87%

The last column shows a percentage of improvement by adding the previous stimulation level (I_{t-1}). Boldface refers to the most effective in each category on the first two columns. SVM, support vector machine; NN, Neural Network; LSTM, long-short-term-memory.

TABLE 9 | Accuracy per class of the most suitable model in this study (LSTM).

Class	0	1	2	3	4
Accuracy	99.76%	87.43%	73.92%	74.17%	0.0%

The most suitable model with the highest accuracy is the combination of LSTM analysis using gyroscope data and the previous stimulation level.

To obtain the best parameters, the grid search was employed on the traditional machine learning algorithms (RF, SVM, and NN) on both feature sets, except for LR. For LR, we did not perform the grid search with this model since there are only four maximum inputs (RMS_x, RMS_y, RMS_z, I_{t-1}), so we decided to use all of them to avoid underfitting the model. **Table 6** shows parameters' choices employed by the grid search for RF, SVM, and NN on both feature sets. For LSTM, we have compared different network's settings manually and chosen the best one, e.g., the number of hidden units, the number of layers, etc. The chosen model of LSTM on both feature sets composed of two layers with 100 hidden units followed by a dense layer with softmax activation. The optimizer was "adam" with the learning rate of 0.001 and the categorical cross-entropy loss. In addition, a feature normalization (StandardScaler in the scikit-learn library) was performed as a data preprocessing for SVM, NN, and LSTM.

Tables 7, **8** show the results in terms of F1 and accuracy, respectively. The results demonstrated that LSTM was the most effective model with F1 = 0.736 and accuracy = 0.865. The success of LSTM is probably found in its time dependency mechanism, so is designed to capture the variation of patient's movement patterns over time. Also, the use of previous stimulation levels (I_{t-1}) played an important role in improving model performance, almost doubling performance on all models and in the most suitable model, LSTM, it improved the performance 149.51% on F1 and 73.87% on accuracy. **Table 9** shows an accuracy per class for the most suitable model. It achieved more than 80% accuracy on most classes, however, it could not capture the data in Class 4 due to a scarcity issue for this class, giving only 0.67% as shown in **Table 2**.

DISCUSSION

In this study, we evaluated the efficacy of EMS in the suppression of classic parkinsonian tremor in 20 PD patients using a Parkinson's glove. The results of tremor reduction were significant and consistent with prior findings (Gallego et al., 2013; Dosen et al., 2015). However, no previous studies have reported quantitative measurements of tremor attenuation after stimulation to allow further comparisons (Jitkritsadakul et al., 2015, 2017). Here, we quantified the duration of the tremor from initiation of EMS to the point after EMS withdrawal when tremor returned to pre-stimulation levels. We found that the mean maximum pulse amplitude applied was 9.45 (SD ± 4.29) mA and the mean stimulation period was 440.7 (SD ± 560.82) seconds and the mean total tremor reset time was 329.90 (SD ± 340.91) seconds. The multiple linear regression model showed that a longest tremor reset time could be obtained by increasing pulse amplitude and increasing the stimulation time. These findings further improve our knowledge on the peripheral mechanism of tremor and the effect of stimulation in the suppression of resting tremor. EMS may act as strong stimuli that can transiently modify tremors, even if the tremor originally occurred from a central origin (Rack and Ross, 1986; Britton et al., 1993; Hallett, 1998; Deuschl et al., 2001).

The Tremor Reset Mechanism

Tremor in PD is generated by the interaction between central and peripheral mechanism (**Supplementary Figure 2**; Hallett, 1998; Deuschl et al., 2000, 2001; McAuley and Marsden, 2000). Early findings on resting tremors in PD suggest they can be reset by an alteration in mechanical conditions at the periphery, including externally imposed movement at a joint or electrical stimulation of nerves and muscles (Mones and Weiss, 1969; Bathien et al., 1980; Lee and Stein, 1981; Britton et al., 1992, 1993). The potential resetting of parkinsonian tremors by modulation of peripheral reflex mechanisms using a short-duration, supramaximal peripheral nerve stimulation was first explored by Mones and Weiss (1969). A spontaneous tremor in the extensor digitorum muscle changed dramatically after the ipsilateral stimulation of median or ulnar nerves with a single 0.5 ms duration, square wave, and supramaximal stimulation and the interval of the post-stimulation tremor bursts decreased when compared with control values. In addition, there was a change in the predicted tremor pattern of the post-stimulation tremor bursts, which were out of phase with the pre-stimulation tremor bursts (Mones and Weiss, 1969). The shortened interval increased gradually on subsequent spontaneous tremor bursts and returned to the control interval value in 750–1,000 ms after nerve stimulation (Mones and Weiss, 1969). Therefore, the pattern of parkinsonian tremor

appeared to be "reset" by the peripheral nerve stimulation. After recording the spontaneous tremor of the extensor indicis muscle after a single 1 ms duration square wave and supramaximal stimulation of the radial nerve, the interval of the next post-stimulation tremor burst was slightly delayed, especially if the stimulation occurred late in the tremor cycle (Bathien et al., 1980). This findings needed to be investigated further to see if there is potential for longer periods of supramaximal stimulation to produce a greater interval for subsequent post-stimulation tremors. Our previous study proposed that resting tremor appeared to be reset after increasing the duration of stimulation (Jitkritsadakul et al., 2015, 2017). After applying EMS using a 10–30-s duration square-wave stimulation, some patients had continuing tremor reduction where a longer duration of stimulation produced a greater duration of reset time (Jitkritsadakul et al., 2015, 2017). The temporary suppression of parkinsonian tremors from EMS may occur via the stretch reflex in muscle fibers (Jitkritsadakul et al., 2015) or by the inhibitory effect of the muscle contraction with Ib fiber rather than Ia fiber (Bathien et al., 1980). Alternatively, EMS may be able to modulate Renshaw cells (Pratt and Jordan, 1987; Alvarez et al., 2013), which create a negative feedback mechanism in the spinal cord and possibly led to tremor suppression (Jitkritsadakul et al., 2015).

The Parkinson's glove is an innovative device with the potential to become an alternative treatment option for patients with medically refractory tremor. This current study is the first that we are aware of that has described the effect of EMS on tremor reduction, and propose a model for calculating tremor reset times. We also identified a machine learning model to predict the pulse amplitude required to achieve the greatest tremor reset time. Using the machine learning model will allow physicians employing this device to identify the most suitable tremor paradigm to suppress and the optimal stimulation protocols to use. However, our study contains certain limitations. Firstly, as this open-label, quasi-experimental study was conducted in a small single group of patients collected from a single PD center in Thailand, it may retain selection and sampling bias that comes with a single group study. However, our study is the ability to recruit the homogeneous PD population with the homogeneous data by selecting a group of PD patients with Class I parkinsonian tremor as confirmed by quantitative tremor analysis, therefore, the characteristic of PD tremor in this study was homogeneous and well represented. Secondly, due to the IRB granted us to permission this treatment as an adjunctive treatment during "on" period when patients were optimized on oral medications, therefore, during stimulation section was conducted during "on" period only. Therefore, this study gave the potential benefit of EMS as an adjunctive treatment for the specific class I parkinsonian tremor. However, for future direction, EMS should be further explored as a possible therapeutic intervention for the different state of tremors in PD (such as "off" period) or the potential usage in other tremor syndromes. Thirdly, the data set that was used to train the model to identify significant tremor reduction was judged by the criteria of significant tremor reduction only. As the impact of EMS on tremor reduction was a transient effect and could not be explained by pre-existing severity of disease or tremor, there are no results to confirm the benefit of EMS in a long-term study. Fourthly, as a longer duration of electrical stimulation is more painful than a shorter duration (Walsh et al., 1998; Tamura et al., 2013), we kept the maximum pulse stimulation below the patients' pain thresholds, delivered as short periods of stimulation to avoid potential side effects of EMS, and, therefore, it is not clear if longer durations of stimulation would support tremor reduction in a long term. Though, the issue of tolerance was not investigated in this study, it has been documented in PD patients with thalamic stimulation (Hariz et al., 1999). Finally, using collected data from the physician's process, we demonstrated that the model could predict a suitable stimulation level based on the current tremor states and the previous stimulation level. However, as the testing phase was conducted using the previous stimulation levels from the collected data, not from the model prediction, the model will require further development before it can be deployed in a real-life patient scenario.

Going forward, it is our aim to use this model to automatically stimulate PD patients to achieve optimal tremor suppression. In the manual process, a physician provides a suitable stimulation level based on the previous pulse amplitude level until a patient shows a significant tremor reduction. To imitate this process, the model is being developed so that the stimulation level will be automatically based on the previous stimulation level predicted by the model. Then, in future work, we can evaluate whether or not the model can achieve tremor reset times similar to that of manual stimulation.

CONCLUSION

Our study provides evidence of the efficacy of EMS in transient tremor reduction among PD patients with medically intractable rest tremor, providing calculations for a model to predict the tremor reset time and evaluation of the best machine-learning model for automatic prediction of the suitable pulse amplitude for stimulation. Greater pulse amplitude and stimulation periods may result in longer tremor reset times. From the machine learning model evaluation, LSTM was identified as the most effective model for the prediction of stimulation levels, and, in future, could be used to automatically adjust stimulation levels, replicating the manual process periods of tremor reset time. Our study also provides more insight into the role of peripheral mechanisms in the origin of parkinsonian tremor. Targeting peripheral mechanisms with strong stimuli may not be able to stop, but could modulate tremor amplitude, even if it is mainly driven from a central origin. The efficacy of EMS should be explored in other tremor syndromes.

DATA AVAILABILITY STATEMENT

The raw data supporting the conclusions of this article will be made available by the authors, without undue reservation.

ETHICS STATEMENT

The studies involving human participants were reviewed and approved by the Institutional Review Board, Faculty of Medicine, Chulalongkorn University (IRB 483/57). The patients/participants provided their written informed consent to participate in this study.

AUTHOR CONTRIBUTIONS

OP and RB designed the research and drafted the work. OP, PV, IW, and CA performed the experiments. OP and PV analyzed the data. All authors contributed to the article and approved the submitted version.

FUNDING

This study was funded by the Technology and Innovation-Based Enterprise Development Fund (TED Fund), the Ministry of Higher Education, Science, Research and Innovation of Thailand, Senior Research Scholar Grant (RTA6280016) of the Thailand Science Research and Innovation (TSRI), International Research Network Grant of the Thailand Research Fund (IRN59W0005), and the Center of Excellence grant of Chulalongkorn University (GCE 6100930004-1).

ACKNOWLEDGMENTS

We thank Chanakarn Chinchatchawal and Akara Supratak from Robolingo Co., Ltd., for preliminary calculating a machine learning model for tremor prediction in this study.

SUPPLEMENTARY MATERIAL

The Supplementary Material for this article can be found online at: https://www.frontiersin.org/articles/10.3389/fnagi.2021.727654/full#supplementary-material

Supplementary Figure 1 | The CONSORT flowchart provides a complete detailed flowchart of this single-arm study.

Supplementary Figure 2 | The complex interaction between central and peripheral (local mechanical-reflex) mechanisms for tremorogenesis. Representation of the origination of PD tremor that develops from the complex interaction between central oscillators and peripheral mechanisms. Bold lines represent the tremor control commanded from central oscillators to peripheral mechanisms Dashed lines represent feedback loops from peripheral mechanisms back to central control oscillators.

Supplementary Material 1 | Translation of protocol synopsis No. 483/57 (NCT02370108).

Supplementary Material 2 | A TREND checklist.

Supplementary Material 3 | Sample size calculation.

REFERENCES

Aich, S., Youn, J., Chakraborty, S., Pradhan, P. M., Park, J. H., Park, S., et al. (2020). A supervised machine learning approach to detect the on/off state in Parkinson's disease using wearable based gait signals. *Diagnostics* 10. doi: 10.3390/diagnostics10060421

Alvarez, F. J., Benito-Gonzalez, A., and Siembab, V. C. (2013). Principles of interneuron development learned from Renshaw cells and the motoneuron recurrent inhibitory circuit. *Ann. N.Y.Acad. Sci.* 1279, 22–31. doi: 10.1111/nyas.12084

Bathien, N., Rondot, P., and Toma, S. (1980). Inhibition and synchronisation of tremor induced by a muscle twitch. *J. Neurol. Neurosurg. Psychiatry* 43, 713–718. doi: 10.1136/jnnp.43.8.713

Benabid, A. L., Pollak, P., Gao, D., Hoffmann, D., Limousin, P., Gay, E., et al. (1996). Chronic electrical stimulation of the ventralis intermedius nucleus of the thalamus as a treatment of movement disorders. *J. Neurosurg.* 84, 203–214. doi: 10.3171/jns.1996.84.2.0203

Bizzego, A., Bussola, N., Chierici, M., Maggio, V., Francescatto, M., Cima, L., et al. (2019). Evaluating reproducibility of AI algorithms in digital pathology with DAPPER. *PLoS Comput. Biol.* 15:e1006269. doi: 10.1371/journal.pcbi.1006269

Bo, A. P., Azevedo-Coste, C., Geny, C., Poignet, P., and Fattal, C. (2014). On the use of fixed-intensity functional electrical stimulation for attenuating essential tremor. *Artiff. Organs* 38, 984–991. doi: 10.1111/aor.12261

Boser, B., Guyon, I., and Vapnik, V. (1992). "A training algorithm for optimal margin classifiers," in *Proceedings of the Fifth Annual Workshop on Computational Learning Theory*.

Britton, T. C., Thompson, P. D., Day, B. L., Rothwell, J. C., Findley, L. J., and Marsden, C. D. (1992). "Resetting" of postural tremors at the wrist with mechanical stretches in Parkinson's disease, essential tremor, and normal subjects mimicking tremor. *Ann. Neurol.* 31, 507–514. doi: 10.1002/ana.410310508

Britton, T. C., Thompson, P. D., Day, B. L., Rothwell, J. C., Findley, L. J., and Marsden, C. D. (1993). Modulation of postural tremors at the wrist by supramaximal electrical median nerve shocks in essential tremor, Parkinson's disease and normal subjects mimicking tremor. *J. Neurol. Neurosurg. Psychiatry* 56, 1085–1089. doi: 10.1136/jnnp.56.10.1085

Connolly, B. S., and Lang, A. E. (2014). Pharmacological treatment of Parkinson disease: a review. *JAMA* 311, 1670–1683. doi: 10.1001/jama.2014.3654

Crosby, N. J., Deane, K. H., and Clarke, C. E. (2003). Beta-blocker therapy for tremor in Parkinson's disease. *Cochrane Database Syst. Rev.* 2003:CD003361.

Deuschl, G., Bain, P., and Brin, M. (1998). Consensus statement of the movement disorder society on tremor. *Adv. Hoc. Sci. Committee. Mov. Disord* 13(Suppl. 3), 2–23. doi: 10.1002/mds.870131303

Deuschl, G., Raethjen, J., Baron, R., Lindemann, M., Wilms, H., and Krack, P. (2000). The pathophysiology of parkinsonian tremor: a review. *J Neurol* 247(Suppl. 5), V33–V48.

Deuschl, G., Raethjen, J., Lindemann, M., and Krack, P. (2001). The pathophysiology of tremor. *Muscle Nerve* 24, 716–735.

Dosen, S., Muceli, S., Dideriksen, J., Romero, J., Rocon, E., Pons, J., et al. (2014). Online tremor suppression using electromyography and low level electrical stimulation. *IEEE Trans Neural. Syst. Rehabil. Eng.* 23, 385–395.

Dosen, S., Muceli, S., Dideriksen, J. L., Romero, J. P., Rocon, E., Pons, J., et al. (2015). Online tremor suppression using electromyography and low-level electrical stimulation. *IEEE Trans Neural. Syst. Rehabil. Eng.* 23, 385–395. doi: 10.1109/tnsre.2014.2328296

Ferreira, J. J., Katzenschlager, R., Bloem, B. R., Bonuccelli, U., Burn, D., Deuschl, G., et al. (2013). Summary of the recommendations of the EFNS/MDS-ES review on therapeutic management of Parkinson's disease. *Eur. J. Neurol.* 20, 5–15. doi: 10.1111/j.1468-1331.2012.03866.x

Gallego, J. A., Rocon, E., Belda-Lois, J. M., and Pons, J. L. (2013). A neuroprosthesis for tremor management through the control of muscle co-contraction. *J. Neuroeng. Rehabil.* 10: 36. doi: 10.1186/1743-0003-10-36

Gallego, J. A., Rocon, E., Roa, J. O., Moreno, J. C., and Pons, J. L. (2010). Real-time estimation of pathological tremor parameters from gyroscope data. *Sensors (Basel)* 10, 2129–2149. doi: 10.3390/s100302129

Hallett, M. (1998). Overview of human tremor physiology. *Mov. Disord* 13(Suppl. 3), 43–48. doi: 10.1002/mds.870131308

Hariz, M. I., Shamsgovara, P., Johansson, F., Hariz, G., and Fodstad, H. (1999). Tolerance and tremor rebound following long-term chronic thalamic stimulation for Parkinsonian and essential tremor. *Stereotact. Funct. Neurosurg.* 72, 208–218. doi: 10.1159/000029728

Helmich, R. C., Hallett, M., Deuschl, G., Toni, I., and Bloem, B. R. (2012). Cerebral causes and consequences of parkinsonian resting tremor: a tale of two circuits? *Brain* 135, 3206–3226. doi: 10.1093/brain/aws023

Helmich, R. C., Janssen, M. J., Oyen, W. J., Bloem, B. R., and Toni, I. (2011). Pallidal dysfunction drives a cerebellothalamic circuit into Parkinson tremor. *Ann. Neurol.* 69, 269–281. doi: 10.1002/ana.22361

Hirschmann, J., Hartmann, C. J., Butz, M., Hoogenboom, N., Ozkurt, T. E., Elben, S., et al. (2013). A direct relationship between oscillatory subthalamic nucleus-cortex coupling and rest tremor in Parkinson's disease. *Brain* 136, 3659–3670. doi: 10.1093/brain/awt271

Hochreiter, S., and Schmidhuber, J. (1997). Long short-term memory. *Neural. Comput.* 9, 1735–1780.

Hughes, A. J., Daniel, S. E., Blankson, S., and Lees, A. J. (1993). A clinicopathologic study of 100 cases of Parkinson's disease. *Arch. Neurol.* 50, 140–148. doi: 10.1001/archneur.1993.00540020018011

Javidan, M., Elek, J., and Prochazka, A. (1992). Attenuation of pathological tremors by functional electrical stimulation. II: clinical evaluation. *Ann. Biomed. Eng.* 20, 225–236. doi: 10.1007/bf02368522

Jimenez, M. C., and Vingerhoets, F. J. (2012). Tremor revisited: treatment of PD tremor. *Parkinsonism Relat. Disord* 18(Suppl. 1), S93–S95.

Jitkritsadakul, O., Thanawattano, C., Anan, C., and Bhidayasiri, R. (2015). Exploring the effect of electrical muscle stimulation as a novel treatment of intractable tremor in Parkinson's disease. *J. Neurol. Sci.* 358, 146–152.

Jitkritsadakul, O., Thanawattano, C., Anan, C., and Bhidayasiri, R. (2017). Tremor's glove-an innovative electrical muscle stimulation therapy for intractable tremor in Parkinson's disease: a randomized sham-controlled trial. *J. Neurol. Sci.* 381, 331–340.

Kartzinel, R., Teychenne, P., Gillespie, M. M., Perlow, M., Gielen, A. C., Sadowsky, D. A., et al. (1976). Bromocriptine and levodopa (with or without carbidopa) in parkinsonism. *Lancet* 2, 272–275. doi: 10.1016/S0140-6736(76)90728-5

Katzenschlager, R., Sampaio, C., Costa, J., and Lees, A. (2003). Anticholinergics for symptomatic management of Parkinson's disease. *Cochrane Database Syst. Rev.* 2003:CD003735. doi: 10.1002/14651858.CD003735

Koller, W., Pahwa, R., Busenbark, K., Hubble, J., Wilkinson, S., Lang, A., et al. (1997). High-frequency unilateral thalamic stimulation in the treatment of essential and parkinsonian tremor. *Ann. Neurol.* 42, 292–299. doi: 10.1002/ana.410420304

Krack, P., Benazzouz, A., Pollak, P., Limousin, P., Piallat, B., Hoffmann, D., et al. (1998a). Treatment of tremor in Parkinson's disease by subthalamic nucleus stimulation. *Mov. Disord* 13, 907–914. doi: 10.1002/mds.870130608

Krack, P., Pollak, P., Limousin, P., Hoffmann, D., Xie, J., Benazzouz, A., et al. (1998b). Subthalamic nucleus or internal pallidal stimulation in young onset Parkinson's disease. *Brain* 121(Pt. 3), 451–457. doi: 10.1093/brain/121.3.451

Larhmam (2018). *SVM Margin*. Available online at: https://en.wikipedia.org/wiki/Support_vector_machine#/media/File:SVM_margin.png (accessed January 17, 2021).

Lee, R. G., and Stein, R. B. (1981). Resetting of tremor by mechanical perturbations: a comparison of essential tremor and parkinsonian tremor. *Ann. Neurol.* 10, 523–531. doi: 10.1002/ana.410100606

Limousin, P., Krack, P., Pollak, P., Benazzouz, A., Ardouin, C., Hoffmann, D., et al. (1998). Electrical stimulation of the subthalamic nucleus in advanced Parkinson's disease. *N. Engl. J. Med.* 339, 1105–1111. doi: 10.1056/NEJM199810153391603

Maneski, L. P., Jorgovanovic, N., Ilic, V., Dosen, S., Keller, T., Popovic, M. B., et al. (2011). Electrical stimulation for the supression of pathological tremor. *Med. Biol. Eng. Comput.* 49, 1187–1193. doi: 10.1007/s11517-011-0803-6

Marjama-Lyons, J., and Koller, W. (2000). Tremor-predominant Parkinson's disease. approaches to treatment. *Drugs Aging* 16, 273–278. doi: 10.2165/00002512-200016040-00003

McAuley, J. H., and Marsden, C. D. (2000). Physiological and pathological tremors and rhythmic central motor control. *Brain* 123(Pt. 8), 1545–1567. doi: 10.1093/brain/123.8.1545

Mones, R. J., and Weiss, A. H. (1969). The response of the tremor of patients with Parkinsonism to peripheral nerve stimulation. *J. Neurol. Neurosurg. Psychiatry* 32, 512–518. doi: 10.1136/jnnp.32.6.512

Olah, C. (2015). *The Repeating Module in an LSTM Contains Four Interacting Layers*. Available online at: https://colah.github.io/posts/2015-08-Understanding-LSTMs/ (accessed January 17, 2021).

Pinter, M. M., Pogarell, O., and Oertel, W. H. (1999). Efficacy, safety, and tolerance of the non-ergoline dopamine agonist pramipexole in the treatment of advanced Parkinson's disease: a double blind, placebo controlled, randomised, multicentre study. *J. Neurol. Neurosurg. Psychiatry* 66, 436–441. doi: 10.1136/jnnp.66.4.436

Pogarell, O., Gasser, T., Van Hilten, J. J., Spieker, S., Pollentier, S., Meier, D., et al. (2002). Pramipexole in patients with Parkinson's disease and marked drug resistant tremor: a randomised, double blind, placebo controlled multicentre study. *J. Neurol. Neurosurg. Psychiatry* 72, 713–720. doi: 10.1136/jnnp.72.6.713

Pratt, C. A., and Jordan, L. M. (1987). Ia inhibitory interneurons and Renshaw cells as contributors to the spinal mechanisms of fictive locomotion. *J. Neurophysiol.* 57, 56–71. doi: 10.1152/jn.1987.57.1.56

Rack, P. M., and Ross, H. F. (1986). The role of reflexes in the resting tremor of Parkinson's disease. *Brain* 109(Pt. 1), 115–141. doi: 10.1093/brain/109.1.115

Sigcha, L., Costa, N., Pavon, I., Costa, S., Arezes, P., Lopez, J. M., et al. (2020). Deep learning approaches for detecting freezing of gait in Parkinson's disease patients through on-body acceleration sensors. *Sensors (Basel)* 20:1895. doi: 10.3390/s20071895

Simpson, J., Mcmillan, H., and Reeve, D. (2013). Reformulating psychological difficulties in people with Parkinson's disease: the potential of a social relational approach to disablism. *Parkinsons Dis.* 2013:608562. doi: 10.1155/2013/608562

Tamura, A., Sonoo, M., Hoshino, S., Iwanami, T., Shimada, H., Miki, T., et al. (2013). Stimulus duration and pain in nerve conduction studies. *Muscle Nerve* 47, 12–16. doi: 10.1002/mus.23446

Taylor, R. (1990). Interpretation of the correlation coefficient : a basic review. *J. Diagn. Med.* 1, 35–39. doi: 10.1177/875647939000600106

Walsh, D. M., Lowe, A. S., Mccormack, K., Willer, J. C., Baxter, G. D., and Allen, J. M. (1998). Transcutaneous electrical nerve stimulation: effect on peripheral nerve conduction, mechanical pain threshold, and tactile threshold in humans. *Arch. Phys. Med. Rehabil.* 79, 1051–1058. doi: 10.1016/S0003-9993(98)90170-8

Williams, R. J., and Zipser, D. (1989). A learning algorithm for continually running fully recurrent neural networks. *Neural. Comput.* 1, 270–280. doi: 10.1162/neco.1989.1.2.270

Yao, L., Brown, P., and Shoaran, M. (2019). Resting tremor detection in Parkinson's disease with machine learning and kalman filtering. *IEEE Biomed. Circ. Syst. Conf.* 2018:BIOCAS.2018.8584721. doi: 10.1109/BIOCAS.2018.8584721

Zhang, D., Poignet, P., Widjaja, F., and Ang, W. T. (2011). Neural oscillator based control for pathological tremor suppression via functional electrical stimulation. *Con. Eng. Prac.* 19, 74–88. doi: 10.1016/j.conengprac.2010.08.009

Zimmermann, R., Deuschl, G., Hornig, A., Schulte-Monting, J., Fuchs, G., and Lucking, C. H. (1994). Tremors in Parkinson's disease: symptom analysis and rating. *Clin. Neuropharmacol.* 17, 303–314. doi: 10.1097/00002826-199408000-00001

Conflict of Interest: The authors declare that the research was conducted in the absence of any commercial or financial relationships that could be construed as a potential conflict of interest.

Publisher's Note: All claims expressed in this article are solely those of the authors and do not necessarily represent those of their affiliated organizations, or those of the publisher, the editors and the reviewers. Any product that may be evaluated in this article, or claim that may be made by its manufacturer, is not guaranteed or endorsed by the publisher.

Copyright © 2021 Phokaewvarangkul, Vateekul, Wichakam, Anan and Bhidayasiri. This is an open-access article distributed under the terms of the Creative Commons Attribution License (CC BY). The use, distribution or reproduction in other forums is permitted, provided the original author(s) and the copyright owner(s) are credited and that the original publication in this journal is cited, in accordance with accepted academic practice. No use, distribution or reproduction is permitted which does not comply with these terms.

frontiers in Aging Neuroscience

ORIGINAL RESEARCH
published: 17 September 2021
doi: 10.3389/fnagi.2021.711009

Disrupted Dynamic Functional Connectivity in Distinguishing Subjective Cognitive Decline and Amnestic Mild Cognitive Impairment Based on the Triple-Network Model

Chen Xue[1†], Wenzhang Qi[1†], Qianqian Yuan[1], Guanjie Hu[2], Honglin Ge[2], Jiang Rao[3], Chaoyong Xiao[1,2] and Jiu Chen[2,4*]*

[1] Department of Radiology, The Affiliated Brain Hospital of Nanjing Medical University, Nanjing, China, [2] Institute of Brain Functional Imaging, Nanjing Medical University, Nanjing, China, [3] Department of Rehabilitation, The Affiliated Brain Hospital of Nanjing Medical University, Nanjing, China, [4] Institute of Neuropsychiatry, The Affiliated Brain Hospital of Nanjing Medical University, Nanjing, China

OPEN ACCESS

Edited by:
Jiehui Jiang,
Shanghai University, China

Reviewed by:
Suping Cai,
Xidian University, China
Xueyan Jiang,
Helmholtz Association of German Research Centers (HZ), Germany

***Correspondence:**
Chaoyong Xiao
xchaoyong@163.com
Jiu Chen
ericcst@aliyun.com

[†] These authors have contributed equally to this work and share first authorship

Received: 17 May 2021
Accepted: 16 August 2021
Published: 17 September 2021

Citation:
Xue C, Qi W, Yuan Q, Hu G, Ge H, Rao J, Xiao C and Chen J (2021) Disrupted Dynamic Functional Connectivity in Distinguishing Subjective Cognitive Decline and Amnestic Mild Cognitive Impairment Based on the Triple-Network Model. Front. Aging Neurosci. 13:711009. doi: 10.3389/fnagi.2021.711009

Background: Subjective cognitive decline and amnestic mild cognitive impairment (aMCI) were widely thought to be preclinical AD spectrum disorders, characterized by aberrant functional connectivity (FC) within the triple networks of the default mode network (DMN), the salience network (SN), and the executive control network (ECN). Dynamic FC (DFC) analysis can capture temporal fluctuations in brain FC during the scan, which static FC analysis cannot. The purpose of the current study was to explore the changes in dynamic FC within the triple networks of the preclinical AD spectrum and further reveal their potential diagnostic value in diagnosing preclinical AD spectrum disorders.

Methods: We collected resting-state functional magnetic resonance imaging data from 44 patients with subjective cognitive decline (SCD), 49 with aMCI, and 58 healthy controls (HCs). DFC analysis based on the sliding time-window correlation method was used to analyze DFC variability within the triple networks in the three groups. Then, correlation analysis was conducted to reveal the relationship between altered DFC variability within the triple networks and a decline in cognitive function. Furthermore, logistic regression analysis was used to assess the diagnostic accuracy of altered DFC variability within the triple networks in patients with SCD and aMCI.

Results: Compared with the HC group, the groups with SCD and aMCI both showed altered DFC variability within the triple networks. DFC variability in the right middle temporal gyrus and left inferior frontal gyrus (IFG) within the ECN were significantly different between patients with SCD and aMCI. Moreover, the altered DFC variability in the left IFG within the ECN was obviously associated with a decline in episodic memory and executive function. The logistic regression analysis showed that multivariable analysis had high sensitivity and specificity for diagnosing SCD and aMCI.

Conclusions: Subjective cognitive decline and aMCI showed varying degrees of change in DFC variability within the triple networks and altered DFC variability within the ECN involved episodic memory and executive function. More importantly, altered DFC variability and the triple-network model proved to be important biomarkers for diagnosing and identifying patients with preclinical AD spectrum disorders.

Keywords: subjective cognitive decline, amnestic mild cognitive impairment, dynamic functional connectivity, resting state functional magnetic resonance imaging, triple network

INTRODUCTION

Alzheimer's disease is a great medical challenge that haunts the world because of its progressive, irreversible, and incurable nature (Jessen et al., 2014a,b). Subjective cognitive decline (SCD) is regarded to be the preclinical stage of AD, and amnestic mild cognitive impairment (aMCI) is considered to be the prodromal stage of AD, both of which have received more attention in recent years (Morris and Cummings, 2005; Jessen et al., 2014a,b; Xue et al., 2019). Patients with SCD, which refers to self-reported memory decline in elderly persons with normal objective cognitive performance, are widely believed to have two times to give rise to aMCI/Alzheimer's disease (AD) than elderly without SCD (Jessen et al., 2014b; Mitchell et al., 2014). Patients with aMCI, which is characterized by subjective memory decline, are thought to have nearly 10 times to progress to AD than healthy elderly people (Bischkopf et al., 2002; Jessen et al., 2014b; Chen et al., 2019; Slot et al., 2019). Due to the lack of effective treatment for AD, comparing and analyzing the neuroimaging characteristics of SCD and aMCI are crucial to research the early biomarkers of the preclinical AD spectrum.

Resting-state functional magnetic resonance imaging, which is a task-independent and powerful imaging modality, has been widely used to investigate the intrinsic functional connectivity networks of neuropsychiatric diseases (Li et al., 2002; Zhang and Raichle, 2010). Of the many intrinsic brain networks, the triple-network model, composed of the default-mode network (DMN), the salience network (SN), and the executive control network (ECN), has been the focus of recent research (Menon, 2011; Joo et al., 2016; Zhan et al., 2016). Numerous studies have suggested that the triple networks can be used to detect the reliability and stability of large-scale connections, which are damaged in neuropsychiatric diseases (He et al., 2014; Joo et al., 2016; Wu et al., 2016; Li et al., 2019). Moreover, the triple-network model provides a common framework for checking the reliable and stable patterns of large-scale connectivity (Menon, 2011). The DMN, mainly located in the ventromedial prefrontal cortex (vmPFC) and posterior cingulate cortex, is activated in internally directed cognitive activities, such as self-referential mental processes and social functions (Raichle et al., 2001; Broyd et al., 2009). The ECN, primarily involved in the lateral posterior parietal cortex and dorsolateral prefrontal cortex, is activated during externally directed higher-order cognitive function, including working memory, decision-making, and attention (Liang et al., 2016). The SN, which primarily includes the anterior cingulate cortex and anterior insula, is associated with affective processes, attention, and interoception (Sridharan et al., 2008; Uddin, 2015). Specifically, when salient events are detected, the SN can activate brain networks, direct the DMN and ECN to perform cognitive tasks, and help the corresponding brain regions to respond to stimuli appropriately (Menon and Uddin, 2010; Menon, 2011). Further study of triple-network model alterations in SCD and aMCI could help us better understand their pathological mechanisms.

Many neuroimaging studies have demonstrated that SCD and aMCI patients showed altered functional connectivity (FC) in the triple networks (Brier et al., 2012; Uddin, 2015; Chand et al., 2017). However, all the aforementioned studies were based on the assumption that the functional networks were spatiotemporally static during MRI scans (Chang and Glover, 2010). Due to the complexity and changing environment of the human brain, the assumption that brain activity remains static is too simplistic and may not reflect the dynamic characteristics of brain activation and connectivity (Preti et al., 2017). Previous rsfMRI studies have suggested that brain FC patterns can be time varying across a short time window; this phenomenon is known as dynamic FC (DFC) (Hutchison et al., 2013). DFC analysis has become an important tool in resting-state functional magnetic resonance imaging (rsfMRI) research by capturing temporal fluctuations in brain FC during the scan (Hutchison et al., 2013). Previous studies have demonstrated that the quantification of DFC disruption might be a sensitive biomarker or a prognostic indicator of disease progression and cognitive function (Long et al., 2019; Finc et al., 2020). Moreover, some studies have highlighted the potential role of DFC analysis in improving the accuracy of disease diagnosis, which made it necessary to apply DFC analysis to the diagnosis of AD spectrum disorders (Lei et al., 2020).

A number of studies found that AD showed altered DFC. Gu et al. suggested that AD showed decreased regional temporal variability, primarily in the temporal, parietal, and somatomotor regions (Gu et al., 2020). The authors also found that disrupted DFC was associated with cognitive function in patients with AD. They claimed that DFC analysis provided novel insight into the pathophysiological mechanisms of AD. In recent years, the research focus has been shifted to preclinical AD spectrum disorders, including SCD and MCI. Dong et al. found that patients with SCD showed both increased and decreased temporal variability compared with healthy controls (HCs) (Dong et al., 2020). Niu et al. found that patients with aMCI showed altered DFC in the prefrontal and parietal cortexes compared with HCs, and the regions were mainly in the DMN

(Niu et al., 2019). Córdova-Palomera et al. suggested that patients with MCI showed altered DFC mainly in the frontal-superior, temporal, and default modes compared with patients with AD (Cordova-Palomera et al., 2017). However, the previous studies did not reveal changes in DFC with the progression of preclinical AD spectrum disorders. It is unclear whether there are common or specific changes in DFC features in SCD and aMCI. Specifically, there are few studies on alterations in DFC variability within the triple networks in patients with SCD and aMCI and their diagnostic value for SCD and aMCI.

Therefore, in the current study, using combined rsfMRI and the classic sliding time-window correlation approach, we aimed to reveal changes in DFC variability within the triple networks in patients with SCD and aMCI, as well as their relationship with cognitive function. We further explored the diagnostic efficiency of DFC variability in patients with SCD and aMCI. We hypothesized that DFC variability within the triple networks in patients with SCD and aMCI had varying degrees of change, and that altered DFC variability of the triple networks may contribute to cognitive decline. Additionally, a comprehensive analysis of DFC temporal variability within the triple networks might serve as an indicator to diagnose and identify SCD and aMCI.

MATERIALS AND METHODS

Subjects

The applied research data were obtained from our in-home database: Nanjing Brain Hospital-Alzheimer's Disease Spectrum Neuroimaging Project (NBH-ADsnp) (Nanjing, China), which is continuously being updated. Related information of the NBH-ADsnp was summarized in *SI Methods*. The research gained approval by the responsible Human Participants Ethics Committee of the Affiliated Brain Hospital of Nanjing Medical University (No. 2018-KY010-01 and No. 2020-KY010-42). All volunteers participated voluntarily and with written informed consent. The current study used 151 data (until January 21, 2020), including 58 healthy control (HC), 44 SCD, and 49 aMCI from the NBH-ADnsp database. The inclusion and exclusion criteria of participants were provided in *SI Method*. All subjects underwent a comprehensive and standardized clinical evaluation interview, including demographic inventory, medical history, neurological and mental status examination, and MRI scan.

Neurocognitive Assessments

Classical and comprehensive neurocognitive assessments were performed for all the participants, including general cognitive functions, episodic memory, executive function, information processing speed, and visuospatial function. Details of the neurocognitive assessments were summarized in *SI Methods*.

MRI Data Acquisition

The details of image acquisition parameters (structure MRI images and rsfMRI images) are provided in *SI Methods*.

Preprocessing of rsfMRI Data

Functional MRI images were analyzed as described in previous studies using the DPABI based on the SPM program, implemented in MATLAB2013b with the following steps (Chen et al., 2016a, 2020): We discarded the first 10 volumes and performed slice-timing correction and head motion correction. The participants with excessive head motion (cumulative translation or rotation of $> 3.$ mm or $3.^0$) were excluded. Subsequently, segmentation and nuisance covariate regression with 24 motion parameters, global signal, white matter signal, and cerebrospinal fluid signal were performed. Then, we selected a filtering frequency of 0.01–0.08 Hz, used segmented T1 image for normalization, and resampled to an isotropic voxel size of 3 mm. Finally, we applied spatial smoothing with a 6-mm full width at half-maximum Gaussian kernel and detrending.

After preprocessing, we further processed the preprocessed data according to the following steps illustrated in **Figure 1**.

Definition of Functional Brain Networks

Seed-based static FC analysis was carried out to extract the triple networks. In the current study, four 10-mm spherical regions of interest (ROIs) centered in the vmPFC (MNI space: 0, 52, and −6) for the anterior DMN (aDMN), posterior cingulated cortex (PCC) (MNI space: 0, −53, and 26) for the posterior DMN (pDMN), right anterior insula (rAI) (MNI space: 38, 22, and −10) for the SN, and dorsolateral prefrontal cortex (MNI space: 48, 12, and 34) for the ECN were created according to previous studies (Wotruba et al., 2014; Chen et al., 2016b; Xue et al., 2019). The average time series of the ROIs in each participant was extracted, and voxel-wise cross-correlation analysis was conducted between the average time series within the ROIs and the whole brain within the GM mask. Fisher's z-transformation was applied to enhance the normality of the correlation coefficients.

Following this, the individual correlation maps from the HC group were subjected to random-effects analysis using a one-sample *t*-test. The threshold was set at a $p < 0.05$ with threshold-free cluster enhancement (TFCE) approach (1,000 random permutations) and family-wise error (FWE) correction. The regions with positive functional connections to the four ROIs were defined as templates for the aDMN, pDMN, SN, and ECN.

Seed-Based DFC Variability Within the Triple Networks

The dynamic brain connectome analysis toolbox (http://restfmri.net/forum/DynamicBC) was used to compute DFC variability within the aDMN, pDMN, SN, and ECN. First, similar to the above static FC analysis, seed-based (vmPFC, PCC, rAI, and dorsolateral prefrontal cortex) voxel-wise DFC was applied to calculate DFC changes in the triple networks. The classic sliding time-window correlation method was used to compute the correlation between each ROI with a width of 40 TRs slid in steps of 2 TR according to previous studies, resulting in the analysis of 96 windows (Lin et al., 2018; Ma et al., 2019). Each obtained correlation coefficients were converted to a z score by the Fisher r-to-z transformation to improve normality. These Fisher's *z*-transformed correlation results were used to further calculate the temporal variation in DFC.

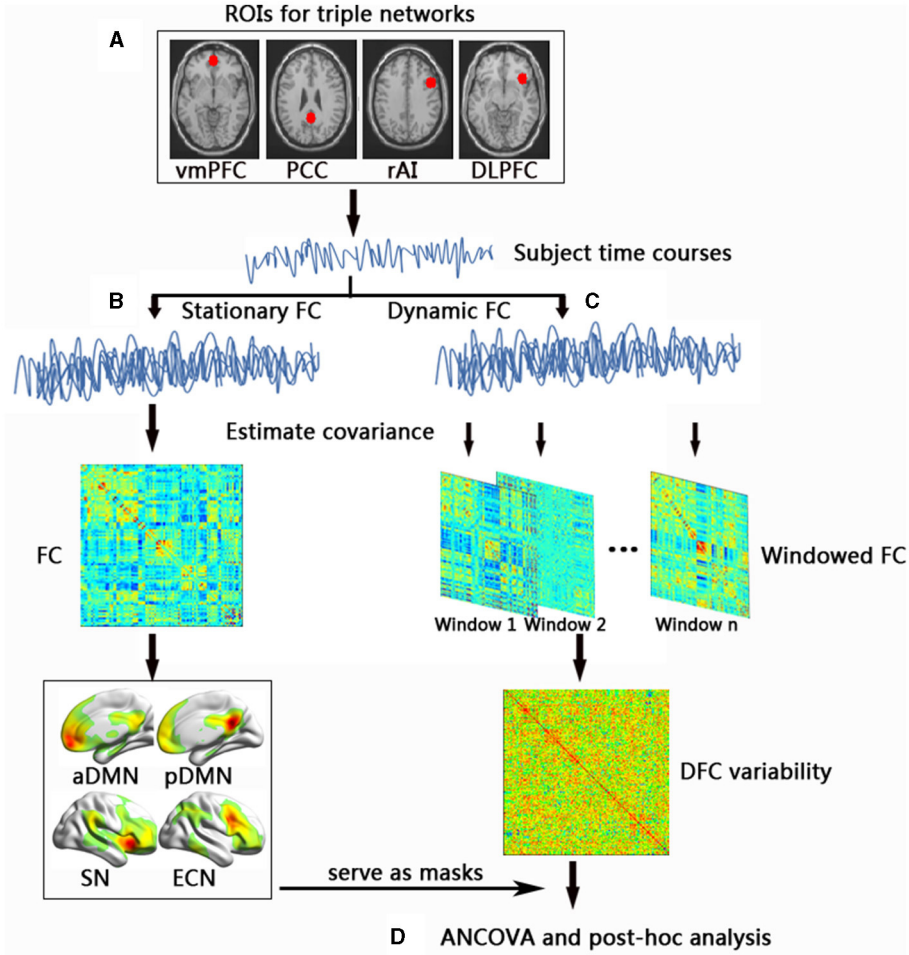

FIGURE 1 | A flow chart for the dynamic functional connectivity analysis in this study. **(A)** For the RS-fMRI data of all subjects, we first used four ROIs to prepare for the next seed-based functional connectivity analysis. **(B)** Then, we adopted stationary functional connectivity analysis and obtained the template of the triple networks. **(C)** We applied the sliding window approach to analyze the dynamic functional connectivity of the obtained 96 windows. Afterward, we calculated dynamic functional connectivity variability across the windows. **(D)** Last, we performed the statistical analysis. ROI, regions of interests; vmPFC, ventromedial prefrontal cortex; PCC, posterior cingulated cortex; rAI, right anterior insula; DLPFC, dorsolateral prefrontal cortex; FC, functional connectivity; DFC, dynamic functional connectivity; aDMN, anterior default mode network; pDMN, posterior default mode network; SN, salience network; ECN, executive control network. ANCOVA, analysis of covariance.

Statistical Analysis

The Statistical Package for the Social Sciences (SPSS) software version 22.0 (IBM, Armonk, NY, USA) was used to analyze the demographic and clinical information. The analysis of covariance (ANCOVA) and chi-squared tests were conducted to compare the demographic and neurocognitive data across the three groups with SCD, aMCI, and HC. Bonferroni's correction with a $p < 0.05$ was used for *post hoc* analysis.

One-way ANCOVA was used to compare the differences in DFC variability in the aDMN, pDMN, SN, and ECN within the corresponding network mask among the three groups with SCD, aMCI, and HC after controlling for the effects of age, gender, and years of education. The non-parametric permutation test with the permutation times of 1,000 was performed in the present study to precisely control the false-positive rate. Corrected $p < 0.05$ and cluster numbers of $\geq$ 20 voxels (cluster size $\geq$ 540 mm^3) were applied to multiple comparisons. The two-sample *t*-test was used for *post hoc* comparisons with the mask from the ANCOVA analysis and age, gender, and years of education as covariates. The significance level was set with a TFCE-FWE corrected $p < 0.05$ and a cluster number of > 9 voxels (cluster size > 243 mm^3).

Significantly, altered DFC variability was extracted with the DPABI and used for the next correlation analysis. Correlation analysis was conducted by SPSS software to explore the relationship between altered DFC variability and cognitive domains with age, gender, and years of education as covariates (Bonferroni-corrected, $p < 0.05$).

Binary Logistic Regression Analysis

Univariate and multivariable analyses of binary logistic regression were conducted in SPSS software to test the diagnostic value of DFC variability in SCD and aMCI. Altered

TABLE 1 | Demographics and clinical measures of three groups, including SCD, aMCI, and HC.

	HC(58)	SCD(44)	aMCI(49)	*F*-values(χ^2)	*P*-values
Age (years)	63.328 ± 6.28	66.000 ± 7.80	63.633 ± 7.58	1.966	0.144
Gender (male/female)	25/33	8/36**	13/36	7.865	0.020[c]
Education level (years)	12.40 ± 2.52	12.33 ± 2.59	10.99 ± 2.95*	4.359	0.014[a]
MMSE scores	28.62 ± 1.24	28.34 ± 1.14	27.22 ± 1.86***/**	13.319	<0.001[ab]
MDRS-2	141.57 ± 2.21	139.89 ± 3.61	136.80 ± 5.10***/***	11.808	<0.001[ab]
MoCA	25.11 ± 2.52	24.64 ± 1.95	22.77 ± 2.98***/**	21.740	<0.001[ab]
SCD-Q	3.51 ± 1.52	6.45 ± 0.89***	5.02 ± 1.92***/***	46.568	<0.001[cab]
Composite Z scores of each cognitive domain					
Episodic memory	0.185 ± 0.080	0.330 ± 0.093	−0.519 ± 0.090***/***	25.178	<0.001[ab]
Information processing speed	0.190 ± 0.084	0.042 ± 0.098	−0.264 ± 0.095**	6.339	0.002[a]
Executive function	0.175 ± 0.065	0.147 ± 0.076	−0.330 ± 0.074***/***	15.166	<0.001[ab]
Visuospatial function	0.068 ± 0.098	0.226 ± 0.114	−0.218 ± 0.111*	3.954	0.021[b]

*Numbers are given as means ± standard deviation, SD unless stated otherwise. Values for age derived from ANCOVA; gender from chi-square test; all clinical measures from ANCOVA with age, gender, years of education as covariates. MMSE, mini-mental state examination; MDRS-2, Mattis Dementia Rating Scale-2; MoCA, the Montreal Cognitive Assessment test; SCD-Q, Subjective Cognitive Decline Questionnaire; [a]post hoc analyses showed a significant group difference between aMCI and HC; [b]post hoc analyses showed a significant group difference between aMCI and SCD; [c]post hoc analyses showed a significant group difference between SCD and HC; *p < 0.05; **p < 0.01; ***p < 0.001; aMCI, amnestic mild cognitive impairment; SCD, subjective cognitive decline; HC, healthy control.*

DFC variability and cognitive function in univariate analysis were included in the multivariable models using backward elimination according to the likelihood ratio with a variable selection criterion of $p < 0.05$. We estimated the receiver-operating characteristic (ROC) curve and the area under the receiver-operating characteristic curve (AUC) to assess the predictive ability of the univariate and multivariable models according to the accuracy, sensitivity, and specificity. A $p < 0.05$ was considered statistically significant.

RESULTS

Demographic and Neurocognitive Characteristics

The demographic and neurocognitive characteristics of all subjects, including 49 with aMCI, 44 with SCD, and 58 with HCs, are shown in **Table 1**. As is expected, the results showed significant differences in cognitive performance. The aMCI group showed significantly lower episodic memory (EM) and executive function (EF) scores compared with both the SCD and HC groups. The aMCI group showed significantly lower information processing speed and visuospatial function compared with the HC group (Bonferroni's *post hoc* correction, $p < 0.05$).

Altered DFC Variability in the Triple Networks in Patients With SCD and aMCI

In the aDMN subnetwork, the ANCOVA results showed significantly altered DFC variability among the three groups, including the right parahippocampal gyrus, right inferior frontal gyrus (IFG), left anterior cingulum gyrus, left caudate, right angular gyrus, right superior temporal gyrus, and bilateral superior frontal gyrus (SFG). Compared with the HC group, the aMCI group showed decreased DFC variability in the right angular and right SFG (TFCE-FWE corrected, $p < 0.05$, cluster number > 9 voxels). All results were obtained with age, gender, and years of education as covariates (**Table 2** and **Figure 2**).

In the pDMN subnetwork, the ANCOVA showed significantly altered DFC variability in the right middle temporal gyrus (MTG) in the three groups. Compared with the HCs, the patients with SCD showed significant decreased DFC variability in the right MTG (TFCE-FWE corrected, $p < 0.05$, cluster number > 9 voxels). All results were obtained with age, gender, and years of education as covariates (**Table 2** and **Figure 2**).

In the SN, the ANCOVA showed significantly altered DFC variability in the left hippocampus, right IFG, left insula, left putamen, left STG, and right IFG. Compared with the group with HC, the group with aMCI showed increased DFC variability in the left putamen while the group with SCD showed increased DFC variability in the left putamen and left insula (TFCE-FWE corrected, $p < 0.05$, cluster number > 9 voxels). All results were obtained with age, gender, and years of education as covariates (**Table 2** and **Figure 3**).

In the ECN, the ANCOVA showed significantly altered DFC variability in the bilateral middle frontal gyrus (MFG), left IFG, and right inferior parietal lobule. Compared with the HCs, the group with SCD showed increased DFC variability in the MFG. Compared with SCD, aMCI showed decreased DFC variability in the right MFG, while increased DFC variability in left IFG (TFCE-FWE corrected, $p < 0.05$, cluster number > 9 voxels). All results were obtained with age, gender, and years of education as covariates (**Table 2** and **Figure 4**).

Behavioral Significance of Altered DFC Variability Within the Triple Networks in Patients With SCD and aMCI

The correlation analysis showed that in the groups with SCD and aMCI, altered DFC variability in the left IFG of the ECN

TABLE 2 | The difference of dynamic functional connectivity variability in default mode network across three groups.

Region(aal)	Peak MNI coordinate			F/t	Cluster number
	x	y	z		
Anterior default mode network					
ANCOVA					
R parahippocampal gyrus	21	−18	−30	6.3284	20
R inferior frontal gyrus	36	24	−24	7.0609	42
B anterior cingulum gyrus	−6	39	3	8.9345	22
L caudate	−9	6	−3	7.232	38
R angular gyrus/superior temporal gyrus	60	−51	21	6.6394	79
R superior frontal gyrus	21	39	27	7.4796	40
L superior frontal gyrus	−21	33	54	7.2538	21
aMCI vs. HC					
R angular gyrus	42	−51	24	−3.0653	18
R superior frontal gyrus	24	39	33	−3.6477	18
Posterior default mode network					
ANCOVA					
R middle temporal gyrus	66	−45	−3	6.9386	21
SCD vs. HC					
R middle temporal gyrus	66	−45	0	−3.1797	10
Salience network					
ANCOVA					
R Hippocampus	39	−27	6	3.8555	20
R superior temporal gyrus	51	−24	6	3.1027	34
L hippocampus	−18	−18	−15	6.3901	49
R inferior frontal gyrus	45	39	−6	7.1029	47
L insula/putamen	−45	12	3	11.4039	252
L superior temporal gyrus	−48	−39	18	6.4033	57
R inferior frontal gyrus	45	15	15	6.6237	28
SCD vs. HC					
L putamen	−30	−3	−3	3.6342	15
L insula	−45	12	3	4.1688	53
aMCI vs. HC					
L putamen	−27	12	−3	4.0464	11
Executive control network					
ANCOVA					
R middle frontal gyrus	33	54	9	7.1346	38
L inferior frontal gyrus	−39	9	24	6.3027	59
R middle frontal gyrus	45	36	21	5.0147	64
L middle frontal gyrus	−42	45	18	7.732	39
R inferior parietal lobule	54	−42	42	8.0083	32
SCD vs. HC					
L middle frontal gyrus	−48	42	21	3.8698	22
aMCI vs. HC					
R middle frontal gyrus	30	57	6	−3.3649	11
L inferior frontal gyrus	−36	15	15	3.7362	14

The x, y, z coordinates are the primary peak locations in the MNI space. Cluster size > 19 voxels in ANCOVA analysis, $p < 0.05$; Cluster size > 10 voxels in post hoc test, $p < 0.05$, TFCE-FWE corrected; L, left; R, right; B, bilateral; aMCI, amnestic mild cognitive impairment; SCD, subjective cognitive decline; HC, healthy control.

was significantly negatively correlated with EM ($r = -0.421$, $p < 0.001$) and EF ($r = -0.382$, $p < 0.001$) (Bonferroni-corrected, $p < 0.05$). Age, gender, and years of education were used as covariates for all these results (**Figure 4**).

Diagnosis and Classification of SCD and aMCI Using Logistic Regression Analysis

The receiver-operating characteristic (ROC) curve of each altered index is shown in **Figure 5**. The best-fitting model

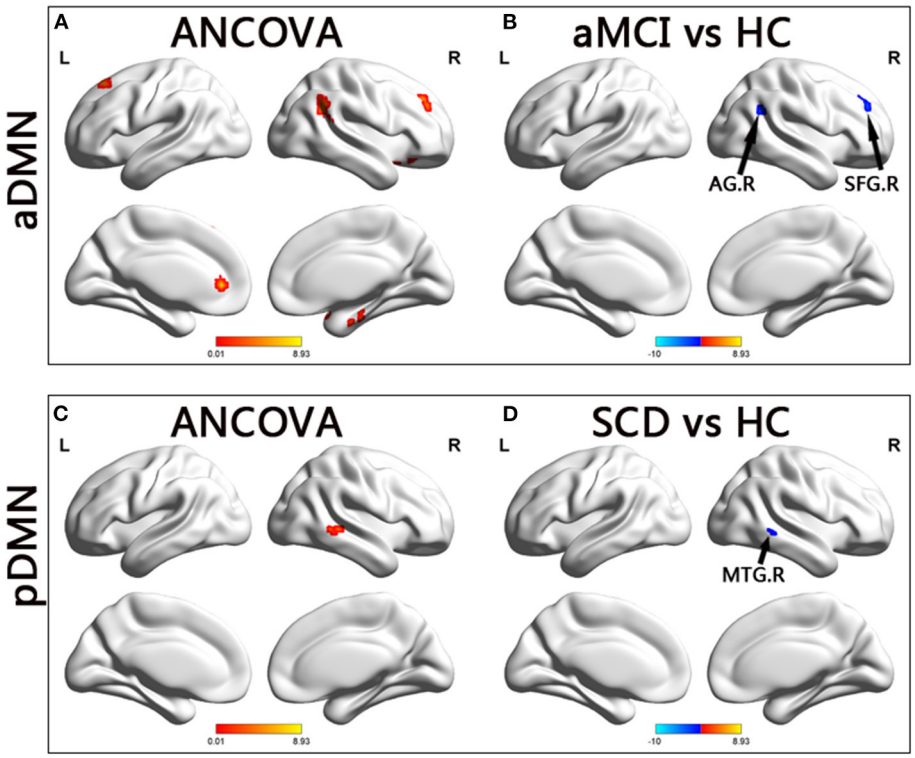

FIGURE 2 | Brain regions exhibiting significant differences in dynamic functional connectivity variability within default mode network. **(A,C)** Brain regions showing significant differences in dynamic functional connectivity variability within the anterior default mode network and posterior default mode network across three groups, including SCD, aMCI, and HC ($p < 0.05$, the cluster size > 19 voxels). **(B,D)** Results of *post hoc* analysis in voxel-wise analysis (TFCE-FWE corrected, cluster size > 9, $p < 0.05$). aDMN, anterior default mode network; pDMN, posterior default mode network; aMCI, amnestic mild cognitive impairment; SCD, subjective cognitive decline; HC, healthy controls; AG, angular gyrus; SFG, superior frontal gyrus; MTG, middle temporal gyrus; R, right.

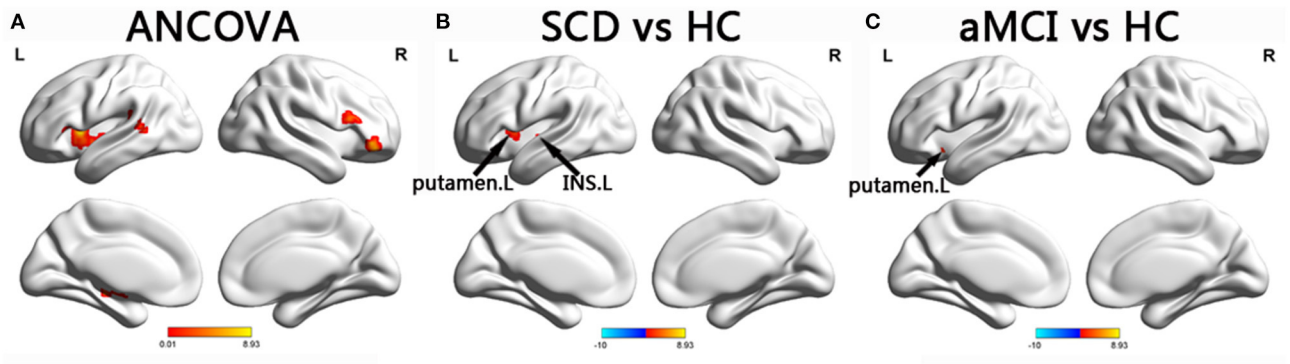

FIGURE 3 | Brain regions exhibiting significant differences in dynamic functional connectivity variability within salience network. **(A)** Brain regions showing significant differences in dynamic functional connectivity variability within the salience network across three groups, including SCD, aMCI, and HC ($p < 0.05$, the cluster size > 19 voxels). **(B,C)** Results of *post hoc* analysis in voxel-wise analysis (TFCE-FWE corrected, cluster size > 9, $p < 0.05$). aDMN, anterior default mode network; pDMN, posterior default mode network; aMCI, amnestic mild cognitive impairment; SCD, subjective cognitive decline; HC, healthy controls; INS, insula; L, left.

was based on the multivariable models, combining altered DFC variability and decreased cognitive function. The AUC in the groups with SCD and HC based on the multivariable model was.877, with 88.6% sensitivity and 75.9% specificity ($p < 0.001$). In the groups with aMCI and HC, the AUC based on the multivariable model was.927, with 75.% sensitivity, and 98.2% specificity ($p < 0.001$). The AUC of the groups of SCD and aMCI based on the multivariable model was.907, with 86.4% sensitivity and 81.8% specificity ($p < 0.001$).

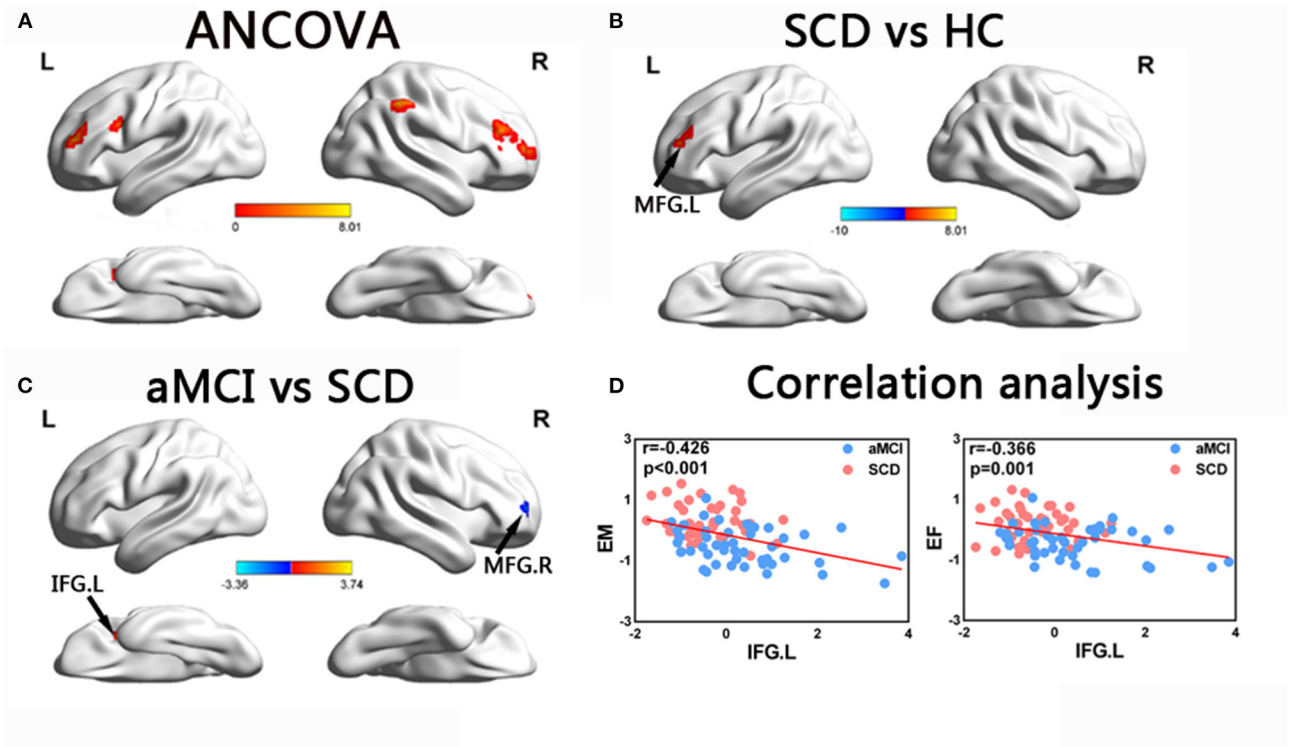

FIGURE 4 | Brain regions exhibiting significant differences in dynamic functional connectivity variability within executive control network and the correlation with cognitive function. **(A)** Brain regions showing significant differences in dynamic functional connectivity variability within the executive control network across three groups, including SCD, aMCI, and HC ($p < 0.05$, the cluster size > 19 voxels). **(B,C)** Results of *post hoc* analysis in voxel-wise analysis (TFCE-FWE corrected, cluster size > 9, $p < 0.05$). **(D)** Results of associations between altered dynamic functional connectivity variability and cognitive function. Age, gender, and years of education were used as covariates of results (Bonferroni corrected, $p < 0.05$). aDMN, anterior default mode network; pDMN, posterior default mode network; aMCI, amnestic mild cognitive impairment; SCD, subjective cognitive decline; HC, healthy controls; MFG, middle frontal gyrus; IFG, inferior frontal gyrus; EM, episodic memory; EF, executive function; R, right; L, left.

DISCUSSION

To the best of our knowledge, the present study was the first to analyze DFC variability in patients with SCD and aMCI based on the triple-network model and the association with cognitive decline. The primary findings of the study were that DFC variability within the triple networks in patients with SCD and aMCI had varying degrees of change. Moreover, altered DFC variability within the ECN was significantly correlated with cognitive performance in patients with SCD and aMCI. Most importantly, altered DFC variability, combined with the triple-network model, can serve as an important biomarker for their higher efficiency in the diagnosis of SCD and aMCI.

The present study showed that the DFC variability within the triple networks, including the DMN, SN, and ECN, was changed to different degrees in patients with SCD and aMCI. The DMN can be divided into the aDMN and pDMN, each of which has been considered to function independently in a wide range of cognitive tasks. Specifically, the aDMN is involved in self-referential mental idealization, while the pDMN is involved in EM retrieval (Xue et al., 2020). In the present study, patients with SCD patients showed decreased DFC variability in the right MTG within the pDMN compared with HCs, whereas patients with aMCI showed decreased DFC variability in the right angular gyrus and right SFG within the aDMN. The impaired brain regions are involved in language processing functions (angular gyrus), spatial orientation (angular gyrus), motor planning and executive (SFG) function, and visual information processing (MTG). This might mean that impairment in the DMN may lead to extensive cognitive decline. Moreover, a prior static FC study indicated that the FC of the aDMN first increased and then decreased with the progression of AD spectrum disease, which was consistent with our results, showing that DFC variability of the aDMN was decreased in patients with aMCI compared with HCs, while the patients with SCD remained stable (Xue et al., 2020). Notably, previous DFC studies demonstrated that higher DFC variability in brain regions may reflect greater complexity and greater information processing ability (Marusak et al., 2017). Decreased DFC variability may indicate the decreased information processing ability of patients with SCD and aMCI (Marusak et al., 2017). The decreased DFC variability within the DMN subnetworks of the patients with SCD in the present study means that patients with SCD already had a tendency toward impaired information processing. In addition, the patients with

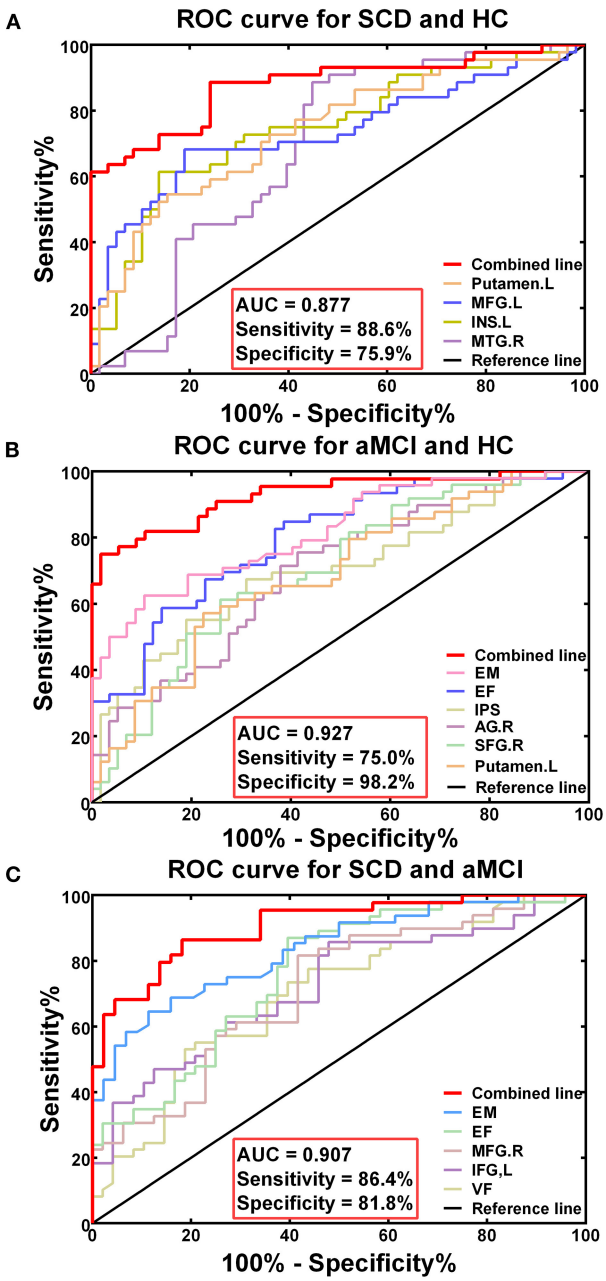

FIGURE 5 | Diagnosis and differentiation of SCD and aMCI based on ROC analysis. **(A)** The ROC curve showing the classification of SCD and HC; **(B)** The ROC curve showing the classification of aMCI and HC; **(C)** The ROC curve showing the classification of aMCI and SCD.

SCD showed altered DFC variability, mainly in the pDMN, whereas the patients with aMCI showed altered DFC variability mainly in the aDMN, which seemed to confirm the specificity of DFC variability within the DMN of patients with AD spectrum disorders.

In our study, the groups with SCD and aMCI both showed increased DFC variability in the left putamen within the SN, while the group with aMCI additionally showed increased DFC variability in the left insula within the SN. The putamen is part of the neostriatum, which was identified as one of the first brain areas affected by amyloid deposition in healthy elderly people (Rodriguez-Vieitez et al., 2016). Previous studies indicated that the putamen was involved in working memory and probabilistic learning and might be an appropriate clinical biomarker of neurodegenerative disease (Bellebaum et al., 2008; Looi et al., 2012). Research studies reported that a decline in the amplitude of low frequency fluctuations and volume of the putamen were significantly related to cognitive decline in patients with AD spectrum disorders (de Jong et al., 2008; Ren et al., 2016). The insula, a major region of the SN, is believed to play an important role in the maintenance of memory performance in the early stage of AD spectrum disorders (Lin et al., 2017). One study suggested that the left insula had the higher node degree and participation coefficient in the brain network and was associated with EM (Xue et al., 2020). The increased DFC variability of the SN in patients verified the "brain reserve" hypothesis that the enhanced FC of the SN in SCD and aMCI might be a compensatory mechanism for decreased DMN function, which resists amyloid protein deposition and maintains relatively normal cognitive function (Cohen et al., 2009; Menon and Uddin, 2010).

Our results showed altered DFC variability within the ECN in patients with SCD and aMCI. The ECN, with the prefrontal lobe as the core, plays an important role in the regulation of cognition and behavior, the integration of perception and memory information, and working memory (Petersen et al., 2019). The MFG and IFG are responsible for executive cognitive function and working memory. The present research found that SCD showed increased DFC variability in the left MFG compared with HCs, whereas patients with aMCI showed decreased DFC variability in the right MFG compared with the patients with SCD. This might indicate that DFC variability decreased as AD spectrum disorder progressed, representing a gradual decline in information-processing ability.

Taken together, we can speculate that patients with SCD and aMCI have a common and unique disruption in the triple networks. The triple networks are involved in a wide range of cognitive tasks through direct or indirect means. The disruption of any network of the triple networks will result in aberrant goal-related stimuli and internal psychological events (Sridharan et al., 2008). Previous research findings suggested that abnormal organization and function of the triple networks were prominent features of neuropsychiatric diseases. However, the specific changes in static FC within the triple networks of patients with SCD and aMCI were inconsistent. For example, some research claimed that aMCI showed increased static FC in the SN, while several reported disrupted static FC in the SN (Brier et al., 2012; Uddin, 2015; Chen et al., 2016b). One possible reason for the inconsistent results may be that the FC pattern was dynamic rather than static during the entire rsfMRI scan, leading to different FC patterns in different scan periods (Wang et al., 2020). Therefore, our study confirmed that the DFC of the triple networks was disrupted in patients with SCD and aMCI, suggesting that

DFC analysis can be used to complement and verify static FC analysis.

The present study showed observably negative associations between altered DFC variability in the left IFG and cognitive domains in patients with SCD and aMCI, including EM and EF. The results demonstrated that disruption of DFC was significantly related to declining cognition performance in patients with SCD and aMCI. As the EM and EF were impaired, DFC variability in patients with SCD and aMCI increased in the left IFG. Moreover, the patients with aMCI exhibited higher DFC variability with the EM and EF impairment compared with patients with SCD. This might mean that the increased DFC variability in the left IFG was to compensate for the impairment of EM and EF in the progression of preclinical AD spectrum disorders. Furthermore, EF refers to the cognitive process of goal-oriented behavior from goal formulation to successful execution and the processing of results (Miller and Cohen, 2001; Diamond, 2013). The correlation between altered DFC variability in the left IFG within the ECN and EF confirmed why the ECN is widely used to investigate the mechanism of altered EF in patients (Brown et al., 2019). Interestingly, patients with SCD and aMCI showed significant correlations between EM and altered DFC variability within ECN. A previous study suggested that EM deficits in patients with aMCI were associated with the right dorsolateral prefrontal cortex functional network (Yuan et al., 2016). Our results provided new evidence for the interaction between impaired EF and memory impairment. Taken together, the study suggested that DFC in SCD and aMCI was disrupted, which extended the current understanding of the functional network and showed the importance of evaluating changes in DFC in patients with preclinical AD spectrum disorders.

The most significant finding in the current study was that the best-fitting model in diagnosing and characterizing SCD and aMCI was based on multivariable models. They combined altered DFC variability within the triple networks and declining cognitive function. It can be seen that the multivariable models had higher AUC values with high sensitivity and specificity compared with univariate models. The model was highly specific for aMCI with 98.2% specificity, so the risk of false-positive errors was very low, suggesting that DFC analysis could be a reliable potential biomarker for diagnosing patients with aMCI. Specifically, DFC variability in the left putamen played a vital role in the diagnosis of SCD, whereas DFC variability of the right angular gyrus played a major role in the diagnosis of aMCI due to its higher AUC values. Meanwhile, DFC variability in the right MFG and left IFG played dominant roles in the differentiation of SCD from aMCI. That distinction might provide additional information in research on specific brain region changes in SCD and aMCI. Additionally, research has indicated that the classification accuracy of static FC was lower than that of DFC because time-averaged analysis could not account for microscopic changes in brain states (Bassett et al., 2013; Allen et al., 2014; Cordova-Palomera et al., 2017). Studies have shown that DFC provided significantly more behavioral information than static FC (Cordova-Palomera et al., 2017; Liegeois et al., 2019). Thus, such reliable methods will have more value for the early detection of AD-related pathology.

LIMITATIONS

Several limitations of the present study showed are acknowledged. First, the patient sample was small, which may have reduced the generalizability of the results. To avoid this problem, we applied a non-parametric permutation test to control the false-positive rate. Moreover, our research group is continuously recruiting new volunteers, and the NBH-ADsnp database is constantly updated, which means we will further verify our conclusions in the future. Secondly, we collected only 8-min-long data on each participant in the current study, resulting in inadequate results. We will take advantage of longer fMRI scan times, such as several hours, to improve the DFC variability estimates in a future study. Lastly, the lack of longitudinal research made it impossible to explore disease transformation in depth. Our research team is following up on the recruited volunteers regularly, and we plan to further explore the longitudinal changes in DFC in the future.

CONCLUSION

The current study revealed common and specific DFC variability abnormalities within the triple networks of patients with SCD and aMCI. Moreover, altered DFC variability in the left IFG within the ECN was significantly correlated with cognitive decline, including EM and EF. More importantly, the best-fitting model in diagnosing and differentiating SCD and aMCI was a multivariable model that combined altered DFC variability (right MTG, left putamen, left insula, and left MFG in distinguishing patients with SCD and HCs; right AG, right SFG, and left putamen in distinguishing patients with aMCI and HCs; and right MFG and left IFG in distinguishing patients with SCD and aMCI) with declined cognitive function. Therefore, our findings suggest that the DFC variability analysis, combined with the triple-network model, can be used as a potential biomarker of preclinical AD spectrum disorders and may help us to understand abnormal cognitive function.

DATA AVAILABILITY STATEMENT

The data analyzed in this study is subject to the following licenses/restrictions: The datasets analyzed in this article are not publicly available. Requests to access the datasets should be directed to Jiu Chen, ericcst@aliyun.com.

ETHICS STATEMENT

The studies involving human participants were reviewed and approved by the responsible Human Participants Ethics Committee of the Affiliated Brain Hospital of Nanjing Medical University. The patients/participants provided their written informed consent to participate in this study. Written informed consent was obtained from the individual(s) for the publication of any potentially identifiable images or data included in this article.

AUTHOR CONTRIBUTIONS

CXu, WQ, CXi, and JC designed the study. CXu, WQ, CXi, JC, QY, GH, HG, and JR collected the data. CXu analyzed the data and prepared the manuscript. All authors contributed to the article and approved the submitted version.

FUNDING

This study was supported by the National Natural Science Foundation of China (No. 81701675); the Key Project supported by Medical Science and Technology Development Foundation, Nanjing Department of Health (No. JQX18005); the Cooperative Research Project of Southeast University-Nanjing Medical University (No. 2018DN0031); the Key Research and Development Plan (Social Development) Project of Jiangsu Province (No. BE2018608); and the Innovation and Entrepreneurship Training Program for College Students in Jiangsu Province (Nos. 201810312061X; 201910312035Z).

SUPPLEMENTARY MATERIAL

The Supplementary Material for this article can be found online at: https://www.frontiersin.org/articles/10.3389/fnagi.2021.711009/full#supplementary-material

REFERENCES

Allen, E. A., Damaraju, E., Plis, S. M., Erhardt, E. B., Eichele, T., and Calhoun, V. D. (2014). Tracking whole-brain connectivity dynamics in the resting state. *Cereb. Cortex* 24, 663–676. doi: 10.1093/cercor/bhs352

Bassett, D. S., Wymbs, N. F., Rombach, M. P., Porter, M. A., Mucha, P. J., and Grafton, S. T. (2013). Task-based core-periphery organization of human brain dynamics. *PLoS Comput. Biol.* 9:e1003171. doi: 10.1371/journal.pcbi.1003171

Bellebaum, C., Koch, B., Schwarz, M., and Daum, I. (2008). Focal basal ganglia lesions are associated with impairments in reward-based reversal learning. *Brain* 131, 829–841. doi: 10.1093/brain/awn011

Bischkopf, J., Busse, A., and Angermeyer, M. C. (2002). Mild cognitive impairment–a review of prevalence, incidence and outcome according to current approaches. *Acta Psychiatr. Scand.* 106, 403–414. doi: 10.1034/j.1600-0447.2002.01417.x

Brier, M. R., Thomas, J. B., Snyder, A. Z., Benzinger, T. L., Zhang, D., Raichle, M. E., et al. (2012). Loss of intranetwork and internetwork resting state functional connections with Alzheimer's disease progression. *J. Neurosci.* 32, 8890–8899. doi: 10.1523/JNEUROSCI.5698-11.2012

Brown, C. A., Schmitt, F. A., Smith, C. D., and Gold, B. T. (2019). Distinct patterns of default mode and executive control network circuitry contribute to present and future executive function in older adults. *Neuroimage* 195, 320–332. doi: 10.1016/j.neuroimage.2019.03.073

Broyd, S. J., Demanuele, C., Debener, S., Helps, S. K., James, C. J., and Sonuga-Barke, E. J. S. (2009). Default-mode brain dysfunction in mental disorders: A systematic review. *Neurosci. Biobehav. Rev.* 33, 279–296. doi: 10.1016/j.neubiorev.2008.09.002

Chand, G. B., Wu, J. J., Hajjar, I., and Qiu, D. Q. (2017). Interactions of the salience network and its subsystems with the default-mode and the central-executive networks in normal aging and mild cognitive impairment. *Brain Connect.* 7, 401–412. doi: 10.1089/brain.2017.0509

Chang, C., and Glover, G. H. (2010). Time-frequency dynamics of resting-state brain connectivity measured with fMRI. *Neuroimage* 50, 81–98. doi: 10.1016/j.neuroimage.2009.12.011

Chen, J., Chen, G., Shu, H., Chen, G., Ward, B. D., Wang, Z., et al. (2019). Predicting progression from mild cognitive impairment to Alzheimer's disease on an individual subject basis by applying the CARE index across different independent cohorts. *Aging* 11, 2185–2201. doi: 10.18632/aging.101883

Chen, J., Duan, X., Shu, H., Wang, Z., Long, Z., Liu, D., et al. (2016a). Differential contributions of subregions of medial temporal lobe to memory system in amnestic mild cognitive impairment: insights from fMRI study. *Sci. Rep.* 6:26148. doi: 10.1038/srep26148

Chen, J., Ma, N., Hu, G., Nousayhah, A., Xue, C., Qi, W., et al. (2020). rTMS modulates precuneus-hippocampal subregion circuit in patients with subjective cognitive decline. *Aging* 13, 1314–1331. doi: 10.18632/aging.202313

Chen, J., Shu, H., Wang, Z., Zhan, Y. F., Liu, D., Liao, W. X., et al. (2016b). Convergent and divergent intranetwork and internetwork connectivity patterns in patients with remitted late-life depression and amnestic mild cognitive impairment. *Cortex* 83, 194–211. doi: 10.1016/j.cortex.2016.08.001

Cohen, A. D., Price, J. C., Weissfeld, L. A., James, J., Rosario, B. L., Bi, W., et al. (2009). Basal cerebral metabolism may modulate the cognitive effects of Abeta in mild cognitive impairment: an example of brain reserve. *J. Neurosci.* 29, 14770–14778. doi: 10.1523/JNEUROSCI.3669-09.2009

Cordova-Palomera, A., Kaufmann, T., Persson, K., Alnaes, D., Doan, N. T., Moberget, T., et al. (2017). Disrupted global metastability and static and dynamic brain connectivity across individuals in the Alzheimer's disease continuum. *Sci. Rep.* 7:40268. doi: 10.1038/srep40268

de Jong, L. W., van der Hiele, K., Veer, I. M., Houwing, J. J., Westendorp, R. G., Bollen, E. L., et al. (2008). Strongly reduced volumes of putamen and thalamus in Alzheimer's disease: an MRI study. *Brain* 131, 3277–3285. doi: 10.1093/brain/awn278

Diamond, A. (2013). Executive functions. *Annu. Rev. Psychol.* 64, 135–168. doi: 10.1146/annurev-psych-113011-143750

Dong, G., Yang, L., Li, C. R., Wang, X., Zhang, Y., Du, W., et al. (2020). Dynamic network connectivity predicts subjective cognitive decline: the Sino-Longitudinal Cognitive impairment and dementia study. *Brain Imaging Behav.* 14, 2692–2707. doi: 10.1007/s11682-019-00220-6

Finc, K., Bonna, K., He, X., Lydon-Staley, D. M., Kuhn, S., Duch, W., et al. (2020). Dynamic reconfiguration of functional brain networks during working memory training. *Nat. Commun.* 11:2435. doi: 10.1038/s41467-020-15631-z

Gu, Y., Lin, Y., Huang, L., Ma, J., Zhang, J., Xiao, Y., et al. (2020). Abnormal dynamic functional connectivity in Alzheimer's disease. *CNS Neurosci. Ther.* 26, 962–971. doi: 10.1111/cns.13387

He, X. X., Qin, W., Liu, Y., Zhang, X. Q., Duan, Y. Y., Song, J. Y., et al. (2014). Abnormal salience network in normal aging and in amnestic mild cognitive impairment and Alzheimer's disease. *Hum. Brain Mapp.* 35, 3446–3464. doi: 10.1002/hbm.22414

Hutchison, R. M., Womelsdorf, T., Allen, E. A., Bandettini, P. A., Calhoun, V. D., Corbetta, M., et al. (2013). Dynamic functional connectivity: promise, issues, and interpretations. *Neuroimage* 80, 360–378. doi: 10.1016/j.neuroimage.2013.05.079

Jessen, F., Amariglio, R. E., van Boxtel, M., Breteler, M., Ceccaldi, M., Chetelat, G., et al. (2014a). A conceptual framework for research on subjective cognitive decline in preclinical Alzheimer's disease. *Alzheimers. Dement.* 10, 844–852. doi: 10.1016/j.jalz.2014.01.001

Jessen, F., Wolfsgruber, S., Wiese, B., Bickel, H., Mosch, E., Kaduszkiewicz, H., et al. (2014b). AD dementia risk in late MCI, in early MCI, and in subjective memory impairment. *Alzheimers. Dement.* 10, 76–83. doi: 10.1016/j.jalz.2012.09.017

Joo, S. H., Lim, H. K., and Lee, C. U. (2016). Three large-scale functional brain networks from resting-state functional MRI in subjects with different levels of cognitive impairment. *Psychiatry Investig.* 13, 1–7. doi: 10.4306/pi.2016.13.1.1

Lei, B., Yu, S., Zhao, X., Frangi, A. F., Tan, E. L., Elazab, A., et al. (2020). Diagnosis of early Alzheimer's disease based on dynamic high order networks. *Brain Imaging Behav.* 15, 276–287. doi: 10.1007/s11682-019-00255-9

Li, C. X., Li, Y. J., Zheng, L., Zhu, X. Q., Shao, B. X., Fan, G., et al. (2019). Abnormal Brain network connectivity in a triple-network model of Alzheimer's disease. *J. Alzheimers Dis.* 69, 237–252. doi: 10.3233/jad-181097

Li, S. J., Li, Z., Wu, G., Zhang, M. J., Franczak, M., and Antuono, P. G. (2002). Alzheimer Disease: evaluation of a functional MR imaging index as a marker. *Radiology* 225, 253–259. doi: 10.1148/radiol.2251011301

Liang, X., Zou, Q., He, Y., and Yang, Y. (2016). Topologically reorganized connectivity architecture of default-mode, executive-control, and salience networks across working memory task loads. *Cereb. Cortex* 26, 1501–1511. doi: 10.1093/cercor/bhu316

Liegeois, R., Li, J., Kong, R., Orban, C., Van De Ville, D., Ge, T., et al. (2019). Resting brain dynamics at different timescales capture distinct aspects of human behavior. *Nat. Commun.* 10:2317. doi: 10.1038/s41467-019-10317-7

Lin, F., Ren, P., Lo, R. Y., Chapman, B. P., Jacobs, A., Baran, T. M., et al. (2017). Insula and inferior frontal gyrus' activities protect memory performance against Alzheimer's disease pathology in old age. *J. Alzheimers. Dis.* 55, 669–678. doi: 10.3233/JAD-160715

Lin, S. J., Vavasour, I., Kosaka, B., Li, D. K. B., Traboulsee, A., MacKay, A., et al. (2018). Education, and the balance between dynamic and stationary functional connectivity jointly support executive functions in relapsing-remitting multiple sclerosis. *Hum. Brain Mapp.* 39, 5039–5049. doi: 10.1002/hbm.24343

Long, Y., Chen, C., Deng, M., Huang, X., Tan, W., Zhang, L., et al. (2019). Psychological resilience negatively correlates with resting-state brain network flexibility in young healthy adults: a dynamic functional magnetic resonance imaging study. *Ann Transl Med* 7, 809. doi: 10.21037/atm.2019.12.45

Looi, J. C., Rajagopalan, P., Walterfang, M., Madsen, S. K., Thompson, P. M., Macfarlane, M. D., et al. (2012). Differential putaminal morphology in Huntington's disease, frontotemporal dementia and Alzheimer's disease. *Aust. N. Z. J. Psychiatry* 46, 1145–1158. doi: 10.1177/0004867412457224

Ma, W. Y., Yao, Q., Hu, G. J., Xiao, C. Y., Shi, J. P., and Chen, J. (2019). Dysfunctional dynamics of intra- and inter-network connectivity in dementia with lewy bodies. *Front. Neurol.* 10:1265. doi: 10.3389/fneur.2019.01265

Marusak, H. A., Calhoun, V. D., Brown, S., Crespo, L. M., Sala-Hamrick, K., Gotlib, I. H., et al. (2017). Dynamic functional connectivity of neurocognitive networks in children. *Hum. Brain Mapp.* 38, 97–108. doi: 10.1002/hbm.23346

Menon, V. (2011). Large-scale brain networks and psychopathology: a unifying triple network model. *Trends Cogn. Sci.* 15, 483–506. doi: 10.1016/j.tics.2011.08.003

Menon, V., and Uddin, L. Q. (2010). Saliency, switching, attention and control: a network model of insula function. *Brain Struct. Funct.* 214, 655–667. doi: 10.1007/s00429-010-0262-0

Miller, E. K., and Cohen, J. D. (2001). An integrative theory of prefrontal cortex function. *Annu. Rev. Neurosci.* 24, 167–202. doi: 10.1146/annurev.neuro.24.1.167

Mitchell, A. J., Beaumont, H., Ferguson, D., Yadegarfar, M., and Stubbs, B. (2014). Risk of dementia and mild cognitive impairment in older people with subjective memory complaints: meta-analysis. *Acta Psychiatr. Scand.* 130, 439–451. doi: 10.1111/acps.12336

Morris, J. C., and Cummings, J. (2005). Mild cognitive impairment (MCI) represents early-stage Alzheimer's disease. *J. Alzheimers. Dis.* 7, 235–239. doi: 10.3233/jad-2005-7306

Niu, H., Zhu, Z., Wang, M., Li, X., Yuan, Z., Sun, Y., et al. (2019). Abnormal dynamic functional connectivity and brain states in Alzheimer's diseases: functional near-infrared spectroscopy study. *Neurophotonics* 6:025010. doi: 10.1117/1.NPh.6.2.025010

Petersen, N., Ghahremani, D. G., Rapkin, A. J., Berman, S. M., Wijker, N., Liang, L., et al. (2019). Resting-state functional connectivity in women with PMDD. *Transl. Psychiatry* 9:339. doi: 10.1038/s41398-019-0670-8

Preti, M. G., Bolton, T. A., and Van De Ville, D. (2017). The dynamic functional connectome: State-of-the-art and perspectives. *Neuroimage* 160, 41–54. doi: 10.1016/j.neuroimage.2016.12.061

Raichle, M. E., MacLeod, A. M., Snyder, A. Z., Powers, W. J., Gusnard, D. A., and Shulman, G. L. (2001). A default mode of brain function. *Proc. Natl. Acad. Sci. U.S.A.* 98, 676–682. doi: 10.1073/pnas.98.2.676

Ren, P., Lo, R. Y., Chapman, B. P., Mapstone, M., Porsteinsson, A., Lin, F., et al. (2016). Longitudinal alteration of intrinsic brain activity in the striatum in mild cognitive impairment. *J. Alzheimers. Dis.* 54, 69–78. doi: 10.3233/JAD-160368

Rodriguez-Vieitez, E., Saint-Aubert, L., Carter, S. F., Almkvist, O., Farid, K., Scholl, M., et al. (2016). Diverging longitudinal changes in astrocytosis and amyloid PET in autosomal dominant Alzheimer's disease. *Brain* 139, 922–936. doi: 10.1093/brain/awv404

Slot, R. E. R., Sikkes, S. A. M., Berkhof, J., Brodaty, H., Buckley, R., Cavedo, E., et al. (2019). Subjective cognitive decline and rates of incident Alzheimer's disease and non-Alzheimer's disease dementia. *Alzheimers. Dement.* 15, 465–476. doi: 10.1016/j.jalz.2018.10.003

Sridharan, D., Levitin, D. J., and Menon, V. (2008). A critical role for the right fronto-insular cortex in switching between central-executive and default-mode networks. *Proc. Natl. Acad. Sci. U.S.A.* 105, 12569–12574. doi: 10.1073/pnas.0800005105

Uddin, L. Q. (2015). Salience processing and insular cortical function and dysfunction. *Nat. Rev. Neurosci.* 16, 55–61. doi: 10.1038/nrn3857

Wang, J. J., Wang, Y., Huang, H. Y., Jia, Y. B., Zheng, S. N., Zhong, S. M., et al. (2020). Abnormal dynamic functional network connectivity in unmedicated bipolar and major depressive disorders based on the triple-network model. *Psychol. Med.* 50, 465–474. doi: 10.1017/s003329171900028x

Wotruba, D., Michels, L., Buechler, R., Metzler, S., Theodoridou, A., Gerstenberg, M., et al. (2014). Aberrant coupling within and across the default mode, task-positive, and salience network in subjects at risk for psychosis. *Schizophr. Bull.* 40, 1095–1104. doi: 10.1093/schbul/sbt161

Wu, X., Li, Q., Yu, X., Chen, K., Fleisher, A. S., Guo, X., et al. (2016). A triple network connectivity study of large-scale brain systems in cognitively normal APOE4 carriers. *Front. Aging Neurosci.* 8, 231. doi: 10.3389/fnagi.2016.00231

Xue, C., Sun, H., Hu, G., Qi, W., Yue, Y., Rao, J., et al. (2020). Disrupted patterns of rich-club and diverse-club organizations in subjective cognitive decline and amnestic mild cognitive impairment. *Front. Neurosci.* 14:575652. doi: 10.3389/fnins.2020.575652

Xue, C., Yuan, B. Y., Yue, Y. Y., Xu, J. N., Wang, S. Y., Wu, M. L., et al. (2019). Distinct disruptive patterns of default mode subnetwork connectivity across the spectrum of preclinical Alzheimer's disease. *Front. Aging Neurosci.* 11:307. doi: 10.3389/fnagi.2019.00307

Yuan, B. Y., Chen, J., Gong, L., Shu, H., Liao, W. X., Wang, Z., et al. (2016). Mediation of episodic memory performance by the executive function network in patients with amnestic mild cognitive impairment: a resting-state functional MRI study. *Oncotarget* 7, 64711–64725. doi: 10.18632/oncotarget.11775

Zhan, Y., Ma, J., Alexander-Bloch, A. F., Xu, K., Cui, Y., Feng, Q., et al. (2016). Longitudinal study of impaired intra- and inter-network brain connectivity in subjects at high risk for Alzheimer's disease. *J. Alzheimers. Dis.* 52, 913–927. doi: 10.3233/JAD-160008

Zhang, D., and Raichle, M. E. (2010). Disease and the brain's dark energy. *Nat. Rev. Neurol.* 6, 15–28. doi: 10.1038/nrneurol.2009.198

Conflict of Interest: The authors declare that the research was conducted in the absence of any commercial or financial relationships that could be construed as a potential conflict of interest.

Publisher's Note: All claims expressed in this article are solely those of the authors and do not necessarily represent those of their affiliated organizations, or those of the publisher, the editors and the reviewers. Any product that may be evaluated in this article, or claim that may be made by its manufacturer, is not guaranteed or endorsed by the publisher.

Copyright © 2021 Xue, Qi, Yuan, Hu, Ge, Rao, Xiao and Chen. This is an open-access article distributed under the terms of the Creative Commons Attribution License (CC BY). The use, distribution or reproduction in other forums is permitted, provided the original author(s) and the copyright owner(s) are credited and that the original publication in this journal is cited, in accordance with accepted academic practice. No use, distribution or reproduction is permitted which does not comply with these terms.

frontiers in Aging Neuroscience

ORIGINAL RESEARCH
published: 28 September 2021
doi: 10.3389/fnagi.2021.713084

Nanopore Single-Molecule Sequencing for Mitochondrial DNA Methylation Analysis: Investigating Parkin-Associated Parkinsonism as a Proof of Concept

*Theresa Lüth[1], Kobi Wasner[2], Christine Klein[1], Susen Schaake[1], Ronnie Tse[1], Sandro L. Pereira[2], Joshua Laß[1], Lasse Sinkkonen[3], Anne Grünewald[1,2] and Joanne Trinh[1]**

[1] Institute of Neurogenetics BMF, University of Lübeck and University Hospital Schleswig-Holstein Campus Lübeck, Lübeck, Germany, [2] Luxembourg Centre for Systems Biomedicine, University of Luxembourg, Belvaux, Luxembourg, [3] Department of Life Sciences and Medicine, University of Luxembourg, Belvaux, Luxembourg

OPEN ACCESS

Edited by:
Kuangyu Shi,
University of Bern, Switzerland

Reviewed by:
Cecilia Beatriz Conde,
Medical Research Institute Mercedes and Martín Ferreyra (INIMEC), Argentina
Yuzuru Imai,
Juntendo University, Japan
Derek Narendra,
National Institutes of Health (NIH), United States

***Correspondence:**
Joanne Trinh
joanne.trinh@neuro.uni-luebeck.de

Received: 21 May 2021
Accepted: 01 September 2021
Published: 28 September 2021

Citation:
Lüth T, Wasner K, Klein C, Schaake S, Tse R, Pereira SL, Laß J, Sinkkonen L, Grünewald A and Trinh J (2021) Nanopore Single-Molecule Sequencing for Mitochondrial DNA Methylation Analysis: Investigating Parkin-Associated Parkinsonism as a Proof of Concept. Front. Aging Neurosci. 13:713084. doi: 10.3389/fnagi.2021.713084

Objective: To establish a workflow for mitochondrial DNA (mtDNA) CpG methylation using Nanopore whole-genome sequencing and perform first pilot experiments on affected *Parkin* biallelic mutation carriers (Parkin-PD) and healthy controls.

Background: Mitochondria, including mtDNA, are established key players in Parkinson's disease (PD) pathogenesis. Mutations in Parkin, essential for degradation of damaged mitochondria, cause early-onset PD. However, mtDNA methylation and its implication in PD is understudied. Herein, we establish a workflow using Nanopore sequencing to directly detect mtDNA CpG methylation and compare mtDNA methylation between Parkin-related PD and healthy individuals.

Methods: To obtain mtDNA, whole-genome Nanopore sequencing was performed on blood-derived from five Parkin-PD and three control subjects. In addition, induced pluripotent stem cell (iPSC)-derived midbrain neurons from four of these patients with PD and the three control subjects were investigated. The workflow was validated, using methylated and unmethylated 897 bp synthetic DNA samples at different dilution ratios (0, 50, 100% methylation) and mtDNA without methylation. MtDNA CpG methylation frequency (MF) was detected using Nanopolish and Megalodon.

Results: Across all blood-derived samples, we obtained a mean coverage of 250.3X (SD ± 80.5X) and across all neuron-derived samples 830X (SD ± 465X) of the mitochondrial genome. We detected overall low-level CpG methylation from the blood-derived DNA (mean MF ± SD = 0.029 ± 0.041) and neuron-derived DNA (mean MF ± SD = 0.019 ± 0.035). Validation of the workflow, using synthetic DNA samples showed that highly methylated DNA molecules were prone to lower Guppy Phred quality scores and thereby more likely to fail Guppy base-calling. CpG methylation in blood- and neuron-derived DNA was significantly lower in Parkin-PD compared to controls (Mann-Whitney U-test $p < 0.05$).

Conclusion: Nanopore sequencing is a useful method to investigate mtDNA methylation architecture, including Guppy-failed reads is of importance when investigating highly methylated sites. We present a mtDNA methylation workflow and suggest methylation variability across different tissues and between Parkin-PD patients and controls as an initial model to investigate.

Keywords: mitochondrial DNA, methylation, Nanopore, third-generation sequencing, Parkinson's disease, Parkin

INTRODUCTION

Given the importance of environmental impact on mtDNA and its association with disease, the investigation of mtDNA CpG methylation is of interest. For example, nuclear genome methylation correlates with age (Benayoun et al., 2015; Jiang and Guo, 2020), and it has been suggested that mtDNA can behave similarly, as an association between age and methylation level of two CpG sites within mtDNA has been observed (Mawlood et al., 2016).

The most common method to detect mtDNA methylation has been bisulfite treatment. With bisulfite treatment, the characterization of the methylation patterns depends on the resistance of 5-methylcytosine (5-mC) to be converted to uracil. However, the secondary and tertiary structure of intact mtDNA may block cytosines from bisulfite conversion, which influences the outcome of the detected methylation levels (Mechta et al., 2017; Owa et al., 2018). Bisulfite conversion-resistant cytosines can lead to an overestimation of mtDNA methylation. To counteract the bias of bisulfite-resistant cytosines, linearization of mtDNA has been recommended (Owa et al., 2018). For linearized mtDNA prior to bisulfite treatment, lower levels of methylation have been observed compared to intact mtDNA (Liu et al., 2016; Mechta et al., 2017). The low levels of methylation have led to suggestions of this being artifactual, suggesting an absence of methylation in the mitochondrial genome altogether (Hong et al., 2013; Mechta et al., 2017). By contrast, there has also been supportive evidence for the presence of mtDNA methylation after linearization (Sun et al., 2018; Patil et al., 2019). Furthermore, cytosines outside of the CpG context have been reported to be relatively highly methylated (Bellizzi et al., 2013; Patil et al., 2019). The level of mtDNA methylation and its biological significance is still under debate. In the specific case of Parkinson's disease (PD), one study has shown altered methylation in the non-coding D-loop region of patient mtDNA (Blanch et al., 2016). In the D-loop, mtDNA replication and transcription are being initiated and there is evidence that methylation can interfere with these processes (Sirard, 2019). In addition, a small decrease of *ND1* methylation was observed which led to an increase in *ND1* expression (Blanch et al., 2016). Thus, how mtDNA methylation affects mtDNA gene expression has not been fully elucidated yet.

Using long-read, single-molecule sequencing technologies like Nanopore sequencing (Deamer et al., 2016), it is possible to overcome limitations of the indirect measurement of methylation with bisulfite treatment, as it can be detected directly from squiggle signals (Xu and Seki, 2020). Nanopore technology enables the direct sequencing of full-length linearized mtDNA in contrast to the shorter fragments obtained from second-generation sequencing (De Coster and Van Broeckhoven, 2019). To our knowledge, there are currently only three studies that have used Nanopore sequencing to investigate mtDNA methylation (Aminuddin et al., 2020; Bicci et al., 2021; Goldsmith et al., 2021). Thus, detecting mtDNA methylation with this novel sequencing technology remains to be thoroughly investigated and validated.

While the main purpose of the study was to establish a pipeline for mtDNA methylation analysis using Nanopore sequencing technology, we included samples from PD patients with Parkin mutations to highlight potential areas of application in neuroscience. Our results suggest that mtDNA methylation exists and that it can be reliably detected by Nanopore sequencing. Moreover, the methodology holds promise for future studies exploring the molecular underpinnings of neurodegenerative diseases. Herein, we focus on the exploration of mtDNA CpG methylation using Nanopore. The present study aimed to (i) establish and validate a workflow to analyze mtDNA CpG methylation from native DNA and (ii) as a pilot, investigate mtDNA methylation from human blood-DNA as well as DNA from induced pluripotent stem cells (iPSC)-derived neurons in a specific Parkin-related PD model.

MATERIALS AND METHODS

Sample Selection

All individuals included in this study provided informed consent and local ethics committee approval at the Research Ethics Boards of the Universities of Luebeck and Luxembourg were obtained. Eight individuals were included (L-13062, L-3244, L-3048, B-125, B-11, L-2131, L-2132 and L-2135). Five of these individuals are PD patients with *Parkin* mutations (Parkin-PD), with three being compound-heterozygous carriers (L-3244, L-13062 and B-11) and two homozygous carriers (L-3048 and B-125) (**Supplementary Table 1**). The other three are healthy control subjects without *Parkin* mutations (L-2131, L-2132 and L-2135). Movement disorder specialists performed the clinical assessments of patients. Genetic screening of the *Parkin* gene was performed with Sanger Sequencing and MLPA from blood-derived DNA, as previously described (Trinh et al., 2019). Blood-derived DNA from all individuals was included as well as DNA from iPSC-derived midbrain neurons generated from four patients (L-3244, L-3048, B-125 and B-11) and three controls (L-2131, L-2132 and L-2135).

Generation of iPSC-derived Neurons

Fibroblast from four patients and three controls were utilized to generate iPSCs as previously described (Seibler et al., 2011). For culturing iPSCs, mTeSR™ complete medium (StemCell Technologies) was used and, subsequently, cells were differentiated into small molecule neural precursor cells (smNPCs) by following an established protocol (Reinhardt et al., 2013). The smNPCs were cultured in N2/B27 medium—Neurobasal (Gibco)/DMEM-F12 (Gibco) 50:50 with 1% B27 lacking vitamin A (ThermoFisher), 1% 200 mM glutamine (Westburg), 1% penicillin-streptomycin (ThermoFisher) and 0.5% N2 (Life Technologies)—supplemented with 3 μM CHIR 99021 (Sigma), 150 μM ascorbic acid (AA) (Sigma) and 0.5 μM purmorphamine (PMA) (Sigma), which was replaced every other day. When smNPCs reached the 15th passage, the differentiation into midbrain neurons was induced. At ∼75% confluence, smNPCs were detached by adding Accutase (Merck Millipore) and subsequently incubated for five min at 37°C and then pelleted by centrifuging for three min at 300 x g at room temperature. Via the Countess II FL Automated Cell Counter (ThermoFisher), smNPCs were counted and 750,000 cells were seeded in 6-well plates coated with Matrigel and covered with N2/B27 medium. N2/B27 medium with 200 μM AA, 1 μM PMA and 100 ng FGF8 (PeproTech) was used for eight days and then for two days N2/B27 medium with 200 μM AA and 0.5 μM PMA. Afterward, the cells were cultured 22 days in N2/B27 medium supplemented with 200 μM AA, 1 ng/mL TGF-β3 (Peprotech), 10 ng/mL GDNF (Peprotech), 20 ng/mL BDNF (PeproTech) and 500 μM dibutyryl-cAMP (Applichem). During this process, the medium was exchanged every other day.

DNA Extraction

DNA extraction from blood was performed for all included individuals with the QIAGEN Blood DNA Mini Kit (Qiagen, Hilden, Germany) following the manufacturer's instructions. In addition, DNA was extracted from iPSC-derived neurons of four patients and three controls using the QIAAmp Minikit (Qiagen).

Library Preparation and Nanopore Sequencing

Whole Genomes

DNA concentration of the blood- and neuron-derived DNA was quantified with Qubit fluorometric quantification using the dsDNA BR Assay Kit (Thermo Fisher Scientific, Waltham, MA, USA). Library preparation of 1.5 μg input DNA from the samples was performed with the Ligation Sequencing Kit (SQK-LSK109) (Oxford Nanopore Technologies, Oxford, United Kingdom) following a Nanopore whole-genome sequencing protocol (premium WGA). To conserve DNA methylation, whole-genome amplification with random primers was omitted from this established protocol (the intended first step of the premium WGA protocol).

Mitochondrial Genome Long-Range PCR

In order to create a negative control and a baseline for methylation calling, the mitochondrial genome of one patient (L-3244) was amplified with a long-range PCR. Two primer sets were used to generate two overlapping PCR products (MTL-F1 5′- AAA GCA CAT ACC AAG GCC AC−3′, MTL-F2 5′- TAT CCG CCA TCC CAT ACA TT−3′, MTL-R1 5′- TTG GCT CTC CTT GCA AGA TT−3′, MTL-R2 5′- AAT GTT GAG CCG TAG ATG CC−3′). The library was prepared using the Nanopore Ligation Sequencing Kit (SQK-LSK109) and multiplexed with the Native Barcoding Expansion (EXP-NBD104).

Synthetic DNA

To further validate the workflow, two types of commercially available 897 bp synthetic DNAs (D4505, Zymo Research, Irvine, CA, USA) were used where all cytosines were modified to 5-mC or unmodified. From these two synthetic DNAs, we created three different dilutions: (1) only methylated DNA (100% methylation), (2) 1:1 dilution of methylated and unmethylated DNA (50% methylation), and (3) only unmethylated DNA (0% methylation).

The DNA concentration was quantified as described above and 1 μg input DNA was used. The library was prepared using the Nanopore Ligation Sequencing Kit (SQK-LSK109) and multiplexed with the Native Barcoding Expansion (EXP-NBD104).

Sequencing

Nanopore sequencing was performed with the MinION or GidION using the R9.4.1 flow cells. The flow cell was primed and loaded according to the manufacturer's instructions. For base-calling, MinKNOW (version 20.10.6) with the integrated Guppy (version 4.2.3) was used. The Guppy base-calling software is available for Nanopore community members (https://community.nanoporetech.com). We aimed to obtain 3 Gigabases (Gb) of data before stopping the run which lasted ∼24 h.

Data Analysis

DNA Methylation Analysis

Base-called Nanopore reads were aligned to the reference sequence (i.e., mitochondrial genome, hg38 assembly), using Minimap2 (version 2.17). DNA methylation in a CpG dinucleotide context was called with Nanopolish (version 0.13.2), a software tool that uses a Hidden Markov Model (HMM) (Simpson et al., 2017). Nanopolish reports the log-likelihood ratio for each observed event (i.e., CpG site within a k-mer sequence). The methylation frequency (MF) was calculated with the default threshold of the log-likelihood ratio. Thus, with a log-likelihood ratio >2 the CpG site was classified as methylated and with a value <-2 the site was classified as unmethylated. In addition, the split-group parameter was used, which provides the MF of each detected CpG site in the reference sequence separately. The MF describes the proportion of reads that support methylation at the given CpG site. In addition, the Megalodon (version 2.2.9) software tool was used as well to investigate mtDNA CpG methylation with the basecall model res_dna_r941_min_modbases_5mC_v001 provided by Rerio (version 4.4.0).

To investigate the methylation of the synthetic DNA, alignment, methylation calling, and calculation of MF were performed. The D5405 reference sequence provided by the

manufacturer was used. Reads that passed Guppy calling, as well as failed reads, were analyzed.

Adjusting the mtDNA Methylation Frequency

To adjust the detected methylation frequency of the blood- and neuron-derived samples, we calculated the false-positive rate (FPR = Number of called methylated cytosines/Number of all called cytosines) as recommended (Goldsmith et al., 2021) from the long-range PCR products. The resulting FPR of Nanopolish and Megalodon for blood- and neuron-derived DNA was subtracted from the methylation frequency of each site. In addition, all sites that showed a methylation frequency >0.2 in a PCR product were excluded from downstream analyses.

Plus- and Minus-Strand Methylation and Comparison With 45S rRNA

To explore heavy-strand (H-strand) and light-strand (L-strand) methylation, methylation calls from Nanopolish were stratified by plus- and minus-strand. The plus-strand represents the L-strand and the minus-strand the H-strand.

In order to compare the MF of mtDNA to a nuclear-encoded gene, we used the *45S rRNA* gene (13 kb core region of the 45S cluster 5). There are multiple copies of the *45S rRNA* gene in the human genome, comparable in size and coverage to the mtDNA. DNA methylation of the *45S rRNA* gene was stratified by plus- and minus-strand to allow comparison to the H- and L-strand of mtDNA.

Coverage and mtDNA Methylation Analysis

To investigate the relationship between coverage and MF, different subsets of the obtained sequencing data (i.e., Fast5 and FastQ files) with increasing coverage were used to detect methylation. The mean coverage and MF of each data set were calculated.

mtDNA Variants Detection

To additionally investigate the frequency of homoplasmic and heteroplasmic variants in the mtDNA, we processed the indexed alignments in BAM format with the Mutserve pipeline (version 2.0.0) (Weissensteiner et al., 2016). Due to the amplification-free approach of our study, the coverage of the mitochondrial genome in our study is below that typically reported in deep mitochondrial sequencing studies. To reduce the detection of artifacts, we set the minimum heteroplasmy level to 0.5 (i.e., 50%).

Statistical Analysis

For statistical analysis, GraphPad Prism software (version 9) was used. To compare median MF between plus- and minus-strand, blood- and neuron-derived mtDNA or patients and controls, the non-parametric Mann-Whitney U test for pairwise comparison was performed. Non-parametric Spearman correlation was used for correlation analyses. All *p*-values were exploratory and not corrected for multiple testing.

RESULTS

We first investigated mtDNA methylation in eight blood-derived samples to establish a workflow. In total, we obtained a mean of 8.6 Gb of data and a read length of 4.9 kb with whole-genome Nanopore sequencing. Alignment to the mitochondrial genome (hg38) resulted in a mean coverage of 250.3X (SD = ±80.5X, **Supplementary Figure 1**). To validate the workflow we assessed the false positive rate, sequencing depth, mitochondrial DNA (NUMTs) contamination as well as plus- and minus-strand differences. We then applied this workflow on a specific Parkinson's disease neuronal model as a pilot.

Mitochondrial DNA CpG Methylation Detected With Nanopolish and Megalodon

We used the Nanopolish software tool to characterize CpG methylation. Overall, we detected low-level CpG methylation (mean MF ± SD = 0.057 ± 0.053) of mtDNA across the eight blood-derived samples (**Figure 1**). Additionally, we used Megalodon, which resulted in low-level mtDNA CpG methylation as well (mean MF ± SD = 0.086 ± 0.068). To access possible false-positive methylation calls, we adjusted the MF for the FPR calculated from the methylation calling of the long-range PCR product ($FPR_{Nanopolish}$ = 0.029, $FPR_{Megalodon}$ = 0.046) and excluded all CpG sites that showed an MF higher than 0.2 in the long-range PCR product from further analysis. After this correction, with Nanopolish there remained 11 unique CpG sites across the blood-derived samples with an MF >0.2 in the following genes: *12S rRNA* (chrM: 807, 1261, 1560), *16S rRNA* (chrM: 3008), *Cytochrome c oxidase, subunit 1* (chrM: 6052), *ATPase6/8* (chrM:8646), *NADH dehydrogenase, subunit 3* (chrM:10399), *NADH dehydrogenase, subunit 4* (chrM:12123), *tRNA-Glutamic acid* (chrM:14696), *tRNA-Threonine* (chrM:15929) and within the non-coding D-loop (chrM:16127). By contrast, with Megalodon there remained 28 unique CpG sites in the following mitochondrial genes: *12S rRNA* (chrM:807, 897, 1022, 1132, 1176, 1215, 1225, 1487), *16S rRNA* (chrM: 2565, 2569, 2571, 2842, 2914, 3077), *NADH dehydrogenase, subunit 1* (chrM: 3405), *tRNA-Methionine* (chrM:4425), *NADH dehydrogenase, subunit 2* (chrM: 4711), *Cytochrome c oxidase, subunit 1* (chrM: 6688), *NADH dehydrogenase, subunit 4* (chrM: 11715), *NADH dehydrogenase, subunit 5* (chrM: 12816, 13364), *tRNA-Glutamic acid* (chrM:14683), *Cytochrome b* (chrM: 15039, 15589, 15759), *tRNA-Threonine* (chrM:15929) and within the non-coding D-loop (chrM:16410). There was a weak correlation between the MF of individual CpG sites detected with Nanopolish and Megalodon (Spearman's r = 0.2924, Spearman's exploratory p-value < 0.0001, **Supplementary Figure 2A**) but a strong correlation between the mean MF of each sample (Spearman's r = 0.7904, Spearman's exploratory p-value = 0.0244, **Supplementary Figure 2B**). The calculated FPR was lower for Nanopolish analysis and the software required less computational resources in our set-up. After the formal comparison, we proceed with Nanopolish in our study. Next, we have analyzed the

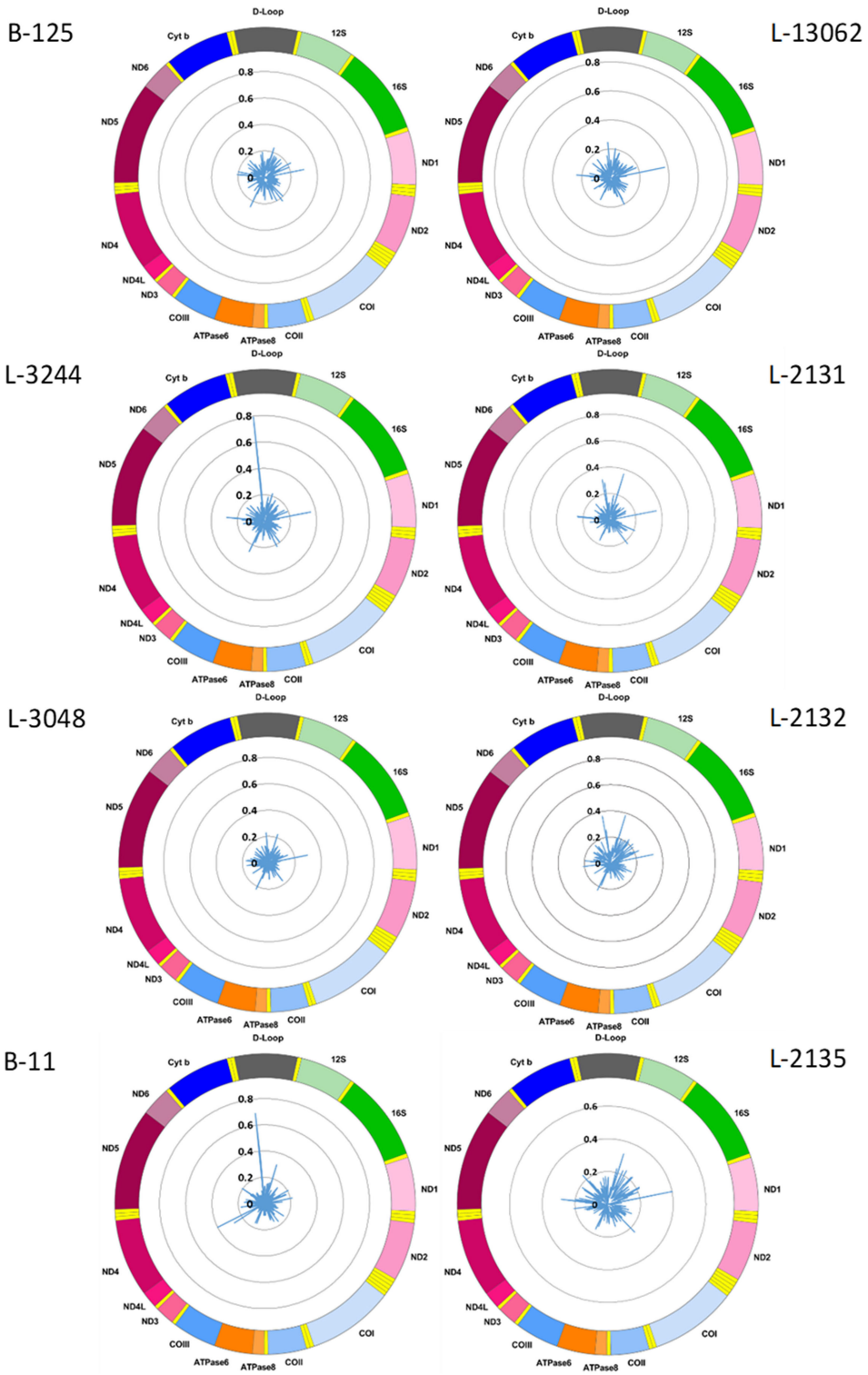

FIGURE 1 | Mitochondrial CpG methylation frequency detected by Nanopore sequencing in eight individuals. Radar chart showing mitochondrial DNA methylation from eight blood-derived DNA samples detected by Nanopolish. Methylation frequency is indicated by blue spikes. 12S, small subunit rRNA; 16S, large subunit rRNA; ND1, NADH dehydrogenase, subunit 1; ND2, NADH dehydrogenase, subunit 2; COI, cytochrome c oxidase, subunit 1; COII, cytochrome c oxidase, subunit 2; ATPase8, ATP synthase, subunit 8; ATPase6, ATP synthase, subunit 6; COIII, cytochrome c oxidase, subunit 3; ND3, NADH dehydrogenase, subunit 3; ND4L, NADH dehydrogenase, subunit 4L; ND4, NADH dehydrogenase, subunit 4; ND5, NADH dehydrogenase, subunit 5; ND6, NADH dehydrogenase, subunit 6; Cyt b, cytochrome b; D-Loop, displacement loop.

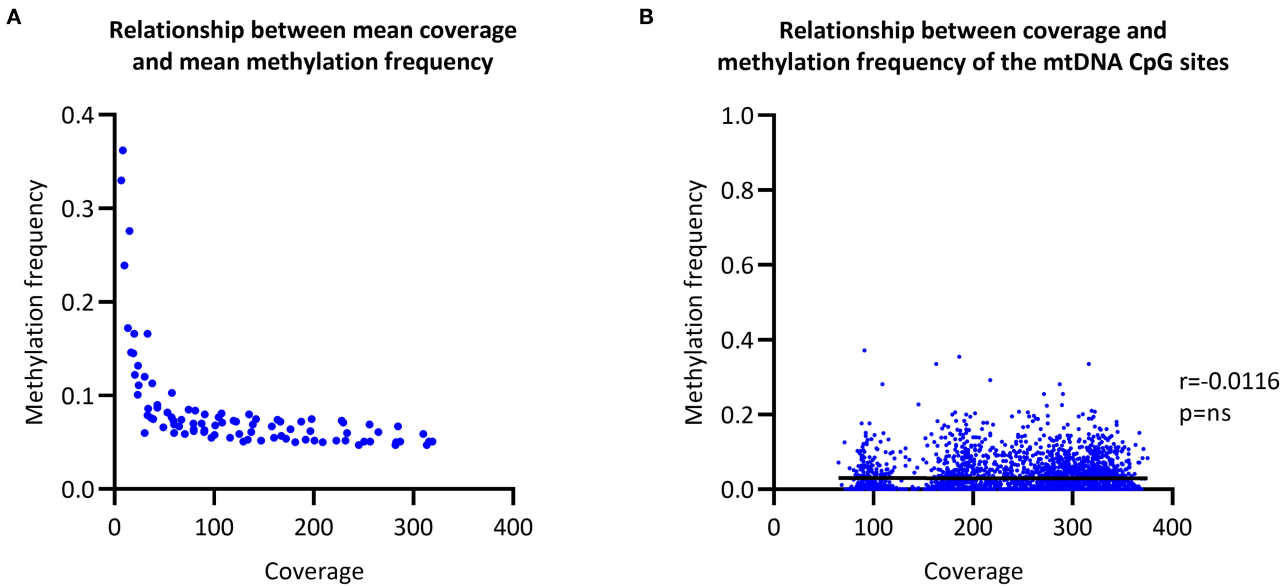

FIGURE 2 | Relationship between coverage and methylation frequency. **(A)** Overall relationship between the mean coverage and mean methylation frequency of different subsections of the obtained sequencing data. **(B)** Overall relationship between the coverage of each individual CpG site and the corresponding methylation frequency. r, Spearman's rank correlation coefficient; p, Spearman's exploratory *p*-value.

number of mtDNA variants and did not detect a difference in heteroplasmic variants likely due to our lower sequencing depth (**Supplementary Table 2**).

Relationship Between the Coverage and Methylation Frequency

To evaluate the relationship between coverage and MF, we increased the coverage of each sample in a step-wise fashion and then called CpG methylation. The raw mean MF for the eight individuals was at ∼0.06 with >100X coverage (**Figure 2A**). In comparison, the raw mean MF detected from the long-range PCR products was at ∼0.03 with >4000X coverage (**Supplementary Figure 3**). There was no correlation between coverage and detected MF when all of the sequencing data was used to call methylation (Spearman's $r = 0.0116$, Spearman's exploratory p-value > 0.05, **Figure 2B**).

Nuclear Mitochondrial DNA

We explored possible NUMTs contamination in our data. NUMTs are transposition of mtDNA into the nuclear genome but most of these segments have sizes shorter than 500 bp (Dayama et al., 2014). Therefore, we filtered the reads by an alignment length to the mtDNA FASTA file of more than 1 kb to exclude possible NUMTs from the analysis. The detected MF after the filtering changed marginally and was strongly correlated to the MF without this filtering step (Spearman's $r = 0.9445$, Spearman's exploratory p-value < 0.0001, **Supplementary Figure 4**).

Heavy- and Light-Strand Methylation Differences

We next explored differences in methylation of the H- and L-strands. As the reference sequence of the mitochondrial genome represents the L-strand, the L-strand is reported as the plus-strand and the H-strand as the minus-strand. The CpG MF detected from the mtDNA plus- and minus-strands was corrected for the FPR, as well. We observed a positive correlation between the plus- and minus-strand MF detected with Nanopolish (Spearman's $r = 0.3214$, Spearman's exploratory p-value < 0.0001, **Figure 3A**).

For comparison, the *45S rRNA* gene was used as a nuclear-encoded comparison, since it has comparable size and coverage to the mtDNA (size = 13 kb, mean coverage = 623X). The overall correlation between plus-strand and minus-strand methylation was stronger in the *45S* rRNA gene compared to mtDNA (Spearman's $r = 0.7011$, Spearman's exploratory p-value < 0.0001, **Figure 3B**).

Our analysis showed that there was a trend for differences in the overall mean MF between mtDNA plus- and minus-strands in six individuals (**Supplementary Figure 5A**, Mann Whitney U-test $p < 0.0382$). However, the difference was not consistent in the same direction and effect sizes were small (difference in mean MF < 0.010). Similar to the mtDNA, the CpG sites in *45S rRNA* showed a trend for differences in the mean MF between plus- and minus-strands in five individuals (**Supplementary Figure 5B**, Mann Whitney U-test $p < 0.0101$, difference in mean MF < 0.014). The number of plus- and minus-strand reads from the mtDNA and *45S rRNA* gene were

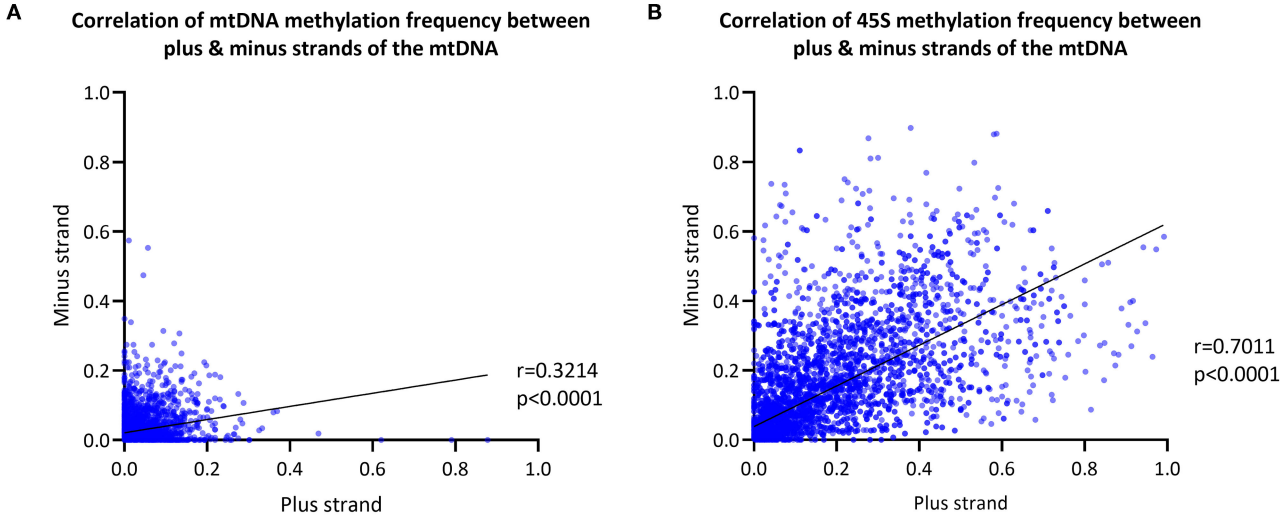

FIGURE 3 | Mitochondrial and *45S rRNA* CpG methylation comparison by strand. **(A)** Correlation between the methylation frequency of the mitochondrial plus- and minus-strand (plus-strand = light-strand, minus-strand = heavy-strand). Data of the six blood-derived samples combined. **(B)** Correlation between the methylation frequency detected from the *45S rRNA* gene plus- and minus-strand. Data of the six blood-derived samples combined. r, Spearman's rank correlation coefficient; p, Spearman's exploratory *p*-value.

comparable (**Supplementary Figures 5C,D**, Mann Whitney U-test $p > 0.05$).

Synthetic DNA

To further validate the workflow and to also include a highly methylated sample, we performed Nanopore sequencing of an 897 bp synthetic methylated and unmethylated control DNA sample at different dilution ratios (0%, 50% and 100%). We obtained a mean of 14 Mb data and a read length of 963 bp. As the three samples were multiplexed for sequencing, barcodes with a length of 40 bp were added on both sides of the DNA fragments, which led to the higher mean read length of 963 bp compared to the 897 bp reference sequence. Alignment resulted in a mean coverage of 5018X (SD = ±424X).

Synthetic DNA Methylation

The CpG methylation of three samples with a ratio of 0, 50 or 100% of methylated synthetic DNA molecules was investigated (**Figure 4A**). In the 0% methylated sample, a mean $MF = 0.021$ (SD ± 0.042) was detected similar to the 50% methylated sample (mean MF ± SD = 0.022 ± 0.038). At particular CpG sites (e.g., D4505:195–350), the detected methylation level in the 0% methylated sample was higher than zero (range of $MF = 0.014$–0.193). In the 100% methylated sample, the detected methylation was higher (mean MF ± SD = 0.262 ± 0.141) compared to the 0% and 50% methylated samples. Nevertheless, the detected MF was lower than the corresponding ratio of methylated DNA molecules in the 50% and 100% methylated samples when we used Nanopolish to call the methylation. Similarly, when we used Megalodon, the detected MF was lower than expected in the 50% (mean MF ± SD = 0.040 ± 0.024) and 100% (mean MF ± SD = 0.535 ± 0.151) methylated sample as well (**Supplementary Figure 6A**).

Investigation of Guppy-Failed Reads

To investigate the possibility of preferential sequencing of unmethylated reads and methylated reads, which do not pass the quality threshold during base-calling, we analyzed Guppy-failed reads. During the Guppy base-calling, the software reports Phred quality scores (qscores) of each read, which indicates the accuracy of the base-calling. Reads with low qscores are classified as failed. Exploring these failed reads only, using Nanopolish, we detected low methylation in the 0% methylated sample (mean MF ± SD = 0.057 ± 0.123) and higher levels in the 50% methylated sample (mean MF ± SD = 0.430 ± 0.168) and the 100% methylated sample (mean MF ± SD = 0.880 ± 0.156). Thus, the detected methylation was overall higher in Guppy-failed reads compared to Guppy-passed reads in all samples (**Figure 4B**). Similarly, when we used Megalodon, the detected MF was higher in the 0% (mean MF ± SD = 0.054 ± 0.070), 50% (mean MF ± SD = 0.645 ± 0.168) and 100% methylated sample (mean MF ± SD = 0.687 ± 0.182) (**Supplementary Figure 6B**).

Including passed and failed reads, the proportion of failed reads was n = 55/6,550 in the 0% methylated sample, n = 26,068/56,577 in the 50% methylated sample and n = 44,505/51,555 in the 100% methylated sample (**Figure 4C**). Thus, the majority of methylated reads will not be analyzed under default Guppy parameters (cutoff value for the mean qscore = 7). In addition, there was a negative correlation between coverage of CpG sites and detected MF with Nanopolish from passed reads in the 100% methylated sample (Spearman's $r = -0.2884$, Spearman's exploratory p-value = 0.0381, **Figure 4D**) and in contrast, there was a trend toward a positive association

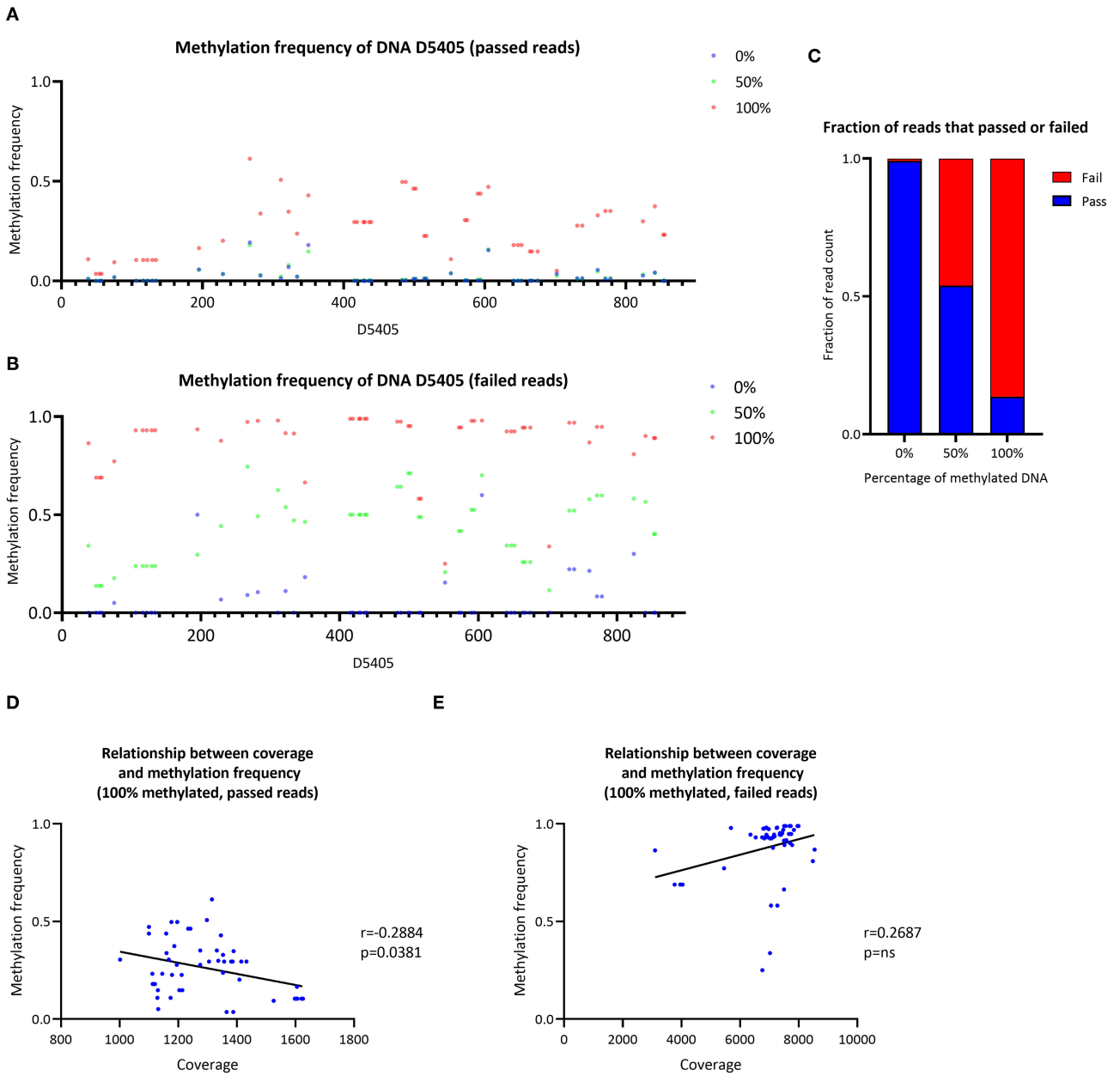

FIGURE 4 | Analysis of synthetic DNA for the validation of the data analysis pipeline. **(A)** Methylation frequency detected by Nanopolish from three samples of synthetic DNA with different proportions of methylated DNA (0, 50 and 100%), only reads that passed Guppy quality threshold were included in the analysis. **(B)** Methylation frequency detected by Nanopolish from three samples of synthetic DNA with different proportions of methylated DNA (0, 50 and 100%), only reads that failed Guppy quality threshold were included in the analysis. **(C)** Stacked bar plot of the fraction of reads that passed (blue) or failed (red) the Guppy quality threshold, stratified by the ratio of methylated reads in the sample. **(D)** Relationship between the coverage and methylation frequency in the sample with 100% methylated reads, only reads that passed Guppy quality threshold were included in the analysis. **(E)** Relationship between the coverage and methylation frequency in the sample with 100% methylated reads, only reads that failed Guppy quality threshold were included in the analysis. r, Spearman's rank correlation coefficient; p, Spearman's exploratory *p*-value.

when the MF was detected from the failed reads (Spearman's $r = 0.2687$, Spearman's exploratory p-value > 0.05, **Figure 4E**). When we used Megalodon, we observed the same trend for a negative association between coverage and MF from passed reads (Spearman's $r = -0.1092$, Spearman's exploratory p-value > 0.05, **Supplementary Figure 5D**) compared to a positive association in failed reads (Spearman's $r = 0.1696$, Spearman's exploratory p-value > 0.05, **Supplementary Figure 5E**).

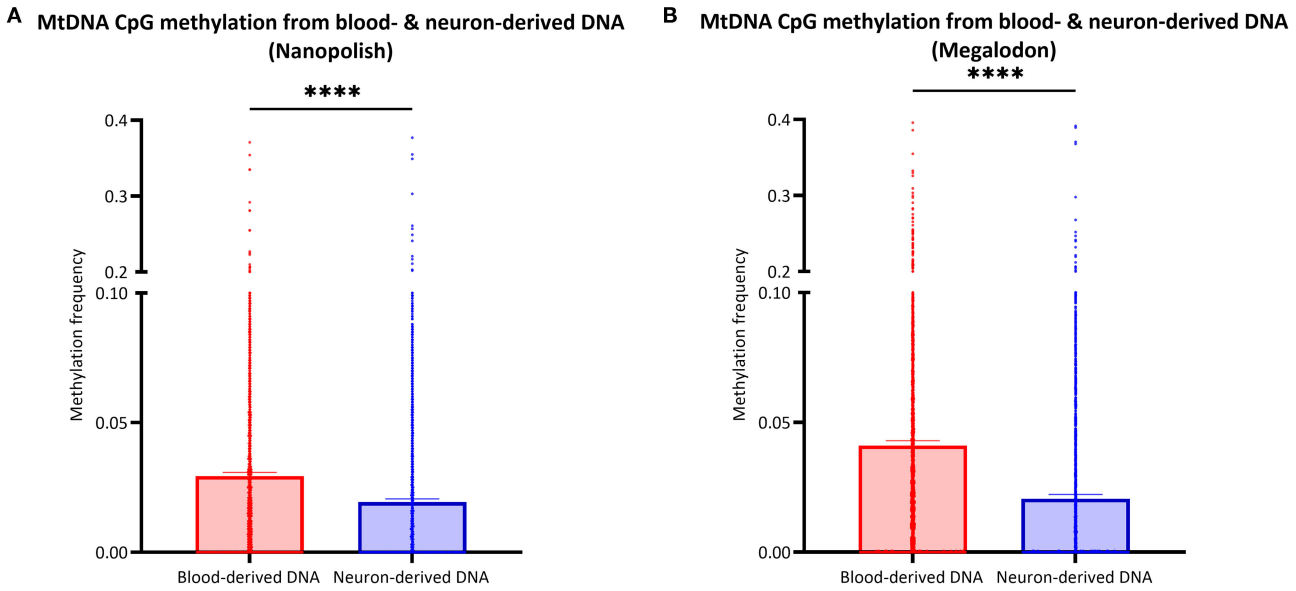

FIGURE 5 | Comparison of mtDNA CpG methylation between blood- and neuron-derived DNA. **(A,B)** The bar plot shows the mtDNA CpG methylation from blood- or neuron-derived DNA (iPSC-derived midbrain neurons) which was either detected with Nanopolish **(A)** or Megalodon **(B)**. Bars indicate means and 95% confidence interval. The asterisks represent the level of significance (*$p \leq 0.05$, **$p \leq 0.01$, ***$p \leq 0.001$, ****$p \leq 0.0001$), p-value = Mann Whitney U-test performed for pairwise comparisons, blood-derived DNA is indicated in red and neuron-derived DNA in blue.

Re-analysis of Mitochondrial Methylation Including Guppy-Failed Reads

To consider the results obtained from the investigation of the synthetic DNA samples, mtDNA methylation was re-analyzed, including Guppy-passed and -failed reads. We obtained a mean coverage of 263X (SD = ±79X) of the mitochondrial genome, which was on average 13X more coverage compared to just including the passed reads. The overall change in the MF was marginal as the correlation was very strong between the MF detected from the passed reads only and the passed and failed reads together (Spearman's $r = 0.9934$, Spearman's exploratory p-value < 0.0001, **Supplementary Figure 7**).

Investigation of Neuron-Derived Mitochondrial DNA

After the validation of our workflow, we compared mtDNA CpG methylation of blood- and neuron-derived DNA. Analogous to the blood-derived mtDNA, we obtained a mean of 7.1 GB of base-called data per sample and a mean read length of 5.6 kb (SD = ±2.1 kb). However, we obtained higher mean coverage of the neuron-derived mtDNA per sample with 830X (SD = ±465X). After the data were corrected for FPR, mtDNA methylation frequency detected with Nanopolish was significantly lower in neuron-derived DNA (mean MF ± SD = 0.019 ± 0.035) compared to blood-derived DNA (mean MF ± SD = 0.029 ± 0.041, Mann Whitney U-test p < 0.0001, **Figure 5A**). A significant difference between blood- and neuron-derived mtDNA CpG methylation was present and in the same direction with Megalodon as well (**Figure 5B**). Significantly higher methylation levels in blood-derived mtDNA were also observed when we included a second independent batch of neuron-derived DNA (**Supplementary Figure 8A**). We analyzed the relationship between blood- and neuron-derived mtDNA of each CpG site for individual participants and observed that the methylation frequency in blood- and neuron-derived mtDNA was correlated (Spearman's r > 0.5659, Spearman's exploratory p-value < 0.0001, **Supplementary Figure 9**).

Comparison of Mitochondrial DNA Methylation in Patients With Parkinson's Disease and Healthy Controls

We included patients with Parkin-PD and healthy control subjects and compared the mtDNA CpG methylation between the groups in a global fashion. There were significantly lower methylation levels in Parkin-PD compared to healthy controls. The difference was present using either Nanopolish or Megalodon. The blood-derived mtDNA mean MF detected with Nanopolish in Parkin-PD was 0.027 (SD = 0.038) compared to 0.034 (SD = ±0.047) in healthy controls (Mann Whitney U-test $p = 0.0002$, **Figure 6A**) and with Megalodon the mean MF was 0.036 (SD = 0.051) in patients compared to 0.048 (SD = 0.065) in control subjects (Mann Whitney U-test $p < 0.0001$, **Figure 6B**). Additionally, in neuron-derived mtDNA, the MF detected with Nanopolish was significantly lower in patients (mean MF ± SD = 0.017 ± 0.034) compared to controls as well (mean MF ± SD = 0.021 ± 0.038, Mann Whitney U-test $p = 0.0268$, **Figure 6C**). Similarly, the MF detected with Megalodon was significantly lower in patients (mean MF ± SD = 0.013 ± 0.031) compared to controls (mean MF ± SD = 0.031 ± 0.053, Mann Whitney U-test $p < 0.0001$, **Figure 6D**). This significant difference was

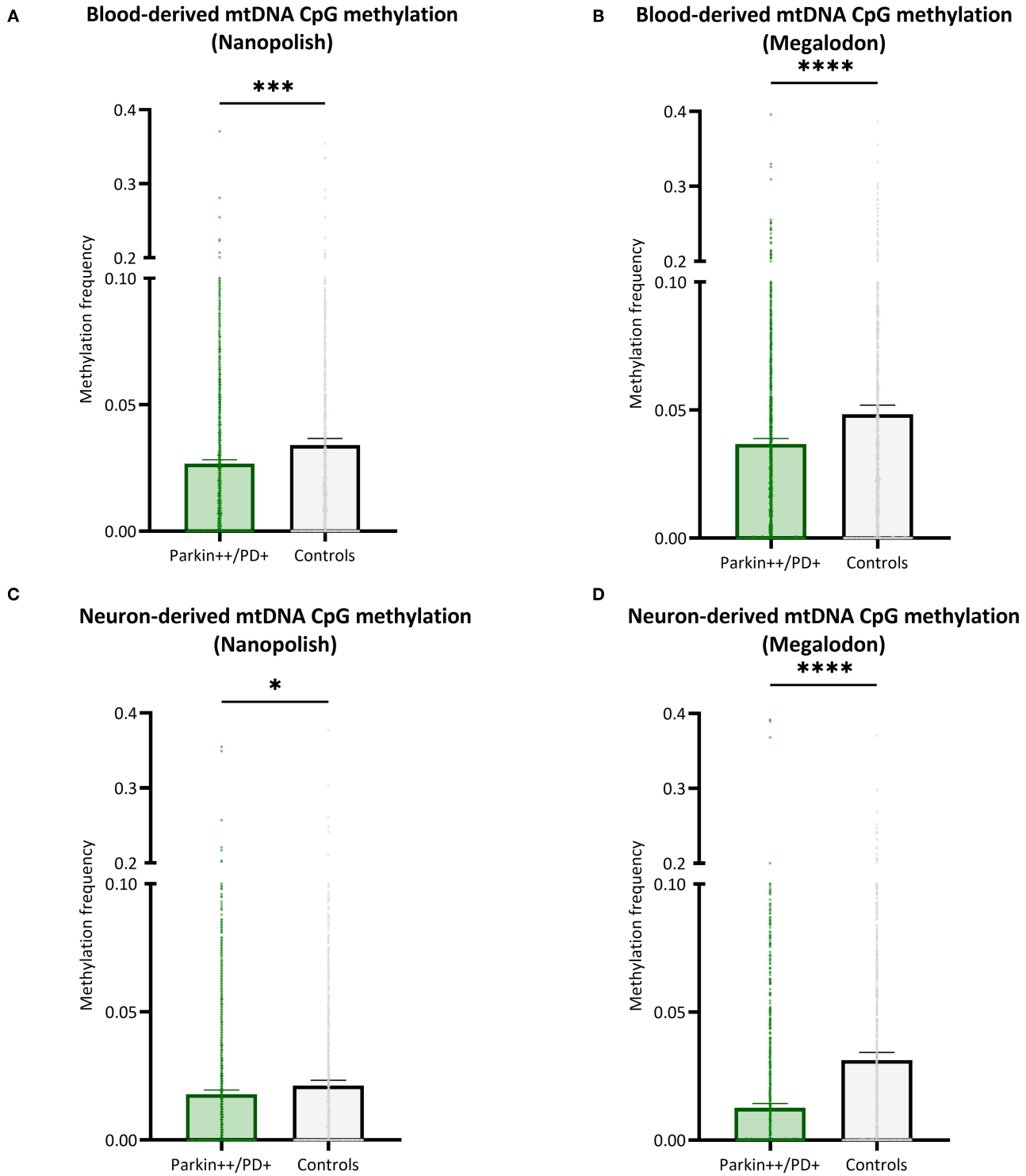

FIGURE 6 | Comparison of mtDNA CpG methylation between patients with Parkin-PD and healthy controls. **(A,B)** The bar plot shows the mtDNA CpG methylation from blood-derived DNA in patients with Parkin-PD and healthy control subjects, which was either detected with Nanopolish **(A)** or Megalodon **(B)**. **(C,D)** The bar plot shows the mtDNA CpG methylation from neuron-derived DNA (iPSC-derived midbrain neurons) in patients with Parkin-PD and healthy control subjects, which was either detected with Nanopolish **(A)** or Megalodon **(B)**. Bars indicate means and 95% confidence interval. The asterisks represent the level of significance (*$p \leq 0.05$, **$p \leq 0.01$, ***$p \leq 0.001$, ****$p \leq 0.0001$), p-value = Mann Whitney U-test performed for pairwise comparisons, Parkin++ = Parkin biallelic; PD+ = PD patient, patients are indicated in green and control subjects in gray.

also present when we included a second independent batch of neuron-derived mtDNA (**Supplementary Figure 8B**). Lastly, we analyzed the relationship between the age at examination of the participants and the overall methylation level on the mtDNA. We did not observe a correlation between the age and the detected mean MF in blood- or neuron-derived DNA ($p > 0.05$, **Supplementary Figure 10**).

DISCUSSION

In this study, we (i) present and validate a workflow to assess mtDNA CpG methylation using whole-genome Nanopore sequencing and (ii) use the present workflow in a specific Parkin-PD model to compare mtDNA methylation of patients and controls as a pilot.

Validation of mtDNA Methylation Analysis Workflow

We performed Nanopore sequencing of native whole-cell DNA and detected overall low-level mtDNA CpG methylation concordant with previous reports that used bisulfite sequencing (van der Wijst et al., 2017; Sun et al., 2018). The D-loop is the longest non-coding region of the mitochondrial genome and there is evidence that CpG methylation happens most prominently at sites within this region (Liu et al., 2016; van der Wijst et al., 2017). Interestingly, we detected higher methylation levels at two CpG sites within the D-loop (chrM: 16359 and 16410), however, these sites were excluded as false-positive calls. The FPR was lower when the methylation was called with Nanopolish compared to Megalodon and there were fewer CpG sites that showed an MF > 0.2 in the amplicon sequencing data, indicating Nanopolish is less prone to false-positive calls in the context of mtDNA CpG methylation. Although there are exceptions at particular sites after the correction of the MF, our results provide further evidence that mtDNA CpG methylation is low in general. Despite the weak concordance of the detected MF of each individual CpG site between Nanopolish and Megalodon, the concordance between the mean MF of each sample detected with the software tools was strong. The discrepancies in detected MF are likely due to different analysis algorithms used by both tools. Megalodon is based on a neural network, uses Guppy base calls of 5mC and maps the reads to a reference to provide per-site methylation data (https://github.com/nanoporetech/megalodon). Nanopolish is based on HMM to classify each CpG site of each read as methylated or unmethylated (Simpson et al., 2017). Additionally, the training strategy and the data sets themselves used to train these tools could contribute to the lower per-site concordance. A recent benchmark study investigated the strength and limitations of the widest used state-of-the-art tools to detect CpG methylation from Nanopore sequencing data, including Megalodon and Nanopolish (Yuen et al., 2021). The results from Megalodon were found to be more consistent with whole-genome bisulfite sequencing data compared to Nanopolish. Both tools showed, however, more disperse and lower per-site accuracy. Given the fact that, in our study, the overall methylation levels of samples are highly correlated between the tools, we used a global approach to assess differences in mtDNA CpG methylation between groups.

To validate if we obtained sufficient sequencing depth, we investigated the relationship between coverage and MF of mtDNA. As the mean MF plateaus at a coverage >100X, our results suggest that at least 100X coverage is necessary to detect mtDNA CpG methylation with Nanopore sequencing. With higher coverage, we did not observe an association between coverage and MF and therefore we concluded that we obtained sufficient sequencing depth to reliably detect mtDNA CpG methylation. Interestingly, a negative association between coverage and the detected MF was shown with whole-genome bisulfite sequencing (Mechta et al., 2017) and there were speculations that bisulfite conversion-resistant cytosines were the culprit. However, the detection of mtDNA methylation from the Nanopore sequencing data does not depend on bisulfite conversion and we observed a plateau of the mean MF after 100X coverage.

Next, we explored possible NUMTs contamination in our data. As these segments are usually shorter than 500 bp (Dayama et al., 2014), we excluded all reads that had an alignment length shorter than 1 kb to the mitochondrial genome reference file from the analysis and recalled CpG methylation. As the detected MF after the filtering only changed marginally, NUMTs contamination did not influence our results.

In the double-stranded mitochondrial genome, the H-strand has a higher purine content (G and A) compared to the L-strand and encodes 12 out of the 13 mitochondrial-encoded proteins (Berk and Clayton, 1974). We explored possible differences in mtDNA H- (minus-) and L- (plus-) strand CpG methylation in comparison to the nuclear-encoded *45S rRNA* gene. Although the correlation between plus- and minus-strand MF was higher in the *45S rRNA* gene, the trend for strand differences in the mtDNA mean MF were minor and without bias toward any specific strand. Still, a previous report suggested differences in H- and L-strand methylation mainly at non-CpG sites (Dou et al., 2019) which could be partially explained by the significantly lower frequency of cytosines in the H-strand (2,196) compared to the L-strand (5,181) (Dou et al., 2019). Methodologically, there was no preferential sequencing for either of the strands, as the number of plus- and minus-strand reads were comparable.

For further validation of our workflow, we used synthetic control DNA samples, which had 0, 50 or 100% methylation of DNA molecules. Highly methylated reads are prone to lower Guppy qscores, highlighted by the higher proportion of failed reads in the 100 and 50% methylated sample compared to the 0% methylated sample. As the detected MF in the 0% methylated sample was higher in the failed reads compared to the passed reads, there is the possibility of more false-positive calls though.

However, since mtDNA CpG methylation levels are low, the addition of the failed reads only marginally influenced the methylation. In fact, concerns about false positives increase when including failed reads, and therefore this is not recommended for quantification of mtDNA methylation. The inclusion of failed

reads may be of importance when analyzing highly methylated samples of nuclear DNA in other research contexts.

Mitochondrial CpG Methylation in Parkinson's Disease

With our analyses in PD patient-derived samples, we bring forth a case that mtDNA methylation does not only exist but can be reliably detected by Nanopore sequencing. This methodology is useful when investigating the molecular underpinnings of neurodegenerative diseases. Our proof-of-concept study in blood and neuronal samples from Parkin mutation carriers serves an example for better illustration. Although the overall methylation levels were low in the blood- and neuron-derived mtDNA, we observed significantly higher methylation in blood-derived mtDNA compared to neuron-derived mtDNA. On the one hand, there is evidence for a negative association between mtDNA methylation and gene expression (Sirard, 2019) and our results may indicate a higher expression of mtDNA genes in neuron-derived DNA. On the other hand, a previous study reported lower mtDNA CpG methylation levels in cell lines compared to tissue-derived DNA (Goldsmith et al., 2021). When exploring iPSC-derived midbrain neurons, lower CpG mtDNA methylation was detected compared to blood and perhaps the reprogramming process also modifies the epigenetics of mtDNA. Additionally, we have observed a correlation between the MF detected at the individual CpG sites in mtDNA derived from blood and neurons. Thus, mtDNA methylation, although lower in neuron-derived mtDNA, appear to be conserved across different cell types.

Importantly, we observed lower methylation levels in Parkin-PD compared to healthy controls, which is evidenced in blood- and neuron-derived mtDNA. A previous study that used targeted bisulfite pyrosequencing to investigate mtDNA CpG methylation has reported lower methylation in patients with PD as well, and more specifically within the D-Loop (Blanch et al., 2016). A recent publication using whole-genome bisulfite sequencing did not show an association between mtDNA methylation and idiopathic PD (Guitton et al., 2021) but an association between mtDNA methylation and transcript levels. In our study, all patients included were biallelic *Parkin* mutation carriers. As Parkin is involved in the degradation of damaged mitochondria and mtDNA maintenance, patients carrying Parkin mutations could be prone to mtDNA dyshomeostasis. Altered methylation levels in Parkin-PD patients could affect the regulation of mtDNA gene expression and thereby contribute to mitochondrial dysfunction. By contrast, further functional studies will be required to investigate if mtDNA methylation and gene expression are causally linked.

As nuclear genome methylation is associated with age (Benayoun et al., 2015; Jiang and Guo, 2020) and similar findings have been reported for mtDNA (Mawlood et al., 2016), we analyzed the relationship between age and mtDNA CpG methylation in both, the blood and neuronal samples, but did not observe a correlation. However, the sample size in our study was limited and we assessed the overall mean methylation level rather than site-specific methylation frequencies.

Review of Literature on mtDNA Nanopore Sequencing

We performed a literature search for the terms "mtDNA" and "Nanopore" and found 47 publications, eight of which performed Nanopore sequencing of human mtDNA (Lindberg et al., 2016; Carter and Hussain, 2017; Zascavage et al., 2019; Aminuddin et al., 2020; Bi et al., 2020; Georgieva et al., 2020; Bicci et al., 2021; Goldsmith et al., 2021) (**Supplementary Figure 11**). In these studies, the coverage of the mitochondrial genome ranged from 60.4X (Aminuddin et al., 2020) to over 10000X (Goldsmith et al., 2021) (**Supplementary Table 3**). In the latter case, extraction of mtDNA from a subcellular fraction was performed before Nanopore sequencing, which enhanced the fraction of sequenced reads that mapped to the mitochondrial genome.

Three out of the six publications investigated mtDNA methylation in the context of cancer research (Aminuddin et al., 2020; Bicci et al., 2021; Goldsmith et al., 2021). In our study, we included patients with Parkin-PD and investigated global differences in mtDNA CpG methylations between patients and control subjects. For the published studies in cancer cells, Nanopolish was used to call methylation from the Nanopore sequencing data (Aminuddin et al., 2020; Bicci et al., 2021; Goldsmith et al., 2021). In addition to Nanopolish, one study used Guppy in combination with Medaka (Goldsmith et al., 2021). Low-level mtDNA methylation in these three studies has been described (Aminuddin et al., 2020; Bicci et al., 2021; Goldsmith et al., 2021), albeit one study evaluated only three specific sites. We also detected overall low-level mtDNA methylation in blood-derived and neuron-derived DNA, in concordance with the reported literature (Aminuddin et al., 2020; Bicci et al., 2021; Goldsmith et al., 2021).

Strengths and Limitations

In our study, we present an optimized protocol for the investigation of mtDNA CpG methylation. We obtained high coverage of the mtDNA as well as the nuclear-encoded *45S rRNA* gene and the synthetic DNA samples. The mean coverage of the mtDNA ranged from 177X to 320X across individuals. Linearization of mtDNA has been recommended to counteract the influence of secondary and tertiary structure in bisulfite-dependent methods (Liu et al., 2016; Mechta et al., 2017; Owa et al., 2018). Thus, we performed T7 Endonuclease I digestion of whole-cell DNA for single-molecule sequencing. Still, the sample size of our study was small with eight included individuals and our analysis was limited to DNA methylation at CpG sites. As previous studies have shown that there is non-CpG methylation present in the mtDNA (Dou et al., 2019; Patil et al., 2019), future workflows should be expanded to include non-CpG methylation as well. In the current study, mtDNA methylation was analyzed in DNA extracted from whole blood, which is the most common source of DNA in genetic research. Unfortunately, some samples were frozen EDTA vials, which precluded cell compositing analyses. By contrast, future studies should be based on fresh blood draws to allow for a correlation of cell type and mtDNA methylation status in a given sample. Another

limitation of this study is that Parkin mutation carriers are rare and an assessment of a larger Parkin-PD cohort is therefore only possible within the framework of international collaborations. Furthermore, due to the high cell culture costs, time and labor-intensive procedure, such mechanistic studies in iPSC-derived cell models are typically limited to a small number of samples. However, while we currently do not have access to additional iPSC lines with biallelic Parkin mutations, we have included an additional independent differentiation of all lines in the study. In this fashion, we could explore the impact of inter-experimental variability on our data set. This validation showed methylation profiles in the control and Parkin-PD patients comparable to the original analysis. Given these limitations, we investigated two different types of genetic material in addition to the 16.5 kb mitochondrial genome to validate our workflow, i.e. an 897 bp synthetic DNA sample and the native 13 kb *45S rRNA* nuclear-encoded gene. To have a comparison of two software tools, we have used Nanopolish and Megalodon to call methylation, which showed high concordance between the mean MF detected for each sample. Additionally, we have corrected our data for false-positive methylation calls individually for Nanopolish and Megalodon. Lastly, all experiments and analyses were performed at the same institute to reduce batch effects. These results highlight that using Nanopore sequencing overcomes the bias that might be introduced by bisulfite-based methods due to conversion-resistant cytosines of the mtDNA. But it is important to note that also with Nanopore sequencing we observed false-positive methylation calls as illustrated by the FPR calculated from the long-range PCR sequencing data. Thus, the software predicting the MF tools might need to be trained with more mtDNA-specific data sets to enhance the accuracy even more.

CONCLUSION

In conclusion, our results suggest the applicability of Nanopore sequencing for the investigation of mtDNA methylation. Overall, we detected low-level CpG methylation of mtDNA with exceptions for certain sites. Our results suggest that highly methylated DNA molecules were more likely to fail Guppy base-calling and therefore bioinformatic pipelines that take Guppy-failed reads into account are recommended for highly methylated samples. Despite our small sample size, we observed significant differences in patients with Parkin-PD, which highlights the importance to further investigate the underlying molecular mechanism and its implication in neurodegeneration. Additionally, an expansion of the workflow to include non-CpG methylation analysis is warranted.

DATA AVAILABILITY STATEMENT

The datasets presented in this study can be found in online repositories. The names of the repository/repositories and accession number(s) can be found below: NCBI SRA, accession numbers: SAMN20956590-SAMN20956606.

ETHICS STATEMENT

The studies involving human participants were reviewed and approved by Research Ethics Boards of the Universities of Luebeck and the Research Ethics Boards of the Universities of Luxembourg. Written informed consent to participate in this study was provided by the participants' legal guardian/next of kin.

AUTHOR CONTRIBUTIONS

JT, CK, AG, LS, and SP contributed to conception and design of the study. TL, KW, SS, RT, JL, and JT contributed to the acquisition and analysis of data. TL, CK, SP, JL, LS, AG, and JT contributed to interpretation of data. TL and JT wrote the first draft of the manuscript. All authors participated in revising the manuscript for intellectual content and approved its final version.

FUNDING

Funding has been obtained from the German Research Foundation (ProtectMove; FOR 2488, GR 3731/5-1; SE 2608/2-1; KO 2250/7-1), the Luxembourg National Research Fund within the ATTRACT (Model-IPD, FNR9631103) and INTER programs (ProtectMove, INTER/DFG/19/14429377), the Personalized Medicine Consortium (PMC) of Luxembourg (PUMP-PRIME grant), the European Community (SysMedPD), the Canadian Institutes of Health Research (CIHR), Peter and Traudl Engelhorn Foundation, and the Joachim Herz Stiftung.

ACKNOWLEDGMENTS

We acknowledge Aurelien Ginolhac for his review of the manuscript and insightful comments and Philip Seibler for expertise in IPSC-derived neuronal models. The study is available as a preprint (Lüth et al., 2021).

SUPPLEMENTARY MATERIAL

The Supplementary Material for this article can be found online at: https://www.frontiersin.org/articles/10.3389/fnagi.2021.713084/full#supplementary-material

REFERENCES

Aminuddin, A., Ng, P. Y., Leong, C. O., and Chua, E. W. (2020). Mitochondrial DNA alterations may influence the cisplatin responsiveness of oral squamous cell carcinoma. *Sci. Rep.* 10:7885. doi: 10.1038/s41598-020-64664-3

Bellizzi, D., D'aquila, P., Scafone, T., Giordano, M., Riso, V., Riccio, A., et al. (2013). The control region of mitochondrial DNA shows an unusual CpG and non-CpG methylation pattern. *DNA Res.* 20, 537–547. doi: 10.1093/dnares/dst029

Benayoun, B. A., Pollina, E. A., and Brunet, A. (2015). Epigenetic regulation of ageing: linking environmental inputs to genomic stability. *Nat. Rev. Mol. Cell Biol.* 16, 593–610. doi: 10.1038/nrm4048

Berk, A. J., and Clayton, D. A. (1974). Mechanism of mitochondrial DNA replication in mouse L-cells: asynchronous replication of strands, segregation of circular daughter molecules, aspects of topology and turnover of an initiation sequence. *J. Mol. Biol.* 86, 801–824. doi: 10.1016/0022-2836(74)90355-6

Bi, C., Wang, L., Fan, Y., Ramos-Mandujano, G., Yuan, B., Zhou, X., et al. (2020). Single-cell individual complete mtDNA sequencing uncovers hidden mitochondrial heterogeneity in human and mouse oocytes. *bioRxiv [preprint]*. doi: 10.1101/2020.12.28.424537

Bicci, I., Calabrese, C., Golder, Z. J., Gomez-Duran, A., and Chinnery, P. F. (2021). Oxford nanopore sequencing-based protocol to detect CpG methylation in human mitochondrial DNA. *bioRxiv [preprint]*. doi: 10.1101/2021.02.20.432086

Blanch, M., Mosquera, J. L., Ansoleaga, B., Ferrer, I., and Barrachina, M. (2016). Altered mitochondrial DNA methylation pattern in Alzheimer disease-related pathology and in Parkinson disease. *Am. J. Pathol.* 186, 385–397. doi: 10.1016/j.ajpath.2015.10.004

Carter, J. M., and Hussain, S. (2017). Robust long-read native DNA sequencing using the ONT CsgG Nanopore system. *Wellcome Open Res.* 2:23. doi: 10.12688/wellcomeopenres.11246.2

Dayama, G., Emery, S. B., Kidd, J. M., and Mills, R. E. (2014). The genomic landscape of polymorphic human nuclear mitochondrial insertions. *Nucleic Acids Res.* 42, 12640–12649. doi: 10.1093/nar/gku1038

De Coster, W., and Van Broeckhoven, C. (2019). Newest methods for detecting structural variations. *Trends Biotechnol.* 37, 973–982. doi: 10.1016/j.tibtech.2019.02.003

Deamer, D., Akeson, M., and Branton, D. (2016). Three decades of Nanopore sequencing. *Nat. Biotechnol.* 34, 518–524. doi: 10.1038/nbt.3423

Dou, X., Boyd-Kirkup, J. D., Mcdermott, J., Zhang, X., Li, F., Rong, B., et al. (2019). The strand-biased mitochondrial DNA methylome and its regulation by DNMT3A. *Genome Res.* 29, 1622–1634. doi: 10.1101/gr.234021.117

Georgieva, D., Liu, Q., Wang, K., and Egli, D. (2020). Detection of base analogs incorporated during DNA replication by nanopore sequencing. *Nucleic Acids Res.* 48:e88. doi: 10.1093/nar/gkaa517

Goldsmith, C., Rodriguez-Aguilera, J. R., El-Rifai, I., Jarretier-Yuste, A., Hervieu, V., Raineteau, O., et al. (2021). Low biological fluctuation of mitochondrial CpG and non-CpG methylation at the single-molecule level. *Sci. Rep.* 11:8032. doi: 10.1038/s41598-021-87457-8

Guitton, R., Dölle, C., Alves, G., Tysnes, O.-B., Nido, G. S., and Tzoulis, C. (2021). Ultra-deep whole genome bisulfite sequencing reveals a single methylation hotspot in human brain mitochondrial DNA. *bioRxiv [preprint]*. doi: 10.1101/2021.03.30.437685

Hong, E. E., Okitsu, C. Y., Smith, A. D., and Hsieh, C. L. (2013). Regionally specific and genome-wide analyses conclusively demonstrate the absence of CpG methylation in human mitochondrial DNA. *Mol. Cell Biol.* 33, 2683–2690. doi: 10.1128/MCB.00220-13

Jiang, S., and Guo, Y. (2020). Epigenetic clock: DNA methylation in aging. *Stem Cells Int.* 2020:1047896. doi: 10.1155/2020/1047896

Lindberg, M. R., Schmedes, S. E., Hewitt, F. C., Haas, J. L., Ternus, K. L., Kadavy, D. R., et al. (2016). A comparison and integration of MiSeq and MinION platforms for sequencing single source and mixed mitochondrial genomes. *PLoS ONE* 11:e0167600. doi: 10.1371/journal.pone.0167600

Liu, B., Du, Q., Chen, L., Fu, G., Li, S., Fu, L., et al. (2016). CpG methylation patterns of human mitochondrial DNA. *Sci. Rep.* 6:23421. doi: 10.1038/srep23421

Lüth, T., Klein, C., Schaake, S., Tse, R., Pereira, S., Lass, J., et al. (2021). Analysis of mitochondrial genome methylation using Nanopore single-molecule sequencing. *bioRxiv [preprint]*. doi: 10.1101/2021.02.05.429923

Mawlood, S. K., Dennany, L., Watson, N., Dempster, J., and Pickard, B. S. (2016). Quantification of global mitochondrial DNA methylation levels and inverse correlation with age at two CpG sites. *Aging (Albany NY)* 8, 636–641. doi: 10.18632/aging.100892

Mechta, M., Ingerslev, L. R., Fabre, O., Picard, M., and Barres, R. (2017). Evidence Suggesting absence of mitochondrial DNA methylation. *Front. Genet.* 8:166. doi: 10.3389/fgene.2017.00166

Owa, C., Poulin, M., Yan, L. Y., and Shioda, T. (2018). Technical adequacy of bisulfite sequencing and pyrosequencing for detection of mitochondria! DNA methylation: sources and avoidance of false-positive detection. *PLos ONE* 13:e0192722. doi: 10.1371/journal.pone.0192722

Patil, V., Cuenin, C., Chung, F., Aguilera, J. R. R., Fernandez-Jimenez, N., Romero-Garmendia, I., et al. (2019). Human mitochondrial DNA is extensively methylated in a non-CpG context. *Nucleic Acids Res.* 47, 10072–10085. doi: 10.1093/nar/gkz762

Reinhardt, P., Glatza, M., Hemmer, K., Tsytsyura, Y., Thiel, C. S., Hoing, S., et al. (2013). Derivation and expansion using only small molecules of human neural progenitors for neurodegenerative disease modeling. *PLoS ONE* 8:e59252. doi: 10.1371/annotation/6a917a2e-df4a-4ad9-99bb-6aa7218b833e

Seibler, P., Graziotto, J., Jeong, H., Simunovic, F., Klein, C., and Krainc, D. (2011). Mitochondrial Parkin recruitment is impaired in neurons derived from mutant PINK1 induced pluripotent stem cells. *J. Neurosci.* 31, 5970–5976. doi: 10.1523/JNEUROSCI.4441-10.2011

Simpson, J. T., Workman, R. E., Zuzarte, P. C., David, M., Dursi, L. J., and Timp, W. (2017). Detecting DNA cytosine methylation using nanopore sequencing. *Nat. Methods* 14, 407–410. doi: 10.1038/nmeth.4184

Sirard, M. A. (2019). Distribution and dynamics of mitochondrial DNA methylation in oocytes, embryos and granulosa cells. *Sci. Rep.* 9:11937. doi: 10.1038/s41598-019-48422-8

Sun, X., Vaghjiani, V., Jayasekara, W. S. N., Cain, J. E., and St John, J. C. (2018). The degree of mitochondrial DNA methylation in tumor models of glioblastoma and osteosarcoma. *Clin. Epigenet.* 10:157. doi: 10.1186/s13148-018-0590-0

Trinh, J., Lohmann, K., Baumann, H., Balck, A., Borsche, M., Bruggemann, N., et al. (2019). Utility and implications of exome sequencing in early-onset Parkinson's disease. *Mov. Disord.* 34, 133–137. doi: 10.1002/mds.27559

van der Wijst, M. G., Van Tilburg, A. Y., Ruiters, M. H., and Rots, M. G. (2017). Experimental mitochondria-targeted DNA methylation identifies GpC methylation, not CpG methylation, as potential regulator of mitochondrial gene expression. *Sci. Rep.* 7:177. doi: 10.1038/s41598-017-00263-z

Weissensteiner, H., Forer, L., Fuchsberger, C., Schopf, B., Kloss-Brandstatter, A., Specht, G., et al. (2016). mtDNA-server: next-generation sequencing data analysis of human mitochondrial DNA in the cloud. *Nucleic Acids Res.* 44, W64–W69. doi: 10.1093/nar/gkw247

Xu, L., and Seki, M. (2020). Recent advances in the detection of base modifications using the nanopore sequencer. *J. Hum. Genet.* 65, 25–33. doi: 10.1038/s10038-019-0679-0

Yuen, Z. W., Srivastava, A., Daniel, R., Mcnevin, D., Jack, C., and Eyras, E. (2021). Systematic benchmarking of tools for CpG methylation detection from nanopore sequencing. *Nat. Commun.* 12:3438. doi: 10.1038/s41467-021-23778-6

Zascavage, R. R., Thorson, K., and Planz, J. V. (2019). Nanopore sequencing: an enrichment-free alternative to mitochondrial DNA sequencing. *Electrophoresis* 40, 272–280. doi: 10.1002/elps.201800083

Conflict of Interest: The authors declare that the research was conducted in the absence of any commercial or financial relationships that could be construed as a potential conflict of interest.

Publisher's Note: All claims expressed in this article are solely those of the authors and do not necessarily represent those of their affiliated organizations, or those of the publisher, the editors and the reviewers. Any product that may be evaluated in this article, or claim that may be made by its manufacturer, is not guaranteed or endorsed by the publisher.

Copyright © 2021 Lüth, Wasner, Klein, Schaake, Tse, Pereira, Laß, Sinkkonen, Grünewald and Trinh. This is an open-access article distributed under the terms of the Creative Commons Attribution License (CC BY). The use, distribution or reproduction in other forums is permitted, provided the original author(s) and the copyright owner(s) are credited and that the original publication in this journal is cited, in accordance with accepted academic practice. No use, distribution or reproduction is permitted which does not comply with these terms.

frontiers in Aging Neuroscience

ORIGINAL RESEARCH
published: 04 October 2021
doi: 10.3389/fnagi.2021.741445

Topological Alterations of Working Memory Impairment in Aged Patients With Vascular Dementia

Cao Zheng[1,2]*, *Rong-Sheng Zhang*[1], *Ting Wan*[1] and *Jun-Sheng Zhao*[1]

[1] Department of Radiation Intervention, Central Hospital of Huanggang City, Huanggang, China, [2] Department of Radiology, Central Hospital of Huanggang City, Huanggang, China

Aneurysmal subarachnoid hemorrhage (aSAH) is a common disease causing vascular dementia. Survivors often suffer from cognitive impairment especially working memory deficit. Currently, lack of theoretical support limits the improvement of cognitive intervention or rehabilitation. It is unclear how the large-scale network differs and to what extent is the brain network affected? Our study aims to provide novel information about the topological characteristics of brain organization, especially "small-world" property. A total of 62 aSAH patients are enrolled in this study. They are divided into two groups according to the syndrome of working memory deficit. Their working memory function is evaluated by TMT-B and AVLT (Chinese version). Functional MRI scan is also performed for detecting resting-state cortical plasticity. We utilized ICA to extract functional sub-networks including working memory network from imaging data. And then we establish binarized network and calculate the small-worldness property as well as local and global efficiency of networks. aSAH group with working memory deficit shows no significant difference of clustering coefficient with control group. Our study discovered significant decrease of characteristic path length indicating an increase of overall routing efficiency. We reason that patients with working memory deficit have to recruit more neuronal resources and thus develops higher overall routing efficiency of local network. This study provides novel information about the neural alterations of aSAH patients with working memory deficit. It might contribute to the understanding of neural mechanism and the improvement of current intervention for vascular dementia.

Keywords: aSAH, vascular dementia, working memory deficit, independent component analysis, small-world

OPEN ACCESS

Edited by:
Woon-Man Kung,
Chinese Culture University, Taiwan

Reviewed by:
Yu Lei,
Fudan University, China
Wei Hung Chang,
National Cheng Kung University, Taiwan

***Correspondence:**
Cao Zheng
20130046@stu.nmu.edu.cn

Received: *14 July 2021*
Accepted: *03 September 2021*
Published: *04 October 2021*

Citation:
Zheng C, Zhang R-S, Wan T and Zhao J-S (2021) Topological Alterations of Working Memory Impairment in Aged Patients With Vascular Dementia. Front. Aging Neurosci. 13:741445. doi: 10.3389/fnagi.2021.741445

INTRODUCTION

Aneurysmal subarachnoid hemorrhage (aSAH) is one common disease which causes vascular dementia. It is traditionally regarded as one severe incident with high mortality and morbidity (Lovelock et al., 2010). The hemorrhagic strike is sudden and deadly because of a high prevalence of occult or undetected intracranial aneurysms (Vernooij, 2007; Vlak et al., 2011). But in the recent decades, there is a tremendous improvement on the overall survival rate of aSAH patients due to the great progress made on early diagnosis and timely intervention.

As the mortality rate is dropping in the last two decades, more patients experience severe neurological sequela after survival. Several studies reported that even those survivors categorized into "mild disability" also suffered from various cognitive impairments such as working memory

deficit, aphasia or alexia (Ørbo et al., 2008). That increases the number of patients who needs rehabilitative care and return to their normal life. As a result, it is of great value to study the cognitive impairment after aSAH. New strategy or improvement of intervention and rehabilitation needs theoretic foundation, which comes from specific description of neural behavior and recovery process.

According to the previous research, short-term memory has been listed as the most important sequela (Mayer et al., 2002; Anderson et al., 2006; Al-Khindi et al., 2010; Scott et al., 2010). Particularly, reports pointed out that working memory deficit is often affected (Sheldon et al., 2012, 2013). This persistent cognitive problem lays a great impact on patients' daily life. Although a number of rehabilitative methods have been applied, most approaches are empirical or experimental (Wong et al., 2016; Huenges Wajer et al., 2017; Stabel et al., 2017). Lacking theoretical support somehow limits the improvement of current rehabilitation. Of course, previous studies have provided insight into the functional alterations of the working memory deficit after aSAH. It reported that aSAH patients with cognitive impairment displayed significant decline of spontaneous neural activity in several cerebral regions (Su, 2018). However, there are still questions about the specific cortical changes of aSAH patients with working memory deficit. (1)To what extent is the brain network of those with memory deficit affected, whole-brain network level or sub-network level? (2) How is the working memory network organized when isolated regions have been proved dysfunctional? Although the existing evidence revealed some functional changes, identifying worthwhile large-scale changes would be a vital advance for clarifying the underlying mechanism of working memory deficit.

In this study, we would extract several sub-networks including working memory network from the resting-state fMRI data. The topological changes of networks instead of activation status of one brain region would be analyzed. We aim to provide novel information about the characteristics of brain organization, especially "small-world" property (Sporns and Zwi, 2004). The comparison would be performed in the aSAH patients with and without working memory deficit in order to reveal more information about the associated neural plasticity.

MATERIALS AND METHODS

Demographics and Ethic Information

A total of 62 aSAH patients who are treated and followed up in our center are identified for neuropsychological assessment and MR scan, including 32 with intact working memory and another 30 with working memory deficit. We only recruit those patients with over 1 year follow-up so that their outcome of cognitive impairment would be identified. Loss Trail Making Test part B (TMT-B) and AVLT (the Chinese version of AVLT, Auditory Verbal Learning Test) is performed for evaluation of cognitive function. Participants' original demographic and clinical status at first admission are retrospectively adopted and compared. The severity of aSAH is examined through head CT of Fisher grade (assessed by a neurologist and a radiologist). Definitive treatment of clipping or coiling is performed within 48 h after first admission.

We select MRI-safe titanium clips as implants in order to produce minimal artifact (Khursheed, 2011). An advanced 3T MR scanner can successfully image brain tissue around implanted titanium aneurysm clips at different spatial ranges depending on the sequence type. The patients enrolled in this study had lesions distant from the regions of interest on fMRI analysis. Most of the clips had limited artifacts 2 mm outside of the boarder. In addition, construction of a spatial confidence boundary of signal integrity, represented numerically by an artifact mask volume, was performed. It was possible to quantify the degree of uncertainty across patients regarding whether the signal in a particular region of the brain was completely or partially affected by clip artifacts.

Inclusion criteria of this study is listed as follows: (1) aged over 18 years; (2) aneurysm diagnosed through digital subtraction angiography; (3) minimum 1 year of follow-up since admission; (4) Right handedness, evaluated by Edinburgh laterality manual test. The exclusion criteria includes: (1) History of aSAH related complications (hydrocephalus, rebleeding or vasospasm); (2) other cerebral surgical or interventional treatment before enrollment; (3) Disturbances in the motor, sensitive or cerebellum assessment. This study is approved by the ethics committee of Ruijin Hospital, Shanghai Jiaotong University Medical School. All participants provided written informed consent according to the Helsinki Statement.

Patients who survived the hemorrhagic attack spent circa 20 days in the neurology and neurosurgery department and another 60 days in a rehabilitation center. Neuroimaging and other tests were performed after discharge and initial rehabilitation, which was usually 75–90 days after admission to our center. A washout period of at least 30 days was used to eliminate the effect of previous medication.

Data Acquisition and Preprocessing

We conduct this study with a GE 3.0T MR System. The parameters of scans are listed as followed: sequence = GRE-EPI, axial slices, scanning order = interleaved [1:2:43 2:2:42], slice number = 43, matrix size = 64 * 64, FOV = 192 * 192 mm, TR/TE = 2,000/30 ms, FA = 90 deg, slice thickness = 3.0 mm, gap = 0 (voxel size 3.0 * 3.0 * 3.0), dummy scan = 6, number of acquisitions = 240, NEX = 1, parallel acceleration = 2, total scan time = 8 min 12 s.

Data Preprocessing

We utilize Statistical Parametric Mapping toolbox (https://www.fil.ion.ucl.ac.uk/spm/) for data preprocessing. The functional data is first adjusted with slicing time procedure for difference of acquisition time. Then head movement correction procedure is performed. Those subjects of which the translational or rotational motion over 2.5 mm or 2.5 degrees would be discarded. In the procedure of realignment, one mean volume is extracted and pointed as the reference image. We perform

spatial normalization of the functional images via standard EPI template. Covariates including head motion parameters, white matter and cerebral spinal fluid BOLD signal would be regressed from functional data. Finally, spatial smoothing with a Gaussian kernel of 6-mm full width at half maximum is performed for denoising.

Independent Component Analysis

We utilize GICA toolbox (Group ICA of fMRI Toolbox, Generally, group independent component analysis with concatenation approach plus back-reconstruction is utilized for these multi-subject analysis (Calhoun et al., 2001). We first perform dimension reduction to the functional data. Afterwards, the number of independent components of subjects decreases to 60. Then temporal concatenation is performed for image connection. All the images are reduced to 40 components at group level with EM (expectation maximization) algorithm. Also, we perform 100 times repetition of infomax algorithm in ICASSO for better robustness. After aggregated spatial maps are estimated, the back reconstruction approach is utilized for extracting subject-specific spatial pattern and time courses. We threshold these maps of spatial weight with a significance level of $p < 0.05$. After revealing spatial pattern of certain component, we manually recognize eight sub-networks including working memory network and so on. This component which shows a spatial pattern of working memory network would be binarized and transformed into a mask. It helps to extract time series of working memory network from the original data. In this procedure, we also determine the spatial coordinate of several peak points which represents the highest possibility of belonging to the current component.

Node and Edge Definition

We aim to explore the difference of small-world property between two groups at both whole brain network and sub-network level. For whole brain network analysis, we use random parcellation and segment the brain into 1,000 nodes. It was proved that the topological property did not depend on the methodology of parcellation (Zalesky et al., 2010). Then, we calculate the functional connectivity between each two nodes. The Pearson correlation of mean time courses in each two nodes are considered as edge.

For sub-network analysis, we first perform an independent component analysis and extract 40 spatial components for the construction of sub-network. Then we manually recognize eight sets of independent components representing eight sub-networks, including basal ganglia network (BGN), dorsal default mode network (d-DMN), visual network (VN), left executive control network (LECN), sensorimotor network (SMN), visual spatial network (VSN), anterior-salience network (a-SN) and working memory network (WMN). For each sub-network, we define each voxel as node and voxel-voxel functional connectivity as edge. In order to balance the scale of edge number of two levels, we adjust the voxel size and resample it into 6 mm^3, which massively reduces the computational work. The networks constructed in this study are all undirected and unweighted. In the calculation, we set the sparsity from 0.05 to 0.50 with an increased step of 0.01.

Analysis of Small-Worldness in Working Memory Network

The major metrics of small-world network involved in this study are clustering coefficient (Cp), characteristic path length (Lp), normalized clustering coefficient γ and normalized characteristic path length λ. Cp of network is calculated as the mean of the clustering coefficients of all the nodes in the network. Clustering coefficient quantifies the extent of local interconnectivity or cliquishness of a network. Decreased Cp implies reduced efficiency in local information transmission and processes (Wang et al., 2016). The mean minimum path length of a node is computed as the average of minimum distances from that node

TABLE 1 | Demographic information of enrolled aSAH subjects.

	Patients without working memory deficit	Patients with working memory deficit	Statistical significance
Age, mean (SEM*)	63.3 (3.3)	62.4 (4.6)	$P > 0.05$
Sex, male (%)	37.5% ($n = 12$)	43% ($n = 13$)	/
Length of hospitalization (days), mean (SEM)	21 (1.23)	23 (1.12)	$P > 0.05$
TMT-B (Second)	165 (45)	221 (72)	$P < 0.05$
AVLT (Chinese Version) -delayed memory	9.33 (0.9)	4.12 (1.1)	$P < 0.05$
AVLT (Chinese Version) -repeat recognition	12.45 (1.0)	7.26 (1.4)	$P < 0.05$
Total number of subjects	N = 32	N = 30	/

**SEM, standard error of mean; TMT-B, trail making test part B; AVLT, auditory verbal learning test.*

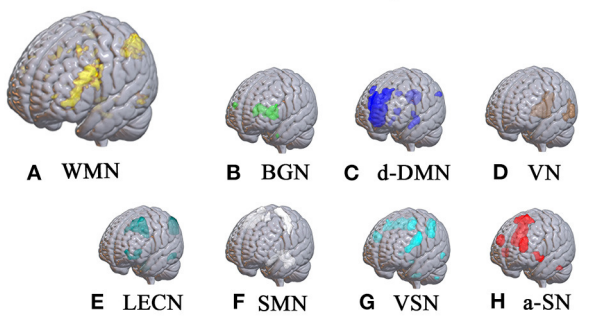

FIGURE 1 | Functional networks extracted from resting-state data with ICA. With ICA approach, we manage to extract 40 components and establish totally 8 sub-networks from the resting data including working memory network **(A)**, basal ganglia network **(B)**, dorsal default mode network **(C)**, visual network **(D)**, left executive control network **(E)**, sensorimotor network **(F)**, visual spatial network **(G)** and anterior salience network **(H)**.

to all the remaining nodes in the network. Lp of network is the average of the mean minimum path lengths of all the nodes in the network. Characteristic path length Lp measures the extent of overall communication efficiency of a network and increased Lp represents a shift toward "regularization" (Suo et al., 2017). As for the isolated nodes in the network, which are totally disconnected with the network, is assigned 0 for clustering coefficient and Inf for path length. For normalization purpose, we also construct random networks as baseline. We calculate the ration of Cp and Lp of target network and same metrics of random network with the same number of nodes and degree distribution (Sporns and Zwi, 2004). In contrast to random network, a network with small-world property has a high normalized clustering coefficients $\gamma(Cp/Cprand) > 1$ and relatively low normalized characteristic path length $\lambda(Lp/Lprand) \approx 1$ (Achard, 2006).

Analysis of Global and Local Efficiency of Whole Brain Network and Sub-networks

The global efficiency of network is the inverse of the harmonic mean of the minimum path length between each pair of nodes. According to the previous studies, global efficiency is a more meaningful measure in parallel information processing than path length (Achard and Bullmore, 2007). On the other hand, the local efficiency reflects the fault tolerance of a network by measuring the capability of its sub-network for information exchange when the index node are eliminated (Latora and Marchiori, 2001). Small-worldness properties, especially the path length is not robust if the network contains disconnected nodes. Therefore, we would also calculate the local and global efficiency of whole brain network as well as those sub-networks to provide supplementary information. Similarly, we create 100 random networks with same nodes number and degree as the target

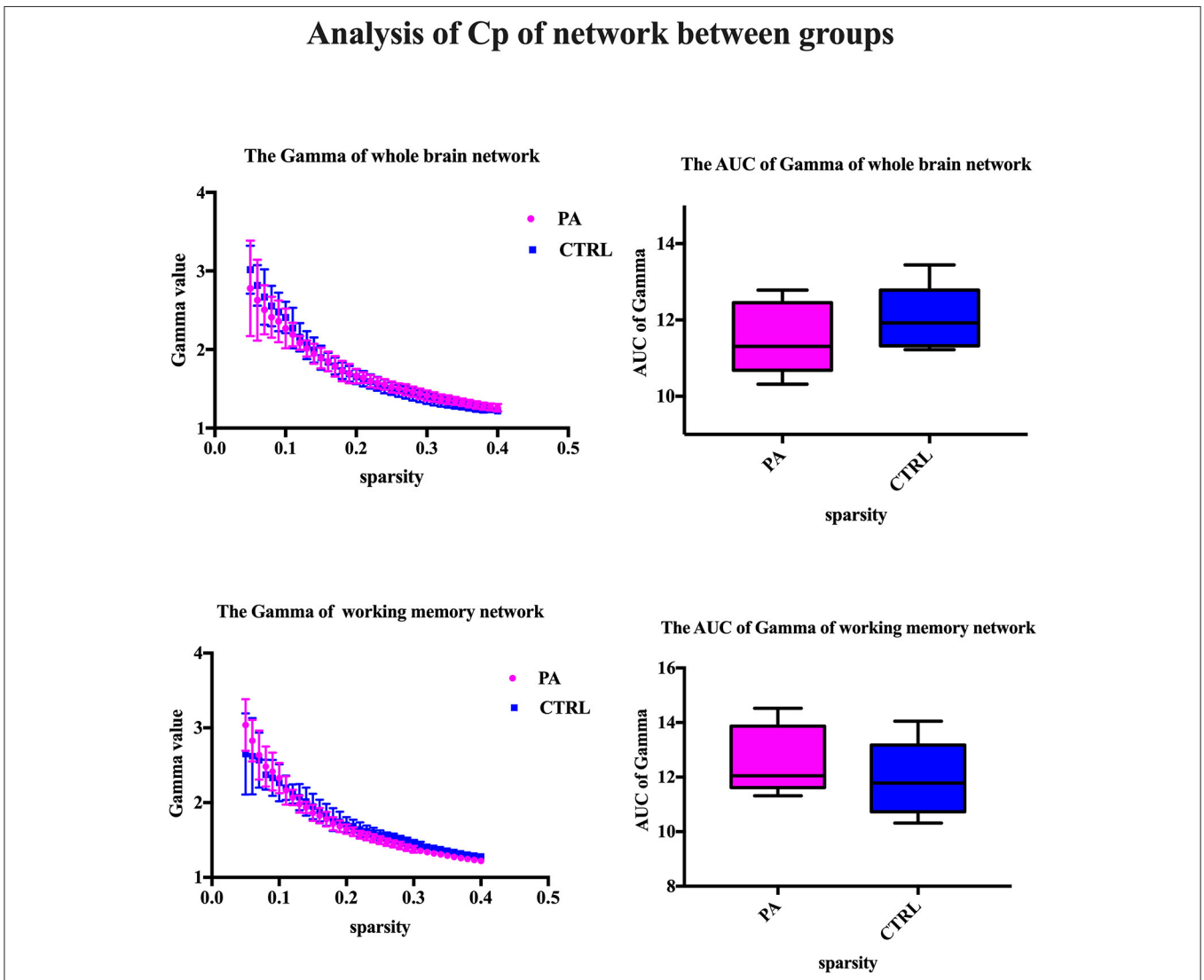

FIGURE 2 | Analysis of Cp of network between groups. We compare the gamma value and its area under curve (AUC), which represents the clustering coefficient of whole brain network or working memory network. The statistical results show no significant difference.

network. Then we compare the efficiency of target network with that of random network.

Statistical Analysis

For metrics of graph theory, multiple comparison methods were applied by utilizing AUC (area under curve) as measurement. For numerical analysis, two sample *T* test was adopted. The statistical threshold was set at $p < 0.05$.

RESULTS

We compare the gender as well as the length of hospitalization and the statistical result shows no significant difference. The AVLT scaling result is 9.33 ± 0.93/12.45 ± 1.02(Mean ± SEM) in control group and 6.21 ± 0.76/9.58 ± 0.87 (Mean ± SEM) in working memory deficit group. The statistical analysis confirms significant decrease of delayed memory function in working memory deficit group (**Table 1**).

After ICA procedure, we extract 40 components and establish totally eight sub-networks from the resting data including working memory network, basal ganglia network, dorsal default mode network, visual network, left executive control network, sensorimotor network, visual spatial network (**Figure 1**). In the analysis of small-worldness analysis, aSAH group with working memory deficit shows no significant difference of clustering coefficient with control group (**Figure 2**). But it shows significant decrease of characteristic path length than control group (**Figure 3**). As for the analysis of local and global efficiency, the result shows no significant difference between groups (**Figure 4**).

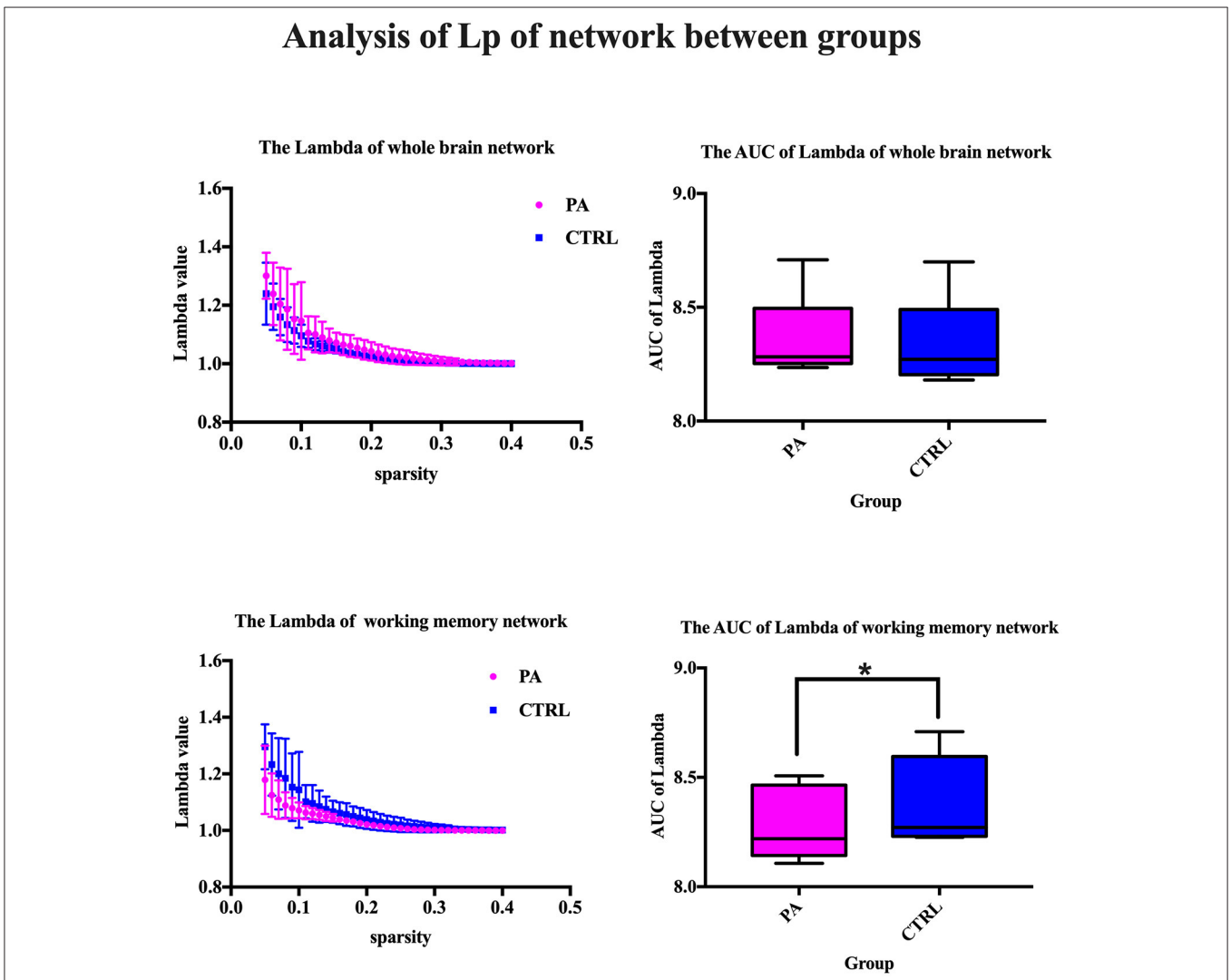

FIGURE 3 | Analysis of Lp of network between groups. We compare the lambda value and its area under curve (AUC), which represents the characteristic path length of whole brain network or working memory network. The statistical results show significant decrease of characteristic path length in control group. *Significant difference of AUC of Lambda between two groups.

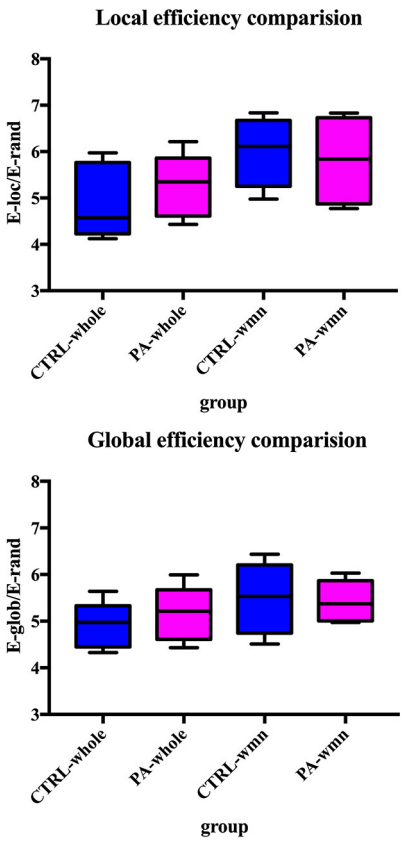

FIGURE 4 | Analysis of local and global efficiency between groups. We compare both local and global efficiency of whole brain network of control group, whole brain network of PA group, working memory network of control group and working memory network of PA group. The statistical results show no significant difference among groups.

DISCUSSION

The detailed alteration of cognitive impairment after aSAH has been always a vital problem for researchers (Welmer et al., 2006; Al-Khindi et al., 2010; Ali et al., 2020). Because improvement on current treatment or development of new interventional strategy depends on our understanding of neural mechanism. However, there is still a long way before the thorough clarification of neural basis, which leads to multiple cognitive impairment including working memory deficit. In fact, the exact neurological change of working memory deficit after aSAH remains unclear.

Our study is motivated by previous research, which indicated persistent memory dysfunction after recovery of aSAH (Ørbo et al., 2008; Schweizer and Macdonald, 2010). Task-dependent BOLD experiment has been utilized to reveal the abnormal cortical activation which is potentially associated with memory deficit (Ellmore et al., 2013). Nevertheless, it is still not sufficient for a detailed description on the neurological change. Because isolated activation of certain brain regions fails to give enough attention to the connective situation between those regions. It is possible to reveal more details about working memory deficit if we consider more about the characteristic of information transmission from an angle of brain network.

On the other hand, the cognitive impairment is believed to trigger very limited response in whole brain scale compared with other task of strong activation. In order to increase our sensitivity of detection, we also include regional functional network to our analysis. The working memory network is localized and identified by ICA, which enables us to extract individual sub-network from group-level data.

Our study provides insight to the topological property of working memory deficit after aSAH. The most important findings could be concluded as followed, (1) The significant alteration of working memory deficit stays in a limited extent, which lies in regional working memory network rather than whole-brain network. (2) Working memory dysfunction promotes higher overall routing efficiency of regional functional network.

The most important result of this study is the significant decrease of characteristic path length. That indicates the surprising increase of overall routing efficiency of working memory network in aSAH patients with working memory deficit, which somehow fails to be in line with former studies (Chung et al., 2019). Previous studies demonstrated that working memory deficit was related with reduced connectivity within the network (Arciniega et al., 2021; Vannest et al., 2021)and other neuron loss or dysfunctionality (Fang et al., 2018; Cheng et al., 2019). Most reports focus on the direct hemodynamic response or adjacent connectivity of regions such as left dorsolateral prefrontal cortex (DLPFC) (Burgess et al., 2010) or parietal cortex (Olesen et al., 2004). Some existing evidence suggested subjects with working memory deficit requires more executive control, and therefore more brain activity, compared to healthy (or faster) individuals in order to perform successfully (Postle et al., 1999; Chang et al., 2011). An exact idea to explain this is the Compensation-Related Utilization of Neural Circuits Hypothesis (Reuter-Lorenz and Cappell, 2008), whereby patients with working memory deficit have to recruit more neuronal resources at lower loads than those with normal memory capacity leaving fewer resources for processing at higher loads. Similar result was found in patients of ADHD with working memory deficit. The imaging study discovered decreased efficiency of DLPFC for high-load visuospatial working memory and greater reliance on posterior spatial attention circuits to store and update spatial position than healthy control youth (Bédard et al., 2014). Actually, it was unclear at the outset whether memory dysfunction would be accompanied by reduced or increased activation. But we could say that the direct task-dependent imaging and large-scale network analysis provide two dimension of information about the detailed neural alteration contributing to the working memory deficit. Of course, the current theory needs larger sample size for confirmation in further study.

We also noticed the insignificant working network in left hemisphere. Previous studies (Owen et al., 2005) reported activation in the left inferior parietal lobe and left precunues

increased along with increasing age. Those regions were implicated in WMN studies. According to this theory, the subjects recruited in our study would display progressive recruitment of these task related frontal and parietal regions that underpin the functional maturation of working memory. In this circumstances, the left working memory system showed more robust architecture than the right one in the face of disease strike.

We perform independent component analysis for separating noise and functional sub-network. We concatenate all the data from both groups and then perform group-level dimensional reduction. It is true that the included images from two groups might differ in their brain signal. But we reason that the extracted spatial pattern of components should be unified in both groups for incoming statistical comparison. As a result, the spatial maps of component representing working memory network is not far different from previous human studies (Damoiseaux et al., 2006, 2008). In addition, our result does not include another pattern of working memory network, in which most of the significant voxels are localized in the left hemisphere. We think this may attribute to the limited sample size of included subjects. The component of right hemispheric working memory network fails to achieve the threshold of within-group significance.

CONCLUSION

Working memory deficit is one severe symptom of vascular dementia patients such as aSAH survivors. Our study discovered significant decrease of characteristic path length, which indicates the increase of overall routing efficiency. We reason that patients with working memory deficit have to recruit more neuronal resources and thus develops higher overall routing efficiency of local network. This study provides novel information about the neural alterations of aSAH patients with working memory deficit. It might contribute to the understanding of its neural mechanism and the improvement of current intervention.

LIMITATION

This study recruited limited number of subjects. However, the disease-triggered cognitive changes require larger sample size to determine.

DATA AVAILABILITY STATEMENT

The raw data supporting the conclusions of this article will be made available by the authors, without undue reservation.

ETHICS STATEMENT

The studies involving human participants were reviewed and approved by IRB of Huanggang Central Hospital. The patients/participants provided their written informed consent to participate in this study. Written informed consent was obtained from the individual(s) for the publication of any potentially identifiable images or data included in this article.

AUTHOR CONTRIBUTIONS

CZ designed the study and wrote the article. R-SZ and TW analyzed the data. J-SZ reviewed this article. All authors contributed to the article and approved the submitted version.

REFERENCES

Achard, S. (2006). A resilient, low-frequency, small-world human brain functional network with highly connected association cortical hubs. *J. Neurosci.* 26, 63–72. doi: 10.1523/JNEUROSCI.3874-05.2006

Achard, S., and Bullmore, E. (2007). Efficiency and cost of economical brain functional networks. *PLoS Comput. Biol.* 3:e17. doi: 10.1371/journal.pcbi.0030017

Ali, A., Bitir, B., Abdullah, T., Sabanci, P. A., Aras, Y., Aydoseli, A., et al. (2020). Gray-to-white matter ratio predicts long-term recovery potential of patients with aneurysmal subarachnoid hemorrhage. *Neurosurg. Rev.* 43, 195–202. doi: 10.1007/s10143-018-1029-y

Al-Khindi, T., Macdonald, R. L., and Schweizer, T. A. (2010). Cognitive and functional outcome after aneurysmal subarachnoid hemorrhage. *Stroke* 41, e519–e536. doi: 10.1161/STROKEAHA.110.581975

Anderson, S. W., Todd, M. M., Hindman, B. J., Clarke, W. R., Torner, J. C., Tranel, D., et al. (2006). Effects of intraoperative hypothermia on neuropsychological outcomes after intracranial aneurysm surgery. *Ann. Neurol.* 60, 518–527. doi: 10.1002/ana.21018

Arciniega, H., Shires, J., Furlong, S., Kilgore-Gomez, A., Cerreta, A., Murray, N. G., et al. (2021). Impaired visual working memory and reduced connectivity in undergraduates with a history of mild traumatic brain injury. *Sci. Rep.* 11:2789. doi: 10.1038/s41598-021-80995-1

Bédard, A.-C. V., Newcorn, J. H., Clerkin, S. M., Krone, B., Fan, J., Halperin, J. M., et al. (2014). Reduced prefrontal efficiency for visuospatial working memory in attention-deficit/hyperactivity disorder. *J. Am. Acad. Child Adolesc. Psychiatry* 53, 1020–1030.e6. doi: 10.1016/j.jaac.2014.05.011

Burgess, G. C., Depue, B. E., Ruzic, L., Willcutt, E. G., Du, Y. P., and Banich, M. T. (2010). Attentional control activation relates to working memory in attention-deficit/hyperactivity disorder. *Biol. Psychiatry* 67, 632–640. doi: 10.1016/j.biopsych.2009.10.036

Calhoun, V. D., Adali, T., Pearlson, G. D., and Pekar, J. J. (2001). A method for making group inferences from functional MRI data using independent component analysis. *Hum. Brain Mapp.* 14, 140–151. doi: 10.1002/hbm.1048

Chang, W. H., Park, Y. H., Ohn, S. H., Park, C., Lee, P. K. W., and Kim, Y.-H. (2011). Neural correlates of donepezil-induced cognitive improvement in patients with right hemisphere stroke: a pilot study. *Neuropsychol. Rehabil.* 21, 502–514. doi: 10.1080/09602011.2011.582708

Cheng, H., Sun, G., Li, M., Yin, M., and Chen, H. (2019). Neuron loss and dysfunctionality in hippocampus explain aircraft noise induced working memory impairment: a resting-state fMRI study on military pilots. *BioSci. Trends* 13, 430–440. doi: 10.5582/bst.2019.01190

Chung, D. Y., Oka, F., Jin, G., Harriott, A., Kura, S., Aykan, S., et al. (2019). Subarachnoid hemorrhage leads to early and persistent functional connectivity and behavioral changes in mice. *Neuroscience* 41, 975–985. doi: 10.1101/826891

Damoiseaux, J. S., Beckmann, C. F., Arigita, E. J. S., Barkhof, F., Scheltens, P.h., Stam, C. J., et al. (2008). Reduced resting-state brain activity in the "default network" in normal aging. *Cereb. Cortex* 18, 1856–1864. doi: 10.1093/cercor/bhm207

Damoiseaux, J. S., Rombouts, S. A. R. B., Barkhof, F., Scheltens, P., Stam, C. J., Smith, S. M., et al. (2006). Consistent resting-state networks across healthy subjects. *Proc. Natl. Acad. Sci.* 103, 13848–13853. doi: 10.1073/pnas.0601417103

Ellmore, T. M., Rohlffs, F., and Khursheed, F. (2013). fMRI of working memory impairment after recovery from subarachnoid hemorrhage. *Front. Neurol.* 4:179. doi: 10.3389/fneur.2013.00179

Fang, X., Wang, Y., Cheng, L., Zhang, Y., Zhou, Y., Wu, S., et al. (2018). Prefrontal dysconnectivity links to working memory deficit in first-episode schizophrenia. *Brain Imaging Behav.* 12, 335–344. doi: 10.1007/s11682-017-9692-0

Huenges Wajer, I. M. C., Visser-Meily, J. M. A., Greebe, P., Post, M. W. M., Rinkel, G. J. E., and van Zandvoort, M. J. E. (2017). Restrictions and satisfaction with participation in patients who are ADL-independent after an aneurysmal subarachnoid hemorrhage. *Top. Stroke Rehabil.* 24, 134–141. doi: 10.1080/10749357.2016.1194557

Khursheed, F. (2011). Artifact quantification and tractography from 3T MRI after placement of aneurysm clips in subarachnoid hemorrhage patients. *BMC Med. Imaging* 11:19. doi: 10.1186/1471-2342-11-19

Latora, V., and Marchiori, M. (2001). Efficient behavior of small-world networks. *Phys. Rev. Lett.* 87:198701. doi: 10.1103/PhysRevLett.87.198701

Lovelock, C. E., Rinkel, G. J. E., and Rothwell, P. M. (2010). Time trends in outcome of subarachnoid hemorrhage: population-based study and systematic review. *Neurology* 74, 1494–1501. doi: 10.1212/WNL.0b013e3181dd42b3

Mayer, S. A., Kreiter, K. T., Copeland, D., Bernardini, G. L., Bates, J. E., Peery, S., et al. (2002). Global and domain-specific cognitive impairment and outcome after subarachnoid hemorrhage. *Neurology* 59, 1750–1758. doi: 10.1212/01.WNL.0000035748.91128.C2

Olesen, P. J., Westerberg, H., and Klingberg, T. (2004). Increased prefrontal and parietal activity after training of working memory. *Nat. Neurosci.* 7, 75–79. doi: 10.1038/nn1165

Ørbo, M., Waterloo, K., Egge, A., Isaksen, J., Ingebrigtsen, T., and Romner, B. (2008). Predictors for cognitive impairment one year after surgery for aneurysmal subarachnoid hemorrhage. *J. Neurol.* 255, 1770–1776. doi: 10.1007/s00415-008-0047-z

Owen, A. M., McMillan, K. M., Laird, A. R., and Bullmore, E. (2005). N-back working memory paradigm: a meta-analysis of normative functional neuroimaging studies. *Hum. Brain Mapp.* 25, 46–59. doi: 10.1002/hbm.20131

Postle, B. R., Berger, J. S., and D'Esposito, M. (1999). Functional neuroanatomical double dissociation of mnemonic and executive control processes contributing to working memory performance. *Proc. Natl. Acad. Sci.* 96, 12959–12964. doi: 10.1073/pnas.96.22.12959

Reuter-Lorenz, P. A., and Cappell, K. A. (2008). Neurocognitive aging and the compensation hypothesis. *Curr. Dir. Psychol. Sci.* 17, 177–182. doi: 10.1111/j.1467-8721.2008.00570.x

Schweizer, T. A., and Macdonald, R. L. (2010). Assessing outcome after subarachnoid hemorrhage. *Nat. Rev. Neurol.* 6, 427–428. doi: 10.1038/nrneurol.2010.94

Scott, R. B., Eccles, F., Molyneux, A. J., Kerr, R. S. C., Rothwell, P. M., and Carpenter, K. (2010). Improved cognitive outcomes with endovascular coiling of ruptured intracranial aneurysms: neuropsychological outcomes from the International Subarachnoid Aneurysm Trial (ISAT). *Stroke* 41, 1743–1747. doi: 10.1161/STROKEAHA.110.585240

Sheldon, S., Macdonald, R. L., Cusimano, M., Spears, J., and Schweizer, T. A. (2013). Long-term consequences of subarachnoid hemorrhage: examining working memory. *J. Neurol. Sci.* 332, 145–147. doi: 10.1016/j.jns.2013.06.021

Sheldon, S., Macdonald, R. L., and Schweizer, T. A. (2012). Free recall memory performance after aneurysmal subarachnoid hemorrhage. *J. Int. Neuropsychol. Soc.* 18, 334–342. doi: 10.1017/S1355617711001780

Sporns, O., and Zwi, J. D. (2004). The small world of the cerebral cortex. *Neuroinformatics* 2, 145–162. doi: 10.1385/NI:2:2:145

Stabel, H. H., Pedersen, A. R., Johnsen, S. P., and Nielsen, J. F. (2017). Rupture of a non-traumatic anterior communicating artery aneurysm: does location of aneurysm associate with functional independence following post-acute in-patient neurorehabilitation? *Top. Stroke Rehabil.* 24, 585–591. doi: 10.1080/10749357.2017.1373973

Su, J. (2018). Memory deficits after aneurysmal subarachnoid hemorrhage: a functional magnetic resonance imaging study. *World Neurosurg.* 111, e500–e506. doi: 10.1016/j.wneu.2017.12.102

Suo, X., Lei, D., Chen, F., Wu, M., Li, L., Sun, L., et al. (2017). Anatomic insights into disrupted small-world networks in pediatric posttraumatic stress disorder. *Radiology* 282, 826–834. doi: 10.1148/radiol.2016160907

Vannest, J., Radhakrishnan, R., Gutierrez-Colina, A. M., Wade, S. L., Maloney, T., Combs, A., et al. (2021). Altered functional network connectivity and working memory dysfunction in adolescents with epilepsy. *Brain Imaging Behav.* doi: 10.1007/s11682-021-00452-5. [Epub ahead of print].

Vernooij, M. W. (2007). Incidental findings on brain MRI in the general population. *N. Engl. J. Med.* 357, 1821–1828. doi: 10.1056/NEJMoa070972

Vlak, M. H., Algra, A., Brandenburg, R., and Rinkel, G. J. (2011). Prevalence of unruptured intracranial aneurysms, with emphasis on sex, age, comorbidity, country, and time period: a systematic review and meta-analysis. *Lancet Neurol.* 10, 626–636. doi: 10.1016/S1474-4422(11)70109-0

Wang, L., Wu, L., Lin, X., Zhang, Y., Zhou, H., Du, X., et al. (2016). Altered brain functional networks in people with Internet gaming disorder: evidence from resting-state fMRI. *Psychiatry Res. Neuroimaging* 254, 156–163. doi: 10.1016/j.pscychresns.2016.07.001

Welmer, A.-K., von Arbin, M., Widén Holmqvist, L., and Sommerfeld, D. K. (2006). Spasticity and its association with functioning and health-related quality of life 18 months after stroke. *Cerebrovasc. Dis.* 21, 247–253. doi: 10.1159/000091222

Wong, G. K. C., Lam, S. W., Wong, A., Ngai, K., Mok, V., and Poon, W. S. (2016). "Early cognitive domain deficits in patients with aneurysmal subarachnoid hemorrhage correlate with functional status," in *Intracranial Pressure and Brain Monitoring XV Acta Neurochirurgica Supplement*, ed B. T. Ang (Cham: Springer International Publishing), 129–132. doi: 10.1007/978-3-319-22533-3_26

Zalesky, A., Fornito, A., Harding, I. H., Cocchi, L., Yücel, M., Pantelis, C., et al. (2010). Whole-brain anatomical networks: does the choice of nodes matter? *NeuroImage* 50, 970–983. doi: 10.1016/j.neuroimage.2009.12.027

Conflict of Interest: The authors declare that the research was conducted in the absence of any commercial or financial relationships that could be construed as a potential conflict of interest.

Publisher's Note: All claims expressed in this article are solely those of the authors and do not necessarily represent those of their affiliated organizations, or those of the publisher, the editors and the reviewers. Any product that may be evaluated in this article, or claim that may be made by its manufacturer, is not guaranteed or endorsed by the publisher.

Copyright © 2021 Zheng, Zhang, Wan and Zhao. This is an open-access article distributed under the terms of the Creative Commons Attribution License (CC BY). The use, distribution or reproduction in other forums is permitted, provided the original author(s) and the copyright owner(s) are credited and that the original publication in this journal is cited, in accordance with accepted academic practice. No use, distribution or reproduction is permitted which does not comply with these terms.

frontiers in Molecular Neuroscience

ORIGINAL RESEARCH
published: 15 October 2021
doi: 10.3389/fnmol.2021.747798

Transcriptomic and Network Meta-Analysis of Frontotemporal Dementias

*Virginie Bottero[1], Fahed Alrafati[1], Jose A. Santiago[2] and Judith A. Potashkin[1]**

[1] Center for Neurodegenerative Diseases and Therapeutics, Chicago Medical School, Discipline of Cellular and Molecular Pharmacology, Rosalind Franklin University of Medicine and Science, North Chicago, IL, United States, [2] NeuroHub Analytics LLC., Chicago, IL, United States

Frontotemporal lobar degeneration (FTLD), also known as frontotemporal dementia (FTD), results in a progressive decline in executive function, leading to behavioral changes, speech problems, and movement disorders. FTD is the second most common cause of young-onset dementia affecting approximately 50–60,000 Americans. FTD exists in familial and sporadic forms, with GRN progranulin and C9orf72 mutations being the most common causes. In this study, we compared the sporadic and familial transcriptome within the cerebellum, frontal cortex, hippocampus, and Brodmann's area 8 of patients with FTD to determine genes and pathways involved in the disease process. Most dysregulated genes expression occurred in the frontal cortex and Brodmann's area 8 for genetic and sporadic forms of FTD, respectively. A meta-analysis revealed 50 genes and 95 genes are dysregulated in at least three brain regions in patients with familial mutations and sporadic FTD patients, respectively. Familial FTD genes centered on the Wnt signaling pathway, whereas genes associated with the sporadic form of FTD centered on MAPK signaling. The results reveal the similarities and differences between sporadic and familial FTD. In addition, valproic acid and additional therapeutic agents may be beneficial in treating patients with FTD.

Keywords: frontotemporal lobars degeneration, frontotemporal dementia, neurodegeneration, Wnt signaling, MAPK signaling, valproic acid

OPEN ACCESS

Edited by:
Jiehui Jiang,
Shanghai University, China

Reviewed by:
Alexandre Henriques,
Neuro-Sys, France
Jack Harry Brelstaff,
University of Cambridge,
United Kingdom

****Correspondence:***
Judith A. Potashkin
judy.potashkin@rosalindfranklin.edu

Specialty section:
This article was submitted to Brain Disease Mechanisms, a section of the journal Frontiers in Molecular Neuroscience

Received: *26 July 2021*
Accepted: *28 September 2021*
Published: *15 October 2021*

Citation:
Bottero V, Alrafati F, Santiago JA and Potashkin JA (2021) Transcriptomic and Network Meta-Analysis of Frontotemporal Dementias. Front. Mol. Neurosci. 14:747798. doi: 10.3389/fnmol.2021.747798

INTRODUCTION

Frontotemporal Lobar Degeneration (FTLD), also known as frontotemporal dementia (FTD), is a spectrum of clinical syndromes characterized by the progressive neurodegeneration of the frontal and temporal lobes of the brain. Damage to these brain regions results in behavioral changes, deficits in language and executive functions (Bott et al., 2014; Bang et al., 2015; Coyle-Gilchrist et al., 2016; Olney et al., 2017). FTD is the third most common cause of dementia after Alzheimer's disease and dementia with Lewy bodies in individuals 65 years and younger, with a prevalence of 15–22/100,000 individuals (Coyle-Gilchrist et al., 2016).

FTD is a complex disorder with a highly clinical, genetic, and pathological heterogeneity. FTD has three clinical subtypes (Bott et al., 2014; Olney et al., 2017; Santiago et al., 2020). The behavioral

variant FTD (Bv-FTD) is the most prevalent, and patients have behavioral deficits and loss of social functioning (Bott et al., 2014). In addition, there are two pathological variants of FTD, one with tau positive inclusions (FTD-tau) and the more prevalent form that is tau and alpha-synuclein negative (FTD-U) (Chen-Plotkin et al., 2008; Prasad et al., 2019).

In the context of genetics, about 40% of FTD patients are familial, 15% of which have an autosomal dominant inheritance pattern. Mutations in over 20 genes have been reported in FTD patients. For instance, mutations in progranulin (GRN), microtubule-associated protein tau (MAPT), and chromosome 9 open reading frame 72 (C9ORF72) are the most common (Woollacott and Rohrer, 2016; Capozzo et al., 2017). Other mutations including fused in sarcoma gene (FUS), TAR-DNA binding protein (TARDBP), valosin-containing protein (VCP), charged multivesicular protein 2B (CHMP2B), TATA box binding protein (TBP), sequestosome 1 (SQSTM1), ubiquilin 2 (UBQLN2), and optineurin (OPTN) have been recognized in less than 5% of the cases (Greaves and Rohrer, 2019).

Despite the progress in defining clinical subtypes and identifying genetic factors, the molecular mechanisms underlying the pathogenesis of FTD remain poorly understood. Several transcriptomic studies have provided insights into some of the dysregulated molecular pathways in FTD. For example, transcriptomic and pathway analyses of the frontal cortex showed marked differences in biological pathways between FTD patients with GRN (+) and without GRN (–) progranulin mutations (Chen-Plotkin et al., 2008). Upregulated genes in FTD GRN (–) subjects associated with lipid metabolism and downregulated genes were involved in the MAPK signaling pathway. Furthermore, upregulated genes in FTD GRN (+) were associated with TGF beta signaling and cell communication, whereas downregulated genes were related to calcium signaling.

Transcriptomic and network biology approaches have been key in the identification of dysregulated pathways and potential therapeutic targets in neurodegenerative diseases (Santiago and Potashkin, 2014; Santiago et al., 2017). Previous work in network-based studies in FTD has unveiled novel disease mechanisms. For example, analysis of a weighted protein-protein interaction network in FTD identified DNA damage response and cell waste disposal as important mechanisms of disease (Ferrari et al., 2017). Similarly, gene co-expression network analysis revealed that FTD genes were enriched in DNA metabolism, transcriptional regulation, and DNA protection in FTD patients' frontal and temporal cortices (Ferrari et al., 2016).

In this study, we compared the transcriptomic profiles from different brain regions, including the cerebellum, frontal cortex, hippocampus, and Brodmann's area 8 from sporadic and familial FTD subjects to identify potential mechanisms of disease and therapeutic targets, particularly pathways that may shed light on the distinction between the familial and sporadic subtypes (Chen-Plotkin et al., 2008; Olney et al., 2017). We incorporated network, pathway, and transcription factor analyses as a means of identifying dysregulated genes in pathways within FTD as well as in the familial and sporadic subtypes.

MATERIALS AND METHODS

Database Mining, Curation, and Meta-Analysis

The NCBI GEO database[1] and ArrayExpress database[2] were searched on June 2020 for studies in which transcriptomic data was available from FTD patients. Three arrays containing samples from patients' brains (E-MTAB-6189, GSE13162 and E-MTAB-656) were identified. The microarrays were curated using the database BaseSpace Correlation Engine (BSCE, Illumina, Inc., San Diego, CA, United States). Unfortunately, the dataset E-MTAB-656 did not meet the quality standards required by the BSCE curation methods. The meta-analysis tool in BSCE used a normalized ranking approach, allowing the elimination of any potential biases introduced by the use of different array platforms or the sample size. Using BSCE for differential gene expression analysis and meta-analysis, negative values, if any, were replaced with the smallest positive number in the dataset. Genes whose mean normalized test and control intensities were both less than the 20th percentile of the combined normalized signal intensities were removed. The activity of the gene in each dataset and the number of datasets in which the gene is differentially expressed were used to determine the scoring and ranking of each gene. The analysis included only genes with an absolute fold-change of 1.2 or greater and a p-value of 0.05 or less. BSCE computes the overlapping p-values between different gene expression datasets using a "Running Fisher" algorithm. *Post hoc* analysis was not performed. Unfortunately, the demographic and clinical information about the study participants publicly available was limited. E-MTAB-6189 sample information only included the age and the post-mortem interval (PMI). The patient information from GSE13162 included the number of male and female patients. Age, sex, and PMI to autopsy were not significantly different between cases and controls. The controls used in GSE13162 were defined as neurologically normal controls and were sampled from the University of Pennsylvania Center for Neurodegenerative Disease Research Brain Bank. The FTD cases were reviewed by a board-certified neuropathologist. In general, the control samples used in these studies were defined as neurologically healthy. Information about drugs, BMI, and comorbidities were not available. The sample population is summarized in **Table 1**.

Pathway Enrichment Analysis

Entrez gene identifiers from the genes identified in the differential gene expression analysis and meta-analyses were imported into NetworkAnalyst for network and pathway analyses (Zhou et al., 2019). The Kyoto Encyclopedia of Genes and Genome (KEGG) pathway database was used as annotation source (Kanehisa and Goto, 2000). The pathways are ranked according to the number of hits and lowest p-value, with the two factors demonstrating a linear relationship. A p-value of less than 0.05 was considered significant. *Post hoc* analysis was not performed.

[1] https://www.ncbi.nlm.nih.gov/gds

[2] https://www.ebi.ac.uk/arrayexpress/

TABLE 1 | Sample population.

	Gender (Male/Female)	Median age (IQR)	PMI (IQR)
GSE13162			
Control	7/4	67 (54–75)	7 (5–14.5)
Familial (GRN + mutation)	3/4	71 (67–77)	6 (5–7)
Sporadic (GRN– mutation)	4/6	64 (53–72)	7.5 (3–11)
E-MTAB-6189			
Control	NA	66.5 (63–74)	5 (3.5–6.5)
Familial	NA	67.5 (58–80)	10 (5–12)
Sporadic	NA	73.5 (65–77)	7.5 (5–13)

IQR: Interquartile range (25th–75th percentile). PMI: Postmortem interval in hours. NA, Non-available.

Gene-Transcription Factors Interaction Analysis

Gene-transcription factors interactome was performed in NetworkAnalyst. Transcription factor and gene target data were derived from the Encyclopedia of DNA Elements (ENCODE) ChIP-seq data, ChIP Enrichment Analysis (ChEA), or JASPAR database (Lachmann et al., 2010; Wang et al., 2013; Fornes et al., 2020). ENCODE uses the BETA Minus Algorithm in which only peak intensity signal < 500 and the predicted regulatory potential score < 1 is used. ChEA transcription factor targets database inferred from integrating literature curated Chip-X data. JASPAR is an open-access database of curated, non-redundant transcription factor-binding profiles. A Venn diagram analysis was performed with the transcription factors identified with each database. Transcription factors were ranked according to network topology measurements, including degree and betweenness centrality.

Gene-miRNA Interaction Analysis

The gene-miRNA interactome was performed in NetworkAnalyst. The Gene-miRNA interactome was carried out from comprehensive experimentally validated miRNA-gene interaction data collected from TarBase v.8.0 and miRTarBase v.8.0 (Chou et al., 2016, 2018; Karagkouni et al., 2018). miRNAs were ranked according to network topology measurements such as degree and betweenness centrality. Venn diagram analysis was used to identify the shared and unique set of miRNAs between familial and sporadic FTD patients. Biological and functional analysis of miRNAs was performed using miRNet 2.0 (Chang et al., 2020). The pathways are ranked according to the number of hits and lowest *p*-value. A *p*-value of less than 0.05 was considered significant. *Post hoc* analysis was not performed. This network software is publicly available and can be accessed at https://www.mirnet.ca/miRNet/upload/MirUploadView.xhtml.

Gene-Chemical Analysis

Protein-chemical associated analysis was performed in NetworkAnalyst, which uses the literature curated gene-chemical database Comparative Toxicogenomics, a genomic resource available to the public that is derived from genes and proteins of toxicologic significance to humans (Mattingly et al., 2003). Chemicals were ranked according to network topology measurements, degree, and betweenness centrality.

RESULTS

Database Mining for Brain Transcriptomic Studies

The Array Express and NCBI GEO databases were searched to identify studies that contained expression data from postmortem brain tissue of FTD patients and age-matched controls. Two independent studies that met our inclusion criteria were identified. Transcriptomic data obtained included sporadic and familial FTD data from four brain regions (frontal cortex, cerebellum, hippocampus, and Brodmann's area 8). The description of the datasets analyzed in this study is presented in **Table 2**. The overall analysis strategy is shown in **Figure 1**.

Analysis of Differentially Expressed Genes in Familial and Sporadic Frontotemporal Dementia Individuals

To identify consensus among the different transcriptomic datasets from FTD patients, we performed a meta-analysis using BSCE (**Supplementary Table 1**). Meta-analysis of the four regions of familial or sporadic FTD microarrays was performed using only the set of dysregulated genes in the same direction with a fold-change of 1.2 or more (**Figure 2**). There were no shared genes between the four brain areas in the transcriptomic profiles from familial FTD subjects. Meta-analysis of the transcriptomic profiles from familial FTD identified 50 genes dysregulated in at least 3 out of 4 studies, including 9 downregulated genes and 41 upregulated genes (**Figure 3** and **Supplementary Table 2**).

TABLE 2 | Datasets used in the study.

Arrays	Platform	Conditions	Brain region	#of Patients (Familial | sporadic)	Gene features (Familial | sporadic)
GSE13162	Affymetrix human genome U133A 2.0 Array	FTD patients with/without progranulin (GRN) mutations (i.e., familial vs. sporadic)	Frontal cortex	10 | 6	2921 | 5835
			Cerebellum	6 | 4	2739 | 1018
			Hippocampus	8 | 5	795 | 1543
E-MTAB-6189	A-GEOD-22844 Affymetrix human clarion D assay	Familial and sporadic FTD with C9ORF72 repeat expansion	Brodmann area 8	10 | 10	635 | 4171

Likewise, a meta-analysis of sporadic FTD transcriptomic profiles identified 4 genes downregulated in the four brain areas: protocadherin 1 (PCDH1), mitogen-activated protein kinase 11 (MAPK11), ectonucleoside triphosphate diphosphohydrolase 4 (ENTPD4), and programmed cell death 5 (PDCD5). In addition, 91 genes were dysregulated in 3 out of the 4 brain areas, including 72 downregulated genes and 19 upregulated genes (**Figure 4** and **Supplementary Table 2**). Interestingly, 3 genes were shared between the familial and sporadic analysis: F-box and leucine-rich repeat protein 8 (FBXL8), versican (VCAN), and sarcospan (SSPN) (**Figures 3**, **4**).

Pathway Analysis of Familial and Sporadic Frontotemporal Dementia Genes

Biological and functional analysis of the familial and sporadic genes was performed using the KEGG database in NetworkAnalyst. Pathway analysis identified 11 and 13 dysregulated pathways in familial and sporadic FTD, respectively (**Figure 5**). All the pathways identified were unique to each FTD. Wnt signaling pathway was the most represented pathway in familial FTD with 3 genes associated (TBL1X, GPC4, and CREBBP). Sporadic FTD genes were predominantly associated with the MAPK signaling pathway. Seven sporadic FTD genes were linked to the MAPK signaling pathway (MAPK11, RASGRP1, CACNA1I, RPSKA4, TAOK2, and NTRK2).

Gene-Transcription Factors Interaction Analysis

To identify the main regulators of familial and sporadic FTD genes, transcription factor analysis was performed on NetworkAnalyst using three different databases (ENCODE, ChEA, and JASPAR). Venn diagram analysis revealed 13 shared transcription factors regulating the familial FTD genes (**Figure 6A** and **Supplementary Table 3**). Transcription factors CEBPB, GATA3, KLF4, and MYB were identified as unique master regulators of familial FTD genes. These transcription factors have been implicated in Alzheimer's disease (Wang et al., 2019; Ndoja et al., 2020). To the best of our knowledge, these transcription factors have not been investigated in FTD models. Likewise, 17 transcription factors were identified as regulating the sporadic FTD genes (**Figure 6B** and **Supplementary Table 3**). In addition, 9 transcription factors were shared between familial and sporadic FTD datasets (**Figure 6C**). Interestingly, sporadic FTD genes were regulated by 8 unique transcription factors, including CTCF, IRF1, MEF2A, REST, SREBF1, SREBF2, STAT3, and ZFX. Among these factors, CTCF, MEF2A, and STAT3 have been associated with Alzheimer's, Huntington's, and Parkinson's diseases (Gonzalez et al., 2007; De Souza et al., 2016; Wu et al., 2017). Transcription factor REST has been associated with the preservation of cognition in Alzheimer's disease, dementia with Lewy bodies, and FTD (Lu et al., 2014).

Gene-miRNA Interaction Analysis

To further study the regulation of the FTD genes' expression, a gene-miRNA interaction network analysis was performed in NetworkAnalyst using 2 different databases (TarBase v.8.0. and miRtarBase v.8.0.). Venn diagram analysis showed that 330 and 338 miRNAs were shared between the databases that potentially regulate the familial and sporadic FTD genes, respectively (**Figure 7** and **Supplementary Table 4**). In addition, 199 miRNAs were shared between the familial and sporadic FTD analyses (**Supplementary Table 4**).

To investigate the functional role of miRNAs in familial and sporadic FTD, we performed a pathway analysis using miRNet 2.0, a web-based platform for miRNAs functional analysis (Chang et al., 2020). Functional analysis of the top miRNAs regulating familial FTD genes associated predominantly with the immune system, angiogenesis, virus replication, and aging whereas miRNAs regulating sporadic FTD genes were enriched in pathways related to cell cycle, cell division, virus replication, cell death, hematopoiesis, T cell differentiation, and cell proliferation (**Supplementary Table 5**).

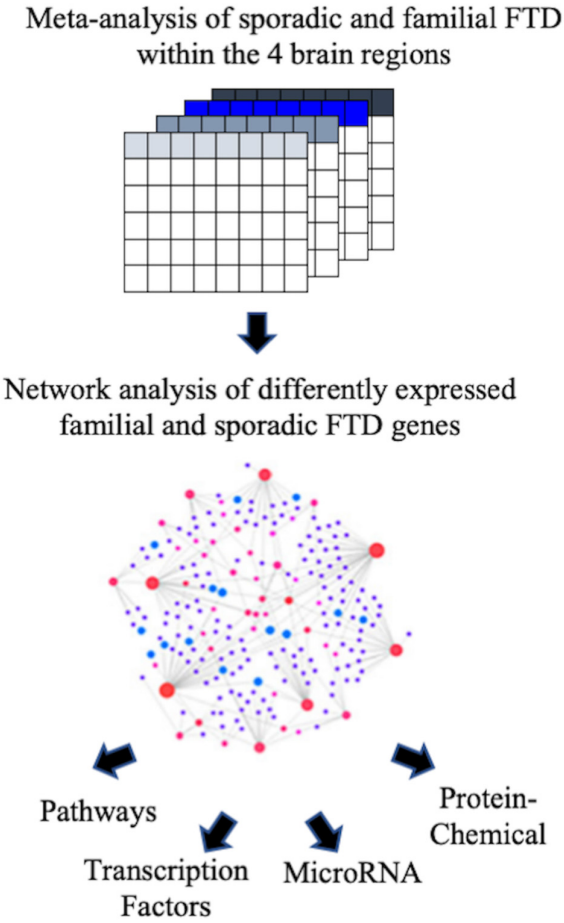

FIGURE 1 | Flowchart of the study. The ArrayExpress and NCBI GEO databases were searched to identify studies that contained expression data from postmortem brain tissue of FTD patients. Microarray data from familial and sporadic FTD patients were curated, and meta-analysis was performed using the BaseSpace Correlation Engine (BSCE, Illumina, Inc., San Diego, CA, United States). The genes were then analyzed for functional pathways, transcription factors, miRNA, and chemical associations.

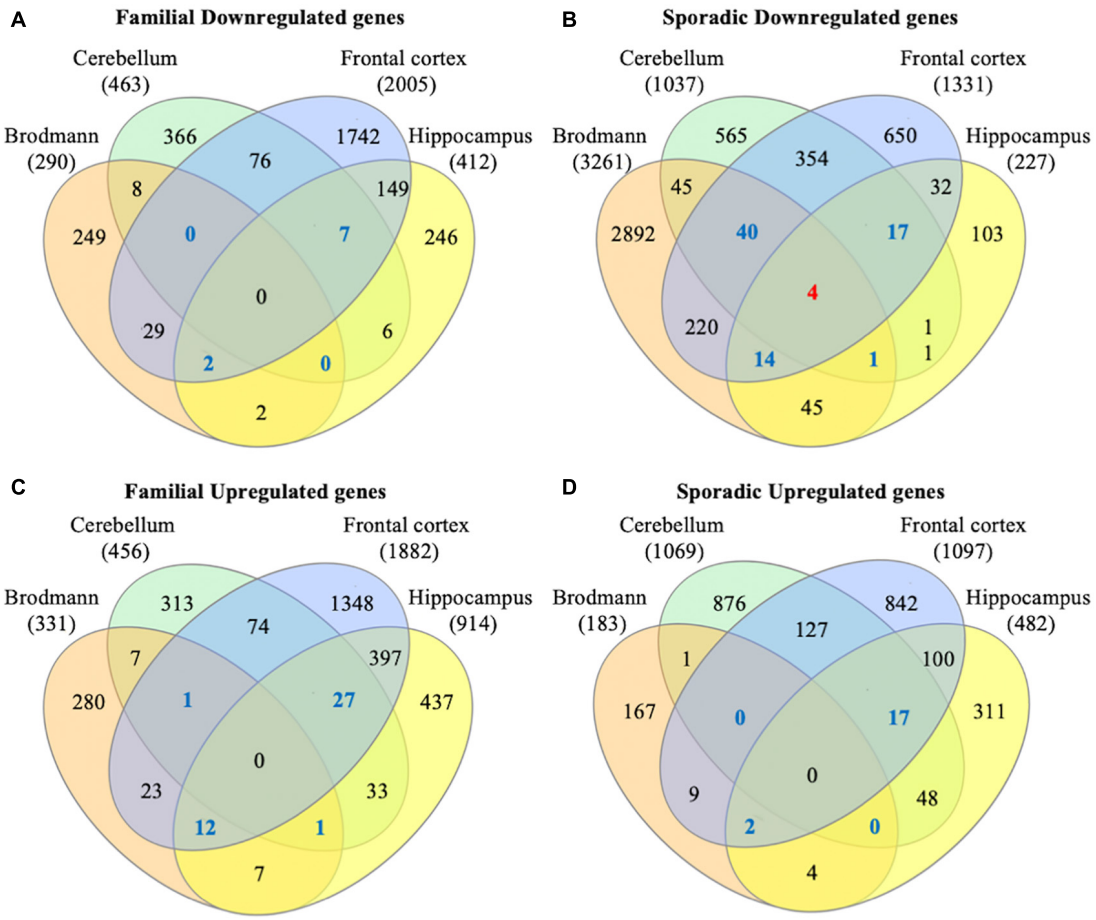

FIGURE 2 | Venn diagram from FTD genes. Differentially expressed genes from familial and sporadic FTD patients were downloaded from curated databases. Venn diagram analysis showed that 50 genes were dysregulated in at least 3 out of the 4 arrays analyzed for familial FTD **(A,B)**, whereas 95 genes were dysregulated in at least 3 out of the 4 arrays for sporadic FTD **(C,D)**. Genes dysregulated in all 4 brain areas are shown in red, and those dysregulated in 3 out of 4 brain areas are shown in blue.

Protein-Chemical Interaction Analysis

A protein–chemical interaction network analysis revealed drugs potentially helpful in treating familial and sporadic FTD. 370 and 504 chemicals were identified from familial and sporadic genes, respectively. The top 10 drugs associated with each FTD were identified in **Figure 8**. 223 chemicals were shared between the familial and sporadic FTD analyses (**Supplementary Table 6**).

DISCUSSION

Meta-Analysis of Familial and Sporadic Frontotemporal Dementia Microarrays

A meta-analysis of the 4 brain regions of familial FTD microarrays identified 50 genes, 41 genes downregulated and 9 upregulated, in 3 out of the 4 studies. Annexin 6 (ANXA6) and adipocyte enhancer binding protein 1 (AEBP1) were the most significantly downregulated and upregulated genes, respectively, in familial FTD subjects compared to non-demented controls. Similarly, analysis of sporadic FTD identified 4 genes downregulated in the four brain areas: PCDH1, MAPK11, ENTPD4, and PDCD5. Although these genes have not been directly implicated in FTD, some have been associated with neurodegeneration. For example, ANXA6 interacts with tau and contributes to tau axonal localization (Gauthier-Kemper et al., 2018). AEBP1 is a transcriptional repressor involved in adipogenesis, macrophage cholesterol homeostasis, and activation of the NFKB pathway (Majdalawieh et al., 2020). Further, AEBP1 is associated with Braak staging and the degree of amyloid deposition, suggesting it is a marker of disease progression in Alzheimer's disease (AD) (Shijo et al., 2018; Piras et al., 2019).

Interestingly, 3 genes were shared between the familial and sporadic FTD subjects, including FBXL8, VCAN, and SSPN. Genetic variants in VCAN are associated with cerebrovascular disease and dementia (Rutten-Jacobs et al., 2018). In addition, VCAN expression is dysregulated in ALS animal models (Mizuno et al., 2008; Forostyak et al., 2014). SSPN is differentially expressed in the blood of Alzheimer's disease

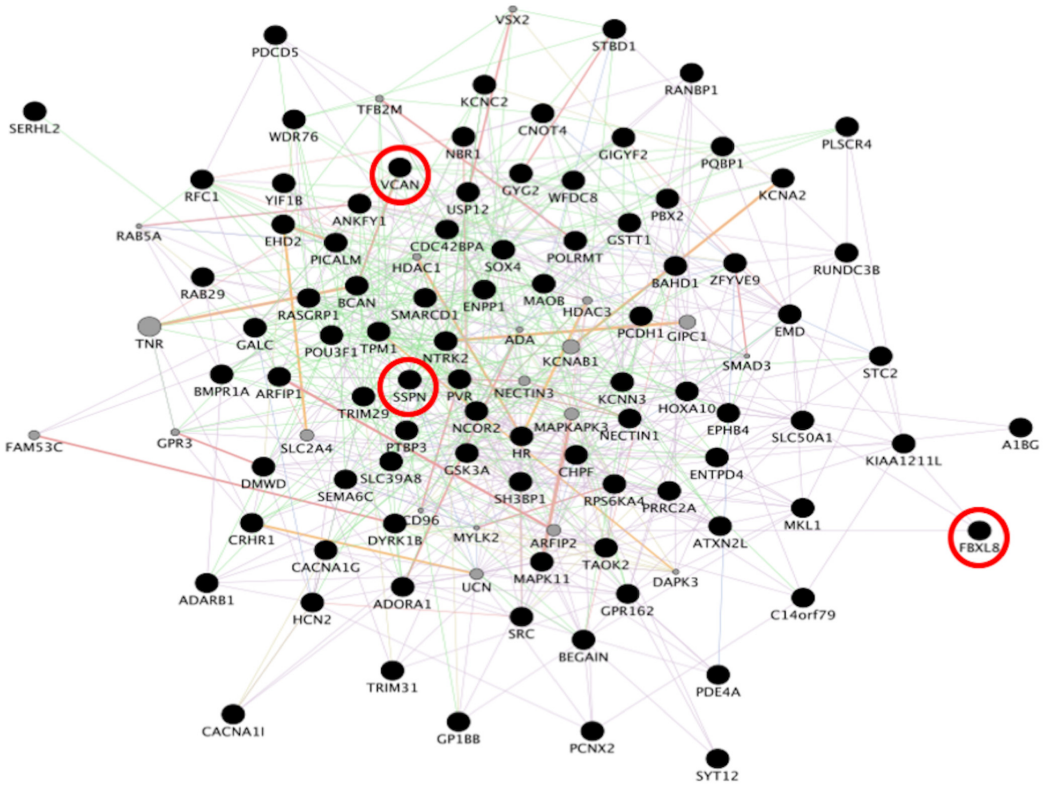

FIGURE 3 | Network analysis from familial FTD genes. Network analysis of the 50 genes dysregulated in sporadic FTD was performed using GeneMANIA in Cytoscape v3.8.0. Input genes are shown in black circles. Purple, blue, and pink lines represent co-expression, co-localization, and physical interactions, respectively. FBXL8, VCAN, and SSPN were dysregulated in both familial and sporadic FTD.

patients (Leandro et al., 2018). The involvement of these genes, however, in FTD is unknown and warrants further investigation.

Biological and Functional Analysis of Familial and Sporadic Frontotemporal Dementia Genes

Biological and functional analysis of dysregulated genes in familial FTD identified several pathways, including WNT signaling, adherens junctions, GABAergic, HIF-1 signaling, glutamatergic synapse, spliceosome, and insulin signaling as the most overrepresented pathways. Familial FTD genes centered on the WNT signaling pathway. This finding reinforces previous investigations reporting a key role of WNT signaling in FTD. For instance, progranulin deficiency compromised neuronal cell survival by targeting WNT signaling *in vitro* and *in vivo* models of FTD (Rosen et al., 2011). Furthermore, the same study reported that upregulation of the WNT receptor Fzd2 promoted neuronal survival *in vitro* (Rosen et al., 2011). Collectively, these findings suggest that targeting WNT signaling is a potential therapeutic route for familial FTD.

Pathway analysis of sporadic FTD genes identified several pathways, including MAPK signaling, platelet activation, starch and sucrose metabolism, dopaminergic synapse, atherosclerosis, and VEGF signaling. Interestingly, sporadic FTD genes centered on MAPK signaling, the most overrepresented pathway. This is not surprising since MAPK signaling has been implicated in several neurodegenerative diseases, including FTD (Chen-Plotkin et al., 2008; Ahmed et al., 2020; Santiago et al., 2020). Of note, dysregulation of genes involved in the MAPK signaling has been reported in FTD subjects with progranulin mutations (Chen-Plotkin et al., 2008). In addition, genetic variants in VEGF conferred susceptibility to sporadic FTD in an Italian population (Borroni et al., 2008). However, there is no evidence of platelet activation, starch and sucrose metabolism, and atherosclerosis in FTD.

Although the association between the WNT and MAPK signaling pathways in familial and sporadic FTD, respectively, could be potentially interesting in the development of personalized treatments, these pathways are also involved in other neurodegenerative diseases. For example, these pathways have been implicated in the pathogenesis of amyotrophic lateral sclerosis (ALS), a fatal neurodegenerative disease that shares a clinical continuum and overlapping genetic factors with FTD. The WNT/β-catenin signaling pathway is responsible for the differentiation of neural stem cells into neurons as well as synaptic stability and plasticity (Jiang et al., 2021). Upregulation of receptors, co-receptors, and modulators of the WNT/β-catenin signaling pathway has been reported in several transgenic animal models and human spinal cord tissues from ALS patients

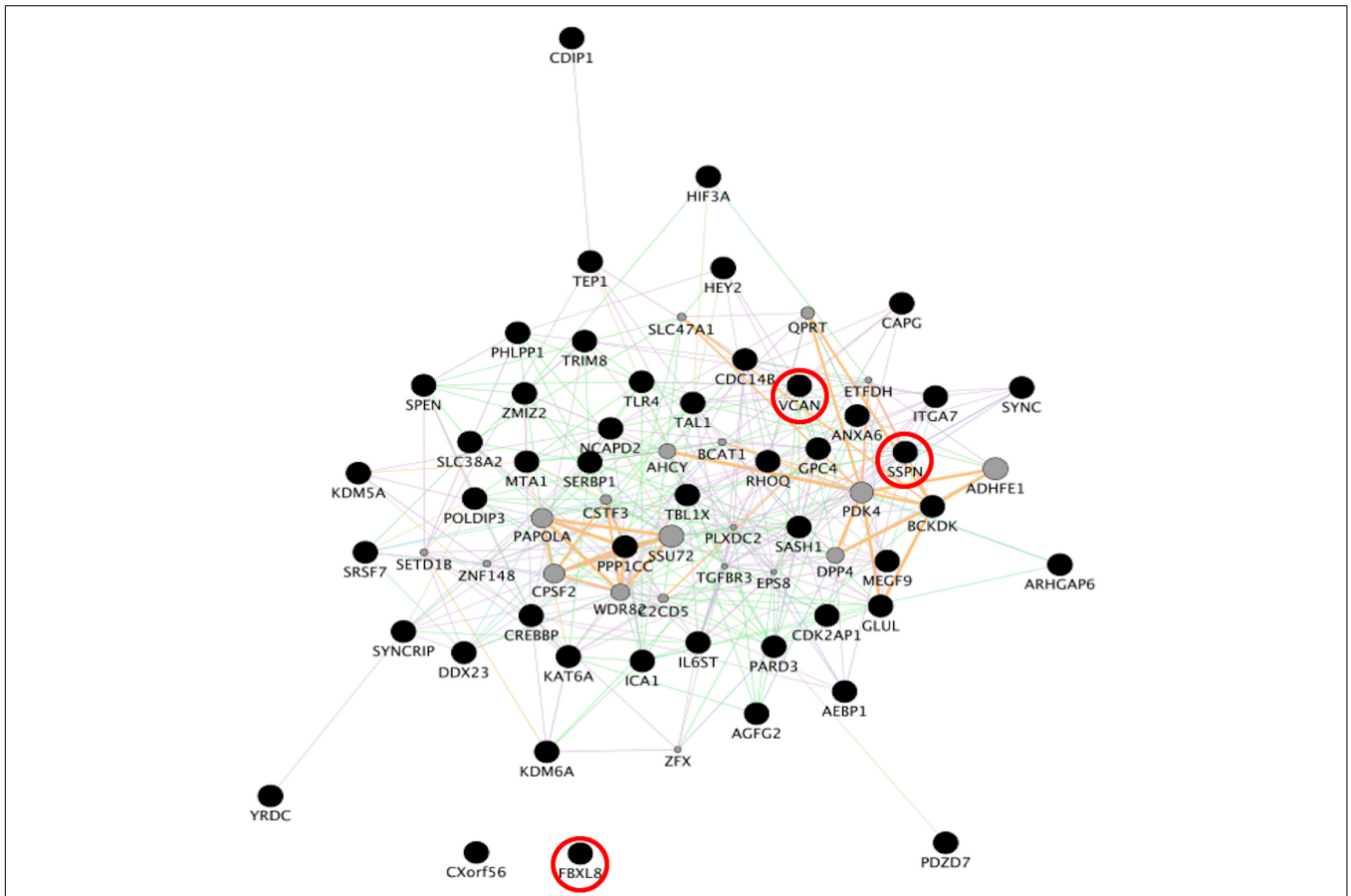

FIGURE 4 | Network analysis from sporadic FTD genes. Network analysis of the set of 96 genes dysregulated in sporadic FTD was performed using GeneMANIA in Cytoscape v3.8.0. Input genes are shown in black circles. Purple, blue, and pink lines represent co-expression, co-localization, and physical interactions, respectively. FBXL8, VCAN, and SSPN were dysregulated in both familial and sporadic FTD.

(Yao et al., 1988; Gonzalez-Fernandez et al., 2019; Jiang et al., 2021). Most of the altered expression of WNT/β-catenin pathway components occur in astrocytes and motor neurons in ALS models (Yao et al., 1988). Interestingly, it is reported that the main drug to treat ALS patients, Riluzole, enhanced WNT/β-catenin signaling in neuronal cells (Biechele et al., 2010). Thus, targeting components of the WNT/β-catenin signaling pathway may be a possible therapeutic route for ALS and FTD. Similarly, dysregulation of MAPK signaling has been associated with ALS. MAPK members are the serine and threonine kinases that play a pivotal role in cellular proliferation, differentiation, apoptosis, and survival (Sahana and Zhang, 2021). Aggregates of abnormally phosphorylated MAPK components and TDP-43 have been found in motor neurons and spinal cord cells of ALS patients under stress conditions (Ayala et al., 2011). This aberrant hyperphosphorylation of MAPK members is associated with several pathophysiological defects involved in ALS including oxidative stress, neuroinflammation, and axonal transport disruption (Ayala et al., 2011). Several MAPK inhibitors have shown promise in various cellular and animal models of ALS and one inhibitor is currently being tested in clinical trials (Sahana and Zhang, 2021). The pathway convergence between ALS and FTD suggests that MAPK inhibitors might represent a potential therapeutic option for FTD patients.

Transcription Factor Analysis

Transcription factor analysis revealed differences in the transcriptional regulation of familial and sporadic FTD genes. Analysis of familial and sporadic FTD genes identified 13 and 17 transcription factors, respectively. Four transcription factors, including CEBPB, GATA3, KLF4, and MYB were identified as unique master regulators of familial FTD genes. Among these transcription factors, the CCAAT enhancer-binding protein beta (CEBPB) and krupple like factor 4 (KLF4) have been documented previously in neurodegenerative diseases. For example, CEBPB regulates pro-inflammatory factors in microglia and is upregulated in AD (Wang et al., 2019; Ndoja et al., 2020).

Furthermore, CEBPB is also increased in the frontal cortex of HIV neurocognitive disorder patients and plays a role in regulating inflammation, metabolism, and autophagy in astroglia (Canchi et al., 2020). Although CEBPB has not been reported in FTD *per se*, the interplay between microglia and neuroinflammation is a central process in all neurodegenerative diseases. Likewise, KLF4 is involved in the microglial release

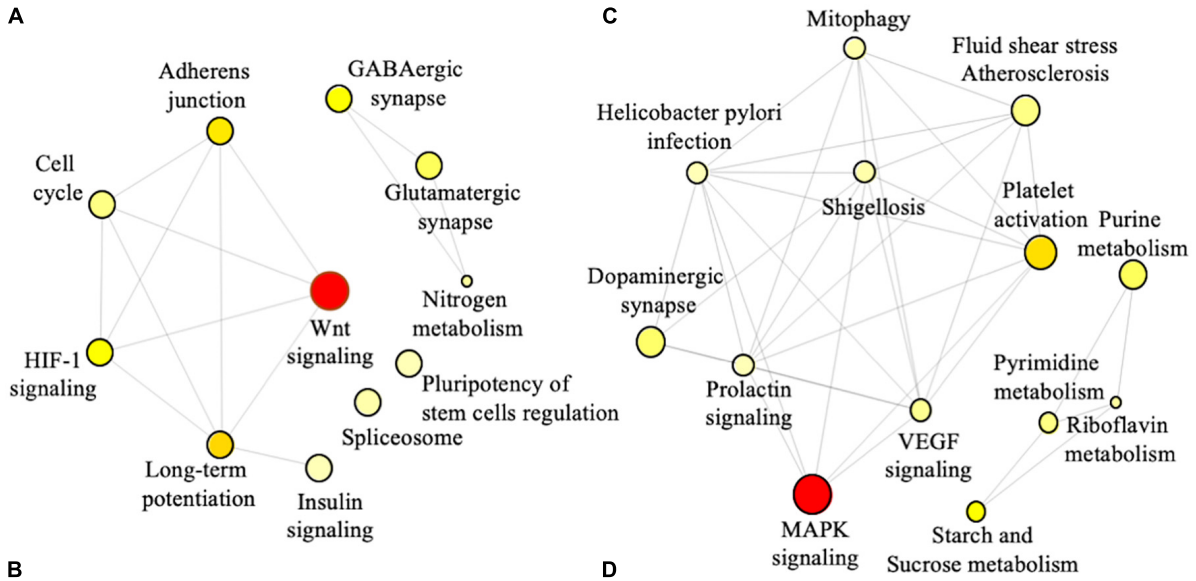

B

Name	Hits	Pval
Wnt signaling pathway	3/158	0.007
Long-term potentiation	2/67	0.013
Adherens junction	2/72	0.015
GABAergic synapse	2/89	0.021
HIF-1 signaling pathway	2/100	0.027
Glutamatergic synapse	2/114	0.034
Cell cycle	2/124	0.040
Nitrogen metabolism	1/17	0.043
Spliceosome	2/134	0.046
Insulin signaling pathway	2/137	0.048
Signaling pathways regulating pluripotency of stem cells	2/139	0.049

D

Name	Hits	Pval
MAPK signaling pathway	7/295	0.0005
Platelet activation	4/124	0.003
Starch and sucrose metabolism	2/36	0.014
Purine metabolism	3/130	0.027
Dopaminergic synapse	3/131	0.028
Fluid shear stress and atherosclerosis	3/139	0.032
Pyrimidine metabolism	2/57	0.033
VEGF signaling pathway	2/59	0.035
Riboflavin metabolism	1/8	0.040
Mitophagy - animal	2/65	0.042
Shigellosis	2/65	0.042
Epithelial cell signaling in Helicobacter pylori infection	2/68	0.046
Prolactin signaling pathway	2/70	0.048

FIGURE 5 | Pathway analysis. Genes identified in the meta-analysis from familial and sporadic FTD subjects were imported into NetworkAnalyst for pathway analysis **(A)** Network analysis of dysregulated pathways in familial FTD subjects. **(B)** Dysregulated pathways in familial FTD subjects. **(C)** Network analysis of dysregulated pathways in sporadic FTD subjects. **(D)** Dysregulated pathways in sporadic FTD subjects. The pathways are ranked according to the number of hits and lowest *p*-value, with the two factors demonstrating a linear relationship.

of pro-inflammatory factors. Overexpression of KLF4 promoted the peptide Aβ42 induced neuroinflammation and neurotoxicity in the brains of transgenic AD model mice (Li et al., 2017). The involvement of these transcription factors in FTD warrants further investigations.

Transcription factor analysis identified 8 unique master regulators of sporadic FTD genes, including CTCF, IRF1, MEF2A, REST, SREBF1, SREBF2, STAT3, and ZFX. Several of these transcription factors have been implicated in neurodegenerative diseases. For instance, CTCF may play a role in regulating Huntington's (HTT) promoter function in Huntington's disease (De Souza et al., 2016). Moreover, the deletion of interferon regulatory factor 1 (IRF1) resulted in cognitive impairment in mice (Mogi et al., 2018). The myocyte enhancer factor 2A (MEF2A) promoted neuronal cell apoptosis *in vitro* and *in vivo* experimental models of Parkinson's disease

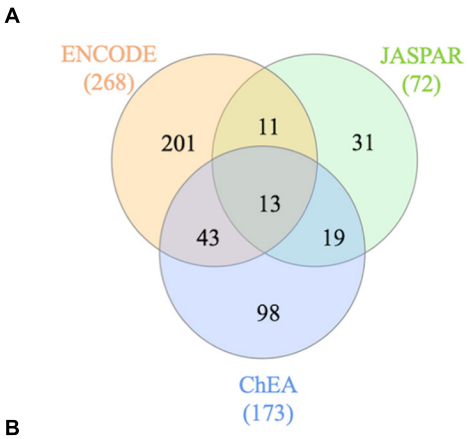

C

Familial FTD	Sporadic FTD
CEBPB	CREB1
CREB1	CTCF
EGR1	EGR1
ELK1	ELK1
GATA2	GATA2
GATA3	IRF1
JUN	JUN
KLF4	MEF2A
MYB	PPARG
PPARG	RELA
RELA	REST
STAT1	SREBF1
YY1	SREBF2
	STAT1
	STAT3
	YY1
	ZFX

FIGURE 6 | Transcription factors regulating FTD genes. **(A)** Transcription factor analysis from the familial FTD genes. **(B)** Transcription factor analysis from the sporadic FTD genes. Transcription factors and gene target data were derived from the ENCODE, ChEA, and JASPAR databases. Shared transcription factors between the 3 databases are shown in **(C)**. The transcription factors shared between familial and sporadic FTD are shown in red, and those unique to the specific FTD are shown in black.

and some of its genetic variants associated with an increased risk of late-onset AD (Gonzalez et al., 2007; Wu et al., 2017). In addition, gene network analysis showed that Amyloid precursor protein (APP) is co-regulated by MEF2A (Wang et al., 2010). The repressor element 1 silencing transcription factor (REST) regulates a network of genes that mediates cell death and stress resistance in AD. Dysregulation of REST has been documented in AD, FTD, and dementia with Lewy bodies, and elevated levels of REST are associated with the preservation of cognition (Lu et al., 2014). Genetic variation in the sterol regulatory element-binding transcription factor 1 (SREBF1), known to play a role in lipid and cholesterol metabolism, is associated with increased susceptibility to dementia and AD (Spell et al., 2004; Carter, 2007; Reynolds et al., 2010). The signal transducer and activator of transcription 3 (STAT3), a major inducer of genes involved in apoptosis, cell growth, and inflammation, has been extensively implicated in neurodegenerative diseases. For example, STAT3 modulates glial activation and Aβ deposition leading to cognitive impairment in AD transgenic models (Toral-Rios et al., 2020). Moreover, inhibition of STAT3 rescued deficits in learning and memory in 5xFAD mice, suggesting it may be a potential therapeutic target for AD (Choi et al., 2020).

miRNAs Regulating Familial and Sporadic Frontotemporal Dementia Genes

To investigate further the differences in regulation between familial and sporadic FTD genes, we performed a miRNA analysis. Functional analysis revealed that miRNAs regulating familial FTD genes were involved in the regulation of the immune system, angiogenesis, virus replication, and aging. In contrast, miRNAs regulating sporadic FTD genes were enriched in pathways related to cell cycle, cell division, virus replication, cell death, hematopoiesis, T cell differentiation, and cell proliferation. These findings, along with the pathways identified at the mRNA level, suggest that different regulatory mechanisms may be involved in the pathogenesis of familial and sporadic FTD patients.

Chemical-Gene Interaction Analysis

Protein chemical network analysis identified several potential therapeutic agents for FTD. Valproic acid was identified as the highest-ranked chemical interacting with both sporadic and FTD genes. Indeed, some studies indicate that valproic acid is involved in WNT/β-catenin and MAPK signaling, pathways

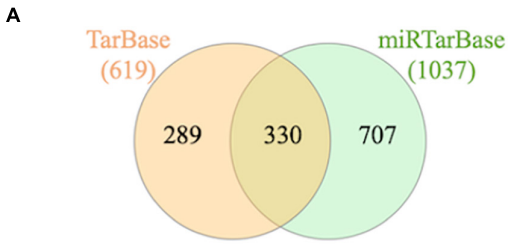

B

	TarBase		MirTarBase	
	Degree	Betweenness	Degree	Betweenness
mir-16-5p	23	4733	8	14142
let-7b-5p	14	1690	6	4352
mir-106b-5p	14	1663	6	3115
mir-93-5p	13	1985.07	5	1814
mir-335-5p	13	1450	12	20341
mir-181a-5p	12	2302	5	8522
mir-17-5p	12	1081	5	2592
mir-15a-5p	11	1134	5	4593
mir-320a	10	1401	7	12069

D

	TarBase		MirTarBase	
	Degree	Betweenness	Degree	Betweenness
mir-1-3p	44	9347	7	4454
mir-124-3p	39	7472	17	48777
mir-16-5p	34	6589	7	7330
let-7b-5p	32	7130	8	11421
mir-34a-5p	28	4553	6	3862
mir-155-5p	27	3819	5	3040
mir-335-5p	18	1294	17	51044
mir-17-5p	17	2346	8	6138
let-7c-5p	17	1837	5	1834
mir-98-5p	17	1781	6	6644
mir-20a-5p	16	1636	7	10645
mir-93-5p	14	1486	9	18607
mir-19b-3p	14	1017	5	2955
mir-106b-5p	13	1203	6	5160
mir-15b-5p	12	526	5	5087
mir-218-5p	10	741	7	6378
mir-92a-3p	10	458	10	9679

FIGURE 7 | Venn diagram analysis of miRNAs. The FTD genes were uploaded to https://www.networkanalyst.ca/NetworkAnalyst/faces/home.xhtml. Gene-microRNA interactome was performed using TarBase v. 8.0 and miRTarBase 8.0. The top miRNAs were determined using a miRTarBase cut-off degree of 5 and TarBase cut-off degree of 10. **(A)** Venn diagram analysis of miRNAs regulating familial FTD. **(B)** Network topology measurements for the top miRNAs regulating familial FTD genes. **(C)** Venn diagram analysis of miRNAs regulating sporadic FTD genes. The miRNAs shared between familial and sporadic FTD are shown in red. **(D)** Network topology measurements for the top miRNAs regulating sporadic FTD genes.

identified in this study as central in familial and sporadic FTD, respectively. For example, valproic acid stimulated neurogenesis in the adult hippocampus of transgenic AD mice through the activation of the WNT/β-catenin signaling pathway (Zeng et al., 2019). In addition, valproic acid promoted the differentiation of spiral ganglion neural stem cells and neurite outgrowth *via* the activation of the WNT/β-catenin signaling pathway (Moon et al., 2018). Furthermore, valproic acid elicited neuroprotective effects in the 1-methyl-4-phenylpyridinium (MPP^+) model of PD in primary dopamine neurons via the activation of the MAPK pathway (Zhang et al., 2017). Further molecular studies in animal and cellular models of FTD will be key to understand the potential therapeutic value of valproic acid in FTD-associated neurodegeneration.

Interestingly, several recent studies have indicated that valproic acid may be a potential drug for neurodegenerative diseases. For instance, valproic acid treatment reduced the expression of pro-inflammatory cytokines and NF-κB signaling in PC12 cells treated with amyloid protein fragments suggesting that it may be neuroprotective via the attenuation of the inflammatory pathways (Zhao et al., 2018). Similarly, valproic acid treatment selectively reduced Aβ42 *in vitro* using 7PA2 cells transfected with human APP (Williams and Bate, 2018). Furthermore, valproic acid restored the physiological function of synapsin I, a synaptic protein important for neurotransmitter release in rat hippocampal neurons exposed to neurotoxic Aβ42 oligomers (Marsh et al., 2017). Recently, a bioinformatic analysis identified valproic acid as a potential drug for dementia (Potashkin et al., 2020). In the context of FTD, valproic acid improved neuropsychiatric symptoms including agitation, without exacerbating Parkinsonism in FTD subjects (Chow and Mendez, 2002).

Nevertheless, some studies have reported negative findings of the use of valproic acid for dementia. For example, an epidemiological study comprising 5,158 patients with bipolar disorder showed that valproic acid treatment increased the risk of dementia by 73–95% (Tsai et al., 2016). In addition, the use of valproic acid is associated with an increased risk of mortality in dementia patients (Kales et al., 2012). Therefore, more research studies into the potential mechanisms of valproic acid are needed to confirm its utility for dementia.

Limitations and Future Research

Several caveats should be kept in mind when interpreting the results from this study. Although the curation methods of BSCE are rigorous, differences in microarray platforms and sample

A

Drug	Degree	Betweenness
Valproic Acid	40	7487
Copper Sulfate	29	4580
Aflatoxin B1	29	3212
4-(5-benzo(1,3)dioxol-5-yl-4-pyridin-2-yl-1H-imidazol-2-yl)benzamide	23	3333
Cyclosporine	23	1720
(6-(4-(2-piperidin-1-ylethoxy)phenyl))-3-pyridin-4-ylpyrazolo(1,5-a)pyrimidine	22	3127
trichostatin A	19	2077
Antirheumatic Agents	19	1987
Benzo(a)pyrene	19	1302
cobaltous chloride	18	2493

B

Drug	Degree	Betweenness
Valproic Acid	44	12416
Aflatoxin B1	36	8214
(6-(4-(2-piperidin-1-ylethoxy)phenyl))-3-pyridin-4-ylpyrazolo(1,5-a)pyrimidine	35	8359
4-(5-benzo(1,3)dioxol-5-yl-4-pyridin-2-yl-1H-imidazol-2-yl)benzamide	35	8050
Cyclosporine	30	4227
Estradiol	29	7674
(+)-JQ1 compound	26	4808
Antirheumatic Agents	25	4334
Silicon Dioxide	25	3434
Copper Sulfate	25	2962

FIGURE 8 | Top 10 Drugs associated with the FTD genes. **(A)** Drug analysis from the familial FTD genes. **(B)** Drug analysis from the sporadic FTD genes. The FTD genes were uploaded to https://www.networkanalyst.ca/NetworkAnalyst/faces/home. A Chemical-gene interactome was performed. Most of the chemicals were shared between familial and sporadic FTD analyses.

collection may bias the results. In addition, the demographic and clinical information about the study participants publicly available was limited. For example, information about drugs, comorbidities, and BMI was not available. Control samples were defined as neurologically healthy, but information about other diseases was not available. These confounding variables might have impacted the results of this study. In addition, FTD is a highly heterogeneous disorder that shares many genetic factors and pathological features with ALS. The results presented in this study are limited to sporadic and FTD with progranulin mutations or C9ORF72 repeat expansion. Therefore, future studies investigating the pathways dysregulated in FTD patients with other common mutations including MAPT, FUS, CHMP2B mutation and will be important to understand the underlying mechanisms in different genetic forms of FTD.

Finally, even though bioinformatic studies, in general, can lead to the identification of novel mechanisms of disease and therapeutics, findings should be confirmed in preclinical cellular and animal models.

CONCLUSION

This study investigated the transcriptomic profiles from different brain regions from FTD subjects to identify pathways that may shed light on the distinction between the familial and sporadic FTD subtypes. We determined that most dysregulated gene expression occurred in the frontal cortex and Brodmann's area 8 for genetic and sporadic forms of FTD, respectively. There were notable differences in the dysregulated pathways between familial and sporadic FTD subjects. We found that familial FTD genes were associated predominantly with the Wnt signaling pathway, whereas sporadic FTD genes were involved in the MAPK signaling. Top miRNAs regulating familial FTD genes associated predominantly with the immune system, angiogenesis, virus replication, and aging, whereas those regulating sporadic FTD genes were related to cell cycle, cell division, virus replication, cell death, hematopoiesis, T cell differentiation, and cell proliferation. In addition, valproic acid was identified as a potential treatment for FTD patients. Nonetheless, valproic acid has been suggested as a treatment for other neurodegenerative diseases, including AD and amyotrophic lateral sclerosis. Collectively, these findings suggest that different mechanisms may drive the disease process in familial and sporadic FTD patients. Further research on the transcriptional regulation and the molecular pathways involved in familial and sporadic FTD forms is warranted.

DATA AVAILABILITY STATEMENT

The original contributions presented in the study are included in the article/**Supplementary Material**, further inquiries can be directed to the corresponding author/s.

AUTHOR CONTRIBUTIONS

VB, FA, JS, and JP conceived and contributed to designs of the methods used in this study, analyzed the data, and wrote the manuscript. All authors have read and approved the final version of the manuscript.

FUNDING

This study was funded by the National Institute on Aging (NIA) grant no. R01AG062176 to JP.

SUPPLEMENTARY MATERIAL

The Supplementary Material for this article can be found online at: https://www.frontiersin.org/articles/10.3389/fnmol.2021.747798/full#supplementary-material

Supplementary Table 1 | BSCE meta-analysis.

Supplementary Table 2 | Pathway analysis.

Supplementary Table 3 | Transcription factors analysis.

Supplementary Table 4 | miRNA analysis.

Supplementary Table 5 | miRNA pathway analysis.

Supplementary Table 6 | Chemical analysis.

REFERENCES

Ahmed, T., Zulfiqar, A., Arguelles, S., Rasekhian, M., Nabavi, S. F., Silva, A. S., et al. (2020). Map kinase signaling as therapeutic target for neurodegeneration. *Pharmacol. Res.* 160:105090. doi: 10.1016/j.phrs.2020.105090

Ayala, V., Granado-Serrano, A. B., Cacabelos, D., Naudi, A., Ilieva, E. V., Boada, J., et al. (2011). Cell stress induces TDP-43 pathological changes associated with ERK1/2 dysfunction: implications in ALS. *Acta Neuropathol.* 122, 259–270. doi: 10.1007/s00401-011-0850-y

Bang, J., Spina, S., and Miller, B. L. (2015). Frontotemporal dementia. *Lancet* 386, 1672–1682. doi: 10.1016/S0140-6736(15)00461-4

Biechele, T. L., Camp, N. D., Fass, D. M., Kulikauskas, R. M., Robin, N. C., White, B. D., et al. (2010). Chemical-genetic screen identifies riluzole as an enhancer of Wnt/beta-catenin signaling in melanoma. *Chem. Biol.* 17, 1177–1182. doi: 10.1016/j.chembiol.2010.08.012

Borroni, B., Ghezzi, S., Agosti, C., Archetti, S., Fenoglio, C., Galimberti, D., et al. (2008). Preliminary evidence that VEGF genetic variability confers susceptibility to frontotemporal lobar degeneration. *Rejuvenation Res.* 11, 773–780. doi: 10.1089/rej.2008.0711

Bott, N. T., Radke, A., Stephens, M. L., and Kramer, J. H. (2014). Frontotemporal dementia: diagnosis, deficits and management. *Neurodegener. Dis. Manag.* 4, 439–454. doi: 10.2217/nmt.14.34

Canchi, S., Swinton, M. K., Rissman, R. A., and Fields, J. A. (2020). Transcriptomic analysis of brain tissues identifies a role for CCAAT enhancer binding protein beta in HIV-associated neurocognitive disorder. *J. Neuroinflam.* 17:112. doi: 10.1186/s12974-020-01781-w

Capozzo, R., Sassi, C., Hammer, M. B., Arcuti, S., Zecca, C., Barulli, M. R., et al. (2017). Clinical and genetic analyses of familial and sporadic frontotemporal dementia patients in Southern Italy. *Alzheimers Dement* 13, 858–869. doi: 10.1016/j.jalz.2017.01.011

Carter, C. J. (2007). Convergence of genes implicated in Alzheimer's disease on the cerebral cholesterol shuttle: APP, cholesterol, lipoproteins, and atherosclerosis. *Neurochem. Int.* 50, 12–38. doi: 10.1016/j.neuint.2006.07.007

Chang, L., Zhou, G., Soufan, O., and Xia, J. (2020). miRNet 2.0: network-based visual analytics for miRNA functional analysis and systems biology. *Nucleic Acids Res.* 48, W244–W251. doi: 10.1093/nar/gkaa467

Chen-Plotkin, A. S., Geser, F., Plotkin, J. B., Clark, C. M., Kwong, L. K., Yuan, W., et al. (2008). Variations in the progranulin gene affect global gene expression in frontotemporal lobar degeneration. *Hum. Mol. Genet.* 17, 1349–1362. doi: 10.1093/hmg/ddn023

Choi, M., Kim, H., Yang, E. J., and Kim, H. S. (2020). Inhibition of STAT3 phosphorylation attenuates impairments in learning and memory in 5XFAD mice, an animal model of Alzheimer's disease. *J. Pharmacol. Sci.* 143, 290–299. doi: 10.1016/j.jphs.2020.05.009

Chou, C. H., Chang, N. W., Shrestha, S., Hsu, S. D., Lin, Y. L., Lee, W. H., et al. (2016). miRTarBase 2016: updates to the experimentally validated miRNA-target interactions database. *Nucleic Acids Res.* 44, D239–D247. doi: 10.1093/nar/gkv1258

Chou, C. H., Shrestha, S., Yang, C. D., Chang, N. W., Lin, Y. L., Liao, K. W., et al. (2018). miRTarBase update 2018: a resource for experimentally validated microRNA-target interactions. *Nucleic Acids Res.* 46, D296–D302. doi: 10.1093/nar/gkx1067

Chow, T. W., and Mendez, M. F. (2002). Goals in symptomatic pharmacologic management of frontotemporal lobar degeneration. *Am. J. Alzheimers Dis. Demen* 17, 267–272. doi: 10.1177/153331750201700504

Coyle-Gilchrist, I. T., Dick, K. M., Patterson, K., Vazquez Rodriquez, P., Wehmann, E., Wilcox, A., et al. (2016). Prevalence, characteristics, and survival of frontotemporal lobar degeneration syndromes. *Neurology* 86, 1736–1743. doi: 10.1212/WNL.0000000000002638

De Souza, R. A., Islam, S. A., McEwen, L. M., Mathelier, A., Hill, A., Mah, S. M., et al. (2016). DNA methylation profiling in human Huntington's disease brain. *Hum. Mol. Genet.* 25, 2013–2030. doi: 10.1093/hmg/ddw076

Ferrari, R., Forabosco, P., Vandrovcova, J., Botia, J. A., Guelfi, S., Warren, J. D., et al. (2016). Frontotemporal dementia: insights into the biological underpinnings of disease through gene co-expression network analysis. *Mol. Neurodegener.* 11:21. doi: 10.1186/s13024-016-0085-4

Ferrari, R., Lovering, R. C., Hardy, J., Lewis, P. A., and Manzoni, C. (2017). Weighted Protein Interaction Network Analysis of Frontotemporal Dementia. *J. Proteome Res.* 16, 999–1013. doi: 10.1021/acs.jproteome.6b00934

Fornes, O., Castro-Mondragon, J. A., Khan, A., van der Lee, R., Zhang, X., Richmond, P. A., et al. (2020). JASPAR 2020: update of the open-access database of transcription factor binding profiles. *Nucleic Acids Res.* 48, D87–D92. doi: 10.1093/nar/gkz1001

Forostyak, S., Homola, A., Turnovcova, K., Svitil, P., Jendelova, P., and Sykova, E. (2014). Intrathecal delivery of mesenchymal stromal cells protects the structure of altered perineuronal nets in SOD1 rats and amends the course of ALS. *Stem Cells* 32, 3163–3172. doi: 10.1002/stem.1812

Gauthier-Kemper, A., Suarez Alonso, M., Sundermann, F., Niewidok, B., Fernandez, M. P., Bakota, L., et al. (2018). Annexins A2 and A6 interact with the extreme N terminus of tau and thereby contribute to tau's axonal localization. *J. Biol. Chem.* 293, 8065–8076. doi: 10.1074/jbc.RA117.000490

Gonzalez, P., Alvarez, V., Menendez, M., Lahoz, C. H., Martinez, C., Corao, A. I., et al. (2007). Myocyte enhancing factor-2A in Alzheimer's disease: genetic analysis and association with MEF2A-polymorphisms. *Neurosci. Lett.* 411, 47–51. doi: 10.1016/j.neulet.2006.09.055

Gonzalez-Fernandez, C., Gonzalez, P., Andres-Benito, P., Ferrer, I., and Rodriguez, F. J. (2019). Wnt Signaling Alterations in the Human Spinal Cord of Amyotrophic Lateral Sclerosis Cases: Spotlight on Fz2 and Wnt5a. *Mol. Neurobiol.* 56, 6777–6791. doi: 10.1007/s12035-019-1547-9

Greaves, C. V., and Rohrer, J. D. (2019). An update on genetic frontotemporal dementia. *J. Neurol.* 266, 2075–2086. doi: 10.1007/s00415-019-09363-4

Jiang, X., Guan, Y., Zhao, Z., Meng, F., Wang, X., Gao, X., et al. (2021). Potential Roles of the WNT Signaling Pathway in Amyotrophic Lateral Sclerosis. *Cells* 10:10040839. doi: 10.3390/cells10040839

Kales, H. C., Kim, H. M., Zivin, K., Valenstein, M., Seyfried, L. S., Chiang, C., et al. (2012). Risk of mortality among individual antipsychotics in patients with dementia. *Am. J. Psychiatry* 169, 71–79. doi: 10.1176/appi.ajp.2011.11030347

Kanehisa, M., and Goto, S. (2000). KEGG: kyoto encyclopedia of genes and genomes. *Nucleic Acids Res.* 28, 27–30. doi: 10.1093/nar/28.1.27

Karagkouni, D., Paraskevopoulou, M. D., Chatzopoulos, S., Vlachos, I. S., Tastsoglou, S., Kanellos, I., et al. (2018). DIANA-TarBase v8: a decade-long collection of experimentally supported miRNA-gene interactions. *Nucleic Acids Res.* 46, D239–D245. doi: 10.1093/nar/gkx1141

Lachmann, A., Xu, H., Krishnan, J., Berger, S. I., Mazloom, A. R., and Ma'ayan, A. (2010). ChEA: transcription factor regulation inferred from integrating genome-wide ChIP-X experiments. *Bioinformatics* 26, 2438–2444. doi: 10.1093/bioinformatics/btq466

Leandro, G. S., Evangelista, A. F., Lobo, R. R., Xavier, D. J., Moriguti, J. C., and Sakamoto-Hojo, E. T. (2018). Changes in Expression Profiles Revealed by Transcriptomic Analysis in Peripheral Blood Mononuclear Cells of Alzheimer's Disease Patients. *J. Alzheimers Dis.* 66, 1483–1495. doi: 10.3233/JAD-170205

Li, L., Zi, X., Hou, D., and Tu, Q. (2017). Kruppel-like factor 4 regulates amyloid-beta (Abeta)-induced neuroinflammation in Alzheimer's disease. *Neurosci. Lett.* 643, 131–137. doi: 10.1016/j.neulet.2017.02.017

Lu, T., Aron, L., Zullo, J., Pan, Y., Kim, H., Chen, Y., et al. (2014). REST and stress resistance in ageing and Alzheimer's disease. *Nature* 507, 448–454. doi: 10.1038/nature13163

Majdalawieh, A. F., Massri, M., and Ro, H. S. (2020). AEBP1 is a Novel Oncogene: Mechanisms of Action and Signaling Pathways. *J. Oncol.* 2020:8097872. doi: 10.1155/2020/8097872

Marsh, J., Bagol, S. H., Williams, R. S. B., Dickson, G., and Alifragis, P. (2017). Synapsin I phosphorylation is dysregulated by beta-amyloid oligomers and restored by valproic acid. *Neurobiol. Dis.* 106, 63–75. doi: 10.1016/j.nbd.2017.06.011

Mattingly, C. J., Colby, G. T., Forrest, J. N., and Boyer, J. L. (2003). The Comparative Toxicogenomics Database (CTD). *Environ. Health Perspect.* 111, 793–795. doi: 10.1289/ehp.6028

Mizuno, H., Warita, H., Aoki, M., and Itoyama, Y. (2008). Accumulation of chondroitin sulfate proteoglycans in the microenvironment of spinal motor neurons in amyotrophic lateral sclerosis transgenic rats. *J. Neurosci. Res.* 86, 2512–2523. doi: 10.1002/jnr.21702

Mogi, M., Iwanami, J., Wang, X. L., Tsukuda, K., Kan-No, H., Bai, H. Y., et al. (2018). Deletion of interferon-regulatory factor-1 results in cognitive impairment. *Hypertens Res.* 41, 809–816. doi: 10.1038/s41440-018-0080-y

Moon, B. S., Lu, W., and Park, H. J. (2018). Valproic acid promotes the neuronal differentiation of spiral ganglion neural stem cells with robust axonal growth. *Biochem. Biophys. Res. Commun.* 503, 2728–2735. doi: 10.1016/j.bbrc.2018.08.032

Ndoja, A., Reja, R., Lee, S. H., Webster, J. D., Ngu, H., Rose, C. M., et al. (2020). Ubiquitin Ligase COP1 Suppresses Neuroinflammation by Degrading c/EBPbeta in Microglia. *Cell* 182, 1156–1169e1112. doi: 10.1016/j.cell.2020.07.011

Olney, N. T., Spina, S., and Miller, B. L. (2017). Frontotemporal Dementia. *Neurol. Clin.* 35, 339–374. doi: 10.1016/j.ncl.2017.01.008

Piras, I. S., Krate, J., Delvaux, E., Nolz, J., Mastroeni, D. F., Persico, A. M., et al. (2019). Transcriptome Changes in the Alzheimer's Disease Middle Temporal Gyrus: Importance of RNA Metabolism and Mitochondria-Associated Membrane Genes. *J. Alzheimers Dis.* 70, 691–713. doi: 10.3233/JAD-181113

Potashkin, J. A., Bottero, V., Santiago, J. A., and Quinn, J. P. (2020). Bioinformatic Analysis Reveals Phosphodiesterase 4D-Interacting Protein as a Key Frontal Cortex Dementia Switch Gene. *Int. J. Mol. Sci.* 21:11. doi: 10.3390/ijms21113787

Prasad, A., Bharathi, V., Sivalingam, V., Girdhar, A., and Patel, B. K. (2019). Molecular Mechanisms of TDP-43 Misfolding and Pathology in Amyotrophic Lateral Sclerosis. *Front. Mol. Neurosci.* 12:25. doi: 10.3389/fnmol.2019.00025

Reynolds, C. A., Hong, M. G., Eriksson, U. K., Blennow, K., Wiklund, F., Johansson, B., et al. (2010). Analysis of lipid pathway genes indicates association of sequence variation near SREBF1/TOM1L2/ATPAF2 with dementia risk. *Hum. Mol. Genet.* 19, 2068–2078. doi: 10.1093/hmg/ddq079

Rosen, E. Y., Wexler, E. M., Versano, R., Coppola, G., Gao, F., Winden, K. D., et al. (2011). Functional genomic analyses identify pathways dysregulated by progranulin deficiency, implicating Wnt signaling. *Neuron* 71, 1030–1042. doi: 10.1016/j.neuron.2011.07.021

Rutten-Jacobs, L. C. A., Tozer, D. J., Duering, M., Malik, R., Dichgans, M., Markus, H. S., et al. (2018). Genetic Study of White Matter Integrity in UK Biobank (N=8448) and the Overlap With Stroke, Depression, and Dementia. *Stroke* 49, 1340–1347. doi: 10.1161/STROKEAHA.118.020811

Sahana, T. G., and Zhang, K. (2021). Mitogen-Activated Protein Kinase Pathway in Amyotrophic Lateral Sclerosis. *Biomedicines* 9:8. doi: 10.3390/biomedicines9080969

Santiago, J. A., Bottero, V., and Potashkin, J. A. (2017). Dissecting the Molecular Mechanisms of Neurodegenerative Diseases through Network Biology. *Front. Aging Neurosci.* 9:166. doi: 10.3389/fnagi.2017.00166

Santiago, J. A., Bottero, V., and Potashkin, J. A. (2020). Transcriptomic and Network Analysis Identifies Shared and Unique Pathways across Dementia Spectrum Disorders. *Int. J. Mol. Sci.* 21:6. doi: 10.3390/ijms21062050

Santiago, J. A., and Potashkin, J. A. (2014). A network approach to clinical intervention in neurodegenerative diseases. *Trends Mol. Med.* 20, 694–703. doi: 10.1016/j.molmed.2014.10.002

Shijo, M., Honda, H., Suzuki, S. O., Hamasaki, H., Hokama, M., Abolhassani, N., et al. (2018). Association of adipocyte enhancer-binding protein 1 with Alzheimer's disease pathology in human hippocampi. *Brain Pathol.* 28, 58–71. doi: 10.1111/bpa.12475

Spell, C., Kolsch, H., Lutjohann, D., Kerksiek, A., Hentschel, F., Damian, M., et al. (2004). SREBP-1a polymorphism influences the risk of Alzheimer's disease in carriers of the ApoE4 allele. *Dement Geriatr. Cogn. Disord* 18, 245–249. doi: 10.1159/000080023

Toral-Rios, D., Patino-Lopez, G., Gomez-Lira, G., Gutierrez, R., Becerril-Perez, F., Rosales-Cordova, A., et al. (2020). Activation of STAT3 Regulates Reactive Astrogliosis and Neuronal Death Induced by AbetaO Neurotoxicity. *Int. J. Mol. Sci.* 21:20. doi: 10.3390/ijms21207458

Tsai, P. S., Liu, I. C., Chiu, C. H., Huang, C. J., and Wang, M. Y. (2016). Effect of valproic acid on dementia onset in patients with bipolar disorder. *J. Affect Disord* 201, 131–136. doi: 10.1016/j.jad.2016.05.010

Wang, S., Sun, H., Ma, J., Zang, C., Wang, C., Wang, J., et al. (2013). Target analysis by integration of transcriptome and ChIP-seq data with BETA. *Nat. Protoc.* 8, 2502–2515. doi: 10.1038/nprot.2013.150

Wang, X., Chen, Y., Wang, X., and Lu, L. (2010). Genetic regulatory network analysis for app based on genetical genomics approach. *Exp. Aging Res.* 36, 79–93. doi: 10.1080/03610730903418729

Wang, Z. H., Xiang, J., Liu, X., Yu, S. P., Manfredsson, F. P., Sandoval, I. M., et al. (2019). Deficiency in BDNF/TrkB Neurotrophic Activity Stimulates delta-Secretase by Upregulating C/EBPbeta in Alzheimer's Disease. *Cell Rep.* 28, 655–669e655. doi: 10.1016/j.celrep.2019.06.054

Williams, R. S. B., and Bate, C. (2018). Valproic acid and its congener propylisopropylacetic acid reduced the amount of soluble amyloid-beta oligomers released from 7PA2 cells. *Neuropharmacology* 128, 54–62. doi: 10.1016/j.neuropharm.2017.09.031

Woollacott, I. O., and Rohrer, J. D. (2016). The clinical spectrum of sporadic and familial forms of frontotemporal dementia. *J. Neurochem.* 138(Suppl. 1), 6–31. doi: 10.1111/jnc.13654

Wu, Q., Yang, X., Zhang, L., Zhang, Y., and Feng, L. (2017). Nuclear Accumulation of Histone Deacetylase 4 (HDAC4) Exerts Neurotoxicity in Models of Parkinson's Disease. *Mol. Neurobiol.* 54, 6970–6983. doi: 10.1007/s12035-016-0199-2

Yao, K. N., Solanto, M. V., and Wender, E. H. (1988). Prevalence of hyperactivity among newly immigrated Chinese-American children. *J. Dev. Behav. Pediatr.* 9, 367–373.

Zeng, Q., Long, Z., Feng, M., Zhao, Y., Luo, S., Wang, K., et al. (2019). Valproic Acid Stimulates Hippocampal Neurogenesis via Activating the Wnt/beta-Catenin Signaling Pathway in the APP/PS1/Nestin-GFP Triple Transgenic Mouse Model of Alzheimer's Disease. *Front. Aging Neurosci.* 11:62. doi: 10.3389/fnagi.2019.00062

Zhang, C., Yuan, X., Hu, Z., Liu, S., Li, H., Wu, M., et al. (2017). Valproic Acid Protects Primary Dopamine Neurons from MPP(+)-Induced Neurotoxicity: Involvement of GSK3beta Phosphorylation by Akt and ERK through the Mitochondrial Intrinsic Apoptotic Pathway. *Biomed. Res. Int.* 2017:8124501. doi: 10.1155/2017/8124501

Zhao, L., Zhu, L., and Guo, X. (2018). Valproic acid attenuates Abeta25-35-induced neurotoxicity in PC12 cells through suppression of mitochondria-mediated apoptotic pathway. *Biomed. Pharmacother.* 106, 77–82. doi: 10.1016/j.biopha.2018.06.080

Zhou, G., Soufan, O., Ewald, J., Hancock, R. E. W., Basu, N., and Xia, J. (2019). NetworkAnalyst 3.0: a visual analytics platform for comprehensive gene expression profiling and meta-analysis. *Nucleic Acids Res.* 47, W234–W241. doi: 10.1093/nar/gkz240

Conflict of Interest: JS was employed by NeuroHub Analytics, LLC.

The remaining authors declare that the research was conducted in the absence of any commercial or financial relationships that could be construed as a potential conflict of interest.

Publisher's Note: All claims expressed in this article are solely those of the authors and do not necessarily represent those of their affiliated organizations, or those of the publisher, the editors and the reviewers. Any product that may be evaluated in this article, or claim that may be made by its manufacturer, is not guaranteed or endorsed by the publisher.

Copyright © 2021 Bottero, Alrafati, Santiago and Potashkin. This is an open-access article distributed under the terms of the Creative Commons Attribution License (CC BY). The use, distribution or reproduction in other forums is permitted, provided the original author(s) and the copyright owner(s) are credited and that the original publication in this journal is cited, in accordance with accepted academic practice. No use, distribution or reproduction is permitted which does not comply with these terms.

frontiers in Aging Neuroscience

ORIGINAL RESEARCH
published: 20 October 2021
doi: 10.3389/fnagi.2021.751913

Methamphetamine and Modulation Functionality of the Prelimbic Cortex for Developing a Possible Treatment of Alzheimer's Disease in an Animal Model

*Bai-Chuang Shyu[1], Zhi-Yue Gao[2], José Jiun-Shian Wu[3], Alan Bo Han He[4], Cai-N Cheng[4,5] and Andrew Chih Wei Huang[4]**

[1] Institute of Biomedical Sciences, Academia Sinica, Taipei, Taiwan, [2] Yuanshan Branch, Taipei Veterans General Hospital, Taipei, Taiwan, [3] Department of Biology, National Tsing Hua University, Hsinchu, Taiwan, [4] Department of Psychology, Fo Guang University, Yilan, Taiwan, [5] Department of Life Sciences, National Central University, Taoyuan City, Taiwan

Alzheimer's disease (AD) is a progressive neurodegenerative condition that causes cognitive impairment and other neuropsychiatric symptoms. Previously, little research has thus far investigated whether methamphetamine (MAMPH) can enhance cognitive function or ameliorate AD symptoms. This study examined whether a low dose of MAMPH can induce conditioned taste aversion (CTA) learning, or can increase plasma corticosterone levels, neural activity, and neural plasticity in the medial prefrontal cortex (mPFC) (responsible for cognitive function), the nucleus accumbens (NAc) and the amygdala (related to rewarding and aversive emotion), and the hippocampus (responsible for spatial learning). Furthermore, the excitations or lesions of the prelimbic cortex (PrL) can affect MAMPH-induced CTA learning, plasma corticosterone levels, and neural activity or plasticity in the mPFC [i.e., PrL, infralimbic cortex (IL), cingulate cortex 1 (Cg1)], the NAc, the amygdala [i.e., basolateral amygdala (BLA) and central amygdala (CeA)], and the hippocampus [i.e., CA1, CA2, CA3, and dentate gyrus (DG)]. In the experimental procedure, the rats were administered either saline or NMDA solutions, which were injected into the PrL to excite or destroy PrL neurons. Additionally, rats received 0.1% saccharin solution for 15 min, followed by intraperitoneal injections of either normal saline or 1 mg/kg MAMPH to induce CTA. A one-way ANOVA was performed to analyze the effects of saccharin intake on CTA, plasma corticosterone levels, and the expression of c-Fos and p-ERK. The results showed that the MAMPH induced CTA learning and increased plasma corticosterone levels. The mPFC, and particularly the PrL and IL and the DG of the hippocampus, appeared to show increased neural activity in c-Fos expression or neural plasticity in p-ERK expression. The excitation of the PrL neurons upregulated neural activity in c-Fos expression and neural plasticity in p-ERK expression in the PrL and IL. In summary, MAMPH may be able to improve cognitive and executive function in the brain and reduce AD symptoms. Moreover, the

OPEN ACCESS

Edited by:
Woon-Man Kung,
Chinese Culture University, Taiwan

Reviewed by:
Wang Min,
Shanghai University, China
Chung-Feng Kao,
National Chung Hsing University, Taiwan

***Correspondence:**
Andrew Chih Wei Huang
chweihuang@mail.fgu.edu.tw

Received: *02 August 2021*
Accepted: *27 September 2021*
Published: *20 October 2021*

Citation:
Shyu B-C, Gao Z-Y, Wu JJ-S, He ABH, Cheng C-N and Huang ACW (2021) Methamphetamine and Modulation Functionality of the Prelimbic Cortex for Developing a Possible Treatment of Alzheimer's Disease in an Animal Model. Front. Aging Neurosci. 13:751913. doi: 10.3389/fnagi.2021.751913

excitatory modulation of the PrL with MAMPH administration can facilitate MAMPH-induced neural activity and plasticity in the PrL and IL of the mPFC. The present data provide clinical implications for developing a possible treatment for AD in an animal model.

Keywords: methamphetamine (MA), conditioned taste aversion (CTA), prelimbic cortex (PrL), corticosterone (CORT), Alzeheimer's disease, rats

INTRODUCTION

Previous studies of methamphetamine (MAMPH) have demonstrated that MAMPH is an addictive drug that induces compulsion, craving, and relapsing behaviors (Kirkpatrick et al., 2012; Mizoguchi and Yamada, 2019). Additionally, chronic MAMPH exposure can cause neurotoxicity, neuroinflammation, and neuronal apoptosis in the central nervous system (Shukla and Vincent, 2020). In this context, MAMPH has led to cognitive impairments and premature brain aging caused by Alzheimer's disease (AD) (Hart et al., 2012; Panenka et al., 2013). However, MAMPH has been beneficial in treating conditions including obesity (Bray, 1993), bipolar depression (Perugi et al., 2017), attention-deficit/hyperactivity disorder (Ramirez et al., 2018), and narcolepsy (Fry, 1998). A fewer research has shown that MAMPH administration may ameliorate some of the behavioral and neuropsychiatric symptoms of AD and could suppress AD-associated proteins and molecular in neurons (Shukla and Vincent, 2020). For example, MAMPH, and a cognitive enhancer, FR121196, boosted memory retention in rats that undertook passive avoidance tasks (Matsuoka et al., 1992). An *in vitro* study demonstrated that the application of MAMPH to the human neuroblastoma SH-SY5Y cell line modulated beta-amyloid precursor protein-cleaving secretases, indicating it may ameliorate cognitive function in AD patients (Shukla et al., 2019). Additionally, long-term, low-dose MAMPH treatments to the dentate granule neuron of the hippocampus slice have facilitated long-term potentiation (LTP) and spinal enlargement (Baptista et al., 2016). Depending on the clinical findings in human models, the administration of psychostimulants (e.g., methylphenidate and amphetamine) could improve the apathy symptom in AD patients (Scherer et al., 2018). Additionally, a one-off, low dose of MAMPH (i.e., 30 mg) appeared to enhance the abilities in attention, information processing speed, and working memory in relation to cognitive performance (Mahoney et al., 2011). Therefore, the low dose of MAMPH may improve behavioral cognitive function, and neuronal activity, or synaptic plasticity.

MAMPH activates different functions in a variety of brain areas (Hart et al., 2012; Shukla and Vincent, 2020). For example, the medial prefrontal cortex (mPFC) comprises the medial (frontal) agranular cortex, the anterior cingulate cortex, the prelimbic cortex (PrL), and the infralimbic cortex (IL) (Morales et al., 2007). It also mediates numerous cognitive functions such as inhibition control, attention, habit formation, spatial learning, working memory, and long-term memory (Riga et al., 2014; Jobson et al., 2021). Regarding aging and dementia, the mPFC is involved in cognitive decline and impairments in cognitive performance (Jobson et al., 2021). In addition, the dense interactivity of the mPFC links to the subcortical regions, including the thalamus, NAc, amygdala, and hippocampus (Riga et al., 2014; Jobson et al., 2021); it also controls certain executive and cognitive functions in these subcortical regions (Dalley et al., 2004). The cingulate cortex area 1 (Cg1) of the mPFC is involved in pain (Vogt and Sikes, 2000), anxiety, and aversion (Singewald et al., 2003). The PrL and IL contribute to MAMPH addiction, which is also associated with conditioned learning (He et al., 2019). Furthermore, the PrL modulates enhancements in aversive stimuli in fear behavior and in rewarding stimuli in drug addiction behavior; conversely, the IL regulates inhibition in fear and facilitation in drug addiction (Peters et al., 2009). Another projected pathway is from the mPFC to the affected brain areas that involve the NAc, which mediates the reward and reinforcement effects of MAMPH addiction (Sun et al., 2013; Cheng et al., 2020). The amygdala was separated into the central amygdala (CeA), which mediates negative emotional responses, and the basolateral amygdala (BLA), which controls the processing of rewarding and aversive stimuli (Tanimoto et al., 2003; Beyeler et al., 2018; Cai et al., 2018). The hippocampus also receives the convey projections from the mPFC and regulates spatial and contextual learning and memory from the subareas of the hippocampus, including the CA1, CA2, CA3, and dentate gyrus (DG) (Jarrard, 1993). Moreover, the hippocampus has been intensively studied in relation to age-related neurological condition, including Alzheimer's disease (Patrylo and Williamson, 2007). Primarily, the DG mediates spatially related information processing as well as representations of spatial memory retention based on the DG's conjunctive encoding and spatial pattern separation, and the encoding of spatial information conveyed to the CA3 (Kesner, 2007). Therefore, the present study tested whether the MAMPH administrations stimulated neuronal activity in brain areas that mediate cognition, rewarding and aversive emotion, and spatial learning and memory.

Previous studies of AD animal models have demonstrated that age is a crucial factor in learning and memory (El Tamer et al., 1992, 1996; Gilbert et al., 2009). For example, in one AD animal model, the intracerebroventricular administration of the cholinotoxic ethylcholine aziridinium (AF64A) resulted in reduced choline acetyltransferase (ChAT) activity and increased acetylcholinesterase (AChE) in the hippocampus of 4- and 12-month-old rats, but no effects were observed in 22-month-old rats, which indicated age-dependent effects on AF64A-mediated cholinotoxicity (El Tamer et al., 1996). A similar study using rats aged 1.5–2 months old (i.e., weighing 250–350 g) showed similar results (El Tamer et al., 1992). Another study examining

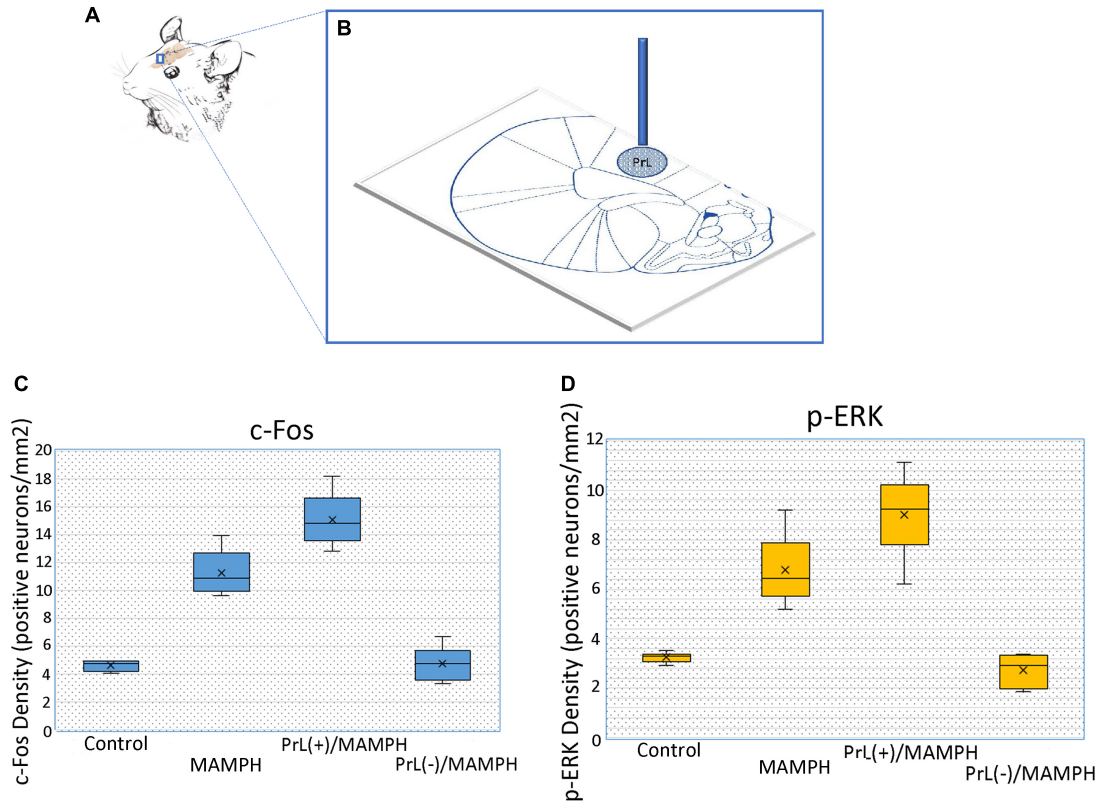

FIGURE 1 | (A) The rat's brain atlas showing the PrL location as a small vertical bar. **(B)** The location of the PrL microinjection. The blue vertical bar represents the buried cannula placement. The spot area indicates the distributions of saline or the NMDA microinjections. The density of **(C)** c-Fos or **(D)** p-ERK in positive neurons/mm^2 in the PrL for the control, MAMPH, PrL (+)/MAMPH, and PrL(–)/MAMPH groups.

rats aged 6 and 24 months showed similar performances for both age groups in olfactory and visual discrimination tasks; however, the 24-month-old rats displayed worse performance in reversal learning and contextual learning tasks than the 6-month-old rats (Gilbert et al., 2009). Therefore, younger rats may be more appropriate when measuring performance on learning and memory tasks. Therefore, the present study used younger rats, aged 1.5–2 months (6–8 weeks) to test the effects of MAMPH on conditioned taste aversion (CTA).

Regarding previous neuroendocrinological data, plasma corticosterone levels secreted from the hypothalamus-pituitary gland-adrenal gland system can serve as stress biomarkers (Piazza et al., 1991; Harvey et al., 2006). Therefore, this study also investigated whether MAMPH administrations elevate plasma corticosterone levels.

Overall, the present study set out to determine the following:

(a) Whether MAMPH administrations induce conditioned learning in the CTA task, increase plasma corticosterone levels, and neural activity (labeling c-Fos expression) or neural plasticity (labeling p-ERK expression) in the Cg1, PrL, and IL of the mPFC; the NAc; the CeA and BLA of the amygdala; and the CA1, CA2, CA3, and DG of the hippocampus.

(b) Whether microinjecting PrL neurons with low or high concentrations of NMDA modulates MAMPH-induced CTA learning, plasma corticosterone levels, and neural activity or neural plasticity in the mPFC (i.e., Cg1, PrL, and IL), NAc, amygdala (i.e., CeA and BLA), and hippocampus (i.e., CA1, CA2, CA3, and DG).

MATERIALS AND METHODS

Animals

All of the 89 male Wistar rats were obtained from BioLasco Taiwan Co., Ltd. At the commencement of the experiment, each rat weighed between 220 and 330 g. The rats were grouped-housed in the colony rooms with two rats in the plastic cage (47 × 26 × 21 cm) containing hardwood laboratory bedding. The colony room was kept at a constant temperature (approximately 23°C ± 2°C) with a 12 h:12 h light/dark cycle (lights on 0600–1800) maintained throughout the experiment. Water and food were freely available, except for rats on the water deprivation regimen who were deprived of water for 23.5 h/day from the water deprivation to the conditioning phase. The experiment was performed in accordance with the Animal Scientific Procedures

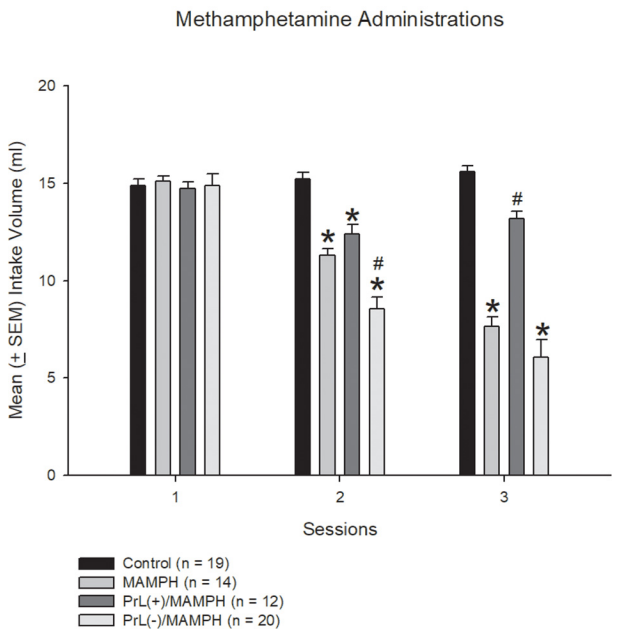

FIGURE 2 | MAMPH-induced conditioned taste aversion tested for behavior using NMDA or saline injections. Mean (± SEM) intake volume of 0.1% saccharin solution for three sessions (with 1 mg/kg of intraperitoneally injected MAMPH) across the control (n = 19), MAMPH (n = 14), PrL (+)/MAMPH (n = 12), and PrL(–)/MAMPH groups (n = 20). PrL(+): Injection of a low concentration of NMDA to excite the PrL neurons; PrL(–): Injection of a high concentration of NMDA to destroy the PrL neurons. Differences in the intake volumes of 0.1% saccharin solution among all groups in each session were analyzed by one-way ANOVA, followed by Tukey's *post hoc* test if a significant difference was appeared among groups. $^{*}p < 0.05$ indicates significant differences compared with the control group; $^{\#}p < 0.05$ indicates significant differences compared with the MAMPH group.

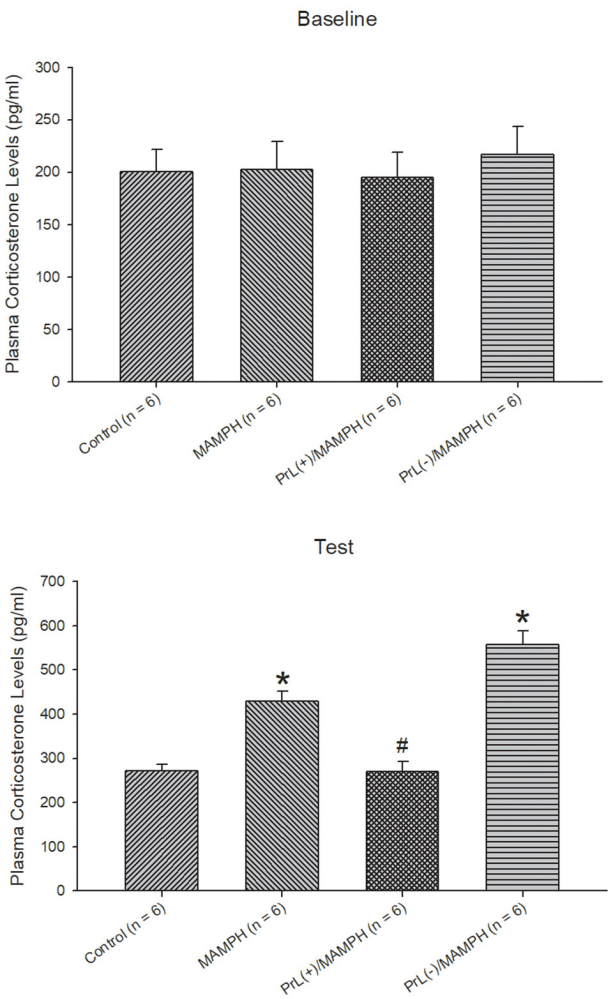

FIGURE 3 | The effect of MAMPH administrations on plasma corticosterone levels were tested using NMDA or saline injections into the PrL. Mean (± SEM) plasma corticosterone levels (pg/ml) were taken for the control (n = 6), MAMPH (n = 6), PrL(+)/MAMPH (n = 6), and PrL(–)/MAMPH groups (n = 6) at the baseline and in the conditioning phase. PrL(+): Injection of a low concentration of NMDA to excite the PrL neurons; PrL(–): Injection of a high concentration of NMDA to destroy the PrL neurons. Plasma corticosterone levels were analyzed by one-way ANOVA, followed by Tukey's *post hoc* test if a significant difference was appeared among groups at the baseline and test phases. $^{*}p < 0.05$ indicates significant differences compared with the control group; $^{\#}p < 0.05$ indicates significant differences compared with the MAMPH group.

Act of 1986 and received approval from the Fo Guang University Institutional Animal Care and Use Committee. The number of animals was limited, and every effort was made to minimize animal suffering during the experiment.

Apparatus

Lickometer was used to measure the intake volume of water or saccharin solution in the study. The lickometer device comprises a wire-mesh cage, a white panel, and a 25-ml burette with 0.1-ml graduations. The burette was mounted in front of the wire-mesh cage inserted through a hole in the white panel. The intake volume of the saccharin solution served to determine the magnitude of the effect of MAMPH on CTA learning.

Microinjection Parameters and Experimental Surgery

For the surgical procedures, a 1-μl volume of either NMDA or saline was left unilaterally injected into the PrL (anterior-posterior: 3.24 mm from bregma; lateral: 0.60 mm from the midline; dorsal-ventral: 3.00 mm from the skull surface) (Paxinos and Watson, 2007). The substances were injected at a rate of 1 μl/10 min, and the needle was left in the PrL for an additional 10 min. To verify the cannula location, a schematic representation of a left unilateral cannula site was used for reference. The blue dot area indicates a microinjection site of saline or NMDA within the PrL (**Figures 1A,B**). **Figures 1C,D** show the density of c-Fos- or p-ERK-positive neurons after the PrL microinjections of saline and low or high concentrations of NMDA solutions before the MAMPH intraperitoneal administrations for the control, MAMPH, PrL(+)/MAMPH, and PrL(–)/MAMPH groups. MAMPH enhanced the density of c-Fos and p-ERK expression in the PrL ($p < 0.05$).

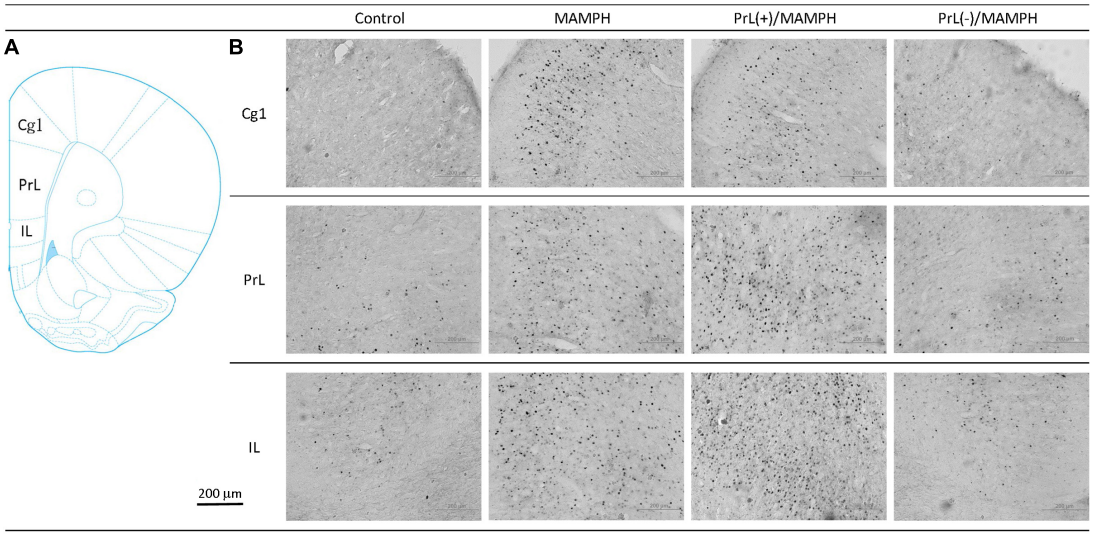

FIGURE 4 | (A) A schematic brain atlas for the Cg1, PrL, and IL of the mPFC. **(B)** Representative photomicrographs of c-Fos expression for the Cg1, PrL, and IL in the control, MAMPH, PrL(+)/MAMPH, and PrL(–)/MAMPH groups. The scale bar represents 200 μm.

The microinjections of low-concentration NMDA significantly increased the density of c-Fos and p-ERK expression compared with the PrL(+)/MAMPH and MAMPH groups ($p < 0.05$). The high concentration of NMDA microinjections in the PrL significantly decreased the density of c-Fos and p-ERK expression compared with the PrL(–)/MAMPH and MAMPH groups ($p < 0.05$; **Figure 1**).

Behavioral Procedure

During the 7-day adaptation phase, the rats were allowed to drink water and eat food freely in their home cage. On Day 0, all rats received anesthesia and surgery. Twenty minutes before anesthesia by sodium pentobarbital injection (50 mg/kg, i.p.), the rats were injected with gentamicin (40 mg/kg, i.p.) and atropine sulfate (0.1 mg, i.p.). After the surgery, the outer cannula was kept in the PrL for the later microinjections of saline or low or high concentrations of NMDA to destroy or excite the PrL neurons. All the rats were then allowed to recover in the home cage for 7 days, with food and water freely available (Days 1–7). Next, the rats were deprived of water for 23.5 h/day for 5 days (Days 8–12). On Day 13, the rats were given microinjections of saline and either a low or high concentration of NMDA into the PrL. Later, the rats were subject to CTA conditioning learning for three trials, which was 0.1% saccharin solution for 15 min and then intraperitoneal injections of 1 mg/kg MAMPH or saline to form CTA learning. During the conditioning phase (Days 13–15), the rats underwent another water deprivation regimen where they were allowed to drink a 0.1% saccharin solution for 15 min from the lickometer device in the morning and then water for 30 min in the home cage in the evening. The rats were then separated into control ($n = 19$), MAMPH ($n = 14$), PrL(+)/MAMPH ($n = 12$), and PrL(–)/MAMPH ($n = 20$) groups. The control group was given microinjections of saline into the PrL and intraperitoneal injections of saline in conditioning; the MAMPH group were given microinjections of saline into the PrL and intraperitoneal injections of MAMPH in conditioning; the PrL(+)/MAMPH group were given microinjections of low concentrations of NMDA into the PrL and intraperitoneal injections of MAMPH in conditioning; and the PrL(–)/MAMPH group were given microinjections of high concentrations of NMDA into the PrL and intraperitoneal injections of MAMPH in conditioning.

Ninety minutes after completing the final trial of the CTA learning test, the rats were humanely sacrificed, and their brains were removed for immunohistochemical staining with c-Fos or p-ERK expression. Additionally, blood was collected to assess plasma corticosterone levels using the ELISA method for baseline (on Day 0) and testing (on Day 15; **Supplementary Figure 1**).

Immunohistochemical Staining

To begin, the rats were sacrificed via a sodium pentobarbital overdose. Later, the rats were conducted using perfusion with 100 ml of 0.1 M sodium phosphate-buffered saline (PBS) followed by 400 ml of 4% paraformaldehyde in a 0.1 M PBS buffer. Next, the brain tissues were dissected and transferred to a 30% sucrose dissolved in a 4% paraformaldehyde solution for cryoprotection. Once the brain tissues sank to the bottom of the solution, the tissues were then frozen with Tissue-Tek® O.C.T. Compound. Next, 40–μm slices of the brain were obtained using a freezing microtome. The slices were labeled using the immunohistochemical staining for c-Fos and p-ERK expression. These free-floating brain slices were then washed for 15 min in 0.1 M PBS, permeabilized in 3% H_2O_2 for 1 h, washed for 20 min three times in 2% PBS tween-20 (PBST), and soaked in 3% normal goat serum and 1% bovine serum albumin for 1 h. Later, all brain slices were washed twice with PBST for 15 min. The slices were incubated at 4°C overnight to carry out c-Fos labeling with primary rabbit anti-Fos antibody (SC-52, 1:1,000; Santa Cruz Biotechnology Inc.) and p-ERK labeling with primary

rabbit anti-p-ERK (GTX50274, 1:500; Genetex Inc.). The slices were then washed twice for 10 min with PBST before being incubated with a biotinylated goat anti-rabbit secondary antibody (1:500; Vector Lab BA-1,000) for 1 h. Later, the brain slices were washed for 10 min with PBS, and the ABC kit (Vector Lab ABC Kit, PK-6100) was used to amplify the bound secondary antibody of the brain slices. The positive expression of c-Fos or p-ERK was counted for the entire brain using ImageJ software. Counting was performed visually at 20x magnification for each brain slice. The c-Fos- or p-ERK density positive neurons were analyzed using the formula: c-Fos or p-ERK numbers/the slice areas (0.88 mm × 0.69 mm ≒ 60.72 mm^2).

Drugs

The MAMPH was obtained from the Food and Drug Administration, Ministry of Health and Welfare, Executive Yuan (Taipei, Taiwan), while the NMDA and sodium chloride were obtained from Sigma-Aldrich (St. Louis, MO). The MAMPH was dissolved in normal saline to a concentration of 1 mg/ml. The sodium saccharin was dissolved in distilled water and prepared in a 0.1% saccharin solution. The saline and MAMPH were injected intraperitoneally at a volume of 1 ml. The study used a low concentration of 2 mg/ml of NMDA and a high concentration of 20 mg/ml, in line with the concentrations suggested by the previous study (Huang et al., 2020).

Statistical Analysis

A one-way ANOVA was performed to analyze the volume of saccharin solution intake to measure MAMPH-injected producing the CTA learning for the control, MAMPH, PrL (+)/MAMPH, PrL(−)/MAMPH groups over the first three sessions. Furthermore, the effect size (i.e., partial η^2) and the power value were performed. When appropriate, Tukey's honestly significant difference (HSD) *post hoc* test was performed for each session. A p-value of < 0.05 was considered significant in all cases. A one-way ANOVA was performed for plasma corticosterone levels and the immunohistochemical staining data for c-Fos and p-ERK expression in the selected brain areas for the control, MAMPH, PrL (+)/MAMPH, and PrL(−)/MAMPH groups at baseline and in the final conditioning (testing phase). Furthermore, the effect size (i.e., partial η^2) and the power value were performed. When appropriate, Tukey's HSD *post hoc* test was conducted for each session. A p-value of < 0.05 was considered significant in all cases.

Partialη^2 is the ratio of variance related to an effect, plus that effect and its associated error variance. The formula was to calculate partialη^2 as follows:

Partialη^2 = SSeffect/(SSeffect + SSerror)

The following rules of thumb are applied to interpret values for partialη^2: 0.01: Small effect size; 0.06: Medium effect size; 0.14 or higher: Large effect size.

Power values are the probability of correctly rejecting a null hypothesis (H0) when it is false. The formula was to calculate power as follows: Power = P(reject H0/H0 is false). A statistical power value is of 0.80 or higher, and the experimental results lead to valid conclusions about the meaning of the results.

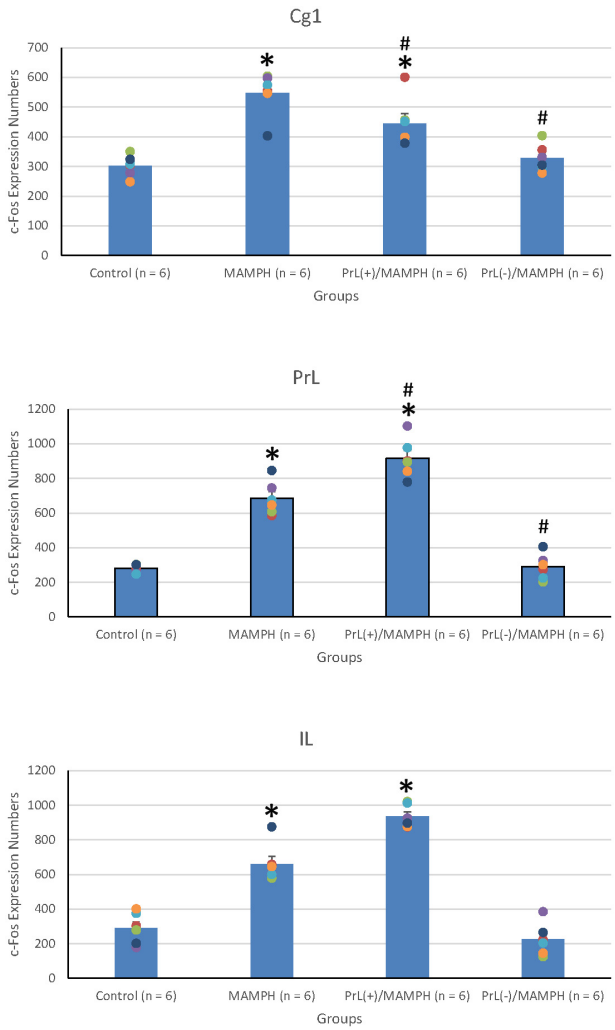

FIGURE 5 | MAMPH administrations were tested to label c-Fos expression in the Cg1, PrL, and IL of the mPFC for the control (n = 6), MAMPH (n = 6), PrL(+)/MAMPH (n = 6), and PrL(−)/MAMPH groups (n = 6) by injecting NMDA or saline into the PrL. PrL(+): injection of a low concentration of NMDA to excite the PrL neurons; PrL(−): injection of a high concentration of NMDA to destroy the PrL neurons. Differences in c-Fos expression levels in the Cg1, PrL, and IL among all groups were analyzed by one-way ANOVA, followed by Tukey's *post hoc* test if a significant difference was appeared among groups. $^*p < 0.05$ indicates significant differences compared with the control group; $^\#p < 0.05$ indicates significant differences compared with the MAMPH group.

RESULTS

The study tested MAMPH administrations associated with PrL modulation over three sessions once a session for the conditioned learning, plasma corticosterone levels, the c-Fos or p-ERK expression for the mPFC, the amygdala, the NAc, and the hippocampus as follows.

In the beginning, we tested the MAMPH administrations induced CTA conditioned learning and the excitation or the lesion of the PrL underlying MAMPH-induced CTA learning. One-way ANOVA was analyzed showed that the factor of group

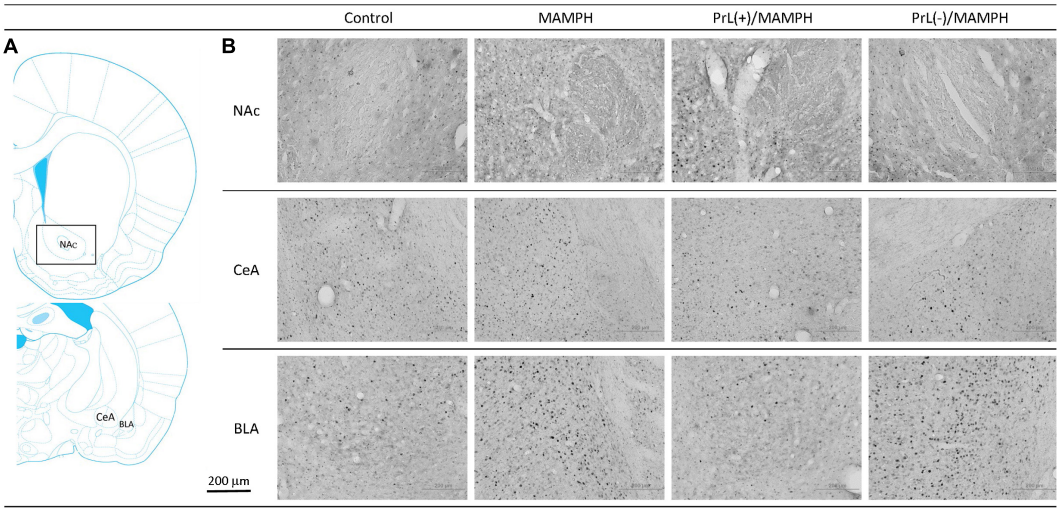

FIGURE 6 | (A) A schematic brain atlas for the NAc, and the amygdala's CeA and BLA. **(B)** Representative photomicrographs of c-Fos expression for the NAc and the amygdala's CeA and BLA in the control, MAMPH, PrL(+)/MAMPH, and PrL(–)/MAMPH groups. The scale bar represents 200 μm.

showed significant differences in session 2 [$F(3, 61) = 40.20$, $p < 0.05$] (partial $\eta^2 = 0.64$, power = 1.00) and in session 3 [$F(3, 61) = 53.00$, $p < 0.05$] (partial $\eta^2 = 0.72$, power = 1.00), but not a significant difference in session 1 [$F(3, 61) = 0.90$, $p > 0.05$] (partial $\eta^2 = 0.00$, power = 0.07). The *post hoc* Tukey's test showed that the saccharin intake volumes of the MAMPH, PrL(+)/MAMPH, and PrL(–)/MAMPH groups during session 2 were significantly reduced compared with the control group ($p < 0.05$). The intake volume of the PrL(–)/MAMPH group was significantly less than that of the MAMPH group ($p < 0.05$). In session 3, the MAMPH and PrL(–)/MAMPH groups showed significantly reduced intake volumes of the saccharin solution; however, the PrL(+)/MAMPH group showed a significant increase in intake volume compared with the MAMPH group. Therefore, we can conclude that MAMPH administration in session 1 did not induce CTA conditioned learning. However, the MAMPH injections in sessions 2 and 3 reduced the saccharin solution intake enough to induce CTA conditioned learning. The high concentrations of NMDA microinjected into the PrL destroyed the PrL neurons. The lesion of the PrL neurons enhanced the MAMPH-induced CTA conditioned learning in session 2. In contrast, the low concentration of NMDA microinjected in the PrL, excited the PrL neurons enough to blunt the MAMPH-induced CTA learning in session 3 (**Figure 2**).

Regarding the analysis of the plasma corticosterone levels, one-way ANOVA analysis indicated that there were no significant differences between the control, MAMPH, PrL(+)/MAMPH, and PrL(–)/MAMPH groups [$F(3, 20) = 0.14$, $p > 0.05$] (partial $\eta^2 = 0.02$, power = 0.07) in the baseline. During the test phase, significant differences were found in group [$F(3, 20) = 33.67$, $p < 0.05$] (partial $\eta^2 = 0.84$, power = 1.00). The *post hoc* Tukey HSD test indicated that plasma corticosterone levels in the MAMPH and PrL(–)/MAMPH groups had increased significantly compared with the control group ($p < 0.05$), while plasma corticosterone levels in the PrL(+)/MAMPH group were significantly less than those in the MAMPH group ($p < 0.05$).

In summary, the test phase MAMPH administrations increased plasma corticosterone levels. Moreover, the lesion of the PrL with MAMPH injections enhanced plasma corticosterone levels but exciting the PrL blunted plasma corticosterone levels compared with the single MAMPH administrations (**Figure 3**).

In order to examine the effects of MAMPH administrations with the PrL modulation in cognitive functions using c-Fos expression, a one-way ANOVA was performed, which indicated that the factor of group was the significant difference in the Cg1 [$F(3, 20) = 19.13$, $p < 0.05$] (partial $\eta^2 = 0.74$, power = 1.00), PrL [$F(3, 20) = 83.40$, $p < 0.05$] (partial $\eta^2 = 0.93$, power = 1.00), and IL [$F(3, 20) = 80.02$, $p < 0.05$] (partial $\eta^2 = 0.92$, power = 1.00). The subareas of the mPFC, such as the Cg1, PrL, and IL, were identified with neural activity labeling c-Fos expression. The *post hoc* Tukey's HSD test revealed that the addition of MAMPH significantly increased c-Fos expression compared with the control group for the Cg1, PrL, and IL ($p < 0.05$). Moreover, the PrL(+)/MAMPH group showed a significant increase in c-Fos expression for PrL and IL ($p < 0.05$). The Cg1 showed a significant decrease in c-Fos expression in the PrL(+)/MAMPH group when compared with the MAMPH group ($p < 0.05$). However, the PrL(–)/MAMPH group was significantly reduced compared to the MAMPH group ($p < 0.05$) in the subareas of the mPFC, including the Cg1, PrL, and the IL (**Figures 4**, **5**). In conclusion, MAMPH administrations may activate neural activity in brain areas associated with cognitive function, including the Cg1, PrL, and IL. The excitation of the PrL neurons increased this neural activity, which was induced by MAMH administration in the PrL and IL. Moreover, the lesion of the PrL neurons blunted MAMPH-induced neural activity in all subareas of the mPFC (i.e., the Cg1, PrL, and IL).

To test MAMPH-induced neural activity and the modulation of the PrL in c-Fos expression, a one-way ANOVA analysis was

performed, which showed that the main factor was significant differences in the NAc [$F(3, 20) = 28.82$, $p < 0.05$] (partial $\eta^2 = 0.80$, power = 1.00), CeA [$F(3, 20) = 0.94$, $p > 0.05$] (partial $\eta^2 = 0.12$, power = 0.22), and BLA [$F(3, 20) = 16.06$, $p < 0.05$] (partial $\eta^2 = 0.69$, power = 1.00). The *post hoc* Tukey's HSD test showed that the MAMPH group significantly increased c-Fos expression in the NAc and BLA but not in the CeA compared with the control group ($p < 0.05$), indicating that MAMPH increased neural activity in the NAc and BLA. In the NAc, c-Fos expression in the PrL(+)/MAMPH group showed no significant differences compared with the MAMPH group ($p > 0.05$). However, the PrL(–)/MAMPH group showed a significant decrease in c-Fos expression compared with the MAMPH group ($p < 0.05$), indicating the lesion of the PrL neurons blocked neural activity in the NAc. In the BLA, the PrL(+)/MAMPH group significantly decreased c-Fos expression compared with the MAMPH group ($p < 0.05$). However, the PrL(–)/MAMPH group did not show any significant differences in c-Fos expression compared with the MAMPH group ($p > 0.05$; **Figures 6**, **7**).

In conclusion, the rewarding and aversive emotion-related brain areas—the NAc and BLA but not the CeA—elicited neural activity following MAMPH administrations. The excitation of the PrL neurons decreased MAMPH-induced neural activity in the BLA. Moreover, the lesion of the PrL neurons blunted MAMPH-elicited neural activity in the NAc.

By analyzing c-Fos expression to elucidate the effect of MAMPH administrations and the modulation of the PrL underlying the MAMPH injections, a one-way ANOVA was conducted, which showed that significant differences occurred in the DG [$F(3, 20) = 66.26$, $p < 0.05$] (partial $\eta^2 = 0.91$, power = 1.00). However, there were no significant differences in the CA1 [$F(3, 20) = 0.74$, $p > 0.05$] (partial $\eta^2 = 0.10$, power = 0.18), CA2 [$F(3, 20) = 0.56$, $p > 0.05$] (partial $\eta^2 = 0.08$, power = 0.15), and CA3 [$F(3, 20) = 0.10$, $p > 0.05$] (partial $\eta^2 = 0.01$, power = 0.06). The *post hoc* Tukey's HSD test showed that, in the DG, c-Fos expression in the MAMPH and the PrL(–)/MAMPH groups increased significantly compared with the control group ($p > 0.05$). The PrL(–)/MAMPH group showed a significant decrease ($p < 0.05$), while the PrL(+)/MAMPH group showed a significant increase ($p < 0.05$) in the DG's c-Fos expression (**Figures 8**, **9**). Therefore, it can be surmised that the addition of MAMPH only elicited neural activity in the DG but not in the other subareas of the hippocampus such as the CA1, CA2, and CA3. In the DG, the excitation of the PrL neurons reduced MAMPH administration-induced neural activity, while the lesion of the DG neurons significantly enhanced MAMPH administration-induced neural activity.

In conclusion, the brain areas associated with spatial learning function, the CA1, CA2, CA3, and DG of the hippocampus, were examined by MAMPH administration and PrL's modulation underlying the MAMPH injections. Only the DG showed neural activity following MAMPH administration. In the DG, the excitation of the PrL neurons blunted MAMPH-induced neural activity, while the lesion of the PrL neurons enhanced MAMPH-induced neural activity.

In order to examine neural plasticity using p-ERK expression labeling in the areas of the brain associated with cognitive function, including the mPFC (e.g., Cg1, PrL, and IL), a one-way ANOVA analysis was performed, which showed that the factor of group was the significant difference in the Cg1 [$F(3, 20) = 11.23$, $p < 0.05$] (partial $\eta^2 = 0.63$, power = 1.00), PrL [$F(3, 20) = 41.04$, $p < 0.05$] (partial $\eta^2 = 0.86$, power = 1.00), and IL [$F(3, 20) = 35.53$, $p < 0.05$] (partial $\eta^2 = 0.84$, power = 1.00).

Additionally, the *post hoc* Tukey's HSD test indicated that p-ERK expression in the MAMPH group increased significantly in the PrL ($p < 0.05$), and IL ($p < 0.05$) compared with the control group, but not in the Cg1 ($p > 0.05$). p-ERK expression increased

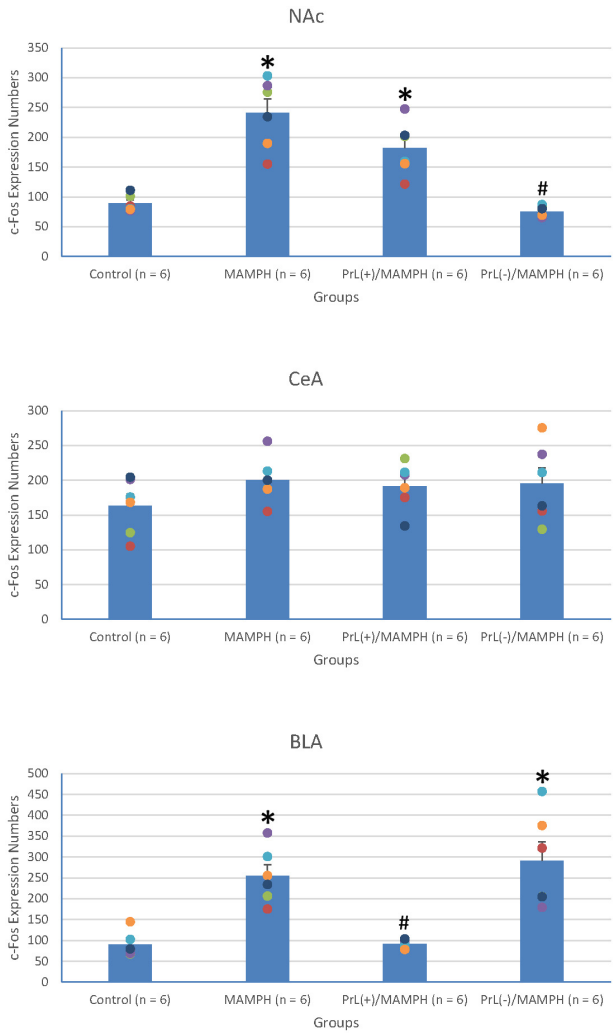

FIGURE 7 | MAMPH administrations were tested to label c-Fos expression in the NAc and the amygdala's CeA, and BLA for the control ($n = 6$), MAMPH ($n = 6$), PrL(+)/MAMPH ($n = 6$), and PrL(–)/MAMPH groups ($n = 6$) by injecting NMDA or saline into the PrL. PrL(+): Injection of a low concentration of NMDA to excite the PrL neurons; PrL(–): Injection of a high concentration of NMDA to destroy the PrL neurons. Differences in c-Fos expression levels in the NAc, CeA, and BLA among all groups were analyzed by one-way ANOVA, followed by Tukey's *post hoc* test if a significant difference was appeared among groups. $^*p < 0.05$ indicates significant differences compared with the control group; $^{\#}p < 0.05$ indicates significant differences compared with the MAMPH group.

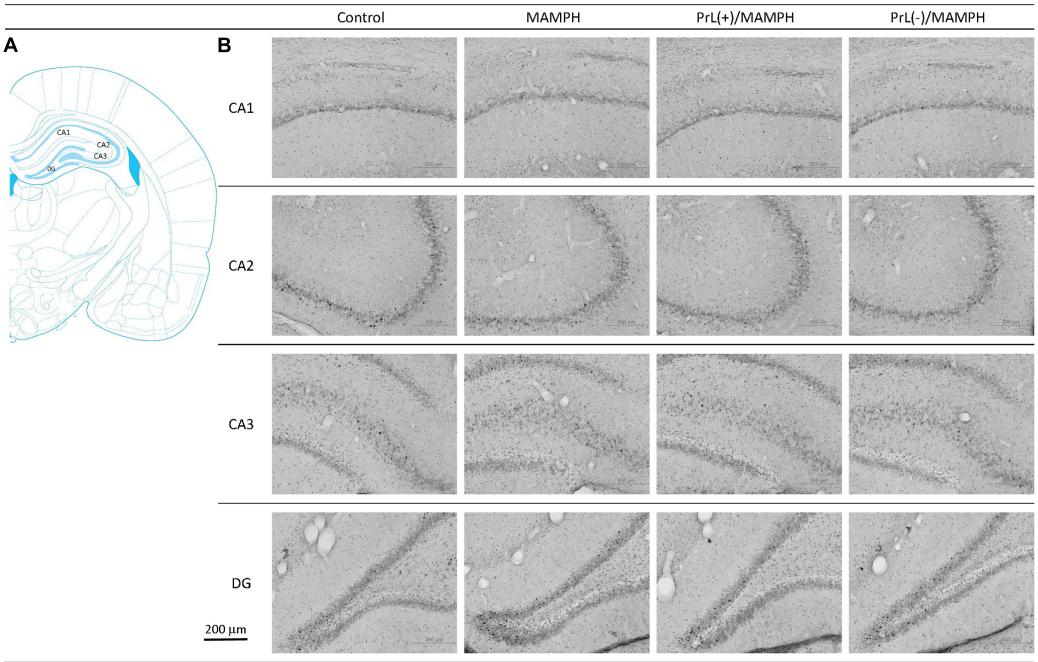

FIGURE 8 | (A) A schematic brain atlas for the CA1, CA2, CA3, and DG of the hippocampus. **(B)** Representative photomicrographs of c-Fos expression for the CA1, CA2, CA3, and DG of the hippocampus in the control, MAMPH, PrL(+)/MAMPH, and PrL(–)/MAMPH groups. The scale bar represents 200 μm.

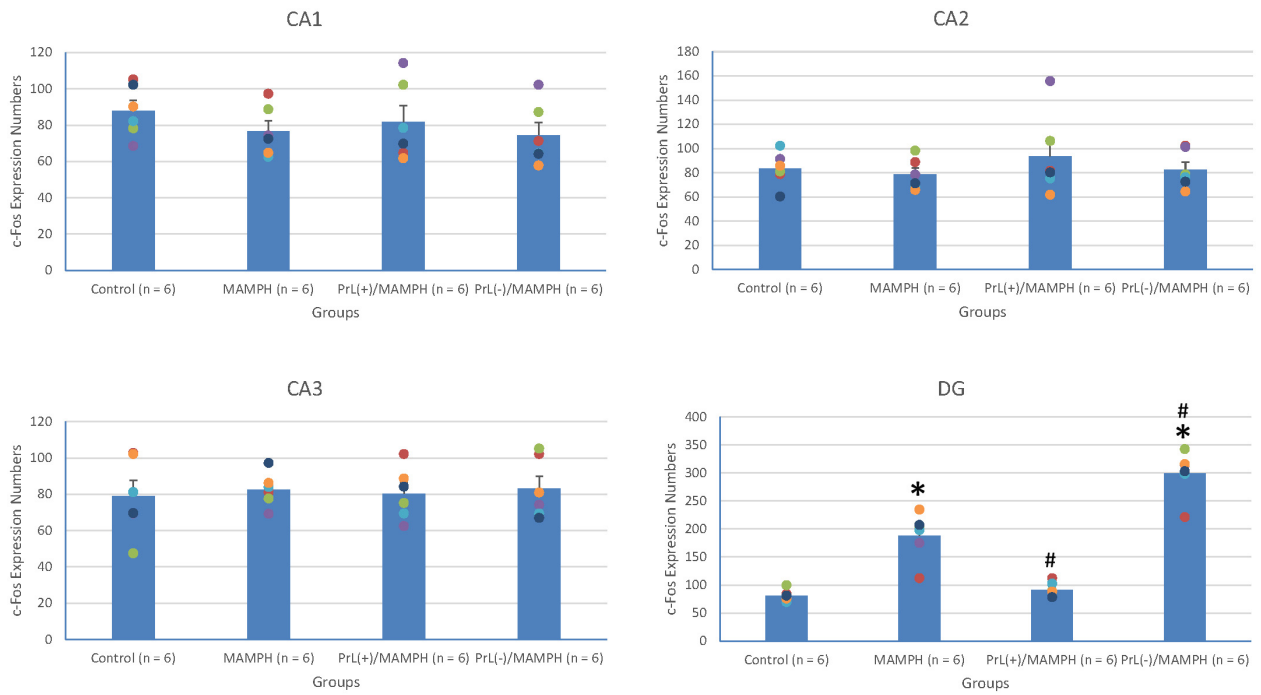

FIGURE 9 | MAMPH administrations were tested in order to label c-Fos expression in the CA1, CA2, CA3, and DG of the hippocampus for the control (n = 6), MAMPH (n = 6), PrL(+)/MAMPH (n = 6), and PrL(–)/MAMPH groups (n = 6) by injecting NMDA or saline into the PrL. PrL(+): injection of a low concentration of NMDA to excite the PrL neurons; PrL(–): Injection of a high concentration of NMDA to destroy the PrL neurons. Differences in c-Fos expression levels in the CA1, CA2, CA3, and DG among all groups were analyzed by one-way ANOVA, followed by Tukey's *post hoc* test if a significant difference was appeared among groups. $^{*}p < 0.05$ indicates significant differences compared with the control group; $^{\#}p < 0.05$ indicates significant differences compared with the MAMPH group.

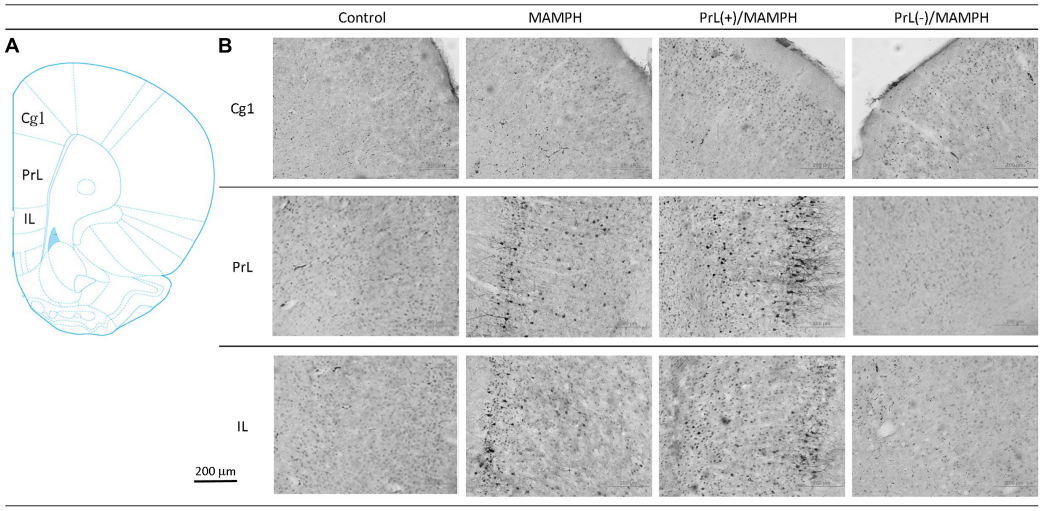

FIGURE 10 | (A) A schematic brain atlas for the Cg1, PrL, and IL of the mPFC. **(B)** Representative photomicrographs of p-ERK expression for the Cg1, PrL, and IL in the control, MAMPH, PrL(+)/MAMPH, and PrL(–)/MAMPH groups. The scale bar represents 200 μm.

significantly in the Cg1, PrL, and IL for the PrL(+)/MAMPH group compared with the MAMPH group ($p < 0.05$). In contrast, p-ERK expression in the PrL(–)/MAMPH group decreased significantly in the PrL and BLA compared with the MAMPH group ($p < 0.05$; **Figures 10**, **11**). Therefore, we can surmise that MAMPH elicited neural plasticity in the PrL and IL but not in the Cg1. The excitation of the PrL neurons enhanced MAMPH-induced neural plasticity throughout the entire mPFC, including the Cg1, PrL, and IL. Additionally, the lesion of the PrL neurons reduced MAMPH-induced neural plasticity in the PrL and IL.

To test the effect of MAMPH administrations and the PrL's modulation underlying the MAMPH injections on p-ERK expression in the rewarding and aversive emotion-related brain areas such as the NAc, CeA, and BLA, a one-way ANOVA analysis showed that the factor of the group was the significant difference in the NAc [$F(3, 20) = 7.71$, $p < 0.05$] (partial $\eta^2 = 0.54$, power = 0.97) and BLA [$F(3, 20) = 45.19$, $p < 0.05$] (partial $\eta^2 = 0.87$, power = 1.00), but not in the CeA [$F(3, 20) = 0.13$, $p > 0.05$] (partial $\eta^2 = 0.02$, power = 0.07). The *post hoc* Tukey's HSD test indicated that p-ERK expression in the MAMPH group increased significantly compared with the control group in the BLA ($p < 0.05$) but not in the NAc and CeA ($p > 0.05$). In the BLA, p-ERK expression in the PrL(+)/MAMPH group decreased significantly compared with the MAMPH group ($p < 0.05$), while it increased significantly in the PrL(–)/MAMPH group compared with the MAMPH group ($p < 0.05$; **Figures 12**, **13**).

In conclusion, MAMPH elicited neural plasticity in the BLA but not in the CeA and NAc. The excitation of the PrL neurons inhibited MAMPH-induced neural plasticity, while the lesion of the PrL neurons enhanced MAMPH-induced neural plasticity in the BLA.

A one-way ANOVA analysis was performed in order to examine MAMPH and the PrL's modulation underlying the MAMPH administrations. The results of p-ERK expression showed that a factor of group was significant difference in the DG [$F(3, 20) = 28.49$, $p < 0.05$] (partial $\eta^2 = 0.81$, power = 1.00) but not the CA1 [$F(3, 20) = 0.41$, $p > 0.05$] (partial $\eta^2 = 0.06$, power = 0.12), CA2 [$F(3, 20) = 2.65$, $p > 0.05$] (partial $\eta^2 = 0.28$, power = 0.56), and CA3 [$F(3, 20) = 1.04$, $p > 0.05$] (partial $\eta^2 = 0.14$, power = 0.24). The *post hoc* Tukey's HSD test showed that p-ERK expression in the MAMPH group increased significantly compared with the control group in the DG ($p < 0.05$). In the DG, p-ERK expression in the PrL(+)/MAMPH decreased significantly compared with the MAMPH group ($p < 0.05$). However, there were no significant differences in p-ERK expression between the PrL(–)/MAMPH group and the MAMPH group in the DG ($p > 0.05$; **Figures 14**, **15**). The administration of MAMPH only appeared to induce neural plasticity in the DG. The excitation of the PrL neurons suppressed MAMPH-induced neural plasticity in the DG, while the lesion of the PrL neurons did not affect MAMPH-induced neural plasticity in the DG.

DISCUSSION

Long-term MAMPH administrations elicited CTA learning and plasma corticosterone levels. At this condition, the brain areas related to cognition, such as the mPFC (e.g., the Cg1, PrL, and IL), the affective areas, such as the rewarding NAc and the aversive and rewarding BLA, and the spatial learning brain area, the DG, activate neural activity for labeling c-Fos expression. Neural plasticity was induced in the PrL, IL, BLA, and DG for labeling p-ERK expression following MAMPH administration. Although microinjections of a low concentration of NMDA enhanced MAMPH-induced neural activity in the brain areas associated with cognitive function (the Cg1, PrL, and IL), the microinjections reduced MAMPH-induced neural activity and plasticity in the BLA and DG. In contrast, microinjections of a high concentration of NMDA reduced MAMPH-induced

neural activity in the Cg1, PrL, and IL, and neural plasticity in the PrL and IL, but increased MAMPH-induced neural activity in the DG and neural plasticity in the BLA and DG (**Supplementary Table 1**).

Comparison With Previous Findings: Methamphetamine Treatments in Alzheimer's Disease in the Animal and Human Models

Previous studies have shown that MAMPH administrations can cause neurotoxicity, inflammation, apoptosis, and cell death, or can also produce ameliorative effects in cognitive enhancement and synaptic plasticity, depending on differing doses, and the trials and durations of MAMPH (Hart et al., 2012; Shukla and Vincent, 2020). The low and medium doses or the one-off or short-term MAMPH administrations can ameliorate cognitive decline and dysfunction in AD patients (Hart et al., 2012; Shukla and Vincent, 2020). However, high doses and long-term use of MAMPH are likely to induce neuropsychiatric symptoms (Scherer et al., 2018) and cognitive dysfunction in AD patients (Hart et al., 2012; Shukla and Vincent, 2020).

Regarding neuronal levels, long-term treatments and high doses of MAMPH can cause neuronal inflammation and neurotoxicity (Panenka et al., 2013; Wood et al., 2014). A previous study on people showed that injecting a low dose of 30 mg MAMPH enhanced working memory, attention, and information processing speed (Mahoney et al., 2011). This human study gave a trial injection of 30 mg MAMPH to the subject. If we assumed that the subject weighed 60 kg, this dose could be translated to approximately 1.36 mg for a rat weighing 300 g (Nair and Jacob, 2016). The present study used a lower dose of MAMPH (1 mg/kg) in rats than in the previous human study, meaning that MAMPH administrations used in the present study may enhance cognitive function and neuronal plasticity but will not cause cognitive decline or neurotoxicity.

As per our anticipatory results, the present data showed that MAMPH administrations elicit CTA learning and increase neural activity in c-Fos expression and neural plasticity in p-ERK expression in the neural substrates related to cognitive function. In the subareas of the mPFC (including the Cg1, PrL, and IL), MAMPH activated CTA learning and memory. Moreover, the DG of the hippocampus, which mediates spatial learning, elicited neural activity and neural plasticity after MAMPH administration. This evidence appears to support results from previous animal and human models. For example, low doses of MAMPH were shown to enhance LTP activity and spinal enlargement in the dentate granule cells of the DG (Baptista et al., 2016). In the passive avoidance conditioning test, rats with MAMPH injections were able to boost their memory, indicating that MAMPH may be a cognitive enhancer that could aid memory retention (Matsuoka et al., 1992). Low concentrations of MAMPH have been shown to increase dopamine transmission and dopamine firing rates, while higher concentrations of MAMPH have reduced dopamine D2 autoreceptor activity and decreased the peak amplitude of dopamine's synaptic currents (Branch and Beckstead, 2012). In an *in vivo* study, a low dose of MAMPH exposure regulated beta-amyloid precursor protein-cleaving secretases and stimulated the soluble amyloid precursor protein alpha for improving cognitive functions in AD patients (Shukla et al., 2019).

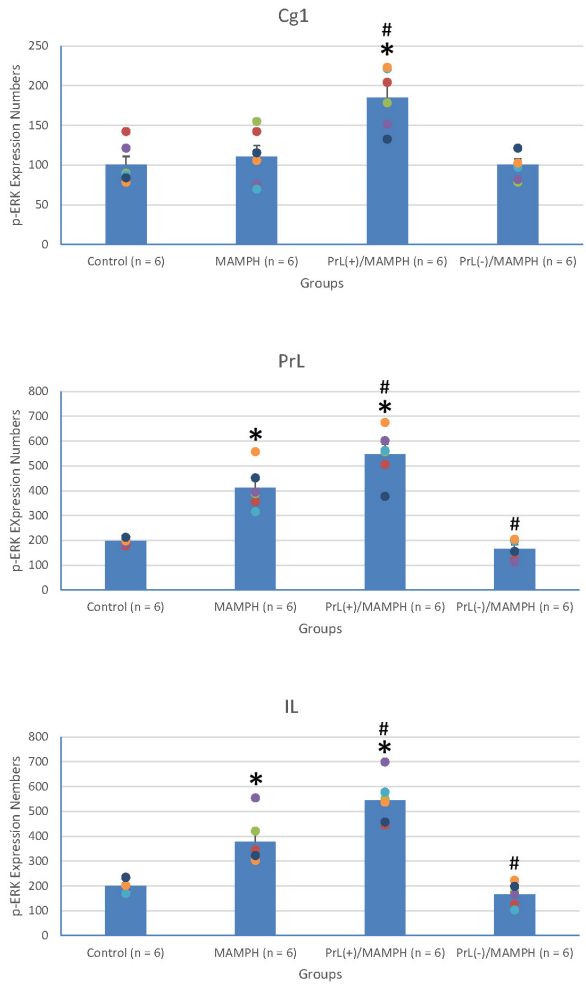

FIGURE 11 | MAMPH administrations were tested to label p-ERK expression in the Cg1, PrL, and IL of the mPFC for the control (n = 6), MAMPH (n = 6), PrL(+)/MAMPH (n = 6), and PrL(–)/MAMPH groups (n = 6) by injecting NMDA or saline into the PrL. PrL(+): Injection of a low concentration of NMDA to excite the PrL neurons; PrL(–): Injection of a high concentration of NMDA to destroy the PrL neurons. Differences in p-ERK expression levels in the Cg1, PrL, and IL among all groups were analyzed by one-way ANOVA, followed by Tukey's *post hoc* test if a significant difference was appeared among groups. *$p < 0.05$ indicates significant differences compared to the Control group; #$p < 0.05$ indicates significant differences compared to the MAMPH group.

In human models, the previous findings are similar to those in animal studies. MAMPH may ameliorate an AD patient's numerous cognitive functions, including visuospatial perception, attention span, inhibition, working memory, long-term memory and learning, and neuropsychiatric symptoms for a specific condition. For example, a low dose or a one-off administration of MAMPH (Hart et al., 2012) could be used as a cognitive enhancer for treating AD symptoms (Shukla and Vincent, 2020).

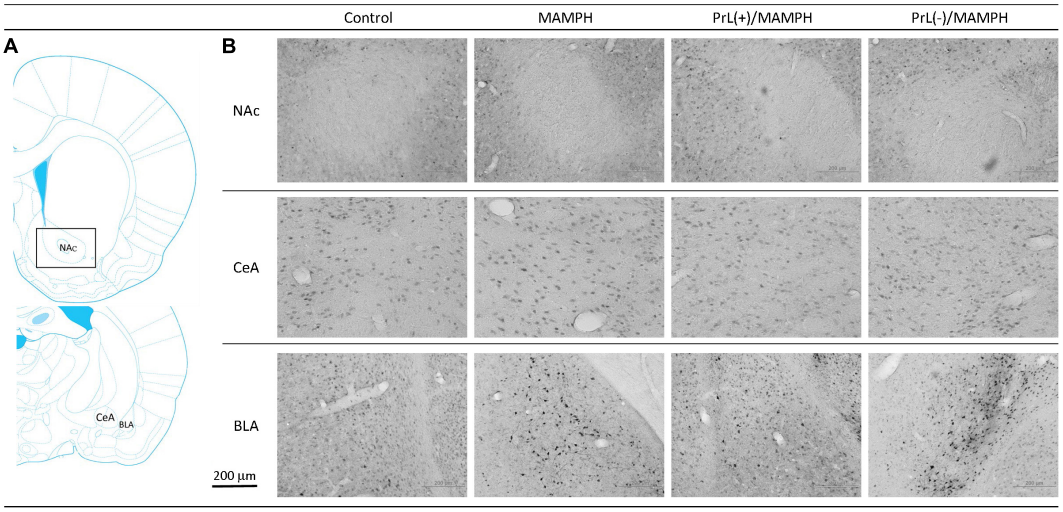

FIGURE 12 | (A) A schematic brain atlas for the NAc and the amygdala's CeA and BLA. **(B)** Representative photomicrographs of p-ERK expression for the NAc and the amygdala's CeA and BLA in the control, MAMPH, PrL(+)/MAMPH, and PrL(–)/MAMPH groups. The scale bar represents 200 μm.

One-off administrations and relatively small concentrations of amphetamine (90, 95, 105 ng/ml) and MAMPH (72, 67, and 59 ng/ml) were found to enhance psychomotor function and perceptual speed in attention studies (Silber et al., 2006). Intermediate doses (12 and 25 mg/70 kg) of MAMPH, applied using intranasal administration, were shown to improve cognitive and psychomotor functions that decreased hit latency, increased maximum tracking speed for improving divided attention performance, and enhanced performance in a total attempt and correct in the digit-symbol-substitution task (Hart et al., 2008). Using 15 and 30 mg MAMPH administration by the intravenous way increased attention, concentration, and psychomotor performance (Johnson et al., 2005). In addition, a low dose of 10 mg MAMPH appeared to increase reaction time in a memory scanning task (Mohs et al., 1980). Psychostimulants (e.g., amphetamine and methylphenidate) can improve apathy symptoms in AD patients (Scherer et al., 2018). In summary, the MAMPH administrations may ameliorate cognitive impairments and neuropsychiatric symptoms and activate neuroactivity and synaptic plasticity. Administrating the specific doses of MAMPH over specific trials and durations could potentially treat AD symptoms in the future.

By contrast, MAMPH administrations can also induce c-Fos or p-ERK expression in the affected brain area- rewarding the NAc and rewarding and aversive the BLA. In this treatment regimen, MAMPH administrations caused drug addiction and negative emotional responses. These adverse effects of MAMPH should also be taken into consideration when developing treatment regimens for AD symptoms.

Prelimbic Cortex Modulation and Methamphetamine Administrations

In the present study, the MAMPH administrations linked to PrL excitation with a low concentration of NMDA enhanced a single MAMPH administration-induced neural activity in c-Fos expression and neural plasticity in p-ERK expression in the PrL and IL of the mPFC. The results indicated that the excitation of the PrL neurons underlying MAMPH administrations upregulated c-Fos expression in neural activity and p-ERK expression in neural plasticity. The PrL may also play a role in enhancing MAMPH's effect on neural activity and plasticity. The involvement of the PrL produces a combined effect for facilitating MAMPH-induced neural activity and plasticity in the mPFC—the area of the brain associated with cognition. Unfortunately, no research currently exists that examines the effect of the PrL in MAMPH's neural activation and cognitive function in animal models. Our findings were associated with the viewpoint that the prefrontal cortex regulates various cognitive and executive functions, including working memory, inhibitory control, decision making, attention, spatial learning, and long-term memory (Dalley et al., 2004; Jobson et al., 2021). In light of this indirect viewpoint, the excitation of the PrL of the mPFC might be expected to enhance cognitive and executive processing in the frontal cortex, thereby facilitating MAMPH-induced neural activity and plasticity in the mPFC, particularly in the PrL and IL.

On the other hand, the PrL excitation inhibited CTA conditioned learning induced by MAMPH and plasma corticosterone levels, whereas the PrL lesion enhanced MAMPH-induced CTA learning and corticosterone levels in the plasma. The present study also indicated that the PrL plays a role in inhibitory control to blunt the aversive CTA learning and corticosterone secretions (Jobson et al., 2021).

The data also showed that the PrL has an inhibitory role for the DG. Regarding the DG, the PrL excitation inhibited the spatial learning brain area (the DG of the hippocampus) in neural activity for c-Fos expression or neural plasticity for p-ERK expression. Conversely, the PrL lesion enhanced neural activity or neural plasticity in the DG of the hippocampus. However, the

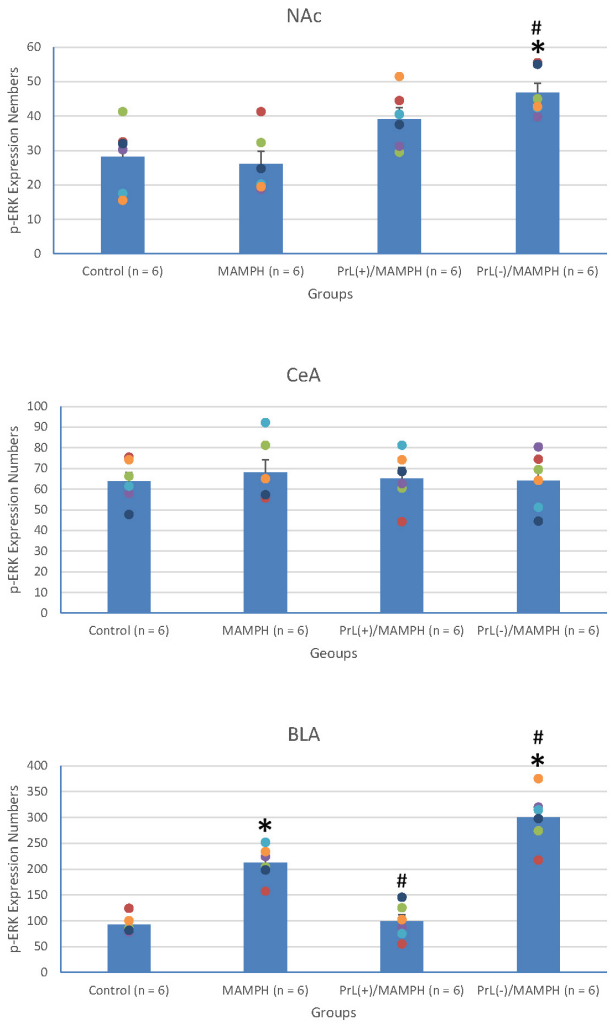

FIGURE 13 | MAMPH administrations were tested in order to label p-ERK expression in the NAc and the amygdala's CeA, and BLA for the control (n = 6), MAMPH (n = 6), PrL(+)/MAMPH (n = 6), and PrL(–)/MAMPH groups (n = 6) by injecting NMDA or saline into the PrL. PrL(+): Injection of a low concentration of NMDA to excite the PrL neurons; PrL(–): Injection of a high concentration of NMDA to destroy the PrL neurons. Differences in p-ERK expression levels in the NAc, CeA, and BLA among all groups were analyzed by one-way ANOVA, followed by Tukey's *post hoc* test if a significant difference was appeared among groups. $^{*}p < 0.05$ indicates significant differences compared with the control group; $^{\#}p < 0.05$ indicates significant differences compared with the MAMPH group.

PrL excitation also inhibited the BLA's neural activity in c-Fos expression and neural plasticity in p-ERK expression, and the PrL lesion increased neural acidity in c-Fos expression and neural plasticity in p-ERK expression, indicating the PrL also plays a role of an inhibitory regulation for the BLA.

It is well known that the mPFC projects different brain areas to mediate distinct functions (Dalley et al., 2004). In the structural aspect, the mPFC interacts significantly with the cortical subregions, including the thalamus, NAc, amygdala, and hippocampus (Riga et al., 2014; Jobson et al., 2021). In the functional aspect, it remains unknown as to whether the mPFC (particularly the PrL) interacted with these subregions, and it always played an inhibitory control to the NAc, amygdala, and hippocampus. Alternatively, it may contribute to regulating the cortical subregions under certain conditions. This emerging issue should be investigated in future studies.

Plasma in Corticosterone Levels and Stress Underlying the Methamphetamine Administrations

Whether or not MAMPH administration affects plasma corticosterone remains uncertain for the following reasons? For example, a high dose of MAMPH (10 mg/kg) caused an increase in plasma corticosterone levels and BDNF for neonatal rats during the postnatal days 11–15 (Grace et al., 2008). However, adolescent mice with acute MAMPH exposure exhibited increased locomotor activity and anxiety behavior, although their plasma corticosterone levels remained steady (Rud et al., 2016). After acute MAMPH administration, female (but not male) mice exhibited a prolonged increase in plasma corticosterone levels, indicating that the animal's sex can affect plasma corticosterone levels after MAMPH administration (Zuloaga et al., 2014). Another study pointed out the importance of the time point, as MAMPH treatments increased plasma corticosterone levels between 1 and 72 h, with the peak point occurring during the first hour (Herring et al., 2008). The results showed that MAMPH administration elevates plasma corticosterone, which might also show that MAMPH enhances stress status. The data were consistent with the above viewpoint that MAMPH-elicited corticosterone levels in plasma and anxiety and aversive behaviors (Grace et al., 2008; Herring et al., 2008). Alternatively, the excitation or lesion of the PrL neurons decreased or increased MAMPH-induced plasma corticosterone levels in the present study. The PrL might also play executive and inhibitory roles in the regulation of MAMPH administration-induced stress effects. This viewpoint is seemingly consistent with the fact that the PrL of the mPFC inhibits neural activity within the amygdala (Laurent and Westbrook, 2008; Koenigs and Grafman, 2009). The mPFC-amygdala pathway conveys a negative valence of the emotion of the amygdala to the mPFC, meaning that the mPFC inhibits the negative emotional response from the amygdala. The balance of the mPFC-amygdala pathway is to maintain the individual's psychological health (Peters et al., 2009; Kim et al., 2011). MAMPH may induce a stress effect and may release plasma corticosterone. However, the PrL's modulation of the mPFC is essential for reducing the stress effect induced by MAMPH administrations.

Experimental Limitations and Emerged Issues

The present study had some experimental limitations. First, the present study used healthy rats to test whether MAMPH administration affected conditioned learning in the mPFC (cognitive function), the NAc, the amygdala (the affected brain areas), or the hippocampus (the spatial learning area) by

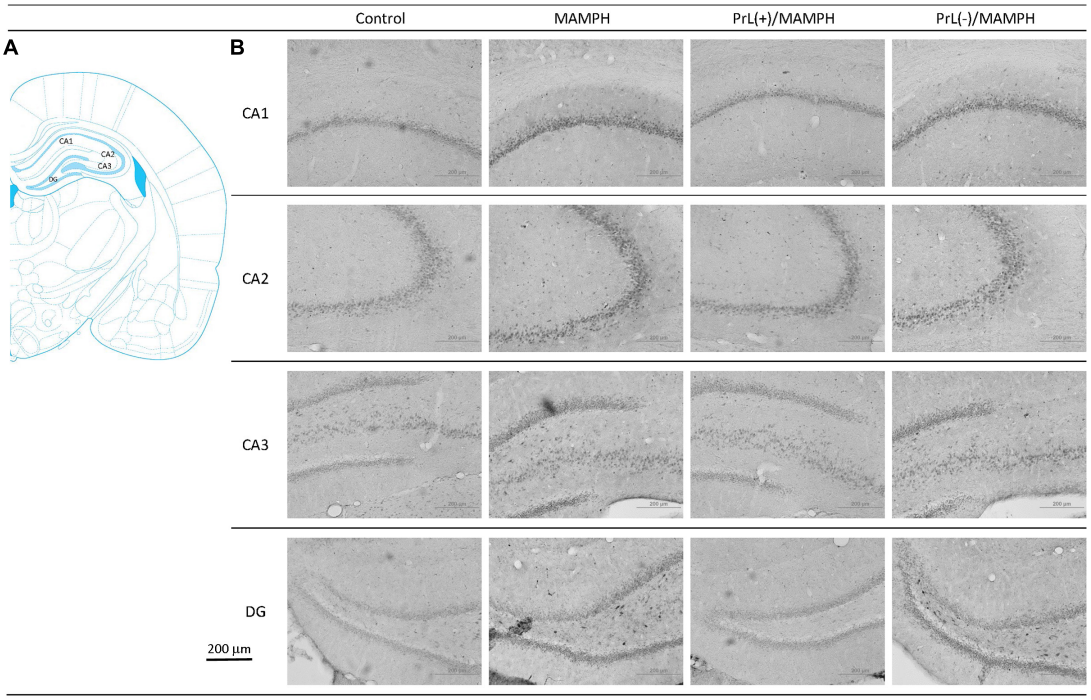

FIGURE 14 | (A) A schematic brain atlas for the CA1, CA2, CA3, and DG of the hippocampus. **(B)** Representative photomicrographs of p-ERK expression for the CA1, CA2, CA3, and DG of the hippocampus in the control, MAMPH, PrL(+)/MAMPH, and PrL(–)/MAMPH groups. The scale bar represents 200 μm.

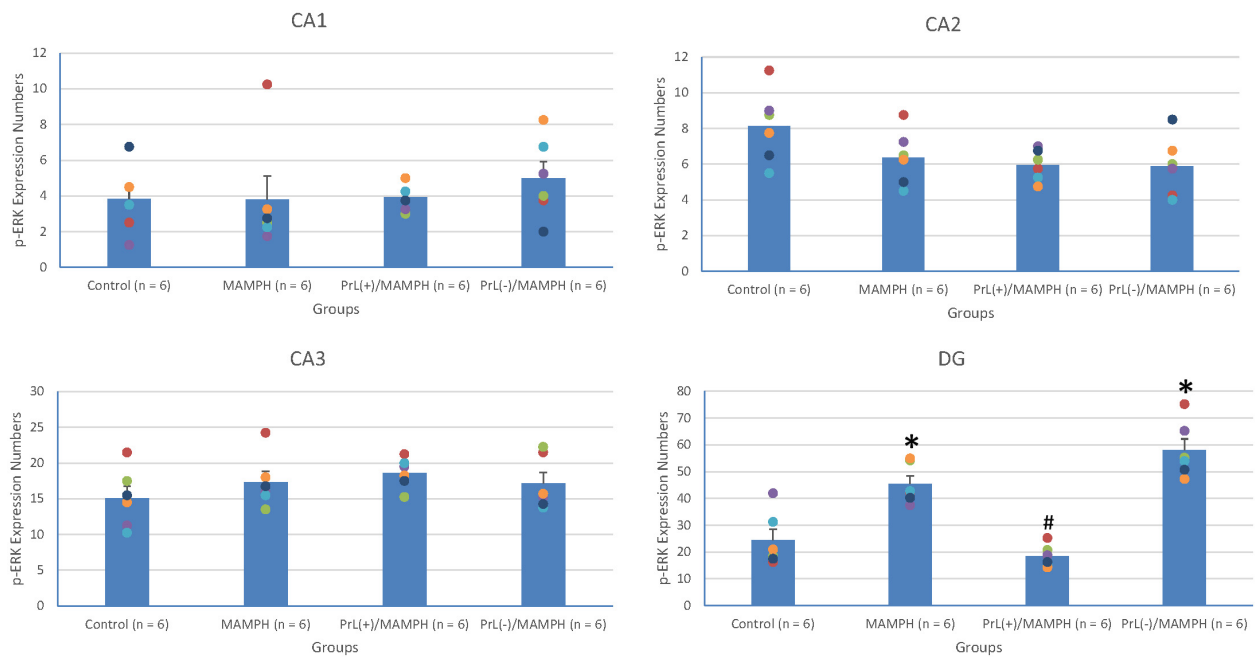

FIGURE 15 | MAMPH administrations were tested to label p-ERK expression in the CA1, CA2, CA3, and DG of the hippocampus for the control (n = 6), MAMPH (n = 6), PrL(+)/MAMPH (n = 6), and PrL(–)/MAMPH groups (n = 6) by injecting NMDA or saline into the PrL. PrL(+): Injection of a low concentration of NMDA to excite the PrL neurons; PrL(–): Injection of a high concentration of NMDA to destroy the PrL neurons. Differences in p-ERK expression levels in the CA1, CA2, CA3, and DG among all groups were analyzed by one-way ANOVA, followed by Tukey's *post hoc* test if a significant difference was appeared among groups. $^{*}p < 0.05$ indicates significant differences compared with the control group; $^{\#}p < 0.05$ indicates significant differences compared with the MAMPH group.

measuring plasma corticosterone levels; neural activity, assessed by measuring c-Fos expression; or neural plasticity, via assessed by measuring p-ERK expression. The study also clarified whether MAMPH administered to the PrL affected CTA, neural activity, or plasticity in the mPFC, NAc, amygdala, and hippocampus. Our study found that the short-term administration of MAMPH serves as a cognitive enhancer in a typical animal model of CTA (Yu et al., 2021); however, the model used in this study was not a typical animal model of AD. Repeating these tests in a suitable animal model of AD [e.g., a transgenic (Weishaupt et al., 2018) or a neurotoxic lesion-induced mouse model (Ando et al., 2002) of AD] and examining the effects on CTA under AD conditions remains necessary in future studies to determine whether these findings are applicable in the AD brain.

Second, this study only used rats aged between 6 and 8 weeks (1.5–2 months). Some studies have suggested that younger rats are suitable for AD animal models (El Tamer et al., 1992, 1996). For example, AD-related animal studies of reversible cholinergic changes have demonstrated that the intracerebroventricular administration of AF64A to induce cholinergic toxicity resulted in decreased ChAT activity and increased AChE activity in the hippocampus and septal regions of young rats (2, 4, and 12 months), whereas older rats, aged 22 months, showed no changes in ChAT and AChE activity (El Tamer et al., 1992, 1996). However, other AD studies have used older animals (Weishaupt et al., 2018). For example, in APP21 transgenic rats aged 19 months, working memory deficits were observed in strategy shifts and facilitated white matter inflammation (Weishaupt et al., 2018). Therefore, rats of different age groups should be tested in future experiments.

In the statistical analysis, Tukey's HSD test was conducted after one-way ANOVA. According to statistical rules, Tukey's HSD test was used for those analyses in which the sample sizes of different groups were equal; however, when the sample size is unequal, the Tukey's HSD equation should be modified using the Tukey-Kramer procedure (Montgomery, 2013). Therefore, when analyses were performed on groups in which the sample size was not equal, the *post hoc* test was conducted using the Tukey-Kramer procedure.

Finally, this study only tested CTA conditioned learning. The CTA animal task is an aversively conditioned learning process; moreover, it is actually an implicit learning and memory task. Therefore, different learning and memory tasks also need to be investigated in order to determine whether MAMPH enhances cognitive performances in other implicit (e.g., reward conditioned learning) and explicit learning and memory tasks in the animal model.

CONCLUSION

Using a low dose of 1 mg/kg MAMPH with three continuous administrations in the present study produced CTA conditioned learning, increases in plasma corticosterone levels, and enhancements in neural activity in c-Fos expression, and neural plasticity in p-ERK expression in the cognitive function areas (the mPFC, e.g., Cg1, PrL, and IL), the affected brain areas (the rewarding NAc and rewarding and aversive BLA), and the spatial learning and memory brain areas (the hippocampus' CA3 and DG). Additionally, the excitation of the PrL neurons induced more enhancements for neural activity and neural plasticity in the PrL and IL of the mPFC's subareas, indicating that a low dose of MAMPH in conjunction with the excitation of PrL neurons might lead to a higher level of neural activity and plasticity than a single MAMPH administration in ameliorating cognitive functions. Therefore, low doses of MAMPH and the modulation of PrL neurons might provide a possible treatment for certain symptoms of AD.

DATA AVAILABILITY STATEMENT

The datasets presented in this study can be found in online repositories. The names of the repository/repositories and accession number(s) can be found in the article/ **Supplementary Material**.

ETHICS STATEMENT

The animal study was reviewed and approved by the Fo Guang University Institutional Animal Care and Use Committee.

AUTHOR CONTRIBUTIONS

B-CS: methodology, validation, investigation, data curation, supervision, and funding acquisition. ZY-G: data curation and project administration. JW: formal analysis and project administration. C-NC: preparing figures and project administration. ABHH: data curation. ACWH: conceptualization, methodology, formal analysis, writing (original draft), writing (review and editing), and funding acquisition. All authors contributed to the article and approved the submitted version.

FUNDING

This present study was supported by a funding grant from the Ministry of Science and Technology of Taiwan to B-CS (MOST-109-2320-B-001-010) and ACWH (MOST 110-2410-H-431-004).

ACKNOWLEDGMENTS

We would like to thank the Institute of Biomedical Sciences of Academia Sinica in Taiwan.

SUPPLEMENTARY MATERIAL

The Supplementary Material for this article can be found online at: https://www.frontiersin.org/articles/10.3389/fnagi.2021.751913/full#supplementary-material

REFERENCES

Ando, S., Kobayashi, S., Waki, H., Kon, K., Fukui, F., Tadenuma, T., et al. (2002). Animal model of dementia induced by entorhinal synaptic damage and partial restoration of cognitive deficits by BDNF and carnitine. *J. Neurosci. Res.* 70, 519–527. doi: 10.1002/jnr.10443

Baptista, S., Lourenco, J., Milhazes, N., Borges, F., Silva, A. P., and Bacci, A. (2016). Long-Term Treatment with Low Doses of Methamphetamine Promotes Neuronal Differentiation and Strengthens Long-Term Potentiation of Glutamatergic Synapses onto Dentate Granule Neurons. *eNeuro* 3:3. doi: 10.1523/ENEURO.0141-16.2016

Beyeler, A., Chang, C. J., Silvestre, M., Leveque, C., Namburi, P., Wildes, C. P., et al. (2018). Organization of Valence-Encoding and Projection-Defined Neurons in the Basolateral Amygdala. *Cell Rep.* 22, 905–918. doi: 10.1016/j.celrep.2017.12.097

Branch, S. Y., and Beckstead, M. J. (2012). Methamphetamine produces bidirectional, concentration-dependent effects on dopamine neuron excitability and dopamine-mediated synaptic currents. *J. Neurophysiol.* 108, 802–809. doi: 10.1152/jn.00094.2012

Bray, G. A. (1993). Use and abuse of appetite-suppressant drugs in the treatment of obesity. *Ann. Intern. Med.* 119(7 Pt 2), 707–713. doi: 10.7326/0003-4819-119-7_part_2-199310011-00016

Cai, Y. Q., Wang, W., Paulucci-Holthauzen, A., and Pan, Z. Z. (2018). Brain Circuits Mediating Opposing Effects on Emotion and Pain. *J. Neurosci.* 38, 6340–6349. doi: 10.1523/JNEUROSCI.2780-17.2018

Cheng, C. N., Wei Huang, A. C., and Wu, S. J. (2020). Roles of nucleus accumbens shell and core in footshock-induced stress altering behavioral sensitization by methamphetamine in acquisition and testing: Running head: stress, nucleus accumbens, and behavioral sensitization. *Behav. Brain Res.* 380:112434. doi: 10.1016/j.bbr.2019.112434

Dalley, J. W., Cardinal, R. N., and Robbins, T. W. (2004). Prefrontal executive and cognitive functions in rodents: neural and neurochemical substrates. *Neurosci. Biobehav. Rev.* 28, 771–784. doi: 10.1016/j.neubiorev.2004.09.006

El Tamer, A., Corey, J., Wulfert, E., and Hanin, I. (1992). Reversible cholinergic changes induced by AF64A in rat hippocampus and possible septal compensatory effect. *Neuropharmacology* 31, 397–402. doi: 10.1016/0028-3908(92)90073-x

El Tamer, A., Wulfert, E., and Hanin, I. (1996). Age-dependent effect of AF64A on cholinergic activity in the septo-hippocampal pathway of the rat brain: decreased responsiveness in aged rats. *Neurosci Lett* 203, 123–126. doi: 10.1016/0304-3940(95)12283-4

Fry, J. M. (1998). Treatment modalities for narcolepsy. *Neurology* 50(2 Suppl. 1), S43–S48. doi: 10.1212/wnl.50.2_suppl_1.s43

Gilbert, P. E., Pirogovsky, E., Brushfield, A. M., Luu, T. T., Tolentino, J. C., and Renteria, A. F. (2009). Age-related changes in associative learning for olfactory and visual stimuli in rodents. *Ann. N. Y. Acad. Sci.* 1170, 718–724. doi: 10.1111/j.1749-6632.2009.03929.x

Grace, C. E., Schaefer, T. L., Herring, N. R., Skelton, M. R., McCrea, A. E., Vorhees, C. V., et al. (2008). (+)-Methamphetamine increases corticosterone in plasma and BDNF in brain more than forced swim or isolation in neonatal rats. *Synapse* 62, 110–121. doi: 10.1002/syn.20470

Hart, C. L., Gunderson, E. W., Perez, A., Kirkpatrick, M. G., Thurmond, A., Comer, S. D., et al. (2008). Acute physiological and behavioral effects of intranasal methamphetamine in humans. *Neuropsychopharmacology* 33, 1847–1855. doi: 10.1038/sj.npp.1301578

Hart, C. L., Marvin, C. B., Silver, R., and Smith, E. E. (2012). Is cognitive functioning impaired in methamphetamine users? A critical review. *Neuropsychopharmacology* 37, 586–608. doi: 10.1038/npp.2011.276

Harvey, B. H., Brand, L., Jeeva, Z., and Stein, D. J. (2006). Cortical/hippocampal monoamines, HPA-axis changes and aversive behavior following stress and restress in an animal model of post-traumatic stress disorder. *Physiol. Behav.* 87, 881–890.

He, A. B. H., Huang, C. L., Kozlowska, A., Chen, J. C., Wu, C. W., Huang, A. C. W., et al. (2019). Involvement of neural substrates in reward and aversion to methamphetamine addiction: Testing the reward comparison hypothesis and the paradoxical effect hypothesis of abused drugs. *Neurobiol. Learn Mem.* 166:107090. doi: 10.1016/j.nlm.2019.107090

Herring, N. R., Schaefer, T. L., Tang, P. H., Skelton, M. R., Lucot, J. P., Gudelsky, G. A., et al. (2008). Comparison of time-dependent effects of (+)-methamphetamine or forced swim on monoamines, corticosterone, glucose, creatine, and creatinine in rats. *BMC Neurosci.* 9:49. doi: 10.1186/1471-2202-9-49

Huang, A. C. W., Yu, Y. H., He, A. B. H., and Ou, C. Y. (2020). Interactions between prelimbic cortex and basolateral amygdala contribute to morphine-induced conditioned taste aversion in conditioning and extinction. *Neurobiol. Learn Mem.* 172:107248. doi: 10.1016/j.nlm.2020.107248

Jarrard, L. E. (1993). On the role of the hippocampus in learning and memory in the rat. *Behav. Neural. Biol.* 60, 9–26. doi: 10.1016/0163-1047(93)90664-4

Jobson, D. D., Hase, Y., Clarkson, A. N., and Kalaria, R. N. (2021). The role of the medial prefrontal cortex in cognition, ageing and dementia. *Brain Commun.* 3:fcab125. doi: 10.1093/braincomms/fcab125

Johnson, B. A., Roache, J. D., Ait-Daoud, N., Wallace, C., Wells, L. T., and Wang, Y. (2005). Effects of isradipine on methamphetamine-induced changes in attentional and perceptual-motor skills of cognition. *Psychopharmacology* 178, 296–302. doi: 10.1007/s00213-004-1998-0

Kesner, R. P. (2007). A behavioral analysis of dentate gyrus function. *Prog. Brain Res.* 163, 567–576. doi: 10.1016/S0079-6123(07)63030-1

Kim, M. J., Loucks, R. A., Palmer, A. L., Brown, A. C., Solomon, K. M., Marchante, A. N., et al. (2011). The structural and functional connectivity of the amygdala: from normal emotion to pathological anxiety. *Behav. Brain Res.* 223, 403–410. doi: 10.1016/j.bbr.2011.04.025

Kirkpatrick, M. G., Gunderson, E. W., Johanson, C. E., Levin, F. R., Foltin, R. W., and Hart, C. L. (2012). Comparison of intranasal methamphetamine and d-amphetamine self-administration by humans. *Addiction* 107, 783–791. doi: 10.1111/j.1360-0443.2011.03706.x

Koenigs, M., and Grafman, J. (2009). Posttraumatic stress disorder: the role of medial prefrontal cortex and amygdala. *Neuroscientist* 15, 540–548. doi: 10.1177/1073858409333072

Laurent, V., and Westbrook, R. F. (2008). Distinct contributions of the basolateral amygdala and the medial prefrontal cortex to learning and relearning extinction of context conditioned fear. *Learn. Mem.* 15, 657–666. doi: 10.1101/lm.1080108

Mahoney, J. J. III, Jackson, B. J., Kalechstein, A. D., De La Garza, R. II, and Newton, T. F. (2011). Acute, low-dose methamphetamine administration improves attention/information processing speed and working memory in methamphetamine-dependent individuals displaying poorer cognitive performance at baseline. *Prog. Neuropsychopharmacol. Biol. Psychiatry* 35, 459–465. doi: 10.1016/j.pnpbp.2010.11.034

Matsuoka, N., Maeda, N., Yamazaki, M., Ohkubo, Y., and Yamaguchi, I. (1992). Effect of FR121196, a novel cognitive enhancer, on the memory impairment of rats in passive avoidance and radial arm maze tasks. *J. Pharmacol. Exp. Ther.* 263, 436–444.

Mizoguchi, H., and Yamada, K. (2019). Methamphetamine use causes cognitive impairment and altered decision-making. *Neurochem. Int.* 124, 106–113. doi: 10.1016/j.neuint.2018.12.019

Mohs, R. C., Tinklenberg, J. R., Roth, W. T., and Kopell, B. S. (1980). Sensitivity of some human cognitive functions to effects of methamphetamine and secobarbital. *Drug Alcohol. Depend* 5, 145–150. doi: 10.1016/0376-8716(80)90191-x

Montgomery, D. C. (2013). *Design and Analysis of Experiments* (Eighth ed.). Hoboken: Wiley.

Morales, G. J., Ramcharan, E. J., Sundararaman, N., Morgera, S. D., and Vertes, R. P. (2007). Analysis of the actions of nucleus reuniens and the entorhinal cortex on EEG and evoked population behavior of the hippocampus. *Annu. Int. Conf. IEEE Eng. Med. Biol. Soc.* 2007, 2480–2484. doi: 10.1109/IEMBS.2007.4352831

Nair, A. B., and Jacob, S. (2016). A simple practice guide for dose conversion between animals and human. *J. Basic Clin. Pharm.* 7, 27–31. doi: 10.4103/0976-0105.177703

Panenka, W. J., Procyshyn, R. M., Lecomte, T., MacEwan, G. W., Flynn, S. W., Honer, W. G., et al. (2013). Methamphetamine use: a comprehensive review of molecular, preclinical and clinical findings. *Drug Alcohol Depend* 129, 167–179. doi: 10.1016/j.drugalcdep.2012.11.016

Patrylo, P. R., and Williamson, A. (2007). The effects of aging on dentate circuitry and function. *Prog. Brain Res.* 163, 679–696. doi: 10.1016/S0079-6123(07)63037-4

Paxinos, G., and Watson, C. (2007). *The rat brain in stereotaxic coordinates*. Burlington, MA: Academic Press.

Perugi, G., Vannucchi, G., Bedani, F., and Favaretto, E. (2017). Use of Stimulants in Bipolar Disorder. *Curr. Psychiatry Rep.* 19:7. doi: 10.1007/s11920-017-0758-x

Peters, J., Kalivas, P. W., and Quirk, G. J. (2009). Extinction circuits for fear and addiction overlap in prefrontal cortex. *Learn. Mem.* 16, 279–288. doi: 10.1101/lm.1041309

Piazza, P. V., Maccari, S., Deminiere, J. M., Le, M., Mormede, P., and Simon, H. (1991). Corticosterone levels determine individual vulnerability to amphetamine self-administration. *Proc. Natl. Acad. Sci. U S A* 88, 2088–2092.

Ramirez, R. L. III, Perez, V. J., and Zamanian, R. T. (2018). Methamphetamine and the risk of pulmonary arterial hypertension. *Curr. Opin. Pulm. Med.* 24, 416–424. doi: 10.1097/MCP.0000000000000513

Riga, D., Matos, M. R., Glas, A., Smit, A. B., Spijker, S., and Van den Oever, M. C. (2014). Optogenetic dissection of medial prefrontal cortex circuitry. *Front. Syst. Neurosci.* 8:230. doi: 10.3389/fnsys.2014.00230

Rud, M. A., Do, T. N., and Siegel, J. A. (2016). Effects of early adolescent methamphetamine exposure on anxiety-like behavior and corticosterone levels in mice. *Neurosci. Lett.* 633, 257–261. doi: 10.1016/j.neulet.2016.09.036

Scherer, R. W., Drye, L., Mintzer, J., Lanctot, K., Rosenberg, P., Herrmann, N., et al. (2018). The Apathy in Dementia Methylphenidate Trial 2 (ADMET 2): study protocol for a randomized controlled trial. *Trials* 19:46. doi: 10.1186/s13063-017-2406-5

Shukla, M., Maitra, S., Hernandez, J. F., Govitrapong, P., and Vincent, B. (2019). Methamphetamine regulates betaAPP processing in human neuroblastoma cells. *Neurosci. Lett.* 701, 20–25. doi: 10.1016/j.neulet.2019.02.023

Shukla, M., and Vincent, B. (2020). The multi-faceted impact of methamphetamine on Alzheimer's disease: From a triggering role to a possible therapeutic use. *Ageing Res. Rev.* 60:101062. doi: 10.1016/j.arr.2020.101062

Silber, B. Y., Croft, R. J., Papafotiou, K., and Stough, C. (2006). The acute effects of d-amphetamine and methamphetamine on attention and psychomotor performance. *Psychopharmacology* 187, 154–169. doi: 10.1007/s00213-006-0410-7

Singewald, N., Salchner, P., and Sharp, T. (2003). Induction of c-Fos expression in specific areas of the fear circuitry in rat forebrain by anxiogenic drugs. *Biol. Psychiatry* 53, 275–283.

Sun, L. L., Zhang, Y., Liu, J. F., Wang, J., Zhu, W. L., Zhao, L. Y., et al. (2013). Role of melanin-concentrating hormone in the nucleus accumbens shell in rats behaviourally sensitized to methamphetamine. *Int. J. Neuropsychopharmacol.* 16, 1767–1780. doi: 10.1017/S1461145713000072

Tanimoto, S., Nakagawa, T., Yamauchi, Y., Minami, M., and Satoh, M. (2003). Differential contributions of the basolateral and central nuclei of the amygdala in the negative affective component of chemical somatic and visceral pains in rats. *Eur. J. Neurosci.* 18, 2343–2350. doi: 10.1046/j.1460-9568.2003.02952.x

Vogt, B. A., and Sikes, R. W. (2000). The medial pain system, cingulate cortex, and parallel processing of nociceptive information. *Prog. Brain Res.* 122, 223–235.

Weishaupt, N., Liu, Q., Shin, S., Singh, R., Agca, Y., Agca, C., et al. (2018). APP21 transgenic rats develop age-dependent cognitive impairment and microglia accumulation within white matter tracts. *J. Neuroinflammation* 15:241. doi: 10.1186/s12974-018-1273-7

Wood, S., Sage, J. R., Shuman, T., and Anagnostaras, S. G. (2014). Psychostimulants and cognition: a continuum of behavioral and cognitive activation. *Pharmacol. Rev.* 66, 193–221. doi: 10.1124/pr.112.007054

Yu, Y., He, A. B., Liou, M., Ou, C., Kozlowska, A., Chen, P., et al. (2021). The Paradoxical Effect Hypothesis of Abused Drugs in a Rat Model of Chronic Morphine Administration. *J. Clin. Med.* 10:15. doi: 10.3390/jcm10153197

Zuloaga, D. G., Johnson, L. A., Agam, M., and Raber, J. (2014). Sex differences in activation of the hypothalamic-pituitary-adrenal axis by methamphetamine. *J. Neurochem.* 129, 495–508. doi: 10.1111/jnc.12651

Conflict of Interest: The authors declare that the research was conducted in the absence of any commercial or financial relationships that could be construed as a potential conflict of interest.

Publisher's Note: All claims expressed in this article are solely those of the authors and do not necessarily represent those of their affiliated organizations, or those of the publisher, the editors and the reviewers. Any product that may be evaluated in this article, or claim that may be made by its manufacturer, is not guaranteed or endorsed by the publisher.

Copyright © 2021 Shyu, Gao, Wu, He, Cheng and Huang. This is an open-access article distributed under the terms of the Creative Commons Attribution License (CC BY). The use, distribution or reproduction in other forums is permitted, provided the original author(s) and the copyright owner(s) are credited and that the original publication in this journal is cited, in accordance with accepted academic practice. No use, distribution or reproduction is permitted which does not comply with these terms.

frontiers in Aging Neuroscience

ORIGINAL RESEARCH
published: 20 October 2021
doi: 10.3389/fnagi.2021.764308

Can Levodopa Challenge Testing Predict the Effect of Deep Brain Stimulation? One-Year Outcomes in a Chinese Cohort

Wei Lin[1,2], Dongliang Shi[1], Dan Wang[1], Likun Yang[2], Yuhai Wang[2] and Lingjing Jin[1,3]**

[1] *Department of Neurology, Tongji Hospital, Tongji University School of Medicine, Shanghai, China,* [2] *Department of Neurosurgery, Joint Logistics Support Unit No. 904 Hospital, School of Medicine, Anhui Medical University, Wuxi, China,* [3] *Neurorehabilitation Center, Yangzhi Rehabilitation Hospital (Shanghai Sunshine Rehabilitation Center), Tongji University School of Medicine, Shanghai, China*

Objective: Our study examined whether levodopa challenge test (LCT) results could predict quality of life (QoL) outcomes after surgery to implant subthalamic nucleus deep brain stimulation (STN-DBS) electrodes to treat advanced Parkinson's disease (PD).

Methods: Forty patients with STN-DBS underwent a follow-up 1 year after implantation surgery to analyze the correlation between preoperative levodopa impact test results and postoperative Unified Parkinson's Disease Rating Scale (UPDRS) III motor score, postoperative PD Questionnaire-39 (PDQ-39) score, and PDQ-39 improvement.

Results: Improvements in QoL were associated with several preoperative characteristics including preoperative UPDRS-III tremor, UPDRS-III tremor (off-60) ($p = 0.049$), UPDRS-III tremor (off-120) ($p = 0.012$), Mini-Mental State Examination ($p = 0.012$), and PDQ-39 ($p = 0.012$) before surgery. Multiple linear regression model using preoperative MMSE [odds ratio (OR) = 0.342, 95% confidence interval (CI) = 0.051–2.297], preoperative UPDRS-III tremor (OR = 2.099, 95% CI = 0.585–7.535), UPDRS-III tremor (off-60) [OR = 1.316, 95% CI = 0.804–2.154, UPDRS-III tremor (off-120) OR = 0.913, 95% CI = 0.691–1.207], correctly classified 88.5% of patients.

Conclusion: Levodopa challenge test results cannot predict the effect of DBS. However, the test can be incorporated into a regression prediction model to the quality of life of PD patients after DBS with other preoperative factors.

Keywords: levodopa (l-dopa), predict, deep brain brain stimulation, outcome, quality of life

OPEN ACCESS

Edited by:
Woon-Man Kung,
Chinese Culture University, Taiwan

Reviewed by:
Xin Wang,
Harvard Medical School, United States
Wb Liu,
Weifang Medical University, China
Wei Lin,
Chang Bing Show Chwan Memorial Hospital, Taiwan

****Correspondence:***
Lingjing Jin
lingjingjin@163.com
Yuhai Wang
wangyuhai67@126.com

Received: *25 August 2021*
Accepted: *13 September 2021*
Published: *20 October 2021*

Citation:
Lin W, Shi D, Wang D, Yang L, Wang Y and Jin L (2021) Can Levodopa Challenge Testing Predict the Effect of Deep Brain Stimulation? One-Year Outcomes in a Chinese Cohort. Front. Aging Neurosci. 13:764308. doi: 10.3389/fnagi.2021.764308

INTRODUCTION

Deep brain stimulation (DBS) was introduced in the early 1990s (Benabid et al., 1987), and it is now considered an important tool to treat patients with advanced Parkinson's disease (PD). Specifically, high-frequency stimulation to the subthalamic nucleus (STN) has been proved as an effective treatment for improving motor function in idiopathic PD. STN implantation can decrease the mean Unified Parkinson's Disease Rating Scale (UPDRS) score by 23% at 6 months postoperatively and reduce parkinsonian motor manifestations (e.g., bradykinesia, rest tremor, and rigidity).

Subthalamic nucleus DBS achieves good clinical outcomes when electrode programming is optimized (Timmermann et al., 2015), the target area is correct, and the patient is suitable to undergo the procedure. Careful monitoring of some indicators of postoperative outcomes can also help improve outcomes.

An increase of ∼30 points in the motor function score on the UPDRS Part III indicates DBS success in patients with PD (Defer et al., 1999; Kleiner-Fisman et al., 2006; Lang et al., 2006; Rodriguez et al., 2007). Available studies point to a strong relationship between quality of life (QoL) and the motor and non-motor features of PD including sleep disturbance, urinary problems, and mood (Freeman et al., 1995; Rodriguez et al., 2007; Anderson and Nutt, 2011).

As early as the 1980s, acute levodopa challenge tests (LCTs) were applied in various scenarios in patients with movement disorders like PD (Anderson and Nutt, 2011). After pharmacologically stimulating central dopamine receptors, dopaminergic transmission outcomes can be clinically observed, reflecting the short-duration response associated with levodopa intake. The LCT has been used in assessments prior to fetal dopamine neuron grafting (Langston et al., 1992; Peschanski et al., 1994; Freeman et al., 1995). LCT has also been used as a screening method for PD diagnosis and the effects of the treatment. However, a clear relationship between LCT results and outcomes has not been elucidated. Some studies indicated that PD patients with better responses on the LCT have greater QoL improvements after DBS (Deuschl et al., 2020). However, controversy still exists with regard to whether LCT results could be a prognostic factor for the response to DBS and patient prognosis (Jiang et al., 2019; Sharma et al., 2019).

Here, we assessed if LCT results and other clinical factors could be useful factors to predict DBS efficacy 1 year after implantation. This study aimed to evaluate the utility of the Levodopa challenge test and other different variables in predicting QoL outcomes after DBS.

MATERIALS AND METHODS

Subjects

A cohort of 17 females and 23 males with idiopathic PD, who underwent bilateral STN DBS implantation in 904th Hospital, were retrospectively enrolled between January 2016 and April 2019. Data such as medical history, sex, education level, age, and anti-Parkinsonism medication usage were recorded. Neuropsychological examinations were performed on all participants in our study. Only those who had idiopathic PD for at least 5 years, according to the criteria in reference (Hughes et al., 1992), and were willing to accept bilateral DBS surgery, were enrolled.

Compared to baseline, the 30% decline in the UPDRS III score was considered the cut-off point for the DBS operation (Merello et al., 2002, 2011). All the subjects were followed for 1 year after DBS surgery and all the tests below were completed.

On average, the subjects at the STN DBS surgery were 61.30 ± 8.97 years old, and the mean disease duration before surgery was 9.98 ± 4.05 years. The mean scores for the Mini-Mental State Examination (MMSE), Montreal Cognitive Assessment Basic (MoCA-B), and PD Questionnaire-39 (PDQ-39) were 27.14 ± 10.32, 19.69 ± 5.35, and 63.20 ± 26.43, respectively. The average levodopa equivalent daily dose (LEDD) was 825.74 ± 421.19 mg.

Study participants provided informed consent as stipulated in the Declaration of Helsinki. The protocol for this study was approved by the Human Studies Institutional Review Board of 904th Hospital.

Clinical Assessments

Motor Parkinsonism was assessed with the UPDRS-III before surgery and 1 year later. Motor assessments were performed at baseline (off-state), and 60 and 120 min following levodopa administration (1.5 times the first morning levodopa equivalent dose).

The UPDRS III was used to assess motor dysfunction improvement. Patients with an improvement rate >30% were indicated for surgery (Defer et al., 1999; Rodriguez et al., 2007). The improvement rate was calculated as [(pre-treatment UPDRS III score – post-treatment UPDRS III score)/pre-treatment UPDRS III] × 100% (Saranza and Lang, 2020). We also calculated the UPDRS III subscores (Williams et al., 2007), including tremor score (UPDRS III item 20, 21), rigidity score (UPDRS III item 22), less movement score (UPDRS III item 23–26, 31), and posturality gait disorder (PIGD) score (UPDRS III item 27–30 + item 18). The LEDD was calculated to determine the dose of dopaminergic treatment (Tomlinson et al., 2010). At 1 year after STN DBS, motor dysfunction evaluation was performed under Stimulation on/Med-off (Stim-on/Med-off).

We employed the PDQ-39 to evaluate QoL (Luo et al., 2010), and postoperative change in PDQ-39 score was the primary outcome. The Scales for Outcomes in Parkinson's disease autonomic dysfunction (SCOPA-AUT) was employed to assess non-motor features (Visser et al., 2004). The MoCA-B and MMSE were utilized to conduct global cognitive function assessment (Tombaugh and McIntyre, 1992; Chen et al., 2016). Quantitative measures of anxiety [Self Rating Anxiety Scale, SAS (Zung, 1974)] and depression [Beck Depression Inventory, BDI; Geriatric Depression Rating Scale, GDS (Jamison and Scogin, 1992)] were also administered. PDQ-39 QOL scores were obtained preoperatively and 1 year postoperatively. The PDQ-39 contains eight subscores [discomfort, community, cognition, social, stigma, emotional, activities of daily living (ADL), and mobility]. The range of scores was from 0 to 100, with 0 indicating the best functional outcome.

Acute Levodopa Challenge Test

The DBS patients underwent LCT before surgery, and a confirmative diagnosis of PD was made by at least one movement disorders doctor in our hospital. Medication off-state was defined as motor dysfunction following at least 12 h of not using PD-related drugs. The medication on-state was considered as having the best motor response following the first levodopa dose (1.5 times the individual morning dose) after the off-state. The use of long-acting dopamine stimulants was halted ∼72 h before the off-state assessment. We calculated the percentage of motor disability

improvement (i.e., objective motor improvement) based on the off-drug state. Motor response assessments were performed at baseline (off-state), and 60 and 120 min following levodopa administration. Anytime there was a decrease of 30% or more in the total UPDRS III score, it was considered as an indicator that the patient was a candidate for DBS. Those who showed <30% improvement on the LCT without on-off fluctuations, dyskinesia, and disabling tremor were excluded and were not tracked.

Surgical Procedure

A high-resolution, volumetric brain magnetic resonance imaging (MRI) was obtained 1 day before surgery followed by a stereotactic head computed tomography (CT) on the morning of surgery. CT and MRI image fusion was then performed to map out the neuronal brain structures in coordinate space by software developed at our institution. The brain target point was selected utilizing a combination of direct and indirect targeting. For this series, STN was a target without cognitive issues. The anterior commissure, the posterior commissure, and a midline plane were identified to anchor the coordinate system. Multiple-pass microelectrode mapping was employed followed by intraoperative test stimulation to verify lead placement. Moreover, a postoperative CT scan was performed and fused to the MRI to assess the lead location. An implantable pulse generator (IPG) was placed approximately 4 weeks after the procedure and DBS programming/medication adjustment was performed by protocol once a month for the first 6 months and then every 3–6 months.

Statistical Analysis

Exploratory stepwise regression model (inclusion criterion relaxed to $p = 0.1$) included changed scores that were significantly correlated with the PDQ-39 change to evaluate how QoL changes were related to postoperative changes in other clinical and disease variables. A second stepwise regression model included baseline variables with significant correlations with PDQ-39 change (pre minus post-PDQ-39) to evaluate preoperative predictors of postoperative QoL. All statistical analyses were carried out with SPSS 26.0 (IBM Corp., Armonk, NY).

Standard Protocol Approvals, Registrations, and Patient Consents

All participants provided written informed consent with a protocol approved by the 904th hospital Ethics Committee.

RESULTS

Patient Characteristics

Of the 40 PD patients included in our observational study, none dropped out during the 1-year follow-up period. There were no major differences before and after DBS for the SCPA-AUT, SAS, BDI, GDS, MMSE, and MoCA-B results. However, DBS surgery markedly improved UPDRS Part III scores (total scores, sub-score in tremor, rigidity, bradykinesia, and PIGD) at 1 year ($p < 0.01$). Surgery also improved QoL based on PDQ-39 and reduced drug usage ($p < 0.01$). Patient data are outlined in **Table 1**.

Correlation Analysis

Acute LCT was carried out on PD patients before surgery, and the results showed >50% improvement in motor dysfunction at both 60 and 120 min.

Quality of life, as measured with the PDQ-39, was improved after STN-DBS compared with baseline. Postoperative scores were significantly reduced on four of the eight PDQ-39 subscales (except in Cognition, Social support, Stigma, and Communication, $p > 0.05$; **Figure 1**).

Correlations between baseline and/or postsurgical change in demographic/disease variables and PDQ-39 change scores in the cohort are displayed in **Table 2**. Improvements in QoL were associated with several preoperative characteristics including preoperative UPDRS-III tremor, UPDRS-III tremor (off-60), UPDRS-III tremor (off-120), MMSE, and PDQ-39 before surgery (all $p < 0.05$). There was no association of QoL improvement and any demographic variable, PD duration, or disease severity as indicated by the UPDRS-III score off medications (**Table 2**).

Regression Model

Multiple linear regression model was established to predict the prognosis of DBS by using preoperative MMSE [odds ratio (OR) = 0.342, 95% confidence interval (CI) = 0.051–2.297], preoperative UPDRS-III tremor (OR = 2.099, 95% CI = 0.585–7.535), UPDRS-III tremor (off-60) [OR = 1.316, 95% CI = 0.804–2.154, UPDRS-III tremor (off-120) (OR = 0.913, 95% CI = 0.691–1.207)], correctly classified 88.5% of patients (C statistic = 0.73, $p < 0.001$, 95% CI = 0.854–1.000; see **Figure 2**).

TABLE 1 | Baseline and postoperative demographic clinical characteristics.

Variable	Pre-DBS	Post-DBS
Gender (female/male)	17/23	
Age	61.30 ± 8.97	
LEDD (mg)	825.74 ± 421.19	451.25 ± 234.66**
MMSE	27.14 ± 10.32	25.22 ± 3.96
MOCA-B	19.69 ± 5.35	19.44 ± 5.00
PDQ-39	63.20 ± 26.43	45.20 ± 29.74**
GDS	45.06 ± 4.40	45.53 ± 4.51
BDI	17.69 ± 8.78	15.34 ± 9.89
SAS	36.44 ± 6.60	37.35 ± 7.29
SCPA-AUT	16.76 ± 9.09	14.09 ± 8.80
UPDRS-III	43.81 ± 13.18	12.35 ± 6.40**
UPDRS-III temor	4.78 ± 5.16	0.73 ± 1.15**
UPDRS-III rigidity	7.76 ± 4.04	0.89 ± 1.08**
UPDRS-III bradykenisia	17.97 ± 5.56	5.24 ± 3.67**
UPDRS-III PIGD	10.57 ± 3.92	4.43 ± 2.24**

MMSE, Mini-Mental State Exam; MoCA-B, Montreal Cognitive Assessment Basic; SAS, Self Rating Anxiety Scale; BDI, Beck Depression Inventory; GDS, Geriatric Depression Rating Scale; PDQ-39, 39-item Parkinson's Disease Questionnaire; LEDD, levodopa equivalent dailydose; UPDRS-III, Unified Parkinson's III total score; SCOPA-AUT, Parkinson's disease autonomic dysfunction.
***P < 0.01.*

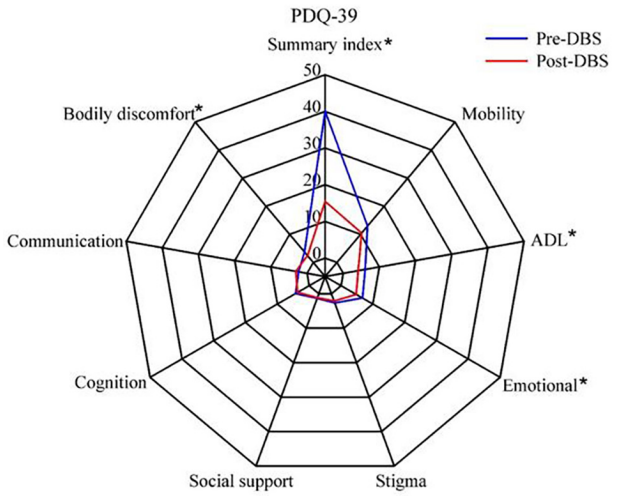

FIGURE 1 | Quality of life in patients with Parkinson's disease before and after subthalamic stimulation. *$P < 0.05$.

DISCUSSION

In our study, STN-DBS surgery was successful in reducing motor impairment through UPDRS-III. It also led to improvements in subscores for tremor, rigidity, bradykinesia, and PIGD. Furthermore, DBS enhanced the overall QoL of PD patients as measured by the PDQ-39, especially for the discomfort, ADL, and emotional subscores. The nearly 28/40 (28 improved and 12 did not in PDQ-39) split between patients reporting improved and stable QoL after STN-DBS was remarkably similar to a recent prospective study (Gorecka-Mazur et al., 2019; Liu et al., 2019).

We extracted four factors as a result of exploratory predictors analysis: UPDRS III-tremor, UPDRS III-tremor (off-60), UPDRS-III tremor (off-120), MMSE, and PDQ-39, including LCT items.

Most prior investigations focused on a postoperative motor function to reflect DBS success from the perspective of the clinician. However, QoL improvement is the main goal of DBS surgery. As such, QoL has been more accepted as the primary outcome. Preoperative clinical characteristics for the long-term effects will be the subject of future investigation. Preoperative QoL was also an important predictor of postoperative QoL ratings. Essentially, patients with poorer preoperative QoL also had relatively worse QoL postoperatively, which is consistent with the high test-retest reliability of the measure.

The MMSE is widely used to screen cognitive function, and it has been used to predict QoL after DBS surgery. A greater improvement in QoL is associated with better cognitive function (Liu et al., 2019). Other groups (Park et al., 2020; Cavallieri et al., 2021) reported practical evidence on PD patients with dementia, indicating worse responses to DBS intervention relative to patients without dementia. This indicates that PD patients with dementia may not show improvement after DBS. We propose that patients with better overall cognitive function may have better postoperative QoL.

The LCT is frequently the first-line screening tool to select suitable patients for DBS (Defer et al., 1999; Kleiner-Fisman et al., 2006; Lang et al., 2006; Rodriguez et al., 2007). However, no guideline has been proposed on the symptoms and pre-surgical response to levodopa or whether LCT can predict outcome (Kleiner-Fisman et al., 2006; Deuschl et al., 2019). Thus, our study aimed to observe if preoperative LCT results before DBS could predict surgery efficacy. For this reason, we placed a strong focus on evaluating the predictive power of our models.

Deep brain stimulation selection criteria to treat advanced PD is based on the "Core Assessment Program for Surgical Interventional Therapies in Parkinson's Disease" (CAPSIT-PD) published in 1999 (Defer et al., 1999). However, most indications in the CAPSIT-PD guidelines were meant to guide candidate selection in the clinical application of DBS worldwide (Munhoz et al., 2016).

Our main finding is that, in a cohort of prospectively recruited recent PD patients who responded well to levodopa in the LCT before DBS surgery (>30% improvement), and

TABLE 2 | Correlations with PDQ-39 change.

	No.	*r*	*P*
UPDRS-III off	40	0.152	0.348
UPDRS-III temor	40	0.314	0.049*
UPDRS-III rigidity	40	−0.030	0.855
UPDRS-III bradykenisia	40	0.021	0.898
UPDRS-III PIGD	40	0.134	0.408
UPDRS-III (OFF-60 min)	40	0.069	0.672
UPDRS-III temor (OFF-60 min)	26	0.494	0.010*
UPDRS-III rigidity (OFF-60 min)	39	−0.042	0.800
UPDRS-III bradykenisia (OFF-60 min)	40	0.027	0.871
UPDRS-III PIGD (OFF-60 min)	40	−0.046	0.777
UPDRS-III (OFF-120)	40	0.102	0.530
UPDRS-III temor (OFF-120)	26	0.483	0.012*
UPDRS-III rigidity (OFF-120)	39	0.100	0.546
UPDRS-III bradykenisia (OFF-12O)	40	0.027	0.871
UPDRS-III PIGD (OFF-120)	40	0.009	0.956
Age	40	0.188	0.246
LEDD (mg)	40	−0.144	0.377
MMSE	40	−0.393	0.012*
MOCA-B	40	−0.234	0.146
Duration	40	0.015	0.926
NMS	40	0.032	0.843
PDQ-39	40	0.392	0.012*
GDS	39	−0.016	0.921
BDI	40	0.084	0.606
SAS	40	0.143	0.378
SCPA-AUT	40	0.095	0.559
RBD	40	−0.113	0.488

MMSE, Mini-Mental State Exam; MoCA-B, Montreal Cognitive Assessment Basic; SAS, Self Rating Anxiety Scale; BDI, Beck Depression Inventory; GDS, Geriatric Depression Rating Scale; PDQ-39, 39-item Parkinson's Disease Questionnaire; LEDD, levodopa equivalent dailydose; UPDRS-III, Unified Parkinson's III total score; SCOPA-AUT, Parkinson's disease autonomic dysfunction.
*$P < 0.05$.

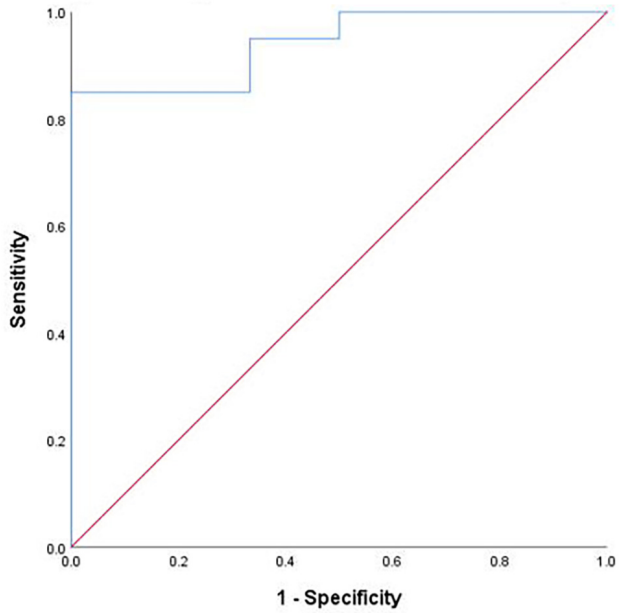

FIGURE 2 | Regression classification accuracy. *Note*: Receiver operating characteristic curve demonstrating the classification accuracy (predicted probability of improved vs not improved quality of life) of the logistic regression. The diagonal dashed line represents chance classification accuracy.

there were relationships between the pre-UPDRS III-tremor, pre-UPDRS III-tremor (off-60), pre-UPDRS III-tremor (off-120), and postoperative QoL. This suggests that tremors can be annoying to patients and therefore impact QoL. The neuroanatomical basis of resting tremor may be different from that of the striatum nigra system. It is generally believed that PD tremor is related to the combined impairment of the cerebello dentato thalamo cortical and basal ganglia–thalamocortical circuits (Poirier et al., 1975; Boecker and Brooks, 2011). Good responsiveness to the drug may reflect good plasticity between the striatum nigra system, ventralis intermediate nucleus, and cerebellum. Specifically, an earlier high response (LCT, off-60, and off-120) indicates more functional reserve. The more obvious tremor decreases during LCT, the more the improvement in postoperative QoL.

The axial symptoms of ineffective levodopa treatment are considered a relative contraindication for surgery, but subjects with camptocormia and Pisa syndrome might be responsive to STN-DBS, even with poor or no amelioration after LCT (Antonini et al., 2018; Artusi et al., 2018; Roediger et al., 2019). There are at least three scenarios where alternative indications for DBS could be used in patients without a sufficient levodopa response: severe dyskinesia, "on/off" motor fluctuations, and medication-refractory tremor (Morishita et al., 2011). This shows that the sensitivity of LCT in screening patients has shortcomings.

Several factors need to be considered in the application of LCT for DBS candidates. Firstly, there are side effects associated with levodopa, and someone may lack tolerance to doses of levodopa that are considered ideal for the effective outcome because of adverse effects (e.g., dyskinesia, sedation, and nausea) that make it difficult to obtain certain information from the LCT. Severe dyskinesia may reduce performance on some indicators on the UPDRS (e.g., rapid alternating movements, hand movement, and finger tapping), suggesting limited improvement in these indicators. Delayed gastric emptying could also affect LCT results (Melamed et al., 1986). Moreover, clinicians should be aware that a UPDRS "on/off" test does not reveal the extent or severity of "on/off" motor fluctuations, which ultimately requires careful history taking and/or formal diary documentation (Hauser et al., 2000, 2006). Finally, LCT threshold values have not been standardized for patients undergoing DBS. Particularly, values vary from 25 to 50% in published surgical series (Hauser et al., 2006; Lang et al., 2006). Clinicians should be aware that higher LCT threshold levels may lead to excluding potentially reasonable DBS candidates, especially those with dyskinesias, fluctuations, and tremors. The response of PD patients to levodopa is different in various Hoehn-Yahr stages, and the responses are also different in the "off" and "on" periods (Müller et al., 2000).

Axial symptoms track disease progression and disability, so accurate presurgical evaluation is necessary for estimating the extent of response after DBS. Indeed, it is dependent on clinical variables such as disease duration, the type of axial symptom (gait often improves after DBS, speech may worsen as a stimulus-related side effect), and interplay with dopaminergic medications. The effect of levodopa on axial symptoms varies greatly among individuals, so it is impossible to predict the efficacy of DBS using this parameter.

A recent meta-analysis of STN DBS outcomes reported a 52% improvement in the UPDRS III motor symptoms after surgery. However, the UPDRS motor scores improved by only 16 and 12.5% at 4-month follow-up (Smeding et al., 2011). These improvements may seem disappointing. However, they fail to measure changes important for an individual patient that contribute to enhanced ADL and QoL scores. The low motor improvement seen in several patients directly supports the notion that DBS impacts levodopa-responsive motor symptoms, but UPDRS III scores may not tell the whole story.

The surgical intervention appears to improve or maintain QoL for the vast majority of patients. Prior DBS research focused on predicting motor improvements after surgery, which reflects the success of DBS from the perspective of the clinician. The recent interest in QoL signals a shift to understanding the characteristics and disease variables that consider success from the perspective of the patient. Our model indicates that UPDRS III-tremor, UPDRS III-tremor (off-60), MMSE, and PDQ-39 before surgery are important indicators of postoperative QoL outcome.

In another study that analyzed 85 PD patients who underwent DBS, the extent of improvement in preoperative LCT motor symptoms was only marginally correlated with better QoL after DBS ($p = 0.053$). That is to say, LCT is probably not sufficiently specific to be considered for accurately predicting postoperative QoL (Floden et al., 2014).

Levodopa treatment of PD is designed to address the issue of excessive dopaminergic neuron death in the substantia nigra and striatum that causes dramatic reductions in dopamine levels. However, the non-motor symptoms that affect the QoL of PD are closely related to norepinephrine (blood pressure),

serotonin (emotion), acetylcholine (cognition), and the locus coeruleus (sleep). Therefore, LCT results alone cannot predict the postoperative QoL. Levodopa remains the primary drug for the treatment of PD. In the pathogenesis of PD, the dopaminergic system is not the only one affected, so it is not comprehensive or accurate to predict the postoperative DBS solely based on levodopa reactivity.

Most prior investigations attempted to predict postoperative motor functions as a measure of DBS success. Researchers have now shifted to QoL outcomes that more accurately reflect disease variables. Our model indicates that UPDRS III-tremor, UPDRS III-tremor (off-60), MMSE, and PDQ-39 scores are useful indicators of postoperative QoL.

Since the overall evaluation of QoL is self-reported, including motor function, cognition, social, and neuropsychological factors, it is necessary to include the above factors in the model, which is also why the curative effect of DBS is difficult to predict.

Subthalamic nucleus DBS can improve the ability of patients to live a normal life by stimulating the sensory motor area of the STN with electrodes, but it does more than improve dopamine secretion. Levodopa treatment for PD is based on excessive dopaminergic neuron death in the substantia nigra and striatum. However, many non-motor features linked to the QoL of patients with PD are closely related to norepinephrine (blood pressure), serotonin (emotion), acetylcholine (cognition), and the locus coeruleus (sleep). Therefore, levodopa efficacy alone cannot predict the postoperative QoL.

The goal of STN-DBS is to reshape the brain functional network of the basal ganglia cortex via effects on the basal ganglia loop. Therefore, from the whole-brain level, we can understand the reason why the LCT test cannot predict the efficacy of DBS. Furthermore, objective biomarkers based on the whole brain are needed to select suitable patients and predict outcomes following DBS.

CONCLUSION

This study confirmed no significant correlation between LCT and PDQ-39 by long-term STN DBS stimulation in PD patients. Although, the improvements in QoL were associated with several preoperative characteristics including preoperative UPDRS-III tremor, UPDRS-III tremor (off-60) ($p = 0.049$), UPDRS-III tremor (off-120) ($p = 0.012$), Mini-Mental State Examination ($p = 0.012$), and PDQ-39 ($p = 0.012$) before surgery. Taken together, our results demonstrate the LCT could not be an objective biomarker for predicting STN DBS QoL for PD.

The primary limitation of this study is the small sample size limiting the strength of correlations and the strength of the modeling or prediction analyses. The predictive model was not further validated in the new DBS population.

DATA AVAILABILITY STATEMENT

The original contributions presented in the study are included in the article/supplementary material, further inquiries can be directed to the corresponding authors.

ETHICS STATEMENT

The studies involving human participants were reviewed and approved by the 904th Hospital Ethics Committee. The patients/participants provided their written informed consent to participate in this study.

AUTHOR CONTRIBUTIONS

All authors listed have made a substantial, direct and intellectual contribution to the work, and approved it for publication.

FUNDING

This work was supported by the Wuxi Health Commission (CSZ0N1729).

ACKNOWLEDGMENTS

We would particularly like to thank all patients and healthy individuals who participated in the study as well as medical staff and research assistants for their contributions to the study.

REFERENCES

Anderson, E., and Nutt, J. (2011). The long-duration response to levodopa: phenomenology, potential mechanisms and clinical implications. *Parkinsonism Relat. Disord.* 17, 587–592. doi: 10.1016/j.parkreldis.2011.03.014

Antonini, A., Stoessl, A. J., Kleinman, L. S., Skalicky, A. M., Marshall, T. S., Sail, K. R., et al. (2018). Developing consensus among movement disorder specialists on clinical indicators for identification and management of advanced Parkinson's disease: a multi-country Delphi-panel approach. *Curr. Med. Res. Opin.* 34, 2063–2073. doi: 10.1080/03007995.2018.1502165

Artusi, C. A., Zibetti, M., Romagnolo, A., Rizzone, M. G., Merola, A., and Lopiano, L. (2018). Subthalamic deep brain stimulation and trunk posture in Parkinson's disease. *Acta Neurol. Scand.* 137, 481–487. doi: 10.1111/ane.12889

Benabid, A. L., Pollak, P., Louveau, A., Henry, S., and de Rougemont, J. (1987). Combined (thalamotomy and stimulation) stereotactic surgery of the VIM thalamic nucleus for bilateral Parkinson disease. *Appl. Neurophysiol.* 50, 344–346. doi: 10.1159/000100803

Boecker, H., and Brooks, D. J. (2011). Resting tremor in Parkinson disease: is the pallidum to blame? *Ann. Neurol.* 69, 229–231. doi: 10.1002/ana.22358

Cavallieri, F., Fraix, V., Bove, F., Mulas, D., Tondelli, M., Castrioto, A., et al. (2021). Predictors of long-term outcome of subthalamic stimulation in Parkinson disease. *Ann. Neurol.* 89, 587–597. doi: 10.1002/ana.25994

Chen, K. L., Xu, Y., Chu, A. Q., Ding, D., Liang, X.-N., Nasreddine, Z. S., et al. (2016). Validation of the Chinese version of montreal cognitive assessment basic for screening mild cognitive impairment. *J. Am. Geriatr. Soc.* 64, e285–e290. doi: 10.1111/jgs.14530

Defer, G. L., Widner, H., Marié, R. M., Rémy, P., and Levivier, M. (1999). Core assessment program for surgical interventional therapies in Parkinson's disease (CAPSIT-PD). *Mov. Disord.* 14, 572–584. doi: 10.1002/1531-8257(199907)14:4<572::AID-MDS1005>3.0.CO;2-C

Deuschl, G., Follett, K. A., Luo, P., Rau, J., Weaver, F. M., Paschen, S., et al. (2019). Comparing two randomized deep brain stimulation trials for Parkinson's disease. *J NEUROSURG* 132, 1376–1384. doi: 10.3171/2018.12.JNS182042

Deuschl, G., Follett, K. A., Luo, P., Rau, J., Weaver, F. M., Paschen, S., et al. (2020). Comparing two randomized deep brain stimulation trials for Parkinson's disease. *J. Neurosurg.* 132, 1376–1384. doi: 10.3171/2018.12.JNS182042

Floden, D., Cooper, S. E., Griffith, S. D., and Machado, A. G. (2014). Predicting quality of life outcomes after subthalamic nucleus deep brain stimulation. *Neurology* 83, 1627–1633. doi: 10.1212/WNL.0000000000000943

Freeman, T. B., Olanow, C. W., Hauser, R. A., Nauert, G. M., Smith, D. A., Borlongan, C. V., et al. (1995). Bilateral fetal nigral transplantation into the postcommissural putamen in Parkinson's disease. *Ann Neurol* 38, 379–388. doi: 10.1002/ana.410380307

Gorecka-Mazur, A., Furgala, A., Krygowska-Wajs, A., Pietraszko, W., Kwinta, B., and Gil, K. (2019). Activities of daily living and their relationship to health-related quality of life in patients with parkinson disease after subthalamic nucleus deep brain stimulation. *World Neurosurg.* 125, e552–e562. doi: 10.1016/j.wneu.2019.01.132

Hauser, R. A., Friedlander, J., Zesiewicz, T. A., Adler, C. H., Seeberger, L. C., O'Brien, C. F., et al. (2000). A home diary to assess functional status in patients with Parkinson's disease with motor fluctuations and dyskinesia. *Clin. Neuropharmacol.* 23, 75–81. doi: 10.1097/00002826-200003000-00003

Hauser, R. A., Russ, H., Haeger, D. A., Bruguiere-Fontenille, M., Müller, T., and Wenning, G. K. (2006). Patient evaluation of a home diary to assess duration and severity of dyskinesia in Parkinson disease. *Clin. Neuropharmacol.* 29, 322–330. doi: 10.1097/01.WNF.0000229546.81245.7F

Hughes, A. J., Daniel, S. E., Kilford, L., and Lees, A. J. (1992). Accuracy of clinical diagnosis of idiopathic Parkinson's disease: a clinico-pathological study of 100 cases. *J. Neurol. Neurosurg. Psychiatry* 55, 181–184. doi: 10.1136/jnnp.55.3.181

Jamison, C., and Scogin, F. (1992). Development of an interview-based geriatric depression rating scale. *Int. J. Aging Hum. Dev.* 35, 193–204. doi: 10.2190/0803-3FBC-6EB0-ACH4

Jiang, J. L., Chen, S. Y., and Tsai, S. T. (2019). Quality of life in patients with Parkinson's disease after subthalamic stimulation: an observational cohort study for outcome prediction. *Ci Ji Yi Xue Za Zhi* 31, 107–112. doi: 10.4103/tcmj.tcmj_92_18

Kleiner-Fisman, G., Herzog, J., Fisman, D. N., Tamma, F., Lyons, K. E., Pahwa, R., et al. (2006). Subthalamic nucleus deep brain stimulation: summary and meta-analysis of outcomes. *Mov. Disord.* 21(Suppl. 14), S290–S304. doi: 10.1002/mds.20962

Lang, A. E., Houeto, J. L., Krack, P., Kubu, C., Lyons, K. E., Moro, E., et al. (2006). Deep brain stimulation: preoperative issues. *Mov. Disord.* 21(Suppl. 14), S171–S196. doi: 10.1002/mds.20955

Langston, J. W., Widner, H., Goetz, C. G., Brooks, D., Fahn, S., Freeman, T., et al. (1992). Core assessment program for intracerebral transplantations (CAPIT). *Mov. Disord.* 7, 2–13. doi: 10.1002/mds.870070103

Liu, F. T., Lang, L. Q., Yang, Y. J., Zhao, J., Feng, R., Hu, J., et al. (2019). Predictors to quality of life improvements after subthalamic stimulation in Parkinson's disease. *Acta Neurol. Scand.* 139, 346–352. doi: 10.1111/ane.13056

Luo, W., Gui, X. H., Wang, B., Zhang, W.-Y., Ouyang, Z.-Y., Guo, Y., et al. (2010). Validity and reliability testing of the Chinese (mainland) version of the 39-item Parkinson's disease questionnaire (PDQ-39). *J. Zhejiang Univ. Sci. B* 11, 531–538. doi: 10.1631/jzus.B0900380

Melamed, E., Bitton, V., and Zelig, O. (1986). Episodic unresponsiveness to single doses of L-dopa in parkinsonian fluctuators. *Neurology* 36, 100–103. doi: 10.1212/WNL.36.1.100

Merello, M., Gerschcovich, E. R., Ballesteros, D., and Cerquetti, D. (2011). Correlation between the movement disorders society unified Parkinson's disease rating scale (MDS-UPDRS) and the unified Parkinson's disease rating scale (UPDRS) during L-dopa acute challenge. *Parkinsonism Relat. Disord.* 17, 705–707. doi: 10.1016/j.parkreldis.2011.07.002

Merello, M., Nouzeilles, M. I., Arce, G. P., and Leiguarda, R. (2002). Accuracy of acute levodopa challenge for clinical prediction of sustained long-term levodopa response as a major criterion for idiopathic Parkinson's disease diagnosis. *Mov. Disord.* 17, 795–798. doi: 10.1002/mds.10123

Morishita, T., Rahman, M., Foote, K. D., Fargen, K. M., Jacobson, C. E. IV, Fernandez, H. H., et al. (2011). DBS candidates that fall short on a levodopa challenge test: alternative and important indications. *Neurologist* 17, 263–268. doi: 10.1097/NRL.0b013e31822d1069

Müller, T., Benz, S., and Przuntek, H. (2000). Choice reaction time after levodopa challenge in parkinsonian patients. *J. Neurol. Sci.* 181, 98–103. doi: 10.1016/S0022-510X(00)00436-6

Munhoz, R. P., Picillo, M., Fox, S. H., Bruno, V., Panisset, M., Honey, C. R., et al. (2016). Eligibility criteria for deep brain stimulation in Parkinson's disease, tremor, and dystonia. *Can. J. Neurol. Sci.* 43, 462–471. doi: 10.1017/cjn.2016.35

Park, K. W., Jo, S., Kim, M. S., Choi, N., Jeon, S. R., Park, H. K., et al. (2020). Cognitive profile as a predictor of the long-term outcome after deep brain stimulation in Parkinson's disease. *J. Neurol. Sci.* 417:117063. doi: 10.1016/j.jns.2020.117063

Peschanski, M., Defer, G., N'Guyen, J. P., Ricolfi, F., Monfort, J. C., Remy, P., et al. (1994). Bilateral motor improvement and alteration of L-dopa effect in two patients with Parkinson's disease following intrastriatal transplantation of foetal ventral mesencephalon. *Brain* 117(Pt 3), 487–499. doi: 10.1093/brain/117.3.487

Poirier, L. J., Filion, M., Larochelle, L., and Péchadre, J. C. (1975). Physiopathology of experimental Parkinsonism in the monkey. *Can. J. Neurol. Sci.* 2, 255–263. doi: 10.1017/S0317167100020357

Rodriguez, R. L., Fernandez, H. H., Haq, I., and Okun, M. S. (2007). Pearls in patient selection for deep brain stimulation. *Neurologist* 13, 253–260. doi: 10.1097/NRL.0b013e318095a4d5

Roediger, J., Artusi, C. A., Romagnolo, A., Boyne, P., Zibetti, M., Lopiano, L., et al. (2019). Effect of subthalamic deep brain stimulation on posture in Parkinson's disease: a blind computerized analysis. *Parkinsonism Relat. Disord.* 62, 122–127. doi: 10.1016/j.parkreldis.2019.01.003

Saranza, G., and Lang, A. E. (2020). Levodopa challenge test: indications, protocol, and guide. *J. Neurol.* 268, 3135–3143.

Sharma, V. D., Lyons, K. E., Nazzaro, J. M., and Pahwa, R. (2019). Deep brain stimulation of the subthalamic nucleus in Parkinson's disease patients over 75 years of age. *J. Neurol. Sci.* 399, 57–60.

Smeding, H. M., Speelman, J. D., Huizenga, H. M., Schuurman, P. R., and Schmand, B. (2011). Predictors of cognitive and psychosocial outcome after STN DBS in Parkinson's disease. *J. Neurol. Neurosurg. Psychiatry* 82, 754–760.

Timmermann, L., Jain, R., Chen, L., Maarouf, M., Barbe, M. T., Allert, N., et al. (2015). Multiple-source current steering in subthalamic nucleus deep brain stimulation for Parkinson's disease (the VANTAGE study): a non-randomised, prospective, multicentre, open-label study. *Lancet Neurol.* 14, 693–701.

Tombaugh, T. N., and McIntyre, N. J. (1992). The mini-mental state examination: a comprehensive review. *J. Am. Geriatr. Soc.* 40, 922–935.

Tomlinson, C. L., Stowe, R., Patel, S., Rick, C., Gray, R., and Clarke, C. E. (2010). Systematic review of levodopa dose equivalency reporting in Parkinson's disease. *Mov. Disord.* 25, 2649–2653.

Visser, M., Marinus, J., Stiggelbout, A. M., and Van Hilten, J. J. (2004). Assessment of autonomic dysfunction in Parkinson's disease: the SCOPA-AUT. *Mov. Disord.* 19, 1306–1312.

Williams, L. N., Seignourel, P., Crucian, G. P., Okun, M. S., Rodriguez, R. L., Skidmore, F. M., et al. (2007). Laterality, region, and type of motor dysfunction correlate with cognitive impairment in Parkinson's disease. *Mov. Disord.* 22, 141–145.

Zung, W. W. (1974). The measurement of affects: depression and anxiety. *Mod. Probl. Pharmacopsychiatry* 7, 170–188.

Conflict of Interest: The authors declare that the research was conducted in the absence of any commercial or financial relationships that could be construed as a potential conflict of interest.

Publisher's Note: All claims expressed in this article are solely those of the authors and do not necessarily represent those of their affiliated organizations, or those of the publisher, the editors and the reviewers. Any product that may be evaluated in this article, or claim that may be made by its manufacturer, is not guaranteed or endorsed by the publisher.

Copyright © 2021 Lin, Shi, Wang, Yang, Wang and Jin. This is an open-access article distributed under the terms of the Creative Commons Attribution License (CC BY). The use, distribution or reproduction in other forums is permitted, provided the original author(s) and the copyright owner(s) are credited and that the original publication in this journal is cited, in accordance with accepted academic practice. No use, distribution or reproduction is permitted which does not comply with these terms.

frontiers in Molecular Neuroscience

BRIEF RESEARCH REPORT
published: 22 October 2021
doi: 10.3389/fnmol.2021.711396

Severe and Regionally Widespread Increases in Tissue Urea in the Human Brain Represent a Novel Finding of Pathogenic Potential in Parkinson's Disease Dementia

Melissa Scholefield[1], Stephanie J. Church[1], Jingshu Xu[1,2], Stefano Patassini[2], Federico Roncaroli[3,4], Nigel M. Hooper[5], Richard D. Unwin[1,6] and Garth J. S. Cooper[1,2]*

[1] Centre for Advanced Discovery & Experimental Therapeutics, Division of Cardiovascular Sciences, School of Medical Sciences, Faculty of Biology, Medicine and Health, The University of Manchester, Manchester Academic Health Science Centre, Manchester, United Kingdom, [2] Faculty of Science, School of Biological Sciences, The University of Auckland, Auckland, New Zealand, [3] Geoffrey Jefferson Brain Research Centre, Manchester Academic Health Science Centre, Manchester, United Kingdom, [4] Division of Neuroscience and Experimental Psychology, School of Biological Sciences, Faculty of Brain and Mental Health, The University of Manchester, Manchester, United Kingdom, [5] Division of Neuroscience & Experimental Psychology, School of Biological Sciences, Faculty of Biology, Medicine and Health, The University of Manchester, Manchester Academic Health Science Centre, Manchester, United Kingdom, [6] Stoller Biomarker Discovery Centre & Division of Cancer Sciences, School of Medical Sciences, Faculty of Biology, Medicine and Health, The University of Manchester, Manchester, United Kingdom

OPEN ACCESS

Edited by:
Woon-Man Kung, Chinese Culture University, Taiwan

Reviewed by:
Baruh Polis, Yale University, United States
Fabricio Ferreira de Oliveira, Elysian Clinic, Brazil

***Correspondence:**
Melissa Scholefield
Melissa.scholefield@postgrad.manchester.ac.uk;
mjscholefield@gmail.com

Specialty section:
This article was submitted to Brain Disease Mechanisms, a section of the journal Frontiers in Molecular Neuroscience

Received: *18 May 2021*
Accepted: *30 September 2021*
Published: *22 October 2021*

Citation:
Scholefield M, Church SJ, Xu J, Patassini S, Roncaroli F, Hooper NM, Unwin RD and Cooper GJS (2021) Severe and Regionally Widespread Increases in Tissue Urea in the Human Brain Represent a Novel Finding of Pathogenic Potential in Parkinson's Disease Dementia. Front. Mol. Neurosci. 14:711396. doi: 10.3389/fnmol.2021.711396

Widespread elevations in brain urea have, in recent years, been reported in certain types of age-related dementia, notably Alzheimer's disease (AD) and Huntington's disease (HD). Urea increases in these diseases are substantive, and approximate in magnitude to levels present in uraemic encephalopathy. In AD and HD, elevated urea levels are widespread, and not only in regions heavily affected by neurodegeneration. However, measurements of brain urea have not hitherto been reported in Parkinson's disease dementia (PDD), a condition which shares neuropathological and symptomatic overlap with both AD and HD. Here we report measurements of tissue urea from nine neuropathologically confirmed regions of the brain in PDD and post-mortem delay (PMD)-matched controls, in regions including the cerebellum, motor cortex (MCX), sensory cortex, hippocampus (HP), substantia nigra (SN), middle temporal gyrus (MTG), medulla oblongata (MED), cingulate gyrus, and pons, by applying ultra-high-performance liquid chromatography-tandem mass spectrometry (UHPLC-MS/MS). Urea concentrations were found to be substantively elevated in all nine regions, with average increases of 3–4-fold. Urea concentrations were remarkably consistent across regions in both cases and controls, with no clear distinction between regions heavily affected or less severely affected by neuronal loss in PDD. These urea elevations mirror those found in uraemic encephalopathy, where equivalent levels are generally considered to be pathogenic, and those previously reported in AD and HD. Increased urea is a widespread metabolic perturbation in brain metabolism common to PDD, AD, and HD, at levels equal to those seen in uremic encephalopathy. This presents a novel pathogenic mechanism in PDD, which is shared with two other neurodegenerative diseases.

Keywords: Parkinson's disease dementia (PDD), Huntington's disease (HD), Alzheimer's disease (AD), urea-analysis, metabolomics (OMICS), mass spectrometry-LC-MS/MS

INTRODUCTION

Parkinson's disease (PD) is the second most common neurodegenerative condition after Alzheimer's disease (AD; Erkkinen et al., 2018). PD is characterised mainly by motor dysfunction including bradykinesia, resting tremor, and rigidity. Up to 80% of patients with PD develop cognitive dysfunction during the course of their disease, usually within 20 years from the diagnosis, designated as Parkinson's disease dementia (PDD; Hely et al., 2008). Neuropathologically, PD and PDD are characterised by extensive loss of dopaminergic neurons in the substantia nigra (SN), and accumulation and progressive spread of misfolded α-synuclein with formation of Lewy bodies and Lewy neuropil threads. Deposition of α-synuclein is thought to begin in the olfactory bulbs and lower brainstem and progress to the midbrain and eventually to the neocortex (Braak et al., 2003; Jellinger, 2019). The severity of α-synuclein deposition in the post-mortem brain is assessed using the Braak staging system.

A conclusive clinical diagnosis of PD/PDD can be challenging due to the heterogeneity of the condition, presence of comorbidities and overlap with other forms of movement disorders and dementia (Irwin et al., 2013; Walker et al., 2019). The hypothesis that different forms of dementia represent a spectrum with common pathogenetic mechanisms has been suggested (Perl et al., 1998; Jellinger and Korczyn, 2018). Studies that search for perturbations in different areas of the brain across different neurodegenerative conditions represent an approach to unveil potential common pathogenetic mechanisms. Previous metabolomics studies have investigated AD and HD and demonstrated widespread increases in brain-tissue urea in both these conditions despite their different clinical phenotypes and genetic alterations (Patassini et al., 2015, 2016; Xu et al., 2016; Handley et al., 2017).

Peripheral blood levels of urea have been reported in PD patients with discordant results including increase in plasma (Glaab et al., 2019), no change in serum (Hatano et al., 2016), decreases in the CSF (Trezzi et al., 2017), and decrease in whole blood concentrations (Troisi et al., 2019). Additionally, none of these studies of peripheral urea distinguished between PD with or without dementia. Conclusions on cerebral tissue levels of this metabolite cannot be inferred from these studies but to our knowledge, brain-tissue urea levels have not previously been reported in PDD.

MATERIALS AND METHODS

Obtaining Tissue for Urea Quantification

For this study, tissues from nine brain regions from nine cases with definitely diagnosed PDD and nine controls were obtained from the University of Miami Brain Endowment Bank, Miami, FL, United States (part of the National Institute of Health NeuroBioBank network). Tissues were dissected from the following human-brain regions: middle temporal gyrus (MTG); motor cortex (MCX); primary visual cortex (PVC); hippocampus (HP); anterior cingulate gyrus (CG); cerebellum, at the level of the dentate nucleus (CB); SN; pons; and medulla oblongata (MED). All available patient metadata for cases and controls were obtained and are herein presented in **Supplementary Tables A2, 3**.

Diagnosis and Severity of Parkinson's Disease Dementia Cases

Cases and controls were diagnosed by the referring neuropathologists of the Miami Brain Endowment Bank. All cases were diagnosed to be of the alpha-synucleinopathy neocortical type, consistent with the clinical phenotype of PDD. Controls did not show any features of neurodegeneration or vascular pathology. The brains were assessed using either Braak staging (Braak et al., 2003) and/or McKeith's staging criteria for Lewy body dementias (McKeith et al., 2005; see **Supplementary Material A**).

Tissue Dissection

Brain samples were cut into sections of 50 mg (±5 mg) for urea quantification using a metal-free ceramic scalpel. Samples were stored in "Safe-Lok" microfuge Eppendorf tubes (Eppendorf AG; Hamburg, Germany) and stored at −80°C prior to extraction.

Urea Quantification

Urea was quantified in brain sample by UHPLC-MS/MS. Brain samples were extracted in 50:50 (v/v) methanol:chloroform containing labelled urea internal standard [Urea-$^{15}N_2$ 98 atom% ^{15}N, 99% (CP), 316830 Sigma-Aldrich, MO, United States]. Extraction blanks containing only the methanol:chloroform:internal standard solvent were prepared. Samples were lysed in a TissueLyser batch bead homogeniser (Qiagen, Manchester, United Kingdom). LC-MS grade water was then added to samples before separation of polar and non-polar phases by centrifugation at 2,400 × *g* for 15 min. The polar methanol phase was transferred to a fresh tube before being dried overnight in a Speedvac centrifugal concentrator (Savant Speedvac, Thermo Scientific, United Kingdom).

Once dried, 0.1% formic acid was added to samples. The resulting solution was transferred to 300-μl autosampler vials, with two blanks containing only 0.1% (v/v) formic acid also prepared. Standard solutions containing a labelled urea internal standard and corresponding unlabelled urea external standards (urea analytical standard, 56180 Supelco, PA, United States) were prepared, containing concentrations of 0–5,000 μM unlabelled urea in 0.1% v/v formic acid. Three QC samples were also prepared containing 10 μm labelled urea and 20, 200, and 2,000 μM unlabelled urea in 0.1% v/v formic acid.

Urea quantification was performed on a TSQ Vantage triple quadrupole mass spectrometer coupled with an Accela UHPLC system (Thermo Fisher Scientific, MA, United States). Separation was carried out on a Hypersil Gold AQ column with a diameter of 2.1 mm, length of 100 mm, and particle size of 1.9 μm (Thermo Fisher Scientific) maintained at 25°C with a 0.5 μm pre-column filter (Thermo Fisher Scientific). Gradient elution was performed using 0.1% formic acid in water (A) and 0.1% formic acid in acetonitrile (B) at 300 μl/min. Urea and labelled urea internal

standard were detected using electrospray ionisation in positive ionisation mode.

Ultra-High-Performance Liquid Chromatography-Tandem Mass Spectrometry Data Analysis

Ultra-high-performance liquid chromatography-tandem mass spectrometry data were analysed using LCQuan software (Thermo Fisher Scientific, MA, United States). Chromatographic peaks were identified based on expected retention time (RT), and compared against labelled urea internal standard peak RTs for each individual QC/standard/sample. Each peak was manually checked for correct identification.

Quantification of urea in samples was performed using the ratio of urea peak area to internal standard peak area and comparison to the standard curve. These concentrations were corrected for sample wet-weight and analysed in GraphPad Prism v8.1.2. (Prism; La Jolla, CA, United States). A non-parametric Mann-Whitney-*U* test was used to determine the significance of case-control differences due to the relatively small sample sizes.

The minimum sample size required to confidently determine case-control differences at a significance level of $p < 0.05$ and $p < 0.01$ was calculated using the sample size calculator from SPH Analytics, Alpharetta, United States.[1]

RESULTS AND DISCUSSION

Cohort Characterisation

Metadata were obtained for all cases and controls, including sex, age, race, ethnicity, post-mortem delay (PMD), brain weight, comorbidities, and cause of death (see **Supplementary Material A** for individual data). There were no significant case-control differences in sex, age at death, PMD or brain weight (**Supplementary Table A1**). All samples had a PMD of 26 h or less, with an average of 19.8 h in controls and 14.6 h in cases.

Due to a lack of available SN tissue for two of the cohort samples, two alternate SN samples were obtained from different donors. These samples were age- and sex-matched, but the cases had a lower PMD than controls (∼6 h, $p = 0.03$; **Supplementary Table A1**). The impact of this is discussed in the section on brain tissue urea findings below.

Brain Tissue Urea Findings in Parkinson's Disease Dementia

Urea levels were increased in PDD cases compared to controls in every region analysed (**Table 1** and **Figure 1**). There was an average 5.5-fold increase in tissue-urea concentrations in the CG of cases compared with controls, and an average ∼3.5- to 4.5-fold increase in cases in every other region.

Inter-regional concentrations of urea were highly consistent in both controls and cases, with no significant differences between any two regions. Control tissue-urea concentrations averaged ∼9.4 mmol/kg and case concentrations 40.0 mmol/kg, showing a substantial, ∼4-fold increase in case-control urea levels across the brain overall.

[1]https://www.sphanalytics.com/sample-size-calculator-using-average-values/

TABLE 1 | Tissue urea concentrations in PDD cases and controls.

Region	Controls ($n = 9$) (mmol/kg)	PDD cases ($n = 9$) (mmol/kg)	Fold-change	*P*-Value
CB	9.6 (2.7–16.4)	35.2 (15.4–55.0)	**3.7**	**0.003**
MCX	9.2 (2.5–16.0)	37.7 (15.7–59.7)	**4.1**	**0.002**
PVC	8.1 (2.3–13.9)	34.9 (14.6–55.2)	**4.3**	**0.001**
HP	9.0 (2.6–15.4)	37.6 (10.7–64.4)	**4.2**	**0.004**
SN	11.6 (3.4–19.9)	45.8 (17.3–74.2)	**3.9**	**0.006**
MTG	11.0 (2.3–19.6)	46.9 (17.9–76.0)	**4.3**	**0.002**
MED	8.5 (2.3–14.7)	38.9 (14.9–62.9)	**4.6**	**0.002**
CG	8.8 (3.0–14.6)	48.4 (17.6–79.1)	**5.5**	**0.0008**
PONS	8.8 (2.2–15.5)	34.2 (15.4–53.0)	**3.9**	**0.003**

Mean tissue-urea concentrations ± 95% confidence intervals expressed in mmol/kg. Significance of case-control differences was determined using the Mann-Whitney-U test wherein P < 0.05 has been considered significant. Fold-changes are cases compared to controls.
Bolded values show significant case-control differences.

Neither of the substituted SN samples showed significant differences in urea concentrations compared with other cases in the cohort (see **Supplementary Material B** for individual values). Case-control differences in SN-urea levels remained significant with exclusion of substituted SN controls C10 and C11.

As sample sizes in this study were small, a study measuring the statistical power of the urea values was conducted. This found a statistical power of over 80% in the CB, MCX, PVC, MED, CG, and PONS, over 70% in the SN and MTG, and a lower value of 68.7% in the HP for $p < 0.05$. This indicates good statistical power in most regions, but highlights the necessity of larger sample sizes for more robust measurements. The same test showed a required sample size of 3 for confident identification of case-control differences at $p < 0.05$ for all regions except the HP, which showed a required sample size of 4.

Comparisons With Brain Urea Concentrations in Alzheimer's Disease and in Huntington's Disease

Our group has previously reported severe and regionally widespread increases in brain-tissue urea concentrations in cases with AD dementia (Xu et al., 2016), and with HD dementia (Patassini et al., 2015, 2016). In these studies, AD and HD brain-tissue urea values were reported from multiple regions compared between cases and matched controls [**Table 2** and **Figure 2**; refs (Patassini et al., 2015, 2016; Xu et al., 2016)].

Although there are some differences in the methodologies used in the two former studies compared with the current one

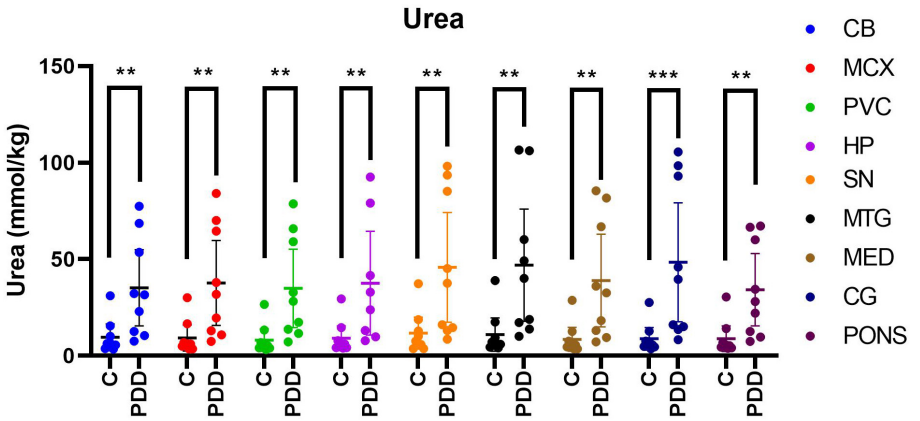

FIGURE 1 | Urea concentrations in PDD cases and matched controls. Mean tissue urea concentrations ± 95% confidence intervals expressed in mmol/kg. Case-control differences were determined by applying the Mann-Whitney-*U* test. $^{**}p < 0.01$ and $^{***}p < 0.001$. C, control; PDD, Parkinson's disease dementia case.

(such as previous use of gas chromatography-mass spectrometry, and some differences in the regions studied; **Figure 2**), case-control tissue-urea fold-changes can be compared between PDD, HD, and AD (**Table 2**) across several brain regions.

Cases and controls in the HD study were slightly younger than those in the current PDD cohort, at an average of around 3 years for controls and 8 years for cases (Patassini et al., 2015, 2016). Moreover, PMD was significantly lower than in the current PDD cohort, at an average of ∼11 h in both cases and controls. Cause of death in the HD cohort was most commonly bronchopneumonia in cases and heart failure in controls, but data on comorbidities and other vascular pathology were unavailable.

TABLE 2 | Urea fold-changes in PDD, AD, and HD.

Region	Fold-change in PDD (this study)	Fold-changes in AD (Xu et al., 2016)	Fold-changes in HD (Patassini et al., 2015)
CB	3.7	4.9	3.6
MCX	4.1	5.0	3.4
PVC	4.3	4.9	3.4
HP	4.2	6.5	3.6
SN	3.9	–	3.5
MTG	4.3	4.7	3.4
MED	4.6	–	–
CG	5.5	5.3	3.5
PONS	3.9	–	–
PUT	–	–	3.7
GP	–	–	3.6
MFG	–	–	3.0
ENT	–	5.6	2.8
Overall	4.3 (3.9–4.6)	5.3 (4.8–5.8)	3.5 (3.2–3.6)

Comparisons of case-control fold-changes in human brain urea levels between PDD, AD, and HD. Case-control differences were significant for every region in every disease. Overall shows mean overall fold-change with ± 95% confidence intervals.

Brain tissue-urea concentrations showed a similar average fold-increase to that measured in PDD of 3.5 in HD cases compared to controls (**Table 2** and **Figure 2**). As in PDD, the increase was observed in the SN, CB, HP, MTG, CG, SCX, and MCX, as well as in other regions not included in the current PDD study, such as the putamen, globus pallidus, middle frontal gyrus, and entorhinal cortex.

The AD cases whose brain-tissue urea levels we measured were similar in age to the current PDD cohort, with an average of ∼70 years in both cases and controls (Xu et al., 2016). PMD was also significantly shorter in this cohort, at an average of 9 h in controls and 7 h in cases. Causes of death were varied in both cases and controls, most commonly being due to heart or lung complications. Comorbidity and vascular pathology metadata were not available. Although absolute tissue-urea concentrations cannot be directly compared to the previous studies in AD brains, there was a higher average case-control fold-change in AD than that observed here in PDD, the average being ∼5.3-fold, but with increases as high as 6.5-fold in the HP (Xu et al., 2016; **Table 2**). Tissue-urea elevations in this AD cohort were observed in the HP, MTG, SCX, MCX, CG, and CB, as well as in the entorhinal cortex (which was not included in the current study). The AD cohort was similar in age to the current PDD cohort.

Comparisons of case-control fold-changes in human brain urea levels between PDD, AD, and HD. Case-control differences were significant for every region in every disease. Overall shows mean overall fold-change with ± 95% confidence intervals.

Additional studies have also confirmed urea increases in AD (Gueli and Taibi, 2013) and HD (Handley et al., 2017) brains, although one study reported decreases in the HD striatum and no change in the HD frontal lobe (Graham et al., 2016). Such discrepancies may be contributed to by differences in methods used or between cohorts, such as differences in PMD. However, we have previously observed that PMD does not affect urea levels for up to 72 h in rat brains (Scholefield et al., 2020), although this may not necessarily also be the case in human brains.

Together, the observations in PDD, AD, and HD suggest a shared pathogenic mechanism in these three diseases, despite

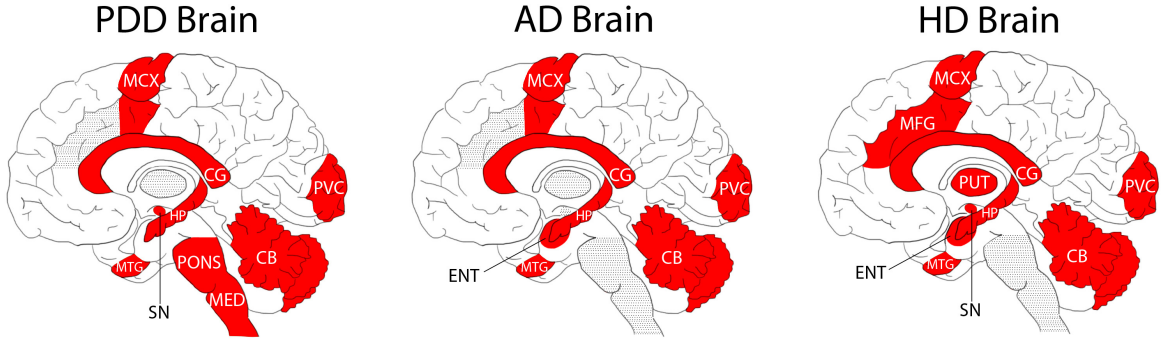

FIGURE 2 | Regional Distribution of Measured Tissue Urea Increases in the PDD, AD, and HD Brain. Areas shaded in red denote significant increases in urea compared to intra-cohort controls. Areas shaded in grey were not investigated in the illustrated studies.

apparent differences in causative processes and symptomology. There appear to be regional differences between diseases with respect to tissue-urea elevations. For example, AD showed the highest increases in the severely affected HP (6.5-fold), whereas in HD the putamen showed slightly higher-than-average elevations (3.7-fold). These regional differences may contribute to differences in severity and pathogenesis in the different conditions. Interestingly, the CG showed the highest urea increase in PDD (5.5-fold); the anterior CG is involved in emotive states and emotionally-coded memories. All other studied regions of the PDD brain showed urea increments of around 3.5- to 4.5-fold. However, there were no statistically significant differences between different PDD-control regions or between different PDD-case regions. Greater power (by increasing the sample size), would probably be required to determine whether the fold-elevation observed in the CG is significantly greater than that of other regions of the PDD brain. If so, it is possible that the prominence of both motor and cognitive dysfunction in PDD correlates with similar tissue urea elevations in areas involved in both cognition and motor control processes–a future investigation into regional tissue urea dysregulation in PD brains without dementia could help elucidate this and would probably be a logical next step.

Urea's main metabolic function is to provide a route for the excretion of nitrogen-containing moieties derived from toxic nitrogen-containing compounds. In the urea cycle, ammonia is converted into urea, which is then excreted from the body *via* the urine. Urea is mainly produced in the liver and is carried to other parts of the body *via* the blood stream. However, it is slow to cross the blood-brain barrier (BBB; Sterns et al., 2015), leading to the question as to whether cerebral urea does in fact enter the brain through the BBB, or whether it is also produced in the brain. There is little evidence for the presence of intracerebral urea cycle activity, although there have been limited observations of partial activity in some studies. For example, some studies have identified increased expression of arginase I (ARG1) mRNA in AD brains and the brains of the APP^{sw} mouse model of AD (Colton et al., 2006), as well as increased arginase activity in human AD brains–accompanied by concurrent decreases in ornithine (Liu et al., 2014). Arginase is the final enzyme of the urea cycle, responsible for conversion of arginine to urea–as such, increased arginase activity could result in increased urea levels. A proteomics study conducted by our own lab on several regions of the AD brain observed arginase II in the CB, but did not observe any case–control changes in the enzyme; ARGI was not identified in any region (Xu et al., 2019). Triple transgenic AD mouse models have also exhibited reduced amyloid-β deposits, microgliosis, and spatial memory deficits with administration of arginase inhibitor L-norvaline (Polis et al., 2018). Administration of an arginase-1 inhibitor has also been found to be protective against midbrain dopaminergic neuronal loss induced in rat brain slice cultures by arginase-1 promoter macelignan (Kiyofuji et al., 2015). A network analysis has also found arginine pathways be enriched in both PD and AD, as well as in amyotrophic lateral sclerosis (Kori et al., 2016), possibly resulting in downstream upregulation of nitric oxide synthesis, leading to hypoxia, which has been implicated in both PD and AD (Virarkar et al., 2013). Together, these results suggest a role for arginase in AD and PD pathology.

However, arginase is only one component of the urea cycle and is not sufficient for complete urea cycle activity; another urea cycle component–ornithine transcarbamylase (OTC)–the enzyme responsible for the conversion of ornithine to citrulline in the urea cycle, was initially reported to be expressed only in AD brains (Bensemain et al., 2009), but has also been observed in healthy control brains in limited amounts (Bernstein et al., 2015, 2017). However, studies attempting to investigate the levels of other urea cycle enzymes in HD sheep model brains for example were unable to identify either OTC or carbamoyl phosphate synthetase I in the striatum (Handley et al., 2017). Additionally, a more recent large-scale proteomic study of six regions of human AD and control brains was unable to identify the presence of either of these urea cycle enzymes at the protein level (Xu et al., 2019). As such, it is possible that upregulation of OTC in AD brains leads to urea cycle activity in the brain that would otherwise not be present, characterised by increased urea and arginase activity and decreased ornithine, but the lack of other urea cycle components makes definite conclusions difficult to draw at this stage. It is not yet known whether increases in OTC are also present in the PDD brain.

Some other urea cycle components such as adenosine (McFarland et al., 2013; Xu et al., 2016; Alonso-Andres et al., 2018), citrulline (Liu et al., 2014), and ornithine (Gueli and Taibi, 2013; Liu et al., 2014) have been reported in the AD brain, as well as the HD brain (Graham et al., 2016; Patassini et al., 2016)—however, as these metabolites are also involved in other metabolic pathways, this does not necessarily indicate urea cycle activity. For example, adenosine is a core component of several widespread co-enzymes such as adenosine triphosphate (ATP), diphosphate (ADP), and monophosphate (AMP) which are crucial to a wide variety of metabolic pathways including the ETC (Nolfi-Donegan et al., 2020), TCA cycle (Madeira, 2018), and purine metabolism (Ichida et al., 2009). As such, it seems likely that cerebral urea may be formed by an alternative process, either by itself or in addition to potential urea cycle activity in the brain.

Several urea cycle intermediates have also been reported to be dysregulated in PD serum, plasma, and CSF. Arginine has been reported by some investigations to be decreased in PD serum (Mally et al., 1997) and CSF (Molina et al., 1997), although other reports have observed no changes in either the serum (Hatano et al., 2016), CSF (Mally et al., 1997; Engelborghs et al., 2003), or plasma (Molina et al., 1997). There is one report of increased citrulline in PD serum (Han et al., 2017), although another investigation reported no change (Hatano et al., 2016), and further reports indicated no change in the CSF (Molina et al., 1997; Engelborghs et al., 2003) or plasma (Iwasaki et al., 1992; Molina et al., 1997). Increases in PD serum ornithine have been reported (Hatano et al., 2016), with varying reports in the CSF of decrease (Molina et al., 1997), increase (Wuolikainen et al., 2016), or no change (Engelborghs et al., 2003). Moreover, no changes have been reported by several groups in studies of plasma ornithine in PD (Iwasaki et al., 1992; Molina et al., 1997; Wuolikainen et al., 2016). None of these urea cycle components have been reported on in the PD/PDD brain itself, and the investigations of peripheral levels in the plasma, CSF, and serum have reported inconsistent results. As such, this entire pathway, and the possibility of partial or whole urea cycle activity in the brain, presents a novel area for future investigation of PDD.

Protein dysregulation and neuronal death may lead to greater protein breakdown, and so to increased urea production. Disruptions to the BBB, as observed in PDD (Sweeney et al., 2018), may result in defective urea clearance from the brain or increased entry of urea from the bloodstream *via* urea transporters. Urea transporters are responsible for regulating movement of urea by facilitating urea diffusion, and are expressed in astrocytes and the BBB as well as outside the brain. Urea transporter B has been shown to be upregulated in the HD CB, which may reflect attempts to clear elevated urea levels in the HD brain (Handley et al., 2017). Urea transporters have not yet been investigated in PD/PDD, but may show similar perturbations to those reported in HD.

Urea accumulation caused by kidney failure is known to be toxic to the brain, leading to a condition called uraemic encephalopathy (Seifter and Samuels, 2011). High urea levels lead to synaptic loss and inhibition of long-term potentiation *via* carbamylation of mTOR in a chronic kidney disease mouse model (Wang H. et al., 2019). Carbamylation is a post-translational modification involving the addition of isocyanate, usually derived from urea, to protein-bound amino-acid residues, causing alterations in the structure and function of the affected proteins. Increased carbamylation has been observed in aging humans (Gorisse et al., 2016), and as a result of chronic kidney disease (Long et al., 2018) as well as in AD with cerebrovascular disease (Gallart-Palau et al., 2017). It has been shown that tau, which is aggregated in AD and also to a lesser degree in PDD, can be carbamylated, resulting in increased amyloid formation and tau accumulation (Guru KrishnaKumar et al., 2018). Whether α-synuclein may also be carbamylated is unknown, but it does contain several potentially susceptible amino-acid residues, which might serve as target sites for carbamylation.

High urea levels in chronic kidney disease and renal failure have also been linked to increased oxidative stress (Vaziri, 2004). Oxidative stress is a well-recognised feature of PD, AD, and HD (Yan et al., 2013; Graham et al., 2016) and is linked to other pathogenic mechanisms including mitochondrial dysfunction and proteinopathy (Ganguly et al., 2017), dysregulated glucose metabolism (Butterfield and Halliwell, 2019), insulin resistance and inflammation (Verdile et al., 2015), and α-synuclein accumulation, oligomerisation, and phosphorylation (Scudamore and Ciossek, 2018; Wang R. et al., 2019). As such, it is possible that elevated urea levels in PDD could contribute to one or more of these known pathogenic mechanisms.

Weaknesses of the current study include small sample sizes of a maximum of 9 v 9 in all three diseases. However, analyses of statistical power show good values, at >80% in most PDD brain regions. Non-parametric tests were also employed due to the small sample size in order to avoid type I errors during statistical analysis. Despite this, larger sample sizes would lead to more robust findings. There are also some regions of the PDD brain that may have been of interest for comparison with other dementias, such as the putamen and caudate nucleus, which are both heavily affected in both PDD and HD. However, this study was limited by the number of available regions for the same donors (which allow for more direct intraregional comparisons of urea concentrations), and also due to our aim of including not only heavily affected regions, but also moderately affected and relatively spared regions. As such, future investigations should try to include such areas, which to our knowledge have yet to be investigated in terms of urea concentrations in PDD. An additional weakness in this study is a lack of additional metadata, such as the duration of Parkinsonism and dementia symptoms in PDD cases, or data on renal functions in donors. Unfortunately, this data was not available for the tissues obtained in this study; although no cases or controls were reported as having renal issues involved in their cause of death, it is unknown whether they had any kidney-related comorbidities before death.

The strengths of this study are the use of highly precise quantitative UHPLC-MS/MS methods, performed in such a way as to make the measured values directly comparable to brain tissues from previous analyses of other dementia diseases. The cohort used for this study was also very

well-matched, with only a small difference in PMD between SN cases and controls. Data was also obtained on donor cause of death and neuropathology–as provided by referring neuropathologists at the brain bank–which is not always available in studies such as these. Statistical tests of study power showed values of >80% in most regions, suggesting good statistical power at $p > 0.05$. Although larger sample sizes are required for further studies, this suggests that a good amount of confidence can be had in the results reported here.

CONCLUSION

In conclusion, this investigation shows widespread urea accumulation throughout the PDD brain, similar to that previously observed in AD and HD, with concentrations comparable to those seen in uremic encephalopathy. This suggests a novel shared pathogenic insult across multiple neurodegenerative conditions and may indicate a common mechanism in the development of cognitive impairment.

DATA AVAILABILITY STATEMENT

The original contributions presented in the study are included in the article/**Supplementary Material**, further inquiries can be directed to the corresponding author/s.

ETHICS STATEMENT

The studies involving human participants were reviewed and approved by Manchester REC (09/H0906/52C5). The patients/participants provided their written informed consent to participate in this study.

AUTHOR CONTRIBUTIONS

MS designed and performed research, analysed and interpreted data, and wrote the first draft and subsequent drafts of the manuscript. SC performed research, analysed data, and read and revised the manuscript. FR, NH, and RU read and revised the manuscript. GC conceived, designed and supervised research, analysed and interpreted data, wrote the manuscript, and bears overall responsibility for the integrity of the study and of the manuscript. JX performed research on previous Auckland AD cohort. SP performed research on previous HD cohort. All authors contributed to the article and approved the submitted version.

FUNDING

This work was funded by grants from: Endocore Research Associates, New Zealand (60147); the Maurice and Phyllis Paykel Trust, New Zealand (3627036; and Travel funding for JX); Lottery Health New Zealand (3626585 and 3702766); the Maurice Wilkins Centre for Molecular Biodiscovery, New Zealand (Tertiary Education Commission 9341-3622506; and Doctoral Scholarship for JX); the Lee Trust, New Zealand; the University of Auckland (Doctoral Student PReSS funding JXU058); the Oakley Mental Health Research Foundation (3456030, 3627092, 3701339, 3703253, and 3702870); the Ministry of Business, Innovation & Employment, New Zealand (UOAX0815); the Neurological Foundation of New Zealand; the Medical Research Council (United Kingdom, MR/L010445/1 and MR/L011093/1); Alzheimer's research United Kingdom (ARUK-PPG2014B-7); the University of Manchester, the CMFT, and the Northwest Regional Development Agency through a combined programme grant to CADET; and was facilitated by the Manchester Biomedical Research Centre and the Greater Manchester Comprehensive Local Research Network.

ACKNOWLEDGMENTS

We thank Michael Anderson for assisting in obtaining the tissues required for this study. *PDD Cohort:* Human tissue was obtained through the NIH Neurobiobank from the University of Miami Brain Endowment Bank. We thank both the banks and donors for supply of these tissues. *Auckland AD and HD cohorts:* We also thank the families of patients with Alzheimer's disease who so generously supported this research through the donation of brain tissue to the New Zealand Neurological Foundation Douglas Human Brain Bank in the Centre for Brain Research, Faculty of Medical and Health.

SUPPLEMENTARY MATERIAL

The Supplementary Material for this article can be found online at: https://www.frontiersin.org/articles/10.3389/fnmol.2021.711396/full#supplementary-material

REFERENCES

Alonso-Andres, P., Albasanz, J. L., Ferrer, I., and Martin, M. (2018). Purine-related metabolites and their converting enzymes are altered in frontal, parietal and temporal cortex at early stages of Alzheimer's disease pathology. *Brain Pathol.* 28, 933–946. doi: 10.1111/bpa.12592

Bensemain, F., Hot, D., Ferreira, S., Dumont, J., Bombois, S., Maurage, C. A., et al. (2009). Evidence for induction of the ornithine transcarbamylase expression in Alzheimer's disease. *Mol. Psychiatry* 14, 106–116. doi: 10.1038/sj.mp.4002089

Bernstein, H. G., Dobrowolny, H., Keilhoff, G., and Steiner, J. (2017). In human brain ornithine transcarbamylase (OTC) immunoreactivity is strongly expressed in a small number of nitrergic neurons. *Metab. Brain Dis.* 32, 2143–2147. doi: 10.1007/s11011-017-0105-2

Bernstein, H. G., Jager, K., Dobrowolny, H., Steiner, J., Keilhoff, G., Bogerts, B., et al. (2015). Possible sources and functions of L-homoarginine in the brain: review of the literature and own findings. *Amino Acids* 47, 1729–1740. doi: 10.1007/s00726-015-1960-y

Braak, H., Del Tredici, K., Rub, U., De Vos, R. A., Jansen Steur, E. N., and Braak, E. (2003). Staging of brain pathology related to sporadic Parkinson's disease. *Neurobiol. Aging* 24, 197–211. doi: 10.1016/S0197-4580(02)00065-9

Butterfield, D. A., and Halliwell, B. (2019). Oxidative stress, dysfunctional glucose metabolism and Alzheimer disease. *Nat. Rev. Neurosci,* 20, 148–160. doi: 10.1038/s41583-019-0132-6

Colton, C. A., Mott, R. T., Sharpe, H., Xu, Q., Van Nostrand, W. E., and Vitek, M. P. (2006). Expression profiles for macrophage alternative activation genes in AD and in mouse models of AD. *J. Neuroinflammation* 3:27. doi: 10.1186/1742-2094-3-27

Engelborghs, S., Marescau, B., and De Deyn, P. P. (2003). Amino acids and biogenic amines in cerebrospinal fluid of patients with Parkinson's disease. *Neurochem. Res.* 28, 1145–1150. doi: 10.1023/A:1024255208563

Erkkinen, M. G., Kim, M. O., and Geschwind, M. D. (2018). Clinical Neurology and epidemiology of the major Neurodegenerative Diseases. *Cold Spring Harb. Perspect. Biol.* 10:a033118. doi: 10.1101/cshperspect.a033118

Gallart-Palau, X., Serra, A., Lee, B. S. T., Guo, X., and Sze, S. K. (2017). Brain ureido degenerative protein modifications are associated with neuroinflammation and proteinopathy in Alzheimer's disease with cerebrovascular disease. *J. Neuroinflammation* 14:175. doi: 10.1186/s12974-017-0946-y

Ganguly, G., Chakrabarti, S., Chatterjee, U., and Saso, L. (2017). Proteinopathy, oxidative stress and mitochondrial dysfunction: cross talk in Alzheimer's disease and Parkinson's disease. *Drug Des. Devel, Ther.* 11, 797–810. doi: 10.2147/DDDT.S130514

Glaab, E., Trezzi, J. P., Greuel, A., Jager, C., Hodak, Z., Drzezga, A., et al. (2019). Integrative analysis of blood metabolomics and PET brain neuroimaging data for Parkinson's disease. *Neurobiol. Dis.* 124, 555–562. doi: 10.1016/j.nbd.2019.01.003

Gorisse, L., Pietrement, C., Vuiblet, V., Schmelzer, C. E., Kohler, M., Duca, L., et al. (2016). Protein carbamylation is a hallmark of aging. *Proc. Natl. Acad. Sci. U.S.A.* 113, 1191–1196. doi: 10.1073/pnas.1517096113

Graham, S. F., Kumar, P. K., Bjorndahl, T., Han, B., Yilmaz, A., Sherman, E., et al. (2016). Metabolic signatures of Huntington's disease (HD): (1)H NMR analysis of the polar metabolome in post-mortem human brain. *Biochim. Biophys. Acta* 1862, 1675–1684. doi: 10.1016/j.bbadis.2016.06.007

Gueli, M. C., and Taibi, G. (2013). Alzheimer's disease: amino acid levels and brain metabolic status. *Neurol. Sci.* 34, 1575–1579. doi: 10.1007/s10072-013-1289-9

Guru KrishnaKumar, V., Baweja, L., Ralhan, K., and Gupta, S. (2018). Carbamylation promotes amyloidogenesis and induces structural changes in Tau-core hexapeptide fibrils. *Biochim. Biophys. Acta Gen. Subj.* 1862, 2590–2604. doi: 10.1016/j.bbagen.2018.07.030

Han, W., Sapkota, S., Camicioli, R., Dixon, R. A., and Li, L. (2017). Profiling novel metabolic biomarkers for Parkinson's disease using in-depth metabolomic analysis. *Mov. Disord.* 32, 1720–1728. doi: 10.1002/mds.27173

Handley, R. R., Reid, S. J., Brauning, R., Maclean, P., Mears, E. R., Fourie, I., et al. (2017). Brain urea increase is an early Huntington's disease pathogenic event observed in a prodromal transgenic sheep model and HD cases. *Proc. Natl. Acad. Sci. U.S.A.* 114, E11293–E11302. doi: 10.1073/pnas.1711243115

Hatano, T., Saiki, S., Okuzumi, A., Mohney, R. P., and Hattori, N. (2016). Identification of novel biomarkers for Parkinson's disease by metabolomic technologies. *J. Neurol, Neurosurg. Psychiatry* 87, 295–301. doi: 10.1136/jnnp-2014-309676

Hely, M. A., Reid, W. G., Adena, M. A., Halliday, G. M., and Morris, J. G. (2008). The Sydney multicenter study of Parkinson's disease: the inevitability of dementia at 20 years. *Mov. Disord.* 23, 837–844. doi: 10.1002/mds.21956

Ichida, K., Hosoyamada, M., Hosoya, T., and Endou, H. (2009). "Primary metabolic and renal hyperuricemia," in *Genetic Diseases of the Kidney*, eds L. P. Lifton, S. Somlo, G. H. Giebisch, and D. W. Seldin (Cambridge, MA: Academic Press). doi: 10.1016/B978-0-12-449851-8.00038-3

Irwin, D. J., Lee, V. M., and Trojanowski, J. Q. (2013). Parkinson's disease dementia: convergence of alpha-synuclein, tau and amyloid-beta pathologies. *Nat. Rev. Neurosci.* 14, 626–636. doi: 10.1038/nrn3549

Iwasaki, Y., Ikeda, K., Shiojima, T., and Kinoshita, M. (1992). Increased plasma concentrations of aspartate, glutamate and glycine in Parkinson's disease. *Neurosci. Lett.* 145, 175–177. doi: 10.1016/0304-3940(92)90015-Y

Jellinger, K. A. (2019). Is Braak staging valid for all types of Parkinson's disease? *J. Neural Trans.* 126, 423–431. doi: 10.1007/s00702-018-1898-9

Jellinger, K. A., and Korczyn, A. D. (2018). Are dementia with Lewy bodies and Parkinson's disease dementia the same disease? *BMC Med.* 16:34. doi: 10.1186/s12916-018-1016-8

Kiyofuji, K., Kurauchi, Y., Hisatsune, A., Seki, T., Mishima, S., and Katsuki, H. (2015). A natural compound macelignan protects midbrain dopaminergic neurons from inflammatory degeneration via microglial arginase-1 expression. *Eur. J. Pharmacol.* 760, 129–135. doi: 10.1016/j.ejphar.2015.04.021

Kori, M., Aydin, B., Unal, S., Arga, K. Y., and Kazan, D. (2016). Metabolic biomarkers and neurodegeneration: a pathway enrichment analysis of Alzheimer's disease, Parkinson's disease, and amyotrophic lateral sclerosis. *OMICS* 20, 645–661. doi: 10.1089/omi.2016.0106

Liu, P., Fleete, M. S., Jing, Y., Collie, N. D., Curtis, M. A., Waldvogel, H. J., et al. (2014). Altered arginine metabolism in Alzheimer's disease brains. *Neurobiol. Aging* 35, 1992–2003. doi: 10.1016/j.neurobiolaging.2014.03.013

Long, J., Vela Parada, X., and Kalim, S. (2018). Protein carbamylation in chronic kidney disease and dialysis. *Adv. Clin. Chem.* 87, 37–67. doi: 10.1016/bs.acc.2018.07.002

Madeira, V. M. C. (2018). Overview of mitochondrial bioenergetics. *Methods Mol. Biol.* 1782, 1–6. doi: 10.1007/978-1-4939-7831-1_1

Mally, J., Szalai, G., and Stone, T. W. (1997). Changes in the concentration of amino acids in serum and cerebrospinal fluid of patients with Parkinson's disease. *J. Neurol. Sci.* 151, 159–162. doi: 10.1016/S0022-510X(97)00119-6

McFarland, N. R., Burdett, T., Desjardins, C. A., Frosch, M. P., and Schwarzschild, M. A. (2013). Postmortem brain levels of urate and precursors in Parkinson's disease and related disorders. *Neurodegener. Dis.* 12, 189–198. doi: 10.1159/000346370

McKeith, I. G., Dickson, D. W., Lowe, J., Emre, M., O'brien, J. T., Feldman, H., et al. (2005). Diagnosis and management of dementia with Lewy bodies: third report of the DLB Consortium. *Neurology* 65, 1863–1872. doi: 10.1212/01.wnl.0000187889.17253.b1

Molina, J. A., Jimenez-Jimenez, F. J., Gomez, P., Vargas, C., Navarro, J. A., Orti-Pareja, M., et al. (1997). Decreased cerebrospinal fluid levels of neutral and basic amino acids in patients with Parkinson's disease. *J. Neurol. Sci.* 150, 123–127. doi: 10.1016/S0022-510X(97)00069-5

Nolfi-Donegan, D., Braganza, A., and Shiva, S. (2020). Mitochondrial electron transport chain: oxidative phosphorylation, oxidant production, and methods of measurement. *Redox Biol.* 37:101674. doi: 10.1016/j.redox.2020.101674

Patassini, S., Begley, P., Reid, S. J., Xu, J., Church, S. J., Curtis, M., et al. (2015). Identification of elevated urea as a severe, ubiquitous metabolic defect in the brain of patients with Huntington's disease. *Biochem. Biophys. Res. Commun.* 468, 161–166. doi: 10.1016/j.bbrc.2015.10.140

Patassini, S., Begley, P., Xu, J., Church, S. J., Reid, S. J., Kim, E. H., et al. (2016). Metabolite mapping reveals severe widespread perturbation of multiple metabolic processes in Huntington's disease human brain. *Biochim. Biophys. Acta* 1862, 1650–1662. doi: 10.1016/j.bbadis.2016.06.002

Perl, D. P., Olanow, C. W., and Calne, D. (1998). Alzheimer's disease and Parkinson's disease: distinct entities or extremes of a spectrum of neurodegeneration? *Ann. Neurol.* 44, S19–S31. doi: 10.1002/ana.410440705

Polis, B., Srikanth, K. D., Elliott, E., Gil-Henn, H., and Samson, A. O. (2018). L-Norvaline reverses cognitive decline and synaptic loss in a murine model of Alzheimer's Disease. *Neurotherapeutics* 15, 1036–1054. doi: 10.1007/s13311-018-0669-5

Scholefield, M., Church, S. J., Xu, J., Robinson, A. C., Gardiner, N. J., Roncaroli, F., et al. (2020). Effects of alterations of post-mortem delay and other tissue-collection variables on metabolite levels in human and rat brain. *Metabolites* 10:438. doi: 10.3390/metabo10110438

Scudamore, O., and Ciossek, T. (2018). Increased oxidative stress exacerbates alpha-synuclein aggregation in vivo. *J. Neuropathol. Exp. Neurol.* 77, 443–453. doi: 10.1093/jnen/nly024

Seifter, J. L., and Samuels, M. A. (2011). Uremic encephalopathy and other brain disorders associated with renal failure. *Semin. Neurol.* 31, 139–143. doi: 10.1055/s-0031-1277984

Sterns, R. H., Silver, S. M., and Hix, J. K. (2015). Urea for hyponatremia? *Kidney Int.* 87, 268–270. doi: 10.1038/ki.2014.320

Sweeney, M. D., Sagare, A. P., and Zlokovic, B. V. (2018). Blood-brain barrier breakdown in Alzheimer disease and other neurodegenerative disorders. *Nat. Rev. Neurol.* 14, 133–150. doi: 10.1038/nrneurol.2017.188

Trezzi, J. P., Galozzi, S., Jaeger, C., Barkovits, K., Brockmann, K., Maetzler, W., et al. (2017). Distinct metabolomic signature in cerebrospinal fluid in early parkinson's disease. *Mov. Disord.* 32, 1401–1408. doi: 10.1002/mds.27132

Troisi, J., Landolfi, A., Vitale, C., Longo, K., Cozzolino, A., Squillante, M., et al. (2019). A metabolomic signature of treated and drug-naive patients with Parkinson's disease: a pilot study. *Metabolomics* 15:90. doi: 10.1007/s11306-019-1554-x

Vaziri, N. D. (2004). Oxidative stress in uremia: nature, mechanisms, and potential consequences. *Semin. Nephrol.* 24, 469–473. doi: 10.1016/j.semnephrol.2004.06.026

Verdile, G., Keane, K. N., Cruzat, V. F., Medic, S., Sabale, M., Rowles, J., et al. (2015). Inflammation and oxidative stress: the molecular connectivity between insulin resistance. Obesity, and Alzheimer's Disease. *Mediators Inflamm* 2015:105828. doi: 10.1155/2015/105828

Virarkar, M., Alappat, L., Bradford, P. G., and Awad, A. B. (2013). L-arginine and nitric oxide in CNS function and neurodegenerative diseases. *Crit. Rev. Food Sci. Nutr.* 53, 1157–1167. doi: 10.1080/10408398.2011.573885

Walker, L., Stefanis, L., and Attems, J. (2019). Clinical and neuropathological differences between Parkinson's disease, Parkinson's disease dementia and dementia with Lewy bodies - current issues and future directions. *J Neurochem* 150, 467–474. doi: 10.1111/jnc.14698

Wang, H., Huang, B., Wang, W., Li, J., Chen, Y., Flynn, T., et al. (2019). High urea induces depression and LTP impairment through mTOR signalling suppression caused by carbamylation. *EBioMedicine* 48, 478–490. doi: 10.1016/j.ebiom.2019.09.049

Wang, R., Wang, Y., Qu, L., Chen, B., Jiang, H., Song, N., et al. (2019). Iron-induced oxidative stress contributes to alpha-synuclein phosphorylation and up-regulation via polo-like kinase 2 and casein kinase 2. *Neurochem. Int.* 125, 127–135. doi: 10.1016/j.neuint.2019.02.016

Wuolikainen, A., Jonsson, P., Ahnlund, M., Antti, H., Marklund, S. L., Moritz, T., et al. (2016). Multi-platform mass spectrometry analysis of the CSF and plasma metabolomes of rigorously matched amyotrophic lateral sclerosis, Parkinson's disease and control subjects. *Mol. Biosyst.* 12, 1287–1298. doi: 10.1039/C5MB00711A

Xu, J., Begley, P., Church, S. J., Patassini, S., Hollywood, K. A., Jullig, M., et al. (2016). Graded perturbations of metabolism in multiple regions of human brain in Alzheimer's disease: snapshot of a pervasive metabolic disorder. *Biochim. Biophys. Acta* 1862, 1084–1092. doi: 10.1016/j.bbadis.2016.03.001

Xu, J., Patassini, S., Rustogi, N., Riba-Garcia, I., Hale, B. D., Phillips, A. M., et al. (2019). Regional protein expression in human Alzheimer's brain correlates with disease severity. *Commun. Biol.* 2:43. doi: 10.1038/s42003-018-0254-9

Yan, M. H., Wang, X., and Zhu, X. (2013). Mitochondrial defects and oxidative stress in Alzheimer disease and Parkinson disease. *Free Radic. Biol. Med.* 62, 90–101. doi: 10.1016/j.freeradbiomed.2012.11.014

Conflict of Interest: The authors declare that the research was conducted in the absence of any commercial or financial relationships that could be construed as a potential conflict of interest.

Publisher's Note: All claims expressed in this article are solely those of the authors and do not necessarily represent those of their affiliated organizations, or those of the publisher, the editors and the reviewers. Any product that may be evaluated in this article, or claim that may be made by its manufacturer, is not guaranteed or endorsed by the publisher.

Copyright © 2021 Scholefield, Church, Xu, Patassini, Roncaroli, Hooper, Unwin and Cooper. This is an open-access article distributed under the terms of the Creative Commons Attribution License (CC BY). The use, distribution or reproduction in other forums is permitted, provided the original author(s) and the copyright owner(s) are credited and that the original publication in this journal is cited, in accordance with accepted academic practice. No use, distribution or reproduction is permitted which does not comply with these terms.

frontiers in Aging Neuroscience

ORIGINAL RESEARCH
published: 25 October 2021
doi: 10.3389/fnagi.2021.736937

Association Between Plasma Amyloid-β and Neuropsychological Performance in Patients With Cognitive Decline

Gyihyaon Yun[1†], Hye Jin Kim[2†], Hyug-Gi Kim[3], Kyung Mi Lee[3], Il Ki Hong[4], Sang Hoon Kim[5], Hak Young Rhee[6], Geon-Ho Jahng[7], Sung Sang Yoon[1], Key-Chung Park[1], Kyo Seon Hwang[2] and Jin San Lee[1]**

[1] Department of Neurology, Kyung Hee University Hospital, Kyung Hee University College of Medicine, Seoul, South Korea, [2] Department of Clinical Pharmacology and Therapeutics, Kyung Hee University College of Medicine, Seoul, South Korea, [3] Department of Radiology, Kyung Hee University Hospital, Kyung Hee University College of Medicine, Seoul, South Korea, [4] Department of Nuclear Medicine, Kyung Hee University Hospital, Kyung Hee University College of Medicine, Seoul, South Korea, [5] Department of Otorhinolaryngology, Head and Neck Surgery, Kyung Hee University Hospital, Kyung Hee University College of Medicine, Seoul, South Korea, [6] Department of Neurology, Kyung Hee University Hospital at Gangdong, Kyung Hee University College of Medicine, Seoul, South Korea, [7] Department of Radiology, Kyung Hee University Hospital at Gangdong, Kyung Hee University College of Medicine, Seoul, South Korea

OPEN ACCESS

Edited by:
Woon-Man Kung,
Chinese Culture University, Taiwan

Reviewed by:
Erik Stoops,
ADx NeuroSciences, Belgium
Julien Rossignol,
Central Michigan University, United States

***Correspondence:**
Kyo Seon Hwang
k.hwang@khu.ac.kr
Jin San Lee
xpist@naver.com

[†] *These authors have contributed equally to this work*

Received: *06 July 2021*
Accepted: *07 October 2021*
Published: *25 October 2021*

Citation:
Yun G, Kim HJ, Kim H-G, Lee KM, Hong IK, Kim SH, Rhee HY, Jahng G-H, Yoon SS, Park K-C, Hwang KS and Lee JS (2021) Association Between Plasma Amyloid-β and Neuropsychological Performance in Patients With Cognitive Decline. Front. Aging Neurosci. 13:736937. doi: 10.3389/fnagi.2021.736937

Objective: To investigate the association between plasma amyloid-β (Aβ) levels and neuropsychological performance in patients with cognitive decline using a highly sensitive nano-biosensing platform.

Methods: We prospectively recruited 44 patients with cognitive decline who underwent plasma Aβ analysis, amyloid positron emission tomography (PET) scanning, and detailed neuropsychological tests. Patients were classified into a normal control (NC, n = 25) or Alzheimer's disease (AD, n = 19) group based on amyloid PET positivity. Multiple linear regression was performed to determine whether plasma Aβ ($Aβ_{40}$, $Aβ_{42}$, and $Aβ_{42/40}$) levels were associated with neuropsychological test results.

Results: The plasma levels of $Aβ_{42/40}$ were significantly different between the NC and AD groups and were the best predictor of amyloid PET positivity by receiver operating characteristic curve analysis [area under the curve of 0.952 (95% confidence interval, 0.892–1.000)]. Although there were significant differences in the neuropsychological performance of cognitive domains (language, visuospatial, verbal/visual memory, and frontal/executive functions) between the NC and AD groups, higher levels of plasma $Aβ_{42/40}$ were negatively correlated only with verbal and visual memory performance.

Conclusion: Our results demonstrated that plasma Aβ analysis using a nano-biosensing platform could be a useful tool for diagnosing AD and assessing memory performance in patients with cognitive decline.

Keywords: Alzheimer's disease, amyloid-β1-40, amyloid-β1-42, memory, blood-based biomarker, cognitive decline, neuropsychological performance

INTRODUCTION

Alzheimer's disease (AD), a neurodegenerative disease, is the most common cause of cognitive impairment and dementia (Jack et al., 2018). The pathophysiology of AD is characterized by extracellular amyloid-β (Aβ) plaques and intracellular tau deposition in the brain (Pereira et al., 2021). Growing evidence suggests that Aβ deposition in the brain initiates AD by inducing a chain of events involving the accumulation of toxic tau, which consequently leads to downstream neurodegeneration (Jack et al., 2013, 2014; Pereira et al., 2021). Pathophysiological changes in AD progress over many years without clinical symptoms or dementia; therefore, early detection of Aβ pathology has clinical significance for the deterioration of cognitive function and the occurrence of dementia.

The detection of Aβ pathology using cerebrospinal fluid (CSF) analysis and *in vivo* amyloid positron emission tomography (PET) scans has shown a high correlation with postmortem findings (Palmqvist et al., 2015; Hansson et al., 2018); however, their use in clinical settings is limited. Considering the advantages in terms of cost, reduced invasiveness, and repeated measurement ability, there is a need for the development of blood-based AD biomarkers. However, since Aβ is present at extremely low levels in the blood (on the scale of pg/mL) (Risacher et al., 2019), a more accurate measurement method with higher sensitivity and selectivity is required for the development of more precise blood-based AD biomarkers. Aβ is produced by proteolytic cleavage of amyloid precursor proteins into a monomeric form by β- and γ-secretases, which are transformed into oligomeric and fibrillar forms, and finally into amyloid plaques (O'Brien and Wong, 2011). With advances in measurement technology, it has become possible to measure various forms of Aβ; however, published results thus far appear to be fairly conflicting, and it has been reported that several factors influence the measurement of Aβ in the blood (Wang et al., 2020).

We previously developed a sensing platform capable of analyzing biomolecules at levels in the range of fg/mL with high accuracy (Kim et al., 2019). Our biosensing platform is manufactured via micro/nano-fabrication technology and detects changes in electrical signals, particularly impedance changes, to quantify fg/mL of biomolecules. Additionally, we quantified the level of plasma Aβ, including the monomeric form, more accurately through the filtration effect induced by the dielectrophoresis (DEP) force. Using this method, we overcame the limitations of Aβ monomer quantification in plasma by mitigating the non-specific binding of matrix factors, and eventually more accurately detected Aβ levels in the blood.

Previous studies have revealed that the oligomeric form of Aβ has neuronal toxicity associated with AD pathology as well as synaptic dysfunction (Lacor et al., 2007; Shankar et al., 2008; Viola and Klein, 2015). In addition, elevated levels of Aβ oligomers in the CSF or blood are negatively correlated with neuropsychological performance in patients with AD (Santos et al., 2012; Wang-Dietrich et al., 2013; Meng et al., 2019). To the best of our knowledge, there have been no studies evaluating the association between the level of plasma Aβ and neuropsychological performance, including monomeric Aβ. Thus, the present study aimed to investigate the association between the level of plasma Aβ ($A\beta_{40}$, $A\beta_{42}$, and $A\beta_{42/40}$) and neuropsychological performance in patients with cognitive decline, classified according to amyloid PET positivity using a highly sensitive nano-biosensing platform. Considering that neuropsychological performance in all cognitive domains, including attention, language, visuospatial, memory, and frontal/executive functions, are impaired in patients with AD (Scheltens et al., 2021), we hypothesized that the level of plasma Aβ would be negatively correlated with neuropsychological performance of all cognitive domains in patients with cognitive decline.

MATERIALS AND METHODS

Reagents and Materials

All reagents and materials are listed in **Supplementary Material**.

Study Participants

We prospectively recruited 44 individuals who underwent plasma Aβ analysis, high-resolution 3.0-T brain magnetic resonance imaging (MRI), ^{18}F-florbetaben PET, and detailed neuropsychological testing (Ahn et al., 2010). The participants comprised 20 patients with subjective cognitive decline (SCD), 7 with amnestic mild cognitive impairment (aMCI), and 17 with probable AD dementia, all of whom had been clinically diagnosed at the Memory Disorders Clinic of Kyung Hee University Hospital (Seoul, Korea) between December 2018 and September 2019. Patients with SCD had subjective memory decline but no objective cognitive dysfunction in any cognitive domain in the detailed neuropsychological tests (Jessen et al., 2014). Patients with aMCI were diagnosed according to the Petersen criteria (Petersen, 2004) with modifications that have been described elsewhere (Seo et al., 2009). Patients with probable AD dementia met the criteria proposed by the National Institute of Neurological and Communicative Disorders and Stroke and the AD and Related Disorders Association (McKhann et al., 1984). Brain MRI confirmed the absence of structural lesions, including cerebral hemorrhage or infarction, hippocampal sclerosis, brain tumors, traumatic encephalomalacia, and vascular malformation. The exclusion criteria included a history of psychological disease, stroke, brain surgery, seizure, head trauma, severe cerebral white matter hyperintensities defined by the modified Fazekas scale (Seo et al., 2009), or current systemic medical diseases that could affect cognition.

Laboratory tests were conducted for all participants to eliminate any other causes of cognitive impairment. These tests included complete blood counts, vitamin B_{12} levels, folate levels, metabolite profiles, thyroid function tests, and syphilis serology. Genomic DNA was extracted from whole blood samples for apolipoprotein E (*APOE*) genotyping according to the manufacturer's instructions (QIAGEN GmbH, Hilden, Germany).

Standard Protocol Approval, Registration, and Patient Consent

Written informed consent was obtained from all participants (surrogates or legally authorized representatives if the patient did not have the cognitive ability to provide consent to study participation) prior to inclusion in the study. The study was approved by the Institutional Review Board (IRB) of Kyung Hee University Hospital (IRB No. 2018-01-023).

Plasma Acquisition and Sampling Protocol

To demonstrate an association between the level of plasma Aβ and neuropsychological performance, we collected approximately 1 mL of blood from each participant in an anticoagulant-treated heparin vacutainer tube (sodium heparin vacutainer, cat. no. 367874; BD Biosciences, Franklin Lakes, NJ). Human plasma was then separated from the blood using an ultra-centrifuge (3,000 rpm at 4°C for 15 min) and transferred into a polypropylene (PP) tube. Finally, the plasma was mixed with 1 × protease inhibitor (Version 09, complete mini-ethylenediaminetetraacetic acid-free) in 10 mM phosphate-buffered saline (PBS), and then approximately 1 mL was aliquoted into fresh 1.5-mL PP tubes. The aliquoted samples were stored frozen (−80°C) and diluted 1/100 in 1 mM PBS buffer immediately prior to plasma analysis.

Fabrication and Modification of the Sensing Platform

The sensing platform was fabricated via a microelectromechanical system (MEMS) (Kim et al., 2016). First, to fabricate the biosensing platform, layers of silicon dioxide (SiO_2) and 300/1500 Å tantalum/platinum (Ta/Pt) were deposited on a 4-inch silicon wafer. Then, the Ta/Pt layers were patterned via photolithography and reactive ion etching (RIE). The single sensing platform consisted of six pairs of interdigitated microelectrodes (IMEs) designed with 30 pairs of electrode fingers with 5-μm spacing and 300-μm length.

Meanwhile, two types of antibodies, 11A50-B10 and 12F4, were immobilized on the surface sensor to analyze $Aβ_{40}$ and $Aβ_{42}$, respectively. The surface of the sensor was cleaned and chemically activated by sequential treatment with piranha cleaning solution (H_2SO_4:H_2O_2 = 4:1), 1% 3-(ethoxydimethylsilyl) propylamine (APMES), and *N*-(3 -dimethyl aminopropyl)-*N*-ethylcarbodiimide hydrochloride /*N*-hydroxysuccinimide (EDC/NHs) cross-linking solution. Then, 10 μL of antibody solution was dropped on the surface of the sensor to immobilize the antibody.

Immunoassay and Signal Analysis

To quantify Aβ, a polydimethylsiloxane (PDMS) microfluidic channel fabricated through the MEMS process was attached to the sensor surface, and 10 μL of Aβ solution diluted into 1 mM PBS and standard human plasma was injected into the channel using a syringe (Kim et al., 2016). Then, using a DG40662 series waveform generator (Rigol Technologies Inc., Beaverton, OR), an alternating current (AC) voltage with an intensity of 0.5 mV and frequency of 60 MHz was applied to encourage a reaction between the antibody and Aβ. This reaction was carried out for 20 min at 25°C, and unbound Aβs were washed with 1 mM PBS after the reaction. The reaction was quantified by comparing the electrical signals (ΔZ) measured before and after the Aβ reaction ($ΔZ_{before}$ and $ΔZ_{after}$, respectively) as follows:

$$|\Delta Z|\,(\%) = \left|\frac{|Z_{after}| - |Z_{before}|}{|Z_{before}|}\right| \times 100$$

Similar to the procedure for quantification of Aβ in PBS and standard plasma, Aβ was quantified in clinical samples to diagnose AD. A single clinical sample was quantified using three

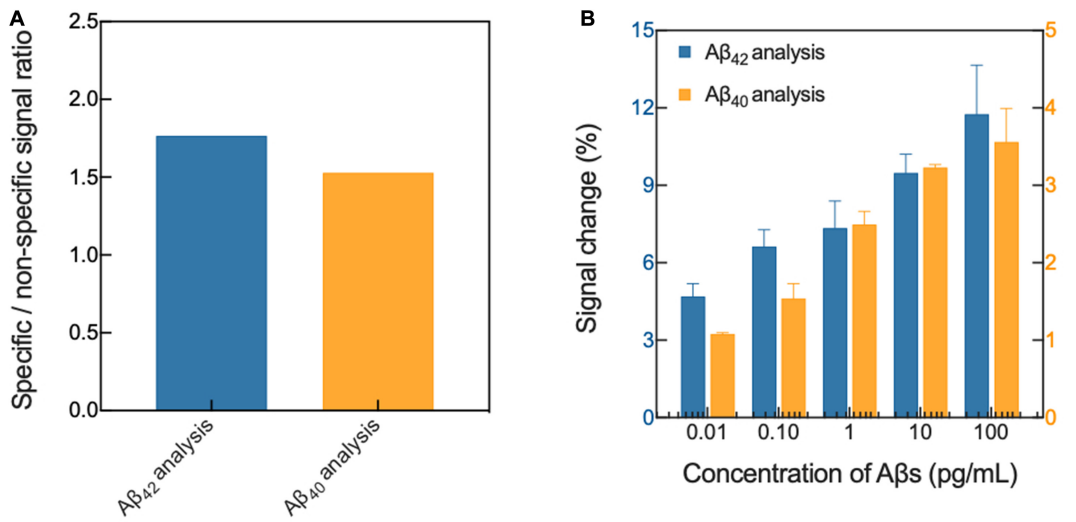

FIGURE 1 | Verification of **(A)** selectivity and **(B)** sensitivity of the biosensor in 1 mM PBS. Aβ, amyloid-β; PBS, phosphate-buffered saline.

sensing platforms (i.e., 18 single IME sensors), and the average of 18 IME signals was used as the final output signal due to the Aβ response in human plasma.

Neuropsychological Testing and Clinical Assessments

All participants underwent detailed neuropsychological tests using the standardized Seoul Neuropsychological Screening Battery (Ahn et al., 2010; Kang et al., 2019). The battery contains tests for attention (Digit Span Forward and Backward), language [Korean version of the Boston Naming Test (K-BNT)], visuospatial function [Rey-Osterrieth Complex Figure Test (RCFT); copying], verbal and visual memory [Seoul Verbal Learning Test (SVLT) and RCFT; immediate and 20-min delayed recall, and recognition], and frontal/executive function [phonemic and semantic Controlled Oral Word Association Test (COWAT) and the Stroop Test; word and color reading]. Age- and education-specific norms for each test based on 447 cognitively normal individuals were used for comparison. Z-scores lower than −1.0 standard deviation (SD) of the age- and education-adjusted norms were considered abnormal. We also used the Mini-Mental State Examination.

Brain Magnetic Resonance Imaging

Structural three-dimensional (3D) T1-weighted images (T1WIs) were acquired using a 3.0-T MRI system (Achieva TX, Philips Medical Systems, Best, The Netherlands) equipped with a 32-channel sensitivity-encoding head coil and multi-transmit technology. The T1WI sequence used was a magnetization-prepared rapid-acquisition gradient-echo sequence with the following parameters: relaxation time = 9.0 ms, echo time = 5.0 ms, flip angle = 8°, field-of-view = 256 × 256 mm^2, and voxel size = 1 × 1 × 1 mm^3.

^{18}F-florbetaben Positron Emission Tomography/CT Acquisition and Analysis

3D static PET images were acquired 90 min after intravenous injection of 296 MBq of 18F-florbetaben using a Gemini TF 16 PET/CT scanner (Philips Healthcare, Cleveland, OH). CT images were acquired from the vertex to the skull base (50 mAs; 120 kVp; slice 2 mm), and 10-mm PET images were immediately acquired over the same region. We used the ordered-subset expectation maximization algorithm (iteration = 3 and subset = 33) to reconstruct 3D PET images in a 128 × 128 × 20 matrix with a voxel size of 2 × 2 × 2 mm^3.

All amyloid PET images were visually assessed and dichotomized as amyloid-positive or amyloid-negative after being reviewed by nuclear medicine physicians who were blinded to the participants' information. Amyloid PET findings were considered positive when the brain amyloid-plaque load (BAPL) score (Barthel et al., 2011) was 2−3, based on visual assessment. Regarding regional cortical tracer uptake (RCTU), image evaluators used the RCTU scoring system (RCTU 1, no tracer uptake; RCTU 2, moderate tracer uptake; and RCTU 3, pronounced tracer uptake) in the lateral temporal cortex, frontal cortex, posterior cingulate cortex/precuneus, and parietal cortex. In terms of RCTU and BAPL correspondence, an RCTU score of 1 in each brain region was considered to be identical to a BAPL score of 1. An RCTU score of 2 in at least one brain region and no score of 3 was considered equivalent to a BAPL score of 2. An RCTU score of 3 in any of the four brain regions was considered a BAPL score of 3. Amyloid-negative status was given

TABLE 1 | Impedance changes according to the concentrations of Aβ spiked in the plasma.

Concentrations, pg/mL	Average impedance change, %	
	$A\beta_{40}$	$A\beta_{42}$
0.01	4.126 (0.369)	3.627 (0.201)
0.1	5.119 (0.102)	4.293 (0.513)
1	5.969 (0.472)	4.548 (0.588)
10	6.784 (0.574)	5.649 (0.655)
100	8.476 (0.935)	6.836 (0.657)

Values are means (SD).
Aβ, amyloid-β.

TABLE 2 | Demographics and clinical characteristics of study participants.

	Total	NC	AD
N	44 (100.0)	25 (56.8)	19 (43.2)
Age, years	69.7 (8.0)	68.4 (6.5)	71.5 (9.5)
Female	31 (70.5)	17 (68.0)	14 (73.7)
Education, years	9.4 (5.6)	10.2 (6.2)	8.5 (4.7)
APOE ε4 status	18 (40.9)	8 (32.0)	10 (52.6)
Hypertension	27 (61.4)	18 (72.0)	9 (47.4)
Diabetes mellitus	15 (34.1)	8 (32.0)	7 (36.8)
Dyslipidemia	25 (56.8)	14 (56.0)	11 (57.9)
History of IHD	5 (11.4)	4 (16.0)	1 (5.3)
History of stroke	8 (18.2)	4 (16.0)	4 (21.1)
Cognitive status			
SCD	20 (45.5)	20 (80.0)	–
aMCI	7 (15.9)	5 (20.0)	2 (10.5)
Dementia	17 (38.6)	–	17 (89.5)
MMSE	21.8 (56.0)	25.1 (4.6)[a]	17.5 (4.8)
Amyloid PET SUVR	1.393 (0.259)	1.198 (0.059)[a]	1.649 (0.182)
Plasma Aβ, fg/mL			
$A\beta_{40}$	219.9 (534.5)	343.8 (676.8)	56.9 (110.2)
$A\beta_{42}$	10,134 (5,095.1)	1,117 (2,798.6)	21,998 (66,717.8)
Plasma Aβ, %			
$A\beta_{40}$	4.520 (0.967)	4.846 (0.906)[a]	4.109 (0.881)
$A\beta_{42}$	4.641 (0.871)	4.320 (0.733)[a]	5.063 (0.858)
$A\beta_{42/40}$ (a.u.)	1.059 (0.256)	0.904 (0.127)[a]	1.263 (0.238)

Values are means (SD) or N (%).
The value of plasma Aβ (%) is the average impedance change of the biosensing platform.
Statistical analyses were performed using the chi-squared test, Fisher's exact test, or Student's t-test.
[a]*Difference between NC and AD, $p < 0.05$.*
NC, normal controls; AD, Alzheimer's disease; N, number; APOE, apolipoprotein E; IHD, ischemic heart disease; SCD, subjective cognitive decline; aMCI, amnestic mild cognitive impairment; MMSE, Mini-Mental State Examination; PET, positron emission tomography; SUVR, standardized uptake value ratio; Aβ, amyloid-β.

to participants with a BAPL score of 1, while amyloid-positive status was given to those with BAPL scores of 2−3.

We also conducted a quantitative amyloid PET analysis using the cortical standardized uptake value ratio (SUVR) in all PET scans. Based on a previous study (Bullich et al., 2017), an SUVR cut-off of ≥ 1.43 was selected as the amyloid positivity criterion. In this study, our visual assessment strongly corresponded with the binarized global ^{18}F-florbetaben PET binding evaluations, as the comparison of the two methods resulted in a high accuracy of 100% [25 participants were amyloid-negative (20 patients with SCD and 5 with aMCI), and 19 were amyloid-positive (2 patients with aMCI and 17 with AD dementia)].

Pattern Analysis of Aβ Accumulation in the Brain

Pattern analysis was performed with MRI and amyloid PET images to visually estimate the relative levels of plasma $A\beta_{40}$ and $A\beta_{42}$ in the brain. First, cortical and subcortical brain regions were automatically segmented using Freesurfer 5.3,[1] following the pipeline described at https://surfer.nmr.mgh.harvard.edu/fswiki/recon-all. Second, ^{18}F-florbetaben PET images were co-registered to the 3D T1WI-labeled data using the Statistical Parametric Mapping Version 12 program (Wellcome Department of Imaging Neuroscience, University College, London, United Kingdom). Amyloid cortical SUVR was determined as the average of the standardized uptake value normalized by the uptake in the cerebellar gray matter, with this reference region being selected from the cerebellum external and cortex segments on MRI. Third, pattern analysis was conducted between Aβ present in the plasma and SUVR in amyloid PET using the coefficient of linear correlation. The results showed the average correlation coefficient in each brain region of interest as color-coded overlays on the representative MR image.

Statistical Analyses

Continuous variables were compared using Student's *t*-test and are presented as the mean ± SD. Categorical variables were compared using the chi-squared test or Fisher's exact test. For multiple comparisons, we performed non-parametric statistical testing as the data were not normally distributed (Kruskal–Wallis one-way analysis of variance with the Dunn test for *post hoc* comparison between individual pairs). Multiple linear regression was performed using vascular risk factors (hypertension, diabetes mellitus, hyperlipidemia, and history of ischemic heart disease and stroke), *APOE* ε4 status, and $A\beta_{40}$, $A\beta_{42}$, and $A\beta_{42/40}$ as independent variables. Statistical significance was set at $p < 0.05$, in two-tailed tests. Statistical analyses were performed using SPSS (version 20.0; IBM, Armonk, NY) and Prism 8 (GraphPad Software, San Diego, CA). Also, to compute the area under the curve (AUC), a receiver operator characteristic (ROC) curve was created using Prism 8. We used a hybrid Wilson/Brown method to compare ROC curves and determine the 95% confidence intervals associated with the sensitivities and specificities (at Youden index thresholds).

[1]http://surfer.nmr.mgh.harvard.edu/

RESULTS

Demonstrating the Platform's Performance in Plasma Aβ Analysis

Our biosensing platform showed high specificity in the analysis of Aβs in 1 mM PBS, depending on the type of immobilized antibody on the surface of the platform (**Figure 1A**). Because the selectivity of the sensor indicates how well the sensor will respond specifically to the target analyte (Bhalla et al., 2016), we compared the output signal of the sensor in Aβ-specific and non-specific binding conditions. In the biosensor in which $A\beta_{42}$-specific antibodies were immobilized, an approximately 1.862-fold higher signal change occurred following the specific binding of $A\beta_{42}$ compared with the change following the non-specific binding of $A\beta_{40}$ (approximately 5.928 ± 0.357% and 3.183 ± 0.318%, respectively; $p < 0.0001$). However, in the biosensor where $A\beta_{42}$-specific antibodies were immobilized, the signal change due to the specific binding of $A\beta_{42}$ was approximately 1.536-fold higher than that due to non-specific binding of $A\beta_{40}$ (approximately 3.325 ± 0.430% and 2.165 ± 0.394%, respectively; $p < 0.01$). In addition, the average impedance variation due to buffer exchange and non-specific adsorption of plasma proteins on the surface of the platform was approximately 2.086 ± 0.585%.

The platform also had excellent sensitivity in the Aβ analysis, and the changes upon specific binding of $A\beta_{42}$ and $A\beta_{40}$ ranged from approximately 3.241 ± 0.053%−10.684 ± 1.296% and from 1.563 ± 0.169% to 3.919 ± 0.632%, respectively, depending on the concentrations of Aβ in 1 mM PBS (**Figure 1B**). In general, the sensitivity of a sensor is defined as the change in the output signal in the sensor as a function of the concentration of the analyte ($S = \Delta\text{signal}/\Delta\text{analyte}$), and is normally calculated from the slope of the linear calibration curve (Morales and Halpern, 2018). Therefore, through a linear regression analysis (linear equation: y = intercept + slope x, the value of the slope signifies the sensitivity of the sensor for Aβ binding), the sensitivities were calculated to be approximately 0.777 ± 0.106 and 1.036 ± 0.091 for $A\beta_{42}$ and $A\beta_{40}$ analysis, respectively. Furthermore, we demonstrated the possibility of highly sensitive analysis of Aβs spiked in standard plasma, and as a result, our sensing platform for the analysis of Aβs spiked in plasma was verified.

Furthermore, we verified that the impedance changes of our sensing platform ranged from approximately 3.627 ± 0.201% to 6.836 ± 0.657% and from 4.126 ± 0.369% to 8.476 ± 0.935%, respectively, depending on the concentrations of Aβ spiked in the plasma (**Table 1**). The results suggested that our sensing platform is useful for plasma Aβ analysis.

Demographics and Plasma Aβ Analysis in Patients With Cognitive Decline

Table 2 shows the demographics and plasma Aβ levels of the study participants. Based on amyloid PET positivity, participants were classified into a normal control (NC, $n = 25$) or AD ($n = 19$) group. The average signal levels of $A\beta_{40}$ ($p = 0.012$) and $A\beta_{42}$ ($p = 0.004$) were significantly different between the NC and AD groups. This difference was clearly reduced when the signal level of $A\beta_{42}$ was divided by that of $A\beta_{40}$ (NC

vs. AD: $p < 0.001$ for $A\beta_{42/40}$) (**Figure 2A**). In addition, the concentration of Aβs, estimated from the impedance changes based on the sensitivity curves of our sensing platform, were calculated (**Supplementary Table 1**). ROC curve analysis demonstrated that the ratio of $A\beta_{42/40}$ was the best predictor of amyloid PET positivity, with the AUC of 0.952 [95% confidence interval (CI), 0.892–1.000] (**Figure 2B**). Participants with $A\beta_{42/40}$ values exceeding 1.016 were considered as AD patients, as this value gave the maximum Youden index with a positive percentage agreement of 0.81 (95% CI, 0.75–0.96) and a negative percentage agreement of 0.95 (95% CI, 0.67–0.83) with amyloid PET positivity.

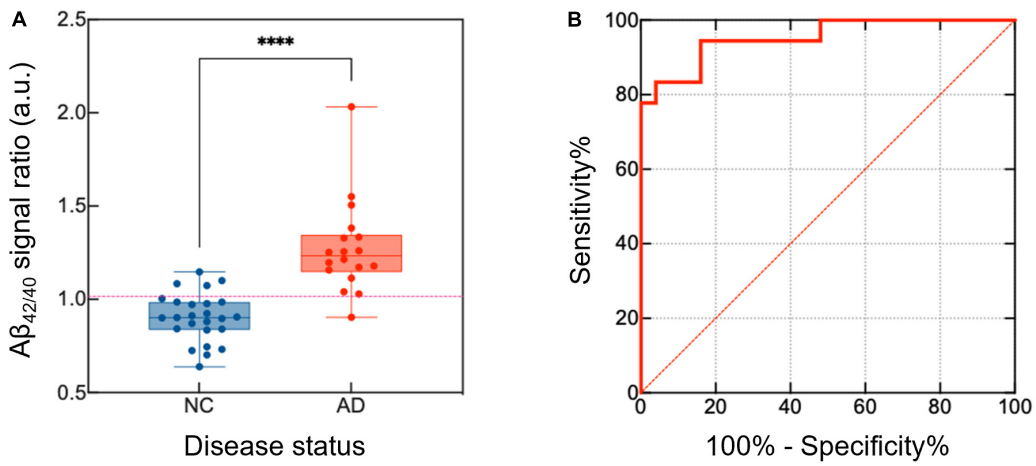

FIGURE 2 | Differentiation of the NC and AD groups based on the analysis of plasma $A\beta_{42/40}$ levels. To distinguish between the NC and AD groups, the relative signal level of $A\beta_{42}$ and $A\beta_{40}$ was calculated. **(A)** The ratio of the signal between the $A\beta_{42}$ and $A\beta_{40}$ was higher in the AD group than in the NC group. **(B)** A high AUC value was calculated using the ROC (AUC = 0.952, 95% CI, 0.892–1.000). *p*-values are indicated with asterisks: ****$p < 0.0001$. NC, normal control; AD, Alzheimer's disease; Aβ, amyloid-β; AUC, area under the curve; ROC, receiver operating curve; CI, confidence interval.

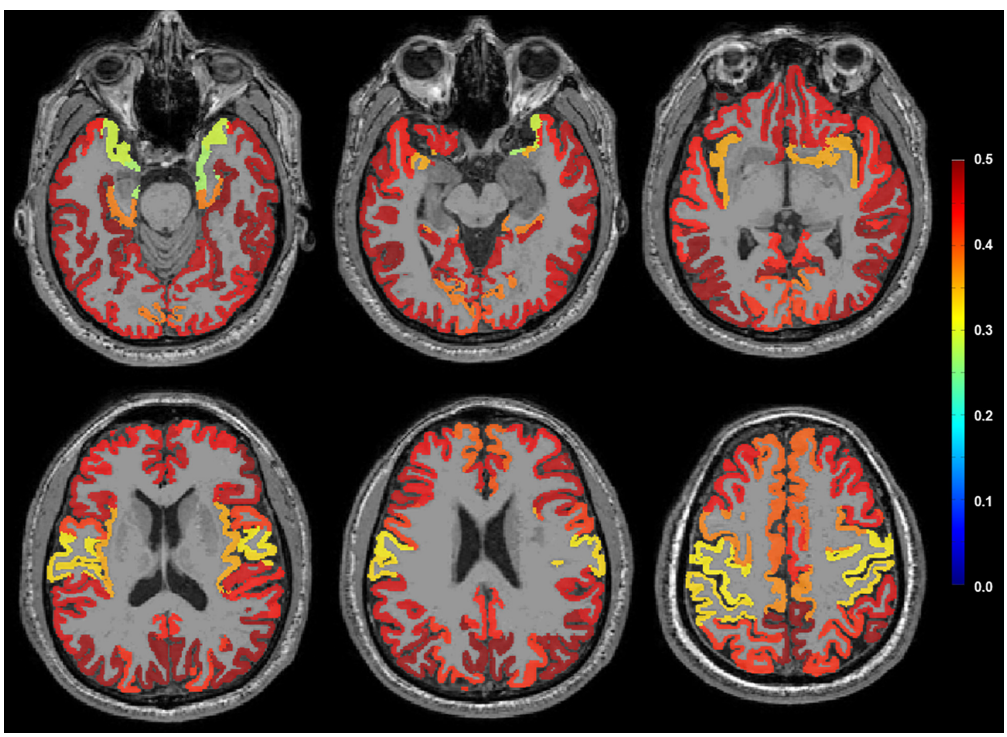

FIGURE 3 | Correlation coefficient (*r*) between plasma $A\beta_{42/40}$ and amyloid PET SUVR on representative MRI using pattern analysis. A moderate positive correlation (red color) was observed in the bilateral frontal, parietal, temporal, and occipital cortices, except the primary motor and sensory cortices. Aβ, amyloid-β; SUVR, standardized uptake value ratio.

Neuroimaging Pattern Analysis Between Plasma $A\beta_{42/40}$ Levels and Amyloid Positron Emission Tomography Standardized Uptake Value Ratio

A topographical pattern of the correlation coefficient (r) between plasma $A\beta_{42/40}$ and amyloid PET SUVR is presented in **Figure 3**. Plasma $A\beta_{42/40}$ and amyloid PET SUVR showed moderate positive correlations in the bilateral frontal, parietal, temporal, and occipital cortices, except for the primary motor and sensory cortices, suggesting a typical pattern of regional deposition for neocortical Aβ in AD.

Neuropsychological Performance in the Normal Control and Alzheimer's Disease Groups

As shown in **Table 3**, we compared neuropsychological performance results between the NC and AD groups. Significant differences were observed in the mean Z-scores of the K-BNT ($p = 0.002$), SVLT [immediate recall ($p < 0.001$), delayed recall ($p < 0.001$), recognition ($p < 0.001$)], RCFT [copy ($p = 0.028$), immediate recall ($p < 0.001$), delayed recall ($p < 0.001$), recognition ($p = 0.001$)], COWAT phonemic total ($p = 0.030$), and Stroop color reading ($p = 0.012$) tasks between the NC and AD groups.

TABLE 3 | Neuropsychological performance in the NC and AD groups.

	NC	AD	*p*-value
Attention			
Digit span forward	–0.41 (0.82)	–0.41 (1.06)	0.995
Digit span backward	–0.35 (0.96)	–0.91 (1.01)	0.067
Language			
K-BNT	–0.66 (1.36)	–2.66 (2.55)	0.002
Visuospatial function			
RCFT copy	0.03 (1.08)	–3.36 (6.03)	0.028
Verbal memory			
SVLT immediate recall	–0.86 (0.82)	–2.05 (1.16)	<0.001
SVLT delayed recall	–0.86 (0.72)	–2.34 (0.96)	<0.001
SVLT recognition	–0.16 (1.10)	–2.61 (2.23)	<0.001
Visual memory			
RCFT immediate recall	–0.40 (0.92)	–1.71 (0.95)	<0.001
RCFT delayed recall	–0.48 (0.96)	–1.92 (0.89)	<0.001
RCFT recognition	–0.37 (0.86)	–2.14 (1.96)	0.001
Frontal/executive function			
COWAT phonemic total	–0.58 (1.00)	–1.43 (1.26)	0.030
Stroop color reading	–0.22 (1.12)	–2.68 (2.97)	0.012

Age- and education-specific Z-scores were used to compare neuropsychological performance between the NC and AD groups.
NC, normal controls; AD, Alzheimer's disease; K-BNT, Korean version of the Boston Naming Test; RCFT, Rey-Osterrieth Complex Figure Test; SVLT, Seoul Verbal Learning Test; COWAT, Controlled Oral Word Association Test.

Association Between the Level of Plasma Aβs and Neuropsychological Test Results

The results of multivariate regression analysis between the levels of plasma Aβ ($A\beta_{40}$, $A\beta_{42}$, and $A\beta_{42/40}$) and neuropsychological performance are presented in **Table 4**. There were no significant correlations between plasma $A\beta_{40}$ and $A\beta_{42}$ levels and neuropsychological performance in the study participants. However, higher levels of plasma $A\beta_{42/40}$ showed a significant negative correlation with the Z-score of the SVLT [immediate recall ($p = 0.014$), delayed recall ($p = 0.006$), recognition ($p = 0.018$)], and RCFT [immediate recall ($p = 0.042$), delayed recall ($p = 0.048$), recognition ($p = 0.005$)] tasks in the study participants.

DISCUSSION

In this study, we investigated the association between plasma Aβ levels and neuropsychological performance in patients with cognitive decline using a highly sensitive nano-biosensing platform fabricated by combining micro/nanotechnology with DEP. We confirmed that our methods for precise AD diagnosis were reliable for the selective analysis of extremely low levels of plasma Aβ, and the neuroimaging pattern analysis supported this result. Unexpectedly, higher levels of plasma $A\beta_{42/40}$ were negatively associated with memory performance in patients with cognitive decline, but not in all cognitive domains. Our results demonstrated that plasma Aβ analysis using a nano-biosensing platform could be a useful tool for diagnosing AD and assessing memory performance in patients with cognitive decline.

We found that the ratio of plasma $A\beta_{42}$ to $A\beta_{40}$ ($A\beta_{42/40}$) was the best predictor of amyloid PET positivity in the study participants, and our findings were consistent with previous results using plasma Aβ analysis (Lue et al., 2017; Park et al., 2017; de Rojas et al., 2018). Our results are also in line with the fact that the combination of $A\beta_{40}$ and $A\beta_{42}$ is more reliable in predicting the risk of developing AD than either biomarker individually (van Oijen et al., 2006). With the remarkable advances in technology to date, there have been efforts to detect Aβ in the CSF and blood using various technical methods (Wang et al., 2020). However, since Aβ levels are approximately 10 times lower in the plasma than in CSF despite the overall protein content being 100-fold higher, the occurrence of strong interference has been raised as a key problem to overcome in plasma Aβ analysis with conventional bioassay systems (Kleinschmidt et al., 2016; Wang et al., 2020). In fact, the concentrations of Aβ in the CSF are present at the level of sub-ng/mL or several ng/mL, while those in the blood are at much lower levels of pg/mL (Yang et al., 2017). This means that the required limit of detection (LoD) for assaying Aβ protein in human blood should be several pg/mL. Previous attempts to demonstrate blood-based AD biomarkers using an enzyme-linked immunosorbent assay (ELISA) have been unsuccessful because the concentration of Aβ is ultralow in AD and the performance of horseradish peroxidase used in ELISA is highly dependent on pH and temperature (Jiao et al., 2018; Lyu et al., 2020). Recently, mass spectrometry-based AD biomarker testing has also been developed to diagnose AD through high-performance measurement of plasma Aβ (Nakamura et al., 2018; Oeckl and Otto, 2019). However, as far as we know, blood-based Aβ assay technologies using ELISA and

TABLE 4 | Correlations of plasma $A\beta_{40}$, $A\beta_{42}$, and $A\beta_{42/40}$ levels with the results of neuropsychological tests.

	Plasma $A\beta_{40}$			Plasma $A\beta_{42}$			Plasma $A\beta_{42/40}$		
	B	**SE**	***p*-value**	***B***	**SE**	***p*-value**	***B***	**SE**	***p*-value**
Attention									
Digit span forward	−0.17	0.15	0.237	0.00	0.16	0.998	0.63	0.56	0.267
Digit span backward	0.05	0.17	0.754	−0.18	0.17	0.310	−0.84	0.63	0.191
Language									
K-BNT	0.25	0.36	0.494	−0.24	0.38	0.529	−2.17	1.36	0.121
Visuospatial function									
RCFT copy	0.93	0.75	0.223	0.53	0.81	0.517	−1.43	2.96	0.632
Verbal memory									
SVLT immediate recall	0.32	0.18	0.078	−0.09	0.19	0.648	−1.69	0.66	0.014
SVLT delayed recall	0.35	0.19	0.078	−0.19	0.21	0.371	−2.02	0.69	0.006
SVLT recognition	0.59	0.35	0.098	−0.13	0.38	0.727	−3.19	1.28	0.018
Visual memory									
RCFT immediate recall	0.19	0.20	0.353	−0.22	0.21	0.301	−1.55	0.73	0.042
RCFT delayed recall	0.11	0.21	0.611	−0.33	0.22	0.135	−1.58	0.77	0.048
RCFT recognition	0.54	0.28	0.057	−0.25	0.30	0.413	−3.00	1.01	0.005
Frontal/executive function									
COWAT phonemic total	0.41	0.24	0.105	−0.17	0.27	0.525	−1.78	0.98	0.078
Stroop color reading	0.69	0.43	0.120	−0.01	0.49	0.980	−2.47	1.61	0.139

Multiple linear regression was performed using vascular risk factors (hypertension, diabetes mellitus, hyperlipidemia, and history of ischemic heart disease and stroke), APOE ε4 status, and $A\beta_{40}$, $A\beta_{42}$, and $A\beta_{42/40}$ as independent variables.

Aβ, amyloid-β; K-BNT, Korean version of the Boston Naming Test; RCFT, Rey-Osterrieth Complex Figure Test; SVLT, Seoul Verbal Learning Test; COWAT, Controlled Oral Word Association Test; APOE, apolipoprotein E.

mass spectrometry demonstrate LoD values in the hundreds of pg/mL (Sehlin et al., 2010; Oeckl and Otto, 2019). In addition, recent studies related to blood-based AD diagnosis have reported that digital ELISA technology, or the single molecule assay (SIMOA), can detect specific N-terminal Aβ peptides in plasma with high accuracy (De Meyer et al., 2020; Thijssen et al., 2021). Immunomagnetic reduction (IMR) technology has also been introduced as a promising blood-based biomarker platform to diagnose AD at early stages (Yang et al., 2017; Lue et al., 2019). IMR has technical advantages over SIMOA: SIMOA use magnetic beads to purify target molecules and this process usually causes loss of target molecules (Yang et al., 2017). However, IMR technology and our nano-biosensing platform both directly measure target molecules using a primary antibody. Furthermore, our platform has the advantage of detecting small biomolecules by precisely detecting changes in electrical signals and maximizing them using DEP (Kim et al., 2019). When Aβ reacts with a specific antibody immobilized on the sensor surface, the electric field formed between the electrodes is affected by Aβ, thus changing the electrical signal of the sensor. Additionally, DEP causes a filtration effect, which enriches Aβ present at extremely low levels in the plasma, enabling a sensitive LoD that can detect the concentrations of plasma Aβ in the range of fg/mL with high accuracy. Using this technology, we could precisely quantify the level of plasma Aβ, including its monomeric form. We suggest that our method is a promising screening tool for identifying AD as a first-line clinical evaluation.

Our major finding in the present study was that plasma $A\beta_{42/40}$ was negatively correlated with memory performance in patients with cognitive decline. The AD group showed poorer neuropsychological performance than the NC group in all cognitive domains except attention. However, in multivariate regression analysis, upon inclusion of age, education, vascular risk factors, and *APOE* ε4 status, higher levels of plasma $A\beta_{42/40}$ showed significant negative correlations with verbal and visual memory performance, including immediate recall, delayed recall, and recognition tests. Therefore, we suggest that the biosensing platform used in this study sensitively reflects the degree of memory impairment in the study participants. Since the introduction of new research frameworks using Aβ, tau, and neurodegeneration, the definition of AD has shifted from a syndromal to a biological construct based on biomarkers that are proxies of pathology (Jack et al., 2018). Accordingly, most research has mainly focused on the application of molecular (PET) and structural (MRI) imaging in the diagnosis of AD. Although remarkable progress has been made in blood-based diagnostic methods for AD, it is unclear whether these methods reflect neuropsychological performance in patients with cognitive decline in clinical settings. Furthermore, most studies using blood-based AD biomarkers have only reported the diagnostic power for the distinction between the NC and AD groups. However, to the best of our knowledge, there have been no reports on which cognitive domains significantly correlate with biomarkers.

Since amnestic syndrome is a typical presentation of AD onset (Cerami et al., 2017), we suggest that our findings in this study have clinical significance in terms of the precise diagnosis of AD and the clinical assessment of memory impairment in patients with cognitive decline. We speculate that there are several explanations for the reason that only the memory domain

was negatively correlated with the level of plasma $A\beta_{42/40}$ in this study. Since our biosensing platform was able to detect the monomers and oligomers among the various forms of Aβ in the blood, we suggest that our precise method could more accurately reflect differences in memory impairment, a core feature of AD, between the NC and AD groups. Alternatively, as various factors that could affect cognitive function even in normal aging were statistically mitigated (Salthouse, 2009; Lee et al., 2018), only the level of plasma $A\beta_{42/40}$ and memory domain may have shown a significant association.

This study has several limitations. First, since our study was conducted using blood samples collected from a cross-sectional study, further validation studies are needed. Second, the statistical power of our analyses was relatively low due to the small sample size. Third, since our method measured the total amount of Aβ present in the plasma (mainly monomers but also oligomers consisting of 10 or fewer monomers with a molecular weight of 3–10 kDa), it was not possible to evaluate the effect of each form on the study results. Finally, our study participants were enrolled from a single memory clinic, which might limit the generalizability of the results. Despite these limitations, we suggest that our study might have clinical significance because plasma Aβ analysis using a highly sensitive nano-biosensing platform could not only be a useful non-invasive method for diagnosing AD, but also showed a significant association with memory performance in patients with cognitive decline. Further investigations with a larger sample size are necessary to clarify the possible relevance of plasma Aβ as a blood-based biomarker for precise AD diagnosis.

DATA AVAILABILITY STATEMENT

The datasets generated for this study are available on request to the corresponding authors.

ETHICS STATEMENT

The studies involving human participants were reviewed and approved by the Institutional Review Board of Kyung Hee University Hospital. The patients/participants provided their written informed consent to participate in this study.

AUTHOR CONTRIBUTIONS

IH and JL: conception, design of the study, and final approval of the manuscript. GY, HK, KL, IH, HR, SY, K-CP, and JL: acquisition of data. GY, HK, H-GK, KL, IH, HR, G-HJ, SY, K-CP, IH, and JL: analysis and interpretation of the data. GY, HK, HR, K-CP, IH, and JL: drafting and revising the manuscript for content. All authors contributed to the article and approved the submitted version.

FUNDING

This work was supported by the National Research Foundation of Korea (NRF) grant funded by the Korean government (Ministry of Science and ICT) (grant nos. NRF-2021R1A2C2004760 and NRF-2021R1C1C1012429) and the Korea Health Industry Development Institute (KHIDI, grant nos. HU21C0053 and HU21C0098).

SUPPLEMENTARY MATERIAL

The Supplementary Material for this article can be found online at: https://www.frontiersin.org/articles/10.3389/fnagi.2021.736937/full#supplementary-material

REFERENCES

Ahn, H. J., Chin, J., Park, A., Lee, B. H., Suh, M. K., Seo, S. W., et al. (2010). Seoul Neuropsychological Screening Battery-dementia version (SNSB-D): a useful tool for assessing and monitoring cognitive impairments in dementia patients. *J. Korean Med. Sci.* 25, 1071–1076. doi: 10.3346/jkms.2010.25.7.1071

Barthel, H., Gertz, H. J., Dresel, S., Peters, O., Bartenstein, P., Buerger, K., et al. (2011). Cerebral amyloid-β PET with florbetaben (18F) in patients with Alzheimer's disease and healthy controls: a multicentre phase 2 diagnostic study. *Lancet Neurol.* 10, 424–435. doi: 10.1016/s1474-4422(11)70077-1

Bhalla, N., Jolly, P., Formisano, N., and Estrela, P. (2016). Introduction to biosensors. *Essays Biochem.* 60, 1–8. doi: 10.1007/978-0-585-37623-3_1

Bullich, S., Seibyl, J., Catafau, A. M., Jovalekic, A., Koglin, N., Barthel, H., et al. (2017). Optimized classification of (18)F-Florbetaben PET scans as positive and negative using an SUVR quantitative approach and comparison to visual assessment. *Neuroimage Clin.* 15, 325–332. doi: 10.1016/j.nicl.2017.04.025

Cerami, C., Dubois, B., Boccardi, M., Monsch, A. U., Demonet, J. F., and Cappa, S. F. (2017). Clinical validity of delayed recall tests as a gateway biomarker for Alzheimer's disease in the context of a structured 5-phase development framework. *Neurobiol. Aging* 52, 153–166. doi: 10.1016/j.neurobiolaging.2016.03.034

De Meyer, S., Schaeverbeke, J. M., Verberk, I. M. W., Gille, B., De Schaepdryver, M., Luckett, E. S., et al. (2020). Comparison of ELISA- and SIMOA-based quantification of plasma Aβ ratios for early detection of cerebral amyloidosis. *Alzheimers Res. Ther.* 12:162.

de Rojas, I., Romero, J., Rodríguez-Gomez, O., Pesini, P., Sanabria, A., Pérez-Cordon, A., et al. (2018). Correlations between plasma and PET beta-amyloid levels in individuals with subjective cognitive decline: the Fundació ACE Healthy Brain Initiative (FACEHBI). *Alzheimers Res. Ther.* 10:119.

Hansson, O., Seibyl, J., Stomrud, E., Zetterberg, H., Trojanowski, J. Q., Bittner, T., et al. (2018). CSF biomarkers of Alzheimer's disease concord with amyloid-β PET and predict clinical progression: a study of fully automated immunoassays in BioFINDER and ADNI cohorts. *Alzheimers Dement.* 14, 1470–1481. doi: 10.1016/j.jalz.2018.01.010

Jack, C. R. Jr., Bennett, D. A., Blennow, K., Carrillo, M. C., Dunn, B., Haeberlein, S. B., et al. (2018). NIA-AA research framework: toward a biological definition of Alzheimer's disease. *Alzheimers Dement.* 14, 535–562. doi: 10.1016/j.jalz.2018.02.018

Jack, C. R. Jr., Knopman, D. S., Jagust, W. J., Petersen, R. C., Weiner, M. W., Aisen, P. S., et al. (2013). Tracking pathophysiological processes in Alzheimer's disease: an updated hypothetical model of dynamic biomarkers. *Lancet Neurol.* 12, 207–216. doi: 10.1016/s1474-4422(12)70291-0

Jack, C. R. Jr., Wiste, H. J., Weigand, S. D., Rocca, W. A., Knopman, D. S., Mielke, M. M., et al. (2014). Age-specific population frequencies of cerebral β-amyloidosis and neurodegeneration among people with normal cognitive function aged 50-89 years: a cross-sectional study. *Lancet Neurol.* 13, 997–1005. doi: 10.1016/s1474-4422(14)70194-2

Jessen, F., Amariglio, R. E., Van Boxtel, M., Breteler, M., Ceccaldi, M., Chételat, G., et al. (2014). A conceptual framework for research on subjective cognitive decline in preclinical Alzheimer's disease. *Alzheimers Dement.* 10, 844–852.

Jiao, L., Zhang, L., Du, W., Li, H., Yang, D., and Zhu, C. (2018). Hierarchical manganese dioxide nanoflowers enable accurate ratiometric fluorescence enzyme-linked immunosorbent assay. *Nanoscale* 10, 21893–21897. doi: 10.1039/c8nr07096b

Kang, S. H., Park, Y. H., Lee, D., Kim, J. P., Chin, J., Ahn, Y., et al. (2019). The cortical neuroanatomy related to specific neuropsychological deficits in Alzheimer's continuum. *Dement. Neurocogn. Disord.* 18, 77–95. doi: 10.12779/dnd.2019.18.3.77

Kim, H. J., Kim, J., Yoo, Y. K., Lee, J. H., Park, J. H., and Hwang, K. S. (2016). Sensitivity improvement of an electrical sensor achieved by control of biomolecules based on the negative dielectrophoretic force. *Biosens. Bioelectron.* 85, 977–985. doi: 10.1016/j.bios.2016.06.081

Kim, H. J., Park, D., Baek, S. Y., Yang, S. H., Kim, Y., Lim, S. M., et al. (2019). Dielectrophoresis-based filtration effect and detection of amyloid beta in plasma for Alzheimer.s disease diagnosis. *Biosens. Bioelectron.* 128, 166–175. doi: 10.1016/j.bios.2018.12.046

Kleinschmidt, M., Schoenfeld, R., Göttlich, C., Bittner, D., Metzner, J. E., Leplow, B., et al. (2016). Characterizing aging, mild cognitive impairment, and dementia with blood-based biomarkers and neuropsychology. *J. Alzheimers Dis.* 50, 111–126. doi: 10.3233/jad-143189

Lacor, P. N., Buniel, M. C., Furlow, P. W., Clemente, A. S., Velasco, P. T., Wood, M., et al. (2007). Abeta oligomer-induced aberrations in synapse composition, shape, and density provide a molecular basis for loss of connectivity in Alzheimer's disease. *J. Neurosci.* 27, 796–807.

Lee, J. S., Kim, S., Yoo, H., Park, S., Jang, Y. K., Kim, H. J., et al. (2018). Trajectories of physiological brain aging and related factors in people aged from 20 to over-80. *J. Alzheimers Dis.* 65, 1237–1246.

Lue, L. F., Kuo, Y. M., and Sabbagh, M. (2019). Advance in plasma AD core biomarker development: current findings from immunomagnetic reduction-based SQUID technology. *Neurol. Ther.* 8, 95–111. doi: 10.1007/s40120-019-00167-2

Lue, L. F., Sabbagh, M. N., Chiu, M. J., Jing, N., Snyder, N. L., Schmitz, C., et al. (2017). Plasma levels of Aβ42 and tau identified probable Alzheimer's dementia: findings in two cohorts. *Front. Aging Neurosci.* 9:226. doi: 10.3389/fnagi.2017.00226

Lyu, Z., Ding, S., Zhang, N., Zhou, Y., Cheng, N., Wang, M., et al. (2020). Single-atom nanozymes linked immunosorbent assay for sensitive detection of Aβ 1-40: a biomarker of Alzheimer's disease. *Research (Wash. DC)* 2020:4724505.

McKhann, G., Drachman, D., Folstein, M., Katzman, R., Price, D., and Stadlan, E. M. (1984). Clinical diagnosis of Alzheimer's disease: report of the NINCDS-ADRDA Work Group under the auspices of Department of Health and Human Services Task Force on Alzheimer's disease. *Neurology* 34, 939–944.

Meng, X., Li, T., Wang, X., Lv, X., Sun, Z., Zhang, J., et al. (2019). Association between increased levels of amyloid-β oligomers in plasma and episodic memory loss in Alzheimer's disease. *Alzheimers Res. Ther.* 11:89.

Morales, M. A., and Halpern, J. M. (2018). Guide to selecting a biorecognition element for biosensors. *Bioconjug. Chem.* 29, 3231–3239. doi: 10.1021/acs.bioconjchem.8b00592

Nakamura, A., Kaneko, N., Villemagne, V. L., Kato, T., Doecke, J., Doré, V., et al. (2018). High performance plasma amyloid-β biomarkers for Alzheimer's disease. *Nature* 554, 249–254. doi: 10.1038/nature25456

O'Brien, R. J., and Wong, P. C. (2011). Amyloid precursor protein processing and Alzheimer's disease. *Annu. Rev. Neurosci.* 34, 185–204. doi: 10.1146/annurev-neuro-061010-113613

Oeckl, P., and Otto, M. (2019). A review on MS-based blood biomarkers for Alzheimer's disease. *Neurol. Ther.* 8, 113–127. doi: 10.1007/s40120-019-00165-4

Palmqvist, S., Zetterberg, H., Mattsson, N., Johansson, P., Minthon, L., Blennow, K., et al. (2015). Detailed comparison of amyloid PET and CSF biomarkers for identifying early Alzheimer disease. *Neurology* 85, 1240–1249. doi: 10.1212/WNL.0000000000001991

Park, J. C., Han, S. H., Cho, H. J., Byun, M. S., Yi, D., Choe, Y. M., et al. (2017). Chemically treated plasma Aβ is a potential blood-based biomarker for screening cerebral amyloid deposition. *Alzheimers Res. Ther.* 9:20. doi: 10.1186/s13195-017-0248-8

Pereira, J. B., Janelidze, S., Ossenkoppele, R., Kvartsberg, H., Brinkmalm, A., Mattsson-Carlgren, N., et al. (2021). Untangling the association of amyloid-β and tau with synaptic and axonal loss in Alzheimer's disease. *Brain* 144, 310–324. doi: 10.1093/brain/awaa395

Petersen, R. C. (2004). Mild cognitive impairment as a diagnostic entity. *J. Intern. Med.* 256, 183–194. doi: 10.1111/j.1365-2796.2004.01388.x

Risacher, S. L., Fandos, N., Romero, J., Sherriff, I., Pesini, P., Saykin, A. J., et al. (2019). Plasma amyloid beta levels are associated with cerebral amyloid and tau deposition. *Alzheimers Dement. (Amst.)* 11, 510–519. doi: 10.1016/j.dadm.2019.05.007

Salthouse, T. A. (2009). Decomposing age correlations on neuropsychological and cognitive variables. *J. Int. Neuropsychol. Soc.* 15, 650–661. doi: 10.1017/S1355617709990385

Santos, A. N., Ewers, M., Minthon, L., Simm, A., Silber, R. E., Blennow, K., et al. (2012). Amyloid-β oligomers in cerebrospinal fluid are associated with cognitive decline in patients with Alzheimer's disease. *J. Alzheimers Dis.* 29, 171–176. doi: 10.3233/JAD-2012-111361

Scheltens, P., De Strooper, B., Kivipelto, M., Holstege, H., Chételat, G., Teunissen, C. E., et al. (2021). Alzheimer's disease. *Lancet* 397, 1577–1590. doi: 10.1016/S0140-6736(20)32205-4

Sehlin, D., Söllvander, S., Paulie, S., Brundin, R., Ingelsson, M., Lannfelt, L., et al. (2010). Interference from heterophilic antibodies in amyloid-β oligomer ELISAs. *J. Alzheimers Dis.* 21, 1295–1301. doi: 10.3233/JAD-2010-100609

Seo, S. W., Cho, S. S., Park, A., Chin, J., and Na, D. L. (2009). Subcortical vascular versus amnestic mild cognitive impairment: comparison of cerebral glucose metabolism. *J. Neuroimaging* 19, 213–219. doi: 10.1111/j.1552-6569.2008.00292.x

Shankar, G. M., Li, S., Mehta, T. H., Garcia-Munoz, A., Shepardson, N. E., Smith, I., et al. (2008). Amyloid-beta protein dimers isolated directly from Alzheimer's brains impair synaptic plasticity and memory. *Nat. Med.* 14, 837–842. doi: 10.1038/nm1782

Thijssen, E. H., Verberk, I. M. W., Vanbrabant, J., Koelewijn, A., Heijst, H., Scheltens, P., et al. (2021). Highly specific and ultrasensitive plasma test detects Abeta(1-42) and Abeta(1-40) in Alzheimer's disease. *Sci. Rep.* 11:9736. doi: 10.1038/s41598-021-89004-x

van Oijen, M., Hofman, A., Soares, H. D., Koudstaal, P. J., and Breteler, M. M. (2006). Plasma Abeta(1-40) and Abeta(1-42) and the risk of dementia: a prospective case-cohort study. *Lancet Neurol.* 5, 655–660. doi: 10.1016/S1474-4422(06)70501-4

Viola, K. L., and Klein, W. L. (2015). Amyloid β oligomers in Alzheimer's disease pathogenesis, treatment, and diagnosis. *Acta Neuropathol.* 129, 183–206. doi: 10.1007/s00401-015-1386-3

Wang, X., Sun, Y., Li, T., Cai, Y., and Han, Y. (2020). Amyloid-β as a blood biomarker for Alzheimer's disease: a review of recent literature. *J. Alzheimers Dis.* 73, 819–832. doi: 10.3233/JAD-190714

Wang-Dietrich, L., Funke, S. A., Kühbach, K., Wang, K., Besmehn, A., Willbold, S., et al. (2013). The amyloid-β oligomer count in cerebrospinal fluid is a biomarker for Alzheimer's disease. *J. Alzheimers Dis.* 34, 985–994. doi: 10.3233/JAD-122047

Yang, S. Y., Chiu, M. J., Chen, T. F., and Horng, H. E. (2017). Detection of plasma biomarkers using immunomagnetic reduction: a promising method for the early diagnosis of Alzheimer's disease. *Neurol. Ther.* 6, 37–56. doi: 10.1007/s40120-017-0075-7

Conflict of Interest: The authors declare that the research was conducted in the absence of any commercial or financial relationships that could be construed as a potential conflict of interest.

Publisher's Note: All claims expressed in this article are solely those of the authors and do not necessarily represent those of their affiliated organizations, or those of the publisher, the editors and the reviewers. Any product that may be evaluated in this article, or claim that may be made by its manufacturer, is not guaranteed or endorsed by the publisher.

Copyright © 2021 Yun, Kim, Kim, Lee, Hong, Kim, Rhee, Jahng, Yoon, Park, Hwang and Lee. This is an open-access article distributed under the terms of the Creative Commons Attribution License (CC BY). The use, distribution or reproduction in other forums is permitted, provided the original author(s) and the copyright owner(s) are credited and that the original publication in this journal is cited, in accordance with accepted academic practice. No use, distribution or reproduction is permitted which does not comply with these terms.

frontiers in Aging Neuroscience

ORIGINAL RESEARCH
published: 12 November 2021
doi: 10.3389/fnagi.2021.774477

Alleviative Effect of Alpha-Lipoic Acid on Cognitive Impairment in High-Fat Diet and Streptozotocin-Induced Type 2 Diabetic Rats

Chih-Yuan Ko[1,2,3,4†‡], Jian-Hua Xu[5†], Yangming Martin Lo[6], Rong-Syuan Tu[7], James Swi-Bea Wu[8‡], Wen-Chung Huang[9] and Szu-Chuan Shen[7‡]*

[1] Department of Clinical Nutrition, The Second Affiliated Hospital of Fujian Medical University, Quanzhou, China, [2] Department of Respiratory and Critical Care Medicine, The Second Affiliated Hospital of Fujian Medical University, Quanzhou, China, [3] School of Public Health, Fujian Medical University, Fuzhou, China, [4] Respiratory Medicine Center of Fujian Province, Quanzhou, China, [5] Department of Tumor Surgery, The Second Affiliated Hospital of Fujian Medical University, Quanzhou, China, [6] Institute for Advanced Study, Shenzhen University, Shenzhen, China, [7] Graduate Program of Nutrition Science, National Taiwan Normal University, Taipei City, Taiwan, [8] Graduate Institute of Food Science and Technology, National Taiwan University, Taipei City, Taiwan, [9] Graduate Institute of Health Industry Technology, Chang Gung University of Science and Technology, Taoyuan City, Taiwan

OPEN ACCESS

Edited by:
Jiehui Jiang,
Shanghai University, China

Reviewed by:
I-Shiang Tzeng,
Chinese Culture University, Taiwan
Tao-Ran Li,
Capital Medical University, China

***Correspondence:**
Szu-Chuan Shen
scs@ntnu.edu.tw

[†]These authors share first authorship

[‡]**ORCID:**
Chih-Yuan Ko
orcid.org/0000-0002-5767-3041
James Swi-Bea Wu
orcid.org/0000-0002-2855-5716
Szu-Chuan Shen
orcid.org/0000-0001-9005-0455

Received: 12 September 2021
Accepted: 21 October 2021
Published: 12 November 2021

Citation:
Ko C-Y, Xu J-H, Lo YM, Tu R-S, Wu JS-B, Huang W-C and Shen S-C (2021) Alleviative Effect of Alpha-Lipoic Acid on Cognitive Impairment in High-Fat Diet and Streptozotocin-Induced Type 2 Diabetic Rats. Front. Aging Neurosci. 13:774477. doi: 10.3389/fnagi.2021.774477

Background: The intricate relationship between type 2 diabetes mellitus (T2DM) and Alzheimer's disease (AD) suggests that insulin is involved in modulating AD-related proteins. Alpha-lipoic acid (ALA) can improve insulin resistance (IR) in diabetic rats. However, the role of ALA in alleviating the cognitive decline of T2DM is not yet clear. This study examined the ameliorative effect of ALA on cognitive impairment, cerebral IR, and synaptic plasticity abnormalities in high-fat diet (HFD) plus streptozotocin (STZ) induced diabetic rats.

Methods: The HFD/STZ-induced T2DM male Wistar rats were orally administered with ALA (50, 100, or 200 mg/kg BW) once a day for 13 weeks. Abilities of cognition were measured with a passive avoidance test and Morris water maze. Specimens of blood and brain were collected for biochemical analysis after the rats were sacrificed. Western blotting was used to determine protein expressions in the hippocampus and cortex in the insulin signaling pathways, long-term potentiation (LTP), and synaptic plasticity-related protein expressions.

Results: Alpha-lipoic acid improved hyperinsulinemia and the higher levels of free fatty acids of the T2DM rats. Behavioral experiments showed that the administration of ALA improved cognitive impairment in HFD/STZ-induced T2DM rats. ALA ameliorated insulin-related pathway proteins [phosphoinositide 3-kinase (PI3K), phospho-protein kinase B (pAkt)/Akt, and insulin-degrading enzyme (IDE)] and the LTP pathway, as well as synaptic plasticity proteins (calmodulin-dependent protein kinase II, cyclic AMP response element-binding protein, and postsynaptic density protein-95) of the cerebral cortex or hippocampus in HFD/STZ-induced T2DM rats.

Conclusion: Our findings suggested that ALA may ameliorate cognition impairment *via* alleviating cerebral IR improvement and cerebral synaptic plasticity in diabetic rats.

Keywords: α-lipoic acid, Alzheimer's disease, cerebral insulin signaling, long-term potentiation, type 2 diabetes

INTRODUCTION

Obesity poses a risk factor for type 2 diabetes mellitus (T2DM). Not only does obesity induce metabolic disorders and insulin resistance (IR), but it also promotes β-cell dysfunction (Eckel et al., 2011). IR is the most prominent symptom of T2DM. When cellular IR occurs, glucose in the blood cannot be effectively used, and the body is in a state of high blood sugar and high insulin for a long time, which leads to an increase in oxidative stress in the body and subsequently causes the body to produce a chronic inflammatory response. Additionally, IR in peripheral tissues can also cause IR in the brain. The role of insulin in the brain can affect neuron development, synapse formation, learning, memory, and glucose regulation (Derakhshan and Toth, 2013). Evidence has demonstrated that T2DM is a risk factor for the development of Alzheimer's disease (AD) or dementia (Chatterjee and Mudher, 2018).

The brain is an organ with high sensitivity to insulin. The functions of brain can be regulated by insulin including neuron development, synapse formation, learning and memory, glucose regulation, and feeding behavior (Derakhshan and Toth, 2013). It has been verified that insulin can penetrate the blood-brain barrier (BBB) through a transporter, consequently regulating the relevant information transmission pathways in the brain (Derakhshan and Toth, 2013). Insulin receptors are transmembrane receptors that are present in the cerebral hippocampus and cortex that play a critical role in the formation of learning memory (Cole et al., 2007). Decreased insulin and related receptor activities were demonstrated with brain IR in postmortem AD brains (Talbot et al., 2012).

Alzheimer's disease causes nerve cell death and brain tissue atrophy; however, the cause of the disease is still not clarified. Plaque deposits formed by β-amyloid (Aβ) and neurofibrillary tangles (NFTs) due to the hyperphosphorylation of Tau proteins are well-known hypothesized causes, since they are considered the main pathological feature of AD (Bloom, 2014). Additionally, hypotheses regarding IR, inflammation, oxidative imbalance, and gene mutations have been proposed (Gu et al., 2016). When generating IR, the main PI3K/protein kinase B (Akt/PKB) of the insulin signal pathway loses activity so that blood sugar cannot be effectively regulated. Meanwhile, glycogen synthase kinase 3β (GSK-3β) is activated. GSK-3β is a key step to increasing phosphorylation of Tau proteins. When Tau proteins are over phosphorylated, they are separated from microtubules and can eventually be aggregated to form NFTs (Špolcová et al., 2014). Moreover, protein glycation is the course and complication of diabetes. Depending on the pathology, Tau protein glycosylation induces the formation of NFTs in the development of AD (Chatterjee and Mudher, 2018).

The brain can scavenge Aβ by various mechanisms, such as protein degradation, glial cell phagocytosis, and transport out of brain nerve cells through the BBB (Ries and Sastre, 2016). However, when IR or hyperinsulinemia occurs, IDEs can degrade and clear Aβ in brain. Insulin and Aβ compete with each other for the IDEs of the brain. Due to the high affinity of insulin and IDEs, Aβ cannot be removed and thus accumulates in the brain prompting further AD pathogenesis (Son et al., 2016).

Moreover, decline of cognitive functions and gradual loss of memory are AD features. The hippocampus serves an important function in learning and memory. Presynaptic neurons mainly use glutamate as a neurotransmitter to connect *N*-methyl-D-aspartate receptors (NMDARs) and non-NMDARs (also known as AMPARs) on postsynaptic neurons. When short-term high-frequency stimulation is given, the postsynaptic potentials increase, and Mg^{2+} on the NMDAR can be repelled to open the channel at this time. When Ca^{2+} enters the synapse and activates the cascade reaction of calmodulin and Ca^{2+}/calmodulin-dependent protein kinase II (CaMKII), long-term potentiation (LTP) is formed (Nicoll, 2017). Aβ and its active fragments can inhibit LTP induced by high-frequency stimulation in the hippocampus of rats. However, the complex mechanisms of hippocampal LTP are not yet entirely understood.

Alpha-lipoic acid (ALA), a natural antioxidant, is widely observed in various plants and animals. Studies have found that it has an anti-inflammatory effect, prevents vascular diseases, reduces cognitive impairment, and alleviates diabetes and related complications (Shay et al., 2009; Fava et al., 2013; Liu et al., 2017; Zhang et al., 2018; Ko et al., 2021). The present study aimed to explore the effects of ALA on improving cognitive impairment, brain IR, and abnormal synaptic plasticity using a high-fat diet (HFD) plus streptozotocin (STZ)-induced T2DM model rats.

MATERIALS AND METHODS

Animal Experimental Procedures

Animal experimental procedures used in this study were adapted from our previous study (Ko et al., 2021). Eight-week-old male Wistar rats were reared in a temperature- (22 ± 1°C) and humidity-controlled (50 ± 20%) room, under a 12-h light/dark cycle (lights on from 08:00 to 20:00), with free access to food and water in the animal room of Taiwan Normal University. The study was approved by the Institutional Animal Care and Use Committee of National Taiwan Normal University with the certificate number 106042.

After adapting to the environment for 1 week, rats were fed a HFD (60% calories from fat) or a normal diet for 4 weeks. HFD-fed rats were then intraperitoneally injected with STZ (Sigma, St. Louis, MO, United States) [30 mg/kg body weight (BW)] to induce diabetes, and then were fed with a HFD for nine more weeks. Thirty-six rats were randomly divided into six groups with six rats in each. The normal group contained rats fed with a normal diet; the DM group contained diabetic rats fed with a HFD alone as the negative control; the DM + PIO group contained diabetic rats fed with a HFD and orally administered pioglitazone (PIO, 30 mg/kg BW) daily for 13 weeks as the positive control; and the DM + ALA50, DM + ALA100, and DM + ALA200 groups, which contained diabetic rats daily fed with a HFD and orally administered 50, 100, or 200 mg/kg BW ALA (Sigma, St. Louis, MO, United States), respectively, for

13 weeks. The dosages used were the same as in our previous study (Ko et al., 2021). All rats were sacrificed at the end of the experiment.

Passive Avoidance Test

The passive avoidance test was slightly modified from a previous study (Elrod and Buccafusco, 1988). Basically, all test subjects were divided into separate rooms with a gate in the middle of the two rooms and an electric shock net at the bottom of the two rooms, but only the electric shock net in the dark room was energized. Before the experiment, the rats were acclimatized in the dark room for 15 min and then the experiment was started.

The first day was the training period. The rat entered from the bright room. When it entered the darkroom completely through the gate, the gate was shut and the rat was given an electric shock for 2 s. After the electric shock was over, the rat stayed in the dark room for f 5 s, and then was put back into the breeding cage before taking records. Rats completed the learning and training within the latency time of the bright room. If the rat had not entered the darkroom within 300 s, it was forced to enter the dark room and an electric shock was given to complete the learning and training process. After completing the learning and training, the next continuous test began and lasted for 3 days, with the exception that at this time, the test subject did not receive any electric shocks. The time the rats stayed in the bright room was recorded, since this test enabled observation of the rat's ability to continue learning and memory.

Morris Water Maze Test

The MWM protocol was adopted from previous studies (Morris, 1984; Vorhees and Williams, 2006). For spatial acquisition, rats performed spatial learning in four separate quadrants every day, and the experiment was repeated for a total of five consecutive days. The rat was placed facing the wall of the pool at the starting position of each quadrant. When the rat was positioned in the water, timing began immediately, and when the rat climbed (touched) the platform, the time was stopped and recorded. The duration of one test was approximately 2 min. If the rat did not reach the underwater platform within 2 min, it was led to face the east and placed on the platform for 15 s. Once the test was completed, another animal was employed for the test in the same quadrant. After all animals had completed the test in the first quadrant, the tests were repeated in the second quadrant until all four quadrants were covered.

To probe the trial measurement, after 24 h of the positioning navigation test, the target platform in the water was removed, and the rat was placed facing the wall of the pool in the relative position of the original target platform before timing started. The time was recorded when passing the original target platform position for the first time. If the time exceeded 30 s, the rat was removed from the water maze.

For a physical function test, the platform was placed in the new quadrant and exposed 2 cm in height above the water surface to make it a visible platform. This test was used to confirm that the rat's visual movement function was normal, and the time was recorded when the rat found the platform.

Tissue Protein Preparation and Measurement

To prepare brain protein samples, 100 mg of the cerebral cortex or hippocampus were mixed with 0.5 mL lysis buffer and ground three times (10 s each time). After 1-h incubation in an ice bath, the homogenized tissue solutions were centrifuged at 20,000 $\times$ *g* under 4°C for 1 h to obtain tissue protein supernatants. The protein concentration was measured at 595 nm using the Bradford method with a Bio-Rad protein assay kit (Hercules, CA, United States).

Western Blot

Aliquots of brain tissue protein samples, each containing 40 μg of protein, were evaluated for the expression of insulin receptor substrate 1 (IRS-1), PI3K, Akt/PKB, pAkt, GSK-3β, pGSK-3β, IDE, pTau (Thr181), Tau, *N*-methyl-D-aspartate receptor (NMDAR)1, NMDAR2β, calmodulin, CaMK II, cyclic AMP response element (CRE)-binding protein (CREB), postsynaptic density protein 95 (PSD-95), and brain derived neurotrophic factor (BDNF). The samples were subjected to 10% sodium dodecyl sulfate-polyacrylamide gel electrophoresis. The separated proteins were electrotransferred to a polyvinylidene difluoride membrane. The membrane was incubated with blocking buffer [phosphate-buffered saline (PBS) containing 0.05% Tween-20 (PBST) and 5% (wt/vol) non-fat dry milk] for 1 h, incubated overnight at 4°C with PBST, and probed with anti-IRS-1 (1906-7), anti-PI3K (60225-1-lg), anti-AKT (9272), anti-pAKT (9271), anti-GSK3β (9315), anti-pGSK3β (9336), anti-Tau (4019), anti-CaMKII (44436), anti-CREB (9197), and anti-IDE (67106-1-lg) antibodies (1:1000; Signalway Antibody, MD, United States), anti-PSD95 (ab18258) and anti-BDNF (ab108383) antibodies (1:1000; Abcam, MA, United States) as well as anti-pTau (GTX50171), anti-NMDAR1 (GTX133097), anti-NMDAR 2β (GTX133099), and anti-calmodulin (GTX52363) antibodies (1:1000; GeneTex, Hsinchu, Taiwan). A 1:5000 dilution of mouse monoclonal α-tubulin (3873) or GAPDH (5174) antibodies (Signalway Antibody, MD, United States) were used to ensure that a constant amount of protein was loaded into each lane of the gel. The membrane was washed three times (5 min each) in PBST, shaken in a solution of horseradish peroxidase-conjugated anti-mouse IgG or anti-rabbit IgG (Genetex, Irvine, CA, United States) secondary, washed three times (5 min each) in PBST, and incubated in enhanced chemiluminescence reagent (Millipore, Darmstadt, Germany). Autoradiography was performed and analyzed using a UVP Biospectrum image system (Level, Cambridge, United Kingdom). Finally, all relevant protein expressions were normalized with α-tubulin or GAPDH.

Blood Samples Collection

Rats were fasted overnight (8-h) and blood was sampled from the tail vessels before they were sacrificed. Blood was collected and centrifuged at 12,000 $\times$ *g* for 8 min to obtain the serum samples. The samples were stored at −80°C before use.

TABLE 1 | Profiles of fasting insulin, free fatty acid, and brain weight in high-fat diet and streptozotocin-induced type 2 diabetic rats treated with alpha-lipoic acid for 13 weeks.

	Normal	DM + PIO	DM	DM + ALA50	DM + ALA100	DM + ALA200
Fasting serum insulin (μg/L)	1.02 ± 0.15^{ab}	0.66 ± 0.06^{b}	1.24 ± 0.23^{a}	0.72 ± 0.14^{b}	0.69 ± 0.03^{b}	0.72 ± 0.07^{b}
Fasting plasma free fatty acid (mmol/L)	0.65 ± 0.05^{b}	0.77 ± 0.06^{b}	1.17 ± 0.07^{a}	0.89 ± 0.03^{ab}	0.86 ± 0.04^{ab}	0.57 ± 0.02^{b}
Brain weight (g)	1.64 ± 0.02^{a}	1.59 ± 0.02^{ab}	1.49 ± 0.05^{b}	1.56 ± 0.03^{ab}	1.61 ± 0.03^{ab}	1.63 ± 0.02^{a}

Normal, Normal diet; DM, high-fat diet (HFD; 60% fat) with STZ (30 mg/kg body weight, i.p.) induced diabetic rats; DM + Pio, DM rats gavaged with pioglitazone (30 mg/kg body weight) for 13 weeks; DM + ALA50, DM rats gavaged with ALA (50 mg/kg body weight) for 13 weeks; DM + ALA100, DM rats gavaged with ALA (100 mg/kg body weight) for 13 weeks; DM + ALA200, DM rats gavaged with ALA (200 mg/kg body weight) for 13 weeks.
Values were calculated as the mean ± SEM, n = 6 for each group.^{a,b}letter is significantly different among all samples tested ($p < 0.05$).

Measurement of Serum Insulin and Plasma Free Fatty Acid

Levels of insulin and FFA were measured by the commercial enzyme-linked immunosorbent assay (ELISA) kits (Mercodia AB and Uppsala, Sweden; Crumlin, Co., Antrim, United Kingdom). Biochemical analyses were conducted according to the supplier's protocols.

Statistical Analyses

Values are presented as the mean ± standard error of the mean using SPSS version 22.0 (SPSS Inc., Chicago, IL, United States). A one-way analysis of variance (ANOVA) and Duncan's multiple range tests were performed. $P < 0.05$ was accepted as statistically significant.

RESULTS

Effects of Alpha-Lipoic Acid on High-Fat Diet/Streptozotocin-Induced Brain Tissue Weight and Serum Insulin in Type 2 Diabetes Mellitus Rats

Serum insulin of the DM group was significantly higher than that of the DM + PIO and ALA groups (**Table 1**). The plasma free fatty acid of the DM group was significantly higher than that of the normal, DM + PIO, and ALA200 groups (**Table 1**). The brain tissue weight of the DM group was significantly lower than that of the normal and ALA200 groups (**Table 1**).

Passive Avoidance Test

The passive avoidance test is an experimental method that utilizes a darkening environment for the rats and was utilized to observe rats' abilities in learning memory. The results from the before-shock experiments showed that when the experimental animals in each experimental group entered the darkroom, the DM + PIO group remained significantly longer than the normal, DM, ALA50, and ALA100 groups (**Figure 1A**). Contrarily, the after-shock results showed that the normal, DM + PIO, and ALA100 groups stayed in the bright room for a significantly longer time than the DM group (**Figure 1A**).

Morris Water Maze

The MWM test is the most commonly used method to assess the spatial learning and memory abilities of rodents (Morris, 1984). For the physical function of MWM, there was no difference in the basic physiological functions (visual and motor abilities) of all rats (**Figure 1B**).

There was no statistical difference in the results between each group on the first and second days of the spatial acquisition test (**Figure 1C**). On the third day of the test, the DM group took significantly more time looking for a platform in the water than the normal, ALA50, ALA100, and ALA200 groups (**Figure 1C**). On the fourth day of the test, only the ALA50 and DM groups had a significant difference. Compared with other groups, the DM group had an increase in time, but there was no statistically significant difference (**Figure 1C**). The results on the last day of the trial showed that the DM group (29.70 ± 8.52 s) exhibited a significantly longer time than the DM + PIO, ALA50, ALA100, and ALA200 groups (**Figure 1C**). The probe trial of MWM was to evaluate the reference memory after the learning experience (Vorhees and Williams, 2006). For the probe trial of MWM, the DM group took a significantly longer time than the other groups (**Figure 1D**).

The Effect of Alpha-Lipoic Acid on the Insulin Signal Pathway in the Cerebral Hippocampus and Cortex in Type 2 Diabetes Mellitus Rats and the Expression of Proteins Related to the Phosphorylation Pathway of Tau Protein

Effects of ALA on expression of proteins of the insulin signal pathway in the cerebral hippocampus (**Figure 2A**) and cortex (**Figure 2F**). The expression of IRS-1 protein in the hippocampus of the ALA200 group was significantly higher than that of the DM group, an increase of 71.5% (**Figure 2B**). There was no statistical difference in the expression level of cortical IRS-1 protein among the groups (**Figure 2G**).

The expression levels of PI3K in the hippocampus of normal, DM + PIO, and ALA200 groups was significantly higher than that of the DM group (**Figure 2C**). The expression level of PI3K in the cortical DM group was lower than that of others, but it was only significantly different from the ALA100 group, which was a significant increase of 68.6% (**Figure 2H**).

The expression levels of pAKT/AKT in the hippocampus of the ALA100 and ALA200 groups was significantly higher than that of the DM group (**Figure 2D**). The ALA200 group of the cortex was significantly higher than in the normal and DM groups (**Figure 2I**).

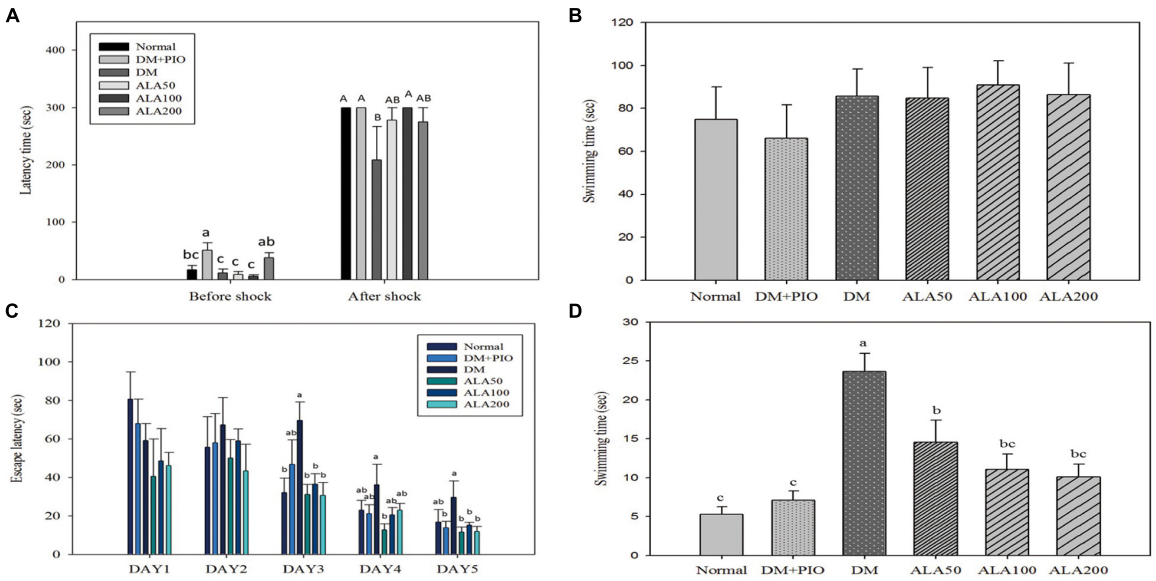

FIGURE 1 | Passive avoidance test **(A)**, physical function **(B)**, spatial acquisition **(C)**, and probe trial **(D)** of Morris Water Maze of high-fat diet and streptozotocin-induced type 2 diabetic rats treated with alpha-lipoic acid for 13 weeks. Normal, Normal diet; DM, high-fat diet (HFD; 60% fat) with STZ (30 mg/kg body weight, i.p.) induced diabetic rats; DM + Pio, DM rats gavaged with pioglitazone (30 mg/kg body weight) for 13 weeks; DM + ALA50, DM rats gavaged with ALA (50 mg/kg body weight) for 13 weeks; DM + ALA100, DM rats gavaged with ALA (100 mg/kg body weight) for 13 weeks; DM + ALA200, DM rats gavaged with ALA (200 mg/kg body weight) for 13 weeks. Values were calculated as the mean ± SEM, $n = 6$ for each group. a–c letter is significantly different among all samples tested before the shock of the passive avoidance test or Morris Water Maze test ($p < 0.05$). A,B letter is significantly different among all samples tested in after shock of passive avoidance test ($p < 0.05$).

The expression levels of pGSK-3β/GSK-3β in the hippocampus of the ALA200 group was significantly higher than that of the normal, DM + PIO, and DM groups (**Figure 2E**). The normal group was significantly higher in the cortex than the DM group (**Figure 2J**).

The expression levels of IDE in the hippocampus of the DM group was significantly higher than that of the normal, DM + PIO, ALA100, and ALA200 groups (**Figure 3A**). The DM group was significantly higher in the cortex than the normal, DM + PIO, and ALA100 groups (**Figure 3B**). However, the expression of pTau (Thr181)/Tau protein in the hippocampus (**Figure 3C**) and cortex (**Figure 3D**) of each group did not reach a statistically significant difference.

The Effect of Alpha-Lipoic Acid on the Expression of Proteins Related to Long-Term Potentiation Related Pathways in the Cerebral Hippocampus and Cortex in Type 2 Diabetes Mellitus Rats

Effects of ALA on expression of proteins of LTP related pathways in the cerebral hippocampus (**Figure 4A**) and cortex (**Figure 4G**). The expression of NMDAR1 protein in the hippocampus (**Figure 4B**) and cortex (**Figure 4H**) of each group did not reach a statistically significant difference.

There was no statistical difference in the expression levels of hippocampus NMDAR2β protein among groups (**Figure 4C**). While the normal group was significantly higher in the cortex than the groups (**Figure 4I**).

The expression levels of calmodulin in the hippocampus of the normal group was significantly higher than that of the DM and ALA200 groups (**Figure 4D**). The DM group was significantly lower in the cortex than the normal, DM + PIO, ALA100, and ALA200 groups (**Figure 4J**).

There was no statistical difference in the expression levels of CaMK II in hippocampus between normal and DM groups, but the DM group was significantly lower than that of the ALA50, ALA100, and ALA200 groups (**Figure 4E**). The ALA200 group was significantly higher in the cortex than the normal and DM groups (**Figure 4K**).

The expression levels of CREB in the hippocampus of the DM group was significantly reduced by 33.6% compared with the ALA100 group (**Figure 4F**). The DM group was significantly lower in the cortex than the normal, DM + PIO, ALA100, and ALA200 groups (**Figure 4L**).

The Effect of Alpha-Lipoic Acid on the Expression of Proteins Related to Synaptic Plasticity in the Cerebral Hippocampus and Cortex in Type 2 Diabetes Mellitus Rats

The expression levels of PSD-95 in the hippocampus (**Figure 5A**) and cortex (**Figure 5B**) of the ALA200 group was significantly higher than that of the DM group. However, the expression

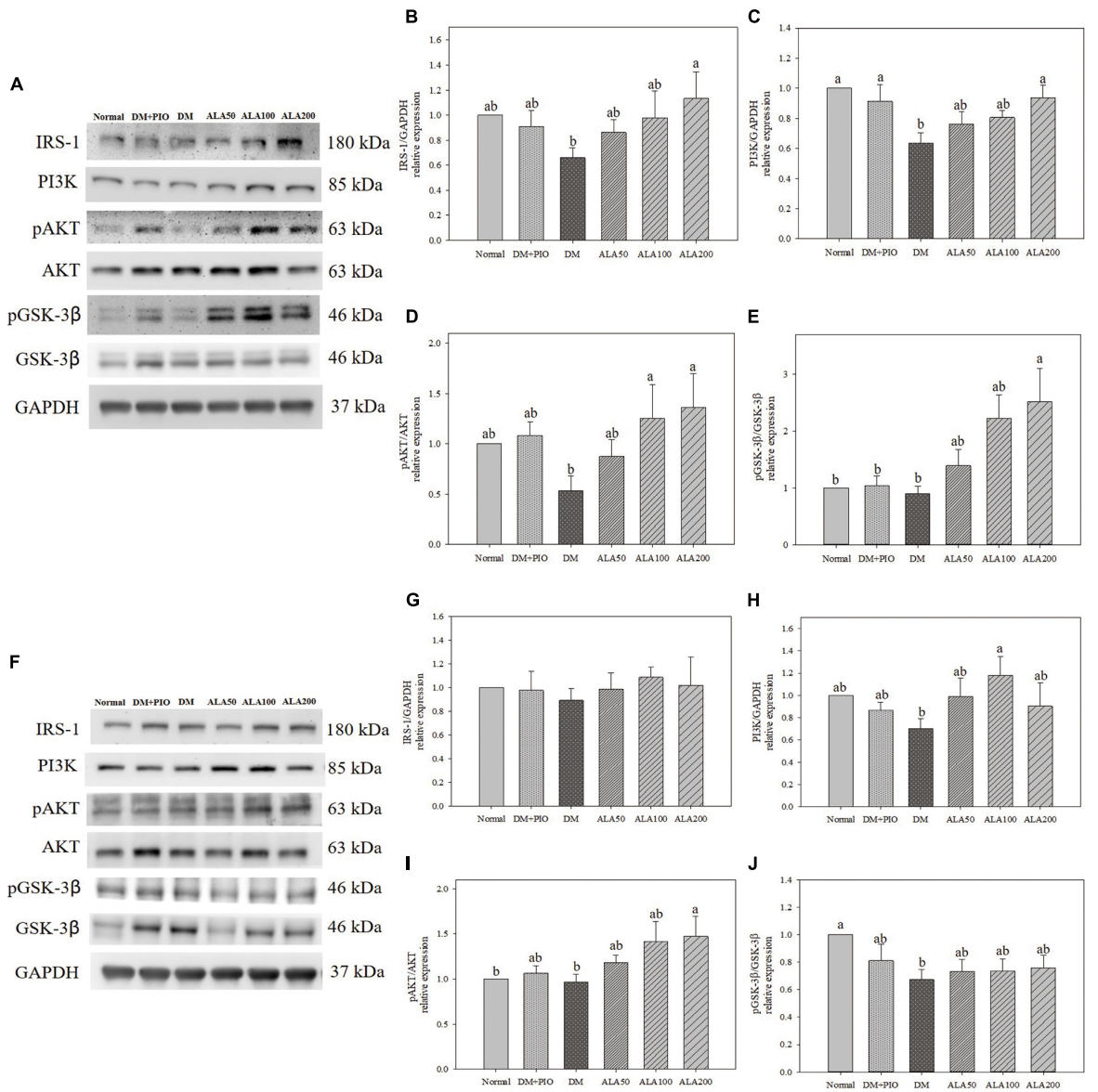

FIGURE 2 | Protein expression levels of the hippocampus **(A)** and cortex **(F)** in quantifying relative IRS-1 **(B,G)**, PI3K **(C,H)**, pAKT/AKT **(D,I)**, and pGSK-3β/GSK-3β **(E,J)** in high-fat diet and streptozotocin-induced type 2 diabetic rats treated with alpha-lipoic acid for 13 weeks. Normal, Normal diet; DM, high-fat diet (HFD; 60% fat) with STZ (30 mg/kg body weight, i.p.) induced diabetic rats; DM + Pio, DM rats gavaged with pioglitazone (30 mg/kg body weight) for 13 weeks; DM + ALA50, DM rats gavaged with ALA (50 mg/kg body weight) for 13 weeks; DM + ALA100, DM rats gavaged with ALA (100 mg/kg body weight) for 13 weeks; DM + ALA200, DM rats gavaged with ALA (200 mg/kg body weight) for 13 weeks. Values were calculated as the mean ± SEM, $n = 6$ for each group. a,b letters indicate significant differences among all samples tested ($p < 0.05$).

of BDNF protein in the hippocampus (**Figure 5C**) and cortex (**Figure 5D**) of each group did not reach a statistically significant difference.

DISCUSSION

In this study, ALA improves hyperinsulinemia and high levels of FFA, and slows brain atrophy caused by T2DM. Additionally, behavioral experiments demonstrated that ALA alleviates cognitive impairment in HFD/STZ-induced T2DM rats. This is the postulated mechanism through which ALA alleviates PI3K of the insulin signal pathway and regulates CaMKII of the LTP-related pathway in the hippocampus and cortex of HFD/STZ-induced T2DM rats (**Figure 6**).

Alpha-lipoic acid can act as a dietary supplement benefit for patients with DM (Shay et al., 2009). A clinical study revealed that ALA (600 mg/day) ameliorates cognitive decline in AD patients with DM (Fava et al., 2013). The underlying molecular mechanisms and therapeutic potential were not clear. IR is

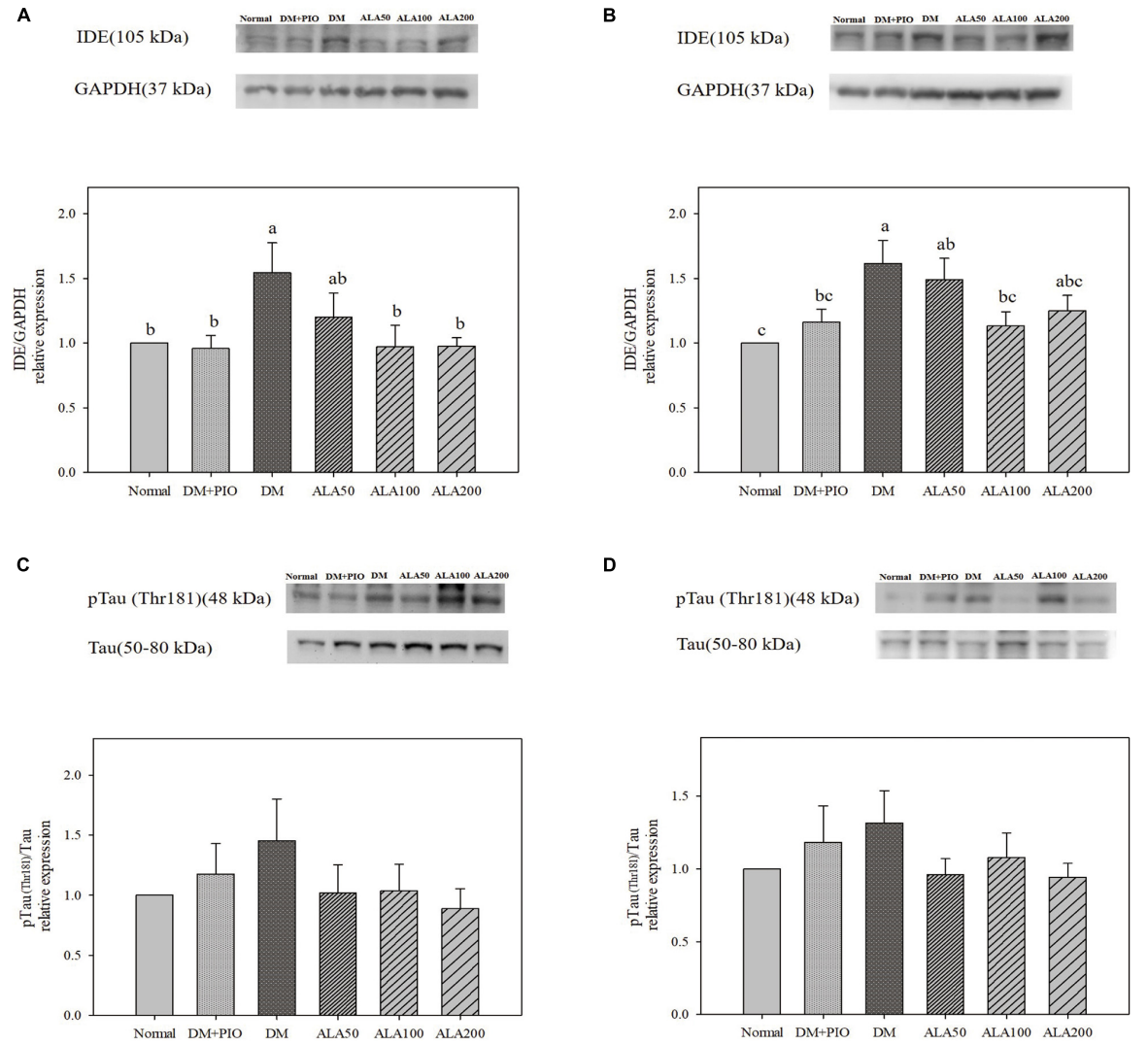

FIGURE 3 | Protein levels of IDE in the hippocampus **(A)** and cortex **(B)**, and pTau (Thr181)/Tau levels in the hippocampus **(C)** and cortex **(D)** in high-fat diet and streptozotocin-induced type 2 diabetic rats treated with alpha-lipoic acid for 13 weeks. Normal, Normal diet; DM, high-fat diet (HFD; 60% fat) with STZ (30 mg/kg body weight, i.p.) induced diabetic rats; DM + Pio, DM rats gavaged with pioglitazone (30 mg/kg body weight) for 13 weeks; DM + ALA50, DM rats gavaged with ALA (50 mg/kg body weight) for 13 weeks; DM + ALA100, DM rats gavaged with ALA (100 mg/kg body weight) for 13 weeks; DM + ALA200, DM rats gavaged with ALA (200 mg/kg body weight) for 13 weeks. Values were calculated as the mean ± SEM, $n = 6$ for each group. a–c letter is significantly different among all samples tested ($p < 0.05$).

deemed to be a common risk factor for DM and AD (Ott et al., 1999). Chronic overnutrition and obesity are signs of IR. The higher concentration of FFA in the body reduces the phosphorylation of tyrosine of IRS-1 and affects the expression of downstream PI3K. ALA effectively reduced the contents of insulin and FFA in diabetic rats, which was consistent with a previous study (Ko et al., 2021). As the time given for HFD increases, the weight of the brain tissue tends to decrease (Lyn-Cook et al., 2009), which is consistent with the results of this study.

AKT plays a critical role in the transmission of insulin signals and regulates cell growth, survival, and metabolism. When IR occurs, insulin signal transmission is inhibited (Huang et al., 2018). In the present study, ALA increased phosphorylation of AKT in the hippocampus and cortex of T2DM rats. Additionally, ALA increased GSK-3β phosphorylation (inactive state) expression in the hippocampus of T2DM rats. The insulin signal pathway of the brain in patients with AD was impaired and the activity of GSK-3β was significantly increased; the activation of GSK-3β in the hippocampus led to phosphorylation of Tau proteins in the T2DM rodent, which further affected memory impairment (Dey et al., 2017). Although the phosphorylation of Tau protein in the ALA treatment group had a tendency to decrease, there was no significant difference in Tau protein between the hippocampus and cortex in this study. Nonetheless, IDE is

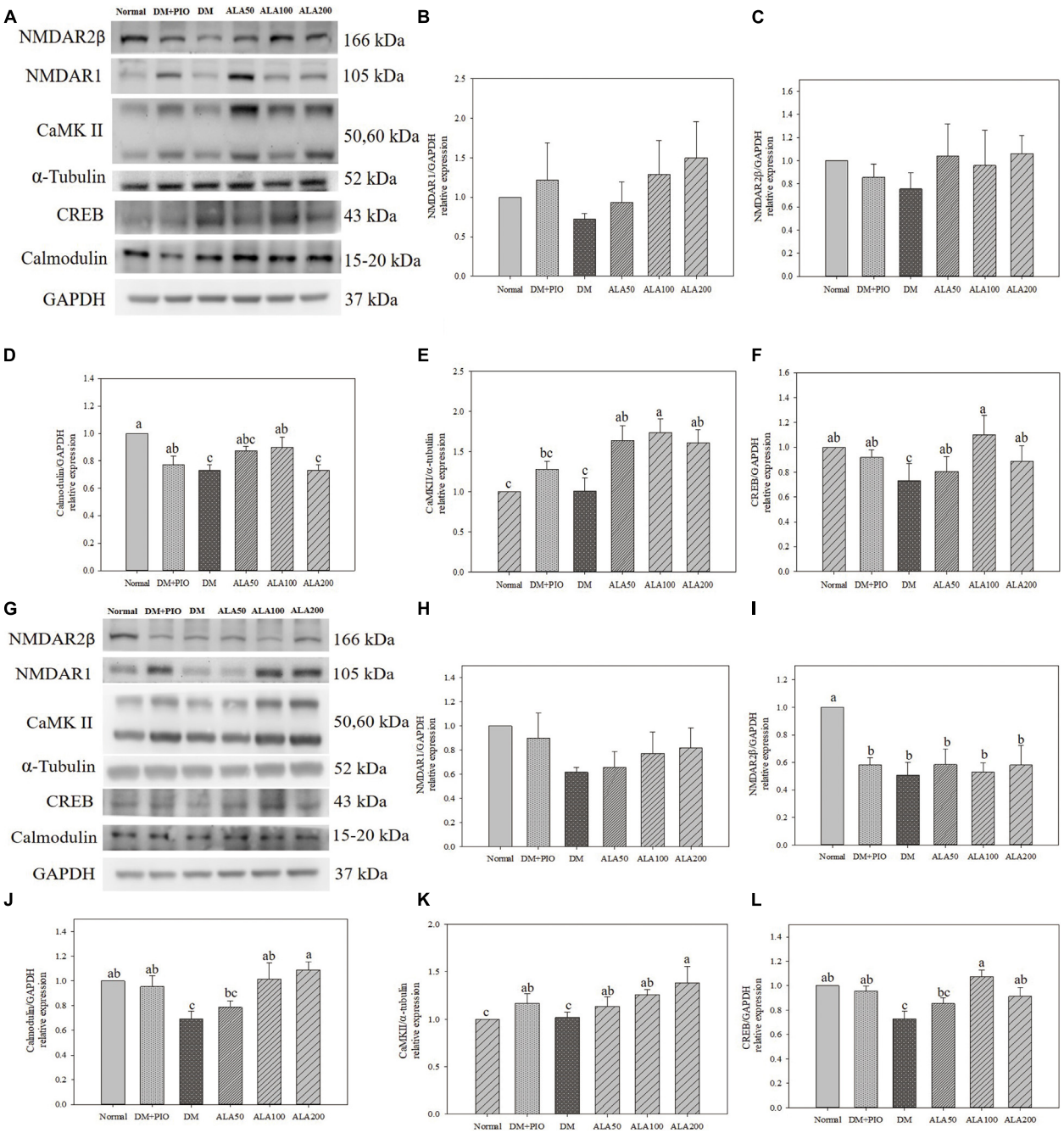

FIGURE 4 | Protein expression levels of the hippocampus **(A)** and cortex **(G)** in quantifying relative NMDAR1 **(B,H)**, NMDAR2β **(C,I)**, calmodulin **(D,J)**, CaMK II **(E,K)**, and CREB **(F,L)** in high-fat diet and streptozotocin-induced type 2 diabetic rats treated with alpha-lipoic acid for 13 weeks. Normal, Normal diet; DM, high-fat diet (HFD; 60% fat) with STZ (30 mg/kg body weight, i.p.) induced diabetic rats; DM + Pio, DM rats gavaged with pioglitazone (30 mg/kg body weight) for 13 weeks; DM + ALA50, DM rats gavaged with ALA (50 mg/kg body weight) for 13 weeks; DM + ALA100, DM rats gavaged with ALA (100 mg/kg body weight) for 13 weeks; DM + ALA200, DM rats gavaged with ALA (200 mg/kg body weight) for 13 weeks. Values were calculated as the mean ± SEM, $n = 6$ for each group. a–c letter is significantly different among all samples tested ($p < 0.05$).

responsible for the degradation of insulin and a major enzyme that breaks down Aβ in the brain. However, the affinity of insulin for IDE is greater than Aβ, which means that insulin and Aβ will compete with each other for IDE. As a result, the occurrence of hyperinsulinemia may result in the accumulation of Aβ (Kazkayasi et al., 2018). Our results showed that the IDE expression of the hippocampus or cortex of HFD/STZ-induced T2DM rats was greater than the other groups, not only in line

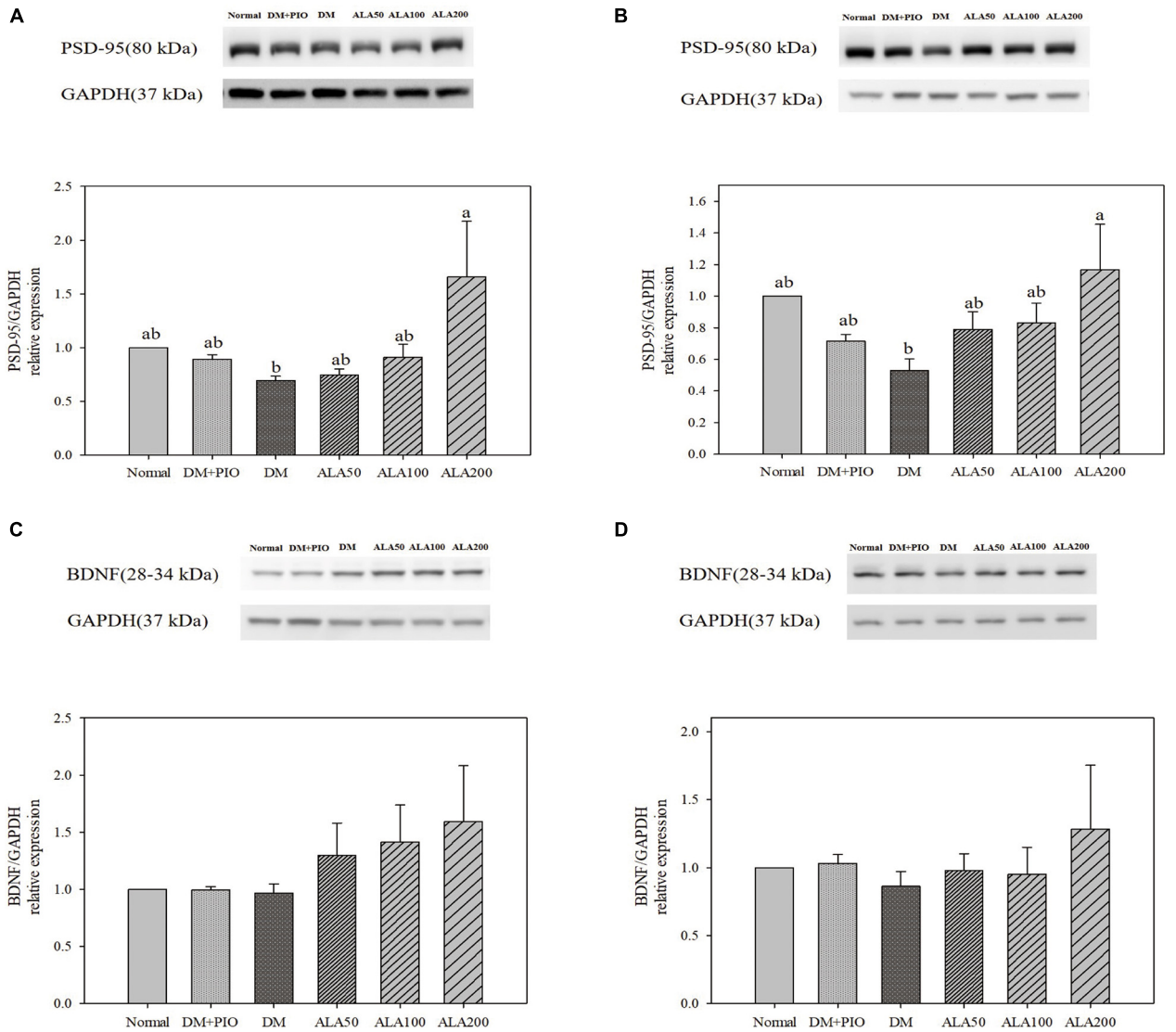

FIGURE 5 | Protein levels of PSD-95 in the hippocampus **(A)** and cortex **(B)**, and BDNF levels in the hippocampus **(C)** and cortex **(D)** in high-fat diet and streptozotocin-induced type 2 diabetic rats treated with alpha-lipoic acid for 13 weeks. Normal, Normal diet; DM, high-fat diet (HFD; 60% fat) with STZ (30 mg/kg body weight, i.p.) induced diabetic rats; DM + Pio, DM rats gavaged with pioglitazone (30 mg/kg body weight) for 13 weeks; DM + ALA50, DM rats gavaged with ALA (50 mg/kg body weight) for 13 weeks; DM + ALA100, DM rats gavaged with ALA (100 mg/kg body weight) for 13 weeks; DM + ALA200, DM rats gavaged with ALA (200 mg/kg body weight) for 13 weeks. Values were calculated as the mean ± SEM, $n = 6$ for each group. a–c letter is significantly different among all samples tested ($p < 0.05$).

with the literature results but also in line with the serum insulin results of this study. Our above findings suggested that ALA alleviates IR of the brain by modulating the IRS-1-insulin signal pathway in HFD/STZ-induced T2DM rats.

Administration of ALA as a dietary supplement in AD patients with DM improved cognitive decline over 16 months on mini-mental state examination scores (Fava et al., 2013). In the present study, ALA improved the memory and learning ability of HFD/STZ-induced T2DM rats. For the passive avoidance test, the consequence of T2DM rats staying in the bright room for a short time was consistent with the results of Firouzjaei et al. (2014). Moreover, in animal models of T1DM, T2DM, AD, and HFD-induced metabolic disorders, on the last day of a space exploration experiment using the WMW protocol, the animals took longer to complete the task than the normal group (Biessels et al., 1998; Cordner and Tamashiro, 2015; Kang et al., 2017). Our results similarly showed that the ALA groups had reduced exploration times. Based on the above results, it is concluded that ALA might modulate in improving the learning memory of T2DM rats.

Long-term potentiation is a memory formation mechanism that relies on the enhancement of synapses. When the NMDAR channel is opened, Ca^{2+} enters the synapse and activates the cascade reaction of calmodulin and CaMKII, and LTP starts to

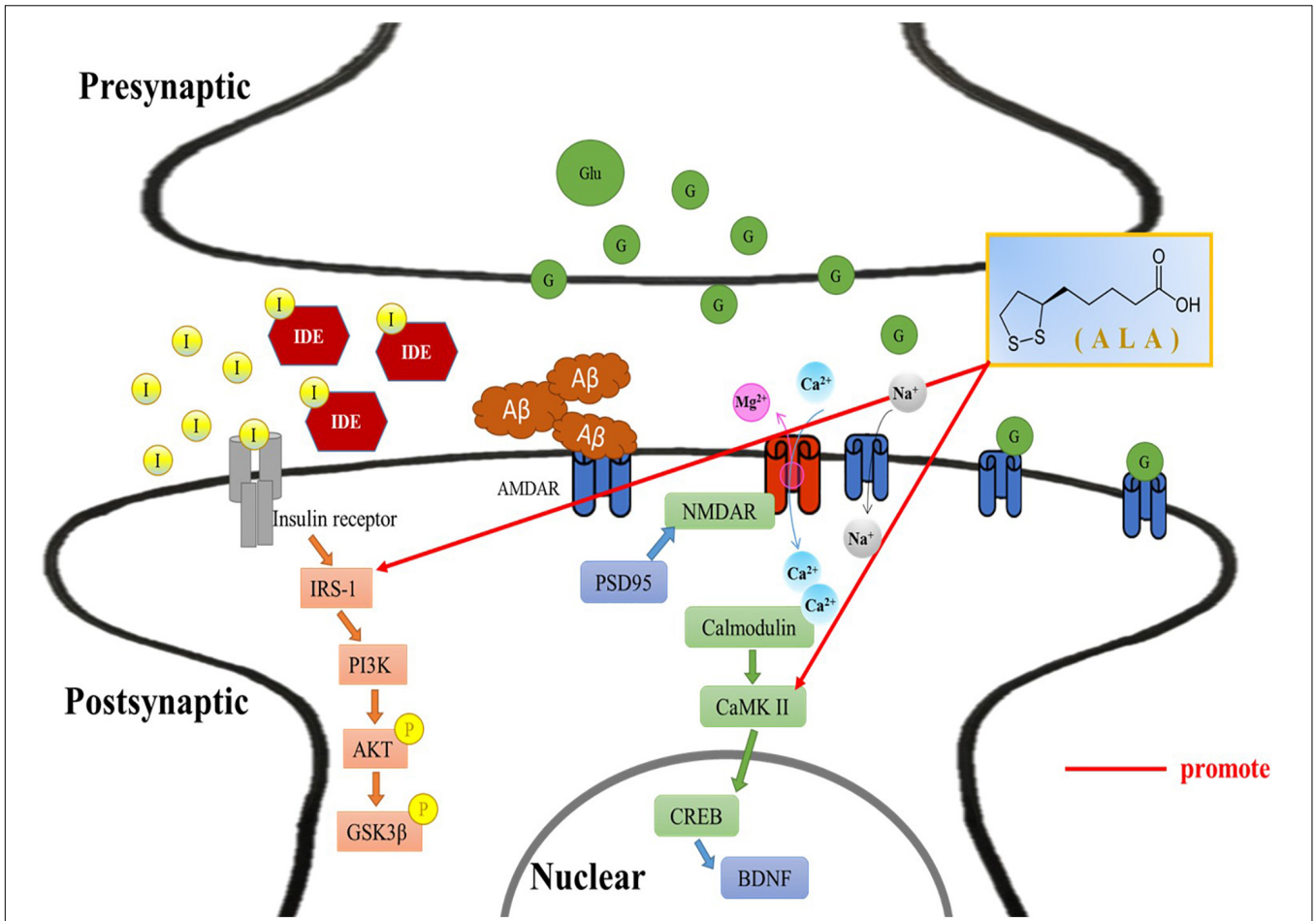

FIGURE 6 | Alleviative mechanism of α-lipoic acid (ALA) in the hippocampus and cortex of T2DM rats induced by HFD/STZ. Postulated mechanism through which ALA alleviates insulin receptor substrate-1 and calmodulin-dependent protein kinase II in the hippocampus and cortex of high-fat diet and streptozotocin-induced type 2 diabetic rats. I, insulin; IDE, insulin-degrading enzyme; IRS-1, insulin receptor substrate 1; PI3K, phosphoinositide 3-kinase; Akt/PKB, protein kinase B; P, phosphorylation; GSK-3β, glycogen synthase kinase 3β; Aβ, β-amyloid; NMDAR, *N*-methyl-D-aspartate receptor; PSD-95, postsynaptic density protein 95; CaMKII, Ca^{2+}/calmodulin-dependent protein kinase II; CREB, cyclic AMP response element-binding protein; BDNF, brain derived neurotrophic factor; Glu/G, glucose; ALA, α-lipoic acid.

work (Nicoll, 2017). Activated CaMKII can also trigger synaptic plasticity (Wang et al., 2014). NMDAR is the receptor and ion channel protein of postsynaptic glutamate, which is very important for synaptic plasticity and memory function (Crump et al., 2001). It has been verified that the accumulation of Aβ can affect the LTP process and impair memory (Pozueta et al., 2013). Unfortunately, the results of this study showed that the two subunit results of NMDA did not reach significant differences among the groups. Preceding studies using HFD-induced obesity accompanied by IR impaired neuronal survival, affected learning memory, and impaired brain synaptic plasticity (Liu et al., 2017). The results of calmodulin and CaMKII in this study showed that ALA treatment could improve obesity and the damage caused by IR to synaptic plasticity. Additionally, the storage of learning and memory is determined by the postsynaptic density. PSD-95 is the most abundant scaffold protein in the postsynaptic density and plays an important role in synaptic plasticity (Chen et al., 2011). CREB induced LTP formation (Silva et al., 1998). Administration of ALA significantly increased the expression of CREB and PSD-95 in the hippocampus and cortex in this study. It is assumed that ALA might increase synaptic plasticity and enhance the effect of learning memory.

CONCLUSION

Administration of ALA for 13 weeks significantly improved the abnormal lipid metabolism and IR of brain in HFD/STZ-induced T2DM rats. Results of passive avoidance and the MWM test showed that ALA ameliorated the learning memory abilities of T2DM rats. Western blot analyses of insulin signaling pathways showed that ALA can improve insulin sensitivity in the brain of T2DM rats, activate insulin signaling pathways, and inhibit the activity of GSK-3β. Expression levels of the LTP pathway downstream proteins showed that ALA can improve synaptic plasticity in T2DM rats. Our results suggested that ALA alleviates

HFD/STZ-induced brain IR in T2DM rats to improve learning memory. However, the detailed mechanism of ALA to improve LTP has yet to be clarified in the future.

DATA AVAILABILITY STATEMENT

The original contributions presented in the study are included in the article/supplementary material, further inquiries can be directed to the corresponding author.

ETHICS STATEMENT

The animal study was reviewed and approved by The Institutional Animal Care and Use Committee of National Taiwan Normal University.

AUTHOR CONTRIBUTIONS

C-YK and S-CS participated in the design of the study and writing the protocol. R-ST carried out all experiments. C-YK, J-HX, YL, JW, W-CH, and S-CS conducted kinds of literature searches and data analyses and writing drafts of the manuscript. All authors contributed to the article and approved the submitted version.

ACKNOWLEDGMENTS

The authors would like to thank the Ministry of Science and Technology of the Republic of China (ROC), Taiwan, for financially supporting this research under contract No. MOST 107-2320-B-003-004-MY3 and academic funding of The Second Affiliated Hospital of Fujian Medical University (Serial No. BS201902).

REFERENCES

Biessels, G. J., Kamal, A., Urban, I. J., Spruijt, B. M., Erkelens, D. W., and Gispen, W. H. (1998). Water maze learning and hippocampal synaptic plasticity in streptozotocin-diabetic rats: effects of insulin treatment. *Brain Res.* 800, 125–135. doi: 10.1016/s0006-8993(98)00510-1

Bloom, G. S. (2014). Amyloid-β and tau: the trigger and bullet in Alzheimer disease pathogenesis. *JAMA Neurol.* 71, 505–508. doi: 10.1001/jamaneurol.2013.5847

Chatterjee, S., and Mudher, A. (2018). Alzheimer's Disease and Type 2 Diabetes: a critical assessment of the shared pathological traits. *Front. Neurosci.* 12:383. doi: 10.3389/fnins.2018.00383

Chen, X., Nelson, C. D., Li, X., Winters, C. A., Azzam, R., Sousa, A. A., et al. (2011). PSD-95 is required to sustain the molecular organization of the postsynaptic density. *J. Neurosci.* 31, 6329–6338. doi: 10.1523/JNEUROSCI.5968-10.2011

Cole, A. R., Astell, A., Green, C., and Sutherland, C. (2007). Molecular connexions between dementia and diabetes. *Neurosci. Biobehav. Rev.* 31, 1046–1063. doi: 10.1016/j.neubiorev.2007.04.004

Cordner, Z. A., and Tamashiro, K. L. (2015). Effects of high-fat diet exposure on learning & memory. *Physiol. Behav.* 152(Pt B), 363–371.

Crump, F. T., Dillman, K. S., and Craig, A. M. (2001). cAMP-dependent protein kinase mediates activity-regulated synaptic targeting of NMDA receptors. *J. Neurosci.* 21, 5079–5088. doi: 10.1523/jneurosci.21-14-05079.2001

Derakhshan, F., and Toth, C. (2013). Insulin and the brain. *Curr. Diabetes Rev.* 9, 102–116.

Dey, A., Hao, S., Wosiski-Kuhn, M., and Stranahan, A. M. (2017). Glucocorticoid-mediated activation of GSK3β promotes tau phosphorylation and impairs memory in type 2 diabetes. *Neurobiol. Aging* 57, 75–83. doi: 10.1016/j.neurobiolaging.2017.05.010

Eckel, R. H., Kahn, S. E., Ferrannini, E., Goldfine, A. B., Nathan, D. M., Schwartz, M. W., et al. (2011). Obesity and type 2 diabetes: what can be unified and what needs to be individualized? *J. Clin. Endocrinol. Metab.* 96, 1654–1663. doi: 10.1210/jc.2011-0585

Elrod, K., and Buccafusco, J. J. (1988). An evaluation of the mechanism of scopolamine-induced impairment in two passive avoidance protocols. *Pharmacol. Biochem. Behav.* 29, 15–21. doi: 10.1016/0091-3057(88)90267-5

Fava, A., Pirritano, D., Plastino, M., Cristiano, D., Puccio, G., Colica, C., et al. (2013). The effect of lipoic acid therapy on cognitive functioning in patients with Alzheimer's Disease. *J. Neurodegener. Dis.* 2013:454253.

Firouzjaei, M. A., Jafari, M. R., Eskandari, M., Anarkoli, I. J., and Alipour, M. (2014). Aminoguanidine changes hippocampal expression of apoptosis-related genes, improves passive avoidance learning and memory in streptozotocin-induced diabetic rats. *Cell Mol. Neurobiol.* 34, 343–350. doi: 10.1007/s10571-013-0018-5

Gu, C., Yang, X., and Huang, L. (2016). Cistanches herba: a neuropharmacology review. *Front. Pharmacol.* 7:289. doi: 10.3389/fphar.2016.00289

Huang, X., Liu, G., Guo, J., and Su, Z. (2018). The PI3K/AKT pathway in obesity and type 2 diabetes. *Int. J. Biol. Sci.* 14, 1483–1496.

Kang, S., Kim, C. H., Jung, H., Kim, E., Song, H. T., and Lee, J. E. (2017). Agmatine ameliorates type 2 diabetes induced-Alzheimer's disease-like alterations in high-fat diet-fed mice via reactivation of blunted insulin signalling. *Neuropharmacology* 113(Pt A), 467–479. doi: 10.1016/j.neuropharm.2016.10.029

Kazkayasi, I., Burul-Bozkurt, N., Ismail, M. A., Merino-Serrais, P., Pekiner, C., Cedazo-Minguez, A., et al. (2018). Insulin deprivation decreases insulin degrading enzyme levels in primary cultured cortical neurons and in the cerebral cortex of rats with streptozotocin-induced diabetes. *Pharmacol. Rep.* 70, 677–683. doi: 10.1016/j.pharep.2018.01.008

Ko, C. Y., Lo, Y. M., Xu, J. H., Chang, W. C., Huang, D. W., Wu, J. S., et al. (2021). Alpha-lipoic acid alleviates NAFLD and triglyceride accumulation in liver via modulating hepatic NLRP3 inflammasome activation pathway in type 2 diabetic rats. *Food Sci. Nutr.* 9, 2733–2742. doi: 10.1002/fsn3.2235

Liu, Z., Patil, I., Sancheti, H., Yin, F., and Cadenas, E. (2017). Effects of lipoic acid on high-fat diet-induced alteration of synaptic plasticity and brain glucose metabolism: a PET/CT and 13C-NMR study. *Sci. Rep.* 7:5391. doi: 10.1038/s41598-017-05217-z

Lyn-Cook, L. E. Jr., Lawton, M., Tong, M., Silbermann, E., Longato, L., Jiao, P., et al. (2009). Hepatic ceramide may mediate brain insulin resistance and neurodegeneration in type 2 diabetes and non-alcoholic steatohepatitis. *J. Alzheimers Dis.* 16, 715–729.

Morris, R. (1984). Developments of a water maze procedure for studying spatiallearning in the rats. *J. Neurosci. Methods* 11, 47–60. doi: 10.1016/0165-0270(84)90007-4

Nicoll, R. A. (2017). A brief history of long-term potentiation. *Neuron* 93, 281–290.

Ott, A., Stolk, R. P., van Harskamp, F., Pols, H. A., Hofman, A., and Breteler, M. M. (1999). Diabetes mellitus and the risk of dementia: the rotterdam study. *Neurology* 53, 1937–1942. doi: 10.1212/wnl.53.9.1937

Pozueta, J., Lefort, R., and Shelanski, M. L. (2013). Synaptic changes in Alzheimer's disease and its models. *Neuroscience* 251, 51–65.

Ries, M., and Sastre, M. (2016). Mechanisms of Aβ clearance and degradation by glial cells. *Front. Aging Neurosci.* 8:160. doi: 10.3389/fnagi.2016.00160

Shay, K. P., Moreau, R. F., Smith, E. J., Smith, A. R., and Hagen, T. M. (2009). Alpha-lipoic acid as a dietary supplement: molecular mechanisms and therapeutic potential. *Biochim. Biophys. Acta* 1790, 1149–1160.

Silva, A. J., Kogan, J. H., Frankland, P. W., and Kida, S. (1998). CREB and memory. *Annu. Rev. Neurosci.* 21, 127–148.

Son, S. M., Cha, M. Y., Choi, H., Kang, S., Choi, H., Lee, M. S., et al. (2016). Insulin-degrading enzyme secretion from astrocytes is mediated by an autophagy-based unconventional secretory pathway in Alzheimer disease. *Autophagy* 12, 784–800. doi: 10.1080/15548627.2016.1159375

Špolcová, A., Mikulášková, B., Kršková, K., Gajdošechová, L., Zórad, Š, Olszanecki, R., et al. (2014). Deficient hippocampal insulin signaling and augmented Tau phosphorylation is related to obesity- and age-induced peripheral insulin resistance: a study in Zucker rats. *BMC Neurosci.* 15:111. doi: 10.1186/1471-2202-15-111

Talbot, K., Wang, H. Y., Kazi, H., Han, L. Y., Bakshi, K. P., Stucky, A., et al. (2012). Demonstrated brain insulin resistance in Alzheimer's disease patients is associated with IGF-1 resistance. IRS-1 dysregulation, and cognitive decline. *J. Clin. Invest.* 122, 1316–1338. doi: 10.1172/jci59903

Vorhees, C. V., and Williams, M. T. (2006). Morris water maze: procedures for assessing spatial and related forms of learning and memory. *Nat. Protoc.* 1, 848–858. doi: 10.1038/nprot.2006.116

Wang, N., Chen, L., Cheng, N., Zhang, J., Tian, T., and Lu, W. (2014). Active calcium/calmodulin-dependent protein kinase II (CaMKII) regulates NMDA receptor mediated postischemic long-term potentiation (i-LTP) by promoting the interaction between CaMKII and NMDA receptors in ischemia. *Neural Plast.* 2014:827161. doi: 10.1155/2014/827161

Zhang, Y. H., Wang, D. W., Xu, S. F., Zhang, S., Fan, Y. G., Yang, Y. Y., et al. (2018). α-Lipoic acid improves abnormal behavior by mitigation of oxidative stress, inflammation, ferroptosis, and tauopathy in P301S Tau transgenic mice. *Redox Biol.* 14, 535–548. doi: 10.1016/j.redox.2017.11.001

Conflict of Interest: The authors declare that the research was conducted in the absence of any commercial or financial relationships that could be construed as a potential conflict of interest.

Publisher's Note: All claims expressed in this article are solely those of the authors and do not necessarily represent those of their affiliated organizations, or those of the publisher, the editors and the reviewers. Any product that may be evaluated in this article, or claim that may be made by its manufacturer, is not guaranteed or endorsed by the publisher.

Copyright © 2021 Ko, Xu, Lo, Tu, Wu, Huang and Shen. This is an open-access article distributed under the terms of the Creative Commons Attribution License (CC BY). The use, distribution or reproduction in other forums is permitted, provided the original author(s) and the copyright owner(s) are credited and that the original publication in this journal is cited, in accordance with accepted academic practice. No use, distribution or reproduction is permitted which does not comply with these terms.

frontiers in Aging Neuroscience

SYSTEMATIC REVIEW
published: 12 November 2021
doi: 10.3389/fnagi.2021.775432

Age Matching Is Essential for the Study of Cerebrospinal Fluid sTREM2 Levels and Alzheimer's Disease Risk: A Meta-Analysis

*Shimin Hu[1,2], Na Pan[1,2], Chunyan Liu[1,2], Yuping Wang[1,2,3] and Tingting Zhang[1,2]**

[1] Department of Neurology, Xuanwu Hospital, Capital Medical University, Beijing, China, [2] Beijing Key Laboratory of Neuromodulation, Beijing, China, [3] Institute of Sleep and Consciousness Disorders, Center of Epilepsy, Beijing Institute for Brain Disorders, Capital Medical University, Beijing, China

Background: Both the genetic and pathological studies link Alzheimer's disease (AD) to the triggering receptor expressed on myeloid cells 2 (TREM2). A large number of studies have explored the value of cerebrospinal fluid (CSF) soluble TREM2 (sTREM2) levels as a biomarker for the diagnosis and prediction of AD; however, the findings are inconsistent. We aimed to review the studies that investigated the association of CSF sTREM2 levels and AD risk, and to provide the recommendations for future research.

Methods and Results: A systematic literature search was performed using the MEDLINE, EMBASE, and Web of Science (all databases) databases. The meta-analysis for the association between the CSF sTREM2 levels and AD risk included 15 studies (17 comparisons) with a total of 1,153 cases and 1,626 controls. The total results showed that the higher CSF sTREM2 levels and AD risk were associated [standardized mean difference (SMD) = 0.428, 95% *CI* (0.213, 0.643), I^2 = 81.1%]. However, the analysis of the subgroup of "age difference $\leq$ 2 years" indicated that sTREM2 was not associated with AD [SMD = 0.090, 95% *CI* (−0.092, 0.272), I^2 = 27.4%] and had a significantly lower heterogeneity. Combining the results of the "age difference of 5–10 years" [SMD = 0.497, 95% *CI* (0.139, 0.855), I^2 = 82.5%] and "age difference > 10 years" [SMD = 0.747, 95% *CI* (0.472, 1.023), I^2 = 50.0%] subgroups showed that the difference in CSF sTREM2 between the AD and control groups was positively correlated with the age difference. A meta-regression analysis showed that the age difference can explain 33.4% of the between-study variance. By conducting further subgroup analyses of the five age-matched studies (495 cases and 364 controls) according to the measurement method, and whether inclusion criteria containing the requirement for pathological evidence of AD, no changes were observed in the corresponding pooled SMD or in the significance of the results. The meta-analysis result of "age difference $\leq$ 2 years" group was robust in the sensitivity analysis.

Conclusion: The available high-quality evidence does not yet support an association between the CSF sTREM2 levels and AD risk. Age matching between the patients with AD and cognitively unimpaired controls was a major influencing factor in the results.

Keywords: Alzheimer's disease, sTREM2, age matching, meta-analysis, cerebrospinal fluid

OPEN ACCESS

Edited by:
Jiehui Jiang,
Shanghai University, China

Reviewed by:
Shi Wu Wen,
Ottawa Hospital Research Institute (OHRI), Canada
Lv Wang,
Monash University, Australia

****Correspondence:***
Tingting Zhang
zhtingting129@163.com

Received: *14 September 2021*
Accepted: *08 October 2021*
Published: *12 November 2021*

Citation:
Hu S, Pan N, Liu C, Wang Y and Zhang T (2021) Age Matching Is Essential for the Study of Cerebrospinal Fluid sTREM2 Levels and Alzheimer's Disease Risk: A Meta-Analysis. Front. Aging Neurosci. 13:775432. doi: 10.3389/fnagi.2021.775432

INTRODUCTION

Alzheimer's disease (AD), as a clinically heterogeneous and complex neurodegenerative disease, is considered the most common type of dementia and induces a heavy burden to the patients and families. The onset of AD is a continuous progressive process that from an asymptomatic state to mild cognitive impairment and to clinical diagnosis of dementia (Morris, 2005). Early risk estimation and identification are essential to prevent or slow down the development of AD, which means the reliable biomarkers are necessary.

Typical pathological features in the brain of the patients with AD are beta-amyloid (Aβ) plaques, intracellular neurofibrillary tangles consisting of hyper-phosphorylated tau fibrils, degeneration of neurons, and loss of synapses, neuroinflammation, and glial activation (Bronzuoli et al., 2016). As the main immune cells in the brain, microglia have been shown to be the important modulators of AD. It is reported that the initial activation of microglia induces phagocytosis of Aβ, prevents oligomer formation, and limits the neurotoxicity of Aβ deposited in plaques; however, its continuous activation and further inflammatory response might accelerate the neurodegeneration (Nordengen et al., 2019). Currently, the inflammatory mechanism of AD has been demonstrated. However, in contrast to the use of classical fluid biomarkers of Aβ and tau proteins, the reliable inflammatory markers in the diagnosis of AD are lacking.

A triggering receptor expressed on myeloid cells 2 (TREM2) is a transmembrane protein with V-immunoglobulin extracellular domains and cytoplasmic tails (Bouchon et al., 2000). In the brain, a TREM2 is almost exclusively expressed by microglia (Sessa et al., 2004). A TREM2 participates in microglia functions, such as survival, proliferation, clustering around plaques, as well as phagocytosis of apoptotic cells and myelin debris (Ulland et al., 2017). Two genome-wide association studies based on different populations published in 2013 showed that a variant (p.R47H) in *TREM2* increased the risk of AD by almost threefold (Guerreiro et al., 2013; Jonsson et al., 2013). It is one of the strongest genetic risk factors for AD following the amyloid-beta precursor protein (*APP*), presenilin-1 (*PSEN1*), and apolipoprotein E (*APOE*). Soluble TREM2 (sTREM2) is generated and released into the extracellular milieu through cleavage of full-length TREM2 by disintegrin and metalloproteinase domain-containing protein 17 (ADAM17) and ADAM10 (Wu et al., 2015; Ulland and Colonna, 2018). A large number of studies have explored the value of cerebrospinal fluid (CSF) sTREM2 levels as a biomarker for the diagnosis and prediction of AD. However, previous studies have reported the conflicting results. A meta-analysis published in 2018 analyzed seven studies and concluded that the CSF sTREM2 levels in the AD cases were increased compared with controls (Liu et al., 2018). However, nine additional relevant articles were published since then, and more than half of the literature showed that the CSF sTREM2 levels are not associated with AD risk (Brosseron et al., 2018; Heywood et al., 2018; Deming et al., 2019; Morenas-Rodríguez et al., 2019; Nordengen et al., 2019; Suarez-Calvet et al., 2019; Banerjee et al., 2020; Knapskog et al., 2020; Van Hulle et al., 2021). Therefore, it is necessary to update the meta-analysis.

This study summarized the studies on the association of CSF sTREM2 and AD risk, with the attempt to find the potential influence factors to interpret the considerable differences of the results reported by these studies and provide recommendations for future research. The previous studies have shown a positive association between the CSF sTREM2 levels and age (Gispert et al., 2016, 2017; Henjum et al., 2016; Piccio et al., 2016; Suarez-Calvet et al., 2016, 2019; Brosseron et al., 2018; Deming et al., 2019; Morenas-Rodríguez et al., 2019; Knapskog et al., 2020). Meanwhile, age is the strongest predictor of AD. To reveal the value of CSF sTREM2 levels in the diagnosis and prediction of AD, the positive results from the studies with age-matched strategy are more credible. Thus, we particularly analyzed the impact of the age difference between the patients with AD and cognitively unimpaired controls on the conclusion of the association between CSF sTREM2 level and AD risk.

METHODS

Literature Search

The databases MEDLINE, EMBASE, and Web of Science (all databases, such as Web of Science Core Collection and BIOSIS Citation Index) were searched up to April 13, 2021 to find the studies evaluating the relationship between CSF sTREM2 level and AD risk. The following keywords were used: (cerebrospinal fluid) AND (TREM2 OR sTREM2 OR "soluble trigger receptor expressed on myeloid cells 2") AND [(Alzheimer's disease) OR (dementia)]. All the reference lists of the resulting primary research reports and relevant reviews were manually searched to identify the additional eligible studies.

Eligible Studies, Data Extraction, and Quality Evaluation

The eligible studies were included in this meta-analysis: (1) investigated the relationship between the CSF sTREM2 levels and AD risk; (2) included a case group of patients with AD and a group of cognitively unimpaired controls; (3) clinical criteria that used to diagnose AD were qualified; (4) provided data with the mean and SD or median and interquartile range (IQR) or median and the minimum and maximum; (5) the studies performed in humans; (6) full text in English. The articles were excluded if they measured sTREM2 concentrations in the postmortem samples, had a sample size of less than 5, or used the samples that overlapped with other studies. Information regarding the first author, year of publication, study location (country), study design, number of patients and controls, diagnostic criteria, measurement methods, the mean and SD of CSF sTREM2 levels, and information for the potential confounding factors (i.e., age) were extracted.

The quality of case-control studies and cohort studies included was evaluated based on the Newcastle-Ottawa Scale (NOS) recommended by the Agency for Healthcare Research and Quality of the United States. Comparability of the cases and

controls on the basis of the design or analysis was evaluated based on whether the age and gender matched. The methodological quality of the cross-sectional studies included was assessed using an 11-item checklist which was recommended by Agency for Healthcare Research and Quality (AHRQ). The studies with NOS scores lower than 5, or AHRQ scores lower than 4 were recognized to be of inferior quality and therefore excluded.

The disputes were resolved by discussion with a third author during data extraction and quality evaluation. If the case or control groups were further divided into subgroups, the data from the subgroups were merged as $n = n_1 + n_2$, $\overline{x} = \frac{n_1\overline{x_1}+n_2\overline{x_2}}{n_1+n_2}$ and $\mathrm{SD} = \sqrt{\frac{(n_1-1)SD_1^2+(n_2-1)SD_2^2+\frac{n_1 n_2}{n_1+n_2}(\overline{x}_1^2+\overline{x}_2^2-2\overline{x}_1\overline{x}_2)}{n_1+n_2-1}}$. When a study provided medians and IQRs (instead of means and SDs), without the minimum or maximum values, we treated the medians as the means and calculated the SDs as SD = IQR/1.35 (Higgins et al., 2021). If the study provided the minimum and maximum, we imputed the means and SDs as described by Hozo et al. (2005).

Statistical Analysis

The association between the CSF sTREM2 level and AD risk was estimated by calculating the pooled standardized mean difference (SMD) and the 95% *CI*. To analyze the potential influences of age difference at the time of lumbar puncture, measurement method, and inclusion criteria containing the requirement for pathological evidence of AD, we performed the subgroup analysis. Based on the age difference between the AD group and the control group at lumbar puncture, the subjects were divided into three subgroups: (1) age difference $\leq$ 2 years, (2) age difference of 5–10 years, and (3) age difference $>$ 10 years. Based on the measurement method, the subjects were divided into three subgroups: (1) enzyme-linked immunosorbent assay (ELISA), (2) mesoscale discovery electrochemiluminescence platform-based assay (MSD) or electrochemiluminescence (ECL) immunoassay, and (3) ultra-performance liquid chromatography-tandem mass spectrometer (UPLC-MS). Additionally, based on the diagnostic criteria, the subjects were divided into two subgroups: (1) with neuropathologic verification, and (2) no relative information. The significance of the pooled SMD was determined using a *Z* test, and the level was set at $p < 0.05$.

Heterogeneity across the studies was assessed using the *Q* test and the I^2 statistic. When significant heterogeneity was observed ($p < 0.1$ in the *Q* test, and $I^2 > 50\%$), a random effects model was used for pooling the data from the primary studies. A meta-regression with restricted maximum likelihood estimation (REML) was performed to assess the potentially important covariate exerting substantial impact on the between-study heterogeneity. The age difference ($\leq$2 years, 5–10 years, and $>$10 years) was included in the meta-regression analysis. The sensitivity analysis was performed by sequentially excluding the individual studies to assess the stability of the results. A funnel-plot asymmetry was assessed using Egger's linear regression test, with $p < 0.05$ representing significant publication bias. All the analyses were performed using STATA 12.0 software (Stata Corporation, College Station, TX, United States), and all the *p* values were two-tailed.

RESULTS

Study Selection

With respect to the association between the CSF sTREM2 levels and AD risk, an initial search identified 184 records of the potentially relevant studies from the databases. Of these, 152 records were excluded based on their title and/or abstract: these were repetitive publications (n = 90), conference abstracts (n = 14), the reports of animal studies (n = 7), the reports of studies that investigated either the outcomes irrelevant to this meta-analysis (n = 18), the markers other than sTREM2 (n = 1), review or meta-analysis (n = 12), protocol (n = 1), the studies of which sTREM2 levels was not measured in CSF (n = 2), the reports of studies that only had *TREM2* gene information (n = 6), or the studies of which did not have a normal cognitive function group (n = 1).

A further 17 articles were excluded after reviewing the full text. These were (1) *TREM2* gene study (n = 2), (2) the studies in which the interviewees were not grouped according to the AD clinical diagnosis criteria (n = 4), (3) study in which the sTREM2 levels were not detected in the control group (n = 1), (4) postmortem samples (n = 1), (5) the studies used the samples that overlapped with other studies (n = 5), (6) the studies in which all the participants had Down syndrome (n = 1), and (7) the studies in which data were shown in figures only (n = 3). The 15 studies (17 comparisons) that were ultimately selected for our meta-analysis included 1,153 cases and 1,626 controls (**Table 1** and **Supplementary Tables 1**, **2**); the process of study selection is shown in **Figure 1**.

Association Between the Cerebrospinal Fluid sTREM2 Levels and Alzheimer's Disease Risk in All Eligible Comparisons

The meta-analysis for the association between the CSF sTREM2 levels and AD risk included 15 studies (17 comparisons) with a total of 1,153 cases and 1,626 controls. The total results showed that a higher CSF sTREM2 level was associated with increased AD risk [SMD = 0.428, 95% *CI* (0.213, 0.643), I^2 = 81.1%] (**Figure 2**).

Of the 17 comparisons, four comparisons had an age difference greater than 10 years, eight comparisons had an age difference from 5–10 years, and five studies had an age difference of 2 years or less. When distinguishing the subgroups by age difference, the heterogeneity decreased substantially in both the subgroup of "age differences $\leq$ 2 years" (I^2 = 27.4%) and the subgroup of "age differences $>$ 10 years" (I^2 = 50.0%). An analysis of the subgroup of "age difference $\leq$ 2 years" indicated that sTREM2 was not associated with AD [SMD = 0.090, 95% *CI* (−0.092, 0.272), I^2 = 27.4%]. An analysis of the subgroup of "age difference of 5–10 years" [SMD = 0.497, 95% *CI* (0.139, 0.855), I^2 = 82.5%], and the subgroup of "age difference $>$ 10 years" [SMD = 0.747, 95% *CI* (0.472, 1.023), I^2 = 50.0%] showed that the CSF sTREM2 levels were associated with AD. The results indicated that the greater the difference in age, the greater the difference in CSF sTREM2 levels between the case group and the control group (**Figure 3** and **Table 2**). The meta-regression

TABLE 1 | The detailed characteristics of all the eligible studies for the association with the cerebrospinal fluid soluble triggering receptor expressed on myeloid cells 2 (CSF sTREM2) levels and Alzheimer's disease (AD).

Author, year	Location	Study Design	Number AD/C	AD diagnosis	Measurement method	Age AD/C	AD pathology	sTREM2 levels, ng/ml Mean (SD)		
								AD	Control	*p*
Van Hulle et al., 2021	United States	CS*	50/606	NIA-AA	ECL immunoassay	72.8/62.4	NI	9.87 (3.46)	8.01 (2.46)	< 0.001
Knapskog et al., 2020	Norway	CC	237/113	NIA-AA	ELISA	70.1/72.3	NI	9.5 (4.8)	8.8 (3.6)	NS
Banerjee et al., 2020	United Kingdom	CC	20/10	NIA-AA	MSD	62.5/62.2	Verification	6.58 (1.84)	7.96 (2.71)	NS
Deming et al., 2019	ADNI	CC	172/169	NINCDS–ADRDA	MSD	74.4/74.5	NI	4.019 (1.946)	3.988 (1.923)	NS
Nordengen et al., 2019	Norway	CC	27/36	NIA-AA	ELISA	67.5/61.1	Verification	4.8 (1.7)	3.1 (0.9)	< 0.001
Morenas-Rodríguez et al., 2019	Spain	CC	36/40	NIA-AA	ELISA	74.6/67.4	Verification	4.3 (2.2)	4.2 (2.3)	NS
Heywood et al., 2018	Italy	CC	13/15	NINCDS-ADRDA	UPLC-MS	72.1/61.0	Verification	261.7 (82.0) mol/ml	154.7 (53.1) mol/ml	< 0.001
Brosseron et al., 2018	Germany	CC	116/85	NIA-AA	MSD	74/67	Verification	4.315 (2.235)	2.994 (2.269)	0.002
Gispert et al., 2017	Spain	CC	15/49	NIA-AA	MSD	67.14/61.92	Verification	0.5866 (0.3589) relative to an internal standard	0.4235 (0.2176) relative to an internal standard	0.035
Suarez-Calvet et al., 2016	Sweden Germany Belgium Spain	CC	200/150	NIA-AA	MSD	73.8/62.4	Verification	5.33 (3.7)	3.07 (1.4)	< 0.001
Piccio et al., 2016	Italy United States	CC	73/107	NINCDS-ADRDA	ELISA	76.6/70.2	NI	1.028 (0.388)	0.832 (0.339)	0.015
Heslegrave et al., 2016	United Kingdom	CC	37/22	IWG2	UPLC-MS	70.5/69.2	Verification	0.2312 (0.0984)	0.1956 (0.0813)	0.0457
	Sweden		24/16			64.3/55.6		0.2305 (0.0970)	0.1713 (0.0652)	0.0312
Henjum et al., 2016	Sweden	CC	25/25	NINCDS-ADRDA	ELISA	76.25/61.75	NI	3.8 (2.22)	3.2 (1.63)	0.76
	Norway		29/50	NIA-AA		68/66	Verification	4.8 (2.67)	4.4 (2)	0.17
Gispert et al., 2016	Spain	CC	23/45	NIA-AA	MSD	66.78/60.98	Verification	3.34 (1.35)	2.40 (1.14)	0.004
Kleinberger et al., 2014	Germany	CC	56/88	NINCDS-ADRDA	ELISA	70.4/60.7	Verification	0.309 (0.191) relative to an internal standard	0.381 (0.174) relative to an internal standard	0.001

*CC, Case-control study; CS, Cross-sectional study; NIA-AA, National Institute on Aging-Alzheimer's Association; NINCDS–ADRDA, National Institute of Neurological and Communicative Disorders and Stroke and the Alzheimer's Disease and Related Disorders Association; IWG2, the revised proposed International Working Group; ECL immunoassay, electrochemiluminescence immunoassay; ELISA, enzyme-linked immunosorbent assay; MSD, mesoscale discovery electrochemiluminescence platform-based assay; UPLC-MS, ultra-performance liquid chromatography-tandem mass spectrometer; NI, no information; NS, non-significant. *Although the subjects in this article were part of a cohort, the authors requested that lumbar punctures were performed within 1 year of cognitive testing. Therefore, we believed this article should more appropriately be classified as a cross-sectional study.*

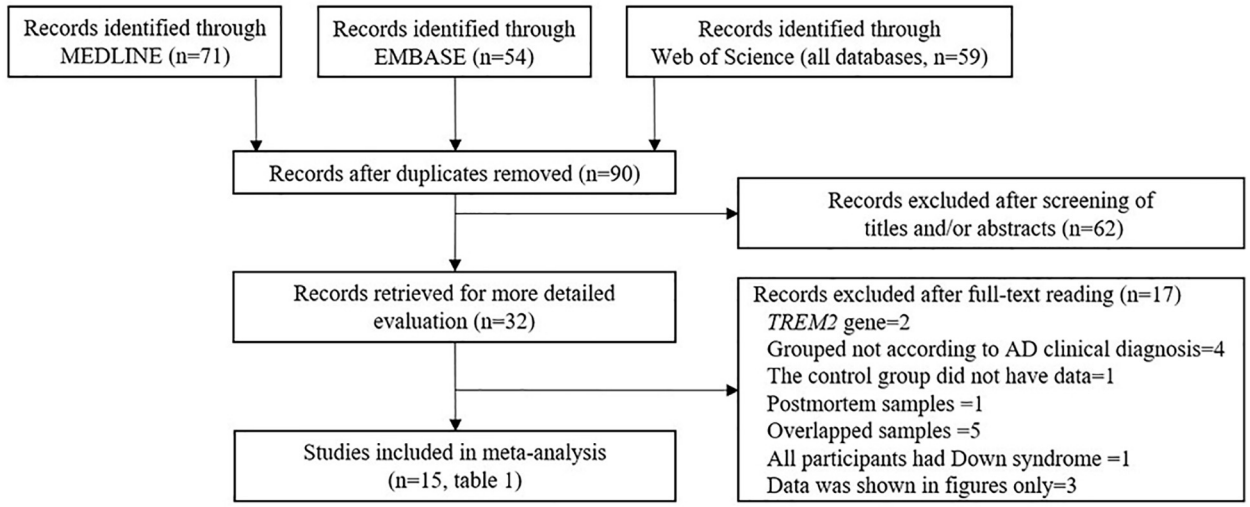

FIGURE 1 | Preferred reporting items for systematic reviews and meta-analyses (PRISMA) flow diagram of the study selection process.

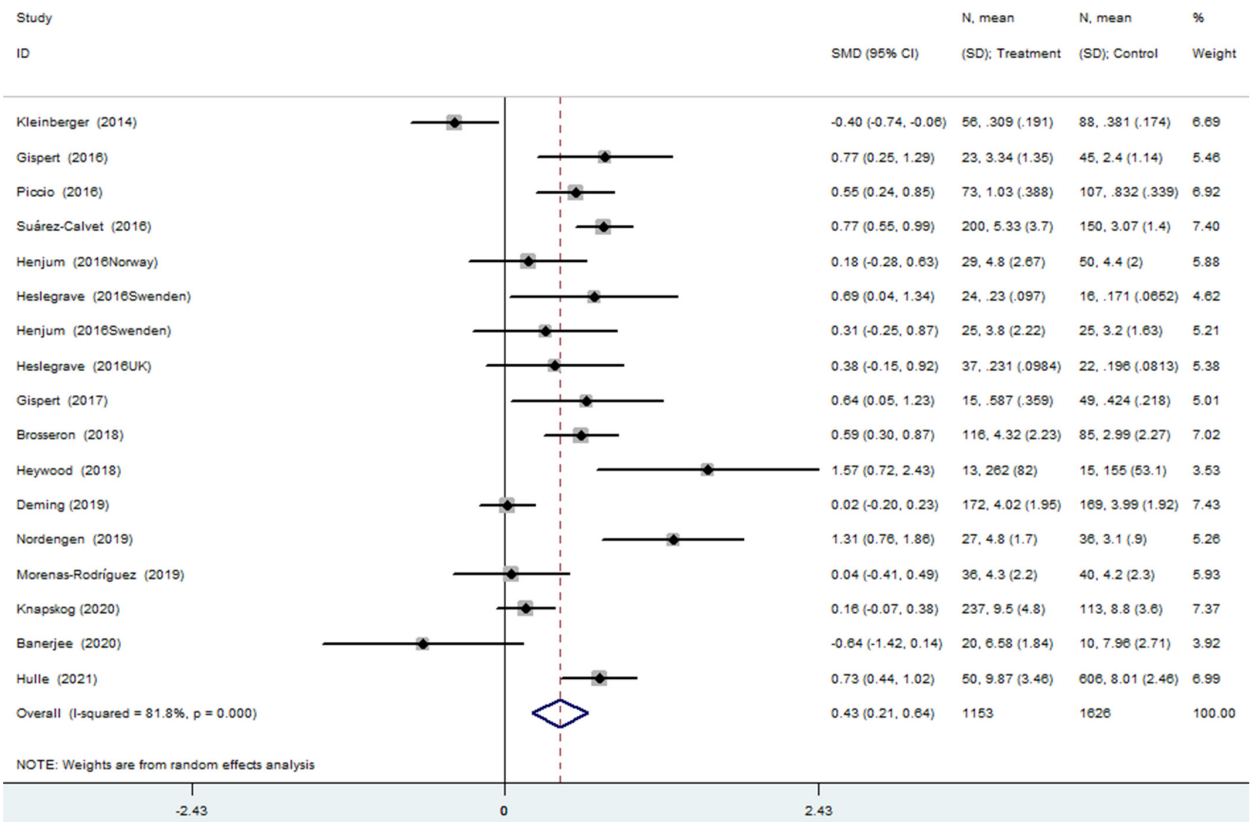

FIGURE 2 | Meta-analysis for the association of the cerebrospinal fluid soluble triggering receptor expressed on myeloid cells 2 (CSF sTREM2) level with Alzheimer's disease (AD) risk using a random effects model.

analysis showed that age difference could explain 33.4% of the between-study variance (coefficient = 0.354, SE = 0.144, $t = 2.45$, and $p = 0.027$).

Subgroup analysis of the 17 comparisons was carried out according to the measurement method and the heterogeneity within each subgroup remained high. The results suggested

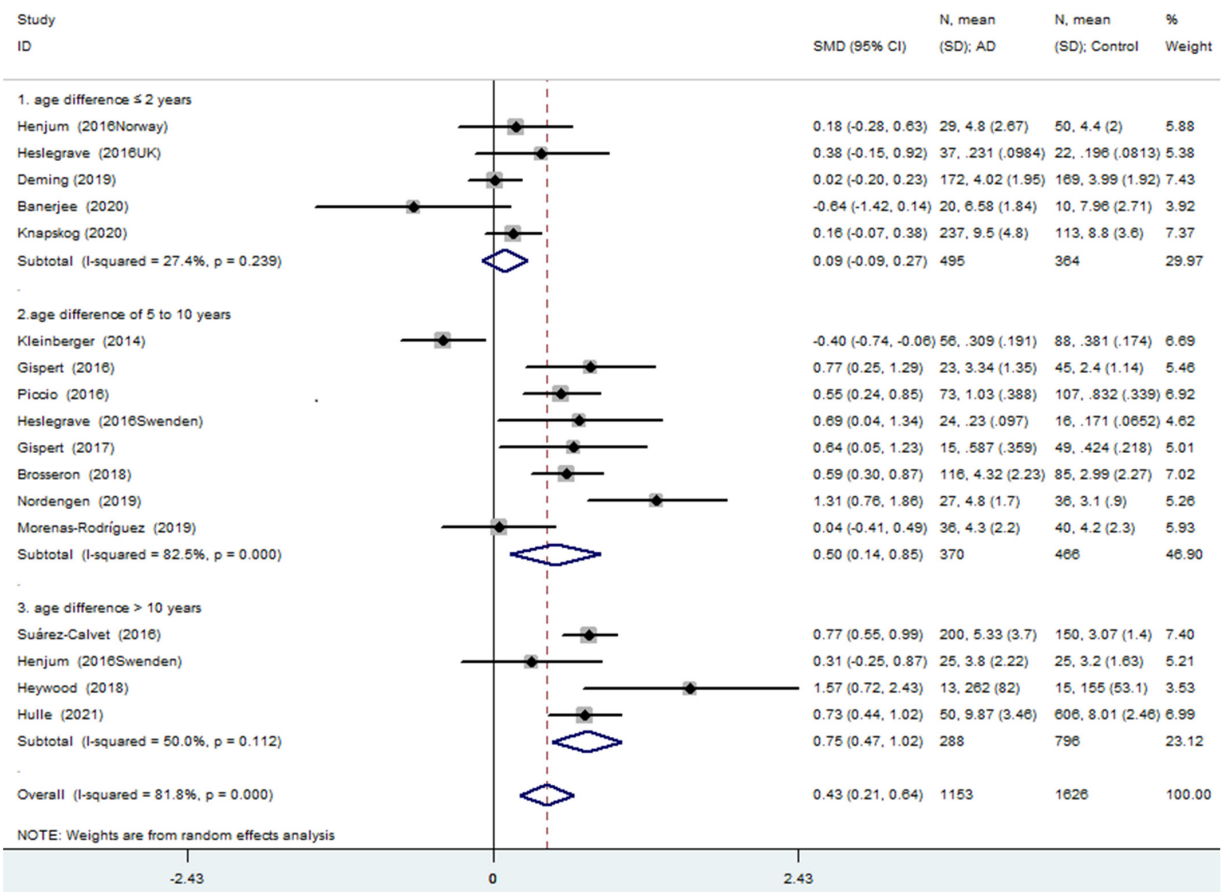

FIGURE 3 | Age difference at a lumbar puncture subgroup analysis using a random effects model.

that the measurement methods might impact the results of the difference in the CSF sTREM2 levels between the patients with AD and controls [ELISA: SMD = 0.280, 95% *CI* (−0.057, 0.616), I^2 = 81.9%; MSD or ECL immunoassay: SMD = 0.463, 95% *CI* (0.144, 0.781), I^2 = 84.1%; UPLC-MS: SMD = 0.810, 95% *CI* (0.179, 1.441), I^2 = 62.5%; **Supplementary Figure 1** and **Table 2**].

Subgroup analysis of the 20 comparisons according to whether the study diagnostic criteria contained AD pathology was conducted. In addition, the data showed a high degree of heterogeneity within each subgroup. The 20 comparisons included the 17 comparisons used for the overall analysis and three additional comparisons. Among the three additional comparisons, two studies (Knapskog et al., 2020; Van Hulle et al., 2021) had group comparisons after further confirmation of AD pathology in addition to the group comparisons according to the clinical AD diagnosis; another one study (Suarez-Calvet et al., 2019) used the same ADNI database as the study by Deming et al. (2019) but had smaller sample size and confirmed AD pathology (as shown in **Supplementary Table 3**). The results suggested that the more demanding the diagnostic criteria, the greater the difference between the two CSF sTREM2 groups [with neuropathologic verification: SMD = 0.477, 95% *CI* (0.236, 0.718), I^2 = 81.0%; no relative information: SMD = 0.342, 95% *CI* (0.060, 0.624), I^2 = 79.2%; **Supplementary Figure 2** and **Table 2**].

Association Between the Cerebrospinal Fluid sTREM2 Levels and Alzheimer's Disease Risk in "Age Difference ≤ 2 Years" Group

A total of five studies with approximately equal age between the patients with AD and cognitively unimpaired controls were included. All of these were the case-control studies involving 495 patients with AD and 364 cognitively unimpaired controls. Two studies were published in 2016 and the other three were published after 2019. Four studies were carried out in Europe and one was in the United States. The mean age of participants in the four studies ranged from 68 to 74 years and the mean age in the remaining study was 62.5 years. In terms of method, two studies used ELISA, two used MSD, and one used UPLC-MS for the measurement of the sTREM2 levels. Three articles had restrictions on the pathological status of AD in both the groups and two had no restrictions.

The meta-analysis of the studies with an age difference within 2 years showed that the CSF sTREM2 levels were not associated

TABLE 2 | Summary of different comparative results of the CSF sTREM2 level with AD risk in all the eligible comparisons.

Category		No. of comparisons	No. of cases	No. of controls	SMD (95% CI)	Z	*p* Value	I^2 %	p_{het}
Overall		17	1,153	1,626	0.428 (0.213, 0.643)	3.90	<0.001	81.8	<0.001
Age difference	≤2 years	5	495	364	0.090 (−0.092, 0.272)	0.97	0.332	27.4	0.239
	5–10 years	8	370	466	0.497 (0.139, 0.855)	2.72	0.007	82.5	<0.001
	>10 years	4	288	796	0.747 (0.472, 1.023)	5.31	<0.001	50.0	0.112
Measurement method	ELISA	7	483	459	0.280 (−0.057, 0.616)	1.63	0.103	81.9	<0.001
	MSD or ECL immunoassay	7	596	1,114	0.463 (0.144, 0.781)	2.85	0.004	84.1	<0.001
	UPLC-MS	3	74	53	0.810 (0.179, 1.441)	2.52	0.012	62.5	0.069
AD pathology	With neuropathologic verification	15*	849	1,316	0.477 (0.236, 0.718)	3.87	<0.001	81.0	<0.001
	No relative information	5	557	1,020	0.342 (0.060, 0.624)	2.38	0.017	79.2	0.001

*SMD, standardized mean difference; p_{het}, p value for heterogeneity; *Compared with the 17 comparisons used for the overall analysis, three additional comparisons were added for the subgroup analysis of AD pathology: specific information was described in the results section.*

with AD and there was little heterogeneity between the studies [SMD = 0.090, 95% *CI* (−0.092, 0.272), I^2 = 27.4%]. Neither the subgroup analysis of the five articles distinguished by the measurement method [ELISA: SMD = 0.161, 95% *CI* (−0.040, 0.363), I^2 = 0%; others: SMD = 0.001, 95% *CI* (−0.413, 0.415), I^2 = 56.2%; **Supplementary Figure 3** and **Table 3**] nor by whether the study diagnostic criteria contained AD pathology [with neuropathologic verification: SMD = 0.103, 95% *CI* (−0.188, 0.394), I^2 = 35.9%; without neuropathologic verification: SMD = 0.083, 95% *CI* (−0.071, 0.237), I^2 = 0%; **Supplementary Figure 4** and **Table 3**] showed association between the CSF sTREM2 level and AD risk.

Publication Bias and Sensitivity Analysis

In the sensitivity analysis of the meta-analysis of "age difference ≤ 2 years" group, one eligible study was excluded at a time to assess the influence of each dataset on the pooled SMD. We observed no changes in the corresponding pooled SMD or in the significance of the results (**Figure 4**), which indicated that our results were significantly stable to the study-selection process. The publication bias was assessed using the Begg's funnel plot and Egger's test (**Figure 5**). The results of Begg's funnel plot and the modified Egger linear regression test showed no publication bias ($Z = -0.24$, $p = 1.000$; $t = -0.34$, $p = 0.753$).

In addition, the meta-analysis of 17 comparisons showed robust results with no publication bias (Begg's test: $Z = 0.45$, $p = 0.650$; Egger's test: $t = 0.62$, $p = 0.542$; **Supplementary Figures 5**, **6**).

DISCUSSION

Main Findings

Our meta-analysis shows that the higher CSF sTREM2 level is related to AD risk, but this association cannot be shown in the studies in which age was matched or showed a similar distribution in the AD and control groups. Greater age differences between the case and control groups would result in a larger difference in CSF sTREM2 levels between groups.

Interpretation

The association between TREM2 and cognitive impairment was first identified through the studies examining the mutations in the patients with Nasu-Hakola disease (NHD) (Paloneva et al., 2002). The patients with NHD are asymptomatic through early adulthood, present with neuropsychiatric symptoms in their fourth decades which are characterized by frontal lobe syndrome and progressive dementia (Montalbetti et al., 2004). The number of microglia was lower in various regions of the brain in the TREM2-deficient mice; and this finding was only confirmed in the aging mice (1–2 years old) (Poliani et al., 2015). Complete lack of *TREM2* affects microglia function in the brain. However, additional risk factors, such as increased age, are probably necessary to elicit neuropsychiatric pathology, at least in mice (Ulland and Colonna, 2018). In neuropathologically normal human brain, the expression of TREM2 is found to be elevated with aging (Forabosco et al., 2013).

TABLE 3 | Summary of different comparative results of CSF sTREM2 level with AD risk in "age difference ≤ 2 years" group.

Category		No. of comparisons	No. of cases	No. of controls	SMD (95% CI)	Z	*p* Value	I^2 %	p_{het}
Age difference ≤ 2 years		5	495	364	0.090 (−0.092, 0.272)	0.97	0.332	27.4	0.239
Measurement method	ELISA	2	266	163	0.161 (−0.040, 0.363)	1.57	0.117	0	0.941
	Others	3	229	201	0.001 (−0.413, 0.415)	< 0.01	0.998	56.2	0.102
AD pathology	With neuropathologic verification	4*	166	204	0.103 (−0.188, 0.394)	0.70	0.487	35.9	0.197
	No relative information	2	409	282	0.083 (−0.071, 0.237)	1.05	0.293	0	0.370

*SMD, standardized mean difference; p_{het}, p value for heterogeneity. *Compared with the five comparisons used for the "age difference ≤ 2 years" analysis, one additional comparison was added for the subgroup analysis of AD pathology: specific information was described in the results section.*

Both the genetic and pathological studies link AD to TREM2. Increased AD risk is thought to be mediated through the reduced TREM2 function (Qin et al., 2021). The TREM2 surface expression declines upon activation of the myeloid cells with the toll-like receptor ligands or inflammatory cytokines. This phenomenon is caused at least in part by the sequential cleavage of membrane-bound TREM2 by proteases that release sTREM2 (Ulland and Colonna, 2018). The sTREM2 levels in CSF could depend on the synthesis rate of TREM2 in largely microglia and peripherally derived macrophages, transport to the cell surface of TREM2, shedding and degradation of the sTREM2 fragment (Henjum et al., 2016). The positive correlation between the CSF sTREM2 level and age is validated in the patients with clinical AD (both MCI and dementia) and clinical cognitively unimpaired individuals, and in the patients with neuropathologically confirmed AD and neuropathologically confirmed cognitively unimpaired individuals (Gispert et al., 2016, 2017; Henjum et al., 2016; Piccio et al., 2016; Suarez-Calvet et al., 2016, 2019; Brosseron et al., 2018; Deming et al., 2019; Morenas-Rodríguez et al., 2019; Knapskog et al., 2020). One Norwegian study with relatively small sample size (27 patients with AD and 36 controls) concluded that the CSF sTREM2 levels were independent of age (Nordengen et al., 2019). In our meta-analysis, the overall analysis showed positive association between the CSF sTREM2 level and AD risk; however, when we only included studies with similar age (age difference ≤ 2 years) between the patients with AD and controls, no association was found between the CSF sTREM2 and AD risk. The result of "age difference ≤ 2 years" subgroup meta-analysis was robust in the sensitivity analysis. Moreover, the heterogeneity between the studies in "age difference ≤ 2 years" subgroup was significantly lower than that in all studies included. These suggest that the negative results of "age difference ≤ 2 years" subgroup should not be ignored. In addition, combining the results of the "age difference of 5–10 years" and "age difference > 10 years" subgroups showed that the difference in CSF sTREM2 between the AD and control groups was positively correlated with the age difference. The large age difference between the AD and control groups is more likely to account for the different CSF sTREM2 levels in the two groups than the association of sTREM2 with AD risk. In addition to the issue of age matching, the mean age of the control group in most of the available studies was less than 65 years old, especially in the studies with a large age difference between the two groups. This makes the results of the overall analysis potentially subject to selection bias. Overall, for future studies we strongly recommend that the age matching between the two groups should be used as an inclusion criterion and that the age of the control group should be fully considered.

An analysis to investigate whether the diagnostic criteria affected the result revealed that the greater difference of CSF sTREM2 between the AD and control groups was shown in the subgroup of studies contained pathological diagnosis. The 95% *CI* of pooled SMD of the subgroup in which the diagnostic criteria were only clinical symptoms was 0.06–0.62, which was very close to "no association." This suggests that the level of CSF sTREM2 may have a higher value as a biomarker for AD when based on pathological diagnosis. However, it must be noted that the studies

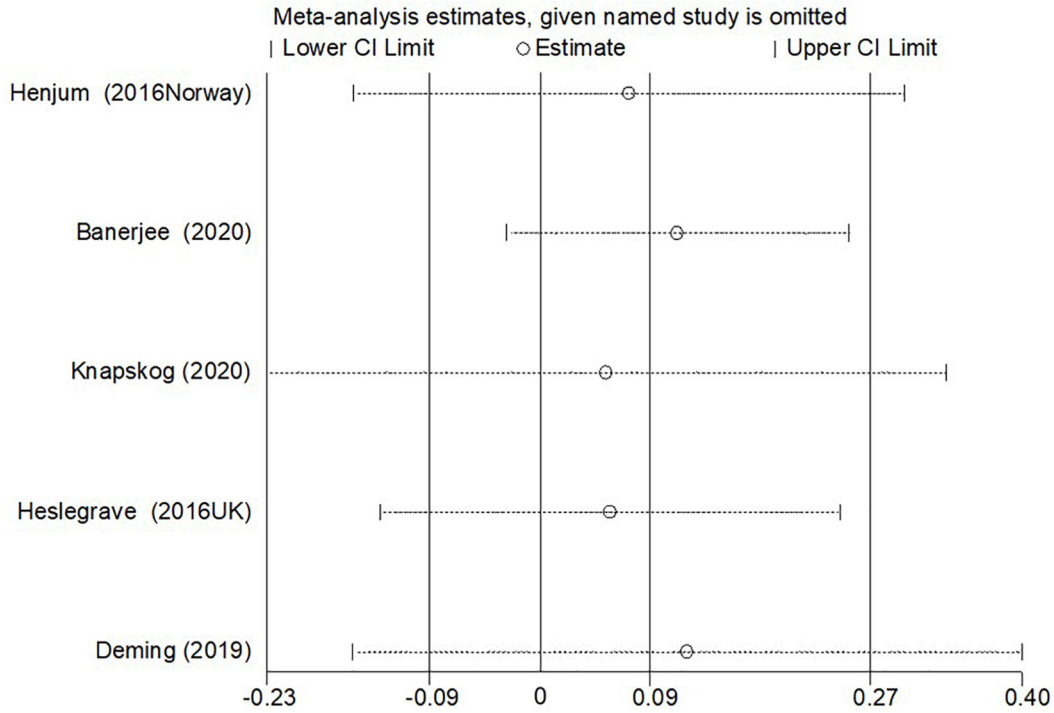

FIGURE 4 | The results of the sensitivity analysis of the CSF sTREM2 level with AD risk in the studies with approximately equal age between the AD group and control group.

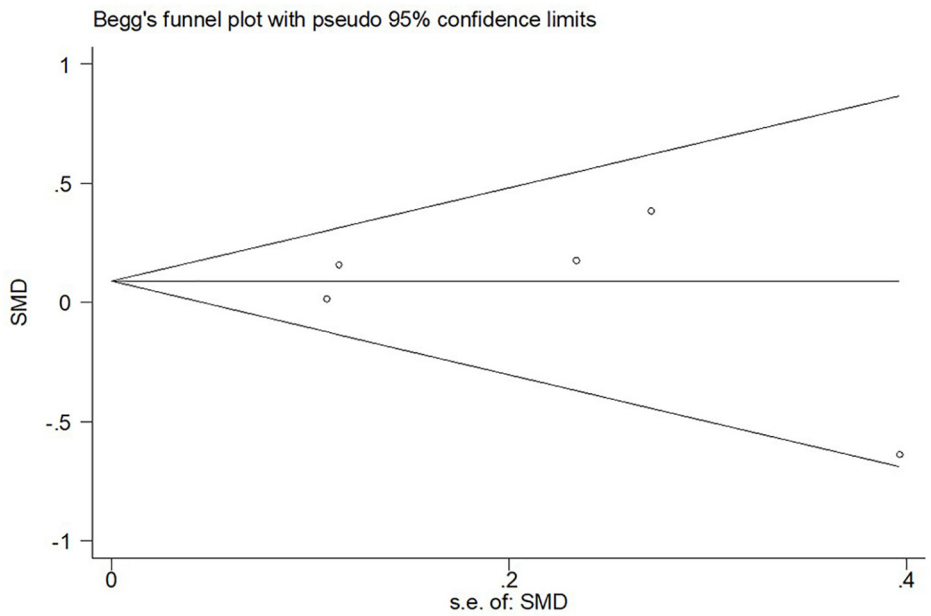

FIGURE 5 | Begg's funnel plot for publication bias test of CSF sTREM2 level with AD risk in the studies with approximately equal age between the AD group and control group.

used uniform pathological diagnosis index and the data showed a high degree of heterogeneity. The reliability of this conclusion needs further study. On the other hand, the clinical diagnosis focusing on the syndromes is still the routine diagnostic strategy because of good accuracy and the limited standardization and utility of biomarkers (Knopman et al., 2001). The value of the

CSF sTREM2 level as a complementary diagnostic marker in the clinical diagnosis may be limited and requires further investigation.

In this study, when the effect of the measurement methods on the results was analyzed, different results were found for different measurement methods. Negative result was shown in the group of studies using ELISA, the simplest and most practical measurement method. Practicality and standardization of CSF sTREM2 as a complementary marker for the clinical diagnosis are yet to be investigated.

This study has certain limitations. First, the heterogeneity within the studies included in the overall analysis was high; therefore, the overall result needs to be interpreted with caution. Second, a total of five studies with approximately equal age between the AD group and the control group were included, involving 495 patients in the AD group and 364 in the control group. It will be necessary to update this meta-analysis in the future when more high-quality literature appears. Last, our study only included the articles written in English, which might have resulted in a language bias.

CONCLUSION

The available high-quality evidence does not support an association between the CSF sTREM2 levels and AD risk. The matching of age between the patients with AD and cognitively unimpaired controls was a major influencing factor in the results.

DATA AVAILABILITY STATEMENT

The original contributions presented in the study are included in the article/**Supplementary Material**, further inquiries can be directed to the corresponding author/s.

AUTHOR CONTRIBUTIONS

SH and NP have searched the databases and extracted the information. YW reviewed the processes of literature search and data extraction. SH did the statistical analysis. SH and CL drafted the manuscript. TZ has revised and expanded the manuscript. All the authors read and approved the final manuscript.

FUNDING

We acknowledge the support by the National Key R&D Program (Nos. 2018YFC1314500 and 2018YFC1314504) and the Natural Science Foundation of Beijing (No. 7212048) within the funding program Open Access Publishing.

SUPPLEMENTARY MATERIAL

The Supplementary Material for this article can be found online at: https://www.frontiersin.org/articles/10.3389/fnagi.2021.775432/full#supplementary-material

REFERENCES

Banerjee, G., Ambler, G., Keshavan, A., Paterson, R. W., Foiani, M. S., Toombs, J., et al. (2020). Cerebrospinal Fluid Biomarkers in Cerebral Amyloid Angiopathy. *J. Alzheimers Dis.* 74, 1189–1201. doi: 10.3233/jad-191254

Bouchon, A., Dietrich, J., and Colonna, M. (2000). Cutting edge: inflammatory responses can be triggered by TREM-1, a novel receptor expressed on neutrophils and monocytes. *J. Immunol.* 164, 4991–4995. doi: 10.4049/jimmunol.164.10.4991

Bronzuoli, M. R., Iacomino, A., Steardo, L., and Scuderi, C. (2016). Targeting neuroinflammation in Alzheimer's disease. *J. Inflamm. Res.* 9, 199–208. doi: 10.2147/JIR.S86958

Brosseron, F., Traschutz, A., Widmann, C. N., Kummer, M. P., Tacik, P., Santarelli, F., et al. (2018). Characterization and clinical use of inflammatory cerebrospinal fluid protein markers in Alzheimer's disease. *Alzheimers Res. Ther.* 10:25. doi: 10.1186/s13195-018-0353-3

Deming, Y., Filipello, F., Cignarella, F., Cantoni, C., Hsu, S., Mikesell, R., et al. (2019). The MS4A gene cluster is a key modulator of soluble TREM2 and Alzheimer's disease risk. *Sci. Transl. Med.* 11:aau2291. doi: 10.1126/scitranslmed.aau2291

Forabosco, P., Ramasamy, A., Trabzuni, D., Walker, R., Smith, C., Bras, J., et al. (2013). Insights into TREM2 biology by network analysis of human brain gene expression data. *Neurobiol. Aging* 34, 2699–2714. doi: 10.1016/j.neurobiolaging.2013.05.001

Gispert, J. D., Monte, G. C., Suarez-Calvet, M., Falcon, C., Tucholka, A., Rojas, S., et al. (2017). The APOE epsilon4 genotype modulates CSF YKL-40 levels and their structural brain correlates in the continuum of Alzheimer's disease but not those of sTREM2. *Alzheimers Dement.* 6, 50–59. doi: 10.1016/j.dadm.2016.12.002

Gispert, J. D., Suárez-Calvet, M., Monté, G. C., Tucholka, A., Falcon, C., Rojas, S., et al. (2016). Cerebrospinal fluid sTREM2 levels are associated with gray matter volume increases and reduced diffusivity in early Alzheimer's disease. *Alzheimers Dement.* 12, 1259–1272. doi: 10.1016/j.jalz.2016.06.005

Guerreiro, R., Wojtas, A., Bras, J., Carrasquillo, M., Rogaeva, E., Majounie, E., et al. (2013). TREM2 variants in Alzheimer's disease. *N. Engl. J. Med.* 368, 117–127. doi: 10.1056/NEJMoa1211851

Henjum, K., Almdahl, I. S., Arskog, V., Minthon, L., Hansson, O., Fladby, T., et al. (2016). Cerebrospinal fluid soluble TREM2 in aging and Alzheimer's disease. *Alzheimers Res. Ther.* 8:17. doi: 10.1186/s13195-016-0182-1

Heslegrave, A., Heywood, W., Paterson, R., Magdalinou, N., Svensson, J., Johansson, P., et al. (2016). Increased cerebrospinal fluid soluble TREM2 concentration in Alzheimer's disease. *Mol. Neurodegener.* 11:3. doi: 10.1186/s13024-016-0071-x

Heywood, W. E., Hallqvist, J., Heslegrave, A. J., Zetterberg, H., Fenoglio, C., Scarpini, E., et al. (2018). CSF pro-orexin and amyloid-beta38 expression in Alzheimer's disease and frontotemporal dementia. *Neurobiol. Aging* 72, 171–176. doi: 10.1016/j.neurobiolaging.2018.08.019

Higgins, J. P. T., Thomas, J., Chandler, J., Cumpston, M., Li, T., Page, M. J., et al. (2021). *Cochrane Handbook for Systematic Reviews of Interventions version 6.2 (updated February 2021)*. London: Cochrane.

Hozo, S. P., Djulbegovic, B., and Hozo, I. (2005). Estimating the mean and variance from the median, range, and the size of a sample. B*MC Med Res Methodol* 5:13. doi: 10.1186/1471-2288-5-13

Jonsson, T., Stefansson, H., Steinberg, S., Jonsdottir, I., Jonsson, P. V., Snaedal, J., et al. (2013). Variant of TREM2 associated with the risk of Alzheimer's disease. *N. Engl. J. Med.* 368, 107–116. doi: 10.1056/NEJMoa1211103

Kleinberger, G., Yamanishi, Y., Suarez-Calvet, M., Czirr, E., Lohmann, E., Cuyvers, E., et al. (2014). TREM2 mutations implicated in neurodegeneration impair cell surface transport and phagocytosis. *Sci. Transl. Med.* 6:243ra286. doi: 10.1126/scitranslmed.3009093

Knapskog, A. B., Henjum, K., Idland, A. V., Eldholm, R. S., Persson, K., Saltvedt, I., et al. (2020). Cerebrospinal fluid sTREM2 in Alzheimer's disease: comparisons

between clinical presentation and AT classification. *Sci. Rep.* 10:15886. doi: 10.1038/s41598-020-72878-8

Knopman, D. S., DeKosky, S. T., Cummings, J. L., Chui, H., Corey-Bloom, J., Relkin, N., et al. (2001). Practice parameter: diagnosis of dementia (an evidence-based review). Report of the Quality Standards Subcommittee of the American Academy of Neurology. *Neurology* 56, 1143–1153. doi: 10.1212/wnl.56.9.1143

Liu, D., Cao, B., Zhao, Y., Huang, H., McIntyre, R. S., Rosenblat, J. D., et al. (2018). Soluble TREM2 changes during the clinical course of Alzheimer's disease: A meta-analysis. *Neurosci. Lett.* 686, 10–16. doi: 10.1016/j.neulet.2018.08.038

Montalbetti, L., Soragna, D., Ratti, M. T., Bini, P., Buscone, S., and Moglia, A. (2004). Nasu-Hakola disease: a rare entity in Italy. Critical review of the literature. *Funct. Neurol.* 19, 171–179.

Morenas-Rodríguez, E., Alcolea, D., Suárez-Calvet, M., Muñoz-Llahuna, L., Vilaplana, E., Sala, I., et al. (2019). Different pattern of CSF glial markers between dementia with Lewy bodies and Alzheimer's disease. *Sci. Rep.* 9:7803. doi: 10.1038/s41598-019-44173-8

Morris, J. C. (2005). Early-stage and preclinical Alzheimer disease. *Alzheimer Dis. Assoc. Disord.* 19, 163–165. doi: 10.1097/01.wad.0000184005.22611.cc

Nordengen, K., Kirsebom, B. E., Henjum, K., Selnes, P., Gisladottir, B., Wettergreen, M., et al. (2019). Glial activation and inflammation along the Alzheimer's disease continuum. *J. Neuroinflamm.* 16:46. doi: 10.1186/s12974-019-1399-2

Paloneva, J., Manninen, T., Christman, G., Hovanes, K., Mandelin, J., Adolfsson, R., et al. (2002). Mutations in two genes encoding different subunits of a receptor signaling complex result in an identical disease phenotype. *Am. J. Hum. Genet.* 71, 656–662. doi: 10.1086/342259

Piccio, L., Deming, Y., Del-Águila, J. L., Ghezzi, L., Holtzman, D. M., Fagan, A. M., et al. (2016). Cerebrospinal fluid soluble TREM2 is higher in Alzheimer disease and associated with mutation status. *Acta Neuropathol.* 131, 925–933. doi: 10.1007/s00401-016-1533-5

Poliani, P. L., Wang, Y., Fontana, E., Robinette, M. L., Yamanishi, Y., Gilfillan, S., et al. (2015). TREM2 sustains microglial expansion during aging and response to demyelination. *J. Clin. Invest.* 125, 2161–2170. doi: 10.1172/JCI77983

Qin, Q., Teng, Z., Liu, C., Li, Q., Yin, Y., and Tang, Y. (2021). TREM2, microglia, and Alzheimer's disease. *Mech. Ageing Dev.* 195:111438. doi: 10.1016/j.mad.2021.111438

Sessa, G., Podini, P., Mariani, M., Meroni, A., Spreafico, R., Sinigaglia, F., et al. (2004). Distribution and signaling of TREM2/DAP12, the receptor system mutated in human polycystic lipomembraneous osteodysplasia with sclerosing leukoencephalopathy dementia. *Eur. J. Neurosci.* 20, 2617–2628. doi: 10.1111/j.1460-9568.2004.03729.x

Suarez-Calvet, M., Kleinberger, G., Araque Caballero, M. A., Brendel, M., Rominger, A., Alcolea, D., et al. (2016). sTREM2 cerebrospinal fluid levels are a potential biomarker for microglia activity in early-stage Alzheimer's disease and associate with neuronal injury markers. *EMBO Mol. Med.* 8, 466–476. doi: 10.15252/emmm.201506123

Suarez-Calvet, M., Morenas-Rodriguez, E., Kleinberger, G., Schlepckow, K., Araque Caballero, M. A., Franzmeier, N., et al. (2019). Early increase of CSF sTREM2 in Alzheimer's disease is associated with tau related-neurodegeneration but not with amyloid-beta pathology. *Mol. Neurodegener.* 14:1. doi: 10.1186/s13024-018-0301-5

Ulland, T. K., and Colonna, M. (2018). TREM2 - a key player in microglial biology and Alzheimer disease. *Nat. Rev. Neurol.* 14, 667–675. doi: 10.1038/s41582-018-0072-1

Ulland, T. K., Song, W. M., Huang, S. C., Ulrich, J. D., Sergushichev, A., Beatty, W. L., et al. (2017). TREM2 Maintains Microglial Metabolic Fitness in Alzheimer's Disease. *Cell* 170, 649–663e613. doi: 10.1016/j.cell.2017.07.023

Van Hulle, C., Jonaitis, E. M., Betthauser, T. J., Batrla, R., Wild, N., Kollmorgen, G., et al. (2021). An examination of a novel multipanel of CSF biomarkers in the Alzheimer's disease clinical and pathological continuum. *Alzheimers Dement.* 17, 431–445. doi: 10.1002/alz.12204

Wu, K., Byers, D. E., Jin, X., Agapov, E., Alexander-Brett, J., Patel, A. C., et al. (2015). TREM-2 promotes macrophage survival and lung disease after respiratory viral infection. *J. Exp. Med.* 212, 681–697. doi: 10.1084/jem.20141732

Conflict of Interest: The authors declare that the research was conducted in the absence of any commercial or financial relationships that could be construed as a potential conflict of interest.

Publisher's Note: All claims expressed in this article are solely those of the authors and do not necessarily represent those of their affiliated organizations, or those of the publisher, the editors and the reviewers. Any product that may be evaluated in this article, or claim that may be made by its manufacturer, is not guaranteed or endorsed by the publisher.

Copyright © 2021 Hu, Pan, Liu, Wang and Zhang. This is an open-access article distributed under the terms of the Creative Commons Attribution License (CC BY). The use, distribution or reproduction in other forums is permitted, provided the original author(s) and the copyright owner(s) are credited and that the original publication in this journal is cited, in accordance with accepted academic practice. No use, distribution or reproduction is permitted which does not comply with these terms.

frontiers in Aging Neuroscience

ORIGINAL RESEARCH
published: 15 November 2021
doi: 10.3389/fnagi.2021.770528

Region-Specific Neurovascular Decoupling Associated With Cognitive Decline in Parkinson's Disease

Song'an Shang[1†], Hongying Zhang[2†], Yuan Feng[1], Jingtao Wu[2], Weiqiang Dou[3], Yu-Chen Chen[1] and Xindao Yin[1*]*

[1] Department of Radiology, Nanjing First Hospital, Nanjing Medical University, Nanjing, China, [2] Department of Radiology, Clinical Medical College, Yangzhou University, Yangzhou, China, [3] MR Research China, GE Healthcare, Beijing, China

OPEN ACCESS

Edited by:
Jiehui Jiang,
Shanghai University, China

Reviewed by:
Jiajia Zhu,
First Affiliated Hospital of Anhui Medical University, China
Ana Margarida Ledo,
University of Coimbra, Portugal

***Correspondence:**
Yu-Chen Chen
chenyuchen1989@126.com
Xindao Yin
y.163yy@163.com

[†] *These authors have contributed equally to this work*

Received: *04 September 2021*
Accepted: *11 October 2021*
Published: *15 November 2021*

Citation:
Shang S, Zhang H, Feng Y, Wu J, Dou W, Chen Y-C and Yin X (2021) Region-Specific Neurovascular Decoupling Associated With Cognitive Decline in Parkinson's Disease. Front. Aging Neurosci. 13:770528. doi: 10.3389/fnagi.2021.770528

Background: Cognitive deficits are prominent non-motor symptoms in Parkinson's disease (PD) and have been shown to involve the neurovascular unit (NVU). However, there is a lack of sufficient neuroimaging research on the associated modulating mechanisms. The objective of this study was to identify the contribution of neurovascular decoupling to the pathogenesis of cognitive decline in PD.

Methods: Regional homogeneity (ReHo), a measure of neuronal activity, and cerebral blood flow (CBF), a measure of vascular responses, were obtained from patients with PD with mild cognitive impairment (MCI) and normal cognition (NC) as well as matched healthy controls (HCs). Imaging metrics of neurovascular coupling (global and regional CBF-ReHo correlation coefficients and CBF-ReHo ratios) were compared among the groups.

Results: Neurovascular coupling was impaired in patients with PD-MCI with a decreased global CBF-ReHo correlation coefficient relative to HC subjects ($P < 0.05$). Regional dysregulation was specific to the PD-MCI group and localized to the right middle frontal gyrus, right middle cingulate cortex, right middle occipital gyrus, right inferior parietal gyrus, right supramarginal gyrus, and right angular gyrus ($P < 0.05$). Compared with HC subjects, patients with PD-MCI showed higher CBF-ReHo ratios in the bilateral lingual gyri (LG), bilateral putamen, and left postcentral gyrus and lower CBF-ReHo ratios in the right superior temporal gyrus, bilateral middle temporal gyri, bilateral parahippocampal gyri, and right inferior frontal gyrus. Relative to the HC and PD-NC groups, the PD-MCI group showed an increased CBF-ReHo ratio in the left LG, which was correlated with poor visual–spatial performance ($r = -0.36$ and $P = 0.014$).

Conclusion: The involvement of neurovascular decoupling in cognitive impairment in PD is regionally specific and most prominent in the visual–spatial cortices, which could potentially provide a complementary understanding of the pathophysiological mechanisms underlying cognitive deficits in PD.

Keywords: Parkinson's disease, neurovascular coupling, cognitive impairment, magnetic resonance imaging, regional homogeneity, cerebral blood flow

INTRODUCTION

Parkinson's disease (PD) is an age-related neurodegenerative disorder with primary pathological features of selective and progressive dopamine depletion and Lewy body deposition, accounting for clinical manifestations with cardinal motor disturbances as well as a spectrum of non-motor dysfunction (Kalia and Lang, 2015; Dickson, 2018). The investigation of cognitive impairment, a prevalent non-motor symptom, has been highlighted due to concerns about its early onset and the associated risk of progression to dementia (Aarsland et al., 2017; Baiano et al., 2020; Ryman and Poston, 2020). Notably, mild cognitive impairment in PD (PD-MCI) has been defined as a transitional stage between normal aging and dementia with a prevalence of 20–30% among those with PD (Baiano et al., 2020). In contrast with the well-characterized pathology in motor symptoms, the cognitive status in patients with PD-MCI deteriorates through the integration of pathological effects, including abnormal neurotransmitter systems (dopaminergic and cholinergic systems) (Olde Dubbelink et al., 2014) and aberrant protein aggregates (α-synuclein and amyloid-β) (Hepp et al., 2016). A comprehensive understanding of the pathophysiological mechanisms in PD-MCI is still needed.

Recent studies have suggested that neurovascular coupling, one of the pivotal mechanisms that maintain homeostasis in the cerebral microenvironment, is disrupted in several pathological conditions, such as AD (Solis et al., 2020), cerebrovascular diseases (Cai et al., 2017), and traumatic brain injury (Jang et al., 2017). In fact, as the primary components of the neurovascular unit (NVU), neurons and the vasculature could also be vulnerable to the involvement of neuroinflammation and oxidative stress in PD (Campolo et al., 2019). Emerging evidence based on a blood oxygen level-dependent (BOLD) approach has revealed that patients with PD-MCI experienced aberrant neuronal activity mainly in cortices in the default mode network (DMN) and motor network, which corresponded to symptomatic presentations (Amboni et al., 2015; Pan et al., 2017; Bezdicek et al., 2018). Meanwhile, cerebral blood flow (CBF) can be quantified as a non-invasive surrogate of metabolic demand by the arterial spin labeling (ASL) approach; such studies with patients with PD-MCI have shown a distribution of parietal–occipital hypoperfusion and a PD-related perfusion pattern (PDRP) that were analogous to radiotracer findings (Melzer et al., 2011; Arslan et al., 2020). However, there is still a paucity of neuroimaging investigations regarding neurovascular decoupling and the consequent cognitive deficits in PD-MCI.

As a functional complex, alterations in neuronal activity and cerebral perfusion in the NVU are interactive rather than independent (Phillips et al., 2016). Recently, a novel imaging metric derived from MRI techniques (BOLD and ASL) was introduced for the assessment of NVU function (Liang et al., 2013). Although some regions of neurovascular decoupling were shown to be involved in cognitive impairment in cerebrovascular disease (Liu et al., 2021), whether the heterogeneous cognitive profiles in PD-MCI are potentially driven by NVU dysregulation is inconclusive. Therefore, this study aimed to investigate neurovascular decoupling in PD-MCI by integrating regional homogeneity (ReHo) information, a measure of neuronal activity, and CBF information, a measure of cerebral perfusion. The intergroup differences in the CBF-ReHo coupling coefficient at the global and regional levels and CBF-ReHo ratios at a voxel-wise level were compared among patients with PD-MCI, patients with PD and normal cognition (PD-NC), and healthy controls (HCs). The correlations between neurovascular decoupling and clinical variables were further explored. We hypothesized that the responsible cortices would be more vulnerable to neurovascular decoupling, yielding potential imaging biomarkers for insight into the underlying pathological processes.

MATERIALS AND METHODS

Patients

In total, 92 right-handed patients with PD from the clinic of movement disorders and 46 matched HC in terms of age, sex, handedness, and years of education from the local community were recruited from May 2019 to April 2021. This study was approved by the Research Ethics Committee of Nanjing Medical University, and written informed consent was obtained from all subjects 24 h before study entry. The Unified Parkinson's Disease Rating Scale Part III (UPDRS-III) and Hoehn–Yahr (H-Y) scale were scored for disease severity and stage of PD, respectively. Levodopa equivalent daily dose (LEED) was also calculated in patients with PD. All subjects received neuropsychological assessments, including the Montreal Cognitive Assessment (MoCA), Hopkins Verbal Learning Test-Revised (HVLT-R), Symbol Digit Modalities Test (SDMT), Trail Making Test (TMT)-A and TMT-B, Boston Naming Test (BNT), and Benton's Judgment of Line Orientation (JoLO), for the assessment of global cognition and five particular cognitive domains. Meanwhile, the Clinical Dementia Rating (CDR) was administered for the evaluation of dementia. All patients were instructed to withhold medication administration 12 h prior to clinical assessment and MRI data acquisition.

Patients were enrolled based on the following inclusion criteria: (1) patients met the United Kingdom Parkinson's

Disease Society Brain Bank Clinical Diagnostic Criteria (Hughes et al., 1992); (2) patients were at a disease stage within the H-Y stages I–III; (3) there was an absence of dementia based on the MDS diagnostic criteria for PD with dementia (Emre et al., 2007); and (4) antiparkinsonian medications with a stable and optimized daily dose were being administered for more than 4 weeks before enrollment. The HC subjects were required to be free of cognitive complaints and obtain scores in the normal range in the neuropsychological assessments. The exclusion criteria for all participants were as follows: (1) atypical or secondary parkinsonism; (2) other diseases involving the central neural system, including neurological or psychiatric diseases, cerebrovascular accident, trauma, and brain tumor; (3) history of alcoholism, smoking, any chronic disorders, or neurological surgery that affect cognitive status; (4) psychotropic or anticholinergic treatment; (5) excessive head motion (displacement >3 mm or rotation >3.0°) during the data preprocessing procedures; and (6) any MRI contraindication or severe hearing or visual loss. Subsequently, patients with PD who fulfilled the proposed Movement Disorders Society Task Force criteria for level I were included in the PD-MCI group, whereas other patients with PD were included in the PD-NC group. The demographic and clinical details are listed in **Table 1**.

MRI Data Acquisition

MRI data for each individual were acquired using a 3.0-Tesla MRI scanner (Discovery MR750, GE Medical Systems, Milwaukee, WI, United States) with a commercial eight-channel phased-array head coil. During acquisition, all subjects wore headphones, were instructed to lie still in a supine position, and to stay awake with their eyes closed. Functional data of the whole brain were acquired using a gradient recalled echo echo-planar imaging sequence as follows: repetition time (TR), 2,000 ms; echo time (TE), 30 ms; flip angle (FA), 90°; slice thickness, 4 mm without gap; field of view (FOV), 240 mm × 240 mm; matrix size, 64 × 64; voxel size, 4.0 mm × 4.0 mm × 4.0 mm; number of time points, 240; each frame included 35 continuous slices that covered the whole brain volume; and total scan time, 480 s. Perfusion data were obtained using a background suppressed three-dimensional pseudocontinuous ASL (pCASL) sequence with the following parameters: TR, 10.5 ms; TE, 4.9 ms; FA, 111°; slice thickness, 4 mm without gap; FOV, 240 mm × 240 mm; matrix size, 128 × 128; labeling duration, 1,500 ms; postlabeling delay, 2,025 ms; number of excitations, 3; number of slices, 36; 8 arms with 512 points per arm; total scan time, 284 s; and units, ml/100 g/min. This sequence also included a fluid-suppressed proton density acquisition with the same image dimensions as the pCASL but without radio frequency labeling for CBF quantitation and image registration. Whole-brain structural images were also acquired using a three-dimensional high-resolution brain volume imaging sequence as follows: TR, 12 ms; TE, 5.1 ms; inversion time, 450 ms; FA, 15°; slice thickness, 1 mm with no gaps; FOV, 240 mm × 240 mm; matrix size, 256 × 256; voxel size, 1 mm × 1 mm × 1 mm; number of slices, 172; and total scan time, 320 s.

Functional Data Preprocessing and Analysis

Data preprocessing was implemented using the Data Processing and Analysis for Brain Imaging toolkit (DPABI, version 4.6[1]) on the basis of statistical parametric mapping (SPM, version 12[2]) running on the MATLAB 2018a platform (MathWorks, Natick, MA, United States). In brief, the main preprocessing steps were as follows: removal of the initial 10 time points; slice timing of the remaining slices; realignment for head-motion correction by excluding subjects with excessive head movement (displacement >3 mm or rotation >3.0°); coregistration based on segmented T1 images; spatial normalization to Montreal Neurological Institute (MNI) space (resampling of 3 mm × 3 mm × 3 mm); linear detrending and temporal band-pass (0.01–0.08 Hz) filtering; and regression of nuisance covariates (i.e., Friston-24 parameters, global signals, white matter signals, and cerebrospinal fluid signals).

Regional homogeneity was applied to assess the regional signal synchronizations (Zang et al., 2004). For each individual, Kendall's coefficient concordance (KCC) was calculated to measure the similarity between the time series of a functional voxel and its 26 neighboring voxels within a whole-brain mask. Finally, the voxel-wise ReHo map was standardized to a *z*-scored map by subtracting the global mean value of gray matter (GM) and then dividing by the SD and further spatially smoothed with a 6-mm full-width at half-maximum (FWHM) Gaussian kernel.

Perfusion Data Preprocessing and Analysis

The CBF images for each subject were obtained using FuncTool software (Version 4.6, GE Medical Systems, Milwaukee, WI, United States) based on a general kinetic model for ASL (Ambarki et al., 2015) and were preprocessed using SPM12 running on the MATLAB 2018a platform. The main preprocessing procedures were as follows: motion and magnetic inhomogeneity correction by excluding subjects with excessive head movement (displacement >3 mm or rotation >3.0°); coregistration based on segmented T1 images and spatial normalization to MNI space (resampling of 3 mm × 3 mm × 3 mm); removal of non-brain tissues; *z*-scored standardization; and spatial smoothing with a 6-mm FWHM Gaussian kernel. Specifically, a relative increase in perfusion with respect to other groups was interpreted as preserved perfusion as previously described.

Neurovascular Coupling Quantitative Analysis

The neurovascular coupling quantitative analysis was performed using the DPABI toolkit. The neurovascular coupling of each subject was quantitatively assessed by calculating the correlation coefficient between the *z*-ReHo map and *z*-CBF map across voxels at the whole-brain GM level (Zhu et al., 2017; Guo et al., 2019). Regional neurovascular coupling (Hu et al., 2019)

[1]http://rfmri.org/dpabi

[2]http://www.fil.ion.ucl.ac.uk/spm

TABLE 1 | Demographic characteristics and scores of clinical assessments.

	HC (n = 46)	PD-NC (n = 47)	PD-MCI (n = 45)	P
Age	61.93 ± 6.51	62.17 ± 10.27	63.11 ± 9.39	0.80
Sex (M/F)	24/22	26/21	24/21	0.95
Education (years)	10.78 ± 3.48	10.53 ± 3.49	10.04 ± 3.50	0.87
Disease duration (years)	N/A	3.55 ± 2.48	3.76 ± 2.33	0.57
UPDRS-III	N/A	28.64 ± 11.19	31.36 ± 10.41	0.25
H-Y stage	N/A	1.66 ± 0.72	1.89 ± 0.82	0.20
LEED	N/A	430.68 ± 146.75	454.04 ± 151.62	0.46
MoCA	28.20 ± 1.19	27.64 ± 1.49	21.16 ± 2.28[a,b]	<0.001
HVLT-R (total)	21.87 ± 3.99	20.77 ± 4.26	18.62 ± 3.58[a,b]	<0.001
HVLT-R (delayed)	7.80 ± 2.21	7.15 ± 2.48	6.51 ± 2.42[a]	<0.001
HVLT-R (recognition)	8.67 ± 2.16	8.26 ± 2.26	7.73 ± 2.03	0.12
SDMT	46.04 ± 11.61	42.43 ± 11.86	37.67 ± 13.08[a]	0.006
TMT-A	62.20 ± 15.61	68.06 ± 19.34	76.11 ± 17.57[a,b]	0.001
TMT-B	123.43 ± 31.43	137.96 ± 33.79	155.02 ± 43.30[a,b]	<0.001
BNT	24.72 ± 3.23	23.17 ± 3.61	18.98 ± 5.17[a,b]	<0.001
JoLO	22.63 ± 4.93	21.02 ± 5.43	17.02 ± 5.14[a,b]	<0.001

Data were represented as mean ± SD; N/A indicates not applicable. [a]Indicates significant difference to the HC group. [b]Indicates significant difference to the PD-NC group.

HC, healthy control; PD, Parkinson's disease; NC, normal cognition; MCI, mild cognitive impairment; M, male; F, female; UPDRS, Unified Parkinson's Disease Rating Scale; H-Y, Hoehn–Yahr; LEED, levodopa equivalent daily dose; MoCA, Montreal Cognitive Assessment; HVLT, Hopkins Verbal Learning Test-Revised; SDMT, Symbol Digit Modalities Test; TMT, Trail Making Test; BNT, Boston Naming Test; JoLO, Benton's Judgment of Line Orientation.

was further analyzed by dividing the whole-brain GM into 90 independent regions based on the automated anatomical labeling (AAL) atlas (Rolls et al., 2020). Given that the spatial preprocessing (registration and spatial smoothing) would induce high dependence of neighboring voxels, the effective degree of freedom (df_{eff}) in across-voxel correlation analyses would be much smaller than the number of voxels within the GM mask. Thus, we conducted the estimation for df_{eff} of across-voxel correlations with the following equation (Liang et al., 2013; Zhu et al., 2017):

$$df_{eff} = \frac{N}{(\mathrm{FWHMx} \times \mathrm{FWHMy} \times \mathrm{FWHMz})/\mathrm{v}} - 2$$

where v represents the voxel volume (3 mm × 3 mm × 3 mm), N represents the number of voxels used in the analyses (48,539), and FWHMx × FWHMy × FWHMz is the average smoothness of the CBF and ReHo maps (9.50 mm × 10.04 mm × 9.87 mm). In this study, df_{eff} of across-voxel correlations was 1,390. In addition, CBF-ReHo ratios (Liang et al., 2013), designed to reflect metabolic energy per unit of neuronal activity, across voxels within the GM mask were calculated with the original values of the metrics and subsequently z-scored for standardization.

Statistical Analysis

The Kolmogorov–Smirnov test was employed to assess demographic and clinical data normality. Intergroup differences in sex distribution and age were analyzed using Chi-square tests or one-way analysis of variance (ANOVA), respectively. The UPDRS-III scores, H-Y stage, disease duration, and LEED between PD subgroups were compared using Mann–Whitney U tests. Kruskal–Wallis H tests (for years of education and MoCA scores) and ANOVAs (for scores of five cognitive domains, metrics of whole-brain GM, and regional neurovascular coupling) were utilized for comparisons among groups, followed by *post hoc* tests with Bonferroni correction. The above analyses were performed using SPSS 22.0 software (version 22.0, SPSS Inc., Chicago, IL, United States), and the significance level was set as a P-value < 0.05.

A voxel-wise one-way analysis of covariance within the GM mask was applied using SPM12 software for the investigations of differences (e.g., with CBF-ReHo ratios) among groups, followed by *post hoc* analysis within the significant clusters. The significance level was set at an uncorrected voxel-wise threshold of $P < 0.001$ and a familywise error (FWE)-corrected cluster-wise threshold of $P < 0.05$. The mean values of each cluster that showed significant intergroup differences were extracted. By using SPSS 19.0 software, the mean values of clusters (CBF-ReHo ratio, CBF values, and ReHo values) among three groups were compared using ANOVA, followed by *post hoc* test with Bonferroni correction; Pearson correlation tests (for normally distributed scores) or Spearman's rank correlation tests (for non-normally distributed scores) were further applied to explore potential associations between values of these clusters and scores from the clinical assessments. A statistically significant threshold was set at a P-value < 0.05. The above analyses were adjusted for covariates, including age, sex, years of education, and GM volume (obtained from segmented T1 data).

RESULTS

Demographic and Neuropsychological Characteristics

The demographic and neuropsychological characteristics of the three groups are summarized in **Table 1**. There were no significant differences in terms of age, sex, or education among

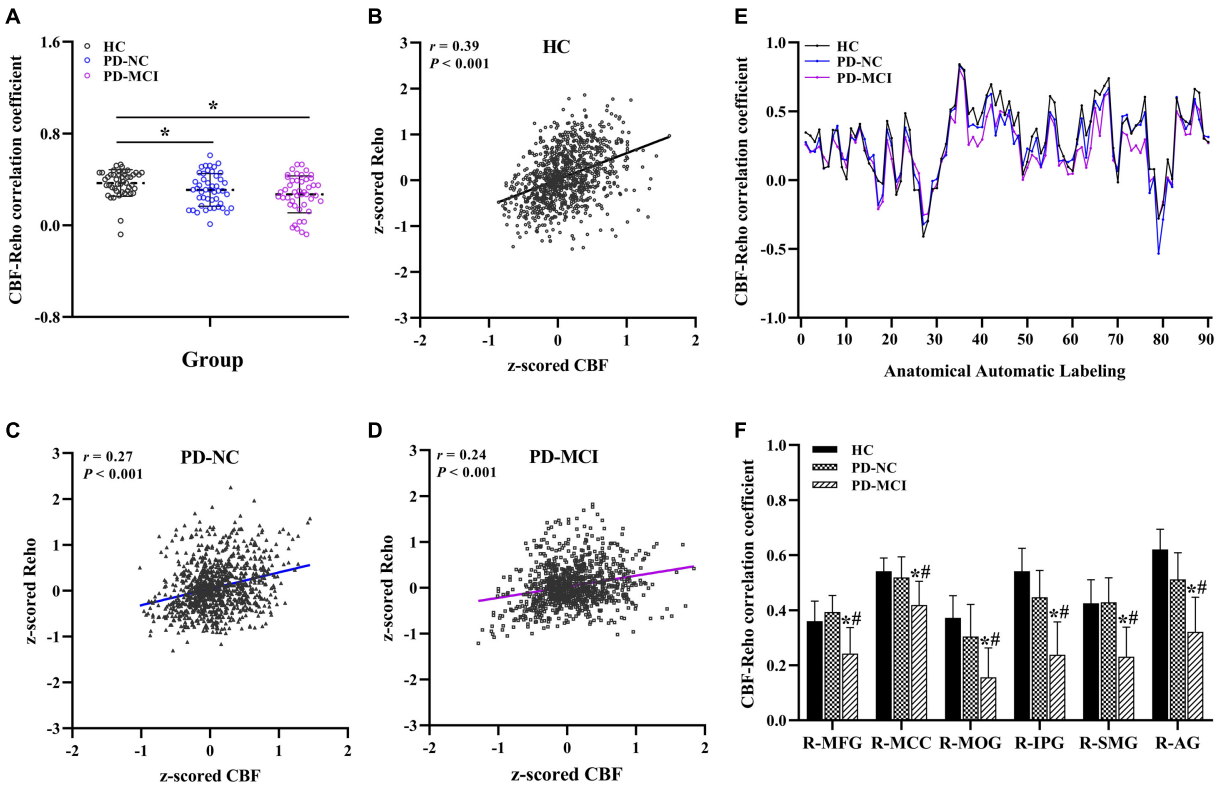

FIGURE 1 | Global and regional neurovascular coupling among groups. The mean CBF-ReHo coupling at the global level among groups **(A)** and representative scatter plots of the spatial correlations across voxels in individuals **(B–D)**; regional neurovascular coupling of CBF-ReHo **(E)** and the significantly different brain regions in the PD-MCI group as compared with HC and PD-NC groups **(F)**. *Indicates significant intergroup difference to HC group; #indicates significant intergroup difference to PD-NC group. CBF, cerebral blood flow; ReHo, regional homogeneity; HC, healthy control; PD, Parkinson's disease; NC, normal cognition; MCI, mild cognitive impairment; R, right; L, left; MFG, middle frontal gyrus; MCC, middle cingulate cortex; MOG, middle occipital gyrus; IPG, inferior parietal gyrus; SMG, supramarginal gyrus; AG, angular gyrus.

the three groups or in disease duration, disease severity, H-Y stage, or LEED between the PD-NC and PD-MCI groups ($P > 0.05$). For the neuropsychological comparisons, patients with PD-MCI suffered from significant impairments within the global cognition and five domains compared with the other two groups ($P < 0.05$). None of the significant differences between the HC and PD-NC groups survived regarding global cognition or the five cognitive domains ($P > 0.05$).

Alterations in Whole-Brain and Regional Cerebral Blood Flow-Regional Homogeneity Correlation Coefficients

Significant differences in the CBF-ReHo correlation coefficients at the whole-brain GM level were found among the groups ($P = 0.005$) (**Figures 1A–D**). Both the PD-MCI and PD-NC groups showed significantly reduced coefficients compared with the HC group ($P = 0.001$ and $P = 0.044$). Although no significant intergroup differences between the PD-NC and PD-MCI groups survived, a downward trend was observed among the groups. Regarding comparisons of the regional CBF-ReHo correlation coefficients, the HC group and PD-NC group showed significant differences relative to the PD-MCI group, which had lower coefficients in the right middle frontal gyrus (MFG), right middle cingulate cortex (MCC), right middle occipital gyrus (MOG), right inferior parietal gyrus (IPG), right supramarginal gyrus (SMG), and right angular gyrus (AG) ($P < 0.05$) (**Figures 1E,F**).

Aberrant Distributions of Cerebral Blood Flow-Regional Homogeneity Ratios and Correlations

The significantly altered CBF-ReHo ratios among the three groups were distributed in the right superior temporal gyrus (STG), left rectus gyrus, bilateral middle temporal gyri (MTG), bilateral putamen, bilateral lingual gyri (LG), and left postcentral gyrus (PoG) (**Figure 2**). Both the PD-NC and PD-MCI groups showed higher CBF-ReHo ratios in the left LG, bilateral putamen, and left PoG and lower CBF-ReHo ratios in the right STG and bilateral MTG (**Figures 3A,B**) than the HC group. Despite these overlapping distributions, the PD-MCI group exhibited more extensive alterations with significantly increased CBF-ReHo ratios in the right LG and lower CBF-ReHo ratios in the bilateral parahippocampal gyri (PhGs) and right inferior frontal gyrus (IFG) (**Figure 3B**). Positive correlations between the mean CBF-ReHo ratio in the left putamen and UPDRS-III scores

survived in both the PD-NC and PD-MCI groups (**Figures 4A,B**). Additionally, a higher CBF-ReHo ratio in the left LG was found in patients with PD-MCI than in patients with PD-NC (**Figure 5A**). Descriptions of significantly different brain regions in the CBF-ReHo ratios among groups are presented in **Tables 2–4**. In the PD-MCI group, the mean CBF-ReHo ratio in the left LG was negatively correlated with JoLO scores (**Figure 5B**). For brain regions with significant group differences in the voxel-based analyses, alterations in CBF-ReHo ratios, CBF, and ReHo are shown in **Figure 6**.

Distribution of Impaired Regional Homogeneity and Cerebral Blood Flow

For the analysis of ReHo maps, the significantly altered ReHo among the three groups was distributed in the right MTG, left STG, bilateral LG, and bilateral PoG. Relative to the HC subjects, higher ReHo values in right MTG and left STG were observed in patients with PD-NC, as well as higher ReHo values in the left PhG and right inferior temporal gyrus in patients with PD-MCI. Both the PD-NC and PD-MCI groups showed decreased ReHo in the bilateral LG and bilateral PoG than the HC group. There was no cluster that survived for the comparison between patients with PD-NC and PD-MCI. Descriptions of significantly different brain regions in the ReHo among groups are presented in **Supplementary Tables 1–3** and **Supplementary Figures 1A–C**.

For the analysis of CBF maps, the significantly altered CBF among the three groups was distributed in the bilateral putamen, right insula, right MTG, left IFG, bilateral thalamus, left calcarine fissure (CF), left PoG, left paracentral lobule (PL), and right MFG. Both the PD-NC and PD-MCI groups showed higher *z*-CBF values in the bilateral putamen, bilateral thalamus, left IFG, left PoG, and left PL and lower *z*-CBF values in the right insula than the HC group. Additionally, decreased perfusion in right AG and left CF was observed in patients with PD-NC, as well as preserved perfusion in left LG and bilateral supplementary motor area and decreased perfusion in right MTG and right MFG in patients with PD-MCI. In comparison with the PD-NC group, the PD-MCI group showed higher *z*-CBF values in left CF and lower *z*-CBF values in right MTG and right MFG. Descriptions of significantly different brain regions in the CBF among groups are presented in **Supplementary Tables 4–7** and **Supplementary Figures 2A–D**.

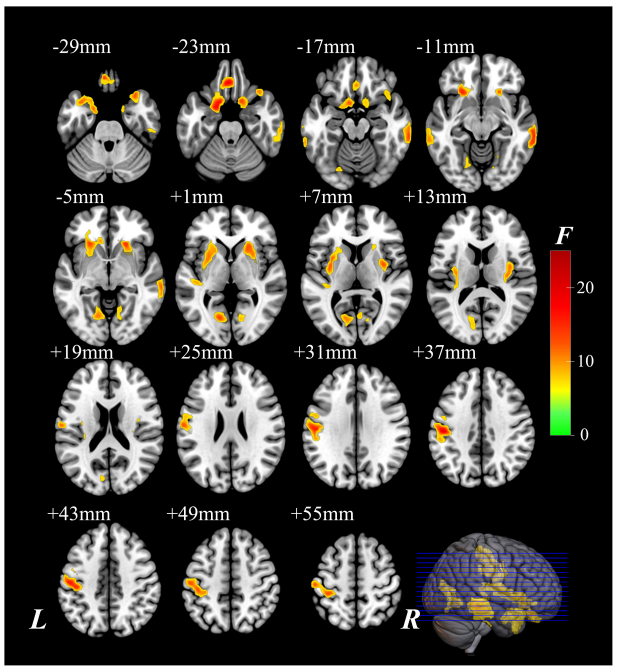

FIGURE 2 | The brain regions with significant differences of the CBF-ReHo ratio among groups. The voxel-based analysis demonstrates the survived clusters among HC, PD-NC, and PD-MCI groups. These clusters are referred to multiple comparisons correction using the FWE rate (a cluster-defining threshold of $P = 0.001$ and a corrected cluster significance of $P < 0.05$). The region with the significant difference among the three groups is shown with warm color. CBF, cerebral blood flow; ReHo, regional homogeneity; HC, healthy control; PD, Parkinson's disease; NC, normal cognition; MCI, mild cognitive impairment; FWE, familywise error; R, right; L, left.

DISCUSSION

Neuroimaging characterization holds the promise of monitoring intrinsic dysfunction and revealing the corresponding pathophysiological mechanisms in PD (Rispoli et al., 2018). This study investigates neurovascular decoupling and resultant deterioration in patients with PD-MCI by integrating informative data obtained from the BOLD and ASL approaches. The PD-MCI group exhibited dysregulation of the NVU at the whole-brain GM level as well as regional disturbances in cognition-related cortices. In comparison with HC subjects, patients with PD-MCI had increased CBF-ReHo ratios in motor-related regions and decreased ratios in the limbic system and prefrontal and temporal cortices. Specifically, a distinct neurovascular decoupling in the LG that involved visuospatial dysfunction was characterized in the PD-MCI group relative to the HC and PD-NC groups. These imaging signatures linked to neurovascular coupling could potentially provide complementary insights into the underlying mechanisms of cognitive impairment during the progression of PD.

As the primary modulating element in the central nervous system, neurovascular coupling that is structurally based on the NVU ensures sufficient blood supply for neuronal activity (Yu et al., 2020). This interaction under normal physiological conditions was observed in our neuroimaging study with global and regional correlations between CBF and ReHo. Although the deleterious repercussions of neurovascular decoupling in those with PD remain poorly elucidated, recent studies have documented aberrant neuronal activity caused by dopaminergic or non-dopaminergic dysfunction as well as impaired cerebral perfusion resulting from disrupted integrity of the blood–brain barrier during the progression of PD (Ztaou et al., 2016; Dohgu et al., 2019; Henderson et al., 2020). Pathological impairments in the NVU might disrupt neurovascular coupling and consequently induce the pathogenesis underlying neurodegenerative disorders (Yan et al., 2020). Thus, our findings of compromised coordination with decreased CBF-ReHo coefficients in patients

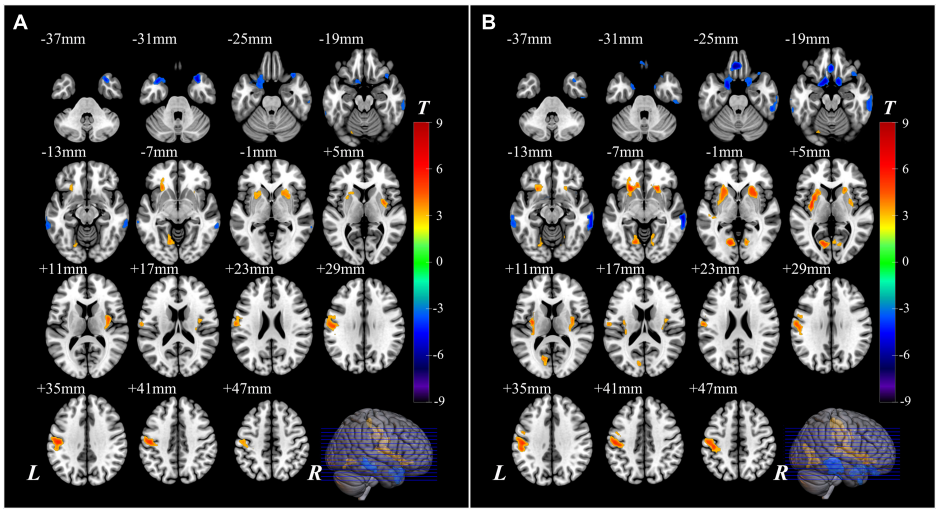

FIGURE 3 | The brain regions with significant intergroup differences of the CBF-ReHo ratio. The voxel-based analysis demonstrates the survived clusters between the HC group and PD-NC group **(A)** and PD-MCI group **(B)**. These clusters are referred to multiple comparisons correction using the FWE rate (a cluster-defining threshold of $P = 0.001$ and a corrected cluster significance of $P < 0.05$). The significantly increased ratio relative to HC in the group is shown with warm color. The significantly decreased ratio relative to HC in the group is shown with cold color. CBF, cerebral blood flow; ReHo, regional homogeneity; HC, healthy control; PD, Parkinson's disease; NC, normal cognition; MCI, mild cognitive impairment; FWE, familywise error; R, right; L, left.

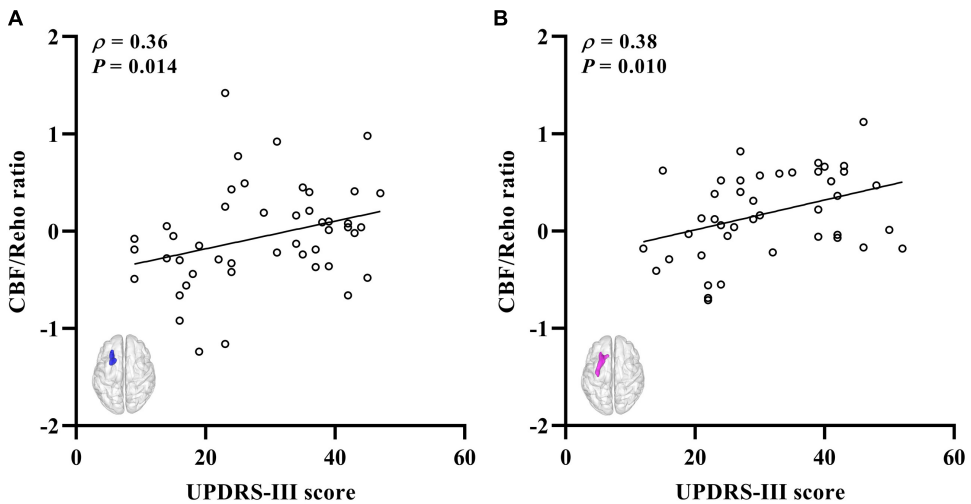

FIGURE 4 | The correlations between the CBF-ReHo ratio and scores of disease severity. **(A)** Correlations for the PD-NC group between the scores of UPDRS-III (*X*-axis) and CBF-ReHo ratio in left putamen (*Y*-axis); **(B)** correlations for the PD-MCI group between the scores of UPDRS-III (*X*-axis) and CBF-ReHo ratio in left putamen (*Y*-axis). CBF, cerebral blood flow; ReHo, regional homogeneity; PD, Parkinson's disease; NC, normal cognition; MCI, mild cognitive impairment; UPDRS, Unified Parkinson's Disease Rating Scale.

with both PD-NC and PD-MCI provide supporting evidence to the concept of neurovascular decoupling in PD, in contrast to independent alterations within each component of the NVU that have been explored by separating imaging modalities.

Guiney et al. (2015) recently proposed a mechanistic link between better neurovascular coupling and cognitive benefits. Emerging studies have concentrated on the investigation of NVU discoordination involved in pathological conditions contributing to cognitive impairment and have yielded convicting findings in AD (Liu et al., 2019), diabetes mellitus (Yan et al., 2020), and cerebrovascular diseases (Eldahshan et al., 2019). Unlike a fundamental pathway involving decoupling in these disorders, however, the underpinning mismatch responsible for the impaired cognitive profiles in PD is more complicated and accompanied by diverse pathological processes and heterogeneous symptoms. Although there was no significant intergroup difference between patients with PD-NC and PD-MCI in the global interaction, this study further explored decoupling at the regional level. Given the engagement in corresponding cognitive functions, the reduced CBF-ReHo coefficients in the

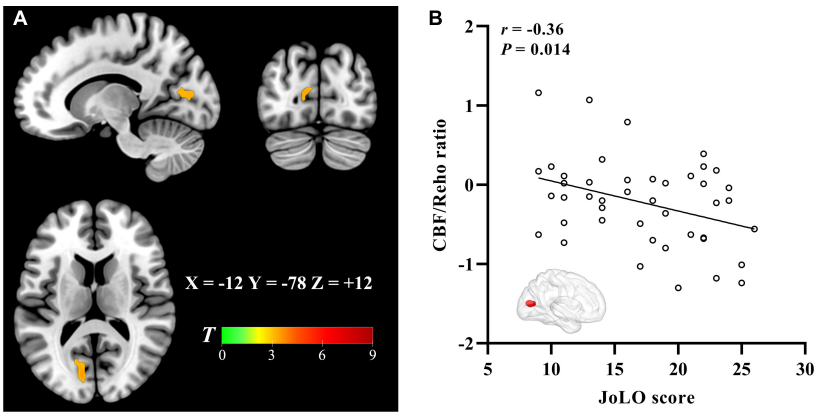

FIGURE 5 | The brain regions with the significant CBF-ReHo ratio difference between PD-MCI and PD-NC groups and correlation to visual–spatial function. The voxel-based analysis demonstrates the survived clusters between PD-MCI and PD-NC groups **(A)**. These clusters are referred to multiple comparisons correction using the FWE rate (a cluster-defining threshold of $P = 0.001$ and a corrected cluster significance of $P < 0.05$). Significantly increased ratio relative to PD-NC in the group is shown with warm color. **(B)** Correlations between the scores of JoLO (*X*-axis) and CBF-ReHo ratio values in the left lingual gyrus (*Y*-axis). CBF, cerebral blood flow; ReHo, regional homogeneity; PD, Parkinson's disease; NC, normal cognition; MCI, mild cognitive impairment; FWE, familywise error; JoLO, Benton's Judgment of Line Orientation.

TABLE 2 | Descriptions of significantly different brain regions in the CBF-ReHo ratio among groups.

Brain regions (AAL)	Peak MNI coordinates (mm)			Peak *F* value	Cluster size (mm^3)
	X	Y	Z		
ANOVA					
Right superior temporal gyrus	12	9	−21	15.62	164
Left rectus gyrus	−6	36	−27	22.58	242
Left middle temporal gyrus	−63	−42	−15	11.97	54
Right middle temporal gyrus	66	−30	−9	16.56	178
Left putamen	−24	24	−9	17.95	296
Right putamen	21	24	−6	15.78	189
Left lingual gyrus	−12	−69	0	14.44	162
Right lingual gyrus	3	−66	9	9.07	61
Left postcentral gyrus	−45	−21	39	21.50	422

These clusters are referred to multiple comparisons correction using the FWE rate (a cluster-defining threshold of P = 0.001 and a corrected cluster significance of P < 0.05).

CBF, cerebral blood flow; ReHo, regional homogeneity; HC, healthy control; PD, Parkinson's disease; NC, normal cognition; MCI, mild cognitive impairment; ANOVA, analysis of variance; AAL, automated anatomical labeling; MNI, Montreal Neurological Institute; FWE, familywise error.

MFG (executive function), the MOG (visual processing), the SMG (language processing), and the MCC, IPG, and AG, major parts of the DMN (higher-order cognitive functions), were specific to the PD-MCI group, confirming that these vulnerable regions were involved in cognitive impairment in PD from the perspective of neurovascular decoupling.

In this study, the aberrant regions of neuronal activity and cerebral perfusion in patients identified with PD-MCI were in line with those explored in previous research (Jia et al., 2018; Guo et al., 2021), although the trends in these alterations were spatially inconsistent in several regions (**Figure 6**). In contrast to decreased neuronal activity in motor-related regions, hypermetabolism was detected, which has been characterized as a remarkable feature of PDRP, resulting from increased energy demand (higher *z*-CBF) driven by activation of the inhibitory pathway (lower ReHo) (Chen et al., 2015). Additionally, other vasoactive mediators (i.e., dopamine and acetylcholine) or factors (i.e., neuroinflammation and oxidative stress) in PD could potentially interfere with neurovascular coupling by modulating the vascular response independent from regulation of neuronal systems (Falquetto et al., 2017; Santaella et al., 2020). Benefiting from the identification of neurovascular coupling within local regions in a voxel-wise manner, the analysis of CBF-ReHo ratios revealed comprehensive details regarding NVU changes and incongruity in patients with PD. We discovered that disproportionate interactions could be subtly reflected in CBF-ReHo ratios when alterations in the NVU were in the opposite direction. In particular, these deviations in coupling were profound within motor-related regions in patients with both PD-NC and PD-MCI. Together with the correlation between neurovascular decoupling in the putamen and disease severity, we deduced that the investigation of neurovascular

TABLE 3 | Descriptions of significantly different brain regions in the CBF-ReHo ratio between HC and PD-NC groups.

Brain regions	Peak MNI coordinates (mm)			Peak *T* value	Cluster size (mm^3)
	X	Y	Z		
PD-NC > HC					
Left lingual gyrus	−12	−66	−9	4.08	49
Left putamen	−27	24	−9	4.60	85
Right putamen	36	−3	9	4.84	123
Left postcentral gyrus	−48	−18	33	5.77	237
PD-NC < HC					
Right superior temporal gyrus	33	15	−30	−5.80	77
Left middle temporal gyrus	−33	9	−30	−4.93	104
Right middle temporal gyrus	66	−30	−18	−4.13	61

These clusters are referred to multiple comparisons correction using the FWE rate (a cluster-defining threshold of P = 0.001 and a corrected cluster significance of P < 0.05).
CBF, cerebral blood flow; ReHo, regional homogeneity; HC, healthy control; PD, Parkinson's disease; NC, normal cognition; AAL, automated anatomical labeling; MNI, Montreal Neurological Institute; FWE, familywise error.

TABLE 4 | Descriptions of significantly different brain regions in the CBF-ReHo ratio between PD-MCI group and HC and PD-NC groups.

Brain regions (AAL)	Peak MNI coordinates (mm)			Peak *T* value	Cluster size (mm^3)
	X	Y	Z		
PD-MCI > HC					
Left putamen	−21	21	−9	6.10	272
Right putamen	21	24	−9	5.25	170
Left lingual gyrus	−12	−69	0	5.57	158
Right lingual gyrus	15	−66	0	4.16	59
Left postcentral gyrus	−48	−21	39	5.86	348
PD-MCI < HC					
Right superior temporal gyrus	33	12	−45	−4.08	23
Left parahippocampal gyrus	−6	36	−27	−6.42	188
Right parahippocampal gyrus	12	9	−21	−5.46	59
Right inferior frontal gyrus	36	21	−18	−3.88	28
Left middle temporal gyrus	−63	−24	−15	−3.98	44
Right middle temporal gyrus	63	−27	−9	−5.70	173
PD-MCI > PD-NC					
Left lingual gyrus	−12	−78	12	3.75	26

These clusters are referred to multiple comparisons correction using the FWE rate (a cluster-defining threshold of P = 0.001 and a corrected cluster significance of P < 0.05).
CBF, cerebral blood flow; ReHo, regional homogeneity; HC, healthy control; PD, Parkinson's disease; NC, normal cognition; MCI, mild cognitive impairment; AAL, automated anatomical labeling; MNI, Montreal Neurological Institute; FWE, familywise error.

decoupling is essential for the elucidation of the underlying mechanism related to movement disorders in PD. The validation of diagnostic/prognostic power for the CBF-ReHo ratio is warranted in further studies.

Divergent cognitive performances are associated with alterations in corresponding brain regions. We found deviations in the coordination in patients with PD-MCI with decreased ratios in the limbic system (STG and PhG) and prefrontal (IFG) and temporal (MTG) cortices, which corresponds well with the vulnerable regions that have been closely implicated in cognitive dysfunction (Adler and Beach, 2016). Importantly, intergroup differences in the LG with a higher CBF-ReHo ratio were identified in this study. As the core hub that manages visual processing function, the LG has been reported to show aberrant functional, metabolic, and structural alterations, contributing to cognitive decline in patients with PD (Kamagata et al., 2011; Lee et al., 2013; Wang et al., 2018). Given the dual syndrome hypothesis proposed within the neuropathological literature (Kehagia et al., 2013), we hypothesized that decoupling in the LG was mainly subtended by cholinergic dysfunction rather than nigrostriatal degradation. Longitudinal studies have implied that impairments in visuospatial processing in patients with PD are superior to declines in episodic memory for the prediction of progression to dementia (Williams-Gray et al., 2009; Wolters et al., 2019). Although the precise pathogenic substrates cannot be distinguished by CBF-ReHo ratios, our correlation analysis demonstrated that decoupling in the LG was associated with poor visual–spatial performance scored using the JoLO scale,

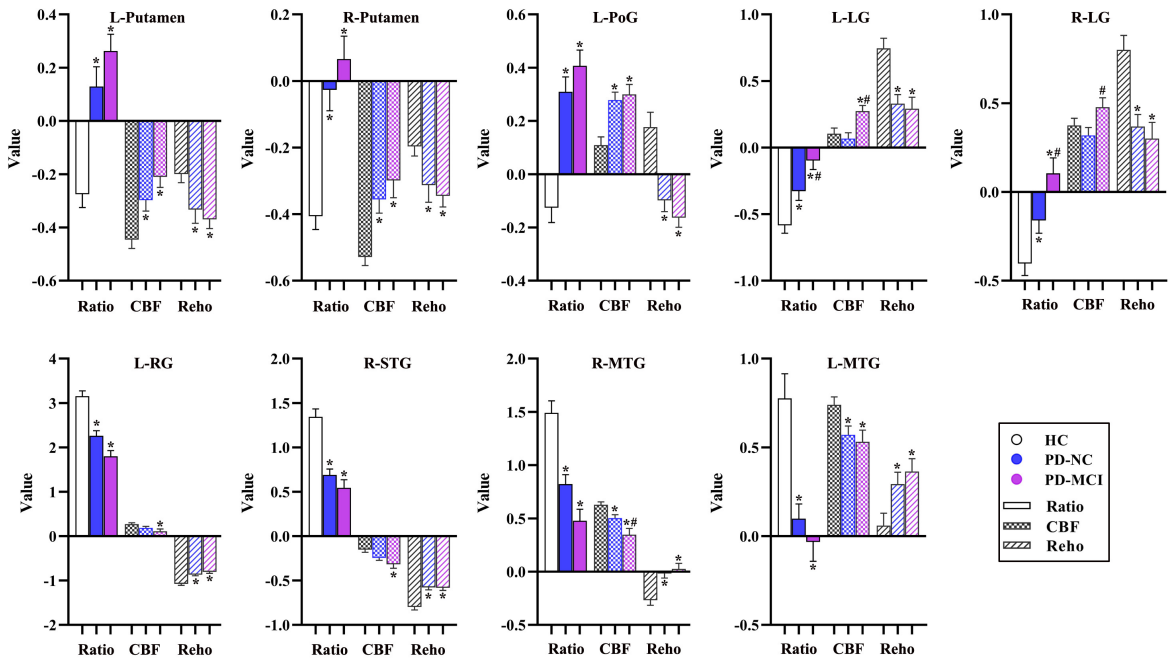

FIGURE 6 | The alterations of CBF-ReHo ratio, CBF, and ReHo in brain regions with significant group differences using the voxel-based analyses. *Indicates significant intergroup difference to the HC group; #indicates significant intergroup difference to the PD-NC group. CBF, cerebral blood flow; ReHo, regional homogeneity; PD, Parkinson's disease; NC, normal cognition; MCI, mild cognitive impairment; L, left; R, right; PoG, postcentral gyrus; LG, lingual gyrus; RG, rectus gyrus; STG, superior temporal gyrus; MTG, middle temporal gyrus.

confirming that this integrated metric of neurovascular coupling could function as a promising imaging biomarker of cognitive decline in patients with PD-MCI.

Several limitations of this study should be mentioned. First, the sample size in this study was relatively small, which might have influenced the statistical analysis. Further longitudinal investigations are required with a larger cohort including individuals with dementia as well as stricter head motion correction. Second, the elucidation of specific neurovascular mechanisms underlying PD-MCI still needs in-depth exploration that directly uses advanced imaging modalities or pathophysiological models. Third, although neuropsychological scales were employed for each cognitive domain, more detailed scales are recommended for the comprehensive understanding of corresponding cognitive performance. Finally, the clinical and MRI data were obtained on the "OFF" medication state to mitigate pharmacological effects. However, medication-free patients are required in future studies to validate our findings.

CONCLUSION

In summary, this study found that patients with PD-MCI show neurovascular decoupling associated with deteriorated motor function and cognitive performance. Most prominently, the LG in patients with PD-MCI showed region-specific effects associated with visual–spatial function characterized by NVU dysfunction, i.e., disrupted CBF-ReHo correlation coefficients and CBF-ReHo ratios. Our research illuminated the involvement of neurovascular decoupling in the neurodegenerative process in PD-MCI and emphasized the potential role of coupling metrics for the mechanistic investigation of the cognitive decline associated with PD.

DATA AVAILABILITY STATEMENT

The original contributions presented in the study are included in the article/**Supplementary Material**, further inquiries can be directed to the corresponding authors.

ETHICS STATEMENT

The studies involving human participants were reviewed and approved by the Research Ethics Committee of Nanjing Medical University. The patients/participants provided their written informed consent to participate in this study.

AUTHOR CONTRIBUTIONS

SS, HZ, and YF made substantial contributions to the conception and design of this study. SS, JW, and WD made substantial contributions to the acquisition of data. SS, HZ, and Y-CC made substantial contributions to the analysis of data. SS, YF, Y-CC, and XY contributed to the interpretations of data. SS and HZ

drafted the first version of the manuscript. All authors revised the draft for intellectual content, gave their final approval of the final version for publication, and agreed to be accountable for all aspects of the work in ensuring that questions related to the accuracy or integrity of any part of this study were appropriately investigated and resolved.

FUNDING

This study was supported by the National Natural Science Foundation of China (No. NSFC81571652), the Natural Science Foundation of Jiangsu Province (No. BK20201118), the Jiangsu Provincial Special Program of Medical Science (No. BE2021604), the Science and Technology Project of Yangzhou (No. YZ2018059), and the "333 Project" of Jiangsu Province (No. BRA2017154).

SUPPLEMENTARY MATERIAL

The Supplementary Material for this article can be found online at: https://www.frontiersin.org/articles/10.3389/fnagi.2021.770528/full#supplementary-material

Supplementary Figure 1 | The brain regions with significant differences of ReHo among groups. The voxel-based analysis demonstrates the survived clusters among HC, PD-NC, and PD-MCI groups **(A)**, between HC and PD-NC groups **(B)**, and between HC and PD-MCI groups **(C)**. These clusters are referred to multiple comparisons correction using the FWE rate (a cluster-defining threshold of $P = 0.001$ and a corrected cluster significance of $P < 0.05$). The region with the significant difference among the three groups is shown with the warm color (for **A**). The significantly increased ratio relative to HC in the group is shown with warm color, and the significantly decreased ratio relative to HC in the group is shown with cold color (for **B,C**). ReHo, regional homogeneity; HC, healthy control; PD, Parkinson's disease; NC, normal cognition; MCI, mild cognitive impairment; FWE, familywise error; R, right; L, left.

Supplementary Figure 2 | The brain regions with significant differences of CBF among groups. The voxel-based analysis demonstrates the survived clusters among HC, PD-NC, and PD-MCI groups **(A)**, between HC and PD-NC groups **(B)**, between HC and PD-MCI groups **(C)**, and between PD-NC and PD-MCI groups **(D)**. These clusters are referred to multiple comparisons correction using the FWE rate (a cluster-defining threshold of $P = 0.001$ and a corrected cluster significance of $P < 0.05$). The region with the significant difference among the three groups is shown with the warm color (for **A**). The significantly increased ratio relative to HC in the group is shown with warm color, and the significantly decreased ratio relative to HC in the group is shown with cold color (for **B,C**). The significantly increased ratio relative to PD-NC in the group is shown with warm color, and the significantly decreased ratio relative to PD-NC in the group is shown with cold color (for **D**). CBF, cerebral blood flow; HC, healthy control; PD, Parkinson's disease; NC, normal cognition; MCI, mild cognitive impairment; FWE, familywise error; R, right; L, left.

REFERENCES

Aarsland, D., Creese, B., Politis, M., Chaudhuri, K. R., Ffytche, D. H., Weintraub, D., et al. (2017). Cognitive decline in Parkinson disease. *Nat. Rev. Neurol.* 13, 217–231. doi: 10.1038/nrneurol.2017.27

Adler, C. H., and Beach, T. G. (2016). Neuropathological basis of nonmotor manifestations of Parkinson's disease. *Mov. Disord.* 31, 1114–1119. doi: 10.1002/mds.26605

Ambarki, K., Wahlin, A., Zarrinkoob, L., Wirestam, R., Petr, J., Malm, J., et al. (2015). Accuracy of parenchymal cerebral blood flow measurements using pseudocontinuous arterial spin-labeling in healthy volunteers. *AJNR Am. J. Neuroradiol.* 36, 1816–1821. doi: 10.3174/ajnr.A4367

Amboni, M., Tessitore, A., Esposito, F., Santangelo, G., Picillo, M., Vitale, C., et al. (2015). Resting-state functional connectivity associated with mild cognitive impairment in Parkinson's disease. *J. Neurol.* 262, 425–434. doi: 10.1007/s00415-014-7591-5

Arslan, D. B., Gurvit, H., Genc, O., Kicik, A., Eryurek, K., Cengiz, S., et al. (2020). The cerebral blood flow deficits in Parkinson's disease with mild cognitive impairment using arterial spin labeling MRI. *J. Neural. Transm. (Vienna)* 127, 1285–1294. doi: 10.1007/s00702-020-02227-6

Baiano, C., Barone, P., Trojano, L., and Santangelo, G. (2020). Prevalence and clinical aspects of mild cognitive impairment in Parkinson's disease: a meta-analysis. *Mov. Disord.* 35, 45–54. doi: 10.1002/mds.27902

Bezdicek, O., Ballarini, T., Ruzicka, F., Roth, J., Mueller, K., Jech, R., et al. (2018). Mild cognitive impairment disrupts attention network connectivity in Parkinson's disease: a combined multimodal MRI and meta-analytical study. *Neuropsychologia* 112, 105–115. doi: 10.1016/j.neuropsychologia.2018.03.011

Cai, W., Zhang, K., Li, P., Zhu, L., Xu, J., Yang, B., et al. (2017). Dysfunction of the neurovascular unit in ischemic stroke and neurodegenerative diseases: an aging effect. *Ageing Res. Rev.* 34, 77–87. doi: 10.1016/j.arr.2016.09.006

Campolo, M., Paterniti, I., Siracusa, R., Filippone, A., Esposito, E., and Cuzzocrea, S. (2019). TLR4 absence reduces neuroinflammation and inflammasome activation in Parkinson's diseases in vivo model. *Brain Behav. Immun.* 76, 236–247. doi: 10.1016/j.bbi.2018.12.003

Chen, Y., Pressman, P., Simuni, T., Parrish, T. B., and Gitelman, D. R. (2015). Effects of acute levodopa challenge on resting cerebral blood flow in Parkinson's Disease patients assessed using pseudo-continuous arterial spin labeling. *PeerJ* 3:e1381. doi: 10.7717/peerj.1381

Dickson, D. W. (2018). Neuropathology of Parkinson disease. *Parkinsonism Relat. Disord.* 46(Suppl. 1), S30–S33. doi: 10.1016/j.parkreldis.2017.07.033

Dohgu, S., Takata, F., Matsumoto, J., Kimura, I., Yamauchi, A., and Kataoka, Y. (2019). Monomeric alpha-synuclein induces blood-brain barrier dysfunction through activated brain pericytes releasing inflammatory mediators in vitro. *Microvasc Res.* 124, 61–66. doi: 10.1016/j.mvr.2019.03.005

Eldahshan, W., Fagan, S. C., and Ergul, A. (2019). Inflammation within the neurovascular unit: focus on microglia for stroke injury and recovery. *Pharmacol. Res.* 147:104349. doi: 10.1016/j.phrs.2019.104349

Emre, M., Aarsland, D., Brown, R., Burn, D. J., Duyckaerts, C., Mizuno, Y., et al. (2007). Clinical diagnostic criteria for dementia associated with Parkinson's disease. *Mov. Disord.* 22, 1689–1707. doi: 10.1002/mds.21507 quiz 1837,

Falquetto, B., Tuppy, M., Potje, S. R., Moreira, T. S., Antoniali, C., and Takakura, A. C. (2017). Cardiovascular dysfunction associated with neurodegeneration in an experimental model of Parkinson's disease. *Brain Res.* 1657, 156–166. doi: 10.1016/j.brainres.2016.12.008

Guiney, H., Lucas, S. J., Cotter, J. D., and Machado, L. (2015). Evidence cerebral blood-flow regulation mediates exercise-cognition links in healthy young adults. *Neuropsychology* 29, 1–9. doi: 10.1037/neu0000124

Guo, W., Jin, W., Li, N., Gao, J., Wang, J., Chang, Y., et al. (2021). Brain activity alterations in patients with Parkinson's disease with cognitive impairment based on resting-state functional MRI. *Neurosci. Lett.* 747:135672. doi: 10.1016/j.neulet.2021.135672

Guo, X., Zhu, J., Zhang, N., Zhang, L., Qi, Y., Cai, H., et al. (2019). Altered neurovascular coupling in neuromyelitis optica. *Hum. Brain Mapp.* 40, 976–986. doi: 10.1002/hbm.24426

Henderson, M. X., Sedor, S., Mcgeary, I., Cornblath, E. J., Peng, C., Riddle, D. M., et al. (2020). Glucocerebrosidase activity modulates neuronal susceptibility to pathological alpha-synuclein insult. *Neuron* 105, 822.e827–836.e827. doi: 10.1016/j.neuron.2019.12.004

Hepp, D. H., Vergoossen, D. L., Huisman, E., Lemstra, A. W., Berendse, H. W., Rozemuller, A. J., et al. (2016). Distribution and load of amyloid-beta pathology in parkinson disease and dementia with lewy bodies. *J. Neuropathol. Exp. Neurol.* 75, 936–945. doi: 10.1093/jnen/nlw070

Hu, B., Yan, L. F., Sun, Q., Yu, Y., Zhang, J., Dai, Y. J., et al. (2019). Disturbed neurovascular coupling in type 2 diabetes mellitus patients: evidence from a comprehensive fMRI analysis. *Neuroimage Clin.* 22:101802. doi: 10.1016/j.nicl.2019.101802

Hughes, A. J., Daniel, S. E., Kilford, L., and Lees, A. J. (1992). Accuracy of clinical diagnosis of idiopathic Parkinson's disease: a clinico-pathological study of 100 cases. *J. Neurol. Neurosurg. Psychiatry* 55, 181–184. doi: 10.1136/jnnp.55.3.181

Jang, H., Huang, S., Hammer, D. X., Wang, L., Rafi, H., Ye, M., et al. (2017). Alterations in neurovascular coupling following acute traumatic brain injury. *Neurophotonics* 4:045007. doi: 10.1117/1.NPh.4.4.045007

Jia, X., Li, Y., Li, K., Liang, P., and Fu, X. (2018). Precuneus dysfunction in Parkinson's disease with mild cognitive impairment. *Front. Aging Neurosci.* 10:427. doi: 10.3389/fnagi.2018.00427

Kalia, L. V., and Lang, A. E. (2015). Parkinson's disease. *Lancet* 386, 896–912. doi: 10.1016/S0140-6736(14)61393-3

Kamagata, K., Motoi, Y., Hori, M., Suzuki, M., Nakanishi, A., Shimoji, K., et al. (2011). Posterior hypoperfusion in Parkinson's disease with and without dementia measured with arterial spin labeling MRI. *J. Magn. Reson. Imaging* 33, 803–807. doi: 10.1002/jmri.22515

Kehagia, A. A., Barker, R. A., and Robbins, T. W. (2013). Cognitive impairment in Parkinson's disease: the dual syndrome hypothesis. *Neurodegener. Dis.* 11, 79–92. doi: 10.1159/000341998

Lee, S. H., Kim, S. S., Tae, W. S., Lee, S. Y., Lee, K. U., and Jhoo, J. (2013). Brain volumetry in Parkinson's disease with and without dementia: where are the differences? *Acta Radiol.* 54, 581–586. doi: 10.1177/0284185113476029

Liang, X., Zou, Q., He, Y., and Yang, Y. (2013). Coupling of functional connectivity and regional cerebral blood flow reveals a physiological basis for network hubs of the human brain. *Proc. Natl. Acad. Sci. U.S.A.* 110, 1929–1934. doi: 10.1073/pnas.1214900110

Liu, X., Cheng, R., Chen, L., Gong, J., Luo, T., and Lv, F. (2021). Altered neurovascular coupling in subcortical ischemic vascular disease. *Front. Aging Neurosci.* 13:598365. doi: 10.3389/fnagi.2021.598365

Liu, X., Hou, D., Lin, F., Luo, J., Xie, J., Wang, Y., et al. (2019). The role of neurovascular unit damage in the occurrence and development of Alzheimer's disease. *Rev. Neurosci.* 30, 477–484. doi: 10.1515/revneuro-2018-0056

Melzer, T. R., Watts, R., Macaskill, M. R., Pearson, J. F., Rueger, S., Pitcher, T. L., et al. (2011). Arterial spin labelling reveals an abnormal cerebral perfusion pattern in Parkinson's disease. *Brain* 134, 845–855. doi: 10.1093/brain/awq377

Olde Dubbelink, K. T., Schoonheim, M. M., Deijen, J. B., Twisk, J. W., Barkhof, F., and Berendse, H. W. (2014). Functional connectivity and cognitive decline over 3 years in Parkinson disease. *Neurology* 83, 2046–2053. doi: 10.1212/WNL.0000000000001020

Pan, P., Zhan, H., Xia, M., Zhang, Y., Guan, D., and Xu, Y. (2017). Aberrant regional homogeneity in Parkinson's disease: a voxel-wise meta-analysis of resting-state functional magnetic resonance imaging studies. *Neurosci. Biobehav. Rev.* 72, 223–231. doi: 10.1016/j.neubiorev.2016.11.018

Phillips, A. A., Chan, F. H., Zheng, M. M., Krassioukov, A. V., and Ainslie, P. N. (2016). Neurovascular coupling in humans: physiology, methodological advances and clinical implications. *J. Cereb Blood Flow Metab.* 36, 647–664. doi: 10.1177/0271678X15617954

Rispoli, V., Schreglmann, S. R., and Bhatia, K. P. (2018). Neuroimaging advances in Parkinson's disease. *Curr. Opin. Neurol.* 31, 415–424. doi: 10.1097/WCO.0000000000000584

Rolls, E. T., Huang, C. C., Lin, C. P., Feng, J., and Joliot, M. (2020). Automated anatomical labelling atlas 3. *Neuroimage* 206:116189. doi: 10.1016/j.neuroimage.2019.116189

Ryman, S. G., and Poston, K. L. (2020). MRI biomarkers of motor and non-motor symptoms in Parkinson's disease. *Parkinsonism Relat. Disord.* 73, 85–93. doi: 10.1016/j.parkreldis.2019.10.002

Santaella, A., Kuiperij, H. B., Van Rumund, A., Esselink, R. A. J., Van Gool, A. J., Bloem, B. R., et al. (2020). Inflammation biomarker discovery in Parkinson's disease and atypical parkinsonisms. *BMC Neurol.* 20:26. doi: 10.1186/s12883-020-1608-8

Solis, E. Jr., Hascup, K. N., and Hascup, E. R. (2020). Alzheimer's disease: the link between amyloid-beta and neurovascular dysfunction. *J. Alzheimers Dis.* 76, 1179–1198. doi: 10.3233/JAD-200473

Wang, Z., Jia, X., Chen, H., Feng, T., and Wang, H. (2018). Abnormal spontaneous brain activity in early parkinson's disease with mild cognitive impairment: a resting-state fMRI study. *Front. Physiol.* 9:1093. doi: 10.3389/fphys.2018.01093

Williams-Gray, C. H., Evans, J. R., Goris, A., Foltynie, T., Ban, M., Robbins, T. W., et al. (2009). The distinct cognitive syndromes of Parkinson's disease: 5 year follow-up of the CamPaIGN cohort. *Brain* 132, 2958–2969. doi: 10.1093/brain/awp245

Wolters, A. F., Van De Weijer, S. C. F., Leentjens, A. F. G., Duits, A. A., Jacobs, H. I. L., and Kuijf, M. L. (2019). Resting-state fMRI in Parkinson's disease patients with cognitive impairment: a meta-analysis. *Parkinsonism Relat. Disord.* 62, 16–27. doi: 10.1016/j.parkreldis.2018.12.016

Yan, C., Zhou, Y., Chen, Q., Luo, Y., Zhang, J. H., Huang, H., et al. (2020). Dysfunction of the neurovascular unit in diabetes-related neurodegeneration. *Biomed. Pharmacother.* 131:110656. doi: 10.1016/j.biopha.2020.110656

Yu, X., Ji, C., and Shao, A. (2020). Neurovascular unit dysfunction and neurodegenerative disorders. *Front. Neurosci.* 14:334. doi: 10.3389/fnins.2020.00334

Zang, Y., Jiang, T., Lu, Y., He, Y., and Tian, L. (2004). Regional homogeneity approach to fMRI data analysis. *Neuroimage* 22, 394–400. doi: 10.1016/j.neuroimage.2003.12.030

Zhu, J., Zhuo, C., Xu, L., Liu, F., Qin, W., and Yu, C. (2017). Altered coupling between resting-state cerebral blood flow and functional connectivity in schizophrenia. *Schizophr. Bull.* 43, 1363–1374. doi: 10.1093/schbul/sbx051

Ztaou, S., Maurice, N., Camon, J., Guiraudie-Capraz, G., Kerkerian-Le Goff, L., Beurrier, C., et al. (2016). Involvement of striatal cholinergic interneurons and M1 and M4 muscarinic receptors in motor symptoms of Parkinson's disease. *J. Neurosci.* 36, 9161–9172. doi: 10.1523/JNEUROSCI.0873-16.2016

Conflict of Interest: The authors declare that the research was conducted in the absence of any commercial or financial relationships that could be construed as a potential conflict of interest.

Publisher's Note: All claims expressed in this article are solely those of the authors and do not necessarily represent those of their affiliated organizations, or those of the publisher, the editors and the reviewers. Any product that may be evaluated in this article, or claim that may be made by its manufacturer, is not guaranteed or endorsed by the publisher.

Copyright © 2021 Shang, Zhang, Feng, Wu, Dou, Chen and Yin. This is an open-access article distributed under the terms of the Creative Commons Attribution License (CC BY). The use, distribution or reproduction in other forums is permitted, provided the original author(s) and the copyright owner(s) are credited and that the original publication in this journal is cited, in accordance with accepted academic practice. No use, distribution or reproduction is permitted which does not comply with these terms.

frontiers in Molecular Neuroscience

ORIGINAL RESEARCH
published: 22 November 2021
doi: 10.3389/fnmol.2021.772584

Genetic Pathways and Functional Subnetworks for the Complex Nature of Bipolar Disorder in Genome-Wide Association Study

Chan-Yen Kuo[1,2†], Tsu-Yi Chen[3,4†], Pei-Hsiu Kao[5‡], Winifred Huang[6‡], Chun-Ruei Cho[5], Ya-Syuan Lai[5], Giou-Teng Yiang[3,4] and Chung-Feng Kao[5,7]*

[1] Department of Research, Taipei Tzu Chi Hospital, Buddhist Tzu Chi Medical Foundation, New Taipei, Taiwan, [2] Department of Nursing, Cardinal Tien College of Healthcare and Management, New Taipei, Taiwan, [3] Department of Emergency Medicine, Taipei Tzu Chi Hospital, Buddhist Tzu Chi Medical Foundation, New Taipei, Taiwan, [4] Department of Emergency Medicine, School of Medicine, Tzu Chi University, Hualien, Taiwan, [5] Department of Agronomy, College of Agriculture and Natural Resources, National Chung Hsing University, Taichung, Taiwan, [6] School of Management, University of Bath, Bath, United Kingdom, [7] Advanced Plant Biotechnology Center, National Chung Hsing University, Taichung, Taiwan

OPEN ACCESS

Edited by:
Jiehui Jiang,
Shanghai University, China

Reviewed by:
Can Sheng,
Capital Medical University, China
Lalu Muhammad Irham,
Ahmad Dahlan University, Indonesia
Suleman Atique,
University of Hail, Saudi Arabia

***Correspondence:**
Chung-Feng Kao
kaoc@nchu.edu.tw;
gcf6@hotmail.com

[†] These authors have contributed equally to this work and share first authorship

[‡] These authors have contributed equally to this work

Specialty section:
This article was submitted to Brain Disease Mechanisms, a section of the journal Frontiers in Molecular Neuroscience

Received: *08 September 2021*
Accepted: *08 October 2021*
Published: *22 November 2021*

Citation:
Kuo C-Y, Chen T-Y, Kao P-H, Huang W, Cho C-R, Lai Y-S, Yiang G-T and Kao C-F (2021) Genetic Pathways and Functional Subnetworks for the Complex Nature of Bipolar Disorder in Genome-Wide Association Study. Front. Mol. Neurosci. 14:772584. doi: 10.3389/fnmol.2021.772584

Bipolar disorder is a complex psychiatric trait that is also recognized as a high substantial heritability from a worldwide distribution. The success in identifying susceptibility loci for bipolar disorder (BPD) has been limited due to its complex genetic architecture. Growing evidence from association studies including genome-wide association (GWA) studies points to the need of improved analytic strategies to pinpoint the missing heritability for BPD. More importantly, many studies indicate that BPD has a strong association with dementia. We conducted advanced pathway analytics strategies to investigate synergistic effects of multilocus within biologically functional pathways, and further demonstrated functional effects among proteins in subnetworks to examine mechanisms underlying the complex nature of bipolarity using a GWA dataset for BPD. We allowed bipolar susceptible loci to play a role that takes larger weights in pathway-based analytic approaches. Having significantly informative genes identified from enriched pathways, we further built function-specific subnetworks of protein interactions using MetaCore. The gene-wise scores (i.e., minimum *p*-value) were corrected for the gene-length, and the results were corrected for multiple tests using Benjamini and Hochberg's method. We found 87 enriched pathways that are significant for BPD; of which 36 pathways were reported. Most of them are involved with several metabolic processes, neural systems, immune system, molecular transport, cellular communication, and signal transduction. Three significant and function-related subnetworks with multiple hotspots were reported to link with several Gene Ontology processes for BPD. Our comprehensive pathway-network frameworks demonstrated that the use of prior knowledge is promising to facilitate our understanding between complex psychiatric disorders (e.g., BPD) and dementia for the access to the connection and clinical implications, along with the development and progression of dementia.

Keywords: genome-wide association study, pathway analysis, functional subnetwork, prior knowledge, bipolar, dementia

INTRODUCTION

Many studies have suggested that there is a strong link between bipolar disorder (BPD) and dementia. BPD could increase the risk of developing some specific syndromes of dementia, especially for older adults (Masouy et al., 2011; Wu et al., 2013; Chen et al., 2015; Almeida et al., 2016; Diniz et al., 2017). Furthermore, Kessing and Andersen (2004) suggested that the rate of dementia is 6% higher for the patients with BPD who get admission to hospital with every episode than for those without BPD. BPD comes from a number of causes, such as ages, the duration of illness, polypharmacy, the presence of clinical comorbidity and so on (Borges et al., 2019). According to the Anatomical evidences, the gray matter volume and prefrontal cortex are both affected as people are suffered from BPD, and both of these two regions in the brain also have an influence on causing dementia (Pavlovic et al., 2011). On the one hand, the reduction of gray matter volume in the left cerebellar hemisphere and vermis volume increases the risk of dementia (Baldaçara et al., 2012). On the other hand, volumes of both hemispheres and the vermis are reduced when people suffered from BPD. Relatedly, Pavlovic et al. (2011) indicated that the dementia associated with BPD has a lot to do with psychosocial and functional impairment. Thus, dementia seems to be serious and inevitable. The significant symptom overlapping between dementia and psychiatric disorders like BPD is particularly an important therapeutic target with diagnostic challenges. Although clinical perspectives and implications with BPD and dementia were discussed previously (Lopes and Fernandes, 2012), the potential biologically functional pathways and molecular mechanisms still remains unclear.

Psychiatric traits are generally complex and multifactorial. Over the last decade, numerous genome-wide association (GWA) studies were conducted to search for susceptibility genes for complex human traits (Hindorffa et al., 2009). More than half or a few million markers in hundreds or thousands of subjects were conducted to increase the explanatory power of the disease heritability. A large number of low-risk genetic variants (usually odds ratios < 1.5) were identified to be involved in the etiology of complex traits (Manolio et al., 2008). However, the associated single-nucleotide polymorphisms (SNPs) and genes in total only account for a small proportion of the heritability for most of complex traits including BPD (Manolio et al., 2009). For instance, the effects of genes identified by linkage scans and association tests can only account for ∼2% of the ∼80% heritability of BPD (Crow, 2011). Many replication studies further demonstrated no replicable support for bipolar candidates (Crow, 2007). The failure in detecting true associations for heritable diseases like BPD might be involved with the "common-disease common-variant" hypothesis and the noise that is inherent in GWA studies and others (Maher, 2008; Gershon et al., 2011). We conducted allelic association tests for each SNP of three GWA datasets of BPD including the Wellcome Trust Consortium (WTCCC), the Genetic Association Information Network (GAIN), and the National Institute of Mental Health (NIMH). Again, only a few markers (*ATMIN*, *CENPN*, *HTR3B,* and *UBR1*) reached the commonly used genome-wide significance threshold level ($p < 5 \times 10^{-8}$) in the WTCCC GWA data, indicating the fact of potential noise inherent in genome-wide approaches. The noise may come from several sources such as small effect sizes at individual SNP level, causal variants (in particular when their minor allele frequency lower than genotyped SNPs) that are not in a complete linkage disequilibrium (LD) with SNPs, no power in inappropriate statistical methods, and others (Yang et al., 2010; Lee et al., 2011). In addition, due to the complexity of BPD, it is a challenge to identify which particular gene markers are the true causes of disease as noises may potentially be introduced due to technical or biological errors in nature (Ideker et al., 2011). This study aims to overcome these problems, in a gene-gene interaction sense, through identifying and finding the missing heritability.

In a GWA study, *p*-values are usually used to represent the statistical significance in the association, and the most significant SNP (*min-p*) of a gene region is selected to represent the significance level of a gene. However, the "*min-p*" approach is biased toward genes saturated with SNPs. Typically, large genes may have a higher gene-wise statistic, and in fact, we have previously observed a negative relationship between *p*-values and gene length (Yang et al., 2011; Kao et al., 2014). Introducing such bias into a subsequent pathway analysis may result in favoring pathways with larger genes. There are several Sidak's correction based methods proposed to correct for a gene-size bias (Sidak, 1967; Saccone et al., 2007; Peng et al., 2010). In particular, a simple method based on the first order statistic (FOSCO) can well correct the gene-size bias by obtaining a gene-level significance for individual genes (Mirina et al., 2012). Although the FOSCO method does not deal with LD structures, its performance is as well as other methods such as GATES and VEGAS, whose computation is based on the LD structure (Mirina et al., 2012).

Bipolar disorder is a complex mental disorder with lifetime prevalence ranging from 8 to 5% in the general population and with a high probability of heritability around 80% (McGuffin et al., 2003; Kessler et al., 2005; Kato, 2007; Merikangas et al., 2008). Previous studies have also suggested the involvement of polygenic and multifactorial features in the pathology of BPD, along with the complex interactions among genes (G × G) and environmental (G × E) factors (Holmans et al., 2009; Pregelj, 2011; Chuang et al., 2013). Recently, we identified and prioritized candidate genes for BPD from multi-dimensional evidence-based data sources, which provide us an opportunity to explore an advanced pathway and network for BPD (Kao et al., 2014). With the combined scores obtained from the prior knowledge of BPD, each of the GWA genes was weighted by the magnitude of association to reduce noise (e.g., false-positive results and publication bias) and increase the effect size in pathway analysis (Pedroso et al., 2012). This hypothesis allows BPD candidates to play a larger role in pathways. The stronger the prior knowledge for BPD of a gene, the larger role the gene plays in pathways. Thus, these genes were regarded as "key genes."

Genes normally cooperate with others having similar or related functions or characteristics to form a complex network of functional interactions to affect diseases, particularly for complex psychiatric traits. Genome-wide association studies provide the

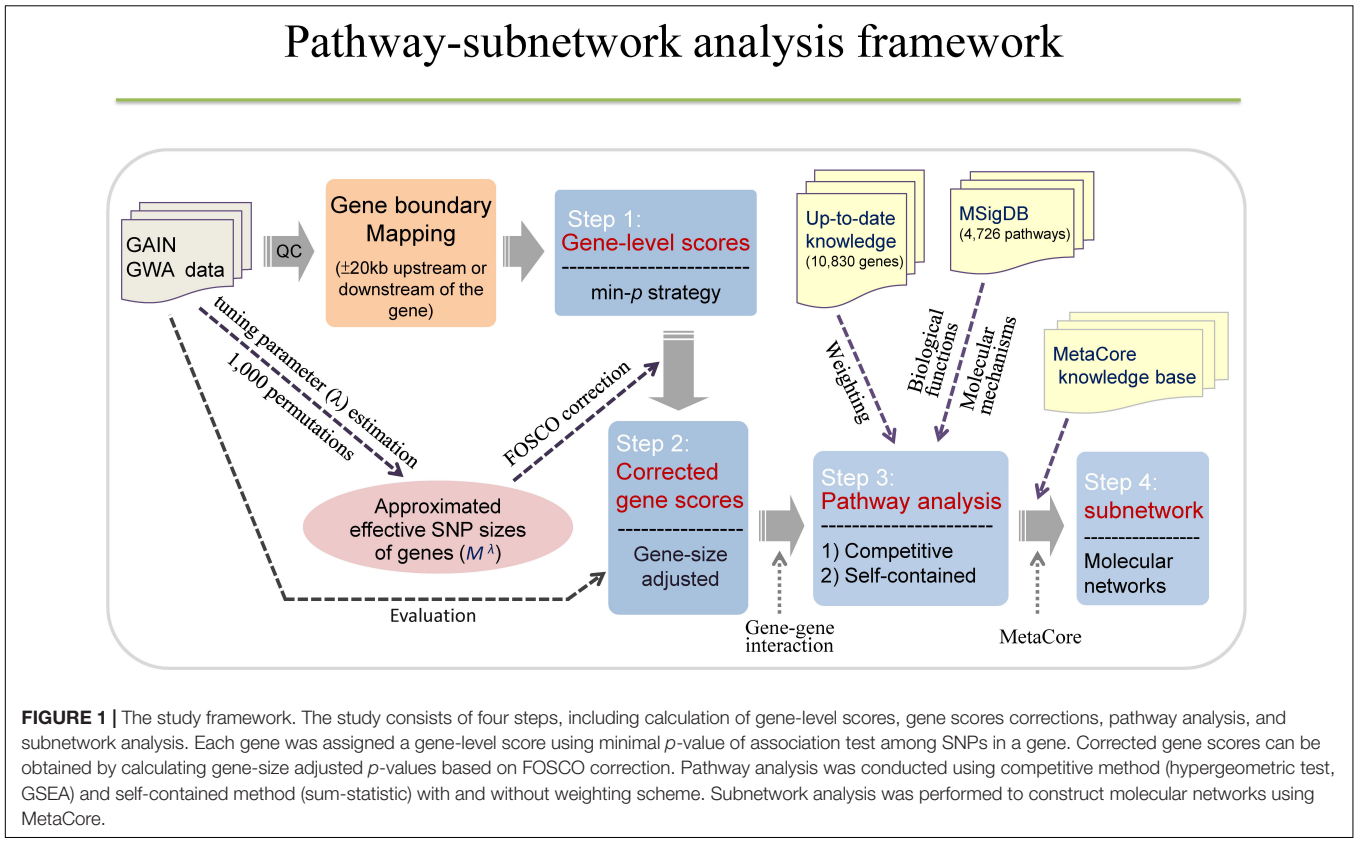

FIGURE 1 | The study framework. The study consists of four steps, including calculation of gene-level scores, gene scores corrections, pathway analysis, and subnetwork analysis. Each gene was assigned a gene-level score using minimal *p*-value of association test among SNPs in a gene. Corrected gene scores can be obtained by calculating gene-size adjusted *p*-values based on FOSCO correction. Pathway analysis was conducted using competitive method (hypergeometric test, GSEA) and self-contained method (sum-statistic) with and without weighting scheme. Subnetwork analysis was performed to construct molecular networks using MetaCore.

potential to account for such complexity. Thus, the pathway analytic strategy provides a basis of a gene-gene interaction to account for the biological relevance of genes and has the potential to detect the synergetic effects of multiple genes that might have been missed in the traditional single-marker association (Holmans, 2010; Fridley and Biernacka, 2011). The network analysis further provides a dynamic interrelationship among proteins to interconnect biological functions and molecular mechanisms, for instance, our previous work in major depressive disorder (Jia et al., 2011a). Most importantly, we want to know how genes aggregated into clusters of similar or related functions and how these components interconnect and function biologically in pathways and networks underlying the BPD. Therefore, pathway-based and network-based analyses are powerful approaches that summarize genetic information from sets of genes. Using such framework has the potential to interpret genes and pathways biologically. Thus, the objective of the present study uses the systems biology strategy to identify the missing heritability of BPD, which provides additional insights into the nature of complex genetic architecture underlying BPD.

Our current study intends to investigate enriched pathways and functional networks for BPD using a large-scale GWA dataset. We first conducted FOSCO method to correct for the gene-size bias by calculating the gene-level statistical significance. Second, we performed a pathway-based analysis using weighted competitive and self-contained methods with a minimum *p*-value approach to extract SNP information at a gene level. Third, we applied the subnetwork analysis to construct molecular networks. More importantly, the strategies used to conduct pathway or network-based analyses in the current study for bipolar potentially boosted our explanatory power to obtain meaningful results for studying the biological functions and molecular mechanisms of bipolar. For a more detailed study framework, please refer to **Figure 1**.

MATERIALS AND METHODS

Genome-Wide Association Dataset

The BPD GWA dataset was accessed through the GAIN database of Genotypes and Phenotypes for bipolar disorders.[1] A total of 1,001 bipolar cases and 1,034 healthy controls of Americans with European ancestry were included in this dataset. The genotyping platform was Affymetrix Genome-Wide Human SNP Array 6.0. After conducting quality control procedures (Manolio et al., 2007), a total of 698,227 SNPs were retained. We assigned a SNP to a gene if it was located within the gene or 20kb upstream or downstream of the gene. Therefore, a total of 416,371 SNPs were mapped into 15,213 protein-coding genes after dealing with aliases in the GAIN GWA dataset of BPD to perform pathway and network analyses. A basic allelic association test was used to calculate the genomic inflation factor for this GWA dataset, which was 1.03. The quantile-quantile plot for all analyzed SNPs

[1]http://www.ncbi.nlm.nih.gov/

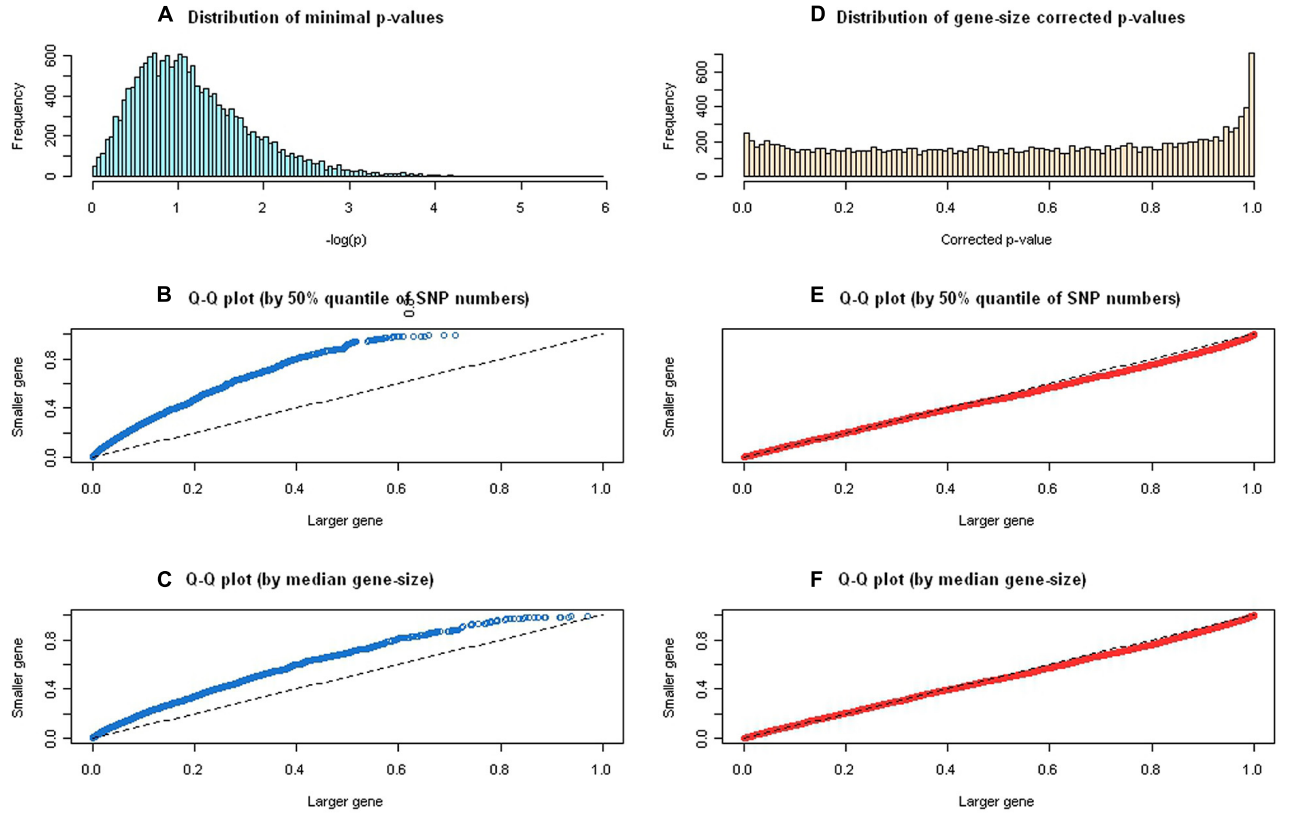

FIGURE 2 | The distribution of minimal *p*-values and quantile-quantile plots before and after gene-size correction. **(A)** Distribution of logarithm of minimal *p*-values was skewed to the right. **(B)** The quantile-quantile plot, using 50% quantile of single-nucleotide polymorphism (SNP) numbers, showed a significant correlation between minimal *p*-values and the gene-size. **(C)** The quantile-quantile plot, using median gene size, showed a significant correlation between minimal *p*-values and the gene size. **(D)** Distribution of logarithm of gene-size corrected *p*-values demonstrated uniformly distributed from [0,1]. **(E)** The quantile-quantile plot, using 50% quantile of SNP numbers, showed no significant correlation between gene-size corrected *p*-values and the gene-size. **(F)** The quantile-quantile plot, using median gene size, showed no significant correlation between gene-size corrected *p*-values and the gene size.

can be found in **Supplementary Figure 2**, indicating a good quality of this GWA dataset.

Bipolar Candidate Genes

We prioritized a list of 10,830 susceptible genes (**Supplementary Data 1**) that were collected from several lines of evidence-based datasets for BPD, including GWA study, association studies, linkage scans, gene expression (including human and animal studies), literature search, and biological regulatory pathways. For each gene, a dataset-specific score (CS_j) was assigned in each data source according to the magnitude of association. All data types were combined using an optimized weighting vector to indicate the priority of the association of a gene with BPD. More detailed information of this gene prioritization procedure can be found in Kao et al. (2014).

Pathway Annotations

To map genes into biological pathways, we used the Molecule Signature Database (MSigDB)[2] annotations. The MSigDB consists of several open public sources of pathway annotations, including Gene Ontology (GO) terms, Kyoto Encyclopedia of Genes and Genomes (KEGG), BioCarta, Reactome, and gene sets compiled from published biomedical literature (Subramanian et al., 2005), which listed 4,726 pathways and 22,429 genes. Pathways with extreme numbers of genes (i.e., 10th percentile of pathway-size distribution, <10 or >380 genes) were removed from analyses to avoid stochastic bias or testing any over-general biological process. This procedure resulted in a total of 4,120 pathways left in the GAIN GWA dataset.

Gene-Wise Statistical Significance Correction of Gene-Size Bias

To obtain a gene-level statistical significance, we first mapped SNPs to a gene (using NCBI build 36) if SNPs were located within the gene region or 20 kb upstream or downstream of the gene, which was suggested as a good gene boundary (Jia et al., 2011b). We used a commonly adopted method to select the most significant SNP (*min-p*, denoted as p^{min}) among M SNPs in a gene region in association tests to represent the significance level of a gene. Because the *p*-values

[2]http://www.broadinstitute.org/gsea/msigdb/index.jsp

are biased toward to a gene-length, we utilized $p^{adj} = 1 - \left(1 - p^{\min}\right)^{M_{eff}}$ to adjust it to the gene-wise statistical significance. We approximated the effective number, or alternatively adjusted number, of SNPs (M_{eff}) using ${}_M{}^{\lambda}$ to correct for the actual number of SNPs (M), where the tuning parameter λ satisfies the correlation between adjusted p-values (p^{adj}) and M is minimal; that is, $\min \left|\text{corr}\left(p^{adj}, M\right)\right|$. The value of the tuning parameter λ can be optimized empirically on permuted genotype data under the null through randomly permuting case/control status of subjects, keeping the genotypes remain the same. If p^{adj} are well corrected for the gene-size, they would be uniformly distributed from [0,1]. For a detailed method, please refer to Mirina et al. (2012).

Statistical Methods for Pathway Enrichment Analysis

We applied three statistical methods to test the enrichment of significant pathways for BPD. According to prior studies, we extended two permutation-based approaches, the Gene Set Enrichment Analysis (GSEA, a competitive method) and the sum-statistic method (a self-contained method), by taking into account prior knowledge on BPD (Wang et al., 2010, 2011). We denoted D as the disease of interest (here is BPD), and $r_j(D)$ as the gene-wise statistic value that defined as the logarithm of adjusted gene-wise p-values of the corresponding to the most significant SNP in gene $j(j = 1, \ldots, N)$. Here we allowed bipolar candidate genes to play a larger role in pathway analyses. A weight ($\geq$1), $w_j = 1 + \frac{CS_j}{\overline{CS}}$, proportional to the prior knowledge (i.e., magnitude of association) is particularly assigned to gene j, where $\overline{CS}$ represents the mean of combined scores of all bipolar candidate genes. Thus, a weighted GSEA (wGSEA) was generalized. A set of genes (g) was first ordered according to the weighted gene-wise statistic values $[w_j r_j(D)]$ so that genes with a stronger significance (or small p-values) are ranked on the top. For each tested pathway (S), an enrichment score (ES) was calculated based on p-values of a gene-set in each pathway. The ES can be written as $ES = \max_{1 \leq j \leq N} \left\{ \sum_{g \in S, j \leq i} \frac{\left|w_j r_j(D)\right|^p}{N_R} - \sum_{g \notin S, j \leq i} \frac{1}{N - N_H} \right\}$ which consists of two parts, namely, gain (if gene is in a pathway) and loss (if gene is not in a pathway), where N_H represents the number of genes in a pathway S and $N_R = \sum_{g \in S} \left|w_j r_j(D)\right|^p$ is the total gain with $p = 1$. The ES was used to evaluate association signals for each annotated pathway. Then, for each pathway, the ES was normalized to compute NES by subtracting the mean of the ES in the permutated data sets, $ES(S^{perm})$, and divided by the standard deviation of $ES(S^{perm})$. We calculated empirical p-values for all pathways using 5,000 permutations to compare the original ES score from the GWA dataset and the permutation datasets (denoted as S^{perm}) by computing the fraction of the numbers of $\left\{ES\left(S^{perm}\right) > ES\left(S\right)\right\}$ divided by the total number of permutations. In a weighted sum-statistic (wSS) method, only genes in a specific pathway were considered, while part of those genes may play a larger role in the pathway. The wSS method calculates the sum of the weighted gene-wise statistic values over the set of genes $\left(\sum_{j=1}^{k} w_j r(D)_j\right)$. Alternatively, a statistical probability hypergeometric model was applied. In the hypergeometric test, we used a cutoff p-value of 0.05 to define significant genes using their gene-wise statistics (i.e., p-values). A p-value based on a hypergeometric distribution for each pathway was computed to describe the probability of interest genes (i.e., significant genes) in a specific pathway without a replacement from the whole GWA genes. We performed the hypergeometric test for all annotated pathways using the GWA dataset for BPD.

Biologically Functional Subnetwork Analysis

To perform the biologically functional subnetwork analysis, we selected genes from 15,213 GAIN GWA genes only if the gene contains at least one SNP having gene-wise statistic $p^{adj} < 0.05$ and the gene provides prior knowledge (i.e., having combined score greater than the total mean of combined scores) as these genes were denoted as seed genes for a further subnetwork analysis. We applied the AUTO expand algorithm in software, MetaCore[3], to these seed genes. A large network was constructed to the initial list of seed nodes (i.e., seed genes). Then, we cut the large network into several subnetworks according to the following procedures. Firstly, we expanded edges from the most relevant nodes (i.e., proximity of a node and traffic/flow through the node) for the outgoing (•→) path direction. Secondly, a flow value was calculated for each of seed nodes, with the flow through it equal to 1, according to algorithm. For example, a node has three incoming flows (each with flow value of 1/4), and then the node receives a flow value of 3/4. On the contrast, if the sum of incoming flows exceeds 1, the resulting flow value will be reduced to 1. Thirdly, we only considered the most connected node and selected the nodes that have the highest flow values. Fourthly, we iterated the process until the included nodes exceeded a default limit of 50. Fifthly, we applied the above steps for ingoing (←•) path direction and merged them into one subnetwork. Sixthly, the nodes selected for the subnetwork from the large network were deleted. Finally, a new subnetwork was reconstructed until no more subnetworks can be generated.

Each subnetwork provides a Z-score that ranks the subnetworks according to their saturation with genes from the initial list of seed nodes. The formula for the Z-score is

$$Z - score = \frac{r^{node} - n^{node}\left(\frac{R^{object}}{N^{node}}\right)}{\sqrt{n^{node}\left(\frac{R^{object}}{N^{node}}\right)\left(1 - \frac{R^{object}}{N^{node}}\right)\left(1 - \frac{R^{object} - 1}{N^{node} - 1}\right)}},$$

where r^{node} and n^{node} represent the number of nodes and the total number of nodes in each subnetwork generated from the seed nodes, respectively, R^{object} represents the number of network objects corresponding to the genes and proteins in the seed nodes, and N^{node} represents the total number of nodes in MetaCore™ database. A high Z-score exhibits that the network is highly saturated with genes from the seed genes. Similar to Z-score, we

[3]http://thomsonreuters.com/products_services/science/systems-biology/

compared the genes in the subnetwork versus the genes not in the subnetwork within the full set of all genes (i.e., MetaCore base knowledge) on maps, and calculated a *p*-value based on the hypergeometric distribution for each subnetwork to estimate the probability for a particular mapping to a subnetwork.

Multiple Testing Corrections

To account for multiple testing problems in the pathway and network analyses, we used the method proposed by Benjamini and Hochberg (1995) to control for the false discovery rate (FDR). We ordered all the *p*-values of pathways and compared each *p*-value $p(i)$ with a threshold of $(i/m)\,q^*$, where m represents the total number of pathways, and q^* represents the significance level. Thus, the procedure controls for the FDR at $q^* = 0.05$ level in this current study, assuming *p*-values are independently distributed under null hypotheses.

RESULTS

A total of 416,371 SNPs were annotated and mapped into 15,213 protein-coding genes in the GAIN GWA study of BPD, which were then mapped to 4,726 annotated pathways in the gene-pathway mapping process. We computationally optimized the tuning parameter λ in the gene-wise statistical significance correction step, and the value 0.85 was estimated iteratively to approximate the effective number of SNPs (see **Supplementary Figure 2**) for calculating gene-size corrected *p*-values using the GAIN GWA study for BPD. **Figure 2** displays the distribution of minimal *p*-values and quantile-quantile plots before and after the gene-size correction. We used 50% quantile of SNP numbers (i.e., >13 SNPs) and median of gene lengths (i.e., >23.15mb) to define a large gene. The distribution of logarithm of minimal *p*-values was skewed to the right (**Figure 2A**) and the quantile-quantile plots were far away from the 45° line (i.e., under null hypothesis of no correlation), which showed a significant correlation ($p = 2.2 \times 10^{-16}$) between minimal *p*-values and the gene-size (**Figures 2B,C**). After adjusted for the gene-length, the corrected *p*-values approximated uniformly distributed from [0,1] (**Figure 2D**) and their quantile-quantile plots followed the 45° line, which exhibit no any correlation ($p = 0.13$) between corrected *p*-values and the gene-size (**Figures 2E,F**).

In total, 87 enriched pathways (see **Supplementary Table 1**) were identified for their biological relevance in BPD using the GAIN GWA dataset after controlling the FDR at the 0.05 level. **Table 1** summarizes 36 significant pathways that were simultaneously enriched in both with or without weighting schemes under competitive methods (*w*GSEA and hypergeometric test) and self-contained method (*w*SS). Of which, 26 pathways were identified in permutation-based approaches (i.e., 22 out of 80 were identified in GSEA and 12 were identified in Sum-statistic, with 8 overlaps). The eight overlapping pathways (six from KEGG and two from Reactome) are drug metabolisms of other enzymes, pentose and glucuronate interconversions, starch and sucrose metabolism, ascorbate and aldarate metabolism, retinol metabolism, porphyrin and chlorophyll metabolism, glucuronidation, and phase II conjugation, which related to drug metabolism, carbohydrate metabolism, metabolism in cofactors and vitamins, xenobiotic metabolism, immune system, cell differentiation, cellular communication, cellular signal transduction, and growth factors. The remaining 18 pathways (3 from KEGG, 6 from GO, 2 from Reactome, and 7 from Curated gene sets) are mainly involved with lipid metabolism, xenobiotics biodegradation and metabolism, ion transport, molecular transport, cellular component, cellular communication, cell differentiation, immune system, growth factors, and oncogenes and translocate cancer genes. From a statistical and probabilistic point of view, 10 enriched pathways (7 from GO and 3 from Curated gene sets) were found significant using the hypergeometric test. Those pathways were structurally mapped to channel activities (i.e., voltage-gated channel activity, gated channel activity, voltage-gated cation channel activity and cation channel activity), molecular transport activities (i.e., cation or ion transmembrane transporter activity and metal ion transmembrane transporter activity), immune system, cell differentiation, cellular communication, cellular signal transduction, transcription factor, and growth factor.

We selected 274 genes (denoted as seed nodes) that show a high chance to associate with BPD (see our selection criteria in Materials and methods) from 15,213 GAIN GWA genes further for a functional subnetwork analysis. The selection of the 274 seed nodes was unlikely to be affected by large genes (correlation coefficient = −0.045, $p = 0.46$). The type and location of the 274 seed nodes were summarized in **Table 2**. These genes were mainly allocated to G-protein coupled receptor (e.g., *GRM1* and *ADRA1B* in plasma membrane), growth factor (e.g., *FGF5* and *TGFA* in extracellular space), ion channel (e.g., *KCNB1* and *CACNA2D* in plasma membrane; *ITPR2* and *NOX5* in cytoplasm), ligand-dependent nuclear receptor (e.g., *NR3C2* in nucleus), transcription regulator (e.g., *PAX* in nucleus; *WHAH* in cytoplasm), transmembrane receptor (e.g., *IL17RA* in plasma membrane; *TSPO* in cytoplasm), transporter (e.g., *ATP6V1B2* in cytoplasm; *SLC16A4* in plasma membrane), and others.

A total of 26 subnetworks were constructed in MetaCore using these 274 seed nodes. The crosstalk information and statistical tests for network saturation of the top three function-related biological subnetworks were listed in **Table 3** and the remaining subnetworks in **Supplementary Table 2**. The top one functional subnetwork (**Figure 3**) was saturated with 22 objects (spanned by 15 seed nodes) and 39 interactions (33 were activation and 6 were inhibition), which has a hub in transcription factor SP1 with 10 activation interactions ($p = 2.33 \times 10^{-20}$, Z-score = 24.35). This subnetwork was involved with several GO processes such as *de novo* posttranslational protein folding, *de novo* protein folding, protein folding, cellular protein complex assembly, and protein polymerization ($p = 9.6 \times 10^{-33} \sim 4.4 \times 10^{-22}$). The top two functional subnetworks (**Figure 4**) were centered around six hubs, including three transcription factors (SMAD3, PAX6, UBF), two generic binding proteins (BLNK, MTS1) and one generic enzyme (HDC), in a high range of crosstalk (ranging from 5 to 14 interactions) with other genes ($p = 3.25 \times 10^{-18}$, Z-score = 21.93). These subnetworks contained 15 objects

TABLE 1 | Significantly enriched pathways in the Genetic Association Information Network (GAIN) genome-wide association (GWA) study for bipolar disorder (BPD) using competitive and self-contained methods with and without weighting scheme.

			Permutation-based								**Probability-based**	
			GSEA				**Sum-statistic**				**Hypergeometric test**	
Annotated pathway[a]	n^{pw}_{GWA}/n^{pw}	n^{pw}_{BPD}	**Equal weight**		**Weighting**		**Equal weight**		**Weighting**			
			ES	p_{BH}[b]	**ES**	p_{BH}[b]	**SS**	p_{BH}[b]	**SS**	p_{BH}[b]	p_{nom}	p_{BH}[b]
KEGG:												
Drug metabolism other enzymes	48/51	26	0.68	**$<10^{-4}$**	0.72	**$<10^{-4}$**	42.24	**$<10^{-4}$**	73.01	**$<10^{-4}$**		
Retinol metabolism	60/64	42	0.67	**$<10^{-4}$**	0.66	**$<10^{-4}$**	53.94	**$<10^{-4}$**	93.48	**$<10^{-4}$**		
Pentose and glucuronate interconversions	25/28	13	0.73	**$<10^{-4}$**	0.78	**$<10^{-4}$**	28.58	**$<10^{-4}$**	50.73	**$<10^{-4}$**		
Porphyrin and chlorophyll metabolism	37/41	19	0.69	**$<10^{-4}$**	0.75	**$<10^{-4}$**	31.95	**$<10^{-4}$**	57.27	**$<10^{-4}$**		
Starch and sucrose metabolism	49/52	32	0.63	**$<10^{-4}$**	0.70	**$<10^{-4}$**	38.81	**$<10^{-4}$**	70.11	**$<10^{-4}$**		
Ascorbate and aldarate metabolism	23/25	12	0.79	**$<10^{-4}$**	0.81	**0.03**	27.54	**$<10^{-4}$**	50.67	**$<10^{-4}$**		
Drug metabolism cytochrome P450	68/72	54					53.22	**$<10^{-4}$**	98.54	**$<10^{-4}$**		
Metabolism of xenobiotics by cytochrome P450	68/70	54					51.41	**$<10^{-4}$**	94.61	**$<10^{-4}$**		
Steroid hormone biosynthesis	51/55	36					38.49	**$<10^{-4}$**	69.22	**$<10^{-4}$**		
GO:												
Extracellular region part	313/332	218	0.49	**$<10^{-4}$**	0.55	**$<10^{-4}$**						
Extracellular space	224/239	155	0.51	**$<10^{-4}$**	0.57	**$<10^{-4}$**						
Ion transport	174/184	108	0.54	**$<10^{-4}$**	0.54	**0.05**						
Substrate specific transmembrane transporter activity	321/341	207	0.49	**$<10^{-4}$**	0.51	**0.05**						
Substrate specific transporter activity	366/388	236	0.48	**$<10^{-4}$**	0.50	**0.05**						
Cytosol	191/202	139	0.50	**0.03**	0.55	**0.03**						
Cation transmembrane transporter activity	201/211	130									1.2×10^{-6}	**0.002**
Ion transmembrane transporter activity	259/275	169									6.7×10^{-6}	**0.006**
Metal ion transmembrane transporter activity	140/145	91									7.3×10^{-6}	**0.006**
Voltage-gated channel activity	70/73	46									3.1×10^{-5}	**0.02**
Gated channel activity	115/121	76									3.8×10^{-5}	**0.02**
Voltage-gated cation channel activity	64/66	41									5.8×10^{-5}	**0.03**
Cation channel activity	115/118	78									6.3×10^{-5}	**0.03**
REACTOME:												
Glucuronidation	17/19	8	0.83	**$<10^{-4}$**	0.81	**$<10^{-4}$**	22.50	**$<10^{-4}$**	37.16	**$<10^{-4}$**		
Phase II conjugation	56/60	35	0.60	**$<10^{-4}$**	0.66	**0.03**	42.18	**$<10^{-4}$**	72.53	**$<10^{-4}$**		
Purine ribonucleoside monophosphate biosynthesis	11/11	6	0.82	**0.03**	0.84	**0.05**						
Biological oxidations	120/127	83					76.62	**$<10^{-4}$**	133.5	**$<10^{-4}$**		
Curated gene-set:												
Riggi ewing sarcoma progenitor UP	375/426	245	0.46	**$<10^{-4}$**	0.54	**$<10^{-4}$**						
Zhang breast cancer progenitors UP	360/448	215	0.46	**$<10^{-4}$**	0.49	**0.03**						
Mullighan mll signature 1 UP	351/389	235	0.46	**0.02**	0.50	**0.03**						
Weber methylated icp in fibroblast	16/16	6	0.76	**0.02**	0.75	**0.03**						
Rizki tumor invasiveness 3D DN	215/234	145	0.49	**0.02**	0.53	**0.05**						
Bonci targets of MIR15A and MIR16_1	81/81	57	0.57	**0.04**	0.61	**0.05**						
Mccabe bound by HOXC6	350/461	228	0.46	**0.05**	0.50	**0.05**						
Martinez response to trabectedin	40/42	27									5.9×10^{-10}	**2.4×10^{-6}**
Manalo hypoxia UP	191/210	127									6.5×10^{-6}	**0.006**
Onder CDH1 targets 2 UP	226/258	159									3.0×10^{-5}	**0.02**

n^{pw}, the number of genes in pathway; n^{pw}_{GWA}, the number of genes on chip; n^{pw}_{BPD}, the number of bipolar candidate genes in pathway (i.e., prior knowledge to BPD); GSEA, gene-set enrichment analysis; ES, enrichment score; SS, sum-statistic; p_{nom}, nominal p-value.

[a] GSEA and Sum-statistic results were based on 5,000 permutations and hypergeometric test results were based on statistical probability model.

[b] The p_{BH} were based on Benjamini and Hochberg (1995) multiple testing correction.

Pathways with p-values highlighted in bold are significantly enriched for their biological relevance in BPD.

TABLE 2 | Type and location of the 274 seed nodes[a] selected from the GAIN GWA genes.

Type	Location	Genes[b]
G-protein coupled receptor	Plasma membrane	*ADRA1B, BAI1, GPR133, GRM1, NMBR, OR2B6, OR9G1, PTGER4*
Growth factor	Extracellular space	*FGF5, NELL1, TGFA*
Ion channel	Plasma membrane	*ACCN3, CACNA2D, CNGA3, KCNB1, KCNIP1, KCNQ1, KCNS1, PKD2L1, SCN3B, TRPC7, TRPV1, TRPV3*
	Cytoplasm	*ITPR2, NOX5, PEX5L*
	Unknown	*NALCN*
Ligand-dependent nuclear receptor	Nucleus	*NR3C2*
transcription regulator	Nucleus	*ADNP, ANKRD55, ATF3, ATF4, BASP1, CDYL, CREBBP, DMRT1, DNMT3L, FANK1, FOXM1, HIF3A, HIVEP2, HNF1B, KIDINS220, MLL4, NCOA1, PAX5, REST, RFX2, SIM1, TCF7L1, VSX1, ZBTB32, ZSCAN2*
	Cytoplasm	*ATF6Y, WHAH*
Transmembrane receptor	Plasma membrane	*CD40, GFRA1, IFNGR1, IL17RA, KIR2DS4, LMBR1, SFRP1, TYROBP*
	Cytoplasm	*TSPO*
Transporter	Cytoplasm	*ABCB8, ATP6V1B2, CCT6B, DOC2A, FABP3, SLC25A13, SYT2, SYT6, VPS26B*
	Plasma membrane	*ATP10B, SLC16A4, SLC17A3, SLC2A13, SLC4A10, VTI1A SLC5A1, SLC5A7, SLC6A15, SORCS2, STXBP3, TM9SF2,*
	Unknown	*SLCO5A1, SYT14*
Peptidase	Cytoplasm	*GZMB, PEPD*
	Extracellular space	*HABP2, MMP7*
	Plasma membrane	*DPP4*
	Unknown	*USP13*
Phosphatase	Plasma membrane	*PPFIA2, PTPRB*
	Cytoplasm	*PPM1A*
Chemical- endogenous mammal	Unknown	*C3*
Cytokine	Extracellular space	*CCL1, IFNA7, IFNG, IL26, WNT2, WNT4*
Enzyme	Cytoplasm	*ADSL, ALDH9A1, BRAF, BTRC, CNOT4, CYP26A1, CYP2C18, FBXL2, GCLM, GM2A, GNPAT, HEXA, HS3ST5, HSP90AA1, IRS1, MGAT4A, MTHFD1L, NAT1, NOS3, PAFAH1B2, PDHX, PLCG2, RAB21, RAB2A, RAB6A, TIAM2, UGT1A1, UGT1A4, UGT1A10, UGT1A8*
	Plasma membrane	*ADCY6, DAGLA, FADS1, GNG7, RAB4B, VNN1*
	Nucleus	*CA9, FNBP1, MAD2L2, SMARCAD1, SMYD3, TARS*
	Extracellular space	*SOD3*
	Unknown	*FAM135A, LCMT2, MBOAT2*
Kinase	Cytoplasm	*CHUK, CSNK1E, DCLK2, DGKH, EIF2AK4, PRKCE, STK4, TAOK2*
	Nucleus	*CDK5, CDK6, VRK2*
	Plasma membrane	*MAGI2, TRAT1, TRIO*
	Unknown	*RBKS, TTBK2*
Other	Cytoplasm	*ADAL, ARC, ARRB1, BAG1, BCAS4, BLNK, CIDEA, CST5, EFHA1, EML1, FAM129B, HBXIP, HSPB6, MFHAS1, NLRP5, NOS1AP, RASGRP3, RIN2, RPS7, SOCS6, STARD10, STARD13, STMN4, SWAP70, TBC1D15, TPM2*
	Extracellular space	*COL28A1, FBLN2, FST, LAMA5, NLRP7, TIMP2*
	Nucleus	*BCL11B, BMS1, CABLES1, CDAN1, FYB, GCKR, HIRIP3, HIST1H2AB, HIST1H3B, HIST1H4B, JRK, MAD1L1, NCAPD3, PCBP3, RANBP3, RASSF2, RBM15, SNRPA, SFRS5, SYNE1, ZFP161, ZMYND11, ZNF260, ZNF295, ZNF461, ZNF564, ZNF592*
	Plasma membrane	*ANK3, BTN2A1, CD276, CD53, CDH19, CDH22, CDH4, CGNL1, DSC3, EPB41L5, KIAA1797, GYPA, NPTN, PLXDC1, RPH3AL, SEZ6L, SGCG, SIRPB1, STOM, TANC1, TLN1, TSPAN15*
	Unknown	*ACTR3B, ADAMTSL3, BICC1, CACNA2D4, CALM3, CCDC122, CDKAL1, CTDSPL2, DNHD1, DPY19L1, FHAD1, GRAMD1B, KRTAP4-5, LONRF1, ODZ4, PHF21B, PSAPL1, SLC38A10, TMEM133, TMEM51, TMEM54, TTC15, TRIM38, TTC39B, TTLL12, WDFY2*

[a] *All selected genes were mapped in the Ingenuity Pathways Analysis (IPA).*
[b] *All genes contained at least one SNP having gene-wise statistic $p^{adj} < 0.05$ and provided information of combined scores greater than the median. Detailed methods of calculating combined scores please refer to Kao et al. (2014).*

(spanned by 14 seed nodes) and 83 interactions (58 were activation and 25 were inhibition), which mainly involve in GO processes of positive regulation of biological process, cellular process, signal transduction, response to stimulus and macromolecule metabolic process ($p = 3.7 \times 10^{-29}$–8.8×10^{-22}). In addition, 16 canonical pathways were presented on the subnetwork. The top three functional subnetworks (**Figure 5**) contained 16 objects (spanned by 14 seed nodes) and 64

TABLE 3 | The top three biologically enriched subnetworks[a].

No	Key subnetwork objects	GO processes	No. of seed nodes	No. of pathways	*p*-value[b]	Z-score[c]
1	DPP4, Ankyrin-B, ADNP, MCR, TAO2	"*de novo*" posttranslational protein folding (26.0%), "*de novo*" protein folding (26.0%), protein folding (31.5%), cellular protein complex assembly (28.8%), protein polymerization (19.2%)	15	0	2.33×10^{-20}	24.35
2	BLNK, Granzyme B, PAX5, C3, Follistatin	positive regulation of biological process (80.0%), positive regulation of cellular process (76.0%), positive regulation of response to stimulus (46.7%), positive regulation of signal transduction (40.0%), positive regulation of macromolecule metabolic process (56.0%)	14	16	3.25×10^{-18}	21.93
3	WNT4, TIMP2, GCKR(MAP4K5), B-Raf, SFRP1	canonical Wnt receptor signaling pathway (28.7%), positive regulation of biological process (82.5%), positive regulation of cellular process (77.5%), non-canonical Wnt receptor signaling pathway (20.0%), signal transduction (83.8%)	14	6	3.25×10^{-18}	21.93

[a]*Results are based on 274 selected genes (seed nodes).* [b]*p-value was calculated using hypergeometric test.* [c]*Z-score was calculated based on MetaCore base knowledge.*

interactions (49 were activation and 15 were inhibition), which have two hubs in a transcription factor (EGR1) and a GPCR receptor (FZD7) with a range from 5 to 18 interactions ($p = 3.25 \times 10^{-18}$, Z-score = 21.93). These subnetworks were involved with several GO processes including canonical and non-canonical Wnt receptor signaling pathways, a positive regulation of biological process and cellular process, and a signal transduction ($p = 3.3 \times 10^{-35}$–1.6×10^{-29}). In addition, six canonical pathways were presented on the subnetwork.

DISCUSSION

A rich and large-scale GWA data has been produced over past few years to document complex traits like BPD. The pathway-based analytics strategy provides an opportunity to uncover enriched pathways that are involved with the etiology of BPD based on prior knowledge of gene functions and molecular mechanisms. In this study, we reported 36 overrepresented pathways using a GWA dataset for BPD in GAIN, where genes in the same pathway were jointly associated with BPD. It is worth noting that many of these genes did not reach significant associations in GWA studies of BPD at a gene-level but reveal their potential roles in pathway-based analyses. In gene-level association analyses of the GAIN GWA study for BPD, the most genome-wide significant loci were found in *GRAMD1B* (rs4936819, $p = 1.2 \times 10^{-6}$), although it did not reach genome-wide significance threshold level at 5×10^{-8}. Not surprisingly, we observed that many genes were included in multiple pathways to increase the risk of BPD but not reported in the GAIN GWA study for BPD. For example, *HTR3B* and *CACNA1C* (the top 6th and 12th in BPD genes) were included in substrate specific transmembrane transporter activity, substrate specific transporter activity, cation transmembrane transporter activity, ion transmembrane transporter activity, metal ion transmembrane transporter activity, gated channel activity, and cation channel activity (Kao et al., 2014). Evidence also supported that *HTR3B* encodes the subunit B of type 3 receptor for 5-hydroxytryptamine (serotonin). It was also found to be a susceptible gene for the development of BPD while *CACNA1C* was reported to be associated with the involvement of calcium channels in the biological mechanisms of BPD (Frank et al., 2004; Kloiber et al., 2012).

Among the 36 enriched pathways, we examined the degree of overlapping for significant genes ($p < 0.05$) in these pathways to evaluate their crosstalk. The resulting number and proportion of overlapping genes were shown in **Supplementary Table 3**. The proportion of significant genes (i.e., contain at least one SNP having $p < 0.05$) among all pathways was between 12 and 88% (average = 49.4%). This demonstrated that these significant pathways were dominated by many genes rather than one single gene. Our results exhibited a low to intermediate level of overlapping across pathways, indicating some crosstalk of molecules in enriched pathways. Among all pair-wise pathway comparisons, 48.4% did not have any significant genes overlapping, 33.6% had a low degree of overlapping (less than 20%), 8.6% had a moderate degree of overlapping (20–70%), and only 9.4% pathways had a high degree of overlapping (more than 70%). The fact that only a few genes were commonly identified in significant pathways for BPD further reflects the difficulty we faced in identifying "the genes" for complex diseases.

Many disease traits are usually caused by the dysfunction of several susceptible gene loci with small main and interaction effects. In fact, there may exist some (or even a few) key genes to dominate particular functions within a specific biological pathway. To capture this, we allowed such genes to play important roles relevant to BPD in the pathway. Thus, a weighting algorithm linking to prior biological knowledge was introduced into our analytic strategies for the pathway analysis. Genes with stronger prior information contributed majorly to the significance of the pathway. We found the number of enriched pathways increased with the proportion of significant genes (i.e., prior information) of a pathway. The development of pathway-based approaches that incorporate prior biological knowledge can identify novel disease susceptibility pathways along with "the key genes," which will greatly facilitate the interpretation of GWA data biologically. Therefore, without highlighting the effects of these key genes in the pathway analysis, it is difficult to interpret their biological mechanisms correctly.

The *min-p* is a commonly used approach to assess association evidence at the gene-level in the pathway-based analysis.

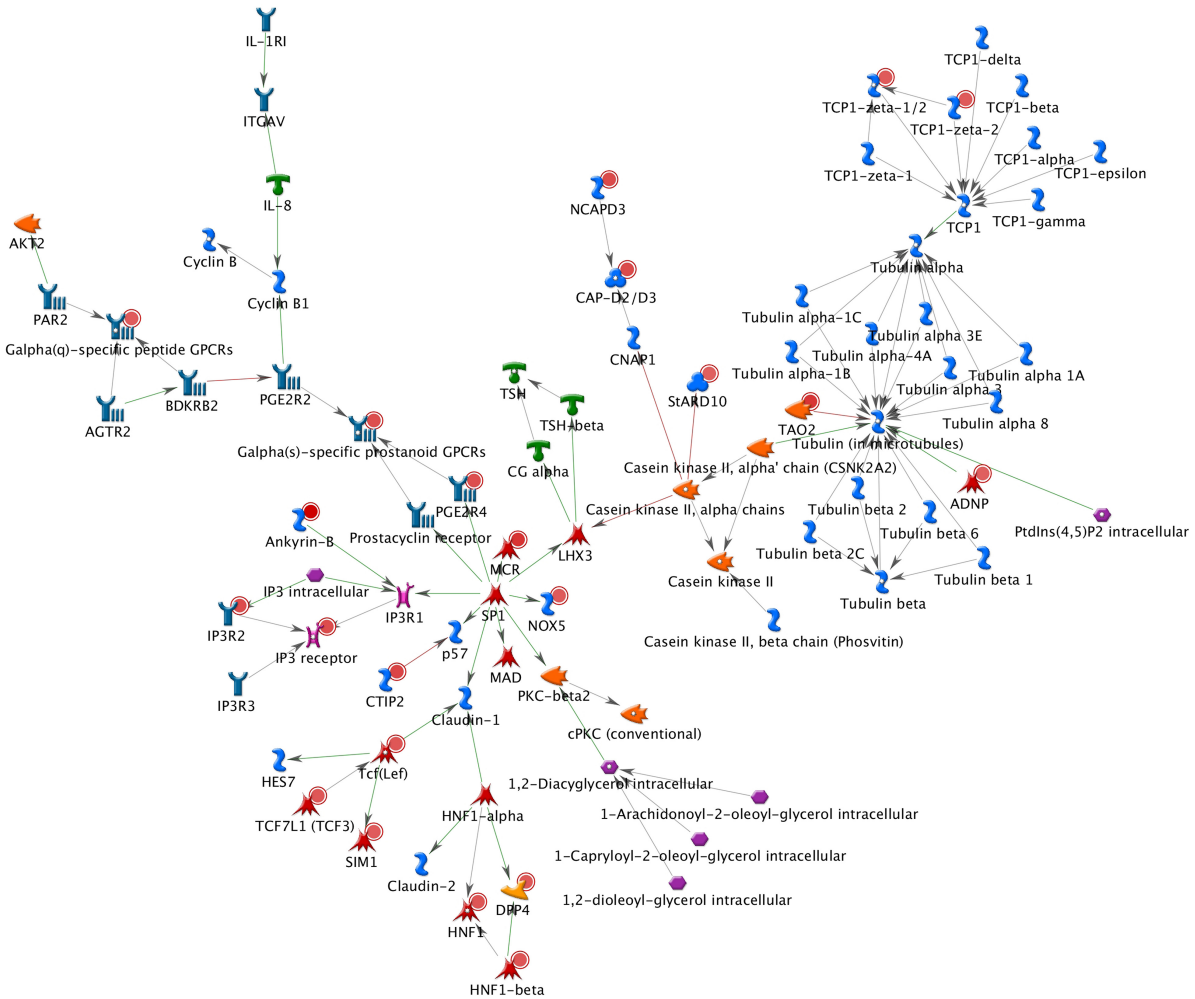

FIGURE 3 | The top one functional subnetwork. This subnetwork was saturated with 22 objects and 39 interactions, with a hub in transcription factor SP1 with 10 activation interactions. Thick cyan lines indicate the fragments of canonical pathways. Upregulated genes are marked with red circles and downregulated with blue circles. Green and red arrows indicate activation and inhibition effect, respectively.

However, using the *min-p* statistic to represent the significance of a gene may be limited. For instance, if a number of markers within a gene region are moderately associated with a disease trait, the signal of such gene may be downweighed by not having "one" particular significant signal. Thus, combining all information of SNPs (i.e., *combined-p*) in a gene can aggregate the overall evidence that the gene-set association and SNPs with moderate effects can be included. Different strategies of defining the gene-level statistic may have substantial influences on results. This seems to be reasonable and also supported by observations evidence (Kao et al., 2012). One possible future direction in defining gene-level statistic is to adopt a mixed approach of using *min-p* and *combined-p*. With the mixed algorithm, an appropriate gene-level statistic will be computed to represent each gene properly.

In this current study, we found several BPD-susceptibility pathways were significantly related to metabolism that is not reported in previous studies using GWA SNPs data. However, there is overwhelming evidence to suggest that many metabolic pathways have been reported to be linked to complex traits, particularly psychiatric disorders (Saxena, 2009; Wood and Wood, 2013). In the past, a meta-analysis of metabolic abnormalities in BPD reported that bipolar patients, particularly patients of older age, are at a high risk for metabolic syndrome (Vancampfort et al., 2013). Priebe et al. (2012) used genome-wide SNP data to search for the presence of copy number variations in 291 early-onset bipolar patients and 872 healthy controls to implement pathways and biological processes. They found many pathways were significantly enriched in drug metabolism, lipid metabolism, and molecular transport, which were in line with our findings. Our results were also consistent with other studies based on using information from allele-specific gene methylation and incorporating information of microRNAs into the pathway analysis in the GAIN GWA study for BPD (Chuang et al., 2013; Shih et al., 2013). Besides, schizophrenia patients were found to be associated with thiol metabolism. In addition,

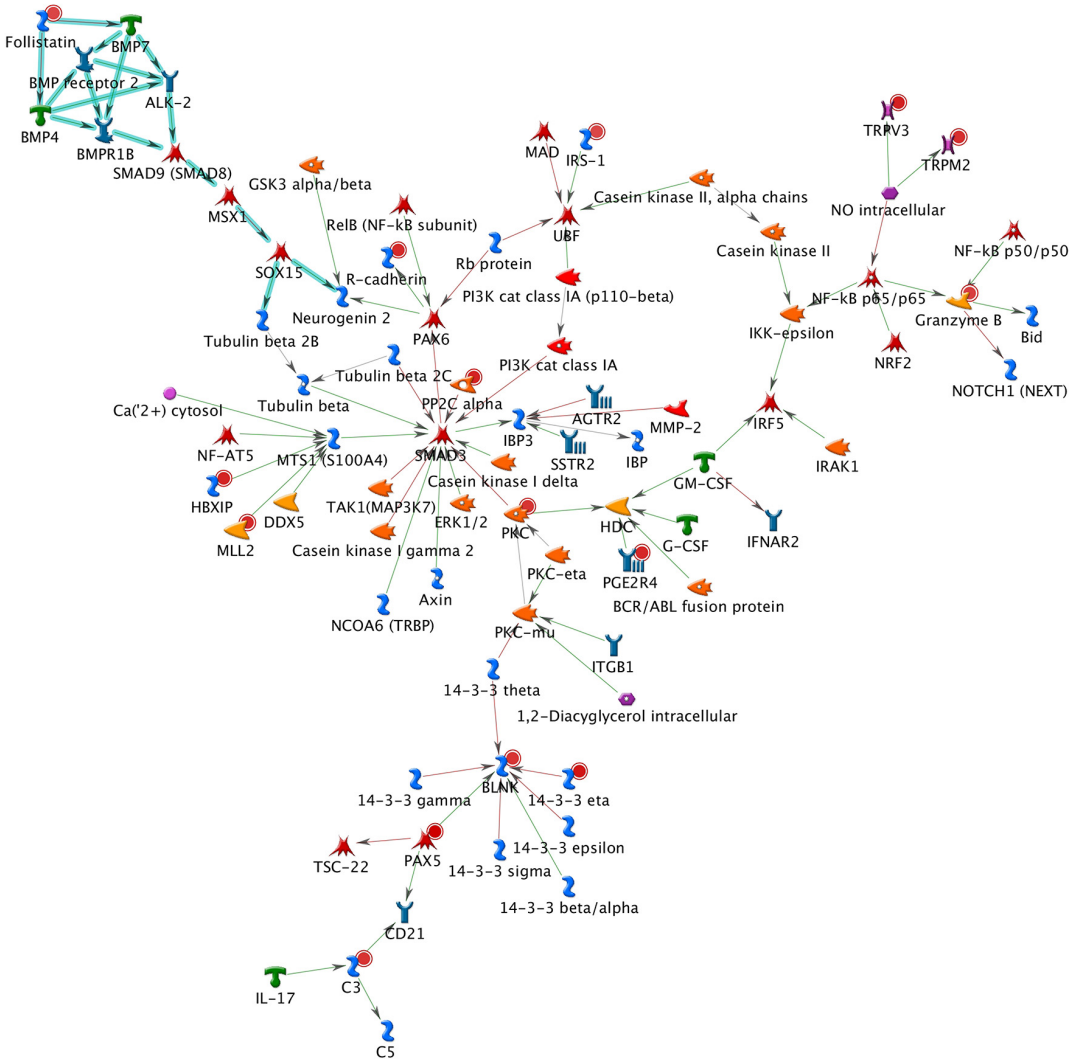

FIGURE 4 | The top two functional subnetwork. This subnetwork contained 15 objects and 83 interactions, which centered around six hubs, including three transcription factors (SMAD3, PAX6, and UBF), two generic binding proteins (BLNK and MTS1), and one generic enzyme (HDC). Thick cyan lines indicate the fragments of canonical pathways. Upregulated genes are marked with red circles and downregulated with blue circles. Green and red arrows indicate activation and inhibition effect, respectively.

abnormalities in metabolic cascades and metabolic disturbances were further observed in schizophrenia patients (Thakore, 2004; Kirkpatrick et al., 2008). Overall, the above evidence suggests that metabolic syndromes and complex psychiatric disorders like BPD appear to share some common in genetic factors, and may contribute to medical co-morbidity, including endocrine disturbances, dysregulation of sympathetic nervous system, and behavior patterns in these patients (Fagiolini et al., 2008). Our results identified nine enriched metabolic pathways that were significantly associated with BPD. These pathways were involved with human metabolic profiles, including drug, cofactors and vitamins, carbohydrate, lipid, and xenobiotics biodegradation. Importantly, human metabolizing systems act as a role of detoxification and transport through specialized enzymatic systems to aid excretion of xenobiotics, including drugs.

The BPD-related subnetworks (**Figures 3–5** and **Table 3**) are complex and sophisticated, involving with several biological processes, cellular processes, signal transduction, metabolic processes, neuronal activities, immune system, and inflammation processes. The most significant subnetwork (**Figure 3**) is primarily related to the activation mechanism of transcription regulation between effects of *SP1* and many proteins (e.g., MAD, Prostacyclin receptor, *NOX5*, *LHX3*, PGE2R4, PKC-beta2, MCR, Claudin-1, p57 and IP3R1). This subnetwork plays a role in cell growth and apoptosis (e.g., *NOX5*), cell differentiation (e.g., *TCF7L1*, also known as *TCF3*), major transcript (e.g., Ankyrin-B), and ion or water transport (e.g., MCR). The second significant subnetwork (**Figure 4**) plays a role in regulating B-cell function and development (e.g., *BLNK*), B-cell differentiation and neural development (e.g., *PAX5*), immune system and inflammatory

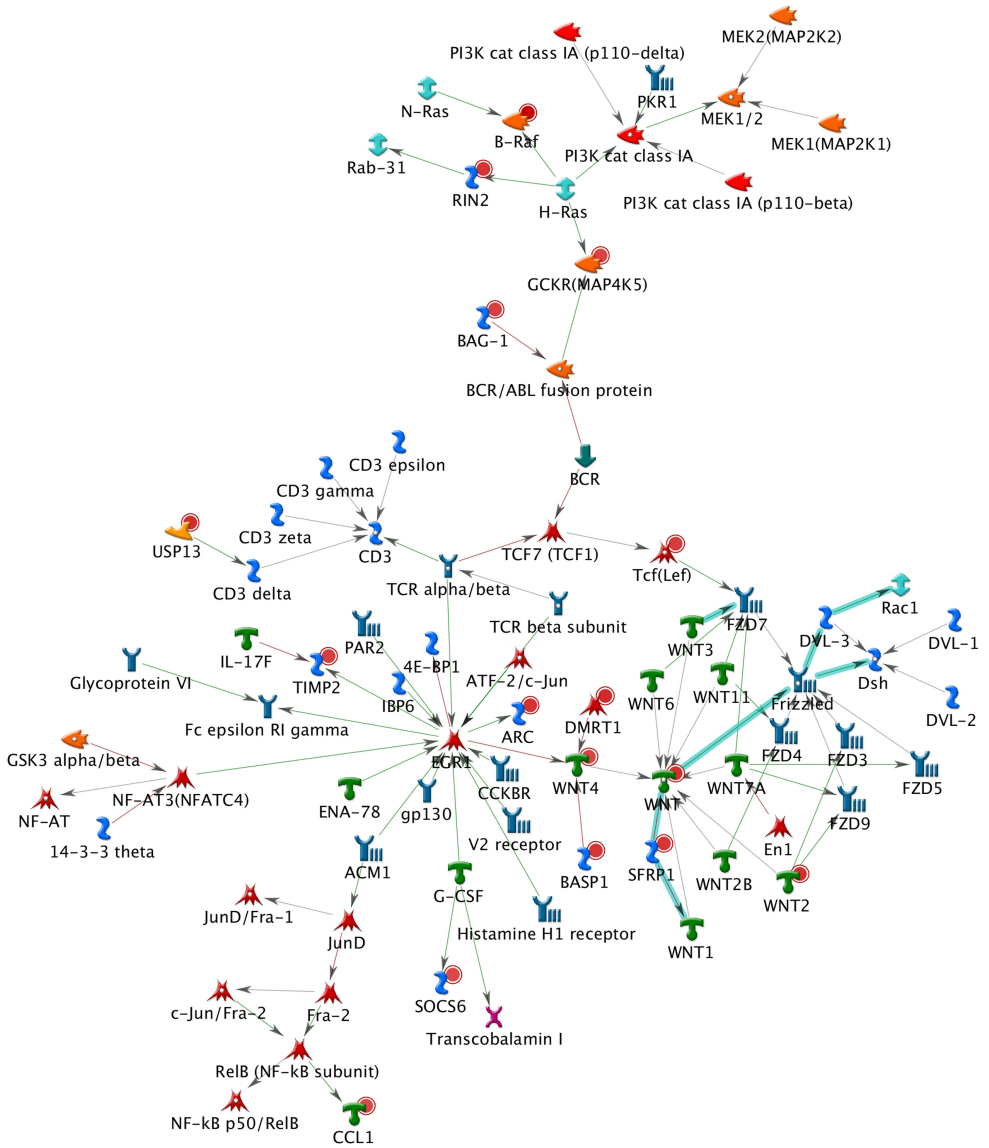

FIGURE 5 | The top three functional subnetwork. This subnetwork contained 16 objects and 64 interactions, with two hubs in a transcription factor (EGR1) and a GPCR receptor (FZD7) with ranging from 5 to 18 interactions. Thick cyan lines indicate the fragments of canonical pathways. Upregulated genes are marked with red circles and downregulated with blue circles. Green and red arrows indicate activation and inhibition effect, respectively.

response (e.g., Granzyme B, *C3*), cellular proliferation and differentiation (e.g., Follistatin), and mediation of the control of cellular processes including cell cycle, neuron growth, ion channel regulation, and immune response (e.g., PKC). The third significant subnetwork (**Figure 5**) is central with two hubs (*EGR1* and *FZD7*). *EGR1* plays a critical role in animal models of maternal behavior on stress responses in the offspring (Weaver et al., 2004). The mechanism underlying the effect of early maternal behavior involves the EGR-mediated regulation of glucocorticoid receptor that may influence psychiatric illness susceptibility and abnormal anxiety-related behaviors later in life (Fish et al., 2004). McGowan et al. (2009) conducted a study in postmortem brains and suggested that similar mechanisms may occur in humans. *FZD7* was also identified to be associated with psychiatric or neurological disorders (Hoseth et al., 2018). This subnetwork plays a role in the response to environmental stress [e.g., *GCKR* (*MAP4K5*)], long-term memory (*ARC*), hippocampal neuron (B-Raf), and in regulating cell growth and differentiation (*SFRP1*). In this study, we identified 26 BPD-related functional subnetworks, which provide us an opportunity to facilitate future follow-up and functional studies for bipolar.

Many enriched pathways and selected genes were significantly associated with BPD in this study. Of which several genes and pathways were discussed and found to be consistent with previous studies. Particularly, six metabolic pathways (drug metabolism, retinol metabolism, pentose and glucuronate interconversions, porphyrin and chlorophyll metabolism, starch and sucrose metabolism, ascorbate and aldarate metabolism)

were connected to dementia. A metabolic-caused dementia is a loss of function in the brain, e.g., cognitive changes and memory loss, that often occurs with certain psychiatric disorders like BPD. For instance, drugs are frequently a cause of dementia, which may impair cognition indirectly through metabolic effects (Starr and Whalley, 1994). Retinol metabolism was connected to an increased risk of dementia development. Retinol hypofunction and impaired transport may contribute to patients with memory impairment in Alzheimer's disease (AD) and dementia (Goodman and Pardee, 2003). Two metabolic pathways, pentose and glucuronate interconversions (Zheng et al., 2019), and starch and sucrose metabolism (Ling et al., 2021) may play roles in learning and cognitive impairment that are caused by abnormal nitric oxide production and monoaminergic neurotransmitters in AD, BPD, and/or dementia patients. Other metabolisms, including porphyrin and chlorophyll metabolism (Wang et al., 2015), and ascorbate and aldarate metabolism (Chen et al., 2011) were biologically or molecularly connected with psychiatric disorders (e.g., AD, BPD) and dementia. We noticed that some of enriched network pathways that were not reported previously suggest that there may be potential links between BPD and the risk of dementia or possibly a chance association.

There are some limitations in our study. First, our pathway analysis relied on the accuracy and completeness of pathway annotation databases (e.g., MSigDB). Some genes may have potential impacts on BPD but not annotated in pathway databases, and they may be excluded from our analyses. Other datasets, such as IPA knowledge base,[4] that provides detail-rich, highly structured knowledge for over 1,582,000 biological and chemical concepts in 19,635 humans, 15,194 mice, and 8,190 rat genes may be helpful to be considered in future analyses though their annotations need to be carefully selected. Second, it is possible that some genes might be falsely reported as significant loci in the literature. Thus, the accuracy of prior information is subjective to the completeness of data sources from the literature and current knowledge. We integrated gene information from different platforms or data sources to construct a combined score for each gene, followed by weighted pathway analysis to obtain more value-added pathway results using all existing genomic evidence and knowledge for BPD. Third, different strategies of defining the gene-level statistic may result in different outcomes in the pathway analysis. Some genes may be dominated by one (or a few) SNP(s) with a strong effect while other genes may be dominated by several SNPs with moderate effects. In this study, we only used the *min-p* statistic to extract information of SNPs for a gene. An advanced approach in calculating gene-level statistics for each gene is to extract SNPs information using both the *min-p* and the *combined-p* (e.g., random effects model or Bayesian statistical methods according to the structure of SNPs in a gene region (Stephens and Balding, 2009). Fourth, our study uses the signals of genetic association, while other genomic information (such as gene expression, gene regulation, etc.) has not been used yet. Concerning other useful genomic datasets, a possible utilization approach is to incorporate all possible genomic information into the pathway analysis. Finally, we only focused on Caucasian populations, using one GWA dataset for the pathway analysis and other for prior information collection (Kao et al., 2014). To generalize the results to the Eastern countries, a meta-analysis (or mega-analysis) of combining different populations (Caucasian and Han Chinese) of GWA data is underway to increase power to uncover the underlying biological mechanisms for BPD.

[4]http://www.ingenuity.com/products/ipa#/

CONCLUSION

Applying our comprehensive framework for the pathway and functional subnetwork analyses is useful for uncovering the underlying mechanisms and networks for complex traits. The evidence-based collection of prior information could benefit from quick accumulated data information and evidence from different aspects, which provides valuable information to quantify the contribution of genes in pathways for complex traits of interest. A number of novel genes that did not show significant associtions with BPD in the original single marker or gene analysis of GWA dataset were found to participate in several pathways, which, jointly with other genes, play roles in the pathogenesis of BPD. Although it remains largely unclear how the defect of pathways is specifically linked to the development of BPD, our identified pathways provided important biological insights into the interpretation of genome-wide association data for BPD. These findings are anticipated to facilitate future follow-up and functional studies for the connection and clinical implications between BPD and dementia.

DATA AVAILABILITY STATEMENT

The GWA data set was accessed through the Genetic Association Information Network (GAIN), database of Genotypes and Phenotypes (dbGaP) accession number phs000017.v3.p1 (http://www.ncbi.nlm.nih.gov/).

AUTHOR CONTRIBUTIONS

C-FK: study conception and design and acquisition of data. C-FK and WH: analysis and interpretation of data. C-FK, C-YK, T-YC, P-HK, WH, C-RC, Y-SL, and G-TY: draft and revise manuscript. All authors read and approved the final manuscript.

FUNDING

This work was supported by grant MOST 109-2320-B-303-004-MY3 from Taiwan Ministry of Science and Technology and grant TCRD-TPE-MOST-109-15 from the Taipei Tzu Chi Hospital, Buddhist Tzu Chi Medical Foundation, New Taipei City, Taiwan. This work was financially supported (in part) by the Advanced Plant Biotechnology Center from The Featured Areas Research Center Program within the framework of the Higher Education Sprout Project by the Ministry of Education (MOE) in Taiwan.

ACKNOWLEDGMENTS

We thank Li-Chung Chuang and Po-Hsiu Kuo for collecting the GWA data and being in charge of data management.

SUPPLEMENTARY MATERIAL

The Supplementary Material for this article can be found online at: https://www.frontiersin.org/articles/10.3389/fnmol.2021.772584/full#supplementary-material

REFERENCES

Almeida, O. P., Mccaul, K., Hankey, G. J., Yeap, B. B., Golledge, J., and Flicker, L. (2016). Risk of dementia and death in community-dwelling older men with bipolar disorder. *Br. J. Psychiatry* 209, 121–126. doi: 10.1192/bjp.bp.115.180059

Baldaçara, L., Borgio, J. G. F., Araújo, C., Nery-Fernandes, F., Lacerda, A. L. T., Moraes, W. A. D. S., et al. (2012). Relationship between structural abnormalities in the cerebellum and dementia, posttraumatic stress disorder and bipolar disorder. *Dement. Neuropsychol.* 6, 203–211. doi: 10.1590/S1980-57642012DN06040003

Benjamini, Y., and Hochberg, Y. (1995). Controlling the false discovery rate: a practical and powerful approach to multiple testing. *J. R. Stat. Soc. Ser. B Methodol.* 57, 289–300. doi: 10.1111/j.2517-6161.1995.tb02031.x

Borges, S. Q., Corrêa, T. X., Trindade, I. O. A., Amorim, R. F. B., and Toledo, M. A. D. V. (2019). Cognitive impairment in bipolar disorder neuroprogression or behavioral variant frontotemporal dementia? *Dement. Neuropsychol.* 13, 475–480. doi: 10.1590/1980-57642018dn13-040016

Chen, K.-D., Chang, P.-T., Ping, Y.-H., Lee, H.-C., Yeh, C.-W., and Wang, P.-N. (2011). Gene expression profiling of peripheral blood leukocytes identifies and validates ABCB1 as a novel biomarker for Alzheimer's disease. *Neurobiol. Dis.* 43, 698–705. doi: 10.1016/j.nbd.2011.05.023

Chen, M.-H., Li, C.-T., Tsai, C.-F., Lin, W.-C., Chang, W.-H., Chen, T.-J., et al. (2015). Risk of subsequent dementia among patients with bipolar disorder or major depression: a nationwide longitudinal study in Taiwan. *J. Am. Med. Dir. Assoc.* 16, 504–508. doi: 10.1016/j.jamda.2015.01.084

Chuang, L.-C., Kao, C.-F., Shih, W.-L., and Kuo, P.-H. (2013). Pathway analysis using information from allele-specific gene methylation in genome-wide association studies for bipolar disorder. *PLoS One* 8:e53092. doi: 10.1371/journal.pone.0053092

Crow, T. (2011). The missing genes: what happened to the heritability of psychiatric disorders? *Mol. Psychiatry* 16, 362–364. doi: 10.1038/mp.2010.92

Crow, T. J. (2007). How and why genetic linkage has not solved the problem of psychosis: review and hypothesis. *Am. J. Psychiatry* 164, 13–21. doi: 10.1176/ajp.2007.164.1.13

Diniz, B. S., Teixeira, A. L., Cao, F., Gildengers, A., Soares, J. C., Butters, M. A., et al. (2017). History of bipolar disorder and the risk of dementia: a systematic review and meta-analysis. *Am. J. Geriatr. Psychiatry* 25, 357–362. doi: 10.1016/j.jagp.2016.11.014

Fagiolini, A., Chengappa, K. N. R., Soreca, I., and Chang, J. (2008). Bipolar disorder and the metabolic syndrome: causal factors, psychiatric outcomes and economic burden. *CNS Drugs* 22, 655–669. doi: 10.2165/00023210-200822080-00004

Fish, E. W., Shahrokh, D., Bagot, R., Caldji, C., Bredy, T., Szyf, M., et al. (2004). Epigenetic programming of stress responses through variations in maternal care. *Ann. N. Y. Acad. Sci.* 1036, 167–180. doi: 10.1196/annals.1330.011

Frank, B., Niesler, B., Nothen, M. M., Neidt, H., Propping, P., Bondy, B., et al. (2004). Investigation of the human serotonin receptor gene HTR3B in bipolar affective and schizophrenic patients. *Am. J. Med. Genet. B Neuropsychiatr.* 131B, 1–5. doi: 10.1002/ajmg.b.30070

Fridley, B. L., and Biernacka, J. M. (2011). Gene set analysis of SNP data: benefits, challenges, and future directions. *Eur. J. Hum. Genet.* 19, 837–843. doi: 10.1038/ejhg.2011.57

Gershon, E. S., Alliey-Rodriguez, N., and Liu, C. (2011). After GWAS: searching for genetic risk for schizophrenia and bipolar disorder. *Am. J. Psychiatry* 168, 253–256. doi: 10.1176/appi.ajp.2010.10091340

Goodman, A. B., and Pardee, A. B. (2003). Evidence for defective retinoid transport and function in late onset Alzheimer's disease. *Proc. Natl. Acad. Sci. U.S.A.* 100, 2901–2905. doi: 10.1073/pnas.0437937100

Hindorffa, L. A., Sethupathy, P., Junkins, H. A., Ramos, E. M., Mehta, J. P., Collins, F. S., et al. (2009). Potential etiologic and functional implications of genome-wide association loci for human diseases and traits. *Proc. Natl. Acad. Sci. U.S.A.* 106, 9362–9367. doi: 10.1073/pnas.0903103106

Holmans, P. (2010). Statistical methods for pathway analysis of genome-wide data for association with complex genetic traits. *Adv. Genet.* 72, 141–179. doi: 10.1016/B978-0-12-380862-2.00007-2

Holmans, P., Green, E. K., Pahwa, J. S., Ferreira, M. A. R., Purcell, S. M., Sklar, P., et al. (2009). Gene ontology analysis of GWA study data sets provides insights into the biology of bipolar disorder. *Am. J. Hum. Genet.* 85, 13–24. doi: 10.1016/j.ajhg.2009.05.011

Hoseth, E. Z., Krull, F., Dieset, I., Mørch, R. H., Hope, S., Gardsjord, E. S., et al. (2018). Exploring the Wnt signaling pathway in schizophrenia and bipolar disorder. *Transl. Psychiatry* 8, 1–10. doi: 10.1038/s41398-018-0102-1

Ideker, T., Dutkowski, J., and Hood, L. (2011). Boosting signal-to-noise in complex biology: prior knowledge is power. *Cell* 144, 860–863. doi: 10.1016/j.cell.2011.03.007

Jia, P., Kao, C.-F., Kuo, P.-H., and Zhao, Z. (2011a). A comprehensive network and pathway analysis of candidate genes in major depressive disorder. *BMC Syst. Biol.* 5:S12. doi: 10.1186/1752-0509-5-S3-S12

Jia, P., Wang, L., Meltzer, H. Y., and Zhao, Z. (2011b). Pathway-based analysis of GWAS datasets: effective but caution required. *Int. J. Neuropsychopharmacol.* 14, 567–572. doi: 10.1017/S1461145710001446

Kao, C. F., Chuang, L. C., and Kuo, P. H. (2014). Risk and information evaluation of prioritized genes for complex traits: application to bipolar disorder. *Am. J. Med. Genet. B Neuropsychiatr. Genet.* 165, 596–606. doi: 10.1002/ajmg.b.32263

Kao, C.-F., Jia, P., Zhao, Z., and Kuo, P.-H. (2012). Enriched pathways for major depressive disorder identified from a genome-wide association study. *Int. J. Neuropsychopharmacol.* 15, 1401–1411. doi: 10.1017/S1461145711001891

Kato, T. (2007). Molecular genetics of bipolar disorder and depression. *Psychiatry Clin. Neurosci.* 61, 3–19. doi: 10.1111/j.1440-1819.2007.01604.x

Kessing, L., and Andersen, P. (2004). Does the risk of developing dementia increase with the number of episodes in patients with depressive disorder and in patients with bipolar disorder? *J. Neurol. Neurosurg. Psychiatry* 75, 1662–1666. doi: 10.1136/jnnp.2003.031773

Kessler, R. C., Berglund, P., Demler, O., Jin, R., Merikangas, K. R., and Walters, E. E. (2005). Lifetime prevalence and age-of-onset distributions of DSM-IV disorders in the national comorbidity survey replication. *Arch. Gen. Psychiatry* 62, 593–602. doi: 10.1001/archpsyc.62.6.593

Kirkpatrick, B., Fernandez-Egea, E., Garcia-Rizo, C., and Bernardo, M. (2008). Differences in glucose tolerance between deficit and nondeficit schizophrenia. *Schizophr. Res.* 107, 122–127. doi: 10.1016/j.schres.2008.09.023

Kloiber, S., Czamara, D., Karbalai, N., Müller-Myhsok, B., Hennings, J., Holsboer, F., et al. (2012). ANK3 and CACNA1C – missing genetic link for bipolar disorder and major depressive disorder in two German case-control samples. *J. Psychiatr. Res.* 46, 973–979. doi: 10.1016/j.jpsychires.2012.04.017

Lee, S. H., Wray, N. R., Goddard, M. E., and Visscher, P. M. (2011). Estimating missing heritability for disease from genome-wide association studies. *Am. J. Hum. Genet.* 88, 294–305. doi: 10.1016/j.ajhg.2011.02.002

Ling, Z., Zhu, M., Liu, X., Shao, L., Cheng, Y., Yan, X., et al. (2021). Fecal fungal dysbiosis in chinese patients with Alzheimer's disease. *Front. Cell Dev. Biol.* 8:1920. doi: 10.3389/fcell.2020.631460

Lopes, R., and Fernandes, L. (2012). Bipolar disorder: clinical perspectives and implications with cognitive dysfunction and dementia. *Depress. Res. Treat.* 2012:275957. doi: 10.1155/2012/275957

Maher, B. (2008). Personal genomes: the case of the missing heritability. *Nature* 456, 18–21. doi: 10.1038/456018a

Manolio, T. A., Brooks, L. D., and Collins, F. S. (2008). A HapMap harvest of insights into the genetics of common disease. *J. Clin. Investig.* 118, 1590–1605. doi: 10.1172/JCI34772

Manolio, T. A., Collins, F. S., Cox, N. J., Goldstein, D. B., Hindorff, L. A., Hunter, D. J., et al. (2009). Finding the missing heritability of complex diseases. *Nature* 461, 747–753. doi: 10.1038/nature08494

Manolio, T. A., Rodriguez, L. L., Brooks, L., Abecasis, G., Psoriasis, T. C. A. S. O., Ballinger, D., et al. (2007). New models of collaboration in genomewide association studies: the genetic association information network. *Nat. Genet.* 39, 1045–1051. doi: 10.1038/ng2127

Masouy, A., Chopard, G., Vandel, P., Magnin, E., Rumbach, L., Sechter, D., et al. (2011). Bipolar disorder and dementia: where is the link? *Psychogeriatrics* 11, 60–67.

McGowan, P. O., Sasaki, A., D'alessio, A. C., Dymov, S., Labonté, B., Szyf, M., et al. (2009). Epigenetic regulation of the glucocorticoid receptor in human brain associates with childhood abuse. *Nat. Neurosci.* 12, 342–348. doi: 10.1038/nn.2270

McGuffin, P., Rijsdijk, F., Andrew, M., Sham, P., Katz, R., and Cardno, A. (2003). The heritability of bipolar affective disorder and the genetic relationship to unipolar depression. *Arch. Gen. Psychiatry* 60, 497–502. doi: 10.1001/archpsyc.60.5.497

Merikangas, K. R., Herrell, R., Swendsen, J., Rossler, W., Ajdacic-Gross, V., and Angst, J. (2008). Specificity of bipolar spectrum conditions in the comorbidity of mood and substance use disorders: results from the Zurich cohort study. *Arch. Gen. Psychiatry* 65, 47–52. doi: 10.1001/archgenpsychiatry.2007.18

Mirina, A., Atzmon, G., Ye, K., and Bergman, A. (2012). Gene size matters. *PLoS One* 7:e49093. doi: 10.1371/journal.pone.0049093

Pavlovic, A., Marley, J., and Sivakumar, V. (2011). Development of frontotemporal dementia in a case of bipolar affective disorder: is there a link? *BMJ Case Rep.* 2011:bcr0920103303. doi: 10.1136/bcr.09.2010.3303

Pedroso, I., Lourdusamy, A., Rietschel, M., Nöthen, M. M., Cichon, S., Mcguffin, P., et al. (2012). Common genetic variants and gene-expression changes associated with bipolar disorder are over-represented in brain signaling pathway genes. *Biol. Psychiatry* 72, 311–317. doi: 10.1016/j.biopsych.2011.12.031

Peng, G., Luo, L., Siu, H., Zhu, Y., Hu, P., Hong, S., et al. (2010). Gene and pathway-based second-wave analysis of genome-wide association studies. *Eur. J. Hum. Genet.* 18, 111–117. doi: 10.1038/ejhg.2009.115

Pregelj, P. (2011). Gene environment interactions in bipolar disorder. *Psychiatr. Danub.* 23, S91–S93.

Priebe, L., Degenhardt, F., Herms, S., Haenisch, B., Mattheisen, M., Nieratschker, V., et al. (2012). Genome-wide survey implicates the influence of copy number variants (CNVs) in the development of early-onset bipolar disorder. *Mol. Psychiatry* 17, 421–432. doi: 10.1038/mp.2011.8

Saccone, S. F., Hinrichs, A. L., Saccone, N. L., Chase, G. A., Konvicka, K., Madden, P. A. F., et al. (2007). Cholinergic nicotinic receptor genes implicated in a nicotine dependence association study targeting 348 candidate genes with 3713 SNPs. *Hum. Mol. Genet.* 16, 36–49. doi: 10.1093/hmg/ddl438

Saxena, U. (2009). Lipid metabolism and Alzheimer's disease: pathways and possibilities. *Expert Opin. Ther. Targets* 13, 331–338. doi: 10.1517/14728220902738720

Shih, W.-L., Kao, C.-F., Chuang, L.-C., and Kuo, P.-H. (2013). Incorporating information of microRNAs into pathway analysis in a genome-wide association study of bipolar disorder. *Front. Genet.* 3:293. doi: 10.3389/fgene.2012.00293

Sidak, Z. (1967). Rectangular confidence regions for the means of multivariate normal distributions. *J. Am. Stat. Assoc.* 62, 626–633. doi: 10.2307/2283989

Starr, J. M., and Whalley, L. J. (1994). Drug-induced dementia. *Drug Saf.* 11, 310–317. doi: 10.2165/00002018-199411050-00003

Stephens, M., and Balding, D. J. (2009). Bayesian statistical methods for genetic association studies. *Nat. Rev. Genet.* 10, 681–690. doi: 10.1016/j.gene.2018.10.057

Subramanian, A., Tamayo, P., Mootha, V. K., Mukherjee, S., Ebert, B. L., Gillette, M. A., et al. (2005). Gene set enrichment analysis: a knowledge-based approach for interpreting genome-wide expression profiles. *Proc. Natl. Acad. Sci. U.S.A.* 102, 15545–15550. doi: 10.1073/pnas.0506580102

Thakore, J. H. (2004). Metabolic disturbance in first-episode schizophrenia. *Br. J. Psychiatry* 184, s76–s79. doi: 10.1192/bjp.184.47.s76

Vancampfort, D., Vansteelandt, K., Correll, C. U., Mitchell, A. J., De Herdt, A., Sienaert, P., et al. (2013). Metabolic syndrome and metabolic abnormalities in bipolar disorder: a meta-analysis of prevalence rates and moderators. *Am. J. Psychiatry* 170, 265–274. doi: 10.1176/appi.ajp.2012.12050620

Wang, C., Zhao, J., Xu, R., Zhao, J., and Duan, S. (2015). Identification of pivotal markers in vascular dementia based on proteomics data. *Dement. Geriatr. Cogn. Disord.* 39, 312–320. doi: 10.1159/000375296

Wang, K., Li, M., and Hakonarson, H. (2010). Analysing biological pathways in genome-wide association studies. *Nat. Rev. Genet.* 11, 843–854. doi: 10.1038/nrg2884

Wang, L., Jia, P., Wolfinger, R. D., Chen, X., and Zhao, Z. (2011). Gene set analysis of genome-wide association studies: methodological issues and perspectives. *Genomics* 98, 1–8. doi: 10.1016/j.ygeno.2011.04.006

Weaver, I. C. G., Cervoni, N., Champagne, F. A., D'alessio, A. C., Sharma, S., Seckl, J. R., et al. (2004). Epigenetic programming by maternal behavior. *Nat. Neurosci.* 7, 847–854. doi: 10.1038/nn1276

Wood, P. L., and Wood, J. A. (2013). Thiol metabolism in schizophrenia: current status. *Curr. Psychiatry Rev.* 9, 136–147. doi: 10.2174/1573400511309020008

Wu, K. Y., Chang, C. M., Liang, H. Y., Wu, C. S., Chia−Hsuan Wu, E., Chen, C. H., et al. (2013). Increased risk of developing dementia in patients with bipolar disorder: a nested matched case–control study. *Bipolar Disord.* 15, 787–794. doi: 10.1111/bdi.12116

Yang, J., Benyamin, B., Mcevoy, B. P., Gordon, S., Henders, A. K., Nyholt, D. R., et al. (2010). Common SNPs explain a large proportion of the heritability for human height. *Nat. Genet.* 142, 565–571. doi: 10.1375/twin.13.6.517

Yang, W., De Las Fuentes, L., Davila-Roman, V. G., and Gu, C. C. (2011). Variable set enrichment analysis in genome-wide association studies. *Eur. J. Hum. Genet.* 19, 893–900. doi: 10.1038/ejhg.2011.46

Zheng, R., Zhang, Z.-H., Zhao, Y.-X., Chen, C., Jia, S.-Z., Cao, X.-C., et al. (2019). Transcriptomic insights into the response of the olfactory bulb to selenium treatment in a mouse model of Alzheimer's disease. *Int. J. Mol. Sci.* 20:2998. doi: 10.3390/ijms20122998

Conflict of Interest: The authors declare that the research was conducted in the absence of any commercial or financial relationships that could be construed as a potential conflict of interest.

Publisher's Note: All claims expressed in this article are solely those of the authors and do not necessarily represent those of their affiliated organizations, or those of the publisher, the editors and the reviewers. Any product that may be evaluated in this article, or claim that may be made by its manufacturer, is not guaranteed or endorsed by the publisher.

Copyright © 2021 Kuo, Chen, Kao, Huang, Cho, Lai, Yiang and Kao. This is an open-access article distributed under the terms of the Creative Commons Attribution License (CC BY). The use, distribution or reproduction in other forums is permitted, provided the original author(s) and the copyright owner(s) are credited and that the original publication in this journal is cited, in accordance with accepted academic practice. No use, distribution or reproduction is permitted which does not comply with these terms.

frontiers in Aging Neuroscience

ORIGINAL RESEARCH
published: 29 November 2021
doi: 10.3389/fnagi.2021.761010

^{18}F-THK5351 Positron Emission Tomography Imaging in Neurodegenerative Tauopathies

Michinori Ezura[1†], Akio Kikuchi[1,2†], Nobuyuki Okamura[3,4*†], Aiko Ishiki[5,6], Takafumi Hasegawa[1], Ryuichi Harada[4], Shoichi Watanuki[7], Yoshihito Funaki[8], Kotaro Hiraoka[7], Toru Baba[9], Naoto Sugeno[1], Shun Yoshida[1], Junpei Kobayashi[1], Michiko Kobayashi[10], Ohito Tano[1], Shun Ishiyama[1], Takaaki Nakamura[1], Ichiro Nakashima[1,10], Shunji Mugikura[11], Ren Iwata[8], Yasuyuki Taki[12], Katsutoshi Furukawa[5,6], Hiroyuki Arai[5], Shozo Furumoto[8], Manabu Tashiro[7], Kazuhiko Yanai[4], Yukitsuka Kudo[5], Atsushi Takeda[9] and Masashi Aoki[1]*

[1] Department of Neurology, Tohoku University Graduate School of Medicine, Sendai, Japan, [2] Department of Occupational Therapy, Yamagata Prefectural University of Health Sciences, Yamagata, Japan, [3] Division of Pharmacology, Faculty of Medicine, Tohoku Medical and Pharmaceutical University, Sendai, Japan, [4] Department of Pharmacology, Tohoku University Graduate School of Medicine, Sendai, Japan, [5] Department of Geriatrics and Gerontology, Institute of Development, Aging and Cancer, Tohoku University, Sendai, Japan, [6] Division of Community of Medicine, Tohoku Medical and Pharmaceutical University, Sendai, Japan, [7] Division of Cyclotron Nuclear Medicine, Cyclotron and Radioisotope Center, Tohoku University, Sendai, Japan, [8] Division of Radiopharmaceutical Chemistry, Cyclotron and Radioisotope Center, Tohoku University, Sendai, Japan, [9] Department of Neurology, National Hospital Organization Sendai Nishitaga Hospital, Sendai, Japan, [10] Division of Neurology, Tohoku Medical and Pharmaceutical University, Sendai, Japan, [11] Department of Diagnostic Radiology, Tohoku University Graduate School of Medicine, Sendai, Japan, [12] Department of Nuclear Medicine and Radiology, Institute of Development, Aging and Cancer, Tohoku University, Sendai, Japan

Introduction: We aimed to determine whether *in vivo* tau deposits and monoamine oxidase B (MAO-B) detection using ^{18}F-THK5351 positron emission tomography (PET) can assist in the differential distribution in patients with corticobasal syndrome (CBS), progressive supranuclear palsy (PSP), and Alzheimer's disease (AD) and whether ^{18}F-THK5351 retention of lesion sites in CBS and PSP can correlate with clinical parameters.

Methods: ^{18}F-THK5351 PET was performed in 35 participants, including 7, 9, and 10 patients with CBS, PSP, and AD, respectively, and 9 age-matched normal controls. In CBS and PSP, cognitive and motor functions were assessed using the Montreal Cognitive Assessment, Addenbrooke's Cognitive Examination–Revised, and Frontal Assessment Battery, Unified Parkinson's Disease Rating Scale Motor Score, and PSP Rating Scale.

Results: ^{18}F-THK5351 retention was observed in sites susceptible to disease-related pathologies in CBS, PSP, and AD. ^{18}F-THK5351 uptake in the precentral gyrus clearly differentiated patients with CBS from those with PSP and AD. Furthermore, ^{18}F-THK5351 uptake in the inferior temporal gyrus clearly differentiated patients with AD

OPEN ACCESS

Edited by:
Chih-Yu Hsu,
Fujian University of Technology, China

Reviewed by:
Masashi Kameyama,
Tokyo Metropolitan Geriatric Hospital and Institute of Gerontology (TMGH-IG), Japan
Amy Christensen,
University of Southern California, United States

***Correspondence:**
Akio Kikuchi
akikuchi@med.tohoku.ac.jp
Nobuyuki Okamura
nookamura@tohoku-mpu.ac.jp

[†]These authors have contributed equally to this work

Received: 19 August 2021
Accepted: 18 October 2021
Published: 29 November 2021

Citation:
Ezura M, Kikuchi A, Okamura N, Ishiki A, Hasegawa T, Harada R, Watanuki S, Funaki Y, Hiraoka K, Baba T, Sugeno N, Yoshida S, Kobayashi J, Kobayashi M, Tano O, Ishiyama S, Nakamura T, Nakashima I, Mugikura S, Iwata R, Taki Y, Furukawa K, Arai H, Furumoto S, Tashiro M, Yanai K, Kudo Y, Takeda A and Aoki M (2021) ^{18}F-THK5351 Positron Emission Tomography Imaging in Neurodegenerative Tauopathies. Front. Aging Neurosci. 13:761010. doi: 10.3389/fnagi.2021.761010

from those with CBS and PSP. Regional ^{18}F-THK5351 retention was associated with the cognitive function in CBS and PSP.

Conclusion: Measurement of the tau deposits and MAO-B density in the brain using ^{18}F-THK5351 may be helpful for the differential diagnosis of tauopathies and for understanding disease stages.

Keywords: tau deposits, ^{18}F-THK5351, positron emission tomography (PET), corticobasal syndrome (CBS), Alzheimer's disease (AD), tauopathy, progressive supranuclear palsy (PSP), monoamine oxidase B (MAO-B)

INTRODUCTION

Tauopathies are a class of neurodegenerative diseases associated with the pathological aggregation of the tau protein in the brain. Progressive supranuclear palsy (PSP), corticobasal degeneration (CBD), and Alzheimer's disease (AD) are common tauopathies. Typical pathological characteristics of PSP include tufted astrocytes, coiled bodies, and globose tangles. Conversely, CBD is pathologically characterized by astrocytic plaques and achromatic and ballooned neurons. Both PSP and CBD are four-repeat tauopathies and show overlapping pathological characteristics. Ultrastructurally, tau proteins in PSP and CBD form straight filaments, while those in AD form paired helical filaments. The clinical characteristics of corticobasal syndrome (CBS) include asymmetric motor symptoms (i.e., Parkinsonism, dystonia, and myoclonus) and cortical dysfunction. The CBS phenotypes include CBD, PSP, and AD. Because of the overlapping clinical symptoms of these diseases, their differential diagnosis is often difficult (Litvan et al., 2003 Osaki et al., 2004; Day et al., 2017).

Positron emission tomography (PET) has been used for the visualization of abnormal protein deposits such as amyloid-β (Klunk et al., 2004), tau, and α-synuclein (Kikuchi et al., 2010). The first generation of tau probes include ^{11}C-PBB3 (Maruyama et al., 2013), ^{18}F-AV-1451 (^{18}F-T807) (Chien et al., 2013; Johnson et al., 2016; Smith et al., 2017a,b), and ^{18}F-THK5351 (Harada et al., 2016; Kikuchi et al., 2016; Brendel et al., 2017; Ishiki et al., 2017; Okamura et al., 2018; Ezura et al., 2019). ^{18}F-THK5351 (Harada et al., 2016 Brendel et al., 2017; Ishiki et al., 2017) was originally developed to visualize tau deposits in the AD brain. However, ^{18}F-THK5351 shows high binding affinity to monoamine oxidase B (MAO-B), which enables astrocytosis visualization in the human brain (Harada et al., 2018; Ishiki et al., 2018; Tago et al., 2019). MAO-B inhibitor prescription has reduced ^{18}F-THK5351 retention on average by 36.7–51.8% (Ng et al., 2017). In several neurodegenerative diseases, one of the prominent changes is reactive astrogliosis associated with the accumulation of misfolded proteins (Leyns and Holtzman, 2017). Therefore, the spatial information of ^{18}F-THK5351 binding is expected to be useful for the early and differential diagnosis of tauopathies and disease progression monitoring. Tau PET studies have been performed in patients with CBS, PSP, and AD (Dani et al., 2016; Coakeley and Strafella, 2017). However, comparative study of these three tauopathies have never been performed at a single center. In the present study, we aim to evaluate the clinical utility of tau deposits and MAO-B PET imaging using ^{18}F-THK5351 for the differential diagnosis and clinical assessment of tauopathies.

MATERIALS AND METHODS

Participants

A total of 35 participants were included in this study: seven patients with probable CBS (**Supplementary Table 1**), nine with probable PSP (Richardson syndrome type), and 10 with probable AD and 9 age-matched normal controls (NCs) (**Table 1**). All of them underwent ^{18}F-THK5351 PET scans. The diagnoses of CBS, PSP, and AD were made based on the modified Cambridge criteria (Mathew et al., 2012), National Institute of Neurological Disorders and Stroke and the Society for PSP (NINDS-SPSP) criteria (Litvan et al., 1996), and National Institute of Neurological and Communicative Disorders and Stroke and the Alzheimer's Disease and Related Disorders Association (NINCDS-ADRDA) criteria (McKhann et al., 1984), respectively. The Mini-Mental State Examination (MMSE), Montreal Cognitive Assessment (MoCA), Addenbrooke's Cognitive Examination–Revised (ACE-R), and Frontal Assessment Battery (FAB) were used to assess the cognitive performance of the participants with CBS and PSP. However, one patient with PSP could not perform the ACE-R and MoCA. Furthermore, the motor functions were assessed using the Unified Parkinson's Disease Rating Scale (UPDRS) motor score and Progressive Supranuclear Palsy Rating Scale (PSPRS) in CBS and PSP. The NC group was comprised of volunteers with no cognitive or motor function impairments nor any observable cerebrovascular lesions through MRI scans. This study protocol was approved by the Ethics Committee of Tohoku University Hospital (approval number, 2016-2-266) and registered to the UMIN Clinical Trials Registry (registration number, UMIN000021819). Written informed consent was obtained from each patient or his/her guardian(s) after they were given a complete description of the study.

Image Acquisition

^{18}F-THK5351 and ^{11}C-Pittsburgh compound B (PiB) were manufactured at the Cyclotron and Radioisotope Center of Tohoku University using a semiautomated system developed in-house. The injectable solutions of ^{18}F-THK5351 and ^{11}C-PiB were obtained with a radiochemical purity of >95% and specific activity of 357 ± 270 and 240 ± 48 GBq/μmol. PET imaging was performed using an Eminence STARGATE scanner

TABLE 1 | Demographic characteristics of CBS, PSP, AD, and NC participants.

	CBS	PSP	AD	NC
Number (M/F)	7 (2/5)	9 (9/0)	10 (7/3)	9 (5/4)
Age (years)				
Mean	69.1 ± 4.85	74.1 ± 5.28	75.6 ± 10.0	71.0 ± 6.44
Range	64–78	66–81	58–88	61–81
Education (years)	11.6 ± 1.13	14.1 ± 2.26	12.4 ± 2.41	12.9 ± 2.52
11C-PiB SUVR in neocort	1.18 ± 0.11#	1.20 ± 0.12#	1.96 ± 0.28	1.14 ± 0.09 #
Cognitive scores				
MMSE score	23.3 ± 6.85	21.8 ± 6.63*	18.9 ± 4.65**	28.8 ± 1.56
MoCA score	18.0 ± 8.41	14.9 ± 4.73	NE	NE
ACE-R score	66.7 ± 27.7	63.9 ± 19.3	NE	NE
FAB score	9.90 ± 4.91	9.00 ± 4.06	NE	NE
Motor scores				
UPDRS motor score	33.7 ± 18.3	38.9 ± 14.6	NE	NE
PSPRS score	34.0 ± 21.7	44.9 ± 19.4	NE	NE
Medication (mg/day)				
L-dopa	191 ± 269	500 ± 249	0	0
Selegiline	0	0	0	0
Amantadine	0	38.9 ± 78.2	20.0 ± 63.2	0
Donepezil	0.71 ± 1.89	0.56 ± 1.67	5.50 ± 4.38	0
Galantamine	0	0	3.20 ± 6.75	0
Memantine	0	1.11 ± 3.33	10.0 ± 10.5	0

The data are expressed as the mean ± standard deviation.
#$p < 0.001$ comparing with AD by the one-way ANOVA for multiple comparisons.
**$p < 0.05$ and **$p < 0.01$ comparing with NC by the one-way ANOVA for multiple comparisons.*
ACE-R, Addenbrooke's cognitive examination–revised; AD, Alzheimer's disease; CBS, corticobasal syndrome; FAB, frontal assessment battery; MMSE, mini-mental state examination; MoCA, Montreal cognitive assessment; NC, normal control; NE, not examined; PiB, Pittsburgh compound B; PSP, progressive supranuclear palsy; PSPRS, progressive supranuclear palsy rating scale; UPDRS, unified Parkinson's disease rating scale.

(Shimadzu, Kyoto, Japan). After rapidly injecting 185-MBq ^{18}F-THK5351 or 296-MBq ^{11}C-PiB, PET images were obtained for 20 min (4 scans × 300 s) from 40 to 60 min or 50–70 min postinjection and used for further analysis. In addition, a 3D volumetric acquisition of a T1-weighted gradient echo sequence produced a gapless series of thin axial sections using a spoiled gradient recall sequence (echo time/repetition time, 3.4/7.2 ms; flip angle, 9°; acquisition matrix, 240 × 256; 1 excitation; field of view, 25.6 cm; slice thickness, 0.8 mm) of a Vantage Titan^{TM} 3T scanner (Canon Medical Systems, Otawara, Japan).

Image Analysis

The standardized uptake value (SUV) images of ^{18}F-THK5351 and ^{11}C-PiB were obtained by normalizing the tissue radioactivity concentration to the injected dose and body weight. The PNEURO module in PMOD software (version 3.6; PMOD Technologies, Zurich, Switzerland) was used to place and evaluate the volumes of interest (VOIs) through an automatic VOI method. The PET images were matched rigidly to the T1-weighted MR images acquired from each participant. Then, the MR images were spatially normalized to the Montreal Neurological Institute T1-MRI template. The VOIs were automatically outlined on the normalized MR images based on the maximum probability atlas constructed by the automated anatomic labeling template used in the PMOD software. Subsequently, they were defined in the 13 regions; precentral, superior frontal, postcentral, and superior parietal gyri, parahippocampus, fusiform and inferior temporal gyri, putamen, pallidum, thalamus, midbrain, cerebral white matter, and cerebellar cortex. In a normal brain, the cerebellum is a region among those with the lowest MAO-B concentrations (Tong et al., 2013). Because tau deposition is usually minimal in the cerebellar cortex, increased MAO-B signals related to tau depositions would be expected to be negligible. Therefore, the regional-to-cerebellar-cortex SUV ratio (SUVR) was used as a tracer retention index.

Neocortical amyloid-β burden was expressed as the average SUVR for the following cortical VOIs: superior frontal, superior parietal, middle and inferior temporal, and posterior cingulate gyri for ^{11}C-PiB. As in the previous studies (Ezura et al., 2019), an ^{11}C-PiB SUVR threshold of 1.5 was used to categorize high and low amyloid-β burden.

Statistical Analysis

The one-way ANOVA and Steel–Dwass test for multiple comparisons was used to identify the group differences in clinical variables (e.g., age, years of education, MMSE score, and ^{11}C-PiB SUVR value) and assess the differences in the regional ^{18}F-THK5351 SUVR values, respectively. Moreover, the group differences in clinical variables including MoCA, ACE-R, FAB, UPDRS motor, and PSPRS scores between CBS and PSP were identified using the Mann–Whitney *U* test. Pearson's correlation coefficients were also calculated to assess the relationship between ^{18}F-THK5351 SUVR values and MMSE, MoCA, ACE-R, FAB, UPDRS motor, and PSPRS scores without the correction for multiple comparisons. Moreover, statistical relations of ^{18}F-THK5351 SUVR values and clinical parameters were calculated based on the region's base and drawn into correlation matrices. The four aforementioned tests were performed using GraphPad Prism 6 software (GraphPad, San Diego, CA, United States). The data were expressed as the mean ± standard deviation.

RESULTS

Clinical Characteristics of the Corticobasal Syndrome, Progressive Supranuclear Palsy, Alzheimer's Disease, and Normal Control Participants

The clinical characteristics of all participants are summarized in **Table 1**. Among the four groups, no significant differences in the age and years of education were noted. However, the MMSE scores in the PSP and AD groups were significantly lower than that in the NC group. No significant differences in the MoCA, ACE-R, FAB, UPDRS motor, and PSPRS scores were

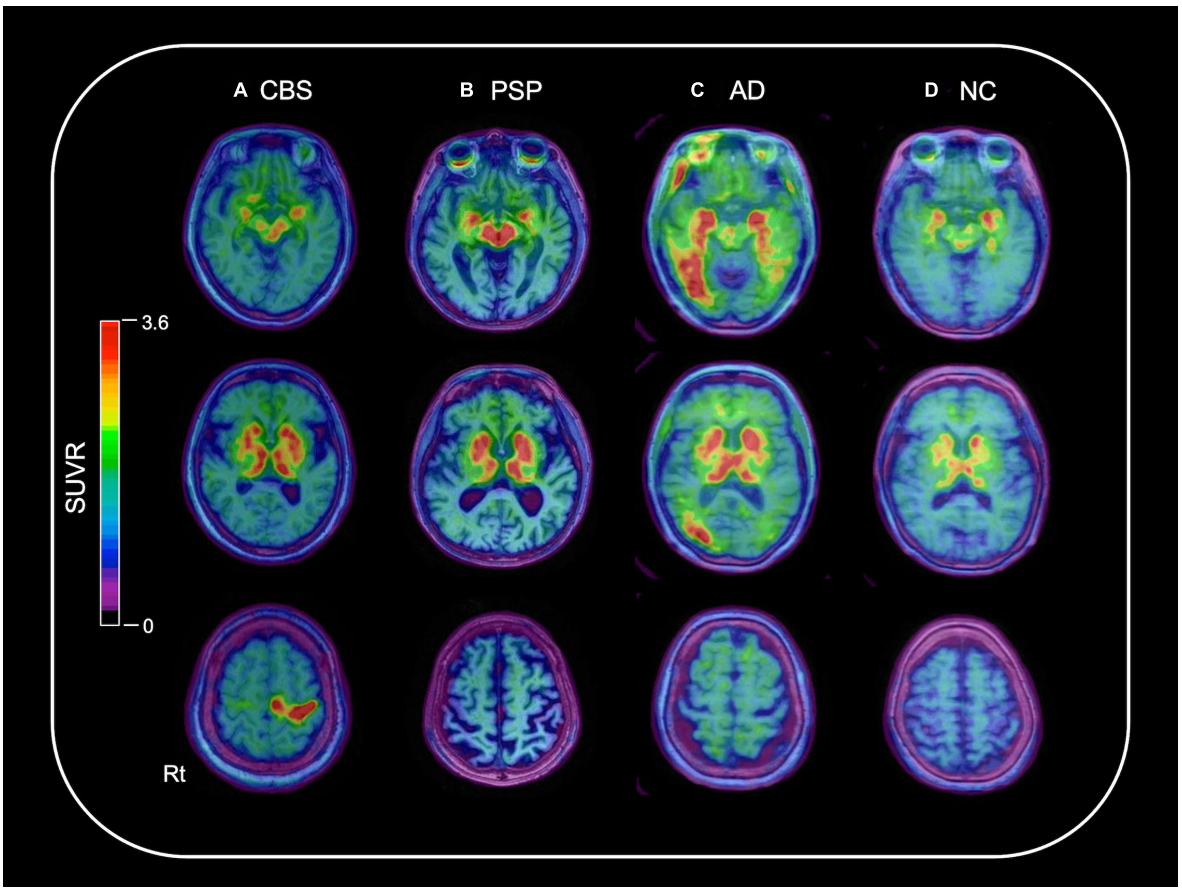

FIGURE 1 | Representative ^{18}F-THK5351 PET images overlaid on the baseline MRI data of the CBS, PSP, AD, and NC participants. A 70-year-old female with corticobasal syndrome (CBS) **(A)**, a 79-year-old male with progressive supranuclear palsy (PSP) **(B)**, and a 74-year-old female with Alzheimer's disease (AD) **(C)** showed high ^{18}F-THK5351 signals in the precentral and postcentral gyri; midbrain; and inferior temporal, fusiform, and parahippocampal gyri, respectively, compared with a 71-year-old female in the normal control (NC) group **(D)**.

TABLE 2 | Regional ^{18}F-THK5351 SUVR values in CBS, PSP, AD, and NC participants.

Region (abbreviation)	CBS	PSP	AD	NC
Precentral gyrus (PreG)	$1.57 \pm 0.23^{Pb,\ Ad,\ Ne}$	1.17 ± 0.10^{Cb}	1.12 ± 0.13^{Cd}	1.02 ± 0.07^{Ce}
Superior frontal gyrus, dorsolateral (SFG)	1.47 ± 0.15^{Na}	1.29 ± 0.08	1.36 ± 0.13	1.16 ± 0.12^{Ca}
Postcentral gyrus (PosG)	1.42 ± 0.23^{Na}	1.17 ± 0.12	1.21 ± 0.12	1.10 ± 0.08^{Ca}
Superior parietal gyrus (SPG)	1.40 ± 0.28^{Na}	1.14 ± 0.13	1.29 ± 0.22	1.04 ± 0.11^{Ca}
Parahippocampus (Par)	2.00 ± 0.15^{Ac}	1.82 ± 0.17^{Ae}	$2.43 \pm 0.20^{Cc,\ Pe,\ Nd}$	2.01 ± 0.12^{Ad}
Fusiform gyrus (FG)	1.56 ± 0.10^{Ae}	1.41 ± 0.14^{Ae}	$2.06 \pm 0.19^{Ce,\ Pe,\ Ne}$	1.60 ± 0.11^{Ae}
Inferior temporal gyrus (ITG)	1.56 ± 0.12^{Ae}	1.38 ± 0.14^{Ae}	$2.11 \pm 0.25^{Ce,\ Pe,\ Ne}$	1.53 ± 0.12^{Ae}
Putamen (Put)	$2.92 \pm 0.37^{Pa,\ Aa,\ Nc}$	2.60 ± 0.29^{Ca}	2.60 ± 0.34^{Ca}	2.48 ± 0.30^{Cc}
Pallidum (Pal)	$3.92 \pm 0.61^{Pa,\ Ae,\ Ne}$	$3.57 \pm 0.41^{Ca\ Aa,\ Nc}$	$3.28 \pm 0.43^{Ce,\ Pa}$	$3.16 \pm 0.41^{Ce,\ Pc}$
Thalamus (Tha)	$2.73 \pm 0.31^{Pa,\ Ae,\ Nb}$	2.38 ± 0.26^{Ca}	2.17 ± 0.20^{Ce}	2.32 ± 0.20^{Cb}
Midbrain (Mid)	$2.66 \pm 0.28^{Ae,\ Nc}$	2.41 ± 0.14^{Aa}	$2.09 \pm 0.24^{Ce,\ Pa}$	2.22 ± 0.15^{Cc}
Cerebral white matter (WM)	1.81 ± 0.1^{Na}	1.61 ± 0.10	1.69 ± 0.11	1.50 ± 0.13^{Ca}

Data are mean ± standard deviation.
$^{a}p < 0.05$, $^{b}p < 0.005$, $^{c}p < 0.001$, $^{d}p < 0.0005$, and $^{e}p < 0.0001$ by Steel–Dwass test for multiple comparisons.
^{C}versus CBS, ^{P}versus PSP, ^{A}versus AD, ^{N}versus NC by Steel–Dwass test for multiple comparisons.
AD, Alzheimer's disease; CBS, corticobasal syndrome; NC, normal control; PSP, progressive supranuclear palsy; SUVR, standardized uptake value ratio.

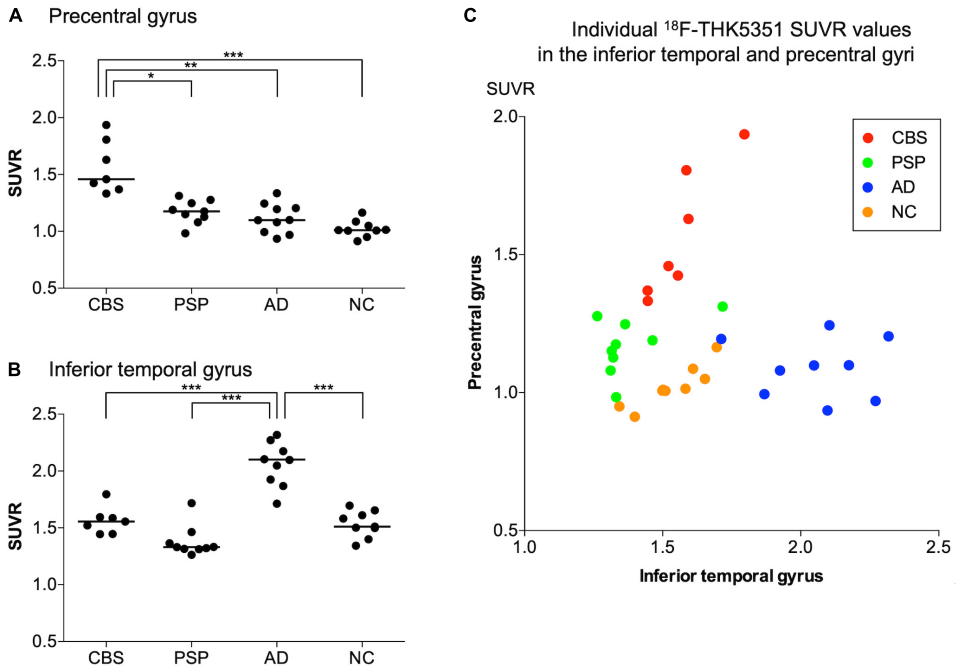

FIGURE 2 | ^{18}F-THK5351 SUVR values in the precentral and inferior temporal gyri. There were significant differences in ^{18}F-THK5351 SUVR values in the precentral gyrus of patients with corticobasal syndrome (CBS) compared with those in the progressive supranuclear palsy (PSP), Alzheimer's disease (AD), and normal control (NC) groups **(A)** and in the inferior temporal gyrus of the patients with AD compared with those in the other groups **(B)**. The scatter chart showed ^{18}F-THK5351 SUVR values in the inferior temporal (x-axis) and precentral (y-axis) gyri of the participants in four groups. The participants with CBS, PSP, AD, and NC are represented by red, green, blue, and orange dots, respectively. The individual bivariate values clearly discriminated the patients among three groups **(C)**. *$p < 0.005$, **$p < 0.0005$, and ***$p < 0.0001$ by Steel–Dwass test for multiple comparisons.

noted between the CBS and PSP groups. Additionally, PiB-PET showed negative neocortical signals in all CBS, PSP, and NC subjects, while all of 10 patients with AD were positive. Therefore, all of CBS patients in this study are possibly CBS-CBD, although it is not pathologically proven.

Clinical Positron Emission Tomography Studies

Figure 1 shows the representative ^{18}F-THK5351 PET images of the CBS, PSP, AD, and NC participants. High ^{18}F-THK5351 signals were noted in the precentral and postcentral gyri of the patients with CBS, midbrain of the patients with PSP, and inferior temporal, fusiform, and parahippocampal gyri of the patients with AD compared with those of the NC participants. All patients with AD in this study showed typical subtype. AD patients showing hippocampal-sparing or limbic-predominant subtypes are not included in this study.

^{18}F-THK5351 SUVR values in the four groups are shown in **Table 2**. In the patients with CBS, ^{18}F-THK5351 retention was significantly greater in the precentral gyrus compared with those in the PSP, AD, and NC groups (**Figure 2A**). This retention was also significantly greater in the inferior temporal and fusiform gyri of the patients with AD than those in the other groups (**Figure 2B**). The individual bivariate ^{18}F-THK5351 SUVR values in the precentral and inferior temporal gyri clearly show the discrimination among three groups (**Figure 2C**). In the patients with CBS and PSP, associations were noted between cognitive performances and spatial distribution of ^{18}F-THK5351 signals (**Figure 3**). **Supplementary Table 2** shows the result of correlation matrices.

DISCUSSION

Clinical and pathological overlaps between CBS and PSP (Armstrong et al., 2013) make the differential diagnosis of CBS and PSP difficult. Thus, several studies have been conducted to explore novel neuroimaging markers (Niethammer et al., 2014; Fujioka et al., 2021). ^{18}F-THK5351 PET showed the characteristic spatial pattern of tracer distribution in CBS, PSP, and AD. High ^{18}F-THK5351 uptake was observed in the precentral and postcentral gyri; midbrain; and inferior temporal, fusiform, and parahippocampal gyri of the patients with CBS, PSP, and AD, respectively (**Figure 1**). These spatial patterns of ^{18}F-THK5351 retention were consistent with the distribution of gliosis in the postmortem analysis of the brains of the patients with CBD, PSP, and AD (Yoshida, 2014; Harada et al., 2018). The precentral gyrus, where patients with CBS showed the highest retention of ^{18}F-THK5351, was the best region for the differentiation between CBS and PSP or AD (**Figure 2A**). Furthermore, the inferior temporal gyrus, where a high density of paired helical filament-tau and associated gliosis have been observed in AD

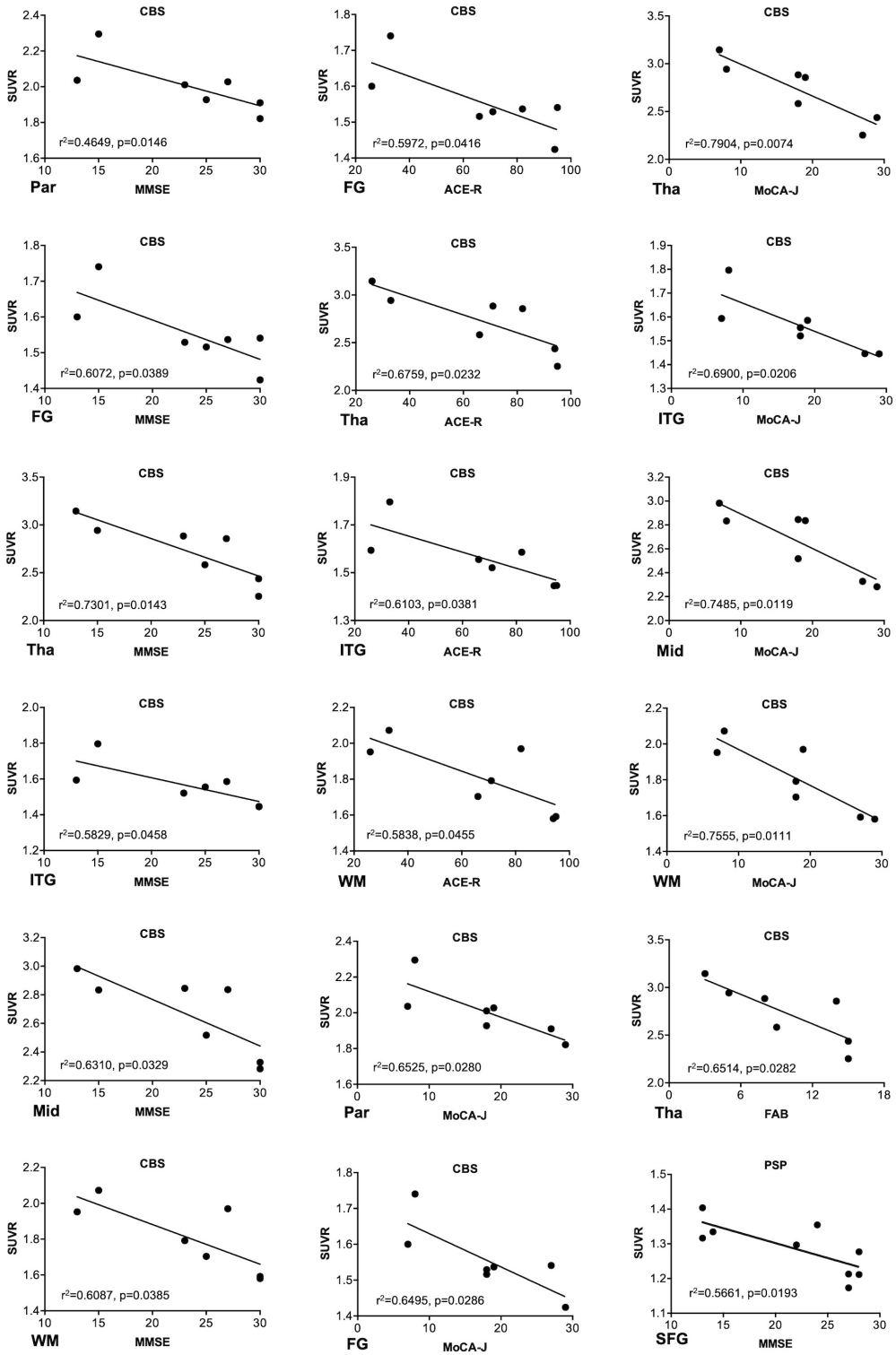

FIGURE 3 | Associations between the regional^{18}F-THK5351 retention and cognitive and motor function scores. The regional^{18}F-THK5351 retention showed associations with the Mini-Mental State Examination (MMSE), Montreal Cognitive Assessment (MoCA), Addenbrooke's Cognitive Examination–Revised (ACE-R), and Frontal Assessment Battery (FAB) scores in corticobasal syndrome (CBS) and MMSE score in progressive supranuclear palsy (PSP). FG, fusiform gyrus; ITG, inferior temporal gyrus; Mid, midbrain; Par, parahippocampus; SFG, superior frontal gyrus (dorsolateral); Tha, thalamus; WM, cerebral white matter. *P* values were uncorrected because of no correction for multiple comparisons.

(Harada et al., 2018), was a good region to differentiate AD from PSP and CBS, because patients with AD showed higher retention of ^{18}F-THK5351 in the region compared to those with CBS and PSP (**Figure 2B**). Thus, the bivariate ^{18}F-THK5351 SUVR values in these two regions clearly distinguished the patients among three groups (**Figure 2C**). Our results suggest that tau deposits and MAO-B imaging by ^{18}F-THK5351 PET is a valuable method for the differential diagnosis of tauopathies. Moreover, one of the advantages of this study is the consistent acquisition of PET images in CBS, PSP, and AD patients in a single center, which minimizes data variability.

In this study, we additionally evaluated the relationship between the clinical parameters and SUVR values of ^{18}F-THK5351. ^{18}F-THK5351 retention was associated with cognitive parameters in the patients with CBS and PSP (**Figure 3**), while no significant association was observed between ^{18}F-THK5351 retention and motor parameters. These results differed from the previous results in PSP (Brendel et al., 2017) and in CBS (Kikuchi et al., 2016). In the prior study, significant relation between the clinical motor severity and ^{18}F-THK5351 retention in midbrain was demonstrated in the patients with PSP (Brendel et al., 2017). Contrarily, all of patients with PSP in the present study met the criteria for the Richardson syndrome type and were administrated with L-dopa (500 ± 249 mg). Supposedly, dopamine-replenishing therapy may somehow alleviate motor dysfunction in PSP and obscure the relationship between the clinical motor and imaging parameters. Further research is needed to clarify the correlations between clinical motor severities and ^{18}F-THK5351 retention in more patients with PSP with various subtypes and stages. On the other hand, our previous report failed to elucidate a meaningful relationship between clinical severities including cognitive dysfunction and ^{18}F-THK5351 retention in patients with CBS because of the very limited small sample size (Kikuchi et al., 2016). ^{18}F-THK5351 PET may be useful to evaluate disease stages in CBS.

Several limitations are noted in this study. Firstly, our sample size was relatively small. Secondly, there was the absence of neuropathological confirmation of clinical diagnosis for all the cases. Thirdly, the current PET data are difficult to interpret due to the non-selective binding properties of ^{18}F-THK5351 to MAO-B and tau. However, because of the substantial reduction of ^{18}F-THK5351 retention after the treatment with the MAO-B inhibitor (Ng et al., 2017), we consider that a majority of the tracer signals in ^{18}F-THK5351 PET are derived from the binding to MAO-B (Ishiki et al., 2018). The elevation of MAO-B level is thought to reflect reactive astrogliosis caused by tau burden in the affected brain regions. Thus, ^{18}F-THK5351 signals reflect a sequence of pathogenic process in tauopathies. In the future, selective PET tracers for MAO-B or four-repeat tau will clarify the association of tau protein accumulation and reactive astrocytosis in the PSP and CBD pathogenesis.

In conclusion, the spatial pattern of ^{18}F-THK5351 PET signals adequately coincided with the disease-related regions and was a good diagnostic marker in neurodegenerative tauopathies. Considering the high binding affinity of THK5351 to tau deposits and MAO-B, ^{18}F-THK5351 PET imaging is a potentially useful technique in the differential diagnosis of tauopathies.

DATA AVAILABILITY STATEMENT

The raw data supporting the conclusions of this article will be made available by the authors, without undue reservation.

ETHICS STATEMENT

The studies involving human participants were reviewed and approved by the Ethics Committee of Tohoku University Hospital (approval number, 2016-2-266). The patients/participants provided their written informed consent to participate in this study.

AUTHOR CONTRIBUTIONS

AK and NO designed the experiments. ME, AK, and NO analyzed and interpreted the data. ME, AK, NO, and TH wrote the manuscript. All authors contributed to the data collection and analysis and reviewed the manuscript.

FUNDING

This study was supported in part by Grants-in-Aid for Scientific Research (C) (23591266, 26461303, and 17K09789) and (B) (24390219 and 15H04900) and Grant-in-Aid for Scientific Research on Innovative Areas (Brain Protein Aging and Dementia Control) (26117003) from the Ministry of Education, Culture, Sports, Science and Technology (MEXT) of Japan and Novartis Research Grants.

SUPPLEMENTARY MATERIAL

The Supplementary Material for this article can be found online at: https://www.frontiersin.org/articles/10.3389/fnagi.2021.761010/full#supplementary-material

REFERENCES

Armstrong, M. J., Litvan, I., Lang, A. E., Bak, T. H., Bhatia, K. P., Borroni, B., et al. (2013). Criteria for the diagnosis of corticobasal degeneration. *Neurology* 80, 496–503. doi: 10.1212/WNL.0b013e31827f0fd1

Brendel, M., Schonecker, S., Hoglinger, G., Lindner, S., Havla, J., Blautzik, J., et al. (2017). [^{18}F]-THK5351 PET Correlates with Topology and Symptom Severity in Progressive Supranuclear Palsy. *Front. Aging. Neurosci.* 9:440. doi: 10.3389/fnagi.2017.00440

Chien, D. T., Bahri, S., Szardenings, A. K., Walsh, J. C., Mu, F., Su, M. Y., et al. (2013). Early clinical PET imaging results with the novel PHF-tau radioligand [F-18]-T807. *J. Alzheimers Dis.* 34, 457–468. doi: 10.3233/JAD-122059

Coakeley, S., and Strafella, A. P. (2017). Imaging tau pathology in Parkinsonisms. *NPJ Parkinsons Dis.* 3:22. doi: 10.1038/s41531-017-0023-3

Dani, M., Brooks, D. J., and Edison, P. (2016). Tau imaging in neurodegenerative diseases. *Eur. J. Nucl. Med. Mol. Imaging* 43, 1139–1150. doi: 10.1007/s00259-015-3231-2

Day, G. S., Lim, T. S., Hassenstab, J., Goate, A. M., Grant, E. A., Roe, C. M., et al. (2017). Differentiating cognitive impairment due to corticobasal degeneration and Alzheimer disease. *Neurology* 88, 1273–1281. doi: 10.1212/WNL.0000000000003770

Ezura, M., Kikuchi, A., Ishiki, A., Okamura, N., Hasegawa, T., Harada, R., et al. (2019). Longitudinal changes in ^{18}F-THK5351 positron emission tomography in corticobasal syndrome. *Eur. J. Neurol.* 26, 1205–1211. doi: 10.1111/ene.13966

Fujioka, S., Morishita, T., Takano, K., Takahashi, N., Kurihara, K., Nishida, A., et al. (2021). A novel diagnostic marker for progressive supranuclear palsy targeting atrophy of the subthalamic nucleus. *J. Neurol. Sci.* 423:117366. doi: 10.1016/j.jns.2021.117366

Harada, R., Okamura, N., Furumoto, S., Furukawa, K., Ishiki, A., Tomita, N., et al. (2016). ^{18}F-THK5351: A Novel PET Radiotracer for Imaging Neurofibrillary Pathology in Alzheimer Disease. *J. Nucl. Med.* 57, 208–214. doi: 10.2967/jnumed.115.164848

Harada, R., Ishiki, A., Kai, H., Sato, N., Furukawa, K., Furumoto, S., et al. (2018). Correlations of ^{18}F-THK5351 PET with Postmortem Burden of Tau and Astrogliosis in Alzheimer Disease. *J. Nucl. Med.* 59, 671–674. doi: 10.2967/jnumed.117.197426

Ishiki, A., Harada, R., Okamura, N., Tomita, N., Rowe, C. C., Villemagne, V. L., et al. (2017). Tau imaging with [^{18}F]THK-5351 in progressive supranuclear palsy. *Eur. J. Neurol.* 24, 130–136. doi: 10.1111/ene.13164

Ishiki, A., Harada, R., Kai, H., Sato, N., Totsune, T., Tomita, N., et al. (2018). Neuroimaging-pathological correlations of [^{18}F]THK5351 PET in progressive supranuclear palsy. *Acta Neuropathol. Commun.* 6:53. doi: 10.1186/s40478-018-0556-7

Johnson, K. A., Schultz, A., Betensky, R. A., Becker, J. A., Sepulcre, J., Rentz, D., et al. (2016). Tau positron emission tomographic imaging in aging and early Alzheimer disease. *Ann. Neurol.* 79, 110–119. doi: 10.1002/ana.24546

Kikuchi, A., Takeda, A., Okamura, N., Tashiro, M., Hasegawa, T., Furumoto, S., et al. (2010). *In vivo* visualization of alpha-synuclein deposition by carbon-11-labelled 2-[2-(2-dimethylaminothiazol-5-yl)ethenyl]-6-[2-(fluoro)ethoxy]benzoxazole positron emission tomography in multiple system atrophy. *Brain* 133, 1772–1778. doi: 10.1093/brain/awq091

Kikuchi, A., Okamura, N., Hasegawa, T., Harada, R., Watanuki, S., Funaki, Y., et al. (2016). *In vivo* visualization of tau deposits in corticobasal syndrome by ^{18}F-THK5351 PET. *Neurology* 87, 2309–2316. doi: 10.1212/WNL.0000000000003375

Klunk, W. E., Engler, H., Nordberg, A., Wang, Y., Blomqvist, G., Holt, D. P., et al. (2004). Imaging brain amyloid in Alzheimer's disease with Pittsburgh Compound-B. *Ann. Neurol.* 55, 306–319. doi: 10.1002/ana.20009

Leyns, C. E. G., and Holtzman, D. M. (2017). Glial contributions to neurodegeneration in tauopathies. *Mol. Neurodegener.* 12:50. doi: 10.1186/s13024-017-0192-x

Litvan, I., Agid, Y., Calne, D., Campbell, G., Dubois, B., Duvoisin, R. C., et al. (1996). Clinical research criteria for the diagnosis of progressive supranuclear palsy (Steele-Richardson-Olszewski syndrome): report of the NINDS-SPSP international workshop. *Neurology* 47, 1–9. doi: 10.1212/WNL.47.1.1

Litvan, I., Bhatia, K. P., Burn, D. J., Goetz, C. G., Lang, A. E., McKeith, I., et al. (2003). Movement Disorders Society Scientific Issues Committee report: SIC Task Force appraisal of clinical diagnostic criteria for Parkinsonian disorders. *Mov. Disord.* 18, 467–486. doi: 10.1002/mds.10459

Maruyama, M., Shimada, H., Suhara, T., Shinotoh, H., Ji, B., Maeda, J., et al. (2013). Imaging of tau pathology in a tauopathy mouse model and in Alzheimer patients compared to normal controls. *Neuron* 79, 1094–1108. doi: 10.1016/j.neuron.2013.07.037

Mathew, R., Bak, T. H., and Hodges, J. R. (2012). Diagnostic criteria for corticobasal syndrome: a comparative study. *J. Neurol. Neurosurg. Psychiatry* 83, 405–410. doi: 10.1136/jnnp-2011-300875

McKhann, G., Drachman, D., Folstein, M., Katzman, R., Price, D., and Stadlan, E. M. (1984). Clinical diagnosis of Alzheimer's disease: report of the NINCDS-ADRDA Work Group under the auspices of Department of Health and Human Services Task Force on Alzheimer's Disease. *Neurology* 34, 939–944. doi: 10.1212/wnl.34.7.939

Ng, K. P., Pascoal, T. A., Mathotaarachchi, S., Therriault, J., Kang, M. S., Shin, M., et al. (2017). Monoamine oxidase B inhibitor, selegiline, reduces ^{18}F-THK5351 uptake in the human brain. *Alzheimers Res. Ther.* 9:25. doi: 10.1186/s13195-017-0253-y

Niethammer, M., Tang, C. C., Feigin, A., Allen, P. J., Heinen, L., Hellwig, S., et al. (2014). A disease-specific metabolic brain network associated with corticobasal degeneration. *Brain* 137, 3036–3046. doi: 10.1093/brain/awu256

Okamura, N., Harada, R., Ishiki, A., Kikuchi, A., Nakamura, T., and Kudo, Y. (2018). The development and validation of tau PET tracers: current status and future directions. *Clin. Transl. Imaging* 6, 305–316. doi: 10.1007/s40336-018-0290-y

Osaki, Y., Ben-Shlomo, Y., Lees, A. J., Daniel, S. E., Colosimo, C., Wenning, G., et al. (2004). Accuracy of clinical diagnosis of progressive supranuclear palsy. *Mov. Disord.* 19, 181–189. doi: 10.1002/mds.10680

Smith, R., Schain, M., Nilsson, C., Strandberg, O., Olsson, T., Hagerstrom, D., et al. (2017a). Increased basal ganglia binding of ^{18}F-AV-1451 in patients with progressive supranuclear palsy. *Mov. Disord.* 32, 108–114. doi: 10.1002/mds.26813

Smith, R., Scholl, M., Widner, H., van Westen, D., Svenningsson, P., Hagerstrom, D., et al. (2017b). In vivo retention of ^{18}F-AV-1451 in corticobasal syndrome. *Neurology* 89, 845–853. doi: 10.1212/WNL.0000000000004264

Tago, T., Toyohara, J., Sengoku, R., Murayama, S., and Ishii, K. (2019). Monoamine Oxidase B Binding of ^{18}F-THK5351 to Visualize Glioblastoma and Associated Gliosis: An Autopsy-Confirmed Case. *Clin. Nucl. Med.* 44, 507–509. doi: 10.1097/RLU.0000000000002564

Tong, J., Meyer, J. H., Furukawa, Y., Boileau, I., Chang, L. J., Wilson, A. A., et al. (2013). Distribution of monoamine oxidase proteins in human brain: implications for brain imaging studies. *J. Cereb. Blood Flow. Metab.* 33, 863–871. doi: 10.1038/jcbfm.2013.19

Yoshida, M. (2014). Astrocytic inclusions in progressive supranuclear palsy and corticobasal degeneration. *Neuropathology* 34, 555–570. doi: 10.1111/neup.12143

Conflict of Interest: NO, SF, and YK declare that this study received funding from GE Healthcare, Clino Ltd. and Sumitomo Electric Industries. The funder was not involved in the study design, collection, analysis, interpretation of data, the writing of this article or the decision to submit it for publication.

Publisher's Note: All claims expressed in this article are solely those of the authors and do not necessarily represent those of their affiliated organizations, or those of the publisher, the editors and the reviewers. Any product that may be evaluated in this article, or claim that may be made by its manufacturer, is not guaranteed or endorsed by the publisher.

Copyright © 2021 Ezura, Kikuchi, Okamura, Ishiki, Hasegawa, Harada, Watanuki, Funaki, Hiraoka, Baba, Sugeno, Yoshida, Kobayashi, Kobayashi, Tano, Ishiyama, Nakamura, Nakashima, Mugikura, Iwata, Taki, Furukawa, Arai, Furumoto, Tashiro, Yanai, Kudo, Takeda and Aoki. This is an open-access article distributed under the terms of the Creative Commons Attribution License (CC BY). The use, distribution or reproduction in other forums is permitted, provided the original author(s) and the copyright owner(s) are credited and that the original publication in this journal is cited, in accordance with accepted academic practice. No use, distribution or reproduction is permitted which does not comply with these terms.

frontiers in Aging Neuroscience

ORIGINAL RESEARCH
published: 30 November 2021
doi: 10.3389/fnagi.2021.761044

Characteristics of Autonomic Dysfunction in Parkinson's Disease: A Large Chinese Multicenter Cohort Study

*Zhou Zhou[1,2†], Xiaoting Zhou[2†], Xiaoxia Zhou[1], Yaqin Xiang[1], Liping Zhu[1], Lixia Qin[1], Yige Wang[1], Hongxu Pan[1], Yuwen Zhao[1], Qiying Sun[2,3], Qian Xu[1,3], Xinyin Wu[4], Xinxiang Yan[1,3], Jifeng Guo[1,3], Beisha Tang[1,2,3,5,6] and Zhenhua Liu[1,3,6]**

[1] Department of Neurology, Xiangya Hospital, Central South University, Changsha, China, [2] Department of Geriatric Neurology, Xiangya Hospital, Central South University, Changsha, China, [3] National Clinical Research Center for Geriatric Disorders, Xiangya Hospital, Central South University, Changsha, China, [4] Department of Public Health, Xiangya School of Medicine, Central South University, Changsha, China, [5] Center for Medical Genetics, School of Life Sciences, Central South University, Changsha, China, [6] Key Laboratory of Hunan Province in Neurodegenerative Disorders, Central South University, Changsha, China

OPEN ACCESS

Edited by:
Woon-Man Kung, Chinese Culture University, Taiwan

Reviewed by:
Marcelo Mendonça, Champalimaud Foundation, Portugal
Jamie Sheard, Independent Researcher, Chattanooga, TN, United States

***Correspondence:**
Zhenhua Liu
liuzhenhua@csu.edu.cn

† These authors have contributed equally to this work

Received: *19 August 2021*
Accepted: *25 October 2021*
Published: *30 November 2021*

Citation:
Zhou Z, Zhou X, Zhou X, Xiang Y, Zhu L, Qin L, Wang Y, Pan H, Zhao Y, Sun Q, Xu Q, Wu X, Yan X, Guo J, Tang B and Liu Z (2021) Characteristics of Autonomic Dysfunction in Parkinson's Disease: A Large Chinese Multicenter Cohort Study. Front. Aging Neurosci. 13:761044. doi: 10.3389/fnagi.2021.761044

Autonomic dysfunction (AutD) is one of the non-motor symptoms (NMSs) in Parkinson's disease (PD). To investigate the prevalence and clinical features of AutD in Chinese patients with PD, a large multicenter cohort of 2,556 individuals with PD were consecutively involved in the Parkinson's Disease and Movement Disorders Multicenter Database and Collaborative Network in China (PD-MDCNC) between January 1, 2017, and December 31, 2019. The assessment of AutD was performed using the Scale for Outcomes in Parkinson's Disease for Autonomic Symptoms (SCOPA-AUT). The evaluation of motor symptoms and other NMSs were performed using well-established scales recommended by the Movement Disorder Society. We found that out of 2,556 patients with PD, 2,333 patients with PD (91.28%) had AutD. Compared with the group of patients with PD without AutD, the group of patients with PD with AutD had older age, older age of onset, longer disease duration, more severe motor symptoms, motor complications, and more frequent NMSs. As for partial correlation analysis, the total SCOPA-AUT score was significantly and positively associated with motor severity scales [Unified Parkinson's Disease Rating Scale (UPDRS) total score] and some of the NMSs [Rapid Eye Movement Sleep Behavior Disorder Questionnaire (RBD), Epworth Sleepiness Scale, Hamilton Depression Scale], Fatigue Severity Scale, and Parkinson's disease questionnaire. PD Sleep Scale was significantly and negatively correlated with AutD. With logistic regression analysis for potentially related factors, age, UPDRS total score, RBD, hyposmia, depression, and fatigue may be associated with PD with AutD. In conclusion, our multicenter cohort study reported the high prevalence of AutD in Chinese PD and revealed the associated factors of PD with AutD.

Keywords: Parkinson's disease, non-motor symptoms, autonomic dysfunction, SCOPA-AUT, PD-MDCNC

INTRODUCTION

Parkinson's disease (PD) is a complex neurodegenerative disorder with a multifactorial origin and varied clinical symptoms. Loss of neurons in the substantia nigra leads to a lack of dopamine in the striatum and the formation of intracellular inclusions containing α-synuclein aggregates that are neuropathological hallmarks of PD (Bloem et al., 2021). PD is characterized by motor symptoms, such as bradykinesia, resting tremor, rigidity, and postural instability, as well as non-motor symptoms (NMSs), including olfactory dysfunction, cognitive dysfunction, neuropsychiatric phenotypes, sleep disturbances, and autonomic dysfunction (AutD) (Schapira et al., 2017).

Dysfunction of the autonomic nervous system, AutD, can occur roughly 5–20 years earlier than the onset of typical PD motor symptoms (Pont-Sunyer et al., 2015; Postuma and Berg, 2016). Symptoms of AutD include, but are not limited to, constipation, urinary urgency, orthostatic hypotension, abnormal perspiration, and photophobia. AutD has been considered as a crucial factor that affects daily living and health-related quality of life (HRQoL) (Merola et al., 2017, 2018; Tomic et al., 2017). Furthermore, it may be associated with faster progression and shorter survival time in patients with PD (De Pablo-Fernandez et al., 2017). Despite the considerable understanding of PD symptoms, the exact pathogenesis of AutD is still largely unknown. Studies that demonstrate neuronal loss and abnormal aggregation of α-synuclein in the autonomic nervous system, including the dorsal motor nucleus of the vagus and sympathetic ganglia, may provide a pathological explanation for PD (Gelpi et al., 2014; Van Den Berge et al., 2021).

Given the high prevalence of AutD (14–84%) and its severe effect on the quality of life of patients, an increasing number of clinical studies have appeared in recent years (Wüllner et al., 2007; Arnao et al., 2015; Merola et al., 2017, 2018; Stankovic et al., 2019). Moreover, NMSs vary between Chinese and Western patients with PD based on the differences in sociodemographic factors, cultural backgrounds, and pharmacogenomics (Chen et al., 2012; Sauerbier et al., 2017). The Scale for Outcomes in PD for Autonomic Symptoms (SCOPA-AUT) has been used to assess the presence and frequency of autonomic symptoms in PD and has shown satisfactory reliability and validity (Visser et al., 2004). However, AutD is significantly diverse among populations (Qin et al., 2019; Wang et al., 2019). NMSs vary between Chinese and Western patients with PD due to disparities in sociodemographic factors, cultural backgrounds, and pharmacogenomics (Chen et al., 2012; Sauerbier et al., 2017). Therefore, the small-scale, monocentric cohorts previously reported in China may not comprehensively reflect the full scope of clinical features found in AutD (Qin et al., 2019; Wang et al., 2019). To overcome this limitation, our study aims to investigate the overall and individual prevalence of AutD, its clinical features, and the correlations among AutD and other PD symptoms in a large multicenter cohort.

MATERIALS AND METHODS

Participants

A total of 3,056 participants were involved from eight movement disorders centers in China from January 1, 2017, to December 31, 2019, as shown in **Supplementary Table 1**. Clinical diagnosis of PD was confirmed by at least one neurological specialist according to the MDS Clinical Diagnostic Criteria for PD (Postuma et al., 2015), including diagnoses of either clinically established PD or clinically probable PD. Exclusion criteria included (1) other diseases that have severe autonomic complications, such as diabetes with $\geq$3 years, severe prostatic hypertrophy, and glaucoma, (2) chronic wasting diseases such as active tuberculosis, hyperthyroidism, chronic atrophic gastritis, renal failure, and anemia with hemoglobin $\leq$ 60 g/L, (3) malignant tumors, and (4) experiencing autonomic side effects confirmed by doctors to be associated with medication consumption, such as severe diarrhea, constipation, fatigue, and sweating. Based on these criteria, 2,556 patients with PD were included in the study (**Figure 1**), and 352 patients with any disease that affects AutD, 69 patients with other chronic wasting diseases, 40 patients with cancer, 29 patients taking any other medicine that clearly affects AutD, and 10 patients who could not finish the interview were excluded.

This study was supported by the Parkinson's Disease and Movement Disorders Multicenter Database and Collaborative Network in China (PD-MDCNC). The data were downloaded from the PD-MDCNC database on December 31, 2019. All patients signed informed consent before entering the study. The study was endorsed by the Ethics Committee of Central South University Xiangya Hospital.

Clinical Assessment

Demographic and clinical characteristics were collected as described in our previous study, including age, gender, body mass index (BMI), age of onset, disease duration, history of smoking, alcohol intake, drinking tea, and pesticide exposure (Zhao et al., 2020). Six autonomic function-related domains were recorded from SCOPA-AUT, including gastrointestinal, urinary, cardiovascular, thermoregulatory, pupillomotor, and sexual domains. Clinical examinations of motor symptoms were performed based on the Unified Parkinson's Disease Rating Scale (UPDRS) and Hoehn and Yahr (H&Y) scale, defining motor subtypes as either tremor dominant (TD), postural instability/gait difficulty (PIGD), or indeterminate group (Stebbins et al., 2013). Motor complications such as dyskinesia, freezing of gait (FOG), and wearing-off were diagnosed by clinicians, and the severity of each was evaluated using UPDRS-IV part A, New Freezing of Gait Questionnaire (NFOG-Q), and the 9-Item End-of-Dose Wearing-Off Questionnaire (WOQ-9), respectively. Levodopa equivalent daily dose (LEDD) was calculated based on a commonly used method (Tomlinson et al., 2010).

In addition to motor symptoms, we evaluated a broad range of NMSs based on the Non-Motor Symptoms Scale (NMSS), Mini-Mental State Examination (MMSE), Rapid Eye Movement

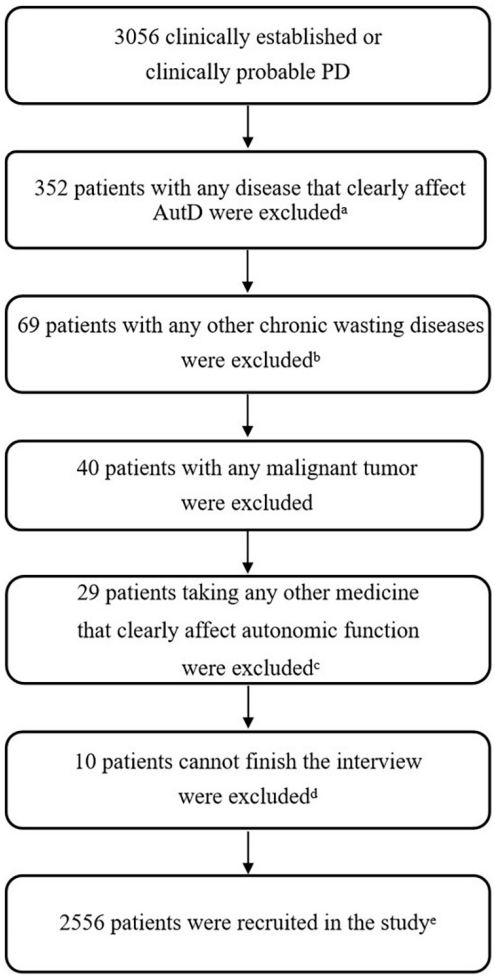

FIGURE 1 | Flowchart of exclusion criteria. [a]Other diseases that have severe autonomic complications, such as diabetes with ≥3 years, severe prostatic hypertrophy, and glaucoma. [b]Chronic wasting diseases such as active tuberculosis, hyperthyroidism, chronic atrophic gastritis, renal failure, and anemia with hemoglobin ≤ 60 g/L. [c]Experiencing autonomic side effects confirmed by doctors that were apparently associated with medication consumption that would affect the evaluation of AutD, such as severe diarrhea, constipation, fatigue, and sweating. [d]10 patients cannot finish the interview due to cognitive impairment. [e]If a patient met two or more of the above exclusion criteria, we took into count for only once. PD, Parkinson's disease; AutD, autonomic dysfunction.

Sleep Behavior Disorder Questionnaire-Hong Kong (RBDQ-HK), Epworth Sleepiness Scale (ESS), sleeping performance by Parkinson's Disease Sleep Scale (PDSS), Hyposmia Rating Scale (HRS), Hamilton Depression Scale (HAMD-17), Fatigue Severity Scale (FSS), and Cambridge-Hopkins questionnaire for restless legs syndrome (CH-RLSq). The quality of life was assessed using Parkinson's Disease Questionnaire-39 item version (PDQ-39). Cognitive impairment was defined as an MMSE total score equal to or less than 24 (Katzman et al., 1988). Hyposmia was defined as a total HRS scale less than 22.5 (Millar Vernetti et al., 2012). Rapid eye movement sleep behavior disorder (RBD) was defined as either a total RBDQ-HK scale not less than 18 or a RBDQ-HK part II score not less than 13 (Li et al., 2010). Restless legs syndrome (RLS) was defined based on the diagnostic criteria of CH-RLSq (Allen et al., 2009; Walters et al., 2014). Excessive daytime sleepiness (EDS) was defined as a total ESS score higher than 9 (Johns, 1991). Fatigue was defined as a FSS mean score not less than 3.3 (Brown et al., 2005). Depression was defined as a total HAMD-17 score higher than 7 (Montgomery and Asberg, 1979).

The evaluations in this study were only conducted once. Both a clinician and a researcher guided the assessments and recorded the results of basic information collection and scale evaluations. Along with patients, and at least one of their primary family caregivers participated in the assessment as well. Before carrying out the assessment, all researchers were trained to ensure equal understanding of the scales used as well as the methods and phrasing for clinical data collection.

Definition of Autonomic Dysfunction

Autonomic dysfunction was defined as a score greater than or equal to one in SCOPA-AUT. A score of zero was regarded as normal autonomic function. Each of the six autonomic domains was categorized as impaired when at least one of the related items was rated. Referring to Merola, patients were further divided into three subgroups according to the number of affected domains: without AutD, with single-domain AutD, and with multiple-domain AutD (Merola et al., 2018).

Statistical Analysis

Continuous variables were analyzed based on one-way ANOVA or using nonparametric tests. Categorical variables were analyzed using the chi-square test.

Partial correlation analysis was used to analyze relationships between SCOPA-AUT score and other clinical variables while better controlling other potential random variables. This analysis included the SCOPA-AUT total score and its 6 subdomains adjusted by age, gender, and disease duration, as well as 12 variables including body BMI, age of onset, LEDD, UPDRS total score, MMSE, RBDQ-HK, ESS, PDSS, HRS, HAMD, FSS, and PDQ-39.

For binary logistic regression analysis, as many variables were converted into categorical variables as possible. A total of 21 variables, including age, gender, BMI, and age of onset, were divided into two groups (earlier or later than 50 years old), disease duration, LEDD, UPDRS total score, motor subtypes, H&Y stage (H&Y was divided into two groups, i.e., stage 1–2.5 and stage 3–5), with or without dyskinesia, wearing-off, FOG, with or without cognition impairment, RBD, EDS, RLS, hyposmia, depression, fatigue, PDSS score, and PDQ-39 were introduced into the model to diagnose the multicollinearity before running the logistic regression analysis. The variance inflation factor (VIF) in the SPSS software was used as a predictor for multicollinearity. Variable with a VIF score less than 10.0 is considered as mild multicollinearity. Among the 21 variables tested, the wearing-off was removed because of its VIF score higher than 10. Statistical significance was defined as $p < 0.05$.

TABLE 1 | Demographic and clinical characteristics of patients with PD.

Characteristics	Total (n = 2,556)	Median (25–75% interquartile)
Age	61.03 ± 10.15	62.00 (54.00–68.00)
Gender ratio (male/total)	52.23%	–
BMI	23.51 ± 4.62	23.51 (20.13–26.67)
Smoking history	25.01%	–
Alcohol intake history	25.14%	–
Drinking tea history	13.44%	–
Pesticide exposure history	11.13%	–
Age of onset	55.67 ± 10.79	56.00 (48.00–63.00)
Disease duration	5.39 ± 4.73	4.00 (2.00–7.00)
LEDD	314.47 ± 264.12	300.00 (150.00–437.50)
Drug-naïve patients	17.04%	
Levodopa	77.28%	–
Non-ergot DR agonists	52.94%	–
COMT inhibitors	7.14%	–
MAO-B inhibitors	10.47%	–
Anticholinergic drugs	15.25%	–
Amantadine	11.36%	–
UPDRS I	2.39 ± 2.06	2.00 (1.00–4.00)
UPDRS II	11.88 ± 6.56	10.00 (8.00–15.00)
UPDRS III	27.20 ± 15.35	25.00 (16.00–35.00)
UPDRS total score	42.96 ± 22.57	39.00 (27.00–55.00)
Tremor score	5.26 ± 4.50	4.00 (2.00–7.00)
Postural and gait score	4.43 ± 3.27	4.00 (2.00–6.00)
Motor subtypes	39.49/13.74/46.77	–
TD/Indeterminate/PIGD (%)		
H&Y stage	2.0 (1.5–3)	–
1	15.38%	–
1.5	13.54%	–
2	22.30%	–
2.5	21.13%	–
3	21.95%	–
4	4.54%	–
5	1.17 %	–
Dyskinesia	16.55%	–
Wearing-off	23.06%	–
FOG	24.78%	–
NMSS	36.06 ± 27.20	31.00 (16.00–50.00)
MMSE	26.37 ± 3.69	27.00 (25.00–29.00)
RBDQ-HK	16.89 ± 17.11	11.00 (3.00–27.00)
ESS	7.80 ± 6.42	7.00 (2.00–12.00)
PDSS	115.22 ± 27.51	121.00 (102.00–135.00)
HRS	19.62 ± 6.29	24.00 (18.00–24.00)
HAMD	6.08 ± 6.04	5.00 (1.00–9.00)
RLS	10.61%	–
FSS	45.87 ± 19.09	48.00 (32.00–64.00)
PDQ-39	29.98 ± 26.44	23.00 (9.00–43.00)

Quantitative data were expressed as mean ± SD. Categorical variables were expressed as percentages.
PD, Parkinson's disease; BMI, body mass index; LEDD, Levodopa equivalent daily dose; DR, dopamine receptor; COMT, catechol-O-methyltransferase; MAO-B, monoamine oxidase-B; UPDRS, Unified Parkinson's Disease Rating Scale; TD, tremor dominant; PIGD, postural instability, and gait difficulty; H&Y, Hoehn and Yahr; FOG, freezing of gait; NMSS, Non-Motor Symptoms Scale; MMSE, Mini-Mental State Examination; RBDQ-HK, Rapid Eye Movement Sleep Behavior Disorder Questionnaire-Hong Kong; ESS, Epworth Sleepiness Scale; PDSS, Parkinson's Disease Sleep Scale; HRS, Hyposmia Rating Scale; HAMD, Hamilton Depression Scale; RLS, restless legs syndrome; FSS, Fatigue Severity Scale; PDQ-39, Parkinson's Disease Questionnaire-39 item version.

All data were analyzed with the IBM SPSS Statistics version 23.0 (IBM Corp., United States) software.

RESULTS

Overview

In the cohort of 2,556 participants with PD (52.23% men and 47.77% women), the mean age was 61.03 ± 10.15 years. The mean age of PD onset was 55.67 ± 10.79 years, with an average disease duration of 5.39 ± 4.73 years. The mean LEDD was 314.47 ± 264.12 mg. Detailed information is shown in **Table 1**.

A large majority of patients in this cohort experienced autonomic dysfunction (2,333 out of 2,556 or 91.28%). The average score of SCOPA-AUT was 9.21 ± 7.39, with a median (25–75% interquartile) of 8 (3–13). The most frequently affected domain in PD with AutD was gastrointestinal (72.30%), followed by urinary (71.05%), thermoregulatory (44.25%), cardiovascular (23.87%), sexual (21.79%), and pupillomotor dysfunction (15.61%). The top five most frequently involved symptoms were nocturia (63.69%), straining for defecation (49.41%), constipation (45.11%), sialorrhea (44.95%), and urinary urgency (37.21%). The top five least frequently involved symptoms were fecal incontinence (2.27%), syncope (2.54%), dysphagia (10.33%), early abdominal fullness (11.35%), and hyperhidrosis during the night (15.14%). An overview of each SCOPA-AUT item is summarized in **Supplementary Table 2**.

Clinical Characteristics of Autonomic Dysfunction

As shown in **Table 2**, we compared the demographic and clinical characteristics of patients with PD who fall under the without AutD group, single-domain AutD group, or multiple-domain AutD group. Statistically significant differences ($p < 0.05$) were observed across age, BMI, history of pesticide exposure, age of onset, disease duration, LEDD, UPDRS I, II, III score, UPDRS total score, postural and gait score, the motor subtypes, H&Y stage, dyskinesia, wearing-off, FOG, MMSE, RBDQ-HK, ESS, PDSS, HRS, HAMD, RLS, FSS, and PDQ-39 score.

TABLE 2 | Demographic and clinical characteristics of patients with PD without and with single-domain and multiple-domain AutD.

Characteristics	Without AutD (*n* = 223)	Single-Domain AutD (*n* = 387)	Multiple-Domain AutD (*n* = 1946)	Total *p-value*	Multiple comparisons adjusted *p-value**		
					$p_{WOA\ VSSDA}$	$p_{WOA\ VSMDA}$	$p_{SDA\ VSMDA}$
Age	55.02 ± 9.82	58.70 ± 10.13	62.18 ± 9.87	**<0.001**	**<0.001**	**<0.001**	**<0.001**
Gender ratio (male)	47.53%	51.94%	52.83%	0.323	–	–	–
BMI	21.16 ± 4.51	22.53 ± 4.51	23.96 ± 4.54	**<0.001**	**0.002**	**<0.001**	**<0.001**
Smoking history	21.15%	25.00%	25.44%	0.400	–	–	–
Alcohol intake history	20.28%	23.95%	25.91%	0.170	–	–	–
Drinking tea history	9.13%	13.87%	13.86%	0.147	–	–	–
Pesticide exposure history	4.48%	10.44%	12.05%	**0.003**	**<0.05**	**<0.05**	>0.05
Age of onset	51.26 ± 11.24	54.51 ± 10.71	56.41 ± 10.62	**<0.001**	**0.004**	**<0.001**	**0.003**
Disease duration	3.96 ± 4.47	4.21 ± 3.69	5.79 ± 4.88	**<0.001**	0.202	**<0.001**	**<0.001**
LEDD	250.02 ± 225.56	281.01 ± 241.23	328.79 ± 271.02	**<0.001**	0.310	**<0.001**	**0.005**
UPDRS I	1.63 ± 1.54	1.83 ± 1.71	2.59 ± 2.13	**<0.001**	0.715	**<0.001**	**<0.001**
UPDRS II	8.25 ± 5.09	9.43 ± 5.03	12.78 ± 6.71	**<0.001**	**0.012**	**<0.001**	**<0.001**
UPDRS III	20.62 ± 12.77	22.97 ± 13.47	28.79 ± 15.61	**<0.001**	0.107	**<0.001**	**<0.001**
UPDRS total score	31.22 ± 18.07	35.21 ± 18.66	45.84 ± 22.96	**<0.001**	**0.033**	**<0.001**	**<0.001**
Tremor score	4.54 ± 3.74	4.92 ± 4.01	5.41 ± 4.66	0.076	–	–	–
Postural and gait score	3.04 ± 2.41	3.36 ± 2.66	4.80 ± 3.37	**<0.001**	0.734	**<0.001**	**<0.001**
Motor subtypes TD/Indeterminate/PIGD (%)	46.19/16.59/37.22	46.77/14.99/38.24	37.31/13.16/49.54	**<0.001**	–	–	–
H&Y stage*	1.5 (1–2.5)	2 (1–2.5)	2.5 (2–3)	**<0.001**	0.119	**<0.001**	**<0.001**
<3	86.10%	83.72%	68.50%	–	–	–	–
≥3	13.90%	16.28%	31.50%	–	–	–	–
Dyskinesia	10.81%	10.85%	18.34%	**<0.001**	>0.05	**<0.05**	**<0.05**
Wearing-off	14.22%	16.09%	25.41%	**<0.001**	>0.05	**<0.05**	**<0.05**
FOG	13.57%	17.73%	27.33%	**<0.001**	>0.05	**<0.05**	**<0.05**
NMSS	16.04 ± 19.51	21.70 ± 18.04	41.22 ± 27.39	–	–	–	–
MMSE	27.66 ± 3.39	27.16 ± 3.27	26.07 ± 3.76	**<0.001**	0.085	**<0.001**	**<0.001**
RBDQ-HK	8.25 ± 11.85	12.15 ± 14.79	18.82 ± 17.56	**<0.001**	**0.003**	**<0.001**	**<0.001**
ESS	5.78 ± 5.90	6.51 ± 6.13	8.29 ± 6.45	**<0.001**	0.434	**<0.001**	**<0.001**
PDSS	124.12 ± 28.45	124.57 ± 24.78	112.32 ± 27.29	**<0.001**	1.000	**<0.001**	**<0.001**
HRS	21.53 ± 4.84	20.58 ± 5.74	19.21 ± 6.48	**<0.001**	0.452	**<0.001**	**<0.001**
HAMD	3.24 ± 5.00	4.15 ± 5.19	6.79 ± 6.12	**<0.001**	**0.038**	**<0.001**	**<0.001**
RLS	8.42%	6.70%	11.63%	**0.013**	>0.05	>0.05	**<0.05**
FSS	37.41 ± 16.97	38.24 ± 18.34	48.36 ± 18.79	**<0.001**	1.000	**<0.001**	**<0.001**
PDQ-39	17.57 ± 20.30	19.86 ± 21.74	33.35 ± 26.97	**<0.001**	0.470	**<0.001**	**<0.001**

Quantitative data were expressed as means ± SD. Categorical variables were expressed as percentages. Bold value means $p < 0.05$.
**H&Y stage was expressed as median (25–75% interquartile), subordinate levels were expressed as percentages.*
AutD, autonomic dysfunction; WOA, without AutD; SDA, single-domain AutD; MDA, multiple-domain AutD.

Next, we performed multiple comparisons to further elucidate the differences among groups. The results showed that age, BMI, age of onset, disease duration, scores of UPDRS II, total UPDRS, RBDQ-HK, and HAMD tended to increase progressively along with the increasing number of affected SCOPA-AUT domains. The above factors showed statistical significance between each multiple comparison of the subgroups ($p < 0.05$). In addition, comparison of disease duration, LEDD, UPDRS I, III score, postural and gait score, the motor subtypes, H&Y stage, the incidence of wearing-off, MMSE, ESS, PDSS, HRS, FSS, and PDQ-39 scores showed statistical significance between without AutD group and the multiple-domain AutD group. However, we did not detect any statistical significance between the without AutD group and the single-domain AutD group. An overview of the comparisons among the three subgroups is summarized in **Table 2**.

The NMSS covers a broad range of non-motor symptoms, encompassing 9 domains and 30 items (Chaudhuri et al., 2007). Three of those domains, including gastrointestinal, urinary, and sexual function domains, are related to autonomic function. To evaluate the autonomic dysfunctions using another alternative scale, as well as to compare its authenticity and reliability with the SCOPA-AUT scale, we performed comparison analysis with different domains of NMSS among AutD subgroups as shown in **Supplementary Table 3** and **Supplementary Figure 1**. The average score of every NMSS domain increases as the affected AutD domains increase. In addition, the scores of the three autonomic-related domains in NMSS were significantly

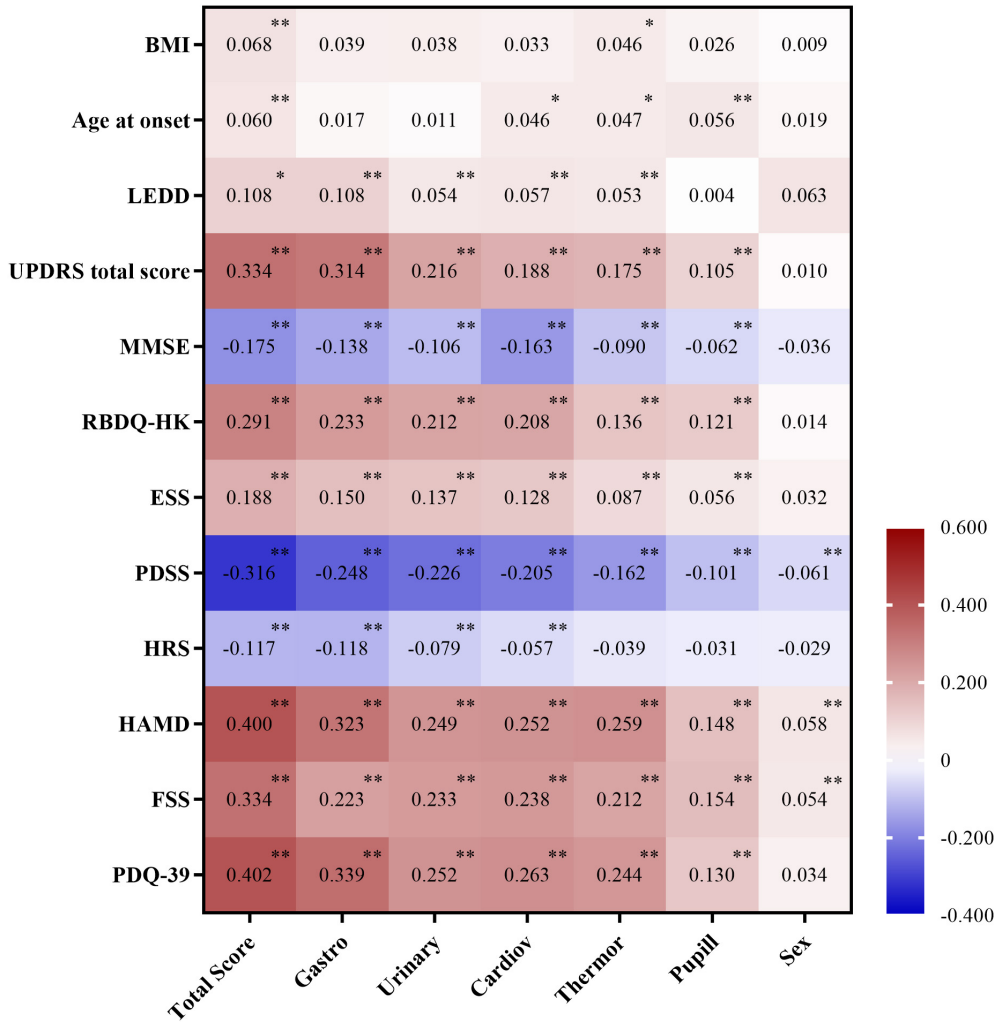

FIGURE 2 | Correlation between Scale for Outcomes in Parkinson's disease for autonomic symptoms (SCOPA-AUT) and clinical factors adjusted by age, gender, and disease duration. Number indicates partial correlation coefficient, $0.01 \leq {}^{*}p < 0.05$, and ${}^{**}p < 0.01$. BMI, body mass index; LEDD, Levodopa equivalent daily dose; UPDRS, Unified Parkinson's Disease Rating Scale; H&Y, Hoehn and Yahr; MMSE, Mini-Mental State Examination; RBDQ-HK, Rapid Eye Movement Sleep Behavior Disorder Questionnaire-Hong Kong; ESS, Epworth Sleepiness Scale; PDSS, Parkinson's Disease Sleep Scale; HRS, Hyposmia Rating Scale; HAMD, Hamilton Depression Scale; FSS, Fatigue Severity Scale; PDQ-39, Parkinson's Disease Questionnaire-39 item version; Gastro, gastrointestinal dysfunction; Urinary, urinary dysfunction; Cardiov, cardiovascular dysfunction; Thermor, thermoregulatory dysfunction; Pupill, pupillomotor dysfunction; Sex, sexual dysfunction.

correlated with that in SCOPA-AUT, which indicates that the scoring system for assessing autonomic symptoms was consistent with both SCOPA-AUT and NMSS scales.

To control for the heterogeneity of patient timelines, we stratified PD cases into three subgroups based on disease duration (less than 3, 3–8, and more than 8 years) and four subgroups based on the age of onset, as shown in **Supplementary Tables 4**, **5**, respectively. The overall SCOPA-AUT score as well as the scores in gastrointestinal, urinary, thermoregulatory, and male sexual domains increased as the disease progressed. However, the cardiovascular and pupillomotor functions were less likely to be associated with disease progression. Additionally, we found that gastrointestinal, urinary, cardiovascular dysfunctions were prone to occur in patients with PD with older disease onset. Conversely, male sexual dysfunctions were more prominent in early-onset patients with PD. The thermoregulatory and pupillomotor functions did not show any significant difference among different diseases of onset subgroups.

Correlation Between Scale for Outcomes in Parkinson's Disease for Autonomic Symptoms and Clinical Factors

The presence and severity of AutD can be affected by diverse clinical factors as some autonomic phenotypes may occur simultaneously with other clinical symptoms. To thoroughly investigate the correlation between SCOPA-AUT and other PD clinical manifestations, we employed partial correlation analysis investigating the SCOPA-AUT total score and its six subdomains (gastrointestinal, urinary, cardiovascular, thermoregulatory,

TABLE 3 | Multivariate logistic regression analysis showing factors that related to PD with AutD.

Variables	Odds ratio	95% CI	*p-value*
Age	1.055	1.036–1.074	<0.001
UPDRS total score	1.022	1.011–1.034	<0.001
RBD (with vs without)	2.138	1.331–3.434	0.002
Hyposmia (with vs without)	1.624	1.090–2.420	0.017
Depression (with vs without)	1.789	1.049–3.052	0.033
Fatigue (with vs without)	1.682	1.086–2.604	0.020

RBD, rapid eye movement sleep behavior disorder.

pupillomotor, and sexual domains). The total SCOPA-AUT score was significantly and positively associated with the motor severity scales (UPDRS total score) and some of the non-motor symptoms, such as ESS and RBD. Meanwhile, the overall score of AutD and almost all the subdomains of AutD, except for the sexual domains, showed a significant correlation with the HAMD, fatigue scale, and PDQ-39, all of which were commonly used methods for the assessment of the quality of life. The gastrointestinal domain turned out to be the most significant contributor among all the domains of the SCOPA-AUT scale. The PDSS, MMSE, and HRS scores, in which lower scores indicate more severe symptoms, were also significantly and negatively correlated with the AutD total score and most of the subdomains. Details are shown in **Figure 2**. Together these results emphasize that autonomic dysfunctions are a key factor affecting the quality of life of patients with PD.

Factors Associated With Autonomic Dysfunction

Since the occurrence of AutD is associated with multiple clinical symptoms as shown in **Figure 2**, a multivariate logistic regression analysis was performed to investigate potential predictors for AutD. NMSS was removed from the logistic regression model as it has shared domains with autonomic dysfunction and was considered to be a confounder of AutD. Additionally, wearing-off was deleted from the variable list due to its high risk of multicollinearity. Detailed results are shown in **Supplementary Table 6**. Variables that are not present in the logistic regression model are shown in **Supplementary Table 7**. The logistic regression model demonstrated that age (OR = 1.055, 95% CI: 1.036–1.074), UPDRS total score (OR = 1.022, 95% CI: 1.011–1.034), RBD (OR = 2.138, 95% CI: 1.331–3.434), hyposmia (OR = 1.624, 95% CI: 1.090–2.420), depression (OR = 1.789, 95% CI: 1.049–3.052), and fatigue (OR = 1.682, 95% CI: 1.086–2.604) may be linked to PD with AutD. All related factors are shown in **Table 3**. In conjunction with the correlation analysis shown in **Figure 2**, the consistent positive correlations between AutD and either RBD, depression, or fatigue indicate that these symptoms are inclined to occur simultaneously, which may suggest a similar underlying mechanism between AutD and these symptoms. Differing from the partial correlation analysis, age of onset, motor symptom severity, and motor complications were not significant AutD predictors in the multivariate logistic regression model.

DISCUSSION

Autonomic dysfunction can present as a wide variety of symptoms, varying greatly between individuals, and is often not well recognized during routine clinical visits, which may be one of the reasons for its diverse prevalence and characteristics from different ethnicities and cohorts (Shulman et al., 2002). The most frequent AutD were constipation (72%), followed by nocturia (65%) as it is summarized in a review manuscript (Chen et al., 2012). The PRIAMO study, which aimed to study the prevalence and presentation of NMSs amongst 1,000 patients with PD, found that more than 98% of the patients had at least one NMS, illustrating the importance of studying these phenotypes in patients with PD (Barone et al., 2009). In a prospective study that involved 101 PD cases, the prevalence of sleep disturbance was 43% as evaluated using the Pittsburgh Sleep Quality Inventory scale. However, neurologists failed to recognize sleep disturbance in 40% of patients in routine clinical examinations (Shulman et al., 2002). In this study, we performed a large-scale, multicenter analysis of AutD in Chinese patients with PD, who seem to be different from the results shown in Western studies. Significant differences in age, gender, motor symptoms, motor complications, and other NMSs domains were shown between patients with PD with and without AutD.

In this study, we found that the most prominently affected autonomic symptoms were urinary dysfunctions with a mean score of 3.40, followed by gastrointestinal dysfunctions. Similar results were observed in a recent study. Qin et al. (2019) in another Chinese cohort including 108 patients with PD at the early and middle stages reported that the most common gastrointestinal AutD were dry mouth (59.26%), followed by constipation (49.07%) and dysgeusia (37.04%). The most common autonomic dysfunctions reported in the PRIAMO study among the non-motor symptoms were fatigue and insomnia (37%) and urgency and nocturia (35%) (Barone et al., 2009). The disparity between the prevalence of AutD in China and western countries may be related to sample size, disease duration, and stage, in addition to racial diversity.

From the partial correlation analysis, both the overall and subdomains of AutD were significantly correlated with motor symptom parameters, such as LEDD and UPDRS total score. Studies have shown similar results that patients with PD with AutD are usually accompanied by severe motor symptoms (Verbaan et al., 2007; Arnao et al., 2015). Besides, AutD was also correlated with most of the non-motor symptoms in the correlation analysis.

From the logistic regression analysis, our results suggested that older age and higher UPDRS total score, consistent with the partial correlation analysis, was related to AutD (Verbaan et al., 2007; Wüllner et al., 2007). Among all the non-motor symptoms, RBD, hyposmia, depression, and fatigue turned out to be potential strong predictors for AutD. RBD, hyposmia, and depression were associated with AutD (Braak et al., 2003; Boeve et al., 2007). Another British cohort including 1,746 early patients with PD (within 3.5 years from PD diagnoses) found that RBD, depression, EDS, and PIGD subtype were significantly

correlated with autonomic severity evaluated using SCOPA-AUT scale (Malek et al., 2017). Their study partially validated the finding in our cohort. The similar results between their study and our Chinese cohort showed that AutD was strongly correlated with these early PD non-motor symptoms. This provided a possible linkage between potential PD pathological change patterns and autonomic disorders progression, but it still needs verification from other clinical cohorts in the future. The hypothesis that NMS may all have mutual influence and permeation can partially explain our result. Several studies have demonstrated that patients with RBD may be affected by an underlying synucleinopathy pathological process that links to AutD, especially orthostatic hypotension and gastrointestinal dysfunction (Ferini-Strambi et al., 2014; Lee et al., 2015; Knudsen et al., 2019). Therefore, RBD and AutD may interact with each other, yielding individual and combined negative effects on PD (Li et al., 2017; Pilotto et al., 2019). Taken as a whole, the obvious significance of the number of and severity of NMS was shown in the PD with AutD group. Our study discovered that the more severe AutD, the worse the PDQ-39 score was, indicating that severe autonomic nervous symptoms may have a great impact on the quality of life of patients.

The scientific nature of the research is a large, multicenter cohort from eight movement disorders centers, and the integrity and coverage of the data collected were satisfactory. Thus, the study relatively reflected authentic clinical characteristics of Chinese PD with AutD. However, there are limitations to our study. First, as a cross-sectional study, it only explains the relationship rather than causality between related factors and AutD. A large longitudinal cohort is warranted to thoroughly elucidate the causal relationship in the future. Second, most of the data in this study are collected by a series of clinical scales to reflect the features of PD with AutD. Although the scales included in the study were recommended by MDS, the relatively subjective way of scoring and rating for individuals is biased. More objective examinations or intelligence-based evaluation in large cohorts may be the future direction to minimize bias.

Of note, the average score of SCOPA-AUT in our study was lower than other Asian studies (Matsushima et al., 2014; Kim et al., 2017; Wang et al., 2019). This may be due to the younger age of patients and stricter inclusion criteria in our cohorts, which excluded patients with PD diagnosed with diseases that affect AutD. Furthermore, our study showed a lower prevalence of symptoms in the sexual domain compared with other Asian studies, which may be due to the hesitation of Chinese patients to answer questions about sex due to cultural norms.

In summary, we studied the prevalence and clinical characteristics of AutD in a large cohort of Chinese patients with PD, which provided an overview of the yet poorly understood Chinese PD with AutD. In the future, long-term follow-up studies will be needed to verify the patterns of AutD in Chinese patients with PD.

DATA AVAILABILITY STATEMENT

The raw data supporting the conclusions of this article will be made available by the authors, without undue reservation.

ETHICS STATEMENT

The studies involving human participants were reviewed and approved by Ethics Committee of Xiangya Hospital of Central South University. The patients/participants provided their written informed consent to participate in this study.

AUTHOR CONTRIBUTIONS

ZZ, XTZ, BT, and ZL: research project–conception and organization and statistical analysis–design and execution of the study. ZZ, XTZ, XXZ, YX, LQ, LZ, YW, HP, YZ, QS, QX, XY, and JG: research project execution and experimental works. ZZ and XTZ: writing the first draft of the manuscript. XW, BT, and ZL: statistical analysis and manuscript–review and critique. All authors read and approved the final manuscript.

FUNDING

This study was supported by the National Natural Science Foundation of China (Grant Nos. 82001359 and U20A20355) and the Hunan Innovative Province Construction Project (Grant No. 2019SK2335).

ACKNOWLEDGMENTS

The authors would like to thank the participants involved in this study and Parkinson's Disease and Movement Disorders Multicenter Database and Collaborative Network in China (PD-MDCNC).

SUPPLEMENTARY MATERIAL

The Supplementary Material for this article can be found online at: https://www.frontiersin.org/articles/10.3389/fnagi.2021.761044/full#supplementary-material

Supplementary Figure 1 | Subdomain correlation of NMSS with SCOPA-AUT. Number indicates partial correlation coefficient, $0.01 \leq {}^{*}p < 0.05$, and ${}^{**}p < 0.01$. NMSS, Non-Motor Symptoms Scale.

REFERENCES

Allen, R. P., Burchell, B. J., MacDonald, B., Hening, W. A., and Earley, C. J. (2009). Validation of the self-completed Cambridge-Hopkins questionnaire (CH-RLSq) for ascertainment of restless legs syndrome (RLS) in a population survey. *Sleep Med.* 10, 1097–1100. doi: 10.1016/j.sleep.2008.10.007

Arnao, V., Cinturino, A., Valentino, F., Perini, V., Mastrilli, S., Bellavia, G., et al. (2015). In patient's with Parkinson disease, autonomic symptoms are frequent

and associated with other non-motor symptoms. *Clin. Autonomic Res.* 25, 301–307. doi: 10.1007/s10286-015-0306-x

Barone, P., Antonini, A., Colosimo, C., Marconi, R., Morgante, L., Avarello, T. P., et al. (2009). The PRIAMO study: a multicenter assessment of nonmotor symptoms and their impact on quality of life in Parkinson's disease. *Mov. Disord.* 24, 1641–1649. doi: 10.1002/mds.22643

Bloem, B. R., Okun, M. S., and Klein, C. (2021). Parkinson's disease. *Lancet* 397, 2284–2303.

Boeve, B. F., Silber, M. H., Saper, C. B., Ferman, T. J., Dickson, D. W., Parisi, J. E., et al. (2007). Pathophysiology of REM sleep behaviour disorder and relevance to neurodegenerative disease. *Brain* 130(Pt 11), 2770–2788. doi: 10.1093/brain/awm056

Braak, H., Del Tredici, K., Rüb, U., de Vos, R. A., Jansen Steur, E. N., and Braak, E. (2003). Staging of brain pathology related to sporadic Parkinson's disease. *Neurobiol. Aging* 24, 197–211. doi: 10.1016/s0197-4580(00)00065-69

Brown, R. G., Dittner, A., Findley, L., and Wessely, S. C. (2005). The Parkinson fatigue scale. *Parkinsonism. Relat. Disord.* 11, 49–55. doi: 10.1016/j.parkreldis.2004.07.007

Chaudhuri, K. R., Martinez-Martin, P., Brown, R. G., Sethi, K., Stocchi, F., Odin, P., et al. (2007). The metric properties of a novel non-motor symptoms scale for Parkinson's disease: results from an international pilot study. *Mov. Disord.* 22, 1901–1911. doi: 10.1002/mds.21596

Chen, W., Xu, Z.-M., Wang, G., and Chen, S.-D. (2012). Non-motor symptoms of Parkinson's disease in China: a review of the literature. *Parkinson. Related Disord.* 18, 446–452. doi: 10.1016/j.parkreldis.2012.02.002

De Pablo-Fernandez, E., Tur, C., Revesz, T., Lees, A. J., Holton, J. L., and Warner, T. T. (2017). Association of autonomic dysfunction with disease progression and survival in Parkinson disease. *JAMA Neurol.* 74, 970–976. doi: 10.1001/jamaneurol.2017.1125

Ferini-Strambi, L., Oertel, W., Dauvilliers, Y., Postuma, R. B., Marelli, S., Iranzo, A., et al. (2014). Autonomic symptoms in idiopathic REM behavior disorder: a multicentre case-control study. *J. Neurol.* 261, 1112–1118. doi: 10.1007/s00415-014-7317-7318

Gelpi, E., Navarro-Otano, J., Tolosa, E., Gaig, C., Compta, Y., Rey, M. J., et al. (2014). Multiple organ involvement by alpha-synuclein pathology in Lewy body disorders. *Mov. Disord.* 29, 1010–1018. doi: 10.1002/mds.25776

Johns, M. W. (1991). A new method for measuring daytime sleepiness: the Epworth sleepiness scale. *Sleep* 14, 540–545. doi: 10.1093/sleep/14.6.540

Katzman, R., Zhang, M. Y., Ouang, Ya, Q., Wang, Z. Y., Liu, W. T., et al. (1988). A Chinese version of the mini-mental state examination; impact of illiteracy in a shanghai dementia survey. *J. Clin. Epidemiol.* 41, 971–978.

Kim, J.-Y., Song, I.-U., Koh, S.-B., Ahn, T.-B., Kim, S. J., Cheon, S.-M., et al. (2017). Validation of the korean version of the scale for outcomes in Parkinson's disease-autonomic. *J. Movement Disord.* 10, 29–34. doi: 10.14802/jmd.16057

Knudsen, K., Fedorova, T. D., Hansen, A. K., Sommerauer, M., Haase, A. M., Svendsen, K. B., et al. (2019). Objective intestinal function in patients with idiopathic REM sleep behavior disorder. *Parkinsonism. Relat. Disord.* 58, 28–34. doi: 10.1016/j.parkreldis.2018.08.011

Lee, H., Cho, Y.-W., and Kim, H. A. (2015). The severity and pattern of autonomic dysfunction in idiopathic rapid eye movement sleep behavior disorder. *Mov. Disord.* 30, 1843–1848. doi: 10.1002/mds.26416

Li, S. X., Wing, Y. K., Lam, S. P., Zhang, J., Yu, M. W. M., Ho, C. K. W., et al. (2010). Validation of a new REM sleep behavior disorder questionnaire (RBDQ-HK). *Sleep Med.* 11, 43–48. doi: 10.1016/j.sleep.2009.06.008

Li, Y., Kang, W., Yang, Q., Zhang, L., Zhang, L., Dong, F., et al. (2017). Predictive markers for early conversion of iRBD to neurodegenerative synucleinopathy diseases. *Neurology* 88, 1493–1500. doi: 10.1212/WNL.0000000000003838

Malek, N., Lawton, M. A., Grosset, K. A., Bajaj, N., Barker, R. A., Burn, D. J., et al. (2017). Autonomic dysfunction in early Parkinson's disease: results from the united kingdom tracking Parkinson's study. *Mov. Disord. Clin. Pract.* 4, 509–516. doi: 10.1002/mdc3.12454

Matsushima, M., Yabe, I., Hirotani, M., Kano, T., and Sasaki, H. (2014). Reliability of the Japanese version of the scales for outcomes in Parkinson's disease-autonomic questionnaire. *Clin. Neurol. Neurosurg* 124, 182–184. doi: 10.1016/j.clineuro.2014.07.007

Merola, A., Romagnolo, A., Comi, C., Rosso, M., Artusi, C. A., Zibetti, M., et al. (2017). Prevalence and burden of dysautonomia in advanced Parkinson's disease. *Mov. Disord.* 32, 796–797. doi: 10.1002/mds.26970

Merola, A., Romagnolo, A., Rosso, M., Suri, R., Berndt, Z., Maule, S., et al. (2018). Autonomic dysfunction in Parkinson's disease: a prospective cohort study. *Mov. Disord.* 33, 391–397. doi: 10.1002/mds.27268

Millar Vernetti, P., Perez Lloret, S., Rossi, M., Cerquetti, D., and Merello, M. (2012). Validation of a new scale to assess olfactory dysfunction in patients with Parkinson's disease. *Parkinsonism Related Disord.* 18, 358–361. doi: 10.1016/j.parkreldis.2011.12.001

Montgomery, S. A., and Asberg, M. (1979). A new depression scale designed to be sensitive to change. *Br. J. Psychiatry* 134, 382–389. doi: 10.1192/bjp.134.4.382

Pilotto, A., Romagnolo, A., Tuazon, J. A., Vizcarra, J. A., Marsili, L., Zibetti, M., et al. (2019). Orthostatic hypotension and REM sleep behaviour disorder: impact on clinical outcomes in alpha-synucleinopathies. *J. Neurol. Neurosurg. Psychiatry* 90, 1257–1263. doi: 10.1136/jnnp-2019-320846

Pont-Sunyer, C., Hotter, A., Gaig, C., Seppi, K., Compta, Y., Katzenschlager, R., et al. (2015). The onset of nonmotor symptoms in Parkinson's disease (the ONSET PD study). *Mov. Disord.* 30, 229–237. doi: 10.1002/mds.26077

Postuma, R. B., and Berg, D. (2016). Advances in markers of prodromal Parkinson disease. *Nat. Rev. Neurol.* 12, 622–634. doi: 10.1038/nrneurol.2016.152

Postuma, R. B., Berg, D., Stern, M., Poewe, W., Olanow, C. W., Oertel, W., et al. (2015). MDS clinical diagnostic criteria for Parkinson's disease. *Mov. Disord.* 30, 1591–1601. doi: 10.1002/mds.26424

Qin, X., Li, X., Xin, Z. E., and Li, Z. (2019). Gastrointestinal dysfunction in Chinese patients with Parkinson's disease. *Parkinson's Dis.* 2019:3897315. doi: 10.1155/2019/3897315

Sauerbier, A., Jitkritsadakul, O., Titova, N., Klingelhoefer, L., Tsuboi, Y., Carr, H., et al. (2017). Non-Motor symptoms assessed by non-motor symptoms questionnaire and non-motor symptoms scale in parkinson's disease in selected asian populations. *Neuroepidemiology* 49, 1–17. doi: 10.1159/000478702

Schapira, A. H. V., Chaudhuri, K. R., and Jenner, P. (2017). Non-motor features of Parkinson disease. *Nat. Rev. Neurosci.* 18, 435–450. doi: 10.1038/nrn.2017.62

Shulman, L. M., Taback, R. L., Rabinstein, A. A., and Weiner, W. J. (2002). Non-recognition of depression and other non-motor symptoms in Parkinson's disease. *Parkinsonism. Relat. Disord.* 8, 193–197. doi: 10.1016/s1353-802000015-13

Stankovic, I., Petrovic, I., Pekmezovic, T., Markovic, V., Stojkovic, T., Dragasevic-Miskovic, N., et al. (2019). Longitudinal assessment of autonomic dysfunction in early Parkinson's disease. *Parkinsonism. Relat. Disord.* 66, 74–79. doi: 10.1016/j.parkreldis.2019.07.008

Stebbins, G. T., Goetz, C. G., Burn, D. J., Jankovic, J., Khoo, T. K., and Tilley, B. C. (2013). How to identify tremor dominant and postural instability/gait difficulty groups with the movement disorder society unified Parkinson's disease rating scale: comparison with the unified Parkinson's disease rating scale. *Mov. Disord.* 28, 668–670. doi: 10.1002/mds.25383

Tomic, S., Rajkovaca, I., Pekic, V., Salha, T., and Misevic, S. (2017). Impact of autonomic dysfunctions on the quality of life in Parkinson's disease patients. *Acta Neurol. Belg.* 117, 207–211. doi: 10.1007/s13760-016-0739-736

Tomlinson, C. L., Stowe, R., Patel, S., Rick, C., Gray, R., and Clarke, C. E. (2010). Systematic review of levodopa dose equivalency reporting in Parkinson's disease. *Mov. Disord.* 25, 2649–2653. doi: 10.1002/mds.23429

Van Den Berge, N., Ferreira, N., Mikkelsen, T. W., Alstrup, A. K. O., Tamguney, G., Karlsson, P., et al. (2021). Ageing promotes pathological alpha-synuclein propagation and autonomic dysfunction in wild-type rats. *Brain* 144, 1853–1868. doi: 10.1093/brain/awab061

Verbaan, D., Marinus, J., Visser, M., van Rooden, S. M., Stiggelbout, A. M., and van Hilten, J. J. (2007). Patient-reported autonomic symptoms in Parkinson disease. *Neurology* 69, 333–341.

Visser, M., Marinus, J., Stiggelbout, A. M., and Van Hilten, J. J. (2004). Assessment of autonomic dysfunction in Parkinson's disease: the SCOPA-AUT. *Mov. Disord.* 19, 1306–1312. doi: 10.1002/mds.20153

Walters, A. S., Frauscher, B., Allen, R., Benes, H., Chaudhuri, K. R., Garcia-Borreguero, D., et al. (2014). Review of diagnostic instruments for the restless legs syndrome/Willis-Ekbom Disease (RLS/WED): critique and recommendations. *J. Clin. Sleep Med.* 10, 1343–1349. doi: 10.5664/jcsm.4298

Wang, X.-Y., Han, Y.-Y., Li, G., and Zhang, B. (2019). Association between autonomic dysfunction and olfactory dysfunction in Parkinson's disease in southern Chinese. *BMC Neurol.* 19:17. doi: 10.1186/s12883-019-1243-1244

Wüllner, U., Schmitz-Hübsch, T., Antony, G., Fimmers, R., Spottke, A., Oertel, W. H., et al. (2007). Autonomic dysfunction in 3414 Parkinson's disease patients enrolled in the German Network on Parkinson's disease (KNP e.V.): the effect of ageing. *Eur. J. Neurol.* 14, 1405–1408. doi: 10.1111/j.1468-1331.2007.01982.x

Zhao, Y., Qin, L., Pan, H., Liu, Z., Jiang, L., He, Y., et al. (2020). The role of genetics in Parkinson's disease: a large cohort study in Chinese mainland population. *Brain* 143, 2220–2234. doi: 10.1093/brain/awaa167

Conflict of Interest: The authors declare that the research was conducted in the absence of any commercial or financial relationships that could be construed as a potential conflict of interest.

Publisher's Note: All claims expressed in this article are solely those of the authors and do not necessarily represent those of their affiliated organizations, or those of the publisher, the editors and the reviewers. Any product that may be evaluated in this article, or claim that may be made by its manufacturer, is not guaranteed or endorsed by the publisher.

Copyright © 2021 Zhou, Zhou, Zhou, Xiang, Zhu, Qin, Wang, Pan, Zhao, Sun, Xu, Wu, Yan, Guo, Tang and Liu. This is an open-access article distributed under the terms of the Creative Commons Attribution License (CC BY). The use, distribution or reproduction in other forums is permitted, provided the original author(s) and the copyright owner(s) are credited and that the original publication in this journal is cited, in accordance with accepted academic practice. No use, distribution or reproduction is permitted which does not comply with these terms.

frontiers in Molecular Neuroscience

ORIGINAL RESEARCH
published: 09 December 2021
doi: 10.3389/fnmol.2021.779436

Effects of Chemogenetic Inhibition of D1 or D2 Receptor-Containing Neurons of the Substantia Nigra and Striatum in Mice With Tourette Syndrome

Lixue Lin[1,2], Yuye Lan[1], He Zhu[3], Lingling Yu[4], Shuang Wu[1], Wangyixuan Wan[1], Yang Shu[5], Hongchun Xiang[6], Tengfei Hou[1], Hong Zhang[1], Yan Ma[2], Wen Su[7] and Man Li[1]**

[1] Department of Neurobiology, School of Basic Medicine, Tongji Medical College, Huazhong University of Science and Technology, Wuhan, China, [2] Department of Rehabilitation, Wuhan No.1 Hospital, Wuhan, China, [3] Institute of Clinical Medicine, Zhanjiang Central People's Hospital, Zhanjiang, China, [4] Institute of Integrated Traditional Chinese and Western Medicine, Tongji Hospital, Tongji Medical College, Huazhong University of Science and Technology, Wuhan, China, [5] Department of Central Laboratory, Affiliated Hospital of Jiangsu University, Zhenjiang, China, [6] Department of Acupuncture and Moxibustion, Union Hospital, Tongji Medical College, Huazhong University of Science and Technology, Wuhan, China, [7] Department of Pediatrics, Wuhan No.1 Hospital, Wuhan, China

As tourette syndrome (TS) is a common neurobehavioral disorder, the primary symptoms of which include behavioral stereotypies. Dysfunction of the substantia nigra–striatum network could be the main pathogenesis of TS, which is closely associated with dopamine (DA) and its receptors. TS is often resistant to conventional treatments. Therefore, it is necessary to investigate the neurobiological mechanisms underlying its pathogenesis. In this study, we investigated whether chemogenetic activation or inhibition of dopaminergic D1 receptor (D1R)- or D2 receptor (D2R)-containing neurons in the substantia nigra pars compacta (SNpc) or dorsal striatum (dSTR) affected the stereotyped behavior and motor functions of TS mice. Intraperitoneal injection of 3,3′-iminodipropionitrile (IDPN) was used to induce TS in mice. Stereotyped behavior test and open-field, rotarod, and grip strength tests were performed to evaluate stereotyped behavior and motor functions, respectively. Immunofluorescence labeling was used to detect the co-labeling of virus fluorescence and D1R or D2R. We found that chemogenetic inhibition of D1R- or D2R-containing neurons in the SNpc and dSTR alleviated behavioral stereotypies and motor functions in TS mice. Chemogenetic activation of D1R-containing neurons in the dSTR aggravated behavioral stereotypies and motor functions in vehicle-treated mice, but neither was aggravated in TS mice. In conclusion, chemogenetic inhibition of D1R- or D2R-containing neurons in the SNpc and dSTR alleviated behavioral stereotypies of TS, providing a new treatment target for TS. Moreover, the activation of D1R-containing neurons in the dSTR may contribute to the pathogenesis of TS, which can be chosen as a more precise target for treatment.

Keywords: tourette syndrome, chemogenetic, dopamine receptors, substantia nigra pars compacta, dorsal striatum

OPEN ACCESS

Edited by:
Jiehui Jiang,
Shanghai University, China

Reviewed by:
Yunping Deng,
University of Tennessee Health Science Center (UTHSC), United States
Vignayanandam Ravindernath Muddapu,
Ecole Polytechnique Fédérale de Lausanne (EPFL), Switzerland
Jing-Ning Zhu,
Nanjing University, China
Adriano Targa,
Instituto de Salud Carlos III (ISCIII), Spain

***Correspondence:**
Wen Su
784404524@qq.com
Man Li
liman73@mails.tjmu.edu.cn

Specialty section:
This article was submitted to Brain Disease Mechanisms, a section of the journal Frontiers in Molecular Neuroscience

Received: *18 September 2021*
Accepted: *09 November 2021*
Published: *09 December 2021*

Citation:
Lin L, Lan Y, Zhu H, Yu L, Wu S, Wan W, Shu Y, Xiang H, Hou T, Zhang H, Ma Y, Su W and Li M (2021) Effects of Chemogenetic Inhibition of D1 or D2 Receptor-Containing Neurons of the Substantia Nigra and Striatum in Mice With Tourette Syndrome. Front. Mol. Neurosci. 14:779436. doi: 10.3389/fnmol.2021.779436

INTRODUCTION

Tourette syndrome (TS) is a common neurobehavioral disorder, the primary symptoms of which include a variety of motor and vocal behavioral stereotypies (Hsu et al., 2021). Male patients have a higher incidence of TS than female patients, and the onset occurs before the age of 18 and lasts for more than 1 year (Ganos and Martino, 2015; Yang et al., 2016). Typically, behavioral stereotypies are defined as rapid, recurrent, and brief movements or vocalizations, the process of which gradually deteriorates (Kawohl et al., 2009). Approximately 90% of patients with TS are accompanied by neuropsychiatric diseases, among which attention-deficit hyperactivity disorder, obsessive-compulsive disorder, and impulse control disorder are the most common complications (Ganos and Martino, 2015). The process of TS reduces the quality of life in patients and puts a heavy burden on the family and society (Dodel et al., 2010; Cen et al., 2020). TS is often resistant to conventional treatments and remains a major therapeutic challenge. It is necessary to investigate the neurobiological mechanisms underlying the pathogenesis of TS and choose more precise intervention targets.

There is sufficient evidence that the basal ganglia plays an important role in the pathophysiology of TS, and the dopamine (DA) system can affect locomotion behavior. The causes of TS are mainly related to abnormalities in the substantia nigra–striatum network (Groenewegen et al., 2003; Jakubovski and Muller-Vahl, 2017; Hamamoto and Kano, 2018), which is closely associated with DA and its receptors. The dopaminergic D1 receptor (D1R) and D2 receptor (D2R) are involved in the direct and indirect pathways of basal ganglia function (Surmeier et al., 2007). Activating D1R can enhance the role of the direct pathway to promote movement, whereas activating D2R can inhibit the indirect pathway (Bromberg-Martin et al., 2010; Lobo et al., 2010; Ferguson et al., 2011). Thus, we wondered whether the manipulation of D1R- or D2R-containing neurons could affect stereotyped behavior in mice with TS, to explore the correlation between DA receptors and the neurobiological mechanism of TS.

Dopaminergic neurons in the substantia nigra pars compacta (SNpc) are the main neurons responsible for DA synthesis in the brain (Lerner et al., 2012). A large amount of DA is released in the neural circuit of SNpc projections to the dorsal striatum (dSTR) (Broderick and Phelix, 1997). In the substantia nigra–striatum network, the dSTR plays an important role in the motor regulation function mediated by the basal ganglia motor regulation pathway (Groenewegen et al., 2003; Rodrigues et al., 2017). Since the dSTR is associated with the early stages of the motor process (Kravitz et al., 2010), it may also be involved in the generation of TS-related behavioral stereotypies. The excessive release of DA in the dSTR can cause abnormal behavioral stereotypies in mice (Liu et al., 2020). After microinjection of the $GABA_A$ antagonist picrotoxin (PTX) into the dSTR, mice showed intermittent rapid, repetitive, and non-rhythmic movements of the head and contralateral limbs, which were similar to the behavioral stereotypies of patients with TS (Pogorelov et al., 2015). Long-term administration of the D2R agonist quinpirole induced TS-related behavioral stereotypies in rats (Nespoli et al., 2018). This suggests that over-release of DA and overactivation of D2R may contribute to TS-related behavioral stereotypies. However, haloperidol, a D2R antagonist, has limited efficacy in the treatment of TS with severe extrapyramidal side effects (Silva et al., 1996; Mogwitz et al., 2013; Egolf and Coffey, 2014). Therefore, it is worthwhile to develop a new intervention method to treat TS, such as chemogenetic strategies.

Studies have shown that neural activity in the SNpc of patients with TS is stronger than that of normal subjects in the presence of spontaneous and non-spontaneous behavioral stereotypies, reflecting the overactivity of SNpc dopaminergic neurons in patients with TS (Baym et al., 2008). D1Rs and D2Rs are distributed on DA neurons in the SNpc, as well as inhibitory interneurons (Yung et al., 1995; Beaulieu and Gainetdinov, 2011; Yang et al., 2019). In addition, D2Rs are distributed on GABAergic projecting neurons of the indirect pathway and inhibitory interneurons in the dSTR (Alcantara et al., 2003; Maurice et al., 2004; Zhang et al., 2009; Jijon-Lorenzo et al., 2018; Brandenburg et al., 2020; Lewis et al., 2020). However, D1R is only expressed on GABAergic projecting neurons of the direct pathway in the dSTR (Avila-Luna et al., 2019; Assali et al., 2021), which is closely related to the regulation of dyskinesia in patients with Parkinson's disease (Calabrese et al., 2020). Therefore, we wondered whether manipulating D1R- or D2R-containing neurons in the SNpc or dSTR by chemogenetic strategies affected behavioral stereotypies in normal and TS mice. We hypothesized that D1R in the dSTR may be a more precise target to treat TS, since it is distributed on only one type of neuron.

3,3′-Iminodipropionitrile (IDPN) is a synthetic organic nitrile, and it is the most commonly used inducer of TS in animal models as its effects can last a long time (Wang et al., 2013, 2021; Zhang et al., 2014; Zhang and Li, 2015a,b; Xie et al., 2016; Chen et al., 2019; Zhao et al., 2020; Liu et al., 2021). Our previous research results also showed that IDPN induced abnormal stereotyped behavior in mice (Lin et al., 2019), which caused a behavioral syndrome in rodents similar to the symptoms of patients with TS, such as featuring lateral and vertical head-shakes, random circling, hyperactivity, and elevated acoustic startle response (Khan and Ibrahim, 2015; Zhang and Li, 2015c; Wang et al., 2021). Therefore, we used IDPN to induce a model of TS in mice. We improved the score sheet of stereotyped behavior based on the typical symptoms of patients with TS and relevant studies, in order to evaluate the stereotyped behavior of mice (Wang et al., 2013; Proietti Onori et al., 2014).

In this study, we investigated whether chemogenetic activation or inhibition of D1R- or D2R-containing neurons in the SNpc or dSTR affected the stereotyped behavior and motor functions of IDPN-induced TS mice, in order to find the neurobiological mechanism of the pathogenesis of TS and choose more precise intervention targets for the treatment of TS.

MATERIALS AND METHODS

Animals

All D1R-cre mice [MMRRC Tg (Drd1a cre) EY262Gsat], D2R-cre mice [MMRRC Tg (Drd2-cre) ER44Gsat], and their wild-type littermate (WT) mice (male, aged 8 weeks, and

18–21g) maintained on a C57BL/6 congenic background were kindly provided by Professor Tonghui Xu (Fudan University, Shanghai, China) (Li et al., 2018). All animal experimental protocols conformed to the Animal Management Rules of the Chinese Ministry of Health, and this study was approved by the Animal Ethics Committee of the Chinese Academy of Medical Sciences. The mice were maintained in a controlled environment with a temperature of 21 ± 1°C and a relative humidity of 60% ± 10% under a 12-h light/dark cycle (lights on at 7 a.m.), and had free access to food and water. The mice were housed individually in standard polypropylene plastic cages (318 mm × 202 mm × 136 mm) with sawdust bedding and water and food *ad libitum* (Xietong Pharmaceutical Biotechnology Limited Liability Company, Jiangsu, China).

Viruses Constructs and Surgery

Chemogenetic strategies: rAAV-hSyn-DIO-hM3D(Gq)-mCherry-WPRE-pA (hM3Dq) or rAAV-hSyn-DIO-hM4D(Gi)-mCherry-WPREs-pA (hM4Di) were microinjected into the bilateral SNpc or dSTR, respectively, of D1R-cre, D2R-cre, or wild-type littermate mice, to activate or inhibit neurons containing dopaminergic D1R and D2R. rAAV-hSyn-DIO-mCherry was selected as the control virus. All viruses used in this study were acquired from Wuhan BrainVTA Scientific and Technical Corporation.

Before surgery, each mouse was anesthetized with isoflurane and fixed in a stereotaxic apparatus (RWD Instruments, China). A 1.5-cm-long longitudinal incision was made along the midline of the skull, and the periosteum was gently removed from the exposed surface of the surgical area. The coordinates of the SNpc were as follows: -3.3 mm from the bregma, 1.6 mm lateral from the midline, and 3.7 mm ventral to the skull. The coordinates of the dSTR were as follows: 0.5 mm from the bregma, 1.5 mm lateral from the midline, and 2.7 mm ventral to the skull. Desired virus vectors (200 nL) were injected into the SNpc or dSTR at a rate of 30 nL per 60 s.

Tourette Syndrome Model

The adaptation period between arrival at the laboratory and the start of testing was 1 week. After 1 week, the vehicle group mice were intraperitoneally (i.p.) injected with saline (0.9%) once a day for 7 consecutive days. The TS group mice were intraperitoneally injected with IDPN (350 mg/kg, Sigma, St. Louis, MO, United States) once a day for 7 consecutive days. The ethological score between each group was balanced, by referring to the evaluation grade of stereotypy (**Table 1**). On the 8th day, the score of stereotyped behavior of mice was greater than or equal to 2 points, which proved a successful IDPN-induced TS model.

Behavioral Tests

Stereotyped Behavior Test

The stereotyped behavior test was conducted by two trained and independent observers who were familiar with the measurements but blinded to the group allocation. They grouped the mice themselves and then randomly tested all mice and scored them according to the random number table method. Finally, the results were correctly counted by an experimenter who was aware of the group allocation. The observers placed the mice in the box and recorded a 30-min video for each mouse. The apparatus used for stereotyped behavior was a round, black plastic box with a diameter of 16 cm and a height of 14 cm, and the camera was placed at the top. The light condition during the observation period was created with an LED tube (consistent with the illumination of the usual living environment of the mouse), which lasted throughout the experiment. Before the test, the observers sprayed the inside and bottom of the box and the transparent lid with 75% alcohol and wiped it with a paper towel. Each animal was observed for 1 min every 5 min for a total of six periods. One or more episodes in accordance with the grades were used to obtain the corresponding score and calculate the average score on the basis of results from two observers, as objective indicators of behavioral changes (**Table 1**).

TABLE 1 | Behavior measurements referring to evaluating grades of stereotypy.

Score	Stereotypy
0	No stereotypy or normal activity[a]
1	Discontinuous circling behavior[b] Occasional head twitching
2	Occasionally vertical dyskinetic head and neck movements Occasional sniffing, licking, and biting
3	Continuous circling behavior, increased body raising Increased sniffing, repetitive grooming (such as paw-to-mouth movements)[c]
4	Increased lateral and vertical dyskinetic head and neck movements

[a] *Such as immobility (no visible movement of the animal).*
[b] *Such as clockwise/counterclockwise circling, loosely circular path traced on the cage floor.*
[c] *Such as head-down sniffing (nose in contact with the floor), grooming (self-cleaning with mouth or paws), and face washing (forepaws moving back and forth from the ears to the snout and mouth).*

Rotarod Test

To assess the motor coordination of mice, they were individually placed on a rotarod (YLS-4C, Yiyan, Jiang, China) for 5 min at 4 rpm at 10:00 a.m. and 5:00 p.m. for 3 days before the formal test, to allow the mice to learn how to use the apparatus. The rotarod moved at an initial speed of 4 rpm and subsequently accelerated to 40 rpm in 5 min. Mice were held by the tail and placed on the rotarod, facing away from the direction of rotation. The falling time after the acceleration began was recorded. Each mouse received three test sessions with at least a 5-min interval between them, and the average time was calculated.

Grip Strength Test

To evaluate the muscle strength of mice, we performed a grip strength test. We followed the manufacturer's instructions for the grip strength meter (YLS-13A, Zhenghua, Anhui, China), and the statistical indicator was the grip force (g). Mice were placed on a base plate (230 mm × 250 mm) in front of a grasping bar. The

bar was fitted to a force transducer connected to a peak amplifier. The mice were pulled with their tails when grasping the bar. The maximal grip force was measured within 20 s.

Open-Field Test

We used a 50 cm × 50 cm black-walled open-field test box, and a camera was installed directly above to record the trajectory. After each mouse was tested, 75% alcohol was sprayed on the test area and wiped with a paper towel, and then the next mouse was placed. During the test, the mice were allowed to move freely in the test area. The test duration for each mouse was 10 min. This study recorded the movement trajectory, total distance (mm), and resting time (s) of each mouse. The data were processed and analyzed using the SuperMaze software (Xinsoft SuperMaze Animal Behavior Analysis System, Shanghai, China).

Immunofluorescence Labeling

On the 24th day, the mice of D1R-cre + Vehicle + Gi + i.p. Saline, D1R-cre + Vehicle + Gq + i.p. Saline, D2R-cre + Vehicle + Gi + i.p. Saline, and D2R-cre + Vehicle + Gq + i.p. Saline group (n = 6 in each) were deeply anesthetized with 1% sodium pentobarbital anesthesia (50 mg/kg, i.p.) and transcardially perfused with 100 mL of 37°C normal saline followed by 50 mL of 4% paraformaldehyde in 0.1 M phosphate buffered saline (PBS, pH 7.4) at 4°C for fixation. The brain tissues were quickly separated and post-fixed for 6–8 h in the same fixative solution and dehydrated in 20% sucrose in 0.1 M PBS for 24 h and 30% sucrose in 0.1 M PBS for 24 h at 4°C. The sections were cut (60 μm in thickness) on a cryostat, mounted onto gelatin-coated slides, and air-dried overnight.

The sections were rinsed in 0.01 M PBS, blocked for 1 h with 5% donkey serum and 0.2% Tween-20 in PBS, and then incubated with the following primary antibodies at 37°C for 1 h and at 4°C overnight: rabbit anti-D1R (1:500, Ab20066, Abcam) and rabbit anti-D2R (1:100, PAA673Mu01, Cloud-Clone). Subsequently, the sections were washed four times in PBS for 5 min and incubated with the corresponding secondary antibodies, donkey anti-rabbit IgG conjugated with DyLight 488 (1:400, 711-545-152, Jackson Immune Research). Sections were washed four times with 0.05% Tween-20 in PBS for 5 min and then cover-slipped. Olympus BX51 fluorescence microscope was used to view the sections, and images were captured using Qimaging Camera and QCapture software. Five to six sections were randomly selected from each mouse. Images were analyzed using the NIH Image J software (Bethesda, MD, United States). The layouts of the images were based on Photoshop CS5 (ADOBE Company, United States).

Data Analysis

All data analyses were conducted using GraphPad Prism 7 (GraphPad Software, Inc., La Jolla, CA, United States). Data are presented as the mean ± SEM. Normality of data was checked by Shapiro–Wilk test. We used one-way ANOVA and Tukey's *post hoc* test to analyze behavioral data between different groups. $P < 0.05$ was considered statistically significant.

RESULTS

The Neurons Containing Dopaminergic D1 Receptor or Dopaminergic D2 Receptor in the Substantia Nigra Pars Compacta or Dorsal Striatum Were Effectively Transfected With hM4Di or hM3Dq

In order to investigate the correlation between the neurons containing D1R or D2R in the SNpc or dSTR and locomotor activities in TS mice, we used D1R-cre, D2R-cre, and their wild-type littermate (WT) mice. The hM3Dq, hM4Di, or control virus was microinjected into the SNpc or dSTR (**Figure 1A**). Then, IDPN was injected intraperitoneally to establish the TS model. After the virus was fully expressed for 3 weeks, behavioral tests were performed (**Figure 1B**).

Immunofluorescence labeling showed that there were co-labels of hM4Di and D1R or D2R, and hM3Dq and D1R or D2R (total co-labeling rate was greater than 90%) in the SNpc (**Supplementary Figure 1**) and dSTR (**Supplementary Figure 2**), respectively, indicating that the microinjection of the virus effectively transfected neurons containing D1R or D2R in the SNpc and dSTR.

Chemogenetic Inhibition of Dopaminergic D1 Receptor-Containing Neurons in the Substantia Nigra Pars Compacta Significantly Alleviated Involuntary Behavioral Stereotypies of Tourette Syndrome Mice

Behavioral tests were performed to explore the changes in locomotor activity in mice after D1R-containing neurons in the SNpc were activated or inhibited by the chemogenetic approach. We found that after injection of saline (i.p. Saline, contrast with CNO), there was no significant difference in the score of stereotyped behavior, total distance, resting time in the open-field test, retention time on the rotarod, and grip force between the WT + Vehicle + mCherry + i.p. Saline group (WT + m) and D1R-cre + Vehicle + mCherry + i.p. Saline group (Veh + m), indicating that the change in genotype of D1R-cre mice had no effect on locomotor activity compared with WT mice ($P > 0.05$, **Figures 2A**, **3B,D** and **Supplementary Figures 3A,C**). In terms of the results of the stereotyped behavior test, the score of stereotyped behavior in each IDPN-induced TS group [D1R-cre + IDPN + mCherry + i.p. Saline group (TS + m), D1R-cre + IDPN + Gq + i.p. Saline group (TS + Gq), and D1R-cre + IDPN + Gi + i.p. Saline group (TS + Gi)] was significantly higher than that of each vehicle group [D1R-cre + Vehicle + mCherry + i.p.Saline group (Veh + m), D1R-cre + Vehicle + Gq + i.p. Saline group (Veh + Gq), and D1R-cre + Vehicle + Gi + i.p. Saline group (Veh + Gi)] ($P < 0.05$, **Figure 2A**), indicating successful modeling.

Thirty minutes after the injection of CNO (i.p. CNO), the scores of stereotyped behavior in each IDPN-induced TS group

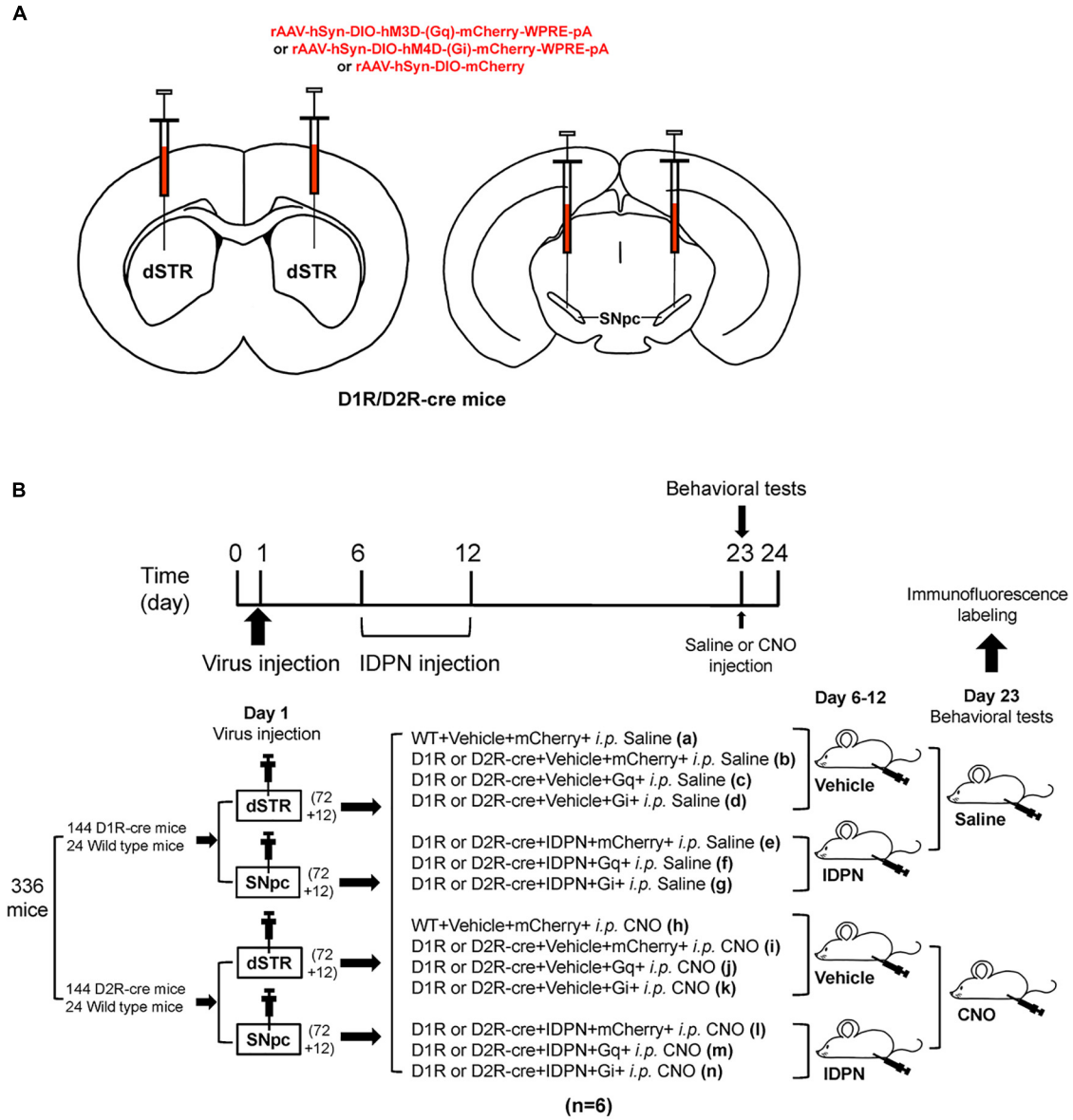

FIGURE 1 | Experimental design. **(A)** Schematic diagram of the virus injection area. **(B)** Experimental design timeline. A total of 336 mice [including 144 D1R-cre mice and 24 wild-type littermate (WT) mice, 144 D2R-cre mice, and 24 WT mice] participated in this experiment. After adaptive feeding for 1 week, they were randomly divided into four large groups (84 mice in each large group), among which 72 D1R-cre mice and 12 WT mice were further divided into two small groups, and 72 D2R-cre mice and 12 WT littermate mice were further divided into two small groups. On the first day, one small group of D1R-cre mice and WT littermate mice, one small group of D2R-cre mice and WT mice were injected with the virus in the bilateral dSTR (200 nL/side), the other two small groups were injected with the virus in the bilateral SNpc (200 nL/side). Eighty-four mice in each large group were randomly divided into 14 groups according to the injections of different drugs or virus, including WT + Vehicle + mCherry + i.p. Saline (group a), D1R or D2R-cre + Vehicle + mCherry + i.p. Saline group (group b), D1R or D2R-cre + Vehicle + Gq + i.p. Saline group (group c), D1R or D2R-cre + Vehicle + Gi + i.p. Saline group (group d), D1R or D2R-cre + IDPN + mCherry + i.p. Saline group (group e), D1R or D2R-cre + IDPN + Gq + i.p. Saline group (group f), D1R or D2R-cre + IDPN + Gi + i.p. Saline group (group g), WT + Vehicle + mCherry + i.p. CNO group (group h), D1R or D2R-cre + Vehicle + mCherry + i.p. CNO group (group i), D1R or D2R-cre + Vehicle + Gq + i.p. CNO group (group j), D1R or D2R-cre + Vehicle + Gi + i.p. CNO group (group k), D1R or D2R-cre + IDPN + mCherry + i.p. CNO group (group l), D1R or D2R-cre + IDPN + Gq + i.p. CNO group (group m) and D1R or D2R-cre + IDPN + Gi + i.p. CNO group (group n) (n = 6 mice in each group). Mice in the groups a, b, e, h, i, and l were injected with a control virus (mCherry). Mice in the groups c, f, j, and m were injected with hM3Dq. Mice in group d, g, k, and n were injected with hM4Di. After the virus injection, all mice were back to the cage to rest for 4 days (days 2–5). On days 6–12, mice in groups e, f, g, l, m, and n were intraperitoneally injected with IDPN at 10:00 a.m. once daily, and mice in the other groups were intraperitoneally injected with 0.9% saline (Vehicle, contrast with IDPN). On the 23rd day, mice in the a–g groups were intraperitoneally injected with 0.9% saline (contrast with CNO), and mice in the h–n groups were intraperitoneally injected with clozapine N-oxide (CNO, Sigma, St. Louis, MO, United States, 1 mg/kg). Thirty minutes later, behavioral tests were carried out to compare the differences between the groups. Brain tissues for immunofluorescence labeled were collected on day 24.

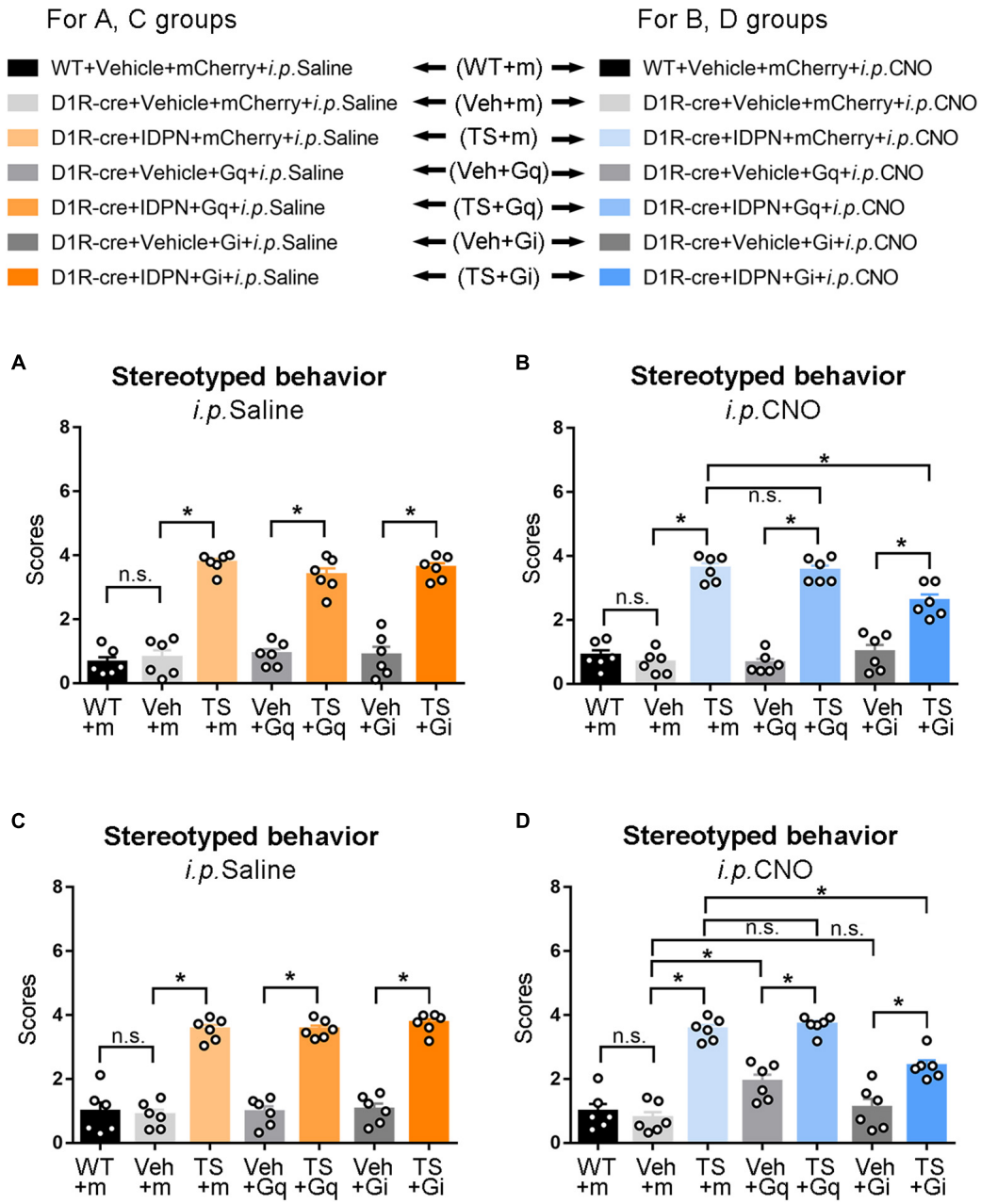

FIGURE 2 | Effects of activation or inhibition of the D1R-containing neurons in the SNpc and dSTR on stereotyped behavior in mice. **(A)** Evaluations of stereotyped behavior scores of mice injected with virus in the SNpc 30 min after the injection of saline (i.p. Saline) in the WT + Vehicle + mCherry + i.p. Saline group (WT + m), D1R-cre + Vehicle + mCherry + i.p. Saline group (Veh + m), D1R-cre + IDPN + mCherry + i.p. Saline group (TS + m), D1R-cre + Vehicle + Gq + i.p. Saline group (Veh + Gq), D1R-cre + IDPN + Gq + i.p. Saline group (TS + Gq), D1R-cre + Vehicle + Gi + i.p. Saline group (Veh + Gi), D1R-cre + IDPN + Gi + i.p. Saline group (TS + Gi) on day 23. **(B)** Evaluations of stereotyped behavior scores of mice injected with virus in the SNpc 30 min after the injection of CNO (i.p. CNO) in the WT + Vehicle + mCherry + i.p. CNO group (WT + m), D1R-cre + Vehicle + mCherry + i.p. CNO group (Veh + m), D1R-cre + IDPN + mCherry + i.p. CNO group (TS + m), D1R-cre + Vehicle + Gq + i.p. CNO group (Veh + Gq), D1R-cre + IDPN + Gq + i.p. CNO group (TS + Gq), D1R-cre + Vehicle + Gi + i.p. CNO group (Veh + Gi), D1R-cre + IDPN + Gi + i.p. CNO group (TS + Gi) on day 23. **(C)** Evaluations of stereotyped behavior scores of mice injected with virus in the dSTR 30 min after the injection of saline (i.p. Saline) in each group on day 23. **(D)** Evaluations of stereotyped behavior scores of mice injected with virus in the dSTR 30 min after the injection of CNO (i.p. CNO) in each group on day 23. Data are expressed as mean ± SEM ($n = 6$ mice in each group), and the black line segment indicates the differences between groups, * represents $P < 0.05$ between marked groups, n.s. represents $P > 0.05$ between marked groups.

(TS + m, TS + Gq, and TS + Gi) was significantly higher than those of each vehicle group (Veh + m, Veh + Gq, and Veh + Gi) ($P < 0.05$, **Figure 2B**), indicating that CNO did not affect the effect of IDPN on the behavioral stereotypies. There was no significant difference in the scores of stereotyped behavior between D1R-cre + IDPN + Gq + i.p. CNO (TS + Gq)

and D1R-cre + IDPN + mCherry + i.p. CNO (TS + m) groups ($P > 0.05$, **Figure 2B**), indicating that chemogenetic activation of D1R-containing neurons in the SNpc did not affect the involuntary behavioral stereotypies in TS mice. Compared with the D1R-cre + IDPN + mCherry + i.p. CNO group (TS + m), the score of stereotyped behavior of D1R-cre + IDPN + Gi + i.p.CNO group (TS + Gi) was significantly decreased ($P < 0.05$, **Figure 2B**), indicating that chemogenetic inhibition of D1R-containing neurons in the SNpc significantly alleviated involuntary behavioral stereotypies in TS mice.

Chemogenetic Activation of Dopaminergic D1 Receptor-Containing Neurons in the Dorsal Striatum Significantly Aggravated Involuntary Behavioral Stereotypies of Vehicle-Treated Mice, While Chemogenetic Inhibition of Dopaminergic D1 Receptor-Containing Neurons in the Dorsal Striatum Significantly Alleviated Involuntary Behavioral Stereotypies of Tourette Syndrome Mice

The change in genotype of D1R-cre mice had no effect on locomotor activity compared with WT mice ($P > 0.05$, **Figures 2C**, **4B,D** and **Supplementary Figures 4A,C**). In terms of the results of the stereotyped behavior test, after the injection of saline (i.p. Saline, contrast with CNO), the score of stereotyped behavior in each IDPN-induced TS model group was significantly higher than that of each vehicle group ($P < 0.05$, **Figure 2C**), indicating successful modeling.

After the injection of CNO (i.p. CNO), the score of stereotyped behavior of the D1R-cre + Vehicle + Gq + i.p. CNO group (Veh + Gq) was significantly higher than that of the D1R-cre + Vehicle + mCherry + i.p. CNO group (Veh + m) ($P < 0.05$, **Figure 2D**), indicating that chemogenetic activation of D1R-containing neurons in the dSTR significantly aggravated involuntary behavioral stereotypies in vehicle-treated mice. At the same time, there was no significant difference in the scores of stereotyped behavior between D1R-cre + Vehicle + Gi + i.p. CNO (Veh + Gi) and D1R-cre + Vehicle + mCherry + i.p. CNO (Veh + m) groups ($P > 0.05$, **Figure 2D**), indicating that chemogenetic inhibition of D1R-containing neurons in the dSTR had no significant effect on involuntary behavioral stereotypies in vehicle-treated mice.

Compared with the D1R-cre + IDPN + mCherry + i.p. CNO group (TS + m), the score of stereotyped behavior of the D1R-cre + IDPN + Gi + i.p.CNO group (TS + Gi) was significantly decreased ($P < 0.05$, **Figure 2D**), indicating that chemogenetic inhibition of D1R-containing neurons in the dSTR significantly alleviated the involuntary behavioral stereotypies in TS mice. There was no significant difference in the scores of stereotyped behavior between D1R-cre + IDPN + Gq + i.p. CNO (TS + Gq) and D1R-cre + IDPN + mCherry + i.p. CNO (TS + m) groups ($P > 0.05$, **Figure 2D**), indicating that chemogenetic activation of D1R-containing neurons in the dSTR did not affect the involuntary behavioral stereotypies in TS mice.

Chemogenetic Inhibition of Dopaminergic D2 Receptor-Containing Neurons in the Substantia Nigra Pars Compacta Significantly Alleviated Involuntary Behavioral Stereotypies of Tourette Syndrome Mice

The change in genotype of D2R-cre mice had no effect on locomotor activity compared with WT mice ($P > 0.05$, **Figures 5A**, **6B,D** and **Supplementary Figures 5A,C**). The score of stereotyped behavior in each TS group was significantly higher than that of each vehicle group ($P < 0.05$, **Figure 5A**), indicating successful modeling.

After the injection of CNO (i.p. CNO), the score of stereotyped behavior in each IDPN-induced TS group (TS + m, TS + Gq, and TS + Gi) was significantly higher than that of each vehicle group (Veh + m, Veh + Gq, and Veh + Gi) ($P < 0.05$, **Figure 5B**), indicating that CNO did not affect the effect of IDPN on the TS model. Compared with the D2R-cre + IDPN + mCherry + i.p. CNO group (TS + m), the score of stereotyped behavior of D2R-cre + IDPN + Gi + i.p.CNO group (TS + Gi) was significantly decreased ($P < 0.05$, **Figure 5B**), indicating that chemogenetic inhibition of D2R-containing neurons in the SNpc significantly alleviated behavioral stereotypies in TS mice. There was no significant difference in the scores of stereotyped behavior between D2R-cre + IDPN + Gq + i.p. CNO (TS + Gq) and D2R-cre + IDPN + mCherry + i.p. CNO (TS + m) groups ($P > 0.05$, **Figure 5B**), indicating that chemogenetic activation of D2R-containing neurons in the SNpc did not affect the involuntary behavioral stereotypies in TS mice.

Chemogenetic Inhibition of Dopaminergic D2 Receptor-Containing Neurons in the Dorsal Striatum Significantly Alleviated Involuntary Behavioral Stereotypies of Tourette Syndrome Mice

The change in genotype of D2R-cre mice had no effect on locomotor activity compared with WT mice ($P > 0.05$, **Figures 5C**, **7B,D** and **Supplementary Figures 6A,C**). After the injection of saline (i.p. Saline), the score of stereotyped behavior in each TS group was significantly higher than that of each vehicle group ($P < 0.05$, **Figure 5C**), indicating successful modeling.

After the injection of CNO (i.p. CNO), the score of stereotyped behavior in each IDPN-induced TS group (TS + m, TS + Gq, and TS + Gi) was significantly higher than that of each vehicle group (Veh + m, Veh + Gq, and Veh + Gi) ($P < 0.05$, **Figure 5D**), indicating that CNO did not affect the effect of IDPN on the TS model. Compared with the D2R-cre + IDPN + mCherry + i.p. CNO group (TS + m), the score of stereotyped behavior of D2R-cre + IDPN + Gi + i.p.CNO group (TS + Gi) was

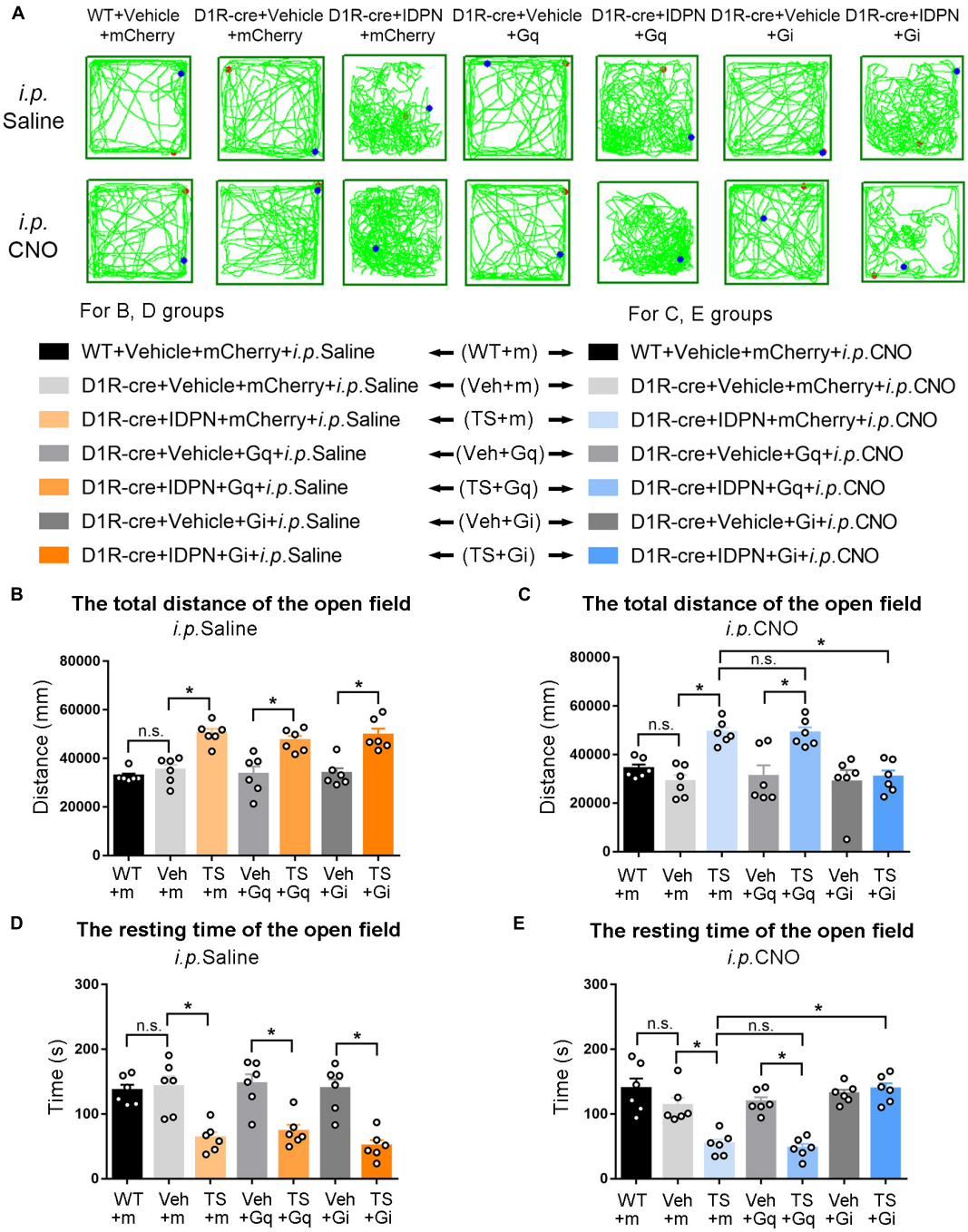

FIGURE 3 | Effects of activation or inhibition of D1R-containing neurons in the SNpc on total distance and resting time in the open-field test in mice. **(A)** Evaluations of the trajectory in the open-field test in mice 30 min after the injection of saline (i.p. Saline) or CNO (i.p. CNO) in the WT + Vehicle + mCherry + i.p. Saline group (WT + m), D1R-cre + Vehicle + mCherry + i.p. Saline group (Veh + m), D1R-cre + IDPN + mCherry + i.p. Saline group (TS + m), D1R-cre + Vehicle + Gq + i.p. Saline group (Veh + Gq), D1R-cre + IDPN + Gq + i.p. Saline group (TS + Gq), D1R-cre + Vehicle + Gi + i.p. Saline group (Veh + Gi), D1R-cre + IDPN + Gi + i.p. Saline group (TS + Gi), WT + Vehicle + mCherry + i.p. CNO group (WT + m), D1R-cre + Vehicle + mCherry + i.p. CNO group (Veh + m), D1R-cre + IDPN + mCherry + i.p. CNO group (TS + m), D1R-cre + Vehicle + Gq + i.p. CNO group (Veh + Gq), D1R-cre + IDPN + Gq + i.p. CNO group (TS + Gq), D1R-cre + Vehicle + Gi + i.p. CNO group (Veh + Gi), D1R-cre + IDPN + Gi + i.p. CNO group (TS + Gi) on day 23. **(B)** Total distance in the open-field test within 10 min in mice of each group 30 min after the injection of saline (i.p. Saline) on day 23. **(C)** Total distance in the open-field test within 10 min in mice of each group 30 min after the injection of CNO (i.p. CNO) on day 23. **(D)** Resting time in the open-field test within 10 min in mice of each group 30 min after the injection of saline (i.p. Saline) on day 23. **(E)** Resting time in the open-field test within 10 min in mice of each group 30 min after the injection of CNO (i.p. CNO) on day 23. Data are expressed as mean ± SEM (n = 6 mice in each group), and the black line segment indicates the differences between groups, * represents $P < 0.05$ between marked groups, and n.s. represents $P > 0.05$ between marked groups.

significantly decreased ($P < 0.05$, **Figure 5D**), indicating that chemogenetic inhibition of D2R-containing neurons in the dSTR significantly alleviated behavioral stereotypies in TS mice. There was no significant difference in the score of stereotyped behavior between D2R-cre + IDPN + Gq + i.p. CNO (TS + Gq) and D2R-cre + IDPN + mCherry + i.p. CNO (TS + m) groups ($P > 0.05$, **Figure 5D**), indicating that chemogenetic activation of D2R-containing neurons in the dSTR did not affect the involuntary behavioral stereotypies in TS mice.

Chemogenetic Inhibition of Dopaminergic D1 Receptor- or Dopaminergic D2 Receptor-Containing Neurons in the Substantia Nigra Pars Compacta and Dorsal Striatum Decreased the Activity in the Open-Field Test of Tourette Syndrome Mice, While Chemogenetic Activation of Dopaminergic D1 Receptor-Containing Neurons in the Dorsal Striatum Increased the Activity in the Open-Field Test of Vehicle-Treated Mice

The results of total distance and resting time of mice in the open-field test were similar to those in the stereotyped behavior test (**Figures 3**, **4**, **6**, **7**). In the open-field test (**Figures 3**, **4**, **6**, **7A** was the trajectory in the open-field test), after the injection of saline (i.p. Saline), compared with each vehicle group (Veh + m, Veh + Gq and Veh + Gi), total distance in the open-field test within 10 min of each TS model group (TS + m, TS + Gq and TS + Gi) was significantly increased ($P < 0.05$, **Figures 3**, **4**, **6**, **7B**), and resting time in the open-field test within 10 min was significantly decreased ($P < 0.05$, **Figures 3**, **4**, **6**, **7D**), indicating that IDPN significantly increased the activity in mice.

After the injection of CNO (i.p. CNO), compared with the TS + m group, total distance of the TS + Gi group was significantly decreased ($P < 0.05$, **Figures 3**, **4**, **6**, **7C**), and resting time was significantly increased ($P < 0.05$, **Figures 3**, **4**, **6**, **7E**). It indicated that after inhibiting D1R- or D2R-containing neurons in the SNpc and dSTR, the activity in the open-field test in TS mice was decreased. Compared with the TS + m group, total distance and resting time of the TS + Gq group did not significantly change ($P > 0.05$, **Figures 3**, **6**, **7C,E**). It indicated that chemogenetic activation of D1R- or D2R-containing neurons in the SNpc- and D2R-containing neurons in the dSTR did not affect the activity in the open-field test in TS mice.

As shown in **Figure 4**, after the injection of CNO (i.p. CNO), compared with the D1R-cre + Vehicle + mCherry + i.p. CNO group (Veh + m), total distance of the D1R-cre + Vehicle + Gq + i.p. CNO group (Veh + Gq) was significantly increased ($P < 0.05$, **Figure 4C**), and resting time was significantly decreased ($P < 0.05$, **Figure 4E**) in the open-field test, indicating that after activating D1R-containing neurons in the dSTR, the activity in the open-field test of the vehicle-treated mice was increased. Compared with the D1R-cre + Vehicle + mCherry + i.p. CNO group (Veh + m), total distance and resting time in the open-field test of the D1R-cre + Vehicle + Gi + i.p. CNO group (Veh + Gi) did not significantly change ($P > 0.05$, **Figures 4C,E**). It indicated that chemogenetic inhibition of D1R-containing neurons in the dSTR did not affect the activity in the open-field test in vehicle-treated mice.

In addition, chemogenetic activation or inhibition of D1R- or D2R-containing neurons in the SNpc and dSTR had no significant effect on motor coordination (**Supplementary Result Section** "Chemogenetic Activation or Inhibition D1R or D2R-Containing Neurons in the SNpc and dSTR Had No Significant Effect on Motor Coordination and Grip Strength in Mice" and **Supplementary Figures 3–6A,B**) and grip strength (**Supplementary Result Section** "Chemogenetic Activation or Inhibition D1R or D2R-Containing Neurons in the SNpc and dSTR Had No Significant Effect on Motor Coordination and Grip Strength in Mice" and **Supplementary Figures 3–6C,D**) of mice.

DISCUSSION

Tourette syndrome is a common neurobehavioral disorder that is closely related to DA and its receptors (Nespoli et al., 2018). A large number of studies have found that dysfunction of the substantia nigra–striatum network could be the main pathogenesis of TS, which is closely associated with the hyperfunction of the nigrostriatal dopaminergic neurons (Zebardast et al., 2013). Our study showed that chemogenetic inhibition of D1R- or D2R-containing neurons in the SNpc and dSTR significantly alleviated involuntary behavioral stereotypies in TS mice. Chemogenetically activating D1R-containing neurons, but not D2R-containing neurons, in the dSTR significantly aggravated behavioral stereotypies in vehicle-treated mice. Chemogenetic activation or inhibition of D1R- or D2R-containing neurons in the SNpc and dSTR had no significant effect on the motor coordination and grip strength of mice, and the results of total distance and the resting time of mice in the open-field test were similar to those of the stereotyped behavior test (**Supplementary Table 1**). Previous studies have shown that the basal ganglia can control different processes of movement by regulating the DA system, thus playing an important role in the pathophysiology of TS (Buot and Yelnik, 2012). The main pathogenesis of TS is the hyperfunction of dopaminergic neurons projecting from the substantia nigra to the striatum (Cui Y. H. et al., 2013), leading to an increased release of DA in the substantia nigra–striatum network, thereby causing TS (Maqsood et al., 2020).

The basal ganglia motor system includes both direct and indirect pathways. D1R and D2R are expressed in the direct and indirect pathways, respectively (Beaulieu and Gainetdinov, 2011). In the direct pathway, the SNpc releases a large amount of DA to activate GABAergic projection neurons in the striatum, which can inhibit the globus pallidus internus (GPi) and substantia nigra pars reticulata (SNpr) (Grillner and Robertson, 2016). The thalamus is normally inhibited by the globus pallidus and

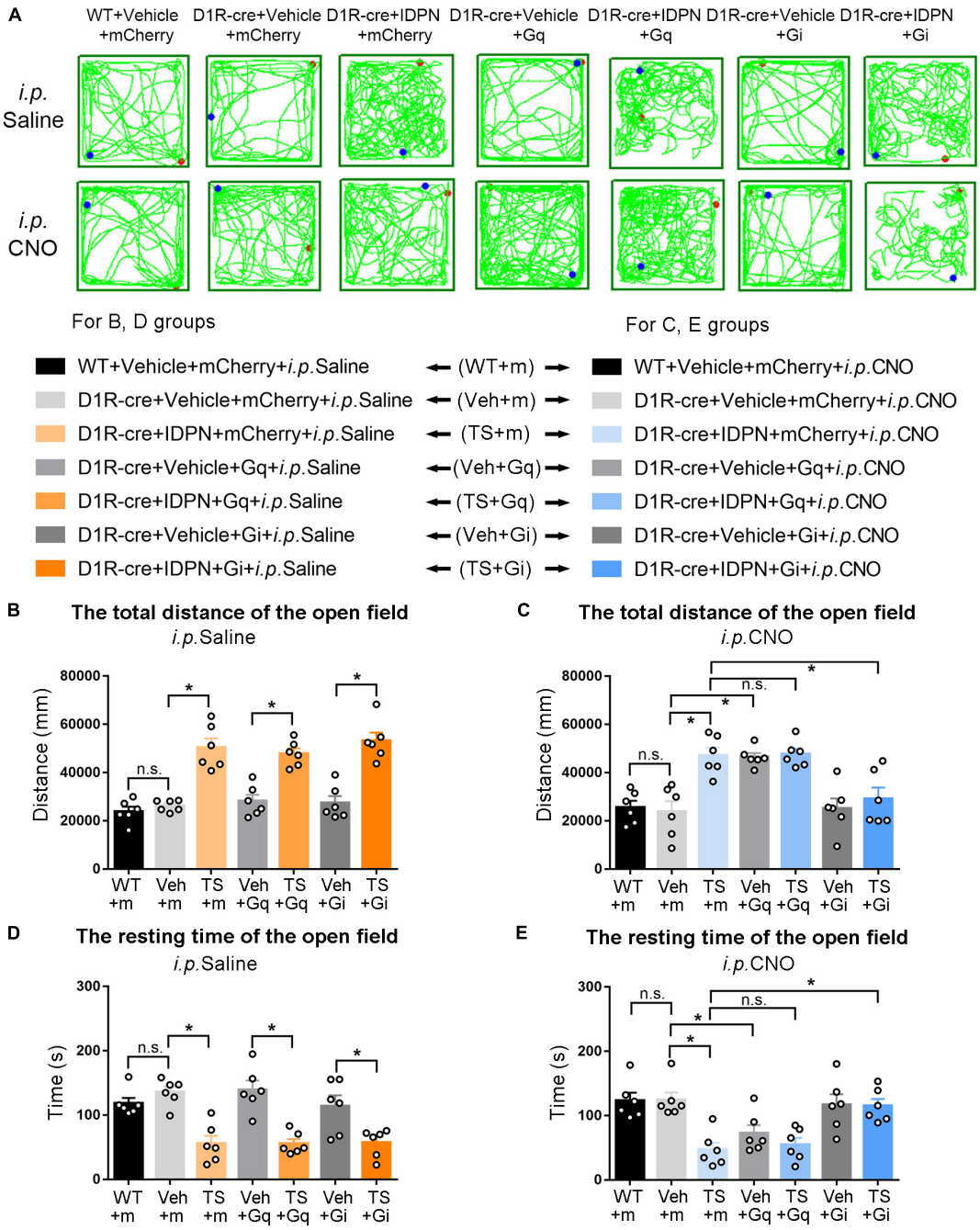

FIGURE 4 | Effects of activation or inhibition of D1R-containing neurons in the dSTR on total distance and resting time in the open-field test in mice. **(A)** Evaluations of the trajectory in the open-field test in mice 30 min after the injection of saline (i.p. Saline) or CNO (i.p. CNO) in the WT + Vehicle + mCherry + i.p. Saline group (WT + m), D1R-cre + Vehicle + mCherry + i.p. Saline group (Veh + m), D1R-cre + IDPN + mCherry + i.p. Saline group (TS + m), D1R-cre + Vehicle + Gq + i.p. Saline group (Veh + Gq), D1R-cre + IDPN + Gq + i.p. Saline group (TS + Gq), D1R-cre + Vehicle + Gi + i.p. Saline group (Veh + Gi), D1R-cre + IDPN + Gi + i.p. Saline group (TS + Gi), WT + Vehicle + mCherry + i.p. CNO group (WT + m), D1R-cre + Vehicle + mCherry + i.p. CNO group (Veh + m), D1R-cre + IDPN + mCherry + i.p. CNO group (TS + m), D1R-cre + Vehicle + Gq + i.p. CNO group (Veh + Gq), D1R-cre + IDPN + Gq + i.p. CNO group (TS + Gq), D1R-cre + Vehicle + Gi + i.p. CNO group (Veh + Gi), D1R-cre + IDPN + Gi + i.p. CNO group (TS + Gi) on day 23. **(B)** Total distance in the open-field test within 10 min in mice of each group 30 min after the injection of saline (i.p. Saline) on day 23. **(C)** Total distance in the open-field test within 10 min in mice of each group 30 min after the injection of CNO (i.p. CNO) on day 23. **(D)** Resting time in the open-field test within 10 min in mice of each group 30 min after the injection of saline (i.p. Saline) on day 23. **(E)** Resting time in the open-field test within 10 min in mice of each group 30 min after the injection of CNO (i.p. CNO) on day 23. Data are expressed as mean ± SEM (n = 6 mice in each group), and the black line segment indicates the differences between groups, * represents $P < 0.05$ between marked groups, and n.s. represents $P > 0.05$ between marked groups.

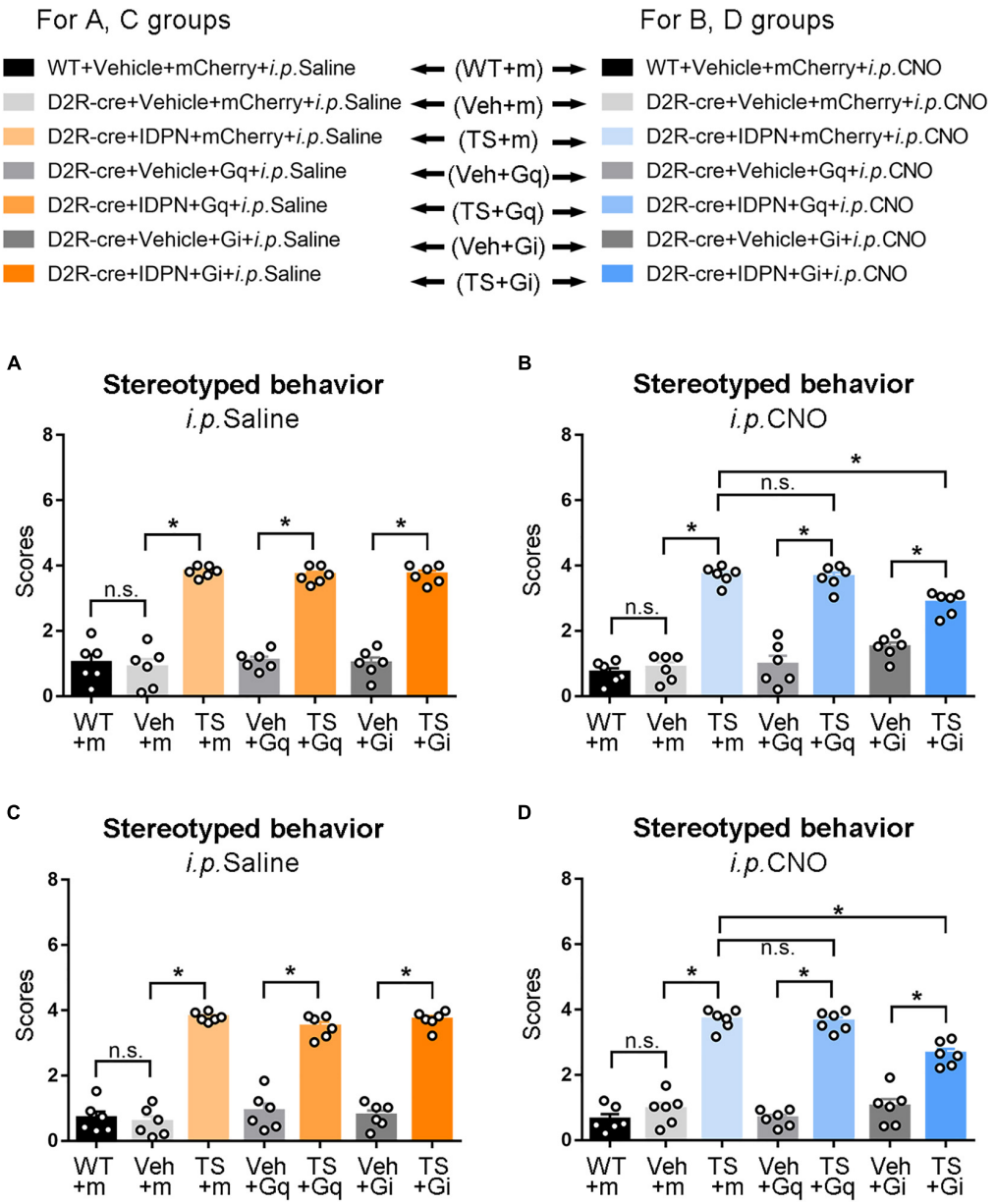

FIGURE 5 | Effects of activation or inhibition of the D2R-containing neurons in the SNpc and dSTR on stereotyped behavior in mice. **(A)** Evaluations of stereotyped behavior scores of mice injected with virus in the SNpc 30 min after the injection of saline (i.p. Saline) in the WT + Vehicle + mCherry + i.p. Saline group (WT + m), D2R-cre + Vehicle + mCherry + i.p. Saline group (Veh + m), D2R-cre + IDPN + mCherry + i.p. Saline group (TS + m), D2R-cre + Vehicle + Gq + i.p. Saline group (Veh + Gq), D2R-cre + IDPN + Gq + i.p. Saline group (TS + Gq), D2R-cre + Vehicle + Gi + i.p. Saline group (Veh + Gi), D2R-cre + IDPN + Gi + i.p. Saline group (TS + Gi) on day 23. **(B)** Evaluations of stereotyped behavior scores of mice injected with virus in the SNpc 30 min after the injection of CNO (i.p. CNO) in the WT + Vehicle + mCherry + i.p. CNO group (WT + m), D2R-cre + Vehicle + mCherry + i.p. CNO group (Veh + m), D2R-cre + IDPN + mCherry + i.p. CNO group (TS + m), D2R-cre + Vehicle + Gq + i.p. CNO group (Veh + Gq), D2R-cre + IDPN + Gq + i.p. CNO group (TS + Gq), D2R-cre + Vehicle + Gi + i.p. CNO group (Veh + Gi), D2R-cre + IDPN + Gi + i.p. CNO group (TS + Gi) on day 23. **(C)** Evaluations of stereotyped behavior scores of mice injected with virus in the dSTR 30 min after the injection of saline (i.p. Saline) in each group on day 23. **(D)** Evaluations of stereotyped behavior scores of mice injected with virus in the dSTR 30 min after the injection of CNO (i.p. CNO) in each group on day 23. Data are expressed as mean ± SEM ($n = 6$ mice in each group), and the black line segment indicates the differences between groups, * represents $P < 0.05$ between marked groups, n.s. represents $P > 0.05$ between marked groups.

the SNpr. When the direct pathway is activated, the thalamus is disinhibited and it sends excitatory impulses back to the cortex, thus promoting movement (**Figure 8**; Cui G. et al., 2013; Dobbs et al., 2016).

In this study, we found that chemogenetic inhibition of D1R- or D2R-containing neurons in the SNpc significantly alleviated behavioral stereotypies in TS mice. In the SNpc, D1R, and D2R are expressed on both dopaminergic neurons

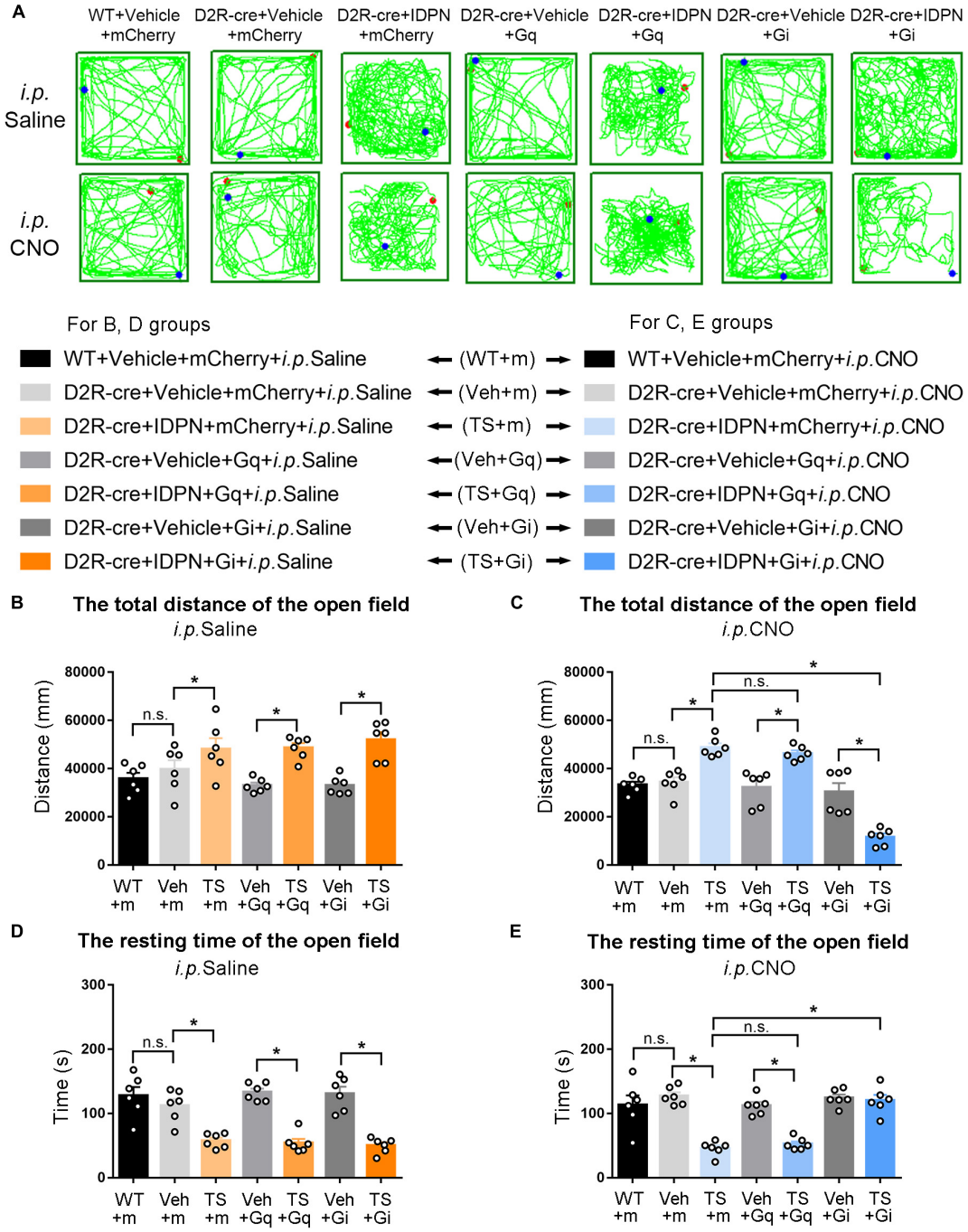

FIGURE 6 | Effects of activation or inhibition of D2R-containing neurons in the SNpc on total distance and resting time in the open-field test in mice. **(A)** Evaluations of the trajectory in the open-field test in mice 30 min after the injection of saline (i.p. Saline) or CNO (i.p. CNO) in the WT + Vehicle + mCherry + i.p. Saline group (WT + m), D2R-cre + Vehicle + mCherry + i.p. Saline group (Veh + m), D2R-cre + IDPN + mCherry + i.p. Saline group (TS + m), D2R-cre + Vehicle + Gq + i.p. Saline group (Veh + Gq), D2R-cre + IDPN + Gq + i.p. Saline group (TS + Gq), D2R-cre + Vehicle + Gi + i.p. Saline group (Veh + Gi), D2R-cre + IDPN + Gi + i.p. Saline group (TS + Gi), WT + Vehicle + mCherry + i.p. CNO group (WT + m), D2R-cre + Vehicle + mCherry + i.p. CNO group (Veh + m), D2R-cre + IDPN + mCherry + i.p. CNO group (TS + m), D2R-cre + Vehicle + Gq + i.p. CNO group (Veh + Gq), D2R-cre + IDPN + Gq + i.p. CNO group (TS + Gq), D2R-cre + Vehicle + Gi + i.p. CNO group (Veh + Gi), D2R-cre + IDPN + Gi + i.p. CNO group (TS + Gi) on day 23. **(B)** Total distance in the open-field test within 10 min in mice of each group 30 min after the injection of saline (i.p. Saline) on day 23. **(C)** Total distance in the open-field test within 10 min in mice of each group 30 min after the injection of CNO (i.p. CNO) on day 23. **(D)** Resting time in the open-field test within 10 min in mice of each group 30 min after the injection of saline (i.p. Saline) on day 23. **(E)** Resting time in the open-field test within 10 min in mice of each group 30 min after the injection of CNO (i.p. CNO) on day 23. Data are expressed as mean ± SEM (n = 6 mice in each group), and the black line segment indicates the differences between groups, * represents $P < 0.05$ between marked groups, and n.s. represents $P > 0.05$ between marked groups.

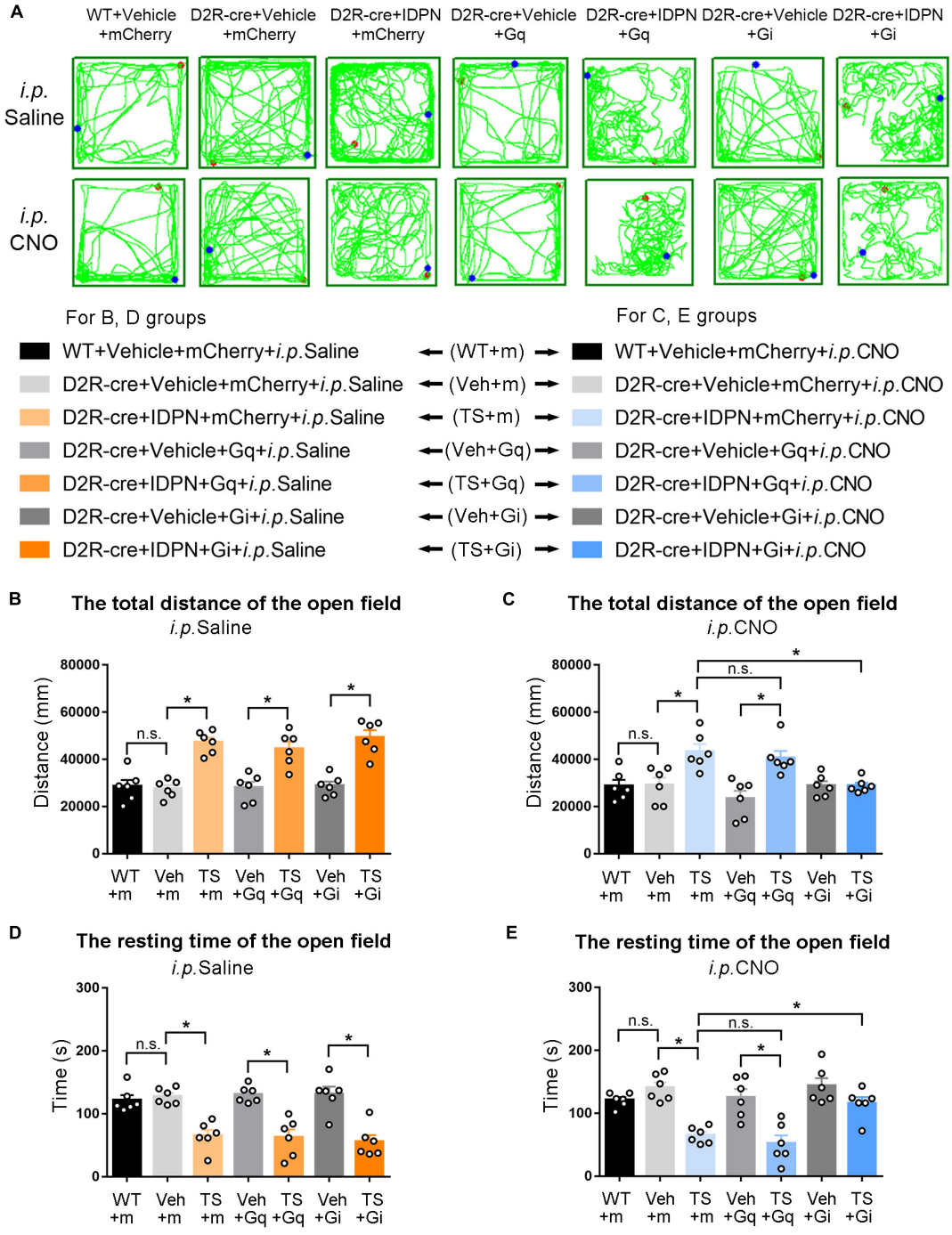

FIGURE 7 | Effects of activation or inhibition of D2R-containing neurons in the dSTR on total distance and resting time in the open-field test in mice. **(A)** Evaluations of the trajectory in the open-field test in mice 30 min after the injection of saline (i.p. Saline) or CNO (i.p. CNO) in the WT + Vehicle + mCherry + i.p. Saline group (WT + m), D2R-cre + Vehicle + mCherry + i.p. Saline group (Veh + m), D2R-cre + IDPN + mCherry + i.p. Saline group (TS + m), D2R-cre + Vehicle + Gq + i.p. Saline group (Veh + Gq), D2R-cre + IDPN + Gq + i.p. Saline group (TS + Gq), D2R-cre + Vehicle + Gi + i.p. Saline group (Veh + Gi), D2R-cre + IDPN + Gi + i.p. Saline group (TS + Gi), WT + Vehicle + mCherry + i.p. CNO group (WT + m), D2R-cre + Vehicle + mCherry + i.p. CNO group (Veh + m), D2R-cre + IDPN + mCherry + i.p. CNO group (TS + m), D2R-cre + Vehicle + Gq + i.p. CNO group (Veh + Gq), D2R-cre + IDPN + Gq + i.p. CNO group (TS + Gq), D2R-cre + Vehicle + Gi + i.p. CNO group (Veh + Gi), D2R-cre + IDPN + Gi + i.p. CNO group (TS + Gi) on day 23. **(B)** Total distance in the open-field test within 10 min in mice of each group 30 min after the injection of saline (i.p. Saline) on day 23. **(C)** Total distance in the open-field test within 10 min in mice of each group 30 min after the injection of CNO (i.p. CNO) on day 23. **(D)** Resting time in the open-field test within 10 min in mice of each group 30 min after the injection of saline (i.p. Saline) on day 23. **(E)** Resting time in the open-field test within 10 min in mice of each group 30 min after the injection of CNO (i.p. CNO) on day 23. Data are expressed as mean ± SEM (n = 6 mice in each group), and the black line segment indicates the differences between groups, * represents $P < 0.05$ between marked groups, and n.s. represents $P > 0.05$ between marked groups.

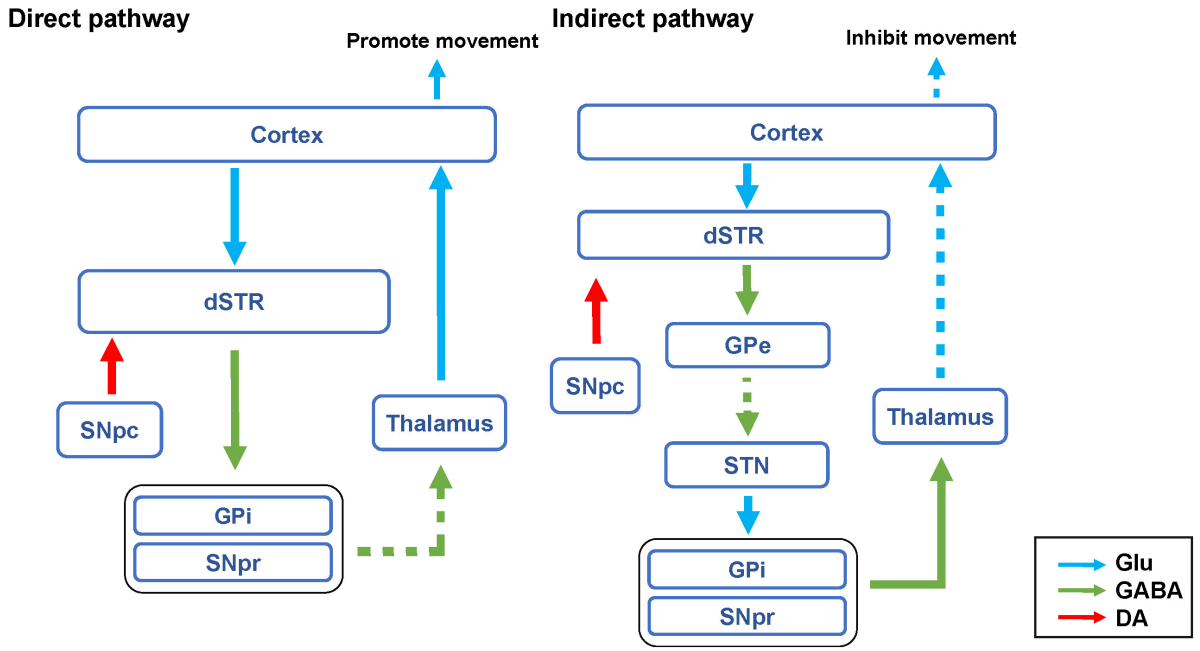

FIGURE 8 | Hypothesis diagram of direct and indirect pathways of basal ganglia motor regulatory system. The blue arrow represents glutamatergic (Glu) neuron transmission. The green arrow indicates GABAergic neuron transmission. The red arrow represents dopaminergic neuron transmission. The solid line represents activation. The dashed line indicates inhibition.

and inhibitory interneurons (**Figures 9A,B**; Yung et al., 1995; Yang et al., 2019). Chemogenetic inhibition of D1R- or D2R-containing dopaminergic neurons may inhibit the release of DA in the direct pathway and reduce movement, thus alleviating involuntary behavioral stereotypies. Although chemogenetic inhibition of D1R- or D2R-containing inhibitory interneurons may disinhibit D1R or D2R-containing dopaminergic neurons, dopaminergic neurons were already inhibited by chemogenetic approach and could not be activated. In our study, D1R- or D2R-containing neurons were manipulating, not D1R or D2R receptors. As a result, chemogenetic inhibition of D1R- or D2R-containing neurons in the SNpc produced the same effects of reducing movement. However, chemogenetic activation of D1R- or D2R-containing neurons in the SNpc did not aggravate the behavioral stereotypies of vehicle-treated and TS mice. It has been demonstrated that D1R or D2R is also expressed in inhibitory interneurons in the SNpc (Cover et al., 2019; Ohira, 2019) and can be activated by a chemogenetic approach to inhibit D1R- or D2R-containing dopaminergic neurons (**Figures 9A,B**). Therefore, chemogenetic activation of D1R- or D2R-containing neurons did not affect movement.

In our study, after inhibiting or activating D1R-containing neurons in the dSTR, the stereotyped behavior of TS or vehicle-treated mice was significantly decreased or increased, respectively. Since D1R is mainly expressed on GABAergic projection neurons but not inhibitory interneurons in the dSTR (**Figure 9C**; Avila-Luna et al., 2019; Assali et al., 2021), chemogenetic inhibition of D1R-containing neurons in the dSTR may inhibit the direct pathway, thus alleviating the stereotyped behavior of the TS model. Although chemogenetically activating D1R-containing neurons might have enhance the direct pathway, it only induced stereotyped behavior in vehicle-treated mice, but did not deteriorate the stereotyped behavior of TS mice. This might be the reason why the behavioral stereotypies of TS mice reached a peak and would not increase further by chemogenetic activation. This suggests that the activation of D1R-containing neurons in the dSTR may be involved in the pathogenesis of TS.

As shown in **Figure 8**, in the indirect pathway, the striatum transmits inhibitory efferent stimuli to the globus pallidus externus (GPe), which in turn disinhibits the subthalamic nucleus (STN), leading to increased excitement of the GPi and SNpr, thus inhibiting the thalamus and weakening the excitement of the cortex (Hadipour-Niktarash et al., 2012). Therefore, the activation of the indirect pathway can inhibit the movement (Freeze et al., 2013). In this study, we found that chemogenetic activation of D2R-containing neurons in the dSTR did not significantly affect the behavioral stereotypies of vehicle-treated mice. This may be due to the activation of various types of D2R-containing neurons in the dSTR, including GABAergic projection neurons that can inhibit movement in indirect pathways, as well as inhibitory GABAergic or acetylcholinergic interneurons, which can inhibit GABAergic projection neurons (**Figure 9D**; Alcantara et al., 2003; Maurice et al., 2004; Zhang et al., 2009; Jijon-Lorenzo et al., 2018; Brandenburg et al., 2020; Lewis et al., 2020). Since

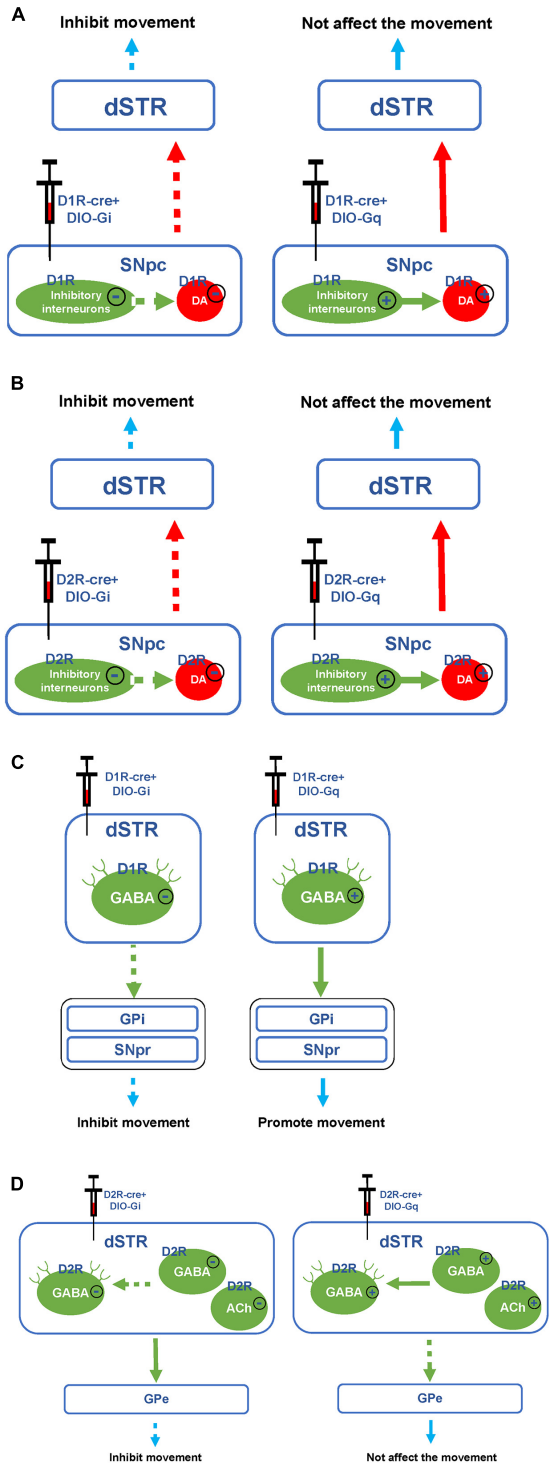

FIGURE 9 | Hypothesis diagram of experimental mechanism. **(A)** Hypothesis diagram of chemogenetic inhibition or activation of D1R-containing neurons in the SNpc. **(B)** Hypothesis diagram of chemogenetic inhibition or activation of D2R-containing neurons in the SNpc. **(C)** Hypothesis diagram of chemogenetic inhibition or activation of D1R-containing neurons in the dSTR. **(D)** Hypothesis diagram of chemogenetic inhibition or activation of D2R-containing neurons in the dSTR. The solid line or plus sign indicates activation. The dashed line or minus sign indicates inhibition.

D2R-containing projection and interneurons played the opposite role in movement, chemogenetic activation of D2R-containing neurons in the dSTR had no significant effect on behavioral stereotypies in mice.

Previous studies have found that enhanced GABA transmission drives bradykinesia following the loss of D2R signaling in medium spiny neurons of the indirect pathway (Lemos et al., 2016). After inhibiting D2R-containing neurons in the dSTR, the involuntary behavioral stereotypies of TS mice were alleviated. This result was different from what we expected, we speculated that this may be because the number of D2R-containing inhibitory interneurons in the dSTR exceeds that of GABAergic projection neurons. After both are chemogenetically inhibited, the activity of inhibitory interneurons is greatly reduced, and GABAergic projection neurons in the indirect pathway are disinhibited, thereby inhibiting movement (**Figure 9D**). Since we found that chemogenetic inhibition of D1R- or D2R-containing neurons in the SNpc and dSTR can alleviate involuntary behavioral stereotypies in TS mice, we speculated that inhibiting D1R- and D2R-containing neurons in the SNpc and dSTR at the same time may have a better therapeutic effect.

In this study, after inhibiting D1R- or D2R-containing neurons in the SNpc or dSTR, the total distance of TS mice in the open-field test was decreased and the resting time was increased, indicating that spontaneous locomotor activities of TS mice were reduced. After activating D1R- but not D2R-containing neurons in the dSTR, the spontaneous locomotor activities of vehicle-treated mice in the open-field test were increased, which was similar to the result of the stereotyped behavior test and mainly due to the expression of D2R but not D1R on inhibitory interneurons in the dSTR. The rotarod test was used to evaluate the motor coordination in mice. Previous studies have shown that chemogenetic activation or inhibition of direct or indirect pathways does not impair motor coordination (Kravitz et al., 2010). Our study found that after activating or inhibiting D1R- or D2R-containing neurons in the SNpc or dSTR, the movement coordination of mice in each group was not affected, which was consistent with previous studies.

Previous studies have demonstrated that D1R and D2R antagonists have extrapyramidal side effects (Peacock et al., 1999). The clinical use of dopaminergic agonists or antagonists can disturb the regulation of blood pressure leading to either hypo- or hypertension, respectively (Gonsai et al., 2018). In addition, chemogenetic strategy is a more precise intervention on a specific target, which is the advantages of this technology. Therefore, we used chemogenetic strategies to selectively activate or inhibit D1R- or D2R-containing neurons in the SNpc or dSTR, which also provided guidance on the clinical treatment of TS, such as deep brain stimulation (DBS). The targets applied for DBS in TS include the STN, the GPi, and the GPe (Rotsides and Mammis, 2013; Andrade and Visser-Vandewalle, 2016; Zhu et al., 2019); the exploration of these brain regions will become our next research direction.

In conclusion, we found that chemogenetic inhibition of D1R- or D2R-containing neurons in the SNpc and dSTR significantly alleviated involuntary behavioral stereotypies in TS mice, which may provide a new approach for the treatment of TS, and help overcome the clinical problem of TS. Moreover, the activation of D1R-containing neurons in the dSTR could also contribute to the occurrence of TS, which may be a more specific target for TS treatment.

DATA AVAILABILITY STATEMENT

The original contributions presented in the study are included in the article/**Supplementary Material**, further inquiries can be directed to the corresponding authors.

ETHICS STATEMENT

All animal experimental protocols conformed to the Animal Management Rules of the Chinese Ministry of Health, and the study was approved by the Animal Ethics Committee of the Chinese Academy of Medical Sciences.

AUTHOR CONTRIBUTIONS

ML and WS conceived and designed the experiments. LL did most of the experiments and analyzed the data. YL, SW, and WW helped with the behavior test experiments. HeZ, LY, and YS helped with the viruses constructs and surgery experiments. HX and TH helped with the immunofluorescence labeling experiments. HoZ and YM helped with analyzing the data. LL, ML, and WS wrote the manuscript. All authors reviewed the manuscript.

FUNDING

This work was supported by the major project of the National Natural Science Foundation of Hubei Province (Grant Number 2015CFA094) and the Huanghe Talents Plan of Wuhan City in 2015.

SUPPLEMENTARY MATERIAL

The Supplementary Material for this article can be found online at: https://www.frontiersin.org/articles/10.3389/fnmol.2021.779436/full#supplementary-material

REFERENCES

Alcantara, A. A., Chen, V., Herring, B. E., Mendenhall, J. M., and Berlanga, M. L. (2003). Localization of dopamine D2 receptors on cholinergic interneurons of the dorsal striatum and nucleus accumbens of the rat. *Brain Res.* 986, 22–29. doi: 10.1016/s0006-8993(03)03165-2

Andrade, P., and Visser-Vandewalle, V. (2016). DBS in tourette syndrome: where are we standing now? *J. Neural Transm.* 123, 791–796. doi: 10.1007/s00702-016-1569-7

Assali, D. R., Sidikpramana, M., Villa, A. P., Falkenstein, J., and Steele, A. D. (2021). Type 1 dopamine receptor (D1R)-independent circadian food anticipatory activity in mice. *PLoS One* 16:e0242897. doi: 10.1371/journal.pone.0242897

Avila-Luna, A., Rios, C., Galvez-Rosas, A., Montes, S., Arias-Montano, J. A., and Bueno-Nava, A. (2019). Chronic administration of the histamine H3 receptor agonist immepip decreases L-Dopa-induced dyskinesias in 6-hydroxydopamine-lesioned rats. *Psychopharmacology* 236, 1937–1948. doi: 10.1007/s00213-019-5182-y

Baym, C. L., Corbett, B. A., Wright, S. B., and Bunge, S. A. (2008). Neural correlates of tic severity and cognitive control in children with Tourette syndrome. *Brain* 131(Pt 1), 165–179. doi: 10.1093/brain/awm278

Beaulieu, J. M., and Gainetdinov, R. R. (2011). The physiology, signaling, and pharmacology of dopamine receptors. *Pharmacol. Rev.* 63, 182–217. doi: 10.1124/pr.110.002642

Brandenburg, C., Soghomonian, J. J., Zhang, K., Sulkaj, I., Randolph, B., Kachadoorian, M., et al. (2020). Increased Dopamine Type 2 gene expression in the dorsal striatum in individuals with autism spectrum disorder suggests alterations in indirect pathway signaling and circuitry. *Front. Cell Neurosci.* 14:577858. doi: 10.3389/fncel.2020.577858

Broderick, P. A., and Phelix, C. F. (1997). I. Serotonin (5-HT) within dopamine reward circuits signals open-field behavior. II. Basis for 5-HT–DA interaction in cocaine dysfunctional behavior. *Neurosci. Biobehav. Rev.* 21, 227–260. doi: 10.1016/s0149-7634(96)00048-6

Bromberg-Martin, E. S., Matsumoto, M., and Hikosaka, O. (2010). Dopamine in motivational control: rewarding, aversive, and alerting. *Neuron* 68, 815–834. doi: 10.1016/j.neuron.2010.11.022

Buot, A., and Yelnik, J. (2012). Functional anatomy of the basal ganglia: limbic aspects. *Rev. Neurol.* 168, 569–575. doi: 10.1016/j.neurol.2012.06.015

Calabrese, V., Di Maio, A., Marino, G., Cardinale, A., Natale, G., De Rosa, A., et al. (2020). Rapamycin, by Inhibiting mTORC1 signaling, prevents the loss of striatal bidirectional synaptic plasticity in a rat model of L-DOPA-Induced Dyskinesia. *Front. Aging Neurosci.* 12:230. doi: 10.3389/fnagi.2020.00230

Cen, S. S., Yu, J., Wang, Q., Deeb, W., Wang, K. L., Shukla, A. W., et al. (2020). Multidisciplinary telemedicine care for tourette syndrome: minireview. *Front. Neurol.* 11:573576. doi: 10.3389/fneur.2020.573576

Chen, J., Leong, P. K., Leung, H. Y., Chan, W. M., Li, Z., Qiu, J., et al. (2019). A chinese herbal formulation, xiao-er-an-shen decoction, attenuates tourette syndrome, possibly by reversing abnormal changes in neurotransmitter levels and enhancing antioxidant status in mouse brain. *Front. Pharmacol.* 10:812. doi: 10.3389/fphar.2019.00812

Cover, K. K., Gyawali, U., Kerkhoff, W. G., Patton, M. H., Mu, C., White, M. G., et al. (2019). Activation of the rostral intralaminar thalamus drives reinforcement through striatal dopamine release. *Cell Rep.* 26, 1389–1398 e1383. doi: 10.1016/j.celrep.2019.01.044

Cui, G., Jun, S. B., Jin, X., Pham, M. D., Vogel, S. S., Lovinger, D. M., et al. (2013). Concurrent activation of striatal direct and indirect pathways during action initiation. *Nature* 494, 238–242. doi: 10.1038/nature11846

Cui, Y. H., Zheng, Y., Jin, Z., He, Y., Chen, X., and Yu, L. P. (2013). [Relationship between tic symptom severity and amplitude of low frequency fluctuation of resting-state functional magnetic resonance imaging of Tourette syndrome]. *Zhonghua Er Ke Za Zhi* 51, 448–452.

Dobbs, L. K., Kaplan, A. R., Lemos, J. C., Matsui, A., Rubinstein, M., and Alvarez, V. A. (2016). Dopamine regulation of lateral inhibition between striatal neurons gates the stimulant actions of cocaine. *Neuron* 90, 1100–1113. doi: 10.1016/j.neuron.2016.04.031

Dodel, I., Reese, J. P., Muller, N., Munchau, A., Balzer-Geldsetzer, M., Wasem, J., et al. (2010). Cost of illness in patients with Gilles de la Tourette's syndrome. *J. Neurol.* 257, 1055–1061.

Egolf, A., and Coffey, B. J. (2014). Current pharmacotherapeutic approaches for the treatment of Tourette syndrome. *Drugs Today* 50, 159–179. doi: 10.1358/dot.2014.50.2.2097801

Ferguson, S. M., Eskenazi, D., Ishikawa, M., Wanat, M. J., Phillips, P. E., Dong, Y., et al. (2011). Transient neuronal inhibition reveals opposing roles of indirect and direct pathways in sensitization. *Nat. Neurosci.* 14, 22–24. doi: 10.1038/nn.2703

Freeze, B. S., Kravitz, A. V., Hammack, N., Berke, J. D., and Kreitzer, A. C. (2013). Control of basal ganglia output by direct and indirect pathway projection neurons. *J. Neurosci.* 33, 18531–18539. doi: 10.1523/jneurosci.1278-13.2013

Ganos, C., and Martino, D. (2015). Tics and tourette syndrome. *Neurol. Clin.* 33, 115–136.

Gonsai, N. H., Amin, V. H., Mendpara, C. G., Speth, R., and Hale, G. M. (2018). Effects of dopamine receptor antagonist antipsychotic therapy on blood pressure. *J. Clin. Pharm. Ther.* 43, 1–7. doi: 10.1111/jcpt.12649

Grillner, S., and Robertson, B. (2016). The basal ganglia over 500 Million years. *Curr. Biol.* 26, R1088–R1100. doi: 10.1016/j.baga.2011.01.090

Groenewegen, H. J., van den Heuvel, O. A., Cath, D. C., Voorn, P., and Veltman, D. J. (2003). Does an imbalance between the dorsal and ventral striatopallidal systems play a role in Tourette's syndrome? a neuronal circuit approach. *Brain Dev.* 25(Suppl. 1), S3–S14. doi: 10.1016/s0387-7604(03)90001-5

Hadipour-Niktarash, A., Rommelfanger, K. S., Masilamoni, G. J., Smith, Y., and Wichmann, T. (2012). Extrastriatal D2-like receptors modulate basal ganglia pathways in normal and Parkinsonian monkeys. *J. Neurophysiol.* 107, 1500–1512. doi: 10.1152/jn.00348.2011

Hamamoto, Y., and Kano, Y. (2018). [Tourette Syndrome]. *Brain Nerve* 70, 1237–1245.

Hsu, C. J., Wong, L. C., and Lee, W. T. (2021). Immunological dysfunction in tourette syndrome and related disorders. *Int. J. Mol. Sci.* 22:853. doi: 10.3390/ijms22020853

Jakubovski, E., and Muller-Vahl, K. R. (2017). [Gilles de la Tourette syndrome: symptoms, causes and therapy]. *Psychother. Psychosom. Med. Psychol.* 67, 252–268.

Jijon-Lorenzo, R., Caballero-Floran, I. H., Recillas-Morales, S., Cortes, H., Avalos-Fuentes, J. A., Paz-Bermudez, F. J., et al. (2018). Presynaptic Dopamine D2 receptors modulate [(3)H]GABA release at striatopallidal terminals via activation of PLC−>IP3−>calcineurin and inhibition of AC−>cAMP−>PKA signaling cascades. *Neuroscience* 372, 74–86. doi: 10.1016/j.neuroscience.2017.12.041

Kawohl, W., Bruhl, A., Krowatschek, G., Ketteler, D., and Herwig, U. (2009). Functional magnetic resonance imaging of tics and tic suppression in Gilles de la Tourette syndrome. *World J. Biol. Psychiatry* 10(4 Pt 2), 567–570. doi: 10.1080/15622970802118356

Khan, H. A., and Ibrahim, K. E. (2015). Pattern of neurobehavioral and organ-specific toxicities of beta, beta'-iminodipropionitrile in mice. *Arch Med. Sci.* 11, 1137–1144. doi: 10.5114/aoms.2015.54871

Kravitz, A. V., Freeze, B. S., Parker, P. R., Kay, K., Thwin, M. T., Deisseroth, K., et al. (2010). Regulation of parkinsonian motor behaviours by optogenetic control of basal ganglia circuitry. *Nature* 466, 622–626. doi: 10.1038/nature09159

Lemos, J. C., Friend, D. M., Kaplan, A. R., Shin, J. H., Rubinstein, M., Kravitz, A. V., et al. (2016). Enhanced GABA transmission drives bradykinesia following loss of dopamine D2 receptor signaling. *Neuron* 90, 824–838. doi: 10.1016/j.neuron.2016.04.040

Lerner, A., Bagic, A., Simmons, J. M., Mari, Z., Bonne, O., Xu, B., et al. (2012). Widespread abnormality of the gamma-aminobutyric acid-ergic system in Tourette syndrome. *Brain* 135(Pt 6), 1926–1936. doi: 10.1093/brain/aws104

Lewis, R. G., Serra, M., Radl, D., Gori, M., Tran, C., Michalak, S. E., et al. (2020). Dopaminergic control of striatal cholinergic interneurons underlies cocaine-induced psychostimulation. *Cell Rep.* 31:107527. doi: 10.1016/j.celrep.2020.107527

Li, Z., Chen, Z., Fan, G., Li, A., Yuan, J., and Xu, T. (2018). Cell-type-specific afferent innervation of the nucleus accumbens core and shell. *Front. Neuroanat.* 12:84. doi: 10.3389/fnana.2018.00084

Lin, L., Yu, L., Xiang, H., Hu, X., Yuan, X., Zhu, H., et al. (2019). Effects of acupuncture on behavioral stereotypies and brain dopamine system in mice as a model of tourette syndrome. *Front. Behav. Neurosci.* 13:239. doi: 10.3389/fnbeh.2019.00239

Liu, S., Tian, M., He, F., Li, J., Xie, H., Liu, W., et al. (2020). Mutations in ASH1L confer susceptibility to Tourette syndrome. *Mol. Psychiatry* 25, 476–490. doi: 10.1038/s41380-019-0560-8

Liu, X., Wang, X., Cao, A., and Zhang, X. (2021). Immune function changes of the IDPN-induced Tourette syndrome rat model. *Int. J. Dev. Neurosci.* 81, 159–166. doi: 10.1002/jdn.10085

Lobo, M. K., Covington, H. E. III, Chaudhury, D., Friedman, A. K., Sun, H., Damez-Werno, D., et al. (2010). Cell type-specific loss of BDNF signaling mimics optogenetic control of cocaine reward. *Science* 330, 385–390. doi: 10.1126/science.1188472

Maqsood, A., Akram, S., and Akram, F. (2020). Chlorpromazine-induced relapse of tourette syndrome in a patient with intellectual disability, attention deficit hyperactivity disorder, and Schizophrenia. *Cureus* 12:e10732. doi: 10.7759/cureus.10732

Maurice, N., Mercer, J., Chan, C. S., Hernandez-Lopez, S., Held, J., Tkatch, T., et al. (2004). D2 dopamine receptor-mediated modulation of voltage-dependent Na+ channels reduces autonomous activity in striatal cholinergic interneurons. *J. Neurosci.* 24, 10289–10301. doi: 10.1523/JNEUROSCI.2155-04.2004

Mogwitz, S., Buse, J., Ehrlich, S., and Roessner, V. (2013). Clinical pharmacology of dopamine-modulating agents in Tourette's syndrome. *Int. Rev. Neurobiol.* 112, 281–349. doi: 10.1016/B978-0-12-411546-0.00010-X

Nespoli, E., Rizzo, F., Boeckers, T., Schulze, U., and Hengerer, B. (2018). Altered dopaminergic regulation of the dorsal striatum is able to induce tic-like movements in juvenile rats. *PLoS One* 13:e0196515. doi: 10.1371/journal.pone.0196515

Ohira, K. (2019). Dopamine stimulates differentiation and migration of cortical interneurons. *Biochem. Biophys. Res. Commun.* 512, 577–583. doi: 10.1016/j.bbrc.2019.03.105

Peacock, L., Jensen, G., Nicholson, K., and Gerlach, J. (1999). Extrapyramidal side effects during chronic combined dopamine D1 and D2 antagonist treatment in *Cebus apella* monkeys. *Eur. Arch. Psychiatry Clin. Neurosci.* 249, 221–226. doi: 10.1007/s004060050090

Pogorelov, V., Xu, M., Smith, H. R., Buchanan, G. F., and Pittenger, C. (2015). Corticostriatal interactions in the generation of tic-like behaviors after local striatal disinhibition. *Exp. Neurol.* 265, 122–128. doi: 10.1016/j.expneurol.2015.01.001

Proietti Onori, M., Ceci, C., Laviola, G., and Macri, S. (2014). A behavioural test battery to investigate tic-like symptoms, stereotypies, attentional capabilities, and spontaneous locomotion in different mouse strains. *Behav. Brain Res.* 267, 95–105. doi: 10.1016/j.bbr.2014.03.023

Rodrigues, S., Salum, C., and Ferreira, T. L. (2017). Dorsal striatum D1-expressing neurons are involved with sensorimotor gating on prepulse inhibition test. *J. Psychopharmacol.* 31, 505–513. doi: 10.1177/0269881116686879

Rotsides, J., and Mammis, A. (2013). The use of deep brain stimulation in Tourette's syndrome. *Neurosurg. Focus* 35:E4.

Silva, R. R., Munoz, D. M., Daniel, W., Barickman, J., and Friedhoff, A. J. (1996). Causes of haloperidol discontinuation in patients with Tourette's disorder: management and alternatives. *J. Clin. Psychiatry* 57, 129–135.

Surmeier, D. J., Ding, J., Day, M., Wang, Z., and Shen, W. (2007). D1 and D2 dopamine-receptor modulation of striatal glutamatergic signaling in striatal medium spiny neurons. *Trends Neurosci.* 30, 228–235.

Wang, D. H., Li, W., Liu, X. F., Zhang, J. M., and Wang, S. M. (2013). Chinese medicine formula "Jian-Pi-Zhi-Dong Decoction" attenuates tourette syndrome via downregulating the expression of dopamine transporter in mice. *Evid. Based Complement. Alternat. Med.* 2013:385685. doi: 10.1155/2013/385685

Wang, Y., Zhao, L., and Li, A. Y. (2021). Gastrodin - A potential drug used for the treatment of Tourette Syndrome. *J. Pharmacol. Sci.* 145, 289–295. doi: 10.1016/j.jphs.2021.01.005

Xie, H., Wang, Z., Ji, Y., Yin, J., Yang, W. H., and Ren, L. M. (2016). [Effects of salidroside on tic behavior of tourette syndrome model rats]. *Zhongguo Zhong Xi Yi Jie He Za Zhi* 36, 90–93.

Yang, C., Zhang, L., Zhu, P., Zhu, C., and Guo, Q. (2016). The prevalence of tic disorders for children in China: a systematic review and meta-analysis. *Medicine* 95:e4354. doi: 10.1097/MD.0000000000004354

Yang, W., Munhall, A. C., and Johnson, S. W. (2019). AMP-activated protein kinase slows D2 dopamine autoreceptor desensitization in substantia nigra neurons. *Neuropharmacology* 158:107705. doi: 10.1016/j.neuropharm.2019.107705

Yung, K. K., Bolam, J. P., Smith, A. D., Hersch, S. M., Ciliax, B. J., and Levey, A. I. (1995). Immunocytochemical localization of D1 and D2 dopamine receptors in the basal ganglia of the rat: light and electron microscopy. *Neuroscience* 65, 709–730. doi: 10.1016/0306-4522(94)00536-e

Zebardast, N., Crowley, M. J., Bloch, M. H., Mayes, L. C., Wyk, B. V., Leckman, J. F., et al. (2013). Brain mechanisms for prepulse inhibition in adults with Tourette syndrome: initial findings. *Psychiatry Res.* 214, 33–41. doi: 10.1016/j.pscychresns.2013.05.009

Zhang, F., and Li, A. (2015a). Dual ameliorative effects of Ningdong granule on dopamine in rat models of Tourette's syndrome. *Sci. Rep.* 5:7731. doi: 10.1038/srep07731

Zhang, F., and Li, A. (2015b). Dual regulating effects of gastrodin on extracellular dopamine concentration in rats models of Tourette's syndrome. *Int. J. Neurosci.* 125, 784–792. doi: 10.3109/00207454.2014.971455

Zhang, F., and Li, A. (2015c). Dual restoring effects of gastrodin on dopamine in rat models of Tourette's syndrome. *Neurosci. Lett.* 588, 62–66. doi: 10.1016/j.neulet.2014.12.051

Zhang, T., Zhang, L., Liang, Y., Siapas, A. G., Zhou, F. M., and Dani, J. A. (2009). Dopamine signaling differences in the nucleus accumbens and dorsal striatum exploited by nicotine. *J. Neurosci.* 29, 4035–4043. doi: 10.1523/JNEUROSCI.0261-09.2009

Zhang, W., Yu, W., Wang, D., Wei, L., Lee, M., and Wang, S. (2014). Effect of "jian-pi-zhi-dong decoction" on gamma-aminobutyric Acid in a mouse model of Tourette syndrome. *Evid. Based Complement. Alternat. Med.* 2014:407509. doi: 10.1155/2014/407509

Zhao, L., Cheng, N., Sun, B., Wang, S., Li, A., Wang, Z., et al. (2020). Regulatory effects of Ningdong granule on microglia-mediated neuroinflammation in a rat model of Tourette's syndrome. *Biosci. Trends* 14, 271–278. doi: 10.5582/bst.2020.03262

Zhu, G. Y., Geng, X. Y., Zhang, R. L., Chen, Y. C., Liu, Y. Y., and Wang, S. Y. (2019). Deep brain stimulation modulates pallidal and subthalamic neural oscillations in Tourette's syndrome. *Brain Behav.* 9:e01450.

Conflict of Interest: The authors declare that the research was conducted in the absence of any commercial or financial relationships that could be construed as a potential conflict of interest.

Publisher's Note: All claims expressed in this article are solely those of the authors and do not necessarily represent those of their affiliated organizations, or those of the publisher, the editors and the reviewers. Any product that may be evaluated in this article, or claim that may be made by its manufacturer, is not guaranteed or endorsed by the publisher.

Copyright © 2021 Lin, Lan, Zhu, Yu, Wu, Wan, Shu, Xiang, Hou, Zhang, Ma, Su and Li. This is an open-access article distributed under the terms of the Creative Commons Attribution License (CC BY). The use, distribution or reproduction in other forums is permitted, provided the original author(s) and the copyright owner(s) are credited and that the original publication in this journal is cited, in accordance with accepted academic practice. No use, distribution or reproduction is permitted which does not comply with these terms.

frontiers in Aging Neuroscience

ORIGINAL RESEARCH
published: 15 December 2021
doi: 10.3389/fnagi.2021.758895

Flavones 7,8-DHF, Quercetin, and Apigenin Against Tau Toxicity *via* Activation of TRKB Signaling in ΔK280 Tau_{RD}-DsRed SH-SY5Y Cells

Ni-Ni Chiang[1†], Te-Hsien Lin[1†], Yu-Shan Teng[1], Ying-Chieh Sun[2], Kuo-Hsuan Chang[3], Chung-Yin Lin[4], Hsiu Mei Hsieh-Li[1], Ming-Tsan Su[1], Chiung-Mei Chen[3] and Guey-Jen Lee-Chen[1]**

[1] Department of Life Science, National Taiwan Normal University, Taipei, Taiwan, [2] Department of Chemistry, National Taiwan Normal University, Taipei, Taiwan, [3] Department of Neurology, Chang Gung Memorial Hospital, Chang Gung University School of Medicine, Taoyuan, Taiwan, [4] Medical Imaging Research Center, Institute for Radiological Research, Chang Gung Memorial Hospital, Chang Gung University, Taoyuan, Taiwan

OPEN ACCESS

Edited by:
Kuangyu Shi,
University of Bern, Switzerland

Reviewed by:
Xavier Xifró,
University of Girona, Spain
Cecilia Beatriz Conde,
Medical Research Institute Mercedes and Martín Ferreyra (INIMEC), Argentina

***Correspondence:**
Chiung-Mei Chen
cmchen@cgmh.org.tw
Guey-Jen Lee-Chen
t43019@ntnu.edu.tw

† These authors have contributed equally to this work

Received: *15 August 2021*
Accepted: *17 November 2021*
Published: *15 December 2021*

Citation:
Chiang N-N, Lin T-H, Teng Y-S, Sun Y-C, Chang K-H, Lin C-Y, Hsieh-Li HM, Su M-T, Chen C-M and Lee-Chen G-J (2021) Flavones 7,8-DHF, Quercetin, and Apigenin Against Tau Toxicity via Activation of TRKB Signaling in ΔK280 Tau_{RD}-DsRed SH-SY5Y Cells. Front. Aging Neurosci. 13:758895. doi: 10.3389/fnagi.2021.758895

Alzheimer's disease (AD) is a progressive neurodegenerative disease with memory loss and cognitive decline. Neurofibrillary tangles (NFTs) formed by hyperphosphorylated Tau protein are one of the pathological hallmarks of several neurodegenerative diseases including AD. Heat shock protein family B (small) member 1 (HSPB1) is a molecular chaperone that promotes the correct folding of other proteins in response to environmental stress. Nuclear factor erythroid 2-like 2 (NRF2), a redox-regulated transcription factor, is the master regulator of the cellular response to excess reactive oxygen species. Tropomyosin-related kinase B (TRKB) is a membrane-bound receptor that, upon binding brain-derived neurotrophic factor (BDNF), phosphorylates itself to initiate downstream signaling for neuronal survival and axonal growth. In this study, four natural flavones such as 7,8-dihydroxyflavone (7,8-DHF), wogonin, quercetin, and apigenin were evaluated for Tau aggregation inhibitory activity and neuroprotection in SH-SY5Y neuroblastoma. Among the tested flavones, 7,8-DHF, quercetin, and apigenin reduced Tau aggregation, oxidative stress, and caspase-1 activity as well as improved neurite outgrowth in SH-SY5Y cells expressing ΔK280 Tau_{RD}-DsRed folding reporter. Treatments with 7,8-DHF, quercetin, and apigenin rescued the reduced HSPB1 and NRF2 and activated TRKB-mediated extracellular signal-regulated kinase (ERK) signaling to upregulate cAMP-response element binding protein (CREB) and its downstream antiapoptotic BCL2 apoptosis regulator (BCL2). Knockdown of TRKB attenuated the neuroprotective effects of these three flavones. Our results suggest 7,8-DHF, quercetin, and apigenin targeting HSPB1, NRF2, and TRKB to reduce Tau aggregation and protect cells against Tau neurotoxicity and may provide new treatment strategies for AD.

Keywords: Tau, Alzheimer's disease, quercetin, apigenin, TRKB agonist, 7,8-dihydroxyflavone

INTRODUCTION

Neurodegenerative disorders tauopathies, including the most common Alzheimer's disease (AD), are characterized by abnormal hyperphosphorylation of microtubule-associated protein Tau that leads to the formation of neurofibrillary tangles (NFTs) and causes gain of toxic function (Iqbal et al., 2005). Tau is mainly expressed in neuronal axons, where it promotes assembly and bundling of microtubules, thereby regulating vesicular transport and apoptosis (Lee et al., 2001). Phosphorylation of Tau has been proposed as the link between oxidative stress, mitochondrial dysfunction, and synaptic failure during early stages of AD (Mondragón-Rodríguez et al., 2013). In retinal ganglion cells of human P301S Tau transgenic mice with early tauopathy, the impairment of tropomyosin-related kinase B (TRKB) signaling is triggered by Tau pathology and mediates the Tau-induced dysfunction of visual response (Mazzaro et al., 2016). In addition, the accumulated asparagine endopeptidase-cleaved N368 Tau N-terminal fragment binds the TRKB receptor on its C terminus and antagonizes neurotrophic signaling to trigger neuronal apoptosis (Xiang et al., 2019).

Tropomyosin-related kinase B, a member of the neurotrophic tyrosine receptor kinase family, is a high-affinity receptor for brain-derived neurotrophic factor (BDNF) (Soppet et al., 1991). Upon BDNF binding, TRKB phosphorylates itself and members of the mitogen-activated protein kinase (MAPK) pathway initiate intracellular signaling cascades (Levine et al., 1996). TRKB is highly expressed in adult hippocampus (Nakagawara et al., 1995), an area of the brain involved in learning and memory. Rapid activation of extracellular signal-regulated kinase (ERK), a member of the MAPK family, by BDNF/TRKB signaling induces phosphorylation of cAMP-response element binding protein (CREB) (Bonni et al., 1999) to stimulate expression of antiapoptotic BCL2 apoptosis regulator (BCL2) (Riccio et al., 1999) for neuronal survival. As a significant risk factor for AD (Coppola et al., 2012), p.A152T Tau variant alters Tau function and toxicity *via* impairing retrograde axonal transport of synaptic vesicles (Butler et al., 2019). As retrograde axonal transport of endosomes mediated by TRKB signaling is essential for dendrite growth of cortical neurons (Zhou et al., 2012), BDNF/TRKB potentiation would be protective in AD.

Structurally, Tau is a prototypical natively unfolded protein (Schweers et al., 1994). Tau binds microtubules through C-terminal highly conserved 18-amino acid repeat domains (Tau_{RD}), which reside at the core of paired helical filaments of NFT (Goedert et al., 1989). The Tau_{RD} with the deletion mutation ΔK280 is highly prone to spontaneous aggregation (Khlistunova et al., 2006). Heat shock protein family B (small) member 1 (HSPB1) can prevent pathological misfolding of Tau by altering the conformation of hyperphosphorylated Tau and rescue hyperphosphorylated Tau-mediated cell death (Shimura et al., 2004). Accumulation of misfolded proteins can cause oxidative stress and compromise nuclear factor erythroid 2-like 2 (NRF2) to incur early events in the pathogenesis of AD (Mota et al., 2015). NRF2 activators have therapeutic effects in AD animal models and in cultured human cells that express the pathology of AD (Bahn and Jo, 2019).

Flavones, common in fruits and vegetables, are a class of flavonoids consisting of a benzene A ring condensed with an oxygenated heterocyclic C ring and phenyl B ring. Flavones are plant secondary metabolites with wide range of biological activity including antioxidant, anti-inflammation, and neuroprotective activity (Kumar and Pandey, 2013; Singh et al., 2014). 7,8-dihydroxyflavone (7,8-DHF), the first reported BDNF-mimetic compound, binds with high affinity and specificity to the TRKB receptor (Jang et al., 2010). In addition to improve memory consolidation processes in rats and mice (Bollen et al., 2013), 7,8-DHF activates TRKB signaling to rescue amyloid-beta (Aβ)-induced neurotoxicity and synaptic dysfunction in transgenic mice expressing five familial AD-linked amyloid beta precursor protein (APP) and presenilin 1 (PS1) mutations [5 × familial Alzheimer's disease (FAD)] (Devi and Ohno, 2012; Zhang et al., 2014). Furthermore, an optimized 7,8-DHF prodrug R13 alleviates Aβ deposition, attenuates the loss of hippocampal synapse, and ameliorates memory deficits in 5 × FAD mice (Chen et al., 2018). We have previously shown neuroprotective effects of 7,8-DHF on neurite length and branch in mouse hippocampal primary neurons under Aβ toxicity and 7,8-DHF-mediated upregulation of neuronal nuclei, p-ERK, and p-CREB in the immunohistochemical staining of mice with oligomeric Aβ injection into hippocampal cornu ammonis area 1 subregion (Fan et al., 2020). In addition, wogonin (5,7-dihydroxy-8-methoxyflavone), a novel inhibitor for mammalian target of rapamycin (mTOR) signaling pathway, strengthens the autophagy to effectively clear Aβ and suppresses Tau protein phosphorylation (Zhu and Wang, 2015). Quercetin (3,3′,4′,5,7-pentahydroxyflavone) decreases β-amyloidosis and tauopathy and protects the cognitive function in APP, PS1, and Tau triple-transgenic AD mouse model (3 × Tg-AD mice) (Sabogal-Guáqueta et al., 2015; Pérez-Corredor et al., 2019). Studies have shown that apigenin (4′,5,7-trihydroxyflavone) ameliorates learning and memory impairment through relieving Aβ burden, suppressing amyloidogenic process, and restoring ERK/CREB/BDNF pathway in APP and PS1 double transgenic AD mice (Zhao et al., 2013). Wogonin, quercetin, and apigenin provide neuroprotection in AD through potentiating HSPB1, NRF2, and TRKB signaling that are not clear. Previously, we have generated human neuroblastoma cells overexpressing ΔK280 Tau_{RD} and used to screen agents that prevent the aggregation and degeneration of cells (Chang et al., 2017). Using this cell model, we demonstrate that 7,8-DHF, quercetin, and apigenin target HSPB1, NRF2, and TRKB to reduce Tau aggregation and protect cells against Tau neurotoxicity, providing new treatment strategies for AD.

MATERIALS AND METHODS

Test Compounds and Biochemical Analysis of Tau Aggregation Inhibition

7,8-dihydroxyflavone, wogonin, quercetin, and apigenin were purchased from Sigma-Aldrich, St. Louis, Mosby, MO, United States. Congo red (Sigma-Aldrich, St. Louis, Mosby, MO, United States), known to bind to the cross β-sheet

structure of amyloid fibrils (Sipe and Cohen, 2000), was included for comparison. For biochemical Tau aggregation inhibition test, bacterial expressed proaggregator ΔK280 Tau_{RD} (Gln^{244}–Glu^{372} of 441-residue human Tau) was prepared as described (Lin et al., 2020). ΔK280 Tau_{RD} protein (20 μM in final 50 μl) was incubated with tested compounds (5–10 μM in 150 mM sodium chloride (NaCl) and 20 mM tris(hydroxymethyl)aminomethane-hydrochloride (Tris–HCl), pH 8.0) at 37°C for 48 h. Then, thioflavin T (5 μM final concentration; Sigma-Aldrich, St. Louis, Mosby, MO, United States), a dye exhibiting enhanced fluorescence upon binding to diverse types of amyloid fibrils (Biancalana and Koide, 2010), was added and incubated for 25 min at room temperature. The formed aggregates reflected by thioflavin T fluorescence intensity was recorded at excitation 420 nm and emission 485 nm by using the FLx800 Fluorescence Microplate Reader (BioTek Instruments Incorporation, Winooski, VT, United States). Half maximal effective concentration (EC_{50}) was calculated using the interpolation method.

1,1-Diphenyl-2-Picrylhydrazyl Radical Scavenging Assay

1,1-diphenyl-2-picrylhydrazyl (DPPH) (Sigma-Aldrich, St. Louis, Mosby, MO, United States), a common stable free radical for antioxidant assay (Li et al., 2008), was used to examine the radical scavenging activity of the studied flavones. DPPH solution (100 μM) was prepared in 95% ethanol. After adding test compounds (10–80 μM), the mixture was vortexed for 15 s and allowed to stand for 30 min at room temperature. Subsequently, the mixture was measured spectrophotometrically at 517 nm (Multiskan GO Microplate Spectrophotometer; Thermo Fisher Scientific, Waltham, MA, United States). The free radical scavenging activity was calculated as the percentage of DPPH discoloration using the formula 1 − (absorbance of sample/absorbance of control) × 100%, with EC_{50} calculated using the interpolation method.

Docking Computation

7,8-dihydroxyflavone is a known potent and selective small-molecule agonist of TRKB (Jang et al., 2010). Using GOLD docking program (Nissink et al., 2002; Verdonk et al., 2003), protein structure of TRKB-d5 domain (pdb code: 1HCF) (Banfield et al., 2001) was utilized to perform docking computation for 7,8-DHF, wogonin, quercetin, and apigenin. In addition to be used to determine the specificity of neurotrophin receptors experimentally (Urfer et al., 1995), the d5 domain was predicted to be the binding site by docking computation (Chitranshi et al., 2015). In docking computations, 10,000, 20,000, 40,000, and 80,000 operations were performed to ensure convergence of the calculated results.

Cells and Culture

Human neuroblastoma SH-SY5Y-derived ΔK280 Tau_{RD}-DsRed cells (Chang et al., 2017) were maintained in Dulbecco's Modified Eagle Medium (DMEM)/F12 supplemented with 10% fetal bovine serum (FBS) (Thermo Fisher Scientific, Waltham, MA, United States), with 5 μg/ml blasticidin and 100 μg/ml hygromycin (InvivoGen, San Diego, CA, United States) added to the growth medium. Retinoic acid (10 μM; Sigma-Aldrich, St. Louis, Mosby, MO, United States) and doxycycline (2 μg/ml; Sigma-Aldrich, St. Louis, Mosby, MO, United States) were used to induce neuronal differentiation and ΔK280 Tau_{RD}-DsRed expression, respectively.

High Content Analyses of ΔK280 Tau_{RD}-DsRed Fluorescence and Oxidative Stress

On day 1, ΔK280 Tau_{RD}-DsRed SH-SY5Y cells were seeded into a 96-well plate (2.5×10^4/well), with retinoic acid (10 μM) added to induce neuronal differentiation (Påhlman et al., 1984). On day 2, cells were pretreated with Congo red, 7,8-DHF, wogonin, quercetin, or apigenin (2.5–10 μM) for 8 h, followed by inducing ΔK280 Tau_{RD}-DsRed expression with doxycycline. On day 8, cells were stained with Hoechst 33342 (0.1 μg/ml; Sigma-Aldrich, St. Louis, Mosby, MO, United States) for 30 min and cell images were automatically recorded at excitation/emission wavelengths of 543/593 nm (ImageXpress Micro Confocal High-Content Imaging System; Molecular Devices, Sunnyvale, CA, United States) and analyzed (MetaXpress High-Content Image Acquisition and Analysis Software; Molecular Devices, Sunnyvale, CA, United States).

For reactive oxygen species (ROS) measurement, dichloro-dihydro-fluorescein diacetate (DCFH-DA) (10 μM; Invitrogen, Carlsbad, CA, United States), a fluorogenic dye that measures hydroxyl, peroxyl, and other ROS activity within cells (Aranda et al., 2013), was added to the cells on day 8 and incubated at 37°C for 30 min. ROS in cells was measured using the High-Content Imaging System, with excitation/emission wavelengths at 482/536 nm.

Real-Time PCR Analysis

As described, ΔK280 Tau_{RD}-DsRed SH-SY5Y cells were seeded on a 6-well plate (5×10^5/well), with retinoic acid addition on day 1, treated with tested compounds (5 or 10 μM), and induced ΔK280 Tau_{RD}-DsRed expression with doxycycline on day 2. On day 8, cells were collected and total RNA was extracted using Trizol reagent (Invitrogen, Carlsbad, CA, United States). The RNA was reverse-transcribed using the SuperScript III Reverse Transcriptase (Invitrogen, Carlsbad, CA, United States). Real-time quantitative PCR was performed using 50 ng complementary DNA (cDNA) with the customized Assays-by-Design probe for DsRed (Chang et al., 2017) and the TaqMan fluorogenic probe for hypoxanthine phosphoribosyltransferase 1 (HPRT1) (4326321E) using the StepOnePlus Real-Time PCR System (Applied Biosystems, Foster City, CA, United States). Fold change was calculated using the formula $2^{\Delta Ct}$, $\Delta C_T = C_T$ (HPRT1) − C_T (DsRed), in which C_T indicates cycle threshold.

Neurite Outgrowth Analysis

As described, ΔK280 Tau_{RD}-DsRed SH-SY5Y cells were seeded on a 24-well plate (5×10^4 cells/well), with induced neuronal differentiation on day 1, treated with test compounds (5 or

10 μM), and induced ΔK280 Tau_{RD}-DsRed expression on day 2. After 7 days, the cells were washed with phosphate-buffered saline (PBS) and fixed in 4% paraformaldehyde in PBS for 10 min. After being permeabilized with 0.1% Triton X-100 in PBS for 10 min and blocked with 3% bovine serum albumin in PBS for 20 min, cells were stained with tubulin beta 3 class III (TUBB3) primary antibody (1:1,000; Covance, Princeton, NJ, United States) at 4°C overnight, followed by goat anti-rabbit Alexa Fluor®555 secondary antibody (1:1,000; Invitrogen, Carlsbad, CA, United States) at room temperature for 3 h. After nuclei were stained with 4′,6-diamidino-2-phenylindole (DAPI) (0.1 μg/ml; Sigma-Aldrich, St. Louis, Mosby, MO, United States) for 30 min, neuronal images from at least 60 individual fields (150–250 neurons per field) per experiment were captured at excitation/emission wavelengths of 531/593 nm using the ImageXpress Micro Confocal High-Content Imaging System (Molecular Devices, Sunnyvale, CA, United States). Neurite total length (μm), process (the number of primary neurites defined as the segments originating from the cell body of a neuron), and branch (the number of secondary neurites extending from primary neurites) were analyzed using the MetaXpress Neurite Outgrowth Application Module (Molecular Devices, Sunnyvale, CA, United States). For each sample, around 6,000 cells were analyzed in each of 3 independent experiments.

Caspase-1, Lactate Dehydrogenase, and Acetylcholinesterase Assays

ΔK280 Tau_{RD}-DsRed SH-SY5Y cells were seeded in a 6-well plate (5×10^5/well) and treated with retinoic acid, test compound, and doxycycline as described. On day 8, cells were collected and lysates were prepared by 6 freeze/thaw cycles. After centrifugation to collect supernatant, caspase-1 activity in 50 μg cell extracts was measured using the ICE Fluorometric Assay Kit (BioVision, Milpitas, CA, United States). The mixture was incubated for 2 h at 37°C and caspase-1 activity was measured with excitation/emission wavelengths at 400/505 nm (FLx800 Fluorescence Microplate Reader; BioTek Instruments Incorporation, Winooski, VT, United States). In addition, the collected cells were lysed by sonication. Acetylcholinesterase (AChE) activity in supernatant was determined using AChE Activity Assay Kit (Sigma-Aldrich, St. Louis, Mosby, MO, United States) with 10 μg cell extracts. The mixture was incubated for 2–10 min at room temperature and absorbance at 412 nm was measured using the Multiskan GO Microplate Spectrophotometer Reader (Thermo Fisher Scientific, Waltham, MA, United States). The release of lactate dehydrogenase (LDH) in culture medium was examined by using the LDH Cytotoxicity Assay Kit (Cayman, Ann Arbor, MI, United States). The absorbance was read at 490 nm with the Multiskan GO Microplate Spectrophotometer Reader.

Ribonucleic Acid Interference

For TRKB knockdown in ΔK280 Tau_{RD}-DsRed SH-SY5Y cells, lentivirus carrying TRKB-targeting (TRCN0000002243, TRCN0000002245, and TRCN0000002246) and negative control scrambled (TRC2.Void) short hairpin RNA (shRNA) were obtained from the National RNAi Core Facility, institute of molecular biology/genomic research center, Academia Sinica, Taipei, Taiwan. On day 1, cells were plated on 24-well plates in the presence of retinoic acid as described. On day 2, the cells were infected with lentivirus (3 multiplicity of infection for each shRNA) in medium with polybrene (8 μg/ml; Sigma-Aldrich, St. Louis, Mosby, MO, United States). On day 3, the culture medium was changed and the cells were pretreated with Congo red (10 μM), 7,8-DHF (5 μM), quercetin (5 μM), or apigenin (10 μM) for 8 h, followed by induction of ΔK280 Tau_{RD}-DsRed expression. On day 9, the cells were collected for TRKB protein analysis or analyzed for neurite outgrowth as described.

Protein Blot Analysis

Total proteins from ΔK280 Tau_{RD}-DsRed SH-SY5Y cells were prepared using lysis buffer containing 50 mM Tris–HCl pH 8.0, 150 mM NaCl, 1 mM ethylene diamine tetra acetic acid pH 8.0, 1 mM ethylene glycol-bis(β-aminoethyl ether)tetraacetic acid pH 8.0, 0.1% sodium dodecyl sulfate (SDS), 0.5% sodium deoxycholate, 1% Triton X-100, and protease (Sigma-Aldrich, St. Louis, Mosby, MO, United States) and phosphatase (Abcam, Cambridge, MA, United States) inhibitor cocktails. After quantitation using a protein assay kit (Bio-Rad, Hercules, CA, United States), proteins (20 μg) were separated on 10% SDS-polyacrylamide gel electrophoresis and blotted to polyvinylidene difluoride membranes (Sigma-Aldrich, St. Louis, Mosby, MO, United States) by reverse electrophoresis. After blocking, the membrane was probed with antibody against DsRed (1:500; BioVision #3994, Milpitas, CA, United States); HSPB1 (1:500; Abcam #ab137748, Cambridge, MA, United States); NRF2 (1:500; Santa Cruz Biotechnology, Santa Cruz, CA, United States #sc-365949); TRKB (1:500; Cell Signaling, Danvers, MA, United States #4603); p-TRKB (Y817) (1:500; Millipore #ABN1381, Billerica, MA, United States); ERK (1:500; Cell Signaling, Danvers, MA, United States #9102); p-ERK (T202/Y204) (1:500; Cell Signaling, Danvers, MA, United States #9101); CREB (1:1,000; Santa Cruz Biotechnology, Santa Cruz, CA, United States #sc-186); p-CREB (S133) (1:1,000; Millipore #06-519, Billerica, MA, United States); BCL2 (1:500; Santa Cruz Biotechnology, Santa Cruz, CA, United States #sc-7382), BCL2-associated X protein (BAX) (1:500; Cell Signaling, Danvers, MA, United States #2772); or glyceraldehyde-3-phosphate dehydrogenase (GAPDH) (as a loading control) (1:1,000; MDBio #30000002, Taipei, Taiwan). The immune complexes were detected by horseradish peroxidase-conjugated goat antimouse (#GTX213111-01) or goat antirabbit (#GTX213110-01) immunoglobulin G (IgG) antibody (1:5,000, GeneTex Incorporation, Irvine, CA, United States) and chemiluminescent substrate (Millipore, Billerica, MA, United States).

Statistical Analysis

Data are presented as mean ± SD. 3 independent tests in 2 or 3 biological replicates were performed in each experiment. Differences between groups were evaluated using the two-tailed Student's *t*-test or the one-way ANOVA with the *post hoc* Tukey's test where appropriate. $p < 0.05$ indicate a statistically significant difference.

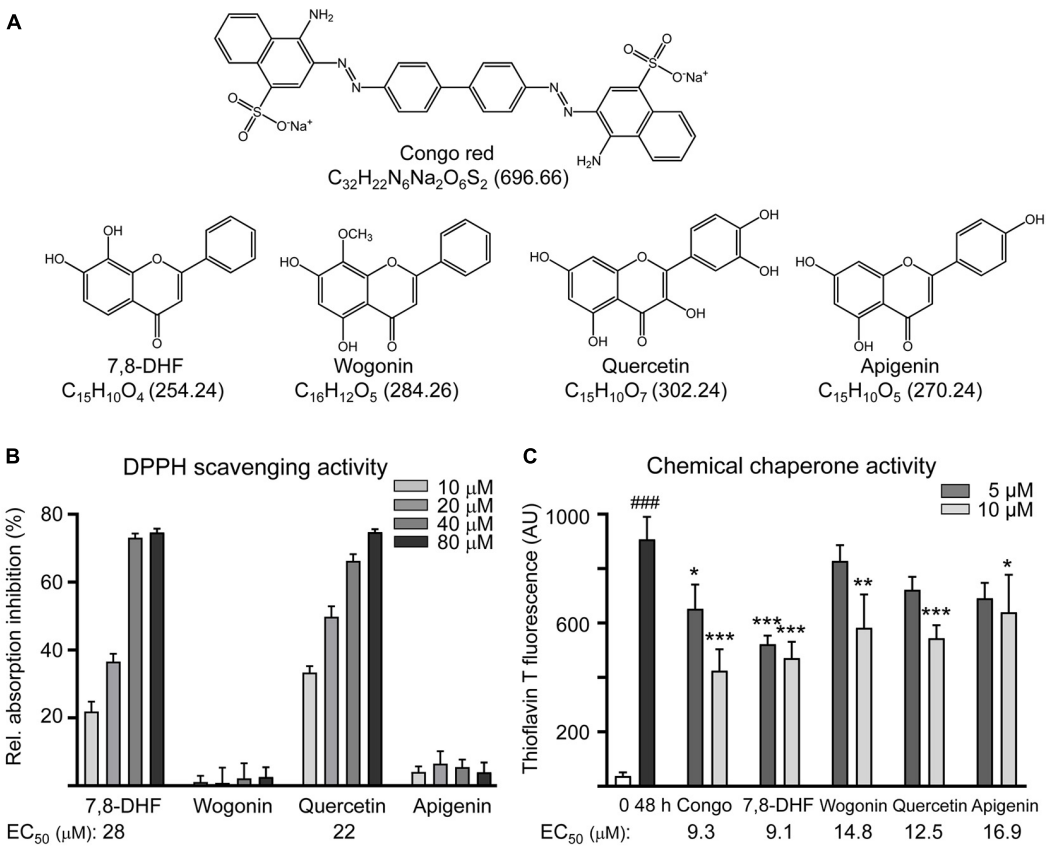

FIGURE 1 | Tested compounds. **(A)** Structure, formula, and molecular weight of Congo red (as a positive control), 7,8-dihydroxyflavone (7,8-DHF), wogonin, quercetin, and apigenin. **(B)** Radical-scavenging activity of tested flavones (10–80 μM) on 1,1-diphenyl-2-picrylhydrazyl (DPPH) ($n = 3$). Shown below are the EC_{50} values. **(C)** ΔK280 Tau_{RD} aggregation inhibition of tested compounds (5–10 μM) by the thioflavin T assay ($n = 3$). p-values: comparisons between 0-h and 48-h incubation ($^{###}p < 0.001$) or between with and without compound addition ($^{*}p < 0.05$, $^{**}p < 0.01$, and $^{***}p < 0.001$) (one-way ANOVA with the *post hoc* Tukey's test). Shown below are the EC_{50} values.

RESULTS

Tested Flavones, Radical Scavenging, and Biochemical Tau Aggregation Inhibition

Natural flavones such as 7,8-DHF, wogonin, quercetin, and apigenin (**Figure 1A**) were examined. Oxidative stress has been recognized as a contributing factor to the progression of AD and preventing oxidative stress is considered as a treatment approach for AD (Poprac et al., 2017). Therefore, the radical scavenging activity of the three flavones (10–80 μM) was first examined. While wogonin and apigenin displayed no radical scavenging activity, 7,8-DHF and quercetin had EC_{50} values of 24 and 25 μM, respectively (**Figure 1B**).

The inhibition of Tau aggregation was measured by measuring thioflavin T binding to *Escherichia coli*-derived 14.7 kDa ΔK280 Tau_{RD} protein using Congo red as a control. EC_{50} values of Congo red, 7,8-DHF, wogonin, quercetin, and apigenin for Tau aggregation inhibition were: 9.3, 9.1, 14.8, 12.5, and 16.9 μM, respectively (**Figure 1C**).

Tropomyosin-Related Kinase B Binding Prediction

The strengths and conformation of wogonin, quercetin, and apigenin binding with neurotrophin-binding domain d5 of TRKB were calculated using 7,8-DHF as a control. As shown in **Figure 2**, the computations predicted docking scores of 44.67, 44.08, 49.77, and 47.91 for 7,8-DHF, wogonin, quercetin, and apigenin, respectively. Quercetin had the top interacting docking score with TRKB receptor among the 3 flavones examined.

Cellular Tau Aggregation Inhibition and Oxidative Stress Reduction in ΔK280 Tau_{RD}-DsRed-Expressing SH-SY5Y Cells

Neuronal differentiated human SH-SY5Y cells were used to evaluate the effects of tested flavones on ΔK280 Tau_{RD} aggregation inhibition, ROS reduction, and HSPB1 and NRF2 expression changes (**Figure 3A**). In these cells, the misfolded ΔK280 Tau_{RD} adversely affected the folding of fused DsRed to decrease DsRed fluorescence (Chang et al., 2017). DsRed fluorescence was measured in wells containing at least 80% cells

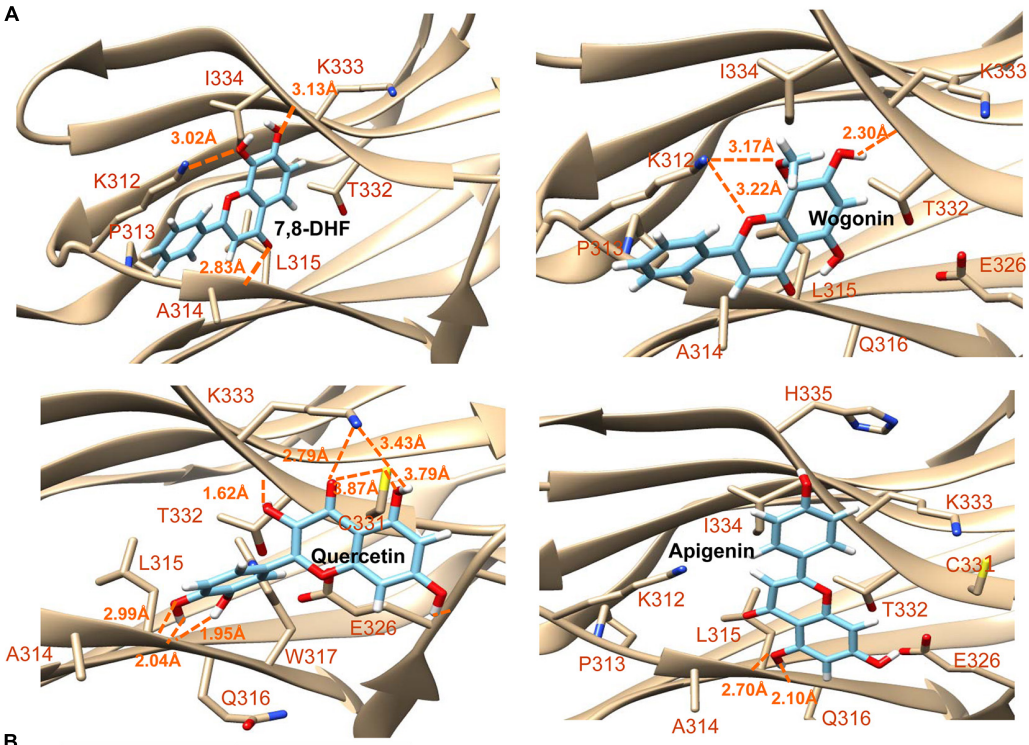

B

Compound	Docking score
7,8-DHF	44.67
Wogonin	44.08
Quercetin	49.77
Apigenin	47.91

C

300 350

7,8-DHF WCIPFTVKGN PKPALQWFYN GAILNESKYI CTKIHVTNHT EYHGCLQLDN
Wogonin WCIPFTVKGN PKPALQWFYN GAILNESKYI CTKIHVTNHT EYHGCLQLDN
Quercetin WCIPFTVKGN PKPALQWFYN GAILNESKYI CTKIHVTNHT EYHGCLQLDN
Apigenin WCIPFTVKGN PKPALQWFYN GAILNESKYI CTKIHVTNHT EYHGCLQLDN

FIGURE 2 | Docking computations of 7,8-DHF, wogonin, quercetin, and apigenin. **(A)** The docking conformations of tested flavones binding to d5 domain (the second immunoglobulin-like domain, 250–340 amino acid residues) of extracellular domain of tropomyosin-related kinase B (TRKB) receptor. The TRKB-d5 domain (ribbon structures) is colored in beige and the wire-frame structures denote the compounds. The labeled amino acids were within 10 Å radii of examined compounds. Carbon, oxygen, hydrogen, and nitrogen atoms of compounds or side chains of surrounding amino acids are shown in light blue, red, white, and blue, respectively. The dotted orange lines indicate hydrogen bond interactions between compounds and proteins. **(B)** The docking scores of 7,8-DHF, wogonin, quercetin, and apigenin calculated by the GOLD program. **(C)** Amino acid residues 301–350 of d5 domain. The amino acids within 10 Å radii of examined compounds are colored in red; the cysteines involved in disulfide linkage are underlined.

remained compared to untreated cells. Congo red, known to attenuate amyloid-like aggregates of neuronal Tau induced by formaldehyde (Nie et al., 2007), was included for comparison. As shown in **Figure 3B**, after normalization of DsRed fluorescence with cell number counted, treatment with Congo red at 5–10 μM (106–108%; $p = 0.018$–0.017), 7,8-DHF at 5 μM (108%; $p = 0.004$), quercetin at 5 μM (106%; $p = 0.004$), or apigenin at 5–10 μM (106–110%; $p = 0.016$–0.010) increased the DsRed fluorescence intensity significantly compared with untreated cells (100%), but treatment with wogonin did not increase the DsRed fluorescence intensity. Under circumstance of over 80% cells remained, treatment of 10 μM Congo red, 5 μM 7,8-DHF, 5 μM quercetin, or 10 μM apigenin did not altered Tau-DsRed RNA level significantly (26.3–30.9-folds, $p > 0.05$) compared with untreated cells (25.6-fold) (**Figure 3C**). Given that wogonin did not show aggregation-inhibiting and free radical scavenging effects, only Congo red, apigenin at 10 μM and 7,8-DHF, quercetin at 5 μM were adopted in the subsequent experiments.

Misfolded Tau may increase the production of ROS (Cente et al., 2006). Thus, we evaluated antioxidative effects of 7,8-DHF, quercetin, and apigenin using DCFH-DA. Induced ΔK280 Tau_{RD}-DsRed expression elevated the ROS level in these cells (112%; $p = 0.005$) and Congo red (10 μM), 7,8-DHF (5 μM), quercetin (5 μM), or apigenin (10 μM) effectively reduced the ROS level associated with ΔK280 Tau_{RD} overexpression (from 112 to 101–98%; $p = 0.008$–0.001) (**Figure 3D**).

We also examined if Congo red, 7,8-DHF, quercetin, and apigenin upregulate HSPB1 and NRF2 expression in ΔK280 Tau_{RD}-DsRed SH-SY5Y cells. As shown in **Figure 3E**, addition of Congo red (10 μM), 7,8-DHF (5 μM), quercetin (5 μM), or apigenin (10 μM) increased soluble ΔK280 Tau_{RD}-DsRed (from 100 to 113–123%; p = 0.098–0.003) and HSPB1 (from 79 to 104–115%; p = 0.016– < 0.001) levels. In addition, addition of Congo red or tested flavones (5 or 10 μM) increased NRF2 protein level (from 82 to 104–112%; p = 0.010– < 0.001), which is essential for defense against ROS.

Caspase-1, AChE Reduction, and Neurite Outgrowth Promotion in ΔK280 Tau_{RD}-DsRed-Expressing SH-SY5Y Cells

In the brains of patients with AD, cholinergic neurons were selectively impaired (Davies and Maloney, 1976) and AChE inhibitors have been used as standard treatment of AD (Citron, 2010). In addition, caspase-1 activation is associated with brain pathology of AD (Heneka et al., 2013) and caspase-1 inhibition alleviates cognitive impairment and neuropathology (Flores et al., 2018) in AD mouse models. Therefore, caspase-1 and AChE activities in compound-treated cells were also evaluated. The overexpression of ΔK280 Tau_{RD} significantly increased caspase-1 activity (118%; p = 0.020) and treatment with Congo red, 7,8-DHF, quercetin, and apigenin (5 or 10 μM) reduced the caspase-1 activity (from 118 to 92–79%; p = 0.002– < 0.001) (**Figure 4A**). Similar changing trend of LDH release was also observed (from 111 to 98–88%), although not significant (p > 0.05) (**Figure 4B**). In SH-SY5Y cells, ΔK280 Tau_{RD} overexpression did not increased AChE activity, but treatment with apigenin (10 μM) reduced AChE activity (from 99 to 74%; p = 0.016) compared to no treatment (**Figure 4C**).

Tau is a microtubule-associated protein that plays a role in mediating neurite outgrowth (Johnson and Stoothoff, 2004). Calpain-cleaved neurotoxic $Tau_{45–230}$ fragment modifies the composition of the neuronal cytoskeleton and impairs neurite elongation in neurons undergoing degeneration (Afreen and Ferreira, 2019). The neurite outgrowth-promoting effect of tested compounds including total neurite length, number of processes, and number of branch points was evaluated. As shown in **Figure 4C**, overexpression of ΔK280 Tau_{RD} significantly decreased neurite length (from 30.8 to 27.8 μm; p = 0.026) and branch (from 0.76 to 0.67; p = 0.010). Treatment with Congo red (10 μM), 7,8-DHF (5 μM), quercetin (5 μM), and apigenin (10 μM) rescued the impairment of neurite length (from 27.8 to 30.7–34.3 μm; p = 0.035– < 0.001) and branch (from 0.67 to 0.74–0.99; p = 0.034– < 0.001).

Molecular Targets of 7,8-DHF, Quercetin, and Apigenin in ΔK280 Tau_{RD}-DsRed-Expressing SH-SY5Y Cells

Tropomyosin-related kinase B is highly expressed in the hippocampus and plays a critical role in memory processes (Kang et al., 1997). Phosphorylation of TRKB at the most C-terminal tyrosine, Y817, leads to activation of ERK and CREB and transcription of BCL2 to promote cell survival (Hausott et al., 2009). The effects of Congo red (10 μM), 7,8-DHF (5 μM), quercetin (5 μM), and apigenin (10 μM) on expression levels of TRKB, ERK, CREB, and BCL2 in ΔK280 Tau_{RD}-DsRed-expressing SH-SY5Y cells were examined (**Figure 5**). Addition of tested flavones increased p-TRKB (Y817) (from 86 to 99–100%; p = 0.039–0.022), p-ERK (T202/Y204) (from 54 to 92–97%; p = 0.105–0.052), p-CREB (S133) (from 76 to 120–123%; p = 0.003–0.001), and downstream BCL2 (from 68 to 119–123%; p = 0.002–0.001) protein levels. In response to the antiapoptotic BCL2 change, addition of tested flavones significantly reduced the expression of proapoptotic BAX (from 128 to 95–91%; p = 0.003–0.002). Although Congo red treatment increased p-TRKB (Y817) (104%; p = 0.003) and p-ERK (T202/Y204) (107%; p = 0.014), changes of p-CREB (S133) (92 vs. 76%), BCL2 (94 vs. 68%), and BAX (122 vs. 128%) were not significant (p > 0.05) in ΔK280 Tau_{RD}-DsRed-expressing SH-SY5Y cells. Due to reduction of the total amount of TRKB (36%; p = 0.001), apigenin induced a significant hyperphosphorylation of TRKB in ΔK280 Tau_{RD}-DsRed-expressing SH-SY5Y cells (p-TRKB/TRKB: 282%; p < 0.001). The reason for observed reduced TRKB level in apigenin-treated cells is not clear.

Tropomyosin-Related Kinase B Knockdown in ΔK280 Tau_{RD}-DsRed-Expressing SH-SY5Y Cells

Since the studied compounds displayed potential to activate TRKB signaling, we knocked down TRKB expression through lentivirus-mediated shRNA targeting in ΔK280 Tau_{RD}-DsRed SH-SY5Y cells to examine if TRKB was the therapeutic target of 7,8-DHF, quercetin, and apigenin (**Figure 6A**). As shown in **Figure 6B**, no significant change of TRKB level (93 vs. 100%; p > 0.05) was observed in scrambled shRNA-infected cells with or without inducing ΔK280 Tau_{RD} expression. While apigenin reduced TRKB level (from 93 to 45%; p < 0.001), addition of Congo red, 7,8-DHF, or quercetin did not affect TRKB level in scrambled shRNA-infected cells expressing ΔK280 Tau_{RD} (83–92 vs. 93%; p > 0.05). However, TRKB-specific shRNA significantly reduced TRKB in ΔK280 Tau_{RD}-DsRed SH-SY5Y cells treated without (from 93 to 30%, p < 0.001) or with (from 92–45 to 33–23%, p = 0.007– < 0.001) compound.

For neurite outgrowth analysis (**Figure 6C**), neurite length (from 30.0 to 26.9 μm; p = 0.030) and branch (from 0.81 to 0.66; p = 0.006) were reduced upon induction of ΔK280 Tau_{RD} expression in scrambled shRNA-infected cells. Congo red, 7,8-DHF, quercetin, or apigenin increased neurite length (from 26.9 to 30.3–33.8 μm; p = 0.013– < 0.001) and branch (from 0.66 to 0.79–0.88; p = 0.022– < 0.001). In line with TRKB knockdown, TRKB-specific shRNA significantly reduced neurite length and branch without (length: from 26.9 to 21.0 μm, p < 0.001; branch: from 0.66 to 0.54, p = 0.049) or with (length: from 30.3–33.8 to 26.4–27.6 μm, p = 0.003– < 0.001; branch: from 0.81–0.88 to 0.67–0.76, p = 0.033–0.009) 7,8-DHF, quercetin, or apigenin addition, but not with Congo red addition (length: 30.7 vs. 30.8 μm, branch: 0.76 vs. 0.79; p > 0.05). These results suggested that 7,8-DHF, quercetin, and apigenin improved neurite outgrowth phonotype by upregulating TRKB signaling.

DISCUSSION

Effective treatments to slow neurodegeneration of AD are still unavailable. BDNF, a well-characterized member of the nerve growth factor family, is expressed in whole brain (Jones and Reichardt, 1990). Binding of BDNF to TRKB receptor activates downstream signaling pathways to promote neuronal growth, survival, and neural plasticity as well as enhance memory formation and storage (Nagahara and Tuszynski, 2011; Lu et al., 2013). The expanding role of BDNF suggests a valuable therapeutic target for AD. However, BDNF has a poor biostability such as the very short plasma half-life and the limited diffusion crossing blood–brain barrier (BBB) (Dittrich et al., 1996). Small compounds that mimic neurotrophic signaling and overcome the pharmacokinetic barrier of BDNF may have greater therapeutic potential (Zeng et al., 2013). In human SH-SY5Y cells expressing proaggregator Tau, we found protective potentials of three natural flavones, 7,8-DHF, quercetin, and apigenin, including reduction of Tau aggregation, ROS and caspase-1, as well as promotion of neurite outgrowth (**Figures 3**, **4**). Similarly, promotion of neurite outgrowth by quercetin in **Figure 4** has been reported in pheochromocytoma cell line (Katebi et al., 2019). TRKB silencing counteracted the neuroprotective effects of these flavones against toxicity of proaggregator Tau (**Figure 6**), demonstrating that the neuroprotective effects of three natural flavones against Tau toxicity were mechanically mediated by increasing p-TRKB (Y817) (**Figure 5**) to enhance TRKB signaling, in addition to directly interfering with Tau aggregate formation (**Figure 1**). As knockdown of TRKB is not complete, the added flavones may still exert a modest neuroprotective effect by binding to the remained TRKB, so that the flavone-treated cells with TRKB knockdown still displayed improved neurite outgrowth compared to those without flavone treatment (**Figure 6**). The mechanism is supported by the

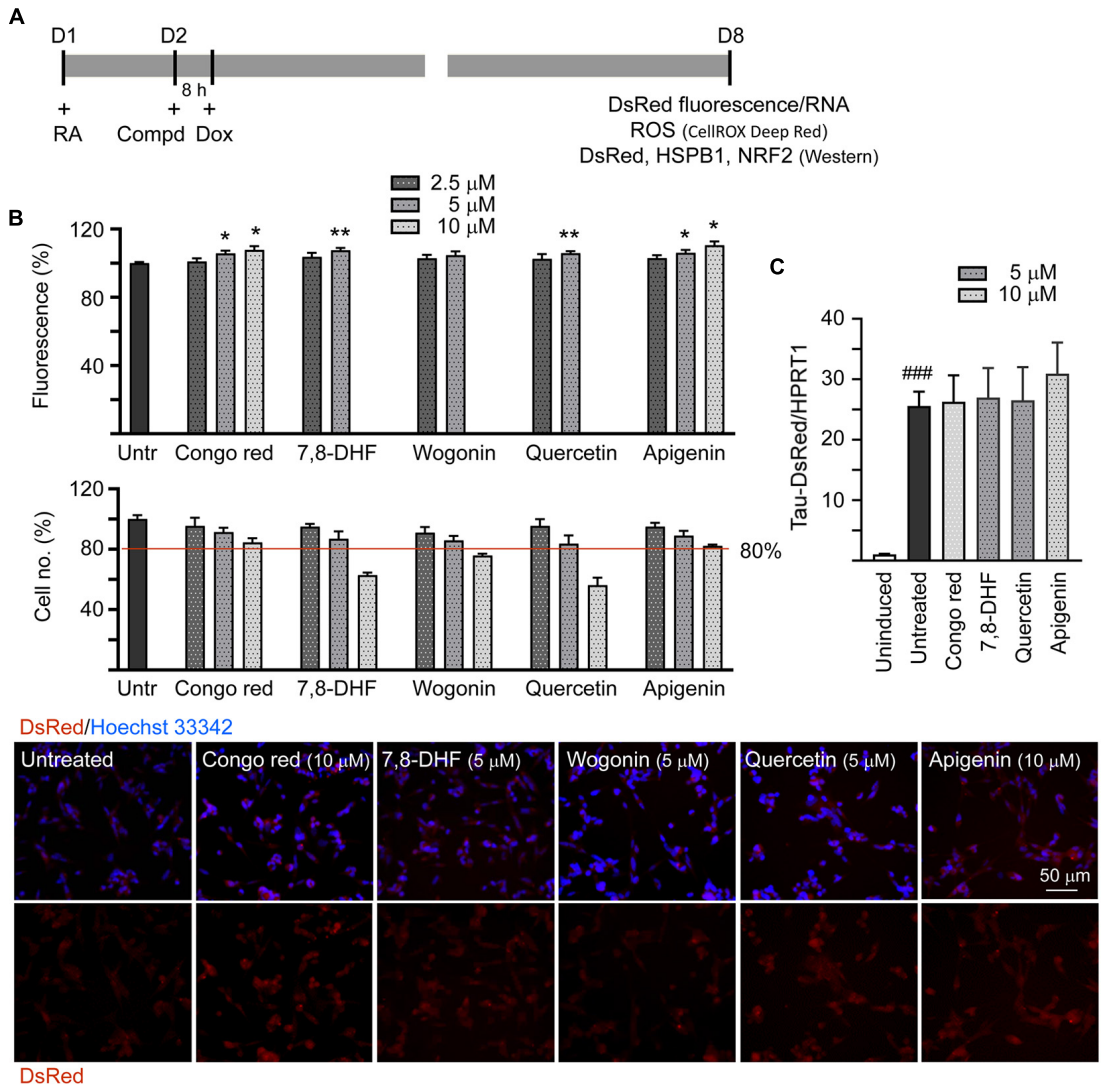

FIGURE 3 | (Continued)

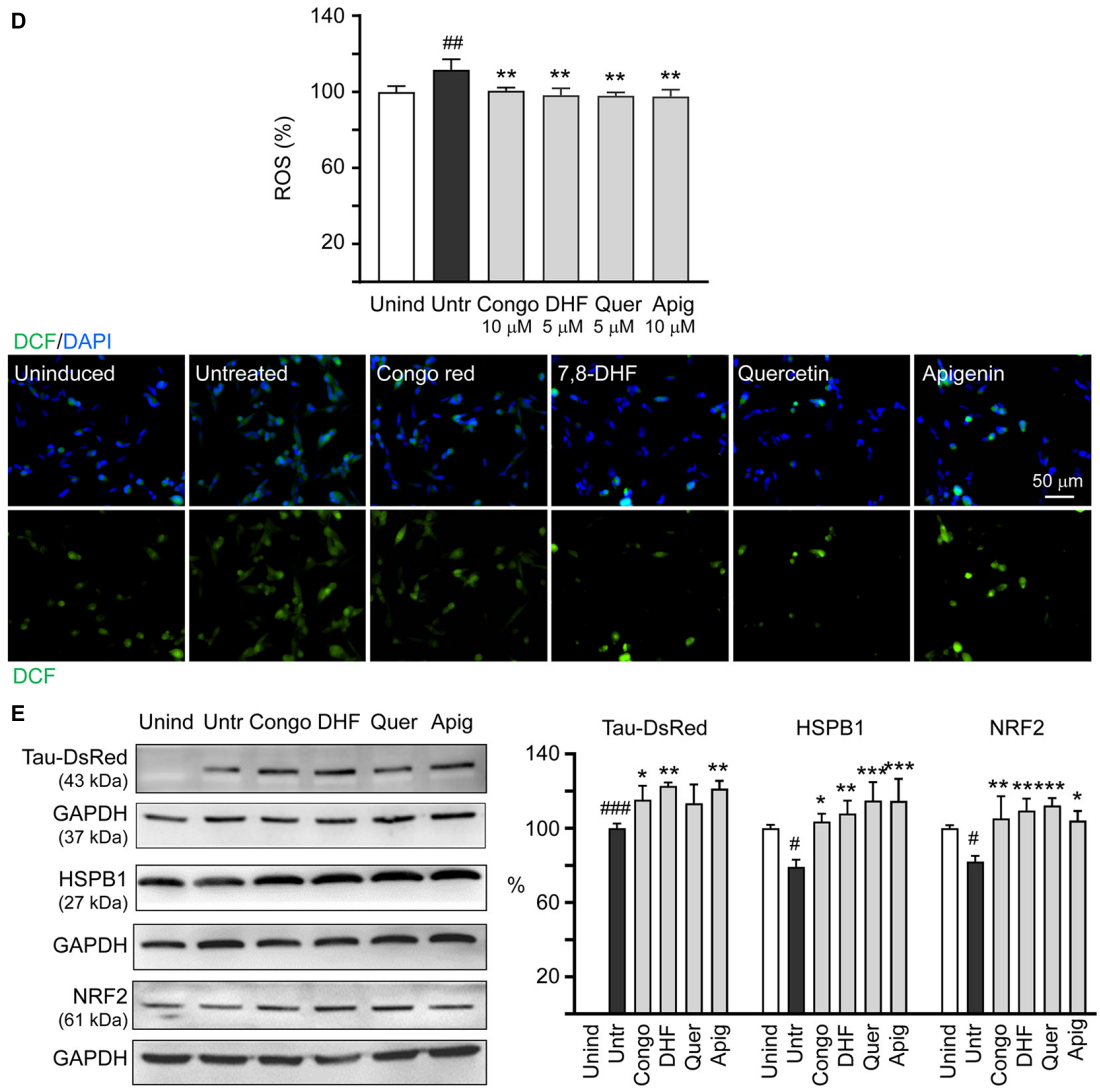

FIGURE 3 | Tau aggregation inhibition and reactive oxygen species (ROS) reduction in SH-SY5Y cells expressing ΔK280 Tau_{RD}-DsRed. **(A)** Experimental flowchart. On day 1, cells were plated with retinoic acid (RA) (10 μM) added to the culture medium. On day 2, Congo red (as a positive control), 7,8-DHF, wogonin, quercetin, or apigenin was added to the cells for 8 h, followed by inducing ΔK280 Tau_{RD}-DsRed expression with doxycycline (Dox) (2 μg/ml) for 6 days. On day 8, ΔK280 Tau_{RD}-DsRed fluorescence/RNA, ROS dichlorofluorescein (DCF stain), as well as DsRed, heat shock protein family B (small) member 1 (HSPB1), and nuclear factor erythroid 2-like 2 (NRF2) protein levels were measured. **(B)** Top: Assessment of DsRed fluorescence with Congo red, 7,8-DHF, wogonin, quercetin, or apigenin (2.5–10 μM) treatment and cell number (obtained by counting Hoechst 33342 stained cell nuclei) analyzed (n = 3). The relative DsRed fluorescence/cell number of untreated cells (Untr) was normalized as 100%. p-values: comparisons between with and without compound addition (*$p < 0.05$, **$p < 0.01$; two-tailed Student's t-test). Bottom: Fluorescent images of ΔK280 Tau_{RD}-DsRed cells with or without Congo red (10 μM), 7,8-DHF (5 μM), wogonin (5 μM), quercetin (5 μM), or apigenin (10 μM) treatment. Nuclei were counterstained with Hoechst 33342 (blue). **(C)** Real-time PCR analysis of Tau_{RD}-DsRed RNA in SH-SY5Y cells uninduced, untreated, or treated with 5 or 10 μM compound (n = 3). HPRT1 was used as an endogenous control to normalize between samples. **(D)** Top: Quantitation of ROS (n = 3) and images of DCF stain (green) of ΔK280 Tau_{RD}-DsRed cells uninduced, untreated, or treated with Congo red (10 μM), 7,8-DHF (5 μM), quercetin (5 μM), or apigenin (10 μM). The relative ROS of uninduced cells was normalized as 100%. Bottom: Images of DCF (green) assay of ΔK280 Tau_{RD}-DsRed cells uninduced, untreated, or treated with Congo red (10 μM), 7,8-DHF (5 μM), quercetin (5 μM), or apigenin (10 μM). Nuclei were counterstained with 4′,6-diamidino-2-phenylindole (DAPI) (blue). **(E)** Immunoblot analysis of Tau_{RD}-DsRed, HSPB1, and NRF2 proteins in SH-SY5Y cells uninduced, untreated, or treated with 5 or 10 μM compound (n = 3). Glyceraldehyde-3-phosphate dehydrogenase (GAPDH) was used as a loading control. To normalize, the HSPB1 or NRF2 expression level in uninduced (Unind) cells was set at 100%. For Tau_{RD}-DsRed, the soluble level in untreated cells (Untr) cells was set at 100%. **(D,E)** p-values: comparisons between untreated vs. uninduced cells ($^{\#}p < 0.05$, $^{\#\#}p < 0.01$, $^{\#\#\#}p < 0.001$) or compound-treated vs. untreated cells (*$p < 0.05$, **$p < 0.01$, ***$p < 0.001$) (one-way ANOVA with the *post hoc* Tukey's test).

high docking scores of the tested compounds binding to the neurotrophin-binding domain d5 of TRKB predicted by the computations (**Figure 2**). The observed neuroprotective effect under the knockdown of TRKB by these flavones may be also attributed to the increased NRF2 to promote neurite outgrowth (Yang et al., 2015).

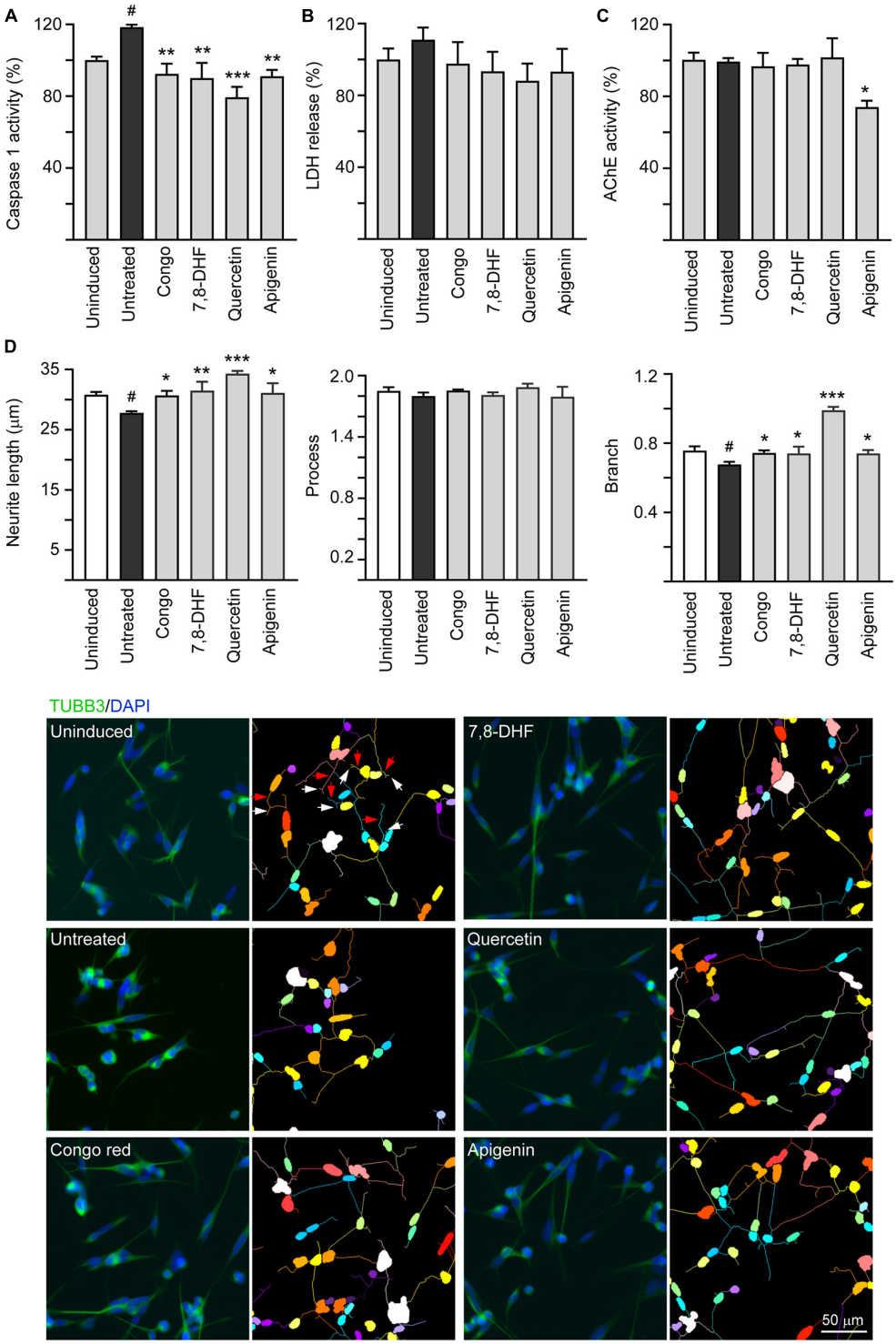

FIGURE 4 | Caspase-1, acetylcholinesterase (AChE) reduction, and neurite outgrowth promotion of 7,8-DHF, quercetin, and apigenin in SH-SY5Y cells expressing ΔK280 Tau_{RD}-DsRed. As described, cells were seeded with RA, treated with Congo red (10 μM), 7,8-DHF (5 μM), quercetin (5 μM), or apigenin (10 μM), and induced ΔK280 Tau_{RD}-DsRed expression with doxycycline for 6 days. On day 8, **(A)** caspase-1 activity, **(B)** lactate dehydrogenase (LDH) release, **(C)** AChE activity, and **(D)** neurite length, process, and branch were analyzed ($n = 3$). To normalize, the relative caspase-1, LDH release, or AChE activity of uninduced cells (Dox -) was set as 100%. Shown on the bottom half of panel **(D)**, there were images of TUBB3 (green)-stained cells, with nuclei counterstained with DAPI (blue) and segmented images with multicolored mask to assign each outgrowth to a cell body for neurite outgrowth quantification. Process and branches in uninduced cells were marked with red and white arrows, respectively. *p*-values: comparisons between induced vs. uninduced cells ($^{\#}p < 0.05$) or compound-treated vs. untreated cells ($^{*}p < 0.05$, $^{**}p < 0.01$, $^{***}p < 0.001$) (one-way ANOVA with the *post hoc* Tukey's test).

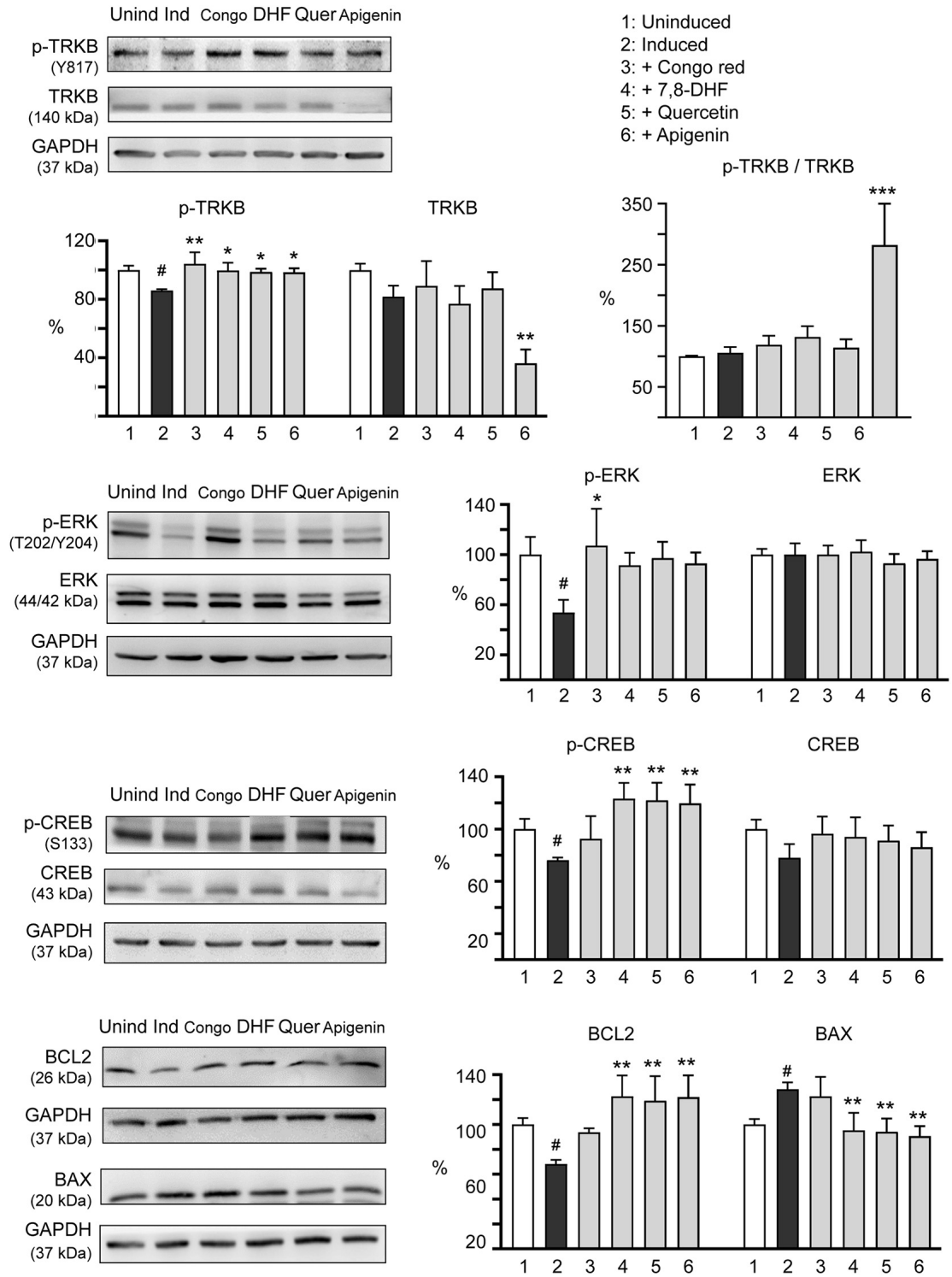

FIGURE 5 | Molecular targets of 7,8-DHF, quercetin, and apigenin in SH-SY5Y cells expressing ΔK280 Tau_{RD}-DsRed. Congo red (10 μM) was included as a negative control. Relative TRKB, p-TRKB (Y817), p-TRKB/TRKB, extracellular signal-regulated kinase (ERK), p-ERK (T202/Y204), cAMP-response element binding protein (CREB), p-CREB (S133), BCL2 apoptosis regulator (BCL2), and BCL2-associated X protein (BAX) protein levels were analyzed through immunoblotting using specific antibodies ($n = 3$). GAPDH was used as a loading control. Relative protein levels are shown on the right side of the representative western blot images. To normalize, the relative protein level in uninduced cells (Dox -) was set as 100%. *p*-values: comparisons between induced and uninduced cells ($^{\#}p < 0.05$) or between treated and untreated cells ($^{*}p < 0.05$, $^{**}p < 0.01$, $^{***}p < 0.001$) (one-way ANOVA with the *post hoc* Tukey's test).

Various natural flavones display antioxidant activity (Pietta, 2000). The majority of neurodegenerative diseases are speculated to originate from cumulative oxidative stress caused by deposition of abnormal aggregated proteins (Grimm et al., 2011). There is clear evidence that ROS is highly upregulated in the brain of tauopathies of the patients and ROS also directly promotes Tau modifications (Haque et al., 2019). Compounds with antioxidative potential may directly serve as chemical chaperone to suppress protein aggregates or quench free oxygen radicals. All the three flavones displayed some degree of chemical chaperone activity to enhance the folding and/or stability of proaggregator Tau (**Figure 1C**). Structural requirements of flavonoids for appreciable radical scavenging activity have been established (Seyoum et al., 2006). Without o-dihydroxy group (catechol structure) in the benzene ring, apigenin has poor antioxidant capacity for scavenging free radicals as assessed using stable radical DPPH (**Figure 1B**).

An alternative way to decrease cellular ROS is by enhancing antioxidative signaling such as NRF2 pathway. Stabilized following oxidative stress, NRF2 induces the expression of antioxidants as well as cytoprotective genes (Vomund et al., 2017). Reduced nuclear levels of NRF2 are observed in postmortem brains of patients with AD (Ramsey et al., 2007) and NRF2 inducer carnosic acid improves learning and memory in 3 × Tg-AD mice (Lipton et al., 2016). In this study, all the three flavones enhanced the expression of NRF2 (**Figure 3E**), supporting the role of 7,8-DHF, quercetin, and apigenin in activating the adaptive response to reduce oxidative stress. The NRF2 expression can be upregulated by AKT serine/threonine kinase 1 (AKT), which is one of the downstream proteins of TRKB activation (Yoo et al., 2017). Therefore, the NRF2 in the ΔK280 Tau_{RD} cell model treated with the three flavones may be increased through TRKB activation, at least partially.

Heat-shock proteins such as HSP90, HSP40, and HSPB1 had been speculated to function as regulators of soluble Tau protein levels (Sahara et al., 2007). As all the three flavones enhanced the expression of HSPB1 for chaperoning misfolded Tau (**Figure 3E**), 7,8-DHF, quercetin, and apigenin may also reduce the Tau-associated ROS through eliminating the misfolded Tau deposits. HSPB1 is transcriptionally upregulated by heat shock transcription factor 1 that can be enhanced by NRF2 (Paul et al., 2018). The HSPB1 expression in the ΔK280 Tau_{RD} cell model treated with the tested compounds may be activated by increased NRF2. However, further studies are required to consolidate the assumption.

Reactive oxygen species-associated neuroinflammation has been well known to be involved in caspase-1 activation and cleavage of proinflammatory cytokines

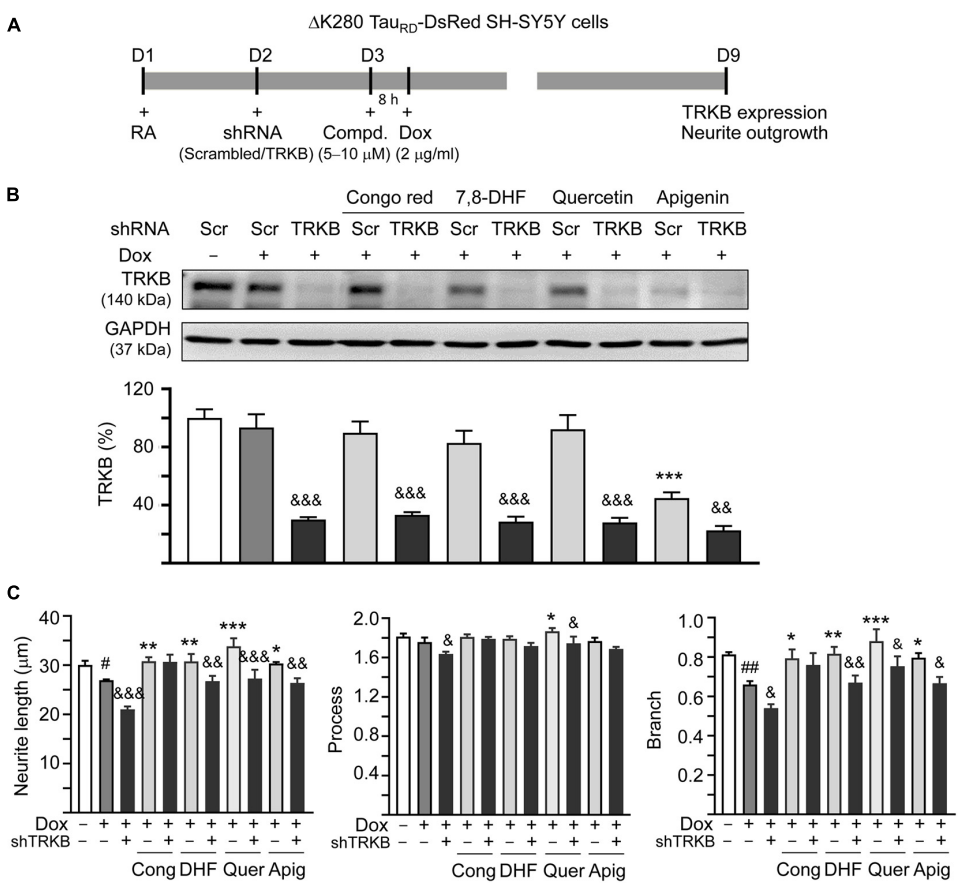

FIGURE 6 | (Continued)

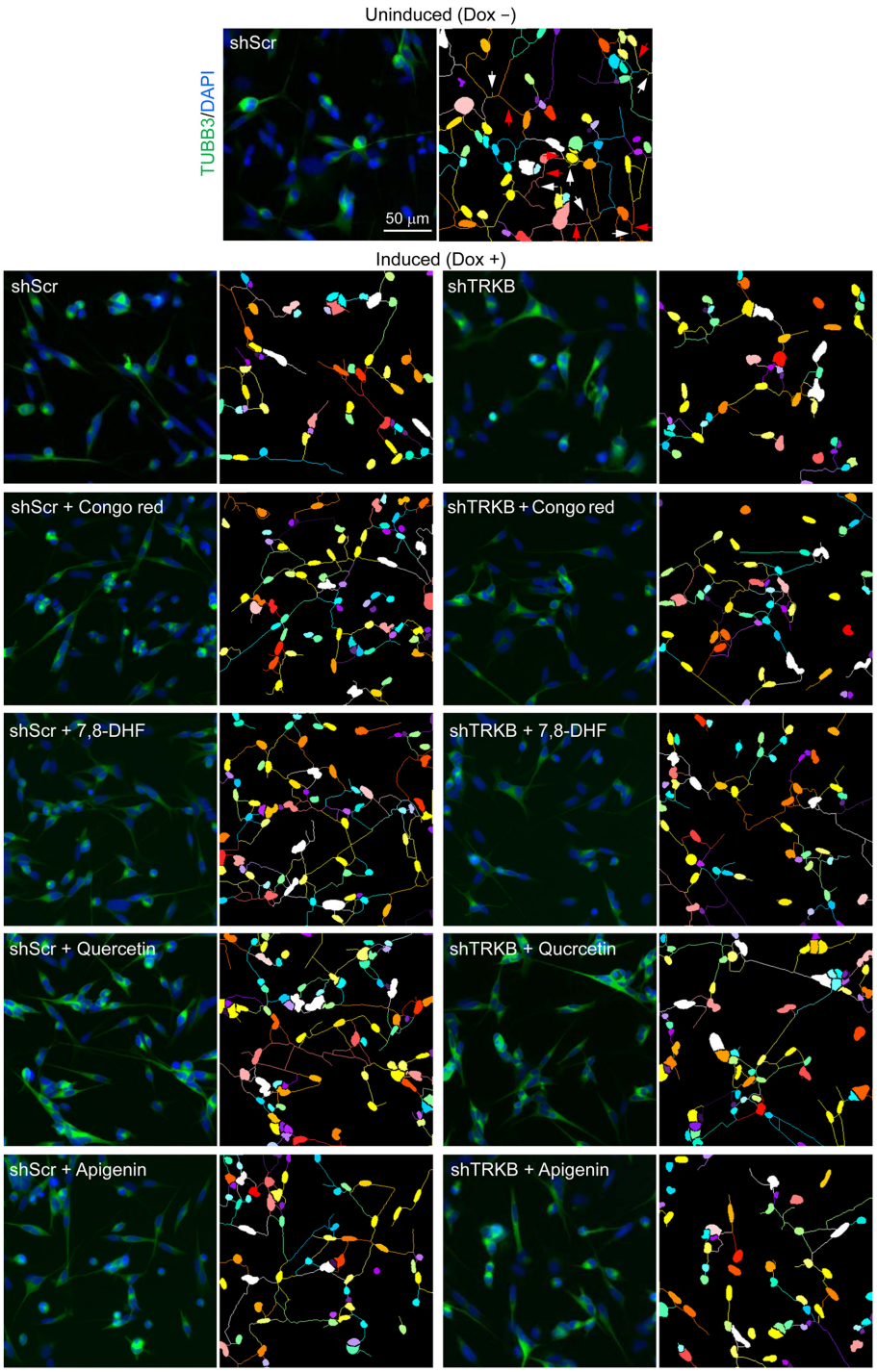

FIGURE 6 | TRKB RNA interference of SH-SY5Y cells expressing ΔK280 Tau_{RD}-DsRed. **(A)** Experimental flowchart. On day 1, ΔK280 Tau_{RD}-DsRed SH-SY5Y cells were plated with RA (10 μM). On day 2, the cells were infected with lentivirus-expressing TRKB-specific or scrambled shRNA. At 24 h postinfection, Congo red (10 μM), 7,8-DHF (5 μM), quercetin (5 μM), or apigenin (10 μM) was added to the cells for 8 h, followed by induction of ΔK280 Tau_{RD}-DsRed expression (Dox, 2 μg/ml) for 6 days. On day 9, the cells were collected for **(B)** TRKB protein (GAPDH as a loading control) and **(C)** neurite outgrowth analyses ($n = 3$). To normalize, the relative TRKB protein of uninduced cells (Dox -) was set as 100%. Shown on the bottom half of panel **(C)**, there were images of TUBB3 (green)-stained cells, with nuclei counterstained with DAPI (blue) and segmented images with multicolored mask to assign each outgrowth to a cell body for neurite outgrowth quantification. Processes and branches in scrambled shRNA-infected uninduced cells were marked with red and white arrows, respectively. *p*-values: comparisons between induced (Dox +) vs. uninduced (Dox -) cells ($^{\#}p < 0.05$, $^{\#\#}p < 0.01$) between compound-treated vs. untreated cells ($^{*}p < 0.05$, $^{**}p < 0.01$, $^{***}p < 0.001$) or between TRKB shRNA-treated vs. scrambled shRNA-treated cells ($^{\&}p < 0.05$, $^{\&\&}p < 0.01$, $^{\&\&\&}p < 0.001$) (one-way ANOVA with the *post hoc* Tukey's test).

(Howley and Fearnhead, 2008). Oxidative stress may also directly activate caspase-1 involved in inflammasome (Bai et al., 2020). Active caspase-1 induces caspase-6 activation that leads to axonal and neuronal degeneration in human primary central nervous system (CNS) cultures (Kaushal et al., 2015). Both the quercetin and apigenin have been reported to suppress inflammasome activation and downstream effector caspase-1 in human diseases induced by inflammatory responses (Yi, 2018). In this study, 7,8-DHF, quercetin, and apigenin counteract increased caspase-1 activity induced by proaggregator Tau (**Figure 4B**), which may be attributed to their free radical-scavenging (**Figure 1B**) or NRF2-enhancing activity (**Figure 3E**) to reduce ROS.

Acetylcholinesterase, an enzyme breaking down the neurotransmitter acetylcholine, is a feasible therapeutic target for treatment of AD (Akıncıoğlu and Gülçin, 2020). Currently AChE inhibitors such as donepezil, rivastigmine, and galantamine are commonly used to increase the level and duration of acetylcholine and facilitate cholinergic transmission in AD (Marucci et al., 2021). It has been shown that AChE activity as well as choline acetyltransferase is reduced in the cerebral cortex of patients with AD and tauopathy, indicating degenerated cholinergic neurons in both the diseases (Shinotoh et al., 2000; Hirano et al., 2006, 2018). However, the AChE activity is increased in frontotemporal dementia with parkinsonism-17 human tau transgenic mice (Silveyra et al., 2012). The findings of AChE activity in human tauopathy and the mouse model are not consistent. Our cell model that did not show significant changes in AChE activity may indicate that AChE activity is still preserved or partially impaired in this model and that inhibiting AChE activity may rescue acetylcholine levels. Among the three flavones examined, only apigenin reduced AChE activity in SH-SY5Y cells expressing proaggregator Tau (**Figure 4C**). Studies have shown that oxidative stress may induce AChE activity (Wang et al., 2019). However, given that all the three flavones in this study can reduce ROS, the reduced AChE activity only by apigenin may be attributed to some unknown mechanism. In the past years, intensive study efforts have been made for developing multitarget anti-Alzheimer compounds that hit several key pathogenic factors of the disease. Hybrid compounds combining a unit of potent and selective AChE inhibitor huprine Y with the 4-hydroxy-3-methoxyphenylpentanone moiety of natural antioxidant 6-shogaol have been documented (Pérez-Areales et al., 2014). In addition, herbal formulations with anticholinesterase and antioxidant activity could be benefit to memory enhancement (Nwidu et al., 2018). Being a dual antioxidant and anticholinesterase agent with tau antiaggregating property (**Figures 1**, **3**, **4**), apigenin emerges as an interesting multitarget anti-AD agent.

Upon BDNF binding, TRKB dimerized and phosphorylated to initiate intracellular signaling such as ERK, leading to activation of transcription factor CREB and downstream antiapoptotic BCL2 for neuronal survival (Walton and Dragunow, 2000). The level of phosphorylated CREB is decreased in the hippocampus of old rats with spatial memory deficits (Kudo et al., 2005; Williams et al., 2008; Xu et al., 2010). BCL2 binds to and inactivates BAX, thereby inhibiting apoptosis (Jonas, 2009). In 3 × Tg-AD mice, Tau provokes downregulation of BCL2 and increases level of BAX to lead to degeneration of cochlear spiral ganglion neurons (Wang and Wu, 2021). In our SH-SY5Y cell model, induction of proaggregated ΔK280 Tau_{RD} expression downregulated BCL2 and upregulated BAX, whereas 7,8-DHF, quercetin, and apigenin rescued changes in these gene expression (**Figure 4**). Although Congo red was used as a control, it did not rescue changes of p-CREB, BCL2, and BAX, which is probably due to its modest neuroprotection effect. In contrast, under the same condition, the tested flavones showed significant improvements in p-CREB, BCL2, and BAX, suggesting their promising therapeutic potential. As crosstalk between pathological Tau phosphorylation and mitochondrial dysfunction exists (Guha et al., 2020) and BCL2 counteracts the mitochondria dysfunction-mediated apoptosis, investigation of mitochondria-related apoptotic pathways through caspase-9 and caspase-3 activation may shed light on the mechanism of how quercetin and apigenin provide antiapoptotic effect on ΔK280 Tau_{RD} cells. There are still other TRKB downstream pathways such as phosphatidylinositol 3-kinase (PI3K)/AKT/mTOR. In the future, investigating if PI3K/AKT/mTOR is also involved in the neuroprotective mechanism of these flavones is warranted. Besides, although our previous study has shown the neuroprotection effects of 7,8-DHF in the primary hippocampal primary neurons and mouse models induced by Aβ (Fan et al., 2020), whether the other two flavones apigenin and quercetin also provide the similar effects either in primary neurons and mouse models should be examined in the future.

In conclusion, our results show that, in addition to 7,8-DHF, quercetin and apigenin activate TRKB signaling to upregulate downstream CREB and BCL2 expressions. In the proaggregator Tau AD cell model, these flavones improve neurite outgrowth, reduce caspase-1 and/or AChE activities by activating TRKB, as well as ameliorating ROS. As multiple pathogenic pathways are involved in AD, the potential of these flavones targeting multiple pathways may have a significant perspective for developing anti-AD drug. The effect of quercetin and apigenin as TRKB agonists should be validated in AD animal models. Assays of mitochondrial function, especially in the light of increased BCL2 expression, would provide a better connection between the reported signaling mechanisms and resulting changes in cell physiology. Also, binding of quercetin and apigenin to the TRKB receptor should be measured using surface plasmon resonance to consolidate the action as agonists of TRKB.

DATA AVAILABILITY STATEMENT

The original contributions presented in the study are included in the article/supplementary material, further inquiries can be directed to the corresponding author/s.

AUTHOR CONTRIBUTIONS

N-NC, T-HL, and Y-ST contributed to the execution of experiments, data analysis, and interpretation. Y-CS, K-HC, C-YL, HH-L, and M-TS contributed to review and editing. C-MC and G-JL-C contributed to the concept and design, data analysis and interpretation, obtained funding, and wrote and finalized the

manuscript. All authors have read and agreed to the published version of the draft of the manuscript.

FUNDING

This study was supported by the grants 108-2320-B-003-001 and 108-2320-B-182A-001 from the Ministry of Science and Technology, Taiwan.

ACKNOWLEDGMENTS

We would like to thank the Molecular Imaging Core Facility of National Taiwan Normal University for the technical assistance. We would like to acknowledge computing resources provided by the National Center of High-Performance Computing to facilitate this study. We would also like to thank the National RNAi Core Facility, Academia Sinica, for technical support.

REFERENCES

Afreen, S., and Ferreira, A. (2019). Altered cytoskeletal composition and delayed neurite elongation in tau45-230-expressing hippocampal neurons. *Neuroscience* 412, 1–15. doi: 10.1016/j.neuroscience.2019.05.046

Akıncıoğlu, H., and Gülçin, İ (2020). Potent acetylcholinesterase inhibitors: potential drugs for Alzheimer's disease. *Mini Rev. Med. Chem.* 20, 703–715. doi: 10.2174/1389557520666200103100521

Aranda, A., Sequedo, L., Tolosa, L., Quintas, G., Burello, E., Castell, J. V., et al. (2013). Dichloro-dihydro-fluorescein diacetate (DCFH-DA) assay: a quantitative method for oxidative stress assessment of nanoparticle-treated cells. *Toxicol. In Vitro* 27, 954–963. doi: 10.1016/j.tiv.2013.01.016

Bahn, G., and Jo, D. G. (2019). Therapeutic approaches to Alzheimer's disease through modulation of NRF2. *Neuromolecular Med.* 21, 1–11. doi: 10.1007/s12017-018-08523-5

Bai, B., Yang, Y., Wang, Q., Li, M., Tian, C., Liu, Y., et al. (2020). NLRP3 inflammasome in endothelial dysfunction. *Cell Death Dis.* 11:776. doi: 10.1038/s41419-020-02985-x

Banfield, M. J., Naylor, R. L., Robertson, A. G., Allen, S. J., Dawbarn, D., and Brady, R. L. (2001). Specificity in Trk receptor:neurotrophin interactions: the crystal structure of TrkB-d5 in complex with neurotrophin-4/5. *Structure* 9, 1191–1199. doi: 10.1016/s0969-2126(01)00681-5

Biancalana, M., and Koide, S. (2010). Molecular mechanism of Thioflavin-T binding to amyloid fibrils. *Biochim. Biophys. Acta* 1804, 1405–1412. doi: 10.1016/j.bbapap.2010.04.001

Bollen, E., Vanmierlo, T., Akkerman, S., Wouters, C., Steinbusch, H. M., and Prickaerts, J. (2013). 7,8-Dihydroxyflavone improves memory consolidation processes in rats and mice. *Behav. Brain Res.* 257, 8–12. doi: 10.1016/j.bbr.2013.09.029

Bonni, A., Brunet, A., West, A. E., Datta, S. R., Takasu, M. A., and Greenberg, M. E. (1999). Cell survival promoted by the Ras-MAPK signaling pathway by transcription-dependent and -independent mechanisms. *Science* 286, 1358–1362. doi: 10.1126/science.286.5443.1358

Butler, V. J., Salazar, D. A., Soriano-Castell, D., Alves-Ferreira, M., Dennissen, F. J. A., Vohra, M., et al. (2019). Tau/MAPT disease-associated variant A152T alters tau function and toxicity via impaired retrograde axonal transport. *Hum. Mol. Genet.* 28, 1498–1514. doi: 10.1093/hmg/ddy442

Cente, M., Filipcik, P., Pevalova, M., and Novak, M. (2006). Expression of a truncated tau protein induces oxidative stress in a rodent model of tauopathy. *Eur. J. Neurosci.* 24, 1085–1090. doi: 10.1111/j.1460-9568.2006.04986.x

Chang, K. H., Lin, C. H., Chen, H. C., Huang, H. Y., Chen, S. L., Lin, T. H., et al. (2017). The potential of indole/indolylquinoline compounds in tau misfolding reduction by enhancement of HSPB1. *CNS Neurosci. Ther.* 23, 4–56. doi: 10.1111/cns.12592

Chen, C., Wang, Z., Zhang, Z., Liu, X., Kang, S. S., Zhang, Y., et al. (2018). The prodrug of 7,8-dihydroxyflavone development and therapeutic efficacy for treating Alzheimer's disease. *Proc. Natl. Acad. Sci. U.S.A.* 115, 578–583. doi: 10.1073/pnas.1718683115

Chitranshi, N., Gupta, V., Kumar, S., and Graham, S. L. (2015). Exploring the molecular interactions of 7,8-dihydroxyflavone and its derivatives with TrkB and VEGFR2 proteins. *Int. J. Mol. Sci.* 16, 21087–21108. doi: 10.3390/ijms160921087

Citron, M. (2010). Alzheimer's disease: strategies for disease modification. *Nat. Rev. Drug Discov.* 9, 387–398. doi: 10.1038/nrd2896

Coppola, G., Chinnathambi, S., Lee, J. J., Dombroski, B. A., Baker, M. C., Soto-Ortolaza, A. I., et al. (2012). Evidence for a role of the rare p.A152T variant in MAPT in increasing the risk for FTD-spectrum and Alzheimer's diseases. *Hum. Mol. Genet.* 21, 3500–3512. doi: 10.1093/hmg/dds161

Davies, P., and Maloney, A. J. (1976). Selective loss of central cholinergic neurons in Alzheimer's disease. *Lancet* 2:1403. doi: 10.1016/s0140-6736(76)91936-x

Devi, L., and Ohno, M. (2012). 7,8-dihydroxyflavone, a small-molecule TrkB agonist, reverses memory deficits and BACE1 elevation in a mouse model of Alzheimer's disease. *Neuropsychopharmacology* 37, 434–444. doi: 10.1038/npp.2011.191

Dittrich, F., Ochs, G., Grosse-Wilde, A., Berweiler, U., Yan, Q., Miller, J. A., et al. (1996). Pharmacokinetics of intrathecally applied BDNF and effects on spinal motoneurons. *Exp. Neurol.* 141, 225–239. doi: 10.1006/exnr.1996.0157

Fan, C. H., Lin, C. W., Huang, H. J., Lee-Chen, G. J., Sun, Y. C., Lin, W., et al. (2020). LMDS-1, a potential TrkB receptor agonist provides a safe and neurotrophic effect for early-phase Alzheimer's disease. *Psychopharmacology (Berl.)* 237, 3173–3190. doi: 10.1007/s00213-020-05602-z

Flores, J., Noël, A., Foveau, B., Lynham, J., Lecrux, C., and LeBlanc, A. C. (2018). Caspase-1 inhibition alleviates cognitive impairment and neuropathology in an Alzheimer's disease mouse model. *Nat. Commun.* 9:3916. doi: 10.1038/s41467-018-06449-x

Goedert, M., Spillantini, M. G., Potier, M. C., Ulrich, J., and Crowther, R. A. (1989). Cloning and sequencing of the cDNA encoding an isoform of microtubule-associated protein tau containing four tandem repeats: differential expression of tau protein mRNAs in human brain. *EMBO J.* 8, 393–399.

Grimm, S., Hoehn, A., Davies, K. J., and Grune, T. (2011). Protein oxidative modifications in the ageing brain: consequence for the onset of neurodegenerative disease. *Free Radic. Res.* 45, 73–88. doi: 10.3109/10715762.2010.512040

Guha, S., Johnson, G. V. W., and Nehrke, K. (2020). The crosstalk between pathological Tau phosphorylation and mitochondrial dysfunction as a key to understanding and treating Alzheimer's disease. *Mol. Neurobiol.* 57, 5103–5120. doi: 10.1007/s12035-020-02084-0

Haque, M. M., Murale, D. P., Kim, Y. K., and Lee, J. S. (2019). Crosstalk between oxidative stress and tauopathy. *Int. J. Mol. Sci.* 20:1959. doi: 10.3390/ijms20081959

Hausott, B., Kurnaz, I., Gajovic, S., and Klimaschewski, L. (2009). Signaling by neuronal tyrosine kinase receptors: relevance for development and regeneration. *Anat. Rec. (Hoboken)* 292, 1976–1985. doi: 10.1002/ar.20964

Heneka, M. T., Kummer, M. P., Stutz, A., Delekate, A., Schwartz, S., Vieira-Saecker, A., et al. (2013). NLRP3 is activated in Alzheimer's disease and contributes to pathology in APP/PS1 mice. *Nature* 493, 674–678. doi: 10.1038/nature11729

Hirano, S., Shinotoh, H., Kobayashi, T., Tsuboi, Y., Wszolek, Z. K., Aotsuka, A., et al. (2006). Brain acetylcholinesterase activity in FTDP-17 studied by PET. *Neurology* 66, 1276–1277. doi: 10.1212/01.wnl.0000208515.50924.94

Hirano, S., Shinotoh, H., Shimada, H., Ota, T., Sato, K., Tanaka, N., et al. (2018). Voxel-based acetylcholinesterase PET study in early and late onset Alzheimer's disease. *J. Alzheimers Dis.* 62, 1539–1548. doi: 10.3233/JAD-170749

Howley, B., and Fearnhead, H. O. (2008). Caspases as therapeutic targets. *J. Cell. Mol. Med.* 12, 1502–1516. doi: 10.1111/j.1582-4934.2008.00292.x

Iqbal, K., Alonso Adel, C., Chen, S., Chohan, M. O., El-Akkad, E., Gong, C. X., et al. (2005). Tau pathology in Alzheimer disease and other tauopathies. *Biochim. Biophys. Acta* 1739, 198–210. doi: 10.1016/j.bbadis.2004.09.008

Jang, S. W., Liu, X., Yepes, M., Shepherd, K. R., Miller, G. W., Liu, Y., et al. (2010). A selective TrkB agonist with potent neurotrophic activities by 7,8-dihydroxyflavone. *Proc. Natl. Acad. Sci. U.S.A.* 107, 2687–2692. doi: 10.1073/pnas.0913572107

Johnson, G. V., and Stoothoff, W. H. (2004). Tau phosphorylation in neuronal cell function and dysfunction. *J. Cell Sci.* 117, 5721–5729. doi: 10.1242/jcs.01558

Jonas, E. A. (2009). Molecular participants in mitochondrial cell death channel formation during neuronal ischemia. *Exp. Neurol.* 218, 203–212. doi: 10.1016/j.expneurol.2009.03.025

Jones, K. R., and Reichardt, L. F. (1990). Molecular cloning of a human gene that is a member of the nerve growth factor family. *Proc. Natl. Acad. Sci. U.S.A.* 87, 8060–8064. doi: 10.1073/pnas.87.20.8060

Kang, H. J., Welcher, A. A., Shelton, D., and Schuman, E. M. (1997). Neurotrophins and time: different roles for TrkB signaling in hippocampal long-term potentiation. *Neuron* 19, 653–664. doi: 10.1016/s0896-6273(00)80378-5

Katebi, S., Esmaeili, A., Ghaedi, K., and Zarrabi, A. (2019). Superparamagnetic iron oxide nanoparticles combined with NGF and quercetin promote neuronal branching morphogenesis of PC12 cells. *Int. J. Nanomedicine* 14, 2157–2169. doi: 10.2147/IJN.S191878

Kaushal, V., Dye, R., Pakavathkumar, P., Foveau, B., Flores, J., Hyman, B., et al. (2015). Neuronal NLRP1 inflammasome activation of Caspase-1 coordinately regulates inflammatory interleukin-1-beta production and axonal degeneration-associated Caspase-6 activation. *Cell Death Differ.* 22, 1676–1686. doi: 10.1038/cdd.2015.16

Khlistunova, I., Biernat, J., Wang, Y., Pickhardt, M., von Bergen, M., Gazova, Z., et al. (2006). Inducible expression of Tau repeat domain in cell models of tauopathy: aggregation is toxic to cells but can be reversed by inhibitor drugs. *J. Biol. Chem.* 281, 1205–1214. doi: 10.1074/jbc.M507753200

Kudo, K., Wati, H., Qiao, C., Arita, J., and Kanba, S. (2005). Age-related disturbance of memory and CREB phosphorylation in CA1 area of hippocampus of rats. *Brain Res.* 1054, 30–37. doi: 10.1016/j.brainres.2005.06.045

Kumar, S., and Pandey, A. K. (2013). Chemistry and biological activities of flavonoids: an overview. *Sci. World J.* 2013:162750. doi: 10.1155/2013/162750

Lee, V. M., Goedert, M., and Trojanowski, J. Q. (2001). Neurodegenerative tauopathies. *Annu. Rev. Neurosci.* 24, 1121–1159. doi: 10.1146/annurev.neuro.24.1.1121

Levine, E. S., Dreyfus, C. F., Black, I. B., and Plummer, M. R. (1996). Selective role for trkB neurotrophin receptors in rapid modulation of hippocampal synaptic transmission. *Mol. Brain Res.* 38, 300–303. doi: 10.1016/0169-328x(96)00025-3

Li, N., Liu, J. H., Zhang, J., and Yu, B. Y. (2008). Comparative evaluation of cytotoxicity and antioxidative activity of 20 flavonoids. *J. Agric. Food Chem.* 56, 3876–3883. doi: 10.1021/jf073520n

Lin, T. H., Chiu, Y. J., Lin, C. H., Lin, C. Y., Chao, C. Y., Chen, Y. C., et al. (2020). Exploration of multi-target effects of 3-benzoyl-5-hydroxychromen-2-one in Alzheimer's disease cell and mouse models. *Aging Cell* 19:e13169. doi: 10.1111/acel.13169

Lipton, S. A., Rezaie, T., Nutter, A., Lopez, K. M., Parker, J., Kosaka, K., et al. (2016). Therapeutic advantage of pro-electrophilic drugs to activate the Nrf2/ARE pathway in Alzheimer's disease models. *Cell Death Dis.* 7:e2499. doi: 10.1038/cddis.2016.389

Lu, B., Nagappan, G., Guan, X., Nathan, P. J., and Wren, P. (2013). BDNF-based synaptic repair as a disease-modifying strategy for neurodegenerative diseases. *Nat. Rev. Neurosci.* 14, 401–416. doi: 10.1038/nrn3505

Marucci, G., Buccioni, M., Ben, D. D., Lambertucci, C., Volpini, R., and Amenta, F. (2021). Efficacy of acetylcholinesterase inhibitors in Alzheimer's disease. *Neuropharmacology* 190:108352. doi: 10.1016/j.neuropharm.2020.108352

Mazzaro, N., Barini, E., Spillantini, M. G., Goedert, M., Medini, P., and Gasparini, L. (2016). Tau-driven neuronal and neurotrophic dysfunction in a mouse model of early tauopathy. *J. Neurosci.* 36, 2086–2100. doi: 10.1523/JNEUROSCI.0774-15.2016

Mondragón-Rodríguez, S., Perry, G., Zhu, X., Moreira, P. I., Acevedo-Aquino, M. C., and Williams, S. (2013). Phosphorylation of tau protein as the link between oxidative stress, mitochondrial dysfunction, and connectivity failure: implications for Alzheimer's disease. *Oxid. Med. Cell. Longev.* 2013:940603. doi: 10.1155/2013/940603

Mota, S. I., Costa, R. O., Ferreira, I. L., Santana, I., Caldeira, G. L., Padovano, C., et al. (2015). Oxidative stress involving changes in Nrf2 and ER stress in early stages of Alzheimer's disease. *Biochim. Biophys. Acta* 1852, 1428–1441. doi: 10.1016/j.bbadis.2015.03.015

Nagahara, A. H., and Tuszynski, M. H. (2011). Potential therapeutic uses of BDNF in neurological and psychiatric disorders. *Nat. Rev. Drug Discov.* 10, 209–219. doi: 10.1038/nrd3366

Nakagawara, A., Liu, X. G., Ikegaki, N., White, P. S., Yamashiro, D. J., Nycum, L. M., et al. (1995). Cloning and chromosomal localization of the human TRK-B tyrosine kinase receptor gene (NTRK2). *Genomics* 25, 538–546. doi: 10.1016/0888-7543(95)80055-q

Nie, C. L., Wang, X. S., Liu, Y., Perrett, S., and He, R. Q. (2007). Amyloid-like aggregates of neuronal tau induced by formaldehyde promote apoptosis of neuronal cells. *BMC Neurosci.* 8:9. doi: 10.1186/1471-2202-8-9

Nissink, J. W., Murray, C., Hartshorn, M., Verdonk, M. L., Cole, J. C., and Taylor, R. (2002). A new test set for validating predictions of protein-ligand interaction. *Proteins* 49, 457–471. doi: 10.1002/prot.10232

Nwidu, L. L., Elmorsy, E., and Carter, W. G. (2018). In vitro anti-cholinesterase and anti-oxidant activity of three standardised polyherbal products used for memory enhancing in ethnomedicine of South-East Nigeria. *Malays. J. Med. Sci.* 25, 27–39. doi: 10.21315/mjms2018.25.2.4

Påhlman, S., Ruusala, A. I., Abrahamsson, L., Mattsson, M. E., and Esscher, T. (1984). Retinoic acid-induced differentiation of cultured human neuroblastoma cells: a comparison with phorbolester-induced differentiation. *Cell Differ.* 14, 135–144. doi: 10.1016/0045-6039(84)90038-1

Paul, S., Ghosh, S., Mandal, S., Sau, S., and Pal, M. (2018). NRF2 transcriptionally activates the heat shock factor 1 promoter under oxidative stress and affects survival and migration potential of MCF7 cells. *J. Biol. Chem.* 293, 19303–19316. doi: 10.1074/jbc.RA118.003376

Pérez-Areales, F. J., Pietro, O. D., Espargaró, A., Vallverdú-Queralt, A., Galdeano, C., Ragusa, I. M., et al. (2014). Shogaol-huprine hybrids: dual antioxidant and anticholinesterase agents with β-amyloid and tau anti-aggregating properties. *Bioorg. Med. Chem.* 22, 5298–5307. doi: 10.1016/j.bmc.2014.07.053

Pérez-Corredor, P., Sabogal-Guáqueta, A. M., Carrillo-Hormaza, L., and Cardona-Gómez, G. P. (2019). Preventive effect of quercetin in a triple transgenic Alzheimer's disease mice model. *Molecules* 24:2287. doi: 10.3390/molecules24122287

Pietta, P. G. (2000). Flavonoids as antioxidants. *J. Nat. Prod.* 63, 1035–1042. doi: 10.1021/np9904509

Poprac, P., Jomova, K., Simunkova, M., Kollar, V., Rhodes, C. J., and Valko, M. (2017). Targeting free radicals in oxidative stress-related human diseases. *Trends Pharmacol. Sci.* 38, 592–607. doi: 10.1016/j.tips.2017.04.005

Ramsey, C. P., Glass, C. A., Montgomery, M. B., Lindl, K. A., Ritson, G. P., Chia, L. A., et al. (2007). Expression of Nrf2 in neurodegenerative diseases. *J. Neuropathol. Exp. Neurol.* 66, 75–85. doi: 10.1097/nen.0b013e31802d6da9

Riccio, A., Ahn, S., Davenport, C. M., Blendy, J. A., and Ginty, D. D. (1999). Mediation by a CREB family transcription factor of NGF-dependent survival of sympathetic neurons. *Science* 286, 2358–2361. doi: 10.1126/science.286.5448.2358

Sabogal-Guáqueta, A. M., Muñoz-manco, J. I., Ramírez, J. R., Lamprea-rodriguez, M., Osorio, E., and Cardona-gómez, G. P. (2015). The flavonoid quercetin ameliorates Alzheimer's disease pathology and protects cognitive and emotional function in aged triple transgenic Alzheimer's disease model mice. *Neuropharmacology* 93, 134–145. doi: 10.1016/j.neuropharm.2015.01.027

Sahara, N., Maeda, S., Yoshiike, Y., Mizoroki, T., Yamashita, S., Murayama, M., et al. (2007). Molecular chaperone-mediated tau protein metabolism counteracts the formation of granular tau oligomers in human brain. *J. Neurosci. Res.* 85, 3098–3108. doi: 10.1002/jnr.21417

Schweers, O., Schonbrunnhanebeck, E., Marx, A., and Mandelkow, E. (1994). Structural studies of tau-protein and Alzheimer paired helical filaments show no evidence for β-structure. *J. Biol. Chem.* 1269, 24290–24297.

Seyoum, A., Asres, K., and El-Fiky, F. K. (2006). Structure-radical scavenging activity relationships of flavonoids. *Phytochemistry* 67, 2058–2070. doi: 10.1016/j.phytochem.2006.07.002

Shimura, H., Miura-Shimura, Y., and Kosik, K. S. (2004). Binding of tau to heat shock protein 27 leads to decreased concentration of hyperphosphorylated tau and enhanced cell survival. *J. Biol. Chem.* 279, 17957–17962. doi: 10.1074/jbc.M400351200

Shinotoh, H., Namba, H., Fukushi, K., Nagatsuka, S., Tanaka, N., Aotsuka, A., et al. (2000). Brain acetylcholinesterase activity in Alzheimer disease measured by positron emission tomography. *Alzheimer Dis. Assoc. Disord.* 14(Suppl. 1), S114–S118. doi: 10.1097/00002093-200000001-00017

Silveyra, M. X., García-Ayllón, M. S., de Barreda, E. G., Small, D. H., Martínez, S., Avila, J., et al. (2012). Altered expression of brain acetylcholinesterase in FTDP-17 human tau transgenic mice. *Neurobiol. Aging* 33, 624.e23–e34. doi: 10.1016/j.neurobiolaging.2011.03.006

Singh, M., Kaur, M., and Silakari, O. (2014). Flavones: an important scaffold for medicinal chemistry. *Eur. J. Med. Chem.* 84, 206–239. doi: 10.1016/j.ejmech.2014.07.013

Sipe, J. D., and Cohen, A. S. (2000). Review: history of the amyloid fibril. *J. Struct. Biol.* 130, 88–98. doi: 10.1006/jsbi.2000.4221

Soppet, D., Escandon, E., Maragos, J., Middlemas, D. S., Reid, S. W., Blair, J., et al. (1991). The neurotrophic factors brain-derived neurotrophic factor and neurotrophin-3 are ligands for the trkB tyrosine kinase receptor. *Cell* 65, 895–903. doi: 10.1016/0092-8674(91)90396-g

Urfer, R., Tsoulfas, P., O'Connell, L., Shelton, D. L., Parada, L. F., and Presta, L. G. (1995). An immunoglobulin-like domain determines the specificity of neurotrophin receptors. *EMBO J.* 14, 2795–2805.

Verdonk, M. L., Cole, J. C., Hartshorn, M. J., Murray, C. W., and Taylor, R. D. (2003). Improved protein-ligand docking using GOLD. *Proteins* 52, 609–623. doi: 10.1002/prot.10465

Vomund, S., Schäfer, A., Parnham, M. J., Brüne, B., and von Knethen, A. (2017). Nrf2, the master regulator of anti-oxidative responses. *Int. J. Mol. Sci.* 18:2772. doi: 10.3390/ijms18122772

Walton, M. R., and Dragunow, M. (2000). Is CREB a key to neuronal survival? *Trends Neurosci.* 23, 48–53. doi: 10.1016/s0166-2236(99)01500-3

Wang, S. E., and Wu, C. H. (2021). Tau phosphorylation and cochlear apoptosis cause hearing loss in 3Tg-AD mouse model of Alzheimer's disease. *Chin. J. Physiol.* 64, 61–71. doi: 10.4103/CJP.CJP_79_20

Wang, X., Li, P., Ding, Q., Wu, C., Zhang, W., and Tang, B. (2019). Observation of acetylcholinesterase in stress-induced depression phenotypes by two-photon fluorescence imaging in the mouse brain. *J. Am. Chem. Soc.* 141, 2061–2068. doi: 10.1021/jacs.8b11414

Williams, C. M., El Mohsen, M. A., Vauzour, D., Rendeiro, C., Butler, L. T., Ellis, J. A., et al. (2008). Blueberry-induced changes in spatial working memory correlate with changes in hippocampal CREB phosphorylation and brain-derived neurotrophic factor (BDNF) levels. *Free Radic. Biol. Med.* 45, 295–305. doi: 10.1016/j.freeradbiomed.2008.04.008

Xiang, J., Wang, Z. H., Ahn, E. H., Liu, X., Yu, S. P., Manfredsson, F. P., et al. (2019). Delta-secretase-cleaved Tau antagonizes TrkB neurotrophic signalings, mediating Alzheimer's disease pathologies. *Proc. Natl. Acad. Sci. U.S.A.* 116, 9094–9102. doi: 10.1073/pnas.1901348116

Xu, J., Rong, S., Xie, B., Sun, Z., Deng, Q., Wu, H., et al. (2010). Memory impairment in cognitively impaired aged rats associated with decreased hippocampal CREB phosphorylation: reversal by procyanidins extracted from the lotus seedpod. *J. Gerontol. A Biol. Sci. Med. Sci.* 65, 933–940. doi: 10.1093/gerona/glq094

Yang, C., Cheng, Y., Zhao, J., and Rong, J. (2015). Releasing Nrf2 to promote neurite outgrowth. *Neural Regen. Res.* 10, 1934–1935. doi: 10.4103/1673-5374.169618

Yi, Y. S. (2018). Regulatory roles of flavonoids on inflammasome activation during inflammatory responses. *Mol. Nutr. Food Res.* 62:e1800147. doi: 10.1002/mnfr.201800147

Yoo, J. M., Lee, B. D., Sok, D. E., Ma, J. Y., and Kim, M. R. (2017). Neuroprotective action of N-acetyl serotonin in oxidative stress-induced apoptosis through the activation of both TrkB/CREB/BDNF pathway and Akt/Nrf2/Antioxidant enzyme in neuronal cells. *Redox Biol.* 11, 592–599. doi: 10.1016/j.redox.2016.12.034

Zeng, Y., Wang, X., Wang, Q., Liu, S., Hu, X., and McClintock, S. M. (2013). Small molecules activating TrkB receptor for treating a variety of CNS disorders. *CNS Neurol. Disord. Drug Targets* 12, 1066–1077. doi: 10.2174/18715273113129990089

Zhang, Z., Liu, X., Schroeder, J. P., Chan, C. B., Song, M., Yu, S. P., et al. (2014). 7,8-dihydroxyflavone prevents synaptic loss and memory deficits in a mouse model of Alzheimer's disease. *Neuropsychopharmacology* 39, 638–650. doi: 10.1038/npp.2013.243

Zhao, L., Wang, J. L., Liu, R., Li, X. X., Li, J. F., and Zhang, L. (2013). Neuroprotective, anti-amyloidogenic and neurotrophic effects of apigenin in an Alzheimer's disease mouse model. *Molecules* 18, 9949–9965. doi: 10.3390/molecules18089949

Zhou, B., Cai, Q., Xie, Y., and Sheng, Z. H. (2012). Snapin recruits dynein to BDNF-TrkB signaling endosomes for retrograde axonal transport and is essential for dendrite growth of cortical neurons. *Cell Rep.* 2, 42–51. doi: 10.1016/j.celrep.2012.06.010

Zhu, Y., and Wang, J. (2015). Wogonin increases β-amyloid clearance and inhibits tau phosphorylation via inhibition of mammalian target of rapamycin: potential drug to treat Alzheimer's disease. *Neurol. Sci.* 36, 1181–1188. doi: 10.1007/s10072-015-2070-z

Conflict of Interest: The authors declare that the research was conducted in the absence of any commercial or financial relationships that could be construed as a potential conflict of interest.

Publisher's Note: All claims expressed in this article are solely those of the authors and do not necessarily represent those of their affiliated organizations, or those of the publisher, the editors and the reviewers. Any product that may be evaluated in this article, or claim that may be made by its manufacturer, is not guaranteed or endorsed by the publisher.

Copyright © 2021 Chiang, Lin, Teng, Sun, Chang, Lin, Hsieh-Li, Su, Chen and Lee-Chen. This is an open-access article distributed under the terms of the Creative Commons Attribution License (CC BY). The use, distribution or reproduction in other forums is permitted, provided the original author(s) and the copyright owner(s) are credited and that the original publication in this journal is cited, in accordance with accepted academic practice. No use, distribution or reproduction is permitted which does not comply with these terms.

frontiers in Aging Neuroscience

ORIGINAL RESEARCH
published: 17 December 2021
doi: 10.3389/fnagi.2021.721217

Structural Covariance Network as an Endophenotype in Alzheimer's Disease-Susceptible Single-Nucleotide Polymorphisms and the Correlations With Cognitive Outcomes

*Hsin-I Chang[1†], Yu-Tzu Chang[2†], Chi-Wei Huang[1], Kuo-Lun Huang[3], Jung-Lung Hsu[3,4,5], Shih-Wei Hsu[6], Shih-Jen Tsai[7,8], Wen-Neng Chang[1], Chen-Chang Lee[6], Shu-Hua Huang[9] and Chiung-Chih Chang[1]**

[1] Department of Neurology, Cognition and Aging Center, Institute for Translational Research in Biomedicine, Kaohsiung Chang Gung Memorial Hospital, Chang Gung University College of Medicine, Kaohsiung, Taiwan, [2] Division of Nephrology, Department of Internal Medicine, National Cheng Kung University Hospital, College of Medicine, National Cheng Kung University, Tainan, Taiwan, [3] Department of Neurology, Chang Gung Memorial Hospital Linkou Medical Center and College of Medicine, Neuroscience Research Center, Chang Gung University, Taoyuan City, Taiwan, [4] Department of Neurology, New Taipei Municipal TuCheng Hospital, New Taipei City, Taiwan, [5] Graduate Institute of Mind, Brain, and Consciousness, Taipei and Brain and Consciousness Research Center, TMU Shuang Ho Hospital, Taipei Medical University, New Taipei City, Taiwan, [6] Department of Radiology, Kaohsiung Chang Gung Memorial Hospital, Chang Gung University College of Medicine, Kaohsiung, Taiwan, [7] Psychiatric Department of Taipei Veterans General Hospital, Taipei, Taiwan, [8] Psychiatric Division, School of Medicine, National Yang-Ming University, Taipei City, Taiwan, [9] Department of Nuclear Medicine, Kaohsiung Chang Gung Memorial Hospital, Chang Gung University College of Medicine, Kaohsiung, Taiwan*

The cognitive manifestations of Alzheimer's disease (AD) are related to brain network degeneration, and genetic differences may mediate network degeneration. Several AD-susceptible loci have been reported to involve amyloid or tau cascades; however, their relationships with gray matter (GM) volume and cognitive outcomes have yet to be established. We hypothesized that single-nucleotide polymorphism genotype groups may interact with apolipoprotein E4 (*ApoE4*) status or independently exert an effect on cognitive outcomes. We also hypothesized that GM structural covariance networks (SCNs) may serve as an endophenotype of the genetic effect, which, in turn, may be related to neurobehavior test scores. Gray matter SCNs were constructed in 324 patients with AD using T1 magnetic resonance imaging with independent component analysis (ICA). We assessed the effects of 15 genetic loci (rs9349407, rs3865444, rs670139, rs744373, rs3851179, rs11136000, rs3764650, rs610932, rs6887649, rs7849530, rs4866650, rs3765728, rs34011, rs6656401, and rs597668) using additive, recessive, and dominant models on cognitive outcomes. Statistical analysis was performed to explore the independent role of each locus, interactions with *ApoE4* status, and relationships to GM ICA network intensity score. For outcome measures, we used the Mini-Mental State Examination (MMSE), Cognitive Abilities Screening Instrument (CASI) total score, and short-term memory (STM) subscores, adjusted for the covariates of education, disease duration, and age. Clinically, the *CD2AP* G allele showed a protective role in MMSE, CASI total, and CASI-STM scores

OPEN ACCESS

Edited by:
Jiehui Jiang,
Shanghai University, China

Reviewed by:
Kuen-Jer Tsai,
National Cheng Kung University, Taiwan
Andrea T. Shafer,
National Institute on Aging, National Institutes of Health (NIH), United States
Woon-Man Kung,
Chinese Culture University, Taiwan

***Correspondence:**
Chiung-Chih Chang
neur099@adm.cgmh.org.tw

† These authors have contributed equally to this work

Specialty section:
This article was submitted to Alzheimer's Disease and Related Dementias, a section of the journal Frontiers in Aging Neuroscience

Received: *06 June 2021*
Accepted: *04 November 2021*
Published: *17 December 2021*

Citation:
Chang H-I, Chang Y-T, Huang C-W, Huang K-L, Hsu J-L, Hsu S-W, Tsai S-J, Chang W-N, Lee C-C, Huang S-H and Chang C-C (2021) Structural Covariance Network as an Endophenotype in Alzheimer's Disease-Susceptible Single-Nucleotide Polymorphisms and the Correlations With Cognitive Outcomes. Front. Aging Neurosci. 13:721217. doi: 10.3389/fnagi.2021.721217

independently or via interactions with non-*ApoE4* status, while the *CR1* A genotype group was associated with lower STM subscores independent of *ApoE4* status. Three loci showed synergic interactions with *ApoE4*: *BIN 1, MS4A6A,* and *FTMT*. Of the 15 meaningful ICA components, 5 SCNs (anterior and posterior hippocampus, right temporal, left thalamus, default mode network) showed relationships with general cognitive performance, in which only the *ApoE4* and *MS4A6A* genotype groups were independently related to the hippocampus network. The genetic loci *MS4A6A, BIN1, CLU, CR1, BIN1, PICALM,* and *FGF1* influenced the networks independently or in synergy. This study suggests that AD-susceptible loci may each exert clinical significance independently through interactions with *ApoE4* status or through SCNs as an endophenotype and that this effect is associated with the cognitive outcomes.

Keywords: Alzheimer's disease, single nucleotide polymorphism, independent component analysis, apolipoprotein E4, structural covariance network, network integrity score

BACKGROUND

The National Institutes on Aging-Alzheimer's Association (NIA-AA) criteria (Jack et al., 2018) incorporate diagnostic biomarkers in the definition of Alzheimer's disease (AD), and the key pathology is the presence of amyloid plaque and neurofibrillary tangles. From a genetic point of view, AD is a complex disease. For late-onset AD, the apolipoprotein E (ApoE) gene is the most significant example of a single-nucleotide polymorphism (SNP) that modifies susceptibility to AD (Singh et al., 2006). The clinical significance of *ApoE4* on brain integrity has been shown in studies of people with AD (Martins et al., 2005), those with mild cognitive impairment (Risacher et al., 2013), and the non-demented elderly (Bretsky et al., 2003; Wisdom et al., 2011). The presence of the *ApoE4* allele (Corder et al., 1993) remains the greatest risk factor for AD (Farrer et al., 1997), responsible for a 3- to 15-fold increase in risk. The synergic effect of the *ApoE4* allele with other genetic loci has been reported in previous studies (Mahley, 1988), which showed that overall pathological cascades may influence neuropsychiatric outcomes (Hall et al., 2014). Although genetic effects have been extensively studied, only a few studies have shown reproducible results. The mechanisms by which ApoE influences the pathogenesis of AD have been proposed, including a role in the clearance of amyloid (Koistinaho et al., 2004; Shi et al., 2017; Ringland et al., 2020). However, whether this is via interactions between APoE4 and amyloid- or tau-related SNPs remains to be explored.

Recent large-scale genome-wide association studies (GWASs) have revealed several SNPs other than *ApoE4* that are associated with susceptibility to AD. In a study by Lambert et al. (2013), a total of 19 GWAS loci were identified using a discovery sample of 17,008 patients with AD and 37,154 controls, followed by replication with 8,572 patients with AD and 11,312 controls. In 2019, a GWAS meta-analysis reported an additional 29 risk loci (Jansen et al., 2019). Collectively termed as AD-susceptible genes, they can only explain a small proportion of the heritability and influence of SNPs for risk prediction, and the results have been inconsistent among different ethnicities. For example, the rs11136000 polymorphism in the clusterin (*CLU*) gene has been significantly associated with AD (Zhu et al., 2018) in Caucasian and Asian populations, but not in people of African or Hispanic descent (Du et al., 2016). Genetic-gray matter (GM) interactions may be different among different ethnicities, and so the genetic effect on the cognitive outcomes may also be different. For AD, structural imaging is one of the most reliable tools to reveal correlations with cognitive measures, while links between reported genotype groups and neuroimaging biomarkers may help to understand how these SNPs modulate GM. The clinical significance of these risk loci and their interactions with brain networks may also help to understand the neurobiology of AD.

Recent research suggests that highly related regions show covariance in morphometric characteristics, the so-called structural covariance. Structural covariance networks (SCNs) have been associated with structural and functional connectivity, while genetic variations, developmental, degenerative, and disease staging have been shown to be important covariates of interest (Alexander-Bloch et al., 2013). SCNs are considered to be reproducible and heritable models that may represent disease-related or genetic-associated changes in topology (Huang et al., 2017; Chang et al., 2018a,b; Chang H. I. et al., 2019). We hypothesized that AD-susceptible genes may have greater covariance in GM and that the SCNs may serve as an endophenotype to reflect the influence of the risk gene. Using spatial independent component analysis (ICA), the structural covariance between topographically distant regions can be modeled without *a priori* knowledge (Biswal et al., 1995, 2010). In addition to fully automated spatial component maps of maximal statistical independence, a network integrity score (NIS) can be calculated for each ICA map. The NIS describes the strength of the individual expression in each network, and a higher NIS indicates a stronger individual expression of the identified network (Beckmann and Smith, 2004; Segall et al., 2012). Once an SCN pattern has been identified to distinguish one group from another, its expression can be prospectively quantified on an individual basis and correlated with the clinical or physiological measures of interest. GM SCNs modeled by ICA may help to clarify SNP-GM relationships, while the NIS can be used as a dependent variable to test the genetic interactions.

The NIA-AA criteria define AD as a disease status because higher diagnostic hierarchy is placed on the *in vivo* demonstration of neuropathological status rather than the presence of clinical symptoms. For a diagnosis of AD, the presence of amyloid and tau protein is essential (Jack et al., 2018). To understand the genetic effects of amyloid or tau on disease progression, we selected 15 amyloid- or tau-related SNPs belonging to the following genetic loci: *CD2AP* (rs9349407) (Furusawa et al., 2019), *CD33* (rs3865444) (Bradshaw et al., 2013; Chen et al., 2021), *MS4AE4* (rs670139) (Karch et al., 2012), *BIN1* (rs744373) (Martiskainen et al., 2015), *PICALM* (rs3851179) (Zhao et al., 2015), *CLU* (rs11136000) (Chibnik et al., 2011), *ABCA7* (rs3764650) (Bamji-Mirza et al., 2016; Zhao Q. F. et al., 2016; Ma et al., 2018), *MS4A6A* (rs610932) (Dos Santos et al., 2017), *FTMT* (rs6887649) (Yang et al., 2015), *SPTLC1* (rs7849530) (Geekiyanage and Chan, 2011), *Intergenic SNP* (rs4866650) (Hohman et al., 2014), p73 (rs3765728) (Wetzel et al., 2008), *FGF1* (rs34011) (Kimura et al., 1994), *CR1* (rs6656401) (Chibnik et al., 2011; Biffi et al., 2012), and *EXOC3L2* (rs597668) (Olgiati et al., 2011). In this study, we first tested whether each SNP exerted an effect on cognitive measures directly or via interactions with ApoE4. Then, we evaluated whether the genetic effects on cognitive measures were via an SCN as an endophenotype.

MATERIALS AND METHODS

This study was conducted in accordance with the Declaration of Helsinki and was approved by the Institutional Review Board of Chang Gung Memorial Hospital. The study participants were treated at the Cognition and Aging Center, Department of General Neurology, Kaohsiung Chang Gung Memorial Hospital. The multidisciplinary team was composed of behavioral neurologists, psychiatrists, neuropsychologists, neuroradiologists, and experts in nuclear medicine. We enrolled patients with AD who were diagnosed according to the International Working Group-2 criteria (Dubois et al., 2014) and further confirmed using amyloid imaging (TW-ADNI[1]) if the consensus panel did not agree on the diagnosis. All of the patients were in a stable condition under acetylcholine esterase inhibitor treatment from the time of diagnosis. The exclusion criteria were a history of clinical stroke, a negative amyloid scan, a modified Hachinski ischemic score > 4, and depression. After checking the inclusion and exclusion criteria, a total of 324 subjects (152 males and 172 females) were included and underwent imaging and genetic tests.

Clinical and Neurobehavioral Assessments

After enrollment, the demographic data of each patient were recorded. We also recorded the time of the first symptom during interviews with family members so that an estimated duration of onset could be calculated. At baseline, a trained neuropsychologist administered the neurobehavioral tests using the Mini-Mental State Examination (MMSE) and Cognitive Abilities Screening Instrument (CASI) total score as a global assessment of cognitive function. The CASI contains nine subdomains. We used attention, verbal fluency, abstract thinking, and mental manipulation subdomain scores to assess executive function (Huang et al., 2013) and orientation, short- and long-term memory, language ability, and drawing as non-executive domains. As the salient feature of AD is short-term memory (STM) impairment, we used CASI-STM subscores as the major outcome for genetic correlations.

Genotyping

Single-nucleotide polymorphism genotyping was performed using MassARRAY technology with iPLEX Gold chemistry (Agena Bioscience, San Diego, CA, United States). The PCR primers and single base extension primers were designed using Assay Design Suite version 2.0 software (Redwood City, CA, United States). The genotyping analysis was performed using an iPLEX Gold Reagent Kit according to the instructions of the manufacturer. Briefly, 1 μl of DNA sample (10 ng/μl) was added to 5 μl of PCR reaction mixture containing 0.2 units of Taq polymerase, 2.5 pmol each of the PCR primers, and 25 mM each of the dNTPs. Thermocycling was started at 94°C for 2 min followed by 45 cycles of 94°C for 30 s, 56°C for 30 s, and 72°C for 1 min, and a final extension was done at 72°C for 1 min. Unincorporated dNTPs were dephosphorylated using 0.3 U of shrimp alkaline phosphatase. Purified amplicons were then subjected to primer extension using an iPLEX Gold Reagent Kit. Primer extension was performed using a cycling program of 94°C for 30 s, followed by 40 cycles of 94°C for 5 s, and 5 cycles of 52°C for 5 s, and 80°C for 5 s within 40 cycles, followed by a final extension at 72°C for 3 min. The extended reaction products were purified using cation exchange resin and then spotted onto a 384-format SpectroCHIP II array using a MassArray Nanodispenser RS1000 (San Diego, CA, United States). Mass determination was done on a MassARRAY Compact Analyzer. The resulting spectra were processed, and alleles were called using MassARRAY Typer 4.0 with model-based cluster analysis to analyze the genotypes of the SNPs. We tested 15 SNPs (rs9349407, rs3865444, rs670139, rs744373, rs3851179, rs11136000, rs3764650, rs610932, rs6887649, rs7849530, rs4866650, rs3765728, rs34011, rs6656401, and rs597668). The risk alleles and minor allele frequencies (MAFs) are listed in **Supplementary Table 1**. The *ApoE* genotype was determined using rs7412 and rs429358. *ApoE4* carriers were defined as those with one or two E4 alleles.

Image Acquisition

Magnetic resonance images were acquired using a 3.0T magnetic resonance imaging (MRI) scanner (Excite, GE Medical Systems, Milwaukee, WI, United States). All MRI images were performed within 3 months of taking the cognitive tests. High-resolution structural images were acquired for spatial normalization using the following protocol: a T1-weighted, inversion-recovery-prepared, three-dimensional, gradient-recalled acquisition in a steady-state sequence with a repetition time/echo time/inversion time of 8,600 ms/minimal/450 ms, a 256 mm × 256 mm field of view, and a 1-mm slice sagittal thickness with a resolution of 0.5 mm × 0.5 mm × 1 mm.

[1]http://tadni.cgmh-mi.com/home

Data Analysis for Neuroimaging Biomarkers

Image preprocessing and statistical analysis were performed using SPM12 (Wellcome Trust Centre of Cognitive Neurology, University College London, United Kingdom[2]). The T1 images were reoriented, realigned, and normalized using the standard Montreal Neurological Institute space. The images were then segmented into GM and white matter. Related tissue segments were used to create a custom template using diffeomorphic anatomical registration with an exponentiated lie algebra approach, which is one of the highest ranking registration methods in patients with AD (Cuingnet et al., 2011). To correct for partial volume effects, the segmentation of tissue type was performed using partial volume estimation. During the modulation step, each voxel of the registered GM image was multiplied by the Jacobian of the warp field that defined the direction and amount of modulation. The modulated and warped GM images were then smoothed using a Gaussian kernel of 8 mm full width at half maximum.

Independent Component Analysis and Network Integrity Score

The preprocessed spatially normalized modified GM images of the patients were concatenated to form a subject series and entered into the ICA process. Spatial ICA was carried out using the Multivariate Exploratory Linear Optimized Decomposition into Independent Components software package version 3.15[3]. The resulting independent components were z-transformed and visualized using a threshold of $z > 1.96$ ($p < 0.05$). In general, the optimal number of components is related to the data size and the research questions. A lower number of components causes a loss of spatial information, while a higher number of components can result in less meaningful components. In this study, we set the number of independent components to 25. Among these 25 components, we determined 15 to be meaningful based on matching them with the published data and templates from a study investigating the social brain across childhood and adolescence (McCormick et al., 2018) and the BrainMap 70-component ICA template[4].

Statistical Analysis

We first tested whether each SNP exerted an effect on cognitive measures directly or via interactions (or synergistically) with *ApoE4*. Next, to evaluate whether the genetic effects on cognitive measures were via the SCN as an endophenotype, we explored the SCN-cognitive and SCN-SNP relationships. The SCN-cognitive relationships were explored using a linear regression model with the cognitive scores as the dependent variable and the NIS of each SCN as the independent variable, adjusted for age, education, and disease duration. Finally, we modeled how the 15 SNPs and *ApoE4* status may affect the GM SCN (and SCN-SNP relationship) using a multivariate linear model.

Clinical data were expressed as mean ± standard deviation. The Student's t-test was used to compare continuous variables, and the chi-square test was used to compare categorical variables. To examine the genotype effects on cognitive outcome measures, we used additive, dominant, and recessive models (Zhao F. et al., 2016). The dichotomization of the SNP genotype into different genetic models was based on the risk allele. Based on the classification, the additive model compared three groups: risk homozygotes, risk heterozygotes, and non-risk homozygotes. For the dominant model, the genotype group was dichotomized into risk (homozygote and heterozygotes) and non-risk groups. For the recessive group, the risk homozygotes were considered to be one group and compared with the risk heterozygotes and non-risk homozygotes. For each SNP, the risk allele is listed in **Supplementary Table 1** according to a literature review of the Chinese-Han population, and binary group stratification was based on the Hardy-Weinberg equation for equilibrium. Using the MMSE, CASI total score, or STM subscore as dependent variables, we also explored the interactions between the susceptible SNPs and ApoE4 status (ApoE4 carriers and non-E4 carriers) using a linear regression model, with education, age, and duration of disease as covariates. All statistical analyses were conducted using SPSS software (SPSS version 22 for Windows®, SPSS Inc., Chicago, IL, United States). Statistical significance was set at $p < 0.05$.

For each component, the intensity was calculated and recorded as NIS, which was then Z-transformed in the regression model. Differences in the ICA NIS of each SNP were calculated using the Student's t-test based on the predefined groups in **Supplementary Table 1**. To understand the clinical significance of each SCN, we used a linear regression model to explore the relationships between outcome measures (MMSE, CASI total score, and executive and non-executive domains) and NIS with education, age, and duration of disease as covariates. In addition, to understand the clinical significance of the identified SCN in the CASI subscores, we also calculated partial correlations between the extracted SCN NIS and the cognitive scores by setting the significance value at $p < 0.05$ and the covariates as age, educational level, and disease duration (years).

Finally, multivariate linear regression analysis was performed to assess the SCN-SNP relationships. Fifteen models were run (one for each SCN NIS), and each model consisted of the following variables: age, sex, the 15 SNPs, and *APOE* E4 status. For the SNPs that showed significance on NIS, we tested the interactions with ApoE4 status. The NIS served as the dependent variable, with the significant SNP, ApoE4, and interaction (SNP*ApoE4) as independent variables. All independent variables were entered in one block and the significance value was set at $p < 0.05$.

RESULTS

Demographic Data of the Patients With Alzheimer's Disease

The demographic data and cognitive test scores are shown in **Table 1**. All of the enrolled patients had early-stage AD, as the mean duration of disease was 0.9 ± 1.12 years. Among the

[2]http://www.fil.ion.ucl.ac.uk/spm/

[3]http://fsl.fmrib.ox.ac.uk/fsl/fslwiki/MELODIC

[4]https://brainmap.org/icns/

TABLE 1 | Demographic data of the 324 patients with Alzheimer's disease.

	Case numbers or scores
Male/Female	152/172
Education (year)	7.8 ± 5.09
Duration of disease (year)	0.9 ± 1.12
ApoE4 carriers (%)	114 (35.19%)
Age (years)	71.6 ± 8.8
Mini-mental state examination	21.1 ± 2.8
Cognition Ability Screening Instrument	
Total score (100)	68.6 ± 24.7
Executive function test (40)	25.5 ± 9.6
Attention (8)	6.3 ± 1.63
Verbal fluency (10)	5.4 ± 3.08
Abstract thinking (12)	8.1 ± 3.12
Mental manipulation (10)	5.7 ± 3.50
Non-executive domains (60)	43.2 ± 15.83
Orientation (18)	13.0 ± 5.71
Short- term memory (12)	6.1 ± 4.11
Long-term memory (10)	8.3 ± 2.42
Language ability (10)	8.1 ± 2.42
Drawing (10)	7.7 ± 2.99

Data presented as mean ± standard deviation. Numbers in parentheses indicate maximal score.

enrolled patients, 114 were E4 carriers (E4 homozygote $n = 14$). The risk alleles *CD2AP, ABCA7, FTMT, SPTLC1, FGF1, CR1,* and *EXOC3L2* were found to be minor alleles (**Supplementary Table 1**). Of note, the MAFs of *FTMT* and *CR1* were extremely low.

For cognitive outcomes (MMSE, CASI total scores, and STM subscores), gender had no effect when controlling for educational level. For those with an educational level ≤ 6 years (elementary school), 7–12 years (high school), and >12 years, none of the comparisons of test scores between the male and female patients were significant. There were age effects on MMSE ($r = -0.23$, $p < 0.0001$), CASI total ($r = -0.259$, $p < 0.0001$), and STM subscores ($r = -0.271$, $p < 0.0001$). The educational effects on MMSE ($r = 0.432$, $p < 0.0001$), CASI total ($r = 0.433$, $p < 0.0001$), and STM subscores ($r = 0.372$, $p < 0.0001$) were also significant.

CD2AP and *CR1* on Cognitive Test Scores

The results of the additive model, dominant model, and recessive model of each SNP on MMSE and CASI are shown in **Tables 2**, **3**. The *CD2AP* G allele was associated with MMSE total score (**Table 2**) or CASI total score (**Table 3**) in the additive or dominant model, and the G allele was associated with higher scores. The *CD2AP* G allele (in the additive or dominant model) was also associated with a higher STM subscore (**Table 4**). The association between the *CD2AP* G allele and cognitive scores showed interactions with the non-*ApoE4* genotype in MMSE (**Table 2**), CASI total score (**Table 3**), and STM subscore (**Table 4**). In the recessive model, the *CR1* A allele was associated with a lower STM subscore (**Table 4**), while the risk of a detrimental effect was independent of *ApoE4* status. Of note, the MAF of the A allele in *CR1* was 0.029.

Effect of Interactions With the *ApoE4* Gene on Short-Term Memory Scores

Short-term memory is the salient feature in AD, and we found three additional SNPs that showed interactions with the *ApoE4* gene: *BIN 1, MS4A6A,* and *FTMT* (**Table 4** and **Supplementary Figure 1**). The E4 allele was related to lower scores in the *BIN 1, FTMT,* and *MS4A6A* alleles. The MAF of the G allele in *FTMT* was 0.082.

Network Spatial Topography and Cognitive Significance Validation

A total of 15 ICA components were constructed and considered to be meaningful networks (**Figure 1**). The MMSE and CASI total scores were considered to indicate general cognitive performance, and their relationships with significant NIS are shown in **Figure 2**. Among the significant networks, the anterior and posterior hippocampus, right temporal, left thalamus, and default mode network were the most important for general cognitive performance. We then used NIS as the dependent variable to explore its relationships with STM, executive domains, and non-executive domains, adjusted for age and educational level. The standardized beta coefficients (95% confidence intervals) and exact *p*-values are reported in **Table 5**. For STM, executive domains, and non-executive domains, the aforementioned five networks (**Figure 2**) showed statistical significance, while the dorsal attentional network also showed statistical significance. Finally, we examined the relationships between CASI subdomains and NIS (**Supplementary Table 2**). The results suggested that the NIS of the anterior and posterior hippocampus, right temporal, right thalamus, lateral cerebellum, and medial cerebellum (all $p < 0.0001$) were consistently related to the cognitive test scores adjusted for age and years of education.

Structural Covariance Networks–Single-Nucleotide Polymorphism Relationships

Using the binary classifications as described in **Supplementary Table 1**, seven SNPs were found to have an independent effect on NIS (**Figure 3**). To avoid possible false positives based on the 16×15 SCN-SNP matrix and a *p*-value of 0.05, we further explored the SCN-SNP relationships (**Table 6**) using a multivariate linear model. The NIS served as the dependent variable, and the independent variables included ApoE4 status, rs9349407, rs3865444, rs670139, rs744373, rs3851179, rs11136000, rs3764650, rs610932, rs6887649, rs7849530, rs4866650, rs3765728, rs34011, rs6656401, and rs597668, adjusted for age and sex. Among the tested 16 genetic loci, the significance of the 7 SNPs (*ApoE4, MS4A6A, BIN1, CLU, CR1, PICALM,* and *FGF1*) showed independent or collinear relationships with the SCNs. The predictive roles of *CLU* and *CR1* on supplementary motor cortex SCNs were independent, and no interactions with ApoE4 were found.

TABLE 2 | General linear model for single nucleotide polymorphisms on mini-mental score examination*.

Gene	Additive model				Dominant model			Recessive model			Interaction with APOE		
	Group	β	*SE*	*p*	β	*SE*	*p*	β	*SE*	*p*	Chi-square	*p*	effects
CD2AP	GG compares to CC (1/3)	9.180	3.8140	0.016	8.968	3.8115	0.019	–1.025	0.8284	0.216	8.065	0.026	Non-E4
rs9349407	CG compares to CC(2/3)	8.437	3.8528	0.029									
CD33	CC compares to AA (1/3)	1.810	2.0389	0.375	2.191	2.0287	0.280	0.875	0.7900	0.268	3.016	0.389	–
rs 3865444	CA compares to AA(2/3)	2.992	2.0962	0.153									
MS4AE4	GG compares to TT (1/3)	0.824	1.1392	0.470	1.054	1.0311	0.307	0.097	0.7921	0.903	3.252	0.354	–
s670139	GT compares to TT (2/3)	1.221	1.0883	0.262									
BIN1	AA compares to GG (1/3)	–0.399	1.2194	0.744	–0.043	1.1009	0.969	0.272	0.7868	0.729	2.559	0.465	–
rs744373	AG compares to GG(2/3)	0.055	1.1708	0.963									
PICALM	CC compares to TT (1/3)	–1.379	1.1078	0.213	–1.294	1.0134	0.202	0.485	0.7764	0.532	2.523	0.471	–
rs3851179	CT compares to TT (2/3)	–1.222	1.0822	0.259									
CLU	CC compares to TT (1/3)	–0.803	1.8222	0.660	–0.310	1.8107	0.864	1.373	0.7766	0.077	3.730	0.292	–
rs11136000	TC compares to TT (2/3)	0.650	1.8792	0.729									
ABCA7	TT compares to GG (1/3)	–0.371	1.1807	0.753	0.108	1.1082	0.922	0.808	0.7645	0.291	6.46	0.091	–
rs3764650	TG compares to GG(2/3)	0.570	1.1754	0.628									
MS4A6A	GG compares to TT (1/3)	–0.270	1.1356	0.806	0.461	1.0307	0.655	1.025	0.7877	0.193	5.518	0.138	–
rs610932	TG compares to TT (2/3)	0.986	1.0831	0.362									
FTMT	AA compares to GG (1/3)	–4.819	6.6353	0.468	–4.801	6.6335	0.469	0.206	1.0325	0.842	1.974	0.160	–
rs6887649	AG compares to GG(2/3)	–4.708	6.6912	0.482									
SPTLC1	AA compares to GG (1/3)	1.647	3.3356	0.622	1.465	3.3362	0.661	–1.030	0.9562	0.28	7.282	0.053	–
rs7849530	AG compares to GG(2/3)	0.661	3.4251	0.847									
Intergenic SNP	AA compares to CC (1/3)	–1.747	2.1482	0.416	–1.742	2.1286	0.670	0.161	0.7768	0.836	5.89	0.117	–
rs4866650	AC compares to CC(2/3)	–1.723	2.1886	0.428									
P73	GG compares to AA (1/3)	0.436	1.1243	0.698	0.456	0.7792	0.559	–0.201	1.0410	0.847	2.549	0.467	–
rs3765728	GA compares to AA(2/3)	0.463	0.8381	0.581									
FGF1	GG compares to AA (1/3)	–0.625	1.2399	0.671	–0.263	1.1872	0.825	0.576	0.7573	0.447	4.296	0.231	–
rs34011	GA compares to AA(2/3)	0.064	1.2681	0.960									
CR1	AA compares to GG (1/3)	–5.326	6.6206	0.421	5.231	6.6324	0.430	–2.032	1.6498	0.218	4.020	0.259	–
rs6656401	GA compares to GG(2/3)	–1.826	1.6971	0.282									
EXOC3L2	TT compares to CC (1/3)	0.138	1.1541	0.905	0.329	1.0693	0.758	0.239	0.7718	0.757	7.673	0.045	Non-E4
rs597668	TC compares to CC(2/3)	0.499	1.1362	0.661									

**Adjusted for education, disease duration and age.*
SE, standard error.

DISCUSSION

Major Findings

In this study, we tested the effects of amyloid- or tau-related genotypes on cognitive measurements and evaluated whether the genetic effects on cognitive measures were via SCNs as an endophenotype. We found that three different mechanisms modulated the relationships among AD-susceptible loci, GM network, and cognitive measures. First, an independent role of the genetic effect on cognitive test scores was found, as the *CD2AP* and *CR1* genotypes were directly related to CASI and MMSE scores. Second, the effects of amyloid- or tau-related genotypes on cognitive measures interacted or had a synergic effect with *ApoE4* status. Finally, we identified several SCNs that may serve as endophenotypes of AD-susceptible loci in predicting cognitive outcomes. The SCNs showing clinical significance with cognitive scores included the hippocampal, temporal, thalamus, default mode network, and dorsal attention network. In multivariate regression, seven genotype groups were found to either exert an independent effect or synergistic effect on these SCNs. As the SCNs were associated with different cognitive domains, the identification of genotype-SCN relationships may help to understand the neurobiology of SNPs on the cognitive features in AD.

Dominant Model Suggested Protection of the *CD2AP* rs9349407 G Allele in Non-E4 Carriers

The role of rs9349407 as a risk SNP in Han Chinese populations has been reported (Xiao et al., 2015); however, the findings have been inconsistent (Jiao et al., 2015). One meta-analysis suggested that rs9349407 C is a risk allele for susceptibility to AD in East Asian, American, Canadian, and European populations (Chen et al., 2015). In our additive and dominant models, patients with AD with the rs9349407 G allele had higher CASI total and STM subscores, especially the non-E4 carriers. The minor allele C of rs9349407 has been associated with neuritic plaque burden,

TABLE 3 | General linear model for single nucleotide polymorphisms on cognitive ability screening instrument total scores*.

Gene	Additive model				Dominant model			Recessive model			Interaction with APOE		
	Group	β	*SE*	*p*	β	*SE*	*p*	β	*SE*	*p*	Chi-square	*p*	effects
CD2AP	GG compares to CC (1/3)	44.091	14.17	0.002	43.245	14.165	0.002	–4.337	3.0951	0.161	5.989	<0.05	Non-E4
rs9349407	CG compares to CC(2/3)	41.125	14.32	0.004									
CD33	CC compares to AA (1/3)	0.406	7.658	0.958	1.048	7.5987	0.890	1.746	2.9576	0.555	2.489	0.477	–
rs 3865444	CA compares to AA(2/3)	2.398	7.8728	0.761									
MS4AE4	GG compares to TT (1/3)	2.26	4.2595	0.596	4.152	3.8605	0.282	1.896	2.9644	0.522	6.002	0.112	–
s670139	GT compares to TT (2/3)	5.514	4.0691	0.175									
BIN1	AA compares to GG (1/3)	0.089	4.4880	0.984	1.080	4.1155	0.793	1.32	2.941	0.654	3.612	0.306	–
rs744373	AG compares to GG(2/3)	1.791	4.3096	0.678									
PICALM	CC compares to TT (1/3)	–3.254	4.1484	0.433	–2.431	3.7963	0.522	1.986	2.9024	0.494	3.117	0.374	–
rs3851179	CT compares to TT (2/3)	–1.733	4.0528	0.669									
CLU	CC compares to TT (1/3)	0.490	6.8294	0.943	1.801	6.7691	0.790	3.333	2.9119	0.252	2.972	0.396	–
rs11136000	TC compares to TT (2/3)	4.358	7.0434	0.536									
ABCA7	TT compares to GG (1/3)	0.127	4.4213	0.977	1.915	4.1498	0.644	2.657	2.8650	0.354	3.034	0.386	–
rs3764650	TG compares to GG(2/3)	3.636	4.4014	0.409									
MS4A6A	GG compares to TT (1/3)	–1.407	4.2567	0.741	0.329	3.8545	0.932	2.588	2.9492	0.380	4.623	0.202	–
rs610932	TG compares to TT (2/3)	1.562	4.0599	0.7									
FTMT	AA compares to GG (1/3)	26.705	24.7683	0.281	26.328	24.7763	0.288	2.905	3.8570	0.451	2.337	0.126	–
rs6887649	AG compares to GG(2/3)	24.296	24.9768	0.331									
SPTLC1	AA compares to GG (1/3)	11.770	12.4733	0.345	11.596	12.4562	0.352	1.663	3.5659	0.641	2.738	0.434	–
rs7849530	AG compares to GG(2/3)	10.829	12.8078	0.398									
Intergenic SNP	AA compares to CC (1/3)	–4.298	8.0343	0.593	–4.654	7.9625	0.559	–0.533	2.9044	0.854	3.990	0.263	–
rs4866650	AC compares to CC(2/3)	–5.279	8.1853	0.519									
P73	GG compares to AA (1/3)	–0.260	4.2196	0.951	1.091	2.9254	0.709	1.076	3.9070	0.783	3.319	0.345	–
rs3765728	GA compares to AA(2/3)	1.606	3.1456	0.610									
FGF1	GG compares to AA (1/3)	–6.776	4.5323	0.144	–5.592	4.4370	0.208	3.584	2.8329	0.206	5.267	0.153	–
rs34011	GA compares to AA(2/3)	–4.123	4.7375	0.384									
CR1	AA compares to GG (1/3)	34.971	24.7119	0.157	34.67	24.7429	0.161	–7.488	6.1687	0.225	3.999	0.135	–
rs6656401	GA compares to GG(2/3)	–5.771	6.3347	0.362									
EXOC3L2	TT compares to CC (1/3)	–2.806	4.3082	0.515	–4.447	3.9970	0.266	–1.65	2.8892	0.568	2.783	0.426	–
rs597668	TC compares to CC(2/3)	–5.899	4.2413	0.164									

**Adjusted for education, disease duration and age.*
SE, standard error.

which may explain why non-E4 carriers with the G allele may have higher cognitive test scores (Shulman et al., 2013).

In this study, we only enrolled patients with clinical AD, and we tested whether risk SNP alleles or protective SNP alleles affected cognitive test scores or SCNs. Although not all of our patients with AD received amyloid scans, our exclusion criteria reduced the possibility of non-AD pathologies. Rs9349407 is a polymorphism in the *CD2AP* gene that translates the scaffolding molecule for signal transduction. Loss of function of *CD2AP* has been linked to enhanced Aβ production, tau-induced neurotoxicity, abnormal neurite structure modulation, and reduced blood-brain barrier integrity, which has been implicated in AD pathogenesis (Dubey et al., 2018; Ramos de Matos et al., 2018).

CR1 rs6656401 A Allele on Cognitive Outcomes

CR1 is an AD susceptibility locus that also influences AD-related traits on neuritic plaque deposition and episodic memory decline. As STM is the salient feature in AD, it was used in this study as a dependent variable in the SNP genetic model analysis. We identified the independent role of the rs6656401 A allele on lower STM subscores, consistent with a previous meta-analysis of greater risk with the minor allele A in AD (Shen et al., 2015). A coding variant in the long homologous repeat D region of the *CR1* gene, rs4844609 (Ser1610Thr), has been associated with episodic memory decline and been shown to account for the known effect of SNP rs6656401 (Keenan et al., 2012). *CR1* risk allele A was a minor allele with a low MAF in this study, and the relationship with lower STM may be due to the small number of patients with the A allele. However, three studies have confirmed the association between AD susceptibility and the rs6656401 A allele in Chinese patients (Zhang et al., 2010; Chen et al., 2012; Jin et al., 2012), although another study showed no association (Li et al., 2011). Rs6656401 is in the *CR1* gene, and complement system activation in the clearance of amyloid has been proposed to be a possible mechanism of the risk associated with rs6656401 (Zhang et al., 2010). Although the independent role of rs6656401

TABLE 4 | General linear model for single nucleotide polymorphisms on cognitive ability screening instrument short-term memory score*.

Gene	Additive model				Dominant model			Recessive Model			Interaction with APOE		
	Group	β	*SE*	*p*	β	*SE*	*p*	β	*SE*	*p*	Chi-square	*p*	Effects
CD2AP	GG compares to CC (1/3)	5.596	2.3663	0.018	5.418	2.3673	0.022	–0.790	0.5135	0.124	7.950	0.019	Non-E4
rs9349407	CG compares to CC(2/3)	4.971	2.3903	0.038									
CD33	CC compares to AA (1/3)	1.086	1.2685	0.392	1.225	1.2594	0.331	0.277	0.4910	0.573	5.597	0.133	–
rs 3865444	CA compares to AA(2/3)	1.518	1.3042	0.244									
MS4AE4	GG compares to TT (1/3)	0.506	0.7078	0.475	0.675	0.6407	0.292	0.095	0.4923	0.847	6.163	0.104	–
s670139	GT compares to TT (2/3)	0.797	0.6762	0.239									
BIN1	AA compares to GG (1/3)	0.488	0.7432	0.511	0.238	0.6819	0.727	–0.442	0.4869	0.364	7.7977	0.046	E4
rs744373	AG compares to GG(2/3)	0.059	0.7136	0.934									
PICALM	CC compares to TT (1/3)	0.035	0.6895	0.960	0.087	0.6308	0.890	0.061	0.4823	0.899	6.756	0.080	–
rs3851179	CT compares to TT (2/3)	0.132	0.6736	0.845									
CLU	CC compares to TT (1/3)	0.024	1.1313	0.983	0.268	1.1236	0.811	0.758	0.4824	0.116	6.739	0.081	–
rs11136000	TC compares to TT (2/3)	0.837	1.1667	0.473									
ABCA7	TT compares to GG (1/3)	1.112	0.7320	0.129	1.159	0.6856	0.091	–0.190	0.4760	0.690	6.606	0.086	–
rs3764650	TG compares to GG(2/3)	1.204	0.7287	0.098									
MS4A6A	GG compares to TT (1/3)	0.509	0.7056	0.470	–0.117	0.6389	0.855	0.632	0.4888	0.196	8.070	0.045	Non-E4
rs610932	TG compares to TT (2/3)	0.162	0.6730	0.809									
FTMT	AA compares to GG (1/3)	5.961	4.1087	0.147	–5.954	4.1075	0.147	0.161	0.6410	0.802	4.598	0.032	E4
rs6887649	AG compares to GG(2/3)	5.921	4.1433	0.153									
SPTLC1	AA compares to GG (1/3)	1.145	2.0743	0.581	1.198	2.0720	0.563	0.188	0.5928	0.751	6.861	0.076	–
rs7849530	AG compares to GG(2/3)	1.429	2.1299	0.502									
Intergenic SNP	AA compares to CC (1/3)	0.597	1.3297	0.653	–0.853	1.3220	0.519	–0.594	–0.4811	0.217	5.203	0.158	–
rs4866650	AC compares to CC(2/3)	1.302	1.3547	0.337									
P73	GG compares to AA (1/3)	0.545	0.7934	0.438	–0.424	0.4876	0.385	0.353	0.6516	0.588	6.753	0.080	–
rs3765728	GA compares to AA(2/3)	0.378	0.5244	0.471									
FGF1	GG compares to AA (1/3)	0.372	0.7702	0.629	–0.299	0.7369	0.685	0.212	0.4705	0.653	4.551	0.208	–
rs34011	GA compares to AA(2/3)	0.208	0.7877	0.792									
CR1	AA compares to GG (1/3)	5.587	4.0857	0.171	5.483	4.1096	0.182	–2.217	1.0189	0.030	4.670	0.198	–
rs6656401	GA compares to GG(2/3)	2.006	1.0473	0.055									
EXOC3L2	TT compares to CC (1/3)	0.131	0.7166	0.855	–0.115	0.6647	0.862	–0.382	0.4793	0.425	7.655	0.054	–
rs597668	TC compares to CC(2/3)	0.333	0.7055	0.637									

**Adjusted for education, disease duration, and age.*
SE, standard error.

minor allele on lower STM was confirmed in this study, it is worth noting that the A allele was a minor allele and the MAF was only 0.029. Therefore, the findings related to *CR1* in this study should be interpreted with caution.

To understand the effect, we also evaluated SCN intensity and explored whether the relationships between the rs6656401 A allele and cognitive test results may have been modulated by SCNs. As shown in our regression model, the dorsal attention SCN intensity and supplementary motor cortex SCN were significantly different between the risk and protective alleles, and the network intensity was also related to the executive and non-executive domains. Therefore, we suggest that the dorsal attention network is the endophenotype of the link between rs6656401 and cognitive outcomes.

Structural Covariance Networks as an Endophenotype Between Risk Single-Nucleotide Polymorphism and Cognitive Test Scores

Based on the relationships between SCN and cognitive test scores, we identified several significant networks that predicted general or isolated cognitive function in the patients (**Table 5**, **Figure 2**, and **Supplementary Table 2**). For these significant networks, we identified independent or synergic effects in seven genotype groups that predicted the network integrity. As the clinical significance of SCNs was established in regression analysis with different cognitive domains, SCNs may have served as the endophenotype between the risk SNP group and cognitive test scores.

ApoE4 Modulated Anterior Hippocampal, Precentral Gyrus, Supplementary Motor Cortex and Determined the Salient Features of Alzheimer's Disease

By definition, SCNs are based on the similarity of the same microstructural variations and thus may be influenced by factors influencing underlying structures such as the expression of common genetic traits during development. The independent role of *ApoE4* on the anterior hippocampus and precentral and supplementary motor cortex SCN was established in this study. As the hippocampal SCN intensity scores were also correlated with STM subscores in our patients with AD, this finding supports the role of *ApoE4* in linking salient cognitive and biosignature features in AD.

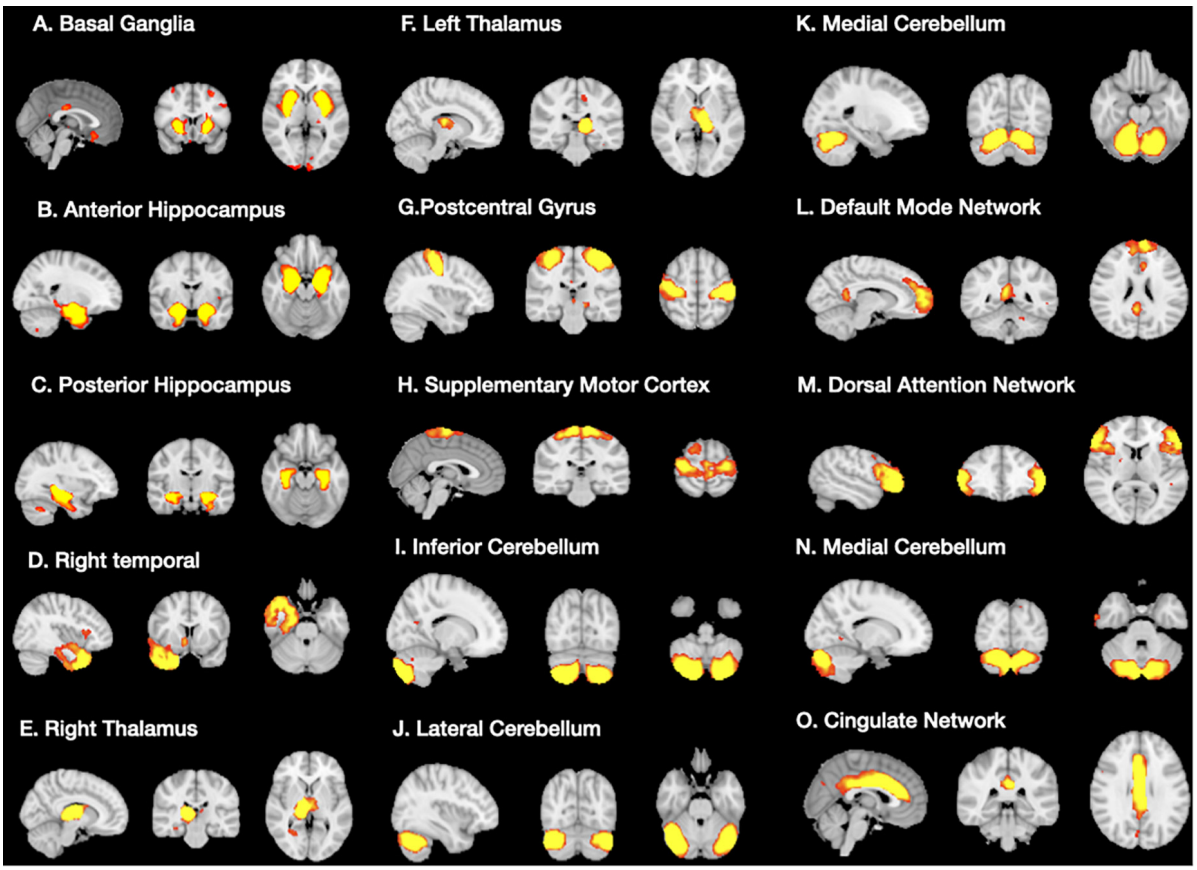

FIGURE 1 | Significant structural covariance network **(A–O)** showing group differences in signal intensities using independent component analysis.

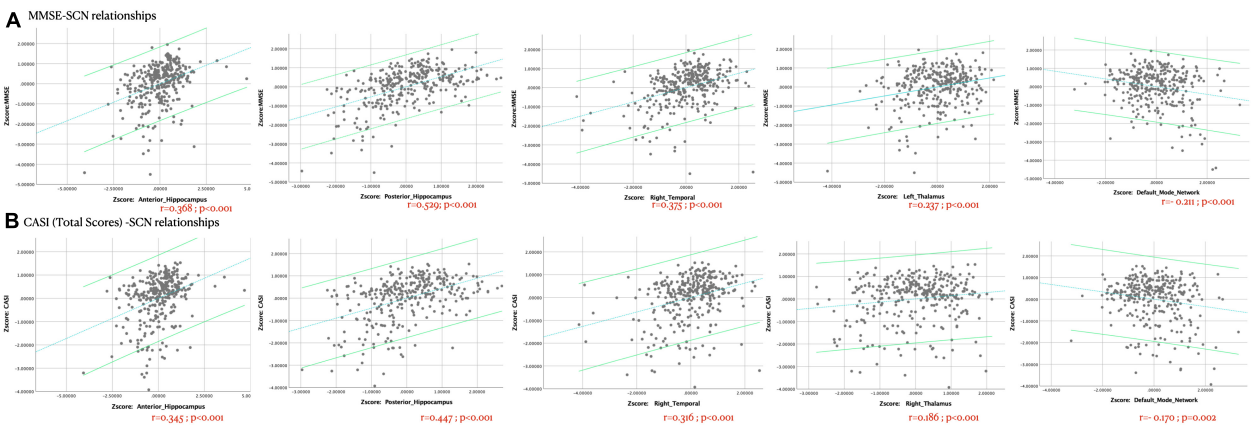

FIGURE 2 | The *Z*-transformed cognitive **(A)** Mini-Mental State Examination [MMSE] or **(B)** Cognitive Ability Screening Instrument [CASI]-structural covariance network relationships, adjusted for age, years of education, and disease duration (years). Dots represent each participant in this study, and the linear relationships and 95% confidence intervals of individuals are shown. *r* = partial correlation coefficient. The exact *p*-values are shown.

An important finding in this study is the relationship between *ApoE4* and the anterior hippocampal area. Traditional cytoarchitectonic distribution of the hippocampus (Frederickson et al., 1983) is a convoluted GM structure encompassing three architectonically distinct regions: the fascia dentata, the CA region (which can be subdivided into CA1–CA4 fields), and the subicular complex. In this study, two hippocampus SCNs in ICA (anterior vs. posterior hippocampus) showed *ApoE4* genotype group differences. The SCN of the hippocampal axis associated with *ApoE4* showing the anterior-posterior axis is

TABLE 5 | Linear regression model between network intensity score analysis and cognitive test scores (Z transformed).

Area		Unstandardized beta; 95% Confidence Interval (*p*-value)		
Index on Figure 1	**Network main structure**	**Short term memory score**	**Non-executive score**	**Executive score**
A	Basal ganglia	–0.312; –0.749 ~0.116 ($p = 0.153$)	–0.343; –1.984 ~1.297 ($p = 0.681$)	–0.533; –1.5 ~0.433 ($p = 0.278$)
B	Anterior hippocampus	1.518; 1.102~1.934 ($p < 0.001$)	6.064; 4.486~7.642 ($p < 0.001$)	2.118; 1.134~3.102 ($p < 0.001$)
C	Posterior hippocampus	2.125; 1.717~2.533 ($p < 0.001$)	7.691; 6.105~9.278 ($p < 0.001$)	3.415; 2.422~4.407 ($p < 0.001$)
D	Right temporal	1.292; 0.872 ~1.712 ($p < 0.001$)	5.045; 3.444 ~6.646 ($p < 0.001$)	2.384; 1.419~3.350 ($p < 0.001$)
E	Right thalamus	0.411; –0.022~0.844 ($p = 0.063$)	2.037; –0.388~3.685 ($p = 0.016$)	1.219; 0.246~2.191 ($p = 0.014$)
F	Left thalamus	0.591; 0.164~1.017 ($p = 0.007$)	2.354; 0.724~3.984 ($p = 0.005$)	1.525; 0.566~2.484 ($p = 0.002$)
G	Postcentral gyrus	–0.477; –0.896~–0.058 ($p = 0.026$)	–1.447; –3.054~–0.151 ($p = 0.078$)	–0.409; –1.361~0.543 ($p = 0.398$)
H	Supplementary motor cortex	–0.439; –0.860~–0.019 ($p = 0.041$)	–1.130; –2.743~0.484 ($p = 0.169$)	–0.685; –1.637~0.267 ($p = 0.158$)
I	Inferior cerebellum	–0.442; –0.859~–0.026 ($p = 0.037$)	–1.917; –3.505~–0.329 ($p = 0.018$)	–0.729; –1.671~0.214 ($p = 0.129$)
J	Lateral cerebellum	–0.181; –0.613~0.251 ($p = 0.410$)	–0.752; –2.404~0.9 ($p = 0.371$)	–0.034; –1.010~0.942 ($p = 0.945$)
K	Medial cerebellum	–0.426; –0.853~0.001 ($p = 0.05$)	–2.595; –4.212~–0.977 ($p = 0.002$)	–1.262; –2.221~–0.303 ($p = 0.01$)
L	Default mode network	0.668; 0.253~1.083 ($p = 0.002$)	1.263; 0.296~2.177 ($p = 0.01$)	2.582; 1.001~4.170 ($p = 0.001$)
M	Dorsal attention network	0.682; 0.273~1.092 ($p = 0.001$)	3.119; 1.566~4.672 ($p = 0.001$)	1.956; 1.042~2.869 ($p = 0.001$)
N	Medial cerebellum	–0.073; –0.493 ~0.346 ($p = 0.731$)	–0.472; –2.075~1.132 ($p = 0.563$)	–0.635; –1.579~0.31 ($p = 0.187$)
O	Cingulate network	–0.085; –0.333~0.504 ($p = 0.688$)	0.567; –1.033~2.168 ($p = 0.486$)	–0.398; –0.546~1.3343 ($p = 0.407$)

consistent with task-related activities or connectivity patterns (Colombo et al., 1998; Przeździk et al., 2019). A similar anterior-posterior organization has recently been reported, suggesting that the gene expression is linked to the distinct molecular gradient in the hippocampus (Vogel et al., 2020). Among the 15 preselected SNPs and *ApoE4*, *ApoE4* had an independent role on the anterior hippocampal axis, in contrast to *MS4A6A* on the posterior axis. The association with cognitive test scores in hippocampal SCN intensity scores and the interactions between the hippocampus and cortical/subcortical structures demonstrate its close integration within large-scale degenerative systems.

MS4A6A Modulated Posterior Hippocampus, Right Thalamus, and Dorsal Attention Networks

A previous study reported interactions between *MS4A* and *CLU* (Lambert et al., 2013) or *CD33* on conferring the risk of AD. Meanwhile, common variants of *MS4A6A* (rs610932), *MS4A4E* (rs670139), *CD33* (rs3865444), *CD2AP* (rs9349407), *CLU*, and *PICALM* have been associated with memory decline (Hollingworth et al., 2011; Naj et al., 2011; Karch et al., 2012). These reports emphasize the risk and role of *MS4A6A* in disease progression, while our results emphasize the role of *MS4A6A* (rs610932) and posterior hippocampus in the clinical features of AD. Similar to a report with a smaller AD cohort (Chang Y. T. et al., 2019), the dissociation of the hippocampus (anterior or posterior) emphasizes the interplay of genetic loci on anatomy.

BIN1 and *CLU* Modulated Default Mode Network Structural Covariance Networks

The most commonly affected brain region in AD studies is the default mode network, and the deposition of amyloid or tau protein is localized in this network (Hansson et al., 2017; Jones et al., 2017). The default mode network is regarded to be an early neuroimaging biosignature (Chang et al., 2015), and a recent report suggested that the default mode network may be comprised of multiple, spatially dissociated but interactive components (Andrews-Hanna et al., 2010), of which two subsystems are of particular interest. Our SCN results of associations with *BIN1* and *CLU* are consistent with cores in the posterior cingulate cortex and anterior medial prefrontal cortex, which is known as the "dorsal medial prefrontal cortex subsystem" (or midline core subsystem). The genetic locus rs744373 near *BIN1* (OR = 1.13; 95% CI, 1.06–1.21 per copy of the minor allele; $p = 1.59 \times 10^{-11}$) has been related to AD, with the possible mechanism involving tau-related cascade (Franzmeier et al., 2019). *BIN1* also modulated the inferior cerebellum and left thalamus and could predict cognitive scores in this study.

Limitations and Methodological Considerations

This study has several limitations. First, we enrolled subjects with early-stage AD, and we did not include a control group or subjects with late-stage AD. As the SNPs were preselected from GWAS results showing significance in AD susceptibility, the inclusion of a control group may have helped to elucidate whether these SNPs exerted similar GM modulation patterns in healthy elderly subjects as in those with AD. However, as these SNPs each exert different functional activities on the pathogenetic mechanisms in AD, the use of a pure AD population may help to maximize the effect of each SNP on regional GM networks. As a structural covariance matrix is defined by estimating the interregional correlations of cortical volumes between all possible pairs of regions defined by anatomy, SCN construction relies on both the spatial patterns of morphometric and signal similarities. Given the differences in brain morphometry in

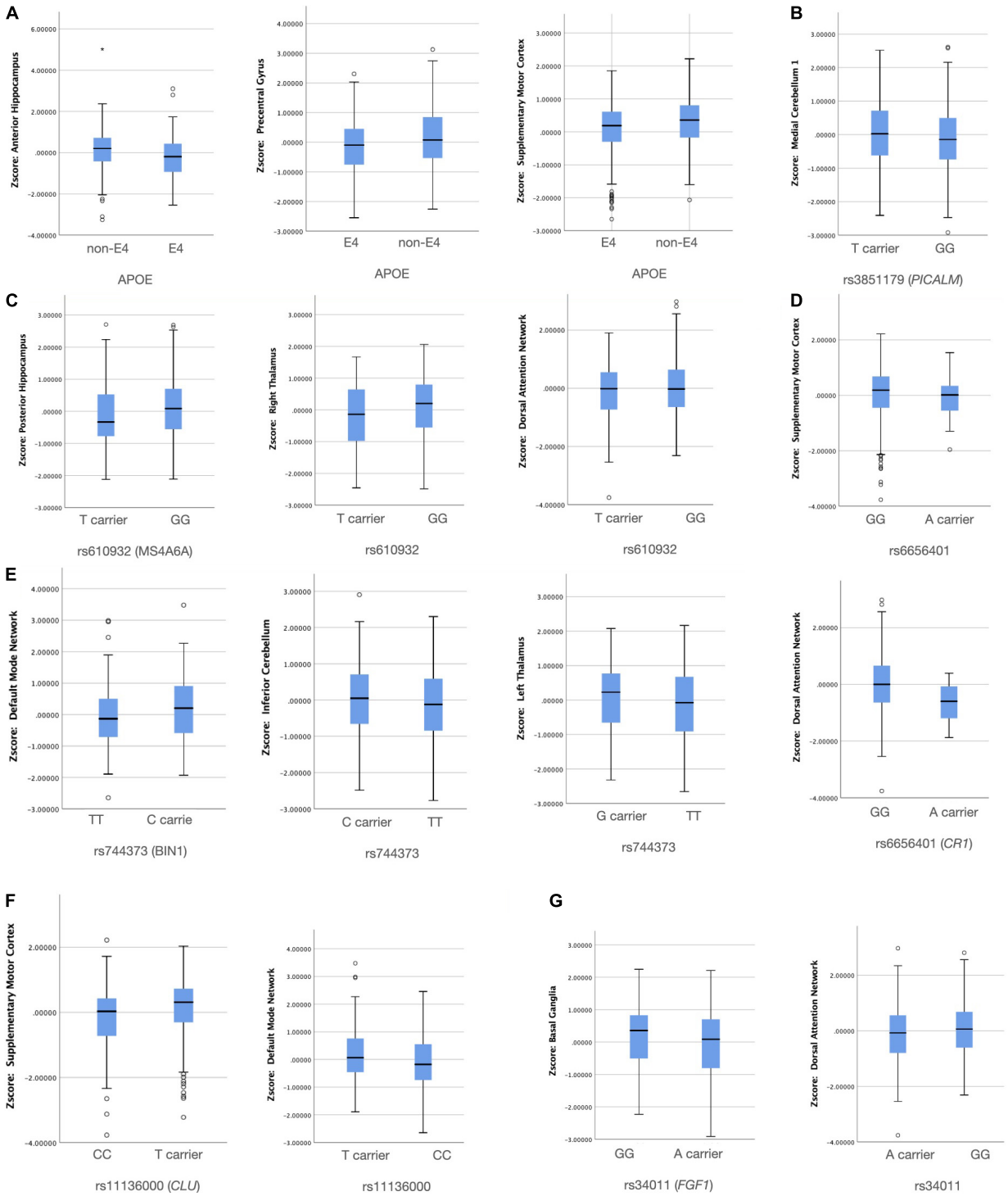

FIGURE 3 | Significant group differences between the risk and non-risk allele **(A–G)** in network intensity score ($p < 0.05$). *X* axis: SNP group, *Y* axis: *Z* transformed network intensity values.

controls, it would be difficult to match all influential factors. In this study, we did not include a late-stage AD group based on two considerations. First, we wanted to examine interactions between SCNs and SNPs in a more uniform population, so only subjects with early-stage AD were included. Second, the enrollment of subjects with late-stage AD may have included SCNs related to disease progression; however, this was not the major purpose of this study. The effects of susceptible

TABLE 6 | Risk allele per structural covariance network of 15 tested single nucleotide polymorphisms (SNP) and ApoE4.

Network	SNP	Risk allele	Unstandardized B (95%CI)	Standardized β	*P*-value
Basal ganglia	*FGF1* (rs34011)	A-carrier	–0.261(–0.026∼–0.497)	–0.142	0.03
Anterior Hippocampus	*ApoE4*	E4 carrier	–0.344 (–0.619∼–0.069)	–0.164	0.014
posterior Hippocampus	*MS4A6A* (rs610932)	T carrier	0.292(0.024∼0.559)	0.154	0.033
Right Thalamus	*MS4A6A* (rs610932)	T carrier	0.417 (0.121∼0.712)	0.199	0.006
Left Thalamus	*BIN1* (rs744373)	TT	–0.294(–0.557∼–0.031)	–0.145	0.028
Precentral Gyrus	*APOE4*	E4	0.421 (0.173–0.669)	0.217	0.001
Supplementary Motor Cortex	*APOE4*	E4 carrier	0.302(0.074∼0.53)	0.169	0.01
	CLU (rs11136000)	CC	0.258(0.032∼0.484)	0.143	0.025
	CR1 (rs6656401)	A carrier	–0.482(—-0.954∼–0.011)	–0.130	0.045
Inferior Cerebellum	*BIN1* (rs744373)	TT	–0.335(–0.607∼–0.062)	–0.161	0.016
Medial Cerebellum	*PICALM (rs3851179)*	GG	–0.266 (–0.521∼–0.011)	–0.135	0.041
Default Mode Network	*CLU* (rs11136000)	CC	–0.313(–0.566∼–0.06)	–0.157	0.016
	BIN1 (rs744373)	TT	0.320(0.063∼0.576)	0.161	0.015
Dorsal Attention Network	*CR1* (rs6656401)	A-carrier	–0.640(–1.184∼–0.096)	0.103	0.021
	FGF1 (rs34011)	A-carrier	0.274(0.025∼0.255)	0.137	0.031
	MS4A6A (rs610932)	T carrier	0.364(0.076∼0.652)	0.175	0.014

The Multivariate linear model was used. Independent variables using ApoE4, rs9349407, rs3865444, rs670139, rs744373, rs3851179, rs11136000, rs3764650, rs610932, rs6887649, rs7849530, rs4866650, rs3765728, rs34011, rs6656401, rs597668, adjusted for age and gender; dependent variable is the network integrity score.

SNPs and disease progression are important scientific questions. However, we focused on the initial hypothesis and tested the endophenotypic role of SCNs in cognitive outcomes in a uniform population with early-stage AD. A larger sample size including subjects with different stages of AD may help to extend the understanding of susceptible SNPs and brain degeneration patterns.

Another limitation is the estimation of the number of components for ICA analysis. Most studies have used 12–30 components in structural networks or resting-state networks. In this study, we constructed SCN networks and filtered the clinical significance of a network using correlation analysis with cognitive measures and by matching with the ICA template (see footnote 4). From a methodological aspect, the groupwise structural covariance analysis relied on the morphological properties of each voxel with the rest of the brain across a group of participants. The registration of the structural data of a single participant to the template involves linear and non-linear deformation that can result in inaccuracies in subregions. In this report, we emphasized well-characterized networks to explain the SNP effect, where the network significance was established by correlations with cognitive measures. Finally, the use of 15 AD-susceptible SNPs to validate the underlying pathological mechanisms may have oversimplified the genetic interactions. However, these SNPs were chosen based on their significance in large-scale GWASs in which they were all involved in amyloid or tau cascades, so the hypothesis was to test their effect on cognitive scores. We only tested interactions between each SNP and *ApoE4* status, as *ApoE4* remains the strongest predictor. The interpretations of interactions between SNPs and SCNs were based on a literature review of possible alterations in functional pathways and may not fully explain the *in vivo* situation. Therefore, the findings should be interpreted with caution.

CONCLUSION AND FUTURE PERSPECTIVES

In AD, our findings demonstrated amyloid or tau-related SNP effects that may influence SCNs independently or synergistically with *ApoE4*. The use of SCNs as an endophenotype allowed us to assume the independent and synergistic role of putative SNPs to predict cognitive measures. The complex interplay among these SNPs in our study suggests that the hierarchical order of SNPs modulates GM networks.

DATA AVAILABILITY STATEMENT

The raw data supporting the conclusions of this article will be made available by the authors, without undue reservation.

ETHICS STATEMENT

The studies involving human participants were conducted in accordance with the Declaration of Helsinki and were reviewed and approved by the Institutional Review Board of Chang Gung Memorial Hospital. Written informed consent to participate in this study was provided by the participants.

AUTHOR CONTRIBUTIONS

C-WH, K-LH, J-LH, S-WH, S-JT, W-NC, C-CL, S-HH, and C-CC contributed to the acquisition and analysis of data. H-IC, Y-TC, and C-CC drafted a significant portion of the manuscript and figures. All authors read and approved the final manuscript.

FUNDING

This work was supported by grants CMRPG8J0522, CMRPG8J0842, and CMRPG8K1531 from Chang Gung Memorial Hospital and 109-2314-B-182A-082 from the Ministry of Science and Technology (MOST), Taiwan, to C-CC.

ACKNOWLEDGMENTS

We thank the Genomics Center for Clinical and Biotechnological Applications of the National Core Facility for Biopharmaceuticals, Taiwan (MOST 109-2740-B-010-002), for genotyping. We thank the participants and their families for their generosity.

SUPPLEMENTARY MATERIAL

The Supplementary Material for this article can be found online at: https://www.frontiersin.org/articles/10.3389/fnagi.2021.721217/full#supplementary-material

Supplementary Figure 1 | Effect of interactions with the *ApoE4* gene on STM scores was found in *CD2AP*, *BIN 1*, *MS4A6A,* and *FTMT*.

REFERENCES

Alexander-Bloch, A., Giedd, J. N., and Bullmore, E. (2013). Imaging structural co-variance between human brain regions. *Nat. Rev. Neurosci.* 14, 322–336. doi: 10.1038/nrn3465

Andrews-Hanna, J. R., Reidler, J. S., Sepulcre, J., Poulin, R., and Buckner, R. L. (2010). Functional-anatomic fractionation of the brain's default network. *Neuron* 65, 550–562. doi: 10.1016/j.neuron.2010.02.005

Bamji-Mirza, M., Li, Y., Najem, D., Liu, Q. Y., Walker, D., Lue, L. F., et al. (2016). Genetic Variations in ABCA7 Can Increase Secreted Levels of Amyloid-beta40 and Amyloid-beta42 Peptides and ABCA7 Transcription in Cell Culture Models. *J. Alzheimers Dis.* 53, 875–892.

Beckmann, C. F., and Smith, S. M. (2004). Probabilistic independent component analysis for functional magnetic resonance imaging. *IEEE Trans. Med. Imaging* 23, 137–152. doi: 10.1109/tmi.2003.822821

Biffi, A., Shulman, J. M., Jagiella, J. M., Cortellini, L., Ayres, A. M., Schwab, K., et al. (2012). Genetic variation at CR1 increases risk of cerebral amyloid angiopathy. *Neurology* 78, 334–341. doi: 10.1212/WNL.0b013e3182452b40

Biswal, B., Yetkin, F. Z., Haughton, V. M., and Hyde, J. S. (1995). Functional connectivity in the motor cortex of resting human brain using echo-planar MRI. *Magn. Reson. Med.* 34, 537–541.

Biswal, B. B., Mennes, M., Zuo, X. N., Gohel, S., Kelly, C., Smith, S. M., et al. (2010). Toward discovery science of human brain function. *Proc. Natl. Acad. Sci. U. S. A.* 107, 4734–4739.

Bradshaw, E. M., Chibnik, L. B., Keenan, B. T., Ottoboni, L., Raj, T., Tang, A., et al. (2013). CD33 Alzheimer's disease locus: altered monocyte function and amyloid biology. *Nat. Neurosci.* 16, 848–850. doi: 10.1038/nn.3435

Bretsky, P., Guralnik, J. M., Launer, L., Albert, M., and Seeman, T. E. (2003). The role of APOE-epsilon4 in longitudinal cognitive decline: MacArthur Studies of Successful Aging. *Neurology* 60, 1077–1081. doi: 10.1212/01.wnl.0000055875.26908.24

Chang, C. C., Chang, Y. T., Huang, C. W., Tsai, S. J., Hsu, S. W., Huang, S. H., et al. (2018a). Associations of Bcl-2 rs956572 genotype groups in the structural covariance network in early-stage Alzheimer's disease. *Alzheimers Res. Ther.* 10:17. doi: 10.1186/s13195-018-0344-4

Chang, C. C., Tsai, S. J., Chen, N. C., Huang, C. W., Hsu, S. W., Chang, Y. T., et al. (2018b). Catechol-O-Methyltransferase Val158Met Polymorphism on Striatum Structural Covariance Networks in Alzheimer's Disease. *Mol. Neurobiol.* 55, 4637–4649. doi: 10.1007/s12035-017-0668-2

Chang, H. I., Chang, Y. T., Tsai, S. J., Huang, C. W., Hsu, S. W., Liu, M. E., et al. (2019). MAOA-VNTR Genotype Effects on Ventral Striatum-Hippocampus Network in Alzheimer's Disease: analysis Using Structural Covariance Network and Correlation with Neurobehavior Performance. *Mol. Neurobiol.* 56, 4518–4529. doi: 10.1007/s12035-018-1394-0

Chang, Y. T., Huang, C. W., Chang, Y. H., Chen, N. C., Lin, K. J., Yan, T. C., et al. (2015). Amyloid burden in the hippocampus and default mode network: relationships with gray matter volume and cognitive performance in mild stage Alzheimer disease. *Medicine* 94:e763. doi: 10.1097/MD.0000000000000763

Chang, Y. T., Mori, E., Suzuki, M., Ikeda, M., Huang, C. W., Lee, J. J., et al. (2019). APOE-MS4A genetic interactions are associated with executive dysfunction and network abnormality in clinically mild Alzheimer's disease. *Neuroimage Clin.* 21:101621. doi: 10.1016/j.nicl.2018.101621

Chen, H., Wu, G., Jiang, Y., Feng, R., Liao, M., Zhang, L., et al. (2015). Analyzing 54,936 Samples Supports the Association Between CD2AP rs9349407 Polymorphism and Alzheimer's Disease Susceptibility. *Mol. Neurobiol.* 52, 1–7. doi: 10.1007/s12035-014-8834-2

Chen, L. H., Kao, P. Y., Fan, Y. H., Ho, D. T., Chan, C. S., Yik, P. Y., et al. (2012). Polymorphisms of CR1, CLU and PICALM confer susceptibility of Alzheimer's disease in a southern Chinese population. *Neurobiol. Aging* 33, 210.e1–210.e7. doi: 10.1016/j.neurobiolaging.2011.09.016

Chen, M. J., Ramesha, S., Weinstock, L. D., Gao, T., Ping, L., Xiao, H., et al. (2021). Extracellular signal-regulated kinase regulates microglial immune responses in Alzheimer's disease. *J. Neurosci. Res.* 99, 1704–1721.

Chibnik, L. B., Shulman, J. M., Leurgans, S. E., Schneider, J. A., Wilson, R. S., Tran, D., et al. (2011). CR1 is associated with amyloid plaque burden and age-related cognitive decline. *Ann. Neurol.* 69, 560–569. doi: 10.1002/ana.22277

Colombo, M., Fernandez, T., Nakamura, K., and Gross, C. G. (1998). Functional differentiation along the anterior-posterior axis of the hippocampus in monkeys. *J. Neurophysiol.* 80, 1002–1005.

Corder, E. H., Saunders, A. M., Strittmatter, W. J., Schmechel, D. E., Gaskell, P. C., Small, G. W., et al. (1993). Gene dose of apolipoprotein E type 4 allele and the risk of Alzheimer's disease in late onset families. *Science* 261, 921–923. doi: 10.1126/science.8346443

Cuingnet, R., Gerardin, E., Tessieras, J., Auzias, G., Lehericy, S., Habert, M. O., et al. (2011). Automatic classification of patients with Alzheimer's disease from structural MRI: a comparison of ten methods using the ADNI database. *Neuroimage* 56, 766–781. doi: 10.1016/j.neuroimage.2010.06.013

Dos Santos, L. R., Pimassoni, L. H. S., Sena, G. G. S., Camporez, D., Belcavello, L., Trancozo, M., et al. (2017). Validating GWAS Variants from Microglial Genes Implicated in Alzheimer's Disease. *J. Mol. Neurosci.* 62, 215–221.

Du, W., Tan, J., Xu, W., Chen, J., and Wang, L. (2016). Association between clusterin gene polymorphism rs11136000 and late-onset Alzheimer's disease susceptibility: a review and meta-analysis of case-control studies. *Exp. Ther. Med.* 12, 2915–2927. doi: 10.3892/etm.2016.3734

Dubey, H., Gulati, K., and Ray, A. (2018). Recent studies on cellular and molecular mechanisms in Alzheimer's disease: focus on epigenetic factors and histone deacetylase. *Rev. Neurosci.* 29, 241–260. doi: 10.1515/revneuro-2017-0049

Dubois, B., Feldman, H. H., Jacova, C., Hampel, H., Molinuevo, J. L., Blennow, K., et al. (2014). Advancing research diagnostic criteria for Alzheimer's disease: the IWG-2 criteria. *Lancet Neurol.* 13, 614–629.

Farrer, L. A., Cupples, L. A., Haines, J. L., Hyman, B., Kukull, W. A., Mayeux, R., et al. (1997). Effects of age, sex, and ethnicity on the association between apolipoprotein E genotype and Alzheimer disease. A meta-analysis. APOE and Alzheimer Disease Meta Analysis Consortium. *JAMA* 278, 1349–1356. doi: 10.1001/jama.278.16.1349

Franzmeier, N., Rubinski, A., Neitzel, J., Ewers, M., and Alzheimer's Disease Neuroimaging Initiative [ADNI] (2019). The BIN1 rs744373 SNP is associated with increased tau-PET levels and impaired memory. *Nat. Commun.* 10:1766. doi: 10.1038/s41467-019-09564-5

Frederickson, C. J., Klitenick, M. A., Manton, W. I., and Kirkpatrick, J. B. (1983). Cytoarchitectonic distribution of zinc in the hippocampus of man and the rat. *Brain Res.* 273, 335–339. doi: 10.1016/0006-8993(83)90858-2

Furusawa, K., Takasugi, T., Chiu, Y. W., Hori, Y., Tomita, T., Fukuda, M., et al. (2019). CD2-associated protein (CD2AP) overexpression accelerates amyloid precursor protein (APP) transfer from early endosomes to the lysosomal degradation pathway. *J. Biol. Chem.* 294, 10886–10899. doi: 10.1074/jbc.RA118.005385

Geekiyanage, H., and Chan, C. (2011). MicroRNA-137/181c regulates serine palmitoyltransferase and in turn amyloid beta, novel targets in sporadic Alzheimer's disease. *J. Neurosci.* 31, 14820–14830. doi: 10.1523/JNEUROSCI.3883-11.2011

Hall, J. R., Wiechmann, A. R., Johnson, L. A., Edwards, M., Barber, R. C., Cunningham, R., et al. (2014). The Impact of APOE Status on Relationship of Biomarkers of Vascular Risk and Systemic Inflammation to Neuropsychiatric Symptoms in Alzheimer's Disease. *J. Alzheimers Dis.* 40, 887–896. doi: 10.3233/JAD-131724

Hansson, O., Grothe, M. J., Strandberg, T. O., Ohlsson, T., Hagerstrom, D., Jogi, J., et al. (2017). Tau Pathology Distribution in Alzheimer's disease Corresponds Differentially to Cognition-Relevant Functional Brain Networks. *Front. Neurosci.* 11:167. doi: 10.3389/fnins.2017.00167

Hohman, T. J., Koran, M. E., Thornton-Wells, T. A., and Alzheimer's Neuroimaging Initiative (2014). Genetic variation modifies risk for neurodegeneration based on biomarker status. *Front. Aging Neurosci.* 6:183. doi: 10.3389/fnagi.2014.00183

Hollingworth, P., Harold, D., Sims, R., Gerrish, A., Lambert, J. C., Carrasquillo, M. M., et al. (2011). Common variants at ABCA7, MS4A6A/MS4A4E, EPHA1, CD33 and CD2AP are associated with Alzheimer's disease. *Nat. Genet.* 43, 429–435. doi: 10.1038/ng.803

Huang, C. W., Chang, W. N., Huang, S. H., Lui, C. C., Chen, N. C., Chang, Y. T., et al. (2013). Impact of homocysteine on cortical perfusion and cognitive decline in mild Alzheimer's dementia. *Eur. J. Neurol.* 20, 1191–1197. doi: 10.1111/ene.12159

Huang, C. W., Hsu, S. W., Tsai, S. J., Chen, N. C., Liu, M. E., Lee, C. C., et al. (2017). Genetic effect of interleukin-1 beta (C-511T) polymorphism on the structural covariance network and white matter integrity in Alzheimer's disease. *J. Neuroinflammation* 14:12. doi: 10.1186/s12974-017-0791-z

Jack, C. R. Jr., Bennett, D. A., Blennow, K., Carrillo, M. C., Dunn, B., Haeberlein, S. B., et al. (2018). NIA-AA Research Framework: toward a biological definition of Alzheimer's disease. *Alzheimers Dement.* 14, 535–562. doi: 10.1016/j.jalz.2018.02.018

Jansen, I. E., Savage, J. E., Watanabe, K., Bryois, J., Williams, D. M., Steinberg, S., et al. (2019). Genome-wide meta-analysis identifies new loci and functional pathways influencing Alzheimer's disease risk. *Nat. Genet.* 51, 404–413.

Jiao, B., Liu, X., Zhou, L., Wang, M. H., Zhou, Y., Xiao, T., et al. (2015). Polygenic Analysis of Late-Onset Alzheimer's Disease from Mainland China. *PLoS One* 10:e0144898. doi: 10.1371/journal.pone.0144898

Jin, C., Li, W., Yuan, J., Xu, W., and Cheng, Z. (2012). Association of the CR1 polymorphism with late-onset Alzheimer's disease in Chinese Han populations: a meta-analysis. *Neurosci. Lett.* 527, 46–49. doi: 10.1016/j.neulet.2012.08.032

Jones, D. T., Graff-Radford, J., Lowe, V. J., Wiste, H. J., Gunter, J. L., Senjem, M. L., et al. (2017). Tau, amyloid, and cascading network failure across the Alzheimer's disease spectrum. *Cortex* 97, 143–159. doi: 10.1016/j.cortex.2017.09.018

Karch, C. M., Jeng, A. T., Nowotny, P., Cady, J., Cruchaga, C., and Goate, A. M. (2012). Expression of novel Alzheimer's disease risk genes in control and Alzheimer's disease brains. *PLoS One* 7:e50976. doi: 10.1371/journal.pone.0050976

Keenan, B. T., Shulman, J. M., Chibnik, L. B., Raj, T., Tran, D., and Sabuncu, M. R. (2012). A coding variant in CR1 interacts with APOE-epsilon4 to influence cognitive decline. *Hum. Mol. Genet.* 21, 2377–2388. doi: 10.1093/hmg/dds054

Kimura, H., Tooyama, I., and McGeer, P. L. (1994). Acidic FGF expression in the surroundings of senile plaques. *Tohoku J. Exp. Med.* 174, 279–293. doi: 10.1620/tjem.174.279

Koistinaho, M., Lin, S., Wu, X., Esterman, M., Koger, D., Hanson, J., et al. (2004). Apolipoprotein E promotes astrocyte colocalization and degradation of deposited amyloid-beta peptides. *Nat. Med.* 10, 719–726. doi: 10.1038/nm1058

Lambert, J. C., Ibrahim-Verbaas, C. A., Harold, D., Naj, A. C., Sims, R., Bellenguez, C., et al. (2013). Meta-analysis of 74,046 individuals identifies 11 new susceptibility loci for Alzheimer's disease. *Nat. Genet.* 45, 1452–1458. doi: 10.1038/ng.2802

Li, H. L., Shi, S. S., Guo, Q. H., Ni, W., Dong, Y., Liu, Y., et al. (2011). PICALM and CR1 variants are not associated with sporadic Alzheimer's disease in Chinese patients. *J. Alzheimers Dis.* 25, 111–117.

Ma, F. C., Zong, Y., Wang, H. F., Li, J. Q., Cao, X. P., and Tan, L. (2018). ABCA7 genotype altered Abeta levels in cerebrospinal fluid in Alzheimer's disease without dementia. *Ann. Transl. Med.* 6:437. doi: 10.21037/atm.2018.07.04

Mahley, R. W. (1988). Apolipoprotein E: cholesterol transport protein with expanding role in cell biology. *Science* 240, 622–630. doi: 10.1126/science.3283935

Martins, C. A., Oulhaj, A., de Jager, C. A., and Williams, J. H. (2005). APOE alleles predict the rate of cognitive decline in Alzheimer disease: a nonlinear model. *Neurology* 65, 1888–1893. doi: 10.1212/01.wnl.0000188871.74093.12

Martiskainen, H., Viswanathan, J., Nykanen, N. P., Kurki, M., Helisalmi, S., Natunen, T., et al. (2015). Transcriptomics and mechanistic elucidation of Alzheimer's disease risk genes in the brain and in vitro models. *Neurobiol. Aging* 36, 1221.e15–28. doi: 10.1016/j.neurobiolaging.2014.09.003

McCormick, E. M., van Hoorn, J., Cohen, J. R., and Telzer, E. H. (2018). Functional connectivity in the social brain across childhood and adolescence. *Soc. Cogn. Affect. Neurosci.* 13, 819–830.

Naj, A. C., Jun, G., Beecham, G. W., Wang, L. S., Vardarajan, B. N., Buros, J., et al. (2011). Common variants at MS4A4/MS4A6E, CD2AP, CD33 and EPHA1 are associated with late-onset Alzheimer's disease. *Nat. Genet.* 43, 436–441.

Olgiati, P., Politis, A. M., Papadimitriou, G. N., De Ronchi, D., and Serretti, A. (2011). Genetics of late-onset Alzheimer's disease: update from the alzgene database and analysis of shared pathways. *Int. J. Alzheimers Dis.* 2011:832379. doi: 10.4061/2011/832379

Przeździk, I., Faber, M., Fernandez, G., Beckmann, C. F., and Haak, K. V. (2019). The functional organisation of the hippocampus along its long axis is gradual and predicts recollection. *Cortex* 119, 324–335. doi: 10.1016/j.cortex.2019.04.015

Ramos de Matos, M., Ferreira, C., Herukka, S. K., Soininen, H., Janeiro, A., Santana, I., et al. (2018). Quantitative Genetics Validates Previous Genetic Variants and Identifies Novel Genetic Players Influencing Alzheimer's Disease Cerebrospinal Fluid Biomarkers. *J. Alzheimers Dis.* 66, 639–652. doi: 10.3233/JAD-180512

Ringland, C., Schweig, J. E., Paris, D., Shackleton, B., Lynch, C. E., Eisenbaum, M., et al. (2020). Apolipoprotein E isoforms differentially regulate matrix metallopeptidase 9 function in Alzheimer's disease. *Neurobiol. Aging* 95, 56–68. doi: 10.1016/j.neurobiolaging.2020.06.018

Risacher, S. L., Kim, S., Shen, L., Nho, K., Foroud, T., Green, R. C., et al. (2013). The role of apolipoprotein E (APOE) genotype in early mild cognitive impairment (E-MCI). *Front. Aging Neurosci.* 5:11. doi: 10.3389/fnagi.2013.00011

Segall, J. M., Allen, E. A., Jung, R. E., Erhardt, E. B., Arja, S. K., Kiehl, K., et al. (2012). Correspondence between structure and function in the human brain at rest. *Front. Neuroinform.* 6:10. doi: 10.3389/fninf.2012.00010

Shen, N., Chen, B., Jiang, Y., Feng, R., Liao, M., Zhang, L., et al. (2015). An Updated Analysis with 85,939 Samples Confirms the Association Between CR1 rs6656401 Polymorphism and Alzheimer's Disease. *Mol. Neurobiol.* 51, 1017–1023. doi: 10.1007/s12035-014-8761-2

Shi, Y., Yamada, K., Liddelow, S. A., Smith, S. T., Zhao, L., Luo, W., et al. (2017). ApoE4 markedly exacerbates tau-mediated neurodegeneration in a mouse model of tauopathy. *Nature* 549, 523–527. doi: 10.1038/nature24016

Shulman, J. M., Chen, K., Keenan, B. T., Chibnik, L. B., Fleisher, A., Thiyyagura, P., et al. (2013). , Genetic susceptibility for Alzheimer disease neuritic plaque pathology. *JAMA Neurol.* 70, 1150–1157.

Singh, P. P., Singh, M., and Mastana, S. S. (2006). APOE distribution in world populations with new data from India and the UK. *Ann. Hum. Biol.* 33, 279–308. doi: 10.1080/03014460600594513

Vogel, J. W., La Joie, R., Grothe, M. J., Diaz-Papkovich, A., Doyle, A., and Vachon-Presseau, E. (2020). A molecular gradient along the longitudinal axis of the human hippocampus informs large-scale behavioral systems. *Nat. Commun.* 11:960. doi: 10.1038/s41467-020-14518-3

Wetzel, M. K., Naska, S., Laliberte, C. L., Rymar, V. V., Fujitani, M., Biernaskie, J. A., et al. (2008). p73 regulates neurodegeneration and phospho-tau accumulation during aging and Alzheimer's disease. *Neuron* 59, 708–721. doi: 10.1016/j.neuron.2008.07.021

Wisdom, N. M., Callahan, J. L., and Hawkins, K. A. (2011). The effects of apolipoprotein E on non-impaired cognitive functioning: a meta-analysis. *Neurobiol. Aging* 32, 63–74. doi: 10.1016/j.neurobiolaging.2009.02.003

Xiao, Q., Liu, Z. J., Tao, S., Sun, Y. M., Jiang, D., Li, H. L., et al. (2015). Risk prediction for sporadic Alzheimer's disease using genetic risk score in the Han Chinese population. *Oncotarget* 6, 36955–36964. doi: 10.18632/oncotarget.6271

Yang, H., Guan, H., Yang, M., Liu, Z., Takeuchi, S., Yanagisawa, D., et al. (2015). Upregulation of mitochondrial ferritin by proinflammatory cytokines: implications for a role in Alzheimer's disease. *J. Alzheimers Dis.* 45, 797–811. doi: 10.3233/JAD-142595

Zhang, Q., Yu, J. T., Zhu, Q. X., Zhang, W., Wu, Z. C., Miao, D., et al. (2010). Complement receptor 1 polymorphisms and risk of late-onset Alzheimer's disease. *Brain Res.* 1348, 216–221. doi: 10.1016/j.brainres.2010.06.018

Zhao, F., Song, M., Wang, Y., and Wang, W. (2016). Genetic model. *J. Cell. Mol. Med.* 20:765.

Zhao, Q. F., Wan, Y., Wang, H. F., Sun, F. R., Hao, X. K., Tan, M. S., et al. (2016). ABCA7 Genotypes Confer Alzheimer's Disease Risk by Modulating Amyloid-beta Pathology. *J. Alzheimers Dis.* 52, 693–703. doi: 10.3233/JAD-151005

Zhao, Z., Sagare, A. P., Ma, Q., Halliday, M. R., Kong, P., Kisler, K., et al. (2015). Central role for PICALM in amyloid-beta blood-brain barrier transcytosis and clearance. *Nat. Neurosci.* 18, 978–987. doi: 10.1038/nn.4025

Zhu, R., Liu, X., and He, Z. (2018). Association between CLU gene rs11136000 polymorphism and Alzheimer's disease: an updated meta-analysis. *Neurol. Sci.* 39, 679–689. doi: 10.1007/s10072-018-3259-8

Conflict of Interest: The authors declare that the research was conducted in the absence of any commercial or financial relationships that could be construed as a potential conflict of interest.

The reviewer K-JT declared a shared affiliation, with no collaboration, with one of the authors, Y-TC, to the handling editor at the time of the review.

Publisher's Note: All claims expressed in this article are solely those of the authors and do not necessarily represent those of their affiliated organizations, or those of the publisher, the editors and the reviewers. Any product that may be evaluated in this article, or claim that may be made by its manufacturer, is not guaranteed or endorsed by the publisher.

Copyright © 2021 Chang, Chang, Huang, Huang, Hsu, Hsu, Tsai, Chang, Lee, Huang and Chang. This is an open-access article distributed under the terms of the Creative Commons Attribution License (CC BY). The use, distribution or reproduction in other forums is permitted, provided the original author(s) and the copyright owner(s) are credited and that the original publication in this journal is cited, in accordance with accepted academic practice. No use, distribution or reproduction is permitted which does not comply with these terms.

frontiers in Molecular Neuroscience

ORIGINAL RESEARCH
published: 21 December 2021
doi: 10.3389/fnmol.2021.739571

Association of the Polygenic Risk Score With the Probability of Prodromal Parkinson's Disease in Older Adults

*Maria I. Maraki[1,2], Alexandros Hatzimanolis[3,4], Niki Mourtzi[5], Leonidas Stefanis[5,6], Mary Yannakoulia[2], Mary H. Kosmidis[7], Efthimios Dardiotis[8], Georgios M. Hadjigeorgiou[8,9], Paraskevi Sakka[10], Alfredo Ramirez[11,12,13,14,15], Benjamin Grenier-Boley[16], Jean-Charles Lambert[16], Stefanie Heilmann-Heimbach[17], Maria Stamelou[5,18], Nikolaos Scarmeas[5,19] and Georgia Xiromerisiou[8]**

[1] Section of Sport Medicine and Biology of Exercise, School of Physical Education and Sport Science, National and Kapodistrian University of Athens, Athens, Greece, [2] Department of Nutrition and Dietetics, School of Health Sciences, Hellenic Mediterranean University, Crete, Greece, [3] Department of Psychiatry, National and Kapodistrian University of Athens Medical School, Eginition Hospital, Athens, Greece, [4] Neurobiology Research Institute, Theodor-Theohari Cozzika Foundation, Athens, Greece, [5] First Department of Neurology, Eginition Hospital, National and Kapodistrian University of Athens Medical School, Athens, Greece, [6] Center of Clinical, Experimental Surgery and Translational Research, Biomedical Research Foundation of the Academy of Athens, Athens, Greece, [7] Laboratory of Cognitive Neuroscience, School of Psychology, Aristotle University of Thessaloniki, Thessaloniki, Greece, [8] School of Medicine, University of Thessaly, Larissa, Greece, [9] Department of Neurology, Medical School, University of Cyprus, Nicosia, Cyprus, [10] Athens Association of Alzheimer's Disease and Related Disorders, Marousi, Greece, [11] Division of Neurogenetics and Molecular Psychiatry, Department of Psychiatry and Psychotherapy, Faculty of Medicine and University Hospital Cologne, University of Cologne, Cologne, Germany, [12] Department of Neurodegenerative Diseases and Geriatric Psychiatry, University Hospital Bonn, Bonn, Germany, [13] German Center for Neurodegenerative Diseases (DZNE Bonn), Bonn, Germany, [14] Department of Psychiatry and Glenn Biggs Institute for Alzheimer's and Neurodegenerative Diseases, San Antonio, TX, United States, [15] Cluster of Excellence Cellular Stress Responses in Aging-Associated Diseases (CECAD), University of Cologne, Cologne, Germany, [16] INSERM, CHU Lille, Institut Pasteur de Lille, U1167-RID-AGE Facteurs de Risque et Determinants Moléculaires des Maladies Liées au Vieillissement, University of Lille, Lille, France, [17] Institute of Human Genetics, School of Medicine and University Hospital Bonn, University of Bonn, Bonn, Germany, [18] Parkinson's Disease and Movement Disorders Department, HYGEIA Hospital, Athens, Greece, [19] Taub Institute for Research in Alzheimer's Disease and the Aging Brain, The Gertrude H. Sergievsky Center, Department of Neurology, Columbia University, New York, NY, United States

OPEN ACCESS

Edited by:
Kuangyu Shi,
University of Bern, Switzerland

Reviewed by:
Gaia Faustini,
University of Brescia, Italy
Christos Proukakis,
University College London, United Kingdom

***Correspondence:**
Georgia Xiromerisiou
georgiaxiromerisiou@gmail.com

Specialty section:
This article was submitted to Brain Disease Mechanisms, a section of the journal Frontiers in Molecular Neuroscience

Received: *11 July 2021*
Accepted: *29 November 2021*
Published: *21 December 2021*

Citation:
Maraki MI, Hatzimanolis A, Mourtzi N, Stefanis L, Yannakoulia M, Kosmidis MH, Dardiotis E, Hadjigeorgiou GM, Sakka P, Ramirez A, Grenier-Boley B, Lambert J-C, Heilmann-Heimbach S, Stamelou M, Scarmeas N and Xiromerisiou G (2021) Association of the Polygenic Risk Score With the Probability of Prodromal Parkinson's Disease in Older Adults. Front. Mol. Neurosci. 14:739571. doi: 10.3389/fnmol.2021.739571

Several studies have investigated the association of the Parkinson's disease (PD) polygenic risk score (PRS) with several aspects of well-established PD. We sought to evaluate the association of PRS with the prodromal stage of PD. We calculated PRS in a longitudinal sample (n = 1120) of community dwelling individuals ≥ 65 years from the HELIAD (The Hellenic Longitudinal Investigation of Aging and Diet) study in order to evaluate the association of this score with the probability of prodromal PD or any of the established risk and prodromal markers in MDS research criteria, using regression multi-adjusted models. Increases in PRS estimated from GWAS summary statistics' ninety top SNPS with $p < 5 \times 10^{-8}$ was associated with increased odds of having probable/possible prodromal PD (i.e., ≥ 30% probability, OR = 1.033, 95%CI: 1.009–1.057 p = 0.006). From the prodromal PD risk markers, significant association

was found between PRS and global cognitive deficit exclusively (p = 0.003). To our knowledge, our study is the first population based study investigating the association between PRS scores and prodromal markers of Parkinson's disease. Our results suggest a strong relationship between the accumulation of many common genetic variants, as measured by PRS, and cognitive deficits.

Keywords: genetics, Parkinsonism, elderly, neurodegeneration, cognition

INTRODUCTION

Currently, several non-motor symptoms have been associated with an increased risk to develop Parkinson's disease (PD) in otherwise healthy individuals, while ongoing research aims to validate a variety of candidate PD biomarkers based on imaging, genetic, proteomic, or metabolomic signatures, supplemented by work on tissue markers accessible to minimally invasive biopsies. In fact, the recently defined MDS research criteria for prodromal PD include a combination of risk and prodromal markers, in an effort to define target populations of future disease modification trials (Heinzel et al., 2019a). Critically, these criteria have been prospectively validated in six independent cohort studies (Fereshtehnejad et al., 2017; Pilotto et al., 2017; Mahlknecht et al., 2018; Mirelman et al., 2018; Giagkou et al., 2020).

Additionally, genetic markers have been integrated in the MDS criteria for prodromal PD in order to improve the accuracy of prodromal PD diagnosis (Heinzel et al., 2019a). Individuals with rare high-penetrance genetic mutations are considered a distinct subgroup with a specific risk according to the mutation. For intermediate strength genetic factors, such as mutations in GBA and LRRK2, the prodromal PD risk is age-dependent and can be calculated, based on the penetrance of mutation and the PD risk, across different age groups. However, the cumulative predictive effect of common and low individual effect strength genetic risk variants has been recently introduced in the criteria. The aforementioned variable, PRS, has been introduced and likelihood-ratio (LR) is estimated according to its value (Heinzel et al., 2019a).

More specifically, polygenic score association analysis examines if a polygenic score, calculated as the cumulative risk of several small effect alleles detected by genome-wide association study (GWAS), confers a high risk for a disease and if the same sets of risk alleles are shared between cohorts/data sets. An influential role for polygenic inheritance in PD is strongly supported by a number of studies, that revealed a significant association between disease risk, age of onset, motor progression, and cognitive decline with polygenic risk scores (PRS), calculated from GWAS summary statistics for PD (Nalls et al., 2019).

However, all studies published today, examined the association of PRS with several aspects of well-established PD. There are no studies that investigate the association of this score with the probability of prodromal PD and its risk markers. In this study, we calculated PRS in a longitudinal sample of community dwelling individuals $\geq$ 65 years from the HELIAD study (The Hellenic Longitudinal Investigation of Aging and Diet) to evaluate the association of this score with the probability of prodromal PD. We further investigated whether there is an association between any of the established risk and prodromal markers in MDS criteria with PRS. The identification of the genetic influence on prodromal phase will allow the detection of a pure association between multiple domains of the disorder and PRS without the interaction of other clinical features.

MATERIALS AND METHODS

Study Population

The Hellenic Longitudinal Investigation of Aging and Diet (HELIAD) is a large-scale, population-based, multidisciplinary study designed to assess the prevalence, incidence, and risk factors of neuropsychiatric conditions of aging in Greece (Dardiotis et al., 2014). We randomly selected participants among community-dwelling individuals from two areas in Greece (age $\geq$ 65, no exclusion criteria), and qualified neurologists and other health professionals collected demographic, medical, environmental, neuropsychological, and lifestyle information. Senior or junior neurologists examined all participants. Details on HELIAD design, participation rates and clinical and neuropsychological evaluation have been previously published (Dardiotis et al., 2014; Ntanasi et al., 2017, 2020; Tsapanou et al., 2017; Kosmidis et al., 2018; Bougea et al., 2019; Maraki et al., 2019a,b; Giagkou et al., 2020). For the present study, we excluded from the analysis those participants who were diagnosed with PD or dementia with Lewy bodies (DLB) and participants for whom the presence or absence of these diagnoses could not be ascertained (Maraki et al., 2019b; Giagkou et al., 2020). The study protocol was approved by the relevant institutional review boards (University of Thessaly, Larisa, Greece, and the National and Kapodistrian University of Athens, Greece, Ethics Committees). All participants or authorized representatives gave their written informed consent prior to participation.

Clinical and Other Assessments

We collected information regarding sociodemographics (e.g., gender, age, years of education, number of vehicles, home size, rental vs. ownership status, type and amount of tobacco use). We used a structured pretested questionnaire to evaluate pesticide exposure and a semiquantitative food frequency questionnaire to evaluate coffee consumption. Physical inactivity was ascertained *via* a leisure activities structured questionnaire. We also collected information regarding medical and neurological conditions, neuropsychiatric symptoms, current medications,

hospitalizations, and injuries of the participants, and information about the medical/neurological histories of the participants' first-degree relatives. In addition, we conducted an extensive structured physical evaluation of the participant, including neurological signs and symptoms. We used the 15-item Geriatric Depression Scale (Fountoulakis et al., 1999) and the 7-item anxiety subscale of the Hospital Anxiety and Depression Scale (Michopoulos et al., 2008) to screen for depressive symptoms and anxiety during the preceding week, respectively. We used the 12-item Medical Outcomes Study Sleep Scale (Hays et al., 2005) to assess the quantitative and qualitative features of sleep during the preceding month and the Blessed Dementia Scale (Blessed et al., 1968) for the perceived changes in performance of daily activities and self-care habits. Parkinsonian signs and symptoms were evaluated using the UPDRSIII (Fahn and Elton, 1987). We also administered a structured questionnaire to determine whether core (e.g., Parkinsonism), suggestive [e.g., REM sleep behavior disorder (RBD)] or supportive features (e.g., systematized delusions) of the revised diagnostic criteria for Dementia with Lewy bodies were present (McKeith et al., 2005; Anastasiou et al., 2017). We also administered the 12-item Neuropsychiatric Inventory (Cummings, 1997). The information obtained was reviewed, and the clinical diagnosis of each participant was reached using published criteria at expert consensus meetings.

Calculation of the Probability of pPD

We collected data for the vast majority of 2019 MDS pPD markers (Berg et al., 2015; Heinzel et al., 2019b): 16 of 21 (seven out of the 10 risk markers and nine out of the 11 prodromal markers) (Maraki et al., 2019b; Giagkou et al., 2020). In more details, the *risk* markers assessed were: sex, pesticide exposure, non-use of caffeine, non-smoking status, presence of 1**st** degree relative with PD, Type 2 Diabetes mellitus (DM2) and physical inactivity. Information on occupational solvent exposure, substantia nigra hyperechogenicity and plasma urate were not available. The *prodromal* markers assessed were: possible RBD, subthreshold parkinsonism, constipation, excessive daytime somnolence, symptomatic orthostatic hypotension, erectile dysfunction, urinary dysfunction, depression or anxiety without depression and global cognitive deficit. Information on olfactory dysfunction and tracer uptake of the presynaptic dopaminergic system (single-photon emission computed tomography or positron emission tomography) were not available. As MDS and recent studies have suggested, pPD probability may be calculated using available markers in each cohort, although may be underestimated when markers are limited (Mahlknecht et al., 2016; Skorvanek et al., 2017). Details on how we evaluated the above risk and prodromal markers can be found in previous publications on the probability of pPD in HELIAD population (Bougea et al., 2019; Maraki et al., 2019a,b; Giagkou et al., 2020; Ntanasi et al., 2020).

We calculated the pPD probability for non-PD/DLB participants, according to MDS guidance (Berg et al., 2015; Mahlknecht et al., 2016; Heinzel et al., 2019b), as previously reported (Bougea et al., 2019; Maraki et al., 2019a,b; Giagkou et al., 2020; Ntanasi et al., 2020). In more detail, we determined prior (pretest) pPD probability according to the participant's age. We calculated the individualized likelihood ratios (LRs) for every risk and prodromal marker; missing values were scored 1.0. We then computed the total risk LR and total prodromal LR separately by multiplying the corresponding markers. Next, these LRs were multiplied to provide the total LR. Then, we calculated the final posttest pPD probability by combining pretest probability with total LR. For the purpose of the present analysis, we used posttest pPD probability as a continuous variable, but also the cut-offs of 30% (possible/probable pPD), 50% and 80% (probable pPD) (Berg et al., 2014, 2015).

Genotyping and Imputation

Genome-wide genotyping was performed for 1,446 individuals in three different centers, at the "Centre National de Recherché en Génétique Humaine" (GNRGH, Evry, France), at Life and Braincenter (Bonn, Germany) and at the Erasmus Medical University (Rotterdam, Netherlands) using the Illumina Infinium Global Screening Array (GSA, GSAsharedCUSTOM_24 + v1.0), as part of the European Alzheimer DNA biobank (EADB) project. Base calling of the raw reads was performed at CNRGH. A detailed description of the EADB genotyping, QC and imputation can be found elsewhere. In summary, variants included in the marker list for removal, provided by Illumina, or variants not uniquely aligned in GRCh37 genome were excluded for further analysis. Moreover, variant intensity quality control (QC), was conducted for all autosomal variants, according to established thresholds, while sex-check was also performed using chromosome X variants (Grove et al., 2013).

Next, we performed sample quality control using PLINK v1.9 software (Purcell et al., 2007; Chang et al., 2015; Chang, 2020). Specifically, samples with missingness > 0.05, sex inconsistencies or with heterozygosity rate that deviated more than ± 6 SD from the mean, were excluded. To identify population outliers, we run Principal Component Analysis (PCA), using as reference dataset the population of 1000 Genome (phase 3) and we projected the combined dataset (1000 GP3 samples and the EADB samples) onto two dimensions, using the flashPCA2 software (Abraham et al., 2017). To control for cryptic relatedness, we excluded individuals with a kinship coefficient more than 0.125 (cut-off for third-degree relatives), yielding a final sample size of 1,120 unrelated individuals.

Regarding quality controls of variants, we excluded variants showing a missingness > 0.05 in at least one genotyping center or having a differential missingness test $P < 10^{-10}$. The Hardy-Weinberg equilibrium test ($p < 5e^{-8}$) was performed only in controls and for each genotyping center/country separately.

To improve the accuracy of imputation, we compared the frequencies of variants (chi-square test) against two reference panels, the population of the Haplotype Reference Consortium r1.1 (HRC) (McCarthy et al., 2016), excluding samples from 1,000 genomes as well as the Finnish and the non-Finnish population of Genome Aggregation Database v3 (gnomAD) (Karczewski et al., 2020). Variants showing a x2 > 3,000 in both HRC and gnomAD or a x2 > 3,000 in one reference panel and not present in the other were excluded. Finally, GWASs were performed between controls

across genotyping centers to assess frequency differences between genotyping centers, using the software SNPTEST (Marchini et al., 2007), under an additive model and adjusting on associated Principal Components (PCs). Variants having a Likelihood Ratio Test of $p < 10^{-5}$ were excluded. Furthermore, we removed ambiguous variants with Minor Allele Frequency (MAF) > 0.4 and we kept only one copy of any duplicated variants, prioritizing the one with the lowest missingness.

All samples and variants, passing the above QC metrics were imputed o Michigan Imputation Server (v1.2.4) (Das et al., 2016), using the TOPMed Freeze 5 reference panel. Phasing and imputation were performed using EAGLE v2.4 and Minimac4 v4-1.0.2 software, respectively.

Polygenic Risk Score Calculation

Imputed dosages for a total of 5,611,082 SNPs with MAF > 0.05, call rate > 95% and imputation quality score > 0.4 were converted to best-guess genotypes for PRS computation. The PRSice software[1] (Choi and O'Reilly, 2019) was utilized to construct PRSs for each individual applying the clumping and thresholding (C + T) method, following the approach originally described by the International Schizophrenia Consortium (International Schizophrenia et al., 2009). Separate PRS for Parkinson's disease were computed, as the weighted sum of the risk increasing alleles that each individual carries at each SNP locus multiplied by the effect size for the reference allele on the basis of large-scale genome-wide association (GWAS) meta-analysis summary data (i.e., discovery samples) (International Schizophrenia et al., 2009). Different sets of SNPs were filtered in the HELIAD sample (i.e., target sample) by applying increasing *p*-value thresholds to the discovery GWAS summary statistics and appropriate linkage disequilibrium (LD)-based SNP clumping (SNP with $r^2 > 0.1$ in 250 kb-windows were removed) was performed to ensure that only independent markers are included in the computed PRS. Markers within the major histocompatibility complex (MHC) LD region on chromosome 6 (hg19; chr6:27–33 Mb) were also excluded from PRS computation process due to the high polymorphic nature of this region.

For each subject, we computed different genome-wide PRSs based on *a priori* set of eight *P*-value thresholds (PT) (i.e., 1e-4, 0.001, 0.05, 0.1, 0.2, 0.3, 0.4, 0.5), to identify the best threshold for predicting the outcomes of interest.

Statistical Analysis

HELIAD participants with available data on PRS and probability of pPD were included in the present analysis. Normality of data was graphically explored using Q-Q plots. Values are presented as means ± SD or medians (Q1, Q3) for continuous, normally and not normally distributed, respectively, and as frequencies (%) for categorical variables. Differences between two groups (e.g., possible vs. not possible pPD, i.e., ≥ vs. < 30% pPD probability etc.) were tested by unpaired *t*-test or Mann–Whitney rank tests for normally and not normally distributed continuous variables, respectively, and Chi-Square tests for categorical variables. Differences between PRS quartiles were tested with one-way ANOVA followed by *post hoc* Student *t*-tests, or Kruskal–Wallis followed by Mann–Whitney rank tests, for normally and not normally distributed continuous, respectively, and Chi-Square tests for categorical variables.

The associations between PRS and probability of pPD (log-transformed data) were evaluated with linear regression analyses or logistic regression analyses [when probability of pPD was treated as dichotomous variable (i.e., ≥ 30% etc., probability of pPD)]. Furthermore, we used linear regression models to investigate relations between PRS and total LR for prodromal or risk markers (log-transformed data). We also used logistic regression analyses to investigate relations between PRS and each prodromal marker. All models were adjusted for MDSC1, MDSC2, age and sex. The PRS was entered into the models both as a continuous variable, as well as quartiles (comparing the fourth-higher *vs*. other quartiles). We did not adjust for age and/or sex when the dependent variable (e.g., probability of pPD) was calculated using age and/or sex among others (see above: calculation of pPD probability). Nevertheless, on a purely exploratory attempt, we calculated supplementary models adjusting for age and sex.

Reported *p*-values are nominal. Statistical significance was set at $p \leq 0.05$. All data were analyzed using SPSS statistical software (SPSS 19.0, SPSS Inc., United States).

Sensitivity Analysis

In an effort to distinguish the association of PRS with cognitive dysfunction in the sole context of pPD we performed additional analysis excluding participants with dementia ($n = 39$) and those with mild cognitive impairment (MCI, $n = 143$). The diagnosis of dementia was based on Diagnostic and Statistical Manual of Mental Disorders -IV-text revision criteria [American Psychiatric Association [APA], 2000] while MCI was diagnosed according to Petersen Criteria (Petersen et al., 2018).

RESULTS

Genotyping and Subjects Characteristics

European ancestry of the cohort samples was confirmed with principal component analysis, as all samples clustered accordingly with European samples from the 1,000 G dataset. We excluded third degree relatives with pihat scores > 0.125 ($n = 130$).

Non-PD/DLB participants were included in our analysis and their main characteristics are shown in **Table 1**. Most participants (745, 66.5%) had less than 5% probability of pPD, while 5.3% of the sample had possible or probable pPD, i.e., 30% or more pPD probability (**Table 1**).

Association of the PRSs With the Probability of pPD

There were no significant associations between any p_T cutoffs (p_T: significance level probability value thresholds for SNP selection in the discovery sample) and the probability of pPD

[1] http://prsice.info/

TABLE 1 | Sample characteristics (n = 1,120).

Characteristics	All
Sex, *n* (%)	
Male	475 (42.4%)
Female	645 (57.6%)
Age (years), mean ± SD	74 ± 5
Years of education, median (Q1, Q3)	6 (4, 9)
Job Type, *n* (%)	
Manual labor	782 (74.9%)
Mental labor	262 (25.1%)
Socioeconomic Status, *n* (%)	
Lower	542 (48.4%)
Higher	578 (51.6%)
PRS, *mean* ± SD	−1.60 ± 12.61
Probability of pPD, *median* (Q1, Q3)	2.74 (1.14, 7.08)
≥80% probability of pPD, *n* (%)	11 (1.0%)
≥50% probability of pPD, *n* (%)	28 (2.5%)
≥30% probability of pPD, *n* (%)	59 (5.3%)

($p > 0.05$). Additionally, for most p_T cutoffs there was no association between PRS and total LR for risk markers ($p > 0.05$) as well as total LR for prodromal markers ($p > 0.05$). However, PRS estimated from 90 top SNPS with $p < 5 \times 10^{-8}$ was significantly higher in the possible/probable pPD group (i.e., in those with 30% or more pPD probability) (2.83 ± 8.85 vs. −1.85 ± 12.75, $p < 0.001$; **Figure 1**) and in those with 50% or more pPD probability (5.09 ± 9.23 vs. −1.77 ± 12.65, $p = 0.001$; **Figure 2**). Logistic regression models adjusted for MDSC1 and MDSC2 showed that increase in PRS was associated with increased odds of having 30 or 50% or more pPD probability (OR = 1.033, 95%CI: 1.009–1.057, $p = 0.006$; OR = 1.052, 95%CI: 1.015–1.089, $p = 0.005$), while further adjustment for age and sex did not change the results (OR = 1.036, 95%CI: 1.011–1.060, $p = 0.004$ and OR = 1.056, 95%CI: 1.019–1.096, $p = 0.003$, respectively).

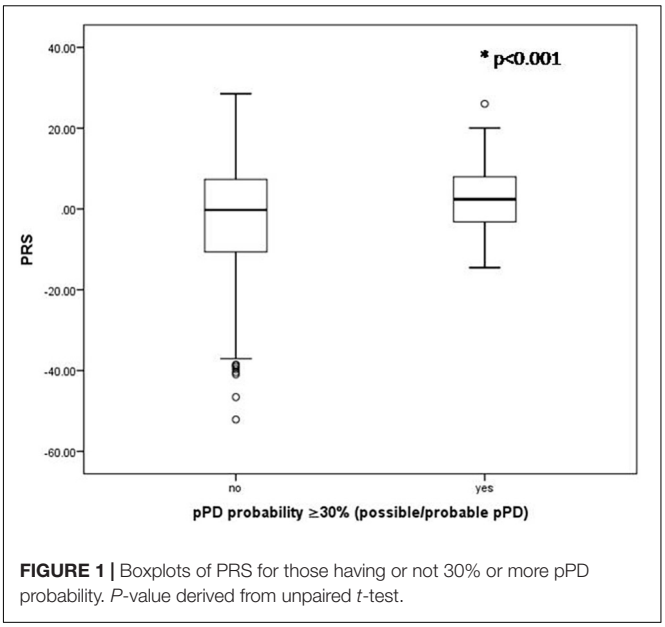

FIGURE 1 | Boxplots of PRS for those having or not 30% or more pPD probability. *P*-value derived from unpaired *t*-test.

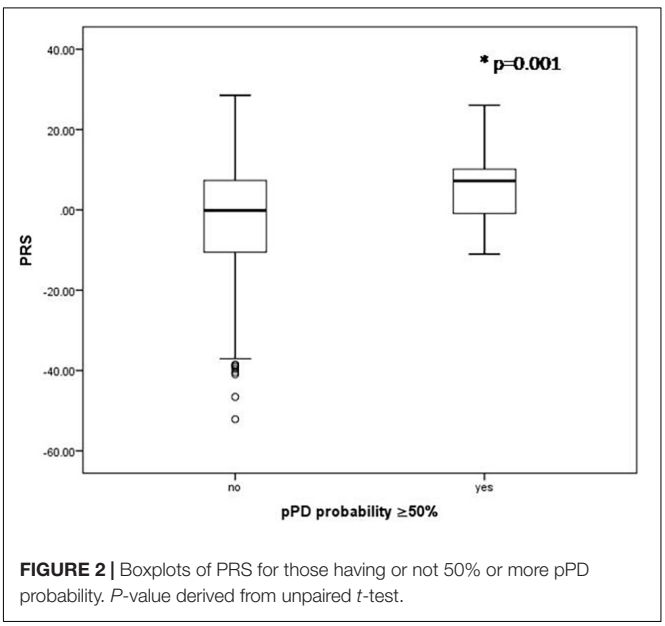

FIGURE 2 | Boxplots of PRS for those having or not 50% or more pPD probability. *P*-value derived from unpaired *t*-test.

Correlations Between PRSs and Prodromal Markers

Results of multi-adjusted logistic regression models (adjusted for MDSC1, MDSC2, age and sex) investigating the association between PRS and each prodromal PD marker revealed significant association between PRS and global cognitive deficit exclusively ($p = 0.003$). Increases in PRS were associated with increased odds of having global cognitive deficit (OR = 1.021, 95%CI: 1.007–1.035, $p = 0.003$). Therefore, those in the higher quartile of PRS had higher odds of having global cognitive deficit, compared to participants in the lower quartile of PRS (OR = 1.923, 95%CI: 1.202–3.076, $p = 0.006$, **Figure 3**).

Sensitivity Analysis

Excluding participants with dementia (n = 39) or additionally removing participants with MCI (n = 143) associations of PRS with global cognitive deficit remained unchanged, i.e., increases in PRS was associated with increased odds of having global cognitive deficit (OR = 1.023, 95%CI: 1.008–1.038, $p = 0.002$; OR = 1.025, 95%CI: 1.007–1.044, $p = 0.007$; respectively), while those in the higher quartile of PRS had higher odds of having global cognitive deficit, compared to participants in the lower quartile of PRS (excluding participants with dementia: OR = 1.990, 95%CI: 1.209–3.277, $p = 0.007$; additionally removing participants with MCI: OR = 2.060, 95%CI: 1.123–3.778, $p = 0.020$).

Increases in PRS were associated with lower individual cognitive domain z scores (memory: $b = -0.005$, 95%CI: −0.008 to −0.001, $p = 0.020$, language: $b = -0.005$, 95%CI: −0.009 to −0.001, $p = 0.015$, attention-speed: $b = -0.010$, 95%CI: −0.016 to −0.005, $p < 0.001$, executive: $b = -0.004$, 95%CI: −0.007 to −0.000, $p = 0.045$) with the exception of visual-spatial

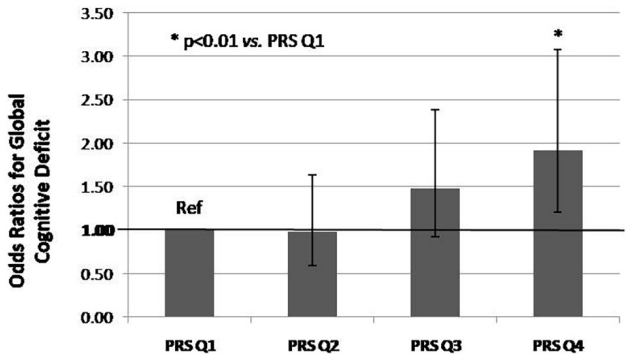

FIGURE 3 | Odd ratios for PD prodromal marker Global Cognitive Deficit by PRS quartile (Q), com-pared to lower quartile in older population (n = 1,120). *P*-values derived from logistic regression models adjusted for MDSC1, MDSC2, age and sex. *P* for trend = 0.002. Q4 vs. Q1: OR = 1.923, 95%CI: 1.202–3.076, p = 0.006.

functioning (b = −0.003, 95%CI: −0.008 to 0.001, p = 0.169). Including all cognitive domains z scores in the same model, PRS was negatively associated with attention-speed z scores (p = 0.012).

Increases in PRS were associated with higher odds of language and attention-speed deficits (OR = 1.015, 95%CI: 1.002–1.027, p = 0.025; OR = 1.013, 95%CI: 1.000–1.026, p = 0.042; respectively). When including deficits of all cognitive domains in the same model, PRS was not associated with any of them ($p > 0.05$), suggesting associative dependency.

When we excluded the prodromal marker of global cognitive deficit from pPD probability calculation, the associations of PRS with increased odds of having 30% or 50% or more pPD probability remained unchanged (OR = 1.031, 95%CI: 1.006–1.056, p = 0.013; OR = 1.048, 95%CI: 1.012–1.085, p = 0.009; respectively).

When we excluded the risk marker of having or not first-degree relative with PD from the calculation of pPD probability, results also remained unchanged, i.e., there were no significant associations of PRS with pPD probability (continuous variable) or total LR for risk markers ($p > 0.05$), while increases in PRS were associated with increased odds of having 30% or 50% or more pPD probability (OR = 1.031, 95%CI: 1.007–1.056, p = 0.010; OR = 1.052, 95%CI: 1.014–1.091, p = 0.006; respectively).

In addition, we performed the analysis splitting the sample according to whether they reported having first-degree relative with PD. In those having first-degree relative with PD (n = 43), we found that PRS was associated with increased pPD probability (continuous and the cut-off of 30% (n = 9), b = 0.017, 95%CI: 0.004–0.030, p = 0.013 and OR = 1.125, 95%CI: 1.011–1.253, p = 0.031; respectively), total LR for prodromal markers (b = 0.023, 95%CI: 0.007–0.039, p = 0.007) and higher odds of subthreshold Parkinsonism (OR = 1.257, 95%CI: 1.018–1.550, p = 0.033). On the other hand, in those had not first-degree relative with PD (n = 1074), PRS was associated with higher odds of having 30% or more pPD probability (OR = 1.024, 95%CI: 1.000–1.050, p = 0.050), 50% or more pPD probability (OR = 1.040, 95%CI: 1.002–1.081, p = 0.041) and global cognitive deficit (OR = 1.020, 95%CI: 1.006–1.034, p = 0.005).

Finally, when we used PRS higher quartile as a pPD risk marker, pPD probability was significantly lower than when we used the presence of first-degree relative with PD [2.50 (1.00, 6.63) vs. 2.74 (1.14, 7.08), p = 0.007]. However, this difference was not significant in those who had not first-degree relative with PD (p = 0.694), since 50% of this sample received the same LR (1.00), while 25% received greater (1.57) and 25% lower LR (0.45) when PRS higher quartile was served as a marker instead of the marker of presence of first-degree relative with PD.

DISCUSSION

In the present study, we explored the effect of genes on prodromal PD by screening and integrating PD- associated SNPs identified from large GWASs and building polygenic risk models. Such PRS reflect the cumulative genome-wide impact of common genetic variation on a given phenotype into a single measure of genetic risk. We used a large population-based cohort which enabled us to obtain more stable effect size estimates and better risk predictions. Several PRS models containing different numbers of SNPs were built for investigating possible associations with probability of pPD and its risk markers. A PRS model based on 90 SNPs (SNPs with a threshold of $p < 5 \times 10^{-8}$ from a large GWASs meta-analysis showed a significant association with pPD. Variants that do not reach GWAS significance do not seem to contribute to the prediction accuracy of pPD in our study.

Previous studies have shown that PRSs differentiated individuals already diagnosed with PD from unaffected individuals and several polygenic analysis have become standard tools for dissecting risk for polygenic disorders and related traits (Nalls et al., 2014). However, there are no studies that examine the relationship between PRS and pPD or with several prodromal markers. The results of our study suggest that PRS may further improve PD risk prediction. Hence, PRS can serve as a promising clinical tool in early screening and identifying at -risk asymptomatic individuals for disease prevention. PRSs could also lead to the reclassification of individuals more accurately into appropriate disease risk categories.

Furthermore, we found a significant correlation between PRS and global cognitive deficit, a prodromal marker of PD. However, we failed to detect other prodromal or risk markers associated with PRS. Additionally, the total LRs of risk markers was not associated with PRS.

This could be partly explained by the fact that several putative risk/protective factors for PD were not included in our analysis. In the HELIAD study, we had information on 13 of 17 MDS markers (eight of 10 prodromal) (Maraki et al., 2019a). Several risk assessments were based on questionnaires and we did not perform any specific tests for certain markers such as polysomnography for RBD, specific smell identification tests for olfactory dysfunction or questionnaires like Gastrointestinal Dysfunction Scale for Parkinson's Disease (GIDS-PD) to quantitatively assess features of gastrointestinal dysfunction (GID) symptoms. Moreover, MDS pPD criteria are

still undergoing validation and each criterion may not specific to pPD or may overlap with other neurodegenerative diseases. Therefore, although we have considered several comorbidities we cannot exclude or calculate the role of others.

For instance, olfactory dysfunction is one of the markers not included in our analysis. Olfactory dysfunction is common in Parkinson's disease (PD) and often predates the diagnosis by years, reflecting early deposition of Lewy pathology, the histologic hallmark of PD, in the olfactory bulb (Fullard et al., 2017). Olfactory function is also correlated with other non-motor features of PD and may serve as a predictor of cognitive decline. Hyposmia/anosmia is often seen in SNCA, GBA and LRRK2 carriers. However, it has variable penetrance in both sporadic and monogenic PD (Chase and Markopoulou, 2020). Therefore, while the hyposmia has been implicated as a "genetic" marker of PD in familial cases it has not been evaluated in our cohort concealing a possible association.

In an effort to explain this significant association of PRS with global cognitive deficit in pPD, we present previous studies showing how cognitive function influences the risk of parkinsonism and the genetic basis of cognition in PD.

Cognitive impairment and dementia are well established disorders in PD. As many as 80% of patients who are alive, 10 years after diagnosis are expected to develop dementia (Davis and Racette, 2016; Aarsland et al., 2017; Darweesh et al., 2017). Based on these findings global cognitive deficit was included in the calculation of risk markers (Heinzel et al., 2019a).

We have also recently reported results from HELIAD study investigating associations between pPD probability and cognitive function showing that higher probability of pPD was associated with lower cognitive performance in all domains. This may reflect a widespread pathologic process and non-dopaminergic pathways involved in neurodegeneration (Bougea et al., 2019).

As far as the genetic background of cognitive deficit concerns, most of the patient cohorts investigating cognitive impairment in PD have used candidate gene approaches so far. For instance, GBA, one of the most important genetic factors for PD, has also been implicated in cognitive impairment in PD (Alcalay et al., 2012; Mata et al., 2016; D'Souza and Rajkumar, 2020). Other studies have assessed the role of LRRK2, MAPT and SNCA for dementia in PD but results have often been inconclusive or not replicated independently (Mata et al., 2014). There were few studies so far that linked the cumulative burden of PD genetic risk factors with patient's cognitive deficit. Thus, a recent study showed that PRS was associated with significantly faster cognitive decline (Paul et al., 2018).

However, the main question, as far as cognitive decline in PD is concerned, is whether this association is driven by phenotypic and pathogenetic links with other neurodegenerative disorders. The sensitivity analysis that we performed, excluding participants with dementia and MCI, enforces the implication of an independent association. Therefore, this significant association between PRS and cognitive deficit is attributed solely to cognitive decline in the context of PD.

The assumption of a distinct genetic component of cognition in PD is supported by a number of studies investigating phenotypic and genotypic links between PD and other associated disorders. The Brainstorm Consortium, collaboration among GWAS meta-analysis consortia for 25 disorders, performed a comprehensive correlation analysis of brain disorders. Neurological disorders showed a limited extend of genetic correlation suggesting greater diagnostic specificity and more distinct etiologies (Brainstorm et al., 2018). The absence of genetic overlap between AD and PD reported that might be indicative of different biological pathways solidifies our findings.

In terms of the distinct cognitive impairment profile detected in PD, there are a number of studies showing that cognitive impairment involves executive, attention visuospatial and memory impairment with the language being usually preserved (Fang et al., 2020). Executive dysfunction is at the root of most cognitive changes in PD while the attentional deficit is always present and has been shown to interfere significantly in the patients' quality of life (Jalakas et al., 2019). Our findings are in consistent with this distinct clinical characteristics and PRS has been associated with them. Attention speed deficit was the most significantly associated cognitive domain with PRS. Declining processing speed in PD seems to have structural correlates with cortical thinning in temporoparietal regions, changes in diffusion MRI, especially in the cingulum tract, and decreased functional connectivity in posterior brain networks (Jalakas et al., 2019). All this evidence highlights even further these interesting associations that we detected at a prodromal stage.

A robust argument that could explain the association of PRS with cognitive deficit in pPD is that many genes that are included in PRS such as GBA, SNCA and MAPT, have been linked with cognitive outcomes in PD separately. For instance, results from the more recent large studies including more than a thousand subjects indicate an effect of SNCA variability on cognitive decline in PD (Guella et al., 2016). *GBA* status has been identified as one of the primary biological factors associated with cognitive status (Phongpreecha et al., 2020). *GBA* carriers had worse performance across most cognitive measures and the effect of this genetic factor on cognitive decline has been highlighted in many studies so far (D'Souza and Rajkumar, 2020). Previous reports on *MAPT* and cognition are mixed, with some studies reporting faster decline in MMSE scores and greater dementia risk in PD patients with the H1 haplotype and others showing a greater association between the H1 haplotype and PD diagnosis among those with dementia (Williams-Gray et al., 2009; Seto-Salvia et al., 2011).

Although evidence supporting an influence of genetics on cognition in PD is beginning to accumulate, the existing studies present variable methodology, conflicting results and limited number of candidate genes. High quality standardized data on cognition is also lacking in most studies. Our study is the only population based prospective study to investigate PRS with many prodromal markers of Parkinson's disease and to highlight a significant association between the accumulation of many common genetic variants and cognitive deficits. The identification of the genetic influence on prodromal phase is even more robust especially when certain criteria on prodromal disorders are well established. This procedure allows the

detection of a pure association between multiple domains of the disorder and the genetic susceptibility without the interaction of other clinical features.

DATA AVAILABILITY STATEMENT

The original contributions presented in the study are included in the article/supplementary material, further inquiries can be directed to the corresponding author/s.

ETHICS STATEMENT

The studies involving human participants were reviewed and approved by institutional review boards (University of Thessaly, Larisa, Greece, and the National and Kapodistrian University of Athens, Greece Ethics Committees). The patients/participants provided their written informed consent to participate in this study.

AUTHOR CONTRIBUTIONS

MM, NS, and GX: conceptualization. MM, AH, NM, LS, MS, NS, and GX: methodology. AH and NM: software. MM, AH, and NM: formal analysis and data curation. MY, MK, ED, GH, PS, NS, and GX: investigation and resources. MM and GX: writing—original draft preparation. AH, NM, MY, LS, and NS: writing—review and editing. GX and NS: supervision. MY, MK, ED, GH, NS, and GX: project administration. NS and GX: funding acquisition. All authors have read and agreed to the published version of the manuscript.

FUNDING

This study was supported by a grant (European Alzheimer DNA BioBank, EADB) from the EU Joint Programme—Neurodegenerative Disease Research (JPND), Inserm UMR1167 is also funded by Inserm, Institut Pasteur de Lille, the Lille Métropole Communauté Urbaine, the French government's LABEX DISTALZ program (development of innovative strategies for a transdisciplinary approach to Alzheimer's disease). This study was also supported by the following grants: IIRG-09-133014 from the Alzheimer's Association; 189 10276/8/9/2011 from the ESPA-EU Program Excellence Grant (ARISTEIA), which is co-funded by the European Social Fund and Greek National Resources, and DY2b/oik.51657/14.4.2009 from the Ministry for Health and Social Solidarity (Greece).

ACKNOWLEDGMENTS

We would like to thank the high-performance computing service of the University of Lille. We would also like to thank all the CEA-CNRGH staff who contributed to sample preparation and genotyping for their excellent technical assistance.

REFERENCES

Aarsland, D., Creese, B., Politis, M., Chaudhuri, K. R., Ffytche, D. H., Weintraub, D., et al. (2017). Cognitive decline in Parkinson disease. *Nat. Rev. Neurol.* 13, 217–231.

Abraham, G., Qiu, Y., and Inouye, M. (2017). FlashPCA2: principal component analysis of Biobank-scale genotype datasets. *Bioinformatics* 33, 2776–2778. doi: 10.1093/bioinformatics/btx299

Alcalay, R. N., Caccappolo, E., Mejia-Santana, H., Tang, M., Rosado, L., Orbe Reilly, M., et al. (2012). Cognitive performance of GBA mutation carriers with early-onset PD: the CORE-PD study. *Neurology* 78, 1434–1440. doi: 10.1212/WNL.0b013e318253d54b

American Psychiatric Association [APA] (2000). *Diagnostic and Statistical Manual of Mental Disorders*, 4th Edn. Washington: American Psychiatric Publishing.

Anastasiou, C. A., Yannakoulia, M., Kosmidis, M. H., Dardiotis, E., Hadjigeorgiou, G. M., Sakka, P., et al. (2017). Mediterranean diet and cognitive health: initial results from the Hellenic Longitudinal Investigation of Ageing and Diet. *PLoS One* 12:e0182048. doi: 10.1371/journal.pone.0182048

Berg, D., Postuma, R. B., Adler, C. H., Bloem, B. R., Chan, P., Dubois, B., et al. (2015). MDS research criteria for prodromal Parkinson's disease. *Mov. Disord.* 30, 1600–1611. doi: 10.1002/mds.26431

Berg, D., Postuma, R. B., Bloem, B., Chan, P., Dubois, B., Gasser, T., et al. (2014). Time to redefine PD? Introductory statement of the MDS Task Force on the definition of Parkinson's disease. *Mov. Disord.* 29, 454–462.

Blessed, G., Tomlinson, B. E., and Roth, M. (1968). The association between quantitative measures of dementia and of senile change in the cerebral grey matter of elderly subjects. *Br. J. Psychiatry* 114, 797–811. doi: 10.1192/bjp.114.512.797

Bougea, A., Maraki, M. I., Yannakoulia, M., Stamelou, M., Xiromerisiou, G., Kosmidis, M. H., et al. (2019). Higher probability of prodromal Parkinson disease is related to lower cognitive performance. *Neurology* 92, e2261–e2272. doi: 10.1212/WNL.0000000000007453

Brainstorm, C., Anttila, V., Bulik-Sullivan, B., Finucane, H. K., Walters, R. K., Bras, J., et al. (2018). Analysis of shared heritability in common disorders of the brain. *Science* 360:eaa8757. doi: 10.1126/science.aap8757

Chang, C. C. (2020). Data Management and Summary Statistics with PLINK. *Methods Mol. Biol.* 2090, 49–65. doi: 10.1007/978-1-0716-0199-0_3

Chang, C. C., Chow, C. C., Tellier, L. C., Vattikuti, S., Purcell, S. M., and Lee, J. J. (2015). Second-generation PLINK: rising to the challenge of larger and richer datasets. *Gigascience* 4:7. doi: 10.1186/s13742-015-0047-8

Chase, B. A., and Markopoulou, K. (2020). Olfactory Dysfunction in Familial and Sporadic Parkinson's Disease. *Front. Neurol.* 11:447. doi: 10.3389/fneur.2020.00447

Choi, S. W., and O'Reilly, P. F. (2019). PRSice-2: polygenic Risk Score software for biobank-scale data. *Gigascience* 8:giz082. doi: 10.1093/gigascience/giz082

Cummings, J. L. (1997). The Neuropsychiatric Inventory: assessing psychopathology in dementia patients. *Neurology* 48, S10–S16. doi: 10.1212/wnl.48.5_suppl_6.10s

Dardiotis, E., Kosmidis, M. H., Yannakoulia, M., Hadjigeorgiou, G. M., and Scarmeas, N. (2014). The Hellenic Longitudinal Investigation of Aging and Diet (HELIAD): rationale, study design, and cohort description. *Neuroepidemiology* 43, 9–14. doi: 10.1159/000362723

Darweesh, S. K. L., Wolters, F. J., Postuma, R. B., Stricker, B. H., Hofman, A., Koudstaal, P. J., et al. (2017). Association Between Poor Cognitive Functioning and Risk of Incident Parkinsonism: the Rotterdam Study. *JAMA Neurol.* 74, 1431–1438. doi: 10.1001/jamaneurol.2017.2248

Das, S., Forer, L., Schonherr, S., Sidore, C., Locke, A. E., Kwong, A., et al. (2016). Next-generation genotype imputation service and methods. *Nat. Genet.* 48, 1284–1287. doi: 10.1038/ng.3656

Davis, A. A., and Racette, B. (2016). Parkinson disease and cognitive impairment: five new things. *Neurol. Clin. Pract.* 6, 452–458. doi: 10.1212/CPJ.0000000000000285

D'Souza, T., and Rajkumar, A. P. (2020). Systematic review of genetic variants associated with cognitive impairment and depressive symptoms in Parkinson's disease. *Acta Neuropsychiatr.* 32, 10–22. doi: 10.1017/neu.2019.28

Fahn, S., and Elton, R. L. (1987). "Unified Parkinson's disease rating scale," in *Recent Developments in Parkinson's Disease*, eds S. Fahn, C. D. Marsden, D. B. Calne, and M. Goldstein (Florham Park: Macmillan Healthcare Information), 153–163.

Fang, C., Lv, L., Mao, S., Dong, H., and Liu, B. (2020). Cognition Deficits in Parkinson's Disease: mechanisms and Treatment. *Parkinsons Dis.* 2020:2076942. doi: 10.1155/2020/2076942

Fereshtehnejad, S. M., Montplaisir, J. Y., Pelletier, A., Gagnon, J. F., Berg, D., and Postuma, R. B. (2017). Validation of the MDS research criteria for prodromal Parkinson's disease: longitudinal assessment in a REM sleep behavior disorder (RBD) cohort. *Mov. Disord.* 32, 865–873. doi: 10.1002/mds.26989

Fountoulakis, K. N., Tsolaki, M., Iacovides, A., Yesavage, J., O'Hara, R., Kazis, A., et al. (1999). The validation of the short form of the Geriatric Depression Scale (GDS) in Greece. *Aging* 11, 367–372. doi: 10.1007/BF03339814

Fullard, M. E., Morley, J. F., and Duda, J. E. (2017). Olfactory Dysfunction as an Early Biomarker in Parkinson's Disease. *Neurosci. Bull.* 33, 515–525. doi: 10.1007/s12264-017-0170-x

Giagkou, N., Maraki, M. I., Yannakoulia, M., Kosmidis, M. H., Dardiotis, E., Hadjigeorgiou, G. M., et al. (2020). Prospective Validation of the Updated Movement Disorders Society Research Criteria for Prodromal Parkinson's Disease. *Mov. Disord.* 35, 1802–1809. doi: 10.1002/mds.28145

Grove, M. L., Yu, B., Cochran, B. J., Haritunians, T., Bis, J. C., Taylor, K. D., et al. (2013). Best practices and joint calling of the HumanExome BeadChip: the CHARGE Consortium. *PLoS One* 8:e68095. doi: 10.1371/journal.pone.0068095

Guella, I., Evans, D. M., Szu-Tu, C., Nosova, E., Bortnick, S. F., Group, S. C. S., et al. (2016). Alpha-synuclein genetic variability: a biomarker for dementia in Parkinson disease. *Ann. Neurol.* 79, 991–999. doi: 10.1002/ana.24664

Hays, R. D., Martin, S. A., Sesti, A. M., and Spritzer, K. L. (2005). Psychometric properties of the Medical Outcomes Study Sleep measure. *Sleep Med.* 6, 41–44. doi: 10.1016/j.sleep.2004.07.006

Heinzel, S., Berg, D., Gasser, T., Chen, H., Yao, C., and Postuma, R. B. (2019a). Disease MDSTFotDoPs. Update of the MDS research criteria for prodromal Parkinson's disease. *Mov. Disord.* 34, 1464–1470.

Heinzel, S., Berg, D., Gasser, T., Chen, H., Yao, C., and Postuma, R. B. (2019b). Update of the MDS research criteria for prodromal Parkinson's disease. *Mov. Disord.* 34, 1464–1470. doi: 10.1002/mds.27802

International Schizophrenia, C., Purcell, S. M., Wray, N. R., Stone, J. L., Visscher, P. M., O'Donovan, M. C., et al. (2009). Common polygenic variation contributes to risk of schizophrenia and bipolar disorder. *Nature* 460, 748–752. doi: 10.1038/nature08185

Jalakas, M., Palmqvist, S., Hall, S., Svard, D., Lindberg, O., Pereira, J. B., et al. (2019). A quick test of cognitive speed can predict development of dementia in Parkinson's disease. *Sci. Rep.* 9:15417. doi: 10.1038/s41598-019-51505-1

Karczewski, K. J., Francioli, L. C., Tiao, G., Cummings, B. B., Alfoldi, J., Wang, Q., et al. (2020). The mutational constraint spectrum quantified from variation in 141,456 humans. *Nature* 581, 434–443.

Kosmidis, M. H., Vlachos, G. S., Anastasiou, C. A., Yannakoulia, M., Dardiotis, E., Hadjigeorgiou, G., et al. (2018). Dementia Prevalence in Greece: the Hellenic Longitudinal Investigation of Aging and Diet (HELIAD). *Alzheimer Dis. Assoc. Disord.* 32, 232–239. doi: 10.1097/WAD.0000000000000249

Mahlknecht, P., Gasperi, A., Djamshidian, A., Kiechl, S., Stockner, H., Willeit, P., et al. (2018). Performance of the Movement Disorders Society criteria for prodromal Parkinson's disease: a population-based 10-year study. *Mov. Disord.* 33, 405–413. doi: 10.1002/mds.27281

Mahlknecht, P., Gasperi, A., Willeit, P., Kiechl, S., Stockner, H., Willeit, J., et al. (2016). Prodromal Parkinson's disease as defined per MDS research criteria in the general elderly community. *Mov. Disord.* 31, 1405–1408. doi: 10.1002/mds.26674

Maraki, M. I., Stefanis, L., Yannakoulia, M., Kosmidis, M. H., Xiromerisiou, G., Dardiotis, E., et al. (2019a). Motor function and the probability of prodromal Parkinson's disease in older adults. *Mov. Disord.* 34, 1345–1353. doi: 10.1002/mds.27792

Maraki, M. I., Yannakoulia, M., Stamelou, M., Stefanis, L., Xiromerisiou, G., Kosmidis, M. H., et al. (2019b). Mediterranean diet adherence is related to reduced probability of prodromal Parkinson's disease. *Mov. Disord.* 34, 48–57. doi: 10.1002/mds.27489

Marchini, J., Howie, B., Myers, S., McVean, G., and Donnelly, P. (2007). A new multipoint method for genome-wide association studies by imputation of genotypes. *Nat. Genet.* 39, 906–913. doi: 10.1038/ng2088

Mata, I. F., Leverenz, J. B., Weintraub, D., Trojanowski, J. Q., Chen-Plotkin, A., Van Deerlin, V. M., et al. (2016). Variants are associated with a distinct pattern of cognitive deficits in Parkinson's disease. *Mov. Disord.* 31, 95–102. doi: 10.1002/mds.26359

Mata, I. F., Leverenz, J. B., Weintraub, D., Trojanowski, J. Q., Hurtig, H. I., Van Deerlin, V. M., et al. (2014). MAPT, and SNCA genes and cognitive performance in Parkinson disease. *JAMA Neurol.* 71, 1405–1412. doi: 10.1001/jamaneurol.2014.1455

McCarthy, S., Das, S., Kretzschmar, W., Delaneau, O., Wood, A. R., Teumer, A., et al. (2016). A reference panel of 64,976 haplotypes for genotype imputation. *Nat. Genet.* 48, 1279–1283. doi: 10.1038/ng.3643

McKeith, I. G., Dickson, D. W., Lowe, J., Emre, M., O'Brien, J. T., Feldman, H., et al. (2005). Diagnosis and management of dementia with Lewy bodies: third report of the DLB Consortium. *Neurology* 65, 1863–1872.

Michopoulos, I., Douzenis, A., Kalkavoura, C., Christodoulou, C., Michalopoulou, P., Kalemi, G., et al. (2008). Hospital Anxiety and Depression Scale (HADS): validation in a Greek general hospital sample. *Ann. Gen. Psychiatry* 7:4.

Mirelman, A., Saunders-Pullman, R., Alcalay, R. N., Shustak, S., Thaler, A., Gurevich, T., et al. (2018). Application of the Movement Disorder Society prodromal criteria in healthy G2019S-LRRK2 carriers. *Mov. Disord.* 33, 966–973. doi: 10.1002/mds.27342

Nalls, M. A., Blauwendraat, C., Vallerga, C. L., Heilbron, K., Bandres-Ciga, S., Chang, D., et al. (2019). Identification of novel risk loci, causal insights, and heritable risk for Parkinson's disease: a meta-analysis of genome-wide association studies. *Lancet Neurol.* 18, 1091–1102. doi: 10.1016/S1474-4422(19)30320-5

Nalls, M. A., Pankratz, N., Lill, C. M., Do, C. B., Hernandez, D. G., Saad, M., et al. (2014). Large-scale meta-analysis of genome-wide association data identifies six new risk loci for Parkinson's disease. *Nat. Genet.* 46, 989–993. doi: 10.1038/ng.3043

Ntanasi, E., Maraki, M., Yannakoulia, M., Stamelou, M., Xiromerisiou, G., Kosmidis, M. H., et al. (2020). Frailty and prodromal Parkinson's disease: results from the HELIAD study. *J. Gerontol. A Biol. Sci. Med. Sci.* 76, 622–629. doi: 10.1093/gerona/glaa191

Ntanasi, E., Yannakoulia, M., Kosmidis, M. H., Anastasiou, C. A., Dardiotis, E., Hadjigeorgiou, G., et al. (2017). Adherence to Mediterranean Diet and Frailty. *J. Am. Med. Dir. Assoc.* 19, 315–322.e2.

Paul, K. C., Schulz, J., Bronstein, J. M., Lill, C. M., and Ritz, B. R. (2018). Association of Polygenic Risk Score With Cognitive Decline and Motor Progression in Parkinson Disease. *JAMA Neurol.* 75, 360–366. doi: 10.1001/jamaneurol.2017.4206

Petersen, R. C., Lopez, O., Armstrong, M. J., Getchius, T. S. D., Ganguli, M., Gloss, D., et al. (2018). Practice guideline update summary: mild cognitive impairment: report of the Guideline Development, Dissemination, and Implementation Subcommittee of the American Academy of Neurology. *Neurology* 90, 126–135. doi: 10.1212/wnl.0000000000004826

Phongpreecha, T., Cholerton, B., Mata, I. F., Zabetian, C. P., Poston, K. L., Aghaeepour, N., et al. (2020). Multivariate prediction of dementia in Parkinson's disease. *NPJ Parkinsons Dis.* 6:20. doi: 10.1038/s41531-020-00121-2

Pilotto, A., Heinzel, S., Suenkel, U., Lerche, S., Brockmann, K., Roeben, B., et al. (2017). Application of the movement disorder society prodromal Parkinson's disease research criteria in 2 independent prospective cohorts. *Mov. Disord.* 32, 1025–1034. doi: 10.1002/mds.27035

Purcell, S., Neale, B., Todd-Brown, K., Thomas, L., Ferreira, M. A., Bender, D., et al. (2007). PLINK: a tool set for whole-genome association and population-based

linkage analyses. *Am. J. Hum. Genet.* 81, 559–575. doi: 10.1086/519795

Seto-Salvia, N., Clarimon, J., Pagonabarraga, J., Pascual-Sedano, B., Campolongo, A., Combarros, O., et al. (2011). Dementia risk in Parkinson disease: disentangling the role of MAPT haplotypes. *Arch. Neurol.* 68, 359–364. doi: 10.1001/archneurol.2011.17

Skorvanek, M., Ladomirjakova, Z., Han, V., Lesko, N., Feketeova, E., Jarcuskova, D., et al. (2017). Prevalence of Prodromal Parkinson's Disease as Defined by MDS Research Criteria among Elderly Patients Undergoing Colonoscopy. *J. Parkinsons Dis.* 7, 481–489. doi: 10.3233/JPD-161036

Tsapanou, A., Gu, Y., O'Shea, D. M., Yannakoulia, M., Kosmidis, M., Dardiotis, E., et al. (2017). Sleep quality and duration in relation to memory in the elderly: initial results from the Hellenic Longitudinal Investigation of Aging and Diet. *Neurobiol. Learn. Mem.* 141, 217–225. doi: 10.1016/j.nlm.2017.04.011

Williams-Gray, C. H., Evans, J. R., Goris, A., Foltynie, T., Ban, M., Robbins, T. W., et al. (2009). The distinct cognitive syndromes of Parkinson's disease: 5 year follow-up of the CamPaIGN cohort. *Brain* 132, 2958–2969. doi: 10.1093/brain/awp245

Conflict of Interest: The authors declare that the research was conducted in the absence of any commercial or financial relationships that could be construed as a potential conflict of interest.

Publisher's Note: All claims expressed in this article are solely those of the authors and do not necessarily represent those of their affiliated organizations, or those of the publisher, the editors and the reviewers. Any product that may be evaluated in this article, or claim that may be made by its manufacturer, is not guaranteed or endorsed by the publisher.

Copyright © 2021 Maraki, Hatzimanolis, Mourtzi, Stefanis, Yannakoulia, Kosmidis, Dardiotis, Hadjigeorgiou, Sakka, Ramirez, Grenier-Boley, Lambert, Heilmann-Heimbach, Stamelou, Scarmeas and Xiromerisiou. This is an open-access article distributed under the terms of the Creative Commons Attribution License (CC BY). The use, distribution or reproduction in other forums is permitted, provided the original author(s) and the copyright owner(s) are credited and that the original publication in this journal is cited, in accordance with accepted academic practice. No use, distribution or reproduction is permitted which does not comply with these terms.

frontiers in Pharmacology

ORIGINAL RESEARCH
published: 22 December 2021
doi: 10.3389/fphar.2021.731483

Liraglutide Improves Cognitive and Neuronal Function in 3-NP Rat Model of Huntington's Disease

Samar M. Shawki[1], *Mohammed A. Saad*[2,3], *Rania M. Rahmo*[1], *Walaa Wadie*[2]* *and Hanan S. El-Abhar*[4]

[1]Department of Pharmacology and Toxicology, Faculty of Pharmacy, Misr International University, Cairo, Egypt, [2]Department of Pharmacology and Toxicology, Faculty of Pharmacy, Cairo University, Cairo, Egypt, [3]School of Pharmacy, Newgiza University, Cairo, Egypt, [4]Department of Pharmacology, Toxicology and Biochemistry, Faculty of Pharmacy, Future University in Egypt, Cairo, Egypt

Huntington's disease (HD) is an autosomal dominant inherited neurodegenerative disease characterized by progressive motor, psychiatric, and cognitive abnormalities. The antidiabetic drug liraglutide possesses a neuroprotective potential against several neurodegenerative disorders; however, its role in Huntington's disease (HD) and the possible mechanisms/trajectories remain elusive, which is the aim of this work. Liraglutide (200 µg/kg, s.c) was administered to rats intoxicated with 3-nitropropionic acid (3-NP) for 4 weeks post HD model induction. Liraglutide abated the 3-NP-induced neurobehavioral deficits (open field and elevated plus maze tests) and histopathological changes. Liraglutide downregulated the striatal mRNA expression of HSP 27, PBR, and GFAP, while it upregulated that of DARPP32. On the molecular level, liraglutide enhanced striatal miR-130a gene expression and TrKB protein expression and its ligand BDNF, while it reduced the striatal protein content and mRNA expression of the death receptors sortilin and p75NTR, respectively. It enhanced the neuroprotective molecules cAMP, p-PI3K, p-Akt, and p-CREB, besides modulating the *p*-GSK-3β/*p*-β-catenin axis. Liraglutide enhanced the antioxidant transcription factor Nrf2, abrogated TBARS, upregulated both Bcl2 and Bcl-XL, and downregulated Bax along with decreasing caspase-3 activity. Therefore, liraglutide exerts a neurotherapeutic effect on 3-NP-treated rats that is, besides the upturn of behavioral and structural findings, it at least partially, increased miR-130a and modulated PI3K/Akt/CREB/BDNF/TrKB, sortilin, and p75NTR, and Akt/GSK-3β/*p*-β-catenin trajectories besides its capacity to decrease apoptosis and oxidative stress, as well as its neurotrophic activity.

Keywords: Huntington's disease, 3-nitropropionic acid, (BDNF)/(TrkB), neurotrophic, liraglutide

OPEN ACCESS

Edited by:
Kuangyu Shi,
University of Bern, Switzerland

Reviewed by:
Vinod Tiwari,
Indian Institute of Technology (BHU), India
Kenneth S. Hettie,
Stanford University, United States

***Correspondence:**
Walaa Wadie
walaa.wadie@pharma.cu.edu.eg

Specialty section:
This article was submitted to Neuropharmacology, a section of the journal Frontiers in Pharmacology

Received: *27 June 2021*
Accepted: *09 November 2021*
Published: *22 December 2021*

Citation:
Shawki SM, Saad MA, Rahmo RM, Wadie W and El-Abhar HS (2021) Liraglutide Improves Cognitive and Neuronal Function in 3-NP Rat Model of Huntington's Disease. Front. Pharmacol. 12:731483. doi: 10.3389/fphar.2021.731483

1 INTRODUCTION

Huntington's disease (HD) is an autosomal dominant, progressive, and devastating neurodegenerative disorder caused by a polyglutamine expansion in exon 1 of the huntingtin gene (Htt) with the primary site of neuron loss is at the striatal part of the basal ganglia (Agrawal and Fox, 2019; Lallani et al., 2019). HD is a rare disease that mainly affects 5–7 individuals per 100,000 population associated with significant morbidity and mortality (Bruzelius et al., 2019). The hallmark features of HD are the presence of abnormal involuntary jerking and writhing movements (progressive chorea) accompanied by cognitive decline. As a consequence, HD patients are burdened with uncontrolled motor deficits,

cognitive impairments, and neuropsychiatric symptoms (Huguet et al., 2019). Altered delivery of brain-derived neurotrophic factor (BDNF) to the striatum and consequently its diminished striatal levels are believed to underlie the high vulnerability of the striatum to neuronal loss in HD (Suelves et al., 2019).

3-Nitropropionic acid (3-NP) is a mitochondrial toxin used to induce HD-like symptoms in rats. This toxin irreversibly inhibits the enzyme succinate dehydrogenase (complex II) of the electron transport chain and Kreb's cycle leading to selective massive loss of GABAergic medium-sized spiny neurons (MSNs) of the striatum, i.e., the typical pathology observed in HD (Cirillo et al., 2019). Despite previous studies, Durães et al., (2018) and Barker and Mason (2019) have stated that HD is still incurable with very limited therapies that target the symptoms only, and the available medications can only lessen some motor, cognitive, and psychiatric symptoms. Another work (Tabrizi et al., 2019) has recounted that strategies that aim at decreasing huntingtin are able to modify HD, a notion that emphasizes the importance of treating the causes of HD rather than mitigating only its symptoms.

Incretin hormones are a group of metabolic hormones, which are rapidly inactivated by dipeptidyl peptidase-4 (DPP-4). One incretin of particular concern is the glucagon-like peptide-1 (GLP-1) that can primarily cross the blood–brain barrier (BBB) to influence quite a lot of cellular pathways within the central nervous system (CNS). Existing research recognizes the critical neurotrophic and neuroprotective effects of GLP-1 on increasing the level of the BDNF in the cortex, hippocampus, and striatum to protect against neuronal apoptosis and improve the neuronal differentiation (Bomba et al., 2018). Hence, the implication of GLP-1 receptors (GLP-1Rs) may afford a promising target for the treatment of HD disease (Yang et al., 2017a).

To overcome the drawback of the short half-life of endogenous GLP-1, several DPP-4 resistant GLP-1 analogs were developed including liraglutide (Lira). Lira is an analog of the endogenous human GLP-1 with 97% of sequence homology (Sharma et al., 2018). Lira is an approved antidiabetic drug that acts as an incretin mimetic GLP-1R agonist and is increasingly used to improve glycemic control, reduce the risk of heart attack, stroke, and cardiovascular death in adults with type 2 diabetes mellitus (T2DM) (Marso et al., 2016). Besides its documented antidiabetic effect, Lira possesses an extrapancreatic neuroprotective potential against models of Parkinson's disease (Badawi et al., 2017), Alzheimer's disease (Zhang et al., 2019a), stroke (Zhao et al., 2018), and diabetes-associated neurodegeneration (Filchenko et al., 2018); however, its possible role in HD models has yet to be determined.

Based on the aforementioned data, we attempt to assess the effect of Lira on the 3-NP-induced HD-like mode through its ability to recover altered cognition and behavior, to restore striatal morphology, and explore some trajectories that can be involved in its therapeutic effect.

2 MATERIALS AND METHODS

2.1 Animals

Adult male Wistar rats weighing 250 ± 20 g were obtained from the National Research Centre (NRC, Giza, Egypt) and were allowed to acclimatize in the animal facility of the Faculty of Pharmacy (Cairo University) for a week prior to starting any experimental procedure. Rats were housed under controlled environmental conditions of constant temperature (25 ± 2°C), on a 12/12-h light/dark cycle. Rats were permitted free access to standard food and water *ad libitum*, and all behavioral tests were carried out in a sound isolated laboratory. The protocols used in this study complied with "The Guide for Care and Use of Laboratory Animals" published by the US National Institutes of Health (NIH publication no. 85–23, revised 2011) and were approved by the Ethics Committee for Animal Experimentation at Faculty of Pharmacy, Cairo University (permit number: PT 2099). All efforts were made to minimize animal suffering and to reduce the number of animals used.

2.2 Drugs and Chemicals

3-NP was purchased from Sigma-Aldrich (St. Louis, MO, USA), freshly prepared daily in normal saline, and neutralized to pH 7.4 with NaOH. It was administered through intraperitoneal (i.p.) route to each animal at a dose of 10 mg/kg body weight. The selection of dose and duration of 3-NP administration was based on published studies (El-Abhar et al., 2018). Liraglutide (Lira) was purchased as a raw material from Sigma-Aldrich Chemical Co. (St. Louis, MO, USA), and the dose was chosen after performing a pilot study in which three different dose levels (50, 100, and 200 μg/kg/day) were injected subcutaneously (s.c.) for 4 weeks (Dong et al., 2017), and different parameters were assessed to aid in dose selection; *viz.*, neurocognitive behavioral tests, body weight, histopathological changes, and striatal contents of phosphorylated cAMP response element-binding protein (p-CREB) and BDNF. Since BDNF can be detected in several brain regions, namely, the cortex, striatum, and hippocampus, the content of BDNF was assessed in these areas in the different groups. According to the results of the pilot study (data not shown) a dose of 200 μg/kg and the striatal area were used for the core study parameters. The concentration of the drugs in the prepared solutions was adjusted, so that the required dose for each 200 g rat was found in 2 ml. All other reagents used were of analytical grade.

2.3 Experimental Design

As depicted in **Figure 1**, 60 rats were randomly allocated into one of four treatment groups ($n = 15$) by a technical assistant who was not involved in the analysis. Animals in groups 1 and 2 were injected with normal saline (i.p.) for 14 days, this was followed by s.c administration of saline or Lira, respectively, for another 28 days. In groups 3 and 4, rats received 3-NP (10 mg/kg dissolved in 0.9% saline; i.p.) for 14 days, followed by an s.c injection of either normal saline or Lira for another 28 days. At the end of the study period, all animals were subjected to behavioral tests that were arranged from the least stressful (open-field test; OFT) to the more stressful (elevated plus maze test; EPM) test with a 2-h rest period between the two tests. All behavioral tests were carried out in an attenuated sound testing room with dim light starting at 6.00 p.m., during the light cycle of the animal.

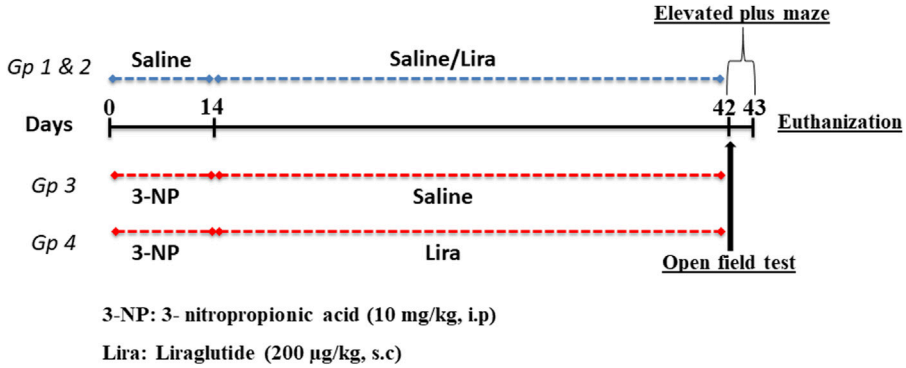

FIGURE 1 | Schematic presentation of the experimental design. The 3-nitropropionic acid (3-NP) (10 mg/kg, i.p.) was injected daily for 14 days, followed by 4 weeks of daily administration of liraglutide (200 µg/kg, s.c.). On days 42 and 43, animals were subjected to behavioral tests and killed on day 43.

Afterward, the rats in each group were divided into three subsets and then euthanized by an overdose of thiopental (100 mg/kg). The brains were then rapidly harvested, and the striata were dissected out and stored at −80°C until analysis using ELISA (n = 6), Western blot (n = 3), and RT-qPCR (n = 3). For the histopathological study, the whole brains of the other three representative animals were fixed in 10% (v/v) formalin.

2.4 Assessment of Parameters

2.4.1 Body Weight

The body weight was measured on the first and last days of the experiment, and the percentage change was calculated in comparison with the initial measurement on the first day as follows:

$$\%\ \text{Change in body weight} = [(\text{weight on day 42} - \text{initial weight})/\text{initial weight}] \times 100$$

2.4.2 Behavioral Assessments

2.4.2.1 Open Field test

The spontaneous locomotor behaviors were assessed using the OFT in which each rat was placed individually into the center of the open field apparatus composed of a square black wooden box (80 × 80 × 40 cm) with smooth polished floor divided into 16 squares 4 × 4 by yellow lines. Summarily, each animal was gently placed in the center of the open field and remote monitored using an overhead camera for 5 min. The apparatus floor and walls were wiped and cleaned after each tested animal with a wet sponge and a dry paper towel to eliminate possible bias due to odors left by previous rats. During the 5-min period, the latency in leaving the starting square and the ambulation (number of squares crossed), grooming, and rearing (number of attempts the animal stretched on its hind limbs with or without forelimb support) frequencies were measured. A line crossing was counted when all four paws crossed over the line (Thangarajan et al., 2016).

2.4.2.2 Elevated Plus Maze Test

Rats were subjected to the EPM using the method described by Kumar et al. (2017) to assess memory retention and cognitive function of the animals. The apparatus consisted of two opposite open arms (50 × 10 cm), crossed with two closed arms of the same dimensions with 40-cm-high walls, connected by a central square (10 × 10 cm); the maze was elevated to a height of 50 cm from the floor. On the first day, each rat was placed individually at one end of an open arm, and the time taken by the rat to move from the open arm to one of the closed arms was recorded as the initial transfer latency (ITL). The rat was allowed to explore the maze for 30 s before being returned to its home cage. In case the animal failed to enter the closed arm within 90 s, the animal was gently pushed into the closed arm, and the ITL for that animal was assigned as 90 s. The retention latency was noted again on the following day, and the percent retention of memory was calculated by the following formula:

$$[\text{Transfer latency (day 42} - \text{day 43)/Transfer latency (day 42)}] \times 100$$

2.4.3 Biochemical Measurements

2.4.3.1 Parameters Assessed by ELISA

The ELISA kits purchased from MyBiosource, Inc. (Southern California, San Diego, CA, United States) were used for estimating the striatal contents of cyclic adenosine monophosphate (cAMP; cat#: MBS018906), BDNF (cat#: MBS355345), and nuclear factor E2-related factor 2 (Nrf-2; cat#: MBS752046), whereas striatal content of thiobarbituric acid reactive substances (TBARS) was measured using a rat ELISA kit (cat#:MD 25 28) purchased from Bio-Diagnostics (Worcestershire, UK). For the determination of caspase-3 activity (cat# ab39401), the corresponding ELISA kit was purchased from Abcam (Cambridge, UK). For all parameters, the assays were performed according to the protocol of the manufacturer. The protein content was quantified according to the method described by Bradford (Camby et al., 2002).

2.4.3.2 Quantitative Real-Time Polymerase Chain Reaction

Total RNA was extracted and purified from the homogenized rat striatal tissue using Qiagen tissue extraction kit (Qiagen, USA), and the purity (A260/A280 ratio) and the concentration of RNA were obtained using spectrophotometry (dual wavelength Beckman, Spectrophotometer, USA). The total RNA (0.5–2 µg)

TABLE 1 | The primer sequences used for RT-qPCR.

Gene	Primer sequence (5′–3′)
miR-130a	Forward: 5′-ACACTCCAGCTGGGGCTCTTTTCACATTGT-3′
	Reverse: 5′-CTCAACTGGTGTCGTGGAGTCGGCAATTCAGTTGAGAGTAGCAC-3′
U6	Forward: 5′-CTCGCTTCGGCAGCACA-3′
	Reverse: 5′-AACGCTTCACGAATTTGCGT-3′
Glial fibrillary acidic protein (GFAP)	Forward: 5′- GCTAATGACTATCGCCGCCAACT-3′
	Reverse: 5′-CTCCTTAATGACCTCGCCATCCC-3′
Heat shock protein 27 (HSP27)	Forward: 5′-ACGAAGAAAGGCAGGATGAA-3′
	Reverse: 5′-GCTCCAGACTGTTCCGACTC-3′
Dopamine- and cAMP-regulated phosphoprotein (DARPP-32)	Forward: 5′-AGTTAGGGGAGCTTCG-3′
	Reverse: 5′-AGTTTCCATCTCTCTGGG-3′
Peripheral benzodiazepine receptor (PBR_	Forward: 5′-TCCTGCTTTCATGACCATTGGGC-3′
	Reverse: 5′-ACAACTGTCCCCGCATGGGACTTAG-3′
p75 neurotrophin receptor (p75NTR)	Forward: 5′-AGGGATGGCGTGACTTTC-3′
	Reverse: 5′-GTTGGCTTCAGGCTTATGC-3′
B-cell lymphoma 2-associated X protein (Bax)	Forward: 5′-CCCTGTGCACTAAAGTGCCCC-3′
	Reverse: 5′-GTCAGATGGACACATGGTG-3′
B-cell lymphoma 2 (Bcl2)	Forward: 5′-CTACGAGTGGGATGCTGGAGG-3′
	Reverse: 5′-GTCAGATGGACACATGGTG-3′
B-cell lymphoma-extra large (Bcl-XL)	Forward: 5′-GATCCCCATGGCAGCAGTAAAGCAAG-3′
	Reverse: 5′- CCCCATCCCGGAAGAGTTCATTCACT-3′
β-Actin	Forward: 5′-GGTCGGTGTGAACGGATTTGG-3′
	Reverse: 5′-ATGTAGGCCATGAGGTCCACC-3′

was used for cDNA conversion using high-capacity cDNA reverse transcription kit (Fermentas, USA) according to the instructions of the manufacturer. Quantitative RT-PCR was performed to assess the gene expression of the glial fibrillary acidic protein (GFAP), heat shock protein 27 (HSP27), dopamine- and cAMP-regulated phosphoprotein (DARPP-32), peripheral benzodiazepine receptor (PBR), p75 neurotrophin receptor (p75NTR), BCL2-associated X (Bax), B-cell lymphoma 2 (Bcl2), B-cell lymphoma-extra large (Bcl-XL), and miR-130a using SYBR Green I. The qPCR amplification and analysis were performed using an Applied Biosystem with software version 3.1 (StepOne™, USA) according to the instructions of the manufacturer. Briefly, 3 µl of random primers (**Table 1**) were added to the 10 µl of RNA, which was denatured for 5 min at 65°C in the thermal cycler. The RNA primer mixture was cooled to 4°C, and the cDNA master mix was prepared according to the kit instructions and added (19 µl) to each sample; this was added to the 13 µl of RNA-primer mixture resulting in 50 µl of cDNA. The last mixture was incubated in the programmed thermal cycler for 1 h at 37°C followed by inactivation of enzymes at 95°C for 10 min and finally cooled at 4°C, then RNA was changed into cDNA. The converted cDNA was stored at −20°C. The relative quantitation (RQ) of the target genes was calculated using the 2−ΔΔCt formula (Livak and Schmittgen, 2001). All values were normalized to the housekeeping gene β-actin, except for miR-130a that was normalized to U6, and presented as fold changes.

2.4.3.3 Western Blot Analysis

After proteins were extracted from striatal tissues using RIPA lysis buffer PL005, equal amounts of the samples were loaded onto 8% sodium dodecyl sulfate-polyacrylamide gels. A sample was separated on a polyacrylamide gel; the procedure was abbreviated as SDS-PAGE (for sodium dodecyl sulfate polyacrylamide gel electrophoresis) according to the molecular weights. Following electrophoresis, parameters were transferred to nitrocellulose membranes (Amersham Bioscience, Piscataway, NJ, USA) using a semidry transfer apparatus (Bio-Rad, Hercules, CA, USA). The membrane was blocked with 5% (w/v) nonfat dry milk in tris-buffered saline with Tween 20 (TBST) buffer and 3% bovine serum albumin (BSA) at room temperature for 1 h to block non-specific binding sites. Subsequently, membranes were incubated with a 1: 1,000 dilution of antibodies from Thermo Fisher Scientific, Inc. (Rockford, IL, USA) against rat tropomyosin receptor kinase B (TrKB; cat.# PA5-86241), sortilin (cat.# PA1-18312), phospho-phosphatidylinositol 3-kinase (pTyr458-PI3Kp85; cat.# PA5-17387), total PI3K (T-PI3K; cat.# PA5-38904), phosphor-protein kinase B (pS473-Akt; cat.# PA5-85513), T-Akt (cat.# PA5-29169), pS133-CREB (cat.# PA1-851B), and T-CREB (cat.# PA1-850), from Abcam (Cambridge, UK), phospho-glycogen synthase kinase (pS9-GSK-3β; cat.# ab131097), and T-GSK-3β (cat.#ab131356), and from Santa Cruz (CA, USA), pS33β-catenin (cat.# sc-57535) and T-β-catenin (cat.# sc-7963) for 1 h at room temperature with constant shaking. Next, membranes were probed with horseradish peroxidase-conjugated goat anti-mouse immunoglobulins (1:2000; Fluka, St. Louis, MO, USA). Eventually, the band intensity was read and analyzed using a ChemiDoc™ imaging system with Image Lab™ software version 5.1 (Bio-Rad Laboratories, Inc., Hercules, CA, USA). The results are displayed as arbitrary unit (AU) after normalization to levels of the β-actin protein.

2.4.4 Histopathological Examination

Brains were carefully removed from three representative animals in different groups, rinsed with ice-cold saline, and immediately fixed with 10% formalin for 24 h. Samples were dehydrated by incubations in serial dilutions of alcohol, cleared with xylene, and embedded in paraffin at 56°C in a hot air oven for 24 h. Coronal

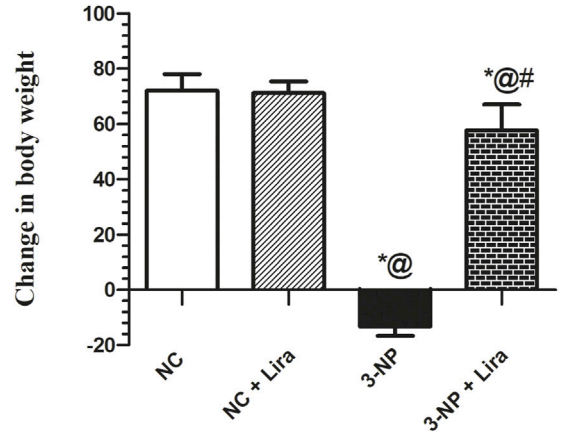

FIGURE 2 | Effect of Lira treatment on body weight in the 3-NP-treated rats. Data are presented as mean ± S.D. (n = 15/group). Statistical analysis was performed using one-way ANOVA followed by Tukey's multiple comparison test; compared with (*) NC, (#) 3-NP, and (@) NC + Lira groups, $p < 0.05$. ANOVA, analysis of variance; Lira, liraglutide; NC, normal control; 3-NP, 3-nitropropionic acid.

brain sections of 4-μm thickness were processed using sledge microtome. Sections were then stained with hematoxylin and eosin (H&E) and examined under a light electric microscope (Olympus CX21, Tokyo, Japan).

2.5 Statistical Analysis

Data are expressed as means ± SD. Statistical analysis and graphical presentations were performed using GraphPad prism software, version 6 (GraphPad Software, Inc., San Diego, CA, USA). One-way ANOVA followed by the Tukey's multiple comparison test was used for statistical evaluation of the difference among means, and the level of significance was set at $p < 0.05$. Data are considered outliers if the data points failed the Dixon test (Dixon, 1954) or if they exceeded four standard deviations of the mean. To ensure sample size sufficiency to establish a statistically significant difference, Mead's "Resource Equation" was used (Mead, 1988).

3 RESULTS

Noteworthy, normal group treated with Lira (NC + Lira) showed no significant changes from the normal control (NC) group in all the measured parameters; hence, all comparisons were conducted relative to NC.

3.1 Effect of Lira on Body Weight

One-way ANOVA showed significant differences among groups on the percent change in body weight (**Figure 2**). Rats in the NC and NC + Lira showed a normal increase in body weight in the 42 days of the experiment. The 3-NP insult, however, resulted in a marked reduction in the final body weight, compared with the NC group. Treatment with Lira bolstered the body weight and obviously raised it, compared with that of 3-NP.

3.2 Effect of Lira on Locomotor Activity Using the Open Field Test

As depicted in **Figure 3**, the OFT revealed hypoactivity and gait abnormalities in 3-NP-untreated rats evidenced by a marked increase in latency time (**Figure 3A**) to reach approximately eightfold that of the NC group. The insult also decreased ambulation (**Figure 3B**), grooming (**Figure 3C**), and rearing (**Figure 3D**) frequencies by about 70%, compared with the NC group. On the other hand, treatment with Lira shortened the latency time by 92%, along with a marked increase in ambulation, grooming, and rearing frequencies to reach approximately threefold the diseased group.

3.3 Effect of Lira on Spatial Long-Term Memory Using the Elevated Plus Maze Test

Figure 4 shows that 3-NP-induced neurodegeneration entailed the long-term memory, where it caused a sixfold delay in the retention transfer latency compared with the vehicle treated group. In contrast, post-administration of Lira significantly abridged the retention latencies by 66% compared with the insult effect. The insult caused a marked reduction in the percentage of memory retention by 133% compared with the NC group. Contrariwise, the Lira-treated group displayed about threefold increment in this assessed parameter when compared with the 3-NP-insulted rats.

3.4 Lira Augments miR-130a and the Cyclic Adenosine Monophosphate/Cyclic Adenosine Monophosphate Response Element-Binding Protein/Brain-Derived Neurotrophic Factor/ Tropomyosin Receptor Kinase B Trajectory

As illustrated in **Figure 5**, the 3-NP administration abated the striatal gene expression of the protective gene miR-130a (**Figure 5A**), as well as the content of cAMP (**Figure 5B**), p-CREB (**Figure 5C**), BDNF (**Figure 5D**), and its receptor TrKB (**Figure 5E**) by about 72%, 66%, 76%, 66%, and 80%, respectively, compared with the 3-NP group. Nevertheless, rats treated with Lira augmented the neuroprotective gene and trail, where it upregulated the gene expression of miR-130a and markedly enhanced the content/protein expression of the c-AMP/CREB axis and its downstream molecules, when compared with the 3-NP group.

3.5 Lira Suppressed Death Receptor and Sortilin

As depicted in **Figure 6**, the 3-NP insult caused an upsurge in the mRNA expression of the death receptor, namely, p75NTR (**Figure 6A**), as well as the protein expression of its coreceptor sortilin (**Figure 6B**), mounted to about seven- and sixfold elevation, respectively, when compared with normal rats. However, Lira post-administration has softened the 3-NP effect and depressed the assessed markers to reach 37% and 45%, respectively, compared with the diseased group.

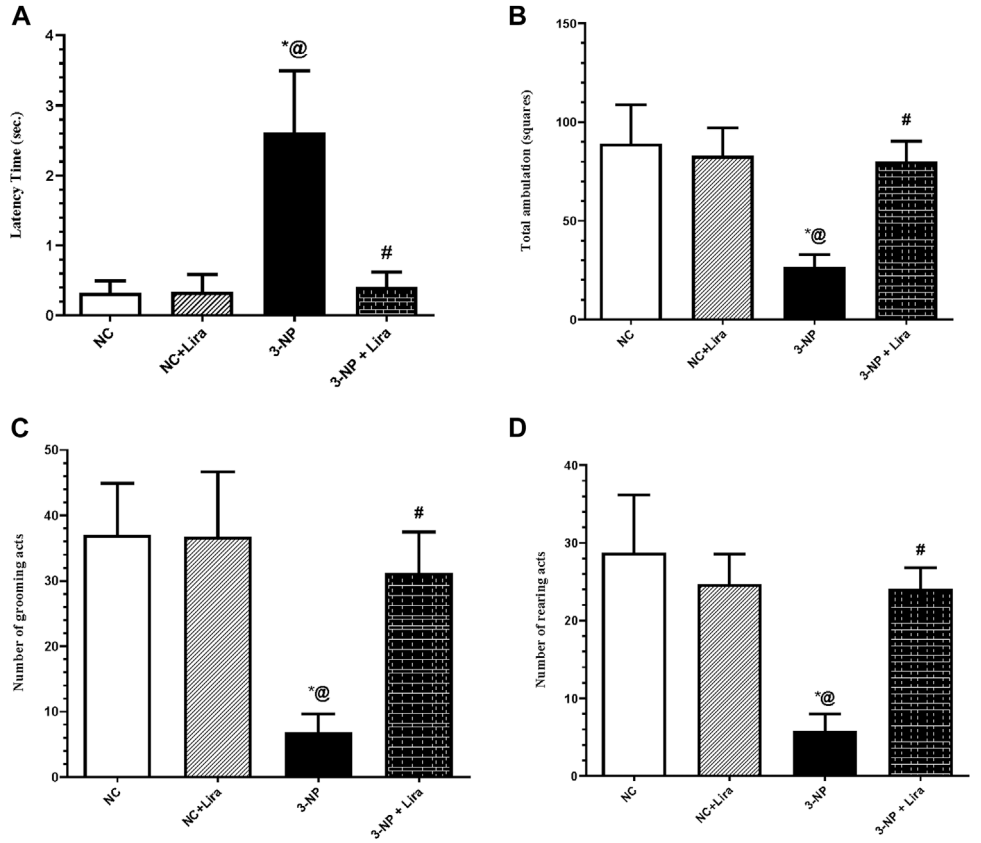

FIGURE 3 | Effect of Lira treatment on the open field test (OFT) **(A)** latency, **(B)** total ambulation, **(C)** number of grooming, and **(D)** rearing acts in 3-NP treated rats. Data are presented as mean ± S.D. (n = 15/group). Statistical analysis was performed using one-way ANOVA followed by Tukey's multiple comparison test; compared with (*) NC, (#) 3-NP, and (@) NC + Lira groups, $p < 0.05$. ANOVA, analysis of variance; Lira, liraglutide; NC, normal control; 3-NP, 3-nitropropionic acid; OFT. open-field test.

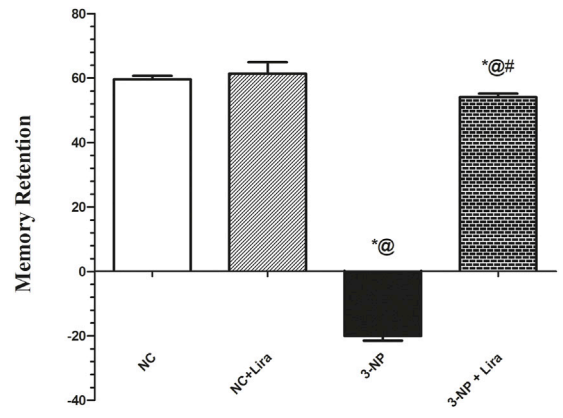

FIGURE 4 | Effect of Lira treatment on the elevated plus maze (EPM). Data are presented as mean ± S.D. (n = 15/group). Statistical analysis was performed using one-way ANOVA followed by Tukey's multiple comparison test; compared with (*) NC, (#) 3-NP, and (@) NC + Lira groups, $p < 0.05$. ANOVA, analysis of variance; EPM, elevated plus maze; Lira, liraglutide; NC, normal control; 3-NP, 3-nitropropionic acid.

3.6 Lira Modulated the PI3K/Akt/GSK-3β/β-Catenin Signaling Pathway

In **Figure 7**, the neurodegenerative effect of 3-NP was accompanied by a sharp decrease in the protein expression of p-PI3K (**Figure 7A**) and its downstream molecule p-Akt (**Figure 7B**). In turn, 3-NP activated the injurious marker GSK-3β documented by the depletion of its inactive/phosphorylated form p-GSK-3β (**Figure 7C**), with the subsequent phosphorylation of its downstream molecule p-β-catenin (**Figure 7D**) to be marked for degradation. However, administration of Lira to intoxicated rats has averted the 3-NP effects, where it turned on the protective axis and heightened the p-PI3K/p-Akt axis and inactivated p-GSK-3β by increasing its phosphorylated form, an effect that was associated by the activation/dephosphorylation of β-catenin, relative to the 3-NP insult.

3.7 Lira Restored Redox Balance and Decreased Neuronal Apoptosis

The 3-NP-induced redox imbalance (**Figure 8**) was evidenced by the 72% suppression of the antioxidant transcription factor Nrf-2

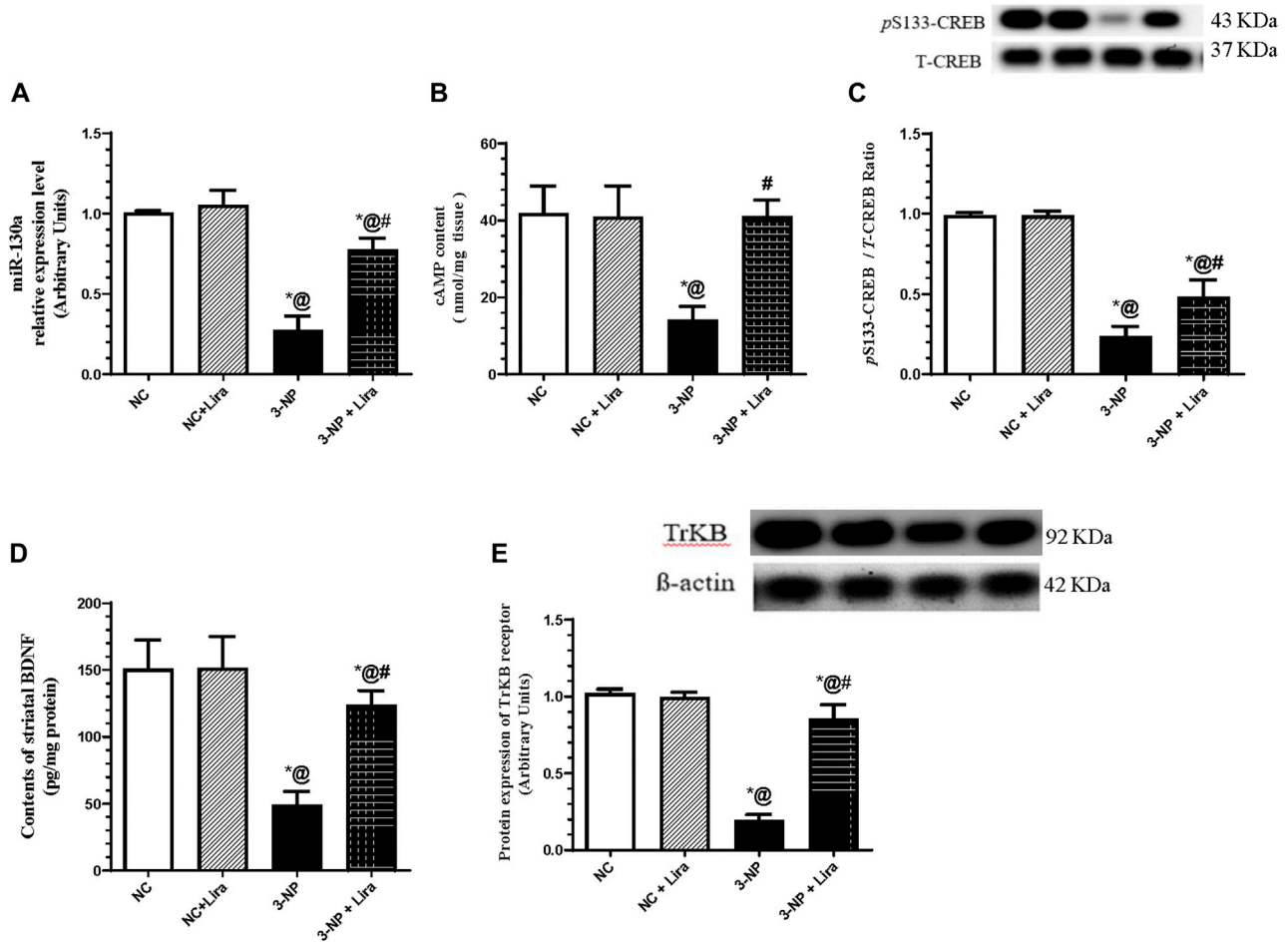

FIGURE 5 | Effect of Lira on gene/protein expression and content of **(A)** miR-130a, **(B)** cAMP, **(C)** p-CREB, **(D)** BDNF, and **(E)** TrKB in 3-NP-treated rats. Data are presented as mean ± S.D. (n = 3–6/group). Statistical analysis was performed using one-way ANOVA followed by Tukey's multiple comparison test; as compared with (*) NC, (#) 3-NP, and (@) NC + Lira groups, $p < 0.05$. ANOVA, analysis of variance; cAMP, cyclic adenosine monophosphate; BDNF, brain-derived neurotrophic factor; p-CREB, phosphor-cAMP response element-binding protein; Lira, liraglutide; miR, micro-RNA; NC, normal control; 3-NP, 3-nitropropionic acid; TrKB. tropomyosin-related kinase receptor.

(**Figure 8A**) effect that was accompanied by the threefold elevation of the lipid peroxidation marker TBARS (**Figure 8B**) compared with normal animals. Additionally, 3-NP enhanced cell apoptotic demise indicated by the 72% reduction in the antiapoptotic marker Bcl-XL (**Figure 8C**), with a 49-fold increase in Bax/Bcl-2 ratio (**Figure 8D**) and a fourfold increase in caspase-3 activity (**Figure 8E**), when compared with the NC group. However, Lira-treated rats displayed a remarkable antioxidant effect verified by its ability to boost striatal Nrf-2 (threefold) that was paralleled by a considerable reduction in striatal TBARS content by 41.5%, compared with the 3-NP-lesioned rats. Moreover, the antiapoptotic activity of Lira was evidenced by the reduction in Bax/Bcl-2 ratio by 95% and caspase-3 activity by 54% compared with the intoxicated group. Besides, it resulted in a threefold elevation in Bcl-XL gene expression compared with the 3-NP rats.

3.8 Lira obliterated Gliosis and Astrocytic Activation, but Enhanced Mature Medium Spiny Neurons

As apparent from **Figure 9**, the 3-NP-intoxicated rats displayed a robust neuroinflammation, ongoing gliosis, and astrocytic activation indicated by the upregulation of the mRNA expression of PBR, HSP27, and GFAP, to about 7.8-, 4.6-, and 5.6-fold, respectively, compared with the NC group. Additionally, the toxin induced a significant neuronal damage as it caused a notable downregulation of the most widely used marker of mature MSNs, DARPP-32, by 73%, when compared with the NC group. Treatment with Lira diversely impeded the upsurge in the assessed parameters; PBR, HSP27, and GFAP reached 32%, 36%, and 32%, respectively, compared with the 3-NP group, while causing an upsurge of the striatal DARPP-32 relative expression (nearly threefold) compared with the 3-NP-lesioned rats.

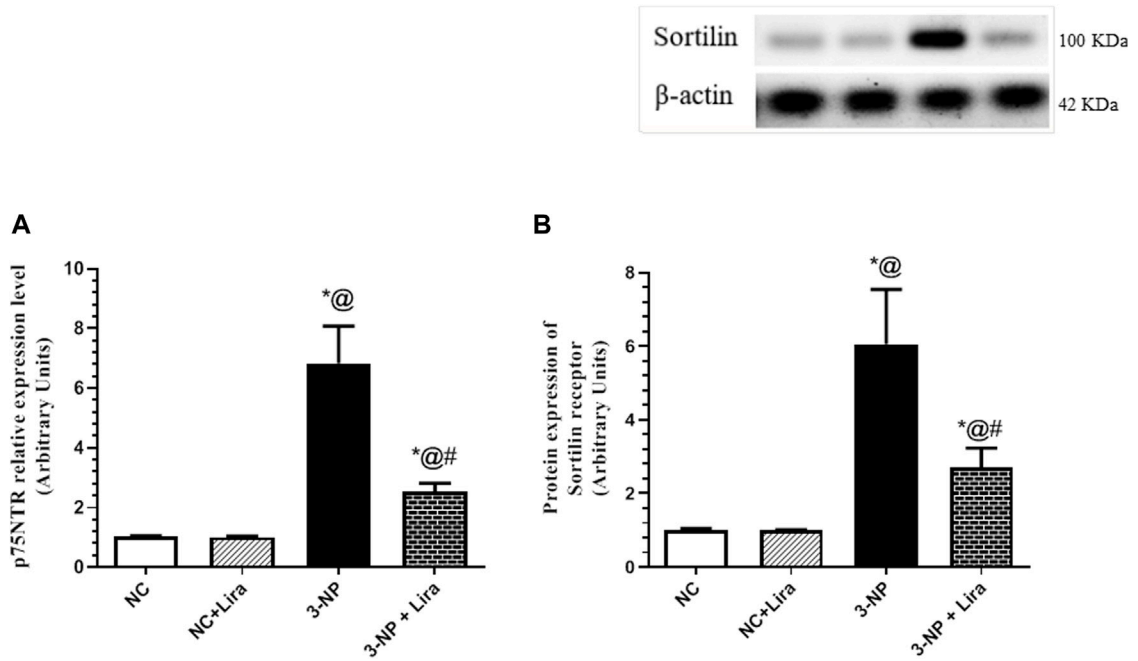

FIGURE 6 | Effect of Lira on gene/protein expression of striatal **(A)** p75NTR and **(B)** sortilin in 3-NP-treated rats. Data are presented as mean ± S.D. (n = 3/group). Statistical analysis was performed using one-way ANOVA followed by Tukey's multiple comparison test; compared with (*) NC, (#) 3-NP, and (@) NC + Lira groups, $p < 0.05$. ANOVA, analysis of variance; p75NTR, p75 neurotrophin receptor; Lira, liraglutide; NC, normal control; 3-NP, 3-nitropropionic acid.

3.9 Lira Improved Structural Alterations

As depicted in **Figure 10**, photomicrograph sections from NC (**Figures 10A–F**) and NC + Lira (**Figures 10G–L**) reveal normal histological structures of neurons in the cerebral cortex, subiculum of the hippocampus, fascia dentate and hilus of the hippocampus, striatum, cerebellum, and medulla oblongata. In contrast, sections of 3-NP reveal focal neuronal degeneration with gliosis in the outer area of the cerebral cortex (**Figure 10M**), while the inner deep area shows focal gliosis, while no histopathological alterations are seen in the subiculum of the hippocampus (**Figure 10N**). However, most of the neurons of the fascia dentate and hilus of the hippocampus show degeneration with nuclear pyknosis (**Figure 10O**). Moreover, a section of the striatum (**Figure 10P**) reveals multiple focal eosinophilic plaques along with diffuse gliosis in between nuclear pyknosis and neuronal degeneration. A section of the cerebellum (**Figure 10Q**) shows congested blood vessels; however, a section of the medulla oblongata (**Figure 10R**) reveals normal histological structures of neurons. On the other hand, sections of the Lira-treated group show normal histological structures of the six assessed areas (**Figures 10S–X**).

4 DISCUSSION

The current study highlighted the potential neuro-therapeutic effect of Lira in a 3-NP-induced HD model. The findings showed that Lira prominently recovered the 3-NP-induced behavioral derangements and degeneration of striatal MSNs; the evident upturn of the neurobehavioral performance was obviously mirrored on the histopathological findings. These findings match that of a previous study, where Lira prevented hippocampal neurodegeneration and cognitive decline following intracerebroventricular injection of streptozotocin in Wistar rats (Palleria et al., 2017).

The improved functional tests have been echoed here using the OFT, which revealed shortened latency time and a noticeable increase in ambulation, grooming, and rearing frequencies in the Lira-treated rats, hindering, thus, the 3-NP effect significantly. In addition, Lira notably abridged the EPM retention latencies that were markedly delayed in the 3-NP group to display a considerable increment in the percentage of memory retention, when compared with that of the insulted rats. The ability of Lira to improve cognitive function was reported in previous models of mild traumatic brain injury (mTBI) (Li et al., 2015), Alzheimer's disease (McClean and Hölscher, 2014), stroke (Zhu et al., 2016), and multiple sclerosis (DellaValle et al., 2016). In the current results, Lira further pinned down its capacity to improve behavioral functions by upregulating the gene expression of DARPP-32, which affects striatal function and plasticity as documented in Parkinson's disease and schizophrenia (Meyer-Lindenberg et al., 2007), as well as models of HD. In this ailment, the protein expression of DARPP-32 was downregulated to mark the early debility of the MSNs in HD (Bibb et al., 2000; Alpaugh et al., 2017) and to concur with our results, as well.

Along with the improved behavior, the administration of Lira also ablated the 3-NP-induced histopathological alterations; the neuro-restorative impact was reflected on the improved structure

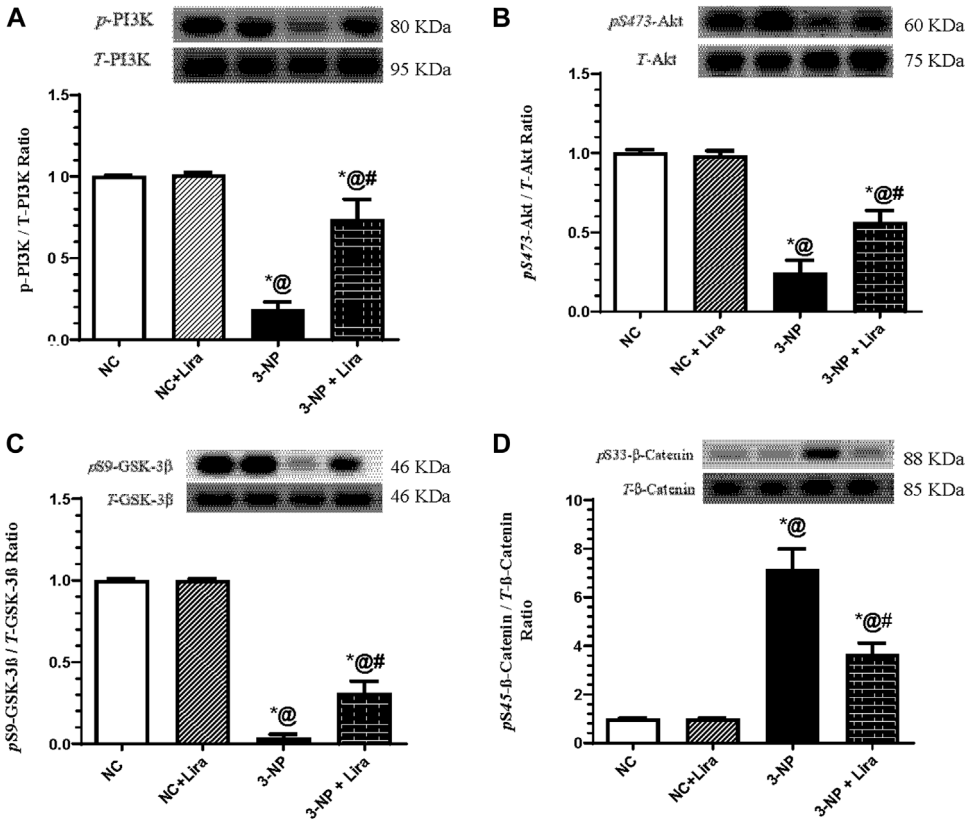

FIGURE 7 | Effect of Lira on protein expression of striatal **(A)** p-PI3K, **(B)** p-Akt, **(C)** p-GSK-3β, and **(D)** p-β-catenin in 3-NP-treated rats. Data are presented as mean ± S.D. (n = 3/group). Statistical analysis was performed using one-way ANOVA followed by Tukey's multiple comparison test; as compared with (*) NC, (#) 3-NP, and (@) NC + Lira groups, $p < 0.05$. ANOVA, analysis of variance; p-Akt, phosphor-protein kinase B; p-GSK-3β, phosphor=glycogen synthase kinase; Lira, liraglutide; NC, normal control; 3-NP, 3-nitropropionic acid; p-PI3K. phospho-phosphoinositide 3-kinase.

that revealed normal cortical, striatal, and hippocampal morphology free of nuclear pyknosis and degeneration. Indeed, the diffuse gliosis detected in the striatum was among the alterations detected here in the present HD model to be further supported by the current augmentation of GFAP that serves as an excellent index of gliosis during neurodegeneration being the main intermediary filament of astrocytes (Brahmachari et al., 2006). However, the post-administration of Lira markedly downregulated GFAP; besides, it downregulated PBR, a hallmark of neuroinflammation that is predominantly expressed in glial cells, including astrocytes and microglia. The aptitude of Lira to abate these markers explains the inactivation of microglia that entailed rescuing striatal neurons in the current HD model. As a support to this notion, a previous study revealed that the use of a mitochondrial PBR antagonist has enhanced mitochondrial function, inactivate microglia, and reduced apoptotic neuronal death and, hence, neuroinflammation in a quinolinic acid-induced HD rat model (Ryu et al., 2005). A third marker assessed here was the HSP27, which is among the markers that increase after brain damage and is also expressed in the astroglia to indicate their activation (Renkawek et al., 1993). Akin to the other glial markers, Lira mitigated HSP27 to reach its normal level and to add to the neurotherapeutic capacity of the antidiabetic drug. These data concur with the findings of a previous study in which orphenadrine, the CNS-acting anti-muscarinic drug, has conferred *in vitro* and *in vivo* neuroprotection against 3-NP-induced neuronal damage, *via* reducing the expression of both HSP27 and PBR density in the striatum of rat brains (Pubill et al., 2001).

On the molecular level, Lira has further signified its neurotherapeutic effect by turning on the neurotrophic signaling hub cAMP/CREB/BDNF/TrKB. In the present work, Lira has enhanced the content of cAMP that was distinctly leveled off by 3-NP. This effect is a sequel of the activation of the receptor GLP-1 to concur the results in an mTBI model (Li et al., 2015). As a downstream to the latter, cAMP stimulates/activates the transcription factor CREB by phosphorylating it at Ser133 (Wang et al., 2018a) to result in a 10- to 20-fold increase in the transcriptional activity of CREB (Tanis et al., 2008), findings that consolidate the present results. In the same context, Lira was recounted to mediate its neuroprotective effect by enhancing the GLP-1 receptor-induced activation of the cAMP/CREB hub (Bao et al., 2015) using primary rat cortical astrocytes.

Upon its translocation to the nucleus, activated CREB endorses the transcription and expression of its target genes BDNF and its cognate receptor TrKB (Nair and Vaidya, 2006; Chou et al., 2020). This verity has been mirrored herein, since following the activated cAMP/p-CREB axis, Lira succeeded to

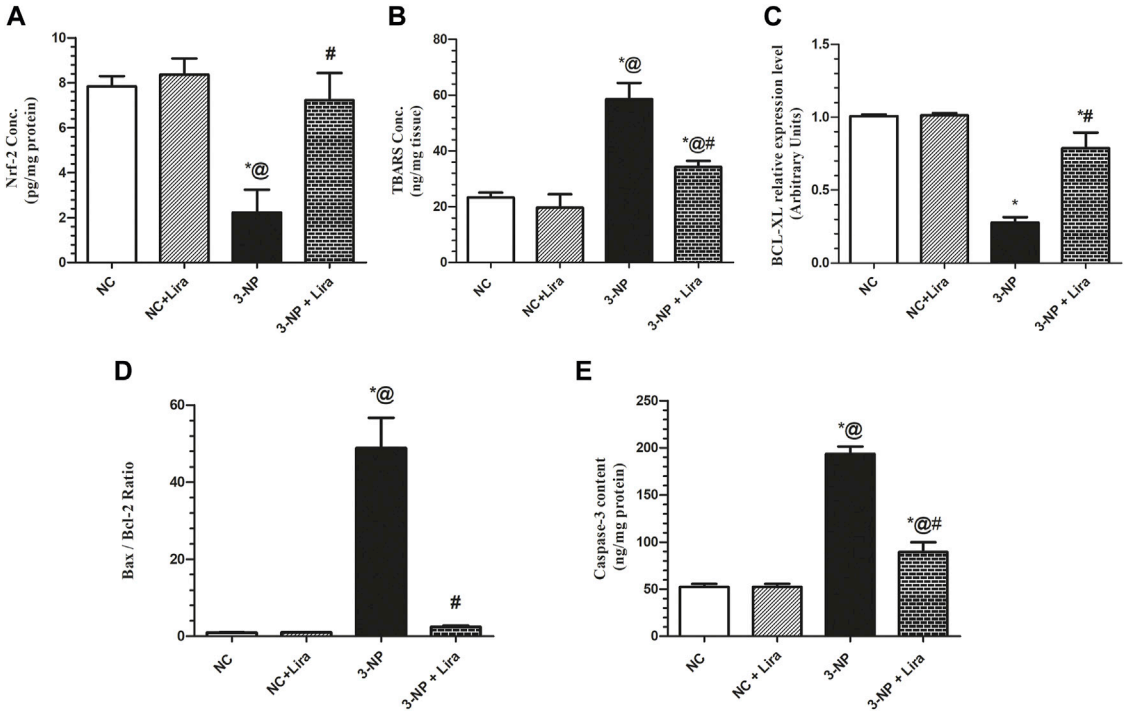

FIGURE 8 | Effect of Lira on protein expression/content of striatal **(A)** Nrf-2, **(B)** TBARS, **(C)** BCL-XL, **(D)** Bax/Bcl-2 ratio, and **(E)** caspase-3 in 3-NP-treated rats. Data are presented as mean ± S.D. (n = 3/group). Statistical analysis was performed using one-way ANOVA followed by Tukey's multiple comparison test; compared with (*) NC, (#) 3-NP, and (@) NC + Lira groups, $p < 0.05$. ANOVA, analysis of variance; Bax, Bcl-2-associated X protein; Bcl-2, B-cell lymphoma 2; BCL-XL, B-cell lymphoma—extra large; Lira, liraglutide; TBARS, malondialdehyde; NC, normal control; 3-NP, 3-nitropropionic acid; Nrf-2, nuclear factor E2-related factor 2.

oppose the effect of 3-NP and augmented the striatal contents of BDNF and the protein expression of its receptor TrKB. In turn, this points for one mechanism by which Lira has mediated its neurotrophic potential, findings that coincide with those of a previous study in a brain trauma model (DellaValle et al., 2014).

Mature BDNF (mBDNF), which is the biologically active form, binds with high affinity to the TrkB receptor and with lower affinity to the death receptor p75NTR (Kowiański et al., 2018) to mediate its beneficial effect. Notably, the mBDNF/TrKB complex is critical for structural (increases in spine density and size) and functional plasticity (LTP), and have important roles in learning and memory (De Vincenti et al., 2019). Earlier studies have highlighted the chief role of the BDNF/TrKB hub in neurogenesis, gliogenesis, neurite outgrowth, development, and maintenance of the basal ganglia in addition to promoting survival and proper function of the striatal neuronal population (Bath and Lee, 2010; Baydyuk and Xu, 2014). This pathway, hence, adds to the mechanisms by which Lira recovered cognitive and behavior functions, as well as antagonizing the 3-NP insult.

To further confine the role of BDNF in the Lira-mediated neuroprotection, the present study is the first to show that Lira has turned off the proBDNF death pathway, where it inhibited the striatal relative expression levels of the proBDNF receptors, *viz.*, p75NTR and sortilin. In agreement with the "yin–yang" hypothesis, mBDNF and its precursor, proBDNF, have opposing effects on the cellular physiology (Gibon et al., 2016). By binding to its pan-neurotrophin receptor, p75NTR, and the co-receptor, sortilin (Lee et al., 2001), proBDNF negatively regulates synaptic transmission and plasticity (Kailainathan et al., 2016). Besides, it inhibits neuronal regeneration, increases the collapse of neurite growth, and promotes apoptotic cell death, as documented here and beforehand (Liu et al., 2018). An earlier study reported that the distressing effects of proBDNF are dependent on the cellular co-expression of both p75NTR and sortilin, and suggested that neurons deficient in p75NTR are resistant to proBDNF-induced apoptosis (Teng et al., 2005). Hence, these facts affirm the present data and further explain the mechanism of Lira and nominate p75NTR to be a valuable therapeutic target (Meeker and Williams, 2014) that contributes significantly to HD progression (Plotkin and Surmeier, 2014).

The binding of mBDNF to its receptor triggers a trail of several signals that crosstalk to mediate its neurogenic effect. The first is the PI3K/Akt signaling pathway, which when turned on presents a central node for complexed functions that modulates diverse multifaceted events resulting in neuronal survival (Sánchez-Alegría et al., 2018). However, the dysregulated PI3K/Akt signaling in neurons has several harmful consequences, such as increased reactive oxygen species (ROS), membrane depolarization, mitochondrial fragmentation, as well as decreased oxidative phosphorylation and ATP production (Kim et al., 2016). In the current work, Lira has activated *p*-PI3K and *p*-Akt to concur with the findings of Yang et al.

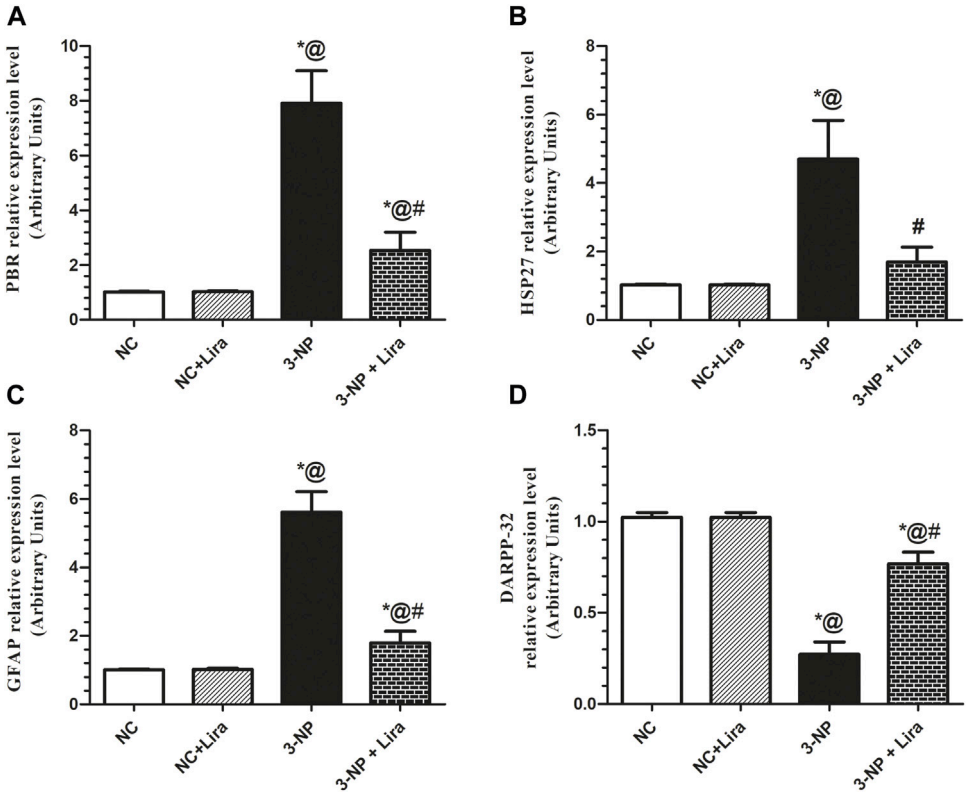

FIGURE 9 | Effect of Lira on mRNA expression of striatal **(A)** PBR, **(B)** HSP27, **(C)** GFAP, and **(D)** DARPP-32 in 3-NP-treated rats. Data are presented as mean ± S.D. (n = 3/group). Statistical analysis was performed using one-way ANOVA followed by Tukey's multiple comparison test; compared with (*) NC, (#) 3-NP, and (@) NC + Lira groups, $p < 0.05$. ANOVA, analysis of variance; DARPP-32, dopamine- and cAMP-regulated phosphoprotein; GFAP, glial fibrillary acidic protein; HSP27, heat shock protein 27; Lira, liraglutide; NC, normal control; 3-NP, 3-nitropropionic acid; PBR, peripheral benzodiazepine receptor.

(2018) in a model of type 2 diabetes, where Lira mediated its neuroprotective effect and improved cognitive function through triggering the PI3K/Akt hub. In turn, the activated Akt plays a crucial role being a central key that manipulated several downstreams and is one of the most multifaceted kinases in the human kinome (Ahn, 2014) that ensures neuron survival (Zhang et al., 2016; Mohamed et al., 2019; Xu et al., 2020). One of the favorable effects of the activated *p*-Akt is its antioxidant (Ali et al., 2018; Wen et al., 2018) and antiapoptotic (Matsuzaki et al., 1999; Pan et al., 2019) potentials, facts that can share a part in verifying the antioxidant and antiapoptotic capacities of Lira that were documented herein.

In fact, oxidative stress (OS) and the disruption of redox homeostasis have long been held as key players in HD progression and pathogenesis (Kumar and Ratan, 2016; Li et al., 2019). The antioxidant capability of *p*-Akt can depend on the adjustment of its downstream molecules; for instance, *p*-Akt induces the expression of Nrf2, a master regulator of cellular redox homeostasis and facilitates its nuclear translocation through its tethering to the nuclear antioxidant response element (ARE). Following this union, a wide array of antioxidant enzymes is generated (Cui et al., 2016) to guard against OS (Tu et al., 2019). This has also been confirmed by previous studies that divulged that activation of the PI3K/Akt pathway induces the expression of Nrf2 to culminate in the decrease of ROS and TBARS levels, as well as neuronal apoptosis as reported here and hitherto (Ali et al., 2018; Liu et al., 2019).

Our results also highlight the role of Akt/GSK-3β/*p*-CREB and β-catenin signaling, another *p*-Akt downstream axis that reinforces its antioxidant and neurotherapeutic effects. In the Lira-treated group, the activation of Akt was tailed by the phosphorylation/inactivation of GSK-3β to concur with an earlier *in vitro* AD model (Zheng et al., 2019). The *p*-GSK-3β is a promiscuous serine-threonine kinase that regulates a wide variety of cellular functions, and its inactivation protects against neuronal toxicity (Goodenough et al., 2004). Indeed, OS brings about GSK-3β overactivation in neuronal cells (Rana and Singh, 2018), while inhibition of the latter is required to control OS in neuronal hippocampal cell lines (Jaworski et al., 2019). Moreover, inhibition of GSK-3β attenuates early stroke injury in a focal ischemic model (Wang et al., 2017). In the same milieu, Mehrafza and coworkers showed that lithium, a known GSK-3 inhibitor, has protected neurons against methamphetamine-induced neurodegeneration *via* turning on the Akt-1/GSK3 and CREB-BDNF signaling pathways, where it was recounted earlier that inactivated GSK-3β endorses the phosphorylation of CREB at Ser133 (Silva-García et al., 2018). This, in turn, allows *p*-CREB to exert its

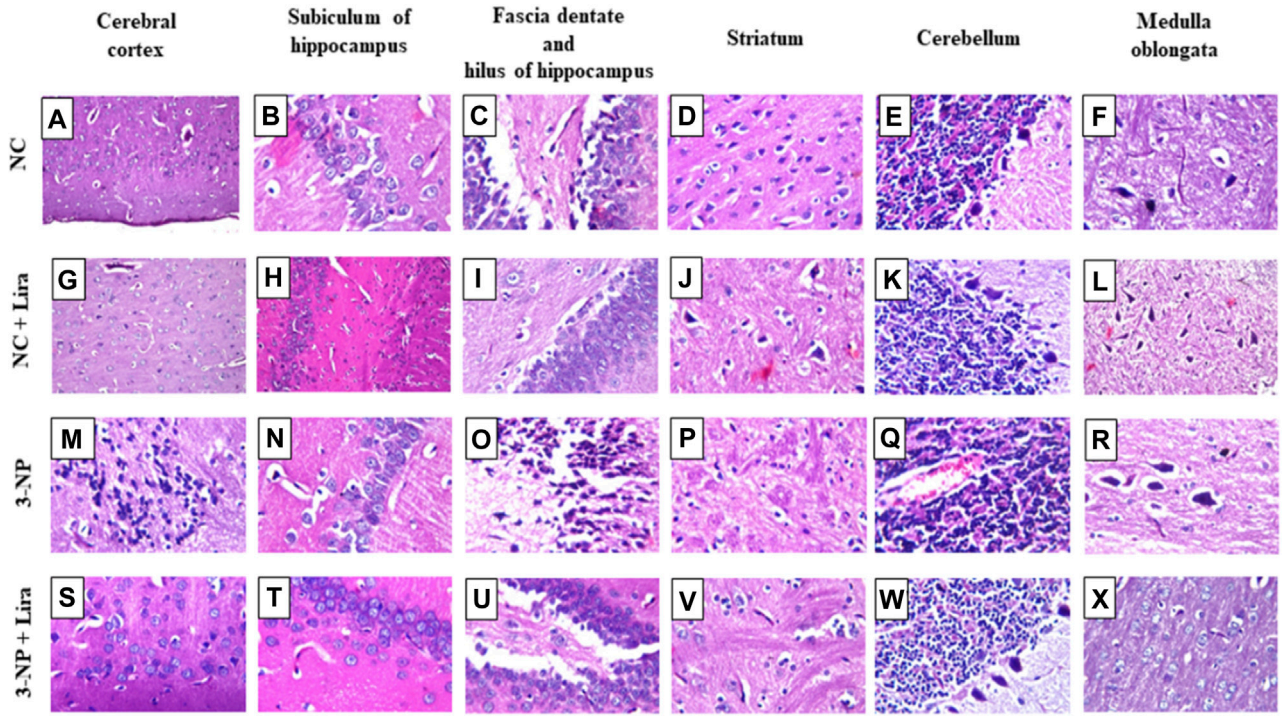

FIGURE 10 | Effect of Lira on 3-NP-induced histologic alterations. Compared with the normal neuronal histological structures seen in **(A–F)** NC and **(G–L)** NC + Lira-treated group, the sections of the 3-NP-intoxicated rats show focal neuronal degeneration with gliosis in **(M)** cerebral cortex, normal morphology of **(N)** hippocampal subiculum, nuclear pyknosis and neuronal degeneration in **(O)** fascia dentate and hilus of the hippocampus, multiple focal eosinophilic plaques with focal gliosis and neuronal damage in **(P)** striatum, congestion of blood vessels in **(Q)** cerebellum, and normal morphology of **(R)** medulla oblongata. Sections of **(S–X)** 3-NP + Lira-treated group show normal histological structures of all assessed six areas (H&E × 80). Lira, liraglutide; NC, normal control; 3-NP, 3-nitropropionic acid.

neuroprotective role as stated earlier by heightening the production of BDNF (Shimizu et al., 2019), which has an imperative role in promoting neuronal survival and differentiation by acting through its TrKB receptor. In a positive uninterrupted loop, BDNF/TrKB reactivates CREB to bestow high neuronal protection (Kowiański et al., 2018). Additionally, the crosstalk between CREB and Nrf2 via CREB-binding protein has been underlined, revealing that CREB transcription could activate the expression of Nrf2 binding partners via an indirect mechanism (Wang et al., 2016) to partake in the verification of the antioxidant capacity of Lira documented herein. These verities synchronize with the current findings, where 3-NP produced a significant reduction in *p*-Akt and, consequently, activated GSK-3β by suppressing its phosphorylation at Ser9. The inhibition of *p*-Akt entailed its downstream trajectory *p*-CREB/BDNF/TrKB to verify the role of neuronal OS in the advancement of 3-NP-induced preferential striatal degeneration, as declared herein and reported hitherto (El-Abhar et al., 2018). However, Lira post-administration resulted in offsetting the effects of 3-NP.

Aside from the GSK-3β/CREB axis, another downstream target of the GSK-3β is β-catenin, which runs inversely to its upstream GSK-3β (Huang et al., 2017). *β*-Catenin is another molecule that is known to have a dynamic role in synaptic plasticity and neurogenesis (Zhang et al., 2011; Yang et al., 2017b). Thus, one can postulate that the antioxidant effect of Lira that helps in mitigating the 3-NP neurodegenerative effect hangs on the central hub *p*-Akt/*p*-GSK-3β with its two downstream molecules *p*-CREB and β-catenin.

The ability of Lira to restore the redox balance aids in increasing cell survival, where OS is well documented to partake in apoptotic cell demise, especially the intrinsic pathway by waning mitochondrial function followed by activation of caspase-3 (Carvour et al., 2008; Méndez-Armenta et al., 2014). Besides, the ability of Lira to downregulate the expression of PBR hinders this pathway too, since as mentioned before, PBR plays a role in mitochondrial permeability transition pore formation (Jorda et al., 2005) and its decrease helps in abrogating cell death (Ryu et al., 2005).

The antiapoptotic potential of Lira also banks on the assessed pathways; indeed, earlier studies underlined the antiapoptotic role of Akt *per se* by phosphorylating the proapoptotic protein Bad, thereby, inhibiting its proapoptotic function (del Peso et al., 1997). In addition, activated Akt prohibits neuronal death effectively by inhibiting the activation of caspase-3 and Bax expression, but induces that of the antiapoptotic molecule Bcl-2, effects that were abolished upon using the specific PI3K inhibitor wortmannin (LY294002) (Matsuzaki et al., 1999). A more recent study showed that Lira protected against cerebral focal ischemia by reducing cell apoptosis *via* activating the PI3K/Akt pathway (Zhu et al., 2016). These studies harmonize with the

present findings, where Lira heightened *p*-Akt and, hence, significantly reduced Bax/Bcl-2 ratio and caspase-3 activity; besides, it resulted in a substantial elevation of Bcl-XL gene expression.

Furthermore, the Akt/GSK-3β/β-catenin and CREB axes play a foremost role in cell survival *via* regulating apoptosis. The downregulation of the defense signal Akt/GSK-3β advocates the neuronal death partially *via* suppressing CREB activity, which correlates with the expression of many survival and proliferation genes (El-Abhar et al., 2018). Moreover, increased CREB activity supports cell survival by boosting the expression of cell-protective proteins, such as Bcl-2 (Cheng et al., 2016) and BDNF (Huang et al., 2015), facts that further back the present findings. Recently, a study by Zhang et al. (2019b) divulged that Lira possesses an antiapoptotic effect by enhancing *p*-CREB and upregulating the expression of the antiapoptotic Bcl-2 in an experimental diabetes model. Not only does CREB but also β-catenin represses apoptosis by inhibiting caspase-3 (Sinha et al., 2015), as well as Bax (Wang et al., 2009), while augmenting Bcl-2 (Manji et al., 2000). These data abet the present results regarding the effect of Lira on the apoptosis-related markers assessed in the present work.

Ample evidence has proclaimed that the role of miRNAs must be considered a vital aspect contributing to the pathogenesis of diverse neurodegenerative diseases as HD through targeting diverse molecules, such as BDNF (Godlewski et al., 2019). Our results showed that treatment with Lira has upregulated miR-130a noticeably, while 3-NP has markedly downregulated it, a finding that braces the neurotherapeutic effect of Lira. One clinical study has reported a marked decrease in the plasma level of miR-130a in acute ischemic stroke patients and was negatively correlated with disease risk and severity (Jin and Xing, 2018), results that may nominate it as a non-invasive promising diagnostic and prognostic biomarker (Eyileten et al., 2018). Meanwhile, the expression of miR-130a was evidently downregulated in PC12 cells after oxygen–glucose deprivation/reperfusion (OGDR) and in rats subjected to ischemic stroke and neurodegeneration. These authors proposed that not only did miR-130 offer protection against cerebral ischemic injury but also its overexpression enhanced the survival of PC12 cells, reduced apoptosis and the overproduction of ROS after OGDR, as well as the cerebral infarct volume in the stroke model. In the same setting, another study reported that miR-130a reduces the blood–brain barrier permeability induced by cerebral ischemia (Wang et al., 2018b). According to the current findings, a crosstalk between miR-130a and the assessed signals can be postulated, a notion that was partly reported in a previous study. The coresearchers revealed that the re-expression of miR-130a enhanced the activation of BDNF-mediated PI3K/Akt signaling pathway by inhibiting PTEN, a mechanism that underlies the neuroprotection against cerebral ischemia–reperfusion injury. However, the correlation between miR-130a and the BDNF/TrKB/PI3K/Akt/GSK-3β/β-catenin/CREB trajectory, as well as the p75NTR–sortilin receptor complex along with the redox imbalance and apoptosis has been reported first in the present work.

In conclusion, the current study has revealed the promising neurotherapeutic potential of Lira against 3-NP-induced HD *via* modulating the crosstalk between cAMP/CREB/BDNF/TrkB, PI3K/Akt/GSK-3β/β-catenin, and GSK-3β/CREB trajectories. In addition, Lira upregulated the newly diagnostic non-invasive promising biomarker, miR-130a, while it curbed the p75NTR–sortilin receptor complex. Meanwhile, Lira purveyed pronounced antioxidant and antiapoptotic potentials in 3-NP model of HD. These mechanisms resulted in an upturn in behavioral and morphological results.

5 LIMITATIONS AND STRENGTHS

The strength of our work is studying the therapeutic effect of the antidiabetic drug Lira against 3-NP-induced HD-like model. The effect was proven through improving cognition and memory, and the upturn of the striatal morphological structure that was altered in the 3-NP-untreated group. On the molecular level, the drug enhanced several survival pathways and abated others that play a role in neurodegeneration.

The limitations of the possible repurposing of Lira is using only one HD model; however, this effect should be attested upon using other HD models. Also, the study use male rats only, and the effect of Lira should also be carried out on different species and genders. Moreover, other signaling pathways have to be evaluated to unveil more therapeutic mechanisms before proceeding to the clinical trials.

DATA AVAILABILITY STATEMENT

The raw data supporting the conclusion of this article will be made available by the authors, without undue reservation.

ETHICS STATEMENT

The animal study was reviewed and approved by the Ethics Committee for Animal Experimentation at the Faculty of Pharmacy, Cairo University (permit number: PT 2099).

AUTHOR CONTRIBUTIONS

EH designed the research. SS performed the research. SM, RR, and WW analyzed the data. All authors wrote and approved the manuscript. All data were generated in-house, and no paper mill was used.

SUPPLEMENTARY MATERIAL

The Supplementary Material for this article can be found online at: https://www.frontiersin.org/articles/10.3389/fphar.2021.731483/full#supplementary-material

REFERENCES

Agrawal, S., and Fox, J. H. (2019). Novel Proteomic Changes in Brain Mitochondria Provide Insights into Mitochondrial Dysfunction in Mouse Models of Huntington's Disease. *Mitochondrion* 47, 318–329. doi:10.1016/j.mito.2019.03.004

Ahn, J. Y. (2014). Neuroprotection Signaling of Nuclear Akt in Neuronal Cells. *Exp. Neurobiol.* 23, 200–206. doi:10.5607/en.2014.23.3.200

Ali, T., Kim, T., Rehman, S. U., Khan, M. S., Amin, F. U., Khan, M., et al. (2018). Natural Dietary Supplementation of Anthocyanins via PI3K/Akt/Nrf2/HO-1 Pathways Mitigate Oxidative Stress, Neurodegeneration, and Memory Impairment in a Mouse Model of Alzheimer's Disease. *Mol. Neurobiol.* 55, 6076–6093. doi:10.1007/s12035-017-0798-6

Alpaugh, M., Galleguillos, D., Forero, J., Morales, L. C., Lackey, S. W., Kar, P., et al. (2017). Disease-modifying Effects of Ganglioside GM1 in Huntington's Disease Models. *EMBO Mol. Med.* 9, 1537–1557. doi:10.15252/emmm.201707763

Badawi, G. A., Abd El Fattah, M. A., Zaki, H. F., and El Sayed, M. I. (2017). Sitagliptin and Liraglutide Reversed Nigrostriatal Degeneration of Rodent Brain in Rotenone-Induced Parkinson's Disease. *Inflammopharmacology* 25 (3), 369–382. doi:10.1007/s10787-017-0331-6

Bao, Y., Jiang, L., Chen, H., Zou, J., Liu, Z., and Shi, Y. (2015). The Neuroprotective Effect of Liraglutide Is Mediated by Glucagon-like Peptide 1 Receptor-Mediated Activation of cAMP/PKA/CREB Pathway. *Cell Physiol. Biochem.* 36, 2366–2378. doi:10.1159/000430199

Barker, R., and Mason, S. L. (2019). The hunt for Better Treatments for Huntington's Disease. *Lancet Neurol.* 18 (2), 131–133. doi:10.1016/S1474-4422(18)30448-4

Bath, K. G., and Lee, F. S. (2010). Neurotrophic Factor Control of Adult SVZ Neurogenesis. *Dev. Neurobiol.* 70, 339–349. doi:10.1002/dneu.20781

Baydyuk, M., and Xu, B. (2014). BDNF Signaling and Survival of Striatal Neurons. *Front. Cel. Neurosci.* 8, 254. doi:10.3389/fncel.2014.00254

Bibb, J. A., Yan, Z., Svenningsson, P., Snyder, G. L., Pieribone, V. A., Horiuchi, A., et al. (2000). Severe Deficiencies in Dopamine Signaling in Presymptomatic Huntington's Disease Mice. *Proc. Natl. Acad. Sci. U S A.* 97, 6809–6814. doi:10.1073/pnas.120166397

Bomba, M., Granzotto, A., Castelli, V., Massetti, N., Silvestri, E., Canzoniero, L. M. T., et al. (2018). Exenatide Exerts Cognitive Effects by Modulating the BDNF-TrkB Neurotrophic axis in Adult Mice. *Neurobiol. Aging* 64, 33–43. doi:10.1016/j.neurobiolaging.2017.12.009

Brahmachari, S., Fung, Y. K., and Pahan, K. (2006). Induction of Glial Fibrillary Acidic Protein Expression in Astrocytes by Nitric Oxide. *J. Neurosci.* 26, 4930–4939. doi:10.1523/JNEUROSCI.5480-05.2006

Bruzelius, E., Scarpa, J., Zhao, Y., Basu, S., Faghmous, J. H., and Baum, A. (2019). Huntington's Disease in the United States: Variation by Demographic and Socioeconomic Factors. *Move. Disord.* 34 (6), 858–865. doi:10.1002/mds.27653

Camby, I., Belot, N., Lefranc, F., Sadeghi, N., de Launoit, Y., Kaltner, H., et al. (2002). Galectin-1 Modulates Human Glioblastoma Cell Migration into the Brain through Modifications to the Actin Cytoskeleton and Levels of Expression of Small GTPases. *J. Neuropathol. Exp. Neurol.* 61 (7), 585–596. doi:10.1093/jnen/61.7.585

Carvour, M., Song, C., Kaul, S., Anantharam, V., Kanthasamy, A., and Kanthasamy, A. (2008). Chronic Low Dose Oxidative Stress Induces Caspase-3 Dependent PKCδ Proteolytic Activation and Apoptosis in a Cell Culture Model of Dopaminergic Neurodegeneration. *Ann. N.Y Acad. Sci.* 1139, 197. doi:10.1196/annals.1432.020

Cheng, C., Tang, N., Kao, S., and Hsieh, C. (2016). Ferulic Acid Administered at Various Time Points Protects against Cerebral Infarction by Activating P38 MAPK/p90RSK/CREB/Bcl-2 Anti-apoptotic Signaling in the Subacute Phase of Cerebral Ischemia-Reperfusion Injury in Rats. *PLoS One* 11, e0155748. doi:10.1371/journal.pone.0155748

Chou, L. Y., Chao, Y. M., Peng, Y. C., Lin, H. C., and Wu, Y. L. (2020). Glucosamine Enhancement of BDNF Expression and Animal Cognitive Function. *Molecules* 25, 3667. doi:10.3390/molecules25163667

Cirillo, G., Cirillo, M., Panetsos, F., Virtuoso, A., and Papa, M. (2019). Selective Vulnerability of Basal Ganglia: Insights into the Mechanisms of Bilateral Striatal Necrosis. *J. Neuropathol. Exp. Neurol.* 78 (2), 123–129. doi:10.1093/jnen/nly123

Cui, Q., Li, X., and Zhu, H. (2016). Curcumin Ameliorates Dopaminergic Neuronal Oxidative Damage via Activation of the Akt/Nrf2 Pathway. *Mol. Med. Rep.* 13, 1381–1388. doi:10.3892/mmr.2015.4657

De Vincenti, A. P., Ríos, A. S., Paratcha, G., and Ledda, F. (2019). Mechanisms that Modulate and Diversify BDNF Functions: Implications for Hippocampal Synaptic Plasticity. *Front. Cel. Neurosci.* 13, 135. doi:10.3389/fncel.2019.00135

del Peso, L., González-Garcıa, M., Page, C., Herrera, R., and Nunez, G. (1997). Interleukin-3-induced Phosphorylation of BAD through the Protein Kinase Akt. *Science* 278, 687–689. doi:10.1126/science.278.5338.687

DellaValle, B., Brix, G. S., Brock, B., Gejl, M., Landau, A. M., Møller, A., et al. (2016). Glucagon-like Peptide-1 Analog, Liraglutide, Delays Onset of Experimental Autoimmune Encephalitis in lewis Rats. *Front. Pharmacol.* 7, 433. doi:10.3389/fphar.2016.00433

DellaValle, B., Hempel, C., Johansen, F. F., and Kurtzhals, J. A. (2014). GLP-1 Improves Neuropathology after Murine Cold Lesion Brain Trauma. *Ann. Clin. Transl. Neurol.* 1, 721–732. doi:10.1002/acn3.99

Dixon, W. J. (1954). Power under Normality of Several Nonparametric Tests. *Ann. Math. Statist.* 25 (3), 610–614. doi:10.1214/aoms/1177728732

Dong, W., Miao, Y., Chen, A., Cheng, M., Ye, X., Song, F., et al. (2017). Delayed Administration of the GLP-1 Receptor Agonist Liraglutide Improves Metabolic and Functional Recovery after Cerebral Ischemia in Rats. *Neurosci. Lett.* 641, 1–7. doi:10.1016/j.neulet.2017.01.045

Durães, F., Pinto, M., and Sousa, E. (2018). Old Drugs as New Treatments for Neurodegenerative Diseases. *Pharmaceuticals (Basel)* 11 (2), 44.

El-Abhar, H., Abd El Fattah, M. A., Wadie, W., and El-Tanbouly, D. M. (2018). Cilostazol Disrupts TLR-4, Akt/GSK-3β/CREB, and IL-6/JAK-2/STAT-3/SOCS-3 Crosstalk in a Rat Model of Huntington's Disease. *PloS One* 13 (9), e0203837. doi:10.1371/journal.pone.0203837

Eyileten, C., Wicik, Z., De Rosa, S., Mirowska-Guzel, D., Soplinska, A., Indolfi, C., et al. (2018). MicroRNAs as Diagnostic and Prognostic Biomarkers in Ischemic Stroke—A Comprehensive Review and Bioinformatic Analysis. *Cells* 7, 249. doi:10.3390/cells7120249

Filchenko, I., Simanenkova, A., Chefu, S., Kolpakova, M., and Vlasov, T. (2018). Neuroprotective Effect of Glucagon-like Peptide-1 Receptor Agonist Is Independent of Glycaemia Normalization in Type Two Diabetic Rats. *Diab. Vasc. Dis. Res.* 15 (6), 567–570. doi:10.1177/1479164118788079

Gibon, J., Barker, P. A., and Séguéla, P. (2016). Opposing Presynaptic Roles of BDNF and ProBDNF in the Regulation of Persistent Activity in the Entorhinal Cortex. *Mol. Brain* 9, 23. doi:10.1186/s13041-016-0203-9

Godlewski, J., Lenart, J., and Salinska, E. (2019). MicroRNA in Brain Pathology: Neurodegeneration the Other Side of the Brain Cancer. *Non-Coding RNA* 5, 20. doi:10.3390/ncrna5010020

Goodenough, S., Conrad, S., Skutella, T., and Behl, C. (2004). Inactivation of Glycogen Synthase Kinase-3β Protects against Kainic Acid-Induced Neurotoxicity *In Vivo*. *Brain Res.* 1026, 116–125. doi:10.1016/j.brainres.2004.08.021

Huang, J., Guo, X., Li, W., and Zhang, H. (2017). Activation of Wnt/β-Catenin Signalling via GSK3 Inhibitors Direct Differentiation of Human Adipose Stem Cells into Functional Hepatocytes. *Scientific Rep.* 7, 1–12. doi:10.1038/srep40716

Huang, W., Cao, J., Liu, X., Meng, F., Li, M., Chen, B., et al. (2015). AMPK Plays a Dual Role in Regulation of CREB/BDNF Pathway in Mouse Primary Hippocampal Cells. *J. Mol. Neurosci.* 56, 782–788. doi:10.1007/s12031-015-0500-2

Huguet, G., Temel, Y., Kádár, E., Pol, S., Casaca-Carreira, J., Segura-Torres, P., et al. (2019). Altered Expression of Dopaminergic Cell Fate Regulating Genes Prior to Manifestation of Symptoms in a Transgenic Rat Model of Huntington's Disease. *Brain Res.* 1712, 101–108. doi:10.1016/j.brainres.2019.01.041

Jaworski, T., Banach-Kasper, E., and Gralec, K. (2019). GSK-3β at the Intersection of Neuronal Plasticity and Neurodegeneration. *Neural Plasticity* 2019, 1–14. doi:10.1155/2019/4209475

Jin, F., and Xing, J. (2018). Circulating miR-126 and miR-130a Levels Correlate with Lower Disease Risk, Disease Severity, and Reduced Inflammatory Cytokine Levels in Acute Ischemic Stroke Patients. *Neurol. Sci.* 39, 1757–1765. doi:10.1007/s10072-018-3499-7

Jorda, E. G., Jimenez, A., Verdaguer, E., Canudas, A. M., Folch, J., Sureda, F. X., et al. (2005). Evidence in Favour of a Role for Peripheral-type Benzodiazepine

Receptor Ligands in Amplification of Neuronal Apoptosis. *Apoptosis* 10, 91–104. doi:10.1007/s10495-005-6064-9

Kailainathan, S., Piers, T. M., Yi, J. H., Choi, S., Fahey, M. S., Borger, E., et al. (2016). Activation of a Synapse Weakening Pathway by Human Val66 but Not Met66 Pro-brain-derived Neurotrophic Factor (proBDNF). *Pharmacol. Res.* 104, 97–107. doi:10.1016/j.phrs.2015.12.008

Kim, D. I., Lee, K. H. Gabr., Gabr, A. A., Choi, G. E. Kim., Kim, J. S., Ko, S. H., et al. (2016). Aβ-Induced Drp1 Phosphorylation through Akt Activation Promotes Excessive Mitochondrial Fission Leading to Neuronal Apoptosis. *Biochim. Biophys. Acta* 1863, 2820–2834. doi:10.1016/j.bbamcr.2016.09.003

Kowiański, P., Lietzau, G., Czuba, E., Waśkow, M., Steliga, A., and Moryś, J. (2018). BDNF: a Key Factor with Multipotent Impact on Brain Signaling and Synaptic Plasticity. *Cell Mol. Neurobiol.* 38, 579–593. doi:10.1007/s10571-017-0510-4

Kumar, A., and Ratan, R. R. (2016). Oxidative Stress and Huntington's Disease: The Good, the Bad, and the Ugly. *J. Huntingtons Dis.* 5, 217–237. doi:10.3233/JHD-160205

Kumar, M., Kaur, D., and Bansal, N. (2017). Caffeic Acid Phenethyl Ester (CAPE) Prevents Development of STZ-ICV Induced Dementia in Rats. *Pharmacogn Mag.* 13 (Suppl. 1), S10–S15. doi:10.4103/0973-1296.203974

Lallani, S. B., Villalba, R. M., Chen, Y., Smith, Y., and Chan, A. W. S. (2019). Striatal Interneurons in Transgenic Nonhuman Primate Model of Huntington's Disease. *Sci. Rep.* 9 (1), 3528. doi:10.1038/s41598-019-40165-w

Lee, R., Kermani, P., Teng, K. K., and Hempstead, B. L. (2001). Regulation of Cell Survival by Secreted Proneurotrophins. *Science* 294, 1945–1948. doi:10.1126/science.1065057

Li, D., Ni, S., Miao, K. S., and Zhuang, C. (2019). PI3K/Akt and Caspase Pathways Mediate Oxidative Stress-Induced Chondrocyte Apoptosis. *Cell Stress Chaperones* 24, 195–202. doi:10.1007/s12192-018-0956-4

Li, Y., Bader, M., Tamargo, I., Rubovitch, V., Tweedie, D., Pick, C. G., et al. (2015). Liraglutide Is Neurotrophic and Neuroprotective in Neuronal Cultures and Mitigates Mild Traumatic Brain Injury in Mice. *J. Neurochem.* 135, 1203–1217. doi:10.1111/jnc.13169

Liu, S., Guo, W., Zhou, H., Tang, L., Feng, S., Zhong, J. H., et al. (2018). proBDNF Inhibits the Proliferation and Migration of OLN-93 O-ligodendrocytes. *Mol. Med. Rep.* 18, 3809–3817. doi:10.3892/mmr.2018.9407

Liu, Y., Zhang, S., Xue, J., Wei, Z., Ao, P., Shen, B., et al. (2019). CGRP Reduces Apoptosis of DRG Cells Induced by High-Glucose Oxidative Stress Injury through PI3K/AKT Induction of Heme Oxygenase-1 and Nrf-2 Expression. *Oxidative Med. Cell. Longevity* 2019, 2053149. doi:10.1155/2019/2053149

Livak, K. J., and Schmittgen, T. D. (2001). Analysis of Relative Gene Expression Data Using Real-Time Quantitative PCR and the 2(-Delta Delta C(T)) Method. *Methods* 25 (4), 402–408. doi:10.1006/meth.2001.1262

Manji, H. K., Moore, G. J., and Chen, G. (2000). Lithium Up-Regulates the Cytoprotective Protein Bcl-2 in the CNS *In Vivo*: A Role for Neurotrophic and Neuroprotective Effects in Manic Depressive Illness. *J. Clin. Psychiatry* 61 (Suppl. 9), 82–96.

Marso, S. P., Daniels, G. H., Brown-Frandsen, K., Kristensen, P., Mann, J. F., Nauck, M. A., et al. (2016). Liraglutide and Cardiovascular Outcomes in Type 2 Diabetes. *N. Engl. J. Med.* 375 (4), 311–322. doi:10.1056/NEJMoa1603827

Matsuzaki, H., Tamatani, M., Mitsuda, N., Namikawa, K., Kiyama, H., Miyake, S., et al. (1999). Activation of Akt Kinase Inhibits Apoptosis and Changes in Bcl-2 and Bax Expression Induced by Nitric Oxide in Primary Hippocampal Neurons. *J. Neurochem.* 73, 2037–2046. doi:10.1046/j.1471-4159.1999.02037.x

McClean, P. L., and Hölscher, C. (2014). Liraglutide Can Reverse Memory Impairment, Synaptic Loss and Reduce Plaque Load in Aged APP/PS1 Mice, a Model of Alzheimer's Disease. *Neuropharmacology* 76, 57–67. doi:10.1016/j.neuropharm.2013.08.005

Mead, R. (1988). *The Design of Experiments: Statistical Principles for Practical Applications*. New York, NY, US: Cambridge University Press.

Meeker, R., and Williams, K. (2014). Dynamic Nature of the P75 Neurotrophin Receptor in Response to Injury and Disease. *J. Neuroimmune Pharmacol.* 9, 615–628. doi:10.1007/s11481-014-9566-9

Méndez-Armenta, M., Nava-Ruíz, C., Juárez-Rebollar, D., Rodríguez-Martínez, E., and Yescas Gómez, P. (2014). Oxidative Stress Associated with Neuronal Apoptosis in Experimental Models of Epilepsy. *Oxidative Med. Cell. Longevity* 2014, 1–12. doi:10.1155/2014/293689

Meyer-Lindenberg, A., Straub, R. E., Lipska, B. K., Verchinski, B. A., Goldberg, T., Callicott, J. H., et al. (2007). Genetic Evidence Implicating DARPP-32 in Human Frontostriatal Structure, Function, and Cognition. *J. Clin. Invest.* 117, 672–682. doi:10.1172/JCI30413

Mohamed, W. A., Salama, R. M., and Schaalan, M. F. (2019). A Pilot Study on the Effect of Lactoferrin on Alzheimer's Disease Pathological Sequelae: Impact of the P-Akt/PTEN Pathway. *Biomed. Pharmacother.* 111, 714–723. doi:10.1016/j.biopha.2018.12.118

Nair, A., and Vaidya, V. A. (2006). Cyclic AMP Response Element Binding Protein and Brain-Derived Neurotrophic Factor: Molecules that Modulate Our Mood. *J. Biosci.* 31, 423–434. doi:10.1007/BF02704114

Palleria, C., Leo, A., Andreozzi, F., Citraro, R., Iannone, M., Spiga, R., et al. (2017). Liraglutide Prevents Cognitive Decline in a Rat Model of Streptozotocin-Induced Diabetes Independently from its Peripheral Metabolic Effects. *Behav. Brain Res.* 321, 157–169. doi:10.1016/j.bbr.2017.01.004

Pan, X. D., Chen, X. L., Ding, S. F., Kou, D., Hu, H. L., and Li, L. (2019). Promethazine Inhibits Neuronal Apoptosis via PI3K/Akt Signaling Pathway in Rats with Cerebral Infarction. *Eur. Rev. Med. Pharmacol. Sci.* 23, 126–134. doi:10.26355/eurrev_201908_18639

Plotkin, J. L., and Surmeier, D. J. (2014). Impaired Striatal Function in Huntington's Disease Is Due to Aberrant p75NTR Signaling. *Rare Dis.* 2, e968482. doi:10.4161/2167549X.2014.968482

Pubill, D., Verdaguer, E., Canudas, A. M., Sureda, F. X., Escubedo, E., Camarasa, J., et al. (2001). Orphenadrine Prevents 3-nitropropionic Acid-Induced Neurotoxicity *In Vitro* and *In Vivo*. *Br. J. Pharmacol.* 132, 693–702. doi:10.1038/sj.bjp.0703869

Rana, A. K., and Singh, D. (2018). Targeting Glycogen Synthase Kinase-3 for Oxidative Stress and Neuroinflammation: Opportunities, Challenges and Future Directions for Cerebral Stroke Management. *Neuropharmacology* 139, 124–136. doi:10.1016/j.neuropharm.2018.07.006

Renkawek, K., Bosman, G. J., and Gaestel, M. (1993). Increased Expression of Heat-Shock Protein 27 kDa in Alzheimer Disease: a Preliminary Study. *Neuroreport* 5, 14–16. doi:10.1097/00001756-199310000-00003

Ryu, J. K., Choi, H. B., and McLarnon, J. G. (2005). Peripheral Benzodiazepine Receptor Ligand PK11195 Reduces Microglial Activation and Neuronal Death in Quinolinic Acid-Injected Rat Striatum. *Neurobiol. Dis.* 20, 550–561. doi:10.1016/j.nbd.2005.04.010

Sánchez-Alegría, K., Flores-León, M., Avila-Muñoz, E., Rodríguez-Corona, N., and Arias, C. (2018). PI3K Signaling in Neurons: A Central Node for the Control of Multiple Functions. *Int. J. Mol. Sci.* 19, 3725. doi:10.3390/ijms19123725

Sharma, D., Verma, S., Vaidya, S., Kalia, K., and Tiwari, V. (2018). Recent Updates on GLP-1 Agonists: Current Advancements & Challenges. *Biomed. Pharmacother.* 108, 952–962. doi:10.1016/j.biopha.2018.08.088

Shimizu, S., Ishino, Y., Takeda, T., Tohyama, M., and Miyata, S. (2019). Antidepressive Effects of Kamishoyosan through 5-HT1AReceptor and PKA-CREB-BDNF Signaling in the Hippocampus in Postmenopausal Depression-Model Mice. *Evidence-Based Complementary & Altern. Med.* 2019, 1–11. doi:10.1155/2019/9475384

Silva-García, O., Rico-Mata, R., Maldonado-Pichardo, M. C., Bravo-Patiño, A., Valdez-Alarcón, J. J., Aguirre-González, J., et al. (2018). Glycogen Synthase Kinase 3α Is the Main Isoform that Regulates the Transcription Factors Nuclear Factor-Kappa B and cAMP Response Element Binding in Bovine Endothelial Cells Infected with Staphylococcus aureus. *Front. Immunol.* 9, 92. doi:10.3389/fimmu.2018.00092

Sinha, A., Tamboli, R. S., Seth, B., Kanhed, A. M., Tiwari, S. K., Agarwal, S., et al. (2015). Neuroprotective Role of Novel Triazine Derivatives by Activating Wnt/β Catenin Signaling Pathway in Rodent Models of Alzheimer's Disease. *Mol. Neurobiol.* 52, 638–652. doi:10.1007/s12035-014-8899-y

Suelves, N., Miguez, A., López-Benito, S., Barriga, G. G., Giralt, A., Alvarez-Periel, E., et al. (2019). Early Downregulation of p75NTR by Genetic and Pharmacological Approaches Delays the Onset of Motor Deficits and Striatal Dysfunction in Huntington's Disease Mice. *Mol. Neurobiol.* 56 (2), 935–953. doi:10.1007/s12035-018-1126-5

Tabrizi, S. J., Ghosh, R., and Leavitt, B. R. (2019). Huntingtin Lowering Strategies for Disease Modification in Huntington's Disease. *Neuron* 101 (5), 801–819. doi:10.1016/j.neuron.2019.01.039

Tanis, K. Q., Duman, R. S., and Newton, S. S. (2008). CREB Binding and Activity in Brain: Regional Specificity and Induction by Electroconvulsive Seizure. *Biol. Psychiatry* 63, 710–720. doi:10.1016/j.biopsych.2007.08.003

Teng, H. K., Teng, K. K., Lee, R., Wright, S., Tevar, S., Almeida, R. D., et al. (2005). ProBDNF Induces Neuronal Apoptosis via Activation of a Receptor Complex of

p75NTR and Sortilin. *J. Neurosci.* 25, 5455–5463. doi:10.1523/JNEUROSCI.5123-04.2005

Thangarajan, S., Ramachandran, S., and Krishnamurthy, P. (2016). Chrysin Exerts Neuroprotective Effects against 3-Nitropropionic Acid Induced Behavioral Despair-Mitochondrial Dysfunction and Striatal Apoptosis via Upregulating Bcl-2 Gene and Downregulating Bax-Bad Genes in Male Wistar Rats. *Biomed. Pharmacother.* 84, 514–525. doi:10.1016/j.biopha.2016.09.070

Tu, W., Wang, H., Li, S., Liu, Q., and Sha, H. (2019). The Anti-inflammatory and Anti-oxidant Mechanisms of the Keap1/Nrf2/ARE Signaling Pathway in Chronic Diseases. *Aging Dis.* 10, 637–651. doi:10.14336/AD.2018.0513

Wang, C., Wang, Z., Xie, J., Wang, T., Wang, X., Xu, Y., et al. (2016). Dl-3-n-butylphthalide-induced Upregulation of Antioxidant Defense Is Involved in the Enhancement of Cross Talk between CREB and Nrf2 in an Alzheimer's Disease Mouse Model. *Neurobiol. Aging* 38, 32–46. doi:10.1016/j.neurobiolaging.2015.10.024

Wang, H., Xu, J., Lazarovici, P., Quirion, R., and Zheng, W. (2018). cAMP Response Element-Binding Protein (CREB): a Possible Signaling Molecule Link in the Pathophysiology of Schizophrenia. *Front. Mol. Neurosci.* 11, 255. doi:10.3389/fnmol.2018.00255

Wang, W., Li, M., Wang, Y., Wang, Z., Zhang, W., Guan, F., et al. (2017). GSK-3β as a Target for protection against Transient Cerebral Ischemia. *Int. J. Med. Sci.* 14, 333. doi:10.7150/ijms.17514

Wang, Y., Wang, M., Xia, Y., Gao, Y., Zhu, Y., Chen, S., et al. (2018). MicroRNA-130a Regulates Cerebral Ischemia–Induced Blood–Brain Barrier Permeability by Targeting Homeobox A5. *FASEB J.* 32, 935–944. doi:10.1096/fj.201700139RRR

Wang, Z., Havasi, A., Gall, J. M., Mao, H., Schwartz, J. H., and Borkan, S. C. (2009). β-Catenin Promotes Survival of Renal Epithelial Cells by Inhibiting Bax. *J. Am. Soc. Nephrol.* 20, 1919–1928. doi:10.1681/ASN.2009030253

Wen, H., Fu, Z., Wei, Y., Zhang, X., Ma, L., Gu, L., et al. (2018). Antioxidant Activity and Neuroprotective Activity of Stilbenoids in Rat Primary Cortex Neurons via the PI3K/Akt Signalling Pathway. *Molecules* 23, 2328. doi:10.3390/molecules23092328

Xu, F., Na, L., Li, Y., and Chen, L. (2020). Roles of the PI3K/AKT/mTOR Signalling Pathways in Neurodegenerative Diseases and Tumours. *Cell Biosci.* 10, 54. doi:10.1186/s13578-020-00416-0

Yang, J. L., Chen, W. Y., and Chen, S. D. (2017). The Emerging Role of GLP-1 Receptors in DNA Repair: Implications in Neurological Disorders. *Int. J. Mol. Sci.* 18 (9), 1861. doi:10.3390/ijms18091861

Yang, K., Chen, Z., Gao, J., Shi, W., Li, L., Jiang, S., et al. (2017). The Key Roles of GSK-3β in Regulating Mitochondrial Activity. *Cell Physiol. Biochem.* 44, 1445–1459. doi:10.1159/000485580

Yang, Y., Fang, H., Xu, G., Zhen, Y., Zhang, Y., Tian, J., et al. (2018). Liraglutide Improves Cognitive Impairment via the AMPK and PI3K/Akt Signaling Pathways in Type 2 Diabetic Rats. *Mol. Med. Rep.* 18, 2449–2457. doi:10.3892/mmr.2018.9180

Zhang, L., Yang, X., Yang, S., and Zhang, J. (2011). The Wnt/β-catenin Signaling Pathway in the Adult Neurogenesis. *Eur. J. Neurosci.* 33, 1–8. doi:10.1111/j.1460-9568.2010.7483.x

Zhang, Q., Xiao, X., Zheng, J., and Li, M. (2019). A Glucagon-like Peptide-1 Analog, Liraglutide, Ameliorates Endothelial Dysfunction through miRNAs to Inhibit Apoptosis in Rats. *Peer-reviewed J.* 7, e6567. doi:10.7717/peerj.6567

Zhang, W., He, H., Song, H., Zhao, J., Li, T., Wu, L., et al. (2016). Neuroprotective Effects of Salidroside in the MPTP Mouse Model of Parkinson's Disease: Involvement of the PI3K/Akt/GSK3β Pathway. *Parkinson's Dis.* 2016, 1–9. doi:10.1155/2016/9450137

Zhang, Y., Xie, J. Z., Xu, X. Y., Hu, J., Xu, T., Jin, S., et al. (2019). Liraglutide Ameliorates Hyperhomocysteinemia-Induced Alzheimer-like Pathology and Memory Deficits in Rats via Multi-Molecular Targeting. *Neurosci. Bull.* 35, 724–734. doi:10.1007/s12264-018-00336-7

Zhao, Y., Yang, B., Huang, L. A., and Zhang, Y. (2018). Liraglutide Ameliorates β-amyloid Deposits and Secondary Damage in the Ipsilateral Thalamus and Sensory Deficits after Focal Cerebral Infarction in Rats. *Front. Neurosci.* 12, 962. doi:10.3389/fnins.2018.00962

Zheng, T., Shi, Y., Zhang, J., Peng, J., Zhang, X., Chen, K., et al. (2019). MiR-130a Exerts Neuroprotective Effects against Ischemic Stroke through PTEN/PI3K/AKT Pathway. *Biomed. Pharmacother.* 117, 109117. doi:10.1016/j.biopha.2019.109117

Zhu, H., Zhang, Y., Shi, Z., Lu, D., Li, T., Ding, Y., et al. (2016). The Neuroprotection of Liraglutide against Ischaemia-Induced Apoptosis through the Activation of the PI3K/AKT and MAPK Pathways. *Sci. Rep.* 6, 26859–26911. doi:10.1038/srep26859

Conflict of Interest: The authors declare that the research was conducted in the absence of any commercial or financial relationships that could be construed as a potential conflict of interest.

Publisher's Note: All claims expressed in this article are solely those of the authors and do not necessarily represent those of their affiliated organizations, or those of the publisher, the editors, and the reviewers. Any product that may be evaluated in this article, or claim that may be made by its manufacturer, is not guaranteed or endorsed by the publisher.

Copyright © 2021 Shawki, Saad, Rahmo, Wadie and El-Abhar. This is an open-access article distributed under the terms of the Creative Commons Attribution License (CC BY). The use, distribution or reproduction in other forums is permitted, provided the original author(s) and the copyright owner(s) are credited and that the original publication in this journal is cited, in accordance with accepted academic practice. No use, distribution or reproduction is permitted which does not comply with these terms.

frontiers in Aging Neuroscience

ORIGINAL RESEARCH
published: 03 January 2022
doi: 10.3389/fnagi.2021.804991

Quantitative Electroencephalography as a Biomarker for Cognitive Dysfunction in Parkinson's Disease

Kevin Novak[1,2†], Bruce A. Chase[1,3†], Jaishree Narayanan[1,2], Premananda Indic[4] and Katerina Markopoulou[1,2]*

[1] Department of Neurology, NorthShore University HealthSystem, Evanston, IL, United States, [2] Department of Neurology, Pritzker School of Medicine, University of Chicago, Chicago, IL, United States, [3] Department of Health Information Technology, Clinical Analytics, NorthShore University HealthSystem, Evanston, IL, United States, [4] Department of Electrical Engineering, The University of Texas at Tyler, Tyler, TX, United States

OPEN ACCESS

Edited by:
Jiehui Jiang,
Shanghai University, China

Reviewed by:
Guosheng Yi,
Duke University, United States
Vilfredo De Pascalis,
Sapienza University of Rome, Italy

***Correspondence:**
Katerina Markopoulou
amarkopoulou@northshore.org

† These authors have contributed equally to this work and share first authorship

Specialty section:
This article was submitted to Parkinson's Disease and Aging-related Movement Disorders, a section of the journal Frontiers in Aging Neuroscience

Received: *29 October 2021*
Accepted: *25 November 2021*
Published: *03 January 2022*

Citation:
Novak K, Chase BA, Narayanan J, Indic P and Markopoulou K (2022) Quantitative Electroencephalography as a Biomarker for Cognitive Dysfunction in Parkinson's Disease. Front. Aging Neurosci. 13:804991. doi: 10.3389/fnagi.2021.804991

Background: Quantitative electroencephalography (qEEG) has been suggested as a biomarker for cognitive decline in Parkinson's disease (PD).

Objective: Determine if applying a wavelet-based qEEG algorithm to 21-electrode, resting-state EEG recordings obtained in a routine clinical setting has utility for predicting cognitive impairment in PD.

Methods: PD subjects, evaluated by disease stage and motor score, were compared to healthy controls ($N = 20$ each). PD subjects with normal (PDN, MoCA 26–30, $N = 6$) and impaired (PDD, MoCA ≤ 25, $N = 14$) cognition were compared. The wavelet-transform based time-frequency algorithm assessed the instantaneous predominant frequency (IPF) at 60 ms intervals throughout entire recordings. We then determined the relative time spent by the IPF in the four standard EEG frequency bands (RTF) at each scalp location. The resting occipital rhythm (ROR) was assessed using standard power spectral analysis.

Results: Comparing PD subjects to healthy controls, mean values are decreased for ROR and RTF-Beta, greater for RTF-Theta and similar for RTF-Delta and RTF-Alpha. In logistic regression models, arithmetic combinations of RTF values [e.g., (RTF-Alpha) + (RTF-Beta)/(RTF-Delta + RTF-Theta)] and RTF-Alpha values at occipital or parietal locations are most able to discriminate between PD and controls. A principal component (PC) from principal component analysis (PCA) using RTF-band values in all subjects is associated with PD status ($p = 0.004$, $\beta = 0.31$, AUC $= 0.780$). Its loadings show positive contribution from RTF-Theta at all scalp locations, and negative contributions from RTF-Beta at occipital, parietal, central, and temporal locations. Compared to cognitively normal PD subjects, cognitively impaired PD subjects have lower median RTF-Alpha and RTF-Beta values, greater RTF-Theta values and similar RTF-Delta values. A PC from PCA using RTF-band values in PD subjects is associated with cognitive status ($p = 0.002$, $\beta = 0.922$, AUC $= 0.89$). Its loadings show positive

contributions from RTF-Theta at all scalp locations, negative contributions from RTF-Beta at central locations, and negative contributions from RTF-Delta at central, frontal and temporal locations. Age, disease duration and/or sex are not significant covariates. No PC was associated with motor score or disease stage.

Significance: Analyzing standard EEG recordings obtained in a community practice setting using a wavelet-based qEEG algorithm shows promise as a PD biomarker and for predicting cognitive impairment in PD.

Keywords: quantitative electroencephalography (QEEG), biomarker, Parkinson's disease, cognitive dysfunction, wavelet-based time-transform algorithm

INTRODUCTION

Parkinson's disease (PD) is characterized by the presence of cardinal motor symptoms including resting tremor, rigidity, bradykinesia and postural instability. Non-motor symptoms including cognitive impairment, anxiety, depression, REM-sleep-behavior disorder, olfactory dysfunction, autonomic dysfunction, orthostatic hypotension, urinary incontinence and constipation are common and often precede the onset of motor symptoms. Cognitive impairment becomes more prevalent as the disease progresses and dementia often develops (Aarsland and Kurz, 2010). The prevalence of dementia in PD may be as high as 75% for disease duration greater than 10 years (Hely et al., 2008). The ability to predict the onset or likelihood of cognitive impairment in PD is important, as impaired cognition is associated with increased morbidity and mortality, decreased quality of life, and increased caregiver burden.

Biomarkers of cognitive dysfunction in PD have been developed (Shi et al., 2010) based on neuroimaging (Poston and Eidelberg, 2009; Arnaldi et al., 2017), genetics (Liu et al., 2017), blood (Lawton et al., 2020) and CSF (Mollenhauer et al., 2017). Over the last decade, analyses of non-stationary EEG data, data where the statistical characteristics change with time, using quantitative electroencephalography (qEEG) methods have been investigated for their ability to distinguish the parkinsonian state and/or predict dementia in PD. Different measures and EEG characteristics have been utilized for this purpose: Fonseca et al. (2009) observed an increase in absolute and relative posterior-delta amplitude in 32 PD patients compared to 26 normal controls; Morita et al. (2011) found an association between a decrease in the spectral ratio of fast-to-slow frequency bands [(Alpha + Beta)/(Theta + Delta)] and a decline in Mini-Mental State Examination (MMSE) scores; Caviness et al. (2015, 2016) reported that an increase in delta-band power was associated with longitudinal changes in neuropsychological testing and distinguished PD patients from controls; and Klassen et al. (2011) found that background frequency and relative power in the theta band were potential predictors of dementia in PD in a cohort of 138 PD subjects, 21 of which had dementia at baseline.

Most of the above-mentioned studies included patients who were undergoing dopaminergic therapy. To address the contributions of potential treatment effects as well as disease–stage, Arnaldi et al. (2017) analyzed EEGs in a cohort of 57 drug-naïve *de novo* PD patients using qEEG and ^{123}I-FP-CIT-SPECT and determined that a mean posterior qEEG frequency of less than 8.3 Hz was a good predictor of cognitive decline in that cohort. Chaturvedi et al. (2017) analyzed high-resolution 256–channel EEG recordings of PD patients and found that theta-power in the left temporal region and the alpha/theta ratio in the central and left regions were able to distinguish PD patients from healthy controls, suggesting a role for regional EEG differences in the disease state. Geraedts et al. (2018) showed that decreased posterior dominant frequency and increased theta power correlate with cognitive impairment in PD. Massa et al. (2020) showed that the alpha/theta ratio was significantly lower in early stage Lewy body disease and in PD without cognitive impairment in comparison to healthy controls and Alzheimer's-disease-associated mild cognitive impairment (MCI-AD). Using qEEG, Schumacher et al. (2020) compared mild cognitive impairment associated with Lewy bodies (MCI-LB) with MCI-AD and reported increased pre-alpha, decreased beta power and slower dominant frequency in MCI-LB, suggesting that early EEG slowing is a specific feature of MCI-LB. Taken together, these studies demonstrate that EEG and qEEG parameters can not only distinguish PD patients from healthy controls, but also serve as potential biomarkers of cognitive impairment in PD and LB-associated diseases. In addition, they point to the association of regional EEG differences with the disease state and degree of cognitive impairment.

An open question is how to best harness the discriminatory ability of qEEG for analyzing non-stationary EEG data for the purpose of distinguishing healthy controls from PD subjects, and cognitively normal from cognitively impaired PD subjects,

Abbreviations: AIC, Aikake information criterion; AUC, Area under the receiver operating characteristic curve; CI, Confidence interval; EEG, Electroencephalogram; EMR, Electronic medical record; FFT, Fast Fourier transform; H&Y, stage Hoehn and Yahr Parkinson's disease stage; IPF, The instantaneous predominant frequency at a scalp location, calculated at 60 ms intervals throughout a resting-state EEG recording; LB, Lewy bodies; MCI, Mild cognitive impairment; MCI-AD, Mild cognitive impairment associated with Alzheimer's disease; MCI-LB, Mild cognitive impairment associated with Lewy bodies; MD, Median; MoCA, Montreal Cognitive Assessment; MT, Median test; MWU, Mann-Whitney *U*-test; PC, Principal component; PCA, Principal components analysis; PD, Parkinson's disease; PDD, Parkinson's disease subjects with impaired cognition (MoCA $\leq$ 25); PDN, Parkinson's disease subjects with normal cognition (MoCA 26-30); qEEG, Quantitative electroencephalography; ROR, Resting occipital rhythm; RTF-band, The relative time spent by the IPF in one of the four standard EEG frequency bands (alpha, beta, delta, or theta) during an entire EEG recording; SD, Standard deviation; STN, Subthalamic nucleus; STN-DBS, Subthalamic nucleus deep brain stimulation; TT, *t*-test (two-tailed); UPDRS-III, Unified Parkinson's Disease Rating Scale, part III (motor score).

in clinical settings where 21-electrode resting-state EEG data is routinely obtained. In this report, we evaluate whether a wavelet-based algorithm has utility for this purpose. Since EEG data can contain multiple independent spectral components that can vary rapidly in their frequency, we hypothesized that PD subjects differ from healthy controls, and cognitively normal PD subjects differ from cognitively impaired PD subjects, in how these spectral components change in frequency. To capture the rapid changes in frequency, we applied a wavelet-based algorithm previously developed by two of us (Indic and Narayanan, 2011) to derive the instantaneous frequency of the EEG signal at multiple time scales. We then determined the instantaneous predominant frequency (IPF, F0) at 60-msec intervals throughout the entire EEG recording at each scalp location and characterized the relative time spent by the IPF in each of the four standard (alpha, beta, delta, theta) EEG frequency bands (RTF). We analyzed these data using logistic regression and principal components analysis (PCA) to assess whether the RTF values in one or more EEG frequency bands (RTF-band) or arithmetic combinations of these values [e.g., the ratio of Alpha + Beta to Delta + Theta, after Morita et al. (2011)] can be used to distinguish PD from healthy control subjects, and within the PD cohort, subjects with normal cognition from subjects with cognitive impairment.

MATERIALS AND METHODS

This retrospective review of patient records and EEG data study was approved by the NorthShore institutional review board.

Study Participants

Twenty PD patients were recruited from one author's (KM) movement disorders clinic. These subjects were medicated with levodopa or dopamine agonists at the time of EEG recording. They remained on medications in consideration of Best Practice and to be consistent with the aim of evaluating whether qEEG analysis of routinely collected EEG data, which would be collected while patients remain on their medications, is productive for discriminating between the groups being studied. The twenty age and sex-matched healthy controls were subjects whose EEGs were performed at our health system following a syncopal episode. Healthy controls had no neurological diagnoses in their medical records and a normal EEG. The average duration of EEG recording was 40 min (range: 30–60 min). The Montreal Cognitive Assessment (MoCA), which is the recommended scale for capturing cognitive changes in PD (Chou et al., 2010), the Unified Parkinson's Disease Rating Scale (UPDRS) part III (motor) (Fahn et al., 1987; Movement Disorder Society Task Force on Rating Scales for Parkinson's Disease, 2003) and the Hoehn and Yahr (H&Y) disease-stage scale (Goetz et al., 2004) scores were obtained as part of the standard clinical evaluation of PD patients in our movement disorders clinic at the NorthShore University HealthSystem (Evanston, IL). Twelve males and eight females were included in each group with an average age of 72.4 (standard deviation (*SD*) 8.1, range 59–85) and 72.7 (*SD* 8.4, range 59–89) years, for PD and control groups, respectively. Clinical features of the PD patients are shown in **Figure 1**.

Quantitative Electroencephalography Analysis

Natus Neuroworks® (Middleton, WI) was used for EEG recording and review. Raw EEG data from each channel were exported to MATLAB (Version 2018. The Math Works Inc., MA) for the wavelet analysis. To capture the rapid variation in frequency in the non-stationary EEG signal, we used an algorithm previously developed by two of us (Indic and Narayanan, 2011) to derive the instantaneous frequencies seen in the EEG signal at multiple time scales. This algorithm uses a continuous wavelet transform, with the Morlet wavelet as the mother wavelet, to complete a time-frequency decomposition of the EEG signal and extract information about simultaneously existing frequencies in the EEG data. It can reliably extract frequency information even in the presence of artifacts, providing they do not have the same frequency content of the EEG (Indic and Narayanan, 2011).

The wavelet transform of the discrete EEG signal is obtained by the convolution of the scaled and translated version of a mother wavelet function with the signal. The convolution is performed N times, N being the length of the EEG signal, using a discrete Fourier transform and wavelet function at each of a set of predefined time scales. We used a dyadic representation of time scales with eight sub-octave scales per octave with a total of 80 scales. The wavelet transformation provides a scalogram—a visual representation plotting the absolute value of the continuous wavelet transform as a function of time and frequency, and so is useful for time-localization of short-duration of high-frequency events as well as frequency localization of low-frequency, longer duration events. At each instant of time, we estimated the peak value of the scalogram. The frequency corresponding to the peak at an instant of time provides the instantaneous predominant frequency (IPF, or F0). The output of the analysis for each EEG channel was the IPF over time, with calculation of the IPF performed every 60 ms. For each channel we calculated the probability of IPF being in one of the four, standard-EEG-frequency bands (delta, theta, alpha, or beta) over the entire EEG recording. We refer to this as the relative time of this frequency (RTF) in each band at that channel.

Analysis of the resting occipital rhythm (ROR) was performed with *Spike2* (Cambridge Electronic Design, Cambridge, United Kingdom) and Igor Pro software (Wave metrics, Lake Oswego, OR). Standard power-spectral-density analysis was performed over a short block of time while the subject was resting with their eyes closed, using a Fast Fourier Transform (FFT).

Statistical Analyses

Since this is a pilot study aimed at evaluating whether the wavelet algorithm previously described by Indic and Narayanan (2011) can be applied to resting-state EEG data to identify features associated with disease (PD vs. healthy control) and cognitive status in PD subjects (normal vs. impaired cognition), there were no published data allowing us to estimate an effect size for the differences that would be seen in either of these groups. Therefore, we could not perform an *a priori* power analysis. We assessed 20 PD and 20 healthy controls; within the PD subjects, six were cognitively normal (PDN, MoCA 26-30) while

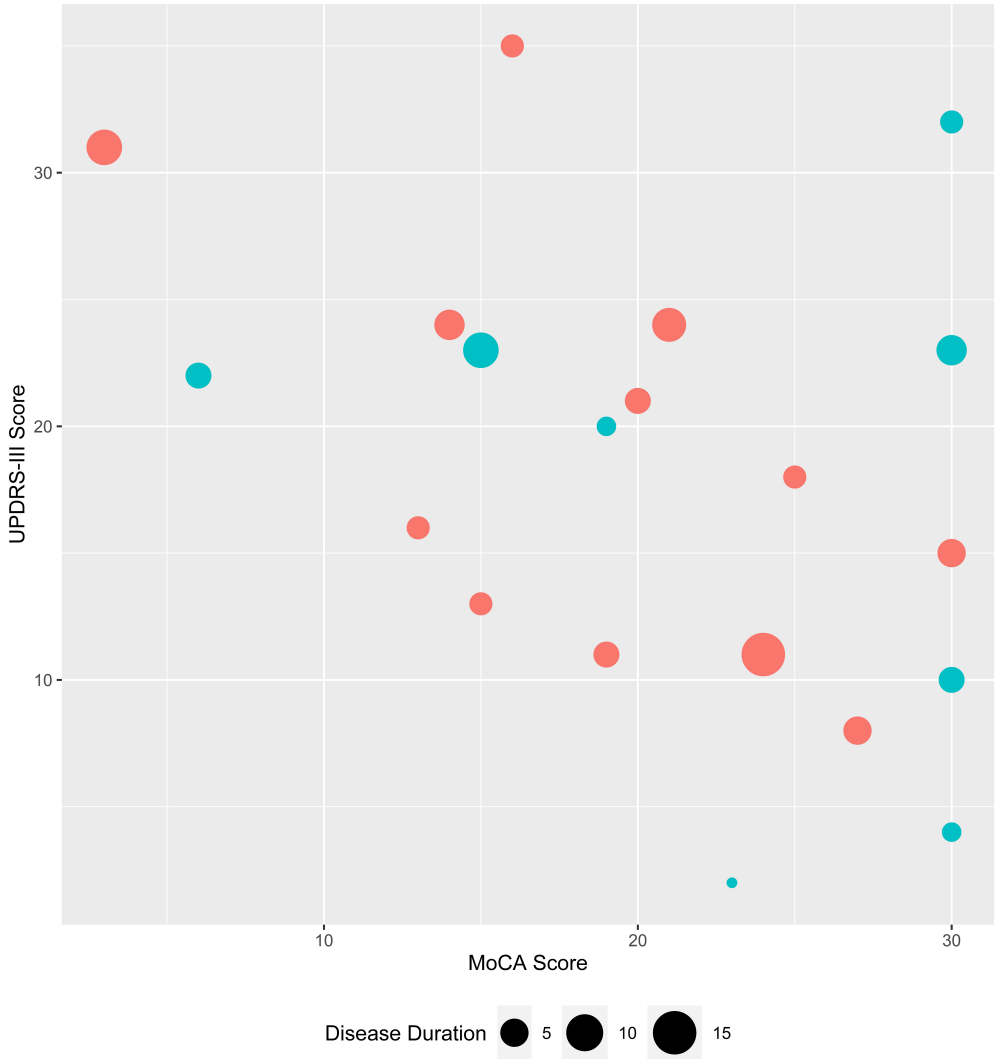

FIGURE 1 | Clinical characteristics of study subjects with Parkinson's disease. MoCA and UPDRS-III scores are plotted for female (teal) and male (coral) PD subjects; symbol size corresponds to disease duration (range: 1–15 years),

14 were cognitively impaired (PDD, MoCA $\leq$ 25). This sample size is comparable to that used in some studies that identified differences in these groups using other EEG analysis methods (see section "Introduction"). We report 95% confidence intervals (CIs) to allow for independent determination of the effect size and range of possible differences with which our data are consistent.

Differences in RTF-band values between subject groups (PD vs. healthy control, PDN vs. PDD) were initially evaluated using both parametric (two-tailed *t*-test (TT) to compare means (*M*) and nonparametric [median test (MT) to compare medians (*MD*), Mann-Whitney *U*-test (MWU) to compare distributions] statistics. Logistic regression models (Stata, vs. 16.1, StataCorp LLC, TX) were used to evaluate associations between subject groups and RTF-band values or, since specific spectral differences have been associated with cognition in previous studies (see Introduction), arithmetic combinations of RTF-band values [(RTF-Alpha + RTF-Beta), (RTF-Alpha + RTF-Beta – RTF-Theta), (RTF-Alpha – RTF-Theta), (RTF-Theta – RTF-Beta), and (RTF-Alpha + RTF-Beta)/(RTF-Delta + RTF-Theta)], by location, focusing on variables with relatively high and similar variance in PD and control subjects. Given the size of groups in our cohort, we sought to minimize overfitting (Peduzzi et al., 1996; Vittinghoff and McCulloch, 2007) in these exploratory models by considering the contributions of only one or two RTF-band variables at once, e.g., RTF-Theta at O1 and O2 or P3 and P4, and interpreted significant models (model p and RTF-band variable $p < 0.05$) as providing evidence of association only if they also passed a link test, a Pearson goodness-of-fit test, and had a McFadden's adjusted R^2 supportive of good model fit (0.2–0.4). The Aikake information criterion (AIC) was used to evaluate whether model fit was improved by including age, sex, and/or disease duration as covariates.

Since we captured four RTF-band values at each of 21 scalp locations in each study subject, we used principal components analysis (PCA), performed in Stata (vs. 16.1) and in *R*,[1] on data from 15 scalp locations to reduce data dimensionality and reduce the likelihood of false discovery. PCA provides an unsupervised method to identify a low-dimensional set of uncorrelated variables that effectively summarize the data obtained from applying the wavelet transform algorithm to EEG data at each scalp location. The RTF-band data for a particular frequency band at different scalp locations tend to be correlated and consequently reflect redundant properties of the recorded brain activity. In the PCAs we performed, we used only RTF-band data, so each PCA used the variance of the RTF-band values obtained at each scalp location to compute uncorrelated principal components (PCs), linear combinations of the RTF-band values that contain the information present in the original data. The principal components separate the information in the original RTF-band data so that each explains a maximal amount of variance, with most of the information compressed into the first several principal components. Our goal in using PCA was to assess whether the scores of any of the PCs, derived only using RTF-band data, are associated with group (PD vs. control, PDN vs. PDD) membership, and identify the RTF-band-location values with strong contributions to that PC.

We performed two different PCAs. In PCA-A, we used RTF-band data from both PD and healthy control subjects, but not any information on disease status, so that we could subsequently evaluate whether any of the principal components, which only accounted for the variance in the RTF-band data, are associated with membership in the PD or the healthy control cohort. In PCA-B, we used RTF-band data only from PD subjects, but not any information on cognitive status, so that we could subsequently evaluate whether any of the principal components, which only accounted for the variance in the RTF-band data from PD subjects, are associated with cognitive status in PD subjects. Both PCAs used RTF-band values, each centered and scaled to have unit variance, for all four bands at locations C3, C4, O1, O2, F3, F4, F7, F8, FP1, FP2, P3, P4, T3, T4, and T5. Data from midline and ear locations were not included in this analysis, and data for location T6 was unavailable. Logistic regression was used to evaluate the association of a PC's scores with group membership. The fit of logistic regression models revealing a significant association between a PC and group membership was evaluated as described above; we also assessed whether any observations had a substantial impact on model fit by evaluating the Pearson residuals, deviance residuals and Pregibon leverage. For PD subjects, linear regression was used to evaluate association of a PC with UPDRS-III score or H&Y stage.

To assess uncertainty in the PC scores obtained from the PCAs, we derived their 95% CIs using a bootstrap method with 1,000 replications, using *PCA.Bootstrap* as implemented in *R* (see text footnote 1) by JLR Villardon. This approach overcomes the limitations of asymptotic approaches to calculate CIs (Babamoradi et al., 2013).

[1]https://CRAN.R-project.org

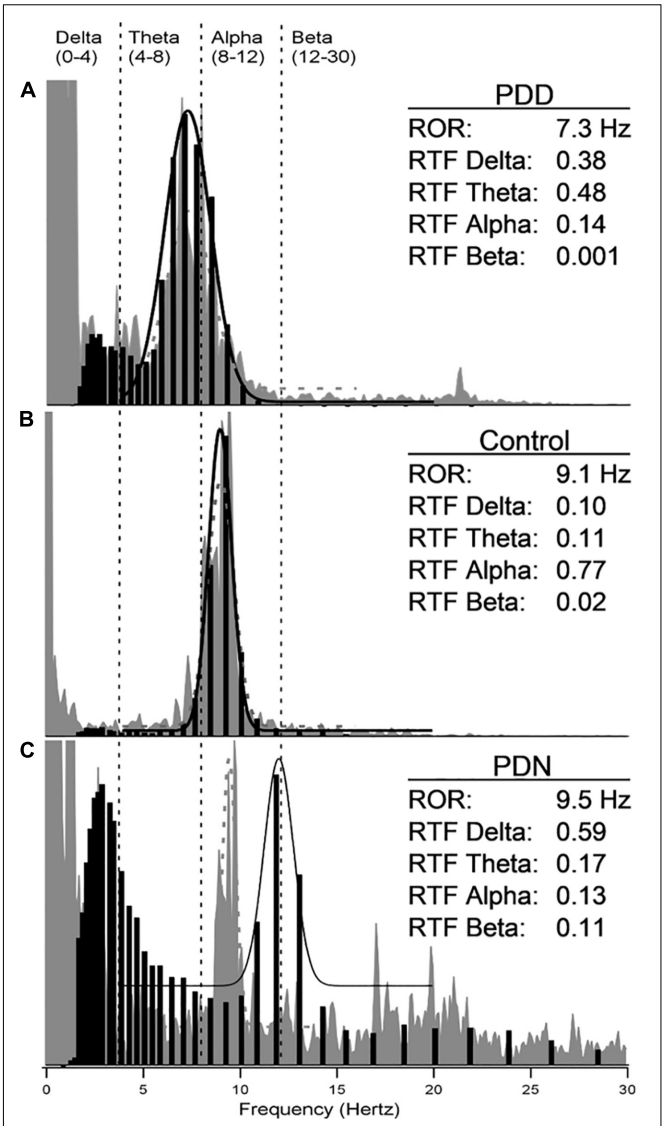

FIGURE 2 | Examples of wavelet-based instantaneous predominant frequency in study subjects. **(A)** (PDD), **(B)** (control), and **(C)** (PDN) show qEEG data obtained at location O1 in the frequency range from 0 to 30 Hz. In gray is the FFT-based resting occipital rhythm (ROR) during 30 s of quiet resting with eyes closed. Black bars show the wavelet-based instantaneous predominant frequency (F0) histogram over the entire recording. A normal curve has been fitted to the FFT (dotted gray) and wavelet-based (black) data over frequencies from 4 to 20 Hz. The ROR and relative times spent by the instantaneous predominant frequency in each EEG band (RTF) are tabulated.

RESULTS

Relationship of Spectral and Wavelet EEG Analysis

To characterize the relationship of the spectral and wavelet analysis during the 30-min EEG recording in a healthy control, PDN and a PDD individual, the spectral peak representing the background ROR (O1 channel) was calculated by fitting a normal curve to the FFT graph for frequencies of 4–20 Hz. A normal

curve was also fit to the histogram of IPF for comparison. Examples of wavelet analysis data in control, PDN and PDD subjects are shown in **Figure 2**. The IPF histogram and FFT-based spectrogram are often, but not always aligned.

A Quantitative Electroencephalography Signature Distinguishes Between the Parkinsonian and Control State

RTF-Band Values Are Associated With Parkinson's Disease and Control Status

We initially evaluated whether mean and median RTF-band values at all scalp locations were different between control and PD subjects. Compared to control subjects, values in PD subjects were lower for RTF-Beta [TT: control $M = 0.0930$, $SD = 0.0547$; PD $M = 0.0474$, $SD = 0.0589$; $t(38) = 2.534$, $p = 0.0155$; MWU: control $MD = 0.07$, PD $MD = 0.02$, $U = 3.030$, $p = 0.0020$; MT: χ^2 (1, N = 40) = 6.4, $p = 0.011$], greater for RTF-Theta [TT: control $M = 0.146$, $SD = 0.069$; PD $M = 0.229$, $SD = 0.125$; $t(38) = -2.599$, $p = 0.0132$; MWU: control $MD = 0.14$, PD $MD = 0.20$, $U = -2.759$, $p = 0.0058$; MT: χ^2 (1, N = 40) = 6.4, $p = 0.011$], and similar for RTF-Delta [TT: control $M = 0.564$, $SD = 0.163$; PD $M = 0.586$, $SD = 0.171$; $t(38) = -0.403$, $p = 0.689$; MWU: control $MD = 0.59$, PD $MD = 0.60$, $U = -0.541$, $p = 0.6017$; MT: χ^2 (1, N = 40) = 0.4, $p = 0.527$] and RTF-Alpha [TT: control $M = 0.186$, $SD = 0.135$; PD $M = 0.138$, $SD = 0.155$; $t(38) = 1.048$, $p = 0.301$; MWU: control $MD = 0.15$, PD $MD = 0.07$, $U = 1.542$, $p = 0.1274$; MT: χ^2 (1, N = 40) = 1.6, $p = 0.206$] (**Figure 3A**).

These results raised the possibility that RTF-band values, possibly in a location-dependent manner, are associated with disease status and degree of cognitive impairment. Therefore, we used logistic regression to explore whether RTF-band values or arithmetic combinations of these values with relatively high variance, which would therefore be more informative for detecting intergroup differences, are associated with disease status. We evaluated arithmetic combinations of RTF-bands that considered the relationships of the faster (alpha and beta) and slower rhythms (delta and theta) in an effort to assess their contribution to the parkinsonian state. A consistent result from these analyses was that RTF-band values in occipital (O1, O2) and parietal (P3, P4) regions were most strongly associated with PD status. The associations were most apparent for arithmetic combinations of RTF-band values [(RTF-Alpha + RTF-Beta)/(RTF-Delta + RTF-Theta), RTF-Alpha + RTF-Beta, RTF-Alpha + RTF-Beta – RTF-Theta, RTF-Alpha – RTF-Theta] and for RTF-Alpha values (**Table 1**).

Significant associations were also seen when RTF-Alpha, RTF-Delta, RTF-Theta, RTF-Alpha-Theta values were evaluated at these scalp locations, when RTF-Beta was evaluated at pairs of

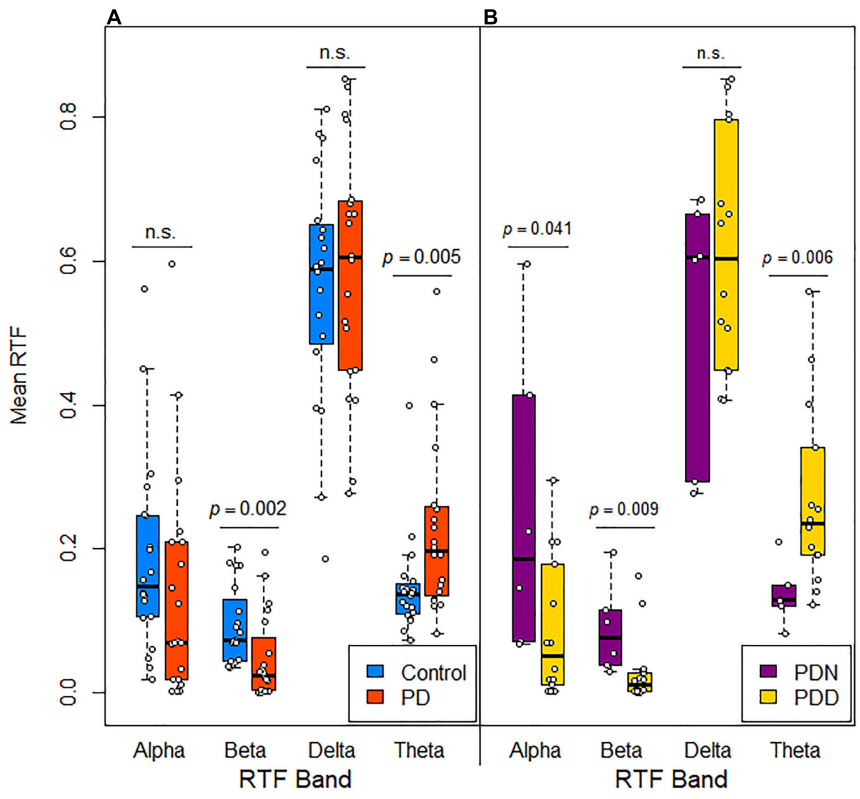

FIGURE 3 | Distribution of mean RTF values in subjects grouped by disease and cognitive status. Box plots with jittered data points show the mean RTF values recorded from all scalp locations for each frequency band in **(A)** control and PD subjects and **(B)** cognitively normal (PDN, MoCA > 25) and cognitively impaired (PDD, MoCA ≤ 25) PD subjects. Significance differences evaluated using a Mann-Whitney *U*-test.

TABLE 1 | Classification of disease status by RTF values at scalp locations using logistic regression.

Scalp locations	RTF or RTF metric evaluated	Variable*	β	95% CI	*P*-value	Area under ROC curve	Classification			McFadden's adjusted R^2	AIC
							Correct (%)	Sensitivity (%)	Specificity (%)		
O1, O2	$\frac{Alpha+Beta}{Delta+Theta}$	O1	30.25	5.53, 54.96	0.016	0.900	77.5	90.0	65.0	0.308	38.385
		O2	−35.71	−64.92, −6.49	0.017						
	Alpha + Beta	O1	45.27	6.83, 83.71	0.021	0.860	75.0	85.0	65.0	0.210	43.804
		O2	−50.58	−90.86, −10.30	0.014						
	Alpha + Beta – Theta	O1	23.94	1.48, 46.39	0.037	0.8625	77.5	85.0	70.0	0.210	43.831
		O2	−28.80	−52.87, −4.74	0.019						
P3, P4	*Alpha*	P3	57.11	11.06, 103.15	0.015	0.850	77.5	85.0	70.0	0.278	40.102
		P4	−64.54	−114.17, −14.91	0.011						
	Alpha – Theta	P3	23.54	5.76, 41.40	0.010	0.860	80.0	85.0	75.0	0.243	41.957
		P4	−30.99	−52.94, −9.05	0.006						
	Alpha + Beta – Theta	P3	12.47	1.172, 23.77	0.031	0.8625	75.0	80.0	70.0	0.170	46.006
		P4	−17.24	−30.30, −4.18	0.010						
	$\frac{Alpha+Beta}{Delta+Theta}$	P3	5.50	0.401, 10.61	0.035	0.8075	67.5	80.0	55.0	0.139	47.76
		P4	−7.823	−14.12, −1.53	0.015						
	Alpha + Beta	P3	16.25	0.577, 31.92	0.042	0.8050	70.0	80.0	60.0	0.098	50.098
		P4	−19.71	−36.34, −3.08	0.020						

**The intercept was not significantly different from zero in all models; all models passed the link test.*

T3, T4 and T5, and, consistent with finding that PD subjects have lower mean RTF-Beta and higher mean RTF-Theta, for mean RTF-Theta or mean RTF-Beta. However, the classification, area under the ROC curve, and model-fit statistics were not as strong as those shown in **Table 1** (see **Supplementary Table 1**).

Age and/or sex were not significant predictors when included in any of these analyses. While including sex and/or age often improved classification, they invariably diminished model fit statistics.

Principal Component Analysis Identifies a Principal Component Able to Distinguish Between Parkinson's Disease and Control Subjects

Since RTF values within a frequency band, and arithmetic combinations of RTF values of different frequency bands tend to be correlated (**Table 2**), we were concerned that co-linearity among variables diluted the precision of the logistic regression analyses. Therefore, we used PCA to reduce data dimensionality and assess whether uncorrelated PCs are associated with PD vs. control status. PCA-A was performed using the only the RTF-band values in each frequency band, from all subjects, at scalp locations C3, C4, O1, O2, F3, F4, F7, F8, FP1, FP2, P3, P4, T3, T4, and T5.

The first five PCs (named here A.PC1 – A.PC5 to avoid confusion with PCs generated in the second PCA-B described below), which explain 91.96% of the total variance (**Figure 4A**) (A.PC1, 42.9%; A.PC2, 27.9%; A.PC3, 13.9%; A.PC4, 4.72%; A.PC5, 2.5%) were each evaluated for a possible association with PD or control status using logistic regression. We found that A.PC2 is associated with PD and control status (model $p = 0.0037$; $\beta = 0.31$, 95% CI: 0.037, 0.59; A.PC2 p value: 0.027; Intercept not significantly different from zero; McFadden's adjusted $R^2 = 0.280$; Goodness-of-fit-test Pearson's $\chi^2 = 46.85$, $p = 0.154$; Link test: pass; AIC = 51.02; Area under ROC curve (AUC): 0.780; Classification: 70% correct, 60% sensitivity, 80% specificity) (**Figures 4B,C**). While A.PC2 remained a significant predictor of disease status in models incorporating sex and age, age and sex, either individually or together, were not significant predictors of disease status. Including them did not improve model fit as evaluated using AIC or McFadden's Adjusted R^2, though including both improved classification (correct: 80.0%; sensitivity: 75%; specificity: 85%; AUC = 0.8225). A.PC1, A.PC3, A.PC4, and A.PC5 were not associated with PD vs. control status (model $p = 0.231$, 0.453, 0.695, 0.355, respectively). A bootstrap analysis deriving the 95% CIs for the A.PC1 and A.PC2 scores for each study subject, as well as other PCA parameters,

TABLE 2 | Correlation between RTF values across all scalp locations.

Band	Mean (Range)
Alpha	0.97 (0.92–0.99)
Beta	0.69 (0.071–0.99)
Delta	0.90 (0.59–0.99)
Theta	0.85 (0.56–0.99)
Alpha – Beta	0.86 (0.37–0.99)
Alpha + Beta – Theta	0.81 (0.22–0.99)
Alpha – Theta	0.90 (0.72–0.99)
Theta – Beta	0.74 (0.034–0.99)
(Alpha + Beta) (Delta + Theta)	0.82 (0.16–0.99)

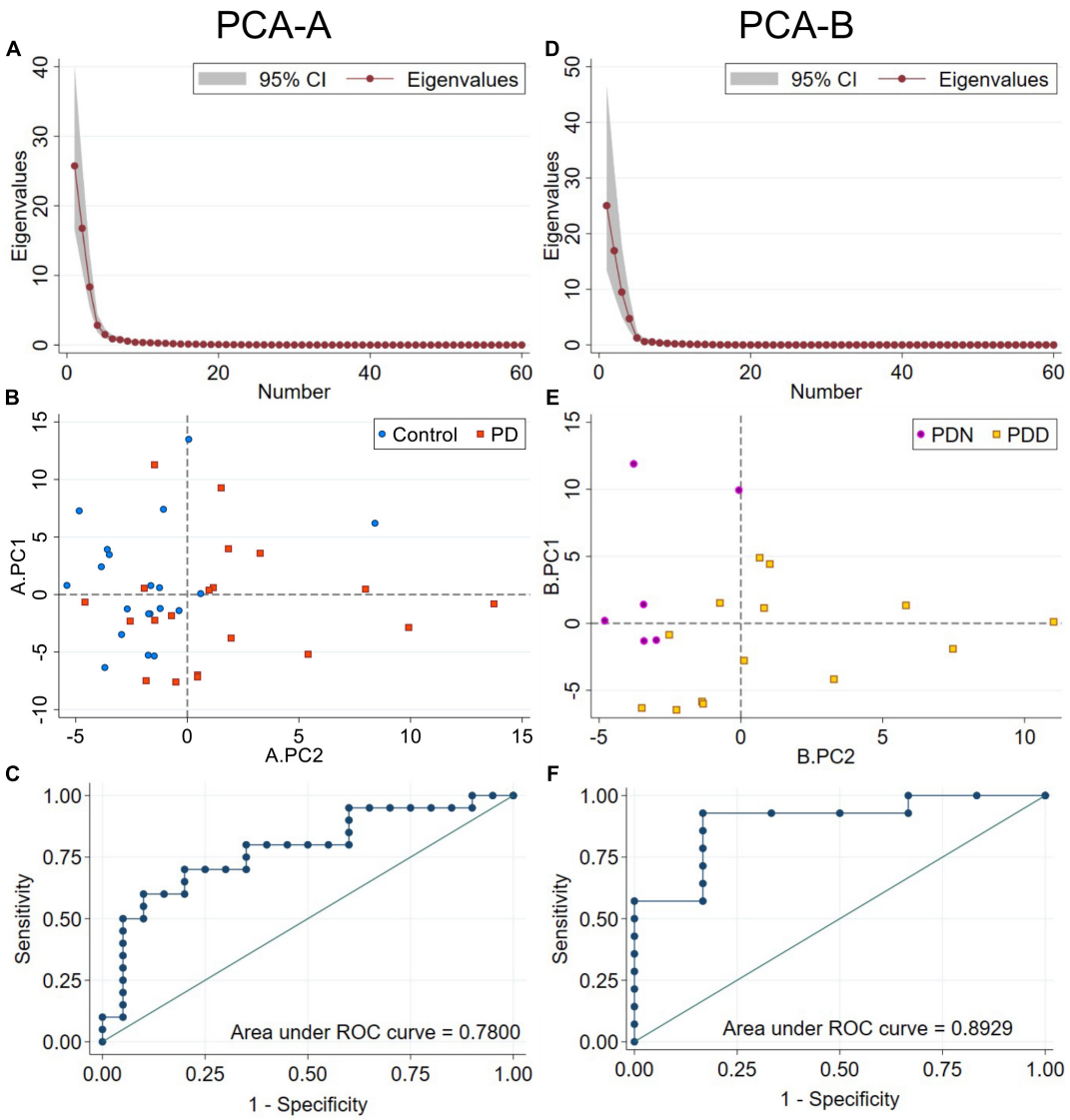

FIGURE 4 | PCA using RTF data for each frequency band at all scalp locations. PCA-A used RTF data from PD and control subjects. **(A)** Scree plot of eigenvalues for PCA-A. Principal components A.PC1–5 account for 92.0% of the total variance. **(B)** Distribution of control (blue circles) and PD (orange squares) subjects by A.PC1 and A.PC2 scores. A.PC2 scores distribute subjects by disease status more effectively than A.PC1 scores. **(C)** ROC curve from a logistic regression model classifying subjects by disease status using A.PC2 scores. PCA-B used RTF data only from PD subjects. **(D)** Scree plot of eigenvalues for PCA-B. Principal components B.PC1–5 account for 95.8% of the total variance. **(E)** Distribution of PDN (MoCA $\geq$ 26, purple circles) and PDD (MoCA $\leq$ 25, gold squares) subjects by B.PC1 and B.PC2 scores. B.PC2 scores distribute PDN from PDD subjects more effectively than B.PC1 scores. **(F)** ROC curve from a logistic regression model classifying PD subjects by PDN vs. PDD status using B.PC2 scores.

indicated that the PCA results are stable and reproducible (**Supplementary Figure 1**).

Examination of the PCA-A loadings revealed that the loadings for A.PC2 have strong, positive and similar levels of contribution from RTF-Theta values at all scalp locations, and strong negative contributions from RTF-Beta values at locations O1, O2, P3, P4, C3, C4, T4, T5, and T6 (**Figure 5A**). These results are congruent with those found in our initial analyses: (1) Compared to control subjects, PD subjects had lower average RTF-Beta and greater average RTF-Theta, and (2) Arithmetic combinations of RTF-band values that include the beta and theta bands at occipital, as well as parietal locations, have utility in discriminating between PD and control subjects.

A Quantitative Electroencephalography Signature Is Associated With Cognitive Status in the Parkinsonian State

We took a similar approach to that used to identify qEEG features distinguishing controls from PD subjects to evaluate whether a qEEG signature is associated with cognitive status in the parkinsonian state. First, we compared the means of

		A					B				
		PCA-A					PCA-B				
Band	Location	A.PC1 (0.429)	A.PC2 (0.279)	A.PC3 (0.139)	A.PC4 (0.047)	A.PC5 (0.025)	B.PC1 (0.417)	B.PC2 (0.282)	B.PC3 (0.158)	B.PC4 (0.079)	B.PC5 (0.029)
RTF-Delta	C3	-0.160	-0.098	-0.030	-0.062	0.064	-0.168	-0.093	-0.043	-0.067	0.268
	C4	-0.176	-0.065	-0.077	-0.094	0.077	-0.174	-0.078	-0.067	-0.090	0.010
	O1	-0.180	-0.066	-0.067	-0.040	-0.006	-0.182	-0.074	-0.065	-0.036	0.117
	O2	-0.181	-0.056	-0.054	0.004	-0.017	-0.184	-0.086	-0.023	0.025	0.006
	F3	-0.172	-0.072	-0.055	0.053	-0.176	-0.171	-0.106	-0.013	0.043	-0.149
	F4	-0.177	-0.070	-0.064	-0.003	-0.022	-0.174	-0.089	-0.034	-0.012	-0.197
	F7	-0.173	-0.094	-0.008	0.003	0.063	-0.170	-0.106	0.011	-0.008	0.126
	F8	-0.178	-0.078	-0.025	-0.024	0.088	-0.178	-0.096	0.017	-0.032	-0.076
	FP1	-0.157	-0.041	-0.007	0.218	-0.311	-0.157	-0.082	-0.013	0.198	-0.138
	FP2	-0.161	-0.059	-0.005	0.219	-0.063	-0.149	-0.077	-0.022	0.204	-0.194
	P3	-0.169	-0.092	-0.016	-0.050	-0.071	-0.179	-0.085	-0.030	-0.045	0.167
	P4	-0.181	-0.061	-0.053	-0.042	-0.031	-0.182	-0.081	-0.033	-0.021	-0.027
	T3	-0.171	-0.087	-0.035	-0.047	0.102	-0.164	-0.111	-0.011	-0.029	0.248
	T4	-0.178	-0.069	-0.062	-0.063	0.078	-0.180	-0.081	-0.049	-0.063	-0.030
	T5	-0.174	-0.087	-0.058	-0.015	0.075	-0.172	-0.110	-0.034	-0.002	0.144
RTF-Theta	C3	-0.018	0.223	0.070	0.064	-0.106	-0.025	0.220	0.014	0.078	-0.212
	C4	0.003	0.231	0.082	0.048	0.007	0.008	0.235	0.025	0.061	0.018
	O1	-0.026	0.218	0.111	-0.102	-0.136	-0.028	0.227	0.057	-0.095	-0.119
	O2	-0.021	0.219	0.108	-0.102	-0.089	-0.012	0.227	0.076	-0.103	-0.043
	F3	0.016	0.222	0.065	0.099	0.168	0.024	0.225	0.022	0.117	0.167
	F4	0.018	0.212	0.080	0.114	0.153	0.023	0.208	0.045	0.123	0.308
	F7	0.004	0.229	0.057	0.050	0.020	-0.014	0.230	0.024	0.073	-0.113
	F8	0.015	0.229	0.068	0.075	0.033	0.011	0.229	0.026	0.083	0.116
	FP1	0.019	0.200	-0.003	0.097	0.342	0.029	0.209	-0.028	0.116	0.280
	FP2	0.027	0.204	0.013	0.125	0.214	0.028	0.195	-0.015	0.166	0.370
	P3	-0.033	0.225	0.086	-0.051	-0.113	-0.039	0.232	0.028	-0.030	-0.144
	P4	-0.015	0.230	0.083	-0.046	-0.033	-0.004	0.234	0.040	-0.039	-0.015
	T3	-0.023	0.218	0.083	0.006	-0.074	-0.044	0.223	0.032	0.004	-0.260
	T4	-0.001	0.232	0.088	-0.022	-0.043	-0.013	0.238	0.040	-0.023	0.017
	T5	-0.023	0.213	0.112	-0.086	-0.146	-0.038	0.225	0.045	-0.078	-0.196
RTF-Alpha	C3	0.175	-0.010	-0.124	-0.031	0.033	0.183	-0.048	-0.090	-0.037	-0.074
	C4	0.175	-0.022	-0.115	0.008	0.002	0.177	-0.054	-0.099	-0.006	0.002
	O1	0.183	-0.025	-0.116	0.003	0.010	0.183	-0.065	-0.090	0.004	0.000
	O2	0.177	-0.039	-0.105	0.010	-0.054	0.179	-0.070	-0.099	0.005	-0.038
	F3	0.182	-0.015	-0.111	-0.005	-0.037	0.182	-0.046	-0.105	0.002	0.017
	F4	0.179	-0.024	-0.109	0.016	-0.051	0.177	-0.052	-0.103	0.029	-0.040
	F7	0.178	-0.032	-0.116	0.020	-0.050	0.180	-0.055	-0.105	0.021	-0.058
	F8	0.179	-0.035	-0.107	0.021	-0.046	0.179	-0.051	-0.112	0.028	-0.007
	FP1	0.174	-0.013	-0.131	-0.007	-0.033	0.174	-0.052	-0.131	0.011	-0.040
	FP2	0.170	-0.017	-0.134	-0.004	-0.065	0.167	-0.054	-0.140	0.013	-0.041
	P3	0.176	-0.007	-0.136	-0.018	0.053	0.181	-0.061	-0.102	-0.021	-0.007
	P4	0.181	-0.030	-0.106	-0.008	0.003	0.179	-0.062	-0.101	-0.016	0.027
	T3	0.176	-0.045	-0.120	0.008	0.026	0.181	-0.064	-0.092	0.006	-0.019
	T4	0.175	-0.048	-0.105	0.018	0.030	0.182	-0.059	-0.092	0.022	0.052
	T5	0.181	-0.039	-0.110	0.015	0.026	0.182	-0.072	-0.079	0.010	0.033
RTF Beta	C3	0.097	-0.110	0.184	0.085	-0.056	0.070	-0.092	0.259	0.087	-0.087
	C4	0.105	-0.113	0.207	0.115	-0.169	0.079	-0.093	0.257	0.109	-0.052
	O1	0.037	-0.126	0.227	0.227	0.191	0.032	-0.079	0.244	0.228	-0.049
	O2	0.043	-0.126	0.206	0.128	0.314	0.074	-0.060	0.217	0.170	0.222
	F3	0.079	-0.086	0.205	-0.241	0.221	0.082	-0.023	0.187	-0.315	0.071
	F4	0.108	-0.080	0.217	-0.191	-0.087	0.101	-0.025	0.204	-0.233	0.065
	F7	0.080	-0.095	0.228	-0.184	-0.130	0.064	-0.050	0.236	-0.227	0.019
	F8	0.090	-0.095	0.227	-0.125	-0.234	0.082	-0.056	0.237	-0.186	0.017
	FP1	0.038	-0.067	0.162	-0.420	0.270	0.035	0.006	0.164	-0.380	0.021
	FP2	0.041	-0.038	0.162	-0.469	0.016	0.033	0.010	0.156	-0.388	0.028
	P3	0.029	-0.128	0.196	0.214	0.197	0.041	-0.085	0.243	0.194	-0.087
	P4	0.063	-0.134	0.217	0.173	0.105	0.082	-0.086	0.240	0.162	0.036
	T3	0.073	-0.122	0.228	0.075	-0.207	0.059	-0.088	0.270	0.069	0.023
	T4	0.062	-0.115	0.238	0.153	-0.190	0.046	-0.086	0.257	0.142	-0.080
	T5	0.053	-0.132	0.240	0.210	0.039	0.040	-0.086	0.252	0.213	0.022

FIGURE 5 | Loadings of uncorrelated principal components from PCAs. **(A)** Loadings from the first five PCs of PCA-A (A.PC1–5), which used RTF values from scalp locations in all subjects. **(B)** Loadings from the first five PCs of PCA-B (B.PC1–5), which used RTF values only from PD subjects. The amount of variance explained by each PC is indicated parenthetically. The intensity and color of shading reflects the strength (stronger = more intense) and type of correlation (red = negative, blue = positive) of the loading with a PC.

the RTF-band values at all scalp locations in PDN (cognitively normal) and PDD (cognitively impaired subjects). Compared to PDN subjects, median values in PDD subjects were lower for RTF-Alpha [MWU: PDN $MD = 0.19$, PDD $MD = 0.05$, $U = 2.062$, $p = 0.0408$; MT: χ^2 (1, N = 20) = 3.81, $p = 0.05$], lower for RTF-Beta [MWU: PDN $MD = 0.08$, PDD $MD = 0.01$,

$U = 2.557$, $p = 0.0087$; MT: χ^2 (1, N = 20) = 8.57, $p = 0.003$], greater for RTF-Theta [MWU: PDN $MD = 0.13$, PDD $MD = 0.24$, $U = -2.638$, $p = 0.0064$; MT: χ^2 (1, N = 20) = 3.81, $p = 0.05$] and similar for RTF-Delta [MWU: PDN $MD = 0.60$, PDD $MD = 0.60$, $U = -0.825$, $p = 0.4095$; MT: χ^2 (1, N = 20) = 0.0, $p = 1.0$] (**Figure 3B**). This suggested that RTF-band values at some locations, or the average RTF-band value across all scalp locations, might be useful to discriminate between PDN and PDD subjects.

To explore this hypothesis, we used logistic regression in an attempt to identify RTF locations and frequency bands associated with cognitive status in the parkinsonian state. While some RTF-band variables (RTF-Theta in C3 and C4, RTF-Theta in O1 and O2, RTF-Theta in P3 and P4; RTF-Beta in C3 and C4, RTF-Beta in T3, T4, or T5) resulted in models with a model $p < 0.05$, either RTF-band variables did contribute significantly to the models, or a link test run after the estimation commands failed, suggesting that none of the models were properly specified (**Supplementary Table 2**).

We therefore evaluated whether PCA could identify uncorrelated PCs useful for classification of PD subjects by their cognitive status (PDN vs. PDD). PCA-B was done using RTF-band values = at the same scalp locations used in PCA-A, but only from PD subjects. The first five PCs (named here B.PC1 – B.PC5 to distinguish them from A.PC1-5 described above) accounted for 95.75 percent of the total variance (B.PC1, 41.73%; B.PC2, 28.23%; B.PC3, 15.83%; B.PC4, 7.86%; B.PC5, 2.89%) (**Figure 4D**). We used logistic regression to evaluate whether any of the first five B.PCs were associated with PDN vs. PDD status. While neither age ($p = 0.634$), disease duration ($p = 0.444$), nor sex ($p = 0.116$) were significantly associated with cognitive status (**Table 3**), since disease duration and age are risk factors for cognitive impairment, we evaluated whether including these covariates improved model-fit statistics. We found that B.PC2 was associated with PDN v PDD status (**Figures 4E,F**), and that including age, disease duration and/or sex as covariates did not improve model fit statistics (**Table 3**). While some models evaluating the association of B.PC1 and the covariates with PDN/PDD status were significant, their model-fit statistics suggested they were not properly specified. Models evaluating the association of B.PC3, B.PC4, and B.PC5 with PDN/PDD status were not significant (model $p = 0.421$, 0.357, 0.326, respectively). As for PCA-A, a bootstrap analysis deriving the 95% CIs associated with B.PC1 and B.PC2 scores, as well as other PCA parameters, indicated that the PCA results are stable and reproducible (**Supplementary Figure 2**).

Examination of the PCA-B loadings revealed that that B.PC2 has positive, similar strong level of contribution from RTF-Theta values at all scalp locations. Less strong are negative contributions from RTF-Beta values at central locations (C3, C4) and RTF-Delta levels at central (C3), frontal (F3, F7, F8), and temporal (T3, T4) locations (**Figure 5B**). Compared to the PCA-A loadings distinguishing between the PD and normal state, the PCA-B loadings distinguishing between normal and impaired cognition in PD that involve RTF-Beta are generally less strong while those involving RTF-Delta are generally stronger.

To address whether qEEG features associated with PDN vs. PDD status might also be associated with the motor or disease state, we used linear regression to evaluate if B.PC1 – B.PC5 scores were associated with scores on UPDRS-III or with H&Y stage. These analyses did not reveal any significant associations (UPDRS-III: B.PC1, $p = 0.498$, $R^2 = 0.0259$; B.PC2, $p = 0.587$, $R^2 = 0.0167$; B.PC3, $p = 0.233$, $R^2 = 0.0267$; B.PC4, $p = 0.536$, $R^2 = 0.0216$; B.PC5, $p = 0.449$, $R^2 = 0.322$. H&Y stage: B.PC1, $p = 0.186$, $R^2 = 0.168$; B.PC2, $p = 0.950$, $R^2 = 0.0004$; B.PC3, $p = 0.961$, $R^2 = 0.0002$; B.PC4, $p = 0.722$, $R^2 = 0.0132$; B.PC5, $p = 0.282$, $R^2 = 0.115$).

DISCUSSION

Here we present a retrospective, cross-sectional analysis of standard EEG recordings in a cohort of PD patients and healthy controls from a clinical practice setting. We demonstrate that the novel application of a wavelet-based transform to these routinely gathered clinical data identifies a qEEG signature that may assist in predicting cognitive dysfunction in PD patients. The EEG data can contain one or more independent spectral components that may exhibit rapid variation in their frequency based on the underlying cortical dynamics. The wavelet transform method can capture these rapid changes in frequency and can help derive the instantaneous frequency of the EEG signal at multiple time scales (Indic and Narayanan, 2011). As such, the wavelet-based analysis used in our study has the advantage of more accurately reflecting the dynamic character of non-stationary EEG signal at any given time, in comparison to the Fourier or Hilbert transform (Wacker and Witte, 2013).

Our results are in full agreement with previous reports indicating that qEEG has utility in distinguishing the parkinsonian state from healthy controls, as well as characterizing the presence of cognitive impairment. In a review of 23 studies assessing cognition in PD, Geraedts et al. (2018) reported that in cross-sectional studies, EEG slowing correlated with cognitive impairment, whereas in longitudinal studies, decreased dominant frequency and increased theta power correlated with cognitive impairment and predicted future cognitive deterioration.

Logistic regression showed that arithmetic combinations of RTF-band values at occipital and parietal locations such as (RTF-Alpha + RTF-Beta)/(RTF-Delta + RTF-Theta) can distinguish between the PD and control states. Furthermore, PCA using RTF-band values from both control and PD subjects identified a PC with contributions from RTF-Theta and RTF-Beta at all scalp locations that can distinguish between PD and control state with an AUC of 0.78. A separate PCA using RTF-band values only from PD subjects identified a PC able to distinguish between PDN and PDD with an AUC of 0.8929. Compared to the PC associated with PD vs. control status, the PC associated with PDN vs. PDD cognitive status had differing contributions from RTF-Delta and RTF-Beta originating in the frontal and occipital regions.

Our analysis highlights the contribution of different EEG dynamics to the parkinsonian vs. non-disease state and

TABLE 3 | Results of logistic regression-based classification of cognitive status in the parkinsonian state by B.PC1, B.PC2, disease duration, age and sex.

Independent variables	Model P	Variable*	β	95% CI	*P*-value	Area under ROC curve	Classification			McFadden's adjusted R^2	AIC	Link test
							Correct (%)	Sensitivity (%)	Specificity (%)			
Disease duration	0.444	Duration	0.134	–0.239, 0.507	0.401	0.5179	70.0	100.0	0.0	–0.140	27.849	Fail
Age	0.634	Age	0.029	–0.093, 0.153	0.637	0.5595	70.0	100.0	0.0	–0.154	28.208	Fail
Sex	0.112	Sex	−1.609	–3.66, 0.446	0.125	0.690	70.0	100.0	0.0	–0.060	25.903	Fail
PC1	0.0340	PC1	−0.236	–0.494, –0.0213	0.072	0.7381	70.0	85.71	33.33	0.020	23.942	Fail
B.PC1 + Disease Duration	0.0945	PC1	−0.231	–0.491, 0.039	0.082	0.7500	70.0	85.71	33.33	–0.052	25.716	Fail
		Duration	0.084	–0.280, 0.449	0.652							
B.PC1 + Age	0.0242	PC1	−0.369	–0.711, –0.026	0.035	0.8571	85.0	92.86	66.67	0.059	22.994	Fail
		Age	0.155	–0.048, 0.358	0.134							
B.PC1 + Sex	0.0282	PC1	−0.297	–0.646, –0.052	0.095	0.8333	70.0	85.71	33.33	0.047	23.298	Fail
		Sex	−1.971	–4.594, 0.653	0.141							
B.PC1 + Disease Duration + Age + Sex*	0.0095	PC1	−0.643	–1.302, 0.0376	0.064	0.9405	85.0	92.86	66.67	0.139	21.04	Fail
		Duration	−0.395	–1.303, 0.512	0.393							
		Age	0.389	–0.177, 0.955	0.178							
		Sex	−5.00	–12.29, 2.29	0.179							
B.PC2	0.0020	PC2	0.922	0.019, 1.925	0.045	0.8929	90.0	92.86	83.33	0.226	18.921	Pass
B.PC2 + Disease Duration	0.0085	PC2	0.985	–0.228, 1.833	0.056	0.8929	90.0	92.86	83.33	0.144	20.984	Pass
PC2 + Age	0.0041	PC2	1.295	0.0151, 2.575	0.047	0.9048	90.0	85.7	66.67	0.205	19.417	Pass
		Age	−0.1424	–0.406, 0.121	0.289							
PC2 + Sex	0.0067	PC2	0.813	–0.100, 1.734	0.084	0.9048	85.0	85.71	83.3	0.164	20.425	Pass
		Sex	−0.957	–3.611, 1.696	0.479							
PC2 + Disease Duration + Age + Sex	0.0250	PC2	1.270	–0.224, 2,765	0.096	0.9048	90.0	92.86	83.33	0.044	23.36	Fail
		Duration	−0.051	–0.588, 0.475	0.850							
		Age	−0.132	–0.420, 0.156	0.368							
		Sex	−0.392	–3.98, 3.19	0.830							

**In all models, the intercept was not significantly different from zero.*

cognitive impairment within the parkinsonian state. Comparing the loadings of the PCs associated with each of these dichotomous states reveals positive associations of RTF-Theta and negative associations of RTF-Delta and RTF-Beta in both the parkinsonian state and cognitive impairment within the parkinsonian state, however, relative to the associations distinguishing the parkinsonian and control state, the negative associations with cognitive impairment in parkinsonian subjects are relatively stronger for RTF-Delta and relatively weaker for RTF-Beta. More specifically, the associations of cognitive impairment with RTF-values in frontal, temporal and occipital locations appear to be relatively stronger for RTF-Delta and relatively weaker for RTF-Beta (**Figure 5**). These findings suggest that the EEG state associated with disease status is not identical to that of cognitive impairment. This difference appears to be specific to the cognitive state as there is no association to the severity of the motor state or disease stage.

Beta oscillations in the basal ganglia have been associated with an anti-kinetic motor state in PD (Little and Brown, 2014). Sustained synchronization between the subthalamic nucleus (STN) and premotor-cortical oscillations likely disrupts normal movement in PD (Sharott et al., 2018). Furthermore, reduction of basal-ganglia beta oscillations by STN deep-brain stimulation (STN-DBS) has been associated with symptomatic improvement (Yin et al., 2021). It is conceivable that the decreased RTF-Beta we observe reflects impaired synchrony between the basal ganglia and the cortex. Cole et al. (2017) showed that non-sinusoidal beta oscillations may underlie cortical pathophysiology in PD and may reflect input synchrony onto the cortex. In that context, it is conceivable that Fourier-based methods fail to fully capture the temporal localization of the frequencies due to the non-stationary nature of EEG data, and so represent the frequencies as present throughout the recording duration. Similarly, the amplitude corresponding to the represented frequencies was depicted as being smooth and present throughout the recording duration. While our study was not designed to assess the role of cortical beta oscillations, the wavelet transform that we used can capture rapid and discrete changes in frequency and as such may more accurately capture the underlying cortical functional state.

Our study has several limitations: One is its retrospective cross-sectional design and a second is its modest sample size. Longitudinal follow-up of the non-demented patients with assessment of the qEEG variables and cognitive status at annual intervals could help confirm the findings of this pilot study. Our measures of effect size will be useful to evaluate sample-size requirements for a larger prospective study. A third limitation is the lack of detailed characterization of the cognitive status of the controls. The controls were selected from the electronic medical record (EMR) and were based on the following criteria: normal EEG, a diagnosis of syncope and absence of a diagnosis of neurological disorder or cognitive impairment. These controls were not clinically assessed and therefore, subtle symptoms associated with later onset of a neurological disease may have been missed.

A fourth limitation is that the PD subjects were on dopaminergic medications when EEGs were recorded. The potential contribution of dopaminergic therapy on brain activity and consequently on the EEG in either the parkinsonian or healthy state cannot be excluded. Dopamine has been shown to modulate cortico-subthalamic activity in in the parkinsonian state and dopaminergic medications lead to coherence in the delta/theta range in the medial and orbitofrontal cortex (Sharma et al., 2021). Furthermore, dopamine can have an effect in the healthy brain by modulating brain dynamics (Braun et al., 2021). Beta oscillations are associated with motor symptoms in PD (van Wijk et al., 2016). Dopaminergic medication can induce changes in phase-amplitude coupling and distributed coherence, which are correlated with changes in rigidity in PD subjects (Miller et al., 2019), so such medication impacts the elevated synchronization seen in PD. Also, dopaminergic medications can be associated with cognitive impairment that may be both brain-region-specific (MacDonald et al., 2011), and dose-dependent (Macdonald and Monchi, 2011). The potential for multifaceted actions of dopamine in the healthy and parkinsonian state does not allow for a clear prediction of how dopaminergic medications would impact RTF-band values in a qEEG analysis. Therefore, the extent to which dopaminergic therapy impacts our findings with respect to cognition warrants further study.

In conclusion, the findings of this retrospective study provide support for the utility of using the novel application of a wavelet-based transform qEEG method to distinguish the parkinsonian state and identify qEEG parameters that can serve as a biomarker for the declining cognitive status in PD patients. Longitudinal assessment of these qEEG parameters and correlation with detailed clinical phenotyping as well as CSF and imaging biomarkers in a larger cohort will provide further insight into PD progression, the progression of cognitive impairment within PD, and the underlying neurodegenerative process.

DATA AVAILABILITY STATEMENT

The datasets presented in this article are not readily available because the data contain protected health information (PHI). The raw data without PHI can be made available on request from the corresponding author. Requests to access the datasets should be directed to corresponding author KM, amarkopoulou@northshore.org.

ETHICS STATEMENT

This was a retrospective study analyzing data obtained as part of standard clinical practice. The studies involving human participants were reviewed and approved by NorthShore University HealthSystem Institutional Review Board. Written informed consent from the patients/participants was not required in this study in accordance with the national legislation and the institutional requirements.

AUTHOR CONTRIBUTIONS

KM, JN, and KN designed the study. PI performed the wavelet analysis. KN and BC performed

data and statistical analysis. All authors participated in editing the manuscript and approved its content.

FUNDING

This study was funded by departmental funds. Open-access publication fees were supported by philanthropic contributions to KM.

ACKNOWLEDGMENTS

We thank the study participants.

SUPPLEMENTARY MATERIAL

The Supplementary Material for this article can be found online at: https://www.frontiersin.org/articles/10.3389/fnagi.2021.804991/full#supplementary-material

REFERENCES

Aarsland, D., and Kurz, M. W. (2010). The epidemiology of dementia associated with Parkinson disease. *J. Neurol. Sci.* 289, 18–22. doi: 10.1016/j.jns.2009.08.034

Arnaldi, D., De Carli, F., Famà, F., Brugnolo, A., Girtler, N., Picco, A., et al. (2017). Prediction of cognitive worsening in de novo Parkinson's disease: Clinical use of biomarkers. *Mov. Disord* 32, 1738–1747. doi: 10.1002/mds.27190

Babamoradi, H., van den Berg, F., and Rinnan, A. (2013). Bootstrap based confidence limits in principal component analysis—A case study. *Chemomet. Intellig. Lab. Syst.* 120, 97–105. doi: 10.1016/j/chemolab.2012.10.007

Braun, U., Harneit, A., Pergola, G., Menara, T., Schäfer, A., Betzel, R. F., et al. (2021). Brain network dynamics during working memory are modulated by dopamine and diminished in schizophrenia. *Nat. Commun.* 12:3478. doi: 10.1038/s41467-021-23694-9

Caviness, J. N., Hentz, J. G., Belden, C. M., Shill, H. A., Driver-Dunckley, E. D., Sabbagh, M. N., et al. (2015). Longitudinal EEG changes correlate with cognitive measure deterioration in Parkinson's disease. *J. Parkinsons Dis.* 5, 117–124. doi: 10.3233/JPD-140480

Caviness, J. N., Utianski, R. L., Hentz, J. G., Beach, T. G., Dugger, B. N., Shill, H. A., et al. (2016). Differential spectral quantitative electroencephalography patterns between control and Parkinson's disease cohorts. *Eur. J. Neurol.* 23, 387–392. doi: 10.1111/ene.12878

Chaturvedi, M., Hatz, F., Gschwandtner, U., Bogaarts, J. G., Meyer, A., Fuhr, P., et al. (2017). Quantitative EEG (QEEG) Measures Differentiate Parkinson's Disease (PD) Patients from Healthy Controls (HC). *Front. Aging Neurosci.* 9:3. doi: 10.3389/fnagi.2017.00003

Chou, K. L., Amick, M. M., Brandt, J., Camicioli, R., Frei, K., Gitelman, D., et al. (2010). Parkinson Study Group Cognitive/Psychiatric Working Group. A recommended scale for cognitive screening in clinical trials of Parkinson's disease. *Mov. Disord* 25, 2501–2507.

Cole, S. R., van der Meij, R., Peterson, E. J., de Hemptinne, C., Starr, P. A., and Voytek, B. (2017). Nonsinusoidal Beta Oscillations Reflect Cortical Pathophysiology in Parkinson's Disease. *J. Neurosci.* 37, 4830–4840. doi: 10.1523/JNEUROSCI.2208-16.2017

Fahn, S., Elton, R., and Members of the Updrs Development Committee. (1987). "The Unified Parkinson's Disease Rating Scale," in *Recent Developments in Parkinson's Disease*, Vol. 2, eds S. Fahn, C. D. Marsden, D. B. Calne, and M. Goldstein (Florham Park: McMellam Health Care Information), 153–163.

Fonseca, L. C., Tedrus, G. M., Letro, G. H., and Bossoni, A. S. (2009). Dementia, mild cognitive impairment and quantitative EEG in patients with Parkinson's disease. *Clin. EEG Neurosci.* 40, 168–172. doi: 10.1177/155005940904000309

Geraedts, V. J., Boon, L. I., Marinus, J., Gouw, A. A., van Hilten, J. J., Stam, C. J., et al. (2018). Clinical correlates of quantitative EEG in Parkinson disease: A systematic review. *Neurology* 91, 871–883. doi: 10.1212/WNL.0000000000006473

Goetz, C. G., Poewe, W., Rascol, O., Sampaio, C., Stebbins, G. T., Counsell, C., et al. (2004). Movement Disorder Society Task Force on Rating Scales for Parkinson's Disease. Movement Disorder Society Task Force report on the Hoehn and Yahr staging scale: status and recommendations. *Mov. Disord* 19, 1020–1028. doi: 10.1002/mds.20213

Hely, M. A., Reid, W. G., Adena, M. A., Halliday, G. M., and Morris, J. G. (2008). The Sydney multicenter study of Parkinson's disease: the inevitability of dementia at 20 years. *Mov Disord.* 23, 837–844. doi: 10.1002/mds.21956

Indic, P., and Narayanan, J. (2011). Wavelet based algorithm for the estimation of frequency flow from electroencephalogram data during epileptic seizure. *Clin. Neurophysiol.* 122, 680–686. doi: 10.1016/j.clinph.2010.10.030

Klassen, B. T., Hentz, J. G., Shill, H. A., Driver-Dunckley, E., Evidente, V. G., Sabbagh, M. N., et al. (2011). Quantitative EEG as a predictive biomarker for Parkinson disease dementia. *Neurology* 77, 118–124. doi: 10.1212/WNL.0b013e318224af8d

Lawton, M., Baig, F., Toulson, G., Morovat, A., Evetts, S. G., Ben-Shlomo, Y., et al. (2020). Blood biomarkers with Parkinson's disease clusters and prognosis: The oxford discovery cohort. *Mov. Disord* 35, 279–287. doi: 10.1002/mds.27888

Little, S., and Brown, P. (2014). The functional role of beta oscillations in Parkinson's disease. *Parkinsonism Relat. Disord.* 20(Suppl. 1), S44–S48. doi: 10.1016/S1353-8020(13)70013-0

Liu, G., Locascio, J. J., Corvol, J. C., Boot, B., Liao, Z., Page, K., et al. (2017). Prediction of cognition in Parkinson's disease with a clinical-genetic score: a longitudinal analysis of nine cohorts. *Lancet Neurol.* 16, 620–629. doi: 10.1016/S1474-4422(17)30122-9

MacDonald, P. A., MacDonald, A. A., Seergobin, K. N., Tamjeedi, R., Ganjavi, H., Provost, J. S., et al. (2011). The effect of dopamine therapy on ventral and dorsal striatum-mediated cognition in Parkinson's disease: support from functional MRI. *Brain* 134(Pt 5), 1447–1463. doi: 10.1093/brain/awr075

Macdonald, P. A., and Monchi, O. (2011). Differential effects of dopaminergic therapies on dorsal and ventral striatum in Parkinson's disease: implications for cognitive function. *Parkinsons Dis.* 2011:572743. doi: 10.4061/2011/572743

Massa, F., Meli, R., Grazzini, M., Fama, F., De Carli, F., Filippi, L., et al. (2020). Utility of quantitative EEG in early Lewy body disease. *Parkinsonism Relat. Disord.* 75, 70–75. doi: 10.1016/j.parkreldis.2020.05.007

Miller, A. M., Miocinovic, S., Swann, N. C., Rajagopalan, S. S., Darevsky, D. M., Gilron, R., et al. (2019). Effect of levodopa on electroencephalographic biomarkers of the parkinsonian state. *J. Neurophysiol.* 122, 290–299. doi: 10.1152/jn.00141.2019

Mollenhauer, B., Caspell-Garcia, C. J., Coffey, C. S., Taylor, P., Shaw, L. M., Trojanowski, J. Q., et al. (2017). Longitudinal CSF biomarkers in patients with early Parkinson disease and healthy controls. *Neurology* 89, 1959–1969. doi: 10.1212/WNL.0000000000004609

Morita, A., Kamei, S., and Mizutani, T. (2011). Relationship between slowing of the EEG and cognitive impairment in Parkinson disease. *J. Clin. Neurophysiol.* 28, 384–387. doi: 10.1097/WNP.0b013e3182273211

Movement Disorder Society Task Force on Rating Scales for Parkinson's Disease (2003). The Unified Parkinson's Disease Rating Scale (UPDRS): status and recommendations. *Mov. Disord* 18, 738–750. doi: 10.1002/mds.10473

Peduzzi, P., Concato, J., Kemper, E., Holford, T. R., and Feinstein, A. R. (1996). A simulation study of the number of events per variable in logistic regression analysis. *J. Clin. Epidemiol.* 49, 1373–1379. doi: 10.1016/s0895-4356(96)00236-3

Poston, K. L., and Eidelberg, D. (2009). Network biomarkers for the diagnosis and treatment of movement disorders. *Neurobiol. Dis.* 35, 141–147. doi: 10.1016/j.nbd.2008.09.026

Schumacher, J., Taylor, J. P., Hamilton, C. A., Firbank, M., Cromarty, R. A., Donaghy, P. C., et al. (2020). Quantitative EEG as a biomarker in mild cognitive impairment with Lewy bodies. *Alzheimers Res. Ther.* 12:82. doi: 10.1186/s13195-020-00650-1

Sharma, A., Vidaurre, D., Vesper, J., Schnitzler, A., and Florin, E. (2021). Differential dopaminergic modulation of spontaneous cortico-subthalamic activity in Parkinson's disease. *Elife* 10:e66057. doi: 10.7554/eLife.66057

Sharott, A., Gulberti, A., Hamel, W., Köppen, J. A., Münchau, A., Buhmann, C., et al. (2018). Spatio-temporal dynamics of cortical drive to human subthalamic nucleus neurons in Parkinson's disease. *Neurobiol. Dis.* 112, 49–62. doi: 10.1016/j.nbd.2018.01.001

Shi, M., Huber, B. R., and Zhang, J. (2010). Biomarkers for cognitive impairment in Parkinson disease. *Brain Pathol.* 20, 660–671. doi: 10.1111/j.1750-3639.2009.00370.x

van Wijk, B. C., Beudel, M., Jha, A., Oswal, A., Foltynie, T., Hariz, M. I., et al. (2016). Subthalamic nucleus phase-amplitude coupling correlates with motor impairment in Parkinson's disease. *Clin. Neurophysiol.* 127, 2010–2019. doi: 10.1016/j.clinph.2016.01.015

Vittinghoff, E., and McCulloch, C. E. (2007). Relaxing the rule of ten events per variable in logistic and Cox regression. *Am. J. Epidemiol.* 165, 710–718. doi: 10.1093/aje/kwk052

Wacker, M., and Witte, H. (2013). Time-frequency techniques in biomedical signal analysis. A tutorial review of similarities and differences. *Methods Inf. Med.* 2013, 279–296. doi: 10.3414/ME12-01-0083

Yin, Z., Zhu, G., Zhao, B., Bai, Y., Jiang, Y., Neumann, W. J., et al. (2021). Local field potentials in Parkinson's disease: A frequency-based review. *Neurobiol. Dis.* 155:105372. doi: 10.1016/j.nbd.2021.105372

Conflict of Interest: The authors declare that the research was conducted in the absence of any commercial or financial relationships that could be construed as a potential conflict of interest.

Publisher's Note: All claims expressed in this article are solely those of the authors and do not necessarily represent those of their affiliated organizations, or those of the publisher, the editors and the reviewers. Any product that may be evaluated in this article, or claim that may be made by its manufacturer, is not guaranteed or endorsed by the publisher.

Copyright © 2022 Novak, Chase, Narayanan, Indic and Markopoulou. This is an open-access article distributed under the terms of the Creative Commons Attribution License (CC BY). The use, distribution or reproduction in other forums is permitted, provided the original author(s) and the copyright owner(s) are credited and that the original publication in this journal is cited, in accordance with accepted academic practice. No use, distribution or reproduction is permitted which does not comply with these terms.

frontiers in Aging Neuroscience

MINI REVIEW
published: 10 January 2022
doi: 10.3389/fnagi.2021.761913

Positron Emission Tomography in Animal Models of Tauopathies

Lei Cao[1,2†], Yanyan Kong[3†], Bin Ji[4], Yutong Ren[5], Yihui Guan[3] and Ruiqing Ni[1,6]*

[1] Institute for Regenerative Medicine, University of Zurich, Zurich, Switzerland, [2] Changes Technology Corporation Ltd., Shanghai, China, [3] PET Center, Huashan Hospital, Fudan University, Shanghai, China, [4] Department of Radiopharmacy and Molecular Imaging, School of Pharmacy, Fudan University, Shanghai, China, [5] Guangdong Robotics Association, Guangzhou, China, [6] Institute for Biomedical Engineering, ETH Zurich and University of Zurich, Zurich, Switzerland

The microtubule-associated protein tau (MAPT) plays an important role in Alzheimer's disease and primary tauopathy diseases. The abnormal accumulation of tau contributes to the development of neurotoxicity, inflammation, neurodegeneration, and cognitive deficits in tauopathy diseases. Tau synergically interacts with amyloid-beta in Alzheimer's disease leading to detrimental consequence. Thus, tau has been an important target for therapeutics development for Alzheimer's disease and primary tauopathy diseases. Tauopathy animal models recapitulating the tauopathy such as transgenic, knock-in mouse and rat models have been developed and greatly facilitated the understanding of disease mechanisms. The advance in PET and imaging tracers have enabled non-invasive detection of the accumulation and spread of tau, the associated microglia activation, metabolic, and neurotransmitter receptor alterations in disease animal models. *In vivo* microPET studies on mouse or rat models of tauopathy have provided significant insights into the phenotypes and time course of pathophysiology of these models and allowed the monitoring of treatment targeting at tau. In this study, we discuss the utilities of PET and recently developed tracers for evaluating the pathophysiology in tauopathy animal models. We point out the outstanding challenges and propose future outlook in visualizing tau-related pathophysiological changes in brain of tauopathy disease animal models.

Keywords: Alzheimer's disease, tau, animal model, positron emission tomography, FTD (fronto-temporal dementia), neurotransmitter, neuroinflammation

OPEN ACCESS

Edited by:
Jiehui Jiang,
Shanghai University, China

Reviewed by:
Elena Rodriguez-Vieitez,
Karolinska Institutet (KI), Sweden
Daichi Sone,
University College London,
United Kingdom

***Correspondence:**
Ruiqing Ni
ni@biomed.ee.ethz.ch

† These authors have contributed equally to this work

Specialty section:
This article was submitted to Neurocognitive Aging and Behavior, a section of the journal Frontiers in Aging Neuroscience

Received: *02 September 2021*
Accepted: *30 November 2021*
Published: *10 January 2022*

Citation:
Cao L, Kong Y, Ji B, Ren Y, Guan Y and Ni R (2022) Positron Emission Tomography in Animal Models of Tauopathies. Front. Aging Neurosci. 13:761913. doi: 10.3389/fnagi.2021.761913

INTRODUCTION

The microtubule-associated protein tau (MAPT) locates intracellularly and is composed of six isoforms, classified into 4-repeat (4R) and 3-repeat (3R) species (Lee et al., 2001; Spillantini and Goedert, 2013). Tauopathy diseases include Alzheimer's disease (AD), primary tauopathy such as progressive supranuclear palsy (PSP), corticobasal degeneration (CBD), and frontotemporal dementia (FTD) with Parkinsonism linked to chromosome 17 and Pick's disease. In AD, amyloid-beta (Aβ) and tau interact synergically in the brain and trigger a complex cascade of biochemical and cellular processes, resulting in neurodegeneration (Busche and Hyman, 2020; Chang et al., 2021b). Tau has been an important target in therapeutics development for AD and primary tauopathies. Immunotherapies semorinemab, gosuranemab (Boxer et al., 2019; Ayalon et al., 2021; Grossman, 2021; Mullard, 2021; Novak et al., 2021), antisense oligonucleotides (DeVos et al., 2017), and aggregation inhibitors are at different stages of clinical trials (Congdon and Sigurdsson, 2018).

Transgenic animal models recapitulating human tauopathy have enabled understanding of disease mechanisms and facilitated the development of treatment strategies (Albert et al., 2019; Roberts et al., 2020; Ayalon et al., 2021). Varieties of transgenic mouse lines with mutations *on MAPT* gene including P301S (PS19), P301L (JNPL3, rTg4510, pR5) (Lewis et al., 2000; Ramsden et al., 2005; Santacruz et al., 2005; Yoshiyama et al., 2007; de Calignon et al., 2012), knock-out hTau (Andorfer et al., 2003), and knock-in (Hashimoto et al., 2019; Saito et al., 2019) mouse models as well as transgenic rat models (Filipcik et al., 2012) have been developed. In addition, 3 × Tg mice and TgF344-AD rats harbor both the Aβ and tauopathy have been widely used (Oddo et al., 2003; Cohen et al., 2013). Recent advances in molecular imaging using PET and MRI have provided valuable insights into the time course of disease pathophysiology in tau animal models, including tau, neuroinflammation, and structural and functional alterations (Ishikawa et al., 2018; Ni et al., 2018; Tagai et al., 2020), thus providing a blueprint for tauopathy disease clinical study.

TAU IMAGING

Different types of tau inclusions in AD and primary tauopathies have been observed. Neuropil thread, neurofibrillary tangles are observed in AD; Oligodendroglial coiled bodies and argyrophilic threads are common in PSP and CBD. For the glial tau inclusions, tufted astrocytes in PSP, and astrocytic plaques in CBD are observed (Lee et al., 2001). The cerebral tau load assessed by PET using various tau imaging tracers associates with brain regional atrophy assessed by using structural MRI and cognitive impairment in patients with AD (La Joie et al., 2020; Ossenkoppele et al., 2020, 2021; Vogel et al., 2021), CBD, and PSP (Robinson et al., 2020; Tagai et al., 2020; Whitwell et al., 2020). Tau spreading and misfolding follow a disease-specific brain region-dependent pattern first in the entorhinal cortex, hippocampus in human (Wegmann et al., 2019), and in transgenic mouse brain (Clavaguera et al., 2009). The onset and severity of the pathology and brain regions of atrophy vary among the different strains. The rTg4510 line develops tauopathy at a young age (4–5 months) and showed atrophy in both the cortex and hippocampus. In contrast, hTau mice mainly show atrophy in the cortex and PS19 mice demonstrate pathology mainly in the brain stem and spinal cord (Lewis et al., 2000; Andorfer et al., 2003; Ramsden et al., 2005; Santacruz et al., 2005; Yoshiyama et al., 2007; de Calignon et al., 2012). MicroPET imaging of tau in tauopathy rodent models has contributed to the development of novel PET tracers, understanding of disease mechanism, and monitoring of treatment effect. Several tau tracers have been tested in tau mouse models including 2,6-disubstituted naphthalene derivative [^{18}F]FDDNP (Teng et al., 2011), pyridinyl-butadienyl-benzothiazole 3 derivatives [^{18}F]PM-PBB3 (APN-1607), [^{11}C]PBB3, [^{11}C]mPBB5 (Maruyama et al., 2013; Ishikawa et al., 2018; Ni et al., 2018; Barron et al., 2020; Tagai et al., 2020), arylquinoline derivatives [^{18}F]THK523 (Fodero-Tavoletti et al., 2011), [^{18}F]THK5351 (Moreno-Gonzalez et al., 2021), [^{18}F]THK5317 (Filip et al., 2021), [^{18}F]THK5117 (Brendel et al., 2016; Chaney et al., 2021), pyridoindole derivative [^{18}F]flortaucipir (Brendel et al., 2018), and lansoprazole derivative [^{18}F]NML (Shao et al., 2012; Fawaz et al., 2014; **Table 1**). Using [^{18}F]THK523, Brendel et al. (2018) showed significantly higher tracer retentions in brains of 6-month-old rTg4510 mice compared with non-transgenic mice or PS1/APP mice with Aβ pathology, indicating specific detection of tau. Brendel et al. (2016) and Chaney et al. (2021) demonstrated that PET using (S)-[^{18}F]THK5117 showed higher tracer uptakes in PS19 biGT mice [glycogen synthase kinase-3β (GSK-3β) × P301L tau] and TgF344 rats compared to non-transgenic littermates, respectively (**Figures 1F,G**). However, Eckenweber et al. (2020) reported that in PS19 mice at 6 month-of-age, (S)-[^{18}F]THK5117 was not able to detect the tau accumulation, although presence of tau accumulation was validated by using *ex vivo* immunohistochemical staining. Moreno-Gonzalez et al. (2021) recently showed an elevated regional [^{18}F]THK5351 PET signaling in brain of PS19 tau mice, correlating with histological levels of tau. However, both the binding assays as well as *in silico* experiment showed that [^{18}F]THK5351 had the limitation of off-target binding to monoamine oxidase B (Ng et al., 2017; Murugan et al., 2019). The most widely used first-generation tau tracer [^{18}F]flortaucipir was reported to showed greater difference compared to [^{18}F]THK5117 in tracer retention in APPswe × P301L vs. non-transgenic mice (Brendel et al., 2018; **Figures 1D,E**). However, *ex vivo* binding and autoradiography from two other studies showed lack of detection using [^{18}F] flortaucipir in rTg4510 mice (Marquié et al., 2015; Ni et al., 2018). PET using [^{11}C]PBB3 imaging for tau has been demonstrated in PS19 (Chang et al., 2021b) and rTg4510 mice (Ishikawa et al., 2018; Ni et al., 2018; Takuwa et al., 2020; **Figures 1A–C**). PS19 mice showed a mainly brainstem and spinal cord tracer retention, while in rTg4510 mice the retention was observed in the cortex and hippocampus in line with the *ex vivo* validation (Maruyama et al., 2013). An age-dependent increase in [^{11}C]PBB3 signal was observed in 7–11-month-old rTg4510 mice, consistent with neuropathological observations (Ni et al., 2018). In addition, the tau load inversely correlated with neocortical volumes assessed by T2 structural MRI, indicating an association between tau and neurodegeneration (Ishikawa et al., 2018; Ni et al., 2018). The disadvantages of [^{11}C]PBB3 include non-negligible binding to Aβ plaques in patients with AD and the short half-life. Thus, the second-generation [^{18}F]PM-PBB3 with improved binding properties was developed to overcome the limitations. Similar observations were reported by Tagai et al. (2020) and Weng et al. (2020) using [^{18}F]PM-PBB3 in rTg4510 mouse models with increased tracer retention in the cortical and hippocampal regions. Among the other second-generation tau tracers, [^{18}F]JNJ-64349311 (Declercq et al., 2017) and [^{18}F]PI-6240 (Kroth et al., 2019) have so far been reported in wild-type mice for brain uptake and biodistribution assessment. In addition, several new tau probes are underdevelopment such as [^{18}F]IBIPF1 (Kaide et al., 2019), [^{18}F]PI-2014 (Gabellieri et al., 2020), [^{18}F]PPQ (Lerdsirisuk et al., 2021), [^{11}C]LM229 (McMurray et al., 2021), [^{18}F]2-phenylquinoxaline derivatives (Zhou K. et al., 2021), antibody-based imaging (Krishnaswamy et al., 2014), and 4R-tau specific tracer [^{18}F]CBD-2115 (Lindberg et al., 2021).

TABLE 1 | Summary of PET imaging in tauopathy animal models.

Target	PET tracer	Animal model	References
Tau	[^{11}C]PBB3	rTg4510 mice	Maruyama et al., 2013; Ishikawa et al., 2018; Ni et al., 2018; Takuwa et al., 2020
		PS19 mice	Maruyama et al., 2013; Barron et al., 2020; Fairley et al., 2021; Ji et al., 2021
	[^{18}F]APN-1607	rTg4510 mice	Tagai et al., 2020; Weng et al., 2020
	[^{18}F]flortaucipir	PS19 mice	Brendel et al., 2018
	[^{18}F]FDDNP	3 × Tg rats	Teng et al., 2011
		TgF344 rats	Cohen et al., 2013
	[^{18}F]THK-5317	APP/Tau rats	Filip et al., 2021
	[^{11}C]THK-5351	P301S mice	Moreno-Gonzalez et al., 2021
	[^{18}F]THK-5105	PS19, biGT mice	Brendel et al., 2016, 2018
	[^{18}F]THK-5117	TgF334 rats	Chaney et al., 2021
	[^{11}C]TH523	rTg4510 mice	Fodero-Tavoletti et al., 2011
	[^{11}C]LM229	PS19 mice	McMurray et al., 2021
	[^{18}F]NML, [^{18}F]LNS	hTau + / + rats	Shao et al., 2012; Fawaz et al., 2014
TSPO	(R)-[^{11}C]PK11195	rTg4510 mice	Ishikawa et al., 2018; Chiquita et al., 2019
		3 × Tg mice	
	[^{18}F]FEBMP	PS19, rTg4510 mice	Barron et al., 2020; Fairley et al., 2021; Ji et al., 2021
	[^{11}C]DAA1106	PS19 mice	Ji et al., 2008
		TgF334 rats	Chaney et al., 2021
	[^{18}F]FEDAA1106	PS19 mice	Maeda et al., 2011; Ji et al., 2021
	[^{11}C]AC-5216	rTg4510 mice	Maeda et al., 2011; Ishikawa et al., 2018; Takuwa et al., 2020; Ji et al., 2021; Zhou X. et al., 2021
		PS19 mice	Ji et al., 2021
	[^{18}F]DPA-714	TgF344 rats	Chaney et al., 2021
	[^{11}C]PBR28	5 × FAD, PS19 mice	Mirzaei et al., 2016; Ji et al., 2021
	[^{125}I]CLINDE	3 × Tg mice, TgF344 rats	Tournier et al., 2019, 2020
	[^{18}F]GE-180	PS19 mice	Eckenweber et al., 2020; Palleis et al., 2021
		TgF344 rats	Chaney et al., 2021
P2Y12R	[^{11}C]AZD1283	rTg4510, PS19 mice	Maeda et al., 2021
OATP1C1	[^{18}F]2B-SRF101	3 × Tg mice	Kreimerman et al., 2019
OGA inhibitor	[^{18}F]MK-8553	rTg4510 mice	Wang et al., 2020
MC-I	[^{18}F]BCPP-EF	rTg4510 mice	Barron et al., 2020
MT	[^{11}C]MPC-6827	PS19 mice	Sai et al., 2020
α7nAChR	[^{18}F]ASEM	TgF334 rats	Chaney et al., 2021
BzR	[^{11}C]flumazenil	rTg4510 mice	Shimojo et al., 2020
mGluR5	(E)-[^{11}C]ABP688	rTg4510 mice	Shimojo et al., 2020
	[^{18}F]FPEB-PET	5 × FAD mice	Lee et al., 2019
CMRglc	[^{18}F]FDG	tauVLW mice	de Cristóbal et al., 2014
		5 × FAD mice	Rojas et al., 2013; Macdonald et al., 2014; Franke et al., 2020
		3 × Tg mice	Sancheti et al., 2013; Adlimoghaddam et al., 2019
		hTau mice	Brendel et al., 2019
		Tg601 mice	Hara et al., 2017
		PS19 mice	Eckenweber et al., 2020
Neutrophil	[^{68}Ga]PEG-cFLFLFK	3 × Tg mice	Kong et al., 2020
Astrocyte	[^{18}F]2B-SRF101, [^{11}C]DED	3 × Tg mice	Kreimerman et al., 2019
Nasal neuron	[^{11}C]GV1-57	rTg4510 mice	Van de Bittner et al., 2017

α7nAChR, a7 nicotinic acetylcholine receptor; BzR, benzodiazepine receptor; CMRglc, cerebral metabolic rate of glucose; [^{11}C]DED, N-(^{11}C-methyl)-L-deuterodeprenyl; mGluR5, metabotropic glutamate receptor 5; FDG, fluorodeoxyglucose; MC-I, mitochondria complex-I; MT, microtubule; OATP1C1, organic anion-transporting polypeptide 1C1; OGA, O-linked N-acetylglucosamine (O-GlcNAc)ase; TSPO, translocator protein; SV2A, synaptic vesicle glycoprotein 2A; NML, N-methyl lansoprazole; WT, wild-type.

NEUROINFLAMMATION IMAGING

Neuroinflammation play an important role in patient with AD and other primary tauopathy diseases as well as in animal models of tauopathy (Heneka et al., 2015; Ising et al., 2019; Wu et al., 2019; Linnerbauer et al., 2020; Richetin et al., 2020; Gaikwad et al., 2021; McAlpine et al., 2021; Palleis et al., 2021), featured by disease associated with microglia activation, reactive astrocytes, and activated cytokines such as complement C3 and interleukin-3. Immunohistochemical

staining showed that synapse loss and microglial activation precede the appearance of tangles in PS19 mice (Yoshiyama et al., 2007). NLR family pyrin domain containing 3 (NLRP3) inflammasome activation was reported to drive tau pathology (Ising et al., 2019). A marked reduction of homeostatic microglial genes was found by single-cell sequencing of microglia isolated from rTg4510 mice, correlating with the degree of neuronal loss (Sobue et al., 2021). Shi et al. (2021a) and Wang C. et al. (2021) showed that microglia promoted apolipoprotein E-dependent neurodegeneration in tau mice (Shi et al., 2019) and that selective removal of astrocytic apolipoprotein E can protect against tau-mediated neurodegeneration and decrease synaptic phagocytosis by microglia. Microglia activation has been shown to occur preceding the tangle formation in tau mice (Yoshiyama et al., 2007). In addition, microglia was activated to engulf neuron containing tau aggregates, turned hypofunctional after phagocytosis, released the seed component of tau aggregates, and, thus, facilitated the spreading of tau in PS19 mice (Bellucci et al., 2004; Brelstaff et al., 2021). Thus, imaging of neuroinflammation in tauopathy mice offers crucial dynamic pathophysiological information and potential diagnostic parameter (Leng and Edison, 2021).

Translocator Protein

The most widely used neuroinflammation probes are those targeting at 18 kDa Translocator Protein (TSPO), locates on the outer mitochondrial membrane, and overexpressed by microglia during activation (Van Camp et al., 2021; Zhou R. et al., 2021). TSPO PET tracers that have been applied in tau animal models include first generation (R)-[^{11}C]PK11195, second generation [^{18}F]FEBMP, [^{18}F]DPA-714, [^{11}C]AC-5216, (^{125}I) CLINDE, [^{11}C]PBR28, [^{18}F]FEDAA1106, and [^{11}C]DAA1106 (Ji et al., 2008, 2021; Maeda et al., 2011; Jacobs and Tavitian, 2012; Mirzaei et al., 2016; Ishikawa et al., 2018; Tournier et al., 2019, 2020; Barron et al., 2020; Takuwa et al., 2020; Chaney et al., 2021; Fairley et al., 2021; Leng and Edison, 2021; Zhou X. et al., 2021), and third generation [^{18}F]GE-180, etc. (Eckenweber et al., 2020; Chaney et al., 2021; Palleis et al., 2021). However, the first generation [^{11}C]PK-11195 has several disadvantages such as high non-specific plasma binding, low signal-to-noise ratio as well as relatively low entrance into the brain and difficulty in quantitative analysis. The second-generation TSPO tracers improved the limitation of [^{11}C]PK-11195 and demonstrated favorable binding properties. However, the binding of second-generation TSPO tracers differs greatly in humans depending on the *rs6971* polymorphism in the *TSPO* gene and can be categorized into high-, mixed-, and low-affinity binders (Owen et al., 2012). This polymorphism adds complexity and introduces high variability among subjects. Therefore, the third-generation TSPO tracers are being developed to overcome this limitation. In preclinical TSPO imaging studies, no evidence with respect to *rs6971* polymorphisms has been reported. Microglia activation assessed by using [^{11}C]PK11195 PET was reported to co-localize with tau and can predict disease progression and tau accumulation assessed by [^{18}F]flortaucipir in patients with PSP (Malpetti et al., 2020, 2021). Takuwa et al. (2020) demonstrated higher [^{11}C]PBB3 uptake (tau accumulation) and [^{18}F]AC-5216 (microglia activation) in rTg4510 mice at 6 month-of-age compared to wild-type littermates. The regional [^{18}F]AC-5216 retention correlated with both the tau level and brain atrophy assessed by T_2 structural MRI (Takuwa et al., 2020). Eckenweber et al. (2020) reported that [^{18}F]GE-180 measures of microglia activation was accompanied by [^{18}F]fluorodeoxyglucose (FDG) reduction with increasing age in PS19 mice at 2–6 months. This microglia activation also predicted the increased tau accumulation assessed by immunohistochemistry and deteriorated spatial learning in the Morris water maze (Eckenweber et al., 2020; **Figures 2A,B**). The specific detection of [^{18}F]GE-180 was demonstrated by serial PET during pharmacological depletion of microglia in PS19 mice (Palleis et al., 2021). Barron et al. (2020), Fairley et al. (2021), and Ji et al. (2021) have assessed microglia activation by using [^{18}F]FEBMP, which showed higher specificity to microglial TSPO and demonstrated increased microglia activation along with increased uptakes of [^{11}C]PBB3 for tau deposits in rTg4510 and PS19 mice.

Beyond Translocator Protein

The probes utilized so far for microglia activation imaging are not specific for a specific activation status (proinflammatory M1 or anti-inflammatory M2) (Jain et al., 2020). TSPO tracers have several limitations such as diverse cellular sources on both the astrocytes and microglia as well as high non-specific binding level (Nutma et al., 2021). Different targets have been pursued for neuroinflammation imaging toward a clearer activation status and have been evaluated in tauopathy animal models. These include tracers for purinergic P2Y12 receptor [[^{11}C]AZD1283], for organic anion-transporting polypeptide 1c1 [[^{18}F]2B-SRF101], and for neutrophil infiltration [(^{68}Ga) PEG-cFLFLFK] (Kreimerman et al., 2019; Kong et al., 2020; Maeda et al., 2021). P2X7 deficiency has been shown to improve plasticity and cognitive abilities in THY-Tau22 mice (Carvalho et al., 2021). Maeda et al. (2021) showed a distinct response of P2Y12 receptor to tau deposits using [^{11}C]AZD1283 by *ex vivo* autoradiography and immunohistochemical staining in rTg4510 and PS19 tau mice. The levels of P2Y12 receptor declined in tau-laden region with increased total level of microglia (Maeda et al., 2021). However, low brain uptake was observed for this tracer, which hinders further *in vivo* usage. Kreimerman et al. (2019) recently reported N-[3-[^{18}F]fluoropropyl] sulfonamide [[^{18}F]2B-SRF101] as a potential astrocytosis tracer in 3 × Tg mice: a higher [^{18}F]2B-SRF101 uptake was observed in the cortex and hippocampus of 3 × Tg compared to control mice, while the N-(^{11}C-methyl)-L-deuterodeprenyl (DED) showed a different uptake pattern.

METABOLISM IMAGING

Cerebral Glucose Metabolism

[^{18}F]FDG is commonly used in assisting the early and differential diagnosis of AD, FTD, and Parkinson's disease, of which regional cerebral glucose hypometabolism is present. Most studies report global cerebral glucose hypometabolism in PS19, tauVLW mice

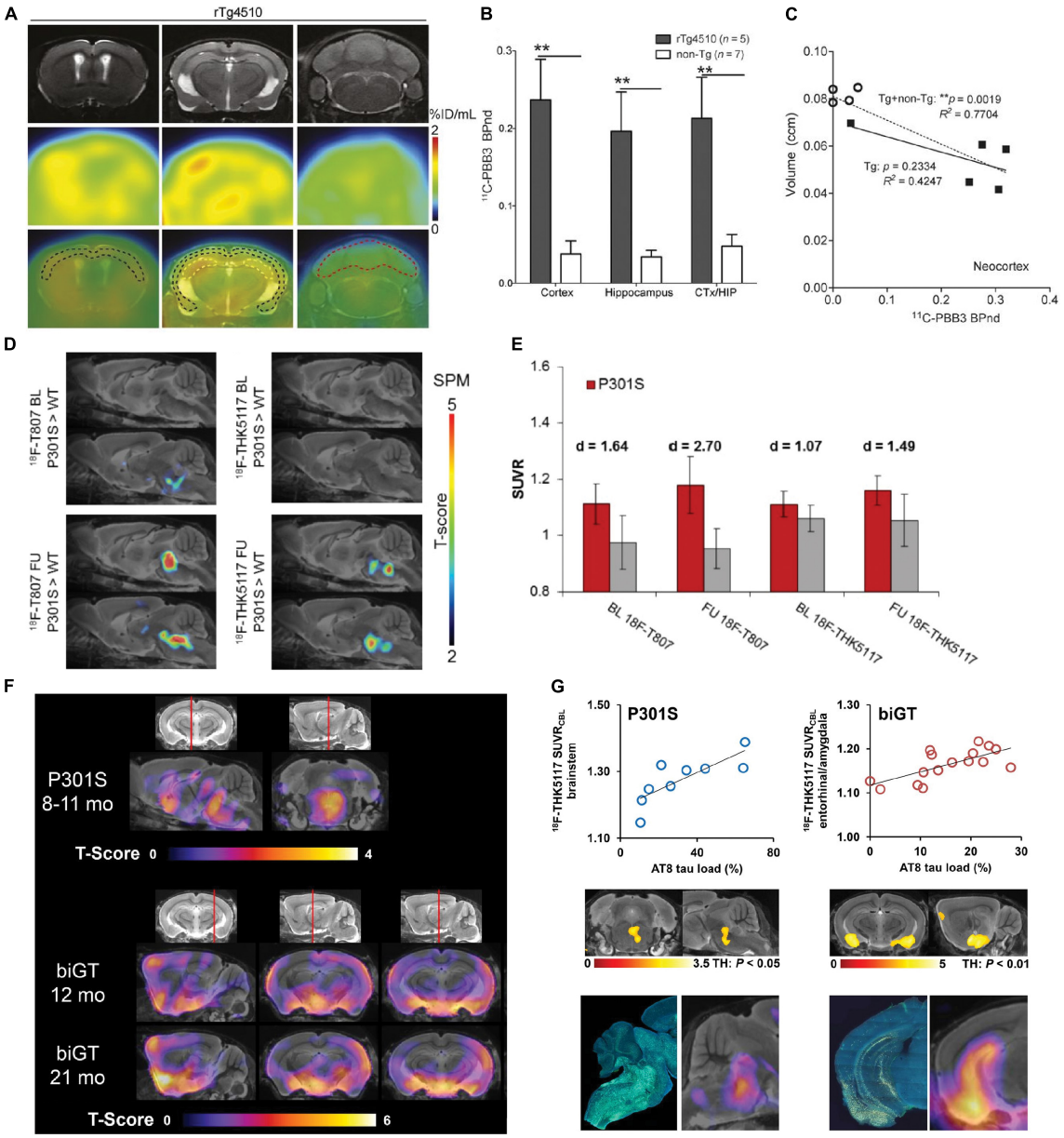

FIGURE 1 | *In vivo* microPET tau imaging in mice **(A)** Representative T_2-weighted MR, PET using [^{11}C]PBB3 and PET/MR images of coronal brain sections of 9-month-old rTg4510 mice showing neocortical, hippocampal, and cerebellar VOIs (black, yellow, and red outlines, respectively). PET images were generated from averaged dynamic data at 30–60 min after injection of [^{11}C]PBB3. **(B)** [^{11}C]PBB3 binding potential in each VOI calculated by simplified reference tissue model with cerebellum as reference tissue and brain volume measured using structural MRI data including calculation of non-displaceable binding potential for neocortex and hippocampus (CTX/HIP). $^{**}p < 0.01$, rTg4510 vs. non-transgenic mice. **(C)** Correlation between [^{11}C]PBB3 non-displaceable binding potential and volume of neocortex and hippocampus in transgenic (•) and non-transgenic (○) mice. $^{**}p < 0.01$, for correlations in the transgenic plus non-transgenic group (Tg + non-Tg, dotted lines) and the transgenic group only (Tg, solid lines). Reproduced from Ni et al. (2018) with permission Society of Nuclear Medicine and Molecular Imaging. **(D)** Statistical parametric mapping (SPM) are depicted upon a MRI mouse atlas and extracerebral voxels are masked. The *t*-score threshold of 2 complies a significance threshold of 0.01 uncorrected. **(E)** Bar graphs show group mean relative standard uptake value (SUVR) of P301S (red) and WT (gray) mice for baseline and follow-up PET measurements of [^{18}F]T807 and [^{18}F]THK5117. Error bars indicate SD and effect sizes are given by Cohen's *d*. Sagittal slices (median and 0.6 mm paramedian) show voxel-wise SPM between transgenic P301S and WT mice at baseline (BL) and follow-up (FU) for [^{18}F]T807 and [^{18}F]THK5117. Reproduced from Brendel et al. (2018) with permission from Frontiers SA. **(F)** Mean voxel-wise z score maps in sagittal and coronal planes of [^{18}F]THK5117 binding for groups of aged P301S vs. pooled WT mice and biGT mice vs. pooled WT mice. Results of 2-sample *t*-test are expressed as z score maps projected on MRI mouse atlas (gray scale). **(G)** Validation of [^{18}F]THK5117 small-animal PET results by immunohistochemical AT8 staining *in vitro* for P301S and biGT mice. Top row shows correlation plots of tau load (%) in corresponding AT8-stained areas with [^{18}F]THK5117 SUVR. Middle row depicts linear regression between tau load (%) and small-animal PET SUVR images projected on MRI mouse atlas. Bottom row illustrates AT8-stained sections from single mice along with their individual SPM-derived z score maps (projected on MRI mouse atlas). Reproduced from Brendel et al. (2016) with permission Society of Nuclear Medicine and Molecular Imaging.

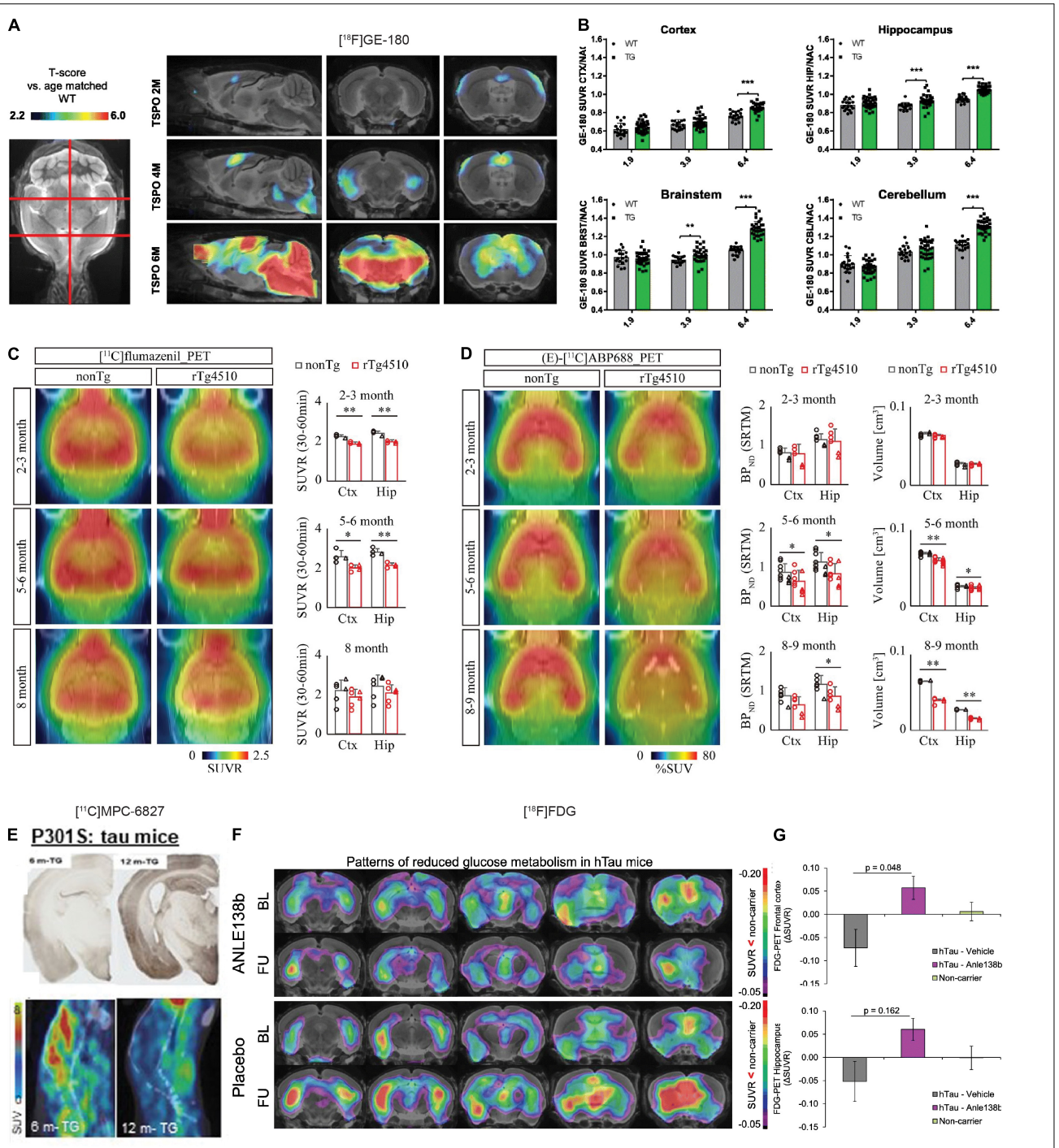

FIGURE 2 | *In vivo* microPET translocator protein (TSPO), synaptic, and metabolic alterations imaging in tauopathy mice. **(A)** Age-dependent exponential increase of 18kDa TSPO expression in different target regions of the brain of P301S tau model mice. n(P301S/WT) = 1.9M, 33/18; 3.9M, 32/17; 6.4M, 29/17. **(B)** Voxel-wise SPM analysis of TSPO expression in the contrast of P301S vs. wild-type mice at different ages. T-score maps are projected upon an MRI template in sagittal and coronal slices. ***$p < 0.001$. Reproduced from Eckenweber et al. (2020) with permission Society of Nuclear Medicine and Molecular Imaging. **(C)** PET assessment of inhibitory synapse with [11C]flumazenil in non-Tg and rTg4510 mice at age 2–3, 5–6, and 8 months after peripheral bolus administration of [11C]flumazenil. Representative PET images generated by averaging dynamic scan data at 30–60 min are shown. Brainstem was set as reference region. *$p < 0.05$; **$p < 0.01$; Student's *t*-test. **(D)** PET assessment of excitatory synapse with (E)-[11C]ABP688 in non-Tg and rTg4510 mice at age 2–3, 5–6, and 8–9 months after peripheral bolus administration of (E)-[11C]ABP688. Representative PET images generated by averaging dynamic scan data at 0–90 min are shown. (E)-[11C]ABP688 PET was analyzed in cortex (Ctx) and hippocampus (Hip) by simple reference tissue model with cerebellum as reference region. *$p < 0.05$ (Mann–Whitney *U* test). Reproduced from Shimojo et al. (2020) with permission from Biomed Central Ltd. (Springer Nature). **(E)** Immunohistochemical tau staining in 6-month- and

(Continued)

FIGURE 2 | 12-month-old transgenic P301S tau mice with their corresponding dynamic 0–45 min microPET/CT images with [^{11}C]MPC-6827 injection. Decrease in [^{11}C]MPC-6827 radioactive uptake with increase in tau loads. Reproduced from Sai et al. (2020) with permission from John Wiley and Sons. **(F)** Serial [^{18}F]fluorodeoxyglucose (FDG)-PET imaging of relative cerebral metabolism at follow-up (FU) imaging 3 months after late-stage novel aggregation-inhibiting oligomer modulator Anle138b treatment in hTau mice, with reduced baseline compared to control mice. **(G)** Quantification of longitudinal changes in relative FDG uptake (ΔSUVR) indicates normalization of cerebral metabolism in the hTau-treated group, while ongoing decrease in hTau-vehicle group. Baseline (BL) at 14.5 months of age and FU at 17.5 months. Reproduced from Brendel et al. (2019) with permission from Springer Nature AG.

as well as in 3 × Tg, 5 × FAD mice with both the amyloid and tau pathologies (Sancheti et al., 2013; Macdonald et al., 2014; DeBay et al., 2017; Hara et al., 2017; Son et al., 2018; Adlimoghaddam et al., 2019; Brendel et al., 2019; Eckenweber et al., 2020; Franke et al., 2020). However, Rojas et al. (2013) reported an increased [^{18}F]FDG uptake resulted from glial activation in 5 × FAD mice compared to wild-type mice. Hara et al. (2017) showed cerebral glucose hypometabolism first in the medial septum measured by using [^{18}F]FDG PET and spread to the hippocampal dentate gyrus in aged Tg601 tau mice. Brendel et al. (2019) demonstrated a reduced [^{18}F]FDG uptake in brain of hTau mice compared to wild-type mice and that treatment using novel aggregation-inhibiting oligomer modulator Anle138b can rescue this reduction in [^{18}F]FDG measures at follow-up scan after treatment (**Figures 2F,G**). Recent study by Xiang et al. (2021) showed that [^{18}F]FDG uptake reflected metabolism derived from microglia and that the increased [^{18}F]FDG might instead due to microglia activation.

Mitochondria

Mitochondrial ATP production is crucial in brain bioenergetics and is associated with brain homeostasis, functions, synaptic plasticity, and neurotransmitter processes (Du et al., 2008). The mitochondrial complex 1 (MC-1) plays an important role in the ATP production process, maintains calcium homeostasis, and regulates the apoptosis pathways. Altered MC1 function has been associated with neuronal toxicity, which contributes to the development of various neurodegenerative diseases including AD, FTD, and Parkinson's disease. Thus, MC-1 has been an attractive target for imaging biomarker indicative of neuronal damage and metabolic changes. As MC-1 locates inside neuron and not microglia or astrocytes, the probe will detect specifically the neuronal metabolism. Several tracers such as [^{18}F]BCPP-EF, [^{18}F]BCPP-BF, [^{18}F]BCPP-EM, and [^{18}F]BMS-747158-02 have been developed (Harada et al., 2013; Tsukada et al., 2014). And among these tracers, [^{18}F]BCPP-EF shows the sufficient brain uptake and a reversible binding pattern. Terada et al. (2021) recently demonstrated reduced uptake of brain [^{18}F]BCPP-EF, associating with [^{11}C]PBB3 measures of tauopathy and cognitive performance in patients with mild AD. In addition, the reduction of [^{18}F]BCPP-EF in the parahippocampus of early-stage AD may precede cerebral glucose hypometabolism assessed by using [^{18}F]FDG (Terada et al., 2020). Barron et al. (2020) and Fairley et al. (2021) showed a reduced [^{18}F]BCPP-EF uptake in the forebrain and hippocampus in rTg4510 mice compared to wild-type mice. Moreover, the [^{18}F]BCPP-EF signal co-localized with tau accumulation assessed by using [^{11}C]PBB3, regional atrophy assayed by structural T_2 MRI, and negatively associated with microglia activation assessed by using [^{18}F]FEBMP in rTg4510 mice (Barron et al., 2020; Fairley et al., 2021).

SYNAPTIC NEUROTRANSMITTER RECEPTORS

Aberrant accumulation of tau, especially the toxic oligomeric type, has been shown to be associated with altered synaptic protein expression, impairment in axonal transport, neurotransmitter deficits (e.g., cholinergic and glutamatergic), and leading to synaptic loss (Lasagna-Reeves et al., 2011; Spires-Jones and Hyman, 2014; Ait-Bouziad et al., 2017; Lo et al., 2019; Chang et al., 2021b). Several receptors have been shown to be involved in the tau-induced neurotoxicity: Tau modulates the N-methyl-D-aspartate (NMDA) receptor-dependent excitotoxicity and depotentiation in mouse models (Miyamoto et al., 2017). M1 and M3 muscarinic receptors have been shown to mediating the tau-induced intracellular calcium increase and alter calcium ion homeostasis (Gómez-Ramos et al., 2008). Oligomeric forms of tau have been shown to impair synaptic function and recognition memory function in mice (Lasagna-Reeves et al., 2011). Neuronal activity, in turn, enhances tau propagation and pathology (Wu et al., 2016). Chang et al. (2021a,b) recently showed that tau reduction reduced the excitation-inhibition ratio and decreased network hypersynchrony. The abnormal accumulation of tau deposits is directly associated with neuronal loss in animal models (Gómez-Isla et al., 1997; Park et al., 2020), gray matter atrophy, and cognitive deficit in AD (Clavaguera et al., 2009; Murray et al., 2011; Nelson et al., 2012; Bejanin et al., 2017; Ossenkoppele et al., 2021). Recent studies have showed a close correlation between postmortem tauopathy and atrophy assessed by structural MRI as well as functional connectivity in patients with CBD and PSP (Spina et al., 2019). Neuronal hyperactivity has been reported to enhance tau spread *in vivo* in tau mice (Wu et al., 2016). Selective disruption of inhibitory synapses led to neuronal hyperexcitability at an early stage of tau pathogenesis in PS19 mice (Shimojo et al., 2020).

Nicotinic Acetylcholine Receptors

The cholinergic system is important for memory and cognitive function. Impairment in cholinergic signaling, cholinesterase, decreased levels of nicotinic acetylcholine receptors (nAChRs) that was found at an early stage of AD and primary tauopathy diseases (Ni et al., 2013; Murley and Rowe, 2018). Several new α7 nAChR tracers have been developed including [^{11}C]NS14492 (Ettrup et al., 2011), [^{18}F]DBT-10 (Hillmer et al., 2016), [^{18}F]YLF-DW (Wang D. et al., 2021), and [^{18}F]ASEM (Horti et al., 2014). In animal models, Chaney et al. (2021) showed using an age-dependent increase in [^{18}F]ASEM uptake in the striatum and nucleus basalis of Meynert in the wild-type rats and was higher compared to that in the TgF344 rats at 18 month-of-age.

[^{18}F]ASEM has also been evaluated in Parkinson's disease animal model with striatal injection of 6-hydroxydopamine, in which a transient increase in the level of α7 nAChR was detected (Vetel et al., 2020). A comparative PET study comparing [^{18}F]ASEM and [^{18}F]DBT-10 indicated that [^{18}F]ASEM harbored better brain uptake and kinetic behavior in non-human primates (Hillmer et al., 2017). [^{18}F]ASEM imaging was reported in patients with mild cognitive impairment (Coughlin et al., 2020), psychosis (Coughlin J. et al., 2018), schizophrenia (Wong et al., 2018), and in healthy aging (Coughlin J. M. et al., 2018). Coughlin et al. (2020) showed an increased cerebral [^{18}F]ASEM measure of α7 nAChR in patients with mild cognitive impairment compared to healthy controls.

Metabotropic Glutamate Receptors

Metabotropic glutamate receptors (mGluRs) play important roles in memory and learning in regulating neuronal cell death and survival (Murley and Rowe, 2018). Among the mGluRs, the mGluR5 subtype has been most implicated in AD and FTD (Lee et al., 2004), with several tracers been developed and evaluated in animal and in human, e.g., [^{18}F]FPEB (Mecca et al., 2020), (E)-[^{11}C]ABP688 (Treyer et al., 2007), and [^{18}F]PSS232 (Sephton et al., 2015; Warnock et al., 2018). Lee et al. (2019) reported a 35% decrease in the cortical and subcortical [^{18}F]FPEB binding in 5 × FAD mice at 9 month-of-age compared to 3 month-of-age. Shimojo et al. (2020) demonstrated a reduced level of inhibitory synapse by using [^{11}C]flumazenil at 2–3 month-of-age and a reduced level of excitatory synapse by using (E)-[^{11}C]ABP688 at 5–6 month-of-age in rTg4510 mice compared to wild-type littermates, preceding tau accumulation and brain regional atrophy (**Figures 2C,D**). Similarly, Treyer et al. (2020) demonstrated a reduced (E)-[^{11}C]ABP688 uptake in the hippocampus and amygdala in patients with AD compared to healthy controls. Mecca et al. (2020) showed an age-dependent reduction of [^{18}F]FPEB-PET level in health control cases probably due to tissue loss. However, conflicting result was reported, where a higher level of [^{18}F]PSS232 binding was detected in autoradiography using postmortem brain slices from AD compared with healthy controls (Müller Herde et al., 2019).

DISCUSSION

Recent advances in PET imaging tracers have enabled *in vivo* visualization of the time course of central pathologies in patients with AD and primary tauopathy diseases as well as in disease animal models (Jacobs and Tavitian, 2012). The multiplex molecular, structural, and functional imaging readouts have provided important etiological insights, facilitating the understanding of disease mechanism (Hoenig et al., 2018; Jacobs et al., 2018; Franzmeier et al., 2019; Hanseeuw et al., 2019; La Joie et al., 2020; Vogel et al., 2020). In this study, we summarize several considerations in further PET studies in tauopathy animal models.

1. Improvement in animal models: Recent studies have indicated that genomic disruption in addition to mutant tau led to neuronal loss in the widely used rTg4510 mouse model (Ramsden et al., 2005; Santacruz et al., 2005). Moreover, the C57BL/6 strain background also impacts on the development of tauopathy in the rTg4510 model (Bailey et al., 2014). Tau propagates more quickly when human tau is knocked into the mouse locus (Gamache et al., 2019). New models such as the knock-in mouse model (Hashimoto et al., 2019; Saito et al., 2019) or non-human primate model (Beckman et al., 2021) that better recapitulate the human tauopathy diseases are essential for evaluation of imaging tracers and for understanding the tau-related pathophysiological alterations.
2. Difference in the structure of tauopathy between animal models and human: The mostly widely used P301L and P301S transgenic mouse models, which overexpress human 4R tau, show accumulation of pretangle, hyperphosphorylated tau, and neurofibrillary tangles in the brain parenchymal. However, the tau fibril structure is different in animal models compared to that in human with 4R tauopathy diseases, partly due to difference in seeding potency, posttranslational modification, cell-type specificity, as well as a much shorter disease development period (Narasimhan et al., 2017). Recent cryogenic electron microscopy study further demonstrated the complexity and structural differences in the folding of tau filaments among AD (3R/4R), primary tauopathy such as CBD (4R), PSP (4R), argyrophilic grain disease (4R), and Pick's disease (3R) (Shi et al., 2021b).
3. Quantification and reference brain region: Different observations across different PET imaging in tauopathy animal models were observed, partly due to the use of different strains and age groups, as the pathophysiology spatial distribution and time course differ among different models. For the quantification of PET tracer uptake, standard uptake value (SUV), percent injected dose per gram (ID%/g), and more advanced reference brain region modeling have been utilized (Kuntner and Stout, 2014). For quantifying tau tracer uptake in animal models, relative SUV (SUVR) was calculated using cerebellum as reference brain region. Difficulty in identifying a suitable reference brain region and high non-specific binding of tracer (such as TSPO tracer) hinder the accuracy of advanced analysis.
4. Emerging synaptic targets: Synaptic loss assessed by PET using synaptic vesicle proteins 2A (SV2A) tracer [^{11}C]UCB-J was recently reported in patients with primary tauopathies (Holland et al., 2020) and in AD (Coomans et al., 2021) where a link between tau [assessed by [^{18}F]flortaucipir] and SV2A was detected. No study has so far been reported using SV2A PET in tauopathy animal models. In addition, other emerging targets such as o-GlcNAcase (Paul et al., 2019; Wang et al., 2020) and GSK-3β (Liang et al., 2016; Hu et al., 2017; Prabhakaran et al., 2017; Bernard-Gauthier et al., 2019; Varlow et al., 2021) that associated with tauopathy remain to be explored in tauopathy models. Pilot study results from microtubule imaging using novel tracer [^{11}C]MPC-6827 in PS19 mice and cynomolgus monkeys showed promising results

(Damuka et al., 2020; Sai et al., 2020), where a decrease level of [^{11}C]MPC-6827 uptake accompanied by an increased level of tau was detected (**Figure 2E**).

5. Imaging microglia activation and astrocytosis: There is a lack of imaging tracers for detecting the dynamic phenotypes of microglia, especially the disease-associated microglia with more specific cellular location and activation status (proinflammatory/anti-inflammatory). Several promising targets are currently under investigation such as purinergic P2X7 receptors, P2Y12 receptors (Beaino et al., 2017, 2020; Van Weehaeghe et al., 2020), cyclooxygenase-1 and cyclooxygenase-2 (Ohnishi et al., 2014, 2016; Shukuri et al., 2016), macrophage colony-stimulating factor 1 receptor (Horti et al., 2019; Zhou X. et al., 2021), cannabinoid receptor type 2 (Savonenko et al., 2015; Ni et al., 2019, 2021a), imidazoline-2 binding sites, and receptor for advanced glycation end products (Cary et al., 2016; Luzi et al., 2020). Recent studies highlighted the role of astrocyte in tau pathology and the associated neurodegeneration (Bussian et al., 2018; Ferrer et al., 2018; Richetin et al., 2020; Maté de Gérando et al., 2021; Wang C. et al., 2021; Wang and Ye, 2021). Tau oligomer exposure was shown to trigger the senescence and toxic subpopulation of astrocytes (Gaikwad et al., 2021; Maté de Gérando et al., 2021). For astrocytosis, imaging several tracers targeting at monoamine oxidase-B [e.g., [^{11}C]deuterium-L-deprenyl and [^{11}C]SMBT-1] (Marutle et al., 2013; Rodriguez-Vieitez et al., 2015, 2016; Schöll et al., 2015; Carter et al., 2019; Bellaver et al., 2021; Ni et al., 2021b) and at imidazoline binding site (I_2-BS) [e.g., [^{11}C]BU99008] have shown promising results (Calsolaro et al., 2021). How the astrocytosis evolves longitudinally in tauopathy animal models remains to be demonstrated.
6. Sex difference: In human, sex modifies APOE ε4 dose effect on brain tau deposition in cognitively impaired individuals. Sex differences in cerebrospinal fluid tau levels and a mediating effect of testosterone were reported (Sundermann et al., 2020). In amyloidosis animal model, higher load of cerebral Aβ level in female compared to male mice and difference in immune system and metabolism have been reported (Eede et al., 2020; Ni, 2021). In tau animal models, the gender influence on the pathophysiology has been less well documented. A recent study showed increased olfactory, motor deficits, and tau pathology in Tau-P301L male mice compared to female mice (Camargo et al., 2021). Imaging of GSK-3β also indicated a sex difference in P301L mouse model with difference in tracer uptake only between male P301L and wild-type mice (Knight et al., 2021). In other studies, no behavioral, structural, and metabolic difference was observed in the P301S (Criver.com, 2021) and P301L mice (Ni et al., 2020; Massalimova et al., 2021). Several histology and behavior studies in 3 × Tg mice have also indicated a higher amyloid load in female mice compared to male mice, while no difference in tau level between groups (Hirata-Fukae et al., 2008; Carroll et al., 2010; Yang et al., 2018). The recent platform such as MODEL-AD provides an excellent platform for comparative studies and further understanding of the phenotype- and sex-related behavioral and pathological differences in the animal models (Oblak et al., 2020; Sukoff Rizzo et al., 2020; Vitek et al., 2020).

In conclusion, PET has provided a systematic non-invasive approaches to probe the spreading of tauopathy and the related neuroinflammatory, metabolic, and synaptic alterations as well as monitoring of treatment effect in tauopathy animal models.

AUTHOR CONTRIBUTIONS

LC, YK, and RN wrote the manuscript draft. All authors contributed to the manuscript and approved the final version of the manuscript.

FUNDING

RN received funding from Helmut Horten Stiftung and Vontobel Stiftung, University of Zurich (reference no. MEDEF-20-021).

REFERENCES

Adlimoghaddam, A., Snow, W. M., Stortz, G., Perez, C., Djordjevic, J., Goertzen, A. L., et al. (2019). Regional hypometabolism in the 3xTg mouse model of Alzheimer's disease. *Neurobiol. Dis.* 127, 264–277. doi: 10.1016/j.nbd.2019.03.008

Ait-Bouziad, N., Lv, G., Mahul-Mellier, A. L., Xiao, S., Zorludemir, G., Eliezer, D., et al. (2017). Discovery and characterization of stable and toxic Tau/phospholipid oligomeric complexes. *Nat. Commun.* 8:1678. doi: 10.1038/s41467-017-01575-4

Albert, M., Mairet-Coello, G., Danis, C., Lieger, S., Caillierez, R., Carrier, S., et al. (2019). Prevention of tau seeding and propagation by immunotherapy with a central tau epitope antibody. *Brain* 142, 1736–1750. doi: 10.1093/brain/awz100

Andorfer, C., Kress, Y., Espinoza, M., de Silva, R., Tucker, K. L., Barde, Y. A., et al. (2003). Hyperphosphorylation and aggregation of tau in mice expressing normal human tau isoforms. *J. Neurochem.* 86, 582–590. doi: 10.1046/j.1471-4159.2003.01879.x

Ayalon, G., Lee, S. H., Adolfsson, O., Foo-Atkins, C., Atwal, J. K., Blendstrup, M., et al. (2021). Antibody semorinemab reduces tau pathology in a transgenic mouse model and engages tau in patients with Alzheimer's disease. *Sci. Transl. Med.* 13:abb2639. doi: 10.1126/scitranslmed.abb2639

Bailey, R. M., Howard, J., Knight, J., Sahara, N., Dickson, D. W., and Lewis, J. (2014). Effects of the C57BL/6 strain background on tauopathy progression in the rTg4510 mouse model. *Mol. Neurodegener.* 9:8. doi: 10.1186/1750-1326-9-8

Barron, A. M., Ji, B., Fujinaga, M., Zhang, M. R., Suhara, T., Sahara, N., et al. (2020). In vivo positron emission tomography imaging of mitochondrial abnormalities in a mouse model of tauopathy. *Neurobiol. Aging* 94, 140–148. doi: 10.1016/j.neurobiolaging.2020.05.003

Beaino, W., Janssen, B., Kooij, G., van der Pol, S. M. A., van Het Hof, B., van Horssen, J., et al. (2017). Purinergic receptors P2Y12R and P2X7R: potential targets for PET imaging of microglia phenotypes in multiple sclerosis. *J. Neuroinflamm.* 14:259. doi: 10.1186/s12974-017-1034-z

Beaino, W., Janssen, B., Kooijman, E., Vos, R., Schuit, R. C., O'Brien-Brown, J., et al. (2020). PET imaging of P2X7R in the experimental autoimmune

encephalomyelitis model of multiple sclerosis using [^{11}C]SMW139. *J. Neuroinflamm.* 17:300. doi: 10.1186/s12974-020-01962-7

Beckman, D., Chakrabarty, P., Ott, S., Dao, A., Zhou, E., Janssen, W. G., et al. (2021). A novel tau-based rhesus monkey model of Alzheimer's pathogenesis. *Alzheimers Dement.* 17, 933–945. doi: 10.1002/alz.12318

Bejanin, A., Schonhaut, D. R., La Joie, R., Kramer, J. H., Baker, S. L., Sosa, N., et al. (2017). Tau pathology and neurodegeneration contribute to cognitive impairment in Alzheimer's disease. *Brain* 140, 3286–3300. doi: 10.1093/brain/awx243

Bellaver, B., Ferrari-Souza, J. P., Uglione da Ros, L., Carter, S. F., Rodriguez-Vieitez, E., Nordberg, A., et al. (2021). Astrocyte Biomarkers in Alzheimer Disease: A Systematic Review and Meta-analysis. *Neurology* [Preprint]. doi: 10.1212/wnl.0000000000012109

Bellucci, A., Westwood, A. J., Ingram, E., Casamenti, F., Goedert, M., and Spillantini, M. G. (2004). Induction of inflammatory mediators and microglial activation in mice transgenic for mutant human P301S tau protein. *Am. J. Pathol.* 165, 1643–1652. doi: 10.1016/s0002-9440(10)63421-9

Bernard-Gauthier, V., Mossine, A. V., Knight, A., Patnaik, D., Zhao, W. N., Cheng, C., et al. (2019). Structural Basis for Achieving GSK-3β Inhibition with High Potency, Selectivity, and Brain Exposure for Positron Emission Tomography Imaging and Drug Discovery. *J. Med. Chem.* 62, 9600–9617. doi: 10.1021/acs.jmedchem.9b01030

Boxer, A. L., Qureshi, I., Ahlijanian, M., Grundman, M., Golbe, L. I., Litvan, I., et al. (2019). Dam: Safety of the tau-directed monoclonal antibody BIIB092 in progressive supranuclear palsy: a randomised, placebo-controlled, multiple ascending dose phase 1b trial. *Lancet Neurol.* 18, 549–558. doi: 10.1016/s1474-4422(19)30139-5

Brelstaff, J. H., Mason, M., Katsinelos, T., McEwan, W. A., Ghetti, B., Tolkovsky, A. M., et al. (2021). Microglia become hypofunctional and release metalloproteases and tau seeds when phagocytosing live neurons with P301S tau aggregates. *Sci. Adv.* 7:eabg4980. doi: 10.1126/sciadv.abg4980

Brendel, M., Deussing, M., Blume, T., Kaiser, L., Probst, F., Overhoff, F., et al. (2019). Late-stage Anle138b treatment ameliorates tau pathology and metabolic decline in a mouse model of human Alzheimer's disease tau. *Alzheimers Res. Ther.* 11:67. doi: 10.1186/s13195-019-0522-z

Brendel, M., Jaworska, A., Probst, F., Overhoff, F., Korzhova, V., Lindner, S., et al. (2016). Small-Animal PET Imaging of Tau Pathology with [^{18}F]-THK5117 in 2 Transgenic Mouse Models. *J. Nucl. Med.* 57, 792–798. doi: 10.2967/jnumed.115.163493

Brendel, M., Yousefi, B. H., Blume, T., Herz, M., Focke, C., Deussing, M., et al. (2018). Comparison of [^{18}F]-T807 and [^{18}F]-THK5117 PET in a Mouse Model of Tau Pathology. *Front. Aging Neurosci.* 10:174. doi: 10.3389/fnagi.2018.00174

Busche, M. A., and Hyman, B. T. (2020). Synergy between amyloid-β and tau in Alzheimer's disease. *Nat. Neurosci.* 23, 1183–1193. doi: 10.1038/s41593-020-0687-6

Bussian, T. J., Aziz, A., Meyer, C. F., Swenson, B. L., van Deursen, J. M., and Baker, D. J. (2018). Clearance of senescent glial cells prevents tau-dependent pathology and cognitive decline. *Nature* 562, 578–582. doi: 10.1038/s41586-018-0543-y

Calsolaro, V., Matthews, P. M., Donat, C. K., Livingston, N. R., Femminella, G. D., Guedes, S. S., et al. (2021). Astrocyte reactivity with late-onset cognitive impairment assessed in vivo using ^{11}C-BU99008 PET and its relationship with amyloid load. *Mol. Psychiatry* [Preprint]. doi: 10.1038/s41380-021-01193-z

Camargo, L. C., Honold, D., Bauer, R., Shah, N. J., Langen, K. J., Willbold, D., et al. (2021). Sex-Related Motor Deficits in the Tau-P301L Mouse Model. *Biomedicines* 9:biomedicines9091160. doi: 10.3390/biomedicines9091160

Carroll, J. C., Rosario, E. R., Kreimer, S., Villamagna, A., Gentzschein, E., Stanczyk, F. Z., et al. (2010). Sex differences in β-amyloid accumulation in 3xTg-AD mice: role of neonatal sex steroid hormone exposure. *Brain Res.* 1366, 233–245. doi: 10.1016/j.brainres.2010.10.009

Carter, S. F., Chiotis, K., Nordberg, A., and Rodriguez-Vieitez, E. (2019). Longitudinal association between astrocyte function and glucose metabolism in autosomal dominant Alzheimer's disease. *Eur. J. Nucl. Med. Mol. Imaging* 46, 348–356. doi: 10.1007/s00259-018-4217-7

Carvalho, K., Martin, E., Ces, A., Sarrazin, N., Lagouge-Roussey, P., Nous, C., et al. (2021). P2X7-deficiency improves plasticity and cognitive abilities in a mouse model of Tauopathy. *Prog. Neurobiol.* 2021:102139. doi: 10.1016/j.pneurobio.2021.102139

Cary, B. P., Brooks, A. F., Fawaz, M. V., Drake, L. R., Desmond, T. J., Sherman, P., et al. (2016). Synthesis and Evaluation of [^{18}F]RAGER: A First Generation Small-Molecule PET Radioligand Targeting the Receptor for Advanced Glycation Endproducts. *ACS Chem. Neurosci.* 7, 391–398. doi: 10.1021/acschemneuro.5b00319

Chaney, A. M., Lopez-Picon, F. R., Serrière, S., Wang, R., Bochicchio, D., Webb, S. D., et al. (2021). Prodromal neuroinflammatory, cholinergic and metabolite dysfunction detected by PET and MRS in the TgF344-AD transgenic rat model of AD: a collaborative multi-modal study. *Theranostics* 11, 6644–6667. doi: 10.7150/thno.56059

Chang, C. W., Shao, E., and Mucke, L. (2021b). Tau: Enabler of diverse brain disorders and target of rapidly evolving therapeutic strategies. *Science* 371:abb8255. doi: 10.1126/science.abb8255

Chang, C. W., Evans, M. D., Yu, X., Yu, G. Q., and Mucke, L. (2021a). Tau reduction affects excitatory and inhibitory neurons differently, reduces excitation/inhibition ratios, and counteracts network hypersynchrony. *Cell Rep.* 37:109855. doi: 10.1016/j.celrep.2021.109855

Chiquita, S., Ribeiro, M., Castelhano, J., Oliveira, F., Sereno, J., Batista, M., et al. (2019). A longitudinal multimodal in vivo molecular imaging study of the 3xTg-AD mouse model shows progressive early hippocampal and taurine loss. *Hum. Mol. Genet.* 28, 2174–2188. doi: 10.1093/hmg/ddz045

Clavaguera, F., Bolmont, T., Crowther, R. A., Abramowski, D., Frank, S., Probst, A., et al. (2009). Transmission and spreading of tauopathy in transgenic mouse brain. *Nat. Cell Biol.* 11, 909–913. doi: 10.1038/ncb1901

Cohen, R. M., Rezai-Zadeh, K., Weitz, T. M., Rentsendorj, A., Gate, D., Spivak, I., et al. (2013). A transgenic Alzheimer rat with plaques, tau pathology, behavioral impairment, oligomeric aβ, and frank neuronal loss. *J. Neurosci.* 33, 6245–6256. doi: 10.1523/jneurosci.3672-12.2013

Congdon, E. E., and Sigurdsson, E. M. (2018). Tau-targeting therapies for Alzheimer disease. *Nat. Rev. Neurol.* 14, 399–415. doi: 10.1038/s41582-018-0013-z

Coomans, E. M., Schoonhoven, D. N., Tuncel, H., Verfaillie, S. C. J., Wolters, E. E., Boellaard, R., et al. (2021). In vivo tau pathology is associated with synaptic loss and altered synaptic function. *Alzheimers Res. Ther.* 13:35. doi: 10.1186/s13195-021-00772-0

Coughlin, J. M., Du, Y., Rosenthal, H. B., Slania, S., Min Koo, S., Park, A., et al. (2018). The distribution of the alpha7 nicotinic acetylcholine receptor in healthy aging: An in vivo positron emission tomography study with [^{18}F]ASEM. *Neuroimage* 165, 118–124. doi: 10.1016/j.neuroimage.2017.10.009

Coughlin, J. M., Rubin, L. H., Du, Y., Rowe, S. P., Crawford, J. L., Rosenthal, H. B., et al. (2020). High Availability of the α7-Nicotinic Acetylcholine Receptor in Brains of Individuals with Mild Cognitive Impairment: A Pilot Study Using (18)F-ASEM PET. *J. Nucl. Med.* 61, 423–426. doi: 10.2967/jnumed.119.230979

Coughlin, J., Du, Y., Crawford, J. L., Rubin, L. H., Behnam Azad, B., Lesniak, W. G., et al. (2018). The availability of the α7 nicotinic acetylcholine receptor in recent-onset psychosis: a study using (18)F-ASEM PET. *J. Nucl. Med.* 2018:213686. doi: 10.2967/jnumed.118.213686

Criver.com (2021). *Characterization of Tau Expressing P301S Mouse Model for Tauopathz Longitudinal Brain Structural and Metabolic Profile*. https://www.criver.com/sites/default/files/resource-files/SP-SFN-17-characterization_tau-expressing-p301s.pdf (accessed November 16, 2021)

Damuka, N., Czoty, P. W., Davis, A. T., Nader, M. A., Nader, S. H., Craft, S., et al. (2020). PET Imaging of [^{11}C]MPC-6827, a Microtubule-Based Radiotracer in Non-Human Primate Brains. *Molecules* 25:molecules25102289. doi: 10.3390/molecules25102289

de Calignon, A., Polydoro, M., Suárez-Calvet, M., William, C., Adamowicz, D. H., Kopeikina, K. J., et al. (2012). Propagation of tau pathology in a model of early Alzheimer's disease. *Neuron* 73, 685–697. doi: 10.1016/j.neuron.2011.11.033

de Cristóbal, J., García-García, L., Delgado, M., Pérez, M., Pozo, M. A., and Medina, M. (2014). Longitudinal assessment of a transgenic animal model of tauopathy by FDG-PET imaging. *J. Alzheimers Dis.* 40(Suppl. 1), S79–S89. doi: 10.3233/jad-132276

DeBay, D. R., Reid, G. A., Macdonald, I. R., Mawko, G., Burrell, S., Martin, E., et al. (2017). Butyrylcholinesterase-knockout reduces fibrillar β-amyloid and conserves 18FDG retention in 5XFAD mouse model of Alzheimer's disease. *Brain Res.* 1671, 102–110. doi: 10.1016/j.brainres.2017.07.009

Declercq, L., Rombouts, F., Koole, M., Fierens, K., Mariën, J., Langlois, X., et al. (2017). Preclinical evaluation of [^{18}F]-JNJ64349311, a novel PET tracer for tau imaging. *J. Nuclear Med.* 58:185199. doi: 10.2967/jnumed.116.185199

DeVos, S. L., Miller, R. L., Schoch, K. M., Holmes, B. B., Kebodeaux, C. S., Wegener, A. J., et al. (2017). Tau reduction prevents neuronal loss and reverses pathological tau deposition and seeding in mice with tauopathy. *Sci. Translat. Med.* 9:eaag0481. doi: 10.1126/scitranslmed.aag0481

Du, F., Zhu, X. H., Zhang, Y., Friedman, M., Zhang, N., Ugurbil, K., et al. (2008). Tightly coupled brain activity and cerebral ATP metabolic rate. *Proc. Natl. Acad. Sci. U S A.* 105, 6409–6414. doi: 10.1073/pnas.0710766105

Eckenweber, F., Medina-Luque, J., Blume, T., Sacher, C., Biechele, G., Wind, K., et al. (2020). Longitudinal TSPO expression in tau transgenic P301S mice predicts increased tau accumulation and deteriorated spatial learning. *J. Neuroinflamm.* 17:208. doi: 10.1186/s12974-020-01883-5

Eede, P., Obst, J., Benke, E., Yvon-Durocher, G., Richard, B. C., Gimber, N., et al. (2020). Interleukin-12/23 deficiency differentially affects pathology in male and female Alzheimer's disease-like mice. *EMBO Rep.* 21:e48530. doi: 10.15252/embr.201948530

Ettrup, A., Mikkelsen, J. D., Lehel, S., Madsen, J., Nielsen, E., Palner, M., et al. (2011). [^{11}C]-NS14492 as a novel PET radioligand for imaging cerebral alpha7 nicotinic acetylcholine receptors: in vivo evaluation and drug occupancy measurements. *J. Nucl. Med.* 52, 1449–1456. doi: 10.2967/jnumed.111.088815

Fairley, L. H., Sahara, N., Aoki, I., Ji, B., Suhara, T., Higuchi, M., et al. (2021). Neuroprotective effect of mitochondrial translocator protein ligand in a mouse model of tauopathy. *J. Neuroinflamm.* 18:76. doi: 10.1186/s12974-021-02122-1

Fawaz, M. V., Brooks, A. F., Rodnick, M. E., Carpenter, G. M., Shao, X., Desmond, T. J., et al. (2014). High Affinity Radiopharmaceuticals Based Upon Lansoprazole for PET Imaging of Aggregated Tau in Alzheimer's Disease and Progressive Supranuclear Palsy: Synthesis, Preclinical Evaluation, and Lead Selection. *ACS Chem. Neurosci.* 5, 718–730. doi: 10.1021/cn500103u

Ferrer, I., García, M. A., González, I. L., Lucena, D. D., Villalonga, A. R., Tech, M. C., et al. (2018). Aging-related tau astrogliopathy (ARTAG): not only tau phosphorylation in astrocytes. *Brain Pathol.* 28, 965–985. doi: 10.1111/bpa.12593

Filip, T., Mairinger, S., Neddens, J., Sauberer, M., Flunkert, S., Stanek, J., et al. (2021). Characterization of an APP/tau rat model of Alzheimer's disease by positron emission tomography and immunofluorescent labeling. *Alzheimer's Res. Therapy* 13:175. doi: 10.1186/s13195-021-00916-2

Filipcik, P., Zilka, N., Bugos, O., Kucerak, J., Koson, P., Novak, P., et al. (2012). First transgenic rat model developing progressive cortical neurofibrillary tangles. *Neurobiol. Aging* 33, 1448–1456. doi: 10.1016/j.neurobiolaging.2010.10.015

Fodero-Tavoletti, M. T., Okamura, N., Furumoto, S., Mulligan, R. S., Connor, A. R., McLean, C. A., et al. (2011). [^{18}F]-THK523: a novel in vivo tau imaging ligand for Alzheimer's disease. *Brain* 134(Pt 4), 1089–1100. doi: 10.1093/brain/awr038

Franke, T. N., Irwin, C., Bayer, T. A., Brenner, W., Beindorff, N., Bouter, C., et al. (2020). In vivo Imaging With [^{18}F]-FDG- and [^{18}F]-Florbetaben-PET/MRI Detects Pathological Changes in the Brain of the Commonly Used 5XFAD Mouse Model of Alzheimer's Disease. *Front. Med.* 7:529. doi: 10.3389/fmed.2020.00529

Franzmeier, N., Rubinski, A., Neitzel, J., Kim, Y., Damm, A., Na, D. L., et al. (2019). Functional connectivity associated with tau levels in ageing, Alzheimer's, and small vessel disease. *Brain* 142, 1093–1107. doi: 10.1093/brain/awz026

Gabellieri, E., Capotosti, F., Molette, J., Sreenivasachary, N., Mueller, A., Berndt, M., et al. (2020). Discovery of 2-(4-(2-fluoroethoxy)piperidin-1-yl)-9-methyl-9H-pyrrolo[2,3-b:4,5-c']dipyridine ([^{18}F]PI-2014) as PET tracer for the detection of pathological aggregated tau in Alzheimer's disease and other tauopathies. *Eur. J. Med. Chem.* 204:112615. doi: 10.1016/j.ejmech.2020.112615

Gaikwad, S., Puangmalai, N., Bittar, A., Montalbano, M., Garcia, S., McAllen, S., et al. (2021). Tau oligomer induced HMGB1 release contributes to cellular senescence and neuropathology linked to Alzheimer's disease and frontotemporal dementia. *Cell Rep.* 36:109419. doi: 10.1016/j.celrep.2021.109419

Gamache, J., Benzow, K., Forster, C., Kemper, L., Hlynialuk, C., Furrow, E., et al. (2019). Factors other than hTau overexpression that contribute to tauopathy-like phenotype in rTg4510 mice. *Nat. Commun.* 10, 2479–2479. doi: 10.1038/s41467-019-10428-1

Gómez-Isla, T., Hollister, R., West, H., Mui, S., Growdon, J. H., Petersen, R. C., et al. (1997). Neuronal loss correlates with but exceeds neurofibrillary tangles in Alzheimer's disease. *Ann. Neurol.* 41, 17–24. doi: 10.1002/ana.410410106

Gómez-Ramos, A., Díaz-Hernández, M., Rubio, A., Miras-Portugal, M. T., and Avila, J. (2008). Extracellular tau promotes intracellular calcium increase through M1 and M3 muscarinic receptors in neuronal cells. *Mol. Cell Neurosci.* 37, 673–681. doi: 10.1016/j.mcn.2007.12.010

Grossman, M. (2021). Lessons learned from a progressive supranuclear palsy trial. *Lancet Neurol.* 20, 162–163. doi: 10.1016/s1474-4422(21)00035-1

Hanseeuw, B. J., Betensky, R. A., Jacobs, H. I. L., Schultz, A. P., Sepulcre, J., Becker, J. A., et al. (2019). Association of Amyloid and Tau With Cognition in Preclinical Alzheimer Disease: A Longitudinal Study. *JAMA Neurol.* 76, 915–924. doi: 10.1001/jamaneurol.2019.1424

Hara, Y., Motoi, Y., Hikishima, K., Mizuma, H., Onoe, H., Matsumoto, S. E., et al. (2017). Involvement of the Septo-Hippocampal Cholinergic Pathway in Association with Septal Acetylcholinesterase Upregulation in a Mouse Model of Tauopathy. *Curr. Alzheimer Res.* 14, 94–103. doi: 10.2174/1567205013666160602235800

Harada, N., Nishiyama, S., Kanazawa, M., and Tsukada, H. (2013). Development of novel PET probes, [^{18}F]BCPP-EF, [^{18}F]BCPP-BF, and [^{11}C]BCPP-EM for mitochondrial complex 1 imaging in the living brain. *J. Labelled Comp. Radiopharm.* 56, 553–561. doi: 10.1002/jlcr.3056

Hashimoto, S., Matsuba, Y., Kamano, N., Mihira, N., Sahara, N., Takano, J., et al. (2019). Tau binding protein CAPON induces tau aggregation and neurodegeneration. *Nat. Commun.* 10:2394. doi: 10.1038/s41467-019-10278-x

Heneka, M. T., Carson, M. J., El Khoury, J., Landreth, G. E., Brosseron, F., Feinstein, D. L., et al. (2015). Neuroinflammation in Alzheimer's disease. *Lancet Neurol.* 14, 388–405. doi: 10.1016/s1474-4422(15)70016-5

Hillmer, A. T., Li, S., Zheng, M. Q., Scheunemann, M., Lin, S. F., Nabulsi, N., et al. (2017). PET imaging of α(7) nicotinic acetylcholine receptors: a comparative study of [^{18}F]ASEM and [^{18}F]DBT-10 in nonhuman primates, and further evaluation of [^{18}F]ASEM in humans. *Eur. J. Nucl. Med. Mol. Imaging* 44, 1042–1050. doi: 10.1007/s00259-017-3621-8

Hillmer, A. T., Zheng, M. Q., Li, S., Scheunemann, M., Lin, S. F., Holden, D., et al. (2016). PET imaging evaluation of [^{18}F]DBT-10, a novel radioligand specific to α7 nicotinic acetylcholine receptors, in nonhuman primates. *Eur. J. Nucl. Med. Mol. Imaging* 43, 537–547. doi: 10.1007/s00259-015-3209-0

Hirata-Fukae, C., Li, H. F., Hoe, H. S., Gray, A. J., Minami, S. S., Hamada, K., et al. (2008). Females exhibit more extensive amyloid, but not tau, pathology in an Alzheimer transgenic model. *Brain Res.* 1216, 92–103. doi: 10.1016/j.brainres.2008.03.079

Hoenig, M. C., Bischof, G. N., Seemiller, J., Hammes, J., Kukolja, J., Onur, A., et al. (2018). Networks of tau distribution in Alzheimer's disease. *Brain* 141, 568–581. doi: 10.1093/brain/awx353

Holland, N., Jones, P. S., Savulich, G., Wiggins, J. K., Hong, Y. T., Fryer, T. D., et al. (2020). Synaptic Loss in Primary Tauopathies Revealed by [(11) C]UCB-J Positron Emission Tomography. *Mov. Disord.* 35, 1834–1842. doi: 10.1002/mds.28188

Horti, A. G., Gao, Y., Kuwabara, H., Wang, Y., Abazyan, S., Yasuda, R. P., et al. (2014). [^{18}F]-ASEM, a radiolabeled antagonist for imaging the α7-nicotinic acetylcholine receptor with PET. *J. Nucl. Med.* 55, 672–677. doi: 10.2967/jnumed.113.132068

Horti, A. G., Naik, R., Foss, C. A., Minn, I., Misheneva, V., Du, Y., et al. (2019). PET imaging of microglia by targeting macrophage colony-stimulating factor 1 receptor (CSF1R). *Proc. Natl. Acad. Sci. U S A.* 116, 1686–1691. doi: 10.1073/pnas.1812155116

Hu, K., Patnaik, D., Collier, T. L., Lee, K. N., Gao, H., Swoyer, M. R., et al. (2017). Development of [^{18}F]Maleimide-Based Glycogen Synthase Kinase-3β Ligands for Positron Emission Tomography Imaging. *ACS Med. Chem. Lett.* 8, 287–292. doi: 10.1021/acsmedchemlett.6b00405

Ishikawa, A., Tokunaga, M., Maeda, J., Minamihisamatsu, T., Shimojo, M., Takuwa, H., et al. (2018). In Vivo Visualization of Tau Accumulation, Microglial Activation, and Brain Atrophy in a Mouse Model of Tauopathy rTg4510. *J. Alzheimers Dis.* 61, 1037–1052. doi: 10.3233/jad-170509

Ising, C., Venegas, C., Zhang, S., Scheiblich, H., Schmidt, S. V., Vieira-Saecker, A., et al. (2019). NLRP3 inflammasome activation drives tau pathology. *Nature* 575, 669–673. doi: 10.1038/s41586-019-1769-z

Jacobs, A. H., and Tavitian, B. (2012). Noninvasive molecular imaging of neuroinflammation. *J. Cereb. Blood Flow Metab.* 32, 1393–1415. doi: 10.1038/jcbfm.2012.53

Jacobs, H. I. L., Hedden, T., Schultz, A. P., Sepulcre, J., Perea, R. D., Amariglio, R. E., et al. (2018). Structural tract alterations predict downstream tau accumulation in amyloid-positive older individuals. *Nat. Neurosci.* 21, 424–431. doi: 10.1038/s41593-018-0070-z

Jain, P., Chaney, A. M., Carlson, M. L., Jackson, I. M., Rao, A., and James, M. L. (2020). Neuroinflammation PET Imaging: Current Opinion and Future Directions. *J. Nucl. Med.* 61, 1107–1112. doi: 10.2967/jnumed.119.229443

Ji, B., Maeda, J., Sawada, M., Ono, M., Okauchi, T., Inaji, M., et al. (2008). Imaging of peripheral benzodiazepine receptor expression as biomarkers of detrimental versus beneficial glial responses in mouse models of Alzheimer's and other CNS pathologies. *J. Neurosci.* 28, 12255–12267. doi: 10.1523/jneurosci.2312-08.2008

Ji, B., Ono, M., Yamasaki, T., Fujinaga, M., Zhang, M. R., Seki, C., et al. (2021). Detection of Alzheimer's disease-related neuroinflammation by a PET ligand selective for glial versus vascular translocator protein. *J. Cereb. Blood. Flow Metab.* 2021:21992457. doi: 10.1177/0271678x21992457

Kaide, S., Watanabe, H., Shimizu, Y., Tatsumi, H., Iikuni, S., Nakamoto, Y., et al. (2019). (18)F-labeled benzimidazopyridine derivatives for PET imaging of tau pathology in Alzheimer's disease. *Bioorg. Med. Chem.* 27, 3587–3594. doi: 10.1016/j.bmc.2019.06.039

Knight, A. C., Varlow, C., Tong, J., and Vasdev, N. (2021). In Vitro and In Vivo Evaluation of GSK-3 Radioligands in Alzheimer's Disease: Preliminary Evidence of Sex Differences. *ACS Pharmacol. Transl. Sci.* 4, 1287–1294. doi: 10.1021/acsptsci.1c00132

Kong, Y., Liu, K., Hua, T., Zhang, C., Sun, B., and Guan, Y. (2020). PET Imaging of Neutrophils Infiltration in Alzheimer's Disease Transgenic Mice. *Front. Neurol.* 11:523798. doi: 10.3389/fneur.2020.523798

Kreimerman, I., Reyes, A. L., Paolino, A., Pardo, T., Porcal, W., Ibarra, M., et al. (2019). Biological Assessment of a [^{18}F]-Labeled Sulforhodamine 101 in a Mouse Model of Alzheimer's Disease as a Potential Astrocytosis Marker. *Front. Neurosci.* 13:734. doi: 10.3389/fnins.2019.00734

Krishnaswamy, S., Lin, Y., Rajamohamedsait, W. J., Rajamohamedsait, H. B., Krishnamurthy, P., and Sigurdsson, E. M. (2014). Antibody-derived in vivo imaging of tau pathology. *J. Neurosci.* 34, 16835–16850. doi: 10.1523/jneurosci.2755-14.2014

Kroth, H., Oden, F., Molette, J., Schieferstein, H., Capotosti, F., Mueller, A., et al. (2019). Discovery and preclinical characterization of [^{18}F]PI-2620, a next-generation tau PET tracer for the assessment of tau pathology in Alzheimer's disease and other tauopathies. *Eur. J. Nucl. Med. Mol. Imaging* 46, 2178–2189. doi: 10.1007/s00259-019-04397-2

Kuntner, C., and Stout, D. (2014). Quantitative preclinical PET imaging: opportunities and challenges. *Front. Phys.* 2:12. doi: 10.3389/fphy.2014.00012

La Joie, R., Visani, A. V., Baker, S. L., Brown, J. A., Bourakova, V., Cha, J., et al. (2020). Prospective longitudinal atrophy in Alzheimer's disease correlates with the intensity and topography of baseline tau-PET. *Sci. Translat. Med.* 12:eaau5732. doi: 10.1126/scitranslmed.aau5732

Lasagna-Reeves, C. A., Castillo-Carranza, D. L., Sengupta, U., Clos, A. L., Jackson, G. R., and Kayed, R. (2011). Tau oligomers impair memory and induce synaptic and mitochondrial dysfunction in wild-type mice. *Mol. Neurodegenerat.* 6:39. doi: 10.1186/1750-1326-6-39

Lee, H. G., Ogawa, O., Zhu, X., O'Neill, M. J., Petersen, R. B., Castellani, R. J., et al. (2004). Aberrant expression of metabotropic glutamate receptor 2 in the vulnerable neurons of Alzheimer's disease. *Acta Neuropathol.* 107, 365–371. doi: 10.1007/s00401-004-0820-8

Lee, M., Lee, H. J., Jeong, Y. J., Oh, S. J., Kang, K. J., Han, S. J., et al. (2019). Age dependency of mGluR5 availability in 5xFAD mice measured by PET. *Neurobiol. Aging* 84, 208–216. doi: 10.1016/j.neurobiolaging.2019.08.006

Lee, V. M., Goedert, M., and Trojanowski, J. Q. (2001). Neurodegenerative tauopathies. *Annu. Rev. Neurosci.* 24, 1121–1159. doi: 10.1146/annurev.neuro.24.1.1121

Leng, F., and Edison, P. (2021). Neuroinflammation and microglial activation in Alzheimer disease: where do we go from here? *Nat. Rev. Neurol.* 17, 157–172. doi: 10.1038/s41582-020-00435-y

Lerdsirisuk, P., Harada, R., Hayakawa, Y., Shimizu, Y., Ishikawa, Y., Iwata, R., et al. (2021). Synthesis and evaluation of 2-pyrrolopyridinylquinoline derivatives as selective tau PET tracers for the diagnosis of Alzheimer's disease. *Nucl. Med. Biol.* 93, 11–18. doi: 10.1016/j.nucmedbio.2020.10.002

Lewis, J., McGowan, E., Rockwood, J., Melrose, H., Nacharaju, P., Van Slegtenhorst, M., et al. (2000). Neurofibrillary tangles, amyotrophy and progressive motor disturbance in mice expressing mutant (P301L) tau protein. *Nat. Genet.* 25, 402–405. doi: 10.1038/78078

Liang, S. H., Chen, J. M., Normandin, M. D., Chang, J. S., Chang, G. C., Taylor, C. K., et al. (2016). Discovery of a Highly Selective Glycogen Synthase Kinase-3 Inhibitor (PF-04802367) That Modulates Tau Phosphorylation in the Brain: Translation for PET Neuroimaging. *Angew Chem. Int. Ed. Engl.* 55, 9601–9605. doi: 10.1002/anie.201603797

Lindberg, A., Knight, A. C., Sohn, D., Rakos, L., Tong, J., Radelet, A., et al. (2021). Radiosynthesis, In Vitro and In Vivo Evaluation of [^{18}F]CBD-2115 as a First-in-Class Radiotracer for Imaging 4R-Tauopathies. *ACS Chem. Neurosci.* 12, 596–602. doi: 10.1021/acschemneuro.0c00801

Linnerbauer, M., Wheeler, M. A., and Quintana, F. J. (2020). Astrocyte Crosstalk in CNS Inflammation. *Neuron* 108, 608–622. doi: 10.1016/j.neuron.2020.08.012

Lo, C. H., Lim, C. K., Ding, Z., Wickramasinghe, S. P., Braun, A. R., Ashe, K. H., et al. (2019). Targeting the ensemble of heterogeneous tau oligomers in cells: A novel small molecule screening platform for tauopathies. *Alzheimers Dement.* 15, 1489–1502. doi: 10.1016/j.jalz.2019.06.4954

Luzi, F., Savickas, V., Taddei, C., Hader, S., Singh, N., Gee, A. D., et al. (2020). Radiolabeling of [(11)C]FPS-ZM1, a receptor for advanced glycation end products-targeting positron emission tomography radiotracer, using a [(11)C]CO(2)-to-[(11)C]CO chemical conversion. *Fut. Med. Chem.* 12, 511–521. doi: 10.4155/fmc-2019-0329

Macdonald, I. R., DeBay, D. R., Reid, G. A., O'Leary, T. P., Jollymore, C. T., Mawko, G., et al. (2014). Early detection of cerebral glucose uptake changes in the 5XFAD mouse. *Curr. Alzheimer. Res.* 11, 450–460. doi: 10.2174/1567205011666140505111354

Maeda, J., Minamihisamatsu, T., Shimojo, M., Zhou, X., Ono, M., Matsuba, Y., et al. (2021). Distinct microglial response against Alzheimer's amyloid and tau pathologies characterized by P2Y12 receptor. *Brain Commun.* 3:fcab011. doi: 10.1093/braincomms/fcab011

Maeda, J., Zhang, M. R., Okauchi, T., Ji, B., Ono, M., Hattori, S., et al. (2011). In vivo positron emission tomographic imaging of glial responses to amyloid-beta and tau pathologies in mouse models of Alzheimer's disease and related disorders. *J. Neurosci.* 31, 4720–4730. doi: 10.1523/jneurosci.3076-10.2011

Malpetti, M., Passamonti, L., Jones, P. S., Street, D., Rittman, T., Fryer, T. D., et al. (2021). Neuroinflammation predicts disease progression in progressive supranuclear palsy. *J. Neurol. Neurosurg. Psychiatry* 92, 769–775. doi: 10.1136/jnnp-2020-325549

Malpetti, M., Passamonti, L., Rittman, T., Jones, P. S., Vázquez Rodríguez, P., Bevan-Jones, W. R., et al. (2020). Neuroinflammation and Tau Colocalize in vivo in Progressive Supranuclear Palsy. *Ann. Neurol.* 88, 1194–1204. doi: 10.1002/ana.25911

Marquié, M., Normandin, M. D., Vanderburg, C. R., Costantino, I. M., Bien, E. A., Rycyna, L. G., et al. (2015). Validating novel tau positron emission tomography tracer [F-18]-AV-1451 (T807) on postmortem brain tissue. *Ann. Neurol.* 78, 787–800. doi: 10.1002/ana.24517

Marutle, A., Gillberg, P. G., Bergfors, A., Yu, W. F., Ni, R. Q., Nennesmo, I., et al. (2013). H-3-Deprenyl and H-3-PIB autoradiography show different laminar distributions of astroglia and fibrillar beta-amyloid in Alzheimer brain. *J. Neuroinflamm.* 10:90. doi: 10.1186/1742-2094-10-90

Maruyama, M., Shimada, H., Suhara, T., Shinotoh, H., Ji, B., Maeda, J., et al. (2013). Imaging of tau pathology in a tauopathy mouse model and in Alzheimer patients compared to normal controls. *Neuron* 79, 1094–1108. doi: 10.1016/j.neuron.2013.07.037

Massalimova, A., Ni, R., Nitsch, R. M., Reisert, M., von Elverfeldt, D., and Klohs, J. (2021). Diffusion Tensor Imaging Reveals Whole-Brain Microstructural Changes in the P301L Mouse Model of Tauopathy. *Neurodegener. Dis.* 2021, 1–12. doi: 10.1159/000515754

Maté de Gérando, A., d'Orange, M., Augustin, E., Joséphine, C., Aurégan, G., Gaudin-Guérif, M., et al. (2021). Neuronal tau species transfer to astrocytes and induce their loss according to tau aggregation state. *Brain* 144, 1167–1182. doi: 10.1093/brain/awab011

McAlpine, C. S., Park, J., Griciuc, A., Kim, E., Choi, S. H., Iwamoto, Y., et al. (2021). Astrocytic interleukin-3 programs microglia and limits Alzheimer's disease. *Nature* [Preprint]. doi: 10.1038/s41586-021-03734-6

McMurray, L., Macdonald, J. A., Ramakrishnan, N. K., Zhao, Y., Williamson, D. W., Tietz, O., et al. (2021). Synthesis and Assessment of Novel Probes for Imaging Tau Pathology in Transgenic Mouse and Rat Models. *ACS Chem. Neurosci.* [Preprint]. doi: 10.1021/acschemneuro.0c00790

Mecca, A. P., McDonald, J. W., Michalak, H. R., Godek, T. A., Harris, J. E., Pugh, E. A., et al. (2020). PET imaging of mGluR5 in Alzheimer's disease. *Alzheimers Res. Ther.* 12:15. doi: 10.1186/s13195-020-0582-0

Mirzaei, N., Tang, S. P., Ashworth, S., Coello, C., Plisson, C., Passchier, J., et al. (2016). In vivo imaging of microglial activation by positron emission tomography with [(11)C]PBR28 in the 5XFAD model of Alzheimer's disease. *Glia* 64, 993–1006. doi: 10.1002/glia.22978

Miyamoto, T., Stein, L., Thomas, R., Djukic, B., Taneja, P., Knox, J., et al. (2017). Phosphorylation of tau at Y18, but not tau-fyn binding, is required for tau to modulate NMDA receptor-dependent excitotoxicity in primary neuronal culture. *Mol. Neurodegenerat.* 12:41. doi: 10.1186/s13024-017-0176-x

Moreno-Gonzalez, I., Edwards, G. A. III, Hasan, O., Gamez, N., Schulz, J. E., Fernandez-Valenzuela, J. J., et al. (2021). Longitudinal Assessment of Tau-Associated Pathology by (18)F-THK5351 PET Imaging: A Histological, Biochemical, and Behavioral Study. *Diagnostics* 11:11101874. doi: 10.3390/diagnostics11101874

Mullard, A. (2021). Failure of first anti-tau antibody in Alzheimer disease highlights risks of history repeating. *Nat. Rev. Drug Discov.* 2021:7. doi: 10.1038/d41573-020-00217-7

Müller Herde, A., Schibli, R., Weber, M., and Ametamey, S. M. (2019). Metabotropic glutamate receptor subtype 5 is altered in LPS-induced murine neuroinflammation model and in the brains of AD and ALS patients. *Eur. J. Nucl. Med. Mol. Imaging* 46, 407–420. doi: 10.1007/s00259-018-4179-9

Murley, A. G., and Rowe, J. B. (2018). Neurotransmitter deficits from frontotemporal lobar degeneration. *Brain* 141, 1263–1285. doi: 10.1093/brain/awx327

Murray, M. E., Graff-Radford, N. R., Ross, O. A., Petersen, R. C., Duara, R., and Dickson, D. W. (2011). Neuropathologically defined subtypes of Alzheimer's disease with distinct clinical characteristics: a retrospective study. *Lancet Neurol.* 10, 785–796. doi: 10.1016/s1474-4422(11)70156-9

Murugan, N. A., Chiotis, K., Rodriguez-Vieitez, E., Lemoine, L., Ågren, H., and Nordberg, A. (2019). Cross-interaction of tau PET tracers with monoamine oxidase B: evidence from in silico modelling and in vivo imaging. *Eur. J. Nucl. Med. Mol. Imaging* 46, 1369–1382. doi: 10.1007/s00259-019-04305-8

Narasimhan, S., Guo, J. L., Changolkar, L., Stieber, A., McBride, J. D., Silva, L. V., et al. (2017). Pathological Tau Strains from Human Brains Recapitulate the Diversity of Tauopathies in Nontransgenic Mouse Brain. *J. Neurosci.* 37, 11406–11423. doi: 10.1523/JNEUROSCI.1230-17.2017

Nelson, P. T., Alafuzoff, I., Bigio, E. H., Bouras, C., Braak, H., Cairns, N. J., et al. (2012). Correlation of Alzheimer disease neuropathologic changes with cognitive status: a review of the literature. *J. Neuropathol. Exp. Neurol.* 71, 362–381. doi: 10.1097/NEN.0b013e31825018f7

Ng, K. P., Pascoal, T. A., Mathotaarachchi, S., Therriault, J., Kang, M. S., Shin, M., et al. (2017). Monoamine oxidase B inhibitor, selegiline, reduces (18)F-THK5351 uptake in the human brain. *Alzheimer's Res. Ther.* 9, 25–25. doi: 10.1186/s13195-017-0253-y

Ni, R. (2021). Positron Emission Tomography in Animal Models of Alzheimer's Disease Amyloidosis. [Preprint]. doi: 10.20944/PREPRINTS202110.0222.V1

Ni, R., Ji, B., Ono, M., Sahara, N., Zhang, M. R., Aoki, I., et al. (2018). Comparative in-vitro and in-vivo quantifications of pathological tau deposits and their association with neurodegeneration in tauopathy mouse models. *J. Nucl. Med.* 59, 960–966. doi: 10.2967/jnumed.117.201632

Ni, R., Marutle, A., and Nordberg, A. (2013). Modulation of α7 nicotinic acetylcholine receptor and fibrillar amyloid-β interactions in Alzheimer's disease brain. *J. Alzheimers Dis.* 33, 841–851. doi: 10.3233/jad-2012-121447

Ni, R., Mu, L., and Ametamey, S. (2019). Positron emission tomography of type 2 cannabinoid receptors for detecting inflammation in the central nervous system. *Acta Pharmacol. Sin.* 40, 351–357. doi: 10.1038/s41401-018-0035-5

Ni, R., Müller Herde, A., Haider, A., Keller, C., Louloudis, G., Vaas, M., et al. (2021a). In vivo Imaging of Cannabinoid Type 2 Receptors: Functional and Structural Alterations in Mouse Model of Cerebral Ischemia by PET and MRI. *Mol. Imaging Biol.* 2021:4. doi: 10.1007/s11307-021-01655-4

Ni, R., Röjdner, J., Voytenko, L., Dyrks, T., Thiele, A., Marutle, A., et al. (2021b). In vitro Characterization of the Regional Binding Distribution of Amyloid PET Tracer Florbetaben and the Glia Tracers Deprenyl and PK11195 in Autopsy Alzheimer's Brain Tissue. *J. Alzheimers Dis.* 80, 1723–1737. doi: 10.3233/jad-201344

Ni, R., Zarb, Y., Kuhn, G. A., Müller, R., Yundung, Y., Nitsch, R. M., et al. (2020). SWI and phase imaging reveal intracranial calcifications in the P301L mouse model of human tauopathy. *Magma* 33, 769–781. doi: 10.1007/s10334-020-00855-3

Novak, P., Kovacech, B., Katina, S., Schmidt, R., Scheltens, P., Kontsekova, E., et al. (2021). ADAMANT: a placebo-controlled randomized phase 2 study of AADvac1, an active immunotherapy against pathological tau in Alzheimer's disease. *Nat. Aging* 1, 521–534. doi: 10.1038/s43587-021-00070-2

Nutma, E., Ceyzériat, K., Amor, S., Tsartsalis, S., Millet, P., Owen, D. R., et al. (2021). Cellular sources of TSPO expression in healthy and diseased brain. *Eur. J. Nuclear Med. Mol. Imaging* [Preprint]. doi: 10.1007/s00259-020-05166-2

Oblak, A. L., Forner, S., Territo, P. R., Sasner, M., Carter, G. W., Howell, G. R., et al. (2020). Model organism development and evaluation for late-onset Alzheimer's disease: MODEL-AD. *Alzheimers Dement.* 6:e12110. doi: 10.1002/trc2.12110

Oddo, S., Caccamo, A., Shepherd, J. D., Murphy, M. P., Golde, T. E., Kayed, R., et al. (2003). Triple-transgenic model of Alzheimer's disease with plaques and tangles: intracellular Abeta and synaptic dysfunction. *Neuron* 39, 409–421. doi: 10.1016/s0896-6273(03)00434-3

Ohnishi, A., Senda, M., Yamane, T., Mikami, T., Nishida, H., Nishio, T., et al. (2016). Exploratory human PET study of the effectiveness of (11)C-ketoprofen methyl ester, a potential biomarker of neuroinflammatory processes in Alzheimer's disease. *Nucl. Med. Biol.* 43, 438–444. doi: 10.1016/j.nucmedbio.2016.04.005

Ohnishi, A., Senda, M., Yamane, T., Sasaki, M., Mikami, T., Nishio, T., et al. (2014). Human whole-body biodistribution and dosimetry of a new PET tracer, [(11)C]ketoprofen methyl ester, for imagings of neuroinflammation. *Nucl. Med. Biol.* 41, 594–599. doi: 10.1016/j.nucmedbio.2014.04.008

Ossenkoppele, R., Lyoo, C. H., Sudre, C. H., van Westen, D., Cho, H., Ryu, Y. H., et al. (2020). Distinct tau PET patterns in atrophy-defined subtypes of Alzheimer's disease. *Alzheimers Dement.* 16, 335–344. doi: 10.1016/j.jalz.2019.08.201

Ossenkoppele, R., Smith, R., Mattsson-Carlgren, N., Groot, C., Leuzy, A., Strandberg, O., et al. (2021). Accuracy of Tau Positron Emission Tomography as a Prognostic Marker in Preclinical and Prodromal Alzheimer Disease: A Head-to-Head Comparison Against Amyloid Positron Emission Tomography and Magnetic Resonance Imaging. *JAMA Neurol.* [Preprint]. doi: 10.1001/jamaneurol.2021.1858

Owen, D. R., Yeo, A. J., Gunn, R. N., Song, K., Wadsworth, G., Lewis, A., et al. (2012). An 18-kDa translocator protein (TSPO) polymorphism explains differences in binding affinity of the PET radioligand PBR28. *J. Cereb. Blood Flow Metabol.* 32, 1–5. doi: 10.1038/jcbfm.2011.147

Palleis, C., Sauerbeck, J., Beyer, L., Harris, S., Schmitt, J., Morenas-Rodriguez, E., et al. (2021). In Vivo Assessment of Neuroinflammation in 4-Repeat Tauopathies. *Mov. Disord.* 36, 883–894. doi: 10.1002/mds.28395

Park, L., Hochrainer, K., Hattori, Y., Ahn, S. J., Anfray, A., Wang, G., et al. (2020). Tau induces PSD95-neuronal NOS uncoupling and neurovascular dysfunction independent of neurodegeneration. *Nat. Neurosci.* 23, 1079–1089. doi: 10.1038/s41593-020-0686-7

Paul, S., Haskali, M. B., Liow, J. S., Zoghbi, S. S., Barth, V. N., Kolodrubetz, M. C., et al. (2019). Evaluation of a PET Radioligand to Image O-GlcNAcase in Brain and Periphery of Rhesus Monkey and Knock-Out Mouse. *J. Nucl. Med.* 60, 129–134. doi: 10.2967/jnumed.118.213231

Prabhakaran, J., Zanderigo, F., Sai, K. K. S., Rubin-Falcone, H., Jorgensen, M. J., Kaplan, J. R., et al. (2017). Radiosynthesis and in Vivo Evaluation of [(11)C]A1070722, a High Affinity GSK-3 PET Tracer in Primate Brain. *ACS Chem. Neurosci.* 8, 1697–1703. doi: 10.1021/acschemneuro.6b00376

Ramsden, M., Kotilinek, L., Forster, C., Paulson, J., McGowan, E., SantaCruz, K., et al. (2005). Age-dependent neurofibrillary tangle formation, neuron loss, and memory impairment in a mouse model of human tauopathy (P301L). *J. Neurosci.* 25, 10637–10647. doi: 10.1523/jneurosci.3279-05.2005

Richetin, K., Steullet, P., Pachoud, M., Perbet, R., Parietti, E., Maheswaran, M., et al. (2020). Tau accumulation in astrocytes of the dentate gyrus induces neuronal dysfunction and memory deficits in Alzheimer's disease. *Nat. Neurosci.* 23, 1567–1579. doi: 10.1038/s41593-020-00728-x

Roberts, M., Sevastou, I., Imaizumi, Y., Mistry, K., Talma, S., Dey, M., et al. (2020). Pre-clinical characterisation of E2814, a high-affinity antibody targeting the microtubule-binding repeat domain of tau for passive immunotherapy in Alzheimer's disease. *Acta Neuropathol. Commun.* 8:13. doi: 10.1186/s40478-020-0884-2

Robinson, J. L., Yan, N., Caswell, C., Xie, S. X., Suh, E., Van Deerlin, V. M., et al. (2020). Primary Tau Pathology, Not Copathology, Correlates With Clinical Symptoms in PSP and CBD. *J. Neuropathol. Exp. Neurol.* 79, 296–304. doi: 10.1093/jnen/nlz141

Rodriguez-Vieitez, E., Ni, R., Gulyás, B., Tóth, M., Häggkvist, J., Halldin, C., et al. (2015). Astrocytosis precedes amyloid plaque deposition in Alzheimer APPswe transgenic mouse brain: a correlative positron emission tomography and in vitro imaging study. *Eur. J. Nucl. Med. Mol. Imaging* 42, 1119–1132. doi: 10.1007/s00259-015-3047-0

Rodriguez-Vieitez, E., Saint-Aubert, L., Carter, S. F., Almkvist, O., Farid, K., Schöll, M., et al. (2016). Diverging longitudinal changes in astrocytosis and amyloid PET in autosomal dominant Alzheimer's disease. *Brain* 139(Pt 3), 922–936. doi: 10.1093/brain/awv404

Rojas, S., Herance, J. R., Gispert, J. D., Abad, S., Torrent, E., Jiménez, X., et al. (2013). Invivo evaluation of amyloid deposition and brain glucose metabolism of 5XFAD mice using positron emission tomography. *Neurobiol. Aging* 34, 1790–1798. doi: 10.1016/j.neurobiolaging.2012.12.027

Sai, K. S., Damuka, N., Mintz, A., Whitlow, C. T., Craft, S., and Macauley-Rambach, S. (2020). [^{11}C]MPC-6827, a microtubule-based PET imaging tracer: A potential early imaging biomarker for AD and other ADRDs. *Alzheimer's Dement.* 16:e037790. doi: 10.1002/alz.037790

Saito, T., Mihira, N., Matsuba, Y., Sasaguri, H., Hashimoto, S., Narasimhan, S., et al. (2019). Humanization of the entire murine Mapt gene provides a murine model of pathological human tau propagation. *J. Biol. Chem.* 294, 12754–12765. doi: 10.1074/jbc.RA119.009487

Sancheti, H., Akopian, G., Yin, F., Brinton, R. D., Walsh, J. P., and Cadenas, E. (2013). Age-dependent modulation of synaptic plasticity and insulin mimetic effect of lipoic acid on a mouse model of Alzheimer's disease. *PLoS One* 8:e69830. doi: 10.1371/journal.pone.0069830

Santacruz, K., Lewis, J., Spires, T., Paulson, J., Kotilinek, L., Ingelsson, M., et al. (2005). Tau suppression in a neurodegenerative mouse model improves memory function. *Science* 309, 476–481. doi: 10.1126/science.1113694

Savonenko, A. V., Melnikova, T., Wang, Y., Ravert, H., Gao, Y., Koppel, J., et al. (2015). Cannabinoid CB2 Receptors in a Mouse Model of Aβ Amyloidosis: Immunohistochemical Analysis and Suitability as a PET Biomarker of Neuroinflammation. *PLoS One* 10:e0129618. doi: 10.1371/journal.pone.0129618

Schöll, M., Carter, S. F., Westman, E., Rodriguez-Vieitez, E., Almkvist, O., Thordardottir, S., et al. (2015). Early astrocytosis in autosomal dominant Alzheimer's disease measured in vivo by multi-tracer positron emission tomography. *Sci. Rep.* 5:16404. doi: 10.1038/srep16404

Sephton, S. M., Herde, A. M., Mu, L., Keller, C., Rüdisühli, S., Auberson, Y., et al. (2015). Preclinical evaluation and test-retest studies of [^{18}F]PSS232, a novel radioligand for targeting metabotropic glutamate receptor 5 (mGlu5). *Eur. J. Nucl. Med. Mol. Imaging* 42, 128–137. doi: 10.1007/s00259-014-2883-7

Shao, X., Carpenter, G. M., Desmond, T. J., Sherman, P., Quesada, C. A., Fawaz, M., et al. (2012). Evaluation of [(11)C]N-Methyl Lansoprazole as a Radiopharmaceutical for PET Imaging of Tau Neurofibrillary Tangles. *ACS Med. Chem. Lett.* 3, 936–941. doi: 10.1021/ml300216t

Shi, Y., Andhey, P. S., Ising, C., Wang, K., Snipes, L. L., Boyer, K., et al. (2021a). Overexpressing low-density lipoprotein receptor reduces tau-associated neurodegeneration in relation to apoE-linked mechanisms. *Neuron* [Preprint]. doi: 10.1016/j.neuron.2021.05.034

Shi, Y., Zhang, W., Yang, Y., Murzin, A. G., Falcon, B., Kotecha, A., et al. (2021b). Structure-based classification of tauopathies. *Nature* [Preprint]. doi: 10.1038/s41586-021-03911-7

Shi, Y., Manis, M., Long, J., Wang, K., Sullivan, P. M., Remolina Serrano, J., et al. (2019). Microglia drive APOE-dependent neurodegeneration in a tauopathy mouse model. *J. Exp. Med.* 216, 2546–2561. doi: 10.1084/jem.20190980

Shimojo, M., Takuwa, H., Takado, Y., Tokunaga, M., Tsukamoto, S., Minatohara, K., et al. (2020). Selective Disruption of Inhibitory Synapses Leading to Neuronal Hyperexcitability at an Early Stage of Tau Pathogenesis in a Mouse Model. *J. Neurosci.* 40, 3491–3501. doi: 10.1523/jneurosci.2880-19.2020

Shukuri, M., Mawatari, A., Ohno, M., Suzuki, M., Doi, H., Watanabe, Y., et al. (2016). Detection of Cyclooxygenase-1 in Activated Microglia During Amyloid Plaque Progression: PET Studies in Alzheimer's Disease Model Mice. *J. Nucl. Med.* 57, 291–296. doi: 10.2967/jnumed.115.166116

Sobue, A., Komine, O., Hara, Y., Endo, F., Mizoguchi, H., Watanabe, S., et al. (2021). Microglial gene signature reveals loss of homeostatic microglia associated with neurodegeneration of Alzheimer's disease. *Acta Neuropathol. Commun.* 9:1. doi: 10.1186/s40478-020-01099-x

Son, Y., Kim, J. S., Jeong, Y. J., Jeong, Y. K., Kwon, J. H., Choi, H.-D., et al. (2018). Long-term RF exposure on behavior and cerebral glucose metabolism in 5xFAD mice. *Neurosci. Lett.* 666, 64–69. doi: 10.1016/j.neulet.2017.12.042

Spillantini, M. G., and Goedert, M. (2013). Tau pathology and neurodegeneration. *Lancet Neurol.* 12, 609–622. doi: 10.1016/S1474-4422(13)70090-5

Spina, S., Brown, J. A., Deng, J., Gardner, R. C., Nana, A. L., Hwang, J.-H. L., et al. (2019). Neuropathological correlates of structural and functional imaging biomarkers in 4-repeat tauopathies. *Brain* 142, 2068–2081. doi: 10.1093/brain/awz122

Spires-Jones, T. L., and Hyman, B. T. (2014). The intersection of amyloid beta and tau at synapses in Alzheimer's disease. *Neuron* 82, 756–771. doi: 10.1016/j.neuron.2014.05.004

Sukoff Rizzo, S. J., Masters, A., Onos, K. D., Quinney, S., Sasner, M., Oblak, A., et al. (2020). Improving preclinical to clinical translation in Alzheimer's disease research. *Alzheimer's Dement.* 6:e12038. doi: 10.1002/trc2.12038

Sundermann, E. E., Panizzon, M. S., Chen, X., Andrews, M., Galasko, D., and Banks, S. J. (2020). Sex differences in Alzheimer's-related Tau biomarkers and a mediating effect of testosterone. *Biol. Sex Differ.* 11:33. doi: 10.1186/s13293-020-00310-x

Tagai, K., Ono, M., Kubota, M., Kitamura, S., Takahata, K., Seki, C., et al. (2020). High-Contrast InVivo Imaging of Tau Pathologies in Alzheimer's and Non-Alzheimer's Disease Tauopathies. *Neuron* 2020:042. doi: 10.1016/j.neuron.2020.09.042

Takuwa, H., Orihara, A., Takado, Y., Urushihata, T., Shimojo, M., Ishikawa, A., et al. (2020). Tracking tau fibrillogenesis and consequent primary phagocytosis of neurons mediated by microglia in a living tauopathy model. *bioRxiv* 2020:368977. doi: 10.1101/2020.11.04.368977

Teng, E., Kepe, V., Frautschy, S. A., Liu, J., Satyamurthy, N., Yang, F., et al. (2011). [F-18]FDDNP microPET imaging correlates with brain Aβ burden in a transgenic rat model of Alzheimer disease: effects of aging, in vivo blockade, and anti-Aβ antibody treatment. *Neurobiol. Dis.* 43, 565–575. doi: 10.1016/j.nbd.2011.05.003

Terada, T., Obi, T., Bunai, T., Matsudaira, T., Yoshikawa, E., Ando, I., et al. (2020). In vivo mitochondrial and glycolytic impairments in patients with Alzheimer disease. *Neurology* 94, e1592–e1604. doi: 10.1212/wnl.0000000000009249

Terada, T., Therriault, J., Kang, M. S. P., Savard, M., Pascoal, T. A., Lussier, F., et al. (2021). Mitochondrial complex I abnormalities is associated with tau and clinical symptoms in mild Alzheimer's disease. *Mol. Neurodegener.* 16:28. doi: 10.1186/s13024-021-00448-1

Tournier, B. B., Tsartsalis, S., Ceyzériat, K., Fraser, B. H., Grégoire, M. C., Kövari, E., et al. (2020). Astrocytic TSPO Upregulation Appears Before Microglial TSPO in Alzheimer's Disease. *J. Alzheimers Dis.* 77, 1043–1056. doi: 10.3233/jad-200136

Tournier, B. B., Tsartsalis, S., Rigaud, D., Fossey, C., Cailly, T., Fabis, F., et al. (2019). TSPO and amyloid deposits in sub-regions of the hippocampus in the 3xTgAD mouse model of Alzheimer's disease. *Neurobiol. Dis.* 121, 95–105. doi: 10.1016/j.nbd.2018.09.022

Treyer, V., Gietl, A. F., Suliman, H., Gruber, E., Meyer, R., Buchmann, A., et al. (2020). Reduced uptake of [^{11}C]-ABP688, a PET tracer for metabolic glutamate receptor 5 in hippocampus and amygdala in Alzheimer's dementia. *Brain Behav.* 10:e01632. doi: 10.1002/brb3.1632

Treyer, V., Streffer, J., Wyss, M. T., Bettio, A., Ametamey, S. M., Fischer, U., et al. (2007). Evaluation of the metabotropic glutamate receptor subtype 5 using PET and [^{11}C]-ABP688: assessment of methods. *J. Nucl. Med.* 48, 1207–1215. doi: 10.2967/jnumed.107.039578

Tsukada, H., Nishiyama, S., Fukumoto, D., Kanazawa, M., and Harada, N. (2014). Novel PET probes [^{18}F]-BCPP-EF and [^{18}F]-BCPP-BF for mitochondrial

complex I: a PET study in comparison with [^{18}F]-BMS-747158-02 in rat brain. *J. Nucl. Med.* 55, 473–480. doi: 10.2967/jnumed.113.125328

Van Camp, N., Lavisse, S., Roost, P., Gubinelli, F., Hillmer, A., and Boutin, H. (2021). TSPO imaging in animal models of brain diseases. *Eur. J. Nucl. Med. Mol. Imaging* [Preprint]. doi: 10.1007/s00259-021-05379-z

Van de Bittner, G. C., Riley, M. M., Cao, L., Ehses, J., Herrick, S. P., Ricq, E. L., et al. (2017). Nasal neuron PET imaging quantifies neuron generation and degeneration. *J. Clin. Invest.* 127, 681–694. doi: 10.1172/jci89162

Van Weehaeghe, D., Van Schoor, E., De Vocht, J., Koole, M., Attili, B., Celen, S., et al. (2020). TSPO Versus P2X7 as a Target for Neuroinflammation: An In Vitro and In Vivo Study. *J. Nucl. Med.* 61, 604–607. doi: 10.2967/jnumed.119.231985

Varlow, C., Mossine, A. V., Bernard-Gauthier, V., Scott, P. J. H., and Vasdev, N. (2021). Radiofluorination of oxazole-carboxamides for preclinical PET neuroimaging of GSK-3. *J. Fluor Chem.* 245:109760. doi: 10.1016/j.jfluchem.2021.109760

Vetel, S., Vercouillie, J., Buron, F., Vergote, J., Tauber, C., Busson, J., et al. (2020). Longitudinal PET Imaging of α7 Nicotinic Acetylcholine Receptors with [^{18}F]ASEM in a Rat Model of Parkinson's Disease. *Mol. Imaging Biol.* 22, 348–357. doi: 10.1007/s11307-019-01400-y

Vitek, M. P., Araujo, J. A., Fossel, M., Greenberg, B. D., Howell, G. R., Rizzo, S. J. S., et al. (2020). Translational animal models for Alzheimer's disease: An Alzheimer's Association Business Consortium Think Tank. *Alzheimer's Dement. Translat. Res. Clin. Intervent.* 6:e12114. doi: 10.1002/trc2.12114

Vogel, J. W., Iturria-Medina, Y., Strandberg, O. T., Smith, R., Levitis, E., Evans, A. C., et al. (2020). Spread of pathological tau proteins through communicating neurons in human Alzheimer's disease. *Nat. Commun.* 11:2612. doi: 10.1038/s41467-020-15701-2

Vogel, J. W., Young, A. L., Oxtoby, N. P., Smith, R., Ossenkoppele, R., Strandberg, O. T., et al. (2021). Four distinct trajectories of tau deposition identified in Alzheimer's disease. *Nat. Med.* 27, 871–881. doi: 10.1038/s41591-021-01309-6

Wang, C., Xiong, M., Gratuze, M., Bao, X., Shi, Y., Andhey, P. S., et al. (2021). Selective removal of astrocytic APOE4 strongly protects against tau-mediated neurodegeneration and decreases synaptic phagocytosis by microglia. *Neuron* 109, 1657.e–1674.e. doi: 10.1016/j.neuron.2021.03.024

Wang, D., Yao, Y., Wang, S., Zhang, H., and He, Z.-X. (2021). The Availability of the α7-Nicotinic Acetylcholine Receptor in Early Identification of Vulnerable Atherosclerotic Plaques: A Study Using a Novel [^{18}F]-Label Radioligand PET. *Front. Bioengine. Biotechnol.* 9:640037. doi: 10.3389/fbioe.2021.640037

Wang, P., and Ye, Y. (2021). Filamentous recombinant human Tau activates primary astrocytes via an integrin receptor complex. *Nat. Commun.* 12:95. doi: 10.1038/s41467-020-20322-w

Wang, X., Li, W., Marcus, J., Pearson, M., Song, L., Smith, K., et al. (2020). MK-8719, a Novel and Selective O-GlcNAcase Inhibitor That Reduces the Formation of Pathological Tau and Ameliorates Neurodegeneration in a Mouse Model of Tauopathy. *J. Pharmacol. Exp. Ther.* 374, 252–263. doi: 10.1124/jpet.120.266122

Warnock, G., Sommerauer, M., Mu, L., Pla Gonzalez, G., Geistlich, S., Treyer, V., et al. (2018). A first-in-man PET study of [^{18}F]PSS232, a fluorinated ABP688 derivative for imaging metabotropic glutamate receptor subtype 5. *Eur. J. Nucl. Med. Mol. Imaging* 45, 1041–1051. doi: 10.1007/s00259-017-3879-x

Wegmann, S., Bennett, R. E., Delorme, L., Robbins, A. B., Hu, M., McKenzie, D., et al. (2019). Experimental evidence for the age dependence of tau protein spread in the brain. *Sci. Adv.* 5:eaaw6404. doi: 10.1126/sciadv.aaw6404

Weng, C. C., Hsiao, I. T., Yang, Q. F., Yao, C. H., Tai, C. Y., Wu, M. F., et al. (2020). Characterization of (18)F-PM-PBB3 ((18)F-APN-1607) Uptake in the rTg4510 Mouse Model of Tauopathy. *Molecules* 25:25071750. doi: 10.3390/molecules25071750

Whitwell, J. L., Tosakulwong, N., Botha, H., Ali, F., Clark, H. M., Duffy, J. R., et al. (2020). Brain volume and flortaucipir analysis of progressive supranuclear palsy clinical variants. *NeuroImage Clin.* 25:102152. doi: 10.1016/j.nicl.2019.102152

Wong, D. F., Kuwabara, H., Horti, A. G., Roberts, J. M., Nandi, A., Cascella, N., et al. (2018). Brain PET Imaging of α7-nAChR with [^{18}F]ASEM: Reproducibility, Occupancy, Receptor Density, and Changes in Schizophrenia. *Int. J. Neuropsychopharmacol.* 21, 656–667. doi: 10.1093/ijnp/pyy021

Wu, J. W., Hussaini, S. A., Bastille, I. M., Rodriguez, G. A., Mrejeru, A., Rilett, K., et al. (2016). Neuronal activity enhances tau propagation and tau pathology in vivo. *Nat. Neurosci.* 19, 1085–1092. doi: 10.1038/nn.4328

Wu, T., Dejanovic, B., Gandham, V. D., Gogineni, A., Edmonds, R., Schauer, S., et al. (2019). Complement C3 Is Activated in Human AD Brain and Is Required for Neurodegeneration in Mouse Models of Amyloidosis and Tauopathy. *Cell Rep.* 28, 2111.e–2123.e. doi: 10.1016/j.celrep.2019.07.060

Xiang, X., Wind, K., Wiedemann, T., Blume, T., Shi, Y., Briel, N., et al. (2021). Microglial activation states drive glucose uptake and FDG-PET alterations in neurodegenerative diseases. *Sci. Transl. Med.* 13:eabe5640. doi: 10.1126/scitranslmed.abe5640

Yang, J.-T., Wang, Z.-J., Cai, H.-Y., Yuan, L., Hu, M.-M., Wu, M.-N., et al. (2018). Sex Differences in Neuropathology and Cognitive Behavior in APP/PS1/tau Triple-Transgenic Mouse Model of Alzheimer's Disease. *Neurosci. Bull.* 34, 736–746. doi: 10.1007/s12264-018-0268-9

Yoshiyama, Y., Higuchi, M., Zhang, B., Huang, S. M., Iwata, N., Saido, T. C., et al. (2007). Synapse loss and microglial activation precede tangles in a P301S tauopathy mouse model. *Neuron* 53, 337–351. doi: 10.1016/j.neuron.2007.01.010

Zhou, K., Yang, F., Li, Y., Chen, Y., Zhang, X., Zhang, J., et al. (2021). Synthesis and Evaluation of Fluorine-18 Labeled 2-Phenylquinoxaline Derivatives as Potential Tau Imaging Agents. *Mol. Pharm.* 18, 1176–1195. doi: 10.1021/acs.molpharmaceut.0c01078

Zhou, R., Ji, B., Kong, Y., Qin, L., Ren, W., Guan, Y., et al. (2021). PET Imaging of Neuroinflammation in Alzheimer's Disease. *Front. Immunol.* 12:3750. doi: 10.1007/s00702-017-1731-x

Zhou, X., Ji, B., Seki, C., Nagai, Y., Minamimoto, T., Fujinaga, M., et al. (2021). PET imaging of colony-stimulating factor 1 receptor: A head-to-head comparison of a novel radioligand, (11)C-GW2580, and (11)C-CPPC, in mouse models of acute and chronic neuroinflammation and a rhesus monkey. *J. Cereb. Blood Flow Metab.* 2021:211004146. doi: 10.1177/0271678x211004146

Conflict of Interest: LC was employed by Changes Technology Corporation Ltd.

The remaining authors declare that the research was conducted in the absence of any commercial or financial relationships that could be construed as a potential conflict of interest.

Publisher's Note: All claims expressed in this article are solely those of the authors and do not necessarily represent those of their affiliated organizations, or those of the publisher, the editors and the reviewers. Any product that may be evaluated in this article, or claim that may be made by its manufacturer, is not guaranteed or endorsed by the publisher.

Copyright © 2022 Cao, Kong, Ji, Ren, Guan and Ni. This is an open-access article distributed under the terms of the Creative Commons Attribution License (CC BY). The use, distribution or reproduction in other forums is permitted, provided the original author(s) and the copyright owner(s) are credited and that the original publication in this journal is cited, in accordance with accepted academic practice. No use, distribution or reproduction is permitted which does not comply with these terms.

frontiers in Aging Neuroscience

ORIGINAL RESEARCH
published: 12 January 2022
doi: 10.3389/fnagi.2021.788723

Effects of α-Lipoic Acid on Phagocytosis of Oligomeric Beta-Amyloid$_{1-42}$ in BV-2 Mouse Microglial Cells

Chih-Yuan Ko[1,2,3,4†‡], Jian-Hua Xu[5†], Yu-Wei Chang[6†], Yangming Martin Lo[7], James Swi-Bea Wu[8‡], Wen-Chung Huang[9] and Szu-Chuan Shen[6‡]*

[1] Department of Clinical Nutrition, The Second Affiliated Hospital of Fujian Medical University, Quanzhou, China, [2] Department of Respiratory and Critical Care Medicine, The Second Affiliated Hospital of Fujian Medical University, Quanzhou, China, [3] School of Public Health, Fujian Medical University, Fuzhou, China, [4] Respiratory Medicine Center of Fujian Province, Quanzhou, China, [5] Department of Tumor Surgery, The Second Affiliated Hospital of Fujian Medical University, Quanzhou, China, [6] Graduate Program of Nutrition Science, National Taiwan Normal University, Taipei, Taiwan, [7] Institute for Advanced Study, Shenzhen University, Shenzhen, China, [8] Graduate Institute of Food Science and Technology, National Taiwan University, Taipei, Taiwan, [9] Graduate Institute of Health Industry Technology, Chang Gung University of Science and Technology, Taoyuan, Taiwan

OPEN ACCESS

Edited by:
Woon-Man Kung,
Chinese Culture University, Taiwan

Reviewed by:
Sachchida Nand Rai,
University of Allahabad, India
Douglas F. Watt,
Lesley University, United States
Nobuyuki Kimura,
National Center for Geriatrics and Gerontology (NCGG), Japan

***Correspondence:**
Szu-Chuan Shen
scs@ntnu.edu.tw

†These authors share first authorship

‡**ORCID:**
Chih-Yuan Ko
orcid.org/0000-0002-5767-3041
James Swi-Bea Wu
orcid.org/0000-0002-2855-5716
Szu-Chuan Shen
orcid.org/0000-0001-9005-0455

Specialty section:
This article was submitted to Alzheimer's Disease and Related Dementias, a section of the journal Frontiers in Aging Neuroscience

Received: 03 October 2021
Accepted: 15 December 2021
Published: 12 January 2022

Citation:
Ko C-Y, Xu J-H, Chang Y-W, Lo YM, Wu JS-B, Huang W-C and Shen S-C (2022) Effects of α-Lipoic Acid on Phagocytosis of Oligomeric Beta-Amyloid$_{1-42}$ in BV-2 Mouse Microglial Cells. Front. Aging Neurosci. 13:788723. doi: 10.3389/fnagi.2021.788723

Background and objectives: This study aimed to investigate the enhancing effect of vitamin-like alpha-lipoic acid (ALA) on phagocytosis of oligomeric beta-amyloid (oAβ)$_{1-42}$ in BV-2 mouse microglial cells.

Methods: An *in vitro* model was established to investigate phagocytosis of oAβ$_{1-42}$ in BV-2 cells. Transmission electron microscopy images indicated that the morphology of prepared oAβ$_{1-42}$ was spherical particles. BV-2 cells treated with ALA were incubated with 5(6)-carboxyfluorescein-labeled oAβ$_{1-42}$ (FAM-oAβ$_{1-42}$) for 24 h, followed by flow cytometer analysis, western blotting, real-time quantitative PCR, and immunocytochemistry (ICC) analysis to assess the *in vitro* phagocytosis ability of oAβ$_{1-42}$.

Results: Alpha-lipoic acid significantly increased messenger RNA (mRNA) expression of the CD36 receptor in BV-2 cells. ICC analysis showed that ALA significantly elevated CD36 protein expression in BV-2 cells both with and without oAβ$_{1-42}$ treatment. Results from the flow cytometry analysis indicated that the CD36 receptor inhibitor significantly attenuated ALA-promoted phagocytosis of FAM-oAβ$_{1-42}$ in BV-2 cells. Moreover, ICC analysis revealed that ALA caused the translocation of peroxisome proliferator-activated receptor-γ (PPAR-γ), which is known to regulate the expression of CD36 mRNA in BV-2 cells. ALA also elevated both the mRNA and protein expression of cyclooxygenase-2 (COX-2), which is a key enzyme involved in the synthesis of 15-deoxy-$^{\Delta 12,14}$-prostaglandin J2 in BV-2 cells.

Conclusion: We postulated that ALA enhances oAβ$_{1-42}$ phagocytosis by upregulating the COX-2/15-deoxy-$^{\Delta 12,14}$-prostaglandin J2/PPAR-γ/CD36 pathway in BV-2 cells. Finally, future studies should be conducted with an *in vivo* study to confirm the findings.

Keywords: α-lipoic acid, microglia, oligomeric beta-amyloid, phagocytosis, Alzheimer's disease (AD)

INTRODUCTION

Alzheimer's disease (AD) is an irreversible neurodegenerative disease with cognitive impairment that accounts for more than half of patients with dementia (Knopman et al., 2021). To date, while the complexity of neurodegeneration continues to be explored and recognized, AD has been characterized in part by excessive extracellular beta-amyloid (Aβ) plaque accumulation, the presence of intracellular tau-containing neurofibrillary tangles, and neuroinflammation in the brain (Erika et al., 2018; Rai et al., 2020; Knopman et al., 2021; Singh et al., 2021). In the brains of patients with AD, synaptic loss can precede neurodegeneration, brain tissue gradually shrinks, which, in turn, leads to a decline in memory and learning abilities of patients, eventually causing dementia (Blennow et al., 2006; Srivastava et al., 2019; Tripathi et al., 2019). Synaptic alterations are actually a critical part of neurodegeneration that are strongly correlated with the morphological lesions of AD, neurotoxicities of tau and Aβ, and cognitive impairment, which induce various neurotoxic effects such as increased inflammation, increased oxidative pressure, and subsequently damages the nerve synapses of the brain (Jack et al., 2019; Srivastava et al., 2019; Knopman et al., 2021). These factors gradually alter the microenvironment system of the brain, which becomes unconducive to the survival of nerve cells. In addition, inflammation plays a hallmark role in progression of AD. Aβ accumulation facilitates activation of immune cells including microglia, astrocytes, and macrophages. Remarkably, when microglia are activated in AD, activated microglia contribute to degraded Aβ accumulation through autophagy or clearance. Additionally, chronically activated microglia stimulating to the release of cytokines, which initiate a proinflammatory cascade and subsequently induce synaptic alterations (Pomilio et al., 2020; Knopman et al., 2021). There is a strong correlation between oligomeric Aβ (oAβ) accumulation in the brain and cognitive ability (Benilova et al., 2012). The oAβ strongly inhibits long-term potentiation of the hippocampal gyrus and causes damage to the nerve synapse, which eventually results in memory deficits in the patient (Walsh et al., 2002; Haass and Selkoe, 2007; Querfurth and LaFerla, 2010; Benilova et al., 2012). Therefore, oAβ is a crucial cause of occurrence of AD; however, the mechanism is still unclear.

Microglial autophagy may be potentially affected for treating AD (Pomilio et al., 2020). Evidence has highlighted that autophagy and antioxidants play core roles in AD (Liu et al., 2015). According to the theory of oxidative stress, numerous antioxidants are associated with the prevention of progression of AD (Su et al., 2008). For example, 15-deoxy-$^{\Delta 12,14}$-prostaglandin J2 (15-deoxy-$^{\Delta 12,14}$-PGJ2), which is produced by cyclooxygenase (COX), has been widely accepted as an anti-inflammatory prostaglandin and its anti-inflammatory mechanism is related to peroxisome proliferator-activated receptor-γ (PPAR-γ) (Scher and Pillinger, 2005). PPAR-γ is the transcription factor of CD36 messenger RNA (mRNA). When the activity of PPAR-γ increases, the transcription of CD36 mRNA increases by cells (Shimizu et al., 2008; Yamanaka et al., 2012). Bujold et al. (2009) successfully linked the mechanisms of COX-2/15-deoxy-$^{\Delta 12,14}$-PGJ2/PPAR-γ/CD36 to elucidate in atherosclerosis. This is a critical mechanism pathway for this study.

The vitamin-like compound, alpha-lipoic acid (ALA), is a thioctic acid- and sulfur-containing organic compound that is a natural biological antioxidant (Packer et al., 1995). It can combat various chronic diseases such as diabetes, its related complications, and hypertension (Thirunavukkarasu et al., 2004; Ko et al., 2021). ALA has also been proven to affect the central nervous system by penetrating the blood–brain barrier (BBB) (Packer et al., 1995). Thus, ALA has been used to study numerous neurodegenerative diseases. One study showed that administering 600 mg/day of ALA to patients with AD can delay the progression of AD (Hager et al., 2007). Study on ALA and AD has largely focused on antioxidation, anti-inflammation, and the promotion of brain glucose metabolism. However, there are limited investigations on the use of ALA to promote the clearance of Aβ by microglia, thereby reducing the neurotoxic effects of Aβ-induced brain oxidative stress, inflammation, and glucose uptake resistance (Holmquist et al., 2007; Maczurek et al., 2008; Farr et al., 2012; Dos Santos et al., 2019; Kim et al., 2019; Choi et al., 2020). Therefore, we evaluated the alleviating effect of ALA on progression of AD and investigated the possible mechanism of ALA in promoting phagocytosis of BV-2 cell oAβ_{1-42} and its association with the COX-2/15-deoxy-$^{\Delta 12,14}$-PGJ2/PPAR-γ/CD36 pathway.

MATERIALS AND METHODS

Cell Culture

The mouse microglial BV-2 cell line used in this study was kindly donated by Professor Fu's laboratory of the College of Medicine, National Taiwan University. BV-2 cells were cultured in an F12 medium without phenol red, containing 100 U/ml penicillin, 100 g/ml streptomycin, and 10% fetal bovine serum (FBS) at 37°C and 5% carbon dioxide (CO_2) (Lu et al., 2007).

Identification of oAβ_{1-42} Aggregation Pattern

The Aβ_{1-42} monomer was purchased from Biopeptide (San Diego, CA, United States). The preparation of oAβ_{1-42} was adopted by the previous study (Yang et al., 2011). The appearance of the prepared oAβ_{1-42} was observed using JEM-1200EX II transmission electron microscopy (TEM) (JEOL, Tokyo, Japan). OAβ_{1-42} was first stained with 1% phosphotungstic acid for

TABLE 1 | Primer sequences for real-time PCR (RT-PCR).

Gene name	Forward (5′-3′)	Reverse (5′-3′)
SR-A1	CTGGACAAACTGGTCCACCT	TCCCCTTCTCTCCCTTTTGT
SR-B1	TTTGGAGTGGTAGTAAAAAGGGC	TGACATCAGGGACTCAGAGTAG
CD36	GAACCACTGCTTTCAAAAACTGG	TGCTGTTCTTTGCCACGTCA
RAGE	ACTACCGAGTCCGAGTCTACC	GTAGCTTCCCTCAGACACACA
COX-2	AGACAGATCATAAGCGA GGACC	CCTCTCCACCAATGACCTGATATT
GAPDH	TGCACCACCAACTGCTTAGC	GGCATGGACTGTGGTCATGAG

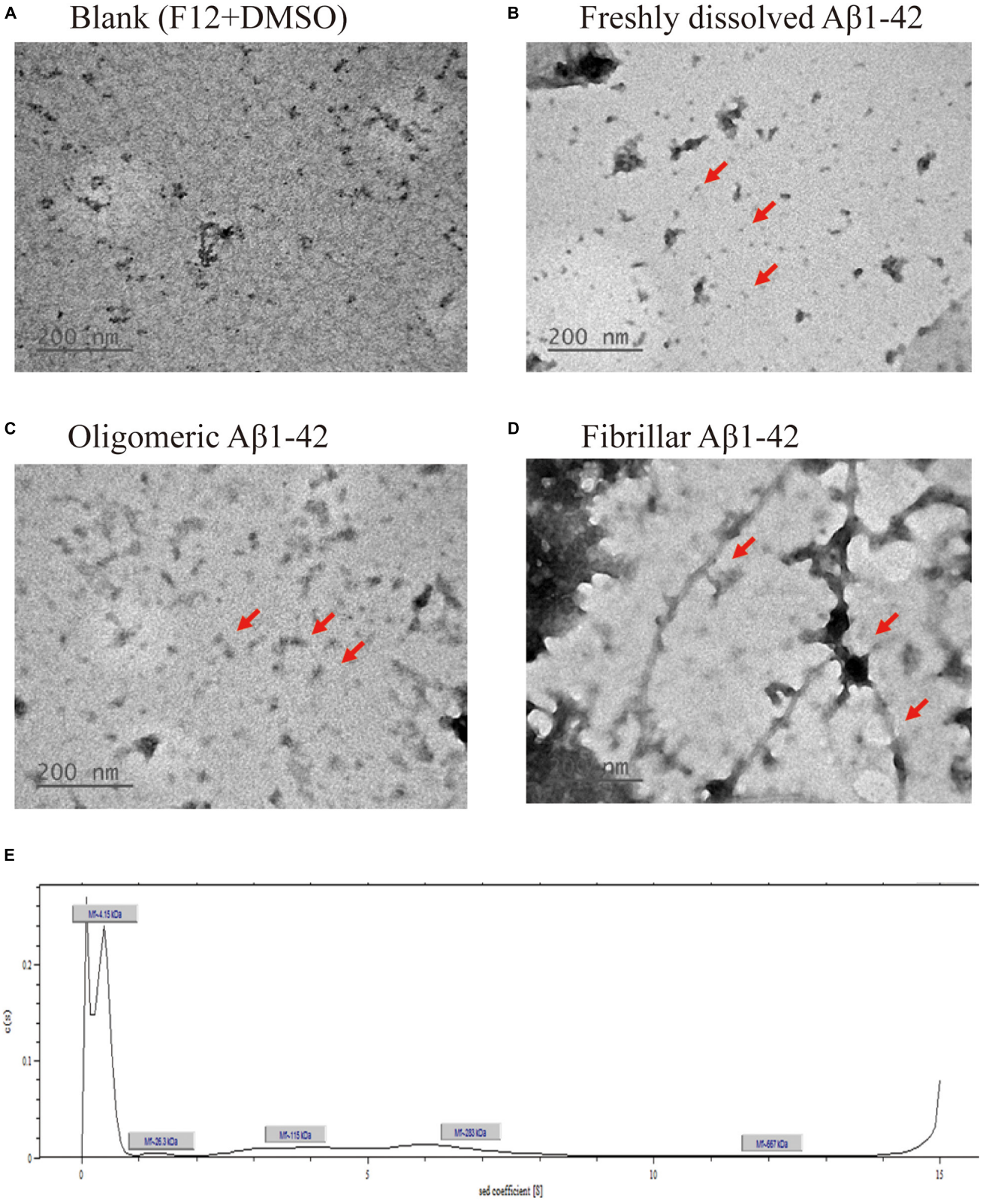

FIGURE 1 | Transmission electron microscopy (TEM), morphological and analytical ultracentrifugation (AUC), and physical characterization analysis of prepared beta-amyloid (Aβ_{1-42}). TEM image of **(A)** blank [F12 medium + dimethyl sulfoxide (DMSO)], **(B)** freshly dissolved Aβ_{1-42}, **(C)** oligomeric Aβ_{1-42}, **(D)** fibrillar Aβ_{1-42}, and **(E)** Sedimentation coefficient analysis of oligomeric Aβ_{1-42} using AUC.

2 min and placed on a 200-mesh copper net for observation. Then, freshly dissolved and fibrillary Aβ_{1-42} was compared to observe whether oAβ_{1-42} had an ideal appearance. In addition, the molecular weight of oAβ_{1-42} was analyzed using XL-A analytical ultracentrifugation (AUC) (Beckman, Palo Alto, CA, United States); the sample was centrifuged at 60,000 rpm and the orientation of the Aβ_{1-42} peptide was detected at a wavelength of 280 nm (Yang et al., 2011). Results of AUC were fitted to the continuous c(s) distribution model using the SEDFIT software[1] and the molecular weight and percentage of aggregation of oAβ_{1-42} were estimated.

Oligomeric Beta-Amyloid$_{1-42}$ Uptake Analysis and Quantification

The fluorescent molecule 5(6)-carboxyfluorescein (FAM) was used as a calibrator to explore the uptake of oAβ_{1-42} in BV-2 cells. When cells uptake oAβ_{1-42}, calibrated by FAM, they were excited by a light with a wavelength of 488 nm and emitted green fluorescence of approximately 517 nm. This fluorescence was detected and accurately quantified using the LSRFortessa Flow Cytometer (BD Biosciences, Franklin Lakes, NJ, United States).

Real-Time Quantitative PCR Analysis

According to the instructions of the manufacturer, the total RNA of cells was extracted using the Direct-zol RNA MiniPrep Kit (Zymo Research, Irvine, CA, United States). RNA concentrations were determined by the ND-1000 Spectrophotometer (NanoDrop®). Complementary DNA (cDNA) was synthesized by adding preisolated RNA and RNA to the cDNA EcoDry^{TM} Premix (Oligo dT; Clontech Laboratories Incorporation, Mountain View, CA, United States). Real-time quantitative PCR was used to analyze genes such as scavenger receptor A1 (SR-A1), scavenger receptor B1 (SR-B1), CD36, receptor for advanced glycation endproducts (RAGE), COX-2, and glyceraldehyde 3-phosphate dehydrogenase (GAPDH). Sequences for the primer sets used in quantitative PCR for each gene are given in **Table 1**. The amplification reactions were performed using the StepOnePlus^{TM} Real-Time PCR System (Applied Biosystems, Foster City, CA, United States). Data were described using the relative quantification method $2^{-\Delta\Delta Ct}$.

Western Blot Analysis

The procedure for Western blot was carried out according to our previous study (Chen et al., 2021). Briefly, the protein concentration in the cell extract was determined using a Bio-Rad protein assay dye reagent (Richmond, Virginia, VA, United States). Aliquots of the supernatant containing 50 μg of protein were separated using sodium dodecyl sulfate polyacrylamide gel electrophoresis (SDS-PAGE) and electrophoretically transferred onto polyvinylidene difluoride membranes. The membranes were then incubated with anti-COX-2 (1:1,000; Cell Signaling Technology, Danvers, MA, United States) and anti-GAPDH (1:5,000; Signalway Antibody Corporation, College Park, MD, United States) antibodies at 4°C overnight. Next, the membranes were incubated with antirabbit immunoglobulin G and washed thrice for 5 min each time. The final images were detected and captured using the UVP Biospectrum Imaging System (Level, Cambridge, United Kingdom). Finally, all the relevant protein expressions were normalized with GAPDH.

[1]https://sedfitsedphat.nibib.nih.gov/software/default.aspx

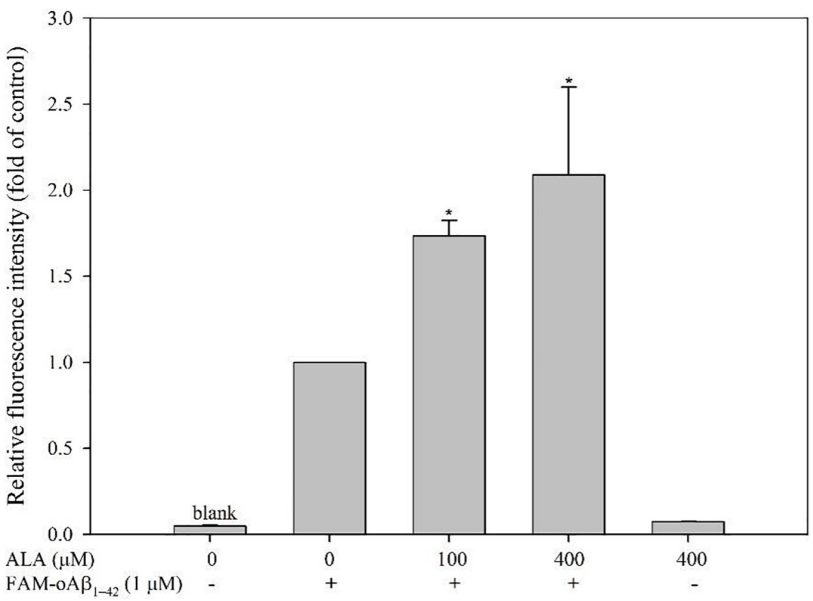

FIGURE 2 | Effect of alpha-lipoic acid (ALA) on 5(6)-carboxyfluorescein (FAM)-oligomeric Aβ (oAβ_{1-42}) uptake in BV-2 mouse microglial cells. BV-2 cells were pretreated with or without ALA (100 or 400 μM) for 30 min, followed by FAM-oAβ_{1-42} treatment for 24 h. Mean fluorescence intensity was detected using a flow cytometer. *$p < 0.05$ vs. the FAM-oAβ_{1-42} group.

Immunocytochemistry

A total of 4×10^4 cells were cultivated on a cover glass. After 24 h, the prepared oAβ_{1-42} was added and incubated for 24 h, fixed with 3% formaldehyde, punched with 0.1% Triton X-100, and placed in phosphate buffered saline with Tween (PBST) containing 5% bovine serum albumin (BSA) for blocking overnight. On the subsequent day, cells were stained with the primary antibody. After the invariable reaction overnight, cells were stained with a secondary antibody of fluorescent molecule Alexa 488 or 647. The nuclei were stained with 4′,6-diamidino-2-phenylindole (DAPI) and observed under an upright fluorescence microscope (Carl Zeiss, Jena, Germany, United Kingdom). Cell fluorescence intensity was analyzed using MetaMorph (Molecular Devices, Sunnyvale, CA, United States).

Detection of Nitric Oxide

A total of 2×10^5 cells were cultured in six-well plates for 24 h, replaced with 1.5 ml Dulbecco's Modified Eagle Medium (DMEM) without FBS and lipopolysaccharides treatment, and cocultured with cells for 24 h. The cell culture fluid was collected and mixed with Griess reagent in a 1:1 manner and reacted for 15 min and absorbance was detected at 540 nm using an ELISA reader.

Analysis of 15-Deoxy-$^{\Delta 12,14}$-PGJ2

A total of 3×10^5 cells were cultured in six-well plates for 24 h, replaced with FBS-free DMEM, and treated with different concentrations of ALA. The cells were pretreated with ALA for 30 min and the vehicle or prepared oAβ_{1-42} was added and cocultivated for 24 h. An ELISA reader was used to analyze the

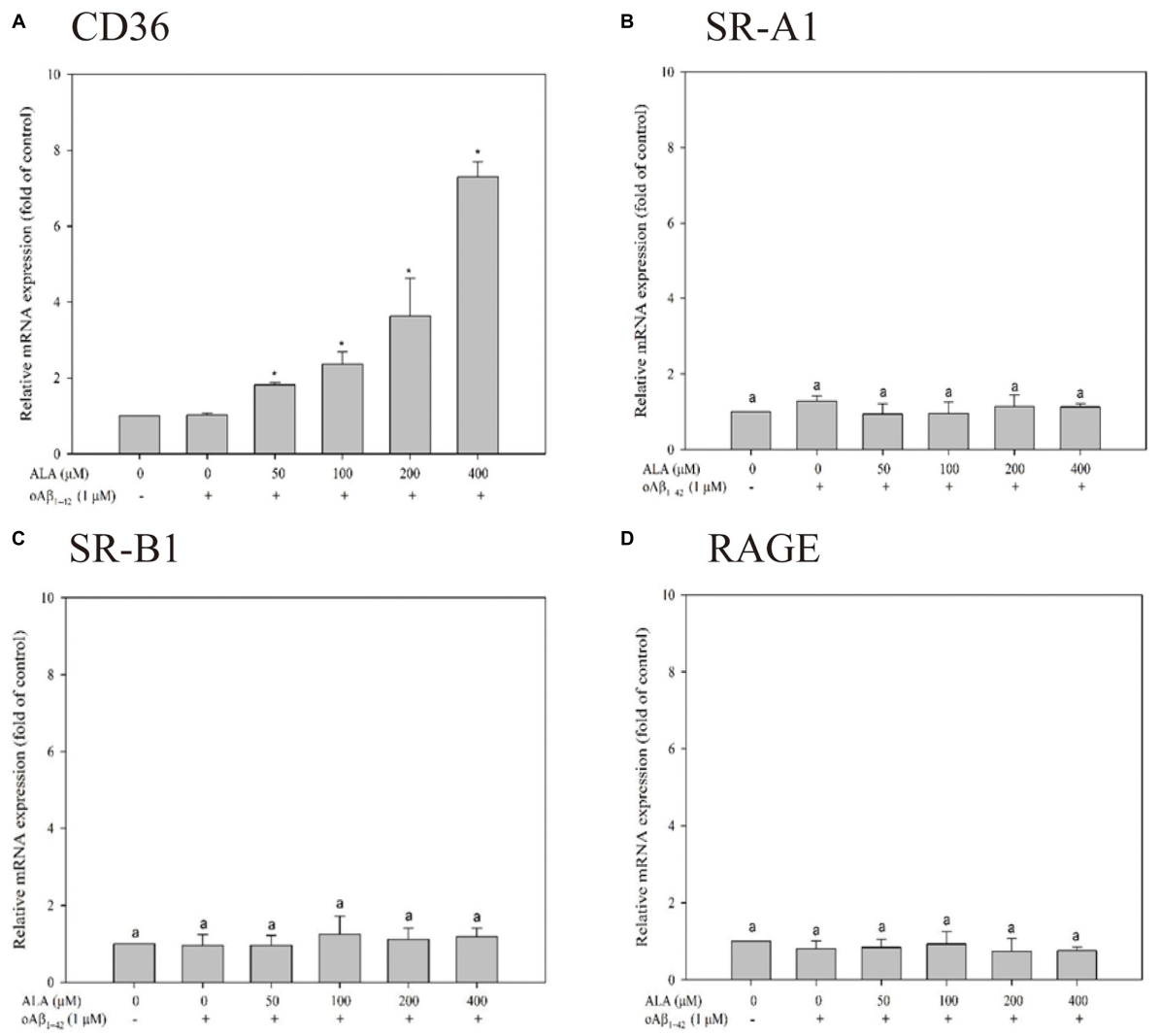

FIGURE 3 | Messenger RNA (mRNA) expression of oAβ_{1-42} phagocytosis-related receptor including CD36 **(A)**, scavenger receptor A1 (SR-A1) **(B)**, scavenger receptor B1 (SR-B1) **(C)**, and receptor for advanced glycation endproducts (RAGE) **(D)** in BV-2 mouse microglial cells. BV-2 cells were pretreated with or without different concentrations of ALA for 30 min, followed by oAβ_{1-42} treatment for 24 h. The relative mRNA expression of CD36, SR-A1, SR-B1, and RAGE was detected using real-time PCR. *$p < 0.05$ vs. the control group.

culture medium. Standard of 15-deoxy-$^{\Delta 12,14}$-PGJ2 was diluted with 400 μM ALA and the 4-parameters logical curve was used to analyze the 15-deoxy-$^{\Delta 12,14}$-PGJ2 concentration of the sample.

Statistical Analyses

Values are presented as the mean ± SD using the SAS version 9.2 (SAS Institute Incorporation, Cary, NC, United States). The one-way ANOVA and Duncan's multiple range tests were performed. $p < 0.05$ was accepted as statistically significant.

RESULTS

Analysis of Transmission Electron Microscopy Appearance and Analytical Ultracentrifugation Physical Properties of Aβ_{1-42}

The appearance of oAβ_{1-42} as a blank group (**Figure 1A**), freshly prepared Aβ_{1-42} (**Figure 1B**), oAβ_{1-42} solution (**Figure 1C**) after 24 h of aggregation at 4°C, and fibrillary Aβ_{1-42} with an apparent fibrous production group (**Figure 1D**) was examined using TEM. AUC was used to analyze the sedimentation coefficient of the prepared oAβ_{1-42} and the molecular weight and friction ratio of oAβ_{1-42} were further fitted using the SEDFIT software, as shown in **Figure 1E**. The molecular weight of the Aβ_{1-42} monomer was approximately 4.6 kDa. Approximately, 50% of Aβ_{1-42} aggregated into an oligomeric form and three primary oligomeric forms with molecular weights of 26.3, 115, and 28 kDa were observed.

Effect of Alpha-Lipoic Acid on Uptake of FAM-oAβ_{1-42} in BV-2 Cells

The fluorescence of BV-2 cells increased by 73.44 ± 8.99% under 100 μM ALA treatment ($p < 0.05$) and fluorescence intensity increased by 108.83 ± 51.07% under 400 μM ALA treatment ($p < 0.05$) compared with the ALA untreated group, which demonstrated a dose-dependent effect. The 400 μM ALA-treated group with untreated FAM-oAβ_{1-42} showed no significant difference in fluorescence from that of the blank group. Therefore, we confirmed that the increase in fluorescence of the BV-2 cells by ALA was not attributed to ALA itself—rather it was caused by an increased uptake of FAM-oAβ_{1-42} (**Figure 2**).

Messenger RNA Expression and oAβ1-42 Phagocytosis-Related Receptors in BV-2 Cells

Cells were treated with 50, 100, 200, and 400 μM ALA compared with the untreated ALA and oAβ group (control group); mRNA expression levels of CD36 were 1.81 ± 0.06, 2.36 ± 0.33, 3.63 ± 1.00, and 7.29 ± 0.39 times for the respective ALA

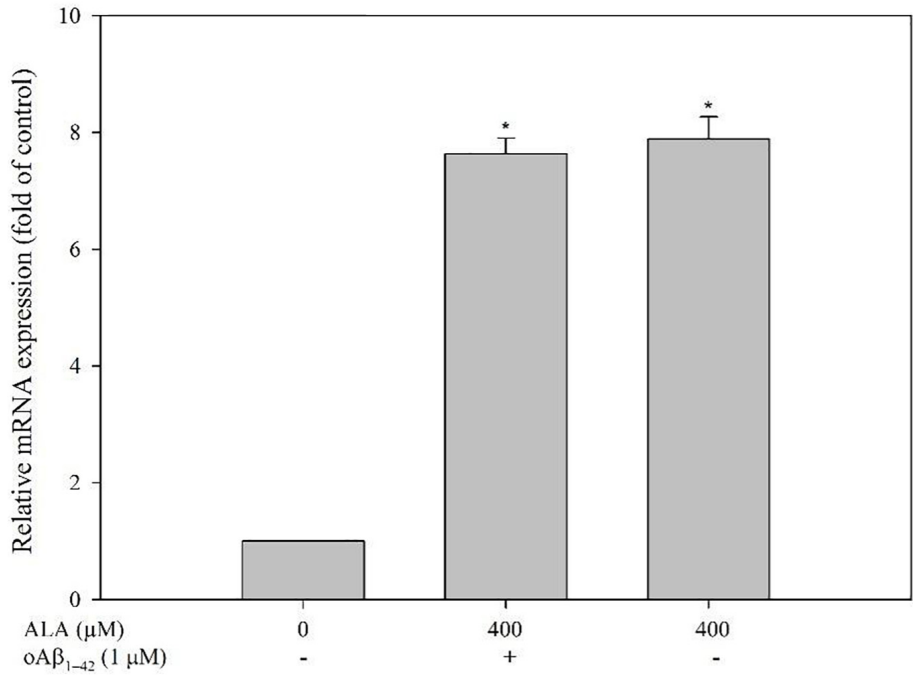

FIGURE 4 | Alpha-lipoic acid elevated CD36 mRNA expression in BV-2 mouse microglial cells. BV-2 cells were pretreated with or without ALA (400 μM) for 30 min, followed by vehicle or oAβ_{1-42} treatment for 24 h. The relative mRNA expression of CD36 was detected using real-time PCR. *$p < 0.05$ vs. the control group.

treatment groups (50, 100, 200, and 400 μM; $p < 0.05$) (**Figure 3A**). However, mRNA expression levels of SR-A1, SR-B1, and RAGE showed no noticeable dose-dependent effect (**Figures 3B–D**). In addition, ALA increased the expression of CD36 mRNA in BV-2 cells that were not treated with oAβ_{1-42} ($p < 0.05$); this result was similar to that of the group treated with 1 μM oAβ_{1-42} ($p < 0.05$) (**Figure 4**).

The expression of ICC-measured CD36 protein is shown in **Figure 5A**. When Alexa 647 was used to stain CD36 on the cell membrane, it appeared red in the image, whereas the

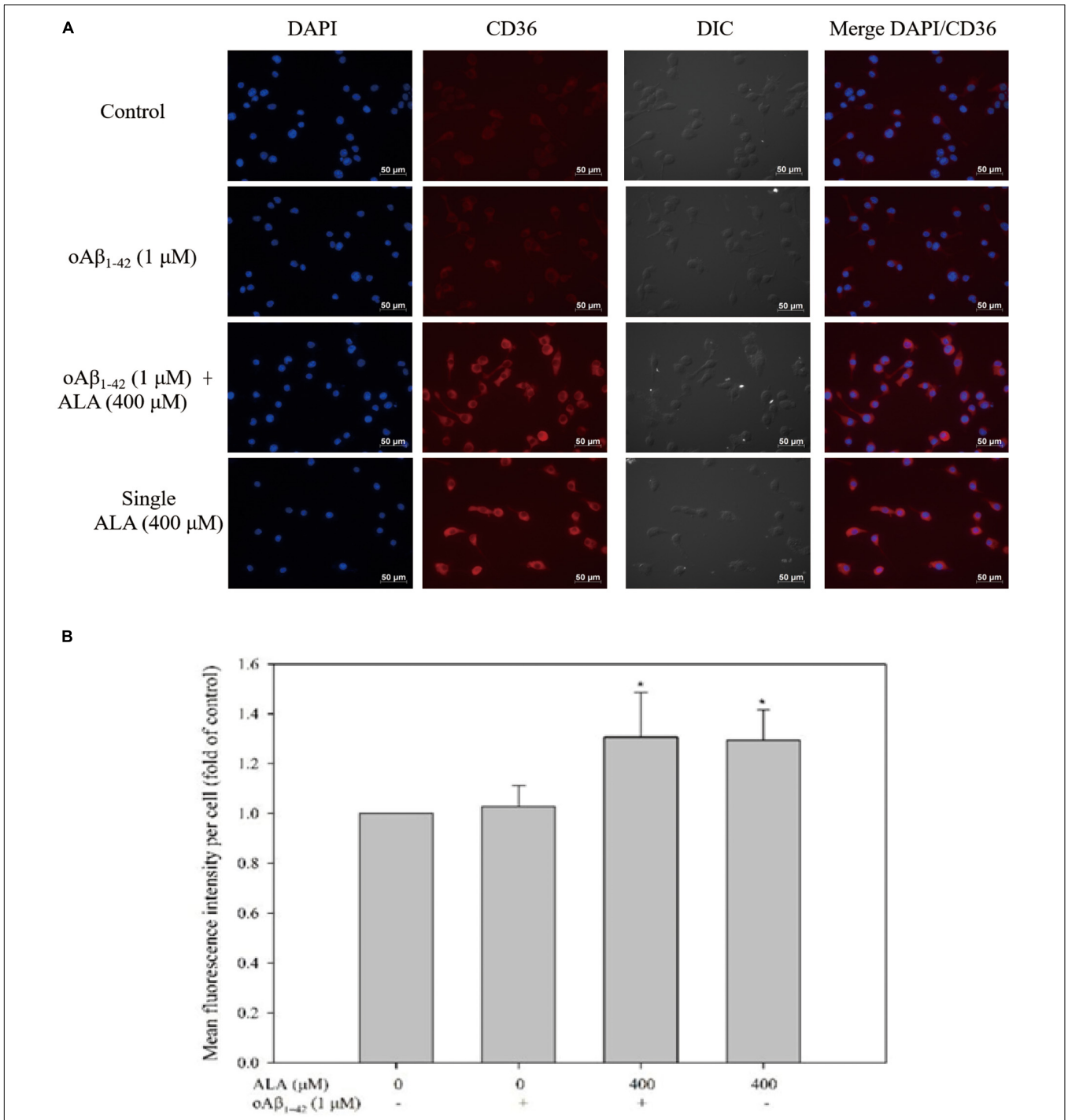

FIGURE 5 | Alpha-lipoic acid elevated CD36 protein expression in BV-2 mouse microglial cells. BV-2 cells were pretreated with or without ALA (400 μM) for 30 min, followed by vehicle or oAβ_{1-42} treatment for 24 h. After treatment, BV-2 cells were immunostained with CD36 antibody (red) and the nuclei were stained with DAPI (blue). **(A)** Fluorescence image from immunocytochemistry. **(B)** Quantification of mean fluorescence intensity per cell. *$p < 0.05$ vs. the control group.

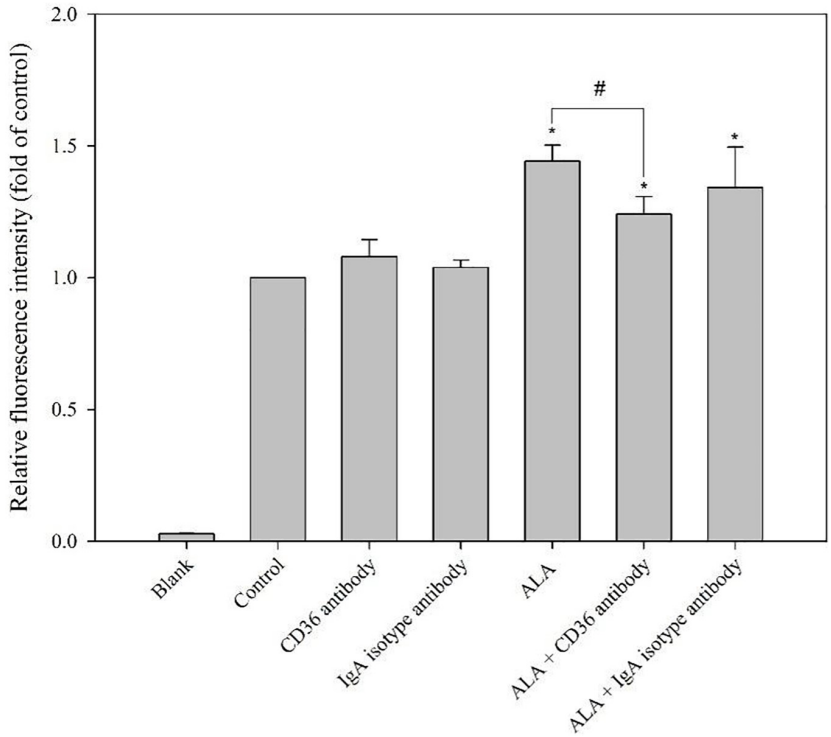

FIGURE 6 | Blocking effect of CD36 antibody on ALA-enhanced phagocytosis ability of FAM-oAβ_{1-42} in BV-2 mouse microglial cells. BV-2 cells were pretreated with or without ALA (400 μM) in the presence of a CD36 antibody or isotype control for 30 min, followed by FAM-oAβ_{1-42} treatment for 24 h. Mean fluorescence intensity was detected using a flow cytometer. $^{*}p < 0.05$ vs. the control group and $^{\#}p < 0.05$ vs. the ALA group.

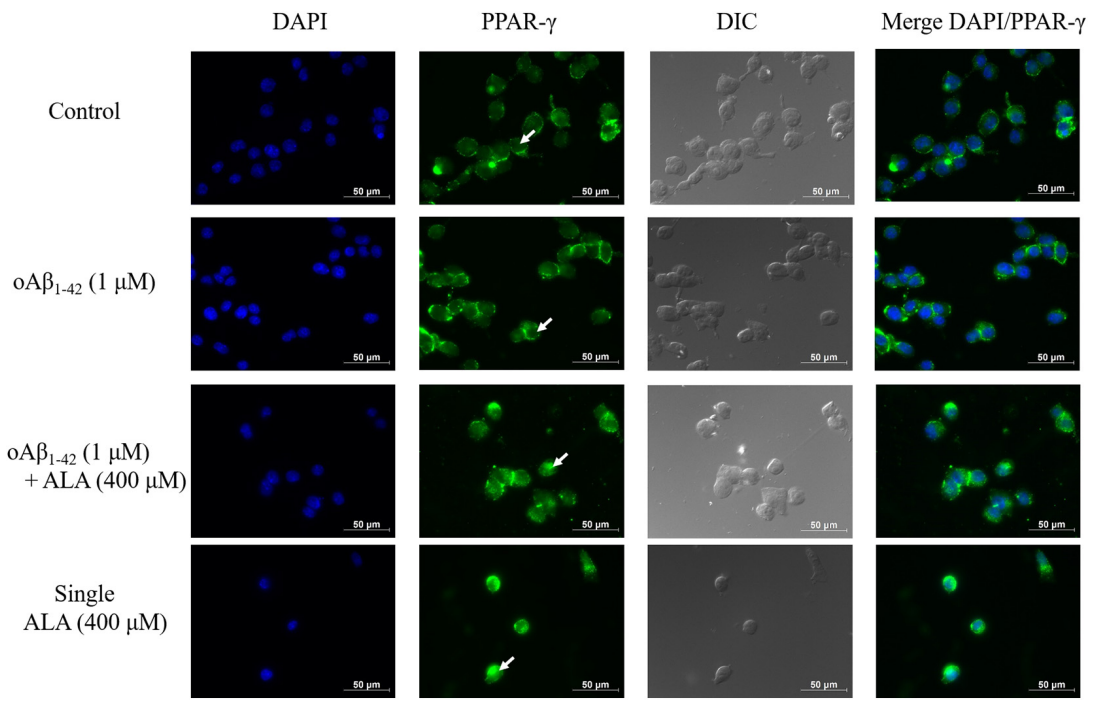

FIGURE 7 | Alpha-lipoic acid caused PPAR-γ translocation from the cytoplasm to the nucleus. BV-2 cells were pretreated with or without ALA (400 μM) for 30 min, followed by vehicle or oAβ_{1-42} treatment for 24 h. After treatment, BV-2 cells were immunostained with PPAR-γ antibody (green) and the nuclei were stained with DAPI (blue).

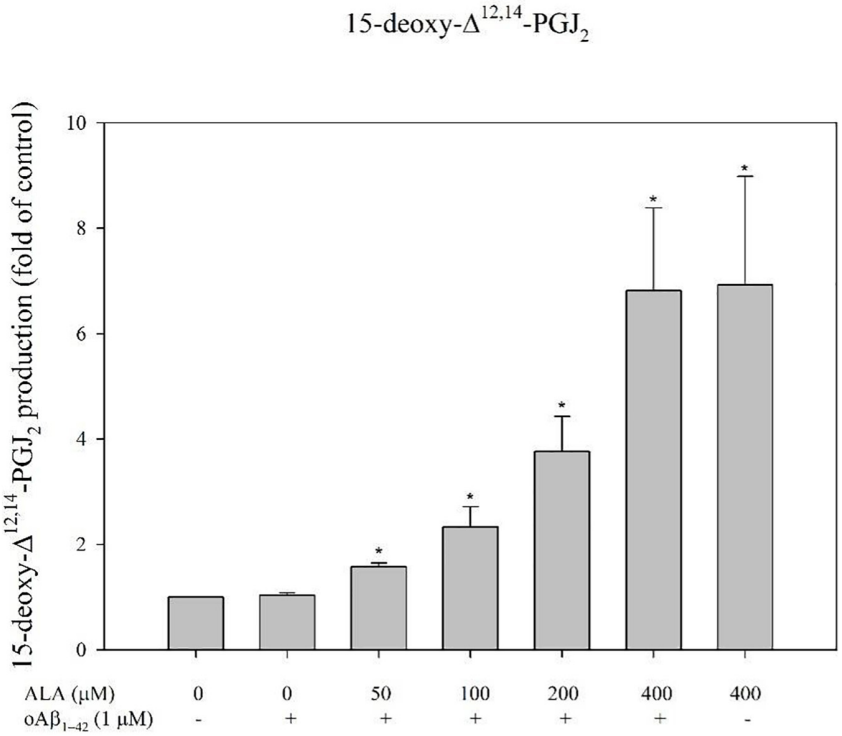

FIGURE 8 | Alpha-lipoic acid promoted 15-deoxy-$^{\Delta 12,14}$-PGJ2 production in BV-2 mouse microglial cells. BV-2 cells were pretreated with or without different concentrations of ALA for 30 min, followed by vehicle or oAβ_{1-42} treatment for 24 h. Relative 15-deoxy-$^{\Delta 12,14}$-PGJ2 production was detected using ELISA. Data are presented as means ± SDs. *$p < 0.05$ vs. the vehicle control group.

nuclei of the BV-2 cells appeared blue when stained with DAPI. The appearance of cells was analyzed to confirm the size and location of the cells using differential interference contrast light paths. Cells treated with ALA promoted the protein expression of CD36. Regardless of whether oAβ_{1-42} was stimulated, CD36 protein expression in BV-2 cells increased with ALA treatment. The fluorescence intensity of the 400 μM ALA treatment group was approximately 1.3 times that of the untreated group ($p < 0.05$) (**Figure 5B**).

The addition of the CD36 antibody significantly reduced the uptake capacity of FAM-oAβ_{1-42} enhanced by ALA. The immunoglobulin A isotype control antibody did not affect the uptake of FAM-oAβ_{1-42} by BV-2 cells. In addition, the CD36 antibody did not affect the ability of BV-2 cells without ALA treatment to take up FAM-oAβ_{1-42}. Results showed that ALA increased the uptake of oAβ_{1-42} by increasing the expression of CD36 ($p < 0.05$) (**Figure 6**).

Alpha-Lipoic Acid Promotes the Translocation of PPAR-γ in BV-2 Cells

When Alexa 488 was used to stain PPAR-γ, it appeared green in the image, whereas the nuclei of the BV-2 cells appeared blue when stained with DAPI, as shown in **Figure 7**. In cells without ALA treatment, most PPAR-γ were located outside the nuclei. Furthermore, cavities were evident in the nucleus, as shown by the white arrow in **Figure 7**. However, in cells treated with ALA, the transcription factor PPAR-γ was translocated and transferred from the cytoplasm to the nucleus and the void area in the nucleus was significantly reduced compared to that of the untreated group. This was observed regardless of whether oAβ_{1-42} was stimulated.

Alpha-Lipoic Acid Causes PPAR-γ Translocation Through COX-2/15-Deoxy-$^{\Delta 12,14}$-PGJ2 in BV-2 Cells

Alpha-lipoic acid promoted BV-2 cells and increased the production of 15-deoxy-$^{\Delta 12,14}$-PGJ2 for the respective ALA treatment groups (50, 100, 200, and 400 μM; $p < 0.05$) (**Figure 8**). For example, in BV-2 cells that were treated with 400 μM ALA for 24 h, the amount of 15-deoxy-$^{\Delta 12,14}$-PGJ2 produced was 6.92 ± 2.06 times that of the untreated group and there was no significant difference from the ALA group cocultured with oAβ_{1-42} (**Figure 8**).

After cocultured with oAβ_{1-42} in BV-2 cells for 24 h, the expression of the COX-2 protein did not differ significantly from that of the untreated oAβ_{1-42} group. However, the expression of the COX-2 protein in BV-2 cells increased with the increase in ALA treatment concentration ($p < 0.05$) (**Figure 9A**). In addition, the expression of COX-2 mRNA in BV-2 cells was similar to the expression of the protein (**Figure 9B**).

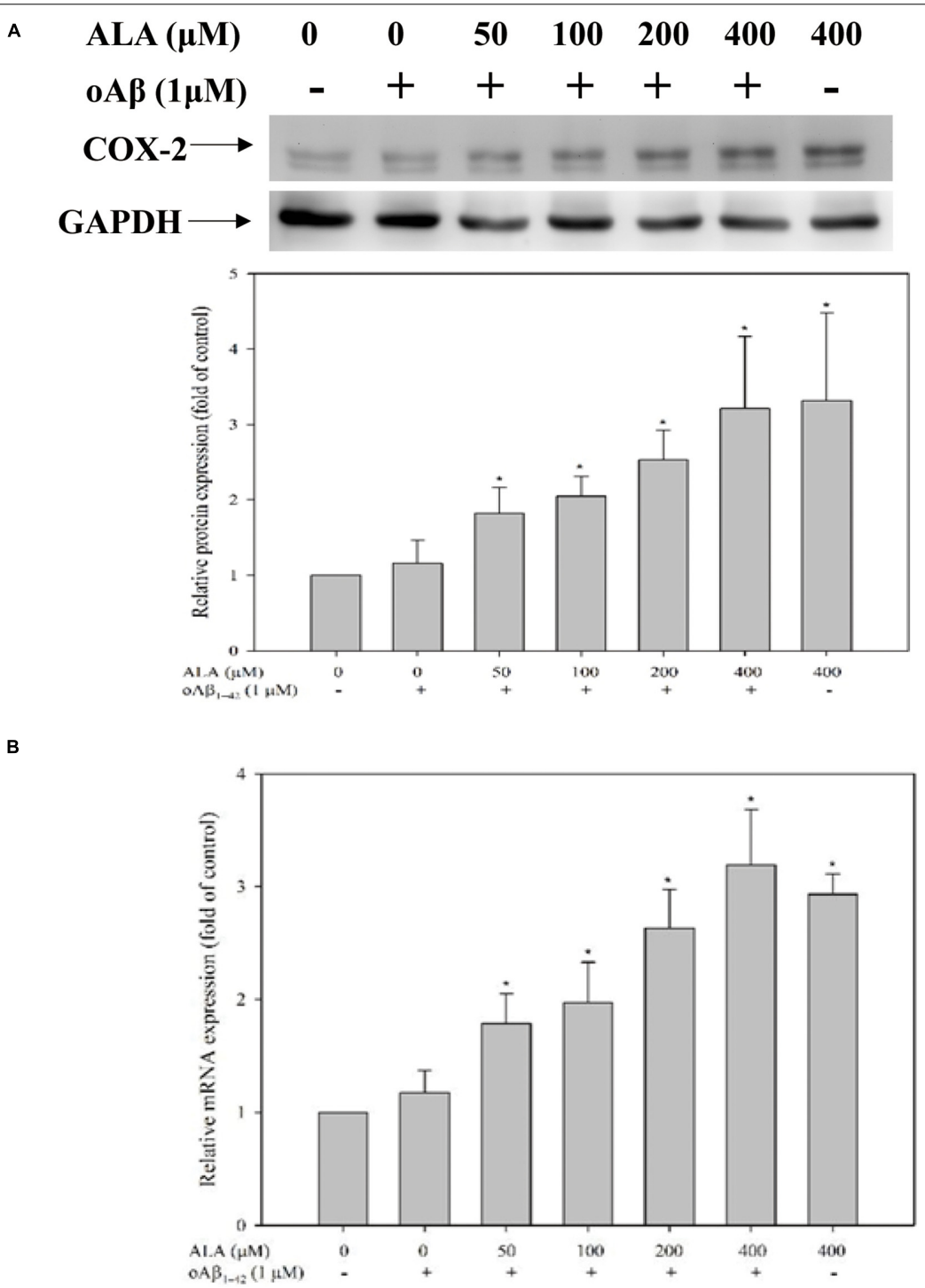

FIGURE 9 | Alpha-lipoic acid elevated cyclooxygenase-2 (COX-2) expression in BV-2 mouse microglial cells. BV-2 cells were pretreated with or without different concentrations of ALA for 30 min, followed by vehicle or oAβ_{1-42} treatment for 24 h. **(A)** The relative COX-2 protein expression was detected using western blotting. **(B)** The relative mRNA expression of COX-2 was determined using real-time PCR. *$p < 0.05$ vs. the vehicle control group.

DISCUSSION

This study demonstrated the possible mechanism of ALA on promoting oAβ_{1-42} uptake in mouse microglial BV-2 cells. ALA treatment increased both the expression of COX-2 mRNA and the COX-2 protein in BV-2 cells. The increase in COX-2 protein expression indirectly accelerated the production of 15-deoxy-$^{\Delta 12,14}$-PGJ2 and acted as a PPAR-γ transcription factor ligand,

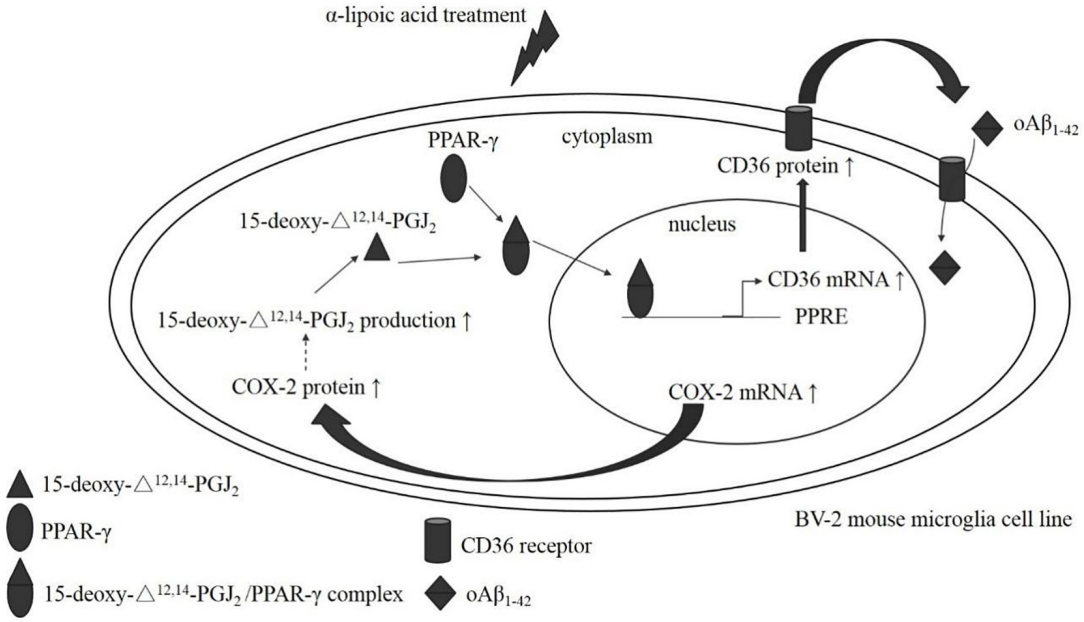

FIGURE 10 | The postulated mechanism of ALA in enhancing oAβ_{1-42} phagocytosis in BV-2 mouse microglial cells. BV-2 mouse microglial cells made a difference after ALA stimulation, which caused the elevation of COX-2 mRNA and the increased translation of the COX-2 protein. Furthermore, the COX-2 protein induced 15-deoxy-$^{\Delta 12,14}$-PGJ2 production and the 15-deoxy-$^{\Delta 12,14}$-PGJ2 acted on the PPAR-γ ligand. Simultaneously, the 15-deoxy-$^{\Delta 12,14}$-PGJ2/PPAR-γ complex translocated from the cytoplasm to the nucleus. PPAR-γ that located the nucleus stimulated the transcription of the CD36 gene, which promoted the synthesis of CD36 mRNA. The increase in CD36 mRNA promoted the translation of the CD36 protein. Finally, the elevated level of the CD36 protein enhanced the phagocytosis of oAβ_{1-42} in BV-2 mouse microglial cells.

which resulted in the translocation and combination of PPAR-γ with peroxisome proliferator hormone response elements. In addition, ALA increased the transcription of CD36 mRNA and increased the translation of CD36 mRNA to the CD36 receptor, which recognized oAβ_{1-42} and triggered the phagocytosis of oAβ_{1-42} in BV-2 cells (**Figure 10**). Thus, our findings suggested that ALA possesses significant potential for regulating the uptake of FAM-oAβ_{1-42} in BV-2 cells. A previous study demonstrated that supplementing 600 mg ALA per day ameliorated the progression of AD (Hager et al., 2007; Fava et al., 2013). However, the mechanism is not well understood. Numerous studies on the alleviating effect of ALA on AD have focused on its antioxidative and anti-inflammatory properties (Maczurek et al., 2008; Farr et al., 2012; Dos Santos et al., 2019; Kim et al., 2019; Choi et al., 2020). We revealed that in addition to antioxidant and anti-inflammatory properties, ALA may also enhance the ability of microglia to eliminate oAβ_{1-42} and subsequently reduce the neurotoxic effect induced by oAβ_{1-42}, which may offer a possible mechanism underlying the prevention of dementia.

It is well established that phagocytosis of oAβ by microglia is accomplished *via* a variety of receptors on the cell membrane such as CD36, SR-A1, SR-B1, and RAGE (Yan et al., 1996; El Khoury et al., 1998; Sokolowski and Mandell, 2011). The scavenger receptor CD36 has been identified as essential in the Aβ-recognition microglia activation (Doens et al., 2017; Dobri et al., 2021). In this study, the mRNA expression of CD36 increased with the increase in the concentration of ALA. We speculate that ALA increases phagocytosis of oAβ_{1-42} in BV-2 cells *via* the CD36 receptor. Additionally, the increase in CD36 mRNA expression in BV-2 cells treated with ALA did not appear to be related to oAβ_{1-42}. In this study, ALA inhibited CD36 receptor expression and subsequently the uptake of FAM-oAβ_{1-42}, but was unable to reverse this progression in BV-2 cells. We speculate that this may be executed solely through CD36, alongside the involvement of other receivers such as Toll-like receptor (TLR)-4 and TLR6 (Stewart et al., 2010). CD36 activation by different ligands is another reason; ligands of microglia in rodents are apoptotic bodies and oxidized low-density protein (Dobri et al., 2021). The CD36 antibody did not inhibit the uptake of FAM-oAβ_{1-42} in BV-2 cells, which is consistent with a previous study (Yang et al., 2011). Increasing the expression of CD36 may promote the ability of microglia to take up Aβ. Results of the Morris water maze test in transplant amyloid precursor protein 23 (APP23) mice showed that the Aβ deposition in the brains of mice in the interleukin-4/interleukin-13 (IL-4/IL-13) treatment group was lower than that in the control group and spatial learning and memory abilities improved significantly more in the treatment group compared with the untreated group, which may be attributed to the increased expression of CD36 by microglia (Kawahara et al., 2012). *In vitro*, it was found that increased expression of CD36 promoted the uptake of oAβ_{1-42} in rat primary type 2 microglia treated with IL-4 (Shimizu et al., 2008). Therefore, we speculate that ALA increases CD36 expression and, subsequently, the CD36 receptor identifies oAβ_{1-42} and initiates downstream phagocytosis.

Peroxisome proliferator-activated receptor-γ has been confirmed as a transcription factor of CD36 mRNA (Shimizu et al., 2008; Yamanaka et al., 2012). In this study, PPAR-γ moved from the cytoplasm to the nucleus under ALA treatment. Thus, the increase in CD36 mRNA facilitated by ALA is related to the increase in the translocation of transcription factor PPAR-γ. The treatment of ALA may increase the activity of PPAR-γ and prevents a variety of diseases (Golbidi et al., 2011; Wang et al., 2013). In a previous study using a PPAR-γ activator, when pioglitazone and DSP-8658 processed rat primary microglia, the expression of CD36 significantly increased and the increase in the CD36 receptor was shown to be the key receptor for pioglitazone and DSP-8658, which promoted the uptake of Aβ_{1-42} by rat primary microglia (Yamanaka et al., 2012). This illustrated the importance of PPAR-γ/CD36 in regulating the uptake of Aβ_{1-42}. PPAR-γ must be combined with its ligand to be translocated. The anti-inflammatory prostaglandin 15-deoxy-$^{\Delta 12,14}$-PGJ2 produced in COX-2 metabolizing polyunsaturated fatty acids is one of the key ligands that activate PPAR-γ (Scher and Pillinger, 2005; Ulivi et al., 2011; Ramer et al., 2013). To date, there has been no evidence demonstrating that ALA promotes the production of 15-deoxy-$^{\Delta 12,14}$-PGJ2 in cells. Therefore, we speculate that anti-inflammatory response mechanism of ALA is linked to the production of 15-deoxy-$^{\Delta 12,14}$-PGJ2 and is involved in PPAR-γ translocation in BV-2 cells. We used the anti-inflammatory properties of ALA to explore PPAR-γ activation and found that BV-2 cells increased the production of 15-deoxy-$^{\Delta 12,14}$-PGJ2 under ALA treatment. This also increased the upstream expression of COX-2, which showed a trend increase with the increase in ALA treatment concentrations. Furthermore, we found that BV-2 cells increased the production of COX-2 mRNA under ALA stimulation, which suggested that ALA increases the translocation of PPAR-γ in BV-2 cells through COX-2/15-deoxy-$^{\Delta 12,14}$-PGJ2.

Study with respect to the effect of ALA on COX-2 expression in microglia is limited. ALA is considered to be a substance with anti-inflammatory activity and COX-2 has a close relationship with inflammation (Wang et al., 2018). Diethylnitrosamine and choline-methionine-deficient diet-induced liver damage and ALA administration in Fischer rats showed that ALA increases hepatic COX-2 protein expression when the liver is damaged. However, this result was not found in the choline-supplemented diet group (Perra et al., 2008). Moreover, ALA did not increase the protein expression of COX-2 in RAW 264.7 cells (Hwang et al., 2015). We believe that this issue has been inadequately explored; although prostaglandin produced by COX-2-metabolizing polyunsaturated fatty acids is partially related to the inflammatory response, it is also partially related to the anti-inflammatory effect. Few studies have focused on the ability of ALA itself to induce COX-2. The best example is 15-deoxy-$^{\Delta 12,14}$-PGJ2, which is a well-known anti-inflammatory prostaglandin and currently, studies on the increase of PPAR-γ translocation by ALA are limited. The results of this study clearly showed a correlation among ALA, 15-deoxy-$^{\Delta 12,14}$-PGJ2, PPAR-γ, and anti-inflammatory effects. Taken together, we speculate that ALA increases the expression of CD36 *via* COX-2/15-deoxy-$^{\Delta 12,14}$-PGJ2/PPAR-γ activation, which may be one of the major mechanisms of oAβ phagocytosis in BV-2 cells. A future study should be conducted with an *in vivo* study to confirm our *in vitro* findings.

CONCLUSION

This study demonstrated that ALA increases phagocytosis of oAβ_{1-42} possibly *via* modulating the COX-2/15-deoxy-$^{\Delta 12,14}$-PGJ2/PPAR-γ/CD36 pathway in microglia. We postulated that ALA enhances mRNA and protein expression of COX-2, increases the production of 15-deoxy-$^{\Delta 12,14}$-PGJ2, acts as a PPAR-γ transcription to elevate CD36 mRNA translation into CD36 protein, and subsequently enhances oAβ_{1-42} phagocytosis in BV-2 cells. These study findings suggest that ALA possesses antidementia potential and offers new insight into the mechanisms underlying the prevention of progression of AD.

DATA AVAILABILITY STATEMENT

The original contributions presented in the study are included in the article/supplementary material, further inquiries can be directed to the corresponding author.

AUTHOR CONTRIBUTIONS

C-YK and S-CS participated in the design of the study and writing the protocol. Y-WC carried out all the experiments. C-YK, J-HX, YL, JW, W-CH, and S-CS conducted kinds of literature searches and data analyses and wrote drafts of the manuscript. All authors contributed to the article and approved the submitted version.

FUNDING

This study was supported by the Ministry of Science and Technology of the Republic of China (ROC), Taiwan, under contract no. MOST 107-2320-B-003-004-MY3, and academic funding of the Second Affiliated Hospital of Fujian Medical University (serial no. BS201902).

ACKNOWLEDGMENTS

Special thanks are due to Fu in the College of Medicine, National Taiwan University for her kindly donation of BV-2 cells.

REFERENCES

Benilova, I., Karran, E., and De Strooper, B. (2012). The toxic Abeta oligomer and Alzheimer's disease: an emperor in need of clothes. *Nat. Neurosci.* 15, 349–357. doi: 10.1038/nn.3028

Blennow, K., de Leon, M. J., and Zetterberg, H. (2006). Alzheimer's disease. *Lancet* 368, 387–403. doi: 10.1016/S0140-6736(06)69113-7

Bujold, K., Rhainds, D., Jossart, C., Febbraio, M., Marleau, S., and Ong, H. (2009). CD36-mediated cholesterol efflux is associated with PPARgamma activation *via* a MAPK-dependent COX-2 pathway in macrophages. *Cardiovasc. Res.* 83, 457–464. doi: 10.1093/cvr/cvp118

Chen, H. J., Ko, C. Y., Xu, J. H., Huang, Y. C., Wu, J. S. B., and Shen, S. C. (2021). Alleviative effect of *Ruellia tuberosa* L. on insulin resistance and abnormal lipid accumulation in TNF-α-treated FL83B mouse hepatocytes. *Evid. Based Complement. Alternat. Med.* 2021:9967910. doi: 10.1155/2021/9967910

Choi, H. R., Ha, J. S., Kim, I. S., and Yang, S. J. (2020). Metformin or α-lipoic acid attenuate inflammatory response and NLRP3 inflammasome in BV-2 microglial cells. *Korean J. Clin. Lab. Sci.* 52, 253–260. doi: 10.15324/kjcls.2020.52.3.253

Dobri, A. M., Dudău, M., Enciu, A. M., and Hinescu, M. E. (2021). CD36 in Alzheimer's disease: an overview of molecular mechanisms and therapeutic targeting. *Neuroscience* 453, 301–311. doi: 10.1016/j.neuroscience.2020.11.003

Doens, D., Valiente, P. A., Mfuh, A. M., Vo, A. X. T., Tristan, A., Carreño, L., et al. (2017). Identification of inhibitors of CD36-amyloid beta binding as potential agents for Alzheimer's disease. *ACS Chem. Neurosci.* 8, 1232–1241. doi: 10.1021/acschemneuro.6b00386

Dos Santos, S. M., Romeiro, C. F. R., Rodrigues, C. A., Cerqueira, A. R. L., and Monteiro, M. C. (2019). Mitochondrial dysfunction and Alpha-lipoic acid: beneficial or harmful in Alzheimer's disease? *Oxid. Med. Cell. Longev.* 2019:8409329. doi: 10.1155/2019/8409329

El Khoury, J., Hickman, S. E., Thomas, C. A., Loike, J. D., and Silverstein, S. C. (1998). Microglia, scavenger receptors, and the pathogenesis of Alzheimer's disease. *Neurobiol. Aging* 19, S81–S84. doi: 10.1016/s0197-4580(98)00036-0

Erika, N. C., Ma'ıra, A. B., Kirsten, L. V., and William, L. K. (2018). The Amyloid-β oligomer hypothesis: beginning of the third decade. *J. Alzheimers Dis.* 64, S567–S610. doi: 10.3233/JAD-179941

Farr, S. A., Price, T. O., Banks, W. A., Ercal, N., and Morley, J. E. (2012). Effect of alpha-lipoic acid on memory, oxidation, and lifespan in SAMP8 mice. *J. Alzheimers Dis.* 32, 447–455. doi: 10.3233/JAD-2012-120130

Fava, A., Pirritano, D., Plastino, M., Cristiano, D., Puccio, G., Colica, C., et al. (2013). The effect of lipoic acid therapy on cognitive functioning in patients with Alzheimer's disease. *J. Neurodegener. Dis.* 2013:454253. doi: 10.1155/2013/454253

Golbidi, S., Badran, M., and Laher, I. (2011). Diabetes and alpha lipoic Acid. *Front. Pharmacol.* 2:69. doi: 10.3389/fphar.2011.00069

Haass, C., and Selkoe, D. J. (2007). Soluble protein oligomers in neurodegeneration: lessons from the Alzheimer's amyloid beta-peptide. *Nat. Rev. Mol. Cell Biol.* 8, 101–112. doi: 10.1038/nrm2101

Hager, K., Kenklies, M., McAfoose, J., Engel, J., and Munch, G. (2007). Alpha-lipoic acid as a new treatment option for Alzheimer's disease–a 48 months follow-up analysis. *J. Neural Transm. Suppl.* 72, 189–193. doi: 10.1007/978-3-211-73574-9_24

Holmquist, L., Stuchbury, G., Berbaum, K., Muscat, S., Young, S., Hager, K., et al. (2007). Lipoic acid as a novel treatment for Alzheimer's disease and related dementias. *Pharmacol. Ther.* 113, 154–164. doi: 10.1016/j.pharmthera.2006.07.001

Hwang, J. S., An, J. M., Cho, H., Lee, S. H., Park, J. H., and Han, I. O. (2015). A dopamine-alpha-lipoic acid hybridization compound and its acetylated form inhibit LPS-mediated inflammation. *Eur. J. Pharmacol.* 746, 41–49. doi: 10.1016/j.ejphar.2014.10.052

Jack, C. R. Jr., Wiste, H. J., Therneau, T. M., Weigand, S. D., Knopman, D. S., Mielke, M. M., et al. (2019). Associations of amyloid, tau, and neurodegeneration biomarker profiles with rates of memory decline among individuals without dementia. *JAMA* 321, 2316–2325. doi: 10.1001/jama.2019.7437

Kawahara, K., Suenobu, M., Yoshida, A., Koga, K., Hyodo, A., Ohtsuka, H., et al. (2012). Intracerebral microinjection of interleukin-4/interleukin-13 reduces beta-amyloid accumulation in the ipsilateral side and improves cognitive deficits in young amyloid precursor protein 23 mice. *Neuroscience* 207, 243–260. doi: 10.1016/j.neuroscience.2012.01.049

Kim, S. M., Ha, J. S., Han, A. R., Cho, S. W., and Yang, S. J. (2019). Effects of α-lipoic acid on LPS-induced neuroinflammation and NLRP3 inflammasome activation through the regulation of BV-2 microglial cells activation. *BMB Rep.* 52, 613–618. doi: 10.5483/BMBRep.2019.52.10.026

Knopman, D. S., Amieva, H., Petersen, R. C., Chételat, G., Holtzman, D. M., Hyman, B. T., et al. (2021). Alzheimer disease. *Nat. Rev. Dis. Primers* 7:33. doi: 10.1038/s41572-021-00269-y

Ko, C. Y., Lo, Y. M., Xu, J. H., Chang, W. C., Huang, D. W., Wu, J. S., et al. (2021). Alpha-lipoic acid alleviates NAFLD and triglyceride accumulation in liver *via* modulating hepatic NLRP3 inflammasome activation pathway in type 2 diabetic rats. *Food Sci. Nutr.* 9, 2733–2742. doi: 10.1002/fsn3.2235

Liu, Z., Li, T., Li, P., Wei, N., Zhao, Z., Liang, H., et al. (2015). The ambiguous relationship of oxidative stress, Tau hyperphosphorylation, and autophagy dysfunction in Alzheimer's disease. *Oxid. Med. Cell. Longev.* 2015:352723. doi: 10.1155/2015/352723

Lu, D. Y., Tang, C. H., Liou, H. C., Teng, C. M., Jeng, K. C., Kuo, S. C., et al. (2007). YC-1 attenuates LPS-induced proinflammatory responses and activation of nuclear factor-kappaB in microglia. *Br. J. Pharmacol.* 151, 396–405. doi: 10.1038/sj.bjp.0707187

Maczurek, A., Hager, K., Kenklies, M., Sharman, M., Martins, R., Engel, J., et al. (2008). Lipoic acid as an anti-inflammatory and neuroprotective treatment for Alzheimer's disease. *Adv. Drug Deliv. Rev.* 60, 1463–1470. doi: 10.1016/j.addr.2008.04.015

Packer, L., Witt, E. H., and Tritschler, H. J. (1995). alpha-Lipoic acid as a biological antioxidant. *Free Radic. Biol. Med.* 19, 227–250. doi: 10.1016/0891-5849(95)00017-r

Perra, A., Pibiri, M., Sulas, P., Simbula, G., Ledda-Columbano, G. M., and Columbano, A. (2008). Alpha-lipoic acid promotes the growth of rat hepatic pre-neoplastic lesions in the choline-deficient model. *Carcinogenesis* 29, 161–168. doi: 10.1093/carcin/bgm205

Pomilio, C., Gorojod, R. M., Riudavets, M., Vinuesa, A., Presa, J., Gregosa, A., et al. (2020). Microglial autophagy is impaired by prolonged exposure to β-amyloid peptides: evidence from experimental models and Alzheimer's disease patients. *Geroscience* 42, 613–632. doi: 10.1007/s11357-020-00161-9

Querfurth, H. W., and LaFerla, F. M. (2010). Alzheimer's disease. *N. Engl. J. Med.* 362, 329–344. doi: 10.1056/NEJMra0909142

Rai, S. N., Singh, C., Singh, A., Singh, M. P., and Singh, B. K. (2020). Mitochondrial dysfunction: a potential therapeutic target to treat Alzheimer's disease. *Mol. Neurobiol.* 57, 3075–3088. doi: 10.1007/s12035-020-01945-y

Ramer, R., Heinemann, K., Merkord, J., Rohde, H., Salamon, A., Linnebacher, M., et al. (2013). COX-2 and PPAR-gamma confer cannabidiol-induced apoptosis of human lung cancer cells. *Mol. Cancer Ther.* 12, 69–82. doi: 10.1158/1535-7163.MCT-12-0335

Scher, J. U., and Pillinger, M. H. (2005). 15d-PGJ2: the anti-inflammatory prostaglandin? *Clin. Immunol.* 114, 100–109. doi: 10.1016/j.clim.2004.09.008

Shimizu, E., Kawahara, K., Kajizono, M., Sawada, M., and Nakayama, H. (2008). IL-4-induced selective clearance of oligomeric beta-amyloid peptide (1-42) by rat primary type 2 microglia. *J. Immunol.* 181, 6503–6513. doi: 10.4049/jimmunol.181.9.6503

Singh, A. K., Rai, S. N., Maurya, A., Mishra, G., Awasthi, R., Shakya, A., et al. (2021). Therapeutic potential of phytoconstituents in management of Alzheimer's disease. *Evid. Based Complement. Alternat. Med.* 2021:5578574. doi: 10.1155/2021/5578574

Sokolowski, J. D., and Mandell, J. W. (2011). Phagocytic clearance in neurodegeneration. *Am. J. Pathol.* 178, 1416–1428. doi: 10.1016/j.ajpath.2010.12.051

Srivastava, P., Tripathi, P. N., Sharma, P., Rai, S. N., Singh, S. P., Srivastava, R. K., et al. (2019). Design and development of some phenyl benzoxazole derivatives as a potent acetylcholinesterase inhibitor with antioxidant property to enhance learning and memory. *Eur. J. Med. Chem.* 163, 116–135. doi: 10.1016/j.ejmech.2018.11.049

Stewart, C. R., Stuart, L. M., Wilkinson, K., van Gils, J. M., Deng, J., Halle, A., et al. (2010). CD36 ligands promote sterile inflammation through assembly of a Toll-like receptor 4 and 6 heterodimer. *Nat. Immunol.* 11, 155–161. doi: 10.1038/ni.1836

Su, B., Wang, X., Nunomura, A., Moreira, P. I., Lee, H. G., Perry, G., et al. (2008). Oxidative stress signaling in Alzheimer's disease. *Curr. Alzheimer Res.* 5, 525–532. doi: 10.2174/156720508786898451

Thirunavukkarasu, V., Anitha Nandhini, A. T., and Anuradha, C. V. (2004). Lipoic acid attenuates hypertension and improves insulin sensitivity, kallikrein activity and nitrite levels in high fructose-fed rats. *J. Comp. Physiol. B* 174, 587–592. doi: 10.1007/s00360-004-0447-z

Tripathi, P. N., Srivastava, P., Sharma, P., Tripathi, M. K., Seth, A., Tripathi, A., et al. (2019). Biphenyl-3-oxo-1,2,4-triazine linked piperazine derivatives as potential cholinesterase inhibitors with anti-oxidant property to improve the learning and memory. *Bioorg. Chem.* 85, 82–96. doi: 10.1016/j.bioorg.2018.12.017

Ulivi, V., Lenti, M., Gentili, C., Marcolongo, G., Cancedda, R., and Descalzi Cancedda, F. (2011). Anti-inflammatory activity of monogalactosyldiacylglycerol in human articular cartilage *in vitro*: activation of an anti-inflammatory cyclooxygenase-2 (COX-2) pathway. *Arthritis Res. Ther.* 13:R92. doi: 10.1186/ar3367

Walsh, D. M., Klyubin, I., Fadeeva, J. V., Cullen, W. K., Anwyl, R., Wolfe, M. S., et al. (2002). Naturally secreted oligomers of amyloid beta protein potently inhibit hippocampal long-term potentiation *in vivo*. *Nature* 416, 535–539. doi: 10.1038/416535a

Wang, K. C., Tsai, C. P., Lee, C. L., Chen, S. Y., Lin, G. J., Yen, M. H., et al. (2013). α-Lipoic acid enhances endogenous peroxisome-proliferator-activated receptor-gamma to ameliorate experimental autoimmune encephalomyelitis in mice. *Clin. Sci.* 125, 329–340. doi: 10.1042/CS20120560

Wang, Q., Lv, C., Sun, Y., Han, X., Wang, S., Mao, Z., et al. (2018). The role of alpha-lipoic acid in the pathomechanism of acute ischemic stroke. *Cell. Physiol. Biochem.* 48, 42–53. doi: 10.1159/000491661

Yamanaka, M., Ishikawa, T., Griep, A., Axt, D., Kummer, M. P., and Heneka, M. T. (2012). PPARgamma/RXRalpha-induced and CD36-mediated microglial amyloid-beta phagocytosis results in cognitive improvement in amyloid precursor protein/presenilin 1 mice. *J. Neurosci.* 32, 17321–17331. doi: 10.1523/JNEUROSCI.1569-12.2012

Yan, S. D., Chen, X., Fu, J., Chen, M., Zhu, H., Roher, A., et al. (1996). RAGE and amyloid-beta peptide neurotoxicity in Alzheimer's disease. *Nature* 382, 685–691. doi: 10.1038/382685a0

Yang, C. N., Shiao, Y. J., Shie, F. S., Guo, B. S., Chen, P. H., Cho, C. Y., et al. (2011). Mechanism mediating oligomeric Abeta clearance by naive primary microglia. *Neurobiol. Dis.* 42, 221–230. doi: 10.1016/j.nbd.2011.01.005

Conflict of Interest: The authors declare that the research was conducted in the absence of any commercial or financial relationships that could be construed as a potential conflict of interest.

Publisher's Note: All claims expressed in this article are solely those of the authors and do not necessarily represent those of their affiliated organizations, or those of the publisher, the editors and the reviewers. Any product that may be evaluated in this article, or claim that may be made by its manufacturer, is not guaranteed or endorsed by the publisher.

Copyright © 2022 Ko, Xu, Chang, Lo, Wu, Huang and Shen. This is an open-access article distributed under the terms of the Creative Commons Attribution License (CC BY). The use, distribution or reproduction in other forums is permitted, provided the original author(s) and the copyright owner(s) are credited and that the original publication in this journal is cited, in accordance with accepted academic practice. No use, distribution or reproduction is permitted which does not comply with these terms.

frontiers in Aging Neuroscience

BRIEF RESEARCH REPORT
published: 13 January 2022
doi: 10.3389/fnagi.2021.788798

Preservation of Retinal Function Through Synaptic Stabilization in Alzheimer's Disease Model Mouse Retina by Lycium Barbarum Extracts

Jinfeng Liu[1], Larry Baum[2,3], Shasha Yu[1,4], Youhong Lin[1], Guoying Xiong[1], Raymond Chuen-Chung Chang[3,5], Kwok Fai So[1,3,6,7] and Kin Chiu[1,3,6]**

[1] Department of Ophthalmology, LKS Faculty of Medicine, The University of Hong Kong, Pokfulam, Hong Kong SAR, China, [2] Department of Psychiatry, LKS Faculty of Medicine, The University of Hong Kong, Pokfulam, Hong Kong SAR, China, [3] State Key Laboratory of Brain and Cognitive Sciences, The University of Hong Kong, Pokfulam, Hong Kong SAR, China, [4] Tianjin Key Lab of Ophthalmology and Visual Science, Clinical College of Ophthalmology, Tianjin Eye Hospital, Nankai University Eye Hospital, Tianjin Eye Institute, Tianjin Medical University, Tianjin, China, [5] Laboratory of Neurodegenerative Diseases, School of Biomedical Sciences, The University of Hong Kong, Pokfulam, Hong Kong SAR, China, [6] Department of Psychology, The University of Hong Kong, Pokfulam, Hong Kong SAR, China, [7] Guangdong-Hongkong-Macau Institute of CNS Regeneration, Jinan University, Guangzhou, China

OPEN ACCESS

Edited by:
Jiehui Jiang,
Shanghai University, China

Reviewed by:
Abdullah Alhomida,
King Saud University, Saudi Arabia
Woon-Man Kung,
Chinese Culture University, Taiwan

***Correspondence:**
Kin Chiu
datwai@hku.hk
Kwok Fai So
hrmaskf@hku.hk

Specialty section:
This article was submitted to Alzheimer's Disease and Related Dementias, a section of the journal Frontiers in Aging Neuroscience

Received: *03 October 2021*
Accepted: *20 December 2021*
Published: *13 January 2022*

Citation:
Liu J, Baum L, Yu S, Lin Y, Xiong G, Chang RC-C, So KF and Chiu K (2022) Preservation of Retinal Function Through Synaptic Stabilization in Alzheimer's Disease Model Mouse Retina by Lycium Barbarum Extracts. Front. Aging Neurosci. 13:788798. doi: 10.3389/fnagi.2021.788798

In Alzheimer's disease (AD), amyloid β deposition-induced hippocampal synaptic dysfunction generally begins prior to neuronal degeneration and memory impairment. *Lycium barbarum* extracts (LBE) have been demonstrated to be neuroprotective in various animal models of neurodegeneration. In this study, we aimed to investigate the effects of LBE on the synapse loss in AD through the avenue of the retina in a triple transgenic mouse model of AD (3xTg-AD). We fed 3xTg-AD mice with low (200 mg/kg) or high (2 g/kg) dose hydrophilic LBE daily for 2 months from the starting age of 4- or 6-month-old. For those started at 6 month age, at 1 month (though not 2 months) after starting treatment, mice given high dose LBE showed a significant increase of a wave and b wave in scotopic ERG. After 2 months of treatment with high dose LBE, calpain-2, calpain-5, and the oxidative RNA marker 8-OHG were downregulated, and presynaptic densities in the inner plexiform layer but not the outer plexiform layer of the retina were significantly increased, suggesting the presynaptic structure of retina was preserved. Our results indicate that LBE feeding may preserve synapse stability in the retina of 3xTg-AD mice, probably by decreasing both oxidative stress and intracellular calcium influx. Thus, LBE might have potential as a neuroprotectant for AD through synapse preservation.

Keywords: Alzheimer's disease, retina, synapse, Lycium barbarum, 8-OHG, calpain-2, calpain-5

INTRODUCTION

The number of people with dementia is about 55 million worldwide in 2021, and is expected to increase to about 140 million by 2050 (World Health Organization., 2021). Alzheimer's disease (AD) is the most common type of dementia (60–70% of cases). It is an evolving humanitarian challenge, with growing numbers due to the aging of the population. In the United States alone, the estimated total healthcare cost for the treatment of AD in 2020 was estimated at $305 billion, and is estimated to increase to more than $1 trillion by 2050 (Wong, 2020). Early detection and diagnosis

of AD, leading to early initiation of current AD therapies, is associated with improved quality of life and economic outcomes. This is despite the modest effectiveness of current AD therapies, therefore finding an improved and affordable treatment would be very important for society.

Transgenic mouse models harboring mutated human genes associated with familial forms of AD are advanced preclinical tools in the study of mechanisms underlying AD. The triple transgenic mouse model of AD (3xTg-AD) incorporates a Swedish amyloid precursor protein (APP) mutation, a human mutant presenilin 1 (PSEN1) gene PS1 (M146V) knock-in, and a tau (P301L) transgene (Oddo et al., 2003). These mice develop intracellular amyloid beta (Aβ), Aβ plaques and neurofibrillary tangle (NFT) like pathology in a progressive and age-dependent manner similar to human AD (Oddo et al., 2003; Edwards et al., 2014). AD disproportionately affects women in both disease prevalence and rate of symptom progression (reviewed by Fisher et al., 2018). 3xTg-AD mice also display faster progression in females than in males. Starting at 6 months of age, female 3xTg-AD mice exhibit greater cognitive deficits than males. This disparity is still evident at 9 months of age, when female mice have significantly higher stress responses (Clinton et al., 2007). Thus, it is crucial to specify sex and age to examine early-stage AD mechanisms and/or novel therapeutic interventions.

In the early stage of AD, memory impairment and loss of hippocampal synapses show up prior to frank neuronal degeneration (Selkoe, 2002; Chen et al., 2019). In early stages of familial AD, neuronal RNA oxidation occurs (Nunomura et al., 2004, 2009; Nunomura and Perry, 2020). Increased oxidative stress (Xu et al., 2021), uncontrolled hyperactivation of a family of cysteine proteases called calpains (Mahaman et al., 2019), and synaptic dysfunction (Jackson et al., 2019) may contribute to the disease process. The abnormal activation of calpain could induce synaptic dysfunction (Chen et al., 2019). Calpain inhibition not only prevented Aβ (1-42) induced Ca^{++} influx and neuronal death in primary cortical neuron culture (Lee et al., 2000), but also decreased the AD-like pathology and cognitive decline in aged 3xTg-AD mice (Medeiros et al., 2012). Mounting evidence indicates that therapeutic approaches aiming to protect against these in the early stage of AD might stop or reverse disease progression (Jackson et al., 2019).

Emerging evidence suggests that visual performance is impaired early in AD (Van Wijngaarden et al., 2017; reviewed by Shah et al., 2017). Visual impairments reported in AD patients include nerve fiber layer thinning, degeneration of retinal ganglion cells (RGC), and changes to vascular parameters (Hart et al., 2016). Moreover, Aβ deposits were observed in multiple layers of the retina, and were significantly associated with brain Aβ burden. The retina (and its related vasculature and optic nerve) shares the same embryological origin as well as some anatomical and physiological properties as the brain (Patton et al., 2005). In transgenic AD animals, retinal abnormalities demonstrated by deterioration in visual function or reactive gliosis were reported (Chidlow et al., 2017; Chiquita et al., 2019a; Zhang et al., 2021). Any neuroprotective agents benefitting the visual system might be useful for AD treatment.

Lycium barbarum (LB) is named Gouqizi in Chinese, and wolfberry in English. It has been used medicinally for more than 2500 years for its abilities to delay aging and improve visual acuity. LB has been regularly consumed by a vast number of people, with little to no side effects, making it a good candidate for an anti-aging agent (Gao et al., 2017). The neuroprotective effect of LB was first demonstrated in animal models of retinal degenerative diseases such as glaucoma, age-related macular degeneration (ARMD) (Chiu et al., 2009). It appears to protect the visual system through four primary processes: neuroprotection, blood-retinal barrier stabilization, antioxidation, and modulation of retinal immune function via the retinal microglial cells and Müller cells (reviewed by Manthey et al., 2017). LB can inhibit two key pro-apoptotic signaling pathways (JNK and PKR) in Aβ peptide neurotoxicity (Chang et al., 2002; Suen et al., 2003; Yu et al., 2005, 2006). The neuroprotective effects of LB were further demonstrated in the preservation of cognitive functions and decrease in Aβ deposition in APPswe/PS1-del9 Tg-AD mice (Zhang et al., 2013; Zhou et al., 2020).

Studies using extracts revealed the beneficial effects of LB. The major LB constituents demonstrating anti-aging properties include LB polysaccharides, carotenoids (zeaxanthin and β-carotene), betaine, flavonoids and vitamins (Gao et al., 2017). Our previous study using hydrophilic extract from LB (LBE) demonstrated the enhancement of retinal light response in the retina of 5xFAD mice (Zhang et al., 2021). Further study in cell culture using the IMG microglial cell line showed that LBE promoted activation of microglia with anti-inflammatory character (M2 polarization) and reduced oligomeric Aβ induced inflammatory reactions in microglia (Sun et al., 2022). LBE also had antioxidant effects under H_2O_2 stimulation of primary mixed glial cells (Zheng et al., 2021). Therefore, if LBE is applied early in AD, disease progression might be significantly delayed.

In the current study, we aimed to explore the effects of LBE feeding on the retinal changes in young female 3xTg AD mice, and to unveil the underlying mechanisms. The evaluation was focused on retinal function changes and RNA oxidation, calpain activation and synaptic proteins in the retina. Because much of retinal function and pathology can be observed non-invasively in living animals and humans, the ability to evaluate treatment effects in the retina would be an invaluable and low cost translational research platform to fulfill an unmet need of healthy aging.

MATERIALS AND METHODS

Animals

3xTg-AD mice [B6;129-Psen1tm1Mpm Tg (APPSwe, tauP301L)1Lfa/J] (Oddo et al., 2003) were purchased from the Jackson Laboratory (stock No. 004807, Bar Harbor, ME, USA). Since the mice are homozygous for mutations in the PS1, APP, and tau genes, we maintained the colony by breeding homozygous 3xTg-AD mice to each other. Non-transgenic C57BL/6J mice were obtained from the Laboratory Animal Unit of the University of Hong Kong and used as wild-type (WT) controls. To reduce sexual dimorphism, especially in the early

stage of AD (from 4 to 8 months), only female mice were used in the study. All animals were maintained in a temperature-controlled room with a 12-h light/dark cycle throughout the observation period. All animal procedures were performed according to the ARRIVE guidelines and were approved by the Committee on the Use of Live Animals in Teaching and Research of the University of Hong Kong. All efforts were taken to minimize the number of animals used and their suffering.

LBE Preparation, Animal Feeding and Grouping

LBE was provided by Eu Yan Sang (HK) Ltd. LB from NingXia Huizu Autonomous Region, the People's Republic of China, was used. The extraction procedure was the same as in our previous report (Sun et al., 2022). Briefly, 2.5 kg of LB was washed and soaked in 40°C ultrapure water for 15 minutes. After 1 h boiling, the filtered drug residues were boiled again. The extracts from two boils were combined and concentrated to 1.25 kg. The final LBE was weighed and diluted in ultrapure water (w/v) to produce a stock solution (100 g/L).

3xTg-AD mice were orally fed with a low dose (200 mg/kg body weight) or high dose (2 g/kg) of LBE daily for 2 months with distilled water feeding as vehicle control, and age-matched C57BL/6J mice with the same treatments were regarded as WT controls. For each age stage (4 and 6 months old), five groups were included: water treated WT mice, high dose LBE treated WT mice, water treated AD mice, low dose LBE treated AD mice, and high dose LBE treated AD mice. Each group consisted of six mice.

Flash Electroretinography

Retinal function was evaluated by an electroretinography (ERG) system (Espion E2 Electrophysiology System, Diagnosys LLC, USA) according to the standard protocol of the International Society for Clinical Electrophysiology of Vision (ISCEV). Mice were anesthetized with intraperitoneal injection of a mixture of ketamine (0.1 mg/g) and xylazine (10 μg/g). The eyes were administered 1% Mydriacyl (Alcon, Fort Worth, USA) to dilate the pupils and 0.5% Alcaine (Alcon, Fort Worth, USA) to reduce cornea sensitivity. ERG signals under a scotopic flash intensity of 3.0 cd·s/m^2 and photopic flash intensity of 22.8 cd·s/m^2 were recorded. Amplitude and latency of ERG signals were filtered and analyzed by Axon pCLAMP 10 (Molecular Devices Corp., Sunnyvale, CA, USA).

Histology and Morphometric Analysis of Retinal Sections

Mice were sacrificed by an overdose of anesthesia with an intraperitoneal injection of Dorminal (0.1–0.15 mg/g). The eyeballs were harvested, fixed, processed and paraffin-embedded for sectioning. Five micrometer thick retinal cross sections with intact optic nerves were deparaffinized and stained with hematoxylin and eosin. Images were captured with a light microscope (Eclipse80i, Nikon) under 40x magnification. Morphometric analysis was carried out as in our previous report (Chan et al., 2012). The thickness of the inner retinal layer (IRL) was measured from inner limiting membrane to the outermost point of the inner nuclear layer (INL), and the outer nuclear layer (ONL), as well as the number of RGC both in the central or peripheral retina, were calculated using Fiji software (NIH, MD, USA).

Immunohistochemical Detection in Retinal Sections

Retinal sections were rehydrated and boiled in 95°C citric acid buffer (10 mM, pH 6.0) for 15 min for antigen retrieval. Sections were then incubated in 10% normal goat serum with 1% bovine serum albumin (Sigma-Aldrich, St. Louis, MO, USA) and 0.1% Triton X-100 (Sigma-Aldrich, St. Louis, MO, USA) in PBS (pH 7.2–7.4) for 1 h at room temperature to block nonspecific binding. Following blocking, sections were incubated with either of the following primary antibodies overnight at 4°C: anti-goat Brn3a (1:500, Santa Cruz, Dallas, USA); anti-mouse PKC-α (1:500, Millipore, Burlington, Massachusetts, USA); anti-rabbit GFAP (1:500, Abcam, Cambridge, UK); anti-rabbit Iba-1(1:500, WAKO, Chou-ku, Osaka, Japan); anti-rabbit synaptophysin (1:500, Abcam); anti-rabbit PSD-95 (1:500, Abcam); anti-rabbit 8-OHG (1:500, Abcam); anti-rabbit calpain-2 (1:200, Thermo Fisher Scientific, Waltham, Massachusetts, USA); or anti-rabbit calpain-5 (1:200, Thermo Fisher Scientific). After washing with PBS, the sections were incubated with Alexa-568 or 488 fluorescent-conjugated goat IgG secondary antibody (1:500; Thermo Fisher Scientific) for 1 h at room temperature. The slides were then washed in PBS and counterstained with 4',6-Diamidino-2-phenylindole (DAPI) (1:1000). Images were captured using a ZEISS LSM 800 Confocal microscope (Carl Zeiss Microscopy GmbH, Germany).

Statistical Analysis

Statistical analysis was performed by *t*-test or one-way ANOVA followed by *post-hoc* analysis using SPSS software for Windows (version 19.0; SPSS, Inc., IL, USA). Data were reported as mean ± SD. A value of $P < 0.05$ was considered significant for statistical analysis.

RESULTS

Age Dependent Retinal Functional Impairment and Accumulation of Intracellular Amyloid in the 3xTg-AD Mice

Retinal function reflected by ERG parameters demonstrated age dependent changes from 4 to 14 months (**Figure 1**). Compared with WT control, the scotopic retinal response in a wave started to decline significantly at age 6 months, followed by a rapid decline between 6 and 8 months (**Figures 1A,C**). Significant decline in b wave could be detected between 6 to 8 months and 9 to 14 months in 3xTg-AD mice. Under light adaptation, the changes in b wave were not significant when compared to WT control. There was significant PhNR reduction at 12 months of age (**Figure 1B**, $^*p < 0.05$). Deterioration of retinal function in ERG might be caused by decreased

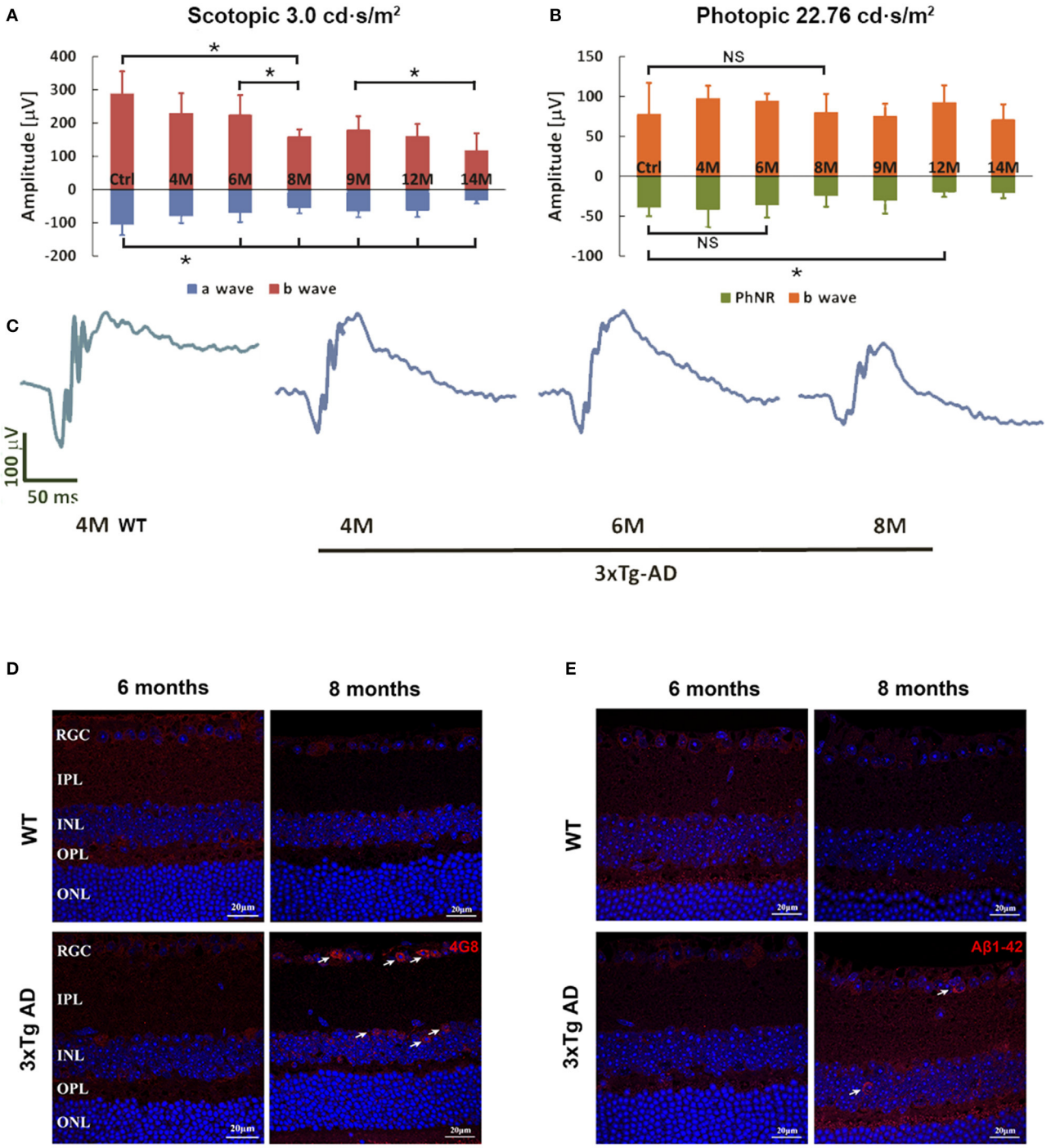

FIGURE 1 | Flash-ERG and amyloid beta (Aβ) deposition in retinas of non-Tg control mice and 3xTg-AD mice at different ages. The scotopic retinal response **(A)** of 3xTg-AD mice started to decline at 6 months of age, followed by a rapid decrease from 6 to 8 months of age **(A,C)**. *$p < 0.05$. Further significant decline in b wave changes can be detected between 6–8 months and 9–14 months. Significant reduction in a wave started at 6 months when compared with non-Tg controls. PhNR detected in the photopic response revealed a significant reduction at 12 months when compared with non-Tg controls **(B)**. *$p < 0.05$; NS, no significant change. Typical ERG wave forms are shown in C. Intracellular Aβ deposition of 4G8 **(D)** and Aβ1-42 **(E)** were detected in the RGCL and INL of retinas of 3xTg-AD mice at 8 months only (arrows). No positive signal could be detected in the non-Tg controls or 6 month old 3xTg-AD retinas. Scale bar: 20 μm.

neuronal activity or connectivity or by loss of retinal neurons. At the age of 8 months, morphometric comparison of the thickness of IRL and ONL, and number of RGC in H&E-stained retinal sections (**Supplementary Figure S1**), did not show any significant changes between WT and 3xTg-AD mice. Further immunohistochemical detection and counting of Brn-3a positive

RGCs, PKC-α labeled retinal bipolar cells and GFAP labeled astrocytes and active Müller cells also confirmed that there was no significant change in the cell densities at the age of 8 months (**Supplementary Figure S2**).

Aβ expression in the retinas of 3xTg-AD mice was detected by two amyloid antibodies, anti-Aβ1-42 and anti-Aβ17-24 (4G8) at the ages of 6 and 8 months, when significant functional changes are found in AD retina. No extracelluar Aβ was detected at either time point. Accumulation of intraneuronal Aβ was found in the ganglion cell layer (GCL) and inner nuclear layer (INL) of the retinas of 3xTg-AD mice at 8 months of age (**Figures 1D,E**). Increased Aβ expression was predominately located in the soma of neurons. Aβ staining was not observed in the retinas of age-matched WT control mice.

LBE Feeding Preserved Retinal Function of 3xTg-AD Mice

The 3xTg-AD mice begin to show impairment on the Morris water maze and inhibitory avoidance, coincident with the onset of intracellular Aβ in the brain at age 4 months. Extracellular Aβ is detectable in the cortex at 6 months of age (Billings et al., 2005). The ages at which feeding was started in this study were chosen as the ages when intracellular (4th month) and extracellular (6th month) Aβ become detectable in the brain. Our previous study using the early onset 5xFAD mouse model found that the retinal function in dark conditions (scotopic response) was enhanced by LBE at 20 g/kg oral feeding (Zhang et al., 2021). In the current study of 3xTg-AD mice, lower doses were chosen because less Aβ accumulation was reported in these mice than in the 5xFAD model. The ERG test was performed at 1 or 2 months after feeding started. As shown in **Figures 2A,B**, no significant changes in scotopic or photopic retinal function were induced by LBE feeding when the feeding started at age 4 months. When the feeding started at age 6 months, 1 month of 2 g/kg LBE gavage significantly increased both a-wave and b-wave amplitude in scotopic ERG compared to the no-feeding 3xTg-AD mice. The same tendency of a-wave and b-wave preservation was observed after 2 months of 2 g/kg LBE feeding, but without statistical significance (**Figures 2C,E**). No significant changes in photopic b-wave or PhNR were observed in LBE-fed 3xTg-AD mice (**Figure 2D**). At 8 months of age, morphometric analysis on the neuronal cell number and Müller cell activation also remained unchanged in 3xTg-AD mice with LBE feeding (**Supplementary Figures S1, S2**).

LBE Feeding Decreased RNA Oxidation and Activation of Calpain-2, Calpain-5 in the Retinas of 3xTg-AD Mice

The guanosine oxidation product 8-hydroxyguanosine (8-OHG) is one of the most abundant and best characterized biomarkers for RNA oxidative lesions (Feyzi et al., 2007). The amount of cellular 8-OHG is a sensitive measurement of oxidative stress and is an RNA damage biomarker (Xu et al., 2021). At 8 months of age, there was an obvious trend of increased 8-OHG in the retinas of water-fed 3xTg-AD mice compared to the age matched WT controls (**Figure 3A**, first lane). Comparing with water-fed mice, LBE oral feeding did not change the 8-OHG level in WT mice, while reducing its level in the 3xTg-AD mice, especially with the high dose (2 g/kg) (**Figure 3B**).

With an increase in age, increased oxidative stress and Aβ deposition, the normally tightly controlled calpain activation regulatory system becomes impaired. Increased calpain activation is involved in the pathogenesis of AD (Mahaman et al., 2019). In the retinas of 3xTg-AD mice, the expression of both calpain-2 (**Figure 3A**, second lane) and calpain-5 (**Figure 3A**, third lane) showed a tendency toward increase compared to WT mice at 8 months of age. While there is no effect of LBE feeding comparing with water feeding in the WT mice, LBE feeding at both doses significantly decreased the expression of calpain-2 and calpain-5 in the retinas of 3xTg-AD mice (**Figures 3C,D**).

LBE Feeding Preserved Impaired Pre-synaptic Densities in Retinas of 3xTg-AD Mice

Synaptic loss is a common pathological change in AD patients and Tg-AD models. Both pre- and post-synaptic proteins were detected in the retinas. While there were no obvious changes in the immunoreactivity of a post-synaptic protein marker (PSD-95) (**Figure 4C**), a pre-synaptic protein marker (synaptophysin) was significantly decreased in the retinal inner plexiform layer (IPL) of 8 month old 3xTg-AD mice (**Figure 4A**). The reduced synaptophysin expression level was restored by LBE feeding, with this restoration reaching significant levels at high dose (**Figure 4B**). Pre-synaptic protein expression in the OPL layer showed a similar but non-significant tendency. Furthermore, we explored post-synaptic changes with PSD-95 staining, and no significant changes were observed in 3xTg-AD mice compared with wild type mice (**Figures 4C,D**).

DISCUSSION

Retinal Aβ aggregation has been reported in various AD transgenic mouse models (reviewed by Chiu et al., 2012). In the current study, we used the retina as a window to study early changes in female 3xTg-AD mice. At the 8th month of age, the retinal function detected by flash ERG revealed a significant decrease of scotopic b-wave in the 3xTg-AD mice compared to WT mice. Morphometric analysis showed no significant loss of neurons in the 3xTg-AD retina. Intracellular Aβ, oxidative RNA marker 8-OHG, and calpain-2 and -5 were increased in the retinal neurons in the RGCL and the INL. The pre-synaptic protein, synaptophysin, was significantly decreased in the IPL of 3xTg-AD mice retinas. Oral feeding of LBE (2 g/kg) starting at 6 months of age decreased the activation of calpain-2 and -5 and restored the synaptophysin expression after 2 months of feeding.

As an extension of the central nervous system, the retina is considered a valuable tool for the study of CNS disorders (London et al., 2013). Accumulating evidence has revealed retinal abnormalities in AD patients, including retinal function impairment and structural changes, such as optic nerve damage, loss of ganglion cells, and retinal thinning (Chiquita et al., 2019b). These facts provided support for the idea to use the retina as

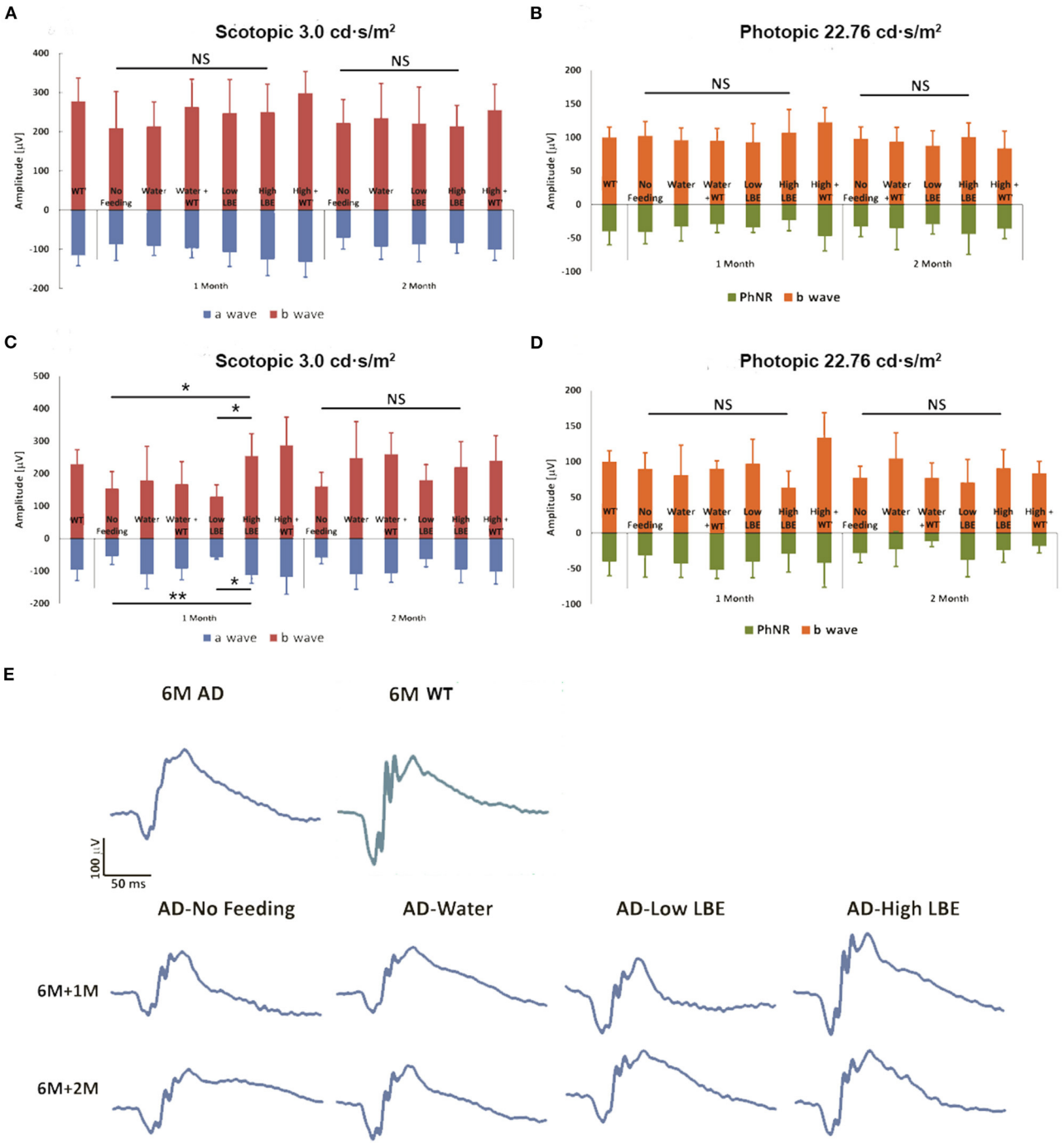

FIGURE 2 | Effect on retinal function of LBE oral feeding started at different ages. LBE feeding started at 4 months or 6 months of age in both non-Tg and 3xTg-AD mice. For two months, two doses [low (200 mg/kg) or high (2 g/kg)] of LBE were given daily, while water served as the control and non-feeding as the age-matched AD control. LBE feeding from age 4 months showed a trend toward better scotopic retinal response for both a-wave and b-wave in 3xTg-AD mice **(A)**. When started at 6 months of age, high dose LBE feeding of 3xTg-AD mice for 1 month showed significantly higher retinal response to scotopic light intensity (3.0 cd·s/m^2) compared to 3xTg-AD mice given only water **(C)**. Photopic b-wave and PhNR, indicating the function of the inner nuclear layer and RGCs, showed no differences among all the groups **(B,D)**. *$p < 0.05$, **$p < 0.01$; NS, no significant change. Typical ERG wave forms of various groups at 1 month and 2 months after the start of feeding **(E)**.

a window into the AD nervous system, to help overcome the difficulty in accessing the brain and the high cost of current modalities, including PET and CSF biomarkers (Liao et al., 2018; Ngolab et al., 2019). More importantly, retinal Aβ plaques tended to show up in the retina prior to brain plaques (Liao et al., 2018). In 3xTg-AD mice, scattered extracellular Aβ deposition in the

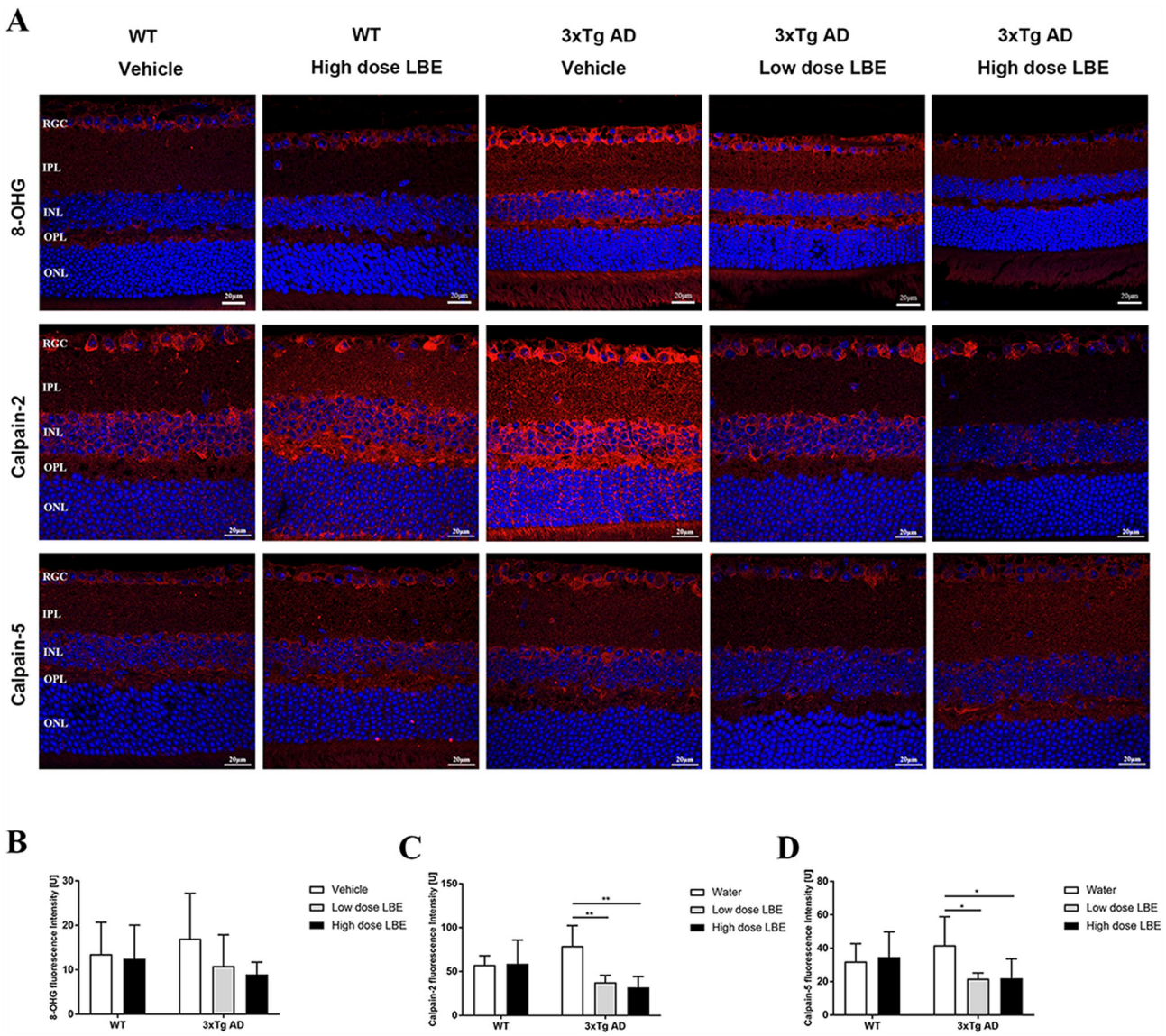

FIGURE 3 | Two months LBE oral feeding downregulated expression of 8-OHG, calpain-2, and calpain-5 in 3xTg-AD mice at the age of 8 months. **(A)** Representative images of 8-OHG, calpain-2, and calpain-5 stained retinal sections of 3xTg-AD mice and age matched non-Tg control mice fed with water, low dose LBE or high dose LBE. Semi-quantification analysis showed increased 8-OHG **(B)**, calpain-2 [**(C)**, * $P < 0.05$; ** $P < 0.01$], and calpain-5 [**(D)**, * $P < 0.05$; **$P < 0.01$] in the retinas of 3xTg-AD mice, which could be suppressed by LBE feeding.

caudal hippocampus existed at the age of 6 months (Belfiore et al., 2019). In this study, intracellular Aβ immunoreactivity (4G8 or Aβ1-42) was detected in the retina at 8 months of age, together with RNA oxidation, calpain activation and reduced synaptophysin expression in the inner retina. These changes might be the reason that significant scotopic retinal function reduction in both a and b wave in the 3xTg-AD mice was detected. Morphometric analysis of the thickness change in the inner and outer retina in H&E retinal sections can be translated to the clinical detection of retinal structure using optical coherence tomography (OCT). Retinal function detected by ERG might be used as an early marker for AD diagnosis. There was no significant change in the retinal thickness using classical histopathology analysis. Moreover, no significant neuronal loss in the retina could be confirmed using immunohistochemical detection of specific cell markers such as Brn-3a and PKC. Loss of synapses in the affected brain regions correlates best with cognitive impairment in AD patients that has been considered as an early mechanism that precedes neuronal loss (Chen et al., 2019). The decrease of retinal function can be explained by the reduction of synaptic protein, especially in the inner retina in the early stage of AD.

A cytoplasmic oxidative RNA nucleoside, 8-OHG, is markedly increased within the hippocampus and temporal neocortex in AD

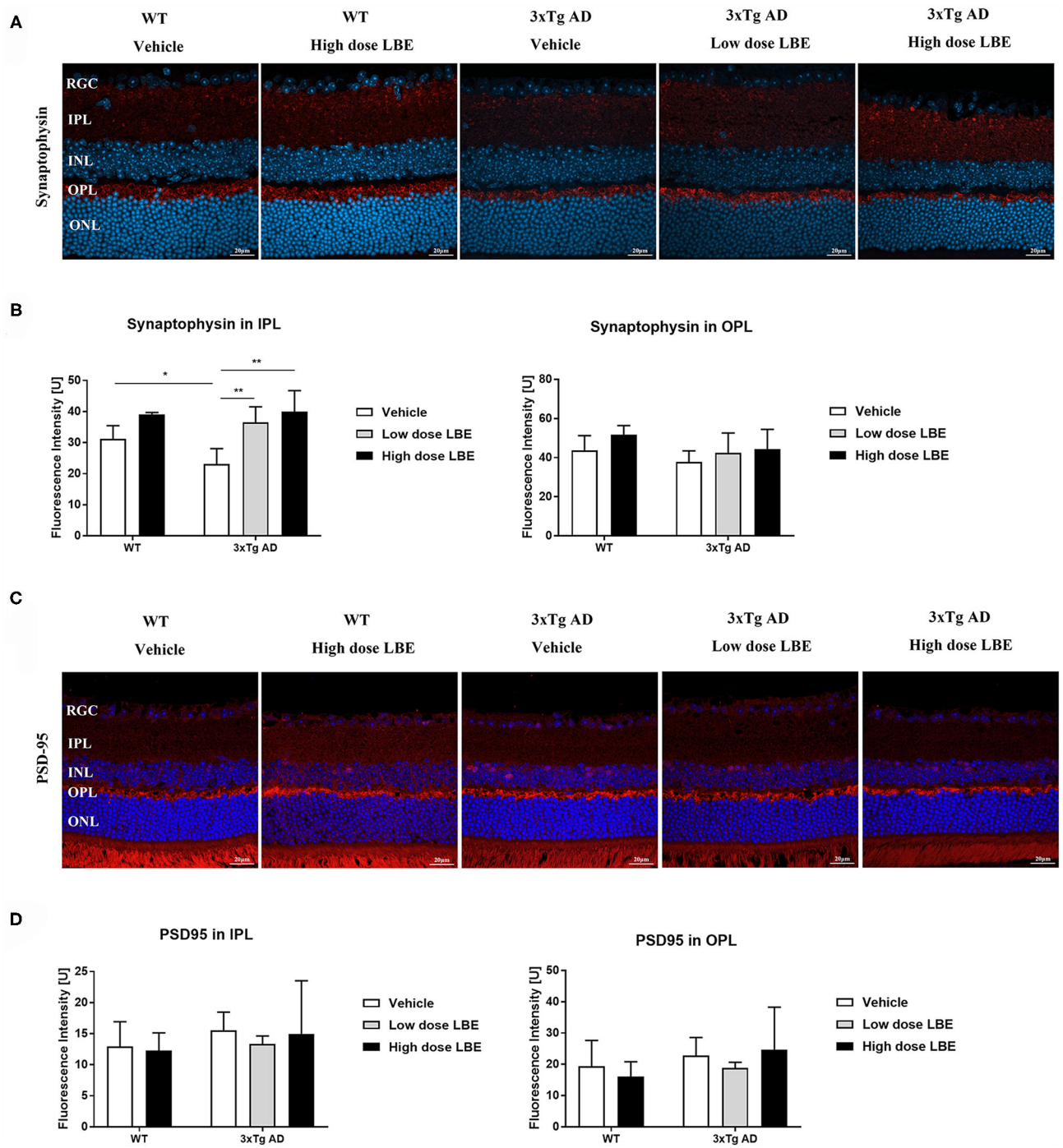

FIGURE 4 | LBE oral feeding significantly preserved presynaptic terminals in 3xTg-AD mice at 8 months of age. **(A)** Representative images of retinal sections stained for the presynaptic marker, synaptophysin, in 8 month old 3xTg-AD mice and age matched non-Tg control mice fed with water, low dose LBE or high dose LBE. Semi-quantification analysis revealed decreased presynaptic densities in the IPL but not the OPL in 8 month old 3xTg-AD mice, and rescue of the decrease by high dose LBE feeding [**(B)**, * $P < 0.05$, ** $p < 0.01$]. Representative images of retinal sections stained for the postsynaptic marker, PSD-95, in 8 month old 3xTg-AD mice and age matched wild type mice fed with water, low dose LBE or high dose LBE **(C)**. No significant changes were observed in postsynaptic densities among all the groups **(D)**.

patients at an early stage of the disease (Nunomura et al., 2009; Nunomura and Perry, 2020). Synaptic dysfunction is closely associated with oxidative stress in AD (Kamat et al., 2016). LBE has been proved to be protective against oxidative damage in various diseases (Gao et al., 2017), and to modulate glial cell function *in vitro* (Zheng et al., 2021). Two months of 2 g/kg

LBE oral feeding starting at 6 months proved the effectiveness of antioxidation and preservation of synaptic function in the retina of 3xTg-AD mice. Although the preserved retinal function can only be significantly detected at the 1 month but not the two-month time point in the LBE-fed 3xTg-AD mice, an increase in animal numbers might reveal a significant effect at 2 months.

In neurodegenerative diseases including AD, abnormal activation of calpains favors Aβ accumulation and tau hyperphosphorylation in neurons and is associated with synaptic dysfunction (Trinchese et al., 2008; Medeiros et al., 2012; Diepenbroek et al., 2014). Upregulated calpain-2 and -5 were detected in the retinas of 8 month-old 3xTg-AD mice. They were down regulated by 2 months of LBE feeding, which also stabilized pre-synaptic protein expression and improved retinal function.

Gliosis is an activation of glial cells in response to central nervous system injury. In the brain tissue of 3xTg-AD mice, increased densities of active astrocytes and microglia were observed at 7 months (Caruso et al., 2013). Activation of astrocytes and Müller cells was also identified in the retinas of 3xTg-AD mice at 8 months of age (Edwards et al., 2014). However, in our study, immunochemical staining of GFAP and Iba-1 did not detect significant changes in astrocytes and microglial cell numbers, respectively, in either the brain or the retina of 8 month old 3xTg-AD mice. These findings may be explained by the fact that neuronal cell damage and extracellular Aβ deposition may be the primary inducers of glial activation in AD, but neither were present in the retinas of the 8 months old 3xTg-AD mice in the current study. Still, a possibility exists that activation of glial cells might have occurred in our mice but may have been too subtle to detect. Oligomeric Aβ induces M1 activation (pro-inflammatory) of the IMG cell line, but pretreatment with LBE shifts the cells to M2 activation (anti-inflammatory) (Sun et al., 2022). Therefore, besides the direct LBE effect on retinal neurons, modulation of retinal glial function cannot be ruled out.

A limitation of this study is that we did not identify which molecular component was responsible for the neuroprotectant activity we examined. However, we used a very simple extraction procedure to make it easy for the general population to use the same method. Therefore, it is possible that, even without pinpointing one chemical for further investigation, this LBE can be quickly and affordably adopted by more patients or even the entire aging population with the ultimate goal of reducing illness and economic burden.

CONCLUSION

Our study demonstrated a protective effect of LBE feeding on synaptic function in the retinas of 3xTg-AD mice. This may be due to the ability of LBE feeding to reduce intracellular RNA oxidation and calpain-2 and -5 hyperactivation, and thus to stabilize synapses. LBE acted through multiple pathways to stabilize retinal function in 3xTg-AD mice. Daily LBE supplementation might be beneficial for neuronal function and survival even during aging in the presence of excess Aβ.

DATA AVAILABILITY STATEMENT

The original contributions presented in the study are included in the article/**Supplementary Material**. Further inquiries can be directed to the corresponding authors.

ETHICS STATEMENT

The animal study was reviewed and approved by Committee on the Use of Live Animals in Teaching and Research of the University of Hong Kong.

AUTHOR CONTRIBUTIONS

KC, KS, and JL: conceptualization. JL, LB, SY, YL, and GX: methodology. JL and GX: data analysis. KC and KS: project administration. JL and LB: writing original draft. KC, LB, and RC: manuscript review and editing. All authors read and approved the final manuscript.

FUNDING

This project was supported by Health and Medical Research Fund (HMRF, Project No: 14151281) and Midstream Research Program for Universities (MRP, Project No: MRP-092-17X) in Hong Kong to KC.

SUPPLEMENTARY MATERIAL

The Supplementary Material for this article can be found online at: https://www.frontiersin.org/articles/10.3389/fnagi.2021.788798/full#supplementary-material

Figure S1 | LBE oral feeding effect on the retinal morphology of 3xTg-AD mice. **(A)** Representative images of H&E-stained retinal sections of 8 month old 3xTg-AD mice and age matched control mice fed with water, low dose LBE or high dose LBE. **(B)** Morphometric analysis revealed no significant changes in the thickness of the IRL or ONL, or in RGC numbers, in LBE-treated mice compared with water-treated 3xTg-AD mice.

Figure S2 | No changes in RGC numbers, retinal bipolar cell numbers, and astrocyte/Müller cell activation were observed in 3xTg-AD mice at 8 months old. **(A)** Representative images of Brn3a, PKC-α, and GFAP stained retinal sections of 8 month old 3xTg-AD mice and age matched wild type mice fed with water, low dose LBE or high dose LBE. **(B)** RGC numbers, retinal bipolar cell numbers, and astrocyte/Müller cell activation showed no significant differences between 3xTg-AD and wild type mice, and between the LBE-treated and water-treated 3xTg-AD mice.

REFERENCES

Belfiore, R., Rodin, A., Ferreira, E., Velazquez, R., Branca, C., Caccamo, A., et al. (2019). Temporal and regional progression of Alzheimer's disease-like pathology in 3xTg-AD mice. *Aging Cell.* 18, e12873. doi: 10.1111/acel.12873

Billings, L. M., Oddo, S., Green, K. N., Mcgaugh, J. L., and Laferla, F. M. (2005). Intraneuronal Abeta causes the onset of early Alzheimer's disease-related cognitive deficits in transgenic mice. *Neuron.* 45, 675–688. doi: 10.1016/j.neuron.2005.01.040

Caruso, D., Barron, A. M., Brown, M. A., Abbiati, F., Carrero, P., Pike, C. J., et al. (2013). Age-related changes in neuroactive steroid levels in 3xTg-AD mice. *Neurobiol Aging.* 34, 1080–1089. doi: 10.1016/j.neurobiolaging.2012.10.007

Chan, T. F., Chiu, K., Lok, C. K., Lau, H. W., So, K. F., and Chang, R. C. (2012). Morphometric analyses of retinal sections. *J Vis Exp*. 3377. doi: 10.3791/3377

Chang, R. C., Suen, K. C., Ma, C. H., Elyaman, W., Ng, H. K., and Hugon, J. (2002). Involvement of double-stranded RNA-dependent protein kinase and phosphorylation of eukaryotic initiation factor-2alpha in neuronal degeneration. *J. Neurochem.* 83, 1215–1225. doi: 10.1046/j.1471-4159.2002.01237.x

Chen, Y., Fu, A. K. Y., and Ip, N. Y. (2019). Synaptic dysfunction in Alzheimer's disease: Mechanisms and therapeutic strategies. *Pharmacol. Ther.* 195, 186–198. doi: 10.1016/j.pharmthera.2018.11.006

Chidlow, G., Wood, J. P., Manavis, J., Finnie, J., and Casson, R. J. (2017). Investigations into retinal pathology in the early stages of a mouse model of alzheimer's disease. *J. Alzheimers Dis.* 56, 655–675. doi: 10.3233/JAD-160823

Chiquita, S., Campos, E. J., Castelhano, J., Ribeiro, M., Sereno, J., Moreira, P. I., et al. (2019a). Retinal thinning of inner sub-layers is associated with cortical atrophy in a mouse model of Alzheimer's disease: a longitudinal multimodal in vivo study. *Alzheimers Res. Ther.* 11, 90. doi: 10.1186/s13195-019-0542-8

Chiquita, S., Rodrigues-Neves, A. C., Baptista, F. I., Carecho, R., Moreira, P. I., Castelo-Branco, M., et al. (2019b). The Retina as a Window or Mirror of the Brain Changes Detected in Alzheimer's Disease: Critical Aspects to Unravel. *Mol. Neurobiol.* 56, 5416–5435. doi: 10.1007/s12035-018-1461-6

Chiu, K., Chan, H. C., Yeung, S. C., Yuen, W. H., Zee, S. Y., Chang, R. C., et al. (2009). Modulation of microglia by Wolfberry on the survival of retinal ganglion cells in a rat ocular hypertension model. *J. Ocul. Biol. Dis. Infor.* 2, 47–56. doi: 10.1007/s12177-009-9023-9

Chiu, K., Chan, T. F., Wu, A., Leung, I. Y., So, K. F., and Chang, R. C. (2012). Neurodegeneration of the retina in mouse models of Alzheimer's disease: what can we learn from the retina? *Age (Dordr).* 34, 633–649. doi: 10.1007/s11357-011-9260-2

Clinton, L. K., Billings, L. M., Green, K. N., Caccamo, A., Ngo, J., Oddo, S., et al. (2007). Age-dependent sexual dimorphism in cognition and stress response in the 3xTg-AD mice. *Neurobiol. Dis.* 28, 76–82. doi: 10.1016/j.nbd.2007.06.013

Diepenbroek, M., Casadei, N., Esmer, H., Saido, T. C., Takano, J., Kahle, P. J., et al. (2014). Overexpression of the calpain-specific inhibitor calpastatin reduces human alpha-Synuclein processing, aggregation and synaptic impairment in [A30P]αSyn transgenic mice. *Hum. Mol. Genet.* 23, 3975–3989. doi: 10.1093/hmg/ddu112

Edwards, M. M., Rodríguez, J. J., Gutierrez-Lanza, R., Yates, J., Verkhratsky, A., and Lutty, G. A. (2014). Retinal macroglia changes in a triple transgenic mouse model of Alzheimer's disease. *Exp. Eye. Res.* 127, 252–260. doi: 10.1016/j.exer.2014.08.006

Feyzi, E., Sundheim, O., Westbye, M. P., Aas, P. A., Vågb,ø, C. B., Otterlei, M., et al. (2007). RNA base damage and repair. *Curr. Pharm. Biotechnol.* 8, 326–331. doi: 10.2174/138920107783018363

Fisher, D. W., Bennett, D. A., and Dong, H. (2018). Sexual dimorphism in predisposition to Alzheimer's disease. *Neurobiol Aging* 70, 308–324. doi: 10.1016/j.neurobiolaging.2018.04.004

Gao, Y., Wei, Y., Wang, Y., Gao, F., and Chen, Z. (2017). Lycium Barbarum: A Traditional Chinese Herb and A Promising Anti-Aging Agent. *Aging Dis.* 8, 778–791. doi: 10.14336/AD.2017.0725

Hart, N. J., Koronyo, Y., Black, K. L., and Koronyo-Hamaoui, M. (2016). Ocular indicators of Alzheimer's: exploring disease in the retina. *Acta. Neuropathol.* 132, 767–787. doi: 10.1007/s00401-016-1613-6

Jackson, J., Jambrina, E., Li, J., Marston, H., Menzies, F., Phillips, K., et al. (2019). Targeting the Synapse in Alzheimer's Disease. *Front. Neurosci.* 13, 735. doi: 10.3389/fnins.2019.00735

Kamat, P. K., Kalani, A., Rai, S., Swarnkar, S., Tota, S., Nath, C., et al. (2016). Mechanism of Oxidative Stress and Synapse Dysfunction in the Pathogenesis of Alzheimer's Disease: Understanding the Therapeutics Strategies. *Mol. Neurobiol.* 53, 648–661. doi: 10.1007/s12035-014-9053-6

Lee, M. S., Kwon, Y. T., Li, M., Peng, J., Friedlander, R. M., and Tsai, L. H. (2000). Neurotoxicity induces cleavage of p35 to p25 by calpain. *Nature.* 405, 360–364. doi: 10.1038/35012636

Liao, H., Zhu, Z., and Peng, Y. (2018). Potential Utility of Retinal Imaging for Alzheimer's Disease: A Review. *Front. Aging Neurosci.* 10, 188. doi: 10.3389/fnagi.2018.00188

London, A., Benhar, I., and Schwartz, M. (2013). The retina as a window to the brain-from eye research to CNS disorders. *Nat. Rev. Neurol.* 9, 44–53. doi: 10.1038/nrneurol.2012.227

Mahaman, Y., a,.R., Huang, F., Kessete Afewerky, H., Maibouge, T. M. S., Ghose, B., et al. (2019). Involvement of calpain in the neuropathogenesis of Alzheimer's disease. *Med. Res. Rev.* 39, 608–630. doi: 10.1002/med.21534

Manthey, A. L., Chiu, K., and So, K. F. (2017). Effects of Lycium barbarum on the Visual System. *Int. Rev. Neurobiol.* 135, 1–27. doi: 10.1016/bs.irn.2017.02.002

Medeiros, R., Kitazawa, M., Chabrier, M. A., Cheng, D., Baglietto-Vargas, D., Kling, A., et al. (2012). Calpain inhibitor A-705253 mitigates Alzheimer's disease-like pathology and cognitive decline in aged 3xTgAD mice. *Am. J. Pathol.* 181, 616–625. doi: 10.1016/j.ajpath.2012.04.020

Ngolab, J., Honma, P., and Rissman, R. A. (2019). Reflections on the Utility of the Retina as a Biomarker for Alzheimer's Disease: A Literature Review. *Neurol. Ther.* 8, 57–72. doi: 10.1007/s40120-019-00173-4

Nunomura, A., Chiba, S., Lippa, C. F., Cras, P., Kalaria, R. N., Takeda, A., et al. (2004). Neuronal RNA oxidation is a prominent feature of familial Alzheimer's disease. *Neurobiol. Dis.* 17, 108–113. doi: 10.1016/j.nbd.2004.06.003

Nunomura, A., Hofer, T., Moreira, P. I., Castellani, R. J., Smith, M. A., and Perry, G. (2009). RNA oxidation in Alzheimer disease and related neurodegenerative disorders. *Acta. Neuropathol.* 118, 151–166. doi: 10.1007/s00401-009-0508-1

Nunomura, A., and Perry, G. (2020). RNA and Oxidative Stress in Alzheimer's Disease: Focus on microRNAs. *Oxid. Med. Cell. Longev.* 2020, 2638130. doi: 10.1155/2020/2638130

Oddo, S., Caccamo, A., Shepherd, J. D., Murphy, M. P., Golde, T. E., Kayed, R., et al. (2003). Triple-transgenic model of Alzheimer's disease with plaques and tangles: intracellular Abeta and synaptic dysfunction. *Neuron.* 39, 409–421. doi: 10.1016/S0896-6273(03)00434-3

Patton, N., Aslam, T., Macgillivray, T., Pattie, A., Deary, I. J., and Dhillon, B. (2005). Retinal vascular image analysis as a potential screening tool for cerebrovascular disease: a rationale based on homology between cerebral and retinal microvasculatures. *J. Anat.* 206, 319–348. doi: 10.1111/j.1469-7580.2005.00395.x

Selkoe, D. J. (2002). Alzheimer's disease is a synaptic failure. *Science.* 298, 789–791. doi: 10.1126/science.1074069

Shah, T. M., Gupta, S. M., Chatterjee, P., Campbell, M., and Martins, R. N. (2017). Beta-amyloid sequelae in the eye: a critical review on its diagnostic significance and clinical relevance in Alzheimer's disease. *Mol. Psychiatry.* 22, 353–363. doi: 10.1038/mp.2016.251

Suen, K. C., Yu, M. S., So, K. F., Chang, R. C., and Hugon, J. (2003). Upstream signaling pathways leading to the activation of double-stranded RNA-dependent serine/threonine protein kinase in beta-amyloid peptide neurotoxicity. *J. Biol. Chem.* 278, 49819–49827. doi: 10.1074/jbc.M306503200

Sun, Z. Q., Liu, J. F., Luo, W., Wong, C. H., So, K. F., Hu, Y., et al. (2022). Lycium barbarum extract promotes M2 polarization and reduces oligomeric amyloid-β-induced inflammatory reactions in microglial cells. *Neural. Regen. Res.* 17, 203–209. doi: 10.4103/1673-5374.314325

Trinchese, F., Fa, M., Liu, S., Zhang, H., Hidalgo, A., Schmidt, S. D., et al. (2008). Inhibition of calpains improves memory and synaptic transmission in a mouse model of Alzheimer disease. *J Clin. Invest.* 118, 2796–2807. doi: 10.1172/JCI34254

Van Wijngaarden, P., Hadoux, X., Alwan, M., Keel, S., and Dirani, M. (2017). Emerging ocular biomarkers of Alzheimer disease. *Clin. Exp. Ophthalmol.* 45, 54–61. doi: 10.1111/ceo.12872

Wong, W. (2020). Economic burden of Alzheimer disease and managed care considerations. *Am J. Manag. Care.* 26, S177–S183. doi: 10.37765/ajmc.2020.88482

World Health Organization. (2021). *"Dementia Fact sheet."* Available online at: https://www.who.int/news-room/fact-sheets/detail/dementia (accessed *September* 2, 2021).

Xu, Z., Huang, J., Gao, M., Guo, G., Zeng, S., Chen, X., et al. (2021). Current perspectives on the clinical implications of oxidative RNA damage in aging research: challenges and opportunities. *Geroscience.* 43, 487–505. doi: 10.1007/s11357-020-00209-w

Yu, M. S., Ho, Y. S., So, K. F., Yuen, W. H., and Chang, R. C. (2006). Cytoprotective effects of Lycium barbarum against reducing stress on endoplasmic reticulum. *Int. J. Mol. Med.* 17, 1157–1161. doi: 10.3892/ijmm.17.6.1157

Yu, M. S., Leung, S. K., Lai, S. W., Che, C. M., Zee, S. Y., So, K. F., et al. (2005). Neuroprotective effects of anti-aging oriental medicine Lycium barbarum against beta-amyloid peptide neurotoxicity. *Exp. Gerontol.* 40, 716–727. doi: 10.1016/j.exger.2005.06.010

Zhang, M., Zhong, L., Han, X., Xiong, G., Xu, D., Zhang, S., et al. (2021). Brain and retinal abnormalities in the 5xFAD mouse model of Alzheimer's disease at early stages. *Front. Neurosci.* 15, 681831. doi: 10.3389/fnins.2021.681831

Zhang, Q., Du, X., Xu, Y., Dang, L., Xiang, L., and Zhang, J. (2013). The effects of Gouqi extracts on Morris maze learning in the APP/PS1 double transgenic mouse model of Alzheimer's disease. *Exp. Ther. Med.* 5, 1528–1530. doi: 10.3892/etm.2013.1006

Zheng, C. W., Zhu, R., Sun, Z. Q., Liu, J. F., So, K. F., and Chiu, K. (2021). The effect of Goji with different origins or different extraction methods on primary mixed glial cells. *Chinese Sci. Bulletin.* 66, 1323. doi: 10.1360/TB-2020-1323

Zhou, Y., Duan, Y., Huang, S., Zhou, X., Zhou, L., Hu, T., et al. (2020). Polysaccharides from Lycium barbarum ameliorate amyloid pathology and cognitive functions in APP/PS1 transgenic mice. *Int. J. Biol. Macromol.* 144, 1004–1012. doi: 10.1016/j.ijbiomac.2019.09.177

Conflict of Interest: The authors declare that the research was conducted in the absence of any commercial or financial relationships that could be construed as a potential conflict of interest.

Publisher's Note: All claims expressed in this article are solely those of the authors and do not necessarily represent those of their affiliated organizations, or those of the publisher, the editors and the reviewers. Any product that may be evaluated in this article, or claim that may be made by its manufacturer, is not guaranteed or endorsed by the publisher.

Copyright © 2022 Liu, Baum, Yu, Lin, Xiong, Chang, So and Chiu. This is an open-access article distributed under the terms of the Creative Commons Attribution License (CC BY). The use, distribution or reproduction in other forums is permitted, provided the original author(s) and the copyright owner(s) are credited and that the original publication in this journal is cited, in accordance with accepted academic practice. No use, distribution or reproduction is permitted which does not comply with these terms.

frontiers in Molecular Neuroscience

ORIGINAL RESEARCH
published: 14 January 2022
doi: 10.3389/fnmol.2021.751570

Netrin-1 Ameliorates Postoperative Delirium-Like Behavior in Aged Mice by Suppressing Neuroinflammation and Restoring Impaired Blood-Brain Barrier Permeability

*Ke Li†, Jiayu Wang†, Lei Chen, Meimei Guo, Ying Zhou, Xiaofeng Li and Mian Peng**

Department of Anesthesiology, Zhongnan Hospital of Wuhan University, Wuhan, China

OPEN ACCESS

Edited by:
Jiehui Jiang,
Shanghai University, China

Reviewed by:
Gabriela Hurtado-Alvarado,
Universidad Nacional Autónoma de México, Mexico
Alessandro Ieraci,
University of Milan, Italy
Jiao Wang,
Shanghai University, China

***Correspondence:**
Mian Peng
mianpeng@whu.edu.cn

† These authors have contributed equally to this work and share first authorship

Specialty section:
This article was submitted to Brain Disease Mechanisms, a section of the journal Frontiers in Molecular Neuroscience

Received: *01 August 2021*
Accepted: *20 December 2021*
Published: *14 January 2022*

Citation:
Li K, Wang J, Chen L, Guo M, Zhou Y, Li X and Peng M (2022) Netrin-1 Ameliorates Postoperative Delirium-Like Behavior in Aged Mice by Suppressing Neuroinflammation and Restoring Impaired Blood-Brain Barrier Permeability. Front. Mol. Neurosci. 14:751570. doi: 10.3389/fnmol.2021.751570

Postoperative delirium (POD) is a common and serious postoperative complication in elderly patients, and its underlying mechanism is elusive and without effective therapy at present. In recent years, the neuroinflammatory hypothesis has been developed in the pathogenesis of POD, in which the damaged blood-brain barrier (BBB) plays an important role. Netrin-1 (NTN-1), an axonal guidance molecule, has been reported to have strong inflammatory regulatory and neuroprotective effects. We applied NTN-1 (45 μg/kg) to aged mice using a POD model with a simple laparotomy to assess their systemic inflammation and neuroinflammation by detecting interleukin-6 (IL-6), interleukin-10 (IL-10), and high mobility group box chromosomal protein-1 (HMGB-1) levels. We also assessed the reactive states of microglia and the permeability of the BBB by detecting cell junction proteins and the leakage of dextran. We found that a single dose of NTN-1 prophylaxis decreased the expression of IL-6 and HMGB-1 and upregulated the expression of IL-10 in the peripheral blood, hippocampus, and prefrontal cortex. Nerin-1 reduced the activation of microglial cells in the hippocampus and prefrontal cortex and improved POD-like behavior. NTN-1 also attenuated the anesthesia/surgery-induced increase in BBB permeability by upregulating the expression of tight junction-associated proteins such as ZO-1, claudin-5, and occludin. These findings confirm the anti-inflammatory and BBB protective effects of NTN-1 in an inflammatory environment *in vivo* and provide better insights into the pathophysiology and potential treatment of POD.

Keywords: postoperative delirium (POD), neuroinflammation, blood brain barrier, microglia cell, Netrin-1

INTRODUCTION

Postoperative delirium (POD) is a state of acute cerebral dysfunction characterized by fluctuating and concurrent disturbances of attention, cognition, sleep-wake rhythm, and consciousness level (Auerbach et al., 2018). It is a common complication occurring mainly within 1 week of surgery and anesthesia (Aldecoa et al., 2017). POD may lead to longer hospital stays, higher hospitalization costs, reduced life independence, increased morbidity and mortality, and long-term cognitive

dysfunction, even dementia (Whitlock et al., 2011; Androsova et al., 2015). Advanced age is an independent risk factor for the incidence of POD (Marcantonio, 2011; Aldecoa et al., 2017). With the increasing aging of the global population, the number of elderly people who need surgical treatment has been growing, as has the occurrence rate of POD. Unfortunately, there are no effective treatments for this complication because of the undefined underlying pathophysiology.

In recent years, an increasing number of studies have shown that the incidence of POD is closely related to neuroinflammation (Whitlock et al., 2011; Maldonado, 2013; Vacas et al., 2013). Aseptic surgical trauma causes a homeostatic inflammatory response in the nervous system with harmful consequences when this response is dysregulated. Surgery can lead to an elevated level of pro-inflammatory cytokines in the systemic circulation, such as interleukin-6 (IL-6) and tumor necrosis factor αnfTNF-NF (Vacas et al., 2013), which are closely associated with the neuroinflammatory cascade that accompanies brain BOLD barrier failure (Rochfort and Cummins, 2015). In this case, pro-inflammatory cytokines and monocyte-derived macrophages enter, leading to the activation of glial cells, including microglia and astrocytes (Terrando et al., 2011; Hu et al., 2018). This process is mainly influenced by bone marrow-derived macrophages (BMDMs), enabling microglia/macrophages to play a two-tier role in the microenvironment of brain injury and repair (Prinz and Priller, 2014; Xiong et al., 2016). The interaction of peripheral immunity with the brain caused by systemic inflammation amplifies the inflammatory response of the central nervous system (CNS) (Matsuda et al., 2019), while the cascade of neuroinflammation leads to synaptic dysfunction and neuronal apoptosis and eventually impairs cognitive function (Girard et al., 2013; Vacas et al., 2013).

At present, possible mechanisms for the transmission of peripheral inflammatory signals to the CNS have been confirmed. First, inflammatory cytokines or macrophages derived from monocytes in peripheral blood passively diffuse into the brain through the damaged blood-brain barrier (BBB) (Terrando et al., 2011). Second, inflammatory factors enter the brain through the damaged BBB via vector-mediated active transport. Third, peripheral inflammatory signals act on the afferent branch of the vagus nerve and activate microglia in the brain to activate the inflammatory response (Cortese and Burger, 2017). In summary, changes in BBB structure and function play a very important role in this process. Yang et al. studied the effect of anesthesia and surgery on BBB permeability using the POD model previously established by our research group. The results showed that exploratory laparotomy in mice under isoflurane inhalation anesthesia caused damage to the BBB and increased permeability of the BBB to 10-kDa dextran (Yang et al., 2017), suggesting that the occurrence of POD in mice may be related to the increased permeability of the BBB due to damage. These findings suggest that POD may be associated with peripheral and neuroinflammation, BBB structural damage, and increased permeability.

Advances in the mechanisms underlying the resolution of acute inflammation have identified a new genus of pro-resolving lipid mediators called "specialized pro-resolving mediators" (SPMs) (Serhan, 2014), which can be increased *in vivo* by Netrin-1 (NTN-1) during acute self-limited inflammation (Dalli and Serhan, 2018). NTN-1 is an axonal guidance molecule involved in physiological and pathological processes such as apoptosis, inflammation, and neurogenesis in the nervous system, as well as in the lungs, heart, and kidneys. In recent years, NTN-1 has been shown to play an active regulatory role in the inflammatory process (Tang et al., 2016). It has also been demonstrated that NTN-1 can limit inflammatory response by participating in inflammatory cascades (Ly et al., 2005). In addition, NTN-1 is considered a survival factor for endothelial cells and can induce neovascularization and vascular remodeling. Overexpression of NTN-1 promotes angiogenesis and improves long-term neurological functions after ischemic stroke. Recent studies have indicated that NTN-1 retains BBB integrity in models of traumatic brain injury and experimental autoimmune encephalomyelitis (Podjaski et al., 2015; Xie et al., 2017). However, there are no reports of the role of NTN-1 in POD.

Based on these discoveries, we proposed the hypothesis that pretreatment with NTN-1 could improve the POD-like behavior of aged mice through its anti-inflammatory effect on the inflammation induced by surgical trauma. To validate this hypothesis, we assessed the effects of NTN-1 on the postoperative behavior of aged mice and inflammatory events in both the periphery nervous system and CNS. In addition, we aimed to determine whether NTN-1 prevents peripheral inflammatory factors from entering the brain by protecting the tightness of the BBB, which plays an important role in preventing peripheral inflammation from metastasizing to the CNS.

MATERIALS AND METHODS

Animals

All procedures were approved by the Animal Ethics Committee of Zhongnan Hospital of Wuhan University, Hubei, China, and all experiments were performed in accordance with the National Institutes of Health Guidelines for the Care and Use of Laboratory Animals. Efforts were made to minimize the number of animals used. C57BL/6J female mice (18 months old, weighing 30–40 g) were purchased from Changsha Tianqin Biotechnology Co. Ltd., Changsha, China. All animals were group-housed at five per cage with free access to food and water. The temperature, humidity, and day-night cycle were maintained according to the standards established by the experimental animal laboratory at Zhongnan Hospital of Wuhan University. The mice were allowed 1 week to acclimatize to the laboratory environment before the experiment.

Experimental Protocol

The mice were randomly divided into four groups: control group, surgery group, surgery + NTN-1 group, and NTN-1 group. NTN-1 group (R&D Systems, 6419-N1-025) was given at 45 μg/kg in phosphate-buffered saline (PBS) and administered through the tail vein with a total volume of 200 μl at 1 h after surgery, while an equal volume of PBS was given in the control group and surgery group. The dose of NTN-1 was based on studies using a subarachnoid hemorrhage model of

acute inflammation with slight modification (Xie et al., 2017). A separate cohort of mice was used for the behavior test experiments, and four cohorts are displayed on the timeline as shown in **Figure 1**.

Postoperative Delirium Mouse Model

A simple laparotomy was performed under isoflurane anesthesia using the methods described in our previous studies (Lu et al., 2020). Specifically, anesthesia was induced and maintained with 1.4% isoflurane in 100% oxygen in a transparent acrylic chamber. After 15 min of induction, the mouse was removed from the chamber and placed on a heating pad to maintain a temperature between 36 and 37°C during the procedure. Isoflurane anesthesia was maintained *via* a cone device. One 16-gauge needle was inserted into the cone near the nose of the mouse to monitor the concentration of isoflurane. A longitudinal midline incision was made from the xiphoid to the 0.5-cm proximal pubic symphysis on the skin, abdominal muscles, and peritoneum. Then, the incision was sutured layer by layer with 5-0 Vicryl thread. At the end of the procedure, EMLA cream (2.5% lidocaine and 2.5% prilocaine) was applied to the incision wound and then repeated every 8 h for 1 day to treat the pain associated with the incision. The procedure lasted approximately 10 min for each mouse, and the mouse was then put back into the anesthesia chamber for up to 2 h to receive the rest of the anesthesia, consisting of 1.4% isoflurane in 100% oxygen. After recovering from the anesthesia, each mouse was returned to a home cage with available food and water. The mice in the control group and the NTN-1 group were placed in their home cages with 100% oxygen for 2 h without surgery.

Behavioral Tests

Behavioral changes were detected using a battery of behavioral tests, including buried food tests, open-field tests, and Y-maze tests, 24 h before (baseline) surgery/anesthesia and at 6, 9, and 24 h, as described in our previous study (Peng et al., 2016). Within each group, separate cohorts were subjected to an assessment of behavior at each time point (n = 10 per cohort). In all tests, the apparatus was cleaned with 75% alcohol after each mouse to remove odors.

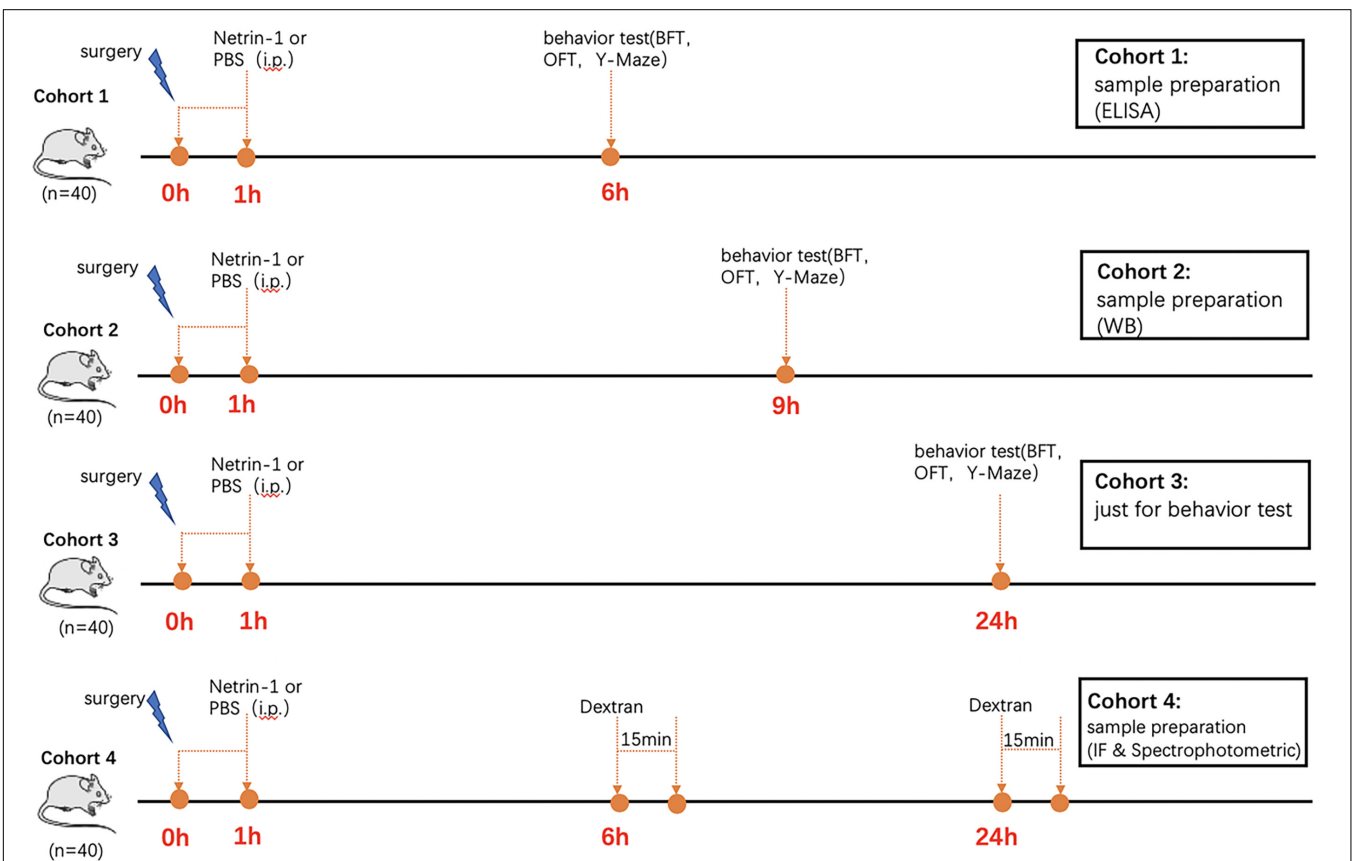

FIGURE 1 | Experimental timeline. The mice were administered Netrin-1 (45 μg/kg) or vehicle control (sterile PBS) at 1 h after surgery (Day 0). The mice in Cohort 1 were used to detect behavior 6 h after surgery. Once the behavior test was completed, they were sacrificed immediately for immunofluorescence and ELISA. The mice in Cohort 2 were used to detect behavior at 9 h after surgery. Once the behavior test was completed, they were sacrificed immediately for WB. The mice in Cohort 3 were used to detect behavior 24 h after surgery. Twenty mice in Cohort 4 were injected intravenously with 100 μl 10-kDa dextran at 6 h after surgery. Fifteen minutes after injection, each mouse was prepared for immunofluorescence. Another 20 mice in Cohort 4 were injected intravenously with 100 μl 10-kDa dextran at 24 h after surgery. Fifteen minutes after injection, each mouse was prepared for spectrophotometric quantification of 10-kDa dextran.

Buried Food Test

The buried food test was carried out as described in previous studies (Zhang et al., 2018; Lu et al., 2020) with modifications. Specifically, 2 days before the buried food test, each mouse received two pieces of sweetened cereal. On the test days, we had each mouse acclimatize for 1 h by placing the home cage with mice in the testing room. The test cage was prepared with clean padding 3 cm high in which we buried one piece of sweetened cereal below the padding. Its location was freely chosen, and it was not visible. We placed the mouse in the center of the cage and measured the latency of eating the food. The latency was defined as the time beginning when the mouse was placed in the cage and ending when the mouse uncovered the food and grasped it with its forepaws and/or teeth, which was used as a measure of organized thinking and attention. When mice found the food pellet within 5 min, they were allowed to eat the food and then were returned to their home cage. If they failed to find the pellet within 5 min, they would be retrieved and the latency was recorded as 300 s.

Open-Field Test

The open-field test was adapted from previous studies (Peng et al., 2016; Meng et al., 2019) with modifications. Each mouse was placed in the center of an open field chamber (40 cm × 40 cm × 40 cm) under dim light and was allowed to move freely for 5 min. The activities were automatically recorded by a video camera connected to Any-Maze animal tracking system software (Xinruan Information Technology Co. Ltd., Shanghai, China), and movement parameters were calculated by the software. The total distance moved (m), time (s) spent in the center of the open field, freezing time (s), and latency (the time in seconds for the mice to reach the location at the first attempt) to the center of the open-field were recorded and analyzed.

Y-Maze Test

Mice underwent testing in the Y-maze test to assess spatial learning and memory ability following surgery/anesthesia (Chen et al., 2014; Wolf et al., 2016). Specifically, the Y-maze was placed in a quiet and illuminated room and consisted of three arms (8 cm × 30 cm × 15 cm) with an angle of 120° between each arm. The three arms included the start arm, in which the mouse started to explore (always open); the novel arm, which was blocked at the first trial but opened at the second trial; and the other arm (always open). The start arm and other arm were designed randomly to avoid spatial memory error. The Y-maze test consisted of two trials separated by an intertrial interval (ITI). The first trial (training) lasted 10 min and allowed the mouse to explore the start arm and the other arm. After 2 h (for the studies 6 and 24 h after the surgery) or 4 h (for the study 9 h after surgery) of ITI, the second trial was conducted. For the second trial, the mouse was placed back in the maze in the same start arm with free access to all arms for 5 min. A video camera, which was linked to the Any-Maze animal tracking system software, was installed 60 cm above the chamber to monitor and analyze the number of entries and time spent in each arm. The time spent in and entries into the novel arms indicated the spatial recognition memory (learned behavior).

Enzyme-Linked Immunosorbent Assay

The mouse IL-6 Enzyme-Linked Immunosorbent Assay (ELISA) kit (ELK Biotechnology, ELK1157), mouse IL-10 ELISA kit (ELK Biotechnology, ELK1143), mouse HMGB-1 ELISA kit (ELK Biotechnology, ELK1440), and mouse NTN-1 ELISA kit (CUSABIO, CSB-EL016127MO) were used to evaluate peripheral or central inflammation and the levels of NTN-1 in the brain tissue at 6 h postoperatively.

Western Blot Analysis

The hippocampus and prefrontal cortex of the mice were harvested 9 h after surgery. Anti-ZO-1 (1:500, Abcam, ab96587), anti-occludin (1:2,000, Abcam, ab167161), and anti-claudin-5 (1:500, Biorbyt, orb214680) antibodies were used to detect the expression of tight junction (TJ)-associated proteins in the hippocampus and prefrontal cortex. Anti-β-actin (1:10,000, TDY Biotech, ab37168) was used to normalize and control for loading differences in protein levels. The bands were measured using image analysis software (AlphaEaseFC software), and changes in protein levels were presented as folds of those in the control group.

Blood-Brain Barrier Permeability Assay

Dextran was used to measure BBB permeability as described in previous studies with modifications (Kutuzov et al., 2018; Bernstein et al., 2020). Specifically, 6 h after surgery, each mouse was injected intravenously with 100 μl 10-kDa dextran Texas Red lysine fixable (4 mg/ml, Invitrogen, D1863). Fifteen minutes after injection, each mouse was anesthetized with 1.4% isoflurane and decapitated. Brain tissue was harvested and fixed with 4% paraformaldehyde overnight at 4°C, cryopreserved in 30% sucrose, and frozen in TissueTek OCT (Sakura). Frozen sections measuring 20 μm were collected and postfixed in 4% PFA at room temperature (20–25°C) for 15 min, washed in PBS and blocked with 10% goat serum (Boster Biologic Technology, China) for 2 h, then permeabilized with 0.5% Triton X-100 and incubated with isolectin B4 (20 μg/ml, I21411, Molecular Probes, San Francisco, CA, United States) for immunostaining to visualize the blood vessels. A Zeiss LSM 510 META microscope was used to detect the fluorescence images of the injected tracer and isolectin under a 40 × objective lens. For each mouse, 20 images of 10 different slices of the hippocampus and prefrontal cortex were randomly selected, and the level of dextran found outside the vessels was analyzed using ImageJ (NIH).

Spectrophotometric quantification of 10-kDa dextran Texas Red from extracts of the hippocampus and prefrontal cortex was carried out at 24 h after surgery. Specifically, each mouse was injected intravenously with 100 μl 10-kDa dextran Texas Red lysine fixable (4 mg/ml, Invitrogen, D1863) 24 h postoperatively. Fifteen minutes after injection, each mouse was deeply anesthetized and perfused with transcranial PBS (150 ml for 5 min). Then, the mice were decapitated, and the hippocampus and prefrontal cortex were harvested. Then, we used 1% Triton X-100 in PBS to homogenize the brain tissue (100 μl/100 mg brain

tissue). The tissue lysates were centrifuged at 16,000 rpm for 20 min, and the fluorescence of the supernatant was measured on a POLAR star Omega fluorometer (BMG Labtech) (ex/em 595/615 nm).

Immunofluorescence

Twenty-four hours after surgery, each mouse was anesthetized with 1.4% isoflurane and perfused transcranially with ice-cold 0.1 M PBS followed by 4% PFA in 0.1 M PBS at pH 7.4. The brains were harvested and fixed in 4% PFA in 0.1 M PBS at 4°C, cryoprotected in 30% sucrose for 72 h, frozen in TissueTek OCT (Sakura), and cut sequentially to 20 μm. After washing in PBS and permeabilization in 0.5% Triton X-100, the sections were blocked with 10% goat serum for 2 h at room temperature to block non-specific binding and washed again in PBS. Then, the sections were incubated with rabbit anti-Iba-1 primary antibody (1:200, Abcam, ab178847) at 4°C overnight. After washing, the sections were incubated with secondary antibody (goat anti-rabbit) conjugated with Alexa Fluor dye 488 from Invitrogen (1:500) at room temperature for 2 h in the dark. Immunolabeled sections were coverslipped with 40,6-diamidino-2-phenylindole (DAPI; Invitrogen) and analyzed using a microscope (Olympus, Tokyo, Japan) equipped with an imaging system. Five high magnifications were chosen in three non-overlapping fields randomly acquired in the hippocampus and prefrontal cortex subregions using a counting frame size of 0.4 mm^2. The images were processed, and the area of the microglia was quantified using ImageJ software (NIH). The area of the selected cells was converted into immunoreactivity, which was calculated as the percentage area density, defined as the number of pixels (positively stained area) divided by the total number of pixels (sum of positively and negatively stained areas) in the imaged field.

Statistical Analysis

Statistical analysis was performed using SPSS version 23.0 (IBM, New York, NY, United States) or GraphPad Prism 6 (GraphPad, New York, NY, United States). The normality of the data was analyzed using the Shapiro-Wilk test, and the data were found to be normally distributed. The quantitative data are expressed as mean ± standard error of the mean (SEM), with the error bars indicating the SEM. Different groups were compared using a one-way ANOVA, followed by the Bonferroni *post hoc* test. We evaluated behavior by calculating a composite Z-score for each mouse. Specifically, the composite Z-score for the mouse was calculated as the sum of the values of 6 Z-scores (latency to eat food, time spent in the center, latency to the center, freezing time, entries to the novel arm, and duration in the novel arm) normalized with the SD for that sum in the controls. Given that the reduction (rather than increase) in time spent in the center and freezing time (open-field test) and the reduction in duration and entries to the novel arm (Y-maze test) indicate impairment of behavior, we multiplied the Z-score values representing these behaviors by one prior to calculating the composite Z-score using these values. The nature of the hypothesis testing was twofold. A value of $p < 0.05$ was considered statistically significant.

RESULTS

Administration of Exogenous Netrin-1 Improves Postoperative Delirium-Like Behavior Induced by Surgery/Anesthesia in Aged Mice

To assess whether surgery/anesthesia affects the general and cognitive behavior of aged mice in this study, we performed a battery of behavioral tests with the food burial test, open-field test, and Y-maze test 24 h before surgery and 6, 9, and 24 h after surgery, as we previously reported (Peng et al., 2016; Lu et al., 2020). Composite Z-scores for each of the 40 mice in the four groups were calculated at 6, 9, and 24 h after surgery ($p < 0.05$, **Figures 2A–C**).

First, we performed a buried food test to explore whether surgery/anesthesia affected the ability of mice to associate odorants with food rewards (Yang and Crawley, 2009). The latency to eat food was markedly increased in the surgery group compared to the control group at 9 h after surgery ($p < 0.01$, **Figure 2D**), while administration of NTN-1 improved the impaired ability to find and eat food induced by surgery/anesthesia ($p < 0.05$, **Figure 2D**). No significant changes were observed between the NTN-1 group and the control group. Surgery/anesthesia-induced impairment in the ability of mice to search for and eat food suggests that surgery/anesthesia might cause the mice to develop changes in behavior (e.g., inattention, disorganized thinking, and altered level of consciousness) associated with delirium.

Then, we executed the open-field test to examine the locomotor ability and exploratory behavior of mice. There were no significant differences in the total distance traveled by mice between the four groups at the three time points after surgery, thus indicating that surgery/anesthesia did not affect the motor function of aged mice (**Figure 2E**). There were no significant differences in latency to the center between the four groups (**Figure 2F**). Surgery/anesthesia significantly decreased the time spent in the center at 9 h after surgery ($p < 0.05$, **Figure 2G**), and preemptive administration of NTN-1 ameliorated this phenomenon at 9 h after surgery ($p < 0.05$, **Figure 2G**). In addition, surgery/anesthesia significantly decreased the freezing time at 9 h after surgery ($p < 0.05$, **Figure 2H**), while preoperative treatment with NTN-1 increased the freezing time at 9 h after surgery ($p < 0.05$, **Figure 2H**). It is worth noting that NTN-1 administration did not change these parameters compared with the control condition (**Figures 2G,H**). These findings suggest that surgery/anesthesia altered the natural behavior of the mice, such as anxiety (time spent in the center) and natural reactions (freezing time).

Finally, we conducted a Y-maze to assess spatial memory in aged mice as previously validated (Wheelan et al., 2015). Surgery/anesthesia significantly reduced both the duration in the novel arm at 9 h after surgery ($p < 0.05$, **Figure 2I**) and the number of entries to the novel arm at 9 h after surgery ($p < 0.05$, **Figure 2J**) as compared with the control condition. Pretreatment with NTN-1 increased the number of entries to the novel arm and duration in the novel arm at 9 h after surgery ($p < 0.05$,

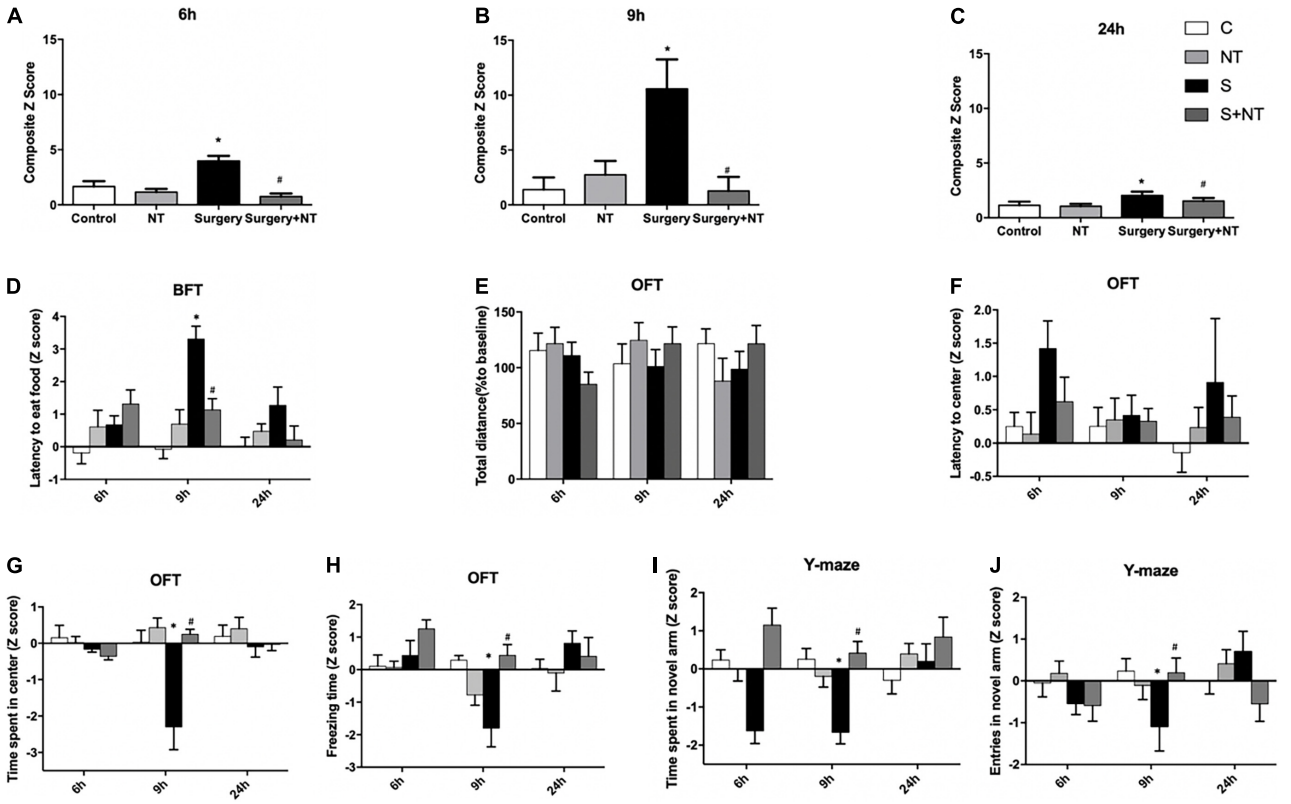

FIGURE 2 | Exogenous recombinant human Netrin-1 (rh-NTN-1) improved POD-like behavior in surgical mice. **(A–C)** Changes in composite Z-scores after rh-NTN-1 treatments *via* tail vein injection at 6, 9, and 24 h postoperatively. **(E,F)** Surgery/anesthesia had no influence on latency to the center or total distance. **(D)** Surgery/anesthesia increased the latency to eat food, while exogenous rh-NTN-1 significantly decreased the latency to eat food at 9 h postoperatively. **(G–J)** Surgery/anesthesia decreased the Z-scores, while exogenous rh-NTN-1 significantly increased the Z-scores at 9 h postoperatively. The data are presented as mean ± standard error of the mean for each group (n = 10 per cohort). $^{*}p < 0.05$ vs. the control group, $^{\#}p < 0.05$ vs. the surgery group.

Figures 2I,J). However, NTN-1 administration alone did not affect the performance of aged mice in the Y-maze test at 9 h after surgery (**Figures 2I,J**).

Taken together, no significant changes were observed between the NTN-1 group and the control group, but prophylaxis with NTN-1 attenuated the impairment of POD behavior of aged mice caused by surgery/anesthesia in a fluctuating way.

Netrin-1 Regulates the Expression of Inflammatory Cytokines After Surgery

To evaluate the effects of NTN-1 on systemic inflammation, we first measured the changes in IL-6, IL-10, and HMGB-1 in blood plasma at 6 h after surgery (Yang et al., 2017). Surgery/anesthesia significantly increased the levels of IL-6 and HMGB-1 ($p < 0.05$, **Figures 3A,C**) but did not change the expression of IL-10 after surgery ($p > 0.05$, **Figure 3B**). Although a single dose of NTN-1 did not completely reverse the increase in pro-inflammatory cytokines to the control condition, it markedly reduced the levels of IL-6 and HMGB-1 after surgery ($p < 0.05$, **Figures 3A,C**). In addition, pretreatment with NTN-1 increased the expression of IL-10, a crucial cytokine during the resolution phase of inflammation after surgery ($p < 0.05$, **Figure 3B**). Second, we measured these cytokines in the hippocampus and prefrontal cortex, which are two key brain regions related to the memory network (Preston and Eichenbaum, 2013; Place et al., 2016), to evaluate the effects of NTN-1 on neuroinflammation at 6 h after surgery. Surgery/anesthesia induced a marked increase in the expression of IL-6 after surgery in both the hippocampus and the prefrontal cortex compared with the control condition ($p < 0.05$, **Figures 3D,G**). Pretreatment with NTN-1 significantly decreased the expression of IL-6 in these brain regions compared with that in the surgery group ($p < 0.05$, **Figures 3D,G**). In addition, pretreatment with NTN-1 increased the expression of IL-10 not only in the hippocampus after surgery ($p < 0.05$, **Figure 3E**) but also in the prefrontal cortex after surgery ($p < 0.05$, **Figure 3H**).

Surgery/Anesthesia Decreases Endogenous Netrin-1 in the Hippocampus and Prefrontal Cortex in Aged Mice

To investigate whether endogenous NTN-1 was involved in the anti-inflammatory and neuroprotective effects, we measured the changes in endogenous NTN-1 in the hippocampus and prefrontal cortex at 6 h after surgery. Our results suggested that

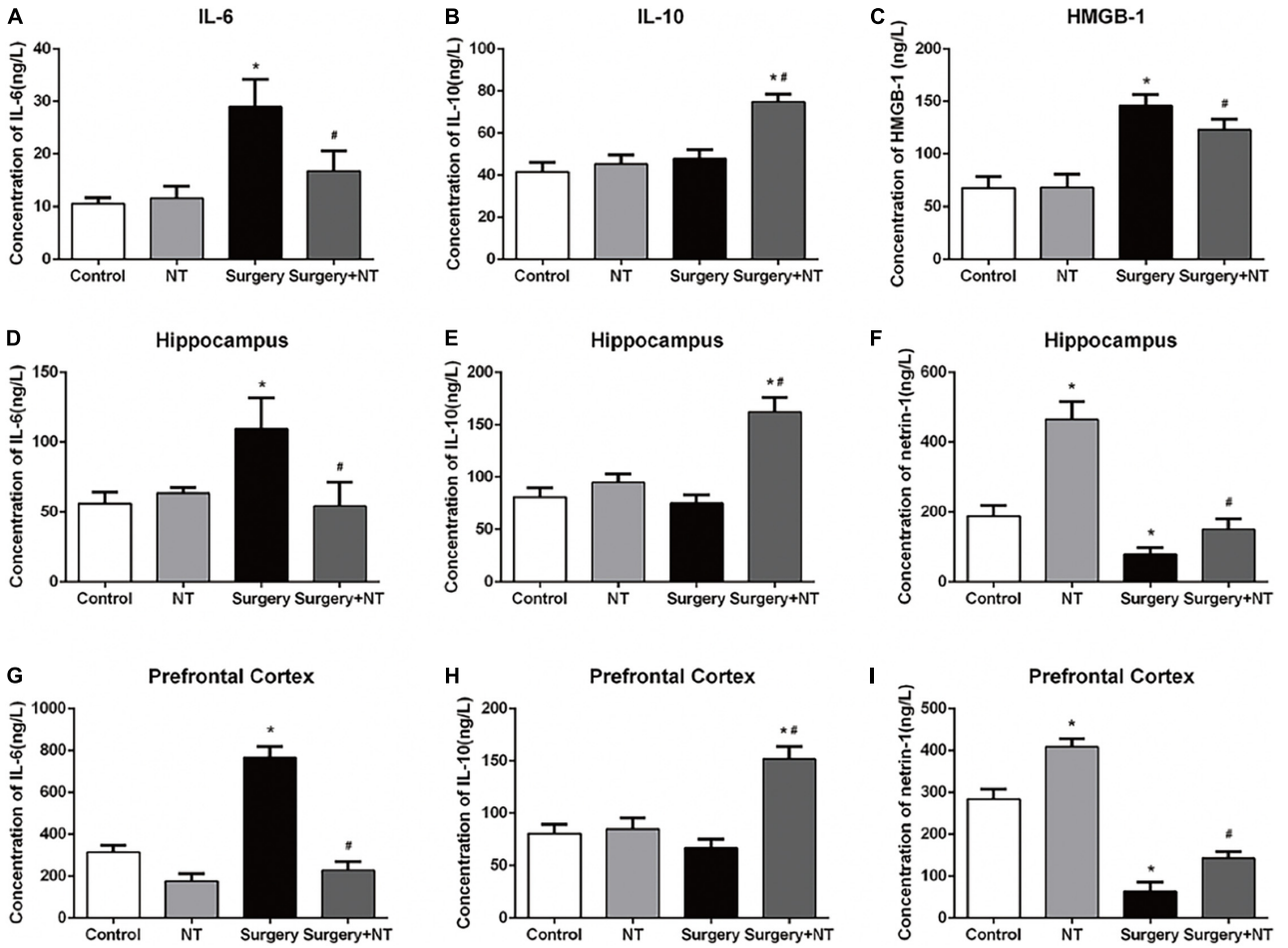

FIGURE 3 | Exogenous recombinant human Netrin-1 decreased the levels of pro-inflammatory cytokines and increased the levels of anti-inflammatory cytokines in the sera, prefrontal cortex, and hippocampus of surgical mice. **(A–C)** Expression levels of IL-6, IL-10, and HMGB-1 in serum at 6 h after surgery/anesthesia. **(D–F)** ELISA was used to detect the expression of IL-6, IL-10, and Netrin-1 in the hippocampus at 6 h postoperatively. **(G–I)** Altered expression of IL-6, IL-10, and Netrin-1 in the prefrontal cortex at 6 h postoperatively. The data are presented as mean ± standard error of the mean for each group (n = 5 per cohort). *$p < 0.05$ vs. the control group, #$p < 0.05$ vs. the surgery group.

surgery/anesthesia significantly decreased the level of NTN-1 in the hippocampus and prefrontal cortex after surgery ($p < 0.05$, **Figures 3F,I**).

Netrin-1 Prevents Neuroinflammation in the Hippocampus and Prefrontal Cortex

We measured the changes in immunoreactivity of Iba-1 in the hippocampus and prefrontal cortex to assess the reactive states of the microglia, which represent the major pathological manifestation of neuroinflammation (Norden et al., 2016; Joshi et al., 2019). NTN-1 attenuated microglial activation by changing the expression of Iba-1. Surgery induced the amoeba-like morphology of microglia and increased the Iba-1 immunoreactivity area in the hippocampus and prefrontal cortex compared with the control condition ($p < 0.05$, **Figures 4A–D**), while preemptive administration of NTN-1 significantly restored the ramified shape of the microglia and reduced the cellular area ($p < 0.05$, **Figures 4A–D**). No significant changes in Iba-1 were observed in the NTN-1 group.

Netrin-1 Prophylaxis Alleviates the Leakage of the Blood-Brain Barrier Induced by Surgery/Anesthesia

It has been reported that destruction of the BBB is linked to delirium and perioperative neurocognitive disorders (Maldonado, 2008; Subramaniyan and Terrando, 2019). Therefore, we used a well-established dye injection trial to investigate the integrity of the BBB (Ben-Zvi et al., 2014; Yang et al., 2017) under the treatment of surgery/anesthesia with or without the administration of NTN-1.

Immunofluorescence images showed that 10-kDa dextran was mainly confined to the vessels in the four groups. The dextran signal was detected in the brain parenchyma around the vessels of mice in the surgery group (**Figure 5A**). To quantitate the

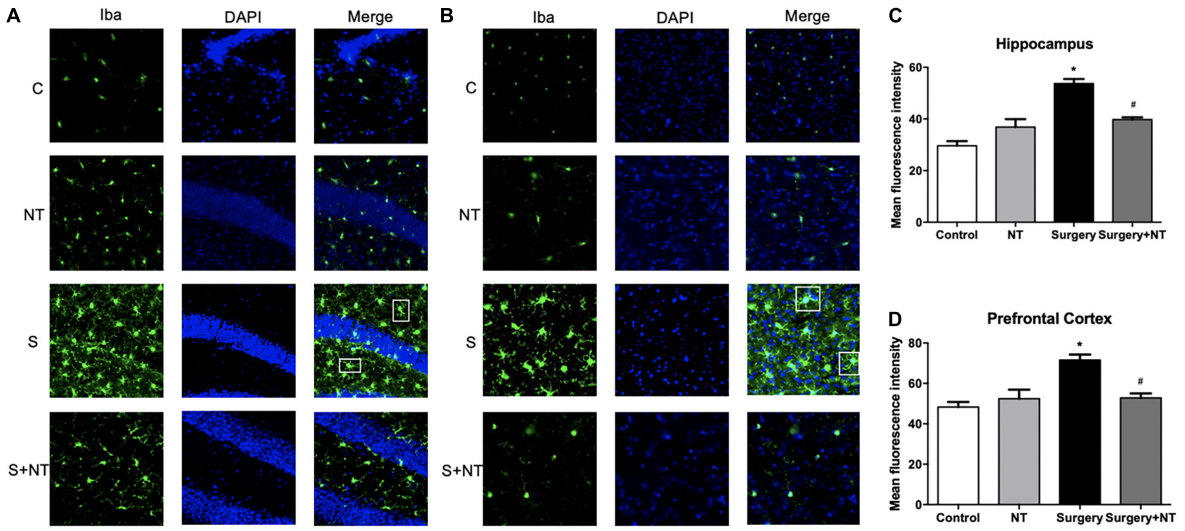

FIGURE 4 | Exogenous recombinant human Netrin-1 decreased the activation of microglia in surgical mice. Activation of microglia in the hippocampus **(A)** and prefrontal cortex **(B)** 24 h postoperatively. **(C,D)** Mean fluorescence intensity in the hippocampus and prefrontal cortex 24 h postoperatively. The data are presented as mean ± standard error of the mean for each group (n = 3 per cohort). $^{*}p < 0.05$ vs. the control group, $^{\#}p < 0.05$ vs. the surgery group.

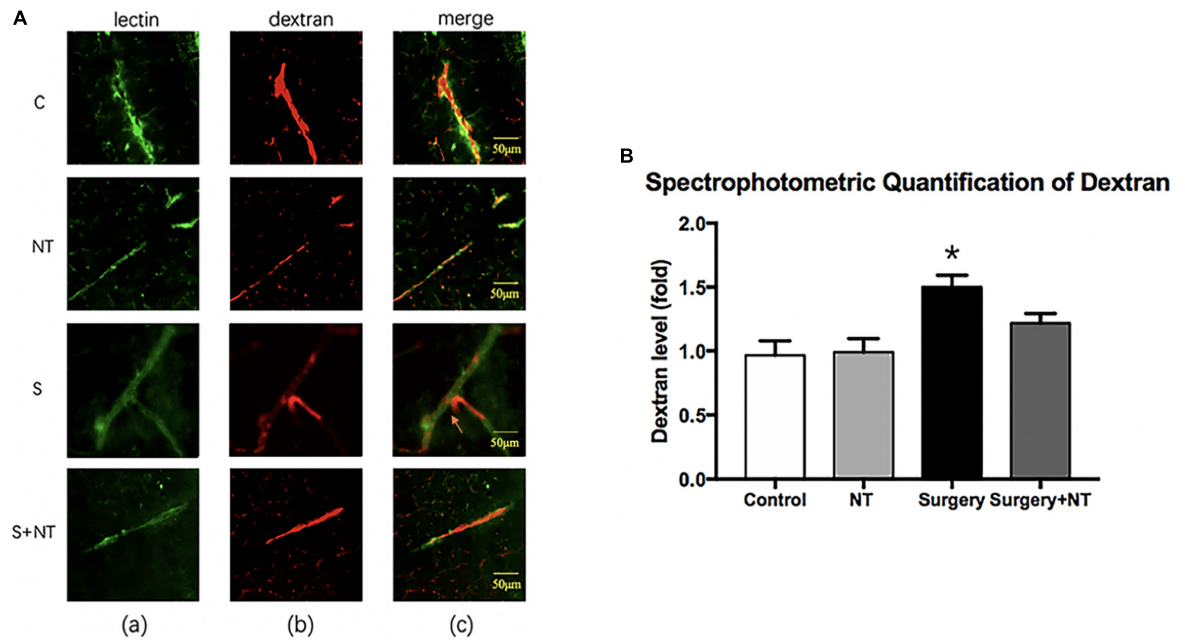

FIGURE 5 | Exogenous recombinant human Netrin-1 attenuates the anesthesia/surgery-induced increase in blood-brain barrier permeability of dextran in the hippocampus of mice. **(A)** Immunostaining of blood vessels (lectin, green, Column a) and dextran (10-kDa dextran, red, Column b) in brain sections from the four groups. The red spots (non-overlapping area) in the column indicate dextran that is not inside the blood vessel (extravascular dextran). N = the total of 150 slides from 5 mice in each group. **(B)** Spectrophotometric quantification of brain dextran (10 kDa) levels. Anesthesia/surgery increases the brain dextran levels of mice compared with those of mice under control conditions. Treatment with rh-NTN-1 attenuates the anesthesia/surgery-induced increase in the extravascular dextran level in mice. The data are presented as mean ± standard error of the mean for each group (n = 5 per cohort). $^{*}p < 0.05$ vs. the control group.

extravascular dextran, spectrophotometric quantification of 10-kDa dextran Texas Red from brain tissue extracts was performed. In the hippocampus, we found that surgery/anesthesia increased the level of extravascular 10-kDa dextran compared with the control condition, while NTN-1 prophylaxis decreased the leakage of dextran induced by surgery/anesthesia ($p < 0.05$, **Figure 5B**).

We next examined the effects of NTN-1 on the expression of occludin, ZO-1, and claudin-5 after surgery (**Figures 6D,H**), which are TJ-associated proteins that maintain the integrity

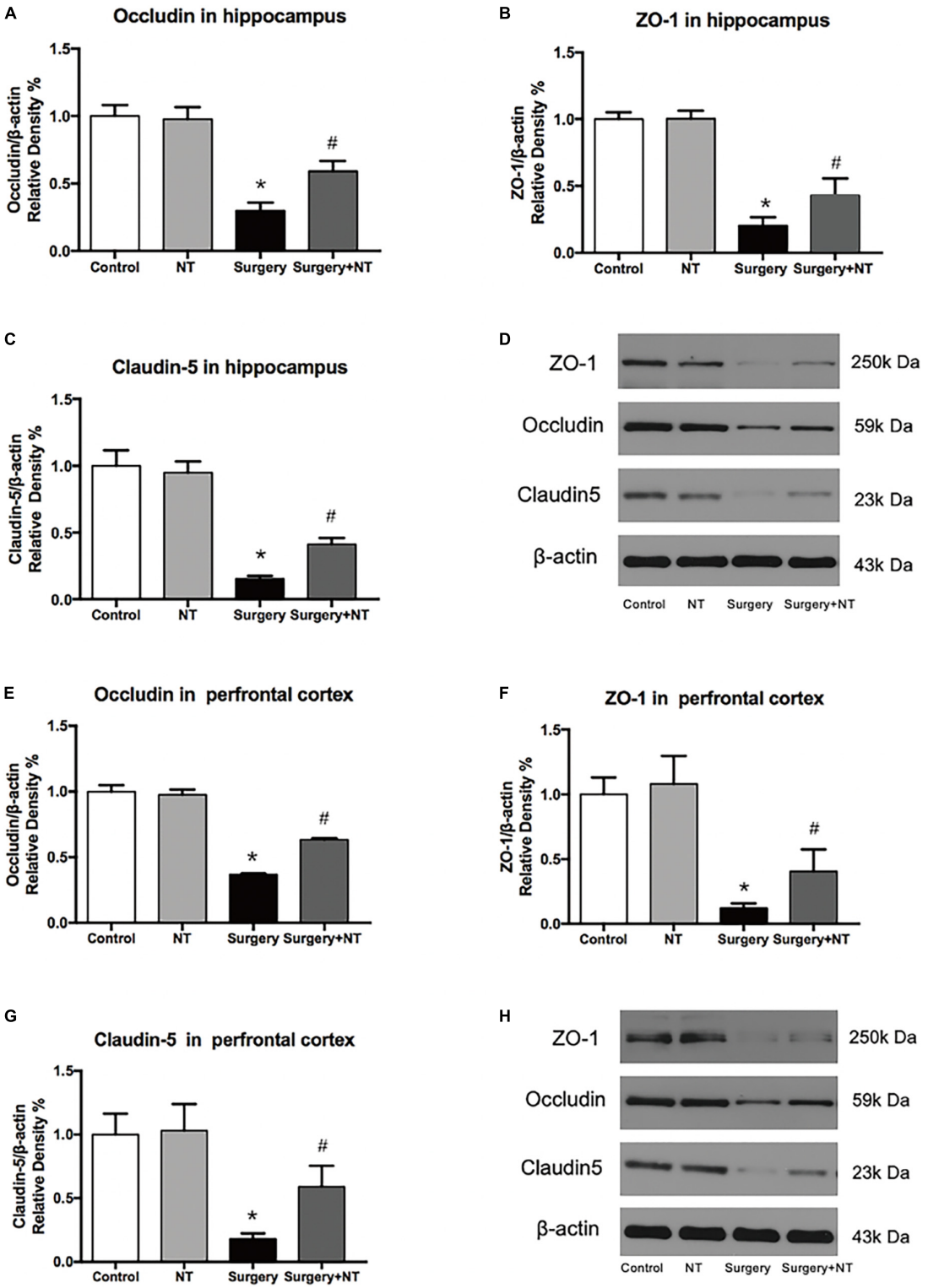

FIGURE 6 | Exogenous recombinant human Netrin-1 attenuates the anesthesia/surgery-induced reduction in cell junction proteins in the hippocampus and prefrontal cortex of mice. Anesthesia/surgery reduced the protein levels of occludin **(A,D,E,H)**, ZO-1 **(B,D,F,H)**, and claudin-5 **(C,D,G,H)** in the hippocampus and prefrontal cortex of mice compared with those of mice under control conditions at 9 h after anesthesia/surgery. Treatment with rh-NTN-1 attenuated these reductions in the levels of occludin **(A,D,E,H)**, ZO-1 **(B,D,F,H)**, and claudin-5 **(C,D,G,H)**. The data are presented as mean ± standard error of the mean for each group ($n = 5$ per cohort). $^*p < 0.05$ vs. the control group, $\#p < 0.05$ vs. the surgery group.

of the BBB (Jiao et al., 2011; Luissint et al., 2012). Using quantitative Western blot, we found that there was a marked decrease in the expression of occludin, ZO-1, and claudin-5 in both the hippocampus and the prefrontal cortex at 9 h after surgery, while pretreatment with NTN-1 significantly attenuated the reduction in these proteins ($p < 0.05$, **Figures 6A–C,E–G**). Preemptive administration of NTN-1 alone did not have any effects on the BBB.

DISCUSSION

In this study, we demonstrate that exogenous NTN-1, an axonal guidance molecule, improves postoperative POD-like behavior in aged mice through its anti-inflammatory and BBB-protecting effects. Our results show that pretreatment with NTN-1 given through the caudal vein remits the systemic inflammatory response and protects the BBB integrity after surgery/anesthesia. In addition, exogenous NTN-1 inhibited neuroinflammation in the hippocampus and prefrontal cortex according to the expression of inflammatory cytokines and reactive states of the microglia in these brain regions. To the best of our knowledge, this is the first study to report the neuroprotective effect of NTN-1 in a mouse model of POD.

Much evidence indicates that neuroinflammation plays an important role in POD. Peripheral aseptic inflammation activates the innate immune system, initiating the inflammatory process that finally leads to POD (Girard et al., 2013; Maldonado, 2013; Saxena and Maze, 2018). In an aseptic surgery environment, cellular trauma releases damage-associated molecular patterns (DAMPs), activates BMDMs by binding to Toll-like receptors (TLRs) *via* high mobility group box-1 (HMGB1), and upregulates the expression of pro-inflammatory cytokines such as IL-1, TNF-α, and IL-6 (Levy et al., 2007; Li R. L. et al., 2013). These cytokines can further activate DAMPs in positive feedback (Huang et al., 2018; Nishigaki et al., 2019) and be released into the circulation to destroy the integrity of the BBB (Li G. et al., 2013; Saxena and Maze, 2018). Our results show that NTN-1 can reduce the release of systemic pro-inflammatory factor IL-6 and increase anti-inflammatory cytokine IL-10 after surgery, which is a vital cytokine after trauma. At the same time, NTN-1 reduced the release of HMGB-1, which is passively released from cells damaged by aseptic trauma and targeted to circulating BMDMs. These findings are consistent with the potent anti-inflammatory activity of NTN-1 in many other disease models associated with inflammation, such as renal ischemia-reperfusion injury (Wang et al., 2008), acute peritonitis (Ariel et al., 2006), and acute pancreatitis (Chen et al., 2012). The migration and aggregation of the white blood cells to the inflammatory site is the central link of the whole inflammatory response. Early studies found that NTN-1 interacts with the UNC-5B receptor expressed on the surface of the white blood cells and inhibits the migration of the white blood cells (Ly et al., 2005). In Alzheimer's disease (AD) rats (Sun et al., 2019), it has been demonstrated that NTN-1 concentrations in serum were positively correlated with the systemic expression of IL-10 (Mosser and Zhang, 2008). Moreover, in acute peritonitis and acute colitis models, NTN-1 inhibits the migration of inflammatory cells and induces the M2 polarization phenotype of macrophages (Mirakaj et al., 2011; Aherne et al., 2012). This further indicates that the changes in peripheral inflammatory factors may be related to the powerful anti-inflammatory effect of NTN-1.

A complete functional BBB is essential for proper homeostatic maintenance and perfusion of the CNS. The unique microvascular endothelial cell monolayer with inflammatory damage that forms the surface of the luminal BBB and leads to increased capillary permeability has been related to various neurological disorders ranging from ischemic stroke and traumatic brain injury to neurodegenerative disease and CNS infections (Hawkins and Davis, 2005). In addition, the neuroinflammatory cascade that typically accompanies BBB failure under these conditions has been strongly associated with elevated levels of pro-inflammatory cytokines such as TNF-α and IL-6 (Rochfort and Cummins, 2015). In models of subarachnoid hemorrhage (Xie et al., 2017), multiple sclerosis (Voortman et al., 2017), and stroke (Yu et al., 2017), NTN-1 has been shown to have a protective effect on the BBB and to improve neurocognitive function, which was also noted in our model. There is compelling evidence that exogenous NTN-1 significantly diminishes the diffusion of dextran in mouse brain-derived endothelial cells *in vitro*. NTN-1-induced barrier tightening is at least partly the consequence of NTN-induced upregulation of TJ molecules. It has been reported that the levels of both the intracellular components of the junctional complex and the transmembrane increased with the response to NTN-1. In addition, junctional proteins were enriched in lipid raft membrane microdomains after NTN-1 treatment of human brain-derived endothelial cells, and these proteins effectively interacted to form functional clusters supporting barrier integrity (Podjaski et al., 2015). Thus, NTN-1 reduces the incidence of POD by reducing the entry of peripheral inflammatory cytokines through impaired flow barriers.

In addition to alleviating the peripheral inflammatory response, NTN-1 also reduces the activation of glial cells and the expression of inflammatory cytokines in the hippocampus and prefrontal cortex. Under non-injurious conditions, microglia promote the essential functions involved in surveillance of the brain parenchyma to maintain homeostasis (Biber et al., 2007). The microglia are activated by one or more pathways following the release of pro-inflammatory cytokines by the innate immune response. The activated microglia quickly transform into a pro-inflammatory phenotype with stout morphology and enhance the production of pro-inflammatory molecules (Saxena and Maze, 2018). These pro-inflammatory cytokines and the debris released by the activated microglia can convert the astrocytes into a neurotoxic A1 reactive subtype (Hinkle et al., 2019; Li et al., 2019), which causes the astrocytes to lose their normal synaptic maintenance and phagocytosis and induces the rapid death of neurons and oligodendrocytes (Hinkle et al., 2019; Li et al., 2019). In our POD model, NTN-1 restored the morphological changes of microglia in both the hippocampus and the prefrontal cortex to their original morphology, representing the transformation of the inflammatory phenotype to the resting state, thereby changing

the pro-inflammatory environment by regulating the secretion of inflammatory cytokines. Herein, it makes sense that pretreatment with NTN-1 facilitates the improvement of POD-like behavior in aged mice since the hippocampus and prefrontal cortex are responsible for shaping emotion, learning, and organizing memory (Dolleman-Van Der Weel et al., 2019; Yavas et al., 2019).

In addition, the regulation of lipid mediators by neuronal circuits might play an important role in the control of inflammation to sterile injury. The vagus nerve regulates the expression of the axonal guidance molecule NTN-1, which can increase SPM production *in vivo* if it upregulates the concentrations of RvD5 and PD1 in the exudate during acute self-limiting inflammation (Dalli and Serhan, 2018; Serhan et al., 2019). Our previous research demonstrated the anti-inflammatory and pro-resolving activities of PD1 in an inflammatory environment and identified the role of PD1 in regulating postoperative inflammation and the consequential POD-like behavior of mice (Zhou et al., 2020). In our study, compared with the control group, the concentration of endogenous NTN-1 in the hippocampus and prefrontal cortex at 6 h postoperatively was significantly reduced. This is most likely the result of endogenous NTN-1 being consumed after participating in the pro-resolution of inflammation by regulating SPM. Therefore, the neuroprotective effect of NTN-1 may be related to this mechanism. Does NTN-1 also inhibit the production of pro-inflammatory mediators by other means? It is essential to explore the underlying mechanism of NTN-1 in inflammation in further investigations.

There are several limitations to our research. First, there are several signaling pathways that have been shown to be involved in anti-inflammatory and vascular endothelial cell protection. An in-depth study of the mechanism of NTN-1 that we need to uncover will open up a novel way to prevent and treat inflammation-related lesions. Second, we have only demonstrated that exogenous prophylactic NTN-1 can improve POD by providing positive anti-inflammatory responses and protective BBB functions after surgery in elderly mice. However, how endogenous NTN-1 changes during this process has not been studied, and NTN-1 small interfering RNA (siRNA) can be used in future studies. Third, because of the frequency of fights between male mice, the occurrence of injuries, and/or the need to live alone, all these have a greater influence on behavior, and so only female mice were used in our experiments. The difference in the prevalence of POD observed between men and women is controversial in the clinic (Edlund et al., 2001; Prendergast et al., 2014; Oh et al., 2016). Perhaps gender differences affect POD development. It is worth including male mice in future studies. Fourth, NTN-1 induces neovascularization and vascular remodeling. Therefore, there may be a risk of developing cancer in older people. NTN-1 expression was elevated in melanoma compared with benign melanocytic lesions. Interference with NTN-1 expression can reduce cancer cell death and promote melanoma progression (Boussouar et al., 2020). The safety and effectiveness of NTN-1 in the clinical treatment of POD deserve further study. Finally, we only assessed the role of microglia in neuroinflammation and ignored astrocytes as important resident immune cells in the CNS, which also play an important role in neuroinflammation. In fact, there are also interactions between microglia and astrocytes in some neurodegenerative diseases (Kwon and Koh, 2020). The effect on astrocytes in POD deserves further investigation in future studies.

CONCLUSION

This study determined that the administration of exogenous NTN-1 could regulate postoperative inflammation and protect the integrity of the BBB to improve POD in aged mice. These findings indicate the potential of NTN-1 as a novel therapy for POD.

DATA AVAILABILITY STATEMENT

The raw data supporting the conclusions of this article will be made available by the authors, without undue reservation.

ETHICS STATEMENT

The animal study was reviewed and approved by Animal Ethics Committee of Zhongnan Hospital of Wuhan University.

AUTHOR CONTRIBUTIONS

KL and JW designed and performed the experiment, collected and analyzed the data, prepared the manuscript, and participated in the statistical analysis. MG and XL were involved in preparing the animal models and participated in interpreting the results. LC contributed to the behavioral testing. YZ was involved in the biochemical analysis. MP contributed to the study concept and design, secured funding for the project, and prepared and critically revised the manuscript. All authors reviewed the manuscript and approved the submitted version.

FUNDING

This research was supported by grants from the National Natural Science Foundation of China (81870851 and 82071208) and the Outstanding Talented Young Doctor Program of Hubei Province (HB20200407).

ACKNOWLEDGMENTS

This manuscript has been released as a preprint at: https://www.researchsquare.com/article/rs-28936/v1.

SUPPLEMENTARY MATERIAL

The Supplementary Material for this article can be found online at: https://www.frontiersin.org/articles/10.3389/fnmol.2021.751570/full#supplementary-material

REFERENCES

Aherne, C. M., Collins, C. B., Masterson, J. C., Tizzano, M., Boyle, T. A., Westrich, J. A., et al. (2012). Neuronal guidance molecule netrin-1 attenuates inflammatory cell trafficking during acute experimental colitis. *Gut* 61, 695–705. doi: 10.1136/gutjnl-2011-300012

Aldecoa, C., Bettelli, G., Bilotta, F., Sanders, R. D., Audisio, R., Borozdina, A., et al. (2017). European Society of Anaesthesiology evidence-based and consensus-based guideline on postoperative delirium. *Eur. J. Anaesthesiol.* 34, 192–214.

Androsova, G., Krause, R., Winterer, G., and Schneider, R. (2015). Biomarkers of postoperative delirium and cognitive dysfunction. *Front. Aging Neurosci.* 7, 112. doi: 10.3389/fnagi.2015.00112

Ariel, A., Fredman, G., Sun, Y. P., Kantarci, A., Van Dyke, T. E., Luster, A. D., et al. (2006). Apoptotic neutrophils and T cells sequester chemokines during immune response resolution through modulation of CCR5 expression. *Nat. Immunol.* 7, 1209–1216. doi: 10.1038/ni1392

Auerbach, R. P., Mortier, P., Bruffaerts, R., Alonso, J., Benjet, C., Cuijpers, P., et al. (2018). WHO World Mental Health Surveys International College Student Project: Prevalence and distribution of mental disorders. *J. Abnorm. Psychol.* 127, 623–638. doi: 10.1037/abn0000362

Ben-Zvi, A., Lacoste, B., Kur, E., Andreone, B. J., Mayshar, Y., Yan, H., et al. (2014). Mfsd2a is critical for the formation and function of the blood-brain barrier. *Nature* 509, 507–511. doi: 10.1038/nature13324

Bernstein, D. L., Zuluaga-Ramirez, V., Gajghate, S., Reichenbach, N. L., Polyak, B., Persidsky, Y., et al. (2020). miR-98 reduces endothelial dysfunction by protecting blood-brain barrier (BBB) and improves neurological outcomes in mouse ischemia/reperfusion stroke model. *J. Cereb. Blood Flow Metab.* 40, 1953–1965. doi: 10.1177/0271678X19882264

Biber, K., Neumann, H., Inoue, K., and Boddeke, H. W. (2007). Neuronal 'On' and 'Off' signals control microglia. *Trends Neurosci.* 30, 596–602. doi: 10.1016/j.tins.2007.08.007

Boussouar, A., Tortereau, A., Manceau, A., Paradisi, A., Gadot, N., Vial, J., et al. (2020). Netrin-1 and Its Receptor DCC Are Causally Implicated in Melanoma Progression. *Cancer Res.* 80, 747–756. doi: 10.1158/0008-5472.CAN-18-1590

Chen, J., Cai, Q. P., Shen, P. J., Yan, R. L., Wang, C. M., Yang, D. J., et al. (2012). Netrin-1 protects against L-Arginine-induced acute pancreatitis in mice. *PLoS One* 7, e46201. doi: 10.1371/journal.pone.0046201

Chen, Y., Liu, X., Jia, X., Zong, W., Ma, Y., Xu, F., et al. (2014). Anxiety- and depressive-like behaviors in olfactory deficient Cnga2 knockout mice. *Behav. Brain Res.* 275, 219–224. doi: 10.1016/j.bbr.2014.08.042

Cortese, G. P., and Burger, C. (2017). Neuroinflammatory challenges compromise neuronal function in the aging brain: Postoperative cognitive delirium and Alzheimer's disease. *Behav. Brain Res.* 322, 269–279. doi: 10.1016/j.bbr.2016.08.027

Dalli, J., and Serhan, C. N. (2018). Immunoresolvents signaling molecules at intersection between the brain and immune system. *Curr. Opin. Immunol.* 50, 48–54. doi: 10.1016/j.coi.2017.10.007

Dolleman-Van Der Weel, M. J., Griffin, A. L., Ito, H. T., Shapiro, M. L., Witter, M. P., et al. (2019). The nucleus reuniens of the thalamus sits at the nexus of a hippocampus and medial prefrontal cortex circuit enabling memory and behavior. *Learn Mem.* 26, 191–205. doi: 10.1101/lm.048389.118

Edlund, A., Lundstrom, M., Brannstrom, B., Bucht, G., and Gustafson, Y. (2001). Delirium before and after operation for femoral neck fracture. *J. Am. Geriatr. Soc.* 49, 1335–1340. doi: 10.1046/j.1532-5415.2001.49261.x

Girard, S., Brough, D., Lopez-Castejon, G., Giles, J., Rothwell, N. J., and Allan, S. M. (2013). Microglia and macrophages differentially modulate cell death after brain injury caused by oxygen-glucose deprivation in organotypic brain slices. *Glia* 61, 813–824. doi: 10.1002/glia.22478

Hawkins, B. T., and Davis, T. P. (2005). The blood-brain barrier/neurovascular unit in health and disease. *Pharmacol. Rev.* 57, 173–185. doi: 10.1124/pr.57.2.4

Hinkle, J. T., Dawson, V. L., and Dawson, T. M. (2019). The A1 astrocyte paradigm: New avenues for pharmacological intervention in neurodegeneration. *Mov. Disord* 34, 959–969. doi: 10.1002/mds.27718

Hu, J., Feng, X., Valdearcos, M., Lutrin, D., Uchida, Y., Koliwad, S. K., et al. (2018). Interleukin-6 is both necessary and sufficient to produce perioperative neurocognitive disorder in mice. *Br. J. Anaesth.* 120, 537–545. doi: 10.1016/j.bja.2017.11.096

Huang, C., Irwin, M. G., Wong, G. T. C., and Chang, R. C. C. (2018). Evidence of the impact of systemic inflammation on neuroinflammation from a non-bacterial endotoxin animal model. *J. Neuroinflam.* 15:147. doi: 10.1186/s12974-018-1163-z

Jiao, H., Wang, Z., Liu, Y., Wang, P., and Xue, Y. (2011). Specific role of tight junction proteins claudin-5, occludin, and ZO-1 of the blood-brain barrier in a focal cerebral ischemic insult. *J. Mol. Neurosci.* 44, 130–139. doi: 10.1007/s12031-011-9496-4

Joshi, A. U., Minhas, P. S., Liddelow, S. A., Haileselassie, B., Andreasson, K. I., Dorn, G. W. II, et al. (2019). Fragmented mitochondria released from microglia trigger A1 astrocytic response and propagate inflammatory neurodegeneration. *Nat. Neurosci.* 22, 1635–1648.

Kutuzov, N., Flyvbjerg, H., and Lauritzen, M. (2018). Contributions of the glycocalyx, endothelium, and extravascular compartment to the blood-brain barrier. *Proc. Natl. Acad. Sci. U S A* 115, E9429–E9438. doi: 10.1073/pnas.1802155115

Kwon, H. S., and Koh, S. H. (2020). Neuroinflammation in neurodegenerative disorders: the roles of microglia and astrocytes. *Transl. Neurodegener.* 9:42. doi: 10.1186/s40035-020-00221-2

Levy, R. M., Mollen, K. P., Prince, J. M., Kaczorowski, D. J., Vallabhaneni, R., Liu, S., et al. (2007). Systemic inflammation and remote organ injury following trauma require HMGB1. *Am. J. Physiol. Regul. Integr. Comp. Physiol.* 293, R1538–R1544. doi: 10.1152/ajpregu.00272.2007

Li, G., Liang, X., and Lotze, M. T. (2013). HMGB1: The Central Cytokine for All Lymphoid Cells. *Front. Immunol.* 4:68. doi: 10.3389/fimmu.2013.00068

Li, R. L., Zhang, Z. Z., Peng, M., Wu, Y., Zhang, J. J., Wang, C. Y., et al. (2013). Postoperative impairment of cognitive function in old mice: a possible role for neuroinflammation mediated by HMGB1, S100B, and RAGE. *J. Surg. Res.* 185, 815–824. doi: 10.1016/j.jss.2013.06.043

Li, T., Chen, X., Zhang, C., Zhang, Y., and Yao, W. (2019). An update on reactive astrocytes in chronic pain. *J. Neuroinflammation* 16:140. doi: 10.1186/s12974-019-1524-2

Lu, Y., Chen, L., Ye, J., Chen, C., Zhou, Y., Li, K., et al. (2020). Surgery/Anesthesia disturbs mitochondrial fission/fusion dynamics in the brain of aged mice with postoperative delirium. *Aging* 12, 844–865. doi: 10.18632/aging.102659

Luissint, A. C., Artus, C., Glacial, F., Ganeshamoorthy, K., and Couraud, P. O. (2012). Tight junctions at the blood brain barrier: physiological architecture and disease-associated dysregulation. *Fluids Barriers CNS* 9:23. doi: 10.1186/2045-8118-9-23

Ly, N. P., Komatsuzaki, K., Fraser, I. P., Tseng, A. A., Prodhan, P., Moore, K. J., et al. (2005). Netrin-1 inhibits leukocyte migration in vitro and in vivo. *Proc. Natl. Acad. Sci. U S A* 102, 14729–14734. doi: 10.1073/pnas.0506233102

Maldonado, J. R. (2008). Pathoetiological model of delirium: a comprehensive understanding of the neurobiology of delirium and an evidence-based approach to prevention and treatment. *Crit. Care Clin.* 24, 789–856. doi: 10.1016/j.ccc.2008.06.004

Maldonado, J. R. (2013). Neuropathogenesis of delirium: review of current etiologic theories and common pathways. *Am. J. Geriatr. Psychiatry* 21, 1190–1222. doi: 10.1016/j.jagp.2013.09.005

Marcantonio, E. R. (2011). In the clinic. Delirium. *Ann. Intern. Med.* 154:11. doi: 10.7326/0003-4819-154-11-201106070-01006

Matsuda, M., Huh, Y., and Ji, R. R. (2019). Roles of inflammation, neurogenic inflammation, and neuroinflammation in pain. *J. Anesth.* 33, 131–139. doi: 10.1007/s00540-018-2579-4

Meng, B., Li, X., Lu, B., Liu, R., Yuan, H., Zhai, X., et al. (2019). The Investigation of Hippocampus-Dependent Cognitive Decline Induced by Anesthesia/Surgery in Mice Through Integrated Behavioral Z-Scoring. *Front. Behav. Neurosci.* 13:282. doi: 10.3389/fnbeh.2019.00282

Mirakaj, V., Gatidou, D., Potzsch, C., Konig, K., and Rosenberger, P. (2011). Netrin-1 signaling dampens inflammatory peritonitis. *J. Immunol.* 186, 549–555. doi: 10.4049/jimmunol.1002671

Mosser, D. M., and Zhang, X. (2008). Interleukin-10: new perspectives on an old cytokine. *Immunol. Rev.* 226, 205–218. doi: 10.1111/j.1600-065X.2008.00706.x

Nishigaki, A., Kawano, T., Iwata, H., Aoyama, B., Yamanaka, D., Tateiwa, H., et al. (2019). Acute and long-term effects of haloperidol on surgery-induced neuroinflammation and cognitive deficits in aged rats. *J. Anesth* 33, 416–425. doi: 10.1007/s00540-019-02646-0

Norden, D. M., Trojanowski, P. J., Villanueva, E., Navarro, E., and Godbout, J. P. (2016). Sequential activation of microglia and astrocyte cytokine expression precedes increased Iba-1 or GFAP immunoreactivity following systemic immune challenge. *Glia* 64, 300–316. doi: 10.1002/glia.22930

Oh, E. S., Sieber, F. E., Leoutsakos, J. M., Inouye, S. K., and Lee, H. B. (2016). Sex Differences in Hip Fracture Surgery: Preoperative Risk Factors for Delirium and Postoperative Outcomes. *J. Am. Geriatr. Soc.* 64, 1616–1621. doi: 10.1111/jgs.14243

Peng, M., Zhang, C., Dong, Y., Zhang, Y., Nakazawa, H., Kaneki, M., et al. (2016). Battery of behavioral tests in mice to study postoperative delirium. *Sci. Rep.* 6:29874. doi: 10.1038/srep29874

Place, R., Farovik, A., Brockmann, M., and Eichenbaum, H. (2016). Bidirectional prefrontal-hippocampal interactions support context-guided memory. *Nat. Neurosci.* 19, 992–994. doi: 10.1038/nn.4327

Podjaski, C., Alvarez, J. I., Bourbonniere, L., Larouche, S., Terouz, S., Bin, J. M., et al. (2015). Netrin 1 regulates blood-brain barrier function and neuroinflammation. *Brain* 138, 1598–1612. doi: 10.1093/brain/awv092

Prendergast, B. J., Onishi, K. G., and Zucker, I. (2014). Female mice liberated for inclusion in neuroscience and biomedical research. *Neurosci. Biobehav. Rev.* 40, 1–5. doi: 10.1016/j.neubiorev.2014.01.001

Preston, A. R., and Eichenbaum, H. (2013). Interplay of hippocampus and prefrontal cortex in memory. *Curr. Biol.* 23, R764–R773.

Prinz, M., and Priller, J. (2014). Microglia and brain macrophages in the molecular age: from origin to neuropsychiatric disease. *Nat. Rev. Neurosci.* 15, 300–312. doi: 10.1038/nrn3722

Rochfort, K. D., and Cummins, P. M. (2015). The blood-brain barrier endothelium: a target for pro-inflammatory cytokines. *Biochem. Soc. Trans.* 43, 702–706. doi: 10.1042/BST20140319

Saxena, S., and Maze, M. (2018). Impact on the brain of the inflammatory response to surgery. *Presse Med.* 47, e73–e81. doi: 10.1016/j.lpm.2018.03.011

Serhan, C. N. (2014). Pro-resolving lipid mediators are leads for resolution physiology. *Nature* 510, 92–101. doi: 10.1038/nature13479

Serhan, C. N., De La Rosa, X., and Jouvene, C. (2019). Novel mediators and mechanisms in the resolution of infectious inflammation: evidence for vagus regulation. *J. Intern Med.* 286, 240–258. doi: 10.1111/joim.12871

Subramaniyan, S., and Terrando, N. (2019). Neuroinflammation and Perioperative Neurocognitive Disorders. *Anesth Analg.* 128, 781–788.

Sun, L., Ju, T., Wang, T., Zhang, L., Ding, F., Zhang, Y., et al. (2019). Decreased Netrin-1 and Correlated Th17/Tregs Balance Disorder in Abeta1-42 Induced Alzheimer's Disease Model Rats. *Front. Aging Neurosci.* 11:124. doi: 10.3389/fnagi.2019.00124

Tang, Z., Xu, C., Zhang, G., and Chen, H. (2016). [Protect role of Netrin-1 in inflammatory response]. *Zhonghua Wei Zhong Bing Ji Jiu Yi Xue* 28, 756–760. doi: 10.3760/cma.j.issn.2095-4352.2016.08.020

Terrando, N., Eriksson, L. I., Ryu, J. K., Yang, T., Monaco, C., Feldmann, M., et al. (2011). Resolving postoperative neuroinflammation and cognitive decline. *Ann. Neurol.* 70, 986–995. doi: 10.1002/ana.22664

Vacas, S., Degos, V., Feng, X., and Maze, M. (2013). The neuroinflammatory response of postoperative cognitive decline. *Br. Med. Bull.* 106, 161–178. doi: 10.1093/bmb/ldt006

Voortman, M. M., Pekar, T., Bachmayer, D., Archelos, J. J., Stojakovic, T., Scharnagl, H., et al. (2017). Serum netrin-1 in relation to gadolinium-enhanced magnetic resonance imaging in early multiple sclerosis. *Mult. Scler. J. Exp. Transl. Clin.* 3:2055217317727294. doi: 10.1177/2055217317727294

Wang, W., Reeves, W. B., and Ramesh, G. (2008). Netrin-1 and kidney injury. I. Netrin-1 protects against ischemia-reperfusion injury of the kidney. *Am. J. Physiol. Renal. Physiol.* 294, F739–F747.

Wheelan, N., Webster, S. P., Kenyon, C. J., Caughey, S., Walker, B. R., Holmes, M. C., et al. (2015). Short-term inhibition of 11beta-hydroxysteroid dehydrogenase type 1 reversibly improves spatial memory but persistently impairs contextual fear memory in aged mice. *Neuropharmacology* 91, 71–76. doi: 10.1016/j.neuropharm.2014.12.005

Whitlock, E. L., Vannucci, A., and Avidan, M. S. (2011). Postoperative delirium. *Minerva Anestesiol.* 77, 448–456.

Wolf, A., Bauer, B., Abner, E. L., Ashkenazy-Frolinger, T., and Hartz, A. M. (2016). A Comprehensive Behavioral Test Battery to Assess Learning and Memory in 129S6/Tg2576 Mice. *PLoS One* 11:e0147733. doi: 10.1371/journal.pone.0147733

Xie, Z., Enkhjargal, B., Reis, C., Huang, L., Wan, W., Tang, J., et al. (2017). Netrin-1 Preserves Blood-Brain Barrier Integrity Through Deleted in Colorectal Cancer/Focal Adhesion Kinase/RhoA Signaling Pathway Following Subarachnoid Hemorrhage in Rats. *J. Am. Heart Assoc.* 2017:6. doi: 10.1161/JAHA.116.005198

Xiong, X. Y., Liu, L., and Yang, Q. W. (2016). Functions and mechanisms of microglia/macrophages in neuroinflammation and neurogenesis after stroke. *Prog. Neurobiol.* 142, 23–44. doi: 10.1016/j.pneurobio.2016.05.001

Yang, M., and Crawley, J. N. (2009). Simple behavioral assessment of mouse olfaction. *Curr. Protoc. Neurosci.* 8:24. doi: 10.1002/0471142301.ns0824s48

Yang, S., Gu, C., Mandeville, E. T., Dong, Y., Esposito, E., Zhang, Y., et al. (2017). Anesthesia and Surgery Impair Blood-Brain Barrier and Cognitive Function in Mice. *Front. Immunol.* 8:902. doi: 10.3389/fimmu.2017.00902

Yavas, E., Gonzalez, S., and Fanselow, M. S. (2019). Interactions between the hippocampus, prefrontal cortex, and amygdala support complex learning and memory. *F1000Res* 2019:8. doi: 10.12688/f1000research.19317.1

Yu, J., Li, C., Ding, Q., Que, J., Liu, K., Wang, H., et al. (2017). Netrin-1 Ameliorates Blood-Brain Barrier Impairment Secondary to Ischemic Stroke via the Activation of PI3K Pathway. *Front. Neurosci.* 11:700. doi: 10.3389/fnins.2017.00700

Zhang, J., Gao, J., Guo, G., Li, S., Zhan, G., Xie, Z., et al. (2018). Anesthesia and surgery induce delirium-like behavior in susceptible mice: the role of oxidative stress. *Am. J. Transl. Res.* 10, 2435–2444.

Zhou, Y., Wang, J., Li, X., Li, K., Chen, L., Zhang, Z., et al. (2020). Neuroprotectin D1 Protects Against Postoperative Delirium-Like Behavior in Aged Mice. *Front. Aging Neurosci.* 12:582674. doi: 10.3389/fnagi.2020.582674

Conflict of Interest: The authors declare that the research was conducted in the absence of any commercial or financial relationships that could be construed as a potential conflict of interest.

Publisher's Note: All claims expressed in this article are solely those of the authors and do not necessarily represent those of their affiliated organizations, or those of the publisher, the editors and the reviewers. Any product that may be evaluated in this article, or claim that may be made by its manufacturer, is not guaranteed or endorsed by the publisher.

Copyright © 2022 Li, Wang, Chen, Guo, Zhou, Li and Peng. This is an open-access article distributed under the terms of the Creative Commons Attribution License (CC BY). The use, distribution or reproduction in other forums is permitted, provided the original author(s) and the copyright owner(s) are credited and that the original publication in this journal is cited, in accordance with accepted academic practice. No use, distribution or reproduction is permitted which does not comply with these terms.

frontiers in Aging Neuroscience

ORIGINAL RESEARCH
published: 17 January 2022
doi: 10.3389/fnagi.2021.819373

Colonic Leucine-Rich Repeat Kinase 2 Expression Is Increased and Associated With Disease Severity in Patients With Parkinson's Disease

Peng-Hsiang Liao[1†], Han-Lin Chiang[2,3†], Chia-Tung Shun[4], Jen-Fan Hang[5], Han-Mo Chiu[6,7], Ming-Shiang Wu[6] and Chin-Hsien Lin[8]*

[1] College of Medicine, National Taiwan University, Taipei, Taiwan, [2] College of Medicine, Graduate Institute of Clinical Medicine, National Taiwan University, Taipei, Taiwan, [3] Department of Neurology, Neurological Institute, Taipei Veterans General Hospital, Taipei, Taiwan, [4] Department of Pathology, National Taiwan University Hospital, Taipei, Taiwan, [5] Department of Pathology and Laboratory Medicine, Taipei Veterans General Hospital, Taipei, Taiwan, [6] Department of Internal Medicine, National Taiwan University Hospital, Taipei, Taiwan, [7] Department of Integrated Diagnostics and Therapeutics, National Taiwan University Hospital, College of Medicine, National Taiwan University, Taipei, Taiwan, [8] Department of Neurology, National Taiwan University Hospital, College of Medicine, National Taiwan University, Taipei, Taiwan

OPEN ACCESS

Edited by:
Woon-Man Kung, Chinese Culture University, Taiwan

Reviewed by:
Ji-Hong Chen, McMaster University, Canada
Byoung Dae Lee, Kyung Hee University, South Korea

***Correspondence:**
Chin-Hsien Lin
chlin@ntu.edu.tw

[†] These authors have contributed equally to this work and share first authorship

Specialty section:
This article was submitted to Parkinson's Disease and Aging-related Movement Disorders, a section of the journal Frontiers in Aging Neuroscience

Received: *21 November 2021*
Accepted: *28 December 2021*
Published: *17 January 2022*

Citation:
Liao P-H, Chiang H-L, Shun C-T, Hang J-F, Chiu H-M, Wu M-S and Lin C-H (2022) Colonic Leucine-Rich Repeat Kinase 2 Expression Is Increased and Associated With Disease Severity in Patients With Parkinson's Disease. Front. Aging Neurosci. 13:819373. doi: 10.3389/fnagi.2021.819373

Background: Mutations in leucine-rich repeat kinase 2 (*LRRK2*) comprise a common genetic risk factor for Parkinson's disease (PD) and inflammatory bowel disease (IBD). We investigated the expression of LRRK2 in colonic biopsies obtained from a cohort of PD patients and healthy controls.

Methods: A cohort of 51 PD patients and 40 age- and gender-matched controls who have colonic biopsied samples were recruited. Among these participants, 26 individuals (12 PD patients and 14 controls) had a series of colon biopsies. For the patients with PD, the first biopsies were taken before the PD diagnosis. The colonic expression of LRRK2 was assayed by immunohistochemical staining.

Results: The fraction of LRRK2-positive cells among the total cell count in biopsied colonic tissues was significantly higher in PD patients than controls (0.81% ± 0.53% vs. 0.45% ± 0.39%; $P = 0.02$). Colonic LRRK2 immunoreactivity was higher in those with *LRRK2* genetic variants compared to those with wild type *LRRK2* (2.44% ± 1.15% vs. 0.21 ± 0.13%, $P < 0.01$). Age had no effect on LRRK2 expression ($P = 0.96$). LRRK2 expression correlated with disease severity in regards to motor symptoms measured by the UPDRS part III scores (r = 6335, $P < 0.001$) and cognitive dysfunction measured by the mini-mental status examination scores ($r = -0.5774$, $P < 0.001$). PD patients in the prodromal phase had a steeper increase in colonic LRRK2 expression compared to controls during the serial colon biopsy assessment ($P < 0.01$).

Conclusion: Colonic LRRK2 expression was increased in PD patients compared to controls, and the expression level correlated with disease severity.

Keywords: Parkinson's disease, colon biopsy, leucine-rich repeat kinase 2, inflammatory bowel diseases, biomarker (BM)

INTRODUCTION

The pathological hallmarks of Parkinson's disease (PD) are progressive dopaminergic neuron loss and the presence of intracellular α-synuclein aggregations, termed Lewy bodies (Kon et al., 2020). Post-mortem studies have shown that the misfolded α-synuclein in PD may start in the enteric nervous system (ENS) of the gastrointestinal tract and subsequently propagate into brain stem nuclei via cell-to-cell transmission through the vagus nerve (Braak et al., 2003a,b). These pathological findings are coherent with clinical observations that the most common preceding symptom of PD is gastrointestinal dysfunction, particularly constipation, which may appear decades prior to the onset of motor symptoms (Savica et al., 2009). These observations prompted the hypothesis that PD is caused by an environmental trigger that alters the gut microenvironment to initiate a pathological process leading to central dopaminergic neurodegeneration through the gut-brain axis (Houser and Tansey, 2017).

Based on this gut-brain axis theory, α-synuclein immunostaining in the gut has received attention as a potential biomarker. However, many of these reports have raised concerns regarding the specificity of enteric α-synuclein expression because its immuno-reactivity has also been observed in healthy individuals and the results are conflicting (Derkinderen et al., 2011; Olanow et al., 2014). These findings suggest that enteric mucosal α-synuclein may play a limited role as a diagnostic biomarker for PD (Visanji et al., 2015; Antunes et al., 2016; Chung et al., 2016). Additionally, the investigation of enteric α-synuclein expression in a cross-sectional design has not contributed further insights into the specific propagation or accumulation of α-synuclein in the disease process of PD. Therefore, a need exists for alternative gastrointestinal biomarkers that reflect disease progression in PD.

Recent epidemiological and genetic evidence has linked PD to inflammatory bowel disease (IBD). Mutations in *Leucine-Rich Repeat Kinase* 2 (*LRRK2*) are the most common genetic factors in familial PD patients (Zimprich et al., 2004). Recent genome-wide association studies (GWAS) also highlighted *LRRK2* is an important risk factor for sporadic PD patients (Chang et al., 2017; Foo et al., 2017). Notably, GWAS have shown that *LRRK2* is also a susceptibility gene for IBD, and IBD is associated with an increased risk of PD (Umeno et al., 2011; Zhu et al., 2019). This genetic link between PD and IBD prompted us to investigate a potential association between the expression levels of LRRK2 in colonic biopsies from patients with PD. Here, we investigated the expression of LRRK2 in routine colonic biopsies from a longitudinal follow-up cohort of PD patients and healthy controls to investigate the changes in LRRK2 expression with the disease course in PD.

MATERIALS AND METHODS

Study Participants

A total of 51 patients with PD and 40 healthy controls who have colon biopsied samples were recruited from National Taiwan University Hospital. Patients were diagnosed with PD according to the United Kingdom PD Society Brain Bank criteria. All patients had received a regular health check-up with colonoscopy. Control participants who required endoscopic colonoscopies for routine medical screening or abdominal discomfort were recruited from the outpatient clinic of the Department of Gastroenterology of the same hospital. Participants were excluded if they were diagnosed with colon cancer, IBD, irritable bowel syndrome, or use of non-steroidal anti-inflammatory drugs, antibiotics, or probiotics within 3 months of specimen collection. All patients with PD were evaluated using the Unified Parkinson's disease Rating Scale part III motor scores (UPDRS-III) and Hoehn-Yahr staging. Neuropsychological evaluations were carried out with the mini-mental state examination (MMSE). All control participants underwent a detailed neurological examination to rule out PD symptoms and cognitive impairment.

Among the 91 participants, 26 (12 PD patients and 14 control participants) underwent a series of colonoscopies with colon biopsies to follow-up on the development of colon polyps. For the patients with PD, the first biopsies were taken before the PD diagnosis. For these 26 participants with serial colonic biopsies, the latest biopsied samples were used for the group comparison between PD patients and controls. We categorized the participants who underwent serial colonic biopsies into five groups: serial group 1, colonic biopsies $\geq$ 8 years before the onset of motor symptoms ($\leq$-8 years); serial group 2, colonic biopsies 3–7 years before the onset of motor symptoms (-7 to -3 years); serial group 3, colonic biopsies 2 years before or after the onset of motor symptoms (-2 to + 2 years); serial group 4, colonic biopsies 3–7 years after the diagnosis of PD (+ 3 to + 7 years); and serial group 5, colonic biopsies $\geq$ 8 years after the onset of motor symptoms ($\geq$+8). The control participants were classified into five groups according to the interval between the biopsied age and the mean age at which PD was diagnosed in the enrolled PD patients. The study protocol was approved by the Institutional Board Committee of National Taiwan University Hospital. Written informed consent was obtained from each participant.

Immunohistochemistry of Biopsied Colonic Tissues

We retrospectively examined the colonic biopsy specimens from patients with PD and controls after they provided written informed consent to participate in the study. Three to four random biopsies were taken from each study participant during colonoscopy using standard biopsy forceps. Immediately after sampling, the tissues were fixed in 4% phosphate-buffered formaldehyde and processed for paraffin embedding. The paraffinized tissue blocks were cut by a microtome into 6-μm-thick sections for immunohistochemical staining. Immunohistochemistry was performed with the BioGenex detection system according to the manufacturer's protocol. Briefly, the paraffin was melted by sequentially incubating the sections in xylene for 30, 5, and 5 min, followed by 5 min each in 100, 95, and 70% alcohol for rehydration. Heat-mediated antigen retrieval was performed in citrate buffer (pH 6.0). Samples

were allowed to cool at room temperature for at least 30 min. Protein blocking was performed for 1 h to prevent non-specific antibody binding. A primary antibody against LRRK2 (Abcam, ab1334741, 1:1000) was diluted to the desired concentration, and then added to the mixture and incubated at 4°C overnight. The next day, samples were incubated in hydrogen peroxide and methanol for 15 min to block endogenous peroxidase activity. The samples were then incubated in super enhancer solution and horseradish peroxidase for 30 min each. The 3,3′-diaminobenzidine (DAB) chromogen was added for color development. Nuclei were stained with hematoxylin. Samples were then dehydrated in different grades of alcohol (70, 95, and 100%), followed by incubation in xylene (twice, 3 min each) and a xylene substitute (NeoClear®, Merck). Sections were air dried and then mounted on slides.

Image Analysis and Quantification of Leucine-Rich Repeat Kinase 2 Expression

Slides were scanned using the Aperio Scanscope XT high-resolution scanner at 40 × magnification (Leica Biosystems, Mt. Waverley, Australia). The scanned files were imported to a computer and analyzed using StrataQuest Analysis software version 6 (TissueGnostics, Vienna, Austria). An experience pathologist (CT Shun) who was blinded to the clinical diagnosis examined each biopsied colonic tissue for staining quality and selected region of interests (ROIs) to avoid areas with colon polyp hyperplasia changes. Each slide was then carefully evaluated by two raters (PH Liao and HL Chiang) to choose ROIs comprising areas without abnormal colon polyp tissues for StrataQuest analysis (**Figures 1A,B**). The scatter plots were created to visualize the positive cells in the source images automatically using the real-time back-gating feature in the software. The cut-off values were designated to discriminate between false events and specific signals based on cell size and staining intensity (Schmid et al., 2015). Within each image, unwanted precipitate staining or areas with poor staining quality were excluded with exclusion masks automatically by the software. Only the mucosa and part of the submucosa areas were included for analysis. Cells that stained positive with both DAB and hematoxylin were counted as positive cells. The total cell count included all cells in unmasked areas within the ROI. The fraction of positive cells among the total cell count was calculated for each ROI.

Genotyping of Risk Variant and Common Mutations in *Leucine-Rich Repeat Kinase 2*

Genomic DNA was extracted from 10 ml of venous blood using standard protocols. The *LRRK2* c.4322G > A (p. R1441H) mutation on exon 31, *LRRK2* c.6035T > C (p.I2012T) and *LRRK2* c.6055G > A (p.G2019S) mutations on exon 41 and *LRRK2* c.7153G4A (p.G2385R) risk polymorphism on exon 48 were genotyped by direct DNA sequencing as previously described (Lin et al., 2008).

Statistical Analysis

Continuous variables were expressed as the mean ± standard deviation. Categorical data were expressed as the number and percentage. Continuous variables were compared between groups using the two-sample Student test, or the non-parametric Mann-Whitney U test when normality could not be assumed. Statistical analyses were performed in GraphPad Prism 8.0 (San Diego, California, United States). *P*-values < 0.05 were considered significant.

RESULTS

Fifty-one patients with PD (mean age at colon biopsy, 69.2 ± 9.2 years; 55% were men) and 40 age- and gender-matched healthy controls (mean age at colon biopsy, 71.8 ± 6.1 years; 65% were men) were included in this study (**Table 1**). Patients with PD had lower cognitive function compared to controls (MMSE scores: 26.8 ± 2.1 vs. 29.2 ± 1.8, respectively, $P < 0.01$).

The fraction of LRRK2-positive cells within the total cell count in colonic biopsies, termed the LRRK2 (+) cell ratio, were not normally distributed in PD patients or controls (**Figure 1C**). Age did not affect the colonic expression of LRRK2 in these two groups (control group: $r = -0.1810$, 95% confidence interval: −0.4736 to 0.1477, $P = 0.26$; PD group: $r = 0.0081$, 95% confidence interval: −0.2758 to 0.2907, $P = 0.96$; **Figure 2A**). We observed that LRRK2 immunostaining in the colonic submucosa and lamina propria was significantly higher in patients with PD compared to controls [**Figures 1D,E**, controls vs. PD patients: 0.45 ± 0.39% (range 0.00–4.22%) vs. 0.81 ± 0.53% (range 0.01–5.03%); $P = 0.02$]. We then genotyped for three common pathogenic mutations (p.R1441C/G/H, p.I2012T, and p.G2019S) and the Asian-specific risk polymorphism (p.G2385R) in *LRRK2*. Among 51 PD patients, three patients carried the *LRRK2* mutations (one with *LRRK2* p.R1441H mutation and the remaining two with *LRRK2* p.I2012T mutations) and 9 had the PD risk p.G2385R polymorphism. Colonic LRRK2 immunoreactivity was higher in those with *LRRK2* genetic variants, especially those with pathogenic mutations, compared to those with wild type *LRRK2* (**Figure 1F**, *LRRK2* mutation carriers vs. *LRRK2* p.G2385R carriers: 3.49 ± 1.79% vs. 1.73 ± 0.52%, $P = 0.02$; *LRRK2* p.G2385R carriers vs. wild type *LRRK2* carriers: 1.73 ± 0.52% vs. 0.21 ± 0.13%, $P = 0.01$; *LRRK2* risk or mutation carriers vs. wild type *LRRK2* carriers: 2.44 ± 1.15% vs. 0.21 ± 0.13%, $P < 0.01$). Among 40 control participants, 2 controls had *LRRK2* p.G2385R risk variant and none had *LRRK2* pathogenic mutations. The colonic expression levels of these two control participants with *LRRK2* p.G2385R variant were 4.22 and 3.24% individually, which expression levels were higher than the average level of the control participants of 0.45 ± 0.39%. Both controls were in the early fifties and had no signs of parkinsonism feature.

We then further examined the relationship between the LRRK2 (+) cell ratio in colon biopsies and the clinical severity of PD in biopsied samples from 51 patients with PD. For motor

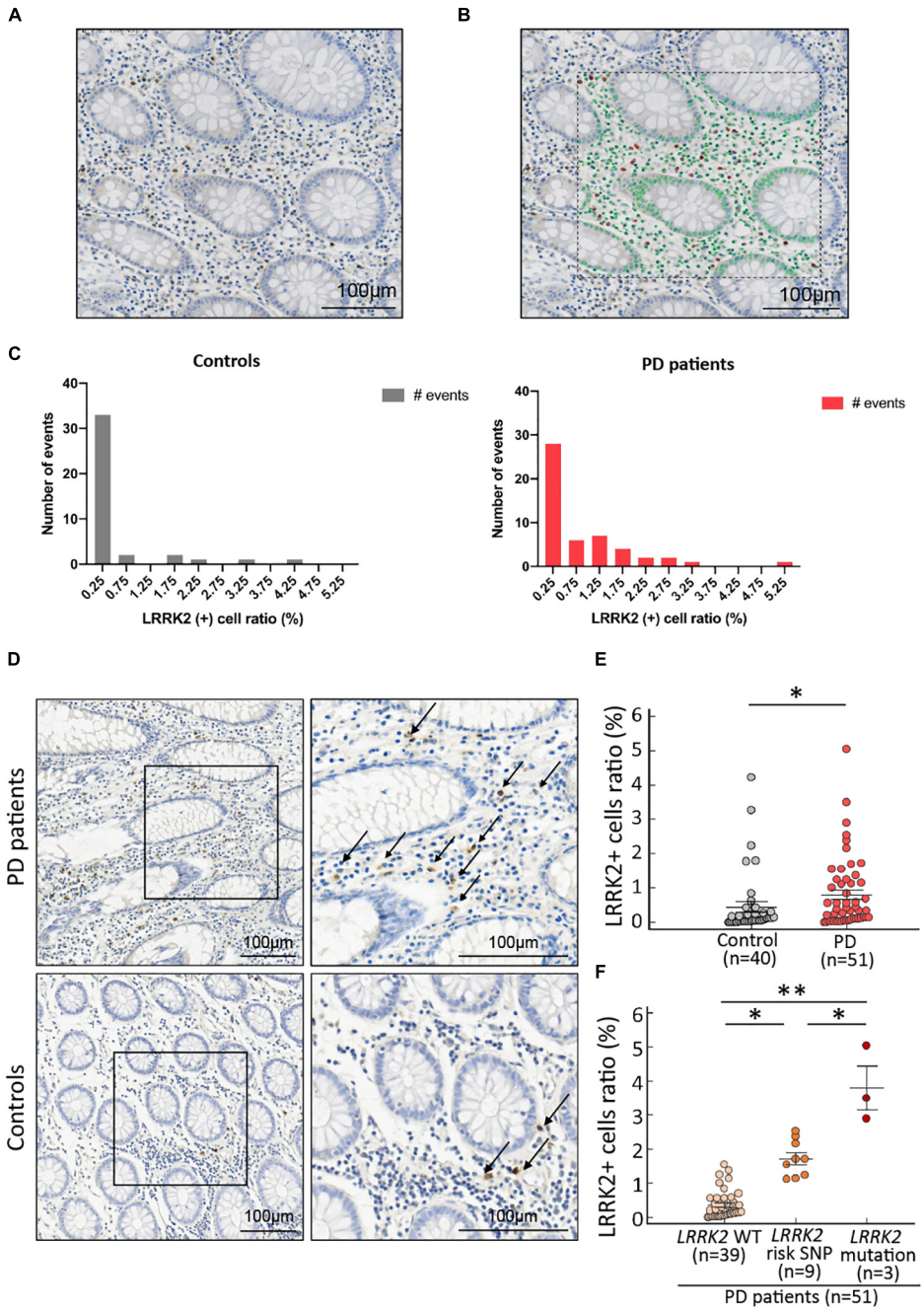

FIGURE 1 | LRRK2 expression in colonic biopsies from PD patients and age- and gender-matched controls. **(A)** Original view of the represented colonic biopsy tissues. **(B)** All nuclei are circled with green lines, and the LRRK2-positive staining detected as positive events are circled in red lines (arrows) by the StrataQuest Analysis software version 6 (TissueGnostics, Vienna, Austria). **(C)** Distribution histograms of the LRRK2-positive ratio in PD patients and controls. **(D)** Representative pictures of LRRK2-positive cells in the submucosa of colonic samples from one 72-year-old male PD patient and one 71-year-old male control participant. Positive events are indicated by arrows. The pictures on the right are the magnification of the framed areas on the left. Scale bar: 100 μm. **(E)** The fractions of LRRK2-positive cells in the total cell counts in colonic biopsies were significantly higher in PD patients than controls ($P = 0.004$ by Mann-Whitney *U*-test). **(F)** The fractions of LRRK2-positive cells in the total cell counts in colonic biopsies from PD patients with wild type or genetic variant in *LRRK2*. $^{*}P < 0.05$; $^{**}P < 0.01$.

symptom severity, the colonic LRRK2 (+) cell ratio correlated with both Hoehn-Yahr stage in the "off" state ($r = 0.6864$, $P < 0.001$) and UPDRS part III motor scores in the "off" stage ($r = 0.6335$, $P < 0.001$; **Figures 2B,C**). The colonic LRRK2 expression level negatively correlated with the MMSE score ($r = -0.5774$, $P < 0.001$; **Figure 2D**), suggesting that a higher LRRK2 expression level is associated with worse cognitive function in patients with PD.

TABLE 1 | Clinical characteristics of all participants in the current study.

Characteristics	Controls (*n* = 40)	PD (*n* = 51)	*P*-value
Current age (years)	73.7 ± 3.6	76.8 ± 11.1	0.47
Age at biopsy (years)[#]	71.8 ± 6.1	69.2 ± 9.2	0.12
Gender (Male,%)	26 (65.0)	28 (54.9)	0.33
MMSE	29.2 ± 1.8	26.8 ± 2.1	<0.01**
Disease duration (years)	N.A.	6.4 ± 1.9	
Hoehn-Yahr stages (on)	N.A.	2.2 ± 1.4	
Hoehn-Yahr stages (off)	N.A.	3.2 ± 1.3	
UPDRS part III scores (on)	N.A.	15.2 ± 8.7	
UPDRS part III scores (off)	N.A.	27.3 ± 12.6	

*Values represent the mean ± standard deviation. PD, Parkinson's disease; MMSE, mini-mental status examination; N.A., not available; UPDRS, unified Parkinson's disease rating scale. **P < 0.01.*

[#]*The age at the most recent biopsy, for patients that received serial biopsies.*

To further elucidate the time-course changes in colonic LRRK2 expression in the disease process of PD, the colonic tissues biopsied from 12 PD patients who had a series of colon biopsied samples (age at the latest biopsy: 75.1 ± 5.8 years; 58% were men) and 14 age- and gender-matched control participants (age at the latest biopsy: 71.4 ± 4.5 years; 57% were men) who underwent a series of colon biopsies were analyzed. Compared to controls, the LRRK2 expression levels started to increase in patients with PD in the prodromal phase, sampling time for which was before the onset of PD motor symptoms (**Figures 3A,B**). Looking at the individual data, the tendency for increased LRRK2 expression varied, as some patients had increased LRRK2 levels before the onset of motor dysfunction and some had steady expression regardless of the disease process (**Figure 3A**). Therefore, the results were further classified into five serial groups according to the sampling time in relation to the age of onset of motor dysfunction in PD group, which was 67 years old. Consistently, the grouping data showed that the colonic LRRK2 expression started to increase before the diagnosis of PD and was higher in PD patients compared to controls in serial group 3 ($P < 0.01$). As PD progressed, the expression of LRRK2 in colonic biopsies increased in accordance with the disease course (**Figure 3B**).

DISCUSSION

This study demonstrated an increase in LRRK2 expression in colonic biopsied specimens from patients with PD compared to age- and gender-matched controls. Among PD patients, the colonic LRRK2 level correlated with disease severity in both motor and cognitive function, and the expression levels were higher in those carrying *LRRK2* risk or pathogenic variants

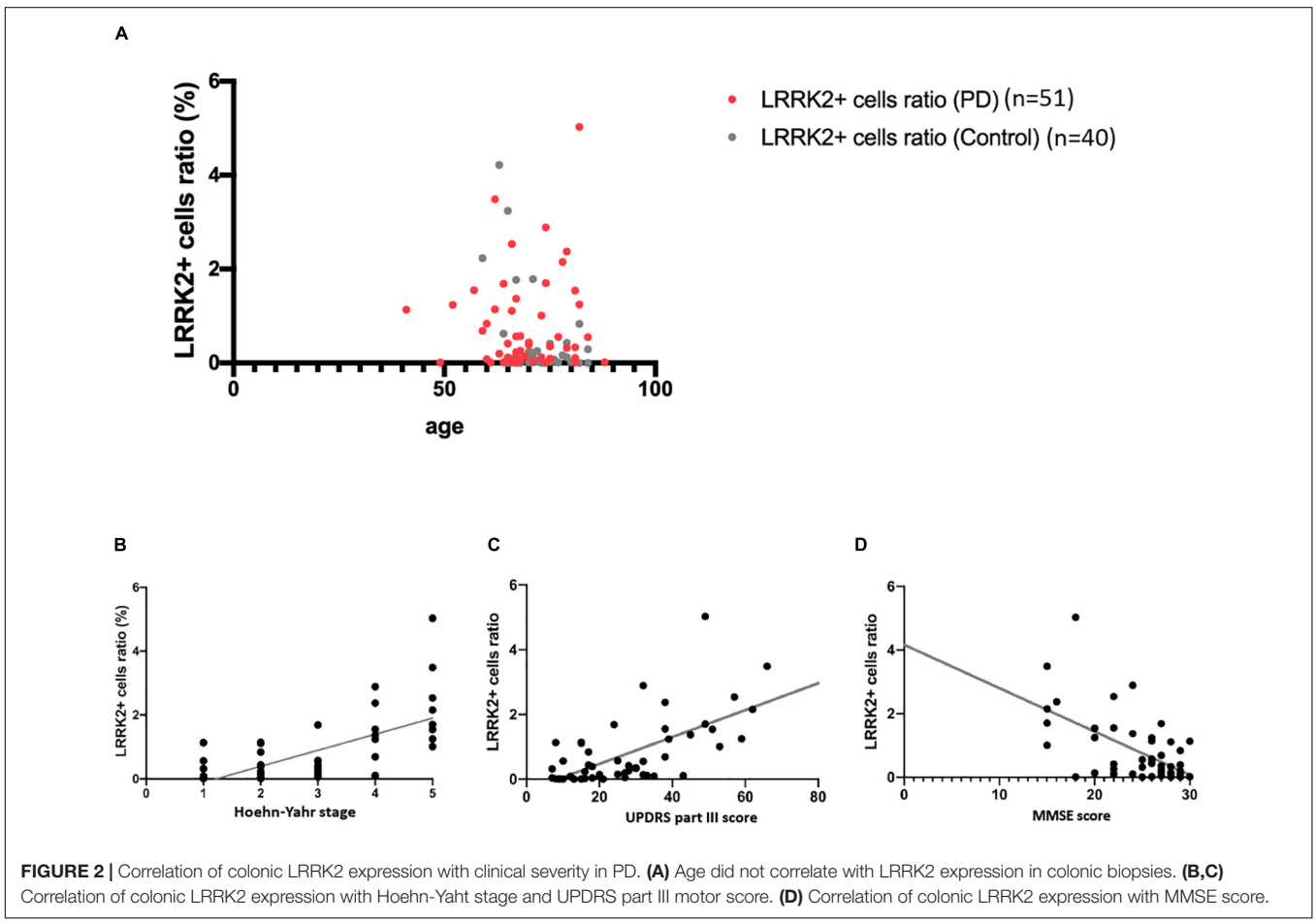

FIGURE 2 | Correlation of colonic LRRK2 expression with clinical severity in PD. **(A)** Age did not correlate with LRRK2 expression in colonic biopsies. **(B,C)** Correlation of colonic LRRK2 expression with Hoehn-Yaht stage and UPDRS part III motor score. **(D)** Correlation of colonic LRRK2 expression with MMSE score.

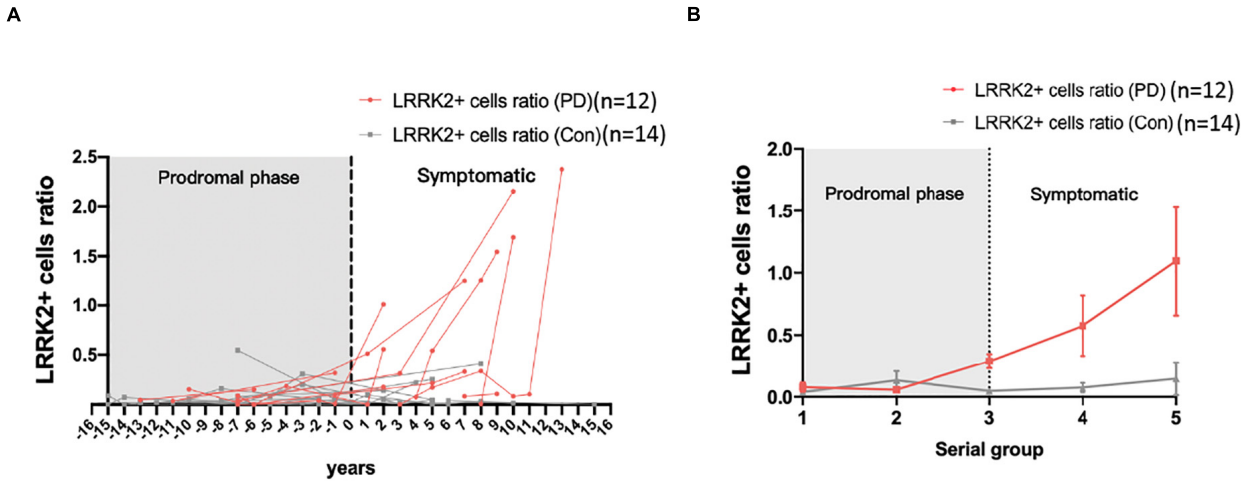

FIGURE 3 | Time-sequential serial analysis of LRRK2 expression in colonic biopsies from patients with PD and controls. **(A)** Individual data for colonic LRRK2 expression from the serial study. **(B)** Grouping analysis of colonic LRRK2 expression was significantly different between PD patients and controls in individual time serial groups.

than those with wild type *LRRK2*. Furthermore, PD patients in the prodromal phase had increased colonic LRRK2 expression compared to controls and, as the disease progressed, the expression of LRRK2 in colonic tissues progressively increased. These results suggest that colonic LRRK2 expression may serve as a surrogate gut-oriented marker of PD.

Routine colonic biopsies typically comprise mucosal and submucosal tissues, including submucosal immune cells and enteric nervous system ganglia and neurites (Lebouvier et al., 2010). Consistent with previous results, the LRRK2 expression in biopsied tissues was low (Westerlund et al., 2008). LRRK2 was detected in the submucosa and lamina propria, but not in intestinal epithelial cells, which is in line with our findings. Evidence has shown that LRRK2 is highly expressed in a subset of mannose receptor-positive macrophages, dendritic cells, and intestinal B cells (Gardet et al., 2010). Notably, the expression of LRRK2 would be activated by the pro-inflammatory cytokine IFN-γ, which would be upregulated by bacteria-induced or gut inflammation, and LRRK2 is an activator of the pro-inflammatory NF-κB pathway, resulting in a vicious cycle of gut inflammation (Gardet et al., 2010). Our observations show a higher colonic expression level of LRRK2 in PD patients compared to controls, especially in those with *LRRK2* risk or mutation carriers, and the expression correlated with disease severity, suggesting that LRRK2 may be involved in the pathophysiology of PD in the very beginning of the disease process that is relevant to the host responses to altered gut microbiota observed in PD (Lin et al., 2019; Romano et al., 2021). Furthermore, reproducibility of the immunostaining and the storage duration of the biopsied samples are critical issues for this kind of retrospective pathology analysis. As the colon biopsied samples analyzed in this study were collected across the time period of 10 years, the stability of the antigen or the targeted protein degradation remains an issue for immunostaining analysis. Antigen decay in archival formalin-fixed paraffin-embedded (FFPE) tissue sections for immunohistochemistry is a well-known phenomenon which may affect the results of the analysis and the length of storage time appears fundamental. A recent study has shown that the immunoreactivities for cytosolic proteins could be preserved for up to 50 years, but nuclear antigens, for example Ki67 and CD31, presented reduced staining intensity in older and aged FFPE blocks (Grillo et al., 2017). As LRRK2 is a cytosolic protein, we assume the immunoreactivity for those biopsied blocks acquired 10 years ago may not decline dramatically. However, a future prospective follow up study analyzing the immunoreactivity of multiple targeted proteins in fresh biopsied samples is needed to confirm our findings.

Emerging evidence has suggested that PD comprises two subtypes. One subtype is the gut-initiated body-first subtype, in which the Lewy body pathology originates in the gut enteric nervous system and then ascends through the vagus nerve and sympathetic connectome to the brainstem. The second subtype is a brain-first subtype in which the Lewy body pathology initially arises in the brain itself or enters through the olfactory bulb, subsequently descending to the peripheral autonomic nervous system (Horsager et al., 2020). Genetic evidence has suggested that LRRK2 is a link between IBD and PD (Umeno et al., 2011; Zhu et al., 2019), and mild intestinal inflammation is common in patients with PD (Forsyth et al., 2011); therefore, it is reasonable to speculate that the colonic LRRK2 expression would be increased in those who are in the body-first subtype of PD. The serial analysis of colonic biopsies in this study showed a diverse pattern of colonic LRRK2 expression from the prodromal phase to the symptomatic stage years after the occurrence of motor dysfunction. Some patients had increased LRRK2 expression compared to healthy controls before the diagnosis of PD, and the LRRK2 level increased along with the disease progression, whereas a minority of the patients did not follow this trend and possessed steady, low LRRK2 levels throughout the disease

course. Although Braak's pathology staging showed that Lewy body pathology initially forms in the gut enteric nervous system (Braak et al., 2003a), alternative neuropathology staging systems for Lewy pathology in some PD patients has shown an amygdala-predominant profile with significantly fewer Lewy bodies in the brainstem or gut, which fits in the brain-first subtype of PD (Raunio et al., 2019). Therefore, we speculate that those with abundant colonic LRRK2 expression or an increased colonic LRRK2 level in the prodromal phase may have associated Lewy body pathology in the gastrointestinal tract. Of note, there were two control participants carrying the *LRRK2* p.G2385R risk variant and having the relatively high levels of colonic LRRK2 expression. Although these two controls did not show evidence of parkinsonism features in their early fifties while receiving colonic biopsy, they should be closely monitored for early prodromal or motor symptoms of PD during follow-up.

Further studies that examine the co-immunostaining of a-synuclein and LRRK2 in those with preceding gastrointestinal symptoms, brainstem dysfunctional symptoms of rapid eye movement sleep behavior disorder or having *LRRK2* risk variants are needed to confirm our hypothesis.

This study had several limitations. First, although we have a large number of colonic biopsied samples for cross-sectional comparison study but only a relatively small number of patients had a series of colonic biopsies in our serial change study. In addition, the participants did not usually undergo serial colonic biopsies at regular intervals, which made time grouping necessary to avoid a lack of data in a certain year influencing the entire analysis. Second, the biopsied samples were taken during routine random colon biopsy and the biopsied anatomic sites may affect the results. Third, in this retrospective study, we did not have the gut symptoms or gastrointestinal questionnaire data of all enrolled participants. Future prospective studies with comprehensively gastrointestinal symptoms combing with food questionnaire are needed. Finally, we did not examine the colonic expression of LRRK2 in different cell types or examine any evidence of gut inflammation. Further studies examining the LRRK2 expression in different neuronal subtypes in the colon, such as choline acetyltransferase (ChAT)-positive, vasoactive intestinal peptide (VIP)-secreting neurons and sympathetic tyrosine hydroxylase-positive neurons, will provide a more comprehensive landscape of LRRK2 expression in individual cell types of PD process. Future studies that investigate the expression of LRRK2 and a-synuclein in individual colonic cell types and inflammatory marker are needed.

CONCLUSION

In conclusion, this study showed that LRRK2 expression is increased in colonic biopsies from PD patients, and the expression level was associated with the clinical severity of PD. Future prospective studies with a larger sample size of participants are needed to confirm our findings.

DATA AVAILABILITY STATEMENT

The original contributions presented in the study are included in the article, further inquiries can be directed to the corresponding author/s.

ETHICS STATEMENT

This study protocol was approved by the Institutional Board Committee of National Taiwan University Hospital. The patients/participants provided their written informed consent to participate in this study.

AUTHOR CONTRIBUTIONS

P-HL, H-LC, and C-HL: study concept and design. P-HL, H-LC, C-TS, H-MC, M-SW, and C-HL: acquisition of data. P-HL, H-LC, J-FH, and C-HL: analysis and interpretation of data. P-HL and C-HL: drafting the manuscript. C-HL: critical revision of the manuscript for important intellectual content, and study supervision. P-HL: statistical analysis. All authors contributed to the article and approved the submitted version.

FUNDING

This work was supported by grants from the National Health Research Institute (NHRI-EX109-10716NC) and the National Taiwan University Hospital (NTUH 109-T18, 109-EDN02, and UN109-011).

ACKNOWLEDGMENTS

We thank all of the participants who joined in this study and the staff of the second core laboratory of National Taiwan University Hospital for their technical support.

REFERENCES

Antunes, L., Frasquilho, S., Ostaszewski, M., Weber, J., Longhino, L., Antony, P., et al. (2016). Similar alpha-Synuclein staining in the colon mucosa in patients with Parkinson's disease and controls. *Mov. Disord.* 31, 1567–1570. doi: 10.1002/mds.26702

Braak, H., Del Tredici, K., Rub, U., De Vos, R. A., Jansen Steur, E. N., and Braak, E. (2003a). Staging of brain pathology related to sporadic Parkinson's disease. *Neurobiol. Aging* 24, 197–211. doi: 10.1016/S0197-4580(02)00065-9

Braak, H., Rub, U., Gai, W. P., and Del Tredici, K. (2003b). Idiopathic Parkinson's disease: possible routes by which vulnerable neuronal types may be subject to neuroinvasion by an unknown pathogen. *J. Neural. Transm.* 110, 517–536. doi: 10.1007/s00702-002-0808-2

Chang, D., Nalls, M. A., Hallgrímsdóttir, I. B., Hunkapiller, J., van der Brug, M., Cai, F., et al. (2017). A meta-analysis of genome-wide association studies identifies 17 new Parkinson's disease risk loci. *Nat. Genet.* 49, 1511–1516. doi: 10.1038/ng.3955

Chung, S. J., Kim, J., Lee, H. J., Ryu, H. S., Kim, K., Lee, J. H., et al. (2016). Alpha-synuclein in gastric and colonic mucosa in Parkinson's disease: limited role as a biomarker. *Mov. Disord.* 31, 241–249. doi: 10.1002/mds.26473

Derkinderen, P., Rouaud, T., Lebouvier, T., Bruley Des Varannes, S., Neunlist, M., and De Giorgio, R. (2011). Parkinson disease: the enteric nervous system spills its guts. *Neurology* 77, 1761–1767. doi: 10.1212/WNL.0b013e318236ef60

Foo, J. N., Tan, L. C., Irwan, I. D., Au, W. L., Low, H. Q., Prakash, K. M., et al. (2017). Genome-wide association study of Parkinson's disease in East Asians. *Hum. Mol. Genet.* 26, 226–232.

Forsyth, C. B., Shannon, K. M., Kordower, J. H., Voigt, R. M., Shaikh, M., Jaglin, J. A., et al. (2011). Increased intestinal permeability correlates with sigmoid mucosa alpha-synuclein staining and endotoxin exposure markers in early Parkinson's disease. *PLoS One* 6:e28032. doi: 10.1371/journal.pone.0028032

Gardet, A., Benita, Y., Li, C., Sands, B. E., Ballester, I., Stevens, C., et al. (2010). LRRK2 is involved in the IFN-gamma response and host response to pathogens. *J. Immunol.* 185, 5577–5585. doi: 10.4049/jimmunol.1000548

Grillo, F., Bruzzone, M., Pigozzi, S., Prosapio, S., Migliora, P., Fiocca, R., et al. (2017). Immunohistochemistry on old archival paraffin blocks: is there an expiry date? *J. Clin. Pathol.* 70, 988–993. doi: 10.1136/jclinpath-2017-204387

Horsager, J., Andersen, K. B., Knudsen, K., Skjaerbaek, C., Fedorova, T. D., Okkels, N., et al. (2020). Brain-first versus body-first Parkinson's disease: a multimodal imaging case-control study. *Brain* 143, 3077–3088. doi: 10.1093/brain/awaa238

Houser, M. C., and Tansey, M. G. (2017). The gut-brain axis: is intestinal inflammation a silent driver of Parkinson's disease pathogenesis? *NPJ Parkinsons. Dis.* 3:3. doi: 10.1038/s41531-016-0002-0

Kon, T., Tomiyama, M., and Wakabayashi, K. (2020). Neuropathology of Lewy body disease: clinicopathological crosstalk between typical and atypical cases. *Neuropathology* 40, 30–39. doi: 10.1111/neup.12597

Lebouvier, T., Neunlist, M., Bruley Des Varannes, S., Coron, E., Drouard, A., N'guyen, J. M., et al. (2010). Colonic biopsies to assess the neuropathology of Parkinson's disease and its relationship with symptoms. *PLoS One* 5:e12728. doi: 10.1371/journal.pone.0012728

Lin, C. H., Chen, C. C., Chiang, H. L., Liou, J. M., Chang, C. M., Lu, T. P., et al. (2019). Altered gut microbiota and inflammatory cytokine responses in patients with Parkinson's disease. *J. Neuroinflammation.* 16:129. doi: 10.1186/s12974-019-1528-y

Lin, C. H., Tzen, K. Y., Yu, C. Y., Tai, C. H., Farrer, M. J., and Wu, R. M. (2008). LRRK2 mutation in familial Parkinson's disease in a Taiwanese population: clinical, PET, and functional studies. *J. Biomed. Sci.* 15, 661–667. doi: 10.1007/s11373-008-9260-0

Olanow, C. W., Wakeman, D. R., and Kordower, J. H. (2014). Peripheral alpha-synuclein and Parkinson's disease. *Mov. Disord.* 29, 963–966. doi: 10.1002/mds.25966

Raunio, A., Kaivola, K., Tuimala, J., Kero, M., Oinas, M., Polvikoski, T., et al. (2019). Lewy-related pathology exhibits two anatomically and genetically distinct progression patterns: a population-based study of Finns aged 85. *Acta Neuropathol.* 138, 771–782. doi: 10.1007/s00401-019-02071-3

Romano, S., Savva, G. M., Bedarf, J. R., Charles, I. G., Hildebrand, F., and Narbad, A. (2021). Meta-analysis of the Parkinson's disease gut microbiome suggests alterations linked to intestinal inflammation. *NPJ Parkinsons. Dis.* 7:27. doi: 10.1038/s41531-021-00156-z

Savica, R., Carlin, J. M., Grossardt, B. R., Bower, J. H., Ahlskog, J. E., Maraganore, D. M., et al. (2009). Medical records documentation of constipation preceding Parkinson disease: a case-control study. *Neurology* 73, 1752–1758. doi: 10.1212/WNL.0b013e3181c34af5

Schmid, M., Dufner, B., Durk, J., Bedal, K., Stricker, K., Prokoph, L. A., et al. (2015). An emerging approach for parallel quantification of intracellular protozoan parasites and host cell characterization using TissueFAXS cytometry. *PLoS One* 10:e0139866. doi: 10.1371/journal.pone.0139866

Umeno, J., Asano, K., Matsushita, T., Matsumoto, T., Kiyohara, Y., Iida, M., et al. (2011). Meta-analysis of published studies identified eight additional common susceptibility loci for Crohn's disease and ulcerative colitis. *Inflamm. Bowel Dis.* 17, 2407–2415. doi: 10.1002/ibd.21651

Visanji, N. P., Marras, C., Kern, D. S., Al Dakheel, A., Gao, A., Liu, L. W., et al. (2015). Colonic mucosal a-synuclein lacks specificity as a biomarker for Parkinson disease. *Neurology* 84, 609–616. doi: 10.1212/WNL.0000000000001240

Westerlund, M., Belin, A. C., Anvret, A., Bickford, P., Olson, L., and Galter, D. (2008). Developmental regulation of leucine-rich repeat kinase 1 and 2 expression in the brain and other rodent and human organs: implications for Parkinson's disease. *Neuroscience* 152, 429–436. doi: 10.1016/j.neuroscience.2007.10.062

Zhu, F., Li, C., Gong, J., Zhu, W., Gu, L., and Li, N. (2019). The risk of Parkinson's disease in inflammatory bowel disease: a systematic review and meta-analysis. *Dig. Liver Dis.* 51, 38–42. doi: 10.1016/j.dld.2018.09.017

Zimprich, A., Biskup, S., Leitner, P., Lichtner, P., Farrer, M., Lincoln, S., et al. (2004). Mutations in LRRK2 cause autosomal-dominant parkinsonism with pleomorphic pathology. *Neuron* 44, 601–607. doi: 10.1016/j.neuron.2004.11.005

Conflict of Interest: The authors declare that the research was conducted in the absence of any commercial or financial relationships that could be construed as a potential conflict of interest.

Publisher's Note: All claims expressed in this article are solely those of the authors and do not necessarily represent those of their affiliated organizations, or those of the publisher, the editors and the reviewers. Any product that may be evaluated in this article, or claim that may be made by its manufacturer, is not guaranteed or endorsed by the publisher.

Copyright © 2022 Liao, Chiang, Shun, Hang, Chiu, Wu and Lin. This is an open-access article distributed under the terms of the Creative Commons Attribution License (CC BY). The use, distribution or reproduction in other forums is permitted, provided the original author(s) and the copyright owner(s) are credited and that the original publication in this journal is cited, in accordance with accepted academic practice. No use, distribution or reproduction is permitted which does not comply with these terms.

frontiers in Aging Neuroscience

ORIGINAL RESEARCH
published: 17 January 2022
doi: 10.3389/fnagi.2021.788765

Intrinsic Brain Activity Alterations in Patients With Mild Cognitive Impairment-to-Normal Reversion: A Resting-State Functional Magnetic Resonance Imaging Study From Voxel to Whole-Brain Level

Qili Hu[1†], Qianqian Wang[2,3†], Yunfei Li[1], Zhou Xie[4], Xiaomei Lin[1], Guofeng Huang[4], LinLin Zhan[5], Xize Jia[2,3] and Xiaohu Zhao[1*]*

[1] Department of Radiology, Shanghai Fifth People's Hospital, Fudan University, Shanghai, China, [2] School of Teacher Education, Zhejiang Normal University, Jinhua, China, [3] Key Laboratory of Intelligent Education Technology and Application of Zhejiang Province, Zhejiang Normal University, Jinhua, China, [4] School of Information and Electronics Technology, Jiamusi University, Jiamusi, China, [5] School of Western Language, Heilongjiang University, Heilongjiang, China

OPEN ACCESS

Edited by:
Jiehui Jiang,
Shanghai University, China

Reviewed by:
Yu Zheng,
Nanjing Medical University, China
Xia-an Bi,
Hunan Normal University, China
Zaixu Cui,
Chinese Institute for Brain Research (CIBR), China
Xiaojun Xu,
Zhejiang University, China

***Correspondence:**
Xize Jia
jiaxize@foxmail.com
Xiaohu Zhao
xhZhao999@263.net

[†] These authors have contributed equally to this work

Specialty section:
This article was submitted to Neurocognitive Aging and Behavior, a section of the journal Frontiers in Aging Neuroscience

Received: 03 October 2021
Accepted: 08 December 2021
Published: 17 January 2022

Citation:
Hu Q, Wang Q, Li Y, Xie Z, Lin X, Huang G, Zhan L, Jia X and Zhao X (2022) Intrinsic Brain Activity Alterations in Patients With Mild Cognitive Impairment-to-Normal Reversion: A Resting-State Functional Magnetic Resonance Imaging Study From Voxel to Whole-Brain Level. Front. Aging Neurosci. 13:788765. doi: 10.3389/fnagi.2021.788765

Mild cognitive impairment (MCI) reversion refers to patients with MCI who revert from MCI to a normal cognitive state. Exploring the underlying neuromechanism of MCI reverters may contribute to providing new insights into the pathogenesis of Alzheimer's disease and developing therapeutic interventions. Information on patients with MCI and healthy controls (HCs) was collected from the Alzheimer's Disease Neuroimaging Initiative database. We redefined MCI reverters as patients with MCI whose logical memory scores changed from MCI to normal levels using the logical memory criteria. We explored intrinsic brain activity alterations in MCI reverters from voxel, regional, and whole-brain levels by comparing resting-state functional magnetic resonance imaging metrics of the amplitude of low-frequency of fluctuation (ALFF), the fractional amplitude of low-frequency fluctuation (fALFF), percent amplitude of fluctuation (PerAF), regional homogeneity (ReHo), and degree centrality (DC) between MCI reverters and HCs. Finally, partial correlation analyses were conducted between cognitive scale scores and resting-state functional magnetic resonance imaging metrics of brain regions, revealing significant group differences. Thirty-two patients with MCI from the Alzheimer's Disease Neuroimaging Initiative database were identified as reverters. Thirty-seven age-, sex-, and education-matched healthy individuals were also enrolled. At the voxel level, compared with the HCs, MCI reverters had increased ALFF, fALFF, and PerAF in the frontal gyrus (including the bilateral orbital inferior frontal gyrus and left middle frontal gyrus), increased PerAF in the left fusiform gyrus, and decreased ALFF and fALFF in the right inferior cerebellum. Regarding regional and whole-brain levels, MCI reverters showed increased ReHo in the left fusiform gyrus and right median cingulate and paracingulate gyri; increased DC in the left inferior temporal gyrus

and left medial superior frontal; decreased DC in the right inferior cerebellum and bilateral insular gyrus relative to HCs. Furthermore, significant correlations were found between cognitive performance and neuroimaging changes. These findings suggest that MCI reverters show significant intrinsic brain activity changes compared with HCs, potentially related to the cognitive reversion of patients with MCI. These results enhance our understanding of the underlying neuromechanism of MCI reverters and may contribute to further exploration of Alzheimer's disease.

Keywords: mild cognitive impairment, Alzheimer's disease, resting-state fMRI, intrinsic brain activity, cognitive reversion

INTRODUCTION

Alzheimer's disease (AD), accounting for 60–80% of all dementia cases, is an irreversible neurodegenerative disease that causes progressive problems with memory, judgment, orientation, and other functions (Dai and He, 2014). It has been reported that every 65 s someone in the United States will be diagnosed with AD, and the number of people aged ≥ 65 years with AD may increase to a projected 13.8 million by 2050[1]. However, the pathogenesis of AD remains unclear, and no drugs or other therapeutic interventions have been proven to be effective.

With an elevated risk of progression to AD (Busse et al., 2006; Petersen et al., 2009; Belleville et al., 2011; Buschert et al., 2011), mild cognitive impairment (MCI) is generally considered a transitional state between normal cognitive functioning and dementia. Research on this mental state has recently increased. Patients with MCI may progress to dementia, maintain stability, or revert to normal (Petersen et al., 2009); thus, most studies have mainly focused on studying MCI-to-dementia or MCI-stable populations and have made considerable contributions in identifying individuals at high risk of developing dementia (Li et al., 2021; Pyun et al., 2021). However, the cognitively normal-to-MCI-to-AD trajectory is not always unidirectional. A large portion of individuals diagnosed with MCI revert to cognitively normal status when reevaluated after ≥ 1 year (up to 30–50%) (Canevelli et al., 2016; Malek-Ahmadi, 2016). Less research attention has been paid to this population, and the neuromechanism underlying cognitive reversion has not been clearly explained. Therefore, further exploration of the neural basis of MCI reverters may contribute to providing new insights into the pathogenesis of AD and developing specific pharmacologic and nonpharmacologic interventions.

Resting-state functional magnetic resonance imaging (rs-fMRI), a widely known tool for investigating brain function, is a promising approach for exploring brain activity alterations (Biswal, 2012). A series of rs-fMRI metrics are used to reflect the intrinsic brain activity from different aspects. At the voxel level, the amplitude of low-frequency fluctuation (ALFF), defined as the mean amplitude of fluctuations within the range of low frequency, directly characterizes the spontaneous activity of each voxel (Zang et al., 2007). The fractional amplitude of low-frequency fluctuation (fALFF), i.e., the ratio of ALFF within a specific low-frequency band to the total blood oxygen level-dependent (BOLD) fluctuation amplitude of the full frequency band (Zou et al., 2008), is regarded as a standardized ALFF-like metric at the single voxel level. The percent amplitude of fluctuation (PerAF), i.e., the percentage of BOLD fluctuations relative to the mean BOLD signal intensity for each time point and averaged across the whole time series (Jia et al., 2020), has better test-retest reliability in both intra-and inter-scanners. Regarding regional and whole-brain levels, regional homogeneity (ReHo) measures the functional synchronization between a given voxel and its neighboring voxels (Zang et al., 2004), and degree centrality (DC) can be used to evaluate intrinsic functional connectivity across the whole brain.

These metrics have attracted significant research interest in the neural mechanisms of individuals with MCI. Studies have identified that regions in those patients, compared with healthy controls (HCs), have decreased or increased ALFF, fALFF, PerAF, ReHo, and DC, which reflects abnormal intrinsic brain activity in widespread areas of patients with MCI (Li et al., 2017; Liu et al., 2018, 2019; Yang et al., 2018; Xiong et al., 2021). Furthermore, a longitudinal study demonstrated that ALFF and fALFF values in some brain regions changed gradually with disease progression, and these metrics were significantly correlated with neuropsychological performance (Yang et al., 2018). These results indicate that ALFF and fALFF may help to detect the underlying pathological mechanism in the AD continuum. Additionally, previous studies have detected several brain regions with higher ALFF in patients with MCI related to those exhibiting functional disruptions in AD, which may indicate a possible compensatory mechanism in the early stage of AD (Wang et al., 2015; Xing et al., 2021). These findings contribute to partly elucidating the functional abnormalities in patients with MCI. To date, the brain functional mechanism in MCI reverters remains unclear, and relatively few studies explore MCI reversion through rs-fMRI.

[1]https://www.alz.org/

Abbreviations: AD, Alzheimer's disease; ADNI, Alzheimer's Disease Neuroimaging Initiative; ALFF, amplitude of low-frequency of fluctuation; BOLD, blood oxygen level dependent; Cerebellum_9_R, right inferior cerebellum; DC, degree centrality; DCG.R, right median cingulate and paracingulate gyri; fALFF, fractional amplitude of low-frequency of fluctuation; FDR, false discovery rate; FFG.L, left fusiform gyrus; GRF, Gaussian Random Field; HCs, healthy controls; INS.L and INS.R, bilateral insular; ITG.L, left inferior temporal gyrus; LM, logical memory; MCI, mild cognitive impairment; MFG.L, left middle frontal gyrus; ORBinf.R, right orbital inferior frontal gyrus; ORBmid.L, left orbital middle frontal gyrus; PerAF, percent amplitude of fluctuation; ReHo, regional homogeneity; rs-fMRI, resting-state functional magnetic resonance imaging; SFGmed.L, left medial superior frontal gyrus.

Therefore, we aimed to perform an exploratory study to indicate the intrinsic brain activity alterations in MCI reverters from different scales by combining various rs-fMRI metrics, namely ALFF, fALFF, PerAF, ReHo, and DC.

The Alzheimer's Disease Neuroimaging Initiative (ADNI) database is a longitudinal multisite observational study of elderly individuals with normal cognition, MCI, and AD (Veitch et al., 2021). In the present study, we obtained information on patients with MCI and healthy controls (HCs) from the ADNI. Currently, the diagnostic criteria for MCI reverters remain controversial. Generally, the most common diagnostic criteria include clinical consensus, neuropsychological tests, and a combination of neuropsychological and daily functional tests (Winblad et al., 2004; Gao et al., 2014; Canevelli et al., 2016; Malek-Ahmadi, 2016; Pandya et al., 2017). Clinical consensus is relatively easily influenced by the clinician's subjective judgment, while the combination of neuropsychological tests and daily functional tests is associated with poor patient compliance and less sensitivity. The use of neuropsychological tests as criteria is an approach that balances sensitivity, reliability, and simplicity. ADNI applied the combination of three neuropsychological tests including clinical dementia rating (CDR), logical memory (LM), and mini-mental state examination (MMSE) as diagnostic criteria of MCI reverters (Petersen et al., 2010). Only patients with MCI that meet all these criteria can be regarded as reverters. Thomas et al. (2019a,b) demonstrated that the standard ADNI MCI criteria may result in certain rates of "false positive" and "false negative" MCI diagnoses, which may be driven by weighting the subjective CDR more heavily than the objective memory test (LM). Further analysis showed that reverters identified by LM were more reliable. These reverters were more closely resemble HCs in terms of positive AD biomarkers (cerebrospinal fluid and genetic susceptibility) and have higher global cognition than those identified by standard AD criteria. Thus, in the current study, we redefined MCI reverters in the ADNI database by applying LM criteria, which may increase the validity of our results.

In this study, we first redefined MCI reverters in the ADNI database using the LM criteria. We then assessed the intrinsic brain activity changes in these patients at the voxel, regional, and whole-brain levels by comparing ALFF, fALFF, PerAF, ReHo, and DC between the MCI-to-normal and HC groups. Finally, we examined the relationship between altered brain activity and clinical features. These results may help us to further understand the underlying neuromechanisms of cognitive reversion.

MATERIALS AND METHODS

Subjects

Data used in the preparation of this article were obtained from the ADNI database[2]. Data collection has been conducted in accordance with the tenets of the Declaration of Helsinki and was approved by the institutional review boards of all participating sites. All subjects and their legal representatives gave written informed consent prior to data collection. We focused on the data acquired from the 3.0 Tesla Siemens Prisma MRI scanner in ADNI 3. The detailed criteria of included subjects in ADNI 3 have been described at http://adni.loni.usc.edu/wp-content/themes/freshnews-dev-v2/documents/clinical/ADNI3_Protocol.pdf. Based on a previous study (Thomas et al., 2019b), we selected 41 patients with MCI-to-normal reversion according to the following criteria: a) LM scores improved from MCI (at first scan) to normal level (at any subsequent scans); b) scores of the Mini-Mental Status Examination (MMSE) were higher than 24 when the LM ability of the patients with MCI was evaluated as normal. Additionally, 66 HCs with no significant neurologic diseases were included.

Data Acquisition

The rs-fMRI, structural MRI, and behavioral data were downloaded. We only included the MRI data of MCI reverters by the time their LM ability was evaluated as normal. The following are the two scanning methods for rs-fMRI data: basic scanning and advanced scanning (multiband scanning). The parameters of the basic scanning were as follows: axial rs-fMRI (eyes open), repetition time/echo time = 3000/30 ms, field of view = 220 × 220 mm, matrix = 64 × 64, flip angle = 90°, voxel size = 3.4 mm × 3.4 mm × 3.4 mm, thick slices = 3.4 mm, number of slices = 48, and total volume = 197. Regarding advanced scanning, the parameters were as follows: axial MB rs-fMRI (eyes open), repetition time/echo time = 607/32 ms, field of view = 220 × 220 mm, matrix = 88 × 88, flip angle = 90°, voxel size = 2.5 mm × 2.5 mm × 2.5 mm, thick slices = 2.5 mm, number of slices = 64, and total volume = 976. All structural MRI data were acquired with the following parameters: accelerated sagittal magnetization prepared-rapid gradient echo, repetition time/echo time = 2300/2.98 ms, inversion time = 900 ms, field of view = 256 × 240 mm, matrix = 256 × 240, voxel size = 1.0 mm × 1.0 mm × 1.0 mm, flip angle = 9°, thick slice = 1.0 mm, and number of slices = 208 (partial basic scanning data = 176). 19 subjects underwent advanced scanning and 50 subjects underwent basic scanning. The scanning method for each subject is shown in **Supplementary Table 1**. The behavioral data, including a series of cognitive scales, are presented in **Supplementary Table 2**.

Data Preprocessing

Data preprocessing was performed using Statistical Parametric Mapping (SPM 12)[3] and the Resting-State fMRI Data Analysis Toolkit plus (RESTplus v.1.24)[4] (Jia et al., 2019) and conducted using MATLAB 2018a platform[5]. All digital imaging and communications in medicine data were converted to neuroimaging informatics technology initiative data. To stabilize the signal of the scanner and to enable subjects to adapt to the environment (Cui et al., 2020), the first 10 volumes of each neuroimaging informatics technology initiative dataset

[2]http://adni.loni.usc.edu/

[3]http://www.fil.ion.ucl.ac.uk/spm

[4]http://restfmri.net/forum/restplus

[5]https://ww2.mathworks.cn/products/matlab.html

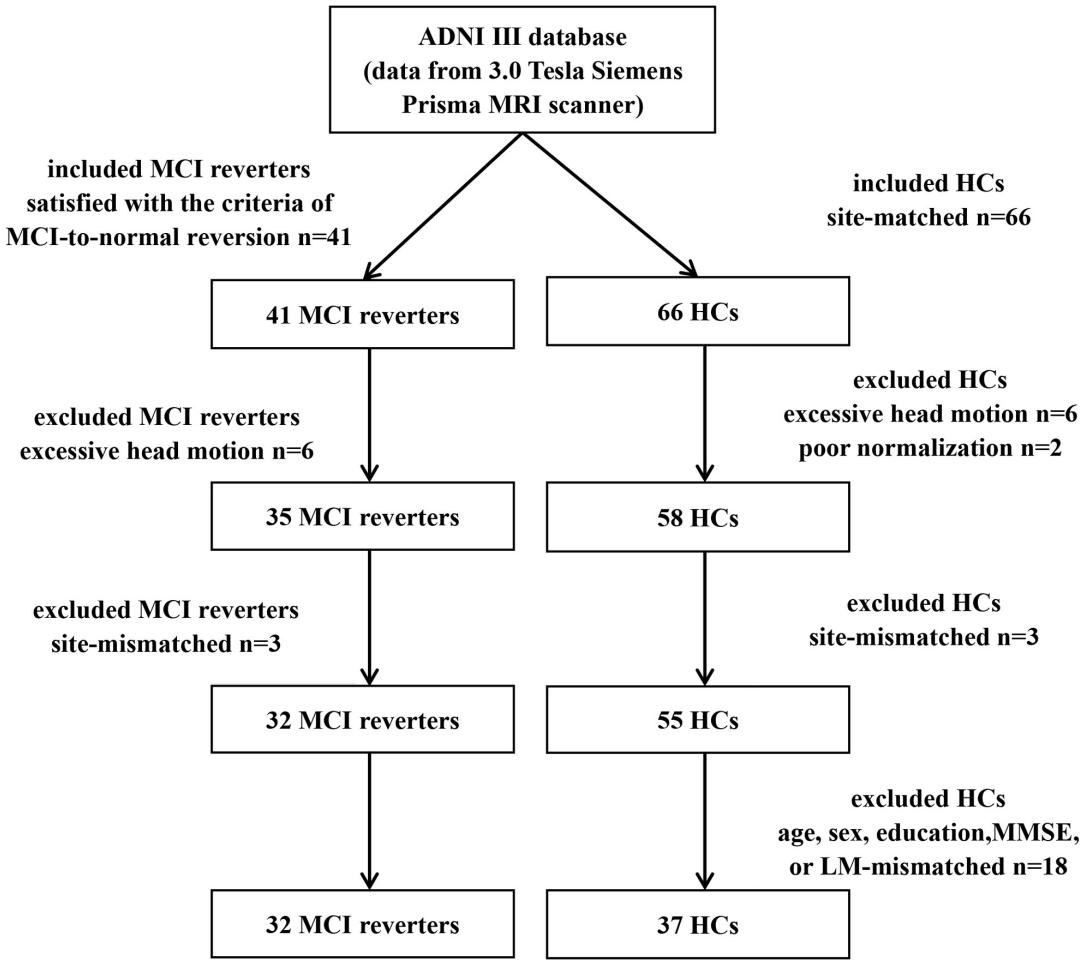

FIGURE 1 | The process of including subjects. HCs, healthy controls; MCI, mild cognitive impairment; n, number.

were discarded. Slice timing was only carried out using the basic scanning data because it is not considered necessary for multiband scanning data (Glasser et al., 2013; Smith et al., 2013). All data were then realigned to correct the head motion. The realigned data were spatially normalized to the Montreal Neurological Institute space via the deformation fields derived from new segmentation of structural images and resampled to 3 mm isotropic voxels. Subsequently, we removed the linear trends and regressed nuisance covariates, including the Friston-24 motion parameters (Friston et al., 1996), white matter signals, and cerebrospinal fluid signals (Chen et al., 2018). Finally, band-pass filtering with 0.01–0.08 Hz was performed. Note that the non-filtering data would be applied in ALFF and fALFF analyses (Wu et al., 2021), because the calculation procedure of ALFF includes the filtering step (Zang et al., 2007) and the fALFF calculation needs data from whole frequency range (Zou et al., 2008). Moreover, considering that spatial smoothing could lead to an overestimation of the local inter-voxel correlations (van den Heuvel et al., 2008) and introduce a bias in computing of ReHo and DC (Zuo et al., 2012), we put the smoothing step after the metrics calculation.

Notably, the process of including subjects was shown in the **Figure 1**. Six MCI reverters and six HCs with excessive head motion (>3 mm translation or >3° rotation), as well as two HCs with poor normalization, were excluded from the next metric calculation. To ensure that each included site involved both MCI reverters and HCs (basic and advanced scanning data in the same site were considered as different sites in these analyses), we also excluded three MCI reverters and three HCs. Additionally, 18 HCs were excluded owing to the mismatch with MCI reverters in age, sex, education, MMSE scores, or LM scores. A list of subjects included in the final analyses is available in **Supplementary Table 1**.

Metrics Calculation

Voxel Level Metrics

ALFF, fALFF, and PerAF belong to a group of voxel-level metrics, reflecting the fluctuation amplitude of the time series for signal voxels from different aspects (Jia et al., 2020). ALFF is the averaged square root at each frequency of the power spectrum at a single voxel across 0.01–0.08 Hz. The time series of a single voxel was transformed to the frequency domain using a fast Fourier

transform, and the power spectrum was obtained. The square root was calculated at each frequency of the power spectrum and the averaged square root obtained across 0.01–0.08 Hz of a single voxel was taken as the ALFF value (Zang et al., 2007). fALFF estimates the relative contribution of low-frequency (0.01–0.08 Hz) to the whole frequency range in the power spectrum. The fALFF value of a single voxel was obtained by calculating the ratio of the amplitude averaged across 0.01–0.08 Hz to that of the whole frequency range (Zou et al., 2008). PerAF is the percentage of resting-state BOLD fluctuations, relative to the mean signal intensity of a given time series. The PerAF value of a single voxel was calculated using the following formula:

$$PerAF = \frac{1}{n}\sum_{i=1}^{n}\left|\frac{X_i - \mu}{\mu}\right| \times 100\%$$

$$\mu = \frac{1}{n}\sum_{i=1}^{n} X_i$$

where, n is the total number of volumes, X_i is the signal intensity at the i_{th} time point, and μ is the mean value of the time series (Jia et al., 2020).

Regional Level Metric

ReHo is widely used to measure intrinsic brain activity in local regions (Zang et al., 2015; Hao et al., 2019). In this study, the ReHo calculation applied the Kendall's coefficient of concordance to measure the similarity of the time series of a given voxel to its nearest 26 neighbors. The Kendall's coefficient of concordance values were calculated using the following formula:

$$W = \frac{\sum (R_i)^2 - n\left(\overline{R}\right)^2}{\frac{1}{12}K^2\left(n^3 - n\right)}$$

where, W is the Kendall's coefficient of concordance value of the given voxel, R_i is the sum rank of the i_{th} volumes, $\overline{R} = (n+1)K/2$ is the mean of the R_i's, K is the number of time series within a cluster (K can be 7, 19, or 27; 27 was used in this study), and n is the number of ranks (Zang et al., 2004).

Whole-Brain Level Metric

We used DC to depict the intrinsic brain activity at the whole-brain level. We calculated Pearson's correlation coefficients (r) of the time series from each pair of voxels in the whole-brain.

$$r_{ij} = \frac{\sum\left[\left(X[t]_i - \overline{X_i}\right)\left(X[t]_j - \overline{X_j}\right)\right]}{\sqrt{\sum\left[\left(X[t]_i - \overline{X_i}\right)^2\left(X[t]_j - \overline{X_j}\right)^2\right]}}$$

where, t is the corresponding volume, and $X[t]_i$ and $X[t]_j$ are the voxel intensities at the i_{th} and j_{th} voxels, respectively in the t_{th} volume. As a result, an $n \times n$ matrix of r values was obtained, where n is the number of voxels in the whole-brain. The binarized DC value of a single voxel (i) is computed by counting the number of voxels which were correlated to the given voxel (i) above a threshold of $r > 0.25$ (Buckner et al., 2009).

$$DC_i = \sum_{r_{ij} > 0.25} 1 \; where \; j = 1 \cdots n, \; i \neq j.$$

Following this, all of the metric maps were calculated with standardization [subtracting the value from each voxel, and divided by the global mean value (Liu et al., 2017; Shan et al., 2020)] and smoothed with a with a Gaussian kernel of 4mm at full width at half-maximum (Wang et al., 2014; Li et al., 2019).We smoothed the unstandardized PerAF for subsequent statistical analyses since it is also used in group comparisons (Jia et al., 2020).

Statistical Analyses

Statistical Product and Service Solutions version (SPSS 26.0, IBM, Armonk, NY, United States) was used for statistical analyses of demographic and cognition data. Comparisons between MCI reverters and HCs were performed using a two-sample t-test for continuous variables and a chi-squared test for categorical variables. For brain intrinsic activity, statistical analyses were performed using data processing and analysis for brain imaging (DPABI 5.1)[6] (Yan et al., 2016). A two-sample t-test was performed to detect differences in each metric of brain intrinsic activity between patients with MCI and HCs, regressing covariates of mean framewise displacement (Jenkinson et al., 2002) and site. The results, which remained after GRF (Gaussian Random Field) correction at two-tailed voxel $p < 0.05$ and a clustering level of $p < 0.05$, were considered to be significant. Additionally, to explore the relationship between cognitive ability and abnormal brain intrinsic activity in MCI reverters, partial correlation analyses were conducted between the cognitive scale scores and brain region metrics with significant group differences, controlling for the site. For the partial correlation analyses, we applied the two thresholds including False Discovery Rate (FDR) corrected $p < 0.05$ and uncorrected $p < 0.05$. We also performed partial correlation analysis controlling for site, age, sex, and education.

RESULTS

Subjects

As shown in **Table 1**, 32 MCI reverters (19 men and 13 women; mean ± SD age, 75.38 ± 7.91 years; mean ± SD education, 16.66 ± 2.48 years; mean ± SD LM score, 13.88 ± 3.18; mean ± SD MMSE score, 28.88 ± 1.36 and 37 HCs (23 men and 14 women; mean ± SD age, 73.38 ± 7.00 years; mean ± SD education, 16.89 ± 2.40 years; mean ± SD LM score, 13.35 ± 3.51; mean ± SD MMSE score, 29.11 ± 0.97) from ADNI 3 were included in the final analysis. There were no significant group differences in age, sex, education, LM score, or MMSE score. The average reversal time of MCI reverters included in this analysis was 5.49 years.

Group Differences in Brain Intrinsic Activity

At the voxel level, MCI reverters had decreased ALFF in the right inferior cerebellum (cerebellum_9_R) and increased ALFF in the left middle inferior frontal gyrus (ORBmid.L) compared with HCs (**Figure 2** and **Table 2**). MCI reverters exhibited decreased

[6]http://rfmri.org/dpabi

TABLE 1 | Demographic and neuropsychological characteristics of the included subjects.

Characteristics	MCI reverters	HCs	p^a
Age (Mean ± SD, year)	75.38 ± 7.91	73.38 ± 7.00	0.270
Sex (M/F)	19/13	23/14	0.813
Education (Mean ± SD, year)	16.66 ± 2.48	16.89 ± 2.40	0.690
LM (Mean ± SD)	13.88 ± 3.18	13.35 ± 3.51	0.521
MMSE (Mean ± SD)	28.88 ± 1.36	29.11 ± 0.97	0.410

[a]p-values for age, education, LM scores, and MMSE scores were obtained using the two-sample t-test, and the p-value for sex was obtained using the chi-squared test.
F, female; HCs, healthy controls; LM, logical memory; M, male; MCI, mild cognitive impairment; MMSE, Mini-Mental State Examination; SD, standard deviation.

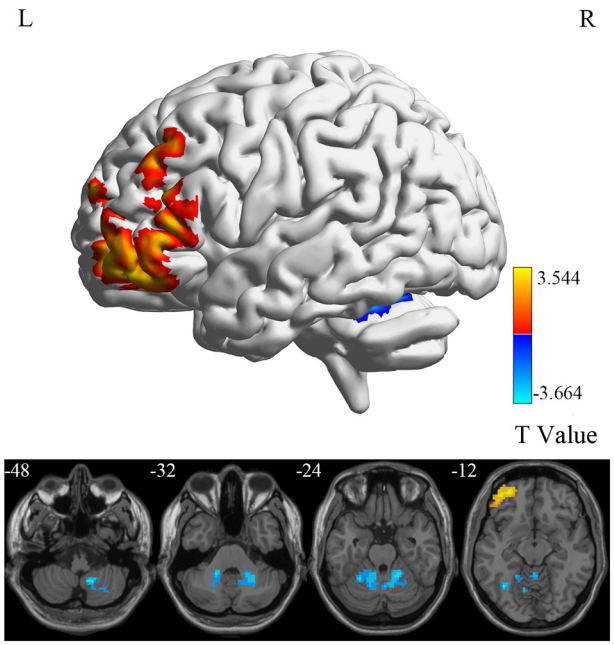

FIGURE 2 | ALFF differences between MCI reverters and HCs. ALFF, amplitude of low-frequency fluctuation; HCs, healthy controls; L, left; MCI, mild cognitive impairment; R, right.

fALFF in the cerebellum_9_R and decreased fALFF in the right orbital inferior frontal gyrus (ORBinf.R) and left middle frontal gyrus (MFG.L) relative to HCs (**Figure 3** and **Table 2**). Regarding PerAF, compared with HCs, MCI reverters showed increased brain intrinsic activity in the ORBinf.R, MFG.L, and left fusiform gyrus (FFG.L; **Figure 4** and **Table 2**). At the regional level, the comparison of ReHo showed group differences between MCI reverters and HCs located in the FFG.L (t = 5.240), right median cingulate, and paracingulate gyri (DCG.R; t = 3.565; **Figure 5** and **Table 2**). Regarding the whole-brain level, as shown in the DC comparison, MCI reverters showed decreased intrinsic brain activity in the cerebellum_9_R, bilateral insular (INS.L and INS.R) and left medial superior frontal gyrus (SFGmed.L) and increased intrinsic brain activity in the left inferior temporal gyrus (ITG.L; **Figure 6**, **Supplementary Table 3**, and **Table 2**).

TABLE 2 | Differences in brain intrinsic activity between MCI reverters and HCs.

Regions	MNI	Cluster	t
	Coordinates	Size	
ALFF			
Cerebellum_9_R	12, −54, −48	736	−3.664
ORBinf.L	−27, 54, −9	381	3.544
fALFF			
Cerebellum_9_R	3, −57, −51	401	−4.001
ORBinf.R	21, 21, −21	309	3.956
MFG.L	−30, 21, 54	319	3.367
PerAF[a]			
ORBinf.R	24, 21, −27	316	4.119
FFG.L	−36, −30, −18	287	3.988
MFG.L	−36, 12, 45	2448	4.741
ReHo			
FFG.L	15, 9, 30	486	5.240
DCG.R	−30, −54.3	328	3.565
DC			
Cerebellum_9_R	15, −48, −51	289	−4.106
INS.L	−42, 3, 3	221	−4.185
SFGmed.L[b]	0, 30, 36	512	−6.219
INS.R[b]	45, 9, −3	600	−4.502
ITG.L[b]	−50, −18, −30	5641	4.599

[a]There is no significant group difference in the standardized PerAF. However, regarding unstandardized PerAF, MCI reverters show significantly increased PerAF in the ORBinf.R, FFG.L, and MFG.L.
*[b]These three clusters belong to a large cluster (7038 voxels; peak coordinate at 0, 30, and 36), with both positive and negative values; therefore, it is reported with separate clusters. The positive regions correspond to the Temporal_Inf_L cluster. The negative regions were dispersed into multiple clusters (**Supplementary Table 3**), mainly located at the SFGmed.L and INS.R.*
ALFF, amplitude of low-frequency fluctuation; Cerebellum_9_R, right inferior cerebellum; DCG.R, right median cingulate and paracingulate gyri; DC, degree centrality; fALFF, fractional amplitude of low-frequency fluctuation; FFG.L, left fusiform gyrus; HCs, healthy controls; INS.L, left insular; INS.R, right insular; MCI, mild cognitive impairment; MFG.L, left middle frontal gyrus; ORBmid.L, left orbital middle frontal gyrus; ORBinf.R, right orbital inferior frontal gyrus; PerAF, percent amplitude of fluctuation; ReHo, regional homogeneity; SFGmed.L, left medial superior frontal gyrus; ITG.L, left inferior temporal gyrus.

Partial Correlations

As presented in **Table 3**, significant partial correlations were found between cognitive scale scores and brain region metrics with significant group differences at a significance level of uncorrected $p < 0.05$, controlling for site. The scatter plots of significant partial correlation results (uncorrected $p < 0.05$) were available in the **Supplementary Figures 1–9**. Notably, no results remained after FDR correction. Besides, the partial correlation results controlling for site, age, sex, and education (**Supplementary Table 4**) were similar to the results controlling for site.

DISCUSSION

In this study, we identified significant intrinsic brain activity changes in MCI reverters compared to HCs on different scales. At the voxel level, MCI reverters showed increased

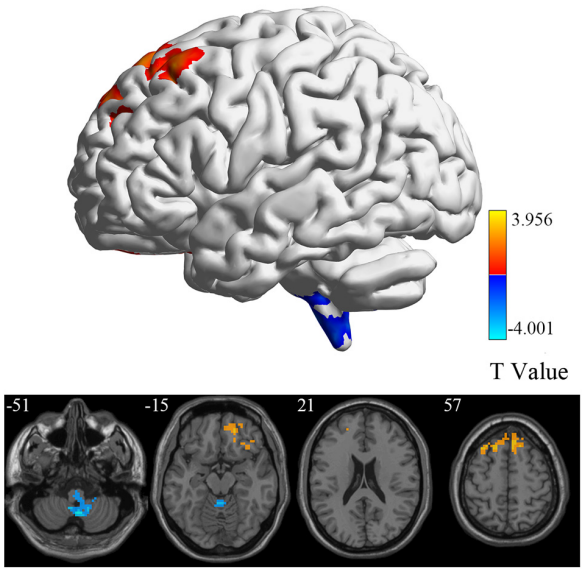

FIGURE 3 | fALFF differences between MCI reverters and HCs. fALFF, fractional amplitude of low-frequency fluctuation; HCs, healthy controls; L, left; MCI, mild cognitive impairment; R, right.

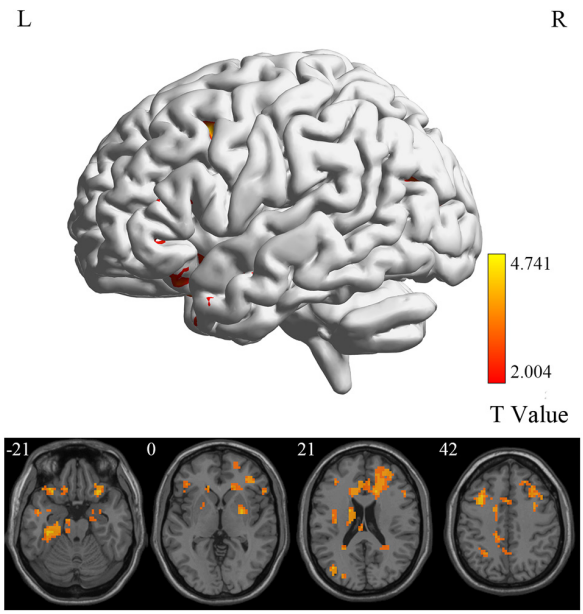

FIGURE 4 | PerAF differences between MCI reverters and HCs. PerAF, percent amplitude of fluctuation; HCs, healthy controls; L, left; MCI, mild cognitive impairment; R, right.

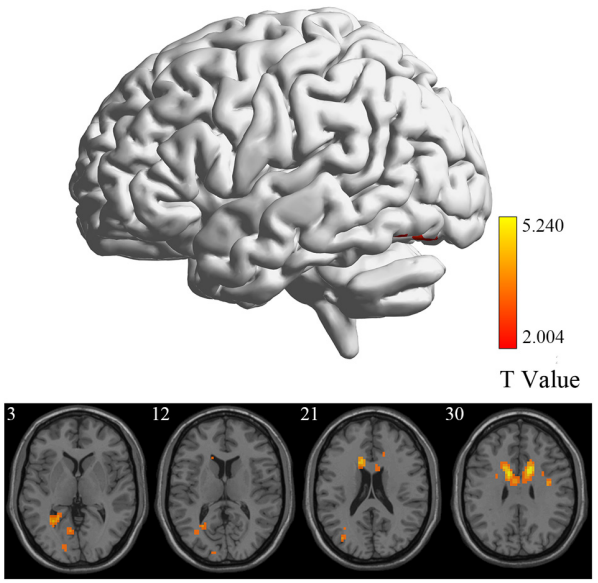

FIGURE 5 | ReHo differences between MCI reverters and HCs. ReHo, regional homogeneity; HCs, healthy controls; L, left; MCI, mild cognitive impairment; R, right.

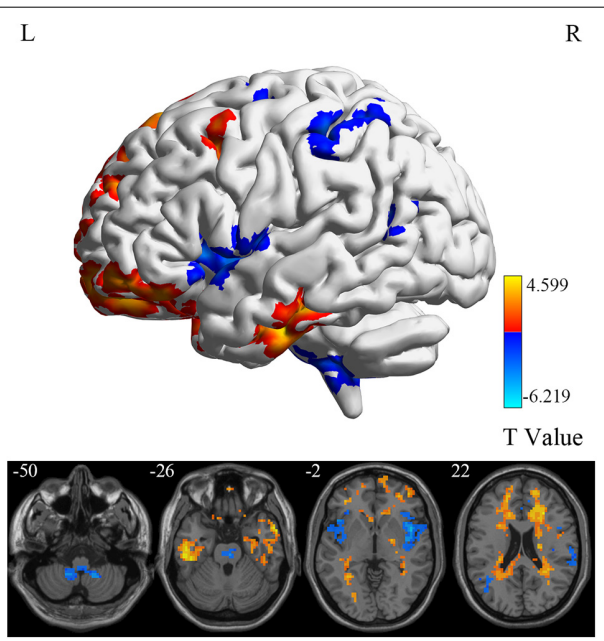

FIGURE 6 | DC differences between MCI reverters and HCs. DC, degree centrality; HCs, healthy controls; L, left; MCI, mild cognitive impairment; R, right.

ALFF, fALFF, and PerAF in the frontal gyrus (including ORBmid.L, ORBinf.R, and MFG.L), increased PerAF in the FFG.L and decreased ALFF and fALFF in the cerebellum_9_R compared with HCs. Regarding regional and whole-brain levels, compared to HCs, patients with MCI showed increased ReHo in the FFG.L, DCG.R; increased DC in the ITG.L and l SFGmed.L; decreased DC in the cerebellum_9_R and INS.L and INS.R.

TABLE 3 | Significant partial correlations between cognitive scale scores and brain region metrics with significant group differences.

Regions	Cognitive scales	Partial correlations	
		r	*p*[a]
ALFF			
ORBmid.L	MOCA	−0.582	0.006**
ORBmid.L	RAVLT_immediate	−0.569	0.007**
ORBmid.L	TMT Parts A	0.499	0.021
fALFF			
Cerebellum_9_R	EcogPtLang	−0.450	0.041
Cerebellum_9_R	EcogPtPlan	−0.483	0.027
Cerebellum_9_R	EcogPtTotal	−0.444	0.044
Cerebellum_9_R	TMT Parts A	−0.475	0.029
MFG.L	EcogSPOrgan	0.514	0.029
PerAF			
ORBinf.R	EcogPtDivatt	−0.496	0.022
MFG.L	RAVLT_immediate	−0.602	0.004**
MFG.L	RAVLT_learning	−0.613	0.003**
MFG.L	RAVLT_perc_forgetting	0.521	0.015
FFG.L	EcogSPVisspat	0.471	0.042
ReHo			
None			
DC			
SFGmed.L	MMSE	0.435	0.049
Cerebellum_9_R	ADASQ4	−0.502	0.020
Cerebellum_9_R	RAVLT_immediate	0.440	0.046
Cerebellum_9_R	RAVLT_learning	0.444	0.044
Cerebellum_9_R	TMT Parts A	−0.550	0.010
Cerebellum_9_R	TMT Parts B	−0.509	0.018
ITG.L	RAVLT_immediate	−0.452	0.040

[a]*The significant level of these results was set at uncorrected $p < 0.05$, and no results remained after FDR correction. The symbol of **indicated the results were significant at the level of uncorrected $p < 0.01$.*

ALFF, amplitude of low-frequency of fluctuation; Cerebellum_9_R, right inferior cerebellum; DC, degree centrality; Divatt, divided attention; EcogPt, Everyday Cognition Test Patient Reported Version; EcogSP, Everyday Cognition Test Study Partner Reported Version; fALFF, fractional amplitude of low-frequency fluctuation; FFG.L, left fusiform gyrus; ITG.L, left inferior temporal gyrus; MFG.L, left middle frontal gyrus; MMSE, Mini-mental State Examination; MOCA, Montreal Cognitive Assessment; ORBmid.L, left orbital middle frontal gyrus; ORBinf.R, right orbital inferior frontal gyrus; Organ, organization; PerAF, percent amplitude of fluctuation; perc, percent; Q4, delayed word recall; RAVLT, Rey Auditory Verbal Learning Test; ReHo, regional homogeneity; SFGmed.L, left medial superior frontal gyrus; TMT, Trail Making Test; Visspat, visuospatial abilities.

Intrinsic Brain Activity Alteration of Mild Cognitive Impairment Reverters at the Voxel Level

ALFF reflects the degree of spontaneous neural activity (Zang et al., 2007) and fALFF is regarded as a standardized ALFF-like metric that has high sensitivity and specificity in the detection of spontaneous brain activity. It should be noted that fALFF is not as reliable as ALFF (Zou et al., 2008; Zuo et al., 2010). In this study, we found that the frontal lobe regions (including the ORBmid.L, ORBinf.R, and MFG.L) in MCI reverters showed increased ALFF and fALFF, while the cerebellum_9_R showed decreased ALFF and fALFF. The frontal lobe is thought to be involved in many high-level cognitive functions (Bae et al., 2021; Wang Y. et al., 2021). Increased frontal cortex connectivity is considered to be associated with increased cognitive control, higher IQ, and higher cognitive performance in young individuals. Therefore, we speculated that the increased neural activity in the frontal lobe regions in MCI reverters may account for the improvement of memory function.

Additionally, we found decreased ALFF and fALFF in the cerebellum_9_R of MCI reverters. According to previous studies, the cerebellum is involved in motor, balance, and cognitive functions (Wagner and Luo, 2020). Transcranial direct current stimulation is a non-invasive brain stimulation technique improving cognitive function in MCI. He et al. (2021) found that fALFF values decreased significantly in the cerebellum of patients with MCI after receiving 10 transcranial direct current stimulation sessions. Accordingly, the decreased ALFF and fALFF in the cerebellum_9_R may contribute to cognitive and motor functional improvement in patients with MCI. PerAF has higher test-retest reliability than conventional ALFF and is markedly higher than fALFF, from both intra- and inter-scanner aspects (Zhao et al., 2018; Jia et al., 2020). The MFG.L also showed decreased PerAF, which is consistent with the ALFF and fALFF results. Increased PerAF was also found in the FFG.L. We believe that the results of ALFF, fALFF, and PerAF may complement each other to increase the validity of the results.

Intrinsic Brain Activity Alteration of Mild Cognitive Impairment Reverters at the Regional and Whole-Brain Level

ReHo is a local index reflecting the local synchronization of the BOLD signal. In this study, the FFG.L and DCG.R of reverters showed increased ReHo, which represented increased local synchronization within these areas. The FFG is involved in the composition of visual regions and contributes markedly in facial recognition (Albonico and Barton, 2017; Liu et al., 2021). It has been thoroughly researched in recent years because of its abnormal structure and function in patients with mental disorders (Hwang et al., 2021; Jalbrzikowski et al., 2021). Patients with MCI have impairments in various domains, including visual-spatial dysfunction. Increased ReHo in the FFG.L is probably conducive to the process of external visual information. The DCG is involved in the composition of the cingulate gyrus, which is the key node in the default mode network and contributes considerably in information transmission and cognitive processing (Wang S. et al., 2021). The increased ReHo values observed in the DCG.R in MCI reverters may be beneficial for completing cognitive tasks.

Degree centrality is representative of the status and role of voxels in the whole-brain network (Buckner et al., 2009). In this study, the right cerebellum, INS.L and INS.R showed decreased DC, while the SFGmed.L and ITG.L showed increased DC. This suggests a reduced and increased, respectively, significance of these regions in the whole-brain. ITG.L and SFGmed.L regions are involved in memory tasks (Sidhu et al., 2013; Bae et al., 2021), and the cerebellum, INS.L, and INS.R are more related to motor and attentional processes (Wagner and Luo, 2020; Song et al., 2021). Previous studies have suggested that patients with AD may use other neurological resources to compensate for the loss of cognitive function in the early stages of the disease

(Grady et al., 2003). Increased DC values in SFGmed.L and ITG.L and decreased DC values in the cerebellum and insula may imply a compensatory mechanism for maintaining memory function.

There are relatively few studies regarding MCI reverters, particularly intrinsic brain activity. Some studies have focused on patients with MCI whose cognitive function improved after treatment. He et.al (He et al., 2021) used the transcranial direct current stimulation in patients with MCI and found that the fALFF and ReHo values changed in multiple areas following tDCS. Brain regions with significant decreases in fALFF values included the INS.R, Precuneus R, and Parietal Sup R, while the FFG.L and Angular R showed significantly increased fALFF values. The brain regions with significantly increased ReHo values involved widespread frontal lobe regions. Another study (Zheng et al., 2021) has found that patients with Ginkgo biloba extract showed significantly decreased ALFF in the left parahippocampal gyrus, FFG.l, right gyrus rectus, and right superior frontal gyrus, while an increase in ALFF in the right middle temporal gyrus. Such brain activity change patterns are not consistent with our results. this may be attributed to our main focus on MCI reverters without clear treatment history. Effects of head motion during image acquisition and signal quality, as well as inconsistent image processing procedures, have also been noted as potential sources of variation.

Intrinsic Brain Activity Alteration of Mild Cognitive Impairment Reverters in the Cerebellum

Another notable finding is the abnormal brain activity in the cerebellum of MCI reverters. Traditionally, the cerebellum has been regarded as an important structure for coordinating intact motor functioning (Colloby et al., 2014). Numerous studies have recently reported that the cerebellum may also contribute to cognitive and affective processing (Grodd et al., 2005; Lin et al., 2020). There are relatively few reports on the changes of cerebellum structure and function in patients with AD. Previous studies pointed out that there is a stepwise decrease in cerebellum gray matter volume change from normal cognition to MCI and AD (Schmahmann, 2010; Tedesco et al., 2011; Tang et al., 2021) [4–6]. Another study (Toniolo et al., 2018) suggested that the cortico-cerebellum functional connectivity in MCI and AD patients were significantly disrupted with different distributions, particularly in the default mode networks and frontoparietal networks region. These results demonstrated the potential role of the cerebellum in AD progression and pathogenesis. Our study indicates that ALFF, fALFF, and DC values in the cerebellum consistently decreased in MCI reverters compared to HCs. These may be valuable and important findings, and future studies of AD should focus more on the cerebellum.

Behavioral Significance of Altered Brain Activity

Correlation analyses were conducted among the neuropsychological scales and rs-fMRI metrics. Many significant partial correlations were found between cognitive scale scores and brain region metrics with significant group differences. Among these, the strongest correlations were found between ALFF and PerAF in the MFG and Rey Auditory Verbal Learning Test scores. The MFG is a major component of the dorsolateral prefrontal cortex mediating higher-order cognitive functions such as executive attention, motor planning, decision making, and theory of mind (Lau et al., 2019; Mateu-Estivill et al., 2021). A previous study (Tang et al., 2021) has shown that AD patients had decreased functional connectivity within the medial frontal gyrus (MFG) compared to HC. Interestingly, MCI patients demonstrated increased functional connectivity within MFG and were positively correlated with memory enhancement. The increased functional connectivity in MFG in MCI patients may serve as a compensatory process. Similarly, this study showed an increased trend of ALFF and perAF values in the MFG of MCI reverters, which may also reflect a compensatory mechanism. However, its negative correlation with Rey Auditory Verbal Learning Test scores suggested that the functional improvement may not be directly subject to the recovery of MFG function. A potential effect may be mediated by the altered functional connection of MFG to the whole brain in reverters (Veitch et al., 2019; Xu et al., 2021). Future studies are required to deeply investigate this possibility and clarify the relationship between alterations in intrinsic brain activity and cognitive reversion. Besides, we found there was no correlation between Reho value and any cognitive scale. We suggested the limited sample size and the inclusion of both amnestic MCI and non-amnestic MCI patients may lead to potential bias.

However, it needs to be noted that these partial correlation results were obtained in a low threshold (uncorrected $p < 0.05$) and no results remained after correction (FDR corrected $p < 0.05$). We mainly attributed this to the small effect size, which likely led to non-significant results at a strict threshold (Jia et al., 2021).

Limitations

This study has several limitations. Firstly, since this is a cross-sectional study, we did not investigate the conversion of MCI to HCs. No baseline rs-fMRI data of MCI reverters were collected. Second, the sample size was relatively modest. In future studies, we would like to combine the rs-fMRI, structural MRI, and other biophysical data with a larger sample and reveal structural and biological substrates underlying these brain activity alterations in MCI reverters.

CONCLUSION

To the best of our knowledge, this is the first study to investigate the intrinsic brain activity changes in MCI reverters. We found that these patients had significantly increased brain activity in regions such as the frontal gyrus (including the ORBmid.L, ORBinf.R, MFG.L, and SFGmed.L), FFG.L, DCG.R, and ITG.L, while decreased brain activities were mainly contained in the cerebellum_9_R, INS.L and INS.R. These alterations are significantly related to cognitive reversion in patients with MCI. These results enhance our understanding of the

neuro-mechanism of cognitive reversion in patients with MCI and provide new insights for developing effective interventions for AD in the future.

DATA AVAILABILITY STATEMENT

The datasets analyzed for this study can be found in the ADNI database, available at: http://adni.loni.usc.edu/. The subject ID of MCI reverters included in this manuscript can be found in **Supplementary Table 1**.

ETHICS STATEMENT

Ethical approval was not provided for this study on human participants because data used in the preparation of this article were obtained from the ADNI. The Alzheimer's Disease Neuroimaging Initiative (ADNI) was approved by the Institutional Review Boards of all participating sites. The patients/participants provided their written informed consent to participate in this study.

AUTHOR CONTRIBUTIONS

QH and XZ designed the study and protocol. YL, ZX, XL, and GH performed the literature search and collected the patient data. QW and XJ performed the image analysis and generated the figures. QH, QW, and LZ wrote the manuscript. XJ and XZ edited and revised the manuscript. All authors contributed to the manuscript and approved the submitted version.

FUNDING

This study was funded by the Science and Technology Commission of Shanghai Municipality under Grants 18411970300 and 201409002200, National Natural Science Foundation of China under Grant 82001898, Shanghai Municipal Health Commission under Grant 201840018, and Medical Specialty of Minhang District (Shanghai) under Grant 2020MWFC01.

ACKNOWLEDGMENTS

We thank Editage (http://editage.com/frontiers/) for the English language editing of this manuscript.

SUPPLEMENTARY MATERIAL

The Supplementary Material for this article can be found online at: https://www.frontiersin.org/articles/10.3389/fnagi.2021.788765/full#supplementary-material

REFERENCES

Albonico, A., and Barton, J. J. S. (2017). Face perception in pure alexia: complementary contributions of the left fusiform gyrus to facial identity and facial speech processing. *Cortex* 96, 59–72. doi: 10.1016/j.cortex.2017.08.029

Bae, J., Jeong, H., Yoon, Y., Bae, C., Lee, H., Paik, S., et al. (2021). Parallel processing of working memory and temporal information by distinct types of cortical projection neurons. *Nat. Commun.* 12:4352. doi: 10.1038/s41467-021-24565-z

Belleville, S., Clément, F., Mellah, S., Gilbert, B., Fontaine, F., and Gauthier, S. (2011). Training-related brain plasticity in subjects at risk of developing Alzheimer's disease. *Brain* 134(Pt 6), 1623–1634. doi: 10.1093/brain/awr037

Biswal, B. B. (2012). Resting state fMRI: a personal history. *Neuroimage* 62, 938–944. doi: 10.1016/j.neuroimage.2012.01.090

Buckner, R. L., Sepulcre, J., Talukdar, T., Krienen, F. M., Liu, H., Hedden, T., et al. (2009). Cortical hubs revealed by intrinsic functional connectivity: mapping, assessment of stability, and relation to Alzheimer's disease. *J. Neurosci.* 29, 1860–1873. doi: 10.1523/jneurosci.5062-08.2009

Buschert, V. C., Friese, U., Teipel, S. J., Schneider, P., Merensky, W., Rujescu, D., et al. (2011). Effects of a newly developed cognitive intervention in amnestic mild cognitive impairment and mild Alzheimer's disease: a pilot study. *J. Alzheimers Dis.* 25, 679–694. doi: 10.3233/jad-2011-100999

Busse, A., Hensel, A., Gühne, U., Angermeyer, M. C., and Riedel-Heller, S. G. (2006). Mild cognitive impairment: long-term course of four clinical subtypes. *Neurology* 67, 2176–2185. doi: 10.1212/01.wnl.0000249117.23318.e1

Canevelli, M., Grande, G., Lacorte, E., Quarchioni, E., Cesari, M., Mariani, C., et al. (2016). Spontaneous reversion of mild cognitive impairment to normal cognition: a systematic review of literature and meta-analysis. *J. Am. Med. Dir. Assoc.* 17, 943–948. doi: 10.1016/j.jamda.2016.06.020

Chen, X., Lu, B., and Yan, C. G. (2018). Reproducibility of R-fMRI metrics on the impact of different strategies for multiple comparison correction and sample sizes. *Hum. Brain Mapp.* 39, 300–318. doi: 10.1002/hbm.23843

Colloby, S. J., O'Brien, J. T., and Taylor, J. P. (2014). Patterns of cerebellar volume loss in dementia with Lewy bodies and Alzheimer's disease: a VBM-DARTEL study. *Psychiatry Res.* 223, 187–191. doi: 10.1016/j.pscychresns.2014.06.006

Cui, Q., Sheng, W., Chen, Y., Pang, Y., Lu, F., Tang, Q., et al. (2020). Dynamic changes of amplitude of low-frequency fluctuations in patients with generalized anxiety disorder. *Hum. Brain Mapp.* 41, 1667–1676. doi: 10.1002/hbm.24902

Dai, Z., and He, Y. J. N. B. (2014). Disrupted structural and functional brain connectomes in mild cognitive impairment and Alzheimer's disease. *Neurosci. Bull.* 30, 217–232. doi: 10.1007/s12264-013-1421-0

Friston, K. J., Williams, S., Howard, R., Frackowiak, R. S., and Turner, R. (1996). Movement-related effects in fMRI time-series. *Magn. Reson. Med.* 35, 346–355. doi: 10.1002/mrm.1910350312

Gao, S., Unverzagt, F. W., Hall, K. S., Lane, K. A., Murrell, J. R., Hake, A. M., et al. (2014). Mild cognitive impairment, incidence, progression, and reversion: findings from a community-based cohort of elderly African Americans. *Am. J. Geriatr. Psychiatry* 22, 670–681. doi: 10.1016/j.jagp.2013.02.015

Glasser, M. F., Sotiropoulos, S. N., Wilson, J. A., Coalson, T. S., Fischl, B., Andersson, J. L., et al. (2013). The minimal preprocessing pipelines for the Human Connectome Project. *Neuroimage* 80, 105–124. doi: 10.1016/j.neuroimage.2013.04.127

Grady, C. L., McIntosh, A. R., Beig, S., Keightley, M. L., Burian, H., and Black, S. E. (2003). Evidence from functional neuroimaging of a compensatory prefrontal network in Alzheimer's disease. *J. Neurosci.* 23, 986–993. doi: 10.1523/jneurosci.23-03-00986.2003

Grodd, W., Hülsmann, E., and Ackermann, H. (2005). Functional MRI localizing in the cerebellum. *Neurosurg. Clin. N. Am.* 16, 77–99. doi: 10.1016/j.nec.2004.07.008

Hao, H., Chen, C., Mao, W., Xia, W., Yi, Z., Zhao, P., et al. (2019). Alterations in resting-state local functional connectivity in obsessive-compulsive disorder. *J. Affect. Disord.* 245, 113–119. doi: 10.1016/j.jad.2018.10.112

He, F., Li, Y., Li, C., Fan, L., Liu, T., and Wang, J. (2021). Repeated anodal high-definition transcranial direct current stimulation over the left dorsolateral

prefrontal cortex in mild cognitive impairment patients increased regional homogeneity in multiple brain regions. *PLoS One* 16:e0256100. doi: 10.1371/journal.pone.0256100

Hwang, H. C., Kim, S. M., and Han, D. H. (2021). Different facial recognition patterns in schizophrenia and bipolar disorder assessed using a computerized emotional perception test and fMRI. *J. Affect. Disord.* 279, 83–88. doi: 10.1016/j.jad.2020.09.125

Jalbrzikowski, M., Hayes, R., Wood, S., Nordholm, D., Zhou, J., Fusar-Poli, P., et al. (2021). Association of structural magnetic resonance imaging measures with psychosis onset in individuals at clinical high risk for developing psychosis: an ENIGMA working group mega-analysis. *JAMA Psychiatry* 78, 753–766. doi: 10.1001/jamapsychiatry.2021.0638

Jenkinson, M., Bannister, P., Brady, M., and Smith, S. (2002). Improved optimization for the robust and accurate linear registration and motion correction of brain images. *Neuroimage* 17, 825–841. doi: 10.1016/s1053-8119(02)91132-8

Jia, X. Z., Sun, J. W., Ji, G. J., Liao, W., Lv, Y. T., Wang, J., et al. (2020). Percent amplitude of fluctuation: a simple measure for resting-state fMRI signal at single voxel level. *PLoS One* 15:e0227021. doi: 10.1371/journal.pone.0227021

Jia, X.-Z., Wang, J., Sun, H.-Y., Zhang, H., Liao, W., Wang, Z., et al. (2019). RESTplus: an improved toolkit for resting-state functional magnetic resonance imaging data processing. *Sci. Bull.* 64, 953–954. doi: 10.1016/j.scib.2019.05.008

Jia, X.-Z., Zhao, N., Dong, H.-M., Sun, J.-W., Barton, M., Burciu, R., et al. (2021). Small P values may not yield robust findings: an example using REST-meta-PD. *Sci. Bull.* 66, 2148–2152. doi: 10.1016/j.scib.2021.06.007

Lau, H., Shahar, S., Mohamad, M., Rajab, N. F., Yahya, H. M., Din, N. C., et al. (2019). Relationships between dietary nutrients intake and lipid levels with functional MRI dorsolateral prefrontal cortex activation. *Clin. Interv. Aging* 14, 43–51. doi: 10.2147/cia.S183425

Li, Y., Fang, Y., Wang, J., Zhang, H., and Hu, B. (2021). Biomarker extraction based on subspace learning for the prediction of mild cognitive impairment conversion. *Biomed. Res. Int.* 2021:5531940. doi: 10.1155/2021/5531940

Li, Y., Jing, B., Liu, H., Li, Y., Gao, X., Li, Y., et al. (2017). Frequency-dependent changes in the amplitude of low-frequency fluctuations in mild cognitive impairment with mild depression. *J. Alzheimers Dis.* 58, 1175–1187. doi: 10.3233/jad-161282

Li, Z., Li, C., Liang, Y., Wang, K., Zhang, W., Chen, R., et al. (2019). Altered functional connectivity and brain network property in pregnant women with cleft fetuses. *Front. Psychol.* 10:2235. doi: 10.3389/fpsyg.2019.02235

Lin, C. Y., Chen, C. H., Tom, S. E., and Kuo, S. H. (2020). Cerebellar volume is associated with cognitive decline in mild cognitive impairment: results from ADNI. *Cerebellum* 19, 217–225. doi: 10.1007/s12311-019-01099-1

Liu, M., Liu, C., Zheng, S., Zhao, K., and Fu, X. J. N. (2021). Reexamining the neural network involved in perception of facial expression: a meta-analysis. *Neurosci. Biobehav. Rev.* 131, 179–191. doi: 10.1016/j.neubiorev.2021.09.024

Liu, X., Chen, J., Shen, B., Wang, G., Li, J., Hou, H., et al. (2018). Altered intrinsic coupling between functional connectivity density and amplitude of low-frequency fluctuation in mild cognitive impairment with depressive symptoms. *Neural Plast.* 2018:1672708. doi: 10.1155/2018/1672708

Liu, X., Tu, Y., Zang, Y., Wu, A., Guo, Z., and He, J. (2019). Disrupted regional spontaneous neural activity in mild cognitive impairment patients with depressive symptoms: a resting-state fMRI study. *Neural Plast.* 2019:2981764. doi: 10.1155/2019/2981764

Liu, Y., Wang, J., Zhang, J., Wen, H., Zhang, Y., Kang, H., et al. (2017). Altered spontaneous brain activity in children with early tourette syndrome: a resting-state fMRI study. *Sci. Rep.* 7:4808. doi: 10.1038/s41598-017-04148-z

Malek-Ahmadi, M. (2016). Reversion from mild cognitive impairment to normal cognition: a meta-analysis. *Alzheimer Dis. Assoc. Disord.* 30, 324–330. doi: 10.1097/wad.0000000000000145

Mateu-Estivill, R., Forné, S., López-Sala, A., Falcón, C., Caldú, X., Sopena, J. M., et al. (2021). Functional connectivity alterations associated with literacy difficulties in early readers. *Brain Imaging Behav.* 15, 2109–2120. doi: 10.1007/s11682-020-00406-3

Pandya, S. Y., Lacritz, L. H., Weiner, M. F., Deschner, M., and Woon, F. L. (2017). Predictors of reversion from mild cognitive impairment to normal cognition. *Dement. Geriatr. Cogn. Disord.* 43, 204–214. doi: 10.1159/000456070

Petersen, R. C., Aisen, P. S., Beckett, L. A., Donohue, M. C., Gamst, A. C., Harvey, D. J., et al. (2010). Alzheimer's Disease Neuroimaging Initiative (ADNI): clinical characterization. *Neurology* 74, 201–209. doi: 10.1212/WNL.0b013e3181cb3e25

Petersen, R. C., Roberts, R. O., Knopman, D. S., Boeve, B. F., Geda, Y. E., Ivnik, R. J., et al. (2009). Mild cognitive impairment: ten years later. *Arch. Neurol.* 66, 1447–1455. doi: 10.1001/archneurol.2009.266

Pyun, J., Park, Y., Lee, K., Kim, S., Saykin, A., Nho, K., et al. (2021). Predictability of polygenic risk score for progression to dementia and its interaction with APOE ε4 in mild cognitive impairment. *Transl. Neurodegener.* 10:32. doi: 10.1186/s40035-021-00259-w

Schmahmann, J. D. (2010). The role of the cerebellum in cognition and emotion: personal reflections since 1982 on the dysmetria of thought hypothesis, and its historical evolution from theory to therapy. *Neuropsychol. Rev.* 20, 236–260. doi: 10.1007/s11065-010-9142-x

Shan, X., Qiu, Y., Pan, P., Teng, Z., Li, S., Tang, H., et al. (2020). Disrupted regional homogeneity in drug-naive patients with bipolar disorder. *Front. Psychiatry* 11:825. doi: 10.3389/fpsyt.2020.00825

Sidhu, M., Stretton, J., Winston, G., Bonelli, S., Centeno, M., Vollmar, C., et al. (2013). A functional magnetic resonance imaging study mapping the episodic memory encoding network in temporal lobe epilepsy. *Brain* 136, 1868–1888. doi: 10.1093/brain/awt099

Smith, S. M., Beckmann, C. F., Andersson, J., Auerbach, E. J., Bijsterbosch, J., Douaud, G., et al. (2013). Resting-state fMRI in the Human Connectome Project. *Neuroimage* 80, 144–168. doi: 10.1016/j.neuroimage.2013.05.039

Song, Y., Xu, W., Chen, S., Hu, G., Ge, H., Xue, C., et al. (2021). Functional MRI-specific alterations in salience network in mild cognitive impairment: an ALE meta-analysis. *Front. Aging Neurosci.* 13:695210. doi: 10.3389/fnagi.2021.695210

Tang, F., Zhu, D., Ma, W., Yao, Q., Li, Q., and Shi, J. (2021). Differences changes in cerebellar functional connectivity between mild cognitive impairment and Alzheimer's disease: a seed-based approach. *Front. Neurol.* 12:645171. doi: 10.3389/fneur.2021.645171

Tedesco, A. M., Chiricozzi, F. R., Clausi, S., Lupo, M., Molinari, M., and Leggio, M. G. (2011). The cerebellar cognitive profile. *Brain* 134(Pt 12), 3672–3686. doi: 10.1093/brain/awr266

Thomas, K. R., Edmonds, E. C., Eppig, J. S., Wong, C. G., Weigand, A. J., Bangen, K. J., et al. (2019a). MCI-to-normal reversion using neuropsychological criteria in the Alzheimer's disease neuroimaging initiative. *Alzheimers Dement.* 15, 1322–1332. doi: 10.1016/j.jalz.2019.06.4948

Thomas, K. R., Eppig, J. S., Weigand, A. J., Edmonds, E. C., Wong, C. G., Jak, A. J., et al. (2019b). Artificially low mild cognitive impairment to normal reversion rate in the Alzheimer's disease neuroimaging initiative. *Alzheimers Dement.* 15, 561–569. doi: 10.1016/j.jalz.2018.10.008

Toniolo, S., Serra, L., Olivito, G., Marra, C., Bozzali, M., and Cercignani, M. (2018). Patterns of cerebellar gray matter atrophy across Alzheimer's disease progression. *Front. Cell. Neurosci.* 12:430. doi: 10.3389/fncel.2018.00430

van den Heuvel, M. P., Stam, C. J., Boersma, M., and Hulshoff Pol, H. E. (2008). Small-world and scale-free organization of voxel-based resting-state functional connectivity in the human brain. *Neuroimage* 43, 528–539. doi: 10.1016/j.neuroimage.2008.08.010

Veitch, D. P., Weiner, M. W., Aisen, P. S., Beckett, L. A., Cairns, N. J., Green, R. C., et al. (2019). Understanding disease progression and improving Alzheimer's disease clinical trials: recent highlights from the Alzheimer's Disease Neuroimaging Initiative. *Alzheimers Dement.* 15, 106–152. doi: 10.1016/j.jalz.2018.08.005

Veitch, D., Weiner, M., Aisen, P., Beckett, L., DeCarli, C., Green, R., et al. (2021). Using the Alzheimer's disease neuroimaging initiative to improve early detection, diagnosis, and treatment of Alzheimer's disease. *Alzheimers Dement'* doi: 10.1002/alz.12422 [Epub ahead of print].

Wagner, M. J., and Luo, L. (2020). Neocortex-cerebellum circuits for cognitive processing. *Trends Neurosci.* 43, 42–54. doi: 10.1016/j.tins.2019.11.002

Wang, L., Li, K., Zhang, Q., Zeng, Y., Dai, W., Su, Y., et al. (2014). Short-term effects of escitalopram on regional brain function in first-episode drug-naive patients with major depressive disorder assessed by resting-state functional magnetic resonance imaging. *Psychol. Med.* 44, 1417–1426. doi: 10.1017/S0033291713002031

Wang, S., Kim, N., Um, Y., Kang, D., Na, H., Lee, C., et al. (2021). Default mode network dissociation linking cerebral beta amyloid retention and depression

in cognitively normal older adults. *Neuropsychopharmacology* 46, 2180–2187. doi: 10.1038/s41386-021-01072-9

Wang, Y., Yin, X., Zhang, Z., Li, J., Zhao, W., and Guo, Z. J. N. (2021). A cortico-basal ganglia-thalamo-cortical channel underlying short-term memory. *Neuron* 109, 3486–3499.e7. doi: 10.1016/j.neuron.2021.08.002

Wang, Y., Zhao, X., Xu, S., Yu, L., Wang, L., Song, M., et al. (2015). Using regional homogeneity to reveal altered spontaneous activity in patients with mild cognitive impairment. *Biomed. Res. Int.* 2015:807093. doi: 10.1155/2015/807093

Winblad, B., Palmer, K., Kivipelto, M., Jelic, V., Fratiglioni, L., Wahlund, L. O., et al. (2004). Mild cognitive impairment–beyond controversies, towards a consensus: report of the international working group on mild cognitive impairment. *J. Intern. Med.* 256, 240–246. doi: 10.1111/j.1365-2796.2004.01380.x

Wu, D., Zhao, H., Gu, H., Han, B., Wang, Q., Man, X., et al. (2021). The effects of rs405509 on APOEepsilon4 non-carriers in non-demented aging. *Front. Neurosci.* 15:677823. doi: 10.3389/fnins.2021.677823

Xing, Y., Fu, S., Li, M., Ma, X., Liu, M., Liu, X., et al. (2021). Regional neural activity changes in Parkinson's disease-associated mild cognitive impairment and cognitively normal patients. *Neuropsychiatr. Dis. Treat* 17, 2697–2706. doi: 10.2147/ndt.S323127

Xiong, J., Yu, C., Su, T., Ge, Q., Shi, W., Tang, L., et al. (2021). Altered brain network centrality in patients with mild cognitive impairment: an fMRI study using a voxel-wise degree centrality approach. *Aging (Albany N. Y.)* 13, 15491–15500. doi: 10.18632/aging.203105

Xu, W., Rao, J., Song, Y., Chen, S., Xue, C., Hu, G., et al. (2021). Altered functional connectivity of the basal nucleus of Meynert in subjective cognitive impairment, early mild cognitive impairment, and late mild cognitive impairment. *Front. Aging Neurosci.* 13:671351. doi: 10.3389/fnagi.2021.671351

Yan, C. G., Wang, X. D., Zuo, X. N., and Zang, Y. F. (2016). DPABI: data processing & analysis for (resting-state) brain imaging. *Neuroinformatics* 14, 339–351. doi: 10.1007/s12021-016-9299-4

Yang, L., Yan, Y., Wang, Y., Hu, X., Lu, J., Chan, P., et al. (2018). Gradual disturbances of the amplitude of low-frequency fluctuations (ALFF) and fractional ALFF in Alzheimer spectrum. *Front. Neurosci.* 12:975. doi: 10.3389/fnins.2018.00975

Zang, Y., Jiang, T., Lu, Y., He, Y., and Tian, L. (2004). Regional homogeneity approach to fMRI data analysis. *Neuroimage* 22, 394–400. doi: 10.1016/j.neuroimage.2003.12.030

Zang, Y. F., He, Y., Zhu, C. Z., Cao, Q. J., Sui, M. Q., Liang, M., et al. (2007). Altered baseline brain activity in children with ADHD revealed by resting-state functional MRI. *Brain Dev.* 29, 83–91. doi: 10.1016/j.braindev.2006.07.002

Zang, Y. F., Zuo, X. N., Milham, M., and Hallett, M. (2015). Toward a meta-analytic synthesis of the resting-state fMRI literature for clinical populations. *Biomed. Res. Int.* 2015:435265. doi: 10.1155/2015/435265

Zhao, N., Yuan, L. X., Jia, X. Z., Zhou, X. F., Deng, X. P., He, H. J., et al. (2018). Intra- and inter-scanner reliability of voxel-wise whole-brain analytic metrics for resting state fMRI. *Front. Neuroinform.* 12:54. doi: 10.3389/fninf.2018.00054

Zheng, Y., Xie, Y., Qi, M., Zhang, L., Wang, W., Zhang, W., et al. (2021). *Ginkgo biloba* extract is comparable with donepezil in improving functional recovery in Alzheimer's disease: results from a multilevel characterized study based on clinical features and resting-state functional magnetic resonance imaging. *Front. Pharmacol.* 12:721216. doi: 10.3389/fphar.2021.721216

Zou, Q. H., Zhu, C. Z., Yang, Y., Zuo, X. N., Long, X. Y., Cao, Q. J., et al. (2008). An improved approach to detection of amplitude of low-frequency fluctuation (ALFF) for resting-state fMRI: fractional ALFF. *J. Neurosci. Methods* 172, 137–141. doi: 10.1016/j.jneumeth.2008.04.012

Zuo, X. N., Di Martino, A., Kelly, C., Shehzad, Z. E., Gee, D. G., Klein, D. F., et al. (2010). The oscillating brain: complex and reliable. *Neuroimage* 49, 1432–1445. doi: 10.1016/j.neuroimage.2009.09.037

Zuo, X. N., Ehmke, R., Mennes, M., Imperati, D., Castellanos, F. X., Sporns, O., et al. (2012). Network centrality in the human functional connectome. *Cereb. Cortex* 22, 1862–1875. doi: 10.1093/cercor/bhr269

Conflict of Interest: The authors declare that the research was conducted in the absence of any commercial or financial relationships that could be construed as a potential conflict of interest.

Publisher's Note: All claims expressed in this article are solely those of the authors and do not necessarily represent those of their affiliated organizations, or those of the publisher, the editors and the reviewers. Any product that may be evaluated in this article, or claim that may be made by its manufacturer, is not guaranteed or endorsed by the publisher.

Copyright © 2022 Hu, Wang, Li, Xie, Lin, Huang, Zhan, Jia and Zhao. This is an open-access article distributed under the terms of the Creative Commons Attribution License (CC BY). The use, distribution or reproduction in other forums is permitted, provided the original author(s) and the copyright owner(s) are credited and that the original publication in this journal is cited, in accordance with accepted academic practice. No use, distribution or reproduction is permitted which does not comply with these terms.

frontiers in Aging Neuroscience

MINI REVIEW
published: 25 January 2022
doi: 10.3389/fnagi.2022.788846

Magnetic Resonance Imaging Markers for Cognitive Impairment in Parkinson's Disease: Current View

*Yanbing Hou and Huifang Shang**

Laboratory of Neurodegenerative Disorders, Department of Neurology, Rare Diseases Center, National Clinical Research Center for Geriatrics, West China Hospital, Sichuan University, Chengdu, China

Cognitive impairment (CI) ranging from mild cognitive impairment (MCI) to dementia is a common and disturbing complication in patients with Parkinson's disease (PD). Numerous studies have focused on neuropathological mechanisms underlying CI in PD, along with the identification of specific biomarkers for CI. Magnetic resonance imaging (MRI), a promising method, has been adopted to examine the changes in the brain and identify the candidate biomarkers associated with CI. In this review, we have summarized the potential biomarkers for CI in PD which have been identified through multi-modal MRI studies. Structural MRI technology is widely used in biomarker research. Specific patterns of gray matter atrophy are promising predictors of the evolution of CI in patients with PD. Moreover, other MRI techniques, such as MRI related to small-vessel disease, neuromelanin-sensitive MRI, quantitative susceptibility mapping, MR diffusion imaging, MRI related to cerebrovascular abnormality, resting-state functional MRI, and proton magnetic resonance spectroscopy, can provide imaging features with a good degree of prediction for CI. In the future, novel combined biomarkers should be developed using the recognized analysis tools and predictive algorithms in both cross-sectional and longitudinal studies.

Keywords: Parkinson's disease, magnetic resonance imaging, biomarker, mild cognitive impairment, dementia

OPEN ACCESS

Edited by:
Jiehui Jiang,
Shanghai University, China

Reviewed by:
Richard Camicioli,
University of Alberta, Canada
Lirong Jin,
Zhongshan Hospital, China
Jong-Min Kim,
Seoul National University Bundang Hospital, South Korea
Paolo Caffarra,
University of Parma, Italy

***Correspondence:**
Huifang Shang
hfshang2002@126.com

Specialty section:
This article was submitted to Parkinson's Disease and Aging-Related Movement Disorders, a section of the journal Frontiers in Aging Neuroscience

Received: *03 October 2021*
Accepted: *03 January 2022*
Published: *25 January 2022*

Citation:
Hou Y and Shang H (2022) Magnetic Resonance Imaging Markers for Cognitive Impairment in Parkinson's Disease: Current View. Front. Aging Neurosci. 14:788846. doi: 10.3389/fnagi.2022.788846

INTRODUCTION

Parkinson's disease (PD) is becoming the fastest-growing neurological disorder. In 2016, globally, approximately 6.1 million people, suffered from PD, and this incidence is further expected to double to more than 12 million by 2040. Cardinal motor symptoms of PD are easy to identify and can be controlled by anti-PD medicine. However, various non-motor symptoms, including cognitive impairment (CI), mood disorders, neuropsychic symptoms, autonomic dysfunction, and pain, greatly aggravate the disability of the affected individuals (Dorsey et al., 2018; Collaborators, 2019; Bloem et al., 2021). CI is a common non-motor symptom that progresses from normal cognition to mild cognitive impairment (MCI), and eventually dementia. Dementia is a common disorder occurring in advanced stages of PD, and MCI, the pre-dementia stage of CI, has certainly attracted great attention in recent years. To promote uniformity in clinical and research applications on

cognition in PD, clinical diagnostic criteria for different stages of CI (MCI and dementia) have been delineated by a panel of experts from the Movement Disorder Society (MDS) Task Force (Emre et al., 2007; Litvan et al., 2012).

The diagnostic criteria of PD patients with MCI (PD-MCI) are as follows: (1) a diagnosis of PD; (2) a gradual decline of the cognitive ability in the level I category based on a brief cognitive assessment or in the level II category based on a more comprehensive neuropsychological assessment including at least two tests for each of five cognitive domains (attention, executive function, language, memory, and visuospatial function); and (3) complete functional independence. Impairment in neuropsychological tests is defined per one to two standard deviations (SDs) below the appropriate norms, a significant decrease in the serial cognitive tests, or a significant decrease from the estimated premorbid levels. The PD patient with MCI according to the level II criteria shows impairment in at least two tests within one single cognitive domain or different cognitive domains (Litvan et al., 2012). Following are the diagnostic criteria of PD patients with dementia (PDD): (1) a diagnosis of PD; (2) progressive impairment in more than one cognitive domain or a significant decrease from premorbid levels; and (3) impaired functional independence (Emre et al., 2007). Based on the MDS Task Force Level II criteria, recent studies report that the frequency of PD-MCI is between 20% and 35% in newly diagnosed PD patients (Broeders et al., 2013; Pedersen et al., 2017). Moreover, according to the clinical criteria, a recent meta-analysis comprising of 41 studies reported that the pooled PD-MCI prevalence is 40% in a total sample of 7,053 PD patients (Baiano et al., 2020). In a prospective population-based study, among the newly diagnosed PD patients with normal cognition at baseline, the cumulative incidence of PD-MCI is 9.9% after 1 year, 23.2% after 3 years, and 28.9% after 5 years of follow-up (Pedersen et al., 2017). Patients with PD-MCI are more likely to eventually develop PDD, and 59.1% of patients with persistent PD-MCI within 1 year develop PDD (Pedersen et al., 2017). The point prevalence of PDD is close to 30% in a PD cohort, and at least 75% of PD patients who survived for more than 10 years are more likely to develop dementia (Aarsland and Kurz, 2010).

Although dementia is a common problem in patients with advanced PD, there are great differences in the rate of cognitive decline and the time of dementia onset in PD patients. Thus, effective markers that can accurately quantify pathological changes are needed to identify PD patients at high risk of developing CI, to predict the progression of cognitive dysfunction, and for ease of their availability. In the last few years, magnetic resonance imaging (MRI) technology, an attractive option, has improved the understanding of the pathophysiology of CI in PD patients, along with establishing potential biomarkers. These biomarkers for cognitive dysfunction in PD were reviewed based on a PubMed search for peer-reviewed articles published between January 2011 and August 2021 using the search terms "marker" OR "biomarker" AND "Parkinson's disease" OR "Parkinson" OR "Parkinson's disease" AND "mild cognitive impairment" OR "MCI" OR "Parkinson's disease dementia" OR "dementia" OR "cognitive impairment" AND "MRI" OR "magnetic resonance imaging". This review provides an update on the recent advances in the emerging role and development of MRI markers for cognitive dysfunction in PD.

STRUCTURAL MAGNETIC RESONANCE IMAGING

Most of the studies in recent years acquired structural MR images using a 3.0 T scanner, and grey matter (GM) abnormalities are extensively examined using either voxel-based morphometry (VBM) or surface-based analyses. Automated and unbiased VBM analysis can be used to estimate the GM volume or concentration differences between groups at the whole-brain level, thus, it has been widely used to quantify regional GM alterations in PD patients with CI. Cortical thickness, the distance between white and pial surfaces, is a more sensitive structural MRI-based measurement to detect early GM changes. The details of imaging methods are presented in **Table 1**. The region of interest (ROI) approach has been used to analyze both cortical and subcortical changes based on an *a priori* hypothesis. Summary findings from structural MRI correlated with cognitive dysfunction in PD are showed in **Table 2**.

Cross-Sectional MR Studies

Cross-sectional results on CI-related GM changes in PD patients remain heterogeneous, and three meta-analyses were conducted to identify the most consistent GM alterations associated with PD-CI (Xu et al., 2016; Mihaescu et al., 2019; Zheng et al., 2019). A meta-analysis study in 2016, using five studies compared 92 PD-MCI patients with 192 PD without CI (PD-NCI) patients, and from ten studies, compared 168 PDD patients with 233 PD without dementia (PD-ND) patients. The authors have reported significantly reduced GM volume in the left superior frontal gyrus (SFG), left superior temporal lobe (STL), and left insula in the PD-MCI group, and in the left SFG, and bilateral STL extending to the hippocampus in the PDD group (Xu et al., 2016). A meta-analysis study in 2019 compared 405 PD-MCI patients with 559 PD-NCI patients from fifteen studies, and compared 178 PDD patients with 278 PD-ND patients from eleven studies. A significantly higher GM atrophy in bilateral dorsolateral prefrontal cortex, left angular gyrus, right supramarginal gyrus, left insula, and midcingulate cortex in the PD-MCI group, and bilateral insula and right hippocampus in the PDD group was reported (Mihaescu et al., 2019). Another meta-analysis study in 2019 consisting of 504 PD-MCI patients and 554 PD-NCI patients from twenty studies reported a drastically remarkable GM atrophy in the left anterior insula extending to the inferior frontal gyrus, and orbital part in the PD-MCI group (Zheng et al., 2019). GM atrophy in the insula and frontal-limbic-temporal regions are robust features of CI in PD, and unilateral-to-bilateral development of structural atrophy is a potential indicator for progression of PD-MCI to PDD. In particular, several studies attempted to analyze GM changes across various stages of cognitive decline by comparing a prospective sample of PD-NCI, PD-MCI, PDD patients, and healthy subjects (HCs).

TABLE 1 | Imaging characteristics of magnetic resonance imaging studies in Parkinson's disease and cognitive impairment.

Modality	MR sequence	Core software/method	Analysis variables	Advantages/disadvantages
Structural imaging	T1-TFE sequence/3D SPGR/MPRAGE	SPM (http://www.fil.ion.ucl.ac.uk/spm)/ Freesurfer (http://surfer.nmr.mgh.harvard.edu)	Voxel-based morphometry (VBM)	It can estimate the gray matter (GM) volume or concentration alterations at the whole-brain level.
		Freesurfer (http://surfer.nmr.mgh.harvard.edu)	Cortical thickness (CTh)	A more sensitive structural MRI-based measurement to detect early GM changes.
MRI related to small-vessel disease	T2-weighted fast spin-echo sequence/FLAIR	Fazekas visual rating scale (Scheltens et al., 1993)	White matter hyperintensity (WMH)	It can reflect pathological white matter (WM) tissue ischemia. It can be assessed on the basis of size and quantity of lesions in a given neuroanatomical location.
		Automated routines (de Boer et al., 2009; Bohnen and Albin, 2011)	WMH	Quantitative assessment of WML burden may be particularly advantageous for assessing changes over time compared with the visual grading.
		Standards for Reporting Vascular Changes on Neuroimaging criteria (Wardlaw et al., 2013)	Perivascular space (PVS)	It is called the Virchow-Robin spaces and is piallined interstitial fluid-filled space surrounding the penetrating vessels.
Neuromelanin-sensitive MRI	T1-weighted FSE sequence	Semi-automated analysis (Sulzer et al., 2018).	Signal intensity	It can depict characteristics of tissue containing neuromelanin.
Quantitative susceptibility mapping (QSM)	3D-fast low-angle shot sequence/3D fast-field echo sequence	Matlab (MathWorks, Natick, MA, United States)/Voxel-based QSM analysis	QSM values	It can quantify susceptibility-changing materials, such as iron accumulation.
Diffusion tensor imaging	Pulsed gradient spin-echo single- shot echo-planar DT MR imaging sequences	FSL Diffusion Toolbox (FMRIB Software Library, Center Software Library, University of Oxford, Oxford, United Kingdom);	Fractional anisotropy (FA)/mean diffusivity (MD)	The directionality of movement, FA, and its total magnitude, MD, both can sensitively detect early microstructural cortical damage.
MRI related to cerebrovascular abnormality	cASL/pASL	ANTs (http://stnava.github.io/ANTs)	Cerebral blood flow (CBF) values	Cerebrovascular abnormalities include altered CBF, cerebral blood volume (CBV), and blood–brain barrier permeability.
	iVASO MRI	Matlab (MathWorks, Natick, MA, United States)/SPM (http://www.fil.ion.ucl.ac.uk/spm)	Arteriolar CBV (CBVa) values	The measurement of changes in CBVa may be more sensitive than measurement of changes in total CBV and CBF.
Resting-state functional MRI	Functional gradient-echo EPI sequence	SPM (http://www.fil.ion.ucl.ac.uk/spm) FSL (http://www.fmrib.ox.ac.uk/fsl/)	Functional connectivity	It can measure intrinsic blood oxygen level-dependent (BOLD) low-frequency signal fluctuations.
Proton magnetic resonance spectroscopy (^{1}H-MRS)	PRESS sequences	Matlab (MathWorks, Natick, MA, United States)/SPM (http://www.fil.ion.ucl.ac.uk/spm)	Average MRS signals	It can reflect the integrity of different elements in the brain, including *N*-acetylaspartate (NAA), choline compounds (Cho), creatine (Cr), and myo-inositol (MI).

cASL, continuous arterial spin labeling; EPI, echo-planar imaging; FLAIR, fluid-attenuated inversion-recovery; FSE, fast spin-echo; iVASO, inflow-based vascular-space-occupancy; MPRAGE, magnetization prepared rapid gradient echo; pASL, pulsed arterial spin labeling; PRESS, point resolved spectroscopy; SPGR, spoiled gradient echo; TFE, turbo field echo.

These typically report a pattern of linear and progressive cortical changes (reduced GM volume or cortical thinning) with increasing levels of CI (Song et al., 2011; Melzer et al., 2012; Pagonabarraga et al., 2013).

Notably, several structural MRI studies focused on assessing the differences in subcortical GM structures or ROIs crucial in the cognitive functions of PD patients. The volume of the hippocampus and substantia innominata (SI), a major source of cholinergic input to the cerebral cortex, progressively decreases corresponding to the cognitive status (Weintraub et al., 2011; Choi et al., 2012). Recent advances in the imaging technology and software analysis tools have made the study of hippocampal subregions *in vivo* a possibility (Iglesias et al., 2015). Smaller cornu ammonis 1 (CA1) and hippocampal-amygdaloid transition

TABLE 2 | Summary findings from structural magnetic resonance imaging studies in Parkinson's disease and cognitive impairment.

Studies		Results
Cross-sectional	Whole brain analysis: Voxel-based meta-analysis/coordinate-based meta-analysis;	**PD-MCI vs. PDNCI:** Gray matter (GM) atrophy in left superior frontal gyrus (SFG), left superior temporal lobe (STL), and left insula (Xu et al., 2016). GM atrophy in bilateral dorsolateral prefrontal cortex, left angular gyrus, right supramarginal gyrus, left insula, and midcingulate cortex (Mihaescu et al., 2019). GM atrophy in the left anterior insula extending to the inferior frontal gyrus, and orbital part (Zheng et al., 2019).
	Voxel-based meta-analysis/coordinate-based meta-analysis;	**PDD vs. PDND:** GM atrophy in the left SFG, bilateral STL extending to hippocampus (Xu et al., 2016). GM atrophy in bilateral insula and right hippocampus (Mihaescu et al., 2019).
		Across various status of cognitive decline: A pattern of linear and progressive cortical changes (reduced GM volume or cortical thinning) (Song et al., 2011; Melzer et al., 2012; Pagonabarraga et al., 2013).
	Subcortical and region of interest analyses:	**PD-MCI vs. PDNCI:** Atrophy in hippocampal subregions [cornu ammonis 1 (CA1) and hippocampal-amygdaloid transition area (HATA)] (Becker et al., 2021), entorhinal cortex (ENT) (Goldman et al., 2012; Jia et al., 2019), amygdala (Schulz et al., 2018), thalamus (Mak et al., 2014; Chen et al., 2016; Schulz et al., 2018), accumbens nucleus (Mak et al., 2014), and nucleus basalis of Meynert (Schulz et al., 2018).
		Across various status of cognitive decline: A progressive decrease in volume of the hippocampus and substantia innominata (SI) (Weintraub et al., 2011; Choi et al., 2012).
Longitudinal	Whole brain analysis:	**PD-MCI vs. PDNCI:** Increased global atrophy (Mak et al., 2017). A higher rate of cortical thinning in frontal/supplementary motor area, parietal-temporal, and occipital cortices (Hanganu et al., 2014; Mak et al., 2015).
	Subcortical and region of interest analyses:	**PD-MCI vs. PDNCI:** A greater progression of cortical thinning in the posterior regions of brain (Garcia-Diaz et al., 2018). A decreased volume in the amygdala and accumbens nucleus (Hanganu et al., 2014; Mak et al., 2015).
	Converters versus non-converters:	**PD-MCI converters vs. non-converters:** GM atrophy in temporal regions and the amygdala/hippocampus structural covariance network at baseline (Wen et al., 2015; Zhou et al., 2020; Chen et al., 2021). Cortical thinning in the anterior cingulate cortex, parietal, temporal, and occipital regions, and GM atrophy in accumbens nucleus at baseline (Mak et al., 2015; Foo et al., 2017a,b; Filippi et al., 2020; Gorges et al., 2020). A higher progression of atrophy in the frontal lobe and longitudinal white matter (WM) volumetric reduction (Wen et al., 2015; Zhou et al., 2020; Chen et al., 2021). A higher progression of atrophy in the thalamus, caudate nucleus, accumbens nucleus and hippocampal subfields (CA2-3) (Mak et al., 2015; Foo et al., 2017a,b; Filippi et al., 2020; Gorges et al., 2020).
		PDD converters vs. non-converters: GM atrophy in uncus, global hippocampus, and hippocampal subfields (presubiculum, subiculum, and CA1) at baseline (Gee et al., 2017; Low et al., 2019). Larger ventricular volume at baseline (Camicioli et al., 2011). Cortical thinning in the precentral gyrus and superior frontal gyrus (RSFG) and anterior cingulate at baseline (Compta et al., 2013). A higher progression of atrophy in the global hippocampus, hippocampal subfields [parasubiculum, presubiculum, granule cell layer of the dentate gyrus (GC-DG), and fimbria] and parahippocampal gyrus (Gee et al., 2017; Low et al., 2019).
		PDD converters vs. PD-MCI non-converters: GM atrophy in prefrontal areas, insular and caudate nucleus, smaller normalized SI volume, and cortical thinning extending from the posterior cortical area into the frontal region, and the frontotemporal cortices (Lee et al., 2014; Chung et al., 2019; Filippi et al., 2020).
	Predictive variables for conversion	**Predictors for PD-MCI conversion:** Baseline volumes of global WM, global hippocampus, and hippocampal subregions (parasubiculum, CA4, GC-DG, and HATA), thalamus, and accumbens nucleus (Kandiah et al., 2014; Wen et al., 2015; Foo et al., 2017a,b).
		Predictors for PDD conversion: Baseline volumes of global hippocampus and hippocampal subregions (presubiculum, subiculum, and CA1), cortical thickness of the medial superior frontal/olfactory cortices, superior frontal/anterior cingulate and precentral regions (Compta et al., 2013; Kandiah et al., 2014; Chung et al., 2019; Low et al., 2019).
		Predictors for CI conversion: A validated AD-spatial pattern of brain atrophy (Tropea et al., 2018). GM volume in the nucleus basalis of Meynert (Ray et al., 2018; Schulz et al., 2018).

CI, cognitive impairment; MCI, mild cognitive impairment; PD, Parkinson's disease; PDD, PD patients with dementia; PD-NCI, PD without CI; PD-ND, PD without dementia.

area (HATA) volumes have been observed in PD-MCI patients relative to the PD-NCI patients (Becker et al., 2021). In addition, as compared with the PD-NCI group, the PD-CI group exclusively exhibits atrophy in the entorhinal cortex (ENT) (Goldman et al., 2012; Jia et al., 2019), amygdala (Schulz et al., 2018), thalamus (Mak et al., 2014; Chen et al., 2016; Schulz et al., 2018), accumbens nucleus (Mak et al., 2014), and nucleus basalis of Meynert (Schulz et al., 2018).

Longitudinal MR Studies

Recent longitudinal studies described the progression patterns of GM changes in PD patients with CI, which can facilitate a better understanding of the mechanism of CI in PD. Patients with PD-MCI show increased global atrophy within 18 months relative to both PD-NCI patients and HCs (Mak et al., 2017). Other studies have also attempted to investigate the longitudinal changes in the cortical and subcortical GM and reported a higher rate of cortical thinning in the frontal/supplementary motor area, parietal-temporal, occipital cortices and a significant decrease in the volume of the amygdala and accumbens nucleus in PD-MCI patients relative to both PD-NCI patients and HCs (Hanganu et al., 2014; Mak et al., 2015). Some longitudinal studies have examined the differential progressive GM loss in the specific cortical regions. A 4-year follow-up study reported that over time, as compared to the PD-NCI patients, those with PD-MCI had significantly greater progression of cortical thinning in the posterior regions of the brain related to visuospatial and visuoperceptual (VS/VP) changes (Garcia-Diaz et al., 2018). Another 4-year follow-up study held the opinion that the hippocampal subfields have different vulnerabilities to the degenerative processes related to aging as well as PD. PD patients and HCs have similar longitudinal changes in CA1, while both PD-NCI and PD-MCI patients have a more severe decline in the anterior and posterior hippocampal segments, implying its predictive value for assessing memory dysfunction (Uribe et al., 2018).

Converters Versus Non-converters

Researchers have examined structural alterations in the brain to predict cognitive decline in PD patients. PD patients with normal cognition at baseline and who develop PD-MCI during follow-up are classified as "PD-MCI converters," while those who remain cognitively asymptomatic during the follow-up are classified as "non-converters." Relative to the non-converters, PD-MCI converters have a significant reduction in GM volume of temporal regions and the amygdala/hippocampus structural covariance network at baseline, along with evidently progressive frontal lobe atrophy and longitudinal white matter (WM) volumetric reduction (Wen et al., 2015; Zhou et al., 2020; Chen et al., 2021). Some studies have further investigated the pattern and progression of cortical thickness and subcortical volumes in PD-MCI converters, and reported a higher degree of anterior cingulate cortex, parietal, temporal, and occipital cortices thinning, atrophy of accumbens nucleus at baseline, and progressive atrophy in the thalamus, caudate nucleus, accumbens nucleus, and CA2-3 of hippocampal subregions (Mak et al., 2015; Foo et al., 2017a,b; Filippi et al., 2020; Gorges et al., 2020).

Non-demented PD patients who progress to PDD during follow-up are classified as "PDD converters." At baseline, relative to the non-converters, PDD converters have lower GM volume in uncus, global hippocampus, and hippocampal subfields (presubiculum, subiculum, and CA1) (Gee et al., 2017; Low et al., 2019), lesser thicknesses of the precentral gyrus and superior frontal gyrus (RSFG) and anterior cingulate (Compta et al., 2013), and larger ventricular volume (Camicioli et al., 2011). Moreover, over time, PDD converters have higher GM atrophy in the global hippocampus, hippocampal subfields [parasubiculum, presubiculum, granule cell layer of the dentate gyrus (GC-DG), and fimbria] and parahippocampal gyrus (Gee et al., 2017; Low et al., 2019). Another study classified PD-MCI patients as PDD converters or PD-MCI non-converters based on whether they are subsequently diagnosed with PDD during follow-up. Relative to PD-MCI non-converters, the PDD converters were found to have lower GM density in prefrontal areas, insular and caudate nucleus, smaller normalized SI volume, and a lesser cortical thickness extending from the posterior cortical area into the frontal region, and the frontotemporal cortices (Lee et al., 2014; Chung et al., 2019; Filippi et al., 2020).

Predictive Variables for Conversion

Baseline volumes of global WM, global hippocampus, and hippocampal subregions (parasubiculum, CA4, GC-DG, and HATA), thalamus, and accumbens nucleus are significant neuroimaging predictors for determining the conversion from PD-NCI to PD-MCI; the baseline global GM volume cannot significantly predict the conversion to PD-MCI (Kandiah et al., 2014; Wen et al., 2015; Foo et al., 2017a,b). Moreover, GM volume in the global hippocampus and hippocampal subregions (presubiculum, subiculum, and CA1), cortical thickness in the medial superior frontal/olfactory cortices, superior frontal/anterior cingulate and precentral regions are significant predictors for the progression to PDD (Compta et al., 2013; Kandiah et al., 2014; Chung et al., 2019; Low et al., 2019).

Growing evidence highlighted that brain regions undergoing neurodegeneration may overlap synergistically with the pathological processes for PD and Alzheimer's disease (AD) (Masliah et al., 2001; Clinton et al., 2010). To determine its association with CI, a validated AD-spatial pattern of brain atrophy (spatial pattern of abnormality for recognition of early AD index, SPARE-AD) was quantified in PD patients with a range of cognitive abilities. The findings support the involvement of hippocampus and parietal-temporal cortex with CI in PD (Weintraub et al., 2012), and affirm the importance of AD biomarkers as effective predictors for CI in PD (Tropea et al., 2018). In addition, autopsies have identified degeneration of the cholinergic basal forebrain, especially in the nucleus basalis of Meynert, causing cortical cholinergic depletion, and eventually leading to the CI in patients with PD and AD (Liu et al., 2015). GM volume in the nucleus basalis of Meynert was a critical cholinergic biomarker to predict CI in PD-NCI patients (Ray et al., 2018; Schulz et al., 2018).

OTHER MAGNETIC RESONANCE IMAGING TECHNIQUES

Magnetic Resonance Imaging Related to Small-Vessel Disease

As a consequence of cerebral small-vessel disease (SVD), white matter hyperintensities (WMHs) in the brain can reflect pathological WM tissue ischemia (Erten-Lyons et al., 2013). PD patients with greater WMH have more severe cognitive deficits and a higher annual rate of change in global cognition (Dadar et al., 2018; Chahine et al., 2019; Chang et al., 2021). The periventricular WMH burden is significantly associated with PD-MCI and severe WMH with PDD; both are independent of cardiovascular risk factors (Huang et al., 2020; Tsai et al., 2021). In addition, heavier temporal WMH burden is associated with worse verbal memory (Chahine et al., 2019), and higher periventricular WMH burden correlates with greater decline in the executive and visuospatial functions (Huang et al., 2020). Therefore, WMH is strongly correlated with CI in PD and may serve as a surrogate marker for CI in PD (Kandiah et al., 2014; Fang et al., 2021). Visible perivascular space (PVS) has also been considered as an imaging biomarker for SVD. A longitudinal MRI-visible PVS study reported higher PVS severity in basal ganglia (BG) as a predictor of cognitive conversion of PD-NCI patients as well as for cognitive decline in PD-MCI patients (Park et al., 2019). Summary findings from other MRI techniques correlated with cognitive dysfunction in PD can be found in **Table 3**.

Neuromelanin-Sensitive Magnetic Resonance Imaging

Neuromelanin-sensitive MRI (NM-MRI) is a promising technique that depicts characteristics of tissue containing neuromelanin, a dark polymer product of noradrenaline metabolism (Nakamura and Sugaya, 2014). The substantia nigra (SN) of the midbrain and the locus coeruleus (LC) within the pons contain large clusters of neuromelanin-producing cells, and the loss of these neuromelanin-containing cells within the two regions is a primary pathological diagnostic criterion for PD. The NM signal intensity of the LC in PD-MCI patients is significantly lower than that of the control subjects, and may serve as an imaging marker for assessing cognitive dysfunction in PD (Li et al., 2019; Prasuhn et al., 2021).

Quantitative Susceptibility Mapping

Quantitative susceptibility mapping (QSM) is another new MRI technique that enables the quantification of susceptibility-changing materials. Iron accumulation has been proposed as a significant pathomechanism for PD, which can be systematically examined using the QSM method. PD-MCI patients have significantly higher QSM values in the orbitofrontal cortex, cuneus, precuneus, fusiform gyrus, and head of the caudate nucleus relative to the PD-NCI patients (Uchida et al., 2019). Meanwhile, PDD patients have significantly higher QSM values in the left hippocampus as compared to non-demented PD patients (Li et al., 2018). These findings suggest the association between CI in PD and cerebral iron burden, which may be an auxiliary biomarker for early detection of CI in PD.

MR Diffusion Imaging

Diffusion tensor imaging (DTI) is an *in vivo* surrogate measure for the microstructural integrity of WM tracts. Using this technique, the rate of 3-dimensional water molecule diffusion through a pulsed-field gradient can be measured. The directionality of movement is quantified as fractional anisotropy (FA) and its total magnitude is measured as mean diffusivity (MD). The decrease in FA and increase in MD within the central nervous system have been proposed as sensitive imaging indicators for detecting early microstructural cortical damage in patients with neurodegenerative disorders.

The PD-MCI patients have a distributed pattern of WM abnormalities in the anterior and superior corona radiata, genu, and body of the corpus callosum, anterior inferior fronto-occipital, uncinate, and superior longitudinal fasciculi relative to PD-NCI patients and HCs (Agosta et al., 2014). Lower FA values in frontotemporoparietal regions, hippocampus, amygdala, thalamus, BG, and higher MD values in hippocampus, ENT, amygdala, thalamus, and nucleus basalis of Meynert relative to PD-NCI patients have been reported in PD-MCI patients (Galantucci et al., 2017; Schulz et al., 2018). PDD patients have significantly lower FA values in the prefrontal WM, hippocampus, and the genu of the corpus callosum relative to the non-demented PD patients (Kamagata et al., 2013; Chen et al., 2015), and lower FA values in both the anterior and the posterior cingulate fiber tracts as compared to HCs (Kamagata et al., 2012). Microstructural abnormalities in WM of PD patients with variant cognitive statuses (PD-NCI, PD-MCI, and PDD) have been investigated to elucidate the pathological processes of CI in PD. The loss of microstructural WM integrity is spatially restricted in PD-NCI patients, while these alterations increase with progressive cognitive deterioration (Hattori et al., 2012; Deng et al., 2013; Melzer et al., 2013).

In a previous study, dynamic MD changes were specifically assessed by a longitudinal approach in newly-diagnosed drug-naïve PD patients. A higher 1-year MD increase in frontal and occipital cortices was found in PD patients relative to HCs, which correlated with changes in the cognitive measures (Sampedro et al., 2019). Moreover, the increased MD values in the nucleus basalis of Meynert can predict the conversion from PD-NCI to PD with CI (Schulz et al., 2018). Thus, further longitudinal investigations are required to establish the clinical utility of DTI as a sensitive biomarker for the pathology of CI in PD.

Magnetic Resonance Imaging Related to Cerebrovascular Abnormality

Emerging evidence supported that cerebrovascular abnormalities including altered cerebral blood flow (CBF), cerebral blood volume (CBV), and blood–brain barrier permeability are linked with pathophysiology in CI. Using the arterial spin labeling (ASL) technique, brain perfusion can be quantitatively assessed in terms of CBF. A pattern of decreased CBF at the posterior part of the brain, mostly in the lateral and medial parietooccipital cortices,

TABLE 3 | Summary findings from other magnetic resonance imaging studies in Parkinson's disease and cognitive impairment.

Modalities	Results	
MRI related to small-vessel disease	White matter hyperintensity (WMH)	PD patients with greater WMH have more severe cognitive deficits and a higher annual rate of change in global cognition (Dadar et al., 2018; Chahine et al., 2019; Chang et al., 2021). The periventricular WMH burden is significantly associated with PD-MCI and severe WMH with PDD (Huang et al., 2020; Tsai et al., 2021). WMH is strongly correlated with CI in PD and may serve as a surrogate marker for CI in PD (Kandiah et al., 2014; Fang et al., 2021).
	Perivascular space (PVS)	Higher PVS severity in basal ganglia (BG) as a predictor of cognitive conversion of PD-NCI patients as well as for cognitive decline in PD-MCI patients (Park et al., 2019).
Neuromelanin-sensitive MRI (NM-MRI)	Signal intensity	**PD-MCI vs. HC** Lower NM signal intensity in the locus coeruleus, which may serve as an imaging marker for assessing cognitive dysfunction in PD (Li et al., 2019; Prasuhn et al., 2021).
Quantitative susceptibility mapping (QSM)	QSM values	**PD-MCI vs. PDNCI** Higher QSM values in the orbitofrontal cortex, cuneus, precuneus, fusiform gyrus, and head of the caudate nucleus (Uchida et al., 2019). **PDD vs. PDND** Higher QSM values in the left hippocampus (Li et al., 2018).
Diffusion tensor imaging	Fractional anisotropy (FA)/mean diffusivity (MD)	**PD-MCI vs. PDNCI** Decreased FA values in the anterior and superior corona radiata, genu, and body of the corpus callosum, anterior inferior fronto-occipital fasciculus (IFOF)/uncinate, and anterior superior longitudinal fasciculi (SLF), frontotemporoparietal regions, hippocampus, BG, amygdala, thalamus (Agosta et al., 2014; Galantucci et al., 2017; Schulz et al., 2018). Increased MD values in hippocampus, entorhinal cortex (ENT), amygdala, thalamus, and nucleus basalis of Meynert (Galantucci et al., 2017; Schulz et al., 2018). **PDD vs. PDND** Decreased FA values in the prefrontal white matter, hippocampus, and the genu of the corpus callosum (Kamagata et al., 2013; Chen et al., 2015). **Across various status of cognitive decline** The loss of microstructural WM integrity was spatially restricted in PD-NCI patients, while these alterations increase with progressive cognitive deterioration (Hattori et al., 2012; Deng et al., 2013; Melzer et al., 2013). **Predictors for CI conversion** The increased MD values in the nucleus basalis of Meynert (Schulz et al., 2018).
MRI related to cerebrovascular abnormality	Cerebral blood flow (CBF) values	**PD-MCI vs. HC** A pattern of decreased CBF at the posterior part of the brain, mostly in the lateral and medial parietooccipital cortices, summarized as "posterior hypoperfusion" (Arslan et al., 2020). Parietal CBF may serve as a potential early biomarker for CI in PD (Pelizzari et al., 2020).
	Arteriolar cerebral blood volume (CBVa) values	**PD-CI vs. HC** A decreasing trend of CBVa in the substantia nigra, caudate nucleus and putamen, and an increasing trend of CBVa in the pre-supplementary motor area and intracalcarine gyrus (Paez et al., 2020).
Resting-state functional MRI	Functional connectivity (FC)	**PD-CI vs. PDNCI** Reduced FC in specific brain regions that are parts of the default mode network (DMN) (Wolters et al., 2019). **Predictors for CI conversion** FC between the medial prefrontal cortex (mPFC) and posterior cingulate cortex (PCC) within DMN at baseline (Zarifkar et al., 2021).
Proton magnetic resonance spectroscopy (^{1}H-MRS)	Average MRS signals	**PD-CI vs. PDNCI** Higher the choline to creatine (Cho/Cr) ratio in the occipital lobe, reduced concentration of *N*-acetylaspartate (NAA) in the middle and superior frontal gray matter regions, and reduced concentration of total Cho and total Cr in the frontal white matter regions (Nie et al., 2013; Chaudhary et al., 2021). Levels of NAA reduced in the dorsolateral prefrontal cortex in the early stage, and progression to the hippocampus in PDD patients (Pagonabarraga et al., 2012). Frontal neuro-metabolism may serve as a promising biomarker for characterizing cognitive deficits in patients with PD (Chaudhary et al., 2021).

CI, cognitive impairment; MCI, mild cognitive impairment; PD, Parkinson's disease; PDD, PD patients with dementia; PD-NCI, PD without CI; PD-ND, PD without dementia.

summarized as "posterior hypoperfusion," has been reported in the PD-MCI group relative to HCs (Arslan et al., 2020), which may be a suitable early biomarker for CI in PD. Parietal CBF correlates to visuomotor skills and also may serve as a potential early biomarker for CI in PD (Pelizzari et al., 2020). Using the inflow-based vascular-space-occupancy (iVASO) MRI approach, potential arteriolar CBV (CBVa) abnormalities reflecting the homeostasis of the most actively regulated segment in the microvasculature can be calculated. A decreasing trend of CBVa in the substantia nigra, caudate nucleus and putamen, and an increasing trend of CBVa in the pre-supplementary motor area and intracalcarine gyrus have been reported in PD-CI patients

relative to HCs (Paez et al., 2020). These exploratory findings provide important information for efforts toward developing potential biomarkers for the risk of CI in PD.

Resting-State Functional Magnetic Resonance Imaging

Resting-state functional MRI (rs-fMRI) can provide a reliable and reproducible tool to examine the functional activity in different brain networks by measuring intrinsic blood oxygen level-dependent (BOLD) low-frequency signal fluctuations. There is a growing interest in using fMRI to investigate the neural basis for CI in PD.

A voxel-based meta-analysis consisting of 289 PD-NCI, 222 PD-MCI, 68 PDD, and 353 HC subjects from seventeen studies showed that PD patients with CI had reduced functional connectivity (FC) in specific brain regions that are parts of the default mode network (DMN) (Wolters et al., 2019). Moreover, notably, increased FC may be the initial manifestation of altered brain function preceding cognitive deficits (transition from PD-NCI to PD-MCI), and these functional disruptions may be considerably associated with a cognitive decline in the progression of PD-related pathology (Gorges et al., 2015; Zhan et al., 2018; Zarifkar et al., 2021). A novel graph-theoretical analysis of functional networks indicates that the topological properties of brain networks are disrupted in PD-MCI patients with reduced long-range connections and enhanced local interconnectedness (Baggio et al., 2014). Moreover, a recent study suggested that PD-MCI patients had an increased random organization of brain networks and altered nodal centralities as compared with HCs (Hou et al., 2020). These results provide a new perspective on the functional basis of CI in PD.

In an exploratory longitudinal study, FC between the medial prefrontal cortex (mPFC) and posterior cingulate cortex (PCC) within DMN at baseline were found to be the best putative predictor for CI in PD (Zarifkar et al., 2021). PD patients with a longitudinal decline in cognitive function have a significant decline in dorsal attention-frontoparietal internetwork (DAN-FPN) strength, which may serve as a prognostic marker for assessing the development of dementia in PD (Campbell et al., 2020).

Proton Magnetic Resonance Spectroscopy

Proton magnetic resonance spectroscopy (^{1}H-MRS) owing to a high natural abundance and magnetic sensitivity of protons in the brain allows for *in vivo* measurements of four major metabolites, that reflect the integrity of different elements in the brain, including *N*-acetylaspartate (NAA), choline compounds (Cho), creatine (Cr), and myo-inositol (MI) (Nie et al., 2013).

The PD-CI patients have higher the choline to creatine (Cho/Cr) ratio in the occipital lobe, reduced concentration of NAA in the middle and superior frontal gray matter regions, and reduced concentration of total Cho and total Cr in the frontal white matter regions relative to PD-CN patients and HCs (Nie et al., 2013; Chaudhary et al., 2021). According to the differential status of CI, levels of NAA in the dorsolateral prefrontal cortex are reduced in the early stage with progression to the hippocampus in PDD patients (Pagonabarraga et al., 2012). Frontal neuro-metabolism may serve as a promising biomarker for characterizing cognitive deficits in patients with PD (Chaudhary et al., 2021).

CONCLUSION

In summary, specific patterns of cognitive neural substrates in PD can be detected using various MRI techniques, and this has become a putative prediction tool for CI in PD. With the advances in image acquisition and analysis technologies, predictors derived from structural MRI are promising for assessing the cognitive dysfunction in PD. Recently, abnormal patterns from other MRI techniques also have emerged as the candidate biomarkers for evaluating the progression of cognitive decline in PD. Given that biomarkers from a single modal MRI cannot completely describe the complexity of pathological substrates of cognitive deficits in PD, we believe that the potential predictors from multi-modal MRI technology using recognized analysis tools and predictive algorithms deserve further investigation. Furthermore, targeted biomarkers for different cognitive domains and the determination of the best combination scheme of biomarkers from multi-modal MRI are the most important issues in the future.

AUTHOR CONTRIBUTIONS

YH prepared the initial manuscript. HS provided content expertise and reviewed the manuscript. Both authors contributed to the article and approved the submitted version.

FUNDING

This present study was supported by the Post-doctor Research Project, West China Hospital, Sichuan University (2020HXBH100 to YH).

REFERENCES

Aarsland, D., and Kurz, M. W. (2010). The epidemiology of dementia associated with Parkinson disease. *J. Neurol. Sci.* 289, 18–22. doi: 10.1016/j.jns.2009.08.034

Agosta, F., Canu, E., Stefanova, E., Sarro, L., Tomic, A., Spica, V., et al. (2014). Mild cognitive impairment in Parkinson's disease is associated with a distributed pattern of brain white matter damage. *Hum. Brain Mapp.* 35, 1921–1929. doi: 10.1002/hbm.22302

Arslan, D. B., Gurvit, H., Genc, O., Kicik, A., Eryurek, K., Cengiz, S., et al. (2020). The cerebral blood flow deficits in Parkinson's disease with mild cognitive impairment using arterial spin labeling MRI. *J. Neural Transm. (Vienna)* 127, 1285–1294. doi: 10.1007/s00702-020-02227-6

Baggio, H. C., Sala-Llonch, R., Segura, B., Marti, M. J., Valldeoriola, F., Compta, Y., et al. (2014). Functional brain networks and cognitive deficits in Parkinson's disease. *Hum. Brain Mapp.* 35, 4620–4634. doi: 10.1002/hbm.22499

Baiano, C., Barone, P., Trojano, L., and Santangelo, G. (2020). Prevalence and clinical aspects of mild cognitive impairment in Parkinson's disease: a meta-analysis. *Mov. Disord.* 35, 45–54. doi: 10.1002/mds.27902

Becker, S., Granert, O., Timmers, M., Pilotto, A., Van Nueten, L., Roeben, B., et al. (2021). Association of hippocampal subfields, CSF biomarkers, and cognition in patients with parkinson disease without dementia. *Neurology* 96, e904–e915. doi: 10.1212/wnl.0000000000011224

Bloem, B. R., Okun, M. S., and Klein, C. (2021). Parkinson's disease. *Lancet* 397, 2284–2303. doi: 10.1016/S0140-6736(21)00218-X

Bohnen, N. I., and Albin, R. L. (2011). White matter lesions in Parkinson disease. *Nat. Rev. Neurol.* 7, 229–236. doi: 10.1038/nrneurol.2011.21

Broeders, M., de Bie, R. M., Velseboer, D. C., Speelman, J. D., Muslimovic, D., and Schmand, B. (2013). Evolution of mild cognitive impairment in Parkinson disease. *Neurology* 81, 346–352. doi: 10.1212/WNL.0b013e31829c5c86

Camicioli, R., Sabino, J., Gee, M., Bouchard, T., Fisher, N., Hanstock, C., et al. (2011). Ventricular dilatation and brain atrophy in patients with Parkinson's disease with incipient dementia. *Mov. Disord.* 26, 1443–1450. doi: 10.1002/mds.23700

Campbell, M. C., Jackson, J. J., Koller, J. M., Snyder, A. Z., Kotzbauer, P. T., and Perlmutter, J. S. (2020). Proteinopathy and longitudinal changes in functional connectivity networks in Parkinson disease. *Neurology* 94, e718–e728. doi: 10.1212/wnl.0000000000008677

Chahine, L. M., Dos Santos, C., Fullard, M., Scordia, C., Weintraub, D., Erus, G., et al. (2019). Modifiable vascular risk factors, white matter disease and cognition in early Parkinson's disease. *Eur. J. Neurol.* 26, 246–e218. doi: 10.1111/ene.13797

Chang, T. C., Chen, Y. C., Huang, Y. C., Lin, W. C., and Lu, C. H. (2021). Systemic oxidative stress and cognitive function in Parkinson's disease with different PWMH or DWMH lesions. *BMC Neurol.* 21:16. doi: 10.1186/s12883-020-02037-z

Chaudhary, S., Kumaran, S. S., Goyal, V., Kalaivani, M., Kaloiya, G. S., Sagar, R., et al. (2021). Frontal lobe metabolic alterations characterizing Parkinson's disease cognitive impairment. *Neurol. Sci.* 42, 1053–1064. doi: 10.1007/s10072-020-04626-9

Chen, B. Y., Fan, G. G., Liu, H., and Wang, S. S. (2015). Changes in anatomical and functional connectivity of Parkinson's disease patients according to cognitive status. *Eur. J. Radiol.* 84, 1318–1324. doi: 10.1016/j.ejrad.2015.04.014

Chen, F. X., Kang, D. Z., Chen, F. Y., Liu, Y., Wu, G., Li, X., et al. (2016). Gray matter atrophy associated with mild cognitive impairment in Parkinson's disease. *Neurosci. Lett.* 617, 160–165. doi: 10.1016/j.neulet.2015.12.055

Chen, Y. S., Chen, H. L., Lu, C. H., Lee, C. Y., Chou, K. H., Chen, M. H., et al. (2021). The corticolimbic structural covariance network as an early predictive biosignature for cognitive impairment in Parkinson's disease. *Sci. Rep.* 11:862. doi: 10.1038/s41598-020-79403-x

Choi, S. H., Jung, T. M., Lee, J. E., Lee, S. K., Sohn, Y. H., and Lee, P. H. (2012). Volumetric analysis of the substantia innominata in patients with Parkinson's disease according to cognitive status. *Neurobiol. Aging* 33, 1265–1272. doi: 10.1016/j.neurobiolaging.2010.11.015

Chung, S. J., Yoo, H. S., Lee, Y. H., Lee, H. S., Ye, B. S., Sohn, Y. H., et al. (2019). Frontal atrophy as a marker for dementia conversion in Parkinson's disease with mild cognitive impairment. *Hum. Brain Mapp.* 40, 3784–3794. doi: 10.1002/hbm.24631

Clinton, L. K., Blurton-Jones, M., Myczek, K., Trojanowski, J. Q., and LaFerla, F. M. (2010). Synergistic Interactions between Abeta, tau, and alpha-synuclein: acceleration of neuropathology and cognitive decline. *J. Neurosci.* 30, 7281–7289. doi: 10.1523/JNEUROSCI.0490-10.2010

Collaborators, G. B. D. N. (2019). Global, regional, and national burden of neurological disorders, 1990–2016: a systematic analysis for the global burden of disease study 2016. *Lancet Neurol.* 18, 459–480. doi: 10.1016/S1474-4422(18)30499-X

Compta, Y., Pereira, J. B., Ríos, J., Ibarretxe-Bilbao, N., Junqué, C., Bargalló, N., et al. (2013). Combined dementia-risk biomarkers in Parkinson's disease: a prospective longitudinal study. *Parkinsonism Relat. Disord.* 19, 717–724. doi: 10.1016/j.parkreldis.2013.03.009

Dadar, M., Zeighami, Y., Yau, Y., Fereshtehnejad, S. M., Maranzano, J., Postuma, R. B., et al. (2018). White matter hyperintensities are linked to future cognitive decline in de novo Parkinson's disease patients. *Neuroimage Clin.* 20, 892–900. doi: 10.1016/j.nicl.2018.09.025

de Boer, R., Vrooman, H. A., van der Lijn, F., Vernooij, M. W., Ikram, M. A., van der Lugt, A., et al. (2009). White matter lesion extension to automatic brain tissue segmentation on MRI. *Neuroimage* 45, 1151–1161. doi: 10.1016/j.neuroimage.2009.01.011

Deng, B. M., Zhang, Y. H., Wang, L. J., Peng, K. R., Han, L. X., Nie, K., et al. (2013). Diffusion tensor imaging reveals white matter changes associated with cognitive status in patients with Parkinson's disease. *Am. J. Alzheimers Dis. Other Dement.* 28, 154–164. doi: 10.1177/1533317512470207

Dorsey, E. R., Sherer, T., Okun, M. S., and Bloem, B. R. (2018). The emerging evidence of the Parkinson pandemic. *J. Parkinsons Dis.* 8, S3–S8. doi: 10.3233/JPD-181474

Emre, M., Aarsland, D., Brown, R., Burn, D. J., Duyckaerts, C., Mizuno, Y., et al. (2007). Clinical diagnostic criteria for dementia associated with Parkinson's disease. *Mov. Disord.* 22, 1689–1707;quiz1837. doi: 10.1002/mds.21507

Erten-Lyons, D., Woltjer, R., Kaye, J., Mattek, N., Dodge, H. H., Green, S., et al. (2013). Neuropathologic basis of white matter hyperintensity accumulation with advanced age. *Neurology* 81, 977–983. doi: 10.1212/WNL.0b013e3182a43e45

Fang, E., Fartaria, M. J., Ann, C. N., Maréchal, B., Kober, T., Lim, J. X., et al. (2021). Clinical correlates of white matter lesions in Parkinson's disease using automated multi-modal segmentation measures. *J. Neurol. Sci.* 427:117518. doi: 10.1016/j.jns.2021.117518

Filippi, M., Canu, E., Donzuso, G., Stojkovic, T., Basaia, S., Stankovic, I., et al. (2020). Tracking cortical changes throughout cognitive decline in Parkinson's disease. *Mov. Disord.* 35, 1987–1998. doi: 10.1002/mds.28228

Foo, H., Mak, E., Chander, R. J., Ng, A., Au, W. L., Sitoh, Y. Y., et al. (2017a). Associations of hippocampal subfields in the progression of cognitive decline related to Parkinson's disease. *Neuroimage Clin.* 14, 37–42. doi: 10.1016/j.nicl.2016.12.008

Foo, H., Mak, E., Yong, T. T., Wen, M. C., Chander, R. J., Au, W. L., et al. (2017b). Progression of subcortical atrophy in mild Parkinson's disease and its impact on cognition. *Eur. J. Neurol.* 24, 341–348. doi: 10.1111/ene.13205

Galantucci, S., Agosta, F., Stefanova, E., Basaia, S., van den Heuvel, M. P., Stojković, T., et al. (2017). Structural brain connectome and cognitive impairment in Parkinson disease. *Radiology* 283, 515–525. doi: 10.1148/radiol.2016160274

Garcia-Diaz, A. I., Segura, B., Baggio, H. C., Uribe, C., Campabadal, A., Abos, A., et al. (2018). Cortical thinning correlates of changes in visuospatial and visuoperceptual performance in Parkinson's disease: a 4-year follow-up. *Parkinsonism Relat. Disord.* 46, 62–68. doi: 10.1016/j.parkreldis.2017.11.003

Gee, M., Dukart, J., Draganski, B., Martin, W. R. W., Emery, D., and Camicioli, R. (2017). Regional volumetric change in Parkinson's disease with cognitive decline. *J. Neurol. Sci.* 373, 88–94. doi: 10.1016/j.jns.2016.12.030

Goldman, J. G., Stebbins, G. T., Bernard, B., Stoub, T. R., Goetz, C. G., and deToledo-Morrell, L. (2012). Entorhinal cortex atrophy differentiates Parkinson's disease patients with and without dementia. *Mov. Disord.* 27, 727–734. doi: 10.1002/mds.24938

Gorges, M., Kunz, M. S., Muller, H. P., Liepelt-Scarfone, I., Storch, A., Dodel, R., et al. (2020). Longitudinal brain atrophy distribution in advanced Parkinson's disease: what makes the difference in "cognitive status" converters? *Hum. Brain Mapp.* 41, 1416–1434. doi: 10.1002/hbm.24884

Gorges, M., Muller, H. P., Lule, D., Consortium, L., Pinkhardt, E. H., Ludolph, A. C., et al. (2015). To rise and to fall: functional connectivity in cognitively normal and cognitively impaired patients with Parkinson's disease. *Neurobiol. Aging* 36, 1727–1735. doi: 10.1016/j.neurobiolaging.2014.12.026

Hanganu, A., Bedetti, C., Degroot, C., Mejia-Constain, B., Lafontaine, A.-L., Soland, V., et al. (2014). Mild cognitive impairment is linked with faster rate of cortical thinning in patients with Parkinson's disease longitudinally. *Brain* 137, 1120–1129. doi: 10.1093/brain/awu036

Hattori, T., Orimo, S., Aoki, S., Ito, K., Abe, O., Amano, A., et al. (2012). Cognitive status correlates with white matter alteration in Parkinson's disease. *Hum. Brain Mapp.* 33, 727–739. doi: 10.1002/hbm.21245

Hou, Y., Wei, Q., Ou, R., Yang, J., Gong, Q., and Shang, H. (2020). Impaired topographic organization in Parkinson's disease with mild cognitive impairment. *J. Neurol. Sci.* 414, 116861. doi: 10.1016/j.jns.2020.116861

Huang, X., Wen, M. C., Ng, S. Y., Hartono, S., Chia, N. S., Choi, X., et al. (2020). Periventricular white matter hyperintensity burden and cognitive impairment in early Parkinson's disease. *Eur. J. Neurol.* 27, 959–966. doi: 10.1111/ene.14192

Iglesias, J. E., Augustinack, J. C., Nguyen, K., Player, C. M., Player, A., Wright, M., et al. (2015). A computational atlas of the hippocampal formation using ex vivo, ultra-high resolution MRI: application to adaptive segmentation of in vivo MRI. *Neuroimage* 115, 117–137. doi: 10.1016/j.neuroimage.2015.04.042

Jia, X., Wang, Z., Yang, T., Li, Y., Gao, S., Wu, G., et al. (2019). Entorhinal cortex atrophy in early, drug-naive Parkinson's disease with mild cognitive impairment. *Aging Dis.* 10, 1221–1232. doi: 10.14336/ad.2018.1116

Kamagata, K., Motoi, Y., Abe, O., Shimoji, K., Hori, M., Nakanishi, A., et al. (2012). White matter alteration of the cingulum in Parkinson disease with and without dementia: evaluation by diffusion tensor tract-specific analysis. *Am. J. Neuroradiol.* 33, 890–895. doi: 10.3174/ajnr.A2860

Kamagata, K., Motoi, Y., Tomiyama, H., Abe, O., Ito, K., Shimoji, K., et al. (2013). Relationship between cognitive impairment and white-matter alteration in Parkinson's disease with dementia: tract-based spatial statistics and tract-specific analysis. *Eur. Radiol.* 23, 1946–1955. doi: 10.1007/s00330-013-2775-4

Kandiah, N., Zainal, N. H., Narasimhalu, K., Chander, R. J., Ng, A., Mak, E., et al. (2014). Hippocampal volume and white matter disease in the prediction of dementia in Parkinson's disease. *Parkinsonism Relat. Disord.* 20, 1203–1208. doi: 10.1016/j.parkreldis.2014.08.024

Lee, J. E., Cho, K. H., Song, S. K., Kim, H. J., Lee, H. S., Sohn, Y. H., et al. (2014). Exploratory analysis of neuropsychological and neuroanatomical correlates of progressive mild cognitive impairment in Parkinson's disease. *J. Neurol. Neurosurg. Psychiatry* 85, 7–16. doi: 10.1136/jnnp-2013-305062

Li, D. T. H., Hui, E. S., Chan, Q., Yao, N., Chua, S. E., McAlonan, G. M., et al. (2018). Quantitative susceptibility mapping as an indicator of subcortical and limbic iron abnormality in Parkinson's disease with dementia. *Neuroimage Clin.* 20, 365–373. doi: 10.1016/j.nicl.2018.07.028

Li, Y., Wang, C., Wang, J., Zhou, Y., Ye, F., Zhang, Y., et al. (2019). Mild cognitive impairment in de novo Parkinson's disease: a neuromelanin MRI study in locus coeruleus. *Mov. Disord.* 34, 884–892. doi: 10.1002/mds.27682

Litvan, I., Goldman, J. G., Troster, A. I., Schmand, B. A., Weintraub, D., Petersen, R. C., et al. (2012). Diagnostic criteria for mild cognitive impairment in Parkinson's disease: movement disorder society task force guidelines. *Mov. Disord.* 27, 349–356. doi: 10.1002/mds.24893

Liu, A. K., Chang, R. C., Pearce, R. K., and Gentleman, S. M. (2015). Nucleus basalis of Meynert revisited: anatomy, history and differential involvement in Alzheimer's and Parkinson's disease. *Acta Neuropathol.* 129, 527–540. doi: 10.1007/s00401-015-1392-5

Low, A., Foo, H., Yong, T. T., Tan, L. C. S., and Kandiah, N. (2019). Hippocampal subfield atrophy of CA1 and subicular structures predict progression to dementia in idiopathic Parkinson's disease. *J. Neurol. Neurosurg. Psychiatry* 90, 681–687. doi: 10.1136/jnnp-2018-319592

Mak, E., Bergsland, N., Dwyer, M. G., Zivadinov, R., and Kandiah, N. (2014). Subcortical atrophy is associated with cognitive impairment in mild Parkinson disease: a combined investigation of volumetric changes, cortical thickness, and vertex-based shape analysis. *AJNR Am. J. Neuroradiol.* 35, 2257–2264. doi: 10.3174/ajnr.A4055

Mak, E., Su, L., Williams, G. B., Firbank, M. J., Lawson, R. A., Yarnall, A. J., et al. (2015). Baseline and longitudinal grey matter changes in newly diagnosed Parkinson's disease: ICICLE-PD study. *Brain* 138, 2974–2986. doi: 10.1093/brain/awv211

Mak, E., Su, L., Williams, G. B., Firbank, M. J., Lawson, R. A., Yarnall, A. J., et al. (2017). Longitudinal whole-brain atrophy and ventricular enlargement in nondemented Parkinson's disease. *Neurobiol. Aging* 55, 78–90. doi: 10.1016/j.neurobiolaging.2017.03.012

Masliah, E., Rockenstein, E., Veinbergs, I., Sagara, Y., Mallory, M., Hashimoto, M., et al. (2001). beta-amyloid peptides enhance alpha-synuclein accumulation and neuronal deficits in a transgenic mouse model linking Alzheimer's disease and Parkinson's disease. *Proc. Natl. Acad. Sci. U.S.A.* 98, 12245–12250. doi: 10.1073/pnas.211412398

Melzer, T. R., Watts, R., MacAskill, M. R., Pitcher, T. L., Livingston, L., Keenan, R. J., et al. (2012). Grey matter atrophy in cognitively impaired Parkinson's disease. *J. Neurol. Neurosurg. Psychiatry* 83, 188–194. doi: 10.1136/jnnp-2011-300828

Melzer, T. R., Watts, R., MacAskill, M. R., Pitcher, T. L., Livingston, L., Keenan, R. J., et al. (2013). White matter microstructure deteriorates across cognitive stages in Parkinson disease. *Neurology* 80, 1841–1849. doi: 10.1212/WNL.0b013e3182929f62

Mihaescu, A. S., Masellis, M., Graff-Guerrero, A., Kim, J., Criaud, M., Cho, S. S., et al. (2019). Brain degeneration in Parkinson's disease patients with cognitive decline: a coordinate-based meta-analysis. *Brain Imaging Behav.* 13, 1021–1034. doi: 10.1007/s11682-018-9922-0

Nakamura, K., and Sugaya, K. (2014). Neuromelanin-sensitive magnetic resonance imaging: a promising technique for depicting tissue characteristics containing neuromelanin. *Neural Regen. Res.* 9, 759–760. doi: 10.4103/1673-5374.131583

Nie, K., Zhang, Y., Huang, B., Wang, L., Zhao, J., Huang, Z., et al. (2013). Marked N-acetylaspartate and choline metabolite changes in Parkinson's disease patients with mild cognitive impairment. *Parkinsonism Relat. Disord.* 19, 329–334. doi: 10.1016/j.parkreldis.2012.11.012

Paez, A. G., Gu, C., Rajan, S., Miao, X., Cao, D., Kamath, V., et al. (2020). Differential changes in arteriolar cerebral blood volume between Parkinson's disease patients with normal and impaired cognition and mild cognitive impairment (MCI) Patients without movement disorder - an exploratory study. *Tomography* 6, 333–342. doi: 10.18383/j.tom.2020.00033

Pagonabarraga, J., Corcuera-Solano, I., Vives-Gilabert, Y., Llebaria, G., García-Sánchez, C., Pascual-Sedano, B., et al. (2013). Pattern of regional cortical thinning associated with cognitive deterioration in Parkinson's disease. *PLoS One* 8:e54980. doi: 10.1371/journal.pone.0054980

Pagonabarraga, J., Gomez-Anson, B., Rotger, R., Llebaria, G., Garcia-Sanchez, C., Pascual-Sedano, B., et al. (2012). Spectroscopic changes associated with mild cognitive impairment and dementia in Parkinson's disease. *Dement. Geriatr. Cogn. Disord.* 34, 312–318. doi: 10.1159/000345537

Park, Y. W., Shin, N. Y., Chung, S. J., Kim, J., Lim, S. M., Lee, P. H., et al. (2019). Magnetic resonance imaging-visible perivascular spaces in basal ganglia predict cognitive decline in Parkinson's disease. *Mov. Disord.* 34, 1672–1679. doi: 10.1002/mds.27798

Pedersen, K. F., Larsen, J. P., Tysnes, O. B., and Alves, G. (2017). Natural course of mild cognitive impairment in Parkinson disease: a 5-year population-based study. *Neurology* 88, 767–774. doi: 10.1212/WNL.0000000000003634

Pelizzari, L., Di Tella, S., Rossetto, F., Laganà, M. M., Bergsland, N., Pirastru, A., et al. (2020). Parietal perfusion alterations in Parkinson's disease patients without dementia. *Front. Neurol.* 11:562. doi: 10.3389/fneur.2020.00562

Prasuhn, J., Prasuhn, M., Fellbrich, A., Strautz, R., Lemmer, F., Dreischmeier, S., et al. (2021). Association of locus coeruleus and substantia nigra pathology with cognitive and motor functions in patients with Parkinson disease. *Neurology* 97, e1007–e1016. doi: 10.1212/wnl.0000000000012444

Ray, N. J., Bradburn, S., Murgatroyd, C., Toseeb, U., Mir, P., Kountouriotis, G. K., et al. (2018). In vivo cholinergic basal forebrain atrophy predicts cognitive decline in de novo Parkinson's disease. *Brain* 141, 165–176. doi: 10.1093/brain/awx310

Sampedro, F., Martínez-Horta, S., Marín-Lahoz, J., Pagonabarraga, J., and Kulisevsky, J. (2019). Longitudinal intracortical diffusivity changes in de-novo Parkinson's disease: a promising imaging biomarker. *Parkinsonism Relat. Disord.* 68, 22–25. doi: 10.1016/j.parkreldis.2019.09.031

Scheltens, P., Barkhof, F., Leys, D., Pruvo, J. P., Nauta, J. J., Vermersch, P., et al. (1993). A semiquantative rating scale for the assessment of signal hyperintensities on magnetic resonance imaging. *J. Neurol. Sci.* 114, 7–12. doi: 10.1016/0022-510x(93)90041-v

Schulz, J., Pagano, G., Fernández Bonfante, J. A., Wilson, H., and Politis, M. (2018). Nucleus basalis of Meynert degeneration precedes and predicts cognitive impairment in Parkinson's disease. *Brain* 141, 1501–1516. doi: 10.1093/brain/awy072

Song, S. K., Lee, J. E., Park, H. J., Sohn, Y. H., Lee, J. D., and Lee, P. H. (2011). The pattern of cortical atrophy in patients with Parkinson's disease according to cognitive status. *Mov. Disord.* 26, 289–296. doi: 10.1002/mds.23477

Sulzer, D., Cassidy, C., Horga, G., Kang, U. J., Fahn, S., Casella, L., et al. (2018). Neuromelanin detection by magnetic resonance imaging (MRI) and its promise as a biomarker for Parkinson's disease. *NPJ Parkinsons Dis.* 4:11. doi: 10.1038/s41531-018-0047-3

Tropea, T. F., Xie, S. X., Rick, J., Chahine, L. M., Dahodwala, N., Doshi, J., et al. (2018). APOE, thought disorder, and SPARE-AD predict cognitive decline in

established Parkinson's disease. *Mov. Disord.* 33, 289–297. doi: 10.1002/mds.27204

Tsai, H. H., Tsai, L. K., Lo, Y. L., and Lin, C. H. (2021). Amyloid related cerebral microbleed and plasma Aβ40 are associated with cognitive decline in Parkinson's disease. *Sci. Rep.* 11:7115. doi: 10.1038/s41598-021-86617-0

Uchida, Y., Kan, H., Sakurai, K., Arai, N., Kato, D., Kawashima, S., et al. (2019). Voxel-based quantitative susceptibility mapping in Parkinson's disease with mild cognitive impairment. *Mov. Disord.* 34, 1164–1173. doi: 10.1002/mds.27717

Uribe, C., Segura, B., Baggio, H. C., Campabadal, A., Abos, A., Compta, Y., et al. (2018). Differential progression of regional hippocampal atrophy in aging and Parkinson's disease. *Front. Aging Neurosci.* 10:325. doi: 10.3389/fnagi.2018.00325

Wardlaw, J. M., Smith, E. E., Biessels, G. J., Cordonnier, C., Fazekas, F., Frayne, R., et al. (2013). Neuroimaging standards for research into small vessel disease and its contribution to ageing and neurodegeneration. *Lancet Neurol.* 12, 822–838. doi: 10.1016/S1474-4422(13)70124-8

Weintraub, D., Dietz, N., Duda, J. E., Wolk, D. A., Doshi, J., Xie, S. X., et al. (2012). Alzheimer's disease pattern of brain atrophy predicts cognitive decline in Parkinson's disease. *Brain* 135(Pt 1), 170–180. doi: 10.1093/brain/awr277

Weintraub, D., Doshi, J., Koka, D., Davatzikos, C., Siderowf, A. D., Duda, J. E., et al. (2011). Neurodegeneration across stages of cognitive decline in Parkinson disease. *Arch. Neurol.* 68, 1562–1568. doi: 10.1001/archneurol.2011.725

Wen, M.-C., Ng, A., Chander, R. J., Au, W. L., Tan, L. C. S., and Kandiah, N. (2015). Longitudinal brain volumetric changes and their predictive effects on cognition among cognitively asymptomatic patients with Parkinson's disease. *Parkinsonism Relat. Disord.* 21, 483–488. doi: 10.1016/j.parkreldis.2015.02.014

Wolters, A. F., van de Weijer, S. C. F., Leentjens, A. F. G., Duits, A. A., Jacobs, H. I. L., and Kuijf, M. L. (2019). Resting-state fMRI in Parkinson's disease patients with cognitive impairment: a meta-analysis. *Parkinsonism Relat. Disord.* 62, 16–27. doi: 10.1016/j.parkreldis.2018.12.016

Xu, Y., Yang, J., Hu, X., and Shang, H. (2016). Voxel-based meta-analysis of gray matter volume reductions associated with cognitive impairment in Parkinson's disease. *J. Neurol.* 263, 1178–1187. doi: 10.1007/s00415-016-8122-3

Zarifkar, P., Kim, J., La, C., Zhang, K., YorkWilliams, S., Levine, T. F., et al. (2021). Cognitive impairment in Parkinson's disease is associated with default mode network subsystem connectivity and cerebrospinal fluid Aβ. *Parkinsonism Relat. Disord.* 83, 71–78. doi: 10.1016/j.parkreldis.2021.01.002

Zhan, Z. W., Lin, L. Z., Yu, E. H., Xin, J. W., Lin, L., Lin, H. L., et al. (2018). Abnormal resting-state functional connectivity in posterior cingulate cortex of Parkinson's disease with mild cognitive impairment and dementia. *CNS Neurosci. Ther.* 24, 897–905. doi: 10.1111/cns.12838

Zheng, D., Chen, C., Song, W., Yi, Z., Zhao, P., Zhong, J., et al. (2019). Regional gray matter reductions associated with mild cognitive impairment in Parkinson's disease: a meta-analysis of voxel-based morphometry studies. *Behav. Brain Res.* 371:111973. doi: 10.1016/j.bbr.2019.111973

Zhou, C., Guan, X. J., Guo, T., Zeng, Q. L., Gao, T., Huang, P. Y., et al. (2020). Progressive brain atrophy in Parkinson's disease patients who convert to mild cognitive impairment. *CNS Neurosci. Ther.* 26, 117–125. doi: 10.1111/cns.13188

Conflict of Interest: The authors declare that the research was conducted in the absence of any commercial or financial relationships that could be construed as a potential conflict of interest.

Publisher's Note: All claims expressed in this article are solely those of the authors and do not necessarily represent those of their affiliated organizations, or those of the publisher, the editors and the reviewers. Any product that may be evaluated in this article, or claim that may be made by its manufacturer, is not guaranteed or endorsed by the publisher.

Copyright © 2022 Hou and Shang. This is an open-access article distributed under the terms of the Creative Commons Attribution License (CC BY). The use, distribution or reproduction in other forums is permitted, provided the original author(s) and the copyright owner(s) are credited and that the original publication in this journal is cited, in accordance with accepted academic practice. No use, distribution or reproduction is permitted which does not comply with these terms.

frontiers in Pharmacology

REVIEW
published: 27 January 2022
doi: 10.3389/fphar.2021.728315

Deciphering the Roles of Metformin in Alzheimer's Disease: A Snapshot

Wang Liao[1,2†], *Jiaxin Xu*[2†], *Bo Li*[3†], *Yuting Ruan*[2,4], *Tian Li*[5*] and *Jun Liu*[1,2*]

[1]Department of Neurology, The Second Affiliated Hospital of Guangzhou Medical University, Guangzhou, China, [2]Department of Neurology, Sun Yat-sen Memorial Hospital, Sun Yat-sen University, Guangzhou, China, [3]Department of Orthopedics, Sun Yat-sen Memorial Hospital, Sun Yat-sen University, Guangzhou, China, [4]Department of Rehabilitation Medicine, The Second Affiliated Hospital of Guangzhou Medical University, Guangzhou, China, [5]School of Basic Medicine, Fourth Military Medical University, Xi'an, China

Alzheimer's disease (AD) is a prevalent neurodegenerative disease predominantly affecting millions of elderly people. To date, no effective therapy has been identified to reverse the progression of AD. Metformin, as a first-line medication for Type 2 Diabetes Mellitus (T2DM), exerts multiple beneficial effects on various neurodegenerative disorders, including AD. Evidence from clinical studies has demonstrated that metformin use contributes to a lower risk of developing AD and better cognitive performance, which might be modified by interactors such as diabetic status and APOE-ε4 status. Previous mechanistic studies have gradually unveiled the effects of metformin on AD pathology and pathophysiology, including neuronal loss, neural dysfunction, amyloid-β (Aβ) depositions, tau phosphorylation, chronic neuroinflammation, insulin resistance, impaired glucose metabolism and mitochondrial dysfunction. Current evidence remains ambiguous and even conflicting. Herein, we review the current state of knowledge concerning the mechanisms of metformin in AD pathology while summarizing current evidence from clinical studies.

Keywords: metformin, Alzheimer's disease, insulin, AMPK, neuroinflammation

OPEN ACCESS

Edited by:
Kuangyu Shi,
University of Bern, Switzerland

Reviewed by:
Woon-Man Kung,
Chinese Culture University, Taiwan
Ewa Krystyna Szczepanska-Sadowska,
Medical University of Warsaw, Poland
Wieslawa Agnieszka Fogel,
Medical University of Lodz, Poland
Sergei V. Fedorovich,
Belarusian State University, Belarus

***Correspondence:**
Tian Li
tian@fmmu.edu.cn
Jun Liu
liujun6@mail.sysu.edu.cn

[†]*These authors have contributed equally to this work*

Specialty section:
This article was submitted to Neuropharmacology, a section of the journal Frontiers in Pharmacology

Received: *22 June 2021*
Accepted: *29 December 2021*
Published: *27 January 2022*

Citation:
Liao W, Xu J, Li B, Ruan Y, Li T and Liu J (2022) Deciphering the Roles of Metformin in Alzheimer's Disease: A Snapshot. Front. Pharmacol. 12:728315. doi: 10.3389/fphar.2021.728315

INTRODUCTION

Alzheimer's disease (AD) is a neurodegenerative disease characterized by a progressive decline of cognitive functions, such as memory and learning, sometimes accompanied by behavioral and psychological symptoms (Apostolova, 2016). With a high morbidity, disability and fatality rate, AD significantly increase global healthcare burden. Unfortunately, its neuropathological hallmarks, amyloid-β (Aβ) plaques and neurofibrillary tangles (NFTs) appear decades before the occurrence of cognitive impairment (Dubois et al., 2014). To date, no effective therapy has been identified to reverse or slow down the progression of AD and improve its clinical outcomes (Schneider et al., 2014). Therefore, early identification of people at higher risk of developing AD and early intervention are now the most practical strategies to reduce AD burden. A broader perspective on the treatment is also urgently needed.

Increasing evidence suggests a positive association between Type 2 Diabetes Mellitus (T2DM) and the risk of developing AD (Schilling, 2016; Yu et al., 2020). Impaired insulin signaling and glucose metabolism, two key mechanisms involved in T2DM, have been found to contribute to AD pathogenesis and progression (Gupta et al., 2011; Kandimalla et al., 2017; Benedict and Grillo, 2018; Boccardi et al., 2019). Researchers have even proposed the term "Type-3-Diabetes" for AD due to the significant association (Kandimalla et al., 2017), which implies the potential of anti-diabetic

medicine to prevent or treat AD. Intranasal insulin has been considered as a promising candidate for AD prevention and treatment due to its safety and current encouraging clinical evidence on its effectiveness (Harris et al., 2020; Hallschmid, 2021). As for other anti-diabetic drugs, including dipeptidyl peptidase (DPP)-IV inhibitors and Glucagon-like peptide-1 (GLP-1) analogues, they were found to decrease neuroinflammation, Aβ load and tau phosphorylation in experimental studies, while clinical evidence is still lacking (McClean et al., 2011; Yang et al., 2013; Kosaraju et al., 2017; Boccardi et al., 2019).

Metformin, one of the first-line medications for T2DM, is a biguanide that lowers plasma glucose concentration mainly by improving insulin resistance and suppressing gluconeogenesis in the liver. Recent studies have further discovered its anti-inflammatory, anti-apoptotic and anti-oxidative effects (Li et al., 2020; Li et al., 2021; Ott et al., 2021; Tanaka et al., 2021). It is also confirmed that metformin can rapidly cross the blood-brain barrier (BBB) and accumulate in different brain regions (Łabuzek et al., 2010), influencing the central nervous system (CNS) (El-Mir et al., 2008). Metformin is now regarded as a magic drug that might benefit various diseases, including AD (Markowicz-Piasecka et al., 2017; Lv and Guo, 2020). Current studies on the effects of metformin on AD and the underlying mechanisms remain limited and controversial. It is also necessary to take its adverse effects into consideration before regarding metformin as a candidate for AD prevention and early-stage treatment. Moreover, it is important to confirm the cognitive safety of long-term metformin use in T2DM patients. The present review is to summarize the current knowledge on this topic and proposes promising directions for further research.

SEARCH STRATEGY AND SELECTION CRITERIA

We initially searched PubMed from inception to June 2021 for English-only publications using predefined search terms for metformin and Alzheimer's disease. We also reviewed the reference list of relevant articles. We included published observational studies and clinical trials exploring the cognitive effect of metformin on people with T2DM or cognitive impairment. As for preclinical studies, we included *in vitro* studies and *in vivo* studies using AD or diabetic or wild-type mouse models. When summarizing the evidence, further search was conducted to collect background information on the mentioned underlying mechanisms such as the association of AMP-activated protein kinase (AMPK) (Hsu et al., 2021) with metformin and AD.

MECHANISMS LINKING METFORMIN WITH AD

The Effects of Metformin on Neuronal Loss and Neural Dysfunction

Metformin treatment was shown to inhibit neuronal loss, the direct cause of cognitive deficits in AD, by promoting neurogenesis and inhibiting pathological neuronal apoptosis in the hippocampus of amyloid precursor protein/presenilin-1 (APP/PS1) mice (West et al., 1994; Ou et al., 2018). Similarly, Chen and others reported that metformin could ameliorate Aβ-induced apoptosis in hippocampal neurons by suppressing c-Jun N-terminal kinase (JNK) activation (Chen B. et al., 2016). Another *in vitro* study demonstrated that in db/db mice, metformin treatment could suppress the activation of caspase-3, one of the essential mediators of apoptosis (Chen F. et al., 2016). In human neural stem cells (hNSCs), co-treatment with metformin restored the Aβ-induced increase in caspase 3/9 activity and cytosolic cytochrome c released from mitochondria in an AMPK-dependent manner, probably leading to a suppression of apoptosis (Chiang et al., 2016). Metformin was also found to decrease apoptotic cell death induced by $A\beta_{25-35}$ in SH-SY5Y cells (Li et al., 2019). However, Picone et al. observed promoted neuronal apoptosis by metformin in the cortex of C57B6/J mice (Picone et al., 2016). Further preclinical studies are warranted to probe the underlying mechanisms and the safety of metformin among nondiabetic and non-AD subjects.

Protein kinase C (PKC) has been known to affect insulin function and memory formation by promoting synaptogenesis (Nelson et al., 2008). Wang et al. showed that metformin enhanced the genesis of human and rodent neurons and promoted spatial memory formation by activating an atypical PKC-CREB-binding protein (aPKC-CBP) signaling pathway in neural precursors (Wang et al., 2012). Furthermore, Syal et al. reported that the activated aPKC-CBP pathway by metformin treatment could reverse impairment of neurogenesis and spatial memory in the 3xTg-AD mouse model by decreasing the expression of monoacylglycerol lipase (Mgll), a hydrolase-producing arachidonic acid (ARA) precursor pool, through degrading endocannabinoid 2-arachidonoyl glycerol (2-AG). Mgll was further considered as a potential biomarker to help identify metformin-responsive AD patients (Mulvihill and Nomura, 2013; Syal et al., 2020).

Metformin was also found to markedly increase the expression of neurotrophic and synapse-related factors (Bdnf, Ngf and Syp) in the brain of APP/PS1 mice (Lu et al., 2020). Pilipenko reported that metformin could restore hippocampal synaptic plasticity in streptozocin (STZ)-induced sporadic AD rats (Pilipenko et al., 2020). In APP/PS1 mice, metformin was shown to improve synaptic defects, including spine loss, inhibit basal synaptic transmission and decrease the expression of surface GluA1 by suppressing the overactivation of cyclin-dependent kinase 5 (Cdk5), which play a critical role in synaptic plasticity (Sheng et al., 2016; Wang et al., 2020). Chen et al. found that metformin potentiated glutamatergic synaptic transmission onto the hippocampal CA1 pyramidal neurons in C57BJ/6 mice (Chen et al., 2020). This promotion by metformin may improve the dysfunction of glutamatergic synapses, which appear in the early stage of AD (Benarroch, 2018).

The Effects of Metformin on Aβ Pathology

The insulin-degrading enzyme (IDE), the protease that cleaves β-forming peptides such as insulin and Aβ, plays a major role in the

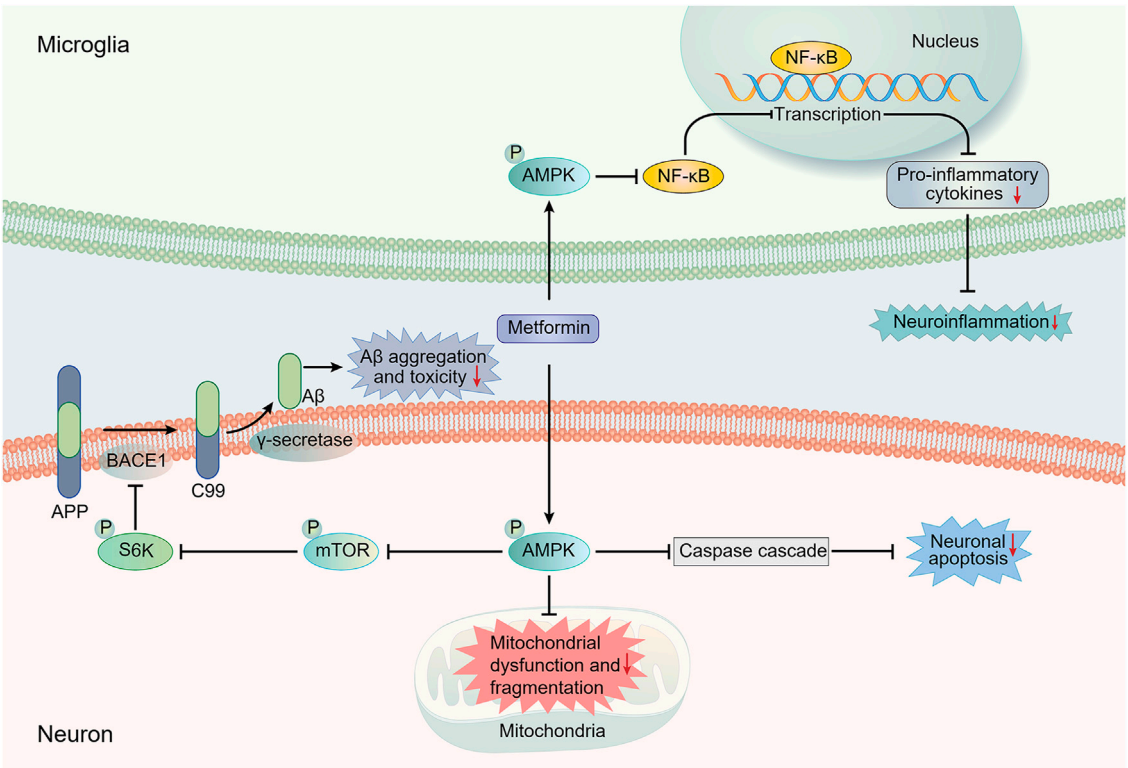

FIGURE 1 | Main potential AMPK-dependent molecule mechanisms involved in the neuroprotective effects of metformin against AD pathology. Most presented mechanistic studies have implied an AMPK-dependent neuroprotective action of metformin against AD. The regulation of AMPK/mTOR/S6K/BACE1 signaling pathway by metformin can result in a reduction in Aβ production, thus decreasing Aβ toxicity. AMPK activation can also suppress the activation of the NF-κB pathway, which is regarded as the central signaling pathway involved in AD neuroinflammation. Moreover, the increased activation of caspase cascade, which is involved in the apoptosis-mediated neurodegeneration, and the impairment of mitochondrial function and morphology induced by Aβ can be inhibited by metformin in an AMPK-dependent manner. AMPK, AMP-activated protein kinase; APP, amyloid precursor protein; Aβ, amyloid-β; BACE1, β-site APP cleaving enzyme-1; mTOR, mechanistic target of rapamycin; NF-κB, Nuclear factor-kappa B; S6K, ribosomal S6 kinase.

crosstalk between T2DM and AD (Kurochkin et al., 2018). Lu et al. proposed that the reduction of Aβ deposition in APP/PS1 mice after metformin usage might be mediated by the increased level of IDE. They also observed a slightly decreased expression of β-secretase BACE1 (one of the key enzymes responsible for the cleavage of APP to produce Aβ) and no significant change in the expression of other Aβ-related secretases (A Disintegrin and metalloproteinase domain-containing protein 10 (ADAM10) and PS1) and transporters (lipoprotein receptor-related protein (LRP1) and receptor for advanced glycation end products (RAGE)) (Lu et al., 2020; Hampel et al., 2021). Ou et al. reported a reduction in BACE1 expression and amyloid plaque accumulation in the hippocampus and cortex of APP/PS1 mice treated with metformin. The reduction was mediated through regulating the AMPK/mTOR/S6K/BACE1 signaling pathway (Ou et al., 2018). It is noteworthy that AMP-activated protein kinase (AMPK) is critical in regulating the effect of metformin on AD pathology (**Figure 1**) (Ou et al., 2018). Previous studies have demonstrated the ability of metformin to activate AMPK thus exerting various effects, including a possible neuroprotective effect on AD pathology (Gupta et al., 2011; Foretz et al., 2014; Yang et al., 2020). As for Aβ transport, Chen et al. reported that metformin could decrease RAGE expression and Aβ influx across the BBB, restoring the abnormal Aβ transport in db/db mice (Chen F. et al., 2016).

However, a previous *in vitro* study showed that metformin alone exerted no significant effect on IDE but up-regulated AMPK-dependent BACE1 expression to increase Aβ generation in N2a695 cells overexpressing APP. A combination with insulin reversed the deleterious effect of metformin, suggesting an important regulatory role of insulin in metformin function (Chen et al., 2009; El Massry et al., 2020). Similarly, overexpression of APP and PS1 in LAN5 neuroblastoma cells treated with metformin was suppressed by insulin. In C57B6/J mice, metformin activated AMPK and increase the levels of APP and BACE1, thus promoting the production of Aβ in the cortex (Picone et al., 2015). Metformin was also found to directly interact with Aβ, leading to the alteration of its aggregation profiles, including a reduction of harmless mature fibrils and stabilization of toxic prefibrillar oligomers, suggesting an increase in Aβ toxicity (Picone et al., 2016).

The Effects of Metformin on Tau Pathology

The underlying mechanisms behind the complex effects of metformin on tau pathology remain elusive. Metformin played

paradoxical roles in tauopathy in the brain of mutant human tau (P301S) transgenic mice, including phosphorylation-suppressing and pro-aggregation effects; the former benefit seemed to be weakened by the latter harm (Barini et al., 2016). Mostafa et al. observed that metformin decreased the level of p-tau in the hippocampus and cortex of mice with scopolamine-induced cognitive impairment, probably through increasing the level of phosphorylated Akt while decreasing that of total Akt (Mostafa et al., 2016). Kickstein et al. also verified the ability of metformin to decrease tau phosphorylation at Ser202 both *in vitro* and *in vivo*, which was dependent on the activation of the mTOR/protein phosphatase 2A (PP2A) signaling pathway and unrelated to AMPK activation (Kickstein et al., 2010). Metformin injection for 18 weeks attenuated the increase of phospho-tau phosphorylated at Ser396 and Thr231 in the hippocampus of obese, leptin-resistant mice with AD-associated brain changes through suppressing the activation of JNK instead of attenuating the decrease of PP2A (Li et al., 2012). Metformin was also found to restrict the spreading of tau pathology and reduce Aβ plaques in APP/PS1 mice injected with tau seeds, probably through promoting microglial autophagy of the two pathologies (Chen et al., 2021). However, Zhang et al. reported that chronic metformin administration increased tau phosphorylation in old ApoE-target replacement (TR) mice, probably through increasing the phosphorylation of GSK-3β at Tyr216 (Zhang et al., 2019). Similarly, Kuhla et al. also reported a metformin-induced increase in tau phosphorylation in ApoE deficient ($ApoE^{-/-}$) mice, a mouse model of tauopathy (Kuhla et al., 2019). Further research is needed to confirm whether ApoE genotypes can modify the effects of metformin.

The Effects of Metformin on Neuroinflammation

Accumulating data have revealed the ability of metformin to modulate chronic neuroinflammation (one of the core pathologies in AD). This includes sustained activation of immune cells such as microglia and increased proinflammatory cytokines (Kinney et al., 2018). Previous studies have proposed that metformin could effectively reduce the levels of proinflammatory cytokines such as tumor necrosis factor-alpha (TNF-α), interleukin 1 beta (IL-1β) and IL-6, in the brain of APP/PS1 mice, which could be attributed to the activation of AMPK/P65 NF-κB signaling pathways observed in the hippocampus (Ou et al., 2018; Lu et al., 2020). Nuclear factor-kappa B (NF-κB) is a well-known pro-inflammatory transcription factor involved in abnormal neuroinflammation in AD (Thawkar and Kaur, 2019). Ou et al. also observed decreased accumulation of activated microglia and astrocytes around Aβ plaques in metformin-treated APP/PS1 mice (Ou et al., 2018). In a mouse model with STZ-induced sporadic AD, microgliosis and astrogliosis were also improved by metformin (Pilipenko et al., 2020). Interestingly, Chen et al. reported enhanced microgliosis around Aβ plaques, promoted microglial phagocytosis and ameliorated autophagy of tau aggregates in metformin-treated APP/PS1 mice initially injected with tau aggregates (Chen et al., 2021). It has been suggested that moderate activation of autophagy is critical in the clearance of protein aggregates, thus delaying progression in the early stage of AD (Li et al., 2017). The difference in microglia activation might be associated with injected tau aggregates stimulation.

The Effects of Metformin on Insulin Resistance and Glucose Metabolism

Mounting evidence has supported a robust correlation between insulin resistance and neurodegenerative changes in AD, such as Aβ accumulation and tau phosphorylation (Kellar and Craft, 2020). It is well established that metformin can alleviate hyperinsulinemia and insulin resistance, secondarily, improving metabolic dysfunction (Kitabchi et al., 2005). Considering the ability of metformin to cross the BBB, it is reasonable to speculate that metformin may directly improve AD-related impairment of insulin signaling and glucose metabolism in the CNS. Gupta et al. reported that metformin treatment could alleviate the insulin resistance and AD-related pathological changes induced by hyper-insulinemic exposure in neuronal cell lines (Gupta et al., 2011).

Glucose hypometabolism has been acknowledged as a key pathophysiological characteristic of AD (Daulatzai, 2017). Metformin effectively increased brain glucose uptake in APP/PS1 mice (Lu et al., 2020). Glucose transporters (GLUTs) deficiency is one of the main causes of the decreased glucose metabolism. GLUT-1 is mainly expressed in BBB endothelial cells and thus plays a crucial role in the glucose transport across the BBB. GLUT-3 is expressed in neurons, and thus it is in charge of glucose uptake into neurons (Shah et al., 2012). Glycogen synthase kinase-3 (GSK-3) is associated with the impairment of glucose tolerance (Pearce et al., 2004). In rats with STZ-induced sporadic AD, metformin elevated the density of GLUT-1 and GLUT-3 but decreased the density of GSK-3 in the hippocampus and cortex, suggesting a normalization of brain glucose transport and uptake (Pilipenko et al., 2020). Niccoli et al. reported that metformin could mimic the impact of overexpressed GLUT-1 to increase neuronal glucose uptake in the adult-onset *Drosophila* model (Niccoli et al., 2016). Thus, metformin treatment could considerably restore the impaired glucose metabolism in the brain.

Other Effects of Metformin on AD

The anti-oxidative property of metformin also plays a vital role in ameliorating AD pathology. In APP/PS1 mice, the increase in superoxide dismutase (SOD) activity and malondialdehyde (MDA) level was attenuated by metformin administration (Lu et al., 2020). In rats with scopolamine-induced cognitive impairment, metformin decreased the level of nitric oxide (NO) and MDA in the frontal cortical and hippocampal tissues (Mostafa et al., 2016). Metformin was also found to inhibit the elevated levels of inflammation and endoplasmic reticulum (ER) stress by high glucose treatment through suppressing the interaction between AMPKα and caveolin1 in primary rat astrocytes (Wang et al., 2021).

TABLE 1 | Representative clinical studies on the effects of metformin on AD. AD, Alzheimer's disease; MCI, mild cognitive impairment; T2DM, type 2 diabetes mellitus.

Authors	Study design	Data source	Participants	Conclusions
Sluggett et al., 2020	Nested case-control study	The National Medication Use and Alzheimer's disease (MEDALZ) study	Community-dwelling Finns with diabetes diagnosed ≥3 years before AD (n = 9,862); Diabetic Controls matched by age, sex, and diabetes duration (n = 19550)	Metformin use (ever use) was not associated with incident AD Long-term and high-dose metformin use was associated with a lower risk of incident AD
Hsu et al., 2011	Cohort study	The National Health Insurance database in Taiwan	Nondemented T2DM patients aged 50 or older taking metformin only (n = 1864) taking sulfonylureas only (n = 3,753) taking both (n = 9,257) taking no anti-diabetic drug (n = 10519)	Compared with no medication, metformin alone reduced the risk of developing dementia by 24%, combined therapy with sulfonylureas by 35%
Orkaby et al., 2017	Cohort study	The National Veterans Administration (VA) clinical and administrative database	US veterans aged 65 or older with T2DM but free of dementia new users of metformin (n = 17200) new users of sulfonylurea (n = 11440)	In veterans <75 years of age, risk of incident dementia was lower among metformin users than sulfonylurea users
Cheng et al., 2014	Cohort study	The National Health Insurance database in Taiwan	Nondemented, nondiabetic participants aged 65 or older developing new-onset T2DM taking metformin alone (n = 1,033) taking sulfonylureas alone (n = 796) taking thiazolidinediones alone (n = 28) not developing new-onset T2DM (n = 62311) during the follow-up from January 2004 to December 2009	The risk effect of T2DM could be weakened by the use of metformin and sulfonylureas (no significant difference was shown between these two drugs)
Imfeld et al., 2012	Case-control study	The United Kingdom-based General Practice Research database	Individuals aged 65 or older with an incident diagnosis of AD (n = 7,086) without dementia and matched by age, sex, general practice, calendar time, and years of history (n = 7,086)	Long-term use of metformin was associated with a slight increase in the risk of developing AD, but no dose-effect relationship was observed
Luchsinger et al., 2016	Randomized placebo-controlled clinical trial	N/A	Individuals aged 55–90 years with aMCI, a BMI of 25 kg/m^2 or higher, without treated diabetes, randomized to take metformin 1,000 mg twice a day for 12 months (n = 40) matching placebo (n = 40)	Metformin usage resulted in greater improvement than placebo in the total recall in the Selective Reminding Test as well as a statistically nonsignificant increase in plasma $A\beta_{42}$
Koenig et al., 2017	Randomized placebo-controlled crossover study	N/A	Nondiabetic subjects with MCI or mild dementia due to AD, randomized to take metformin then placebo for 8 weeks each (n = 10) placebo then metformin for 8 weeks each (n = 10)	Metformin treatment was significantly associated with improved executive functioning, and trends suggested improved learning/memory and attention by metformin
Wu et al., 2020	Observational study	The National Alzheimer's Coordinating Center database	T2DM patients using a hypoglycemic medication with normal cognition (n = 1,192) taking metformin (n = 824) with AD (n = 807) taking metformin (n = 473)	Metformin treatment exerted a memory benefit over time among cognitively normal people. There was no association between metformin and memory decline in AD, but metformin was associated with a greater decline in delayed memory specifically among APOE ε4 carriers
Moore et al., 2013	Observational study	The Primary Research in Memory (PRIME) clinics study, the Australian Imaging, Biomarkers and Lifestyle (AIBL) study of aging, and the Barwon region of southeastern Australia	Patients with AD (n = 480) patients with MCI (n = 187) cognitively intact individuals (n = 687)	Metformin use was associated with impaired cognitive performance, which could be alleviated by vitamin B_{12} and calcium supplements

Mitochondrial dysfunction has been identified as an early event of AD (Desler et al., 2018). Exposure to Aβ could result in an impairment of mitochondrial function and morphology in hNSCs. Co-treatment with metformin, however, was found to protect against the impairment, which was dependent on AMPK activation (Chiang et al., 2016). An *in vivo* study using SAMP8 mice of sporadic AD reported that metformin decreased the level of APPc99 and pTau404 expression, which was associated with improved mitochondrial function in previous studies (Reddy, 2011; Pera et al., 2017; Farr et al., 2019). However, metformin treatment for 3 months was found to increase the levels of the translocase of the outer membrane 40 (TOM40), hexokinase I

(HKI) and voltage-dependent anion-selective channels 1 (VDAC) and influence their conformation in the cortex region of C57B6/J mice, suggesting impairment of mitochondrial permeability transition pores and membrane channels, thereby leading to mitochondrial dysfunction (Picone et al., 2016).

Growing evidence has indicated an anti-degenerative benefit from the inhibition of acetylcholinesterase (AChE), the enzyme secreted into the synaptic cleft to inactivate acetylcholine (ACh) by cholinergic neurons (Krishnan et al., 2003; Ferreira-Vieira et al., 2016; Cavedo et al., 2017; Moss, 2020). Gupta found that metformin could inhibit the increase of AChE activity by 34.9% in insulin-resistant neuroblastoma cells (Gupta et al., 2011). Bhutada et al. reported a decrease in the activity of choline esterase (ChE) after chronic metformin treatment in the hippocampus of rats with STZ-induced diabetes (Bhutada et al., 2011). In the rat model of STZ-induced sporadic AD, metformin inhibited AChE activity in the hippocampal CA1 and CA3. Interestingly, metformin alone increased AChE activity in similar regions of non-AD rats (Pilipenko et al., 2020), probably implying an interaction between metformin and some AD-related pathophysiological change induced by STZ.

CLINICAL EVIDENCE

Current epidemiological studies regarding the effects of metformin on the risk of AD remain still scanty and contradictory (**Table 1**). Most studies set the outcome as the onset of all-cause cognitive dysfunctions such as dementia and the participants as T2DM patients. A meta-analysis conducted in 2018 have shown that treatment with metformin could effectively lower the risk of subsequent dementia by 34% in elderly people with T2DM (Campbell et al., 2018). Consistently, a recent longitudinal study among community-dwelling diabetic patients in Finland suggested that long-term high-dose metformin use could decrease the risk of AD in elderly diabetic patients (Sluggett et al., 2020). Similarly, Wu et al. observed an association between metformin treatment and less memory decline over time in cognitively normal T2DM patients. Interestingly, this association was not observed among the APOE ε4 carriers, which implied an interaction between APOE ε4 carrier status and metformin (Wu et al., 2020). Orkaby et al. found that the protective association between metformin and dementia risk could also be modified by age, race, level of HbA1c and renal function. Compared with sulfonylurea, metformin could significantly lower the risk of dementia only among T2DM patients aged 75 or younger who were white, or had good renal function or HbA1C values ≥ 7% (Orkaby et al., 2017). These findings have implied that it is necessary to identify the subgroups of people that can benefit from metformin use for the prevention of cognitive impairment.

Metformin was also found to have a greater preventive effect than thiazolidinediones (Cheng et al., 2014). A combination of metformin and sulfonylurea could reduce the risk of dementia by 35% compared with no medication use, exhibiting better safety and efficacy (Hsu et al., 2011). A previous case-control study by Imfeld et al. reported an association between long-term metformin use and a slightly higher risk of developing AD, but no dose-effect relationship was observed (Imfeld et al., 2012). The cases and controls were not matched on diabetes diagnosis, which was in fact an important confounder in this study, likely leading to this inconsistent finding.

Several studies have also investigated whether metformin could exert a cognitive benefit in patients with cognitive impairment (**Table 1**). There have been two small-scale randomized clinical trials showing positive results. Luchsinger et al. found that metformin 1,000 mg twice a day for 12 months could result in greater improvement than placebo use in selective reminding test (SRT) as well as a statistically nonsignificant increase of plasma $A\beta_{42}$ in overweight patients with amnestic mild cognitive impairment (aMCI) (Luchsinger et al., 2016). Another randomized crossover study patients with MCI or mild dementia due to AD suggested that metformin use could contribute to an improvement of executive function (Koenig et al., 2017). However, in the longitudinal study by Wu et al., no relationship was found between metformin treatment and longitudinal memory change among all T2DM patients with aMCI or AD dementia. Further analysis showed an association between metformin use and faster decline in delayed memory among the APOE ε4 carriers, implying that the adverse interaction between metformin and APOE-ε4 genotype or AD pathology might neutralize the neuroprotective effect of metformin itself (Wu et al., 2020). A small-scale cross-sectional study reported an association between metformin use and worse cognitive performance among diabetic patients, which might be mediated by vitamin B_{12} deficiency (Moore et al., 2013). The contradictions in the findings above might stem from the insufficient sample sizes of clinical trials and different diabetic status of participants.

In conclusion, current evidence has mainly suggested a cognitive benefit of metformin among cognitive normal T2DM patients while its cognitive effect on T2DM patients with AD seems negative. The underlying mechanisms of the adverse interaction between metformin and APOE-ε4 genotype or AD pathology need to be uncovered. Further works are warranted to identify the characteristics of people who benefit from metformin for the prevention or treatment of cognitive impairment. Large-scale, placebo-controlled randomized clinical trials are also needed to determine whether these effects can be generalized among population without T2DM. It will provide valuable insights into the underlying mechanisms if measuring AD biomarkers such as Aβ, phosphorylated tau (p-tau) and total tau (t-tau) in cerebrospinal fluid (CSF) and brain atrophy in future clinical research.

CONCLUSIONS AND FUTURE PERSPECTIVES

This review mainly focuses on the clinical and mechanistic evidence on the effects of metformin on AD. The specific mechanisms linking T2DM to AD and the general pharmacological mechanisms are reviewed briefly.

Most clinical evidence has suggested that metformin, as a first-line glucose-lowering medication, helps lower the risk of AD among people with T2DM. Potential explanations include an improvement in the various macrovascular disorders associated with T2DM and the specific neuroprotective function of metformin reviewed above (Hsu et al., 2011; Cheng et al., 2014; Orkaby et al., 2017; Campbell et al., 2018; Sluggett et al., 2020; Wu et al., 2020). It is important to note that the effect of metformin on AD pathology is independent of glycemic control. However, current evidence failed to support the therapeutic role of metformin. Although most animal studies have suggested a neuroprotective role of metformin among APP/PS1 mice, clinical studies found no significant cognitive benefit of metformin among subjects with cognitive impairment due to AD (Moore et al., 2013; Wu et al., 2020).

Both preclinical and clinical studies have implied an interaction between metformin and ApoE carrier status (Kuhla et al., 2019; Zhang et al., 2019; Wu et al., 2020). Moreover, there are no studies probing the impact of metformin on non-diabetes subjects with normal cognitive function. It is necessary to identify the characteristics of people who get protection from metformin against AD. The modifiers such as APOE-ε4 genotype should also be taken into consideration when prescribing antidiabetic medication. It would be interesting to compare the effects generated by metformin and insulin treatment since there has been encouraging evidence suggesting the effectiveness of intranasal insulin treatment in AD (Boccardi et al., 2019). It is still unclear about the interactions between metformin and other common anti-AD drugs. Further investigation is needed to demonstrate whether their combination can be more effective in the fight against AD.

The poor oral absorption and gastrointestinal adverse effects significantly limited the clinical application of metformin. Researchers have attempted to design and synthesize prodrugs of metformin with higher lipophilicity to improve permeability and passive transcellular absorption. There have been several lipophilic sulfenamide prodrugs designed and shown to achieve better absorption (Huttunen et al., 2009; Huttunen et al., 2013). Furthermore, Rautio et al. synthesized novel sulfonamide prodrugs that would only be bioactivated by glutathione-S-transferase after oral absorption, which further improved the bioavailability of metformin (Rautio et al., 2014). Further studies are warranted to design new prodrug structures or other techniques making metformin reach the CNS more precisely.

After oral administration, metformin is delivered to the CNS *via* cerebral blood flow (CBF) and transported across the BBB. It is important to note that CBF reduction and the impairment of BBB integrity are early events occurred in AD pathogenesis, which may influence the uptake of metformin across the BBB (Kisler et al., 2017). Interestingly, a clinical trial by Koenig et al. showed that metformin might also affect CBF, as superior and middle orbitofrontal CBF was increased after 8 weeks of metformin treatment (Koenig et al., 2017). In Wistar rats, metformin was reported to efficiently cross the BBB and differently accumulate in brain regions, including hippocampus and frontal cortex after chronic oral administration for 3 weeks (Łabuzek et al., 2010). The patterns of metformin accumulation in different brain structures under AD pathology is still unclear. Further research is needed to confirm the appropriate dose and duration of metformin use required to produce sufficient protective effects against AD while causing less adverse effects.

AUTHOR CONTRIBUTIONS

WL and JX were responsible for original draft preparation. BL reviewed and edited the text. YR designed the graph and the table. JL and TL supervised and gave opinions on the manuscript. JX and TL revised the manuscript.

FUNDING

This study was supported financially by National Natural Science Foundation of China (82101271, 82171178), Guangdong Basic and Applied Basic Research Foundation (2020A1515110317, 2021A1515010705, 2020A1515010210).

ACKNOWLEDGMENTS

This language was edited by the Native Speakers' Group of Sun Yat-sen Memorial Hospital of Sun Yat-sen University.

REFERENCES

Apostolova, L. G. (2016). Alzheimer Disease. *Continuum (Minneap Minn)* 22 (2 Dementia), 419–434. doi:10.1212/con.0000000000000307

Barini, E., Antico, O., Zhao, Y., Asta, F., Tucci, V., Catelani, T., et al. (2016). Metformin Promotes Tau Aggregation and Exacerbates Abnormal Behavior in a Mouse Model of Tauopathy. *Mol. Neurodegener* 11, 16. doi:10.1186/s13024-016-0082-7

Benarroch, E. E. (2018). Glutamatergic Synaptic Plasticity and Dysfunction in Alzheimer Disease: Emerging Mechanisms. *Neurology* 91 (3), 125–132. doi:10.1212/wnl.0000000000005807

Benedict, C., and Grillo, C. A. (2018). Insulin Resistance as a Therapeutic Target in the Treatment of Alzheimer's Disease: A State-Of-The-Art Review. *Front. Neurosci.* 12, 215. doi:10.3389/fnins.2018.00215

Bhutada, P., Mundhada, Y., Bansod, K., Tawari, S., Patil, S., Dixit, P., et al. (2011). Protection of Cholinergic and Antioxidant System Contributes to the Effect of Berberine Ameliorating Memory Dysfunction in Rat Model of Streptozotocin-Induced Diabetes. *Behav. Brain Res.* 220 (1), 30–41. doi:10.1016/j.bbr.2011.01.022

Boccardi, V., Murasecco, I., and Mecocci, P. (2019). Diabetes Drugs in the Fight against Alzheimer's Disease. *Ageing Res. Rev.* 54, 100936. doi:10.1016/j.arr.2019.100936

Campbell, J. M., Stephenson, M. D., de Courten, B., Chapman, I., Bellman, S. M., and Aromataris, E. (2018). Metformin Use Associated with Reduced Risk of Dementia in Patients with Diabetes: A Systematic Review and Meta-Analysis. *J. Alzheimers Dis.* 65 (4), 1225–1236. doi:10.3233/JAD-180263

Cavedo, E., Grothe, M. J., Colliot, O., Lista, S., Chupin, M., Dormont, D., et al. (2017). Reduced Basal Forebrain Atrophy Progression in a Randomized

Donepezil Trial in Prodromal Alzheimer's Disease. *Sci. Rep.* 7 (1), 11706. doi:10.1038/s41598-017-09780-3

Chen, B., Teng, Y., Zhang, X., Lv, X., and Yin, Y. (2016). Metformin Alleviated Aβ-Induced Apoptosis via the Suppression of JNK MAPK Signaling Pathway in Cultured Hippocampal Neurons. *Biomed. Res. Int.* 2016, 1421430. doi:10.1155/2016/1421430

Chen, F., Dong, R. R., Zhong, K. L., Ghosh, A., Tang, S. S., Long, Y., et al. (2016). Antidiabetic Drugs Restore Abnormal Transport of Amyloid-β across the Blood-Brain Barrier and Memory Impairment in Db/db Mice. *Neuropharmacology* 101, 123–136. doi:10.1016/j.neuropharm.2015.07.023

Chen, W. B., Chen, J., Liu, Z. Y., Luo, B., Zhou, T., and Fei, E. K. (2020). Metformin Enhances Excitatory Synaptic Transmission onto Hippocampal CA1 Pyramidal Neurons. *Brain Sci.* 10 (10), 706. doi:10.3390/brainsci10100706

Chen, Y., Zhao, S., Fan, Z., Li, Z., Zhu, Y., Shen, T., et al. (2021). Metformin Attenuates Plaque-Associated Tau Pathology and Reduces Amyloid-β burden in APP/PS1 Mice. *Alzheimers Res. Ther.* 13 (1), 40. doi:10.1186/s13195-020-00761-9

Chen, Y., Zhou, K., Wang, R., Liu, Y., Kwak, Y. D., Ma, T., et al. (2009). Antidiabetic Drug Metformin (GlucophageR) Increases Biogenesis of Alzheimer's Amyloid Peptides via Up-Regulating BACE1 Transcription. *Proc. Natl. Acad. Sci. U S A.* 106 (10), 3907–3912. doi:10.1073/pnas.0807991106

Cheng, C., Lin, C. H., Tsai, Y. W., Tsai, C. J., Chou, P. H., and Lan, T. H. (2014). Type 2 Diabetes and Antidiabetic Medications in Relation to Dementia Diagnosis. *J. Gerontol. A. Biol. Sci. Med. Sci.* 69 (10), 1299–1305. doi:10.1093/gerona/glu073

Chiang, M. C., Cheng, Y. C., Chen, S. J., Yen, C. H., and Huang, R. N. (2016). Metformin Activation of AMPK-dependent Pathways Is Neuroprotective in Human Neural Stem Cells against Amyloid-Beta-Induced Mitochondrial Dysfunction. *Exp. Cel Res* 347 (2), 322–331. doi:10.1016/j.yexcr.2016.08.013

Daulatzai, M. A. (2017). Cerebral Hypoperfusion and Glucose Hypometabolism: Key Pathophysiological Modulators Promote Neurodegeneration, Cognitive Impairment, and Alzheimer's Disease. *J. Neurosci. Res.* 95 (4), 943–972. doi:10.1002/jnr.23777

Desler, C., Lillenes, M. S., Tønjum, T., and Rasmussen, L. J. (2018). The Role of Mitochondrial Dysfunction in the Progression of Alzheimer's Disease. *Curr. Med. Chem.* 25 (40), 5578–5587. doi:10.2174/0929867324666170616110111

Dubois, B., Feldman, H. H., Jacova, C., Hampel, H., Molinuevo, J. L., Blennow, K., et al. (2014). Advancing Research Diagnostic Criteria for Alzheimer's Disease: the IWG-2 Criteria. *Lancet Neurol.* 13 (6), 614–629. doi:10.1016/S1474-4422(14)70090-0

El Massry, M., Alaeddine, L. M., Ali, L., Saad, C., and Eid, A. A. (2021). Metformin: A Growing Journey from Glycemic Control to the Treatment of Alzheimer's Disease and Depression. *Curr. Med. Chem.* 28, 2328–2345. doi:10.2174/0929867327666200908114902

El-Mir, M. Y., Detaille, D., R-Villanueva, G., Delgado-Esteban, M., Guigas, B., Attia, S., et al. (2008). Neuroprotective Role of Antidiabetic Drug Metformin against Apoptotic Cell Death in Primary Cortical Neurons. *J. Mol. Neurosci.* 34 (1), 77–87. doi:10.1007/s12031-007-9002-1

Farr, S. A., Roesler, E., Niehoff, M. L., Roby, D. A., McKee, A., and Morley, J. E. (2019). Metformin Improves Learning and Memory in the SAMP8 Mouse Model of Alzheimer's Disease. *J. Alzheimers Dis.* 68 (4), 1699–1710. doi:10.3233/JAD-181240

Ferreira-Vieira, T. H., Guimaraes, I. M., Silva, F. R., and Ribeiro, F. M. (2016). Alzheimer's Disease: Targeting the Cholinergic System. *Curr. Neuropharmacol* 14 (1), 101–115. doi:10.2174/1570159x13666150716165726

Foretz, M., Guigas, B., Bertrand, L., Pollak, M., and Viollet, B. (2014). Metformin: from Mechanisms of Action to Therapies. *Cell Metab* 20 (6), 953–966. doi:10.1016/j.cmet.2014.09.018

Gupta, A., Bisht, B., and Dey, C. S. (2011). Peripheral Insulin-Sensitizer Drug Metformin Ameliorates Neuronal Insulin Resistance and Alzheimer's-like Changes. *Neuropharmacology* 60 (6), 910–920. doi:10.1016/j.neuropharm.2011.01.033

Hallschmid, M. (2021). Intranasal Insulin for Alzheimer's Disease. *CNS Drugs* 35 (1), 21–37. doi:10.1007/s40263-020-00781-x

Hampel, H., Vassar, R., De Strooper, B., Hardy, J., Willem, M., Singh, N., et al. (2021). The β-Secretase BACE1 in Alzheimer's Disease. *Biol. Psychiatry* 89 (8), 745–756. doi:10.1016/j.biopsych.2020.02.001

Harris, S., Abrahamson, M. J., Ceriello, A., Charpentier, G., Evans, M., Lehmann, R., et al. (2020). Clinical Considerations when Initiating and Titrating Insulin Degludec/Liraglutide (IDegLira) in People with Type 2 Diabetes. *Drugs* 80 (2), 147–165. doi:10.1007/s40265-019-01245-3

Hsu, C.-C., Peng, D., Cai, Z., and Lin, H.-K. (2021). AMPK Signaling and its Targeting in Cancer Progression and Treatment. *Semin. Cancer Biol.* doi:10.1016/j.semcancer.2021.04.006

Hsu, C. C., Wahlqvist, M. L., Lee, M. S., and Tsai, H. N. (2011). Incidence of Dementia Is Increased in Type 2 Diabetes and Reduced by the Use of Sulfonylureas and Metformin. *J. Alzheimers Dis.* 24 (3), 485–493. doi:10.3233/JAD-2011-101524

Huttunen, K. M., Leppänen, J., Laine, K., Vepsäläinen, J., and Rautio, J. (2013). Convenient Microwave-Assisted Synthesis of Lipophilic Sulfenamide Prodrugs of Metformin. *Eur. J. Pharm. Sci.* 49 (4), 624–628. doi:10.1016/j.ejps.2013.05.023

Huttunen, K. M., Mannila, A., Laine, K., Kemppainen, E., Leppänen, J., Vepsäläinen, J., et al. (2009). The First Bioreversible Prodrug of Metformin with Improved Lipophilicity and Enhanced Intestinal Absorption. *J. Med. Chem.* 52 (14), 4142–4148. doi:10.1021/jm900274q

Imfeld, P., Bodmer, M., Jick, S. S., and Meier, C. R. (2012). Metformin, Other Antidiabetic Drugs, and Risk of Alzheimer's Disease: a Population-Based Case-Control Study. *J. Am. Geriatr. Soc.* 60 (5), 916–921. doi:10.1111/j.1532-5415.2012.03916.x

Kandimalla, R., Thirumala, V., and Reddy, P. H. (2017). Is Alzheimer's Disease a Type 3 Diabetes? A Critical Appraisal. *Biochim. Biophys. Acta Mol. Basis Dis.* 1863 (5), 1078–1089. doi:10.1016/j.bbadis.2016.08.018

Kellar, D., and Craft, S. (2020). Brain Insulin Resistance in Alzheimer's Disease and Related Disorders: Mechanisms and Therapeutic Approaches. *Lancet Neurol.* 19 (9), 758–766. doi:10.1016/s1474-4422(20)30231-3

Kickstein, E., Krauss, S., Thornhill, P., Rutschow, D., Zeller, R., Sharkey, J., et al. (2010). Biguanide Metformin Acts on Tau Phosphorylation via mTOR/protein Phosphatase 2A (PP2A) Signaling. *Proc. Natl. Acad. Sci. U S A.* 107 (50), 21830–21835. doi:10.1073/pnas.0912793107

Kinney, J. W., Bemiller, S. M., Murtishaw, A. S., Leisgang, A. M., Salazar, A. M., and Lamb, B. T. (2018). Inflammation as a central Mechanism in Alzheimer's Disease. *Alzheimers Dement (N Y)* 4, 575–590. doi:10.1016/j.trci.2018.06.014

Kisler, K., Nelson, A. R., Montagne, A., and Zlokovic, B. V. (2017). Cerebral Blood Flow Regulation and Neurovascular Dysfunction in Alzheimer Disease. *Nat. Rev. Neurosci.* 18 (7), 419–434. doi:10.1038/nrn.2017.48

Kitabchi, A. E., Temprosa, M., Knowler, W. C., Kahn, S. E., Fowler, S. E., Haffner, S. M., et al. (2005). Role of Insulin Secretion and Sensitivity in the Evolution of Type 2 Diabetes in the Diabetes Prevention Program: Effects of Lifestyle Intervention and Metformin. *Diabetes* 54 (8), 2404–2414. doi:10.2337/diabetes.54.8.2404

Koenig, A. M., Mechanic-Hamilton, D., Xie, S. X., Combs, M. F., Cappola, A. R., Xie, L., et al. (2017). Effects of the Insulin Sensitizer Metformin in Alzheimer Disease: Pilot Data from a Randomized Placebo-Controlled Crossover Study. *Alzheimer Dis. Assoc. Disord.* 31 (2), 107–113. doi:10.1097/WAD.0000000000000202

Kosaraju, J., Holsinger, R. M. D., Guo, L., and Tam, K. Y. (2017). Linagliptin, a Dipeptidyl Peptidase-4 Inhibitor, Mitigates Cognitive Deficits and Pathology in the 3xTg-AD Mouse Model of Alzheimer's Disease. *Mol. Neurobiol.* 54 (8), 6074–6084. doi:10.1007/s12035-016-0125-7

Krishnan, K. R., Doraiswamy, P. M., Weisler, R., Perdomo, C., Ieni, J. R., Rogers, S., et al. (2003). Randomized, Placebo-Controlled Trial of the Effects of Donepezil on Neuronal Markers and Hippocampal Volumes in Alzheimer's Disease. *Am. J. Psychiatry* 160 (11), 2003–2011. doi:10.1176/appi.ajp.160.11.2003

Kuhla, A., Brichmann, E., Rühlmann, C., Thiele, R., Meuth, L., and Vollmar, B. (2019). Metformin Therapy Aggravates Neurodegenerative Processes in ApoE-/- Mice. *J. Alzheimers Dis.* 68 (4), 1415–1427. doi:10.3233/JAD-181017

Kurochkin, I. V., Guarnera, E., and Berezovsky, I. N. (2018). Insulin-Degrading Enzyme in the Fight against Alzheimer's Disease. *Trends Pharmacol. Sci.* 39 (1), 49–58. doi:10.1016/j.tips.2017.10.008

Łabuzek, K., Suchy, D., Gabryel, B., Bielecka, A., Liber, S., and Okopień, B. (2010). Quantification of Metformin by the HPLC Method in Brain Regions, Cerebrospinal Fluid and Plasma of Rats Treated with Lipopolysaccharide. *Pharmacol. Rep.* 62 (5), 956–965. doi:10.1016/s1734-1140(10)70357-1

Li, J., Deng, J., Sheng, W., and Zuo, Z. (2012). Metformin Attenuates Alzheimer's Disease-like Neuropathology in Obese, Leptin-Resistant Mice. *Pharmacol. Biochem. Behav.* 101 (4), 564–574. doi:10.1016/j.pbb.2012.03.002

Li, L. X., Liu, M. Y., Jiang, X., Xia, Z. H., Wang, Y. X., An, D., et al. (2019). Metformin Inhibits Aβ25-35 -induced Apoptotic Cell Death in SH-Sy5y Cells. *Basic Clin. Pharmacol. Toxicol.* 125 (5), 439–449. doi:10.1111/bcpt.13279

Li, Q., Liu, Y., and Sun, M. (2017). Autophagy and Alzheimer's Disease. *Cell Mol Neurobiol* 37 (3), 377–388. doi:10.1007/s10571-016-0386-8

Li, T., Providencia, R., Mu, N., Yin, Y., Chen, M., Wang, Y., et al. (2021). Association of Metformin Monotherapy or Combined Therapy with Cardiovascular Risks in Patients with Type 2 Diabetes Mellitus. *Cardiovasc. Diabetol.* 20 (1), 30. doi:10.1186/s12933-020-01202-5

Li, T., Yin, Y., Mu, N., Wang, Y., Liu, M., Chen, M., et al. (2020). Metformin-Enhanced Cardiac AMP-Activated Protein Kinase/Atrogin-1 Pathways Inhibit Charged Multivesicular Body Protein 2B Accumulation in Ischemia-Reperfusion Injury. *Front Cel Dev Biol* 8, 621509. doi:10.3389/fcell.2020.621509

Lu, X. Y., Huang, S., Chen, Q. B., Zhang, D., Li, W., Ao, R., et al. (2020). Metformin Ameliorates Aβ Pathology by Insulin-Degrading Enzyme in a Transgenic Mouse Model of Alzheimer's Disease. *Oxid Med. Cel Longev* 2020, 2315106. doi:10.1155/2020/2315106

Luchsinger, J. A., Perez, T., Chang, H., Mehta, P., Steffener, J., Pradabhan, G., et al. (2016). Metformin in Amnestic Mild Cognitive Impairment: Results of a Pilot Randomized Placebo Controlled Clinical Trial. *J. Alzheimers Dis.* 51 (2), 501–514. doi:10.3233/JAD-150493

Lv, Z., and Guo, Y. (2020). Metformin and its Benefits for Various Diseases. *Front. Endocrinol. (Lausanne)* 11, 191. doi:10.3389/fendo.2020.00191

Markowicz-Piasecka, M., Sikora, J., Szydłowska, A., Skupień, A., Mikiciuk-Olasik, E., and Huttunen, K. M. (2017). Metformin - a Future Therapy for Neurodegenerative Diseases : Theme: Drug Discovery, Development and Delivery in Alzheimer's Disease Guest Editor: Davide Brambilla. *Pharm. Res.* 34 (12), 2614–2627. doi:10.1007/s11095-017-2199-y

McClean, P. L., Parthsarathy, V., Faivre, E., and Hölscher, C. (2011). The Diabetes Drug Liraglutide Prevents Degenerative Processes in a Mouse Model of Alzheimer's Disease. *J. Neurosci.* 31 (17), 6587–6594. doi:10.1523/jneurosci.0529-11.2011

Moore, E. M., Mander, A. G., Ames, D., Kotowicz, M. A., Carne, R. P., Brodaty, H., et al. (2013). Increased Risk of Cognitive Impairment in Patients with Diabetes Is Associated with Metformin. *Diabetes Care* 36 (10), 2981–2987. doi:10.2337/dc13-0229

Moss, D. E. (2020). Improving Anti-neurodegenerative Benefits of Acetylcholinesterase Inhibitors in Alzheimer's Disease: Are Irreversible Inhibitors the Future? *Int. J. Mol. Sci.* 21 (10), 3438. doi:10.3390/ijms21103438

Mostafa, D. K., Ismail, C. A., and Ghareeb, D. A. (2016). Differential Metformin Dose-dependent Effects on Cognition in Rats: Role of Akt. *Psychopharmacology (Berl)* 233 (13), 2513–2524. doi:10.1007/s00213-016-4301-2

Mulvihill, M. M., and Nomura, D. K. (2013). Therapeutic Potential of Monoacylglycerol Lipase Inhibitors. *Life Sci.* 92 (8-9), 492–497. doi:10.1016/j.lfs.2012.10.025

Nelson, T. J., Sun, M. K., Hongpaisan, J., and Alkon, D. L. (2008). Insulin, PKC Signaling Pathways and Synaptic Remodeling during Memory Storage and Neuronal Repair. *Eur. J. Pharmacol.* 585 (1), 76–87. doi:10.1016/j.ejphar.2008.01.051

Niccoli, T., Cabecinha, M., Tillmann, A., Kerr, F., Wong, C. T., Cardenes, D., et al. (2016). Increased Glucose Transport into Neurons Rescues Aβ Toxicity in Drosophila. *Curr. Biol.* 26 (17), 2291–2300. doi:10.1016/j.cub.2016.07.017

Orkaby, A. R., Cho, K., Cormack, J., Gagnon, D. R., and Driver, J. A. (2017). Metformin vs Sulfonylurea Use and Risk of Dementia in US Veterans Aged ≥65 Years with Diabetes. *Neurology* 89 (18), 1877–1885. doi:10.1212/WNL.0000000000004586

Ott, C., Jung, S., Korn, M., Kannenkeril, D., Bosch, A., Kolwelter, J., et al. (2021). Renal Hemodynamic Effects Differ between Antidiabetic Combination Strategies: Randomized Controlled Clinical Trial Comparing Empagliflozin/linagliptin with Metformin/insulin Glargine. *Cardiovasc. Diabetol.* 20 (1), 178. doi:10.1186/s12933-021-01358-8

Ou, Z., Kong, X., Sun, X., He, X., Zhang, L., Gong, Z., et al. (2018). Metformin Treatment Prevents Amyloid Plaque Deposition and Memory Impairment in APP/PS1 Mice. *Brain Behav. Immun.* 69, 351–363. doi:10.1016/j.bbi.2017.12.009

Pearce, N. J., Arch, J. R., Clapham, J. C., Coghlan, M. P., Corcoran, S. L., Lister, C. A., et al. (2004). Development of Glucose Intolerance in Male Transgenic Mice Overexpressing Human Glycogen Synthase Kinase-3beta on a Muscle-specific Promoter. *Metabolism* 53 (10), 1322–1330. doi:10.1016/j.metabol.2004.05.008

Pera, M., Larrea, D., Guardia-Laguarta, C., Montesinos, J., Velasco, K. R., Agrawal, R. R., et al. (2017). Increased Localization of APP-C99 in Mitochondria-Associated ER Membranes Causes Mitochondrial Dysfunction in Alzheimer Disease. *Embo j* 36 (22), 3356–3371. doi:10.15252/embj.201796797

Picone, P., Nuzzo, D., Caruana, L., Messina, E., Barera, A., Vasto, S., et al. (2015). Metformin Increases APP Expression and Processing via Oxidative Stress, Mitochondrial Dysfunction and NF-Kb Activation: Use of Insulin to Attenuate Metformin's Effect. *Biochim. Biophys. Acta* 1853 (5), 1046–1059. doi:10.1016/j.bbamcr.2015.01.017

Picone, P., Vilasi, S., Librizzi, F., Contardi, M., Nuzzo, D., Caruana, L., et al. (2016). Biological and Biophysics Aspects of Metformin-Induced Effects: Cortex Mitochondrial Dysfunction and Promotion of Toxic Amyloid Pre-fibrillar Aggregates. *Aging (Albany NY)* 8 (8), 1718–1734. doi:10.18632/aging.101004

Pilipenko, V., Narbute, K., Pupure, J., Langrate, I. K., Muceniece, R., and Kluša, V. (2020). Neuroprotective Potential of Antihyperglycemic Drug Metformin in Streptozocin-Induced Rat Model of Sporadic Alzheimer's Disease. *Eur. J. Pharmacol.* 881, 173290. doi:10.1016/j.ejphar.2020.173290

Rautio, J., Vernerová, M., Aufderhaar, I., and Huttunen, K. M. (2014). Glutathione-S-transferase Selective Release of Metformin from its Sulfonamide Prodrug. *Bioorg. Med. Chem. Lett.* 24 (21), 5034–5036. doi:10.1016/j.bmcl.2014.09.019

Reddy, P. H. (2011). Abnormal Tau, Mitochondrial Dysfunction, Impaired Axonal Transport of Mitochondria, and Synaptic Deprivation in Alzheimer's Disease. *Brain Res.* 1415, 136–148. doi:10.1016/j.brainres.2011.07.052

Schilling, M. A. (2016). Unraveling Alzheimer's: Making Sense of the Relationship between Diabetes and Alzheimer's Disease1. *J. Alzheimers Dis.* 51 (4), 961–977. doi:10.3233/JAD-150980

Schneider, L. S., Mangialasche, F., Andreasen, N., Feldman, H., Giacobini, E., Jones, R., et al. (2014). Clinical Trials and Late-Stage Drug Development for Alzheimer's Disease: an Appraisal from 1984 to 2014. *J. Intern. Med.* 275 (3), 251–283. doi:10.1111/joim.12191

Shah, K., Desilva, S., and Abbruscato, T. (2012). The Role of Glucose Transporters in Brain Disease: Diabetes and Alzheimer's Disease. *Int. J. Mol. Sci.* 13 (10), 12629–12655. doi:10.3390/ijms131012629

Sheng, Y., Zhang, L., Su, S. C., Tsai, L. H., and Julius Zhu, J. (2016). Cdk5 Is a New Rapid Synaptic Homeostasis Regulator Capable of Initiating the Early Alzheimer-like Pathology. *Cereb. Cortex* 26 (7), 2937–2951. doi:10.1093/cercor/bhv032

Sluggett, J. K., Koponen, M., Bell, J. S., Taipale, H., Tanskanen, A., Tiihonen, J., et al. (2020). Metformin and Risk of Alzheimer's Disease Among Community-Dwelling People with Diabetes: A National Case-Control Study. *J. Clin. Endocrinol. Metab.* 105 (4), dgz234. doi:10.1210/clinem/dgz234

Syal, C., Kosaraju, J., Hamilton, L., Aumont, A., Chu, A., Sarma, S. N., et al. (2020). Dysregulated Expression of Monoacylglycerol Lipase Is a Marker for Anti-diabetic Drug Metformin-Targeted Therapy to Correct Impaired Neurogenesis and Spatial Memory in Alzheimer's Disease. *Theranostics* 10 (14), 6337–6360. doi:10.7150/thno.44962

Tanaka, A., Shimabukuro, M., Teragawa, H., Okada, Y., Takamura, T., Taguchi, I., et al. (2021). Comparison of the Clinical Effect of Empagliflozin on Glycemic and Non-glycemic Parameters in Japanese Patients with Type 2 Diabetes and Cardiovascular Disease Treated with or without Baseline Metformin. *Cardiovasc. Diabetol.* 20 (1), 160. doi:10.1186/s12933-021-01352-0

Thawkar, B. S., and Kaur, G. (2019). Inhibitors of NF-Kb and P2X7/NLRP3/Caspase 1 Pathway in Microglia: Novel Therapeutic Opportunities in Neuroinflammation Induced Early-Stage Alzheimer's Disease. *J. Neuroimmunol* 326, 62–74. doi:10.1016/j.jneuroim.2018.11.010

Wang, G., Cui, W., Chen, S., Shao, Z., Li, Y., Wang, W., et al. (2021). Metformin Alleviates High Glucose-Induced ER Stress and Inflammation by Inhibiting the Interaction between Caveolin1 and AMPKα in Rat Astrocytes. *Biochem. Biophys. Res. Commun.* 534, 908–913. doi:10.1016/j.bbrc.2020.10.075

Wang, J., Gallagher, D., DeVito, L. M., Cancino, G. I., Tsui, D., He, L., et al. (2012). Metformin Activates an Atypical PKC-CBP Pathway to Promote Neurogenesis and Enhance Spatial Memory Formation. *Cell Stem Cell* 11 (1), 23–35. doi:10.1016/j.stem.2012.03.016

Wang, Y., Zhao, J., Guo, F. L., Gao, X., Xie, X., Liu, S., et al. (2020). Metformin Ameliorates Synaptic Defects in a Mouse Model of AD by

Inhibiting Cdk5 Activity. *Front Cel Neurosci* 14, 170. doi:10.3389/fncel.2020.00170

West, M. J., Coleman, P. D., Flood, D. G., and Troncoso, J. C. (1994). Differences in the Pattern of Hippocampal Neuronal Loss in normal Ageing and Alzheimer's Disease. *Lancet* 344 (8925), 769–772. doi:10.1016/s0140-6736(94)92338-8

Wu, C. Y., Ouk, M., Wong, Y. Y., Anita, N. Z., Edwards, J. D., Yang, P., et al. (2020). Relationships between Memory Decline and the Use of Metformin or DPP4 Inhibitors in People with Type 2 Diabetes with normal Cognition or Alzheimer's Disease, and the Role APOE Carrier Status. *Alzheimers Dement* 16 (12), 1663–1673. doi:10.1002/alz.12161

Yang, L., Jiang, Y., Shi, L., Zhong, D., Li, Y., Li, J., et al. (2020). AMPK: Potential Therapeutic Target for Alzheimer's Disease. *Curr. Protein Pept. Sci.* 21 (1), 66–77. doi:10.2174/1389203720666190819142746

Yang, Y., Zhang, J., Ma, D., Zhang, M., Hu, S., Shao, S., et al. (2013). Subcutaneous Administration of Liraglutide Ameliorates Alzheimer-Associated Tau Hyperphosphorylation in Rats with Type 2 Diabetes. *J. Alzheimers Dis.* 37 (3), 637–648. doi:10.3233/jad-130491

Yu, J. T., Xu, W., Tan, C. C., Andrieu, S., Suckling, J., Evangelou, E., et al. (2020). Evidence-based Prevention of Alzheimer's Disease: Systematic Review and Meta-Analysis of 243 Observational Prospective Studies and 153 Randomised Controlled Trials. *J. Neurol. Neurosurg. Psychiatry* 91 (11), 1201–1209. doi:10.1136/jnnp-2019-321913

Zhang, J., Lin, Y., Dai, X., Fang, W., Wu, X., and Chen, X. (2019). Metformin Treatment Improves the Spatial Memory of Aged Mice in an APOE Genotype-dependent Manner. *FASEB J.* 33 (6), 7748–7757. doi:10.1096/fj.201802718R

Conflict of Interest: The authors declare that the research was conducted in the absence of any commercial or financial relationships that could be construed as a potential conflict of interest.

Publisher's Note: All claims expressed in this article are solely those of the authors and do not necessarily represent those of their affiliated organizations, or those of the publisher, the editors and the reviewers. Any product that may be evaluated in this article, or claim that may be made by its manufacturer, is not guaranteed or endorsed by the publisher.

Copyright © 2022 Liao, Xu, Li, Ruan, Li and Liu. This is an open-access article distributed under the terms of the Creative Commons Attribution License (CC BY). The use, distribution or reproduction in other forums is permitted, provided the original author(s) and the copyright owner(s) are credited and that the original publication in this journal is cited, in accordance with accepted academic practice. No use, distribution or reproduction is permitted which does not comply with these terms.

frontiers in Aging Neuroscience

ORIGINAL RESEARCH
published: 01 February 2022
doi: 10.3389/fnagi.2021.792951

Computer-Aided Classification Framework of Parkinsonian Disorders Using ^{11}C-CFT PET Imaging

Jiahang Xu[2†], Qian Xu[1†], Shihong Liu[3†], Ling Li[1], Lei Li[2,4], Tzu-Chen Yen[5], Jianjun Wu[6], Jian Wang[6], Chuantao Zuo[1,7,8,9], Ping Wu[1,7] and Xiahai Zhuang[2*]*

[1] PET Center, Huashan Hospital, Fudan University, Shanghai, China, [2] School of Data Science, Fudan University, Shanghai, China, [3] School of Computer Science, University of Nottingham, Nottingham, United Kingdom, [4] School of Biomedical Engineering, Shanghai Jiao Tong University, Shanghai, China, [5] Nuclear Medicine and Molecular Imaging Center, Linkou Chang Gung Memorial Hospital, Chang Gung University, Taoyuan, Taiwan, [6] Department of Neurology, Huashan Hospital, Fudan University, Shanghai, China, [7] National Center for Neurological Disorders & National Clinical Research Center for Aging and Medicine, Huashan Hospital, Fudan University, Shanghai, China, [8] Human Phenome Institute, Fudan University, Shanghai, China, [9] Institute of Functional and Molecular Medical Imaging, Fudan University, Shanghai, China

OPEN ACCESS

Edited by:
Chih-Yu Hsu,
Fujian University of Technology, China

Reviewed by:
Muh-Shi Lin,
Kuang Tien General Hospital, Taiwan
Ruixue Cui,
Chinese Academy of Medical Sciences and Peking Union Medical College, China

***Correspondence:**
Ping Wu
wupingpet@fudan.edu.cn
Xiahai Zhuang
zxh@fudan.edu.cn

[†]These authors have contributed equally to this work

Specialty section:
This article was submitted to Parkinson's Disease and Aging-related Movement Disorders, a section of the journal Frontiers in Aging Neuroscience

Received: *11 October 2021*
Accepted: *27 December 2021*
Published: *01 February 2022*

Citation:
Xu J, Xu Q, Liu S, Li L, Li L, Yen T-C, Wu J, Wang J, Zuo C, Wu P and Zhuang X (2022) Computer-Aided Classification Framework of Parkinsonian Disorders Using ^{11}C-CFT PET Imaging. Front. Aging Neurosci. 13:792951. doi: 10.3389/fnagi.2021.792951

Purpose: To investigate the usefulness of a novel computer-aided classification framework for the differential diagnosis of parkinsonian disorders (PDs) based on ^{11}C-methyl-N-2β-carbomethoxy-3β-(4-fluorophenyl)-tropanel (^{11}C-CFT) positron emission tomography (PET) imaging.

Methods: Patients with different forms of PDs—including Parkinson's disease (PD), multiple system atrophy (MSA) and progressive supranuclear palsy (PSP)—underwent dopamine transporter (DAT) imaging with ^{11}C-CFT PET. A novel multistep computer-aided classification framework—consisting of magnetic resonance imaging (MRI)-assisted PET segmentation, feature extraction and prediction, and automatic subject classification—was developed. A random forest method was used to assess the diagnostic relevance of different regions to the classification process. Finally, the performance of the computer-aided classification system was tested using various training strategies involving patients with early and advanced disease stages.

Results: Accuracy values for identifying PD, MSA, and PSP were 85.0, 82.2, and 89.7%, respectively—with an overall accuracy of 80.4%. The caudate and putamen provided the highest diagnostic relevance to the proposed classification framework, whereas the contribution of midbrain was negligible. With the exception of sensitivity for diagnosing PSP, the strategy comprising both early and advanced disease stages performed better in terms of sensitivity, specificity, positive predictive value, and negative predictive value within each PDs subtype.

Conclusions: The proposed computer-aided classification framework based on ^{11}C-CFT PET imaging holds promise for improving the differential diagnosis of PDs.

Keywords: ^{11}C-CFT PET imaging, computer-aided diagnosis, Parkinson's disease, multiple system atrophy, progressive supranuclear palsy

INTRODUCTION

Parkinsonian disorders (PDs) are a heterogeneous group of neurological disorders characterized by tremor, bradykinesia, rigidity, and poor postural stability. Parkinson's disease (PD)—the most common PDs occurring in the elderly (Pringsheim et al., 2014)—should be differentiated by other atypical parkinsonian syndromes (APSs), including multiple system atrophy (MSA) and progressive supranuclear palsy (PSP) (Fahn et al., 2011). A correct differential diagnosis between PD, MSA, and PSP is paramount not only for proper treatment allocation and prognostication, but also for correct implementation of clinical trials focusing on disease-modifying drugs. Unfortunately, an accurate diagnosis remains challenging both because of a consistent overlap of signs and symptoms and the presence of atypical manifestations—especially in early disease stages (Steele et al., 1964). The key pathogenic mechanisms of PDs consist of a progressive neuronal loss in the substantia nigra of midbrain (Burns et al., 1983) and the occurrence of dopaminergic dysfunction in the striatum (Hantraye et al., 1992; Strafella et al., 2017). Although PDs were found to have different midbrain neuronal loss and striatal dopaminergic dysfunction patterns, their effect in PDs classification remains to be discussed (Martin-Bastida et al., 2017).

DAT PET imaging is clinically useful to differentiate PDs from conditions unrelated to dopaminergic dysfunction (e.g., essential tremor and drug-induced or psychogenic parkinsonism) (Benamer et al., 2000; Marshall et al., 2006; Thobois et al., 2019). However, its use in differentiation among PDs remains elusive. Knudsen et al. (2004) demonstrated that patients with PD have significantly higher striatal asymmetry than those with MSA, whereas Ilgin and coworkers (Ilgin et al., 1999) reported that PD is characterized by a more pronounced loss of DAT in the posterior putamen compared with PSP. However, studies have shown that regional analysis of DAT PET images does not allow differentiating between PD and MSA (Pirker et al., 2000;

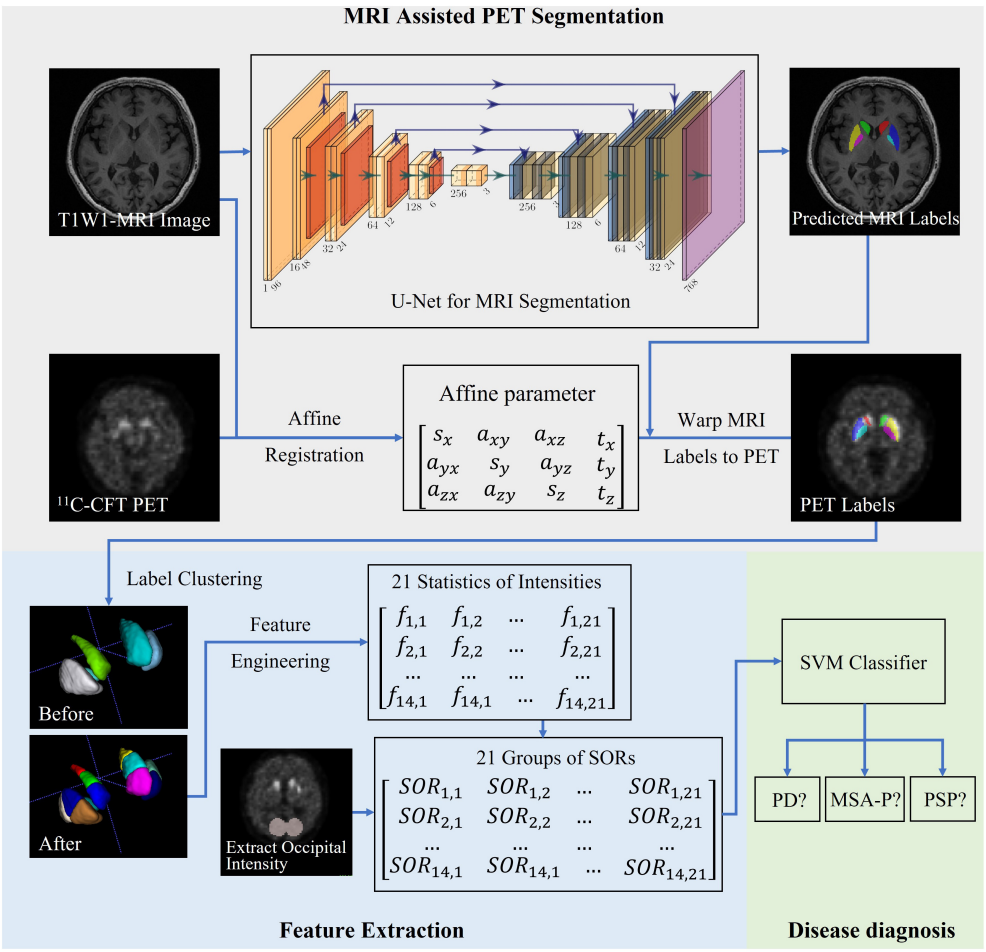

FIGURE 1 | Visual representation of the proposed computer-aided classification framework. Magnetic resonance imaging (MRI)-assisted ^{11}C-CFT PET segmentation was followed by feature extraction and prediction. The final step consisted of automatic subject classification in each of the three diagnostic groups (PD, MSA, and PSP).

Varrone et al., 2001; Perju-Dumbrava et al., 2012). Therefore, in current practice, patients considered with PDs frequently undergo two different PET protocols, i.e., DAT PET for excluding disorders unrelated to dopaminergic dysfunction and ^{18}F-FDG PET for PDs differentiation (Zhao et al., 2012), which is costly and time-consuming.

Recently, computer-aided medical diagnosis has emerged as a valuable tool to extract information from medical images in the context of early-stage PDs (Teune et al., 2014; Tripathi et al., 2016; Matthews et al., 2018; Xu et al., 2019). In this scenario, this study was undertaken to investigate the clinical utility of a novel computer-aided classification framework for PDs using ^{11}C-methyl-N-2β-carbomethoxy-3β-(4-fluorophenyl)-tropanel (^{11}C-CFT) DAT PET imaging.

MATERIALS AND METHODS

Subjects

A total of 107 patients with PDs were recruited from the Department of Neurology, Huashan Hospital, Fudan University (Shanghai, China). Another group of 22 normal controls (NC) was recruited as reference for PDs patients in the aspect of DAT binding level. All participants were screened by two experts in the field of movement disorders before PET imaging. Follow-up was continued for at least one year. The clinical diagnosis of "definite" PD was made according to the UK Brain Bank criteria (Hughes et al., 1992) and confirmed using the Movement Disorder Society clinical diagnostic criteria (Postuma et al., 2015). All of the patients with MSA and PSP conformed to the second consensus statement on the diagnosis of "probable" MSA (Gilman et al., 2008) and the consensus diagnostic criteria for "probable" PSP (NINDS-SPSP) (Litvan et al., 1996), respectively. Exclusion criteria were as follows: history of other neurological or psychiatric disorders; use of neuroleptics; and presence of structural brain lesions on MRI (i.e., masses, white matter changes, ischemia, or hemorrhage). The UPDRS motor examination (items 18–31) and the Hoehn and Yahr (H&Y) stage were determined within 2 h of PET imaging and at least 12 h after discontinuation of antiparkinsonian medications (Wu et al., 2013). The study patients were divided into patients with early-stage (ES) and advanced-stage (AS) disease (duration threshold: 24 months). Ethical approval was granted by the Institutional Review Board of the Huashan Hospital and written consent was obtained from all participants.

Data Acquisition

PET images were acquired using a Siemens Biograph 64 PET/CT scanner (Siemens, Munich, Germany) in the three-dimensional (3D) mode. A computed tomography (CT) transmission scan was initially performed for attenuation correction. A PET scan of 15 min was started 60 min after the intravenous injection of 370 MBq of ^{11}C-CFT. During scanning, patients laid comfortably in supine position in a room with dimmed lighting and low background noise (Huang et al., 2020). MRI data were acquired using the T1-weighted 3D inversion recovery spoiled gradient recalled acquisition (IR-SPGR) technique, as previously described (Bu et al., 2018). PET and MRI scans were performed within one week of each other.

TABLE 1 | General characteristics of the study patients ($n = 107$) and normal controls (NC) ($n = 22$).

	PD	MSA	PSP	NC
Disease stage, ES%	22.0%	45.9%	40.0%	–
Sex, male%	64.0%	67.6%	80.0%	77.7%
Age, years	61.54 ± 7.41	59.24 ± 7.58	65.00 ± 8.32	64.91 ± 6.91
Disease duration, years	3.53 ± 1.99	2.32 ± 1.37	2.82 ± 1.67	–
UPDRS-III	21.94 ± 9.69	30.13 ± 14.42	23.90 ± 12.87	–
Dose equivalent, mg	275.8 ± 301.0	267.5 ± 329.9	161.3 ± 196.9	–

Data are given as counts or means ± standard deviations. PD, Parkinson's disease; MSA, multiple system atrophy; PSP, progressive supranuclear palsy; ES, early-stage; UPDRS-III, Unified Parkinson's Disease Rating Scale – part III.

Diagnostic Methods

Figure 1 provides a workflow of the proposed multistep computer-aided classification framework—which consisted of MRI-assisted PET segmentation, feature extraction and prediction, and automatic subject classification. The detailed procedures have been previously described (Xu et al., 2019).

MRI-Assisted PET Segmentation and Feature Extraction

A U-net was implemented to carry out segmentation analysis of the striatum—including the bilateral caudate, putamen, pallidus and midbrain—on MRI images. Bilateral occipital areas were segmented using the ITK-SNAP software package. The U-net—which consists of an encoder-decoder network with skip connections—is based on an optimized convolutional neural network (CNN) (Ronneberger et al., 2015; Wong et al., 2018). Segmented MRI images were thoroughly aligned to the corresponding PET images by traditional registration methods using the C++ programming language, and the resulting transformation matrix was subsequently used to transform the label information of the MRI image onto the PET image (Xu et al., 2019). Based on the segmentation results, the bilateral caudate and putamen were further divided into three subregions with an equal volume (anterior, middle, and posterior) achieved by a k-means clustering algorithm in Python (Ng et al., 2006). Features were extracted by determining the volumes of tracer uptake from a total of 16 subregions. The striatal-to-occipital ratio (SOR) of the extracted features was calculated for normalization purposes.

SVM Classification Analysis

Machine learning of the extracted features and diagnostic classifications were implemented using the software machine learning library Scikit-learn 0.22.0 (https://pypi.org/project/scikit-learn). The selection of the most suitable classifier was performed by comparing the diagnostic performances with

TABLE 2 | Average SOR values and bilateral asymmetric indexes for parkinsonism groups and normal controls (NC).

					p value					
	PD	**MSA**	**PSP**	**NC**	**PD vs. MSA**	**PD vs. PSP**	**MSA vs. PSP**	**PD vs. NC**	**MSA vs. NC**	**PSP vs. NC**
SOR values										
Anterior caudate	0.90 ± 0.53	1.02 ± 0.83	0.58 ± 0.40	1.65 ± 0.65	ns	ns	ns	***	**	***
Middle caudate	0.52 ± 0.44	0.62 ± 0.59	0.25 ± 0.22	1.26 ± 0.77	ns	ns	*	***	**	***
Posterior caudate	0.25 ± 0.25	0.32 ± 0.36	0.14 ± 0.13	0.70 ± 0.55	ns	ns	ns	***	*	***
Anterior putamen	1.13 ± 0.48	1.26 ± 0.88	1.03 ± 0.37	2.25 ± 0.74	ns	ns	ns	***	***	***
Middle putamen	0.65 ± 0.34	1.06 ± 0.93	0.67 ± 0.29	1.98 ± 0.91	ns	ns	ns	***	**	***
Posterior putamen	0.46 ± 0.30	0.77 ± 0.86	0.55 ± 0.29	1.50 ± 0.88	ns	ns	ns	***	*	**
Asymmetric index										
Anterior caudate	1.06 ± 0.84	1.00 ± 0.71	0.97 ± 0.71	0.74 ± 0.66	ns	ns	ns	ns	ns	ns
Middle caudate	1.28 ± 0.90	1.50 ± 0.91	1.57 ± 0.83	0.89 ± 0.82	ns	ns	ns	ns	*	*
Posterior caudate	1.41 ± 0.72	1.78 ± 0.86	1.54 ± 0.71	1.24 ± 0.84	ns	ns	ns	ns	ns	ns
Anterior putamen	0.63 ± 0.38	0.40 ± 0.41	0.31 ± 0.22	0.25 ± 0.23	**	*	ns	***	ns	ns
Middle putamen	0.76 ± 0.50	0.45 ± 0.47	0.39 ± 0.40	0.29 ± 0.28	**	**	ns	***	ns	ns
Posterior putamen	0.67 ± 0.55	0.59 ± 0.44	0.52 ± 0.56	0.45 ± 0.36	ns	ns	ns	ns	ns	ns

*Data are given as means ± standard deviations. PD, Parkinson's disease; MSA, multiple system atrophy; PSP, progressive supranuclear palsy; ns, no significant difference; *p < 0.05, **p < 0.01, ***p < 0.001.*

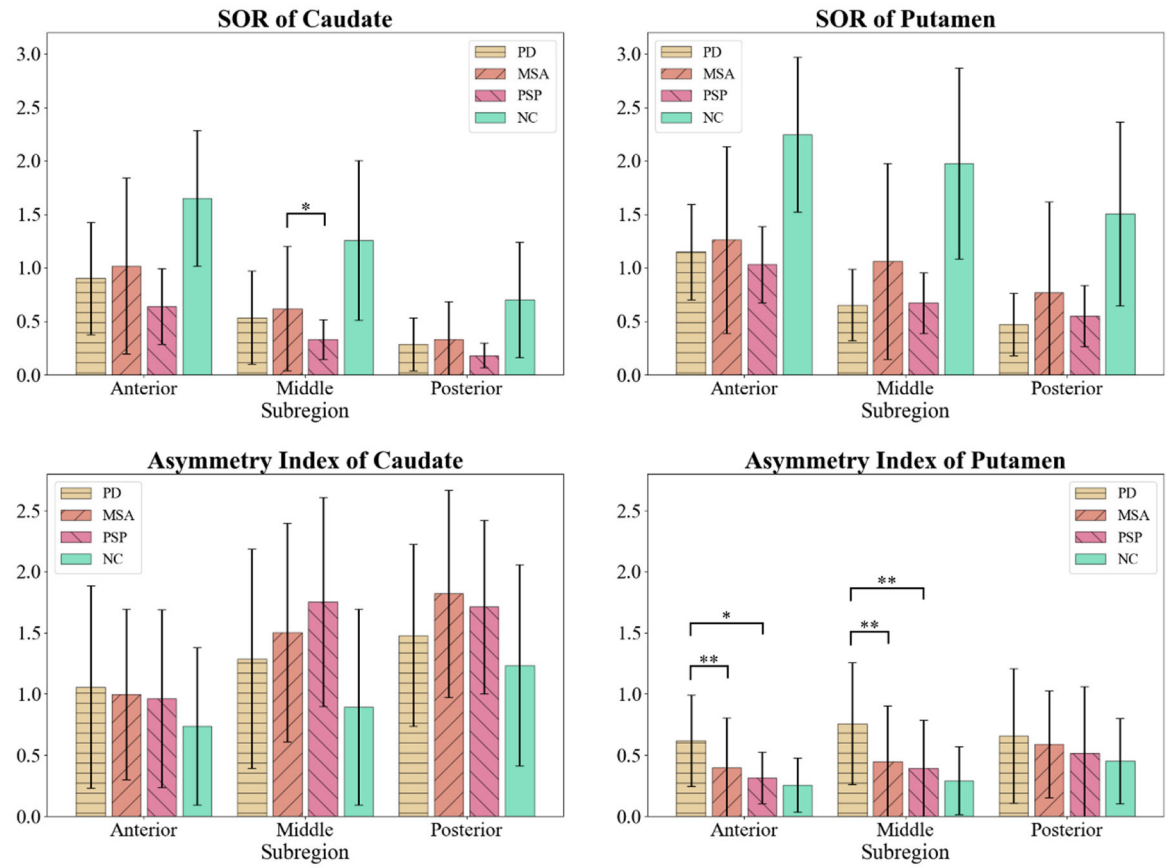

FIGURE 2 | Comparison of SOR values and bilateral asymmetric indexes among parkinsonism groups and normal controls (NC). *$p < 0.05$; **$p < 0.01$. SOR value of middle caudate was lower in PSP group than MSA group. Asymmetric indexes of anterior and middle putamen were elevated in PD group compared with all other groups.

TABLE 3 | Diagnostic performances of the proposed computer-aided classification framework for the binary classification of different parkinsonian disorders.

Classification group	Accuracy	AUC	Sensitivity	Specificity	PPV	NPV
PD vs. others	85.0%	85.0%	84.0%	86.0%	84.0%	86.0%
MSA vs. others	82.2%	80.1%	73.0%	87.1%	75.0%	85.9%
PSP vs. others	89.7%	82.1%	70.0%	94.3%	73.7%	93.2%

PD, Parkinson's disease; MSA, multiple system atrophy; PSP, progressive supranuclear palsy; AUC, area under curve; PPV, positive predictive value; NPV, negative predictive value.

TABLE 4 | Confusion matrix and diagnostic performances of the multi-class classification system of different parkinsonian disorders.

SVM classification	Diagnostic categories (SOT)			PPV/NPV
	PD	MSA	PSP	
PD	**43**	5	4	82.7%/87.3%
MSA	6	**29**	2	78.4%/88.6%
PSP	1	3	**14**	77.7%/93.3%
Sensitivity/specificity	86.0%/84.2%	78.4%/88.6%	70.0%/95.4%	

SVM, support vector machine; SOT, standard of truth; PD, Parkinson's disease; MSA, multiple system atrophy; PSP, progressive supranuclear palsy; PPV, positive predictive value; NPV, negative predictive value. The number of true positive subjects are marked in bold.

various algorithms on the specified dataset—including SVM (Haller et al., 2012; Long et al., 2012), logistic regression (Tripathi et al., 2016) and random forest algorithm (Gray et al., 2013). Owing to its capacity to handle high-dimensional feature spaces with high efficiency, a linear SVM classifier with squared hinge loss was selected for performing the classification task. All of the parameters of the SVM solver were optimized for subsequent experiments.

Training Strategies for Early-Stage Patients

The ES and AS groups consisted of 36 and 71 patients, respectively. The classification performances in different subsetting of ES and AS patients was tested using four strategies, as follows: (1) 71 AS + 35 ES/1 ES (training on both the ES and AS groups, and test on the ES group with a leave-one-out cross-validation strategy); (2) 35 ES/1 ES (training and testing on the ES group with a leave-one-out cross-validation strategy); (3) 71 AS/36 ES (training on the AS group and testing on the ES group); and (4) 36 AS/36 ES (training and testing on the AS group, with the size of the training set made equal to the ES group).

Statistical Analysis

We assessed demographic and clinical data with ANOVA, Kruskal-Wallis, and χ^2 tests, as appropriate. The accuracy, sensitivity, specificity, positive predictive value (PPV), and negative predictive value (NPV) for the binary and multiclass classification of each PDs was determined. Areas under the receiver operating characteristic (ROC) curve (AUCs) were calculated to assess the diagnostic accuracy. The potential added value of the inclusion of midbrain for the purpose of multiclass classification was assessed using the McNemar's test. All above analyses were carried out in GraphPad Prism, version 8.0.1 (Graph Pad Inc., San Diego, CA, USA). Statistical significance was determined by a two-tailed p value < 0.05. The relative contribution of each striatal subregion to the classification process was determined using the random forest method based on Python. and visualized with the BrainNet Viewer (Xia et al., 2013).

RESULTS

Subjects

Of the 107 participants, 50, 37, and 20 were clinically diagnosed with PD, MSA, and PSP, respectively. Demographic and clinical characteristics of subjects and normal controls are shown in **Table 1.**

Detailed DAT distribution of patient groups are shown in **Table 2**; **Figure 2**. Average SOR values of both sides of subregions, and asymmetric indexes [(SOR of the higher side) - (SOR of the lower side)] / (average SOR of both sides) were calculated out and compared. Compared with NC group, patient groups revealed a significant decline of SOR values. However, almost no significant difference was found among parkinsonism groups. Of note, asymmetric indexes of anterior and middle putamen were significantly elevated in PD group compared with all the other groups. At the same time, MSA and PSP group performed higher asymmetric indexes in middle caudate than NC subjects.

Binary and Multiclass Classification of Parkinsonian Disorders

The goal of binary classification was to discriminate between one subtype of PDs and the remaining two. The accuracy values of this classification for distinguishing PD, MSA, and PSP from the other two diagnostic groups were 85.0, 82.2, and 89.7% respectively. The AUCs from ROC curve analysis were 85.0, 80.1, and 82.1% respectively. The sensitivity, specificity, PPV, and NPV for the diagnosis are shown in **Table 3**.

The overall accuracy of multiclass classification—defined as the proportion of instances being correctly predicted across all study participants—was 80.4%. The sensitivity and specificity of multiclass classification are shown in **Table 4**. The NPV was similar for the three diagnostic categories (∼90%), whereas the PPV was higher for PD (**Table 3).**

Diagnostic Results According to Different Training Strategies

We next investigated the classification accuracies for ES patients using the above-mentioned four different training strategies. Strategy 1 resulted in the highest accuracy (77.8%), which was

TABLE 5 | Diagnostic performances of the four different training strategies.

Strategy (training/testing)	Accuracy	Error count (errors/total)	Diagnostic group	Sensitivity	Specificity	PPV	NPV
1 71 AS+ 35 ES/1 ES	**77.8%**	8/36	PD	**90.9%**	80.0%	66.7%	**95.2%**
			MSA	**88.2%**	**84.2%**	**83.3%**	**88.9%**
			PSP	37.5%	**100.0%**	**100.0%**	**84.9%**
2 35 ES/1 ES	69.4%	11/36	PD	63.6%	**88.0%**	**70.0%**	84.6%
			MSA	76.5%	79.0%	76.5%	79.0%
			PSP	**62.5%**	85.7%	55.6%	88.9%
3 71 AS/36 ES	58.3%	15/36	PD	54.5%	76.0%	50.0%	79.2%
			MSA	82.4%	57.9%	63.6%	78.6%
			PSP	37.5%	96.4%	50.0%	79.4%
4 35 AS/36 ES	55.6%	16/36	PD	54.6%	76.0%	50.0%	79.2%
			MSA	70.6%	57.9%	60.0%	68.7%
			PSP	25.0%	92.9%	50.0%	81.3%

PPV, positive predictive value; NPV, negative predictive value; AS, advanced stage; ES, early stage; PD, Parkinson's disease; MSA, multiple system atrophy; PSP, progressive supranuclear palsy. The strategy column reports different combinations of training subjects while maintaining test subjects constant. Best performing values are marked in bold.

TABLE 6 | Relative contribution of different regions to the computer-aided classification framework.

Region	Contribution	Region	Contribution
Anterior caudate (R)	0.113	Anterior caudate (L)	0.072
Middle caudate (R)	0.099	Posterior caudate (R)	0.067
Middle putamen (R)	0.092	Middle caudate (L)	0.064
Posterior caudate (L)	0.077	Pallidum (L)	0.054
Middle putamen (L)	0.076	Anterior putamen (L)	0.053
Posterior putamen (R)	0.075	Anterior putamen (R)	0.048
Posterior putamen (L)	0.072	Pallidum (R)	0.038

R, right; L, left. Diagnostic characteristics were not adjusted. The sum of all relative contribution values is 1.

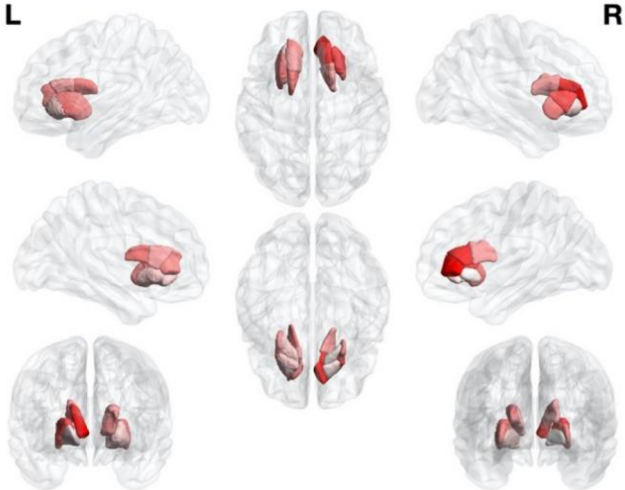

FIGURE 3 | Relative contribution of different components of the striatum to the proposed computer-aided classification framework. Intensity of colors reflects the magnitude of contribution.

found to decrease in a stepwise fashion from strategy 1 to strategy 4 (**Table 5**). The sensitivity, specificity, PPV and NPV obtained with the application of strategy 1 were 90.9, 80.0, 66.7, and 95.2%, respectively, for the diagnosis of PD; 88.2, 84.2, 83.3, and 88.9%, respectively, for the diagnosis of MSA; and 37.5, 100.0, 100.0, and 84.9%, respectively, for the diagnosis of PSP.

Relative Contribution of Subregional Features to the Diagnostic Classification

The caudate contributed more prominently (49.2%) than the putamen (41.6%) and pallidum (9.2%) to the classification process. Specifically, anterior caudate (18.5%), middle putamen (16.8%), and middle caudate (16.3%) contributed more than posterior putamen (14.7%), posterior caudate (14.4%), anterior putamen (10.1%), and pallidum (9.2%). The relative contributions of different striatal subregions to the diagnostic classification are summarized in **Table 6** and visualized with the BrainNet Viewer (**Figure 3**) and. The addition of the midbrain resulted in a slight improvement in terms of accuracy (1.8%), without a significant effect ($p = 0.683$) on multiclass classification. Training based on midbrain alone resulted in a poor diagnostic accuracy (48.6%) (**Table 7**).

DISCUSSION

In the current study, we demonstrate the feasibility of a novel computer-aided classification framework for PDs based on ^{11}C-CFT PET imaging. Specifically, the accuracy values of the proposed strategy for identifying PD, MSA, and PSP were 85.0, 82.2, and 89.7%, respectively—with an overall accuracy in the context of PDs of 80.4%. The caudate and putamen had the highest diagnostic relevance within the proposed classification strategy, whereas the contribution of the midbrain was negligible. If independently validated, our results may set the stage to

TABLE 7 | Accuracy of different combinations of regions of interest.

Strategy	Midbrain + striatum	Midbrain	Striatum	*p* value
Accuracy	82.2%	48.6%	80.4%	0.683

(1) Midbrain + striatum: the classifier was trained using features extracted from both midbrain and striatum; (2) Midbrain: the classifier was trained using features extracted only from midbrain; (3) Striatum only: the classifier was trained using features extracted only from striatum. p value refers to the difference between the analysis with the extracted features from midbrain + striatum and striatum.

the application of the proposed computer-aided classification approach for distinguishing among PD, MSA, and PSP.

While PD is generally characterized by a relatively preserved DAT binding in the caudate during early disease stages followed by a rostrocaudal progression in dopaminergic denervation, diffuse striatal impairment is typical of both MSA and PSP (Georgiopoulos et al., 2015). A recent meta-analysis provided a comprehensive comparison of striatal presynaptic dopaminergic function across the spectrum of PDs (Kaasinen et al., 2019). Compared with PD and MSA, PSP is characterized by the most pronounced loss of DAT function at both caudate and putamen; in addition, caudate DAT binding is lower in patients with MSA than in those with PD (Kaasinen et al., 2019). Other studies have shown that different quantitative indices of DAT PET imaging—including the specific binding ratio, the putamen-to-caudate ratio, and the asymmetry index—are capable of discriminating with high accuracy between PDs and non-synucleinopathy diseases (Georgiopoulos et al., 2015; Iwabuchi et al., 2019). However, the clinical utility of the indexes in distinguishing between different PDs remains questionable (Eerola et al., 2005; Georgiopoulos et al., 2015; Buchert et al., 2019). In our study, subregion-to-subregion comparison showed rare difference among PDs groups, while asymmetric indexes of anterior and middle putamen could distinguish between PD patients and the others on group level.

Recently, the application of a SVM diagnostic framework to ^{123}I-FP-CIT PET data by Nicastro et al. (2019) led to an accuracy for binary classification of PDs ranging between 62.9 and 83.7%. The accuracy values for binary and multiclass classification in this current study were as high as 82.2–89.7 and 80.4%, respectively, which were even in accordance with those reported in recent studies based on ^{18}F-FDG PET imaging (**Supplementary Table 1**). Accordingly, additional features which had been detected by deep learning were integrated to achieve the relative high accuracy in the classification task.

In an effort to identify the most powerful training strategy, we tested a total of four different approaches in different combinations of patients with ES and AS disease—with the highest accuracy (77.8%) being observed for the combined ES+AS group. Notably, the accuracy in patients with AS was lower (55.6–58.3%) than that observed in patients with ES (69.4%). With the exception of sensitivity for the diagnosis of PSP, the ES+AS strategy performed better in terms of sensitivity, specificity, PPV, and NPV for each PDs subtype. These results suggest that DAT PET imaging of patients with AS markedly improves the classification results of patients with ES, while the opposite does not occur. We therefore believe that future replication efforts on the clinical utility of our computer-aided classification system should include both patients with ES and AS.

Another interesting finding from our study is that the greatest contribution to the classification process was attributable to the caudate and putamen, whereas the role of pallidum was negligible. Amongst the intranuclear subregions, the anterior caudate and the middle putamen contributed more prominently to the diagnostic classification. Notably, patients with idiopathic PD are characterized by an uneven pattern of intrastriatal dopaminergic loss (Kish et al., 1988) and differences in terms of intrastriatal dopaminergic loss may exist between different PDs (Ilgin et al., 1999; Knudsen et al., 2004). However, the addition of midbrain to our computer-aided classification system did not significantly improve accuracy ($p = 0.683$). These results may stem from a similar extent of midbrain dopaminergic neuron loss across different PDs, although published data in the field remain inconclusive (Hirsch et al., 1988; Fearnley and Lees, 1991; Martin-Bastida et al., 2017). An alternative explanation is that our computer-aided classification framework is unable to capture existing differences with respect to midbrain dopaminergic neuron loss, ultimately making their diagnostic contribution for distinguishing between different PDs not significant.

The present study has several limitations that merit comment. Firstly, the sample size is relatively small and validation studies on the data with larger sample size and from multiple centers are required. Secondly, the transparency of the whole pipeline could be compromised as a tradeoff of the accuracy when we extracted features for semantic segmentation via deep neural networks (Adadi and Berrada, 2018). The proposed pipeline should be further optimized to be more user-friendly and achieve better classification performance.

In conclusion, we described a user-friendly, semi-automatic computer-aided classification framework for PDs based on ^{11}C-CFT PET imaging. The proposed approach is capable of extracting subtle image information and holds promise to improve the differential diagnosis of PD, MSA, and PSP in both research and clinical settings. However, replication in independent samples is paramount for ensuring external validity of our data.

DATA AVAILABILITY STATEMENT

The original contributions presented in the study are included in the article/**Supplementary Material**, further inquiries can be directed to the corresponding author/s.

ETHICS STATEMENT

The studies involving human participants were reviewed and approved by Institutional Review Board at Huashan Hospital. The patients/participants provided their written informed consent to participate in this study.

AUTHOR CONTRIBUTIONS

XZ and PW: conception and design. JWu, JWa, PW, CZ, QX, and LiL: data acquisition. JX, SL, XZ, LeL, T-CY, QX, CZ, and PW: data analysis and interpretation. JX, SL, and QX: drafting the manuscript. PW, XZ, and CZ: review and critique. All authors contributed to the article and approved the submitted version.

FUNDING

The work was supported by grants from the National Natural Science Foundation of China (61971142, 62111530195, 62011540404, 81771483, 81671239, 81971641, and 81361120393), the Research Project of Shanghai Health Commission (2020YJZX0111), the Clinical Research Plan of SHDC (SHDC2020CR1038B), the Shanghai Municipal Science and Technology Major Project (2017SHZDZX01), Youth Medical Talents-Medical Imaging Practitioner Program funded by Shanghai Municipal Health Commission and Shanghai Medical and Health Development Foundation [SHWRS (2020)_087], and the Fujian Province Joint Funds for the Innovation of Science and Technology (2019Y9070).

SUPPLEMENTARY MATERIAL

The Supplementary Material for this article can be found online at: https://www.frontiersin.org/articles/10.3389/fnagi.2021.792951/full#supplementary-material

REFERENCES

Adadi, A., and Berrada, M. (2018). Peeking inside the black-box: a survey on explainable artificial intelligence (xai). *IEEE Access* 6, 52138–52160. doi: 10.1109/ACCESS.2018.2870052

Benamer, H. T., Patterson, J., Grosset, D. G., Booij, J., De Bruin, K., Van Royen, E., et al. (2000). Accurate differentiation of parkinsonism and essential tremor using visual assessment of [123I]-FP-CIT SPECT imaging: the [123I]-FP-CIT study group. *Mov. Disord.* 15, 503–510. doi: 10.1002/1531-8257(200005)15:3<503::AID-MDS1013>3.0.CO;2-V

Bu, L.-L., Liu, F.-T., Jiang, C.-F., Guo, S.-S., Yu, H., Zuo, C.-T., et al. (2018). Patterns of dopamine transporter imaging in subtypes of multiple system atrophy. *Acta Neurol. Scand.* 138, 170–176. doi: 10.1111/ane.12932

Buchert, R., Buhmann, C., Apostolova, I., Meyer, P. T., and Gallinat, J. (2019). Nuclear imaging in the diagnosis of clinically uncertain parkinsonian syndromes. *Deutsches Ärzteblatt Int.* 116:747. doi: 10.3238/arztebl.2019.0747

Burns, R. S., Chiueh, C. C., Markey, S. P., Ebert, M. H., Jacobowitz, D. M., and Kopin, I. J. (1983). A primate model of parkinsonism: selective destruction of dopaminergic neurons in the pars compacta of the substantia nigra by N-methyl-4-phenyl-1, 2, 3, 6-tetrahydropyridine. *Proc. Natl. Acad. Sci.* 80, 4546–4550. doi: 10.1073/pnas.80.14.4546

Eerola, J., Tienari, P. J., Kaakkola, S., Nikkinen, P., and Launes, J. (2005). How useful is [123I]β-CIT SPECT in clinical practice? *J. Neurol. Neurosurg. Psychiatry* 76, 1211–1216. doi: 10.1136/jnnp.2004.045237

Fahn, S., Jankovic, J., and Hallett, M. (2011). *Chapter 4 – Parkinsonism: Clinical Features and Differential Diagnosis. Principles and Practice of Movement Disorder.* Amsterdam: Elsevier. 66–92. doi: 10.1016/B978-1-4377-2369-4.00004-4

Fearnley, J. M., and Lees, A. J. (1991). Ageing and Parkinson's disease: substantia nigra regional selectivity. *Brain* 114, 2283–2301. doi: 10.1093/brain/114.5.2283

Georgiopoulos, C., Davidsson, A., Engström, M., Larsson, E.-M., Zachrisson, H., and Dizdar, N. (2015). The diagnostic value of dopamine transporter imaging and olfactory testing in patients with parkinsonian syndromes. *J. Neurol.* 262, 2154–2163. doi: 10.1007/s00415-015-7830-4

Gilman, S., Wenning, G., Low, P., a., Brooks, D., Mathias, C., et al. (2008). Second consensus statement on the diagnosis of multiple system atrophy. *Neurology* 71, 670–676. doi: 10.1212/01.wnl.0000324625.00404.15

Gray, K. R., Aljabar, P., Heckemann, R. A., Hammers, A., Rueckert, D., Initiative, A. D. N., et al. (2013). Random forest-based similarity measures for multi-modal classification of Alzheimer's disease. *NeuroImage* 65:167–175. doi: 10.1016/j.neuroimage.2012.09.065

Haller, S., Badoud, S., Nguyen, D., Garibotto, V., Lovblad, K., and Burkhard, P. (2012). Individual detection of patients with Parkinson's disease using support vector machine analysis of diffusion tensor imaging data: initial results. *Am. J. Neuroradiol.* 33, 2123–2128. doi: 10.3174/ajnr.A3126

Hantraye, P., Brownell, A., Elmaleh, D., Spealman, R., Wüllner, U., Brownell, G., et al. (1992). Dopamine fiber detection by [11C]-CFT and PET in a primate model of parkinsonism. *Neuroreport* 3, 265–268. doi: 10.1097/00001756-199203000-00013

Hirsch, E., Graybiel, A. M., and Agid, Y. A. (1988). Melanized dopaminergic neurons are differentially susceptible to degeneration in Parkinson's disease. *Nature* 334, 345–348. doi: 10.1038/334345a0

Huang, Z., Jiang, C., Li, L., Xu, Q., Ge, J., Li, M., et al. (2020). Correlations between dopaminergic dysfunction and abnormal metabolic network activity in rem sleep behavior disorder. *J. Cereb. Blood Flow Metab.* 40, 552–562. doi: 10.1177/0271678X19828916

Hughes, A. J., Daniel, S. E., Kilford, L., and Lees, A. J. (1992). Accuracy of clinical diagnosis of idiopathic Parkinson's disease: a clinico-pathological study of 100 cases. *J. Neurol. Neurosurg. Psychiatry* 55, 181–184. doi: 10.1136/jnnp.55.3.181

Ilgin, N., Zubieta, J., Reich, S., Dannals, R., Ravert, H., and Frost, J. (1999). PET imaging of the dopamine transporter in progressive supranuclear palsy and Parkinson's disease. *Neurology* 52, 1221–1221. doi: 10.1212/WNL.52.6.1221

Iwabuchi, Y., Nakahara, T., Kameyama, M., Yamada, Y., Hashimoto, M., Matsusaka, Y., et al. (2019). Impact of a combination of quantitative indices representing uptake intensity, shape, and asymmetry in dat spect using machine learning: comparison of different volume of interest settings. *EJNMMI Res.* 9, 1–8. doi: 10.1186/s13550-019-0477-x

Kaasinen, V., Kankare, T., Joutsa, J., and Vahlberg, T. (2019). Presynaptic striatal dopaminergic function in atypical parkinsonism: a meta analysis of imaging studies. *J. Nuclear Med.* 60, 1757–1763. doi: 10.2967/jnumed.119.227140

Kish, S. J., Shannak, K., and Hornykiewicz, O. (1988). Uneven pattern of dopamine loss in the striatum of patients with idiopathic Parkinson's disease. *N. Engl. J. Med.* 318, 876–880. doi: 10.1056/NEJM198804073181402

Knudsen, G., Karlsborg, M., Thomsen, G., Krabbe, K., Regeur, L., Nygaard, T., et al. (2004). Imaging of dopamine transporters and d 2 receptors in patients with parkinson's disease and multiple system atrophy. *Eur. J. Nucl. Med. Mol. Imaging* 31, 1631–1638. doi: 10.1007/s00259-004-1578-x

Litvan, I., Agid, Y., Calne, D., Campbell, G., Dubois, B., Duvoisin, R., et al. (1996). Clinical research criteria for the diagnosis of progressive supranuclear palsy (steele-richardson-olszewski syndrome): report of the ninds-spsp international workshop. *Neurology* 47:1–9. doi: 10.1212/WNL.47.1.1

Long, D., Wang, J., Xuan, M., Gu, Q., Xu, X., Kong, D., et al. (2012). Automatic classification of early Parkinson's disease with multi-modal MR imaging. *PLoS ONE* 7:e47714. doi: 10.1371/journal.pone.0047714

Marshall, V. L., Patterson, J., Hadley, D. M., Grosset, K. A., and Grosset, D. G. (2006). Two-year follow-up in 150 consecutive cases with normal dopamine transporter imaging. *Nuclear Med. Commun.* 27, 933–937. doi: 10.1097/01.mnm.0000243374.11260.5b

Martin-Bastida, A., Pietracupa, S., and Piccini, P. (2017). Neuromelanin in parkinsonian disorders: an update. *Int. J. Neurosci.* 127, 1116–1123. doi: 10.1080/00207454.2017.1325883

Matthews, D. C., Lerman, H., Lukic, A., Andrews, R. D., Mirelman, A., Wernick, M. N., et al. (2018). FDG PET parkinson's disease-related pattern as a biomarker for clinical trials in early stage disease. *NeuroImage* 20, 572–579. doi: 10.1016/j.nicl.2018.08.006

Ng, H., Ong, S., Foong, K., Goh, P.-S., and Nowinski, W. (2006). "Medical image segmentation using k-means clustering and improved watershed algorithm," in *2006 IEEE Southwest Symposium on Image Analysis and Interpretation* (Denver, CO). doi: 10.1109/SSIAI.2006.1633722

Nicastro, N., Wegrzyk, J., Preti, M. G., Fleury, V., Van de Ville, D., Garibotto, V., et al. (2019). Classification of degenerative parkinsonism subtypes by support-vector-machine analysis and striatal 123I-FP-CIT indices. *J. Neurol.* 266, 1771–1781. doi: 10.1007/s00415-019-09330-z

Perju-Dumbrava, L. D., Kovacs, G. G., Pirker, S., Jellinger, K., Hoffmann, M., Asenbaum, S., et al. (2012). Dopamine transporter imaging in autopsy-confirmed Parkinson's disease and multiple system atrophy. *Mov. Disor.* 27, 65–71. doi: 10.1002/mds.24000

Pirker, W., Asenbaum, S., Bencsits, G., Prayer, D., Gerschlager, W., Deecke, L., et al. (2000). [123I]β-CIT SPECT in multiple system atrophy, progressive supranuclear palsy, and corticobasal degeneration. *Mov. Disord.* 15, 1158–1167. doi: 10.1002/1531-8257(200011)15:6<1158::AID-MDS1015>3.0.CO;2-0

Postuma, R. B., Berg, D., Stern, M., Poewe, W., Olanow, C. W., Oertel, W., et al. (2015). MDS clinical diagnostic criteria for Parkinson's disease. *Mov. Disord.* 30, 1591–1601. doi: 10.1002/mds.26424

Pringsheim, T., Jette, N., Frolkis, A., and Steeves, T. D. (2014). The prevalence of Parkinson's disease: a systematic review and meta-analysis. *Mov. Disord.* 29, 1583–1590. doi: 10.1002/mds.25945

Ronneberger, O., Fischer, P., and Brox, T. (2015). U-net: Convolutional networks for biomedical image segmentation, in *International Conference on Medical Image Computing and Computer-Assisted Intervention* (Munich). doi: 10.1007/978-3-319-24574-4_28

Steele, J. C., Richardson, J. C., and Olszewski, J. (1964). Progressive supranuclear palsy: a heterogeneous degeneration involving the brain stem, basal ganglia and cerebellum with vertical gaze and pseudobulbar palsy, nuchal dystonia and dementia. *Arch. Neurol.* 10, 333–359. doi: 10.1001/archneur.1964.00460160003001

Strafella, A. P., Bohnen, N. I., Perlmutter, J. S., Eidelberg, D., Pavese, N., Van Eimeren, T., et al. (2017). Molecular imaging to track Parkinson's disease and atypical parkinsonisms: new imaging frontiers. *Mov. Disord.* 32, 181–192. doi: 10.1002/mds.26907

Teune, L. K., Renken, R. J., de Jong, B. M., Willemsen, A. T., van Osch, M. J., Roerdink, J. B., et al. (2014). Parkinson's disease-related perfusion and glucose metabolic brain patterns identified with PCASL-MRI and FDG-PET imaging. *NeuroImage* 5, 240–244. doi: 10.1016/j.nicl.2014.06.007

Thobois S., Prange S., Scheiber C., and Broussolle E. (2019). What a neurologist should know about PET and SPECT functional imaging for parkinsonism: A practical perspective. *Parkinsonism Relat Disord.* 59:93–100. doi: 10.1016/j.parkreldis.2018.08.016

Tripathi, M., Tang, C. C., Feigin, A., De Lucia, I., Nazem, A., Dhawan, V., et al. (2016). Automated differential diagnosis of early parkinsonism using metabolic brain networks: a validation study. *J. Nuclear Med.* 57, 60–66. doi: 10.2967/jnumed.115.161992

Varrone, A., Marek, K. L., Jennings, D., Innis, R. B., and Seibyl, J. P. (2001). [123I]β-CIT SPECT imaging demonstrates reduced density of striatal dopamine transporters in Parkinson's disease and multiple system atrophy. *Mov. Disord.* 16, 1023–1032. doi: 10.1002/mds.1256

Wong, K. C., Moradi, M., Tang, H., and Syeda-Mahmood, T. (2018). "3D segmentation with exponential logarithmic loss for highly unbalanced object sizes," in *International Conference on Medical Image Computing and Computer-Assisted Intervention* (Cham). doi: 10.1007/978-3-030-00931-1_70

Wu, P., Wang, J., Peng, S., Ma, Y., Zhang, H., Guan, Y., et al. (2013). Metabolic brain network in the chinese patients with Parkinson's disease based on 18F-FDG PET imaging. *Parkinsonism Relat. Disord.* 19, 622–627. doi: 10.1016/j.parkreldis.2013.02.013

Xia, M., Wang, J., and He, Y. (2013). Brainnet viewer: a network visualization tool for human brain connectomics. *PLoS ONE* 8:e68910. doi: 10.1371/journal.pone.0068910

Xu, J., Jiao, F., Huang, Y., Luo, X., Xu, Q., Li, L., et al. (2019). A fully automatic framework for Parkinson's disease diagnosis by multi-modality images. *Front. Neurosci.* 13:874. doi: 10.3389/fnins.2019.00874

Zhao, P., Zhang, B., and Gao, S. (2012). 18 [f]-fdg PET study on the idiopathic Parkinson's disease from several parkinsonian-plus syndromes. *Parkinsonism Relat. Disord.* 18, S60–S62. doi: 10.1016/S1353-8020(11)70020-7

Conflict of Interest: The authors declare that the research was conducted in the absence of any commercial or financial relationships that could be construed as a potential conflict of interest.

Publisher's Note: All claims expressed in this article are solely those of the authors and do not necessarily represent those of their affiliated organizations, or those of the publisher, the editors and the reviewers. Any product that may be evaluated in this article, or claim that may be made by its manufacturer, is not guaranteed or endorsed by the publisher.

Copyright © 2022 Xu, Xu, Liu, Li, Li, Yen, Wu, Wang, Zuo, Wu and Zhuang. This is an open-access article distributed under the terms of the Creative Commons Attribution License (CC BY). The use, distribution or reproduction in other forums is permitted, provided the original author(s) and the copyright owner(s) are credited and that the original publication in this journal is cited, in accordance with accepted academic practice. No use, distribution or reproduction is permitted which does not comply with these terms.

frontiers in Aging Neuroscience

ORIGINAL RESEARCH
published: 08 February 2022
doi: 10.3389/fnagi.2022.783773

Stereopsis and Eye Movement Abnormalities in Parkinson's Disease and Their Clinical Implications

Fang Ba[1], Tina T. Sang[2], Wenjing He[3], Jaleh Fatehi[4], Emanuel Mostofi[5] and Bin Zheng[3]*

[1] Division of Neurology, Department of Medicine, University of Alberta, Edmonton, AB, Canada, [2] Faculty of Science, University of Alberta, Edmonton, AB, Canada, [3] Surgical Simulation Research Lab, Department of Surgery, University of Alberta, Edmonton, AB, Canada, [4] Division of Neurology, Department of Medicine, University of Alberta, Edmonton, AB, Canada, [5] Faculty of Medicine and Dentistry, University of Alberta, Edmonton, AB, Canada

Background: Parkinson's disease (PD) is not exclusively a motor disorder. Among non-motor features, patients with PD possess sensory visual dysfunctions. Depth perception and oculomotor deficits can significantly impact patients' motor performance. Stereopsis and eye behavioral study using 3D stimuli may help determine their implications in disease status.

Objective: The objective of this study is to investigate stereopsis and eye movement abnormalities in PD with reliable tools and their correlation with indicators of PD severity. We hypothesize that patients with PD exhibit different eye behaviors and that these differences may correlate to the severity of motor symptoms and cognitive status.

Methods: Control and PD participants were first evaluated for visual acuity, visual field, contrast acuity, and stereo perception with 2D and Titmus stereotests, followed by the assessment with a 3D active shutter system. Eye movement behaviors were assessed by a Tobii X2-60 eye tracker.

Results: Screening visual tests did not reveal any differences between the PD and control groups. With the 3D active shutter system, the PD group demonstrated significantly worse stereopsis. The preserved cognitive function was correlated to a more intact stereo function. Patients with PD had longer visual response times, with a higher number of fixations and bigger saccade amplitude, suggesting fixation stabilization difficulties. Such changes showed a positive correlation with the severity of motor symptoms and a negative correlation with normal cognitive status.

Conclusion: We assessed stereopsis with a 3D active shutter system and oculomotor behaviors with the Tobii eye tracker. Patients with PD exhibit poorer stereopsis and impaired oculomotor behaviors during response time. These deficits were correlated with PD motor and cognitive status. The visual parameters may potentially serve as the clinical biomarkers for PD.

Keywords: Parkinson's disease, stereopsis, extraocular movements, biomarker, cognition

OPEN ACCESS

Edited by:
Jiehui Jiang,
Shanghai University, China

Reviewed by:
Luming Li,
Tsinghua University, China
Juanjuan Jiang,
Shanghai University, China

****Correspondence:***
Fang Ba
fb@ualberta.ca

Specialty section:
This article was submitted to Parkinson's Disease and Aging-related Movement Disorders, a section of the journal Frontiers in Aging Neuroscience

Received: *26 September 2021*
Accepted: *10 January 2022*
Published: *08 February 2022*

Citation:
Ba F, Sang TT, He W, Fatehi J, Mostofi E and Zheng B (2022) Stereopsis and Eye Movement Abnormalities in Parkinson's Disease and Their Clinical Implications. Front. Aging Neurosci. 14:783773. doi: 10.3389/fnagi.2022.783773

INTRODUCTION

Along with the cardinal motor symptoms of Parkinson's disease (PD), patients with PD possess sensory visual and oculomotor dysfunctions. Visual signs and symptoms of PD may include defects in extraocular movement (Pinkhardt and Kassubek, 2011), pupillary function (Micieli et al., 1991; Wang et al., 2016), and higher-level complex visual tasks (Armstrong, 2017). Among these dysfunctions, impairment in depth perception–namely the ability to judge distance, the shape of an object, and the speed of movements–can significantly impact patients' motor performance when impaired. It was reported that patients with PD yield more errors when making 3D judgments (Trick et al., 1994; Maschke et al., 2006; Kim et al., 2011). Patients with PD were notably impaired in spatial orientation (left–right and front–back), immediate visual-spatial recognition memory for mirror image patterns, 3D constructional skills, visual-spatial attention, and 3D mental rotation (Natsopoulos et al., 1993). Multiple factors in the central and peripheral visual pathway may work congruently in contributing to the pathology of depth perception in PD.

Difficulties in navigation due to stereopsis impairments can make patients with PD more susceptible to falls and injuries (Armstrong, 2011, 2017) and might contribute to changes in walking speed (Young et al., 2010). It has been noted that patients with PD with abnormal stereopsis performed significantly worse in motor function tests than those with normal stereopsis (Kim et al., 2011; Sun et al., 2014). The Hoehn and Yahr (H&Y) stages and Unified PD Rating Scale motor scores (UPDRS-III) were higher in PD patients with abnormal stereopsis than those with normal stereopsis (Sun et al., 2014), suggesting a coupling between stereopsis and motor performance in PD, or the association of depth perception difficulties with the progression of PD. In addition, patients with PD with freezing of gait (FOG) had worse stereopsis than those without FOG (Alhassan et al., 2020). However, there is limited knowledge on how depth perception in patients with PD changes as the disease progresses. Some evidence has also indicated that patients with drug naïve PD showed decreased stereopsis, raising the question that this specific visual change might be an early disease indicator (Kim et al., 2011).

The motor symptoms of PD can be treated using dopamine replacement therapy or surgical interventions, i.e., deep brain stimulation. Strong literature is still lacking for medical and surgical treatment of non-motor symptoms of PD, including visual sensory impairments. Sometimes, PD treatments can also cause visual side effects (Armstrong, 2011) notably visual hallucinations. On the other hand, it has been observed that subthalamic deep brain stimulation can improve eye movement abnormality, namely smooth pursuit and saccade (Fawcett et al., 2010; Yugeta et al., 2010; Nilsson et al., 2013; Antoniades et al., 2014). Taken together, stereopsis and eye movement behaviors can be further studied to determine their clinical implications in disease status.

To date, there is scarce scientific research on the stereoscopic functions in patients with PD due to limitations in methodologies and the lack of prospective observations. The widely used Titmus Stereotest and Random-Dot Stereogram showed some evidence of abnormal stereopsis in a group of older PD patients (68.6 ± 8.98 years) with a poor cognitive function (Kim et al., 2011). However, one should note that these stereotests assess binocular disparity without assessing the monocular function. Although the stereopsis is the perception of depth created by binocular cues, with horizontal disparities between the two retinal images being the primary cue for depth, any domain of the monocular peripheral pathways, such as acuity, color, contrast, relative size, texture gradients, and motion parallax, may impact 3D vision during abnormal. Without confirming a relative intact afferent monocular function, stereoscopic assessment is unreliable.

Several studies compared the validity, reliability, and effectiveness of different stereo tests, i.e., Random-Dot Stereogram, Titmus, Frisby, Lang II, and the conclusion was varied (Garmham and Sloper, 2006; Heron and Lages, 2012; Westheimer, 2013; Momeni-Moghadam et al., 2021). As a screening test, random-dot stereograms may not be the best choice to evaluate stereo blindness as correct perception not only requires normal stereopsis but also other higher cortical processes. The test does not differentiate between peripheral and central deficits. For these reasons, software-based stereo tests were established, which could be installable and adaptable to different possible visualization setups and devices (Gadia et al., 2014). Such a test was designed to test stereo acuity and blindness using the same visualization conditions and setup adopted for the tasks to perform, as well as offering better control of parameters like luminance levels. The test can be performed on a 3D TV display based on active shutter systems to produce depth perception. This method of depth perception evaluation is distinct from conventional stereo tests as the shutter system is actually optical rather than mechanical when it comes to forming 3D imaging. Another advantage of using 3D TV systems as a stereo measurement tool is that it allows participants to be tested from different distances, e.g., from the presented stimuli on the screen, and based on the results of the software-based test, stereo acuity can be calculated.

To form 3D images, both eyes receive slightly different images of a visual scene. Therefore, the adjustment aligning the two eyes is necessary to reconcile this disparity and achieve a cohesive 3D vision. To assess stereopsis, eye movements should also be taken into consideration. Using eye movement behaviors, i.e., fixation patterns as an index, they may provide insights into 3D perception as well as motor performance in PD. Some previous studies have shown that eye movement patterns are sensitive to 3D shapes (Vishwanath and Kowler, 2004; Wexler and Ouarti, 2008). In PD, saccade and vergence eye movements are reported to be abnormal (Gupta et al., 2021)–e.g., patients with PD experience increased reaction time in direction errors and slow saccade (Chan et al., 2005; Perkins et al., 2021), interfering with the perception of depth and dimensionality critical for normal balance control and the prevention of falls (Urwyler et al., 2014). Eye-tracking technology provides a simple and non-invasive yet effective way to assess the oculomotion that reflects the brain function (Sweeney et al., 1998; Tseng et al., 2013).

TABLE 1 | Demographic and clinical characteristics of patients with Parkinson's disease (PD) (n = 62).

Clinical characteristics	Control (24)	Parkinson's Patients (20)	*P*-value
Age (years)	62.2 ± 7.5	66.8 ± 8.4	0.059
Sex (M:F)	13:11	11:9	>0.25
Disease course (years)	N/A	9.8 ± 4.7	
UPDRS-III	N/A	18.9 ± 8.2	
LEDD (mg)	N/A	1219.7 ± 719.9	
MoCA	27.8 ± 1.8	25.8 ± 2.8	0.10
Visual Acuity (logMAR)			
OD	0.11 ± 0.13	0.16 ± 0.12	0.08
OS	0.11 ± 0.12	0.11 ± 0.12	>0.25
OU	0.04 ± 0.14	0.05 ± 0.13	>0.25
Contrast acuity (Pelli-Robson log unit)	2.0	2.0	>0.25
Titmus stereotest (seconds of arc)	47.0 ± 25.6	58.4 ± 24.7	>0.25
3D TV Stereo acuity (seconds of arc)	40.1 ± 29.3	74.1 ± 35.7	0.005*

*M, male; F, female; UPDRS-III, Unified Parkinson's Disease Rating Scale-Part III; LEDD, levodopa equivalent daily dose; MoCA, Montreal Cognitive Assessment; OD, oculus dextrus; OS, oculus sinister; OU, oculus uterque. *p < 0.05.*

The objectives of the current study are to investigate the stereo function in PD using 3D active shutter visualization technology, taking the monocular cues into consideration when testing stereopsis, as well as investigating the oculomotor function. We propose that with the software-based system using 3D TV, even subtler deficits of stereo perception in PD can be detected. In addition, with the eye-tracking technology capturing patients' eye response to stimuli, we aim to reveal a visual searching strategy. We hypothesize that patients with PD may exhibit a poor stereo function and different eye movement behaviors, and the types and degree of such changes may correlate to the severity of motor symptoms and certain non-motor symptoms, such as cognitive function.

MATERIALS AND METHODS

Patients with PD aged 40–70 years old and with H&Y stage one to four were recruited from the Parkinson and Movement Disorders Program (PMDP) at the University of Alberta along with age- and sex-matched healthy controls (HCs). Community volunteers without neurological disorders were recruited as HCs. About 20 patients with PD and 24 HCs participated in this study (**Table 1**). All patients with PD were assessed at PMDP and the Surgical Simulation Research Lab at the University of Alberta. PD subjects were assessed by movement disorder neurologists, and the diagnosis of idiopathic PD was based on UK PD Society Brain Bank criteria (Hughes et al., 2002). Patients with PD were optimally treated with PD medications. The study was approved by the University of Alberta Ethics Review Board, and all participants provided written informed consent prior to participation. The exclusion criteria were atypical or secondary parkinsonism, confounding medical or psychiatric condition(s), dementia or any condition that prevents patients from signing consent, other neurological diseases leading to motor dysfunction, and visual acuity of at least 20/40 in either eye.

Clinical Assessments

All participated patients with PD were evaluated for their motor symptoms using the UPDRS-III and H&Y stage. Medication usage summarized as levodopa equivalent daily dose (LEDD) (Tomlinson et al., 2010) for each patient is shown in **Table 1**. At the study enrollment, other demographic and clinical information, i.e., educational level, duration of the disease, and cognitive testing with Montreal Cognitive assessment (MoCA), were obtained by a movement disorder neurologist or the research coordinator.

Visual and Stereo Screening and Stereo Acuity Tests

Visual acuity was tested using the Snellen chart. Corrected visual acuity was recorded for each eye followed by binocular vision. Contrast sensitivity was performed using the Pelli-Robson test. People with abnormal visual acuity (worse than 20/40) and contrast sensitivity were excluded as these abnormalities may represent optic nerve or retina pathologies, as well as media opacities and macular disease that may skew the stereo perception results. Screening stereopsis was performed with 2D pictures demonstrating the depth estimation from image structure, which was based on whole scene structures that do not rely on specific objects (Li et al., 2006). With 2D images, study participants were asked to estimate the depth relationship in each picture. Using three pictures, we show two or three objects of uniform size that are distributed in depth (**Supplementary Figure 1**). The closest object will project to a retinal image with the largest angular size. The other farther objects projected to retinal images are relatively smaller. The study participants were asked to provide a cue to the depth judging the relative sizes of the objects. If the mistakes were made, the participants will be excluded from further assessment. None misjudged depth with the 2D pictures. In addition, the standard and widely used Titmus stereotest (Stereo Optical Co., Inc., Chicago, IL, United States) was utilized. These tests can reveal stereo perception difficulties as well as compare and validate the results from the 3D monitor active shutter system.

Stereo Acuity Function Test With 3D Active Shutter System

After the screening tests, study participants were examined for stereoacuity functions. The visual stimuli were presented on a 3D monitor active shutter system. A 24-inch 3D video monitor (Tobii 1750 LCD Monitor, Tobii Technology, Stockholm, Sweden) was used for a test (**Figure 1A**). The active shutter system uses a special pair of shutter glasses containing a liquid crystal layer. The images were set at a refresh rate of 60 frames/s. We were able to perform the assessment of stereo perception of the participant directly on the device they would use for the stereoscopic working task. The display has a resolution of 2,470 × 1,240 pixels, at a 60 Hz refresh rate. It is equipped with passive stereoscopic visualization based on circularly polarized filters. The pixel display is equal to or similar to most of

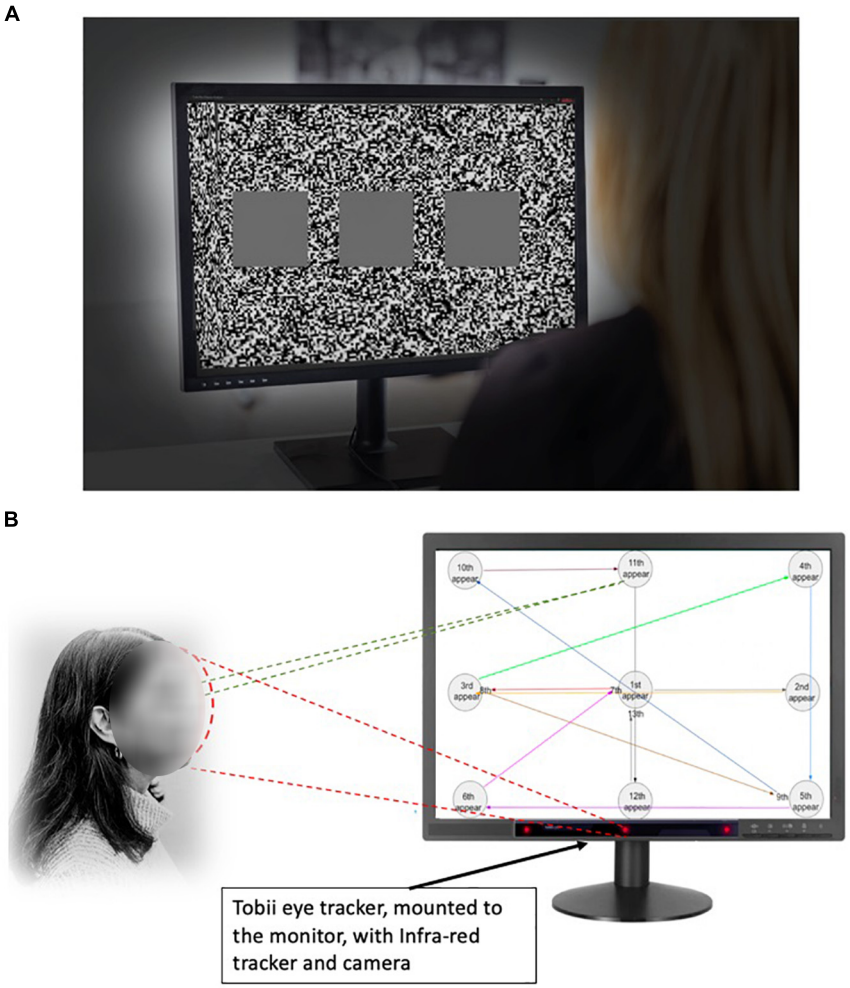

FIGURE 1 | Experimental settings to evaluate stereopsis with the 3D monitor active shutter system. **(A)** The 3D monitor active shutter system. The visual stimuli were presented on a 3D monitor using a 24-inch 3D video monitor. A special pair of shutter glasses containing a liquid crystal layer was used. The images were set at a refresh rate of 60 frames/s. The visual stimuli for each testing position consisted of a set of three squares, placed side-by-side placed in the foreground with a fixed white noise background. One of the squares, randomly decided, was of a one-pixel disparity while the others are presented at zero parallax. **(B)** The eye-tracking system. The Tobii eye tracker was installed beneath the 3D TV monitor. The gaze "hot spots" and position data can be extracted from the TV watching. The participants were asked to track a moving object with their gaze as it appeared on the screen at 13 positions in a predetermined order, and the speed of appearing/disappearing of the visual object remained the same.

the standard desktop monitors. Knowing the distance and the angle of view between the screen and the participant, the disparity among the test images can be calculated (Gadia et al., 2014). The test was performed with the lights off. In this phase, the participants were asked to complete a visual task while seated in eight different positions, varying in the distance (0.7/1.4/2.1/2.8 m) and viewing angle (45° and 90°) (Gadia et al., 2014). The task entailed a sequence of 10 visual stimuli. Each test was consisted of a set of three squares, placed side-by-side placed in the foreground with a fixed background (a white noise random-dots pattern). One of the squares, randomly decided, was of a one-pixel disparity while the others are presented at zero parallax. The participant must verbally report which square was perceived in front of the others. Black background for 2 s was shown before the next test image. The order of the subject's position and the order of the stimuli presented were counterbalanced. The accuracy of the stereo perception was calculated and recorded. The stereo acuity corresponding to the positions are 160, 100, 63, 50, 40, 32, 26, and 20 arc seconds, respectively (Eidolab, 2014). The participants were instructed to not guess and to report the absence of disparity according to their perception. We analyzed the stereo acuity in two ways. First, for the absolute acuity, for any given set of 10 stimuli, if the accuracy was less than 70%, the stereo acuity was assigned to the previously tested level. The choice of using 10 stimuli was to minimize the chance of guessing. Second, we used the percent accuracy for each participant at a given acuity level from 160 to 12.5 arc seconds. Another method used in the current study was to utilize the percentage accuracy at each tested arc second to compare which method is more sensitive to detect

stereo abnormalities. The normal stereo acuity was deemed to be between 32 and 63 arc seconds. The choice of using percent accuracy was to determine whether it is a more sensitive measure, as in the methods described by Gadia et al., they observed substantial equivalence of the two tests, down to the disparity of 26 arc seconds. From 20 to 12.5 arc seconds, the software-based test detects more abnormalities (Gadia et al., 2014).

Oculomotion Patterns

We evaluated the eye motion pattern to reveal specific eye behaviors, namely saccades and fixations in patients with PD. The Tobii X2-60 eye tracker (Tobii Technology, Inc., Danderyd, Sweden) was installed beneath the 3D TV to record subjects' eye movements. Equipped with the two hidden IR cameras, Tobii X2-60 captured gaze location over the TV screen at 60 Hz after calibration. The choice of eye tracker at 60 Hz is constrained by the simultaneous use of a stereoscopic display in our study. The reported resolution of Tobii X2-60 was 0.5 visual degrees when the eye tracker was placed at an ideal distance from the participant. The built-in software allowed the synchronization and analysis of the gaze data (eye motion trajectory) when the images were shown on the screen.

To perform the eye tracking, participants were asked to track the moving object with their gaze as it appeared on the screen at 13 positions in a predetermined order. The speed of the appearing and disappearing visual object remained the same. During the entire trial, participant's eye movements were recorded by the Tobii X2-60 eye tracker (**Figure 1B**). The visual response time was measured on each object's appearance, calculating from the time when the target appeared to the moment when the eyes gazed upon it.

Statistical Analysis

The differences between patients with PD and HCs in a visual and contrast acuity, visual field, stereo screening with the 2D pictures and Titmus Stereotest, stereo acuity using the 3D TV shutter system, and the eye-tracking measures were compared using the Mann–Whitney *U*-test. The correlation between stereopsis and eye-tracking parameters with UPDRS motor scores, LEDD, course of the disease, and MoCA were evaluated using univariate regression models. Standardized estimated regression coefficients (β) and the coefficients of multiple determination (R) were calculated. $p < 0.05$ was considered as significant.

RESULTS

Between the control and PD groups, patients with PD were 5.6 years older. Among the 20 patients with PD recruited (**Table 1**), 45% had a moderate disease with an H&Y ≥III. The mean LEDD was 1,220 ± 720 mg, with a disease duration of 10 ± 5 years at the time of assessment. Patients with PD had a lower MoCA score than control but they were not statistically significant. There were no differences in visual acuity (OD, $p = 0.41$; OA, $p = 0.88$; OU, $p = 0.30$), visual field ($p > 0.99$), and contrast acuity ($p > 0.99$). With the stereo acuity between 32 and 63 arc seconds being considered normal, the stereopsis with the 2D pictures and the Titmus stereotest revealed normal results in both groups (**Figure 2**).

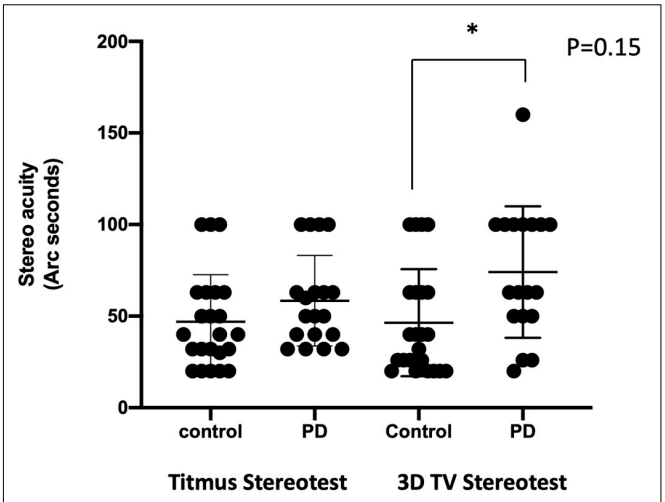

FIGURE 2 | Comparison of the stereo acuity using different methods. Stereo acuity (acuity in arc seconds) assessment with Titmus stereotest was shown on the left, and the 3D active shutter system was shown on the right. *, $p = 0.15$, with Mann–Whitney *U*-test.

Stereo Acuity Function Test With the 3D Monitor Active Shutter System

With the 3D active shutter system measuring absolute acuity, the PD group had a significantly worse stereo acuity (74 ± 36 arc seconds) when compared with the control group (40 ± 29, $p = 0.005$, **Figure 2**). Patients with PD performed the best at the most optimal position—0.7 m right in front of the monitor (160 arc seconds). With the percent accuracy method, the 3D active shutter system was clearly more sensitive in detecting the deficit in stereopsis compared to the Titmus stereotest. It is notable that even at 160 arc seconds, 45% of patients with PD were already making mistakes in their 3D perception, while only 16.7% of control individuals misjudged the disparity. We observed significant changes in stereo perception starting at 63 arc seconds in patients with PD judging the percent accuracy (**Figures 3A–D**, $p < 0.05$). LEDD was negatively correlated with the stereo acuity ($r = -0.5$, $p = 0.037$, **Figure 4A**), and there was a trend that UPDRS-III was negatively correlated with the stereo acuity ($r = -0.42$, $p = 0.067$). However, disease course on its own did not have any correlation with stereo acuity. In addition, in patients with PD, a preserved cognitive function (near normal MoCA score) was linked to a more intact stereo acuity ($r = 0.51$, $p = 0.015$) (**Figure 4B**). These observations suggested that poorer stereo perception can be related to disease severity. These correlations are representative of what holds for the levels of disparity between 63 and 20 arc seconds.

Using the absolute stereo acuity measured with the 3D active shutter system, no correlation was observed between the acuity with the UPDRS-III score, LEDD, duration of the disease, or

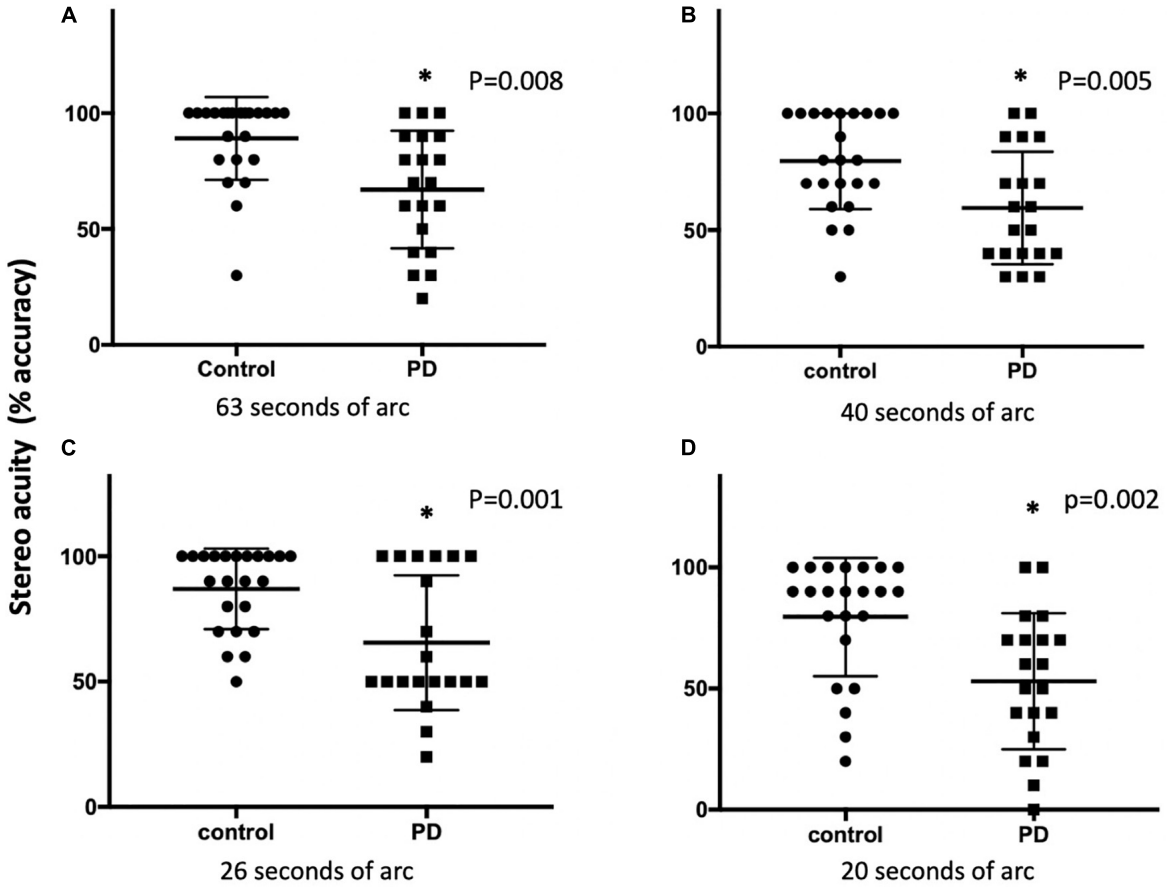

FIGURE 3 | The stereo acuity between the control and PD groups using the 3D active shutter system at 63 **(A)**, 50 **(B)**, 40 **(C)**, and 26 **(D)** arc seconds. The stereopsis was presented as percent accuracy. *$p < 0.05$, with Mann–Whitney *U*-test. PD, Parkinson's disease.

MoCA. There was no correlation detected between the stereo acuity measured with the Titmus stereotest with the clinical features in the PD group.

Eye-Tracking Analysis

Using the Tobii eye tacking system, the response time of the PD group (444 ± 73 ms) was significantly longer than that of the control group (409 ± 62 ms, $p = 0.014$).

Although patients with PD tended to perform worse, no significant differences were observed in the total number of fixations (17 ± 9 vs. 19 ± 8), average fixation duration (274 ± 124 vs. 280 ± 107 ms), average saccade amplitude (7.4° ± 3.2° vs.8.2° ± 3.3°), or the total number of saccades (31 ± 8 vs. 34 ± 9) between control and PD groups. However, when analyzing the response time between the target disappearing and the next target appearing, the number of fixations was higher (1.4 ± 0.9 vs.1.5 ± 1.1, $p < 0.01$) in the PD group, suggesting that patients with PD expressed difficulties in keeping their fixation on the fixation point when compared with the control group. The number of fixations during response time was correlated with the severity of motor symptoms as reflected by UPDRS-III (**Figure 5A**, $p = 0.007$, $r^2 = 0.35$), while the number of saccades during response time was correlated with MoCA (**Figure 5B**, $p = 0.016$, $r^2 = 0.28$).

DISCUSSION

Our current study demonstrated significant stereo deficits in PD, a longer response time with eye gazing, and less accurate saccades and fixations when evaluating these visual functions with easy to use, non-invasive methods, namely the 3D active shuttered system and Tobii eye tracker. The abnormalities in both stereopsis and oculomotor behavior were linked to the severity of the motor symptoms and cognitive status. One main focus is the application of stereo function as a possible marker in PD motor function. These tests are not routinely done in clinical settings. The widely used methodology in assessing stereopsis also has certain limitations. We demonstrated that the software-based stereo assessment is easy to use and may be more sensitive to detect stereo dysfunction, and such dysfunction is correlated to PD clinical features, i.e., motor and cognitive status.

Stereopsis is a complex process, which is dependent on an initial encoding of disparity in the striate cortex (Cumming and DeAngelis, 2001; Westheimer, 2009). Patients with PD with

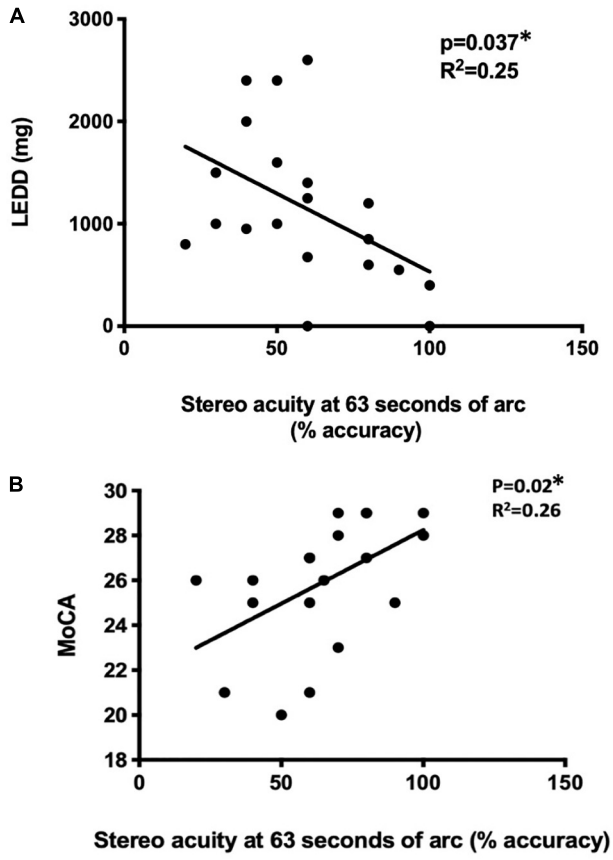

FIGURE 4 | The correlation of disease status with stereo acuity. Disease severity was reflected by LEDD **(A)** and cognitive function was assessed MoCA **(B)**. *$p < 0.05$, using univariate regression models. LEDD, levodopa equivalent daily dose (mg), MoCA, Montreal Cognitive Assessment.

abnormal stereopsis demonstrated non-dominant extrastriate cortical atrophy (Koh et al., 2013). It is known that sensory integration is abnormal in PD. Several dopamine pathways are present in the human brain. Aside from the known deficits in the striatonigral pathway in PD individuals, the same has been seen in the ventral tegmental pathway and additional pathways that connect the ventral tegmentum to the amygdala, hippocampus, cingulate gyrus, and olfactory bulb (Weil et al., 2016; Armstrong, 2017). There is also significantly less activity in the visual cortex of people with PD (Nguyen-Legros, 1988; Harnois and Di Paolo, 1990). In addition, cerebral metabolic rates for glucose are decreased by up to 23% in the primary visual cortex of patients with PD (Eberling et al., 1994). There is a dopamine deficit in the retina and other structures in the peripheral visual system that can weaken visual function, which is related to poor stereopsis (Botha and Carr, 2012). For instance, a previous study has demonstrated that the peripheral visual pathway (i.e., color perception) can contribute to the stereo deficit (Sun et al., 2014). However, in our study design, we excluded individuals with abnormal visual acuity and contrast acuity, and with the screen visual tests, there were no differences between the control and PD groups. These tests are within the normal range, suggesting relatively intact peripheral afferent pathways. Therefore, the observed stereo deficit is most likely central in origin.

The basal ganglia are considered as a "sensory analyzer" engaged in central somatosensory control. The interconnections between the cortex, the basal ganglia, and the thalamus form an indirect basal ganglia-sensory loop (Boecker et al., 1999). Multiple sensory perception domains are abnormal in PD (Jobst et al., 1997; Cury et al., 2016; Hwang et al., 2016; Lester et al., 2017). Visual perception deficit is known to interfere with PD patients' motor function, and the impairment in depth perception has a profound impact on patients' navigation, mobility, and daily activities (Trick et al., 1994; Maschke et al., 2006; Kim et al., 2011). Therefore, it is necessary to consider clinical testing of the stereoscopic abilities of patients with PD, given how it impacts an individual's functional status. In clinical practice, stereopsis is neither routinely assessed nor addressed in this population although patients may report visual deficits on widely used clinical questionnaires, i.e., Parkinson's Non-motor Symptoms Questionnaire (Chaudhuri et al., 2006). To date, methods for stereo assessment include 2D imaging estimates, verbal estimates of depth perception (Ehgoetz Martens et al., 2013), Titmus stereotest (Kim et al., 2011; Sun et al., 2014), stereopsis questionnaires when recalling a video clip on a 3D TV (Lee et al., 2015), randomly placed dots that move as orthographic projections of a sphere on a screen (White et al., 2017), and a recording of the visually evoked potential associated with different 2D and 3D stimuli (Severac Cauquil et al., 2017). There are limitations with these methodologies, e.g., the main monocular cues, as well as the oculomotor function are not considered with the most widely used Titmus stereotest. The current study focused on stereopsis functions in patients with PD using the software-based 3D TV active shutter system, considering the monocular function and eye movement abnormalities. The active shutter system was proven to be more sensitive in detecting stereo deficits, especially subtler deficits in stereo perception in PD (**Figure 2**). We noticed that when the disparity was below the threshold of normal acuity (63 arc seconds, corresponding to the detail size on a 20/20 Snellen chart), there was a steeper decrement of performance in patients with PD. The stereopsis deficit was negatively correlated with LEDD. In addition, the degree of stereopsis change showed a trend of negative correlation with disease severity in PD, as reflected by UPDRS-III in our study. The relationship between motor performance and stereopsis was previously reported by Sun et al.–patients with PD with decreased stereopsis had a higher UPDRS-III score and worse motor function (Sun et al., 2014), consistent with our observations.

In PD, the cognitive function has been shown to correlate with performance in visual tasks. Patients with higher Mattis attention subscores performed better, and those who were able to maintain more steady attention during the visual discrimination task obtained logically better performances (Severac Cauquil et al., 2017). A more recent study with the stereopsis questionnaire and Titmus stereotest compared HCs with PD and patients with Alzheimer's disease, and revealed no differences in the Titmus

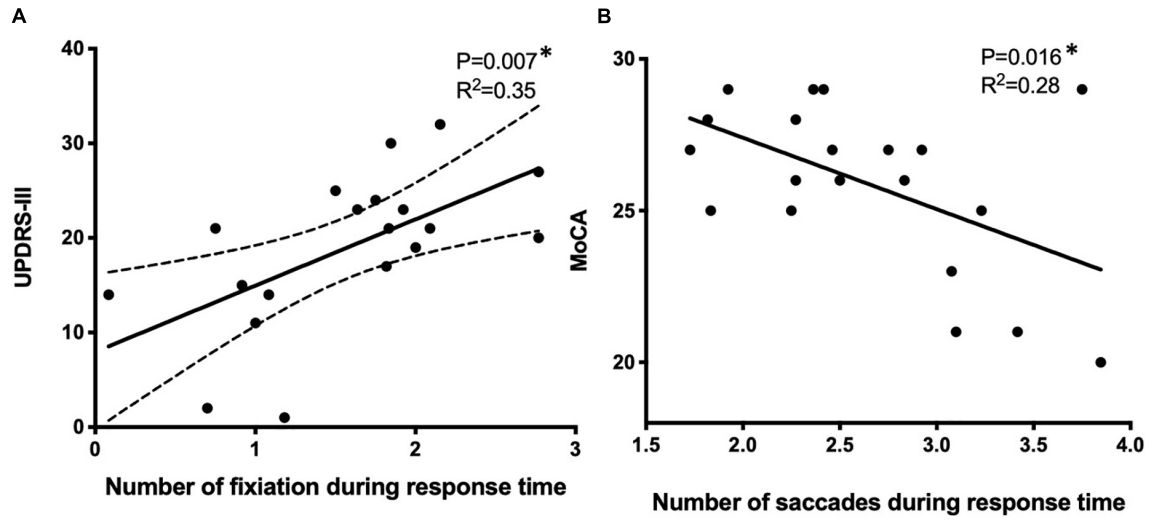

FIGURE 5 | The correlation of eye motion trajectory with disease status using the univariate linear regression model. Eye motion trajectory data were analyzed against UPDRS-III **(A)** and MoCA **(B)**. *$p < 0.05$, using univariate regression models. UPDRS-III, Unified Parkinson's Disease Rating Scale, MoCA, Montreal Cognitive Assessment.

stereotest results among groups; however, in patients with PD, cognitive functions (MoCA scores) were correlated with the scores of the stereopsis questionnaire (Lee et al., 2015). Although patients with PD in that study have poor cognitive performance compared with our PD cohort, the results are similar to our observations. Therefore, our findings and previous reports on stereopsis abnormalities in PD and the associated cognitive decline may indicate behavioral complications of PD and the progression of the disease. As such, the presence of stereopsis dysfunction might serve as a clinical biomarker of PD to predict disease progression and outcomes.

Reductions in dopamine levels in the basal ganglia and frontal cortex also contribute to higher level oculomotor movements (Hikosaka et al., 2000). In our study with the eye-tracking system, we observed a prolonged visual response time in patients with PD compared to the control subjects. The visual response is an important component of information processing as it indexes the speed of stimulus processing and response programming (Rao et al., 1985). It connects visual scanning to movement reaction, which is considered a sensitive variable for measuring information processing of the oculomotion pathway. Patients with PD showed disturbed default mode network connectivity with the brain regions that are involved in visual processing and attentional network (Rektorova et al., 2014). In addition, the reconciliation of visual disparity with vergence and saccade movements is an essential step to form a cohesive 3D vision. In PD, saccade and vergence eye movements are reported to be abnormal (Gupta et al., 2021), interfering with the perception of depth and dimensionality critical for normal balance control and prevention of falls (Urwyler et al., 2014). Although vergence is not directly assessed in this study, it is known that under normal circumstances, the abrupt changes in the 3D gaze shift occur with the congruent movements of vergence and saccade (Erkelens et al., 1989; Zee et al., 1992; Rambold et al., 2002); and in PD, the gaze shifting strategy of the two eyes was incongruent (Gupta et al., 2021).

Stereopsis and visual response time are important in dynamic situations, which require rapid visual functions (Bauer et al., 2001). To date, there is still insufficient knowledge on how visual-locomotion coupling in patients with PD changes as the disease progresses. We found an impaired saccade movement and fixation. A very few studies that tested stereopsis performance can provide a combined analysis of stereo acuity while assessing ocular trajectory and response time at the same time, such an observation is a strength of our current study. Our observations in the link between visual behavior and motor and cognitive deficits suggest that such visual parameters can potentially serve as the clinical markers in PD when combined with other clinical, biochemical, and imaging biomarkers.

Although we did not observe significant differences in the average saccade amplitude or the total number of saccades between the control and PD groups, the saccadic movements were abnormal and manifested as more peaks and unstable fixations in patients with PD, which are consistent with the known characteristic multistep sequence of eye movements, namely the discrete small saccades in PD (DeJong and Jones, 1971).

There are a few limitations to this study. This is a single centered study with relatively small sample size. We did not have any *de novo* patients with PD as we are a tertiary referral center. We did not assess whether there is a difference in the visual behaviors during the OFF and ON medication states. All tests were done during the ON state. We did not test vergence directly—however, the saccade and fixation abnormality may indicate a deficit in vergence, which also impacts stereopsis. In the future, we plan to recruit more patients with further testing during both OFF

and ON states to determine whether stereopsis and oculomotor behaviors can predict the response to treatments. We also plan to continue with a prospective study to observe how these visual functions evolve as disease progresses. In addition, we used 60 Hz as a sampling rate in our study, which is relatively low. Leube et al. (2017) compared eye trackers at 60 and 120 Hz with a 1,000-Hz eye tracker in a reading task. The saccade detection was generally adequate at 60 and 120 Hz, while the 120-Hz eye tracker was better in measuring the duration of the saccade than that of the 60 Hz. The number and duration of fixations were not significantly different between 60 and 120 Hz frequencies (Leube et al., 2017). While 120 Hz sampling results in higher accuracy in the detection of fast eye movements and fixation durations, which is necessary for a reading task. However, the design of our study is different. In contrast to the reading task, our study was testing initiation and velocity of saccade from one target to the next, to compare the PD individuals with age-matched controls. Such a task does not require the same high sampling rate as in reading. The differences observed at 60 Hz are still valid.

In conclusion, with the combination of the software-based 3D shutter system with oculomotor assessment, the current study revealed that patients with PD exhibit poorer stereopsis and impaired visual response time. The degree of stereo perception and visual response deficits reflected the clinical characteristics of PD. Our study suggested a potential role of testing these visual functions in patients with PD and also indicated stereo deficits and the possibility of impaired response time in PD to potentially serve as clinical biomarkers in PD research.

DATA AVAILABILITY STATEMENT

The raw data supporting the conclusions of this article will be made available by the authors, without undue reservation.

ETHICS STATEMENT

The studies involving human participants were reviewed and approved by the University of Alberta Ethics Review Board. The patients/participants provided their written informed consent to participate in this study.

AUTHOR CONTRIBUTIONS

FB: research project – conception and organization, statistical analysis – design, execution, and review and critique, and manuscript – wrote the first draft and review and critique. TS: research project – organization and execution, statistical analysis – design and execution, and manuscript – wrote the first draft and review and critique. WH: research project – execution, statistical analysis – execution and review and critique, and manuscript – review and critique. JF and EM: research project – execution and manuscript – review and critique. BZ: research project – conception and organization, and manuscript – review and critique. All authors contributed to the article and approved the submitted version.

FUNDING

The current study is supported by the Kaye fund to FB and BZ.

ACKNOWLEDGMENTS

We acknowledge all study participants for their time and support.

SUPPLEMENTARY MATERIAL

The Supplementary Material for this article can be found online at: https://www.frontiersin.org/articles/10.3389/fnagi.2022.783773/full#supplementary-material

Supplementary Figure 1 | Screening stereopsis with 2D images. In the 2D pictures, two or three objects of uniform size were shown that are distributed in depth. The study participants were asked to provide a cue to the depth judging the relative sizes of the objects.

REFERENCES

Alhassan, M., Hovis, J. K., and Almeida, Q. J. (2020). Stereopsis and ocular alignment in Parkinson's disease patients with and without freezing of gait symptoms. *Clin. Exp. Opt.* 103, 513–519. doi: 10.1111/cxo.12961

Antoniades, C. A., Bogacz, R., Kennard, C., FitzGerald, J. J., Aziz, T., and Green, A. L. (2014). Deep brain stimulation abolishes slowing of reactions to unlikely stimuli. *J. Neurosci.* 34, 10844–10852. doi: 10.1523/JNEUROSCI.1065-14.2014

Armstrong, R. A. (2011). Visual symptoms in Parkinson's disease. *Parkinsons Dis.* 2011:908306. doi: 10.4061/2011/908306

Armstrong, R. A. (2017). Visual dysfunction in Parkinson's Disease. *Int. Rev. Neurobiol.* 134, 921–946. doi: 10.1016/bs.irn.2017.04.007

Bauer, A., Dietz, K., Kolling, G., Hart, W., and Schiefer, U. (2001). The relevance of stereopsis for motorists: a pilot study. *Graefes Arch. Clin. Exp. Ophthalmol.* 239, 400–406. doi: 10.1007/s004170100273

Boecker, H., Ceballos-Baumann, A., Bartenstein, P., Weindl, A., Siebner, H. R., Fassbender, T., et al. (1999). Sensory processing in Parkinson's and Huntington's disease: investigations with 3D H(2)(15)O-PET. *Brain* 122(Pt 9), 1651–1665. doi: 10.1093/brain/122.9.1651

Botha, H., and Carr, J. (2012). Attention and visual dysfunction in Parkinson's disease. *Parkinsonism Relat. Disord.* 18, 742–747. doi: 10.1016/j.parkreldis.2012.03.004

Chan, F., Armstrong, I. T., Pari, G., Riopelle, R. J., and Munoz, D. P. (2005). Deficits in saccadic eye-movement control in Parkinson's disease. *Neuropsychologia* 43, 784–796. doi: 10.1016/j.neuropsychologia.2004.06.026

Chaudhuri, K. R., Martinez-Martin, P., Schapira, A. H., Stocchi, F., Sethi, K., Odin, P., et al. (2006). International multicenter pilot study of the first comprehensive self-completed nonmotor symptoms questionnaire for Parkinson's disease: the NMSQuest study. *Mov. Disord.* 21, 916–923. doi: 10.1002/mds.20844

Cumming, B. G., and DeAngelis, G. C. (2001). The physiology of stereopsis. *Annu. Rev. Neurosci.* 24, 203–238. doi: 10.1146/annurev.neuro.24.1.203

Cury, R. G., Galhardoni, R., Fonoff, E. T., Perez Lloret, S., Dos Santos Ghilardi, M. G., Barbosa, E. R., et al. (2016). Sensory abnormalities and pain in Parkinson disease and its modulation by treatment of motor symptoms. *Eur. J. Pain* 20, 151–165. doi: 10.1002/ejp.745

DeJong, J. D., and Jones, G. M. (1971). Akinesia, hypokinesia, and bradykinesia in the oculomotor system of patients with Parkinson's disease. *Exp. Neurol.* 32, 58–68. doi: 10.1016/0014-4886(71)90165-8

Eberling, J. L., Richardson, B. C., Reed, B. R., Wolfe, N., and Jagust, W. J. (1994). Cortical glucose metabolism in Parkinson's disease without dementia. *Neurobiol. Aging* 15, 329–335. doi: 10.1016/0197-4580(94)90028-0

Ehgoetz Martens, K. A., Ellard, C. G., and Almeida, Q. J. (2013). Dopaminergic contributions to distance estimation in Parkinson's disease: a sensory-perceptual deficit? *Neuropsychologia* 51, 1426–1434. doi: 10.1016/j.neuropsychologia.2013.04.015

Eidolab (2014). *EidoLab*. Available online at: http://eidomatica.di.unimi.it/index.php/research/stereo/stereotest (accessed August, 2018).

Erkelens, C. J., Van der Steen, J., Steinman, R. M., and Collewijn, H. (1989). Ocular vergence under natural conditions. I. Continuous changes of target distance along the median plane. *Proc. R. Soc. Lond. B Biol. Sci.* 236, 417–440. doi: 10.1098/rspb.1989.0030

Fawcett, A. P., Gonzalez, E. G., Moro, E., Steinbach, M. J., Lozano, A. M., and Hutchison, W. D. (2010). Subthalamic nucleus deep brain stimulation improves saccades in Parkinson's disease. *Neuromodulation* 13, 17–25. doi: 10.1111/j.1525-1403.2009.00246.x

Gadia, D., Garipoli, G., Bonanomi, C., Albani, L., and Rizzi, A. (2014). Assessing stereo blindness and stereo acuity on digital displays. *Displays* 35, 206–212. doi: 10.1016/j.displa.2014.05.010

Garmham, L., and Sloper, J. (2006). Effect of age on adult stereoacuity as measured by different type of stereotests. *Br. J. Ophthal.* 90, 91–95. doi: 10.1136/bjo.2005.077719

Gupta, P., Beylergil, S., Murray, J., Kilbane, C., Ghasia, F. F., and Shaikh, A. G. (2021). Computational models to delineate 3D gaze-shift strategies in Parkinson's disease. *J. Neural. Eng.* 18:0460a5. doi: 10.1088/1741-2552/ac123e

Harnois, C., and Di Paolo, T. (1990). Decreased dopamine in the retinas of patients with Parkinson's disease. *Invest. Ophthalmol. Vis. Sci.* 31, 2473–2475.

Heron, S., and Lages, M. (2012). Screening and sampling in studies of binocular vision. *Vis. Res.* 62, 228–234. doi: 10.1016/j.visres.2012.04.012

Hikosaka, O., Takikawa, Y., and Kawagoe, R. (2000). Role of the basal ganglia in the control of purposive saccadic eye movements. *Physiol. Rev.* 80, 953–978. doi: 10.1152/physrev.2000.80.3.953

Hughes, A. J., Daniel, S. E., Ben-Shlomo, Y., and Lees, A. J. (2002). The accuracy of diagnosis of parkinsonian syndromes in a specialist movement disorder service. *Brain* 125(Pt 4), 861–870. doi: 10.1093/brain/awf080

Hwang, S., Agada, P., Grill, S., Kiemel, T., and Jeka, J. J. (2016). A central processing sensory deficit with Parkinson's disease. *Exp. Brain Res.* 234, 2369–2379. doi: 10.1007/s00221-016-4642-4

Jobst, E. E., Melnick, M. E., Byl, N. N., Dowling, G. A., and Aminoff, M. J. (1997). Sensory perception in Parkinson disease. *Arch. Neurol.* 54, 450–454. doi: 10.1001/archneur.1997.00550160080020

Kim, S. H., Park, J. H., Kim, Y. H., and Koh, S. B. (2011). Stereopsis in drug naive Parkinson's disease patients. *Can. J. Neurol. Sci.* 38, 299–302. doi: 10.1017/s0317167100011501

Koh, S. B., Suh, S. I., Kim, S. H., and Kim, J. H. (2013). Stereopsis and extrastriate cortical atrophy in Parkinson's disease: a voxel-based morphometric study. *Neuroreport* 24, 229–232. doi: 10.1097/WNR.0b013e32835edbc5

Lee, C. N., Ko, D., Suh, Y. W., and Park, K. W. (2015). Cognitive functions and stereopsis in patients with Parkinson's disease and Alzheimer's disease using 3-dimensional television: a case controlled trial. *PLoS One* 10:e0123229. doi: 10.1371/journal.pone.0123229

Lester, M. E., Cavanaugh, J. T., Foreman, K. B., Shaffer, S. W., Marcus, R., and Dibble, L. E. (2017). Adaptation of postural recovery responses to a vestibular sensory illusion in individuals with Parkinson disease and healthy controls. *Clin. Biomech.* 48, 73–79. doi: 10.1016/j.clinbiomech.2017.07.008

Leube, A., Rifai, K., and Rifai, K. (2017). Sampling rate influences saccade detection in mobile eye tracking of a reading task. *J. Eye Mov. Res.* 10:10.16910/jemr.10.3.3. doi: 10.16910/jemr.10.3.3

Li, B., Xu, D., Feng, S., Wu, A., and Yang, X. (2006). *Perceptual Depth Estimation from a Single 2D Image Based on Visual Perception Theory*. Berlin: Springer.

Maschke, M., Gomez, C. M., Tuite, P. J., Pickett, K., and Konczak, J. (2006). Depth perception in cerebellar and basal ganglia disease. *Exp. Brain Res.* 175, 165–176. doi: 10.1007/s00221-006-0535-2

Micieli, G., Tassorelli, C., Martignoni, E., Pacchetti, C., Bruggi, P., Magri, M., et al. (1991). Disordered pupil reactivity in Parkinson's disease. *Clin. Auton. Res.* 1, 55–58. doi: 10.1007/bf01826058

Momeni-Moghadam, H., Kundart, J., Ehsani, M., and Gholami, K. (2011). *The Comparison of Stereopsis with TNO and Titmus Tests in Symptomatic and Asymptomatic University Students*. Boston, FL: American Academy of Optometry Annual Meeting.

Natsopoulos, D., Bostantzopoulou, M. S., Katsarou, Z., Grouios, G., and Mentenopoulos, G. (1993). Space deficits in Parkinson's disease patients: quantitative or qualitative differences from normal controls? *Behav. Neurol.* 6, 193–206. doi: 10.3233/BEN-1993-6404

Nguyen-Legros, J. (1988). Functional neuroarchitecture of the retina: hypothesis on the dysfunction of retinal dopaminergic circuitry in Parkinson's disease. *Surg. Radiol. Anat.* 10, 137–144. doi: 10.1007/bf02307822

Nilsson, M. H., Patel, M., Rehncrona, S., Magnusson, M., and Fransson, P. A. (2013). Subthalamic deep brain stimulation improves smooth pursuit and saccade performance in patients with Parkinson's disease. *J. Neuroeng. Rehabil.* 10:33. doi: 10.1186/1743-0003-10-33

Perkins, J. E., Janzen, A., Bernhard, F. P., Wilhelm, K., Brien, D. C., Huang, J., et al. (2021). Saccade, pupil, and blink responses in rapid eye movement sleep behavior disorder. *Mov. Disord.* 36, 1720–1726. doi: 10.1002/mds.28585

Pinkhardt, E. H., and Kassubek, J. (2011). Ocular motor abnormalities in Parkinsonian syndromes. *Parkinsonism Relat. Disord.* 17, 223–230. doi: 10.1016/j.parkreldis.2010.08.004

Rambold, H., Sprenger, A., and Helmchen, C. (2002). Effects of voluntary blinks on saccades, vergence eye movements, and saccade-vergence interactions in humans. *J. Neurophysiol.* 88, 1220–1233. doi: 10.1152/jn.2002.88.3.1220

Rao, S. L., Gangadhar, B. N., Keshavan, M. S., Hegde, A. S., and Nardev, G. (1985). Reaction time deficits in post traumatic syndrome. *Indian J. Psychiatry* 27, 63–65.

Rektorova, I., Krajcovicova, L., Marecek, R., Novakova, M., and Mikl, M. (2014). Default mode network connectivity patterns associated with visual processing at different stages of Parkinson's disease. *J. Alzheimers Dis.* 42(Suppl. 3), S217–S228. doi: 10.3233/JAD-132684

Severac Cauquil, A., Ory-Magne, F., Jardine, V., Galitzky, M., Rosito, M., Brefel-Courbon, C., et al. (2017). Parkinson's patients can rely on perspective cues to perceive 3D space. *Brain Res.* 1663, 161–165. doi: 10.1016/j.brainres.2017.03.017

Sun, L., Zhang, H., Gu, Z., Cao, M., Li, D., and Chan, P. (2014). Stereopsis impairment is associated with decreased color perception and worse motor performance in Parkinson's disease. *Eur. J. Med. Res.* 19:29. doi: 10.1186/2047-783X-19-29

Sweeney, J. A., Luna, B., Srinivasagam, N. M., Keshavan, M. S., Schooler, N. R., Haas, G. L., et al. (1998). Eye tracking abnormalities in schizophrenia: evidence for dysfunction in the frontal eye fields. *Biol. Psychiatry* 44, 698–708. doi: 10.1016/s0006-3223(98)00035-3

Tomlinson, C. L., Stowe, R., Patel, S., Rick, C., Gray, R., and Clarke, C. E. (2010). Systematic review of levodopa dose equivalency reporting in Parkinson's disease. *Mov. Disord.* 25, 2649–2653. doi: 10.1002/mds.23429

Trick, G. L., Kaskie, B., and Steinman, S. B. (1994). Visual impairment in Parkinson's disease: deficits in orientation and motion discrimination. *Optom. Vis. Sci/* 71, 242–245. doi: 10.1097/00006324-199404000-00002

Tseng, P. H., Cameron, I. G., Pari, G., Reynolds, J. N., Munoz, D. P., and Itti, L. (2013). High-throughput classification of clinical populations from natural viewing eye movements. *J. Neurol.* 260, 275–284. doi: 10.1007/s00415-012-6631-2

Urwyler, P., Nef, T., Killen, A., Collerton, D., Thomas, A., Burn, D., et al. (2014). Visual complaints and visual hallucinations in Parkinson's disease. *Parkinsonism Relat. Disord.* 20, 318–322. doi: 10.1016/j.parkreldis.2013.12.009

Vishwanath, D., and Kowler, E. (2004). Saccadic localization in the presence of cues to three-dimensional shape. *J. Vis.* 4, 445–458. doi: 10.1167/4.6.4

Wang, C. A., McInnis, H., Brien, D. C., Pari, G., and Munoz, D. P. (2016). Disruption of pupil size modulation correlates with voluntary motor preparation deficits in Parkinson's disease. *Neuropsychologia* 80, 176–184. doi: 10.1016/j.neuropsychologia.2015.11.019

Weil, R. S., Schrag, A. E., Warren, J. D., Crutch, S. J., Lees, A. J., and Morris, H. R. (2016). Visual dysfunction in Parkinson's disease. *Brain* 139, 2827–2843. doi: 10.1093/brain/aww175

Westheimer, G. (2009). The third dimension in the primary visual cortex. *J. Physiol.* 587(Pt 12), 2807–2816. doi: 10.1113/jphysiol.2009.170175

Westheimer, G. (2013). Clinical evaluation of stereopsis. *Vis. Res.* 90, 38–42. doi: 10.1016/j.visres.2012.10.005

Wexler, M., and Ouarti, N. (2008). Depth affects where we look. *Curr. Biol.* 18, 1872–1876. doi: 10.1016/j.cub.2008.10.059

White, K. D., Skidmore, F. M., Hammond, J., and Heilman, K. M. (2017). The visual kinetic depth effect is altered with Parkinson's disease. *Parkinsonism Relat. Disord.* 37, 97–100. doi: 10.1016/j.parkreldis.2017.01.004

Young, D. E., Wagenaar, R. C., Lin, C. C., Chou, Y. H., Davidsdottir, S., Saltzman, E., et al. (2010). Visuospatial perception and navigation in Parkinson's disease. *Vis. Res.* 50, 2495–2504. doi: 10.1016/j.visres.2010.08.029

Yugeta, A., Terao, Y., Fukuda, H., Hikosaka, O., Yokochi, F., Okiyama, R., et al. (2010). Effects of STN stimulation on the initiation and inhibition of saccade in Parkinson disease. *Neurology* 74, 743–748. doi: 10.1212/WNL.0b013e3181d31e0b

Zee, D. S., Fitzgibbon, E. J., and Optican, L. M. (1992). Saccade-vergence interactions in humans. *J. Neurophysiol.* 68, 1624–1641. doi: 10.1152/jn.1992.68.5.1624

Conflict of Interest: The authors declare that the research was conducted in the absence of any commercial or financial relationships that could be construed as a potential conflict of interest.

Publisher's Note: All claims expressed in this article are solely those of the authors and do not necessarily represent those of their affiliated organizations, or those of the publisher, the editors and the reviewers. Any product that may be evaluated in this article, or claim that may be made by its manufacturer, is not guaranteed or endorsed by the publisher.

Copyright © 2022 Ba, Sang, He, Fatehi, Mostofi and Zheng. This is an open-access article distributed under the terms of the Creative Commons Attribution License (CC BY). The use, distribution or reproduction in other forums is permitted, provided the original author(s) and the copyright owner(s) are credited and that the original publication in this journal is cited, in accordance with accepted academic practice. No use, distribution or reproduction is permitted which does not comply with these terms.

frontiers in Aging Neuroscience

ORIGINAL RESEARCH
published: 09 February 2022
doi: 10.3389/fnagi.2022.788571

A Spatiotemporal Brain Network Analysis of Alzheimer's Disease Based on Persistent Homology

Jiacheng Xing[1,2], *Jiaying Jia*[1], *Xin Wu*[2] *and Liqun Kuang*[1]*

[1] School of Data Science and Technology, North University of China, Taiyuan, China, [2] Department of Computer Science, University of Birmingham, Birmingham, United Kingdom

Current brain network studies based on persistent homology mainly focus on the spatial evolution over multiple spatial scales, and there is little research on the evolution of a spatiotemporal brain network of Alzheimer's disease (AD). This paper proposed a persistent homology-based method by combining multiple temporal windows and spatial scales to study the spatiotemporal evolution of brain functional networks. Specifically, a time-sliding window method was performed to establish a spatiotemporal network, and the persistent homology-based features of such a network were obtained. We evaluated our proposed method using the resting-state functional MRI (rs-fMRI) data set from Alzheimer's Disease Neuroimaging Initiative (ADNI) with 31 patients with AD and 37 normal controls (NCs). In the statistical analysis experiment, most network properties showed a better statistical power in spatiotemporal networks than in spatial networks. Moreover, compared to the standard graph theory properties in spatiotemporal networks, the persistent homology-based features detected more significant differences between the groups. In the clustering experiment, the brain networks on the sliding windows of all subjects were clustered into two highly structured connection states. Compared to the NC group, the AD group showed a longer residence time and a higher window ratio in a weak connection state, which may be because patients with AD have not established a firm connection. In summary, we constructed a spatiotemporal brain network containing more detailed information, and the dynamic spatiotemporal brain network analysis method based on persistent homology provides stronger adaptability and robustness in revealing the abnormalities of the functional organization of patients with AD.

Keywords: Alzheimer's disease, brain network, functional magnetic resonance imaging, dynamic functional connectivity, persistent homology, sliding window

OPEN ACCESS

Edited by:
Jiehui Jiang,
Shanghai University, China

Reviewed by:
Bin Wang,
Taiyuan University of Technology, China
Yin Guimei,
Taiyuan Normal University, China

***Correspondence:**
Liqun Kuang
kuang@nuc.edu.cn

Specialty section:
This article was submitted to Neurocognitive Aging and Behavior, a section of the journal Frontiers in Aging Neuroscience

Received: *02 October 2021*
Accepted: *10 January 2022*
Published: *09 February 2022*

Citation:
Xing J, Jia J, Wu X and Kuang L (2022) A Spatiotemporal Brain Network Analysis of Alzheimer's Disease Based on Persistent Homology. Front. Aging Neurosci. 14:788571. doi: 10.3389/fnagi.2022.788571

INTRODUCTION

Alzheimer's disease (AD) (Scheltens et al., 2021) is one of the classic chronic neurodegenerative diseases, which is considered as a common form of dementia. With the progress of this disease, it gradually spread to different brain regions, thus greatly affecting the patient's daily life (Patterson, 2018). Currently, the resting-state functional MRI (rs-fMRI) (Engels et al., 2017) has become an important technology to explore brain functional networks. A lot of early brain functional

alterations related to AD pathophysiology have been reported using various brain network analysis methods (Hallquist and Hillary, 2018; Marquez and Yassa, 2019; Mill et al., 2020). Most of these methods assume that the functional connectivity is constant during the brain imaging process, which may ignore some key time-varying information of the brain network caused by healthy brain or nervous system diseases. Therefore, it is necessary to study dynamic functional connectivity based on temporal dynamics (Preti et al., 2017).

Currently, the main methods used in the dynamic functional connectivity analysis include sliding window analysis, clustering analysis, time-frequency coherence analysis, and dynamic graph theory analysis (Preti et al., 2017). Among them, a large number of studies (Chen et al., 2016, 2021; de Vos et al., 2018; Lei et al., 2021) have adopted the time-sliding window approach to analyze the time-varying domain of functional connectivity. In this way, an entire rs-fMRI time series is divided into multiple subseries. For each segment, a functional connectivity network is constructed to measure the short-term correlation between the brain regions. Thus, all networks constructed from all segments describe the dynamics of the short-term functional connectivity over time. Further, the volatility between specific time points or time windows is observed by some network metrics. Specifically, a dynamic graph theory-based analysis method has developed a series of network metrics (Hallquist and Hillary, 2018; Sporns, 2018) to detect the differences of brain network structures over time in rs-fMRI research. Using the method of sliding window, more differences between the groups in a dynamic brain network can be observed, which cannot be seen in a static brain network. Multiple time windows provide more temporal evolution information for the brain network analysis. However, the spatial evolution information is missing as the brain network is measured on a single fixed spatial scale.

Recently, persistent homology (Edelsbrunner and Harer, 2010) is an important research tool of topological data analysis, which focuses on exploring topological invariants with the increase of spatial scales. In the process of spatial scale change, the topological feature with a shorter duration is considered as noise, and the feature with a longer duration is used to represent an essential feature (Giusti et al., 2016). Compared with the traditional graph theory method, it can better reveal topological changes in space and avoid the problem of scale threshold selection. Some studies have successfully applied the persistent homology technology to analyze the brain network structure of AD (Kuang et al., 2019a, 2020b), epilepsy (Choi et al., 2014), autism spectrum disorder, attention-deficit hyperactivity disorder (Lee et al., 2012, 2017), etc. In our prior study on AD brain networks (Kuang et al., 2019a), we have proposed an integrated persistent feature (IPF) based on persistent homology that achieves holistic descriptions of spatial dynamics of the brain network. We have also found that the IPF is more robustness than graph theory-based metrics in our prior studies (Kuang et al., 2019a,b, 2020a,b). However, all existing studies on persistent homology only focus on the feature invariants in the process of spatial dynamics, but no literature studies have reported the influence of the change of time window on feature invariants.

In summary, there are a few available frameworks that can simultaneously quantify the brain network structure both in the time domain and in the spatial domain. As the time-sliding window approach can produce multiple dynamic time windows for studying the characteristics of time-varying connectivity, and the persistent homology method has been verified to be good at measuring the characteristics of space-varying connectivity, we propose a novel method combining spatial scale filtrations of persistent homology with temporal sliding windows. We hypothesize that such generated spatiotemporal network dynamics may improve the performance of detecting AD-induced topological changes in the rs-fMRI analysis, and the derived network properties based on persistent homology may be used as the potential biomarkers for AD imaging.

In this paper, we develop a persistent homology-based method by combining multiple temporal windows and spatial scales to study the spatiotemporal evolution of brain functional networks. Specifically, a time-sliding window method is performed to establish a spatiotemporal network and the persistent homology-based features of such a network are obtained. In our experiments, we evaluate our proposed method using rs-fMRI data set with 31 patients with AD and 37 normal controls (NCs). We test whether the proposed method provides stronger adaptability and robustness in revealing the abnormalities of the functional organization of patients with AD.

MATERIALS AND METHODS

For each participant, the processing and analysis pipeline is summarized in **Figure 1**. Initially, the rs-fMRI data were acquired and preprocessed using well-known toolboxes (Step 1). Then, each subject's blood oxygen-level dependent (BOLD) signals within each region of interest (ROI) were obtained and divided into some segments by moving a sliding window over it (Step 2). For each subject, we then constructed a spatial network (Step 3) from the entire BOLD signals, as well as a series of spatiotemporal networks (Step 4) from the divided signal segments. Further, we applied a clustering analysis to spatiotemporal networks to verify whether the network structures of AD and NC are different (Step 5). Finally, we measured the network topology properties (Step 7) of each subject using the two kinds of methods, i.e., traditional graph theory and novel persistent homology based on graph filtration (Giusti et al., 2016) (Step 6). The specific steps are described in the following subsections.

Data Acquisition and Preprocessing

The data used in the preparation of this article were obtained from the Alzheimer's Disease Neuroimaging Initiative (ADNI) database[1] (Jack et al., 2008; Jagust et al., 2010), which are used to measure the progression of mild cognitive impairment (MCI) and early AD. The rs-fMRI data set was acquired from ADNI-2 in this study. Specifically, the 3.0T Philips MRI scanner was used to scan the brain of the subjects, and a high-resolution rs-fMRI three-dimensional image was acquired by an echo plane imaging

[1] adni.loni.usc.edu

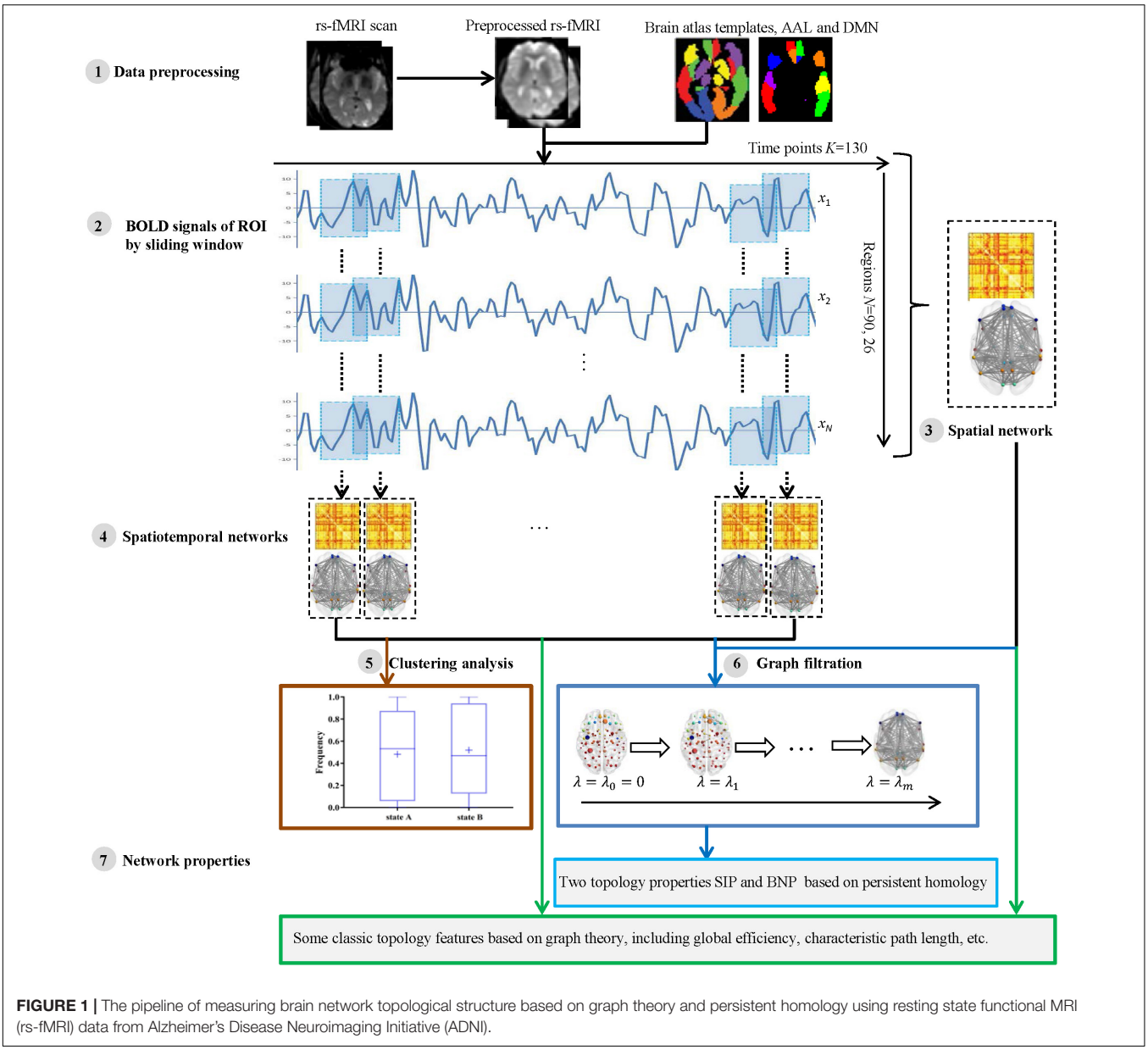

FIGURE 1 | The pipeline of measuring brain network topological structure based on graph theory and persistent homology using resting state functional MRI (rs-fMRI) data from Alzheimer's Disease Neuroimaging Initiative (ADNI).

(EPI) sequence. The acquisition parameters are as follows: echo time (TE) = 30 ms, turning angle = 80°, slice thickness = 3.3 mm, slice number = 48, matrix size = 64 × 64, repetition time (TR) = 3,000 ms, and time point volume = 140.

In this study, we used the commonly available rs-fMRI data of the ADNI database and screened the subjects' age, education level, and gender. Thus, there were a total of 68 AD and NC studies. Then, spm12[2] and DPARSF toolboxes[3] (Yan and Zang, 2010) were applied for rs-fMRI data preprocessing. The specific steps are as follows.

Firstly, for each subject, the first 10 time points of rs-fMRI images were discarded to improve the signal-to-noise ratio and achieve signal stability. The remaining 130 time points were used for further analysis.

Secondly, the time correction was applied according to the acquisition time difference between the scanning layers. The slice at TR/2 time point was used as the reference scanning layer, and other scanning layers were aligned to it to ensure that the acquisition of each slice corresponds to the same time point.

Further, a spatial correction was applied. Each subject's functional images were aligned to the Montreal Institute of Neurology (MNI) space according to its structural image (T1 image).

Then, spatial smoothing with a Gaussian kernel of 4 × 4 × 4 mm full width at half maximum, linear trend removal, band-pass filtering (0.01–0.08 Hz), and global signal regression were carried out in turn.

[2]http://www.fil.ion.ucl.ac.uk/spm/

[3]http://restfmri.net/forum/DPARSF

Finally, a covariate regression analysis was used to eliminate the signal fluctuation caused by a cerebrospinal fluid signal, white matter signal, and head movement.

As there is still a controversy on whether to eliminate the whole brain signal, this study did not regress the whole brain signal. At the end of the experiment, the data of head displacement more than 1 mm or of head-motion rotation more than 1° were excluded.

Construction of Brain Networks

We constructed the two modes of brain network, i.e., spatial network and spatiotemporal network. A spatial network was established according to the brain partition template on spatially anatomical labeling, while a spatiotemporal network was constructed by sliding a time series window.

Construction of Spatial Network

According to standard automated anatomical labeling (AAL) atlas (Tzourio-Mazoyer et al., 2002), the whole brain is spatially divided into 90 ROIs. In this paper, we also studied another subnetwork of AAL with 26 ROIs, i.e., default mode network (DMN). After image preprocessing, the average rs-fMRI time series (a total of 130 time series, $K = 130$) of each brain region were summarized, and the Pearson correlation coefficient between each pair of ROIs was defined as its functional connectivity. Therefore, the spatial brain network of each subject was constructed and represented as an adjacency matrix with a size of 90 × 90 or 26 × 26 ($N = 90$ or 26). Specifically, each ROI represents a node, and the edge weight between ROI i and j is defined based on Pearson correlation, i.e.,

$$w_{ij} = 1 - \frac{cov\left(x_i, x_j\right)}{\sigma_{x_i}\sigma_{x_j}} = 1 - \frac{\sum_{k=1}^{N}\left(x_{ik} - \bar{x}_i\right)\left(x_{jk} - \bar{x}_j\right)}{\sqrt{\sum_{k=1}^{N}\left(x_{ik} - \bar{x}_i\right)^2}\sqrt{\sum_{k=1}^{N}\left(x_{jk} - \bar{x}_j\right)^2}}, \quad (1)$$

where $x_i = (x_{i1}, x_{i2}, \cdots, x_{iN})$ and $x_j = (x_{j1}, x_{j2}, \cdots, x_{jN})$ are the time series of BOLD signals at the ith and jth ROI, respectively.

Construction of Spatiotemporal Network Based on Sliding Time Window

In this study, a sliding window method (Chen et al., 2016, 2021; de Vos et al., 2018; Lei et al., 2021) was performed to establish a spatiotemporal network as shown in **Figure 2**. A detailed construction process is described as follows.

First, a conical window was created by convoluting a sliding time series window with a Gaussian kernel (σ = 3TR). Compared with the traditional rectangle, the conical window has the advantage of reducing the weight of boundary time points when the subsequence window is sliding. The sliding window width W was set to 20TR (60 s) because previous studies have shown that a window width of 30–60 s is able to successfully capture resting-state functional connectivity fluctuations (Preti et al., 2017).

Then, for each subject, we moved the sliding window gradually in the step of one TR each time and thus produced $(K - W + 1)$ subsequences of time windows. Here, $K = 130$ is the length of the time series.

Further, for each time window i, an observation distance matrix C_i ($i = 1, 2, K - W + 1$) was generated based on Pearson correlation according to Equation (1), and the size of matrix is $N \times N$ (N is the number of ROI, $N = 90$ or 26).

Thus, each subject had a series of time-varying matrices, which could capture the dynamic changes of functional connectivity during the resting-state scanning. A time-varying matrix is used as a spatiotemporal network (see step 4 in **Figure 1**).

Finally, to quantify fluctuations in the connectivity time courses, some summary measures have been used, such as their SD (Preti et al., 2017; de Vos et al., 2018) or covariance (Chen et al., 2016). In this study, for each subject, we calculated a SD matrix across all time-varying matrices to quantitatively estimate the stability of functional connectivity over time.

Spatiotemporal Network Clustering Analysis

In this study, we propose a novel method based on persistent homology to detect the differences of dynamic functional networks between AD and NC groups. However, the mostly applied strategy in this area is the state extraction of dynamic functional connectivity through k-means clustering (Preti et al., 2017). To verify the effectiveness of our proposed method, we also use the traditional method to conduct experiments on spatiotemporal networks. Specifically, we used k-means clustering (de Vos et al., 2018) to capture the state changes of functional connectivity in a dynamic time series, and then analyzed the differences between the groups of all patients with AD and NC subjects in the identical states of dynamic functional connectivity. The k-means clustering method uses a distance function to cluster data into different clusters in an iterative manner. It clustered the time-varying matrices of all sliding windows of all individuals into k clustering states. The similarity within the cluster is very high, while the similarity between the clusters is extremely low. In this study, the k-means algorithm was applied to a series of time-varying matrices according to its Manhattan distance (Allen et al., 2014).

We further observed each clustering state from two aspects, window ratio and average residence time using the DynamicBC toolbox (Liao et al., 2014). Specifically, the window ratio is calculated as the proportion of staying in a given state window, and the average residence time represents the number of consecutive windows belonging to a state.

Network Properties

In this study, network measurement methods based on graph theory and persistent homology were used to measure brain functional organization.

Graph Theory-Based Network

Graph theory analysis methods (Sporns, 2018) have been widely used in the study of brain network topology structure. This paper mainly used the currently widely used graph theory indicators. We measured the global and local transmission capabilities of the network (global efficiency and local efficiency)

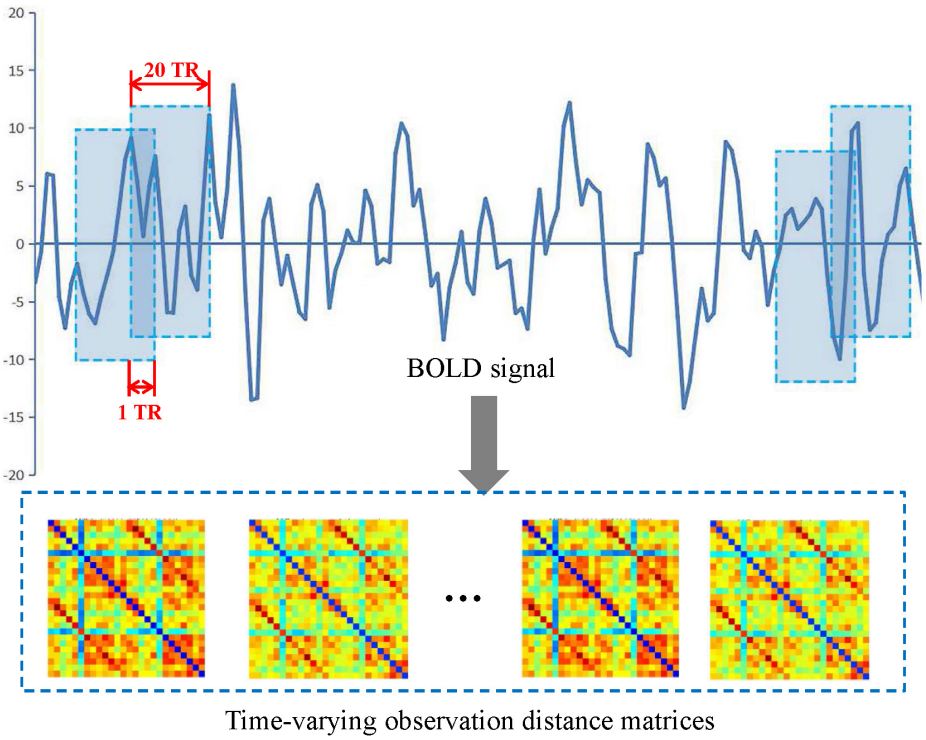

FIGURE 2 | Construction of a spatiotemporal brain network by the sliding window method.

(De Pasquale et al., 2016), the shortest path between the brain regions (characteristic path length) (Brier et al., 2014), the importance of nodes (eigenvector centrality) (Binnewijzend et al., 2014), the degree of clustering of nodes (clustering coefficient) (Rauchmann et al., 2021), the characteristics of the small-world network (Watts and Strogatz, 1998), and the minimum eccentricity of nodes (network radius) (Fujita et al., 2017). As these graph theory indicators usually measure the brain network on a fixed scale, the brain network needs to be filtered before measuring its structure. The statistical analysis of connectivity has been commonly used to filter the network. Specifically, we deleted the edges that were not significantly connected in the brain network ($p > 0.05$) to obtain a sparse structure (Smith and Nichols, 2009; Wang et al., 2013). Then, we applied a brain connectivity toolbox[4] (Rubinov and Sporns, 2010) on the filtered brain network to calculate these graph theory-based indicators.

Persistent Homology-Based Network Properties

Persistent homology (Edelsbrunner and Harer, 2010) is a mathematical concept from the algebraic topology. The typical approach of persistent homology is Betty number plot (BNP) (Lee et al., 2012; Giusti et al., 2016), which can distinguish persistent features from noise in graph filtering and is considered as a useful feature descriptor. It has been successfully used in brain network research based on fluorodeoxyglucose-positron emission tomography (FDG-PET) and MRI data in some neurodegenerative diseases (Lee et al., 2012, 2017; Choi et al., 2014). In our previous research, we proposed an IPF (Kuang et al., 2019a), which integrates a connected component aggregation cost with BNP to realize the spatial evolution of the overall graph. The IPF is defined as follows:

$$IPF_{\lambda_i} = \begin{cases} \frac{m-i}{m(m-1)} \sum_{k=i+1}^{m-1} \lambda_k, & 0 \le i \le m-2 \\ 0\,. & i = m-1 \end{cases}, \quad (2)$$

where m is the maximum number of connected components, λ is a series of filtration values ($\lambda_0 = 0 < \lambda_1 < \lambda_2 < \ldots < \lambda_{m-1}$) generated by all edge weights of the maximum connected components of the brain network (see step 6 in **Figure 1**).

Further, the medical field tends to use a single indicator to measure biomarkers. Because IPF is a monotonically decreasing convergence function, the slope of IPF (SIP) is used as an index to quantify the dynamic research of AD brain network. We have successfully applied the SIP to AD brain network analysis in our prior studies (Kuang et al., 2019a,b, 2020a,b). Our opensource code of persistent homology can be downloaded at http://gsl.lab.asu.edu/software/IPF.

Statistical Test

A two-sample t-test was performed on the brain network properties based on graph theory and persistent homology, as well as clustering states. $p < 0.05$ indicates that the difference

[4]https://sites.google.com/site/bctnet/

between the two groups is statistically significant. We used Matlab (R2017a) for statistical test.

RESULTS

Demographic Information

The experimental participants were obtained from ADNI-2.[5] Details of demographic characteristics are shown in **Table 1**. There were 31 AD subjects aged 60–90 years old in rs-fMRI data set. To conduct a comparative study with the patient group, 37 matched NC subjects were selected in this study. Diagnostic classification was made by ADNI investigators using the established criteria. The Clinical Dementia Rating (CDR) global score of any AD patient was no less than 1, while that of NC subject was 0. There are no significant differences in age, education, and gender between the groups. However, there is a significant difference in Mini-Mental Status Examination (MMSE) scores (Folstein et al., 1975). In addition, the displacement of head movement in any subject's image is less than 1 mm, and the rotation angle in any direction is less than 1°.

Whole Brain Network Properties

In this study, the properties based on graph theory and persistent homology methods were used for the whole brain network analysis using AAL atlas. Their statistical differences between groups are shown in **Table 2** using a two-sample *t*-test.

In the network measurement using graph theory-based properties, the network radius showed significant differences between patients with AD and subjects with NC (*AD*: 6.17 ± 2.63; *NC*: 5.97 ± 2.64, $p = 0.0493$) in a spatial network. However, other network properties based on the graph theory could not detect any significant differences between the groups either in a spatial or spatiotemporal network.

Then, in the network measurement using persistent homology-based properties, the SIP index showed very significant differences between the groups in a spatial network (*AD*: -0.67 ± 0.13; *NC*: -0.75 ± 0.10, $p = 0.008 < 0.01$), so does the BNP index (*AD*: -257.16 ± 43.18; *NC*: -283.12 ± 56.82, $p = 0.041 < 0.05$). Moreover, in the spatiotemporal network measurement, the group difference of BNP is more significant (*AD*: -718.53 ± 84.92; *NC*: -793.13 ± 109.96, $p = 0.0030$, much less than 0.041) than in a spatial network, and so is SIP (*AD*: -0.52 ± 0.11; *NC*: -0.59 ± 0.09, $p = 0.002 < 0.008$).

To sum up, the differences of persistent homology indicators between AD and NC are significantly greater than those of graph theory indicators. Moreover, their group differences in a spatiotemporal network are more significant than those in a spatial network. It suggests that a brain spatiotemporal network analysis based on persistent homology is more likely to explore potential biomarkers.

Brain Default Mode Network Properties

Default mode network is a functional subnetwork with the strongest variability in the study of AD, which contains the most obvious areas of brain atrophy. In this study, 26 areas (Vriend et al., 2018) in AAL were identified as the ROIs of DMN. The statistical differences of network properties between the groups in the DMN atlas are shown in **Table 3**.

In the study of DMN based on the graph theory method, there is no significant difference in the small-world attribute in the spatial DMN ($p > 0.05$), but it shows a very significant difference in the spatiotemporal network (*AD*: 1.03 ± 0.02; *NC*: 1.02 ± 0.01, $p = 0.007$), suggesting a small-world attribute could detect subtle time variability in the spatiotemporal DMN. In addition, it can be seen that the eigenvector centrality has very significant differences between the groups in both the spatial network (*AD*: 0.1046 ± 0.01; *NC*: 0.1047 ± 0.01, $p = 0.009$) and spatiotemporal network (*AD*: 0.1946 ± 0.01; *NC*: 0.1950 ± 0.01, $p = 0.017$), while there is no difference in the whole brain study.

Then, in the study of DMN based on persistent homology, both SIP and BNP detected significant differences between the groups in spatial and spatiotemporal networks. Especially in the spatiotemporal DMN, the SIP (*AD*: -0.69 ± 0.12; *NC*: -1.46 ± 0.10, $p = 0.003$) and BNP (*AD*: -171.41 ± 32.24; *NC*: -198.84 ± 34.08, $p = 0.001$) have very significant group differences.

In general, the spatiotemporal DMN properties based on persistent homology performed the best. Research on the persistent homology of spatiotemporal DMN is more likely to distinguish AD from NC, and it is more likely to explore the potential biomarkers for AD imaging.

Spatiotemporal Network Clustering Results

To determine the optimal number of clusters k, we took k from 2 to 9 and repeated the test 100 times for each value. The experimental result is shown in **Figure 3**, where the solid point represents the best number of clusters. Here, the most suitable number of clusters was $k = 2$. The Silhouette score and Calinski–Harabasz index were used to evaluate the effectiveness of the clustering results. We further check the optimal number of clusters using a fivefold cross-validation. The average distance of test sets was calculated while selecting different cluster numbers, as shown in **Figure 4**. The error distance reached the minimum when the cluster number was 2, suggesting that the optimal value of k was 2 again. Thus, the AD and NC subjects' varying-time

[5]http://adni.loni.usc.edu

TABLE 1 | Demographic information of experimental subjects.

	AD (n = 31)	NC (N = 37)	p-value
Age	74.0 ± 6.1	74.1 ± 6.2	0.7486
Education	15.4 ± 3.9	16.1 ± 3.6	0.4267
Gender (male/female)	16/15	15/22	0.6033
MMSE	22.8 ± 3.4	28.8 ± 1.6	0.0015
CDR score	≥ 1	0	–

Data are presented as mean ± SD.
AD, Alzheimer's disease; NC, normal control; MMSE, Mini-Mental State Examination; CDR, clinical dementia rating.

TABLE 2 | Statistical *p*-values of different network properties between Alzheimer's disease (AD) and normal control (NC) groups in automated anatomical labeling (AAL).

Network mode	Graph theory-based properties						Persistent homology-based properties		
	GE	LE	CPL	EC	CC	SW	NR	SIP	BNP
Spatial network	0.075	0.828	0.484	0.092	0.357	0.763	0.049*	0.008**	0.041*
Spatiotemporal network	0.230	0.642	0.518	0.086	0.327	0.119	0.311	0.002**	0.003**

*$p < 0.05$; **$p < 0.01$.
GE, global efficiency; LE, local efficiency; CPL, characteristic path length; EC, eigenvector centrality; CC, clustering coefficient; SW, small-world attribute; NR, network radius; SIP, slope of integrated persistent feature plot; BNP, Betty number plot.

TABLE 3 | Statistical *p*-values of different network properties between AD and NC groups in a default mode network (DMN).

Network mode	Graph theory-based properties						Persistent homology-based properties		
	GE	LE	CPL	EC	CC	SW	NR	SIP	BNP
Spatial network	0.058	0.960	0.619	0.009**	0.230	0.074	0.164	0.004**	0.049*
Spatiotemporal network	0.177	0.447	0.353	0.017*	0.145	0.007**	0.547	0.003**	0.001**

*$p < 0.05$; **$p < 0.01$.
GE, global efficiency; LE, local efficiency; CPL, characteristic path length; EC, eigenvector centrality; CC, clustering coefficient; SW, small-world attribute; NR, network radius; SIP, slope of integrated persistent feature plot; BNP, Betty number plot.

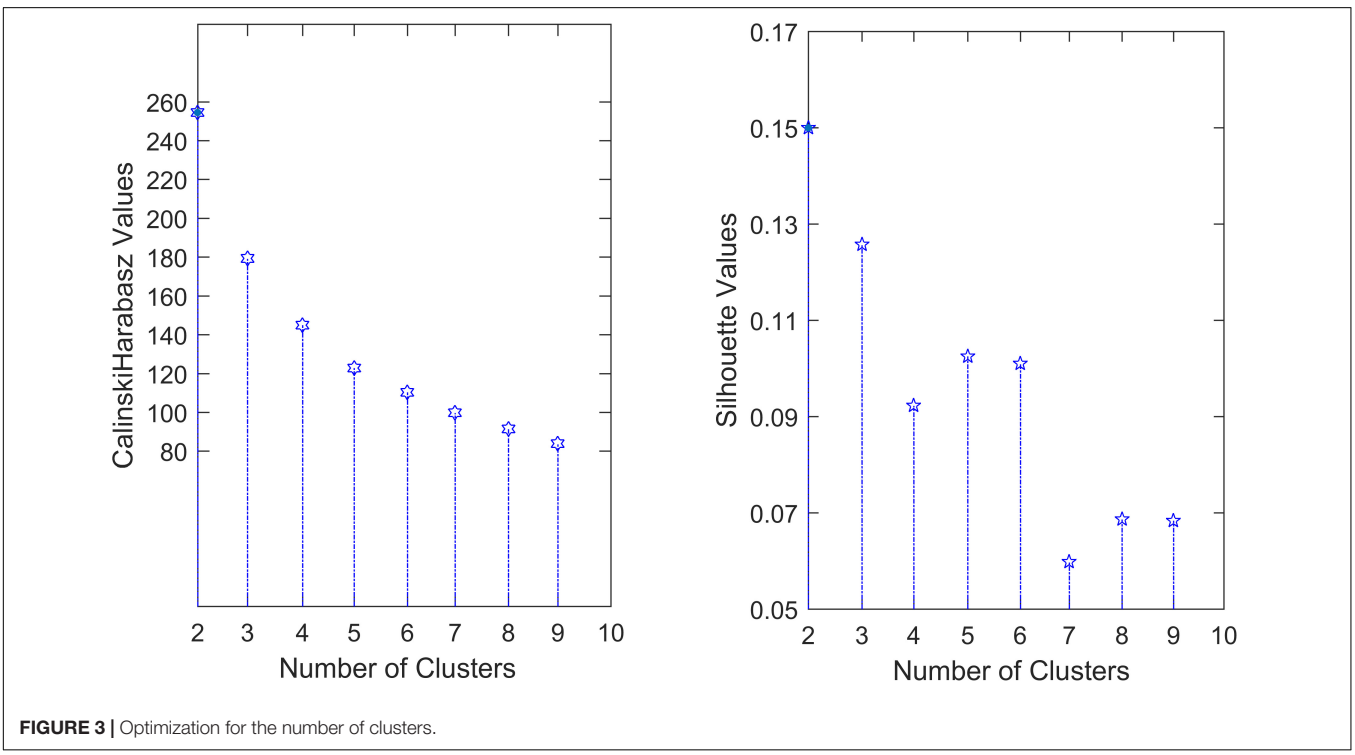

FIGURE 3 | Optimization for the number of clusters.

matrices of sliding windows were clustered into two highly structured functional connectivity states separately.

We calculated a specific functional connectivity matrix (i.e., cluster center) for all windows in each state, and each element in the matrix was the median value of the corresponding element belonging to a state in all window matrices. The cluster center diagrams of the whole brain network and DMN are shown in **Figures 5**, **6**, respectively, where maps correspond to the number of windows in a state, and the color bar represents the Pearson correlation coefficient value. It can be seen that state A is a stronger connection state, and state B is a sparser one. In the whole brain network clustering (see **Figure 5**), the window ratio of patients with AD in state A is reduced by about 5% compared with NC subjects, while it increases accordingly in state B. Similarly, in the DMN clustering (see **Figure 6**), compared with NC subjects, the window ratio of patients with AD in state B (*AD*: 0.67 ± 0.05; *NC*: 0.47 ± 0.06, $p < 0.05$) is significantly higher.

Further, the results of average residence time are shown in **Figures 7**, **8**. It is calculated by averaging the number of consecutive windows before changing from one to another state.

FIGURE 4 | Cross-validation to determine the number of clusters.

The number of consecutive windows of AD in state B is relatively large, either in the whole brain network (see **Figure 7**, AD: 40 ± 8 windows; NC: 27 ± 5 windows, $p < 0.05$), or in DMN (see **Figure 8**, *AD*: 47 ± 8; *NC*: 28 ± 6, $p < 0.05$).

In summarily, the clustering results of the DMN subnetwork were similar to those of the whole brain network, and the difference between the AD and NC group was more significant. The brain network of patients with AD is more likely to stay in state B, a weak connection state.

DISCUSSION

Present Findings

This paper studies the differences of spatiotemporal network dynamics between patients with AD and NCs in the whole brain network and its subnetwork DMN. There are three main findings in this study.

First, the spatiotemporal dynamics method combining a sliding window and persistent homology performs better than existing methods in the AD brain network analysis, and the persistent homology-based measures can be used as a potential biomarker. In our experiment, most of the network properties were more powerful in the spatiotemporal brain network than in

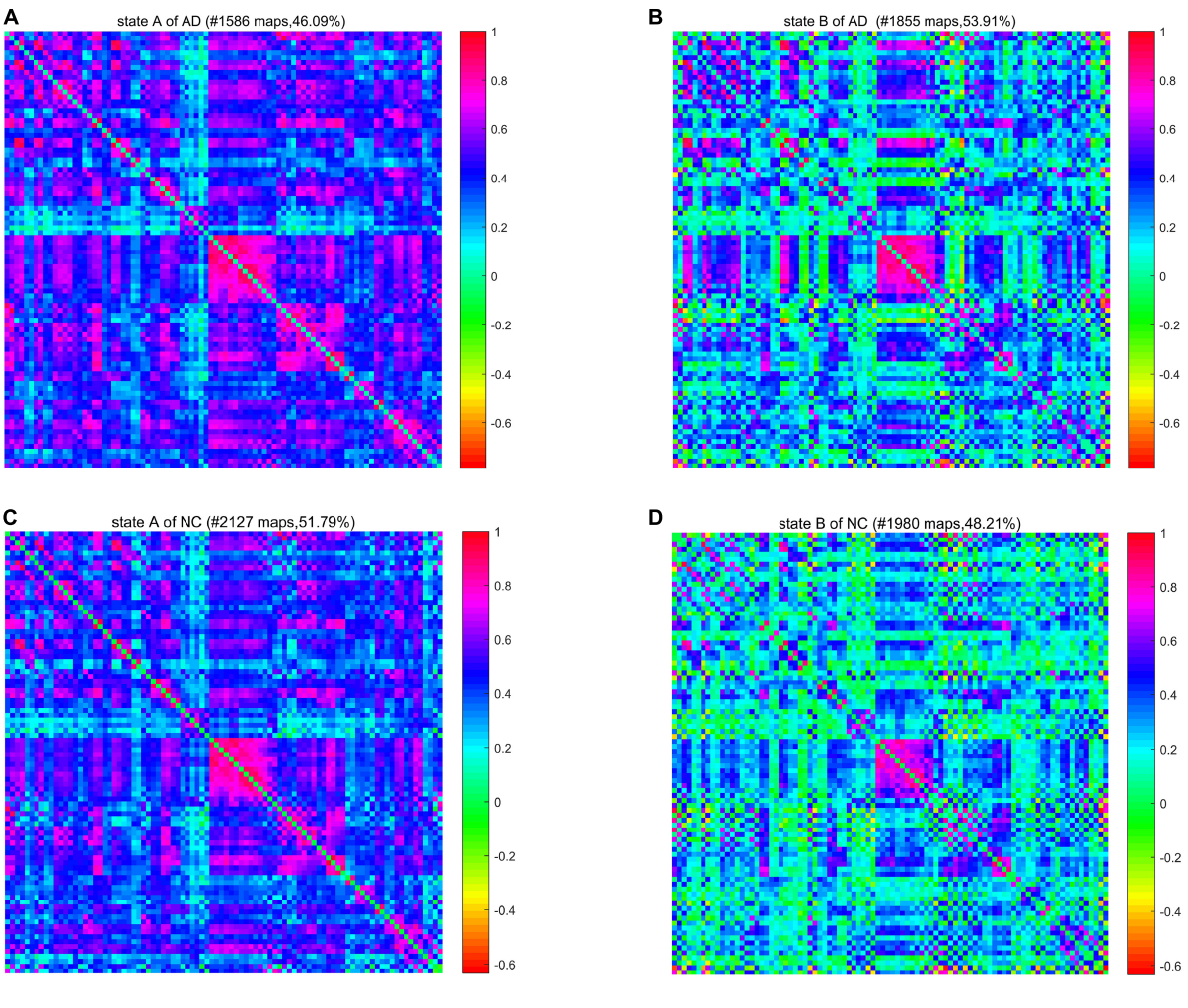

FIGURE 5 | The cluster center diagram of spatiotemporal automated anatomical labeling (AAL) networks for Alzheimer's disease (AD) and normal control (NC).

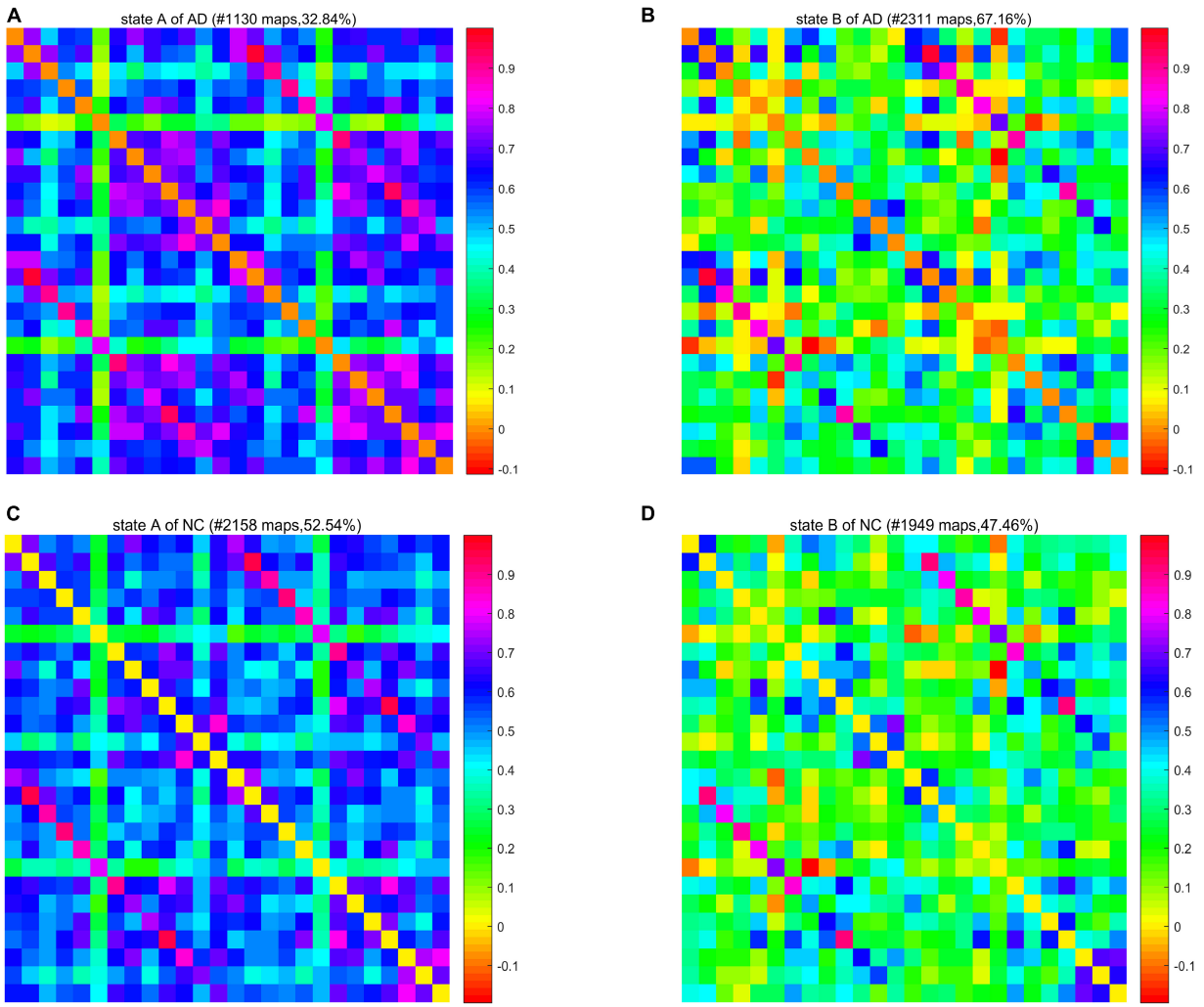

FIGURE 6 | The cluster center diagram of spatiotemporal default mode networks (DMNs) for AD and NC.

the spatial brain network, particularly two persistent homology-based properties. Both SIP and BNP detected significant group differences ($p < 0.01$) in a spatiotemporal network after introducing time-varying information, in both the whole brain network and DMN subnetwork. In addition, in the DMN, the small-world attribute of a spatiotemporal network ($p < 0.01$) is significantly different from that of a spatial network ($p > 0.05$). In general, the brain spatiotemporal network could provide a more subtle temporal variability than a spatial network.

Second, in the study on the AD brain network, the DMN is a more suitable network than the whole brain network. The difference between groups of most network properties in DMN was more apparent than that in the whole brain network. In the DMN measurement using the graph theory method, the eigenvector centrality detected very significant differences between the groups in both spatial and spatiotemporal networks, while there was no difference in the whole brain study. Similarly, there was no significant difference in the small-world attribute in the whole brain network, but there was a very significant difference in the spatiotemporal DMN. Overall, the DMN is more likely to distinguish AD from NC, and it is more likely to explore the potential biomarkers for AD imaging.

Finally, the clustering results show that AD tends to be in the weak connection state. The window ratio and the average residence time in the weak connection state were relatively higher for patients with AD than those of NC. It may be due to the fact that patients with AD have not established a firm connection.

Experimental Result Analysis of Proposed Method

As the persistent homology-based features are monotonically decreasing convergence functions according to filtration values, both the network properties BNP and SIP can be considered as the information diffusion rate or convergence rate in the process of reaching a fully connected component. In this study, in both the whole brain network and DMN, the values of the BNP group and the SIP group showed the same pattern of

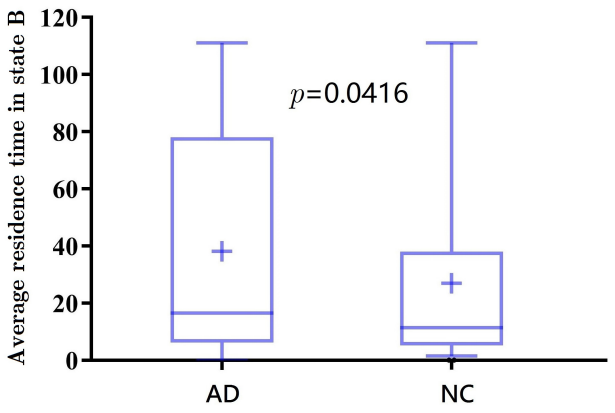

FIGURE 7 | The average residence time of spatiotemporal AAL networks for AD and NC.

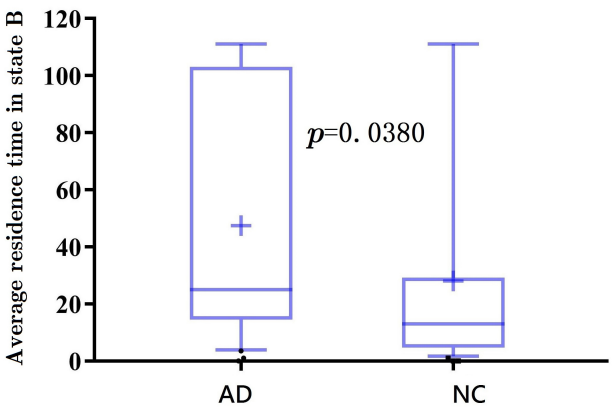

FIGURE 8 | The average residence time of spatiotemporal DMNs for AD and NC.

| AD| < | NC|, with a significance in the level $p < 0.01$ based on a two-sample *t*-test. The fact that the BNP and SIP curves of the AD group are not as steep as those of the NC group may mean that the information diffusion speed in the AD group is slow. Because the persistent homology-based features measure the topology of the whole brain network, it is reasonable to speculate that the slow convergence rate is caused by the reduction of functional integration of the whole brain, which may further lead to cognitive defects in patients with AD.

Further, we apply the traditional method of cluster analysis to verify the abovementioned assumption. The spatiotemporal networks of AD and NC individuals were clustered into two states. One shows the pattern with a stronger connectivity in the brain region, and another presents the pattern with less connection definitions and a lower connectivity. Moreover, the brain network of patients with AD were more likely to stay in a weak connection state. This finding confirms the abovementioned assumption about the weak integration ability of AD brain network. Therefore, our proposed method based on persistent homology provides a novel viewpoint of the overall tissue injury and the interruption of neuronal integration in patients with AD dementia.

Clinical Potential of Spatiotemporal Brain Network

We proposed a novel method to construct and measure a spatiotemporal network based on persistent homology (i.e., spatiotemporal network + persistent homology-based properties). We compared our experimental results with two dynamic spatiotemporal methods and two static spatial methods for a functional connectivity analysis, including spatiotemporal network + graph theory-based properties, spatiotemporal network + *k*-means clustering, spatial network + persistent homology-based properties, and spatial network + graph theory-based properties. Because the strength of functional connectivity varies in the range of seconds to minutes, it is important to analyze the differences between different time periods, forming temporal dynamics. Only a spatiotemporal brain network is able to capture the inner dynamic nature of connectivity alterations, therefore the dynamic spatiotemporal methods are demonstrated to be more powerful to distinguish the AD group from the NC group than the static spatial methods without time-varying information, as shown in **Tables 2**, **3**.

Further, in dynamic spatiotemporal network analyses, after sliding time windows, the state extraction through *k*-means clustering and the network topology measurement have been the two most widely applied strategies (Preti et al., 2017). The former technique enables to detect differences between AD and NC groups based on the dynamical occurrence and connectivity strength of connectivity states. Then, the latter technique allows to refine the meaning of the observed spatial differences across groups using some network metrics. With graph theory-based network properties, various non-trivial topological features, including small-world organization, modular structure, and highly connected hubs, have been observed to be disrupted in patients with AD (Sporns, 2018; Kuang et al., 2019a). Moreover, the persistent homology-based network properties allow to address dynamic abnormalities at a more global level, where the evolution of the global pattern of connectivity contributed by all scales is probed.

In summary, the dynamic spatiotemporal network analysis provides more completed functional alterations in connectivity, which cannot be depicted by a stationary analysis. Such kinds of technique have a greater potential for clinical applications in AD.

Limitation and Future Works

Although the promising results were obtained by applying the two suggested network properties SIP and BNP based on persistent homology to discriminate spatiotemporal networks between AD and NC groups, there are some important caveats. First, most network properties showed a better statistical power in spatiotemporal networks in ADNI data set. To validate the robustness of the proposed method, we will further study on other independent data sets. Then, current research is limited to the analysis of the rs-fMRI data collected in a single time period and does not verify multiple time periods. In the future,

we will study the longitudinal trajectories (Dautricourt et al., 2021) of functional brain dynamics over multiple time periods. Last but not least, although this article interprets the temporal dynamics of the functional brain network well and has obtained good experimental results, a correlation analysis with behavioral data should be performed in the future.

CONCLUSION

This work measured the functional brain network structure of the whole brain network and its subnetwork DMN on rs-fMRI data set. A novel method is proposed based on our prior work of persistent homology. We combine multiple temporal windows and spatial scales to study the spatiotemporal brain dynamics. Most network properties show a better statistical power in spatiotemporal networks than in spatial networks, and the persistent homology-based features detected more significant differences between AD and NC groups than the standard graph theory properties. Moreover, the brain network of patients with AD is more likely to stay in a weak connection state in a clustering study. To the best of our knowledge, this is the first study applying persistent homology to analyze the spatiotemporal brain network. This study offers a novel insight into revealing the abnormalities of the functional organization of patients with AD.

DATA AVAILABILITY STATEMENT

Publicly available datasets were analyzed in this study. This data can be found here: http://adni.loni.usc.edu.

ETHICS STATEMENT

Written informed consent was obtained from the individual(s) for the publication of any potentially identifiable images or data included in this article.

AUTHOR CONTRIBUTIONS

JX and LK designed the study. LK acquired the data. JX, XW, and LK analyzed and interpreted the results of the data. JX and JJ drafted the manuscript. JX and LK revised the manuscript. All authors contributed to the article and approved the submitted version.

FUNDING

This research was funded by the Natural Science Foundation of Shanxi Province of China (201901D111150 to LK) and the Research Project Supported by Shanxi Scholarship Council of China (2020-113 to LK).

ACKNOWLEDGMENTS

Data collection and sharing for this project were funded by the ADNI (National Institutes of Health Grant U01 AG024904) and DOD ADNI (Department of Defense award number W81XWH-12-2-0012). ADNI was funded by the National Institute on Aging, the National Institute of Biomedical Imaging and Bioengineering, and through generous contributions from the following: AbbVie, Alzheimer's Association; Alzheimer's Drug Discovery Foundation; Araclon Biotech; BioClinica, Inc.; Biogen; Bristol-Myers Squibb Company; CereSpir, Inc.; Cogstate; Eisai Inc.; Elan Pharmaceuticals, Inc.; Eli Lilly and Company; EuroImmun; F. Hoffmann-La Roche Ltd. and its affiliated company Genentech, Inc.; Fujirebio; GE Healthcare; IXICO Ltd.; Janssen Alzheimer Immunotherapy Research & Development, LLC.; Johnson & Johnson Pharmaceutical Research & Development LLC.; Lumosity; Lundbeck; Merck & Co., Inc.; Meso Scale Diagnostics, LLC.; NeuroRx Research; Neurotrack Technologies; Novartis Pharmaceuticals Corporation; Pfizer Inc.; Piramal Imaging; Servier; Takeda Pharmaceutical Company; and Transition Therapeutics. The Canadian Institutes of Health Research is providing funds to support ADNI clinical sites in Canada. Private sector contributions are facilitated by the Foundation for the National Institutes of Health (www.fnih.org). The grantee organization is the Northern California Institute for Research and Education, and the study was coordinated by the Alzheimer's Therapeutic Research Institute at the University of Southern California. ADNI data are disseminated by the Laboratory for Neuro Imaging at the University of Southern California.

REFERENCES

Allen, E. A., Damaraju, E., Plis, S. M., Erhardt, E. B., Eichele, T., and Calhoun, V. D. (2014). Tracking whole-brain connectivity dynamics in the resting state. *Cereb. Cortex* 24, 663–676.

Binnewijzend, M. A. A., Adriaanse, S. M., Van der Flier, W. M., Teunissen, C. E., de Munck, J. C., Stam, C. J., et al. (2014). Brain network alterations in Alzheimer's disease measured by Eigenvector centrality in fMRI are related to cognition and CSF biomarkers. *Hum. Brain Mapp.* 35, 2383–2393. doi: 10.1002/hbm.22335

Brier, M. R., Thomas, J. B., Fagan, A. M., Hassenstab, J., Holtzman, D. M., Benzinger, T. L., et al. (2014). Functional connectivity and graph theory in preclinical Alzheimer's disease. *Neurobiol. Aging* 35, 757–768.

Chen, Q., Lu, J. M., Zhang, X., Sun, Y., Chen, W. Q., Li, X., et al. (2021). Alterations in dynamic functional connectivity in individuals with subjective cognitive decline. *Front. Aging Neurosci.* 13:646017. doi: 10.3389/fnagi.2021.646017

Chen, X. B., Zhang, H., Gao, Y., Wee, C. Y., Li, G., Shen, D. G., et al. (2016). High-Order resting-state functional connectivity network for MCI classification. *Hum. Brain Mapp.* 37, 3282–3296. doi: 10.1002/hbm.23240

Choi, H., Kim, Y. K., Kang, H., Lee, H., Im, H.-J., Kim, E. E., et al. (2014). Abnormal metabolic connectivity in the pilocarpine-induced epilepsy rat model: a multiscale network analysis based on persistent homology. *NeuroImage* 99, 226–236.

Dautricourt, S., de Flores, R., Landeau, B., Poisnel, G., Vanhoutte, M., Delcroix, N., et al. (2021). Longitudinal changes in hippocampal network connectivity in Alzheimer's disease. *Ann. Neurol.* 90, 391–406. doi: 10.1002/ana.26168

De Pasquale, F., Della Penna, S., Sporns, O., Romani, G., and Corbetta, M. (2016). A dynamic core network and global efficiency in the resting human brain. *Cereb. Cortex* 26, 4015–4033.

de Vos, F., Koini, M., Schouten, T. M., Seiler, S., van der Grond, J., Lechner, A., et al. (2018). A comprehensive analysis of resting state fMRI measures to

classify individual patients with Alzheimer's disease. *Neuroimage* 167, 62–72. doi: 10.1016/j.neuroimage.2017.11.025

Edelsbrunner, H., and Harer, J. (2010). *Computational Topology: an Introduction*. Providence, RI: American Mathematical society.

Engels, M. M. A., van der Flier, W. M., Stam, C. J., Hillebrand, A., Scheltens, P., and van Straaten, E. C. W. (2017). Alzheimer's disease: the state of the art in resting-state magnetoencephalography. *Clin. Neurophysiol.* 128, 1426–1437. doi: 10.1016/j.clinph.2017.05.012

Folstein, M. F., Folstein, S. E., and McHugh, P. R. (1975). "Mini-mental state": a practical method for grading the cognitive state of patients for the clinician. *J. Psychiatric Res.* 12, 189–198.

Fujita, A., Takahashi, D. Y., Balardin, J. B., Vidal, M. C., and Sato, J. R. (2017). Correlation between graphs with an application to brain network analysis. *Comput. Stat. Data Anal.* 109, 76–92. doi: 10.1016/j.csda.2016.11.016

Giusti, C., Ghrist, R., and Bassett, D. S. (2016). Two's company, three (or more) is a simplex : algebraic-topological tools for understanding higher-order structure in neural data. *J. Comput. Neurosci.* 41, 1–14. doi: 10.1007/s10827-016-0608-6

Hallquist, M. N., and Hillary, F. G. (2018). Graph theory approaches to functional network organization in brain disorders: a critique for a brave new small-world. *Network Neurosci.* 3, 1–26. doi: 10.1162/netn_a_00054

Jack, C. R., Bernstein, M. A., Fox, N. C., Thompson, P., Alexander, G., Harvey, D., et al. (2008). The Alzheimer's disease neuroimaging initiative (ADNI): MRI methods. *J. Magn. Reson. Imaging* 27, 685–691.

Jagust, W. J., Bandy, D., Chen, K., Foster, N. L., Landau, S. M., Mathis, C. A., et al. (2010). The Alzheimer's disease neuroimaging initiative positron emission tomography core. *Alzheimer's Dementia* 6, 221–229.

Kuang, L., Han, X., and Chen, K. (2019a). A concise and persistent feature to study brain resting-state network dynamics: findings from the Alzheimer's disease Neuroimaging Initiative. *Hum. Brain Mapp.* 40, 1062–1081. doi: 10.1002/hbm.24383

Kuang, L., Zhao, D., Xing, J., Chen, Z., Xiong, F., and Han, X. (2019b). Metabolic Brain Network Analysis of FDG-PET in Alzheimer's disease using kernel-based persistent features. *Molecules* 24:2301. doi: 10.3390/molecules24122301

Kuang, L. Q., Gao, Y., Chen, Z. Y., Xing, J. C., Xiong, F. G., and Han, X. (2020a). White matter brain network research in Alzheimer's disease using persistent features. *Molecules* 25:2472. doi: 10.3390/molecules25112472

Kuang, L. Q., Jia, J. Y., Zhao, D. Y., Xiong, F. G., Han, X., and Wang, Y. L. (2020b). Default mode network analysis of APOE genotype in cognitively unimpaired subjects based on persistent homology. *Front. Aging Neurosci.* 12:188. doi: 10.3389/fnagi.2020.00188

Lee, H., Kang, H., Chung, M. K., Kim, B.-N., and Lee, D. S. (2012). Persistent brain network homology from the perspective of dendrogram. *IEEE Trans. Med. Imaging* 31, 2267–2277.

Lee, H., Kang, H., Chung, M. K., Lim, S., Kim, B. N., and Lee, D. S. (2017). Integrated multimodal network approach to PET and MRI based on multidimensional persistent homology. *Hum. Brain Mapp.* 38, 1387–1402.

Lei, B. Y., Yu, S. Z., Zhao, X., Frangi, A. F., Tan, E. L., Elazab, A., et al. (2021). Diagnosis of early Alzheimer's disease based on dynamic high order networks. *Brain Imaging Behav.* 15, 276–287. doi: 10.1007/s11682-019-00255-9

Liao, W., Wu, G. R., Qiang, X., Ji, G. J., Zhang, Z., Zang, Y. F., et al. (2014). DynamicBC: a MATLAB toolbox for dynamic brain connectome analysis. *Brain Connect.* 4:780.

Marquez, F., and Yassa, M. A. (2019). Neuroimaging biomarkers for Alzheimer's disease. *Mol. Neurodegener.* 14:21. doi: 10.1186/s13024-019-0325-5

Mill, R. D., Gordon, B. A., Balota, D. A., and Cole, M. W. (2020). Predicting dysfunctional age-related task activations from resting-state network alterations. *Neuroimage* 221:117167. doi: 10.1016/j.neuroimage.2020.117167

Patterson, C. (2018). *World Alzheimer Report 2018*. London: Alzheimer's Disease International.

Preti, M. G., Bolton, T. A. W., and Van De Ville, D. (2017). The dynamic functional connectome: State-of-the-art and perspectives. *Neuroimage* 160, 41–54. doi: 10.1016/j.neuroimage.2016.12.061

Rauchmann, B.-S., Ersoezlue, E., Stoecklein, S., Keeser, D., Brosseron, F., Buerger, K., et al. (2021). Resting-State network alterations differ between Alzheimer's disease atrophy subtypes. *Cereb. Cortex* 31, 4901–4915. doi: 10.1093/cercor/bhab130

Rubinov, M., and Sporns, O. (2010). Complex network measures of brain connectivity: uses and interpretations. *NeuroImage* 52, 1059–1069.

Scheltens, P., De Strooper, B., Kivipelto, M., Holstege, H., Chetelat, G., Teunissen, C. E., et al. (2021). Alzheimer's disease. *Lancet* 397, 1577–1590. doi: 10.1016/s0140-6736(20)32205-4

Smith, S. M., and Nichols, T. E. (2009). Threshold-free cluster enhancement: addressing problems of smoothing, threshold dependence and localisation in cluster inference. *Neuroimage* 44, 83–98. doi: 10.1016/j.neuroimage.2008.03.061

Sporns, O. (2018). Graph theory methods: applications in brain networks. *Dial. Clin. Neurosci.* 20, 111–121.

Tzourio-Mazoyer, N., Landeau, B., Papathanassiou, D., Crivello, F., Etard, O., Delcroix, N., et al. (2002). Automated anatomical labeling of activations in SPM using a macroscopic anatomical parcellation of the MNI MRI single-subject brain. *NeuroImage* 15, 273–289.

Vriend, C., van den Heuvel, O. A., Berendse, H. W., van der Werf, Y. D., and Douw, L. (2018). Global and subnetwork changes of the structural connectome in de novo Parkinson's disease. *Neuroscience* 386, 295–308. doi: 10.1016/j.neuroscience.2018.06.050

Wang, J., Zuo, X., Dai, Z., Xia, M., Zhao, Z., Zhao, X., et al. (2013). Disrupted functional brain connectome in individuals at risk for Alzheimer's disease. *Biol. Psychiatry* 73, 472–481. doi: 10.1016/j.biopsych.2012.03.026

Watts, D. J., and Strogatz, S. H. (1998). Collective dynamics of 'small-world' networks. *Nature* 393:440.

Yan, C., and Zang, Y. (2010). DPARSF: a MATLAB toolbox for" pipeline" data analysis of resting-state fMRI. *Front. Sys. Neurosci.* 4:13. doi: 10.3389/fnsys.2010.00013

Conflict of Interest: The authors declare that the research was conducted in the absence of any commercial or financial relationships that could be construed as a potential conflict of interest.

Publisher's Note: All claims expressed in this article are solely those of the authors and do not necessarily represent those of their affiliated organizations, or those of the publisher, the editors and the reviewers. Any product that may be evaluated in this article, or claim that may be made by its manufacturer, is not guaranteed or endorsed by the publisher.

Copyright © 2022 Xing, Jia, Wu and Kuang. This is an open-access article distributed under the terms of the Creative Commons Attribution License (CC BY). The use, distribution or reproduction in other forums is permitted, provided the original author(s) and the copyright owner(s) are credited and that the original publication in this journal is cited, in accordance with accepted academic practice. No use, distribution or reproduction is permitted which does not comply with these terms.

frontiers in Aging Neuroscience

ORIGINAL RESEARCH
published: 10 February 2022
doi: 10.3389/fnagi.2022.788166

The Frontal and Cerebellar Metabolism Related to Cognitive Dysfunction in Multiple System Atrophy

Cong Shen[1†], Qi-Si Chen[1†], Chuan-Tao Zuo[2], Feng-Tao Liu[1‡] and Jian Wang[1*‡]*

[1] Department of Neurology and National Research Center for Aging and Medicine & National Center for Neurological Disorders, State Key Laboratory of Medical Neurobiology, Huashan Hospital, Fudan University, Shanghai, China, [2] Positron Emission Tomography (PET) Center at Huashan Hospital, Institute of Functional and Molecular Medical Imaging, Human Phenome Institute, Fudan University, Shanghai, China

OPEN ACCESS

Edited by:
Kenneth S. Hettie, Stanford University, United States

Reviewed by:
Jungho Cha, Icahn School of Medicine at Mount Sinai, United States
Liping Fu, China-Japan Friendship Hospital, China

***Correspondence:**
Feng-Tao Liu
liufengtao@fudan.edu.cn
Jian Wang
wangjian_hs@fudan.edu.cn

[†] These authors have contributed equally to this work

[‡] These authors jointly supervised the work

Specialty section:
This article was submitted to Neurocognitive Aging and Behavior, a section of the journal Frontiers in Aging Neuroscience

Received: *01 October 2021*
Accepted: *11 January 2022*
Published: *10 February 2022*

Citation:
Shen C, Chen Q-S, Zuo C-T, Liu F-T and Wang J (2022) The Frontal and Cerebellar Metabolism Related to Cognitive Dysfunction in Multiple System Atrophy. Front. Aging Neurosci. 14:788166. doi: 10.3389/fnagi.2022.788166

Background: Cognitive dysfunctions have been reported in multiple system atrophy (MSA). However the underlying mechanisms remain to be elucidated. This study aimed to explore the possible cerebral metabolism associated with domain-specific cognitive performances in MSA.

Methods: A total of 84 patients were diagnosed as probable or possible MSA, comprised of 27 patients as MSA with predominant parkinsonism (MSA-P) and 57 patients as MSA with predominant cerebellar ataxia (MSA-C). The comprehensive neuropsychological tests and ^{18}F-fluorodeoxyglucose (^{18}F-FDG) positron emission tomography (PET) imaging were performed. *Z*-score was calculated to non-dimensionalize and unify indicators of different tests in the domains of executive function, attention, language, memory, and visuospatial function. Correlations between specific *Z*-score and cerebral ^{18}F-FDG uptake were analyzed using statistical parametric mapping. The cognition-related metabolic differences between patients with MSA-P and MSA-C were analyzed using the *post-hoc* test.

Results: *Z*-scores of the domains including attention, executive function, and language correlated positively with the metabolism in the superior/inferior frontal gyrus and cerebellum, but negatively with that in the insula and fusiform gyrus ($p < 0.001$). No significant differences in neuropsychological performances and frontal metabolism were found between patients with MSA-P and MSA-C. Only lower metabolism in the cerebellum was observed in MSA-C.

Conclusion: Metabolic changes in the frontal lobe and cerebellum may participate in the cognitive impairments of patients with MSA. Nevertheless, cognitive and corresponding metabolic differences between the two subtypes of MSA still need more exploration.

Keywords: cognitive impairment, ^{18}F-fluorodeoxyglucose, fronto-striatal dopamine signaling, cerebellum, multiple system atrophy

INTRODUCTION

Multiple system atrophy (MSA) is a sporadic, adult-onset neurodegenerative disorder, with the classical clinical presence of progressive autonomic failure, parkinsonism, and/or cerebellar ataxia (Wenning et al., 1997; Stefanova et al., 2009; Fanciulli and Wenning, 2015). Although dementia is a non-supporting item according to the second consensus statement on the diagnosis of MSA (Gilman et al., 2008), accumulating data showed great evidence for possible cognitive decline in MSA. Specifically, nearly half of the patients with MSA presented with cognitive impairments in some epidemiological data, with a broad spectrum of injury (Brown et al., 2010; Stankovic et al., 2014; Shen et al., 2021). At present, however, the underlying mechanisms of cognitive impairments in MSA are still far from being clearly understood. In the study of patients with MSA with mild dementia and aphasia, atrophy and neuronal cell loss were observed macroscopically and microscopically in the frontal lobe (Konagaya et al., 1999). Subsequent studies have compared the pathological burden degrees of glial cytoplasmic inclusions (GCIs) and neuronal cytoplasmic inclusions (NCIs) between MSA with normal cognition (MSA-NC) and MSA with cognitive impairment (MSA-CI; Cykowski et al., 2015; Homma et al., 2016; Koga et al., 2017; Jellinger, 2020; Miki et al., 2020). However, these results were variable and uncertain, which might be partially attributed to the small sample size.

The ^{18}F-fluorodeoxyglucose (^{18}F-FDG) positron emission tomography (PET) imaging can reflect the cerebral metabolic changes and disclose disease-specific alterations (Eckert et al., 2005, 2008). In our previous report, MSA-CI exhibited lower glucose metabolism in the left middle and superior frontal lobe, compared with MSA-NC (Shen et al., 2021). Nevertheless, the cerebral metabolic changes related to detailed cognitive performances in MSA remain to be further explored. In addition, the previous studies on comparisons of the profile and severity of cognitive dysfunction between two MSA subtypes, MSA with predominant parkinsonism (MSA-P) and MSA with predominant cerebellar ataxia (MSA-C; Gilman et al., 2008) remained limited and controversial (Kawai et al., 2008; Chang et al., 2009; Santangelo et al., 2020). Therefore, the comparison of cognition-related cerebral metabolism in different MSA subtypes will be helpful to understand the intrinsic pathological characteristics, which has not been reported earlier.

In this study, we aimed to detect the underlying cerebral metabolic changes by ^{18}F-FDG PET imaging related to domain-specific cognitive dysfunctions in patients with MSA. Furthermore, we compared the neuropsychological performances and cognition-related brain metabolism between the two subtypes of MSA preliminarily.

PARTICIPANTS AND METHODS

Subjects

A total of 84 patients diagnosed with probable or possible MSA were recruited in the Department of Neurology, Huashan Hospital, Fudan University between February 2012 and May 2019. The clinical diagnosis and categorization between MSA-P and MSA-C were made according to the second consensus statement on the diagnosis of MSA published in 2008 (Gilman et al., 2008). Demographic information including age, age at onset, sex, disease duration, and education degree were systematically collected. All patients included neither had head injury nor had other neurological or psychiatric diseases.

This study was approved by the Human Studies Institutional Review Board, Huashan Hospital, Fudan University. Written informed consents were obtained from the participants before entering this study in accordance with the Declaration of Helsinki.

Motor and Neuropsychological Assessments

Motor disability was evaluated by the Unified Parkinson's Disease Rating Scale III (UPDRS III) in all participants in a Med-Off state, which means that the patients were off anti-parkinsonism drugs for more than 12 h. Global cognitive status and cognitive dysfunction in five domains covering attention, executive function, memory, visuospatial function, and language were assessed using Mini-Mental State Examination (MMSE) and a series of comprehensive neuropsychological tests, which were as follows: attention by the Symbol Digit Modalities Test (SDMT; Sheridan et al., 2006) and part A of Trail-Making Test (TMT-A; Zhao et al., 2013); executive function by the part C of Stroop Color-Word Test (CWT-C; Steinberg et al., 2005) and part B of Trail-Making Test (TMT-B; Zhao et al., 2013); memory function by the Auditory Verbal Learning Test (AVLT; Guo et al., 2009) and delayed recall task of the Rey-Osterrieth Complex Figure Test (CFT-delay recall) (Caffarra et al., 2002); visuospatial function by copy task of Rey-Osterrieth Complex Figure Test (CFT; Caffarra et al., 2002) and the Clock Drawing Test (CDT; Ricci et al., 2016); and language ability by Animal Verbal Fluency Test (AVFT) and Boston Naming Test (BNT; Lucas et al., 2005). To eliminate dimensional differences in tests and quantify impairments of cognition, neuropsychological results of each test of all patients were transformed into *Z*-score using the mean and SD of the norm data from healthy controls of similar age and education in the Shanghai area (Wu et al., 2018; Shen et al., 2021): *Z*-score = (test score - mean score of norm data)/SD of norm data (when data was a score) or *Z*-score = (mean time of norm data - test time)/SD of norm data (when data were a time metrics) (Wu et al., 2018). *Z*-score less than −1.5 was defined to be the impairment in each test and *Z*-score of each cognition domain was calculated using the average *Z*-score of two tests in the same cognition domain.

^{18}F-Fluorodeoxyglucose Positron Emission Tomography Scan and Image Processing

^{18}F-fluorodeoxyglucose PET imaging was acquired in all patients within 1 month before or after the clinical assessment in the Huashan Hospital. Patients were instructed to be fasting for at least 6 h in an off-drug state before the scan. Forty-five minutes resting after injection of ^{18}F-FDG (185 MBq), a short

CT scan, and subsequent 10-min PET scan was performed by a Siemens Biograph 64 PET/CT (Siemens, Munich, Germany) in the three-dimensional (3D) mode in a dimly lit and quiet room. Images were subsequently reconstructed using a 3D ordered-subset expectation-maximization algorithm (4 iterations; 24 subsets; Gaussian filter, 2 mm; zoom, 3). Reconstructed images had a matrix size of 168 × 168 × 148 and a voxel size of $2 \times 2 \times 1.5\ mm^3$.

Positron emission tomography images were transformed for further processing using the MRIcron tool (output format: hdr/img). Then, images were processed by statistical parametric mapping (SPM5) software operated in MATLAB platform (Mathworks Inc., Sherborn, MA, United States). First, the original images were spatially normalized to normative stereotactic Montreal Neurological Institute (MNI) space using default [^{15}O]-H2O PET template (Della Rosa et al., 2014)[1]. Second, they were smoothed through a three-dimensional Gaussian filter with 10-mm full-width at half-maximum (FWHM).

To compare the metabolic characteristics between MSA-P and MSA-C, the two-sample *t*-test was used with age, sex, disease duration, and UPDRS score as covariates according to the general linear model at each voxel in SPM. To assess whether metabolic characteristics in a specific brain region would correlate with *Z*-score in each cognitive domain, the multiple regression model established by us previously (Ge et al., 2015; Wu et al., 2018) was applied first to detect clusters with peak threshold set at $P < 0.001$ over whole brain regions and extent threshold set as 120 voxels ($960\ mm^3$) and further to highlight clusters survived after a false discovery rate (FDR) correction at $p < 0.05$. In this step, education degree and UPDRS III score were both included as covariates to eliminate the effect of these factors. The differences in global metabolic values were modeled by analysis of covariance (ANCOVA) to minimize intersubject variability and improve signal-noise ratios. Exact coordinates and corresponding brain regions of detected clusters were ascertained through an MNI-to-Talairach conversion using Talairach–Daemon software (Research Imaging Center, University of Texas Health Science Center, San Antonio, TX, United States). The SPM maps for positive and negative correlations were superpositioned on a standard T1-weighted MRI brain template. Then, the spherical volume of interest (VOI) (4 mm radius) with the center of the circle at the peak voxel of the cluster was constructed, and metabolic value in each VOI was quantified using ScAnVP software (Version 5.9.1; Center for Neuroscience, the Feinstein Institute for Medical Research, Manhasset, NY, United States). To eliminate the individual differences in global metabolic value, the normalized regional cerebral metabolic rate of glucose (rCMRglc) was calculated by the following formula: [VOI value/whole-brain metabolism] × 100%.

Statistical Analysis

Differences in the demographic information, clinical characteristics, and neuropsychological performances between MSA-P and MSA-C were analyzed through Student's *t*-test in continuous and normally distributed data. Pearson's χ^2 test was used in categorical data. Mann–Whitney U test was used in continuous and non-parametric data. The *post-hoc* correlation analysis between *Z*-score in the specific cognitive domain and normalized rCMRglc in each VOI was performed through Pearson correlation and linear regression analyses. In the *post-hoc* metabolic comparison between patients with MSA-P and MSA-C, multiple comparisons *via* the Benjamini–Hochberg procedure were performed to control the FDR. Statistical analyses were performed using SPSS software (SPSS for Windows, version 22.0; SPSS Inc., Chicago, IL, United States). $p < 0.05$ was considered statistically significant.

RESULTS

Clinical Characteristics and Neuropsychological Performances in Patients With Multiple System Atrophy

Demographic, clinical, and detailed neuropsychological information of the total 84 patients with MSA was depicted in **Table 1**. The mean age at onset was 54.89 ± 7.97 years, and the mean disease duration was 26.80 ± 20.69 months. Patients with MSA were divided into two subtypes according to their predominant clinical symptoms, including 27 patients with MSA-P and 57 patients with MSA-C. No group differences were found for age at onset and education, but differences were observed in age, sex, disease duration, and UPDRS III score (**Table 1**). Both subtypes had considerable and extensive cognitive impairments in each domain represented by number and percentage of impairment as follows: attention, MSA-P, 18(67%), MSA-C, 30(53%); executive function, MSA-P, 13(48%), MSA-C, 32(56%); memory, MSA-P, 18(67%), MSA-C, 25(44%); visuospatial function, MSA-P, 12(44%), MSA-C, 22(39%); language, MSA-P, 10(37%), MSA-C, 21(37%). Compared with patients with MSA-C, patients with MSA-P performed worse on the attention domain, judging by a lower *Z*-score of attention domain and two corresponding tests (SDMT and TMT-A) ($p < 0.05$). However, this difference in attention performance was not significant after adjusting age, sex, disease duration, and UPDRS score factors.

The Regional Metabolism Correlating With Cognitive Declines in Multiple System Atrophy

Global metabolic values did not correlate with any *Z*-score in five domains (regression analysis: absolute value $r \leq 0.07$, $p \geq 0.40$). However, the positive and negative correlations between the regional ^{18}F-FDG metabolism and the cognitive *Z*-score in the five domains were detected (**Figure 1**).

The brain regions correlated positively to the *Z*-score of the separate cognitive domain were described as follows, respectively: attention with left inferior frontal gyrus, left superior frontal gyrus, left medial frontal gyrus, and right cerebellum (uvula and cerebellar tonsil); executive function with left inferior frontal gyrus, left middle frontal gyrus, left cerebellum (uvula), and right

[1] www.fil.ion.ucl.ac.uk/spm/spm99.html

TABLE 1 | Demographic, clinical characteristics, and neuropsychological performance in 84 patients with multiple system atrophy (MSA).

	Total MSA (*n* = 84)	MSA-P (*n* = 27)	MSA-C (*n* = 57)	*p*
Age (years)	57.12 (8.01)	59.89 (7.21)	55.81 (8.10)	0.028
Age at onset (years)	54.89 (7.97)	57.08 (7.14)	53.85 (8.19)	0.082
Sex (male)	51	11	40	0.010
MSA duration (months)	26.80 (20.69)	33.70 (25.50)	23.53 (17.28)	0.034
Education (years)	10.82 (3.19)	10.67 (3.33)	10.90 (3.14)	0.761
UPDRS III score_OFF	33.58 (15.42)	48.37 (15.80)	26.58 (9.02)	<0.001
MMSE	26.43 (2.80)	26.48 (2.41)	26.40 (2.98)	0.906
Attention	48 (57%)	18 (67%)	30 (53%)	0.225
Z score	−1.58 (1.62)	−2.28 (1.90)	−1.24 (1.37)	0.005
SDMT score	23.56 (13.09)	19.33 (12.36)	25.56 (13.04)	0.041
TMT-A time	90.73 (46.98)	111.19 (57.78)	81.04 (37.73)	0.018
Executive function	45 (54%)	13 (48%)	32 (56%)	0.493
Z score	−1.10 (1.18)	−1.10 (1.32)	−1.09 (1.12)	0.990
CWT-C score	41.30 (6.82)	43.26 (6.21)	40.37 (6.94)	0.069
TMT-B time	203.58 (80.81)	223.26 (101.01)	194.26 (68.31)	0.125
Memory	43 (51%)	18 (67%)	25 (44%)	0.051
Z score	−1.12 (1.10)	−1.32 (1.10)	−1.03 (1.09)	0.260
AVLT				
-Short delayed recall	3.99 (2.25)	3.63 (2.42)	4.16 (2.16)	0.317
-Long delayed recall	3.77 (2.22)	3.56 (2.52)	3.88 (2.09)	0.539
-cued recall	3.77 (2.42)	3.26 (2.47)	4.02 (2.38)	0.182
CFT-delay recall	11.71 (6.97)	10.30 (5.74)	12.39 (7.44)	0.201
Visuospatial function	34 (40%)	12 (44%)	22 (39%)	0.610
Z score	−1.42 (1.48)	−1.39 (1.25)	−1.43 (1.58)	0.897
CFT-copy score	27.74 (7.43)	26.93 (7.73)	28.12 (7.32)	0.494
CDT score	19.25 (7.10)	20.19 (6.82)	18.81 (7.24)	0.409
Language	31 (37%)	10 (37%)	21 (37%)	0.986
Z score	−1.05 (1.08)	−0.95 (0.97)	−1.11 (1.13)	0.534
AVFT score	13.37 (4.44)	13.15 (4.54)	13.47 (4.43)	0.756
BNT score	21.57 (4.37)	22.30 (4.26)	21.23 (4.42)	0.298

Data are shown in mean (SD) or number (%) of impairment or N. p-value represents the significance level of t-test performed for each item between patients with MSA-P and MSA-C. MSA-P, MSA with predominant parkinsonism; MSA-C, MSA with predominant cerebellar ataxia; UPDRS, Unified Parkinson's Disease Rating Scale; MMSE, Mini-Mental State Examination; SDMT, Symbol Digit Modalities Test; TMT, Trail Making Test; CWT-C, Stroop Color-Word Test C; AVLT, Auditory Verbal Learning Test; CFT, the Rey-Osterrieth Complex Figure Test; CDT, Clock Drawing Test; AVFT, Animal Verbal Fluency Test; BNT, Boston Naming Test.

cerebellum (pyramis and inferior semilunar lobule); language with left superior frontal gyrus, left middle frontal gyrus, left cerebellum (pyramis and uvula), and right cerebellum (tuber, pyramis, cerebellar tonsil, and declive); memory with inferior frontal gyrus; and visuospatial function with left cerebellum (pyramis) (**Figure 1** and **Table 2**).

However, the brain regions associated negatively with the *Z*-score of the separate cognitive domain were shown as follows, respectively: attention with right fusiform gyrus and right insula; executive function with right fusiform gyrus and right inferior temporal gyrus; language with left anterior cingulate, right middle temporal gyrus, and right fusiform gyrus; and memory with right fusiform gyrus and right inferior occipital gyrus (**Figure 1** and **Table 3**).

Moreover, the *post-hoc* correlations between the *Z*-score in separate cognition domain and the normalized rCMRglc in each significant brain region were calculated, with the correlation coefficients listed in **Tables 2**, **3**. The scatterplots and relationships of cognition and metabolic value in 11 representative regions are shown in **Figure 2**.

Cognition-Related Regional Metabolism in Two Subtypes of Multiple System Atrophy

Compared with patients with MSA-C, increased metabolism mainly in the bilateral cerebellum while decreased metabolism in bilateral putamen was observed in MSA-P, with no difference in frontal gyrus (**Supplementary Table 1**).

Considering the unadjusted cognitive differences in the attention domain between MSA-P and MSA-C, the comparisons of regional metabolism in attention-related areas mentioned above between two subtypes are presented in **Figure 3** and **Table 4**. However, no significant metabolic intergroup differences were observed in the left inferior frontal gyrus, superior frontal gyrus, medial frontal gyrus, right fusiform gyrus, right postcentral gyrus, and right insula. Only the metabolism in the right cerebellum (including uvula and cerebellar tonsil) was significantly lower in patients with MSA-C than patients with MSA-P after adjustment for confounders and *post-hoc* correction for multiple comparisons.

In addition, correlations between metabolism and the cognitive *Z*-score in the five domains separately in two subtypes are shown in **Supplementary Tables 2**, **3**. Cognition in patients with MSA-C correlated positively with metabolism in the frontal lobe and cerebellum, negatively with that in the fusiform gyrus and insula, whereas the clusters correlated with cognition in patients with MSA-P were limited to the cerebellum (positively) and temporal lobe (negatively).

DISCUSSION

In this study, there were three main findings. First and most importantly, lesions in the domains of attention, executive function, and language (*Z*-scores) correlated positively with the metabolism in the frontal gyrus and cerebellum and negatively with the insula and fusiform gyrus. Second, the attention function tended to be more severely impaired in MSA-P than in MSA-C, though significance did not sustain after adjusting confounders. Third, among all the attention-related brain regions, there was only lower metabolism of the cerebellum in MSA-C than in MSA-P.

^{18}F-fluorodeoxyglucose PET imaging can detect cerebral glucose metabolism and offer us some hints for mechanisms in neural hubs or networks behind cognitive impairments in

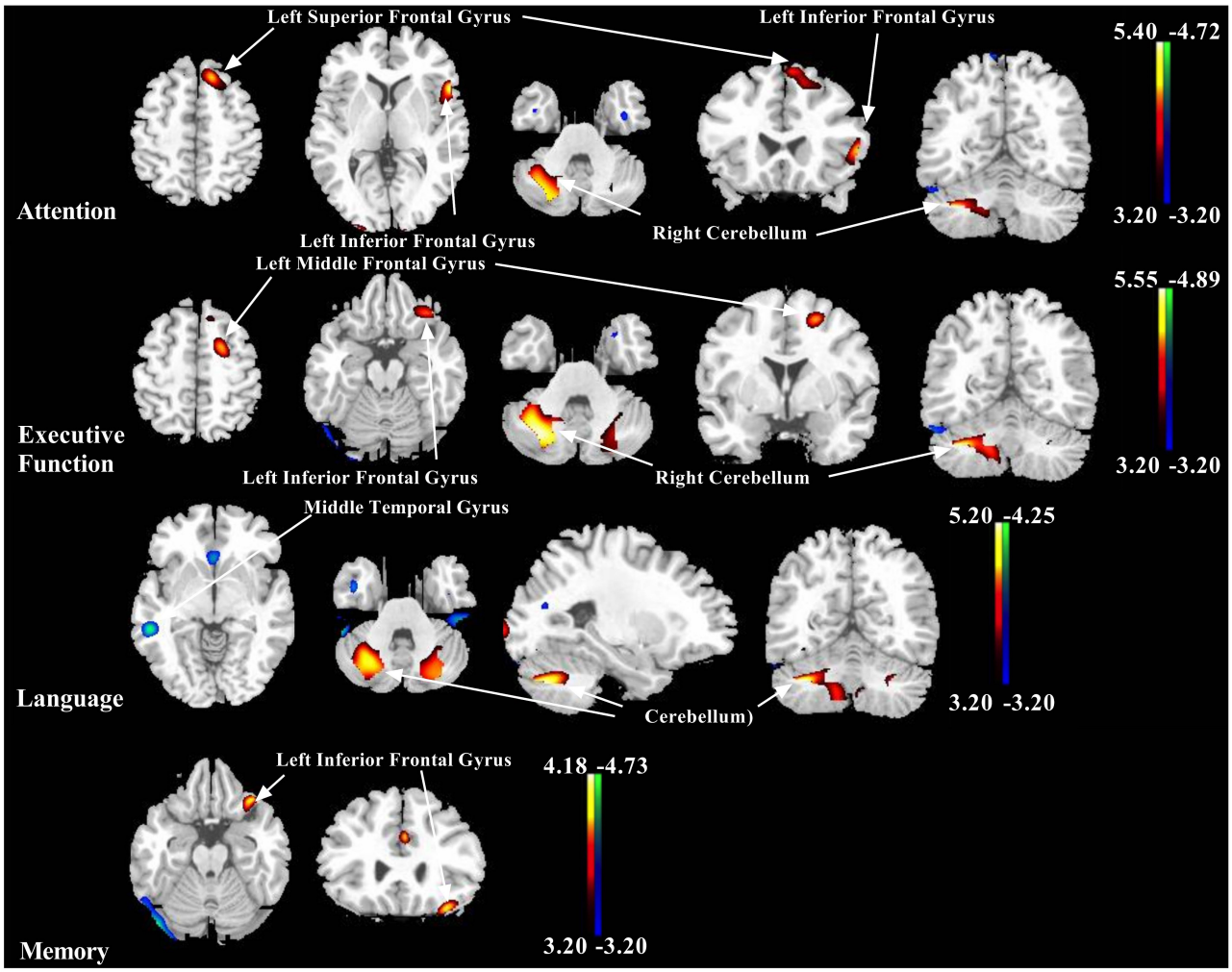

FIGURE 1 | Representative images showing correlations between *Z*-score of each cognitive domain and ^{18}F-fluorodeoxyglucose (^{18}F-FDG) metabolism in patients with multiple system atrophy (MSA). Positive relationships are displayed with a red-yellow scale while negative relationships are displayed using a blue-green scale. Both are overlaid on a structural magnetic resonance image (MRI) brain template. White arrows show the representative brain regions. The thresholds of the color bars indicate *T*-values, and voxel threshold was set at $p < 0.001$.

patients with MSA. In our analysis, metabolism in the frontal gyrus and cerebellum showed a great correlation with the severity of cognitive impairments in attention, executive function, and language domains.

The lower metabolism in the frontal gyrus of patients with MSA with worse cognition might suggest the disruption of frontostriatal dopamine signaling. The prefrontal cortex, as a key hub in the executive network, is associated with working memory and selective attention (Elliott, 2003; Gratwicke et al., 2015). Dopamine released from the substantia nigra and ventral tegmental area modulates prefrontal D2 receptors and facilitates cognitive flexibility (Floresco and Magyar, 2006). In previous neuropathology studies, there was a significant loss of neurons in the frontal cortex in patients with MSA with executive dysfunction compared with those with normal executive function (Salvesen et al., 2017). Analogously, (Fiorenzato et al., 2017) found that MSA-CI had focal volume reduction in the left middle frontal lobe compared with MSA-NC through voxel-based morphometry. Particularly, the study by Chang et al. (2009) showed that memory scores were well associated with prefrontal lobe atrophy. In addition, our hypothesis of striatofrontal differentiation in patients with MSA-CI was supported by the finding from FDG study by Kim et al. (2017), in which the glucose metabolism in the striatum was the most powerful determinant to metabolism in the frontal gyrus in the patients with MSA but not in healthy controls. Considering all these studies together, we believed that the frontostriatal network was involved in cognitive dysfunction in patients with MSA.

Besides the well-known motor function, the cerebellum is also involved in maintaining the functions of working memory, language, and social cognition. As previously reported, cerebellar lesions could lead to executive dysfunctions, deficits in visuospatial processing, and linguistic skills, termed cerebellar cognitive affective syndrome (Schmahmann and Sherman, 1998;

TABLE 2 | Brain regions in the 84 patients with MSA exhibiting positive correlations between the *Z*-score of cognitive domains and regional brain metabolism adjusting for education and Unified Parkinson's Disease Rating Scale (UPDRS) score.

Domains	Regions	BA	MNI coordinate			*Z* max	Cluster size (mm^3)	Pearson correlation coefficient
			x	y	z			
Attention	Left Inferior Frontal Gyrus #	45	−56	18	4	4.97	2,936	0.5612
	Left Superior Frontal Gyrus	8	−14	28	52	4.43	3,184	0.4160
	Left Superior Frontal Gyrus	6	−8	24	58	3.94	3,184	0.4183
	Left Medial Frontal Gyrus	6	−6	42	40	3.23	3,184	0.2747
	Right Uvula (Cerebellum) #	/	30	−72	−36	4.55	3,600	0.3190
	Right Cerebellar Tonsil (Cerebellum)	/	14	−58	−42	3.71	3,600	0.1943
Executive function	Left Middle Frontal Gyrus #	6	−22	0	54	4.37	1,632	0.4857
	Left Inferior Frontal Gyrus	47	−36	30	−20	4.10	1,312	0.4578
	Left Uvula (Cerebellum)	/	−28	−68	−36	3.67	1,280	0.3073
	Right Pyramis (Cerebellum) #	/	28	−68	−38	5.09	5,296	0.4758
	Right Inferior Semi-Lunar Lobule (Cerebellum)	/	24	−64	−50	3.48	5,296	0.3136
Language	Left Middle Frontal Gyrus	11	−32	38	−20	3.60	1,064	0.2883
	Left Superior Frontal Gyrus	11	−38	46	−16	3.45	1,064	0.2330
	Left Pyramis (Cerebellum) #	/	−22	−74	−42	4.19	3,168	0.3997
	Left Uvula (Cerebellum) #	/	−30	−80	−36	4.46	3,168	0.3793
	Right Tuber (Cerebellum) #	/	34	−66	−36	4.81	5,208	0.4574
	Right Pyramis (Cerebellum) #	/	26	−72	−38	4.70	5,208	0.4547
	Right Cerebellar Tonsil	/	6	−56	−50	4.19	5,208	0.3801
	Right Declive (Cerebellum)	/	34	−66	−14	4.05	960	0.4508
Memory	Left Inferior Frontal Gyrus	47	−36	28	−22	3.75	1,000	0.4088
Visuospatial function	Left Pyramis (Cerebellum)	/	−28	−66	−36	3.60	1,160	0.3240

Statistical threshold: $p < 0.001$. # indicates the cluster survived after FDR correction, $p < 0.05$. Pearson correlation coefficient evaluates correlations between Z-score in cognitive domain and normalized rCMRglc. BA, Brodmann area; MNI, Montreal Neurological Institute; and UPDRS, Unified Parkinson's Disease Rating Scale III.

TABLE 3 | Brain regions in the 84 patients with MSA exhibiting negative correlations between the *Z*-score of cognitive domains and regional brain metabolism adjusting for education and UPDRS score.

Domain	Regions	BA	MNI coordinate			*Z* max	Cluster size (mm^3)	Pearson correlation coefficient
			x	y	z			
Attention	Right Fusiform Gyrus	20	58	−34	−32	4.42	3,256	−0.4717
	Right Fusiform Gyrus	37	60	−52	−28	3.60	3,256	−0.3563
	Right Fusiform Gyrus	19	50	−72	−22	3.26	3,256	−0.2992
	Right Postcentral Gyrus	2	42	−28	32	3.92	3,032	−0.4284
	Right Insula	13	40	−10	26	3.80	3,032	−0.4841
	Right Insula	13	38	−22	28	3.60	3,032	−0.4676
Executive function	Right Fusiform Gyrus	20	56	−36	−32	4.56	4,464	−0.4900
	Right Inferior Temporal Gyrus	37	62	−48	−28	3.84	4,464	−0.4225
Language	Left Anterior Cingulate	24	0	24	−8	3.72	1,024	−0.3978
	Right Middle Temporal Gyrus	/	54	−38	−6	4.03	1,728	−0.4089
	Right Fusiform Gyrus	20	58	−42	−32	3.90	1,128	−0.3894
	Right Fusiform Gyrus	37	60	−52	−28	3.50	1,128	−0.3344
	Right Fusiform Gyrus	20	50	−30	−34	3.20	1,128	−0.3349
Memory	Right Fusiform Gyrus	19	46	−80	−22	4.43	2,824	−0.4503
	Right Inferior Occipital Gyrus	17	24	−100	−18	3.33	2,824	−0.3420

Statistical threshold: $p < 0.001$. None of the clusters survived after FDR correction, $p < 0.05$. Pearson correlation coefficient evaluates correlations between Z-score in the cognitive domain and normalized rCMRglc. BA, Brodmann area; MNI, Montreal Neurological Institute.

Buckner, 2013). In study by Kawabata et al. (2019) with resting-state fMRI, it was reported that Addenbrooke's Cognitive Examination-Revised scores correlated strongly with functional connectivity between the cerebellum and the medial prefrontal/anterior cingulate cortices. All these studies indicated extensive disruptions in fronto-cerebellar networks in patients with MSA. In this study, we found the reduced metabolism in the frontal lobe and cerebellum associated with

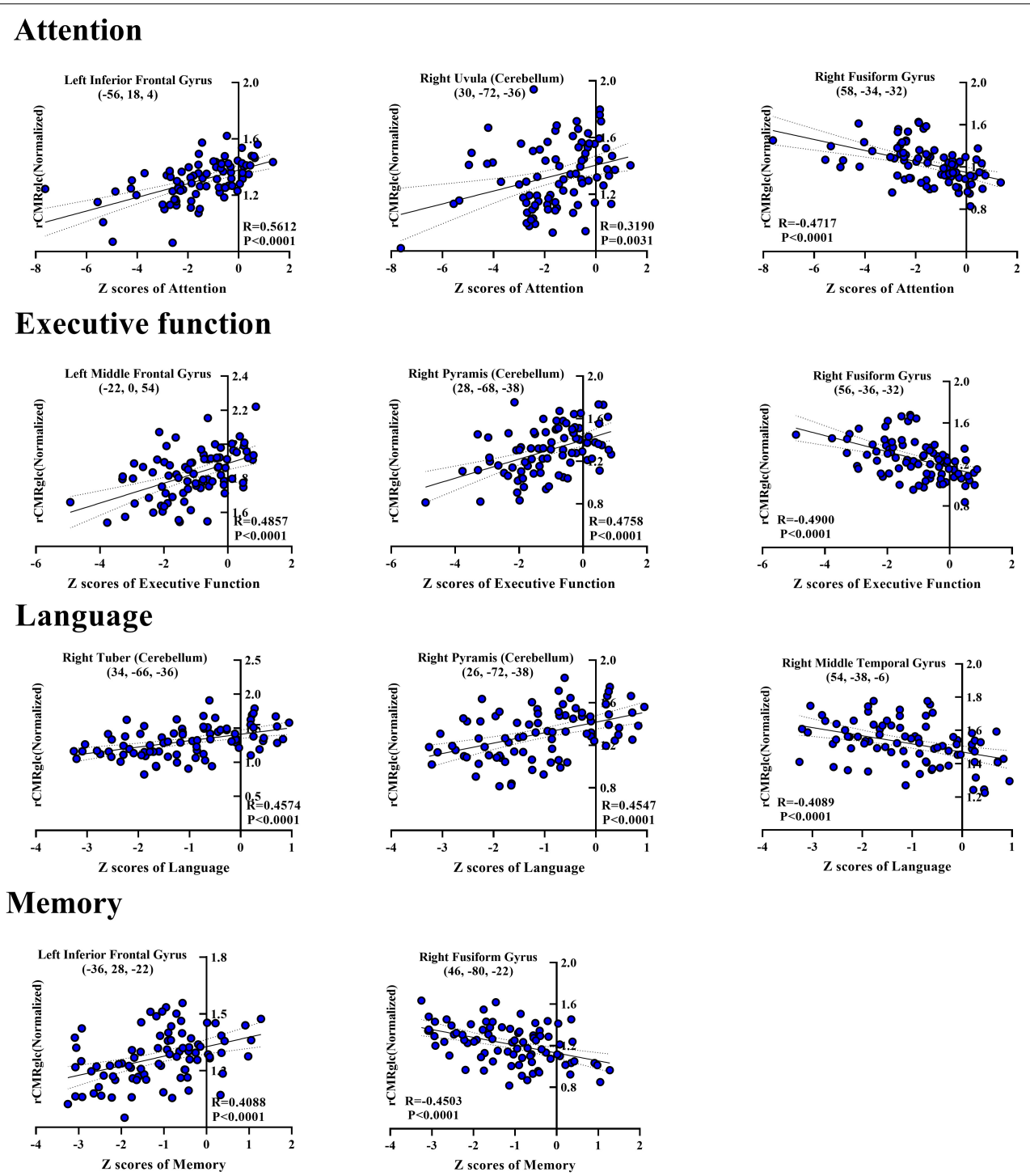

FIGURE 2 | Scatterplots showing correlations between *Z*-score of each cognitive domain and normalized regional glucose metabolic activities for the significantly correlated regions in the *post-hoc* analysis. Each blue-filled circle represents one patient with *Z*-score of specific cognitive domain and regional cerebral metabolic rate of glucose (rCMRglc) in certain brain region. *R*-value means the correlation coefficients. rCMRglc, regional cerebral metabolic rate of glucose.

severer cognitive injury, possibly supported by the role of cerebellum degeneration in cognitive impairments.

Furthermore, the cognitive impairments in MSA-P and MSA-C were evaluated and compared in this study. As previously reported, some studies suggested the patients with MSA-P showed more deteriorated cognitive functions (Kawai et al., 2008; Li et al., 2021), some found patients with MSA-C performing worse on specific cognitive tests (Chang et al., 2009;

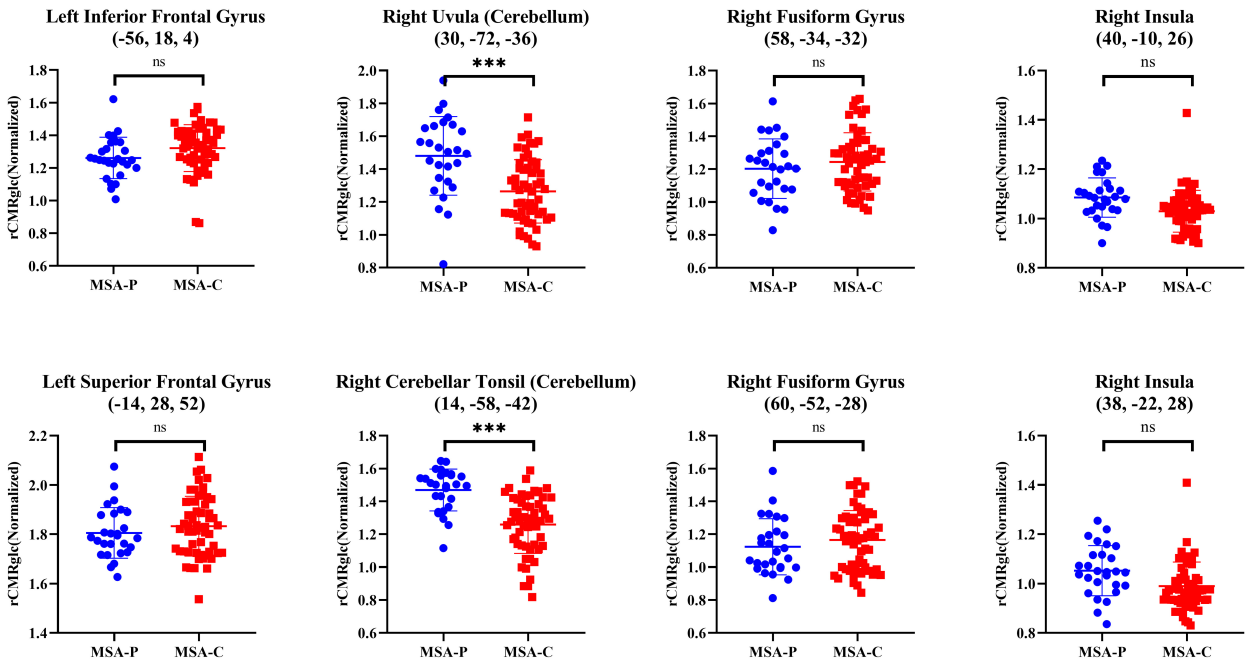

FIGURE 3 | Differences of normalized rCMRglc in representative attention-related regions between two subtypes of patients with MSA. The error bars represent SD. $^{***}p < 0.0001$; $^{*}p < 0.01$; $^{ns}p > 0.05$. rCMRglc, regional cerebral metabolic rate of glucose; MSA-P, multiple system atrophy with predominant parkinsonism; MSA-C, multiple system atrophy with cerebellar ataxia.

TABLE 4 | Differences of regional brain metabolism in attention-related areas between patients with MSA with predominant parkinsonism (MSA-P) and MSA with predominant cerebellar ataxia (MSA-C).

Domains	Regions	BA	MNI coordinate			MSA-P	MSA-C	*p*	*p*[a]
			x	*y*	*z*	(*n* = 27)	(*n* = 57)		
Attention	Left Inferior Frontal Gyrus	45	−56	18	4	1.26 (0.13)	1.32 (0.14)	0.065	0.959
	Left Superior Frontal Gyrus	8	−14	28	52	1.81 (0.10)	1.83 (0.12)	0.314	0.965
	Left Superior Frontal Gyrus	6	−8	24	58	1.79 (0.09)	1.82 (0.10)	0.175	0.981
	Left Medial Frontal Gyrus	6	−6	42	40	1.75 (0.08)	1.77 (0.09)	0.458	0.965
	Right Uvula (Cerebellum)	/	30	−72	−36	1.48 (0.24)	1.26 (0.19)	<0.0001	<0.0001
	Right Cerebellar Tonsil (Cerebellum)	/	14	−58	−42	1.47 (0.13)	1.26 (0.18)	<0.0001	<0.0001
	Right Fusiform Gyrus	20	58	−34	−32	1.20 (0.18)	1.24 (0.18)	0.325	0.055
	Right Fusiform Gyrus	37	60	−52	−28	1.12 (0.17)	1.17 (0.18)	0.315	0.055
	Right Fusiform Gyrus	19	50	−72	−22	1.29 (0.19)	1.31 (0.19)	0.532	0.115
	Right Postcentral Gyrus	2	42	−28	32	1.10 (0.10)	1.08 (0.09)	0.303	0.965
	Right Insula	13	40	−10	26	1.08 (0.08)	1.03 (0.08)	0.005	0.202
	Right Insula	13	38	−22	28	1.05 (0.10)	0.99 (0.10)	0.008	0.223

Data are shown in mean (SD) of normalized rCMRglc in each attention-related region in patients with MSA-P and MSA-C. p-value represents the significance level of t-test performed for normalized rCMRglc in each attention-related region between patients with MSA-P and MSA-C. [a]p-value represents the significance level for normalized rCMRglc in each attention-related region between patients with MSA-P and MSA-C after adjustment for age, sex, disease duration, and UPDRS score and application of the post-hoc correction for multiple comparisons. MSA-P, multiple system atrophy with predominant parkinsonism; MSA-C, multiple system atrophy with predominant cerebellar ataxia; BA, Brodmann area; MNI, Montreal Neurological Institute.

Barcelos et al., 2018), while the rest showed no difference (Siri et al., 2013; Santangelo et al., 2020). In our study, patients with MSA-P performed poorly in the domain of attention, to a weak degree that did not survive after adjusting confounding factors. Therefore, we could not make any definite conclusion on the differences in cognitive dysfunctions between two MSA subtypes so far.

Among attention-related brain regions in this study, we found regional metabolism in the superior/inferior/medial frontal gyrus showing no difference between MSA-P and MSA-C, but metabolism in the cerebellum was lower in MSA-C. Kawai et al. (2008) found cerebellar hypoperfusion in MSA-C, and hypoperfusion in right putamen in MSA-P when comparing brain perfusion between MSA-P and MSA-C. Given significant

differences in motion spectrum between MSA-P and MSA-C, the metabolic pattern in putamen and cerebellum was essentially distinct. Therefore, there is not enough evidence to support whether hypermetabolism in the cerebellum in MSA-P could explain the unadjusted difference of attention performance between two types of MSA. More studies with rigorous design are needed to answer this question.

Our study had several strengths. First, our study sample size was relatively large compared with the previous reports. Second, the neuropsychological tests applied in this study were comprehensive to cover the five domains. However, several limitations should also be admitted. Partial volume effect (PVE) correction was not performed due to the incomplete data of MRI. In future studies, rigorous results performed based on PVE correction in newly recruited patients are warranted. Moreover, the demographic information of patients with MSA-P and MSA-C was mismatched, and the sample size of MSA-P was relatively small in our study. Further study with a more paired and more complete population is needed to confirm the neuropsychological and metabolic comparisons between the two groups. In addition, double-dipping problem causing selective bias was another limitation. It derived from performing MSA-P and MSA-C comparison after extracting metabolic values from statistically significant regions. We hope that another independent data set in the future could confirm our results.

CONCLUSION

The frontal lobe and cerebellum participated in the pathogenesis of cognitive impairments in MSA in this ^{18}F-FDG PET imaging study. Longitudinal studies with specific radioligands are needed to clarify the unique role of dopaminergic deficiency and misfolded protein burden in the development of cognition decline in MSA.

DATA AVAILABILITY STATEMENT

The raw data supporting the conclusions of this article will be made available by the authors, without undue reservation.

ETHICS STATEMENT

The studies involving human participants were reviewed and approved by the Human Studies Institutional Review Board, Huashan Hospital, Fudan University. The patients/participants provided their written informed consent to participate in this study.

AUTHOR CONTRIBUTIONS

JW and F-TL were involved in the conception and design of the study. CS and Q-SC took part in the acquisition, screening, and analysis of data. CS was responsible for figures and tables. CS, Q-SC, and F-TL wrote the first draft of the manuscript. C-TZ, F-TL, and JW revised the manuscript. All authors contributed to the article and approved the submitted version.

FUNDING

This study was supported by the National Nature Science Foundation of China (Grant Numbers: 81701250, 91949118, 81771372, 81671239, and 81971641), the Ministry of Science and Technology of China (Grant Numbers: 2016YFC1306500 and 2016YFC1306504), the Shanghai Sailing Program (No. 18YF1403100), the Shanghai Municipal Science and Technology Major Project (No. 2018SHZDZX01) and ZJ Lab, and Project of Chinese Academy of Sciences (SKLN-201904).

ACKNOWLEDGMENTS

We are grateful to all the patients who took part in this study.

SUPPLEMENTARY MATERIAL

The Supplementary Material for this article can be found online at: https://www.frontiersin.org/articles/10.3389/fnagi.2022.788166/full#supplementary-material

REFERENCES

Barcelos, L. B., Saad, F., Giacominelli, C., Saba, R. A., de Carvalho Aguiar, P. M., Silva, S. M. A., et al. (2018). Neuropsychological and clinical heterogeneity of cognitive impairment in patients with multiple system atrophy. *Clin. Neurol. Neurosurg.* 164, 121–126. doi: 10.1016/j.clineuro.2017.10.039

Brown, R. G., Lacomblez, L., Landwehrmeyer, B. G., Bak, T., Uttner, I., Dubois, B., et al. (2010). Cognitive impairment in patients with multiple system atrophy and progressive supranuclear palsy. *Brain* 133(Pt 8), 2382–2393. doi: 10.1093/brain/awq158

Buckner, R. L. (2013). The cerebellum and cognitive function: 25 years of insight from anatomy and neuroimaging. *Neuron* 80, 807–815. doi: 10.1016/j.neuron.2013.10.044

Caffarra, P., Vezzadini, G., Dieci, F., Zonato, F., and Venneri, A. (2002). Rey-Osterrieth complex figure: normative values in an Italian population sample. *Neurol. Sci.* 22, 443–447. doi: 10.1007/s100720200003

Chang, C. C., Chang, Y. Y., Chang, W. N., Lee, Y. C., Wang, Y. L., Lui, C. C., et al. (2009). Cognitive deficits in multiple system atrophy correlate with frontal atrophy and disease duration. *Eur. J. Neurol.* 16, 1144–1150. doi: 10.1111/j.1468-1331.2009.02661.x

Cykowski, M. D., Coon, E. A., Powell, S. Z., Jenkins, S. M., Benarroch, E. E., Low, P. A., et al. (2015). Expanding the spectrum of neuronal pathology in multiple system atrophy. *Brain* 138(Pt 8), 2293–2309. doi: 10.1093/brain/awv114

Della Rosa, P. A., Cerami, C., Gallivanone, F., Prestia, A., Caroli, A., Castiglioni, I., et al. (2014). A standardized [18F]-xFDG-PET template for spatial normalization in statistical parametric mapping of dementia. *Neuroinformatics* 12, 575–593. doi: 10.1007/s12021-014-9235-4

Eckert, T., Barnes, A., Dhawan, V., Frucht, S., Gordon, M. F., Feigin, A. S., et al. (2005). FDG PET in the differential diagnosis of parkinsonian disorders. *Neuroimage* 26, 912–921. doi: 10.1016/j.neuroimage.2005.03.012

Eckert, T., Tang, C., Ma, Y., Brown, N., Lin, T., Frucht, S., et al. (2008). Abnormal metabolic networks in atypical parkinsonism. *Mov. Disord.* 23, 727–733. doi: 10.1002/mds.21933

Elliott, R. (2003). Executive functions and their disorders. *Br. Med. Bull.* 65, 49–59. doi: 10.1093/bmb/65.1.49

Fanciulli, A., and Wenning, G. K. (2015). Multiple-system atrophy. *N. Engl. J. Med.* 372, 249–263. doi: 10.1056/NEJMra1311488

Fiorenzato, E., Weis, L., Seppi, K., Onofrj, M., Cortelli, P., Zanigni, S., et al. (2017). Brain structural profile of multiple system atrophy patients with cognitive impairment. *J. Neural Transm.* 124, 293–302. doi: 10.1007/s00702-016-1636-0

Floresco, S. B., and Magyar, O. (2006). Mesocortical dopamine modulation of executive functions: beyond working memory. *Psychopharmacology (Berl)* 188, 567–585. doi: 10.1007/s00213-006-0404-5

Ge, J., Wu, P., Peng, S., Yu, H., Zhang, H., Guan, Y., et al. (2015). Assessing cerebral glucose metabolism in patients with idiopathic rapid eye movement sleep behavior disorder. *J. Cereb. Blood Flow Metab.* 35:1902. doi: 10.1038/jcbfm.2015.208

Gilman, S., Wenning, G. K., Low, P. A., Brooks, D. J., Mathias, C. J., Trojanowski, J. Q., et al. (2008). Second consensus statement on the diagnosis of multiple system atrophy. *Neurology* 71, 670–676. doi: 10.1212/01.wnl.0000324625.00404.15

Gratwicke, J., Jahanshahi, M., and Foltynie, T. (2015). Parkinson's disease dementia: a neural networks perspective. *Brain* 138(Pt 6), 1454–1476. doi: 10.1093/brain/awv104

Guo, Q., Zhao, Q., Chen, M., Ding, D., and Hong, Z. (2009). A comparison study of mild cognitive impairment with 3 memory tests among Chinese individuals. *Alzheimer Dis. Assoc. Disord.* 23, 253–259. doi: 10.1097/WAD.0b013e3181999e92

Homma, T., Mochizuki, Y., Komori, T., and Isozaki, E. (2016). Frequent globular neuronal cytoplasmic inclusions in the medial temporal region as a possible characteristic feature in multiple system atrophy with dementia. *Neuropathology* 36, 421–431. doi: 10.1111/neup.12289

Jellinger, K. A. (2020). Neuropathological findings in multiple system atrophy with cognitive impairment. *J. Neural Transm.* 127, 1031–1039. doi: 10.1007/s00702-020-02201-2

Kawabata, K., Hara, K., Watanabe, H., Bagarinao, E., Ogura, A., Masuda, M., et al. (2019). Alterations in cognition-related cerebello-cerebral networks in multiple system atrophy. *Cerebellum* 18, 770–780. doi: 10.1007/s12311-019-01031-7

Kawai, Y., Suenaga, M., Takeda, A., Ito, M., Watanabe, H., Tanaka, F., et al. (2008). Cognitive impairments in multiple system atrophy: MSA-C vs MSA-P. *Neurology* 70(16 Pt 2), 1390–1396. doi: 10.1212/01.wnl.0000310413.04462.6a

Kim, H. W., Oh, M., Oh, J. S., Oh, S. J., Lee, S. J., Chung, S. J., et al. (2017). Striatofrontal deafferentiation in MSA-P: evaluation with [18F]FDG brain PET. *PLoS One* 12:e0169928. doi: 10.1371/journal.pone.0169928

Koga, S., Parks, A., Uitti, R. J., van Gerpen, J. A., Cheshire, W. P., Wszolek, Z. K., et al. (2017). Profile of cognitive impairment and underlying pathology in multiple system atrophy. *Mov. Disord.* 32, 405–413. doi: 10.1002/mds.26874

Konagaya, M., Sakai, M., Matsuoka, Y., Konagaya, Y., and Hashizume, Y. (1999). Multiple system atrophy with remarkable frontal lobe atrophy. *Acta Neuropathol.* 97, 423–428. doi: 10.1007/s004010051008

Li, N., Yang, T., Ran, W., Zhang, X., Wang, Y., Xu, Z., et al. (2021). A study on the characteristics of cognitive function in patients with multiple system atrophy in China. *Sci. Rep.* 11:4995. doi: 10.1038/s41598-021-84393-5

Lucas, J. A., Ivnik, R. J., Smith, G. E., Ferman, T. J., Willis, F. B., Petersen, R. C., et al. (2005). Mayo's older African Americans normative studies: norms for boston naming test, controlled oral word association, category fluency, animal naming, token test, WRAT-3 reading, trail making test, stroop test, and judgment of line orientation. *Clin. Neuropsychol.* 19, 243–269. doi: 10.1080/13854040590945337

Miki, Y., Foti, S. C., Hansen, D., Strand, K. M., Asi, Y. T., Tsushima, E., et al. (2020). Hippocampal alpha-synuclein pathology correlates with memory impairment in multiple system atrophy. *Brain* 143, 1798–1810. doi: 10.1093/brain/awaa126

Ricci, M., Pigliautile, M., D'Ambrosio, V., Ercolani, S., Bianchini, C., Ruggiero, C., et al. (2016). The clock drawing test as a screening tool in mild cognitive impairment and very mild dementia: a new brief method of scoring and normative data in the elderly. *Neurol. Sci.* 37, 867–873. doi: 10.1007/s10072-016-2480-6

Salvesen, L., Winge, K., Brudek, T., Agander, T. K., Løkkegaard, A., and Pakkenberg, B. (2017). Neocortical neuronal loss in patients with multiple system atrophy: a stereological study. *Cereb. Cortex* 27, 400–410. doi: 10.1093/cercor/bhv228

Santangelo, G., Cuoco, S., Picillo, M., Erro, R., Squillante, M., Volpe, G., et al. (2020). Evolution of neuropsychological profile in motor subtypes of multiple system atrophy. *Parkinsonism Relat. Disord.* 70, 67–73. doi: 10.1016/j.parkreldis.2019.12.010

Schmahmann, J. D., and Sherman, J. C. (1998). The cerebellar cognitive affective syndrome. *Brain* 121(Pt 4), 561–579. doi: 10.1093/brain/121.4.561

Shen, C., Chen, L., Ge, J. J., Lu, J. Y., Chen, Q. S., He, S. J., et al. (2021). Cerebral metabolism related to cognitive impairments in multiple system atrophy. *Front. Neurol.* 12:652059. doi: 10.3389/fneur.2021.652059

Sheridan, L. K., Fitzgerald, H. E., Adams, K. M., Nigg, J. T., Martel, M. M., Puttler, L. I., et al. (2006). Normative symbol digit modalities test performance in a community-based sample. *Arch. Clin. Neuropsychol.* 21, 23–28. doi: 10.1016/j.acn.2005.07.003

Siri, C., Duerr, S., Canesi, M., Delazer, M., Esselink, R., Bloem, B. R., et al. (2013). A cross-sectional multicenter study of cognitive and behavioural features in multiple system atrophy patients of the parkinsonian and cerebellar type. *J. Neural Transm.* 120, 613–618. doi: 10.1007/s00702-013-0997-x

Stankovic, I., Krismer, F., Jesic, A., Antonini, A., Benke, T., Brown, R. G., et al. (2014). Cognitive impairment in multiple system atrophy: a position statement by the Neuropsychology Task Force of the MDS multiple system atrophy (MODIMSA) study group. *Mov. Disord.* 29, 857–867. doi: 10.1002/mds.25880

Stefanova, N., Bucke, P., Duerr, S., and Wenning, G. K. (2009). Multiple system atrophy: an update. *Lancet Neurol.* 8, 1172–1178. doi: 10.1016/S1474-4422(09)70288-1

Steinberg, B. A., Bieliauskas, L. A., Smith, G. E., and Ivnik, R. J. (2005). Mayo's older americans normative studies: age- and IQ-adjusted norms for the trail-making test, the stroop test, and MAE controlled oral word association test. *Clin. Neuropsychol.* 19, 329–377. doi: 10.1080/13854040590945210

Wenning, G. K., Tison, F., Ben Shlomo, Y., Daniel, S. E., and Quinn, N. P. (1997). Multiple system atrophy: a review of 203 pathologically proven cases. *Mov. Disord.* 12, 133–147. doi: 10.1002/mds.870120203

Wu, L., Liu, F. T., Ge, J. J., Zhao, J., Tang, Y. L., Yu, W. B., et al. (2018). Clinical characteristics of cognitive impairment in patients with Parkinson's disease and its related pattern in (18) F-FDG PET imaging. *Hum. Brain Mapp.* 39, 4652–4662. doi: 10.1002/hbm.24311

Zhao, Q., Guo, Q., Li, F., Zhou, Y., Wang, B., and Hong, Z. (2013). The Shape Trail Test: application of a new variant of the Trail making test. *PLoS One* 8:e57333. doi: 10.1371/journal.pone.0057333

Conflict of Interest: The authors declare that the research was conducted in the absence of any commercial or financial relationships that could be construed as a potential conflict of interest.

Publisher's Note: All claims expressed in this article are solely those of the authors and do not necessarily represent those of their affiliated organizations, or those of the publisher, the editors and the reviewers. Any product that may be evaluated in this article, or claim that may be made by its manufacturer, is not guaranteed or endorsed by the publisher.

Copyright © 2022 Shen, Chen, Zuo, Liu and Wang. This is an open-access article distributed under the terms of the Creative Commons Attribution License (CC BY). The use, distribution or reproduction in other forums is permitted, provided the original author(s) and the copyright owner(s) are credited and that the original publication in this journal is cited, in accordance with accepted academic practice. No use, distribution or reproduction is permitted which does not comply with these terms.

frontiers in Aging Neuroscience

ORIGINAL RESEARCH
published: 10 February 2022
doi: 10.3389/fnagi.2021.789054

^{18}F-APN-1607 Tau Positron Emission Tomography Imaging for Evaluating Disease Progression in Alzheimer's Disease

Xiaojun Xu[1,2], Weiwei Ruan[1,2], Fang Liu[1,2], Yongkang Gai[1,2], Qingyao Liu[1,2], Ying Su[3], Zhihou Liang[3], Xun Sun[1,2] and Xiaoli Lan[1,2]**

[1] Department of Nuclear Medicine, Union Hospital, Tongji Medical College, Huazhong University of Science and Technology, Wuhan, China, [2] Hubei Province Key Laboratory of Molecular Imaging, Wuhan, China, [3] Department of Neurology, Union Hospital, Tongji Medical College, Huazhong University of Science and Technology, Wuhan, China

OPEN ACCESS

Edited by:
Jiehui Jiang,
Shanghai University, China

Reviewed by:
Chuantao Zuo,
Fudan University, China
Jung Lung Hsu,
Chang Gung University, Taiwan

***Correspondence:**
Xun Sun
xun_sun@hust.edu.cn
Xiaoli Lan
xiaoli_lan@hust.edu.cn

Specialty section:
This article was submitted to Alzheimer's Disease and Related Dementias, a section of the journal Frontiers in Aging Neuroscience

Received: 04 October 2021
Accepted: 20 December 2021
Published: 10 February 2022

Citation:
Xu X, Ruan W, Liu F, Gai Y, Liu Q, Su Y, Liang Z, Sun X and Lan X (2022) ^{18}F-APN-1607 Tau Positron Emission Tomography Imaging for Evaluating Disease Progression in Alzheimer's Disease. Front. Aging Neurosci. 13:789054. doi: 10.3389/fnagi.2021.789054

Purpose: ^{18}F-APN-1607 is a novel tau positron emission tomography (PET) tracer characterized with high binding affinity for 3– and 4-repeat tau deposits. The aim was to analyze the spatial distribution of ^{18}F-APN-1607 PET imaging in Alzheimer's disease (AD) subjects with different stages and to investigate the relationship between the change of tau deposition and overall disease progression.

Methods: We retrospectively analyzed the ^{18}F-APN-1607 PET imaging of 31 subjects with clinically and imaging defined as AD. According to the Mini-Mental State Examination (MMSE) score, patients were divided into three groups, namely, mild ($\geq$21, n = 7), moderate (10–20, n = 16), and severe ($\leq$9, n = 8). PET imaging was segmented to 70 regions of interest (ROIs) and extracted the standard uptake value (SUV) of each ROI. SUV ratio (SUVR) was calculated from the ratio of SUV in different brain regions to the cerebellar cortex. The regions were defined as positive and negative with unsupervised cluster analysis according to SUVR. The SUVRs of each region were compared among groups with the one-way ANOVA or Kruskal–Wallis H test. Furthermore, the correlations between MMSE score and regional SUVR were calculated with Pearson or Spearman correlation analysis.

Results: There were no significant differences among groups in gender (χ^2 = 3.814, P = 0.161), age of onset (P = 0.170), age (P = 0.109), and education level (P = 0.065). With the disease progression, the ^{18}F-APN-1607 PET imaging showed the spread of tau deposition from the hippocampus, posterior cingulate gyrus (PCG), and lateral temporal cortex (LTC) to the parietal and occipital lobes, and finally to the frontal lobe. Between the mild and moderate groups, the main brain areas with significant differences in ^{18}F-APN-1607 uptake were supplementary motor area (SMA), cuneus, precuneus, occipital lobule, paracentral lobule, right angular gyrus, and parietal, which could be used for early disease progression assessment ($P < 0.05$). There were significant differences in the frontal lobe, right temporal lobe, and fusiform gyrus between the moderate and severe

groups, which might be suitable for the late-stage disease progression assessment ($P < 0.05$).

Conclusion: ^{18}F-APN-1607 PET may serve as an effective imaging marker for visualizing the change pattern of tau protein deposition in AD patients, and its uptake level in certain brain regions is closely related to the severity of cognitive impairment. These indicate the potential of ^{18}F-APN-1607 PET for the *in vivo* evaluation of the progression of AD.

Keywords: Alzheimer's disease, ^{18}F-APN-1607, tau, positron emission tomography, progression

INTRODUCTION

Alzheimer's disease (AD) is the most common cause of dementia in elderly people, which is mainly manifested as learning and memory impairment, aphasia, agnosia, impairment of visual and spatial skills, change in abstract thinking, and gradual impairment of daily functions (Longhe, 2020). So far, AD could not be prevented or cured, and therefore, early diagnosis and disease evaluation were critical to treatment and prognosis.

Although the details of the pathological mechanism of AD were not completely clear, the main pathological features were extracellular plaques composed of Aβ-amyloid (Aβ) and intracellular neurofibrillary tangles (NFTs) composed of hyperphosphorylated tau protein. It was generally believed that the above-mentioned pathological changes had appeared more than 10 years before the appearance of clinical symptoms (Cho et al., 2016). Autopsy studies had shown that, compared with Aβ plaque density, NFT was believed to be more directly related to neuron loss and synaptic dysfunction and therefore more closely related to AD cognitive impairment (Hadjichrysanthou et al., 2020).

The latest development of positron emission tomography (PET) imaging allowed *in vivo* visualizing and tracking of the pathophysiological changes of AD and was currently the best method for non-invasive detection of AD neuropathology (Chandra et al., 2019; Chételat et al., 2020; Villa et al., 2020). National Institute of Aging, Alzheimer's Association (NIA-AA) had made it clear that, regardless of cognitive symptoms, AD could be determined only based on abnormal Aβ and tau protein deposition (Jack et al., 2018).

Aβ aggregation measured by amyloid PET has been confirmed to be a feasible biomarker of AD (Jack et al., 2018; Chételat et al., 2020; Jiao et al., 2021). According to available reports, the sensitivity of Aβ PET imaging was comparable to that of autopsy as the gold standard (Chételat et al., 2020; Jiao et al., 2021). However, Aβ plaques reach a plateau in the early stage of the disease, and Aβ load did not show a good correlation with the severity of symptoms and the progression of the later stage of the disease. Therefore, amyloid PET imaging alone was considered insufficient to assess the severity of AD, which limited its value in clinical practice (Koychev et al., 2017; Chételat et al., 2020).

Tau pathology had been proved to be highly related to neurodegeneration and cognitive ability decline, so it may be used as one of the biomarkers for disease severity (Cho et al., 2016; Hadjichrysanthou et al., 2020). The latest development of molecular probes targeting tau made it possible to image tau deposition with PET *in vivo* non-invasively and dynamically, which suggested a reliable method to characterize AD (Villemagne et al., 2014; Baghel et al., 2019; Teng et al., 2019; Zhao et al., 2019; Chételat et al., 2020; Cho et al., 2020). Moreover, studies had shown that tau PET uptake was positively correlated with cortical atrophy and disease severity and could reflect the pathological stage of AD (Baghel et al., 2019; Chételat et al., 2020; Cho et al., 2020).

Based on ^{11}C-PBB3 tracer, the derivative ^{18}F-PM-PBB3 (also known as ^{18}F-APN-1607) had been synthesized and proved with better imaging properties. Both preclinical and clinical studies had proved that ^{18}F-APN-1607 highly selectively combined with the pathological tau of AD and could visualize the spatial distribution of tau deposition in AD (Ni et al., 2018; Hsu et al., 2020; Weng et al., 2020; Tagai et al., 2021). In addition, it also found that ^{18}F-APN-1607 uptake was closely related to the cognitive changes, and the regional uptakes of AD-related cortical areas were significantly correlated with Alzheimer's Disease Assessment Scale-Cognitive section (ADAS-cog) score, indicating that tau deposition may be related to the clinical severity of AD (Hsu et al., 2020).

Although there are some publications on ^{18}F-APN-1607 PET, as a relative novel tracer, some questions are yet to be answered. The relationship and change patterns are needed to be verified between the uptake level of ^{18}F-APN-1607 in different brain regions and AD progression, which is important to understand the trajectory of the disease and find the objective evidence for judging the stage of AD. Therefore, the purpose of this study was to explore the spatial distribution of tau protein deposition with ^{18}F-APN-1607 PET in different severity AD patients and in-depth dig the correlation between the regional uptake and the overall disease progression.

MATERIALS AND METHODS

Patients

The study was approved by the Ethics Committee of Tongji Medical College, Huazhong University of Science and Technology, and registered at clinical trail.gov (NCT number 05003830). Written informed consents were obtained from all participants.

We retrospectively analyzed the ^{18}F-APN-1607 PET imaging and clinical characteristics of the AD (AD-MCI or AD-Dementia) patients diagnosed in our hospital from July 2020 to July 2021. Inclusion criteria were (1) patients were diagnosed strictly in accordance with the 2011 NIA-AA diagnostic criteria (Jack et al., 2011); (2) patients confirmed as positive for β-amyloid (Aβ) deposition with PET imaging by visual assessment; and (3) patients underwent ^{18}F-APN-1607 PET imaging in 2 months after the amyloid PET imaging. Exclusion criteria were (1) patients with significant cerebrovascular disease, with multiple or extensive cerebral infarction; (2) patients with dementia or cognition dysfunction due to other reasons, such as Parkinson's disease dementia, vascular dementia, frontotemporal dementia, Lewy body dementia, and so on; (3) people with drug or alcohol abuse or dependence; (4) patients with history of epilepsy; (5) people with claustrophobia or other reasons who could not cooperate with the examination; and (6) patients who showed obvious movement during PET scanning which affected image quality and image interpretation.

Clinical Assessment

The primary clinical parameters including the gender, age, age of onset, and education level were consulted and recorded. The cognitive function was assessed using the Mini-Mental State Examination (MMSE) score. According to the MMSE score, patients were divided into three groups: mild (≥21), moderate (10–20), and severe (≤9) (Abdullah et al., 2020). The clinical assessment was completed by two physicians (YS and ZL).

Image Acquisition and Reconstruction

Nervous system-related drugs were stopped for more than 12 h before scanning. The precursor of APN-1607 was obtained from APRINOIA Therapeutics (Suzhou, China). According to the method described before (Weng et al., 2020), ^{18}F-APN-1607 was prepared on an ^{18}F-multifunction synthesizer (GE TRACERlab FxFn), and the radiochemical purity was >95%. ^{18}F-APN-1607 was administrated intravenously (3.7–5.5 MBq/kg) under the green light-emitting diode light (510 nm) illumination. Resting for 60 min, the PET scanning was completed with hybrid PET/MR (3.0 T, SIGNA TOF-PET/MR, GE Healthcare). During 20 min PET acquisition, the 3D T1-weighted imaging [three-dimensional gradient echo sequence, flip angle = 12°, time of echo (TE)/time of repetition (TR) = 2.6/6.9 ms, bandwidth = 50 kHz, FOV = 24 cm × 24 cm, matrix = 384 × 384] was obtained simultaneously. The PET data were reconstructed using the ordered subsets expectation maximum (OSEM) algorithm (FOV = 30 cm × 30 cm, matrix = 192 × 192, filter cutoff = 3.0 mm, subsets = 28, iterations = 3), and the time-of-flight (TOF) technique was utilized for the reconstruction. The PET attenuation correction for PET/MR was atlas-based MRI attenuation correction, combined with Dixon water-fat separation methods.

Data Processing

The data processing for the ^{18}F-APN-1607 mainly contained two steps: the structural brain segmentation and standard uptake value (SUV) extraction for regions of interest (ROIs). SUV ratio (SUVR) was calculated from the ratio of SUV in different brain regions to the cerebellar cortex. All imaging data were converted to neuroimaging informatics technology initiative (NIfTI) format with the MRIcron tool. The 3D T1 images were normalized to the Montreal Neurological Institute (MNI) standard space. Seventy brain regions were segmented based on the atlas template from the automated anatomical labeling atlas[1]. The brain segmentation was performed on the 3D-T1 sequence, and divided into brain parenchyma, ventricle, and cerebrospinal fluid. The choroid plexus, containing in the part of the ventricle, had been screened out. Due to the simultaneous acquisition of PET and MRI, the extracted 70 regional ROIs from 3D T1 imaging could be directly transferred to binary mask and used to extract the SUV of corresponding ROIs from PET images. The detailed processing could be found in our previous study (Ruan et al., 2020). The data processing was performed by the SPM12 (see text footnote 1) and MATLAB 2020b (MathWorks, Natick, MA, United States).

Statistical Analysis

We assumed that the SUV ratio (SUVR) of the ROIs conformed to a Gaussian distribution (Krishna and Narasimha Murty, 1999). The unsupervised clustering was performed on the SUVR of each participant and performed a 2-class *k*-means clustering to determine the positive and negative ROI (**Supplementary Figure 1**). In each group, one positive region was defined as ≥50% subjects with positive in the same region. In the following statistics, the difference of SUVR in every brain ROIs among the three groups (i.e., mild, moderate, and severe) was tested statistically. The method used was one-way ANOVA if the data met normality and homogeneity of variance; otherwise, the Kruskal–Wallis *H* test was used. Furthermore, the correlations between MMSE score and ^{18}F-APN-1607 SUVR were analyzed for every brain ROIs with Pearson correlation analysis. $P < 0.05$ was considered a statistically significant difference. All the statistical analyses were performed with SPSS (version 21; IBM).

RESULTS

Participant Characteristics

A total of 31 clinically defined probable AD subjects were included in this study. **Table 1** illustrates their demographic and clinical features. On average, the participants aged 60.5 ± 7.2 years (range: 51–75 years), and 54.8% (17/31) were men. The average education level of the patients was 10.0 ± 4.3 years (range: 3–22 years). The average MMSE score was 14.5 ± 7.9 (range: 1–29).

According to the MMSE score, patients were divided into three groups, namely, mild (≥21, n = 7), moderate (10–20, n = 16), and severe (≤9, n = 8). There were no statistically significant differences among different groups in gender (χ^2 = 3.814, P = 0.161), age of onset (P = 0.170), age (P = 0.109), and education level (P = 0.065).

[1]http://www.gin.cnrs.fr/en/tools/aal-aal2/

TABLE 1 | Demographic and clinical features of the subjects.

Characteristics	Mean ± SD	Range	MMSE groups			*P*-value
			Mild (*n* = 7)	Moderate (*n* = 16)	Severe (*n* = 8)	
Gender						
Male	17		5	6	6	0.161
Female	14		2	10	2	
Age of onset	57.58 ± 7.74	46–73	62.29 ± 8.40	56.81 ± 7.50	55.25 ± 6.45	0.170
Age of PET scan	60.45 ± 7.22	51–75	65.43 ± 7.09	59.31 ± 7.03	58.38 ± 6.46	0.109
Education (y)	9.97 ± 4.32	3–22	12.14 ± 4.14	8.25 ± 3.19	11.50 ± 5.40	0.065
MMSE score	14.52 ± 7.89	1–29	26.14 ± 1.77	14.25 ± 2.79	4.88 ± 2.36	0.000

MMSE, Mini-Mental State Examination.
Mean ± SD is indicated for continuous variables. P-value referred to the difference in clinical characteristics among the three groups.

Distribution of ^{18}F-APN-1607 Uptake in Different Groups

Unsupervised cluster analysis showed that AD patients had different degrees of tau deposition in multiple brain regions. The ^{18}F-APN-1607-positive regions in the mild group mainly included the hippocampus, parahippocampal gyrus, amygdala, lateral temporal cortex (LTC), supramarginal gyrus (SMG), angular gyrus, posterior cingulate gyrus (PCG), and precuneus (**Figure 1B**, red area). In the moderate group, the positive regions expanded to the occipital lobe, cuneus, and parietal superior/inferior lobules (**Figure 1B**, orange area). In the severe group, except the regions mentioned ahead, the frontal lobe also became positive (**Figure 1B**, yellow area). Among all AD patients, the temporal lobe was the first involved, followed by the occipital, parietal, and, finally, the frontal lobe. **Figure 1A** shows the ^{18}F-APN-1607 PET images of 3 AD subjects belonging to mild, moderate, and severe groups, respectively.

Regional ^{18}F-APN-1607 Uptake Level in Different Groups

Among the three groups, except hippocampus, parahippocampal gyrus, amygdala, PCG, SMG, superial frontal gyrus (FGs), left middle and inferior frontal gyrus (FGm and FGi), and left parietal lobe, significant differences of ^{18}F-APN-1607 uptake were noticed in other brain regions (**Figures 2A,B** and **Supplementary Table 1**).

Between the mild and moderate groups, significant differences could be observed in supplementary motor area (SMA), cuneus, precuneus, paracentral lobule, and left occipital lobe (**Figure 2C**, $P < 0.05$). The uptake was significantly different in the frontal lobe (operculum, orbital, and rectus gyrus) and right lateral temporal between the moderate and severe groups (**Figure 2D**, $P < 0.05$).

Correlation Between Regional ^{18}F-APN-1607 Uptake and Mini-Mental State Examination Score

In the regions with significant difference among groups, the linear regression method was applied to analyze the correlation between MMSE score and regional SUVR. As the inter-group difference and correlation were similar in both sides of the precentral gyrus, SMA, PCG, precuneus, cuneus, hippocampus, lateral temporal lobe, and occipital lobe, the scatter diagrams were displayed including bilateral of the corresponding regions. For the frontal lobe (middle and inferior gyrus), angular gyrus, and parietal lobe, the scatter diagrams were displayed only for the right side because the inter-group difference was discovered to be unilateral. There was no significant correlation between the MMSE and SUVR in PCG and hippocampus ($r = -0.175$, $P = 0.173$; $r = -0.105$, $P = 0.416$). The other regions showed a strong negative correlation (r range: $-0.401 \sim -0.631$, $P < 0.05$; **Figure 3** and **Supplementary Table 1**).

DISCUSSION

^{18}F-APN-1607 was a novel PET tracer targeting tau protein which is one of the important factors for AD pathological changes. Our results showed that with the disease progression, the ^{18}F-APN-1607 PET imaging showed the spread of tau deposition from the hippocampus, posterior cingulate gyrus (PCG), and lateral temporal cortex (LTC) to the parietal and occipital lobes, and finally to the frontal lobe. Uptake levels of ^{18}F-APN-1607 in some brain areas may help to assess the degrees of AD progression, including supplementary motor area (SMA), cuneus, precuneus, occipital lobule, paracentral lobule, right angular gyrus, and parietal for early-stage evaluation; and frontal lobe, right temporal lobe, and fusiform gyrus for AD late-stage progression. These suggested that ^{18}F-APN-1607 PET may serve as an effective imaging marker for visualizing the change of tau protein deposition in AD patients, and its uptake pattern in different brain regions may relate to the progress of cognitive impairment.

According to the Braak staging of AD-related neurofibrillary changes (Braak and Braak, 1995; Braak et al., 2006), six stages of disease propagation could be distinguished with respect to the location of the tangle-bearing neurons and the severity of changes (transentorhinal stages I–II: clinically silent cases; limbic stages III–IV: incipient AD; neocortical stages V–VI: fully developed AD). This stage pattern was derived from the histopathological staining at autopsy. Then, tau tracer could be used to describe the spatiotemporal pattern of tau deposition

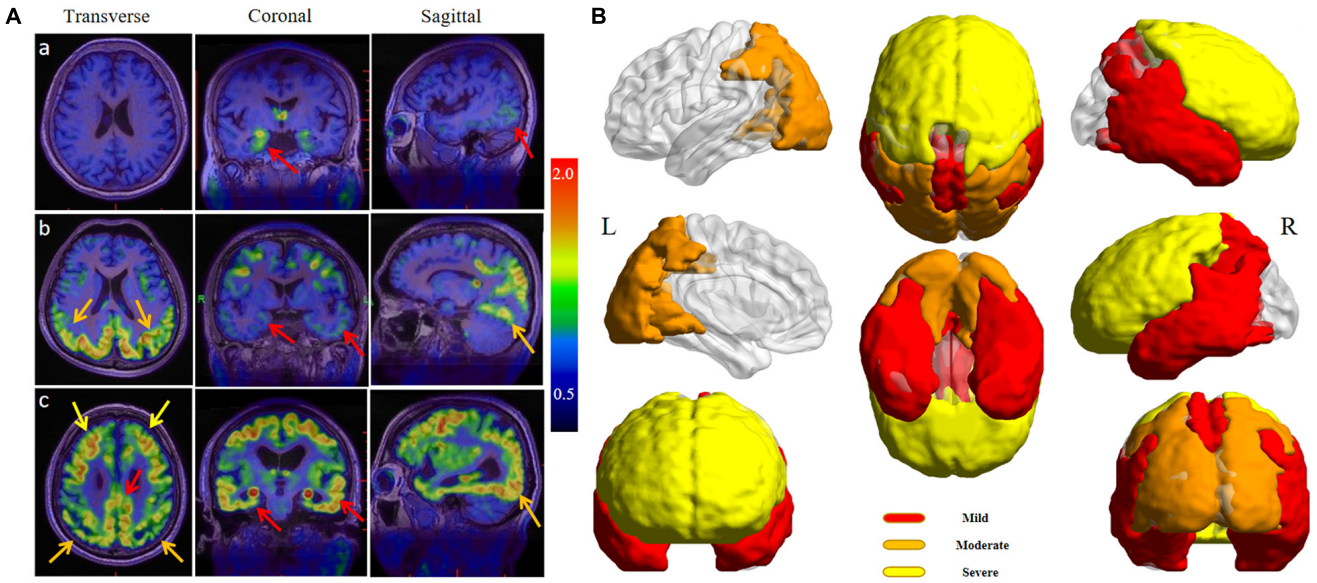

FIGURE 1 | (A) ^{18}F-APN-1607 PET/MR fusion images of three AD patients with varying degrees. **(a)** A 67-year-old woman complained of memory decline for 2 years (MMSE = 26, mild group), and the uptake of ^{18}F-APN-1607 could be seen in the hippocampus and posterolateral temporal cortex (red arrows). **(b)** A 54-year-old man was with progressive memory loss for 5 years and aggravated for 2 years (MMSE = 18, moderate group), and the high uptake was expanded to the parietal and occipital lobes (orange arrows). **(c)** A 67-year-old man suffered from memory loss for 7 years and self-care disabled for 6 months (MMSE = 5, severe group), and high uptake had been spread to the whole brain including the frontal lobe (yellow arrows). **(B)** The full-view sketch map for expanding the tau deposits according to the ^{18}F-APN-1607 PET. The deposition was started from the medial and lateral temporal lobes, posterior cingulate gyrus (PCG), and precuneus (red areas), then spread to the parietal and occipital cortex (orange areas), and finally affected the frontal lobe (yellow areas). L means left and R means right.

in AD patients, which had been replicated by tau-PET imaging studies *in vivo* (Koychev et al., 2017; Baghel et al., 2019; Das et al., 2019; Zhao et al., 2019; Cho et al., 2020; Hsu et al., 2021; Seemiller et al., 2021). In our study, 31 AD patients were divided into 3 groups (i.e., mild, moderate, and severe) according to the MMSE score. ^{18}F-APN-1607 PET imaging revealed that the temporal lobe area (hippocampus, parahippocampal gyrus, amygdala, and LTC), PCG, precuneus, SMG, and angular gyrus were the most affected regions in the mild group. Then, in the moderate group, the high uptake was expanded to the occipital lobe, cuneus, and parietal superior/inferior lobules. In the severe group, the frontal lobe also became positive. This topographical progression of tau distribution was generally consistent with the Braak staging system, which means the ^{18}F-APN-1607 PET imaging could be applied for visualizing disease progression in AD patients. In recent researches, 4 distinct spatiotemporal trajectories of tau pathology were identified in AD, including previously described limbic-predominant and medial temporal lobe-sparing patterns, while also discovering posterior and lateral temporal patterns resembling atypical clinical variants of AD (Vogel et al., 2021). In our study, the affected areas in the early stage were wider than those reported, which may be due to the mixture of the different subtypes and different standards to divide the stage.

Alzheimer's disease was considered as a continuum (Jack et al., 2011), in which different regions presented different deposition models. Which region could be conducted to evaluate the disease progression? To answer this question, the SUVRs of each region were compared among different groups in our study, and many regions possessed significant differences. Furthermore, a good negative correlation between MMSE score and regional SUVR was also presented (r range: -0.401 to -0.631, $P < 0.05$). It was similar to the earlier reported results (Koychev et al., 2017; Baghel et al., 2019; Zhao et al., 2019; Ossenkoppele et al., 2021). Pontecorvo et al. (2017) reported that in Aβ-positive AD patients, neocortical tau tracer retention increased with the severity of the diagnosis. In the study by Hsu et al. (2020), the increased pattern of ^{18}F-APN-1607 tau deposition was also proved regional, and the SUVR was significantly positively correlated with ADAS-cog and Clinical Dementia Rating Scale Sum of Boxes (CDR-SB) score in the frontal lobe, parietal lobe, temporal lobe, occipital lobe, anterior cingulate gyrus, posterior cingulate gyrus, precuneus, and parahippocampus ($P < 0.01$). These findings and the results from our study suggested that ^{18}F-APN-1607 PET imaging could be served as an effective imaging marker to evaluate the disease progression.

In this study, we found that the change, deposition area, and extension of tau protein deposition in different brain regions may be in accordance with the aggravation of the disease. In the early stage, positive tau expression may be found in the medial temporal lobe area (hippocampus, parahippocampal gyrus, and amygdala) and PCG. However, the SUVR did not increase further along with the decline of MMSE score, and no statistical difference was found among the three groups ($P > 0.05$). In the previous report (Hsu et al., 2020), there was also no significant correlation between the hippocampus

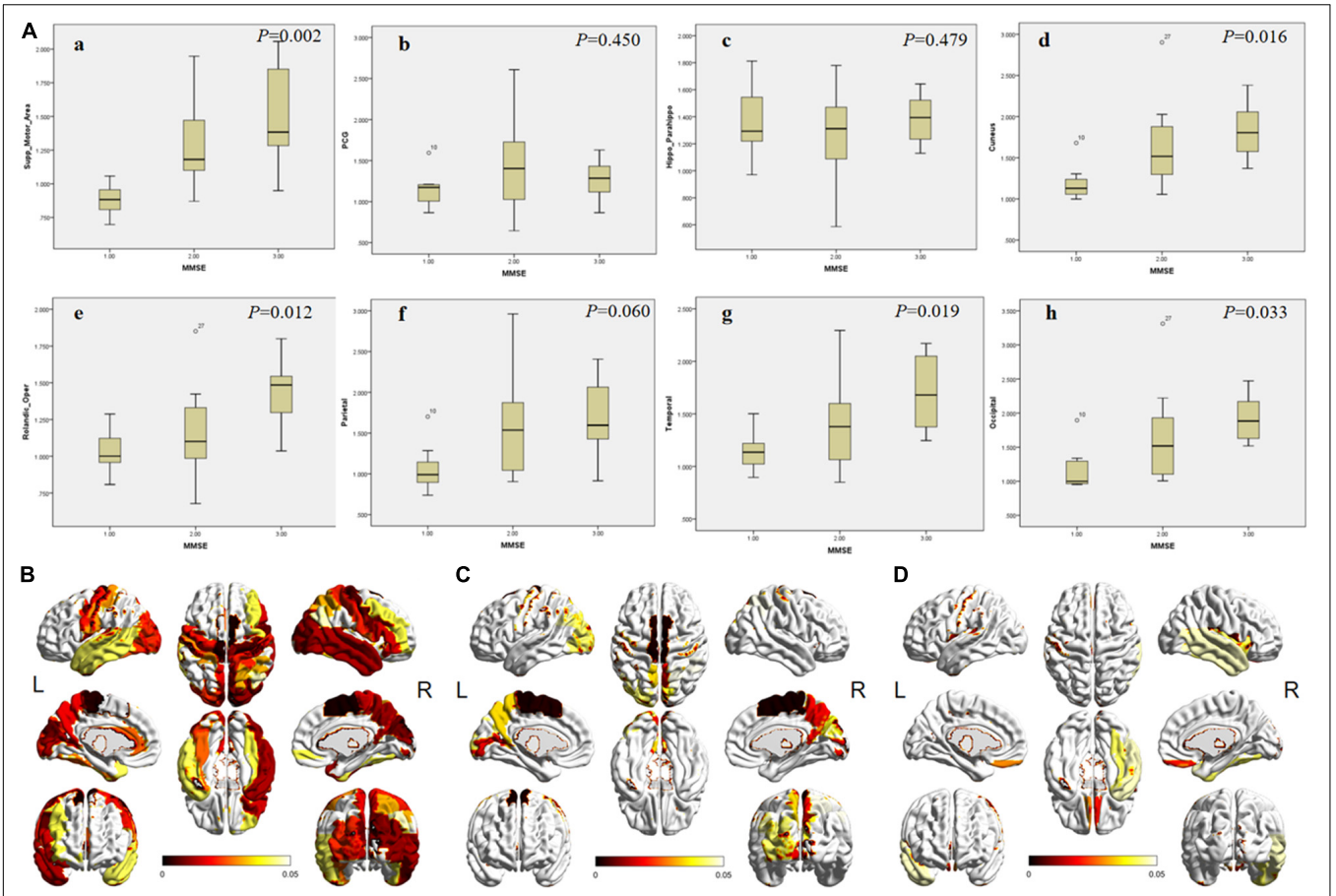

FIGURE 2 | The differences of SUVR in specific brain areas among patients in different MMSE groups. **(A)** The box plot of the SUVR in specific brain areas [**(a)** SMA; **(b)** PCG; **(c)** hippocampus; **(d)** cuneus; **(e)** frontal; **(f)** parietal; **(g)** lateral temporal; and h, occipital cortex) in different groups. 1, 2, and 3 on the abscissa represent mild, moderate, and severe groups, respectively. The *P*-values among groups are shown in the upper right corner. **(B–D)** The full view of regions with significant differences in ^{18}F-APN-1607 uptake. The color bar represents the *P*-value. **(B)** The overall difference among the three groups. **(C)** The difference between the mild and moderate groups. **(D)** The difference between the moderate and severe groups. SMA, supplementary motor area; PCG, posterior cingulate gyrus. L means left and R means right.

and ADAS-cog score (P = 0.53). Then, positive tau deposition could be seen in the lateral temporal lobe presenting as the continual uptake increasing from the early stage to the advanced stage. Next, positive findings appeared in parietal lobe, occipital lobe, cuneus, and precuneus, experiencing a significant increasing trend of SUVR. Notably, the deposition of tau in the frontal region may indicate the middle-late stages.

In our study, although the change modes of tracer uptake were different in various brain regions, the trends were nearly consistent with the Braak pathological pattern, in which tau aggregates spread from the medial temporal lobe and build up in larger quantities throughout the neocortex (Braak and Braak, 1995). Pathological tau might undergo cell-to-cell transmission, resulting in the transformation of normal tau in the recipient cell into misfolded tau and the formation of tau aggregates (Braak and Del Tredici, 2016; Peng et al., 2020). The ^{18}F-APN-1607 PET might reveal the detailed pattern of tau deposition and the pathological progression in AD patients. The changes of the uptake in different brain regions might provide the information to evaluate the staging and clinical manifestation. The medial temporal lobe area and PCG, which presented positive in the early stage but without further increase, might serve as the marker just for early diagnosis. In the lateral temporal lobe, the uptake was continuously increased, which might be an area to monitor the overall progression. Considering the significant change during certain stage, the parietal or occipital lobe might be a monitoring site for the fast progress in the early stage, while the high uptake in the frontal lobe might be a marker for the advanced stage.

The current research still had certain limitations. First, the sample size was relatively small, which might limit the interpretation of the results and need to be expanded in the future study. Second, as a relatively new tracer, compared with other tau tracers, the sensitivity of ^{18}F-APN-1607 in detecting tau deposition for early-stage AD was uncertain. In addition, although the MMSE score was a useful screening tool to evaluate the cognitive function (Folstein et al., 1975; Zhao et al., 2019; Jiao et al., 2020), it had limited value in assessing

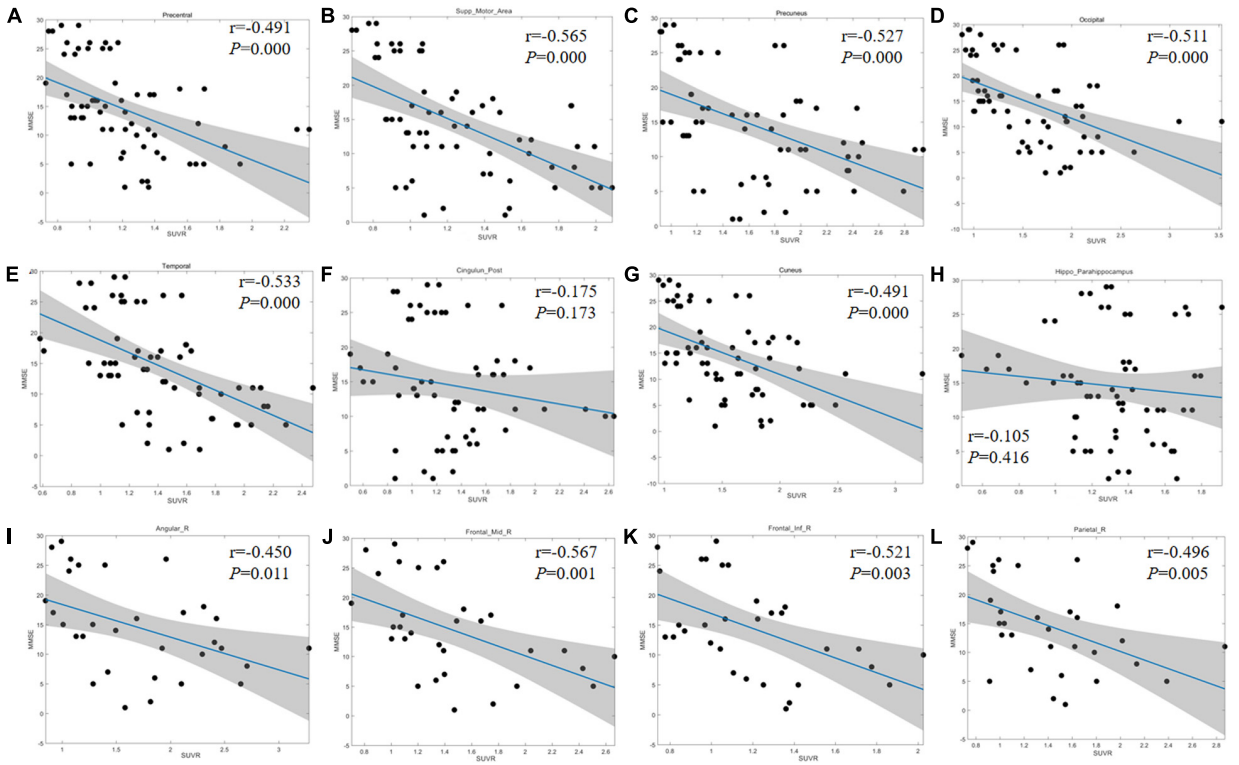

FIGURE 3 | Linear regression results between MMSE score and regional SUVR. **(A–H)** Correlation coefficient graph of the bilateral precentral gyrus **(A)**, SMA **(B)**, precuneus **(C)**, occipital lobe **(D)**, lateral temporal lobe **(E)**, PCG **(F)**, cuneus **(G)**, and hippocampus **(H)**. **(I–L)** Correlation coefficient graph of the right side of angular gyrus **(I)**, FGm **(J)**, FGi **(K)**, and parietal lobe **(L)**. The gray area shows the 95% confidence interval area. The blue solid lines refer to the mean fitting curves. SMA, supplementary motor area; PCG, posterior cingulate gyrus; FGm, middle frontal gyrus; FGi, inferior frontal gyrus.

the severity of AD, and more cognitive tests are required for evaluation. Future researches should focus on the prospective longitudinal study of ^{18}F-APN-1607 PET imaging, supplemented by other biomarkers and more clinical information, which may provide further reliable evidence for the application of tau PET in AD.

CONCLUSION

This study showed that ^{18}F-APN-1607 PET imaging could help to clarify the spatial distribution of tau deposition in AD patients and presented a negative correlation between ^{18}F-APN-1607 uptake in specific brain regions and overall severity of cognitive impairment. In summary, ^{18}F-APN-1607 PET may be an effective imaging marker for visualization and tracking of tau protein spreading in the brain of AD patients and possessed the potential to evaluate the disease progression of AD.

DATA AVAILABILITY STATEMENT

The original contributions presented in the study are included in the article/**Supplementary Material**, further inquiries can be directed to the corresponding author/s.

ETHICS STATEMENT

The studies involving human participants were reviewed and approved by the Ethics Committee of Tongji Medical College, Huazhong University of Science and Technology. The participants provided their written informed consent to participate in this study.

AUTHOR CONTRIBUTIONS

XL substantially contributed to the conception and design, and revised the manuscript critically for important intellectual content. XS interpreted the data and revised the manuscript critically for important intellectual content. XX acquired, analyzed, and interpreted most of the data and drafted the article. WR acquired the PET images and analyzed some data. QL and YG prepared the compound ^{18}F-APN-1607. YS and ZL provided the clinical information and made the diagnosis. All authors read and approved the final manuscript.

FUNDING

This work was supported by the National Natural Science Foundation of China (Nos. 81701759 and 81901735), Hubei

Technical Innovation Major Project (No. 2017ACA182), and Clinical Research Physician Program of Tongji Medical College, Huazhong University of Science and Technology (No. 5001530008).

ACKNOWLEDGMENTS

We sincerely thank the subjects who participated in this study. We also thank Ma Ling [He Kang Corporate Management (SH) Co., Ltd.] for her assistance in the data processing. We would like to acknowledge Tzu-Chen Yen for her guidance on this study. We are grateful for the support from APRINOIA Therapeutics (Suzhou, China) who provided us with precursor and technique instruction for the synthesis of ^{18}F-APN-1607.

SUPPLEMENTARY MATERIAL

The Supplementary Material for this article can be found online at: https://www.frontiersin.org/articles/10.3389/fnagi.2021.789054/full#supplementary-material

REFERENCES

Abdullah, L., Crawford, F., Tsolaki, M., Börjesson-Hanson, A., Olde Rikkert, M., Pasquier, F., et al. (2020). The Influence of Baseline Alzheimer's Disease Severity on Cognitive Decline and CSF Biomarkers in the NILVAD Trial. *Front. Neurol.* 11:149. doi: 10.3389/fneur.2020.00149

Baghel, V., Tripathi, M., Parida, G., Gupta, R., Yadav, S., Kumar, P., et al. (2019). In Vivo Assessment of Tau Deposition in Alzheimer Disease and Assessing Its Relationship to Regional Brain Glucose Metabolism and Cognition. *Clin. Nucl. Med.* 44, e597–e601. doi: 10.1097/RLU.0000000000002791

Braak, H., Alafuzoff, I., Arzberger, T., Kretzschmar, H., and Del Tredici, K. (2006). Staging of Alzheimer disease-associated neurofibrillary pathology using paraffin sections and immunocytochemistry. *Acta Neuropathol.* 112, 389–404. doi: 10.1007/s00401-006-0127-z

Braak, H., and Braak, E. (1995). Staging of Alzheimer's disease-related neurofibrillary changes. *Neurobiol. Aging* 16, 271–284. doi: 10.1016/0197-4580(95)00021-6

Braak, H., and Del Tredici, K. (2016). Potential Pathways of Abnormal Tau and α-Synuclein Dissemination in Sporadic Alzheimer's and Parkinson's Diseases. *Cold Spring Harb. Perspect. Biol.* 8:a023630. doi: 10.1101/cshperspect.a023630

Chandra, A., Valkimadi, P. E., Pagano, G., Cousins, O., Dervenoulas, G., Politis, M., et al. (2019). Applications of amyloid, tau, and neuroinflammation PET imaging to Alzheimer's disease and mild cognitive impairment. *Hum. Brain Mapp.* 40, 5424–5442. doi: 10.1002/hbm.24782

Chételat, G., Arbizu, J., Barthel, H., Garibotto, V., and Drzezga, A. (2020). Amyloid-pet and 18f-fdg-pet in the diagnostic investigation of alzheimer's disease and other dementias. *Lancet Neurol.* 19, 951–962. doi: 10.1016/S1474-4422(20)30314-8

Cho, H., Baek, M. S., Lee, H. S., Lee, J. H., Ryu, Y. H., and Lyoo, C. H. (2020). Principal components of tau positron emission tomography and longitudinal tau accumulation in Alzheimer's disease. *Alzheimer's Res. Ther.* 12:114. doi: 10.1186/s13195-020-00685-4

Cho, H., Choi, J. Y., Hwang, M. S., Kim, Y. J., Lee, H. M., Lee, H. S., et al. (2016). In vivo cortical spreading pattern of tau and amyloid in the Alzheimer disease spectrum. *Anna. Neurol.* 80, 247–258. doi: 10.1002/ana.24711

Das, S. R., Xie, L., Wisse, L., Vergnet, N., Ittyerah, R., Cui, S., et al. (2019). In vivo measures of tau burden are associated with atrophy in early Braak stage medial temporal lobe regions in amyloid-negative individuals. *Alzheimer's Dement.* 15, 1286–1295. doi: 10.1016/j.jalz.2019.05.009

Folstein, M. F., Folstein, S. E., and McHugh, P. R. (1975). Mini-mental state". A practical method for grading the cognitive state of patients for the clinician. *J. Psychiatric Res.* 12, 189–198. doi: 10.1016/0022-3956(75)90026-6

Hadjichrysanthou, C., Evans, S., Bajaj, S., Siakallis, L. C., McRae-McKee, K., de Wolf, F., et al. (2020). The dynamics of biomarkers across the clinical spectrum of Alzheimer's disease. *Alzheimer's Res. Therapy* 12:74. doi: 10.1186/s13195-020-00636-z

Hsu, J. L., Lin, C. H., Chen, P. L., Lin, K. J., and Chen, T. F. (2021). Genetic study of young-onset dementia using targeted gene panel sequencing in Taiwan. *Am. J. Med. Genet. B Neuropsychiatr. Genet.* 186, 67–76. doi: 10.1002/ajmg.b.32836

Hsu, J. L., Lin, K. J., Hsiao, I. T., Huang, K. L., Liu, C. H., Wu, H. C., et al. (2020). The Imaging Features and Clinical Associations of a Novel Tau PET Tracer-18F-APN1607 in Alzheimer Disease. *Clin. Nucl. Med.* 45, 747–756. doi: 10.1097/RLU.0000000000003164

Jack, C. R. Jr., Albert, M. S., Knopman, D. S., McKhann, G. M., Sperling, R. A., Carrillo, M. C., et al. (2011). Introduction to the recommendations from the National Institute on Aging-Alzheimer's Association workgroups on diagnostic guidelines for Alzheimer's disease. *Alzheimer's Dement.* 7, 257–262. doi: 10.1016/j.jalz.2011.03.004

Jack, C. R. Jr., Bennett, D. A., Blennow, K., Carrillo, M. C., Dunn, B., Haeberlein, S. B., et al. (2018). NIA-AA Research Framework: toward a biological definition of Alzheimer's disease. *Alzheimer's Dement.* 14, 535–562. doi: 10.1016/j.jalz.2018.02.018

Jiao, B., Liu, H., Guo, L., Liao, X., Zhou, Y., Weng, L., et al. (2021). Performance of plasma amyloid β, total tau, and neurofilament light chain in the identification of probable Alzheimer's disease in South China. *Front. Aging Neurosci.* 13:749649. doi: 10.3389/fnagi.2021.749649

Jiao, F., Yi, F., Wang, Y., Zhang, S., Guo, Y., Du, W., et al. (2020). The Validation of Multifactor Model of Plasma Aβ 42 and Total-Tau in Combination With MoCA for Diagnosing Probable Alzheimer Disease. *Front. Aging Neurosci.* 12:212. doi: 10.3389/fnagi.2020.00212

Koychev, I., Gunn, R. N., Firouzian, A., Lawson, J., Zamboni, G., Ridha, B., et al. (2017). PET Tau and Amyloid-β Burden in Mild Alzheimer's Disease: divergent Relationship with Age, Cognition, and Cerebrospinal Fluid Biomarkers. *J. Alzheimers Dis.* 60, 283–293. doi: 10.3233/JAD-170129

Krishna, K., and Narasimha Murty, M. (1999). Genetic K-means algorithm. *IEEE Trans. Syst. Man. Cybern. C Appl. Rev.* 29, 433–439. doi: 10.1109/3477.764879

Longhe, Z. (2020). 2020 Alzheimer's disease facts and figures. *Alzheimer's Dement.* 16, 391–460. doi: 10.1002/alz.12068

Ni, R., Ji, B., Ono, M., Sahara, N., Zhang, M. R., Aoki, I., et al. (2018). Comparative In Vitro and In Vivo Quantifications of Pathologic Tau Deposits and Their Association with Neurodegeneration in Tauopathy Mouse Models. *J. Nucl. Med.* 59, 960–966. doi: 10.2967/jnumed.117.201632

Ossenkoppele, R., Leuzy, A., Cho, H., Sudre, C. H., Strandberg, O., Smith, R., et al. (2021). The impact of demographic, clinical, genetic, and imaging variables on tau PET status. *Eur. J. Nucl. Med. Mol. Imaging* 48, 2245–2258. doi: 10.1007/s00259-020-05099-w

Peng, C., Trojanowski, J. Q., and Lee, V. M. (2020). Protein transmission in neurodegenerative disease. *Nat. Rev. Neurol.* 16, 199–212. doi: 10.1038/s41582-020-0333-7

Pontecorvo, M. J., Devous Sr, M. D., Navitsky, M., Lu, M., Salloway, S., Schaerf, F. W., et al. (2017). Relationships between flortaucipir PET tau binding and amyloid burden, clinical diagnosis, age and cognition. *Brain J. Neurol.* 140, 748–763. doi: 10.1093/brain/aww334

Ruan, W., Sun, X., Hu, X., Liu, F., Hu, F., Guo, J., et al. (2020). Regional SUV quantification in hybrid PET/MR, a comparison of two atlas-based automatic brain segmentation methods. *EJNMMI Res.* 10:60. doi: 10.1186/s13550-020-00648-8

Seemiller, J., Bischof, G. N., Hoenig, M. C., Tahmasian, M., van Eimeren, T., Drzezga, A., et al. (2021). Indication of retrograde tau spreading along Braak stages and functional connectivity pathways. *Eur. J. Nucl. Med. Mol. Imaging* 48, 2272–2282. doi: 10.1007/s00259-020-05183-1

Tagai, K., Ono, M., Kubota, M., Kitamura, S., Takahata, K., Seki, C., et al. (2021). High-Contrast In Vivo Imaging of Tau Pathologies in Alzheimer's and Non-Alzheimer's Disease Tauopathies. *Neuron* 109, 42–58.e8. doi: 10.1016/j.neuron.2020.09.042

Teng, E., Ward, M., Manser, P. T., Sanabria-Bohorquez, S., Ray, R. D., Wildsmith, K. R., et al. (2019). Cross-sectional associations between [18F]GTP1 tau PET and cognition in Alzheimer's disease. *Neurobiol. Aging* 81, 138–145. doi: 10.1016/j.neurobiolaging.2019.05.026

Villa, C., Lavitrano, M., Salvatore, E., and Combi, R. (2020). Molecular and Imaging Biomarkers in Alzheimer's Disease: a Focus on Recent Insights. *J. Pers. Med.* 10:61. doi: 10.3390/jpm10030061

Villemagne, V. L., Furumoto, S., Fodero-Tavoletti, M. T., Mulligan, R. S., Hodges, J., Harada, R., et al. (2014). In vivo evaluation of a novel tau imaging tracer for Alzheimer's disease. *Eur. J. Nucl. Med. Mol. Imaging* 41, 816–826. doi: 10.1007/s00259-013-2681-7

Vogel, J. W., Young, A. L., Oxtoby, N. P., Smith, R., Ossenkoppele, R., Strandberg, O. T., et al. (2021). Four distinct trajectories of tau deposition identified in Alzheimer's disease. *Nat. Med.* 27, 871–881. doi: 10.1038/s41591-021-01309-6

Weng, C. C., Hsiao, I. T., Yang, Q. F., Yao, C. H., Tai, C. Y., Wu, M. F., et al. (2020). Characterization of 18F-PM-PBB3 (18F-APN-1607) Uptake in the rTg4510 Mouse Model of Tauopathy. *Molecules* 25:1750. doi: 10.3390/molecules25071750

Zhao, Q., Liu, M., Ha, L., Zhou, Y., Alzheimer's Disease Neuroimaging Initiative (2019). Quantitative 18F-AV1451 Brain Tau PET Imaging in Cognitively Normal Older Adults. *Front. Neurol.* 10:486. doi: 10.3389/fneur.2019.00486

Conflict of Interest: The authors declare that the research was conducted in the absence of any commercial or financial relationships that could be construed as a potential conflict of interest.

Publisher's Note: All claims expressed in this article are solely those of the authors and do not necessarily represent those of their affiliated organizations, or those of the publisher, the editors and the reviewers. Any product that may be evaluated in this article, or claim that may be made by its manufacturer, is not guaranteed or endorsed by the publisher.

Copyright © 2022 Xu, Ruan, Liu, Gai, Liu, Su, Liang, Sun and Lan. This is an open-access article distributed under the terms of the Creative Commons Attribution License (CC BY). The use, distribution or reproduction in other forums is permitted, provided the original author(s) and the copyright owner(s) are credited and that the original publication in this journal is cited, in accordance with accepted academic practice. No use, distribution or reproduction is permitted which does not comply with these terms.

frontiers in Aging Neuroscience

ORIGINAL RESEARCH
published: 14 February 2022
doi: 10.3389/fnagi.2022.783996

Cerebrospinal Fluid Biomarkers in Cerebral Amyloid Angiopathy: New Data and Quantitative Meta-Analysis

Nils G. Margraf[1†], Ulf Jensen-Kondering[2,3†], Caroline Weiler[1], Frank Leypoldt[1,4], Walter Maetzler[1], Sarah Philippen[1], Thorsten Bartsch[1], Charlotte Flüh[5], Christoph Röcken[6], Bettina Möller[1], Georg Royl[7], Alexander Neumann[3], Norbert Brüggemann[7,8], Benjamin Roeben[9,10], Claudia Schulte[9,10], Benjamin Bender[11], Daniela Berg[1,9] and Gregor Kuhlenbäumer[1]*

[1] Department of Neurology, University Medical Center Schleswig-Holstein, Campus Kiel, Kiel University, Kiel, Germany, [2] Department of Radiology and Neuroradiology, University Medical Center Schleswig-Holstein, Campus Kiel, Kiel University, Kiel, Germany, [3] Department of Neuroradiology, University Medical Center Schleswig-Holstein, Campus Lübeck, Lübeck, Germany, [4] Institute of Clinical Chemistry, University Medical Center Schleswig-Holstein, Kiel/Lübeck, Germany, [5] Department of Neurosurgery, University Medical Center Schleswig-Holstein, Campus Kiel, Kiel University, Kiel, Germany, [6] Department of Pathology, University Medical Center Schleswig-Holstein, Campus Kiel, Kiel University, Kiel, Germany, [7] Department of Neurology, University Medical Center Schleswig Holstein, Campus Lübeck, Lübeck, Germany, [8] Institute of Neurogenetics, University of Lübeck, Lübeck, Germany, [9] Department of Neurodegeneration, Hertie Institute for Clinical Brain Research, University of Tübingen, Tübingen, Germany, [10] German Center for Neurodegenerative Diseases, University of Tübingen, Tübingen, Germany, [11] Department of Neuroradiology, Diagnostical and Interventional Neuroradiology, University Hospital of Tübingen, Tübingen, Germany

OPEN ACCESS

Edited by:
Jiehui Jiang,
Shanghai University, China

Reviewed by:
Mitsuru Shinohara,
National Center for Geriatrics and Gerontology (NCGG), Japan
Amy Renee Nelson,
University of South Alabama, United States

***Correspondence:**
Nils G. Margraf
n.margraf@neurologie.uni-kiel.de

[†]These authors have contributed equally to this work and share first authorship

Received: 27 September 2021
Accepted: 03 January 2022
Published: 14 February 2022

Citation:
Margraf NG, Jensen-Kondering U, Weiler C, Leypoldt F, Maetzler W, Philippen S, Bartsch T, Flüh C, Röcken C, Möller B, Royl G, Neumann A, Brüggemann N, Roeben B, Schulte C, Bender B, Berg D and Kuhlenbäumer G (2022) Cerebrospinal Fluid Biomarkers in Cerebral Amyloid Angiopathy: New Data and Quantitative Meta-Analysis. Front. Aging Neurosci. 14:783996. doi: 10.3389/fnagi.2022.783996

Background: To evaluate the diagnostic accuracy of cerebrospinal fluid (CSF) biomarkers in patients with probable cerebral amyloid angiopathy (CAA) according to the modified Boston criteria in a retrospective multicentric cohort.

Methods: Beta-amyloid 1-40 (Aβ40), beta-amyloid 1-42 (Aβ42), total tau (t-tau), and phosphorylated tau 181 (p-tau^{181}) were measured in 31 patients with probable CAA, 28 patients with Alzheimer's disease (AD), and 30 controls. Receiver-operating characteristics (ROC) analyses were performed for the measured parameters as well as the Aβ42/40 ratio to estimate diagnostic parameters. A meta-analysis of all amenable published studies was conducted.

Results: In our data Aβ42/40 (AUC 0.88) discriminated best between CAA and controls while Aβ40 did not perform well (AUC 0.63). Differentiating between CAA and AD, p-tau^{181} (AUC 0.75) discriminated best in this study while Aβ40 (AUC 0.58) and Aβ42 (AUC 0.54) provided no discrimination. In the meta-analysis, Aβ42/40 (AUC 0.90) showed the best discrimination between CAA and controls followed by t-tau (AUC 0.79), Aβ40 (AUC 0.76), and p-tau^{181} (AUC 0.71). P-tau^{181} (AUC 0.76), Aβ40 (AUC 0.73), and t-tau (AUC 0.71) differentiated comparably between AD and CAA while Aβ42 (AUC 0.54) did not. In agreement with studies examining AD biomarkers, Aβ42/40

discriminated excellently between AD and controls (AUC 0.92–0.96) in this study as well as the meta-analysis.

Conclusion: The analyzed parameters differentiate between controls and CAA with clinically useful accuracy (AUC > ∼0.85) but not between CAA and AD. Since there is a neuropathological, clinical and diagnostic continuum between CAA and AD, other diagnostic markers, e.g., novel CSF biomarkers or other parameters might be more successful.

Keywords: cerebral amyloid angiopathy (CAA), cerebrospinal fluid (CSF), high-precision electro-chemiluminescence immunoassay (ECLIA), Boston criteria, Alzheimer's dementia (AD)

INTRODUCTION

Cerebral amyloid angiopathy (CAA) is the most frequent cause of lobar hemorrhage in the elderly. Its diagnosis predicts future hemorrhagic and ischemic complications (Yamada, 2000; Viswanathan and Steven, 2008; Wilson and Werring, 2017; Puy and Cordonnier, 2019). CAA is diagnosed using the modified Boston criteria (Linn et al., 2010). In clinical practice, the diagnosis of CAA is largely based on neuroradiological criteria because brain biopsies are rarely performed.

The direct measurement of amyloid proteins and other protein markers in cerebrospinal fluid (CSF) has been addressed in patients with sporadic CAA suggesting that measurement of beta-amyloid 1-40 (Aβ40), beta-amyloid 1-42 (Aβ42), total tau (t-tau), and phosphorylated tau 181 (p-tau^{181}) in CSF might differentiate CAA from controls as well as from Alzheimer's disease (AD) patients (Verbeek et al., 2009; Hernandez-Guillamon et al., 2012; Renard et al., 2012, 2016; Li et al., 2015; Martínez-Lizana et al., 2015; Charidimou et al., 2018; Banerjee et al., 2020). The Aβ42/40 discriminates excellently between AD and controls and changes of the Aβ40/42 ratio have been suggested to play a role in animal models of CAA (Janelidze et al., 2016; Gervaise-Henry et al., 2017; Doecke et al., 2020).

Beta-amyloid 1-40 more than Aβ42 is the main driver of beta-amyloid deposition in the wall of small cerebral arteries while Aβ42 is more important than Aβ40 in amyloid plaque formation in AD (Viswanathan and Greenberg, 2011). The results of previous diagnostic studies were inhomogeneous and a diagnostic algorithm including cut-off values is lacking. In particular, the difficult differentiation between CAA and AD patients might be caused by the overlapping pathomechanisms (Kester et al., 2014; Greenberg et al., 2020).

We aimed to determine the diagnostic value of CSF Aβ40, Aβ42, t-tau, and p-tau^{181} and the ratio Aβ42/40 (mathematically equivalent to: Aβ40/42) using an automated high-precision electro-chemiluminescence immunoassay (ECLIA) in a large sample of patients with probable CAA. The modified Boston criteria were used as the diagnostic standard for CAA. Also, we performed a quantitative meta-analysis of all amenable studies of CSF parameters in CAA. Diagnostic parameters in our samples, as well as the meta-analysis, were determined using receiver-operating characteristics (ROC) analysis.

MATERIALS AND METHODS

Participants

We retrospectively included three groups between May 2014 and November 2019 at the University Medical Center Schleswig-Holstein (Kiel and Lübeck) and the University Hospital Tübingen: CAA, AD, and control participants.

Cerebral Amyloid Angiopathy Group

Inclusion criteria for the CAA group were (1) probable CAA or probable CAA with supporting pathology according to the modified Boston criteria (**Table 1**); (2) availability of a diagnostic cranial MRI including a gradient-echo T2* or susceptibility-based sequence (SWI, SWIp, or veno BOLD); and (3) availability of a CSF sample within 3 months before or after the cerebral MRI grafted for clinical purposes during the diagnostic work-up.

Patients with possible CAA according to the modified Boston criteria (**Table 1**) or any genetically determined or inflammatory forms of CAA were excluded.

Alzheimer's Disease Group

Inclusion criteria for the AD group were (1) fullfilment of the diagnostic criteria of Alzheimer's dementia according to the National Institute on Aging and Alzheimer's Association (NIA-AA) (Jack et al., 2011); (2) availability of a diagnostic cranial MRI including a gradient-echo T2* or susceptibility-based sequence (SWI, SWIp, or veno BOLD); and (3) availability of a CSF sample within 3 months before or after the cerebral MRI grafted for clinical purposes during the diagnostic work-up.

Exclusion criteria were imaging features of probable CAA according to the modified Boston criteria (**Table 1**).

Control Group

Controls were recruited at the University Medical Center Schleswig-Holstein (Kiel and Lübeck) and the University Hospital Tübingen with biomaterial from the Hertie Institute for Clinical Brain Research Biobank (Tübingen) or the UKSH biobank at the Institute of Clinical Chemistry.

Inclusion criteria for the control group were (1) complaints suggestive of neurologic disease, but no evidence of organic central nervous system disease was found after thorough diagnostic work-up and (2) availability of a CSF sample within 3 months before or after the occurrence of neurological complaints.

TABLE 1 | Modified Boston criteria for the diagnosis of CAA.

Definite CAA	Full postmortem examination demonstrating: • Lobar, cortical, or corticosubcortical hemorrhage • Severe CAA with vasculopathy • Absence of other diagnostic lesion
Probable CAA with supporting pathology	Clinical data and pathologic tissue (evacuated hematoma or cortical biopsy) demonstrating: • Lobar, cortical, or corticosubcortical hemorrhage • Some degree of CAA in specimen • Absence of other diagnostic lesion
Probable CAA	Clinical data and MRI or CT demonstrating: • Multiple hemorrhages restricted to lobar, cortical, or corticosubcortical regions (cerebellar hemorrhage allowed) or • Single lobar, cortical, or corticosubcortical hemorrhage and focal or disseminated superficial siderosis • Age ≥ 55 years • Absence of other cause of hemorrhage or superficial siderosis
Possible CAA	Clinical data and MRI or CT demonstrating: • Single lobar, cortical, or corticosubcortical hemorrhage • Focal or disseminated superficial siderosis • Age ≥ 55 years • Absence of other cause of hemorrhage or superficial siderosis

Exclusion criteria were the evidence or a history of a disease of the central nervous system including abnormal routine CSF parameters or if available, relevant pathological findings in a cranial MRI.

We excluded patients from all groups with a competing central nervous system disease that might increase the level of any of the analyzed CSF parameters. Patients with cerebral infarcts >1.5 cm in diameter or an intracerebral hemorrhage within 4 months before the lumbar puncture were excluded to rule out elevated values for the axonal damage marker t-tau (Hjalmarsson et al., 2014). We only made an exception for CAA patients whose surgical treatment of hemorrhages resulted in a pathological verification of CAA ($n = 5$). In these cases, we confirmed that the CSF t-tau concentrations were in the typical range of the other CAA patients. Further, patients who had a history of heart-lung-machine (HLM) procedures were also excluded because HLM treatment can mimic CAA on MRI scans (Jeon et al., 2010).

All MRI scans including the radiological classification of the CAA cases were reviewed and rated by a board-certified neuroradiologist (UJ-K) blinded to history, clinical diagnosis and laboratory parameters. Imaging parameters were rated based on the STRIVE criteria (Wardlaw et al., 2013).

Furthermore, we matched the three groups on a group level according to sex and age.

Clinical Data

We extracted clinical data (age, sex, date and reason of hospital admission, pre-existing diseases, medication and blood coagulation parameters on admission, risk factors for vascular diseases, date and reason of MRI and lumbar puncture, and results of cognitive assessments) from the medical records.

Cerebrospinal Fluid Analysis

Cerebrospinal fluid was stored at −80° in participating biobanks following lumbar puncture. All participating biobanks used polypropylene primary tubes and samples were frozen at −80°C in polypropylene secondary tubes within maximal 48 h at 4°C. Samples were retrieved for this study and kept on dry ice until the time of measurements. Samples were thawed and aliquoted for measurements into certified polypropylene tubes immediately before measurement. Analysis was performed on a fully automated platform (FujiRebio LumiPulse) using dedicated ECLIA assay chemistry (FujiRebio©) according to the manufacturer's protocols including calibration and controls. All analytes were measured within 2 days using single measurements. Predetermined coefficients of variations (CV) for this approach showed intra- and inter-assay variations of <4% for Aβ40, Aβ42, p-Tau, and 7% for t-tau across the whole measurement range. The reader, a board certified laboratory physician (FL), extracting the data was blinded to history, clinical diagnosis and other laboratory parameters of the study participants. The assay is approved and in routine clinical use at the University Hospital Schleswig-Holstein, Kiel.

Statistics

We used R version 3.6.3 for all analyses. We assessed age and biomarker concentration differences between the three study groups (CAA, AD, and controls) using analysis-of-variance (ANOVA) and *post hoc* Tukey test if applicable. To analyze the sex distribution between groups we used Fisher's exact test and for differences in biomarker concentrations between sexes the unpaired *t*-tests per group. The correlation between CSF storage time and biomarker concentrations was analyzed using Kendall rank correlation analysis. To assess the diagnostic value of the CSF biomarkers we used ROC-analysis in pairwise comparisons between the diagnostic groups. ROC analyses were performed using the pROC-package (version 1.16.2) including calculation of the area under the curve (AUC) and its confidence intervals as well as sensitivity, specificity, and cut-off values optimized using the Youden index. We compared the AUCs between biomarkers using the function "roc.test" from the pROC package for statistically significant differences. The statistical significance threshold was $p < 0.05$.

The Ethics Committee of the Medical Faculty of the University of Kiel, Lübeck and Tübingen approved this retrospective study (B 255/18, AZ19-108, and 864/2016BO2). The study was conducted following the World Medical Association Declaration of Helsinki. Anonymized data will be shared by request with any qualified investigator.

Study Selection and Statistics of the Meta-Analysis

We [two board certified neurologists (GK and NGM)] searched PubMed (up to May 1st, 2020) with the search term: (CAA OR cerebral amyloid angiopathy OR cerebral-amyloid-angiopathy)

AND (cerebrospinal fluid OR CSF) and in addition, the Cochrane database[1] and the clinical trials database[2]. We found no studies in the Cochrane or Clinical Trials database. From 197 entries in PubMed, we selected 18 studies, which had done analysis of at least one of the following four biomarkers: Aβ40, Aβ42, t-tau, and p-tau^{181}. Next, we checked whether studies fulfilled the following four hierarchical inclusion criteria: (1) sporadic CAA diagnosed according to the original or modified Boston criteria, (2) a control group, either healthy or suffering from conditions without known influence on biomarker levels, (3) measurement of Aβ40, Aβ42, t-tau, and p-tau^{181} in CSF, and (4) individual biomarker data extractable from figures or tables. The following reasons for exclusion were agreed on in consensus: studies on animals, studies on CAA-related inflammation, case reports and letters to the editor. The flow chart (**Figure 1**) illustrates the selection process according to the PRISMA criteria. If more than one reason for exclusion of a study was present, only the most important reasons for exclusion were given in **Figure 1**. Four studies showed a strong sample overlap and we used only one of them for the meta-analysis. We extracted scatterplots with individual level CSF concentrations of the biomarkers from the included publications and determined individual level biomarker concentrations with the software "PlotDigitizer"[3] as previously described (Jelicic Kadic et al., 2016). We used frequency histograms to examine the distribution of biomarker concentrations in the control group for compatibility with a normal distribution. Per study, we calculated the mean and SD of each biomarker in the control group. *Z*-scores were calculated for every sample in each study per biomarker by subtracting the mean of the control group from each value in the study and dividing the result by the SD of the control group. We performed ROC analysis on the *Z*-scores as described. Subsequently, we report the results of the meta-analysis including all retrieved studies without our study (WO) and including our study (ALL).

[1] www.cochrane.org

[2] www.ClinicalTrials.gov

[3] plotdigitizer.sourceforge.net

RESULTS

Clinical and MRI Data

In the CAA group we included 31 patients, including 26 patients with probable CAA and 5 patients with probable CAA with supporting pathology according to the modified Boston criteria. A total of 13 patients presented with pathologies on cranial MRI (intracranial hemorrhage $n = 3$, subarachnoid hemorrhage $n = 3$, acute infarct <1.5 cm $n = 7$). In these cases, we confirmed that the CSF t-tau concentrations were in the typical range of the other

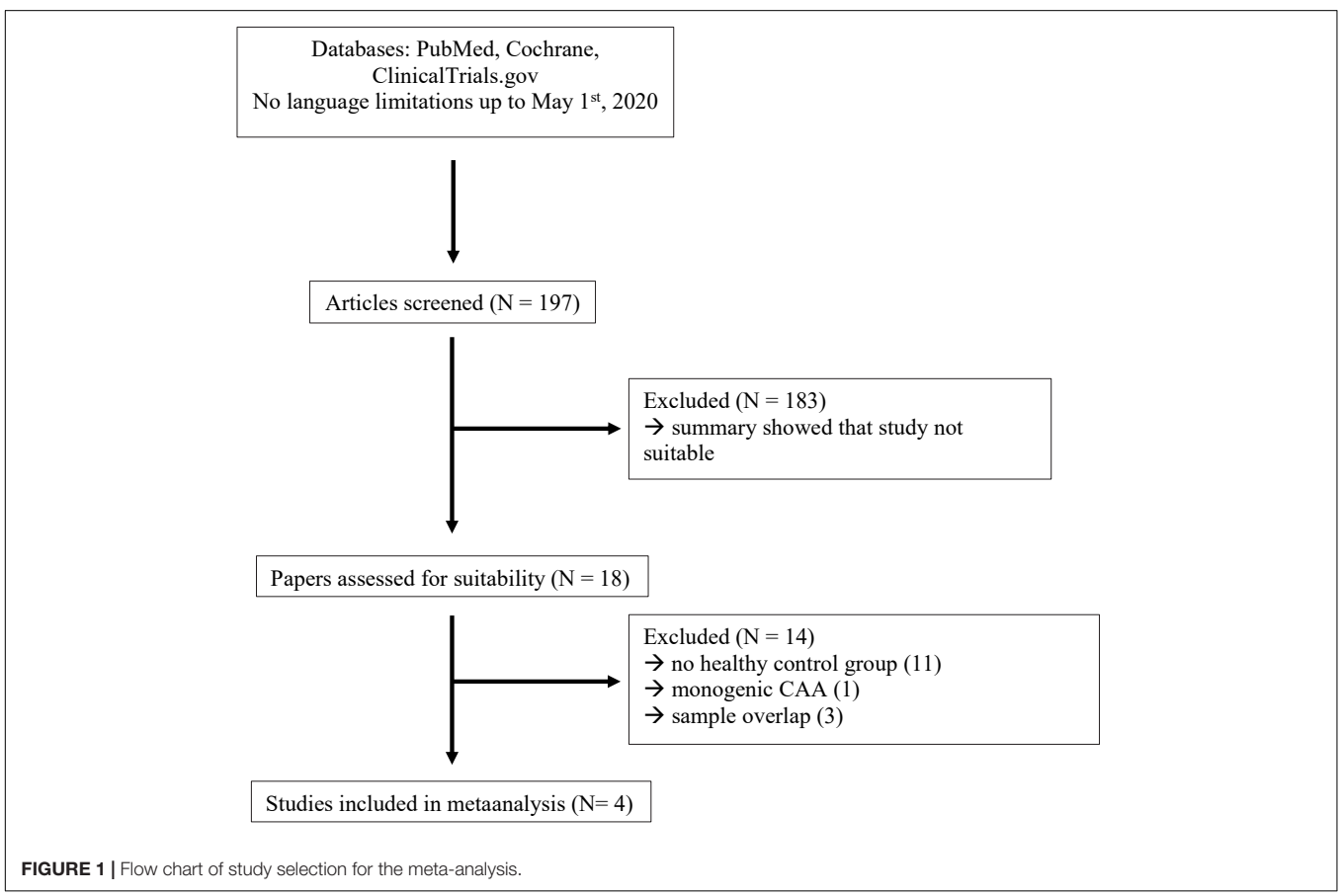

FIGURE 1 | Flow chart of study selection for the meta-analysis.

CAA patients (as indicated by red dots in **Figure 2**). A total of 13 patients were categorized as "demented" and 7 patients as having a mild cognitive impairment based on a neuropsychological screening test as performed during hospital stay [Mini Mental Status Examination, Montreal Cognitive Assessment, Mattis Dementia Rating Scale or DemTect (Kalbe et al., 2004)]. Four patients showed no cognitive deficits and no information was available in seven patients.

In the AD group we included 28 patients. Two of the AD patients (both with one microbleed each, in cerebellar and periventricular location, respectively, not compatible with possible or probable CAA) exhibited cerebral microbleeds.

In the control group we included 30 patients. A total of 12 patients presented with complaints suggestive of neurologic disease, but no evidence of organic neurologic disease was found after thorough diagnostic work-up, 9 patients had a peripheral neurological disease, 2 patients had a muscle disease, and 7 participants were healthy controls without a neurological disease from the biobank of the Hertie Institute, Tübingen. A total of 14 patients (47%) had a cerebral MRI available for review. A neuropsychological screening available in seven patients (23%) showed no indication of dementia.

Table 2 summarizes the main characteristics of the three groups. Age ($p = 0.08$, ANOVA) and gender distribution ($p = 0.4$, Chi square) did not differ significant between the three groups. Most of the MRIs were performed at 1.5 T (79%), however, that was consistent between the three groups ($p = 0.9$, Chi square). A majority (59%) of MRIs included a susceptibility-based sequence instead of a GRE T2* with significantly more susceptibility-based sequences performed in the CAA group than in the other groups (87 vs. 36 vs. 43%, $p = 0.00002$, Fischer's exact test).

TABLE 2 | Clinical and MRI patients characteristics.

		CAA ($n = 31$)	AD ($n = 28$)	Controls ($n = 30$)
Center (*n*/%)		Kiel: 22/71 Lübeck: 4/13 Tübingen: 5/16	Kiel: 13/47 Lübeck: 4/14 Tübingen: 11/39	Kiel: 17/57 Lübeck: 4/13 Tübingen: 9/30
Gender (female) (*n*/%)		13/42%	16/57	17/56
Age years [mean (SD)]		75.1 (5.3)	71.1 (7.7)	72.5 (7.8)
MRI field strength (*n*/%)	1.5 Tesla	25/81	22/79	11/79
	3 Tesla	6/19	6/21	3/21
Sequence (*n*/%)	Susceptibility based	27/87	10/36	6/43
	T2* GRE	4/13	18/64	0/0
ICH (*n*/%)	Acute	3/10	0/0	0/0
	Chronic	5/16	0/0	0/0
cSS (*n*/%)		14/45	0/0	0/0
SAH (*n*/%)		3/10	0/0	0/0
Acute infarct^{+} (*n*/%)	Embolic	3/10	0/0	0/0
	Lacune	4/13	0/0	0/0
Chronic infarct (*n*/%)	Embolic	3/10	3/11	1§ /3
	Lacune	7/23	2/7	0/0

AD, Alzheimer's disease; CAA, cerebral amyloid angiopathy; cSS, cortical superficial siderosis; GRE, gradient-echo; ICH, intracranial hemorrhage; N/A, not available; SAH, subarachnoid hemorrhage.
$^{+}$Cerebral infarcts <1.5 cm in diameter.
§ Asymptomatic, diagnosed on MRI.

Cerebrospinal Fluid Data

We analyzed the CSF parameters Aβ40, Aβ42, t-tau, and p-tau^{181} and the ratio Aβ42/40 which is mathematically equivalent to the multiplicative inverse Aβ40/42. **Table 3** and **Figure 2** show a comparison of biomarker concentrations between groups. Aβ42 was decreased in both the AD and CAA group when compared to the control group but there was no significant difference between CAA and AD. Aβ40 did not differ significantly between CAA, AD, and controls. T-tau and p-tau^{181} were highest in the AD group followed by the CAA group and controls and all group differences were significant (**Figure 2**).

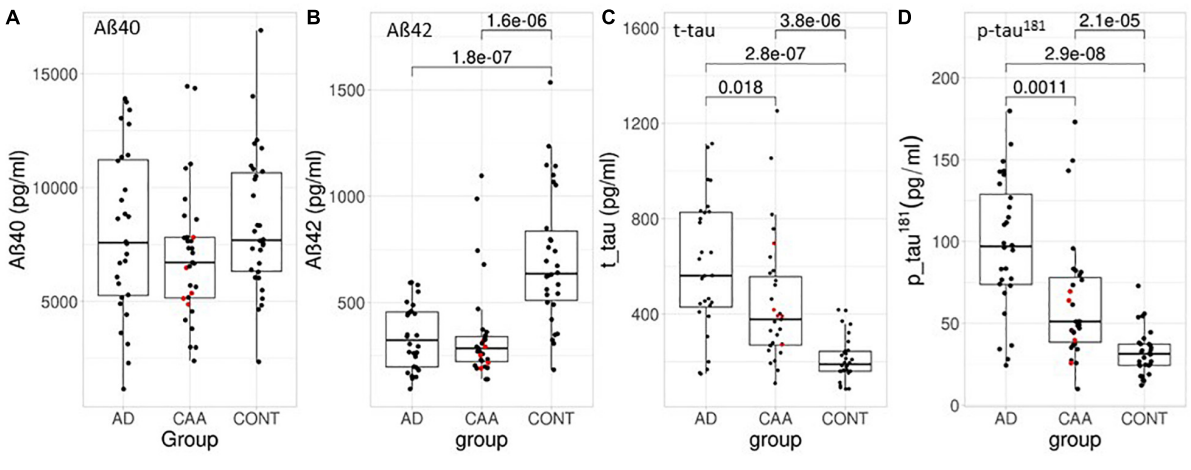

FIGURE 2 | Box- and scatterplots of the CSF biomarker values in this study per diagnostic group. **(A)** Aβ40, **(B)** Aβ42, **(C)** t-tau, and **(D)** p-tau^{181}. Red dots indicate the pathologically confirmed CAA samples. All concentrations in pg/ml. The box encompasses 50% of the samples and the whiskers extend 1.5 quartiles to each side of the box. Significant differences are indicated including *p*-values.

TABLE 3 | Cerebrospinal fluid parameters of the samples in our study.

Parameter	CAA *n* = 31 Mean (SD)	AD *n* = 28 Mean (SD)	CONT *n* = 30 Mean (SD)	ANOVA *p*-value
Aβ40	7008 (2896)	7997 (3649)	8443 (3102)	0.21
Aβ42	347 (228)	340 (154)	709 (317)	<0.01
T-tau	444 (259)	597 (280)	211 (91)	<0.01
P-tau^{181}	62 (37)	98 (41)	32 (14)	<0.01

*AD, Alzheimer's disease; CAA, cerebral amyloid angiopathy; CONT, controls; ANOVA across all three groups. Significant differences between pairs are indicated in **Figure 2**.*

Most CSF biomarker concentrations in samples of patients with probable CAA with supporting pathology were within the interquartile range and the remaining ones were located within the range of ±1.5 quartiles of all values (indicated by red dots in **Figure 2**). The same applied to patients with other acute radiological findings as described above and indicated in **Table 2**.

Cerebrospinal fluid-storage time did not correlate with biomarker concentrations (Aβ40 $p = 0.21$, Aβ42 $p = 0.42$, t-tau $p = 0.08$, p-tau^{181} $p = 0.12$) and biomarker concentrations did not differ significantly between sexes within a diagnostic group (p-value range: 0.09–0.98). **Figure 3A** and **Table 4** show the ROC curves, the key diagnostic parameters, AUC with 95% confidence interval, sensitivity, and specificity.

For the comparison between controls vs. AD we observed the largest AUCs of 0.92 for p-tau^{181} and Aβ42/40, for the comparison controls vs. CAA we observed the largest AUC of 0.88 for Aβ42/40, and for the comparison AD vs. CAA we observed the largest AUC of 0.75 for p-tau^{181}.

For the comparison between controls with AD and CAA patients, respectively, the AUC did not differ significantly between all markers except Aβ40 which showed a significantly smaller AUC (**Table 4** and **Figure 3A**). The same was true for the comparison between AD and CAA patients for p-tau^{181}, t-tau, and Aβ42/40 while Aβ40 and Aβ42 performed significantly worse.

The Youden index optimized measures of sensitivity and specificity (**Table 4**), should be interpreted with caution. ROC curves are jagged due to the relatively small sample size and some ROC curves (e.g., Aβ42 for Alzheimer vs. CAA) run for long stretches nearly parallel to the bisecting line. This indicates that several sensitivity/specificity combinations would result in nearly equal Youden indices.

Meta-Analysis

We identified five studies including this study suitable for a meta-analysis based on individual CSF biomarker concentrations (**Figure 1**). **Table 5** gives an overview of these studies incorporating in total 90 CAA patients, 204 AD patients, and 134 controls. We used Z-scores to harmonize the biomarker data generated on different laboratory platforms between studies. Subsequently, we performed the same ROC analyses as for the data in this study. **Table 4** provides the key diagnostic parameter data for this study as well as the meta-analyses including absolute cut-off values for our study and optimal cut-off Z-values for the meta-analysis. **Figure 3B** shows the ROC plots for the meta-analysis of all studies (ALL) and **Figure 3C** for the meta-analysis without this study (WO). The differentiation between controls and AD was excellent in both meta-analyses with an AUC of 0.96 for the Aβ42/40 ratio in the ALL and the WO analysis. Aβ42 (AUC 0.88 ALL, 0.89 WO) was significantly worse and Aβ40 (AUC 0.53 ALL and WO) did not provide any differentiation at all. Aβ42/40 (AUC 0.9 for ALL and WO) and Aβ42 (AUC 0.89 ALL, 0.91 WO) alone showed comparable AUCs in the analysis of controls vs. CAA. T-tau, Aβ40, and p-tau^{181} performed worse. P-tau (AUC 0.76 ALL, 0.78 WO), Aβ40 (AUC 0.73 ALL, 0.80 WO), and t-tau (AUC 0.71 ALL, 0.72 WO) showed comparable differentiation between AD and CAA while Aβ42 (AUC 0.54 ALL, 0.60 WO) did not separate these diagnoses.

DISCUSSION

Taken together, the results of this study and the meta-analyses indicate that CSF Aβ42 and the Aβ42/40 ratio separates controls from CAA patients with good accuracy (AUC 0.86–0.91). However, the differentiation between AD and CAA on the basis of CSF standard parameters proves to be more difficult. Our quantitative meta-analysis of all amenable CAA studies on CSF parameters utilizing control groups shows that Aβ40, t-tau, and p-tau^{181} yield very similar diagnostic results for AD vs. CAA with an AUC in the range of 0.71–0.80. In our opinion, these values are insufficient to justify routine clinical use.

In contrast to the meta-analysis, Aβ40 did not differentiate between AD and CAA (AUC 0.58) in our study. Especially the size of the actual CAA group is larger than in all preceding studies investigating this topic, and also the control group is larger than in almost all previous studies [except (Verbeek et al., 2009)]. Additional strengths are the use of highly accurate CSF analysis using an automated platform with minimal variation coefficient and strict adherence to diagnostic criteria. The main limitation of the study is its retrospective design. Also, complete and homogeneous neuropsychological test data would have been of great use to us, enabling us to correlate CSF biomarker concentrations not only with the diagnostic category but also with cognitive performance. We speculate that this could be one factor influencing the performance of Aβ40 as a biomarker for CAA (van Oijen et al., 2006). In contrast to the studies by Verbeek et al. (2009), Renard et al. (2012, 2016), and Banerjee et al. (2020), most CAA patients in our cohort were cognitively impaired. We included these patients because they fulfilled the modified Boston criteria that do not contain a statement concerning the cognitive status. We included patients over a long period of time (2014–2019) in three large tertiary care centers and thus believe that they depict a representative sample of CAA patients encountered in clinical practice. On the other hand, a large proportion of the CAA patients in the study by Martínez-Lizana et al. (2015) were also cognitively impaired and while the number of cases was low, results shown in their Figure 2 suggest that Aβ40 does not reliably differentiate between AD and CAA. Due to the small number of cases

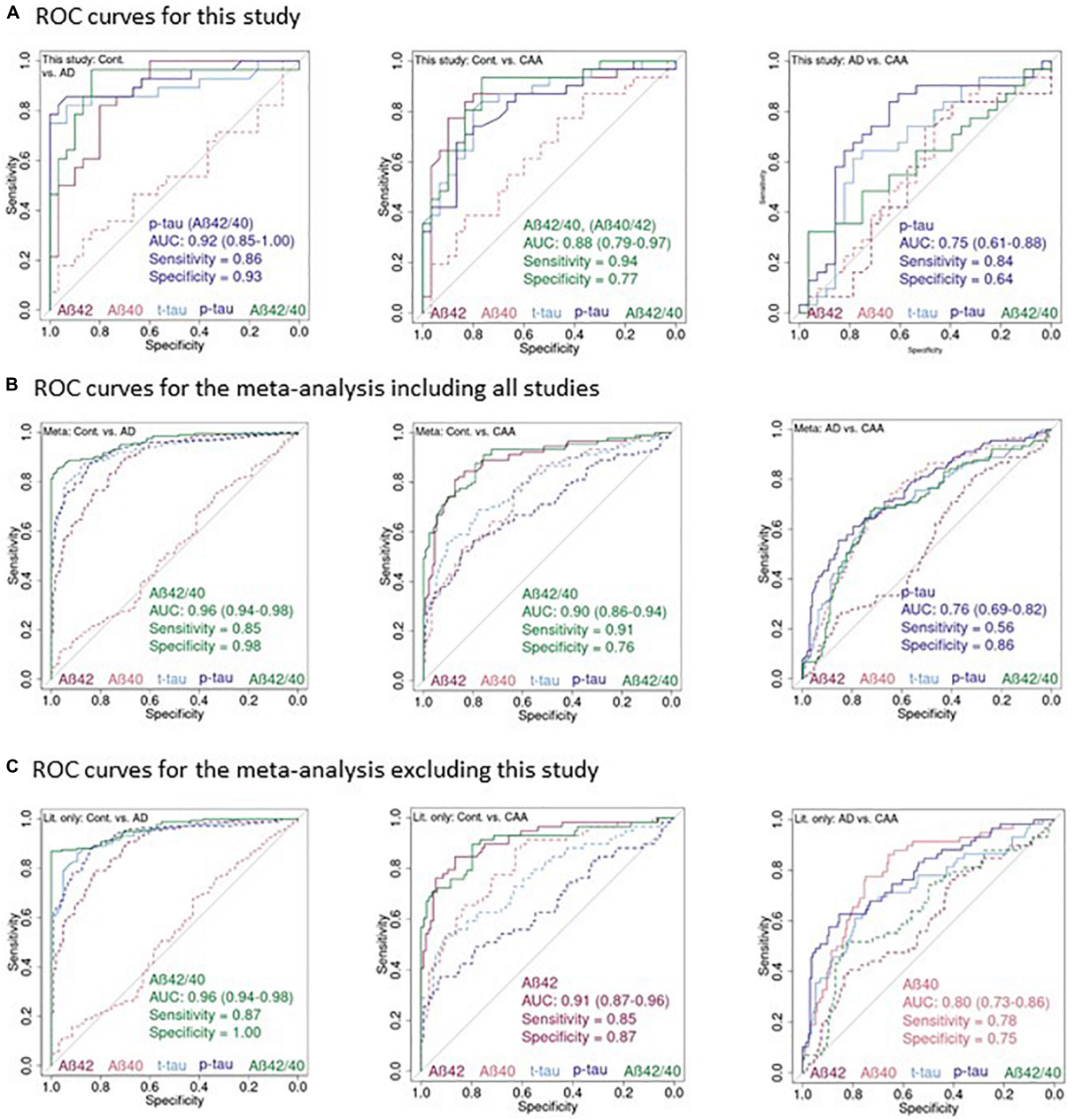

FIGURE 3 | Receiver-operating characteristics curves for the CSF parameters in our study and the meta-analyses. **(A)** ROC plots of Aβ40, Aβ42, t-tau, p-tau^{181}, and Aβ42/40 in this study for: controls vs. AD, controls vs. CAA, AD vs. CAA. **(B)** The same plots as in **(A)** for the meta-analysis including this study. **(C)** And excluding this study. CSF parameters corresponding to the lines are color-coded at the bottom of the plots. Solid lines: parameter with the highest AUC and parameters with an AUC not significantly different from the highest AUC. Dashed line: parameters with a significantly smaller AUC compared to the one with the highest AUC. Text insert: AUC, 95% confidence interval of the AUC, sensitivity, specificity of the parameter with the highest AUC and, if applicable name of additional parameter with identical AUC.

in our study a comparison between demented (n = 17) and non-demented (n = 4) CAA patients did not yield any statistically meaningful results.

Since the modified Boston criteria rely in large part on imaging criteria and microbleed detection, the choice of sequence is crucial. Susceptibility based sequences can detect substantially more microbleeds (Cheng et al., 2013). Due to the retrospective nature of the study we could not fully harmonize the use of image parameters and sequences across centers and we thus cannot fully rule out that this introduced a selection bias. However, the established diagnostic criteria for the diagnosis of CAA and AD, namely the modified Boston criteria and the NIA-AA were fulfilled for all subjects. A further source of error is the unknown relationship between CSF parameters and APOE4 allele status,

TABLE 4 | Diagnostic parameters determined in this study and the meta-analyses.

This study	Parameter	AUC (95% CI)	Sensitivity (95% CI)	Specificity (95% CI)	*Z*-score cut-off	Measured cut-off
cont/ad	Aβ40	0.53 (0.38–0.69)	0.32 (0.14–0.5)	0.83 (0.7–0.97)	−0.21	5904
cont/ad	Aβ42	0.87 (0.78–0.96)	0.82 (0.68–0.96)	0.8 (0.67–0.93)	−0.2	490
cont/ad	**P-tau^{181}**	**0.92 (0.85–1)**	**0.86 (0.71–0.96)**	**0.93 (0.83–1)**	**0.38**	**55**
cont/ad	T-tau	0.89 (0.8–0.99)	0.82 (0.68–0.93)	0.93 (0.83–1)	0.92	381
cont/ad	**Aβ42/40**	**0.92 (0.83–1)**	**0.96 (0.89–1)**	**0.83 (0.7–0.93)**	**−1.22**	**0.06**
cont/caa	Aβ40	0.63 (0.49–0.77)	0.77 (0.61–0.9)	0.47 (0.3–0.63)	0.99	7950
cont/caa	Aβ42	0.86 (0.76–0.96)	0.77 (0.61–0.9)	0.9 (0.77–1)	−0.71	347
cont/caa	P-tau^{181}	0.82 (0.71–0.93)	0.68 (0.52–0.84)	0.87 (0.73–0.97)	−0.36	45
cont/caa	T-tau	0.85 (0.75–0.94)	0.81 (0.65–0.94)	0.8 (0.67–0.93)	−0.1	258
cont/caa	**Aβ42/40**	**0.88 (0.79–0.97)**	**0.94 (0.84–1)**	**0.77 (0.6–0.9)**	**−0.58**	**0.07**
ad/caa	Aβ40	0.58 (0.43–0.73)	0.81 (0.68–0.94)	0.46 (0.29–0.64)	1.38	8618
ad/caa	Aβ42	0.54 (0.39–0.7)	0.74 (0.58–0.9)	0.5 (0.32–0.68)	−0.75	338
ad/caa	**P-tau^{181}**	**0.75 (0.61–0.88)**	**0.84 (0.71–0.94)**	**0.64 (0.46–0.82)**	**2.35**	**83**
ad/caa	T-tau	0.68 (0.54–0.82)	0.61 (0.45–0.77)	0.79 (0.61–0.93)	1.13	406
ad/caa	Aβ42/40	0.61 (0.46–0.75)	0.32 (0.16–0.48)	0.96 (0.89–1)	−1.4	0.05
Meta-analysis excluding this study	**Parameter**	**AUC (95% CI)**	**Sensitivity (95% CI)**	**Specificity (95% CI)**	***Z*-score cut-off**	**Measured cut-off**
cont/ad	Aβ40	0.53 (0.46–0.6)	0.68 (0.61–0.74)	0.43 (0.33–0.52)	0.19	N/A
cont/ad	Aβ42	0.89 (0.85–0.93)	0.79 (0.73–0.85)	0.83 (0.75–0.89)	−0.96	N/A
cont/ad	P-tau^{181}	0.93 (0.9–0.96)	0.89 (0.84–0.93)	0.84 (0.76–0.9)	0.78	N/A
cont/ad	T-tau	0.94 (0.91–0.96)	0.86 (0.81–0.91)	0.89 (0.84–0.95)	1.04	N/A
cont/ad	**Aβ42/40**	**0.96 (0.94–0.98)**	**0.87 (0.82–0.91)**	**1 (1–1)**	**−1.93**	**N/A**
cont/caa	Aβ40	0.82 (0.75–0.89)	0.88 (0.79–0.95)	0.63 (0.53–0.72)	−0.42	N/A
cont/caa	**Aβ42**	**0.91 (0.87–0.96)**	**0.85 (0.75–0.93)**	**0.87 (0.8–0.93)**	**−1.17**	**N/A**
cont/caa	P-tau^{181}	0.65 (0.56–0.74)	0.37 (0.25–0.49)	0.92 (0.88–0.97)	1.47	N/A
cont/caa	T-tau	0.76 (0.68–0.84)	0.53 (0.39–0.66)	0.91 (0.86–0.96)	1.31	N/A
cont/caa	Aβ42/40	0.9 (0.85–0.96)	0.9 (0.81–0.97)	0.8 (0.71–0.87)	−0.83	N/A
ad/caa	**Aβ40**	**0.8 (0.73–0.86)**	**0.78 (0.67–0.88)**	**0.75 (0.68–0.81)**	**−0.73**	**N/A**
ad/caa	Aβ42	0.6 (0.51–0.68)	0.39 (0.27–0.53)	0.84 (0.78–0.89)	−2.14	N/A
ad/caa	P-tau^{181}	0.78 (0.71–0.86)	0.63 (0.51–0.75)	0.85 (0.8–0.91)	1.06	N/A
ad/caa	T-tau	0.72 (0.64–0.8)	0.68 (0.56–0.8)	0.73 (0.67–0.79)	2.07	N/A
ad/caa	Aβ42/40	0.65 (0.56–0.73)	0.52 (0.4–0.64)	0.82 (0.77–0.88)	−2.95	N/A
Meta-analysis including this study	**Parameter**	**AUC (95% CI)**	**Sensitivity (95% CI)**	**Specificity (95% CI)**	***Z*-score cut-off**	**Measured cut-off**
cont/ad	Aβ40	0.53 (0.47–0.59)	0.75 (0.7–0.81)	0.33 (0.24–0.41)	0.46	N/A
cont/ad	Aβ42	0.88 (0.85–0.92)	0.88 (0.84–0.93)	0.72 (0.63–0.79)	−0.6	N/A
cont/ad	P-tau^{181}	0.93 (0.9–0.95)	0.88 (0.84–0.92)	0.84 (0.78–0.9)	0.78	N/A
cont/ad	T-tau	0.93 (0.9–0.96)	0.88 (0.83–0.92)	0.87 (0.81–0.92)	0.96	N/A
cont/ad	**Aβ42/40**	**0.96 (0.94–0.98)**	**0.85 (0.8–0.9)**	**0.98 (0.94–1)**	**−1.74**	**N/A**
cont/caa	Aβ40	0.76 (0.69–0.82)	0.87 (0.8–0.93)	0.54 (0.44–0.63)	−0.2	N/A
cont/caa	Aβ42	0.89 (0.84–0.94)	0.81 (0.73–0.89)	0.87 (0.81–0.93)	−1.17	N/A
cont/caa	P-tau^{181}	0.71 (0.63–0.78)	0.52 (0.42–0.62)	0.84 (0.78–0.9)	0.86	N/A
cont/caa	T-tau	0.79 (0.73–0.85)	0.69 (0.6–0.78)	0.78 (0.71–0.85)	0.59	N/A
cont/caa	**Aβ42/40**	**0.9 (0.86–0.94)**	**0.91 (0.84–0.97)**	**0.76 (0.68–0.83)**	**−0.73**	**N/A**
ad/caa	Aβ40	0.73 (0.67–0.79)	0.74 (0.65–0.83)	0.65 (0.58–0.71)	−0.48	N/A
ad/caa	Aβ42	0.54 (0.47–0.61)	0.81 (0.72–0.89)	0.32 (0.25–0.38)	−1.16	N/A
ad/caa	**P-tau^{181}**	**0.76 (0.69–0.82)**	**0.56 (0.46–0.66)**	**0.86 (0.8–0.9)**	**1.06**	**N/A**
ad/caa	T-tau	0.71 (0.64–0.77)	0.66 (0.56–0.76)	0.73 (0.67–0.79)	2.11	N/A
ad/caa	Aβ42/40	0.69 (0.63–0.76)	0.67 (0.57–0.76)	0.73 (0.67–0.78)	−2.86	N/A

CONT, controls; AD, Alzheimer's disease; CAA, cerebral amyloid angiopathy; AUC, area under the curve in the ROC analysis; Z-score cut-off, Z-score used as cut-off to determine optimal sensitivity and specificity in the metaanalysis. Measured cut-off: cut-off of directly measured parameters to determine optimal sensitivity and specificity in this stud. N/A, not applicable. Bold: parameter with the highest AUC.

TABLE 5 | Characteristics of the studies in the meta-analysis.

Study	Group demographics (*n*, age, and cognitive status)	Diagnostic criteria CAA (MRI sequence), AD	Method of CSF analysis	Results
Verbeek et al., 2009	– **CAA:** *n* = 17, age 62.8 ± 11.9 years (mean, SD), not demented – **AD:** *n* = 72, age 69.4 ± 8.3 years (mean, SD) – **Controls:** *n* = 58, age 61.0, ± 8.7 years (mean, SD), no neurological disorders	CAA: probable or definite per Boston criteria (T2*) AD: NINCDS-ADRDA	ELISA (Innogenetics, NV, Gent, Belgium)	• Aβ40 and Aβ42 decreased in CAA vs. AD and controls • T-tau and p-tau^{181} increased in CAA vs. controls but decreased vs. AD
Martínez-Lizana et al., 2015	– **CAA:** *n* = 19 [12 CAA without SAH, age 69.8 years (mean), 7 CAA with SAH, age 79.1 years (mean)], predominantly MCI/dementia – **AD:** *n* = 42, age 67.6, 50.6–79.8 (mean, range) – **Controls:** *n* = 20, age 66.5, 55.7–77.5 (mean, range), no cognitive complaints, normal neuropsychological evaluation	CAA: possible or probable per modified Boston criteria (T2*) AD: NINCDS-ADRDA	ELISA (Innogenetics, NV, Gent, Belgium)	• Aβ40 and Aβ42 decreased in CAA vs. controls but not AD • T-tau increased in CAA vs. controls • T-tau and p-tau^{181} increased in AD vs. CAA
Renard et al., 2016	– **CAA:** *n* = 13, age 73 years (median), no pre-existing cognitive deficits as reported by patient or family – **AD:** *n* = 42, age 73 years (median) – **Controls:** *n* = 16, age 70 years (median), no neurological diseases related to amyloid deposition, no healthy controls	CAA: possible or probable per Boston criteria (T2*, optional SWI) AD: NIA-AA	ELISA (Innogenetics, NV, Gent, Belgium)	• Aβ42 decreased in CAA vs. controls but not AD • Aβ40 CAA decreased in CAA vs. AD but not controls • T-tau decreased in CAA vs. AD, decreased in CAA vs. controls • P-tau^{181} increased in CAA vs. AD but not controls
Banerjee et al., 2020	– **CAA:** *n* = 10, age 68.6 ± 3.0 years (mean, SD), MMSE ≥ 23 – **AD:** *n* = 20, age 62.5 ± 4.1 years (mean, SD) – **Controls:** *n* = 10, age 62.2 ± 5.4 years (mean, SD), no significant neurological disease	CAA: probable per modified Boston criteria AD: amnestic symptoms, CSF criteria	ECL, Meso Scale Discovery V-PLEX Aβ peptide panel 1; ELISA (Innotest, Fujirebio Europe, Gent, Belgium)	• Aβ40 and Aβ42 decreased in CAA vs. AD and controls • P-tau^{181} and p-tau^{181} increased in AD vs. CAA and controls, but not CAA vs. controls
Our study	– **CAA:** *n* = 31, age 75.1 ± 5.3 years (mean, SD), 54% demented – **AD:** *n* = 28, age 71.1 ± 7.7 years (mean, SD) – **Controls:** *n* = 30, age 72.5 ± 7.8 years (mean, SD) 1/4 healthy controls, 1/3 peripheral neurological diseases	CAA: probable or probable with supporting pathology per modified Boston criteria (SWI, T2*) AD: NIA-AA	Lumipulse 2. Gen. FujiRebio	• Aβ42 decreased in CAA vs. controls and AD vs. controls but not CAA vs. AD • Aβ40 not different in CAA, AD, and controls • T-tau and p-tau^{181} decreased in CAA vs. AD group, and CAA vs. controls and AD vs. controls

AD, Alzheimer's disease; CAA, cerebral amyloid angiopathy; SAH, atraumatic convexal subarachnoid hemorrhage; CSF, cerebrospinal fluid; ECL, electrochemiluminescence; ELISA, enzyme-linked immunosorbent assay; MCI, mild cognitive impairment; NIA-AA, National Institute on Aging and Alzheimer's Association; NINCDS-ADRDA, National Institute of Neurological and Communicative Disorders and Stroke and the Alzheimer's Disease and Related Disorders Association; SWI, susceptibility-weighted imaging.

which was not systematically captured in this study. Further, it has to be noted that CAA is considered an umbrella diagnosis with a spectrum of different manifestations concerning the presence of, e.g., atraumatic SAH, cortical siderosis, intracranial parenchymal hemorrhage, and clinical features such as cognitive impairment, presence of transient focal neurological episodes. It is unknown whether all these different manifestations share the same pathophysiological mechanism and degree of amyloid deposition and thus its concentration in CSF.

Absolute values of CSF biomarker measurements differ between different laboratories and using different methodologies. Therefore, they are not directly comparable even though all assay manufacturers use the same concentration units (pg/ml). To extract the maximum amount of data possible from published studies we re-digitized the published plots to get individual level biomarker concentrations. To homogenize measurements between different publications we generated *Z*-scores. The main limitation of this strategy is its dependence on a representative control sample providing the mean and SD of controls. Control samples in all studies were too small to represent a control population with confidence. However, we checked frequency histograms for compatibility with a normal distribution and think that the excellent differentiation between controls and AD patients, with sensitivity and specificities of Aβ42/40, Aβ42, t-tau, and p-tau^{181} comparable to widely accepted literature values (Blennow et al., 2010) argues in favor of a valid meta-analysis. In addition, the confidence intervals of the AUC decrease with increasing sample size as expected. Further, this is the first meta-analysis on CSF parameters in CAA calculating and reporting standard parameters such as AUC and performing a ROC analysis.

A limitation of all currently available studies is the use of the original or modified Boston criteria on the level of a possible or probable CAA as the gold standard instead of the pathological diagnosis based on a full post-mortem examination or a biopsy. As opposed to some of the previous studies we could include patients with supporting histology. All patients with pathological samples (probable CAA with supporting pathology) in our study suggest that CSF biomarker values in pathologically supported cases are in the same range as the ones without pathological

support. This argues in favor of these criteria even in the category "probable" that is mainly based on radiological data. However, in four hospital-based MRI-neuropathological studies the Boston criteria for probable CAA cases showed sensitivities between 42–77% and specificities of 88–100% (Greenberg and Charidimou, 2018). In practice, brain biopsies are rarely conducted, thus the clinician frequently has to rely solely on the MRI and clinical parameters to decide on a future stroke prophylaxis and faces a difficult decision concerning oral anticoagulation or thrombolysis (Banerjee et al., 2017).

The idea to use CSF parameters to diagnose CAA rests on the assumption that assessing the pathological agent itself might improve diagnostic accuracy and could help to make the diagnosis earlier and maybe facilitating opportunities to prevent the progression of the disease in the future (Tanaka et al., 2020). Nevertheless, this study and the quantitative meta-analysis underlines that the differentiation between CAA and AD using CSF parameters analyzed in this study proves to be difficult. One reason could be the overlap in disease mechanisms, both involving Aβ40 and Aβ42 pathology (Noguchi-Shinohara et al., 2017). However, it might be possible to find other CSF biomarkers which are better suited to differentiate between CAA and AD. Current studies of AD biomarkers focus more and more on plasma biomarkers. Most of these studies aim to replace CSF by plasma using the same biomarkers, facilitating sample acquisition. It is unlikely that the discriminatory power of the biomarkers analyzed in this study is higher in plasma than CSF.

If Aβ is not cleared by perivascular drainage from the CSF, it might be deposited as neuritic plaques in the brain parenchyma or as CAA in vessel walls (Greenberg et al., 2020). Since the pathologic noxious agents (Aβ40 and Aβ42) are basically identical in CAA and AD, the diagnostic differentiation of CAA and AD should focus on the secondary consequences of the disease process as reflected in the modified Boston criteria with its emphasis on neuroradiological findings. Furthermore, neuropsychological testing could offer additional help. AD shows a cortical pattern with an emphasis on memory impairment, while CAA patients suffer mainly from subcortical cognitive disabilities, such as attention and executive deficits (Case et al., 2016). Another option might be amyloid-PET but availability, cost, and radiation exposure limit its use (Charidimou et al., 2017). Finally, quantification of diagnostic criteria (e.g., of microbleeds) might improve the modified Boston criteria and might even help estimate the risk of intracerebral hemorrhage (Tsai et al., 2017; Wilson and Werring, 2017).

In conclusion, our study and meta-analysis suggest that Aβ40, Aβ42, t-tau, and p-tau^{181} and the Aβ42/40 ratio are useful in the differentiation between control subjects and CAA patients. However, these markers do not differentiate well enough between AD and CAA patients to be useful in clinical routine. Maybe other diagnostical approaches as mentioned before might be helpful.

DATA AVAILABILITY STATEMENT

The raw data supporting the conclusions of this article will be made available by the authors upon reasonable request, without undue reservation.

ETHICS STATEMENT

The studies involving human participants were reviewed and approved by the Ethics Committee of the Medical Faculty of the University of Kiel, Lübeck and Tübingen. The ethics committee waived the requirement of written informed consent for participation.

AUTHOR CONTRIBUTIONS

NGM, UJ-K, CW, and GK contributed to conception and design of the study and organized data handling. GK performed the statistical analysis. GK and NGM wrote the first draft of the manuscript. UJ-K and FL wrote sections of the manuscript. All authors contributed to data acquisition and analysis and manuscript revision, read, and approved the submitted version.

ACKNOWLEDGMENTS

We acknowledge financial support by Land Schleswig-Holstein within the funding program Open Access Publikationsfonds.

REFERENCES

Banerjee, G., Ambler, G., Keshavan, A., Paterson, R. W., Foiani, M. S., Toombs, J., et al. (2020). Cerebrospinal fluid biomarkers in cerebral amyloid angiopathy. *J. Alzheimers Dis.* 74, 1189–1201. doi: 10.3233/jad-191254

Banerjee, G., Carare, R., Cordonnier, C., Greenberg, S. M., Schneider, J. A., Smith, E. E., et al. (2017). The increasing impact of cerebral amyloid angiopathy: essential new insights for clinical practice. *J. Neurol. Neurosurg. Psychiatry* 88, 982–994. doi: 10.1136/jnnp-2016-314697

Blennow, K., Hampel, H., Weiner, M., and Zetterberg, H. (2010). Cerebrospinal fluid and plasma biomarkers in Alzheimer disease. *Nat. Rev. Neurol.* 6, 131–144. doi: 10.1038/nrneurol.2010.4

Case, N. F., Charlton, A., Zwiers, A., Batool, S., McCreary, C. R., Hogan, D. B., et al. (2016). Cerebral amyloid angiopathy is associated with executive dysfunction and mild cognitive impairment. *Stroke* 47, 2010–2016. doi: 10.1161/strokeaha.116.012999

Charidimou, A., Farid, K., and Baron, J. C. (2017). Amyloid-PET in sporadic cerebral amyloid angiopathy: a diagnostic accuracy meta-analysis. *Neurology* 89, 1490–1498. doi: 10.1212/wnl.0000000000004539

Charidimou, A., Friedrich, J. O., Greenberg, S. M., and Viswanathan, A. (2018). Core cerebrospinal fluid biomarker profile in cerebral amyloid angiopathy: a meta-analysis. *Neurology* 90, e754–e762. doi: 10.1212/wnl.0000000000005030

Cheng, A. L., Batool, S., McCreary, C. R., Lauzon, M. L., Frayne, R., Goyal, M., et al. (2013). Susceptibility-weighted imaging is more reliable than T2*-weighted gradient-recalled echo MRI for detecting microbleeds. *Stroke* 44, 2782–2786. doi: 10.1161/STROKEAHA.113.002267

Doecke, J. D., Perez-Grijalba, V., Fandos, N., Fowler, C., Villemagne, V. L., Masters, C. L., et al. (2020). Total Abeta42/Abeta40 ratio in plasma predicts amyloid-PET status, independent of clinical AD diagnosis. *Neurology* 94, e1580–e1591. doi: 10.1212/WNL.0000000000009240

Gervaise-Henry, C., Watfa, G., Albuisson, E., Kolodziej, A., Dousset, B., Olivier, J. L., et al. (2017). Cerebrospinal fluid Abeta42/Abeta40 as a means to limiting

tube- and storage-dependent pre-analytical variability in clinical setting. *J. Alzheimers Dis.* 57, 437–445. doi: 10.3233/JAD-160865

Greenberg, S. M., Backskai, B. J., Hernandez-Guillamon, M., Pruzin, J., Sperling, R., and van Veluw, S. J. (2020). Cerebral amyloid angiopathy and Alzheimer disease - one peptide, two pathways. *Nat. Rev. Neurol.* 16, 30–42. doi: 10.1038/s41582-019-0281-2

Greenberg, S. M., and Charidimou, A. (2018). Diagnosis of cerebral amyloid angiopathy: evolution of the boston criteria. *Stroke* 49, 491–497. doi: 10.1161/strokeaha.117.016990

Hernandez-Guillamon, M., Delgado, P., Penalba, A., Rodriguez-Luna, D., Molina, C. A., Rovira, A., et al. (2012). Plasma β-amyloid levels in cerebral amyloid angiopathy-associated hemorrhagic stroke. *Neurodegener. Dis.* 10, 320–323. doi: 10.1159/000333811

Hjalmarsson, C., Bjerke, M., Andersson, B., Blennow, K., Zetterberg, H., Aberg, N. D., et al. (2014). Neuronal and glia-related biomarkers in cerebrospinal fluid of patients with acute ischemic stroke. *J. Cent. Nerv. Syst. Dis.* 6, 51–58. doi: 10.4137/JCNSD.S13821

Jack, C. R. Jr., Albert, M. S., Knopman, D. S., McKhann, G. M., Sperling, R. A., Carrillo, M. C., et al. (2011). Introduction to the recommendations from the National Institute on Aging-Alzheimer's Association workgroups on diagnostic guidelines for Alzheimer's disease. *Alzheimers Dement.* 7, 257–262. doi: 10.1016/j.jalz.2011.03.004

Janelidze, S., Zetterberg, H., Mattsson, N., Palmqvist, S., Vanderstichele, H., Lindberg, O., et al. (2016). CSF Abeta42/Abeta40 and Abeta42/Abeta38 ratios: better diagnostic markers of Alzheimer disease. *Ann. Clin. Transl. Neurol.* 3, 154–165. doi: 10.1002/acn3.274

Jelicic Kadic, A., Vucic, K., Dosenovic, S., Sapunar, D., and Puljak, L. (2016). Extracting data from figures with software was faster, with higher interrater reliability than manual extraction. *J. Clin. Epidemiol.* 74, 119–123. doi: 10.1016/j.jclinepi.2016.01.002

Jeon, S. B., Lee, J. W., Kim, S. J., Chung, C. H., Kwon, S. U., Choi, C. G., et al. (2010). New cerebral lesions on T2*-weighted gradient-echo imaging after cardiac valve surgery. *Cerebrovasc. Dis.* 30, 194–199. doi: 10.1159/000317108

Kalbe, E., Kessler, J., Calabrese, P., Smith, R., Passmore, A. P., Brand, M., et al. (2004). DemTect: a new, sensitive cognitive screening test to support the diagnosis of mild cognitive impairment and early dementia. *Int. J. Geriatr. Psychiatry* 19, 136–143. doi: 10.1002/gps.1042

Kester, M. I., Goos, J. D., Teunissen, C. E., Benedictus, M. R., Bouwman, F. H., Wattjes, M. P., et al. (2014). Associations between cerebral small-vessel disease and Alzheimer disease pathology as measured by cerebrospinal fluid biomarkers. *JAMA Neurol.* 71, 855–862. doi: 10.1001/jamaneurol.2014.754

Li, Y. F., Ge, F. F., Zhang, Y., You, H., and Zhang, Z. X. (2015). Cerebrospinal fluid biomarkers in dementia patients with cerebral amyloid angiopathy. *Chin. Med. Sci. J.* 30, 170–173. doi: 10.1016/s1001-9294(15)30042-0

Linn, J., Halpin, A., Demaerel, P., Ruhland, J., Giese, A. D., Dichgans, M., et al. (2010). Prevalence of superficial siderosis in patients with cerebral amyloid angiopathy. *Neurology* 74, 1346–1350. doi: 10.1212/WNL.0b013e3181dad605

Martínez-Lizana, E., Carmona-Iragui, M., Alcolea, D., Gómez-Choco, M., Vilaplana, E., Sánchez-Saudinós, M. B., et al. (2015). Cerebral amyloid angiopathy-related atraumatic convexal subarachnoid hemorrhage: an ARIA before the tsunami. *J. Cereb. Blood Flow Metab.* 35, 710–717. doi: 10.1038/jcbfm.2015.25

Noguchi-Shinohara, M., Komatsu, J., Samuraki, M., Matsunari, I., Ikeda, T., Sakai, K., et al. (2017). Cerebral amyloid angiopathy-related microbleeds and cerebrospinal fluid biomarkers in Alzheimer's disease. *J. Alzheimers. Dis.* 55, 905–913. doi: 10.3233/jad-160651

Puy, L., and Cordonnier, C. (2019). Sporadic cerebral amyloid angiopathy. *Geriatr. Psychol. Neuropsychiatr. Vieil.* 17, 73–82. doi: 10.1684/pnv.2018.0776

Renard, D., Castelnovo, G., Wacongne, A., Le Floch, A., Thouvenot, E., Mas, J., et al. (2012). Interest of CSF biomarker analysis in possible cerebral amyloid angiopathy cases defined by the modified Boston criteria. *J. Neurol.* 259, 2429–2433. doi: 10.1007/s00415-012-6520-8

Renard, D., Gabelle, A., Hirtz, C., Demattei, C., Thouvenot, E., and Lehmann, S. (2016). Cerebrospinal fluid Alzheimer's disease biomarkers in isolated supratentorial cortical superficial siderosis. *J. Alzheimers Dis.* 54, 1291–1295. doi: 10.3233/jad-160400

Tanaka, M., Saito, S., Inoue, T., Satoh-Asahara, N., and Ihara, M. (2020). Potential therapeutic approaches for cerebral amyloid angiopathy and Alzheimer's disease. *Int. J. Mol. Sci.* 21:1992. doi: 10.3390/ijms21061992

Tsai, H. H., Tsai, L. K., Chen, Y. F., Tang, S. C., Lee, B. C., Yen, R. F., et al. (2017). Correlation of cerebral microbleed distribution to amyloid burden in patients with primary intracerebral hemorrhage. *Sci. Rep.* 7:44715. doi: 10.1038/srep44715

van Oijen, M., Hofman, A., Soares, H. D., Koudstaal, P. J., and Breteler, M. M. (2006). Plasma Abeta(1-40) and Abeta(1-42) and the risk of dementia: a prospective case-cohort study. *Lancet Neurol.* 5, 655–660. doi: 10.1016/S1474-4422(06)70501-4

Verbeek, M. M., Kremer, B. P., Rikkert, M. O., Van Domburg, P. H., Skehan, M. E., and Greenberg, S. M. (2009). Cerebrospinal fluid amyloid beta(40) is decreased in cerebral amyloid angiopathy. *Ann. Neurol.* 66, 245–249. doi: 10.1002/ana.21694

Viswanathan, A., and Greenberg, S. M. (2011). Cerebral amyloid angiopathy in the elderly. *Ann. Neurol.* 70, 871–880. doi: 10.1002/ana.22516

Viswanathan, A. G., and Steven, M. (2008). Chapter 38 Intracerebral hemorrhage. *Handb. Clin. Neurol.* 93, 767–790.

Wardlaw, J. M., Smith, E. E., Biessels, G. J., Cordonnier, C., Fazekas, F., Frayne, R., et al. (2013). Neuroimaging standards for research into small vessel disease and its contribution to ageing and neurodegeneration. *Lancet Neurol.* 12, 822–838. doi: 10.1016/S1474-4422(13)70124-8

Wilson, D., and Werring, D. J. (2017). Antithrombotic therapy in patients with cerebral microbleeds. *Curr. Opin. Neurol.* 30, 38–47. doi: 10.1097/wco.0000000000000411

Yamada, M. (2000). Cerebral amyloid angiopathy: an overview. *Neuropathology* 20, 8–22. doi: 10.1046/j.1440-1789.2000.00268.x

Conflict of Interest: The authors declare that the research was conducted in the absence of any commercial or financial relationships that could be construed as a potential conflict of interest.

Publisher's Note: All claims expressed in this article are solely those of the authors and do not necessarily represent those of their affiliated organizations, or those of the publisher, the editors and the reviewers. Any product that may be evaluated in this article, or claim that may be made by its manufacturer, is not guaranteed or endorsed by the publisher.

Copyright © 2022 Margraf, Jensen-Kondering, Weiler, Leypoldt, Maetzler, Philippen, Bartsch, Flüh, Röcken, Möller, Royl, Neumann, Brüggemann, Roeben, Schulte, Bender, Berg and Kuhlenbäumer. This is an open-access article distributed under the terms of the Creative Commons Attribution License (CC BY). The use, distribution or reproduction in other forums is permitted, provided the original author(s) and the copyright owner(s) are credited and that the original publication in this journal is cited, in accordance with accepted academic practice. No use, distribution or reproduction is permitted which does not comply with these terms.

frontiers in Aging Neuroscience

REVIEW
published: 17 February 2022
doi: 10.3389/fnagi.2022.780811

Role of Specialized Pro-resolving Mediators in Reducing Neuroinflammation in Neurodegenerative Disorders

Jana Ponce[1†], Arzu Ulu[2†], Corrine Hanson[1], Erin Cameron-Smith[3], John Bertoni[3], Jenna Wuebker[4], Alfred Fisher[5], Ka-Chun Siu[1], Vivien Marmelat[6], Jiri Adamec[7] and Danish Bhatti[3]*

[1] Division of Medical Nutrition Education, College of Allied Health Professions, University of Nebraska Medical Center, Omaha, NE, United States, [2] Division of Biomedical Sciences, School of Medicine, University of California, Riverside, Riverside, CA, United States, [3] Department of Neurological Sciences, College of Medicine, University of Nebraska Medical Center, Omaha, NE, United States, [4] Department of Pharmaceutical and Nutrition Care, Nebraska Medicine, Omaha, NE, United States, [5] Department of Internal Medicine, College of Medicine, University of Nebraska Medical Center, Omaha, NE, United States, [6] Department of Biomechanics, College of Education, Health, and Human Sciences, University of Nebraska - Omaha, Omaha, NE, United States, [7] Department of Biochemistry, College of Arts and Sciences, University of Nebraska - Lincoln, Lincoln, NE, United States

OPEN ACCESS

Edited by:
Woon-Man Kung, Chinese Culture University, Taiwan

Reviewed by:
Sachchida Nand Rai, University of Allahabad, India
Andrew C. W. Huang, Fo Guang University, Taiwan

***Correspondence:**
Jana Ponce
jana.ponce@unmc.edu

[†] These authors have contributed equally to this work and share first authorship

Specialty section:
This article was submitted to Alzheimer's Disease and Related Dementias, a section of the journal Frontiers in Aging Neuroscience

Received: *21 September 2021*
Accepted: *21 January 2022*
Published: *17 February 2022*

Citation:
Ponce J, Ulu A, Hanson C, Cameron-Smith E, Bertoni J, Wuebker J, Fisher A, Siu K-C, Marmelat V, Adamec J and Bhatti D (2022) Role of Specialized Pro-resolving Mediators in Reducing Neuroinflammation in Neurodegenerative Disorders. Front. Aging Neurosci. 14:780811. doi: 10.3389/fnagi.2022.780811

Alzheimer's disease (AD) and Parkinson's disease (PD) are neurodegenerative disorders that affect millions of individuals worldwide. As incidence of these conditions increases with age, there will undoubtedly be an increased prevalence of cases in the near future. Neuroinflammation is a hallmark in the development and progression of neurodegenerative diseases and prevention or resolution of chronic neuroinflammation may represent a novel approach to treatment. The present review highlights the potential of the anti-inflammatory and pro-resolving effects of polyunsaturated fatty acid (PUFA)-derived mediators (Specialized Pro-resolving Mediators—SPM) in neurodegenerative disorders. PUFA-derived SPM are biosynthesized in response to chemicals produced from acute inflammatory responses. Preclinical studies from both AD and PD models suggest a dysregulation of SPM and their receptors in neurological disorders. Decreased SPM may be due to inadequate substrate, an imbalance between SPM and pro-inflammatory mediators or a disruption in SPM synthesis. SPMs hold great promise for neuroprotection in AD by altering expression of pro-inflammatory genes, modulating macrophage function, serving as a biomarker for AD status, and promoting resolution of neuroinflammation. In PD, data suggest SPM are able to cross the blood-brain barrier, inhibit microglial activation and decrease induced markers of inflammation, possibly as a result of their ability to downregulate NFκB signaling pathways. Several *in vivo* and *in vitro* studies suggest a benefit from administration of SPMs in both neurodegenerative disorders. However, extrapolation of these outcomes to humans is difficult as no models are able to replicate all features of AD or PD. Minimal data evaluating these PUFA-derived metabolites in humans with neurodegenerative disorders are available and a gap in knowledge exists regarding behavior of SPM and their receptors in patients with these conditions. There is also large gap in our knowledge regarding which lipid

mediator would be most effective in which model of AD or PD and how dietary intake or supplementation can impact SPM levels. Future direction should include focused, translational efforts to investigate SPM as an add-on (in addition to standard treatment) or as standalone agents in patients with neurodegenerative disorders.

Keywords: neurodegenerative disorder, Parkinson's disease, Alzheimer's disease, neuroinflammation, specialized pro-resolving lipid mediator (SPM), omega-3 fatty acids, omega-6 fatty acid, polyunsaturated fatty acids

INTRODUCTION

Millions of people worldwide are living with neurodegenerative disorders, making these conditions a significant public health problem. Today, 5 million suffer from Alzheimer's disease (AD) and 1 million Americans suffer from Parkinson's disease (PD) (Checkoway et al., 2011). Neurodegenerative disorders are associated with substantial mental, physical, and social impairment, which can lead to decreased quality of life. In addition, these conditions are a significant economic burden to society with a yearly direct cost of hospitalizations and medications of $25.4 billion (Kowal et al., 2013). Increased prevalence of neurodegenerative diseases is, in part, due to the aging population (Cova et al., 2017). While genetic and environmental factors for many neurodegenerative disorders have been identified, age remains the primary risk factor (Hou et al., 2019). By 2060, the U.S. census bureau estimates the number of Americans ages 65 and older is projected to nearly double from 52 million in 2018 to 95 million. As incidence of neurodegenerative diseases increases with age, there will undoubtedly be an increased prevalence of cases. In fact, a study by the Parkinson's Foundation estimates the number of PD cases will rise to 1.24 million by 2030 (Marras et al., 2018). Without a known cure, prevention and the slowing of progression of these diseases in an aging population are paramount.

Neuroinflammation is a hallmark in aging as well as in the development and progression of neurodegenerative diseases (Carson et al., 2006; Wang et al., 2015a; Chen et al., 2016; Rai et al., 2016; Niranjan, 2018). The term refers to a variety of immune responses to an initial stimulus in the central nervous system, resulting in increased levels of cytokines, chemokines, and free radical production. Degree of neuroinflammation depends on the primary insult, context and duration (DiSabato et al., 2016). An efficient pro-resolution mechanism is essential for tissue homeostasis and the prevention of chronic neuroinflammation, which can lead to recruitment of immune cells, edema, tissue damage, and the activation of microglial cells (Serhan et al., 2000; Serhan, 2014). Microglia activation is an early feature that occurs in almost any neuronal physiology change. Activation of microglial cells has been shown to occur early in the pathological process of AD and PD (McGeer et al., 1988; Barcia et al., 2003; Croisier et al., 2005; Leng and Edison, 2021) and continues through the late stages. Activated microglial cells are responsible for the production of many cytokines including tumor necrosis factor-α (TNF-α), interleukin-1β (IL-1β), and chemokines. Additionally, microglial activation results in the production of vascular cell adhesion molecule-1 (VCAM-1) and intracellular cell adhesion molecule-1 (ICAM-1) which lead to dopamine neuron apoptosis or death (Benner et al., 2008; Wypijewska et al., 2010; Phani et al., 2012). Chronic microglia activation and neuroinflammation resulting in pro-inflammatory cytokines are associated with motor and cognitive function loss (Dinarello, 2000; Franceschi et al., 2007; Gyengesi et al., 2019).

Inhibiting pro-inflammatory mediators, reducing microglial activation and improving neuronal survival could be effective therapeutic strategies to mitigate the development and progression of neurodegenerative disorders. Interestingly, polyunsaturated fatty acids (PUFAs) have recently been found to serve as substrates for the biosynthesis of specialized pro-resolving lipid mediators (SPM) that promote the endogenous resolution of inflammation (Bannenberg and Serhan, 2010; Serhan, 2014). This discovery has prompted investigations into the ability of SPM to decrease neuroinflammation and downstream effects such as motor and cognitive decline. This review aims to summarize key research findings of these fatty acid (FA)-derived mediators as potential prevention or treatment for neuroinflammation in neurodegenerative disorders.

POLYUNSATURATED FATTY ACIDS, SPECIALIZED PRO-RESOLVING LIPID MEDIATORS AND AGING

PUFAs are long-chain fat molecules that have more than one unsaturated carbon bond. Humans are unable to synthesize these long chain fatty acids and are required in the diet to prevent clinical deficiency. PUFAs are often divided into two major classes: omega (n)-3 and (n)-6 FAs. Alpha-linolenic acid (ALA), eicosapentaenoic acid (EPA), and docosahexaenoic acid (DHA) are the primary n-3 FAs. ALA (18:3) is present in plant oils such as flaxseed, soybean, and canola oils and can be converted to EPA and DHA in the liver (Beadle et al., 1965; Astorg, 2004). However, with a very low conversion rate of 0–4%, ingesting EPA and DHA directly from foods is the best way to increase levels in the body (Plourde and Cunnane, 2007). Major forms of n-6 FAs include linoleic acid (LA) (18:2) and arachidonic acid (ARA) (C20:4). LA is derived from vegetable and meat sources while ARA is metabolized from LA. Low n-3 intake is a common characteristic of the Western diet due to low intakes of foods such as fatty fish and nuts (Simopoulos, 2002). N-6 FAs are consumed at a disproportionately high level in a standard Western diet compared to n-3 due to high intakes of meat, processed foods, soy, and corn oils (Astorg, 2004).

Beneficial effects of n-3 FA, such as DHA and EPA have been well-recognized in brain health (Alessandri et al., 2004; Virtanen et al., 2013). They regulate gene expression and signaling pathways involved in neurotransmitter release, inflammation, and immunity (Basselin et al., 2012; Orr et al., 2013). N-3 FAs compete with their n-6 counterparts such as ARA as substrates for enzymes (cytochrome P450, COX, LOX) that generate numerous bioactive fatty acids, namely "eicosanoids," which regulate inflammation and immunity. ARA is released from phospholipid membranes with the action of phospholipase 2 (PLA2) in response to inflammation; and *in vitro* studies suggest that different types of PLA enzymes have different preferences for DHA vs. ARA as a substrate (Mouchlis et al., 2018). In support of these observations, iPLA2 KO mice display reduced DHA metabolism and increased tendency to neuroinflammation, while iPLA2 is highly expressed in the brain (Yang et al., 2019). This is of importance, because DHA is the most abundant n-3 FA in the brain and DHA metabolism-generating bioactive lipid mediators not only have anti-inflammatory effects, but also have effects in resolution of inflammation (Serhan et al., 2004, 2015). Moreover, n-3 FA show their beneficial effects, in part, through their bioactive metabolites, SPMs, that are involved in resolution of inflammation and tissue repair (Levy and Serhan, 2014). During acute inflammation, ARA-derived metabolites such as prostaglandins are produced to recruit neutrophils to the inflammation site. This process reaches homeostasis by a mechanism involving some prostaglandin metabolites and activation of anti-inflammatory cytokines (Buckley et al., 2014). To further promote resolution of inflammation, SPMs are biosynthesized with a process called "lipid mediator class switching" which temporarily switches pro-inflammatory metabolite biosynthesis to SPM production (Levy et al., 2001; Levy and Serhan, 2014). SPM derived from n-3 include the resolvin D (RvD)-, maresin (MaR)-, and protectin- series from DHA and the resolvin E (RvE)- series from EPA, while those derived from the n-6, ARA, include leukotrienes and lipoxins (**Figure 1**) (Ryan and Godson, 2010; Serhan et al., 2011). This process stops monocyte and PMN recruitment and activates the tissue repair process by recruiting M2-like macrophages and regulatory T-cells.

SPM are biosynthesized in response to chemicals produced from acute inflammatory responses. However, published studies agree that SPM levels are decreased in animals and humans with PD and AD despite chronic inflammatory insult (Zhu et al., 2016; Krashia et al., 2019). Decreased SPM may be due to inadequate EPA, DHA, or ARA substrate, an imbalance between SPM and pro-inflammatory mediators or a disruption in SPM synthesis. Several epidemiological studies suggest that increased n-3 PUFA intake is associated with decreased risk or improved outcomes in neurodegenerative disorders (de Lau et al., 2006; Aden et al., 2011; Zhang et al., 2016). However, intake of n-3 is low in a standard Western diet pattern and lower serum levels have been significantly associated with age (Strike et al., 2016). While proposed dietary reference intakes (DRI) for combined EPA and DHA are 250–500 mg per day (Harris et al., 2009), data from the National Health and Nutrition Examination Survey (NHANES) show intake of DHA and EPA of adults 51 + were 63 ± 2 and 23 ± 1 mg/day, respectively (Papanikolaou et al., 2014). Decreased intake and inadequate serum levels of n-3 may be even lower in the elderly and patients with neurodegenerative disorders due to dysphagia, anorexia, and feeding difficulties. Deprivation of n-3 has been shown to decrease levels of DHA, increase markers of brain AA, and increase nitric oxide (NO) and lipid peroxide levels in the brain (Orr and Bazinet, 2008; Cardoso et al., 2014). This phenomenon may be due, in part, to failed resolution of inflammation due to inadequate SPM production.

SPECIALIZED PRO-RESOLVING LIPID MEDIATORS IN ALZHEIMER'S DISEASE

The leading cause of dementia worldwide, AD is a progressive neurodegenerative disease that leads to a decline in cognitive function. The amyloid cascade is the most accepted hypothesis to explain AD pathogenesis with the main hallmarks of AD being neuritic plaques composed of amyloid beta (Aβ) peptides and neurofibrillary tangles (NFTs) made up of hyperphosphorylated microtubule-associated protein (p-tau) (Iqbal et al., 2010; Barage and Sonawane, 2015). Neuroinflammation is a common feature in AD evidenced by elevated plasma and postmortem levels of pro-inflammatory cytokines as well as significant dysfunction in inflammation resolution pathways (Wang et al., 2015c). While there is a potential benefit of NSAIDs for modulating neuroinflammation in psychiatric diseases (Astorg, 2004), epidemiological studies in neurodegenerative disorders are inconclusive. Given that NSAIDs target early phase of inflammation and can halt inflammation resolution by preventing the biosynthesis of n-3 and n-6 fatty acid-derived SPMs, alternative options appear necessary.

Several studies investigated the dysregulation of inflammation resolution in neurodegenerative diseases. A study by Wang et al. (2015b) compared SPM levels in postmortem cerebrospinal fluid (CSF) (15 AD patients) and brain tissues (10 AD patients) of AD patients, patients with mild (20 patients, MCI) and subjective (21 patients) cognitive impairment (SCI) and non-demented control subjects. This study found lower CSF levels of lipoxin A4 (LXA4, an arachidonic acid derived SPM) in AD patients as compared to MCI and SCI patients, while no significant differences were observed for the DHA-derived RvD1. However, the two SPMs showed a strong positive correlation with each other as well as with mini-mental state examination test, suggesting that SPMs are important in cognition. Similarly, ARA-derived LXA4 and leukotriene B4 (LTB4), and DHA-derived MaR1 levels were lower in the hippocampus of AD patients as compared to control subjects, which was confirmed with both ELISA and LC/MS/MS analysis in this study. These findings were consistent with the heightened levels of the pro-inflammatory prostaglandins in AD brains as compared to control subjects. This study also showed increased levels of SPM receptors, ALX and FPR2 (LXA4 and RvD1 receptors, respectively), and the EPA-derived RvE1 receptor, chemerin receptor 23 (ChemR23) on both glial cells, mainly astrocytes and neurons, in the hippocampus of AD brains as compared to control subjects. However, no correlation was observed between ALX/FPR2 or LXA4/RvD1

levels and tau proteins. Heightened SPM receptor levels were also accompanied by increased hippocampal levels of 15-LOX2, a key enzyme in LXA4 biosynthesis; PPARγ, a nuclear receptor involved in SPM action; and reduced anti-inflammatory cytokine IL-10 in AD brains as compared to controls. Many PUFA-derived lipid mediators are ligands for PPARγ, which is anti-inflammatory and is involved in adipogenesis. Overall, this study showed significant dysregulation of SPMs and an attempt at inflammation resolution to compensate for the pro-inflammatory environment by increasing SPM receptors, an SPM biosynthetic enzyme (15-LOX2) and PPARγ in the AD brain. Also, this study suggests that measuring SPMs in CSF has potential for AD diagnosis and monitoring disease progression. Another study by Emre et al. (2020), reported a comprehensive evaluation of the relationship of AD pathology including early onset AD and MCI, and the distribution of SPM receptors in AD brains. Similar to the findings of Wang et al. (2015b), the BLT1 (LTB4 receptor, and partial agonist for RvE-1) and ChemR23, EPA-derived RvE-1 receptors, were expressed in neurons, astrocytes and microglia of the hippocampal regions, basal forebrain and cingulate gyrus, with higher expression in the AD brains as compared to healthy controls. The receptor expression correlated well with inflammatory markers in microglia and astrocytes, as well as with Braak staging, a measure of disease pathology. Given these findings, and variable expression pattern of these two receptors throughout the brain, the authors hypothesized that these two receptors might modulate neuroinflammation in response to both pro-inflammatory and resolution mediators during both the acute and resolution phases of inflammation.

In a follow-up study by the same group (Zhu et al., 2016), SPMs derived from ARA, EPA, and DHA were detectable in the entorhinal cortex (ENT) brain region which is important for memory and thus, important for AD. While ARA-derived lipoxins did not differ between controls and AD brains, RvD5, MaR1, and protectin D1 (PD1) were lower in AD brains than in controls. Also, the pro-inflammatory PGD2 levels were higher in the AD brains as compared to controls. Direct effects of LXA4, RvD1, and PD1 on cell viability and cell survival were tested on neuroblastoma cells. All tested SPMs were effective in improving cell viability and survival. In Aβ42 stressed/activated microglia, treatment with MaR1 resulted in reduction of Aβ42-induced increase in Cd11b (causes hyper-adhesion) and CD40, respectively. Moreover, MaR1 but not RvD1, PDX (isomer of PD1), or LXA4 increased phagocytosis of Aβ42 in human microglial cells. In addition, SPM receptors GPR32 and ALX/FPR2 were found to be expressed in differentiated neuroblastoma and microglial cells in this study. Another study by Zhao et al. (2012) assessed the role of neuroprotection D1 (NPD1), a lipid mediator derived from DHA in AD pathology. Like LXA4 and LTB4, NPD1 is also reduced in AD brain. Its pro-resolving activity in AD pathology appears to alter Aβ42 release from aging brain cells. To understand if NPD1 is one of the mechanisms through which DHA exhibits its neuroprotective and anti-inflammatory effects in the brain, Zhao et al. (2012) used a transgenic mouse model of AD (PS1, APP, and tau-transgenic) as well as Aβ42 treated aging human neuronal-glial (HNG) co-culture. Age-related decreases were found in hippocampus for both DHA and NPD1 in AD mice as compared to age-matched controls (4 months vs. 12–13-month-old). Similarly, in co-culture experiments with HNG, NPD1 showed neuroprotective effects by reducing cytotoxicity and apoptosis in Aβ42 stressed cells and by down-regulating pro-inflammatory and pro-apoptotic genes [cyclooxygenase-2 (COX-2), tumor necrosis factor-α (TNFα) and B94] while improving cell survival. In addition, NPD1 altered the beta-amyloid precursor (βAPP) protein processing in a dose-dependent manner and stimulated a non-amyloidogenic pathway. The effects of NPD1 on this βAPP processing was in part mediated by modulation of the activity of secretase enzymes (i.e., increase in ADAM10 and decrease in BACE1), which are key enzymes in this process and this effect of NPD1 was dependent on PPARγ.

Yin et al. (2019), investigated the effects of DHA-derived SPM MaR1 in AD. Using a model with Aβ42 infusion into the brain followed by MaR1 injections, they found that treatment with MaR1 reduced the Aβ42-induced increase in pro-inflammatory cytokines and improved AD pathology at the cellular (reduced activation of microglia and astrocyte) and behavioral level (improved learning and memory deficits as measured by escape latency in Morris Water Maze test). Furthermore, MaR1 treatment resulted in upregulation of PI3K/AKT, ERK survival pathway and inhibition of pro-inflammatory proteins, apoptosis, and autophagy, all of which are consistent with effective resolution of inflammation.

Lee et al. (2020), examined the mechanisms of how aspirin-triggered SPM generation occur in a murine model of AD. In their study, they found that a serine residue on COX-2 is acetylated by N-acetyl sphingosine (N-As), and in turn this results in SPM generation. In their *in vivo* model, they found that microglia have reduced levels of N-As and subsequent reduced generation of SPM. These results were further corroborated by a rescue experiment where they treated AD mice with N-As, which increased acetylated COX-2, SPM generation and increased phagocytosis by microglia. Resolution of inflammation in the brain further improved cognitive function in these mice.

RvD1 prevents cognitive decline in animal models (Koivisto et al., 2014), improves Aβ phagocytosis and regulates inflammation in patients with AD (Mizwicki et al., 2013; Fiala et al., 2015; Wang et al., 2015b). Mizwicki et al. (2013), conducted a case control study where they assessed the role of nutraceutical products, DHA-derived RvD1 and vitamin D3 (1, 25-dihydroxyvitamin D3) in peripheral blood mononuclear cells (PBMCs) of healthy subjects (n = 3) and AD patients (n = 5). Their hypothesis was based on previous evidence showing that microglia and associated phagocytosis of Aβ are dysfunctional in AD patients, and vitamin D3 and RvD1 can genetically modulate macrophage response and improve phagocytosis, respectively (Menegaz et al., 2011; Fiala et al., 2015). Treatment of PBMCs with RvD1 and vitamin D3, resulted in a concentration dependent increase in phagocytosis, and decrease in apoptosis in AD macrophages. These changes occurred via specific receptors, that is GPR32 and protein disulfide isomerase A3 receptors for RvD1 and vitamin D3, respectively. Despite the low number of patients in this study, evaluation of 84 inflammatory genes using a RT2 Profiler (inflammatory/autoimmune gene array)

in PBMCs separated the patients into two distinct groups, group 1 with mainly decreased toll-like receptors (TLRs) and Interleukin (IL) Receptor (IL1R1); group 2 with increased transcription of TLRs and cytokines. Regardless of the TLR status, IL1RN, ITGB2 (integrin B2) and nuclear factor kB (NFκB) genes were upregulated, and some of the chemokines and their receptors chemokine ligand (CCL)2, CCL7, CCR1, and IL6R were downregulated as compared to controls, which revealed a unique genetic signature that can serve as a biomarker for isolated AD. Also, when different forms of Aβ proteins were tested on these PBMCs, there was an overall significant upregulation of inflammatory gene transcription in both group 1 and group 2 patients with slight differences in the presence of different Aβ forms as compared to healthy control PBMCs. Both RvD1 and vitamin D3 treatment showed distinct effects on Aβ-induced inflammatory gene expression for group 1 and 2 patients as compared to controls. Both RvD1 and vitamin D3 also decreased $sA\beta_{42}$ stimulated increase in cytokines (vitamin D3 was more potent than RvD1) in one of the group 2 patients. Overall, this study showed that RvD1 and vitamin D3 modulates inflammation and macrophage function in AD PBMCs and have potential as treatment improving macrophage phagocytosis of Aβ proteins in AD.

Hopperton et al. (2018), investigated the role of elevated brain levels of n-3 PUFAs on neuroinflammation and AD pathology using *fat-1* transgenic mice that can convert n-6 PUFAs to n-3 PUFAs, and wild-type mice fed either an n-3 (2% fish oil) rich or 10% safflower oil rich diet (low n-3, high n-6 PUFA). In their study, mice were infused with the amyloid β 1–40 peptide to induce neuroinflammation and AD pathology. They found that the amyloid peptide infused mice that were receiving the safflower oil but not the mice receiving the fish oil supplementation had the gene expression signature associated with increased inflammation. In contrast to other studies discussed here, this study was not able to find any differences in eicosanoids in response to different diets or to amyloid β infusion, and could not detect protectin, maresin and D- and E-series SPMs derived from n-3 and n-6 PUFAs. However, some other metabolites that are precursors to SPM were detected. For example, 4-HDHA, an autoxidative product derived from DHA, was found to be higher in the hippocampus of *fat-1* mice as compared to WT mice receiving the safflower oil diet. An EPA-derived 17(18)-EpETE metabolite was found to be elevated in WT mice receiving the fish oil diet, and its less active metabolite 17(18)-DiHETE was found to be elevated in both *fat-1* and WT mice receiving the fish oil diet as compared to WT mice receiving the safflower oil diet. The authors hypothesized that the 17(18)-EpETE metabolite might be protective against AD due to its vasodilatory and PAPRγ mediated actions.

SPECIALIZED PRO-RESOLVING LIPID MEDIATORS IN PARKINSON'S DISEASE

PD is a progressive nervous system disorder characterized by dopaminergic (DA) neuron loss in the substantia nigra (SN) (Hughes et al., 1992). Clinical symptoms include tremor, rigidity and bradykinesia (Levy et al., 2009), while the histopathological hallmark includes the presence of α-synuclein (α-syn)-rich Lewy bodies in neurons of the CNS (Lee and Trojanowski, 2006). Both experimental and clinical studies have reported that neuroinflammation and oxidative stress markedly contribute to the etiology of PD (Wang et al., 2015a; Chen et al., 2016; Rai et al., 2016, 2017a,b; Niranjan, 2018). Harmful inflammatory mediators have been found to deteriorate DA neurons (Stoll et al., 2000; Sawada et al., 2006) and aggregated α-syn can induce microglial activation or proliferation and inflammatory cytokine release in PD (Zhang et al., 2005; Su et al., 2008; Beraud et al., 2013) even earlier than the occurrence of DA cell death (Zhang et al., 2005; Beraud et al., 2013). Recently, research has shown that specific, bioactive compounds are able to reduce these deleterious effects in PD models (Singh et al., 2018; Rai et al., 2019; Zahra et al., 2020). SPM may be beneficial in patients with PD by preventing or inhibiting chronic neuroinflammation and preserving DA neurons.

Xu et al. (2013) demonstrated the ability of DHA-derived SPM to ameliorate the pro-inflammatory response of lipopolysaccharide (LPS)-induced murine microglial cells. ELISA and RT-PCR showed pretreatment with RvD1 significantly inhibited NO, TNF-α, and IL-1β and TNF- α, IL-1β, and inducible nitric oxide synthase (iNOS) mRNA expression, respectively. Further, RvD1 inhibited the activity of NFκB, 1 (AP-1) DNA binding and prevented the activation of phosphorylation of mitogen-activated protein kinase (MAPK) signaling pathways extracellular signal-related kinase (ERK)1/2 and p38 MAPK. In another study, the ability of RvD1 to inhibit the progression of an experimental model of PD by suppressing inflammation was investigated by Xu et al. (2017). Here, different RvD1 concentrations (50, 100, and 200 nM) were administered prior to 1-methyl-4-phenylpyridium ion (MPP+) treatment in an *in vitro* PD model (PC12 cells). MPP^+ affects dopamine neuron loss by entering nigrostriatal neurons by way of dopamine transporters and impacts SN neuronal loss (Birla et al., 2019; Singh et al., 2020). Fluorescein (FITC) and MTT assay revealed RvD1 (100 and 200 nM) dose-dependently inhibited upregulation of PC12 apoptosis and cellular damage. Consistent with previous research in microglial cells, RvD1 inhibited elevation of TNF-α in the PC12 model and inhibited p-P38, p-ERK, and NF-kB p50 signaling pathways (Xu et al., 2013).

Tian et al. (2015) assessed the impact of an n-3-derived lipid mediator on substantia nigra pars compacta (SNpc) *in vivo* on an LPS-induced animal model and on pro-inflammatory cytokine expression *in vitro* in microglia. The group first aimed to evaluate the development of behavioral defects, neuronal damage in the nigrostriatal dopaminergic system. Following LPS injection, Sprague Dawley (SD) rats received different concentrations of intrathecal RvD2 injections (25, 50, or 100 ng/kg) for 27 days. RvD2 treatment significantly decreased apomorphine-elicited rotational cycles, with rotational cycles decreasing with increased SPM dose. RvD2 also inhibited the tyrosine hydroxylase (TH)-positive neurons loss of the SN in LPS-treated rats. In a separate experiment, pretreatment of LPS-induced microglial cells (CD11b +) with RvD2 (2.5, 5, 10, 20 μmol/L) significantly inhibited activation in the SNpc by

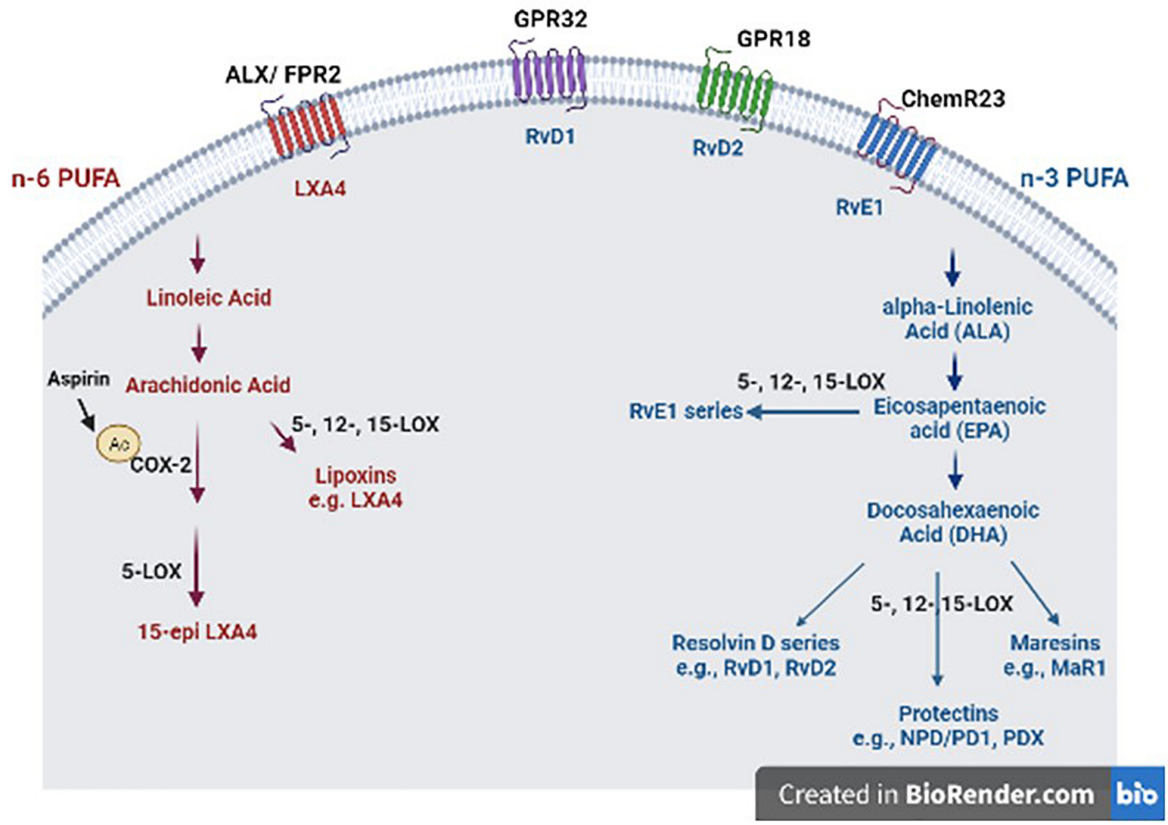

FIGURE 1 | Specialized pro-resolving mediators (SPM) and their receptors. These SPM are derived from omega (n)-3 and n-6 polyunsaturated fatty acids (PUFAS) in response to chemicals produced from acute inflammatory responses. ALX/FPR2, formyl peptide receptor 2; LXA4, lipoxin A4; GPR32, G protein-coupled receptor 32; RvD1, resolvin D1; GPR18, G protein-coupled receptor 18; RvD2, resolvin D2; ChemR23, chemerin receptor 23; RvE1, resolvin E1; COX-2, cyclooxygenase-2; LOX, lipoxygenase; MaR1, maresin 1; NPD/DP1, neuroprotectin/protectin D1.

19, 25, and 43% with increasing dose. Further, RvD2 was able to inhibit the TLR4/NFκB signaling pathway as well as NFκB p65 mRNA expression by reducing the nuclear translocation of NFκB p65 in microglial cells. Further, RT-PCR revealed RvD2 significantly inhibited pro-inflammatory factors, mRNA expression and reduced level of intracellular ROS as shown by fluorescence microscopy.

Given the relationship between neuroinflammation and α-syn and that the presence of α-syn is pathogenic in PD (Zhang et al., 2005; Beraud et al., 2013). Krashia et al. (2019) investigated the effects of DHA-derived SPM in a bacterial artificial chromosome (BAC) transgenic gene model (Syn rats) that overexpresses human α-syn. Syn rats displayed features common in PD, such as progressive DA cell loss, reduced striatal DA outflow and motor deficits. Neuroinflammation was also present, as evidenced by cytokine production and region-specific microglia activation in the midbrain, striatum and hippocampus. To evaluate if these neuroinflammatory changes were associated with changes in inflammation resolution, levels of RvD1 and RvD2 were assessed in the CSF and plasma of Syn rats. Compared with age-matched controls, CSF levels of RvD1, but not RvD2, were higher in 4-month-old Syn rats. The increase was age dependent compared with 2-month-old Syn rats and was coupled with a corresponding decrease in plasma SPM. When levels were measured in 18-month-old rats, CSF and plasma levels of RvD1 were lower compared with age-matched controls. In an attempt to observe the ability of SPM to prevent neuronal and motor deficits secondary to chronic inflammation, RvD1 (i.p.0.2 μg/kg) was injected into Syn rats twice per week for 8 consecutive weeks starting at 2 months of age. In this experiment, early and chronic SPM treatment prevented changes in plasma IFN-γ levels, microglia activation and peripheral monocyte levels, while also preventing functional deficits and motor impairments (Krashia et al., 2019). Treated animals displayed normal crossing into the center zone in an open field test and improved performance on the accelerating rotarod compared to saline-treated animals, providing evidence that the RvD1 pathway can efficiently prevent neurophysiological and motor defects in Syn rats. In addition, Krashia et al. (2019) also examined levels of SPM (RvD1 and RvD2) and cytokines in the CSF and plasma of early PD patients

(n = 8) and healthy age-matched controls (n = 8). In one of the only studies examining SPM levels in humans, patients diagnosed with PD (symptom duration 13 ± 5 months, untreated and mildly affected) showed significantly higher levels of IL-4 in the CSF and IFN-γ and IL-10 in the plasma compared with controls. Interestingly, levels of RvD1 in both the CSF and plasma were significantly lower (p = 0.049 and p = 0.007, respectfully). However, no differences in RvD2 were detected between groups.

DISCUSSION

Both AD and PD preclinical studies discussed here suggest a dysregulation of the SPM levels and their receptors in disease condition as compared to healthy individuals. In both conditions, several studies suggest a benefit from administration of SPMs in various models (**Table 1**). SPMs hold great promise for neuroprotection in AD by altering gene expression of pro-inflammatory genes, modulating macrophage function, serving as a biomarker for AD status, and promoting resolution of neuroinflammation. In PD, data from *in vitro*, *in vivo,* and observational studies suggest SPM are able to cross the blood-brain barrier, inhibit microglial activation and decrease induced markers of inflammation, possibly as a result of their ability to downregulate NFκB signaling pathways (Xu et al., 2013, 2017; Tian et al., 2015). Further, treatment with these lipid-derived mediators may improve behavioral deficit as a result of the protection of DA neurons and prevents the onset of PD by attenuating neuroinflammation.

Many *in vitro* systems, including immortalized cell lines, patient derived iPSCs or iPSC-derived cell lines, and organoids have been used in studying neurodegenerative disorders. Some of the main problems of using *in vitro* cultures for the study of neurodegenerative disorders is the lack of blood brain barrier, interactions between brain cells resulting from the growth of cells as 2D monolayers (Konnova and Swanberg, 2018). These problems were overcome by using 3D cultures, organoids, scaffolds, microfluidics platform to mimic blood flow etc. Cell systems mimicking the blood-brain barrier has been recently reviewed by Peng et al. (2021). Neuroinflammation associated with neurodegeneration can be mimicked by more advanced 3D glial cell culture systems as well as co-culture of microglia, neuroblastoma and endothelial cells (Tu et al., 2019; Yin et al., 2020). These 3D systems can recapitulate the extracellular aggregation of amyloid beta as in AD (Choi et al., 2016) and aggregation of alpha-synuclein in neurons differentiated from iPSCs derived from PD patients (Oh, 2019).

To study the pathology and progression of neurodegenerative disorders, mouse models have been established using neurotoxin (environmental toxins, rotenone and paraquat,

TABLE 1 | Impact of PUFA-derived lipid mediators on neuroinflammation in *in vitro* and *in vivo* neurodegenerative disease models.

Author	Model	PUFA-derived mediators	Effect on neuroinflammation
Wang et al. (2015b)	Post-mortem brain tissue (no neuroinflammation model)	N/A	N/A
	Aβ40-exposed PBMCs	SPM Substrate (1.7 g DHA, 0.6 g EPA)	N/A
Emre et al. (2020)	Post-mortem brain tissue (no neuroinflammation model)	N/A	N/A
Zhu et al. (2016)	STS-induced apoptosis in neuroblastoma cells	LXA4	Improvement
		MaR1	Improvement
		RvD1	Improvement
		PDX	Improvement
	Aβ42 phagocytosis in human microglia	LXA4	No effect
		MaR1	Improvement
		RvD1	No effect
		PDX	No effect
	Aβ42 stressed/activated microglia	MaR1	Improvement
Zhao et al. (2012)	Aβ42-treated HNG	NDP1	Improvement
Yin et al. (2019)	Aβ42-treated C57BL/6 mouse hippocampus	MAR1	Improvement
Lee et al. (2020)	Murine AD	Aspirin-triggered SPM	Improvement
Koivisto et al. (2014)	Microglia activation of APP/PS1 Mice	SPM Substrate (fish-oil based diet)	Improvement
Fiala et al. (2015)	Aβ42-exposed PBMCs	SPM Substrate, RvD1 (1 g DHA, 1 g EPA)	Improvement
Mizwicki et al. (2013)	AD patient PBMCs	RvD1 + Vitamin D3	Improvement
Hopperton et al. (2018)	Aβ40-exposed mice	SPM Substrate (fish-oil based diet)	Improvement
Xu et al. (2013)	LPS-induced murine microglial cells	RvD1	Improvement
Xu et al. (2017)	MPP + treated PC12	RvD1	Improvement
Tian et al. (2015)	LPS-induced SD rats	RvD2	Improvement
	LPS-induced CD11b +	RvD2	Improvement
Krashia et al. (2019)	Syn Rats	RvD1	Improvement

PUFA, Polyunsaturated Fatty Acid; 3xTg-AD mice, harboring PS1 (M146V), APP (Swe) and tau (P301L) human transgenes; Aβ40, amyloid beta 1-40; PBMC, Peripheral blood mononuclear cells; SPM, Specialized pro-resolving mediator; DHA, Docosahexaenoic acid; EPA, Eicosapentaenoic acid; STS, Staurosporine; LXA4, Lipoxin A4; MaR1, Maresin-1; RvD1, Resolvin D1; PDX, Protectin D Isomer; Aβ42, Amyloid Beta 1–42; HNG, human neuronal-glial co-culture; NDP1, Neuroprotectin D1; AD, Alzheimer's disease; LPS, Lipopolysaccharide; MPP+, 1-methyl-4-phenylpyridium; SD, Sprague Dawley; RvD2, Resolvin D2.

MPTP, 6-OHDA) and genetic approaches (knockout mouse models and conditional knockout mouse models) (Konnova and Swanberg, 2018); however, none of these murine models seem to capture all features of disease. Considering the mouse models also vary, it is not always possible to extrapolate results from one model to another. One of the important differences where the effects of treatments as well as novel treatments like SPM might differ is the varying degree of neuroinflammation in these models. Studies have shown that neuroinflammation has an important role in the pathogenesis of neurodegenerative diseases regardless of genetic or toxin-induced models, as evidenced by the presence of activated microglia in postmortem SN, as well as increased levels of pro-inflammatory cytokines in the CSF and serum of patients (Wang et al., 2015b; Zhu et al., 2016; Krashia et al., 2019). Supporting this evidence, injection of LPS into SN has been shown to induce neurotoxicity, activate microglia and cause neurodegeneration in DA and non-dopaminergic neurons (Tufekci et al., 2011). Litteljohn et al. (2010) compared different toxin-induced PD models. These toxins have differences in their mechanisms of action, yet all lead to the loss of DA neurons. The timing of SPM treatment is another issue that needs to be addressed in preclinical studies. For example, their prophylactic effects as well as therapeutic effects need to be addressed in mouse models of disease. One of the challenges of AD and PD is that patients show variability in their symptoms, age of diagnosis, as well as disease progression.

Minimal data evaluating these PUFA-derived metabolites in humans with neurodegenerative disorders are available and a gap in knowledge exists regarding behavior of SPM and their receptors in patients with these conditions. There is also large gap in our knowledge regarding which SPMs would be most effective in which model of AD or PD and how dietary intake or supplementation can impact SPM levels. Previous work suggests PUFA supplementation may increase plasma levels of lipid-derived mediators in humans under a stressed state (Nordgren et al., 2019). However, there is a current paucity of data regarding baseline SPM levels in patients with neurodegenerative disorders as well as amount of substrate needed to result in a potential clinical improvement. One way to approach these issues is to determine SPM levels in different stages of the disease in both AD and PD, which might be addressed in preclinical or clinical studies. Further, as growing evidence demonstrates overlapping clinical and neuropathologic features of the two conditions, the role of SPM in resolving inflammation in Parkinson's dementia should also be investigated. As of now, there are no human studies looking into differences in individuals regarding SPM receptor expression or which SPMs would be most helpful to reduce neuroinflammation in AD patients. Furthermore, SPMs affect microglia activation, which can change the course of events from pro-inflammatory to anti-inflammatory depending on the M1/M2 polarization status, and this can lead to neurotoxic or neuroprotective effects. Despite the differences in major symptoms (memory vs. physical), similar issues related to SPMs are also relevant in PD due to the common neuroinflammatory mechanisms. In both diseases, the long-term effects of SPM supplements should be tested to uncover any unfavorable effects or any repair pathways that might be affected by SPM treatment. To the best of our knowledge, there are limited studies investigating the roles of SPMs in AD or PD, and no studies report any adverse effects of SPMs in these disease states. Nevertheless, some studies report that some survival pathways are activated, for example PI3K/Akt survival pathway, which is a pathway that is also implicated in cancers and resistance in cancer therapy. Therefore, the nuances of SPM treatment would need to be defined in AD and PD patients once it acquires clinical use. Large epidemiological studies seeking to understand the effect of diet on SPM levels would be most useful. The ability of SPM to prevent or resolve chronic neuroinflammation may represent a novel approach to treatment. Future direction should include focused, translational efforts to investigate SPM as an add-on (in addition to standard treatment) or as standalone agents in patients with neurodegenerative disorders.

AUTHOR CONTRIBUTIONS

JP, AU, CH, and DB: conceptualization. JW, AU, and CH: methodology. DB, JB, EC-S, AF, K-CS, VM, and JA: validation. JP and AU: investigation, data curation, and writing—original draft preparation. DB, JB, CH, JW, EC-S, AF, K-CS, VM, and JA: writing—review and editing. JP, AU, and CH: visualization. DB: supervision and project administration. All authors contributed to the article and approved the submitted version.

FUNDING

This research was funded by a grant from the University of Nebraska Collaboration Initiative.

REFERENCES

Aden, E., Carlsson, M., Poortvliet, E., Stenlund, H., Linder, J., Edstrom, M., et al. (2011). Dietary intake and olfactory function in patients with newly diagnosed Parkinson's disease: a case-control study. *Nutr. Neurosci.* 14, 25–31. doi: 10.1179/174313211X12966635733312

Alessandri, J. M., Guesnet, P., Vancassel, S., Astorg, P., Denis, I., Langelier, B., et al. (2004). Polyunsaturated fatty acids in the central nervous system: evolution of concepts and nutritional implications throughout life. *Reprod Nutr. Dev.* 44, 509–538. doi: 10.1051/rnd:2004063

Astorg, P. (2004). Dietary N-6 and N-3 polyunsaturated fatty acids and prostate cancer risk: a review of epidemiological and experimental evidence. *Cancer Causes Control.* 15, 367–386. doi: 10.1023/B:CACO.0000027498.94238.a3

Bannenberg, G., and Serhan, C. N. (2010). Specialized pro-resolving lipid mediators in the inflammatory response: an update. *Biochim. Biophys. Acta.* 1801, 1260–1273. doi: 10.1016/j.bbalip.2010.08.002

Barage, S. H., and Sonawane, K. D. (2015). Amyloid cascade hypothesis: Pathogenesis and therapeutic strategies in Alzheimer's disease. *Neuropeptides* 52, 1–18. doi: 10.1016/j.npep.2015.06.008

Barcia, C., Fernandez Barreiro, A., Poza, M., and Herrero, M. T. (2003). Parkinson's disease and inflammatory changes. *Neurotox Res.* 5, 411–418.

Basselin, M., Ramadan, E., and Rapoport, S. I. (2012). Imaging brain signal transduction and metabolism via arachidonic and docosahexaenoic acid in

animals and humans. *Brain Res. Bull.* 87, 154–171. doi: 10.1016/j.brainresbull.2011.12.001

Beadle, J. B., Just, D. E., Morgan, R. E., and Reiners, R. A. (1965). Composition of Corn Oil. *J. Am. Oil Chem. Soc.* 42, 90–95.

Benner, E. J., Banerjee, R., Reynolds, A. D., Sherman, S., Pisarev, V. M., Tsiperson, V., et al. (2008). Nitrated alpha-synuclein immunity accelerates degeneration of nigral dopaminergic neurons. *PLoS One* 3:e1376. doi: 10.1371/journal.pone.0001376

Beraud, D., Hathaway, H. A., Trecki, J., Chasovskikh, S., Johnson, D. A., Johnson, J. A., et al. (2013). Microglial activation and antioxidant responses induced by the Parkinson's disease protein alpha-synuclein. *J. Neuroimmune Pharmacol.* 8, 94–117. doi: 10.1007/s11481-012-9401-0

Birla, H., Rai, S. N., Singh, S. S., Zahra, W., Rawat, A., Tiwari, N., et al. (2019). Tinospora cordifolia Suppresses Neuroinflammation in Parkinsonian Mouse Model. *Neuromolecular. Med.* 21, 42–53. doi: 10.1007/s12017-018-08521-7

Buckley, C. D., Gilroy, D. W., and Serhan, C. N. (2014). Proresolving lipid mediators and mechanisms in the resolution of acute inflammation. *Immunity* 40, 315–327. doi: 10.1016/j.immuni.2014.02.009

Cardoso, H. D., dos Santos Junior, E. F., de Santana, D. F., Goncalves-Pimentel, C., Angelim, M. K., and Isaac, A. R. (2014). Omega-3 deficiency and neurodegeneration in the substantia nigra: involvement of increased nitric oxide production and reduced BDNF expression. *Biochim. Biophys. Acta.* 1840, 1902–1912. doi: 10.1016/j.bbagen.2013.12.023

Carson, M. J., Thrash, J. C., and Walter, B. (2006). The cellular response in neuroinflammation: The role of leukocytes, microglia and astrocytes in neuronal death and survival. *Clin. Neurosci. Res.* 6, 237–245. doi: 10.1016/j.cnr.2006.09.004

Checkoway, H., Lundin, J. I., and Kelada, S. N. (2011). Neurodegenerative diseases. *IARC Sci. Publ.* 163, 407–419.

Chen, W. W., Zhang, X., and Huang, W. J. (2016). Role of neuroinflammation in neurodegenerative diseases (Review). *Mol. Med. Rep.* 13, 3391–3396. doi: 10.3892/mmr.2016.4948

Choi, S. H., Kim, Y. H., Quinti, L., Tanzi, R. E., and Kim, D. Y. (2016). 3D culture models of Alzheimer's disease: a road map to a "cure-in-a-dish". *Mol. Neurodegener.* 11:75. doi: 10.1186/s13024-016-0139-7

Cova, I., Markova, A., Campini, I., Grande, G., Mariani, C., and Pomati, S. (2017). Worldwide trends in the prevalence of dementia. *J. Neurol. Sci.* 379, 259–260.

Croisier, E., Moran, L. B., Dexter, D. T., Pearce, R. K., and Graeber, M. B. (2005). Microglial inflammation in the parkinsonian substantia nigra: relationship to alpha-synuclein deposition. *J. Neuroinflammation.* 2:14. doi: 10.1186/1742-2094-2-14

de Lau, L. M., Koudstaal, P. J., Hofman, A., and Breteler, M. M. (2006). Subjective complaints precede Parkinson disease: the rotterdam study. *Arch. Neurol.* 63, 362–365. doi: 10.1001/archneur.63.3.noc50312

Dinarello, C. A. (2000). Proinflammatory cytokines. *Chest* 118, 503–508.

DiSabato, D. J., Quan, N., and Godbout, J. P. (2016). Neuroinflammation: the devil is in the details. *J. Neurochem.* 139(Suppl. 2), 136–153. doi: 10.1111/jnc.13607

Emre, C., Hjorth, E., Bharani, K., Carroll, S., Granholm, A. C., and Schultzberg, M. (2020). Receptors for pro-resolving mediators are increased in Alzheimer's disease brain. *Brain Pathol.* 30, 614–640. doi: 10.1111/bpa.12812

Fiala, M., Halder, R. C., Sagong, B., Ross, O., Sayre, J., Porter, V., et al. (2015). omega-3 Supplementation increases amyloid-beta phagocytosis and resolvin D1 in patients with minor cognitive impairment. *FASEB J.* 29, 2681–2689. doi: 10.1096/fj.14-264218

Franceschi, C., Capri, M., Monti, D., Giunta, S., Olivieri, F., Sevini, F., et al. (2007). Inflammaging and anti-inflammaging: a systemic perspective on aging and longevity emerged from studies in humans. *Mech. Ageing Dev.* 128, 92–105. doi: 10.1016/j.mad.2006.11.016

Gyengesi, E., Rangel, A., Ullah, F., Liang, H., Niedermayer, G., Asgarov, R., et al. (2019). Chronic Microglial Activation in the GFAP-IL6 Mouse Contributes to Age-Dependent Cerebellar Volume Loss and Impairment in Motor Function. *Front. Neurosci.* 13:303. doi: 10.3389/fnins.2019.00303

Harris, W. S., Mozaffarian, D., Lefevre, M., Toner, C. D., Colombo, J., Cunnane, S. C., et al. (2009). Towards establishing dietary reference intakes for eicosapentaenoic and docosahexaenoic acids. *J. Nutr.* 139, 804S–819S. doi: 10.3945/jn.108.101329

Hopperton, K. E., Trepanier, M. O., James, N. C. E., Chouinard-Watkins, R., and Bazinet, R. P. (2018). Fish oil feeding attenuates neuroinflammatory gene expression without concomitant changes in brain eicosanoids and docosanoids in a mouse model of Alzheimer's disease. *Brain Behav. Immun.* 69, 74–90. doi: 10.1016/j.bbi.2017.11.002

Hou, Y., Dan, X., Babbar, M., Wei, Y., Hasselbalch, S. G., Croteau, D. L., et al. (2019). Ageing as a risk factor for neurodegenerative disease. *Nat. Rev. Neurol.* 15, 565–581. doi: 10.1038/s41582-019-0244-7

Hughes, A. J., Daniel, S. E., Kilford, L., and Lees, A. J. (1992). Accuracy of clinical diagnosis of idiopathic Parkinson's disease: a clinico-pathological study of 100 cases. *J. Neurol. Neurosurg. Psychiatry* 55, 181–184. doi: 10.1136/jnnp.55.3.181

Iqbal, K., Liu, F., Gong, C. X., and Grundke-Iqbal, I. (2010). Tau in Alzheimer disease and related tauopathies. *Curr. Alzheimer Res.* 7, 656–664. doi: 10.2174/156720510793611592

Koivisto, H., Grimm, M. O., Rothhaar, T. L., Berkecz, R., Lutjohann, D. D., Giniatullina, R., et al. (2014). Special lipid-based diets alleviate cognitive deficits in the APPswe/PS1dE9 transgenic mouse model of Alzheimer's disease independent of brain amyloid deposition. *J. Nutr. Biochem.* 25, 157–169. doi: 10.1016/j.jnutbio.2013.09.015

Konnova, E. A., and Swanberg, M. (2018). "Animal Models of Parkinson's Disease," in *Parkinson's Disease: Pathogenesis and Clinical Aspects*, eds T. B. Stoker and J. C. Greenland (Brisbane, QLD: Codon Publications).

Kowal, S. L., Dall, T. M., Chakrabarti, R., Storm, M. V., and Jain, A. (2013). The current and projected economic burden of Parkinson's disease in the United States. *Mov. Disord.* 28, 311–318. doi: 10.1002/mds.25292

Krashia, P., Cordella, A., Nobili, A., La Barbera, L., Federici, M., Leuti, A., et al. (2019). Blunting neuroinflammation with resolvin D1 prevents early pathology in a rat model of Parkinson's disease. *Nat. Commun.* 10:3945.

Lee, J. Y., Han, S. H., Park, M. H., Song, I. S., Choi, M. K., Yu, E., et al. (2020). N-AS-triggered SPMs are direct regulators of microglia in a model of Alzheimer's disease. *Nat. Commun.* 11:2358. doi: 10.1038/s41467-020-16080-4

Lee, V. M., and Trojanowski, J. Q. (2006). Mechanisms of Parkinson's disease linked to pathological alpha-synuclein: new targets for drug discovery. *Neuron* 52, 33–38. doi: 10.1016/j.neuron.2006.09.026

Leng, F., and Edison, P. (2021). Neuroinflammation and microglial activation in Alzheimer disease: where do we go from here? *Nat. Rev. Neurol.* 17, 157–172. doi: 10.1038/s41582-020-00435-y

Levy, B. D., Clish, C. B., Schmidt, B., Gronert, K., and Serhan, C. N. (2001). Lipid mediator class switching during acute inflammation: signals in resolution. *Nat. Immunol.* 2, 612–619. doi: 10.1038/89759

Levy, B. D., and Serhan, C. N. (2014). Resolution of acute inflammation in the lung. *Annu. Rev. Physiol.* 76, 467–492. doi: 10.1146/annurev-physiol-021113-170408

Levy, O. A., Malagelada, C., and Greene, L. A. (2009). Cell death pathways in Parkinson's disease: proximal triggers, distal effectors, and final steps. *Apoptosis* 14, 478–500. doi: 10.1007/s10495-008-0309-3

Litteljohn, D., Mangano, E., Clarke, M., Bobyn, J., Moloney, K., and Hayley, S. (2010). Inflammatory mechanisms of neurodegeneration in toxin-based models of Parkinson's disease. *Parkinsons Dis.* 2011:713517. doi: 10.4061/2011/713517

Marras, C., Beck, J. C., Bower, J. H., Roberts, E., Ritz, B., Ross, G. W. et al. (2018). Prevalence of ParkinsonŠs disease across North America. *NPJ Parkinsons Dis.* 4:21. doi: 10.1194/jlr.P055418

McGeer, P. L., Itagaki, S., Boyes, B. E., and McGeer, E. G. (1988). Reactive microglia are positive for HLA-DR in the substantia nigra of Parkinson's and Alzheimer's disease brains. *Neurology* 38, 1285–1291. doi: 10.1212/wnl.38.8.1285

Menegaz, D., Mizwicki, M. T., Barrientos-Duran, A., Chen, N., Henry, H. L., and Norman, A. W. (2011). Vitamin D receptor (VDR) regulation of voltage-gated chloride channels by ligands preferring a VDR-alternative pocket (VDR-AP). *Mol. Endocrinol.* 25, 1289–1300. doi: 10.1210/me.2010-0442

Mizwicki, M. T., Liu, G., Fiala, M., Magpantay, L., Sayre, J., Siani, A., et al. (2013). 1alpha,25-dihydroxyvitamin D3 and resolvin D1 retune the balance between amyloid-beta phagocytosis and inflammation in Alzheimer's disease patients. *J. Alzheimers Dis.* 34, 155–170. doi: 10.3233/JAD-121735

Mouchlis, V. D., Chen, Y., McCammon, J. A., and Dennis, E. A. (2018). Membrane Allostery and Unique Hydrophobic Sites Promote Enzyme Substrate Specificity. *J. Am. Chem. Soc.* 140, 3285–3291. doi: 10.1021/jacs.7b12045

Niranjan, R. (2018). Recent advances in the mechanisms of neuroinflammation and their roles in neurodegeneration. *Neurochem. Int.* 120, 13–20. doi: 10.1016/j.neuint.2018.07.003

Nordgren, T. M., Anderson Berry, A., Van Ormer, M., Zoucha, S., Elliott, E., Johnson, R., et al. (2019). Omega-3 fatty acid supplementation, pro-resolving

mediators, and clinical outcomes in maternal-infant pairs. *Nutrients* 11:98. doi: 10.3390/nu11010098

Oh, Y. (2019). Patient-specific pluripotent stem cell-based Parkinson's disease models showing endogenous alpha-synuclein aggregation. *BMB Rep.* 52, 349–359. doi: 10.5483/BMBRep.2019.52.6.142

Orr, S. K., and Bazinet, R. P. (2008). The emerging role of docosahexaenoic acid in neuroinflammation. *Curr. Opin. Investig. Drugs* 9, 735–743.

Orr, S. K., Palumbo, S., Bosetti, F., Mount, H. T., Kang, J. X., Greenwood, C. E., et al. (2013). Unesterified docosahexaenoic acid is protective in neuroinflammation. *J. Neurochem.* 127, 378–393. doi: 10.1111/jnc.12392

Papanikolaou, Y., Brooks, J., Reider, C., and Fulgoni, V. L. III (2014). U.S. adults are not meeting recommended levels for fish and omega-3 fatty acid intake: results of an analysis using observational data from NHANES 2003-2008. *Nutr. J.* 13:31. doi: 10.1186/1475-2891-13-31

Peng, Y., Chu, S., Yang, Y., Zhang, Z., Pang, Z., and Chen, N. (2021). Neuroinflammatory in vitro cell culture models and the potential applications for neurological disorders. *Front. Pharmacol.* 12:671734. doi: 10.3389/fphar.2021.671734

Phani, S., Loike, J. D., and Przedborski, S. (2012). Neurodegeneration and inflammation in Parkinson's disease. *Parkinsonism Relat. Disord.* 18(Suppl. 1), S207–S209. doi: 10.1016/S1353-8020(11)70064-5

Plourde, M., and Cunnane, S. C. (2007). Extremely limited synthesis of long chain polyunsaturates in adults: implications for their dietary essentiality and use as supplements. *Appl. Physiol. Nutr. Metab.* 32, 619–634. doi: 10.1139/H07-034

Rai, S. N., Birla, H., Singh, S. S., Zahra, W., Patil, R. R., Jadhav, J. P., et al. (2017a). Mucuna pruriens Protects against MPTP Intoxicated Neuroinflammation in Parkinson's Disease through NF-kappaB/pAKT Signaling Pathways. *Front. Aging Neurosci.* 9:421. doi: 10.3389/fnagi.2017.00421

Rai, S. N., Birla, H., Zahra, W., Singh, S. S., and Singh, S. P. (2017b). Immunomodulation of Parkinson's disease using Mucuna pruriens (Mp). *J. Chem. Neuroanat.* 85, 27–35. doi: 10.1016/j.jchemneu.2017.06.005

Rai, S. N., Yadav, S. K., Singh, D., and Singh, S. P. (2016). Ursolic acid attenuates oxidative stress in nigrostriatal tissue and improves neurobehavioral activity in MPTP-induced Parkinsonian mouse model. *J. Chem. Neuroanat.* 71, 41–49. doi: 10.1016/j.jchemneu.2015.12.002

Rai, S. N., Zahra, W., Singh, S. S., Birla, H., Keswani, C., Dilnashin, H., et al. (2019). Anti-inflammatory Activity of Ursolic Acid in MPTP-Induced Parkinsonian Mouse Model. *Neurotox Res.* 36, 452–462. doi: 10.1007/s12640-019-00038-6

Ryan, A., and Godson, C. (2010). Lipoxins: regulators of resolution. *Curr. Opin. Pharmacol.* 10, 166–172. doi: 10.1016/j.coph.2010.02.005

Sawada, M., Imamura, K., and Nagatsu, T. (2006). Role of cytokines in inflammatory process in Parkinson's disease. *J. Neural. Transm. Suppl.* 70, 373–381.

Serhan, C. N. (2014). Pro-resolving lipid mediators are leads for resolution physiology. *Nature* 510, 92–101. doi: 10.1038/nature13479

Serhan, C. N., Chiang, N., and Dalli, J. (2015). The resolution code of acute inflammation: Novel pro-resolving lipid mediators in resolution. *Semin. Immunol.* 27, 200–215. doi: 10.1016/j.smim.2015.03.004

Serhan, C. N., Clish, C. B., Brannon, J., Colgan, S. P., Chiang, N., and Gronert, K. (2000). Novel functional sets of lipid-derived mediators with antiinflammatory actions generated from omega-3 fatty acids via cyclooxygenase 2-nonsteroidal antiinflammatory drugs and transcellular processing. *J. Exp. Med.* 192, 1197–1204. doi: 10.1084/jem.192.8.1197

Serhan, C. N., Gotlinger, K., Hong, S., and Arita, M. (2004). Resolvins, docosatrienes, and neuroprotectins, novel omega-3-derived mediators, and their aspirin-triggered endogenous epimers: an overview of their protective roles in catabasis. *Prostaglandins Lipid Mediat.* 73, 155–172. doi: 10.1016/j.prostaglandins.2004.03.005

Serhan, C. N., Krishnamoorthy, S., Recchiuti, A., and Chiang, N. (2011). Novel anti-inflammatory–pro-resolving mediators and their receptors. *Curr. Top. Med. Chem.* 11, 629–647. doi: 10.2174/1568026611109060629

Simopoulos, A. P. (2002). The importance of the ratio of omega-6/omega-3 essential fatty acids. *Biomed. Pharmacother.* 56, 365–379.

Singh, S. S., Rai, S. N., Birla, H., Zahra, W., Kumar, G., Gedda, M. R., et al. (2018). Effect of Chlorogenic Acid Supplementation in MPTP-Intoxicated Mouse. *Front. Pharmacol.* 9:757. doi: 10.3389/fphar.2018.00757

Singh, S. S., Rai, S. N., Birla, H., Zahra, W., Rathore, A. S., Dilnashin, H., et al. (2020). Neuroprotective Effect of Chlorogenic Acid on Mitochondrial Dysfunction-Mediated Apoptotic Death of DA Neurons in a Parkinsonian Mouse Model. *Oxid Med. Cell Longev.* 2020:6571484. doi: 10.1155/2020/6571484

Stoll, G., Jander, S., and Schroeter, M. (2000). Cytokines in CNS disorders: neurotoxicity versus neuroprotection. *J. Neural. Transm. Suppl.* 59, 81–89. doi: 10.1007/978-3-7091-6781-6_11

Strike, S. C., Carlisle, A., Gibson, E. L., and Dyall, S. C. (2016). A High Omega-3 Fatty Acid Multinutrient Supplement Benefits Cognition and Mobility in Older Women: a Randomized, Double-blind, Placebo-controlled Pilot Study. *J. Gerontol. A Biol. Sci. Med. Sci.* 71, 236–242. doi: 10.1093/gerona/glv109

Su, X., Maguire-Zeiss, K. A., Giuliano, R., Prifti, L., Venkatesh, K., and Federoff, H. J. (2008). Synuclein activates microglia in a model of Parkinson's disease. *Neurobiol. Aging* 29, 1690–1701. doi: 10.1016/j.neurobiolaging.2007.04.006

Tian, Y., Zhang, Y., Zhang, R., Qiao, S., and Fan, J. (2015). Resolvin D2 recovers neural injury by suppressing inflammatory mediators expression in lipopolysaccharide-induced Parkinson's disease rat model. *Biochem. Biophys. Res. Commun.* 460, 799–805. doi: 10.1016/j.bbrc.2015.03.109

Tu, D., Gao, Y., Yang, R., Guan, T., Hong, J. S., and Gao, H. M. (2019). The pentose phosphate pathway regulates chronic neuroinflammation and dopaminergic neurodegeneration. *J. Neuroinflammation* 16:255. doi: 10.1186/s12974-019-1659-1

Tufekci, K. U., Genc, S., and Genc, K. (2011). The endotoxin-induced neuroinflammation model of Parkinson's disease. *Parkinsons Dis.* 2011:487450.

Virtanen, J. K., Siscovick, D. S., Lemaitre, R. N., Longstreth, W. T., Spiegelman, D., Rimm, E. B., et al. (2013). Circulating omega-3 polyunsaturated fatty acids and subclinical brain abnormalities on MRI in older adults: the Cardiovascular Health Study. *J. Am. Heart Assoc.* 2:e000305. doi: 10.1161/JAHA.113.000305

Wang, Q., Liu, Y., and Zhou, J. (2015a). Neuroinflammation in Parkinson's disease and its potential as therapeutic target. *Transl. Neurodegener.* 4:19.

Wang, X., Zhu, M., Hjorth, E., Cortes-Toro, V., Eyjolfsdottir, H., Graff, C., et al. (2015c). Resolution of inflammation is altered in Alzheimer's disease. *Alzheimers Dement* 11, e1–e2. doi: 10.1016/j.jalz.2013.12.024

Wang, X., Hjorth, E., Vedin, I., Eriksdotter, M., Freund-Levi, Y., Wahlund, L. O., et al. (2015b). Effects of n-3 FA supplementation on the release of proresolving lipid mediators by blood mononuclear cells: the OmegAD study. *J. Lipid Res.* 56, 674–681.

Wypijewska, A., Galazka-Friedman, J., Bauminger, E. R., Wszolek, Z. K., Schweitzer, K. J., Dickson, D. W., et al. (2010). Iron and reactive oxygen species activity in parkinsonian substantia nigra. *Parkinsonism Relat. Disord.* 16, 329–333. doi: 10.1016/j.parkreldis.2010.02.007

Xu, J., Gao, X., Yang, C., Chen, L., and Chen, Z. (2017). Resolvin D1 Attenuates Mpp+-Induced Parkinson Disease via Inhibiting Inflammation in PC12 Cells. *Med. Sci. Monit.* 23, 2684–2691. doi: 10.12659/msm.901995

Xu, M. X., Tan, B. C., Zhou, W., Wei, T., Lai, W. H., Tan, J. W., et al. (2013). Resolvin D1, an endogenous lipid mediator for inactivation of inflammation-related signaling pathways in microglial cells, prevents lipopolysaccharide-induced inflammatory responses. *CNS Neurosci. Ther.* 19, 235–243. doi: 10.1111/cns.12069

Yang, B., Fritsche, K. L., Beversdorf, D. Q., Gu, Z., Lee, J. C., Folk, W. R., et al. (2019). Yin-Yang Mechanisms Regulating Lipid Peroxidation of Docosahexaenoic Acid and Arachidonic Acid in the Central Nervous System. *Front. Neurol.* 10:642. doi: 10.3389/fneur.2019.00642

Yin, P., Wang, X., Wang, S., Wei, Y., Feng, J., and Zhu, M. (2019). Maresin 1 Improves Cognitive Decline and Ameliorates Inflammation in a Mouse Model of Alzheimer's Disease. *Front. Cell Neurosci.* 13:466. doi: 10.3389/fncel.2019.00466

Yin, P., Wang, S., Wei, Y., Wang, X., Zhang, J., Yin, X., et al. (2020). Maresin1 decreased microglial chemotaxis and ameliorated inflammation induced by amyloid-beta42 in neuron-microglia co-culture models. *J. Alzheimers Dis.* 73, 503–515. doi: 10.3233/JAD-190682

Zahra, W., Rai, S. N., Birla, H., Singh, S. S., Rathore, A. S., Dilnashin, H., et al. (2020). Neuroprotection of Rotenone-Induced Parkinsonism by Ursolic Acid in PD Mouse Model. *CNS Neurol. Disord Drug Targets* 19, 527–540. doi: 10.2174/1871527319666200812224457

Zhang, W., Wang, T., Pei, Z., Miller, D. S., Wu, X., Block, M. L., et al. (2005). Aggregated alpha-synuclein activates microglia: a process leading to disease progression in Parkinson's disease. *FASEB J.* 19, 533–542. doi: 10.1096/fj.04-2751com

Zhang, Y., Chen, J., Qiu, J., Li, Y., Wang, J., and Jiao, J. (2016). Intakes of fish and polyunsaturated fatty acids and mild-to-severe cognitive impairment risks:

a dose-response meta-analysis of 21 cohort studies. *Am. J. Clin. Nutr.* 103, 330–340. doi: 10.3945/ajcn.115.124081

Zhao, W., Varghese, M., Vempati, P., Dzhun, A., Cheng, A., Wang, J., et al. (2012). Caprylic triglyceride as a novel therapeutic approach to effectively improve the performance and attenuate the symptoms due to the motor neuron loss in ALS disease. *PLoS One* 7:e49191. doi: 10.1371/journal.pone.0049191

Zhu, M., Wang, X., Hjorth, E., Colas, R. A., Schroeder, L., Granholm, A. C., et al. (2016). Pro-Resolving Lipid Mediators Improve Neuronal Survival and Increase Abeta42 Phagocytosis. *Mol. Neurobiol.* 53, 2733–2749. doi: 10.1007/s12035-015-9544-0

Conflict of Interest: The authors declare that the research was conducted in the absence of any commercial or financial relationships that could be construed as a potential conflict of interest.

Publisher's Note: All claims expressed in this article are solely those of the authors and do not necessarily represent those of their affiliated organizations, or those of the publisher, the editors and the reviewers. Any product that may be evaluated in this article, or claim that may be made by its manufacturer, is not guaranteed or endorsed by the publisher.

Copyright © 2022 Ponce, Ulu, Hanson, Cameron-Smith, Bertoni, Wuebker, Fisher, Siu, Marmelat, Adamec and Bhatti. This is an open-access article distributed under the terms of the Creative Commons Attribution License (CC BY). The use, distribution or reproduction in other forums is permitted, provided the original author(s) and the copyright owner(s) are credited and that the original publication in this journal is cited, in accordance with accepted academic practice. No use, distribution or reproduction is permitted which does not comply with these terms.

frontiers in Aging Neuroscience

MINI REVIEW
published: 28 February 2022
doi: 10.3389/fnagi.2022.810860

The Disease Modification Conundrum in Parkinson's Disease: Failures and Hopes

Zoltan Mari[1]* *and Tiago A. Mestre*[2]

[1] *Parkinson's and Movement Disorders Program, Cleveland Clinic Lou Ruvo Center for Brain Health, Las Vegas, NV, United States,* [2] *Division of Neurology, Department of Medicine, Parkinson's Disease and Movement Disorders Center, The Ottawa Hospital Research Institute, University of Ottawa, Ottawa, ON, Canada*

In the last half-century, Parkinson's disease (PD) has played a historical role in demonstrating our ability to translate preclinical scientific advances in pathology and pharmacology into highly effective clinical therapies. Yet, as highly efficacious symptomatic treatments were successfully developed and adopted in clinical practice, PD remained a progressive disease without a cure. In contrast with the success story of symptomatic therapies, the lack of translation of disease-modifying interventions effective in preclinical models into clinical success has continued to accumulate failures in the past two decades. The ability to stop, prevent or mitigate progression in PD remains the "holy grail" in PD science at the present time. The large number of high-quality disease modification clinical trials in the past two decades with its lessons learned, as well as the growing knowledge of PD molecular pathology should enable us to have a deeper understanding of the reasons for past failures and what we need to do to reach better outcomes. Periodic reviews and mini-reviews of the unsolved disease modification conundrum in PD are important, considering how this field is rapidly evolving along with our views and understanding of the possible explanations.

Keywords: Parkinson's disease, neuroprotection, biomarkers, animal modeling, synucleinopathy

OPEN ACCESS

Edited by:
Chih-Yu Hsu,
Fujian University of Technology, China

Reviewed by:
Nirosen Vijiaratnam,
University College London, United Kingdom
Enrique Urrea-Mendoza,
Prisma Health Neuroscience Associates, United States
Ellen Sidransky,
National Human Genome Research Institute (NHGRI), United States

***Correspondence:**
Zoltan Mari
mariz@ccf.org

Specialty section:
This article was submitted to Parkinson's Disease and Aging-related Movement Disorders, a section of the journal Frontiers in Aging Neuroscience

Received: *08 November 2021*
Accepted: *03 January 2022*
Published: *28 February 2022*

Citation:
Mari Z and Mestre TA (2022) The Disease Modification Conundrum in Parkinson's Disease: Failures and Hopes. Front. Aging Neurosci. 14:810860. doi: 10.3389/fnagi.2022.810860

INTRODUCTION

PD and movement disorder specialist clinicians frequently encounter patients inquiring about a "cure" for PD, or at least when it will be possible to slow down the progression of their disease. Almost as often as we are asked about a "cure" for PD, patients share popular media news, reporting curative treatments being imminent or on the verge of discovery. Such experiences in movement disorders clinics around the globe are a reminder of the critical unmet need for effective disease modification in PD, but also for accurate and effective messaging to the PD community. While there are effective, well-established symptomatic PD treatments (Armstrong and Okun, 2020), the present enormous societal burden associated with PD (GBD 2016 Parkinson's Disease Collaborators, 2018) is only expected to grow in an aging population (Dorsey et al., 2018), if no disease-modifying therapies in PD are available in clinical practice.

What are the missing pieces to the puzzle of successful disease modification in PD? To attempt to understand the conundrum, we start by reflecting on the history of PD. The first clinical description by James Parkinson was based on a few people, some of them random pedestrians fortuitously observed on the street (Parkinson, 1922). With the introduction of levodopa/carbidopa,

symptomatic treatments (Goetz, 2011) came about to improve the diagnostic signs and symptoms of parkinsonism, in what became a true revolution to improve the lives of people living with Parkinson's (PwP). As more treatments for core motor features of parkinsonism emerged and were further enhanced over the subsequent decades, none could be associated with slowing the relentless progression of PD.

Yet, hope emerged a couple of decades ago due to our growing understanding of PD pathophysiology and subsequent development of PD models. Early animal models relied on toxin-based interventions such as 1-methyl-4-phenyl-1,2,3,6-tetrahydropyridine (MPTP), which selectively destroyed neural structures (Langston, 2017), including and chiefly the nigrostriatal system, known to be core to PD pathology. Even though there were concerns raised about the true value of the MPTP model early on (Mari and Bodis-Wollner, 1997), it became the gold standard testing ground for therapeutic developments, targeting (A) symptomatic and (B) disease modification treatments alike. At the time, those two conceptually different therapeutic goals were not necessarily seen as distinctly separate from each other from the preclinical modeling perspective as they are today. With time, the limitations of animal modeling of neurodegenerative diseases have been recognized. For a recent review (see Dawson et al., 2018).

In fact, since the discovery of the MPTP model, the lack of successful translation from preclinical positive results to efficacy demonstrated in PD human trials has undermined the initial optimism about animal modeling. The "Valley of death" in PD disease modification populated by innumerous failures, such as the various NET-PD trials (Tilley and Galpern, 2007), the ADAGIO trial (Rascol et al., 2016), the more recent α-Synuclein immunotherapy trials (ClinicalTrials.gov, 2021) and Ven-glustat trial (Peterschmitt et al., 2021a,b), are testimony to the gaps in the planning and design of disease modification trials not properly recognized and addressed so far. There has been increasing interest and attention in the PD scientific community to this conundrum (Espay, 2021; Lungu et al., 2021) and this invited Mini Review aims to further add to the discussion.

FROM PRECLINICAL SUCCESS TO CLINICAL DISAPPOINTMENT: POSSIBLE REASONS BEHIND FAILED THERAPEUTIC TRANSLATION AND THE HOPE TO CORRECT THEM

In the following subsections, we review some possible contributors to the lack of translational success from preclinical to clinical therapeutic development for disease modification in PD, along with a brief ("mini") assessment on the hopes of correcting or mitigating each of these obstacles. When applicable, we list specific reasons for hope in each of these subsections, with the most relevant specific points numbered (1) (2) (3) accordingly. While we intend these assessments to help shape a framework for therapeutic development in PD, they are not expected to fully address these complex challenges (Ransohoff, 2018).

Timing Woes

In preclinical studies, researchers are in full control of *timing*, both in terms of the administration of a putative disease-modifying (or neuroprotective) intervention and the inception of a PD-like condition. In other words, preclinical studies can examine the effect of an intervention with arbitrary (optimized) timing relative to the onset of the pathology induced experimentally, which is not possible in real-world PD therapeutic clinical development. Administering a disease-modifying intervention at the earliest possible time in the natural history of a neurodegenerative disease is likely more effective and thus desirable, as it opens a window of opportunity for an intervention to effectively interfere *earlier* in the neurodegenerative process, before the "horses are out of the barn." A path forward in PD is the ability to recognize earlier pre-symptomatic, pre-clinical, and prodromal states of PD and to accurately define the risk of phenoconversion over time. Regarding the risk of phenoconversion over time, it is essential to be able to detect the earliest and more subtle changes relevant to disease inception, but also to use validated biomarkers of ongoing pathology and disease stage/progression. The latter is perhaps the greatest challenge for already symptomatic disease stages, as time to phenoconversion may already be considered as an established efficacy outcome in disease modification clinical trials involving prodromal/pre-symptomatic stages.

Estimating and monitoring disease risk and expected time to phenoconversion would be greatly helpful in preclinical management and advice. For example, a patient with a known mutation in one of the PD risk genes may have a certain lifetime risk of PD at an earlier point in life, which may change later in life (for example due to certain environmental exposures or epigenetic effects). Hopefully easily, inexpensively, and passively monitorable parameters or functions (for example keyboard use, speech, change in autonomic functions, motor speed, habits, sleep, etc.) could raise alerts pointing to a possibly changing risk of impeding phenoconversion. At that point, individual patient's risk could be further evaluated by high specificity and sensitivity testing (such as dopamine nuclear imaging). Once their risk of phenoconversion is established and reaches a certain threshold, the risk and benefit of any disease modifying intervention may be determined taking that into account. This may be particularly important if future, putative disease modifying interventions carry substantial risk of side effects or irreversible complications.

Mini Assessment

It is not expected that clinicians and human clinical trials will ever be in full control of the timing of administration of candidate disease modifying interventions relative to disease inception. However, there still is hope, when it comes to timing woes.

(1) Efforts to target *de novo* patients (and especially subjects at a prodromal stage) can move the timing of a disease modification intervention to a point closer to the presumed inception.

(2) A more ambitious hope is to target those at-risk for PD using a population-based risk-monitoring approach, possibly identifying at-risk individuals earlier in the natural history of the disease. To that end, likely a combination of a validated biomarker is needed with rigorous diagnostic criteria for at-risk PD (Mantri et al., 2019). The ubiquitous nature and technological improvements of consumer-grade monitoring devices could potentially act as part of such population-based screening for impending phenoconversion by alerting individuals of concerning changes in their level of daily activities (motor or non-motor) and functioning, related to pre-symptomatic PD.
(3) Finally, it is also possible that general preventative measures can be safely applied to the general population (such as exercise, removal of toxic contamination from food and drinking water) which, in turn, may impact the risk of incident PD.

No Perfect Model of Parkinson's Disease: The Unnatural Nature of "Pure and Simple" Preclinical Designs

The heterogeneity of sporadic PD remains an active field of research to accurately understand pathophysiology and the impact of independent and simultaneous pathologies, with the intention to inform prognosis, and shape therapeutic development for target-/group-, and individual specific disease-modifying therapies (Mestre et al., 2021). Heterogeneity among individual patients is significant to the point that PD may be more appropriately called a syndrome with multiple causes (Devos et al., 2021).

In preclinical experiments, the design is traditionally driven to simplify and dissect a specific pathological pathway. To accomplish this preclinical goal, "noise" needs to be reduced or eliminated. As part of such deliberate effort, in preclinical models, biological heterogeneity, co-morbidities, and inter-individual variability is attempted to be minimized or eliminated. But this simplification to create "pure" models may then undermine how preclinical models accurately represent their respective human condition. For example, cross-seeding in multiple proteinopathies is a recognized phenomenon in parkinsonian disorders (Williams et al., 2020) and the interplay with other pathologies outside of proteinopathies is also known (Motyl et al., 2021).

In the clinical arena, despite efforts to adopt restrictive eligibility criteria in clinical trials, study participants have intrinsically greater heterogeneity compared with preclinical (animal) models, which typically use nearly identical individuals within the animal cohort. In human studies, beyond the heterogeneity of PD itself as established clinically, there is also the intra-cohort heterogeneity with respect to factors outside of PD itself, including the individuals' age, genome, their environmental exposures, and comorbidities. Usually these areas of heterogeneity among study subjects are not fully accounted for in human clinical trials, even if most do exclude independent neurological comorbidities. The way these various sources of heterogeneity may affect how patients respond to a disease modifying intervention, even when they otherwise possess a common pathological target relevant to the tested intervention, is still largely unknown. Such consideration is generally excluded from creating preclinical models. Consequently, at the present time, a preclinical model of PD is likely to fail as it is not an accurate representation of a very important aspect of sporadic PD, which is heterogeneity of the sample.

In face of the disconnect between the human (heterogeneous) PD and its (homogeneous) preclinical models, an approach that could gap this bridge in drug development may be the ability to select study participants based on the proposed mechanism of action of the experimental intervention being tested, what constitutes an enrichment strategy. This approach would diminish the heterogeneity among individuals of a study cohort in one important way. A biomarker-driven phenotyping (Espay et al., 2017, 2020) may inform this approach. The rule in the past has been that disease modification clinical trials almost exclusively used enrollment criteria based on clinical diagnostic criteria for PD, thus the enrichment strategy promoted by a few authors has been uncommon.

Nevertheless, some recent efforts indicate that the field may be moving forward from clinical diagnostic criteria-based enrollment. One example is the SURE-PD3 trial, where the study design purposely used an enrichment strategy (serum urate below the population median concentration), based on the expected mechanism of action of inosine, the study intervention (Parkinson Study Group et al., 2021). Although, this particular study failed to meet its primary endpoint, we believe it to be an important example of how a biomarker-defined specific sub-population of PD, beyond just meeting clinical diagnostic criteria, can be feasibly employed in a large multicenter clinical trial. As discussed elsewhere in this mini-review, there of course may be a number of potential other reasons for failure, besides the reliance on clinical diagnostic criteria only in disease modifying trials. One example of enrichment of the study population could be the use of PET scanning to identify PD patients with evidence of microglial activation for interventions targeting microglia (Yun et al., 2018; Muzio et al., 2021).

Another example of selective inclusion criteria beyond just meeting clinical diagnostic criteria is represented by a trial of azathioprine, an immunosuppressant medication, to investigate whether suppressing the peripheral immune system can be disease-modifying in PD. In this trial, a prognostic risk score (Greenland et al., 2020) was adopted and those at higher risk of progression were included.

A caveat for restricting PD enrollment to patients with a unique molecular abnormality carries financial and logistical challenges, which can make such an approach less attractive (Lungu et al., 2021). Also, while we strongly believe that anchoring enrollment for disease modifying trials solely on clinical diagnostic criteria is suboptimal, merely correcting this issue alone may not automatically guarantee success, for the possibility of several other errors in trial design. To highlight that cautionary note, the selection of PD patients carrying specific GBA mutations did not save the Ven-glustat trial from failure, with the unexpected finding that those allocated to active treatment and carriers of a less severe GBA mutation

had a greater progression on efficacy outcomes (Peterschmitt et al., 2021a,b), again bringing attention to the complexity and multifactorial nature of the problem.

Mini Assessment

To address the consistently failing preclinical-to-clinical translation in PD therapeutic development, it is paramount that a major characteristic of human populations in clinical trials, i.e., natural heterogeneity among individuals of the sample, is represented in preclinical models, especially if the target population is sporadic PD, for a better understanding of the impact of a novel experimental therapy from a biological and outcome perspective. At the same time, and along the lines of a more rational and solid drug development, disease modification trials should not settle at using only clinical diagnostic criteria for study eligibility, without an "enrichment strategy," e.g., incorporating biomarker-driven inclusion criteria, linked to the putative mechanism of action of the experimental therapy being developed.

(1) Preclinical models should replicate human disease in more than one way. While it is necessary that the individuals of a preclinical experimental cohort share the targeted specific abnormality, heterogeneity in other aspects among individuals of the sample (their age, genetic background, presence/absence of unrelated other pathologies/comorbidities) is desirable, for better representation of a human clinical trial population. This premise is different from current standards, complex, and challenging—yet theoretically possible. For example, injection of α-synuclein fibril seeds combined with adeno-associated virus (AAV)-mediated overexpression of human α-synuclein (Thakur et al., 2017) may be done in an otherwise heterogeneous group of rats. Also, recent developments in mRNA technology could also add tools to create specific changes in protein expression (Kallen and Thess, 2014) in otherwise heterogeneous group of experimental animals. With such approach, it may be possible for investigators to create the same molecular pathological process in an otherwise heterogeneous cohort. The hope is that preclinical efficacy of an intervention may translate better from such models to human trials.

(2) Generic and broad inclusion of clinically defined PD populations for disease modification studies have been motivated by feasibility and financial considerations, while also a necessary compromise due to lack of validated biomarkers in most circumstances. However, the use of an enrichment strategy with more restrictive enrollment criteria, narrowing the study population on the basis of well-defined pharmacodynamic biomarkers of the studied therapeutic target, could offer an attractive starting point for success in disease modification in PD. Similar suggestions have been made recently by others (Espay et al., 2020; Devos et al., 2021). The enormous investment in disease modification clinical trials over the past couple of decades should convince stakeholders that the strategy of "just keep doing the same" will likely only lead to further waste of time and resources, whereas the concept of a well-informed "less is more" rationale proposed here could not only be scientifically sound, but financially pertinent, as it may yield a new opportunity of turning failure to success.

(3) To achieve this ambitious but necessary shift in strategy and vision, stronger collaborations between preclinical and clinical scientist are necessary. "Bench-to-bedside-and-back-again" frameworks may lead to innovation that could address this disconnect.

While seemingly contradictory on the issue of heterogeneity in study cohorts, points (1) and (2) are in fact complementary. To best imagine this, we propose that current standards of animal modeling and clinical testing of disease modification interventions in PD are two ends of a spectrum with regards to sample heterogeneity among individuals within study cohorts. Preclinical experiments make a painstaking effort to eliminate any and all such heterogeneity, whereas human clinical trials employing phenomenology-based clinical diagnostic criteria to select their study population make no actual effort to homogenize their sample in a way relevant to the tested intervention. While the latter point has been discussed elsewhere (Devos et al., 2021; Espay, 2021; Mestre et al., 2021), the purpose of animal modeling is to achieve a more accurate representation of a human disease that better supports testing in humans in a continuum where prior studies inform future studies and reduce risk of failures and yield for success. To improve PD preclinical models, better representation of the human sample's heterogeneity (in age, comorbidities, past environmental exposures, etc.) is necessary.

Targets: The Age of Discovery

The discovery of the nigrostriatal dopaminergic system and the possibility to replenish the deficient neurochemical state of dopamine observed in PD (Carlsson et al., 1957; Hornykiewicz, 1966; Cotzias et al., 1969) led to a prolific therapeutic development. The Nobel prize in the year 2000 was awarded to Arvid Carlsson (1923–2018) and Lees et al. (2015) for the discovery of dopamine and its role in human movement and it is a testimony to the impact of these scientific breakthroughs. It is not an hyperbole that this discovery created a revolutionary momentum in the development of neurological treatments not previously imagined. In contrast, the series of failures in disease modification trials cast a shadow on the feasibility of neuroprotective treatment targets thus far identified and the ability of candidate treatments aimed at those targets to slow down PD progression (Lungu et al., 2021). Therefore, despite all the earlier breakthroughs relative to dopamine that became major milestones in human neuroscience, we are living in a new age in need of discovering new targets in PD with a renewed promise of disease modification. Examples include the development of therapeutics targeting specific genetic forms of PD such as GBA-related PD (Peterschmitt et al., 2021a,b) and LRRK2-associated PD (Schneider and Alcalay, 2020) with ongoing clinical trials, as well as the identification of new molecular fingerprints and other pathophysiological mechanisms in PD neurodegeneration that may be targeted in the future for development of novel therapies (Zeng et al., 2018). This growing knowledge may allow in the

future to define the disease subtypes based on specific disease mechanisms at the molecular level; targets potentially associated with the potential for a disease modification intervention, even prior to the emergence of a motor phenotype and independent of a clinical diagnosis.

Mini Assessment

To improve better disease modifying clinical trials in PD and our chance for success, new treatment targets are need.

(1) Developing a new classification system of PD etiologies will be needed considering cases with a well-defined cause to broader categories of multifactorial and idiopathic etiology.
(2) It is also critical to revise clinical trial designs to place great emphasis on a robust connection between therapeutic target and study population definition, and (in select cases of proof-of-concept trials) a linked endpoint. We will further discuss endpoints in the next section.
(3) A "cocktail" of multi-target therapeutic intervention may prove to be a more successful intervention in the future for disease modification. It is unlikely, even in case of study population selected based on a single cause, such as gene-defined forms of PD, that a single target will be sufficient for successful disease modification.

The Importance of the "Right" Endpoints: The Era of Biomarkers

How do we objectively measure progression in PD? A commonly cited reason for failure of PD disease modification trials is the lack of perfect progression endpoints; that the "gold standard," the Movement Disorder Society's Unified Parkinson's Disease Rating Scale (MDS-UPDRS), should be viewed more as a "bronze standard." A known floor effect, intra- and inter-rater reliability issues, and great susceptibility to symptomatic treatment related variability (Teshuva et al., 2019; Trifonova et al., 2020) make the MDS-UPDRS suboptimal as a primary outcome measure in trials of disease modification. Consequently, there have been calls to use a more complex multi-domain characterization of the PD clinical syndrome One proposed solution is the so-called "digital phenotyping" of PD (Bhidayasiri and Mari, 2020), with the necessary technology and resources becoming available, it is becoming a reality to use more objective digital measures capturing a variety of measures in a multitude of motor and non-motor domains (Dorsey et al., 2020). Research on progression biomarkers remains one of the most relevant field in the area of disease modification research in PD (Marek et al., 2011; Espay et al., 2020). A leading challenge affecting the adoption of reliable biomarkers, including digital, clinical, imaging, biological/biofluid, neuropsychological, and others, remains centered on their proper validation. The complexity of this challenge, further complicated by the influence of commercial developments and interests, represents no smaller barrier than any of the others outlined in previous sections in this mini-review. However, there are increasingly credible efforts to solve this difficult riddle (Espay et al., 2019; Adams et al., 2020; Schneider et al., 2021). The Parkinson Progression Marker Initiative (PPMI) is one of those projects. PPMI is the largest longitudinal study to pursue imaging and biofluid markers of progression in PD (Marek et al., 2011) that aims to provide a comprehensive PD phenotype including not only non-treated PD with a recent clinical diagnosis, but also for subjects deemed to be at a prodromal stage. While so far PPMI has not produced revolutionary breakthroughs, its design, scope, and methods are constantly adapting to new data and are setting new specific goals, having produced significant advances in our understanding of PD pathophysiology, natural history, and ways to more precisely measure disease progression (Rahmim et al., 2017).

Mini Assessment

Along with the other key contributors to past failures of disease modification trials in PD, solving the problem of best endpoints is equally critical. Several ideas come into consideration.

(1) Rather than validating candidate progression biomarkers against existing standards, they may need to be validated against disease-relevant and even disease subtype-, stage-, study-, target-, or individual-specific outcomes, as discussed in a recent review (Bhidayasiri and Mari, 2020).
(2) Deep phenotyping or digital phenotyping (Bhidayasiri and Mari, 2020; Dorsey et al., 2020) would need to sensibly combine a variety of biomarkers and measures.
(3) A scientist and science-driven approach that appropriately regulates industry participation will be required for success (Espay et al., 2019; Lungu et al., 2021). The explosion of consumer electronic technology has led to the burgeoning offerings of consumer fitness and health monitoring products that overlap and encroach the zone of healthcare grade devices, often developed by the same companies as consumer grade monitoring technology. The financial conflicts of interests apply in this area of research and development similarly to other areas, but regulatory response to the rapidly changing field of study simply could not keep up the pace, adding another layer of complexity.

DISCUSSION

The conundrum we are faced with a lost in translation of promising preclinical results into human clinical trial success for PD disease modification qualifies as a crisis. In PD, we are now searching ways to identify the opportunities in this crisis. As outlined at the end of each section above, we do have an opportunity as well as a mandate to change directions, introduce new concepts and experimental protocols, *both* in the preclinical and clinical research realms. Learning from the lessons of over more than two decades of failed disease modification clinical trials in PD, we believe that increased collaboration and coordination across basic and clinical scientists, further increased funding and support from public, foundation, and private industry sources will need to come together to ignite a paradigm shift. It is also necessary that the scientific agenda in PD be primarily academically driven, while industry influence is properly balanced by a scientifically rigorous agenda.

For example, in North America, an academically based not-for-profit research network of credentialed movement disorder specialists and clinical trial experts, such as the PSG and the Michael J. Fox Foundation, can be an ally and advisor to industry sponsors in the development and advise on and oversee the conduction of modern clinical trial designs. Various platforms for scientists and projects, including special interest groups, workshops, and themed symposia within existing large international conferences or new platforms bringing together scientists from all sides can be an effective way of learning from each other and promote broader collaborations.

With an enormous public health need for effective treatments to slow, and ideally prevent the progression of PD, the PD research community is under tremendous pressure to solve this conundrum. We hope that an improved understanding of the likely contributors to past failures can pave the way to success with the creation of animal models that more accurately represent the human disease, the design better clinical trials, with targeted patient selection, and more sensitive and specific biomarkers as endpoints.

AUTHOR CONTRIBUTIONS

ZM developed first draft. Both authors contributed to final draft.

REFERENCES

Adams, J. L., Dorsey, E. R., Steinman, A., Kangarloo, T., Alexander, R., Tracey, B., et al. (2020). WATCH-PD: wearable Assessments in the Clinic and Home in Parkinson's Disease: study Design and Update. *Mov. Disord.* 35, S386–S387.

Armstrong, M. J., and Okun, M. S. (2020). Diagnosis and Treatment of Parkinson Disease: a Review. *JAMA* 323, 548–560. doi: 10.1001/jama.2019.22360

Bhidayasiri, R., and Mari, Z. (2020). Digital phenotyping in Parkinson's disease: empowering neurologists for measurement-based care. *Parkinson. Relat. Disord.* 80, 35–40. doi: 10.1016/j.parkreldis.2020.08.038

Carlsson, A., Lindqvist, M., and Magnusson, T. (1957). 3,4-Dihydroxyphenylalanine and 5-Hydroxytryptophan as Reserpine Antagonists. *Nature* 180, 1200–1200. doi: 10.1038/1801200a0

ClinicalTrials.gov (2021). *A Study to Evaluate the Efficacy of Prasinezumab (RO7046015/PRX002) in Participants With Early Parkinson's Disease (PASADENA)*. United States: ClinicalTrials.gov. Available: https://clinicaltrials.gov/ct2/show/NCT03318523 [Accessed].

GBD 2016 Parkinson's Disease Collaborators (2018). Global, regional, and national burden of Parkinson's disease, 1990-2016: a systematic analysis for the Global Burden of Disease Study 2016. *Lancet Neurol.* 17, 939–953. doi: 10.1016/S1474-4422(18)30295-3

Cotzias, G. C., Papavasi, P. S., and Gellene, R. (1969). Modification of Parkinsonism - Chronic Treatment with L-Dopa. *New Engl. J. Med.* 280, 337–45. doi: 10.1056/nejm196902132800701

Dawson, T. M., Golde, T. E., and Lagier-Tourenne, C. (2018). Animal models of neurodegenerative diseases. *Nat. Neurosci.* 21, 1370–1379.

Devos, D., Hirsch, E., and Wyse, R. (2021). Seven Solutions for Neuroprotection in Parkinson's Disease. *Mov. Disord.* 36, 306–316. doi: 10.1002/mds.28379

Dorsey, E. R., Omberg, L., Waddell, E., Adams, J. L., Adams, R., Ali, M. R., et al. (2020). Deep Phenotyping of Parkinson's Disease. *J. Parkinsons Dis.* 10, 855–873.

Dorsey, E. R., Sherer, T., Okun, M. S., and Bloem, B. R. (2018). The Emerging Evidence of the Parkinson Pandemic. *J. Parkinsons Dis.* 8, S3–S8. doi: 10.3233/JPD-181474

Espay, A. J. (2021). Of Synuclein and Other Demons. *J. Alzheimers Dis.* 83, 1391–1393.

Espay, A. J., Hausdorff, J. M., Sanchez-Ferro, A., Klucken, J., Merola, A., Bonato, P., et al. (2019). A roadmap for implementation of patient-centered digital outcome measures in Parkinson's disease obtained using mobile health technologies. *Mov. Disord.* 34, 657–663. doi: 10.1002/mds.27671

Espay, A. J., Kalia, L. V., Gan-Or, Z., Williams-Gray, C. H., Bedard, P. L., Rowe, S. M., et al. (2020). Disease modification and biomarker development in Parkinson disease: revision or reconstruction? *Neurology* 94, 481–494. doi: 10.1212/WNL.0000000000009107

Espay, A. J., Schwarzschild, M. A., Tanner, C. M., Fernandez, H. H., Simon, D. K., Leverenz, J. B., et al. (2017). Biomarker-driven phenotyping in Parkinson's disease: a translational missing link in disease-modifying clinical trials. *Mov. Disord.* 32, 319–324. doi: 10.1002/mds.26913

Goetz, C. G. (2011). The history of Parkinson's disease: early clinical descriptions and neurological therapies. *Cold Spring Harb Perspect Med.* 1:a008862. doi: 10.1101/cshperspect.a008862

Greenland, J. C., Cutting, E., Kadyan, S., Bond, S., Chhabra, A., and Williams-Gray, C. H. (2020). Azathioprine immunosuppression and disease modification in Parkinson's disease (AZA-PD): a randomised double-blind placebo-controlled phase II trial protocol. *BMJ Open* 10:e040527. doi: 10.1136/bmjopen-2020-040527

Hornykiewicz, O. (1966). Dopamine (3-Hydroxytyramine) and Brain Function. *Pharmacol. Rev.* 18, 925–64.

Kallen, K. J., and Thess, A. (2014). A development that may evolve into a revolution in medicine: mRNA as the basis for novel, nucleotide-based vaccines and drugs. *Ther. Adv. Vaccines* 2, 10–31. doi: 10.1177/2051013613508729

Langston, J. W. (2017). The MPTP Story. *J. Parkinsons Dis.* 7, S11–S19.

Lees, A. J., Tolosa, E., and Olanow, C. W. (2015). Four pioneers of L-dopa treatment: arvid Carlsson, Oleh Hornykiewicz, George Cotzias, and Melvin Yahr. *Mov. Disord.* 30, 19–36. doi: 10.1002/mds.26120

Lungu, C., Cedarbaum, J. M., Dawson, T. M., Dorsey, E. R., Faraco, C., Federoff, H. J., et al. (2021). Seeking progress in disease modification in Parkinson disease. *Parkinsonism Relat. Disord.* 90, 134–141. doi: 10.1016/j.parkreldis.2021.09.006

Mantri, S., Morley, J. F., and Siderowf, A. D. (2019). The importance of preclinical diagnostics in Parkinson disease. *Parkinsonism Relat. Disord.* 64, 20–28. doi: 10.1016/j.parkreldis.2018.09.011

Marek, K., Jennings, D., Lasch, S., Siderowf, A., Tanner, C., Simuni, T., et al. (2011). The Parkinson Progression Marker Initiative (PPMI). *Progress Neurobiol.* 95, 629–635.

Mari, Z., and Bodis-Wollner, I. (1997). *MPTP-induced Parkinsonian Syndrome in Man and Animals: how Good is the Model*. New York: John Wiley & Sons. 189–228.

Mestre, T. A., Fereshtehnejad, S. M., Berg, D., Bohnen, N. I., Dujardin, K., Erro, R., et al. (2021). Parkinson's Disease Subtypes: critical Appraisal and Recommendations. *J. Parkinsons Dis.* 11, 395–404. doi: 10.3233/JPD-202472

Motyl, J. A., Strosznajder, J. B., Wencel, A., and Strosznajder, R. P. (2021). Recent Insights into the Interplay of Alpha-Synuclein and Sphingolipid Signaling in Parkinson's Disease. *Int. J. Mol. Sci.* 22:6277. doi: 10.3390/ijms22126277

Muzio, L., Viotti, A., and Martino, G. (2021). Microglia in Neuroinflammation and Neurodegeneration: from Understanding to Therapy. *Front. Neurosci.* 15:742065. doi: 10.3389/fnins.2021.742065

Parkinson, J. (1922). An essay on the shaking palsy. *Arch. Neurol. Psychiatry* 7, 683–710.

Parkinson Study Group, S.-P. D. I., Schwarzschild, M. A., Ascherio, A., Casaceli, C., Curhan, G. C., Fitzgerald, R., et al. (2021). Effect of Urate-Elevating Inosine on Early Parkinson Disease Progression: the SURE-PD3 Randomized Clinical Trial. *JAMA* 326, 926–939. doi: 10.1001/jama.2021.10207

Peterschmitt, M. J., Giladi, N., Alcalay, R. N., Simuni, T., Marek, K., and Investigators, M.-P. (2021a). "Ven-glustat In Parkinson's Disease Patients with a GBA Mutation: resultsFrom Part 2 of the Phase 2 MOVES-PD Trial" in *15th International Conference on Alzheimer's & Parkinson's Diseases* (Virtual).

Peterschmitt, M. J., Saiki, H., Hatano, T., Gasser, T., Isaacson, S. H., Gaemers, S. J. M., et al. (2021b). Safety, Pharmacokinetics, and Pharmacodynamics of

Oral Venglustat in Patients with Parkinson's Disease and a GBA Mutation: results from Part 1 of the Randomized, Double-Blinded, Placebo-Controlled MOVES-PD Trial. *J. Parkinsons Dis.* doi: 10.3233/JPD-212714 [Epub ahead of print].

Rahmim, A., Huang, P., Shenkov, N., Fotouhi, S., Davoodi-Bojd, E., Lu, L., et al. (2017). Improved prediction of outcome in Parkinson's disease using radiomics analysis of longitudinal DAT SPECT images. *Neuroimage Clin.* 16, 539–544. doi: 10.1016/j.nicl.2017.08.021

Ransohoff, R. M. (2018). All (animal) models (of neurodegeneration) are wrong. Are they also useful? *J. Exp. Med.* 215, 2955–2958. doi: 10.1084/jem.20182042

Rascol, O., Hauser, R. A., Stocchi, F., Fitzer-Attas, C. J., Sidi, Y., Abler, V., et al. (2016). Long-term effects of rasagiline and the natural history of treated Parkinson's disease. *Mov. Disord.* 31, 1489–1496. doi: 10.1002/mds.26724

Schneider, R. B., Omberg, L., Macklin, E. A., Daeschler, M., Bataille, L., Anthwal, S., et al. (2021). Design of a virtual longitudinal observational study in Parkinson's disease (AT-HOME PD). *Ann. Clin. Transl. Neurol.* 8, 308–320. doi: 10.1002/acn3.51236

Schneider, S. A., and Alcalay, R. N. (2020). Precision medicine in Parkinson's disease: emerging treatments for genetic Parkinson's disease. *J. Neurol.* 267, 860–869. doi: 10.1007/s00415-020-09705-7

Teshuva, I., Hillel, I., Gazit, E., Giladi, N., Mirelman, A., and Hausdorff, J. M. (2019). Using wearables to assess bradykinesia and rigidity in patients with Parkinson's disease: a focused, narrative review of the literature. *J. Neural. Transm.* 126, 699–710. doi: 10.1007/s00702-019-02017-9

Thakur, P., Breger, L. S., Lundblad, M., Wan, O. W., Mattsson, B., Luk, K. C., et al. (2017). Modeling Parkinson's disease pathology by combination of fibril seeds and alpha-synuclein overexpression in the rat brain. *Proc. Natl. Acad. Sci. U. S. A.* 114, E8284–E8293. doi: 10.1073/pnas.1710442114

Tilley, B. C., and Galpern, W. R. (2007). Screening potential therapies: lessons learned from new paradigms used in Parkinson disease. *Stroke* 38, 800–803. doi: 10.1161/01.STR.0000255227.96365.37

Trifonova, O. P., Maslov, D. L., Balashova, E. E., Urazgildeeva, G. R., Abaimov, D. A., Fedotova, E. Y., et al. (2020). Parkinson's Disease: available Clinical and Promising Omics Tests for Diagnostics, Disease Risk Assessment, and Pharmacotherapy Personalization. *Diagnostics* 10:339. doi: 10.3390/diagnostics10050339

Williams, T., Sorrentino, Z., Weinrich, M., Giasson, B. I., and Chakrabarty, P. (2020). Differential cross-seeding properties of tau and alpha-synuclein in mouse models of tauopathy and synucleinopathy. *Brain Commun.* 2:fcaa090. doi: 10.1093/braincomms/fcaa090

Yun, S. P., Kam, T.-I., Panicker, N., Kim, S., Oh, Y., Park, J. S., et al. (2018). Block of A1 astrocyte conversion by microglia is neuroprotective in models of Parkinson's disease. *Nat. Med.* 24, 931–938. doi: 10.1038/s41591-018-0051-5

Zeng, X. S., Geng, W. S., Jia, J. J., Chen, L., and Zhang, P. P. (2018). Cellular and Molecular Basis of Neurodegeneration in Parkinson Disease. *Front. Aging Neurosci.* 10:109. doi: 10.3389/fnagi.2018.00109

Conflict of Interest: The authors were the Chair (TM) and Co-Chair (ZM) of the PSG's "Motor Features Working Group" and in that capacity advise a variety of sponsors on clinical trial design related matters. ZM has received consulting fees from Global Kinetics Corporation, served as Medical Chief Officer for Neuraly, Inc., and holds shares of nQ Medical Inc., GB Sciences, and D&D Pharmatech, Inc. TM reports speaker honorarium from Abbvie, and International Parkinson and Movement Disorder Society; consultancies from CHDI Foundation/Management, Sunovion, Valeo Pharma, Roche, nQ Medical and Merz; advisory board from Abbvie; Biogen, Sunovion, Medtronic, and research funding from EU Joint Programme—Neurodegenerative Disease Research, uOBMRI, Roche, Ontario Research Fund, CIHR, MJFF, Parkinson Canada, PDF/PSG, LesLois Foundation, PSI Foundation, Parkinson Research Consortium and Brain Canada.

Publisher's Note: All claims expressed in this article are solely those of the authors and do not necessarily represent those of their affiliated organizations, or those of the publisher, the editors and the reviewers. Any product that may be evaluated in this article, or claim that may be made by its manufacturer, is not guaranteed or endorsed by the publisher.

Copyright © 2022 Mari and Mestre. This is an open-access article distributed under the terms of the Creative Commons Attribution License (CC BY). The use, distribution or reproduction in other forums is permitted, provided the original author(s) and the copyright owner(s) are credited and that the original publication in this journal is cited, in accordance with accepted academic practice. No use, distribution or reproduction is permitted which does not comply with these terms.

frontiers in Aging Neuroscience

ORIGINAL RESEARCH
published: 01 March 2022
doi: 10.3389/fnagi.2022.781480

Mild Cognitive Impairment Subtypes Are Associated With Peculiar Gait Patterns in Parkinson's Disease

Marianna Amboni[1,2], Carlo Ricciardi[3,4], Sofia Cuoco[1], Leandro Donisi[4,5], Antonio Volzone[1], Gianluca Ricciardelli[6], Maria Teresa Pellecchia[1], Gabriella Santangelo[7], Mario Cesarelli[3,4] and Paolo Barone[1]*

[1] Department of Medicine, Surgery and Dentistry, Center for Neurodegenerative Diseases (CEMAND), University of Salerno, Fisciano, Italy, [2] Istituto di Diagnosi e Cura (IDC) Hermitage-Capodimonte, Naples, Italy, [3] Department of Electrical Engineering and Information Technology, University of Naples Federico II, Naples, Italy, [4] Istituti Clinici Scientifici Maugeri Istituto di Ricovero e Cura a Carattere Scientifico (IRCCS), Telese Terme, Italy, [5] Department of Advanced Biomedical Sciences, University of Naples Federico II, Naples, Italy, [6] Department of Medicine, Azienda Ospedaliera Universitaria OO. RR. San Giovanni di Dio e Ruggi D'Aragona, Salerno, Italy, [7] Department of Psychology, University of Campania Luigi Vanvitelli, Caserta, Italy

OPEN ACCESS

Edited by:
Woon-Man Kung, Chinese Culture University, Taiwan

Reviewed by:
Saul Martinez-Horta, Hospital de la Santa Creu i Sant Pau, Spain
Davide Maria Cammisuli, University of Milan, Italy
Daniel Collerton, Newcastle University, United Kingdom

***Correspondence:**
Marianna Amboni
mamboni@unisa.it

Specialty section:
This article was submitted to Parkinson's Disease and Aging-related Movement Disorders, a section of the journal Frontiers in Aging Neuroscience

Received: *22 September 2021*
Accepted: *31 January 2022*
Published: *01 March 2022*

Citation:
Amboni M, Ricciardi C, Cuoco S, Donisi L, Volzone A, Ricciardelli G, Pellecchia MT, Santangelo G, Cesarelli M and Barone P (2022) Mild Cognitive Impairment Subtypes Are Associated With Peculiar Gait Patterns in Parkinson's Disease. Front. Aging Neurosci. 14:781480. doi: 10.3389/fnagi.2022.781480

Background: Mild cognitive impairment (MCI) is frequent in Parkinson's disease (PD) and represents a risk factor for the development of dementia associated with PD (PDD). Since PDD has been associated with disability, caregiver burden, and an increase in health-related costs, early detection of MCI associated with PD (PD-MCI) and its biomarkers is crucial.

Objective: Given that gait is considered a surrogate marker for cognitive decline in PD, the aim of this study was to compare gait patterns in PD-MCI subtypes in order to verify the existence of an association between specific gait features and particular MCI subtypes.

Methods: A total of 67 patients with PD were consecutively enrolled and assessed by an extensive clinical and cognitive examination. Based on the neuropsychological examination, patients were diagnosed as patients with MCI (PD-MCI) and without MCI (no-PD-MCI) and categorized in MCI subtypes. All patients were evaluated using a motion capture system of a BTS Bioengineering equipped with six IR digital cameras. Gait of the patients was assessed in the ON-state under three different tasks (a single task and two dual tasks). Statistical analysis included the *t*-test, the Kruskal–Wallis test with *post hoc* analysis, and the exploratory correlation analysis.

Results: Gait pattern was poorer in PD-MCI vs. no-PD-MCI in all tasks. Among PD-MCI subtypes, multiple-domain PD-MCI and amnestic PD-MCI were coupled with worse gait patterns, notably in the dual task.

Conclusion: Both the magnitude of cognitive impairment and the presence of memory dysfunction are associated with increased measures of dynamic unbalance, especially in dual-task conditions, likely mirroring the progressive involvement of posterior cortical networks.

Keywords: MCI (mild cognitive impairment), Parkinsion's disease (PD), gait analysis, gait pattern characteristics, cognitive decline

INTRODUCTION

Cognitive decline is frequent in Parkinson's disease (PD) even in the early stages, and it occurs as a dysfunction in executive, attention, memory, language, and visuospatial domains (Barone et al., 2011). The full spectrum of cognitive skills in PD spans from normal cognition, through mild cognitive impairment (PD-MCI), to PD dementia (PDD) (Aarsland et al., 2017). A recent meta-analysis has shown that PD-MCI has a pooled prevalence of 40%, which is associated with older age, lower education, longer disease duration, higher levodopa equivalent daily dose, more severe motor symptoms, postural instability/gait difficulty motor subtype, poorer quality of life, and higher levels of apathy and depression (Baiano et al., 2020). In addition, PD-MCI represents a risk factor for the development of PDD (Hoogland et al., 2017; Saredakis et al., 2019), with a higher rate of conversion to dementia in the amnestic PD-MCI subtype relative to the non-amnestic PD-MCI subtype (Chung et al., 2019). Since PDD has been associated with increased disability, caregiver burden, and risk for institutionalization with a consequent increase in health-related costs (Svenningsson et al., 2012), the early detection of MCI and its biomarkers is crucial for the identification of a PD subpopulation at a higher risk of worse disease progression (Mollenhauer et al., 2014).

Cognition and gait in PD appear to be closely related in complex ways. Gait is no longer considered merely an automated motor task but an activity requiring multiple cognitive skills, ensuring safe mobility (Amboni et al., 2013). In a previous study, we have shown that dysfunctions in specific gait parameters that are poorly responsive to levodopa and are highly sensitive to dual-task conditions are associated with PD-MCI, and visuospatial impairment is strongly associated with instability in patients with PD (Amboni et al., 2012). On the one hand, these findings are in line with the hypothesis that dopa-resistant gait components and cognitive dysfunction might share common non-dopaminergic network dysfunction (Nonnekes et al., 2016); on the other hand, they are consistent with the recent findings that balance control would rely on posterior cortical networks (Morris et al., 2019). Moreover, we have provided insight into the chronological relationship between gait and cognitive decline in patients with PD, by showing that step length during a cognitive task on medication predicts subsequent executive/attention dysfunction (Amboni et al., 2018).

More recently, several studies have focused on the ability of gait analysis to distinguish subjects with MCI and different types of dementias. In particular, Mc Ardle et al. (2020) have shown that wearable sensors-based gait analysis was able to identify subjects with MCI, dementia with Lewy bodies (DLB), Alzheimer's disease (AD), and PDD (Mc Ardle et al., 2020), whereas de Oliveira Silva et al. (2020) could distinct healthy controls and also patients with MCI and AD by using a videogrammetry system (de Oliveira Silva et al., 2020). In addition, gait-based machine learning approaches were able to discriminate different types of MCI, such as patients with PD-MCI and non-PD-MCI (Chen et al., 2020) or to detect the presence of MCI in PD (Ricciardi et al., 2020). Finally, Xie et al. (2019) employed an inertial-sensor-based wearable instrument to distinguish patients with amnestic MCI and cognitively normal subjects.

At present, studies comparing quantitative gait measures in PD-MCI subtypes are lacking. The main aim of this study was to compare gait patterns in PD-MCI subtypes in order to verify the existence of an association between specific gait features and particular MCI subtypes. This could shed further light both on the neurobiological substrate of different neuropsychological profiles and on the relationship between gait and cognition in PD.

MATERIALS AND METHODS

Study Design and Population

The study sample consisted of 67 patients with PD, consecutively enrolled between February 2018 and June 2021. Participants were selected from patients referred to the Movement Disorders Unit of the Institute for Diagnosis and Care Hermitage-Capodimonte of Naples and the Center for Neurodegenerative Diseases of the University of Salerno. All patients fulfilled the Movement Disorder Society (MDS) clinical diagnostic criteria for PD (Postuma et al., 2015). The inclusion criteria were as follows: age $\geq$ 45 years; Hoehn and Yahr (H&Y) score $\leq$ 3; disease duration $<$ 10 years; and antiparkinsonian treatment at a stable dosage during the previous 4 weeks. The exclusion criteria were as follows: gait requiring assistance; dementia according to the clinical diagnostic criteria for PDD (Emre et al., 2007); clinically significant comorbidities, including other neurological disorders, orthopedic diseases, or cardiovascular/respiratory diseases; anticholinergic or neuroleptic treatment; and brain surgery.

Standard Protocol Approvals, Registrations, and Patient Consent

This study was performed in accordance with the 1964 Declaration of Helsinki and was approved by Campania Sud, the reference ethics committee of the Center for Neurodegenerative Diseases of the University of Salerno. Written informed consent was obtained from all subjects.

Clinical and Cognitive Evaluations

All subjects were evaluated using a detailed assessment that included demographic, clinical, and anthropometric data. In addition, they completed the Italian version of the Montreal Cognitive Assessment (MoCA) and an extensive neuropsychological battery comprising the following tests: (1) the Rey Auditory 15-word Learning Test, immediate recall and delayed recall, and the Rey-Osterrieth complex figure delayed recall for the memory domain (Caltagirone et al., 1979; Caffarra et al., 2002); (2) the Stroop Color-Word Test and the Trail Making Test B-A for the attention domain (Giovagnoli et al., 1996; Barbarotto et al., 1998); (3) Phonological verbal fluency and the Clock Drawing Test for the executive domain (Caltagirone et al., 1979; Siciliano et al., 2016); (4) the Benton's Judgment of Line Orientation and the Constructional apraxia test for the visuospatial domain (Spinnler and Tognoni, 1987; Ferracuti et al., 2000); and (5) Actions and objects naming tests for the language domain (Capasso and Miceli, 2001).

The test scores were corrected for current normative values. All neuropsychological tests were administered to the patients during the pharmacological ON-state. The diagnosis of PD-MCI by level II category and PD-MCI subtyping were based on the neuropsychological assessment according to the Movement Disorders Society Task Force guidelines (Litvan et al., 2012).

Gait Analysis

All patients underwent gait analysis through a BTS Bioengineering system. The SMART DX is an optical system equipped with six IR cameras, two video cameras, two force plates, a set of passive markers, and an elaborator. The Davis protocol was used for all subjects, comprising the following four phases (Davis et al., 1991):

1. Collection of anthropometric measures of the patient (height, weight, and leg length).
2. Positioning of 22 reflective markers on specific points of the body of the patient.
3. The standing phase, consists of acquiring the patient while standing up on the force plate.
4. The walking phase on a straight path of 10 m during three different tasks including one single task and two dual tasks, namely:
    a. GAIT: normal gait (single task).
    b. MOT: walking while carrying a tray with two glasses filled with water (dual task).
    c. COG: walking while serial subtracting 7s starting from 100 (dual task).

Each task was performed four times.

Prior to commencing the trials, all participants were trained to walk at a normal pace at their usual speed, without any instructions to prioritize walking or performing the concomitant task. This procedure generated a report from which spatial and temporal parameters were extracted.

All participants were evaluated in the self-defined best "ON-state" while receiving their typical dopaminergic drugs.

Statistical Analysis

The statistical analysis was conducted by using Statistical Package for Social Science (SPSS, version 25). First, spatial and temporal variables of gait analysis were compared between patients with PD-MCI and with no-PD-MCI; then, they were compared among patients with no-PD-MCI, with single-domain PD-MCI, and with multiple-domain PD-MCI; and finally, they were compared among patients with no-PD-MCI, with non-amnestic PD-MCI, and with amnestic PD-MCI.

The *t*-test was used to compare two groups; since the analyzed samples contained more than 30 subjects, a normal distribution of the data is fair. Whereas, to compare three groups, given the small sample size for each group, the Kruskal–Wallis test was applied, and when significant, subsequent appropriate *post-hoc* tests were used in order to make the pairwise comparisons, thus correcting the *p*-values for multiple comparisons. Finally, an exploratory correlation study through the coefficient of Spearman was performed between spatiotemporal parameters and neuropsychological test scores.

Alpha significance level was set to $p < 0.05$ for all statistical analyses.

RESULTS

Thirty-two out of 67 patients were diagnosed as PD-MCI and 35 patients as no-PD-MCI. The 2 groups did not significantly differ on demographic and anthropometric variables, but they showed a trend toward significance on age ($p = 0.053$). When comparing clinical variables, the two groups differed significantly on the Movement Disorder Society Unified Parkinson's Disease Rating Scale (MDS-UPDRS) part III ($p = 0.014$) and, consequently, showed a trend toward significance on total MDS-UPDRS ($p = 0.050$) (**Table 1**).

Parkinson's Disease-Mild Cognitive Impairment vs. No-Parkinson's Disease-Mild Cognitive Impairment

Statistical *analyses* comparing all spatial and temporal gait parameters between patients with no-PD-MCI and PD-MCI are presented in **Table 2**.

In all three tasks, patients with PD-MCI exhibited poorer gait patterns when compared with patients with no-PD-MCI. In comparison with patients with no-PD-MCI, patients with PD-MCI exhibited shortened cycle and step length in all tasks ($p < 0.05$). In addition, in the MOT task, PD-MCI vs. no-PD-MCI showed increased stance phase and reduced swing and single-support phases ($p < 0.05$), whereas, in the COG task, they exhibited increased stance phase mainly due to longer double-support stance phase duration, increased swing and step variabilities, and reduced velocity ($p > 0.05$).

TABLE 1 | Comparison of demographic and clinical features between patients with Parkinson's disease (PD) without mild cognitive impairment (MCI) (no-PD-MCI) and with MCI (PD-MCI).

Variables	No-PD-MCI (*N* = 35)	PD-MCI (*N* = 32)	*p*-value
Age (years)	61.70 ± 7.36	65.70 ± 9.11	0.053
BMI	27.30 ± 2.95	28.2 ± 3.97	0.286
Disease duration (years)	4.46 ± 2.52	5.25 ± 2.50	0.207
Hoehn and Yahr	1.75 ± 0.41	1.92 ± 0.31	0.068
LEDD (mg)	495.00 ± 381.30	563.50 ± 380.20	0.465
MDS-UPDRS-Part I	6.54 ± 4.07	9.03 ± 7.07	0.088
MDS-UPDRS-Part II	6.97 ± 4.68	7.72 ± 5.64	0.556
MDS-UPDRS-Part III	20.1 ± 6.66	24.80 ± 8.65	**0.014**
MDS-UPDRS-Part IV	1.86 ± 3.02	1.44 ± 2.86	0.420
Total MDS-UPDRS	35.50 ± 12.10	43.00 ± 18.50	0.050

PD, Parkinson's Disease; MCI, Mild Cognitive Impairment; BMI, Body Mass Index; LEDD, Levodopa Equivalent Daily Dose; MDS-UPDRS, Movement Disorder Society Unified Parkinson's Disease Rating Scale.
Significant p-values are provided in bold.

TABLE 2 | Comparison of all gait parameters (mean ± *SD*) between patients with PD without MCI (no-PD-MCI) and with MCI (PD-MCI).

Features	Unit of measure	No-PD-MCI	PD-MCI	*p*-value
GAIT				
Cycle duration	s	1.10 ± 0.11	1.09 ± 0.10	0.800
Stance duration	s	0.66 ± 0.07	0.67 ± 0.08	0.849
Swing duration	s	0.44 ± 0.05	0.43 ± 0.04	0.303
Swing duration variability	s	0.05 ± 0.06	0.04 ± 0.02	0.377
Stance phase	%	59.90 ± 2.24	60.90 ± 1.64	0.054
Swing phase	%	39.60 ± 1.69	39.20 ± 1.62	0.279
Single-support phase	%	39.40 ± 2.60	39.20 ± 1.63	0.639
Double-support phase	%	10.20 ± 1.57	11.30 ± 3.29	0.074
Mean velocity	m/s	1.07 ± 0.15	0.99 ± 0.16	0.075
Mean velocity	% height/s	63.30 ± 9.01	60.20 ± 10.00	0.179
Cadence	steps/min	108.60 ± 12.60	110.80 ± 10.50	0.442
Cycle length	m	1.160 ± 0.12	1.07 ± 0.15	**0.007**
Cycle length	% height	69.70 ± 6.08	65.2 ± 10.13	**0.031**
Step length	m	0.56 ± 0.09	0.48 ± 0.13	**0.007**
Step length variability	m	0.17 ± 0.39	0.33 ± 0.54	0.169
Step width	m	0.09 ± 0.04	0.11 ± 0.07	0.312
MOT				
Cycle duration	s	1.09 ± 0.12	1.07 ± 0.10	0.403
Stance duration	s	0.66 ± 0.08	0.66 ± 0.07	0.903
Swing duration	s	0.44 ± 0.50	0.45 ± 0.19	0.677
Swing duration variability	s	0.04 ± 0.03	0.03 ± 0.02	0.715
Stance phase	%	60.14 ± 1.45	61.12 ± 2.20	**0.039**
Swing phase	%	39.86 ± 1.45	38.86 ± 2.20	**0.035**
Single-support phase	%	39.93 ± 1.59	38.85 ± 2.17	**0.026**
Double-support phase	%	11.37 ± 3.24	11.96 ± 2.81	0.431
Mean velocity	m/s	1.05 ± 0.15	0.98 ± 0.19	0.077
Mean velocity	% height/s	62.64 ± 8.88	59.22 ± 10.49	0.154
Cadence	steps/min	111.10 ± 12.32	112.80 ± 10.16	0.528
Cycle length	m	1.13 ± 0.13	1.03 ± 0.17	**0.013**
Cycle length	% height	67.73 ± 6.97	63.07 ± 10.45	**0.034**
Step length	m	0.55 ± 0.08	0.48 ± 0.13	**0.009**
Step length variability	m	0.10 ± 0.18	0.25 ± 0.57	0.163
Step width	m	0.10 ± 0.05	0.11 ± 0.06	0.850
COG				
Cycle duration	S	1.14 ± 0.14	1.17 ± 0.16	0.358
Stance duration	s	0.70 ± 0.09	0.74 ± 0.11	0.146
Swing duration	s	0.44 ± 0.05	0.44 ± 0.06	0.902
Swing duration variability	s	0.03 ± 0.02	0.06 ± 0.05	**0.022**
Stance phase	%	61.30 ± 1.89	62.70 ± 2.19	**0.009**
Swing phase	%	38.70 ± 1.90	38.60 ± 5.27	0.898
Single-support phase	%	38.30 ± 2.83	37.70 ± 2.21	0.339
Double-support phase	%	11.70 ± 1.66	13.90 ± 4.10	**0.007**
Mean velocity	m/s	0.95 ± 0.16	0.81 ± 0.18	**0.001**
Mean velocity	% height/s	57.30 ± 9.33	49.50 ± 11.20	**0.003**
Cadence	steps/min	106.60 ± 12.90	104.10 ± 13.50	0.450
Cycle length	m	1.07 ± 0.12	0.94 ± 0.18	**0.001**
Cycle length	% height	64.50 ± 6.47	57.50 ± 12.90	**0.006**
Step length	m	0.53 ± 0.08	0.41 ± 0.12	**0.000**
Step length variability	m	0.09 ± 0.24	0.37 ± 0.50	**0.006**
Step width	m	0.12 ± 0.12	0.12 ± 0.07	0.808

PD, Parkinson's Disease; MCI, Mild Cognitive Impairment; GAIT, normal gait; MOT, walking while carrying a tray with two glasses filled of water; COG, walking while serial subtracting 7s starting from 100.
Significant p-values are provided in bold.

No-Parkinson's Disease-Mild Cognitive Impairment vs. Single-Domain Parkinson's Disease-Mild Cognitive Impairment vs. Multiple-Domain Parkinson's Disease-Mild Cognitive Impairment

When subtyping PD-MCI according to the number of affected cognitive domains, 7 patients were categorized as single-domain PD-MCI and 25 patients as multiple-domain PD-MCI. **Table 3** shows the comparison of all spatial and temporal gait parameters among no-PD-MCI, single-domain PD-MCI, and multiple-domain PD-MCI with subsequent *post-hoc* tests when appropriate.

In all three tasks, step and cycle lengths showed statistically significant differences among the three groups ($p < 0.05$); *post hoc* comparisons revealed significantly shortened step and cycle lengths in multiple-domain PD-MCI vs. no-PD-MCI ($p < 0.05$). Moreover, in the MOT task, the stance phase, the swing phase, the single-support phase, and velocity resulted statistically different among the three groups; the *post hoc* analysis disclosed reduced swing and single-support phases in multiple-domain PD-MCI vs. no-PD-MCI ($p < 0.05$).

In the COG task, swing phase and step length variabilities, the stance and swing phases, the double-support phase, and velocity were significantly different among the three groups ($p < 0.05$); the *post hoc* analysis revealed increased swing phase and step length variabilities, longer stance and double-support phases, and reduced velocity in multiple-domain PD-MCI as compared to no-PD-MCI ($p < 0.05$).

No-Parkinson's Disease-Mild Cognitive Impairment vs. Amnestic Parkinson's Disease-Mild Cognitive Impairment vs. Non-amnestic Parkinson's Disease-Mild Cognitive Impairment

When subtyping PD-MCI based on the presence of memory impairment, 21 patients were diagnosed as amnestic PD-MCI and 11 patients as non-amnestic PD-MCI. **Table 4** shows the comparison of all spatial and temporal gait parameters among no-PD-MCI, amnestic PD-MCI, and non-amnestic PD-MCI using subsequent *post-hoc* tests when appropriate.

In all three tasks, the cycle length normalized for height resulted to be significantly different among the three groups ($p < 0.05$); in the GAIT and COG tasks, *post hoc* comparisons revealed significantly shortened cycle length normalized for height in amnestic PD-MCI vs. no-PD-MCI ($p < 0.05$). In addition, in the COG task, swing phase and step length variabilities, stance duration, stance and double-support phases, velocity, and cycle and step lengths were significantly different among the three groups ($p < 0.05$). The *post hoc* analysis revealed increased swing phase and step length variabilities, increased stance and double-support phases, reduced velocity, and shortened cycle and step lengths in amnestic PD-MCI as compared to no-PD-MCI ($p < 0.05$); the *post hoc* analysis also unveiled shortened step length in non-amnestic PD-MCI vs. no-PD-MCI ($p < 0.001$).

Exploratory Correlation Analysis Between Gait Parameters and Neuropsychological Test Scores

The correlation analysis was performed between the neuropsychological tests scores and the spatiotemporal gait parameters under the COG dual task, as these gait variables were most related to cognition in the previous analysis. Significant correlations were obtained for the global cognition scale MoCA, which correlated with the cycle duration ($r = -0.664$, $p = 0.004$), the stance duration ($r = -0.678$, $p = 0.003$), the stance phase ($r = -0.540$, $p = 0.025$), the swing phase ($r = 0.554$, $p = 0.021$), the single-support phase ($r = 0.554$, $p = 0.021$), the double-support phase ($r = -0.537$, $p = 0.026$), and the cadence ($r = -0.660$, $p = 0.004$).

Among the domain-specific neuropsychological tests, only the Benton's Judgment of Line Orientation Test exhibited a significant correlation (between 0.500 and 0.600) with a gait parameter, namely mean velocity ($r = 0.550$, $p < 0.001$) (**Supplementary Figure 1**).

DISCUSSION

To our knowledge, this is the first study evaluating quantitative walking parameters in MCI subtypes in PD. After confirming that PD-MCI is associated with the dysfunction of several spatial and temporal gait parameters, especially in dual-task conditions, in this study, we showed that multiple-domain PD-MCI and amnestic PD-MCI are coupled with worse gait patterns.

Comparison of Gait Features in Parkinson's Disease-Mild Cognitive Impairment vs. No-Parkinson's Disease-Mild Cognitive Impairment

Consistent with previous findings (Amboni et al., 2012, 2018; Morris et al., 2016, 2019), patients with PD-MCI as compared to patients with no-PD-MCI showed predominant dysfunctions on spatial gait features, i.e., reduced cycle and step length, which were evident in both single and dual task. Under dual-task conditions, PD-MCI exhibited increased stance phase, mainly in double support, and augmented the measures of variability, i.e., swing duration variability and step length variability, which are all indicators of dynamic instability (Plotnik et al., 2011). These findings further support the detrimental effect of the dual task on gait performance, especially on dynamic balance, in patients with cognitive decline (Amboni et al., 2013; Bishnoi and Hernandez, 2020; Ricciardi et al., 2020) with a subsequent increased risk of falling. In fact, the sensitizing role of dual task relies on its peculiar mechanism that leads to a competition for attention resources that collapse when a cognitive reserve is reduced (Amboni et al., 2013). It is worth noting that, since all patients were on medication during gait analysis, the observed gait variable dysfunctions may mirror their levodopa-resistant nature.

TABLE 3 | Comparison of all gait parameters (mean ± *SD*) among no-PD-MCI, single-domain PD-MCI, and multiple-domain PD-MCI.

Features	No-PD-MCI (0)	Single-domain PD-MCI (1)	Multiple-domain PD-MCI (2)	*p*-value Kruskal–wallis	*p*-value *post hoc*
GAIT					
Cycle duration	1.10 ± 0.11	1.09 ± 0.10	1.09 ± 0.10	0.986	
Stance duration	0.66 ± 0.07	0.66 ± 0.06	0.67 ± 0.08	0.998	
Swing duration	0.44 ± 0.05	0.44 ± 0.04	0.43 ± 0.03	0.692	
Swing duration variability	0.05 ± 0.06	0.05 ± 0.01	0.03 ± 0.02	0.101	
Stance phase	59.90 ± 2.24	60.10 ± 1.07	61.00 ± 1.70	0.159	
Swing phase	39.60 ± 1.69	39.90 ± 1.05	39.00 ± 1.70	0.337	
Single-support phase	39.40 ± 2.60	39.90 ± 1.05	39.00 ± 1.70	0.311	
Double-support phase	10.20 ± 1.57	10.20 ± 1.47	11.5 ± 3.56	0.279	
Mean velocity	1.07 ± 0.15	1.08 ± 0.08	0.98 ± 0.17	0.142	
Mean velocity% h/s	63.30 ± 9.01	64.00 ± 5.05	59.30 ± 10.7	0.266	
Cadence	108.60 ± 12.60	110.80 ± 9.67	110.80 ± 10.90	0.829	
Cycle length	1.16 ± 0.12	1.18 ± 0.04	1.05 ± 0.15	**0.020**	**2-0 0.032**
Cycle length % h	69.70 ± 6.08	69.30 ± 1.73	64.20 ± 11.00	**0.005**	**2-0 0.005**
Step length	0.56 ± 0.09	0.57 ± 0.07	0.46 ± 0.13	**0.012**	**2-0 0.015**
Step length variability	0.17 ± 0.39	0.13 ± 0.22	0.38 ± 0.59	0.263	
Step width	0.09 ± 0.04	0.10 ± 0.05	0.11 ± 0.07	0.933	
MOT					
Cycle duration	1.09 ± 0.12	1.05 ± 0.09	1.07 ± 0.10	0.632	
Stance duration	0.66 ± 0.08	0.63 ± 0.06	0.66 ± 0.07	0.478	
Swing duration	0.44 ± 0.50	0.42 ± 0.04	0.46 ± 0.21	0.391	
Swing duration variability	0.04 ± 0.03	0.03 ± 0.03	0.03 ± 0.02	0.381	
Stance phase	60.10 ± 1.45	59.50 ± 2.17	61.50 ± 2.07	**0.024**	1-2 0.096 0-2 0.064
Swing phase	39.90 ± 1.45	40.50 ± 2.17	38.50 ± 2.07	**0.019**	**2-0 0.050**
Single-support phase	39.90 ± 1.59	40.50 ± 2.19	38.50 ± 2.02	**0.015**	**2-0 0.039**
Double-support phase	11.40 ± 3.24	11.40 ± 3.39	12.10 ± 2.72	0.210	
Mean velocity	1.05 ± 0.15	1.12 ± 0.17	0.94 ± 0.19	**0.034**	2-0 0.088 2-1 0.119
Mean velocity % h/s	62.60 ± 8.90	66.50 ± 9.50	57.60 ± 10.15	**0.034**	2-0 0.105 2-1 0.101
Cadence	111.10 ± 12.30	115.33 ± 9.90	112.30 ± 10.30	0.665	
Cycle length	1.13 ± 0.13	1.16 ± 0.08	1.00 ± 0.17	**0.008**	**2-0 0.015**
Cycle length % h	67.70 ± 6.90	68.80 ± 5.70	61.70 ± 10.90	**0.003**	**2-0 0.003**
Step length	0.55 ± 0.08	0.56 ± 0.06	0.46 ± 0.13	**0.018**	**2-0 0.015**
Step length variability	0.10 ± 0.18	0.13 ± 0.22	0.28 ± 0.62	0.659	
Step width	0.10 ± 0.05	0.11 ± 0.06	0.11 ± 0.06	0.815	
COG					
Cycle duration	1.14 ± 0.14	1.18 ± 0.16	1.18 ± 0.16	0.677	
Stance duration	0.70 ± 0.09	0.72 ± 0.08	0.74 ± 0.11	0.396	
Swing duration	0.44 ± 0.05	0.46 ± 0.09	0.43 ± 0.05	0.998	
Swing duration variability	0.03 ± 0.02	0.05 ± 0.04	0.06 ± 0.05	**0.024**	**2-0 0.022**
Stance phase	61.30 ± 1.89	61.60 ± 2.21	62.90 ± 2.15	**0.019**	**2-0 0.015**
Swing phase	38.70 ± 1.90	43.60 ± 10.70	37.40 ± 2.02	**0.016**	2-0 0.061 2-1 0.052
Single-support phase	38.30 ± 2.83	38.70 ± 2.41	37.50 ± 2.14	0.137	
Double-support phase	11.70 ± 1.66	13.90 ± 3.65	13.90 ± 4.26	**0.030**	**2-0 0.039**
Mean velocity	0.95 ± 0.16	0.92 ± 0.12	0.79 ± 0.19	**0.002**	**2-0 0.001**
Mean velocity % h/s	57.30 ± 9.33	53.80 ± 7.57	48.50 ± 11.80	**0.008**	**2-0 0.006**
Cadence	106.50 ± 12.90	104.20 ± 12.90	104.10 ± 13.90	0.732	
Cycle length	1.07 ± 0.12	1.05 ± 0.09	0.92 ± 0.19	**0.002**	**2-0 0.002**
Cycle length % h	64.50 ± 6.47	62.1 ± 7.28	56.40 ± 13.80	**0.001**	**2-0 0.001**
Step length	0.53 ± 0.08	0.44 ± 0.10	0.40 ± 0.12	**0.000**	**2-0 0.000**
Step length variability	0.09 ± 0.24	0.39 ± 0.39	0.37 ± 0.53	**0.002**	**2-0 0.004**
Step width	0.12 ± 0.12	0.14 ± 0.11	0.11 ± 0.07	0.796	

No-PD-MCI, Patients with Parkinson's Disease without Mild Cognitive Impairment; PD-MCI, Patients with Parkinson's Disease with Mild Cognitive Impairment; GAIT, normal gait; MOT, walking while carrying a tray with two glasses filled of water; COG, walking while serial subtracting 7s starting from 100.
Significant p-values are provided in bold.

TABLE 4 | Comparison of all gait parameters (mean ± *SD*) among no-PD-MCI, amnestic PD-MCI, and non-amnestic PD-MCI.

Features	No-PD-MCI (0)	Amnestic PD-MCI (1)	Non-amnestic PD-MCI (2)	*p*-value Kruskal–wallis	*p*-value *post hoc*
GAIT					
Cycle duration	1.10 ± 0.11	1.11 ± 0.10	1.05 ± 0.10	0.272	
Stance duration	0.66 ± 0.07	0.68 ± 0.08	0.64 ± 0.06	0.235	
Swing duration	0.44 ± 0.05	0.43 ± 0.03	0.42 ± 0.05	0.337	
Swing duration variability	0.05 ± 0.06	0.04 ± 0.02	0.03 ± 0.02	0.995	
Stance phase	59.90 ± 2.24	61.1 ± 1.75	60.40 ± 1.33	0.147	
Swing phase	39.60 ± 1.69	38.90 ± 1.75	39.60 ± 1.32	0.324	
Single-support phase	39.40 ± 2.60	38.90 ± 1.76	39.70 ± 1.31	0.304	
Double-support phase	10.20 ± 1.57	11.80 ± 3.83	10.20 ± 1.53	0.121	
Mean velocity	1.07 ± 0.15	0.97 ± 0.18	1.04 ± 0.10	0.333	
Mean velocity % h/s	63.3 ± 9.01	59.10 ± 11.70	62.20 ± 5.41	0.368	
Cadence	108.60 ± 12.60	108.50 ± 10.10	115.00 ± 10.60	0.241	
Cycle length	1.16 ± 0.12	1.07 ± 0.17	1.09 ± 0.12	0.125	
Cycle length % h	69.7 ± 6.08	65.10 ± 11.70	65.40 ± 6.68	**0.022**	**1-0 0.034**
Step length	0.56 ± 0.10	0.48 ± 0.13	0.47 ± 0.14	0.065	
Step length variability	0.17 ± 0.39	0.34 ± 0.61	0.32 ± 0.42	0.254	
Step width	0.09 ± 0.04	0.09 ± 0.05	0.14 ± 0.09	0.508	
MOT					
Cycle duration	1.09 ± 0.12	1.09 ± 0.09	1.03 ± 0.10	0.220	
Stance duration	0.66 ± 0.08	0.68 ± 0.08	0.62 ± 0.05	0.116	
Swing duration	0.44 ± 0.50	0.47 ± 0.23	0.41 ± 0.05	0.204	
Swing duration variability	0.04 ± 0.03	0.03 ± 0.02	0.03 ± 0.02	0.928	
Stance phase	60.10 ± 1.45	61.50 ± 2.31	60.50 ± 1.91	0.174	
Swing phase	39.90 ± 1.45	38.50 ± 2.30	39.50 ± 1.91	0.157	
Single-support phase	39.90 ± 1.59	28.50 ± 2.28	39.50 ± 1.88	0.143	
Double-support phase	11.40 ± 3.24	12.20 ± 3.06	11.60 ± 2.35	0.387	
Mean velocity	1.05 ± 0.15	0.95 ± 0.22	1.01 ± 0.12	0.245	
Mean velocity % h/s	62.60 ± 8.90	58.10 ± 10.30	61.3 ± 6.59	0.311	
Cadence	111.10 ± 12.30	110.40 ± 9.00	117.60 ± 10.90	0.198	
Cycle length	1.13 ± 0.13	1.03 ± 0.19	1.05 ± 0.12	0.086	
Cycle length % h	67.70 ± 6.97	63.20 ± 12.10	62.90 ± 6.96	**0.022**	1-0 0.076 2-0 0.076
Step length	0.55 ± 0.08	0.48 ± 0.13	0.48 ± 0.12	0.072	
Step length variability	0.10 ± 0.18	0.27 ± 0.66	0.22 ± 0.34	0.637	
Step width	0.10 ± 0.05	0.10 ± 0.06	0.11 ± 0.06	0.839	
COG					
Cycle duration	1.14 ± 0.14	1.21 ± 0.15	1.11 ± 0.16	0.108	
Stance duration	0.70 ± 0.09	0.77 ± 0.10	0.69 ± 0.10	**0.048**	1-0 0.095
Swing duration	0.44 ± 0.05	0.45 ± 0.05	0.43 ± 0.07	0.356	
Swing duration variability	0.03 ± 0.02	0.06 ± 0.06	0.04 ± 0.02	**0.021**	**1-0 0.021**
Stance phase	61.30 ± 1.90	63.20 ± 1.9	61.80 ± 2.40	**0.013**	**1-0 0.009**
Swing phase	38.70 ± 1.90	38.50 ± 6.40	38.60 ± 1.90	0.129	
Single-support phase	38.30 ± 2.80	37.30 ± 2.20	38.60 ± 1.90	0.095	
Double-support phase	11.70 ± 1.70	14.1 ± 4.20	13.70 ± 4.00	**0.024**	**1-0 0.025**
Mean velocity	0.95 ± 0.16	0.79 ± 0.19	0.84 ± 0.17	**0.005**	**1-0 0.006**
Mean velocity % h/s	57.30 ± 9.30	48.70 ± 11.70	51.00 ± 10.50	**0.011**	**1-0 0.011**
Cadence	106.50 ± 12.90	100.90 ± 12.10	110.00 ± 14.60	0.127	
Cycle length	1.07 ± 0.12	0.94 ± 0.17	0.94 ± 0.22	**0.009**	**1-0 0.015**
Cycle length % h	64.50 ± 6.50	57.90 ± 13.10	56.70 ± 13.40	**0.004**	**1-0 0.006**
Step length	0.53 ± 0.08	0.40 ± 0.13	0.42 ± 0.10	**0.000**	**2-0 0.009 1-0 0.001**
Step length variability	0.09 ± 0.24	0.44 ± 0.57	0.23 ± 0.32	**0.001**	**1-0 0.001**
Step width	0.11 ± 0.12	0.11 ± 0.07	0.12 ± 0.08	0.800	

No-PD-MCI, Patients with Parkinson's Disease without Mild Cognitive Impairment; PD-MCI, Patients with Parkinson's Disease with Mild Cognitive Impairment; GAIT, normal gait; MOT, walking while carrying a tray with two glasses filled of water; COG, walking while serial subtracting 7s starting from 100.
Significant p-values are provided in bold.

Comparison of Gait Features in Parkinson's Disease-Mild Cognitive Impairment Subtypes

While comparing PD-MCI subtypes based on the number of affected cognitive domains, the magnitude of gait impairment resulted to be directly related to the severity of cognitive dysfunction. In particular, multiple-domain PD-MCI vs. no-PD-MCI showed impaired spatial gait measures, such as shortened step and cycle length, in all three tasks, and increased measures of dynamic unbalance, similar to raised variability measures and increased double-support phase, during dual tasks. On the contrary, single-domain PD-MCI as compared to no-PD-MCI did not display any significant difference on gait features neither in single nor in dual task. Nevertheless, the *post hoc* analysis did not reveal even any significant difference when comparing gait patterns in patients with single-domain PD-MCI and patients with multiple-domain PD-MCI, thus suggesting a spectrum of dysfunction concurrently involving gait and cognition spanning across cognitively intact patients with PD, patients with single-domain PD, and patients with multiple-domain PD.

When confronting PD-MCI subtypes based on the nature of the affected cognitive domain, such as the presence of memory dysfunction, patients with amnestic PD-MCI, as compared to patients with no-PD-MCI and patients with non-amnestic PD-MCI, mainly showed increased dynamic instability during the COG task, evidenced by augmented variability measures and increased double-support phase. In addition, patients with both amnestic PD-MCI and non-amnestic PD-MCI vs. patients with no-PD-MCI subjects displayed reduced step length during the COG task. Again, we might speculate on the pairwise comparisons and infer a grading of gait dysfunction that is the greatest in patients with amnestic PD-MCI, intermediate in patients with non-amnestic PD-MCI, and the smallest in patients with no-PD-MCI. The present findings would be consistent with the progression of neurodegeneration from the anterior to the posterior cortical areas, likely involving also non-dopaminergic networks (Devos et al., 2010), which expresses with the concurrent occurrence of peculiar gait and neuropsychological dysfunction (**Figure 1**).

As regards walking abnormalities, previous imaging studies (Beauchet et al., 2014; Lo et al., 2017) showed that dynamic steadiness is linked to posterior brain networks, whereas more recent findings suggested the involvement of widespread cortical areas important for sensory, cognitive, and motor functions (Jayakody et al., 2020). In fact, dynamic stability is a complex activity requiring integration and control of multiple components, such as the integration of different sensory information, postural adjustments, and motor planning. As concerns cognitive dysfunction, several studies in patients with PD have demonstrated that, as the cognitive decline progresses, the cortical volume, especially in temporoparietal regions, decreases with parallel decay on memory (Lee et al., 2010; Mak et al., 2015; Pereira et al., 2015; Yildiz et al., 2015). In addition, since both multiple-domain PD-MCI and amnestic PD-MCI have been associated with the increased risk of conversion to dementia (Janvin et al., 2006; Hoogland et al., 2017; Chung et al., 2019), the increased dynamic instability, especially in dual task, might represent a possible marker of progression toward PDD. Nevertheless, further longitudinal studies are needed to investigate this speculation.

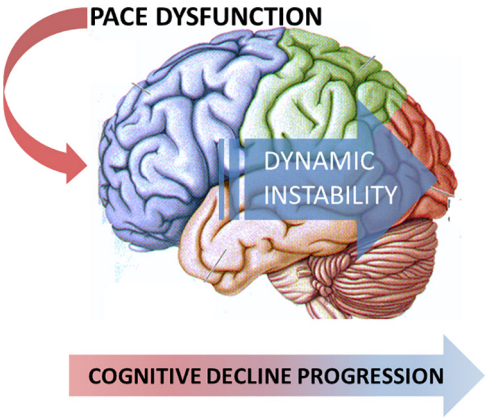

FIGURE 1 | Model of the neurodegeneration progression from the anterior to the posterior cortical areas that express the concurrent occurrence of peculiar gait and neuropsychological dysfunction.

Due to the cross-sectional design of this study, these findings cannot allow any assumption about a causative relationship between posterior cortical-based cognitive deficit and dynamic instability. In other words, our findings show an association between distinctive neuropsychological profiles and specific walking abnormalities, but they cannot establish whether peculiar cognitive dysfunctions can directly contribute to the expression of particular gait patterns.

As regards the exploratory correlation analysis between spatiotemporal gait parameters during the COG dual-task and neuropsychological tests scores, only the MoCA score, a global cognition rating, correlated with gait parameters mirroring dynamic instability, thus further supporting the relationship between the severity of cognitive dysfunction and the extent of gait impairment. In fact, when analyzing correlations between domain-specific neuropsychological tests and gait variables, we found only a correlation between a visuospatial test, namely, the Benton's Judgment of Line Orientation Test, and velocity, a raw measure underlain by multiple gait adaptations. The latter findings are not surprising since the relationship between gait and cognition would reflect common network dysfunction, expressing a collapse on both gait and cognitive skills, probably without strict correlations between walking variables and isolated cognitive test scores. Further studies on larger samples are needed to better explore this issue.

This study has some limitations. First, due to the relatively small sample size, we could not classify and, therefore, compare PD-MCI subtypes immediately according to the four categories, namely, single amnesic PD-MCI, single non-amnesic PD-MCI, multiple amnesic PD-MCI, and multiple non-amnesic PD. Although we recognized that this classification could directly show distinctive gait patterns in PD-MCI subtypes, we envisaged that the separate comparisons, i.e., single- vs. multiple-domain

PD-MCI and amnestic vs. non-amnestic PD-MCI, may represent a reliable method to capture the relative burden of the quantity and quality of cognitive dysfunction on walking features. Second, since the single-domain PD-MCI group included only seven patients, this could have introduced a bias in the interpretation of data; however, this low prevalence is fairly consistent with the findings of a recent meta-analysis reporting that single-domain subtype occurs only in about one-third of patients with PD-MCI (Baiano et al., 2020). Third, we did not include an age-matched control group in our analysis. This arguably could better highlight the difference between the PD-MCI subtypes; nevertheless, a direct comparison with a control group was beyond the purpose of this study. Finally, when comparing demographic and clinical features, we found that PD-MCI vs. no-PD-MCI showed a significant difference on MDS-UPDRS III and a trend toward significance on age, and this might have had an influence on our findings. Nevertheless, such differences reflect two of the main clinical features associated with MCI, namely, older age and more severe motor symptoms, as consistently reported in the literature (Baiano et al., 2020), suggesting a tight relationship among MCI, age, and more severe motor impairment. In other terms, the gait patterns observed in MCI and its subtypes reflect the contribution of all these features that are indissociable in a real-life clinical setting.

CONCLUSION

In conclusion, this study demonstrates that PD-MCI subtypes are associated with different gait patterns. Notably, both the magnitude of cognitive impairment and the presence of memory dysfunction are associated with the increased measures of dynamic unbalance, especially in dual-task condition, likely mirroring the progressive involvement of posterior cortical networks that are concurrently revealed by distinctive cognitive profiles and walking patterns. Additionally, our findings may suggest speculative clues for integrated therapeutic approaches, which could range from cognitive therapy (cognitive training interventions and use of cognitive pharmacological therapy) for improving walking performance to specific walking programs for enhancing cognitive function.

DATA AVAILABILITY STATEMENT

The raw data supporting the conclusions of this article will be made available by the authors, without undue reservation.

ETHICS STATEMENT

The studies involving human participants were reviewed and approved by Campania Sud, the Reference Ethics Committee of the Center for Neurodegenerative Diseases of the University of Salerno. The patients/participants provided their written informed consent to participate in this study.

AUTHOR CONTRIBUTIONS

MA and PB contributed to conception and design of the study. CR, SC, AV, and GR organized the database. CR, LD, and MC performed the statistical analysis. MA and CR wrote the first draft of the manuscript. MP and GS wrote sections of the manuscript. All authors contributed to manuscript revision, read, and approved the submitted version.

SUPPLEMENTARY MATERIAL

The Supplementary Material for this article can be found online at: https://www.frontiersin.org/articles/10.3389/fnagi.2022.781480/full#supplementary-material

Supplementary Figure 1 | Scatterplot representing the correlation between the Benton's Judgment of Line Orientation Test score and mean velocity under COG dual task.

REFERENCES

Aarsland, D., Creese, B., Politis, M., Chaudhuri, K. R., Ffytche, D. H., Weintraub, D., et al. (2017). Cognitive decline in Parkinson disease. *Nat. Rev. Neurol.* 13, 217–231.

Amboni, M., Barone, P., and Hausdorff, J. M. (2013). Cognitive contributions to gait and falls: evidence and implications. *Mov. Disord* 28, 1520–1533. doi: 10.1002/mds.25674

Amboni, M., Barone, P., Iuppariello, L., Lista, I., Tranfaglia, R., Fasano, A., et al. (2012). Gait patterns in Parkinsonian patients with or without mild cognitive impairment. *Mov. Disord* 27, 1536–1543. doi: 10.1002/mds.25165

Amboni, M., Iuppariello, L., Iavarone, A., Fasano, A., Palladino, R., Rucco, R., et al. (2018). Step length predicts executive dysfunction in Parkinson's disease: a 3-year prospective study. *J. Neurol.* 265, 2211–2220. doi: 10.1007/s00415-018-8973-x

Baiano, C., Barone, P., Trojano, L., and Santangelo, G. (2020). Prevalence and clinical aspects of mild cognitive impairment in Parkinson's disease: a meta-analysis. *Mov. Disord* 35, 45–54. doi: 10.1002/mds.27902

Barbarotto, R., Laiacona, M., Frosio, R., Vecchio, M., Farinato, A., and Capitani, E. (1998). A normative study on visual reaction times and two Stroop colour-word tests. *Ital. J. Neurol. Sci.* 19, 161–170. doi: 10.1007/BF00831566

Barone, P., Aarsland, D., Burn, D., Emre, M., Kulisevsky, J., and Weintraub, D. (2011). Cognitive impairment in nondemented Parkinson's disease. *Mov. Dis.* 26, 2483–2495.

Beauchet, O., Annweiler, C., Celle, S., Bartha, R., Barthélémy, J. C., and Roche, F. (2014). Higher gait variability is associated with decreased parietal gray matter volume among healthy older adults. *Brain Topogr.* 27, 293–295. doi: 10.1007/s10548-013-0293-y

Bishnoi, A., and Hernandez, M. E. (2020). Dual task walking costs in older adults with mild cognitive impairment: a systematic review and meta-analysis. *Aging Ment. Health* 6, 1–12. doi: 10.1080/13607863.2020.1802576

Caffarra, P., Vezzadini, G., Dieci, F., Zonato, F., and Venneri, A. (2002). Rey–Osterrieth complex figure: normative values in an Italian population sample. *Neurol. Sci.* 22, 443–447. doi: 10.1007/s100720200003

Caltagirone, C., Gainotti, G., Masullo, C., and Miceli, G. (1979). Validity of some neuropsychological test in the assessment of mental deterioration. *Acta Psychiatr. Scand.* 60, 50–56.

Capasso, R., and Miceli, G. (2001). *Esame Neuropsicologico per l'Afasia, ENPA*. Milan: Springer.

Chen, P. H., Lien, C. W., Wu, W. C., Lee, L. S., and Shaw, J. S. (2020). Gait-Based Machine Learning for Classifying Patients with Different Types of Mild Cognitive Impairment. *J. Med. Syst.* 44:107. doi: 10.1007/s10916-020-01578-7

Chung, S. J., Park, Y. H., Yun, H. J., Kwon, H., Yoo, H. S., Sohn, Y. H., et al. (2019). Clinical relevance of amnestic versus non-amnestic mild cognitive impairment subtyping in Parkinson's disease. *Eur. J. Neurol.* 26, 766–773. doi: 10.1111/ene.13886

Davis, R. B. III, Ounpuu, S., Tyburski, D., and Gage, J. R. (1991). A gait analysis data collection and reduction technique. *Hum. Mov. Sci.* 10, 575–587. doi: 10.1016/0167-9457(91)90046-z

de Oliveira Silva, F., Ferreira, J. V., Plácido, J., Chagas, D., Praxedes, J., Guimarães, C., et al. (2020). Gait analysis with videogrammetry can differentiate healthy elderly, mild cognitive impairment, and Alzheimer's disease: a cross-sectional study. *Exp. Geront.* 131:110816. doi: 10.1016/j.exger.2019.110816

Devos, D., Defebvre, L., and Bordet, R. (2010). Dopaminergic and non-dopaminergic pharmacological hypotheses for gait disorders in Parkinson's disease. *Fundam Clin. Pharmacol.* 24, 407–421. doi: 10.1111/j.1472-8206.2009.00798.x

Emre, M., Aarsland, D., Brown, R., Burn, D. J., Duyckaerts, C., Mizuno, Y., et al. (2007). Clinical diagnostic criteria for dementia associated with Parkinson's disease. *Mov. Disord.* 22, 1689–1707. doi: 10.1002/mds.21507

Ferracuti, S., Sacco, R., Cannoni, E., Hufty, A. M., Silvan, A. B., Hamster, K., et al. (2000). *Contributi per un Assessment Neuropsicologico di Benton AL*. Florence: Organizzazioni Speciali.

Giovagnoli, A. R., Del Pesce, M., Mascheroni, S., Simoncelli, M., Laiacona, M., and Capitani, E. (1996). Trail making test: normative values from 287 normal adult controls. *Ital. J. Neurol. Sci.* 17, 305–309. doi: 10.1007/BF01997792

Hoogland, J., Boel, J. A., de Bie, R. M. A., Geskus, R. B., Schmand, B. A., Dalrymple-Alford, J. C., et al. (2017). Mild cognitive impairment as a risk factor for Parkinson's disease dementia. *Mov. Disord* 32, 1056–1065. doi: 10.1002/mds.27002

Janvin, C. C., Larsen, J. P., Aarsland, D., and Hugdahl, K. (2006). Subtypes of mild cognitive impairment in Parkinson's disease: progression to dementia. *Mov. Disord.* 21, 1343–1349. doi: 10.1002/mds.20974

Jayakody, O., Breslin, M., Beare, R., Blumen, H. M., Srikanth, V. K., and Callisaya, M. L. (2020). Regional Associations of Cortical Thickness With Gait Variability-The Tasmanian Study of Cognition and Gait. *J. Gerontol. A Biol. Sci. Med. Sci.* 75, 1537–1544. doi: 10.1093/gerona/glaa118

Lee, J. E., Park, H. J., Song, S. K., Sohn, Y. H., Lee, J. D., and Lee, P. H. (2010). Neuroanatomic basis of amnestic MCI differs in patients with and without Parkinson disease. *Neurology* 75, 2009–2016. doi: 10.1212/WNL.0b013e3181ff96bf

Litvan, I., Goldman, J. G., Tröster, A. I., Schmand, B. A., Weintraub, D., Petersen, R. C., et al. (2012). Diagnostic criteria for mild cognitive impairment in Parkinson's disease: Movement Disorder Society Task Force guidelines. *Mov. Disord* 27, 349–356. doi: 10.1002/mds.24893

Lo, O. Y., Halko, M. A., Zhou, J., Harrison, R., Lipsitz, L. A., and Manor, B. (2017). Gait Speed and Gait Variability Are Associated with Different Functional Brain Networks. *Front. Aging Neurosci.* 29:390. doi: 10.3389/fnagi.2017.00390

Mak, E., Su, L., Williams, G. B., Firbank, M. J., Lawson, R. A., Yarnall, A. J., et al. (2015). Baseline and longitudinal grey matter changes in newly diagnosed Parkinson's disease: ICICLE-PD study. *Brain* 138, 2974–2986. doi: 10.1093/brain/awv211

Mc Ardle, R., Del Din, S., Galna, B., Thomas, A., and Rochester, L. (2020). Differentiating dementia disease subtypes with gait analysis: feasibility of wearable sensors? *Gait Posture* 76, 372–376. doi: 10.1016/j.gaitpost.2019.12.028

Mollenhauer, B., Rochester, L., Chen-Plotkin, A., and Brooks, D. (2014). What can biomarkers tell us about cognition in Parkinson's disease? *Mov. Disord* 29, 622–633. doi: 10.1002/mds.25846

Morris, R., Lord, S., Bunce, J., Burn, D., and Rochester, L. (2016). Gait and cognition: Mapping the global and discrete relationships in ageing and neurodegenerative disease. *Neurosci. Biobehav. Rev.* 64, 326–345. doi: 10.1016/j.neubiorev.2016.02.012

Morris, R., Martini, D. N., Smulders, K., Kelly, V. E., Zabetian, C. P., Poston, K., et al. (2019). Cognitive associations with comprehensive gait and static balance measures in Parkinson's disease. *Parkinsonism Relat. Disord.* 69, 104–110. doi: 10.1016/j.parkreldis.2019.06.014

Nonnekes, J., Timmer, M. H., de Vries, N. M., Rascol, O., Helmich, R. C., and Bloem, B. R. (2016). Unmasking levodopa resistance in Parkinson's disease. *Mov. Disord* 31, 1602–1609. doi: 10.1002/mds.26712

Pereira, J. B., Aarsland, D., Ginestet, C. E., Lebedev, A. V., Wahlund, L. O., Simmons, A., et al. (2015). Aberrant cerebral network topology and mild cognitive impairment in early Parkinson's disease. *Hum. Brain Mapp.* 36, 2980–2995. doi: 10.1002/hbm.22822

Plotnik, M., Giladi, N., Dagan, Y., and Hausdorff, J. M. (2011). Postural instability and fall risk in Parkinson's disease. Impaired dual tasking, pacing, and bilateral coordination of gait during the "ON" medication state. *Exp. Brain Res.* 210, 529–538. doi: 10.1007/s00221-011-2551-0

Postuma, R. B., Berg, D., Stern, M., Poewe, W., Olanow, C. W., Oertel, W., et al. (2015). MDS clinical diagnostic criteria for Parkinson's disease. *Mov. Disord.* 30, 1591–1601.

Ricciardi, C., Amboni, M., De Santis, C., and Ricciardelli, G. (2020). "Machine learning can detect the presence of Mild cognitive impairment in patients affected by Parkinson's Disease," in *2020 IEEE International Symposium on Medical Measurements and Applications*, (MeMeA), 1–6.

Saredakis, D., Collins-Praino, L. E., Gutteridge, D. S., Stephan, B. C. M., and Keage, H. A. D. (2019). Conversion to MCI and dementia in Parkinson's disease: a systematic review and meta-analysis. *Parkinsonism Relat. Disord* 2019, 30215–30219. doi: 10.1016/j.parkreldis.2019.04.020

Siciliano, M., Santangelo, G., D'Iorio, A., Basile, G., Piscopo, F., Grossi, D., et al. (2016). Rouleau version of the Clock Drawing Test: age- and education-adjusted normative data from a wide Italian sample. *Clin. Neuropsychol.* 30, 1501–1516. doi: 10.1080/13854046.2016.1241893

Spinnler, H., and Tognoni, G. (1987). Standardizzazione e taratura italiana di una batteria di test neuropsicologici. *Ital. J. Neurol. Sci.* 8, 1–120.

Svenningsson, P., Westman, E., Ballard, C., and Aarsland, D. (2012). Cognitive impairment in patients with Parkinson's disease: diagnosis, biomarkers, and treatment. *Lancet Neurol.* 11, 697–707. doi: 10.1016/S1474-4422(12)70152-7

Xie, H., Wang, Y., Tao, S., Huang, S., Zhang, C., and Lv, Z. (2019). Wearable Sensor-Based Daily Life Walking Assessment of Gait for Distinguishing Individuals With Amnestic Mild Cognitive Impairment. *Front. Aging Neurosci.* 11:285. doi: 10.3389/fnagi.2019.00285

Yildiz, D., Erer, S., Zarifoğlu, M., Hakyemez, B., Bakar, M., Karli, N., et al. (2015). Impaired cognitive performance and hippocampal atrophy in Parkinson disease. *Turk. J. Med. Sci.* 2015, 1173–1177.

Conflict of Interest: The authors declare that the research was conducted in the absence of any commercial or financial relationships that could be construed as a potential conflict of interest.

Publisher's Note: All claims expressed in this article are solely those of the authors and do not necessarily represent those of their affiliated organizations, or those of the publisher, the editors and the reviewers. Any product that may be evaluated in this article, or claim that may be made by its manufacturer, is not guaranteed or endorsed by the publisher.

Copyright © 2022 Amboni, Ricciardi, Cuoco, Donisi, Volzone, Ricciardelli, Pellecchia, Santangelo, Cesarelli and Barone. This is an open-access article distributed under the terms of the Creative Commons Attribution License (CC BY). The use, distribution or reproduction in other forums is permitted, provided the original author(s) and the copyright owner(s) are credited and that the original publication in this journal is cited, in accordance with accepted academic practice. No use, distribution or reproduction is permitted which does not comply with these terms.

frontiers in Aging Neuroscience

ORIGINAL RESEARCH
published: 04 March 2022
doi: 10.3389/fnagi.2022.807903

Unified Deep Learning-Based Mouse Brain MR Segmentation: Template-Based Individual Brain Positron Emission Tomography Volumes-of-Interest Generation Without Spatial Normalization in Mouse Alzheimer Model

Seung Yeon Seo[1,2†], Soo-Jong Kim[1,2,3,4†], Jungsu S. Oh[1], Jinwha Chung[1,5], Seog-Young Kim[1,5], Seung Jun Oh[1], Segyeong Joo[2] and Jae Seung Kim[1]*

[1] Department of Nuclear Medicine, Asan Medical Center, University of Ulsan College of Medicine, Songpa-gu, South Korea, [2] Department of Biomedical Engineering, Asan Medical Center, University of Ulsan College of Medicine, Songpa-gu, South Korea, [3] Department of Health Sciences and Technology, Samsung Advanced Institute for Health Sciences & Technology (SAIHST), Sungkyunkwan University, Songpa-gu, South Korea, [4] Department of Intelligent Precision Healthcare Convergence, Sungkyunkwan University, Suwon-si, South Korea, [5] Department of Convergence Medicine, Asan Medical Center, University of Ulsan College of Medicine, Songpa-gu, South Korea

Although skull-stripping and brain region segmentation are essential for precise quantitative analysis of positron emission tomography (PET) of mouse brains, deep learning (DL)-based unified solutions, particularly for spatial normalization (SN), have posed a challenging problem in DL-based image processing. In this study, we propose an approach based on DL to resolve these issues. We generated both skull-stripping masks and individual brain-specific volumes-of-interest (VOIs—cortex, hippocampus, striatum, thalamus, and cerebellum) based on inverse spatial normalization (iSN) and deep convolutional neural network (deep CNN) models. We applied the proposed methods to mutated amyloid precursor protein and presenilin-1 mouse model of Alzheimer's disease. Eighteen mice underwent T2-weighted MRI and ^{18}F FDG PET scans two times, before and after the administration of human immunoglobulin or antibody-based treatments. For training the CNN, manually traced brain masks and iSN-based target VOIs were used as the label. We compared our CNN-based VOIs with conventional (template-based) VOIs in terms of the correlation of standardized uptake value ratio (SUVR) by both methods and two-sample *t*-tests of SUVR % changes in target VOIs before and after treatment. Our deep CNN-based method successfully generated brain parenchyma mask and target VOIs, which shows no significant difference from conventional VOI methods in SUVR correlation analysis, thus establishing methods of template-based VOI without SN.

Keywords: mouse brain, deep convolutional-neural-network (CNN), inverse-spatial-normalization (iSN), skull-stripping, template-based volume of interest (VOI)

OPEN ACCESS

Edited by:
Woon-Man Kung,
Chinese Culture University, Taiwan

Reviewed by:
Zhen Fan,
Fudan University, China
Goo-Rak Kwon,
Chosun University, South Korea

***Correspondence:**
Jungsu S. Oh
jungsu_oh@amc.seoul.kr;
jungsu.oh@gmail.com

† These authors have contributed equally to this work and share first authorship

Specialty section:
This article was submitted to Alzheimer's Disease and Related Dementias, a section of the journal Frontiers in Aging Neuroscience

Received: *02 November 2021*
Accepted: *17 January 2022*
Published: *04 March 2022*

Citation:
Seo SY, Kim S-J, Oh JS, Chung J, Kim S-Y, Oh SJ, Joo S and Kim JS (2022) Unified Deep Learning-Based Mouse Brain MR Segmentation: Template-Based Individual Brain Positron Emission Tomography Volumes-of-Interest Generation Without Spatial Normalization in Mouse Alzheimer Model. Front. Aging Neurosci. 14:807903. doi: 10.3389/fnagi.2022.807903

INTRODUCTION

^{18}F-fluorodeoxyglucose positron emission tomography (^{18}F-FDG PET) is a useful imaging technique that enables the investigation of glucose metabolism-based functional imaging not only in human brains but also in mouse brains (Som et al., 1980; Bascunana et al., 2019).

Because mouse brains have different shapes and sizes, spatial normalization (SN) of individual brain PET and/or magnetic resonance imaging (MRI) onto standard anatomical spaces is required for objective statistical evaluation (Ma et al., 2005). Moreover, we can apply common volume-of-interest (VOI) templates for spatially normalized individual brain PET and MR images, which can be directly used without labor-intensive manual tracing and further can define individual brain-specific VOIs using inverse transformation of SN.

To do this, PET-based SN (i.e., the SN of individual PET images onto a ligand-specific PET template) can be conducted, but SN using PET alone may be vulnerable to local uptake changes, and disease-specific uptake patterns may not be optimal compared to SN based on anatomical information. Moreover, MR-based SN has been preferred to project individual brain PET and/or MR images into a template space (Ashburner and Friston, 1999; Gispert et al., 2003) because MRI is independent of changes in uptake patterns due to diseases in PET images and is advantageous in terms of anatomical precision.

In human brain studies, many neuroimage analysis tools including statistical parametric mapping (SPM), FMRIB Software Library (FSL—Woolrich et al., 2009; Jenkinson et al., 2012), and Elastix (Klein et al., 2010; Shamonin et al., 2014) have been widely used to perform SN. However, there are limitations in the use of these tools in mouse brain research due to various differences between human and mouse brains, such as the scale, shape, and image contrast (including distribution of gray matter).

In some human brain studies, the template used for SN was skull-stripped to avoid potential spatial misregistration due to soft tissues around the skull and brain (Acosta-Cabronero et al., 2008). Because most mouse brain templates have been based on skull-stripped images, skull-stripping has been considered a prerequisite for the SN of mouse brain MRI and/or PET images (Fein et al., 2006; Feo and Giove, 2019).

Template-based (also known as atlas-based) brain skull-stripping and brain VOI segmentation methods in mouse brain MRIs have shown accurate segmentation performance in prior studies (Nie and Shen, 2013; Feo and Giove, 2019). In these studies, PET or MRI images of individual brains were registered onto predefined templates of average mouse brains using affine transformations, occasionally followed by non-linear registration for more precise registration of the individual brains onto a brain template. Subsequently, the template brain skull-stripping results were used as starting (or seeding) points to define the individual brain skull-stripping and segmentation. Although these methods were relatively accurate, most of them were applied semiautomatically, not only resulting in SN with reduced reliability due to inter- and intrarater reliability issues (Yasuno et al., 2002; Kuhn et al., 2014) but also involving a time-consuming process. In addition, degradation of image quality may occur (in preserving the integrity of the original voxel intensities), because SN requires spatial transformation of the images onto a template, which, in turn, requires image intensity interpolation.

Recently, several deep learning (DL)-based skull-stripping methods have been studied. Hsu et al. (2020) devised a DL-based framework to automatically identify mouse brains in MR images. The brain mask was generated using MR image patches randomly cropped as input of the 2D U-Net architecture. For the evaluation of the model, a manually traced brain mask by an anatomical expert and a brain mask generated by the model were evaluated by Dice coefficient and Jaccard index and also positive predictive value and sensitivity, and the results showed better performance than conventional methods (Chou et al., 2011; Oguz et al., 2014; Liu et al., 2020). Similarly, De Feo et al. (2021) proposed multitask U-Net (MU-Net) to accomplish skull-stripping and region segmentation. 128 T2 MR image from 32 mice at 4 different ages were used as inputs to perform the training and validation of their proposed model, and five manually traced regions consisting of cortical, hippocampus, ventricular, striatum, and brain masks were used as labels. They demonstrated that MU-Net was able to effectively reduce the inter- and intrarater variability that occurs when skull-stripping and region segmentation are performed manually and showed better performance than the latest multiatlas segmentation methods (Jorge Cardoso et al., 2013; Ma et al., 2014).

By contrast, DL-based SN has been a very challenging problem involving many DL-based medical image preprocessing steps. Recently, an interesting DL-based "pseudo" PET template generation method (as the preprocessing of amyloid PET SN) has been developed using a convolutional autoencoder and a generative adversarial network (Kang et al., 2018). Nonetheless, this class of methods commonly generates a "pseudo" linearly or non-linearly registered individual brain onto the template using a convolutional neural network (CNN), instead of estimating the actual spatial transformation of the individual images onto the template, inevitably requiring additional efforts for the final SN. Another class of CNN-based spatial registration methods has been developed, called spatial transformer networks (STNs, Jaderberg et al., 2015). However, most of them are demonstrated as 2D registration and linear (rigid body or affine) transformation tools. Although a diffeomorphic transformer network was recently developed by Detlefsen et al. (2018) using a continuous piecewise affine-based transformation, its validation study as

Abbreviations: ^{18}F-FDG PET, ^{18}F-fluorodeoxyglucose positron emission tomography; SN, spatial normalization; MRI, magnetic resonance imaging; VOI, volume-of-interest; SPM, statistical parametric mapping; FSL, FMRIB Software Library; MU-Net, multitask U-Net; CNN, convolutional neural network; STNs, spatial transformer networks; iVOIs, inversely normalized VOIs; CT, computed tomography; FP-CIT, fluoro-propyl-carbomethoxy-iodophenyl-tropane; AC, attenuation correction; APP, amyloid precursor protein; PS, presenilin; AD, Alzheimer's disease; T2 MR, T2-weighted MR; nanoPM, nanoScan PET/MRI 1 Tesla; FOV, field of view; leaky ReLU, leaky rectified linear unit; Adam, adaptive moment estimation; DSC, Dice similarity coefficient; ASSD, average symmetric surface distance; SEN, sensitivity; and PPV, positive predictive value; true positive (TP); FN, false negative; TN, true negative; FP, false positive; SUV, standardized uptake value; SUVR, standardized uptake value ratio; VOI_{DL}, DL-generated mask; VOI_{iGT}, DL label mask; VOI_{GT}, template-based ground-truth VOI; % change, percentage change.

an SN tool for PET or MR images has not been conducted thus far. Notably, a DL model-based SN of Tau PET has been developed, which repeatedly estimates the sets of rigid and affine transformations using a CNN (Alvén et al., 2019). Although rigid and affine transformations have been implemented and evaluated, a non-rigid deformation has not been. Moreover, this class of methods requires a complicated CNN architecture consisting of cascades of many regression and spatial transformer layers, that is, numerous CNN parameters to be estimated. This reduces the clinical feasibility of these methods in that considerable amounts of data are required for effective training. Taken together, thus far, the SN problem in isolation has not been fully resolved, even in recent DL-based literature, including not only image segmentation (Delzescaux et al., 2010; Bai et al., 2012; Nie and Shen, 2013; Feo and Giove, 2019) but also apparently more challenging image generation methods, such as PET-based MR generation, to support SN (Choi et al., 2018). Considering that DL-based image generation can resolve these challenging issues of medical image preprocessing, we were motivated to reformulate the challenging SN problem into a more easily tractable image generation problem of VOI segmentation. To bridge SN and segmentation, we used the useful approach of iSN.

The iSN process involves the operation of generating the inverse of a deformation field and resampling a spatially normalized image back to the original space (i.e., an individual brain space—Ashburner et al., 2000). Indeed, we can generate inversely normalized VOIs (iVOIs) in an individual brain space by applying the iSN technique to VOI templates, as performed in many neuroimaging studies. Representatively, neuroimage analysis tools such as MarsBar and the deformation toolbox of SPM conduct iSN-based VOI analysis in an individual (native) brain space and have been frequently used in many brain PET quantification studies (Kim et al., 2010, 2015; Cho et al., 2014). Specifically, computed tomography (CT)-based SN was used for ^{18}F-fluoro-propyl-carbomethoxy-iodophenyl-tropane (^{18}F-FP-CIT) PET analysis using an inverse-transformed automatic anatomical label (AAL) VOI template in the two previous studies (Cho et al., 2014; Kim et al., 2015). Similarly, iVOIs were defined using the iSN of the Brodmann area or callosal template VOIs as the seed points for diffusion tensor tractography (Oh et al., 2007, 2009). Although attenuation correction (AC) can be conducted directly using CT transmission data in conventional PET/CT, it is difficult to conduct AC in PET/MR. To resolve this issue, several studies have employed template-based AC (Hofmann et al., 2009, 2011; Wollenweber et al., 2013; Sekine et al., 2016). In particular, Sekine et al. (2016) projected an atlas-based pseudo-CT to a patient-specific PET/MR space using iSN methods, which generated a single-head atlas from multiple CT head images.

Inspired by these concepts, we developed a new method for generating the iVOI labels of a deep CNN in an individual brain space. Consequently, we could reduce the abovementioned complicated problem of SN for the final VOI quantification into a much simpler problem of VOI segmentation in an individual brain space that is straightforwardly tractable for modern deep CNNs such as U-Net.

Recently, individual brain-specific VOI generation methods such as the FreeSurfer software (Lehmann et al., 2010), which can produce highly concordant VOIs with respect to manually traced ground-truth VOIs, have been frequently used in many neuroimaging studies. By contrast, template-based VOI approaches such as SPM present better or equal performance than individual brain space VOIs in terms of test–retest reproducibility (Palumbo et al., 2019). Considering this information, our previous iSN-based template VOI defined in the individual brain space leverages the strengths of both methods. Employing the iSN method, we can avoid image deformation, whose magnitude can be described using the Jacobian determinant of the deformation fields (Ashburner and Friston, 2000), which can lead to differences between the effective voxel sizes of PET images in individual brain and template spaces.

In this regard, herein, we propose a unified deep CNN framework designed to conduct not only mouse brain parenchyma segmentation (i.e., skull-stripping) but also to generate target VOIs (i.e., cortex, hippocampus, striatum, thalamus, and cerebellum) in an individual brain space. This is achieved using VOI templates defined in mouse MR or PET templates without SN onto a template to facilitate automatic precision ^{18}F-FDG PET analysis with MR-based iVOI using deep CNN. Consequently, we could reduce the relatively complicated brain VOI generation (by skull-stripping and SN) for precise PET quantification to a more tractable problem of DL-based iVOI segmentation in an individual brain space without conducting SN. This approach can avoid the complicated preprocessing steps for skull-stripping and SN for target VOI generation, which prevents the unwanted time-consuming process of semiautomatic skull-stripping and reduces the inter- and intrarater reliability issues. In addition, our DL-based method can perform precise PET image analysis without a network of complicated structures for SN (Kang et al., 2018; Alvén et al., 2019).

MATERIALS AND METHODS

Data

Eighteen transgenic mice expressing an amyloid precursor protein (APP) and presenilin (PS)-1 Alzheimer's disease (AD) mouse model underwent brain ^{18}F-FDG PET and T2-weighted MR (T2 MR) imaging. The PET images were acquired by nanoScan PET/MRI 1 Tesla (nanoPM—Mediso Medical Imaging Systems, Budapest, Hungary). Eighteen mice were anesthetized with isoflurane (1.5–2%) and received an intravenous injection of ^{18}F-FDG (0.15 m Ci/0.2 cc). After the acquisition of T2-weighted fast spin-echo MRI by nanoPM, the PET static images were acquired for 20 min in list mode and were reconstructed using the ordered subset maximum-likelihood algorithm using the abovementioned T2-weighted MR-based AC in the Nucline software (Reinvent Systems For Science & Discovery, Mundolsheim, France) in the following parameters—energy window: 250–750 keV; coincidence mode: 1–3; Tera-tomo3D full detector; regularization: normal; iteration x subset: 8 × 6; voxel size: 0.4 mm. The MR images were acquired using a Bruker 7.0T MRI Small Animal Scanner (Bruker, Massachusetts, United States) reconstruction options of T2 MR images as

follows—repetition time: 4,500 ms; echo time: 38.52 ms; field of view (FOV): 20 mm x 20 mm; slice thickness: 0.8 mm; matrix: 256 × 256; respiration gating was applied.

Preprocessing

All image preprocessing was performed using SPM 12 software (SPM12; Wellcome Trust Centre for Neuroimaging, London, United Kingdom) implemented in MATLAB R2018a (The MathWorks Inc.) and MRIcro (Chris Rorden, Columbia, South Carolina, United States). First, the acquired T2 MR images and ^{18}F-FDG PET images were converted from DICOM format to Analyze format using MRIcro. PET images were coregistered onto MR images to match different FOVs and slice thicknesses. For brain parenchyma mask generation DL, the entire mouse brain was manually traced using in-house software (Asan Medical Center Nuclear Medicine Toolkit for Image Quantification of Excellence—ANTIQUE) (Han et al., 2016). To achieve a more precise SN of the PET image, deformation fields generated by spatial normalizing T2 MR images to the T2 MR template were applied to the corresponding PET images. In addition, to obtain

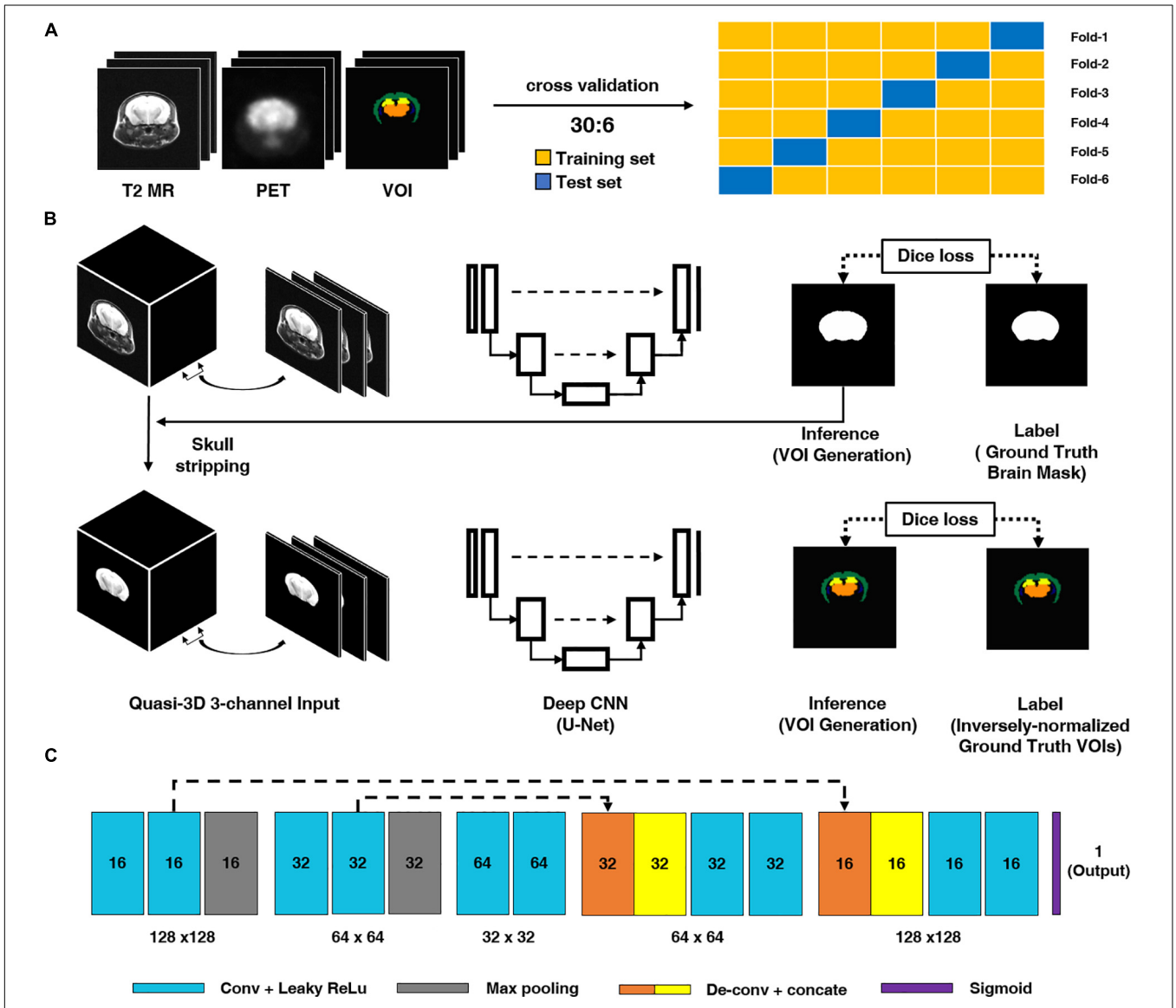

FIGURE 1 | Schematic diagram of the proposed deep CNN model. **(A)** We conducted six-fold crossvalidation for training and test set separation. **(B)** Brain parenchymal mask generation deep CNN. For model training, T2-weighted magnetic resonance (T2 MR) imaging was used as an input and manually traced brain mask was used as a label. **(B)** Inversely normalized volumes-of-interest (iVOIs) in individual brain space generation through deep CNN. For training the deep CNN model, skull-stripped T2 MR was used as the model input and iVOI template was used as the VOIs in individual space (the label for the model). **(C)** Deep CNN (i.e., U-Net) structure used in this study. The light blue box represents a 3 × 3 convolution and a leaky ReLU followed by max pooling, expressed in gray boxes. The orange and yellow boxes denote the 2 × 2 deconvolution and concatenation operations to increase the accuracy of localization. The dash arrow represents the copying skip connections. The dash arrow represents the copying skip connections. deep CNN, deep convolutional neural network.

a label image of the "iVOI template" (i.e., VOI template-based and iSN-based VOIs in an individual brain space) generation model, an inverse deformation field was generated and resampled from the VOI template space to the individual image space. This was achieved using the deformation toolbox of SPM, by performing inverse transformation of the deformation fields that map the individual brains onto the template brain. A quantitative evaluation of the PET images by a VOI template was used as the gold standard.

Deep Convolutional Neural Network

A CNN is a DL model that enables training while maintaining spatial information and thus allows efficient learning with a lighter architecture than a conventional neural network architecture, that is, fully connected network. For image feature extraction in a CNN, the filters (also known as kernels) in the convolution layers transform the input images into convolution-based filtered output images, termed feature maps. F represents a feature map and is calculated using the following equation:

$$\mathrm{F}[m,\ n] \ = \ (I * k)[m,\ n] \ = \ \sum_i \sum_j k[i,j]\, I[m-i, n-j]$$

where I represents the input image, k represents a kernel, and m and n represent the index of the rows and columns of the resulting matrix, respectively. For each convolution layer, the shape of the output data is changed according to the filter size, stride, and max pooling size and if zero-padding is applied or not. In this study, we used a quasi-3D U-Net for the deep CNN architecture and an input comprising three consecutive slices for the T2 MR images to generate a brain mask for skull-stripping and an iVOI template in an individual space, as illustrated in **Figure 1**. Specifically, we used three consecutive slice-based multichannel

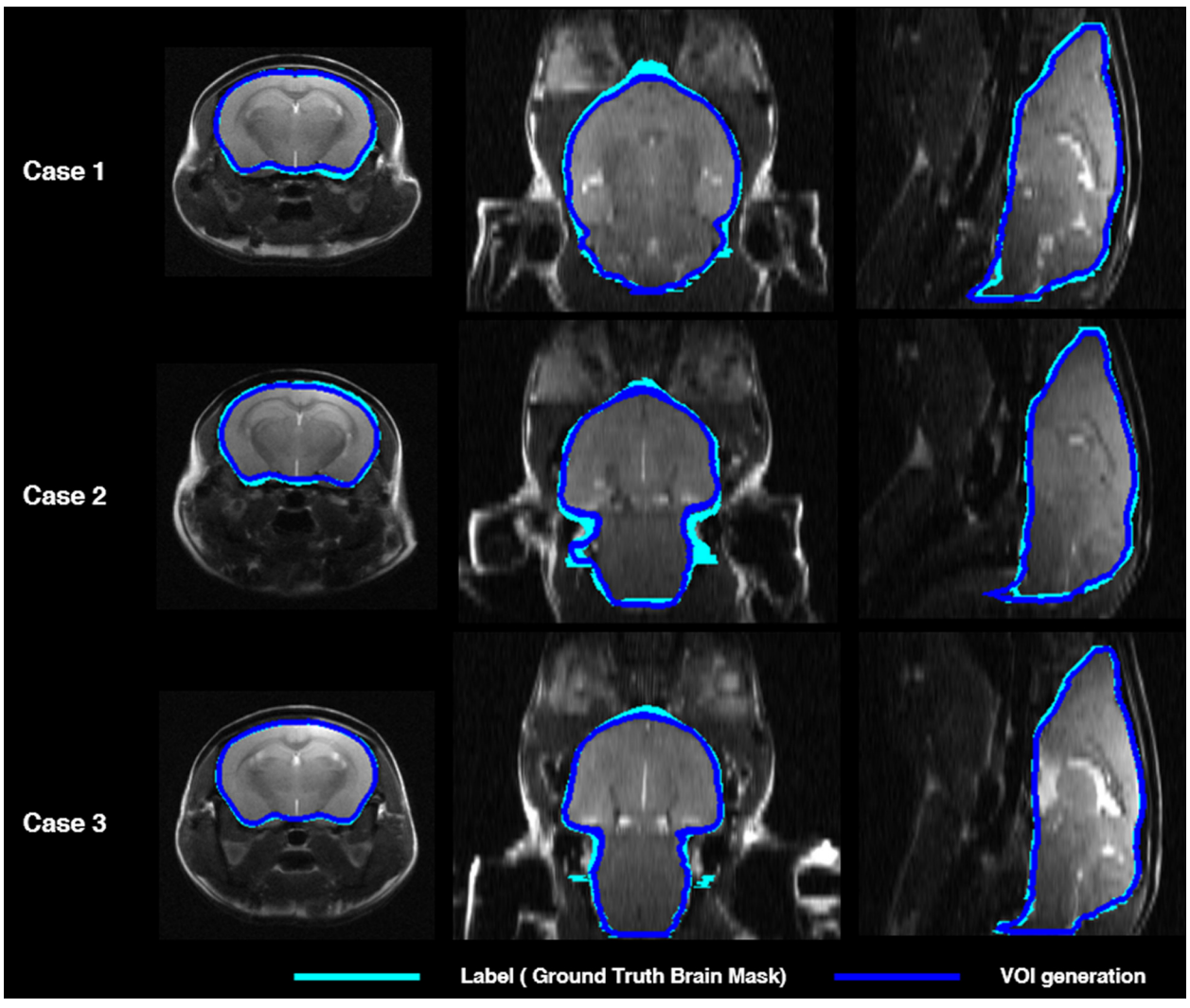

FIGURE 2 | Comparison of mouse brain parenchyma mask contours between manually traced brain mask (light blue) and deep CNN-predicted brain mask (blue) in three cases. The left shows the axial plane, the middle the coronal plane, and the right shows the sagittal plane. deep CNN, deep convolutional neural network.

inputs for the generation of each VOI slice; this 2D-like approach can generate as large amount of training data, as a 2D approach (see **Supplementary Material** for the comparison of the results of the quasi-3D and 2D approaches). We believe that such an approach can additionally overcome the limitations of the small amounts of mouse data. Moreover, the consecutive slice-based information allows the U-Net architecture to generate a highly continuous VOI by referring to the information of contiguous slices. U-Net consists of an end-to-end CNN architecture using a contracting path of the images and an expanding path for localization and residual learning of images to output layers. The contraction path consists of a 3 × 3 convolution followed by a 2 × 2 max pooling using a leaky rectified linear unit (leaky ReLU) as the activation function. The expansion path consists of a 2 × 2 deconvolution for upsampling and a 3 × 3 convolution using a leaky ReLU after concatenating with the context captured in the contraction path to increase the accuracy of localization. To train a DL CNN for skull-stripping mask generation, the abovementioned consecutive axial slices of T2 MR images were used as multichannel input, and manually traced binary brain masks were used as labels. A similar qausi-3D approach was also used in the training of iVOI template generation model, where an iVOI template in an individual space was used as the label. As the U-Net input, the skull-stripping mask generation model and the iVOI template generation model used 70 slices of transaxial MR and the corresponding skull-stripped MR, respectively, and the input dimension was 70 slices × N, 128, 128, 3 channel, where N is the number of mice used in the training set.

To overcome the small amount of data available for training set, data augmentation was performed through shift, rotation, and shear transformations. We used a Dice loss function and an adaptive moment estimation (Adam) optimizer to fit deep CNN parameters. The training was performed with an initial learning rate of 1e-5 with 25 batches. Our deep CNN model was implemented using Keras (version 2.2.4)-based code in the Python programming language with a backbone of TensorFlow (version 1.12.0) running on a GeForce NVIDIA GTX 1080 GPU and an Intel® Xeon® E5-2640 CPU. To regularize the generated

TABLE 1 | Our unified deep neural network assessment through the mean and standard deviation of Dice similarity coefficient (DSC), average symmetric surface distance (ASSD) (mm), sensitivity (SEN), and positive predictive value (PPV) between DL labels and DL-generated brain masks and inversely normalized target VOIs (cortex, hippocampus, striatum, thalamus, and cerebellum) in six-fold crossvalidation.

	N-fold	Brain mask	Cortex	Hippocampus	Striatum	Thalamus	Cerebellum
DSC	Fold-1	0.96 ± 0.01	0.78 ± 0.02	0.68 ± 0.2	0.62 ± 0.18	0.76 ± 0.12	0.66 ± 0.05
	Fold-2	0.95 ± 0.01	0.78 ± 0.01	0.76 ± 0.07	0.72 ± 0.03	0.72 ± 0.11	0.69 ± 0.04
	Fold-3	0.96 ± 0.01	0.79 ± 0.01	0.66 ± 0.1	0.66 ± 0.04	0.74 ± 0.11	0.7 ± 0.01
	Fold-4	0.98 ± 0.02	0.77 ± 0.04	0.74 ± 0.08	0.74 ± 0.11	0.78 ± 0.03	0.72 ± 0.03
	Fold-5	0.96 ± 0.01	0.77 ± 0.02	0.68 ± 0.13	0.75 ± 0.08	0.77 ± 0.08	0.68 ± 0.02
	Fold-6	0.98 ± 0.02	0.75 ± 0.02	0.61 ± 0.13	0.59 ± 0.06	0.76 ± 0.12	0.69 ± 0.02
	Total	0.97 ± 0.01	0.77 ± 0.02	0.69 ± 0.14	0.68 ± 0.13	0.76 ± 0.01	0.71 ± 0.03
ASSD (mm)	Fold-1	0.01 ± 0.00	0.08 ± 0.01	0.11 ± 0.06	0.2 ± 0.13	0.12 ± 0.03	0.12 ± 0.01
	Fold-2	0.01 ± 0.00	0.09 ± 0.0	0.12 ± 0.06	0.08 ± 0.01	0.09 ± 0.01	0.09 ± 0.01
	Fold-3	0.01 ± 0.0	0.08 ± 0.0	0.11 ± 0.04	0.1 ± 0.01	0.02 ± 0.04	0.11 ± 0.01
	Fold-4	0.02 ± 0.01	0.09 ± 0.01	0.12 ± 0.07	0.11 ± 0.04	0.04 ± 0.02	0.05 ± 0.01
	Fold-5	0.01 ± 0.00	0.09 ± 0.01	0.12 ± 0.08	0.1 ± 0.02	0.12 ± 0.01	0.07 ± 0.01
	Fold-6	0.01 ± 0.0	0.09 ± 0.0	0.16 ± 0.08	0.11 ± 0.02	0.22 ± 0.08	0.15 ± 0.02
	Total	0.01 ± 0.00	0.17 ± 0.0	0.12 ± 0.07	0.12 ± 0.06	0.1 ± 0.00	0.01 ± 0.00
SEN	Fold-1	0.91 ± 0.02	0.76 ± 0.05	0.67 ± 0.29	0.6 ± 0.15	0.68 ± 0.02	0.61 ± 0.05
	Fold-2	0.94 ± 0.02	0.81 ± 0.04	0.66 ± 0.11	0.6 ± 0.06	0.65 ± 0.05	0.64 ± 0.12
	Fold-3	0.93 ± 0.02	0.77 ± 0.03	0.53 ± 0.19	0.65 ± 0.08	0.69 ± 0.05	0.71 ± 0.14
	Fold-4	0.97 ± 0.02	0.73 ± 0.06	0.7 ± 0.15	0.65 ± 0.14	0.69 ± 0.01	0.75 ± 0.05
	Fold-5	0.88 ± 0.04	0.78 ± 0.07	0.55 ± 0.22	0.56 ± 0.12	0.66 ± 0.12	0.68 ± 0.08
	Fold-6	0.87 ± 0.01	0.72 ± 0.07	0.52 ± 0.25	0.58 ± 0.08	0.64 ± 0.02	0.72 ± 0.07
	Total	0.92 ± 0.02	0.76 ± 0.06	0.61 ± 0.22	0.61 ± 0.16	0.67 ± 0.05	0.69 ± 0.09
SPE	Fold-1	1.0 ± 0.0	1.0 ± 0.0	1.0 ± 0.0	1.0 ± 0.0	0.99 ± 0.0	0.99 ± 0.0
	Fold-2	1.0 ± 0.0	1.0 ± 0.0	1.0 ± 0.0	1.0 ± 0.0	0.99 ± 0.0	0.99 ± 0.00
	Fold-3	1.0 ± 0.0	1.0 ± 0.0	1.0 ± 0.0	1.0 ± 0.0	0.99 ± 0.0	1.0 ± 0.0
	Fold-4	1.0 ± 0.0	1.0 ± 0.0	1.0 ± 0.0	1.0 ± 0.0	1.0 ± 0.0	1.0 ± 0.0
	Fold-5	1.0 ± 0.0	1.0 ± 0.0	1.0 ± 0.0	1.0 ± 0.0	1.0 ± 0.0	1.0 ± 0.0
	Fold-6	1.0 ± 0.0	1.0 ± 0.0	1.0 ± 0.0	1.0 ± 0.0	1.0 ± 0.0	1.0 ± 0.0
	Total	1.0 ± 0.0	1.0 ± 0.0	1.0 ± 0.0	1.0 ± 0.0	0.99 ± 0.0	0.99 ± 0.0
PPV	Fold-1	0.98 ± 0.01	0.8 ± 0.03	0.65 ± 0.14	0.88 ± 0.04	0.73 ± 0.01	0.68 ± 0.03
	Fold-2	0.99 ± 0.01	0.76 ± 0.02	0.67 ± 0.06	0.81 ± 0.03	0.8 ± 0.06	0.78 ± 0.07
	Fold-3	0.99 ± 0.0	0.8 ± 0.02	0.67 ± 0.09	0.82 ± 0.05	0.78 ± 0.03	0.71 ± 0.03
	Fold-4	0.99 ± 0.0	0.81 ± 0.01	0.6 ± 0.03	0.8 ± 0.06	0.82 ± 0.03	0.65 ± 0.02
	Fold-5	0.99 ± 0.01	0.76 ± 0.03	0.72 ± 0.11	0.8 ± 0.04	0.77 ± 0.03	0.74 ± 0.03
	Fold-6	0.99 ± 0.0	0.8 ± 0.05	0.58 ± 0.07	0.76 ± 0.01	0.78 ± 0.02	0.68 ± 0.04
	Total	0.99 ± 0.0	0.79 ± 0.04	0.65 ± 0.1	0.81 ± 0.06	0.78 ± 0.03	0.71 ± 0.01

mask by the deep CNN, we conducted postprocessing in several steps, different from other studies that used complicated postprocessing methods such as graph cuts (Jimenez-Carretero et al., 2019; Kim et al., 2020; Hu et al., 2021). First, the mask predicted by DL was converted into a binary mask, and erosion and dilation were sequentially performed (also known as the "open" operator) to remove noisy false positives (FPs). Subsequently, 3D-connected component analysis-based kill-islands and fill-holes were conducted to reduce FPs and false negatives (FNs), respectively.

Performance Evaluation

To avoid overfitting issue and also to increase the generalization ability of the deep CNN, we conducted six-fold crossvalidation for training and test set separation. Of a total 36 samples obtained by 2 scans before and after treatment in 18 mice, 30 samples (15 mice × 2 scans) were used as the training set. The remaining 6 samples (3 mice × 2 scans) were used as the testing set in each fold of the training or test set pair to ensure that the slices of the same mouse are not split as training or test samples. To assess the concordance between predicted and label masks, we measured the Dice similarity coefficient (DSC), average symmetric surface distance (ASSD), sensitivity (SEN), and positive predictive value (PPV). DSC is the most representative indicator used for image segmentation evaluation. It directly compares the results of the two image segmentations, which indicate their similarity. The average symmetrical surface distance is the average of all distances from a point at the boundary of the machine segment region to the boundary of the ground truth. The SEN is defined as the proportion of true positive (TP) results among TP and FN. The SPE is defined as the proportion of true negative (TN) among TN and FP. PPV is defined as the proportion of TP among TP and FP. Formulas are provided for the five methods as follows, where P is the predicted mask of our network, and G is the label used in deep CNN (See following equations for the details).

$$Dice\ Similarity\ Coefficient\ =\ \frac{2\,|P \cap G|}{|P| + |G|},$$

$$Average\ Symmetric\ Surface\ Distance$$

$$= \frac{\sum_{m\in\partial(M)} \min_{g\in\partial(G)} \|p-g\| \sum_{g\in\partial(G)} \min_{m\in\partial(M)} \|g-p\|}{|\partial\,(P)| + |\partial\,(G)|}$$

$$Sensitivity\ =\ \frac{TP}{\mathrm{TP}\ +\ \mathrm{FN}},$$

$$Specificity\ =\ \frac{\mathrm{TN}}{\mathrm{TN}\ +\ \mathrm{FP}},$$

$$Positive\ Precitive\ Value\ =\ \frac{\mathrm{TP}}{\mathrm{TP}\ +\ \mathrm{FP}}.$$

Standardized uptake value (SUV), the most representative and simplest method of determining activities in PET images, is widely used for PET (semi)quantitative analysis. SUV can be

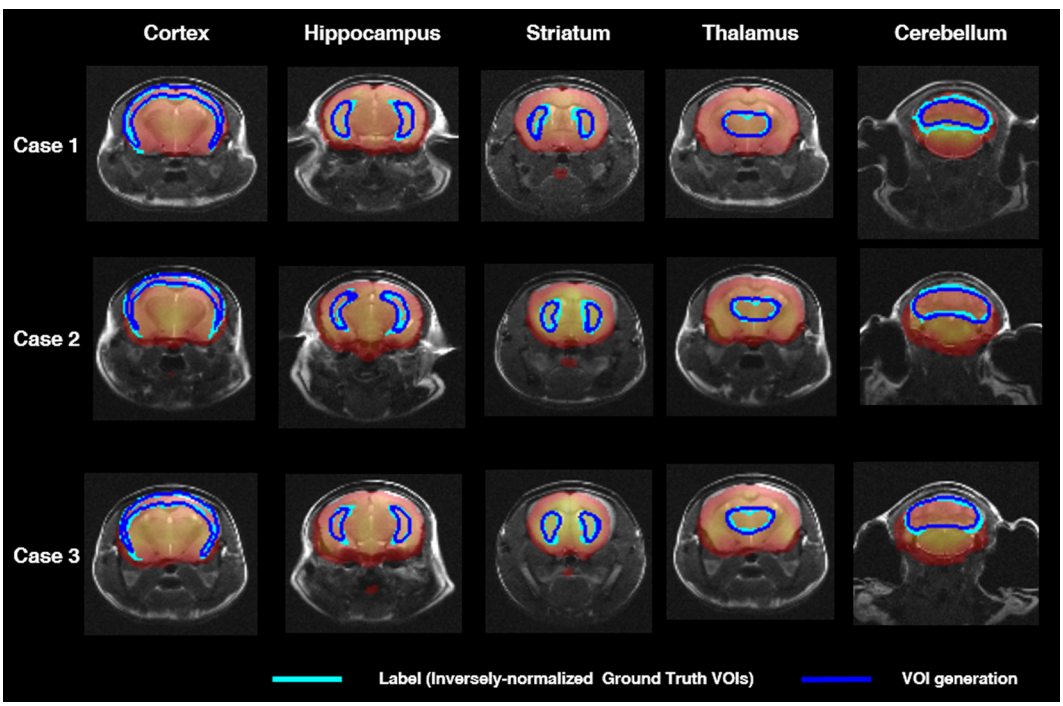

FIGURE 3 | Segmentation comparison of target VOIs (i.e., cortex, hippocampus, striatum, thalamus, cerebellum) in axial plane of three mice. The light blue contour represents deep learning label masks which are iVOI templates. The blue contour represents an iVOI template in an individual space generated by the proposed deep CNN. iVOI, inversely normalized VOI; deep CNN, deep convolutional neural network.

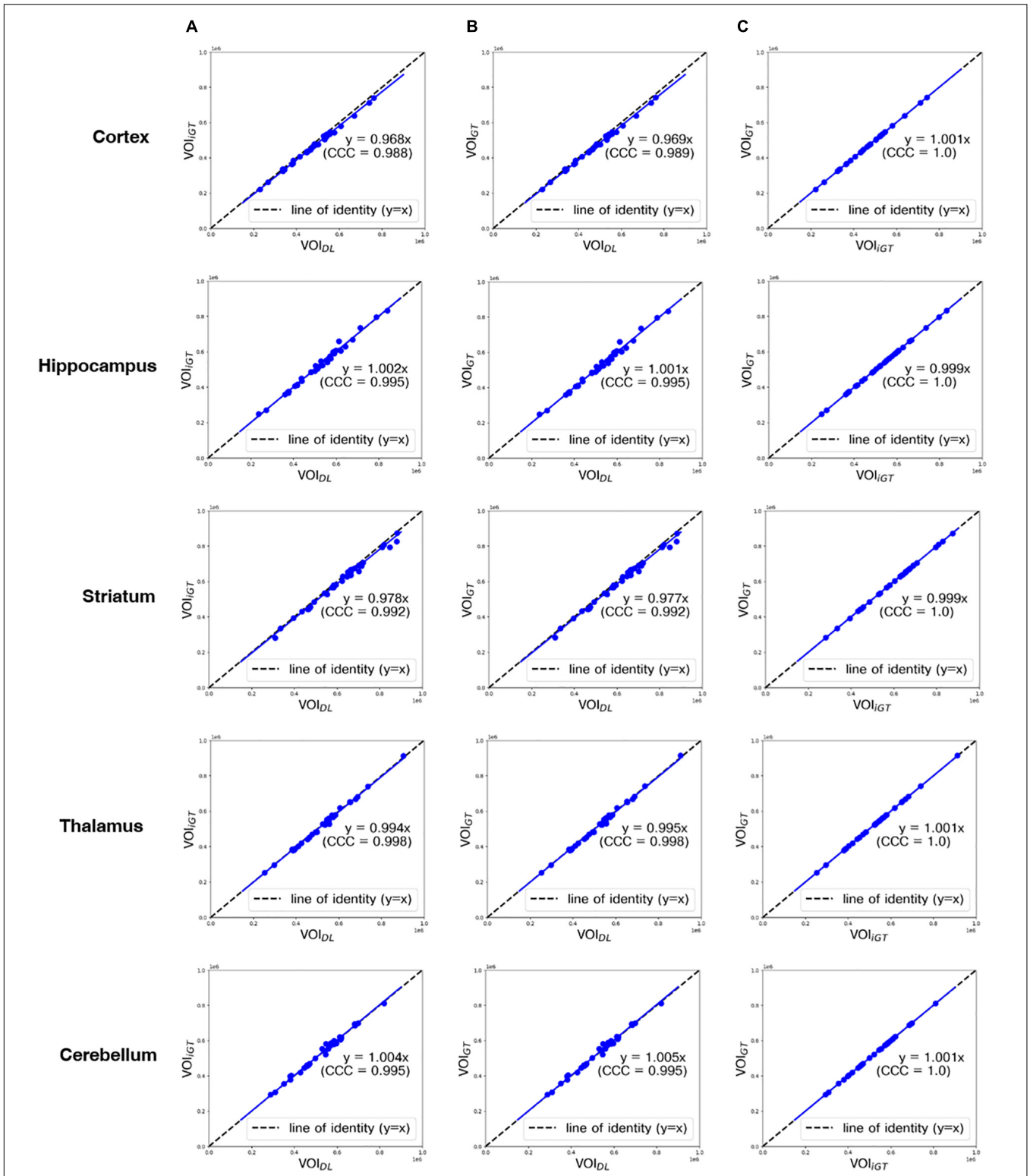

FIGURE 4 | Correlation analysis between all mean counts (blue dot) obtained using VOI_{DL}, VOI_{iGT}, and VOI_{GT} in all target VOIs from the first to the fifth row (cortex, hippocampus, striatum, thalamus, and cerebellum, respectively). CCC represents a measure of reliability based on covariation and correspondence. The line of identity (dashed line) is depicted as a reference line. Cortex, hippocampus, striatum, thalamus, and cerebellum are represented sequentially from the top row. **(A)** Correlation analysis between each mean count obtained using VOI_{DL} and VOI_{iGT}. **(B)** Correlation analysis between each mean count obtained using VOI_{DL} and VOI_{GT}. **(C)** Correlation analysis between each mean count obtained using VOI_{iGT} and VOI_{GT} VOI_{DL}, deep-learning generated-VOI; VOI_{iGT}, deep learning (inverse-normalized ground-truth) label VOI; VOI_{GT}, template-based ground-truth VOI; CCC, concordance correlation coefficient.

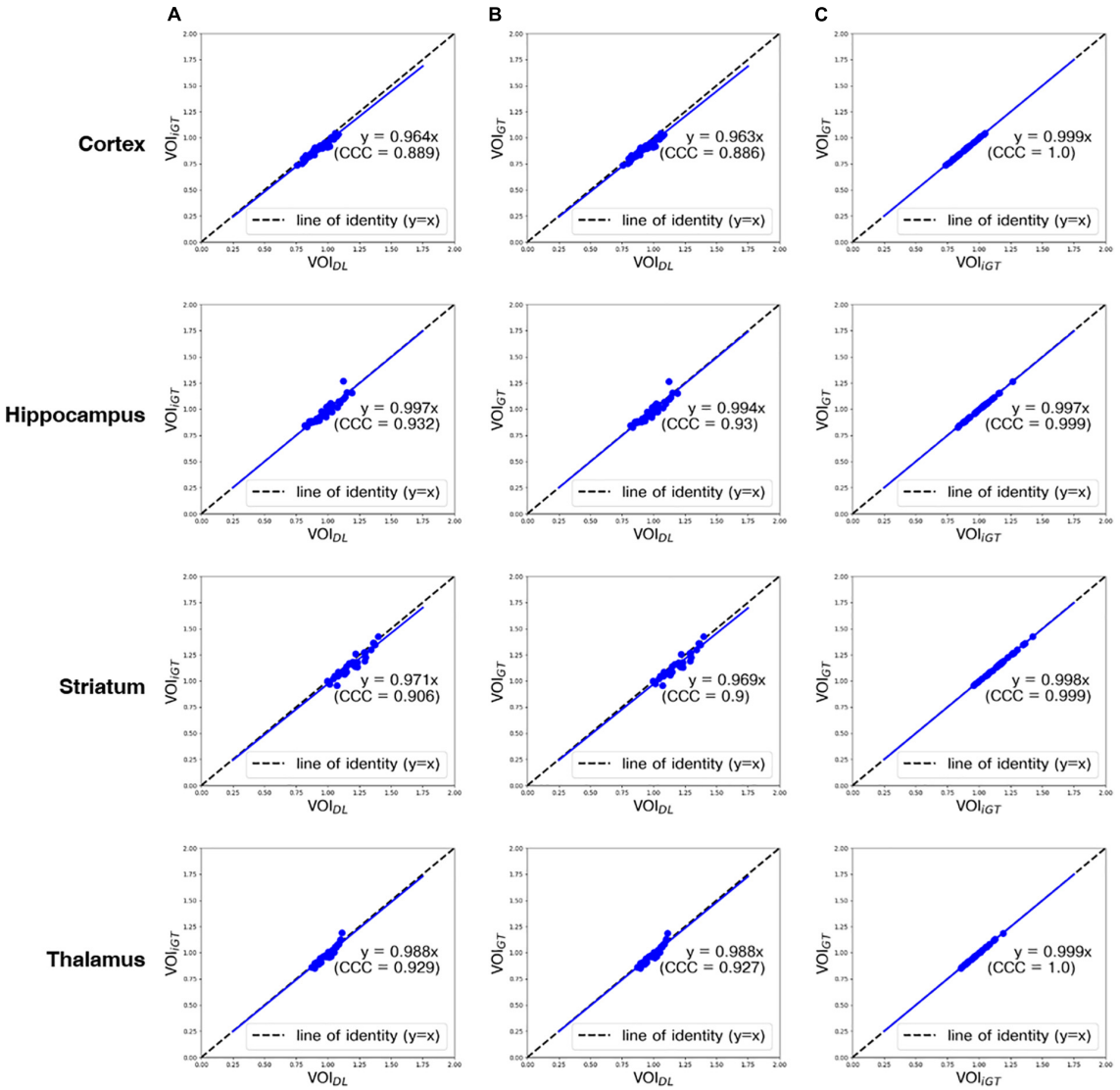

FIGURE 5 | Correlation analysis between all mean SUVRs (blue dot) obtained using VOI_{DL}, VOI_{iGT}, and VOI_{GT} in all target VOIs from the first to the fourth rows (cortex, hippocampus, striatum, and thalamus, respectively). Concordance correlation coefficient represents a measure of reliability based on covariation and correspondence. The line of identity (dashed line) is depicted as a reference line. Cortex, hippocampus, striatum, and thalamus are represented sequentially from the top row. **(A)** Correlation analysis between mean SUVRs obtained using VOI_{DL} and VOI_{iGT}. **(B)** Correlation analysis between mean SUVRs obtained using VOI_{DL} and VOI_{GT}. **(C)** Correlation analysis between each mean SUVRs obtained using VOI_{iGT} and VOI_{GT} VOI_{DL}, deep learning generated VOI; VOI_{iGT}, deep learning label VOI; VOI_{GT}, template-based VOI; CCC, concordance correlation coefficient.

calculated by the equation below.

$$\text{SUV (t)} = \frac{C_{PET}(t)}{ID/BW},$$

where $C_{PET}(t)$ is the radioactivity measured from an image acquired at the time t, ID is the injected dose at t = 0, and BW is the animal's body weight. The ratio of the SUV from target region and reference region within the same PET image is commonly called standardized uptake value ratio (SUVR). In ^{18}F-FDG PET, a PET image is obtained based on glucose uptake metabolism after sufficient time elapses, following the injection of the tracer into the body. Then, SUVR was calculated by dividing target regions of glucose metabolism depending on the disease, with constant glucose uptake regions at all times regardless of the disease. In this study, the SUVR evaluation was conducted on four major regions: cortex, hippocampus, thalamus, and stratum. We chose the cerebellum as a reference region, which seems to be free of plaques in the AD mouse model.

$$\text{SUVR} = \frac{SUV_{target}}{SUV_{reference}} = \frac{C_{img,\ target}}{C_{img,\ reference}}.$$

To assess our DL-based method, mean count and SUVR were calculated by the following three different methods:

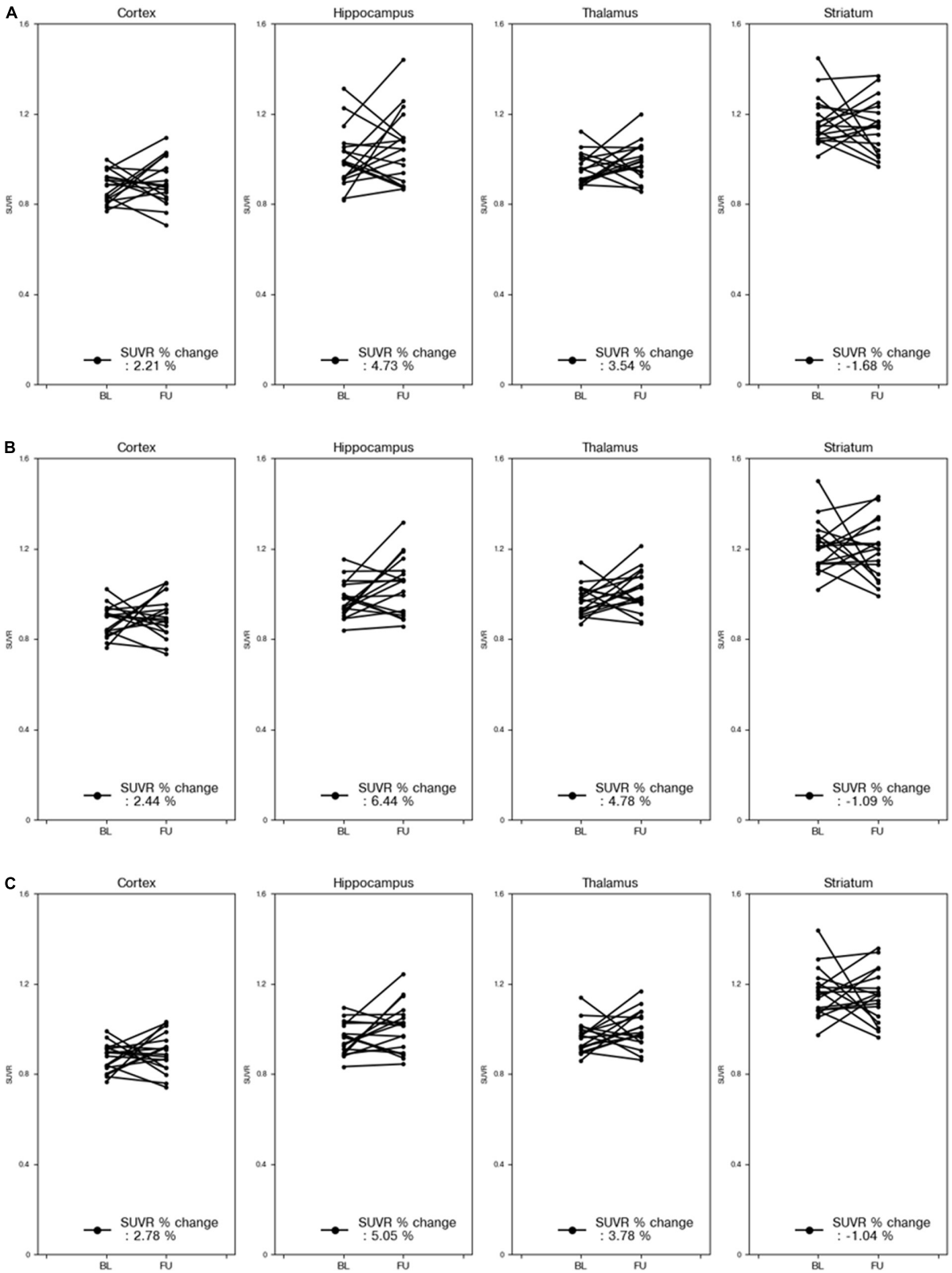

FIGURE 6 | % changes in SUVR for each part of 18 mice before and after treatment. The reference area of the SUVR was the cerebellum. Percent change in SUVR obtained using VOI_{DL} **(A)**. Percent change in SUVR obtained using VOI_{iGT} **(B)**. Percent change in SUVR obtained using VOI_{GT} **(C)**. Results for cortex, hippocampus, striatum, and thalamus are presented sequentially from the left column. VOI_{DL}, deep learning generated VOI; VOI_{iGT}, deep learning label VOI; VOI_{GT}, template-based VOI; baseline (BL—before treatment); follow-up (FU—after treatment).

DL-generated mask (VOI_{DL}), DL label mask (i.e., inversely normalized template (ground-truth) VOIs, VOI_{iGT}), and template-based ground-truth VOI (VOI_{GT}). Then, correlation analysis was conducted between these methods. In addition, we compared percentage change (% change) in SUVR before and after the treatment of 18 mice obtained by the abovementioned three masks by qualitative assessment and quantitative assessment by conducting paired or unpaired two-sample *t*-tests.

RESULTS

Deep Convolutional Neural Network for Automatic Generation of Brain Mask for Skull-Stripping

Figure 2 shows the comparisons in the brain skull-stripping mask generated by the proposed deep CNN (i.e., U-Net) (blue contour) and a manually traced brain mask (light blue contour) in three mice. All three mice showed high visual consistency without significant differences.

Table 1 shows the concordance of brain masks generated by a deep CNN and manually traced masks in terms of the DSC, ASSD, SEN, SPE, and PPV. Mean DSC reached 0.97, mean ASSD was less than 0.01 mm, and mean SEN reached 0.92. In addition, both mean SPE and mean PPV were greater than 0.99. In summary, there was no significant difference between the brain mask generated by our DL-based method and the manually traced mask in the six-fold crossvalidation.

Deep Convolutional Neural Network for Automatic Generation of Inversely Normalized VOI Template in Individual Brain Space

We conducted a qualitative visual assessment and quantitative assessment of VOI_{DL} and VOI_{iGT} to evaluate the performance of the proposed deep CNN model. In addition, we conducted a correlation analysis between mean count in each VOI obtained using VOI_{DL}, VOI_{iGT}, and VOI_{GT} and correlation analysis between each mean SUVR using the abovementioned VOI method. In addition, % change of SUVR between PET images before and after treatment was analyzed through a two-sample *t*-test for each VOI mask.

Figure 3 shows axial slices of VOI_{DL} (blue contour) and VOI_{iGT} (light blue contour) in target VOIs (cortex, hippocampus, stratum, thalamus, and cerebellum). There was no significant difference between VOI_{DL} and VOI_{iGT} in cortex, cerebellum, and thalamus and also in the relatively small areas of the hippocampus and striatum.

In **Table 1**, VOI_{DL} and VOI_{iGT} of 36 mice in target VOIs (cortex, hippocampus, striatum, thalamus, and cerebellum) were evaluated by calculating the average of DSC, ASSD, SEN, SPE, and PPV. The DSC for each target VOI was 0.77, 0.69, 0.68, 0.76, 0.69, the ASSD was 0.17, 0.12, 0.12, 0.1, and 0.01 mm, SEN was 0.76, 0.61, 0.61, 0.67, and 0.69, SPE was 1.0, 1.0, 1.0, 0.99, and 0.99, and PPV was 9, 0.65, 0.81, 0.78, and 0.71, respectively, which indicates that our DL model generated target VOIs well.

In **Figure 4**, the mean counts obtained by VOI_{DL}, VOI_{iGT}, and VOI_{GT} were significantly ($p < 0.001$) correlated with one another in all target VOIs. In addition, as shown in **Figure 4B**, the mean count obtained by VOI_{GT} in template space tended to be slightly underestimated compared to the mean count obtained by VOI_{DL} in individual space. Furthermore, we conducted a correlation analysis between each mean SUVR obtained using VOI_{DL}, VOI_{iGT}, and VOI_{GT} in all target VOIs (**Figure 5**). For SUVR analysis, cerebellum was used as a reference region, that is, SUV (or mean count) of target regions was normalized by that of cerebellum. In all target VOIs, mean SUVR obtained through VOI_{DL}, VOI_{iGT}, and VOI_{GT} was significantly ($p < 0.001$) correlated with one another. As shown in **Figure 5B**, in the hippocampus and thalamus, the mean SUVR obtained by VOI_{GT} in template space and the VOI_{DL} in individual space was almost identical, whereas in the cortex and striatum, the mean SUVR obtained by VOI_{GT} was underestimated compared to the mean SUVR obtained by VOI_{DL}.

Figure 6 compares the % changes of the SUVRs in each VOI before and after treatment using VOI_{DL}, VOI_{iGT}, and VOI_{GT} for 18 mice. Regardless of the three types of masks, there was no significant difference between the mean SUVR % changes obtained by each mask. Moreover, the degrees of increase in the mean SUVRs in the cortex, hippocampus, and thalamus were similar, and the degree of decrease in those in the striatum was similar. In addition, we did not find significant differences in the SUVR% changes of all target VOIs before and after treatment of three methods (DL-based method and SN/iSN-based conventional methods) by both paired and unpaired two-sample *t*-tests ($p > 0.3$ and $p > 0.8$, respectively).

DISCUSSION AND CONCLUSION

Spatial normalization of individual brain PET images onto standard anatomical spaces is required for objective statistical evaluation (Feo and Giove, 2019). However, several steps of the preprocessing were semiautomatic, which causes time-consuming problems and inter- and intrarater problem. A precise SN method through DL has also been devised and has recently attracted considerable attention. However, despite the use of a complicate network of structures, the method still has difficulty in performing complete SN from affine transformation to non-linear transformation (Alvén et al., 2019), and an additional SN process is required to generate a PET pseudotemplate (Kang et al., 2018) or a method of generating MR from a PET image (Choi et al., 2018). In addition, many studies have considered the use of iSN for PET quantitative analysis (Kim et al., 2010, 2015; Cho et al., 2014). Inspired by this, we generated an iVOI template to reformulate the complicated and difficult-to-implement SN problem into a relatively simpler problem of VOI segmentation for PET quantification. Overall, we have devised a unified CNN framework for brain mask generation to skull-stripping and generate an iVOI template in individual space to

perform precise PET quantification without any additional efforts of skull-stripping and SN.

With regard to DL for brain parenchyma segmentation, as shown in **Figure 2**, manually traced brain mask contours (lightblue) and DL-based contours (blue) were almost identical in visual assessment. Moreover, DSC reached 0.97, ASSD was less than 0.01 mm, and SEN and PPV were higher than 0.92 and 0.99 (**Table 1**) compared between these two masks, confirming good agreement from a quantitative perspective as well. With regard to DL for iVOI template segmentation, mean count and SUVR obtained by VOI_{iGT} and VOI_{DL} were significantly ($p < 0.001$) correlated with each other in all target VOIs (**Figures 3A**, **4A**). In addition, each of the mean count and SUVR obtained with template-based VOI (i.e., VOI_{GT}) and individual space VOI (i.e., VOI_{DL}, VOI_{iGT}) showed a significant ($p < 0.001$) correlation between each VOI methods (**Figures 3B,C**, **4B,C**). However, the mean count and SUVR obtained by VOI_{GT} tended to be slightly underestimated compared to that obtained by VOI_{iGT} and VOI_{DL} in hippocampus and striatum. We believe that our method can avoid image intensity degradation problems that may occur in preprocessing, including SN. Consequently, the % change of SUVR in the target VOI showed the same tendency in each of the three methods. In summary, the proposed DL-based method using an iVOI template in individual space that does not require SN has been developed as new method of PET quantitative assessment, avoiding variation between intra- and interrater that can occur in the process of drawing a brain mask or in the preprocessing. In addition, we showed a comparable level of segmentation performance using lighter neural network structures (i.e., CNNs with fewer training parameters—fewer channels and simple convolutional blocks) as compared to conventional mouse brain studies (Hsu et al., 2020; De Feo et al., 2021). Furthermore, our DL-based iVOI method has reformulated the PET SN problem for precise PET quantification, which remains challenging despite using a complicate network that requires a considerable parameter estimation (Choi et al., 2018; Kang et al., 2018; Alvén et al., 2019), with an easy-to-handle image generation method for target VOIs using inversely normalized template VOIs.

This study involves several limitations. First, we only had small number of data, consisting of 18 mice. Although the data were inflated using consecutive axial slices of T2 MR as multichannels input of the deep CNN and using data augmentation, this was not sufficient. Second, because this study was carried out with only in-house mice with a specific disease (i.e., Alzheimer's disease), there is a possibility that the trained model may be specialized to our data. Therefore, as in study by De Feo et al. (2021), model validation should be warranted with more data and various types of mice in the near future. Third, our method is dependent on MR images because we generated iVOI templates using parameters based on SN of MR images onto MR templates in the process of generating label used for deep CNN training. However, corresponding MR images are not always available in PET image analyses. In this regard, we should consider further studies for generating iVOI templates only with PET images. Finally, one of the strengths of this study is that because we used a PET/MRI system registration of PET, MR is straightforward in nature compared to existing methods. Nonetheless, we believe that our proposed approach may be readily applied to ordinary PET or PET/CT scanners with additional MR images as well. In this regard, a further study on a more unified deep CNN with PET input and iVOI defined by MR should be warranted in the near future.

In conclusion, we proposed a unified deep CNN-based model that can generate mouse brain parenchyma masks and iVOI templates in individual brain space without any effort for skull-stripping and SN. Through qualitative and quantitative evaluations, our proposed model has shown identical quantification of regional glucose metabolism (i.e., mean SUV of each VOI) forming line of identity between ground truth (conventional template) methods-based mean SUV/SUVR and DL-based mean SUV/SUVR (**Figures 4**, **5**, respectively) and also concordant patterns of mean SUVR treatment-induced change between ground truth and DL methods. These results show that the proposed approach comprises a new method for PET image analysis by reformulating the SN problem, which has been difficult to implement despite of recent advances in DL techniques, into a segmentation problem using iVOI template generation in an individual brain space.

DATA AVAILABILITY STATEMENT

The datasets presented in this article are not readily available because because this study cohort is not open for public use. Requests to access the datasets should be directed to JO, jungsu.oh@gmail.com.

ETHICS STATEMENT

The animal study was reviewed and approved by the Institutional Animal Care and Use Committee (IACUC), Asan Institute for Life Sciences, Asan Medical Center.

AUTHOR CONTRIBUTIONS

SS, S-JK, and JO contributed to study conceptualization, data acquisition, data analysis, data interpretation, writing, and editing of the manuscript. JC, S-YK, and SO contributed to data acquisition and data interpretation. SJ and JK contributed to study conceptualization, data interpretation, and editing of the manuscript. All authors contributed to the article and approved the submitted version.

FUNDING

This work was supported by the National Research Foundation of Korea (NRF) grant funded by the Korean Government

(Ministry of Science and ICT; nos. NRF-2020M2D9A1094074 and 2021R1A2C3009056) and by a grant from the Korea Health Technology R&D Project through the Korea Health Industry Development Institute (KHIDI), funded by the Ministry of Health & Welfare, Republic of Korea (HI18C2383).

ACKNOWLEDGMENTS

We appreciate Neuracle Science, Co. Ltd. for allowing us to use the collaboration research data of the Center for Bio-imaging of New Drug Development (C-BiND), Asan Institute for Life Sciences, to demonstrate the strength of our DL-based VOI generation method in Alzheimer mice model to be published as this manuscript original article (to Jae Keun Lee and Bong Cheol Kim et al.).

SUPPLEMENTARY MATERIAL

The Supplementary Material for this article can be found online at: https://www.frontiersin.org/articles/10.3389/fnagi.2022.807903/full#supplementary-material

REFERENCES

Acosta-Cabronero, J., Williams, G. B., Pereira, J. M., Pengas, G., and Nestor, P. J. (2008). The impact of skull-stripping and radio-frequency bias correction on grey-matter segmentation for voxel-based morphometry. *Neuroimage* 39, 1654–1665. doi: 10.1016/j.neuroimage.2007.10.051

Alvén, J., Heurling, K., Smith, R., Strandberg, O., Schöll, M., Hansson, O., et al. (2019). "A Deep Learning Approach to MR-less Spatial Normalization for Tau PET Images," in *22nd International Conference on Medical Image Computing and Computer-Assisted Intervention (MICCAI 2019)*, (Shenzhen: MICCAI).

Ashburner, J., Andersson, J. L., and Friston, K. J. (2000). Image registration using a symmetric prior–in three dimensions. *Hum. Brain Mapp.* 9, 212–225. doi: 10.1002/(SICI)1097-0193(200004)9:4<212::AID-HBM3<3.0.CO;2-\#

Ashburner, J., and Friston, K. J. (1999). Nonlinear spatial normalization using basis functions. *Hum. Brain Mapp.* 7, 254–266.

Ashburner, J., and Friston, K. J. (2000). Voxel-based morphometry–the methods. *Neuroimage* 11, 805–821. doi: 10.1006/nimg.2000.0582

Bai, J., Trinh, T. L., Chuang, K. H., and Qiu, A. (2012). Atlas-based automatic mouse brain image segmentation revisited: model complexity vs. image registration. *Magn. Reson. Imaging* 30, 789–798. doi: 10.1016/j.mri.2012.02.010

Bascunana, P., Thackeray, J. T., Bankstahl, M., Bengel, F. M., and Bankstahl, J. P. (2019). Anesthesia and Preconditioning Induced Changes in Mouse Brain [(18)F] FDG Uptake and Kinetics. *Mol. Imaging Biol.* 21, 1089–1096. doi: 10.1007/s11307-019-01314-9

Cho, H., Kim, J. S., Choi, J. Y., Ryu, Y. H., and Lyoo, C. H. (2014). A computed tomography-based spatial normalization for the analysis of [18F] fluorodeoxyglucose positron emission tomography of the brain. *Korean J. Radiol.* 15, 862–870. doi: 10.3348/kjr.2014.15.6.862

Choi, H., Lee, D. S., and Alzheimer's Disease Neuroimaging Initiative (2018). Generation of Structural MR Images from Amyloid PET: application to MR-Less Quantification. *J. Nucl. Med.* 59, 1111–1117. doi: 10.2967/jnumed.117.199414

Chou, N., Wu, J., Bai Bingren, J., Qiu, A., and Chuang, K. H. (2011). Robust automatic rodent brain extraction using 3-D pulse-coupled neural networks (PCNN). *IEEE Trans. Image Process.* 20, 2554–2564. doi: 10.1109/TIP.2011.2126587

De Feo, R., Shatillo, A., Sierra, A., Valverde, J. M., Grohn, O., Giove, F., et al. (2021). Automated joint skull-stripping and segmentation with Multi-Task U-Net in large mouse brain MRI databases. *Neuroimage* 229:117734. doi: 10.1016/j.neuroimage.2021.117734

Delzescaux, T., Lebenberg, J., Raguet, H., Hantraye, P., Souedet, N., and Gregoire, M. C. (2010). Segmentation of small animal PET/CT mouse brain scans using an MRI-based 3D digital atlas. *Annu. Int. Conf. IEEE Eng. Med. Biol. Soc.* 2010, 3097–3100. doi: 10.1109/IEMBS.2010.5626106

Detlefsen, N. S., Freifeld, O., and Hauberg, S. (2018). "Deep Diffeomorphic Transformer Networks," in *2018 IEEE/CVF Conference on Computer Vision and Pattern Recognition*, (Salt Lake City: IEEE), 4403–4412. doi: 10.1016/j.neuroimage.2020.117161

Fein, G., Landman, B., Tran, H., Barakos, J., Moon, K., Di Sclafani, V., et al. (2006). Statistical parametric mapping of brain morphology: sensitivity is dramatically increased by using brain-extracted images as inputs. *Neuroimage* 30, 1187–1195. doi: 10.1016/j.neuroimage.2005.10.054

Feo, R., and Giove, F. (2019). Towards an efficient segmentation of small rodents' brain: a short critical review. *J. Neurosci. Methods* 323, 82–89. doi: 10.1016/j.jneumeth.2019.05.003

Gispert, J. D., Pascau, J., Reig, S., Martínez-Lázaro, R., Molina, V., García-Barreno, P., et al. (2003). Influence of the normalization template on the outcome of statistical parametric mapping of PET scans. *Neuroimage* 19, 601–612. doi: 10.1016/s1053-8119(03)00072-7

Han, S., Oh, M., Oh, J. S., Lee, S. J., Oh, S. J., Chung, S. J., et al. (2016). Subregional Pattern of Striatal Dopamine Transporter Loss on 18F FP-CIT Positron Emission Tomography in Patients With Pure Akinesia With Gait Freezing. *JAMA Neurol.* 73, 1477–1484. doi: 10.1001/jamaneurol.2016.3243

Hofmann, M., Bezrukov, I., Mantlik, F., Aschoff, P., Steinke, F., Beyer, T., et al. (2011). MRI-based attenuation correction for whole-body PET/MRI: quantitative evaluation of segmentation- and atlas-based methods. *J. Nucl. Med.* 52, 1392–1399. doi: 10.2967/jnumed.110.078949

Hofmann, M., Pichler, B., Schölkopf, B., and Beyer, T. (2009). Towards quantitative PET/MRI: a review of MR-based attenuation correction techniques. *Eur. J. Nucl. Med. Mol. Imaging* 36, 93–104. doi: 10.1007/s00259-008-1007-7

Hsu, L. M., Wang, S., Ranadive, P., Ban, W., Chao, T. H., Song, S., et al. (2020). Automatic Skull Stripping of Rat and Mouse Brain MRI Data Using U-Net. *Front. Neurosci.* 14:568614. doi: 10.3389/fnins.2020.568614

Hu, Y. C., Mageras, G., and Grossberg, M. (2021). Multi-class medical image segmentation using one-vs-rest graph cuts and majority voting. *J. Med. Imaging* 8:034003. doi: 10.1117/1.Jmi.8.3.034003

Jaderberg, M., Simonyan, K., Zisserman, A., and Kavukcuoglu, K. (2015). "Spatial transformer networks," in *Proceedings of the 28th International Conference on Neural Information Processing Systems - Volume 2*, (Montreal: MIT Press).

Jenkinson, M., Beckmann, C. F., Behrens, T. E., Woolrich, M. W., and Smith, S. M. (2012). FSL. *Neuroimage* 62, 782–790. doi: 10.1016/j.neuroimage.2011.09.015

Jimenez-Carretero, D., Bermejo-Peláez, D., Nardelli, P., Fraga, P., Fraile, E., San José Estépar, R., et al. (2019). A graph-cut approach for pulmonary artery-vein segmentation in noncontrast CT images. *Med. Image Anal.* 52, 144–159. doi: 10.1016/j.media.2018.11.011

Jorge Cardoso, M., Leung, K., Modat, M., Keihaninejad, S., Cash, D., Barnes, J., et al. (2013). STEPS: similarity and Truth Estimation for Propagated Segmentations and its application to hippocampal segmentation and brain parcellation. *Med. Image Anal.* 17, 671–684. doi: 10.1016/j.media.2013.02.006

Kang, S. K., Seo, S., Shin, S. A., Byun, M. S., Lee, D. Y., Kim, Y. K., et al. (2018). Adaptive template generation for amyloid PET using a deep learning approach. *Hum. Brain Mapp.* 39, 3769–3778. doi: 10.1002/hbm.24210

Kim, H., Jung, J., Kim, J., Cho, B., Kwak, J., Jang, J. Y., et al. (2020). Abdominal multi-organ auto-segmentation using 3D-patch-based deep convolutional neural network. *Sci. Rep.* 10:6204. doi: 10.1038/s41598-020-63285-0

Kim, J. S., Cho, H., Choi, J. Y., Lee, S. H., Ryu, Y. H., Lyoo, C. H., et al. (2015). Feasibility of Computed Tomography-Guided Methods for Spatial Normalization of Dopamine Transporter Positron Emission Tomography Image. *PLoS One* 10:e0132585. doi: 10.1371/journal.pone.0132585

Kim, J. S., Lee, J. S., Park, M. H., Kim, K. M., Oh, S. H., Cheon, G. J., et al. (2010). Feasibility of template-guided attenuation correction in cat brain PET imaging. *Mol. Imaging Biol.* 12, 250–258. doi: 10.1007/s11307-009-0277-1

Klein, S., Staring, M., Murphy, K., Viergever, M. A., and Pluim, J. P. (2010). elastix: a toolbox for intensity-based medical image registration. *IEEE Trans. Med. Imaging* 29, 196–205. doi: 10.1109/TMI.2009.2035616

Kuhn, F. P., Warnock, G. I., Burger, C., Ledermann, K., Martin-Soelch, C., and Buck, A. (2014). Comparison of PET template-based and MRI-based image processing in the quantitative analysis of C11-raclopride PET. *EJNMMI Res.* 4:7. doi: 10.1186/2191-219X-4-7

Lehmann, M., Douiri, A., Kim, L. G., Modat, M., Chan, D., Ourselin, S., et al. (2010). Atrophy patterns in Alzheimer's disease and semantic dementia: a comparison of FreeSurfer and manual volumetric measurements. *Neuroimage* 49, 2264–2274. doi: 10.1016/j.neuroimage.2009.10.056

Liu, Y., Unsal, H. S., Tao, Y., and Zhang, N. (2020). Automatic Brain Extraction for Rodent MRI Images. *Neuroinformatics* 18, 395–406. doi: 10.1007/s12021-020-09453-z

Ma, D., Cardoso, M. J., Modat, M., Powell, N., Wells, J., Holmes, H., et al. (2014). Automatic structural parcellation of mouse brain MRI using multi-atlas label fusion. *PLoS One* 9:e86576. doi: 10.1371/journal.pone.0086576

Ma, Y., Hof, P. R., Grant, S. C., Blackband, S. J., Bennett, R., Slatest, L., et al. (2005). A three-dimensional digital atlas database of the adult C57BL/6J mouse brain by magnetic resonance microscopy. *Neuroscience* 135, 1203–1215. doi: 10.1016/j.neuroscience.2005.07.014

Nie, J., and Shen, D. (2013). Automated segmentation of mouse brain images using multi-atlas multi-ROI deformation and label fusion. *Neuroinformatics* 11, 35–45. doi: 10.1007/s12021-012-9163-0

Oguz, I., Zhang, H., Rumple, A., and Sonka, M. (2014). RATS: rapid Automatic Tissue Segmentation in rodent brain MRI. *J. Neurosci. Methods* 221, 175–182. doi: 10.1016/j.jneumeth.2013.09.021

Oh, J. S., Kubicki, M., Rosenberger, G., Bouix, S., Levitt, J. J., McCarley, R. W., et al. (2009). Thalamo-frontal white matter alterations in chronic schizophrenia: a quantitative diffusion tractography study. *Hum. Brain Mapp.* 30, 3812–3825. doi: 10.1002/hbm.20809

Oh, J. S., Song, I. C., Lee, J. S., Kang, H., Park, K. S., Kang, E., et al. (2007). Tractography-guided statistics (TGIS) in diffusion tensor imaging for the detection of gender difference of fiber integrity in the midsagittal and parasagittal corpora callosa. *Neuroimage* 36, 606–616. doi: 10.1016/j.neuroimage.2007.03.020

Palumbo, L., Bosco, P., Fantacci, M. E., Ferrari, E., Oliva, P., Spera, G., et al. (2019). Evaluation of the intra- and inter-method agreement of brain MRI segmentation software packages: a comparison between SPM12 and FreeSurfer v6.0. *Phys. Med.* 64, 261–272. doi: 10.1016/j.ejmp.2019.07.016

Sekine, T., Buck, A., Delso, G., Ter Voert, E. E., Huellner, M., Veit-Haibach, P., et al. (2016). Evaluation of Atlas-Based Attenuation Correction for Integrated PET/MR in Human Brain: application of a Head Atlas and Comparison to True CT-Based Attenuation Correction. *J. Nucl. Med.* 57, 215–220. doi: 10.2967/jnumed.115.159228

Shamonin, D., Bron, E., Lelieveldt, B., Smits, M., Klein, S., and Staring, M. (2014). Fast Parallel Image Registration on CPU and GPU for Diagnostic Classification of Alzheimer's Disease. *Front. Neuroinform.* 7:50. doi: 10.3389/fninf.2013.00050

Som, P., Atkins, H. L., Bandoypadhyay, D., Fowler, J. S., MacGregor, R. R., Matsui, K., et al. (1980). A fluorinated glucose analog, 2-fluoro-2-deoxy-D-glucose (F-18): nontoxic tracer for rapid tumor detection. *J. Nucl. Med.* 21, 670–675.

Wollenweber, S. D., Ambwani, S., Delso, G., Lonn, A. H. R., Mullick, R., Wiesinger, F., et al. (2013). Evaluation of an Atlas-Based PET Head Attenuation Correction Using PET/CT & MR Patient Data. *IEEE Trans. Nucl. Sci.* 60, 3383–3390. doi: 10.1109/TNS.2013.2273417

Woolrich, M. W., Jbabdi, S., Patenaude, B., Chappell, M., Makni, S., Behrens, T., et al. (2009). Bayesian analysis of neuroimaging data in FSL. *Neuroimage* 45, S173–S186. doi: 10.1016/j.neuroimage.2008.10.055

Yasuno, F., Hasnine, A. H., Suhara, T., Ichimiya, T., Sudo, Y., Inoue, M., et al. (2002). Template-based method for multiple volumes of interest of human brain PET images. *Neuroimage* 16, 577–586. doi: 10.1006/nimg.2002.1120

Conflict of Interest: The authors declare that the research was conducted in the absence of any commercial or financial relationships that could be construed as a potential conflict of interest.

Publisher's Note: All claims expressed in this article are solely those of the authors and do not necessarily represent those of their affiliated organizations, or those of the publisher, the editors and the reviewers. Any product that may be evaluated in this article, or claim that may be made by its manufacturer, is not guaranteed or endorsed by the publisher.

Copyright © 2022 Seo, Kim, Oh, Chung, Kim, Oh, Joo and Kim. This is an open-access article distributed under the terms of the Creative Commons Attribution License (CC BY). The use, distribution or reproduction in other forums is permitted, provided the original author(s) and the copyright owner(s) are credited and that the original publication in this journal is cited, in accordance with accepted academic practice. No use, distribution or reproduction is permitted which does not comply with these terms.

frontiers in Aging Neuroscience

ORIGINAL RESEARCH
published: 10 March 2022
doi: 10.3389/fnagi.2022.841297

A Novel Elastomeric UNet for Medical Image Segmentation

Sijing Cai[1,2], *Yi Wu*[1,3]* *and Guannan Chen*[1,3]*

[1] *Key Laboratory of Optoelectronic Science and Technology for Medicine of Ministry of Education, Fujian Provincial Key Laboratory of Photonics Technology, Fujian Normal University, Fuzhou, China,* [2] *School of Electronic & Electrical Engineering and Physics, Fujian University of Technology, Fuzhou, China,* [3] *Fujian Provincial Engineering Technology Research Center of Photoelectric Sensing Application, Fujian Normal University, Fuzhou, China*

Medical image segmentation is of important support for clinical medical applications. As most of the current medical image segmentation models are limited in the U-shaped structure, to some extent the deep convolutional neural network (CNN) structure design is hard to be accomplished. The design in this study mimics the way the wave is elastomeric propagating, extending the structure from both the horizontal and spatial dimensions for realizing the Elastomeric UNet (EUNet) structure. The EUNet can be divided into two types: horizontal EUNet and spatial EUNet, based on the propagation direction. The advantages of this design are threefold. First, the training structure can be deepened effectively. Second, the independence brought by each branch (a U-shaped design) makes the flexible design redundancy available. Finally, a horizontal and vertical series-parallel structure helps on feature accumulation and recursion. Researchers can adjust the design according to the requirements to achieve better segmentation performance for the independent structural design. The proposed networks were evaluated on two datasets: a self-built dataset (multi-photon microscopy, MPM) and publicly benchmark retinal datasets (DRIVE). The results of experiments demonstrated that the performance of EUNet outperformed the UNet and its variants.

Keywords: Parkinson's disease, medical image segmentation, convolutional neural network (CNN), elastomeric UNet, UNet

OPEN ACCESS

Edited by:
Woon-Man Kung,
Chinese Culture University, Taiwan

Reviewed by:
Yuh-Chung Lin,
Sanda University, China
Ming Zhao,
Yangtze University, China

***Correspondence:**
Yi Wu
wuyi@fjnu.edu.cn
Guannan Chen
edado@fjnu.edu.cn

Specialty section:
This article was submitted to Neurocognitive Aging and Behavior, a section of the journal Frontiers in Aging Neuroscience

Received: *22 December 2021*
Accepted: *10 January 2022*
Published: *10 March 2022*

Citation:
Cai S, Wu Y and Chen G (2022) A Novel Elastomeric UNet for Medical Image Segmentation. Front. Aging Neurosci. 14:841297. doi: 10.3389/fnagi.2022.841297

INTRODUCTION

With the popularization of medical imaging technology, such as magnetic resonance imaging (MRI), computed tomography (CT), positron emission tomography (PET), ultrasonic imaging, digital pathology, and microscopy, medical imaging technology plays an important role in clinical medicine to emerge the structure of human organs, tissues, and cells (Taruttis and Ntziachristos, 2015; Papadopoulos et al., 2017; Pang et al., 2020). The morphology of *in vivo* cells is an intuitive reflection of cell structure and function, and the analysis of it is a significant part of histopathology and clinical medicine to carry out clinical medical diagnosis and genetic research on aging, cell, and tissue expression of Alzheimer's and Parkinson's diseases (Li et al., 2010; Haft-Javaherian et al., 2019; Ye et al., 2020). Research on aging morphology and molecular mechanism of skin cells (especially *in vivo* skin cells) is an effective means for clinical medical research, such as skin aging and refractory skin wounds, and can provide the basis for aging cell research of a variety of aging-related diseases (e.g., cardiovascular disease, osteoporosis, and Parkinson's disease) (Loeser, 2009; Aspray and Hill, 2019; Sun, 2020). Cortical angiography was used to explore the influences

of Alzheimer's disease and cellular senescence on capillaries (Haft-Javaherian et al., 2019). The incidence of melanoma in patients with Parkinson's disease was studied by multiphoton imaging tracking, the dynamic process of melanocytic lesions (Balu et al., 2017; Lentsch et al., 2019; Ye et al., 2020). Image segmentation is an active research topic within medical image technology, which accounts for 70% of the international image processing competitions. As a basilic step in the medical image process, medical image segmentation separates the medical image into different regions with analogous characteristics to segment the regions of interest (ROI) and extract interrelated features. The role of medical image segmentation is to improve the intuitiveness of medical images and reduce man-made mistakes. Accurate medical image segmentation is difficult to achieve, owing to the data scarcity and image complexity, such as noisy background and intensity in-homogeneity.

The broad classification of medical image segmentation technology is traditional segmentation, such as thresholds, morphological methods (Chen et al., 2015) and clustering techniques, and deep-learning segmentation rest on CNN. Although various traditional algorithms have been designed to segment the medical images, the accuracy of segmentation is still difficult to improve. The fully convolutional network (FCN) designed by Long et al., 2015 is an end-to-end pixel-wise segmentation with a 20% amelioration of mean IOU than 2012 (Long et al., 2015). On account of significant improvement in the field of medical image segmentation by deep CNN, diverse variants of CNN are employed to segment medical images. As the development of FCN, UNet was applied to biomedical image segmentation by symmetric U-shaped architecture and skip connections yielding more accurate properties (Ronneberge et al., 2015). The improvement of UNet performance is apt to stagnate by the increase of depth. As a consequence, the diverse variants of UNet had been explored in the past 5 years for medical image segmentation (Li H. et al., 2018; Zhang et al., 2018; Liu et al., 2020). Inspired by the ResNet framework, a residual neural network with U-shape named U-ResNet was explored by Ibtehaz and Rahman (2020) and Drozdzal et al. (2016). In the same way, H-DenseUnet had been proposed to segment liver tumor mixed DenseNet to UNet by Li X. et al. (2018) and Cai et al. (2020). Another recent relevant work was Mask-RCNN, a novel UNet structure introduced by Vuola et al. (2019) through combining UNet and Mask-RCNN for nucleus segmentation. A U-shaped structure with dilated convolution path named Modified UNet was implemented by Zhao et al. (2019). UNet + + was employed to alleviate the *a priori* unknown of depth by Zhou et al. (2020), and the restrictive fusion architecture of UNet skip connections was also optimized in it. A UNet-like network entitled DSC-Net was performed to segment thymoma from CT images by Li et al. (2021). Another variant of UNet called X-Net was designed to segment liver and tumor by Chi et al. (2021). So far, however, the improved models still adopt a U-shaped structure, namely, the symmetrical single branch down-up sampling U-shaped structure. The performance of UNet is difficult to ameliorate, and the technical challenges of expanding the network size of UNet and extracting detailed information have prevented this architecture from being more accurate in medical imaging segmentation. Breaking the U-shaped architecture is an inevitable choice to overcome the technical bottleneck.

The purpose of this study was to design a flexible elastic expansion convolution operation to enhance the boundary detail extraction ability of the model and extend it to the segmentation of public medical image datasets by adjusting parameters through experiments. An elastomeric UNet (EUNet) has been proposed to address the limitations of U-shaped architecture, and the experimental validation demonstrates its effectiveness of it.

METHODOLOGY

UNet Model and Its Variants

UNet was first proposed stemming from FCN. As shown in **Figure 1**, the U-shaped architecture of UNet is illustrated using three elements, namely, a contracting path, an expansive path, and skip connections. The key idea is to connect symmetric contracting path and expansive path by skip connections, where the convolutional operations are employed to extract features and upsampled operations are utilized to locate the ROI.

UNet + + is designed to overcome the two defects of UNet, *a priori* unknown of depth and the restrictive fusion architecture of skip connections. U-shapes with varying depths are integrated to relieve the *a priori* unknown of depth, and a pruning scheme is devised to accelerate convergence in UNet + +. Aggregation feature scheme instead of skip connections is executed in the up-sampling path to extract multi-scale features (Li X. et al., 2018).

Modified UNet extract varying scale features by introducing dilated convolution into U-shaped architecture (Cai et al., 2020). Each feature extraction operation consists of two steps. The first step is feature extraction operation through two convolution paths: one path is composed of ordinary convolution operation, and the other one uses dilated convolution for feature extraction. The second step is to complete feature fusion through a "concatenate" operation. A bigger receptive field is acquired in this way. Dilated convolution and conventional convolution coverage of receptive fields are the same when the dilate rate equals 1, the coverage goes to 5×5 when the dilate rate to 2 (Xia et al., 2020; Amer et al., 2021). Compared with the conventional convolution performed regular range feature extraction on fixed regions, the dilated convolution obtains larger receptive fields by the dilation rate.

Proposed Model: Elastomeric UNet

The proposed model is built on the coding-decoding mechanisms, while novel structural breakthroughs are proposed over the original structure by adding a spatially extended network layer to improve the accuracy. Two types of EUNet, namely, horizontal EUNet and spatial EUNet, are introduced in this section, which include three extension structures of horizontal EUNet and two structures of spatial EUNet.

Horizontal Elastomeric UNet

Owing to the elastomeric wave horizontal transmission, the structure of horizontal EUNet was stretched horizontally by

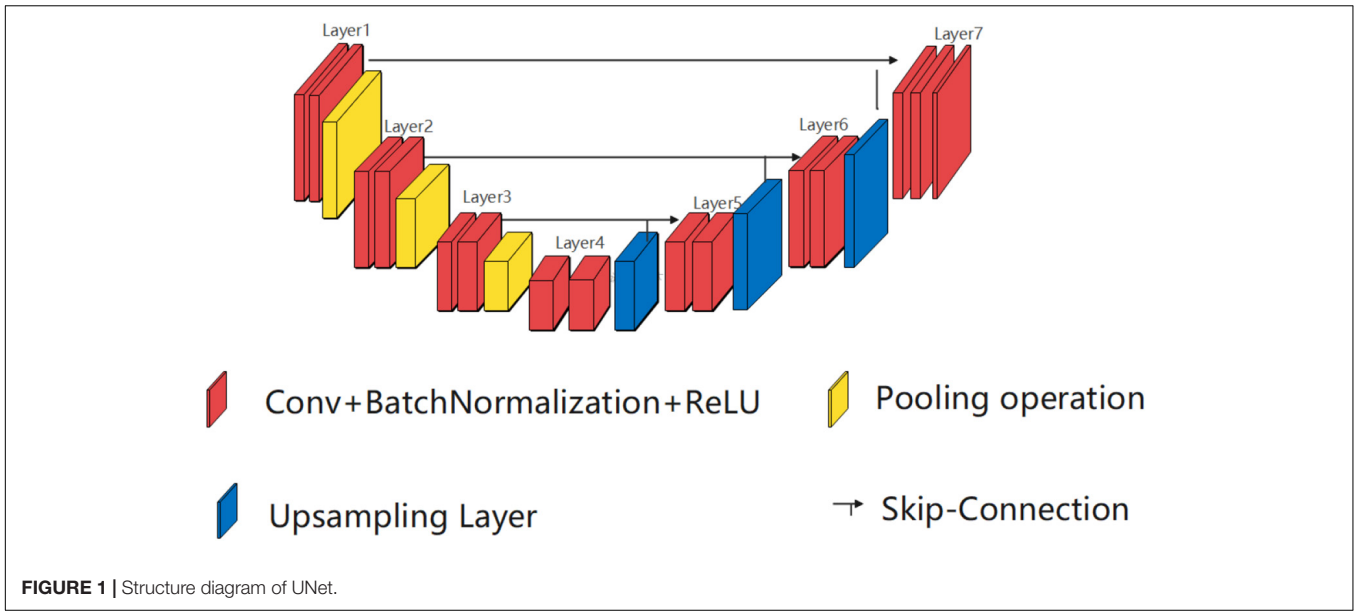

FIGURE 1 | Structure diagram of UNet.

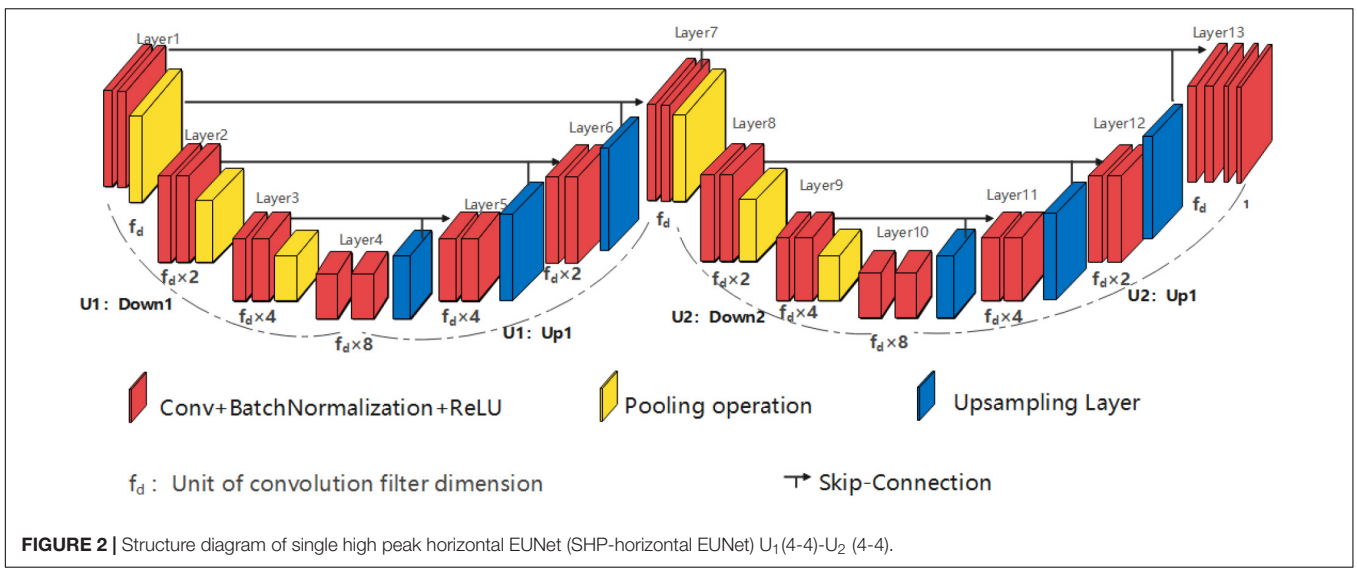

FIGURE 2 | Structure diagram of single high peak horizontal EUNet (SHP-horizontal EUNet) $U_1(4\text{-}4)\text{-}U_2(4\text{-}4)$.

multiple feature extraction and spatial location algorithm to improve the segmentation accuracy. Horizontal EUNet expands the network by means of continuous U-shaped structure cascading and provides three structures according to the amounts of U-shaped structures that are cascaded: single-peak, double-peak, and three-peak horizontal EUNet. In the light of the position of wave peak, each structure is further characterized into two forms, i.e., low peak network and high peak network. There is less difference in performance between low peak and high peak networks, so this study introduces high peak networks.

Single High Peak Horizontal Elastomeric UNet

Single high peak horizontal EUNet (SHP-horizontal EUNet) contains a wave peak yielded W-shaped architecture. Due to twice consecutive down-up sampling, the feature extraction and space location operation were performed twice in the network to achieve more accurate pixel-to-pixel segmentation results. **Figure 2** shows the structure of SHP-horizontal EUNet $U_1(4\text{-}4)\text{-}U_2(4\text{-}4)$, which includes two symmetrical down-up paths forming a W-like structure. The input layer Lay_1 and the output layer Lay_{13} of SHP-horizontal EUNet are located at both ends of the "W" shape on the same height and symmetrical to each other. The peak layer is also at the same height as the input/output layer. The outcome of the output layer is the cascaded output of the input/output layer and peak layer. There are two four-layered capture paths for feature extraction, indicating $Down_1$ path (Lay1–Lay4) and $Down_2$ path (Lay7–Lay10), and two extended paths for spatial information location, Up_1 path (Lay4–Lay7) and Up_2 path (Lay10–Lay13). Each down-layer is comprised of two convolutions to extract information and a pooling operation to reduce dimension for data compression,

and each up-layer consists of a concatenate, an up-sampling, and two convolution operations. Batch normalization (BN) layers normalize the input value to improve the convergence of the gradient. $Down_1$-Up_1 form U_1(4-4) structure, i.e., four layers of down-sampling and four layers of up-sampling, connected through the skip connections, and the structure of corresponding layers is completely symmetric. For instance, the resolution and dimension of Lay_2 and Lay_6 are the same, which is due to the skip connections. The network configuration is shown in **Table 1**.

Researchers can flexibly adjust the structure of the network according to the characteristics of input pictures, such as using the SHP-horizontal EUNet U_1(4-4)-U_2(3-3). That is to say, the number of the sampling layer for different U-shaped structures is independent which means that researchers can determine how many layers are to be hired accordingly. For the dataset with image resolution between 128 and 600, it is recommended to adopt a small sampling structure with 4–5 layers. It is recommended to adopt a 4–5 layer sampling structure with a convolution filter equaled to (3 × 3). Generally, the below rules need to be followed:

① SHP-horizontal EUNet consists of two U-shaped structures. The input layer, wave peak layer, and output layer are at the same height.
② The down-sampling and up-sampling paths are completely symmetrical in each U-shaped structure, and different U-shaped structures are independent of each other, for example, there is no connection relationship between Lay2 and Lay8.
③ The wave peak layer should have three groups of convolutional operations, namely, the cascaded input layer of the output layer, the output layer itself, and the output of the wave peak layer.

Single low peak horizontal EUNet (SLP-horizontal EUNet) can also be designed, and the design principle is similar to SHP-horizontal EUNet. The input layer and the output layer of SLP-horizontal EUNet are also located at both ends of the "W" shape on the same height and symmetrical to each other. The difference between SHP- and SLP-horizontal EUNet is that the peak position is one layer lower than the input/output layer, as shown in **Figure 3**.

Double High Peak Horizontal Elastomeric UNet

Similar to the SHP-horizontal EUNet structure, the double high peak horizontal EUNet (DHP-horizontal EUNet) is composed of three independent and fully symmetrical U-shaped structures by in-series connection. As shown in **Figure 4**, DHP-horizontal EUNet U_1(4-4)-U_2(4-4)-U_3(4-4) is adopted in this section, which can be adjusted by the designer according to their needs, such as DHP-horizontal EUNet U_1(5-5)-U_2(3-3)-U_3(4-4).

Three High Peak Horizontal Elastomeric UNet

Consisting of four consecutive independent U-shaped structures, the three high peak horizontal EUNet (THP-horizontal EUNet)

TABLE 1 | Architecture and parameters of single high peak horizontal elastomeric U-Net (SHP-horizontal EUNet).

Layer	Configuration of SHP-Horizontal EUNet	Feature size
Input	–	128×128
Layer1	f_d×1, 3×3, Conv f_d×1, 3×3, Conv 2×2, Pooling	128×128
Layer2	f_d×2, 3×3, Conv f_d×2, 3×3, Conv 2×2, Pooling	64×64
Layer3	f_d×4, 3×3, Conv f_d×4, 3×3, Conv 2×2, Pooling	32×32
Layer4	f_d×8, 3×3, Conv f_d×8, 3×3, Conv 0.5, Dropout	16×16
Layer5	f_d×4, 2×2, Conv, 2×2, UpSampling Axis=3, concatenate f_d×4, 3×3, Conv f_d×4, 3×3, Conv	32×32
Layer6	f_d×2, 2×2, Conv, 2×2, UpSampling Axis=3, concatenate f_d×2, 3×3, Conv f_d×2, 3×3, Conv	64×64
Layer7	f_d×1, 2×2, Conv, 2×2, UpSampling Axis=3, concatenate f_d×1, 3×3, Conv f_d×1, 3×3, Conv 2×2, Pooling	128×128
Layer8	f_d×2, 3×3, Conv f_d×2, 3×3, Conv 2×2, Pooling	64×64
Layer9	f_d×4, 3×3, Conv f_d×4, 3×3, Conv 2×2, Pooling	32×32
Layer10	f_d×8, 3×3, Conv f_d×8, 3×3, Conv 0.5, Dropout	16×16
Layer11	f_d×4, 2×2, Conv, 2×2, UpSampling Axis=3, concatenate f_d×4, 3×3, Conv f_d×4, 3×3, Conv	32×32
Layer12	f_d×2, 2×2, Conv, 2×2, UpSampling Axis=3, concatenate f_d×2, 3×3, Conv f_d×2, 3×3, Conv	64×64
Layer13	f_d×1, 2×2, Conv, 2×2, UpSampling Axis=3, concatenate f_d×1, 3×3, Conv f_d×1, 1×1, Conv	128×128
Output	2, 3×3, Conv 1, 1×1, Conv	128×128

The second column illustrates the configuration of SHP-horizontal EUNet, and the third column denotes the output size of the feature map (MPM dataset).

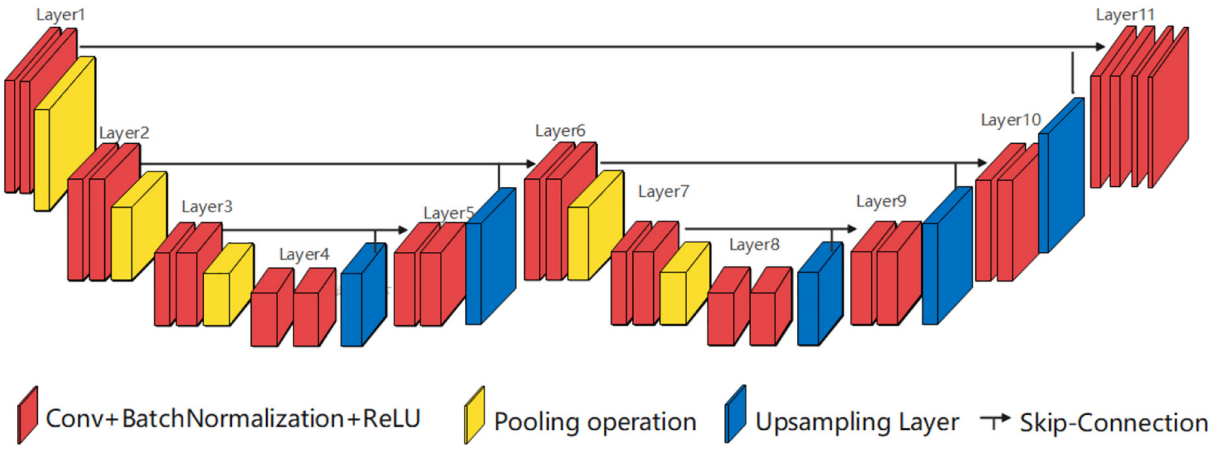

FIGURE 3 | Structure diagram of single low peak horizontal EUNet (SLP-horizontal EUNet) $U_1(4\text{-}3)\text{-}U_2(3\text{-}4)$.

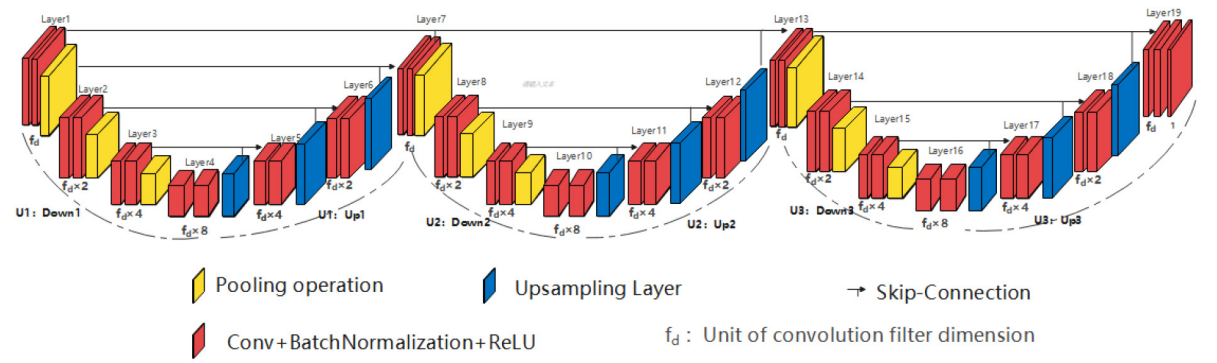

FIGURE 4 | Structure diagram of double high peak horizontal EUNet (DHP-horizontal EUNet) $U_1(4\text{-}4)\text{-}U_2\ (4\text{-}4)\text{-}U_3(4\text{-}4)$.

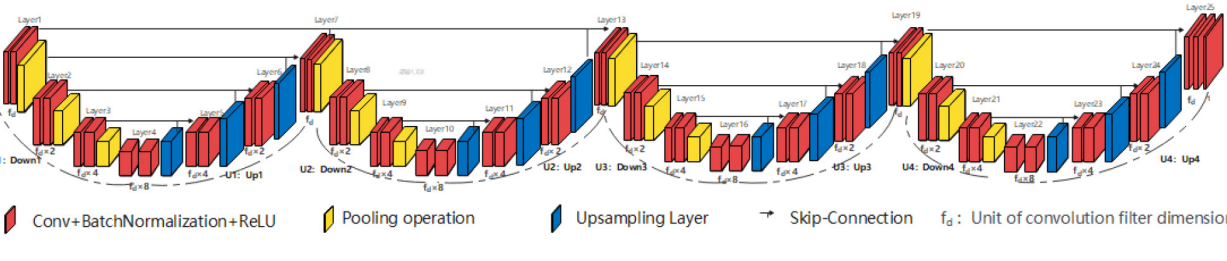

FIGURE 5 | Structure diagram of three high peak horizontal EUNet (THP-horizontal EUNet) $U_1(4\text{-}4)\text{-}U_2(4\text{-}4)\text{-}U_3(4\text{-}4)\text{-}U_4(4\text{-}4)$.

resembles SHP-horizontal EUNet structure which has four consecutive symmetrical U-shaped structures. As shown in **Figure 5**, different U-shaped structure is independent of each other. THP-horizontal EUNet $U_1(4\text{-}4)\text{-}U_2(4\text{-}4)\text{-}U_3(4\text{-}4)\text{-}U_4(4\text{-}4)$ is exhibited in this section.

Spatial Elastomeric UNet

The spatial EUNet extends the network structure from both horizontal and vertical dimensions. The continuous cascade mode of horizontal EUNet is used on the horizontal dimension of spatial EUNet, and random seeds are used to generate multiple independent parallel branches on the vertical dimension. This design provides two spatial EUNet structures, which are double branches and three branches, denoting as U*UNet and U*U*UNet.

*Double Branch Network: U*UNet*

U*UNet, as shown in **Figure 6**, is composed of two U-shaped parallel U_1 and U^1, within $Lay1_1\text{-}Lay4\text{-}Lay1_7$ forms U_1 path and $Lay1^1\text{-}Lay4\text{-}Lay1^7$ forms U^1 path. Each path of U*UNet adopting full symmetric down-up sampling mode for feature extraction and location information recovery, such as the path U_1, is

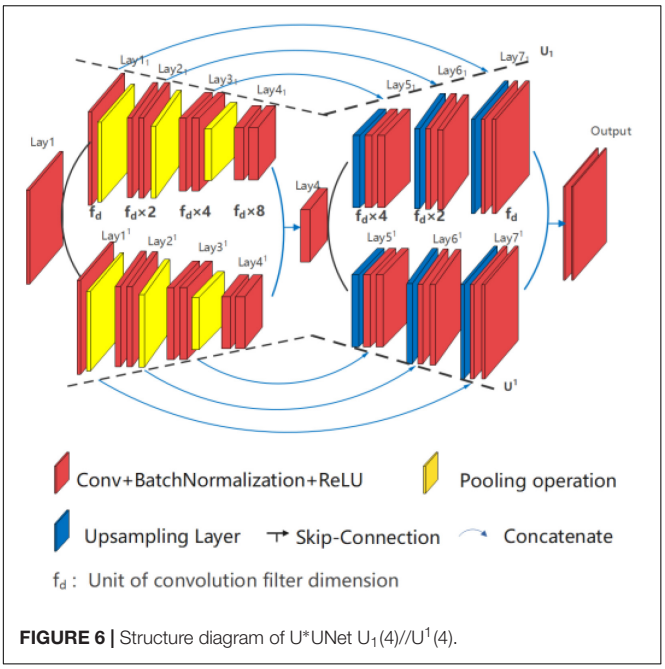

FIGURE 6 | Structure diagram of U*UNet $U_1(4)//U^1(4)$.

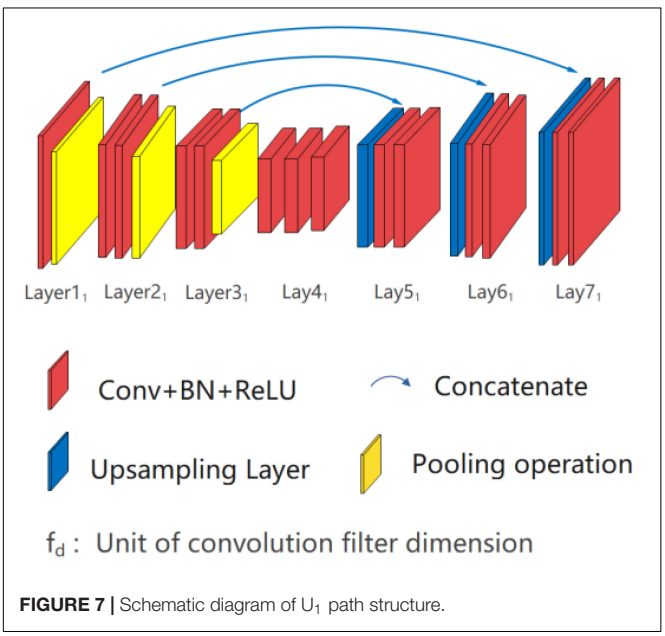

FIGURE 7 | Schematic diagram of U_1 path structure.

shown in **Figure 7**. The separation operation is implemented in the input layer (Lay1) and peak layer (Lay4) to form two paths, and therefore, the convergence operation is executed at the valley ($Lay4_1$ and $Lay4^1$) and output layer ($Lay7_1$ and $Lay7^1$). Separation operation utilizes different random seeds for convolution operation, while merge operation is carried out for convergence. In addition, the two U-shaped paths are independent of each other, so multiform nesting, such as Densenet and Resnet, can be performed independently in each path on the basis of design requirements. This study does not do any nesting, but only provides the basic form of the running results.

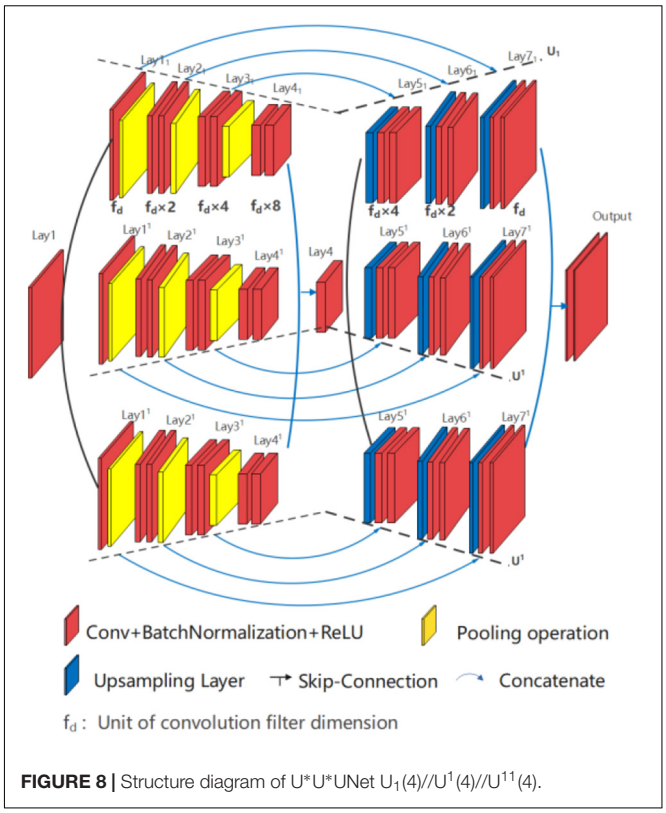

FIGURE 8 | Structure diagram of U*U*UNet $U_1(4)//U^1(4)//U^{11}(4)$.

The architecture design of U*UNet is as follows:

① U*UNet is composed of two in-parallel connected U-shaped structures.
② Each path contains an independent symmetrical U-shaped structure.
③ The fuse output is realized through skip connecting *via* the wave valley and the output layer.

*Three Branch Network: U*U*UNet*

The structure of U*U*UNet is similar to U*UNet, with three U-shaped branches connected in parallel, as shown in **Figure 8**. Three branches are formed by convolutional division operation through the input layer (Lay1) and the wave valley (Lay4), on which the jump-connection aggregation is further taken place through the wave valley ($Lay4_1$, $Lay4^1$, and $Lay4^{11}$) and the output layer ($Lay7_1$, $Lay7^1$, and $Lay7^{11}$). Researchers can take other forms of nested superposition in different branches regarding different research targets.

Various structures of EUNet can be employed, i.e., signal peak U*UNet $U_1(5)//U^1(5)$-$U_2(5)//U^2(5)$ can be devised and signal peak U*UNet $U_1(3)//U^1(3)$-$U_2(5)$ can also be planned. For example, signal peak U*UNet $U_1(5)//U^1(5)$-U_2 $(5)//U^2$ (5) is shown in **Figure 9**. The signal peak U*UNet follows the design principle of horizontal EUNet in the horizontal direction with two consecutive down-up sampling structures. Its space expansion mode is the same as that of U*U Net. To sum up, the designer can design flexibly according to the dataset

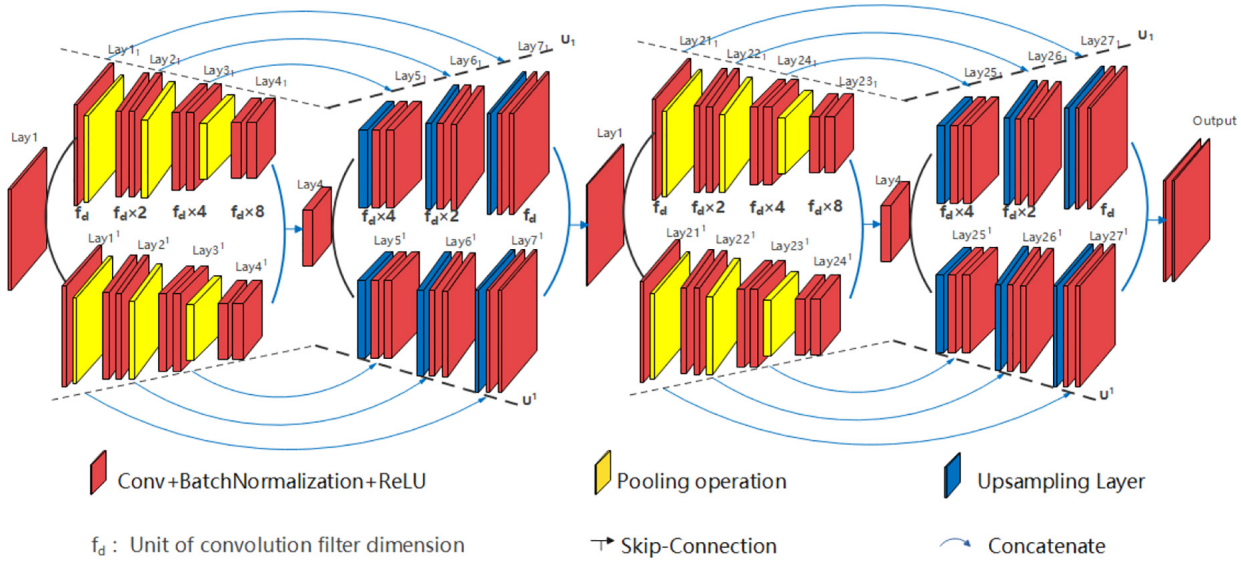

FIGURE 9 | Structure diagram of signal peak U*UNet $U_1(4)//U^1(4)\text{-}U_2(4)//U^2(4)$.

features, and design requirements for each path of EUNet are independent.

EXPERIMENT AND RESULTS

Dataset

All architectures proposed in the study were evaluated on two datasets, namely, the multi-photon microscopy (MPM) publicly benchmark retinal datasets (DRIVE). The self-built MPM imaging datasets were obtained by femtosecond home-testing Ti:Sa laser with a field view of 200 × 200 μm. An imaging system was carried out on Inc., Zeiss LSM 510 META with Plan-Neofluar objective. The testing data were taken from the dorsal forearm of the volunteer with a resolution of 128 × 128 pixels. Informed consent from each volunteer was acquired. The MPM dataset contains 90 images in.png format, of which 60 images are used for training, and the remaining 30 images are disposed of for testing. The DRIVE dataset contains 40 color retina images in.tif format, of which 20 images are used for training, and the remaining 20 images are disposed of for testing. The resolution of each image is 584 × 565 pixels at 45° field of view (Taruttis and Ntziachristos, 2015). The common medical image segmentation evaluation metrics suggested in the ISBI 2016 challenge (Ye et al., 2020) were used for benchmarking, including accuracy, precision, specificity, and mIOU. All networks were executed in Keras 2.24 with TensoFlow-GPU backend using Python 3.5.2. The training was implemented on a Microsoft Windows machine configured with GeForce GTX 1080Ti. All segmentation operations for two datasets were performed using the Dice coefficient loss function.

TABLE 2 | Segmentation performance comparison between *EUNet* and U-shaped network in MPM dataset.

Method		Accuracy	Precision	Specificity	mIOU
UNet		88.90	92.69	84.85	77.90
UNet + + (L3)		88.59	92.01	83.67	77.41
UNet + + (L4)		88.10	91.30	82.08	76.49
Dilated UNet(L1)		88.33	94.20	88.79	77.42
Dilated UNet(L2)		87.52	90.06	79.11	75.29
Dilated UNet(L3)		87.35	89.92	78.81	74.99
Horizontal EUNet	SP- Horizontal EUNet	91.25	96.24	92.82	82.38
	DP-Horizontal EUNet	91.58	95.88	91.88	83.02
	TP- Horizontal EUNet	91.48	94.94	89.82	82.70
Spatial EUNet	U*UNet	91.54	94.66	89.19	82.77
	U*U*UNet	91.21	93.40	86.33	81.99

Results

A series of experiments on MPM and DRIVE datasets was conducted to evaluate the performance between EUNet and U-shaped network (UNet, UNet + +, and Dilated UNet). The UNet and its variants were chosen because other deep network structures do not work well for the low resolution of MPM.

The Segmentation Results of the Multi-Photon Microscopy Dataset

In this section, the proposed EUNet was evaluated based on MPM. EUNet model adopts a 4-layered structure, for example, SHP-horizontal EUNet represents SHP-horizontal EUNet U1 (4-4)-U2 (4-4). The segmentation performance comparison between the proposed EUNet and the U-shaped network is summarized in **Table 2**, in which the segmentation results are also based on the accuracy, precision, specificity, and mIOU.

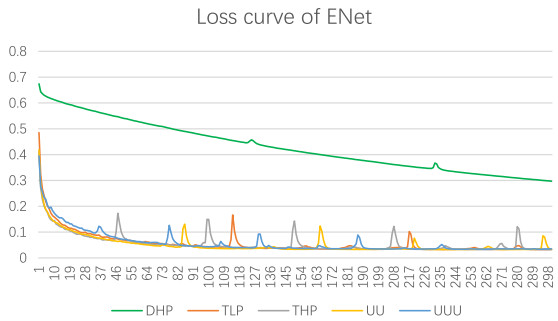

FIGURE 10 | Segmentation loss curve for MPM dataset.

UNet + + (L3) and UNet + + (L4) represent three-layered and four-layered nested structures, respectively, while dilated UNet(L1) denotes that the top layer using dilated convolution instead of convolution and (L2) means that the top two layers employ dilated convolution in down-sampling, and so on. UNET + + and dilated UNet perform comparably of MPM dataset, which segmentation accuracy is lower than that of UNet. Dilation convolution is not effective in small resolution datasets, especially with the deepening of dilated convolution. The performance of EUNet proposed in this article all show improvements based upon the U-shape network, where the average accuracy, precision, Specificity, and mIOU achieve 91.41%, 95.02%, 90%, and 82.57% respectively, yielding average improvement of 2.51 and 4.67 points in accuracy and mIOU than UNet respectively. EUNet shows good convergence, as shown in **Figure 10**.

For a better understanding of performance for each model intuitively, segmentation results of UNet, DHP-horizontal EUNet, and U*UNet are illustrated in **Figure 11**. It can be seen from the figure that EUNet embodies better boundary segmentation by comparing the outline detail in the second, third, and fourth images. In addition, it is noteworthy that more accurate edge feature extraction is achieved by U*UNet.

The Segmentation Results of the DRIVE Dataset

In this section, EUNet and U-shaped networks were tested and verified based on the DRIVE dataset. Each EUNet model adopts a 5-layered structure, for example, SHP-horizontal EUNet represents SHP-horizontal EUNet U1 (5-5)–U2 (5-5). **Table 3** shows the segmentation results that were assessed in the light of accuracy, precision, specificity, and mIOU.

As seen, expansion networks bring as a result to significant improvement for DRIVE dateset, which with average improvement of 0.38 points over UNet. Among the space expansion networks, the performance of U*U*UNet is the best, the accuracy of U*U*UNet is up to 96.56%, which is higher than that of UNet 0.59%. The precision of U*UNet is 85.42%, which is higher than that of UNet 4.22%. Experimental results showed that the proposed EUNet provided good performance than UNet. Compared with the UNET in the DRIVE dataset, the Dilated UNet has reduced performance, and the average accuracy is reduced by 2.21 points, which is lower than that of EUNet by 2.59 points. The results show that expansion convolution performs better inmedium resolution datasets, such as DRIVE dataset.

Partial segmentation results are illustrated in **Figure 12**. As shown in the figure, more details can be described by elastomeric networks. The best background noise processing ability is shown by U*UNet.

DISCUSSION

In general, the overall performance of MPM cell segmentation is limited by the amount of dataset and the resolution size. Based on preliminary work, this study provides EUNet. According to

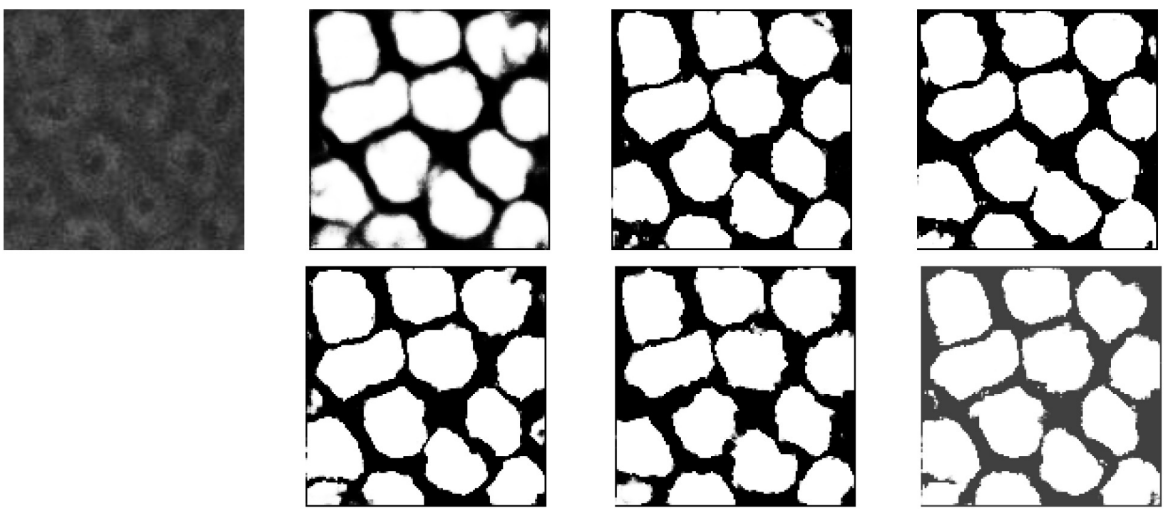

FIGURE 11 | Segmentation results for MPM dataset. Row 1, column 2: UNet; row 1, column 3: UNet + + (L4); row 1, column 4: dilated UNet(L2); row 2, column 2: DHP-horizontal EUNet; row 2, column 3: U*UNet; row 1, column 4: U*U*UNet.

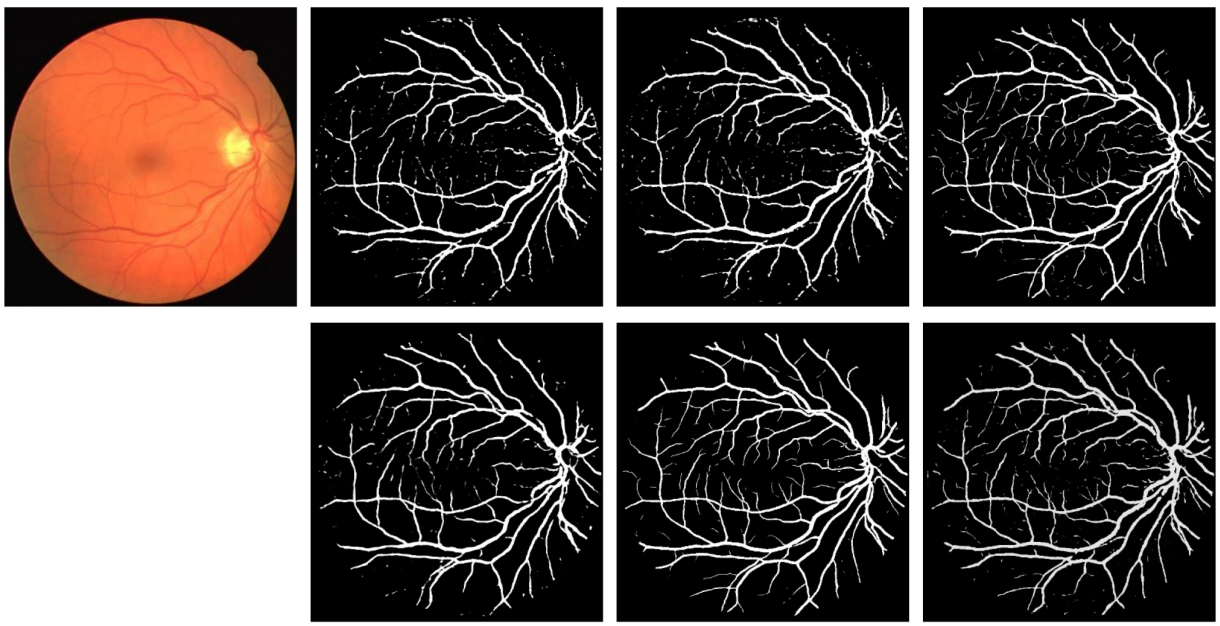

FIGURE 12 | Segmentation results for DRIVE dataset. Row 1, column 2: UNet; row 1, column 3: UNet + + (L4); row 1, column 4: dilated UNet(L2); row 2, column 2: DHP-horizontal EUNet; row 2, column 3: U*Unet; row 1, column 4: U*U*UNet.

their different structural characteristics, each network embodies different segmentation characteristics, as follows:

In summary, the main contributions of this study include:

(1) We proposed EUNet for medical image segmentation. This network provides the possibility for the malleable development of networks through the horizontal and vertical extension of the elastomeric wave, which greatly breaks through the shackles of traditional structures.

(2) Each corresponding peak layer and valley layer of the branch are operated by fusion convolution in spatial EUNet to realize the multipath information complement and to overcome the position information loss caused by down-sampling.

(3) Every path in this study maintains relative independence, which provides flexible redundancy for researchers. Designers can flexibly design diverse structural variants based on image characteristics and the consideration of Res-Net and Dense-Net. For example, the researcher can carry out multi-form nesting in any U-shaped path regarding the design demand or choose different segmentation model parameters to adjust in different paths (e.g., Conv (3)-Conv (3) can be employed in one path, Conv (3)-Conv (1)-Conv (3) can be utilized in the other path in U*UNet, and so forth).

TABLE 3 | Segmentation performance comparison between EUNet and U-shaped network in DRIVE.

Method		Accuracy	Precision	Specificity	mIOU
UNet		95.97	81.20	98.28	79.15
UNet + + (L3)		93.41	61.42	95.12	72.30
UNet + + (L4)		94.57	72.42	97.43	73.60
Dilated UNet(L1)		94.11	73.99	98.02	70.14
Dilated UNet(L2)		94.16	76.51	98.35	69.69
Dilated UNet(L3)		93.88	75.24	98.33	68.26
Dilated UNet(L4)		92.89	65.71	97.48	65.36
Horizontal EUNet	SHP-Horizontal EUNet	96.15	83.62	98.56	78.75
	DHP-Horizontal EUNet	96.36	83.12	98.44	80.17
	THP- Horizontal EUNet	96.22	81.69	98.27	77.43
Spatial EUNet	U*UNet	96.48	85.42	98.71	79.79
	U*U*UNet	96.56	83.19	98.39	82.03

CONCLUSION

A novel EUNet is presented in this study to overcome the fixed U-shaped structure of medical image segmentation, which is desirable for the research of Parkinson's disease and gene aging. Multiple expansion-contraction paths are provided to extract edge detailed features. Convergence is executed to strengthen the fusion of local and global information in peak and valley layers of different branches. The datasets employed in this design were MPM and DRIVE datasets to verify the effectiveness of EUNet. The experimental results demonstrate that the EUNet all show good accuracy and robustness in two datasets. The detailed description is strengthened, and the multi-scale

features are fully described by adding feature channels. The consecutive expand-contract path fully explores the dependency of context information and enhances the association feature representation of each semantic class to make the detailed expression of the image edge clearer. Moreover, the model provides a very flexible and extensible structure for future medical image segmentation owing to the relative independence of each U-shaped structure. Researchers can design each U-shaped structural level, functional structure, and parameter model independently according to the characteristics of the segmented images, which will further offer unprecedented room for segmentation resolution improvement.

DATA AVAILABILITY STATEMENT

The data analyzed in this study is subject to the following licenses/restrictions: this is the *in vivo* skin cell dataset. Requests to access these datasets should be directed to caisijing@163.com.

ETHICS STATEMENT

The studies involving human participants were reviewed and approved by Fujian Normal University. The patients/participants provided their written informed consent to participate in this study. Written informed consent was obtained from the individual(s) for the publication of any potentially identifiable images or data included in this article.

AUTHOR CONTRIBUTIONS

YW: responsible for the overall planning of the project. SC: responsible for CNN model design, improvement and implementation, experimental test and data analysis. GC: responsible for providing experimental data and model design guidance. All authors contributed to the article and approved the submitted version.

FUNDING

This work was supported in part by the National Natural Science Foundation of China (Nos. U1805262 and 61901117), Fujian provincial Research Project, China (Nos. 2021G02006, 2021L3010, and 2020J01879), by the Program for Changjiang Scholars and Innovative Research Team in University (IRT_15R10), by the Special Funds of the Central Government Guiding Local Science and Technology Development (2020L3008 and 2021L3010), by Key provincial scientific and technological innovation projects (2021G02006), the United Fujian Provincial Health and Education Project for Tackling the Key Research of China (2019-WJ-03), and by Fujian Photoelectric Sensing Application Engineering Technology Research Center (2021002).

REFERENCES

Amer, A., Ye, X., and Janan, F. (2021). "Residual dilated U-net for the segmentation Of COVID-19 infection from CT images," in *Proceedings of the IEEE/CVF International Conference on Computer Vision (ICCV) Workshops*, Seoul, 462–470. doi: 10.1109/ICCVW54120.2021.00056

Aspray, T. J., and Hill, T. R. (2019). Osteoporosis and the ageing skeleton. *Subcell. Biochem.* 91, 453–476. doi: 10.1007/978-981-13-3681-2_16

Balu, M., Lentsch, G., Korta, D. Z., König, K., Kelly, K. M., Tromberg, B. J., et al. (2017). In vivo multiphoton-microscopy of picosecond-laser induced optical breakdown in human skin, lasers in surgery and medicine. *Lasers Surg. Med.* 49, 555–562. doi: 10.1002/lsm.22655

Cai, S., Tian, Y., Lui, H., Zeng, H., Wu, Y., and Chen, G. (2020). Dense-UNet: a novel multiphoton in vivo cellular image segmentation model based on a convolutional neural network. *Quant. Imaging Med. Surg.* 10, 1275–1285. doi: 10.21037/qims-19-1090

Chen, G., Lui, H., and Zeng, H. (2015). Image segmentation for integrated multiphoton microscopy and reflectance confocal microscopy imaging of human skin in vivo. *Quant. Imaging Med. Surg.* 5, 17–22. doi: 10.3978/j.issn.2223-4292.2014.11.02

Chi, J., Han, X., Wu, C., Wang, H., and Ji, P. (2021). X-Net: multi-branch UNet-like network for liver and tumor segmentation from 3D abdominal CT scans. *Neurocomputing* 459, 81–96. doi: 10.1016/j.neucom.2021.06.021

Drozdzal, M., Vorontsov, E., Chartrand, G., Kadoury, S., and Pal, C. (2016). "The importance of skip connections in biomedical image segmentation," in *Deep Learning and Data Labeling for Medical Applications. DLMIA 2016, LABELS 2016. Lecture Notes in Computer Science*, Vol. 10008 ed. G. Carneiro, D. Mateus, L. Peter, A. Bradley, J. M. R. S. Tavares, V. Belagiannis, et al. (Cham: Springer). doi: 10.1016/j.media.2019.02.006

Haft-Javaherian, M., Fang, L., Muse, V., Schaffer, C. B., Nishimura, N., and Sabuncu, M. R. (2019). Deep convolutional neural networks for segmenting 3D in vivo multiphoton images of vasculature in Alzheimer disease mouse models. *PLoS One* 14:e0213539. doi: 10.1371/journal.pone.0213539

Ibtehaz, N., and Rahman, M. S. (2020). MultiResUNet : rethinking the U-Net architecture for multimodal biomedical image segmentation. *Neural Netw.* 121, 74–87. doi: 10.1016/j.neunet.2019.08.025

Lentsch, G., Valdebran, M., Harris, R. M., Barr, R. J., Smith, J., Linden, K., et al. (2019). "Recent advances in multiphoton microscopy for clinical skin imaging," in *Proceedings of the Biophotonics Congress: Optics in the Life Sciences Congress*, Vancouver. doi: 10.1364/NTM.2019.NM2C.1

Li, H., Zhygallo, A., and Menze, B. (2018). "Automatic brain structures segmentation 985 using deep residual dilated U-Net," in *Proceedings of the International MICCAI Brainlesion Workshop*, Vol. 26, (Berlin: Springer), 385–393. doi: 10.1007/978-3-030-11723-8_39

Li, J., Sun, W., Feng, X., Xing, G., von Deneen, K. M., Wang, W., et al. (2021). A dense connection encoding–decoding convolutional neural network structure for semantic segmentation of thymoma. *Neurocomputing* 451, 1–11. doi: 10.1016/j.neucom.2021.04.023

Li, X., Chen, H., Qi, X., Dou, Q., Fu, C.-W., and Heng, P.-A. (2018). H-DenseUNet: hybrid densely connected UNet for liver and tumor segmentation from CT volumes. *IEEE Trans. Med. Imaging* 12, 2663–2674. doi: 10.1109/TMI.2018.2845918

Li, Z., Krishnaswamy, V., Jiang, S., Davis, S. C., Srinivasan, S., Paulsen, K. D., et al. (2010). Rapid magnetic resonance-guided near-infrared mapping to image pulsatile hemoglobin in the breast. *Opt. Lett.* 35, 3964–3966. doi: 10.1364/OL.35.003964

Liu, L., Cheng, J., Quan, Q., Wu, F.-X., Wang, Y.-P., and Wang, J. (2020). A survey on U-shaped networks in medical image segmentations. *Neurocomputing* 409, 244–258. doi: 10.1016/j.neucom.2020.05.070

Loeser, R. F. (2009). Aging and osteoarthritis: the role of chondrocyte senescence and aging changes in the cartilage matrix. *Osteoarthr. Cartil.* 17, 971–979. doi: 10.1016/j.joca.2009.03.002

Long, J., Shelhamer, E., and Darrell, T. (2015). "Fully convolutional networks for semantic segmentation," in *Proceedings of the 2015 IEEE Conference on Computer Vision and Pattern Recognition (CVPR)* (Boston, MA: IEEE).

Pang, S., Pang, C., Zhao, L., Chen, Y., Su, Z., Zhou, Y., et al. (2020). SpineParseNet: spine parsing for volumetric MR image by a two-stage segmentation framework with semantic image representation. *IEEE Trans. Med. Imaging* 40, 262–273. doi: 10.1109/TMI.2020.3025087

Papadopoulos, I. N., Jouhanneau, J.-S., Poulet, J. F. A., and Judkewitz, B. (2017). Scattering compensation by focus scanning holographic aberration probing (F-SHARP). *Nat. Photonics* 11, 116–123. doi: 10.1038/nphoton.2016.252

Ronneberge, O., Fischer, P., and Brox, T. (2015). "U-Net: convolutional networks for biomedical image segmentation," in *Medical Image Computing and Computer-Assisted Intervention – MICCAI 2015. MICCAI 2015. Lecture Notes in Computer Science*, Vol. 9351, eds N. Navab, J. Hornegger, W. Wells, and A. Frangi (Cham: Springer).

Sun, Y. (2020). *A Dissertation Submitted to Shanghai Jiao Tong University for the Degree of Philosophy Doctor[D]*. Shanghai: Shanghai Jiao Tong University.

Taruttis, A., and Ntziachristos, V. (2015). Advances in real-time multispectral optoacoustic imaging and its applications. *Nat. Photonics* 9, 219–227. doi: 10.1038/nphoton.2015.29

Vuola, A. O., Akram, S. U., and Kannala, J. (2019). "Mask-RCNN and U-Net ensembled for nuclei segmentation," in *Proceedings of the 2019 IEEE 16th International Symposium on Biomedical Imaging* (Venice: IEEE), 8–11.

Xia, H., Sun, W., Song, S., and Mou, X. (2020). Md-Net: multi-scale dilated convolution network for CT images segmentation. *Neural Process. Lett.* 51, 2915–2927. doi: 10.1007/s11063-020-10230-x

Ye, Q., Wen, Y., Al-Kuwari, N., and Chen, X. (2020). Association between Parkinson's disease and melanoma: putting the pieces together. *Front. Aging Neurosci.* 12:60. doi: 10.3389/fnagi.2020.00060

Zhang, J., Jin, Y., Xu, J., Xu, X., and Zhang, Y. (2018). Mdu-net: multi-scale densely connected u-net for biomedical image segmentation. *arXiv preprint*. arXiv:1812.00352.

Zhao, B., Soraghan, J., Di Caterina, G., and Grose, D. (2019). "Segmentation of head and neck tumours using modified U-net," in *Proceedings of the 27th European Signal Processing Conference (EUSIPCO)* (A Coruna: IEEE), 2–6.

Zhou, Z., Siddiquee, M. M. R., Tajbakhsh, N., and Liang, J. (2020). UNet++: redesigning skip connections to exploit multiscale features in image segmentation. *J. IEEE Trans. Med. Imaging* 13, 1856–1867. doi: 10.1109/TMI.2019.2959609

Conflict of Interest: The authors declare that the research was conducted in the absence of any commercial or financial relationships that could be construed as a potential conflict of interest.

Publisher's Note: All claims expressed in this article are solely those of the authors and do not necessarily represent those of their affiliated organizations, or those of the publisher, the editors and the reviewers. Any product that may be evaluated in this article, or claim that may be made by its manufacturer, is not guaranteed or endorsed by the publisher.

Copyright © 2022 Cai, Wu and Chen. This is an open-access article distributed under the terms of the Creative Commons Attribution License (CC BY). The use, distribution or reproduction in other forums is permitted, provided the original author(s) and the copyright owner(s) are credited and that the original publication in this journal is cited, in accordance with accepted academic practice. No use, distribution or reproduction is permitted which does not comply with these terms.

frontiers in Aging Neuroscience

ORIGINAL RESEARCH
published: 18 March 2022
doi: 10.3389/fnagi.2022.752858

Identification of Potential Driver Genes and Pathways Based on Transcriptomics Data in Alzheimer's Disease

*Liang-Yong Xia, Lihong Tang, Hui Huang and Jie Luo**

School of Biomedical Engineering, Shanghai Jiao Tong University, Shanghai, China

Alzheimer's disease (AD) is one of the most common neurodegenerative diseases. To identify AD-related genes from transcriptomics and help to develop new drugs to treat AD. In this study, firstly, we obtained differentially expressed genes (DEG)-enriched coexpression networks between AD and normal samples in multiple transcriptomics datasets by weighted gene co-expression network analysis (WGCNA). Then, a convergent genomic approach (CFG) integrating multiple AD-related evidence was used to prioritize potential genes from DEG-enriched modules. Subsequently, we identified candidate genes in the potential genes list. Lastly, we combined deepDTnet and SAveRUNNER to predict interaction among candidate genes, drug and AD. Experiments on five datasets show that the CFG score of *GJA1* is the highest among all potential driver genes of AD. Moreover, we found *GJA1* interacts with AD from target-drugs-diseases network prediction. Therefore, candidate gene *GJA1* is the most likely to be target of AD. In summary, identification of AD-related genes contributes to the understanding of AD pathophysiology and the development of new drugs.

Keywords: Alzheimer's disease, transcriptomics, drug repurposing, deep learning, drug-target interaction

OPEN ACCESS

Edited by:
Chih-Yu Hsu,
Fujian University of Technology, China

Reviewed by:
Lorenzo Farina,
Sapienza University of Rome, Italy
Christoph Preuss,
Jackson Laboratory, United States

****Correspondence:***
Jie Luo
jieluo@sjtu.edu.cn

Specialty section:
This article was submitted to Alzheimer's Disease and Related Dementias, a section of the journal Frontiers in Aging Neuroscience

Received: *03 August 2021*
Accepted: *21 February 2022*
Published: *18 March 2022*

Citation:
Xia L-Y, Tang L, Huang H and Luo J (2022) Identification of Potential Driver Genes and Pathways Based on Transcriptomics Data in Alzheimer's Disease. Front. Aging Neurosci. 14:752858. doi: 10.3389/fnagi.2022.752858

INTRODUCTION

Alzheimer's disease (AD) is one of the most common neurodegenerative diseases, accounting for the majority of dementia patients (Wood, 2018; Darby et al., 2019). AD is estimated to affect in 13.8 million individuals in the United States (US), with 7.0 million being aged 85 years or older by 2050 (Alzheimer's Association, 2018; Cummings et al., 2019). Currently, genetic factor are believed to be partially responsible for AD (Xu et al., 2018). Genome-wide association studies (GWAS) have also revealed that some single nucleotide polymorphisms (SNPs) contribute to AD disease onset (Hao et al., 2019; Andrews et al., 2020). These include common variants such as amyloid protein precursor (*APP*), presenilin-1 (*PSEN1*), presenilin-2 (*PSEN2*) and apolipoprotein E (*APOE*). *PSEN1*, *PSEN2* and *APP* genes are clear pathogenic genes of early-onset AD (Lanoiselée et al., 2017). *APOE*, as the only identified risk gene for late-onset AD, can increase the rate of cognitive decline (Wijsman et al., 2011). Different microRNAs (miRNAs) are also involved in the pathophysiology of AD (Femminella et al., 2015). For example, miRNA-377 promotes cell proliferation and inhibits cell apoptosis by regulating the expression level of cadherin 13 (CDH13), thus participating in the occurrence and development of AD (Liu et al., 2018). Long non-coding RNAs (lncRNAs) have been widely reported to be associated with a variety of physiological

and pathological processes, such as AD. Brain cytoplasmic RNA is a kind of lncRNA, and the overexpression of brain cytoplasmic may lead to synaptic/dendritic degeneration in AD (Doxtater et al., 2020). Despite the fact that remarkable advances have been made in the understanding of the genetic basis of AD, there is no disease modifying therapy for AD. Identification of AD-related genes from transcriptomics becomes an attractive strategy for finding potential targets for drug therapy.

Gene expression profiling of transcriptomic datasets of AD and normal brain samples has identified potential genes and contributed to the search for potential targets (Patel et al., 2019). Correlation networks are often used to analyze gene expression data and gather biologically-relevant information from genes with similar co-expression patterns. At present, the two most commonly used gene co-expression network algorithms are SWItchMiner (SWIM) (Falcone et al., 2019) and Weighted Gene Correlation Network Analysis (WGCNA) (Nangraj et al., 2020; Ren et al., 2020). SWIM constructs an unweighted correlation network using local and global graph attributes to mine genes, known as switch genes, that have been shown to be associated with drastic changes in cell phenotypes, such as cancer development. WGCNA builds a correlation network that can be weighted or unweighted, and identifies related genes by measuring the centrality of a gene in the network. However, SWIM does not consider scale-free networks. The most notable characteristic of a scale-free network is the relative commonness of vertices with a degree that greatly exceeds the average. The highest-degree nodes are often referred to as "hubs" and are considered to have a specific purpose in their network. WGCNA is based solely on a scale-free network that is used to determine the relationships between genes, thereby enabling the identification of modules (clusters) of highly correlated genes, and the hub gene in each module. WGCNA is ideal for the identification of gene modules and key genes that contribute to phenotypic traits. Here, we used WGCNA to mine AD-specific modules from DEGs of AD and normal samples and identified candidate genes of from AD-specific modules.

Studying target-drug-disease network has contributed to the search for candidate genes of AD. In recent years, deep learning has been applied in biomedical and artificial intelligence fields, and many deep learning frameworks have been used to deal with the prediction problem of drug-target interaction (DTIs) (Xia et al., 2019). Öztürk et al. (2018) proposed a convolutional neural network (CNN)-based method based on using only sequence information and performing DTIs prediction on Davis and KIBA dataset. Rayhan et al. developed the FRnet-DTI, which is using autoenconder and CNN for feature extraction and classification, respectively (Chu et al., 2021). Zeng et al. (2020a) utilized cascade deep forest and arbitrary-order neighboring algorithms to predict DTIs. Zeng et al. (2020b) developed deepDTnet, a deep learning methodology for new target identification and drug repurposing in a heterogeneous network embedding 15 types of chemical, genomic, phenotypic, and cellular network profiles. Lots of works has been proposed for drug repurposing. Zeng et al. (2019) presented deepDR (deep learning-based drug repositioning), to systematically infer new drug-disease relationships for *in silico* drug repurposing. Fiscon et al. (2021) proposed SAveRUNNER, which predicts drug-disease associations by quantifying the interplay between the drug targets and the disease-specific proteins in the human interactome via a novel network-based similarity measure that prioritizes associations between drugs and diseases locating in the same network neighborhoods. Here, we combined deepDTnet and SAveRUNNER to predict interaction among candidate genes, drug and AD.

In this paper, we aimed to search potential driver genes for AD from DEGs based on multiple transcriptomics dataset. We hypothesized that the DEGs might be regulated by several candidate genes in the DEG-enriched coexpression modules/networks by WGCNA. We used CFG score as a measurement of the likelihood for candidate genes to be AD targets. Further, we combined deepDTnet and SAveRUNNER to predict interaction between candidate genes and AD based on gene-drug-disease network in **Figure 1**.

MATERIALS AND METHODS

AD Expression Data Collection and Preprocessing

Our dataset came from the AlzData and ADNI database. For AlzData, Xu et al. constructed new database AlzData (http://www.alzdata.org/) including, hippocampus (HP), entorhinal cortex (EC), frontal cortex (FC), and temporal cortex (TC). The original four microarray data come from Gene Expression Omnibus (GEO) (https://www.ncbi.nlm.nih.gov/geo), by searching with the keyword "Alzheimer." Data retrieval has been performed using the following series of criteria: 1) AD-related expression profiles in the ArrayExpress database (https://www.ebi.ac.uk/arrayexpress/) were checked to avoid potential omissions; 2) Studies with no genome-wide probes or few probes were filtered; 3) For those GSE series with possibly duplicated samples or identical sample resource, we retained the one with a larger sample size and excluded another; 4) Only expression profiles of human postmortem brain tissues from HP, EC, FC, and TC, which were main regions affected by AD, were included; 5) Data retrieval and quality control were double-checked by two investigators. To ensure data quality, samples that were younger than 50 years old, or were outliers in our principal component analysis (PCA) of expression distribution, were excluded from this study.

For ADNI data (http://adni.loni.usc.edu), Gene expression profiling from peripheral blood samples collected using PAXgene tubes for RNA analysis was performed on the Affymetrix Human Genome U219 Array (www.affymetrix.com, Santa Clara, CA) for ADNI and on the Illumina Whole-Genome DASL assay (www.illumina.com, San Diego, CA) for AddNeuroMed and MCSA. All probe sets were mapped and annotated with reference to the human genome (hg19). Raw microarray expression values were pre-processed followed by standard quality control (QC) procedures on samples and probe sets. Briefly, raw expression values were pre-processed using the robust multi-chip average normalization method. We checked discrepancies between the reported sex and sex determined from sex-specific gene expression data including XIST and USP9Y and also

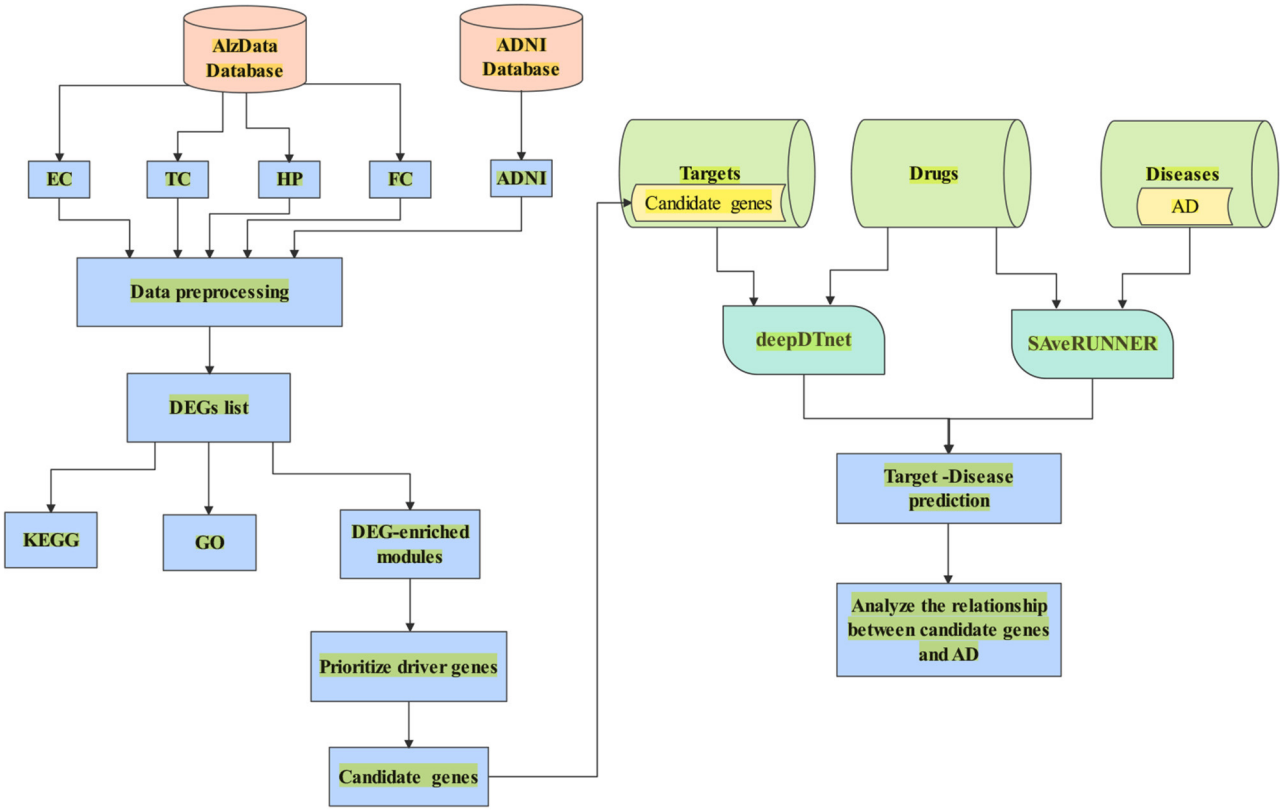

FIGURE 1 | A flowchart of the whole study. (1) Data collection from AlzData and ADNI; (2) Data preprocessing (e.g., eliminating the samples with missing data); (3) DEGs regarded with $|logFC| > 0.1$ and $FDR < 0.05$; (4) Enrichment of biological process analyzed by DAVID 6.8; (5) Use WGCNA to find AD-specific module; (6) Prioritize driver genes of AD by CFG score; (7) candidate genes with $CFG \geq 5$ are identified. (8) Collect the dataset of target, drug and disease; (9) Combine deepDTnet and SAveRUNNER to predict association between candidate genes and AD.

evaluated whether SNP genotypes were matched with genotypes predicted from gene expression data.

In this study, we only consider gene expression data and binary classification problem (control vs. AD). After data processing, e.g., eliminating the samples with missing data, altogether, we have 467 controls and 309 AD from five dataset for subsequent analyses in total, including EC (39 vs. 39), HP (67 vs. 74), FC (128 vs. 104), TC (39 vs. 52) and ADNI (194 vs. 40). Detailed information of each dataset is shown in **Table 1**.

Statistical Analysis

Genes with log2 fold change greater than 0.1 ($|logFC| > 0.1$) and FDR smaller than 0.05 ($FDR < 0.05$) were defined as DEGs in AD patients in the each dataset. Functional enrichment of the DEGs was produced from Database for DAVID 6.8, which now provides a comprehensive set of functional annotation tools for investigators to understand biological meaning behind large list of genes. For obtained list of DEGs, DAVID 6.8 is able to identify enriched biological themes, particularly KEGG pathway and GO terms (Huang et al., 2007). Differential expression analysis was conducted by R package limma and the Benjamini-Hochberg's method was used to correct for multiple comparisons (Xu et al., 2018).

Weighted Gene Co-expression Network Analysis

We used R package WGCNA to perform the weighted correlation network analysis. For genes i and j, the correlation coefficient is r_{ij}, we define the correlation intensity : $a_{ij} = r_{ij}^{\beta}$, which depends on the choice of power β (the power value ranging from 1 to 20). When the independence is more than 0.80, the scale-free network is obtained by screening the appropriate power value. Finally, the adjacency matrix was transformed into topological overlap matrix (TOM). Once the network is built through the TOM, it is converted to a distance matrix (1-TOM) to use it as the basis for clustering. A dynamic tree-cutting algorithm is then applied to the dendrogram to generate a partition of disjunct sets of genes. In addition, we extracted the corresponding gene information of each module for further analysis (Botía et al., 2017).

deepDTnet and SAveRUNNER

In this study, we combined deepDTnet and SAveRUNNER to predict interaction between candidate genes and AD. deepDTnet and SAveRUNNER were applied to predict the interactions of candidate genes/targets and drugs and relationship drugs and diseases, respectively.

TABLE 1 | Brief descriptions for five datasets.

Dataset	AlzData				Alzheimer's disease neuroimaging initiative
	Entorhinal cortex	Hippocampus	Frontal cortex	Temporal cortex	
Abbreviation	EC	HP	FC	TC	ADNI
No.of.gene	15361	16313	11779	15462	49387
Sample size(Control/AD)	78 (39/39)	141 (67/74)	232 (128/104)	91 (39/52)	234 (194/40)
Age	80 (29.6)	81.7 (9.6)	83 (9.4)	81 (8.7)	74.3 (6.5)
Male/Female/Unknown	35/43/0	68/73/0	99/111/22	32/41/18	116/118/0
Aβ	NA	NA	NA	NA	1142.9 (494.9)
Tau	NA	NA	NA	NA	25.4 (11.6)

These datasets come from AlzData and ADNI, respectively. Each dataset has multiple features. SDs are given in parentheses.

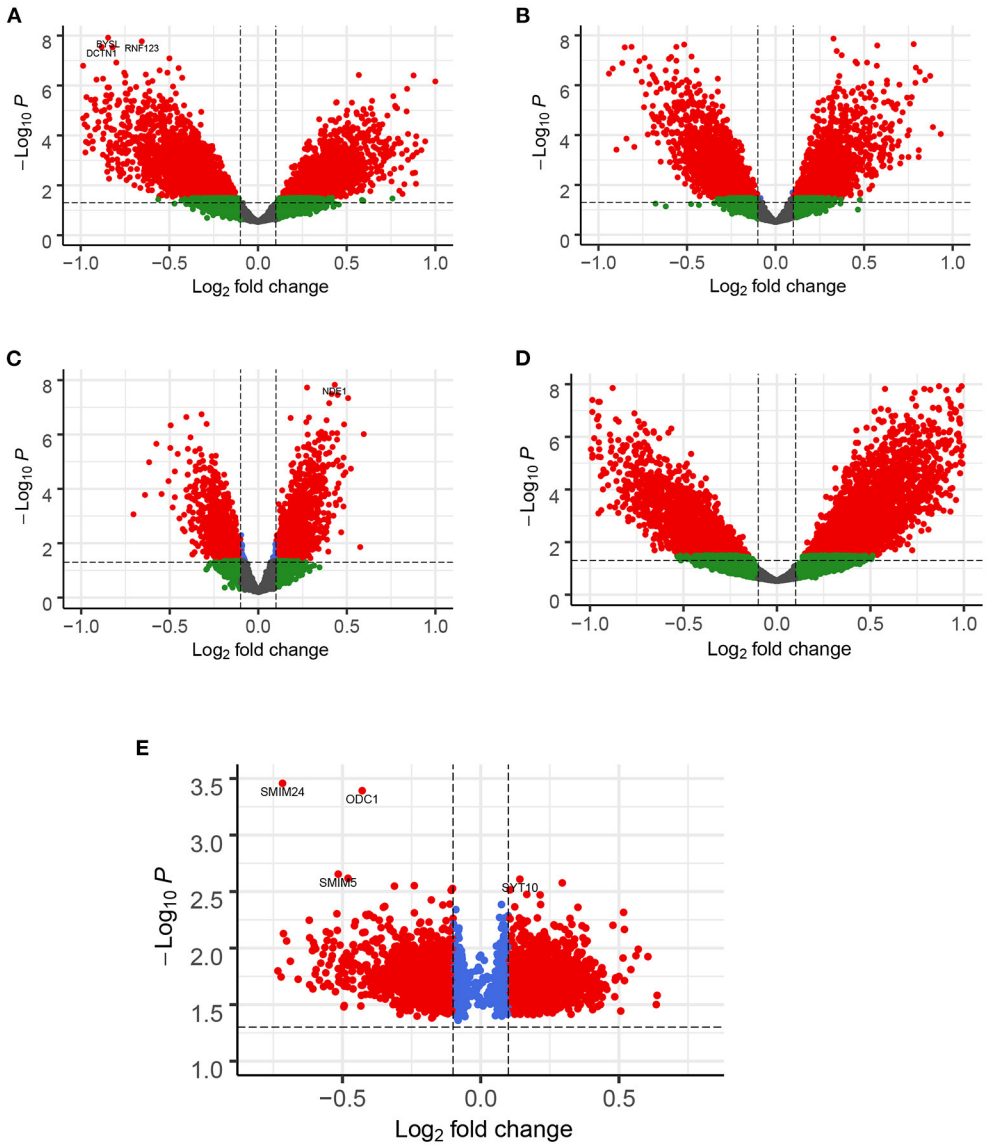

FIGURE 2 | Enhanced Volcano for illustrating DEGs in all datasets. The gene with $|logFC| > 0.1$ and $FDR < 0.05$ as DEGs shown in red node. **(A)** EC, **(B)** HP, **(C)** FC, **(D)** TC and **(E)** ADNI. Note: in ADNI dataset, DEGs by counting the frequency of 3 or above out of 10 occurrences.

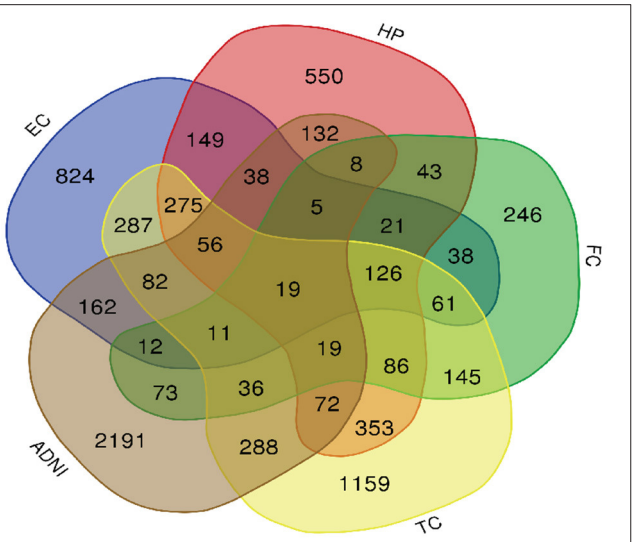

FIGURE 3 | Venn diagram is used to represent relationships between EC (blue), HP (red), FC (green), TC (yellow) and ADNI (brown).

Firstly, deepDTnet uses stacked denoising autoencoder (SDAE) to obtain low-dimensional embedding for both drugs and targets. A SDAE model minimizes the regularized problem and tackles reconstruction error, defined as follows:

$$min_{w_l,b_l}||x-\hat{x}||_F^2+\lambda\sum_l||W_l||_F^2 \quad (1)$$

where x is input sample x(a vector); L is the number of layers, w_l is weight matrix, and b_l is bias vector of layer $l \in \{1,.,L\}$. λ is a regularization parameter and $||.||_F$ denotes the Frobenius norm. The middle layer is the key that enables SDAE to reduce dimensionality and extract effective representations of side information.

Subsequently, Positive Unlabeled-matrix completion is used to predict unknown drug-target pairs. Assume the drug-target interaction matrix is given as $P \in R^{N_d \times N_t}$, where N_d is the number of drugs and N_t is the number of targets. When $P_{ij} = 1$, infers drug i is linked to target j while zero indicates the relationship is unobserved. The optimization problem of our model is parameterized as:

$$\min_{i,j} \sum_{(i,j)\in\Omega^+}(P_{ij}-x_iWH^Ty_j^T)^2+\alpha\sum_{(i,j)\in\Omega^-}(P_{ij}-x_iWH^Ty_j^T)^2+\lambda(||W||_F^2+||H||_F^2) \quad (2)$$

where the set $\Omega \in N_d \times N_t$ is the observed entries from the true underlying matrix that includes both positive and negative entries, such that $\Omega = \Omega^+ \cup \Omega^-$, let Ω^+ denotes the observed samples and Ω^-denotes the missing entries chosen as negatives. Under the assumption that the matrix is modeled to be low rank, i.e., $W \in N_d \times k$ and $H \in N_t \times k$, and these matrices share a low dimensional latent space, satisfying $k \leqslant N_d, N_t$. For biased inductive matrix completion, the value α is the key parameter, λ is a regularization parameter. Next, we approximate the likelihood of the pairwise interaction score between drug i and target j as:

$$Score(i,j) = x_iWH^Ty_j^T \quad (3)$$

where the higher score means a higher possibility that drug i is correlated with target j.

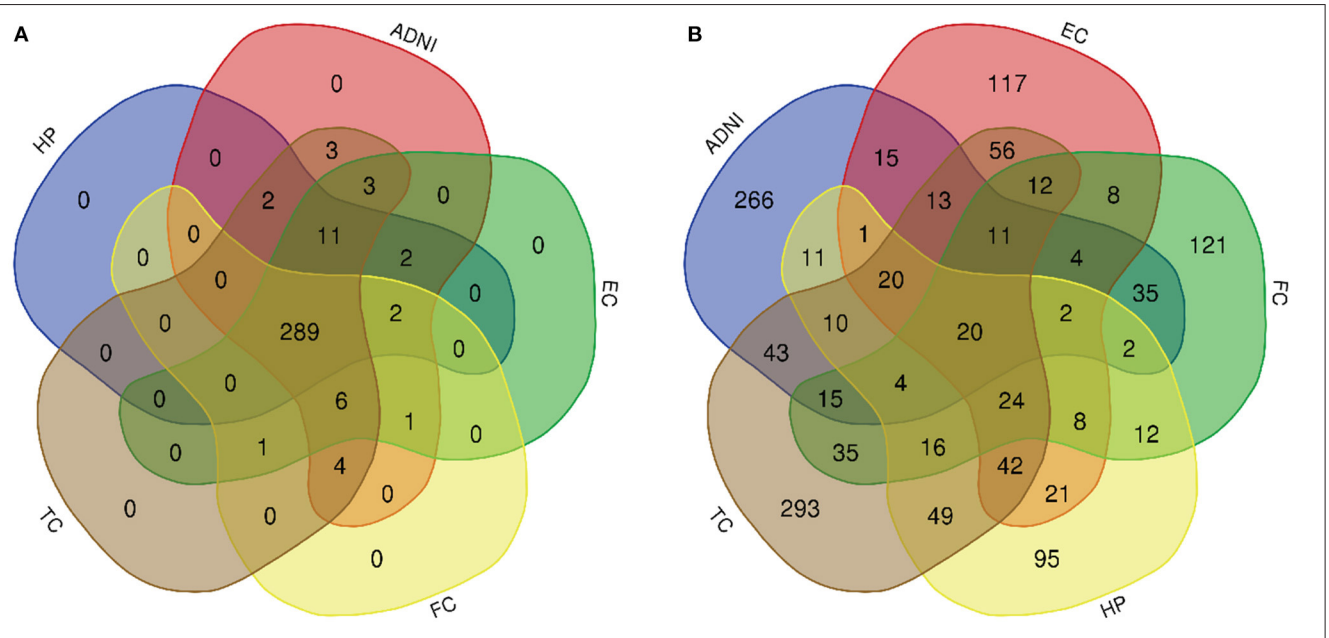

FIGURE 4 | Venn diagram is used to represent relationships between multiple datasets. **(A)** KEGG pathway and **(B)** GO term.

TABLE 2 | Significant KEGG pathways obtained from DAVID ($P < 0.005$).

ID	Description	ID	Description
hsa00020	Citrate cycle (TCA cycle)	hsa04966	Collecting duct acid secretion
hsa00190	Oxidative phosphorylation	hsa05010	Alzheimer's disease
hsa00260	Glycine, serine and threonine metabolism	hsa05012	Parkinson's disease
hsa00620	Pyruvate metabolism	hsa05014	Amyotrophic lateral sclerosis
hsa01200	Carbon metabolism	hsa05016	Huntington disease
hsa01210	2-Oxocarboxylic acid metabolism	hsa05017	Spinocerebellar ataxia
hsa01230	Biosynthesis of amino acids	hsa05020	Prion disease
hsa01522	Endocrine resistance	hsa05022	Pathways of neurodegeneration - multiple diseases
hsa03050	Proteasome	hsa05032	Morphine addiction
hsa04010	MAPK signaling pathway	hsa05033	Nicotine addiction
hsa04070	Phosphatidylinositol signaling system	hsa05110	Vibrio cholerae infection
hsa04071	Sphingolipid signaling pathway	hsa05120	Epithelial cell signaling in Helicobacter pylori infection
hsa04110	Cell cycle	hsa05131	Shigellosis
hsa04120	Ubiquitin mediated proteolysis	hsa05132	Salmonella infection
hsa04137	Mitophagy - animal	hsa05140	Leishmaniasis
hsa04140	Autophagy - animal	hsa05145	Toxoplasmosis
hsa04144	Endocytosis	hsa05152	Tuberculosis
hsa04145	Phagosome	hsa05163	Human cytomegalovirus infection
hsa04152	AMPK signaling pathway	hsa05167	Kaposi sarcoma-associated herpesvirus infection
hsa04211	Longevity regulating pathway	hsa05169	Epstein-Barr virus infection
hsa04218	Cellular senescence	hsa05202	Transcriptional misregulation in cancer
hsa04260	Cardiac muscle contraction	hsa05205	Proteoglycans in cancer
hsa04360	Axon guidance	hsa05212	Pancreatic cancer
hsa04625	C-type lectin receptor signaling pathway	hsa05214	Glioma
hsa04666	Fc gamma R-mediated phagocytosis	hsa05215	Prostate cancer
hsa04721	Synaptic vesicle cycle	hsa05219	Bladder cancer
hsa04722	Neurotrophin signaling pathway	hsa05220	Chronic myeloid leukemia
hsa04723	Retrograde endocannabinoid signaling	hsa05223	Non-small cell lung cancer
hsa04920	Adipocytokine signaling pathway	hsa05225	Hepatocellular carcinoma
hsa04932	Non-alcoholic fatty liver disease	hsa05235	PD-L1 expression and PD-1 checkpoint pathway in cancer
hsa04961	Endocrine and other factor-regulated calcium reabsorption		

Then, to quantify the vicinity between drug and disease modules, SAveRUNNER implements a novel network similarity measure:

$$f(p) = \frac{1}{1 + e^{-c[\frac{(1+QC)(m-p)}{m}d]}} \quad (4)$$

Where p is the network proximity measure defined: $p(T, S) = \frac{1}{\|T\|}\sum_{t\in T} mim_{s\in S}d(t, s)$ that represents the average shortest path length between drug targets t in the drug module T and the nearest disease genes s in the disease module S; QC is the quality cluster score; m is $max(p)$; c and d are the steepness and the midpoint of $f(p)$, respectively.

Finally, via deepDTnet and SAveRUNNER, we identified newly the relationship among candidate genes, drug and neurodegenerative diseases, which is including AD.

More detail about deepDTnet and SAveRUNNER could be found in previous study (Zeng et al., 2020b; Fiscon et al., 2021).

Convergent Functional Genomics

The potential driver genes was prioritized from AD-specific modules by CFG method, which integrated various levels of AD-related evidence (Ayalew et al., 2012; Xu et al., 2018). The range of CFG score was from 0 to 5, with 5 indicating highest priority. There were five AD-related evidence:1) Genetic association. If a gene had at least one locus being significantly associated with AD based on the summary statistics from the International Genomics of Alzheimer's Project [IGAP], 1 point was assigned; otherwise zero point. 2) Genetic regulation of gene expression. If a gene was associated with Expression Quantitative Trait Loci (eQTLs) showing an AD-risk in IGAP data, 1 point was assigned; otherwise zero point. 3) Protein-protein interaction. If a gene was physically interacted with any AD core genes (*APP*, *PSEN1*, *PSEN2*, *APOE*, or *MAPT*), 1 point was assigned; otherwise zero point. 4) Expression correlation with AD pathology. If the expression level of a gene was correlated with AD pathology in AD mice, 1 point was assigned; otherwise zero point. 5) Early alteration in AD mouse brain. If a gene showed differential expression in hippocampus of 2-month-old AD mice compared with age matched wild-type mice, 1 point was assigned; otherwise zero point.

RESULTS

DEG Detection

A total of 776 samples and 108,302 genes from multiple transcriptomic datasets were compiled for DEGs detection. Besides, for ADNI dataset, we randomly chose 40 samples from the control in 10 times and selected gene with frequency greater than or equal to 3. Each red node represented DEG for five datasets in **Figure 2**. We identified 7,567 DEG(2166 EC, 1952 HP, 949 FC, 3075 TC and 3204 ADNI) for subsequent analyses. About 6 19% of the total genes could be identified as DEGs. Among the DEG list in all five datasets, the expression patterns of well-known AD risk genes, such as APP, PSEN1, PSEN2, APOE and MAPT were only slightly altered or unchanged in AD patients. In addition, 19 genes had a consistently differential expression from EC, HP, FC, TC and ADNI (**Figure 3**). We investigated functional enrichment of the AD-related DEGs. The 7,567 target genes in the network were enriched in 324 KEGG pathway and 1,381 GO terms in **Figure 4**. We identified 61 KEGG pathway and 324 GO terms ($P < 0.005$), respectively. As shown in **Table 2**, we also found several pathways have been reported to be associated with AD, including Alzheimer's disease pathway, *MAPK* signaling pathway and AMPK signaling pathway. Top 20 significantly KEGG pathway selected was exhibited for each dataset in **Figure 5**. Besides, these GO terms are divided into ontologies based on a hierarchical relations. Specifically, DEGs related to the biological processes for synaptic-related functions were significant enriched in **Table 3**, such as chemical synaptic

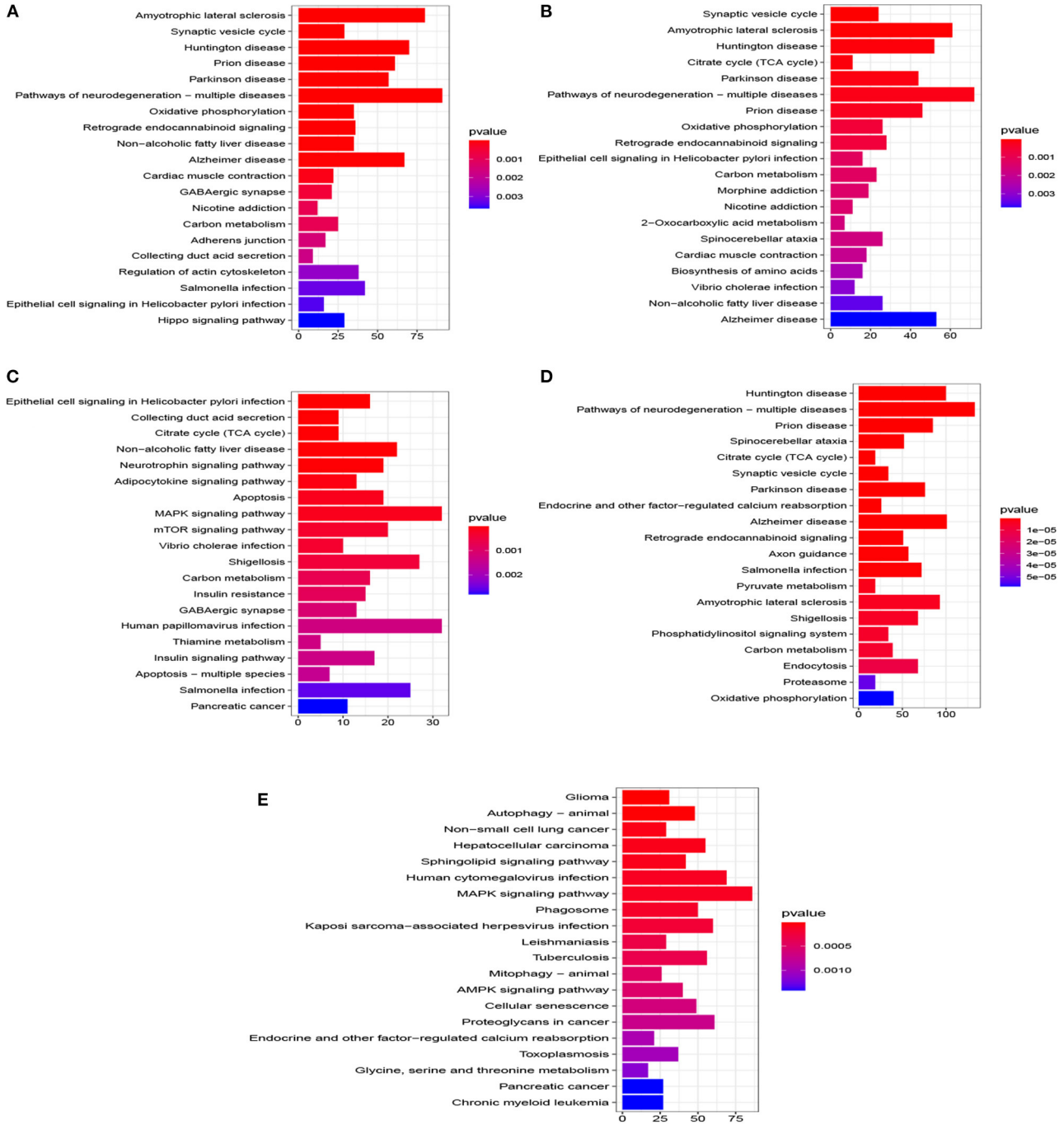

FIGURE 5 | Top 20 pathway of KEGG for five datasets ($P < 0.005$). **(A)** EC, **(B)** HP, **(C)** FC, **(D)** TC, and **(E)** ADNI.

transmission, regulation of postsynaptic membrane potential, synaptic vesicle exocytosis, synaptic transmission, GABAergic, regulation of synaptic transmission, glutamatergic, synaptic vesicle endocytosis and long-term synaptic potentiation. In addition, they were associated with neuron-related processes, including neurotransmitter secretion, neuron projection morphogenesis, negative regulation of neuron apoptotic process and negative regulation of neuron projection development.

We used WGCNA to divide the DEGs into several highly related gene modules. As shown in **Figure 6**, a very significant positive correlation was observed between five modules and AD for five dataset. A modular size was ranged from 96 to 142 genes

TABLE 3 | Significant GO terms obtained from DAVID ($P < 0.005$).

ID	Term
GO:0002223	Stimulatory C-type lectin receptor signaling pathway
GO:0006888	ER to Golgi vesicle-mediated transport
GO:0048015	Phosphatidylinositol-mediated signaling
GO:0038128	ERBB2 signaling pathway
GO:0007249	I-kappaB kinase/NF-kappaB signaling
GO:0006672	ceramide metabolic process
GO:0000165	MAPK cascade
GO:0045944	Positive regulation of transcription from RNA polymerase II promoter
GO:0007269	Neurotransmitter secretion
GO:0035329	Hippo signaling
GO:0006120	Mitochondrial electron transport, NADH to ubiquinone
GO:0042776	Mitochondrial ATP synthesis coupled proton transport
GO:0070125	Mitochondrial translational elongation
GO:0032981	Mitochondrial respiratory chain complex I assembly
GO:0007409	Axonogenesis
GO:0048812	Neuron projection morphogenesis
GO:0043524	Negative regulation of neuron apoptotic process
GO:0007268	Chemical synaptic transmission
GO:0060078	Regulation of postsynaptic membrane potential
GO:0016079	Synaptic vesicle exocytosis
GO:0048813	Dendrite morphogenesis
GO:0090263	Positive regulation of canonical Wnt signaling pathway
GO:0009967	Positive regulation of signal transduction
GO:0051932	Synaptic transmission, GABAergic
GO:0046034	ATP metabolic process
GO:0070933	Histone H4 deacetylation
GO:0007420	Brain development
GO:0007417	Central nervous system development
GO:0035357	Peroxisome proliferator activated receptor signaling pathway
GO:0015986	ATP synthesis coupled proton transport
GO:0040029	Regulation of gene expression, epigenetic
GO:0007399	Nervous system development
GO:0051966	Regulation of synaptic transmission, glutamatergic
GO:0048488	Synaptic vesicle endocytosis
GO:0010977	Negative regulation of neuron projection development
GO:0060071	Wnt signaling pathway, planar cell polarity pathway
GO:0006521	Regulation of cellular amino acid metabolic process
GO:2000310	Regulation of N-methyl-D-aspartate selective glutamate receptor activity
GO:0038061	NIK/NF-kappaB signaling
GO:0035418	Protein localization to synapse
GO:0060291	Long-term synaptic potentiation

The first column is GO terms ID; the second column is the name of GO terms.

that might reflect the different layers and complexity of gene regulation in the AD brain. These five AD-specific modules were used for identifying potential driver genes for AD etiology and pathology. We obtained potential driver genes from each AD-specific modules for every dataset. Finally, after removing the overlap genes, we have 602 candidate genes from 5 AD-specific modules in total, including EC (107), HP(140), FC(142), TC(136) and ADNI(96). We hypothesized that the higher the CFG score is, the more likely the candidate genes are to be AD targets. We chose 40 genes with $CFG \geq 4$ for subsequent analyses.

Identification and Prioritization of Potential Driver Genes

The 40 potential driver genes are prioritized by the CFG method based on AlzData database, which is integrated various levels of AD-related data in **Table 4**. For each gene, we showed the eQLT, GWAS, PPI, Early_DEG, Pathology correlation $A\beta$ and Tau ($CFG \geq 4$), and CFG score. We found that several genes were validated by previous studies from literatures. For example, *GJA1*, also known as connexin 43, shows upregulated mRNA and protein levels in AD (Ren et al., 2018). Specific reductions of RPH3A immunoreactivity compared with aged controls. *RPH3A* loss correlated with dementia severity, cholinergic deafferentation, and increased $A\beta$ concentrations. Furthermore, *RPH3A* expression is selectively downregulated in cultured neurons treated with $A\beta$ 25–35 peptides (Tan et al., 2014). *CASP6* activity is intimately associated with the pathologies that define AD, correlates well with lower cognitive performance in aged individuals, and is involved in axonal degeneration in several cellular and *in vivo* animal models (LeBlanc, 2013). The levels of angiotensinogen (*AGT*) is increased in the cerebrospinal fluid of patients with mild cognitive impairment and AD (Mateos et al., 2011). The stromal cell-derived factor 1 (SDF1), known as chemokine *CXCL12*, was a proinflammatory chemokine, highly expressed in the central nervous system. They may regulate synaptic transmission in excitability neurons and modulate neuroglial communication. *CXCL12* was detected in plasma and hippocampus AD patients. Levels of this chemokine were considerably decreased compared to the control group (Dulewicz et al., 2020). In summary, combining WGCNA with CFG offer a useful tool to prioritize potential genes for AD.

Candidate Genes *GJA1*

As shown in **Table 4**, the CFG score of *GJA1* is the highest among all potential genes and regarded as candidate gene. We combined deepDTnet and SAveRUNNER to search association between candidate genes *GJA1* and AD based on target-drug-disease network. As shown in **Figure 7**, the network is constructed 13 drugs, a candidate genes *GJA1* and neurodegenerative diseases. 11 newly drug-target interaction and 13 newly drug-disease association are identified by deepDTnet and SAveRUNNER, respectively. Especially, we found that dopamine were validated by previous studies from literatures. Dopamine, a compound of the catecholamine and phenethylamine families playing important roles in the human brain, was predicted by deepDR to be associated with AD. Such a prediction can be supported by a previous study indicating that lack of dopamine in the brain may cause some of the earliest symptoms of Alzheimer (Zeng et al., 2019). In AD, the dysfunction of dopaminergic transmission has been hypothesized as a new player in the pathophysiology of AD. Dopamine acts through five different types of receptors, generally distinct in two main subclasses: D1-like [comprising

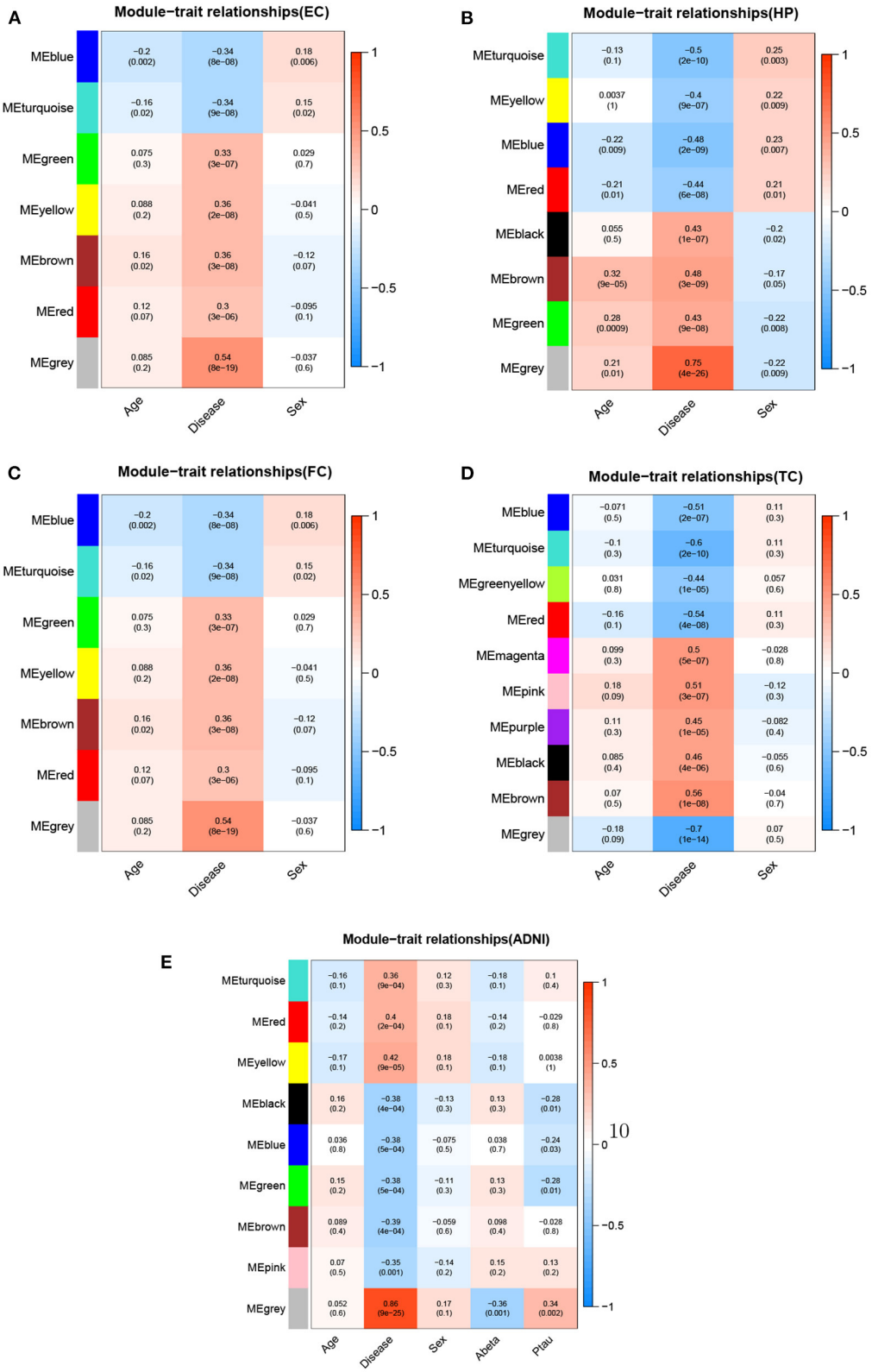

FIGURE 6 | Module-trait relationships for five datasets.Each row represents different gene co-expression modules, and each column represents different clinical phenotypes. Number represent correlation coefficients and P-values are in parenthesis. Correlation strength is represented by continuous color, with red being positive, blue being negative. **(A)** EC, **(B)** HP, **(C)** FC, **(D)** TC, and **(E)** ADNI.

TABLE 4 | The 40 potential driver genes are prioritized by the CFG method based on AlzData database.

Gene	AD-related evidence						CFG
	eQTL	GWAS	PPI	Early_DEG	Pathology cor		
					(Aβ)	(Tau)	
GJA1	2	2	*PSEN1, MAPT, APOE*	yes	0.388^{**}	0.131^{ns}	5
FOXO1	1	0	*PSEN2*	yes	0.270^{ns}	0.526^{*}	4
PRKX	3	NA	*PSEN1*	yes	0.352^{*}	-0.023^{ns}	4
RPH3A	5	2	-	yes	-0.199^{ns}	-0.738^{**}	4
CASP6	5	0	*APP, PSEN1, PSEN2, MAPT*	yes	0.482^{***}	0.738^{**}	4
CRMP1	1	3	*MAPT*	NA	-0.304^{*}	-0.506^{ns}	4
RGS4	1	32	-	yes	-0.419^{**}	-0.579^{*}	4
NPTX2	1	1	-	yes	-0.688^{***}	-0.783^{***}	4
RPS27	1	0	*PSEN2*	yes	0.503^{***}	0.662^{**}	4
MEGF10	3	8	-	yes	0.559^{***}	0.120^{ns}	4
AP2A1	1	0	*APP, PSEN2, MAPT*	yes	-0.277^{ns}	-0.585^{*}	4
PITPNC1	10	1	-	yes	-0.128^{ns}	-0.638^{*}	4
AGT	1	0	*APP, PSEN1, APOE*	yes	-0.359^{*}	0.002^{ns}	4
AQP4	7	4	-	yes	0.800^{***}	0.275^{ns}	4
MYT1L	3	12	-	yes	-0.488^{***}	-0.583^{*}	4
IQGAP1	1	0	*PSEN1*	yes	0.310^{*}	0.282^{ns}	4
IGFBP7	8	0	*MAPT, APOE*	yes	0.353^{*}	0.510^{ns}	4
CITED2	1	0	*APP, PSEN1, APOE*	yes	-0.433^{**}	-0.772^{***}	4
SMAD1	16	1	*APP, APOE*	NA	-0.332^{*}	-0.497^{ns}	4
CDH7	0	1	*PSEN1*	yes	-0.345^{*}	-0.691^{**}	4
MSRB2	5	2	-	yes	0.32^{*}	0.609^{*}	4
DBI	1	1	-	yes	0.780^{***}	0.718^{**}	4
PELI2	2	0	*PSEN2*	yes	0.591^{***}	-0.107^{ns}	4
AVEN	1	1	-	yes	0.525^{***}	0.008^{ns}	4
F13A1	7	3	*APP, APOE*	NA	0.195^{ns}	0.623^{*}	4
SLA	1	0	*PSEN1, MAPT*	yes	0.114^{ns}	0.662^{**}	4
ADAMTS20	2	17	-	yes	0.085^{ns}	0.587^{*}	4
RARB	6	2	*PSEN2*	yes	-0.064^{ns}	-0.387^{ns}	4
SDC2	8	3	*PSEN1, PSEN2, MAPT, APOE*	yes	0.041^{ns}	0.086^{ns}	4
DCN	8	0	*APP, PSEN1, MAPT, APOE*	yes	-0.416^{**}	0.546^{*}	4
CCR5	1	0	*APP*	yes	0.769^{***}	0.616^{*}	4
GPRC5B	2	41	-	yes	0.307^{*}	-0.248^{ns}	4
IRF5	1	0	*APP, PSEN1, PSEN2, MAPT, APOE*	yes	0.879^{***}	0.839^{***}	4
IGFBP7	8	0	*MAPT, APOE*	yes	0.353^{*}	0.510^{ns}	4
CXCL12	1	0	*APP, PSEN2, MAPT, APOE*	yes	0.432^{**}	-0.069^{ns}	4
CREM	1	0	*PSEN1, MAPT, APOE*	yes	-0.439^{**}	-0.396^{ns}	4
EHHADH	14	0	*MAPT, APOE*	yes	0.438^{**}	-0.022^{ns}	4
SLC1A3	7	1	-	yes	0.651^{***}	0.494^{ns}	4
VAV3	0	5	*MAPT*	yes	0.319^{*}	-0.284^{ns}	4
IL15	2	18	-	yes	0.623^{***}	0.685^{**}	4

*"NA," not applicable due to missing related data for the target gene. AD, Alzheimer's disease; CFG, convergent functional genomics score based on the total number of lines of AD-related evidence; DEG, differentially expressed gene; eQTL, the total number of risk SNPs based on the IGAP data setthat were able to regulate expression of the target gene; GWAS, the total number of risk SNPs within the target gene based on the IGAP data set; PPI, AD core genes (APP, PSEN1, PSEN2, MAPT, and APOE) that had a significant protein-protein interaction with the target genes; Early_DEG: target gene is differentially expressed in AD mouse models before AD pathology emergence; Expression correlation of the target gene and AD pathology in AD mice was performed for the Aβ line AD mice in Mouse (marked as Aβ) and the Tau line AD mice in Mouse (marked as Tau). *$P < 0.05$; **$P < 0.01$; ***$P < 0.001$.*

the dopamine 1 receptor (D1R) and the dopamine 5 receptor (D5R)]; and D2-like [comprising the dopamine 2 receptor (D2R), dopamine 3 receptor (D3R) and the dopamine 4 receptor (D4R)]. Pan et al. found that dopamine, D1R and D2R concentration levels were decreased in patients with AD compared with controls. Moreover, decreased levels of dopamine and D2-like

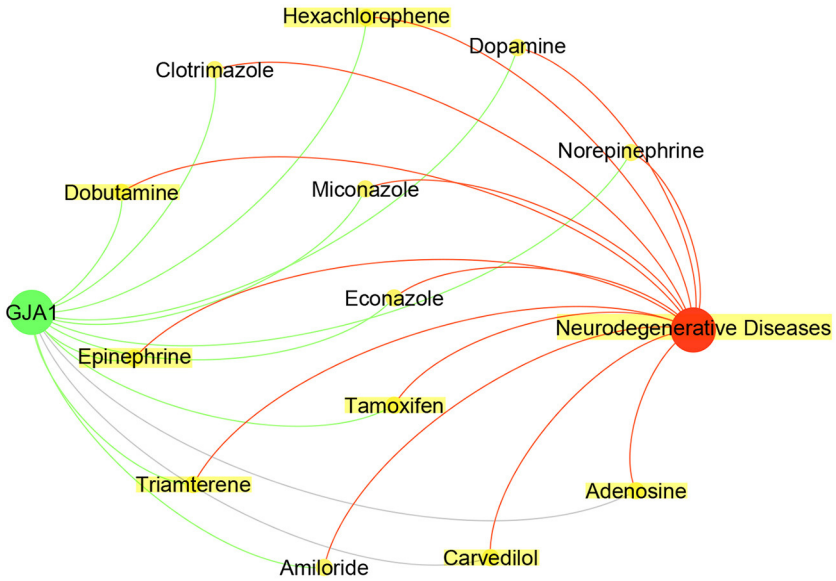

FIGURE 7 | Drug-GJA1-disease interaction network. The network contained candidate target GJA1 (green), Neurodegenerative Diseases (red) and 13 drugs (yellow).Gray indicate known interaction. Green and red lines and newly predicted interactions using deepDTnet and SAveRUNNER, respectively.

receptors were linked with the pathophysiology of AD because of their strong higher rank correlations with AD (Pan et al., 2020). To conclude, candidate genes *GJA1* is the most likely to be targets of AD.

DISCUSSION

Pathway enrichment analysis was performed to interpret the function of these DEGs. KEGG pathway analysis for the 7,567 DEGs were significantly enriched in one KEGG pathway "*MAPK* signaling pathway," which is composed of ERK, P38, and JNK. In the adult nervous system, ERK activation is necessary for synaptic plasticity and memory formation (Du et al., 2019). In the brains of AD patients, P38 is highly expressed. $A\beta$-induced P38 activation increases tau phosphorylation and promotes the amyloidogenic processing of APP (Giraldo et al., 2014; Gourmaud et al., 2015). In a mouse model of AD, the JNK signaling pathway is overactivated in the spine before cognitive decline (Sclip et al., 2014). These studies indicate that the overactivation of MAPK signaling pathway could cause the occurrence of AD. Therefore, preventing MAPK overactivation is effective strategy in order to reduce $A\beta$ deposition, Tau hyperphosphorylation, neuronal apoptosis, and memory impairment. MAPKs could be potential targets for novel and effective therapeutics of AD (Yenki et al., 2013; Feld et al., 2014).

GO term analysis indicated that the 7,567 DEGs were mainly involved in chemical synaptic transmission, regulation of postsynaptic membrane potential, synaptic vesicle exocytosis, synaptic transmission, GABAergic synapses, regulation of synaptic transmission, glutamatergic, synaptic vesicle endocytosis, long-term synaptic potentiation, neurotransmitter secretion, neuron projection morphogenesis, negative regulation of neuron apoptotic process and negative regulation of neuron projection development. Damage to neuronal and synaptic function has always been considered an important pathological feature of neurodegenerative diseases, and decreased synaptic activity is also considered to be the most relevant pathological feature of AD cognitive impairment (Wu et al., 2019). For example, the downregulation of GABAergic synapses is closely related to the loss of GABAergic inhibition (Kim et al., 2020). Studies have found that GABAergic neurotransmission is closely related to various aspects of AD pathology, including $A\beta$ toxicity and Tau hyperphosphorylation (Kadoyama et al., 2021). The level of GABA inhibitory neurotransmitter in AD patients was significantly reduced, suggesting that AD has insufficient synaptic function and neuronal transmission (Schmitz et al., 2017). In addition, In a mouse model of AD indicate that the impairment of hippocampal neurogenesis may be mediated by GABAergic signal dysfunction or the imbalance between excitatory and inhibitory synapses (Sun et al., 2009). Therefore, GABAergic synapses not only plays an important role in the function of the hippocampus, but also in the pathogenesis of AD.

LIMITATIONS

There are some limitations in this study. First, although we identified 23 potential driver genes of AD by the WGCNA and CFG method, these approaches could be used to prioritize genes rather than to identify true causal genes. Therefore, further biological validation of the identified genes are necessary in future studies. Second, 4 of 5 datasets were downloaded from AlzData, which only retained the common genes from different studies during the cross-platform normalization. Third, the

sample size of EC, HP and TC available for analyze was still limited, and the larger sample size of FC and ADNI might have a greater influence on the results. Fourth, the rapid development of various omics provide new opportunities for understanding of AD. However, we only used transcriptomics dataset to identify potential driver genes of AD. Finally, more potential genes of AD were not considered. Deep learning has capacity to dig out more hidden gene in data and is a machine learning algorithm based on artificial neural network, which is a computational model inspired by the structure of human brain. The main difference between deep learning and traditional artificial neural network lies in the scale and complexity of network structure. The networks of deep learning have a larger number of hidden layers, while traditional artificial neural networks usually have only one hidden layer. This is due to the lack of big data and GPU hardware technical support in the last century. Due to the emergence of more powerful CPU and GPU hardware, deep learning with more hidden layers is proposed on the basis of artificial neural network, and more nodes can be used in each hidden layer (Esteva et al., 2019; Zou et al., 2019).

CONCLUSIONS

In this study, we identified potential driver genes from AD-specific modules using multiple transcriptomics datasets and observed that DEGs were enriched with several pathways significantly by DAVID 6.8, which are consistent with observations from previous studies. Moreover, through studying of WGCNA, CFG and drug-target-disease network prediction, candidate gene GJA1 is the most likely to be targets of AD, actually reported in previous study. In summary, identification of AD-related genes contributes to the understanding of AD pathophysiology and the development of new drugs. In summary, Our results contribute to understanding pathophysiology of AD and looking for candidates drug targets.

DATA AVAILABILITY STATEMENT

The original contributions presented in the study are publicly available. This data can be found here: https://github.com/Macau-LYXia/Transcriptomics-Data-for-AD. Data used in the preparation of this article were obtained from the AlzData (http://www.alzdata.org/) and Alzheimer's Disease Neuroimaging Initiative (ADNI) database (adni.loni.usc.edu).

AUTHOR CONTRIBUTIONS

L-YX and LT contributed to collect data sets and analyze data. L-YX, LT, HH, and JL contributed to the interpretation of the results and revised the manuscript. L-YX took the lead in writing the manuscript. All authors contributed to the article and approved the submitted version.

FUNDING

This work was supported by China Postdoctoral Science Foundation (2020M671125) and start-up grant of the Shanghai Jiao Tong University (WF220408213).

REFERENCES

Alzheimer's Association. (2018). 2018 Alzheimer's disease facts and figures. *Alzheimers Dement*. 14, 367–429. doi: 10.1016/j.jalz.2018.02.001

Andrews, S. J., Fulton-Howard, B., and Goate, A. (2020). Interpretation of risk loci from genome-wide association studies of Alzheimer's disease. *Lancet Neurol.* 19, 326–335. doi: 10.1016/S1474-4422(19)30435-1

Ayalew, M., Le-Niculescu, H., Levey, D., Jain, N., Changala, B., Patel, S., et al. (2012). Convergent functional genomics of schizophrenia: from comprehensive understanding to genetic risk prediction. *Mol. Psychiatry* 17, 887–905. doi: 10.1038/mp.2012.37

Botía, J. A., Vandrovcova, J., Forabosco, P., Guelfi, S., D'Sa, K., Hardy, J., et al. (2017). An additional k-means clustering step improves the biological features of wgcna gene co-expression networks. *BMC Syst. Biol.* 11, 1–16. doi: 10.1186/s12918-017-0420-6

Chu, Y., Shan, X., Chen, T., Jiang, M., Wang, Y., Wang, Q., et al. (2021). Dti-mlcd: predicting drug-target interactions using multi-label learning with community detection method. *Brief. Bioinformatics* 22, bbaa205. doi: 10.1093/bib/bbaa205

Cummings, J., Lee, G., Ritter, A., Sabbagh, M., and Zhong, K. (2019). Alzheimer's disease drug development pipeline: 2019. *Alzheimers Dementia* 5, 272–293. doi: 10.1016/j.trci.2019.05.008

Darby, R. R., Joutsa, J., and Fox, M. D. (2019). Network localization of heterogeneous neuroimaging findings. *Brain* 142, 70–79. doi: 10.1093/brain/awy292

Doxtater, K., Tripathi, M. K., and Khan, M. M. (2020). Recent advances on the role of long non-coding rnas in Alzheimer's disease. *Neural Regenerat. Res.* 15, 2253. doi: 10.4103/1673-5374.284990

Du, Y., Du, Y., Zhang, Y., Huang, Z., Fu, M., Li, J., et al. (2019). Mkp-1 reduces aβ generation and alleviates cognitive impairments in Alzheimer's disease models. *Signal Transduct. Targeted Therapy* 4, 1–12. doi: 10.1038/s41392-019-0091-4

Dulewicz, M., Kulczynska-Przybik, A., Borawski, B., Klimkowicz-Mrowiec, A., Pera, J., Slowik, A., et al. (2020). The cerebrospinal fluid stromal cell-derived factor 1 (cxcl12) concentration in Alzheimer's disease: biomarkers (non-neuroimaging)/novel biomarkers. *Alzheimers Dementia* 16, e042573. doi: 10.1002/alz.042573

Esteva, A., Robicquet, A., Ramsundar, B., Kuleshov, V., DePristo, M., Chou, K., et al. (2019). A guide to deep learning in healthcare. *Nat. Med.* 25, 24–29. doi: 10.1038/s41591-018-0316-z

Falcone, R., Conte, F., Fiscon, G., Pecce, V., Sponziello, M., Durante, C., et al. (2019). Braf v600e-mutant cancers display a variety of networks by swim analysis: Prediction of vemurafenib clinical response. *Endocrine* 64, 406–413. doi: 10.1007/s12020-019-01890-4

Feld, M., Krawczyk, M. C., Sol Fustinana, M., Blake, M. G., Baratti, C. M., Romano, A., et al. (2014). Decrease of erk/mapk overactivation in prefrontal cortex reverses early memory deficit in a mouse model of Alzheimer's disease. *J. Alzheimers Dis.* 40, 69–82. doi: 10.3233/JAD-131076

Femminella, G. D., Ferrara, N., and Rengo, G. (2015). The emerging role of micrornas in Alzheimer's disease. *Front. Physiol.* 6, 40. doi: 10.3389/fphys.2015.00040

Fiscon, G., Conte, F., Farina, L., and Paci, P. (2021). Saverunner: a network-based algorithm for drug repurposing and its application to covid-19. *PLoS Comput. Biol.* 17, e1008686. doi: 10.1371/journal.pcbi.1008686

Giraldo, E., Lloret, A., Fuchsberger, T., and Vi na, J. (2014). Aβ and tau toxicities in Alzheimer's are linked via oxidative stress-induced p38 activation: protective role of vitamin e. *Redox Biol.* 2, 873–877. doi: 10.1016/j.redox.2014.03.002

Gourmaud, S., Paquet, C., Dumurgier, J., Pace, C., Bouras, C., Gray, F., et al. (2015). Increased levels of cerebrospinal fluid jnk3 associated with amyloid pathology: links to cognitive decline. *J. Psychiatry Neurosci*. 40, 151. doi: 10.1503/jpn.140062

Hao, S., Wang, R., Zhang, Y., and Zhan, H. (2019). Prediction of AlzheimerŠs disease-associated genes by integration of gwas summary data and expression data. *Front. Genet*. 9, 653. doi: 10.3389/fgene.2018.00653

Huang, D. W., Sherman, B. T., Tan, Q., Kir, J., Liu, D., Bryant, D., et al. (2007). David bioinformatics resources: expanded annotation database and novel algorithms to better extract biology from large gene lists. *Nucleic Acids Res*. 35(Suppl_2), W169ŰW175. doi: 10.1093/nar/gkm415

Kadoyama, K., Matsuura, K., Takano, M., Otani, M., Tomiyama, T., Mori, H., et al. (2021). Proteomic analysis involved with synaptic plasticity improvement by gabaa receptor blockade in hippocampus of a mouse model of AlzheimerŠs disease. *Neurosci. Res*. 165, 61–68. doi: 10.1016/j.neures.2020.04.004

Kim, S., Kim, H., Park, D., Kim, J., Hong, J., Kim, J. S., et al. (2020). Loss of iqsec3 disrupts gabaergic synapse maintenance and decreases somatostatin expression in the hippocampus. *Cell Rep*. 30, 1995–2005. doi: 10.1016/j.celrep.2020.01.053

Lanoiselée, H.-M., Nicolas, G., Wallon, D., Rovelet-Lecrux, A., Lacour, M., Rousseau, S., et al. (2017). App, psen1, and psen2 mutations in early-onset Alzheimer disease: a genetic screening study of familial and sporadic cases. *PLoS Med*. 14, e1002270. doi: 10.1371/journal.pmed.1002270

LeBlanc, A. C. (2013). Caspase-6 as a novel early target in the treatment of Alzheimer's disease. *European Journal of Neuroscience* 37, 2005–2018. doi: 10.1111/ejn.12250

Liu, F., Zhang, Z., Chen, W., Gu, H., and Yan, Q. (2018). Regulatory mechanism of microrna-377 on cdh13 expression in the cell model of AlzheimerŠs disease. *Eur. Rev. Med. Pharmacol. Sci* 22, 2801–2808. doi: 10.26355/eurrev_201805_14979

Mateos, L., Ismail, M.-A.-M., Gil-Bea, F.-J., Leoni, V., Winblad, B., Björkhem, I., et al. (2011). Upregulation of brain renin angiotensin system by 27-hydroxycholesterol in Alzheimer's disease. *J. Alzheimers Dis*. 24, 669–679. doi: 10.3233/JAD-2011-101512

Nangraj, A. S., Selvaraj, G., Kaliamurthi, S., Kaushik, A. C., Cho, W. C., and Wei, D. Q. (2020). Integrated ppi-and wgcna-retrieval of hub gene signatures shared between barrett's esophagus and esophageal adenocarcinoma. *Front. Pharmacol*. 11, 881. doi: 10.3389/fphar.2020.00881

Öztürk, H., Özgür, A., and Ozkirimli, E. (2018). Deepdta: deep drug-target binding affinity prediction. *Bioinformatics* 34, i821Űi829. doi: 10.1093/bioinformatics/bty593

Pan, X., Kaminga, A. C., Jia, P., Wen, S. W., Acheampong, K., and Liu, A. (2020). Catecholamines in alzheimer's disease: a systematic review and meta-analysis. *Front. Aging Neurosci*. 12, 184. doi: 10.3389/fnagi.2020.00184

Patel, H., Dobson, R. J., and Newhouse, S. J. (2019). A meta-analysis of AlzheimerŠs disease brain transcriptomic data. *J. Alzheimers Dis*. 68, 1635–1656. doi: 10.3233/JAD-181085

Ren, R., Zhang, L., and Wang, M. (2018). Specific deletion connexin43 in astrocyte ameliorates cognitive dysfunction in app/ps1 mice. *Life Sci*. 208, 175–191. doi: 10.1016/j.lfs.2018.07.033

Ren, Z.-H., Shang, G.-P., Wu, K., Hu, C.-Y., and Ji, T. (2020). Wgcna co-expression network analysis reveals ilf3-as1 functions as a cerna to regulate ptbp1 expression by sponging mir-29a in gastric cancer. *Front. Genet*. 11, 39. doi: 10.3389/fgene.2020.00039

Schmitz, T. W., Correia, M. M., Ferreira, C. S., Prescot, A. P., and Anderson, M. C. (2017). Hippocampal gaba enables inhibitory control over unwanted thoughts. *Nat. Commun*. 8, 1–12. doi: 10.1038/s41467-017-00956-z

Sclip, A., Tozzi, A., Abaza, A., Cardinetti, D., Colombo, I., Calabresi, P., et al. (2014). c-jun n-terminal kinase has a key role in Alzheimer disease synaptic dysfunction *in vivo*. *Cell Death Dis*. 5, e1019Űe1019. doi: 10.1038/cddis.2013.559

Sun, B., Halabisky, B., Zhou, Y., Palop, J. J., Yu, G., Mucke, L., et al. (2009). Imbalance between gabaergic and glutamatergic transmission impairs adult neurogenesis in an animal model of Alzheimer's disease. *Cell Stem Cell* 5, 624–633. doi: 10.1016/j.stem.2009.10.003

Tan, M. G., Lee, C., Lee, J. H., Francis, P. T., Williams, R. J., Ramírez, M. J., et al. (2014). Decreased rabphilin 3a immunoreactivity in AlzheimerŠs disease is associated with aβ burden. *Neurochem. Int*. 64, 29–36. doi: 10.1016/j.neuint.2013.10.013

Wijsman, E. M., Pankratz, N. D., Choi, Y., Rothstein, J. H., Faber, K. M., Cheng, R., et al. (2011). Genome-wide association of familial late-onset Alzheimer's disease replicates bin1 and clu and nominates cugbp2 in interaction with apoe. *PLoS Genet* 7, e1001308. doi: 10.1371/journal.pgen.1001308

Wood, I. C. (2018). The contribution and therapeutic potential of epigenetic modifications in AlzheimerŠs disease. *Front. Neurosci*. 12, 649. doi: 10.3389/fnins.2018.00649

Wu, M., Fang, K., Wang, W., Lin, W., Guo, L., and Wang, J. (2019). Identification of key genes and pathways for AlzheimerŠs disease via combined analysis of genome-wide expression profiling in the hippocampus. *Biophysics Reports* 5, 98–109. doi: 10.1007/s41048-019-0086-2

Xia, L.-Y., Yang, Z.-Y., Zhang, H., and Liang, Y. (2019). Improved prediction of drug-target interactions using self-paced learning with collaborative matrix factorization. *J. Chem. Inf. Model*. 59, 3340–3351. doi: 10.1021/acs.jcim.9b00408

Xu, M., Zhang, D.-F., Luo, R., Wu, Y., Zhou, H., Kong, L.-L., et al. (2018). A systematic integrated analysis of brain expression profiles reveals yap1 and other prioritized hub genes as important upstream regulators in Alzheimer's disease. *Alzheimers Dementia* 14, 215–229. doi: 10.1016/j.jalz.2017.08.012

Yenki, P., Khodagholi, F., and Shaerzadeh, F. (2013). Inhibition of phosphorylation of jnk suppresses aβ-induced er stress and upregulates prosurvival mitochondrial proteins in rat hippocampus. *J.Mol. Neurosci*. 49, 262–269. doi: 10.1007/s12031-012-9837-y

Zeng, X., Zhu, S., Hou, Y., Zhang, P., Li, L., Li, J., et al. (2020a). Network-based prediction of drug-target interactions using an arbitrary-order proximity embedded deep forest. *Bioinformatics* 36, 2805–2812. doi: 10.1093/bioinformatics/btaa010

Zeng, X., Zhu, S., Liu, X., Zhou, Y., Nussinov, R., and Cheng, F. (2019). deepdr: a network-based deep learning approach to *in silico* drug repositioning. *Bioinformatics* 35, 5191–5198. doi: 10.1093/bioinformatics/btz418

Zeng, X., Zhu, S., Lu, W., Liu, Z., Huang, J., Zhou, Y., et al. (2020b). Target identification among known drugs by deep learning from heterogeneous networks. *Chem. Sci*. 11, 1775–1797. doi: 10.1039/C9SC04336E

Zou, J., Huss, M., Abid, A., Mohammadi, P., Torkamani, A., and Telenti, A. (2019). A primer on deep learning in genomics. *Nat. Genet*. 51, 12–18. doi: 10.1038/s41588-018-0295-5

Conflict of Interest: The authors declare that the research was conducted in the absence of any commercial or financial relationships that could be construed as a potential conflict of interest.

Publisher's Note: All claims expressed in this article are solely those of the authors and do not necessarily represent those of their affiliated organizations, or those of the publisher, the editors and the reviewers. Any product that may be evaluated in this article, or claim that may be made by its manufacturer, is not guaranteed or endorsed by the publisher.

Copyright © 2022 Xia, Tang, Huang and Luo. This is an open-access article distributed under the terms of the Creative Commons Attribution License (CC BY). The use, distribution or reproduction in other forums is permitted, provided the original author(s) and the copyright owner(s) are credited and that the original publication in this journal is cited, in accordance with accepted academic practice. No use, distribution or reproduction is permitted which does not comply with these terms.

frontiers in Aging Neuroscience

ORIGINAL RESEARCH
published: 29 March 2022
doi: 10.3389/fnagi.2022.814893

Aberrant Volume-Wise and Voxel-Wise Concordance Among Dynamic Intrinsic Brain Activity Indices in Parkinson's Disease: A Resting-State fMRI Study

Yuan Tian[1,2], Hai-Bo Chen[1], Xin-Xin Ma[1], Shu-Hua Li[1], Chun-Mei Li[3], Shao-Hui Wu[1,2], Feng-Zhi Liu[1,2], Yu Du[1,2], Kai Li[1] and Wen Su[1,2]**

[1] Department of Neurology, Beijing Hospital, National Center of Gerontology, Institute of Geriatric Medicine, Chinese Academy of Medical Sciences, Beijing, China, [2] Graduate School of Peking Union Medical College, Dongcheng, Beijing, China, [3] Department of Radiology, Beijing Hospital, National Center of Gerontology, Institute of Geriatric Medicine, Chinese Academy of Medical Sciences, Beijing, China

OPEN ACCESS

Edited by:
Kuangyu Shi,
University of Bern, Switzerland

Reviewed by:
David Eidelberg,
Northwell Health, United States
Mahdieh Ghasemi,
University of Neyshabur, Iran

***Correspondence:**
Kai Li
likai_bjh@hotmail.com
Wen Su
suwendy@126.com

Specialty section:
This article was submitted to Parkinson's Disease and Aging-related Movement Disorders, a section of the journal Frontiers in Aging Neuroscience

Received: 14 November 2021
Accepted: 07 March 2022
Published: 29 March 2022

Citation:
Tian Y, Chen H-B, Ma X-X, Li S-H, Li C-M, Wu S-H, Liu F-Z, Du Y, Li K and Su W (2022) Aberrant Volume-Wise and Voxel-Wise Concordance Among Dynamic Intrinsic Brain Activity Indices in Parkinson's Disease: A Resting-State fMRI Study. Front. Aging Neurosci. 14:814893. doi: 10.3389/fnagi.2022.814893

Researches using resting-state functional magnetic resonance imaging (rs-fMRI) have applied different regional measurements to study the intrinsic brain activity (IBA) of patients with Parkinson's disease (PD). Most previous studies have only examined the static characteristics of IBA in patients with PD, neglecting the dynamic features. We sought to explore the concordance between the dynamics of different rs-fMRI regional indices. This study included 31 healthy controls (HCs) and 57 PD patients to calculate the volume-wise (across voxels) and voxel-wise (across periods) concordance using a sliding time window approach. This allowed us to compare the concordance of dynamic alterations in frequently used metrics such as degree centrality (DC), global signal connectivity (GSC), voxel-mirrored heterotopic connectivity (VMHC), the amplitude of low-frequency fluctuations (ALFF), and regional homogeneity (ReHo). We analyzed the changes of concordance indices in the PD patients and investigated the relationship between aberrant concordance values and clinical/neuropsychological assessments in the PD patients. We found that, compared with the HCs, the PD patients had lower volume concordance in the whole brain and lower voxel-wise concordance in the posterior cerebellar lobe, cerebellar tonsils, superior temporal gyrus, and supplementary motor region. We also found negative correlations between these concordance alterations and patients' age. The exploratory results contribute to a better understanding of IBA alterations and pathophysiological mechanisms in PD.

Keywords: Parkinson's disease, resting-state fMRI, intrinsic brain activity, volume-wise concordance, voxel-wise concordance

INTRODUCTION

Parkinson's disease (PD) is characterized by the decrease of dopaminergic neurons in the nigrostriatal pathway, resulting in a neurodegenerative disorder with progressive movement disorders (Kalia and Lang, 2015). Moreover, non-motor symptoms such as emotional disorders and cognitive impairment are also common in PD patients (Rana et al., 2015; Raza et al., 2019).

Many neuroimaging studies have demonstrated that several regions of the brain are also impacted in PD patients (Weingarten et al., 2015). Resting-state functional magnetic resonance imaging (rs-fMRI) has also been widely used to study the IBA in PD, including both brain functional connectivity (FC; Tessitore et al., 2019) and regional cerebral neuronal activity (Yue et al., 2020), which has produced inconsistent results. Some meta-analyses of neuroimaging data have attempted to identify abnormalities in the consistency of IBA patterns in PD, such as studying the amplitude of low-frequency fluctuations (ALFF; Pan et al., 2017; Wang et al., 2018) or regional homogeneity (ReHo; Pan et al., 2016), and functional connectivity network (Tahmasian et al., 2017). There are also relevant studies on the degree centrality (DC; Guo et al., 2020; Chen et al., 2021), and voxel-minored homotopic connectivity (VMHC; Luo et al., 2015). However, most current rs-fMRI research in PD patients has focused on static characteristics of human brain activity and neglected the dynamic properties of IBA in the temporal dimension (Hutchison et al., 2013). In recent years, the sliding window approach has demonstrated the altered dynamic functional connectivity (dFC) of IBA in individuals with common neuropsychiatric disorders such as Alzheimer's disease (de Vos et al., 2018), major depressive disorder (Hosenfeld et al., 2015), and primary generalized epilepsy (Liu et al., 2017).

Many studies have assessed dFC in PD and demonstrated that dynamical changes in IBA were associated with motor (Kim et al., 2017) and cognitive impairments (Fiorenzato et al., 2019). However, it is not enough to focus only on the dynamic functional connectivity features, because much information is found in the fluctuations of regional neural activity (Yu et al., 2019). Different rs-fMRI indicators represent different IBA aspects. The degree of integration is represented by the concordance between the different dynamic regional indices. Yan et al. investigated the volume-wise and voxel-wise concordance between these regional measures and found they demonstrated stable inter-individual differences that were correlated with age (Yan et al., 2017). Fu et al. found consistency in the changes in dynamic ALFF and dynamic FC over time, and this consistency differed between patients with schizophrenia and HCs (Fu et al., 2018). Whether the consistency between regional indicators is abnormal in PD patients remains a direction to be explored. Previous studies on dynamic indicators in PD have been performed with the dynamical amplitude of low-frequency fluctuation (dALFF) analysis (Zhang et al., 2019). Though the PD patients exhibit abnormalities in dynamic and static brain activity, the concordance between different dynamic regional indices remains unclear. In this study, we compared the differences in volume-wise and voxel-wise concordance among IBA measures between PD patients and HCs to explore the pathophysiological mechanisms of PD.

MATERIALS AND METHODS

Participants

We recruited 67 individuals with PD and 34 healthy controls. Both groups were similar in age and gender and had no history of neurological or mental disorders. In this study, all the PD patients were diagnosed based on the diagnostic criteria established by the United Kingdom Parkinson's Disease Society [17]. The Helsinki Declaration was closely followed at every step of this study. Before participating in the trial, all participants were required to provide written informed consent. This research was conducted according to all relevant regulations and laws and the study was authorized by the hospital's ethical review committee. All of the individuals were right-handed. We have ruled out conditions such as deep brain stimulation, head trauma, moderate to severe tremors in the head, alcohol/drug abuse, dementia, and other mental and neurological issues. When all PD medications were stopped for 12 h, all patients with Parkinson's disease were administered an MRI and non-motor/motor function tests in an "off" state: several demographic and clinical questions were posed to each PD participant. These tests included the Mini-Mental State Examination (MMSE), the Hamilton Depression Rating Scale (HAMD), the Hamilton Anxiety Rating Scale (HAMA), the Non-Motor Symptoms Questionnaire (NMSQ), the Unified Parkinson's Disease Rating Scale (UPDRS), and the Hoehn-Yahr staging. Additionally, the MMSE was used to examine the participants in the control group.

MRI Data Acquisition

MRI scans were performed on all patients at Beijing Hospital using a 3.0-T scanner (Achieva TX; Philips Medical Systems, Best, Netherlands). During the scan, the participants were instructed to remain motionless, relax, close their eyes, and maintain their alertness. The use of foam cushion and headphones helped to keep the scanning noise and head movements to a minimum. The following settings were used to generate high-resolution T1-weighted images (three-dimensional turbo field echo): field of view (FOV) = 240 × 240 mm, echo time (TE) = 3.0 ms, repetition time (TR) = 7.4 ms, flip angle = 8°, slice thickness = 1.2 mm, matrix size = 256 × 256, voxel dimensions = 0.94 × 0.94 × 1.20 mm, 140 slices. The functional pictures were generated using the following parameters: FOV = 240 × 240 mm, flip angle = 90, TR = 3,000 ms, TE = 35 ms, voxel dimensions 3.75 × 3.75 × 4.00 mm, matrix size = 64 × 64, slices = 33, time points = 210, slice thickness = 4 mm.

Resting-State Functional Magnetic Resonance Imaging Data Preprocessing

Data preprocessing for the rs-fMRI was performed using RESTPlus V 1.2 (Jia et al., 2019) and the SPM12 program[1] in MATLAB (MathWorks, Inc., Natick, MA, United States). Ten volumes were initially eliminated to stabilize the magnetization and adjust it to the subject's magnetic fields. Participants with head motion above 2 mm in displacement or 2° in rotation were then excluded from the study (**Supplementary Table 1**). The remaining 200 volumes were adjusted according to the slice time and readjusted to account for the head motion. Individual T1WI pictures were co-registered to the mean functional images, and then segmented into the cerebrospinal fluid (CSF), white matter,

[1] www.fifil.ion.ucl.ac.uk/spm

and gray matter. The functional volume of each individual was segmented and then normalized to the Montreal Neurological Institute (MNI) space using the Diffeomorphic Anatomical Registration Through Exponentiated Lie Algebra (DARTEL) toolbox for two-dimensional anatomical registration. They were then resampled to 3 mm isotropic voxels (Ashburner, 2007), which were used to determine the functional volumes of each individual. The rs-fMRI indices were extracted after functional volumes were smoothed with a 6-mm full width at half maximum (FWHM) Gaussian kernel, and the linear trend of the time course was eliminated. The volumes were then filtered with a bandpass filter between 0.01 and 0.08 Hz. The nuisance covariate regression included the Friston 24-head motion parameters, white matter and CSF signals (Power et al., 2012).

Calculation of Dynamic Resting-State Functional Magnetic Resonance Imaging Measures

The dynamic rs-fMRI measures and their concordance were computed using DPABI V6.0 (Yan et al., 2016). Sliding time window analysis was used to examine the temporal dynamics of the five rs-fMRI measurements listed below. The preprocessed functional data from each participant was subjected to hamming windows (window size = 30 TR; window step = 1 TR) in order to produce a series of BOLD signal windows. For each window, the dynamics of these rs-fMRI measurements were then calculated (**Supplementary Figures 1**, **2**).

(1) Amplitude of low-frequency fluctuation (ALFF): We used a Fast Fourier Transform to create the power spectrum by transforming the BOLD time course to a frequency domain (FFT). In this study, ALFF was defined as the mean power spectrum in a particular low-frequency band (0.01–0.1 Hz) (Zang et al., 2007), while fALFF was defined as the ratio of the power spectrum in the low-frequency band (0.01–0.1 Hz) to the entire power spectrum in the frequency range (Zou et al., 2008). Because ALFF is sensitive when evaluating aberrant brain activity in individuals with neuropsychiatric illnesses, we only used ALFF in the concordance analysis (de Vos et al., 2018).

(2) Regional homogeneity (ReHo): Regional brain activity was quantified using the ReHo method, which presumes that neural activity is more likely to occur in a cluster than in a single voxel, and is thus more consistent. Kendall's coordination coefficient (Kendall's W) was obtained when the time series of a particular voxel was compared with the time series of its nearest neighbors (Zang et al., 2004).

(3) Voxel-mirrored homotopic connectivity (VMHC): To enhance the relationship between symmetric voxels, we converted the functional pictures to a symmetric space from a functional image space. We then averaged all of the normalized T1 pictures to obtain a mean T1 image. This was then averaged with its left and right mirror counterparts to create a group-specific symmetrical template using the mean T1 image as a guide. The non-linear registration of each subject was then adjusted to the standard space using the symmetric template and the functional data of each subject was changed to the symmetric space using the symmetric template. The Pearson's correlation coefficient between the time series of the symmetric inter-hemispheric counterpart and the time series of each voxel was defined as the Pearson's correlation coefficient between any pair of symmetric inter-hemispheric voxels (Zuo et al., 2010).

TABLE 1 | Clinical and demographic characteristics of the Parkinson's disease (PD) patients and the healthy controls (HCs).

	PD	HCs	*p*-value
No. of subjects	57	31	
Age	64.16 ± 8.13	62.42 ± 7.19	0.322
Gender (male/female)	28/29	16/15	0.823
Disease duration	6.49 ± 3.59	N/A	N/A
HAMA	10.21 ± 5.49	N/A	N/A
HAMD	9.30 ± 5.14	N/A	N/A
MMSE	28.05 ± 1.95	27.71 ± 2.25	0.458
NMSQ	11.30 ± 5.32	N/A	N/A
H-Y staging	2.20 ± 0.69	N/A	N/A
UPDRS	49.90 ± 18.82	N/A	N/A

PD, Parkinson's disease; HCs, healthy controls; M, male; F, female; MMSE, mini-mental status examination; HAMA, hamilton anxiety rating scale; HAMD, hamilton depression rating scale; NMSQ, non-motor symptoms questionnaire; H-Y staging, Hoehn-Yahr staging; UPDRS, unified Parkinson's disease rating scale.

(4) Degree centrality (DC): DC is defined as the number of edges connecting a node (binary graphs) or the total of their weights (weighted graphs). The Pearson correlation coefficients were between the BOLD time courses of all pairs of voxels, after which a gray matter functional connectivity matrix was constructed for each participant. The DC was calculated as the total number of positive functional connections larger than the threshold of 0.25 between a specific voxel and all other voxels in the gray matter surrounding that voxel (Zuo et al., 2012).

(5) Global signal connectivity (GSC): The gray matter correlation coefficient (GSC) was determined as the Pearson's correlation coefficient between the mean time course and the BOLD time course of each voxel throughout the whole gray matter. The Fisher Z transformation was then applied to the resulting GSC maps for further analysis (Hahamy et al., 2014).

Volume-Wise and Voxel-Wise Concordance

Since Kendall's W is a non-parametric statistic that does not require distributional assumptions and is not impacted by scale discrepancies between these rs-fMRI indices, it was used to quantify the volume and voxel consistency among them (Yan et al., 2017). We calculated two kinds of consistency among the five abovementioned dynamic indices: (1) the volume-wise consistency index is an index reflecting global-level consistency and used Kendall's W to calculate rs-fMRI indices in each subject's brain in the scan and across all time windows; (2) the voxel-wise concordance index used Kendall's W to calculate each voxel coordination across time windows and provided an interactive voxel concordance map (Yan et al., 2017).

Statistical Analysis

A two-sample *t*-test was used to assess the demographic information and neuropsychological scale scores of each group.

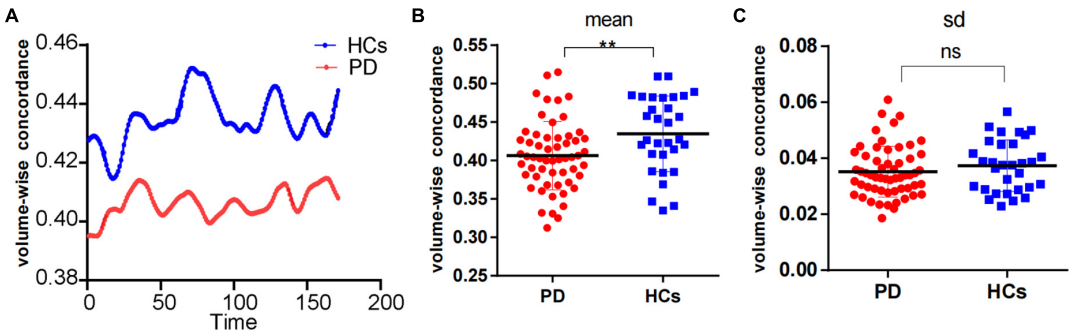

FIGURE 1 | Comparison of volume-wise concordance indices between PD patients and HCs. **(A)** Volume-wise concordance time series of the mean value in PD patients and HCs. **(B)** Comparison of mean volume-wise concordance indices. **(C)** Comparison of the SD of volume-wise concordance indices. PD, Parkinson's disease; HCs, healthy controls. SD, Standard deviation. $^{**}P < 0.01$; ns, no significance.

TABLE 2 | Comparison of volume-wise concordance indices between PD patients and HCs.

	PD	HCs	P
Mean	0.41 ± 0.04	0.44 ± 0.05	0.007
SD	0.035 ± 0.01	0.037 ± 0.01	0.299

PD, Parkinson's disease; HCs, healthy controls; SD, standard deviation.

The quantitative data were showed as a mean ± standard deviation. The chi-square test was used to compare participant gender characteristics across groups, while the inter-group volume-wise concordance was also analyzed using a two-sample *t*-test. Clinical data were analyzed using SPSS (SPSS Version 21.0. Inc., Chicago, IL, United States). $P < 0.05$ was considered significant. The normalized voxel-wise concordance maps of each rs-fMRI index were then compared between the two groups using ANCOVA analysis using DPABI V6.0. Age and gray matter volume (GMV) were included as covariates and subsequently adjusted by regression throughout the statistical analysis to reduce the impact of confounding factors. The voxel-level and cluster-level $P < 0.05$ significance levels were used to correct multiple comparisons using a Gaussian random field correction (GRF) with a voxel-level $P < 0.001$ and cluster-level $P < 0.05$ (Chen et al., 2018). The concordance indices were extracted from areas with significant between group differences and the correlations between the extracted concordance indices values and HAMA, HAMD, NMSQ, MMSE, UPSR scores, H-Y staging, and disease duration were assessed using Spearman correlation analyses.

RESULTS

Demographic and Clinical Characteristics

This research assessed a total of 57 individuals with PD and 31 HCs. Four PD patients and two controls were excluded from the study because they were left-handed. Five PD patients and one healthy control were omitted from the study due to excessive head motion. One PD disease patient was excluded from the study due to low picture quality. **Table 1** summarizes the demographic and clinical data. No statistically significant differences were found in the MMSE scores, age, and gender between the PD and the HCs ($p > 0.05$). **Table 1** summarizes demographic and clinical data. There were no differences in the age, gender, or MMSE scores between PD patients and HCs ($p > 0.05$).

Volume-Wise Concordance Alterations in Parkinson's Disease

We observed a significant degree of volume-wise concordance across the whole brain in the HCs and PD patients (mean Kendall's $W \geq =0.4$), indicating a high degree of spatial distribution consistency across these rs-fMRI measurements. The mean value of volume consistency significantly differed between the two groups ($P = 0.007$), indicating a statistically significant difference between the two groups. However, there was no statistically significant difference in the standard deviation (SD) of volume-wise concordance ($P = 0.299$) (**Figure 1** and **Table 2**). We also identified statistically significant negative associations between volume-wise concordance and age/UPDRS scores in individuals with PD ($r = =-0.439, -0.309$; $P = =0.001, 0.019$) (**Figure 2**).

Voxel-Wise Concordance Alterations in Parkinson's Disease

As displayed in **Figure 3**, inter-group comparisons indicated that PD patients exhibited worse voxel-wise concordance than the HCs in the following regions: the cerebellum posterior lobe (CPL), cerebellar tonsil (CTO), superior temporal gyrus (STG), and supplementary motor area (SMA) (GRF, voxel level, $p < 0.001$; cluster level, $p < 0.05$) (**Figure 3** and **Table 3**). Additionally, the Spearman correlation analyses demonstrated a connection between age/MMSA scores and voxel-wise concordance values in the left CPL between PD patients and HCs ($r = =-0.282, 0.331$; $P = =0.033, 0.012$) (**Figure 4A**). The concordance value in the CTO is negatively correlated with UPDRS scores ($r = =-0.269$; $P = =0.043$)

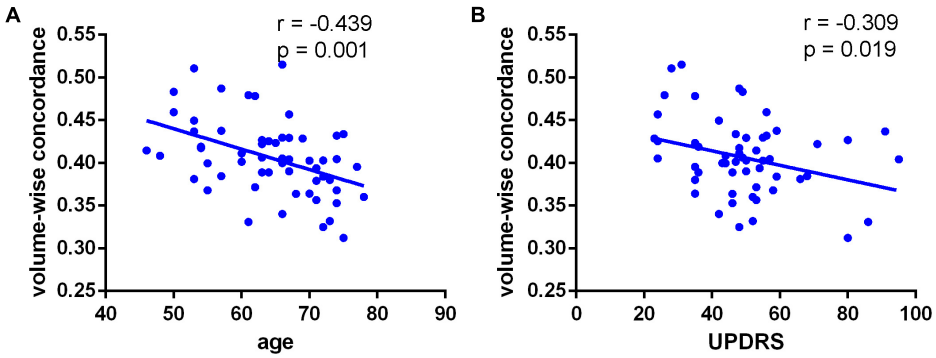

FIGURE 2 | Negative associations between volume-wise concordance and age **(A)** UPDRS **(B)** scores in individuals with PD (r = –0.439, –0.309; P = 0.001, 0.019).

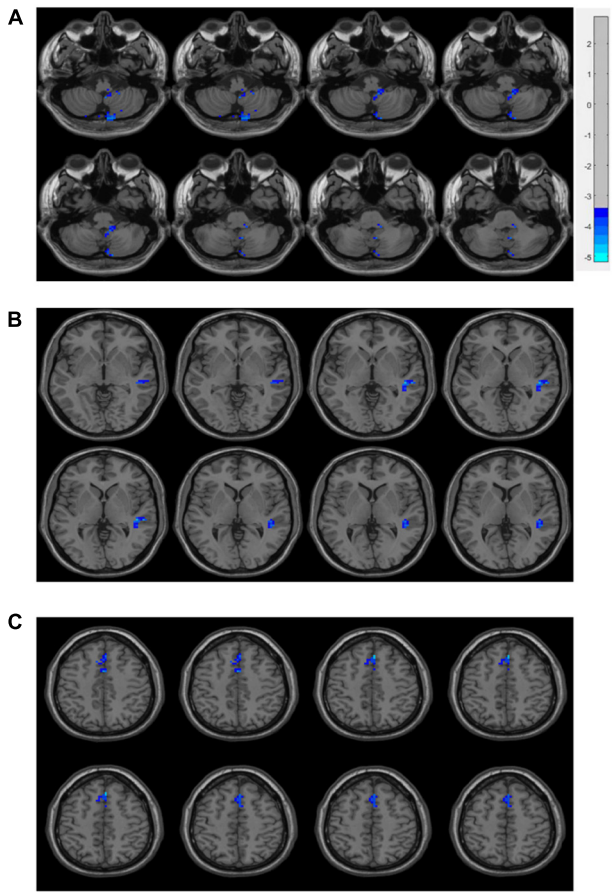

FIGURE 3 | Brain regions of voxel-wise concordance differences between PD patients and HCs: the cerebellum posterior lobe (CPL) and cerebellar tonsil (CTO) **(A)**, superior temporal gyrus (STG) **(B)**, and supplementary motor area (SMA) **(C)**.

(**Figure 4B**), and there is a negative association between age, UPDRS scores, and the concordance values in STG (r = =−0.278, −0.304; P = =0.036, 0.021) (**Figures 4C–E**).

DISCUSSION

Concordance abnormalities in rs-fMRI brain activity data were significantly altered in PD patients based on a dynamic analytic technique. PD patients had worse voxel concordance in certain cerebral regions and lower volume concordances throughout the whole brain than did the healthy controls. Furthermore, age was related to changes in volume concordance, and motor symptoms and age were associated with decreases in voxel concordance regions. This demonstrates that coordination in Parkinson's patients is clinically meaningful.

Previous research has applied various static and dynamic indicators to explore the characteristics of spontaneous brain activity in PD patients, which provided helpful information about certain brain regions (Li et al., 2018; Wang et al., 2018; Filippi et al., 2019). However, certain regions demonstrated various degrees of dysfunction, and some measures were the only way of detecting functional impairments in certain brain regions. The distinctions and overlaps between these rs-fMRI measures remain unknown. Resting-state indicators are constantly being developed, leading researchers to examine the consistency between multiple indices. Therefore, based on the dynamic nature of IBA, we further investigated the concordance of different rs- fMRI indices. Different indices reflect different aspects of IBA, which means that their concordance can be measured by reflecting the integration

TABLE 3 | Brain regions of voxel-wise concordance differences between PD patients and HCs.

Brain regions	Size (voxels)	MNI coordinates (mm)			Peak value
		X	Y	Z	
Right CPL	142	18	−75	−54	−5.1893
Left CPL	69	−18	−69	−57	−4.5713
Right CTO	32	6	−57	−39	−4.7521
Right STG	51	45	−27	0	−4.8072
SMA	83	3	27	48	−4.7717

CPL, cerebellum posterior lobe; CTO, cerebellar tonsil; STG, superior temporal gyrus; SMA, supplementary motor area.

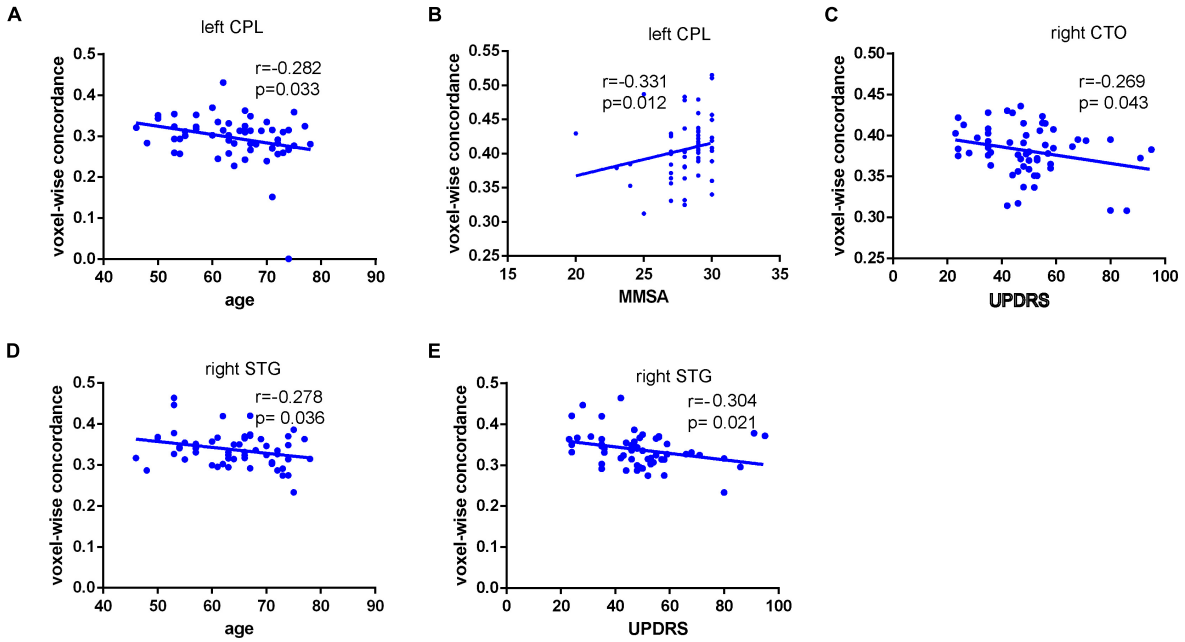

FIGURE 4 | Connection between age/MMSA scores and voxel-wise concordance value in the left CPL in PD patients from HCs (r = –0.282,0.331; P = 0.033, 0.012). **(A,B)** Negative correlation between concordance value in the CTO and UPDRS scores (r = –0.269; P = 0.043). **(C)** Negative association between age, UPDRS scores, and the concordance value in STG (r = –0.278, –0.304; P = 0.036, 0.021) **(D,E)**.

of different functional levels (Yan et al., 2017). The volume-wise concordance demonstrates the consistency of the spatial distribution of these rs-fMRI values. As previously reported (Yan et al., 2017), a high degree of spatial distribution consistency was observed with high volume-wise concordance in HCs (mean Kendall's $W > 0.4$). We also observed volume-wise concordance in PD patients (mean Kendall's W≈0.4), which was significantly lower than HCs. This indicates a less consistent spatial distribution, which could be due to the inconsistent pattern of spatial variation of rs-fMRI measurements in PD. Moreover, the inter-voxel agreement reflects the concordance of temporal dynamics between these rs-fMRI measures. In this study, the frontal lobe, temporal gyrus, and cerebellum of PD patients displayed decreased voxel-wise concordance. The reason for voxel-wise concordance disruptions could be the inconsistent pattern of temporal dynamic changes in rs-fMRI measurements. For detecting regional functional abnormalities, voxel-wise concordance may be the novel symbols based on the single rs-fMRI measurements. For example, concordance studies have been performed on schizophrenia (Zhu et al., 2018), subjective cognitive decline (SCD; Yang et al., 2021), and Alzheimer's disease (AD; Chen et al., 2021), which have identified abnormalities in spontaneous dynamic brain activity and integration.

The SMA is located on the medial side of the cerebral hemisphere, in front of the primary motor cortex. It is closely related to motor planning, learning, and cognitive functions (Nachev et al., 2008). The SMA is connected to the basal ganglia through the thalamus, forming the striatal-thalamocortical loop (STC loop). On the other hand, the SMA connects to the cerebellum through the thalamus to form the cerebellum-thalamocortical loop (CTC loop). Studies have demonstrated that the primary pathogenesis of PD is damage to the STC loop, which disrupts the intracranial control circuit and causes a relatively active CTC loop to compensate for functional deficits caused by this damage (Palmer et al., 2010). PD patients have impaired SMA function, which decreases connectivity between the SMA and other functional brain areas and results in motor impairments in PD patients (Yu et al., 2007; Prodoehl et al., 2010; Wu et al., 2010).

Parkinson's disease patients struggle in rhythm recognition assignments. The right STG plays a crucial role in this process and increased activity in the right STG region suggests inhibited temporal auditory perception (Vikene et al., 2019). The medial temporal lobe is an important center of emotional integration and is associated with motor control, self-perception, and emotional regulation (Paus et al., 1996). While PD has typically been characterized by motor impairment, it can also produce several different non-motor symptoms (Reichmann et al., 2016). We found a significant correlation between the UPDRS score and the voxel-wise concordance value of STG. This could represent enhanced temporal lobe activity as a compensatory mechanism for impaired motor symptoms.

The cerebellum coordinates somatic balance, muscle tone, and casual movements, and is a key node in the CTC loop, controlling and influencing somatic movements (Yang et al., 2013; Hanakawa et al., 2017). Prior studies have found that neuronal activity in cerebellar hemispheres increases in patients with PD compared with HCs (Yu et al., 2007), and that deep stimulation of the subthalamic nuclei inhibits glucose metabolism in the cerebellum

(Hilker et al., 2004). Therefore, increased neuronal activity in the cerebellum of PD patients could be functional compensation for the hypofunction of the basal ganglia (Lewis et al., 2007). Several studies have demonstrated that Parkinson's tremor is closely related to the CTC loop (Hacker et al., 2012; Helmich et al., 2012; Zhang et al., 2015). Additionally, pathological and compensatory effects are believed to result from the cerebellum in PD patients. Certain clinical symptoms could be caused by pathological cerebellar alterations resulting from degeneration of aberrant drives from the basal ganglia, dopaminergic system, and dopaminergic therapy. This compensatory effect could help maintain both functional motor and non-motor systems (Wu and Hallett, 2013). Additionally, recruitment of the CTC circuit is positively related with the severity of symptoms or development in PD of mild to moderate stages (Sen et al., 2010). Neuronal activity in the cerebellar hemispheres is increased in patients with PD compared to HCs (Yu et al., 2007), and its deep stimulation of the subthalamic nuclei clusters aligns glucose metabolism in the cerebellar brain (Hilker et al., 2004). Pathological damages increase in severity as the disease progresses, while the compensatory effect may weaken or fail altogether (Jankovic, 2005). This study demonstrates that concordance indexes in the posterior cerebellar lobes and cerebellar tonsil decreased in PD patients and that concordance values are correlated with age, motor, and non-motor symptoms. This indicates that neuronal activity increased, which compensates for decreases in the STC loop function.

LIMITATION

This study has some limitations. First, the size of this study sample was insufficient; therefore, a study with a larger number of participants is necessary. For the concordance studies, we only used five common rs-fMRI measures since these data-driven measures are less likely to be influenced by variables such as component selection in independent component analysis and seed specification in seed-based correlation analysis. Accounting for additional rs-fMRI measurements could allow for better IBA characteristics and a more nuanced understanding of the physiological mechanisms responsible for these activities.

CONCLUSION

In conclusion, this study demonstrates that PD patients have altered patterns of coherence obtained from rs-fMRI across several routine IBA measurements. We believe that concordance measures can provide novel insights into IBA mechanisms in PD patients.

DATA AVAILABILITY STATEMENT

The raw data supporting the conclusions of this article will be made available by the authors, without undue reservation.

ETHICS STATEMENT

The studies involving human participants were reviewed and approved by Beijing Hospital. The patients/participants provided their written informed consent to participate in this study.

AUTHOR CONTRIBUTIONS

WS, H-BC, and KL conceived and designed the experiments. YT and KL analyzed the fMRI data. C-ML was responsible for the fMRI scan and helped perform fMRI data analyses. WS, S-HL, and H-BC recruited the subjects. X-XM, F-ZL, S-HW, and YD collected the demographic, clinical, and neuropsychological information of the subjects. YT, KL, and WS wrote the manuscript. All authors read and approved the final manuscript.

FUNDING

This study was funded by the National Key Research and Development Program of China (No. 2020YFC2006404, 2020YFC2006402, and 2020YFC2006400), the project "National Major Multidisciplinary Cooperative Diagnosis and Treatment Capacity Building Project" from the National Health Commission of the People's Republic of China, Beijing Hospital grant (BJ-2021-182), the National Key R&D Program of China (No. 2017YFC1310200), and the 12th Five-year Plan for National Science and Technology Supporting Program (Nos. 2012BAI10B03 and 2012BAI10B04).

ACKNOWLEDGMENTS

We are grateful for the cooperation of all participants.

SUPPLEMENTARY MATERIAL

The Supplementary Material for this article can be found online at: https://www.frontiersin.org/articles/10.3389/fnagi.2022.814893/full#supplementary-material

REFERENCES

Ashburner, J. (2007). A fast diffeomorphic image registration algorithm. *Neuroimage* 38, 95–113. doi: 10.1016/j.neuroimage.2007.07.007

Chen, X., Lu, B., and Yan, C. G. (2018). Reproducibility of R-fMRI metrics on the impact of different strategies for multiple comparison correction and sample sizes. *Hum. Brain Mapp.* 39, 300–318. doi: 10.1002/hbm.23843

Chen, X., Onur, O. A., Richter, N., Fassbender, R., Gramespacher, H., Befahr, Q., et al. (2021). Concordance of intrinsic brain connectivity measures is disrupted in Alzheimer's Disease. *Brain Connect.* [Epub ahead of print]. doi: 10.1089/brain.2020.0918

de Vos, F., Koini, M., Schouten, T. M., Seiler, S., van der Grond, J., Lechner, A., et al. (2018). A comprehensive analysis of resting state fMRI measures to

classify individual patients with Alzheimer's disease. *Neuroimage* 167, 62–72. doi: 10.1016/j.neuroimage.2017.11.025

Filippi, M., Spinelli, E. G., Cividini, C., and Agosta, F. (2019). Resting state dynamic functional connectivity in neurodegenerative conditions : a review of magnetic resonance imaging findings. *Front. Neurosci.* 13:657. doi: 10.3389/fnins.2019.00657

Fiorenzato, E., Strafella, A. P., Kim, J., Schifano, R., Weis, L., Antonini, A., et al. (2019). Dynamic functional connectivity changes associated with dementia in Parkinson's disease. *Brain* 142, 2860–2872. doi: 10.1093/brain/awz192

Fu, Z., Tu, Y., Di, X., Du, Y., Pearlson, G. D., Turner, J. A., et al. (2018). Characterizing dynamic amplitude of low-frequency fluctuation and its relationship with dynamic functional connectivity: an application to schizophrenia. *Neuroimage* 180, 619–631. doi: 10.1016/j.neuroimage.2017.09.035

Guo, M. R., Ren, Y., Yu, H. M., Yang, H. G., Cao, C. H., Li, Y. M., et al. (2020). Alterations in degree centrality and functional connectivity in Parkinson's disease patients with freezing of gait: a resting-state functional magnetic resonance imaging study. *Front. Neurosci.* 14:582079. doi: 10.3389/fnins.2020.582079

Hacker, C. D., Perlmutter, J. S., Criswell, S. R., Ances, B. M., and Snyder, A. Z. (2012). Resting state functional connectivity of the striatum in Parkinson's disease. *Brain* 135, 3699–3711. doi: 10.1093/brain/aws281

Hahamy, A., Calhoun, V., Pearlson, G., Harel, M., Stern, N., Attar, F., et al. (2014). Save the global: global signal connectivity as a tool for studying clinical populations with functional magnetic resonance imaging. *Brain Connect.* 4, 395–403. doi: 10.1089/brain.2014.0244

Hanakawa, T., Goldfine, A. M., and Hallett, M. (2017). A common function of basal ganglia-cortical circuits subserving speed in both motor and cognitive domains. *eNeuro* 4:ENEURO.0200-17.2017. doi: 10.1523/ENEURO.0200-17.2017

Helmich, R. C., Hallett, M., Deuschl, G., Toni, I., and Bloem, B. R. (2012). Cerebral causes and consequences of parkinsonian resting tremor: A tale of two circuits? *Brain* 135, 3206–3226. doi: 10.1093/brain/aws023

Hilker, R., Voges, J., Weisenbach, S., Kalbe, E., Burghaus, L., Ghaemi, M., et al. (2004). Subthalamic nucleus stimulation restores glucose metabolism in associative and limbic cortices and in cerebellum: evidence from a FDG-PET Study in Advanced Parkinson's Disease. *J. Cereb. Blood Flow Metab.* 24, 7–16. doi: 10.1097/01.WCB.0000092831.44769.09

Hosenfeld, B., Bos, E. H., Wardenaar, K. J., Conradi, H. J., van der Maas, H. L. J., Visser, I., et al. (2015). Major depressive disorder as a nonlinear dynamic system: bimodality in the frequency distribution of depressive symptoms over time. *BMC Psychiatry* 15:222. doi: 10.1186/s12888-015-0596-5

Hutchison, R. M., Womelsdorf, T., Allen, E. A., Bandettini, P. A., Calhoun, V. D., Corbetta, M., et al. (2013). Dynamic functional connectivity: promise, issues, and interpretations. *Neuroimage* 80, 360–378. doi: 10.1016/j.neuroimage.2013.05.079

Jankovic, J. (2005). Progression of Parkinson Disease. *Arch. Neurol.* 62, 351–352. doi: 10.1001/archneur.62.3.351

Jia, X., Li, Y., Li, K., Liang, P., and Fu, X. (2019). Precuneus dysfunction in Parkinson's disease with mild cognitive impairment. *Front. Aging Neurosci.* 11:427. doi: 10.3389/fnagi.2018.00427

Kalia, L. V., and Lang, A. E. (2015). Parkinson's disease. *Lancet* 386, 896–912. doi: 10.1016/S0140-6736(14)61393-3

Kim, J., Criaud, M., Cho, S. S., Díez-Cirarda, M., Mihaescu, A., Coakeley, S., et al. (2017). Abnormal intrinsic brain functional network dynamics in Parkinson's disease. *Brain* 140, 2955–2967. doi: 10.1093/brain/awx233

Lewis, M. M., Slagle, C. G., Smith, A. B., Truong, Y., Bai, P., McKeown, M. J., et al. (2007). Task specific influences of Parkinson's disease on the striato-thalamo-cortical and cerebello-thalamo-cortical motor circuitries. *Neuroscience* 147, 224–235. doi: 10.1016/j.neuroscience.2007.04.006

Li, K., Su, W., Li, S. H., Jin, Y., and Chen, H. B. (2018). Resting State fMRI: a valuable tool for studying cognitive dysfunction in PD. *Parkinsons Dis.* 2018:6278649. doi: 10.1155/2018/6278649

Liu, F., Wang, Y., Li, M., Wang, W., Li, R., Zhang, Z., et al. (2017). Dynamic functional network connectivity in idiopathic generalized epilepsy with generalized tonic – Clonic Seizure. *Hum. Brain Mapp.* 38, 957–973. doi: 10.1002/hbm.23430

Luo, C., Guo, X., Song, W., Zhao, B., Cao, B., Yang, J., et al. (2015). Decreased resting-state interhemispheric functional connectivity in Parkinson ' s Disease. *Biomed Res. Int.* 2015:692684. doi: 10.1155/2015/692684

Nachev, P., Kennard, C., and Husain, M. (2008). Functional role of the supplementary and pre-supplementary motor areas. *Nat. Rev. Neurosci.* 9, 856–869. doi: 10.1038/nrn2478

Palmer, S. J., Li, J., Wang, Z. J., and McKeown, M. J. (2010). Joint amplitude and connectivity compensatory mechanisms in Parkinson's disease. *Neuroscience* 166, 1110–1118. doi: 10.1016/j.neuroscience.2010.01.012

Pan, P., Zhan, H., Xia, M., Zhang, Y., Guan, D., and Xu, Y. (2016). Aberrant Regional homogeneity in Parkinson's disease : a voxel -wise meta-analysis of resting-state functional magnetic resonance imaging studies. *Neurosci. Biobehav. Rev.* 72, 223–231. doi: 10.1016/j.neubiorev.2016.11.018

Pan, P., Zhang, Y., Liu, Y., Zhang, H., Guan, D., and Xu, Y. (2017). Abnormalities of regional brain function in Parkinson's disease: a meta-analysis of resting state functional magnetic resonance imaging studies. *Sci. Rep.* 7:40469. doi: 10.1038/srep40469

Paus, T., Tomaiuolo, F., Otaky, N., Petrides, M., Atlas, J., Morris, R., et al. (1996). Human cingulate and paracingulate sulci: pattern, variability, asymmetryand probabilistic map. *Cereb. Cortex* 6, 207–214. doi: 10.1093/cercor/6.2.207

Power, J. D., Barnes, K. A., Snyder, A. Z., Schlaggar, B. L., and Petersen, S. E. (2012). NeuroImage Spurious but systematic correlations in functional connectivity MRI networks arise from subject motion. *Neuroimage* 59, 2142–2154. doi: 10.1016/j.neuroimage.2011.10.018

Prodoehl, J., Spraker, M., Corcos, D., Comella, C., and Vaillancourt, D. (2010). Blood oxygenation level-dependent activation in basal ganglia nuclei relates to specific symptoms in de novo Parkinson's disease. *Mov. Disord.* 25, 2035–2043. doi: 10.1002/mds.23360

Rana, A. Q., Ahmed, U. S., Chaudry, Z. M., and Vasan, S. (2015). Parkinson's disease: a review of non-motor symptoms. *Expert Rev. Neurother.* 15, 549–562. doi: 10.1586/14737175.2015.1038244

Raza, C., Anjum, R., and Shakeel, N. U. A. (2019). Parkinson's disease: mechanisms, translational models and management strategies. *Life Sci.* 226, 77–90. doi: 10.1016/j.lfs.2019.03.057

Reichmann, H., Brandt, M. D., and Klingelhoefer, L. (2016). The nonmotor features of Parkinson's disease: pathophysiology and management advances. *Curr. Opin. Neurol.* 29, 467–473. doi: 10.1097/WCO.0000000000000348

Sen, S., Kawaguchi, A., Truong, Y., Lewis, M. M., and Huang, X. (2010). Dynamic changes in cerebello-thalamo-cortical motor circuitry during progression of Parkinson's disease. *Neuroscience* 166, 712–719. doi: 10.1016/j.neuroscience.2009.12.036

Tahmasian, M., Eickhoff, S. B., Giehl, K., Schwartz, F., Herz, D. M., Drzezga, A., et al. (2017). Resting-state functional reorganization in Parkinson's disease: an activation likelihood estimation meta-analysis. *Cortex* 92, 119–138. doi: 10.1016/j.cortex.2017.03.016

Tessitore, A., Cirillo, M., and De Micco, R. (2019). Functional connectivity signatures of Parkinson's disease. *J. Parkinsons Dis.* 9, 637–652. doi: 10.3233/JPD-191592

Vikene, K., Skeie, G. O., and Specht, K. (2019). Compensatory task-specific hypersensitivity in bilateral planum temporale and right superior temporal gyrus during auditory rhythm and omission processing in Parkinson ' s disease. *Sci. Rep.* 9:12623. doi: 10.1038/s41598-019-48791-0

Wang, J., Zhang, J. R., Zang, Y. F., and Wu, T. (2018). Consistent decreased activity in the putamen in Parkinson's disease: a meta-analysis and an independent validation of resting-state fMRI. *Gigascience* 7:giy071. doi: 10.1093/gigascience/giy071

Weingarten, C. P., Sundman, M. H., Hickey, P., and Chen, N. K. (2015). Neuroimaging of Parkinson's disease: expanding views. *Neurosci. Biobehav. Rev.* 59, 16–52. doi: 10.1016/j.neubiorev.2015.09.007

Wu, T., and Hallett, M. (2013). The cerebellum in Parkinson's disease. *Brain* 136, 696–709. doi: 10.1093/brain/aws360

Wu, T., Wang, L., Hallett, M., Li, K., and Chan, P. (2010). Neural correlates of bimanual anti-phase and in-phase movements in Parkinson's disease. *Brain* 133, 2394–2409. doi: 10.1093/brain/awq151

Yan, C., Wang, X., Zuo, X., and Zang, Y. (2016). DPABI : data processing & analysis for (Resting-State) brain imaging. *Neuroinformatics* 14, 339–351. doi: 10.1007/s12021-016-9299-4

Yan, C. G., Yang, Z., Colcombe, S. J., Zuo, X. N., and Milham, M. P. (2017). Concordance among indices of intrinsic brain function: Insights from inter-individual variation and temporal dynamics. *Sci. Bull.* 62, 1572–1584. doi: 10.1016/j.scib.2017.09.015

Yang, H., Zhou, X. J., Zhang, M.-M., Zheng, X. N., Zhao, Y. L., and Wang, J. (2013). Changes in spontaneous brain activity in early Parkinson's disease. *Neurosci. Lett.* 549, 24–28. doi: 10.1016/j.neulet.2013.05.080

Yang, Y., Zha, X., Zhang, X., Ke, J., Hu, S., Wang, X., et al. (2021). Dynamics and concordance abnormalities among indices of intrinsic brain activity in individuals with subjective cognitive decline: a temporal dynamics resting-state functional magnetic resonance imaging analysis. *Front. Aging Neurosci.* 12:584863. doi: 10.3389/fnagi.2020.584863

Yu, H., Sternad, D., Corcos, D. M., and Vaillancourt, D. E. (2007). Role of hyperactive cerebellum and motor cortex in Parkinson's disease. *Neuroimage* 35, 222–233. doi: 10.1016/j.neuroimage.2006.11.047

Yu, Y., Li, Z., Lin, Y., Yu, J., Peng, G., Zhang, K., et al. (2019). Depression affects intrinsic brain activity in patients with mild cognitive impairment. *Front. Neurosci.* 13:1333. doi: 10.3389/fnins.2019.01333

Yue, Y., Jiang, Y., Shen, T., Pu, J., Lai, H. Y., and Zhang, B. (2020). ALFF and ReHo mapping reveals different functional patterns in early- and Late-Onset Parkinson's Disease. *Front. Neurosci.* 14:141. doi: 10.3389/fnins.2020.00141

Zang, Y., Jiang, T., Lu, Y., He, Y., and Tian, L. (2004). Regional homogeneity approach to fMRI data analysis. *Neuroimage* 22, 394–400. doi: 10.1016/j.neuroimage.2003.12.030

Zang, Y. F., Yong, H., Chao-Zhe, Z., Qing-Jiu, C., Man-Qiu, S., Meng, L., et al. (2007). Altered baseline brain activity in children with ADHD revealed by resting-state functional MRI. *Brain Dev.* 29, 83–91. doi: 10.1016/j.braindev.2006.07.002

Zhang, C., Dou, B., Wang, J., Xu, K., Zhang, H., Sami, M. U., et al. (2019). Dynamic alterations of spontaneous neural activity in Parkinson's disease: a resting-state fMRI Study. *Front. Neurol.* 10:1052. doi: 10.3389/fneur.2019.01052

Zhang, J., Wei, L., Hu, X., Xie, B., Zhang, Y., Wu, G. R., et al. (2015). Akinetic-rigid and tremor-dominant Parkinson's disease patients show different patterns of intrinsic brain activity. *Parkinsonism Relat. Disord.* 21, 23–30. doi: 10.1016/j.parkreldis.2014.10.017

Zhu, J., Zhu, D.-M., Qian, Y., Li, X., and Yu, Y. (2018). Altered spatial and temporal concordance among intrinsic brain activity measures in schizophrenia. *J. Psychiatr. Res.* 106, 91–98. doi: 10.1016/j.jpsychires.2018.09.015

Zou, Q. H., Zhu, C. Z., Yang, Y., Zuo, X. N., Long, X. Y., Cao, Q. J., et al. (2008). An improved approach to detection of amplitude of low-frequency fluctuation (ALFF) for resting-state fMRI: fractional ALFF. *J. Neurosci. Methods* 172, 137–141. doi: 10.1016/j.jneumeth.2008.04.012

Zuo, X. N., Ehmke, R., Mennes, M., Imperati, D., Castellanos, F. X., Sporns, O., et al. (2012). Network centrality in the human functional connectome. *Cereb. Cortex* 22, 1862–1875. doi: 10.1093/cercor/bhr269

Zuo, X. N., Kelly, C., Di Martino, A., Mennes, M., Margulies, D. S., Bangaru, S., et al. (2010). Growing together and growing apart: regional and sex differences in the lifespan developmental trajectories of functional homotopy. *J. Neurosci.* 30, 15034–15043. doi: 10.1523/JNEUROSCI.2612-10.2010

Conflict of Interest: The authors declare that the research was conducted in the absence of any commercial or financial relationships that could be construed as a potential conflict of interest.

Publisher's Note: All claims expressed in this article are solely those of the authors and do not necessarily represent those of their affiliated organizations, or those of the publisher, the editors and the reviewers. Any product that may be evaluated in this article, or claim that may be made by its manufacturer, is not guaranteed or endorsed by the publisher.

Copyright © 2022 Tian, Chen, Ma, Li, Li, Wu, Liu, Du, Li and Su. This is an open-access article distributed under the terms of the Creative Commons Attribution License (CC BY). The use, distribution or reproduction in other forums is permitted, provided the original author(s) and the copyright owner(s) are credited and that the original publication in this journal is cited, in accordance with accepted academic practice. No use, distribution or reproduction is permitted which does not comply with these terms.

frontiers in Aging Neuroscience

REVIEW
published: 29 March 2022
doi: 10.3389/fnagi.2022.807909

Therapeutic Devices for Motor Symptoms in Parkinson's Disease: Current Progress and a Systematic Review of Recent Randomized Controlled Trials

Joji Fujikawa[1], Ryoma Morigaki[1,2], Nobuaki Yamamoto[1,3], Teruo Oda[1], Hiroshi Nakanishi[2], Yuishin Izumi[3] and Yasushi Takagi[1,2]*

[1] Department of Advanced Brain Research, Institute of Biomedical Sciences, Graduate School of Medicine, Tokushima University, Tokushima, Japan, [2] Department of Neurosurgery, Institute of Biomedical Sciences, Graduate School of Medicine, Tokushima University, Tokushima, Japan, [3] Department of Neurology, Institute of Biomedical Sciences, Graduate School of Medicine, Tokushima University, Tokushima, Japan

Background: Pharmacotherapy is the first-line treatment option for Parkinson's disease, and levodopa is considered the most effective drug for managing motor symptoms. However, side effects such as motor fluctuation and dyskinesia have been associated with levodopa treatment. For these conditions, alternative therapies, including invasive and non-invasive medical devices, may be helpful. This review sheds light on current progress in the development of devices to alleviate motor symptoms in Parkinson's disease.

Methods: We first conducted a narrative literature review to obtain an overview of current invasive and non-invasive medical devices and thereafter performed a systematic review of recent randomized controlled trials (RCTs) of these devices.

Results: Our review revealed different characteristics of each device and their effectiveness for motor symptoms. Although invasive medical devices are usually highly effective, surgical procedures can be burdensome for patients and have serious side effects. In contrast, non-pharmacological/non-surgical devices have fewer complications. RCTs of non-invasive devices, especially non-invasive brain stimulation and mechanical peripheral stimulation devices, have proven effectiveness on motor symptoms. Nearly no non-invasive devices have yet received Food and Drug Administration certification or a CE mark.

Conclusion: Invasive and non-invasive medical devices have unique characteristics, and several RCTs have been conducted for each device. Invasive devices are more effective, while non-invasive devices are less effective and have lower hurdles and risks. It is important to understand the characteristics of each device and capitalize on these.

Keywords: Parkinson's disease, tremor, freezing of gait (FOG), gait, stimulation, invasive medical devices, non-invasive medical device

OPEN ACCESS

Edited by:
Woon-Man Kung,
Chinese Culture University, Taiwan

Reviewed by:
Joan Cabestany,
Universitat Politecnica de Catalunya, Spain
Robert LeMoyne,
Northern Arizona University, United States

****Correspondence:***
Ryoma Morigaki
morigaki.riyoma.1@tokushima-u.ac.jp

Received: *02 November 2021*
Accepted: *14 January 2022*
Published: *29 March 2022*

Citation:
Fujikawa J, Morigaki R, Yamamoto N, Oda T, Nakanishi H, Izumi Y and Takagi Y (2022) Therapeutic Devices for Motor Symptoms in Parkinson's Disease: Current Progress and a Systematic Review of Recent Randomized Controlled Trials. Front. Aging Neurosci. 14:807909. doi: 10.3389/fnagi.2022.807909

INTRODUCTION

Parkinson's disease (PD) is a neurodegenerative disorder caused by the progressive loss of dopaminergic neurons in the midbrain (Lang and Lozano, 1998; Kalia and Lang, 2015). Its cardinal motor symptoms include tremor, rigidity, bradykinesia/akinesia, and postural instability (Dubois and Pillon, 1997). Pharmacotherapy is the mainstay treatment for patients with PD, and levodopa is the most effective drug for managing motor symptoms (Poewe and Mahlknecht, 2020). However, side effects such as dyskinesia and the on/off phenomenon have been associated with levodopa treatment (Holloway et al., 2004). Moreover, its effectiveness has decreased over the years (Obeso et al., 2017).

Invasive surgical alternatives to pharmacological treatments include stereotactic thalamotomy, deep brain stimulation (DBS), spinal cord stimulation (SCS), and continuous infusion of levodopa-carbidopa or apomorphine therapy. DBS is a widely used medical device therapy and surgical standard for patients with PD (Kleiner-Fisman et al., 2006). The use of SCS in patients with PD is promising for relieving concurrent pain conditions. The delivery of Duodopa® intestinal gel directly into the small intestine reduces fluctuating motor symptoms and improves the quality of life (Olanow et al., 2014). However, the risk associated with the implantation of these invasive medical devices is a burden for patients with PD. For example, DBS may cause irreversible intracranial hemorrhages (Kleiner-Fisman et al., 2006).

Recently, alternative non-pharmacological/non-surgical approaches have been explored to alleviate PD symptoms. Non-invasive medical devices are mainly effective for improving tremors, freezing of gait (FOG), and gait. Emerging non-invasive medical devices primarily include management devices for tremors, non-invasive brain stimulation (NIBS), cueing devices for FOG, non-invasive vagus nerve stimulation (nVNS), vibrotactile stimulation devices, mechanical/electrical peripheral stimulation, and photobiomodulation devices. Each device adapts to different body parts (**Figure 1**) and has different properties and effects. In this study, we review emerging therapeutic devices for motor symptoms in PD.

Abbreviations: aDBS, adaptive deep brain stimulation; AMPS, automated mechanical peripheral stimulation; BDNF, brain-derived neurotrophic factor; cDBS, conventional deep brain stimulation; DBS, deep brain stimulation; DLPFC, dorsolateral prefrontal cortex; EEG, electroencephalography; EMG, electromyography; EMS, electrical muscle stimulation; ET, essential tremor; FDA, Food and Drug Administration; fMRI, functional magnetic resonance imaging; FTM-TRS, Fahn-Tolosa-Marin Tremor Rating Scale; GPi, internal globus pallidus; FOG, freezing of gait; FOGQ, Freezing of Gait Questionnaire score; FSCV, fast scan cyclovoltammetry; LCIG, continuous infusion of levodopa-carbidopa gel; LFPs, local field potentials; M1, primary motor cortex; NIBS, non-invasive brain stimulation; nVNS, non-invasive vagus nerve stimulation; PBM, photobiomodulation; PD, Parkinson's disease; POT, primary orthostatic tremor; RCT, randomized controlled trial; rTMS, repetitive transcranial magnetic stimulation; PMC, premotor cortex; RMS, root mean square; ROM, range of motion; rTSMS, repetitive trans-spinal magnetic stimulation; SCS, spinal cord stimulation; SEMG, surface electromyography; sES, sensory electrical stimulation; SMA, supplementary motor area; STN, subthalamic nucleus; tDCS, transcranial direct current stimulation; TEEDs, total electrical energy delivered to the tissues per second; TETRAS, the Tremor Research Group's Essential Tremor Rating Assessment Scale; tsDCS, trans-spinal direct current stimulation; TUG, timed up and go; UPDRS, the Unified Parkinson's Disease Rating Scale; VIM, ventral intermediate nucleus of the thalamus; VNS, vagus nerve stimulation.

METHODS

A narrative literature review and a systematic review of randomized control trials (RCTs) were conducted. These reviews summarized recent invasive and non-invasive medical devices and their effects on PD patients in the past 10 years. The search method is shown in **Figure 2**. All searches were performed on PubMed and Scopus. The study screening was done independently by two reviewers, JF and RM First, we searched for MeSH term "Parkinson's disease." English language literature in the past 10 years was reviewed. Next, we added the device name to the search terms and performed a search for each device, as shown in **Figure 2**. Articles found in this search were screened based on title and abstract, then based on the full text. In the narrative literature review, we selected literature related to motor symptoms. For the systematic review, RCTs were extracted out from the search results. We manually reviewed these papers and selected the ones that fit. The RCT studies selected from the search are shown in **Table 1**.

RESULTS

Narrative Literature Review

Deep Brain Stimulation

DBS is the surgical standard for patients with movement disorders such as PD, essential tremor (ET), and dystonia. DBS is a highly effective and widely used treatment for PD patients and is probably the most important advance in PD treatment since the introduction of levodopa (Kleiner-Fisman et al., 2006; Benabid et al., 2009; Bronstein et al., 2011). The target of stimulation is either the subthalamic nucleus (STN) or internal globus pallidus (GPi) (Sako et al., 2014). The ventral intermediate nucleus of the thalamus (VIM) is also used to improve tremors (Morigaki et al., 2011a,b). Recently, advanced imaging sequences have enabled direct visualization of anatomical targets, and patient-specific DBS has been performed (Neudorfer et al., 2022). DBS has been demonstrated to improve motor function including FOG (Krack et al., 2003; Huang et al., 2018), camptocormia (Sako et al., 2009; Chan et al., 2018), tremor (Morigaki et al., 2011a,b), and cognitive dysfunction. Although DBS has a lower complication rate than stereotactic thalamotomy (Tasker, 1998; Pahwa et al., 2001), intracranial hemorrhage and infection still occur in 3.9 and 1.6% of the patients, respectively (Kleiner-Fisman et al., 2006). There is also a risk of secondary psychiatric effects (Piasecki and Jefferson, 2004; Kinoshita et al., 2018). Long-term effects have been shown to last for more than 10 years for tremors. In many cases, activity of daily living can be maintained for a long time, and patient satisfaction remains high even after 10 years of follow-up (Hitti et al., 2019). However, since DBS is not effective for all patients, it is necessary to determine if the patient is an appropriate candidate. It is also important to confirm the diagnosis of idiopathic PD. A thorough neurological

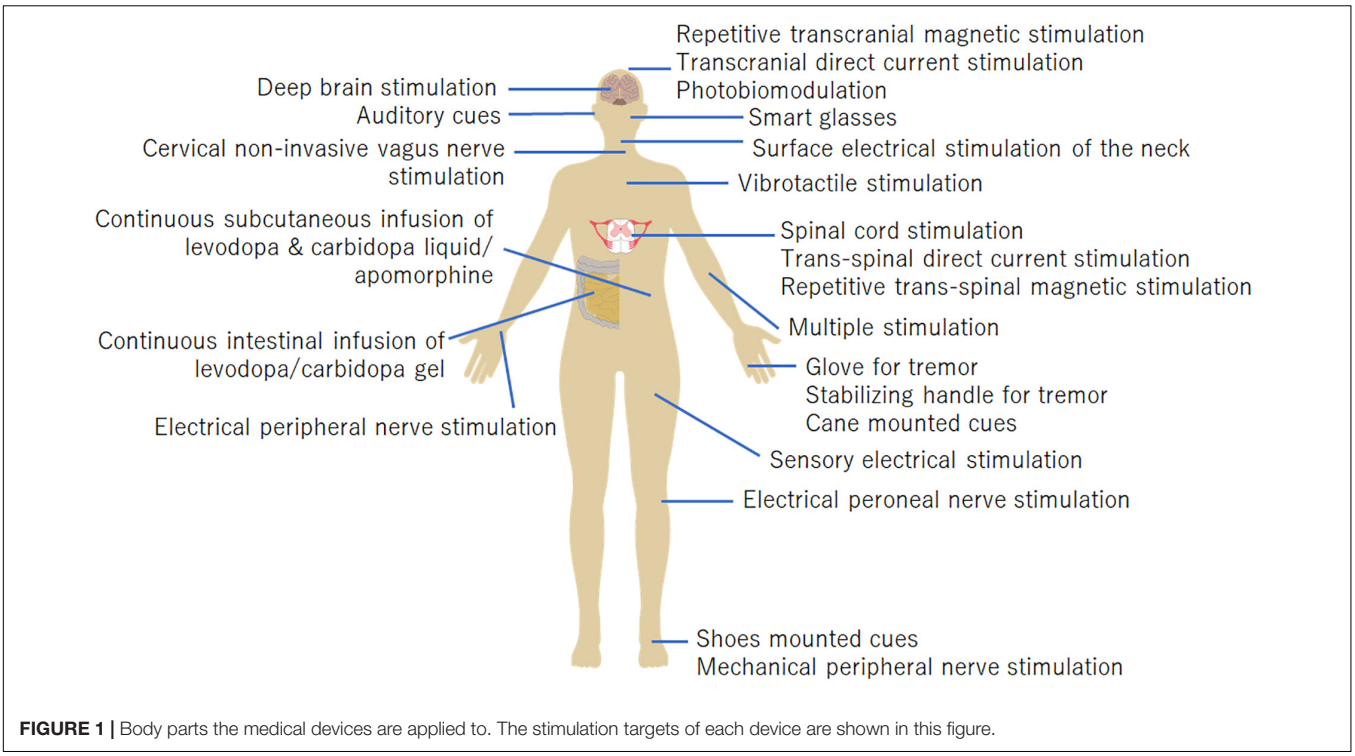

FIGURE 1 | Body parts the medical devices are applied to. The stimulation targets of each device are shown in this figure.

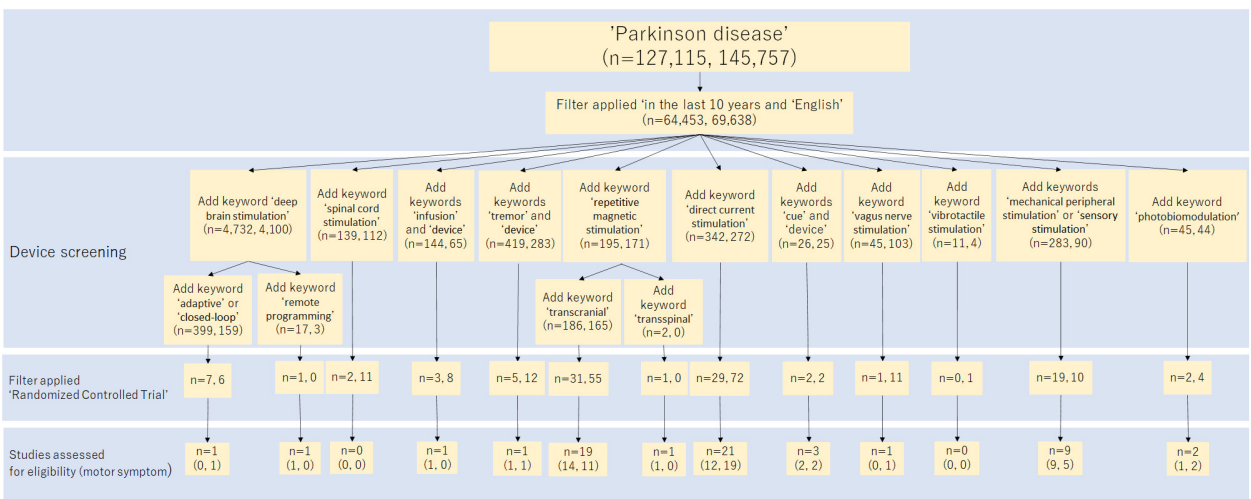

FIGURE 2 | Flow diagram of the study selection process in the systematic review. This diagram shows how to search for studies in a systematic review. The numbers in parentheses show the breakdown of the number of search hits, with PubMed and Scopus listed in that order.

examination is necessary because some neurological disorders can mimic the signs and symptoms of idiopathic PD (Machado et al., 2006). Also, DBS effects for gait impairment, postural instability, postural abnormalities, FOG, and other axial motor signs are under debate (Fasano et al., 2015). Expert opinion showed that the risk/benefit ratio in the elderly for STN DBS is not very favorable; unlike STN DBS, there is no clinical indication that the outcome of VIM DBS is in any way affected by age. It must be determined on an individual basis, considering the need for treatment, risk factors for complications, and general life expectancy (Lang et al., 2006). The precise underlying mechanisms of DBS remain a matter of debate. A leading hypothesis is that DBS restores aberrant neuronal firing to non-pathological rates by applying high-frequency trains of electrical stimulation (Muller and Robinson, 2018). DBS devices are also increasing in functionality as research advances, such as a variety of stimulation methods [interleaved stimulation (Wojtecki et al., 2011; Baumann et al., 2012; Aquino et al., 2019), dual-target stimulation (Hollingworth et al., 2017), directional stimulation (Schupbach et al., 2017), current steering (Barbe et al., 2014)],

TABLE 1 | Randomized controlled trials of medical devices.

Device/Method	Invasive/Non-invasive	CE marking and FDA certification for PD	References	Subject	Efficacy
Adaptive DBS	Invasive	CE marking and FDA approved	Sasaki et al., 2021	12 PD patients	Both programed using a standard of care and the closed-loop algorithm improved UPDRS Part III scores and sensor-based predominantly, but there was no significant difference between the two methods. Median UPDRS Part III was 37.5 points at baseline, 22.0 points for programed using a standard of care and 23.5 points (20.3–27.0) for a closed-loop algorithm. The programming steps were significantly reduced in the closed-loop compared to the existing method.
DBS with remote programming	Invasive	CE marking and FDA approved	Li et al., 2017	64 PD patients	Bilateral wireless programming STN -DBS significant decrease in the UPDRS motor scores were observed for the test group in the off-medication state (25.08 ± 1.00) vs. the control group (4.20 ± 1.99).
LCIG	Invasive	CE marking and FDA approved	Olanow et al., 2014	66 PD patients	LCIG significantly reduced "Off" time by a mean (± SE) of 1.91 ± 0.57 h ($P = 0.0015$) and increased "On" time without troublesome dyskinesia by a mean of 1.86 ± 0.65 h ($P = 0.006$).
Tremor's glove	Non-invasive	Not approved	Jitkritsadakul et al., 2017	30 PD patients	During stimulation, significant reduction in RMS angular velocity (as percentage) in every axis and peak magnitude in axis (x-, y-) and UPDRS tremor score (glove : 5.27 ± 2.19, sham : 4.93 ± 2.37) were found with Tremor's glove compared to the sham groups ($p < 0.05$, each).
rTMS over M1	Non-invasive	Not approved	Benninger et al., 2012	26 PD patients	50 Hz rTMS did not improve gait, bradykinesia, global and motor UPDRS.
			Maruo et al., 2013	21 PD patients	rTMS over M1 significantly improved UPDRS Part III, visual analog scale, the walking test, self-assessment motor score, and finger tapping measurement. No significant improvement was observed in depression and apathy scales.
			Yang et al., 2013	20 PD patients	Effectiveness study of combination of rTMS and treadmill training. Significant time effects on almost all corticomotor and functional variables and it suggested combination of rTMS and treadmill training improve walking performance.
			Kim et al., 2015	17 PD patients	The TUG and UPDRS Part III showed significant ameliorations over time.
			Chang et al., 2016	8 patients with atypical parkinsonism	FOGQ, turn steps, TUG task and UPDRS Part III revealed significant improvements.
			Cohen et al., 2018	42 PD patients	A study of repetitive deep transcranial magnetic stimulation using H5 coils. Although repetitive deep transcranial magnetic stimulation treatment exhibited some motor improvements, we could not demonstrate an advantage for real treatment over sham.
			Khedr et al., 2019	52 PD patients	Comparing the effects of 20 and 1 Hz. Both improve PD motor function, but 20 Hz rTMS is more effective.
rTMS over SMA	Non-invasive	Not approved	Chung et al., 2020	51 PD patients	The 1 and 25 Hz rTMS groups produced a greater improvement in fastest walking speed at 1 day and 3 months postintervention than the sham group.
			Shirota et al., 2013	106 PD patients	At week 20, 1 Hz stimulation showed an improvement of 6.84 points on the UPDRS Part III.
			Sayin et al., 2014	17 PD patients	1 Hz rTMS reduced levodopa-induced dyskinesias lasting 24 h without altering motor performance
			Ma et al., 2019	28 PD patients with FOG	Beneficial effects on FOG and some gait parameters, but no improvement in sequence effects.
			Mi et al., 2019	30 PD patients with FOG	Significantly decreased FOGQ (up to -2.13 points, 95% CI -2.97 to -1.29). Significant improvements of UPDRS Part III (up to -6.69, 95%CI -8.73 to -4.66) and gait variables.
			Ji et al., 2021	42 PD patients	UPDRS Part III score significant decrease in the rTMS group (from 28.0 ± 2.12 at baseline to 20.6 ± 1.82 at Week 2; $p < 0.0001$).
rTMS over DLPFC	Non-invasive	Not approved	Li et al., 2015	132 PD patients	Comparison of the effects of istradefylline and rTMS. There was no significant difference in the UPDRS Part III score, and istradefylline and rTMS had comparable efficacy and tolerability.

(Continued)

TABLE 1 | Continued

Device/Method	Invasive/Non-invasive	CE marking and FDA certification for PD	References	Subject	Efficacy
			Zhuang et al., 2020	33 PD patients	Compared to baseline, active rTMS showed significant improvement in the UPDRS Part III and Non-motor Symptom Questionnaire at 1 month, and the change in scores persisted for 3 months after rTMS intervention.
rTMS over M1, SMA, DLPFC	Non-invasive	Not approved	Lee et al., 2014	20 patients with parkinsonism	tDCS over M1 and DLPFC were significant improvements in TUG test times and UPDRS Part III scores.
			Yokoe et al., 2018	19 PD patients	rTMS over M1 or SMA was able to significantly improve motor symptoms, but it could not clearly improve mood disorders.
rTMS over M1, DLPFC	Non-invasive	Not approved	Brys et al., 2016	50 PD patients	tDCS over M1 was able to significantly improve motor function; there was no benefit from combining M1 and DLPFC stimulation.
rTMS over M1, PFC	Non-invasive	Not approved	Spagnolo et al., 2020	59 PD patients	rTMS (M1-PFC and M1 combined) significantly greater improvement compared to sham in UPDRS Part III total score ($p = 0.007$), tremor subscore ($p = 0.011$), and lateralized sub-scores ($p = 0.042$ for the more affected side; $p = 0.012$ for the less affected side).
Multitarget tDCS (M1 and left DLPFC)	Non-invasive	Not approved	Dagan et al., 2018	20 PD patients with FOG	Significant improvements of TUG, and the Stroop test.
			Manor et al., 2021	77 PD patients with FOG	Decreased self-reported FOG severity and increased daily living step counts. However, demonstrated no advantage for tDCS in laboratory-based FOG-provoking test.
tDCS over M1	Non-invasive	Not approved	Valentino et al., 2014	10 PD patients	Reduction in number and duration of freezing of gait episodes, significant improvements of UPDRS Part III.
			Cosentino et al., 2017	14 PD patients	tDCS induced significant changes in cortical excitability and motor performances of both hands significantly improved.
			Broeder et al., 2019	10 PD patients and 10 healthy control subjects	Funnel task on a touch-sensitive tablet was found significant reduction in upper limb freezing episodes.
tDCS over DLPFC	Non-invasive	Not approved	Beretta et al., 2020b	24 PD patients	tDCS over M1 improved the postural response to external perturbation in PD, with better response observed for 2 mA compared with 1 mA.
			Swank et al., 2016	10 PD patients	Participants performed TUG single and dual task conditions. It did not significantly improve gait.
			Lattari et al., 2017	17 PD patients	Investigate the impact on functional mobility and balance. Significant improvement in Berg Balance Scale, Dynamic Gait Index, TUG.
			Bueno et al., 2019	20 PD patients	Statistically significant differences were found for Trail Making Test part B in active and sham groups. For the Verbal Fluency test differences were found only within the group that received real stimulation.
			Mishra and Thrasher, 2021	20 PD patients	In the dual-task condition, participants walked faster at 15 min ($p = 0.017$) and 30 min ($p < 0.01$) after anodal tDCS ceased compared to sham. Similarly, participants generated a higher number of words per minute at 15 min ($p = 0.017$), and 30 min ($p < 0.01$) after anodal tDCS ceased compared to sham.
tDCS with physical training	Non-invasive	Not approved	Kaski et al., 2014b	16 PD patients	tDCS with physical training increased gait velocity (mean = 29.5%, $SD = 13$; $p < 0.01$) and improved balance (pull test: mean = 50.9%, $SD = 37$; $p = 0.01$) compared with tDCS alone.
			Schabrun et al., 2016	16 PD patients	Gait speed, step length and cadence improved in the active and sham groups, under all dual-task conditions. This effect was maintained at follow-up. There was no difference between the active and sham tDCS groups.

(Continued)

TABLE 1 | Continued

Device/Method	Invasive/Non-invasive	CE marking and FDA certification for PD	References	Subject	Efficacy
			Costa-Ribeiro et al., 2017	22 PD patients	tDCS + cueing gait training group and sham tDCS + cueing gait training group demonstrated similar gains in all outcome measures, except for the stride length. The number of participants who showed minimal clinically important differences was similar between groups.
			Fernandez-Lago et al., 2017	18 PD patients	Evaluated the combination of treadmill walking and tDCS over M1. It improved walking performance and modulated spinal and corticospinal parameters in a similar way.
			Yotnuengnit et al., 2018	53 PD patients	After intervention, group 1 (only tDCS) demonstrated a significant increase in gait speed by 0.13–0.14 m/s (17.8–19.2%) and an increase in step length by 5.9–6.1 cm (14.0–14.5%), whereas group 2 (tDCS and physical therapy) revealed a significant increase in gait speed by 0.10–0.13 m/s (14.9–19.4%) and step length by 4.5–5.4 cm (10.6–12.8%) and group 3 (sham tDCS and physical therapy) showed a significant increase in gait speed by 0.09–0.14 m/s (13.0–20.3%) and step length by 3.0–5.4 cm (6.8–12.3%).
			Horiba et al., 2019	18 PD patients	Mirror visual feedback combined with tDCS over M1. Apply tDCS, the number of ball rotations in accordance with input-output function at 150% intensity was significantly increased after day 1 and retained until day 2.
			Conceicao et al., 2021	17 PD patients	Investigated the effects of tDCS over the prefrontal cortex with cycling. Participants decreased step time variability (effect size: -0.4), shortened simple and choice reaction times (effect sizes: -0.73 and -0.57, respectively), and increased PFC activity.
			Lee and Kim, 2021	30 PD patients	tDCS combined with visual cueing training. Results showed a significant decrease in UPDRS Part III score and a significant increase in functional gait assessment and cadence.
tDCS over SMA, M1	Non-invasive	Not approved	da Silva et al., 2018	17 PD patients	Significant group difference with gait cadence (P = .014, *d* = 0.87), indicating its reduction after tDCS (-0.28 [-1.16, 0.01] steps/s) compared with sham tDCS group (0.17 [0.00, 0.40] steps/s).
tDCS over primary and premotor cortices	Non-invasive	Not approved	Kaski et al., 2014a	1 PD patient	Evaluated the combination of tango dance and tDCS. Significant improvements of trunk velocity and TUG.
tDCS of the cerebellum	Non-invasive	Not approved	Lima de Albuquerque et al., 2020	22 PD patient	Evaluated motor performance by a visuomotor isometric precision grip task and a rapid arm movement task. From results indicate that an acute application of tDCS of the cerebellum does not enhance motor performance in hand and arm tasks in PD.
tDCS over the left sensorimotor (anode) and right frontal areas (cathode)	Non-invasive	Not approved	Schoellmann et al., 2019	10 PD patients and 10 healthy control subjects	Motor UPDRS Part III hemibody score of the right upper extremity (items 22–25) improved. Neurophysiological features indicated a motor-task-specific modulation of activity and coherence from 22 to 27 Hz after tDCS.
rTSMS	Non-invasive	Not approved	Arii et al., 2014	37 PD patients with camptocormia	Evaluated immediate effect of rTSMS on camptocormia. The flexion angle in the standing position significantly decreased by a mean of 10.9° and flexion angle while sitting significantly decreased by 8.1°.
Cueing by smart glass (Google Glass)	Non-invasive	Not approved	Zhao et al., 2016	12 PD patients with FOG	Participants were overall positive about the usability of the Google Glass. However, freezing of gait did not significantly decrease.
Laser light visual cueing	Non-invasive	Not approved	Bunting-Perry et al., 2013	22 PD patients with FOG	The laser beam applied as a visual cue. However, it did not diminish freezing of gait.

(Continued)

TABLE 1 | Continued

Device/Method	Invasive/Non-invasive	CE marking and FDA certification for PD	References	Subject	Efficacy
Visual cues combined with treadmill training	Non-invasive	Not approved	Schlick et al., 2016	23 PD patients	Combining visual cues with treadmill training significantly improved TUG, gait speed, and stride length as compared to not combining the two.
nVNS	Non-invasive	Not approved	Mondal et al., 2021	33 PD patients with FOG	The velocity increased by 16% ($p = 0.018$), step length increased by 11% ($p = 0.021$), and step time reduced by 16% ($p = 0.003$) in the active nVNS group.
Mechanical peripheral stimulation	Non-invasive	CE marking and FDA approved (Gondola)	Barbic et al., 2014	16 PD patients	Mechanical stimulation of the feet increases stride length and gait speed, increases upright rotation speed, and decreases step count.
			Quattrocchi et al., 2015	11 PD patients	Automatic mechanical peripheral stimulation was found to increase resting-state functional connectivity in the sensorimotor cortex, striatum, and cerebellum.
			Galli et al., 2018	28 PD patients and 32 healthy control subjects	Mean velocity, stride length, ankle ROM, and knee ROM significantly improved ($P < 0.05$) after the sessions compared with pre-sessions only in the intervened group.
			Kleiner et al., 2018	30 PD patients	Significant for gait asymmetry [$F(3, 204) = 7.420$; $P = 0.0001$], mean step length [$F(3, 201) = 3.570$; $P = 0.015$], step length coefficient of variation [$F(3, 207) = 7.093$; $P = 0.0001$], step time variability standard deviation [$F(3, 210) = 3.223$; $P = 0.024$], step time variability coefficient of variation [$F(3, 210) = 5.503$; $P = 0.001$], and gait velocity [$F(3, 210) = 5.070$; $P = 0.027$].
			Pagnussat et al., 2018	33 PD patients	Effective stimulation group showed significantly higher serum levels of brain-derived neurotrophic factor and lower serum levels of cortisol compared to sham stimulation group. Gait velocity, stride length, and TUG performance were significantly improved in effective stimulation group.
			Pinto et al., 2018	30 PD patients	Significant improvement in hip internal-external rotation between intervened and sham-control group ($P = 0.018$). Hip internal-external rotation, stride length, step length, and gait speed were significantly improved ($P \sim 0.000$) after eight sessions compared to pre-conditions.
			Prusch et al., 2018	33 PD patients	No positive effects on center of pressure parameters (no positive effect in improving static postural control).
			Pagnussat et al., 2020	25 PD patients	There were no changes in brain activity by task-based fMRI. Resting-state fMRI showed increase in brain connectivity in areas related to sensory processing and sensorimotor integration.
Surface electrical stimulation of the neck (submental region)	Non-invasive	Not approved	Baijens et al., 2013	90 PD patients with dysphagic	No statistically significant differences in fiber optic endoscopic evaluation of swallowing and videofluoroscopy of swallowing outcome variables were found.
Photobiomodulation	Non-invasive	Not approved	Santos et al., 2019	35 PD patients	Significantly improved the walking speed in the fast rhythm of the 10 m walking test by an average of 0.33 m/s.
			Liebert et al., 2021	12 PD patients	Measures of mobility, cognition, dynamic balance, and fine motor skill were significantly improved ($p < 0.05$) with photobiomodulation treatment for 12 weeks and up to 1 year.

DBS, deep brain stimulation; DLPFC, Dorsolateral prefrontal cortex; FDA, Food and Drug Administration; fMRI, functional magnetic resonance imaging; FOG, Freezing of Gait; FOG-Q, Freezing of Gait Questionnaire score; LCIG, continuous infusion of levodopa-carbidopa gel; M1, Primary motor cortex; nVNS, non-invasive vagus nerve stimulation; PD, Parkinson's disease; PFC, pre-frontal cortices; RCT, randomized controlled trial; RMS, the root mean square; ROM, range of motion; rTMS, repetitive transcranial magnetic stimulation; rTSMS, repetitive trans-spinal magnetic stimulation; SMA, supplementary motor area; STN, subthalamic nucleus; tDCS, transcranial direct current stimulation; TUG, timed up and go; UPDRS, the Unified Parkinson's Disease Rating Scale.

and support for magnetic resonance imaging (Larson et al., 2008; McElcheran et al., 2019). Studies have also been conducted to investigate the corresponding effects on stimulus frequency (Karl et al., 2020). Stimulation parameters may change the effects and long-term consequences. In this section, we introduce two emerging technologies in DBS: adaptive DBS (aDBS) and remote programming for DBS adjustment, both of which have seen significant growth and attention in recent years.

Adaptive Deep Brain Stimulation

DBS devices that operate on the principle of closed-loop interaction are called aDBS. A closed-loop system can sense the effect of stimulation and adjust the stimulation in response to the observed effect. Recently, a closed-loop stimulation technology based on local field potentials (LFPs) in target structures as biomarkers has been used for the treatment of PD subjects (Marceglia et al., 2009; Giannicola et al., 2010; Little et al., 2013; Sasaki et al., 2021). Compared to the cortical neural signals such as electroencephalography (EEG), electrocorticography, and magnetoencephalography, LFP signals from deep electrodes provide direct changes in basal ganglia function (Einevoll et al., 2013). In PD, increased synchrony of neuronal networks in the beta band (13–35 Hz) is associated with reduced segregation of parallel processes, leading to reduced specificity of motor programs (Mink, 1996; Pessiglione et al., 2005). The amplitude of spectral peaks in the beta band correlates with the severity of symptoms (Neumann et al., 2016, 2017) and is reduced by dopaminergic medication and DBS (Kuhn et al., 2009). Beta-power is an ideal candidate for aDBS as a biomarker (Marceglia et al., 2009; Giannicola et al., 2010; Little et al., 2013) and aDBS using LFPs has been confirmed to have advantages over conventional DBS (cDBS). aDBS reportedly prevents several complications related to cDBS, including gait and speech disturbances, and was appropriately modulated by levodopa administration, with a further reduction in stimulation, potentially preventing excessive combined therapy and dyskinesias (Little et al., 2016a,b). Bocci et al. (2021) reported that the Unified PD Rating Scale (UPDRS) part III scores, the Rush scale for dyskinesias, and the total electrical energy delivered to the tissues per second (TEEDs) were significantly lower in the aDBS session during an 8-h stimulation protocol, in conjunction with chronic levodopa assumption and without restriction on patients' activities. The safety and effectiveness of aDBS stimulation compared to cDBS in a daily session in terms of motor performance and TEEDs in patients with PD are shown. Little et al. (2013) compared the effectiveness of aDBS with that of cDBS. aDBS showed 66% (unblinded) and 50% (blinded) improvements in motor scores, which were 29% (unblind) and 27% (blinded) significantly better than cDBS. These improvements were achieved with a 56% reduction in stimulation time and a significant reduction in energy requirements compared to cDBS.

In the future, a closed-loop system that uses neurotransmitters such as dopamine, histamine, adenosine, serotonin, and glutamate release as a control variable has been proposed (Griessenauer et al., 2010; Shon et al., 2010; Chang et al., 2012a,b; Chang et al., 2013). A 30-minute baseline of dopamine during a DBS surgery was quantified using microdialysis (Kilpatrick et al., 2010). Kishida et al. (2011, 2016) performed the voltammetric measurement of real-time dopamine dynamics in patients with PD using fast scan cyclovoltammetry (FSCV). One study targeted another neurotransmitter, adenosine. Real-time in vivo FSCV neurochemical recordings in patients with tremors showed that DBS induces adenosine release concurrent with tremor arrest (Chang et al., 2012b). It has become clear that although clinical monitoring of neurotransmitters is technically feasible, and these sensing technologies need to be improved to measure dopamine over long periods (days, months, years). This will require the development of technologies that can solve current problems such as biofouling and material degradation to enable reliable long-term recording. Furthermore, the improvement of current biosensors or the development of new biosensors to accommodate chronic implantation and the method for information processing and decision making are also essential.

Remote Programming for Deep Brain Stimulation Adjustment

Remote DBS programming has been implemented in clinical practice (Li et al., 2017; Zhang et al., 2020; Ma et al., 2021; Xu et al., 2021). Unfortunately, many patients do not achieve the expected DBS outcome due to inadequate or suboptimal programming (Farris and Giroux, 2013). Optimization of DBS parameters is usually attained within three to 6 months, during four to five programming sessions (Bronstein et al., 2011). Additionally, the parameters need to be adjusted over the long term to maintain this effect. The physician responsible for postoperative programming should be an expert in both DBS and medical management of PD patients, but patients living in remote areas may have inadequate access and thus may not receive adequate adjustments. Thus, teleprogramming has received increasing attention in recent years, partly because of the coronavirus disease 2019 pandemic. Ma et al. (2021) followed 90 patients for a total of 386 remote programming visits over 27 months. Their questionnaire survey demonstrated that each remote programming visit saved $\geq$ 2000 Chinese yuan for 76.7% of the patients and $\geq$ 12 h for 90.0% of the patients, compared with the on-site programming visit. Respondents also rated the acceptability of the remote programming platform highly. Moreover, 89% of the patients were satisfied with the remote programming. Significant improvement in UPDRS Part III was also achieved in another study of 32 patients conducted by Xu et al. (2021). LeMoyne et al. (2019a,b, 2020a,b,c) quantified the tremor of PD patients via a wireless inertial sensor system with connectivity to Cloud computing resources attached to the dorsal side of the hand and successfully classified the stimulus amplitude of DBS. Machine learning was used for classification, with neural networks, J48 decision trees, K-nearest neighbor, support vector machine, logistic regression, and random forest, achieving 100% accuracy in certain conditions. An online system for handling such objective and quantitative data is essential for remote DBS coordination.

Spinal Cord Stimulation

The use of SCS in patients with PD is promising for relieving concurrent pain conditions (Fenelon et al., 2012; Cai et al., 2020). Notably, SCS has recently also been shown to be effective for locomotive symptoms in patients with PD (Hassan et al., 2013); therefore, SCS might be a viable alternative therapy to DBS for the management of PD symptoms (Pinto de Souza et al., 2017). Santana et al. (2014) showed that SCS at the upper thoracic level in a primate model of PD improved freezing, hypokinesia, postural instability, and bradykinesia, which is associated with a reduction in beta-frequency oscillation within the cortico-basal ganglia circuitry.

In human case reports, high cervical SCS (C2-C3) yielded incongruent results (Thevathasan et al., 2010; Hassan et al., 2013). Cervical SCS with tonic waveform requires a long latency (more than 3 months) for motor improvement (Mazzone et al., 2019). Contrastingly, the improvement by cervical SCS with burst waveform stimulation showed acute and larger improvements in motor symptoms, including tremor, gait parameters, and pain (Mazzone et al., 2019). Similarly, thoracic SCS (T6-T12) reduced gait impairment, rigidity, abnormal posture, and tremor (Agari and Date, 2012; Fenelon et al., 2012; Landi et al., 2013; Nishioka and Nakajima, 2015; Samotus et al., 2018; Hubsch et al., 2019). Thoracic SCS with burst waveform stimulation also improves pain, gait, and stooping posture (Kobayashi et al., 2018; Furusawa et al., 2020). Some authors have advocated SCS as a possible salvage therapy for DBS with decreased efficacy over the years (Agari and Date, 2012; Landi et al., 2013; Akiyama et al., 2017; Pinto de Souza et al., 2017). However, a 1-year single prospective open-label pilot study revealed no beneficial effect of thoracic SCS in six pain-free advanced PD patients with significant axial symptoms (Prasad et al., 2020). The possibility of quick habituation for tonic stimulation is advocated for the gradual loss of clinical benefit in axial symptoms over time and the ongoing pilot trial of cyclic stimulation (Cury et al., 2020).

The major complications of SCS include infection, lead migration or breakage, subcutaneous hematoma, and discomfort due to the pulse generator (Nissen et al., 2019). The infection rate is 3–6% (Nissen et al., 2019); however, the majority of SCS studies in patients with PD were either uncontrolled or controlled trials with small sample sizes. Thus, well-designed clinical trials, including double-blind and placebo-controlled arms with large sample sizes and specific stimulation protocols are warranted to generate solid evidence regarding the effectiveness of SCS (Fonoff et al., 2019; Rahimpour et al., 2021).

Continuous Infusion of Levodopa-Carbidopa or Apomorphine Therapy

PD patients are mainly treated with oral administration of levodopa and dopamine agonists during the early stage (Fahn and Sulzer, 2004). However, the duration of the response to treatment becomes shorter, and side effects—such as hallucinations—are marked as the progression of the disease stage. Complications such as fluctuations, including the wearing-off phenomenon and dyskinesia, can be seen in patients who have been receiving long-term oral levodopa (Eggert et al., 2008). This fluctuation of symptoms might be caused by the short half-life of levodopa (Nyholm et al., 2005). Continuous drug delivery, allowing for continuous dopaminergic stimulation, is necessary for patients with advanced-stage PD (van Laar, 2003; Nyholm et al., 2005; Gershanik and Jenner, 2012). Dopaminergic stimulation can be prolonged by two methods: the simultaneous administration of enzyme inhibitors to prevent the metabolism of levodopa and continuous administration of dopaminergic agents, not orally. Continuous levodopa administration was reported to be effective for the reduction of dyskinesia and off-time by stabilizing plasma levodopa/carbidopa levels and providing continuous stimulation of dopaminergic receptors in the striatum (Sage et al., 1988; Politis et al., 2017).

The methods currently available for continuous infusion are subcutaneous apomorphine, levodopa/carbidopa liquid, and enteral levodopa/carbidopa gel (Duodopa®, Abbott, Allschwil, Switzerland). Continuous subcutaneous apomorphine infusion is effective on motor function and alleviates motor fluctuations in patients with PD and, it can also significantly reduce off-time (Garcia Ruiz et al., 2008). Various types of apomorphine infusion approaches such as inhale, patch pump, and sublingual administrations have been developed (Titova and Chaudhuri, 2016). In recent years, the efficacy of these approaches on motor function has been assessed (Olanow et al., 2020) and sublingual apomorphine has received Food and Drug Administration (FDA) approval (Larson and Simuni, 2022). Duodopa® can be delivered to the jejunum via a percutaneous gastrojejunostomy tube, which is connected to a portable infusion pump filled with Duodopa®. Duodopa® intestinal gel can shorten off-time while extending on-time without dyskinesia (Olanow et al., 2014). Furthermore, Slevin et al. (2015) and Merola et al. (2016) investigated on-time with/without troublesome dyskinesia with Duodopa® treatment. Although there was no significant difference in on-time with troublesome dyskinesia between the control and Duodopa® groups, significant differences were observed in on-time without troublesome dyskinesia and off-time, suggesting that Duodopa® had a positive effect. However, the pooled results showed that Duodopa® intestinal infusion did not significantly improve the UPDRS total score, including parts II and III (Wang et al., 2018). Contrastingly, a cost-utility analysis was performed in the United Kingdom and showed that Duodopa® intestinal infusion increased quality-adjusted life years while also being cost-effective. Thus, it seems that Duodopa® is effective in reducing fluctuating motor symptoms and improving quality of life, and so might be a useful tool to treat patients with advanced-stage PD. The most frequent adverse events associated with Duodopa® were surgery-associated adverse events, such as infection and inflammation, which may be associated with morbidity and mortality in some patients. Tube obstruction, dislocation of the catheter tip, pump failure, and pull-out of the tube were reported to be related to the infusion system. Furthermore, drug-induced events, such as hallucinations, dystonia, worsened dyskinesia, acute peripheral neuropathy, psychosis, weight loss, and homocysteine concentrations have also been reported (Nyholm, 2012).

In recent years, another method for continuous levodopa administration is the continuous subcutaneous infusion of levodopa using ND0612 (NeuroDerm, Rehovot, Israel)

(Olanow et al., 2021). ND0612 is a drug/device combination consisting of a subcutaneous pump and a liquid formulation. This formulation contains excipients to allow for low infusion rates. ND0612 administrates a liquid levodopa/carbidopa continuously, that stabilizes plasma levodopa levels compared to standard oral levodopa (Giladi et al., 2021). Olanow et al. (2021) evaluated the potential benefits of a 14-h (waking day) infusion compared to a 24-h infusion. The off-time for the overall population was significantly reduced by 2.0 h compared to baseline. On-time with no troublesome dyskinesia was significantly increased from baseline by 3.3 h, and on-time with moderate/severe dyskinesia was also significantly reduced by 1.2 h. The reduction in off-time was 1.5 h larger in the 24-h group than in the 14-h group. Notably, complete resolution of off-time was observed in 42% of patients in the 24-h group. Therefore, subcutaneous administration might both avoid fluctuations in absorption resulting from delayed gastric emptying and reduce surgical risks compared to Duodopa® (Nilsson et al., 1998; Nyholm and Lennernas, 2008). Poewe et al. (2021) evaluated the 1-year safety data of ND0612. After evaluation by 214 patients, most patients experienced infusion site reactions such as particularly nodules (30.8%) and hematomas (25.2%). However, most cases were mild to moderate, and only 10.3% of the patient discontinued treatment. This indicated that ND0612 is generally safe.

Continuous subcutaneous infusion of apomorphine has been developed by Mitsubishi Tanabe/Neuroderm as ND0701. ND0701 is a novel concentrated apomorphine formulation for apomorphine-based continuous subcutaneous infusion. A study by Ramot et al. (2018) and Larson and Simuni (2022) showed that it was safe and well-tolerated and had similar bioavailability to commercially available apomorphine formulations.

Non-invasive Devices for Tremor

Tremor is the most common movement disorder and is defined as a rhythmic, involuntary oscillating movement (Bhatia et al., 2018). ET is the most common tremor worldwide. Although ET affects any part of the body, this tremor occurs most often in the hands, especially at the time of action—such as drinking and writing. Contrastingly, approximately 70% of PD patients also experience a tremor during the course of illness (Martin et al., 1973; Hughes et al., 1993; Pal et al., 2002), although this resting tremor tends to be a pill-rolling tremor, which looks like holding a pill between the thumb and forefinger and rolling it around. For patients with PD, tremor is one of the most disabling symptoms, in addition to slowed movement, rigid muscles, and postural balance impairment. Although resting tremor is a well-known symptom of PD, postural tremor associated with PD can cause more disability than typical resting tremors (Lance et al., 1963; Koller et al., 1989). Furthermore, tremor can be associated with a certain degree of shame in social situations among PD patients. Thus, the management of tremors may be important for patients with PD to improve their activities of daily living.

Active Devices

Pharmacological treatments can suppress tremors; for instance, levodopa and propranolol are used to alleviate resting tremors; primidone and propranolol for hand postural tremors; and beta-blockers, anticholinergic drugs, and primidone for kinetic tremor (Zesiewicz et al., 2011; Shanker, 2019; Poewe and Mahlknecht, 2020). However, although medication may be useful for suppressing tremors, it may incur mental or physical side effects such as addiction, hypotension, decrement of heart rate, and a feeling of thirst. Approximately 30% of patients with tremors do not respond to pharmacological treatment or experience intolerable secondary effects (Koller and Vetere-Overfield, 1989). Moreover, up to 56% of patients eventually discontinue their medication because of these secondary effects or a lack of efficacy (Diaz and Louis, 2010). For patients with tremors unresponsive to medication, stereotactic surgery—such as DBS, gamma knife radiosurgery, and focused ultrasound—can be a viable alternative. However, considering the severe side effects and complications caused by both medication and surgical intervention, non-surgical device treatments for reducing tremors may represent a good solution.

Active devices transfer external force or energy from devices into nerves and/or muscles to reduce tremors (**Table 2**). These devices also measure tremor characteristics using a gyroscope, accelerometer, and electromyogram. Peripheral nerve stimulation has been reported to be useful in reducing tremors—especially in patients with ET (Kim et al., 2020; Yu et al., 2020; Reis et al., 2021)—and is thought to evoke central activity via VIM, a thalamic target widely accepted to improve tremor with DBS (Morigaki et al., 2011a,b; Morigaki and Goto, 2015). Lin et al. (2018) reported the effect of median and radial nerve stimulation using a wrist band in patients with PD. They compared the tremor research group's ET rating assessment scale and spiral drawing tasks pre- and post-stimulation and the scores decreased significantly after stimulation.

The Cala One device (Cala Health, CA, United States) was the first wearable electrical nerve stimulator approved by the FDA (Beringhause et al., 1989). The clinical trial using the new version of the device, Cala TRIO™ (Cala Health, CA, United States), was completed in 2019 (Hendriks et al., 1991). An accelerometer built into this device can assess the frequency of tremors, which enables the individualized calibration of the stimulation intensity. The Cala TRIO™ includes two working electrodes positioned over the median and radial nerves deliver electrical signals that intermittently excite these nerves, while the VIM is stimulated through peripheral sensory nerves of the median and radial nerves, similar to DBS (Bathien et al., 1980; Hanajima et al., 2004a,b). A study with five patients with tremors due to either ET or PD demonstrated its efficacy for tremor suppression (Dosen et al., 2015). Jitkritsadakul et al. (2017) reported the tremor glove to be a medical device that incorporates a tremor detection module and electrical muscle stimulation (EMS) to suppress resting hand tremors. This device included an adjustable glove with embedded inertial sensors and an EMS module, a control box that can be attached to the belt, and a smartphone with the device's application installed. The glove was worn on the most affected hand. Results showed that the tremor glove effectively suppressed intractable resting hand tremor among patients with PD with no serious adverse events.

TABLE 2 | Summary of non-invasive devices for patients with tremor.

Device/Method	CE marking and FDA certification	References	Subject	Efficacy	Adverse event
Cala ONE	FDA-approved Class II medical device	Beringhause et al., 1989	77 patients with ET	Improvement of upper limb TETRAS tremor score and subject related ADL score	Irritation, discomfort, burns
Cala TRIO™	FDA-registered Class I medical device	Hendriks et al., 1991	205 patients with ET	Improvement of upper limb TETRAS tremor score and subject related ADL score	Irritation, discomfort, burns
MOTIMOVE	CE marking approved	Popovic Maneski et al., 2011	3 patients with ET and 4 patients with PD	67% tremor suppression	Muscles fatigue
Tremor's Glove	Not approved	Jitkritsadakul et al., 2017	30 patients with PD	Reduced UPDRS score	Muscles fatigue
Tremor Neurorobot	Not approved	Gallego et al., 2013	4 patients with ET and 2 patients with PD	52% tremor suppression	Muscles fatigue
Vib-Bracet	Not approved	Buki et al., 2018	1 patient with PD	85% Tremor suppression	Not reported
Liftware Steady™	FDA approved	Sabari et al., 2019	15 patients with ET	Improvement of the Fahn-Tolosa-Marin Tremor Rating Scale during eating, and transferring objects 73% tremor suppression	Not reported

ADL, activity of daily living; ET, essential tremor; FDA, Food and Drug Administration; PD, Parkinson's disease; TETRAS, the Tremor Research Group's Essential Tremor Rating Assessment Scale; UPDRS, the Unified Parkinson's Disease Rating Scale.

The MOTIMOVE system (3F-Fit Fabricando Faber, Serbia) has multiple stimulators that can selectively activate antagonistic muscles in the forearms. This system delivers an out-of-phase stimulation. A pilot study of MOTIMOVE showed 67% tremor suppression in patients with ET and PD (Popovic Maneski et al., 2011). The TREMOR neurorobot is similar to the MOTIMOVE system and comprises electrodes to provide stimulation, sensors to evaluate biomechanical signals of tremor, and a controller. The device uses co-contraction methods that apply continuous stimulation to antagonistic muscles to increase limb stiffness and reportedly showed a 52% tremor suppression (Gallego et al., 2013).

Orthostatic tremor is characterized by unsteadiness in standing and improvement when sitting or walking (Lee et al., 2011), and has been reported in elderly patients with PD. Primary orthostatic tremor (POT) is a rare disorder characterized by 13–18 Hz tremors in the legs when standing and is often refractory to medical treatment. Lamy et al. (2021) investigated the potential beneficial effects of trans-spinal direct current stimulation (tsDCS) in POT. Their results showed that cathodal-tsDCS reduced both tremor amplitude and frequency and lowered corticospinal excitability, whereas anodal-tsDCS reduced tremor frequency only. A single session of tsDCS significantly improved POT-induced instability; thus, Lamy et al. (2021) hypothesized that tsDCS may induce spinal and supraspinal effects via ascending pathways.

Passive Devices

Contrastingly, passive devices absorb vibration energy by damping (**Table 2**). A passive device using a viscous beam and a hand orthosis using air dashpots have been reported (Kotovsky and Rosen, 1998; Takanokura et al., 2011). Buki et al. (2018) reported on a passive absorber, dubbed the vib-bracelet, a tremor attenuation device that was designed to operate as a dynamic vibration absorber. The vib-bracelet does not include any motors or sensors and is relatively light and compact. Meanwhile, the Liftware Steady™ (Liftware, United States) has an electronic stabilizing handle and a variety of attachments such as a spoon, fork, and spork, allowing patients with tremors to eat more easily. The handle contains sensors to detect motion and an onboard computer to differentiate between involuntary and voluntary movements. Sabari et al. (2019) compared the Liftware Steady™, standard spoon, weighted spoon (with standard handle and built-up handle), and swivel spoon. Reportedly, participants tended to select either a weighted spoon with a standard handle or the Liftware Steady™. A positive change in the Fahn-Tolosa-Marin Tremor Rating Scale, indicating improvement in tremors, has been shown in a pilot study (Sabari et al., 2019).

Non-invasive Devices for Gait Impairments

Patients with PD manifest gait disturbances and falls, which cause a significant reduction in their quality of life. The gait of PD patients is characterized by decreased step length, angular displacement, the velocity of the lower and upper limbs, high variability in step timing, poor bilateral coordination, and asymmetrical leg function (Lewis et al., 2003). Patients with PD also have a common and paroxysmal symptom termed FOG.

FOG is defined as "an episodic inability (lasting seconds) to generate effective stepping in the absence of any known cause other than parkinsonism or high-level gait disorders" (Giladi and Nieuwboer, 2008). Generally, the initiation of walking requires coordination between locomotion, postural stability, and sensory-motor integration (Hass et al., 2005; Mille et al., 2012). Patients with PD have impaired kinesthesia due to degeneration of this system, resulting in inadequate motor planning to initiate movement, which causes FOG (Konczak et al., 2009). FOG is considered to be a motor manifestation of PD and appears in a significant number of patients as the disease progresses (Giladi and Nieuwboer, 2008), affecting up to 81% of patients after 20 years of disease progression (Hely et al., 2008). It is also one of the main causes of difficulty in walking and deteriorating quality of life (Moore et al., 2007; Perez-Lloret et al., 2014; Walton et al., 2015). Additionally, FOG can increase the risk of falls and cause fractures (Riancho-Zarrabeitia and Delgado-Alvarado, 2017), making freeze control an important issue. The mechanisms underlying FOG are still highly debated. However, impaired sensory processing primarily arising from the proprioceptive system is speculated to be important (Tan et al., 2011). Unfortunately, current pharmacological or surgical treatment has limited efficacy for FOG. Bilateral DBS of the STN may improve FOG during the off-period (Krack et al., 2003) but may be insufficient for long-term benefits (Kim et al., 2019) and FOG in the on-period (Davis et al., 2006). Therefore, alternative non-pharmacological/non-surgical approaches are being explored in an attempt to improve FOG. This section hereafter describes the specific methods for improving gait and FOG.

Non-invasive Brain Stimulation

Among several NIBS techniques, repetitive transcranial magnetic stimulation (rTMS) is particularly effective in modulating corticospinal excitability (Pascual-Leone et al., 1994; Zanjani et al., 2015). rTMS affects cortical networks both during and 1 h after stimulation (Hallett et al., 1999). rTMS can both modify the excitability of local interneurons (local effects) and induce changes in the excitability of spatially distant, but functionally interconnected, cortical areas (network effects) (Hallett et al., 2000).

High-frequency rTMS stimulation (> 5 Hz), applied to the primary motor cortex (M1), efficiently improved the motor symptoms of PD subjects (Khedr et al., 2003; Lefaucheur et al., 2004; Elahi et al., 2009; Zanjani et al., 2015). Specifically, gait performance has been improved by stimulating the leg region of the motor cortex (Maruo et al., 2013; Lee et al., 2014; Kim et al., 2015; Yokoe et al., 2018). In addition to the M1, the supplementary motor area (SMA) and pre-SMA are also used as targets for stimulation. Accumulating evidence suggests that the SMA plays a pivotal role in the pathogenesis of FOG (Snijders et al., 2011; Shine et al., 2013; Peterson et al., 2014). Several studies have explored the clinical efficacy of high-frequency rTMS over the SMA on FOG in patients with PD (Lee et al., 2014; Mi et al., 2019; Mi et al., 2020). Lee et al. (2014) explored the therapeutic effect of rTMS on the SMA and M1. In the study, the number of freezing episodes was significantly decreased after SMA stimulation, and there was a trend for a greater reduction in freezing episodes with SMA stimulation than M1 stimulation. Mi et al. (2019) investigated the effect of rTMS on the SMA with a 4-week follow-up and found significant improvements and interaction effects in the Freezing of Gait Questionnaire score and UPDRS Part III. The pre-SMA is one of the major regions that connect to the basal ganglia and prefrontal cortex and is implicated in the regulation of emotion, motor function, and behavior. A resting-state functional magnetic resonance imaging study indicated that high-frequency rTMS over the SMA confers a beneficial effect jointly by normalizing abnormal brain functional connectivity patterns specifically associated with FOG in addition to normalizing overall disrupted connectivity patterns seen in PD (Mi et al., 2020).

Eye movement disorders have been documented in PD subjects, especially in patients with FOG (Terao et al., 2013). Saccades are controlled by various brain regions and different patterns of saccade impairment reflect pathologies in the corresponding brain regions (Anderson and MacAskill, 2013). Patients with FOG show significantly worse anti-saccade performance, indicating mutually impaired inhibitory control for gait and anti-saccade (Ewenczyk et al., 2017). Okada et al. (2021) confirmed that bilateral 10 Hz rTMS to the leg region of the MC improved MDS-UPDRS motor scores and the anti-saccade success rate, both of which require adequate inhibition of the reflexive response. The improvement in the anti-saccade success rate was correlated with that of the postural instability gait difficulty sub-scores of the MDS-UPDRS (Okada et al., 2021).

Repetitive trans-spinal magnetic stimulation (rTSMS) has been confirmed to improve camptocormia, a treatment-resistant postural abnormality observed in patients with PD. Arii et al. (2014) compared rTSMS (a train of 40 stimuli) groups to sham stimulation groups in patients with PD subjects with camptocormia. The flexion angle in the standing position significantly decreased by a mean of 10.9° after rTSMS but showed no change after sham stimulation. The flexion angle while sitting significantly decreased by 8.1° after rTSMS, whereas the sham treatment had no significant effect. The authors speculated that the effect of rTSMS was possibly due to a blockade of afferent sensory nerve fibers or disruption of akinetic corticostriatal activity.

Transcranial direct current stimulation (tDCS) is a NIBS method that modulates cortical activity. tDCS induces synaptic plasticity changes after stimulation, which has lasting effects (Nitsche and Paulus, 2000) and has some advantages over rTMS. tDCS is less expensive, provides a reliable sham stimulation condition, may lead to longer-lasting modulatory effects of cortical function, and is easy to administer and perform. In animal models, tDCS increased extracellular striatal dopamine levels (Tanaka et al., 2013). Recent systematic reviews have confirmed that tDCS improves motor function in patients with PD (Ferrucci et al., 2016; Lee et al., 2019; Beretta et al., 2020a). In these studies, tDCS protocols primarily targeted motor and prefrontal cortices (e.g., the M1 and dorsolateral prefrontal cortex [DLPFC]) since brain activation patterns in these brain regions are highly involved in successful locomotion performance in patients with PD. Anodal tDCS to the M1 has been shown to significantly improve motor performance and gait in patients

with PD. A significant improvement in gait with a reduction in the number and duration of FOG episodes, along with a significant reduction in the UPDRS Part III score, was observed after anodal stimulation (Valentino et al., 2014). Thus, tDCS could potentially be used in walking training and has the potential to enhance its benefits (Kaski et al., 2014b; Schabrun et al., 2016; Costa-Ribeiro et al., 2017; Yotnuengnit et al., 2018). Some studies have shown that tDCS, in addition to gait training, did not produce clinically important effects on gait speed, stride length, or cadence in people with mild to moderate disabilities associated with PD (Nascimento et al., 2021).

The DLPFC plays an essential role in dual-tasking that requires flexibility between the two tasks performed simultaneously (Collette et al., 2005). Therefore, tDCS stimulation of the DLPFC mainly affects cognitive function. Bueno et al. (2019) showed improvements in verbal fluency and reaction time on the Stroop test. A systematic review confirmed that certain cognitive deficits in PD were improved by anterior cranial tDCS (Dinkelbach et al., 2017; Putzolu et al., 2018; Mishra and Thrasher, 2021). Multitarget stimulation of motor (M1) and cognitive (left DLPFC) networks showed greater improvement than M1 stimulation only or sham stimulation in both the Timed Up and Go (TUG) and the Stroop tests (Dagan et al., 2018).

Photobiomodulation (PBM) is also being considered for use in PD therapy. PBM therapy uses a narrow wavelength band of non-thermal light (LED or laser) to modulate the cellular response and it acts at the cellular and mitochondrial levels. In recent years, transcranial PBM therapy for mental disorders such as depression and neurodegenerative diseases such as Alzheimer's disease and PD has been attracting attention (Hamblin, 2016). Liebert et al. (2021) conducted an RCT to evaluate the efficacy of PBM in reducing the clinical signs of PD. In this study, 12 participants with idiopathic PD underwent PBM therapy for up to 52 weeks. The primary outcome measure was mobility assessment using TUG which showed significant improvements. Moreover, cognition, dynamic balance, and fine motor skills were significantly improved.

As aforementioned, various effects have been reported for each NIBS device. Especially for FOG and postural abnormality, treatment with invasive devices such as DBS is less effective, therefore it is expected to be an alternative or adjunctive treatment for patients with these conditions. However, relatively few studies have been conducted on severely injured patients, which may limit the interpretation of the results.

Cueing Device for Freezing of Gait

Cueing with external stimuli has also been used to assist patients with PD with FOG. Various effects have been reported, and the European guidelines on PD strongly recommend the use of cues to improve walking speed (Keus et al., 2014). Studies investigating the effect of cues on the disease stage show that the effect of cues can be obtained from the early stages of PD and increases as the disease progresses (Lirani-Silva et al., 2019). External stimulus cues for improving FOG are mainly classified into spatial information that informs the user where to guide the action (e.g., floor lines) and temporal cues that provide information about the timing of movement (e.g., metronome, vibration stimuli). An example of a visual cue is the horizontal line on the floor, which has been shown to improve gait, stride length, and the beginning of walking (Lewis et al., 2000; Jiang and Norman, 2006; Lim et al., 2006). In addition, laser visual cues are often used to improve gait performance, such as stride length and walking speed (Donovan et al., 2011; Buated et al., 2012; Ferraye et al., 2016; Tang et al., 2019). Some laser cues have been developed with lasers built into the cane (Buated et al., 2012) or attached to shoes (Ferraye et al., 2016). Another study comparing the effect of a lateral line on the floor and a wearable laser light showed that the step length increased under both conditions, but the improvement in the sequence effect—which refers to the gradual decrease in amplitude—only occurs with a lateral line on the floor (Cao et al., 2020). The presentation of cues using smart glasses has also been considered as an application of this emerging technology (Zhao et al., 2016; Janssen et al., 2017), but concerns have been expressed about the specifications of smart glasses, such as weight and the reduction of the field of view due to the frame (Janssen et al., 2017).

Some studies have also shown that auditory cues can improve FOG (Delval et al., 2014; Lopez et al., 2014; Ginis et al., 2017a; Spildooren et al., 2017). Patients with PD release their anticipatory postural adjustments more quickly when auditory cueing is applied. Monotonous external inputs, such as a metronome, are often used with/without other non-auditory cues (Bachlin et al., 2010; Espay et al., 2010; Hove et al., 2012; Baram et al., 2016; Ginis et al., 2016, 2017b; Zhao et al., 2016). Hove et al. (2012) used a non-linear limit-cycle oscillator to interactively generate a rhythmic pacing sequence using the information on the number of steps taken from a shoe-mounted foot pressure sensor to improve walking.

However, some side effects of these cueing devices have also been identified. People with PD demonstrated cue dependency, expressed as a decline in movement after cue removal (Nieuwboer et al., 2009; Spildooren et al., 2012; Vercruysse et al., 2012). It has also been suggested that external cues may have a negative effect on increasing gait variability because they increase the cognitive load, as all steps need to be coordinated to synchronize (Yogev et al., 2005). These characteristics limit the effectiveness of simple cueing. To apply appropriate cueing at the required moment, effective FOG detection technologies are warranted. Ginis et al. (2017b) proposed an intelligent system in which an inertial sensor attached to the foot was used to obtain the average cadence, and auditory cues and auditory feedback were triggered only when the cadence deviated from the reference by more than 5%. This method significantly reduced cadence deviation compared to the use of normal cues. Additionally, Bachlin et al. (2010) developed a wearable system that initiated auditory cueing only when FOG was detected. Moreover, some studies have shown self-generating internal cues while singing a song instead of providing cues successfully improves gait externally (Harrison et al., 2019). The effect of internal cueing, in the form of singing, vs. external cueing, in the form of listening to music, gait was examined in people with and without PD. Internal cueing significantly improved cadence compared to external cueing (Harrison et al., 2018), and external cueing increased gait

variability whereas internal cues did not (Harrison et al., 2019; Horin et al., 2020). Since higher gait variability is associated with falls, this finding is important for stable walking when addressing PD with FOG.

Non-invasive Vagus Nerve Stimulation

Invasive vagus nerve stimulation (VNS), delivered by a surgically implanted device, has been approved as an adjunctive neuromodulation therapy for epilepsy (Terry, 2014). VNS is supposed to affect various brain regions through direct effects on the nucleus tractus solitarius and locus coeruleus (Kraus et al., 2007; Oshinsky et al., 2014). Anti-inflammatory properties of VNS have been suggested (Corcoran et al., 2005; Majoie et al., 2011) and potential applications to a wide range of inflammatory disorders have been advocated (Bonaz et al., 2016). Neuroinflammation has been implicated in the pathogenesis of PD (Akiyama et al., 2000); therefore, VNS may be effective in the treatment of PD.

Recently, the development of portable, non-invasive VNS (nVNS) devices has simplified this treatment modality (Yuan and Silberstein, 2016). Notably, the application of nVNS in patients with PD has shown beneficial effects for FOG (Mondal et al., 2019). In the study, the application of 2 × 120 s acute nVNS improved the number of steps taken while turning and reduced UPDRS Part III scores in patients with FOG induced by PD by two-dimensional spatiotemporal gait parameter analysis. These short-term effects are most likely due to indirect activation of central neural circuits, including noradrenergic projections from the locus coeruleus (Johnson and Wilson, 2018), a brain region implicated in the pathogenesis of FOG (Ono et al., 2016). Morris et al. (2019) found significant improvement in step length variability in patients with PD after a single application of cervical nVNS.

A randomized, double-blind, sham-controlled crossover study in which nVNS was applied three times a day for 1 month to confirm the long-term effects of cervical nVNS (Mondal et al., 2021), showed improvement in motor function in patients with PD and a significant reduction in serum inflammatory markers. Intriguingly, the analysis of serum biomarkers after nVNS showed a reduction in neuroinflammatory markers (Tumor Necrosis Factor-α) along with increased brain-derived neurotrophic factor (BDNF), which implicated increased neuroplasticity. Given that neuroinflammation has been implicated in the pathogenesis of PD (Akiyama et al., 2000), nVNS may have disease-modifying effects.

Vibrotactile Stimulation Devices

Vibration stimuli to the muscles act as a powerful proprioceptive input and strongly affect the motion perception during extremity movements of healthy people and patients with various neurological disorders (Cohen and Starr, 1985; Han et al., 2014). Peripheral vibrotactile stimulation has been shown to improve bradykinesia, FOG, gait impairment, and postural instability in patients with PD, possibly by affecting the central pattern generator in a desynchronized state (Zehr and Haridas, 2003; Volpe et al., 2014; Pereira et al., 2016; Syrkin-Nikolau et al., 2018; Peppe et al., 2019; Serio et al., 2019; Spolaor et al., 2021; Tan et al., 2021). Three possible mechanisms for how vibration stimuli work against FOG in patients with PD have been laid forth: (i) a cueing effect, (ii) modulation effect against impairment in dealing with conflicting cognitive/attentional resources, and (iii) enhanced proprioceptive processing (Pereira et al., 2016).

Peripheral vibrotactile stimulation delivered by a C-2 tactor glove (Engineering Acoustics Inc., Florida, United States) with high-frequency trains in a patterned sequence acutely improved gait asymmetry, arrhythmicity, and wrist bradykinesia in patients with PD (Syrkin-Nikolau et al., 2018). The study indicated that peripheral vibrotactile stimulation is safe and its effect continues even 1 month after stimulation. The use of light-touch contact is being considered as another approach. Light-touch contact is a phenomenon in which a part of the body lightly (<1 N) touches a stable surface to obtain sensory feedback about the orientation of the body and limbs in space, which can activate the postural muscles and adjust the axial tension of the body's posture. Light-touch contact has also been found to attenuate postural sway in patients with PD, although this is a commonly occurring effect (Franzen et al., 2012; Rabin et al., 2013). Walking has been found to improve the center of gravity shift and improve gait initiation (Ditthaphongphakdee and Gaogasigam, 2021). A wearable device using vibration stimuli on the fingertips provides tactile feedback reportedly improved body balance in normal subjects (Shima et al., 2021) and may also be effective for PD subjects.

Although the improvement rates were small, muscle vibration therapy in the lower limbs using eight vibrators (60 Hz) made by the study authors, significantly improved stride length and walking speed in patients with PD (Han et al., 2014). Another study reported that hand-made vibratory devices embedded in elastic insoles (70 Hz), where the vibratory device senses the pressure on the sole and delivers the vibration stimulus during walking, decreased stride variability while increasing walking speed, stride duration, stride length, and cadence in patients with PD (Novak and Novak, 2006). Admittedly, these changes were significant but small. Another study placed the CUE1 (Charco Neurotech Ltd., London, United Kingdom) on the patient's sternum to produce focused vibrotactile pulsatile stimuli (Tan et al., 2021). Since this device was effective for FOG when it was turned on before the FOG episodes, the authors hypothesized that CUE1 has a cueing effect in addition to enhanced proprioceptive stimuli. Another study revealed that focal vibration training using Equistasi® (Equistasi®, Italy) improved postural stability in patients with PD. The Equistasi® is composed of nanotechnological particles that transform the body temperature into a mechanical high-frequency vibration (0.8 N, 9000 Hz). The device is attached over the seventh cervical vertebra and on each soleus muscle-tendon to alleviate gait disturbances and postural instability (Volpe et al., 2014; Peppe et al., 2019; Serio et al., 2019; Spolaor et al., 2021). RCTs using Equistasi® showed significantly improved motor performance in patients with PD.

Another study revealed that a custom-made vibration device (100 Hz and 1.2 mm of amplitude) attached to the less affected limb moderately alleviated FOG in patients with PD when vibration is applied following FOG onset (Pereira et al., 2016). Importantly, no positive effects for FOG were identified

when the vibration device was applied before the FOG onset, which indicated that vibration did not serve as an external cue in the study. Additionally, vibration stimuli did not exert a positive effect when the more affected limb triggered attentional processing by vibration, indicating that the modulation effect of choosing conflicting cognitive/attentional resources is unlike the mechanism underpinning the effect (Pereira et al., 2016). Given that improper sensory feedback causes worsening of movements (Nieuwboer et al., 2009), vibration stimuli in the lower extremities strongly enhance proprioceptive information and play an important role in controlling posture and balance (Sorensen et al., 2002; Pereira et al., 2016), and the more preserved side of the basal ganglia seems to properly process the enhanced proprioceptive information (Pereira et al., 2016). Upper limb freezing in PD patients with FOG is associated with decreased activation in the basal ganglia and increased activation in the frontal lobes, including the supplementary and primary motor cortices, which indicated the impairment in the indirect pathway-driven non-selective inhibitory program through the cortico-basal ganglia-thalamo-cortical feedback loop in FOG pathogenesis (Vercruysse et al., 2014). Since local vibration stimuli are reported to evoke focused activation of motor cortical circuits (Rosenkranz and Rothwell, 2003), they may help focus on the desired movements through the thalamus.

Mechanical/Electrical Peripheral Stimulation Devices

Peripheral sensory deficits, particularly reduced plantar sensitivity, have been reported in PD (Pratorius et al., 2003; Nolano et al., 2008). This reduction may result from the loss of cutaneous receptors, encapsulated endings, or free nerve endings (Nolano et al., 2008), and is associated with reduced control of compensatory stepping and impaired balance, which causes falls (Pratorius et al., 2003; Kerr et al., 2010).

Textured insoles significantly decreased mediolateral postural sway, which indicated an improvement in standing balance (Qiu et al., 2013). The continuous use of textured insoles for 1-week increased stride length, and the effect continued for another week without textured insoles (Lirani-Silva et al., 2017). Ribbed insoles produce a significant increase in single-limb support time and normalization of the muscle activation sequence of the tibialis anterior in patients with PD (Jenkins et al., 2009). As described in the previous section, vibration stimulation at the soles increased walking speed and improved stride variability in PD subjects (Novak and Novak, 2006). However, the improvement rates in these studies were usually under 20%.

The automated mechanical peripheral stimulation (AMPS) device Gondola^{TM} (Gondola Medical Technologies SA, Switzerland) has been proven effective for addressing motor impairment in patients with PD. Immediate and long-term increases in stride length and gait speed with Gondola^{TM} have been reported (Kleiner et al., 2015; Stocchi et al., 2015). The benefit was maintained for 10 days after the last treatment (Stocchi et al., 2015). Based on these studies, a randomized controlled clinical trial using Gondola^{TM} was performed involving patients with PD, and Gondola^{TM} promoted faster walking with longer strides after 6–8 stimulation sessions (Galli et al., 2018; Kleiner et al., 2018; Pagnussat et al., 2018, 2020; Pinto et al., 2018). Contrastingly, there was no positive effect in terms of improving static postural control in individuals with PD and FOG (Prusch et al., 2018). Interestingly, patients with PD who underwent treatment with Gondola^{TM} showed higher serum BDNF and lower serum cortisol levels in accordance with improvements in gait parameters (Pagnussat et al., 2018). Gondola^{TM} did increase gait velocity and resting-state brain connectivity between the basal ganglia and sensory-related brain areas (insular and somatosensory cortices) in PD subjects. Gait velocity is positively correlated with increased connectivity between the sensory, motor, and supplementary motor cortices (Pagnussat et al., 2020). These findings may help elucidate the mechanism by which AMPS influences gait.

The electrical stimulation of the common peroneal nerve immediately improved average stride length during a three-min walk and reduced the frequency of falls and FOG during an 8-week stimulation period which diminished 4 weeks after the cessation (Mann et al., 2008). A single randomized controlled trial (RCT) showed significant improvement in 10 m walking speed at week 18 compared to the standard care group (Taylor et al., 2021). However, the decrease in the UPDRS score was not significant and the improvement in 10 m walking speed disappeared 4 weeks following the stimulation session.

To reduce FOG, the use of a "fixed" rhythmic sensory electrical stimulation (sES) cueing strategy has been proposed (Rosenthal et al., 2018). sES cueing was delivered by a voltage-controlled two-channel stimulator and skin surface electrodes were placed over the hamstring or quadriceps muscle. In this study, nine patients with PD walked while receiving sES cueing and their performance was evaluated. Results showed that sES cueing significantly reduces the time taken for the walking task and in the number of FOG episodes by 14.23 and 58.28, respectively.

Systematic Review

For the systematic review, we identified RCT studies in the last 10 years (2011–2021). Concerning the invasive devices, RCTs for DBS and LCIG were extracted. These devices have already received FDA certification and a CE mark and are currently being used. The results show a higher efficacy than non-invasive devices. There were no RCTs on SCS and continuous subcutaneous infusion of levodopa.

As represented in **Table 1**, most RCTs refer to non-invasive devices. RCTs for tremors and cueing devices were few despite many devices having been developed. In contrast, extensive RCTs of rTMS and tDCS for various targets and frequencies have been performed. Most of the rTMS studies showed improvement in motor function as assessed by TUG and UPDRS Part III. rTMS is FDA approved for obsessive-compulsive disorder and depression but has not yet been approved for PD. Several studies have targeted M1 for the improvement of motor function, and most of them have shown that it improves motor function. The second most common target was SMA; some studies showed improvement in FOG as well as improvement in motor function. tDCS has also been used to target M1 and DLPFC. tDCS over M1 has been reported to improve motor function. tDCS over DLPFC may not directly improve motor function, but may improve performance under certain conditions, such as dual-tasking. The effects of tDCS, when used in combination with

physical training, have also been studied extensively. There are multiple reports of improved gait performance when stimulated in conjunction with walking. Mechanical/electrical peripheral stimulation devices have also been the subject of many RCTs, which have reported effectiveness in gait performance. Most of the studies have been with Gondola^{TM}, a device that is FDA certificated and CE marked. As shown in **Table 1**, RCTs have been conducted on other non-invasive devices and have shown improvement in motor symptoms, but the number of studies is small, and certification has not been obtained. There is a big difference between invasive and non-invasive treatments in terms of treatment effectiveness. For example, when comparing the improvement of UPDRS Part III, DBS may have an effect of more than 15 points, while non-invasive devices usually have an effect of a few points, and none of them improve by more than 10 points.

DISCUSSION

This paper describes the progress made in the development of therapeutic devices for motor symptoms in patients with PD. We have conducted a narrative literature review and a systematic review of recent RCTs. Generally, invasive devices are more effective than non-invasive devices in terms of improving motor function in patients with PD. DBS has a striking effect on motor symptoms in PD subjects and, specifically, aDBS is more effective than cDBS, pointing to the importance of instrumental advances. Little et al. (2013) confirmed that motor scores improved during aDBS were 27% better than cDBS. In the future, it is expected that a closed-loop system in which the release of neurotransmitters is a control variable will be realized by FSCV and that a more accurate DBS system might be developed. SCS with burst waveform stimulation showed acute and larger improvements in both motor symptoms, including tremor and gait parameters (Kobayashi et al., 2018; Furusawa et al., 2020). Continuous infusion of levodopa-carbidopa via an intestinal infusion (Duodopa®) system has also demonstrated significantly decreased off-time and increased on-time without troublesome dyskinesia (Olanow et al., 2014). In recent years, as a less invasive method, the continuous subcutaneous infusion of levodopa or apomorphine using ND0612 or ND0701 was also developed (Ramot et al., 2018; Olanow et al., 2021; Larson and Simuni, 2022). The effects of these invasive medical devices are usually drastic.

Regarding non-invasive medical devices, we introduced several devices that are effective for tremors, gait, and FOG. These devices have seen improved efficacy and have the advantage of being non-surgical and easy to use. Thus, each device has its characteristics and effects, and the proper selection and use of these devices will result in more effective treatment. As shown in the systematic review, a growing number of high-evidence studies of non-invasive devices have been conducted in recent years. In particular, rTMS has been subjected to meta-analysis and is more reliable than other devices (Elahi et al., 2009; Zanjani et al., 2015). The meta-analysis revealed that targeting M1 improved UPDRS and that targeting multiple brain regions had a short-term effect on functional locomotion. In addition, improvement in gait was reported when combined with physical training (Kaski et al., 2014b; Costa-Ribeiro et al., 2017; Yotnuengnit et al., 2018; Lee and Kim, 2021). rTMS and tDCS have been studied for different stimulation targets, and different effects were reported for each. A relatively large number of RCTs implies that researchers who performed rTMS and tDCS have some confidence in their efficacy on motor symptoms in patients with PD. Further research is required to determine the best treatment method and target. Significant effects have also been reported for other non-invasive devices, such as nVNS, vibrotactile stimulation devices, mechanical peripheral stimulation, and sensory electrical stimulation by RCT. Non-invasive devices are less effective than invasive devices, but easy-to-use and less invasive characteristics make their use more feasible and easier. They may grow more prevalent in the upcoming decade. They also have the potential to become standard treatments for PD in the next generation.

The devices introduced in this paper include prototypes, which need to be further developed for practical use. Since it is important to develop safe and reliable products, it is very important to make effective, reliable, and easy-to-use gold-standard criteria to evaluate them.

AUTHOR CONTRIBUTIONS

JF, RM, and NY designed and drafted the manuscript. All authors revised and approved the final version of the manuscript.

FUNDING

This work was supported by the Terumo Life Science Foundation, JSPS KAKENHI Grant Numbers 20K17932 and 16KK0182. Department of Advanced Brain Research was supported by the Beauty Life Corporation.

REFERENCES

Agari, T., and Date, I. (2012). Spinal cord stimulation for the treatment of abnormal posture and gait disorder in patients with Parkinson's disease. *Neurol. Med. Chir.* 52, 470–474. doi: 10.2176/nmc.52.470

Akiyama, H., Barger, S., Barnum, S., Bradt, B., Bauer, J., Cole, G. M., et al. (2000). Inflammation and Alzheimer's disease. *Neurobiol. Aging* 21, 383–421. doi: 10.1016/s0197-4580(00)00124-x

Akiyama, H., Nukui, S., Akamatu, M., Hasegawa, Y., Nishikido, O., and Inoue, S. (2017). Effectiveness of spinal cord stimulation for painful camptocormia with Pisa syndrome in Parkinson's disease: a case report. *BMC Neurol.* 17:148. doi: 10.1186/s12883-017-0926-y

Anderson, T. J., and MacAskill, M. R. (2013). Eye movements in patients with neurodegenerative disorders. *Nat. Rev. Neurol.* 9, 74–85. doi: 10.1038/nrneurol.2012.273

Aquino, C. C., Duffley, G., Hedges, D. M., Vorwerk, J., House, P. A., Ferraz, H. B., et al. (2019). Interleaved deep brain stimulation for dyskinesia management in Parkinson's disease. *Mov. Disord.* 34, 1722–1727. doi: 10.1002/mds.27839

Arii, Y., Sawada, Y., Kawamura, K., Miyake, S., Taichi, Y., Izumi, Y., et al. (2014). Immediate effect of spinal magnetic stimulation on camptocormia in

Parkinson's disease. *J. Neurol. Neurosurg. Psychiatry* 85, 1221–1226. doi: 10.1136/jnnp-2014-307651

Bachlin, M., Plotnik, M., Roggen, D., Giladi, N., Hausdorff, J. M., and Troster, G. (2010). A wearable system to assist walking of Parkinson's disease patients. *Methods Inf. Med.* 49, 88–95. doi: 10.3414/ME09-02-0003

Baijens, L. W., Speyer, R., Passos, V. L., Pilz, W., van der Kruis, J., Haarmans, S., et al. (2013). Surface electrical stimulation in dysphagic Parkinson patients: a randomized clinical trial. *Laryngoscope* 123, E38–E44. doi: 10.1002/lary.24119

Baram, Y., Aharon-Peretz, J., Badarny, S., Susel, Z., and Schlesinger, I. (2016). Closed-loop auditory feedback for the improvement of gait in patients with Parkinson's disease. *J. Neurol. Sci.* 363, 104–106. doi: 10.1016/j.jns.2016.02.021

Barbe, M. T., Maarouf, M., Alesch, F., and Timmermann, L. (2014). Multiple source current steering–a novel deep brain stimulation concept for customized programming in a Parkinson's disease patient. *Parkinsonism Relat. Disord.* 20, 471–473. doi: 10.1016/j.parkreldis.2013.07.021

Barbic, F., Galli, M., Dalla Vecchia, L., Canesi, M., Cimolin, V., Porta, A., et al. (2014). Effects of mechanical stimulation of the feet on gait and cardiovascular autonomic control in Parkinson's disease. *J. Appl. Physiol. (1985)* 116, 495–503. doi: 10.1152/japplphysiol.01160.2013

Bathien, N., Rondot, P., and Toma, S. (1980). Inhibition and synchronisation of tremor induced by a muscle twitch. *J. Neurol. Neurosurg. Psychiatry* 43, 713–718. doi: 10.1136/jnnp.43.8.713

Baumann, C. R., Imbach, L. L., Baumann-Vogel, H., Uhl, M., Sarnthein, J., and Surucu, O. (2012). Interleaving deep brain stimulation for a patient with both Parkinson's disease and essential tremor. *Mov. Disord.* 27, 1700–1701. doi: 10.1002/mds.25221

Benabid, A. L., Chabardes, S., Mitrofanis, J., and Pollak, P. (2009). Deep brain stimulation of the subthalamic nucleus for the treatment of Parkinson's disease. *Lancet Neurol.* 8, 67–81. doi: 10.1016/S1474-4422(08)70291-6

Benninger, D. H., Iseki, K., Kranick, S., Luckenbaugh, D. A., Houdayer, E., and Hallett, M. (2012). Controlled study of 50-Hz repetitive transcranial magnetic stimulation for the treatment of Parkinson disease. *Neurorehabil. Neural Repair.* 26, 1096–1105. doi: 10.1177/1545968312445636

Beretta, V. S., Conceicao, N. R., Nobrega-Sousa, P., Orcioli-Silva, D., Dantas, L., Gobbi, T. B., et al. (2020a). Transcranial direct current stimulation combined with physical or cognitive training in people with Parkinson's disease: a systematic review. *J. Neuroeng. Rehabil.* 17:74. doi: 10.1186/s12984-020-00701-6

Beretta, V. S., Vitorio, R., Nobrega-Sousa, P., Conceicao, N. R., Orcioli-Silva, D., Pereira, M. P., et al. (2020b). Effect of different intensities of transcranial direct current stimulation on postural response to external perturbation in patients with Parkinson's disease. *Neurorehabil. Neural Repair.* 34, 1009–1019. doi: 10.1177/1545968320962513

Beringhause, S., Rosen, M., and Huang, S. (1989). "Evaluation of a damped joystick for people disabled by intention tremor," in *Proceedings of the 12th Annual Conference on Rehabilitation Technology*, New Orleans, LA.

Bhatia, K. P., Bain, P., Bajaj, N., Elble, R. J., Hallett, M., Louis, E. D., et al. (2018). Consensus statement on the classification of tremors. from the task force on tremor of the International Parkinson and Movement Disorder Society. *Mov. Disord.* 33, 75–87. doi: 10.1002/mds.27121

Bocci, T., Prenassi, M., Arlotti, M., Cogiamanian, F. M., Borrellini, L., Moro, E., et al. (2021). Eight-hours conventional versus adaptive deep brain stimulation of the subthalamic nucleus in Parkinson's disease. *NPJ Parkinsons Dis.* 7:88. doi: 10.1038/s41531-021-00229-z

Bonaz, B., Sinniger, V., and Pellissier, S. (2016). Anti-inflammatory properties of the vagus nerve: potential therapeutic implications of vagus nerve stimulation. *J. Physiol.* 594, 5781–5790. doi: 10.1113/JP271539

Broeder, S., Heremans, E., Pinto Pereira, M., Nackaerts, E., Meesen, R., Verheyden, G., et al. (2019). Does transcranial direct current stimulation during writing alleviate upper limb freezing in people with Parkinson's disease? A pilot study. *Hum. Mov. Sci.* 65, 142–153. doi: 10.1016/j.humov.2018.02.012

Bronstein, J. M., Tagliati, M., Alterman, R. L., Lozano, A. M., Volkmann, J., Stefani, A., et al. (2011). Deep brain stimulation for Parkinson disease: an expert consensus and review of key issues. *Arch. Neurol.* 68:165. doi: 10.1001/archneurol.2010.260

Brys, M., Fox, M. D., Agarwal, S., Biagioni, M., Dacpano, G., Kumar, P., et al. (2016). Multifocal repetitive TMS for motor and mood symptoms of Parkinson disease: a randomized trial. *Neurology* 87, 1907–1915. doi: 10.1212/WNL.0000000000003279

Buated, W., Sriyudthsak, M., Sribunruangrit, N., and Bhidayasiri, R. (2012). A low-cost intervention for improving gait in Parkinson's disease patients: a cane providing visual cues. *Eur. Geriatr. Med.* 3, 126–130. doi: 10.1016/j.eurger.2012.01.006

Bueno, M. E. B., do Nascimento Neto, L. I., Terra, M. B., Barboza, N. M., Okano, A. H., and Smaili, S. M. (2019). Effectiveness of acute transcranial direct current stimulation on non-motor and motor symptoms in Parkinson's disease. *Neurosci. Lett.* 696, 46–51. doi: 10.1016/j.neulet.2018.12.017

Buki, E., Katz, R., Zacksenhouse, M., and Schlesinger, I. (2018). Vib-bracelet: a passive absorber for attenuating forearm tremor. *Med. Biol. Eng. Comput.* 56, 923–930. doi: 10.1007/s11517-017-1742-7

Bunting-Perry, L., Spindler, M., Robinson, K. M., Noorigian, J., Cianci, H. J., and Duda, J. E. (2013). Laser light visual cueing for freezing of gait in Parkinson disease: a pilot study with male participants. *J. Rehabil. Res. Dev.* 50, 223–230. doi: 10.1682/jrrd.2011.12.0255

Cai, Y., Reddy, R. D., Varshney, V., and Chakravarthy, K. V. (2020). Spinal cord stimulation in Parkinson's disease: a review of the preclinical and clinical data and future prospects. *Bioelectron. Med.* 6:5. doi: 10.1186/s42234-020-00041-9

Cao, S. S., Yuan, X. Z., Wang, S. H., Taximaimaiti, R., and Wang, X. P. (2020). Transverse strips instead of wearable laser lights alleviate the sequence effect toward a destination in Parkinson's disease patients with freezing of gait. *Front. Neurol.* 11:838. doi: 10.3389/fneur.2020.00838

Chan, A. K., Chan, A. Y., Lau, D., Durcanova, B., Miller, C. A., Larson, P. S., et al. (2018). Surgical management of camptocormia in Parkinson's disease: systematic review and meta-analysis. *J. Neurosurg.* 131, 368–375. doi: 10.3171/2018.4.JNS173032

Chang, S. Y., Jay, T., Munoz, J., Kim, I., and Lee, K. H. (2012a). Wireless fast-scan cyclic voltammetry measurement of histamine using WINCS–a proof-of-principle study. *Analyst* 137, 2158–2165. doi: 10.1039/c2an16038b

Chang, S. Y., Kim, I., Marsh, M. P., Jang, D. P., Hwang, S. C., Van Gompel, J. J., et al. (2012b). Wireless fast-scan cyclic voltammetry to monitor adenosine in patients with essential tremor during deep brain stimulation. *Mayo Clin. Proc.* 87, 760–765. doi: 10.1016/j.mayocp.2012.05.006

Chang, S. Y., Kimble, C. J., Kim, I., Paek, S. B., Kressin, K. R., Boesche, J. B., et al. (2013). Development of the Mayo Investigational Neuromodulation Control System: toward a closed-loop electrochemical feedback system for deep brain stimulation. *J. Neurosurg.* 119, 1556–1565. doi: 10.3171/2013.8.JNS122142

Chang, W. H., Kim, M. S., Cho, J. W., Youn, J., Kim, Y. K., Kim, S. W., et al. (2016). Effect of cumulative repetitive transcranial magnetic stimulation on freezing of gait in patients with atypical Parkinsonism: a pilot study. *J. Rehabil. Med.* 48, 824–828. doi: 10.2340/16501977-2140

Chung, C. L., Mak, M. K., and Hallett, M. (2020). Transcranial magnetic stimulation promotes gait training in Parkinson disease. *Ann. Neurol.* 88, 933–945. doi: 10.1002/ana.25881

Cohen, L. G., and Starr, A. (1985). Vibration and muscle contraction affect somatosensory evoked potentials. *Neurology* 35, 691–698. doi: 10.1212/wnl.35.5.691

Cohen, O. S., Rigbi, A., Yahalom, G., Warman-Alaluf, N., Nitsan, Z., Zangen, A., et al. (2018). Repetitive deep TMS for Parkinson disease: a 3-month double-blind, randomized sham-controlled study. *J. Clin. Neurophysiol.* 35, 159–165. doi: 10.1097/WNP.0000000000000455

Collette, F., Olivier, L., Van der Linden, M., Laureys, S., Delfiore, G., Luxen, A., et al. (2005). Involvement of both prefrontal and inferior parietal cortex in dual-task performance. *Brain Res. Cogn. Brain Res.* 24, 237–251. doi: 10.1016/j.cogbrainres.2005.01.023

Conceicao, N. R., Gobbi, L. T. B., Nobrega-Sousa, P., Orcioli-Silva, D., Beretta, V. S., Lirani-Silva, E., et al. (2021). Aerobic exercise combined with transcranial direct current stimulation over the prefrontal cortex in Parkinson disease: effects on cortical activity, gait, and cognition. *Neurorehabil. Neural Repair.* 35, 717–728. doi: 10.1177/15459683211019344

Corcoran, C., Connor, T. J., O'Keane, V., and Garland, M. R. (2005). The effects of vagus nerve stimulation on pro- and anti-inflammatory cytokines in humans: a preliminary report. *Neuroimmunomodulation* 12, 307–309. doi: 10.1159/000087109

Cosentino, G., Valentino, F., Todisco, M., Alfonsi, E., Davi, R., Savettieri, G., et al. (2017). Effects of more-affected vs. less-affected motor cortex tDCS in Parkinson's disease. *Front. Hum. Neurosci.* 11:309. doi: 10.3389/fnhum.2017.00309

Costa-Ribeiro, A., Maux, A., Bosford, T., Aoki, Y., Castro, R., Baltar, A., et al. (2017). Transcranial direct current stimulation associated with gait training in Parkinson's disease: a pilot randomized clinical trial. *Dev. Neurorehabil.* 20, 121–128. doi: 10.3109/17518423.2015.1131755

Cury, R. G., Carra, R. B., Capato, T. T. C., Teixeira, M. J., and Barbosa, E. R. (2020). Spinal cord stimulation for Parkinson's disease: dynamic habituation as a mechanism of failure? *Mov. Disord.* 35, 1882–1883. doi: 10.1002/mds.28271

da Silva, D. C. L., Lemos, T., de Sa, F. A., Horsczaruk, C. H. R., Pedron, C. A., de Carvalho, R. E., et al. (2018). Effects of acute transcranial direct current stimulation on gait kinematics of individuals with Parkinson disease. *Top. Geriatr. Rehabil.* 34, 262–268.

Dagan, M., Herman, T., Harrison, R., Zhou, J., Giladi, N., Ruffini, G., et al. (2018). Multitarget transcranial direct current stimulation for freezing of gait in Parkinson's disease. *Mov. Disord.* 33, 642–646. doi: 10.1002/mds.27300

Davis, J. T., Lyons, K. E., and Pahwa, R. (2006). Freezing of gait after bilateral subthalamic nucleus stimulation for Parkinson's disease. *Clin. Neurol. Neurosurg.* 108, 461–464. doi: 10.1016/j.clineuro.2005.07.008

Delval, A., Moreau, C., Bleuse, S., Tard, C., Ryckewaert, G., Devos, D., et al. (2014). Auditory cueing of gait initiation in Parkinson's disease patients with freezing of gait. *Clin. Neurophysiol.* 125, 1675–1681. doi: 10.1016/j.clinph.2013.12.101

Diaz, N. L., and Louis, E. D. (2010). Survey of medication usage patterns among essential tremor patients: movement disorder specialists vs. general neurologists. *Parkinsonism Relat. Disord.* 16, 604–607. doi: 10.1016/j.parkreldis.2010.07.011

Dinkelbach, L., Brambilla, M., Manenti, R., and Brem, A. K. (2017). Non-invasive brain stimulation in Parkinson's disease: exploiting crossroads of cognition and mood. *Neurosci. Biobehav. Rev.* 75, 407–418. doi: 10.1016/j.neubiorev.2017.01.021

Ditthaphongphakdee, S., and Gaogasigam, C. (2021). The effects of light touch cue on gait initiation in patients with Parkinson's disease. *J. Bodyw. Mov. Ther.* 26, 187–192. doi: 10.1016/j.jbmt.2020.08.009

Donovan, S., Lim, C., Diaz, N., Browner, N., Rose, P., Sudarsky, L. R., et al. (2011). Laserlight cues for gait freezing in Parkinson's disease: an open-label study. *Parkinsonism Relat. Disord.* 17, 240–245. doi: 10.1016/j.parkreldis.2010.08.010

Dosen, S., Muceli, S., Dideriksen, J. L., Romero, J. P., Rocon, E., Pons, J., et al. (2015). Online tremor suppression using electromyography and low-level electrical stimulation. *IEEE Trans. Neural. Syst. Rehabil. Eng.* 23, 385–395. doi: 10.1109/TNSRE.2014.2328296

Dubois, B., and Pillon, B. (1997). Cognitive deficits in Parkinson's disease. *J. Neurol.* 244, 2–8. doi: 10.1007/pl00007725

Eggert, K., Schrader, C., Hahn, M., Stamelou, M., Russmann, A., Dengler, R., et al. (2008). Continuous jejunal levodopa infusion in patients with advanced Parkinson disease: practical aspects and outcome of motor and non-motor complications. *Clin. Neuropharmacol.* 31, 151–166. doi: 10.1097/wnf.0b013e31814b113e

Einevoll, G. T., Kayser, C., Logothetis, N. K., and Panzeri, S. (2013). Modelling and analysis of local field potentials for studying the function of cortical circuits. *Nat. Rev. Neurosci.* 14, 770–785. doi: 10.1038/nrn3599

Elahi, B., Elahi, B., and Chen, R. (2009). Effect of transcranial magnetic stimulation on Parkinson motor function–systematic review of controlled clinical trials. *Mov. Disord.* 24, 357–363. doi: 10.1002/mds.22364

Espay, A. J., Baram, Y., Dwivedi, A. K., Shukla, R., Gartner, M., Gaines, L., et al. (2010). At-home training with closed-loop augmented-reality cueing device for improving gait in patients with Parkinson disease. *J. Rehabil. Res. Dev.* 47, 573–581. doi: 10.1682/jrrd.2009.10.0165

Ewenczyk, C., Mesmoudi, S., Gallea, C., Welter, M. L., Gaymard, B., Demain, A., et al. (2017). Antisaccades in Parkinson disease: a new marker of postural control? *Neurology* 88, 853–861. doi: 10.1212/WNL.0000000000003658

Fahn, S., and Sulzer, D. (2004). Neurodegeneration and neuroprotection in Parkinson disease. *NeuroRx* 1, 139–154. doi: 10.1602/neurorx.1.1.139

Farris, S., and Giroux, M. (2013). Retrospective review of factors leading to dissatisfaction with subthalamic nucleus deep brain stimulation during long-term management. *Surg. Neurol. Int.* 4:69. doi: 10.4103/2152-7806.112612

Fasano, A., Aquino, C. C., Krauss, J. K., Honey, C. R., and Bloem, B. R. (2015). Axial disability and deep brain stimulation in patients with Parkinson disease. *Nat. Rev. Neurol.* 11, 98–110. doi: 10.1038/nrneurol.2014.252

Fenelon, G., Goujon, C., Gurruchaga, J. M., Cesaro, P., Jarraya, B., Palfi, S., et al. (2012). Spinal cord stimulation for chronic pain improved motor function in a patient with Parkinson's disease. *Parkinsonism Relat. Disord.* 18, 213–214. doi: 10.1016/j.parkreldis.2011.07.015

Fernandez-Lago, H., Bello, O., Mora-Cerda, F., Montero-Camara, J., and Fernandez-Del-Olmo, M. A. (2017). Treadmill walking combined with anodal transcranial direct current stimulation in Parkinson disease: a pilot study of kinematic and neurophysiological effects. *Am. J. Phys. Med. Rehabil.* 96, 801–808. doi: 10.1097/PHM.0000000000000751

Ferraye, M. U., Fraix, V., Pollak, P., Bloem, B. R., and Debu, B. (2016). The laser-shoe: a new form of continuous ambulatory cueing for patients with Parkinson's disease. *Parkinsonism Relat. Disord.* 29, 127–128. doi: 10.1016/j.parkreldis.2016.05.004

Ferrucci, R., Mameli, F., Ruggiero, F., and Priori, A. (2016). Transcranial direct current stimulation as treatment for Parkinson's disease and other movement disorders. *Basal Ganglia* 6, 53–61. doi: 10.1016/j.baga.2015.12.002

Fonoff, E. T., de Lima-Pardini, A. C., Coelho, D. B., Monaco, B. A., Machado, B., Pinto de Souza, C., et al. (2019). Spinal cord stimulation for freezing of gait: from bench to bedside. *Front. Neurol.* 10:905. doi: 10.3389/fneur.2019.00905

Franzen, E., Paquette, C., Gurfinkel, V., and Horak, F. (2012). Light and heavy touch reduces postural sway and modifies axial tone in Parkinson's disease. *Neurorehabil. Neural Repair.* 26, 1007–1014. doi: 10.1177/1545968312437942

Furusawa, Y., Matsui, A., Kobayashi-Noami, K., Kojima, Y., Tsubouchi, A., Todoroki, D., et al. (2020). Burst spinal cord stimulation for pain and motor function in Parkinson's disease: a case series. *Clin. Park. Relat. Disord.* 3, 100043. doi: 10.1016/j.prdoa.2020.100043

Gallego, J. A., Rocon, E., Belda-Lois, J. M., and Pons, J. L. (2013). A neuroprosthesis for tremor management through the control of muscle co-contraction. *J. Neuroeng. Rehabil.* 10:36. doi: 10.1186/1743-0003-10-36

Galli, M., Vicidomini, C., Rozin Kleiner, A. F., Vacca, L., Cimolin, V., Condoluci, C., et al. (2018). Peripheral neurostimulation breaks the shuffling steps patterns in Parkinsonian gait: a double blind randomized longitudinal study with automated mechanical peripheral stimulation. *Eur. J. Phys. Rehabil. Med.* 54, 860–865. doi: 10.23736/S1973-9087.18.05037-2

Garcia Ruiz, P. J., Sesar Ignacio, A., Ares Pensado, B., Castro Garcia, A., Alonso Frech, F., Alvarez Lopez, M., et al. (2008). Efficacy of long-term continuous subcutaneous apomorphine infusion in advanced Parkinson's disease with motor fluctuations: a multicenter study. *Mov. Disord.* 23, 1130–1136. doi: 10.1002/mds.22063

Gershanik, O., and Jenner, P. (2012). Moving from continuous dopaminergic stimulation to continuous drug delivery in the treatment of Parkinson's disease. *Eur. J. Neurol.* 19, 1502–1508. doi: 10.1111/j.1468-1331.2011.03593.x

Giannicola, G., Marceglia, S., Rossi, L., Mrakic-Sposta, S., Rampini, P., Tamma, F., et al. (2010). The effects of levodopa and ongoing deep brain stimulation on subthalamic beta oscillations in Parkinson's disease. *Exp. Neurol.* 226, 120–127. doi: 10.1016/j.expneurol.2010.08.011

Giladi, N., Gurevich, T., Djaldetti, R., Adar, L., Case, R., Leibman-Barak, S., et al. (2021). ND0612 (levodopa/carbidopa for subcutaneous infusion) in patients with Parkinson's disease and motor response fluctuations: a randomized, placebo-controlled phase 2 study. *Parkinsonism Relat. Disord.* 91, 139–145. doi: 10.1016/j.parkreldis.2021.09.024

Giladi, N., and Nieuwboer, A. (2008). Understanding and treating freezing of gait in Parkinsonism, proposed working definition, and setting the stage. *Mov. Disord.* 23(Suppl. 2), S423–S425. doi: 10.1002/mds.21927

Ginis, P., Heremans, E., Ferrari, A., Bekkers, E. M. J., Canning, C. G., and Nieuwboer, A. (2017a). External input for gait in people with Parkinson's disease with and without freezing of gait: one size does not fit all. *J. Neurol.* 264, 1488–1496. doi: 10.1007/s00415-017-8552-6

Ginis, P., Heremans, E., Ferrari, A., Dockx, K., Canning, C. G., and Nieuwboer, A. (2017b). Prolonged walking with a wearable system providing intelligent auditory input in people with Parkinson's disease. *Front. Neurol.* 8:128. doi: 10.3389/fneur.2017.00128

Ginis, P., Nieuwboer, A., Dorfman, M., Ferrari, A., Gazit, E., Canning, C. G., et al. (2016). Feasibility and effects of home-based smartphone-delivered automated feedback training for gait in people with Parkinson's disease: a pilot randomized

controlled trial. *Parkinsonism Relat. Disord.* 22, 28–34. doi: 10.1016/j.parkreldis.2015.11.004

Griessenauer, C. J., Chang, S. Y., Tye, S. J., Kimble, C. J., Bennet, K. E., Garris, P. A., et al. (2010). Wireless Instantaneous Neurotransmitter Concentration System: electrochemical monitoring of serotonin using fast-scan cyclic voltammetry–a proof-of-principle study. *J. Neurosurg.* 113, 656–665. doi: 10.3171/2010.3.JNS091627

Hallett, M., Epstein, C. M., Berardelli, A., Sackeim, H., and Maccabee, P. (2000). Topics in transcranial magnetic stimulation. *Suppl. Clin. Neurophysiol.* 53, 301–311. doi: 10.1016/s1567-424x(09)70173-4

Hallett, M., Wassermann, E. M., Pascual-Leone, A., and Valls-Sole, J. (1999). Repetitive transcranial magnetic stimulation. The International Federation of Clinical Neurophysiology. *Electroencephalogr. Clin. Neurophysiol. Suppl.* 52, 105–113.

Hamblin, M. R. (2016). Shining light on the head: photobiomodulation for brain disorders. *BBA Clin.* 6, 113–124. doi: 10.1016/j.bbacli.2016.09.002

Han, J., Kim, E., Jung, J., Lee, J., Sung, H., and Kim, J. (2014). Effect of muscle vibration on spatiotemporal gait parameters in patients with Parkinson's disease. *J. Phys. Ther. Sci.* 26, 671–673. doi: 10.1589/jpts.26.671

Hanajima, R., Chen, R., Ashby, P., Lozano, A. M., Hutchison, W. D., Davis, K. D., et al. (2004a). Very fast oscillations evoked by median nerve stimulation in the human thalamus and subthalamic nucleus. *J. Neurophysiol.* 92, 3171–3182. doi: 10.1152/jn.00363.2004

Hanajima, R., Dostrovsky, J. O., Lozano, A. M., Hutchison, W. D., Davis, K. D., Chen, R., et al. (2004b). Somatosensory evoked potentials (SEPs) recorded from deep brain stimulation (DBS) electrodes in the thalamus and subthalamic nucleus (STN). *Clin. Neurophysiol.* 115, 424–434. doi: 10.1016/j.clinph.2003.09.027

Harrison, E. C., Horin, A. P., and Earhart, G. M. (2018). Internal cueing improves gait more than external cueing in healthy adults and people with Parkinson disease. *Sci. Rep.* 8:15525. doi: 10.1038/s41598-018-33942-6

Harrison, E. C., Horin, A. P., and Earhart, G. M. (2019). Mental singing reduces gait variability more than music listening for healthy older adults and people with Parkinson disease. *J. Neurol. Phys. Ther.* 43, 204–211. doi: 10.1097/NPT.0000000000000288

Hass, C. J., Waddell, D. E., Fleming, R. P., Juncos, J. L., and Gregor, R. J. (2005). Gait initiation and dynamic balance control in Parkinson's disease. *Arch. Phys. Med. Rehabil.* 86, 2172–2176. doi: 10.1016/j.apmr.2005.05.013

Hassan, S., Amer, S., Alwaki, A., and Elborno, A. (2013). A patient with Parkinson's disease benefits from spinal cord stimulation. *J. Clin. Neurosci.* 20, 1155–1156. doi: 10.1016/j.jocn.2012.08.018

Hely, M. A., Reid, W. G., Adena, M. A., Halliday, G. M., and Morris, J. G. (2008). The Sydney multicenter study of Parkinson's disease: the inevitability of dementia at 20 years. *Mov. Disord.* 23, 837–844. doi: 10.1002/mds.21956

Hendriks, J., Rosen, M., Berube, N., and Aisen M. A. (1991). "A second-generation joystick for people disabled by tremor," in *Proceedings of the 14th Annual RESNA Conference*, Kansas, MO.

Hitti, F. L., Ramayya, A. G., McShane, B. J., Yang, A. I., Vaughan, K. A., and Baltuch, G. H. (2019). Long-term outcomes following deep brain stimulation for Parkinson's disease. *J. Neurosurg.* 132, 205–210. doi: 10.3171/2018.8.JNS182081

Hollingworth, M., Sims-Williams, H. P., Pickering, A. E., Barua, N., and Patel, N. K. (2017). Single electrode deep brain stimulation with dual targeting at dual frequency for the treatment of chronic pain: a case series and review of the literature. *Brain Sci.* 7:9. doi: 10.3390/brainsci7010009

Holloway, R. G., Shoulson, I., Fahn, S., Kieburtz, K., Lang, A., Marek, K., et al. (2004). Pramipexole vs levodopa as initial treatment for Parkinson disease: a 4-year randomized controlled trial. *Arch. Neurol.* 61, 1044–1053. doi: 10.1001/archneur.61.7.1044

Horiba, M., Ueki, Y., Nojima, I., Shimizu, Y., Sahashi, K., Itamoto, S., et al. (2019). Impaired motor skill acquisition using mirror visual feedback improved by transcranial direct current stimulation (tDCS) in patients with Parkinson's disease. *Front. Neurosci.* 13:602. doi: 10.3389/fnins.2019.00602

Horin, A. P., Harrison, E. C., Rawson, K. S., and Earhart, G. M. (2020). People with Parkinson disease with and without freezing of gait respond similarly to external and self-generated cues. *Gait Posture* 82, 161–166. doi: 10.1016/j.gaitpost.2020.09.005

Hove, M. J., Suzuki, K., Uchitomi, H., Orimo, S., and Miyake, Y. (2012). Interactive rhythmic auditory stimulation reinstates natural 1/f timing in gait of Parkinson's patients. *PLoS One* 7:e32600. doi: 10.1371/journal.pone.0032600

Huang, C., Chu, H., Zhang, Y., and Wang, X. (2018). Deep brain stimulation to alleviate freezing of gait and cognitive dysfunction in Parkinson's disease: update on current research and future perspectives. *Front. Neurosci.* 12:29. doi: 10.3389/fnins.2018.00029

Hubsch, C., D'Hardemare, V., Ben Maacha, M., Ziegler, M., Patte-Karsenti, N., Thiebaut, J. B., et al. (2019). Tonic spinal cord stimulation as therapeutic option in Parkinson disease with axial symptoms: effects on walking and quality of life. *Parkinsonism Relat. Disord.* 63, 235–237. doi: 10.1016/j.parkreldis.2019.02.044

Hughes, A. J., Daniel, S. E., Blankson, S., and Lees, A. J. (1993). A clinicopathologic study of 100 cases of Parkinson's disease. *Arch. Neurol.* 50, 140–148. doi: 10.1001/archneur.1993.00540020018011

Janssen, S., Bolte, B., Nonnekes, J., Bittner, M., Bloem, B. R., Heida, T., et al. (2017). Usability of three-dimensional augmented visual cues delivered by smart glasses on (Freezing of) gait in Parkinson's disease. *Front. Neurol.* 8:279. doi: 10.3389/fneur.2017.00279

Jenkins, M. E., Almeida, Q. J., Spaulding, S. J., van Oostveen, R. B., Holmes, J. D., Johnson, A. M., et al. (2009). Plantar cutaneous sensory stimulation improves single-limb support time, and EMG activation patterns among individuals with Parkinson's disease. *Parkinsonism Relat. Disord.* 15, 697–702. doi: 10.1016/j.parkreldis.2009.04.004

Ji, G. J., Liu, T., Li, Y., Liu, P., Sun, J., Chen, X., et al. (2021). Structural correlates underlying accelerated magnetic stimulation in Parkinson's disease. *Hum. Brain Mapp.* 42, 1670–1681. doi: 10.1002/hbm.25319

Jiang, Y., and Norman, K. E. (2006). Effects of visual and auditory cues on gait initiation in people with Parkinson's disease. *Clin. Rehabil.* 20, 36–45. doi: 10.1191/0269215506cr925oa

Jitkritsadakul, O., Thanawattano, C., Anan, C., and Bhidayasiri, R. (2017). Tremor's glove-an innovative electrical muscle stimulation therapy for intractable tremor in Parkinson's disease: a randomized sham-controlled trial. *J. Neurol. Sci.* 381, 331–340. doi: 10.1016/j.jns.2017.08.3246

Johnson, R. L., and Wilson, C. G. (2018). A review of vagus nerve stimulation as a therapeutic intervention. *J. Inflamm. Res.* 11, 203–213. doi: 10.2147/JIR.S163248

Kalia, L. V., and Lang, A. E. (2015). Parkinson's disease. *Lancet* 386, 896–912. doi: 10.1016/S0140-6736(14)61393-3

Karl, J. A., Ouyang, B., Goetz, S., and Metman, L. V. (2020). A novel DBS paradigm for axial features in Parkinson's disease: a randomized crossover study. *Mov. Disord.* 35, 1369–1378. doi: 10.1002/mds.28048

Kaski, D., Dominguez, R. O., Allum, J. H., Islam, A. F., and Bronstein, A. M. (2014b). Combining physical training with transcranial direct current stimulation to improve gait in Parkinson's disease: a pilot randomized controlled study. *Clin. Rehabil.* 28, 1115–1124. doi: 10.1177/0269215514534277

Kaski, D., Allum, J. H., Bronstein, A. M., and Dominguez, R. O. (2014a). Applying anodal tDCS during tango dancing in a patient with Parkinson's disease. *Neurosci. Lett.* 568, 39–43. doi: 10.1016/j.neulet.2014.03.043

Kerr, G. K., Worringham, C. J., Cole, M. H., Lacherez, P. F., Wood, J. M., and Silburn, P. A. (2010). Predictors of future falls in Parkinson disease. *Neurology* 75, 116–124. doi: 10.1212/WNL.0b013e3181e7b688

Keus, S., Munneke, M., Graziano, M., Paltamaa, J., Pelosin, E., Domingos, J., et al. (2014). *On Behalf of the Guideline Development Group. 2014. European Physiotherapy Guideline for Parkinson's Disease*. Nijmegen: KNGF/ParkinsonNet.

Khedr, E. M., Al-Fawal, B., Abdel Wraith, A., Saber, M., Hasan, A. M., Bassiony, A., et al. (2019). The effect of 20 Hz versus 1 Hz repetitive transcranial magnetic stimulation on motor dysfunction in Parkinson's disease: which is more beneficial? *J. Parkinsons Dis.* 9, 379–387. doi: 10.3233/JPD-181540

Khedr, E. M., Farweez, H. M., and Islam, H. (2003). Therapeutic effect of repetitive transcranial magnetic stimulation on motor function in Parkinson's disease patients. *Eur. J. Neurol.* 10, 567–572. doi: 10.1046/j.1468-1331.2003.00649.x

Kilpatrick, M., Church, E., Danish, S., Stiefel, M., Jaggi, J., Halpern, C., et al. (2010). Intracerebral microdialysis during deep brain stimulation surgery. *J. Neurosci. Methods* 190, 106–111. doi: 10.1016/j.jneumeth.2010.04.013

Kim, J., Wichmann, T., Inan, O. T., and Deweerth, S. P. (2020). A wearable system for attenuating essential tremor based on peripheral nerve stimulation. *IEEE J. Transl. Eng. Health Med.* 8:2000111. doi: 10.1109/JTEHM.2020.2985058

Kim, M. S., Chang, W. H., Cho, J. W., Youn, J., Kim, Y. K., Kim, S. W., et al. (2015). Efficacy of cumulative high-frequency rTMS on freezing of gait in Parkinson's disease. *Restor. Neurol. Neurosci.* 33, 521–530. doi: 10.3233/RNN-140489

Kim, R., Kim, H. J., Shin, C., Park, H., Kim, A., Paek, S. H., et al. (2019). Long-term effect of subthalamic nucleus deep brain stimulation on freezing of gait in Parkinson's disease. *J. Neurosurg.* 131, 1797–1804. doi: 10.3171/2018.8.JNS18350

Kinoshita, M., Nakataki, M., Morigaki, R., Sumitani, S., Goto, S., Kaji, R., et al. (2018). Turning on the left side electrode changed depressive state to manic state in a Parkinson's disease patient who received bilateral subthalamic nucleus deep brain stimulation: a case report. *Clin. Psychopharmacol. Neurosci.* 16, 494–496. doi: 10.9758/cpn.2018.16.4.494

Kishida, K. T., Saez, I., Lohrenz, T., Witcher, M. R., Laxton, A. W., Tatter, S. B., et al. (2016). Subsecond dopamine fluctuations in human striatum encode superposed error signals about actual and counterfactual reward. *Proc. Natl. Acad. Sci. U.S.A.* 113, 200–205. doi: 10.1073/pnas.1513619112

Kishida, K. T., Sandberg, S. G., Lohrenz, T., Comair, Y. G., Saez, I., Phillips, P. E., et al. (2011). Sub-second dopamine detection in human striatum. *PLoS One* 6:e23291. doi: 10.1371/journal.pone.0023291

Kleiner, A., Galli, M., Gaglione, M., Hildebrand, D., Sale, P., Albertini, G., et al. (2015). The Parkinsonian gait spatiotemporal parameters quantified by a single inertial sensor before and after automated mechanical peripheral stimulation treatment. *Parkinsons Dis.* 2015:390512. doi: 10.1155/2015/390512

Kleiner, A. F. R., Souza Pagnussat, A., Pinto, C., Redivo Marchese, R., Salazar, A. P., and Galli, M. (2018). Automated mechanical peripheral stimulation effects on gait variability in individuals with Parkinson disease and freezing of gait: a double-blind, randomized controlled trial. *Arch. Phys. Med. Rehabil.* 99, 2420–2429. doi: 10.1016/j.apmr.2018.05.009

Kleiner-Fisman, G., Herzog, J., Fisman, D. N., Tamma, F., Lyons, K. E., Pahwa, R., et al. (2006). Subthalamic nucleus deep brain stimulation: summary and meta-analysis of outcomes. *Mov. Disord.* 21(Suppl. 14), S290–S304. doi: 10.1002/mds.20962

Kobayashi, R., Kenji, S., Taketomi, A., Murakami, H., Ono, K., and Otake, H. (2018). New mode of burst spinal cord stimulation improved mental status as well as motor function in a patient with Parkinson's disease. *Parkinsonism Relat. Disord.* 57, 82–83. doi: 10.1016/j.parkreldis.2018.07.002

Koller, W. C., and Vetere-Overfield, B. (1989). Acute and chronic effects of propranolol and primidone in essential tremor. *Neurology* 39, 1587–1588. doi: 10.1212/wnl.39.12.1587

Koller, W. C., Vetere-Overfield, B., and Barter, R. (1989). Tremors in early Parkinson's disease. *Clin. Neuropharmacol.* 12, 293–297. doi: 10.1097/00002826-198908000-00006

Konczak, J., Corcos, D. M., Horak, F., Poizner, H., Shapiro, M., Tuite, P., et al. (2009). Proprioception and motor control in Parkinson's disease. *J. Mot. Behav.* 41, 543–552. doi: 10.3200/35-09-002

Kotovsky, J., and Rosen, M. J. (1998). A wearable tremor-suppression orthosis. *J. Rehabil. Res. Dev.* 35, 373–387.

Krack, P., Batir, A., Van Blercom, N., Chabardes, S., Fraix, V., Ardouin, C., et al. (2003). Five-year follow-up of bilateral stimulation of the subthalamic nucleus in advanced Parkinson's disease. *N. Engl. J. Med.* 349, 1925–1934. doi: 10.1056/NEJMoa035275

Kraus, T., Hosl, K., Kiess, O., Schanze, A., Kornhuber, J., and Forster, C. (2007). BOLD fMRI deactivation of limbic and temporal brain structures and mood enhancing effect by transcutaneous vagus nerve stimulation. *J. Neural Transm. (Vienna)* 114, 1485–1493. doi: 10.1007/s00702-007-0755-z

Kuhn, A. A., Tsui, A., Aziz, T., Ray, N., Brucke, C., Kupsch, A., et al. (2009). Pathological synchronisation in the subthalamic nucleus of patients with Parkinson's disease relates to both bradykinesia and rigidity. *Exp. Neurol.* 215, 380–387. doi: 10.1016/j.expneurol.2008.11.008

Lamy, J. C., Varriale, P., Apartis, E., Mehdi, S., Blancher-Meinadier, A., Kosutzka, Z., et al. (2021). Trans-spinal direct current stimulation for managing primary orthostatic tremor. *Mov. Disord.* 36, 1835–1842. doi: 10.1002/mds.28581

Lance, J. W., Schwab, R. S., and Peterson, E. A. (1963). Action tremor and the cogwheel phenomenon in Parkinson's disease. *Brain* 86, 95–110. doi: 10.1093/brain/86.1.95

Landi, A., Trezza, A., Pirillo, D., Vimercati, A., Antonini, A., and Sganzerla, E. P. (2013). Spinal cord stimulation for the treatment of sensory symptoms in advanced Parkinson's disease. *Neuromodulation* 16, 276–279. doi: 10.1111/ner.12005

Lang, A. E., Houeto, J. L., Krack, P., Kubu, C., Lyons, K. E., Moro, E., et al. (2006). Deep brain stimulation: preoperative issues. *Mov. Disord.* 21(Suppl. 14), S171–S196. doi: 10.1002/mds.20955

Lang, A. E., and Lozano, A. M. (1998). Parkinson's disease. Second of two parts. *N. Engl. J. Med.* 339, 1130–1143. doi: 10.1056/NEJM199810153391607

Larson, D., and Simuni, T. (2022). New dopaminergic therapies for PD motor complications. *Neuropharmacology* 204:108869. doi: 10.1016/j.neuropharm.2021.108869

Larson, P. S., Richardson, R. M., Starr, P. A., and Martin, A. J. (2008). Magnetic resonance imaging of implanted deep brain stimulators: experience in a large series. *Stereotact. Funct. Neurosurg.* 86, 92–100. doi: 10.1159/000112430

Lattari, E., Costa, S. S., Campos, C., de Oliveira, A. J., Machado, S., and Maranhao Neto, G. A. (2017). Can transcranial direct current stimulation on the dorsolateral prefrontal cortex improves balance and functional mobility in Parkinson's disease? *Neurosci. Lett.* 636, 165–169. doi: 10.1016/j.neulet.2016.11.019

Lee, H. K., Ahn, S. J., Shin, Y. M., Kang, N., and Cauraugh, J. H. (2019). Does transcranial direct current stimulation improve functional locomotion in people with Parkinson's disease? A systematic review and meta-analysis. *J. Neuroeng. Rehabil.* 16:84. doi: 10.1186/s12984-019-0562-4

Lee, S. A., and Kim, M. K. (2021). The effect of transcranial direct current stimulation combined with visual cueing training on motor function, balance, and gait ability of patients with Parkinson's disease. *Medicina (Kaunas)* 57, 1146. doi: 10.3390/medicina57111146

Lee, S. Y., Chung, E. J., Kim, Y. J., and Kim, S. J. (2011). Dopa responsive slow orthostatic tremor in Parkinson's disease. *J. Mov. Disord.* 4, 82–84. doi: 10.14802/jmd.11019

Lee, S. Y., Kim, M. S., Chang, W. H., Cho, J. W., Youn, J. Y., and Kim, Y. H. (2014). Effects of repetitive transcranial magnetic stimulation on freezing of gait in patients with Parkinsonism. *Restor. Neurol. Neurosci.* 32, 743–753. doi: 10.3233/RNN-140397

Lefaucheur, J. P., Drouot, X., Von Raison, F., Menard-Lefaucheur, I., Cesaro, P., and Nguyen, J. P. (2004). Improvement of motor performance and modulation of cortical excitability by repetitive transcranial magnetic stimulation of the motor cortex in Parkinson's disease. *Clin. Neurophysiol.* 115, 2530–2541. doi: 10.1016/j.clinph.2004.05.025

LeMoyne, R., Mastroianni, T., Whiting, D., and Tomycz, N. (2019a). Preliminary network centric therapy for machine learning classification of deep brain stimulation status for the treatment of Parkinson's disease with a conformal wearable and wireless inertial sensor. *Adv. Parkinsons Dis.* 8, 75–91. doi: 10.4236/apd.2019.84007

LeMoyne, R., Mastroianni, T., Whiting, D., and Tomycz, N. (2019b). "Wearable and wireless systems with internet connectivity for quantification of Parkinson's disease and essential tremor characteristics," in *Wearable and Wireless Systems for Healthcare II. Smart Sensors, Measurement and Instrumentation*, ed. S. C. Mukhopadhyay (Singapore: Springer), 79–97. doi: 10.1007/978-981-13-5808-1_7

LeMoyne, R., Mastroianni, T., Whiting, D., and Tomycz, N. (2020a). "Application of deep learning to distinguish multiple deep brain stimulation parameter configurations for the treatment of Parkinson's disease," in *Proceedings of the 19th IEEE International Conference on Machine Learning and Applications (ICMLA)*, Miami, FL. doi: 10.1109/ICMLA51294.2020.00178

LeMoyne, R., Mastroianni, T., Whiting, D., and Tomycz, N. (2020b). Distinction of an assortment of deep brain stimulation parameter configurations for treating Parkinson's disease using machine learning with quantification of tremor response through a conformal wearable and wireless inertial sensor. *Adv. Parkinsons Dis.* 9, 21–39. doi: 10.4236/apd.2020.93003

LeMoyne, R., Mastroianni, T., Whiting, D., and Tomycz, N. (2020c). Parametric evaluation of deep brain stimulation parameter configurations for Parkinson's disease using a conformal wearable and wireless inertial sensor system and machine learning. *Annu. Int. Conf. IEEE Eng. Med. Biol. Soc.* 2020, 3606–3611. doi: 10.1109/EMBC44109.2020.9175408

Lewis, G. N., Byblow, W. D., and Walt, S. E. (2000). Stride length regulation in Parkinson's disease: the use of extrinsic, visual cues. *Brain* 123(Pt 10), 2077–2090. doi: 10.1093/brain/123.10.2077

Lewis, S. J., Dove, A., Robbins, T. W., Barker, R. A., and Owen, A. M. (2003). Cognitive impairments in early Parkinson's disease are accompanied by reductions in activity in frontostriatal neural circuitry. *J. Neurosci.* 23, 6351–6356. doi: 10.1523/JNEUROSCI.23-15-06351.2003

Li, D., Zhang, C., Gault, J., Wang, W., Liu, J., Shao, M., et al. (2017). Remotely programmed deep brain stimulation of the bilateral subthalamic nucleus for the treatment of primary parkinson disease: a randomized controlled trial investigating the safety and efficacy of a novel deep brain stimulation system. *Stereotact. Funct. Neurosurg.* 95, 174–182. doi: 10.1159/000475765

Li, Z. J., Wu, Q., and Yi, C. J. (2015). Clinical efficacy of istradefylline versus rTMS on Parkinson's disease in a randomized clinical trial. *Curr. Med. Res. Opin.* 31, 2055–2058. doi: 10.1185/03007995.2015.1086994

Liebert, A., Bicknell, B., Laakso, E. L., Heller, G., Jalilitabaei, P., Tilley, S., et al. (2021). Improvements in clinical signs of Parkinson's disease using photobiomodulation: a prospective proof-of-concept study. *BMC Neurol.* 21:256. doi: 10.1186/s12883-021-02248-y

Lim, E. C. H., Tan, T. M., and Seet, R. C. S. (2006). LASER-assisted device (LAD) for start hesitation and freezing in Parkinson's disease. *Case Rep. Clin. Pract. Rev.* 7, 92–95.

Lima de Albuquerque, L., Pantovic, M., Clingo, M., Fischer, K., Jalene, S., Landers, M., et al. (2020). An acute application of cerebellar transcranial direct current stimulation does not improve motor performance in Parkinson's disease. *Brain Sci.* 10:735. doi: 10.3390/brainsci10100735

Lin, P. T., Ross, E. K., Chidester, P., Rosenbluth, K. H., Hamner, S. R., Wong, S. H., et al. (2018). Noninvasive neuromodulation in essential tremor demonstrates relief in a sham-controlled pilot trial. *Mov. Disord.* 33, 1182–1183. doi: 10.1002/mds.27350

Lirani-Silva, E., Lord, S., Moat, D., Rochester, L., and Morris, R. (2019). Auditory cueing for gait impairment in persons with Parkinson disease: a pilot study of changes in response with disease progression. *J. Neurol. Phys. Ther.* 43, 50–55. doi: 10.1097/NPT.0000000000000250

Lirani-Silva, E., Vitorio, R., Barbieri, F. A., Orcioli-Silva, D., Simieli, L., and Gobbi, L. T. B. (2017). Continuous use of textured insole improve plantar sensation and stride length of people with Parkinson's disease: a pilot study. *Gait Posture* 58, 495–497. doi: 10.1016/j.gaitpost.2017.09.017

Little, S., Beudel, M., Zrinzo, L., Foltynie, T., Limousin, P., Hariz, M., et al. (2016a). Bilateral adaptive deep brain stimulation is effective in Parkinson's disease. *J. Neurol. Neurosurg. Psychiatry* 87, 717–721. doi: 10.1136/jnnp-2015-310972

Little, S., Tripoliti, E., Beudel, M., Pogosyan, A., Cagnan, H., Herz, D., et al. (2016b). Adaptive deep brain stimulation for Parkinson's disease demonstrates reduced speech side effects compared to conventional stimulation in the acute setting. *J. Neurol. Neurosurg. Psychiatry* 87, 1388–1389. doi: 10.1136/jnnp-2016-313518

Little, S., Pogosyan, A., Neal, S., Zavala, B., Zrinzo, L., Hariz, M., et al. (2013). Adaptive deep brain stimulation in advanced Parkinson disease. *Ann. Neurol.* 74, 449–457. doi: 10.1002/ana.23951

Lopez, W. O., Higuera, C. A., Fonoff, E. T., Souza Cde, O., Albicker, U., and Martinez, J. A. (2014). Listenmee and Listenmee smartphone application: synchronizing walking to rhythmic auditory cues to improve gait in Parkinson's disease. *Hum. Mov. Sci.* 37, 147–156. doi: 10.1016/j.humov.2014.08.001

Ma, J., Gao, L., Mi, T., Sun, J., Chan, P., and Wu, T. (2019). Repetitive transcranial magnetic stimulation does not improve the sequence effect in freezing of gait. *Parkinsons Dis.* 2019:2196195. doi: 10.1155/2019/2196195

Ma, Y., Miao, S., Zhou, R., Zhang, Q., Chen, H., and Liang, Y. (2021). Application of remote deep brain stimulation programming for Parkinson's disease patients. *World Neurosurg.* 147, e255–e261. doi: 10.1016/j.wneu.2020.12.030

Machado, A., Rezai, A. R., Kopell, B. H., Gross, R. E., Sharan, A. D., and Benabid, A. L. (2006). Deep brain stimulation for Parkinson's disease: surgical technique and perioperative management. *Mov. Disord.* 21(Suppl. 14), S247–S258. doi: 10.1002/mds.20959

Majoie, H. J., Rijkers, K., Berfelo, M. W., Hulsman, J. A., Myint, A., Schwarz, M., et al. (2011). Vagus nerve stimulation in refractory epilepsy: effects on pro- and anti-inflammatory cytokines in peripheral blood. *Neuroimmunomodulation* 18, 52–56. doi: 10.1159/000315530

Mann, G. E., Finn, S. M., and Taylor, P. N. (2008). A pilot study to investigate the feasibility of electrical stimulation to assist gait in Parkinson's disease. *Neuromodulation* 11, 143–149. doi: 10.1111/j.1525-1403.2008.00157.x

Manor, B., Dagan, M., Herman, T., Gouskova, N. A., Vanderhorst, V. G., Giladi, N., et al. (2021). Multitarget transcranial electrical stimulation for freezing of gait: a randomized controlled trial. *Mov. Disord.* 36, 2693–2698. doi: 10.1002/mds.28759

Marceglia, S., Fiorio, M., Foffani, G., Mrakic-Sposta, S., Tiriticco, M., Locatelli, M., et al. (2009). Modulation of beta oscillations in the subthalamic area during action observation in Parkinson's disease. *Neuroscience* 161, 1027–1036. doi: 10.1016/j.neuroscience.2009.04.018

Martin, W. E., Loewenson, R. B., Resch, J. A., and Baker, A. B. (1973). Parkinson's disease. Clinical analysis of 100 patients. *Neurology* 23, 783–790. doi: 10.1212/wnl.23.8.783

Maruo, T., Hosomi, K., Shimokawa, T., Kishima, H., Oshino, S., Morris, S., et al. (2013). High-frequency repetitive transcranial magnetic stimulation over the primary foot motor area in Parkinson's disease. *Brain Stimul.* 6, 884–891. doi: 10.1016/j.brs.2013.05.002

Mazzone, P., Viselli, F., Ferraina, S., Giamundo, M., Marano, M., Paoloni, M., et al. (2019). High cervical spinal cord stimulation: a one year follow-up study on motor and non-motor functions in Parkinson's disease. *Brain Sci.* 9:78. doi: 10.3390/brainsci9040078

McElcheran, C. E., Golestanirad, L., Iacono, M. I., Wei, P. S., Yang, B., Anderson, K. J. T., et al. (2019). Numerical simulations of realistic lead trajectories and an experimental verification support the efficacy of parallel radiofrequency transmission to reduce heating of deep brain stimulation implants during MRI. *Sci. Rep.* 9:2124. doi: 10.1038/s41598-018-38099-w

Merola, A., Espay, A. J., Romagnolo, A., Bernardini, A., Rizzi, L., Rosso, M., et al. (2016). Advanced therapies in Parkinson's disease: long-term retrospective study. *Parkinsonism Relat. Disord.* 29, 104–108. doi: 10.1016/j.parkreldis.2016.05.015

Mi, T. M., Garg, S., Ba, F., Liu, A. P., Liang, P. P., Gao, L. L., et al. (2020). Repetitive transcranial magnetic stimulation improves Parkinson's freezing of gait via normalizing brain connectivity. *NPJ Parkinsons Dis.* 6:16. doi: 10.1038/s41531-020-0118-0

Mi, T. M., Garg, S., Ba, F., Liu, A. P., Wu, T., Gao, L. L., et al. (2019). High-frequency rTMS over the supplementary motor area improves freezing of gait in Parkinson's disease: a randomized controlled trial. *Parkinsonism Relat. Disord.* 68, 85–90. doi: 10.1016/j.parkreldis.2019.10.009

Mille, M. L., Creath, R. A., Prettyman, M. G., Johnson Hilliard, M., Martinez, K. M., Mackinnon, C. D., et al. (2012). Posture and locomotion coupling: a target for rehabilitation interventions in persons with Parkinson's disease. *Parkinsons Dis.* 2012:754186. doi: 10.1155/2012/754186

Mink, J. W. (1996). The basal ganglia: focused selection and inhibition of competing motor programs. *Prog. Neurobiol.* 50, 381–425. doi: 10.1016/s0301-0082(96)00042-1

Mishra, R. K., and Thrasher, A. T. (2021). Transcranial direct current stimulation of dorsolateral prefrontal cortex improves dual-task gait performance in patients with Parkinson's disease: a double blind, sham-controlled study. *Gait Posture* 84, 11–16. doi: 10.1016/j.gaitpost.2020.11.012

Mondal, B., Choudhury, S., Banerjee, R., Roy, A., Chatterjee, K., Basu, P., et al. (2021). Non-invasive vagus nerve stimulation improves clinical and molecular biomarkers of Parkinson's disease in patients with freezing of gait. *NPJ Parkinsons Dis.* 7:46. doi: 10.1038/s41531-021-00190-x

Mondal, B., Choudhury, S., Simon, B., Baker, M. R., and Kumar, H. (2019). Noninvasive vagus nerve stimulation improves gait and reduces freezing of gait in Parkinson's disease. *Mov. Disord.* 34, 917–918. doi: 10.1002/mds.27662

Moore, O., Peretz, C., and Giladi, N. (2007). Freezing of gait affects quality of life of peoples with Parkinson's disease beyond its relationships with mobility and gait. *Mov. Disord.* 22, 2192–2195. doi: 10.1002/mds.21659

Morigaki, R., and Goto, S. (2015). "Deep brain stimulation for essential tremor," in *Deep Brain Stimulation for Neurological Disorders*, ed. T. Itakura (Cham: Springer), 135–155. doi: 10.1007/978-3-319-08476-3_11

Morigaki, R., Nagahiro, S., Kaji, R., and Goto, S. (2011a). "Current use of thalamic surgeries for treating movement disorders," in *Thalamus: Anatomy, Functions and Disorders*, ed. J. L. Song (New York, NY: Nova Science Publishers, Inc), 1–31.

Morigaki, R., Nagahiro, S., Kaji, R., and Goto, S. (2011b). "Thalamic deep brain stimulation for Parkinson's disease," in *Diagnosis and Treatment of Parkinson's Disease*, ed. A. Q. Rana (London: InTech), 233–252. doi: 10.1007/s007010100024

Morris, R., Yarnall, A. J., Hunter, H., Taylor, J. P., Baker, M. R., and Rochester, L. (2019). Noninvasive vagus nerve stimulation to target gait impairment in Parkinson's disease. *Mov. Disord.* 34, 918–919. doi: 10.1002/mds.27664

Muller, E. J., and Robinson, P. A. (2018). Quantitative theory of deep brain stimulation of the subthalamic nucleus for the suppression of pathological rhythms in Parkinson's disease. *PLoS Comput. Biol.* 14:e1006217. doi: 10.1371/journal.pcbi.1006217

Nascimento, L. R., do Carmo, W. A., de Oliveira, G. P., Arêas, F. Z. D. S., and Dias, F. M. V. (2021). Transcranial direct current stimulation provides no clinically important benefits over walking training for improving walking in Parkinson's disease: a systematic review. *J. Physiother.* 67, 190–196. doi: 10.1016/j.jphys.2021.06.003

Neudorfer, C., Kroneberg, D., Al-Fatly, B., Goede, L., Kubler, D., Faust, K., et al. (2022). Personalizing deep brain stimulation using advanced imaging sequences. *Ann. Neurol.* 1–15. doi: 10.1002/ana.26326

Neumann, W. J., Degen, K., Schneider, G. H., Brucke, C., Huebl, J., Brown, P., et al. (2016). Subthalamic synchronized oscillatory activity correlates with motor impairment in patients with Parkinson's disease. *Mov. Disord.* 31, 1748–1751. doi: 10.1002/mds.26759

Neumann, W. J., Staub-Bartelt, F., Horn, A., Schanda, J., Schneider, G. H., Brown, P., et al. (2017). Long term correlation of subthalamic beta band activity with motor impairment in patients with Parkinson's disease. *Clin. Neurophysiol.* 128, 2286–2291. doi: 10.1016/j.clinph.2017.08.028

Nieuwboer, A., Rochester, L., Muncks, L., and Swinnen, S. P. (2009). Motor learning in Parkinson's disease: limitations and potential for rehabilitation. *Parkinsonism Relat. Disord.* 15(Suppl. 3), S53–S58. doi: 10.1016/S1353-8020(09)70781-3

Nilsson, D., Hansson, L. E., Johansson, K., Nystrom, C., Paalzow, L., and Aquilonius, S. M. (1998). Long-term intraduodenal infusion of a water based levodopa-carbidopa dispersion in very advanced Parkinson's disease. *Acta Neurol. Scand.* 97, 175–183. doi: 10.1111/j.1600-0404.1998.tb00633.x

Nishioka, K., and Nakajima, M. (2015). Beneficial Therapeutic effects of spinal cord stimulation in advanced cases of Parkinson's disease with intractable chronic pain: a case series. *Neuromodulation* 18, 751–753. doi: 10.1111/ner.12315

Nissen, M., Ikaheimo, T. M., Huttunen, J., Leinonen, V., and von Und Zu Fraunberg, M. (2019). Long-Term outcome of spinal cord stimulation in failed back surgery syndrome: 20 years of experience with 224 consecutive patients. *Neurosurgery* 84, 1011–1018. doi: 10.1093/neuros/nyy194

Nitsche, M. A., and Paulus, W. (2000). Excitability changes induced in the human motor cortex by weak transcranial direct current stimulation. *J. Physiol.* 527(Pt 3), 633–639. doi: 10.1111/j.1469-7793.2000.t01-1-00633.x

Nolano, M., Provitera, V., Estraneo, A., Selim, M. M., Caporaso, G., Stancanelli, A., et al. (2008). Sensory deficit in Parkinson's disease: evidence of a cutaneous denervation. *Brain* 131(Pt 7), 1903–1911. doi: 10.1093/brain/awn102

Novak, P., and Novak, V. (2006). Effect of step-synchronized vibration stimulation of soles on gait in Parkinson's disease: a pilot study. *J. Neuroeng. Rehabil.* 3:9. doi: 10.1186/1743-0003-3-9

Nyholm, D. (2012). Duodopa(R) treatment for advanced Parkinson's disease: a review of efficacy and safety. *Parkinsonism Relat. Disord.* 18, 916–929. doi: 10.1016/j.parkreldis.2012.06.022

Nyholm, D., and Lennernas, H. (2008). Irregular gastrointestinal drug absorption in Parkinson's disease. *Expert Opin. Drug Metab. Toxicol.* 4, 193–203. doi: 10.1517/17425255.4.2.193

Nyholm, D., Nilsson Remahl, A. I., Dizdar, N., Constantinescu, R., Holmberg, B., Jansson, R., et al. (2005). Duodenal levodopa infusion monotherapy vs oral polypharmacy in advanced Parkinson disease. *Neurology* 64, 216–223. doi: 10.1212/01.WNL.0000149637.70961.4C

Obeso, J. A., Stamelou, M., Goetz, C. G., Poewe, W., Lang, A. E., Weintraub, D., et al. (2017). Past, present, and future of Parkinson's disease: a special essay on the 200th Anniversary of the Shaking Palsy. *Mov. Disord.* 32, 1264–1310. doi: 10.1002/mds.27115

Okada, K. I., Takahira, M., Mano, T., Uga, T., Konaka, K., Hosomi, K., et al. (2021). Concomitant improvement in anti-saccade success rate and postural instability gait difficulty after rTMS treatment for Parkinson's disease. *Sci. Rep.* 11:2472. doi: 10.1038/s41598-021-81795-3

Olanow, C. W., Espay, A. J., Stocchi, F., Ellenbogen, A. L., Leinonen, M., Adar, L., et al. (2021). Continuous subcutaneous levodopa delivery for Parkinson's disease: a randomized study. *J. Parkinsons Dis.* 11, 177–186. doi: 10.3233/JPD-202285

Olanow, C. W., Factor, S. A., Espay, A. J., Hauser, R. A., Shill, H. A., Isaacson, S., et al. (2020). Apomorphine sublingual film for off episodes in Parkinson's disease: a randomised, double-blind, placebo-controlled phase 3 study. *Lancet Neurol.* 19, 135–144. doi: 10.1016/S1474-4422(19)30396-5

Olanow, C. W., Kieburtz, K., Odin, P., Espay, A. J., Standaert, D. G., Fernandez, H. H., et al. (2014). Continuous intrajejunal infusion of levodopa-carbidopa intestinal gel for patients with advanced Parkinson's disease: a randomised, controlled, double-blind, double-dummy study. *Lancet Neurol.* 13, 141–149. doi: 10.1016/S1474-4422(13)70293-X

Ono, S. A., Sato, T., and Muramatsu, S. (2016). Freezing of gait in Parkinson's disease is associated with reduced 6-[(18)F]Fluoro-l-m-tyrosine uptake in the locus coeruleus. *Parkinsons Dis.* 2016:5430920. doi: 10.1155/2016/5430920

Oshinsky, M. L., Murphy, A. L., Hekierski, H. Jr., Cooper, M., and Simon, B. J. (2014). Noninvasive vagus nerve stimulation as treatment for trigeminal allodynia. *Pain* 155, 1037–1042. doi: 10.1016/j.pain.2014.02.009

Pagnussat, A. S., Kleiner, A. F. R., Rieder, C. R. M., Frantz, A., Ehlers, J., Pinto, C., et al. (2018). Plantar stimulation in parkinsonians: from biomarkers to mobility – randomized-controlled trial. *Restor. Neurol. Neurosci.* 36, 195–205. doi: 10.3233/RNN-170744

Pagnussat, A. S., Salazar, A. P., Pinto, C., Redivo Marchese, R., Rieder, C. R. M., Alves Filho, J. O., et al. (2020). Plantar stimulation alters brain connectivity in idiopathic Parkinson's disease. *Acta Neurol. Scand.* 142, 229–238. doi: 10.1111/ane.13253

Pahwa, R., Lyons, K. E., Wilkinson, S. B., Troster, A. I., Overman, J., Kieltyka, J., et al. (2001). Comparison of thalamotomy to deep brain stimulation of the thalamus in essential tremor. *Mov. Disord.* 16, 140–143. doi: 10.1002/1531-8257(200101)16:1<140::aid-mds1025<3.0.co;2-t

Pal, P. K., Samii, A., and Calne, D. B. (2002). "Cardinal features of early Parkinson's disease," in *Parkinson's Disease Diagnosis and Clinical Management*, eds S. Factor and W. J. Weiner (New York, NY: Demos Medical Publishing, Inc), 41–56.

Pascual-Leone, A., Valls-Sole, J., Wassermann, E. M., and Hallett, M. (1994). Responses to rapid-rate transcranial magnetic stimulation of the human motor cortex. *Brain* 117(Pt 4), 847–858. doi: 10.1093/brain/117.4.847

Peppe, A., Paravati, S., Baldassarre, M. G., Bakdounes, L., Spolaor, F., Guiotto, A., et al. (2019). Proprioceptive focal stimulation (Equistasi®) may improve the quality of gait in middle-moderate Parkinson's disease patients. Double-Blind, double-dummy, randomized, crossover, Italian multicentric study. *Front. Neurol.* 10:998. doi: 10.3389/fneur.2019.00998

Pereira, M. P., Gobbi, L. T., and Almeida, Q. J. (2016). Freezing of gait in Parkinson's disease: evidence of sensory rather than attentional mechanisms through muscle vibration. *Parkinsonism Relat. Disord.* 29, 78–82. doi: 10.1016/j.parkreldis.2016.05.021

Perez-Lloret, S., Negre-Pages, L., Damier, P., Delval, A., Derkinderen, P., Destee, A., et al. (2014). Prevalence, determinants, and effect on quality of life of freezing of gait in Parkinson disease. *JAMA Neurol.* 71, 884–890. doi: 10.1001/jamaneurol.2014.753

Pessiglione, M., Guehl, D., Rolland, A. S., Francois, C., Hirsch, E. C., Feger, J., et al. (2005). Thalamic neuronal activity in dopamine-depleted primates: evidence for a loss of functional segregation within basal ganglia circuits. *J. Neurosci.* 25, 1523–1531. doi: 10.1523/JNEUROSCI.4056-04.2005

Peterson, D. S., Pickett, K. A., Duncan, R., Perlmutter, J., and Earhart, G. M. (2014). Gait-related brain activity in people with Parkinson disease with freezing of gait. *PLoS One* 9:e90634. doi: 10.1371/journal.pone.0090634

Piasecki, S. D., and Jefferson, J. W. (2004). Psychiatric complications of deep brain stimulation for Parkinson's disease. *J. Clin. Psychiatry* 65, 845–849. doi: 10.4088/jcp.v65n0617

Pinto, C., Pagnussat, A. S., Rozin Kleiner, A. F., Marchese, R. R., Salazar, A. P., Rieder, C. R. M., et al. (2018). Automated mechanical peripheral stimulation improves gait parameters in subjects with Parkinson disease and freezing of

gait: a randomized clinical trial. *Am. J. Phys. Med. Rehabil.* 97, 383–389. doi: 10.1097/PHM.0000000000000890

Pinto de Souza, C., Hamani, C., Oliveira Souza, C., Lopez Contreras, W. O., Dos Santos Ghilardi, M. G., Cury, R. G., et al. (2017). Spinal cord stimulation improves gait in patients with Parkinson's disease previously treated with deep brain stimulation. *Mov. Disord.* 32, 278–282. doi: 10.1002/mds.26850

Poewe, W., and Mahlknecht, P. (2020). Pharmacologic treatment of motor symptoms associated with Parkinson disease. *Neurol. Clin.* 38, 255–267. doi: 10.1016/j.ncl.2019.12.002

Poewe, W., Stocchi, F., Arkadir, D., Ebersbach, G., Ellenbogen, A. L., Giladi, N., et al. (2021). Subcutaneous levodopa infusion for Parkinson's disease: 1-year data from the open-label BeyoND study. *Mov. Disord.* 36, 2687–2692. doi: 10.1002/mds.28758

Politis, M., Sauerbier, A., Loane, C., Pavese, N., Martin, A., Corcoran, B., et al. (2017). Sustained striatal dopamine levels following intestinal levodopa infusions in Parkinson's disease patients. *Mov. Disord.* 32, 235–240. doi: 10.1002/mds.26848

Popovic Maneski, L., Jorgovanovic, N., Ilic, V., Dosen, S., Keller, T., Popovic, M. B., et al. (2011). Electrical stimulation for the suppression of pathological tremor. *Med. Biol. Eng. Comput.* 49, 1187–1193. doi: 10.1007/s11517-011-0803-6

Prasad, S., Aguirre-Padilla, D. H., Poon, Y. Y., Kalsi-Ryan, S., Lozano, A. M., and Fasano, A. (2020). Spinal cord stimulation for very advanced Parkinson's disease: a 1-year prospective trial. *Mov. Disord.* 35, 1082–1083. doi: 10.1002/mds.28065

Pratorius, B., Kimmeskamp, S., and Milani, T. L. (2003). The sensitivity of the sole of the foot in patients with Morbus Parkinson. *Neurosci. Lett.* 346, 173–176. doi: 10.1016/s0304-3940(03)00582-2

Prusch, J. S., Kleiner, A. F. R., Salazar, A. P., Pinto, C., Marchese, R. R., Galli, M., et al. (2018). Automated mechanical peripheral stimulation and postural control in subjects with Parkinson's disease and freezing of gait: a randomized controlled trial. *Funct. Neurol.* 33, 206–212.

Putzolu, M., Pelosin, E., Ogliastro, C., Lagravinese, G., Bonassi, G., Ravaschio, A., et al. (2018). Anodal tDCS over prefrontal cortex improves dual-task walking in Parkinsonian patients with freezing. *Mov. Disord.* 33, 1972–1973. doi: 10.1002/mds.27533

Qiu, F., Cole, M. H., Davids, K. W., Hennig, E. M., Silburn, P. A., Netscher, H., et al. (2013). Effects of textured insoles on balance in people with Parkinson's disease. *PLoS One* 8:e83309. doi: 10.1371/journal.pone.0083309

Quattrocchi, C. C., de Pandis, M. F., Piervincenzi, C., Galli, M., Melgari, J. M., Salomone, G., et al. (2015). Acute modulation of brain connectivity in Parkinson Disease after automatic mechanical peripheral stimulation: a pilot study. *PLoS One* 10:e0137977. doi: 10.1371/journal.pone.0137977

Rabin, E., Chen, J., Muratori, L., DiFrancisco-Donoghue, J., and Werner, W. G. (2013). Haptic feedback from manual contact improves balance control in people with Parkinson's disease. *Gait Posture* 38, 373–379. doi: 10.1016/j.gaitpost.2012.12.008

Rahimpour, S., Gaztanaga, W., Yadav, A. P., Chang, S. J., Krucoff, M. O., Cajigas, I., et al. (2021). Freezing of gait in Parkinson's disease: invasive and noninvasive neuromodulation. *Neuromodulation* 24, 829–842. doi: 10.1111/ner.13347

Ramot, Y., Nyska, A., Adar, L., Durlach, C., Fishelovitch, D., Sacco, G., et al. (2018). ND0701, a novel formulation of apomorphine for subcutaneous infusion, in comparison to a commercial apomorphine formulation: 28-day pharmacokinetic study in minipigs and a phase I Study in healthy volunteers to assess the safety, tolerability, pharmacokinetics and relative bioavailability. *CNS Drugs* 32, 443–454. doi: 10.1007/s40263-018-0512-x

Reis, C., Arruda, B. S., Pogosyan, A., Brown, P., and Cagnan, H. (2021). Essential tremor amplitude modulation by median nerve stimulation. *Sci. Rep.* 11:17720. doi: 10.1038/s41598-021-96660-6

Riancho-Zarrabeitia, L., and Delgado-Alvarado, M. (2017). Bone health in Parkinson's disease. *Clin. Rev. Bone Miner. Metab.* 15, 99–114. doi: 10.1007/s12018-017-9232-x

Rosenkranz, K., and Rothwell, J. C. (2003). Differential effect of muscle vibration on intracortical inhibitory circuits in humans. *J. Physiol.* 551(Pt 2), 649–660. doi: 10.1113/jphysiol.2003.043752

Rosenthal, L., Sweeney, D., Cunnington, A. L., Quinlan, L. R., and ÓLaighin, G. (2018). Sensory electrical stimulation cueing may reduce freezing of gait episodes in Parkinson's disease. *J. Healthc. Eng.* 2018:4684925. doi: 10.1155/2018/4684925

Sabari, J., Stefanov, D. G., Chan, J., Goed, L., and Starr, J. (2019). Adapted feeding utensils for people with Parkinson's-related or essential tremor. *Am J Occup Ther* 73, 7302205120p1–7302205120p9. doi: 10.5014/ajot.2019.030759

Sage, J. I., Trooskin, S., Sonsalla, P. K., Heikkila, R., and Duvoisin, R. C. (1988). Long-term duodenal infusion of levodopa for motor fluctuations in parkinsonism. *Ann. Neurol.* 24, 87–89. doi: 10.1002/ana.410240116

Sako, W., Miyazaki, Y., Izumi, Y., and Kaji, R. (2014). Which target is best for patients with Parkinson's disease? A meta-analysis of pallidal and subthalamic stimulation. *J. Neurol. Neurosurg. Psychiatry* 85, 982–986. doi: 10.1136/jnnp-2013-306090

Sako, W., Nishio, M., Maruo, T., Shimazu, H., Matsuzaki, K., Tamura, T., et al. (2009). Subthalamic nucleus deep brain stimulation for camptocormia associated with Parkinson's disease. *Mov. Disord.* 24, 1076–1079. doi: 10.1002/mds.22529

Samotus, O., Parrent, A., and Jog, M. (2018). Spinal cord stimulation therapy for gait dysfunction in advanced Parkinson's disease patients. *Mov. Disord.* 33, 783–792. doi: 10.1002/mds.27299

Santana, M. B., Halje, P., Simplicio, H., Richter, U., Freire, M. A. M., Petersson, P., et al. (2014). Spinal cord stimulation alleviates motor deficits in a primate model of Parkinson disease. *Neuron* 84, 716–722. doi: 10.1016/j.neuron.2014.08.061

Santos, L., Olmo-Aguado, S. D., Valenzuela, P. L., Winge, K., Iglesias-Soler, E., Arguelles-Luis, J., et al. (2019). Photobiomodulation in Parkinson's disease: a randomized controlled trial. *Brain Stimul.* 12, 810–812. doi: 10.1016/j.brs.2019.02.009

Sasaki, F., Oyama, G., Sekimoto, S., Nuermaimaiti, M., Iwamuro, H., Shimo, Y., et al. (2021). Closed-loop programming using external responses for deep brain stimulation in Parkinson's disease. *Parkinsonism Relat. Disord.* 84, 47–51. doi: 10.1016/j.parkreldis.2021.01.023

Sayin, S., Cakmur, R., Yener, G. G., Yaka, E., Ugurel, B., and Uzunel, F. (2014). Low-frequency repetitive transcranial magnetic stimulation for dyskinesia and motor performance in Parkinson's disease. *J. Clin. Neurosci.* 21, 1373–1376. doi: 10.1016/j.jocn.2013.11.025

Schabrun, S. M., Lamont, R. M., and Brauer, S. G. (2016). Transcranial direct current stimulation to enhance dual-task gait training in Parkinson's disease: a pilot RCT. *PLoS One* 11:e0158497. doi: 10.1371/journal.pone.0158497

Schlick, C., Ernst, A., Botzel, K., Plate, A., Pelykh, O., and Ilmberger, J. (2016). Visual cues combined with treadmill training to improve gait performance in Parkinson's disease: a pilot randomized controlled trial. *Clin. Rehabil.* 30, 463–471. doi: 10.1177/0269215515588836

Schoellmann, A., Scholten, M., Wasserka, B., Govindan, R. B., Kruger, R., Gharabaghi, A., et al. (2019). Anodal tDCS modulates cortical activity and synchronization in Parkinson's disease depending on motor processing. *Neuroimage Clin.* 22:101689. doi: 10.1016/j.nicl.2019.101689

Schupbach, W. M. M., Chabardes, S., Matthies, C., Pollo, C., Steigerwald, F., Timmermann, L., et al. (2017). Directional leads for deep brain stimulation: opportunities and challenges. *Mov. Disord.* 32, 1371–1375. doi: 10.1002/mds.27096

Serio, F., Minosa, C., De Luca, M., Conte, P., Albani, G., and Peppe, A. (2019). Focal vibration training (Equistasi[§]) to improve posture stability. a retrospective study in Parkinson's disease. *Sensors (Basel)* 19:2101. doi: 10.3390/s19092101

Shanker, V. (2019). Essential tremor: diagnosis and management. *BMJ* 366, l4485. doi: 10.1136/bmj.l4485

Shima, K., Shimatani, K., and Sakata, M. (2021). A wearable light-touch contact device for human balance support. *Sci. Rep.* 11:7324. doi: 10.1038/s41598-021-85687-4

Shine, J. M., Matar, E., Ward, P. B., Bolitho, S. J., Pearson, M., Naismith, S. L., et al. (2013). Differential neural activation patterns in patients with Parkinson's disease and freezing of gait in response to concurrent cognitive and motor load. *PLoS One* 8:e52602. doi: 10.1371/journal.pone.0052602

Shirota, Y., Ohtsu, H., Hamada, M., Enomoto, H., Ugawa, Y., and Research Committee on rTMS Treatment of Parkinson's Disease (2013). Supplementary motor area stimulation for Parkinson disease: a randomized controlled study. *Neurology* 80, 1400–1405. doi: 10.1212/WNL.0b013e31828c2f66

Shon, Y. M., Chang, S. Y., Tye, S. J., Kimble, C. J., Bennet, K. E., Blaha, C. D., et al. (2010). Comonitoring of adenosine and dopamine using the wireless

instantaneous neurotransmitter concentration system: proof of principle. *J. Neurosurg.* 112, 539–548. doi: 10.3171/2009.7.JNS09787

Slevin, J. T., Fernandez, H. H., Zadikoff, C., Hall, C., Eaton, S., Dubow, J., et al. (2015). Long-term safety and maintenance of efficacy of levodopa-carbidopa intestinal gel: an open-label extension of the double-blind pivotal study in advanced Parkinson's disease patients. *J. Parkinsons Dis.* 5, 165–174. doi: 10.3233/JPD-140456

Snijders, A. H., Leunissen, I., Bakker, M., Overeem, S., Helmich, R. C., Bloem, B. R., et al. (2011). Gait-related cerebral alterations in patients with Parkinson's disease with freezing of gait. *Brain* 134(Pt 1), 59–72. doi: 10.1093/brain/awq324

Sorensen, K. L., Hollands, M. A., and Patla, E. (2002). The effects of human ankle muscle vibration on posture and balance during adaptive locomotion. *Exp. Brain Res.* 143, 24–34. doi: 10.1007/s00221-001-0962-z

Spagnolo, F., Fichera, M., Chieffo, R., Dalla Costa, G., Pisa, M., Volonte, M. A., et al. (2020). Bilateral repetitive transcranial magnetic stimulation with the H-Coil in Parkinson's disease: a randomized, sham-controlled study. *Front. Neurol.* 11:584713. doi: 10.3389/fneur.2020.584713

Spildooren, J., Vercruysse, S., Heremans, E., Galna, B., Verheyden, G., Vervoort, G., et al. (2017). Influence of cueing and an attentional strategy on freezing of gait in parkinson disease during turning. *J. Neurol. Phys. Ther.* 41, 129–135. doi: 10.1097/NPT.0000000000000178

Spildooren, J., Vercruysse, S., Meyns, P., Vandenbossche, J., Heremans, E., Desloovere, K., et al. (2012). Turning and unilateral cueing in Parkinson's disease patients with and without freezing of gait. *Neuroscience* 207, 298–306. doi: 10.1016/j.neuroscience.2012.01.024

Spolaor, F., Romanato, M., Annamaria, G., Peppe, A., Bakdounes, L., To, D. K., et al. (2021). Relationship between muscular activity and postural control changes after proprioceptive focal stimulation (Equistasi[§]) in middle-moderate Parkinson's disease patients: an explorative study. *Sensors (Basel)* 21:560. doi: 10.3390/s21020560

Stocchi, F., Sale, P., Kleiner, A. F., Casali, M., Cimolin, V., de Pandis, F., et al. (2015). Long-term effects of automated mechanical peripheral stimulation on gait patterns of patients with Parkinson's disease. *Int. J. Rehabil. Res.* 38, 238–245. doi: 10.1097/MRR.0000000000000120

Swank, C., Mehta, J., and Criminger, C. (2016). Transcranial direct current stimulation lessens dual task cost in people with Parkinson's disease. *Neurosci. Lett.* 626, 1–5. doi: 10.1016/j.neulet.2016.05.010

Syrkin-Nikolau, J., Neuville, R., O'Day, J., Anidi, C., Miller Koop, M., Martin, T., et al. (2018). Coordinated reset vibrotactile stimulation shows prolonged improvement in Parkinson's disease. *Mov. Disord.* 33, 179–180. doi: 10.1002/mds.27223

Takanokura, M., Sugahara, R., Miyake, N., Ishiguro, K., Muto, T., and Sakamoto, K. (2011). "Upper-limb orthoses implemented with airdashpot for suppression of a pathological tremor in daily activities," in *Proceedings of the ISB Conference*, Brussels.

Tan, T., Almeida, Q. J., and Rahimi, F. (2011). Proprioceptive deficits in Parkinson's disease patients with freezing of gait. *Neuroscience* 192, 746–752. doi: 10.1016/j.neuroscience.2011.06.071

Tan, X. S., Pierres, F., Dallman-Porter, A., Hardie-Brown, W., and Kwon, K. Y. (2021). Focused vibrotactile stimulation with cueing effect on freezing of gait in Parkinson's disease: two case reports. *J. Mov. Disord.* 14, 236–238. doi: 10.14802/jmd.21076

Tanaka, T., Takano, Y., Tanaka, S., Hironaka, N., Kobayashi, K., Hanakawa, T., et al. (2013). Transcranial direct-current stimulation increases extracellular dopamine levels in the rat striatum. *Front. Syst. Neurosci.* 7:6. doi: 10.3389/fnsys.2013.00006

Tang, L., Xu, W., Li, Z., Chen, Y., Chen, H., Yu, R., et al. (2019). Quantitative gait analysis for laser cue in Parkinson's disease patients with freezing of gait. *Ann. Transl. Med.* 7:324. doi: 10.21037/atm.2019.05.87

Tasker, R. R. (1998). Deep brain stimulation is preferable to thalamotomy for tremor suppression. *Surg. Neurol.* 49, 145–53; discussion153–4. doi: 10.1016/s0090-3019(97)00459-x

Taylor, P. N., Sampson, T., Beare, B., Donavon-Hall, M., Thomas, P. W., Marques, E., et al. (2021). The effectiveness of peroneal nerve functional electrical simulation for the reduction of bradykinesia in Parkinson's disease: a feasibility study for a randomised control trial. *Clin. Rehabil.* 35, 546–557. doi: 10.1177/0269215520972519

Terao, Y., Fukuda, H., Ugawa, Y., and Hikosaka, O. (2013). New perspectives on the pathophysiology of Parkinson's disease as assessed by saccade performance: a clinical review. *Clin. Neurophysiol.* 124, 1491–1506. doi: 10.1016/j.clinph.2013.01.021

Terry, R. S. Jr. (2014). "Vagus nerve stimulation therapy for epilepsy," in *Epilepsy Topics*, ed. M. D. Holms (London: InTech), 139–160. doi: 10.5772/58332

Thevathasan, W., Mazzone, P., Jha, A., Djamshidian, A., Dileone, M., Di Lazzaro, V., et al. (2010). Spinal cord stimulation failed to relieve akinesia or restore locomotion in Parkinson disease. *Neurology* 74, 1325–1327. doi: 10.1212/WNL.0b013e3181d9ed58

Titova, N., and Chaudhuri, K. R. (2016). Apomorphine therapy in Parkinson's and future directions. *Parkinsonism Relat. Disord.* 33(Suppl. 1), S56–S60. doi: 10.1016/j.parkreldis.2016.11.013

Valentino, F., Cosentino, G., Brighina, F., Pozzi, N. G., Sandrini, G., Fierro, B., et al. (2014). Transcranial direct current stimulation for treatment of freezing of gait: a cross-over study. *Mov. Disord.* 29, 1064–1069. doi: 10.1002/mds.25897

van Laar, T. (2003). Levodopa-induced response fluctuations in patients with Parkinson's disease: strategies for management. *CNS Drugs* 17, 475–489. doi: 10.2165/00023210-200317070-00002

Vercruysse, S., Gilat, M., Shine, J. M., Heremans, E., Lewis, S., and Nieuwboer, A. (2014). Freezing beyond gait in Parkinson's disease: a review of current neurobehavioral evidence. *Neurosci. Biobehav. Rev.* 43, 213–227. doi: 10.1016/j.neubiorev.2014.04.010

Vercruysse, S., Spildooren, J., Heremans, E., Vandenbossche, J., Wenderoth, N., Swinnen, S. P., et al. (2012). Abnormalities and cue dependence of rhythmical upper-limb movements in Parkinson patients with freezing of gait. *Neurorehabil. Neural Repair.* 26, 636–645. doi: 10.1177/1545968311431964

Volpe, D., Giantin, M. G., and Fasano, A. (2014). A wearable proprioceptive stabilizer (Equistasi[§]) for rehabilitation of postural instability in Parkinson's disease: a phase II randomized double-blind, double-dummy, controlled study. *PLoS One* 9:e112065. doi: 10.1371/journal.pone.0112065

Walton, C. C., Shine, J. M., Hall, J. M., O'Callaghan, C., Mowszowski, L., Gilat, M., et al. (2015). The major impact of freezing of gait on quality of life in Parkinson's disease. *J. Neurol.* 262, 108–115. doi: 10.1007/s00415-014-7524-3

Wang, L., Li, J., and Chen, J. (2018). Levodopa-carbidopa intestinal gel in Parkinson's disease: a systematic review and meta-analysis. *Front. Neurol.* 9:620. doi: 10.3389/fneur.2018.00620

Wojtecki, L., Vesper, J., and Schnitzler, A. (2011). Interleaving programming of subthalamic deep brain stimulation to reduce side effects with good motor outcome in a patient with Parkinson's disease. *Parkinsonism Relat. Disord.* 17, 293–294. doi: 10.1016/j.parkreldis.2010.12.005

Xu, J., Wang, J., Keith, S., Zhang, M., Yang, C., Yuan, Q., et al. (2021). Management of Parkinson's disease patients after DBS by remote programming: preliminary application of single center during quarantine of 2019-nCoV. *J. Neurol.* 268, 1295–1303. doi: 10.1007/s00415-020-10273-z

Yang, Y. R., Tseng, C. Y., Chiou, S. Y., Liao, K. K., Cheng, S. J., Lai, K. L., et al. (2013). Combination of rTMS and treadmill training modulates corticomotor inhibition and improves walking in Parkinson disease: a randomized trial. *Neurorehabil. Neural Repair.* 27, 79–86. doi: 10.1177/1545968312451915

Yogev, G., Giladi, N., Peretz, C., Springer, S., Simon, E. S., and Hausdorff, J. M. (2005). Dual tasking, gait rhythmicity, and Parkinson's disease: which aspects of gait are attention demanding? *Eur. J. Neurosci.* 22, 1248–1256. doi: 10.1111/j.1460-9568.2005.04298.x

Yokoe, M., Mano, T., Maruo, T., Hosomi, K., Shimokawa, T., Kishima, H., et al. (2018). The optimal stimulation site for high-frequency repetitive transcranial magnetic stimulation in Parkinson's disease: a double-blind crossover pilot study. *J. Clin. Neurosci.* 47, 72–78. doi: 10.1016/j.jocn.2017.09.023

Yotnuengnit, P., Bhidayasiri, R., Donkhan, R., Chaluaysrimuang, J., and Piravej, K. (2018). Effects of transcranial direct current stimulation plus physical therapy on gait in patients with Parkinson disease: a randomized controlled trial. *Am. J. Phys. Med. Rehabil.* 97, 7–15. doi: 10.1097/PHM.0000000000000783

Yu, J. Y., Rajagopal, A., Syrkin-Nikolau, J., Shin, S., Rosenbluth, K. H., Khosla, D., et al. (2020). Transcutaneous afferent patterned stimulation therapy reduces

hand tremor for one hour in essential tremor patients. *Front. Neurosci.* 14:530300. doi: 10.3389/fnins.2020.530300

Yuan, H., and Silberstein, S. D. (2016). Vagus nerve and vagus nerve stimulation, a comprehensive review: part II. *Headache* 56, 259–266. doi: 10.1111/head.12650

Zanjani, A., Zakzanis, K. K., Daskalakis, Z. J., and Chen, R. (2015). Repetitive transcranial magnetic stimulation of the primary motor cortex in the treatment of motor signs in Parkinson's disease: a quantitative review of the literature. *Mov. Disord.* 30, 750–758. doi: 10.1002/mds.26206

Zehr, E. P., and Haridas, C. (2003). Modulation of cutaneous reflexes in arm muscles during walking: further evidence of similar control mechanisms for rhythmic human arm and leg movements. *Exp. Brain Res.* 149, 260–266. doi: 10.1007/s00221-003-1377-9

Zesiewicz, T. A., Elble, R. J., Louis, E. D., Gronseth, G. S., Ondo, W. G., Dewey, R. B. Jr., et al. (2011). Evidence-based guideline update: treatment of essential tremor: report of the quality standards subcommittee of the American Academy of Neurology. *Neurology* 77, 1752–1755. doi: 10.1212/WNL.0b013e318236f0fd

Zhang, J., Hu, W., Chen, H., Meng, F., Li, L., and Okun, M. S. (2020). Implementation of a novel bluetooth technology for remote deep brain stimulation programming: the pre- and post-COVID-19 Beijing experience. *Mov. Disord.* 35, 909–910. doi: 10.1002/mds.28098

Zhao, Y., Nonnekes, J., Storcken, E. J., Janssen, S., van Wegen, E. E., Bloem, B. R., et al. (2016). Feasibility of external rhythmic cueing with the Google Glass for improving gait in people with Parkinson's disease. *J. Neurol.* 263, 1156–1165. doi: 10.1007/s00415-016-8115-2

Zhuang, S., Wang, F. Y., Gu, X., Wu, J. J., Mao, C. J., Gui, H., et al. (2020). Low-frequency repetitive transcranial magnetic stimulation over right dorsolateral prefrontal cortex in Parkinson's disease. *Parkinsons Dis.* 2020:7295414. doi: 10.1155/2020/7295414

Conflict of Interest: The authors declare that the research was conducted in the absence of any commercial or financial relationships that could be construed as a potential conflict of interest.

Publisher's Note: All claims expressed in this article are solely those of the authors and do not necessarily represent those of their affiliated organizations, or those of the publisher, the editors and the reviewers. Any product that may be evaluated in this article, or claim that may be made by its manufacturer, is not guaranteed or endorsed by the publisher.

Copyright © 2022 Fujikawa, Morigaki, Yamamoto, Oda, Nakanishi, Izumi and Takagi. This is an open-access article distributed under the terms of the Creative Commons Attribution License (CC BY). The use, distribution or reproduction in other forums is permitted, provided the original author(s) and the copyright owner(s) are credited and that the original publication in this journal is cited, in accordance with accepted academic practice. No use, distribution or reproduction is permitted which does not comply with these terms.

frontiers | Frontiers in Aging Neuroscience

CASE REPORT
published: 01 April 2022
doi: 10.3389/fnagi.2022.809972

Directional DBS of the Fornix in Alzheimer's Disease Achieves Long-Term Benefits: A Case Report

*Juan A. Barcia[1†], María Aurora Viloria[2†], Raquel Yubero[3,4], Leyre Sanchez-Sanchez-Rojas[5,6], Amanda López[7,8], Bryan Andrew Strange[9], María Cabrera[10], Leonides Canuet[11], Pedro Gil[2] and Cristina Nombela[5,12]**

[1] Departamento de Cirugía, Facultad de Medicina, Servicio de Neurocirugía, Hospital Clínico San Carlos, Universidad Complutense de Madrid, IdISSC, Madrid, Spain, [2] Departamento de Medicina, Facultad de Medicina, Servicio de Geriatría, Hospital Clínico San Carlos, Universidad Complutense de Madrid, IdISSC, Madrid, Spain, [3] Departamento de Neurología, Hospital Quirón Salud, Madrid, Spain, [4] Universidad Pontificia de Comillas, Madrid, Spain, [5] Grupo de Investigación en Neurociencias Aplicadas, Hospital Clínico San Carlos, IdISSC, Madrid, Spain, [6] Departamento de Medicamentos Veterinarios, Agencia Española del Medicamento y Producto Sanitario, Madrid, Spain, [7] Unidad de Investigación y Ensayos Clínicos, Instituto de Investigación Sanitaria Hospital Clínico San Carlos, Madrid, Spain, [8] Facultad de Salud, Universidad Internacional de la Rioja, Logroño, Spain, [9] Laboratory for Clinical Neuroscience, Centro de Tecnología Biomédica, Universidad Politécnica de Madrid, Campus de Montegancedo, Madrid, Spain, [10] Servicio de Medicina Nuclear, Hospital Clínico San Carlos, IdISSC, Madrid, Spain, [11] Departamento de Neurología, Hospital Nuestra Señora del Rosario, Madrid, Spain, [12] Departamento de Psicología Biológica y de la Salud, Facultad de Psicología, Universidad Autónoma de Madrid, Madrid, Spain

Background: Current treatments for Alzheimer's disease (AD) modulate global neurotransmission but are neither specific nor anatomically directed. Tailored stimulation of target nuclei will increase treatment efficacy while reducing side effects. We report the results of the first directional deep brain stimulation (dDBS) surgery and treatment of a patient with AD in an attempt to slow the progression of the disease in a woman with multi-domain, amnestic cognitive status.

Methods: We aimed to assess the safety of dDBS in patients with AD using the fornix as stimulation target (primary objective) and the clinical impact of the stimulation (secondary objective). In a registered clinical trial, a female patient aged 81 years with a 2-year history of cognitive decline and diagnoses of AD underwent a bilateral dDBS surgery targeting the fornix. Stimulation parameters were set between 3.9 and 7.5 mA, 90 μs, 130 Hz for 24 months, controlling stimulation effects by 18F-fluoro-2-deoxy-D-glucose (18F-FDG) scans (baseline, 12 and 24 months), magnetoencephalography (MEG) and clinical/neuropsychological assessment (baseline, 6, 12, 18, and 24 months).

Results: There were no important complications related to the procedure. In general terms, the patient showed cognitive fluctuations over the period, related to attention and executive function patterns, with no meaningful changes in any other cognitive functions, as is shown in the clinical dementia rating scale (CDR = 1) scores over the 24 months. Such stability in neuropsychological scores corresponds to the stability of the brain metabolic function, seen in PET scans. The MEG studies described low functional connectivity at baseline and a subsequent increase in the number of significant connections, mainly in the theta band, at 12 months.

OPEN ACCESS

Edited by:
Chih-Yu Hsu,
Fujian University of Technology, China

Reviewed by:
Hugo Geerts,
Certara UK Limited, United Kingdom
Jin San Lee,
Kyung Hee University, South Korea

***Correspondence:**
Cristina Nombela
cristina.nombela@uam.es

[†] These authors have contributed equally to this work and share first authorship

Specialty section:
This article was submitted to Alzheimer's Disease and Related Dementias, a section of the journal Frontiers in Aging Neuroscience

Received: *05 November 2021*
Accepted: *17 January 2022*
Published: *01 April 2022*

Citation:
Barcia JA, Viloria MA, Yubero R, Sanchez-Sanchez-Rojas L, López A, Strange BA, Cabrera M, Canuet L, Gil P and Nombela C (2022) Directional DBS of the Fornix in Alzheimer's Disease Achieves Long-Term Benefits: A Case Report. Front. Aging Neurosci. 14:809972. doi: 10.3389/fnagi.2022.809972

Conclusion: The dDBS stimulation in the fornix seems to be a safe treatment for patients in the first stage of AD. Effects on cognition seem to be mild to moderate during the first months of stimulation and return to baseline levels after 24 months, except for verbal fluency.

Clinical Trial Registration: [https://clinicaltrials.gov/ct2/show/NCT03290274], identifier [NCT03290274].

Keywords: Alzheimer's disease, directional deep brain stimulation, fornix (brain), clinical trial, neuropsychology

INTRODUCTION

According to the WHO, approximately 50 million people have Alzheimer's disease (AD) or other dementias worldwide, and this figure is expected to increase three times by 2050 (Hebert et al., 2003; Brookmeyer et al., 2011). AD is a neurodegenerative disorder with cortical and subcortical features, altering the circuits involved in cognitive functions such as memory and attention, among others. Until now, advances in early diagnosis and pharmacological treatment have not led to a significant change in the prognosis of AD (Jakobs et al., 2020). Current therapies modulate neurotransmission and alleviate some symptoms, increasing the quality of life of patients and relatives, but they do not really modify the course of the disease. The tendency to study personalised treatments aims to provide anatomically directed therapies (De Matteis et al., 2018). Therefore, it is necessary to propose alternative approaches, such as deep brain stimulation (DBS), a technique that allows us to modulate the activity of the affected areas to normalise their function. This technique has shown a greater efficacy and safety in other disorders typical of elderly patients, such as Parkinson's disease.

Just a few nuclei may work as candidates for DBS stimulation, one of which is the fornix (Senova et al., 2020). The fornix is a voluminous axonal tract that constitutes the main route of entry and exit of information to the hippocampus and the medial temporal lobe (Jakobs et al., 2020). In 2010, a phase I trial targeted the fornix in 6 patients with mild AD. After a 1-year follow-up, there were improvements in glucose metabolism levels and a slowdown in the progression of general cognitive impairment, memory in particular (Laxton et al., 2010). A later study observed stability at the cognitive level and enhanced glucose metabolism in the mesial temporal area after 12 months of stimulation in the fornix in a patient with mild cognitive impairment (Fontaine et al., 2013; Fontaine and Santucci, 2021). Another phase II clinical trial ($n = 42$ patients) demonstrated the safety of the treatment. The results indicated that efficacy varied with age: patients under 65 had a marked worsening after 1 year of stimulation. In contrast, those over 65 years of age showed a slight improvement in the cognitive sphere (Lozano et al., 2016). Similar results appeared in a later study (Targum et al., 2021).

From the methodological point of view, technical advances provide significant improvements in DBS. Although advanced stimulation offered a real-time adaptation of the stimulation provided, directional DBS (dDBS) allows more accuracy. The radially segmented design of directional electrodes reduces side effects by personalising the stimulation area: delivering either a perpendicular field or a shaped one using anodes and cathodes to steer stimulation in a particular direction (Liu et al., 2020). The use of directional electrodes targetting the fornix and rechargeable batteries in patients with AD has not yet been reported.

This study aimed to assess the safety of dDBS stimulation in the fornix in a patient with mild AD (primary objective) and (secondary objective) to assess the effects of the treatment. For the latter, we evaluated the changes at metabolic, functional, and neuropsychological levels for 24 months.

This case study is part of a clinical trial designed to assess the safety and test the effect of dDBS stimulation in either fornix or the nucleus basalis of Meynert (NBM). The case reported corresponds to patient 1, who underwent a fornix dDBS surgery. There were no other patients involved in the study.

MATERIALS AND METHODS

The patient was selected in the context of a clinical trial to assess the effect of deep brain stimulation in Alzheimert's disease Estimulación Cerebral Profunda en Enfermedad de Alzheimer (ECP-EA) at the Hospital Clínico San Carlos (Madrid, Spain). Inclusion criteria for this clinical trial were (i) age between 50 and 80 years; (ii) AD diagnosis (Dubois et al., 2016) established by a specialist within the past 12 months; (iii) positive amyloid PET scan; (iv) Mini-Mental State Exam (MMSE) score between 20 and 26 points inclusive; (v) clinical dementia rating (CDR) scale score of 1; (vi) use of cholinesterase inhibitors or memantine for 1 year at least, and deterioration in the MMSE and Alzheimer's Disease Assessment Scale-Cognitive Subscale (ADAS-Cog) scores; (vii) absence of delusions, hallucinations or other psychiatric disorders, no neurological findings, no significant concurrent medical illness, including hypertension (rated as moderate or severe) and no history of stroke or cerebral vascular disease; and (viii) patient willing and able to provide consent. The study had approval from the Hospital Clínico San Carlos Ethics Committee (code: ECP-EA - CI 13/448). The study is registered at clinicaltrials.gov under the trial name "Clinical Trial to Evaluate the Efficacy and Security of Deep Brain Stimulation in Alzheimer's Disease (ECP-EA)," registration number: NCT03290274 (https://clinicaltrials.gov/ct2/show/NCT03290274).

Case Presentation

A female patient aged 81 years diagnosed with AD joined the NCT03290274–ECP-EA clinical trial in 2017. She was diagnosed with AD 1 year earlier (2016), presenting recent memory loss, space disorientation, lack of attention, and difficulties in decision-making.

The participant was right-handed and had 8 years of official education. Her medical history was notable for high blood pressure, deep vein thrombosis in the lower-left limb, hiatal hernia, and cataract surgery. After diagnosis, the participant started a regimen of donepezil 10 mg, omeprazole 20 mg, losartan 50 mg, and simvastatin 40 mg. Family history was negative for AD.

At the medical history screening visit, a review was conducted of all previous diagnostic tests, neuropsychological assessments, and specific assessments for dementia (see below). On that visit, the patient signed the informed consent form and received a copy. The baseline assessments (1 week before surgery) included a physical examination, vital signs (blood pressure, pulse, and temperature), and complete blood count with differential and comprehensive metabolic panel, electrocardiogram, chest X-ray, and neuroimaging scans, such as magnetoencephalography (MEG), magnetic resonance imaging (MRI) with diffusion tensor imaging, 18F-fluoro-2-deoxy-D-glucose PET (18F-FDG-PET) and amyloid-β PET scans. The electrocardiogram showed sinus rhythm (70 bpm) and isolated supraventricular extrasystoles. Brain MRI indicated moderate cerebral and temporal medial atrophy, and amyloid-β PET was positive for amyloid deposits. The MEG study showed a somewhat disconnected brain, dominated mainly by few, relatively weak, connections, especially in both temporal regions. All data were compatible with AD diagnoses.

Assessment Procedures

The patient underwent a specific assessment for AD, using the MMSE (Folstein et al., 1975), the CDR (Morris, 1997), and the ADAS-Cog (Rosen et al., 1984) to evaluate the cognitive changes over time.

The patient also underwent an extensive neuropsychological assessment to explore her cognitive performance, including verbal memory, working memory, processing speed, and executive and attentional functions. The neuropsychological assessment included the Word List Test from the Wechsler Memory Scale (WMS) (Weschler, 2008), Direct and Reverse Digit Span, Symbol Digit from WAIS-IV (Weschler, 2008), Trail Making Test Parts A (TMT-A) and B (TMT-B) (Reitan and Wolfson, 1993), and Phonological Verbal Fluencies from the Controlled Oral Word Association Test (COWAT) (Loonstra et al., 2001) and Semantic Verbal Fluency (Benton, 1968). Scores for the neuropsychological assessment at baseline and along the two-years follow up is available in **Table 1**. Before surgery, structural and functional data were acquired on a 3T Siemens TRIO system (Siemens, Erlangen, Germany). A standard eight-channel head coil was used to acquire MPRAGE T1-weighted anatomical images with 1 mm^3 resolution [repetition time (TR), 2,300 ms; echo time (TE), 2.98 ms; flip angle, 9°] and diffusion-weighted images. White matter connectivity was quantified using probabilistic tractography with FDT Probtrackx 2.0 (Behrens et al., 2007).

The neuroimaging assessment also included an 18F-FDG-PET scan. PET images were generated using a PET-CT Siemens Biograph True Point platform integrating a 6-slice detector with the latest-generation PET scanner featuring a lutetium oxyorthosilicate crystal array. Static amyloid PET-CT images were acquired 90 min after intravenous injection of 216 MBq of 18F-florbetaben. Acquisition time was 15 min. The patient fasted a minimum of 6 h before the 18-FDG-PET scans. FDG (mean dose: 185 MBq) was administered intravenously 30 min before images were taken. During this time, the patient rested in a dark room with her eyes closed. Glucose levels had been checked previously and found to be lower than 150 mg/dl.

Magnetoencephalography was conducted using a 306-channel Elekta Neuromag® (Elekta Oy, Helsinki, Finland). The data ranging from 1 to 45 Hz were filtered by removing ocular and cardiac artefacts were removed by the independent component analysis (ICA) method. The signal was decomposed into functionally distinct frequency bands, such as delta (1–4 Hz), theta (4–8 Hz), alpha (8–12 Hz), beta (12–30 Hz), and gamma (30–45 Hz). Contemporarily, the cortex surface was divided into 68 regions of interest (ROIs) based on the Brainstorm default atlas (Desikan et al., 2006). The time series of each ROI was extracted by taking the average of all the signals coming from the dipoles of that region. With the aim of measuring functional connectivity between all pairs of regions (68×68) for each frequency band (Lachaux et al., 1999), the time series of the sources were extracted with the phase-locking value (PLV) algorithm. Details of the assessment timeline appear in **Figure 1**.

Therapeutic Intervention

Presurgery

On the day before the operation, a volumetric CT scan (Philips® Brilliance 64 CT Scanner) was performed in hospital and fused with contrast-enhanced T1 MR and T2 volumetric images. The process included a 3T MRI and CT for navigation planning, presurgery. Initially, the columns of both fornices were identified and a target was selected, 2 mm anterior and parallel to the vertical portion of the fornix. The most ventral contact was located 2 mm above the dorsal surface of the optic tract, approximately 5 mm from the midline.

Surgery

The Vercise Cartesia Directional Leads (Boston Scientific®, Iberica) for dDBS were implanted under NeuroNavigator and fluoroscopic control in the awake patient. Then, intraoperative stimulation was applied to identify beneficial or adverse effects, including unpleasant sensations (sweating, hallucinations, visual sensations, or paraesthesia). Later, a subcutaneous pulse generator (M365DB12000 Vercise™ Gevia System) was implanted in the abdomen, together with subcutaneous connections from the electrodes to the generator under general anaesthesia. A brain CT scan was performed to rule out complications (pneumocephalus or bleeding) on the day of surgery. On the day after surgery, another CT scan was performed to confirm the correct location of the electrodes.

TABLE 1 | Neuropsychological and clinical scores during the study.

		Pre-Surgery	Follow-up			
TESTS	**Subscales**	**Time 0**	**6 months**	**12 months**	**18 months**	**24 months**
ADAS-Cog	Word Recall Task	17	17	16	18	17
	Following Commands	0	0	0	4	0
	Constructional Praxis	3	2	2	1	1
	DelayWordRecal	7	10	10	10	9
	Naming Objects	0	0	0	0	0
	Ideational Praxis	2	1	2	1	2
	Orientation	2	2	6	3	7
	Word Recognition	4	10	10	12	10
	Remembering Direc	0	1	0	0	0
	Spoken Language	0	0	0	0	0
	Word-Finding Difficulty	1	2	2	1	0
	Comprehension	0	0	0	0	1
	Concentration	1	0	1	1	0
	TOTAL	37	45	49	51	47
	TOTAL	37	45	49	51	47
Maze ADAS-Cog	Secs	14	9	5	6	20
	Error	0	0	0	0	0
Cancelation ADAS-Cog	Correct	20	22	16	15	18
	Error	0	0	0	0	0
MMSE	Orientation	7	7	5	6	3
	Fixation	3	3	3	3	3
	Attention & calculation	1	5	4	5	5
	Memory	2	0	0	0	0
	Language	8	9	8	7	8
	total	19	24	18	19	17
WMS	Learning	20; Pe 11	25; Pe 10	20; Pe 8	15; Pe 6	17; Pe 7
	Immediate Memory	5	3	2	0	2
	Long Term Memory	0; Pe 6	0; Pe 6	0; Pe 6	0; Pe 6	0; Pe 6
	Recognition	12; Pe 4	16; Pe 6	14; Pe 5	4; Pe 2	15; Pe 5
Phonological	Average	8	10	9	10	10
Fluency	F	10	8	9	11	10
	A	6; Pc 41-51	15; Pc 98	9; Pc 72-81	10; Pc 82-89	10; Pc 82-89
	S	9; Pc41-59	8; Pc 41-59	10; Pc 41-59	10; Pc 41-59	11; PC 90-92
Semantic		7	9	8	10	8
Fluency	Animals	6; Pc<1	9; Pc 3-5	8; Pc 2	12; Pc 11-18	n/a
	Fruits	7	9	7	10	8
Digit Span	Forwards	6; Pc 82-89	6; Pc 82-89	5; Pc 41-59	6; Pc 82-89	6; Pc 82-89
	Backwards	4; Pc 72-81	5; Pc 90-94	4; Pc 72-81	5; Pc 90-94	4; Pc 72-81
Letter-Number WAIS		3	3	3		3
Coding	Score	31; Pc 60-71	28; Pc41-59	37; Pc 72-81	n/a	n/a
	Error	0	0	0	n/a	n/a
Symbol Search	Score	17	20	17	n/a	n/a
	Error	2	0	1	n/a	n/a
TMT	A-Time	68; Pc 29-40	62; Pc 41-59	47; Pc 60-71	55; Pc 41-59	68; Pc 29-40
	A-Error	0	0	0	0	0
	B-Time	151;Pc 29-40	120;Pc41-59	208; Pc 19-28	150; Pc 29-40	95; Pc 72-81
	B-Error	1	4	4	3	7
CDR-Clinical Dementia Rating		1	1	1	1	1

These tests were standardised in a Spanish population, and values provided stand for raw scores and percentile scores (right-hand side of the cell). For Wechsler Memory Scale (WMS), values provided stand for raw scores and standardised scores (not percentiles). "n/a" stands for missing values.

Postsurgery

The patient was monitored in the intensive care unit for 24 h after the operation. Subsequently, the patient was shifted to the ward and monitored for 3 days before being discharged without significant events. At 1 week after the surgery, monopolar stimulation therapy was started in the bilateral fornix at threshold intensity (90 μs, 130 Hz) to verify the presence of side effects. Then, stimulation was monopolar, the 2 negative distal electrodes and the positive casing, as follows: a) right hemisphere, 7.5 mA: contacts 2 (–30%), 4 (–30%), 5 (–20%), 7 (–20%) and housing positive (+ 100%); b) left hemisphere, 3.9 mA: contacts 4 (30%), 5 (–70%) and housing positive (+ 100%). For more details, see **Figure 1**.

At 1 month after discharge, the patient was admitted to neurosurgery for suspected infection from an implanted dDBS device. An urgent chest ultrasound revealed a

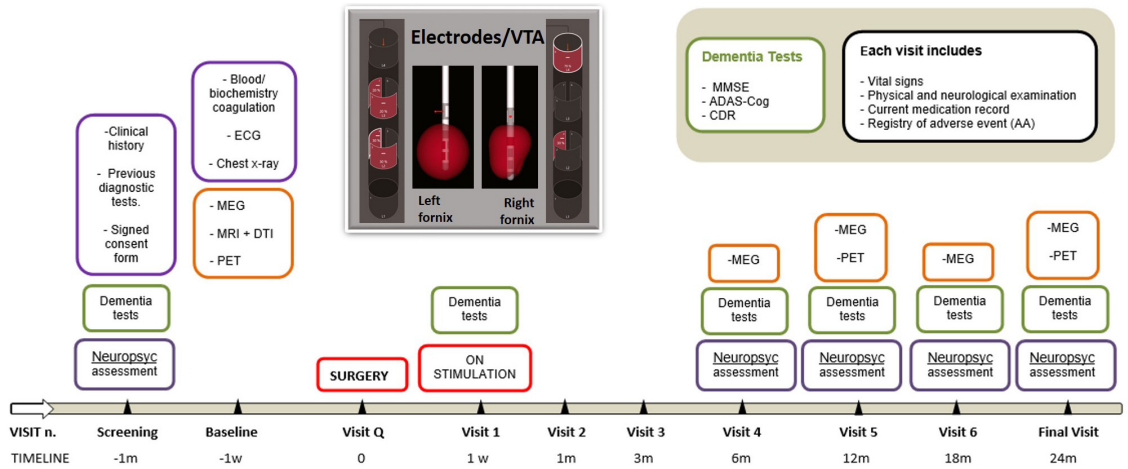

FIGURE 1 | The timeline of the study.

liquid collection surrounding the implanted device but not extending beyond the chest pocket itself. The medical staff prescribed an antibiotic treatment (meropenem and línezolid). During her stay, the patient then remained clinically stable; the inflammatory signs in the area of the implanted stimulator battery progressively reduced. She completed the 2-week antibiotic cycle and was discharged 14 days later.

The medication remained unchanged throughout the trial. The same pattern of stimulation was maintained over 24 months, with visits scheduled after 1 week and 1, 3, 6, 12, 18, and 24 months from the start of stimulation (**Figure 1**). Subsequent protocol visits were attended by the geriatrician, neurosurgeon, and neuropsychologist.

Follow-Up and Outcomes

Follow-up continued in the memory unit of the geriatric service according to the ECP-EA protocol, in the absence of adverse events.

RESULTS

Neuropsychology

The basal cognitive assessment of the patient showed scores below the average in most of the tasks applied: ADAS-Cog, MMSE, WMS list of words, verbal fluency, and processing speed. At 6 months after the surgery, the scores showed mild improvement in tasks related to executive and attentional patterns: TMT-A; TMT-B, digit span backward, verbal fluency, and mazes of the ADAS-Cog. No changes were observed in the patient's performance of any other tasks. In general terms, the patient showed cognitive fluctuations over the period, related to attention and executive function patterns, with no meaningful changes in any other cognitive functions, as is shown in the CDR scores over 24 months.

Neuroimaging Data

At baseline, the MEG study indicated few, relatively weak connections, especially between both temporal regions, whereas the PET study showed mild temporal hypometabolism. These data agreed with the moderate cortical atrophy described in the MRI scan at baseline, particularly in the medial temporal regions.

The comparison between the PET studies at baseline and the 1- and 2-year follow-ups indicated no progression in the mild bilateral hypometabolism described in the mesial temporal regions at baseline (**Figure 2**).

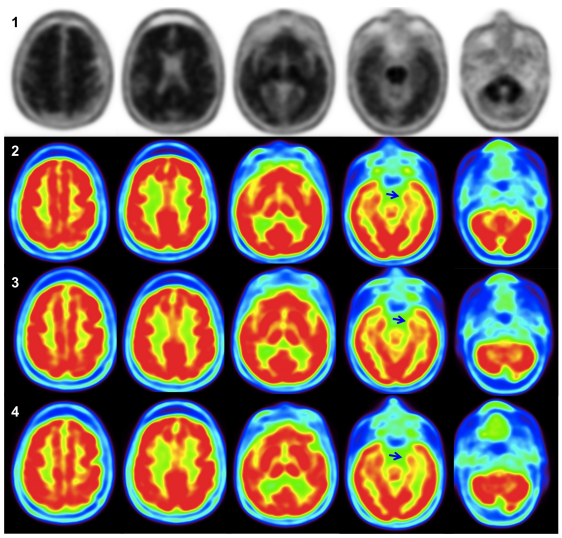

FIGURE 2 | In amyloid PET images **(1)**, the uptake of the grey matter equals that of the white matter in the lateral temporal, parietal, posterior cingulum/precuneus, and especially in the frontal lobe, thus being considered a positive study for amyloid deposition. 18F-FDG-PET images at diagnosis **(2)** show only mild mesial hypometabolism, predominantly in the left hemisphere (blue arrow). 18F-FDG-PET studies showed no evolution of hypometabolism at 1 year **(3)**, and 2 years after diagnosis **(4)** (blue arrows).

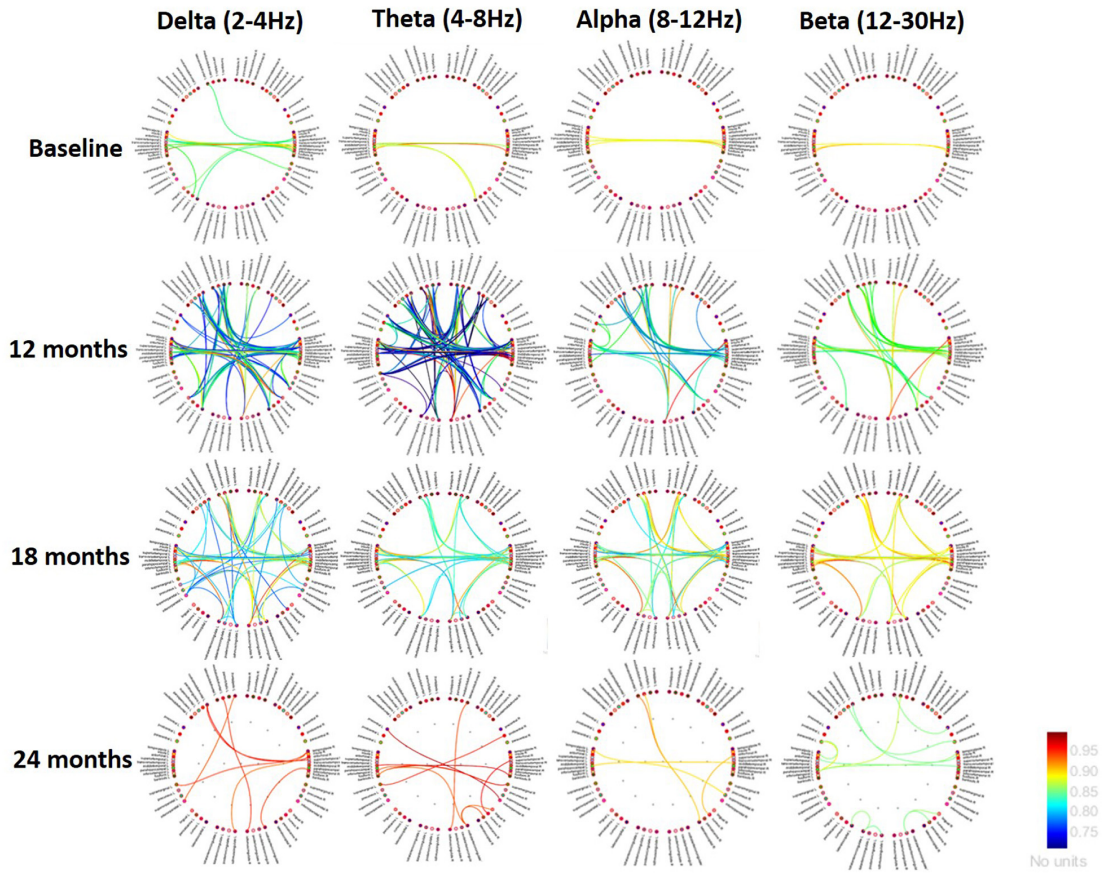

FIGURE 3 | Changes in brain connectivity from the initial study to the end of follow-up (24 months). Red and yellow lines indicate an increase in connectivity, while the blue lines show a decreasing pattern. Functional connections predominate in the bilateral mid-temporal regions with cingulate areas and, to a lesser extent, with frontomedial and orbitofrontal areas. In other words, the connectivity between the temporal and limbic areas remains quite strong. Low frequencies show an earlier decrease in connectivity, but the latest studies would indicate a pattern of reorganisation of activity.

Magnetoencephalography recordings were conducted at baseline, 6, 12, 18, and 24 months after surgery. Baseline MEG images were derived from the connectivity analysis between all brain areas of the first recording. This helped us to define the connectivity threshold for poststimulation comparisons. At baseline, very few areas were functionally connected or synchronised, particularly at the bilateral temporal level. After 6 months of dDBS stimulation, there was an increased number of significant connections, mainly in the theta band. In particular, we found significant changes in both interhemispheric and intrahemispheric functional connectivity affecting temporal areas, with a predominant pattern of significant hypoconnectivity. After 12 months of stimulation, we found important connectivity changes. At 18 months, the effect persisted but to a lesser degree, and at 24 months there remained a low number of connections, showing, in particular, relative hyperconnectivity, as is usually seen in the early stages of AD.

Clinical Impression

The clinical and neuropsychological evaluation indicates that, after implantation of the electrodes in the fornix (bilateral), the patient managed to remain cognitively stable during 2 years of follow-up, showing slight cognitive and functional deterioration in the last evaluation.

The patient showed good adherence (attending appointments for clinical visits, scans, and assessments). Both patient and relatives verbally declared satisfaction with the treatment and the effects. No subsequent diagnostic or complications were reported.

Finally, on the last visit of the ECP-EA clinical trial, the patient presented Katz B (urinary incontinence), requiring help for all instrumental activities but walking without additional support.

DISCUSSION

Alzheimer's disease is an increasingly prevalent, serious social and health problem worldwide. Current medication provides relief from symptoms, but disease progression remains intact. This study describes the first dDBS intervention in a patient with AD by stimulating the fornix in both hemispheres. After completing the 24-month follow-up according to the protocol, we can conclude that dDBS of

the fornix constitutes a safe procedure, without serious side effects and well-tolerated, in agreement with a previous study. Regarding the efficacy of this therapeutic option, the cognitive and functional stability of the patient was observed during the whole study. The stimulation provided a transient cognitive conversion at the neuropsychological and functional levels (as assessed by PET and MEG), by increasing brain metabolism and neural connectivity in the temporal brain hubs.

Regarding the MEG findings, hypersynchronisation in the theta and other frequency bands has been reported in association with a negative impact on cognition in early AD and with tau/amyloid-β pathology (Canuet et al., 2012, 2015). Thus, this evidence supports the pattern of stimulation-induced theta hypoconnectivity underlying early cognitive improvements in this patient with AD (**Figure 3**).

This clinical case formed part of a dDBS clinical trial intended to test its efficacy in two targets: the fornix (main input and output data mainstream of the hippocampus and media temporal lobe) and the NBM. The stimulation of the NBM responded to the hypothesis of reduced acetylcholine level at the cortical level in patients with AD. By random assignment, the first patient enrolled successfully underwent the fornix stimulation. Previous studies reported moderate beneficial effects of both fornix and NBM in AD. Specifically, DBS of NBM showed moderate improvements in cognitive measures in advanced patients (Zhang et al., 2021) and metabolic changes (Kuhn et al., 2015). Studies on evoked potential techniques showed benefits on auditory processing, linking DBS to normalisation of the P50 component under stimulation (vs. sham) (Dürschmid et al., 2020). Some additional effects have been observed in the counteraction of nutritional status deterioration and progressive weight loss (Noreik et al., 2015), together with abnormal thermoregulation (Zhang et al., 2021). In the case of fornix stimulation, relevant clinical trials have verified safety, but efficacy remains elusive. In general, the effect of fornix stimulation ranges from a reduction in the rate of cognitive decline to some possible improvements (Laxton et al., 2010; Fontaine et al., 2013; Leoutsakos et al., 2019). These changes correlated with increases in the glucose metabolism of the temporal and parietal lobes (Laxton et al., 2010) and hippocampal size (Sankar et al., 2015). One of the variables that may explain the differences among studies is the age or the status of the patients and the treatment being more beneficial in those aged over 65 (Lozano et al., 2016; Leoutsakos et al., 2019; Targum et al., 2021).

Although most of the studies used similar instruments to assess the changes related to brain stimulation, the suitability of these instruments needs to be considered. The MMSE and ADAS-Cog were designed specifically for AD and were supposed to detect changes in the progression of each case. Interestingly, opposite results are shown in the scores obtained in MMSE and ADAS-Cog for the effect of stimulation: the increase of 10 points in ADAS-Cog from the first evaluation to the last evaluation (50th percentile) contrasts with the 2-point decrease in MMSE (percentile < 1). This disparity shows that the two tests measure quite different things (Wouters, 2010). In the presymptomatic stages of the disease, the changes are slight and difficult to detect (Snyder et al., 2014), which must be considered when applying these techniques in the early stages of the disease. In this study, we consider the relevance of using a variety of scales, in addition to ADAS-Cog and MMSE, to allow the detection of subtle changes. The effect of the stimulation seems to depend, in fact, on the duration of the therapy. At 6 months, the effects relate essentially to the memory sphere, while at 12 months, an improvement in executive functions begins. Longer studies will be needed if we are to verify the stability in semantic fluency and executive functions.

The majority of DBS studies in AD (either fornix, NBM, or ventral capsule stimulation) include a follow-up period of 6–12 months (Laxton et al., 2010; Fontaine et al., 2013; Kuhn et al., 2015; Lozano et al., 2016; Scharre et al., 2018; Targum et al., 2021). In our study, four post-surgery assessments were conducted during a 24-month follow-up period, as in the study of Leoutsakos (Leoutsakos et al., 2019). Although some variations occurred in the neuropsychological scores, the general instruments reported no changes, mimicking baseline scores. Our results support the possibility that the effect of the stimulation has a peak at 12 months, which means that the follow-up period of future studies should perhaps also be 24 months. In addition, the maintenance of the baseline cognitive performance after 24 months is significant, contrary to our previous understanding of the standard progression of this disorder. These data also outline the range of possible effects linked to dDBS. They will help to establish a frame of reference for planning future studies and to state realistic objectives in cognitive rehabilitation.

One of the main limitations of the study was the difficulty in recruiting. In general terms, patients do not identify DBS as a current treatment for AD, and therefore they reject it (Fontaine et al., 2013). If future research is to assess the eventual benefits of this therapy more reliably in patients with AD, it will need to use a representative sample.

The range of therapeutic options for AD is as wide and complex as its etiopathogenesis. In the future, researchers must focus on those options that offer the highest levels of selectivity and therapeutic potential and provide the best balance of risks and benefits. It is becoming increasingly important to develop multidimensional treatments, ones that are neither focussed on a single strategy nor exclusively based on pharmacological treatment. They must be combined, translationally, with physiotherapy, neuropsychology, and occupational training (Elmaleh et al., 2019), in attempting to slow down the progression of the disease.

DATA AVAILABILITY STATEMENT

The original contributions presented in the study are included in the article, further inquiries can be directed to the corresponding author.

ETHICS STATEMENT

The study involving human participants were reviewed and approved by the Hospital Clínico San Carlos Ethics Committee (code: ECP-EA – C.I. 13/448). The patient provided her written informed consent to participate in this study and for the publication of any potentially identifiable images or data included in this article.

AUTHOR CONTRIBUTIONS

JB was involved in the conceptualisation and design of the study, interpretation of results and supervision. MV, CN, AL, and LS-S-R were involved in conceptualisation and revising. MC and LC were responsible for neuroimaging acquisition, analysis and results. RY and MV were involved in data acquisition, analysis, and interpretations of results. CN was in charge of the manuscript drafting. JB, MV, CN, RY, MC, LC, AL, BS, PG, and LS-S-R were involved in the critical revision of the manuscript.

FUNDING

This study (FIS12/0598) was supported by the Instituto de Salud Carlos III (Plan Estatal de I + D + i 2012–2015) and cofinanced by the European Development Regional Fund (ERDF). CN has a Francisco Tomás y Valiente Fellowship (MIAS-UAM). This study is framed in the research project entitled "Criminal Law and Human Behaviour" (RTI2018-097838-B-I00) granted by the Spain Ministry for Science, Innovation, and Universities of Spain (PI: Eduardo Demetrio Crespo). This study is also framed in the research consortia NEUROCENTRO-CM, funded by Comunidad de Madrid (grant number NEUROCENTRO-B2017/BMD-3760).

ACKNOWLEDGMENTS

We thank the patient and her relatives for their disinterested support and collaboration. We also thank the DBS team of Boston Scientific Ibérica for their technical support throughout the study and in the VTA reconstruction.

REFERENCES

Behrens, T. E. J., Johansen Berg, H., Jbabdi, S., Rushworth, M. F. S., and Woolrich, M. W. (2007). Probabilistic diffusion tractography with multiple fibre orientations: what can we gain? *NeuroImage* 34, 144–155. doi: 10.1016/j.neuroimage.2006.09.018

Benton, A. L. (1968). Differential behavioral effects in frontal lobe disease. *Neuropsychologia* 6, 53–60. doi: 10.1016/0028-3932(68)90038-9

Brookmeyer, R., Evans, D. A., Hebert, L., Langa, K. M., Heeringa, S. G., Plassman, B. L., et al. (2011). National estimates of the prevalence of Alzheimer's disease in the United States. *Alzheimers Dement.* 7, 61–73. doi: 10.1016/j.jalz.2010.11.007

Canuet, L., Pusil, S., López, M. E., Bajo, R., Pineda-Pardo, J. Á, Cuesta, P., et al. (2015). Network disruption and cerebrospinal fluid amyloid-beta and phospho-tau levels in mild cognitive impairment. *J. Neurosci.* 35, 10325–10330. doi: 10.1523/JNEUROSCI.0704-15.2015

Canuet, L., Tellado, I., Couceiro, V., Fraile, C., Fernandez-Novoa, L., Ishii, R., et al. (2012). Resting-State Network Disruption and APOE Genotype in Alzheimer ' s Disease?: a lagged Functional Connectivity Study. *PLoS One* 7:e46289. doi: 10.1371/journal.pone.0046289

De Matteis, L., Martín-Rapún, R., and de la Fuente, J. M. (2018). Nanotechnology in Personalised Medicine: a Promising Tool for Alzheimer's Disease Treatment. *Curr. Med. Chem.* 25, 4602–4615. doi: 10.2174/0929867324666171012112026

Desikan, R. S., Ségonne, F., Fischl, B., Quinn, B. T., Dickerson, B. C., Blacker, D., et al. (2006). An automated labeling system for subdividing the human cerebral cortex on MRI scans into gyral based regions of interest. *NeuroImage* 31, 968–980. doi: 10.1016/j.neuroimage.2006.01.021

Dubois, B., Hampel, H., Feldman, H. H., Scheltens, P., Aisen, P., Andrieu, S., et al. (2016). Preclinical Alzheimer's disease: definition, natural history, and diagnostic criteria. *Alzheimers Dement.?* 12, 292–323. doi: 10.1016/j.jalz.2016.02.002

Dürschmid, S., Reichert, C., Kuhn, J., Freund, H. J., Hinrichs, H., and Heinze, H. J. (2020). Deep brain stimulation of the nucleus basalis of Meynert attenuates early EEG components associated with defective sensory gating in patients with Alzheimer disease – a two-case study. *Eur. J. Neurosci.* 51, 1201–1209. doi: 10.1111/ejn.13749

Elmaleh, D. R., Farlow, M. R., Conti, P. S., Tompkins, R. G., Kundakovic, L., and Tanzi, R. E. (2019). Developing Effective Alzheimer's Disease Therapies: clinical Experience and Future Directions. *J. Alzheimers Dis.* 71, 715–732. doi: 10.3233/JAD-190507

Folstein, M. F., Folstein, S. E., and McHugh, P. R. (1975). Mini-mental state". A practical method for grading the cognitive state of patients for the clinician. *J. Psychiatr. Res.* 12, 189–198. doi: 10.1016/0022-3956(75)90026-6

Fontaine, D., Deudon, A., Lemaire, J. J., Razzouk, M., Viau, P., Darcourt, J., et al. (2013). Symptomatic Treatment of Memory Decline in Alzheimer's Disease by Deep Brain Stimulation: a Feasibility Study. *J. Alzheimers Dis.* 34, 315–323. doi: 10.3233/JAD-121579

Fontaine, D., and Santucci, S. (2021). Deep brain stimulation in Alzheimer's disease. *Int. Rev. Neurobiol.* 159, 69–87. doi: 10.1016/bs.irn.2021.06.005

Hebert, L. E., Scherr, P. A., Bienias, J. L., Bennett, D. A., and Evans, D. A. (2003). Alzheimer Disease in the US Population. *Arch. Neurol.* 60:1119. doi: 10.1001/archneur.60.8.1119

Jakobs, M., Lee, D. J., and Lozano, A. M. (2020). 'Modifying the progression of Alzheimer's and Parkinson's disease with deep brain stimulation. *Neuropharmacology* 171:107860. doi: 10.1016/j.neuropharm.2019.107860

Kuhn, J., Hardenacke, K., Shubina, E., Lenartz, D., Visser-Vandewalle, V., Zilles, K., et al. (2015). Deep brain stimulation of the nucleus basalis of meynert in early stage of Alzheimer's dementia. *Brain Stimul.* 8, 838–839. doi: 10.1016/j.brs.2015.04.002

Lachaux, J.-P., Rodriguez, E., Martinerie, J., and Varela, F. J. (1999). Measuring phase synchrony in brain signals. *Hum. Brain Mapp.* 8, 194–208. doi: 10.1002/(SICI)1097-019319998:4<194::AID-HBM4<3.0.CO;2-C

Laxton, A. W., Tang-Wai, D. F., McAndrews, M. P., Zumsteg, D., Wennberg, R., Keren, R., et al. (2010). A phase I trial of deep brain stimulation of memory circuits in Alzheimer's disease. *Ann. Neurol.* 68, 521–534. doi: 10.1002/ana.22089

Leoutsakos, J. S., Yan, H., Anderson, W. S., Asaad, W. F., Baltuch, G., Burke, A., et al. (2019). Deep Brain Stimulation Targeting the Fornix for Mild Alzheimer Dementia (the ADvance Trial): a Two Year Follow-up Including Results of Delayed Activation. *J. Alzheimers Dis.* 64, 597–606. doi: 10.3233/JAD-180121

Liu, H., Temel, Y., Boonstra, J., and Hescham, S. (2020). The effect of fornix deep brain stimulation in brain diseases. *Cell. Mol. Life Sci.* 77, 3279–3291. doi: 10.1007/s00018-020-03456-4

Loonstra, A. S., Tarlow, A. R., and Sellers, A. H. (2001). COWAT Metanorms Across Age, Education, and Gender. *Appl. Neuropsychol.* 8, 161–166. doi: 10.1207/S15324826AN0803_5

Lozano, A. M., Fosdick, L., Chakravarty, M. M., Leoutsakos, J. M., Munro, C., Oh, E., et al. (2016). A Phase II Study of Fornix Deep Brain Stimulation in Mild Alzheimer's Disease. *J. Alzheimers Dis.* 54, 777–787. doi: 10.3233/JAD-160017

Morris, J. C. (1997). Clinical dementia rating: a reliable and valid diagnostic and staging measure for dementia of the Alzheimer type. *Int. Psychogeriatr.* 9, 173–176. doi: 10.1017/s1041610297004870

Noreik, M., Kuhn, J., Hardenacke, K., Lenartz, D., Bauer, A., Bührle, C. P., et al. (2015). Changes in Nutritional Status after Deep Brain Stimulation of the Nucleus Basalis of Meynert in Alzheimer's Disease–Results of a Phase I Study. *J. Nutr. Health Aging* 19, 812–818. doi: 10.1007/s12603-015-0595-8

Reitan, R. M., and Wolfson, D. (1993). *The Halstead-Reitan Neuropsychological Test Battery: Theory and Clinical Interpretation*, 2nd Editio Edn. Tucson: Neuropsychology Press.

Rosen, W. G., Mohs, R. C., and Davis, K. L. (1984). A new rating scale for Alzheimer's disease. *Am. J. Psychiatry* 141, 1356–1364. doi: 10.1176/ajp.141.11.1356

Sankar, T., Chakravarty, M. M., Bescos, A., Lara, M., Obuchi, T., Laxton, A. W., et al. (2015). 'Deep Brain Stimulation Influences Brain Structure in Alzheimer's Disease. *Brain Stimul.* 8, 645–654. doi: 10.1016/j.brs.2014.11.020

Senova, S., Fomenko, A., Gondard, E., and Lozano, A. M. (2020). Anatomy and function of the fornix in the context of its potential as a therapeutic target. *J. Neurol. Neurosurg. Psychiatry* 91, 547–559. doi: 10.1136/jnnp-2019-322375

Scharre, D. W., Weichart, E., Nielson, D., Zhang, J., Agrawal, P., Sederberg, P. B., et al. (2018). 'Deep Brain Stimulation of Frontal Lobe Networks to Treat Alzheimer's Disease. *J. Alzheimers Dis.* 62, 621–633. doi: 10.3233/JAD-170082

Snyder, P. J., Kahle-Wrobleski, K., Brannan, S., Miller, D. S., Schindler, R. J., DeSanti, S., et al. (2014). Assessing cognition and function in Alzheimer's disease clinical trials: do we have the right tools? *Alzheimers Dement.* 10, 853–860. doi: 10.1016/j.jalz.2014.07.158

Targum, S. D., Fosdick, L., Drake, K. E., Rosenberg, P. B., Burke, A. D., Wolk, D. A., et al. (2021). Effect of age on clinical trial outcome in participants with probable Alzheimer's disease. *J. Alzheimers Dis.* 82, 1243–1257. doi: 10.3233/JAD-210530

Weschler, D. (2008). *Wechsler Adult Intelligence Scale - Fourth Edition*. Statistics Solutions.

Wouters, H. (2010). Three sides of the same coin: measuring global cognitive impairment with the MMSE, ADAS-cog and CAMCOG. *Int. J. Geriatr. Psychiatry* 25, 770–779. doi: 10.1002/gps.2402

Zhang, W., Liu, W., Patel, B., Chen, Y., Wang, K., Yang, A., et al. (2021). Case Report: deep Brain Stimulation of the Nucleus Basalis of Meynert for Advanced Alzheimer's Disease. *Front. Hum. Neurosci.* 15:645584. doi: 10.3389/fnhum.2021.645584

Conflict of Interest: The authors declare that the research was conducted in the absence of any commercial or financial relationships that could be construed as a potential conflict of interest.

Publisher's Note: All claims expressed in this article are solely those of the authors and do not necessarily represent those of their affiliated organizations, or those of the publisher, the editors and the reviewers. Any product that may be evaluated in this article, or claim that may be made by its manufacturer, is not guaranteed or endorsed by the publisher.

Copyright © 2022 Barcia, Viloria, Yubero, Sanchez-Sanchez-Rojas, López, Strange, Cabrera, Canuet, Gil and Nombela. This is an open-access article distributed under the terms of the Creative Commons Attribution License (CC BY). The use, distribution or reproduction in other forums is permitted, provided the original author(s) and the copyright owner(s) are credited and that the original publication in this journal is cited, in accordance with accepted academic practice. No use, distribution or reproduction is permitted which does not comply with these terms.

frontiers | Frontiers in Pharmacology

REVIEW
published: 07 April 2022
doi: 10.3389/fphar.2022.805388

Molecular Mechanisms and Therapeutic Strategies for Levodopa-Induced Dyskinesia in Parkinson's Disease: A Perspective Through Preclinical and Clinical Evidence

Ritam Bandopadhyay[1], *Nainshi Mishra*[1], *Ruhi Rana*[1], *Gagandeep Kaur*[1], *Mohammed M. Ghoneim*[2], *Sultan Alshehri*[3], *Gulam Mustafa*[4], *Javed Ahmad*[5], *Nabil. A. Alhakamy*[6] *and Awanish Mishra*[7*†]

[1]*Department of Pharmacology, School of Pharmaceutical Sciences, Lovely Professional University, Phagwara, India,* [2]*Department of Pharmacy Practice, College of Pharmacy, AlMaarefa University, Ad Diriyah, Saudi Arabia,* [3]*Department of Pharmaceutics, College of Pharmacy, King Saud University, Riyadh, Saudi Arabia,* [4]*College of Pharmacy (Boys), Al-Dawadmi Campus, Shaqra University, Riyadh, Saudi Arabia,* [5]*Department of Pharmaceutics, College of Pharmacy, Najran University, Najran, Saudi Arabia,* [6]*Department of Pharmaceutics, Faculty of Pharmacy, King Abdulaziz University, Jeddah, Saudi Arabia,* [7]*Department of Pharmacology and Toxicology, National Institute of Pharmaceutical Education and Research (NIPER)—Guwahati, Guwahati, India*

Parkinson's disease (PD) is the second leading neurodegenerative disease that is characterized by severe locomotor abnormalities. Levodopa (L-DOPA) treatment has been considered a mainstay for the management of PD; however, its prolonged treatment is often associated with abnormal involuntary movements and results in L-DOPA-induced dyskinesia (LID). Although LID is encountered after chronic administration of L-DOPA, the appearance of dyskinesia after weeks or months of the L-DOPA treatment has complicated our understanding of its pathogenesis. Pathophysiology of LID is mainly associated with alteration of direct and indirect pathways of the cortico-basal ganglia-thalamic loop, which regulates normal fine motor movements. Hypersensitivity of dopamine receptors has been involved in the development of LID; moreover, these symptoms are worsened by concurrent non-dopaminergic innervations including glutamatergic, serotonergic, and peptidergic neurotransmission. The present study is focused on discussing the recent updates in molecular mechanisms and therapeutic approaches for the effective management of LID in PD patients.

Keywords: Parkinson's disease, levodopa, levodopa-induced dyskinesia, pathophysiology, bradykinesia

OPEN ACCESS

Edited by:
Kuangyu Shi,
University of Bern, Switzerland

Reviewed by:
Félix Javier Jiménez-Jiménez,
Hospital Universitario del Sureste, Spain
Jingjie Li,
Zunyi Medical University, China

****Correspondence:***
Awanish Mishra
awanish1985@gmail.com
awanish@niperguwahati.in

†ORCID:
Awanish Mishra
orcid.org/0000-0001-7863-5581

Specialty section:
This article was submitted to Neuropharmacology, a section of the journal Frontiers in Pharmacology

Received: *30 October 2021*
Accepted: *21 February 2022*
Published: *07 April 2022*

Citation:
Bandopadhyay R, Mishra N, Rana R, Kaur G, Ghoneim MM, Alshehri S, Mustafa G, Ahmad J, Alhakamy NA and Mishra A (2022) Molecular Mechanisms and Therapeutic Strategies for Levodopa-Induced Dyskinesia in Parkinson's Disease: A Perspective Through Preclinical and Clinical Evidence. Front. Pharmacol. 13:805388. doi: 10.3389/fphar.2022.805388

1 INTRODUCTION

Parkinson's disease (PD) is a life-threatening progressive neurodegenerative disease, which is characterized by severe locomotor impairments including bradykinesia, tremor, and rigidity (Kalia and Lang, 2015; Mishra et al., 2021; Angelopoulou et al., 2021; Ahmad et al., 2022; Kaur et al., 2022). These symptoms are the manifestation of substantia nigral dopaminergic neuron loss (Kalia and Lang, 2015). Other abnormalities associated with PD are cognitive defects, psychiatric

abnormalities, and neurodegenerative implications of levodopa-induced dyskinesia (LID) (Schapira et al., 2017). Levodopa (L-DOPA) is highly efficient and is the medication used for the mitigation of PD, but its prolonged use gives rise to motor abnormalities including dyskinesia. Dyskinesia may be mild at first but may develop into a debilitating symptom and may affect the quality of life of patients. More than 50% of patients with PD develop LID after 5 years of continuous treatment with L-DOPA, which worsens the quality of life in these patients (Fabbrini et al., 2007; Wu et al., 2019; Maan et al., 2020; Mandal et al., 2020).

Various types of movement disorders have been observed in LID which majorly include dystonia, myoclonus, chorea, or their combination. Generally, dyskinesia appears in the neck, jaw, tongue, face, waist, shoulder, trunk, and leg (Li et al., 2020). There are three types of dyskinesias identified to date, off-period dystonia, peak dose dyskinesia, and diphasic dyskinesia (Fabbrini and Guerra, 2021). Off-time dyskinesia is usually encountered during the night or early morning. Thus, administration of L-DOPA formulations having a longer half-life at night can be an effective way to treat off-time dyskinesia (Vijayakumar and Jankovic, 2016). However, diphasic dyskinesia is treated by increasing the dose of dopaminergic drugs administered; contrarily, treatment of peak dose dyskinesia is generally performed by reducing the dose of dopaminergic drug administered. However, in some cases, reduction of L-DOPA treatment leads to worsening of motor side effects (Fox et al., 2018). The management of LID remains a matter of grave concern as the diagnosis of the type of dyskinesia is a challenging issue. Furthermore, different types of dyskinesias can respond differently to a particular treatment.

LID is currently thought to be related to pre-/postsynaptic changes resulting in dopaminergic imbalance. Dyskinesia is associated with a series of events that include potent stimulation of dopamine (DA) receptors, low-protein and genetic mutations, and abnormalities in non-DA transmission (Bezard and Brotchie, 2001). Therefore, animal models are designed to explore the mechanisms involved in LID and to identify new pathological targets for drugs. Current mice and primate disease models are created by inducing PD by using MPTP or 6-OHDA toxins and then inducing LID by administering a daily dosage of L-DOPA (Bezard and Brotchie, 2001; Brotchie et al., 2007). In this article, we have discussed the pathophysiology, treatment trends of LID, and various preclinical and clinical evidence regarding this.

2 BASIC PATHOPHYSIOLOGY OF L-DOPA-INDUCED DYSKINESIA

The mechanism of LID is not clearly understood. However, continuous research has found that continued damage of nigral dopaminergic neurons produces deformities in the connection of the motor cortex and the striatum and makes a functional disturbance in basal ganglia, which can lead to the generation of involuntary abnormal movements, that is, LID (Bezard and Brotchie, 2001). The quantity and period of drug exposure play a crucial role in the development of dyskinesia. Along with that, the severity of LID also depends on the extent of neurodegeneration. PD patients and MPTP-treated primates having a higher degree of dopaminergic neuron degeneration show dyskinetic symptoms after the administration of L-DOPA. In general, rising and falling of the plasma L-DOPA level is the main reason for dyskinesia and motor defect (Thanvi et al., 2007).

Along with the advancement of the disease, the equal dosage of L-DOPA, which is generally required for alleviation of PD symptoms, causes dyskinesia. The main cause for this altered response pattern is not clear; however, the literature suggests that disturbance in between pre- and postsynaptic nigrostriatal DA transmission leads to motor complications. A schematic diagram describing major signaling abnormalities associated with LID in PD patients has been illustrated in **Figure 1**.

2.1 Improper Dopamine Storage, Neurotransmission, and Postsynaptic Alteration

Exogenously administered L-DOPA, a dopamine precursor, is converted to DA and stored in the vesicles of presynaptic dopaminergic neurons, which upon receiving stimuli releases it. This conversion and storage also take place inside the serotonergic nerve terminals. Even most of the exogenously administered L-DOPA is taken up by the serotonergic neurons and converted to DA. Dopamine transporter (DAT) transports this converted DA into the synaptic vesicles, where it is stored and released in a physiologically regulated manner (Corsi et al., 2021). Mainly, D_2 autoreceptors and DAT buffer the release of DA into the synaptic cleft (Navailles and De Deurwaerdère et al., 2012). However, serotonergic neurons lack these mechanisms; thus, the physiological fine-tuning of DA release is absent in them. With the progression of disease neurodegeneration, the number of dopaminergic terminals which are required to modulate the production and controlled release of DA decreases. With the progression of time, dopaminergic neurons start to degenerate and serotonergic neurons become more relevant, and eventually, most of the striatal DA gets released, as false transmitters, from the serotonergic nerve terminals (Corsi et al., 2021). At an advanced stage of PD, a vast portion of dopaminergic neurons are lost, and the serotonergic terminal is mainly providing the DA release and conversion, which are devoid of the molecular mechanism for DA release management and feedback control. As a result, the DA concentration cannot be regulated, which leads to an abnormal swing in extracellular DA concentration following oral administration of L-DOPA (Mosharov et al., 2015; Fabbrini and Guerra, 2021). Fluctuations in the dopamine release patterns from the presynaptic neuron terminals give rise to abnormal responses, which were then carried out by postsynaptic neurons. These abnormal responses then give rise to fluctuations in motor coordination.

An important pathophysiological factor for LID is the shorter half-life after oral administration of L-DOPA, which produces a non-physiological pulsatile dopaminergic stimulus in the stratum region of the brain. This condition makes the intermediate level of DA dependent on the pharmacokinetics of external L-DOPA. Thus, the improvement from PD symptoms gets dependent on

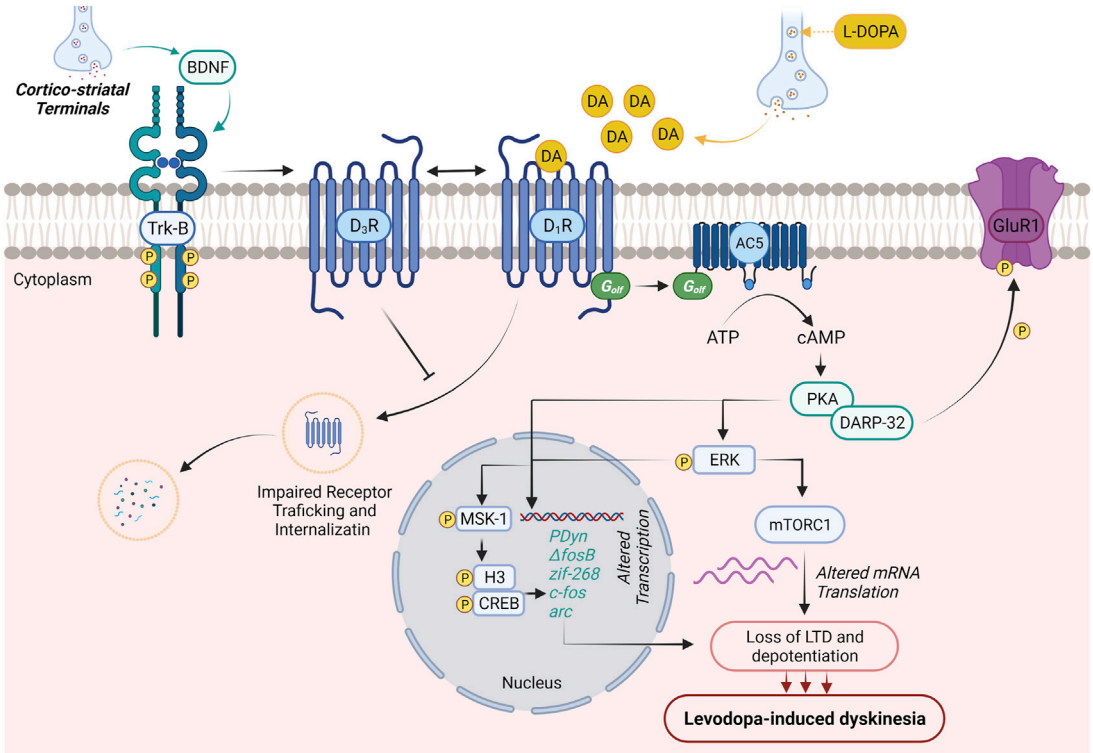

FIGURE 1 | Molecular neurobiology of levodopa-induced dyskinesia. DA production generally regulates voluntary movements. In PD patients, initial dopaminergic neurodegeneration in substantia nigra pars compacta is asymptomatic. Loss of striatal–nigral neuronal sensitizes the D1 receptor on the medium spiny neurons of the direct pathway. This results in initial motor symptoms of PD (dyskinesia). The treatment with L-DOPA improves the initial motor symptoms and promotes BDNF release from corticostriatal neurons. The expressed BDNF potentiates the expression of D3Rs through the activation of Trκ-B receptors in nigrostriatal medium spiny neurons. Enhanced expression of D3Rs suppresses internalization and abnormal trafficking of membrane-bound D1Rs, thus intensifying D1R sensitization and associated dyskinesia. Activation of D1R by DA (released through L-DOPA) results in the activation of D1R/Gαolf/adenylyl cyclase 5 (AC5) machinery in nigrostriatal medium spiny neurons and causes cAMP-mediated hyperexpression of protein kinase A (PKA) and DARPP-32. The abnormal PKA/DARPP-32 expression results in hyper-phosphorylation of GluR1 and promotes the excitability of medium spiny neurons contributing to the loss of long-term depression and depotentiation and development of LID. On the other hand, activation of D1R results in the Ras/Raf/MEK/ERK signaling pathway, which further potentiates Ras/Raf machinery and regulates various transcription and translation processes regulating LID. PKA/DARPP-32 and/or ERK/Elk/MSK1 signaling migrates to the nucleus, leads to phosphorylation of CREB/histone H3, and augments the expression of immediate early genes (prodynorphin and ΔFosB), which are reported to contribute to the development of LID. Activated ERK further elevates mTORC1 expression-mediated mRNA translation and worsens LID.

the administration of the L-DOPA dose. All these abnormalities ultimately give rise to progressive loss of the dopaminergic nerves (Bastide et al., 2015; Leta et al., 2019; Chen et al., 2020). Gradually, degeneration of presynaptic nigral neurons results in loss of DA in peak dose dyskinesia. After a few years of treatment, a new kind of dyskinesia starts to occur, which is known as wearing off dyskinesia. In this condition, worsening of PD symptoms takes place when the next dose of L-DOPA is due, and it improves after taking the new dose (Bezard and Brotchie, 2001; Bézard et al., 2003).

L-DOPA-induced aberrant dyskinetic activity could be due to deleterious plastic neurological implications at the postsynaptic levels. Between several different ideas supporting the role of postsynaptic variables in LID, one theory proposes that L-DOPA causes a stimulatory priming effect in Parkinson's disease sufferers (Nadjar et al., 2009). Chronic introductions to medications that function as direct or indirect stimulants of cerebral DAT can cause sensitization to their cognitive stimulating characteristics, resulting in priming (behavioral sensitization). As a result, priming might occur in both drug usage and LID (Calabresi et al., 2008). Apparently, two required prerequisites for the induction and maintenance of LID that are thought to be a result of priming: high L-DOPA dosages and extensive DA denervation. L-DOPA generates dyskinesia with a constant spectrum of severity in dyskinetic rats, when given an appropriate dose, and results in severe striatal DA depletion (Calabresi et al., 2010).

Chronic drug therapy appears to cause unfavorable plastic alterations, which mostly occur in the postsynaptic region. After systemic administration of L-DOPA, this syndrome causes an excessively significant rise in extracellular DA (Abercrombie et al., 1990), which is coupled with defective monoamine oxidase-mediated DA breakdown, which further increases extracellular striatal DA concentration (Wachtel and Abercrombie, 1994). These huge changes in extracellular DA concentrations could then provoke abnormal postsynaptic responses. The increasing degradation of nigrostriatal dopaminergic neurons, which produces a reduction in DA

holding space, is responsible for the difference between the severity of different disease phases. As a result, changes in L-DOPA fractions in the brain are solely dependent on the drug dosing period (Metman et al., 2000). Moreover, relative to stable responses, PET scans revealed fast oscillations in brain DA levels in individuals with PD and LID. Even though the drug-dosing cycle plays an important part in the vulnerability toward dyskinesias, other peripheral (gastric emptying and ingestion) and central (changes in precursor drug buildup in serotonergic neurons) elements are likely to play a part in the illness (Calabresi et al., 2010).

One further area which has lately been examined in mice persistently treated with L-DOPA, following unilateral 6-hydroxydopamine-induced lesion, is the anatomical location for the manifestation of LID (Buck et al., 2010). Dyskinesias were induced by locally injecting L-DOPA into the lesioned striatum, and on the other hand, regional L-DOPA administration of a similar dose in the ipsilateral globus pallidus and substantia nigra pars reticulata did not elicit dyskinesias, implying that the striatum is a particular target region for the activation of previously existent dyskinesias (Calabresi et al., 2010).

2.2 Altered Dopaminergic Pathways and Receptors

Three signaling pathways, PKA/DARPP-32, ERK, and mTORC1, were identified, which exert significant involvement in the pathophysiology of LID. All these pathways are interrelated and are activated by a common intercellular cascade triggered in nigrostriatal SPNs expressing D1 receptors. Chronic L-DOPA administration activates all of them, which alters the striatal synaptic plasticity. DARPP-32 signaling was observed to regulate ERK and mTORC1 pathways (Santini et al., 2012; Torkaman-Boutorabi et al., 2012).

Recent studies have demonstrated that D1 receptor activation leads to Shp-2 activation, which leads to activation of ERK1/2 and mTOR phosphorylation. This, in turn, induces the LID expression. This effect can easily be reversed by using a D1 receptor antagonist, which downregulates the end product of the D1R/Shp-2 pathway, p-mTOR, and p-ERK1/2 (Calabrese et al., 2020). Rapamycin was observed to be selectively affecting the mTORC1 pathway, without affecting DARPP-32 signaling, ERK pathway, and AMPA, NMDA expression (Santini et al., 2012).

After the onset of LID, the potential of D1 receptors to get associated with PKA and ERK1/2 increases. However, it was observed that after 2 weeks of L-DOPA treatment, D1 receptor-associated activation of PKA and ERK1/2 got blocked, due to oversensitivity of dSPNs (Wu et al., 2018). The D1R-dependent ERK1/2 phosphorylation was observed to be modulated by mGluR5, which modulates the mGluR5/PLC/PKC pathway without influencing PKA activity (Jones-Tabah et al., 2020). D1 receptor activation leads to activation of the D1R/cAMP/PKA pathway, which upregulates the expression of the $G\alpha_{olf}$ protein. $G\alpha_{olf}$ is a major stimulating G-protein, which upon activation upregulates the expression of cAMPs (Fieblinger et al., 2014). It was observed that chronic administration of L-DOPA increases the expression of $G\alpha_{olf}$ in striatonigral SPNs and decreases its expression in striatopallidal SPNs (Alcacer et al., 2012). Knocking out casein kinase 2 (CK2) protein was also found to be linked with reduced $G\alpha_{olf}$ protein expression in striatonigral SPNs. This also reduced the severity of LID. However, knockdown of CK2 in striatopallidal SPNs leads to increased severity of LID, which can be easily reversed by co-administration of caffeine and L-DOPA (Goto, 2017).

Upregulated Nurr1 transcription factor was found to be associated with increased cortically evoked firing rate and increased spine density of SPNs. Leucine-rich repeat kinase 2 (LRRK2) was observed to be influencing D1/D2 receptor-activated pathways. Interaction between them is not well understood, but this can help researchers to control LID in a better way (Sellnow et al., 2020). An anchoring protein, PSD95, dictates the distribution of dopaminergic receptors in the brain. An increased expression was noticed in DA depleted brain, which lowers the diffusion of D1R in the brain (Zhang J. et al., 2014; Divito et al., 2015). The expression of parkin protein also gets impaired, which leads to abnormal involuntary movements (Porras et al., 2012). Ca2+/calmodulin-dependent protein kinase IIα (CaMKIIα) binds to the same domain where the $G_{\alpha i}$ domain is located on the D2 receptor. This also indicates CaMKIIα D2 receptor activity *via* the adenyl cyclase signaling pathway. In the case of LID, increased interaction between CaMKIIα and D2 receptors was observed, and reduction in CaMKIIα concentration reduces LID, just like a D2 receptor agonist (Lyons et al., 2013).

An increased expression of D3 receptors was reported in animals with severe LID. An associated increase in the expression of GABA release was also noticed. D3 receptors can also perform the D1 receptor modulation action *via* affecting the ERK pathway. Upon deletion of the D3 receptor, levels of FosB, ERK, and H3 activities decreased along with the alleviation of LID symptoms, with no effect on L-DOPA treatment (Zhang S. et al., 2014; Albarrán-Bravo et al., 2019). A lack of D5 receptors is also associated with increased LID severity and decreased response to the L-DOPA symptoms (Payer et al., 2016).

2.3 Glutamatergic Hypothesis

In the past two decades, other than the dopaminergic system, numerous, non-dopaminergic systems are also observed to be involved in the pathophysiology of LID. First, significantly increased glutamatergic neurotransmission was observed in basal ganglia and the thermo-cortical circuit. In glutamate, ionotropic and metabotropic glutamate receptors are mainly involved in the excitatory effect. An excessive amount of AMPA and NMDA receptors were observed to be situated at the striatum of the patients and animals suffering from LID (Sgambato-Faure and Cenci, 2012; Guerra et al., 2019). Moreover, a histological study has shown that Glu (related to NMDA) is elevated in the striatum of the dyskinetic patients, but it has not shown any presence in non-dyskinetic patients. The sentence should be corrected as following: Abnormal glutamate release has been linked to development of LID in PD patients (Ahmed et al.,

2011). Confirmation of the link between the elevated level of Glu and LID is also coming from pharmacological studies by using NMDA receptor antagonist drugs. By this, it has been confirmed that NMDA antagonist drugs are decreasing dyskinesia in animals and humans (Jongsma et al., 2001; Morin and Di Paolo, 2014).

It was also observed that metabotropic glutamate receptors (mGluR) are involved in the pathophysiology of LID. Additionally, Glu intracellular signaling is modulated by the MGlu receptor without affecting Glu excitatory action on synaptic neurotransmission. In the GPCR (G-protein coupling receptor), normally, three groups of mGlu are present, and they differ in ligand binding profile and sequence homology (Sebastianutto and Cenci, 2018). In the group 1 receptors (MGluR1, MGluR5) interact with phospholipase C beta and control intracellular calcium release by the inositol triphosphate formation along with protein kinase C activation. Both the group 2 (MGluR2, MGluR3) and group 3 receptors (MGluR4, MGluR6, MGluR7, and MGluR8) interact with the inhibitory G-protein and inhibit the formation of cAMP (Rondard and Pin, 2015; Sebastianutto and Cenci, 2018). Striatal PKA-related glutamatergic signaling and glutamatergic receptors (AMPA) play an important role in the expression and occurrence of LIDs. AMPA antagonists directly act on the glutamate receptors situated in M1 and are proven effective in alleviating LID. NMDA antagonists do not alleviate LID in rats when used as a monotherapy, but when co-administered with AMPA antagonists, they show LID-alleviating properties. This combination also potentiates the AMPA antagonists (Lindenbach et al., 2016).

2.4 Serotonergic Hypothesis

Serotonergic neurons convert 5-HT into DA, sort it, and then release it. This mechanism is referred to as the presynaptic serotonergic LID mechanism (Rylander et al., 2010; Sahin et al., 2014). As discussed earlier, serotonergic neurons play a critical role in the release of DA, and continuing this path, pharmacological lysis of serotonin raphe projections have shown to be blocking LID development in dyskinetic rats (Carta et al., 2007). As discussed earlier, in the advanced stages of PD, false dopaminergic neurotransmission is a serious pathological implication in the manifestation of LID symptoms. It was further established in hemiparkinsonian rats, where demolition of serotonergic innervation in the striatal region of the brain results in complete restoration of LID-like condition (Carta et al., 2007). The same effect was observed in non-dyskinetic rats upon removal of serotonergic afferents (Carta et al., 2007). Furthermore, an association of serotonergic innervations and serotonergic autoreceptors with the pathophysiology of LID was confirmed using other animal models also (Muñoz et al., 2008; Lindgren et al., 2010; Beaudoin Gobert et al., 2015). On the other hand, worsening of LID symptoms was observed after inducing the serotonergic innervations (exerts a tropic effect on serotonergic axons) in the striatum of parkinsonian rats, denoting that the striatum is the most important point of serotonergic implications (Tronci et al., 2017). Many articles support that irregular serotonergic movements are involved in the pathophysiology of LID. The involvement of the serotoninergic system in LID is supported by data showing significant striatal hyper-innervation in the parkinsonian animal (Gagnon et al., 2016). However, the serotonergic implication is not only restricted to the striatal region but also affects the parts wherever the serotonin innervation is present (Carta et al., 2018). Long-term L-DOPA administration was noticed to decrease basal serotonin release and metabolism, with associated downregulation of serotonin tissue content in the brain (Navailles et al., 2011). Thus, prolonged L-DOPA-induced reduction in 5-HT synaptic functionality may be implicated not only in the development of LIDs but also in the onset of non-motor health consequences of L-DOPA medication, such as anxiousness or melancholy, in which the serotonergic system plays a role (Navailles et al., 2011).

Radiological analysis has revealed an upregulation of serotonin transporter (SERT) expression in LID-affected patients (Sahin et al., 2014). Chronic L-DOPA treatment causes brain neurotrophic factor (BNDF) overexpression, which is associated with axonal growth of serotonin neurons, and further activates cAMP/PKA and mTORC pathways (Gagnon et al., 2016). In dopamine-depleted brains of PD-affected monkeys, striata and areas of dopaminergic denervation were found to be denser in SERT positive axons (Inden et al., 2012). Various selective serotonin reuptake inhibitors (SSRIs), like citalopram, paroxetine, and fluoxetine, decrease LID when co-administered with L-DOPA, while no such effects were observed with DA agonist, apomorphine. Thus, uptake blockage of serotonin is the preferred mechanism of anti-dyskinetic action (Bishop et al., 2012; Miguelez et al., 2016).

$5HT_{1A}$ and $5HT_{2B}$ receptors are also passively involved in the prognosis of LID. They exist as autoreceptors in the axons and cell bodies of the serotonergic nerves and as heteroreceptors on striatal, as well as cortical neurons. As heteroreceptors, they control the release of GABA and glutamate in the cortical and striatal regions. As discussed earlier, the release of glutamate has some serious implications in LID. Thus, the activation of the $5HT_{1A}$ receptor leads to a release of glutamate, which exacerbates the LID symptoms (Carta et al., 2018). The role of serotoninergic system in LID has been validated through the animal models of 5HT1A and 5HT2B receptor agonists (animals having normalized serotoninergic receptor expression) and they have attenuated the dyskinetic symptoms produced by the L-DOPA administration. For example, vilazodone is a serotoninergic reuptake inhibitor and partial $5HT_{1A}$ agonist class of drug, which decreases the developing effect of LID without any interruption in motor effects of L-DOPA in 6-hydroxyDA-lesioned hemiparkinsonian rats (Meadows et al., 2018).

3 APPROACHES FOR MANAGEMENT OF LEVODOPA-INDUCED DYSKINESIA: PRECLINICAL STATUS

The management of LID is often complicated as its pathogenesis is poorly understood. Based on the preclinical evidence, surgical

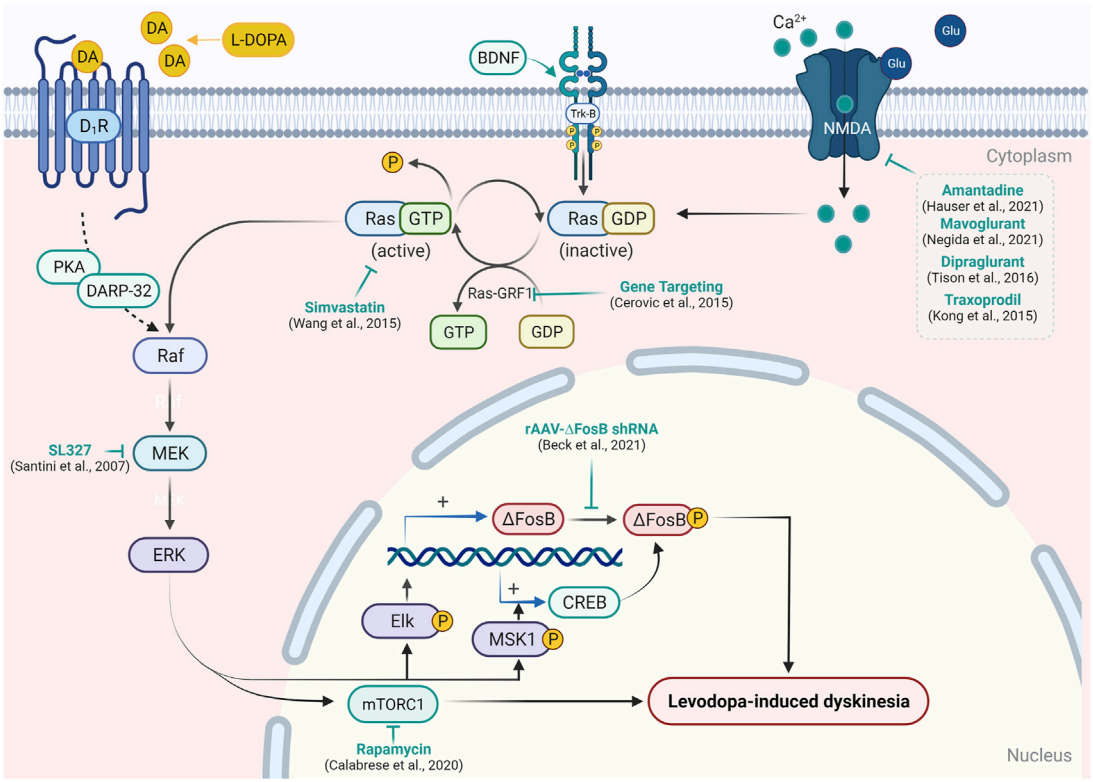

FIGURE 2 | Targeting signaling upstream/downstream of Ras/Raf/MEK/ERK pathway modulation in LID. In the experimental model of PD, L-DOPA administration causes abnormal activation of the RAS/RAF/ERK pathway and results in the emergence of dyskinetic behavior. Activation of D1R, Trk-B, or NMDA receptor causes activation of RAS-GDP molecular switch by Ras-guanyl nucleotide-releasing factor 1 (Ras-GRF1), which facilitates the conversion of RAS-GTP to Ras-GDP. Ras-GDP further causes the activation of Raf protein kinase, which in turn leads to the phosphorylation of mitogen-activated protein kinase/ERK kinase (MEK) and ERK. Activation of ERK enhances expression of the transcription factor ΔFosB- and ERK-dependent activation of mTORC1, which results in the inhibition of long-term depression in striatal neurons and development of the abnormal involuntary movement in PD patients. Attenuation of Ras-GRF1 in the knock-out mice model results in the attenuation of LID. A similar reduction in LID was resulted in the inhibition of Ras (by simvastatin) and MEK (by SL327) expression. On the other hand, the inhibition of ΔFosB by short hairpin RNA and blockade of mTORC1 by rapamycin has been shown to mitigate LID. Various NMDA receptor antagonists have also been reported to reduce the expression of the Ras/Raf pathway and support their efficacy in LID.

and pharmacological approaches for the management of LID have been elaborated.

3.1 Pharmacological Approaches

For so many years, L-DOPA, which is a prodrug, is very effective in the treatment of parkinsonian motor symptoms. Chronic use of L-DOPA leads to several complications in PD patients. Response fluctuations and dyskinesia are examples of these complications. As a result, the management of the use of L-DOPA for treatment becomes a very important aspect. Many approaches participate that decide the best use of L-DOPA for the treatment of PD. Chemical approaches include two types of therapy, that is, dopaminergic therapy and non-dopaminergic therapy (Hauser et al., 2006; Encarnacion and Hauser, 2008). Recent updates on therapeutic interventions for LID (Santini et al., 2007; Kong et al., 2015; Wang et al., 2015; Calabrese et al., 2020; Beck et al., 2021) have been summarized in **Supplementary Table S1** and illustrated in **Figure 2**.

3.1.1 Improving Dopaminergic Therapy

LID is motor complications arising from pulsatile DA concentration in the brain. Theoretically, reaching a steady state of DA expression can precipitate dyskinesia. Thus, researchers have focused on developing therapies that provide continuous dopaminergic stimulation (CDS) to the brain. By doing this, the antiparkinsonian effects will remain unchanged, but it will be achieved without encountering dyskinesias.

Steady administration of L-DOPA abridged the risk of LID (Bibbiani et al., 2005). Many experimental studies showed that Parkinson's patients are more prone to dyskinesia with L-DOPA than DA agonist monotherapy. The reason can be that DA agonists have more affinity for D2 receptors than D1 receptors (Sharma et al., 2015). Therefore, to manage dyskinesia in PD patients, the first step is to lessen the dose of L-DOPA during dopaminergic therapy given to the patient, but in some cases, it will worsen parkinsonism. Apart from this, we can also give repeated small doses of L-DOPA (Mazzucchi et al., 2015). During the management of dyskinesia, the focus is always to prevent the

progress of dyskinesia and reduce the severity of dyskinesia. Instead of an intermediate release, the controlled release formulations of L-DOPA are helpful in delaying dyskinesia (Lee, 2001). Along with L-DOPA, dopaminomimetics having a longer half-life are administered to decrease pulsatile stimulation of DA receptors. In selected cases, COMT inhibitors are included as an example amantadine, which is recently given adjuvant to L-DOPA.

3.1.2 Replacement With Other Dopaminergic Agents

As previously mentioned, prolonged formulation of DA agonists can be used in dyskinesia management because of their selective nature toward D2 receptors. D1 receptors are mainly responsible for emerging dyskinesia. Cabergoline, pramipexole, and ropinirole decreases the development of dyskinesia as compared to L-DOPA monotherapy during initial therapy in PD patients (Binde et al., 2020). DA agonists promote more continuous stimulation and restrict postsynaptic changes, which play the main role in L-DOPA inducing dyskinesia (Jenner, 2004). Pergolide, which is another example of a DA receptor agonist, delays the motor complication more than L-DOPA therapy (Bychkov et al., 2007). Bromocriptine monotherapy also lessens motor complication (Hussain et al., 2018).

Pramipexole, a D3 agonist, balances D1 DA receptor supersensitivity-associated LID. Early use of pramipexole not only prevents dyskinesia but also helps to treat motor fluctuations. Ropinirole is another example of a DA receptor agonist. Studies have claimed that ropinirole significantly lowers dyskinesia as compared to L-DOPA. Prolonged release of ropinirole has the potency to delay dyskinesia more than the increased dose of L-DOPA in patients. Rotigotine, a D1 receptor agonist, can also be used as a replacement for L-DOPA to prevent dyskinesia, but more investigation is required (Hutny et al., 2021).

3.1.3 Adjuvant Therapy With L-DOPA

Catechol-O-methyltransferase inhibitors, also called COMT inhibitors, increase the obtainability of L-DOPA in the brain. The progress of dyskinesia can be overcome in PD patients by maintaining the plasma concentration of drugs in the body (Rascol et al., 2015). Entacapone and tolcapone are the drugs that help to reduce fluctuation in the concentration of L-DOPA. The only disadvantage is that tolcapone leads to liver toxicity. This disadvantage results in the development of new drugs which are safer and have enhanced activity (Deane et al., 2004). Opicapone belongs to the third-generation COMT inhibitor, a drug having safer and enhanced activity. This drug increases the bioavailability of L-DOPA, which has been proved in many experimental studies. Dyskinesia, insomnia, and dizziness are the disadvantages of opicapone (Hutny et al., 2021).

MAO-B inhibitors like safinamide, which also act on the glutamatergic system, help to improve the bioavailability of L-DOPA and increase its availability in spiny neuron synaptic clefts (Grégoire et al., 2013). In another study, safinamide is modulating the glutamate expression in the striatal region. Due to this, it has depicted significant motor complication reduction properties, without inducing troublesome dyskinesia. This fact can support its clinical use as an add-on therapy in the management of LID (Gardoni et al., 2018). Safinamide increases the bioavailability of L-DOPA when used as an ad on therapy, which makes this combination more effective in reducing motor complications (Schaeffer et al., 2014).

From a modification point of view, some alterations in therapy are included. The first modification is related to dose: the dose selection should be in a way that it gives more benefit. One experimental study proved that in the initial stages of treatment, if we give a dose of L-DOPA more than 600 mg, it may increase the chances of dyskinesia (Lee, 2001). In a modification, the dose of DA receptor agonists may increase or the daily dose of L-DOPA may decrease. Treatment of diphasic dyskinesia is more complex. In treatment therapy of diphasic dyskinesia, the addition of DA agonists or drugs that prolong L-DOPA, that is, COMT inhibitors or monoamine oxidase B inhibitors, are administered. D3 receptor antagonist IRL790 can also be given to a patient for maintaining psychomotor stability (Schaeffer et al., 2014; Hutny et al., 2021).

3.1.4 Formulation-Based Approaches for Improved L-DOPA Therapy

Numbers of new formulations have been discovered by drug repurposing methods to manage dyskinesia induced by L-DOPA. The working of the new drug should be in a way that it reduces L-DOPA-induced dyskinesia but should not have any effect on antiparkinsonian activity. Scientists have tried to know the mechanism involved in the occurrence and expression of symptoms in LID. Pharmacokinetics of L-DOPA play an important role in the treatment of LID. We can achieve constant plasma levels by improving the delivery of a drug into the body (Rascol et al., 2015). XP21279 is a L-DOPA prodrug, which is converted into L-DOPA by carboxylesterases. This prodrug has a stable plasma concentration and can be used to diminish LID (Savola et al., 2003). CVT-301, an example of inhaled L-DOPA formulation used in PD patients, has also proven its ability in the improvement of motor complications (Stocchi et al., 2018).

L-DOPA/benserazide (polylactic-glycosic acid) microspheres (LBM), a novel therapeutic approach, have shown to be effective as an antiparkinsonian therapy without inducing dyskinesias. The effect was shown in a dose-dependent manner. LBM was observed to be not activating the D1R/Shp-2/ERK1/2 pathway, which was found to be activated in the 6-hydroxy DA rat model of LID (Fiorentini et al., 2013; Wan et al., 2017). These results were like the previous results, where it was observed that LBM reduces the frequency of LID. In various animal models, it was found that PKA/DARPP-32 signaling activation increases tau protein phosphorylation, which leads to subsequent activation of SNPs and results in LID. Dose-dependent inhibition of PKA/DARPP-32 signaling, tau protein phosphorylation, and activation of SNPs were also examined in LBM-treated animals. Thus, in the case of LBM-treated animals, the amount of dyskinesia encountered was also less frequent (Xie et al., 2014). Chitosan-coated nanoliposomes (CCN) is another advanced way to improve DA delivery in the brain. In Parkinsonian rats treated with

CCN, it was observed that the induction of LID is less than that of L-DOPA-treated animals. CCN was observed to be reducing the expression of ERK1/2, DARPP-32, and FosB/DFosB, which were found to be upregulated in LID (Cao et al., 2016).

3.1.5 Non-Dopaminergic Approaches

Non-dopaminergic activity influences symptomatic development, neurodegenerative processes and, more importantly, the development of available therapeutic adverse effects including LID. It has identified defects in several non-dopaminergic aspects of the pathway inside the basal ganglia. During the past few years, researchers have started to identify improper signaling *via* glutamatergic, adrenergic, serotonergic (5HT), cannabinoid, and opioid pathways in both stimulation and activation of LID at the cellular level (Brotchie, 2005).

3.1.5.1 Adenosine A_{2A} Receptor Antagonists

Adenosine receptors play a crucial role in the development of LID. Adenosine interacts closely with DA and regulates the excessive glutamate neurotransmission in PD as well as LID (Morin et al., 2016). Adenosine A_{2A} receptor antagonists were observed to be reducing excessive striato-pallidal and subthalamic neuronal activity (Blandini and Armentero, 2012). In a study, it was observed that MPTP-treated monkeys with dyskinesia have an upregulated expression of adenosine A_{2A} receptor, compared with non-dyskinetic MPTP treated monkeys (Morin et al., 2016). Hence, adenosine receptors have gained increased attention from researchers.

ST1535, an adenosine A2 receptor antagonist, was examined to be effective as an antiparkinsonian agent, and it significantly reduces the requirement of L-DOPA dose. Thus, using this as an add-on therapy along with L-DOPA may significantly delay the development of LID (Rose et al., 2006). Caffeine also shows adenosine A2 receptor antagonism action. It was examined that caffeine was able to alleviate LID symptoms in 6-OHDA-treated mice. The mechanism of action was found to be blockage of adenosine A_1 or A_{2A} receptors (Xiao et al., 2011). Istradefylline, another adenosine A2 receptor antagonist, was observed to be effective in improving motor complications associated with PD without provoking dyskinesia. Therefore, it has the potential to be used as a monotherapy in PD; in that way, it will eliminate the occurrence of LID. However, more research is required to explore its potential (Uchida et al., 2015). Contrastingly, SCH 412348, an adenosine A2 receptor antagonist, does not alleviate LID when co-administered with L-DOPA in 6-OHDA-treated rats (Jones et al., 2013). Thus, using a combination therapy of L-DOPA and adenosine A2 receptor antagonists to treat LID might not carry that much potential. However, more research is needed to confirm it.

3.1.5.2 Adrenergic Receptor Antagonists

The adrenergic system also plays a crucial role in the development of PD and LID. In a study, it was observed that the noradrenergic system modulates the LID severity. In that same study, it was also demonstrated that in 6-OHDA-treated hemiparkinsonian rats, the use of alpha- and beta-adrenergic receptor blockers can alleviate the development of LID (Barnum et al., 2012). Alpha-2 adrenergic receptor blockers idazoxan, rauwolscine, and yohimbine were also observed to be reducing LID in the MPTP-lesioned primate PD model. Idazoxan as monotherapy has no beneficial effect on PD or LID, but when it was used in combination with L-DOPA, it not only alleviated LID but also increased the t_{max} more than two times (Paredes-Rodriguez et al., 2020). Propranolol, a potent beta-adrenergic receptor blocker, was also observed to be reducing LID in hemiparkinsonian rats. The researchers found that LID-alleviating effects of propranolol were mediated *via* mitigation of L-DOPA-induced extra physiological efflux of DA (Bhide et al., 2015). Fipamezole (JP-1730) is also a potent alpha-2-adrenergic blocker. It was observed to be reducing LID in MPTP-lesioned primate PD models. The combination of fipamezole and L-DOPA increases the duration of action of L-DOPA by 66%, compared with L-DOPA alone (Savola et al., 2003). Thus, adrenergic receptor antagonists have great potential as an adjunct to classical L-DOPA therapy. It can be beneficial in increasing the duration of the therapy and providing continuous dopaminergic stimulation.

3.1.5.3 Glutamatergic Antagonists

There are two types of glutamatergic receptors: First is ionotropic glutamatergic receptors (iGluRs) that mediate fast excitatory neurotransmission, and the second one is metabotropic glutamatergic receptors (mGluR) that mediate slow excitatory neurotransmission. iGluRs are classified into NMDA, AMPA, and kainite (KA) receptors (Morin and Di Paolo, 2014; Fabbrini and Guerra, 2021). Higher striatal expression of NMDA and AMPA receptors was reported previously in MPTP-treated dyskinetic monkeys (Morin and Di Paolo, 2014). However, NMDA and AMPA receptor blockage was observed to be alleviating the development of LID in 6-OHDA rats (Fabbrini and Guerra, 2021).

Mavoglurant is an antagonist for the glutamate mGluR5 receptor. Ionotropic and metabotropic glutamate receptor antagonists are subjected to examination for their possible involvement in the alleviation of LID since overactivity of glutamatergic pathways has been linked to the development of LID in animal models (Jimenez-Urbieta et al., 2015; Trenkwalder et al., 2016a; Negida et al., 2021). The striatum is rich in metabotropic mGlu5 receptors, which are related to NMDA receptors. mGlu5 receptor antagonists appeared to be beneficial in correcting aberrant movements in 6-hydroxy DA (6-OHDA)-lesioned macaques in preclinical trials. Human trials of mavoglurant, a metabotropic mGlu5 receptor antagonist, have had mixed results. In addition, the medication has been linked to several potentially dangerous side effects such as hallucinations and dizziness. MGluR4PAM in several animal models of PD, a positive allosteric modulator of mGluR4 (VU0364770), elicits significant antiparkinsonian effects, but it fails to affect the development and evolution of LID in unilaterally 6-OHDA-lesioned rats (Iderberg et al., 2015; Tison et al., 2016).

Traxoprodil is an NR2B subunit-specific NMDA receptor antagonist. It was observed that administration of traxoprodil revealed 30% reduction in LID severity, but there was no

reduction in motor abnormalities or certain cognitive difficulties associated with therapy (Nutt et al., 2008; Kong et al., 2015). Memantine functions as a non-competitive NMDA receptor antagonist. In an experiment with 6-ODHA-lesioned rats, both memantine and amantadine greatly decreased LID, but the alleviating effect of memantine was found to be, in a few days, showing a rapid tolerance to the anti-dyskinetic action of this medicine (Jankovic and Clarence-Smith, 2011). In contrast, riluzole, an NMDA receptor antagonist, did not elicit any anti-dyskinetic effect (Bara-Jimenez et al., 2006). CI-1041, another NMDA receptor antagonist, was observed to be inhibiting the development of LID in parkinsonian monkeys. The mechanism of action observed was the downregulation of the striatal mGlu5 receptor (Hadj et al., 2004).

3.1.5.4 Serotonergic Agonists

Chronic L-DOPA therapy and decreased DA levels in the brain lead to alterations in the brain's serotonergic system. It was observed that modification of the serotonergic system exerts an inhibitory effect on LID. However, careful administration is required as an overdose of serotonergic agonists can lead to symptomatology (5-HT syndrome), which shows PD-like symptoms (Hernandez et al., 2019). Buspirone, a partial 5-HT1A receptor agonist, was examined to be preventing the development of LID in rats without altering the STN electrical activity. An observed mechanism was found to be the regulation of GABA and Glu release, along with burst activity in pars reticular of SN (SNr) (Vegas-Suárez et al., 2020).

8-Hydroxy-2-dipropylaminotetralin (8-OH-DPAT), a 5-HT1A receptor agonist, was reported to be reducing LID development *via* downregulating D1 and D2 agonism-induced cortical gamma overactivity. However, associated frequent 5-HT syndrome development limits its further application (Nahimi et al., 2012; Dupre et al., 2016). SSRIs were also evaluated for this purpose. Citalopram, an SSSRI, was observed to be alleviating LID development without inducing 5-HT syndrome (Lindenbach et al., 2015). Another 5-HT_{1A} receptor agonist, BMY-14802, was also evaluated to be showing LID reducing effect in a dose-dependent manner. It not only reduces L-DOPA-induced dyskinesias but reduction of DA agonism-induced dyskinesias was also reported. The chances of developing 5-HT syndrome after treatment were also very low as its activity can be easily reversed by using a 5-HT1A receptor antagonist (Bhide et al., 2013). 5-HT_3 receptor antagonism is another possible checkpoint in the treatment of LID. Ondansetron, a well-known 5-HT_3 receptor antagonist, was examined for this purpose. After 23 days of continuous co-administration with L-DOPA, a significant reduction in LID development was noticed between Ondansetron + L-DOPA-treated group and only L-DOPA-treated groups. These results suggest that 5-HT_3 receptor antagonism carries potential in controlling the development of LID, but more research is needed to explore its maximum potential (Aboulghasemi et al., 2018).

Serotonin precursor, 5-hydroxy-tryptophan (5-HTP), was also examined to bear anti-dyskinetic properties. The basic mechanism of its activity is the upregulation of cytoplasmic serotonin, which competes with DA in serotonergic neurons and decreases the DA release from nerve terminals (Maffei, 2020). 5-HTP was reported to be alleviating LID in 6-OHDA-treated PD mice. When co-administered with L-DOPA, it neither loses its LID-alleviating properties nor decreases the antiparkinsonian effect of L-DOPA (Tronci et al., 2013). Thus, it can serve as a potent adjunct to L-DOPA therapy, which can minimize the development of LID.

In rat models of LID, levetiracetam has been found to decrease abnormal involuntary movements in a dose-dependent manner. While the mechanism for this improvement is unknown, it is thought to occur as a result of its effect at many locations in the LID cascade, including a change in the expression of specific transcription factors and phosphorylated kinases in the striatum (Du et al., 2015). In an MPTP non-human monkey model of PD, levetiracetam was observed to enhance the effects of amantadine (Hill et al., 2004). Levetiracetam has been proven to be effective in treating LID in several open-label clinical studies (Tousi and Subramanian, 2005).

3.1.5.5 Opioid Drugs

The idea that increased signaling by opioid peptides may promote to the development of LID has piqued interest for more than a decade because the opioids affect the neurotransmission in the basal ganglia, and significant alteration in opioid signaling is generally encountered in PD patients (Johansson et al., 2001). Thus, drugs modulating this system can prove to be an effective alternative therapy to the standard anti-dyskinetic therapy.

Combination treatment of L-DOPA and nalbuphine (κ subtype agonist and μ subtype antagonist) was examined to be downregulating the expression of various LID markers, like ΔFosB, prodynorphin, dynorphin A, Cdk5, and Thr34 phosphorylation of DARPP-32, to normalized levels. No adverse events were encountered during this study. The sedative effect of nalbuphine was also not induced by L-DOPA (Potts et al., 2015). To find out the potential of μ receptor antagonism monotherapy in alleviating LID, another study was performed on the 6-OHDA PD rat model. In this experiment, it was found that selective μ receptor antagonism is not able to improve dyskinesias in rats (Bartlett et al., 2020b). Thus, the results obtained by using the L-DOPA and nalbuphine combination therapy might be an outcome of the therapy's dualistic nature. However, μ receptor agonism monotherapy was able to downgrade the incidence of LID in the MPTP parkinsonian rat model (Hutny et al., 2021).

Mu-delta opioid receptor agonism can also be beneficial in the treatment of LID. Lactomorphin, a mu-delta opioid receptor agonist, was examined to exert antiparkinsonian activity along with reduced incidence of dyskinesia in 6-OHDA-treated male SD rats. It reduced the AIM score significantly when compared with the untreated animals (Flores et al., 2018). Cyprodime, ADC-02520849, and ADC-02265510 are three opioid receptor agonists. They were examined to be alleviating LID symptoms along with reduction of LID severity scores in MPTP-treated primate models of PD (Bezard et al., 2020). Thus, the use of opioid drugs is an effective pharmacotherapeutic way to reduce

dyskinesias associated with L-DOPA treatment. However, much research is needed to evaluate such possibilities.

3.1.5.6 Nitric Oxide Modulators

Loss of dopaminergic neurons in the substantia nigra of the brain is the main characteristic feature of PD. However, along with DA depletion hindrance in nitric oxide (NO), neurotransmission was also observed to be hindered during PD. DA by direct acting on DA receptors situated in the striatal nNOS interneurons facilitates NO production. In PD, there is a significant decrease in the expression of nNOS-containing neurons and nNOS mRNAs. NO is proven to play a crucial role in the control of motor functions (Pierucci et al., 2011; Lorenc-Koci et al., 2017). Thus, it can be concluded that NO hypofunction can play a crucial role in the development of PD and LID.

In a study, it was observed that when NO donor molsidomine was co-administered with L-DOPA, the expression of DA gets increased, which in turn decreases the incidence of LID (Lorenc-Koci et al., 2013). The anti-dyskinetic property of molsidomine was also demonstrated in genetically susceptible PD mice (Solís et al., 2015). Upregulation of NO-soluble guanylyl cyclase–cGMP signaling also plays a vital role in LID. Methylene blue, a potent inhibitor of it, can alleviate LID, when co-administered with L-DOPA or when injected into the lateral ventricle of the brain as a monotherapy (Pierucci et al., 2011; Bariotto-Dos-Santos et al., 2019). Thus, the use of NO modulators carries the potential to be included in the management of LID. However, clinical evidence regarding this is still missing in the literature. More research is required to reveal its true potential in the management of LID.

4 CLINICAL MANAGEMENT OF LEVODOPA-INDUCED DYSKINESIA

4.1 Surgical Approaches

Neurosurgical approaches have shown to be the most effective in providing sustained relief from LID in PD patients. Mainly, neurosurgical approaches associated with basal ganglia and cerebral cortex have shown to be the most effective in treating LID.

4.1.1 Deep Brain Stimulation

DBS is a highly effective and the most preferred procedure in LID patients having advanced PD, drug refractoriness, and motor complications associated with L-DOPA therapy (Fasano et al., 2012; Munhoz et al., 2014). Various randomized control trials (RCTs) have proven that DBS reduces the PD symptoms, dyskinesias, and reduces the need for dopaminergic stimulation in LID (Kopell et al., 2006; Nazzaro et al., 2013). There are mainly two widely persuaded targets in the human brain that are being stimulated by DBS, that is, subthalamic nucleus (STN) and globus pallidus internus (GPi). Many RCTs have proven STN DBS and GPi DBS to be more successful in alleviating LID symptoms than medical treatment (Deuschl et al., 2006; Weaver et al., 2009). Few studies have demonstrated that STN DBS is more effective at reducing the required medication dose in LID, and these studies have also confirmed that STN DBS application does not lead to worse neuropsychiatric and cognitive outcomes than those of GPi DBS (Odekerken et al., 2016; Xie et al., 2016; Elgebaly et al., 2018). There are some conflicting pieces of evidence, whether the beneficial mechanism of DBS in LID is due to its direct stimulation, reduction of L-DOPA dosage, or a blend of both. However, some studies suggested that the effects are target-dependent. Like in the case of GPi DBS, the dyskinesia scores (UPDRS IV) get improved without reducing the required L-DOPA dose (Volkmann et al., 2004; Follett et al., 2010; Moro et al., 2010; Odekerken et al., 2016; Bonenfant et al., 2017), whereas in the case of STN DBS, the mechanism is of mixed type (Castrioto et al., 2011; Zibetti et al., 2011; Munhoz et al., 2014; Krishnan et al., 2016).

Classical DBS is mainly based on frame-based and frameless stereotactic methods with microelectrode recording (MER, for electrode placement confirmation). Portable imaging techniques (O-arm) have also been used in some studies, with or without the use of MER, to improve the accuracy and safety associated with DBS target placement (Burchiel et al., 2013; Frizon et al., 2018). Another technique, namely, frameless iMRI-guided DBS, was successfully investigated to have significantly greater accuracy than that of the classical DBS. It uses interventional magnetic resonance imaging (iMRI), and the electrode placement in it is guided by a skull-mounted aiming device. It is performed in anesthetized patients with the assistance of a real-time MRI scanner. The real-time MRI can account for the brain shift after the skull is opened, contrary to the classical DBS, where stereotactic placement based on preoperative imaging is the only option (Nakajima et al., 2011). A second-generation iMRI-guided DBS with improved operator control and fully integrated software has also been reported to be used with even greater lead placement accuracy and favorable patient outcomes (Ostrem et al., 2016).

Recently, frame-based stereotactic DBS has also been used along with iMRI (Matias et al., 2018). The iMRI-guided DBS has certain advantages over classical DBS, like improved electrode placement accuracy, streamlined procedure (as the patients are anesthetized), improved patient compliance (as performed under general anesthesia), faster lead placement times, and incorporation of MER for target confirmation (Ostrem et al., 2013). The iMRI-guided DBS is a very costly procedure, along with the logistical challenges of maintaining detectable intraoperative MRI and scheduling the procedure time on a diagnostic scanner. So, the cost to benefit ratio for patients included in this procedure must be evaluated with great importance (Azmi et al., 2016).

Classical DBS needs calibration for every patient to avoid side effects like dyskinesia, as incorrect stimulation parameters can lead to dyskinesia. To address this drawback, an adaptive or closed-loop DBS has been developed. In adaptive DBS, a sensory electrode and a modulating electrode are applied on the motor cortex and basal ganglia region, respectively. They help in monitoring the brain activity patterns associated with dyskinesia. Upon detection of these patterns, a feedback loop gets activated, which decreases the stimulation delivered to the target region (Swann et al., 2018). An adaptive DBS study was successfully performed using a novel narrowband gamma

oscillation as a biomarker for dyskinesia in the motor cortex to modulate the target stimulation delivered (Swann et al., 2018). They also reported 38–45% less energy consumption than classical DBS to maintain the same therapeutic efficacy (Dastin-van Rijn et al., 2021). Recently, more responsive adaptive DBS systems have been developed using accelerometer-based technology, which detects movements by utilizing peripheral kinematic sensors to detect dyskinesia (Rojas Cabrera et al., 2020).

4.1.2 Surgical Ablation

Surgical ablation is another well-persuaded procedure in LID. Ablation of globus pallidus is preferred when several factors, like situations with fewer resources, difficulties in follow-up for several years, and risk of complications from electrode implantation, make DBS less practical to follow (Sharma et al., 2020). Unilateral pallidotomy has shown to result in long-lasting and sustained improvement of LID, tremor, rigidity, bradykinesia, gait, and balance. Contralateral and ipsilateral improvements in LID were also reported by following this procedure (Vitek et al., 2003; Upadhyay et al., 2015). However, it was reported that bilateral STN DBS produced greater improvements in motor and bradykinesia symptoms than unilateral pallidotomy (Esselink et al., 2004).

Ultrasound ablation or focused ultrasound ablation is a newly developed and minimally invasive procedure, which has been successfully examined to be highly effective in the treatment of LID (Magara et al., 2014; Na et al., 2015; Schlesinger et al., 2015; Zaaroor et al., 2018). It is a magnetic resonance-guided focused ultrasound (MRgFUS) technique, which has been successfully incorporated with pallidothalamic tractotomy (Fine et al., 2000) and unilateral pallidotomy (Na et al., 2015) procedures, and it resulted in better outcomes than conventional surgical ablation procedures. Focused ultrasound ablation showed to improve the UPDRS motor scores and contralateral dyskinesia scores in LID patients (Magara et al., 2014; Na et al., 2015; Schlesinger et al., 2015; Zaaroor et al., 2018). Thus, it has great potential in the management of LID.

4.1.3 Transcranial Magnetic Stimulation

TMS is one newly implemented non-pharmacological method to treat LID. TMS is a non-surgical procedure, in which a specific area of cortex is stimulated by recurrent single pulse electromagnetic conduction that emerges from a coil, which is coupled to a pulse generator. It has been observed that the excitability in the cortical region gets increased after application of high-frequency stimulation, and it gets decreased by the application of low-frequency stimulation, but in the case of theta-burst stimulation (TBS), intermittent stimulation increases cortical excitability, whereas continuous stimulation reverses (Pascual-Leone et al., 1994; Chen et al., 1997; Huang et al., 2005).

A study suggests that LID is mainly a manifestation of primary disinhibition of motor cortex and secondary excessive outflow of pallidothalamocortical motor loop (during peak dosing) (Rascol et al., 1998). Overlapping of these quantifiable cortical changes with LID symptoms provides strong evidence toward the involvement of cortical dysfunction in the pathophysiology of LID (Rascol et al., 1998). Thus, applying stimulation to the cortex region to undo its dysfunctions is a rational LID treatment approach.

Although some studies have demonstrated that repetitive TMS (rTMS) with lower frequency (1 Hz) can produce a significant decrease of dyskinesia symptoms in patients, but the effect is not long term, recurrent rTMS treatment is needed to maintain the reduced dyskinesia state for a longer duration of time (Wagle-Shukla et al., 2007; Filipović et al., 2009). However, the long-term effects of rTMS are still debatable as there are study limitations like insufficient statistical power, protocol variation, short follow-up period, and lack of standardized control procedure. Due to these limitations, the dopaminergic effects of rTMS are not proven yet (Strafella et al., 2006; Elahi et al., 2009; Benninger et al., 2012).

4.1.4 Implanted Motor Cortex Stimulation

MCS is a neurosurgical procedure that allows implantation in both epidural and subdural levels, and due to that, long-term, repetitive electromagnetic stimulation is delivered to the cortex. However, epidural implantations are preferred over subdural implantations because of no dampening of therapeutic stimulation by CSF and less serious complications in it (Bezard et al., 1999; Saitoh et al., 2003; Manola et al., 2005; Delavallee et al., 2008). MCS works on the same principles as TMS. The mechanism of action of the MCS procedure is uncertain, but some studies on primate PD models have proven that "electromagnetic stimulation dampens the abnormal oscillations taking place between the cortex and basal ganglia in PD, normalizes hyperactive structures in these areas, and reactivates hypoactive structures" (Drouot et al., 2004; Lefaucheur, 2009). Implanted MCS has shown promising results in reducing L-DOPA dose; hence, delaying the onset of LID (Canavero and Paolotti, 2000; Cilia et al., 2007). However, some studies have reported conflicting results. In those studies, it has been observed that a lower frequency of stimulation produced negative results, whereas higher frequency stimulation produced positive results (Lefaucheur, 2009). Despite these conflicting results, implanted MCS has great potential in the management of LID. Further research can fortify its application in LID with greater effectiveness.

4.2 Pharmacotherapeutic Approaches

Pathological knowledge of LID has increased vastly in the last decade. Many pharmacotherapeutic approaches have shown promising results in their preclinical studies, but their clinical results are not satisfactory. The present clinical status of LID management has been summarized in **Supplementary Table S2**.

There is profound evidence present in the literature regarding the treatment of LID. The main goal of LID treatment has been the reduction or prevention of LID or to reduce its onset, maintaining the excellent antiparkinsonian effect of L-DOPA (good on time). To achieve this goal, researchers have mainly focused to reduce the L-DOPA dose, providing continuous

dopaminergic stimulation, and identifying non-dopaminergic targets to treat LID.

Continuous usage of lower doses of L-DOPA is the most preferred clinical strategy in the management of LID (Scott et al., 2016). There is a clear correlation between the dose of L-DOPA used and the severity and likelihood of the dyskinesia developed. It was observed that PD patients receiving higher doses of L-DOPA are more likely to develop LID (Fahn, 1999; Verschuur et al., 2019). Along with that, adjuvant therapy of DA agonists and MAO inhibitors was also evaluated in various seminal studies, with an aim of reducing the L-DOPA dose; thus, delaying the onset of LID (Holloway et al., 2005; Watts et al., 2010). However, no long-term benefit has been observed. A new extent release capsule of carbidopa and L-DOPA named IPX066 has also been discovered. This capsule contains immediate and sustained-release pellets, and has become superior over L-DOPA + carbidopa + entacapone in the treatment of PD (Hauser et al., 2013). L-DOPA carbidopa subcutaneous pumps are also used in PD patients. This subcutaneous pump helps reduce fluctuation in L-DOPA concentrations (Giladi et al., 2015).

Due to the failure of these approaches, the concept of continuous dopaminergic stimulation (CDS) has emerged. This technique makes use of longer acting dopaminergic agents, which provide more constant and long-lasting dopaminergic stimulation to the dopaminergic receptors. Rotigotine, apomorphine-like drugs, entacapone/L-DOPA, and L-DOPA carbidopa intestinal gel (LICG)-like formulation approaches have been taken to provide CDS, but they have proven beneficial only in advanced PD and not in LID. However, they are reported to be reducing the occurrence of motor complications and dyskinesia. Thus, using them along with other preventive medication can increase the quality of life of patients suffering from LID (Olanow et al., 2020).

DBS is the most effective technique by which CDS and subsequent alleviation from LID can be achieved. Stimulation of the subthalamic nucleus and internal globus pallidus has shown to be beneficial in LID as it induces the striatal DA release, which provides more sustained CDS (Fox et al., 2018). However, despite the benefits, cost, lack of accessibility, invasiveness, and side effect profile limit their use on human subjects (Buhmann et al., 2017).

MAO-B inhibition has also proven to be effective in the management of LID. Safinamide is a water-soluble orally given aminoamide that has two mechanisms of action: MAO-B inhibition and glutamate release inhibition. In a two-year period, in PD, a prospective double-blind placebo-controlled study is being conducted. Safinamide treatment was found to reduce the motor complications without worsening PD complications (Borgohain et al., 2014). When compared to placebo, long-term usage of safinamide did not increase the risk of dyskinesia, and 100 mg of safinamide per day reduced dyskinesia in patients who had more severe dyskinesia at baseline and was well accepted by patients (Borgohain et al., 2014).

Zonisamide works *via* increasing DA production, inhibiting MAO-B, inhibiting glutamate release, and inhibiting sodium and T-type calcium channels, among other things. Since studies indicated an improvement in PD symptoms with a very low frequency of side responses such as dyskinesia and hallucination, zonisamide has been approved in Japan for use as a supplementary therapy in PD patients. Zonisamide lowers off-time in PD patients with wearing off, according to a double-blind RCT including 422 patients (Murata et al., 2015). Zonisamide is effective in the treatment of PD motor symptoms, although it is still considered experimental for other indications, such as the therapy of LIDs (Seppi et al., 2011).

Along with dopaminergic alteration, scientists have identified many non-dopaminergic targets/add-on therapies also. Metabotropic glutamate receptor agonism is one the most promising aspect of it. Dipraglurant and mavoglurant (AFQ056), two selective metabotropic glutamate receptor agonists, have shown to be significantly reducing dyskinesia without worsening PD symptoms (Stocchi et al., 2013; Tison et al., 2016). Amongst them, dipraglurant has shown a significant reduction in peak dose dyskinesia, along with rapid absorption (T_{max} = 1 h) (Tison et al., 2016). This fact can support the rational use of dipraglurant in the management of acute peak dose dyskinesia cases, but its efficacy in such cases is yet to be evaluated. However, in another clinical study, mavoglurant (AFQ056) has failed to show LID-alleviating effects (Negida et al., 2021). Thus, the use of mavoglurant in the management of LID is questionable.

Out of several add-on therapies evaluated, amantadine, which is a non-selective NMDA receptor antagonist, is the most widely used and has proven to be the most effective add-on treatment in clinical studies (Fox et al., 2018; Hauser et al., 2021; He et al., 2021). Extended-release formulations of it were observed to be significantly increasing the on time, but it does not affect the dyskinesia (Hauser et al., 2021). However, due to side effects like confusion and hallucinations, their human application is limited (Hubsher et al., 2012). FDA has approved the use of a long-acting amantadine formulation for LID treatment in 2017. It provides a more stable plasma concentration and bioavailability than that of the immediate release forms, that is, supporting the concept of CDS (Müller and Möhr, 2019). In one phase III clinical study, it was observed that single daily dosing of amantadine significantly reduces LID in comparison to placebo-treated group (Pahwa et al., 2015; Paik et al., 2018). In another study of extended-release amantadine formulation, it was observed that a reduced level of LID was achieved, and that reduced expression was maintained for a median treatment period of 1.9 years (Tanner et al., 2020). However, its chronic clinical use for a longer period still needs to be evaluated. 100 mg of amantadine twice daily resulted in a significant decrease in total dyskinesia by 24%, and a significant reduction in duration of dyskinesia was also observed in a single double-blind placebo-controlled study involving 24 patients (Snow et al., 2000). Dyskinesias deteriorated within a week in patients who stopped using amantadine, according to a 3-month multicenter double-blind RCT comparing patients who were kept on amantadine vs. those who switched to a placebo. Apathy and tiredness were more common worsening conditions in these individuals (Friedman et al., 2014). Though the effects of amantadine anti-dyskinetic were thought to disappear after a few months, clinical investigation on 32 PD patients with LID,

who received amantadine for more than a year, has shown improvement in dyskinesia. In contrast, some studies suggested that the anti-dyskinetic effect was not the same (Wolf et al., 2010). The findings revealed that amantadine remained efficient in treating dyskinesia longer than a year after therapy began, with no adverse signs recorded in patients. The LID symptoms were observed to deteriorate in the group which received a placebo treatment. Furthermore, chronic amantadine treatment was associated with the development of hallucinations, sedation, myoclonus, livedo reticularis, hair loss, and edema (Seppi et al., 2011; Vijverman and Fox, 2014), which suggests the careful monitoring of the patients.

Another most promising non-dopaminergic approach to treat LID is the 5-HT (5-HT_{1A} and 5-HT_{1B}) receptor agonism. 5-HT_{1A} and 5-HT_{1B} receptor agonism have also gained research interest, as serotonergic stimulation is associated with DA release and activation of 5-HT_{1A}, 5-HT_{1B} receptors, which can lead to increased serotonin release in the brain (Carta et al., 2007). Eltoprazine, a 5-HT_{1A}, and a 5-HT_{1B} receptor agonist have been shown to be alleviating dyskinesia without interfering with the L-DOPA activity. It was also reported to be well tolerated amongst the patients (Svenningsson et al., 2015). Thus, this can be a possible add-on therapy to L-DOPA in controlling LID. In a randomized placebo-controlled double-blind pilot trial of nine PD patients, on time without dyskinesia or with non-troublesome dyskinesia increased significantly (Zesiewicz et al., 2005). Another multicenter double-blind placebo-controlled crossover experiment in 38 individuals with LID found that LID at dosages of 500 and 1,000 mg per day resulted in a substantial reduction in time (Stathis et al., 2011). However, a nine-patient open-label trial found that levetiracetam was not well tolerated in PD patients, with most patients experiencing sleepiness and increasing dyskinesia (Lyons and Pahwa, 2006).

In a phase 1 or 2 a dose-finding trial, eltoprazine, an agonist of presynaptic 5-HT_{1A} and 5-HT_{1B} receptors, established its anti-dyskinetic efficacy at 5 or 7.5 mg without affecting normal motor responses to L-DOPA (Svenningsson et al., 2015). Pardoprunox is a partial and full agonist at D_2 and D_3 receptors, as well as a low-affinity agonist at D4, α-2 adrenergic, and $5HT_7$ receptors. Because of its partial agonist action at DA receptors, this medication is thought to have a reduced risk of dyskinesia than other DA agonists. An RCT found a substantial increase in on time without bothersome dyskinesias when pardoprunox was titrated to as high as 42 mg per day (Hauser et al., 2009). A 12-week randomized placebo-controlled trial found that pardoprunox rose on time without causing troublesome dyskinesia, although the research had a high dropout rate, owing to gastrointestinal side effects, somnolence, and insomnia, as well as fast titration to higher dosages (Rascol et al., 2012).

Dipraglurant was studied in PD patients with moderate or severe LID in a phase IIa, randomized, placebo-controlled, double-blind, parallel-group trial. The primary goal was to establish safety and tolerability, and secondary goals were set to improve abnormal involuntary movements. A total of 46 (88.5%) dipraglurant-treated patients and 18 (75%) placebo patients experienced adverse events, with no significant changes in safety monitoring measures. Treatment with dipraglurant was linked with substantial effects on the mAIMS, but the durability of this initial impact is unknown, as there was no significant between-group difference at the study's conclusion point (Tison et al., 2013). The impact of the mGluR-5 negative allosteric modulator dipraglurant on LID reduction without worsening of parkinsonism observed in one RCT suggests that this drug merits further research.

In Japan, istradefylline, an agonist of adenosine A_{2A} receptor, has been approved as a supplement to L-DOPA therapy for PD patients (Mizuno and Kondo, 2013). Its impact on locomotor disturbances and LID is debatable. In a placebo-controlled, double-blinded RCT containing 373 PD affected volunteers with motor abnormalities, it was found that by applying istradefylline along with L-DOPA, the off-time associated with L-DOPA therapy was significantly reduced, although dyskinesia was the most encountered adverse effect (Vorovenci, and Antonini, 2015). Preladenant, an adenosine A_{2A} receptor antagonist, was observed to be improving the on time associated with L-DOPA therapy, without changing the dyskinesia state in individuals with moderate to severe PD in a double-blinded, placebo-controlled RCT (Hauser et al., 2015). Preladenant was observed to be increasing the on time of L-DOPA, without severe dyskinesia in two double-blinded, placebo-controlled, phase III studies. However, the results obtained were not significant when compared with the placebo-treated group (Hauser et al., 2015). Caffeine is a commonly prescribed psychostimulant that works by blocking adenosine A2A and A1 receptors, which inhibits adenosine propagation (Fredholm et al., 1999). Caffeine causes a persistent and dose-dependent increase in DARPP-32 phosphorylation at Thr75, according to new research. Caffeine's impact is greatest at 7.5 mg/kg, which also induces a sustained increase in motor activity. Caffeine's capacity to enhance DARPP-32 phosphorylation at Thr75 is most likely mediated by adenosine A2A receptor inhibition as SCH 58261, a specific A2A receptor antagonist, similarly increases phosphoThr75 levels (Lindskog et al., 2002).

Clozapine, in numerous trials, including a placebo-controlled, double-blinded study, was observed to be decreasing the severity of LID (Durif et al., 2004; Seppi et al., 2011). Clozapine's specific mechanism of action is unknown, but antagonistic binding to striatal DA receptor type 2 (D2) and serotonin type 2A receptors has been postulated (5-HT2A receptors). However, worries regarding possible side effects limit the use of clozapine for dyskinesia treatment. Insomnia, sialorrhea, asthenia, and possible severe toxicities, such as agranulocytosis in around 0.7 percent of patients, seizures, and myocarditis, were among the most prevalent side effects observed. Because of concerns regarding possible neutropenia, the constant neutrophil count was to be monitored for 12 months while on this drug (Pahwa et al., 2006; Seppi et al., 2011; Hack et al., 2014).

PET investigations in PD patients with LID show abnormalities in opioid receptors in the basal ganglia and

elsewhere (Piccini et al., 1997). Furthermore, in rodent and primate models of LID, the expression and levels of opioid receptors are changed throughout the basal ganglia (Johansson et al., 2001). While there are numerous methodological variations across the trials, it appears that blocking opioid transmission in a fashion that is not selective for opioid receptor subtypes has no anti-dyskinetic effect in humans when used in conjunction with L-DOPA. This was proven in recent research in individuals with LID, where an intravenous infusion of the non-subtype-selective opioid antagonist naloxone at a dosage that had previously been shown to offer effective opioid transmission-blocking was unable to decrease opioid transmission (Fox et al., 2004).

Many other drugs which have shown promising results in the reduction of LID severity in animal models have failed to show their activity in clinical studies. Perampanel, topiramate, AQW051, rislenemdaz, vitamin D, and nitric oxide modulators (Lees et al., 2012; Kobylecki et al., 2014; Trenkwalder et al., 2016b; Herring et al., 2017; Habibi et al., 2018) are a few examples of it. Topiramate, an anti-epileptic drug, was even reported to be increasing the severity of dyskinesia in patients. Five patients were even withdrawn from the study due to increased dyskinesia (Kobylecki et al., 2014). However, more research is still required to fully understand these variations.

5 PROBLEMS IN THE CONVERSION OF PRECLINICAL EFFECTIVITY TO CLINICAL STAGE

The first challenge faced is the difference between the disease models used to evaluate effectivity in animals and humans. The animal models used for this purpose do not fully replicate the complex human neurodegenerative patterns and variations that can take place inside a human body. The gold standard preclinical model, that is, the MPTP-lesioned primate model of PD, is generally dopaminergic and non-progressive, but in the case of humans, there is the involvement of complex pathogenic pathways and progressive neurodegeneration. This fact can explain the lack of conversion of efficacious results from the preclinical to clinical phase (Fox and Brotchie, 2019).

Also, finding of equivalent dose between the preclinical to clinical phases is difficult. As an example, naftazone (CVXL0107), a glutamate inhibitor, showed to reduce LID in the MPTP-lesioned primate model of PD, but in a multicenter, crossover, double-blinded randomized control trial (DBRCT), it failed to alleviate the LID symptoms (Mattei et al., 1999; Brotchie et al., 2007; Corvol et al., 2019). The authors of this study have interpreted that the unsuccessful results are either due to a mismatch between L-DOPA/naftazone or due to inappropriate dosing. Famotidine, a selective H2 receptor antagonist, also failed to show clinical efficacy despite being effective in the preclinical studies. The reason behind this failure is poor BBB permeability (Johnston et al., 2010; Mestre et al., 2014). Another shortcoming of preclinical studies is that the animal models used cannot properly measure the tolerability in human subjects. Many drugs like topiramate and 5-HT1A antagonists have shown poor tolerability in human subjects, despite being efficacious in the preclinical studies (Goetz et al., 2017; Huot et al., 2017).

Measurement of LID severity in clinical trials is a difficult task. In preclinical studies, many objective rating scales are used to measure the LID severity, which are similar to objective rating scales used in clinical studies (UDYRS part III). This depends upon the patient's perception of dyskinesia severity, and it provides no information about the level of disability. Along with that, lack of awareness of mild dyskinesia in PD is well documented (Hung et al., 2010). Thus, the results obtained from these scales are quite inaccurate, unreliable, and are subjected to recall bias (Stone et al., 2002; Papapetropoulos, 2012). However, some advanced technologies have been evaluated for the measurement of LID, and they were found to be producing more accurate and reliable results. Implementation of sensors to aid these technologies in measuring the severity and endpoints can also be an objective step that can produce more accurate results (Lopane et al., 2015; Ossig et al., 2016; Delrobaei et al., 2017).

The placebo effect in the evaluation of novel therapies alleviating LID is well observed in various studies. As an example, in a trial involving sarizotan, a 5HT1A agonist, the on time of LID was reduced by up to 1.5 h/day in the placebo-treated group, while the observed reduction in the LID on time was 2 h/day in the intervention group (Goetz et al., 2007; Goetz et al., 2008). The placebo effect is profound in the trials involving PD patients. The main underlying reason can be the reward effect associated with the DA pathology (Quattrone et al., 2018), that is, in blinded studies, after taking the placebo, there is a release of DA in the subject's brain. These effects can lead to false-positive results and can mask the underlying effect of a novel therapy. Thus, understanding the placebo effect can guide the trial design of future clinical trials.

6 CONCLUSION

LID is a common and difficult condition to treat PD patients. Clinical phenomenology for LID varies, but the three types are high-dose dyskinesia, dressing off or off-period dyskinesia, and diphasic dyskinesia. The exact mechanism of action is not known for dyskinesia, but both presynaptic and postsynaptic methods are effective in the pathogenesis of LID, and the management of dyskinesia depends on the type of dyskinesia encountered and thereafter, is treated. Reduction of dyskinesia is dependent on the dose like peak-dose dyskinesia, while the addition of long-acting formulations is effective in wearing-off dyskinesia. Infusion and surgical procedures are working on all kinds of dyskinesia. Along with that, various other drug targets have also been identified like serotonergic and glutamatergic systems. Targeting these targets as an add-on therapy has proven to be very beneficial in the management of epilepsy. Chemical management with a neurosurgical approach is the

future of the management of dyskinesia. Despite various advancements, the preclinical to clinical conversion rate is very low in the case of newly discovered drugs. Also, measuring the severity of dyskinesia has been challenging. More focus should be given to developing a progressive neurodegenerative animal model; a more unified LID measurement scale that does not depend on the patient's perception is needed. Neurosurgical stimulation for primary mitigation, along with drug treatment as maintenance therapy, should be a rational approach going into the future. However, this combination is yet to be tested on humans.

AUTHOR CONTRIBUTIONS

Conceptualization: AM and JA; methodology: NM, RB, and AM; formal analysis: AM, NM, and GM; resources: NM, RR, RB, and GS; data curation: AM, NM, GS, and RB; writing—original draft preparation: NM, RR, RB, GS, and AM; writing—review and editing: JA, SA, MG, and GM; visualization: AM and RB; and supervision: AM, JA, SA, and MG.

FUNDING

The Deanship of Scientific Research (DSR) at King Abdulaziz University, Jeddah, Saudi Arabia, has funded this project, under grant no. (FP-86-42).

ACKNOWLEDGMENTS

The author AM would like to acknowledge the Department of Pharmaceuticals, Ministry of Chemical and Fertilizers, Govt. of India, and National Institute of Pharmaceutical Education and Research (NIPER), Guwahati, for the necessary infrastructure and facilities. The images were "Created with BioRender.com."

SUPPLEMENTARY MATERIAL

The Supplementary Material for this article can be found online at: https://www.frontiersin.org/articles/10.3389/fphar.2022.805388/full#supplementary-material

REFERENCES

Abercrombie, E. D., Bonatz, A. E., and Zigmond, M. J. (1990). Effects of L-Dopa on Extracellular Dopamine in Striatum of normal and 6-Hydroxydopamine-Treated Rats. *Brain Res.* 525 (1), 36–44. doi:10.1016/0006-8993(90)91318-b

Aboulghasemi, N., Hadipour Jahromy, M., and Ghasemi, A. (2018). Anti-dyskinetic Efficacy of 5-HT3 Receptor Antagonist in the Hemi-Parkinsonian Rat Model. *IBRO Rep.* 6, 40–44. doi:10.1016/j.ibror.2018.12.001

Ahmad, J., Haider, N., Khan, M. A., Md, S., Ghoneim, M. M., Alshehri, S., et al. (2022). Novel Therapeutic Interventions for Combating Parkinson's Disease and Prospects of Nose-To-Brain Drug Delivery. *Biochem. Pharmacol.* 195, 114849. doi:10.1016/j.bcp.2021.114849

Ahmed, I., Bose, S. K., Pavese, N., Ramlackhansingh, A., Turkheimer, F., Hotton, G., et al. (2011). Glutamate NMDA Receptor Dysregulation in Parkinson's Disease with Dyskinesias. *Brain* 134 (Pt 4), 979–986. doi:10.1093/brain/awr028

Albarrán-Bravo, S., Ávalos-Fuentes, J. A., Cortés, H., Rodriguez-Sánchez, M., Leyva-García, N., Rangel-Barajas, C., et al. (2019). Severity of Dyskinesia and D3R Signaling Changes Induced by L-DOPA Treatment of Hemiparkinsonian Rats Are Features Inherent to the Treated Subjects. *Biomolecules* 9 (9), 431. doi:10.3390/biom9090431

Alcacer, C., Santini, E., Valjent, E., Gaven, F., Girault, J. A., and Hervé, D. (2012). Gα(olf) Mutation Allows Parsing the Role of cAMP-dependent and Extracellular Signal-Regulated Kinase-dependent Signaling in L-3,4-Dihydroxyphenylalanine-Induced Dyskinesia. *J. Neurosci.* 32 (17), 5900–5910. doi:10.1523/JNEUROSCI.0837-12.2012

Altwal, F., Moon, C., West, A. R., and Steiner, H. (2020). The Multimodal Serotonergic Agent Vilazodone Inhibits L-DOPA-Induced Gene Regulation in Striatal Projection Neurons and Associated Dyskinesia in an Animal Model of Parkinson's Disease. *Cells* 9 (10), 2265. doi:10.3390/cells9102265

Angelopoulou, E., Nath Paudel, Y., Piperi, C., and Mishra, A. (2021). Neuroprotective Potential of Cinnamon and its Metabolites in Parkinson's Disease: Mechanistic Insights, Limitations, and Novel Therapeutic Opportunities. *J. Biochem. Mol. Toxicol.*, e22711. doi:10.1002/jbt.22711

Arakawa, K., Yuge, N., and Maehara, S. (2020). Ameliorative Effects of a Phosphodiesterase 10A Inhibitor, MR1916 on L-DOPA-Induced Dyskinesia in Parkinsonian Rats. *Pharmacol. Rep.* 72 (2), 443–448. doi:10.1007/s43440-020-00060-y

Azmi, H., Gupta, F., Vukic, M., Kreitner, J., Kera, E., Nicola, G., et al. (2016). Interventional Magnetic Resonance Imaging-Guided Subthalamic Nucleus Deep Brain Stimulation for Parkinson's Disease: Patient Selection. *Surg. Neurol. Int.* 7 (Suppl. 19), S557–S563. doi:10.4103/2152-7806.187537

Bara-Jimenez, W., Dimitrova, T. D., Sherzai, A., Aksu, M., and Chase, T. N. (2006). Glutamate Release Inhibition Ineffective in Levodopa-Induced Motor Complications. *Mov Disord.* 21 (9), 1380–1383. doi:10.1002/mds.20976

Bariotto-Dos-Santos, K., Padovan-Neto, F. E., Bortolanza, M., Dos-Santos-Pereira, M., Raisman-Vozari, R., Tumas, V., et al. (2019). Repurposing an Established Drug: an Emerging Role for Methylene Blue in L-DOPA-Induced Dyskinesia. *Eur. J. Neurosci.* 49 (6), 869–882. doi:10.1111/ejn.14079

Barnum, C. J., Bhide, N., Lindenbach, D., Surrena, M. A., Goldenberg, A. A., Tignor, S., et al. (2012). Effects of Noradrenergic Denervation on L-DOPA-Induced Dyskinesia and its Treatment by α- and β-adrenergic Receptor Antagonists in Hemiparkinsonian Rats. *Pharmacol. Biochem. Behav.* 100 (3), 607–615. doi:10.1016/j.pbb.2011.09.009

Bartlett, M. J., Flores, A. J., Ye, T., Smidt, S. I., Dollish, H. K., Stancati, J. A., et al. (2020a). Preclinical Evidence in Support of Repurposing Sub-anesthetic Ketamine as a Treatment for L-DOPA-Induced Dyskinesia. *Exp. Neurol.* 333, 113413. doi:10.1016/j.expneurol.2020.113413

Bartlett, M. J., So, L. Y., Szabò, L., Skinner, D. P., Parent, K. L., Heien, M. L., et al. (2020b). Highly-selective M-Opioid Receptor Antagonism Does Not Block L-DOPA-Induced Dyskinesia in a Rodent Model. *BMC Res. Notes* 13 (1), 149. doi:10.1186/s13104-020-04994-7

Bastide, M. F., Meissner, W. G., Picconi, B., Fasano, S., Fernagut, P. O., Feyder, M., et al. (2015). Pathophysiology of L-Dopa-Induced Motor and Non-motor Complications in Parkinson's Disease. *Prog. Neurobiol.* 132, 96–168. doi:10.1016/j.pneurobio.2015.07.002

Beaudoin-Gobert, M., Epinat, J., Météreau, E., Duperrier, S., Neumane, S., Ballanger, B., et al. (2015). Behavioural Impact of a Double Dopaminergic and Serotonergic Lesion in the Non-human Primate. *Brain* 138 (Pt 9), 2632–2647. doi:10.1093/brain/awv183

Beck, G., Zhang, J., Fong, K., Mochizuki, H., Mouradian, M. M., and Papa, S. M. (2021). Striatal ΔFosB Gene Suppression Inhibits the Development of Abnormal Involuntary Movements Induced by L-Dopa in Rats. *Gene Ther.* 28, 760–770. doi:10.1038/s41434-021-00249-710.1038/s41434-021-00249-7

Bélanger, N., Grégoire, L., Tahar, A. H., and Bédard, P. J. (2003). Chronic Treatment with Small Doses of Cabergoline Prevents Dopa-Induced Dyskinesias in Parkinsonian Monkeys. *Mov. Disord.* 18 (12), 1436–1441. doi:10.1002/mds.10589

Benninger, D. H., Iseki, K., Kranick, S., Luckenbaugh, D. A., Houdayer, E., and Hallett, M. (2012). Controlled Study of 50-Hz Repetitive Transcranial Magnetic

Stimulation for the Treatment of Parkinson Disease. *Neurorehabil. Neural Repair* 26 (9), 1096–1105. doi:10.1177/1545968312445636

Bezard, E., Boraud, T., Nguyen, J. P., Velasco, F., Keravel, Y., and Gross, C. (1999). Cortical Stimulation and Epileptic Seizure: a Study of the Potential Risk in Primates. *Neurosurgery* 45 (2), 346–350. doi:10.1097/00006123-199908000-00030

Bezard, E., Brotchie, J. M., and Gross, C. E. (2001). Pathophysiology of Levodopa-Induced Dyskinesia: Potential for New Therapies. *Nat. Rev. Neurosci.* 2 (8), 577–588. doi:10.1038/35086062

Bézard, E., Ferry, S., Mach, U., Stark, H., Leriche, L., Boraud, T., et al. (2003). Attenuation of Levodopa-Induced Dyskinesia by Normalizing Dopamine D3 Receptor Function. *Nat. Med.* 9 (6), 762–767. doi:10.1038/nm875

Bezard, E., Li, Q., Hulme, H., Fridjonsdottir, E., Nilsson, A., Pioli, E., et al. (2020). M Opioid Receptor Agonism for L-DOPA-Induced Dyskinesia in Parkinson's Disease. *J. Neurosci.* 40 (35), 6812–6819. doi:10.1523/JNEUROSCI.0610-20.2020

Bhide, N., Lindenbach, D., Barnum, C. J., George, J. A., Surrena, M. A., and Bishop, C. (2015). Effects of the Beta-Adrenergic Receptor Antagonist Propranolol on Dyskinesia and L-DOPA-Induced Striatal DA Efflux in the Hemi-Parkinsonian Rat. *J. Neurochem.* 134 (2), 222–232. doi:10.1111/jnc.13125

Bhide, N., Lindenbach, D., Surrena, M. A., Goldenberg, A. A., Bishop, C., Berger, S. P., et al. (2013). The Effects of BMY-14802 against L-DOPA- and Dopamine Agonist-Induced Dyskinesia in the Hemiparkinsonian Rat. *Psychopharmacology (Berl)* 227 (3), 533–544. doi:10.1007/s00213-013-3001-4

Bibbiani, F., Costantini, L. C., Patel, R., and Chase, T. N. (2005). Continuous Dopaminergic Stimulation Reduces Risk of Motor Complications in Parkinsonian Primates. *Exp. Neurol.* 192 (1), 73–78. doi:10.1016/j.expneurol.2004.11.013

Binde, C. D., Tvete, I. F., Gåsemyr, J. I., Natvig, B., and Klemp, M. (2020). Comparative Effectiveness of Dopamine Agonists and Monoamine Oxidase Type-B Inhibitors for Parkinson's Disease: a Multiple Treatment Comparison Meta-Analysis. *Eur. J. Clin. Pharmacol.* 76 (12), 1731–1743. doi:10.1007/s00228-020-02961-6

Bishop, C., George, J. A., Buchta, W., Goldenberg, A. A., Mohamed, M., Dickinson, S. O., et al. (2012). Serotonin Transporter Inhibition Attenuates L-DOPA-Induced Dyskinesia without Compromising L-DOPA Efficacy in Hemi-Parkinsonian Rats. *Eur. J. Neurosci.* 36 (6), 2839–2848. doi:10.1111/j.1460-9568.2012.08202.x

Blandini, F., and Armentero, M. T. (2012). New Pharmacological Avenues for the Treatment of L-DOPA-Induced Dyskinesias in Parkinson's Disease: Targeting Glutamate and Adenosine Receptors. *Expert Opin. Investig. Drugs* 21 (2), 153–168. doi:10.1517/13543784.2012.651457

Boi, L., Pisanu, A., Greig, N. H., Scerba, M. T., Tweedie, D., Mulas, G., et al. (2019). Immunomodulatory Drugs Alleviate L-Dopa-Induced Dyskinesia in a Rat Model of Parkinson's Disease. *Mov Disord.* 34 (12), 1818–1830. Erratum in: Mov. Disord. 2021;36(1):275. PMID: 31335998. doi:10.1002/mds.27799

Bonenfant, J., Drapier, S., Houvenaghel, J. F., Naudet, F., Haegelen, C., Sauleau, P., et al. (2017). Pallidal Stimulation in Parkinson's Patients with Contraindications to Subthalamic Target: A 3 Years Follow-Up. *Parkinsonism Relat. Disord.* 34, 20–25. doi:10.1016/j.parkreldis.2016.10.007

Borgohain, R., Szasz, J., Stanzione, P., Meshram, C., Bhatt, M. H., Chirilineau, D., et al. (2014). Two-year, Randomized, Controlled Study of Safinamide as Add-On to Levodopa in Mid to Late Parkinson's Disease. *Mov. Disord.* 29 (10), 1273–1280. doi:10.1002/mds.25961

Brotchie, J., Johnston, T., Fox, S., Zerr, P., Tiberghien, F., and Bossi, L. (2007). FP0011 Extends the Duration of the Anti-parkinsonian Actions of L-DOPA and Reduces L-DOPA-Induced Dyskinesia in the MPTP-Lesiones Macaque Model of Parkinson's Disease. FP0011 Extends Durat. Anti-parkinsonian Actions LDOPA Reduces L-DOPA-Induced Dyskinesia MPTP-Lesiones Macaque Model Park. *Dis.* 2007, S96.

Brotchie, J. M. (2005). Nondopaminergic Mechanisms in Levodopa-Induced Dyskinesia. *Mov. Disord.* 20 (8), 919–931. doi:10.1002/mds.20612

Buck, K., Voehringer, P., and Ferger, B. (2010). Site-specific Action of L-3,4-Dihydroxyphenylalanine in the Striatum but Not Globus Pallidus and Substantia Nigra Pars Reticulata Evokes Dyskinetic Movements in Chronic L-3,4-Dihydroxyphenylalanine-Treated 6-Hydroxydopamine-Lesioned Rats. *Neuroscience* 166 (2), 355–358. doi:10.1016/j.neuroscience.2009.12.032

Buhmann, C., Huckhagel, T., Engel, K., Gulberti, A., Hidding, U., Poetter-Nerger, M., et al. (2017). Adverse Events in Deep Brain Stimulation: A Retrospective Long-Term Analysis of Neurological, Psychiatric and Other Occurrences. *PLoS One* 12 (7), e0178984. doi:10.1371/journal.pone.0178984

Burchiel, K. J., McCartney, S., Lee, A., and Raslan, A. M. (2013). Accuracy of Deep Brain Stimulation Electrode Placement Using Intraoperative Computed Tomography without Microelectrode Recording. *J. Neurosurg.* 119 (2), 301–306. doi:10.3171/2013.4.JNS122324

Bychkov, E., Ahmed, M. R., Dalby, K. N., and Gurevich, E. V. (2007). Dopamine Depletion and Subsequent Treatment with L-DOPA, but Not the Long-Lived Dopamine Agonist Pergolide, Enhances Activity of the Akt Pathway in the Rat Striatum. *J. Neurochem.* 102 (3), 699–711. doi:10.1111/j.1471-4159.2007.04586.x

Calabrese, V., Di Maio, A., Marino, G., Cardinale, A., Natale, G., De Rosa, A., et al. (2020). Rapamycin, by Inhibiting mTORC1 Signaling, Prevents the Loss of Striatal Bidirectional Synaptic Plasticity in a Rat Model of L-DOPA-Induced Dyskinesia. *Front. Aging Neurosci.* 12, 230. doi:10.3389/fnagi.2020.00230

Calabresi, P., Di Filippo, M., Ghiglieri, V., and Picconi, B. (2008). Molecular Mechanisms Underlying Levodopa-Induced Dyskinesia. *Mov. Disord.* 23 (Suppl. 3), S570–S579. doi:10.1002/mds.22019

Calabresi, P., Di Filippo, M., Ghiglieri, V., Tambasco, N., and Picconi, B. (2010). Levodopa-induced Dyskinesias in Patients with Parkinson's Disease: Filling the Bench-To-Bedside gap. *Lancet Neurol.* 9 (11), 1106–1117. doi:10.1016/S1474-4422(10)70218-0

Canavero, S., and Paolotti, R. (2000). Extradural Motor Cortex Stimulation for Advanced Parkinson's Disease: Case Report. *Mov. Disord.* 15 (1), 169–171. doi:10.1002/1531-8257(200001)15:1<169::aid-mds1030>3.0.co;2-w

Cao, X., Hou, D., Wang, L., Li, S., Sun, S., Ping, Q., et al. (2016). Effects and Molecular Mechanism of Chitosan-Coated Levodopa Nanoliposomes on Behavior of Dyskinesia Rats. *Biol. Res.* 49 (1), 32. doi:10.1186/s40659-016-0093-4

Carta, M., and Björklund, A. (2018). The Serotonergic System in L-DOPA-Induced Dyskinesia: Pre-clinical Evidence and Clinical Perspective. *J. Neural Transm. (Vienna)* 125 (8), 1195–1202. doi:10.1007/s00702-018-1865-5

Carta, M., Carlsson, T., Kirik, D., and Björklund, A. (2007). Dopamine Released from 5-HT Terminals Is the Cause of L-DOPA-Induced Dyskinesia in Parkinsonian Rats. *Brain* 130 (Pt 7), 1819–1833. doi:10.1093/brain/awm082

Castrioto, A., Lozano, A. M., Poon, Y. Y., Lang, A. E., Fallis, M., and Moro, E. (2011). Ten-year Outcome of Subthalamic Stimulation in Parkinson Disease: a Blinded Evaluation. *Arch. Neurol.* 68 (12), 1550–1556. doi:10.1001/archneurol.2011.182

Chang, F. C., Kwan, V., van der Poorten, D., Mahant, N., Wolfe, N., Ha, A. D., et al. (2016). Intraduodenal Levodopa-Carbidopa Intestinal Gel Infusion Improves Both Motor Performance and Quality of Life in Advanced Parkinson's Disease. *J. Clin. Neurosci.* 25, 41–45. doi:10.1016/j.jocn.2015.05.059

Chen, R., Classen, J., Gerloff, C., Celnik, P., Wassermann, E. M., Hallett, M., et al. (1997). Depression of Motor Cortex Excitability by Low-Frequency Transcranial Magnetic Stimulation. *Neurology* 48 (5), 1398–1403. doi:10.1212/wnl.48.5.1398

Chen, X., Wang, Y., Wu, H., Cheng, C., and Le, W. (2020). Research Advances on L-DOPA-Induced Dyskinesia: from Animal Models to Human Disease. *Neurol. Sci.* 41 (8), 2055–2065. doi:10.1007/s10072-020-04333-5

Cilia, R., Laguna, J., Cassani, E., Cereda, E., Pozzi, N. G., Isaias, I. U., et al. (2017). Mucuna Pruriens in Parkinson Disease: A Double-Blind, Randomized, Controlled, Crossover Study. *Neurology* 89 (5), 432–438. doi:10.1212/WNL.0000000000004175

Cilia, R., Landi, A., Vergani, F., Sganzerla, E., Pezzoli, G., and Antonini, A. (2007). Extradural Motor Cortex Stimulation in Parkinson's Disease. *Mov. Disord.* 22 (1), 111–114. doi:10.1002/mds.21207

Corsi, S., Stancampiano, R., and Carta, M. (2021). Serotonin/dopamine Interaction in the Induction and Maintenance of L-DOPA-Induced Dyskinesia: An Update. *Prog. Brain Res.* 261, 287–302. doi:10.1016/bs.pbr.2021.01.032

Corvol, J. C., Durif, F., Meissner, W. G., Azulay, J. P., Haddad, R., Guimarães-Costa, R., et al. (2019). Naftazone in Advanced Parkinson's Disease: An Acute L-DOPA challenge Randomized Controlled Trial. *Parkinsonism Relat. Disord.* 60, 51–56. doi:10.1016/j.parkreldis.2018.10.005

Dastin-van Rijn, E. M., Provenza, N. R., Calvert, J. S., Gilron, R., Allawala, A. B., Darie, R., et al. (2021). Uncovering Biomarkers during Therapeutic

Neuromodulation with PARRM: Period-Based Artifact Reconstruction and Removal Method. *Cel. Rep. Methods* 1 (2), 100010. doi:10.1016/j.crmeth.2021.100010

Deane, K. H., Spieker, S., and Clarke, C. E. (2004). Catechol-O-methyltransferase Inhibitors for Levodopa-Induced Complications in Parkinson's Disease. *Cochrane Database Syst. Rev.* (4), CD004554. doi:10.1002/14651858.CD004554.pub2

Delavallée, M., Abu-Serieh, B., de Tourchaninoff, M., and Raftopoulos, C. (2008). Subdural Motor Cortex Stimulation for central and Peripheral Neuropathic Pain: A Long-Term Follow-Up Study in a Series of Eight Patients. *Neurosurgery* 63, 101–108. [discussion: 105-108]. doi:10.1227/01.NEU.0000335076.24481.B6

Delrobaei, M., Baktash, N., Gilmore, G., McIsaac, K., and Jog, M. (2017). Using Wearable Technology to Generate Objective Parkinson's Disease Dyskinesia Severity Score: Possibilities for Home Monitoring. *IEEE Trans. Neural Syst. Rehabil. Eng.* 25 (10), 1853–1863. doi:10.1109/TNSRE.2017.2690578

Deuschl, G., Schade-Brittinger, C., Krack, P., Volkmann, J., Schäfer, H., Bötzel, K., et al. (2006). A Randomized Trial of Deep-Brain Stimulation for Parkinson's Disease. *N. Engl. J. Med.* 355 (9), 896–908. Erratum in: N. Engl. J. Med. 2006 Sep 21;355(12):1289. PMID: 16943402. doi:10.1056/NEJMoa060281

Divito, C. B., Steece-Collier, K., Case, D. T., Williams, S. P., Stancati, J. A., Zhi, L., et al. (2015). Loss of VGLUT3 Produces Circadian-dependent Hyperdopaminergia and Ameliorates Motor Dysfunction and L-Dopa-Mediated Dyskinesias in a Model of Parkinson's Disease. *J. Neurosci.* 35 (45), 14983–14999. doi:10.1523/JNEUROSCI.2124-15.2015

Drouot, X., Oshino, S., Jarraya, B., Besret, L., Kishima, H., Remy, P., et al. (2004). Functional Recovery in a Primate Model of Parkinson's Disease Following Motor Cortex Stimulation. *Neuron* 44 (5), 769–778. doi:10.1016/j.neuron.2004.11.023

Du, H., Nie, S., Chen, G., Ma, K., Xu, Y., Zhang, Z., et al. (2015). Levetiracetam Ameliorates L-DOPA-Induced Dyskinesia in Hemiparkinsonian Rats Inducing Critical Molecular Changes in the Striatum. *Parkinsons Dis.* 2015, 253878. doi:10.1155/2015/253878

Dupre, K. B., Cruz, A. V., McCoy, A. J., Delaville, C., Gerber, C. M., Eyring, K. W., et al. (2016). Effects of L-Dopa Priming on Cortical High Beta and High Gamma Oscillatory Activity in a Rodent Model of Parkinson's Disease. *Neurobiol. Dis.* 86, 1–15. doi:10.1016/j.nbd.2015.11.009

Durif, F., Debilly, B., Galitzky, M., Morand, D., Viallet, F., Borg, M., et al. (2004). Clozapine Improves Dyskinesias in Parkinson Disease: a Double-Blind, Placebo-Controlled Study. *Neurology* 62 (3), 381–388. doi:10.1212/01.wnl.0000110317.52453.6c

Elahi, B., Elahi, B., and Chen, R. (2009). Effect of Transcranial Magnetic Stimulation on Parkinson Motor Function-Ssystematic Review of Controlled Clinical Trials. *Mov. Disord.* 24 (3), 357–363. doi:10.1002/mds.22364

Elgebaly, A., Elfil, M., Attia, A., Magdy, M., and Negida, A. (2018). Neuropsychological Performance Changes Following Subthalamic versus Pallidal Deep Brain Stimulation in Parkinson's Disease: a Systematic Review and Metaanalysis. *CNS Spectr.* 23 (1), 10–23. doi:10.1017/S1092852917000062

Encarnacion, E. V., and Hauser, R. A. (2008). Levodopa-induced Dyskinesias in Parkinson's Disease: Etiology, Impact on Quality of Life, and Treatments. *Eur. Neurol.* 60 (2), 57–66. doi:10.1159/000131893

Espadas, I., Keifman, E., Palomo-Garo, C., Burgaz, S., García, C., Fernández-Ruiz, J., et al. (2020). Beneficial Effects of the Phytocannabinoid Δ9-THCV in L-DOPA-Induced Dyskinesia in Parkinson's Disease. *Neurobiol. Dis.* 141, 104892. doi:10.1016/j.nbd.2020.104892

Esselink, R. A., de Bie, R. M., de Haan, R. J., Lenders, M. W., Nijssen, P. C., Staal, M. J., et al. (2004). Unilateral Pallidotomy versus Bilateral Subthalamic Nucleus Stimulation in PD: a Randomized Trial. *Neurology* 62 (2), 201–207. doi:10.1212/01.wnl.0000103235.12621.c3

Fabbrini, A., and Guerra, A. (2021). Pathophysiological Mechanisms and Experimental Pharmacotherapy for L-Dopa-Induced Dyskinesia. *J. Exp. Pharmacol.* 13, 469–485. doi:10.2147/JEP.S265282

Fabbrini, G., Brotchie, J. M., Grandas, F., Nomoto, M., and Goetz, C. G. (2007). Levodopa-induced Dyskinesias. *Mov. Disord.* 22 (10), 1379–1523. doi:10.1002/mds.21475

Fahimi, Z., and Jahromy, M. H. (2018). Effects of Blackberry (Morus Nigra) Fruit Juice on Levodopa-Induced Dyskinesia in a Mice Model of Parkinson's Disease. *J. Exp. Pharmacol.* 10, 29–35. doi:10.2147/JEP.S161782

Fahn, S. (2006). A New Look at Levodopa Based on the ELLDOPA Study. *J. Neural Transm. Suppl.* (70), 419–426. doi:10.1007/978-3-211-45295-0_63

Fahn, S. (1999). Parkinson Disease, the Effect of Levodopa, and the ELLDOPA Trial. Earlier vs Later L-DOPA. *Arch. Neurol.* 56 (5), 529–535. doi:10.1001/archneur.56.5.529

Fasano, A., Daniele, A., and Albanese, A. (2012). Treatment of Motor and Non-motor Features of Parkinson's Disease with Deep Brain Stimulation. *Lancet Neurol.* 11 (5), 429–442. doi:10.1016/S1474-4422(12)70049-2

Fieblinger, T., Sebastianutto, I., Alcacer, C., Bimpisidis, Z., Maslava, N., Sandberg, S., et al. (2014). Mechanisms of Dopamine D1 Receptor-Mediated ERK1/2 Activation in the Parkinsonian Striatum and Their Modulation by Metabotropic Glutamate Receptor Type 5. *J. Neurosci.* 34 (13), 4728–4740. doi:10.1523/JNEUROSCI.2702-13.2014

Filipović, S. R., Rothwell, J. C., van de Warrenburg, B. P., and Bhatia, K. (2009). Repetitive Transcranial Magnetic Stimulation for Levodopa-Induced Dyskinesias in Parkinson's Disease. *Mov. Disord.* 24 (2), 246–253. doi:10.1002/mds.22348

Fine, J., Duff, J., Chen, R., Chir, B., Hutchison, W., Lozano, A. M., et al. (2000). Long-term Follow-Up of Unilateral Pallidotomy in Advanced Parkinson's Disease. *N. Engl. J. Med.* 342 (23), 1708–1714. doi:10.1056/NEJM200006083422304

Fiorentini, C., Savoia, P., Savoldi, D., Barbon, A., and Missale, C. (2013). Persistent Activation of the D1R/Shp-2/Erk1/2 Pathway in L-DOPA-Induced Dyskinesia in the 6-Hydroxy-Dopamine Rat Model of Parkinson's Disease. *Neurobiol. Dis.* 54, 339–348. doi:10.1016/j.nbd.2013.01.005

Flores, A. J., Bartlett, M. J., Root, B. K., Parent, K. L., Heien, M. L., Porreca, F., et al. (2018). The Combination of the Opioid Glycopeptide MMP-2200 and a NMDA Receptor Antagonist Reduced L-DOPA-Induced Dyskinesia and MMP-2200 by Itself Reduced Dopamine Receptor 2-like Agonist-Induced Dyskinesia. *Neuropharmacology* 141, 260–271. doi:10.1016/j.neuropharm.2018.09.005

Follett, K. A., Weaver, F. M., Stern, M., Hur, K., Harris, C. L., Luo, P., et al. (2010). Pallidal versus Subthalamic Deep-Brain Stimulation for Parkinson's Disease. *N. Engl. J. Med.* 362 (22), 2077–2091. doi:10.1056/NEJMoa0907083

Fox, S., Silverdale, M., Kellett, M., Davies, R., Steiger, M., Fletcher, N., et al. (2004). Non-subtype-selective Opioid Receptor Antagonism in Treatment of Levodopa-Induced Motor Complications in Parkinson's Disease. *Mov. Disord.* 19 (5), 554–560. doi:10.1002/mds.10693

Fox, S. H., and Brotchie, J. M. (2019). Viewpoint: Developing Drugs for Levodopa-Induced Dyskinesia in PD: Lessons Learnt, what Does the Future Hold? *Eur. J. Neurosci.* 49 (3), 399–409. doi:10.1111/ejn.14173

Fox, S. H., Katzenschlager, R., Lim, S. Y., Barton, B., de Bie, R. M. A., Seppi, K., et al. (2018). International Parkinson and Movement Disorder Society Evidence-Based Medicine Review: Update on Treatments for the Motor Symptoms of Parkinson's Disease. *Mov. Disord.* 33 (8), 1248–1266. Erratum in: Mov Disord. 2018;33(12):1992. PMID: 29570866. doi:10.1002/mds.27372

Fox, S. H., Metman, L. V., Nutt, J. G., Brodsky, M., Factor, S. A., Lang, A. E., et al. (2017). Trial of Dextromethorphan/quinidine to Treat Levodopa-Induced Dyskinesia in Parkinson's Disease. *Mov. Disord.* 32 (6), 893–903. doi:10.1002/mds.26976

Fredholm, B. B., Bättig, K., Holmén, J., Nehlig, A., and Zvartau, E. E. (1999). Actions of Caffeine in the Brain with Special Reference to Factors that Contribute to its Widespread Use. *Pharmacol. Rev.* 51 (1), 83–133.

Frizon, L. A., Shao, J., Maldonado-Naranjo, A. L., Lobel, D. A., Nagel, S. J., Fernandez, H. H., et al. (2018). The Safety and Efficacy of Using the O-Arm Intraoperative Imaging System for Deep Brain Stimulation Lead Implantation. *Neuromodulation* 21 (6), 588–592. doi:10.1111/ner.12744

Frouni, I., Hamadjida, A., Kwan, C., Bédard, D., Nafade, V., Gaudette, F., et al. (2019). Activation of mGlu2/3 Receptors, a Novel Therapeutic Approach to Alleviate Dyskinesia and Psychosis in Experimental Parkinsonism. *Neuropharmacology* 158, 107725. doi:10.1016/j.neuropharm.2019.107725

Gagnon, D., Gregoire, L., Di Paolo, T., and Parent, M. (2016). Serotonin Hyperinnervation of the Striatum with High Synaptic Incidence in Parkinsonian Monkeys. *Brain Struct. Funct.* 221 (7), 3675–3691. doi:10.1007/s00429-015-1125-5

Gardoni, F., Morari, M., Kulisevsky, J., Brugnoli, A., Novello, S., Pisanò, C. A., et al. (2018). Safinamide Modulates Striatal Glutamatergic Signaling in a Rat Model

of Levodopa-Induced Dyskinesia. *J. Pharmacol. Exp. Ther.* 367 (3), 442–451. doi:10.1124/jpet.118.251645

Giladi, N., Caraco, Y., Gureritch, T., Imam, S., Ahmad, M. Z., and Mishra, A. (2015). Pharmacokinetics and Safety of ND0612L (L-DOPA/carbidopa for Subcutaneous Infusion): Results from a Phase II Study in Moderate to Severe Parkinson's Disease. *Neurology* 84 (Suppl. l), P1.187.

Goetz, C. G., Damier, P., Hicking, C., Laska, E., Müller, T., Olanow, C. W., et al. (2007). Sarizotan as a Treatment for Dyskinesias in Parkinson's Disease: a Double-Blind Placebo-Controlled Trial. *Mov. Disord.* 22 (2), 179–186. doi:10.1002/mds.21226

Goetz, C. G., Laska, E., Hicking, C., Damier, P., Müller, T., Nutt, J., et al. (2008). Placebo Influences on Dyskinesia in Parkinson's Disease. *Mov. Disord.* 23 (5), 700–707. doi:10.1002/mds.21897

Goetz, C. G., Stebbins, G. T., Chung, K. A., Nicholas, A. P., Hauser, R. A., Merkitch, D., et al. (2017). Topiramate as an Adjunct to Amantadine in the Treatment of Dyskinesia in Parkinson's Disease: A Randomized, Double-Blind, Placebo-Controlled Multicenter Study. *Mov. Disord.* 32 (9), 1335–1336. doi:10.1002/mds.27092

Goto, S. (2017). Striatal Gαolf/cAMP Signal-dependent Mechanism to Generate Levodopa-Induced Dyskinesia in Parkinson's Disease. *Front. Cell Neurosci.* 11, 364. doi:10.3389/fncel.2017.00364

Grégoire, L., Jourdain, V. A., Townsend, M., Roach, A., and Di Paolo, T. (2013). Safinamide Reduces Dyskinesias and Prolongs L-DOPA Antiparkinsonian Effect in Parkinsonian Monkeys. *Parkinsonism Relat. Disord.* 19 (5), 508–514. doi:10.1016/j.parkreldis.2013.01.009

Guerra, A., Suppa, A., D'Onofrio, V., Di Stasio, F., Asci, F., Fabbrini, G., et al. (2019). Abnormal Cortical Facilitation and L-Dopa-Induced Dyskinesia in Parkinson's Disease. *Brain Stimul.* 12 (6), 1517–1525. doi:10.1016/j.brs.2019.06.012

Habibi, A. H., Anamoradi, A., Shahidi, G. A., Razmeh, S., Alizadeh, E., and Kokhedan, K. M. (2018). Treatment of Levodopainduced Dyskinesia with Vitamin D: A Randomized, Double-Blind, Placebo-Controlled Trial. *Neurol. Int.* 10 (3), 7737. doi:10.4081/ni.2018.7737

Hack, N., Fayad, S. M., Monari, E. H., Akbar, U., Hardwick, A., Rodriguez, R. L., et al. (2014). An Eight-Year Clinic Experience with Clozapine Use in a Parkinson's Disease Clinic Setting. *PLoS One* 9 (3), e91545. doi:10.1371/journal.pone.0091545

Hadj Tahar, A., Grégoire, L., Bangassoro, E., and Bédard, P. J. (2000). Sustained Cabergoline Treatment Reverses Levodopa-Induced Dyskinesias in Parkinsonian Monkeys. *Clin. Neuropharmacol.* 23 (4), 195–202. doi:10.1097/00002826-200007000-00005

Hadj Tahar, A., Grégoire, L., Darré, A., Bélanger, N., Meltzer, L., and Bédard, P. J. (2004). Effect of a Selective Glutamate Antagonist on L-Dopa-Induced Dyskinesias in Drug-Naive Parkinsonian Monkeys. *Neurobiol. Dis.* 15 (2), 171–176. doi:10.1016/j.nbd.2003.10.007

Hauser, R. A., Bronzova, J., Sampaio, C., Lang, A. E., Rascol, O., Theeuwes, A., et al. (2009). Safety and Tolerability of Pardoprunox, a New Partial Dopamine Agonist, in a Randomized, Controlled Study of Patients with Advanced Parkinson's Disease. *Eur. Neurol.* 62 (1), 40–48. doi:10.1159/000216839

Hauser, R. A., Hsu, A., Kell, S., Espay, A. J., Sethi, K., Stacy, M., et al. (2013). Extended-release Carbidopa-Levodopa (IPX066) Compared with Immediate-Release Carbidopa-Levodopa in Patients with Parkinson's Disease and Motor Fluctuations: a Phase 3 Randomised, Double-Blind Trial. *Lancet Neurol.* 12 (4), 346–356. doi:10.1016/S1474-4422(13)70025-5

Hauser, R. A., McDermott, M. P., and Messing, S. (2006). Factors Associated with the Development of Motor Fluctuations and Dyskinesias in Parkinson Disease. *Arch. Neurol.* 63 (12), 1756–1760. doi:10.1001/archneur.63.12.1756

Hauser, R. A., Stocchi, F., Rascol, O., Huyck, S. B., Capece, R., Ho, T. W., et al. (2015). Preladenant as an Adjunctive Therapy with Levodopa in Parkinson Disease: Two Randomized Clinical Trials and Lessons Learned. *JAMA Neurol.* 72 (12), 1491–1500. doi:10.1001/jamaneurol.2015.2268

Hauser, R. A., Walsh, R. R., Pahwa, R., Chernick, D., and Formella, A. E. (2021). Amantadine ER (Gocovri®) Significantly Increases on Time without Any Dyskinesia: Pooled Analyses from Pivotal Trials in Parkinson's Disease. *Front. Neurol.* 12, 645706. doi:10.3389/fneur.2021.645706

He, J.-M., Wu, Z.-B., Cai, N.-Q., and Lin, Y. (2021). Levodopa-Induced Ocular Dyskinesia in an Early-Onset Parkinson Disease Patient with GBA Mutation. *Clin. Neuropharm* 44, 201–204. doi:10.1097/WNF.0000000000000484

Hernandez, M., Walsh, M., Stead, T., Quinones, A., and Ganti, L. (2019). Serotonin Syndrome in the Emergency Department. *Cureus* 11 (12), e6307. doi:10.7759/cureus.6307

Herring, W. J., Assaid, C., Budd, K., Vargo, R., Mazenko, R. S., Lines, C., et al. (2017). A Phase Ib Randomized Controlled Study to Evaluate the Effectiveness of a Single-Dose of the NR2B Selective N-Methyl-D-Aspartate Antagonist MK-0657 on Levodopa-Induced Dyskinesias and Motor Symptoms in Patients with Parkinson Disease. *Clin. Neuropharmacol* 40 (6), 255–260. doi:10.1097/WNF.0000000000000241

Hill, M. P., Ravenscroft, P., Bezard, E., Crossman, A. R., Brotchie, J. M., Michel, A., et al. (2004). Levetiracetam Potentiates the Antidyskinetic Action of Amantadine in the 1-Methyl-4-Phenyl-1,2,3,6-Tetrahydropyridine (MPTP)-Lesioned Primate Model of Parkinson's Disease. *J. Pharmacol. Exp. Ther.* 310 (1), 386–394. doi:10.1124/jpet.104.066191

Holloway, R. G., Shoulson, I., Fahn, S., Kieburtz, K., Lang, A., Marek, K., et al. (2004). Parkinson Study Group. Pramipexole vs. Levodopa as Initial Treatment for Parkinson Disease: A 4-Year Randomized Controlled Trial. *Arch. Neurol.* 61 (7), 1044–1053. doi:10.1001/archneur.61.7.1044

Huang, Y. Z., Edwards, M. J., Rounis, E., Bhatia, K. P., and Rothwell, J. C. (2005). Theta Burst Stimulation of the Human Motor Cortex. *Neuron* 45 (2), 201–206. doi:10.1016/j.neuron.2004.12.033

Hubsher, G., Haider, M., and Okun, M. S. (2012). Amantadine: the Journey from Fighting Flu to Treating Parkinson Disease. *Neurology* 78 (14), 1096–1099. doi:10.1212/WNL.0b013e31824e8f0d

Hung, S. W., Adeli, G. M., Arenovich, T., Fox, S. H., and Lang, A. E. (2010). Patient Perception of Dyskinesia in Parkinson's Disease. *J. Neurol. Neurosurg. Psychiatry* 81 (10), 1112–1115. doi:10.1136/jnnp.2009.173286

Huot, P., Sgambato-Faure, V., Fox, S. H., and McCreary, A. C. (2017). Serotonergic Approaches in Parkinson's Disease: Translational Perspectives, an Update. *ACS Chem. Neurosci.* 8 (5), 973–986. doi:10.1021/acschemneuro.6b00440

Hussain, R., Zubair, H., Pursell, S., and Shahab, M. (2018). Neurodegenerative Diseases: Regenerative Mechanisms and Novel Therapeutic Approaches. *Brain Sci.* 8 (9), 177. doi:10.3390/brainsci8090177

Hutny, M., Hofman, J., Klimkowicz-Mrowiec, A., and Gorzkowska, A. (2021). Current Knowledge on the Background, Pathophysiology and Treatment of Levodopa-Induced Dyskinesia-Literature Review. *J. Clin. Med.* 10 (19), 4377. doi:10.3390/jcm10194377

Iderberg, H., Maslava, N., Thompson, A. D., Bubser, M., Niswender, C. M., Hopkins, C. R., et al. (2015). Pharmacological Stimulation of Metabotropic Glutamate Receptor Type 4 in a Rat Model of Parkinson's Disease and L-DOPA-Induced Dyskinesia: Comparison between a Positive Allosteric Modulator and an Orthosteric Agonist. *Neuropharmacology* 95, 121–129. doi:10.1016/j.neuropharm.2015.02.023

Inden, M., Abe, M., Minamino, H., Takata, K., Yoshimoto, K., Tooyama, I., et al. (2012). Effect of Selective Serotonin Reuptake Inhibitors via 5-HT1A Receptors on L-DOPA-Induced Rotational Behavior in a Hemiparkinsonian Rat Model. *J. Pharmacol. Sci.* 119 (1), 10–19. doi:10.1254/jphs.12003fp

Jankovic, J., and Clarence-Smith, K. (2011). Tetrabenazine for the Treatment of Chorea and Other Hyperkinetic Movement Disorders. *Expert Rev. Neurother.* 11 (11), 1509–1523. doi:10.1586/ern.11.149

Jenner, P. (2004). Avoidance of Dyskinesia: Preclinical Evidence for Continuous Dopaminergic Stimulation. *Neurology* 62 (Suppl. 1), S47–S55. doi:10.1212/wnl.62.1_suppl_1.s47

Jiménez-Urbieta, H., Gago, B., de la Riva, P., Delgado-Alvarado, M., Marin, C., and Rodriguez-Oroz, M. C. (2015). Dyskinesias and Impulse Control Disorders in Parkinson's Disease: From Pathogenesis to Potential Therapeutic Approaches. *Neurosci. Biobehav. Rev.* 56, 294–314. doi:10.1016/j.neubiorev.2015.07.010

Johansson, P. A., Andersson, M., Andersson, K. E., and Cenci, M. A. (2001). Alterations in Cortical and Basal Ganglia Levels of Opioid Receptor Binding in a Rat Model of L-DOPA-Induced Dyskinesia. *Neurobiol. Dis.* 8 (2), 220–239. doi:10.1006/nbdi.2000.0372

Johnston, T. H., van der Meij, A., Brotchie, J. M., and Fox, S. H. (2010). Effect of Histamine H2 Receptor Antagonism on Levodopa-Induced Dyskinesia in the MPTP-Macaque Model of Parkinson's Disease. *Mov. Disord.* 25 (10), 1379–1390. doi:10.1002/mds.23069

Jones, N., Bleickardt, C., Mullins, D., Parker, E., and Hodgson, R. (2013). A2A Receptor Antagonists Do Not Induce Dyskinesias in Drug-Naive or L-Dopa Sensitized Rats. *Brain Res. Bull* 98, 163–169. doi:10.1016/j.brainresbull.2013.07.001

Jones-Tabah, J., Mohammad, H., Hadj-Youssef, S., Kim, L. E. H., Martin, R. D., Benaliouad, F., et al. (2020). Dopamine D1 Receptor Signalling in Dyskinetic Parkinsonian Rats Revealed by Fiber Photometry Using FRET-Based Biosensors. *Sci. Rep.* 10 (1), 14426. doi:10.1038/s41598-020-71121-8

Jongsma Wallin, H., Danielsen, N., Johnston, J. M., Gratto, K. A., Karchewski, L. A., and Verge, V. M. (2001). Exogenous NT-3 and NGF Differentially Modulate PACAP Expression in Adult Sensory Neurons, Suggesting Distinct Roles in Injury and Inflammation. *Eur. J. Neurosci.* 14 (2), 267–282. doi:10.1046/j.0953-816x.2001.01641.x

Kalia, L. V., and Lang, A. E. (2015). Parkinson's Disease. *Lancet* 386 (9996), 896–912. doi:10.1016/S0140-6736(14)61393-3

Kaur, G., Rathod, S. S. S., Ghoneim, M. M., Alshehri, S., Ahmad, J., Mishra, A., et al. (2022). DNA Methylation: A Promising Approach in Management of Alzheimer's Disease and Other Neurodegenerative Disorders. *Biology (Basel)* 11 (1), 90. doi:10.3390/biology11010090

Ko, W. K. D., Li, Q., Cheng, L. Y., Morelli, M., Carta, M., and Bezard, E. (2017). A Preclinical Study on the Combined Effects of Repeated Eltoprazine and Preladenant Treatment for Alleviating L-DOPA-Induced Dyskinesia in Parkinson's Disease. *Eur. J. Pharmacol.* 813, 10–16. doi:10.1016/j.ejphar.2017.07.030

Kobylecki, C., Burn, D. J., Kass-Iliyya, L., Kellett, M. W., Crossman, A. R., and Silverdale, M. A. (2014). Randomized Clinical Trial of Topiramate for Levodopa-Induced Dyskinesia in Parkinson's Disease. *Parkinsonism Relat. Disord.* 20 (4), 452–455. doi:10.1016/j.parkreldis.2014.01.016

Kong, M., Ba, M., Liu, C., Zhang, Y., Zhang, H., and Qiu, H. (2015). NR2B Antagonist CP-101,606 Inhibits NR2B Phosphorylation at Tyrosine-1472 and its Interactions with Fyn in Levodopa-Induced Dyskinesia Rat Model. *Behav. Brain Res.* 282, 46–53. doi:10.1016/j.bbr.2014.12.059

Kopell, B. H., Rezai, A. R., Chang, J. W., and Vitek, J. L. (2006). Anatomy and Physiology of the Basal Ganglia: Implications for Deep Brain Stimulation for Parkinson's Disease. *Mov. Disord.* 21 (Suppl. 14), S238–S246. doi:10.1002/mds.20958

Krishnan, S., Prasad, S., Pisharady, K. K., Sarma, G., Sarma, S. P., and Kishore, A. (2016). The Decade after Subthalamic Stimulation in Advanced Parkinson's Disease: A Balancing Act. *Neurol. India* 64 (1), 81–89. doi:10.4103/0028-3886.173663

Lee, C. S. (2001). L-DOPA-induced Dyskinesia: Mechanisms and Management. *Br. Columbia Med. J.* 43 (4), 206–209.

Lees, A., Fahn, S., Eggert, K. M., Jankovic, J., Lang, A., Micheli, F., et al. (2012). Perampanel, an AMPA Antagonist, Found to Have No Benefit in Reducing "off" Time in Parkinson's Disease. *Mov. Disord.* 27 (2), 284–288. doi:10.1002/mds.23983

Lefaucheur, J. P. (2009). Treatment of Parkinson's Disease by Cortical Stimulation. *Expert Rev. Neurother.* 9 (12), 1755–1771. doi:10.1586/ern.09.132

Leta, V., Jenner, P., Chaudhuri, K. R., and Antonini, A. (2019). Can Therapeutic Strategies Prevent and Manage Dyskinesia in Parkinson's Disease? an Update. *Expert Opin. Drug Saf.* 18 (12), 1203–1218. doi:10.1080/14740338.2019.1681966

Lewitt, P. A., Hauser, R. A., Lu, M., Nicholas, A. P., Weiner, W., Coppard, N., et al. (2012). Randomized Clinical Trial of Fipamezole for Dyskinesia in Parkinson Disease (FJORD Study). *Neurology* 79 (2), 163–169. doi:10.1212/WNL.0b013e31825f0451

Li, C., Xue, L., Liu, Y., Yang, Z., Chi, S., and Xie, A. (2020). Zonisamide for the Treatment of Parkinson Disease: A Current Update. *Front Neurosci.* 14, 574652. doi:10.3389/fnins.2020.574652

Lindenbach, D., Conti, M. M., Ostock, C. Y., George, J. A., Goldenberg, A. A., Melikhov-Sosin, M., et al. (2016). The Role of Primary Motor Cortex (M1) Glutamate and GABA Signaling in L-DOPA-Induced Dyskinesia in Parkinsonian Rats. *J. Neurosci.* 36 (38), 9873–9887. doi:10.1523/JNEUROSCI.1318-16.2016

Lindenbach, D., Palumbo, N., Ostock, C. Y., Vilceus, N., Conti, M. M., and Bishop, C. (2015). Side Effect Profile of 5-HT Treatments for Parkinson's Disease and L-DOPA-Induced Dyskinesia in Rats. *Br. J. Pharmacol.* 172 (1), 119–130. doi:10.1111/bph.12894

Lindgren, H. S., Andersson, D. R., Lagerkvist, S., Nissbrandt, H., and Cenci, M. A. (2010). L-DOPA-Induced Dopamine Efflux in the Striatum and the Substantia Nigra in a Rat Model of Parkinson's Disease: Temporal and Quantitative Relationship to the Expression of Dyskinesia. *J. Neurochem.* 112 (6), 1465–1476. doi:10.1111/j.1471-4159.2009.06556.x

Lindskog, M., Svenningsson, P., Pozzi, L., Kim, Y., Fienberg, A. A., Bibb, J. A., et al. (2002). Involvement of DARPP-32 Phosphorylation in the Stimulant Action of Caffeine. *Nature* 418 (6899), 774–778. doi:10.1038/nature00817

Lohse, A., Meder, D., Nielsen, S., Lund, A. E., Herz, D. M., Løkkegaard, A., et al. (2020). Low-frequency Transcranial Stimulation of Pre-supplementary Motor Area Alleviates Levodopa-Induced Dyskinesia in Parkinson's Disease: a Randomized Cross-Over Trial. *Brain Commun.* 2 (2), fcaa147. doi:10.1093/braincomms/fcaa147

Lopane, G., Mellone, S., Chiari, L., Cortelli, P., Calandra-Buonaura, G., and Contin, M. (2015). Dyskinesia Detection and Monitoring by a Single Sensor in Patients with Parkinson's Disease. *Mov. Disord.* 30, 1267–1271. doi:10.1002/mds.26313

Lopez-Lopez, A., Labandeira, C. M., Labandeira-Garcia, J. L., and Muñoz, A. (2020). Rho Kinase Inhibitor Fasudil Reduces L-DOPA-Induced Dyskinesia in a Rat Model of Parkinson's Disease. *Br. J. Pharmacol.* 177 (24), 5622–5641. doi:10.1111/bph.15275

Lorenc-Koci, E., Czarnecka, A., Kamińska, K., Knutelska, J., Zygmunt, M., and Dudek, M. (2017). Contribution of the Nitric Oxide Donor Molsidomine and the Antiparkinsonian Drug L-DOPA to the Modulation of the Blood Pressure in Unilaterally 6-OHDA-Lesioned Rats. *Pharmacol. Rep.* 69 (1), 29–35. doi:10.1016/j.pharep.2016.09.022

Lorenc-Koci, E., Czarnecka, A., Lenda, T., Kamińska, K., and Konieczny, J. (2013). Molsidomine, a Nitric Oxide Donor, Modulates Rotational Behavior and Monoamine Metabolism in 6-OHDA Lesioned Rats Treated Chronically with L-DOPA. *Neurochem. Int.* 63 (8), 790–804. doi:10.1016/j.neuint.2013.09.021

Lyons, D., de Jaeger, X., Rosen, L. G., Ahmad, T., Lauzon, N. M., Zunder, J., et al. (2013). Opiate Exposure and Withdrawal Induces a Molecular Memory Switch in the Basolateral Amygdala between ERK1/2 and CaMKIIα-dependent Signaling Substrates. *J. Neurosci.* 33 (37), 14693–14704. doi:10.1523/JNEUROSCI.1226-13.2013

Lyons, K. E., and Pahwa, R. (2006). Efficacy and Tolerability of Levetiracetam in Parkinson Disease Patients with Levodopa-Induced Dyskinesia. *Clin. Neuropharmacol.* 29 (3), 148–153. doi:10.1097/01.WNF.0000220814.48360.F4

Maan, G., Sikdar, B., Kumar, A., Shukla, R., and Mishra, A. (2020). Role of Flavonoids in Neurodegenerative Diseases: Limitations and Future Perspectives. *Curr. Top Med. Chem.* 20 (13), 1169–1194. doi:10.2174/1568026620666200416085330

Maffei, M. E. (2020). 5-Hydroxytryptophan (5-HTP): Natural Occurrence, Analysis, Biosynthesis, Biotechnology, Physiology and Toxicology. *Int. J. Mol. Sci.* 22 (1), 181. doi:10.3390/ijms22010181

Magara, A., Bühler, R., Moser, D., Kowalski, M., Pourtehrani, P., and Jeanmonod, D. (2014). First Experience with MR-Guided Focused Ultrasound in the Treatment of Parkinson's Disease. *J. Ther. Ultrasound* 2, 11. doi:10.1186/2050-5736-2-11

Mandal, M., Jaiswal, P., and Mishra, A. (2020). Role of Curcumin and its Nanoformulations in Neurotherapeutics: A Comprehensive Review. *J. Biochem. Mol. Toxicol.* 34 (6), e22478. doi:10.1002/jbt.22478

Manola, L., Roelofsen, B. H., Holsheimer, J., Marani, E., and Geelen, J. (2005). Modelling Motor Cortex Stimulation for Chronic Pain Control: Electrical Potential Field, Activating Functions and Responses of Simple Nerve Fibre Models. *Med. Biol. Eng. Comput.* 43 (3), 335–343. doi:10.1007/BF02345810

Matias, C. M., Frizon, L. A., Nagel, S. J., Lobel, D. A., and Machado, A. G. (2018). Deep Brain Stimulation Outcomes in Patients Implanted under General Anesthesia with Frame-Based Stereotaxy and Intraoperative MRI. *J. Neurosurg.* 129 (6), 1572–1578. doi:10.3171/2017.7.JNS171166

Mattei, C., Molgó, J., Joseph, X., Israel, M., and Bloy, C. (1999). Naftazone Reduces Glutamate Cerebro Spinal Fluid Levels in Rats and Glutamate Release from Mouse Cerebellum Synaptosomes. *Neurosci. Lett.* 271 (3), 183–186. doi:10.1016/s0304-3940(99)00552-2

Mazzucchi, S., Frosini, D., Bonuccelli, U., and Ceravolo, R. (2015). Current Treatment and Future Prospects of Dopa-Induced Dyskinesias. *Drugs Today (Barc)* 51 (5), 315–329. doi:10.1358/dot.2015.51.5.2313726

Meadows, S. M., Conti, M. M., Gross, L., Chambers, N. E., Avnor, Y., Ostock, C. Y., et al. (2018). Diverse Serotonin Actions of Vilazodone Reduce L-3,4-Dihidroxyphenylalanine-Induced Dyskinesia in Hemi-Parkinsonian Rats. *Mov. Disord.* 33 (11), 1740–1749. doi:10.1002/mds.100

Meloni, M., Puligheddu, M., Sanna, F., Cannas, A., Farris, R., Tronci, E., et al. (2020). Efficacy and Safety of 5-Hydroxytryptophan on Levodopa-Induced Motor Complications in Parkinson's Disease: A Preliminary Finding. *J. Neurol. Sci.* 415, 116869. doi:10.1016/j.jns.2020.116869

Mestre, T. A., Shah, B. B., Connolly, B. S., de Aquino, C., Al Dhakeel, A., Walsh, R., et al. (2014). Famotidine, a Histamine H2 Receptor Antagonist, Does Not Reduce Levodopa-Induced Dyskinesia in Parkinson's Disease: A Proof-Of-Concept Study. *Mov. Disord. Clin. Pract.* 1 (3), 219–224. doi:10.1002/mdc3.12061

Metman, L. V., Konitsiotis, S., and Chase, T. N. (2000). Pathophysiology of Motor Response Complications in Parkinson's Disease: Hypotheses on the Why, where, and what. *Mov. Disord.* 15 (1), 3–8. doi:10.1002/1531-8257(200001)15:1<3::aid-mds1003>3.0.co;2-e

Miguelez, C., Navailles, S., De Deurwaerdère, P., and Ugedo, L. (2016). The Acute and Long-Term L-DOPA Effects Are Independent from Changes in the Activity of Dorsal Raphe Serotonergic Neurons in 6-OHDA Lesioned Rats. *Br. J. Pharmacol.* 173 (13), 2135–2146. doi:10.1111/bph.13447

Mishra, A., Mishra, P. S., Bandopadhyay, R., Khurana, N., Angelopoulou, E., Paudel, Y. N., et al. (2021). Neuroprotective Potential of Chrysin: Mechanistic Insights and Therapeutic Potential for Neurological Disorders. *Molecules* 26, 6456. doi:10.3390/molecules26216456

Mizuno, Y., and Kondo, T.Japanese Istradefylline Study Group (2013). Adenosine A2A Receptor Antagonist Istradefylline Reduces Daily off Time in Parkinson's Disease. *Mov. Disord.* 28 (8), 1138–1141. doi:10.1002/mds.25418

Möller, J. C., Oertel, W. H., Köster, J., Pezzoli, G., and Provinciali, L. (2005). Long-term Efficacy and Safety of Pramipexole in Advanced Parkinson's Disease: Results from a European Multicenter Trial. *Mov. Disord.* 20 (5), 602–610. doi:10.1002/mds.20397

Morin, N., and Di Paolo, T. (2014). Pharmacological Treatments Inhibiting Levodopa-Induced Dyskinesias in MPTP-Lesioned Monkeys: Brain Glutamate Biochemical Correlates. *Front. Neurol.* 5, 144. doi:10.3389/fneur.2014.00144

Morin, N., Morissette, M., Grégoire, L., and Di Paolo, T. (2016). mGlu5, Dopamine D2 and Adenosine A2A Receptors in L-DOPA-Induced Dyskinesias. *Curr. Neuropharmacol.* 14 (5), 481–493. doi:10.2174/1570159x14666151201185652

Moro, E., Lozano, A. M., Pollak, P., Agid, Y., Rehncrona, S., Volkmann, J., et al. (2010). Long-term Results of a Multicenter Study on Subthalamic and Pallidal Stimulation in Parkinson's Disease. *Mov. Disord.* 25 (5), 578–586. doi:10.1002/mds.22735

Mosharov, E. V., Borgkvist, A., and Sulzer, D. (2015). Presynaptic Effects of Levodopa and Their Possible Role in Dyskinesia. *Mov. Disord.* 30 (1), 45–53. doi:10.1002/mds.26103

Müller, T., and Möhr, J. D. (2019). Recent Clinical Advances in Pharmacotherapy for Levodopa-Induced Dyskinesia. *Drugs* 79 (13), 1367–1374.

Munhoz, R. P., Cerasa, A., and Okun, M. S. (2014). Surgical Treatment of Dyskinesia in Parkinson's Disease. *Front. Neurol.* 5, 65. doi:10.3389/fneur.2014.00065

Muñoz, A., Li, Q., Gardoni, F., Marcello, E., Qin, C., Carlsson, T., et al. (2008). Combined 5-HT1A and 5-HT1B Receptor Agonists for the Treatment of L-DOPA-Induced Dyskinesia. *Brain* 131 (Pt 12), 3380–3394. doi:10.1093/brain/awn235

Murata, M., Hasegawa, K., Kanazawa, I., Fukasaka, J., Kochi, K., and Shimazu, R.Japan Zonisamide on PD Study Group (2015). Zonisamide Improves Wearing-Off in Parkinson's Disease: A Randomized, Double-Blind Study. *Mov. Disord.* 30 (10), 1343–1350. doi:10.1002/mds.26286

Na, Y. C., Chang, W. S., Jung, H. H., Kweon, E. J., and Chang, J. W. (2015). Unilateral Magnetic Resonance-Guided Focused Ultrasound Pallidotomy for Parkinson Disease. *Neurology* 85 (6), 549–551. doi:10.1212/WNL.0000000000001826

Nadjar, A., Gerfen, C. R., and Bezard, E. (2009). Priming for L-Dopa-Induced Dyskinesia in Parkinson's Disease: a Feature Inherent to the Treatment or the Disease? *Prog. Neurobiol.* 87 (1), 1–9. doi:10.1016/j.pneurobio.2008.09.013

Nahimi, A., Høltzermann, M., Landau, A. M., Simonsen, M., Jakobsen, S., Alstrup, A. K., et al. (2012). Serotonergic Modulation of Receptor Occupancy in Rats Treated with L-DOPA after Unilateral 6-OHDA Lesioning. *J. Neurochem.* 120 (5), 806–817. doi:10.1111/j.1471-4159.2011.07598.x

Nakajima, T., Zrinzo, L., Foltynie, T., Olmos, I. A., Taylor, C., Hariz, M. I., et al. (2011). MRI-guided Subthalamic Nucleus Deep Brain Stimulation without Microelectrode Recording: Can We Dispense with Surgery under Local Anaesthesia? *Stereotact Funct. Neurosurg.* 89 (5), 318–325. doi:10.1159/000330379

Navailles, S., Bioulac, B., Gross, C., and De Deurwaerdère, P. (2011). Chronic L-DOPA Therapy Alters central Serotonergic Function and L-DOPA-Induced Dopamine Release in a Region-dependent Manner in a Rat Model of Parkinson's Disease. *Neurobiol. Dis.* 41 (2), 585–590. doi:10.1016/j.nbd.2010.11.007

Navailles, S., and De Deurwaerdère, P. (2012). Imbalanced Dopaminergic Transmission Mediated by Serotonergic Neurons in L-DOPA-Induced Dyskinesia. *Parkinsons Dis.* 2012, 323686. doi:10.1155/2012/323686

Nazzaro, J. M., Lyons, K. E., and Pahwa, R. (2013). Deep Brain Stimulation for Essential Tremor. *Handb. Clin. Neurol.* 116, 155–166. doi:10.1016/B978-0-444-53497-2.00013-9

Negida, A., Ghaith, H. S., Fala, S. Y., Ahmed, H., Bahbah, E. I., Ebada, M. A., et al. (2021). Mavoglurant (AFQ056) for the Treatment of Levodopa-Induced Dyskinesia in Patients with Parkinson's Disease: a Meta-Analysis. *Neurol. Sci.* 42 (8), 3135–3143. doi:10.1007/s10072-021-05319-7

Nutt, J. G., Gunzler, S. A., Kirchhoff, T., Hogarth, P., Weaver, J. L., Krams, M., et al. (2008). Effects of a NR2B Selective NMDA Glutamate Antagonist, CP-101,606, on Dyskinesia and Parkinsonism. *Mov. Disord.* 23 (13), 1860–1866. doi:10.1002/mds.22169

Odekerken, V. J., Boel, J. A., Schmand, B. A., de Haan, R. J., Figee, M., van den Munckhof, P., et al. (2016). GPi vs STN Deep Brain Stimulation for Parkinson Disease: Three-Year Follow-Up. *Neurology* 86 (8), 755–761. doi:10.1212/WNL.0000000000002401

Oertel, W., Eggert, K., Pahwa, R., Tanner, C. M., Hauser, R. A., Trenkwalder, C., et al. (2017). Randomized, Placebo-Controlled Trial of ADS-5102 (Amantadine) Extended-Release Capsules for Levodopa-Induced Dyskinesia in Parkinson's Disease (EASE LID 3). *Mov. Disord.* 32 (12), 1701–1709. doi:10.1002/mds.27131

Ogawa, M., Zhou, Y., Tsuji, R., Kasahara, J., and Goto, S. (2019). Intrastriatal Memantine Infusion Dampens Levodopa-Induced Dyskinesia and Motor Deficits in a Mouse Model of Hemiparkinsonism. *Front. Neurol.* 10, 1258. doi:10.3389/fneur.2019.01258

Oki, M., Kaneko, S., Morise, S., Takenouchi, N., Hashizume, T., Tsuge, A., et al. (2017). Zonisamide Ameliorates Levodopa-Induced Dyskinesia and Reduces Expression of Striatal Genes in Parkinson Model Rats. *Neurosci. Res.* 122, 45–50. doi:10.1016/j.neures.2017.04.003

Olanow, C. W., Calabresi, P., and Obeso, J. A. (2020). Continuous Dopaminergic Stimulation as a Treatment for Parkinson's Disease: Current Status and Future Opportunities. *Mov. Disord.* 35 (10), 1731–1744. doi:10.1002/mds.28215

Ory-Magne, F., Corvol, J. C., Azulay, J. P., Bonnet, A. M., Brefel-Courbon, C., Damier, P., et al. (2014). Withdrawing Amantadine in Dyskinetic Patients with Parkinson Disease: the AMANDYSK Trial. *Neurology* 82 (11), 300–307. doi:10.1212/WNL.0000000000000050

Ossig, C., Antonini, A., Buhmann, C., Classen, J., Csoti, I., Falkenburger, B., et al. (2016). Wearable Sensor-Based Objective Assessment of Motor Symptoms in Parkinson's Disease. *J. Neural Transm. (Vienna)* 123 (1), 57–64. doi:10.1007/s00702-015-1439-8

Ostrem, J. L., Galifianakis, N. B., Markun, L. C., Grace, J. K., Martin, A. J., Starr, P. A., et al. (2013). Clinical Outcomes of PD Patients Having Bilateral STN DBS Using High-Field Interventional MR-Imaging for lead Placement. *Clin. Neurol. Neurosurg.* 115 (6), 708–712. doi:10.1016/j.clineuro.2012.08.019

Ostrem, J. L., Ziman, N., Galifianakis, N. B., Starr, P. A., Luciano, M. S., Katz, M., et al. (2016). Clinical Outcomes Using ClearPoint Interventional MRI for Deep Brain Stimulation lead Placement in Parkinson's Disease. *J. Neurosurg.* 124 (4), 908–916. doi:10.3171/2015.4.JNS15173

Pahwa, R., Factor, S. A., Lyons, K. E., Ondo, W. G., Gronseth, G., Bronte-Stewart, H., et al. (2006). Practice Parameter: Treatment of Parkinson Disease with Motor Fluctuations and Dyskinesia (An Evidence-Based Review): Report of the

Quality Standards Subcommittee of the American Academy of Neurology. *Neurology* 66 (7), 983–995. doi:10.1212/01.wnl.0000215250.82576.87

Pahwa, R., Tanner, C. M., Hauser, R. A., Isaacson, S. H., Nausieda, P. A., Truong, D. D., et al. (2017). ADS-5102 (Amantadine) Extended-Release Capsules for Levodopa-Induced Dyskinesia in Parkinson Disease (EASE LID Study): A Randomized Clinical Trial. *JAMA Neurol.* 74 (8), 941–949. doi:10.1001/jamaneurol.2017.0943

Pahwa, R., Tanner, C. M., Hauser, R. A., Sethi, K., Isaacson, S., Truong, D., et al. (2015). Amantadine Extended Release for Levodopa-Induced Dyskinesia in Parkinson's Disease (EASED Study). *Mov. Disord.* 30 (6), 788–795. doi:10.1002/mds.26159

Paik, J., and Keam, S. J. (2018). Amantadine Extended-Release (GOCOVRI™): A Review in Levodopa-Induced Dyskinesia in Parkinson's Disease. *CNS Drugs* 32 (8), 797–806. doi:10.1007/s40263-018-0552-2

Papapetropoulos, S. S. (2012). Patient Diaries as a Clinical Endpoint in Parkinson's Disease Clinical Trials. *CNS Neurosci. Ther.* 18 (5), 380–387. doi:10.1111/j.1755-5949.2011.00253.x

Paredes-Rodriguez, E., Vegas-Suarez, S., Morera-Herreras, T., De Deurwaerdere, P., and Miguelez, C. (2020). The Noradrenergic System in Parkinson's Disease. *Front. Pharmacol.* 11, 435. doi:10.3389/fphar.2020.00435

Pascual-Leone, A., Valls-Solé, J., Wassermann, E. M., and Hallett, M. (1994). Responses to Rapid-Rate Transcranial Magnetic Stimulation of the Human Motor Cortex. *Brain* 117 (Pt 4), 847–858. doi:10.1093/brain/117.4.847

Payer, D. E., Guttman, M., Kish, S. J., Tong, J., Adams, J. R., Rusjan, P., et al. (2016). D3 Dopamine Receptor-Preferring [11C]PHNO PET Imaging in Parkinson Patients with Dyskinesia. *Neurology* 86 (3), 224–230. doi:10.1212/WNL.0000000000002285

Piccini, P., Weeks, R. A., and Brooks, D. J. (1997). Alterations in Opioid Receptor Binding in Parkinson's Disease Patients with Levodopa-Induced Dyskinesias. *Ann. Neurol.* 42 (5), 720–726. doi:10.1002/ana.410420508

Pierucci, M., Galati, S., Valentino, M., Di Matteo, V., Benigno, A., Pitruzzella, A., et al. (2011). Nitric Oxide Modulation of the Basal Ganglia Circuitry: Therapeutic Implication for Parkinson's Disease and Other Motor Disorders. *CNS Neurol. Disord. Drug Targets* 10 (7), 777–791. doi:10.2174/187152711798072329

Poewe, W., Chaudhuri, K. R., Bergmann, L., and Antonini, A. (2019). Levodopa-carbidopa Intestinal Gel in a Subgroup of Patients with Dyskinesia at Baseline from the GLORIA Registry. *Neurodegener. Dis. Manag.* 9 (1), 39–46. doi:10.2217/nmt-2018-0034

Porras, G., Berthet, A., Dehay, B., Li, Q., Ladepeche, L., Normand, E., et al. (2012). PSD-95 Expression Controls L-DOPA Dyskinesia through Dopamine D1 Receptor Trafficking. *J. Clin. Invest.* 122 (11), 3977–3989. doi:10.1172/JCI59426

Potts, L. F., Park, E. S., Woo, J. M., Dyavar Shetty, B. L., Singh, A., Braithwaite, S. P., et al. (2015). Dual κ-agonist/μ-antagonist Opioid Receptor Modulation Reduces Levodopa-Induced Dyskinesia and Corrects Dysregulated Striatal Changes in the Nonhuman Primate Model of Parkinson Disease. *Ann. Neurol.* 77 (6), 930–941. doi:10.1002/ana.24375

Quattrone, A., Barbagallo, G., Cerasa, A., and Stoessl, A. J. (2018). Neurobiology of Placebo Effect in Parkinson's Disease: What We Have Learned and where We Are Going. *Mov. Disord.* 33 (8), 1213–1227. doi:10.1002/mds.27438

Rascol, O., Bronzova, J., Hauser, R. A., Lang, A. E., Sampaio, C., Theeuwes, A., et al. (2012). Pardoprunox as Adjunct Therapy to Levodopa in Patients with Parkinson's Disease Experiencing Motor Fluctuations: Results of a Double-Blind, Randomized, Placebo-Controlled, Trial. *Parkinsonism Relat. Disord.* 18 (4), 370–376. doi:10.1016/j.parkreldis.2011.12.006

Rascol, O., Perez-Lloret, S., and Ferreira, J. J. (2015). New Treatments for Levodopa-Induced Motor Complications. *Mov. Disord.* 30 (11), 1451–1460. doi:10.1002/mds.26362

Rascol, O., Sabatini, U., Brefel, C., Fabre, N., Rai, S., Senard, J. M., et al. (1998). Cortical Motor Overactivation in Parkinsonian Patients with L-Dopa-Induced Peak-Dose Dyskinesia. *Brain* 121 (Pt 3), 527–533. doi:10.1093/brain/121.3.527

Rojas Cabrera, J. M., Price, J. B., Rusheen, A. E., Goyal, A., Jondal, D., Barath, A. S., et al. (2020). Advances in Neurochemical Measurements: A Review of Biomarkers and Devices for the Development of Closed-Loop Deep Brain Stimulation Systems. *Rev. Anal. Chem.* 39 (1), 188–199. doi:10.1515/revac-2020-0117

Rondard, P., and Pin, J. P. (2015). Dynamics and Modulation of Metabotropic Glutamate Receptors. *Curr. Opin. Pharmacol.* 20, 95–101. doi:10.1016/j.coph.2014.12.001

Rose, S., Jackson, M. J., Smith, L. A., Stockwell, K., Johnson, L., Carminati, P., et al. (2006). The Novel Adenosine A2a Receptor Antagonist ST1535 Potentiates the Effects of a Threshold Dose of L-DOPA in MPTP Treated Common Marmosets. *Eur. J. Pharmacol.* 546 (1-3), 82–87. doi:10.1016/j.ejphar.2006.07.017

Rylander, D., Parent, M., O'Sullivan, S. S., Dovero, S., Lees, A. J., Bezard, E., et al. (2010). Maladaptive Plasticity of Serotonin Axon Terminals in Levodopa-Induced Dyskinesia. *Ann. Neurol.* 68 (5), 619–628. doi:10.1002/ana.22097

Sahin, G., Thompson, L. H., Lavisse, S., Ozgur, M., Rbah-Vidal, L., Dollé, F., et al. (2014). Differential Dopamine Receptor Occupancy Underlies L-DOPA-Induced Dyskinesia in a Rat Model of Parkinson's Disease. *PLoS One* 9 (3), e90759. doi:10.1371/journal.pone.0090759

Saitoh, Y., Kato, A., Ninomiya, H., Baba, T., Shibata, M., Mashimo, T., et al. (2003). Primary Motor Cortex Stimulation within the central Sulcus for Treating Deafferentation Pain. *Acta Neurochir Suppl.* 87, 149–152. doi:10.1007/978-3-7091-6081-7_31

Sanna, A., Follesa, P., Puligheddu, M., Cannas, A., Serra, M., Pisu, M. G., et al. (2020). Cerebellar Continuous Theta Burst Stimulation Reduces Levodopa-Induced Dyskinesias and Decreases Serum BDNF Levels. *Neurosci. Lett.* 716, 134653. doi:10.1016/j.neulet.2019.134653

Sano, H., and Nambu, A. (2019). The Effects of Zonisamide on L-DOPA-Induced Dyskinesia in Parkinson's Disease Model Mice. *Neurochem. Int.* 124, 171–180. doi:10.1016/j.neuint.2019.01.011

Santini, E., Feyder, M., Gangarossa, G., Bateup, H. S., Greengard, P., and Fisone, G. (2012). Dopamine- and cAMP-Regulated Phosphoprotein of 32-kDa (DARPP-32)-dependent Activation of Extracellular Signal-Regulated Kinase (ERK) and Mammalian Target of Rapamycin Complex 1 (mTORC1) Signaling in Experimental Parkinsonism. *J. Biol. Chem.* 287 (33), 27806–27812. doi:10.1074/jbc.M112.388413

Santini, E., Valjent, E., Usiello, A., Carta, M., Borgkvist, A., Girault, J. A., et al. (2007). Critical Involvement of cAMP/DARPP-32 and Extracellular Signal-Regulated Protein Kinase Signaling in L-DOPA-Induced Dyskinesia. *J. Neurosci.* 27 (26), 6995–7005. doi:10.1523/JNEUROSCI.0852-07.2007

Savola, J. M., Hill, M., Engstrom, M., Merivuori, H., Wurster, S., McGuire, S. G., et al. (2003). Fipamezole (JP-1730) Is a Potent Alpha2 Adrenergic Receptor Antagonist that Reduces Levodopa-Induced Dyskinesia in the MPTP-Lesioned Primate Model of Parkinson's Disease. *Mov. Disord.* 18 (8), 872–883. doi:10.1002/mds.10464

Sayın, S., Cakmur, R., Yener, G. G., Yaka, E., Uğurel, B., and Uzunel, F. (2014). Low-frequency Repetitive Transcranial Magnetic Stimulation for Dyskinesia and Motor Performance in Parkinson's Disease. *J. Clin. Neurosci.* 21 (8), 1373–1376. doi:10.1016/j.jocn.2013.11.025

Schaeffer, E., Pilotto, A., and Berg, D. (2014). Pharmacological Strategies for the Management of Levodopa-Induced Dyskinesia in Patients with Parkinson's Disease. *CNS Drugs* 28 (12), 1155–1184. doi:10.1007/s40263-014-0205-z

Schapira, A. H. V., Chaudhuri, K. R., and Jenner, P. (2017). Non-motor Features of Parkinson Disease. *Nat. Rev. Neurosci.* 18 (7), 509–450. Erratum in: Nat. Rev. Neurosci. 2017;18(8):509. PMID: 28592904. doi:10.1038/nrn.2017.6210.1038/nrn.2017.91

Schlesinger, I., Eran, A., Sinai, A., Erikh, I., Nassar, M., Goldsher, D., et al. (2015). MRI Guided Focused Ultrasound Thalamotomy for Moderate-To-Severe Tremor in Parkinson's Disease. *Parkinsons Dis.* 2015, 219149. doi:10.1155/2015/219149

Scott, N. W., Macleod, A. D., and Counsell, C. E. (2016). Motor Complications in an Incident Parkinson's Disease Cohort. *Eur. J. Neurol.* 23 (2), 304–312. doi:10.1111/ene.12751

Sebastianutto, I., and Cenci, M. A. (2018). mGlu Receptors in the Treatment of Parkinson's Disease and L-DOPA-Induced Dyskinesia. *Curr. Opin. Pharmacol.* 38, 81–89. doi:10.1016/j.coph.2018.03.003

Sellnow, R. C., Steece-Collier, K., Altwal, F., Sandoval, I. M., Kordower, J. H., Collier, T. J., et al. (2020). Striatal Nurr1 Facilitates the Dyskinetic State and Exacerbates Levodopa-Induced Dyskinesia in a Rat Model of Parkinson's Disease. *J. Neurosci.* 40 (18), 3675–3691. doi:10.1523/JNEUROSCI.2936-19.2020

Seppi, K., Weintraub, D., Coelho, M., Perez-Lloret, S., Fox, S. H., Katzenschlager, R., et al. (2011). The Movement Disorder Society Evidence-Based Medicine Review Update: Treatments for the Non-motor Symptoms of Parkinson's Disease. *Mov. Disord.* 26 Suppl 3 (S3), S42–S80. doi:10.1002/mds.23884

Sgambato-Faure, V., and Cenci, M. A. (2012). Glutamatergic Mechanisms in the Dyskinesias Induced by Pharmacological Dopamine Replacement and Deep Brain Stimulation for the Treatment of Parkinson's Disease. *Prog. Neurobiol.* 96 (1), 69–86. doi:10.1016/j.pneurobio.2011.10.005

Sharma, S., Singh, S., Sharma, V., Singh, V. P., and Deshmukh, R. (2015). Neurobiology of L-DOPA Induced Dyskinesia and the Novel Therapeutic Strategies. *Biomed. Pharmacother.* 70, 283–293. doi:10.1016/j.biopha.2015.01.029

Sharma, V. D., Patel, M., and Miocinovic, S. (2020). Surgical Treatment of Parkinson's Disease: Devices and Lesion Approaches. *Neurotherapeutics* 17 (4), 1525–1538. doi:10.1007/s13311-020-00939-x

Snow, B. J., Macdonald, L., Mcauley, D., and Wallis, W. (2000). The Effect of Amantadine on Levodopa-Induced Dyskinesias in Parkinson's Disease: a Double-Blind, Placebo-Controlled Study. *Clin. Neuropharmacol.* 23 (2), 82–85. doi:10.1097/00002826-200003000-00004

Solís, O., Espadas, I., Del-Bel, E. A., and Moratalla, R. (2015). Nitric Oxide Synthase Inhibition Decreases L-DOPA-Induced Dyskinesia and the Expression of Striatal Molecular Markers in Pitx3(-/-) Aphakia Mice. *Neurobiol. Dis.* 73, 49–59. doi:10.1016/j.nbd.2014.09.010

Stathis, P., Konitsiotis, S., Tagaris, G., and Peterson, D.VALID, and PD Study Group (2011). Levetiracetam for the Management of Levodopa-Induced Dyskinesias in Parkinson's Disease. *Mov. Disord.* 26 (2), 264–270. doi:10.1002/mds.23355

Stocchi, F., Fabbri, L., Vecsei, L., Krygowska-Wajs, A., Monici Preti, P. A., and Ruggieri, S. A. (2007). Clinical Efficacy of a Single Afternoon Dose of Effervescent Levodopa-Carbidopa Preparation (CHF 1512) in Fluctuating Parkinson Disease. *Clin. Neuropharmacol.* 30 (1), 18–24. doi:10.1097/01.WNF.0000236762.77913.C6

Stocchi, F., Rascol, O., Destee, A., Hattori, N., Hauser, R. A., Lang, A. E., et al. (2013). AFQ056 in Parkinson Patients with Levodopa-Induced Dyskinesia: 13-week, Randomized, Dose-Finding Study. *Mov. Disord.* 28 (13), 1838–1846. doi:10.1002/mds.25561

Stocchi, F., Vacca, L., Stirpe, P., and Torti, M. (2018). Pharmacokinetic Drug Evaluation of CVT-301 for the Treatment of Parkinson's Disease. *Expert Opin. Drug Metab. Toxicol.* 14 (12), 1189–1195. doi:10.1080/17425255.2018.1550483

Stone, A. A., Shiffman, S., Schwartz, J. E., Broderick, J. E., and Hufford, M. R. (2002). Patient Non-compliance with Paper Diaries. *BMJ* 324 (7347), 1193–1194. doi:10.1136/bmj.324.7347.1193

Strafella, A. P., Ko, J. H., and Monchi, O. (2006). Therapeutic Application of Transcranial Magnetic Stimulation in Parkinson's Disease: the Contribution of Expectation. *Neuroimage* 31 (4), 1666–1672. doi:10.1016/j.neuroimage.2006.02.005

Strecker, K., Adamaszek, M., Ohm, S., Wegner, F., Beck, J., and Schwarz, J. (2012). The 5-Ht1a-Receptor Agonist Flibanserin Reduces Drug-Induced Dyskinesia in RGS9-Deficient Mice. *J. Neural Transm. (Vienna)* 119 (11), 1351–1359. doi:10.1007/s00702-012-0815-x

Svenningsson, P., Rosenblad, C., Af Edholm Arvidsson, K., Wictorin, K., Keywood, C., Shankar, B., et al. (2015). Eltoprazine Counteracts L-DOPA-Induced Dyskinesias in Parkinson's Disease: a Dose-Finding Study. *Brain* 138 (Pt 4), 963–973. doi:10.1093/brain/awu409

Swann, N. C., de Hemptinne, C., Thompson, M. C., Miocinovic, S., Miller, A. M., Gilron, R., et al. (2018). Adaptive Deep Brain Stimulation for Parkinson's Disease Using Motor Cortex Sensing. *J. Neural Eng.* 15 (4), 046006. doi:10.1088/1741-2552/aabc9b

Tanner, C. M., Pahwa, R., Hauser, R. A., Oertel, W. H., Isaacson, S. H., Jankovic, J., et al. (2020). EASE LID 2: A 2-Year Open-Label Trial of Gocovri (Amantadine) Extended Release for Dyskinesia in Parkinson's Disease. *J. Parkinsons Dis.* 10 (2), 543–558. doi:10.3233/JPD-191841

Thanvi, B., Lo, N., and Robinson, T. (2007). Levodopa-induced Dyskinesia in Parkinson's Disease: Clinical Features, Pathogenesis, Prevention and Treatment. *Postgrad. Med. J.* 83 (980), 384–388. doi:10.1136/pgmj.2006.054759

Tison, F., Keywood, C., Wakefield, M., Durif, F., Corvol, J. C., Eggert, K., et al. (2016). A Phase 2A Trial of the Novel mGluR5-Negative Allosteric Modulator Dipraglurant for Levodopa-Induced Dyskinesia in Parkinson's Disease. *Mov. Disord.* 31 (9), 1373–1380. doi:10.1002/mds.26659

Tison, F., Durif, F., Corvol, J. C., Eggert, K., Trenkwalder, C., Lew, M., et al. (2013). Safety, Tolerability and Anti-dyskinetic Efficacy of Dipraglurant, a Novel mGluR5 Negative Allosteric Modulator (NAM) in Parkinson's Disease (PD) Patients with L-DOPA-Induced Dyskinesia (LID)(S23.004). *Neurology* 80.

Tohge, R., Kaneko, S., Morise, S., Oki, M., Takenouchi, N., Murakami, A., et al. (2021). Zonisamide Attenuates the Severity of Levodopa-Induced Dyskinesia via Modulation of the Striatal Serotonergic System in a Rat Model of Parkinson's Disease. *Neuropharmacology* 198, 108771. doi:10.1016/j.neuropharm.2021.108771

Torkaman-Boutorabi, A., Shahidi, G. A., Choopani, S., Rezvani, M., Pourkosary, K., Golkar, M., et al. (2012). The Catechol-O-Methyltransferase and Monoamine Oxidase B Polymorphisms and Levodopa Therapy in the Iranian Patients with Sporadic Parkinson's Disease. *Acta Neurobiol. Exp. (Wars)* 72 (3), 272–282.

Tousi, B., and Subramanian, T. (2005). The Effect of Levetiracetam on Levodopa Induced Dyskinesia in Patients with Parkinson's Disease. *Parkinsonism Relat. Disord.* 11 (5), 333–334. doi:10.1016/j.parkreldis.2004.11.003

Trenkwalder, C., Berg, D., Rascol, O., Eggert, K., Ceballos-Baumann, A., Corvol, J. C., et al. (2016b). A Placebo-Controlled Trial of AQW051 in Patients with Moderate to Severe Levodopa-Induced Dyskinesia. *Mov. Disord.* 31 (7), 1049–1054. doi:10.1002/mds.26569

Trenkwalder, C., Stocchi, F., Poewe, W., Dronamraju, N., Kenney, C., Shah, A., et al. (2016a). Mavoglurant in Parkinson's Patients with L-Dopa-Induced Dyskinesias: Two Randomized Phase 2 Studies. *Mov. Disord.* 31 (7), 1054–1058. doi:10.1002/mds.26585

Tronci, E., Lisci, C., Stancampiano, R., Fidalgo, C., Collu, M., Devoto, P., et al. (2013). 5-Hydroxy-tryptophan for the Treatment of L-DOPA-Induced Dyskinesia in the Rat Parkinson's Disease Model. *Neurobiol. Dis.* 60, 108–114. doi:10.1016/j.nbd.2013.08.014

Tronci, E., Napolitano, F., Muñoz, A., Fidalgo, C., Rossi, F., Björklund, A., et al. (2017). BDNF Over-expression Induces Striatal Serotonin Fiber Sprouting and Increases the Susceptibility to L-DOPA-Induced Dyskinesia in 6-OHDA-Lesioned Rats. *Exp. Neurol.* 297, 73–81. doi:10.1016/j.expneurol.2017.07.017

Tsunekawa, H., Takahata, K., Okano, M., Ishikawa, T., Satoyoshi, H., Nishimura, T., et al. (2018). Selegiline Increases on Time without Exacerbation of Dyskinesia in 6-Hydroxydopamine-Lesioned Rats Displaying L-Dopa-Induced Wearing-Off and Abnormal Involuntary Movements. *Behav. Brain Res.* 347, 350–359. doi:10.1016/j.bbr.2018.03.002

Uchida, S., Soshiroda, K., Okita, E., Kawai-Uchida, M., Mori, A., Jenner, P., et al. (2015). The Adenosine A2A Receptor Antagonist, Istradefylline Enhances Anti-parkinsonian Activity Induced by Combined Treatment with Low Doses of L-DOPA and Dopamine Agonists in MPTP-Treated Common Marmosets. *Eur. J. Pharmacol.* 766, 25–30. doi:10.1016/j.ejphar.2015.09.028

Upadhyay, G., Shankar, S., and Srivastava, R. K. (2015). Stem Cells in Neurological Disorders: Emerging Therapy with Stunning Hopes. *Mol. Neurobiol.* 52 (1), 610–625. doi:10.1007/s12035-014-8883-6

Utsumi, H., Okuma, Y., Kano, O., Suzuki, Y., Iijima, M., Tomimitsu, H., et al. (2013). Evaluation of the Efficacy of Pramipexole for Treating Levodopa-Induced Dyskinesia in Patients with Parkinson's Disease. *Intern. Med.* 52 (3), 325–332. doi:10.2169/internalmedicine.52.8333

Vegas-Suárez, S., Pisanò, C. A., Requejo, C., Bengoetxea, H., Lafuente, J. V., Morari, M., et al. (2020). 6-Hydroxydopamine Lesion and Levodopa Treatment Modify the Effect of Buspirone in the Substantia Nigra Pars Reticulata. *Br. J. Pharmacol.* 177 (17), 3957–3974.

Verschuur, C. V. M., Suwijn, S. R., Boel, J. A., Post, B., Bloem, B. R., van Hilten, J. J., et al. (2019). Randomized Delayed-Start Trial of Levodopa in Parkinson's Disease. *N. Engl. J. Med.* 380 (4), 315–324. doi:10.1056/NEJMoa1809983

Vijayakumar, D., and Jankovic, J. (2016). Drug-Induced Dyskinesia, Part 1: Treatment of Levodopa-Induced Dyskinesia. *Drugs* 76 (7), 759–777. doi:10.1007/s40265-016-0566-3

Vijverman, A. C., and Fox, S. H. (2014). New Treatments for the Motor Symptoms of Parkinson's Disease. *Expert Rev. Clin. Pharmacol.* 7 (6), 761–777. doi:10.1586/17512433.2014.966812

Vitek, J. L., Bakay, R. A., Freeman, A., Evatt, M., Green, J., McDonald, W., et al. (2003). Randomized Trial of Pallidotomy versus Medical Therapy for Parkinson's Disease. *Ann. Neurol.* 53 (5), 558–569. doi:10.1002/ana.10517

Volkmann, J., Allert, N., Voges, J., Sturm, V., Schnitzler, A., and Freund, H. J. (2004). Long-term Results of Bilateral Pallidal Stimulation in Parkinson's Disease. *Ann. Neurol.* 55 (6), 871–875. doi:10.1002/ana.20091

Vong, L. B., Sato, Y., Chonpathompikunlert, P., Tanasawet, S., Hutamekalin, P., and Nagasaki, Y. (2020). Self-assembled Polydopamine Nanoparticles Improve Treatment in Parkinson's Disease Model Mice and Suppress Dopamine-Induced Dyskinesia. *Acta Biomater.* 109, 220–228. doi:10.1016/j.actbio.2020.03.021

Vorovenci, R. J., and Antonini, A. (2015). The Efficacy of Oral Adenosine A(2A) Antagonist Istradefylline for the Treatment of Moderate to Severe Parkinson's Disease. *Expert Rev. Neurother.* 15 (12), 1383–1390. doi:10.1586/14737175.2015.1113131

Wachtel, S. R., and Abercrombie, E. D. (1994). L-3,4-dihydroxyphenylalanine-induced Dopamine Release in the Striatum of Intact and 6-Hydroxydopamine-Treated Rats: Differential Effects of Monoamine Oxidase A and B Inhibitors. *J. Neurochem.* 63 (1), 108–117. doi:10.1046/j.1471-4159.1994.63010108.x

Wagle-Shukla, A., Angel, M. J., Zadikoff, C., Enjati, M., Gunraj, C., Lang, A. E., et al. (2007). Low-frequency Repetitive Transcranial Magnetic Stimulation for Treatment of Levodopa-Induced Dyskinesias. *Neurology* 68 (9), 704–705. doi:10.1212/01.wnl.0000256036.20927.a5

Wan, Y., Wu, N., Song, L., Wang, X., Liu, Z., Yuan, W., et al. (2017). Levodopa/Benserazide Loaded Microspheres Alleviate L-Dopa Induced Dyskinesia through Preventing the Over-expression of D1R/Shp-2/ERK1/2 Signaling Pathway in a Rat Model of Parkinson's Disease. *Front. Aging Neurosci.* 9, 331. doi:10.3389/fnagi.2017.00331

Wang, T., Cao, X., Zhang, T., Shi, Q., Chen, Z., and Tang, B. (2015). Effect of Simvastatin on L-DOPA-Induced Abnormal Involuntary Movements of Hemiparkinsonian Rats. *Neurol. Sci.* 36 (8), 1397–1402. doi:10.1007/s10072-015-2127-z

Wang, W. W., Zhang, X. R., Lin, J. Y., Zhang, Z. R., Wang, Z., Chen, S. Y., et al. (2019). Levodopa/Benserazide PLGA Microsphere Prevents L-Dopa-Induced Dyskinesia via Lower β-Arrestin2 in 6-Hydroxydopamine Parkinson's Rats. *Front. Pharmacol.* 10, 660. doi:10.3389/fphar.2019.00660

Watts, R. L., Lyons, K. E., Pahwa, R., Sethi, K., Stern, M., Hauser, R. A., et al. (2010). 228 Study Investigators. Onset of Dyskinesia With Adjunct Ropinirole Prolonged-Release or Additional Levodopa in Early Parkinson's Disease. *Mov. Disord.* 25 (7), 858–866. doi:10.1002/mds.22890

Weaver, F. M., Follett, K., Stern, M., Hur, K., Harris, C., Marks, W. J., Jr, et al. (2009). Bilateral Deep Brain Stimulation vs Best Medical Therapy for Patients with Advanced Parkinson Disease: a Randomized Controlled Trial. *JAMA* 301 (1), 63–73. doi:10.1001/jama.2008.929

Wictorin, K., and Widner, H. (2016). Memantine and Reduced Time with Dyskinesia in Parkinson's Disease. *Acta Neurol. Scand.* 133 (5), 355–360. doi:10.1111/ane.12468

Wolf, E., Seppi, K., Katzenschlager, R., Hochschorner, G., Ransmayr, G., Schwingenschuh, P., et al. (2010). Long-term Antidyskinetic Efficacy of Amantadine in Parkinson's Disease. *Mov. Disord.* 25 (10), 1357–1363. doi:10.1002/mds.23034

Wu, J., Lim, E. C., Nadkarni, N. V., Tan, E. K., and Kumar, P. M. (2019). The Impact of Levodopa Therapy-Induced Complications on Quality of Life in Parkinson's Disease Patients in Singapore. *Sci. Rep.* 9 (1), 9248. doi:10.1038/s41598-019-45110-5

Wu, N., Wan, Y., Song, L., Qi, C., Liu, Z., and Gan, J. (2018). The Abnormal Activation of D1R/Shp-2 Complex Involved in Levodopa-Induced Dyskinesia in 6-Hydroxydopamine-Lesioned Parkinson's Rats. *Neuropsychiatr. Dis. Treat* 14, 1779–1786. doi:10.2147/NDT.S162562

Xiao, D., Cassin, J. J., Healy, B., Burdett, T. C., Chen, J. F., Fredholm, B. B., et al. (2011). Deletion of Adenosine A_1 or $A(_2A)$ Receptors Reduces L-3,4-Dihydroxyphenylalanine-Induced Dyskinesia in a Model of Parkinson's Disease. *Brain Res.* 1367, 310–318. doi:10.1016/j.brainres.2010.08.099

Xie, C. L., Shao, B., Chen, J., Zhou, Y., Lin, S. Y., and Wang, W. W. (2016). Effects of Neurostimulation for Advanced Parkinson's Disease Patients on Motor Symptoms: A Multiple-Treatments Meta-Analysas of Randomized Controlled Trials. *Sci. Rep.* 6, 25285. doi:10.1038/srep25285

Xie, C. L., Wang, W. W., Zhang, S. F., Yuan, M. L., Che, J. Y., Gan, J., et al. (2014). Levodopa/benserazide Microsphere (LBM) Prevents L-Dopa Induced Dyskinesia by Inactivation of the DR1/PKA/P-Tau Pathway in 6-OHDA-Lesioned Parkinson's Rats. *Sci. Rep.* 4, 7506. doi:10.1038/srep07506

Yu, S. J., Chen, S., Yang, Y. Y., Glotfelty, E. J., Jung, J., Kim, H. K., et al. (2020). PT320, Sustained-Release Exendin-4, Mitigates L-DOPA-Induced Dyskinesia in a Rat 6-Hydroxydopamine Model of Parkinson's Disease. *Front. Neurosci.* 14, 785. doi:10.3389/fnins.2020.00785

Zaaroor, M., Sinai, A., Goldsher, D., Eran, A., Nassar, M., and Schlesinger, I. (2018). Magnetic Resonance-Guided Focused Ultrasound Thalamotomy for Tremor: a Report of 30 Parkinson's Disease and Essential Tremor Cases. *J. Neurosurg.* 128 (1), 202–210. doi:10.3171/2016.10.JNS16758

Zesiewicz, T. A., Sullivan, K. L., Maldonado, J. L., Tatum, W. O., and Hauser, R. A. (2005). Open-label Pilot Study of Levetiracetam (Keppra) for the Treatment of Levodopa-Induced Dyskinesias in Parkinson's Disease. *Mov. Disord.* 20 (9), 1205–1209. doi:10.1002/mds.20563

Zhang J., J., Saur, T., Duke, A. N., Grant, S. G., Platt, D. M., Rowlett, J. K., et al. (2014). Motor Impairments, Striatal Degeneration, and Altered Dopamine-Glutamate Interplay in Mice Lacking PSD-95. *J. Neurogenet.* 28 (1-2), 98–111. doi:10.3109/01677063.2014.892486

Zhang, S., Xie, C., Wang, Q., and Liu, Z. (2014). Interactions of CaMKII with Dopamine D2 Receptors: Roles in Levodopa-Induced Dyskinesia in 6-hydroxydopamine Lesioned Parkinson's Rats. *Sci. Rep.* 4, 6811. doi:10.1038/srep06811

Zhang, Z. R., Zhang, X. R., Luan, X. Q., Wang, X. S., Wang, W. W., Wang, X. Y., et al. (2019). Striatal Overexpression of β-arrestin2 Counteracts L-Dopa-Induced Dyskinesia in 6-hydroxydopamine Lesioned Parkinson's Disease Rats. *Neurochem. Int.* 131, 104543. doi:10.1016/j.neuint.2019.104543

Zibetti, M., Merola, A., Rizzi, L., Ricchi, V., Angrisano, S., Azzaro, C., et al. (2011). Beyond Nine Years of Continuous Subthalamic Nucleus Deep Brain Stimulation in Parkinson's Disease. *Mov. Disord.* 26 (13), 2327–2334. doi:10.1002/mds.23903

Conflict of Interest: The authors declare that the research was conducted in the absence of any commercial or financial relationships that could be construed as a potential conflict of interest.

Publisher's Note: All claims expressed in this article are solely those of the authors and do not necessarily represent those of their affiliated organizations, or those of the publisher, the editors, and the reviewers. Any product that may be evaluated in this article, or claim that may be made by its manufacturer, is not guaranteed or endorsed by the publisher.

Copyright © 2022 Bandopadhyay, Mishra, Rana, Kaur, Ghoneim, Alshehri, Mustafa, Ahmad, Alhakamy and Mishra. This is an open-access article distributed under the terms of the Creative Commons Attribution License (CC BY). The use, distribution or reproduction in other forums is permitted, provided the original author(s) and the copyright owner(s) are credited and that the original publication in this journal is cited, in accordance with accepted academic practice. No use, distribution or reproduction is permitted which does not comply with these terms.

frontiers | Frontiers in Aging Neuroscience

ORIGINAL RESEARCH
published: 20 April 2022
doi: 10.3389/fnagi.2022.870844

Intelligent Healthcare System Using Patients Confidential Data Communication in Electrocardiogram Signals

*Ming Zhao[1], Shuo-Tsung Chen[2], Tzu-Li Chen[2], Shu-Yi Tu[3], Cheng-Ta Yeh[4], Fang-Yu Lin[5] and Hao-Chun Lu[6,7]**

[1] School of Computer Science, Yangtze University, Jingzhou, China, [2] Department of Industrial Engineering and Management, National Taipei University of Technology, Taipei, Taiwan, [3] Department of Mathematics, University of Michigan-Flint, Flint, MI, United States, [4] Department of Information Management, Fu Jen Catholic University, New Taipei City, Taiwan, [5] Graduate Institute of Business Administration, Fu Jen Catholic University, New Taipei City, Taiwan, [6] Department of Cardiology, Linkou Chang Gung Memorial Hospital, Taoyuan, Taiwan, [7] Department of Industrial and Business Management, Chang Gung University, Taoyuan, Taiwan

OPEN ACCESS

Edited by:
Jiehui Jiang, Shanghai University, China

Reviewed by:
Yao-Chin Wang, Taipei Medical University, Taiwan
Wenying Du, Capital Medical University, China

***Correspondence:**
Hao-Chun Lu
haoclu@gmail.com

Specialty section:
This article was submitted to Neurocognitive Aging and Behavior, a section of the journal Frontiers in Aging Neuroscience

Received: *07 February 2022*
Accepted: *28 February 2022*
Published: *20 April 2022*

Citation:
Zhao M, Chen S-T, Chen T-L, Tu S-Y, Yeh C-T, Lin F-Y and Lu H-C (2022) Intelligent Healthcare System Using Patients Confidential Data Communication in Electrocardiogram Signals. Front. Aging Neurosci. 14:870844. doi: 10.3389/fnagi.2022.870844

With the advent of the aging era, healthcare and elderly care have become the focus of medical care, especially the care of the elderly with dementia. Patients' confidential data hiding is a useful technology for healthcare and patient information privacy. In this study, we implement an intelligent healthcare system using the multiple-coefficient quantization technology in transform domain to hide patients' confidential data into electrocardiogram (ECG) signals obtained by ECG sensor module. In embedding patients' confidential data, we first consider a non-linear model for optimizing the quality of the embedded ECG signals. Next, we apply simulated annealing (SA) to solve the non-linear model so as to have good signal-to-noise ratio (SNR), root mean square error (RMSE), and relative RMSE (rRMSE). Accordingly, the distortion of the PQRST complexes and the ECG amplitude is very small so that the embedded confidential data can satisfy the requirements of physiological diagnostics. In end devices, one can receive the ECG signals with the embedded confidential data and without the original ECG signals. Experimental results confirm the effectiveness of our method, which remains high quality for each ECG signal with the embedded confidential data no matter how the quantization size Q is increased.

Keywords: multiple-coefficient, transform domain, non-linear model, simulated annealing, dementia

INTRODUCTION

In recent years, most countries around the world are facing the advent of the age of old age. Healthcare and long-term care have become the focus of medical care, especially the care of the elderly with dementia. Electrocardiogram (ECG) represents the human heart's electrical activity, and hence it can be used as a reference for the analysis of cardiac pathology and cardiovascular system diagnostics. So, ECG contains a very important bio-information that has to be protected

and transmitted on the Internet. It is necessary to apply information hiding technology on the ECG to protect patient rights and information.

Research on the protection of ECG information by watermarking or hiding techniques is still an important issue. Kong and Feng (2001) and Engin et al. (2005) propose a simple data hiding method for ECG signals, but the method is not blind. Zheng and Qian (2008) and Zheng et al. (2009) proposed a wavelet-domain ECG data hiding method in non-QRS complex frames to ensure the restoration of almost un-distorted ECG signals. Kaur et al. (2010) presented the safe transmission of ECG signals in wireless networks by using a blind hiding method. Ibaida et al. (2010) improved the watermarking technique of least significant bit (LSB) and applied this improved technique to hide healthcare information in an ECG signal. Ibaida et al. (2011) presented a watermarking technique to embed patient biomedical information into ECG signals so as to ensure patient/ECG linkage integrity, and is suitable for a wearable sensor-net health monitoring system. However, the selection of embedding location is difficult.

In Guo and Zhou (2012) and He et al. (2012), a Haar wavelet transform with 7 levels decomposition is adopted to transform the ECG signal, and then the synchronization code combined with watermark are embedded into the low-frequency sub-band of level 7 to have good signal-to-noise ratio (SNR) and bit error rate (BER). However, the quality of all watermarked ECG signals decreases when the embedding strength increases. Moreover, Guo and Zhou (2012) presented a model of single-channel electromyography blind recognition. Dey et al. (2012a) embedded reversible binary bits to be watermark in the photoplethysmography (PPG) signal and extracted them by an error prediction algorithm. Dey et al. (2012b) presented a new session-based blind watermarking scheme by hiding a binary watermark image into the ECG signal. However, the methods in Dey et al. (2012a,b) are not blind. Ayman and Ibrahim (2013) developed a wavelet-based information hiding technique to protect patient confidential data by combining encryption and scrambling. Their method applied wavelet transform to ECG signal to hide the related patient confidential data and physiological information. In Chen et al. (2014) and Tseng et al. (2014), single-coefficient quantization in transform domain is applied to the digital watermark encryption technology on the ECG for protecting patient rights and information. By this method, the changes in the PQRST complexes and amplitude of the ECG signal are very small. Jero et al. (2015) and Jero and Ramu (2016) used curvelet transforms to identify the coefficients that store the crucial information about diagnosis. The novelty of their approach is the usage of curvelet transform for ECG steganography, adaptive selection of watermark location, and a new threshold selection algorithm. In Swierkosz and Augustyniak (2018), an original time-frequency watermarking technique with an adaptive beat-to-beat lead-independent data container design is implemented. The authors tested six wavelets, six coding bit depth values, and two types of watermark content to find the conditions that are necessary for watermarked ECG to maintain the compliance with International Electrotechnical Commission (IEC) requirements for interpretation performance. Sanivarapu et al. (2020) proposed a wavelet method-based watermarking scheme for patient information hiding in the ECG as a QR image. They first converted the 1D-ECG signal to 2D-ECG image using Pan–Tompkins algorithm, and then used a wavelet transform to decompose the 2D-ECG image. They then decompose the detail coefficient of wavelet and the QR image using QR decomposition for embedding data.

In this study, we install ECG sensor module on patients to obtain their ECG and propose a new information hiding technology for the ECG. As ECG has high requirements for accuracy, we rewrite SNR and amplitude-quantization as performance index and constraint to obtain an optimization model for embedding patients' confidential data into ECGs imperceptibly. The optimization model is then solved by simulated annealing (SA) algorithms and applied to embed patients' confidential data. By network transmission, one can receive the ECGs embedded with the confidential data in the other end and extract the confidential data without the original ECG. In experiments, we evaluated the relation between embedding strength Q and SNR, embedding strength Q and root mean square error (RMSE), and embedding strength Q and similarity. Experimental results confirm the effectiveness of our method, which remains high quality for each ECG signal with the embedded confidential data no matter how the quantization size Q is increased.

The rest of this article is as follows. Section 2 reviews some preliminaries including ECG principle, discrete wavelet transform (DWT), discrete Fourier transform (DFT), discrete cosine transform (DCT), and SA. Section 3 presents the proposed SA-based quantization embedding method for hiding patient confidential data into ECG signals. Section 4 shows experimental results and discussion. Conclusions are finally drawn in Section 5.

PRELIMINARIES

In this section, we review some preliminaries including ECG principle, DWT, DFT, DCT, and SA.

Electrocardiogram Signal

The abbreviation ECG denotes the electrocardiogram wave, named by the Dutch physiologist W. Einthoven (the inventor of the ECG). As shown in **Figure 1**, he classified one cardiac cycle into P, Q, R, S, and T complex waves (Burrus et al., 1998). The ECG diagnosis mainly depends on the PQRST waves. Therefore, it is necessary to maintain the shape of these waveforms when we add information into ECG signals or perform ECG signals compression.

Discrete Wavelet Transform

The DWT is a technique attained by scales and translates a mother wavelet $\psi(x)$. The normalized scaling functions and wavelets are defined as,

$$\varphi_{i,n}(t) = 2^{\frac{i}{2}} h_i \varphi(2^i \text{t-n})$$

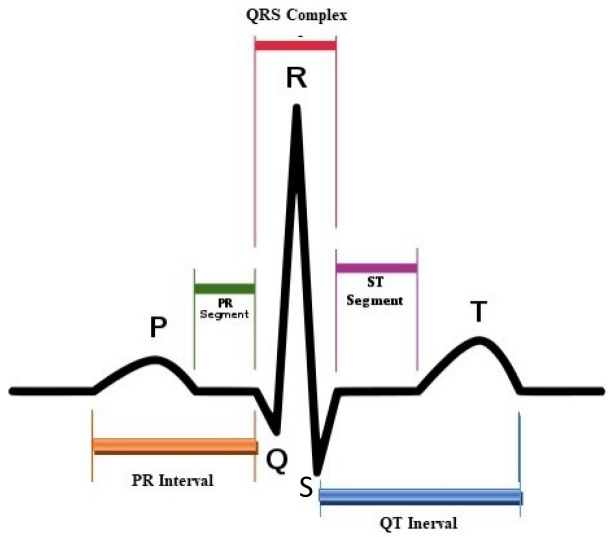

FIGURE 1 | ECG signal.

$$\psi_{i,n}(t) = 2^{i/2} g_i \psi(2^i \text{t-n})$$

where i and n denote the scale and translation parameters, and h_i and $g_i$are the low-pass and high-pass filters, respectively. It should be noted that orthogonal wavelet basis functions are adopted to ease the work in calculating coefficients expansion so that an input signal can be decomposed into several non-overlapping multi-resolution sub-bands, including low-frequency sub-bands and high-frequency sub-bands (Oran Brigham, 1988; Mallat, 1989, 1999).

Discrete Fourier Transform

The DFT converts a finite sequence of equally spaced samples of a function into a same-length sequence of equally spaced samples of the discrete-time Fourier transform (DTFT), which is a complex-valued function of frequency. Since it deals with a finite amount of data, it can be implemented in computers by numerical algorithms or even dedicated hardware. These implementations usually employ efficient fast Fourier transform (FFT) algorithms, so much so that the terms "FFT" and "DFT" are often used interchangeably (Rao and Yip, 1990; Oppenheim et al., 1999).

Discrete Cosine Transform

The DCT expresses a finite sequence of data points in terms of a sum of cosine functions oscillating at different frequencies. In particular, a DCT is a Fourier-related transform similar to the DFT but using only real numbers (Rao and Yip, 1990; Granville et al., 1994).

Simulated Annealing

Simulated annealing is an artificial intelligent algorithm, which utilizes probabilistic concept to approximate the global optimum of a given function. Specifically, It uses a metaheuristic method to approximate global optimization in a large discrete search space. In general, SA algorithm works as follows. At each time step, SA algorithm gives a solution randomly close to the current one, evaluates its quality, and then decides to move to it or to stay with the current solution based on either one of two probabilities between which it chooses based on the fact that the new solution is better or worse than the current one. During the search, the temperature is progressively decreased from an initial positive value to zero, and this affects the two probabilities: at each step, the probability of moving to a better new solution is either kept as 1 or is changed toward a positive value; instead, the probability of moving to a worse new solution is progressively changed toward zero (Bouttier and Gavra, 2019). The implementation of SA algorithm is easy because of its simple concept and computation.

PROPOSED INTELLIGENT HEALTHCARE SYSTEM

This section first shows the proposed amplitude-quantization hiding technique for confidential data communication and private information protection in the transform domain of ECGs, as shown in **Figure 2**. Next, we provide the architecture of the proposed intelligent multiple-coefficient quantization hiding system for patients' confidential data communication.

Information Hiding

As shown in **Figure 2**, the information hiding and detection proposed in this study is introduced as follows. Let $S = \{s_1, s_2, \cdots, s_N\}$ denote an ECG signal with total length N sample points. We then perform three transforms, DWT, DCT, and DFT, independently on the ECG signal$S = \{s_1, s_2, \cdots, s_N\}$so that the binary bits $B = \{m_i\}$ can be hidden into the coefficients of each transform domain. Finally, the hidden ECG signal is obtained and denoted by $\tilde{S} = \{\tilde{s}_1, \tilde{s}_2, \cdots, \tilde{s}_N\}$. The details of the hiding process for each transform are listed below.

DWT: In the information hiding, we first apply Haar DWT with orthogonal wavelet bases to decompose an ECG signal into several non-overlapping sub-bands. In order not to distort or

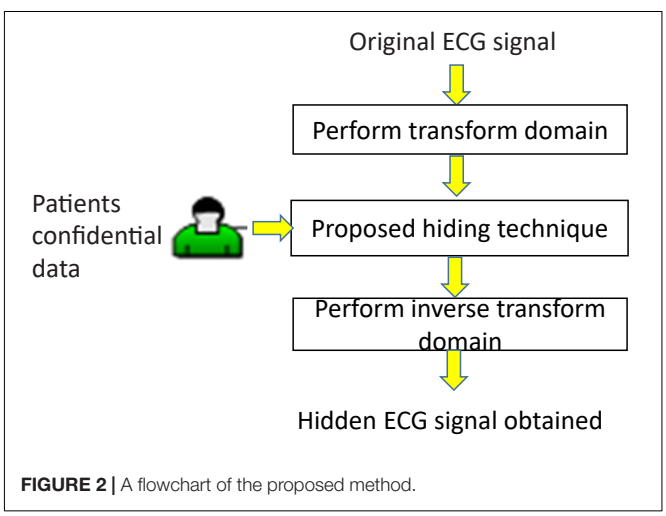

FIGURE 2 | A flowchart of the proposed method.

disturb the original ECG as much as possible, we hide the binary bits $B = \{m_i\}$ into the DWT lowest-frequency coefficients by the following rule,

$$\sum_{i=1}^{N} |\tilde{c}_i| = \begin{cases} \left\lfloor \sum_{i=1}^{N} |c_i| \Big/ Q \right\rfloor Q + {}^{3Q}\!/_{4}, & \text{if } m_i = 1 \\ \left\lfloor \sum_{i=1}^{N} |c_i| \Big/ Q \right\rfloor Q + {}^{Q}\!/_{4}, & \text{if } m_i = 0 \end{cases}$$

where $\{c_i\}$ and $\{\tilde{c}_i\}$ are the DWT lowest-frequency coefficients before and after hiding, respectively; Q is the hiding strength. By performing the inverse DWT (IDWT), the hidden ECG signal $\tilde{S}$ is obtained and the information hiding is completed.

DCT: The hiding rule for DCT multiple coefficients is the same as for DWT. Similarly, we hide the binary bits $B = \{m_i\}$ into the DCT lowest-frequency coefficients $\{c_i\}$, respectively.

DFT: The hiding rule for DFT multiple coefficients is the same as for DWT. Similarly, we hide the binary bits $B = \{m_i\}$ into the DFT lowest-frequency coefficients $\{c_i\}$, respectively.

Theoretically, an ECG signal is modified when embedding patient confidential information. The modification is usually called a distortion. In order to reduce the distortion of ECG signal, we consider the maximum of SNR which is defined as,

$$SNR = -10 \log \left[\sum_{i=1}^{N} (\tilde{s}_i - s_i)^2 \Big/ \sum_{i=1}^{N} s_i^2 \right]$$

where $\{s_i\}$ represents the original ECG signal sample points, and $\{\tilde{s}_i\}$ represents the unknown embedded (or modified) ECG signal sample points. Since we implement the DWT with orthogonal wavelet bases, the SNR can be rewritten to the form,

$$SNR = -10 \log \left[\sum_{i=1}^{N} (|\tilde{c}_i| - |c_i|)^2 \Big/ \sum_{i=1}^{N} |c_i|^2 \right]$$

From the point of view on maximizing SNR, we consider to determine the unknown values of $\{\tilde{c}_i\}_{i=0}^{N}$ by using the following optimization models.

- If the bit $b_i = 1$ is embedded into $\{c_i | 1 \le i \le N\}$, $\sum_{i=1}^{N} |c_i|$ is modified to $\sum_{i=1}^{N} |\tilde{c}_i|$ by,

  $$\text{maximize} \quad -10 \log \left[\sum_{i=1}^{N} (|\tilde{c}_i| - |c_i|)^2 \Big/ \sum_{i=1}^{N} |c_i|^2 \right]$$

  $$\text{subject to} \sum_{i=1}^{N} |\tilde{c}_i| = \left\lfloor \sum_{i=1}^{N} |c_i| \Big/ Q \right\rfloor Q + \frac{3}{4} Q$$

- If the bit $b_i = 1$ is embedded into $\{c_i | 1 \le i \le N\}$, $\sum_{i=1}^{N} |c_i|$ is modified to $\sum_{i=1}^{N} |\tilde{c}_i|$ by,

  $$\text{maximize} \quad -10 \log \left[\sum_{i=1}^{N} (|\tilde{c}_i| - |c_i|)^2 \Big/ \sum_{i=1}^{N} |c_i|^2 \right]$$

  $$\text{subject to} \sum_{i=1}^{N} |\tilde{c}_i| = \left\lfloor \sum_{i=1}^{N} |c_i| \Big/ Q \right\rfloor Q + \frac{1}{4} Q$$

Due to the fact that the algorithm of SA is easy to be implemented by its simple concept and calculation mentioned in section "Simulated Annealing," especially for embedded system, we adopt SA to solve the optimization models approximately. In other words, we apply SA to obtain the optimal solutions of $\{\tilde{c}_i\}_{i=0}^{N}$ approximately. At each time step in SA, the algorithm randomly selects a solution close to the current one, measures its quality, and then decides to move to it or to stay with the current solution based on either one of two probabilities between which it chooses on the basis of the fact that the new solution is better or worse than the current one. During the search, the temperature is progressively decreased from an initial positive value to zero, which affects the two probabilities: at each step, the probability of moving to a better new solution is either kept as 1 or is changed toward a positive value; instead, the probability of moving to a worse new solution is progressively changed toward zero. In this section, we adopt SA to approach the optimal solution of the proposed optimization model. The detailed procedure of SA in solving the proposed optimization model is introduced in the following steps.

Step 1: Setting the initial value for parameters including initial solution C_0, initial temperature T_0, final temperature T_f, cooling rate r, and number of iteration D for each temperature T, where $T_0 \le T \le T_f$.

Step 2: For each $d = 1,\ldots,D$ in a temperature T, do the following repeatedly:

(1) Produce a new solution $C'' = \{|c_1''|, |c_2''|, \cdots, |c_n''|\}$ randomly and calculate the difference $\Delta E = E(C'') - E(C') = \left\{ -10 \log \left[\sum_{i=1}^{n} \left(|c_i''| - |c_i|\right)^2 \Big/ \sum_{i=1}^{N} |c_i|^2 \right] - \left(-10 \log \left[\sum_{i=1}^{N} \left(|c_i'| - |c_i|\right)^2 \Big/ \sum_{i=1}^{N} |c_i|^2 \right]\right) \right\}$ between current solution $C' = \{|c_1'|, |c_2'|, \cdots, |c_n'|\}$ and the new solution (neighbors) $C'' = \{|c_1''|, |c_2''|, \cdots, |c_n''|\}$.

(2) The probability of making the transition from the current solution to a new solution (neighbors) is specified by an acceptance probability function $P(\Delta E, T)$ that depends on ΔE and T.

$$P(\Delta E, T) = \begin{cases} 1, & if\ \Delta E \le 0 \\ e^{\left(\frac{-\Delta E}{T}\right)}, & if\ \Delta E > 0 \end{cases}$$

In case $\Delta E \le 0$, the probability function $P(\Delta E, T)$ is equal to 1 indicating that the current solution S is replaced by new solution S'. In case $\Delta E > 0$, the current solution S is replaced by the new solution S' when probability function $P(\Delta E, T) = e^{\left(\frac{-\Delta E}{T}\right)}$ is greater than a threshold $H \in (0, 1)$.

Step 3: When step 2 is finished, the temperature T is decreased by a cooling rate r to a new temperature $T = rT$.

Step 4: Check if temperature T reaches the final temperature T_f to stop SA.

After applying SA to embed patients' essential body functions into ECG signal S, we obtain an embedded ECG signal $\tilde{S}$, respectively.

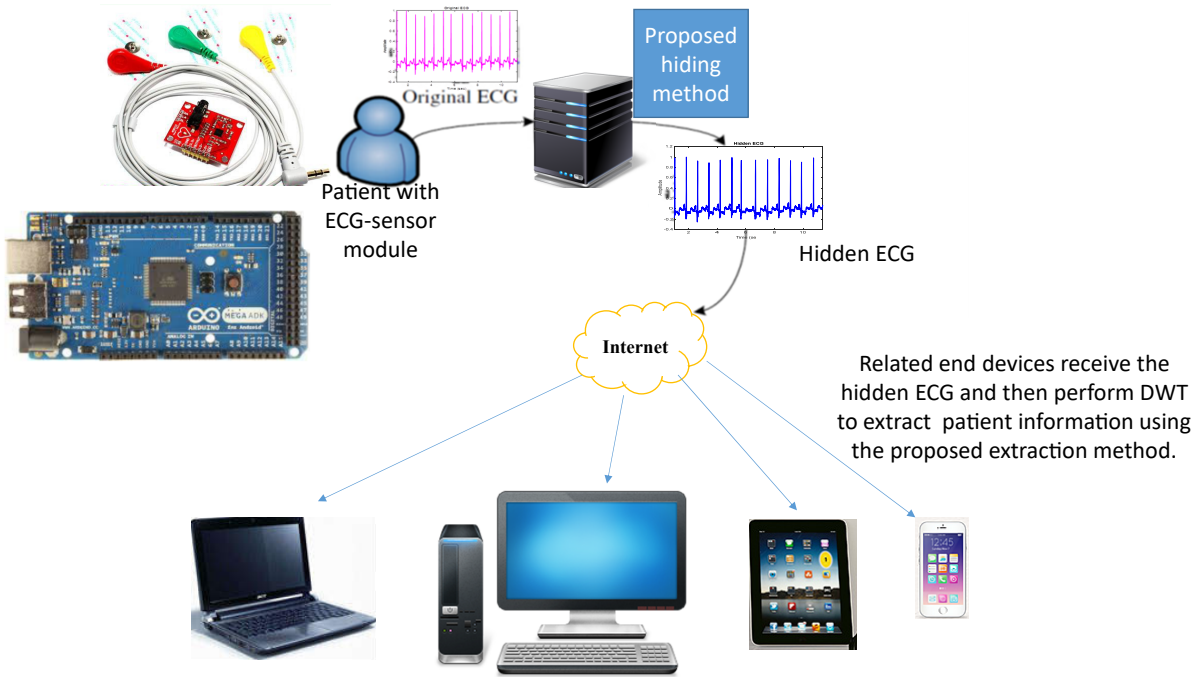

FIGURE 3 | Proposed intelligent multiple-coefficient quantization hiding and communication system for patients' confidential data.

Information Detection

In the information detection, similar to the information hiding mentioned earlier, we first perform the transforms, DWT, DCT, and DFT on the test ECG signals, respectively. Next, we detect binary bits $\{m_i^*\}$ from the hidden coefficients $\{\tilde{c}_i\}$ of the DWT, DCT, and DFT by the following rule:

$$m_i^* = \begin{cases} 1, \text{ if } \sum_{i=1}^{N} |\tilde{c}_i| - \left\lfloor \sum_{i=1}^{N} |\tilde{c}_i| / Q \right\rfloor Q \geq Q/2 \\ 0, \text{ if } \sum_{i=1}^{N} |\tilde{c}_i| - \left\lfloor \sum_{i=1}^{N} |\tilde{c}_i| / Q \right\rfloor Q < Q/2 \end{cases}$$

Architecture of the Proposed System

Figure 3 shows the architecture of the proposed intelligent multiple-coefficient quantization hiding system for patients' confidential data communication. First, we install ECG-sensor module, including electrode patch, AD8232 ECG sensor, and Arduino, on patients or dementia patients to obtain their ECG. As the ECG-sensor module shown in the upper left corner of **Figure 3**, three electrode patches are installed on patient body and connected to AD8232 ECG sensor. At the same time, AD8232 is connected to Arduino which outputs the ECG data to a computer. Next, as in subsections "Information Hiding" and "Information Detection," we hide the patient's information into the ECG signal in the transform domain by performing DWT/DFT/DCT and IDWT/inverse DFT (IDFT)/inverse DCT (IDCT). At the other end, the embedded patients confidential data are extracted after the hidden ECG is received through wireless communication and we perform transform domain DWT/DFT/DCT on the hidden ECG.

EXPERIMENTS AND DISCUSSION

In experiments, we apply the ECG data obtained from ECG sensor module to test the proposed method on each ECG signal with length 4,096 samples represented by 16-bit. To have more embedding capacity, we set N to 2. The evaluation of experimental results and discussion are listed in section 4.1. Limitation and future research plan are listed in section 4.2.

Experimental Results and Discussion

Without generality, the performance of the proposed scheme is evaluated by SNR, similarity, and RMSE, which are formulated as follows:

$$\text{SNR} = -10 \log_{10} \left(\frac{\sum_{i=1}^{N} (\tilde{s}_i - s_i)^2}{\sum_{i=1}^{N} s_i^2} \right),$$

$$\text{Similarity}\left(S, \tilde{S}\right) = \frac{\sum_{i=1}^{N} s_i \tilde{s}_i}{\sum_{i=1}^{N} \tilde{s}_i^2},$$

$$\text{RMSE} = \sqrt{\frac{1}{N} \sum_{i=1}^{N} (\tilde{s}_i - s_i)^2},$$

where s_i and $\tilde{s}_i$ denote original ECG signal sample point and hidden ECG signal sample point, respectively.

The proposed method provides good quality for each hidden ECG signal. For example, **Figures 4A,B** show the original ECG signal and hidden ECG signal using DWT lowest-frequency coefficients in 5-level decomposition for dataset ID 1. They look

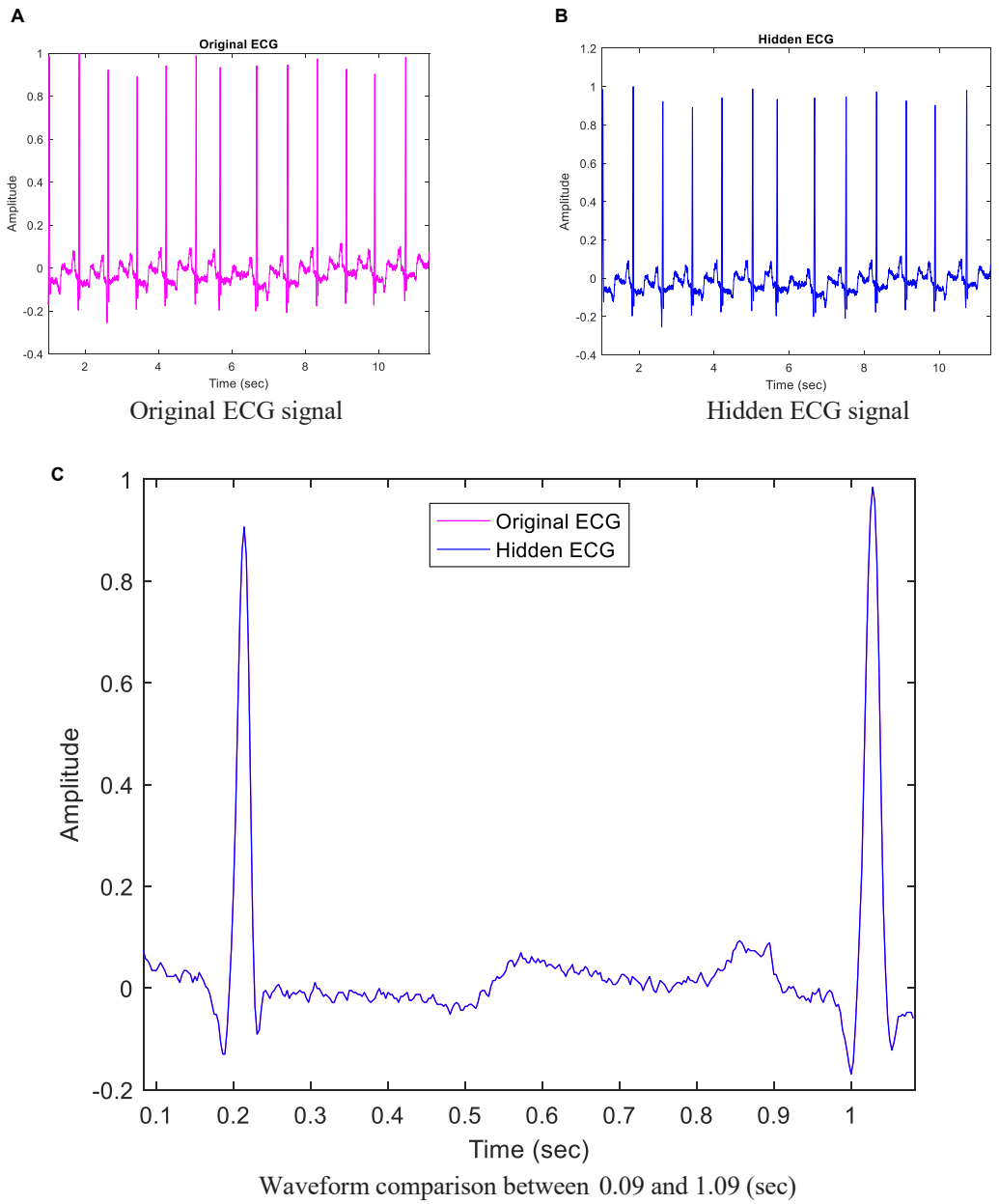

FIGURE 4 | Comparison between original electrocardiogram (ECG) signal and hidden ECG signal for dataset ID 1. **(A)** Original ECG signal. **(B)** Hidden ECG signal. **(C)** Waveform comparison between 0.09 and 1.09 s.

almost indistinguishable. As shown in **Figure 4C**, the purple curve represents the original ECG signals, and the blue curve represents the hidden ECG signals using DWT and quantization size $Q = 4000$.

Moreover, as shown in **Table 1**, the proposed method applies SA to optimize the quality of each hidden ECG signal and then improve the drawback that the quality of each hidden ECG signal is greatly reduced as the quantization size Q is increased. In other words, our method remains high quality, with good RMSE and SNR, for each hidden ECG signal under sufficient hiding capacity no matter how the quantization size Q is increased. In addition, both DFT and DCT also have the same effect on RMSE and SNR.

Limitation and Future Research Plan

There are some limitations in the proposed system. The two limitations in our system are that the ECG signals embedded with patients' confidential data are transmitted to the receiver with an upload speed with a limit of 75 Mbps and a download speed with a limit of 300 Mbps. In future research plan, we will reduce the size of the sensor module and the computer and have a waterproof case without affecting the function.

TABLE 1 | Experimental results for the three transforms: discrete wavelet transform (DWT), discrete cosine transform (DCT), and discrete Fourier transform (DFT).

ID	Method	Domain	Q	Amplitude similarity	SNR	RMSE	Interval RMSE in ECG			
							PR	QRS	ST	QT
1	Chen et al., 2014	DWT (Level 5)	500	1	40.26	36.86	0	0	0.028	0
			2000	1	32.74	69.64	0	0	0	0
			10000	1	20.75	126.13	0	0	0	0
		DFT	500	1	61.13	3.74	0	0	0	0
			2000	1	50.09	7.49	0	0	0	0
			10000	0.99	38.11	29.79	0	0	0	0
		DCT	500	0.99	26.62	198.90	0	0	0	0
			2000	0.98	17.85	434.41	0	0	0	0
			10000	0.81	4.73	1964.4	0	0	0	0
	Proposed	DWT (Level 5)	500	0.99	38.46	50.92	0	0	0	0
			2000	0.99	38.44	50.99	0	0	0	0
			10000	0.99	38.55	50.41	0	0	0	0
		DFT	500	1	33.74	91.61	0	0	0	0
			2000	1	31.73	110.41	0	0	0	0
			10000	1	32.09	106.01	0	0	0	0
		DCT	500	1	46.08	21.17	0	0	0	0
			2000	1	45.70	22.10	0	0	0	0
			10000	1	45.58	22.41	0	0	0	0
2	Chen et al., 2014	DWT (Level 5)	500	1	40.78	35.95	0	0.002	0.002	0
			2000	1	31.67	72.57	0	0	0	0
			10000	1	20.31	141.47	0	0	0	0
		DFT	500	1	60.01	3.72	0	0	0	0
			2000	1	51.56	7.35	0	0	0	0
			10000	1	38.33	30.03	0	0	0	0
		DCT	500	0.99	25.68	204.19	0	0	0	0
			2000	0.98	16.94	443.70	0	0	0	0
			10000	0.78	2.94	1982.1	0	0	0	0
	Proposed	DWT (Level 5)	500	1	32.59	92.49	0	0	0	0
			2000	1	32.71	91.01	0	0	0	0
			10000	0.99	32.29	95.49	0	0	0	0
		DFT	500	0.99	31.36	106.28	0	0	0	0
			2000	0.99	31.76	101.53	0	0	0	0
			10000	0.99	32.19	96.61	0	0	0	0
		DCT	500	1	35.13	68.85	0	0	0	0
			2000	1	35.33	67.26	0	0	0	0
			10000	1	35.27	67.53	0	0	0	0
3	Chen et al., 2014	DWT (Level 5)	500	0.99	43.10	34.84	0	0	0	0
			2000	0.99	35.05	69.96	0	0	0	0
			10000	0.99	20.46	265.70	0	0	0	0
		DFT	500	1	62.52	3.72	0	0	0	0
			2000	1	51.49	7.45	0	0	0	0
			10000	1	39.42	29.95	0	0	0	0
		DCT	500	0.99	28.02	197.89	0	0	0	0
			2000	0.99	19.42	423.11	0	0	0	0
			10000	0.87	5.43	1886.2	0	0	0	0
	Proposed	DWT (Level 5)	500	1	34.25	96.58	0	0	0	0
			2000	1	34.23	96.84	0	0	0	0
			10000	1	32.83	113.84	0	0	0	0
		DFT	500	0.99	27.32	302.95	0	0	0	0
			2000	0.99	26.54	331.65	0	0	0	0
			10000	0.99	27.61	293.19	0	0	0	0
		DCT	500	1	28.27	169.43	0	0	0	0
			2000	1	28.36	167.42	0	0	0	0
			10000	1	28.54	166.77	0	0	0	0

(Continued)

TABLE 1 | (Continued)

ID	Method	Domain	Q	Amplitude similarity	SNR	RMSE	Interval RMSE in ECG			
							PR	QRS	ST	QT
5	Chen et al., 2014	DWT (Level 5)	500	1	40.56	36.07	0.002	0.002	0	0
			2000	1	33.65	63.48	0	0	0	0
			10000	1	19.05	270.75	0	0	0	0
		DFT	500	1	62.23	3.74	0	0	0	0
			2000	1	52.16	7.53	0	0	0	0
			10000	0.99	38.22	29.77	0	0	0	0
		DCT	500	0.99	27.27	209.75	0	0	0	0
			2000	0.99	19.62	450.70	0	0	0	0
			10000	0.85	3.76	1980.2	0	0	0	0
	Proposed	DWT (Level 5)	500	1	26.21	258.11	0	0	0	0
			2000	1	26.95	238.72	0	0	0	0
			10000	1	26.78	253.62	0	0	0	0
		DFT	500	0.99	28.32	156.43	0	0	0	0
			2000	0.99	28.54	157.12	0	0	0	0
			10000	0.99	28.61	156.37	0	0	0	0
		DCT	500	1	34.17	94.74	0	0	0	0
			2000	1	34.11	95.42	0	0	0	0
			10000	1	34.25	94.08	0	0	0	0
6	Chen et al., 2014	DWT (Level 5)	500	0.99	41.56	37.21	0.051	0	0	0
			2000	0.99	34.20	68.96	0	0	0	0
			10000	0.99	20.67	260.17	0	0	0	0
		DFT	500	1	62.46	3.76	0.697	0.019	0.019	0
			2000	1	53.47	7.50	0	0	0	0
			10000	0.99	40.45	29.62	0	0	0	0
		DCT	500	0.99	27.84	202.645	0	0	0	0
			2000	0.99	19.26	431.98	0	0	0	0
			10000	0.86	3.41	1897.0	0	0	0	0
	Proposed	DWT (Level 5)	500	0.99	26.16	317.65	0	0	0	0
			2000	0.99	26.34	327.15	0	0	0	0
			10000	0.99	26.76	322.48	0	0	0	0
		DFT	500	0.99	27.18	166.33	0	0	0	0
			2000	0.99	27.09	167.05	0	0	0	0
			10000	0.99	27.46	166.46	0	0	0	0
		DCT	500	1	31.41	134.54	0	0	0	0
			2000	1	32.26	129.75	0	0	0	0
			10000	1	32.18	128.96	0	0	0	0
7	Chen et al., 2014	DWT (Level 5)	500	1	41.96	33.04	0	0	0	0
			2000	1	35.15	68.28	0	0	0	0
			10000	0.99	20.75	284.63	0	0	0	0
		DFT	500	1	64.46	3.70	0	0	0	0
			2000	1	55.37	7.47	0	0	0	0
			10000	1	41.24	30.21	0	0	0	0
		DCT	500	0.98	29.58	205.58	0	0	0	0
			2000	0.99	19.76	450.82	0	0	0	0
			10000	0.88	5.43	2092.6	0	0	0	0
	Proposed	DWT (Level 5)	500	1	28.83	283.36	0	0	0	0
			2000	1	28.39	297.09	0	0	0	0
			10000	1	28.56	291.09	0	0	0	0
		DFT	500	0.99	25.96	160.33	0	0	0	0
			2000	0.99	25.74	161.05	0	0	0	0
			10000	0.99	25.36	161.46	0	0	0	0
		DCT	500	1	46.58	29.02	0	0	0	0
			2000	1	46.00	31.05	0	0	0	0
			10000	1	46.22	28.54	0	0	0	0

CONCLUSION

Based on the proposed optimization model and SA algorithm, we apply multiple-coefficients quantization technology to propose a new method for embedding patients' confidential data into ECG signals in the transform domain. After testing ECG data sets by using the proposed embedding method, the difference between the embedded ECG signal and the original one is very small and negligible for physiological diagnostics. In addition, the proposed method improves the drawback that the quality of each embedded ECG signal is greatly reduced as the quantization size Q is increased. At the end devices, the embedded patients' confidential data are extracted after the embedded ECG is received through internet transmission and we perform DWT on the embedded ECG.

DATA AVAILABILITY STATEMENT

The original contributions presented in the study are included in the article/supplementary material, further inquiries can be directed to the corresponding author.

AUTHOR CONTRIBUTIONS

S-TC: conceptualization and methodology. S-TC, F-YL, and T-LC: software. S-TC, C-TY, and S-YT: validation. S-TC, MZ, and H-CL: writing – review and editing. All authors have read and agreed to the published version of the manuscript.

REFERENCES

Ayman, I., and Ibrahim, K. (2013). Wavelet-based ECG steganography for protecting patient confidential information in point-of-care systems. *IEEE Trans. Biomed. Eng.* 60, 3322–3330. doi: 10.1109/TBME.2013.2264539

Bouttier, C., and Gavra, I. (2019). Convergence rate of a simulated annealing algorithm with noisy observations. *J. Mach. Learn. Res.* 20, 127–171. doi: 10.1016/j.compbiolchem.2009.11.002

Burrus, C. S., Gopinath, R. A., and Gao, H. (1998). *Introduction to Wavelet Theory and Its Application*. Hoboken, NJ: Prentice-Hall.

Chen, S.-T., Guo, Y.-J., Huang, H.-N., Kung, W.-M., Tseng, K.-K., and Tu, S.-Y. (2014). Hiding patients confidential data in the ECG signal via transform-domain quantization scheme. *J. Med. Syst.* 38:54. doi: 10.1007/s10916-014-0054-9

Dey, N., Biswas, S., Roy, A. B., Das, A., and Chowdhuri, S. S. (2012a). "Analysis of photoplethysmographic signals modified by reversible watermarking technique using prediction-error in wireless telecardiology," in *Proceedings of the First International Conference on Intelligent Infrastructure the 47th Annual National Convention of Computer Society of India* CSI (New York, NY: McGraw-Hill) (accessed December 2, 2012).

Dey, N., Mukhopadhyay, S., Das, A., and Chaudhuri, S. S. (2012b). Analysis of P-QRS-T components modified by blind watermarking technique within the electrocardiogram signal for authentication in wireless telecardiology using DWT. *Int. J. Image Graph. Signal Process.* 4, 33–46.

Engin, M., Çidam, O., and Engin, E. Z. (2005). Wavelet transformation based watermarking technique for human electrocardiogram (ECG). *J. Med. Syst.* 29, 589–594. doi: 10.1007/s10916-005-6126-0

Granville, V., Krivanek, M., and Rasson, J.-P. (1994). Simulated annealing: a proof of convergence. *IEEE Trans. Pattern Anal. Mach. Intell.* 16, 652–656.

Guo, Y., and Zhou, D. (2012). Single channel surface electromyography blind recognition model based on watermarking. *J. Vib. Control* 18, 42–47.

He, X., Tseng, K. K., Huang, H. H., Chen, S. T., Tu, S. Y., Zeng, F., et al. (2012). "Wavelet-based quantization watermarking for ECG signals," in *Proceedings of the 2012 International Conference on Computing, Measurement, Control and Sensor Network, (CMCSN)*, Taiyuan, 233–236. doi: 10.1007/s10916-016-0608-0

Ibaida, A., Khalil, I., and van Dhiah, A. S. (2010). "Embedding patients confidential data in ECG signal for healthcare information system," in *Proceeding of the 32nd Annual International Conference of the IEEE EMBS*, Buenos Aires, 3891–3894. doi: 10.1109/IEMBS.2010.5627671

Ibaida, A., Khalil, I., and van Schyndel, R. (2011). "A low complexity high capacity ECG signal watermark for wearable sensor-net health monitoring system," in *Proceedings of the Computing in Cardiology* (CinC), Hangzhou, 393–396.

Jero, S. E., Palaniappan, R., and Ramakrishnan, S. (2015). ECG steganography using curvelet transform. *Biomed. Signal Process. Control* 22, 161–169. doi: 10.3390/s20102941

Jero, S. E., and Ramu, P. (2016). Curvelets-based ECG steganography for data security. *Electron. Lett.* 52, 283–285. doi: 10.1049/el.2015.3218

Kaur, S., Farooq, O., Singhal, R., and Ahuja, B. S. (2010). "Digital watermarking of ECG data for secure wireless communication," in *Proceedings of the 2010 International Conference on Recent Trends in Information, Telecommunication and Computing* (ITC2010), Kochi, 140–144. doi: 10.1109/ITC.2010.96

Kong, X., and Feng, R. (2001). Watermarking medical signals for telemedicine. *IEEE Trans. Inf. Technol. Biomed.* 5, 195–201. doi: 10.1109/4233.945290

Mallat, S. (1989). A theory for multiresolution signal decomposition: the wavelet representation. *IEEE. Trans. Pattern Anal. Mach. Intell.* 11, 674–693. doi: 10.1109/34.192463

Mallat, S. (1999). *A Wavelet Tour of Signal Processing*, 2nd Edn. Cambridge, MA: Academic Press. doi: 10.1016/B978-012466606-1/50008-8

Oppenheim, Alan, V., Schafer, R. W., and Buck, J. R. (1999). *Discrete-time Signal Processing*. Upper Saddle River, N.J: Prentice Hall.

Oran Brigham, E. (1988). *The Fast Fourier Transform and its Applications*. Hoboken, NJ: Prentice Hall.

Rao, K. R., and Yip, P. (1990). *Discrete Cosine Transform: Algorithms, Advantages, Applications*. Boston: Academic Press. doi: 10.1016/B978-0-08-092534-9.50007-2

Sanivarapu, P. V., Kandala, N. V. P. S., Rajesh, N. V., Rajasekhar Reddy, N., and Sekhar Reddy, C. (2020). Patient data hiding into ECG signal using watermarking in transform domain. *Phys. Eng. Sci. Med.* 43, 213–226. doi: 10.1007/s13246-019-00838-2

Swierkosz, A., and Augustyniak, P. (2018). Optimizing wavelet ECG watermarking to maintain measurement performance according to industrial standard. *Sensors* 18:3401. doi: 10.3390/s18103401

Tseng, K.-K., He, X., Kung, W.-M., Chen, S.-T., Liao, M., and Huang, H.-N. (2014). Wavelet-based watermarking and compression for ECG signals with verification evaluation. *Sensors* 14, 3721–3736. doi: 10.3390/s140203721

Zheng, K. M., and Qian, X. (2008). "Reversible data hiding for electrocardiogram signal based on wavelet transforms," in *Proceedings of the 2008 International Conference on Computational Intelligence and Security* (CIS2008), Suzhou, 295–299. doi: 10.1007/s10916-016-0608-0

Zheng, K. M., Tang, L. W., and Qian, X. (2009). Watermarking technology for electrocardiogram signal certification. *Comput. Eng. Appl.* 45, 231–233.

Conflict of Interest: The authors declare that the research was conducted in the absence of any commercial or financial relationships that could be construed as a potential conflict of interest.

Publisher's Note: All claims expressed in this article are solely those of the authors and do not necessarily represent those of their affiliated organizations, or those of the publisher, the editors and the reviewers. Any product that may be evaluated in this article, or claim that may be made by its manufacturer, is not guaranteed or endorsed by the publisher.

Copyright © 2022 Zhao, Chen, Chen, Tu, Yeh, Lin and Lu. This is an open-access article distributed under the terms of the Creative Commons Attribution License (CC BY). The use, distribution or reproduction in other forums is permitted, provided the original author(s) and the copyright owner(s) are credited and that the original publication in this journal is cited, in accordance with accepted academic practice. No use, distribution or reproduction is permitted which does not comply with these terms.

frontiers | Frontiers in Aging Neuroscience

ORIGINAL RESEARCH
published: 25 April 2022
doi: 10.3389/fnagi.2022.849932

Statistical Parametric Mapping in Amyloid Positron Emission Tomography

*Natasha M. Smith[1†], Jeremy N. Ford[2,3†], Arsalan Haghdel[1], Lidia Glodzik[2], Yi Li[2], Debra D'Angelo[4], Arindam RoyChoudhury[4], Xiuyuan Wang[2], Kaj Blennow[5,6], Mony J. de Leon[2] and Jana Ivanidze[2]**

[1] Department of Radiology and MD Program, Weill Cornell Medicine, New York City, NY, United States, [2] Department of Radiology, Weill Cornell Medicine, New York City, NY, United States, [3] Department of Radiology, Massachusetts General Hospital, Boston, MA, United States, [4] Department of Population Health Sciences, Weill Cornell Medicine, New York City, NY, United States, [5] Department of Neuroscience and Physiology, University of Gothenburg, Mölndal, Sweden, [6] Clinical Neurochemistry Laboratory, Sahlgrenska University Hospital, Mölndal, Sweden

OPEN ACCESS

Edited by:
Kuangyu Shi,
University of Bern, Switzerland

Reviewed by:
Weiwei Ruan,
Huazhong University of Science and Technology, China
Ganna Blazhents,
University of Freiburg Medical Center, Germany
Anna Rubinski,
LMU Munich University Hospital, Germany

***Correspondence:**
Jana Ivanidze
jai9018@med.cornell.edu

† These authors have contributed equally to this work and share first authorship

Specialty section:
This article was submitted to Alzheimer's Disease and Related Dementias, a section of the journal Frontiers in Aging Neuroscience

Received: *06 January 2022*
Accepted: *21 March 2022*
Published: *25 April 2022*

Citation:
Smith NM, Ford JN, Haghdel A, Glodzik L, Li Y, D'Angelo D, RoyChoudhury A, Wang X, Blennow K, de Leon MJ and Ivanidze J (2022) Statistical Parametric Mapping in Amyloid Positron Emission Tomography. Front. Aging Neurosci. 14:849932. doi: 10.3389/fnagi.2022.849932

Alzheimer's disease (AD), the most common cause of dementia, has limited treatment options. Emerging disease modifying therapies are targeted at clearing amyloid-β (Aβ) aggregates and slowing the rate of amyloid deposition. However, amyloid burden is not routinely evaluated quantitatively for purposes of disease progression and treatment response assessment. Statistical Parametric Mapping (SPM) is a technique comparing single-subject Positron Emission Tomography (PET) to a healthy cohort that may improve quantification of amyloid burden and diagnostic performance. While primarily used in 2-[^{18}F]-fluoro-2-deoxy-D-glucose (FDG)-PET, SPM's utility in amyloid PET for AD diagnosis is less established and uncertainty remains regarding optimal normal database construction. Using commercially available SPM software, we created a database of 34 non-*APOE* ε4 carriers with normal cognitive testing (MMSE > 25) and negative cerebrospinal fluid (CSF) AD biomarkers. We compared this database to 115 cognitively normal subjects with variable AD risk factors. We hypothesized that SPM based on our database would identify more positive scans in the test cohort than the qualitatively rated [^{11}C]-PiB PET (QR-PiB), that SPM-based interpretation would correlate better with CSF Aβ42 levels than QR-PiB, and that regional z-scores of specific brain regions known to be involved early in AD would be predictive of CSF Aβ42 levels. Fisher's exact test and the kappa coefficient assessed the agreement between SPM, QR-PiB PET, and CSF biomarkers. Logistic regression determined if the regional z-scores predicted CSF Aβ42 levels. An optimal z-score cutoff was calculated using Youden's index. We found SPM identified more positive scans than QR-PiB PET (19.1 vs. 9.6%) and that SPM correlated more closely with CSF Aβ42 levels than QR-PiB PET (kappa 0.13 vs. 0.06) indicating that SPM may have higher sensitivity than standard QR-PiB PET images. Regional analysis demonstrated the z-scores of the precuneus, anterior cingulate and posterior cingulate were predictive of CSF Aβ42 levels [OR (95% CI) 2.4 (1.1, 5.1) $p = 0.024$; 1.8 (1.1, 2.8) $p = 0.020$; 1.6 (1.1, 2.5) $p = 0.026$]. This study demonstrates the utility of using SPM with a "true normal" database and suggests that SPM enhances diagnostic performance in AD in the clinical setting through its quantitative approach, which will be increasingly important with future disease-modifying therapies.

Keywords: SPM, PET, Alzheimer's disease, dementia, amyloid

INTRODUCTION

Alzheimer's disease (AD) is the most common cause of dementia worldwide, affecting over five million people in the United States alone. Without disease-modifying therapies, the annual cost to Medicare and Medicaid is expected to surpass $1 trillion by 2050 (Association, 2019). In addition to clinical criteria, cerebrospinal fluid (CSF) biomarkers (Shaw et al., 2018), plasma biomarkers (Zetterberg and Blennow, 2021), and positron emission tomography (PET) with 2-[^{18}F]-fluoro-2-deoxy-D-glucose (FDG) have become a cornerstone of AD diagnosis and staging in both research and clinical settings. Specifically, appropriate use of FDG-PET adds clinically valuable information in the diagnostic workup of neurodegenerative disorders and is cost-effective (Silverman et al., 2002), providing a rationale for reimbursement from the Centers for Medicare and Medicaid Services (CMS) (Phurrough et al., 2004).

With the launch of amyloid-targeting therapies such as aducanumab into the clinic, amyloid-targeting PET tracers are poised to have increasing relevance in diagnosis and disease monitoring. At present, despite targeting a principal pathologic substrate, FDA-approved amyloid-binding PET tracers such as [^{18}F]-florbetapir, [^{18}F]-florbetaben, and [^{18}F]-flutemetamol are not typically reimbursed outside of a clinical trial (Cohen et al., 2015), leaving patients to cover the high cost. Another amyloid tracer, [^{11}C]-labeled Pittsburgh compound B (PiB), is used almost exclusively in research settings. Notably, PiB was the first widely used amyloid PET tracer and is often used as a reference standard to make comparisons between FDA-approved [^{18}F]-labeled amyloid-targeting agents (Landau et al., 2014; Adamczuk et al., 2016; Amadoru et al., 2020). Altogether, amyloid PET agents enhance diagnostic confidence and change management in 20–60% of patients attending memory clinics, guiding decision making on the use of acetylcholinesterase inhibitors (de Wilde et al., 2018; Rabinovici et al., 2019).

In the interpretation of amyloid-targeted PET images, there is significant interrater disagreement with kappa coefficients as low as 0.50 (Lilly, 2013), requiring dedicated training for standardized interpretation (Clark et al., 2011). Amyloid PET scans in normal subjects demonstrate non-amyloid binding in the white matter, possibly to myelin basic protein (Veronese et al., 2015), whereas uptake in neocortical structures is minimal or absent. As validated at post-mortem, in the setting of AD pathology and cortical amyloid-β deposits, there is increased cortical radiotracer avidity, leading to a loss of gray-white matter differentiation on amyloid-targeted cross-sectional PET imaging (Clark et al., 2011). For a standard amyloid PET image, a scan is considered positive if there are: (1) two or more brain areas larger than a single cortical gyrus in which there is reduced or absent gray-white differentiation or (2) one or more areas in which gray matter radioactivity is intense and clearly exceeds amyloid-avidity in adjacent white matter (Lilly, 2013). There is robust sensitivity in the detection of amyloid-β plaques with this standardized interpretation procedure; however, suboptimal interrater variability persists (Clark et al., 2012; Joshi et al., 2012). In the era of amyloid-targeting therapies such as aducanumab, any significant degree of disagreement would be unacceptable given the high cost of the drug and the potential adverse outcome of cerebral edema and hemorrhage (Barakos et al., 2013). Furthermore, this standard qualitative approach provides a binary interpretation which is suboptimal for longitudinal studies and precludes imaging-based treatment response assessment.

Statistical parametric mapping (SPM) is a technique which allows comparison of standardized uptake values (SUVs) within select regions in a given patient to a normal cohort. The technique has been mostly widely and successfully used with FDG-PET (Ishii et al., 2001; Kim et al., 2016). In addition to the quantitative data provided by SPM, semiquantitative data is provided as stereotactic surface projections (SSPs), 3D renderings of the brain showing z-scores as color values. Compared to standard PET images, SPM for FDG-PET has been shown to improve diagnostic performance by multiple groups (Yakushev et al., 2009; Mosconi et al., 2013; Della Rosa et al., 2014; Perani et al., 2014; Ford et al., 2021).

Feasibility of SPM has been demonstrated with [^{11}C]-PiB (Ziolko et al., 2006) and more recently with [^{18}F]-labeled amyloid-targeting agents (Lilja et al., 2016; Doré et al., 2019; Tanyaluck Thientunyakit et al., 2021). This approach enables the interpreter to quantify amyloid burden rather than offering a binary "positive" or "negative" interpretation. However, direct comparisons of SPM interpretations with standard PET interpretations have been limited. Moreover, a potential pitfall is subject selection for the normal cohort database required for SPM. Up to 30–40% of cognitively normal elderly may have significant amyloid burden on PET, a proportion that is higher among apolipoprotein E (APOE) ε4 carriers (Mielke et al., 2012). The frequency of *APOE* ε4 carriers in the general population is 19.5%, of these, 1.2% are homozygous for ε4 (Jia et al., 2020). A normal database that is enriched with amyloid positive subjects and *APOE* ε4 carriers could diminish sensitivity, risking not identifying patients who could potentially benefit from amyloid-targeting therapeutics.

In addition to FDG and amyloid PET, CSF biomarkers such as total-tau (t-tau), phosphorylated-tau (p-tau), and Aβ42 can provide additional information about disease state and progression. For example, low levels of CSF Aβ42 and high levels of CSF t-tau and p-tau can identify symptomatic AD with a sensitivity and specificity above 80% (Zou et al., 2020). These biomarkers can also be used to identify preclinical AD before symptom onset. Several studies have demonstrated that reduction in CSF Aβ42 levels occur before cognitive decline (Skoog et al., 2003; Gustafson et al., 2007; Stomrud et al., 2007). In a prospective longitudinal study, Bateman et al. found that CSF Aβ42 levels may start to decline 25 years before the onset of AD symptoms, whereas amyloid deposition as measured by [^{11}C]-PiB PET and CSF levels of t-tau start to increase 15 years before symptom onset (Bateman et al., 2012). While the CSF levels of Aβ42, t-tau, and p-tau are not a gold standard for predicting or diagnosing AD as other factors may affect the CSF levels of these proteins (Blennow and Hampel, 2003), they are nonetheless a valuable source of information especially in a preclinical, cognitively normal cohort. By using subjects with normal (non-AD range) CSF biomarkers to construct a database, we can be more assured that we have a normal cohort, with

low likelihood of having AD-type pathology. Conversely, by obtaining CSF protein levels of a test cohort we can identify cognitively normal individuals at higher risk for developing AD.

Therefore, our purpose was to construct a database of [^{11}C]-PiB PET scans from cognitively normal, non-*APOE* ε4 carriers with negative cerebrospinal fluid (CSF) biomarkers for AD and to use SPM on a test cohort of cognitively normal subjects with variable AD risk factors. We hypothesized that SPM based on our database reference cohort would identify more scans as positive in our test cohort than the qualitatively rated [^{11}C]-PiB PET (QR-PiB). We further hypothesized that the SPM-based interpretation would correlate better with CSF Aβ42 levels than QR-PiB, and that regional z-scores of specific brain regions known to be involved early in AD, including the precuneus, anterior cingulate, and posterior cingulate would be predictive of CSF Aβ42 levels, whereas the orbitofrontal gyri and middle temporal gyri, similarly sized regions not known to be involved early in AD, would not be predictive.

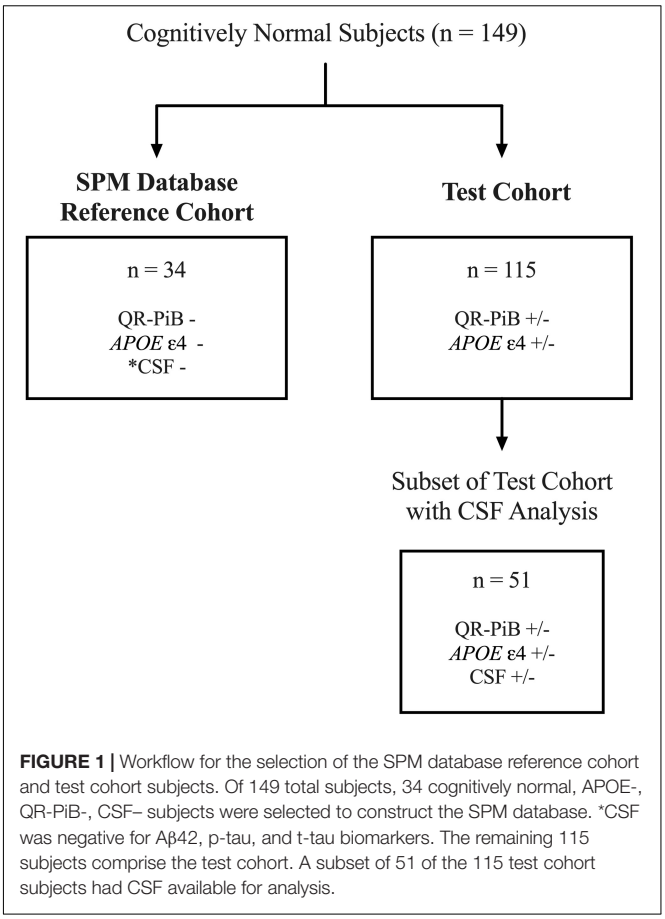

FIGURE 1 | Workflow for the selection of the SPM database reference cohort and test cohort subjects. Of 149 total subjects, 34 cognitively normal, APOE-, QR-PiB-, CSF– subjects were selected to construct the SPM database. *CSF was negative for Aβ42, p-tau, and t-tau biomarkers. The remaining 115 subjects comprise the test cohort. A subset of 51 of the 115 test cohort subjects had CSF available for analysis.

MATERIALS AND METHODS

Patient Enrollment

We performed a retrospective analysis of a prospectively enrolled cohort of volunteers who were recruited in IRB approved NIH supported longitudinal studies of normal aging, M. J. de Leon, principal investigator (PI). Subjects were enrolled between 2009 and 2013. Exclusion criteria were mild cognitive impairment, a score > 17 on the 17-item Hamilton Depression Scale, brain tumor, neocortical infarction, and axis I disorders. Of note, a subset of this cohort was previously studied (Glodzik et al., 2014, 2015, 2016; Mosconi et al., 2017, 2018, 2021). After applying exclusion criteria, 149 subjects remained. Subjects were divided into either the SPM database reference cohort (n = 34) or the test cohort (n = 115). **Figure 1** illustrates the workflow of patient selection.

Imaging: Positron Emission Tomography and Computed Tomography Images

Positron emission tomography (PET)/Computed tomography (CT) images were acquired on General electric (GE) Discovery LS PET/CT and Siemens Biograph PET/CT 64 slice. Two physician-raters with experience in QR-PiB (YL, 13 years of experience; LG, 8 years of experience) provided qualitative interpretations of the QR-PiB images as either positive or negative. The QR-PiB scans were then classified as either positive (both raters identified the scan as positive), indeterminate (only one rater identified the scan as positive), or negative (both raters identified the scan as negative).

Statistical Parametric Mapping Database Construction

[^{11}C]-PiB PET data from PET/CT cases were post-processed using the syngo.via (Siemens Healthineers, Erlangen, Germany) MI Neurology Workflow (n = 34). This process involves alignment of PET to the CT using a rigid registration algorithm. Adequate co-registration of PET and anatomical data was confirmed visually by NS, a medical student with four years of neuroradiology research experience and JF, a neuroradiology fellow. To create the atlas, PET images were fit to the Montreal Neurological Institute (MNI) standard space and smoothing was accomplished with an isotropic Gaussian filter of size 12 mm fullwidth at half-maximum. This was followed by intensity normalization to the cerebellum at 75% brightest voxels per the manufacturer's recommendation in order to mitigate minor imprecisions of region location. A PET template was used to guide the registration of PET data to the MNI geometry. The cerebellum protocol was chosen over automated whole brain because Aβ deposition is low in the cerebellum at all stages of normal and disease (Rowe et al., 2007).

Statistical Parametric Mapping Analysis

The test cohort (n = 115) had both QR-PiB and SPM analysis performed. These two analyses were conducted separately and were blinded to the raters. For the SPM analysis, the images were parsed into Automated Anatomical Labeling (AAL) regions, which have been described previously (Tzourio-Mazoyer et al., 2002). A z-score [(Patient SUV-Healthy Atlas SUV)/Healthy Atlas Standard Deviation] was generated for each AAL region and SSP visualizations with color map gradients were created. The color map provided a visual representation of the number of standard deviations (z-score) each region was above or below the normal database.

Each SSP generated by the SPM analysis was blinded and presented to the same two raters that graded the original QR-PiB scans. Prior to rating, the raters were oriented to the color map and trained on clear examples of positive and negative SSP's from known AD and non-AD subjects. The SSP's of the test cohort were graded independently by each rater and assigned a score according to the Likert scale (1 = definitely negative, 2 = probably negative, 3 = indeterminate, 4 = probably positive, 5 = definitely positive). In order to convert the scores to a binary output for comparison against the QR-PiB, the scores from the two raters were averaged and the SSP image was rated as negative (average score < 3), indeterminate (average score = 3), or positive (average score > 3). A subset of the test cohort underwent CSF sampling and analysis ($n = 51$).

Lumbar Puncture, Cerebrospinal Fluid Collection, and Aβ42 Evaluation

Cerebrospinal fluid was collected by lumbar punctures performed between late morning and early afternoon using a 25-gauge needle guided by fluoroscopy. The CSF samples were centrifuged for 10 min at 1,500 g at 4°C, aliquoted into 0.25 mL polypropylene tubes and then stored at −80°C until assayed. CSF Aβ42 (pg/mL), p-tau (pg/mL), and t-tau (pg/mL) were blindly analyzed in batch mode using enzyme-linked immunosorbent assay (ELISA) (Innotest, Innogenetics/Fujirebio, Ghent, Belgium). The procedures for the lumbar puncture and CSF handling are published (Spiegel et al., 2016). Each CSF biomarker was classified as positive or negative based on the cutoff values as defined by Miners et al. (2019). A positive AD range for each biomarker was defined as Aβ42 < 550 pg/mL, p-tau > 60 pg/mL, or t-tau > 400 pg/mL (Miners et al., 2019).

Statistical Analysis

Categorical variables are presented as counts or percentages and continuous variables are presented as means ± standard deviations (SD). The Fisher's exact test was employed to compare the number of patients who received positive, negative, and indeterminate ratings between SPM and QR-PiB alone. Agreement between QR-PiB, SPM and CSF was assessed using the kappa coefficient (κ). In order to assess differences in age and *APOE* ε4 status between those with positive and negative QR-PiB reads, *p*-values were calculated using the unpaired *t*-test for age and two-tailed Fisher exact test for *APOE* ε4 status. Next, a regional analysis was performed on five regions of interest: the anterior cingulate gyrus, the posterior cingulate gyrus, precuneus, middle temporal gyrus, and orbitofrontal gyrus. The anterior cingulate, posterior cingulate, and precuneus were selected given their known early involvement in Aβ deposition (Huang et al., 2013; Grothe et al., 2017; Palmqvist et al., 2017). The middle temporal gyrus and orbitofrontal gyrus, which may be involved in advanced AD, are not known to be specific or early involved regions. A logistic regression model was employed to determine if the z-scores from each studied region predicted a positive rating of the AD biomarker, Aβ42 (<550 pg/mL). For any region whose z-score was a significant predictor of the outcome, an optimal z-score cutoff was calculated using Youden's index, derived from receiver operating characteristic (ROC) curves, to distinguish positive from negative cases (**Supplementary Figure 1**).

RESULTS

Statistical Parametric Mapping Database

A subset of 34 subjects from the cohort of 149 were selected for construction of the database (**Figure 1**). In order to be included in the reference database all subjects had to be cognitively normal with a Mini-Mental State Exam (MMSE) ≥ 25, be *APOE* ε4 negative on both alleles, be negative on QR-PiB, and have CSF levels of Aβ42, phosphorylated tau (p-tau), and total-tau (t-tau) in the non-AD range as defined by Miners et al. and described in the Materials and Methods section (Miners et al., 2019). Clinical and demographic characteristics of the SPM database reference cohort are outlined in **Table 1**.

Statistical Parametric Mapping Analysis

The test cohort is comprised of the 115 remaining subjects (**Figure 1**). None of the subjects used to construct the SPM database were used in the test cohort. Clinical and demographic characteristics of the test cohort are outlined in **Table 2**. Of the 115 subjects, all had QR-PiB scans and 51 had additional CSF analysis. All patients were cognitively normal with a Mini-Mental State Exam (MMSE) of 29 ± 0.89. Despite all having normal cognition, subjects varied in terms of AD risk factors. 48.7% of subjects were *APOE* ε4 + , 13% had a positive or indeterminate QR-PiB scan, and of the subjects with CSF, 41.2% had Aβ42 levels in the AD range, 27.5% had p-tau levels in the AD range, and 15.6% had t-tau in the AD range (**Table 3**). *APOE* ε4 positivity was defined as positive for the presence of ε4 on at least one allele (*APOE* X/ε4).

Statistical parametric mapping analysis was performed on the test cohort of 115 patients. Representative QR-PiB images and respective SPM maps are shown in **Figure 2**. Results of the SPM analysis are displayed in **Table 4**. Use of SPM resulted in statistically significant differences in the categorization of cases. Of note, SPM identified 19.1% of cases as positive while QR-PiB identified only 9.6%. SPM also had a higher proportion of indeterminate cases relative to QR-PiB (7.0 vs. 3.5%).

TABLE 1 | Cohort characteristics of the statistical parametric mapping (SPM) database.

Number of subjects	34
Gender (M/F)	12/22
Race (White/Non-White)	31/3
Education (years) ± SD	17 ± 1.7
APOE ε4 status (−/+)	34/0
Age in years at time of PET scan ± SD	62 ± 7.5
Age in years at time of CSF ± SD	62 ± 7.5
Average time in years between CSF and PET acquisition ± SD	0.25 ± 0.31
MMSE ± SD [Range]	29 ± 1.0 [26–30]
QR-PiB (−/+)	34/0
CSF (−/+)	34/0

TABLE 2 | Cohort characteristics of the test group.

Number of subjects	115
Gender (M/F)	36/79
Race (White/Non-White)	99/16
Education (years) ± SD	17 ± 1.9
APOE ε4 status (−/+/unknown)	51/56/8
Age in years at time of PET scan ± SD	59.6 ± 11.5
Age in years at time of CSF ± SD	64.4 ± 9.1
Average time in years between CSF and PET acquisition ± SD	0.35 ± 0.42
MMSE ± SD [Range]	29 ± 0.89 [26–30]

TABLE 3 | Cerebrospinal fluid results of the test group.

CSF (+/−) (*n* = 51)	Aβ42: 21/30 p-tau: 11/40 t-tau: 8/43
CSF Aβ42 pg/mL (avg ± SD)	653 ± 227.4
CSF p-tau pg/mL (avg ± SD)	46 ± 20.1
CSF t-tau pg/mL (avg ± SD)	293 ± 169.8

There were eight subjects that were positive on both SPM and QR-PiB. There were 14 subjects who were positive on SPM, but negative or indeterminate on QR-PiB (SPM +, QR-PiB I/−). We found that the SPM +, QR-PiB I/− subjects were older than the average of the entire cohort (p = 0.0104) and were more likely to be *APOE* ε4 positive (p = 0.0369) (**Table 5**). The subjects who tested positive on QR-PiB (n = 11) were similarly on average older than the average of the entire cohort (p = 0.0331), but unlike the SPM positive group were not more likely to be *APOE* ε4 positive (p = 0.5219) (**Table 6**).

TABLE 4 | Diagnostic rating by test type.

Test type	Diagnostic rating			Fisher's exact test *p*-value
	Positive (*N* = 33)	Indeterminate (*N* = 12)	Negative (*N* = 185)	
SPM	22 (19.1%)	8 (7.0%)	85 (73.9%)	0.002
QR-PiB	11 (9.6%)	4 (3.5%)	100 (87.0%)	

Table 7 demonstrates that the SPM +, QR-PiB I/− subjects (n = 14) did not differ significantly in age from the QR-PiB + subjects (n = 11) (p = 0.8458), but were more likely to be *APOE* ε4 positive (p = 0.0393). These results are visually represented in **Figure 3**.

There were three subjects that were positive on QR-PiB, but negative on SPM. All three subjects had an SPM score of 2.5. Two of the three discordant subjects had CSF; the CSF was negative for all three AD biomarkers (Aβ42, p-tau, and t-tau).

Within the test cohort, a subset of 51 subjects also had CSF. The degree of agreement between SPM and QR-PiB was fair (κ = 0.33). SPM had a stronger correlation with the CSF Aβ42 levels than QR-PiB (κ = 0.13 vs. 0.06) (**Table 8**).

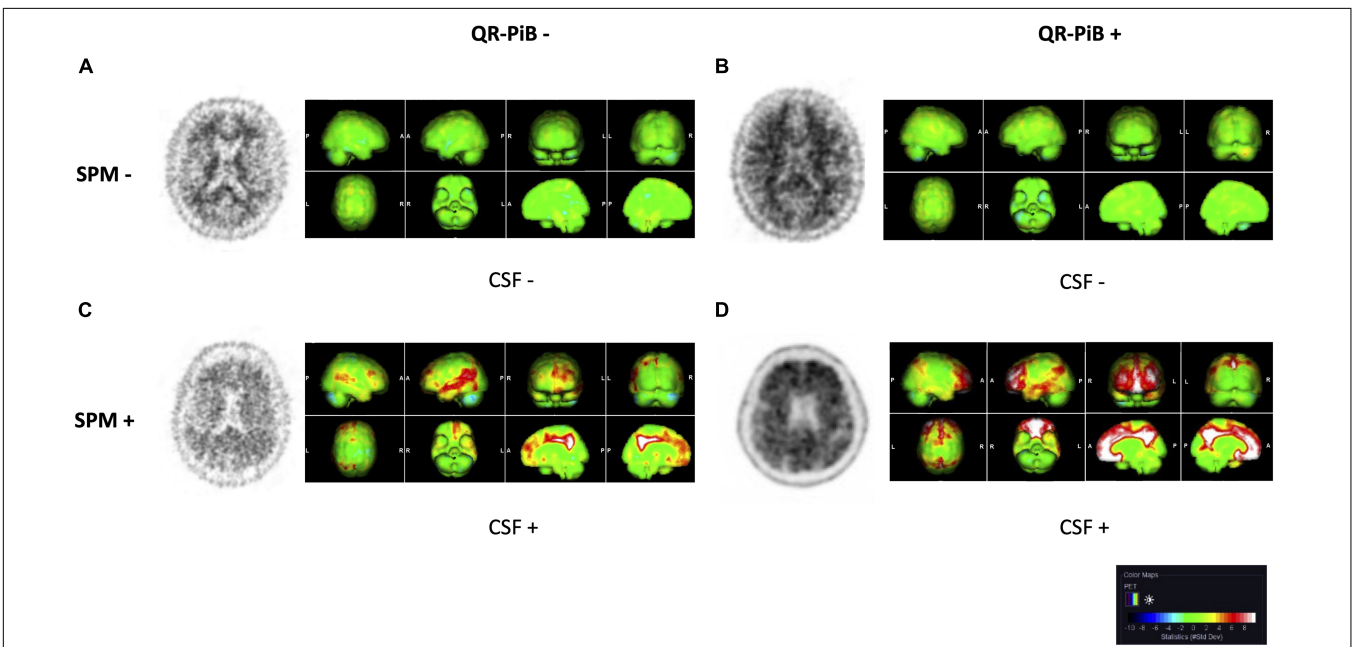

FIGURE 2 | QR-PiB and SPM projections for four cases from the test cohort that represent the spectrum of cases seen in our study. Rows represent SPM− and SPM+ cases, and columns represent QR-PiB− and QR-PiB+ cases. The CSF Aβ42 biomarker status of each case is listed below the SSP. **(A)** A QR-PiB−, SPM−, CSF− subject (69 y/o, M, MMSE: 29, *APOE* ε4−, t-tau = 470 pg/mL, p-tau = 76 pg/mL, Aβ42 = 942 pg/mL). **(B)** A QR-PiB+, SPM−, CSF− subject (58 y/o, F, MMSE: 30, *APOE* ε4−, t-tau = 295 pg/mL, p-tau = 59 pg/mL, Aβ42 = 1,090 pg/mL). **(C)** A QR-PiB−, SPM+, CSF+ subject (73 y/o, M, MMSE: 30, *APOE* ε4+, t-tau = 236 pg/mL, p-tau = 38 pg/mL, Aβ42 = 496 pg/mL). **(D)** A QR-PiB+, SPM+, CSF+ subject (76 y/o, F, MMSE: 29, *APOE* ε4+, t-tau = 705 pg/mL, p-tau = 71 pg/mL, Aβ42 = 465 pg/mL).

TABLE 5 | Entire test cohort vs. statistical parametric mapping (SPM) positive, QR-PiB indeterminate/negative.

	Entire cohort (*n* = 115)	SPM+, QR-PiB I/− (*n* = 14)	*p*-value
Age in years at time of PET scan ± SD	59.6 ± 11.5	68.18 ± 13.0	0.0104
APOE ε4 status (−/+/unknown)	51/56/8	2/11/1	0.0369

TABLE 6 | Entire test cohort vs. QR-PiB positive.

	Entire cohort (*n* = 115)	QR-PiB + (*n* = 11)	*p*-value
Age in years at time of PET scan ± SD	59.6 ± 11.5	64.86 ± 12.7	0.0331
APOE ε4 status (−/+/unknown)	51/56/8	6/4/1	0.5219

TABLE 7 | QR-PiB positive vs. statistical parametric mapping (SPM) positive, QR-PiB indeterminate/negative.

	QR-PiB+ (*n* = 11)	SPM+, QR-PiB I/− (*n* = 14)	*p*-value
Age in years at time of PET scan ± SD	64.86 ± 12.7	68.18 ± 13.0	0.8458
APOE ε4 status (−/+/unknown)	6/4/1	2/11/1	0.0393

Next, we performed a regional analysis of five regions to determine if any regions were good predictors of the CSF Aβ42 levels (**Table 9**). The anterior cingulate gyrus [OR: 1.6 (95% CI 1.1, 2.5)], posterior cingulate gyrus [OR: 1.8 (95% CI 1.1, 2.8)], and precuneus [OR: 2.4 (95% CI 1.1, 5.1)], were found to be significant predictors of the CSF Aβ42 levels. The middle orbitofrontal gyrus and middle temporal gyrus were not statistically significant predictors of CSF Aβ42 levels.

DISCUSSION

We present the construction of a database of cognitively normal subjects who underwent QR-PiB for subsequent application of SPM analysis and direct comparison with QR-PiB interpretation. We were able to construct the database from a cohort of cognitively normal volunteers who had previously been enrolled in a prospective study, and for whom CSF protein data and *APOE* genetics data was also available. With exception of proof-of-concept studies (Ziolko et al., 2006; Lilja et al., 2016; Doré et al., 2019; Tanyaluck Thientunyakit et al., 2021), head-to-head studies comparing amyloid PET SPM to QR-PiB image interpretation have been limited. Two representative studies (Harn et al., 2017; Petrover et al., 2021) used commercially available databases for SPM analysis with [^{18}F]-Florbetapir and [^{18}F]-Florbetaben, respectively. Both studies demonstrated that SPM improved diagnostic confidence and performance; however, the commercially available databases utilized were comprised of "negative scans" confirmed by expert review without the aid of *APOE* ε4 status and CSF biomarkers. Given the persistent interrater variability among trained interpreters of QR-PiB (Clark et al., 2012; Joshi et al., 2012), it is conceivable that positive scans could be included. Additionally, the fact that CSF biomarker data was not used to construct these databases opens the possibility that subjects with early CSF changes indicative of preclinical AD could be included given that CSF changes can occur up to 25 years before the onset of cognitive symptoms and up to 10 years before QR-PiB changes (Bateman et al., 2012). It is important to note that while positive CSF biomarkers provide valuable adjunct information and convey a degree of increased risk, they are not by themselves diagnostic and as such there is no universally accepted standard for the CSF cutoffs. For the purposes of this study we used the threshold set forth by Miners et al. (2019). Subjects with normal CSF criteria per this threshold were considered to be lower risk for later development of AD.

We used [^{11}C]-PiB PET to create and test an amyloid PET database for SPM, using commercially available software (syngo.via MI Neurology analysis tool). A particular advantage of this software over alternatives is that it is clinically integrated which allows for easier clinical translation and has the potential for widespread use. The SPM approach also has the potential to be applied to other PET radiotracers targeting amyloid, tau, or other biomarkers of neurodegeneration.

Our study demonstrates that use of SPM for amyloid-targeted PET may improve sensitivity given that more positive scans were identified relative to interpretation of the standard QR-PiB image (19.1 vs. 9.6%). This invokes the question of whether these represent true or false positives, but given the cross-sectional nature of our study we are not able to identify those individuals who go on to develop AD versus those who do not. Taking this limitation into account, our correlation with CSF biomarkers suggests a greater proportion of cases interpreted as positive are true positives given the greater concordance of SPM with AD biomarkers relative to the QR-PiB interpretation (kappa coefficient 0.13 vs. 0.06). The exact incidence of true versus false positives could be identified with future prospective longitudinal studies. While the kappa coefficient between CSF biomarkers and SPM interpretation appears low, it is important to reiterate that these subjects are cognitively normal, and if indeed there is AD pathology, they would be early in the disease process. Among cognitively normal, amnestic MCI, and AD subjects, it has been shown that CSF Aβ42 does not correlate with cognitive scores (Vemuri et al., 2009). Moreover, AD-type changes in CSF may be a feature of normal aging (Toledo et al., 2015) and may be present in up to one-third of cognitively normal subjects (De Meyer et al., 2010).

Of note, there was a higher proportion of indeterminate cases with the use of SPM (7.0 vs. 3.5%). One potential explanation for this is that the raters had never used SPM before to determine amyloid status and received limited training, whereas the raters were well-versed in the interpretation of QR-PiB. Therefore, additional training in SPM interpretation is likely to increase rater confidence, similar to the effect that training had on standard PET interpretation (Clark et al., 2011). The reader unfamiliarity with interpreting SPM for amyloid

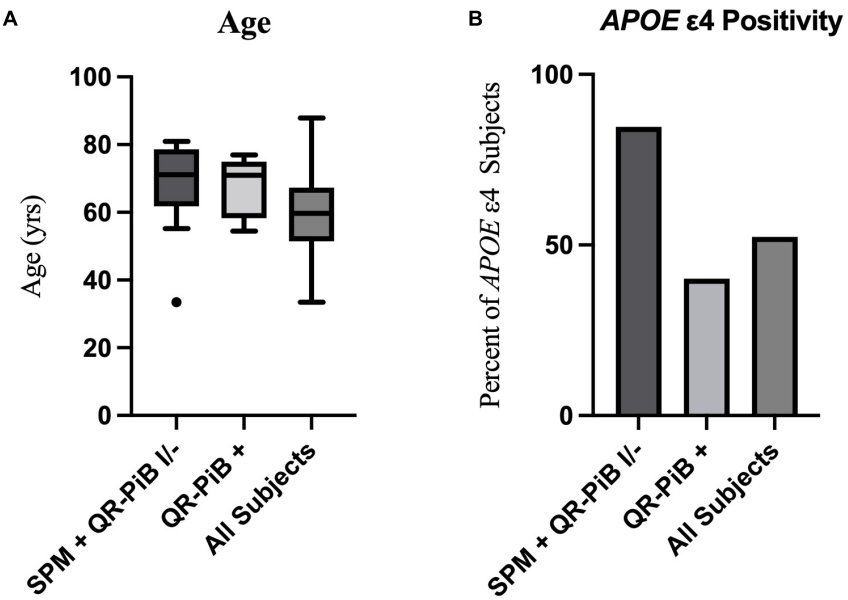

FIGURE 3 | A visual representation of the age distribution with a Tukey box and whisker plot (outlier, black dot) **(A)** and percent of *APOE* ε4 positive subjects **(B)** in the SPM +, QR-PiB I/− subgroup (n = 14), the QR-PiB + subgroup (n = 11), and the entire test cohort (All Subjects, n = 115). There is no significant difference in age between the SPM+, QR-PiB I/− subgroup and the QR-PiB + subgroup **(A)**, but the SPM+, QR-PiB I/− subgroup identifies a higher percentage of *APOE* ε4 positive subjects than the QR-PiB + subgroup **(B)**.

PET and the subsequent higher number of indeterminate cases likely contributed to the low kappa coefficient representing the correlation between the SPM read and the CSF Aβ42 levels. Further training with SPM and validation of quantifiable z-score cutoffs could serve to further increase the correlation. Nonetheless, SPM-naïve raters still identified more positive cases with the use of SPM.

There were three cases that were QR-PiB positive, SPM negative. In total, these represent only 2.6% of the entire test cohort. A study by Ikonomovic et al. (2018) found the rate of false positives on amyloid PET, even among experienced raters such as ours, to be 2.8%. In addition, the lack of CSF amyloid biomarkers favors the qualitative reads to have been false positives, possibly due to poor scan quality, scan timing, or cortical atrophy (Apostolova et al., 2016).

When we further examined the cases that were identified as positive on SPM, but negative or indeterminate on QR-PiB we found that SPM, similar to QR-PiB, identified individuals whose average age was significantly higher than that of the entire cohort (SPM p = 0.0104, QR-PiB p = 0.0331). Given that amyloid deposition increases with age, this is in line with what would be expected (Mormino and Papp, 2018; Zhang et al., 2021). Interestingly, SPM was able to identify a higher proportion of *APOE* ε4 positive individuals (p = 0.0369) than were present in the entire cohort whereas QR-PiB did not identify more *APOE* ε4 positive subjects (p = 0.5219). This indicates SPM may be able to identify *APOE* ε4 subjects with increased sensitivity over QR-PiB.

Future work will focus on establishing region-specific z-score cutoffs. Certain regions such as the precuneus and posterior cingulate are known to have early accumulation of Aβ42 (Karas et al., 2007; Grothe et al., 2017; Mi et al., 2017; Palmqvist et al., 2017). Palmqvist et al. demonstrated that 15 of 68 cortical regions including the precuneus, anterior cingulate, and posterior cingulate had an increased rate of amyloid accumulation in cognitively normal subjects with low levels of CSF Aβ42 (CSF+) but negative ^{18}F-florbetapir PET scans (PET-) indicating these regions accumulate Aβ early in the disease process (Bateman et al., 2012; Palmqvist et al., 2017). As such, global z-score analysis could underemphasize the pivotal role that select regions may have in portending progression of AD.

TABLE 8 | Diagnostic rating agreement.

Comparison	Kappa coefficient
SPM vs. CSF Aβ42 (P/N)	0.13
QR-PiB vs. CSF Aβ42 (P/N)	0.06
SPM vs. QR-PiB (P/I/N)	0.33

P = positive, I = indeterminate, N = negative.

TABLE 9 | Logistic regression using regional Z-score to predict cerebrospinal fluid (CSF) Aβ42 levels (n = 51).

Region	OR (95% CI)	p-value	Optimal Z-score cut-off
Anterior cingulate gyrus	1.6 (1.1, 2.5)	0.026	2.00
Posterior cingulate gyrus	1.8 (1.1, 2.8)	0.020	0.50
Precuneus	2.4 (1.1, 5.1)	0.024	1.20
Middle frontal gyrus, orbital part	1.3 (1.0, 1.8)	0.084	–
Middle temporal gyrus	1.3 (1.0, 1.8)	0.080	–

Even in the absence of z-score cutoffs, visual interpretation of SPM SSPs alone provides improvements in diagnostic performance relative to interpretation of preprocessed PET images. This has been well-validated with the use of FDG-PET for dementia diagnosis (Perani et al., 2014). Perani et al. demonstrated that visual interpretation of SSPs rather than standard FDG-PET improved sensitivity for the detection of neurodegenerative disorders from 78 to 96% and increased specificity from 50 to 84%. The interpretation of SSP maps from FDG-PET in conjunction with z-scores reflects how FDG-PET SPM is currently used in clinical practice, and we foresee a similar role for SPM in amyloid PET.

While we were able to identify region specific cutoffs for our dataset, these specific cutoffs may not be generalizable given that our population was largely cognitively normal (MMSE $\geq$ 25). In the clinical setting, amyloid PET scans are ordered in patients who usually demonstrate cognitive impairment. A Cochrane review on FDG-PET for dementia highlights that it has been challenging to establish thresholds given the heterogeneity of study populations (Morbelli et al., 2015). Nonetheless, we believe greater standardization is achievable with amyloid PET, and hope to explore valid, region-specific z-score thresholds in future studies of clinical populations.

In our region-specific analysis, the precuneus had the highest odds-ratio in predicting CSF Aβ42 levels. While this data was collected from a single timepoint, it suggests early involvement of the precuneus in AD pathology, concordant with other studies demonstrating early precuneus involvement in AD (Karas et al., 2007; Mi et al., 2017). Interestingly, the anterior cingulate demonstrated a higher odds ratio than the posterior cingulate, which is seemingly discordant from FDG-PET related findings (Minoshima et al., 1997; Brown et al., 2014; Ford et al., 2021). However, there is evidence that amyloid deposits may occur early in the anterior cingulate in AD (Grothe et al., 2017; Palmqvist et al., 2017). Future longitudinal studies in cognitively normal individuals using our SPM database could further illuminate the sequence of amyloid deposition in preclinical AD and normal aging.

There are several notable limitations of this study. There is lack of diversity in the enrolled population this retrospective analysis was based on, with the cohort of volunteers primarily comprised of persons identifying as Caucasian; enrollment of a diverse population reflecting the population affected by cognitive impairment and dementia will be prioritized in future prospective studies. Moreover, the mean age of the normal database was 62 $\pm$ 7.5 years, which may be less relevant for elderly patients (e.g., >80 years old). Furthermore, the CSF biomarkers applied here are somewhat inadequate given that specificities and positive predictive values are insufficient to diagnose AD prior to meeting clinical criteria (Hertze et al., 2010). Also, as mentioned, AD-type CSF biomarkers (De Meyer et al., 2010; Toledo et al., 2015) and amyloid deposition (Mielke et al., 2012) may be expected findings of normal aging. Longitudinal assessment with SPM would be the most suitable approach to confirm which region-based z-score cutoffs are clinically relevant and predictive of future conversion to AD. Another noteworthy limitation is that the amyloid PET scans were acquired from 2009 to 2013, and there have since been improvements on multiple fronts in amyloid PET, including motion correction (Brendel et al., 2015) as well as the utilization of low-dose technique in conjunction with deep learning (Chen et al., 2019). As such, to ensure accuracy of SPM analysis, future prospective studies will require the construction of new reference databases to match acquisition and post-processing protocols that incorporate these technical advances.

Emerging therapeutic options for AD, including amyloid targeting antibodies such as aducanumab (Cummings et al., 2021), underscore the critical need for early and accurate identification of AD pathology. Amyloid targeted PET with SPM analysis can take PET interpretation from a primarily qualitative to a quantitative approach, allowing more accurate quantification of cortical amyloid burden, and laying the basis for longitudinal follow up in the context of treatment response assessment. With further validation, SPM with amyloid PET may become routine in clinical practice, analogous to FDG PET for dementia evaluation. Given the high-cost of current and future amyloid-modulating therapies, and given ongoing considerations by the Centers for Medicare and Medicaid Services to lift PET payment restrictions (Stempniak, 2021), it is conceivable that amyloid PET with SPM will eventually become reimbursable from third party payers, thereby increasing access to this important diagnostic tool within the population-at-large.

DATA AVAILABILITY STATEMENT

The raw data supporting the conclusions of this article will be made available by the authors, without undue reservation.

ETHICS STATEMENT

The studies involving human participants were reviewed and approved by Weill Cornell Medicine IRB. The patients/participants provided their written informed consent to participate in this study.

AUTHOR CONTRIBUTIONS

JI, NS, and JF: conceptualization and writing—original draft. MdL: participant enrollment, PET image acquisition, and CSF collection. KB: CSF protein analysis. NS and XW: data curation. YL and LG: qualitative PET review and scoring and SPM image review and scoring. NS, JF, AH, and JI: SPM database construction. AH, NS, and JF: SPM analysis of test cohort. DD'A, AR, and NS: statistical analysis. All authors: writing—review and editing and approved the submitted version.

FUNDING

This work was funded by the Weill Cornell Medical College Dean's Jumpstart Award (PI: JI). It was additionally funded by NIH-NIA grants RO1AG13616, RO1AG12101, RF1AG057570, and R56AG058913 (PI: MdL) and R01AG057848 (PI: YL).

ACKNOWLEDGMENTS

We would like to thank Drs. Guenther Platsch and Marcus Steward from Siemens Healthineers for their technical assistance with the SPM database construction in syngo.via.

SUPPLEMENTARY MATERIAL

The Supplementary Material for this article can be found online at: https://www.frontiersin.org/articles/10.3389/fnagi.2022.849932/full#supplementary-material

Supplementary Figure 1 | Receiver operating characteristic (ROC) curves generated for the anterior cingulate **(A)**, posterior cingulate **(B)**, and precuneus **(C)** regions. An optimal z-score cutoff for each region was calculated using Youden's index.

REFERENCES

Adamczuk, K., Schaeverbeke, J., Nelissen, N., Neyens, V., Vandenbulcke, M., Goffin, K., et al. (2016). Amyloid imaging in cognitively normal older adults: comparison between 18 F-flutemetamol and 11 C-Pittsburgh compound B. *Eur. J. Nuclear Med. Mol. Imag.* 43, 142–151. doi: 10.1007/s00259-015-3156-9

Amadoru, S., Doré, V., Mclean, C. A., Hinton, F., Shepherd, C. E., Halliday, G. M., et al. (2020). Comparison of amyloid PET measured in Centiloid units with neuropathological findings in Alzheimer's disease. *Alzheimer's Res. Ther.* 12:22. doi: 10.1186/s13195-020-00587-5

Apostolova, L. G., Haider, J. M., Goukasian, N., Rabinovici, G. D., Chételat, G., Ringman, J. M., et al. (2016). Critical review of the Appropriate Use Criteria for amyloid imaging: effect on diagnosis and patient care. *Alzheimers Dement* 5, 15–22. doi: 10.1016/j.dadm.2016.12.001

Association, A. S. (2019). 2019 Alzheimer's disease facts and figures. *Alzheimer's Dement.* 15, 321–387. doi: 10.1016/j.jalz.2019.01.010

Barakos, J., Sperling, R., Salloway, S., Jack, C., Gass, A., Fiebach, J., et al. (2013). MR imaging features of amyloid-related imaging abnormalities. *Am. J. Neuroradiol.* 34, 1958–1965. doi: 10.3174/ajnr.A3500

Bateman, R. J., Xiong, C., Benzinger, T. L., Fagan, A. M., Goate, A., Fox, N. C., et al. (2012). Clinical and biomarker changes in dominantly inherited Alzheimer's disease. *N Engl. J. Med.* 367, 795–804. doi: 10.1056/NEJMoa1202753

Blennow, K., and Hampel, H. (2003). CSF markers for incipient Alzheimer's disease. *Lancet Neurol.* 2, 605–613. doi: 10.1016/s1474-4422(03)00530-1

Brendel, M., Högenauer, M., Delker, A., Sauerbeck, J., Bartenstein, P., Seibyl, J., et al. (2015). Improved longitudinal [18F]-AV45 amyloid PET by white matter reference and VOI-based partial volume effect correction. *Neuroimage* 108, 450–459. doi: 10.1016/j.neuroimage.2014.11.055

Brown, R. K., Bohnen, N. I., Wong, K. K., Minoshima, S., and Frey, K. A. (2014). Brain PET in suspected dementia: patterns of altered FDG metabolism. *Radiographics* 34, 684–701. doi: 10.1148/rg.343135065

Chen, K. T., Gong, E., De Carvalho Macruz, F. B., Xu, J., Boumis, A., Khalighi, M., et al. (2019). Ultra–low-dose 18F-florbetaben amyloid PET imaging using deep learning with multi-contrast MRI inputs. *Radiology* 290, 649–656. doi: 10.1148/radiol.2018180940

Clark, C. M., Mintun, M. A., and Pontecorvo, M. J. (2011). Florbetapir-PET Imaging and Postmortem β-Amyloid Pathology—Reply. *Jama* 305, 1857–1858. doi: 10.1001/jama.2011.579

Clark, C. M., Pontecorvo, M. J., Beach, T. G., Bedell, B. J., Coleman, R. E., Doraiswamy, P. M., et al. (2012). Cerebral PET with florbetapir compared with neuropathology at autopsy for detection of neuritic amyloid-β plaques: a prospective cohort study. *Lancet Neurol.* 11, 669–678. doi: 10.1016/S1474-4422(12)70142-4

Cohen, J. P., Dong, J., Lu, C. Y., and Chakravarthy, R. (2015). Restricting access to florbetapir: medicare coverage criteria for diagnostics and drugs are inconsistent. *BMJ* 351:h3333. doi: 10.1136/bmj.h3333

Cummings, J., Aisen, P., Apostolova, L. G., Atri, A., Salloway, S., and Weiner, M. (2021). Aducanumab: Appropriate Use Recommendations. *J. Prev. Alzheimers Dis.* 8, 398–410.

De Meyer, G., Shapiro, F., Vanderstichele, H., Vanmechelen, E., Engelborghs, S., De Deyn, P. P., et al. (2010). Diagnosis-independent Alzheimer disease biomarker signature in cognitively normal elderly people. *Arch. Neurol.* 67, 949–956. doi: 10.1001/archneurol.2010.179

de Wilde, A., Van Der Flier, W. M., Pelkmans, W., Bouwman, F., Verwer, J., Groot, C., et al. (2018). Association of amyloid positron emission tomography with changes in diagnosis and patient treatment in an unselected memory clinic cohort: the ABIDE project. *JAMA Neurol.* 75, 1062–1070. doi: 10.1001/jamaneurol.2018.1346

Della Rosa, P. A., Cerami, C., Gallivanone, F., Prestia, A., Caroli, A., Castiglioni, I., et al. (2014). A standardized [18F]-FDG-PET template for spatial normalization in statistical parametric mapping of dementia. *Neuroinformatics* 12, 575–593. doi: 10.1007/s12021-014-9235-4

Doré, V., Bullich, S., Rowe, C. C., Bourgeat, P., Konate, S., Sabri, O., et al. (2019). Comparison of 18F-florbetaben quantification results using the standard Centiloid, MR-based, and MR-less CapAIBL§approaches: validation against histopathology. *Alzheimer's Dement.* 15, 807–816. doi: 10.1016/j.jalz.2019.02.005

Ford, J. N., Sweeney, E. M., Skafida, M., Glynn, S., Amoashiy, M., Lange, D. J., et al. (2021). Heuristic scoring method utilizing FDG-PET statistical parametric mapping in the evaluation of suspected Alzheimer disease and frontotemporal lobar degeneration. *Am. J. Nucl. Med. Mol. Imag.* 11, 313–326.

Glodzik, L., Kuceyeski, A., Rusinek, H., Tsui, W., Mosconi, L., Li, Y., et al. (2014). Reduced glucose uptake and Aβ in brain regions with hyperintensities in connected white matter. *Neuroimage* 100, 684–691. doi: 10.1016/j.neuroimage.2014.06.060

Glodzik, L., Rusinek, H., Kamer, A., Pirraglia, E., Tsui, W., Mosconi, L., et al. (2016). Effects of vascular risk factors, statins, and antihypertensive drugs on PiB deposition in cognitively normal subjects. *Alzheimers Dement* 2, 95–104. doi: 10.1016/j.dadm.2016.02.007

Glodzik, L., Rusinek, H., Li, J., Zhou, C., Tsui, W., Mosconi, L., et al. (2015). Reduced retention of Pittsburgh compound B in white matter lesions. *Eur. J. Nucl. Med. Mol. Imag.* 42, 97–102. doi: 10.1007/s00259-014-2897-1

Grothe, M. J., Barthel, H., Sepulcre, J., Dyrba, M., Sabri, O., Teipel, S. J., et al. (2017). In vivo staging of regional amyloid deposition. *Neurology* 89, 2031–2038. doi: 10.1212/wnl.0000000000004643

Gustafson, D. R., Skoog, I., Rosengren, L., Zetterberg, H., and Blennow, K. (2007). Cerebrospinal fluid beta-amyloid 1-42 concentration may predict cognitive decline in older women. *J. Neurol. Neurosurg. Psychiatry* 78, 461–464. doi: 10.1136/jnnp.2006.100529

Harn, N. R., Hunt, S. L., Hill, J., Vidoni, E., Perry, M., and Burns, J. M. (2017). Augmenting amyloid PET interpretations with quantitative information improves consistency of early amyloid detection. *Clin. Nuclear Med.* 42, 577–581. doi: 10.1097/RLU.0000000000001693

Hertze, J., Minthon, L., Zetterberg, H., Vanmechelen, E., Blennow, K., and Hansson, O. (2010). Evaluation of CSF biomarkers as predictors of Alzheimer's disease: a clinical follow-up study of 4.7 years. *J. Alzheimer's Dis.* 21, 1119–1128. doi: 10.3233/jad-2010-100207

Huang, K.-L., Lin, K.-J., Hsiao, I.-T., Kuo, H.-C., Hsu, W.-C., Chuang, W.-L., et al. (2013). Regional amyloid deposition in amnestic mild cognitive

impairment and Alzheimer's disease evaluated by [18F] AV-45 positron emission tomography in Chinese population. *PLoS One* 8:e58974. doi: 10.1371/journal.pone.0058974

Ikonomovic, M. D., Fantoni, E. R., Farrar, G., and Salloway, S. (2018). Infrequent false positive [(18)F]flutemetamol PET signal is resolved by combined histological assessment of neuritic and diffuse plaques. *Alzheimers Res. Ther.* 10:60. doi: 10.1186/s13195-018-0387-6

Ishii, K., Willoch, F., Minoshima, S., Drzezga, A., Ficaro, E. P., Cross, D. J., et al. (2001). Statistical brain mapping of 18F-FDG PET in Alzheimer's disease: validation of anatomic standardization for atrophied brains. *J. Nucl. Med.* 42, 548–557.

Jia, L., Xu, H., Chen, S., Wang, X., Yang, J., Gong, M., et al. (2020). The APOE ε4 exerts differential effects on familial and other subtypes of Alzheimer's disease. *Alzheimers Dement* 16, 1613–1623. doi: 10.1002/alz.12153

Joshi, A. D., Pontecorvo, M. J., Clark, C. M., Carpenter, A. P., Jennings, D. L., Sadowsky, C. H., et al. (2012). Performance characteristics of amyloid PET with florbetapir F 18 in patients with Alzheimer's disease and cognitively normal subjects. *J. Nuclear Med.* 53, 378–384. doi: 10.2967/jnumed.111.090340

Karas, G., Scheltens, P., Rombouts, S., Van Schijndel, R., Klein, M., Jones, B., et al. (2007). Precuneus atrophy in early-onset Alzheimer's disease: a morphometric structural MRI study. *Neuroradiology* 49, 967–976. doi: 10.1007/s00234-007-0269-2

Kim, J., Cho, S. G., Song, M., Kang, S. R., Kwon, S. Y., Choi, K. H., et al. (2016). Usefulness of 3-dimensional stereotactic surface projection FDG PET images for the diagnosis of dementia. *Medicine* 95:e5622. doi: 10.1097/MD.0000000000005622

Landau, S., Thomas, B., Thurfjell, L., Schmidt, M., Margolin, R., Mintun, M., et al. (2014). Amyloid PET imaging in Alzheimer's disease: a comparison of three radiotracers. *Eur. J. Nuclear Med. Mol. Imag.* 41, 1398–1407. doi: 10.1007/s00259-014-2753-3

Lilja, J., Thurfjell, L., and Sörensen, J. (2016). Visualization and quantification of 3-dimensional stereotactic surface projections for 18F-Flutemetamol PET using variable depth. *J. Nuclear Med.* 57, 1078–1083. doi: 10.2967/jnumed.115.169169

Lilly, E. (2013). *Package Insert: Florbetapir*. Available online at: https://pi.lilly.com/us/amyvid-uspi.pdf [accessed on Nov 12, 2021].

Stempniak, M. (2021). *Imaging Advocate Applauds CMS' Decision to Lift Longstanding PET Payment Restriction. Radiology Business*. Available online at: https://www.radiologybusiness.com/topics/economics/imaging-cms-decision-pet-payment-restriction-oncology [accessed on Dec 18, 2021]

Mi, Z., Abrahamson, E. E., Ryu, A. Y., Fish, K. N., Sweet, R. A., Mufson, E. J., et al. (2017). Loss of precuneus dendritic spines immunopositive for spinophilin is related to cognitive impairment in early Alzheimer's disease. *Neurobiol. Aging* 55, 159–166. doi: 10.1016/j.neurobiolaging.2017.01.022

Mielke, M. M., Wiste, H. J., Weigand, S. D., Knopman, D. S., Lowe, V. J., Roberts, R. O., et al. (2012). Indicators of amyloid burden in a population-based study of cognitively normal elderly. *Neurology* 79, 1570–1577. doi: 10.1212/WNL.0b013e31826e2696

Miners, J. S., Kehoe, P. G., Love, S., Zetterberg, H., and Blennow, K. (2019). CSF evidence of pericyte damage in Alzheimer's disease is associated with markers of blood-brain barrier dysfunction and disease pathology. *Alzheimers Res. Ther.* 11:81. doi: 10.1186/s13195-019-0534-8

Minoshima, S., Giordani, B., Berent, S., Frey, K. A., Foster, N. L., and Kuhl, D. E. (1997). Metabolic reduction in the posterior cingulate cortex in very early Alzheimer's disease. *Ann. Neurol.* 42, 85–94. doi: 10.1002/ana.410420114

Morbelli, S., Garibotto, V., Van De Giessen, E., Arbizu, J., Chételat, G., Drezgza, A., et al. (2015). A Cochrane review on brain [^{18}F]FDG PET in dementia: limitations and future perspectives. *Eur. J. Nucl. Med. Mol. Imag.* 42, 1487–1491.

Mormino, E. C., and Papp, K. V. (2018). Amyloid Accumulation and Cognitive Decline in Clinically Normal Older Individuals: Implications for Aging and Early Alzheimer's Disease. *J. Alzheimers Dis.* 64, S633–S646. doi: 10.3233/JAD-179928

Mosconi, L., Berti, V., Dyke, J., Schelbaum, E., Jett, S., Loughlin, L., et al. (2021). Menopause impacts human brain structure, connectivity, energy metabolism, and amyloid-beta deposition. *Sci. Rep.* 11:10867. doi: 10.1038/s41598-021-90084-y

Mosconi, L., Berti, V., Quinn, C., Mchugh, P., Petrongolo, G., Varsavsky, I., et al. (2017). Sex differences in Alzheimer risk: brain imaging of endocrine vs chronologic aging. *Neurology* 89, 1382–1390. doi: 10.1212/WNL.0000000000004425

Mosconi, L., Rahman, A., Diaz, I., Wu, X., Scheyer, O., Hristov, H. W., et al. (2018). Increased Alzheimer's risk during the menopause transition: a 3-year longitudinal brain imaging study. *PLoS One* 13:e0207885. doi: 10.1371/journal.pone.0207885

Mosconi, L., Rinne, J. O., Tsui, W. H., Murray, J., Li, Y., Glodzik, L., et al. (2013). Amyloid and metabolic positron emission tomography imaging of cognitively normal adults with Alzheimer's parents. *Neurobiol. Aging* 34, 22–34. doi: 10.1016/j.neurobiolaging.2012.03.002

Palmqvist, S., Schöll, M., Strandberg, O., Mattsson, N., Stomrud, E., Zetterberg, H., et al. (2017). Earliest accumulation of β-amyloid occurs within the default-mode network and concurrently affects brain connectivity. *Nat. Commun.* 8:1214. doi: 10.1038/s41467-017-01150-x

Perani, D., Della Rosa, P. A., Cerami, C., Gallivanone, F., Fallanca, F., Vanoli, E. G., et al. (2014). Validation of an optimized SPM procedure for FDG-PET in dementia diagnosis in a clinical setting. *Neuroimage Clin.* 6, 445–454. doi: 10.1016/j.nicl.2014.10.009

Petrover, D., Giliberto, L., Clouston, S., Gordon, M., and Franceschi, A. (2021). Semiquantitative Approach to Amyloid PET Interpretation in Clinical Practice. *Soc. Nuclear Med.* 62:1068.

Phurrough, S., Salive, M., Richardson, S., and Cano, C. (2004). *Decision Memo for Positron Emission Tomography (FDG) and Other Neuroimaging Devices for Suspected Dementia*. Baltimore: Centers for Medicare & Medicaid Services.

Rabinovici, G. D., Gatsonis, C., Apgar, C., Chaudhary, K., Gareen, I., Hanna, L., et al. (2019). Association of amyloid positron emission tomography with subsequent change in clinical management among Medicare beneficiaries with mild cognitive impairment or dementia. *Jama* 321, 1286–1294. doi: 10.1001/jama.2019.2000

Rowe, C. C., Ng, S., Ackermann, U., Gong, S. J., Pike, K., Savage, G., et al. (2007). Imaging beta-amyloid burden in aging and dementia. *Neurology* 68, 1718–1725.

Shaw, L. M., Arias, J., Blennow, K., Galasko, D., Molinuevo, J. L., Salloway, S., et al. (2018). Appropriate use criteria for lumbar puncture and cerebrospinal fluid testing in the diagnosis of Alzheimer's disease. *Alzheimers Dement* 14, 1505–1521. doi: 10.1016/j.jalz.2018.07.220

Silverman, D. H., Gambhir, S. S., Huang, H.-W. C., Schwimmer, J., Kim, S., Small, G. W., et al. (2002). Evaluating early dementia with and without assessment of regional cerebral metabolism by PET: a comparison of predicted costs and benefits. *J. Nuclear Med.* 43, 253–266.

Skoog, I., Davidsson, P., Aevarsson, O., Vanderstichele, H., Vanmechelen, E., and Blennow, K. (2003). Cerebrospinal fluid beta-amyloid 42 is reduced before the onset of sporadic dementia: a population-based study in 85-year-olds. *Dement Geriatr. Cogn. Disord.* 15, 169–176. doi: 10.1159/000068478

Spiegel, J., Pirraglia, E., Osorio, R. S., Glodzik, L., Li, Y., Tsui, W., et al. (2016). Greater specificity for cerebrospinal fluid P-tau231 over P-tau181 in the differentiation of healthy controls from Alzheimer's disease. *J. Alzheimers Dis.* 49, 93–100. doi: 10.3233/JAD-150167

Stomrud, E., Hansson, O., Blennow, K., Minthon, L., and Londos, E. (2007). Cerebrospinal fluid biomarkers predict decline in subjective cognitive function over 3 years in healthy elderly. *Dement Geriatr. Cogn. Disord.* 24, 118–124. doi: 10.1159/000105017

Tanyaluck Thientunyakit, M., Chakmeedaj Sethanandha, M., Weerasak Muangpaisan, M., and Satoshi Minoshima, M. (2021). 3D-SSP analysis for amyloid brain PET imaging using 18F-florbetapir in patients with Alzheimer's dementia and mild cognitive impairment. *Med. J. Malaysia* 76, 493–501.

Toledo, J. B., Zetterberg, H., Van Harten, A. C., Glodzik, L., Martinez-Lage, P., Bocchio-Chiavetto, L., et al. (2015). Alzheimer's disease cerebrospinal fluid biomarker in cognitively normal subjects. *Brain* 138, 2701–2715.

Tzourio-Mazoyer, N., Landeau, B., Papathanassiou, D., Crivello, F., Etard, O., Delcroix, N., et al. (2002). Automated anatomical labeling of activations in SPM using a macroscopic anatomical parcellation of the MNI MRI single-subject brain. *Neuroimage* 15, 273–289. doi: 10.1006/nimg.2001.0978

Vemuri, P., Wiste, H., Weigand, S., Shaw, L., Trojanowski, J., Weiner, M., et al. (2009). MRI and CSF biomarkers in normal, MCI, and AD subjects: diagnostic discrimination and cognitive correlations. *Neurology* 73, 287–293. doi: 10.1212/WNL.0b013e3181af79e5

Veronese, M., Bodini, B., García-Lorenzo, D., Battaglini, M., Bongarzone, S., Comtat, C., et al. (2015). Quantification of [11C] PIB PET for imaging myelin in the human brain: a test—retest reproducibility study in high-resolution research tomography. *J. Cereb. Blood Flow Metabol.* 35, 1771–1782. doi: 10.1038/jcbfm.2015.120

Yakushev, I., Hammers, A., Fellgiebel, A., Schmidtmann, I., Scheurich, A., Buchholz, H. G., et al. (2009). SPM-based count normalization provides excellent discrimination of mild Alzheimer's disease and amnestic mild cognitive impairment from healthy aging. *Neuroimage* 44, 43–50. doi: 10.1016/j.neuroimage.2008.07.015

Zetterberg, H., and Blennow, K. (2021). Moving fluid biomarkers for Alzheimer's disease from research tools to routine clinical diagnostics. *Mol. Neurodegener* 16:10. doi: 10.1186/s13024-021-00430-x

Zhang, K., Mizuma, H., Zhang, X., Takahashi, K., Jin, C., Song, F., et al. (2021). PET imaging of neural activity, β-amyloid, and tau in normal brain aging. *Eur. J. Nucl. Med. Mol. Imag.* 48, 3859–3871. doi: 10.1007/s00259-021-05230-5

Ziolko, S. K., Weissfeld, L. A., Klunk, W. E., Mathis, C. A., Hoge, J. A., Lopresti, B. J., et al. (2006). Evaluation of voxel-based methods for the statistical analysis of PIB PET amyloid imaging studies in Alzheimer's disease. *Neuroimage* 33, 94–102. doi: 10.1016/j.neuroimage.2006.05.063

Zou, K., Abdullah, M., and Michikawa, M. (2020). Current Biomarkers for Alzheimer's Disease: From CSF to Blood. *J. Pers. Med.* 10:85.

Conflict of Interest: The authors declare that the research was conducted in the absence of any commercial or financial relationships that could be construed as a potential conflict of interest.

Publisher's Note: All claims expressed in this article are solely those of the authors and do not necessarily represent those of their affiliated organizations, or those of the publisher, the editors and the reviewers. Any product that may be evaluated in this article, or claim that may be made by its manufacturer, is not guaranteed or endorsed by the publisher.

Copyright © 2022 Smith, Ford, Haghdel, Glodzik, Li, D'Angelo, RoyChoudhury, Wang, Blennow, de Leon and Ivanidze. This is an open-access article distributed under the terms of the Creative Commons Attribution License (CC BY). The use, distribution or reproduction in other forums is permitted, provided the original author(s) and the copyright owner(s) are credited and that the original publication in this journal is cited, in accordance with accepted academic practice. No use, distribution or reproduction is permitted which does not comply with these terms.

frontiers | Frontiers in Aging Neuroscience

ORIGINAL RESEARCH
published: 26 April 2022
doi: 10.3389/fnagi.2022.810125

Deep Learning-Based Multilevel Classification of Alzheimer's Disease Using Non-invasive Functional Near-Infrared Spectroscopy

*Thi Kieu Khanh Ho[1], Minhee Kim[2], Younghun Jeon[3], Byeong C. Kim[4], Jae Gwan Kim[2], Kun Ho Lee[5,6,7], Jong-In Song[3] and Jeonghwan Gwak[1,8,9,10]**

[1] Department of Software, Korea National University of Transportation, Chungju, South Korea, [2] Department of Biomedical Science and Engineering, Gwangju Institute of Science and Technology, Gwangju, South Korea, [3] School of Electrical Engineering and Computer Science, Gwangju Institute of Science and Technology, Gwangju, South Korea, [4] Department of Neurology, Chonnam National University Medical School, Gwangju, South Korea, [5] Gwangju Alzheimer's Disease and Related Dementias Cohort Research Center, Chosun University, Gwangju, South Korea, [6] Department of Biomedical Science, Chosun University, Gwangju, South Korea, [7] Korea Brain Research Institute, Daegu, South Korea, [8] Department of Biomedical Engineering, Korea National University of Transportation, Chungju, South Korea, [9] Department of AI Robotics Engineering, Korea National University of Transportation, Chungju, South Korea, [10] Department of IT and Energy Convergence (BK21 FOUR), Korea National University of Transportation, Chungju, South Korea

OPEN ACCESS

Edited by:
Kuangyu Shi,
University of Bern, Switzerland

Reviewed by:
Anubha Gupta,
Indraprastha Institute of Information Technology Delhi, India
Arcangelo Merla,
University of Studies G. d'Annunzio Chieti and Pescara, Italy

***Correspondence:**
Jeonghwan Gwak
james.han.gwak@gmail.com;
jgwak@ut.ac.kr

Specialty section:
This article was submitted to Alzheimer's Disease and Related Dementias, a section of the journal Frontiers in Aging Neuroscience

Received: *06 November 2021*
Accepted: *01 March 2022*
Published: *26 April 2022*

Citation:
Ho TKK, Kim M, Jeon Y, Kim BC, Kim JG, Lee KH, Song J-I and Gwak J (2022) Deep Learning-Based Multilevel Classification of Alzheimer's Disease Using Non-invasive Functional Near-Infrared Spectroscopy. Front. Aging Neurosci. 14:810125. doi: 10.3389/fnagi.2022.810125

The timely diagnosis of Alzheimer's disease (AD) and its prodromal stages is critically important for the patients, who manifest different neurodegenerative severity and progression risks, to take intervention and early symptomatic treatments before the brain damage is shaped. As one of the promising techniques, functional near-infrared spectroscopy (fNIRS) has been widely employed to support early-stage AD diagnosis. This study aims to validate the capability of fNIRS coupled with Deep Learning (DL) models for AD multi-class classification. First, a comprehensive experimental design, including the resting, cognitive, memory, and verbal tasks was conducted. Second, to precisely evaluate the AD progression, we thoroughly examined the change of hemodynamic responses measured in the prefrontal cortex among four subject groups and among genders. Then, we adopted a set of DL architectures on an extremely imbalanced fNIRS dataset. The results indicated that the statistical difference between subject groups did exist during memory and verbal tasks. This presented the correlation of the level of hemoglobin activation and the degree of AD severity. There was also a gender effect on the hemoglobin changes due to the functional stimulation in our study. Moreover, we demonstrated the potential of distinguished DL models, which boosted the multi-class classification performance. The highest accuracy was achieved by Convolutional Neural Network-Long Short-Term Memory (CNN-LSTM) using the original dataset of three hemoglobin types (0.909 $\pm$ 0.012 on average). Compared to conventional machine learning algorithms, DL models produced a better classification performance. These findings demonstrated the capability of DL frameworks on the imbalanced class distribution analysis and validated the great potential of fNIRS-based approaches to be further contributed to the development of AD diagnosis systems.

Keywords: Alzheimer's disease, fNIRS, multi-class classification, deep learning – artificial neural network (DL-ANN), CNN-LSTM

INTRODUCTION

The incidence of age-related dementia has increased dramatically as the world population is aging. Dementia was estimated to affect 50 million people worldwide in 2018 and is expected to exceed 150 million people within 30 years (Alzheimer's Disease International, 2018). Alzheimer's disease (AD) is one of the most well-known causes of dementia, accounting for nearly two-thirds of all dementia patients (Alzheimer's Association, 2019). AD is characterized by the progressive impairment of both cognitive and memory abilities due to a consequence of the significant loss of neurons in the nervous system (Veitch et al., 2019) or disruption of nerve cell communications by the presence of extracellular Amyloid-Beta (Aβ) peptide plaques and neurofibrillary tangles (NFT), which typically develop decades before the symptoms manifest (Lowe et al., 2019). Since AD first destroys brain cells related to language and memory brain regions, patients suffer from confusion, memory loss, speech impediment, poor problem-solving skills, and difficulty in daily communication. Then, other brain regions for controlling breathing and heart functionality would deteriorate, eventually leading to death. Patients with AD are generally diagnosed in late stages, by which point existing treatments can only decelerate the speed of cognitive declines. As such, a prompt diagnosis to facilitate proper treatments of preclinical and its prodromal stages is significantly crucial. Besides fundamental exams, such as patient interview, Mini-Mental State Examination (MMSE), and physical and neurobiological exams, reliable and powerful neuroimaging techniques, such as from functional magnetic resonance imaging (fMRI) (Cheng et al., 2019), structural magnetic resonance imaging (sMRI) (Wang et al., 2016), positron-emission tomography (PET) (Alster et al., 2019), electroencephalography (EEG) (Mazaheri et al., 2018), or diffusion tensor imaging (DTI) (Hwang et al., 2019) techniques, are desperately needed to furnish more informative diagnosis approach. However, these techniques usually appeal to the clinical interaction between doctors and patients, whilst a more flexible paradigm of doctor-patient interaction is preferable.

Functional near-infrared spectroscopy (Naseer and Hong, 2015) is a scalp-located and non-invasive technique which measures the neural activity using the concentration of oxygenated (HbO) and deoxygenated (Hb) hemoglobin in the brain by calculating by the blood-oxygen-level-dependent effect (Ferrari and Quaresima, 2012). fNIRS offers a variety of advantages over the aforementioned neuroimaging methods, such as a relatively high temporal resolution, absence of ionizing radiation, low cost, high portability, lightweight implementation, and lower susceptibility to motion artifacts during experiments (Lancia et al., 2018; Ho et al., 2019). Unlike commonly sizeable systems (e.g., fMRI, PET, EEG), which prevent the daily activity acquisition in the brain, fNIRS enables the brain measurement with much less intrusive form factors when performing tasks to not interrupt the actual behavior of participants. In AD studies, specifically, fNIRS has verified its own potential (Zeller et al., 2010; Perpetuini et al., 2017). Araki et al. (2014) presented a significant difference in the cerebral blood flows of patients with AD under the effects of memantine. Hemodynamic responses between healthy controls (HC) and patients with AD were also distinguished (Metzger et al., 2016; Li et al., 2019), whilst mild cognitive impairment (MCI) – an early stage of AD – was differentiated from those in the HC group (Ghafoor et al., 2019). These studies have demonstrated that patients with AD typically exhibit lower levels of activation in specific brain regions compared to the HC group during cognitive tasks. In addition, fNIRS is well operable with EEG in the multimodal integration to reinforce the diagnosis accuracy (Fazli et al., 2012). Nevertheless, these previous studies have solely distinguished AD from HC using cognitive tests, whereas different AD stages remain unknown and the pathological mechanism of AD progression has not yet been thoroughly documented. Therefore, in this study, multiple subject groups were recruited and participated in different evaluation tasks (cognitive, memory, and language) to comprehensively compare and evaluate the capability of fNIRS in AD diagnosis.

Machine learning (ML) techniques have been a fundamental element involved in any computer-aided diagnosis systems for the automated prediction of neurological disorders. A Bayes classifier was applied to determine the utility of the eye-tracker, heat flux and median absolute deviation, electrocardiogram armband, EEG headset, and heart rate monitor (Haapalainen et al., 2010). A Gaussian mixture model was used to measure the mental workload of a mental arithmetic task through eye-tracking data (Chen and Epps, 2013). The capability of multiple learning algorithms, including logistic regression, decision trees, naïve Bayes, 1-nearest neighbor, and multilayer perceptron, was evaluated on heart rate data. Subsequently, ML has gained much attention in fNIRS studies. Support vector machines (SVMs) and adaptive boosting as traditional ML algorithms were utilized to distinguish stress levels from the resting states of subjects during Stroop task experiments (Solovey et al., 2014). Logistic regression and SVMs in mental workload classification were also verified (Benerradi et al., 2019).

Despite being successfully applied on signal domains, extracting and selecting features in appropriate ways are still considered as main drawbacks of conventional ML. The cost of these supervised learning methods increases with respect to parameters. As such, these algorithms require a huge amount of labeled training data. Meanwhile, theoretical and biological arguments have strongly recommended a model which is composed of multilayers of nonlinear processing with few labeled inputs in correspondence with human brain activity. Therefore, deep architectures such as Convolutional Neural Network (CNN) and Recurrent Neural Network (RNN) as two common forms of Artificial Neural Network (ANN) have unsurprisingly come to our top priorities in terms of solving optimization problems, automated feature extractions, and multi-class classification tasks. Deep learning (DL) models have been adopted a diversity of applications in practice. CNNs have drawn extensive attention in image classification using various frameworks, such as VGG-16 (Simonyan and Zisserman, 2014) and Residua-Net (He et al., 2016), while RNNs depict connections between computing units that formulate a directed graph along a sequence, thus is popular in time-series data analyses, such as machine translation,

time-series prediction, or speech recognition (Lokesh et al., 2019; Wright et al., 2019).

Although the DL-based approach has earned great success in various computer vision tasks, its potential in AD classification using fNIRS are not substantially achievable. First, various preprocessing steps are required since the amplitude and the length of signals are different from patient to patient. Second, a sufficiently large number of datasets is mandatory to efficiently train a DL model. Thus, either an adequate number of original data or artificial data from augmentation or resampling techniques is required. Third, it is arduous to obtain an efficient conversion approach to express medical signals in the form of carrying pertinent information in CNN. Moreover, feeding inputs to a RNN network and training it with gradient descent algorithms (Ruder, 2016), such as long-term independence, remain challenges. To address these challenges, researchers have recently paid exceptional efforts to develop the 1 Dimensional-Convolutional Neural Network (1D-CNN) which can capture spatial-temporal information of signals and long short-term memory (LSTM), as one type of RNNs, which can train and avoid the so-called vanishing gradient issue. Therefore, it is of great interest and importance to address the aforementioned challenges in our study.

The main contributions of this study are summarized as follows: (1) we presented the comprehensive experimental protocol, including cognitive, memory, and verbal tests to investigate the diverse patterns of AD progression, thereby facilitating the investigation of hemodynamic response differences between the HC group and three stages of patients with AD; (2) we inspected the significant differences of oxygen hemodynamic concentrations between subject groups and between gender; and (3) we demonstrated the potential of fNIRS in AD multi-class classification using four DL architectures.

The remainder of this paper is organized as follows: Section "Related Works" briefly presents the related works concerning AD studies using fNIRS and DL techniques. In section "Materials and Methods," we describe materials, including the experimental protocols, fNIRS datasets, pre-processing steps, and DL models for multi-class classification tasks in detail. Section "Experimental Results" summarizes the experimental classification results. In section "Conclusions and Future Works," we conclude the paper with our main contributions and some suggestions for future works.

RELATED WORKS

Functional near-infrared spectroscopy is a non-invasive way of measuring cerebral hemodynamic change using near-infrared rays (Yücel et al., 2017). Irani et al. (2007) proved the relatively superior spatial-resolution of fNIRS compared to EEG/Magnetoencephalography (MEG). fNIRS was used to successfully distinguish signals from nearby measured brain regions, thus avoiding fake correlations as induced by EEG/MEG (Sonkaya, 2018). Moreover, from a practical point of view, fNIRS is portable, safe, quiet, relatively inexpensive, easy to handle, has fewer restrictions on subjects, compatible with iron metals, and feasible for long-term continuous and repeated measurements at short intervals. These advantages outweigh the merits of other neuroimaging techniques in the study of neurological disorders and psychiatric disorders such as dementia and brain-related disorders. Many studies have examined the validity of using fNIRS to compare the hemodynamic response in HC and patients with AD, and demonstrated that patients with AD showed lower activation in specific brain regions during various cognitive tasks than normal people's (Beishon et al., 2017; Vermeij et al., 2017; Liao et al., 2019). Hock et al. (1997) reported that there was a decrease in HbO and Total Hemoglobin (HbT) given a verbal fluency task (VFT) in the parietal cortex of patients with AD. Arai et al. (2006) revealed that HbO concentrations were significantly reduced in the frontal and bilateral parietal areas of the AD group, whereas the hemoglobin activation was only lower in the right parietal area of the MCI group. These findings suggest that fNIRS holds the promising potential to detect AD, even at early stages.

To monitor the declined cognitive function of AD, it is essential to further define a classification scheme. Recent studies have adopted ML on the classification of AD stages. With the development of computational resources, the application of ML algorithms has enabled the work of AD stage labeling based on a classification model, which is beyond the traditional analysis. Cicalese et al. (2020) presented a linear discriminant analysis (LDA) algorithm applied on a hybrid EEG-fNIRS dataset to classify four subject groups (8 HC, 8 MCI, 6 MAD, and 7 MSAD) given a random digit encoding-retrieval task. Their results indicated that the right prefrontal and left parietal regions were relevant to AD progression. The integrated EEG-fNIRS feature set achieved a higher accuracy (79.31%) compared to using EEG (65.52%) or fNIRS (58.62%) alone. Yang et al. (2018) aimed to investigate MCI assessment using statistical analysis and an LDA algorithm to differentiate MCI from HC. They yielded an effective ML tool for early prediction of AD using digital biomarkers and fNIRS (Yang and Hong, 2019). Despite its popularity, conventional ML algorithms have been criticized for their poor performance on raw data, not being limited to on bio-signal domains, and for the prerequisite step of manually extracting informative features (Plis et al., 2014; LeCun et al., 2015).

The ability to achieve features with higher orders of abstraction and complexity compared to conventional ML, such as SVM, makes DL better suited for detecting scattered, complex, and subtle patterns of the data. In addition, an integral facet of DL to differentiate it from other ML methods is that features are not manually engineered. Instead, DL learns the data in an end-to-end manner, resulting in a more objective and less bias-prone process (Plis et al., 2014). Proven for its superior image classification and recognition capabilities, CNN has motivated the development of a CNN-based taxonomy for early-stage AD detection (Vieira et al., 2017). This review paper identified a total of 25 articles relevant to DL studies of psychiatric and neurological disorders, including AD-related concerns. First, the diagnostic studies aimed to classify patients from HC. Second, studies on conversion to illness used the baseline scan from individuals who were predicted as being at high risk of developing a psychiatric or neurologic abnormality. Finally, studies on

predicting the treatment response employed the baseline scan from subjects with a neurological or psychiatric diagnosis to predict the subsequent treatment response. The accuracies of DL architectures from those articles were also reported to testify DL feasibility in discriminating between more than two classes (HC, MCI, and AD).

Oh et al. (2019) presented volumetric CNN-based approaches [convolutional autoencoder (CAE)-based unsupervised learning and supervised transfer learning] for four binary classification tasks (AD vs. HC, progressive MCI vs. HC, stable MCI vs. HC, and progressive MCI vs. stable MCI) and a gradient-based visualization task of the spatial attention. They discovered the important AD-related biomarker using an MRI dataset from Alzheimer's Disease Neuroimaging Initiative (ADNI) database without human intervention (Oh et al., 2019). The experimental results showed that their proposed models achieved favorable performance and comparable efficiency to current state-of-the-art models. Meanwhile, the multimodal DL approach has exerted to incorporate different types of inputs and DL models to boost the AD classification accuracy. Lee et al. (2019) extracted multiple features from MRI, cohort data, and cerebrospinal fluid (CSF) data and adopted an RNN to predict AD. Suk and Shen (2013) employed MMSE, MRI, PET, and CSF to discriminate AD from MCI. Feng et al. (2019) fed MRI and PET data to the incorporated framework of 3D-CNN and LSTM.

Previous AD studies have validated not only the potential of fNIRS in assisting clinicians/practitioners to distinguish different AD groups from a HC group, but also the potential of DL on AD analysis. However, to the best of our knowledge, there are several issues that remain unsolved and needed to be addressed. The comprehensive experiment design with different tasks to investigate AD patterns and the DL classification frameworks for AD studies using imbalanced fNIRS datasets have not been thoroughly documented. We, therefore, conducted entire experiments (cognitive, memory, and verbal tests) and verified a collection of four DL models to differentiate the HC group from three levels of AD progression using the fNIRS dataset.

MATERIALS AND METHODS

Subjects

Early-phase AD is hardly characterized since it precedes for years as an asymptomatic AD that is not comparable to the normal aging process. However, using neuropathological biomarkers from the cerebrospinal fluid and several brain imaging techniques, the sequence of AD development is distinguishable from that of aging in a cognitively unimpaired healthy state that does not have AD biomarkers. Hence, the National Research Center for Dementia and Chonnam National University Hospital (Gwangju, South Korea) recruited senior citizens living in Gwangju and adjacent cities to approach this objective. By conducting a series of medical examinations (MMSE, PET, MRI, and patient interview), subjects were diagnosed with disease stages according to the guidelines from the National Institute of Neurological and Communicative Disorders and Stroke (NINCDS)-Alzheimer's Disease and Related Disorders Association (ADRDA) Work Group (McKhann et al., 1984), the National Institute on Aging and Alzheimer's Association (NIA-AA) (Jack et al., 2011), and International Working Group (IWG) (Cummings et al., 2013). Subjects with a mental and/or behavioral disorder were excluded from this cohort.

The final subject groups included HCs (cognitively normal individuals), asymptomatic AD (abbreviated as aAD: cognitively normal individuals, the amyloid positive in PET was found), prodromal AD (abbreviated as pAD: mild brain dysfunction symptoms such as short-term memory deficits, impaired insight, irritability, dysphoric mood, and anxiety), and AD dementia (abbreviated as ADD: deterioration of memory, language, social abilities that severely effect on daily life) groups. A total of 140 subjects were involved in this study: HC class (n = 53, age = 72.7 $\pm$ 5.3 years), aAD class (n = 28, age = 74.5 $\pm$ 4.3 years), pAD class (n = 50, age = 75.8 $\pm$ 3.9 years), and ADD class (n = 9, age = 75.4 $\pm$ 6.8 years).

All subjects had no previous experience with our experimental protocol. The purpose of the research and the written consent form were furnished and agreed upon by each subject prior to conducting the experiment. The experimental procedure was approved by the International Review Board at the Gwangju Institute of Science and Technology. The demographic information of participants is summarized in **Table 1**.

Functional Near-Infrared Spectroscopy Device and Data Preprocessing

Figure 1A represents the fNIRS device setup. fNIRS signals from six channels located in the prefrontal cortex region were recorded. The device was built in the laboratory, and the probe consisted of a pair of source and detector, light-emitting diode (LED; OE-MV7385-P, Opto ENG, South Korea) and photodiodes (Opt101, Texas Instruments). The LED had dual wavelengths (730 and 850 nm). Channels 1, 2, and 3 measured signals in the right prefrontal region while channels 4, 5, and 6 measured signals in the left prefrontal region. While channels 2, 3, 5, and 6 were far-channels (30 mm) and the signals obtained from these channels presented the cerebral hemodynamic response, channels 1 and 4 were known as near-channels since the distance between the source and the detector was very close (8 mm) in order to measure the superficial layer from the head. The photodiode located in between channel 3 and channel 5 was 15 mm distant from the Fpz point in the 10–20 EEG system.

The signal sampling rate was set to 8 Hz. Each channel was visually inspected during the experiment, and channels exhibiting large spikes were marked as noise and excluded from the study. The changes in the concentration of hemoglobin [HbO, Hb, and

TABLE 1 | Subject demographics.

	HC	aAD	pAD	ADD
Number	53	28	50	9
Age ± SD (years)	72.7 ± 5.3	74.5 ± 4.3	75.8 ± 3.9	75.4 ± 6.8
Gender (M/F)	21/32	15/13	31/17	4/5
MMSE ± SD	27.0 ± 4.2	26.9 ± 2.5	26.0 ± 3.2	20.2 ± 4.8
Education ± SD	9.8 ± 4.7	10.2 ± 5.2	10.6 ± 5.2	8.5 ± 5.3

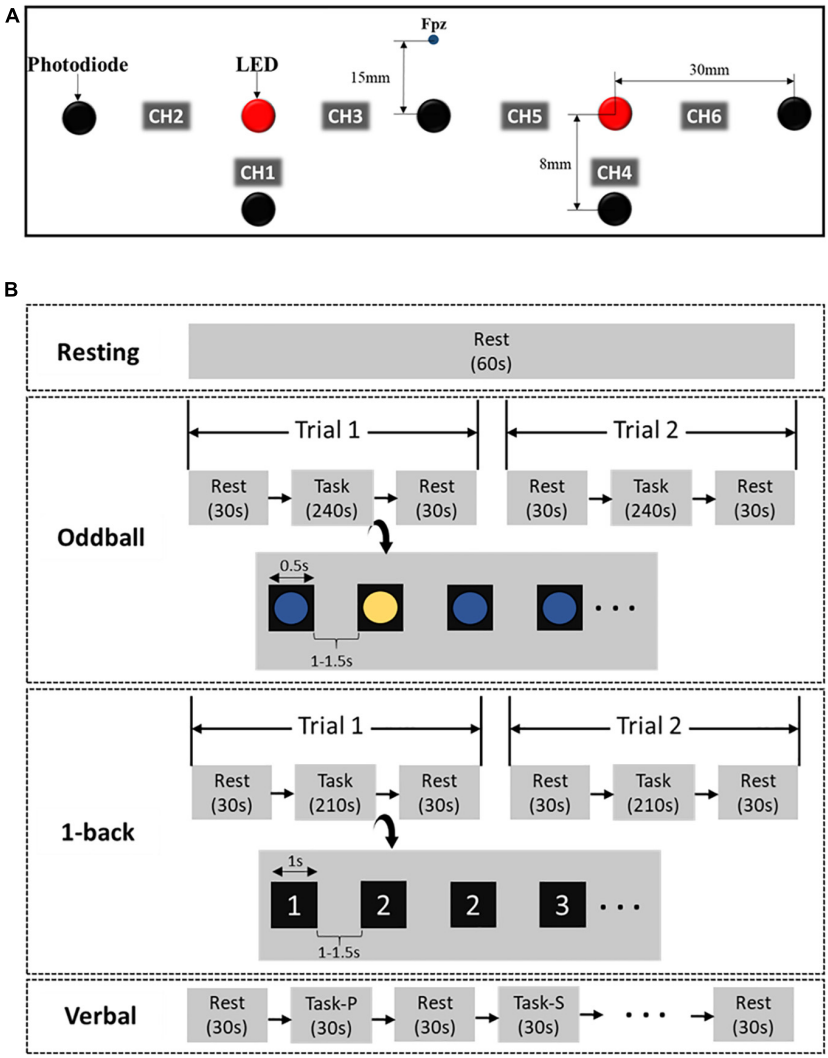

FIGURE 1 | fNIRS device setup **(A)** and experimental protocol **(B)** (s, second; P, phonemic; S, semantic).

total hemoglobin (THb)] were computed by the modified Beer–Lambert law (Swinehart, 1962). To remove artifacts, a low-pass filter with a cutoff frequency of 0.5 Hz was applied. Although we utilized four channels in our previous studies (Nguyen et al., 2019) where the near-channels were excluded by employing the extraction algorithm since their function was to get rid of the skin and skull noise from the far-channels, it is crucial to consider inputs from all channels to be fed to proposed DL frameworks in this present study.

Experimental Protocol

Subjects were requested to sit in a comfortable chair situated in a confined room to reduce environmental disturbances and minimize their body movements during experiments. In our experiment, subjects underwent a resting stage and three brain functional tasks, including Oddball (cognitive ability test), 1-back (memory ability test), and Verbal fluency (language ability test). First, subjects calmly watched a white cross appeared on the monitor screen for 60 s during the resting period. Subjects also had 30 s for resting in a similar way before and after each experimental task.

Second, the blue and yellow circles appeared alternately, and subjects were asked to report the color of each ball in the Oddball task. The yellow circle rarely appeared compared to the blue one. Subjects were asked to pay attention to the occurrence of the circle and press "0" if the yellow circle presented. Each colored circle appeared for 0.5 s, and a blank screen appeared for 1–1.5 s between the circles. The task took 5 min and was recorded twice.

Third, a consecutive series of numbers, from 1 to 3, randomly appeared on the screen in the 1-back task. The appearance of each number lasted for only a second. Subjects were requested to remember a number which was selected and previously presented in one trial. Subjects then pressed the "0" button likewise. The task took 5 min and was also recorded twice.

Lastly, a total of six Korean phonemic and semantic words alternately appeared on the screen in the Verbal fluency task.

Initially, a letter appeared alone (i.e., "a"), and subjects would continuously recite complete words that start with the letter (i.e., "anniversary"). If a white cross appeared on the screen, they would stop speaking and carefully glare at the screen until the next semantic word appeared. When the semantic word (i.e., "animal") appeared, the subjects would continuously recite certain animals (i.e., "Lion"). Each trial block took for 30 s, and there was a 30-s resting state between trials. This process was repeatedly conducted, and the Verbal task took approximately 7 min.

In total, every subject performed six sub-tasks in the order of Resting, Oddball (trial 1), Oddball (trial 2), 1-back (trial 1), 1-back (trial 2), and Verbal fluency. All procedures took around 30 min, including the break time between tasks (see **Figure 1B**). Any subject who was not able to fulfill any of these sub-tasks was excluded from our analysis.

Proposed Deep Learning Models

As a subcategory of ML, DL is inspired by the structure and function of the brain, the so-called biological neural networks (NNs). A DL model is made of the basic building block of NNs which are trained on the large-scale labeled dataset(s) to learn functions from the original data without manually extracting features, as most of the conventional ML algorithms do. CNN, denoted as one of the most well-known forms of DL, has been demonstrating its robust performances in the computer vision community where the inputs usually include high dimensional features (i.e., each pixel of an image is a dimension). Hence, it is pertinent to perform on a long sequence of data and is easy to implement. Meanwhile, employing RNN, which can handle the temporal data through modeling the underlying dynamic behaviors of time series sequences, is natural. However, since the sequence data is generated from electrodes that are closely located, there is a strong correlation in time within the sequence. Directly learning sequences with noises from RNNs is very challenging. LSTM or the recently invented Generated Recurrent Units (GRUs) can settle the vanishing or explosion of gradient loss. Due to the early-stopping strategy used during the training process, it is certainly expected that no severe overfitting can be observed. Lastly, to take synergetic advantage of CNN and LSTM, a mixed model including CNN followed by LSTM, where CNN acts as an effective decoder for LSTM layers, is seemingly interesting to build.

1D-Convolutional Neural Network

Since the input size of fNIRS data is different from acquainted image datasets with more than one dimension, a 1D-CNN is necessarily done in the time domain. In this work, with the idea of using 2 dimensional stacks for time-specific activity, the CNN model was employed to decompose and feed-forward a 1D fNIRS signal that was known as a precomputed spectrogram or time-frequency. CNN consisted of one 1D convolutional layer, one 1D max-pooling layer, and two linear layers. Batch normalization was used before the activation function, and dropout was used for regularization. A grid search of convolutional filter number, filter size, pooling size, batch size, number of units per layer, stride, and learning rate was done to optimize hyper-parameters, as shown in **Supplementary Table 1**.

Long Short-Term Memory

To discriminate the subtle spatial-temporal change in the fNIRS feature space associated with different progressive stages of AD, a solution capable of remembering and ultimately aggregating transitions across the dataset is required. LSTM, with the attention mechanism, has been known as a wide-ranging method utilized for distinctly learning and classifying bio-signal time-series datasets (Tsiouris et al., 2018; Zhang et al., 2018, 2019) on fNIRS (Yoo et al., 2018; Sirpal et al., 2019). Thus, it triggered us to apply LSTM to improve the classification performance using fNIRS by focusing on the crucial task-relevant features from different time-steps. Compared to classic approaches in such aforementioned classifiers, RNN or LSTM particularly requires no or almost no feature engineering that an fNIRS dataset is able to feed directly into the network. We utilized the "many to one" architecture, which means using time series of feature vectors (one vector per time step) to convert them to a probability matrix at the output layer.

An LSTM network consists of cells whose outputs evolve through the network based on the content of past memory. The cell has a common cell state, keeping long-term dependences along the entire LSTM chain. The flow information is then monitored by the input gate i_t and the forget gate f_t, hence allowing the network to decide whether to forget the previous state C_{t-1} or to update the current state C_t with new information. The output of each cell, namely, hidden state, is controlled by an output gate o_t that allows the cell to compute its output given the updated cell state (see **Figure 2A**). These states of an LSTM model are formulated by the following formula:

$$i_t = \sigma(W_i \cdot \left[h_{t-1},\ x_t\right] + b_i), \tag{1}$$

$$f_t = \sigma(W_f \cdot \left[h_{t-1},\ x_t\right] + b_f), \tag{2}$$

$$C_t = f_t * C_{t-1} + i_t * tanh(W_c \cdot \left[h_{t-1},\ x_t\right] + b_c), \tag{3}$$

$$o_t = \sigma(W_o \cdot \left[h_{t-1},\ x_t\right] + b_o), \tag{4}$$

$$h_t = o_t * tanh(C_t), \tag{5}$$

where $\sigma(x) = \frac{1}{1+e^{-x}}$, x_t is the input features fed into the cell, h_t is the hidden state at time step t, C_{t-1} is the cell state at time step t, W_i, W_f, W_c, W_o are the weights, and b_i, b_f, b_c, b_o are the biases obtained during the backpropagation process. We thereby proposed an LSTM architecture with three stacked layers and a fully connected layer with rectified linear units (ReLU) function to predict the probability of each class (see **Figure 2B**).

Several hyper-parameters for the LSTM network were thoroughly explored and tuned to earn the best classification results. Concretely, these hyper-parameters encompassed the recurrent depth, LSTM hidden layer size, batch size, and training epochs. Three stacked LSTM layers (D_0, D_1, D_2) and the weight matrix L_2 regularization coefficient was applied for each LSTM layer. In addition, other variables such as learning rate (l_r) and the amount of lambda loss were used for stochastic Adam

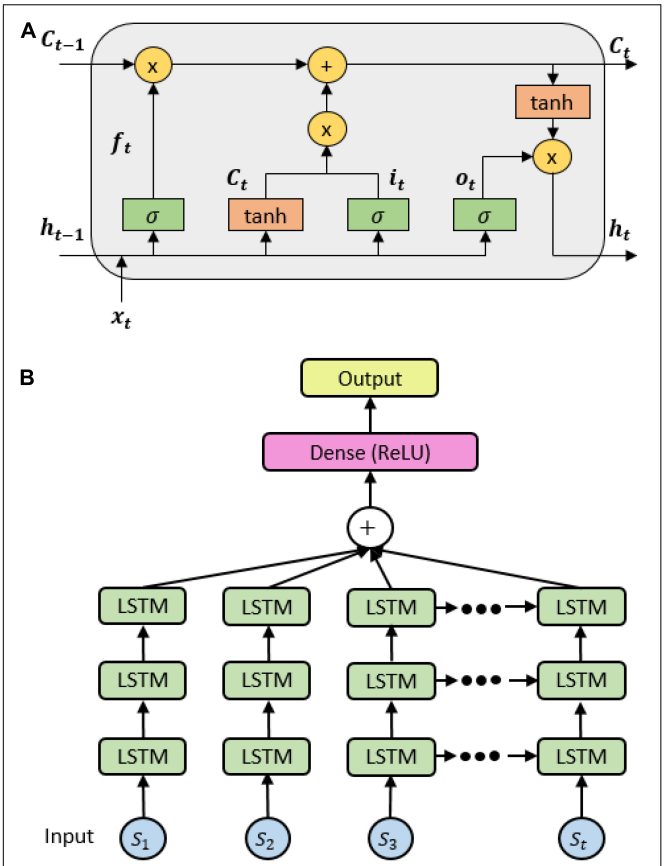

FIGURE 2 | (A) A long short-term memory (LSTM) cell internal mechanism; **(B)** the stacked LSTM architecture.

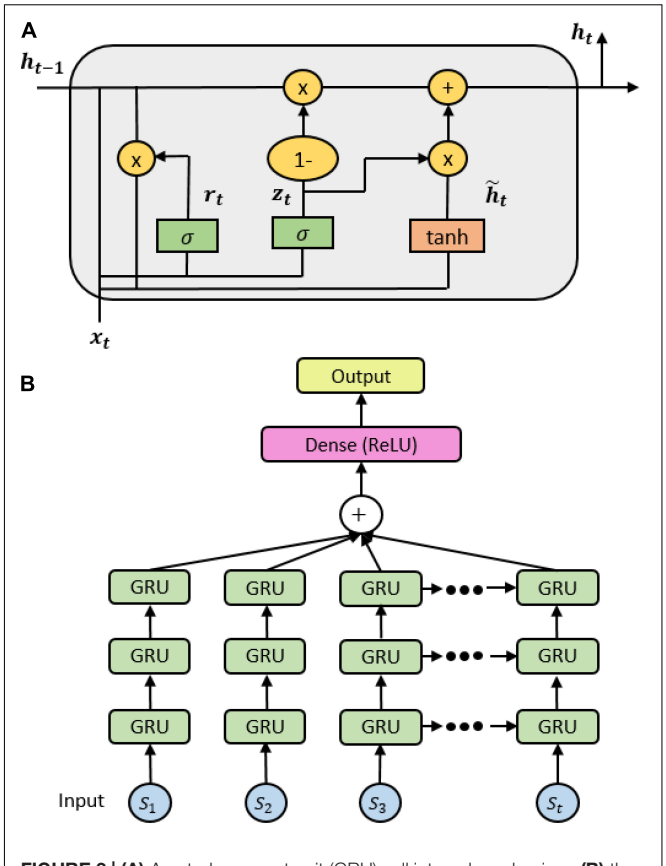

FIGURE 3 | (A) A gated recurrent unit (GRU) cell internal mechanism; **(B)** the stacked GRU architecture.

optimizer. **Supplementary Table 2** presents the optimal values for these parameters.

Gated Recurrent Units

As similar to the precedent LSTM, gated recurrent units (GRU) is newly created for the solution of short-term memory. An internal mechanism called gates is also needed to regulate the flow of information. However, GRU gets rid of the cell state and uses the hidden state to transfer information. It includes only two gates: a reset gate which is another gate used to decide how much past information can be forgotten, and an update gate which acts similar to the forget and input gate of LSTM which decides what information can be discarded and what new information can be complemented (see **Figure 3A**). These states of a GRU model are formulated by following formulas:

$$z_t = \sigma(W_z \cdot [h_{t-1}, x_t]) \quad (6)$$

$$r_t = \sigma(W_r \cdot [h_{t-1}, x_t]) \quad (7)$$

$$\tilde{h}_t = tanh(W \cdot [r_t * h_6 t - 1, x_t]), \quad (8)$$

$$h_t = (1 - z_t) * h_{t-1} + z_t * \tilde{h}_t) \quad (9)$$

Due to its fewer tensor operations, GRU trains data faster than LSTM. It also has a faster convergence, but it is unlikely to guarantee which one outperforms others. In practice, we built a GRU model with the same architecture of LSTM, excluding the module used in the current layers. Three GRU layers were stacked, followed by a fully connected layer and an output layer (see **Figure 3B**). Batch-normalization and the ReLU activation function were applied in the fully connected layer. The output layer was computed by the cross-entropy loss with a soft-max layer. More details of chosen parameters are depicted in **Supplementary Table 3**.

A Mixed Model: Long Short-Term Memory Model Coupled With Convolutional Neural Network Decoder

Inspired by the phenomenal performance of the hybrid CNN-RNN in both the spatial domain (Dutta et al., 2018) and the spatial-temporal domain (Yang et al., 2018; Shi et al., 2019), we employed a CNN layer as a decoder for original input data, followed by multiple LSTM layers to cope with the decoded temporal data, and a fully connected layer where the cross-entropy loss with a soft-max function was computed for classification (see **Supplementary Table 4**). We let a CNN layer extract multiple high-level features from the raw data by using a substantially large filter size and stride. The sequence was thus

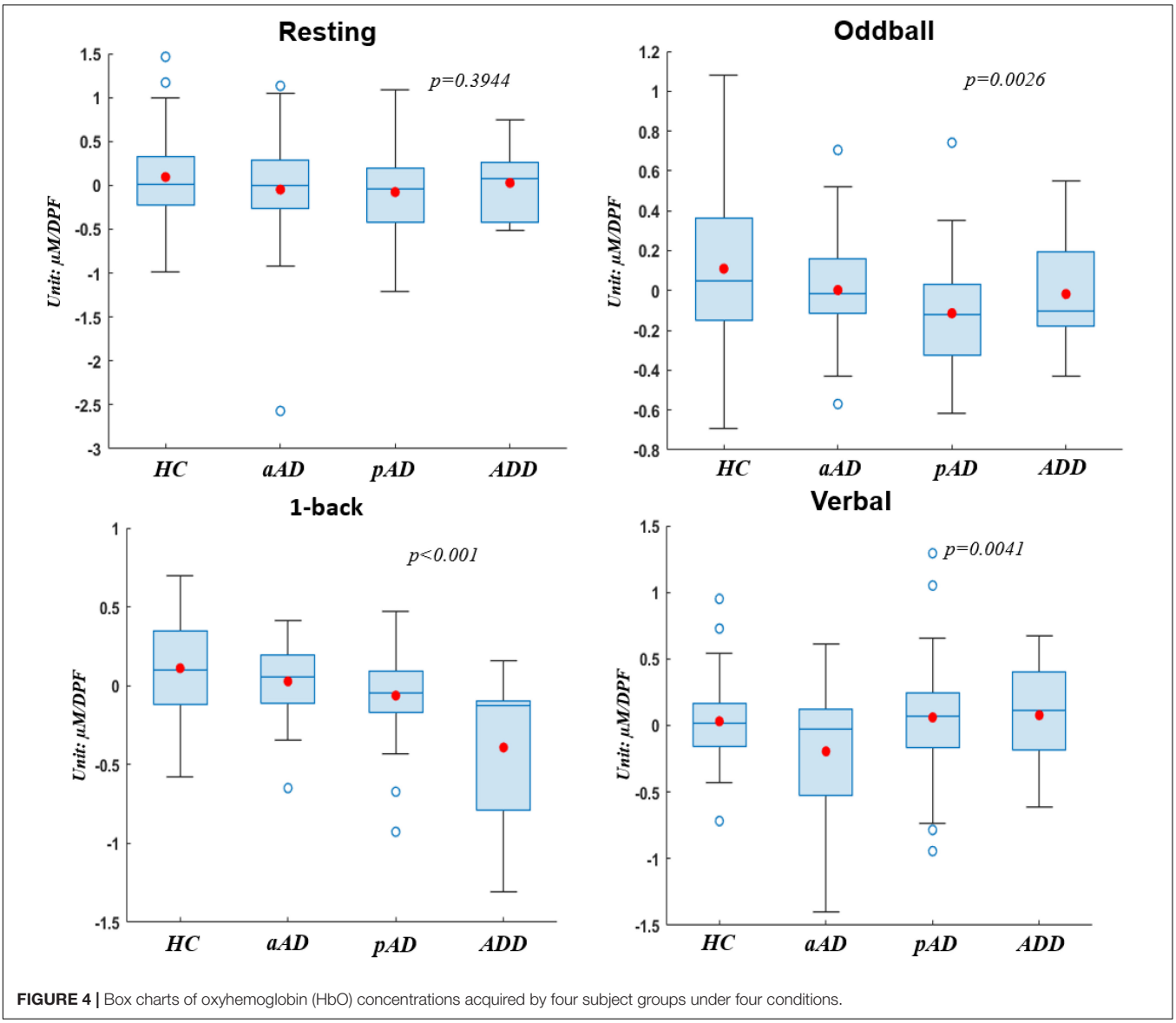

FIGURE 4 | Box charts of oxyhemoglobin (HbO) concentrations acquired by four subject groups under four conditions.

decoded into multiple shorter sequences symbolizing different high-level temporal features.

EXPERIMENTAL RESULTS

Statistical Analysis: The Change of Oxygen Hemoglobin Concentrations

To clearly evaluate the change of hemoglobin concentrations among four subject groups who underwent four experimental stages, we utilized the utmost distinguishable observation from HbO over other hemoglobin types of reduced hemoglobin (HbR) and THb in this part. **Figure 4** presents the box chart distributions of HbO obtained from each experimental protocol to compare HC with each level of AD severity. Note that the typical hemodynamic response of brain activation is accompanied by an increase of HbO concentrations (Mangrum et al., 2018). On each box, the central mark is median, the red filled circle is the mean, the edges of each box are the 25th and 75th percentiles, the whiskers denote the standard error of the mean, and the empty blue circle show outliners. All statistical analyses were performed with a significant level at 0.05 as the cutoff of significance, and each box chart was given a p-value.

Regarding the difference among subject groups, all groups did not show significant differences ($p > 0.05$) during the resting period, whereas there existed significant differences during the other three experimental tasks ($p < 0.05$). The HC group (values were greater than zero) consistently presented much higher hemodynamic activations than other groups. This indicates that normal people had the highest response and had no difficulty when they performed all the brain ability tasks. Meanwhile, on the second place of AD severity level, pAD patients showed lower values than HC and aAD during resting,

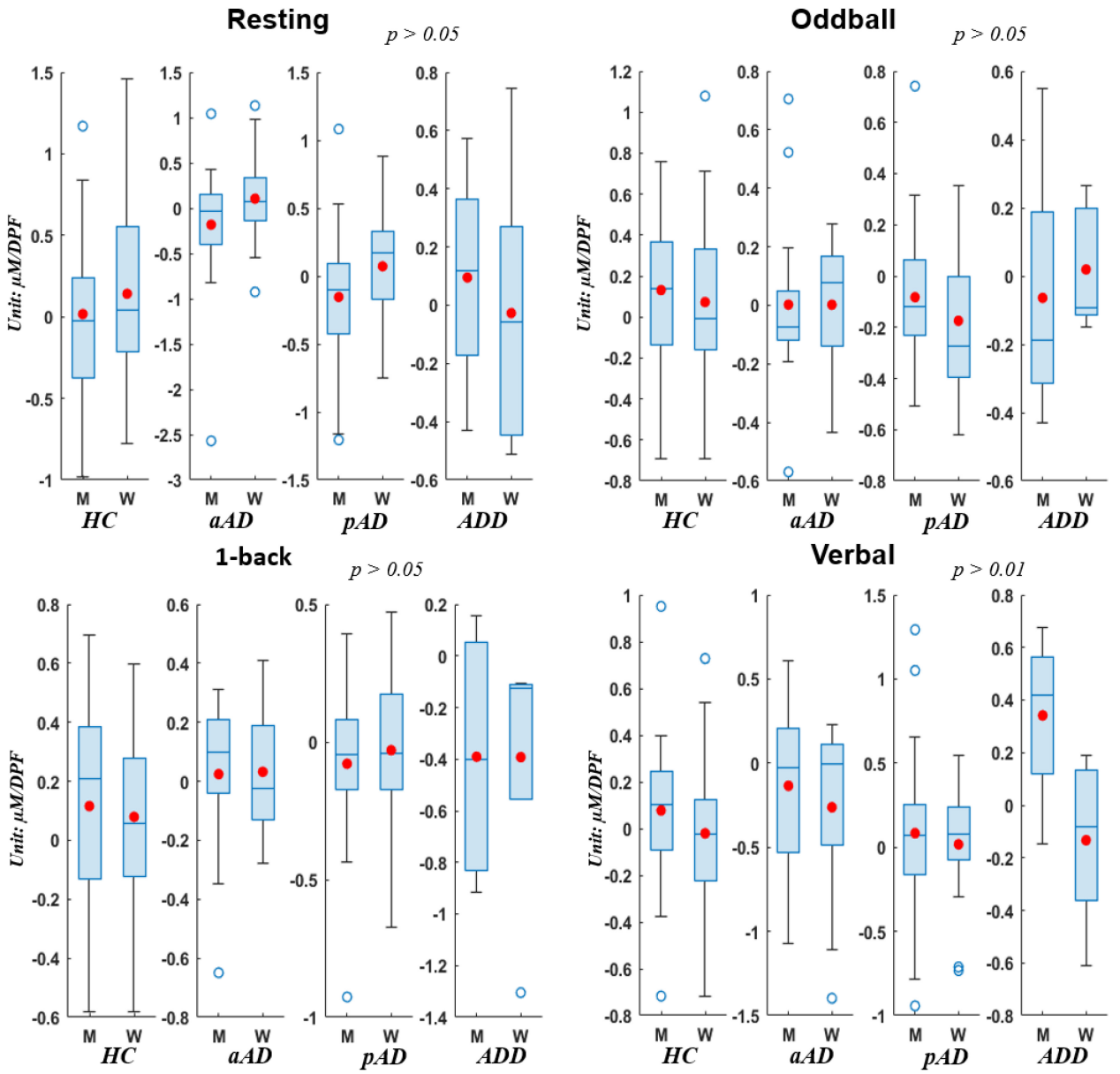

FIGURE 5 | Box charts of HbO concentrations acquired by Men (M) and Women (W) of four subject groups under four conditions.

oddball, and 1-back tasks. This verifies that pAD patients noted lower activations of hemodynamic responses compared with HC and patients with aAD in the resting period, cognitive ability, and memory ability tests. More interestingly, the significantly statistical difference between subject groups did exist during the 1-back task ($p < 0.001$). Each group behaved and responded differently in this memory task, and their response was perfectly correlated with the degree of AD severity. ADD patients, in particular, denoted the lowest hemodynamic activation, followed by pAD, aAD, and HC.

In addition, we testified the change of HbO concentrations via box chart distributions for all conditions when subjects were sub-grouped by gender (see **Figure 5**). In general, there was no significant difference between men and women who underwent all three conditions ($p > 0.05$ for resting, oddball, and 1-back stages) whilst there existed relatively important disparity among gender in the verbal stage. Further, men from all four subject groups presented much higher levels of hemodynamic activations than women in most conditions except the resting period in which men from HC, aAD, and pAD groups showed lower hemodynamic activations. This finding suggested that the frontal changes in HbO concentrations during cognitive, memory, and verbal tasks were stronger in men compared to women. Hence, there was a gender effect on relative hemoglobin changes due to the functional stimulation in our study that achieved similar observations from previous studies on evaluating hemodynamic

TABLE 2 | Comparison of classification metric results as shown by four proposed deep learning (DL) models using original data.

Class	Accuracy			Precision			Recall			F1-Score		
	HbO	HbR	THb	HbO	HbR	THb	HbO	HbR	THb	HbO	HbR	THb
1D-Convolutional Neural Network (1D-CNN)												
HC	0.863	0.853	0.866	0.884	0.862	0.870	0.863	0.853	0.866	0.848	0.852	0.862
aAD	0.826	0.817	0.779	0.847	0.879	0.819	0.826	0.817	0.779	0.806	0.810	0.774
pAD	0.854	0.861	0.876	0.878	0.842	0.912	0.854	0.861	0.876	0.849	0.860	0.875
ADD	0.774	0.731	0.786	0.778	0.864	0.772	0.754	0.711	0.736	0.749	0.710	0.735
Mean	0.829	0.815	0.827	0.847	0.862	0.843	0.824	0.810	0.814	0.813	0.808	0.811
Long Short-term memory (LSTM)												
HC	0.897	0.855	0.875	0.913	0.835	0.903	0.897	0.855	0.875	0.893	0.850	0.874
aAD	0.830	0.836	0.848	0.904	0.907	0.927	0.830	0.836	0.848	0.837	0.835	0.836
pAD	0.867	0.863	0.879	0.887	0.900	0.925	0.867	0.863	0.879	0.858	0.874	0.872
ADD	0.781	0.761	0.795	0.764	0.762	0.747	0.751	0.731	0.735	0.751	0.721	0.732
Mean	0.844	0.829	0.849	0.867	0.851	0.875	0.836	0.821	0.834	0.835	0.820	0.828
Gated Recurrent Units (GRUs)												
HC	0.816	0.765	0.771	0.839	0.850	0.810	0.816	0.765	0.771	0.812	0.760	0.774
aAD	0.792	0.727	0.741	0.811	0.808	0.785	0.792	0.727	0.741	0.770	0.719	0.739
pAD	0.811	0.779	0.805	0.837	0.868	0.849	0.811	0.779	0.805	0.808	0.778	0.805
ADD	0.705	0.695	0.705	0.721	0.764	0.736	0.705	0.695	0.705	0.706	0.697	0.708
Mean	0.781	0.742	0.756	0.802	0.823	0.795	0.781	0.742	0.756	0.774	0.738	0.756
CNN-LSTM												
HC	0.918	0.907	0.917	0.938	0.905	0.918	0.918	0.907	0.917	0.898	0.902	0.913
aAD	0.879	0.855	0.889	0.865	0.872	0.917	0.839	0.855	0.859	0.835	0.853	0.864
pAD	0.880	0.893	0.907	0.902	0.890	0.910	0.880	0.893	0.907	0.876	0.894	0.907
ADD	0.797	0.799	0.793	0.781	0.839	0.771	0.767	0.799	0.753	0.767	0.806	0.746
Mean	0.868	0.864	0.877	0.871	0.877	0.879	0.851	0.864	0.859	0.844	0.864	0.858

activations based on gender inclusion criteria (Shoemaker et al., 2001; Auger et al., 2016).

Classification Performance of Deep Learning Models

To precisely validate the potential of deep learning approaches, the original dataset (three hemoglobin types) was used. Four models were built, including 1D-CNN, stacked LSTM, stacked GRU, and a mixed CNN-LSTM. To enhance the classification performance, we segmented the training signals into nonoverlapping fragments with a specified window length. Each split window was assigned a label associated with its ground truth. Then, we ran eight classifier algorithms to differentiate the HC group from the three levels of AD severity. DL models were then adopted to differentiate the HC group from the three levels of AD severity. Five-fold cross-validation was used to evaluate the model's performance using accuracy-based measurements (Accuracy, Precision, Recall, and F1-score).

In regard to the efficacy of the DL models, all models achieved average accuracies above 80% using all three types of hemoglobin (i.e., accuracies of 82.9, 84.4, 78.1, and 86.8% with HbO type are associated with the performance of 1D-CNN, LSTM, GRU, and CNN-LSTM, respectively). Based on our observations, although LSTM and GRU models had similar concepts of preventing the vanishing gradient problem, their performance in AD multi-classification using fNIRS were exposed differently. GRU was simpler with only two gates, was trained faster, and more computationally efficient, but GRU obtained much lower accuracies than LSTM on all three hemoglobin classes. This indicates that LSTM could outperform GRU since LSTM resembled the theory of remembering longer sequences with a memory unit. This made LSTM more sophisticated and able to produce the network stability in dealing with the fNIRS task, which requires modeling the long-distance relation. In addition, LSTM achieved a higher classification accuracy than 1D-CNN. That is, LSTM, which included less feature compatibility, handled arbitrary input/output lengths, and used its internal memory and time-series information to process the arbitrary sequences of the input, was well-suited for the fNIRS temporal data compared to 1D-CNN.

More importantly, CNN-LSTM outperformed others (86.8, 86.4, and 87.7% corresponding to HbO, HbR, and THb, respectively). CNN and LSTM were not mutually exclusive since

either of them could perform image and time-series classification tasks. The model integration could yield an opportunity to bond the two network types to facilitate effectiveness. A CNN alone would be unable to process fNIRS as the input to be classified as it is visually complicated with the temporal characteristic. Meanwhile, the high-level features that were extracted from long sequences of fNIRS signals by CNN were considerably easy for LSTM to deal with due to its shorter lengths. In detail, the highest accuracy averaged among three hemoglobin types was 87.7% and could occasionally peak to values up to 88.9% at some moments of luck during the training process. This relied on how LSTM weights got initialized at the beginning of training. This means that LSTM was able to correctly identify the movement type using decoded CNN features. Thus, CNN-LSTM was more robust in classifying HC with three different AD stages compared to 1D-CNN and LSTM alone. **Table 2** generally denotes the robust performance of the DL model of CNN-LSTM on all three hemoglobin types with higher means in terms of different classification metrics than those obtained by other DL models. Regarding the effects of subject group types, since we had an extremely imbalanced dataset (for all three types of hemoglobin concentrations), it is predictable that DL models could easily classify the majority classes (i.e., HC and pAD). As a result, we obtained accuracies with higher means and lower SD on HC and pAD, while groups of patients with aAD and patients with ADD achieved lower classification accuracies.

The training's session progress of CNN-LSTM, including Training and Validation accuracies (**Figure 6A** and losses **Figure 6B**), is presented. Initially, the validation loss was slightly similar or lower than the training loss. As long as the validation loss was higher, we would stop the training. In addition, both training and validation accuracies should approach to 1. This demonstrates that the training of CNN-LSTM was exposed to have a stable and accurate performance. As shown in **Figure 6C**, the overall confusion matrix which was obtained visualized the prediction accuracy of CNN-LSTM by comparing the actual and predicted classes. The overall confusion matrix was produced by the full set of actual and predicted classes to visualize the performance and effectiveness of the algorithms. In particular, for each of five splits, we fitted the training data to the model, and the fitted model was used to predict the classes in the current fold. All actual classes and predicted classes were then appended after fivefolds. The model nearly predicted HC correctly (six misclassified samples), aAD (five misclassified samples), pAD class (five misclassified samples), and ADD (three misclassified samples) in the total of 140 patients.

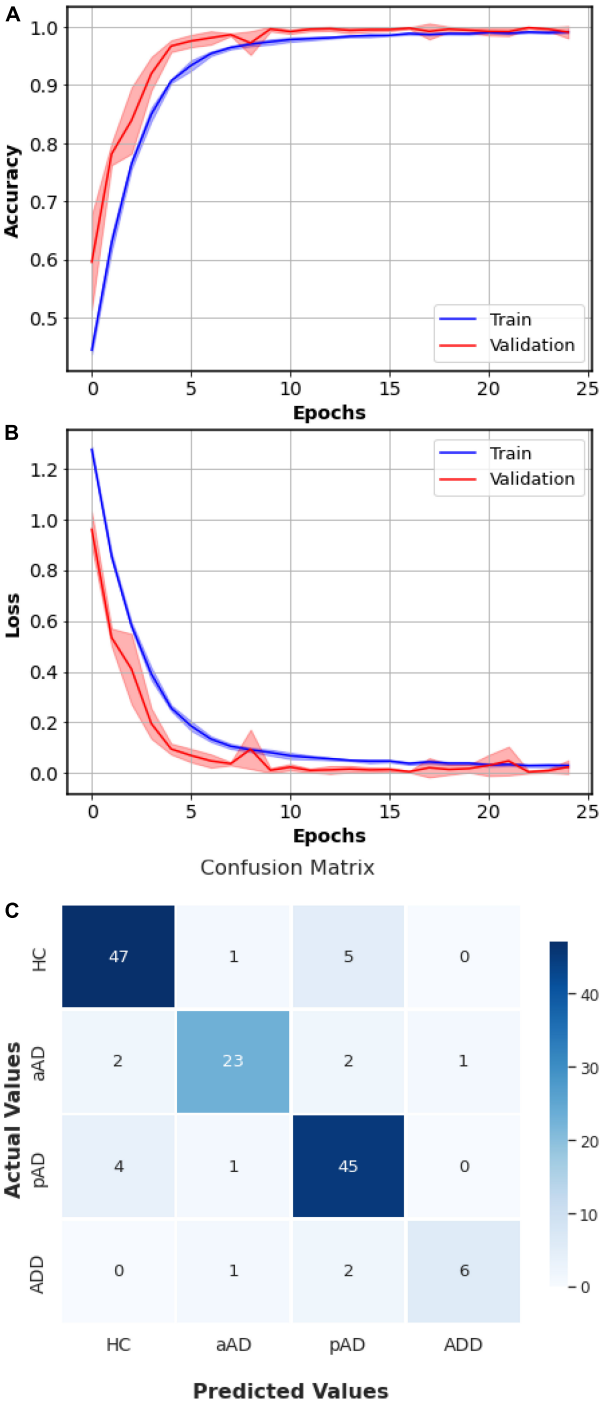

FIGURE 6 | Summarized history of Cognitive Neural Network-Long Short-Term Memory (CNN-LSTM) model's accuracies **(A)** and losses **(B)** and conclusive confusion matrix **(C)** of the fivefold cross validation. In the accuracy and loss curves, the solid lines indicate the mean and the shadow areas represent the ranges over the fivefolds.

Comparison of the Performance of Deep Learning-Based Approaches With Traditional Machine Learning Classifiers

To empirically verify the potential of DL techniques in AD classification using fNIRS, we compared them with the performances of seven conventional ML algorithms, including:

- Linear Discriminant Analysis (LDA) (Li et al., 2006): A set of n samples $\{x_1, x_2, \ldots, x_n\}$was assigned to four AD classes. We calculated the intra-class M_{intra} and inter-class M_{inter} matrices samples (discriminant features) and performed the classification task on the transformed space using the Euclidean distance with the

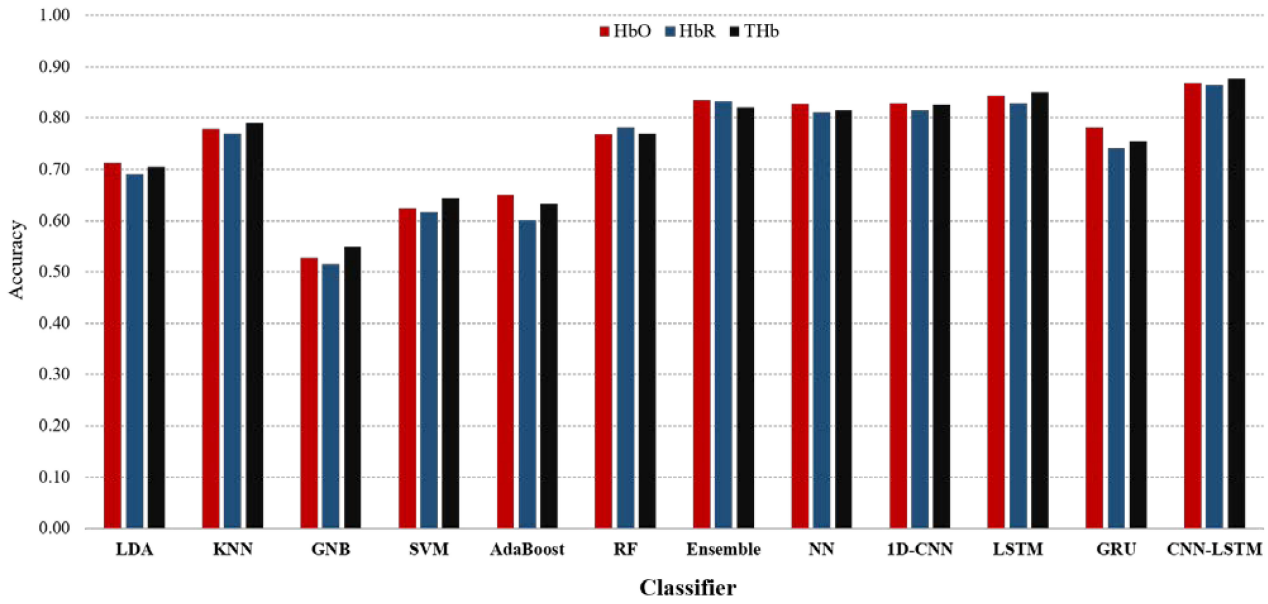

FIGURE 7 | Classification comparisons of accuracy between eight machine learning (ML) classifiers and four DL models using original HB datasets.

200 epochs training. LDA offered an elegant way to reduce dimension and to possibly classify four classes using those discriminant features.

- K-Nearest Neighbors (KNN) (Zhang and Zhou, 2007): $K = 4$ (number of clusters) was assigned as the most optimal value. The KNN algorithm computed the distance between each data point and its cluster centroid and minimized the error. The point located at a minimum distance from the testing point was supposed to belong to the same class. After 200 epochs, KNN could capture the distant proximity for four class-classification. However, its performance gradually slowed down as the number of data points increased.
- Gaussian Naive Bayes (GNB) (Griffis et al., 2016): We computed the prior $P(c)$ and posterior probability $P(x|c)$. Then, the conditional probability for each class (given a test sample) was calculated $P(c_i|x)$ based on the Naive Bayes (NB) theory. The class presenting the highest probability among the four classes was predicted as the target class. GNB was the simplest and easiest algorithm among all conventional ML methods.
- Support Vector Machine (SVM) (Lee and Lee, 2007): To non-linearly separate four classes, SVM was applied to construct the decision hyperplanes whereby the margin of the classifier was maximized. The sigmoid kernel trick was employed to do the data transformation and seek optimal boundaries between classes, although this mimicked the idea of the two-layer perception and generated less errors when dealing with non-linear fNIRS data. The number of epochs was not assigned since SVM would stop training when the margin error was very trivial. In addition, no further optimization was required. The time-consuming and computationally intensive resources were more demanding compared to previous classifiers.
- Adaptive Boosting (AdaBoost) (Hastie et al., 2009): A weak classifier was initially built to generate class labels using unweighted training samples. If any misclassified data point was found during training, the weight of that training point was boosted and updated to the next classifier. The procedure was repeated while each classifier had its own score. The final classifier was defined by the linear combination of 1,000 weak classifiers to boost accuracy. The number of estimators was 200 to control the boosting process, and the higher amount of training time was inevitable.
- Random Forest (RF) (Gray et al., 2013): Starting with the selection of arbitrary samples from the given dataset, a decision tree was built for each sample and produced predicted classes. RF consisted of multiple decision trees that would vote for each class. The class was then selected based on the most votes to be the final prediction. The max depth of the tree was set as 8 and the number of estimators was 200. RF was trained several times, and the random state was fixed to guarantee the same sequence of samples and to achieve a deterministic behavior.
- Ensemble Learning (Kang et al., 2015): Six base classifiers (aforementioned algorithms) were integrated to yield a strong and diverse set of base learners to find the optimal combination. By selecting features from these weak learners via a meta-classifier, it was not easily vulnerable to overfitting. We predicted the final class label using the hard (majority) voting method. The result was explicitly equal or better than the best of base classifiers although, it costed longer training time and features. demanding memory.

- Neural Network (NN) (Amato et al., 2013): Compared to previous ML algorithms, NN could learn non-linear and complex relationships of inputs and outputs to constitute better generalization and classification accuracies. After training NN with different settings of hyper-parameters, we came up with the final set of neurons: an input layer, the set of hidden neurons (100-80-50) organized in the form of three hidden layers, and an output layer (four neurons). We manually selected a ReLU activation function, Adam optimizer, 1e-5 learning rate, and 500-iteration duration. NN was relatively hard to train and required a large number of parameters.

As presented in **Figure 7**, among traditional ML algorithms, the highest accuracy was obtained by Ensemble (82.9% in average), followed by NN, KNN, RF, LDA, SVM, AdaBoost, and GNB (81.8, 77.9, 77.2, 70.3, 63.9, 62.7, and 53.0%, respectively). This indicates that NN was substantially flexible to adopt our adequate data size without considering any feature-engineering steps or structured data and was able to learn high-level features in an end-to-end manner. Meanwhile, most of the features to be identified (to reduce the complexity), split into different parts (to make patterns more tangible), and recombined in the final stage were all preliminary steps for other ML classifiers. However, the obtained result was somewhat poor. In contrast, DL or CNN-LSTM, in particular, validated its robust performance to scale the accuracy up to 87.7%. The results revealed that CNN-LSTM obtained the highest accuracies, tallying with three hemoglobin types, followed by LSTM, NN, 1D-CNN, and Ensemble. In general, the DL algorithms outperform the ML algorithms. Among them, CNN-LSTM elevates accuracy to 3% compared to NN (as the best performance of the ML algorithms).

CONCLUSION AND FUTURE WORKS

Developing an approach to identify individuals before or during the earliest stages of AD, with the hope that the urgent intervention could significantly prevent the onset of clinical symptoms, is desperately needed. Due to somewhat similar symptomologies shared by moderate AD with other neurological disorders, the difficulty of monitoring AD progression that results in diagnostic uncertainties and the subsequent suspension of prompt treatments still remains. Therefore, this present study, on one hand, aimed to present the potential capability of fNIRS in AD analysis. A cohort of 140 participants ranging from HC to three severity levels of patients with AD was included. We verified that there were significant oscillations of hemoglobin concentrations recorded from the prefrontal cortex regions among four subject groups and among gender using an intensive experimental design (cognitive, memory, and verbal fluency tests). On the other hand, a collection of DL architectures demonstrated its potential application to fundamentally advance the search for AD multi-classification using fNIRS signals. Three groups of pathological patients with AD were remarkably distinguished from HC with the top highest accuracy of 90.91 and 90.04% achieved by CNN-LSTM and LSTM, respectively. More importantly, DL could better learn complex and abstract representations of an imbalanced fNIRS dataset and presented its outperformance compared to seven traditional ML classifiers in AD analysis. These findings, thereby, furnish preliminary evidence supporting the potential roles of fNIRS coupled with DL to accurately diagnose and assess the AD severity in future development.

Although this study has yielded the feasibility of utilizing different DL models on the fNIRS dataset to discriminate patients at diverse AD stages, several improvements would be required for the future works. First, it is critically crucial to represent the property of hemodynamic responses of three hemoglobin types of fNIRS signals, such as variance, kurtosis, skewness, or initial dips, to precisely quantify the difference among four groups. Second, since the DL performance counted on the relatively small sample size, which could easily lead to the misclassification problem, either a larger cohort or advanced augmentation techniques used for bio-signal domains should be carried out to extend our present findings. Lastly, although CNN-LSTM was very powerful to result in competitive classification performance, other advanced DL architectures should be developed.

DATA AVAILABILITY STATEMENT

The datasets presented in this article are not readily available because the research was conducted with the research support of the National Research Foundation of Korea and Gwangju Metropolitan City, and approval from the relevant institutions is required. Requests to access the datasets should be directed to JG, james.han.gwak@gmail.com; jgwak@ut.ac.kr.

ETHICS STATEMENT

The studies involving human participants were reviewed and approved by IRB Committee of Gwangju Institute of Science and Technology (from IRB No. 20180629-HR-36-07-01 to 20180629-HR-36-07-05). The patients/participants provided their written informed consent to participate in this study.

AUTHOR CONTRIBUTIONS

TH and JG designed the study and wrote the original draft. MK, JK, and JG designed the experimental protocol. MK and JK designed the NIRS system. BK, KL, and J-IS contributed to the collection of patient samples and related data. MK conducted fNIRS data preprocessing steps. TH conducted the experiments and analyzed the obtained results. JG edited the final manuscript. All authors reviewed the manuscript and gave final approval for the manuscript submission.

FUNDING

This research was supported by the Brain Research Program through the National Research Foundation of Korea (NRF) funded by the Ministry of Science, ICT and Future Planning

(2016M3C7A1905475), the Basic Science Research Program through the National Research Foundation of Korea (NRF) funded by the Ministry of Education (Grant No. NRF-2020R1I1A3074141), "Regional Innovation Strategy (RIS)" through the National Research Foundation of Korea(NRF) funded by the Ministry of Education (MOE) [2021RIS-001(1345341783)], and Healthcare AI Convergence Research & Development Program through the National IT Industry Promotion Agency of Korea (NIPA) funded by the Ministry of Science and ICT (No. S1601-20-1016).

SUPPLEMENTARY MATERIAL

The Supplementary Material for this article can be found online at: https://www.frontiersin.org/articles/10.3389/fnagi.2022.810125/full#supplementary-material

REFERENCES

Alster, P., Madetko, N. K., Koziorowski, D. M., Królicki, L., Budrewicz, S., and Friedman, A. (2019). Accumulation of tau protein, metabolism and perfusion—application and efficacy of positron emission tomography (PET) and single photon emission computed tomography (SPECT) imaging in the examination of progressive supranuclear palsy (PSP) and corticobasal syndrome (CBS). *Front. Neurol.* 10:101. doi: 10.3389/fneur.2019.00101

Alzheimer's Association (2019). 2019 Alzheimer's disease facts and figures. *Alzheimers Dement.* 15, 321–387. doi: 10.1016/j.jalz.2019.01.010

Alzheimer's Disease International (2018). *World Alzheimer Report 2018. The State of the Art of Dementia Research: New Frontiers*. London: Alzheimer's Disease International, 32–36.

Amato, F., López, A., Peña-Méndez, E. M., Vaňhara, P., Hampl, A., and Havel, J. (2013). Artificial neural networks in medical diagnosis. *J. Appl. Biomed.* 11, 47–58.

Arai, H., Takano, M., Miyakawa, K., Ota, T., Takahashi, T., Asaka, H., et al. (2006). A quantitative near-infrared spectroscopy study: a decrease in cerebral hemoglobin oxygenation in Alzheimer's disease and mild cognitive impairment. *Brain Cogn.* 61, 189–194. doi: 10.1016/j.bandc.2005.12.012

Araki, T., Wake, R., Miyaoka, T., Kawakami, K., Nagahama, M., Furuya, M., et al. (2014). The effects of combine treatment of memantine and donepezil on Alzheimer's disease patients and its relationship with cerebral blood flow in the prefrontal area. *Int. J. Geriatr. Psychiatry* 29, 881–889. doi: 10.1002/gps.4074

Auger, H., Bherer, L., Boucher, É, Hoge, R., Lesage, F., and Dehaes, M. (2016). Quantification of extra-cerebral and cerebral hemoglobin concentrations during physical exercise using time-domain near infrared spectroscopy. *Biomed. Opt. Express* 7, 3826–3842. doi: 10.1364/BOE.7.003826

Beishon, L., Haunton, V. J., Panerai, R. B., and Robinson, T. G. (2017). Cerebral hemodynamics in mild cognitive impairment: a systematic review. *J. Alzheimers Dis.* 59, 369–385. doi: 10.3233/JAD-170181

Benerradi, J., Maior, H. A., Marinescu, A., Clos, J., and Wilson, M. L. (2019). "Exploring machine learning approaches for classifying mental workload using fNIRS data from HCI tasks," in *Proceedings of the Halfway to the Future Symposium*, Vol. 2019, Nottingham, 1–11.

Chen, S., and Epps, J. (2013). Automatic classification of eye activity for cognitive load measurement with emotion interference. *Comput. Methods Programs Biomed.* 110, 111–124. doi: 10.1016/j.cmpb.2012.10.021

Cheng, J., Yang, H., and Zhang, J. (2019). Donepezil's effects on brain functions of patients with Alzheimer disease: a regional homogeneity study based on resting-state functional magnetic resonance imaging. *Clin. Neuropharmacol.* 42:42. doi: 10.1097/WNF.0000000000000324

Cicalese, P. A., Li, R., Ahmadi, M. B., Wang, C., Francis, J. T., Selvaraj, S., et al. (2020). An EEG-fNIRS hybridization technique in the four-class classification of Alzheimer's disease. *J. Neurosci. Methods* 336:108618. doi: 10.1016/j.jneumeth.2020.108618

Cummings, J. L., Dubois, B., Molinuevo, J. L., and Scheltens, P. (2013). International work group criteria for the diagnosis of Alzheimer disease. *Med. Clin.* 97, 363–368. doi: 10.1016/j.mcna.2013.01.001

Dutta, K., Krishnan, P., Mathew, M., and Jawahar, C. (2018). "Improving cnn-rnn hybrid networks for handwriting recognition," in *Proceedings of the 2018 16th International Conference on Frontiers in Handwriting Recognition (ICFHR)* (Niagara Falls, NY: IEEE), 80–85.

Fazli, S., Mehnert, J., Steinbrink, J., Curio, G., Villringer, A., Müller, K. R., et al. (2012). Enhanced performance by a hybrid NIRS–EEG brain computer interface. *Neuroimage* 59, 519–529. doi: 10.1016/j.neuroimage.2011.07.084

Feng, C., Elazab, A., Yang, P., Wang, T., Zhou, F., Hu, H., et al. (2019). Deep learning framework for Alzheimer's disease diagnosis via 3D-CNN and FSBi-LSTM. *IEEE Access* 7, 63605–63618. doi: 10.1109/access.2019.2913847

Ferrari, M., and Quaresima, V. (2012). A brief review on the history of human functional near-infrared spectroscopy (fNIRS) development and fields of application. *Neuroimage* 63, 921–935. doi: 10.1016/j.neuroimage.2012.03.049

Ghafoor, U., Yaqub, M. A., and Hong, K.-S. (2019). "Performance evaluation of temporal features for detection of mild cognitive impairment: an fNIRS study," in *Proceedings of the 2019 International Automatic Control Conference (CACS)* (Keelung: IEEE), 1–6. doi: 10.3389/fnagi.2020.00141

Gray, K. R., Aljabar, P., Heckemann, R. A., Hammers, A., Rueckert, D., and Alzheimer's Disease Neuroimaging Initiative (2013). Random forest-based similarity measures for multi-modal classification of Alzheimer's disease. *Neuroimage* 65, 167–175. doi: 10.1016/j.neuroimage.2012.09.065

Griffis, J. C., Allendorfer, J. B., and Szaflarski, J. P. (2016). Voxel-based Gaussian naïve Bayes classification of ischemic stroke lesions in individual T1-weighted MRI scans. *J. Neurosci. Methods* 257, 97–108.

Haapalainen, E., Kim, S., Forlizzi, J. F., and Dey, A. K. (2010). ", Psycho-physiological measures for assessing cognitive load," in *Proceedings of the 12th ACM international conference on Ubiquitous computing*, Copenhagen, 301–310.

Hastie, T., Rosset, S., Zhu, J., and Zou, H. (2009). Multi-class adaboost. *Stat. Interf.* 2, 349–360. doi: 10.4310/sii.2009.v2.n3.a8

He, K., Zhang, X., Ren, S., and Sun, J. (2016). "Deep residual learning for image recognition," in *Proceedings of the IEEE Conference on Computer Vision and Pattern Recognition*, Las Vegas, NV, 770–778.

Ho, T. K. K., Gwak, J., Park, C. M., and Song, J.-I. (2019). Discrimination of mental workload levels from multi-channel fNIRS using deep leaning-based approaches. *IEEE Access* 7, 24392–24403. doi: 10.1109/access.2019.2900127

Hock, C., Villringer, K., Müller-Spahn, F., Wenzel, R., Heekeren, H., Schuh-Hofer, S., et al. (1997). Decrease in parietal cerebral hemoglobin oxygenation during performance of a verbal fluency task in patients with Alzheimer's disease monitored by means of near-infrared spectroscopy (NIRS)—correlation with simultaneous rCBF-PET measurements. *Brain Res.* 755, 293–303. doi: 10.1016/s0006-8993(97)00122-4

Hwang, S. J., Adluru, N., Kim, W. H., Johnson, S. C., Bendlin, B. B., and Singh, V. (2019). Associations between positron emission tomography amyloid pathology and diffusion tensor imaging brain connectivity in pre-clinical Alzheimer's disease. *Brain Connect.* 9, 162–173. doi: 10.1089/brain.2018.0590

Irani, F., Platek, S. M., Bunce, S., Ruocco, A. C., and Chute, D. (2007). Functional near infrared spectroscopy (fNIRS): an emerging neuroimaging technology with important applications for the study of brain disorders. *Clin. Neuropsychol.* 21, 9–37. doi: 10.1080/13854040600910018

Jack, C. R. Jr., Albert, M. S., Knopman, D. S., McKhann, G. M., Sperling, R. A., Carrillo, M. C., et al. (2011). Introduction to the recommendations from the national institute on aging-Alzheimer's association workgroups on diagnostic guidelines for Alzheimer's disease. *Alzheimers Dement.* 7, 257–262.

Kang, S., Cho, S., and Kang, P. (2015). Multi-class classification via heterogeneous ensemble of one-class classifiers. *Eng. Appl. Artif. Intell.* 43, 35–43. doi: 10.1016/j.engappai.2015.04.003

Lancia, S., Cofini, V., Carrieri, M., Ferrari, M., and Quaresima, V. (2018). Are ventrolateral and dorsolateral prefrontal cortices involved in the computerized Corsi block-tapping test execution? An fNIRS study. *Neurophotonics* 5:011019. doi: 10.1117/1.NPh.5.1.011019

LeCun, Y., Bengio, Y., and Hinton, G. (2015). Deep learning. *Nature* 521, 436–444.

Lee, D., and Lee, J. (2007). Domain described support vector classifier for multi-classification problems. *Pattern Recogn.* 40, 41–51.

Lee, G., Nho, K., Kang, B., Sohn, K.-A., and Kim, D. (2019). Predicting Alzheimer's disease progression using multi-modal deep learning approach. *Sci. Rep.* 9:1952. doi: 10.1038/s41598-018-37769-z

Li, R., Nguyen, T., Potter, T., and Zhang, Y. (2019). Dynamic cortical connectivity alterations associated with Alzheimer's disease: an EEG and fNIRS integration study. *Neuroimage Clin.* 21:101622. doi: 10.1016/j.nicl.2018.101622

Li, T., Zhu, S., and Ogihara, M. (2006). Using discriminant analysis for multi-class classification: an experimental investigation. *Knowl. Inf. Syst.* 10, 453–472. doi: 10.1007/s10115-006-0013-y

Liao, J., Li, T., Dong, W., Wang, J., Tian, J., Liu, J., et al. (2019). Reduced prefrontal-temporal cortical activation during verbal fluency task in obsessive-compulsive disorder: a multi-channel near-infrared spectroscopy study. *J. Psychiatr. Res.* 109, 33–40. doi: 10.1016/j.jpsychires.2018.11.006

Lokesh, S., Kumar, P. M., Devi, M. R., Parthasarathy, P., and Gokulnath, C. (2019). An automatic tamil speech recognition system by using bidirectional recurrent neural network with self-organizing map. *Neural Comput. Appl.* 31, 1521–1531. doi: 10.1007/s00521-018-3466-5

Lowe, V. J., Lundt, E. S., Albertson, S. M., Przybelski, S. A., Senjem, M. L., Parisi, J. E., et al. (2019). Neuroimaging correlates with neuropathologic schemes in neurodegenerative disease. *Alzheimers Dement.* 15, 927–939. doi: 10.1016/j.jalz.2019.03.016

Mangrum, W., Hoang, Q. B. P. B., Amrhein, T. J., Maxfield, C. M., Song, A. W., and Merkle, E. (2018). *Duke Review of MRI Principles: Case Review Series E-Book*. Philadelphia, PA: Elsevier Health Sciences.

Mazaheri, A., Segaert, K., Olichney, J., Yang, J. C., Niu, Y. Q., Shapiro, K., et al. (2018). EEG oscillations during word processing predict MCI conversion to Alzheimer's disease. *Neuroimage Clin.* 17, 188–197.

McKhann, G., Drachman, D., Folstein, M., Katzman, R., Price, D., and Stadlan, E. M. (1984). Clinical diagnosis of Alzheimer's disease: report of the NINCDS-ADRDA work group* under the auspices of department of health and human services task force on Alzheimer's disease. *Neurology* 34, 939–939. doi: 10.1212/wnl.34.7.939

Metzger, F. G., Schopp, B., Haeussinger, F. B., Dehnen, K., Synofzik, M., Fallgatter, A. J., et al. (2016). Brain activation in frontotemporal and Alzheimer's dementia: a functional near-infrared spectroscopy study. *Alzheimers Res. Ther.* 8, 1–12. doi: 10.1186/s13195-016-0224-8

Naseer, N., and Hong, K.-S. (2015). fNIRS-based brain-computer interfaces: a review. *Front. Hum. Neurosci.* 9:3.

Nguyen, T., Kim, M., Gwak, J., Lee, J. J., Choi, K. Y., Lee, K. H., et al. (2019). Investigation of brain functional connectivity in patients with mild cognitive impairment: a functional near-infrared spectroscopy (fNIRS) study. *J. Biophotonics* 12:e201800298. doi: 10.1002/jbio.201800298

Oh, K., Chung, Y.-C., Kim, K. W., Kim, W.-S., and Oh, I.-S. (2019). Classification and visualization of Alzheimer's disease using volumetric convolutional neural network and transfer learning. *Sci. Rep.* 9:18150.

Perpetuini, D., Bucco, R., Zito, M., and Merla, A. (2017). Study of memory deficit in Alzheimer's disease by means of complexity analysis of fNIRS signal. *Neurophotonics* 5:011010. doi: 10.1117/1.NPh.5.1.011010

Plis, S. M., Hjelm, D. R., Salakhutdinov, R., Allen, E. A., Bockholt, H. J., Long, J. D., et al. (2014). Deep learning for neuroimaging: a validation study. *Front. Neurosci.* 8:229. doi: 10.3389/fnins.2014.00229

Ruder, S. (2016). An overview of gradient descent optimization algorithms. *arXiv* [preprint] arXiv:1609.04747,

Shi, X., Wang, T., Wang, L., Liu, H., and Yan, N. (2019). "Hybrid convolutional recurrent neural networks outperform CNN and RNN in task-state EEG detection for Parkinson's disease," in *Proceedings of the 2019 Asia-Pacific Signal and Information Processing Association Annual Summit and Conference (APSIPA ASC)* (Lanzhou: IEEE), 939–944.

Shoemaker, J. K., Hogeman, C. S., Khan, M., Kimmerly, D. S., and Sinoway, L. I. (2001). Gender affects sympathetic and hemodynamic response to postural stress. *Am. J. Physiol. Heart Circ. Physiol.* 281, H2028–H2035. doi: 10.1152/ajpheart.2001.281.5.H2028

Simonyan, K., and Zisserman, A. (2014). Very deep convolutional networks for large-scale image recognition. *arXiv* [preprint] arXiv:1409.1556,

Sirpal, P., Kassab, A., Pouliot, P., Nguyen, D. K., and Lesage, F. (2019). fNIRS improves seizure detection in multimodal EEG-fNIRS recordings. *J. Biomed. Opt.* 24:051408. doi: 10.1117/1.JBO.24.5.051408

Solovey, E. T., Zec, M., Garcia Perez, E. A., Reimer, B., and Mehler, B. (2014). "Classifying driver workload using physiological and driving performance data: two field studies," in *Proceedings of the SIGCHI Conference on Human Factors in Computing Systems*, Toronto, ON, 4057–4066.

Sonkaya, A. R. (2018). The use of functional near infrared spectroscopy technique in neurology. *NeuroQuantology* 16:87. doi: 10.1255/jnirs.266

Suk, H.-I., and Shen, D. (2013). "Deep learning-based feature representation for AD/MCI classification," in *Proceedings of the International Conference on Medical Image Computing and Computer-Assisted Intervention* (Berlin: Springer), 583–590. doi: 10.1007/978-3-642-40763-5_72

Swinehart, D. F. (1962). The beer-lambert law. *J. Chem. Educ.* 39:333.

Tsiouris, KM, Pezoulas, V. C., Zervakis, M., Konitsiotis, S., Koutsouris, D. D., and Fotiadis, D. I. (2018). A long short-term memory deep learning network for the prediction of epileptic seizures using EEG signals. *Comput. Biol. Med.* 99, 24–37. doi: 10.1016/j.compbiomed.2018.05.019

Veitch, D. P., Weiner, M. W., Aisen, P. S., Beckett, L. A., Cairns, N. J., Green, R. C., et al. (2019). Understanding disease progression and improving Alzheimer's disease clinical trials: recent highlights from the Alzheimer's disease neuroimaging initiative. *Alzheimers Dement.* 15, 106–152. doi: 10.1016/j.jalz.2018.08.005

Vermeij, A., Kessels, R. P., Heskamp, L., Simons, E. M., Dautzenberg, P. L., and Claassen, J. A. (2017). Prefrontal activation may predict working-memory training gain in normal aging and mild cognitive impairment. *Brain Imaging Behav.* 11, 141–154. doi: 10.1007/s11682-016-9508-7

Vieira, S., Pinaya, W. H., and Mechelli, A. (2017). Using deep learning to investigate the neuroimaging correlates of psychiatric and neurological disorders: methods and applications. *Neurosci. Biobehav. Rev.* 74, 58–75. doi: 10.1016/j.neubiorev.2017.01.002

Wang, S., Zhang, Y., Liu, G., Phillips, P., and Yuan, T.-F. (2016). Detection of Alzheimer's disease by three-dimensional displacement field estimation in structural magnetic resonance imaging. *J. Alzheimers Dis.* 50, 233–248. doi: 10.3233/JAD-150848

Wright, A., Damskägg, E.-P., and Välimäki, V. (2019). "Real-time black-box modelling with recurrent neural networks," in *Proceedings of the 22nd International Conference on Digital Audio Effects (DAFx-19)*, Birmingham.

Yang, D., and Hong, K.-S. (2019). "Comparison of neural biomarker assessment methods for early detection of Alzheimer's disease," in *Proceedings of the 2019 International Conference on Mechatronics, Robotics and Systems Engineering (MoRSE)* (Bali: IEEE), 34–39.

Yang, Y., Wu, Q., Qiu, M., Wang, Y., and Chen, X. (2018). "Emotion recognition from multi-channel EEG through parallel convolutional recurrent neural network," in *Proceedings of the 2018 International Joint Conference on Neural Networks (IJCNN)* (Lanzhou: IEEE), 1–7.

Yoo, S.-H., Woo, S.-W., and Amad, Z. (2018). "Classification of three categories from prefrontal cortex using LSTM networks: fNIRS study," in *Proceedings of the 2018 18th International Conference on Control, Automation and Systems (ICCAS)* (PyeongChang: IEEE), 1141–1146.

Yücel, M. A., Selb, J. J., Huppert, T. J., Franceschini, M. A., and Boas, D. A. (2017). Functional near infrared spectroscopy: enabling routine functional brain imaging. *Curr. Opin. Biomed. Eng.* 4, 78–86. doi: 10.1016/j.cobme.2017.09.011

Zeller, J. B., Herrmann, M. J., Ehlis, A.-C., Polak, T., and Fallgatter, A. J. (2010). Altered parietal brain oxygenation in Alzheimer's disease as assessed with near-infrared spectroscopy. *Am. J. Geriatr. Psychiatry* 18, 433–441. doi: 10.1097/JGP.0b013e3181c65821

Zhang, D., Yao, L., Zhang, X., Wang, S., Chen, W., and Boots, R. (2018). "Cascade and parallel convolutional recurrent neural networks on EEG-based intention recognition for brain computer interface," in *Proceedings of the The 32nd AAAI Conference on Artifical Intelligence (AAAI-18)*, New Orleans, LA, 1703–1710. doi: 10.1109/TCYB.2019.2905157

Zhang, G., Davoodnia, V., Sepas-Moghaddam, A., Zhang, Y., and Etemad, A. (2019). Classification of hand movements from EEG using a deep attention-based LSTM network. *IEEE Sensors J.* 20, 3113–3122. doi: 10.1109/jsen.2019.2956998

Zhang, M.-L., and Zhou, Z.-H. (2007). ML-KNN: a lazy learning approach to multi-label learning. *Pattern Recogn.* 40, 2038–2048. doi: 10.1016/j.patcog.2006.12.019

Conflict of Interest: The authors declare that the research was conducted in the absence of any commercial or financial relationships that could be construed as a potential conflict of interest.

Publisher's Note: All claims expressed in this article are solely those of the authors and do not necessarily represent those of their affiliated organizations, or those of the publisher, the editors and the reviewers. Any product that may be evaluated in this article, or claim that may be made by its manufacturer, is not guaranteed or endorsed by the publisher.

Copyright © 2022 Ho, Kim, Jeon, Kim, Kim, Lee, Song and Gwak. This is an open-access article distributed under the terms of the Creative Commons Attribution License (CC BY). The use, distribution or reproduction in other forums is permitted, provided the original author(s) and the copyright owner(s) are credited and that the original publication in this journal is cited, in accordance with accepted academic practice. No use, distribution or reproduction is permitted which does not comply with these terms.

frontiers | Frontiers in Aging Neuroscience

ORIGINAL RESEARCH
published: 30 May 2022
doi: 10.3389/fnagi.2022.844066

Effects of Sex on the Relationship Between Apolipoprotein E Gene and Serum Lipid Profiles in Alzheimer's Disease

Jiajia Fu[1], Yan Huang[2], Ting Bao[2], Ruwei Ou[1], Qianqian Wei[1], Yongping Chen[1], Jing Yang[1], Xueping Chen[1] and Huifang Shang[1]**

[1] *Laboratory of Neurodegenerative Disorders, National Clinical Research Center for Geriatrics, Department of Neurology, West China Hospital, Sichuan University, Chengdu, China,* [2] *Health Management Center, West China Hospital, Sichuan University, Chengdu, China*

OPEN ACCESS

Edited by:
Kuangyu Shi,
University of Bern, Switzerland

Reviewed by:
Nutjaree Jeenduang,
Walailak University, Thailand
Safaa Tayel,
Menoufia University, Egypt

***Correspondence:**
Xueping Chen
chenxueping0606@sina.com
Huifang Shang
hfshang2002@163.com

Specialty section:
This article was submitted to Alzheimer's Disease and Related Dementias, a section of the journal Frontiers in Aging Neuroscience

Received: *27 December 2021*
Accepted: *08 April 2022*
Published: *30 May 2022*

Citation:
Fu J, Huang Y, Bao T, Ou R, Wei Q, Chen Y, Yang J, Chen X and Shang H (2022) Effects of Sex on the Relationship Between Apolipoprotein E Gene and Serum Lipid Profiles in Alzheimer's Disease. Front. Aging Neurosci. 14:844066. doi: 10.3389/fnagi.2022.844066

Background: Sex is an important factor in studying the relationship between the *APOE* gene, lipid profiles, and AD. However, few studies have focused on the effect of sex on lipids in AD and normal controls with different *APOE* genes.

Materials and Methods: A total of 549 participants, including 298 AD patients and 251 body mass index (BMI)-matched healthy controls (HCs), were enrolled. Lipid profiles and *APOE* genes in both AD patients and HCs were determined.

Results: (1) TC and LDL were higher in AD patients than in HCs, only in *APOEε4* carrying populations, but not in non-carrying populations. (2) TC and LDL were higher in *APOEε4* allele carriers than in non-carriers, only in AD populations, but not in HCs. (3) The TC of *APOEε2* carriers was lower than that of non-carriers in the male AD population, but not in the female AD population, female HCs, and male HCs. (4) The increased LDL level may increase the risk of AD in female people carrying *APOEε 4*.

Conclusion: The TC and LDL levels of *APOEε4* carriers were higher than those of non-carriers, and the effect was more significant in the female AD population. The TC levels in *APOEε2* carriers were lower than those in non-carriers, which was more significant in the male AD population.

Keywords: Alzheimer's disease, lipid profiles, sex, *APOEε4*, *APOEε2*

INTRODUCTION

Alzheimer's disease (AD) is the most common neurodegenerative dementia disease which is characterized by insidious onset, progressive memory failure, cognitive impairment, and behavioral and psychological manifestations. The etiology and pathogenesis of AD are still unclear, and the development of AD could be the result of interaction between multiple genetic and environmental risk factors (Poirier et al., 2014). The most specific genetic risk factor for late-onset AD is the Apolipoprotein (*APO*) *E* gene (Corder et al., 1993). The ε2, ε3, and ε4 alleles of the *APOE* gene,

located on chromosome 19q13.2, constitute a common polymorphism in most populations (Corder et al., 1993). The *APOEε4* allele is shown to be associated with a higher risk of AD and greater disease severity, whereas the *APOEε2* allele has an opposite role (Corder et al., 1993). Patients with AD have a higher frequency of *APOEε4* allele than control participants (Isbir et al., 2001). An epidemiology study showed that the frequency of the *APOEε4* allele varied drastically among different populations; it occurs in about 25% African Americans, 15% Caucasians, and 7% Chinese (Corbo and Scacchi, 1999).

There are plenty of studies focusing on the correlation between dyslipidemia and AD, but most of them are trying to explore the effect of cholesterol (TC) on AD. A previous study has shown that high serum TC level in middle age is a risk factor for AD and AD-related pathology (Anstey et al., 2008). Cerebrovascular risk factors, such as high cholesterol, had a mild combined effect on the earlier onset of AD (de Oliveira et al., 2014). High TC level in the brain was proven to play an important role in the process of amyloid-β (Aβ)-induced AD (Refolo et al., 2000). TC and low-density lipoprotein (LDL) were shown to be involved in the pathogenesis of AD by increasing amyloid accumulation and disrupting the cell cycle (Wu et al., 2019), but late-life hypercholesterolemia might also slow cognitive decline, particularly when in combination with other cerebrovascular risk factors, possibly due to enhanced cerebral perfusion (de Oliveira et al., 2015). However, a longitudinal study did not show significant associations of high cholesterol with cognitive or functional changes in AD (de Oliveira et al., 2018). Some studies have found that serum HDL levels were lower in AD patients (Merched et al., 2000), and were inversely associated with cognitive impairment, but opposite reports also existed (Launer et al., 2001).

The lipid profiles were also found to be associated with the *APOE*, but the results were inconsistent (Isbir et al., 2001; Hoshino et al., 2002). Previous studies found that the levels of LDL and TC in *APOEε4* carriers increased or tended to be increased compared with non-carriers (Sun et al., 2014). However, Isbir et al. (2001) showed a decreasing trend, and Hall et al. (2006) found no statistical differences. It was also reported that AD patients carrying the *APOEε2* allele had lower TC and LDL levels and higher HDL levels than AD patients carrying the *APOEε4* allele (Sabbagh et al., 2006), but other studies did not find statistical significance (Isbir et al., 2001). de Oliveira et al. (2017) considered that *APOEε4 non*-carriers might enhance lipid availability to protect neuronal membranes, thus overcoming their supposed dysfunction in cholesterol metabolism, while *APOEε4* carriers have inefficient neural repair mechanisms.

In addition, sex can affect *APOEε4* allele-associated cognitive impairment. The risk of AD or MCI conversion was higher in female *APOEε4* allele carriers than that in male *APOEε4* allele carriers (Kim et al., 2015). There was a stronger correlation between *APOEε4* and CSF Tau levels in women than in men (Liu et al., 2021). The gender-specific *APOE* haplotype interactions can alter the response to anticholinesterase therapy (MacGowan et al., 1998). Among the females treated with anticholinesterase, the individuals carrying the *APOEε4* allele presented a poor response to treatment than those carrying other *APOE* alleles, and the anticholinesterase reactivity in the males was superior to that in the females (MacGowan et al., 1998). Some studies found that TC was significantly higher in women with AD (Oliveira et al., 2016). However, few studies have focused on the effect of sex on lipids in AD and normal controls with different *APOE* genes.

Therefore, sex is an important factor affecting the interaction between the *APOE* gene and lipid profiles in AD. The sex-related difference is also crucial for precision therapy. Few studies have clearly elucidated the effect of sex on lipids in AD and normal controls with different *APOE* genes. In order to explore the relationship between lipid profiles, *APOE* gene, and sex in AD, we examined the lipid profiles in AD patients and healthy controls (HCs) with different *APOE* alleles and analyzed the effect of sex on lipid profiles in both AD patients and HCs with different *APOE* genes.

MATERIALS AND METHODS

Participants

Alzheimer's disease patients admitted to West China Hospital of Sichuan University from January 2020 to January 2021 were recruited, and trained doctors diagnosed AD according to the NINCDS-ADRDA and DSM V (McKhann et al., 1984; dermann and Fleischhacker, 2016). Detailed medical history-taking and physical examination were performed. Individuals without any disease in the central nervous system and normal cognitive function were recruited as healthy controls (HCs) during the same period, and they were matched for body mass index (BMI) to the AD group. The patients received the standardized assessments, including the Mini-mental State Examination (MMSE), the Montreal Cognitive Assessment (MoCA), and magnetic resonance imaging (MRI). AD patients with MMSE scores higher than 25 were excluded. Since MMSE has shown not to be adequate in detecting MCI and clinical signs of dementia, and MoCA is superior to MMSE in identifying MCI (Pinto et al., 2019), HCs with MoCA scores higher than 22 were included in the present study. All participants with vascular dementia (VaD), cardiopathy, hypertension, diabetes mellitus, demyelinating diseases, white matter lesions, obesity, fatty liver and other diseases closely related to blood lipids were excluded. The study was approved by the ethics committee of West China Hospital of Sichuan University. All AD patients and control participants gave their written informed consent to participate in the investigation.

Measurements

All blood samples were routinely collected in the early morning when patients were fasting. The serum lipid profiles, including TC, triglycerides (TG), LDL, and HDL, were measured by homogeneous enzyme colorimetry on Roche/Hitachi Cobas C analyzer. DNA was isolated from blood cells.

Samples were amplified by the polymerase chain reaction amplified samples (ABI 7500 FAST, Applied Biosystems, Thermo Fisher Scientific, Waltham, MA, United States). *APOE* haplotypes were determined according to the manufacturer's instruction using an *APOE* haplotype determinating kit (Memorigen

Biotech, Xiamen, China). The kit is based on fluorescent PCR technology, using three pairs of detection reagents that can specifically recognize two single nucleotide polymorphisms (RS429358 and RS7412) of *APOE* gene type 2, 3 and 4, respectively, to identify and amplify the samples. When the sample contained *APOE* allele matched with the amplification system, PCR amplification reaction would take place in the system. The exonuclease activity at the 5–3 end of DNA polymerase would degrade the fluorescent-labeled DNA molecular probe by enzyme digestion. After degradation by enzyme digestion, the probe could be stimulated with a fluorescence signal and detected by the monitoring system.

Statistical Analyses

SPSS software 26.0 version (IBM, Armonk, NY, United States) was used for data analysis. The χ^2 test was used to compare allele frequencies among groups. An independent *t*-test was used to compare lipid profiles in patients with different *APOE* haplotypes or sex. For those groups with significant age differences, age was adjusted by covariance analysis, for non-normal distribution data were used for non-parametric ANOVA (Kruskal–Wallis) and a non-parametric Mann–Whitney *U* test. Logistic regression was used to analyze the influences of various variables on the risk of disease. Two-tailed $p < 0.05$ was considered statistically significant. Table data are expressed as the means ± standard deviation (SD), and image values are expressed as the mean (standard error).

RESULTS

A total of 549 participants (298 AD patients, 251 HCs) were included in the study. The mean (SD) age of AD patients was 76.07 (7.12) years old, and the HCs were 65.85 (11.33) years old, so the age factor was adjusted in the subsequent lipid analyses (**Supplementary Material 1** – adjusting for age). There were 113 male (185 female) people in AD and 103 male (148 female) people in HCs. In AD patients, the mean (SD) course of the disease was 2.5 (2.52) years, the mean (SD) of MMSE score was 18 (5.21), the mean (SD) of MOCA was 12.48 (3.56) (**Table 1**). There was no significant difference in statin use between the AD and the HCs groups (**Table 1**). Additional adjustments for the statin use did not change the statistical significance of the results of lipid analyses (**Supplementary Material 2** – adjusting for age and the stain use).

APOE Gene Analysis in Alzheimer's Disease Patients and Healthy Controls

There were significant differences in the haplotype frequency of *APOEε4*, *APOEε2,* and *APOEε3* between the AD and HCs (**Table 1**). A significantly higher proportion of *APOEε4* carriers and a lower proportion of *APOEε2* carriers were found in the AD group than in the HCs (**Table 1**). There was no significant difference in the proportion of *APOEε3* carriers between AD group and HCs group, and the state of *APOEε3* allele carrying had no effect on lipid profiles (**Supplementary Material 3**).

Comparison of Lipid Profiles Between Alzheimer's Disease Patients and Healthy Controls

The levels of TG were insignificant between AD and HCs groups (**Figure 1**). The levels of TC and LDL in the AD group were higher than those in the HCs group (**Figures 2A**, **3A**). In the subgroup analysis based on *APOE* alleles, AD patients carrying *APOEε4* had higher levels of TC and LDL than HCs with *APOEε4* allele; AD patients without *APOEε2* allele had increased TC and LDL levels than HCs without *APOEε2* allele (**Figures 2B**, **3B**). In subgroup analysis based on sex, TC and LDL levels in the AD group were significantly higher than in the HCs group in both sexes (**Figures 2B**, **3B**). A subgroup analysis combined sex and *APOE* haplotypes showed that TC and LDL levels were higher in AD patients than in HCs, which were only found in female *APOEε4* carriers or male *APOEε2* non-carriers (**Figures 2D**, **3D**). In addition, serum HDL level in the AD group was higher than those in the HCs group (**Figure 4A**). Subgroup analysis showed that the change of HDL level was found in populations with *APOEε4* allele and without *APOEε2* allele (**Figure 4B**), as well as in male non-*APOEε2* carriers and male *APOEε4* carriers (**Figure 4D**).

Comparison of Lipid Profiles Between *APOEε4* Allele-Carriers and Non-*APOEε4* Allele-Carriers

The levels of TC and LDL in the *APOEε4* carriers were higher than those in non-*APOEε4* carriers (**Figures 2A**, **3A**). In the subgroup analysis based on disease, we found that AD patients with *APOEε4* had significantly higher levels of TC and LDL than AD patients without *APOEε4* (**Figures 2B**, **3B**). No differences in the levels of TC and LDL between HCs with and without *APOEε4* (**Figures 2B**, **3B**). Furthermore, In the subgroup analysis based on sex, significantly higher levels of TC and LDL were only found in female AD patients with *APOEε4* than without *APOEε4* female AD patients (**Figures 2D**, **3D**). However, no differences were found between male AD patients with and without *APOEε4* (**Figures 2D**, **3D**).

Comparison of Lipid Profiles Between *APOEε2* Allele-Carriers and Non-*APOEε2* Allele-Carriers

The levels of TC and LDL in the *APOEε2* carriers were lower than those in non-*APOEε2* carriers (**Figures 2A**, **3A**). In the subgroup analysis based on sex and disease, similar changes in LDL levels were found in almost all subgroups except the female control population (**Figures 3B–D**). The TC levels were lower in AD patients with the *APOEε2* allele than in AD patients without the *APOEε2* allele, but no such change was observed in the HCs (**Figure 2B**). In addition, the TC of *APOEε2* carriers was lower than that of non-carriers in the male AD population, but there was no such change in the female AD population, female HCs, and male HCs (**Figure 2D**).

Comparison of Lipid Profiles Between the Male and the Female

The TC, HDL, and LDL levels in the female population were higher than the male population (**Figures 2A**, **3A**, **4A**). In order to exclude the effect of disease and *APOE* gene, subgroup analyses were performed, and the results showed that sex had similar effects on TC and LDL in AD patients, *APOEε4* carriers, and *APOEε2* non-carriers (**Figures 2B,C**, **3B,C**). In the control participants and *APOEε4* non-carriers, TC and HDL in the female population were higher than the male population (**Figures 2B,C**, **4B,C**).

Complex Interactions Exist Between Alzheimer's Disease, *APOE* Haplotypes, Lipid Profiles, and Sex

Age, gender, disease course of AD, *APOEε4,* and blood lipids level were considered influencing factors for Logistics regression analysis, and we found that age and *APOE4* were important risk factors, while the blood lipids were not significantly related with AD. When TG, TC, HDL, and LDL were taken as targets to study the relationship with AD, no correlation was found between lipid profiles and AD through logistics regression analysis. However, in the subgroup analysis, adjusted *APOE* and sex, we found that LDL increased the risk of AD in females with the *APOEε4* allele, that is, for every 1 unit increase in LDL, the risk of AD increased 898.46 times in the female population with *APOEε4* ($P = 0.04$). Therefore, the increased LDL level may increase the risk of AD in female people carrying *APOEε 4*.

DISCUSSION

This study found that LDL and TC serum levels in AD patients were higher than those in HCs, consistent with previous studies (Wang et al., 2020). In addition, we found higher HDL levels in AD patients compared to controls. A prospective study published in 2021 reported very high serum HDL cholesterol levels as

TABLE 1 | *APOE* gene and sex distribution in AD group and HCs group (mean ± standard deviation).

		AD (*n* = 298)	HCs (*n* = 251)	t/χ^2	*p*-value
Age at examination, year		76.07 ± 7.12	65.85 ± 11.33	12.38	< 0.001
Course of the disease, year		2.54 ± 2.52			
Education (>12 yearsr/<12 year)		134/164	131/120	2.85	0.09
MoCA scores		12.48 ± 5.21	24.00 ± 1.48	21.43	< 0.001
MMSE scores		18 ± 3.56			
APOEε4	*APOEε4* +, n (%)	149 (50.00%)	38 (20.30%)	73.73	< 0.001
APOEε2	*APOEε2* +, n (%)	18 (6.00%)	53 (21.10%)	27.50	< 0.001
APOEε3	*APOEε3* +, n (%)	280 (93.96%)	236 (94.02%)	0.00	0.975
Sex	Male, n (%)	113 (37.92%)	103 (41.04%)	0.55	0.457
	Female, n (%)	185 (62.08%)	148 (58.96%)	0.55	0.457
Subtypes				79.340	< 0.001
	ε2/ε2, ε2/ε3, ε3/ε3, n (%)	149 (41.20%)	213 (58.80%)	73.72	< 0.001
	ε2/ε4, ε3/ε4, n (%)	131 (44.00%)	35 (13.90%)	58.19	< 0.001
	ε4/ε4, n (%)	18 (6.00%)	3 (1.20%)	8.69	0.003
APOE haplotypes				99.46	< 0.001
	ε2/ε2, n (%)	0	5 (0.90%)	5.99	0.02
	ε2/ε3, n (%)	18 (6.00%)	41 (16.30%)	15.05	< 0.001
	ε3/ε3, n (%)	131 (44.00%)	167 (66.50%)	27.98	< 0.001
	ε2/ε4, n (%)	0	7 (2.80%)	8.46	0.004
	ε3/ε4, n (%)	131 (44.00%)	28 (11.20%)	71.26	< 0.001
	ε4/ε4, n (%)	18 (6.00%)	3 (1.20%)	8.69	0.003
The stain use		12 (4.00%)	8 (3.20%)	0.274	0.601
	APOEε4 +	7 (4.70%)	2 (5.30%)	0.021	0.884
	APOEε4 -	5 (3.40%)	6 (2.80%)	0.086	0.769
	APOEε2 +	1 (5.60%)	1 (1.90%)	0.661	0.416
	APOEε2 -	11 (3.90%)	7 (3.50%)	0.049	0.824
	Male	5 (4.40%)	3 (2.90%)	0.345	0.557
	Female	7 (3.80%)	5 (3.40%)	0.039	0.844

AD, Alzheimer's disease; HCs, healthy controls; APOEε4+, APOEε4 carriers; APOEε2+, APOEε2 carriers; APOEε3+, APOEε3 carriers; MMSE, the Mini-mental State Examination; MoCA, the Montreal Cognitive Assessment.

APOEε2 carriers included APOEε2/2, APOEε2/3, and APOEε2/4, and APOEε2 non-carriers included APOEε3/3, APOEε3/4, and APOEε 4/4.

APOEε3 carriers included APOEε2/3, APOEε3/3, and APOEε3/4, and APOEε3 non-carriers included APOEε2/2, APOEε2/4, and APOEε 4/4.

APOEε4 carriers included APOEε2/4, APOEε3/4, and APOEε4/4, and APOEε4 non-carriers included APOEε2/2, APOEε2/3, and APOEε 3/3.

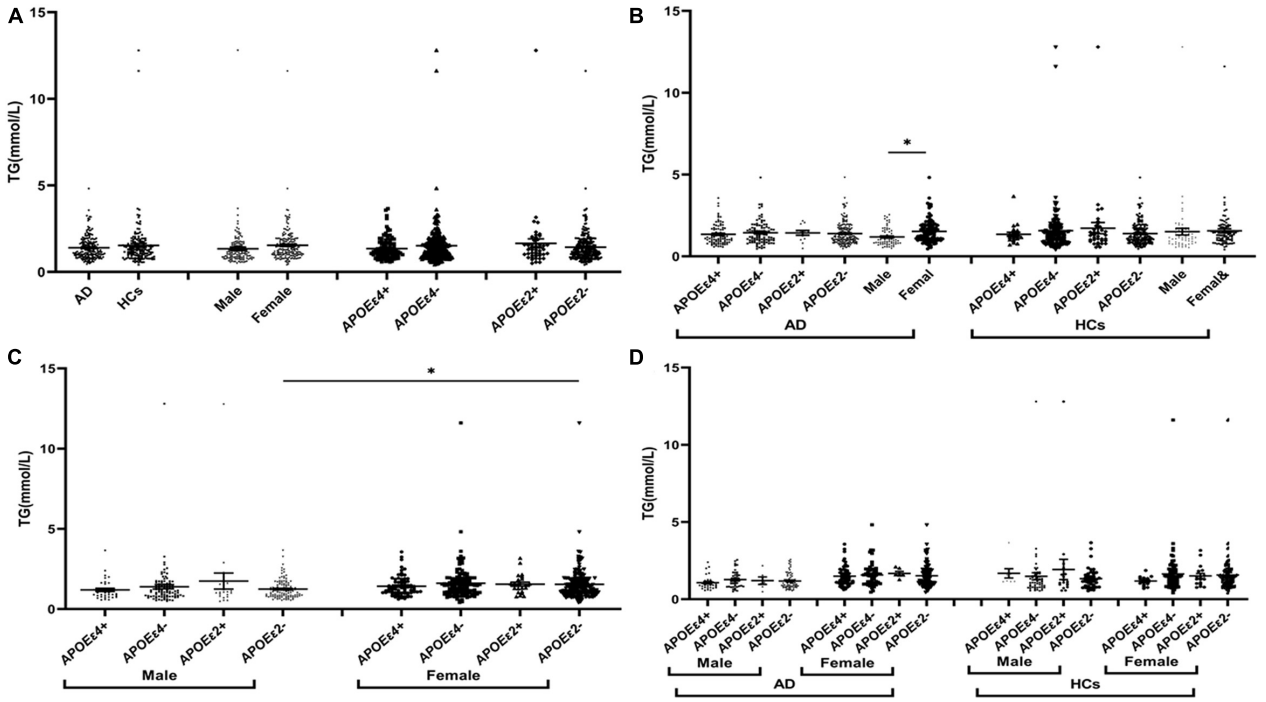

FIGURE 1 | The levels of TG in different populations. *$P < 0.05$; Values are expressed as mean (standard error). AD, Alzheimer's disease; HCs, healthy controls; *APOEε4+*, *APOEε4* carriers; *APOEε2+*, *APOEε2* carriers.

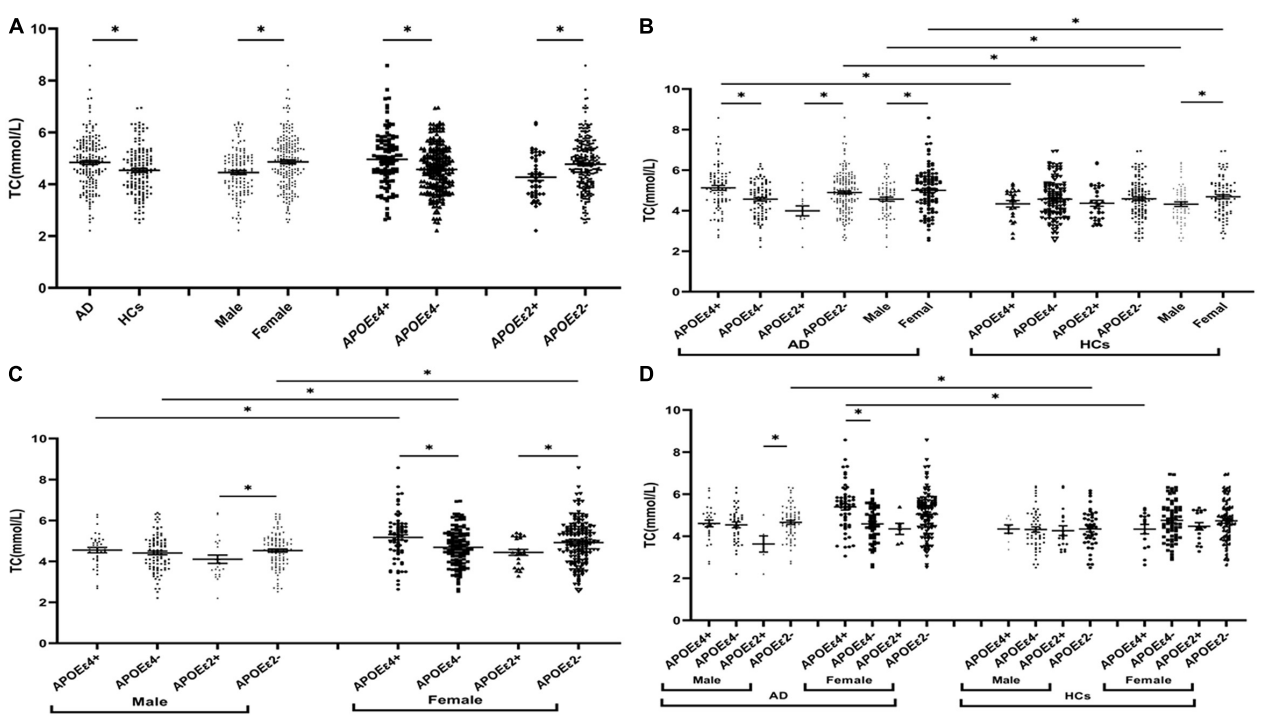

FIGURE 2 | The levels of TC in different populations. *$P < 0.05$; Values are expressed as mean (standard error). AD, Alzheimer's disease; HCs, healthy controls; *APOEε4+*, *APOEε4* carriers; *APOEε2+*, *APOEε2* carriers.

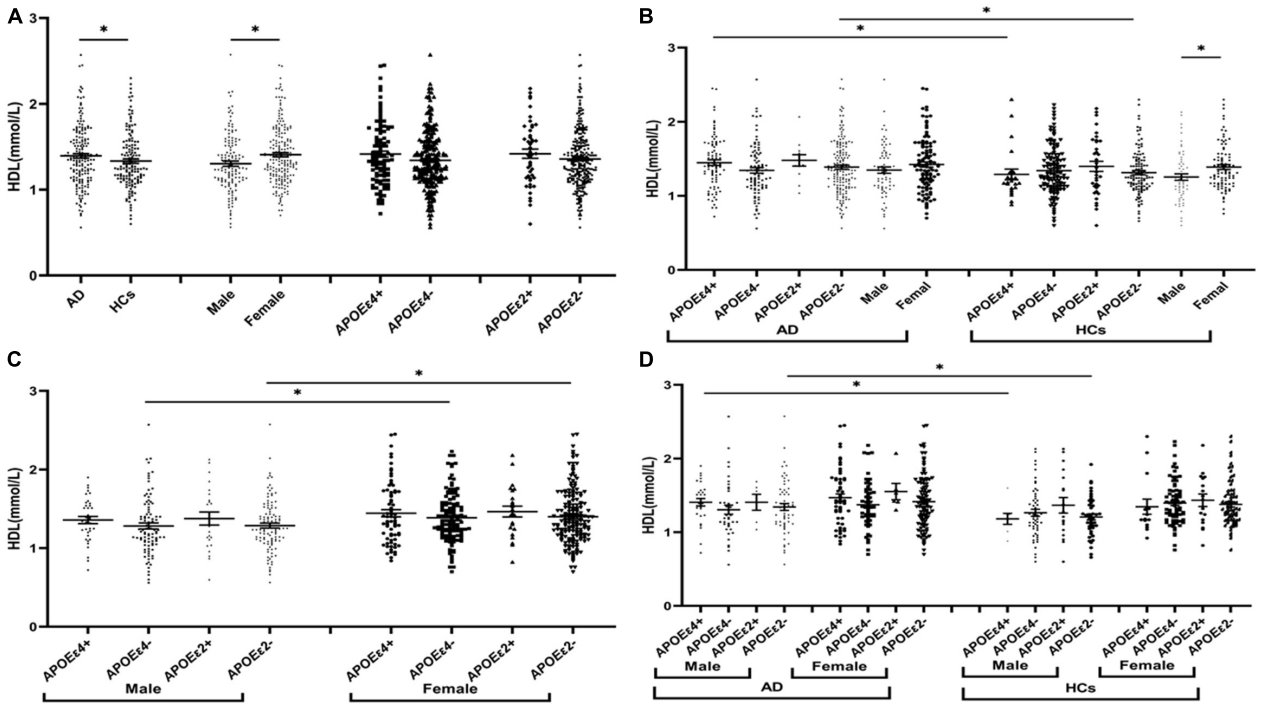

FIGURE 3 | The levels of LDL in different populations. *$P < 0.05$; Values are expressed as mean (standard error). AD, Alzheimer's disease; HCs, healthy controls; *APOEε4+*, *APOEε4* carriers; *APOEε2+*, *APOEε2* carriers.

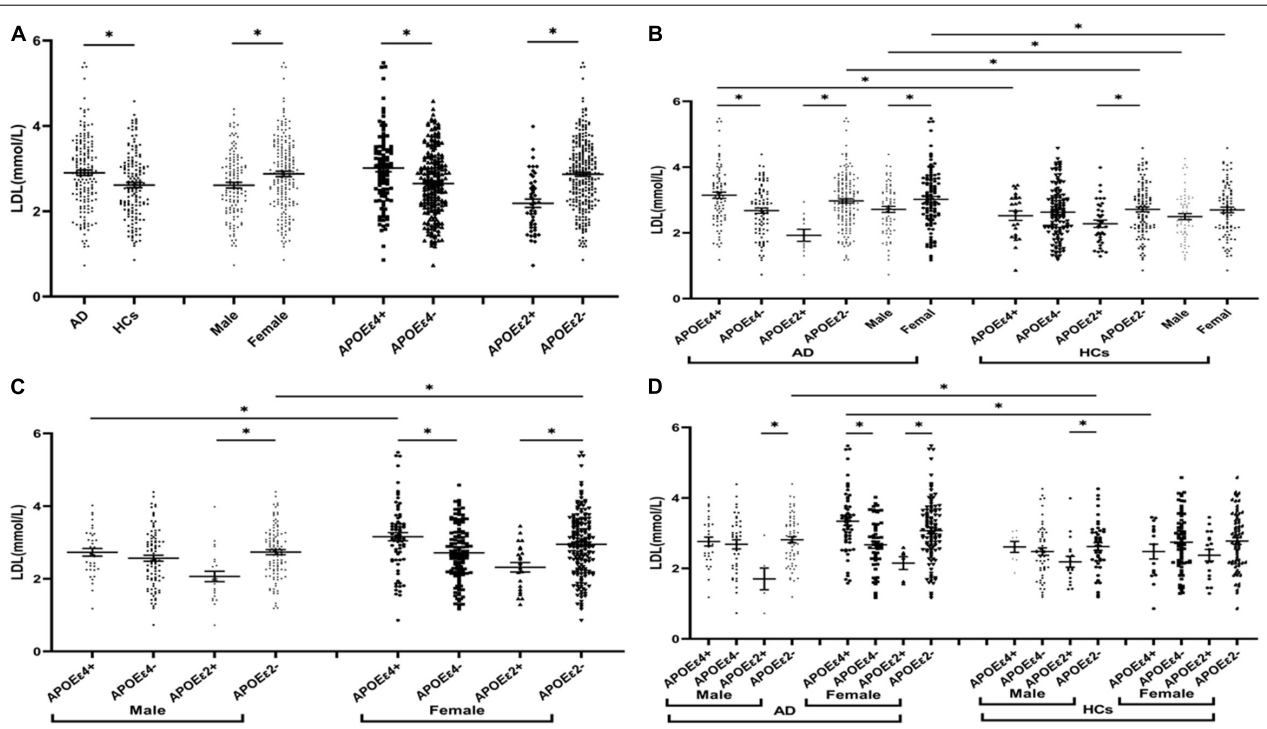

FIGURE 4 | The levels of HDL in different populations. *$P < 0.05$; Values are expressed as mean (standard error). AD, Alzheimer's disease; HCs, healthy controls; *APOEε4+*, *APOEε4* carriers; *APOEε2+*, *APOEε2* carriers.

an independent risk factor for either dementia or AD and suggested that elevated HDL may serve as a serum biomarker for assessing the risk of dementia (Kjeldsen et al., 2021). However, a prospective study with approximately 7,000 French people found that HDL was not associated with AD (Schilling et al., 2017). A meta-analysis that combined all relevant studies before 2017 showed that HDL was not associated with AD in later life (Anstey et al., 2017). Marsillach et al. (2020) point out that functional HDL is more important in disease rather than HDL cholesterol levels. Therefore, more attention should be paid to the interaction between HDL functional subtypes and AD.

In the AD population, the TC and LDL levels were increased in the *APOEε4* carriers compared to the non-*APOEε4* carriers, and this alteration was not found in the control population. In *APOEε4* allele carriers, the TC and LDL levels in the AD patients were higher than those in control participants, but these differences in TC and LDL were not found in non-*APOEε4* carriers. These findings indicated that the involvement of *APOEε4* in AD could be associated with lipid profiles. Similarly, Wang et al. (2020) found that the levels of TC in the AD population carrying *APOEε4* were higher than those without *APOEε4*, while no such change was observed in healthy controls. However, Raygani et al. (2006) found these lipid changes between *APOEε4* carriers and non-*APOEε4* carriers in both AD and controls. In addition, we also found that LDL may increase the risk of AD in females with the *APOEε4* allele. A previous study showed that the association of elevated midlife TC level with late-life AD was not altered after adjusting for the *APOEε4* allele (Kivipelto et al., 2002), but another study showed decreasing TC after midlife may represent a risk marker for late-life cognitive impairment (Solomon et al., 2007), and these studies did not take into account the role of sex. Therefore, further research and exploration are needed to verify if the effect of *APOEε4* on lipid profiles is gender-specific in AD.

In subgroup analyses based on sex showed that TC and LDL in the AD group were higher than those of the control group in both male and female populations. In the female population, TC and LDL were higher in *APOEε4* carriers than in non-*APOEε4* carriers, but no change was found in the male population. Several recent studies have shown that sex can alter the risk of the *APOEε4* allele, and female people with *APOEε4* have a higher risk of AD than male carriers (Kim et al., 2015). Women aged 65–75 with *APOEε4* had a higher risk of AD than men and had higher levels of tau in the cerebrospinal fluid (CSF) (Liu et al., 2021). A significant sex-specific association was found between CSF apolipoprotein E and AD biomarkers in Liu's study. In women, baseline CSF apolipoprotein E was significantly associated with longitudinal changes in baseline CSF Aβ and tau, but no longitudinal association was observed in men (Liu et al., 2021). In addition, a recent study on brain metabolism found that the exponential function of brain metabolism in females declines more rapidly than the linear function in males when young and more slowly in old age. The explanation for this could be a greater brain reserve in men, indicating that men have a greater capacity to withstand more pathology than women (Zhang et al., 2017). Our study found that the effect of the *APOEε4* allele on TC and LDL metabolism is significantly altered in female AD patients, but not in male AD patients, so we think the difference may also be related to metabolic reserve.

The effect of the *APOEε4* allele on lipid profiles in women was greater than that in men, but the effect of the *APOEε2* allele on lipid profiles was different from the *APOEε4* allele. In this study, the individuals were stratified according to the presence of the *APOEε2* allele, and we found that the role of the *APOEε2* allele in lipid levels was affected by the disease of AD. In the AD population, the TC level in *APOEε2* carriers was lower than those in non-carriers, but these changes were not found in the HCs. Although the TC level of *APOEε2* carriers was lower than that of non-carriers in both male and female populations, such change was only found in the male AD population, but not in the male HCs, female HCs, and female AD population. Therefore, we hypothesized that reducing TC by *APOEε2* allele seems to be more biased in male AD populations. Human studies have shown that the *APOEε2* allele is associated with decreased Aβ deposition in the brain of non-dementia elderly individuals and AD patients, and protects against cognitive impairment in individuals over 90 years of age with high levels of Aβ in the brain (Serrano-Pozo et al., 2015). *In vitro* and *in vivo* studies have shown that *APOEε2* provides protection independent of Aβ pathology through multiple potential pathways, including the regulatory role of *APOEε2* in lipid metabolism (Huang et al., 2019).

It is well known that the main component of senile plaques is Aβ, which is the main pathological basis of AD. Aβ is produced by the double cleavage of amyloid precursor protein (APP) by β-secretase and γ-secretase. APP, β-secretase and γ-secretase are located in lipid rafts, a type of membrane-bound cholesterol, where APP metabolism occurs. The level of 27-OH cholesterol circulating in the blood is proportional to the level of cholesterol, and there is a concentration-driven flux of 27-OH cholesterol circulating into the brain. The accumulation of 27-OH cholesterol was found to be the most significant change in the brain cholesterol profile of AD patients, and part of this accumulation may be influenced by circulating cholesterol levels. High levels of 27-OH cholesterol increase the formation of Aβ by antagonizing the inhibition of 24S-hydroxyl cholesterol (Feringa and van der Kant, 2021). It is speculated that the increase of tag-rich lipoprotein in the ε4 vector *APOE* may increase its affinity for LDLR, which ultimately reduces LDL intake and increases circulating plasma cholesterol. *APOEε4* has been shown to contribute to AD susceptibility by disrupting lipid and cholesterol levels. One study used correlation analysis to detect gene expression patterns in *APOEε4*-positive and *APOEε4*-negative elderly men and women. A large number of genes with the same *APOE* expression pattern were found in *APOEε4*-positive individuals but not in *APOEε4*-negative individuals. *APOEε4*-positive women tended to be larger than *APOEε4*-positive men and *APOEε4*-negative controls. The classification of genes is concerned with hormones involved in oxidation, inflammatory lipid metabolism, and immune processes. A significant triple interaction was observed in the brain region/sex/genotype of γ-secretase, which is closely associated with AD and is thought to play a role in APP processing (Hsu et al., 2019). This may explain the finding in this study that high LDL levels may increase the risk of AD in female people with the *APOEε4* allele. Therefore,

more attention should be paid to lipid profiles of different genders and APOE genotypes in the future study of AD, especially women who carry the *APOE4* allele.

In general, cholesterol and *APOEε4* gene are major factors affecting the development of AD, but current studies have found that statins may have a protective effect before the onset of AD, and once the onset of the disease, statins become inefficient or ineffective (Li et al., 2010). A longitudinal study in 2021 evaluated the association between statin use (the time-varying status and the dose-response relationship) and the incidence of AD, and found that statin use was not associated with an increased incidence of AD (Jeong et al., 2021). In this study, The proportion of statin use was small and adjustment for statin use did not significantly affect lipid profile results. However, this study was a cross-sectional result, and it is worthwhile to further explore whether statins benefit female AD patients with *APOE4* allele in longitudinal follow-up because these subpopulations have more significant changes in TC and LDL.

CONCLUSION

The TC and LDL levels of *APOEε4* allele carriers were higher than those of non-carriers, and the effect was more significant in the AD and female population. High LDL levels may increase the risk of AD in female people with the *APOEε4* allele. The TC levels in *APOEε2* allele carriers were lower than those in non-carriers, and the effect was more significant in the male AD population. Further prospective studies focusing on the relationship between the *APOE* gene, sex, lipid profiles, and AD are essential to confirm our findings, and special attention should be paid to female AD patients with the *APOEε4* allele and male AD patients carrying the *APOEε2* allele when regulating the blood lipids.

LIMITATIONS

This study has the following limitations. First, due to the large difference in whether AD patients take medication, type of medication, and dose, there is no stratification according to medication. Second, this study did not analyze the relationship between lipid profiles and AD severity due to limited data. Thirdly, This study was cross-sectional and lacks the dynamic changes and correlation of lipid profiles with time and disease. Fourthly, this study is a single-center, small-sample study, which needs to be verified by a larger sample and multi-center study.

DATA AVAILABILITY STATEMENT

The original contributions presented in the study are included in the article/**Supplementary Material**, further inquiries can be directed to the corresponding author/s.

ETHICS STATEMENT

The studies involving human participants were reviewed and approved by the Ethics Committee of West China Hospital of Sichuan University. The patients/participants provided their written informed consent to participate in this study.

AUTHOR CONTRIBUTIONS

JF contributed to the compilation of articles and data analysis. YH and TB contributed to the selection and data entry of healthy controls. RO, QW, YC, and JY contributed to the screening and data entry of AD patients. XC and HS contributed to the review, editing and scientific research thinking, and methods. All authors read and approved the manuscript.

FUNDING

This study was supported by grant from the National Key Research and Development Program of China (Grant No. 2017YFC09007703), grant from Science and Technology Planning Project in Sichuan Province (Grant No. 2020YJ0281), 1·3·5 Project for Disciplines of Excellence, West China Hospital, Sichuan University (Grant No. ZYJC18038), and Cadres Health Care Project in Sichuan Province (Grant No. 2019-112).

ACKNOWLEDGMENTS

We gratefully acknowledge the AD patients for their participation in this study.

SUPPLEMENTARY MATERIAL

The Supplementary Material for this article can be found online at: https://www.frontiersin.org/articles/10.3389/fnagi.2022.844066/full#supplementary-material

Supplementary Material 1

Supplementary Table 1 | Comparison of lipids between AD and HCs groups (Adjusting for age); Values are expressed as mean (standard deviation); AD, Alzheimer's disease; HCs, healthy controls; *APOEε4+*, *APOEε4* carriers; *APOEε2+*, *APOEε2* carriers; Male and *APOEε4+*, male *APOEε4* carriers; Male and *APOEε4−*, male *APOEε4* non-carriers; Female and *APOEε4+*, female *APOEε4* carrier; Female and *APOEε4−*, female *APOEε4* non-carrier; Male and *APOEε2+*, male *APOEε2* carriers; Male and *APOEε2−*, male *APOEε2* non-carriers; Female and *APOEε2+*, female *APOEε2* carrier; Female and *APOEε2−*, female *APOEε2* non-carrier.

Supplementary Table 2 | Comparison of lipids between *APOEε4+* group and *APOEε4−* group (Adjusting for age); Values are expressed as mean (standard deviation); AD, Alzheimer's disease; HCs, healthy controls; Male and AD, male patients with Alzheimer's disease; Female and AD, female patients with Alzheimer's disease; Male and HCs, male healthy controls; Female and HCs, healthy female controls.

Supplementary Table 3 | Comparison of lipids between *APOEε2+* group and *APOEε2−* group (Adjusting for age); Values are expressed as mean (standard deviation); AD, Alzheimer's disease; HCs, healthy controls; Male and AD, male patients with Alzheimer's disease; Female and AD, female patients with Alzheimer's disease; Male and HCs, male healthy controls; Female and HCs, healthy female controls.

Supplementary Table 4 | Comparison of lipids between male and female (Adjusting for age); Values are expressed as mean (standard deviation); AD, Alzheimer's disease; HCs, healthy controls; *APOEε4+*, *APOEε4* carrier.

Supplementary Material 2

Supplementary Table 1 | Comparison of lipids between AD and HCs groups (Adjusting for age and the stain use); Values are expressed as mean (standard deviation); AD, Alzheimer's disease; HCs, healthy controls; *APOEε4+*, *APOEε4* carriers; *APOEε2+*, *APOEε2* carriers; Male and *APOEε4+*, male *APOEε4* carriers; Male and *APOEε4−*, male *APOEε4* non-carriers; Female and *APOEε4+*, female *APOEε4* carrier; Female and *APOEε4−*, female *APOEε4* non-carrier; Male and *APOEε2+*, male *APOEε2* carriers; Male and *APOEε2−*, male *APOEε2* non-carriers; Female and *APOEε2+*, female *APOEε2* carrier; Female and *APOEε2−*, female *APOEε2* non-carrier.

Supplementary Table 2 | Comparison of lipids between *APOEε4+* group and *APOEε4−* group (Adjusting for age and the stain use); Values are expressed as mean (standard deviation); AD, Alzheimer's disease; HCs, healthy controls; Male and AD, male patients with Alzheimer's disease; Female and AD, female patients with Alzheimer's disease; Male and HCs, male healthy controls; Female and HCs, healthy female controls.

Supplementary Table 3 | Comparison of lipids between *APOEε2+* group and *APOEε2−* group (Adjusting for age and the stain use); Values are expressed as mean (standard deviation); AD, Alzheimer's disease; HCs, healthy controls; Male and AD, male patients with Alzheimer's disease; Female and AD, female patients with Alzheimer's disease; Male and HCs, male healthy controls; Female and HCs, healthy female controls.

Supplementary Table 4 | Comparison of lipids between male and female (Adjusting for age and the stain use); Values are expressed as mean (standard deviation); AD, Alzheimer's disease; HCs, healthy controls; *APOEε4+*, *APOEε4* carrier.

Supplementary Material 3

Supplementary Table 1 | Comparison of lipids between AD and HCs groups (Adjusting for age); Values are expressed as mean (standard deviation); AD, Alzheimer's disease; HCs, healthy controls; *APOEε3+*, *APOEε3* carriers; Male and *APOEε3+*, male *APOEε3* carriers; Male and *APOEε3−*, male *APOEε3* non-carriers; Female and *APOEε3+*, female *APOEε3* carrier; Female and *APOEε3−*, female *APOEε3* non-carrier.

Supplementary Table 2 | Comparison of lipids between *APOEε3+* group and *APOEε3−* group (Adjusting for age); Values are expressed as mean (standard deviation); AD, Alzheimer's disease; HCs, healthy controls.

REFERENCES

Anstey, K. J., Ashby-Mitchell, K., and Peters, R. (2017). Updating the Evidence on the Association between Serum Cholesterol and Risk of Late-Life Dementia: review and Meta-Analysis. *J. Alzheimers Dis.* 56, 215–228. doi: 10.3233/JAD-160826

Anstey, K. J., Lipnicki, D. M., and Low, L. F. (2008). Cholesterol as a risk factor for dementia and cognitive decline: a systematic review of prospective studies with meta-analysis. *Am. J. Geriatr. Psychiatry* 16, 343–354. doi: 10.1097/JGP.0b013e31816b72d4

Corbo, R. M., and Scacchi, R. (1999). Apolipoprotein E (*APOE*) allele distribution in the world. Is *APOE**4 a 'thrifty' allele? *Ann. Hum. Genet.* 63(Pt 4), 301–310. doi: 10.1046/j.1469-1809.1999.6340301.x

Corder, E. H., Saunders, A. M., Strittmatter, W. J., Schmechel, D. E., Gaskell, P. C., Small, G. W., et al. (1993). Gene dose of apolipoprotein E type 4 allele and the risk of Alzheimer's disease in late onset families. *Science* 261, 921–923. doi: 10.1126/science.8346443

de Oliveira, F. F., Bertolucci, P. H., Chen, E. S., and Smith, M. C. (2014). Risk factors for age at onset of dementia due to Alzheimer's disease in a sample of patients with low mean schooling from São Paulo. *Brazil. Int. J. Geriatr. Psychiatry* 29, 1033–1039. doi: 10.1002/gps.4094

de Oliveira, F. F., Chen, E. S., Smith, M. C., and Bertolucci, P. H. F. (2017). Longitudinal lipid profile variations and clinical change in Alzheimer's disease dementia. *Neurosci. Lett.* 646, 36–42. doi: 10.1016/j.neulet.2017.03.003

de Oliveira, F. F., de Almeida, S. S., Chen, E. S., Smith, M. C., Naffah-Mazzacoratti, M. D. G., and Bertolucci, P. H. F. (2018). Lifetime Risk Factors for Functional and Cognitive Outcomes in Patients with Alzheimer's Disease. *J. Alzheimers Dis.* 65, 1283–1299. doi: 10.3233/JAD-180303

de Oliveira, F. F., Pivi, G. A., Chen, E. S., Smith, M. C., and Bertolucci, P. H. (2015). Risk factors for cognitive and functional change in one year in patients with Alzheimer's disease dementia from São Paulo, Brazil. *J. Neurol. Sci.* 359, 127–132. doi: 10.1016/j.jns.2015.10.051

dermann, F., and Fleischhacker, W. W. (2016). Psychotic disorders in DSM-5 and ICD-11. *CNS Spectr.* 21, 349–354. doi: 10.1017/S1092852916000316

Feringa, F. M., and van der Kant, R. (2021). Cholesterol and Alzheimer's Disease; From Risk Genes to Pathological Effects. *Front. Aging Neurosci.* 13:690372. doi: 10.3389/fnagi.2021.690372

Hall, K., Murrell, J., Ogunniyi, A., Deeg, M., Baiyewu, O., Gao, S., et al. (2006). Cholesterol, *APOE* haplotype, and Alzheimer disease: an epidemiologic study of Nigerian Yoruba. *Neurology* 66, 223–227. doi: 10.1212/01.wnl.0000194507.39504.17

Hoshino, T., Kamino, K., and Matsumoto, M. (2002). Gene dose effect of the *APOE*-epsilon4 allele on plasma HDL cholesterol level in patients with Alzheimer's disease. *Neurobiol. Aging.* 23, 41–45. doi: 10.1016/s0197-4580(01)00252-4

Hsu, M., Dedhia, M., Crusio, W. E., and Delprato, A. (2019). Sex differences in gene expression patterns associated with the APOE4 allele. *F1000Res* 8:387. doi: 10.12688/f1000research.18671.2

Huang, Y. A., Zhou, B., Nabet, A. M., Wernig, M., and Südhof, T. C. (2019). Differential Signaling Mediated by *APOEε2*, *APOE3*, and *APOEε4* in Human Neurons Parallels Alzheimer's Disease Risk. *J. Neurosci.* 39, 7408–7427. doi: 10.1523/JNEUROSCI.2994-18.2019

Isbir, T., Agaçhan, B., Yilmaz, H., Aydin, M., Kara, I., Eker, E., et al. (2001). Apolipoprotein-E gene polymorphism and lipid profiles in Alzheimer's disease. *Am. J. Alzheimers Dis. Other Demen.* 16, 77–81. doi: 10.1177/153331750101600207

Jeong, S. M., Shin, D. W., Yoo, T. G., Cho, M. H., Jang, W., Lee, J., et al. (2021). Association between statin use and Alzheimer's disease with dose response relationship. *Sci. Rep.* 11:15280. doi: 10.1038/s41598-021-94803-3

Kim, S., Kim, M. J., Kim, S., Kang, H. S., Lim, S. W., Myung, W., et al. (2015). Gender differences in risk factors for transition from mild cognitive impairment to Alzheimer's disease: a CREDOS study. *Compr. Psychiatry* 62, 114–122. doi: 10.1016/j.comppsych.2015.07.002

Kivipelto, M., Helkala, E. L., Laakso, M. P., Hänninen, T., Hallikainen, M., Alhainen, K., et al. (2002). Apolipoprotein E epsilon4 allele, elevated midlife total cholesterol level, and high midlife systolic blood pressure are independent risk factors for late-life Alzheimer disease. *Ann. Intern. Med.* 137, 149–155. doi: 10.7326/0003-4819-137-3-200208060-00006

Kjeldsen, E. W., Thomassen, J. Q., Juul Rasmussen, I., Nordestgaard, B. G., Tybjærg-Hansen, A., Frikke-Schmidt, R., et al. (2021). Plasma HDL cholesterol and risk of dementia - observational and genetic studies. *Cardiovasc. Res.* 2021:cvab164. doi: 10.1093/cvr/cvab164

Launer, L. J., White, L. R., Petrovitch, H., Ross, G. W., and Curb, J. D. (2001). Cholesterol and neuropathologic markers of AD: a population-based autopsy study. *Neurology* 57, 1447–1452. doi: 10.1212/wnl.57.8.1447

Li, G., Shofer, J. B., Rhew, I. C., Kukull, W. A., Peskind, E. R., McCormick, W., et al. (2010). Age-varying association between statin use and incident Alzheimer's disease. *J. Am. Geriatr. Soc.* 58, 1311–1317. doi: 10.1111/j.1532-5415.2010.02906.x

Liu, Y., Song, J. H., Xu, W., Hou, X. H., Li, J. Q., Yu, J., et al. (2021). The Associations of Cerebrospinal Fluid APOE and Biomarkers of Alzheimer's Disease: exploring Interactions With Sex. *Front. Neurosci.* 15:633576. doi: 10.3389/fnins.2021.633576

MacGowan, S. H., Wilcock, G. K., and Scott, M. (1998). Effect of gender and apolipoprotein E haplotype on response to anticholinesterase therapy in Alzheimer's disease. *Int. J. Geriatr. Psychiatry* 13, 625–630. doi: 10.1002/(sici)1099-1166(199809)13:9<625::aid-gps835>3.0.co;2-2

Marsillach, J., Adorni, M. P., Zimetti, F., Papotti, B., Zuliani, G., Cervellati, C., et al. (2020). HDL Proteome and Alzheimer's Disease: evidence of a Link. *Antioxidants* 9:1224. doi: 10.3390/antiox9121224

McKhann, G., Drachman, D., Folstein, M., Katzman, R., Price, D., and Stadlan, E. M. (1984). Clinical diagnosis of Alzheimer's disease: report of the NINCDS-ADRDA Work Group under the auspices of Department of Health and Human Services Task Force on Alzheimer's Disease. *Neurology* 34, 939–944. doi: 10.1212/wnl.34.7.939

Merched, A., Xia, Y., Visvikis, S., Serot, J. M., and Siest, G. (2000). Decreased high-density lipoprotein cholesterol and serum apolipoprotein AI concentrations are highly correlated with the severity of Alzheimer's disease. *Neurobiol. Aging.* 21, 27–30. doi: 10.1016/s0197-4580(99)00103-7

Oliveira, F. F., Chen, E. S., Smith, M. C., and Bertolucci, P. H. (2016). Predictors of Cognitive and Functional Decline in Patients With Alzheimer Disease Dementia From Brazil. *Alzheimer Dis. Assoc. Disord.* 30, 243–250. doi: 10.1097/WAD.0000000000000117

Pinto, T. C. C., Machado, L., Bulgacov, T. M., Rodrigues-Júnior, A. L., Costa, M. L. G., et al. (2019). Is the Montreal Cognitive Assessment (MoCA) screening superior to the Mini-Mental State Examination (MMSE) in the detection of mild cognitive impairment (MCI) and Alzheimer's Disease (AD) in the elderly? *Int. Psychogeriatr.* 31, 491–504. doi: 10.1017/S1041610218001370

Poirier, J., Miron, J., Picard, C., Gormley, P., Théroux, L., Breitner, J., et al. (2014). Apolipoprotein E and lipid homeostasis in the etiology and treatment of sporadic Alzheimer's disease. *Neurobiol. Aging* 35(Suppl. 2), S3–S10. doi: 10.1016/j.neurobiolaging.2014.03.037

Raygani, A. V., Rahimi, Z., Kharazi, H., Tavilani, H., and Pourmotabbed, T. (2006). Association between apolipoprotein E polymorphism and serum lipid and apolipoprotein levels with Alzheimer's disease. *Neurosci. Lett.* 408, 68–72. doi: 10.1016/j.neulet.2006.08.048

Refolo, L. M., Malester, B., LaFrancois, J., Bryant-Thomas, T., Wang, R., et al. (2000). Hypercholesterolemia accelerates the Alzheimer's amyloid pathology in a transgenic mouse model. *Neurobiol. Dis.* 7, 321–331. doi: 10.1006/nbdi.2000.0304

Sabbagh, M. N., Sandhu, S., Kolody, H., Lahti, T., Silverberg, N. B., and Sparks, D. L. (2006). Studies on the effect of the apolipoprotein E haplotype on the lipid profile in Alzheimer's disease. *Curr. Alzheimer Res.* 3, 157–160. doi: 10.2174/156720506776383013

Schilling, S., Tzourio, C., Soumaré, A., Kaffashian, S., Dartigues, J. F., Ancelin, M. L., et al. (2017). Differential associations of plasma lipids with incident dementia and dementia subtypes in the 3C Study: A longitudinal, population-based prospective cohort study. *PLoS Med.* 14:e1002265. doi: 10.1371/journal.pmed.1002265

Serrano-Pozo, A., Qian, J., Monsell, S. E., Betensky, R. A., Hyman, B. T., et al. (2015). *APOE*ε2 is associated with milder clinical and pathological Alzheimer disease. *Ann. Neurol.* 77, 917–929. doi: 10.1002/ana.24369

Solomon, A., Kåreholt, I., Ngandu, T., Winblad, B., Nissinen, A., Tuomilehto, J., et al. (2007). Serum cholesterol changes after midlife and late-life cognition: twenty-one-year follow-up study. *Neurology* 68, 751–756. doi: 10.1212/01.wnl.0000256368.57375.b7

Sun, L., Hu, C., Zheng, C., Huang, Z., Lv, Z., Huang, J., et al. (2014). Gene-gene interaction between CETP and APOE polymorphisms confers higher risk for hypertriglyceridemia in oldest-old Chinese women. *Exp. Gerontol.* 55, 129–133. doi: 10.1016/j.exger.2014.04.003

Wang, P., Zhang, H., Wang, Y., Zhang, M., and Zhou, Y. (2020). Plasma cholesterol in Alzheimer's disease and frontotemporal dementia. *Transl. Neurosci.* 11, 116–123. doi: 10.1515/tnsci-2020-0098

Wu, Y., Wang, Z., Jia, X., Zhang, H., Zhang, H., Li, J., et al. (2019). Prediction of Alzheimer's disease with serum lipid levels in Asian individuals: a meta-analysis. *Biomarkers* 24, 341–351. doi: 10.1080/1354750X.2019.1571633

Zhang, H., Wu, P., Ziegler, S. I., Guan, Y., Wang, Y., Ge, J., et al. (2017). Data-driven identification of intensity normalization region based on longitudinal coherency of 18F-FDG metabolism in the healthy brain. *Neuroimage* 146, 589–599. doi: 10.1016/j.neuroimage.2016.09.031

Conflict of Interest: The authors declare that the research was conducted in the absence of any commercial or financial relationships that could be construed as a potential conflict of interest.

Publisher's Note: All claims expressed in this article are solely those of the authors and do not necessarily represent those of their affiliated organizations, or those of the publisher, the editors and the reviewers. Any product that may be evaluated in this article, or claim that may be made by its manufacturer, is not guaranteed or endorsed by the publisher.

Copyright © 2022 Fu, Huang, Bao, Ou, Wei, Chen, Yang, Chen and Shang. This is an open-access article distributed under the terms of the Creative Commons Attribution License (CC BY). The use, distribution or reproduction in other forums is permitted, provided the original author(s) and the copyright owner(s) are credited and that the original publication in this journal is cited, in accordance with accepted academic practice. No use, distribution or reproduction is permitted which does not comply with these terms.

frontiers | Frontiers in Aging Neuroscience

ORIGINAL RESEARCH
published: 30 May 2022
doi: 10.3389/fnagi.2022.818871

Check for updates

Alzheimer's Disease Diagnosis and Biomarker Analysis Using Resting-State Functional MRI Functional Brain Network With Multi-Measures Features and Hippocampal Subfield and Amygdala Volume of Structural MRI

Uttam Khatri and Goo-Rak Kwon for the Alzheimer's Disease Neuroimaging Initiative†*

Department of Information and Communication Engineering, Chosun University, Gwangju, South Korea

OPEN ACCESS

Edited by:
Woon-Man Kung,
Chinese Culture University, Taiwan

Reviewed by:
Jungsu S. Oh,
University of Ulsan, South Korea
Oezguer A. Onur,
University of Cologne, Germany

***Correspondence:**
Goo-Rak Kwon
grkwon@chosun.ac.kr

†*Data used in the preparation of this article were obtained from the ADNI database (adni.loni.usc.edu). As such, the investigators within the ADNI contributed to the design and implementation of ADNI and/or provided data but did not participate in the analysis or writing of this report. A complete listing of ADNI investigators can be found at: http://adni.loni.usc.edu/wp-content/uploads/how_to_apply/ADNI_Acknowledgement_List.pdf*

Specialty section:
This article was submitted to Alzheimer's Disease and Related Dementias, a section of the journal Frontiers in Aging Neuroscience

Received: *20 November 2021*
Accepted: *01 March 2022*
Published: *30 May 2022*

Citation:
Khatri U and Kwon G-R (2022) Alzheimer's Disease Diagnosis and Biomarker Analysis Using Resting-State Functional MRI Functional Brain Network With Multi-Measures Features and Hippocampal Subfield and Amygdala Volume of Structural MRI. Front. Aging Neurosci. 14:818871. doi: 10.3389/fnagi.2022.818871

Accurate diagnosis of the initial phase of Alzheimer's disease (AD) is essential and crucial. The objective of this research was to employ efficient biomarkers for the diagnostic analysis and classification of AD based on combining structural MRI (sMRI) and resting-state functional MRI (rs-fMRI). So far, several anatomical magnetic resonance imaging (MRI) imaging markers for AD diagnosis have been identified. The use of cortical and subcortical volumes, the hippocampus, and amygdala volume, as well as genetic patterns, has proven to be beneficial in distinguishing patients with AD from the healthy population. The fMRI time series data have the potential for specific numerical information as well as dynamic temporal information. Voxel and graphical analyses have gained popularity for analyzing neurodegenerative diseases, such as Alzheimer's and its prodromal phase, mild cognitive impairment (MCI). So far, these approaches have been utilized separately for the diagnosis of AD. In recent studies, the classification of cases of MCI into those that are not converted for a certain period as stable MCI (MCIs) and those that converted to AD as MCIc has been less commonly reported with inconsistent results. In this study, we verified and validated the potency of a proposed diagnostic framework to identify AD and differentiate MCIs from MCIc by utilizing the efficient biomarkers obtained from sMRI, along with functional brain networks of the frequency range .01–.027 at the resting state and the voxel-based features. The latter mainly included default mode networks (amplitude of low-frequency fluctuation [ALFF], fractional ALFF [ALFF], and regional homogeneity [ReHo]), degree centrality (DC), and salience networks (SN). Pearson's correlation coefficient for measuring fMRI functional networks has proven to be an efficient means for disease diagnosis. We applied the graph theory to calculate nodal features (nodal

degree [ND], nodal path length [NL], and between centrality [BC]) as a graphical feature and analyzed the connectivity link between different brain regions. We extracted three-dimensional (3D) patterns to calculate regional coherence and then implement a univariate statistical *t*-test to access a 3D mask that preserves voxels showing significant changes. Similarly, from sMRI, we calculated the hippocampal subfield and amygdala nuclei volume using Freesurfer (version 6). Finally, we implemented and compared the different feature selection algorithms to integrate the structural features, brain networks, and voxel features to optimize the diagnostic identifications of AD using support vector machine (SVM) classifiers. We also compared the performance of SVM with Random Forest (RF) classifiers. The obtained results demonstrated the potency of our framework, wherein a combination of the hippocampal subfield, the amygdala volume, and brain networks with multiple measures of rs-fMRI could significantly enhance the accuracy of other approaches in diagnosing AD. The accuracy obtained by the proposed method was reported for binary classification. More importantly, the classification results of the less commonly reported MCIs vs. MCIc improved significantly. However, this research involved only the AD Neuroimaging Initiative (ADNI) cohort to focus on the diagnosis of AD advancement by integrating sMRI and fMRI. Hence, the study's primary disadvantage is its small sample size. In this case, the dataset we utilized did not fully reflect the whole population. As a result, we cannot guarantee that our findings will be applicable to other populations.

Keywords: Alzheimer's disease, rs-fMRI, brain network, DMN, SN, features selection, machine learning, SVM

INTRODUCTION

With the increase and the prevalence of age-related mental decline, researchers have been increasingly interested in studying pathological and regular aging in an attempt to identify early markers of neuronal disease. Indeed, due to the high expense and pharmaceutical burden of progressive disorder on the national healthcare system, research targeted at providing a timely and differential assessment of these disorders is essential. Alzheimer's disease (AD) is the most prevalent neurodegeneration disease in the world, impacting millions of individuals (2020 Alzheimer's disease facts and figures, 2020). The identification of precise and accurate biomarkers of early AD advancement will aid researchers and doctors in the development of novel medications and the monitoring of their efficacy, as well as reduce the time and expense of clinical examination. The National Institute of Neurologic and Communication Disorders and Stroke and the Alzheimer's disease and Related Disorders Association (NINCDS-ADRDA) created clinical diagnostic guidelines for AD based on the binary method in the 1980s. The importance of cognitive deterioration in the detection of AD is mentioned in this technique (McKhann et al., 1984). Later, neuropathological evidence in the form of neurofibrillary tangles and senile plaques (Hyman and Trojanowski, 1997) was introduced. AD diagnostic regulation was enhanced in 2011 by the National Institute on Aging-Association Alzheimer's Group. Additional features can be obtained by measuring cerebrospinal fluid (CSF), neurogenetic approach, tau, amyloid, and neuronal damage features as assessed by neuroimaging analysis, including MRI, positron emission tomography (PET), and functional MRI (fMRI). The use of biomarkers, such as the Mini-Mental State Examination (MMSE) score, magnetic resonance imaging (MRI) biomarkers (such as normalized whole-brain volume and hippocampal volume), and CSF biomarkers (amyloid–42, tau), as well as combined metabolic disorders, to detect AD and predict mild cognitive impairment (MCI) conversion shows promising future (van Maurik et al., 2017). MRI and PET imaging alterations allow for the determination of atrophic areas and amyloid/metabolism indicators (Zhang et al., 2011; Garali et al., 2018), allowing for the detection of AD even at an early stage (Jack et al., 2019). Because of the non-invasive nature of MRI, a lot of work has gone into improving the MRI processing scheme in order to uncover MRI-associated markers that may be used to increase the efficiency of Alzheimer's diagnosis. There is a lot of evidence that various anatomical brain areas are damaged at different stages of the pathology, with the amygdala, hippocampus, and entorhinal cortex being the first to be impacted. Despite the fact that these areas are responsible for AD, they have yet to be thoroughly investigated. The hippocampal sub-regions are widely recognized to have a key part in the short-to-long-term memory assimilation process. The hippocampus region is more likely to be the first section of the brain to deteriorate. Furthermore, clinical research has revealed that the hippocampus region is one of the most often utilized and effective biomarkers for detecting the transition from MCI to AD (Platero et al., 2019; Liu et al., 2020). Despite this, due to the low resolution

of MRI, it is commonly treated as a single entity. With major advancements in high-resolution MRI image data acquisition techniques, new possibilities for studying specific hippocampal sub-regions have emerged. CA1 volume measures were found to be more sensitive than total hippocampal volumetry for detecting structural alterations in the early stages of AD (Zheng et al., 2018). Hippocampus sub-regions have also been connected to age-related memory loss and certain features of memory patterns (Zheng et al., 2018). As a result, early identification of AD or its prodromal stage, MCI (Petersen, 2004) is critical for consistent and effective diagnosis, that can assist to slow the course of the disease. As an intermediate stage of Alzheimer's, individuals with MCI are commonly marked by a cognitive and functional decline in the regular aging process and is affected by memory decline without the disorder (Petersen, 2004; Angelucci et al., 2010), which is commonly characterized by the overall decline in cognition on various brain regions. MCI is considered as prior AD (Petersen, 2004). Individuals with MCI develop Alzheimer's subsequently, wherein symptoms emerge over the period of 2–3 years on average (Lopez et al., 2012). An eventual community support analysis in the old individual indicated that the transition rate of MCI from Alzheimer's to various forms of dementia is approximately 10–15% every year (Wei et al., 2016). Previous research advises some individuals cannot transit to Alzheimer's, and quite continue in stable form clinically for a long time, which is considered as stable MCI (MCIs), whereas MCI that converts to AD is referred to as MCIc. Previous research from Alzheimer's analysis advocates the hypothesis that Alzheimer's is commonly characterized by a functional disconnection of the neuronal pattern and functional connectivity (FC) of various brain areas, which is also shown in the initial stage of MCI or even before the transition to Alzheimer's (Bishop et al., 2010; Clem et al., 2017; de Vos et al., 2018).

Biomarkers obtained from various imaging techniques, such as PET, resting-state fMRI (rs-fMRI), and structural MRI (sMRI), have shown beneficial aspects in the MCI and AD diagnosis (Ju et al., 2019). Particularly, the fMRI technique presents a wide analysis platform to quantify the functional patterns of the brain by calculating the correlation among intrinsic blood-oxygen-level-dependent (BOLD) frequency variation in multiple brain areas at resting state. Being sensitive to various brain region spontaneous neuronal activity, BOLD signal can be therefore utilized as an effective noninvasive biomarker for analyzing neuronal disease at a whole-brain level such as Alzheimer's. FC, which gives the temporal interaction of BOLD frequency among various brain areas, can reveal how structurally isolated and functionally related brain regions communicate. Therefore, a functional network study utilizing fMRI images will serve an immense potentiality for automated disease diagnosis. A large literature has analyzed AD-generated alteration in functional networks on rs-fMRI (Hojjati et al., 2017; Zhang et al., 2019). The rs-fMRI presents the insight on a dynamic imaging modality for pathological identification of FC not only in an individual with Alzheimer's but also in those with other neuropsychiatric or neurological disorders (Greicius, 2008). Evidence from previous studies indicates that functional relation at the resting state shows the connection link of work-related knowledge (Ito et al., 2017), in which functional networks have proven to be highly valuable and sensitive markers for Alzheimer's (Sheline et al., 2010). Grieder et al. (2018) advise that loss in cognitive ability in AD individual are directly connected to the brain network complexity pattern. In a previous fMRI study, FC has been reported to indicate Alzheimer's related cognitive impairment in older individuals with healthy cognition, AD, and MCI (Lin et al., 2018). Some fMRI analyses also indicated that the pathophysiology of Alzheimer's is correlated with statistical alteration of regional spontaneous low-frequency BOLD variation coherence estimation in the relaxed phase. For voxel-wise analysis, the metrics used in these studies included regional homogeneity (ReHo) (Zang et al., 2004; He et al., 2007); the amplitude of low-frequency fluctuation (ALFF) (Zou et al., 2008; Li et al., 2017), and fractional ALFF (fALFF). These studies showed that the precuneus (PCu) and the posterior cingulate cortex (PCC) had the larger ReHo abnormality among Alzheimer's as compared to cognitively normal individuals ($p < 0.05$). The fALFF along with ALFF analysis on fMR images (Han et al., 2011) suggested, individuals with MCI are characterized by reduced fALFF measure in the larger brain areas, which includes temporal cortices and occipital. The FC of rs-fMRI (Li et al., 2017), indicated, a brain area with major FC was highly presented in the default mode network (DMN) regions (Hafkemeijer et al., 2012; Zhang et al., 2020) and primarily affect the PCC and bilateral PCu (Dai et al., 2015). Both AD and aMCI have been found to target large-scale networks, including reduced DMN connectivity and increased salience network (SN) (Greicius et al., 2004; Zhou et al., 2010; Zhou and Seeley, 2014) connectivity, as well as aberrant connectivity between networks (Brier et al., 2012) in AD and disturbed connectivity in aMCI, especially in relation to the DMN (Lee et al., 2016; Yang et al., 2017; Zhang et al., 2017), using resting-state functional connectivity methods that quantify the temporal synchrony between brain regions. These are all statistically important discoveries for cluster-level comparison. Yet, the classification potential of the above-indicated biomarker identified the individual with MCI/AD into one of the categories (MCI/AD vs. healthy controls [HC]), which is a highly complex work as compared to the study of different groups (Rathore et al., 2017). Recently, another analysis recommended that the biomarkers retrieved from functional networks assessment and machine learning techniques using rs-fMRI provide an effective framework for accurate and efficient identification. Chen et al. (2011) utilized large-scale networks (LSN) technique with 95% area under the curve (AUC) to classify patients into amnestic MCI (aMCI) and cognitively healthy. Challis et al. (2015) presented the GP-LR technique with SVM and obtained an accuracy of 75% to diagnose healthy individuals from aMCI. Khazaee et al. (2015) utilized time series from a brain network with linear SVM as a classifier to identify disease individuals, their experimental result achieved 100% accuracy on classification. This could be due to the limited number of sample and their feature reduction technique which was the single-variable Fischer score method. In another study, they utilized features obtained both spatial and temporal variation from dynamic connectivity networks (DCNs). Finally, they combined it as a feature to evaluate the multi-kernel technique along with

manifold regularization multi-task feature learning and obtained 78.8% of accuracy for the identification of EMCI and LMCI (Jie et al., 2018). It has been proven that a functional graph measure with a machine learning technique using rs-fMRI can precisely identify individuals with MCI, individuals with Alzheimer's, and healthy control (Xiang et al., 2013).

However, large of the literature collected MCIs and MCIc groups into a single MCI group (He et al., 2008; Khazaee et al., 2015), and very few works of literature have analyzed the potentiality of rs-fMRI to identify differences among the two groups (Khazaee et al., 2015). In addition, Zuo et al. (2010) categorized the BOLD frequency into five frequency bands. Brain function in individuals with AD and MCI was significantly different at hippocampus, medial prefrontal, and posterior cingulate regions in these frequency bands. From this framework, we aimed to assess the potency for diagnostic classification to differentiate MCIs and MCIc, along with other groups, by using the biomarkers obtained from sMRI and functional brain networks during the resting state. Based on the classification results, to discover highly sensitive biomarkers, we can recognize accurately and precisely why sensitive biomarkers in the brain altered with disease advancement. We hypothesized that providing cognitive training and appropriate treatment for an individual's highly sensitive brain area at various phases in disease advancement can avert the growth of Alzheimer's conversion. It is better to observe that large of the abovementioned rs-fMRI technique utilized only time-series networks to compare different groups. However, using only time series for a feature vector obtained by rs-fMRI modality is possibly not precise to present the spatiotemporal pattern of the whole brain (He et al., 2008).

Volume alterations in the hippocampus and amygdala are considered a primary feature of AD and are utilized as a diagnostic indication. In Alzheimer's patients, hippocampal and amygdala atrophy generally spreads to other parts of the brain (Josephs et al., 2017; Feng et al., 2018). Anatomical MR imaging can be used to visualize the pattern of hippocampus amygdala, cortical, and subcortical atrophy. Which is important in the clinical diagnosis of AD (Feng et al., 2018). Therefore, the fundamental aim of this framework was to analyze the sMRI and rs-fMRI data to their full potential by combining hippocampal sub-volume, amygdala nuclei volume of sMRI, brain networks, and multi-measure voxel-based features of rs-fMRI to identify AD. Firstly, the cortical and subcortical segmentation was performed with Freesurfer (version 6), and then hippocampus subfield and amygdala nuclei volume segmentation was performed with Freesurfer's segmentHA_T1.sh function (Fischl, 2012). Secondly, we processed the signal into the 0.01–0.027 Hz frequency band at the resting phase. Thereafter, we created a brain network by evaluating Pearson's correlation coefficients among time series of the entire brain region. Afterward, we performed a threshold operation to obtain a binary undirected brain network. Subsequently, we obtained graph elements, such as global efficiency, local efficiency, characteristic path length, clustering coefficient, and SmallWorlds, to calculate the parameters of functional brain networks. Likewise, we obtained maps of three-dimensional (3D) regional coherence (fALFF, ALFF, ReHo, and DC) for each patient. After this we implemented univariate statistical two-sample *t*-tests for the entire 3D-brain area among training classes to obtain an analysis mask that preserved the original set of significant voxel-based features, generating notable differences in any one of the voxel measures, that is, fALFF, ReHo, FALFF, and DC. In this study, we also applied brain networks and voxel features separately, and finally, we combined both sMRI and rs-fMRI features. At the feature selection stage, we implemented and analyzed three different feature selection techniques to obtain the optimal features. To achieve unbiased classification performance, SVM with the cross-validation method (CV) was implemented as a classifier. More importantly, we also compare the performance of our model with the ensemble learning approach using Random Forest (RF) classifiers.

MATERIALS AND METHODS

Participants

Data used in the preparation of this article were obtained from the AD Neuroimaging Initiative (ADNI)[1] database. The ADNI was launched in 2003 as a public-private partnership, led by Principal Investigator Michael W. Weiner, MD. The primary goal of ADNI has been to test whether serial MRI, PET, other biological markers, and clinical and neuropsychological assessment can be combined to measure the progression of MCI and early AD. Individual inclusion criteria for subjects were mentioned in the ADNI conduct. The included individuals were between the ages of 53 and 93 years. All individuals were able and willing to endure all test procedures, along with neuroimaging, and admitted to a longitudinal investigation. Psychoactive treatment was not included in the assessment. In this framework, we obtained data for all individuals accessible on the ADNI webpage. In total, 213 individuals were included as either AD ($n = 63$), MCIs ($n = 37$), MCIc ($n = 45$), or HC ($n = 68$), matched with age and sex ratio. Group categories were sorted through the functional activities questionaries (FAQ) record between 0 and 4, the Mini-Mental State Examination (MMSE) record 26–30, and the Geriatric Depression Scale (GDS) record between 0 and 4. For the MCI case, the FAQ record was 0–16, the MMSE record was 24–30, and the GDS record was 0–13. For the MCIc case, the FAQ record was 0–18, the MMSE record was 18–30, and the GDS record was 0–10.

For the AD case, the individual had a global CDR score of 1, an FAQ score of 3–28, an MMSE score of 14–24, and a GDS score of 0–7. Individuals with MCI who had been followed for less than 18 months and did not convert were not included in this study. **Table 1** presents the demographic report of individuals who participated in the study, including the sex ratios and mean age for each category. Statistically significant differences in the clinical and demographic features were assessed among these categories, Student's *t*-test was utilized at a.05 significance level. We did not notice significant changes ($p > 0.05$) among the category in sex ratio or age. For unbiased evaluation of performance, group classifications were randomly shuffled and

[1]http://adni.loni.usc.edu/

split into k subgroup. For model evaluation training, datasets were trained and classification performance was measured on diagnostic sensitivity, specificity, F1-score, and Cohen's Kappa index on the independent testing set. Sex and age distribution were preserved on the splitting procedure.

Structural MRI Preprocessing

From the ADNI webpage, we obtained 1.5-T T1-weighted MR images. The MRI scans were collected using Philips, GE, or Siemens Medical system scanners from data centers. Because the acquisition methodology of each scanner was different, ADNI performed an image normalization step. Image corrections encompassed calibration, image geometry distortion due to gradient non-linearity (grad-warp), a decrease in intensity non-uniformity due to waves, or a decrease in residual intensity non-uniformity of the 1.5-T scans utilized by ADNI. On the ADNI website, we can get more information regarding the sMRI. All scans had a resolution of 176×256×256 and were spaced 1 mm apart. We used the Freesurfer[2] (version 6) (Fischl, 2012) toolbox to pre-process the collected sMRI images in our experiment.

Resting-State Functional MRI Image Acquisition

Philips Medical sMRI scanner of 3 T was utilized to obtain the fMR images. The rs-fMR images were acquired through the ADNI webpage. At the time of image acquisition, patients were asked to not to think, to lie in the scanner, and to relax. The parameters sequences were as follows: TR = 3,000 ms, plus sequence = GR, flip angle = 800°, TE = 30 ms, data matrix = 64 × 64, slice thickness = 3.33 mm, pixel spacing X = 3.31 mm and Y = 3.31 mm, axial slices = 48, time points = 140, and no slice gap.

Resting-State Functional MRI Preprocessing

Image processing procedures were achieved by utilizing Data Processing Assistant for Resting-State fMRI (DPARSF) (Yan and Zang, 2010) containing Statistical Parametric Mapping (SPM)[3] and Resting-State fMRI Data Analysis Toolkit (REST)[4]. For stabilization and adaptation of individuals, participants' first 10 time points were removed followed by correction of the last slice time. To compensate for the effect of head motion realignment, spatial transformation of a six-parameter rigid body was used. All spatial motion displacements were performed for <3 mm and <30° of rotation in each direction. Further, co-registration of rs-fMR images to 3D-T1 structural high-resolution images was carried out. The Montreal Neurological Institute (MNI) space was undertaken to normalize 3D-T1 structural MR images by non-linear wrapping based on Diffeomorphic Anatomical Registration *via* Exponential Lie Algebra (DARTEL). Individual fMRI images were then spatially normalized to the MNI field utilizing the parameters collected from the normalization of the structural image and simultaneously resampling them into 3-mm isotropic voxels. The 6-mm full-width half-maximum Gaussian kernel was utilized on normalized individual rs-fMR data. Linear detrending and band-pass filtering at 0.01–0.027 Hz were performed. The 6-mm FWHM Gaussian kernel for spatial smoothing was implemented. The six head motion parameter, the global mean signal, the white matter (WM), and the CSF signal were discarded as nuisance variance to decrease the motion effects and non-neuronal BOLD variation (Hojjati et al., 2018). Similarly, for voxel-based features, mask images were obtained according to the subject specialized normalized T1 anatomical images. The voxel measures within the mask were utilized for the analysis. The mask images obtained were utilized for developing various testing in further investigation and analyses.

[2]http://surfer.nmr.mgh.harvard.edu/

[3]http://www.fil.ion.ucl.ac.uk/spm

[4]http://restfmri.net

TABLE 1 | Neuropsychological and demographic characteristics of participants.

Group	AD (n = 63)	MCIs (n = 37)	MCIc (n = 45)	HC (n = 68)
Sex (M/F)	37/26	15/22	27/18	33/35
Age	74.51 ± 7.18	73.32 ± 7.58	73.81 ± 7.91	76.37 ± 7.13
FAQ score	19.95 ± 7.73	1.72 ± 2.15	7.23 ± 7.18	0.14 ± 0.37
NPI-Q score	4.85 ± 5.13	1.87 ± 1.75	2.78 ± 2.85	0.37 ± 0.83
GDS score	2.32 ± 2.87	1.28 ± 1.05	2.35 ± 2.95	1.19 ± 1.95
MMSE score	19.95 ± 5.15	29.12 ± 1.03	25.17 ± 3.45	29.25 ± 1.75
CDR	0.94 ± 0.27	0.50 ± 0.0	0.50 ± 0.28	0.00 ± 0.13

Values are means or numbers ± standard deviations.
MMSE, mini-mental examination; NPI-Q, neuropsychiatric inventory questionnaire; FAQ, functional activities questionaries; GDS, geriatric depression scale.

Proposed Framework

Figure 1 represents the proposed procedure used in this framework. The first step of the framework was to prepare and process the sMRI (hippocampal subfield, amygdala volume) and rs-fMRI images to obtain the corresponding time series and whole-brain 3D measurements. From time-series data, we constructed the brain network. Similarly, we obtained the fALFF, ReHo, ALFF, DC, and SN feature vectors from 3D measures. From brain network construction, we obtained a nodal degree (ND), betweenness centrality (BC), and the nodal path length (NL). Similarly, for the voxel-based 3D structural model, we retrieved a 3D mask that determined a set of "effective" voxels to conduct statistical univariate t-tests. Thereafter, we combined the hippocampal-amygdala subfield volume (sMRI), the brain network, and voxel-based feature vectors (rs-fMRI) for the final classification. We then applied the feature reduction technique on the integrated training features set to choose highly significant features vectors to train the SVM and the RF classifiers. We finally obtained significant feature rank and fed the feature vectors as the training sample, and we also obtained the testing sample for classification. Owing to the limited size of the dataset, we utilized a CV of 10-fold to validate the diagnosis performance of the classification for the proposed framework. While performing the 10-fold CV, 90% of the total sample was utilized for the training process and the remaining 10% for testing.

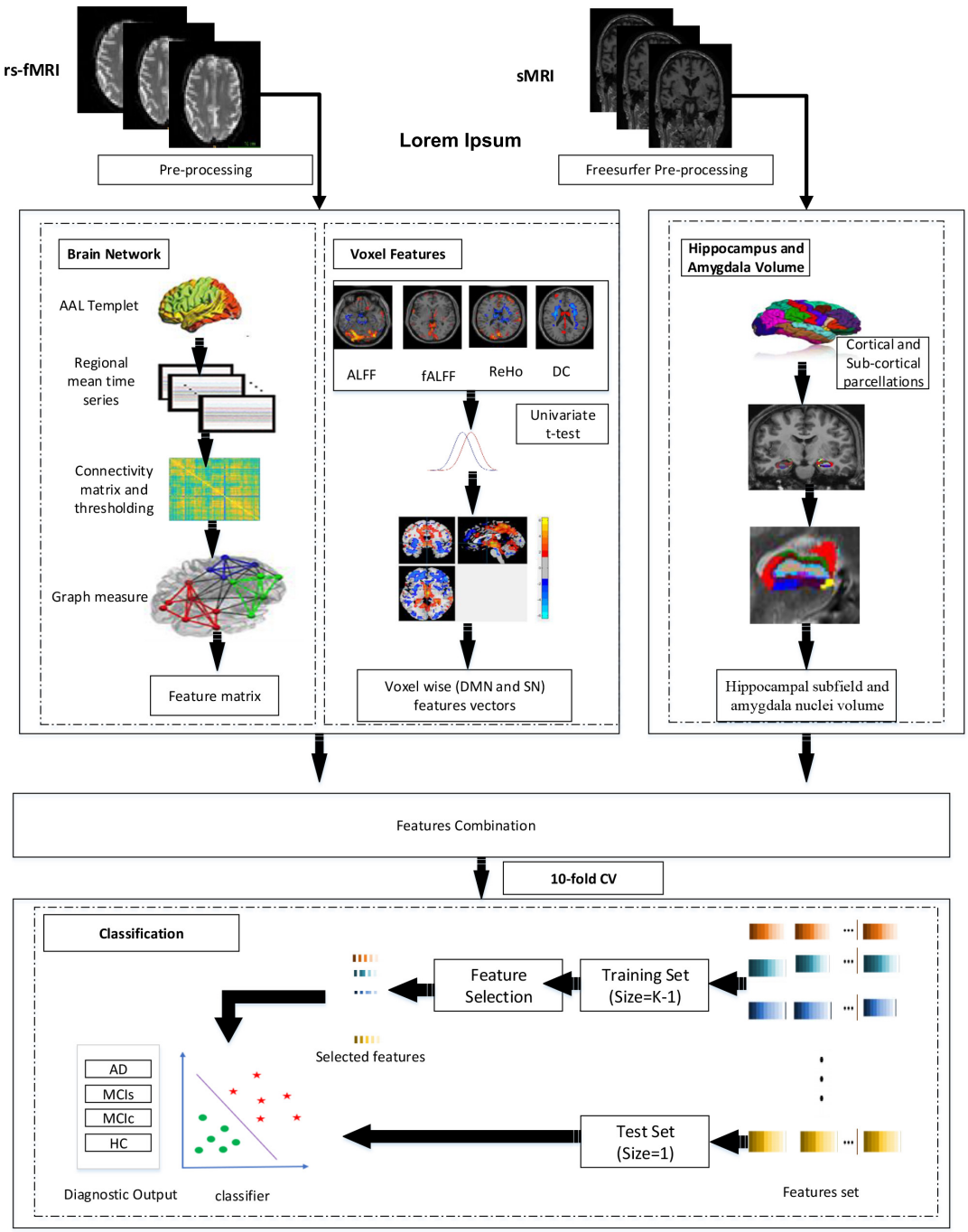

FIGURE 1 | Overview of the proposed framework.

Hippocampal Subfield and Amygdala Nuclei Volume

Hippocampal subregions in MRI have been demonstrated to play a role in predicting AD in those with moderate symptoms (van Maurik et al., 2017). It is more crucial to assess the sub-volume of the hippocampus in order to compute atrophy measures on the hippocampal subfield more precisely and to identify AD in individuals with MCI as well as normal controls (Zheng et al., 2018). Hippocampal segmentation was carried out utilizing the Freesurfer (Fischl, 2012) software in our procedure. First, the cortical and subcortical segmentation was performed with Freesurfer (version 6), and then the hippocampal subfield and amygdala nuclei volume segmentation were performed with Freesurfer's segmentHA_T1.sh function (Fischl, 2012), and

details can be found at[5]. Hippocampus atrophy is thought to be a key indicator of AD (Sørensen et al., 2017). The hippocampal subregion parcellation approach, provided by Freesurfer, was finally used to estimate hippocampal subregions and amygdala nuclei subfields (version 6). This program creates a computational parcellation of the amygdala and hippocampal regions using an atlas-based probabilistic Bayesian interface and ultra-high resolution *ex-vivo* MRI imaging data (0.1–0.15 mm isotropic). Simultaneous segmentation of both structures ensures that there is no overlap between them and that there is no chance of a gap between them (Saygin et al., 2017). The subiculum, the presubiculum, the parasubiculum, the cornu amonis fields 1, 2/3, and 4 (referred to as CA1, CA3, and CA4), the granule cell sheet of the Dentate Gyrus (DG), a transition of Hippocampus-Amygdaloid Area (HATA), the fimbria (a white matter area), the molecular coat of DG, the fissure region of the hippocampus, and the tail of the hippocampus are the 12 regions, as illustrated in **Figure 2**. Similarly, the accessory basal and basal, the central medial, the lateral, the cortical, and the anterior amygdala regions, the para laminar nucleus, and the Cortico-Amygdaloid Transition Area (CTA) are the nine subregions of the amygdala.

[5]https://surfer.nmr.mgh.harvard.edu/fswiki/HippocampalSubfieldsAndNucleiOfAmygdala

Functional Network Construction

The brain network nodes were constructed by parcellation of the entire brain into 90 regions of interest by utilizing the automated anatomical labeling (AAL) template that gives an entire functional division of the cortex (Tzourio-Mazoyer et al., 2002). The time series obtained inside every voxel of the 90 regions of interest were averaged, which produced signals that served as the nodal features. Pearson's correlation coefficient among the time series of the entire brain region was used to construct the value of the edges for networks. Then, Fischer's *r*-to-*z* conversion was practiced on the rough random connectivity matrix to enhance the partial correlation coefficient uniformity (Risacher et al., 2009; Wee et al., 2012). The obtained matrix is symmetrical diagonally with zero value (Zhan et al., 2013). The sparsity threshold was utilized to define the value of the possible edges on an individual's brain networks. The threshold serves as the connection cost for networks, which is explained as the ratio of the total possible number of connections to the suprathreshold relation within the brain networks (Sanz-Arigita et al., 2010). There is no straightforward approach to define a single sparseness threshold because various sparseness drive various analysis outcomes (He et al., 2009; Hojjati et al., 2018). This experiment examined each network at costs ranging from 5 to 25% at 1% intervals. In addition, we also carried

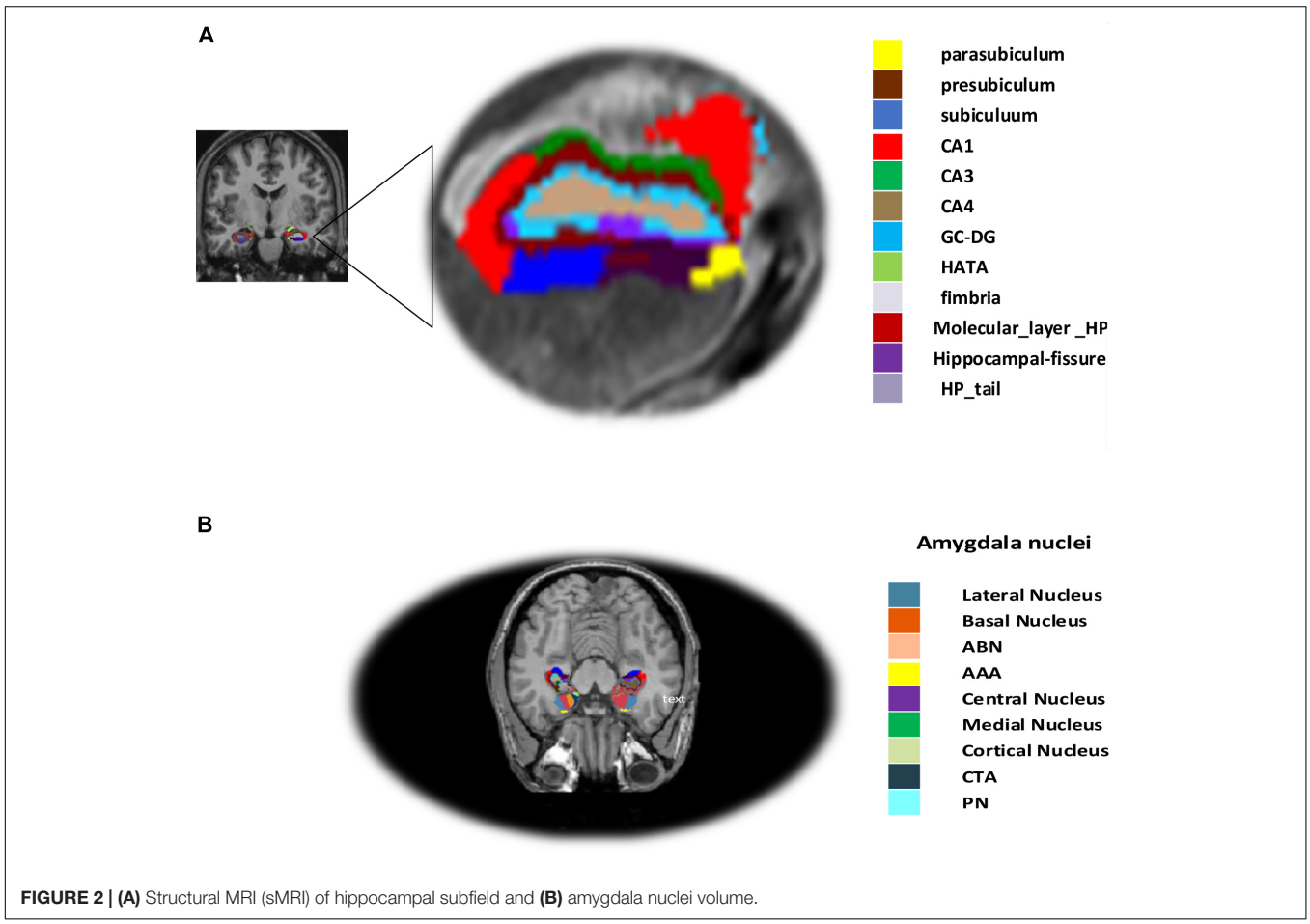

FIGURE 2 | (A) Structural MRI (sMRI) of hippocampal subfield and **(B)** amygdala nuclei volume.

out an analysis over various threshold values to examine the excellent threshold value (Fornito et al., 2010). To create efficient network parameters statistically fascinating variations in network parameters among different classification groups on various sparsity levels were measured.

Brain Network Feature Extraction

Entire brain networks parameters were calculated and evaluated utilizing the Matlab 2019a[6] program and matlab_bgl[7]. All graph matrices were evaluated using the undirected connectivity matrix on 0.01–0.027 Hz frequency band. To retrieve dynamic features and eliminate largely redundant matrix features, we computed five global graph parameters for the undirected graphs. These five global graph parameters are as follows: local efficiency, global efficiency, clustering coefficient, characteristic path length, and small-worldness (Tan et al., 2019). In the feature extraction section, we extracted brain network features for 270 nodal features of the brain network, in which ND, NL, and BC were calculated for further study and for the classification framework. In short, for the obtained node i, ND, NL, and BC were defined as follows:

$$L_i = \frac{\sum_{j \neq i \in V} L_{ij}}{(V-1)} \quad (1)$$

$$K_i = \sum_{j \in V} b_{ij} \quad (2)$$

$$B_i = \sum_{i \neq j \neq m \in V} \frac{S_{jm}(i)}{S_{jm}} \quad (3)$$

where L_{ij} represents the minimal number of edges among nodes i and j, V represents the range of the graph, b_{ij} represents the network structure among nodes i and j, S_{jm} represents producing the shortest path length number among nodes m and j, $S_{jm}(i)$ where indicated the shortest path number over the node i among nodes m and j. Possibly, path length L_i calculates the pace of the message that is carried *via* a specific node, each node degree K_i corresponds to the connected link number to the particular node; the larger the value of b_i, the higher the meaning of node i to the communication link within the networks, which reflect the information interaction level in the brain network.

Voxel-Wise Features Extraction

In this study, we illustrated voxel-base feature estimation from rs-fMR utilizing the REST toolbox pipeline. These voxel features can be classified into DMN (ReHo, fALFF, and ALFF), DC, and SN. We utilized the ReHo voxel to examine the regional brain activity amid the phase of the brain at resting. The Kendall's Coefficient of Concordance (KCC) approach was utilized to calculate the voxel-wise features. Individual ReHo maps were obtained from all brain voxels for individual subjects. A higher ReHo value was obtained for the voxel consisting of its closest neighbors, and brain voxel features were obtained for a larger regional coherence within a cluster. Larger analyses in recent literature indicated the potentiality of ReHo in recent clinical practice (Zang et al., 2004; He et al., 2007). Similarly, the ALFF measure estimates the regional spontaneous activities of the brain, and fALFF is an improved version of ALFF. The time series were transformed and filtered to the frequency region utilizing a fast Fourier transform (FFT) followed by its corresponding power range. The fALFF is a modified domain of ALFF, which is characterized by the average amplitude ratio within the low-frequency range. A large body of literature on the brain has indicated the unusualness level of the particular signal in brain regions for a disease class as related to a control class while employing statistical univariate tests (Arbabshirani et al., 2017). Recently, many works of literature have utilized *t*-tests to calculate descriptive biomarkers from neuroimaging for machine learning (Chaves et al., 2009; Wee et al., 2012). The main results of the statistical analysis tests are generally carried out using *p*-values. We generated a diagnostic feature estimation, that is, ReHo, fALFF, ALFF, and DC, among two classification groups at the threshold value of $p < 0.05$. The correlation cluster size on the defined threshold ($p = 0.05$) associated with the respective voxel *p*-value was determined by Monte–Carlo simulations using the AlphaSim tool embedded in REST to calculate the cluster value and the cluster size. Similarly, for SN, we utilized a well-validated region of interest (ROI) that included 12 posterior and 7 anterior SN nodes accessible at[8] and were extracted using independent component analysis (Shirer et al., 2012).

Features Selection Techniques

The number of features per subject, as in the neuroimaging study, is extremely high in comparison to the number of patients, a phenomenon known as the curse of dimensionality. Furthermore, dealing with a large number of features might be problematic because of the computational limitations of dealing with high-dimensional data, which can lead to overfitting. Feature selection is a step that comes before the classification problem and helps to minimize the dimensionality of a feature by choosing the right features and leaving out the wrong ones. This stage reduces the computing time for the training and testing datasets, speeding up the classification process and improving classification accuracy. To remove duplication and dependence, we first normalized the extracted features using the standard scalar function from the Scikit-learn module (Pedregosa et al., 2011), which modifies the dataset in such a manner that its distribution has a mean of 0 and a unit variance of 1. Features selection techniques utilized in this model are described below.

Least Absolute Shrinkage and Selection Operation

The least absolute shrinkage and selection (LASSO) method (Tibshirani, 1996) is a dynamic process and is utilized to select the significant features set. This method is basically based on regularization and feature elimination. The LASSO technique helps to reduce the residual sum of squares present in the analysis by ordinary least square regression (OLS), which places a constraint on the absolute sum values of the design framework.

[6]https://www.mathworks.com

[7]https://github.com/dgleich/matlab_bgl

[8]http://nitrc.org/projects/bnv/

LASSO measures model coefficients β by minimization of the function below:

$$RSS_{LASSO}(\beta_i, \beta_0) = \underset{\beta}{arg\,min}\left[\sum_{i=1}^{n}\left(y_i - (\beta_i x_i + \beta_0)^2 + \alpha\sum_{j=1}^{k}|\beta_j|\right)\right] \quad (4)$$

where x_j represent the data input at observation j and a vector k, and n represent the observation sample. y_j represent the observation response at i. α is a user-defined non-negative parameter for regularization that controls the penalty strength. If α is largely sufficient, then parameters are compelled to be zero, ultimately leading to generating only efficient features vector. When α tends to zero, the model turn to OLS with the most efficient features vector (Hanyu et al., 2010).

Support Vector Machine-Recursive Feature Elimination

The support vector machine-recursive feature elimination (SVM-RFE) method is basically a multivariate wrapper technique based on the backward feature elimination technique, which precisely adopts a model and eliminates the less relevant feature vector till the specific number of relevant features is obtained. The ranking principle for the SVM-RFE is identical to the SVM technique. After this, the features that acquired the lowest rank is eliminated because it has the lowest response on evaluation, while the other feature vectors are selected for the SVM model in another iteration. All the irrelevant feature vectors were removed based on the repeated sequential procedure. Entire feature vectors are graded according to the elimination rank. A detailed explanation of the SVM-RFE technique can be explored in a preceding article (Guyon et al., 2002). In this study, after the implementation of SVM-RFE, the highly informative training feature vectors were kept which boosted cross-validated performance accuracy to train the classifiers.

Joint Mutual Information

Mutual information (MI) can be applied to evaluate any arbitrary relation among random variables in the information theory (Kraskov et al., 2004). Truly, the MI among two arbitrary variables, X and Y, is a calculation of the measure of knowledge on Y given by X or, reversely, on X supplied by Y. If X and Y are independent, that is, if X has no message about Y and vice versa, then mutual information between them is zero. For two random variables, X and Y, MI is calculated as

$$I(X;Y) = H(X) - H(X/Y) = H(Y) - H(Y/X) = H(X) + H(Y) - H(X;Y) \quad (5)$$

where H(.) is entropy, $H(X/Y)$ and $H(Y/X)$ represent conditional entropies, respectively, and similarly, $H(X;Y)$ represent joint entropy for X and Y, which are calculated as

$$H(X) = \int_x P_X(x)\log P_X(X)dx \quad (6)$$

$$H(Y) = -\int_y P_Y(y)\log P_Y(y)dy \quad (7)$$

$$h(X;Y) = -\int_x\int_y P_{X,Y}(x,y)\log P_{X,Y}(x,y)dxdy \quad (8)$$

where $P_x(x)$ and $P_y(y)$ represent marginal density value and $P_{x,y}(X,y)$ defined the joint probability density value for X and Y, correspondingly. The function which defines the marginal density are:

$$P_X(x) = \int_y P_{X,Y}(x,y)dy \quad (9)$$

$$P_Y(y) = \int_x P_{X,Y}(x,y)dx \quad (10)$$

By substituting Eqs. 6, 7, 8 in Eq.5, the MI equation will be

$$I(X;Y) = \oint_x\int_y P_{X,Y}(x,y)\log\frac{P_{X,Y}(x,y)}{P_X(x)P_Y(y)}dxdy \quad (11)$$

The discrete form of the equation can be represented by the integration over summation in the date for all possible values. Therefore, estimation of $P_{x,y}(x,y)$ is required to calculate the Joint Mutual Information (JMI) between X and Y. The discrete form of JMI is represented by the below equation.

$$I(X;Y) = \sum_{x\in X}\sum_{r\in Y} P_{X,Y}(x,y)\log\frac{P_{X,Y}(x,y)}{P_X(x)P_Y(y)} \quad (12)$$

when F_k is one of the traits in a set of traits $\{F_1, F_2, \ldots, F_k\}$ and Y is an outcome that can be assumed by the trait, and the MI technique can pick the efficient trait. The process usually treats the trait as an independent random variable and is sort in a descending order based on their mutual information according to the obtained value Y, which selects the top n number of features. The process is conditioned by parsimonious and proper feature vectors that should (i) not be highly correlated among them and (ii) be individually relevant. JMI is shared among $\{F_1, F_2, \ldots, F_k\}$ and Y is highlighted at Eq. 13, where F_k and Y represent the elements of F_k and Y, correspondingly.

$$I(F_1, F_2, \ldots, F_k) = \sum_{f_1\in F_1}\sum_{f_2\in F_2}\cdots\sum_{f_k\in F_k}\sum_{y\in Y} P(f_1, f_2, \ldots, f_k, y)\log\frac{P(f_1, f_2, \ldots, f_k, y)}{P(f_1, f_2, \ldots, f_k)P(y)} \quad (13)$$

A JMI feature elimination technique initializes from an empty feature of trait, which iteratively calculates $F_i s$ and is added to the empty set, creating the optimum increment measure in the JMI among the feature vectors and the results. JMI is considered to be a highly stable and a flexible feature reduction technique amid all the information-theoretic feature elimination techniques established until now.

Random Forest Classifier

Random Forest is an ensemble learning approach, originally developed by Breiman (2001) to address regression and classification problems. The implementation of RF is based on the parameters set up, among which is the number of features in each branch and the number of trees. Previous studies noted that the optimum results could be obtained by setting default parameters (Immitzer et al., 2012; Zhang and Roy, 2017). However, studies conducted by Liaw and Wiener (2002) suggested that the larger the number of trees the more stable will the results be. In another study, Breiman (2001) noted that using more number of trees may not be beneficial for performance, but there is also no negative effect for the model. In another piece of literature, Feng et al. (2015) analyzed that, with the number of trees = 200, RF could reach precise results. Regarding the split parameter, many previous studies utilized the default parameter value $\sqrt{p}$; where p represented the number of predictor variables (Duro et al., 2012). However, in our model, we set a number of trees = 100, 200, 500, and 1000; split = 1:10 with a step size 1 to obtain the optimal performance. RF classifiers were implemented using the Scikit-learn Python library (Pedregosa et al., 2011).

Support Vector Machine Classifier

As a supervised learning technique, SVM (Cortes and Vapnik, 1995) divides the classification group by finding the best hyperplane. By training data, SVM is trained in a given features space. Thereafter, that test dataset is classified according to its arrangement in the n-dimensional vector field. SVM has been practiced in numerous neuroimaging fields (Zhang et al., 2011; Collij et al., 2016) and is recognized as one of the highly robust machine learning tools in the area of neuroscience. Mathematically, in a 2D field, a linearly separable features vector can be separated by a line. A line equation is defined by $y = ax + b$. By replacing x with x_1 and y with x_2, the equation will become $a(x1 - x2) + b = 0$. If we stipulate $x = (x1, x2)$ and $w = (a - 1)$, we get $w.x + b = 0$, which gives the hyperplane equation. The hyperplane equation with a linearly separable output has the following form:

$$f(y) = z^{T\phi}.(y) + b \tag{14}$$

where y represents the input data, z^T represent a hyperplane, and $\phi(y)$ represents a function that map vector y into a high dimension. The elements z and b are appropriately scaled by the equal value, and the selected hyperplane in equation (14) remains stable. Furthermore, hyperplane can be making an exclusive pair of (z,b), which is represented by below formulation:

$$\min |z^{T\phi}.(y_i) + b| = 1, \quad i = 1, \ldots, N, \tag{15}$$

where $y_1, y_2, \ldots, y_N$ represent the training vector. The hyperplane in equation (15) are recognized as canonical hyperplanes. The hyperplane is represented as below:

$$z^{T\phi}.(x) + b = 0, \quad \textit{which is same as}$$
$$z^{T\phi}.(y) = 0(\textit{which has more dimensions}) \tag{16}$$

For a feature x that does not fit the obtained hyperplane, the equation below represents it (Cortes and Vapnik, 1995):

$$z^{T\phi}.(x) + b = \pm s||z|| \tag{17}$$

where s is the measure of vector x to the defined hyperplane. Therefore, the output vector *fy* from SVM is exactly equivalent to the distance *sx* and z vector for the obtained hyperplane. Furthermore, in this study, we have utilized the kernel-support vector method, which is good to deal with the non-linear issue with the help of the linear classification method and which engages in swapping of the linearly un-classifiable vector into linearly classifiable. The concept inside this idea is a linearly unclassifiable vector that might be linearly classifiable in high dimensions. The kernel is mathematically defined as,

$$K(x, y) = (x, y)^d \tag{18}$$

where x and y represent features in the input and d represents the kernel element. Gaussian radial bias functions are represented by:

$$K(x, y) = \exp\left(-\frac{||x - y||^2}{2\sigma^2}\right) \tag{19}$$

where x and y represent two samples input, which are vectors in input $||x - y||^2$ that can be represented as Euclidean distance in the square form among two features. σ represents kernel elements. Sigmoid function derived from the neural networks was used for activation, and the bipolar sigmoid function is utilized often for an artificial neuron, which is represented by

$$K(x, y) = \tanh(\propto x^T y + c) \tag{20}$$

where x and y represent features in the input and $\propto$, c represents the kernel elements.

The SVM classifier was implemented by utilizing the Scikit-learn library (Pedregosa et al., 2011). The Scikit-learn library internally utilized LIBSVM (Chang and Lin, 2011) to handle all calculations. To obtain optimal classification accuracy, hyperparameters; cost c and γ (kernel width) of SVM must be tuned. With the aid of grid search and a 10-fold CV, these tuned optimal hypermeter values are automatically selected from the specified range of c = 1 to 9 and $\gamma = 1e^{-4}$ to 1. CV is a popular data shuffling and resampling technique for evaluating the generalization idea for the design of a predictive model and for preventing the underfitting or overfitting of the classifiers. CV is widely utilized in predictive modalities such as classification problems. In such types of issue, a framework is fitted with a known dataset, which is known as the training set, and a set of unknown samples against that model is evaluated, as the test set. The purpose is to have a testing sample for the model in the training stage and to then demonstrate how the process adopts various unknown datasets. Each phase of the CV engages the partition of the data samples into independent datasets, followed by an analysis of an individual sample. Subsequently, the study is validated on new independent subsets called testing samples. To lessen variability, numerous phases of CV are carried out by several partitions, after which an average of the results is considered. CV is a powerful procedure for evaluating model

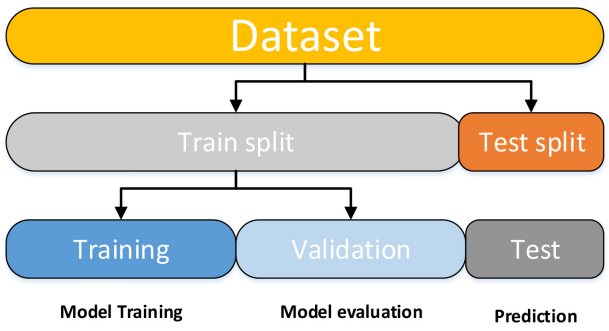

FIGURE 3 | The data splitting stage is depicted in a diagram.

performance. Moreover, the data split features were applied in our model. The training data is used to train the machine learning (ML) classifier for subject group prediction across the provided features. After that, the classifier will be fine-tuned and tested on holdout data. To begin, model training entails a procedure in which ML passes the trained data *via* a process in which the classifier uncovers the train data patterns. As a result, the parameters are passed through to the target variables. As stated, our goal was to develop an ML classifier for the specific purpose of accurately identifying patients with AD and HC. We used supervised and ensemble learning models to propose an efficient ML classifier in the classification of subjects with AD to predict the AD patient status given a collection of independent variables. For crossvalidation purposes, we partitioned the dataset into three subgroups using this procedure. One set (test data) is used to forecast model performance, while the other two sets (training and validation) are used to evaluate model performance by training against new data. We randomly divided the entire dataset into a 70:30 ratio after data preparation, with 70% utilized for training and 30% used for testing. This will allow the system to generate fresh combinations each time the model is run, allowing for the most accurate prediction. The training dataset was divided into two subsets for training and validation after model training. **Figure 3** is a brief explanation of each model.

In this study, accuracy, specificity, sensitivity, F1-score, and Receiver Operating Characteristic (ROC) curves were used for performing validation of the classifiers. We also calculated Cohen's kappa values for each class group, which represent interrater reliability between two classes (Cohen, 1960). Kappa calculates the proportion of information scores in a table's principal diagonal and then adjusts them for the amount of agreement that might be expected by chance alone. For two raters, the formula is $K = \frac{p_0 - p_e}{1 - p_e}$, where is the relative observed agreement between raters and is the hypothetical probability of chance agreement. In this method, we referred to HC as negative samples, patients with AD as positive samples, TN represents the number of negative sample sets that are correctly classified, total positive (TP) denotes the number of positive samples correctly categorized, false positive (FP) denotes the portion of negative dataset classified as positive, and false-negative (FN) denotes the number of positive datasets classified as negative samples. The accuracy, specificity, precision, and area under the curve are defined as follows:

$$accuracy = \frac{TP + TN}{TP + FP + FN + TN} \quad (21)$$

$$specificity = \frac{TN}{TN + FP} \quad (22)$$

$$sensitivity = \frac{TP}{TP + FN} \quad (23)$$

The ROC curve, which is a curve obtained by plotting the TP rate versus the FP rate, can calculate the diagnostic capability of a binary classifier. The area under the ROC curve is proportional to the classifier performance.

RESULTS

Findings From a Demographic and Clinical Approach

In AD over HC, AD over MCI, MCI over HC, and MCIs over MCIc, there was no significant age difference between groups. In all group combinations, however, there was a significant difference in MMSE ($P > 0.05$) and CDR ($P > 0.05$). AD has a male-predominant gender percentage while HC has a female-predominant gender percentage, whereas MCIs and MCIc have a female- and male-predominance percentage, respectively. Male dominance in AD is 58.73%, while female dominance in HC is 51.47%; whereas female and male dominance in MCIs and MCIc is 59.45 and 60%, respectively. These variables are described and analyzed in-depth in **Table 1**.

Highly Sensitive Brain Network Features

This section presents the top brain network features obtained by the JMI algorithm. Details about the selected network feature number and location of the AAL brain regions with their connectivity in the circular graph are presented in **Figure 4** below. The feature reduction using the JMI method preserves all of the following attributes: betweenness centrality (BC), nodal path length (NL), and nodal degree (ND) features. We noted that, for all group classification NL trait contributed more as compared to the other two network features. The features selected show roughly similar features for the AD vs. HC and the MCIs vs. MCIc group and include the right precentral gyrus (PreCG.R), the left middle temporal gyrus (MTG.L), the left superior temporal gyrus (STG.L), the hippocampus (HIP.L and R), the amygdala left (AMYG.L), and the cuneal cortex right (CUN.R). For AD vs. MCI classification, the hippocampus (HIP.L and R), the cuneal cortex left (CUN.L), and the amygdala were selected along with other brain regions; similarly, for the HC vs. MCI group classification, the left middle temporal gyrus (MTG.L), the hippocampus (HIP.L and R), and the amygdala (AMYG.L and R) were selected along with other brain regions as shown in **Figure 4**. From this, we can conclude that the most affected brain region for all group classification analysis was mainly located on the middle temporal gyrus, the hippocampus, and the amygdala area

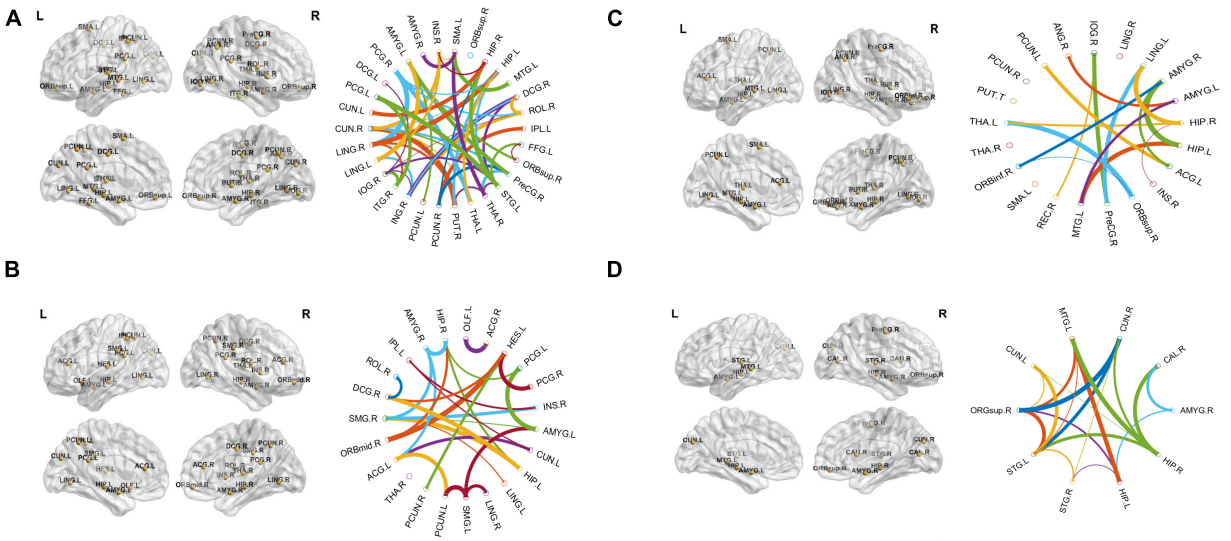

FIGURE 4 | The location and networks of cortical regions with the highly discriminative attribute of top brain regions (BrainNet Viewer)[8] and their corresponding circular connectivity (circularGraph) (http://www.mathworks.com/matlabcentral/fileexchange/48576-circulargraph): **(A)** Alzheimer's disease (AD) vs. healthy control (HC) group, **(B)** AD vs. mild cognitive impairment (MCI) group, **(C)** HC vs. MCI group, **(D)** stable MCI (MCIs) vs. converted MCI (MCIc) group.

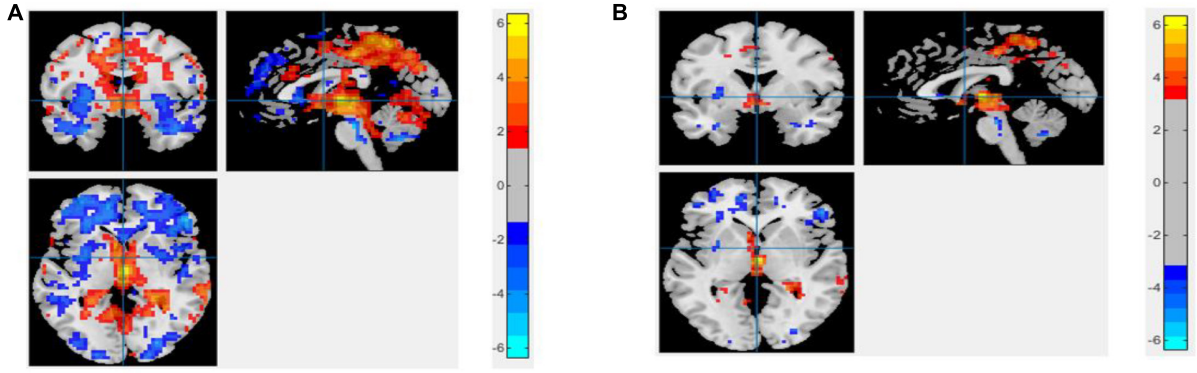

FIGURE 5 | An univariate statistical two-sample test on region of homogeneity (ReHo) voxel maps among two classification groups **(A)** AD vs. HC **(B)** MCIs vs. MCIc. The threshold value was set to $p < 0.05$. The hot and cold bar represent negative and positive changes.

followed by other brain regions. The location and brain region of these brain features are presented in **Supplementary Tables 1–4**.

Voxel-Based Sensitive Features

The region showing significant alteration in a univariate *t*-test are vital in achieving highly accurate differential prediction of the AD, MCI, and HC groups. For the optimal classification accuracy, previous studies (Arbabshirani et al., 2017) used the univariate statistical *t*-test to compute the group difference in the voxel-based analysis in the machine learning method. The main outcomes of the calculation are relied on statistical tests generally represented by *p*-values. Afterward, the excellent *p*-value only preserves the effective brain regions. Using the *t*-test of different group analyses, we created an analytically significant mask that preserved only the significant voxels difference between the two groups at $p < 0.05$ for ReHo, ALFF, and fALFF obtained from rs-fMR images. Consequently, adjusted individual voxel *p*-values of.05 were determined. Afterward, for SN, we utilized a well-validated region of interest (ROI) that included 12 posterior and 7 anterior SN nodes accessible at[9] and were extracted using independent component analysis (Shirer et al., 2012), as presented in **Supplementary Figure 5** and **Supplementary Table 5**. Similarly, to do a full-brain study of the areas impacted by AD and MCI, we utilized a frequently used graph-based metric of network architecture called degree centrality (DC). Individual network centrality maps were created in a voxel-by-voxel manner within the study mask. First, a voxel-based whole-brain correlation analysis was performed on the preprocessed functional runs. A correlation matrix was created by correlating the time course of each voxel inside

[9]http://findlab.stanford.edu/research.html

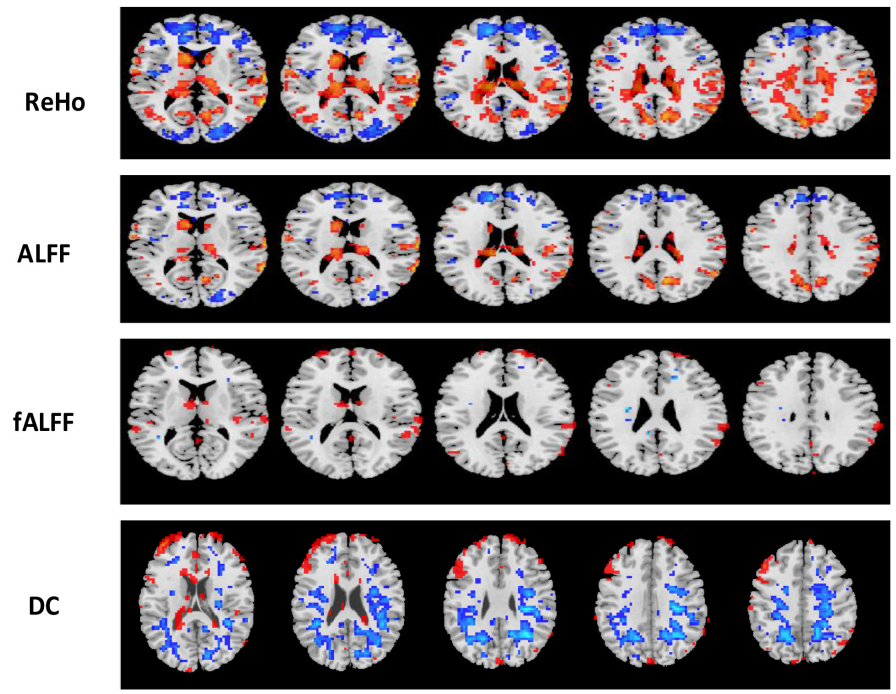

FIGURE 6 | Univariate *t*-test difference maps between two classification groups, AD vs. HC, of four voxel maps.

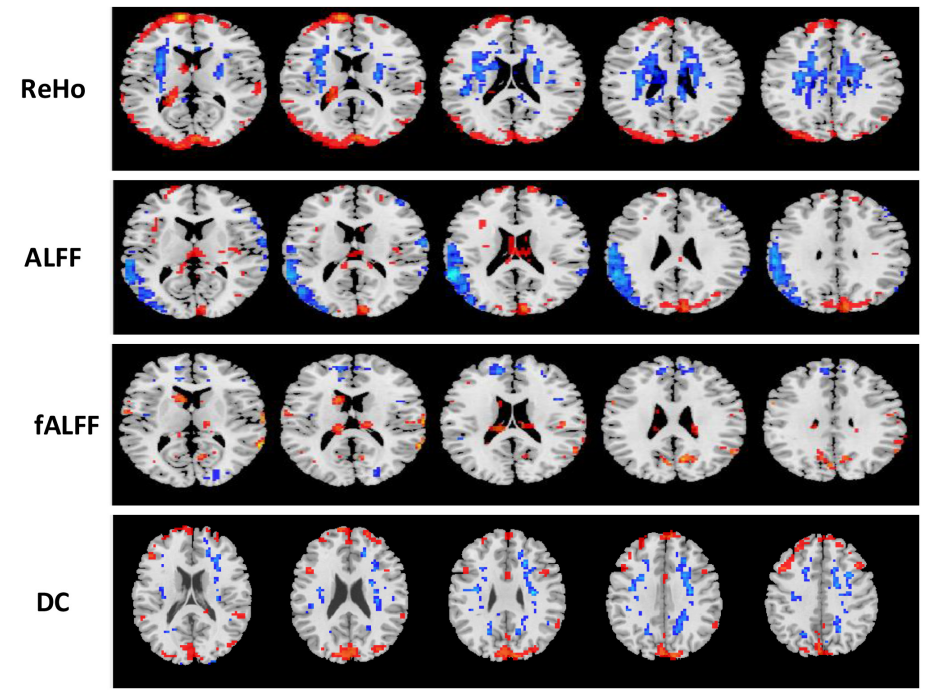

FIGURE 7 | Univariate *t*-test difference maps between two classification groups MCIs vs. MCIc, of four voxel maps.

the gray matter mask from each participant with the time course of every other voxel. The DC was calculated as the sum of the weights of the significant weighted connections for each voxel using an undirected adjacency matrix created by thresholding the correlation at $r > 0.25$ (Zuo et al., 2012). Finally, the DC on a voxel-by-voxel basis is calculated at the

individual level. The highly significant brain regions obtained on the voxel-based analysis for the proposed method are shown in **Figures 5–7** and in **Supplementary Figures 6, 7**. We have also presented the information of peak regions and their corresponding MNI co-ordinate in **Supplementary Tables 6, 9**. The most discriminative patterns obtained on the process and all information from regional coherence measures were calculated. This can suggest that various parts of the brain region go through various functional alterations because of MCI and Alzheimer's. Therefore, to accomplish optimal diagnostic accuracy of the classification framework, it should cover the complementary information about altered brain patterns. One major discovery of this framework is that the effective and important regional voxel-based features can complement the brain network features obtained from the rs-fMRI data and structural features from sMRI.

Classification Results

In this section, we evaluated the diagnostic performance of the purposed method on sMRI of the hippocampus, the amygdala features along with brain network features, and the voxel-based features of rs-fMRI and have combined all of them with that of SVM and RF classifiers for respective binary classification. We implemented and analyzed the three features obtained from sMRI and rs-fMRI images separately as well as combined. We used the hippocampus and the amygdala volume, as well as voxel features, as complementary features for the brain network, which help to improve the classification accuracy for AD and MCI diagnosis. The combined procedure shows great potential for the classification task with higher AUC, accuracy, better sensitivity, and precision. For brain network features, we measured the different features such as ND, NL, and BC. Through a series of threshold values in the cost, 5–25% of best and stable results were utilized for diagnostic classification of each group, which is presented in **Supplementary Figures 1–4**. Similarly, for voxel-based features, we calculated the five voxel features, namely ReHo, ALFF, fALFF, DC, and SN: group difference univariate *t*-test. We evaluated our feature reduction and classification algorithm on feature vectors using a 10-fold CV. First, we partition the data into 10 equal-sized subsets (folds) which contain 90% subset for training and the remaining 10% of the test subjects. Then, features selection was carried out on the training subsets. We implemented the distinct features selection algorithm to select the important feature sets to optimize the classifier performance. Based on the obtained top selected features set, SVM and RF classifiers were trained. Because each feature had a distinct scale, we linearly ascended each training feature to simulate to a range between 0 and 1 in our case; the same scaling procedure was then used on the test dataset. In our scenario, the RBF kernel outperforms other kernels because of the modest number of features used. For each test and training subset, we implemented independent feature selection to escape the feature selection bias amid a 10-fold CV. We measured cross-validated accuracy for classifiers on a given number of feature sets and plotted the numbers of selected features against the accuracy as shown in **Figure 8** for each group classification.

Finally, we evaluated the AUC as shown in **Figure 9**, and accuracy, sensitivity, specificity, F1-score, and Cohen's Kappa in **Figure 10** for individual and combined feature set and different features selection algorithm as presented in **Tables 2–5**. **Table 2** presents the classification of AD against HC. In this study, we compared the performance of different features selection methods on the different feature sets with SVM and RF classifiers. The Joint Mutual Information (JMI) feature reduction technique with SVM classifiers outperforms all other techniques contemplated with the highest AUC and accuracy. For AD vs. HC diagnostic classification, the integrated (Hippocampal + Amygdala + BN + Voxel) feature vectors performed well in comparison with individual feature set with 97.03% AUC, 95.87% accuracy, 97.35% sensitivity, and 95.95% specificity along with 96.33% F1-score and.913 Cohen's Kappa index, respectively. We did not notice the significant classification difference between the SVM-RFE, and LASSO features selection algorithm for AD vs. HC. In comparison with the RF classifier, there was 1–6% better performance in terms of accuracy with SVM for AD vs. HC classification on different features vectors, but we noticed slightly better specificity for combined features with LASSO for RF classifier. For voxel features with JMI feature selection, we noticed the same pattern for RF classifiers that perform equally with SVM classifiers in terms of accuracy. For hippocampal and amygdala volume, RF classifiers with SVM-RFE features selection show good performance in terms of F1-score. Similarly, for the classification performance of AD vs. MCI as shown in **Table 3**, we obtained the 94.03% AUC, 92.45% accuracy, 95.98% sensitivity along with 90.45% specificity, 93.75% F1-score, and.9105 of Cohen's Kappa index, respectively. For HC vs. MCI classification as shown in **Table 4**, we achieved the highest classification accuracy on the JMI feature selection method. Although there was not much difference between the individual features method, JMI significantly improved for the combination of the hippocampal, amygdala, brain network, and voxel-based features sets with 92.06% AUC, 90.35% accuracy, and 94.34% sensitivity along with 92.11% specificity, 94.13% F1-score, and.9035 of Cohen's Kappa score. More importantly, from the results presented in **Tables 2–5**, brain network features perform well as compared to the hippocampal, amygdala (sMRI), and voxel-based (rs-fMRI) features for individual features in most of the cases.

Similarly, the classification performance for the less commonly reported group of MCIs vs. MCIc using different features selection methods is listed in **Table 5**. Like the previous pattern, the highest diagnostic classification results in terms of AUC, accuracy, specificity, and sensitivity were calculated with the JMI feature selection method as compared to other features selection technique. However, for MCIs vs. MCIc classification, there was no significant difference between the performance of SVM-RFE and the LASSO feature selection as compared to other different group classifications as shown in **Tables 2–5**. For the MCIs vs. MCIc classification, we obtained the 91.08% AUC, 88.03% accuracy, 94.85% sensitivity, and 89.71% specificity along with 93.17% of F1-score, and.8831 of Cohen's Kappa index, respectively, for combined feature

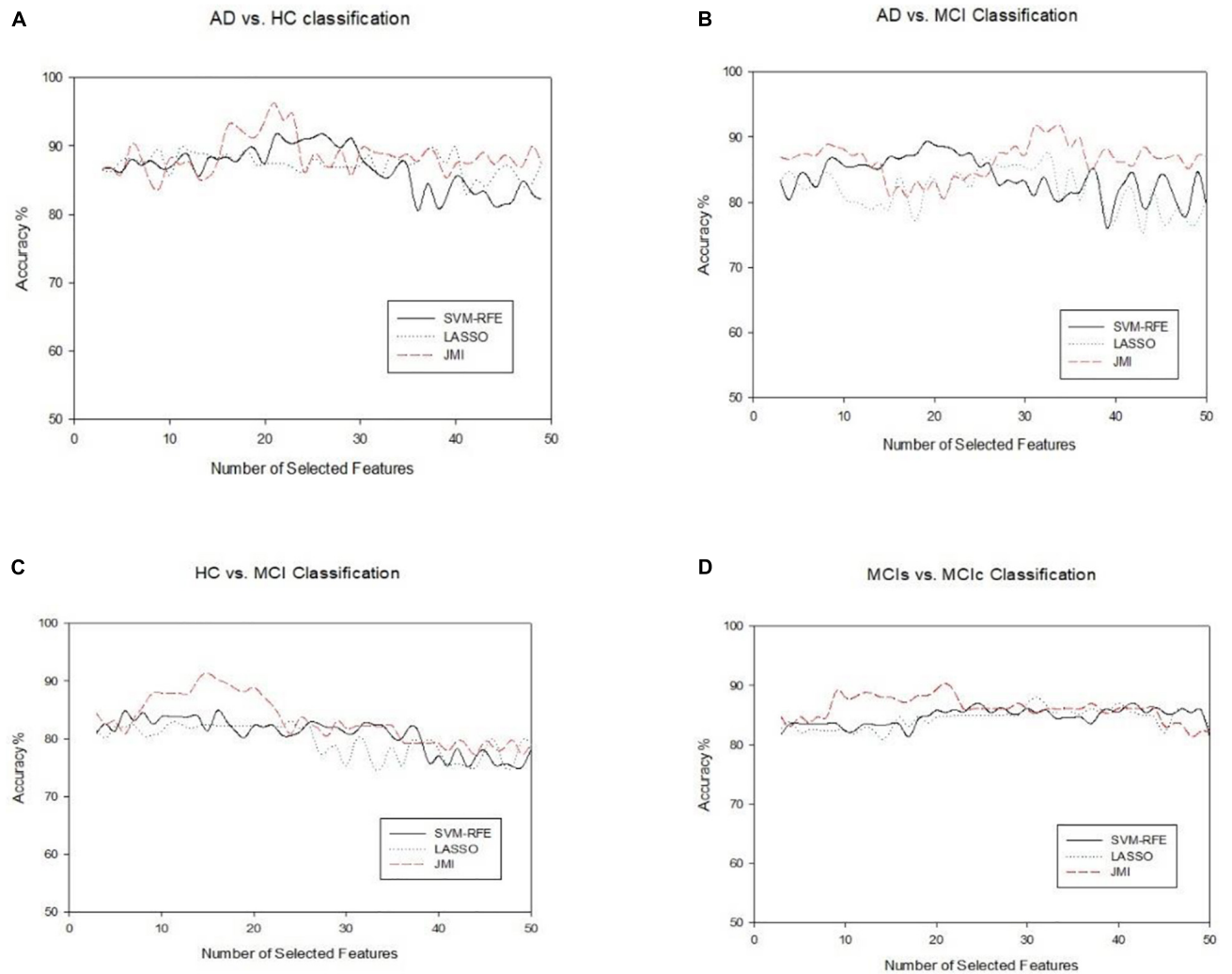

FIGURE 8 | An illustration of the performance of three feature selection algorithms for classifying four different groups on combined features vectors **(A)** AD vs. HC, **(B)** AD vs. MCI, **(C)** HC vs. MCI, and **(D)** MCIs vs. MCIc. The *x*-axis represents the number of selected features, while the *y*-axis represents the classification accuracy.

set, i.e., hippocampal and amygdala features (sMRI) as well as BN and Voxel (rs-fMRI) features. From **Table 5** for the MCIs vs. MCIc classification, SVM-RFE and LASSO feature selection method also shows the potential to compete the JMI feature selection with 90.19% and 89.75% AUC along with 85.32% and 85.11% accuracy, respectively. We also observed that accuracy is significantly increased while classifying MCIs vs. MCIs by integrating hippocampal and amygdala volume of sMRI along with brain networks and voxel features of rs-fMRI. Overall, we noticed that, as compared with RF classifiers, SVM classifiers perform better for almost all feature selection techniques and all three different kinds of feature sets. This may be due to lesser training data than the number of feature set. SVM is better than RF when there were a large number of features and lesser training data and RF is better for multiclass problems, while SVM is better for binary classification.

From all these reported results, it has clear evidence that the utilization of JMI as features selection algorithm for MCI and AD against HC classification and conversion prediction of MCI shows the great potentiality using SVM classifiers with a combination of structural features (hippocampal and amygdala), brain networks, and voxel-based (rs-fMRI) features. More importantly, the AUC curve as illustrated in **Figure 9** below for all classification groups shows that the proposed model was quite stable.

DISCUSSION

Alzheimer's disease can be detected earlier, which can aid with therapy and avoid brain tissue damage. For the diagnosis of AD, researchers have used a variety of statistical and machine learning models. In clinical research, the MMSE score, MRI

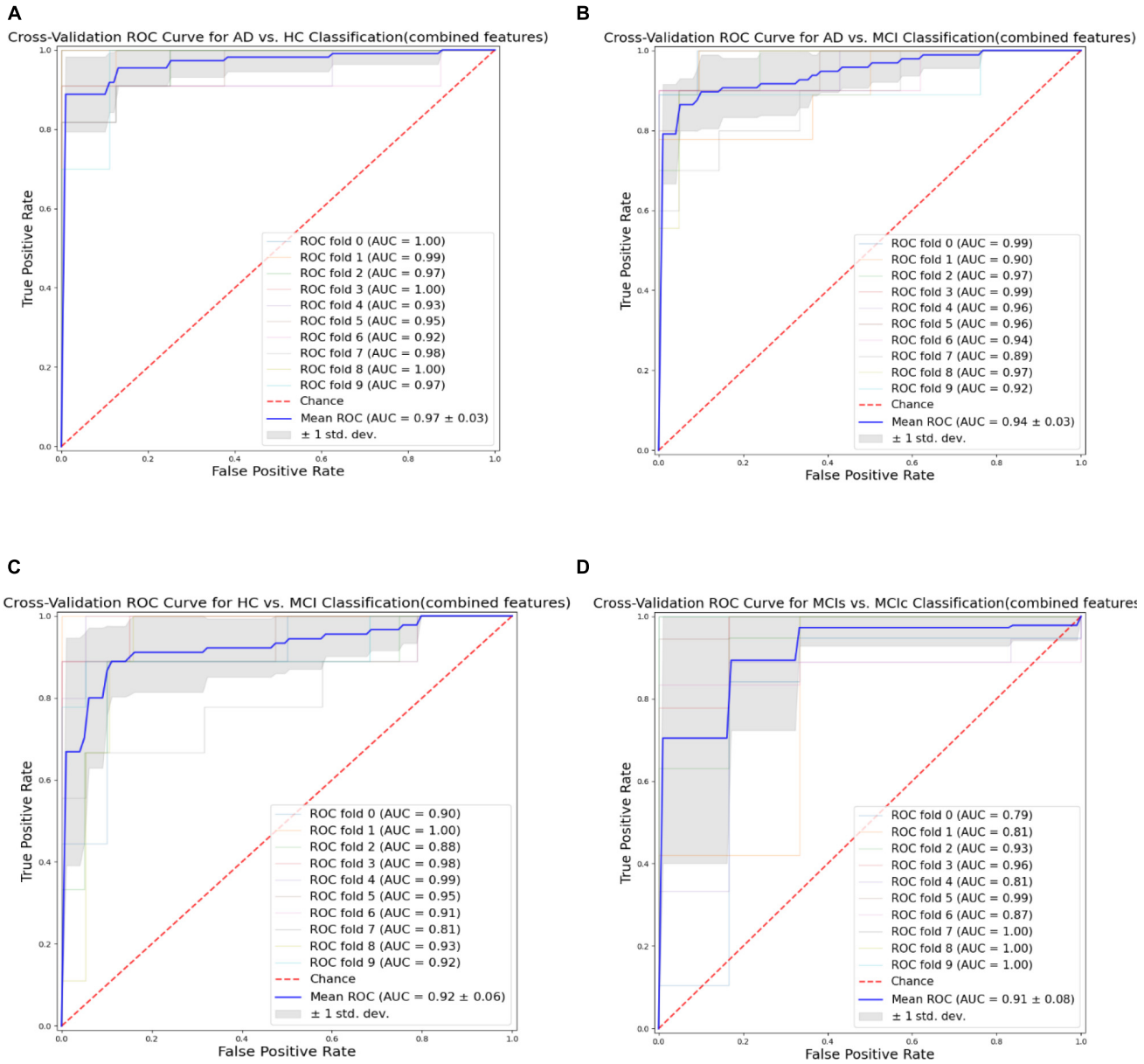

FIGURE 9 | Receiver operating characteristics (ROC) curve for **(A)** the AD vs. HC group, **(B)** the AD vs. MCI group, **(C)** the HC vs. MCI group, and **(D)** the MCIs vs. MCIc group for combined features vectors: Hippocampus, amygdala, brain network (BN), and voxel (Combined).

analysis (normalized whole-brain volume, hippocampal volume), biomarkers based on CSF, such as amyloid–42, and combined biomarkers have shown a great potentiality for AD diagnosis (van Maurik et al., 2017). The closeness between AD MRI data and normal healthy MRI data of older persons makes detection of AD difficult. A recent study suggested that decreased hippocampus subfield volumes have been commonly observed in dementia disorders such as AD and dementia with Lewy bodies (DLB) (Delli Pizzi et al., 2016; Mak et al., 2016, 2017). The volumes of the CA1, CA2-3, CA4, DG, and total subiculum (subiculum, presubiculum, and parasubiculum) are reduced in AD, according to one study (Mak et al., 2017). Similarly, the rs-fMRI data not only involve peculiar numerical features but also present rich dynamic temporal information. Several works of literature that relied on rs-fMR have been tested and verified for the diagnostic classification of MCI and Alzheimer's from the healthy population. However, those previous studies either focus only on structural features, the graph theory approach, or the voxel-based approach and lose the full potentiality of combing structural features (hippocampal-amygdala) and brain network with voxel-based features. Therefore, to examine the full possibility of rs-fMRI and sMRI on AD diagnosis, we presented insights into the performance for diagnostic classification of all four binary classification groups by combining the hippocampus

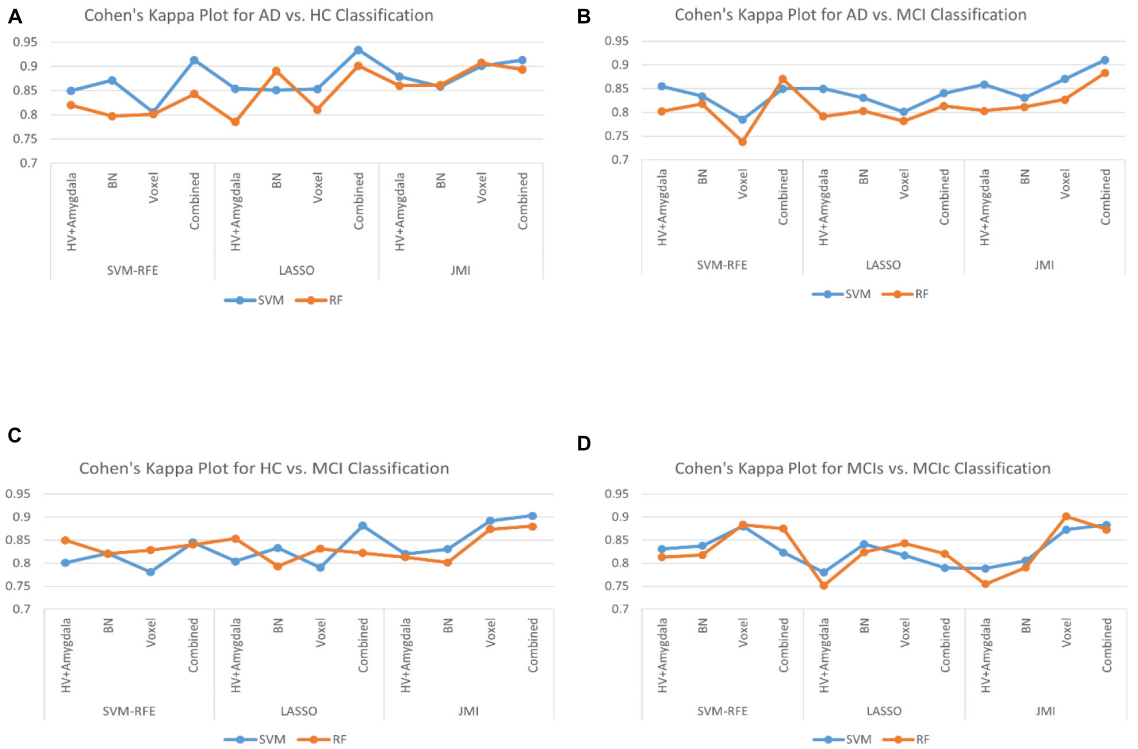

FIGURE 10 | The Cohen's Kappa index for **(A)** AD vs. HC group, **(B)** AD vs. MCI group, **(C)** HC vs. MCI group, and **(D)** MCIs vs. MCIc group for individual and combined feature set and different feature selection algorithm.

TABLE 2 | A 10-fold cross-validated binary classification performance for Alzheimer's disease (AD) vs. healthy control (HC) groups using support vector machine (SVM) and Random Forest (RF) classifiers.

		Performance Matrix										
		SVM						RF				
Feature selection method	**Features**	**AUC**	**ACC**	**SEN**	**SPE**	**F1**	**Cohen's Kappa**	**ACC**	**SEN**	**SPE**	**F1**	**Cohen's Kappa**
SVM-RFE	HV + Amygdala	87.12	84.51	91.13	85.07	85.45	0.8501	78.03	86.12	86.33	87.13	0.8201
	BN	90.42	90.13	81.04	85.12	84.13	0.8713	88.47	87.35	90.07	82.15	0.7972
	Voxel	92.17	88.97	90.71	95.09	88.46	0.8055	84.78	92.01	86.42	84.13	0.8013
	Combined	93.14	92.98	95.03	92.71	83.78	0.9131	91.05	91.23	88.88	82.23	0.8430
LASSO	HV + Amygdala	85.99	82.75	82.03	87.59	82.20	0.8538	80.05	75.43	83.11	84.05	0.7851
	BN	90.07	88.95	95.04	84.45	85.77	0.8512	87.74	86.71	91.08	87.71	0.8903
	Voxel	91.75	88.13	92.14	93.25	90.65	0.8531	87.31	90.45	87.72	76.11	0.8113
	Combined	95.95	94.13	93.53	95.51	84.38	0.9345	90.46	93.04	84.22	84.11	0.9012
JMI	HV + Amygdala	89.45	85.33	89.05	84.83	86.15	0.8791	80.85	87.59	82.2	85.38	0.8601
	BN	93.95	92.75	93.03	89.08	92.45	0.8583	87.75	87.47	90.35	91.37	0.8614
	Voxel	94.41	92.46	95.43	88.81	91.15	0.9010	92.51	95.00	85.87	93.15	0.9071
	Combined	97.03	95.87	97.35	95.95	96.33	0.9130	93.23	95.31	94.93	92.37	0.8935

subfield and the amygdala nuclei volume from sMRI along with brain network and voxels-based features (ReHo, fALFF, ALFF, DC, and SN) from rs-fMRI. Besides this, we also proposed the different feature selection algorithms for the classification of AD vs. HC, AD vs. MCI, HC vs. MCI, and the less commonly reported group, MCIs vs. MCIc. Our experimental outcome indicated that each feature set is important to achieving good classification performance.

Several recent works of literature have analyzed the neuroimaging method for discriminative classification of AD, with the target on patients with MCI, who may or may not convert to Alzheimer's, and identifying an individual

TABLE 3 | A 10-fold cross-validated binary classification performance for AD vs. mild cognitive impairment (MCI) groups using SVM and RF classifiers.

		Performance Matrix										
		SVM						RF				
Feature selection method	**Features**	**AUC**	**ACC**	**SEN**	**SPE**	**F1**	**Cohen's Kappa**	**ACC**	**SEN**	**SPE**	**F1**	**Cohen's Kappa**
SVM-RFE	HV + Amygdala	85.27	78.14	87.91	84.73	82.75	0.855	77.45	83.18	84.17	84.18	0.8021
	BN	91.42	84.85	95.12	87.45	88.13	0.8342	80.25	90.43	84.56	77.45	0.8178
	Voxel	85.32	82.83	84.51	93.13	83.52	0.7847	81.75	92.53	84.98	81.78	0.7380
	Combined	93.71	87.18	92.45	90.14	91.75	0.8501	86.45	88.37	84.73	82.51	0.8703
LASSO	HV + Amygdala	84.9	80.83	93.11	87.04	84.19	0.8503	78.51	82.58	78.95	84.45	0.7913
	BN	90.34	88.74	94.45	90.87	87.14	0.8305	85.91	90.98	87.42	83.31	0.8033
	Voxel	86.73	85.24	95.01	88.11	85.46	0.8013	85.41	91.21	84.63	78.98	0.7818
	Combined	93.91	90.45	94.46	91.71	89.58	0.8401	87.75	92.13	90.03	85.54	0.8135
JMI	HV + Amygdala	82.75	81.27	87.72	81.27	88.35	0.8587	79.31	83.24	81.18	85.03	0.8035
	BN	91.73	91.32	94.43	87.17	88.75	0.8309	86.08	87.53	88.14	84.23	0.8118
	Voxel	92.08	88.01	93.13	89.57	91.33	0.8703	87.89	93.58	89.13	85.85	0.8273
	Combined	94.03	92.45	95.98	90.45	93.75	0.9105	90.75	95.15	87.73	91.03	0.8831

TABLE 4 | A 10-fold cross-validated binary classification performance for HC vs. MCI using SVM and RF classifiers.

		Performance Matrix										
		SVM						RF				
Feature selection method	**Features**	**AUC**	**ACC**	**SEN**	**SPE**	**F1**	**Cohen's Kappa**	**ACC**	**SEN**	**SPE**	**F1**	**Cohen's Kappa**
SVM-RFE	HV + Amygdala	82.85	77.32	90.54	84.13	84.71	0.8010	76.53	86.15	90.23	78.97	0.8501
	BN	86.01	85.42	84.12	81.47	84.13	0.8210	78.56	84.45	88.11	78.47	0.8203
	Voxel	87.31	86.53	93.12	87.89	85.45	0.7809	84.01	90.35	88.75	80.10	0.8283
	Combined	91.21	85.21	93.45	92.11	88.79	0.8451	84.36	87.84	85.01	79.45	0.8401
LASSO	HV + Amygdala	84.92	76.95	87.3	82.08	82.83	0.8045	75.03	85.91	90.07	87.18	0.8531
	BN	87.42	82.15	88.63	87.45	84.88	0.8331	81.52	87.38	82.88	85.45	0.7933
	Voxel	87.13	80.45	86.85	91.12	86.91	0.7903	78.96	88.45	86.23	76.14	0.8311
	Combined	90.03	84.74	85.77	91.03	90.11	0.8815	82.41	87.15	82.95	80.75	0.8220
JMI	HV + Amygdala	83.57	79.45	88.45	79.85	83.50	0.8201	77.13	78.95	85.52	85.15	0.8130
	BN	91.83	86.15	92.09	94.15	87.71	0.8305	83.87	91.54	84.35	81.33	0.8015
	Voxel	90.57	86.43	85.15	86.01	91.23	0.8917	84.25	88.32	83.03	89.77	0.8738
	Combined	92.06	90.35	94.34	92.11	94.13	0.9035	85.15	91.12	85.31	84.95	0.8805

TABLE 5 | A 10-fold cross-validated binary classification performance for stable MCI (MCIs) vs. converted MCI (MCIc) groups using SVM and RF classifiers.

		Performance Matrix										
		SVM						RF				
Feature selection method	**Features**	**AUC**	**ACC**	**SEN**	**SPE**	**F1**	**Cohen's Kappa**	**ACC**	**SEN**	**SPE**	**F1**	**Cohen's Kappa**
SVM-RFE	HV + Amygdala	83.35	76.43	82.75	78.41	82.14	0.8310	75.02	80.37	85.3	79.41	0.8129
	BN	88.32	84.46	90.11	85.27	90.17	0.8375	80.45	87.52	91.15	80.14	0.8175
	Voxel	84.54	83.25	91.95	88.11	83.52	0.8805	80.34	86.33	80.17	84.75	0.8835
	Combined	90.19	85.32	92.87	88.03	88.73	0.8231	82.13	84.85	87.85	87.02	0.8750
LASSO	HV + Amygdala	85.23	75.10	86.35	83.57	82.17	0.7803	74.91	74.74	81.50	77.13	0.7512
	BN	86.37	80.98	92.84	86.38	84.56	0.8415	76.89	84.77	80.11	77.91	0.8240
	Voxel	84.33	84.45	90.37	87.33	89.47	0.8170	82.31	86.13	84.71	79.79	0.8430
	Combined	89.75	85.11	92.37	90.15	85.12	0.7897	83.39	91.18	84.27	84.18	0.8203
JMI	HV + Amygdala	85.52	78.45	88.5	84.05	83.14	0.7888	77.54	79.57	82.35	79.09	0.7545
	BN	88.73	84.38	94.17	91.13	90.03	0.8055	82.45	87.31	81.41	90.93	0.7905
	Voxel	87.97	85.14	92.77	87.53	91.11	0.8730	84.24	90.34	82.59	88.15	0.9015
	Combined	91.08	88.03	94.85	89.71	93.17	0.8831	85.31	92.17	87.15	90.57	0.8733

AUC, area under curve; ACC, accuracy; SEN, sensitivity; SPE, specificity; F1, F-score; SVM, support vector machine; RF, random forest; SVM-RFE, SVM recursive feature elimination; LASSO, least absolute shrinkage and selection operation; JMI, joint mutual information; HV, hippocampus volume; BN, brain networks).

with Alzheimer's from HC. However, it is hard to do a direct comparison with the existing state-of-art methods due to the majority of works of literature utilizing different datasets and classification methods, which both significantly affected the performance accuracy. With the combination of different feature selections with different classifiers for AD vs. HC and MCIs vs. MCIc, the binary classification of previous works of literature has reported the accuracy of different ranges as shown in **Tables 6**, **7**. These works of literature utilized the ADNI database to evaluate their proposed method, and we can clearly see that the classification accuracy was influenced by the number of subjects, and the accuracy decreased as the number of subjects increased. As reported in the Results section, the highest classification accuracy for AD vs. HC and MCIs vs. MCIc obtained in this study is 95.87 and 88.03%, using the combination of the features with JMI feature selection, which is visualized in **Figure 11**. If we compare the obtained results for AD vs. HC and MCIs vs. MCIc classification; our framework outperforms the current state-of-art method. The majority of the studies, including Khazaee et al. (2015) and Lama and Kwon (2021), have utilized a limited number of datasets because of the limited number of fMRI data availability in the ADNI data bank. For MCIs vs. MCIc, the accuracy of prior approaches (Khazaee et al., 2015; Zhang et al., 2021) for constructing brain networks was lower than that of the current study since they solely analyzed functional aspects. Only Hojjati et al. (2017) classified diseases using the rs-fMRI graph theory and the machine learning technique (mRMR, FS) with a 91.4% classification accuracy. However, the sample size (of only 18 people) was insufficient, and the result was not generally representative. In this study, we used rs-fMRI and sMRI features to perform binary classifications and found that combining structural and functional MRI data improved classification performance. In our proposed framework, we found that combined sMRI (hippocampal subfield and amygdala nuclei volume) and rs-fMRI (brain networks and voxel) outperformed a single sMRI or rs-fMRI model for two-group classifications (MCIs and MCIc) with improvement in accuracy (Ardekani et al., 2017; Zhang et al., 2021) as shown in **Table 7**. As a result, in the current work, we proposed to combine sMRI and rs-fMRI for disease classification. Schouten et al. used sMRI and fMRI to differentiate 16 patients with AD from 22 normal controls. They discovered that integrating features from two modalities increases classification performance, and they attained an accuracy of 89.5% in AD vs. HC classification (Schouten et al., 2016). All the state-of-art studies presented here analyzed and performed the classification task and made a conclusion. Furthermore, we also carried out our proposed method using ADNI dataset with a larger number of individuals as compared to existing works of literature with cross-validation. It was challenging to identify MCIc subjects since we utilized baseline sMRI and rs-fMRI images in these participants and they transitioned to AD 6 to 36 months later. They exhibited heterogeneity in their conversion time to AD, ranging from 6 to 36 months. Patients with MCIc who converted to AD over a longer period of time (e.g., 36 months) may have a comparable brain network and structure at baseline as compared to patients with MCIs who did not convert to AD. The brain networks and structures of patients with MCIc who progressed to AD in a shorter period (e.g., at 6 months) may on the other hand be comparable to those of patients with AD. In addition, individuals with MCIc were the only unstable group of patients that progressed from MCI to AD over the 36-month follow-up period. In fact, for at least 36 months, patients in the MCIs, AD, and HC groups remained stable and did not transition to another group. Furthermore, we noticed instability in patients with MCIc, as some of them converted to AD and then returned to MCI after 36 months. Unlike earlier research, our study examined not only the conversion sensitivity of the two groups of patients MCIs/MCIc but also analyzed the brain regions of other patient groups. The highly responsive brain regions selected from the two groups are listed in **Figure 4** and

TABLE 6 | Performance comparison of AD vs. HC with state-of-the-art methods.

References	Cohort	Features	Classifier	Accuracy	AUC
de Vos et al., 2018	AD/HC(77/173)	FC matrices, FC dynamics, ALFF	Group Lasso LR	–	85%
Khazaee et al., 2015	AD/HC (34/45)	Graph measures	Naïve Bayes	93.30%	–
Lama and Kwon, 2021	AD/HC (31/31)	Brain Network	LSVM	90.63%	N/A
Our method	**AD/HC (33/35)**	**sMRI, Brain Network and Voxel features of rs-fMRI**	**SVM**	**96.95%**	**98**

Bold value represents the results obtained form proposed method.

TABLE 7 | Performance comparison of MCIs vs. MCIc with state-of-the-art methods.

References	Cohort	Features	Classifier	Accuracy	AUC
Moradi et al., 2015	sMCI/pMCI (100/16)	MRI, age and cognitive measure	LDS	82.72%	0.902
Ardekani et al., 2017	sMCI/pMCI (78/86)	Hippocampal volumetric (sMRI)	RF	82.30%	N/A
Hojjati et al., 2017	MCIc/MCInc (18/62)	rs-fMRI, graph theory	SVM	91.40%	N/A
Zhang et al., 2021	MCIc/MCInc (30/35)	rs-fMRI, sMRI, graph theory	SVM	84.71%	0.88
Our method	**MCIs/MCIc (30/31)**	**sMRI, Brain Network and Voxel features of rs-fMRI**	**SVM**	**87.78%**	**93.8**

Bold value represents the results obtained form proposed method.

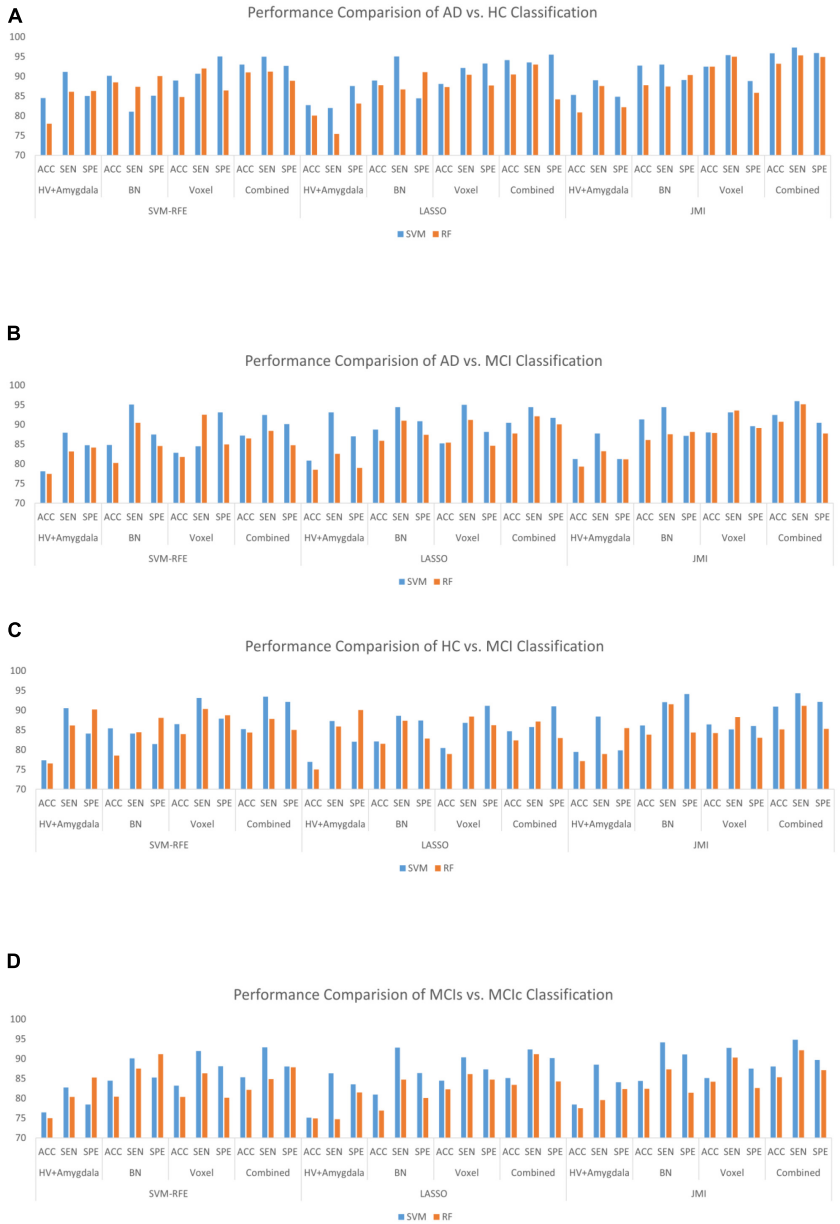

FIGURE 11 | Bar graph with different features selection methods **(A)** the AD vs. HC group, **(B)** the AD vs. MCI group, **(C)** the HC vs. MCI group, and **(D)** the MCIs vs. MCIc group on different feature vectors: Hippocampal-amygdala volume, Brain Network (BN), Voxel, and combined features set.

Supplementary Tables 1–4. It is also worth mentioning that betweenness centrality contributed 70–75% of the features for brain networks and 30–35% for the feature combination. Our findings imply that the betweenness centrality in a functional network conveys more disease information and that the top selected features are more responsive to more efficient detection for MCIs vs. MCIc and HC vs. MCI. Our findings are consistent with earlier research, and these specific brain areas have been linked to AD and MCI conversion (Liu et al., 2013). The importance of numerous brain areas in MCI pathology has long been acknowledged.

Previous studies noted the network distortion in the temporal lobe area in individuals with Alzheimer's (He et al., 2009). In other studies (Liu et al., 2013) also noted the functional loss in the middle temporal gyrus (MTG) and PreCG in AD patients. In comparison with previous literature, we notice that the temporal lobe area may be more damaged in the AD and initial MCI. The MTG was highly sensitive in the feature selection for MCI and AD classification. The nodal degree in the superior temporal gyrus (STG), Cuneus (CUN), precentral gyrus (PreCG), and MTG as well as the betweenness centrality in the hippocampus (HIP), Amygdala (AMYG), and inferior temporal

gyrus (ITG) were shown to be discriminative in distinguishing AD from HC. Similar trends were followed by MCIs from MCIc classification. The nodal degree in the STG, middle temporal gyrus (MTG), and CUN as well as the betweenness centrality in the amygdala (AMYG) and Hippocampus (HIP) were shown to be discriminative in distinguishing MCIs from MCIc **Supplementary Table 4**. In summary, the highly sensitive features were selected for the brain network using the JMI algorithm. Moreover, the selected brain area carries more information about the disease with more sensitive features which leads to more accurate performance. The temporal region plays an important role in MCI and AD. We also suggested that the other region such as the caudate nucleus, superfrontal gyrus, orbitofrontal cortex, occipital, etc. regions for further exploration of the disease pathology in AD.

Limitations

Our study has a few drawbacks. First, the sample size is limited, which may impair the robustness of the group's statistical analysis. Further analysis with a bigger sample size with different datasets should be carried out. The unbalance data is another drawback. We aimed to analyze high-quality data with more balanced samples for feature selection and classification in the future or to design a more robust approach that enhances classification accuracy and generalization; the model's generalization should be considered by using a different database besides ADNI. Because the ADNI database is growing, future research should acquire a bigger sample and should balance the number of individuals. Future research should also look at different networks analysis and classification approaches in different phases of AD, as well as the interpretability of functional brain abnormalities. The ability to evaluate the models' resilience across numerous data sets will be required. We think that the follow-up data within the subject can better show the brain area where the sensitive features of the altered biomarker are present in terms of subject design. More significant and accurate findings may be produced if participants may record follow-up data through cognitive training while also maintaining a baseline control.

CONCLUSION

Alzheimer's disease is an irreversible and a leading health problem in older age; it is important to consider the protective response and to slow down the onset of the advancement of Alzheimer's. Thus, the proper identification of various stages of Alzheimer's and MCI progression is important. In this article, we utilized the hippocampal subfield and the amygdala nuclei volume obtained from sMRI in combination with brain network features and multi-measure features obtained from rs-fMRI. So far, several anatomical MRI imaging biomarkers for AD diagnosis have been identified. The use of the cortical and subcortical volume, the hippocampus, and the amygdala volume has proven to be beneficial in distinguishing patients with AD from the healthy population. Similarly, the rs-fMRI data provides specific numerical information but also contributes to the rich dynamic temporal correlation. However, those preceding studies used either of the biomarker hippocampal subfield and amygdala volume, brain networks, or voxel-based multi-measure features separately. Thus, to analyze the full potentiality of sMRI and rs-fMRI in AD identification, we utilized the combined features in our studies. Additionally, we utilized and compared the different features selection algorithm to select the optimal feature set to obtain the maximum classification accuracy. We also compared the performance of SVM with an RF classifier. From the results obtained, JMI feature selection with the SVM algorithm among all others significantly improved the performance accuracy.

DATA AVAILABILITY STATEMENT

Publicly available datasets were analyzed in this study. This data can be found here: the dataset used in this study were acquired from ADNI homepage, which is available freely for all researcher and scientist for experiments on Alzheimer's disease and can be easily downloaded from ADNI websites: http://adni.loni.usc.edu/about/contact-us/. The raw data supporting the conclusions of this article will be made available by the authors, without undue reservation.

ETHICS STATEMENT

The studies involving human participants were reviewed and approved by IRB no. is 2-1041055-AB-N-01-2019-45/2020-72 in Chosun University. The patients/participants provided their written informed consent to participate in this study.

AUTHOR CONTRIBUTIONS

UK developed the concept and handled the analysis. G-RK reviewed the concept and verified the results. Both authors reviewed and contributed to the manuscript and have approved the final version.

FUNDING

This research was supported by the National Research Foundation of Korea (NRF) grant funded by the Korea government (MSIT) (No. NRF-2021R1I1A3050703). And this research was supported by the Brain Korea 21 Four Program through the National Research Foundation of Korea (NRF) funded by the Ministry of Education (4299990114316).

ACKNOWLEDGMENTS

Data collection and sharing for this project were funded by the Alzheimer's Disease Neuroimaging Initiative (ADNI) (National Institutes of Health Grant U01 AG024904) and DOD ADNI (Department of Defense award number W81XWH-12-2-0012). As such, the investigators within the ADNI

contributed to the design and implementation of ADNI and/or provided data but did not participate in the analysis or writing of this report. A complete listing of ADNI investigators can be found at: http://adni.loni.usc.edu/wpcontent/uploads/how_to_apply/ADNI_Acknowledgement_List.pdf, accessed on 6 April 2022. ADNI is funded by the National Institute on Aging, the National Institute of Biomedical Imaging and Bioengineering, and through generous contributions from the following: AbbVie, Alzheimer's Association; Alzheimer's Drug Discovery Foundation; Araclon Biotech; BioClinica, Inc.; Biogen; Bristol-Myers Squibb Company; CereSpir, Inc.; Cogstate; Eisai Inc.; Elan Pharmaceuticals, Inc.; Eli Lilly and Company; EuroImmun; F. Hoffmann-La Roche Ltd. and its affiliated company Genentech, Inc.; Fujirebio; GE Healthcare; IXICO Ltd.; Janssen Alzheimer Immunotherapy Research & Development, LLC.; Johnson & Johnson Pharmaceutical Research and Development LLC.; Lumosity; Lundbeck; Merck & Co., Inc.; Meso Scale Diagnostics, LLC.; NeuroRx Research; Neurotrack Technologies; Novartis Pharmaceuticals Corporation; Pfizer Inc.; Piramal Imaging; Servier; Takeda Pharmaceutical Company; and Transition Therapeutics. The Canadian Institutes of Health Research provide funds to ADNI clinical sites in Canada. Private-sector contributions are facilitated by the Foundation for support of the National Institutes of Health (https://www.fnih.org, accessed on 11 August 2021). The grantee organization is the Northern California Institute for Research and Education, and the study is coordinated by the Alzheimer's Therapeutic Research Institute at the University of Southern California. ADNI data are disseminated by the Laboratory for Neuro Imaging at the University of Southern California.

SUPPLEMENTARY MATERIAL

The Supplementary Material for this article can be found online at: https://www.frontiersin.org/articles/10.3389/fnagi.2022.818871/full#supplementary-material

REFERENCES

2020 Alzheimer's disease facts and figures (2020). 2020 Alzheimer's disease facts and figures. *Alzheimers Dement.* 16, 391–460. doi: 10.1002/alz.12068

Angelucci, F., Spalletta, G., di Iulio, F., Ciaramella, A., Salani, F., Colantoni, L., et al. (2010). Alzheimer's disease (AD) and mild cognitive impairment (MCI) patients are characterized by increased BDNF serum levels. *Curr. Alzheimer Res.* 7, 15–20. doi: 10.2174/156720510790274473

Arbabshirani, M. R., Plis, S., Sui, J., and Calhoun, V. D. (2017). Single subject prediction of brain disorders in neuroimaging: promises and pitfalls. *Neuroimage* 145, 137–165. doi: 10.1016/j.neuroimage.2016.02.079

Ardekani, B. A., Bermudez, E., Mubeen, A. M., and Bachman, A. H. (2017). Prediction of incipient Alzheimer's disease dementia in patients with mild cognitive impairment. *J. Alzheimers Dis.* 55, 269–281. doi: 10.3233/JAD-160594

Bishop, N. A., Lu, T., and Yankner, B. A. (2010). Neural mechanisms of ageing and cognitive decline. *Nature* 464, 529–535. doi: 10.1038/nature08983

Breiman, L. (2001). Random forests. *Mach. Learn.* 45, 5–32. doi: 10.1023/A:1010933404324

Brier, M. R., Thomas, J. B., Snyder, A. Z., Benzinger, T. L., Zhang, D., Raichle, M. E., et al. (2012). Loss of intranetwork and internetwork resting state functional connections with Alzheimer's disease progression. *J. Neurosci. Off. J. Soc. Neurosci.* 32, 8890–8899. doi: 10.1523/JNEUROSCI.5698-11.2012

Challis, E., Hurley, P., Serra, L., Bozzali, M., Oliver, S., and Cercignani, M. (2015). Gaussian process classification of Alzheimer's disease and mild cognitive impairment from resting-state fMRI. *Neuroimage* 112, 232–243. doi: 10.1016/j.neuroimage.2015.02.037

Chang, C.-C., and Lin, C.-J. (2011). LIBSVM: a library for support vector machines. *ACM Trans. Intell. Syst. Technol.* 2:27. doi: 10.1145/1961189.1961199

Chaves, R., Ramírez, J., Górriz, J. M., López, M., Salas-Gonzalez, D., Alvarez, I., et al. (2009). SVM-based computer-aided diagnosis of the Alzheimer's disease using t-test NMSE feature selection with feature correlation weighting. *Neurosci. Lett.* 461, 293–297. doi: 10.1016/j.neulet.2009.06.052

Chen, G., Ward, B. D., Xie, C., Li, W., Wu, Z., Jones, J. L., et al. (2011). Classification of Alzheimer disease, mild cognitive impairment, and normal cognitive status with large-scale network analysis based on resting-state functional MR imaging. *Radiology* 259, 213–221. doi: 10.1148/radiol.10100734

Clem, M. A., Holliday, R. P., Pandya, S., Hynan, L. S., Lacritz, L. H., and Woon, F. L. (2017). Predictors that a diagnosis of mild cognitive impairment will remain stable 3 years later. *Cogn. Behav. Neurol. Off. J. Soc. Behav. Cogn. Neurol.* 30, 8–15. doi: 10.1097/WNN.0000000000000119

Cohen, J. (1960). A coefficient of agreement for nominal scales. *Educ. Psychol. Meas.* 20, 37–46. doi: 10.1177/001316446002000104

Collij, L. E., Heeman, F., Kuijer, J. P. A., Ossenkoppele, R., Benedictus, M. R., Möller, C., et al. (2016). Application of machine learning to arterial spin labeling in mild cognitive impairment and Alzheimer disease. *Radiology* 281, 865–875. doi: 10.1148/radiol.2016152703

Cortes, C., and Vapnik, V. (1995). Support-vector networks. *Mach. Learn.* 20, 273–297. doi: 10.1007/BF00994018

Dai, Z., Yan, C., Li, K., Wang, Z., Wang, J., Cao, M., et al. (2015). Identifying and mapping connectivity patterns of brain network hubs in Alzheimer's disease. *Cereb. Cortex* 25, 3723–3742. doi: 10.1093/cercor/bhu246

de Vos, F., Koini, M., Schouten, T. M., Seiler, S., van der Grond, J., Lechner, A., et al. (2018). A comprehensive analysis of resting state fMRI measures to classify individual patients with Alzheimer's disease. *Neuroimage* 167, 62–72. doi: 10.1016/j.neuroimage.2017.11.025

Delli Pizzi, S., Franciotti, R., Bubbico, G., Thomas, A., Onofrj, M., and Bonanni, L. (2016). Atrophy of hippocampal subfields and adjacent extrahippocampal structures in dementia with Lewy bodies and Alzheimer's disease. *Neurobiol. Aging* 40, 103–109. doi: 10.1016/j.neurobiolaging.2016.01.010

Duro, D. C., Franklin, S. E., and Dubé, M. G. (2012). A comparison of pixel-based and object-based image analysis with selected machine learning algorithms for the classification of agricultural landscapes using SPOT-5 HRG imagery. *Remote Sens. Environ.* 118, 259–272. doi: 10.1016/j.rse.2011.11.020

Feng, F., Wang, P., Zhao, K., Zhou, B., Yao, H., Meng, Q., et al. (2018). Radiomic features of hippocampal subregions in Alzheimer's disease and amnestic mild cognitive impairment. *Front. Aging Neurosci.* 10:290. doi: 10.3389/fnagi.2018.00290

Feng, Q., Liu, J., and Gong, J. (2015). UAV remote sensing for urban vegetation mapping using random forest and texture analysis. *Remote Sens.* 7, 1074–1094. doi: 10.3390/rs70101074

Fischl, B. (2012). FreeSurfer. *Neuroimage* 62, 774–781. doi: 10.1016/j.neuroimage.2012.01.021

Fornito, A., Zalesky, A., and Bullmore, E. T. (2010). Network scaling effects in graph analytic studies of human resting-state fMRI data. *Front. Syst. Neurosci.* 4:22. doi: 10.3389/fnsys.2010.00022

Garali, I., Adel, M., Bourennane, S., and Guedj, E. (2018). Histogram-based features selection and volume of interest ranking for Brain PET image classification. *IEEE J. Transl. Eng. Health Med.* 6, 1–12. doi: 10.1109/JTEHM.2018.2796600

Greicius, M. (2008). Resting-state functional connectivity in neuropsychiatric disorders. *Curr. Opin. Neurol.* 21, 424–430. doi: 10.1097/WCO.0b013e328306f2c5

Greicius, M. D., Srivastava, G., Reiss, A. L., and Menon, V. (2004). Default-mode network activity distinguishes Alzheimer's disease from healthy aging: Evidence from functional MRI. *Proc. Natl. Acad. Sci. U.S.A.* 101, 4637–4642. doi: 10.1073/pnas.0308627101

Grieder, M., Wang, D. J. J., Dierks, T., Wahlund, L.-O., and Jann, K. (2018). Default mode network complexity and cognitive decline in mild Alzheimer's disease. *Front. Neurosci.* 12:770. doi: 10.3389/fnins.2018.00770

Guyon, I., Weston, J., Barnhill, S., and Vapnik, V. (2002). Gene selection for cancer classification using support vector machines. *Mach. Learn.* 46, 389–422. doi: 10.1023/A:1012487302797

Hafkemeijer, A., van der Grond, J., and Rombouts, S. A. R. B. (2012). Imaging the default mode network in aging and dementia. *Biochim. Biophys. Acta BBA Mol. Basis Dis.* 1822, 431–441. doi: 10.1016/j.bbadis.2011.07.008

Han, Y., Wang, J., Zhao, Z., Min, B., Lu, J., Li, K., et al. (2011). Frequency-dependent changes in the amplitude of low-frequency fluctuations in amnestic mild cognitive impairment: a resting-state fMRI study. *Neuroimage* 55, 287–295. doi: 10.1016/j.neuroimage.2010.11.059

Hanyu, H., Sato, T., Hirao, K., Kanetaka, H., Iwamoto, T., and Koizumi, K. (2010). The progression of cognitive deterioration and regional cerebral blood flow patterns in Alzheimer's disease: a longitudinal SPECT study. *J. Neurol. Sci.* 290, 96–101. doi: 10.1016/j.jns.2009.10.022

He, Y., Chen, Z., and Evans, A. (2008). Structural insights into aberrant topological patterns of large-scale cortical networks in Alzheimer's disease. *J. Neurosci.* 28, 4756–4766. doi: 10.1523/JNEUROSCI.0141-08.2008

He, Y., Chen, Z., Gong, G., and Evans, A. (2009). Neuronal networks in Alzheimer's disease. *Neurosci. Rev. J. Bringing Neurobiol. Neurol. Psychiatry* 15, 333–350. doi: 10.1177/1073858409334423

He, Y., Wang, L., Zang, Y., Tian, L., Zhang, X., Li, K., et al. (2007). Regional coherence changes in the early stages of Alzheimer's disease: a combined structural and resting-state functional MRI study. *Neuroimage* 35, 488–500. doi: 10.1016/j.neuroimage.2006.11.042

Hojjati, S. H., Ebrahimzadeh, A., Khazaee, A., Babajani-Feremi, A., Alzheimer's Disease Neuroimaging Initiative (2017). Predicting conversion from MCI to AD using resting-state fMRI, graph theoretical approach and SVM. *J. Neurosci. Methods* 282, 69–80. doi: 10.1016/j.jneumeth.2017.03.006

Hojjati, S. H., Ebrahimzadeh, A., Khazaee, A., Babajani-Feremi, A., Alzheimer's Disease Neuroimaging Initiative (2018). Predicting conversion from MCI to AD by integrating rs-fMRI and structural MRI. *Comput. Biol. Med.* 102, 30–39. doi: 10.1016/j.compbiomed.2018.09.004

Hyman, B. T., and Trojanowski, J. Q. (1997). Consensus recommendations for the postmortem diagnosis of Alzheimer disease from the National Institute on Aging and the Reagan Institute Working Group on diagnostic criteria for the neuropathological assessment of Alzheimer disease. *J. Neuropathol. Exp. Neurol.* 56, 1095–1097. doi: 10.1097/00005072-199710000-00002

Immitzer, M., Atzberger, C., and Koukal, T. (2012). Tree species classification with random forest using very high spatial resolution 8-band WorldView-2 satellite data. *Remote Sens.* 4, 2661–2693. doi: 10.3390/rs4092661

Ito, T., Kulkarni, K. R., Schultz, D. H., Mill, R. D., Chen, R. H., Solomyak, L. I., et al. (2017). Cognitive task information is transferred between brain regions via resting-state network topology. *Nat. Commun.* 8:1027. doi: 10.1038/s41467-017-01000-w

Jack, C. R., Therneau, T. M., Weigand, S. D., Wiste, H. J., Knopman, D. S., Vemuri, P., et al. (2019). Prevalence of biologically vs clinically defined alzheimer spectrum entities using the national institute on aging-Alzheimer's association research framework. *JAMA Neurol.* 76, 1174–1183. doi: 10.1001/jamaneurol.2019.1971

Jie, B., Liu, M., and Shen, D. (2018). Integration of temporal and spatial properties of dynamic connectivity networks for automatic diagnosis of brain disease. *Med. Image Anal.* 47, 81–94. doi: 10.1016/j.media.2018.03.013

Josephs, K. A., Dickson, D. W., Tosakulwong, N., Weigand, S. D., Murray, M. E., Petrucelli, L., et al. (2017). Rates of hippocampal atrophy and presence of post-mortem TDP-43 in patients with Alzheimer's disease: a longitudinal retrospective study. *Lancet Neurol.* 16, 917–924. doi: 10.1016/S1474-4422(17)30284-3

Ju, R., Hu, C., Zhou, P., and Li, Q. (2019). Early diagnosis of Alzheimer's disease based on resting-state brain networks and deep learning. *IEEE/ACM Trans. Comput. Biol. Bioinform.* 16, 244–257. doi: 10.1109/TCBB.2017.2776910

Khazaee, A., Ebrahimzadeh, A., and Babajani-Feremi, A. (2015). Identifying patients with Alzheimer's disease using resting-state fMRI and graph theory. *Clin. Neurophysiol. Off. J. Int. Fed. Clin. Neurophysiol.* 126, 2132–2141. doi: 10.1016/j.clinph.2015.02.060

Kraskov, A., Stögbauer, H., and Grassberger, P. (2004). Estimating mutual information. *Phys. Rev. E* 69:066138. doi: 10.1103/PhysRevE.69.066138

Lama, R. K., and Kwon, G.-R. (2021). Diagnosis of Alzheimer's disease using brain network. *Front. Neurosci.* 15:605115. doi: 10.3389/fnins.2021.605115

Lee, E.-S., Yoo, K., Lee, Y.-B., Chung, J., Lim, J.-E., Yoon, B., et al. (2016). Default mode network functional connectivity in early and late mild cognitive impairment. *Alzheimer Dis. Assoc. Disord.* 30, 289–296. doi: 10.1097/WAD.0000000000000143

Li, Y., Jing, B., Liu, H., Li, Y., Gao, X., Li, Y., et al. (2017). Frequency-dependent changes in the amplitude of low-frequency fluctuations in mild cognitive impairment with mild depression. *J. Alzheimers Dis. JAD* 58, 1175–1187. doi: 10.3233/JAD-161282

Liaw, A., and Wiener, M. (2002). Classification and Regression by randomForest. *R News* 2:5.

Lin, Q., Rosenberg, M. D., Yoo, K., Hsu, T. W., O'Connell, T. P., and Chun, M. M. (2018). Resting-state functional connectivity predicts cognitive impairment related to Alzheimer's disease. *Front. Aging Neurosci.* 10:94. doi: 10.3389/fnagi.2018.00094

Liu, C. Y., Krishnan, A. P., Yan, L., Smith, R. X., Kilroy, E., Alger, J. R., et al. (2013). Complexity and synchronicity of resting state blood oxygenation level-dependent (BOLD) functional MRI in normal aging and cognitive decline. *J. Magn. Reson. Imaging JMRI* 38, 36–45. doi: 10.1002/jmri.23961

Liu, M., Li, F., Yan, H., Wang, K., Ma, Y., Shen, L., et al. (2020). A multi-model deep convolutional neural network for automatic hippocampus segmentation and classification in Alzheimer's disease. *Neuroimage* 208:116459. doi: 10.1016/j.neuroimage.2019.116459

Lopez, O. L., Becker, J. T., Chang, Y.-F., Sweet, R. A., DeKosky, S. T., Gach, M. H., et al. (2012). Incidence of mild cognitive impairment in the Pittsburgh Cardiovascular Health Study-Cognition Study. *Neurology* 79, 1599–1606. doi: 10.1212/WNL.0b013e31826e25f0

Mak, E., Gabel, S., Su, L., Williams, G. B., Arnold, R., Passamonti, L., et al. (2017). Multi-modal MRI investigation of volumetric and microstructural changes in the hippocampus and its subfields in mild cognitive impairment, Alzheimer's disease, and dementia with Lewy bodies. *Int. Psychogeriatr.* 29, 545–555. doi: 10.1017/S1041610216002143

Mak, E., Su, L., Williams, G. B., Watson, R., Firbank, M., Blamire, A., et al. (2016). Differential atrophy of hippocampal subfields: a comparative study of dementia with lewy bodies and Alzheimer disease. *Am. J. Geriatr. Psychiatry* 24, 136–143. doi: 10.1016/j.jagp.2015.06.006

McKhann, G., Drachman, D., Folstein, M., Katzman, R., Price, D., and Stadlan, E. M. (1984). Clinical diagnosis of Alzheimer's disease: report of the NINCDS-ADRDA Work Group under the auspices of department of health and human services task force on Alzheimer's disease. *Neurology* 34, 939–944. doi: 10.1212/wnl.34.7.939

Moradi, E., Pepe, A., Gaser, C., Huttunen, H., and Tohka, J. (2015). Machine learning framework for early MRI-based Alzheimer's conversion prediction in MCI subjects. *Neuroimage* 104, 398–412. doi: 10.1016/j.neuroimage.2014.10.002

Pedregosa, F., Varoquaux, G., Gramfort, A., Michel, V., Thirion, B., Grisel, O., et al. (2011). Scikit-learn: machine learning in python. *J. Mach. Learn. Res.* 12, 2825–2830. doi: 10.1080/13696998.2019.1666854

Petersen, R. C. (2004). Mild cognitive impairment as a diagnostic entity. *J. Intern. Med.* 256, 183–194. doi: 10.1111/j.1365-2796.2004.01388.x

Platero, C., Lin, L., and Tobar, M. C. (2019). longitudinal neuroimaging hippocampal markers for diagnosing Alzheimer's disease. *Neuroinformatics* 17, 43–61. doi: 10.1007/s12021-018-9380-2

Rathore, S., Habes, M., Iftikhar, M. A., Shacklett, A., and Davatzikos, C. (2017). A review on neuroimaging-based classification studies and associated feature extraction methods for Alzheimer's disease and its prodromal stages. *Neuroimage* 155, 530–548. doi: 10.1016/j.neuroimage.2017.03.057

Risacher, S. L., Saykin, A. J., West, J. D., Shen, L., Firpi, H. A., McDonald, B. C., et al. (2009). Baseline MRI predictors of conversion from MCI to probable AD in the ADNI cohort. *Curr. Alzheimer Res.* 6, 347–361. doi: 10.2174/156720509788929273

Sanz-Arigita, E. J., Schoonheim, M. M., Damoiseaux, J. S., Rombouts, S. A. R. B., Maris, E., Barkhof, F., et al. (2010). Loss of 'small-world' networks in Alzheimer's

disease: graph analysis of fMRI resting-state functional connectivity. *PLoS One* 5:e13788. doi: 10.1371/journal.pone.0013788

Saygin, Z. M., Kliemann, D., Iglesias, J. E., van der Kouwe, A. J. W., Boyd, E., Reuter, M., et al. (2017). High-resolution magnetic resonance imaging reveals nuclei of the human amygdala: manual segmentation to automatic atlas. *Neuroimage* 155, 370–382. doi: 10.1016/j.neuroimage.2017.04.046

Schouten, T. M., Koini, M., de Vos, F., Seiler, S., van der Grond, J., Lechner, A., et al. (2016). Combining anatomical, diffusion, and resting state functional magnetic resonance imaging for individual classification of mild and moderate Alzheimer's disease. *Neuroimage Clin.* 11, 46–51. doi: 10.1016/j.nicl.2016.01.002

Sheline, Y. I., Morris, J. C., Snyder, A. Z., Price, J. L., Yan, Z., D'Angelo, G., et al. (2010). APOE4 allele disrupts resting state fMRI connectivity in the absence of amyloid plaques or decreased CSF Aβ42. *J. Neurosci. Off. J. Soc. Neurosci.* 30, 17035–17040. doi: 10.1523/JNEUROSCI.3987-10.2010

Shirer, W. R., Ryali, S., Rykhlevskaia, E., Menon, V., and Greicius, M. D. (2012). Decoding subject-driven cognitive states with whole-brain connectivity patterns. *Cereb. Cortex* 22, 158–165. doi: 10.1093/cercor/bhr099

Sørensen, L., Igel, C., Pai, A., Balas, I., Anker, C., Lillholm, M., et al. (2017). Differential diagnosis of mild cognitive impairment and Alzheimer's disease using structural MRI cortical thickness, hippocampal shape, hippocampal texture, and volumetry. *Neuroimage Clin.* 13, 470–482. doi: 10.1016/j.nicl.2016.11.025

Tan, B., Liu, Q., Wan, C., Jin, Z., Yang, Y., and Li, L. (2019). Altered functional connectivity of alpha rhythm in obsessive-compulsive disorder during rest. *Clin. EEG Neurosci.* 50, 88–99. doi: 10.1177/1550059418804378

Tibshirani, R. (1996). Regression Shrinkage and selection via the Lasso. *J. R. Stat. Soc. Ser. B Methodol.* 58, 267–288. doi: 10.1111/j.2517-6161.1996.tb02080.x

Tzourio-Mazoyer, N., Landeau, B., Papathanassiou, D., Crivello, F., Etard, O., Delcroix, N., et al. (2002). Automated anatomical labeling of activations in SPM using a macroscopic anatomical parcellation of the MNI MRI single-subject brain. *Neuroimage* 15, 273–289. doi: 10.1006/nimg.2001.0978

van Maurik, I. S., Zwan, M. D., Tijms, B. M., Bouwman, F. H., Teunissen, C. E., Scheltens, P., et al. (2017). Interpreting biomarker results in individual patients with mild cognitive impairment in the Alzheimer's biomarkers in daily practice (ABIDE) project. *JAMA Neurol.* 74, 1481–1491. doi: 10.1001/jamaneurol.2017.2712

Wee, C.-Y., Yap, P.-T., Zhang, D., Denny, K., Browndyke, J. N., Potter, G. G., et al. (2012). Identification of MCI individuals using structural and functional connectivity networks. *Neuroimage* 59, 2045–2056. doi: 10.1016/j.neuroimage.2011.10.015

Wei, R., Li, C., Fogelson, N., and Li, L. (2016). Prediction of conversion from mild cognitive impairment to Alzheimer's disease using MRI and structural network features. *Front. Aging Neurosci.* 8:76. doi: 10.3389/fnagi.2016.00076

Xiang, J., Guo, H., Cao, R., Liang, H., and Chen, J. (2013). An abnormal resting-state functional brain network indicates progression towards Alzheimer's disease. *Neural Regen. Res.* 8, 2789–2799. doi: 10.3969/j.issn.1673-5374.2013.30.001

Yan, C., and Zang, Y. (2010). DPARSF: a MATLAB toolbox for "pipeline" data analysis of resting-state fMRI. *Front. Syst. Neurosci.* 4:13. doi: 10.3389/fnsys.2010.00013

Yang, H., Wang, C., Zhang, Y., Xia, L., Feng, Z., Li, D., et al. (2017). Disrupted causal connectivity anchored in the posterior cingulate cortex in amnestic mild cognitive impairment. *Front. Neurol.* 8:10. doi: 10.3389/fneur.2017.00010

Zang, Y., Jiang, T., Lu, Y., He, Y., and Tian, L. (2004). Regional homogeneity approach to fMRI data analysis. *Neuroimage* 22, 394–400. doi: 10.1016/j.neuroimage.2003.12.030

Zhan, L., Jahanshad, N., Jin, Y., Toga, A. W., McMahon, K. L., de Zubicaray, G. I., et al. (2013). "Brain network efficiency and topology depend on the fiber tracking method: 11 tractography algorithms compared in 536 subjects," in *Proceedings of the 2013 IEEE 10th International Symposium on Biomedical Imaging*, San Francisco, CA, 1134–1137. doi: 10.1109/ISBI.2013.6556679

Zhang, D., Wang, Y., Zhou, L., Yuan, H., Shen, D., and Alzheimer's Disease Neuroimaging Initiative (2011). Multimodal classification of Alzheimer's disease and mild cognitive impairment. *Neuroimage* 55, 856–867. doi: 10.1016/j.neuroimage.2011.01.008

Zhang, H. K., and Roy, D. P. (2017). Using the 500m MODIS land cover product to derive a consistent continental scale 30m Landsat land cover classification. *Remote Sens. Environ.* 197, 15–34. doi: 10.1016/j.rse.2017.05.024

Zhang, L., Zuo, X.-N., Ng, K. K., Chong, J. S. X., Shim, H. Y., Ong, M. Q. W., et al. (2020). Distinct BOLD variability changes in the default mode and salience networks in Alzheimer's disease spectrum and associations with cognitive decline. *Sci. Rep.* 10:6457. doi: 10.1038/s41598-020-63540-4

Zhang, T., Liao, Q., Zhang, D., Zhang, C., Yan, J., Ngetich, R., et al. (2021). Predicting MCI to AD conversation using integrated sMRI and rs-fMRI: machine learning and graph theory approach. *Front. Aging Neurosci.* 13:688926. doi: 10.3389/fnagi.2021.688926

Zhang, T., Zhao, Z., Zhang, C., Zhang, J., Jin, Z., and Li, L. (2019). Classification of early and late mild cognitive impairment using functional brain network of resting-state fMRI. *Front. Psychiatry* 10:572. doi: 10.3389/fpsyt.2019.00572

Zhang, Y.-W., Zhao, Z.-L., Qi, Z., Hu, Y., Wang, Y.-S., Sheng, C., et al. (2017). Local-to-remote cortical connectivity in amnestic mild cognitive impairment. *Neurobiol. Aging* 56, 138–149. doi: 10.1016/j.neurobiolaging.2017.04.016

Zheng, F., Cui, D., Zhang, L., Zhang, S., Zhao, Y., Liu, X., et al. (2018). The volume of hippocampal subfields in relation to decline of memory recall across the adult lifespan. *Front. Aging Neurosci.* 10:320. doi: 10.3389/fnagi.2018.00320

Zhou, J., Greicius, M. D., Gennatas, E. D., Growdon, M. E., Jang, J. Y., Rabinovici, G. D., et al. (2010). Divergent network connectivity changes in behavioural variant frontotemporal dementia and Alzheimer's disease. *Brain J. Neurol.* 133, 1352–1367. doi: 10.1093/brain/awq075

Zhou, J., and Seeley, W. W. (2014). Network dysfunction in Alzheimer's disease and frontotemporal dementia: implications for psychiatry. *Biol. Psychiatry* 75, 565–573. doi: 10.1016/j.biopsych.2014.01.020

Zou, Q.-H., Zhu, C.-Z., Yang, Y., Zuo, X.-N., Long, X.-Y., Cao, Q.-J., et al. (2008). An improved approach to detection of amplitude of low-frequency fluctuation (ALFF) for resting-state fMRI: fractional ALFF. *J. Neurosci. Methods* 172, 137–141. doi: 10.1016/j.jneumeth.2008.04.012

Zuo, X.-N., Di Martino, A., Kelly, C., Shehzad, Z. E., Gee, D. G., Klein, D. F., et al. (2010). The oscillating brain: complex and reliable. *Neuroimage* 49, 1432–1445. doi: 10.1016/j.neuroimage.2009.09.037

Zuo, X.-N., Ehmke, R., Mennes, M., Imperati, D., Castellanos, F. X., Sporns, O., et al. (2012). Network centrality in the human functional connectome. *Cereb. Cortex* 22, 1862–1875. doi: 10.1093/cercor/bhr269

Conflict of Interest: The authors declare that the research was conducted in the absence of any commercial or financial relationships that could be construed as a potential conflict of interest.

Publisher's Note: All claims expressed in this article are solely those of the authors and do not necessarily represent those of their affiliated organizations, or those of the publisher, the editors and the reviewers. Any product that may be evaluated in this article, or claim that may be made by its manufacturer, is not guaranteed or endorsed by the publisher.

Copyright © 2022 Khatri and Kwon. This is an open-access article distributed under the terms of the Creative Commons Attribution License (CC BY). The use, distribution or reproduction in other forums is permitted, provided the original author(s) and the copyright owner(s) are credited and that the original publication in this journal is cited, in accordance with accepted academic practice. No use, distribution or reproduction is permitted which does not comply with these terms.

Advantages of publishing in Frontiers

OPEN ACCESS
Articles are free to read for greatest visibility and readership

FAST PUBLICATION
Around 90 days from submission to decision

HIGH QUALITY PEER-REVIEW
Rigorous, collaborative, and constructive peer-review

TRANSPARENT PEER-REVIEW
Editors and reviewers acknowledged by name on published articles

Frontiers
Avenue du Tribunal-Fédéral 34
1005 Lausanne | Switzerland

Visit us: www.frontiersin.org
Contact us: frontiersin.org/about/contact

REPRODUCIBILITY OF RESEARCH
Support open data and methods to enhance research reproducibility

DIGITAL PUBLISHING
Articles designed for optimal readership across devices

FOLLOW US
@frontiersin

IMPACT METRICS
Advanced article metrics track visibility across digital media

EXTENSIVE PROMOTION
Marketing and promotion of impactful research

LOOP RESEARCH NETWORK
Our network increases your article's readership